META 2025 Torremolinos - Spain

The 15th International Conference on Metamaterials, Photonic Crystals and Plasmonics



July 22 – 25, 2025
Torremolinos - Spain

Proceedings

ISSN 2429-1390

metaconferences.org

META 2025 Torremolinos - Spain

The 15th International Conference on Metamaterials, Photonic Crystals and Plasmonics

Edited by

Khaled Mnaymneh | National Research Council, Canada
Said Zouhdi | Paris-Saclay University, France

TABLE OF CONTENT

ORGANIZATION I COMMITTEES 4

SPONSORS I EXHIBITORS 6

PLENARY SPEAKERS 9

KEYNOTE SPEAKERS 15

TUTORIAL 28

GUIDELINES FOR PRESENTERS 29

USEFUL INFORMATION 30

TABLE OF CONTENTS 33

AIP Publishing

Proudly sponsoring META 2025

Our mission is to advance, promote, and serve the physical sciences for the benefit of humanity by breaking barriers to open, fair research communication and empowering researchers to accelerate global progress.

Explore our resources and programs designed to connect your work to a legacy of foundational discoveries and new ideas, and to a community of peers and institutions around the world.

LEARN MORE

publishing.aip.org

ORGANIZATION I COMMITTEES

Conference Chairs



Khaled Mnaymneh
National Research Council
Canada



Said Zouhdi
Paris–Saclay University
France

Local Organizing Committee

Arcady Zhukov — Chair (Spain)

Abdulrahman M. Alsaadi (Korea)
Daniel Arenas Ortega (Spain)
Luca Assogna (Italy)
Yijia Cheng (China)
Karam Choukri (France)
Mohammadhossein Khosravi (Germany)
Oussama Korichi (Finland)
Ning Lyu (Germany)
Runpeng Miao (Italy)
Andrea Rossini (Italy)
Natalia Salakhova (Russia)
Junze Shao (Saudi Arabia)
Junaid Ahmed Uqaili (Spain)

International Advisory Committee

Harry Atwater Harry (USA)
Federico Capasso (USA)
Nader Engheta (USA)
Ortwin Hess (UK)
Teruya Ishihara (Japan)
Yuri Kivshar (Australia)
Graeme W. Milton (USA)
Manuel N.-Vesperinas (Spain)
Susumu Noda (Japan)
Franco Nori (Japan & USA)
Masaya Notomi (Japan)
Vladimir Shalaev (USA)
David R. Smith (USA)
Martin Wegener (Germany)
Xiang Zhang (Hong Kong)
Nikolay Zheludev (UK)

Technical Program Committee

Pierre-Michel Adam (France)
Ishwar Aggarwal (USA)
Antonio Ambrosio (Italy)
Benfeng Bai (China)
Xavier Begaud (France)
Maha Ben Rhouma (France)
Henri Benisty (France)
Jamal Berakdar (Germany)
Svetlana V. Boriskina (USA)
Che Ting Chan (Hong Kong)
Debashis Chanda (USA)
Pai-Yen Chen (USA)
Johan Christensen (Spain)
Alfredo De Rossi (France)
Alexander Dmitriev (Sweden)
Mohamed Farhat (Saudi Arabia)
Monika Fleischer (Germany)
Denis Garoli (Italy)
Alexander Govorov (USA)
Tatjana Gric (Lithuania)
Jean-Philippe Groby (France)
Kotaro Kajikawa (Japan)
Eugene Kamenetskii (Israel)
Howard (Ho Wai) Lee (USA)
Jensen Li (Hong Kong)
Qiang Li (China)
Yang Li (China)
Anatole Lupu (France)
Nicolò Maccaferri (Sweden)
Martin McCall (UK)
Marco Miniaci (France)
Taiichi Otsuji (Japan)
Willie Padilla (USA)
Dorota Pawlak (Poland)
Lucia Petti (Italy)
Virginie Ponsinet (France)
Giorgio Quaranta (Switzerland)
Jun Suk Rho (Korea)
Junichi Takahara (Japan)
Takuo Tanaka (Japan)
Hong Wei (China)
Chung-Tse Michael Wu (Taiwan)
Arcady Zhukov (Spain)

Special Sessions Organizers

Guillermo Acuna (Switzerland)
Ashod Aradian (France)
Benfeng Bai (China)
Angela Barreda (Spain)
Henri Benisty (France)
Jamal Berakdar (Germany)
Miguel Beruete (Spain)
Sergey I. Bozhevolnyi (Denmark)
Stefano Corni (Italy)
Sébastien Cueff (France)
Fei Ding (Denmark)
Li Ge (USA)
Tommaso Giovannini (Italy)
Alejandro G. Gonzalez (Spain)
Tatjana Gric (Lithuania)
Yael Gutierrez (Spain)
Han Htoon (USA)
Libai Huang (USA)
Baohua Jia (Lithuania)
Alina Karabchevsky (Israel)
Guixin Li (China)
Zhenfei Li (China)
Iñigo Liberal (Spain)
Eduardo L. Fraguas (Spain)
Anatole Lupu (France)
Konstantinos Makris (Greece)
Dorota Pawlak (Poland)
Virginie Ponsinet (France)
Aswathi K. Sivan (Switzerland)
Hiroshi Sugimoto (Japan)
Alicia Torres-García (Spain)
Alessandro Veltri (Ecuador)
Hong Wei (China)
Jin Zhang (Finland)
Weiren Zhu (China)
Peter Zijlstra (Netherlands)

Special Symposia Organizers



Jerome Plain
France



Alexander Govorov
USA



Davy Gérard
France



Pedro H. Martinez
Singapore



Junsuk Rho
Korea



Hakjoo Lee
Korea



Namkyoo Park
Korea



Seong Ok Han
Korea



Howard Lee
USA



Pin-Chieh Wu
Taiwan



Wen-Hui Cheng
Taiwan



Eugene
Kamenetskii
Israel



Marco Miniaci
France



Jensen Li
Hong Kong



Philippe Groby
France



Vincent Pagneux
France



Noé Jiménez
Spain



Maha Ben Rhouma
FranceMM

SPONSORS I EXHIBITORS

Gold Sponsors

AIP Publishing's mission is to advance, promote, and serve the physical sciences for the benefit of humanity. We connect our authors and readers to a living legacy of published science, to peers and institutions across the globe, and to myriad services, tools, and platforms which expand the impact and reach of groundbreaking scientific work.
Learn more at https://pubs.aip.org/aip/apq.

At **ASML** we're changemakers! Our growing team of over 40,000 people and 140 nationalities provides leading chipmakers with the hardware, software and services to mass produce patterns on silicon. We're probably part of the device you're reading this on right now.

Headquartered in Europe's prolific tech hub, the Brainport Eindhoven region in the Netherlands, we have over 60 locations globally and annual net sales of €28 billion in 2024. Want to be part of progress? Visit www.asml.com/careers.

Silver Sponsors

LINBOU Nearfield has been established since 2016, by a group of academic researchers specialized in field-matter interaction. Over the past 9 years, LINBOU has been providing customized electromagnetic and acoustic field scanners that are being used in top institutions, and achieving results in top journals such as Nature, Nature Materials, Nature Physics, etc. The field scanners are capable of visualizing electromagnetic / acoustic field interaction with materials, in either Cartesian coordinates by xyz stage or polar coordinates by rotating stage. Besides research-level scanners, LINBOU also provides teaching-level scanners with teaching experiments. Feel free to contact info@linbou.com for further information.

Learn more at https://www.linbou.com.

Founded in 2003, **PHASICS**, offers state-of-the-art optics metrology and imaging solutions. With over 20 years of expertise, their QuadriWave Lateral Shearing Interferometry (QWLSI) technology delivers ultra-high resolution, sub-nanometric sensitivity, and a wide dynamic range.

PHASICS' Quantitative Phase Microscopy (QPM) solutions support a broad range of applications—from optical metasurface characterization to refractive index variation measurements in bulk materials, and temperature mapping in thermonanoplasmonics.

Learn more at https://www.phasics.com.



The **MetacMed** - Acoustic and mechanical metamaterials for biomedical and energy harvesting applications, project is a European Doctoral Network (DN) funded by the European Commission under the Horizon 2022 Marie Sklodowska-Curie Action (MSCA), Grant Agreement n° 101119738, duration 48 months. MetacMed started on the 1st of March 2024, and will provide world-class interdisciplinary training to 12 Doctoral Candidates (DCs) in the area of acoustic and mechanical metamaterials for biomedical and energy harvesting applications. It consists of a well-balanced consortium that spans four European countries, plus Switzerland and the UK and incorporates academic, research centers and SMEs, interdisciplinary and inter-sectoral aspects of DC skill development.

Please, visit https://www.metacmed.eu for further details about the research program, DCs projects, and application procedures to follow.

Other Partners

Université Paris-Saclay is a research university based in Paris, France. Université Paris-Saclay offers a comprehensive and varied range of Undergraduate, Master's and PhD degrees, renowned internationally thanks to the University's reputation for research excellence and the commitment of its academic staff. The University's constituent faculties, institutes and component institutions all contribute to the curricula with cutting-edge specialized courses in Science and Engineering, Life Sciences and Health, and Social Sciences and Humanities.
Université Paris-Saclay is ranked 1st in France and 12th in the world according to the Academic Ranking of World Universities (ARWU).

AEM - Advanced Electromagnetics is a peer-reviewed, Gold Open Access journal. It covers recent international research results in the general field of Electromagnetic Waves, Antennas and Propagation. Authors of articles published in Advanced Electromagnetics retain the copyright of their articles and are free to reproduce and disseminate their work (under a Creative Commons Attribution License). AEM is widely indexed and has a Scopus CiteScore of 2.9 (2024).



Nanophotonics (De Gruyter) covers recent international research results, specific developments in the field and novel applications. It publishes all article in a Gold Open Access model and belongs to the top journals in the field. Nanophotonics focuses on the interaction of photons with nano-structures, such as carbon nano-tubes, nano metal particles, nano crystals, semiconductor nano dots, photonic crystals, tissue and DNA.

Advanced Devices & Instrumentation is an online-only Open Access journal published in affiliation with Beijing Institute of Aerospace Control Devices (BIACD) and distributed by the American Association for the Advancement of Science (AAAS). Like all partners participating in the Science Partner Journal program, Advanced Devices & Instrumentation is editorially independent from the Science family of journals and BIACD is responsible for all content published in the journal. To learn more about the Science Partner Journal program, visit the SPJ program homepage.

PLENARY SPEAKERS



Robert W. Boyd

University of Ottawa (Canada) & University of Rochester (USA)

Applications of highly nonlinear epsilon-near-zero materials in photonics

Robert W. Boyd received the B.S. degree in physics from the Massachusetts Institute of Technology and the Ph.D. degree in physics in 1977 from the University of California at Berkeley. His Ph.D. thesis was supervised by Charles Townes and involved the use of nonlinear optical techniques in infrared detection for astronomy. Professor Boyd joined the faculty of the Institute of Optics of the University of Rochester in 1977 and in July 2001 he became the M. Parker Givens Professor of Optics. In 2010, he became Professor of Physics and Canada Excellence Research Chair in Quantum Nonlinear Optics at the University of Ottawa. His research interests include studies of nonlinear optical interactions, studies of the nonlinear optical properties of materials, the development of photonic devices including photonic biosensors, and studies of the quantum statistical properties of nonlinear optical interactions. Professor Boyd has written two books, co-edited two anthologies, published over 200 research papers, and has been awarded five patents. He is a fellow of the Optical Society of America and of the American Physical Society and is the past chair of the Division of Laser Science of the American Physical Society.

Applications of highly nonlinear epsilon-near-zero materials in photonics
Optical materials display extremely large nonlinear response in a spectral band around their plasma frequency. This presentation reviews the origin of this behavior and provides examples of such materials and of applications enabled by this response.



Nader Engheta

University of Pennsylvania (USA)

Metastructures That Compute and Optimize

Nader Engheta is the H. Nedwill Ramsey Professor at the University of Pennsylvaniain Philadelphia with affiliations in the Departments of Electrical and Systems Engineering, Physics and Astronomy, Bioengineering, and Materials Science and Engineering. He received his BS degree from the University of Tehran, and his MS and Ph.D. degrees from Caltech. His current research activities span a broad range of areas including optics, metamaterials, electrodynamics, microwaves, photonics, nano-optics, graphene photonics, imaging and sensing inspired by eyes of animal species, microwave and optical antennas, and physics and engineering of fields and waves. He has received several awards for his research including the 2023 Benjamin Franklin Medal in Electrical Engineering, Election to the American Academy of Arts and Sciences (2023), Caltech Distinguished Alumni Award (2023), the 2020 Isaac Newton Medal and Prize from the Institute of Physics (UK), the 2020 Max Born Award from the OPTICA (formerly Optical Society), the 2019 Ellis Island Medal of Honor, the 2018 IEEE Pioneer Award in Nanotechnology, the 2022 Hermann Anton Haus Lecture at MIT, the 2015 SPIE Gold Medal, the 2014 Balthasar van der Pol Gold Medal from the International Union of Radio Science (URSI), the 2017 William Streifer Scientific Achievement Award, the Canadian Academy of Engineeringas an International Fellow the Fellow of US National Academy of Inventors (NAI), the IEEE Electromagnetics Award, the Vannevar Bush Faculty Fellowship Awardfrom DoD, the Wheatstone Lecture in King's College London, 2006 Scientific American Magazine 50 Leaders in Science and Technology, and the Guggenheim Fellowship. He is a Fellow of nine international scientificand technical organizations, i.e., IEEE, OPTICA, APS, MRS, SPIE, URSI, AAAS, IOP and NAI. He has received the honorary doctoral degrees from the Aalto University in Finland in 2016, the University of Stuttgart, Germany in 2016, and Ukraine's National Technical University Kharkov Polytechnic Institute in 2017.

Metastructures That Compute and Optimize

I will present some of the most recent results of our ongoing research projects on nonlocal metasurfaces and metastructures that perform ultrafast analog computation, such as vector-matrix multiplication, matrix inversion, constrained optimization, equation solving, etc. I will also discuss how incoherent light can be used for certain analog computations.



Ortwin Hess

Trinity College Dublin (Ireland)

Nanoplasmonic Quantum Photonics

Ortwin Hess currently holds the Chair Professorship of Quantum Nanophotonics and an SFI Research Professorship in the School of Physics and the CRANN Institute of Trinity College Dublin, The University of Dublin, Ireland. He is Editor-in-Chief of the gold open-access journal APL Quantum. Ortwin is a Fellow of the Institute of Physics (FInstP), a Fellow of Optica (formerly OSA) and a Professorial Fellow of Trinity College Dublin. Previously, Ortwin held the Leverhulme Chair in Metamaterials in the Blackett Laboratory at Imperial College London, UK. From 2003 to 2010 he was a full professor at the University of Surrey (Guildford, UK) and visiting professor at Stanford University, USA, and at the Ludwig-Maximilians University of Munich, Germany. Ortwin obtained the Dr.-rer-nat. (PhD) degree from the Technical University of Berlin, Germany in 1993 and the Habilitation (Dr.-habil.) at the University of Stuttgart, Germany in 1997. Ortwin's research interests bridge quantum nanophotonics with semiconductor and metamaterials physics, laser science and bio-medical photonics. He discovered the 'trapped-rainbow' principle, had the idea of stopped-light lasing and made defining contributions to the fields of spatio-temporal dynamics of semiconductor lasers, ultraslow light in metamaterials, complex quantum dot photonics and photonic crystals and strong coupling in nanoplasmonics. Ortwin pioneered active nanoplasmonics and optical metamaterials with quantum gain for which he has been awarded the Royal Society Rumford Medal.

Nanoplasmonic Quantum Photonics
Nanoplasmonic quantum photonics revolutionizes quantum information technologies by enabling room-temperature quantum operations through extreme nanoscale field confinement and strong photon-emitter coupling. This facilitates ultrafast single-photon emission, multipartite entanglement, near-field coupling, and quantum sensing, enhanced by quantum nanoplasmonic coherent perfect absorption, paving the way for practical quantumdevices operable at ambient conditions.



Stefanie Kroker

Technische Universität Braunschweig (Germany)

Routes for integrated photonics and meta-optics in quantum technologies and precision experiments

Stefanie Kroker studied Physics at Friedrich Schiller University in Jena/Germany and Universidad de Granada/Spain. She did her PhD with the Institute of applied Physics at Friedrich Schiller University in 2014 and became assistant professor at TU Braunschweig and the German national metrology institute, PTB in 2016. In 2020 Stefanie Kroker received the Science Award Lower Saxony and in 2021 she was appointed to a full professorship at TU Braunschweig. She is a member of the German clusters of excellence QuantumFrontiers and PhoenixD. Since 2023 she is associate editor of the journal APL Quantum. Stefanie's research covers nanophotonic and integrated optical systems for applications in sensing, high-precision metrology and quantum technologies. In 2024 she received a Consolidator Grant from the European Research Council.

Routes for integrated photonics and meta-optics in quantum technologies and precision experiments

Integrated photonics and meta-optics enable compact, precise light control, advancing optical metrology in applications like atomic clocks and gravitational wave detectors. This work explores nanophotonic devices for precision experiments and atom chips, focusing on light-matter interactions and the impact of material properties on performance and precision.



Gloria Platero Coello

ICMM-CSIC (Spain)

Robust Edge States in Topological Lattices for Quantum information Transfer

Gloria Platero Coello Gloria Platero is Research Professor at the Materials Science Institute of Madrid, at the CSIC (Spanish Research Council), which is located at the excellence Campus CSIC-UAM (Autonomous University of Madrid). She leads the group at ICMM: “New Platforms and Nanodevices for Quantum Simulation and Quantum Computation” https://wp.icmm.csic.es/npqsic/ and belongs to the University Institute Gregorio Millán on Nanoscience and Industrial Mathematics (Carlos III University of Madrid). She has given over hundred invited, keynote or plenary talks in international conferences and she has been invited to give seminars and to make stays in many research centers all over the world. She has been Mercator Fellow at the University of Regensburg. Supervisor of many PhD students, most of them are working successfully in Academia. She is Fellow or the APS (Quantum Information), and Secretary of the C8 IUPAP Commission on Semiconductor Physics. She will be Chair on January 2025. Her research belongs to the field of Quantum Nanotechnologies. She investigates the theory of spin qubits in quantum dot arrays, their manipulation and the transfer of quantum information in these systems, for quantum computation purposes. She also investigates hybrid systems: superconducting cavities coupled to qubits, where photons are the flying qubits. Time periodic driven systems is one of her main topics of research. She investigates as well, in different platforms as photonic crystals, the role of topological edge states for the transfer of quantum information.

Robust Edge States in Topological Lattices for Quantum information Transfer
This talk will deal with the transfer of quantum information using protected topological edge states. I will discuss the long-range transfer in a dimer chain, a 1D topological insulator, and in the Creutz-Ladder lattice and the role of topological domain walls to speed up the particle transfer.



Eli Yablonovitch

IUC Berkeley (USA)

What I Wish I Had Known, as I Searched for the First 3d Photonic Bandgap

Eli Yablonovitch is a Professor of Electrical Engineering and Computer Sciences at UC Berkeley, where he holds the James & Katherine Lau Chair in Engineering. He is the Director of the NSF Center for Energy Efficient Electronics Science (E3S), a multi-University Center headquartered at Berkeley.
Prof. Yablonovitch introduced the idea that strained semiconductor lasers could have superior performance due to reduced valence band (hole) effective mass. With almost every human interaction with the internet, optical telecommunication occurs by strained semiconductor lasers. He is regarded as a Father of the Photonic BandGap concept, and he coined the term "Photonic Crystal". The geometrical structure of the first experimentally realized Photonic bandgap, is sometimes called “Yablonovite”. In his photovoltaic research, Yablonovitch introduced the 4(n squared) (“Yablonovitch Limit”) light-trapping factor that is in worldwide use, for almost all commercial solar panels. His mantra that "a great solar cell also needs to be a great LED”, is the basis of the world record solar cells: single-junction 29.1% efficiency; dual-junction 31.5%; quadruple-junction 38.8% efficiency; all at 1 sun. His startup company Ethertronics Inc., has shipped over 2 billion cellphone antennas.
Prof. Yablonovitch is elected as a Member of the National Academy of Engineering, the National Academy of Sciences, the American Academy of Arts & Sciences, and is a Foreign Member of the Royal Society of London. He has been awarded the Buckley Prize of the American Physical Society, the Isaac Newton Medal of the UK Institute of Physics, the Rank Prize (UK), the Harvey Prize (Israel), the IEEE Photonics Award, the IET Mountbatten Medal (UK), the Julius Springer Prize (Germany), the R.W. Wood Prize, the W. Streifer Scientific Achievement Award, and the Adolf Lomb Medal. He also has an honorary Ph.D. from the Royal Institute of Technology, Stockholm, & the Hong Kong Univ. of Science & Technology, and is honorary Professor at Nanjing University.

What I Wish I Had Known, as I Searched for the First 3d Photonic Bandgap
The first 3-dimensional Photonic Bandgap was found by Edison-ian search, trial-and-error, guided by physical intuition. The 4-year search was beset by pseudo-gaps, and required deep physical insights to find the right geometry (diamond unit cell in a face-centered-cubic lattice). Nonetheless, there do exist mathematical techniques for 3d geometry optimization that could have led to the right structure more quickly.

KEYNOTE SPEAKERS



Andrea Alù

City University of New York (USA)

Space-time metamaterials

Andrea Alù is a Distinguished Professor at the City University of New York (CUNY), the Founding Director of the Photonics Initiative at the CUNY Advanced Science Research Center, and the Einstein Professor of Physics at the CUNY Graduate Center. He received his Laurea (2001) and PhD (2007) from the University of Roma Tre, Italy, and, after a postdoc at the University of Pennsylvania, he joined the faculty of the University of Texas at Austin in 2009, where he was the Temple Foundation Endowed Professor until Jan. 2018. Dr. Alù is a Fellow of the National Academy of Inventors (NAI), the American Association for the Advancement of Science (AAAS), the Institute of Electrical and Electronic Engineers (IEEE), the Materials Research Society (MRS), Optica, the International Society for Optics and Photonics (SPIE) and the American Physical Society (APS). He is the President of Metamorphose, a Highly Cited Researcher since 2017, a Simons Investigator in Physics, the director of the Simons Collaboration on Extreme Wave Phenomena Based on Symmetries, and the Editor in Chief of Optical Materials Express. He has received several scientific awards, including the NSF Alan T. Waterman award, the Blavatnik National Award for Physical Sciences and Engineering, the IEEE Kiyo Tomiyasu Award, the ICO Prize in Optics, the OSA Adolph Lomb Medal, and the URSI Issac Koga Gold Medal.

Space-time metamaterials
In this talk, I will discuss my group's recent work in the area of space-time metamaterials, with an emphasis on the use of abrupt time switching and spatio-temporal modulation patterns for efficient frequency translation and energy manipulation.



Harry Atwater

California Institute of Technology (USA)

Active Metastructures – Tailoring Space-Time and Breaking Reciprocity

Harry Atwater is the Otis Booth Leadership Chair of the Division of Engineering and Applied Science, and the Howard Hughes Professor of Applied Physics and Materials Science at the California Institute of Technology. Atwater's scientific effort focuses on nanophotonic light-matter interactions. His work spans fundamental nanophotonic phenomena and applications, including active wavefront shaping of light using metasurfaces, optical propulsion of lightsails, quantum and 2D nanophotonics as well as solar energy conversion, on earth and in space.

Atwater was an early pioneer in nanophotonics and plasmonics and gave a name to the field of plasmonics in 2001. He is Chair of the LightSail Committee for the Breakthrough Starshot program. Currently Atwater is also the Director for the Liquid Sunlight Alliance (LiSA), a Department of Energy Hub program for solar fuels, and was also the founding Editor in Chief of the journal ACS Photonics. Atwater is a Member of the US National Academy of Engineering, a Fellow of APS, MRS, SPIE and Optica, a Web of Science Highly Cited Researcher from 2014-2023, and is recipient of numerous awards, including the 2021 von Hippel Award of the Materials Research Society.

Active Metastructures – Tailoring Space-Time and Breaking Reciprocity
In this talk, I will discuss approaches to spatiotemporal wavefront control in active metastructures that can modify energy and momentum states of light, break reciprocity via space-time modulation, and break Kirchhoff's radiation law via action of external or internal magnetic fields.



Renaud Bachelot

Université de Technologie of Troyes (France) & Nanyang Technological University (Singapore)

Hybrid plasmonic nanosystems based on weak and strong coupling

Renaud Bachelot is a full professor of physics at the University of Technology of Troyes (UTT) that he joined in 1996 after graduate studies and PhD at the University of Paris-Cité and ESPCI graduate school (Paris, University PSL). His area of expertise includes nano-optics, nanophotonics, near-field optics, local light/polymer interaction, scanning probe microscopy, nano-optoelectronics and hybrid nanoplasmonics. He recently joined the CINTRA Lab (CNRS/NTU/CINTRA) as an Adjunct Senior Research Scientist. At UTT, R. Bachelot is the director of the Graduate School "Nanooptics & Nanophotonics" (nano-phot.utt.fr) including both master and PhD programs. From 2011 to 2019, RB has been the director of the Light, nanomaterials nanotechnologies CNRS Laboratory involving more than 100 people (l2n.utt.fr). His national and international influence includes current and past activities and positions such as (e.g.) adjunct professor at the LuMin Laboratory (University of Paris-Saclay), Board Member of the Faculty of Physics of Sorbonne University, elected board member of the French Society of Physics, condensed matter section division, adjunct-professor of the Shanghai University (since 2019, "1000-talents" award since 2020), invited scholar in Argonne National Laboratory, USA, and chair of the NFO-15 international conference that took place in August 2018 in Troyes, France. RB has (co)supervised 24 PhD students and is the co-author of more than 130 peer-reviewed articles (H=46, cf. google scholar), 10 book chapters and 5 patents.

Hybrid plasmonic nanosystems based on weak and strong coupling
Hybrid plasmonic nanosystems based on weak or strong coupling are discussed in terms of controlling the spatial distribution, and associated symmetry, of the active medium in the vicinity of the metallic nanocavities.



Guillaume Baffou

Institut Fresnel - CNRS (France)

Wavefront microscopy for nanophotonics

Guillaume Baffou is a CNRS researcher at the Institut Fresnel in Marseille, France. He graduated from the Ecole Normale Superieure de Cachan (now ENS Paris-Saclay) and earned his Ph.D. in Nanoscience from Paris XI University in 2007. Following his doctorate, he undertook a postdoctoral fellowship at ICFO, Barcelona, where he worked on plasmonics and related photothermal effects under the supervision of Prof. Romain Quidant. In 2010, he joined the CNRS and the Institut Fresnel. His contributions to research at the intersection of optics, thermodynamics, and small-scale biology have earned him several honors, including the CNRS Bronze Medal in 2015. In 2018, he was awarded an ERC Consolidator Grant. Most recently, during the 2023–2024 academic year, he spent a year at Columbia University in New York on a Fulbright grant, collaborating with Prof. Rafael Yuste's team.

Wavefront microscopy for nanophotonics
Cross-grating wavefront microscopy (CGM) consists of the association of a 4-wave diffraction grating and a camera separated by millimeter distance. We show how CGM can be used to measure the optical properties of nanoparticles, 2D material a metasurfaces, such as the complex optical polarizability, conductivity, refractive indices, and cross-sections.



Konstantin Bliokh

Donostia International Physics Center (Spain)

Chiral Vortices, Skyrmions, Möbius Strips: From Nanooptics to Ocean Waves

Konstantin Bliokh received the MSc and PhD degrees in physics from the Kharkov National University (Ukraine) in 1998 and 2001, respectively. After that, he worked as a research scientist at the Institute of Radio Astronomy (Ukraine, 2001–2009). He was a post-doctoral fellow at Bar-Ilan University (Israel, 2003–2005), a visiting research scientist at Technion–Israel Institute of Technology (Israel, 2007), a Linkage International research fellow at the Australian National University (Australia, 2008–2009), a Marie Curie research fellow at the National University of Ireland (Ireland, 2009–2011), an associate professor at the Australian National University (Australia, 2015–2019), and a senior research scientist at RIKEN (Japan, 2011–2024). Starting from 2024, he is an Ikerbasque Professor at the Donostia International Physics Center (Spain). His ongoing research areas include: complex wave systems, geometric phases, spin-orbit interactions, wave momentum and angular momentum, wave vortices, wave-matter interactions, etc. He has co-authored more than 130 scientific papers, reviews, and book chapters.

Vortices, Skyrmions, Möbius Strips: From Nanooptics to Ocean Waves
I will present recent theoretical and experimental results on: (i) subwavelength high-intensity vortices around 'holes' in 2D wave systems: from polaritons to ocean waves, (ii) Bessel-type vortices, displacement-field skyrmions, and polarization Möbius strips in sound and water waves, and (iii) manipulation of floating particles using topologically structured water waves.



Alexandra Boltasseva

Purdue University (USA)

Quasi-2D Materials: From Tailorable Photonics to New Physics

Alexandra Boltasseva is a Ron and Dotty Garvin Tonjes Distinguished Professor of Electrical and Computer Engineering with courtesy appointment in Materials Engineering at Purdue University. She received her PhD in electrical engineering at Technical University of Denmark, DTU in 2004. Boltasseva specializes in nanophotonics, quantum photonics, and optical materials. She is the 2023 recipient of the R.W. Wood Prize (Optica, formerly Optical Society of America), 2022 Guggenheim Fellow, 2018 Blavatnik National Award for Young Scientists Finalist and received the 2013 Institute for Electrical and Electronics Engineers (IEEE) Photonics Society Young Investigator Award, 2013 Materials Research Society (MRS) Outstanding Young Investigator Award, the 2011 MIT Technology Review Top Young Innovator (TR35), the 2009 Young Researcher Award in Advanced Optical Technologies from the University of Erlangen-Nuremberg, Germany, and the Young Elite-Researcher Award from the Danish Council for Independent Research (2008). She is a Fellow of the National Academy of Inventors (NAI), MRS, IEEE, Optica, and SPIE. She served on MRS Board of Directors and is former Editor-in-Chief for Optical Materials Express journal.

Quasi-2D Materials: From Tailorable Photonics to New Physics
We discuss the designer-like characteristics of MXenes, achievable with the choice of transition metal and control of stoichiometry, remarkable tailorability of properties of TD materials with the thickness, and ultra-fast TCOs response. We also explore new device concepts for flat optics/metasurfaces.



Kai Chang

Zhejiang University (China)

Exotic Exciton Phases in Two-Dimensional Quantum Materials

Kai Chang is a chair professor at the School of Physics, Zhejiang University. His research focuses on semiconductor physics and device physics, topological quantum matter and spintronics for decades. He has published more than 200 SCI papers including Nature sub-journals, PRL and other SCI papers. He won the second-class prize of the National Natural Science Award in 2004, and was awarded the 2013 Chinese Physical Society Huang Kun Solid State Physics and Semiconductor Physical Science Award. In 2019, he was elected as an academician of the Chinese Academy of Sciences. He is currently a member of the C8 Committee on Semiconductor Physics of the International Union of Pure and Applied Physics (IUPAP).

Exotic Exciton Phases in Two-Dimensional Quantum Materials
Exciton insulator phases has attracted intensive interests in 2D systems. We demonstrate the existence of topological exciton in InAs/GaSb quantum wells resilient to intense in-plane magnetic fields, identify conventional and novel topological exciton density waves in van der Waals systems, and propose light-engineered exciton supersolidity in heterostructures.



Zhigang Chen

Nankai University (China)

Empowering Topological Photonics for OAM Manipulation

Zhigang Chen is currently a Chair Professor at Nankai University, a recipient of China's National Overseas High-Level Talent Program, and a Chief Scientist of a National Key R&D Program. His research interests include nonlinear optics, topological photonics, and optical trapping and manipulation. Dr. Chen is a Fellow of both Optica and the American Physical Society (APS). He has served as an editor or editorial board member for several journals, including Light: Science & Applications, Laser & Photonics Reviews, Optics Letters, Science Bulletin, and Advances in Physics: X. He has also chaired numerous international conferences, including CLEO-Fundamental Science and the Nonlinear Optics Topical Meeting.

Empowering Topological Photonics for OAM Manipulation
In this talk, we present a few demonstrated examples of topology-driven photonic applications based on the simplest topological model. Building on these foundations, we introduce our design and implementation of more advanced photonic structures that enable robust optical vortex transport and effective manipulation of orbital angular momentum (OAM).



Karin Everschor-Sitte

University of Duisburg-Essen (Germany)

Rethinking Linking - Topology in Magnetism, and Plasmonics

Karin Everschor-Sitte is a professor of Theoretical Physics at the University of Duisburg-Essen in Germany. Her main scientific research fields are the complex fundamental physics of topological magnetic textures and spintronics-based unconventional computing. After completing her PhD at the University of Cologne in 2012, Karin Everschor-Sitte worked as a postdoc at the Technical University Munich and then received a DAAD postdoctoral fellowship to conduct research at the University of Texas at Austin. Followed by a period as a postdoc, she led an Emmy Noether group at the Johannes Gutenberg University Mainz, from 2016 to 2021. In 2018, she received the Hertha-Sponer-Prize, and in 2024, she was honored as the Wohlfarth Lecturer.

Rethinking Linking - Topology in Magnetism, and Plasmonics
Topology in physics explores robust, fault-tolerant states of matter aiming at practical applications. Similar topological structures arise in magnetism, optics, and plasmonics despite differing physics. A challenge is understanding them when traditional mathematical topological frameworks are not necessarily applicable. Linking and geometry offer intuitive ways to describe these complex textures.



Vivian Ferry

University of Minnesota (USA)

Computational Models of Light Management in Photovoltaics and LEDs

Vivian Ferry is an Associate Professor in the Department of Chemical Engineering and Materials Science at the University of Minnesota. Prior to joining Minnesota, she was a Postdoctoral Fellow at Lawrence Berkeley National Laboratory working with Prof. A. Paul Alivisatos , and she received her PhD in Chemistry from the California Institute of Technology working with Prof. Harry A. Atwater. Her work in nano-optics and optical materials has resulted in more than 50 journal publications. Her research includes fundamentals of optical materials and applications, including chiral materials, phase-change materials, luminescent materials and composites, large-area fabrication of nanostructures, and applications to energy, sensing, and optoelectronic devices. She is the recipient of an NSF CAREER award, an Air Force Office of Scientific Research Young Investigator Award, the Marion Milligan Mason Award for Women in the Chemical Sciences, the SPIE Early Career Achievement Award, and was named as one of Technology Review's 35 Innovators under 35.

Computational Models of Light Management in Photovoltaics and LEDs
This talk will discuss the computational models for light management strategies in photovoltaics, including systems that integrate luminescent solar concentrators in greenhouses and reduce the temperature of outdoor panels.



Mark C. Hersam

Northwestern University (USA)

Chemically Functionalized 2D Materials for Quantum Photonic Science and Technology

Mark C. Hersam is the Walter P. Murphy Professor of Materials Science and Engineering, Director of the Materials Research Center, and Chair of the Materials Science and Engineering Department at Northwestern University. He also holds faculty appointments in the Departments of Chemistry, Applied Physics, Medicine, and Electrical Engineering. He earned a B.S. in Electrical Engineering from the University of Illinois at Urbana-Champaign (UIUC) in 1996, M.Phil. in Physics from the University of Cambridge (UK) in 1997, and Ph.D. in Electrical Engineering from UIUC in 2000. His research interests include nanoelectronic materials, additive manufacturing, scanning probe microscopy, renewable energy, sensors, neuromorphic computing, and quantum information science. Dr. Hersam has received several honors including the Presidential Early Career Award for Scientists and Engineers, TMS Robert Lansing Hardy Award, MRS Mid-Career Researcher Award, AVS Medard Welch Award, U.S. Science Envoy, MacArthur Fellowship, and eight Teacher of the Year Awards. Dr. Hersam has been repeatedly named a Clarivate Analytics Highly Cited Researcher with over 700 peer-reviewed publications that have been cited more than 78,000 times. An elected member of the American Academy of Arts and Sciences, National Academy of Engineering, and National Academy of Inventors with over 170 issued and pending patents, Dr. Hersam has founded two companies, NanoIntegris and Volexion, which are suppliers of nanoelectronic and battery materials, respectively. Dr. Hersam is a Fellow of MRS, ACS, ECS, AVS, APS, AAAS, SPIE, and IEEE, and also serves as an Executive Editor of ACS Nano.

Chemically Functionalized 2D Materials for Quantum Photonic Science and Technology
Chemical functionalization allows tailoring of the properties of 2D materials and the degree of coupling across heterointerfaces. In this talk, the prospects of 2D materials for quantum photonic science and technology will be discussed with a focus on how chemical functionalization can enhance quantum emission in 2D transition metal dichalcogenides.



Maria Kafesaki

University of Crete & FORTH (Greece)

Empowering chiral metamaterials with gain materials

Maria Kafesaki is Professor in the Dept. of Materials Science and Engineering of the University of Crete and Adjunct Researcher at the Institute of Electronic Structure and Laser (IESL) of Foundation for Research and Technology Hellas (FORTH). She obtained her Ph.D. from the Physics Department of the University of Crete, Greece. She has worked as post-doctoral researcher in CSIC in Madrid, Spain, and in IESL of FORTH. Her current research is on the area of electromagnetic wave propagation in periodic and random media, with emphasis on metamaterials, where she has large theoretical and computational experience. She has more than 140 publications in refereed journals and more than 80 invited talks at international conferences/schools and Institutions. She has participated in many European projects as well as in the organization of many international conferences and schools. She is Fellow of Optica.

Empowering chiral metamaterials with gain materials
We will review our recent works on chiral metamaterials involving gain materials and on chiral metamaterials combining gain and loss. Special attention will be given to parity-time symmetric chiral metamaterials and to chiral metamaterials for circularly polarized laser emission.



Alexander V. Kildishev

Purdue University (USA)

Beyond the Voigt lineshapes: Efficient statistics-convolved approximants in the time domain

Alexander V. Kildishev works on theory and numerical modeling for nanophotonics. He has had several breakthrough results on negative refractive index metamaterials, optical artificial magnetic structures, loss compensation in metamaterials, plasmonic nanolasers, optical metasurfaces, optical cloaks, and hyperlenses. His current interests also cover the AI-driven inverse design of metadevices in optics and acoustics. He has been included on the Highly Cited Researchers List for the years of 2018, 2022, and 2023 in Web of Science (WOS), which recognizes world-class researchers selected for their exceptional research performance with multiple highly cited papers that rank in the top 1% by citations in the cross-field category. Prof. Kildishev is a Fellow of Optica (OSA).

Beyond the Voigt lineshapes: Efficient statistics-convolved approximants in the time domain
We present a minimax-based approach for efficient time-domain modeling of optical responses from materials with disorder. The utility of our approach, generally applicable to symmetric and non-symmetric disorder statistics, is demonstrated by the non-classical oscillator, relaxation, and conductivity models, achieving the shortest possible numerical stencil for a given controlled accuracy.



Philippe Lalanne

Institut d'Optique - CNRS (France)

Tailoring the visual appearance with correlated-disorder metasurfaces

Philippe Lalanne currently works as a CNRS Research Scientist in Bordeaux. He is an expert in nanoscale electrodynamics. Over the course of his career, he has introduced novel modal theories, established general principles for designing high-Q microcavities, clarified the role of plasmons in the extraordinary optical transmissions, and demonstrated the first high-NA optical metalenses using high-index nanostructures during the late 1990s. Presently, his research interest focuses on the non-Hermitian interaction of light with nanoresonators and disordered optical metasurfaces. From 2018 to 2022, he held the role of Director for the GDR Ondes that gathers the French community working on electromagnetic waves. He received several distinctions, including the prestigious 2023 ERC Advanced grant. He is a fellow of IOP, SPIE and OPTICA.

Tailoring the visual appearance with correlated-disorder metasurfaces
We will review our current effort to model the resonance of individual resonators and collections of them with various theories, including quasinormal modes expansion and multiple scattering.



Howard Lee

UC Irvine (USA)

Functional "Meta"-Optical Fibers for Advanced Imaging and Endoscopy

Howard Lee is currently an Associate Professor in the Department of Physics and Astronomy at UC Irvine. Before joining UCI in 2020, he was an Associated Professor in the Department of Physics at Baylor University and IQSE Fellow and visiting professor in the Institute for Quantum Science and Engineering (IQSE) at TexasA&M. He was a Postdoctoral Fellow at the Caltech, working with Prof. Harry Atwater in active plasmonics/metasurfaces. He received his PhD in Physics from the Max Planck Institute for the Science of Light in Germany in 2012 under the supervision of Prof. Philip Russell. His work on nano-optics, plasmonics/metasurfaces, and fiber optics has led to 50 journal publications in various journals, such as Science, Nano Letters, Advanced Materials, as well as 100 invited talks and 180 conference papers. Dr. Lee is a recipient of a 2025 IEEE Photonics Society Distinguished Lecturer, a 2024 SPIE Fellow, a 2023 Finalist of Moore Inventor Fellow, a 2023 UCI Beall Innovation Award in Physical Sciences, a 2022 Finalist of Moore Inventor Fellow, a 2021 iCANX Young Scientist Awarcd, a 2021 Finalist of Rising Stars of Light, 2020 SPIE Rising Researcher, a 2019 DARPA Director's Fellowship, a 2019 IEEE OGC Young Scientist Award, a 2018 NSF CAREER Award, a 2017 DARPA Young Faculty Award, a 2018 OSA Ambassador, and a 2017 APS Robert S. Hyer Award. He has strong passion in promoting optical sciences and physics to students and the general public, and in serving for the professional communities. He organized more than 25 technical sessions in nanophotonics/metasurfaces in international conferences (Optica, META, PQE, MRS, IEEE) and serves as Lead Symposium Organizer for plasmonic/metasurface symposiums at 2019-2025 MRS Fall Meeting and 2020-2025 MRS Spring Meeting (organized > 2000 presentations).

Functional "Meta"-Optical Fibers for Advanced Imaging and Endoscopy
In this talk, I will review the various material platforms (metallic, dielectric, and compound structures) and geometric platforms which have been utilized in "meta"-fiber devices to date. I will present our recent development of "Meta"-optical fiber, an advanced optical fiber integrated with emerging metasurface concepts. I will present the development of ultrathin optical metalens which is cascaded on the facet of optical fiber that enables advanced optical functions via wavefront shaping such as light focusing.



Konstantinos Makris

University of Crete - FORTH (Greece)

Non-normality, Pseudospectra and Exponential sensitivity

Konstantinos Makris is Associate Professor in the Department of Physics, of the University of Crete and Affiliated Researcher at the Institute of Electronic Structure and Laser (IESL) of Foundation for Research and Technology Hellas (FORTH). He obtained his PhD in Theoretical Photonics from the School of Optics and Photonics (CREOL-FCPE) at the University of Central Florida, Orlando (USA) in 2008. From 2008 until 2010 he was a postdoctoral researcher at Ecole Polytechnique Federale de Lausanne (EPFL), Switzerland. During 2011 he was Lecturer at Institute for Theoretical Physics of Vienna University of Technology (TU-Wien), Austria. From 2012 until 2015 he was a Marie Curie fellow between Princeton University, USA and TU-Wien, Austria. His current research interests lie on non-Hermitian physics, nonlinear optics, photonics lattices and wave propagation in complex media. He has more than 100 publications in refereed journals and more than 60 invited talks-colloquia at international conferences/schools and Institutions. In 2022 he was awarded an ERC consolidator grant related to open disorder systems. He was also elected as a 2023 Fellow of OPTICA (former OSA).

Non-normality, Pseudospectra and Exponential sensitivity
In the context of non-Hermitian photonics, we present recent results regarding non-normal optical waveguides. We investigate photonic lattices with gain/loss, as well as, asymmetric couplings and study their spectral and dynamical response based on pseudospectra theory. The recent notions of exponential sensitivity, and power eigenchannels will be also discussed.



Marco Miniaci

IEMN-CNRS (France)

Bioinspired metamaterials

Marco Miniaci is a permanent researcher at the French National Scientific Research Centre (CNRS) appointed at the Institute of Electronics, Microelectronics and Nanotechnology (IEMN) of Villeneuve D'Ascq, in France. His research interests cover theoretical, numerical, and experimental aspects of wave propagation and structural mechanics of phononic crystals and elastic metamaterials. Marco Miniaci currently is the principal investigator of the ERC StG « POSEIDON » (dealing with bioinspired metamaterials, topological protection and underwater acoustics), coordinator of the MAGNIFIC HORIZON-CL4-2022-RESILIENCE-01-10 (dealing with materials for a next generation of (nano-)opto-eòectro-mechanical systems), and participate into the MetAcMed HORIZON-MSCA-2022-DN-01 (dealing with acoustic and mechanical metamaterials for biomedical and energy harvesting applications).

Bioinspired metamaterials



Sir John Pendry

Imperial College London (UK)

Talk 1. Quantum Aspects of Light Propagation in Time-Varying Media

Talk 2. Modulating Optical Properties in Time Using Plasmonic Resonances

John Pendry has worked at the Blackett Laboratory, Imperial College London, since 1981. His research at Imperial College reflects his broad interests in physics but has recently concentrated on optics and electromagnetism in general. In collaboration with scientists at The Marconi Company he designed a series of 'metamaterials' whose properties owed more to their micro-structure than to the constituent materials. The metamaterial concept caught on and now is a major topic not only of research activity, but also of application to 5G and 6G network technology, MRI, satellite communications and much else, though popular interest has concentrated on his design for a cloak of invisibility.

Talk 1. Quantum Aspects of Light Propagation in Time-Varying Media
Recent experiments demonstrate ultra-fast modulation of refractive indices opening up the field of space-time modulation. Breaking time invariance presents new challenges to theory with the removal of conservation of energy/frequency. New conservation laws are emerging which deepen our understanding of these systems.

Talk 2. Modulating Optical Properties in Time Using Plasmonic Resonances
Plasmonic effects in Indium Tin Oxide enable rapid switching of transparency which can be exploited to modulate THz radiation on a fs time scale.



Kaushik Senguptav

Princeton University (USA)

AI to Discover and Synthesize Sub-terahertz Chips beyond Human Intuition

Kaushik Sengupta received his Ph.D. in Electrical Engineering from Caltech in 2012. Dr. Sengupta joined the Department of Electrical and Computer Engineering at Princeton University, Princeton, NJ, as a Faculty Member in 2013, where he is currently a Professor. His research interests include novel chip-scale architectures for intelligent sensing and communication for a wide range of emerging applications.
Dr. Sengupta is an IEEE Fellow. He received the DARPA Young Faculty Award in 2018, the Bell Labs Prize in 2017, the Young Investigator Program Award from the ONR in 2017, the 2015 Microwave Prize, and multiple best paper awards in IEEE IMS and RFIC. He served as a Distinguished Lecturer for the IEEE Solid-State Circuits Society from 2019 to 2020 and for the IEEE Microwave Theory and Technology Society from 2021 to 2023. He is a recipient of the 2021 IEEE Microwave Theory and Technology Outstanding Young Engineer Award and the 2022 IEEE Solid-state Circuits New Frontier Award. He currently serves as the co-chair of the IEEE Solid-state Directions Sub-committee and as a technical advisor for the wireless start-up company, GuRu, based in Pasadena, CA. His group received IEEE Journal of Solid-State Circuits Best Paper of the Year in 2023.

AI to Discover and Synthesize Sub-terahertz Chips beyond Human Intuition
Traditionally, chip-scale high-frequency system design has been in the domain of the experts. We demonstrate here for the first time how AI can not only allow design times that are orders of magnitude faster, but also unearth new sub-THz chip architectures that are beyond human intuition.



Vladimir M. Shalaev

Purdue University (UK)

Silicon Quantum Photonics

Vladimir M. Shalaev, Scientific Director for Nanophotonics at Birck Nanotechnology Center and Distinguished Professor of Electrical and Computer Engineering at Purdue University, specializes in nanophotonics, plasmonics, optical metamaterials and quantum photonics. Prof. Shalaev has received several awards for his research, including the APS Frank Isakson Prize for Optical Effects in Solids, the Optica (formerly, Optical Society of America) Max Born Award for his pioneering contributions to the field of optical metamaterials, the Willis E. Lamb Award for Laser Science and Quantum Optics, IEEE Photonics Society William Streifer Scientific Achievement Award, Rolf Landauer medal of the ETOPIM (Electrical, Transport and Optical Properties of Inhomogeneous Media) International Association, the UNESCO Medal for the development of nanosciences and nanotechnologies, and the OSA and SPIE Goodman Book Writing Award. Prof. Shalaev is recognized as a Highly Cited Researcher in physics by the Web of Science Group for 7 consecutive years, in 2017-2023. He is a Fellow of the IEEE, APS, SPIE, MRS and Optica.

Silicon Quantum Photonics
We discuss scalable quantum photonics circuitry based on room-temperature single-photon emitters in silicon nitride that we recently discovered in this technologically important material platform. We also consider integration of SiN single-photon emitters with waveguides as well as the quantum emission enhancement through integration with resonant cavities and plasmonic nanostructures.



Marin Soljačić

MIT (USA)

Certain intersections of AI and Photonics

Marin Soljačić is a Professor of Physics at MIT. He is a founder of a few companies, including WiTricity Corporation (2007) and Lightelligence (2017). His main research interests are in artificial intelligence as well as electromagnetic phenomena, focusing on nanophotonics, non-linear optics, and wireless power transfer. He is a co-author of more than 300 scientific articles, more than 100 issued US patents, and he has been invited to give more than 100 invited talks at conferences and universities around the world. He is a recipient of the Adolph Lomb medal from the Optical Society of America (2005), and the TR35 award of the Technology Review magazine (2006). In 2008, he was awarded a MacArthur fellowship "genius" grant. He is an international member of the Croatian Academy of Engineering since 2009. In 2011 he became a Young Global Leader (YGL) of the World Economic Forum. In 2014, he was awarded Blavatnik National Award, as well as Invented Here! (Boston Patent Law Association). In 2017, he was awarded "The Order of the Croatian Daystar, with the image of Ruđer Bošković", the Croatian President's top medal for Science. In 2017, the Croatian President also awarded him with "The Order of the Croatian Interlace" medal. He was a Highly Cited Researcher according to WoS for 2019, 2020, 2021, 2022 & 2023. In 2023, he was awarded Max Born award of Optica.

Certain intersections of AI and Photonics
This talk will explore how photonics can enhance AI hardware and how AI can accelerate photonics research. Topics will include large language models for scientific discovery and robotics for photonics experiments, highlighting key opportunities and challenges at this intersection.



Clivia M. Sotomayor Torres

Iberian Nanotechnology Laboratory - INL (Portugal)

Spectral Frequency Response of Hypersonic Phonons in a Non-Trivial Topological Waveguide

Clivia M. Sotomayor Torres obtained her PhD in Physics in 1984 from the University of Manchester, UK. She held tenured academic appointments at Saint Andrews and Glasgow universities in the UK, at Wuppertal University in Germany and was a research professor at the National university of Ireland University College Cork (Tyndall National Institute). From 2007 to 2023 she was an ICREA research professor and group leader of the Phononic and Photonic Nanostructures group at the ICN2 in Spain. Clivia received awards from the Royal Society of Edinburgh, the Nuffield Foundation and an Amelia Earhart Fellowship from ZONTA International (USA). She carries out research in the science and engineering of phononic nanostructures, nanophotonics and thermal transport. In 2020 she was elected to the Academia Europaea. She is holder of an European Research Council advanced grant investigating phonon transport in topological waveguides. Since September 2023 she is the Director General of the International Iberian Nanotechnology Laboratory (INL) in Braga, Portugal, where she has set up a new research group.

Spectral Frequency Response of Hypersonic Phonons in a Non-Trivial Topological Waveguide
The spectral frequency response of a hypersonic phononic wave propagating along a non-trivial topological waveguide is obtained by laser Doppler vibrometry. The guided mode at 2.115 GHz is shown to propagate with minimal loss..



Vincent Tourna

Laboratory of Acoustics - CNRS, Le Mans University (France)

Transition waves in multistable mechanical metamaterials

Vincent Tournat currently holds a Research Professor position at CNRS and conducts research in the field of nonlinear waves and acoustics at the Laboratory of Acoustics at Le Mans University in France. VT graduated with a major in solid state physics, acoustics & wave physics and defended his PhD thesis on nonlinear acoustics in granular materials in 2003. He then spent the year 2004 as a postdoc at Hokkaido University, Japan, working on laser picosecond ultrasonics, prior to starting at CNRS. During his first years at CNRS, he established two research groups on acoustics of granular media and laser ultrasonics, then participated in developing two other areas of research in his department, ultrasonic non-destructive testing, and acoustic metamaterials. For the last decade, his research focuses on nonlinear waves in flexible mechanical metamaterials. From 2007 to 2022, VT led the "Acoustics and Mechanics of Materials" research team of more than 50 people. His research achievements have been awarded prizes on several occasions, including the CNRS Bronze Medal in 2010 and the Silver Whistle early career award by the International Commission on Ultrasonics (ICU) in 2013. Until 2024, he has been the director of the Institut d'Acoustique - Graduate School (http://iags.univ-lemans.fr) created in 2017 and awarded the national label "Graduate School" (a selection of few Institutes comprising high impact research laboratories, departments, as well as recognized master, engineering and doctoral curriculae). VT has been regularly invited for research visits in Japan, Chile, Spain, USA and he is a visiting research Professor at Harvard University since September 2022. https://perso.univ-lemans.fr/ vtournat/

Transition waves in multistable mechanical metamaterials
I will highlight the fundamentals and a selection of recent results on transition waves triggering, propagation, and discuss some of their potential applications. In general, these reconfiguration fronts obey nonlinear reaction-diffusion equations and show specific properties not necessarily found in other waves supported by periodic and/or nonlinear media.



Seokho Yun

Samsung Advanced Institute of Technology - SAIT (Korea)

AI-Driven Photonics: From Metaphotonics to Silicon Photonics Integration

Seokho Yun is the Vice President of Technology at the Samsung Advanced Institute of Technology (SAIT), where he leads the Photonics Research Team, advancing research and development in meta-photonics and silicon photonics. His expertise lies in meta-photonics and silicon photonics, with a strong focus on enhancing device performance, enabling miniaturization, and pioneering innovative functionalities. He earned his Ph.D. in Electrical Engineering from Pennsylvania State University and conducted postdoctoral research at the Materials Research Science & Engineering Center, specializing in metamaterials and plasmonics applications.
Since joining Samsung Electronics in 2012, he has played a key role in leading meta-photonics sensor projects. Under his leadership, in February 2025, his team successfully commercialized the world's first image sensor integrating meta-photonic color-routing nanostructures. As the demand for high-speed data processing continues to accelerate in the AI era, he is spearheading the development of next-generation ultra-high-speed optical interconnect technologies based on silicon photonics. Additionally, he is driving research on the convergence of silicon photonics and meta-photonics, shaping the future of photonics innovation.

AI-Driven Photonics: From Metaphotonics to Silicon Photonics Integration
As we enter the AI era, photonics is evolving beyond boundaries. This keynote explores advances in metaphotonics and silicon photonics—enabling next-generation image sensors, LiDAR, micro-LED displays, and optical interconnects. Their convergence opens new pathways to compact, power-efficient, and high-performance devices that elevate the capabilities of future optical systems.



Nikolay Zheludev

University of Southampton (UK)

Photonic Metamaterial Time Crystals and Timetronics

Nikolay Zheludev 's research interest are in nanophotonics and metamaterials. He is the Deputy Director of the Optoelectronics Research Centre in Southampton University, UK. Prof. Zheludev is elected as a Fellow of the Royal Society (UK) and Member of the USA National Academy of Engineering. He is a Fellow of the European Physical Society (EPS), the Optical Society (OSA) and the Institute of Physics (London). He has been awarded the Michael Faraday Gold Medal, Thomas Young Medal and President of Singapore Science and Technology Award.

Photonic Metamaterial Time Crystals and Timetronics
We discuss recent developments in understanding functionalities and developing applications of time crystals - a new state of matter, a many-body interacting system that exhibits a spontaneous mobilization transition to the robust state of oscillation, breaking time translation symmetry under an infinitely small change of the external driving force.

TUTORIAL



Prof. Andrea Alù

City University of New York (USA)

Wednesday 23th July
14:00 - 15:00 — Torremolinos

Nonlocal metasurfaces

Andrea Alù is a Distinguished Professor at the City University of New York (CUNY), the Founding Director of the Photonics Initiative at the CUNY Advanced Science Research Center, and the Einstein Professor of Physics at the CUNY Graduate Center. He received his Laurea (2001) and PhD (2007) from the University of Roma Tre, Italy, and, after a postdoc at the University of Pennsylvania, he joined the faculty of the University of Texas at Austin in 2009, where he was the Temple Foundation Endowed Professor until Jan. 2018. Dr. Alù is a Fellow of the National Academy of Inventors (NAI), the American Association for the Advancement of Science (AAAS), the Institute of Electrical and Electronic Engineers (IEEE), the Materials Research Society (MRS), Optica, the International Society for Optics and Photonics (SPIE) and the American Physical Society (APS). He is the President of Metamorphose, a Highly Cited Researcher since 2017, a Simons Investigator in Physics, the director of the Simons Collaboration on Extreme Wave Phenomena Based on Symmetries, and the Editor in Chief of Optical Materials Express. He has received several scientific awards, including the NSF Alan T. Waterman award, the Blavatnik National Award for Physical Sciences and Engineering, the IEEE Kiyo Tomiyasu Award, the ICO Prize in Optics, the OSA Adolph Lomb Medal, and the URSI Issac Koga Gold Medal.

Nonlocal metasurfaces
The use of engineered nonlocal responses in metasurfaces has been recently unveiled as a paradigm for extreme wave control, enabling rational control over space, time, frequency and momentum of the incoming signals, as well as analog-based image processing and computing. Several recent demonstrations of metasurfaces performing edge-detection and image-processing using engineered spatial nonlocality have shown a path towards ultrafast, efficient, massively parallel analog image processing based on passive devices, which holds the promise for being extended towards general analog computing platforms. Space-time nonlocal metasurfaces performing the space- and time-derivatives of the incoming signal were also envisioned by tailoring their frequency and momentum dispersion. In this tutorial, I will discuss the basics of nonlocality engineering in metasurfaces and their various implementations and opportunities for this field of research, showcasing compact meta-structures with reconfigurable properties that can perform mathematical operations, solve compact mathematical problems and address the issues of reprogrammability and cascaded responses. I will discuss how these findings may open exciting opportunities for applications in imaging, automotive vehicles, sensing and computing, and serve as a pre-processing tool for simplifying complex computing architectures.

The tutorial is free and open to all META conference attendees.

GUIDELINES FOR PRESENTERS

Oral Presentations

Each session room is equipped with a stationary computer connected to a LCD projector. Presenters must load their presentation files in advance onto the session computer. Technician personnel will be available to assist you.

Scheduled time slots for oral presentations are 15 mn for regular, 20 mn for invited presentations, 30 mn for keynote talks and 35 mn for plenary talks, including questions and discussions. Presenters are required to report to their session room and to their session Chair at least 15 minutes prior to the start of their session.

The session chair must be present in the session room at least 15 minutes before the start of the session and must strictly observe the starting time and time limit of each paper.

Poster Presentations

Presenters are requested to stand by their posters during their session. One poster board, A0 size (118.9 x 84.1 cm), in portrait orientation, will be available for each poster. Pins or thumbtacks are provided to mount your posters on the board. All presenters are required to mount their papers 30mn before the session and remove them at the end of their sessions. Posters must prepared using the standard AES poster template (available on the conference website).

USEFUL INFORMATION

Venue

META 2025 will be held at
Palacio de Congresos y Exposiciones de la Costa del Sol
3 Calle Mexico, 29620 Torremolinos (Spain)

https://palacio-congresos.es

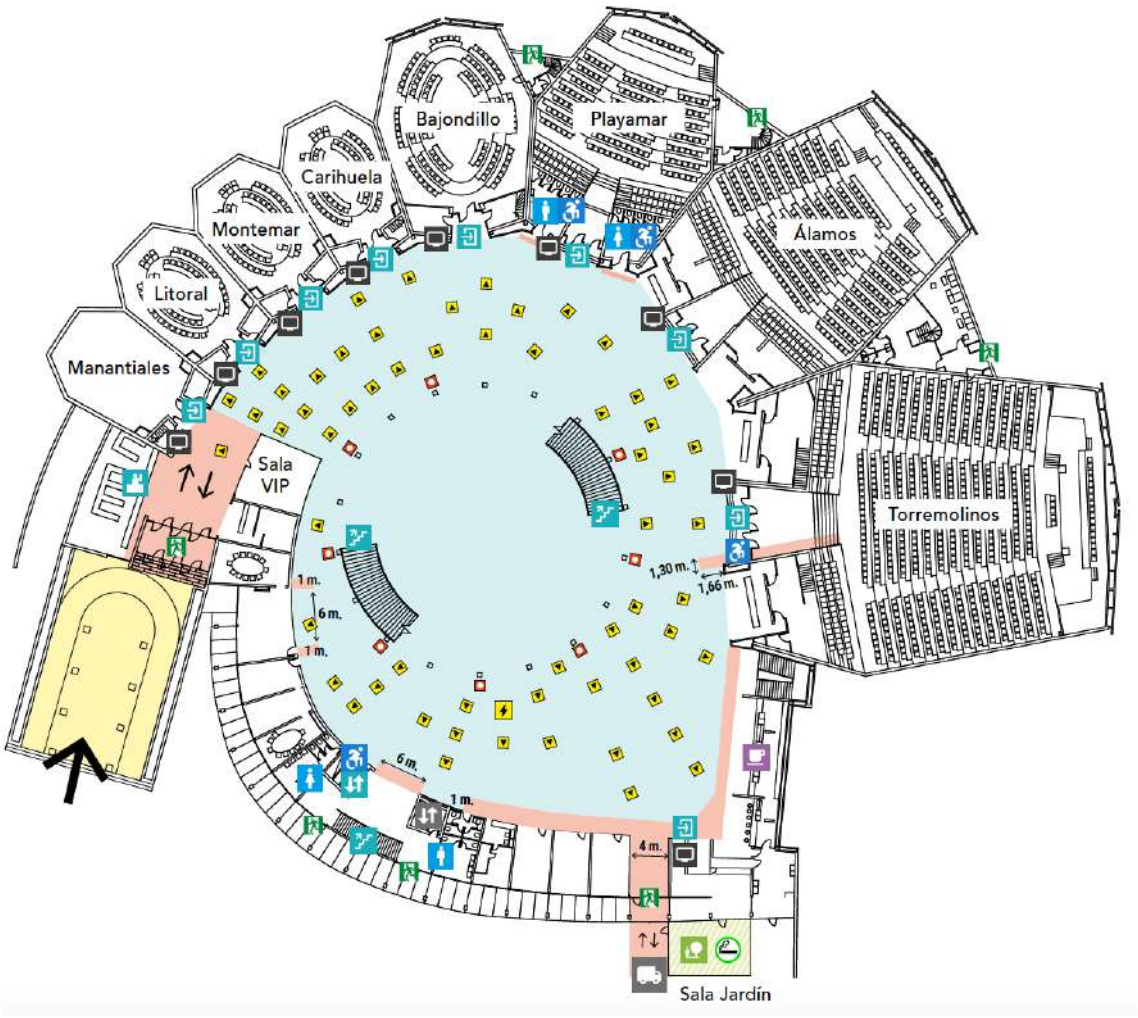


Opened in October 1970, the Palacio de Congresos y Exposiciones de Torremolinos (Congress and Exhibition Centre) was the result of a project designed in 1967 by the architects Rafael de la Hoz and Gerardo Olivares James. The building, which became the state heritage property in 1971.

The complex is built on an estate of 70,000 square meters, of which 18,000 square meters are gardens. Situated in a privileged location in the municipality of Torremolinos and located in the upper area of the town on a hill overlooking the sea, the Congress Center is an icon of Malaga's coastal landscape.



The building is arranged in a circular format around which the various auditoriums, meeting rooms, administrative offices and annexed buildings are distributed. The central hall is presided over by its most iconic visual symbol, an emblem of convention and business tourism in Spain: a large translucent dome with an unprecedented crystal lamp hanging from the center of the exposed radial roof, falling like drops in a waterfall spilling over the center of the composition.



Getting to Venue

Getting to Torremolinos from Malaga Airport

Torremolinos is around 8km away from Malaga international airport. You can go from the airport to the city center by taxi, by train or by bus.

Taxi

The airport has a well-signposted taxi rank outside the arrivals area of Terminal T3. Make sure that the taxi driver has started the taximeter at the beginning of the journey (minimum fare). We recommend requesting a receipt for any complaint or claim.

Train

The new suburban train station in the new Terminal T3 building links the airport with Torremolinos city centre and other cities like Benalmadena and Fuengirola in one direction, and it links Malaga city center in the other direction.

The train station is situated underground and accessed via escalators. It is well signposted and can be reached via the square outside arrivals or outside departures. Before the station entry barriers you will see several self-service tickets machines on your right where you can buy your tickets.

The first train to Torremolinos leaves the airport at 05:32, leaving every 20-30 minutes until the last train at 23.42. Line: C1. Estimated travel time: 10 minutes.

Bus

You will find the bus stop straight in front of you outside the arrivals area of Terminal T3 on the side of the road where there are a couple of shelters with seats. You will also see a ticket office in the left hand corner of the arrivals forecourt where you should purchase your tickets for the journey. Line: Torremolinos-Benalmadena-Airport. Estimated travel time: 30 minutes.

Getting to Torremolinos from Malaga train station

There are two train stations in the centre of Malaga : Maria Zambrano and Centro Alameda. Maria Zambrano station provides high-speed (AVE) and long-distance links to many Spanish cities like Barcelona, Cordoba, Madrid, Santiago de Compostela, Seville, etc, as well as local and regional routes.

You can take Line C1 from any of the two stations to reach Torremolinos. The estimated travel time is 20 minutes. You can check the timetables on the website of the national rail company RENFE.

Getting to Torremolinos from Malaga bus station

Malaga bus station is located at the street "Paseo de los Tilos" very near Maria Zambrano train station. So it will be very easy to take a bus or a train from this station. You can take bus line Malaga-Torremolinos. Estimated travel time: 20 minutes.

TABLE OF CONTENTS

Plenary presentations

Applications Of Highly Nonlinear Epsilon-near-zero Materials In Photonics (pp. 90)
Robert Boyd

Nanoplasmonic Quantum Photonics (pp. 91)
Ortwin Hess

Robust Edge States in Topological Lattices for Quantum information Transfer (pp. 93)
J. Zurita, C. E. Creffield, Gloria Platero Coello

Routes for Integrated Photonics and Meta-Optics in Quantum Technologies and Precision Experiments (pp. 94)
Stefanie Kroker, M. Gaedtke, S. Häfner, L. Shelling Neto, S. Sauer, M. Schittenhelm, A. Sorokina, N. Wagner

Metastructures That Compute and Optimize (pp. 95)
Nader Engheta

What I Wish I Had Known, as I Searched for the First 3d Photonic Bandgap (pp. 96)
Eli Yablonovitch

Keynote presentations

Modulating Optical Properties In Time Using Plasmonic Resonances (pp. 99)
John Pendry

Quantum Aspects Of Light Propagation In Time-varying Media (pp. 100)
John Pendry

Chemically Functionalized 2D Materials for Quantum Photonic Science and Technology (pp. 101)
Mark Hersam

Empowering chiral metamaterials with gain materials (pp. 102)
Ioannis Katsantonis, Anna Tasolamprou, Maria Kafesaki

Photonic Metamaterial Time Crystals And Timetronics (pp. 104)
Nikolay Zheludev

Computational Models Of Light Management In Photovoltaics And Leds (pp. 105)
Vivian Ferry

Rethinking Linking - Topology In Magnetism, And Plasmonics (pp. 106)
Maria Azhar, Ross Knapman, Philipp Gessler, Alexander Neuhaus, Pascal Dreher, Frank Meyer zu Heringdorf, Karin Everschor-Sitte

Space-time Metamaterials (pp. 108)
Andrea Alu

Wavefront Microscopy For Nanophotonics (pp. 109)
Guillaume Baffou

Vortices, Skyrmions, Möbius Strips: From Nanooptics To Ocean Waves (pp. 111)
Konstantin Bliokh

Hybrid Plasmonic Nanosystems Based On Weak And Strong Coupling (pp. 113)
Minyu Chen, Yuqing Zhao, Sylvie Marguet, Safi Jradi, Ali Issa, Anne Laure Baudrion, Jerome Plain, Christophe Couteau, Cuong Dang, Alexander Govorov, Renaud Bachelot

Certain Intersections Of Ai And Photonics (pp. 115)
Marin Soljacic

Spectral Frequency Response Of Hypersonic Phonons In A Non-Trivial Topological Waveguide (pp. 116)

O. R. Ranjbar-Naeini, O. Florez, M. D. Koijam, B. Djafari-Rouhani, Y. Pennec, T. Makkonen, O.M.E. Ylivaara, S. Pourjamal, J. Ahopelto, Clivia M. Sotomayor Torres

AI To Discover And Synthesize Sub-Terahertz Chips Beyond Human Intuition (pp. 118)
Kaushik Sengupta

Tailoring The Visual Appearance With Correlated-Disorder Metasurfaces (pp. 119)
M. Chen, T. Wu, A. Agreda, M. Tréguer-Delapierre, K. Vynck, R. Pacanowski, Philippe Lalanne

Silicon Quantum Photonics (pp. 121)
Vladimir Shalaev

Quasi-2d Materials: From Tailorable Photonics To New Physics (pp. 122)
Alexandra Boltasseva

A Large Language Model Agent for Autonomous Inverse Metamaterial Design (pp. 123)
Willie Padilla, D. Lu, J. M. Malof

Exotic Exciton Phases in Two-Dimensional Quantum Materials (pp. 124)
Wenkai Lou, Kai Chang

AI-Driven Photonics: From Metaphotonics to Silicon Photonics Integration (pp. 127)
Seokho Yun

Beyond the Voigt lineshapes: Efficient statistics-convolved approximants in the time domain (pp. 128)
L. J. Prokopeva, Alexander V. Kildishev

Non-Normality, Pseudospectra and Exponential Sensitivity (pp. 129)
Konstantinos Makris

Active Metastructures – Tailoring Space-Time and Breaking Reciprocity (pp. 130)
Harry Atwater

Functional “Meta”-Optical Fibers for Advanced Imaging and Endoscopy (pp. 131)
Ho Wai (Howard) Lee, Andrew Palmer, Yucheng Jin, Jin Yan, Beyonce Hu, Harvey Lin, Stuart Love, David Dang, M. Father, L. Liu, A. Teoh

Bio-inspired hierarchical phononic crystals and metamaterials (pp. 132)
Marco Miniaci

Transition Waves in Multistable Mechanical Metamaterials (pp. 133)
Vincent Tournat

Empowering Topological Photonics for OAM Manipulation (pp. 134)
Zhigang Chen

Tutorial

Nonlocal Metasurfaces (pp. 136)
Andrea Alu

New trends in nanophotonics and advanced materials

Photonic Crystal Information Processing Chips (pp. 138)
Xiaoyong Hu, Kun Liao

Advanced Self-powered Room-temperature Nir Plasmonic Photodetection And Reconstructive Spectroscopy (pp. 139)
Eslam Abubakr, Shiro Saito, Hironori Suzuki, Tetsuo Kan

Holotomography In Optics And X-ray: Advancing The Study Of Metamaterials (pp. 141)

Yongkeun Park

Momentum-Direct Infrared Interlayer Exciton and Photodetection in WSe2/InSe Heterostructures (pp. 143)
Jiong Yang, Chao Zhang

Accelerating Topological Pumps On Integrated Photonic Chips (pp. 145)
Wange Song

Enhancing Brightness And Directional Control Of Dark Excitons Via All-dielectric Metasurfaces (pp. 146)
Angela Barreda, Sebastian Klimmer, Giancarlo Soavi, Isabelle Staude

Dna Identification Using Surface-enhanced Raman Spectroscopy (sers) And Surface Plasmon Resonance (spr) Sensors: Identification Of Brca1 Gene Mutation Variants In Clinical Samples (pp. 148)
Agata Kowalczyk, Anna Nowicka, Aleksandra Michalowska, Michal Duszczyk, Malgorzata Sikorska, Jan Weyher, Sebastian Zieba, Artur Kowalik, Andrzej Kudelski

Topological Photonic Devices Based On Artificial Gauge Fields (pp. 150)
Cuicui Lu

Engineering Complex Structured Beams With Flat Optics (pp. 152)
Xianzhong Chen, Hammad Ahmed, Chunmei Zhang

Conducting Polymer-cellulose Devices For Tunable Infrared And Thz Optics (pp. 154)
Chaoyang Kuang, Shangzhi Chen, M. P. Jonsson

Spectroscopy Of Single Metal Nanoparticles For Single-molecule Biosensing (pp. 156)
Peter Zijlstra

Arbitrarily Configurable Nonlinear Topological Modes (pp. 157)
Duanduan Wan, Kai Bai, Meng Xiao

Mems-tunable Metasurfaces For Dynamic Vortex Beam Generation (pp. 158)
Chuanshuo Wang, Chao Meng, Lili Gui, Paul C. V. Thrane, Xianglong Mei, Hao Chen, Fei Ding, Kun Xu, Sergey I. Bozhevolny

Edge Bound State In The Continuum On Silicon Pillar Photonic Crystal (pp. 160)
Rodrigo Sato, Christian Vinther Bertelsen, Maxim Nikitin, Elena Lopez Aymerich, Radu Malreanu, Winnie Edith Svendsen, Andrei V. Lavrinenko, Osamu Takayama

Sub-wavelength Optical Lattice In 2d Materials (pp. 162)
Supratik Sarkar, Mahmoud Jalali Mehrabad, Daniel G. Suarez-Forero, Liuxin Gu, You Zhou, Mohammad Hafezi

Metasurface-Enhanced Single-Shot 3D Imaging for High-Precision Biological and Industrial Applications (pp. 164)
Huijie Hao, Jian Liu, Xumin Ding

All-optical control and detection of broken time-reversal symmetry and topological nonlinear optics (pp. 166)
Giancarlo Soavi

Creation of Novel Scattering Singularities in Generic Non-Hermitian Systems Probed Through Complex Time Delay (pp. 168)
Jared Erb, Nadav Shaibe, Thomas M. Antonsen, Steven Anlage

Non-noble metal plasmonic nanostructures (pp. 170)
Michal Horák, Michael Foltýn, Tomáš Šikola

Characterizing the mechanical properties of single bacteria in air by multimode tracking nanomechanical resonators (pp. 172)
Alicia Aparicio Millán, Elena Sentre Arribas, Jose Jaime Ruz, Sergio García López, Priscila Monteiro Kosaka, Montserrat Calleja, Javier Tamayo, Eduardo Gil Santos

High-resolution photothermal imaging using mid-infrared photo-induced force microscopy - modeling and experiment (pp. 174)
Maryam Ali, Shohely T. Anindo, Robin Schneider, Christin David, Daniela Täuber

Hyperuniform Disordered Materials for Solar and Solar-Thermal Absorbers (pp. 176)
Marian Florescu

Developing quantitative multiscale models for nonlinear molecular plasmonics (pp. 178)
Maxim Sukharev

Metasurface with gap and collective surface plasmon modes (pp. 180)
Anatoliy Pinchuk, Yeshchenko Oleg

Nonlocal metasurfaces and thin film devices for all-optical image processing and phase contrast imaging (pp. 182)
Ann Roberts

Chern insulators: nonlinearity and switching (pp. 184)
Justin Cole

Active Conducting Polymer Plasmonics and Metasurfaces (pp. 185)
Magnus Jonsson

Microenvironment Responsive Bio-Acoustic Metamaterials for Precision Medicine (pp. 186)
Hanchuan Tang

Tailored Resonant Metasurfaces for Enhanced Third-order Nonlinear Optics (pp. 188)
Hailun Xie, Lili Gui, Kun Xu

Structurally engineered phosphors for high color-conversion efficiency (pp. 190)
Tae-Yun Lee, Hansol Lee, Heonsu Jeon

Investigate the Growth of (multi)metallic nanoparticles Synthesized by physical vapor deposition (pp. 192)
Julien Ramade, Maël Costes, Sophie Camelio, Sophie Rousselet, Frederic Pailloux, Marc Marteau, Kevin Dusaillant, David Babonneau

Time-resolved vector polarimetry for identifying topological features of surface plasmon polaritons (pp. 194)
Pascal Dreher, Alexander Neuhaus, Timothy Davis, Bettina Frank, Harald Giessen, Frank Meyer zu Heringdorf

Single Crystals of Two-Dimensional Layered Perovskite Heterostructures (pp. 196)
Alexander Schleusener, Mehrdad Faraji, Martina Borreani, Linhan Li, Miao-Ling Lin, PingHeng Tan, Sirous Khabbaz Abkenar, Giorgio Divitini, Roman Krahne

Development of three-dimensional bulk metamaterials suppliable as meta-atomic grains (pp. 198)
Yoshiaki Kanamori

Large-diameter Infrared Si Metalenses through Deep-UV Lithography (pp. 200)
Kai Sun, Xingzhao Yan, Jordan Scott, James Monks, Jun-Yu Ou, Otto Muskens

Plasmonic nanohole array for tumor cell and tissue biosensing (pp. 202)
Alfredo Franco, Dolores Ortiz, Carlos Velásquez, Víctor García-Milán, Sara Marcos, Rubén Martin-Laez, Fernando Moreno, José Luis Fernández-Luna

Near-Infrared Photodetector Enhancement via Plasmonic Diffraction (pp. 204)
Soh Uenoyama

Reconfigurable Plasmonics Enabled by Phase Change Materials (pp. 206)
Yael Gutierrez, Gonzalo Santos, Capucine Laprais, Lofti Berguiga, Saul Vazquez Miranda, Mateusz Rebarz, Shirly Espinoza, Sebastien Cueff, Maria Losurdo

Recognition of Shiga Toxins by Plasmonic SERS Metasurface PCA Assisted (pp. 207)
Massimo Rippa, Alessia Milano, Valentina Marchesano, Domenico Sagnelli, Bryan Guilcapi, Amalia D'Avino, Maurizio Brigotti, Stefano Morabito, Joseph Zyss, Lucia Petti

Boosting the magnetic response of a composite nanostructure in the near-visible region with a Fano resonance (pp. 209)
Maximilian Grimmer, Monika Fleischer

Electric field induced second order nonlinearity in amorphous As2S3, SiOx and SiNx (pp. 211)

Laurids Wardenberg, Krishna Koundinya Upadhyayula, Georg von Freymann, Vadim Talalaev, Michael Hanke, Andre Kühling, Joerg Schilling

Superconducting Nanowire Single Photon Detectors for photon counting applications in the mid-infrared (pp. 213)

Dmitry Morozov, Daniel Kuznesof, Ciaran Lennon, Umberto Nasti, Robert H. Hadfield

Freestanding Ultra-thin Bic Membrane Metasurface For High-q Surface Emission In The Visible (pp. 215)

Chih-Zong Deng, Ya-Lun Ho

Steering Plasmonic Optical Losses Using Alkali Metals (pp. 217)

Yuhan Yang, Jie Liang, Lin Zhou

Manipulation Of Light Propagation In Photonic Crystals Via Non-hermitian Photonic Band Engineering (pp. 219)

Takuya Inoue, Masahiro Yoshida, Susumu Noda

Exploration Of Optical Chirality Based On The Orbital Angular Momentum Of Light Using A Single Chiral Metallic Nanostructure As A Probe (pp. 221)

Shun Hashiyada, An'an Wu, Yoshito Tanaka

Susceptibility Invariance And Disorder-induced Statistical Properties In Time-varying Media (pp. 223)

Bo Zhou, Enzong Wu, Zuojia Wang

Scalable Integration Of Multiple Single-photon Sources For Fiber Quantum Network (pp. 225)

Woong Bae Jeon, Donghyun Park, Jongsung Moon, Kyu-Young Kim, Mohamed Benyoucef, Je-Hyung Kim

Second-order Coherence Of Bose-einstein Condensation In Plasmonic Lattices (pp. 227)

Evgeny Mamonov, Sioneh Eyvazi, Lukas Freter, Päivi Törmä

Optical Picometrology (pp. 229)

Kevin F. MacDonald, Thomas A. Grant, Cheng-Hung Chi, Huanli Zhou, Anton N. Vetlugin, Eric Plum, Stefan Rotter, Nikolay I. Zheludev

Negative Frequency Generation And Temporal Diffraction (pp. 230)

Euan Hendry

Self-hydridized Plasmonic Excitations And Hot Electron Generation In Aluminum Nanorods (pp. 232)

J. Martin, O. Avalos-Ovando, T. Simon, G. Arditi, F. Lamaze, J. Proust, L. Tizei, M. Kociak, A. Govorov, O. Stéphan, Davy Gerard

Enhancing Thermoplasmonic Sensing Via Plasmonic Nanoplatforms (pp. 233)

Andreea Campu, Simion Astilean, Monica Focsan

Low-loss Resonant Nonlinear Nanophotonics In The Visible Spectral Range Using Wafer-bonded Crystalline Alinp (pp. 234)

Radoslaw Kolkowski, Seyed Ahmad Shahahmadi, Serguei Novikov, Jani Oksanen, Andreas Liapis, Huayu Bai, Timo Stolt, Matti Kaivola, Andriy Shevchenko

Fluorescence-based Chiral Sensing With Silicon Metasurfaces (pp. 236)

Tom Sistermans, Artemijs Krimovs, Robert Pal, Alberto Curto

Nanophotonics For Integrated Chiroptical Sensing Of Drug Solutions (pp. 238)

Raju Adhikary, Ambaresh Sahoo, Massimiliano Aschi, Isabella Daidone, Matteo Silvestri, Matteo Venturi, Giovanna Salvitti, Carino Ferrante, Paola Benassi, Davide Tedeschi, Andrea Marini

Large-area Nanohelices As Chiral Metasurface For Engineering Optical Chirality (pp. 240)

Thu H. H. Le, Hisako Sato, Takuo Tanaka

Transition Metal Dichalcogenide Lateral Heterostructure-based Excitonic Platform For Photonics And Optoelectronics (pp. 243)

Hassan Lamsaadi, Aurélien Cuche, Gonzague Agez, Ioannis Paradisanos, Dorian Beret, Laurent Lombez, Pierre Renucci, Delphine Lagarde, Xavier Marie, Ziyang Gan, Antony George, Kenji Watanabe, Takashi Taniguchi, Andrey Turchanin, Nicolas Combe, Bernhard Urbaszek, Jean-Marie Poumirol, Vincent Paillard

Wavefront Engineering Of Microcavity-empowered Multi-resonant Metasurfaces (pp. 245)
Shih-Hsiu Huang, Hsiu-Ping Su, Zijin Yang, Yuzhi Shi, Qinghua Song, Pin Chieh Wu

Photonics And Ai For Next-generation Smart Applications (pp. 246)
Luigi Di Lauro, A Aadhi, Imtiaz Alamgir, Pavel Dmitriev, Bennet Fischer, Celine Mazoukh, Nicolas Perron, Evgeny Viktorov, Anton Kovalev, Armaghan Eshaghi, Mario Chemnitz, Piotr Roztocki, Shervin Vakili, Brent Little, Sai Chu, David Moss, Roberto Morandotti

Optical Pulling Forces For 3-dimensional Motion Control In Plasmonic Nanomotors (pp. 248)
Guillermo Serrera, Yoshito Y. Tanaka, Pablo Albella

Nonlinear Optics In The Xuv Spectral Range (pp. 250)
Luca Assogna, Emiliano Principi, Matteo Silvestri, Ambaresh Sahoo, Giovanni Batignani, Giuseppe Fumero, Laura Foglia, Riccardo Mincigrucci, Davide Tedeschi, Claudio Masciovecchio, Tullio Scopigno, Andrea Marini, Carino Ferrante

Labyrinthine Magnetic Domains In Epitaxial Magnetooptical Garnet Films For Synchrotron Analysis And Optical Modulator Applications (pp. 252)
Taichi Goto

Quasi-babinet Principle In Dielectric Resonators And Mie Voids (pp. 254)
Masoud Hamidi, Kirill Koshelev, S. Gladyshev, A. C. Valero, M. Hentschel, H. Giessen, Y. Kivshar, Thomas Weiss

Chiral Semiconductor Nanophotonics (pp. 256)
Alberto G. Curto

Resonant Light Absorption Driving By Bound States In The Continuum In Hybrid metasurfaces (pp. 258)
Andrey Evlyukhin, M. A. Poleva, C. Rockstuhl

Multilayer And Microbead Structures For Ultraviolet To Near Infrared Spectroscopic Applications Based On Metal-free Phosphors (pp. 260)
David Hernandez-Pinilla, Barun Kumar Barman, Keisuke Watanabe, Hiroyuki Yamada, Thien Duc Ngo, Tadaaki Nagao

Exfoliation Of Millimeter-sized Flakes Of 2d Transition Metal Dichalcogenides On Arbitrary Substrates (pp. 262)
Ermes Peci, Riccardo Galafassi, Valentina Venturino, Emma Spotorno, Francesca Telesio, Michele Magnozzi, Maurizio Canepa, Francesco Bisio

Design Of Broadband Multilayer Metamaterials Based On Genetic Algorithm And Neural Network (pp. 264)
Kotaro Kajikawa

Surface Acoustic Wave Stimulated Brillouin Scattering (pp. 266)
Moritz Merklein

Permittivity-driven Ultrafast Photonic Bound States In The Continuum (pp. 267)
Andreas Tittl

Enhanced Sensing With Ultrastrong Coupling Condition (pp. 269)
Wen-Hui (Sophia) Cheng, Alexis Angelo R. Garcia, Cheng-An Mao

Self-illuminated Plasmonic Biosensor Enabled By Inelastic Tunnelingluminescence (pp. 270)
Jihye Lee, Yina Wu, Ivan Sinev, Mikhail Masharin, Sotirios Papadopoulos, Eduardo Dias, Lujun Wang, Ming Lun Tseng, Seunghwan Moon, Jong-Souk Yeo, Lukas Novotny, Javier Garcia de Abajo, Hatice Altug

Characteristics Of Optical Chiral Fields Around Nanostructures Revealed By Scanning Near-field Optical Microscopy (pp. 272)
Kohei Imura

Hybrid Photoresists In Multi-photon Lithography: Optical Properties Andpost-processing Strategies (pp. 274)
Dimitra Ladika, Michalis Stavrou, Gordon Zyla, Artur Harnik, Frederik Dumur, Mikas Vengris, Maria Kafesaki, David Gray, Saulius Juodlazis, Mangirdas Malinauskas, Maria Farsari

Exploring Channelrhodopsin-2 And Gold Nanoparticle Interaction For Optogenetics (pp. 276)
Roberto Messina, Luca Bellucci, Stefano Corni, Lucia Cascino, Stefania D'Agostino, Laura Zanetti Polzi

Neural Network-optimized Multifunctional Metasurfaces For Adaptive High-frequency Wireless Communication (pp. 278)
Miguel Beruete, Damián Rodríguez-Trujillo, Alicia E. Torres-García, Mikel Aldea, Jorge Teniente, Asier Marzo-Perez

Temporal Topological Aharonov-bhom Phase In Quantum-systems Under Electric And Gravitational Scalar Potentials (pp. 280)
Michael Tobar, Michael Hatzon, Graeme Flower, Maxim Goryachev, Jeremy Bourhill, Raymond Chiao, Nader Inan, Michael Scheibner, Jay Sharping, Douglas Singleton

Two-dimensional Semiconductors For On-chip Polarization-sensitive Photodetectors (pp. 282)
Marcos Guimaraes

Controlled Synthesis Of Silver-coated Gold Nanostars For Tunable Optical Properties (pp. 283)
Nicolas Pazos Perez

Tailoring The Emission And The Photodynamics Of Quantum Emitters With Simple And Optimized High-index Dielectric Nanostructures (pp. 285)
Swaroop Palai, Mélodie Humbert, Romain Hernandez, Peter Wiecha, Jonas Muller, Etienne Palleau, Frank Fournel, Vincent Larrey, Aurélie Lecestre, Guilhem Larrieu, Christian Girard, Vincent Paillard, Laurence Ressier, Aurelien Cuche

Optimising Cross-polarisation Conversion Of Ghost Hyperbolic Polaritons With A Twist (pp. 287)
Mark Cunningham, Rair Macêdo

Broadband Third Harmonic Generation Through Strong Coupling Between All-dielectric Metasurfaces And Epsilon-near-zero Materials (pp. 290)
Hui-Hsin Hsiao

Efficient Modeling Of Particle Acceleration In Structured Dielectric Waveguides Driven By Short-pulse Laser Excitation (pp. 292)
Andrea Locatelli, Gino Sorbello, Davide Guarnera, Roberta Palmeri, Giorgio Mauro, Giuseppe Torrisi, Nunzio Salerno, Davide Rocco, Luca Vincetti

Nonlinear Photonics In Low-index Time-varying Systems (pp. 294)
Marcello Ferrera, Wallace Jaffray, Sven Stengel

Continuous Translational Symmetry Breaking Metamaterial Design For Photonic Integrated Circuits To Free Space Outcouplers (pp. 296)
Alexei Azarov, Dhriti Maurya, Daron Westly, Vladimir Aksyuk

Optical Fresnel Zone Plate Lenses Fabricated Entirely Of colored Photoresist With I-line Stepper (pp. 298)
Kuniaki Konishi

Integrating Superconductors With Silicon Photonic Circuits For High-performance Quantum Optic Applications (pp. 300)
Jeff Young, Mohammad Khalifa, Phillip Kirwin, Joseph Salfi

Recent Progress In Metasurface Fluorescence Biosensors: Expansion Of The Targets To Next-generation Nucleic Acid Biomarkers (pp. 302)
Masanobu Iwanaga

Anisotropic Nonlinearities In Crystalline Gold And How To Exploit Them (pp. 304)
Sergejs Boroviks, Olivier Martin

Fabrication Of Polymer Structures In The Sub-micron Range As Potential Landscapes For Photon Bose-einstein Condensates Via Direct Laser Writing (pp. 306)
Sven Enns, Julian Schulz, Kirankumar Karkihalli Umesh, Frank Vewinger, Georg von Freymann

Scanning Near-field Optical Microscopy On Hyperuniform Disordered Photonic Materials (pp. 308)
Nicoletta Granchi, Gabriele Calusi, Kris Stokkereit, Matteo Lodde, Camilla Gonzini, Andrea Fiore, Marian Florescu, Francesca Intonti

Spectroscopic Proof Of The Non-thermal Reactant Activation in Plasmon-photocatalysis (pp. 310)
Zee Hwan Kim

Active Modulation Of Optical Response In Transparent Conducting Oxide Films (pp. 312)

Stefania Benedetti, Alessandro di Bona, Sergio D'Addato, Alexandr Petrov, Piero Torelli, michele Magnozzi, Stefano Colace, Maurizio Canepa, Francesco Bisio

Photonic Force Microscopy In Front Of Epsilon-near-zero (enz) Surfaces (pp. 314)

Maria Grazia Donato, Michael Hinczewski, Theodore Letsou, Mohamed ElKabbash, Rosalba Saija, Pietro Giuseppe Gucciardi, Nader Engheta, Giuseppe Strangi, Onofrio Maria Maragò

Extracting Resonances In Nanophotonic Systems From Light Scattering Simulations (pp. 316)

Felix Binkowski, Fridtjof Betz, Lin Zschiedrich, Sven Burger, Martin Hammerschmidt

Towards Photonic Orbitronics: Exploiting The Orbital Angular Momentum Of Light (pp. 318)

Max Weber, Julian Schulz, Ian Heil, Christina Jörg, Georg von Freymann

Direct Determination Of Carrier Parameters In Plasmonic Indium Tin Oxide Nanocrystals Exploiting Magnetoplasmonic Modulation (pp. 320)

Alessio Gabbani, Elisa Della Latta, Xiaoyan Li, Andrea Scarperi, Francesca Martini, Francesco Biccari, Mathieu Kociak, Marco Geppi, Silvia Borsacchi, Francesco Pineider

Chiral Metasurface Photodetectors For Circular-polarization-selective Phase Contrast Imaging (pp. 322)

Ahmet Erturan, Jianing Liu, Maliheh Azimi Roueini, Nicolas Malamug, Lei Tian, Roberto Paiella

Harmonic Generation From Aluminium And Gold Nanolayers And Nanogratings: Bound And Hot Electron Contributions (pp. 324)

Shroddha Mukhopadhyay, Crina Cojocaru, Maria Antonietta Vincenti, Kent Hallman, Michael Scalora, Jose Trull

Hyperbolic Plasmon Polaritons In Van A Der Waals Crystal At Visible Frequencies (pp. 326)

Andrea Mancini, Giacomo Venturi, Nicola Melchioni, Stefano Chiodini, Antonio Ambrosio

Femtosecond Laser Delamination Cavities And Their Applications (pp. 328)

Pavel Varlamov, Akira Barros, Aditya Swaminathan, Jan Marx, Andreas Ostendorf, Anna Semisalova, Denys Makarov, Alexey Lomonosov, Paolo Vavassori, Yannis Laplace, Michele Raynaud, Vasily Temnov

UV Upconversion In Lanthanides-doped Thin Films Assisted By Photonic Crystals. (pp. 330)

Damien Rinnert, Emmanuel Drouard, Antonio Pereira, Céline Chevalier, Aziz Benamrouche, Benjamin Fornacciari, Hai Son Nguyen, Gilles Ledoux, Christian Seassal

Miniaturized Microfluidic Plasmonic Chip For Enhanced Biosensing (pp. 332)

Andreea Campu, Daria Stoia, Dana Maniu, Simion Astilean, Marc Lamy de la Chapelle, Monica Focsan

Natural Hyperbolic Van Der Waals Materials Towards Low-loss Near Unity Linear Dichroism (pp. 333)

Nicola Melchioni, Andrea Mancini, Lin Nan, Anastasiia Efimova, Giacomo Venturi, Antonio Ambrosio

Two-dimensional Gold Flakes For Nonlinear And Low-loss Plasmonics (pp. 335)

Alexey Krasavin, Chenxinyu Pan, Lufang Liu, Anatoly Zayats, Limin Tong, Pan Wang, Zhenxin Wang

Infrared Electroluminescence And Energy Transfer In Hbn-encapsulated Graphene Devices Under High Bias Voltage (pp. 336)

Yannick De Wilde

Unified Framework For Enhancing Chiral Light-matter Interactions (pp. 338)

Chloe Doiron

Fabrication Of Plasmonic Transition Metal Nitride Thin Films And Nano-arrays (pp. 340)

Ryan Bower, Ethan Muir, Gwilherm Kerherve, Bruno Rente, Arutiun Ehiasarian, Peter Petrov

Multilayer Structures For Broadband Switchable Absorption And Switchable Radiative Cooling Based On Phase-change Materials (pp. 342)

Georgios Veronis, Md Tanvir Emrose, Ming Zhou, Shanhui Fan

Detection Of Ammonia In Water Using Self-assembled Plasmonic Colorimetric Sensor (pp. 343)

M. Soudi, P. Cencillo-Abad, S. Ghimire, Debashis Chanda, Kausik Mukhopadhyay

Visualization Of Thermal Extraction Process Achieved By Metamaterial Absorber (pp. 345)
Wakana Kubo

Twisted Moiré Metasurfaces With Emissive Gap Layers Enabling Giant And Tunable Chiral Emission (pp. 347)
Zijie Jiang, Zhao Sun, Zhuofei Gan, Wen-Di Li

Optimization Of Photonic Structures For Cmos Image Sensors Using Adjoint Sensitivity (pp. 348)
Rishad Arfin, Jeongwoo Son, Jens Niegemann, Dylan McGuire, Mohamed H. Bakr

Modulation And Amplification Of Waves By Metasurfaces (pp. 350)
Ilya Shadrivov

Negative Refraction Of Light Using Atoms Instead Of Metamaterials (pp. 351)
L. Ruks, K. E. Ballantine, Janne Ruostekoski

Development of A Silicon Nitride Platform for Next Photonic Integrated Circuits (pp. 353)
Brahim Ahammou, Narges Dalvand, Boris Le Drogoff, Youssef Ouldhnini, Abir Radi, Majid Taghavi Dehaghani, Kulbir Kaur Ghuman, Joëlle Margot, Michael Ménard, Mohamed Chaker

Vectorial Metasurface For Polarization Encoding And Imaging (pp. 354)
Fengjun Li, Zilan Deng, Xiangping Li

Highly Sensitive Cmos Image Sensor Integrating Color-routing Nanostructures (pp. 355)
Choonlae Cho, Sangyun Lee, Sookyoung Roh, Sungmo Ahn, Suyeon Lee, Junho Lee, Subeom Song, Seokho Yun

Non-lorentzian Effects For Exciton-plasmon Systems At Strong Coupling (pp. 357)
Tigran Shahbazyan

Sub-1-volt, Reconfigurable Gires-tournois Resonators For Colored Monopixel Array (pp. 359)
Young Min Song

Single-shot Weak Measurement For Spin Hall Effect Of Light Using A Metasurface (pp. 361)
Minkyung Kim

Laser Color Printing On Disordered Metal-dielectric Multilayer Structures (pp. 363)
Piotr Nyga, Michal Nowak, Marcin Woszto, Tomasz Wojciechowski, Bartosz Bartosewicz, Przemyslaw Wachulak

The General Boundary Conditions For All Interfaces, Including Arbitrary Moving Metasurfaces And Instantaneous Changes In Constitutive Relations. (pp. 365)
Jonathan Gratus, Simon Horsely, Martin McCall

Harnessing The Power Of Mid-infrared Metasurfaces For Ultrafast And High-efficiency All-optical Modulation (pp. 367)
The Linh Pham, Amirmostafa Amirjani, Kacper Pilarczyk, Nils Deßmann, Thanh Tung Nguyen, Ewald Janssens

Injecting Physics Knowledge In Neural Networks For A Wide Range Of Photonic Devices: Qnm-net (pp. 369)
Viktor Lilja, Albin Svärdsby, Timo Gahlmann, Philippe Tassin

Suspended Algaas Integrated Nonlinear Photonics (pp. 371)
Changzheng Sun, Yuqian Zhang, Bing Xiong, Jian Wang, Zhibiao Hao, Lai Wang, Yanjun Han, Hongtao Li, Lin Gan, Yi Luo

Far-field Petahertz Sampling Of Plasmonic Fields (pp. 373)
Kai-Fu Wong, Weiwei Li, Z. Wang, V. Wanie, E. Mansson, D. Hoeing, J. Blöchl, T. Nubbemeyer, A. Azzeer, A. Trabatton, Holger Lange, Francesca Calegari, Matthias F. Kling

Degenerate Metasurface Eigenstates: Coupling And Interfering For Maximum-chiral Optics (pp. 375)
Maxim Gorkunov, Alexander Antonov, Yuri Kivshar

Non-hermitian Skin Effect In Lossy Anisotropic Nanophotonic Systems (pp. 377)
Yuto Moritake, Nozomi Ogawa, Issei Takeda, Masaya Notomi

Electrically Tunable Free-electron Nonlinearity In Heavily-doped Ingaas (pp. 379)

Valeria Giliberti, Tommaso Venanzi, Andrea Rossetti, Huatian Hu, Raffaella Polito, Andrea Notargiacomo, Antonio Valletta, Francesco Mattioli, Adel Bousseksou, Gregoire Beaudoin, Isabelle Sagnes, Raffaele Colombelli, Markus Ludwig, Daniele Brida, Marialilia Pea, Cristian Ciracì, Michele Ortolani

Material Aspects For Ultra-stable Laser Interferometers (pp. 381)

Nico Wagner, Bess Fang, Sebastian Häfner, Michael Hartman, Michael Jetter, Thomas Legero, Mateusz Naroznik, Michael Zimmer, Stefanie Kroker

Ultrafast Plasmonic Hot Carriers: From Light Generation To Pulsed Photocatalysis (pp. 383)

Andrea Schirato, Yang Luo, Shaoxiang Sheng, Giulio Cerullo, Alessandro Alabastri, Manish Garg, Peter Nordlander, Giuseppe Della Valle

Chiral Photoacoustic Spectroscopy On Plasmonic Materials (pp. 385)

Claudia Skubisz, Emilija Petronijevic, Grigore Leahu, Teemu Hakkarainen, Eero Koivusalo, Mircea Guina, Roberto Li Voti, Concita Sibilia, Alessandro Belardini

Next-generation Implantable Neural Probes: Advanced Photonics On The Tip Of Multimode optical Fibers For Enhanced Endoscopic Sensing (pp. 387)

Linda Piscopo, Maria Samuela Andriani, Luciana Algieri, Liam Collard, Di Zheng, Muhammad Fayyaz Kashif, Cinzia Montinaro, Mohammadrahim Kazemzadeh, Stella Aslanoglou, Filippo Pisano, Antonio Balena, Marco Bianco, Marco Pisanello, Barbara Spagnolo, Michele Scaraggi, Tommaso Fellin, Massimo De Vittorio, Ferruccio Pisanello

Incident Light Selective Metasurfaces (pp. 389)

Kuang-Yu Yang

Precision Fabrication Of Nanoscopic Europium Emittersutilizing Electron Beam Lithography (pp. 391)

Marijn Rikers, Ayesheh Bashiri, Ángela Barreda, Michael Steinert, Duk-Yong Choi, Thomas Pertsch, Isabelle Staude

Controlled Electrophoretic Deposition Of Nanoparticle Films And Their Applications In Light Emitting Diodes (pp. 393)

Ning Liu, Anthony Mullen, Lin Lyu, Yongliang Zhang, Nandita Biswas, Kevin M. Ryan

Classical-Quantum Correspondence In Photonic Temporal Crystals (pp. 395)

Bumki Min

Harnessing Plasmonic Nanostructures For Selective Light-driven Co_2 Reduction (pp. 396)

Anjalie Edirisooriya, Zelio Fusco Beck, Ning Lyu, Christin David, Fiona Beck

Complex Modulation Of Light In Polarization And Space Using Laser-written Multi-plane Light Conversion (pp. 398)

Oussama Korichi, Markus Hiekkamäki, Robert Fickler

Integration Technique Of Micro- And Nano-lasers On Si By Epitaxial Growth Using Iii-v-on-si Wafer (pp. 400)

Takuro Fujii, Koji Takeda, Erina Kanno, Takuma Tsurugaya, Tomonari Sato, Shinji Matsuo

New Materials For Metaoptics From Infrared (ir) To Deep-ultraviolet (duv) (pp. 402)

Zeng Wang

Probing Nanoscale Light-matter Interactions With Fast Electrons And Near-field Optical Probes (pp. 403)

Carlos Maciel Escudero, Ermin Malic, Rainer Hillenbrand, Javier Aizpurua

Automated Design Of One-dimensional Photonic Crystals For Surface Wave Enhanced Chiroptical Spectroscopy (pp. 405)

Jonathan Barolak, Francesco Michelotti, Agostino Occhicone, Marco Finazzi, Paolo Biagioni, Giovanni Pellegrini

Exponentially Sensitive Lattices: Pseudospectral Scalings (pp. 407)

Ioannis Kiorpelidis, Konstantinos G. Makris

Subwavelength Metamaterials For High-performance Power And Modal Control In Silicon Photonics (pp. 409)

Raquel Fernández de Cabo, Alejandro Sánchez-Sánchez, Yijun Yang, Daniele Melati, Carlos Alonso-Ramos, Pavel Cheben, Aitor V. Velasco, David González-Andrade

Unconventional Phenomena From Space-time Modulation Of Dispersive Media (pp. 411)

Carlo Rizza, Alessandra Contestabile, Maria Antonietta Vincenti, Giuseppe Castaldi, Michael Scalora, Vincenzo Galdi

Engineered Single-photon Emitters In Materials For Integrated Quantum Photonics (pp. 413)
Alexander Senichev, Zachariah O. Martin, Samuel Peana, Pranshu Maan, Artem Kryvobok, Demid Sychev, Alexei S. Lagutchev, Alexandra Boltasseva, Vladimir M. Shalaev

Optical Fiber Microstructure Devices Inscribed By Femtosecond Laser And Their Sensing Applications (pp. 415)
Xuewen Shu

Multi-Temperature Modeling Of Hot-Carrier Dynamics In Photonic Metastructures (pp. 417)
Andrea Schirato, Giulia Crotti, Giuseppe Della Valle

Effect Of Disorder In 3d Photonic Networks On Their Photonic Band Gaps (pp. 419)
Florin Hemmann, Vincent Glauser, Ullrich Steiner, Matthias Saba

Nano-Optomechanical Disk Resonators: Operating Principles And Sensing Applications (pp. 421)
Elena Sentre-Arribas, Alicia Aparicio-Millán, Ivan Favero, Aristide Lemaître, Oscar Malvar, Jose Jaime Ruz, Montserrat Calleja, Javier Tamayo, Eduardo Gil-Santos

Ab Initio Simulation Of Nonlinear Optical Response In Periodic Semiconducting Nanostructures (pp. 423)
Mitsuharu Uemoto

Lasing Emission From Guided Mode-Assisted Quasi-Bound States In The Continuum In All-Dielectric Metasurfaces (pp. 425)
Ayesheh Bashiri, Aleksandr Vaskin, Muyi Yang, Katsuya Tanaka, Marijn Rikers, Thomas Pertsch, Isabelle Staude

Real-Space Renormalization Group On Topological Scattering Under Strong Disorder (pp. 427)
Zhe Zhang, Romain Fleury

Photodegradation Of Dyes Using Fe3O4-Au-Pd Hybrid Nanoparticles Synthesized Liquid-Phase (pp. 429)
Yukie Yokota, Taiga Uehara, Mao Takeda

Photonic Antiferromagnetic Topological Insulator With A Single Surface Dirac Cone (pp. 431)
Yihao Yang

Spin-Orbit Coupling And Tunable Lasing In Liquid-Crystal-based Photonic 1d Crystals (pp. 433)
Jacek Szczytko, Marcin Muszyński, Pavel Kokhanchik, Przemyslaw Oliwa, Piotr Kapuscinski, Daniil Bobylev, Eva Oton, Rafal Mazur, Przemyslaw Morawiak, Wiktor Piecek, Przemyslaw Kula, Witold Bardyszewski, Barbara Piętka, Dmitry Solnyshkov, Guillaume Malpuech

Room-Temperature Exciton-Polariton Condensation In Prism-Shaped Gan Microcavity Structures (pp. 435)
Yong-Hoon Cho

High-Temperature Superfluorescence In Perovskites (pp. 436)
Kenan Gundogdu

Multipartite Light-Matter Interactions In Hybrid 2d-Material Nanophotonic Cavities (pp. 437)
Chenjiang Qian, Viviana Villafañe, Pedro Soubelet, Andreas V. Stier, Jonathan J. Finley

From Exceptional Point To Bound States In The Continuum And From Lasing To Coherent Perfect Absorption, Or There And Back Again Using Non-hermitian Metasurfaces (pp. 438)
Yaoyao Liang, Yara El Droubi, Liubov Ivzhenko, Maciej Krawczyk, Andriy Serebryannikov, Anatole Lupu

Chirality Transfer In Silicon Nanoparticles With Chiral Molecules (pp. 440)
Hiroshi Sugimoto, Hiroki Kasai, Kento Shintani, Shahin Ghamari, Frank Vollmer, Minoru Fujii

Imaging Method Of The Photodegradation Mechanism At The Nanoscale Over A Gold Metasurface (pp. 442)
Marlo Vega, Paul-Ludovic Karsenti, Paul G. Charette, Julien Moreau, Michael Canva, Jean-François Bryche

Non-Hermitian Dynamics In Bosonic Systems: Classical And Quantum Realizations (pp. 443)
Yogesh Joglekar

Past, Present And Future Of Mass Diffusion Metamaterials (pp. 444)
Juan Manuel Restrepo Florez

Enhanced Photo-Excitation Of Spin-Forbidden Gray Exciton In 2d Materials By Using Spin-Orbit-Coupled Vector Vortex Beams (pp. 445)
Shun-Jen Cheng

Higher-Order Mie Resonant Metasurfaces For Ultrafast All-Optical Light Manipulation (pp. 447)
Claudio Hail, Lior Michaeli, Harry Atwater

Snapshot Polarimetric Stereoscopic Imaging And On-Chip High Dynamic Range Correction System (pp. 448)
Shuming Wang

Building Complex Nanophotonic Device With Self-Assembled Colloidal Particles (pp. 450)
Weihua Zhang

Van Der Waals Polaritonic Crystals And Their Applications In Thz Detection (pp. 451)
Huanjun Chen, Ximiao Wang, Shaojing Liu, Hongjia Zhu, Shaozhi Deng

Plasmonic Sensing On Nanofibers For In Vivo Protein Measurement In The Brain (pp. 452)
Jean-Francois Masson, M. H. Jodaylami

Ultrafast Manipulation Of Collective Modes Via Chiral Fermions In A Charge Density Wave Weyl Semimetal (pp. 453)
L. Cheng, Z. X. Wei, Y. G. Yao, Jingbo Qi

Coexisting And Cooperating Light-matter Interaction Regimes In Apolaritonic Photovoltaic System (pp. 455)
Roberto Termine, Vincenzo Caligiuri, Svetlana Siprova, Attilio Golemme, Aniket Patra, Giuseppe E. Lio, Antonio De Luca

Nanostructured Surfaces For Enhanced Spectroscopy And Nonlinear Optics (pp. 456)
Luca Razzari

Configurable Quantum Simulator For Few Atoms In A Super-Resolved Optical Tweezers (pp. 457)
Vincent Mancois, Kelvin Lim, Haijun Wu, Yijie Shen, David Wilkowski

Optical Skyrmions From Metamaterials (pp. 458)
Yijie Shen, Nilo Mata-Cervera

Thermal Photonics For Advanced Energy Conversion Systems (pp. 459)
Atsushi Sakurai

Quadrupole Topological Phase Constructed By Gyromagnetic Photonic Crystal (pp. 460)
Peiheng Zhou, Gui-Geng Liu, Qindong Xie, Longjiang Deng, Baile Zhang

Polarization Optics Using Nonlocal Dielectric Metasurfaces (pp. 461)
Yu Geun Ki, Changhyun Lee, SeokJae Yoo, Soo Jin Kim

Extreme-Ultraviolet Spatiotemporal Optical Vortices (pp. 463)
Rodrigo Martin-Hernandez, Guan Gui, Luis Plaja, Henry Kapteyn, Margaret Murnane, Miguel Ángel Porras, Chen-Ting Liao, Carlos Hernandez-Garcia

Optical Properties Of Nanoporous Gold And Their Change Upon Electrochemical Oxidation (pp. 465)
Maurice Pfeiffer, Xinyan Wu, Manfred Eich, Alexander Petrov

Low-Loss Phase Change Materials For Integrated Photonics (pp. 466)
Ioannis Zeimpekis, A. Shoaa, Q. Luo, I. Johnson, D. Lawson, L. Rozaqi, P. Deoli, D. Trubacs, S. Blundell, O. L. Muskens, F. Gardes

Optical Response In Twisted Bilayer Graphene (pp. 467)
M. Sanchez, J. Gonzalez, Tobias Stauber

Heterostrucutred Photonic Media For Phz Optoelectronics Applications (pp. 469)
Václav Hanus, Beatrix Fehér, Peter Dombi

Modifying Perovskite Solar Cell Architecture To Limit The Effective Radiative Recombination To Enhance The Open Circuit Voltage (pp. 470)

Martina D'Andrea, R. Runjun, F. Bernal-Texca, Jordi Martorell

Active IR and THz Light Modulators Based on Epsilon-Near Zero InAs and GaSb Semiconductor Frequency-Selective Surfaces (pp. 471)

Julien Guise, Fernando Gonzalez-posada Flores, Stephan Blin, Thierry Taliercio

High-Speed Self-Biased 2d Ins Photodetector (pp. 473)

Srinivasa Tamalampudi, Ghada Dushaq, Mahmoud Rasras

Integrated Photonic Platforms For Nonlinear Light Generation In The Ultraviolet And Visible Regions (pp. 475)

Natale Pruiti, Elissa McKay, Eugenio Di Gaetano, Cosmin Suciu, Daniel Kelly, Stuart May, Marc Sorel

Colloidal Self-Assembly As Templating For 3d Second-harmonic Photonic Crystals (pp. 476)

Thomas Kainz, Helena Weigand, Ülle-Linda Talts, Rachel Grange, Ullrich Steiner, Viola Vogler-Neuling

Multi-Photon Lithography For Advanced Micro-optics And Large-Area Metasurfaces (pp. 478)

Gordon Zyla, Dimitra Ladika, Vasileia Melissinaki, Michalis Stavrou, Ivan Kassamakov, Savvas Papamakarios, Dimitrios Zografopoulos, Anna Christoforidou, George Kenanakis, Odysseas Tsilipakos, Mangirdas Malinauskas, Maria Farsari

Strong Light-Matter Interaction In Dielectric Hybrid Metasurfaces (pp. 479)

Giorgio Adamo, Marco Marangi, Alexander M Dubrovkin, Andrea Zacheo, Cesare Soci

Rapid, Full-wafer Fabrication Of All-inorganic, High-efficiency Metaoptics And Ar Waveguides Via Additive Nanoimprint Lithography (pp. 480)

James Watkins

Monolithic Integration For Silicon Photonics (pp. 481)

Frederic Gardes, Ilias Skandalos, Xingshi Yu, Afrooz Shoaa, Qianbin Luo, Thalia Dominguez Bucio, Ipsita Chakraborty, Michele Paparella, Ioannis Zeimpekis, Huiyun` liu, Alwyn Seeds

Controlling And Applying The Loss Of Electromagnetic Metasurface Based On Machine Learning (pp. 482)

Peng Fu, Yang Guo, Changzhi Gu

Development Of Plasmonic Components For Artificial Neural Networks (pp. 483)

Martin Aeschlimann

DNA Origami Self-Assembled Diamond Lattice Photonic Crystals (pp. 484)

Xin Yin, Gregor Posnjak, Paul Butler, Oliver Bienek, Mihir Dass, Seungwoo Lee, Ian Sharp, Tim Liedl

Photon Manipulation with the Interface of Synthetic Temporal Photonic Lattices (pp. 486)

Bing Wang

Nonlinear and Optomechanical Applications Harnessing Silicon Nanostructures (pp. 488)

P. Nuño Ruano, J. Zhang, D. González-Andrade, H. E. B. Ferhart, T. T. D. Dinh, D. Medina-Quiroz, S. Edmond, P. Cheben, D. Marris-Morini, E. Cassan, L. Vivien, N. D. Lanzillotti-Kimura, Carlos Alonso Ramos

Cavity-Induced Attractive Interactions in Van der Waals Quantum Material (pp. 489)

F. Helmrich, T. F. Nova, H. S. Adlong, I. Khanonkin, E. Jöchl, M. Kroner, G. Scalari, J. Faist, Atac Imamoglu

BICs and Quasi-BICs in Unpatterned Media (pp. 490)

Rodrigo Berte, T. Possmayer, A. Tittl, L. de S. Menezes, S. A. Maier

Flat Band Finetuning and its Photonic Applications (pp. 491)

Sergej Flach

Programmable Nanophotonic Devices with Low-loss Phase-Change Materials (pp. 492)

Fouad Bentata, Capucine Laprais, Stéphane Monfray, Nicolas Baboux, Xavier Letartre, Guillaume Saint-Girons, Patrice Genevet, Lotfi Berguiga, Sébastien Cueff

Near-Unity Absorption in Semiconductor Nanowire Metasurfaces (pp. 493)

Michael Reimer

Switching of Topological Edge Transmission in Si Photonics Platform (pp. 494)
Tomohiro Amemiya, Sho Okada, Liyan Hu, Qianshuo Wang, XingXiang Wang, Xiao Hu

Second Harmonic Generation of High-Coherence Light in Si3N4 Microresonators (pp. 495)
Kerry Vahala, Z. Yuan, B. Li, J. Ge, P. Liu, M. Li, J.-Y. Liu, Y. Yu, H.-J. Chen, J. Bowers

Very Large-Scale Integration for Fibers (VLSI-Fi): Assembling Fiber-Embedded Photonics and Optoelectronics by Melt-Shaping Multimaterial Cores (pp. 496)
Alexander Gumennik

Bulk Embedded Laue type Photonic Crystals (pp. 498)
Darius Gailevičius, E. Aleksandravicius, G. Tamošauskas, G. Kontenis, A. Dubietis, K. Staliūnas

Overcoming Integration Challenges in Photonic AI Accelerators (pp. 500)
Angel Ortega-Gomez, Nikolaos Farmakidis, Håvard Hem Toftevaag, Yi Zhang, Harish Bhaskaran

Plasmonic Nanoparticle Synthesis and characterization: Harnessing Enhanced Visible Absorption for Dye Molecule Applications (pp. 502)
Amina Badir, Siham Refki, Zouheir Sekkat

Interfacing the brain by photonic technologies (pp. 503)
Massimo De Vittorio, F. Pisanello

Modeling Electromagnetic Wave Interactions With Ferroelectric Vortex Lattices In The Sub-thz Regime (pp. 504)
Marvin Degen, Ramaz Khomeriki, Vakhtang Jandieri, Jan T. Svejda, Pingjuan L. Werner, Douglas H. Werner, Jamal Berakdar, Daniel Erni

Metamaterial Grating Distributed Feedback Laser Spatial Coupled-mode Modelling (pp. 506)
Henri Benisty, Yaoyao Liang, Abderrahim Ramdane, Anatole Lupu

Discretization effects in topological plasmonics (pp. 508)
Alexander Neuhaus, Pascal Dreher, Frank Meyer zu Heringdorf

Terahertz metasurface for realizing high-Q chiral BICs (pp. 510)
Xinyue Liang, Jian Liu, Xumin Ding

Transport Properties Of Coupled-resonator Phononic Graphene Ribbons (pp. 512)
Rafael Méndez-Sánchez, Yael Hernández-Espinosa, Edgar Sotelo-Parra, Angel M. Martínez-Argüello

Orienting Fluorophores For Highly Efficient Plasmonic Nanoantennas (pp. 514)
Karol Kolataj, Aleksandra Adamczyk, Guillermo Acuna

Mechanically Machinable, Printable Photonic Materials (pp. 516)
Jong G. Ok, Minwook Kim, Kwangjun Kim

Linear Logic Operations In A Quasi-Digital System (pp. 517)
Ross Glyn Macdonald, Alex Yakovlev, Victor Pacheco-Peña

Emitting properties of a-Si:C:H-coated 2D-opaline photonic crystals (pp. 519)
S. I. Pavlov, M. E. Bochkarev, S. A. Dyakov, V. G. Golubev, S. A. Grudinkin, Mikhail Limonov, A. B. Pevtsov

Hybrid Nanomaterials and Metastructures for Photonics, Sensing and Energy

Rhodium Nanospheres For Expanding Plasmonic Applications With Uv And Visible Light (pp. 522)
Vincenzo Amendola

Multiplexed, Label-free Biosensing With Plasmonic Nanoparticles (pp. 524)
Stephan Kastner, Andre Heewig, Florian Seier, Andrea Csaki, Wolfgang Fritzsche

Plasmonic Nanostructures On Paper Lateral Flow Assays For Point-of-care Testing (pp. 526)
Nianqiang Wu

Colloidal Synthesis Of Chiral Plasmonic Nanocomposites Via Circularly Polarized Light Irradiation (pp. 528)
Koichiro Saito, Yoshihiro Nemoto, Yoshie Ishikawa

Magnetic Micro- And Nanorods For Viscosity Imaging Using Heterodyne Holography (pp. 530)
Clémence Gentner, Zhu Zhang, Jean-François Berret, Pascal Berto, Hadrien Robert, Robert Kuszelewicz, Gilles Tessier

Chiral Photogrowth On Plasmonic Nanostructures Under Circularly Polarized Light (pp. 532)
Lucas Vazquez Besteiro

Directional Light Scattering In Mie-resonant Si Particles With Ultra-thin Plasmonic Shells (pp. 533)
Emmanuel Idowu, Kevin O'Connor, Jonathan Veinot, Sabrina Lacomme, Julien Proust, Jérôme Plain, Xiaoyan Li, Mathieu Kociak, Alexandre Baron, Virginie Ponsinet, Lucien Roach, Peter Wiecha, Glenna Drisko

Chiral Silicon Meta Biosensors (pp. 535)
Dominic J.P. Koyroytsaltis-McQuire, Rahul Kumar, Tamas Javorfi, Giuliano Siligardi, Adiran Lapthorn, Nikolaj Gadegaard, Malcolm Kadodwala

Chiro-optical Microscopy Of Plasmonic Materials And Chiral Near-field Interaction With Molecules And Materials (pp. 536)
Hiromi Okamoto, Shun Hashiyada, Hyo-Yong Ahn, Junsuke Yamanishi

Chiral Photochemical Amplification In Mesoporous Plasmonic Shurikens Demonstrating Asymmetric Catalysis (pp. 538)
Olga Guselnikova, Pavel Postnikov, Markus Valtiner, Jonathan P. Hill, Joel Henzie, Daniel T. Payne, Martin Kartau, Iliyana Samardzhieva, George Lefroy Brookes, Malcolm Kadodwala, Alexander O. Govorov, Affar S. Karimullah, Yusuke Yamauchi

Photocatalytic hydrogen evolution with plasmonic and photonic nanomaterials (pp. 542)
Alberto Naldoni

From Symmetry to Chirality: Near-Field Optical Activity in Achiral Gold Nanoparticles (pp. 543)
Minyu Chen, Thinhinane Aoudjit, Baozhong Deng, Yuqing Zhao, Ali Issa, Sylvie Marguet, Davy Gerard, Lucas Vázquez Besteiro, Safi Jradi, Bin Wei, Alexander Govorov, Tao Xu, Renaud Bachelot

Plasmonic Materials for Healthcare and Solar Energy Harvesting Applications (pp. 545)
Fang Xie

Pancake Meta-photonics: Stacking Layers To Prepare Quasi-3d Metasurfaces (pp. 546)
Shunsuke Murai

Sensing Mechanical Resonances Of Living Human Cells Using Nanomechanical Resonators (pp. 547)
Jose Jaime Ruz, Verónica Puerto-Belda, Carmen Millá, Álvaro Cano, Marina Lopez Yubero, Sergio García, Priscila Kosaka, Montserrat Calleja, Javier Tamayo

Organic Optoelectronic Devices And Biofunctionalized Nanoplasmonic Gratings: Integration Into Miniaturized Optical Biosensors (pp. 549)
Margherita Bolognesi, Mario Prosa, Stefano Toffanin

Dna Origami Self-assembled Optical Antennas For Single-photon Chiral Emission (pp. 551)
Fangjia Zhu, Maximilian Lengauer, Maria Sanz-Paz, Karol Kolataj, Sophie Brasselet, Guillermo Acuna

Experimental Femtosecond Pulse Trains For Time-modulation Metamaterials In The Terahertz Spectral Band (pp. 552)
William Wardley, C. M. Hooper, I. R. Hooper, S. A. R. Horsley, E. Hendry

Attomolar Sensing Of Cancer Markers Using A Novel Plasmonic Nanocomposite Thin Film For Early Stage Disease Diagnosis (pp. 554)
Manon Gireau, Fusheng Du, Joelle Youssef, Georges Humbert, Shuwen Zeng, Corinne Champeaux, Frédéric Dumas-Bouchiat

Topological Thermal Emitters (pp. 556)
Said Ergoktas

DNA Sensing With Whispering Gallery Mode Microlasers (pp. 557)
Soraya Caixeiro, Robert Dörrenhaus, Anna Popczyk, Marcel Schubert, Stephanie Kath-Schorr, Malte C. Gather

(Photo-) catalytic Activity Of Sub-5nm Gold Nanoparticles Limited By Coulomb Repulsion (pp. 558)

Monalisa Garai, Thomas A. Klar

Collective Behavior Of A Plasmonic Particle Array With A Chiral Arrangement Under Modal Coupling Regime (pp. 560)
Tomoya Oshikiri

Photocatalysis And Local Growth Driven By Plasmonic Hot Electrons (pp. 562)
Eva Yazmin Santiago

Hybrid Tmdc/plasmonic Systems (pp. 563)
Ermes Peci, Emma Spotorno, Michele Magnozzi, Lorenzo Ramò, Valentina Venturino, Maria Caterina Giordano, Maurizio Canepa, Francesco Bisio

Statistical Evaluation And Dipole Determination By Polarimetric Spectroscopy Yielding The Orientation Of Gold Nanorods (pp. 565)
P. Christian Simo, Annika Mildner, Michaela Zbytovska, Dieter P. Kern, Monika Fleischer

Single-particle Chiral Optical Microscope With High Precision (pp. 567)
Wei-Shun Chang, Angel Thomas, Vidhi Singla, Oscar Avalos Ovando, Trang Nguyen, Tamie Vo, Alexander Govorov

Photoluminescence-based Polarization Conversion In Quantum Rods Aggregate-containing Hybrid Polymer System (pp. 568)
Yutaka Okazaki, Yoshihiro Kawahara, Shoma Kimura, Hayaki Shimizu, Kan Hachiya, Takashi Sagawa

Meta-Atoms Based On Self-assembly Of Gold Nanoparticle On Polymer Microspheres (pp. 570)
Hiroshi Yabu

Hot-electron Dynamics And Speciality Optical Fibres For Quantum Applications (pp. 572)
Kristina Rusimova

Experimental Measurement Of Nanoscale Circular Dichroism In Plasmonic Chiral Structures Using Electron Beams (pp. 574)
Malo Bézard, Simon Garrigou, Yves Auad, Jérémie Béal, Hugo Lourenço-Martins, Davy Gérard, Mathieu Kociak

Highly Efficient And Reversible Chirality Transfer Between Protein And Achiral Plasmonic Assemblies (pp. 576)
Ziwei Zhou, Ningwei Sun, Nina Tverdokhleb, Artur Movsesyan, Anja Maria Steiner, Patrick T. Probst, Vaibhav Gupta, Bo Yin, Nicolás Pazos-Peréz, Ramón A. Álvarez-Puebla, Mirjam Hofmaier, Martin Müller, Holger Merlitz, Olga Guskova, Yaroslava G. Yingling, Franziska Lissel, Tobias A. F. König, Zhiming Wang, Alexander O. Govorov, Nicholas A. Kotov

Surface Plasmon Enhanced Photocatalysis (pp. 578)
Dongling Ma

Sensing 3d Electromagnetic Landscapes With Enhanced Quantum Light-matter Interaction At The Single-molecule And Nanometer Resolution (pp. 580)
R. Margoth Cordova Castro

Reconfigurable Integrated Photonics For Next-Generation Optical Computing And Quantum Technologies (pp. 582)
Alina Karabchevsky

Colloidal Quantum Optoelectronics (pp. 583)
Hilmi Volkan Demir

From Hairy Particles To Particle-Based Metamaterials (pp. 584)
Andreas Fery

Hyperdoped silicon nanocrystals embedded in a silica matrix for infrared plasmonics (pp. 586)
Clavel Berclis Kengne, Xavier Devaux, Mathieu Stoffel, Michel Vergnat, Hervé Rinnert

Controlled Self-assembly Of Polymer-grafted Nanoparticles Toward Hyperuniform Materials (pp. 588)
Kyoungweon Park, Derek Huang, Kenya Hazell, Anesia Auguste, Andrew Gillman, Rich Vaia, Larry Drummy

A Platform for Single-Crystal Nanomaterials and Metasurfaces with Application in Nanophotonics, Sensing and Energy Harvesting (pp. 590)

Sasan V. Grayli, Albert Adserias, Finlay MacNab, Gary Leach

Photopolymerized Molecularly Imprinted Polymers for Plasmonic Sensing Platforms (pp. 592)
A. Khitous, C. Molinaro, Olivier Soppera

Finite Element Analysis of Light Scattering in Resonant Multi-Dielectric Coverslips for Enhanced Total Internal Reflection Fluorescence Microscopy (pp. 594)
Y. Toumi, R. Gurram, F. Lemarchand, A. Moreau, C. Favard, J. Lumeau, G. Demesy, Aude Lereu

Metasurfaces by Two-Photon Polymerization Gray Scale Lithography (pp. 596)
Dewa Ade-Onojobi, Kiernan E. Arledge, Xitlali G. Juarez, Nazli Rasouli, Chase T. Ellis, Joseph G. Tischler

Hybrid Self-assembled Plasmonic Metasurfaces For Applications In Photonics (pp. 598)
Tomas Tamulevičius, Klaudijus Midveris, Gvidas Klyvis, Tomas Klinavičius, Asta Tamulevičienė, Mindaugas Juodėnas, Domantas Peckus, Joel Henzie, Sigitas Tamulevičius

Environmental Permittivity-asymmetric Bic Metasurfaces With Electrical Reconfigurability (pp. 600)
Haiyang Hu, Wenzheng Lu, Alexander Antonov, Rodrigo Berté, Stefan A. Maier, Andreas Tittl

High-resolution And Broadband Metafiber Refraction Index Sensors (pp. 602)
Jiyong Wang, L. Zhang, M. Qiu

N-Heterocyclic Carbene As Robust And Conductive Linkages To Couple Gold Nanoparticles and Conductive Polymers (pp. 603)
Ningwei Sun, Franziska Lissel

Biocompatible Plasmonic Nanoparticle-doped Hydrogel For Facile Optical Detection Of Cortisol (pp. 605)
Alexandra Nicolae-Maranciuc, Dan Chicea, Andreea Campu

Nanocomposite Materials For Biosensors Made By A Dual Pulsed Laser Source (pp. 606)
Manon Gireau, Fusheng Du, Joelle Youssef, Georges Humbert, Shuwen Zeng, Corinne Champeaux, Frédéric Dumas-Bouchiat

Silicon Nanoparticle Arrays for Studies on Colloidal WS2 Nanosheets (pp. 608)
Melanie Sommer, Markus Fröhlich, Lukas Lang, P. Christian Simo, Jannika Lauth, Monika Fleischer

Silver Nanocubes Decorated Silicon Nanostructures Used As 3d Active Sers Platforms For Detection Of Microplastics (pp. 610)
Adina Boldeiu, Pericle Varasteanu, Oana Brancoveanu, Gabriel Craciun, Razvan Pascu, Andrei Avram, Cosmin Romanitan, Iuliana Mihalache, Mihaela Kusko

Angularly Resolved Optical Response of Organic Molecules in Single and Collective Plasmonic Gold Nanosphere ystems (pp. 612)
Felix Schneider, Daniel Schäfer, Sebastian Schlücker, Alfred J. Meixner, Dai Zhang

Synthesis of silver and gold nanoparticles with tunable plasmonic properties for light-assisted anticancer therapy (pp. 614)
Aleš Panáček, Lucie Válková, Lucie Hochvaldová, Anastassiya Pedan, Hana Kolářová, Libor Kvítek

Advanced passive and active metasurfaces and zero-index materials

Nonlocal Metalens For Far-field Label-free Super-resolution Imaging (pp. 617)
Bohan Zhang, Yuanmu Yang

Room-temperature, Tunable Lasing From Quasi-2d Perovskites Integrated With Plasmonic Lattices (pp. 618)
Yu-Jung Lu

Symmetry-breaking And Disorder-assisted Bound States In The Continuum (pp. 620)
Qinghua Song

Shaping Photon Emission With Emitter-coupled Metasurfaces (pp. 622)
Fei Ding

Nonlinear Optics Driven By Out-of-equilibrium Electron Dynamics In Epsilon-near-zero Media (pp. 623)
Matteo Silvestri, Ambaresh Sahoo, Luca Assogna, Matteo Venturi, Raju Adhikary, Paola Benassi, Carino Ferrante, Davide Tedeschi, Alessandro Ciattoni, Andrea Marini

Terahertz Modulators Enabled By Vanadium Dioxide: From Materials Optimization To Devices (pp. 625)
Xi Wang

Electrochemically-tunable Oxide Materials For Metasurfaces (pp. 627)
Vivian Ferry

Electrochemically Active Mid-ir Metasurfaces Based On Conjugated Polymers (pp. 629)
Po-Chun Hsu

Thermo-optical Effects In Nanoantennas And Metasurfaces (pp. 631)
Giulia Tagliabue

Heterogeneous High-entropy Alloy (hea) Plasmonics For Superior And Low-cost Photocatalytic Hydrogen Evolution Reaction (her) (pp. 632)
Chun-Yen Chen, Yu-Hsuan Cheng, Alex Sam, Arya Pilakunnath, Ta-Jen Yen

Accelerating The Design Of Photonic Metamaterials With Artificial Intelligence (pp. 634)
Yongmin Liu

Dynamic Ir Beam Steering And Switching With Active Metasurfaces (pp. 636)
Min Seok Jang

Towards Tunable Metamaterial-based Torque Sensing (pp. 637)
Michael Töfferl, Alexander Schossmann, Maximilian Saiko, Peter Banzer, Alexander Bergmann

Active And Dynamic Optical Phase Gradient Metasurfaces Enabled By Resonant Nanophotonics And Electro-Optic Materials (pp. 639)
David Barton, Sahil Dagli, Sina Abedini Dereshgi, Jennifer Dionne

Metasurface For Multi-Functional Edge Imaging And Quantitative Phase Imaging (pp. 641)
Zhaowei Liu

Highly Confined, Low-Loss Infrared Phonon Polaritons In Perovskite Oxide Membranes (pp. 642)
Yin Liu

Liquid-Metal-Based Reconfigurable Metasurfaces For Display And Sensing Applications (pp. 643)
Peter Qiang Liu

Metasurface-Based Optical Elements For Biomedical Applications (pp. 644)
S. Vyas, C. H. Chu, JerLiang Yeh, Yuan Luo

Confinement-Induced Nonlocality, Topological Darkness, And Goos-Hänchen Effect Enhancement In Transdimensional Plasmonic Film Systems (pp. 646)
Igor Bondarev, Svend-Age Biehs

Ultra-Sensitive Infrared Gas Molecular Measurement Using Three-Dimensional Broadband Metasurface Absorber (pp. 648)
Takuo Tanaka

Nonreciprocal And Directional Control Of Infrared Emissivity In Semiconductor Enz Systems (pp. 650)
Aaswath Raman

Multi-Layer Flat Optics: Challenges And Opportunities (pp. 651)
Ahmed Dorrah

Far-Field Radiation And Polarization Engineering Using Luminescent Metasurfaces (pp. 653)
Elise Bailly, Anne Nguyen, Jean-Paul Hugonin, Jean-Jacques Greffet, Benjamin Vest

Multi-polar High Quality Factor Metasurfaces (pp. 655)

Mark Lawrence, Bo Zhao, Shuqin Dai, Samuel Ameyaw, Lin Lin

Nanofocusing of the Orbital Angular Momentum Laser Beam for Nanoimaging (pp. 656)
Zhenrong Zhang

Metasurface for Bioimaging and Thermal Radiation Management (pp. 657)
Guangwei Hu

Merging Nanophotonics and Optical Fibers for Flexible Beam Control Using 3D Nanoprinting (pp. 659)
Markus Schmidt, Bennet Fischer, Matthias Zeisberger, Mohammad Khosravi, Shahrzad Hosseinabadi, Oleh Yermakov

High Contrast Nanoscale Chirality Imaging (pp. 660)
Seongmin Im, Gayatri Chandran, Yang Zhao

Bright and Dark Lasing in Nanoplasmonic Metasurfaces (pp. 662)
Ortwin Hess

Tunable focus manipulation in multicore meta-fibers through 3D nanoprinted phase-only holograms (pp. 664)
Mohammadhossein Khosravi, Torsten Wieduwilt, Matthias Zeisberger, Adrian Lorenz, Markus Schmidt

Transient Optical Symmetry Breaking For The Ultrafast Switching Of A Metasurface Quasi-bic (pp. 666)
Giulia Crotti, Andrea Schirato, Olesiya Pashina, Olga Sergaeva, Mihail Petrov, Costantino De Angelis, Giuseppe Della Valle

Addressing The Challenge Of Phase-only Dynamic Modulation Of Transmissive Metasurfaces (pp. 668)
Juyoung Kim, Ruzan Sokhoyan, Harry Atwater, Min Seok Jang

All-dielectric Electrically-tunable Metasurface For Efficient Beam Steering (pp. 670)
Junghyun Park, Byung Gil Jeong, Sun Il Kim, Minkyung Lee, Young Kim, Jang-Woo You, Wontaek Seo, Byung-Hoon Ko, Seokho Yun

Optical Charge Trap Memory Based On Graphene/zno Heterostructures For Long-term Retention And Adaptive Learning (pp. 672)
Junhyung Kim, Seungmin Shin, Hyeongdoh Lee, Min Seok Jang, Himchan Cho

Dynamic Multi-Wavelength Coded Aperture Imaging Using Reconfigurable Metasurfaces (pp. 674)
Reza Marzban, Hamed Abiri, Ali Adibi

Dynamic Control Of Bound States In The Continuum By Mems-enabled Hybridization Of 1d And 2d Metasurfaces (pp. 676)
Fedor Kovalev, Mariusz Martyniuk, Andrey Miroshnichenko, Ilya Shadrivov

Chirality, magnetism, and magnetoelectricity: Separate phenomena and joint effects in metamaterial structures

A Qed Theory Of Discriminatory Ret Mediated By One Or Two Polarisable Molecules (pp. 679)
Akbar Salam

Theory Of Unidirectional Magnetoresistance In Nanoscale Bilayers (pp. 681)
Xiangrong Wang

New Topological Magnetic Photonic Crystals (pp. 684)
Che Ting Chan

Development Of Carbon Fiber Composites With Ferromagnetic Microwire Inclusions For Free Space Microwave Sensing (pp. 686)
Valentina Zhukova, Johan Malm, Christer Johansson, Rafael García-Etxabe, Francisco Javier Vallejo, Peio Olaskoaga, Arcady Zhukov

Spin Current Generation Due To Differential Rotation (pp. 688)
Mamoru Matsuo

Experimentally Testing The Spontaneous Disentanglement Hypothesis Using A Ferri--magnetic Resonator (pp. 689)
Eyal Buks

Optical Quasiparticles Induced Structured Materials (pp. 691)
Takashige Omatsu

Topological Magneto-optical Effect In Skyrmion-hosting Mott Insulator (pp. 693)
Yoshihiro Okamura, R. Shimizu, K. Okigami, S. Okumura, N. Kanazawa, Y. Tokura, T. Morimoto, Y. Takahashi

Listening To Nanostructures' Absorption And Chirality: Widely Tunable Photo-acoustic Spectroscopy (pp. 694)
Emilija Petronijevic, Claudia Skubisz, Grigore Leahu, Concita Sibilia, Roberto Li Voti, Alessandro Belardini

Optical Force Nanoscopy Of Circular Dichroism In Photoinduced Force Microscopy (pp. 696)
Junsuke Yamanishi, H.-Y. Ahn, H. Okamoto

Two-color Laser Driven Novel Phenomena In Solids: Detection Of Symmetries And Control Of Photocurrent (pp. 698)
Masahiro Sato, Minoru Kanega, Mina Udono

Uv-plasmonics For Surface-enhanced Spectroscopies (pp. 700)
Bjoern Reinhard

Helicity-dependent Optical Control Of The Magnetization Emerging From The Zeeman Energy (pp. 702)
Amir Capua

Observation Of Large Nonreciprocal Propagation Constants In Zero-index Magneto-optical Meta-waveguides (pp. 703)
Yucong Yang, Yueyang Liu, Yang Li, Lei Bi

Attosecond Magnetism: Ultrafast Control Of Magnetic Phases And Novel Probes (pp. 705)
Ofer Neufeld

Extreme Light Manipulation: Hyperbolic Plasmon Polaritons And Subcycle Orbitalangular Momentum Control (pp. 707)
Antonio Ambrosio

Tailoring Broadband Large Chiral Response In All-dielectric Twisted L-shape Metamaterial Platforms (pp. 708)
Ufuk Kilic, Eva Schubert, Christos Argyropoulos, Mathias Schubert

Spin-charge Dynamics Of Topological Magnetic Textures In Kondo-lattice Magnets (pp. 710)
Masahito Mochizuki

Microwave-modulated optomagnet as a tunable nanosource ofspin-waves (pp. 712)
Vage Karakhanyan, Miguel Suarez, Marina Raschetti, Thierry Grosjean, Anna Duvakina, Mingran Xu, Axel Deenen, Andrea Mucchietto, Dirk Grundler

Inverse Design of Chiral Structures for Giant Helical Dichroism (pp. 714)
Munseong Bae, Chia-Chun Pan, Hongtao Wang, Jaesung Lim, Ranjith Unnithan, Joel Yang, Sejeong Kim, Haejun Chung

Magnonic φ Josephson Junctions and Synchronized Precession (pp. 716)
Kouki Nakata, Ji Zou, Jelena Klinovaja, Daniel Loss

Classifying Fragile Topology Using Matrix Homotopy (pp. 718)
Alexander Cerjan

Electromagnetic Helicity in Twisted Cavity Resonators (pp. 719)
Jeremy Bourhill, Emma Paterson, Maxim Goryachev, Michael Tobar

Electrical control of ultrastrong coupling of 2-dimensional electronic systems to single meta-atoms (pp. 721)
Elsa Jöchl, Felix Helmrich, Anna-Lydia Vieli, Lucy Hale, Deniz Turan, Mona Jarrahi, Mattias Beck, Atac Imamoglu, Jerome Faist, Tobia Nova, Giacomo Scalari

Chiral Polaritons in Bulk van der Waals Metasurfaces (pp. 723)
Alexander Antonov, Connor Heimig, Maxim Gorkunov, Yuri Kivshar, Andreas Tittl

Fluctuation-Driven Phenomena in Chiral and Indefinite-Gain Systems (pp. 725)
Daigo Oue, Mario Silveirinha

Unified Dipolar Interactions in Bispinor Formalism and the Energy Symmetry Sphere (pp. 727)
Sebastian Golat, Alex J. Vernon, Francisco J. Rodriguez Fortuno

Topological And Geometric Effects In Magnetic Nanowires (pp. 729)
Oleksandr Pylypovskyi

Terahertz Pulse Shaping And Chirality Control Using Magnetic Heterostructures (pp. 731)
Weipeng Wu, Wilder Acuna, Zhixiang Huang, Xi Wang, Lars Gundlach, Matthew Doty, Joshua Zide, Benjamin Jungfleisch

Enantioselective Molecular Sensing By Chiral Gold Helicoid Nanoparticles (pp. 733)
Jeong Hyun Han, Ki Tae Nam

Dynamics Of Softened Spin Waves In Thin Films With Perpendicular Anisotropy At Temporal Interfaces (pp. 735)
Krzysztof Sobucki, Nikodem Leśniewski, Pawel Gruszecki

A Multiscale Approach To Molecular Nanoplasmonics: From Sers To Chiroptical Spectroscopies (pp. 737)
Tommaso Giovannini

Chiral Modes In Photonic Integrated Waveguides (pp. 739)
Iago Diez, Daniel Arenas-Ortega, Josep Martínez-Romeu, Alejandro Martínez

Magneto Nanophotonics Platform Based On Monocrystalline Yttrium Iron Garnets (pp. 741)
Yasutomo Ota, Siyuan Gao, Kota Taniguchi, Takeru Yambe, Yuta Tanimura, Satoshi Iwamoto

Microwave-to-optical Quantum Transduction Mediated By Antiferromagnetic Magnons In Antiferromagnets (pp. 743)
Akihiko Sekine, Ryo Murakami, Yoshiyasu Doi

Excitations And Light-matter Interactions In Polar Topologies (pp. 745)
Suyash Rijal, Yousra Nahas, Sergei Prokhorenko, Laurent Bellaiche

Quantum Theory Of Polarization In Inhomogeneous Crystals And Its Relation To Orbital Magnetoelectric Effect (pp. 747)
Nobuhiro Arai, Yang Gao, Di Xiao, Shuichi Murakami

Optical Response Of Periodic Arrays Of Graphene Nanostructures Under Static Magnetic Fields (pp. 748)
Juan R. Deop-Ruano, Mikkel H. Eriksen, Juan J. Alvarez-Serrano, Alejandro Manjavacas, Joel D. Cox

Nonlinear Response Of Truly Chiral Phonons: Light-induced Phonon Angular Momentum And Peltier Effect (pp. 750)
Hiroaki Ishizuka, Masahiro Sato

Nano-squeezing Of Optical Chirality Via Topology-optimized 3d Nanogap Antennas (pp. 752)
Atsushi Taguchi

Magnetoelectric Effect In Antiferromagnetic Chern Insulators (pp. 754)
Tomoki Hirosawa, Daichi Komine, Nobuo Furukawa

Enhanced Chiral Sensing And Unambiguous Enantiomer Differentiation With Achiral Anisotropic Photonic Metasurfaces (pp. 755)
Sotiris Droulias

What Is And What Is Not A Good Measure For Enhanced Chiroptical Response? (pp. 757)
Thomas Weiss

Emergent Chirality, Antiskyrmions And Bloch Skyrmions In Ferroelectrics (pp. 759)
Jiri Hlinka

Ultrafast Tacos (pp. 760)
J. Terentjevas, P. Vindel-Zandbergen, L. Rego, F. Morales, A. Ordóñez, O. Smirnova, David Ayuso

Coherent Dynamics Of A Magnon Bose-einstein Condensate - Temporal Coherence And Correlation Characteristics (pp. 762)
Oleksandr Serha

Electron-phonon Interaction In Chiral Crystal: Angular Momentum And Phonon Chirality (pp. 763)
Junichiro Kishine, T. Tateishi, A. Kato

Spin Polarization Induced By Nonequilibrium Fluctuation Near The Surface In Chiral Metals (pp. 765)
Yusuke Kato

Sensing And Generating Structured And Twisted Light Through Photonic Integrated Circuits (pp. 767)
Marko Šimić, J. Butow, V. Sharma, D. Brandmuller, J. S. Eismann, Peter Banzer

Thz Metastructures Using Spintronic Thz Emitters (pp. 769)
Christian Bohley, Ramaz Khomeriki, Vakhtang Jandieri, Dominik Schulz, Benjamin Schwager, Björn Niedzielski, Jamal Berakdar

Tunable Of Universal Quantum States At Weyl Semimetal Interstitial Interfaces With Magnetic Textures (pp. 771)
Eklavya Thareja, Gina Pantano, Ilya Vekhter, Jacob Gayles

Nonlinear Chiral Quantum Photonics (pp. 773)
Nir Rotenberg

Symmetry In Magnetoelectric Electromagnetism (pp. 774)
Eugene Kamenetskii

One-Way Transparency At Custom Wavelengths Via A Layered Magnetoelectric Window (pp. 776)
Artem Kuzmenko, Alexander Mukhin, Alexey Shuvaev, Andrei Pimenov, David Szaller

Skyrmion Hall Effect In Altermagnets (pp. 778)
Zhejunyu Jin, Zhaozhuo Zeng, Yunshan Cao, Peng Yan

Optically And Magnetically Responsive Metamaterial Capsules For Drug Delivery (pp. 779)
Pavel Ginzburg

Microwave Coherent Storage Based On The Long Lifetime Cavity Electromechanical System (pp. 781)
Tiefu Li

Can The Spinterface Model Explain All Different Ciss Related Effects? (pp. 782)
Amos Sharoni, S. Alwan, Yonatan Dubi

Plasmonic Nanocrystals For Hot Electron Generation And Chiral Photochemistry (pp. 784)
Alexander Govorov

Manipulating Light-driven Nanoscale Vectorial Currents (pp. 785)
Hou-Tong Chen

Planar Dielectric Structures With Mirror Symmetry Broken By Substrate As Versatile Sources Of Chiral Light (pp. 787)
Alena Mamonova, Polina Kovaleva, Alexander Antonov, Maxim Gorkunov

Band Structure Evolution in Quaternary Magnetic Semiconductors for Photonic and Spintronic Applications (pp. 789)
Oksana Yastrubchak, N. Tataryn, S. Mamykin, V. Romanyuk, O. Kondratenko, L. Borkovska, L. Khomenkova, X. Liu, B. A. Assaf, J. Furdyna, Y. Ichiyanagi, M. Sawicki, J. Sadowski

Novel Sensing Technique For Non-destructive Composites Monitoring (pp. 792)
Valentina Zhukova, P. Corte-León, A. Allue, K. Gondra, J. M. Blanco, Arcady Zhukov

The Generation Of Two Distinct Berry Phases On The Surface Of A Twisted Triangular Möbius Cavity Resonator (pp. 794)
Emma Paterson, Michael Tobar, Maxim Goryachev, Jeremy Bourhill

Architectured Elastic and Acoustic Metamaterials & Phononic Crystals

A Template-aided Versatile Approach For Creating Metamaterials (pp. 797)
Rui Xu, Denys Makarov

Acoustic Lattice Resonances and eGneralised Rayleigh-Bloch Waves (pp. 798)
Malte Peter, Luke Bennetts, Gregory Chaplain, Stuart Hawkins, Kei Matsushima, Tim Starkey

Reconfigurable Topological Insulators And Acoustic Devices Based On An Electroacoustic Material Platform (pp. 800)
Michael Leamy

Elastic Spin Angular Momentum In Continuum And Metamaterials Rod Structures (pp. 802)
Jinfeng Zhao, Yuxuan Zhang, Yongdong Pan

Periodic Infilled Trench Barriers For Rayleigh Wave Attenuation In Saturated Soil (pp. 804)
Zhifei Shi, Shuyin Cai, An Chen

Simulation Of Acoustic Metamaterial Lens Imaging Under Complex-frequency Excitation In A Real-frequency Solver (pp. 806)
Tuo Liu

Vibrational Dynamics Of Single Supported Plasmonic Nanodisks (pp. 808)
Nathan Berrit, Clément Panais, Noelle Lascoux, Sylvie Marguet, Natalia Del Fatti, Aurélien Crut

Mechanically time-modulated 2D phononic crystal (pp. 810)
Dmitrii Shymkiv, Matthew Li, Ying Wu, Arkadii Krokhin

Enhanced ultrasound focusing through dense barrier (pp. 812)
Zhongming Gu, Jie Zhu

Optomechanical Photonic Crystal Cavities Based on Silicon and Hybrid Nanopillars for Integrated Force Sensing (pp. 814)
Daniel Navarro Urrios

Time-resolved two-dimensional imaging of GHz acoustic waves in phononic crystalsand metamaterials (pp. 816)
Osamu Matsuda

Surface acoustic waves-driven magnon spin Hall effect in atomically thin van der Waals antiferromagnets (pp. 818)
Ryotaro Sano, Yuya Ominato, Mamoru Matsuo

Acoustic trapping, emission enhancement, and harvesting from bound states in the continuum (pp. 820)
Sibo Huang, Yong Li, Jie Zhu, Din Ping Tsai

Maximizing the modal effective mass of metamaterial resonators through topology optimization (pp. 822)
Vanessa Cool, Willem Jaspers, Berkay Biçer, Claus Claeys, Elke Deckers

Spectral Methods For Designing Quasiperiodic Metamaterials (pp. 824)
Bryn Davies

Tunable Phonon-electron Fano Resonance In Si Nanoparticles Via Electromagnetic Confinement And Anharmonic Decay In Engineered Media (pp. 826)
Michel Kazan

Distinct Exceptional Points in Hermitian Phononic Laminates (pp. 828)
Ariel Fishman, Ben Lustig, Guy Elbaz, Alan Muhafra, Venkatesh Varma, Gal Shmuel

Band Structure Engineering In Artificial Phononic Trans-polyamynoborane With First And Second-nearest Neighbors (pp. 830)
Rafael Méndez-Sánchez, Yonatan Betancur-Ocampo, Bryan Manjarrez-Montañez, Angel M. Martínez-Argüello

Realizations Of Acoustic And Elastic Meta-structures To Reduce Noise And Vibration (pp. 832)
Wonju Jeon

Locally Resonant Mosaic Meta-plate (pp. 834)

Nan Gao, Vicente Romero-García, Jean-Philippe Groby, Ping Sheng

Conditions For Weak Scattering In Flexural Waves (pp. 836)
Mario Lázaro, Vicent Romero-García, Luis M. García-Raffi

Towards A Generalized Theory For Aeroacoustic Metacontinua (pp. 838)
Umberto Iemma, Giada Colombo

Acoustic And Mechanical Features Of Polymer Colloidal Crystals - Brillouin Spectroscopy Studies (pp. 840)
Bartlomiej Graczykowski

Locally Resonant Elastic Metagratings: Theory, Experiment, And Applications (pp. 842)
Liyun Cao, Y. -F. Wang, B. Assouar, Y. -S. Wang

Applications Of Mechanical Metamaterials In Microsystems: Challenges And Perspectives (pp. 844)
Valentina Zega

Developing Active Acoustic Metamaterials Using Magneto-rheological Fluids (pp. 846)
Richard Watson

Accurate Fem Investigation Of Acoustic Properties In Aerospace Sandwich Structures With Metamaterial Core (pp. 848)
Maria Cinefra, Martino Carlo Moruzzi, Marco Petrolo, Matteo Filippi, Giuseppe Petrone

Hypersonic Surface Acoustic Wave In A Nanomembrane (pp. 850)
Omid Reza Ranjbar Naeini, Tapani Makkonen, Oili M.E Ylivaara, Jouni Ahopelto, Clivia M Sotomayor Torres

Metastructures: New Approaches To Enhancing Disaster Resilience And Reduced Embodied Carbon (pp. 852)
Oreste S. Bursi, Tugberk Guner

On The Practical Use Of Wooden Logs Sonic Crystals As Road Traffic Noise Barriers (pp. 854)
Paulo Amado-Mendes, Luis Godinho

Topological Modes In Phononic Waveguide Interfaces (pp. 856)
Koijam Monika Devi, Clivia M. SotomayorTorres, Yan Pennec, Bahram Djafari-rouhani

When Acoustic Artificial Materials Meet Artificial Intelligence: Ai-empowered Metamaterials And Their Applications (pp. 858)
Bin Liang, Jingjing Liu, Jing Yang, Jianchun Cheng

Sound-absorbing Metasurface Using Hybrid Resonators With Embeded Necks And Micro-perforations (pp. 860)
Hyeonbin Ryoo, Ki Yong Lee, Wonju Jeon

Unlocking Large-scale Metasurface Fabrication With Electron Beam Lithography Through Algorithmic Patterning (pp. 862)
Michael Kahl, Frank Nouvertné, Rainer Schmid, Volker Boegli

A Non-diffracting Resonant Angular Filter (pp. 864)
Tristan Lawrie, Gregor Tanner, Gregory Chaplain

Phase-matching Holographic Metasurfaces For Accurate Acoustic Image Generation (pp. 866)
Víctor Vegas-Luque, Diana Andrés Bautista, Alba Eroles Simó, Juan José Rodríguez García, Francisco Camarena Femenia, Noé Jiménez González

Visualization Of Topological Edge And Boundary Modes In Mechanical Metamaterials (pp. 868)
Motonobu Tomoda, Konosuke Yamaguchi, Gun Yoon, Hayato Takeda, Ryoya Minami, Osamu Matsuda, Oliver Wright

Compact Elastic Plate For Bound State In The Continuum (pp. 870)
Zhihui Wen, Marc Marti-Sabaté, Yabin Jin, Daniel Torrent, Yegao Qu

Topological Phase Transitions And Edge States In Ssh-type Elastic Systems With Periodic And Disordered Non-hermitian Modulations (pp. 872)
Runcheng Cai, Yabin Jin, Yan Pennec, Xiaoying Zhuang, Bahram Djafari Rouhani

Skewing Of Guided Waves In Anisotropic Plates Close To Zero-group-velocity Points (pp. 874)
Daniel Kiefer, Sylvain Mezil, Claire Prada

Elastic-wave Control Based On Non-hermitian Metasurfaces (pp. 876)
Bing Li, Bochen Ren, Jiali Cheng

Acoustic Metasurfaces For High-resolution Imaging Of Additively Manufactured Metals (pp. 878)
Hrishikesh Danawe, Raguez Taha, Talha Khan, Didem Ozevin, Serife Tol

Electromechanical Excitation Of Nanostructures By Bulk Acoustic Wave Transducers (pp. 880)
Tapani Makkonen, Oili Ylivaara, Sara Pourjamal, Jouni Ahopelto

Nanocrystalline Silicon For Optomechanical Metamaterials (pp. 882)
Gloria Conte, Omid Reza Ranjbar Naeini, Cristiana Alves, Oliver Schraidt, Oili Ylivaara, Sara Pourjamal, Jouni Ahopelto, Clivia Mafra Sotomayor Torres

Tailoring Ghz Surface Acoustic Waves By Spatial Modulation Of Ultrashort Light Pulses (pp. 884)
Olga Boyko, F. Soldevila, V. Bochkarev, L. Belliard

Temperonic Metamaterials: Shaping Wave-like Temperature Oscillations On The Ultrafast Time Scale. (pp. 886)
Giulio Benetti, Marco Gandolfi, Riccardo Rurali, Claudio Giannetti, Francesco Banfi

Interaction Of Sloshing Water Waves With A Vertically Oscillating Plate (pp. 888)
Magdalini Koukouraki, Philippe Petitjeans, Agnès Maurel, Vincent Pagneux

Perfect Absorption Of Flexural Waves In Vibration Transmission Problems Via Coupled Monopolar-dipolar Resonant Scatterers (pp. 890)
Daniele Giannini, Jean-Philippe Groby

Ultrafast Phononic Manipulation Of Magnetization (pp. 892)
Carl Davies

Controlling The Propagation Of 20 Ghz Coherent Acoustic Phonons In An Optophononic Waveguide (pp. 894)
Edson Rafael Cardozo de Oliveira, Chushuang Xiang, Sathyan Sandeep, Konstantinos Papatryfonos, Martina Morassi, Luc Le Gratiet, Abdelmounaim Harouri, Isabelle Sagnes, Aristide Lemaitre, Omar Ortiz, Martin Esmann, Daniel Lanzillotti-Kimura

Wave Locking In Periodically Folded Beams: Influence Of Modelling Choices On Complete Band Gap Prediction (pp. 896)
Elisabetta Manconi, Farzad Tatar

Sensitivity And Nonlinear Effects In Non-Hermitian Quasi-Periodic Lattices (pp. 898)
Ananya Ghatak, Dimitrios H. Kaltsas, Manas Kulkarni, Konstantinos G. Makris

Luneburg Lens for Surface Water Waves (pp. 900)
S. M. Kuznetsova, V. F. dal Poggetto, M. Mazzotti, M. Onorato, V. Pagneux, M. Miniaci

Design of Underwater Noise Reduction Ultra-Thin Metabarriers (pp. 902)
Vinicius Fonseca Dal Poggetto, M. Miniaci

Ultrathin architected plates and their applications (pp. 904)
Igor Bargatin

Optomechanical Su-Schrieffer-Heeger States in a Nanobeam Cavity (pp. 906)
Hicham Mangach, Abdellatif Gueddida, Ricardo Alcorta-Galvan, Gaëtan Lévêque, Marco Miniaci, Yan Pennec, Bahram Djafari-Rouhani

Springtronics: Towards advanced information processing in elastic metamaterials (pp. 908)
Finn Bohte, Sima Zahedi Fard, Parisa Omidvar, Theophile Louvet, Saeed Zohoori, Marc Serra-Garcia

Wave Dispersion Analysis Of Frame-shear Wall Building Structures Based On The Periodic Structure Theory (pp. 910)
Zhibao Cheng, Jiaming Li, Peng Pan, Jing Sun

Transforming room acoustics with causality-driven dual-function passive metamaterials (pp. 912)

Eric Ballestero, Yang Meng, Ping Sheng, Vincent Tournat, Vicente Romero-García, Jean-Philippe Groby

Nonreciprocal Acoustic Wave Control With Field-transforming Metasurface (pp. 914)
Xinhua Wen, Choonlae Cho, Xinghong Zhu, Namkyoo Park, Jensen Li

Momentum-resolved Studies Of Plasmon - Acoustic Phonon Interactions In An Acoustoplasmonic Metamaterial (pp. 917)
Anuj Kumar Dhiman, Hritika Dongre, Karol Zaleski, Piotr Graczyk, Bartlomiej Graczykowski, Thomas Vasileiadis

Customized Inverse Design Of Quasi-zero-stiffness Metamaterials By Topology Optimization (pp. 919)
Chao Ma, Kun Wu

Realization Of Weyl Elastic Metamaterials with Spin Skyrmions (pp. 921)
Yuang Pan, Yihao Yang

Numerical And Experimental Investigation Of Multi-stable Metastructures Endowed With Free-standing Bistable Locally Resonant Unit Cells (pp. 922)
Tugberk Guner, O. S. Bursi, M. Broccardo

Multimode Phonon Lasing In A Self-modulated Silicon Optomechanical Crystal Cavity (pp. 930)
David Alonso Tomás, Carlos Mas Arabi, Carles Milián, Néstor E. Capuj, Alejandro Martínez, Daniel Navarro Urrios

A Reconfigurable Coding Acoustic Metasurface Based On Coiling Units (pp. 932)
Jie Hu, Hao Zhou, Haoxiang Li

Observation Of Oriented Landau Levels And Helical Zero Modes In Berry Dipole Acoustic Crystals (pp. 934)
Qingyang Mo, Riyi Zheng, Cuicui Lu, Xueqin Huang, Zhengyou Liu, Shuang Zhang

Design Principle And Application Exploration Of Water-to-air Vibroacoustic Metasurfaces (pp. 936)
Hong-Tao Zhou, Yan-Feng Wang, Yue-Sheng Wang

Vibration And Sound Radiation Reduction By Meta-plate With Rainbow Reflection Effect (pp. 938)
Feng Liu, Yan-Feng Wang, Yue-Sheng Wang

Quadratic Weyl Semimetal And Topological Double Negative Refraction In Phononic Crystals (pp. 940)
Yating Yang

High-performance Nanotriboelectric Generator Integrating An Acoustic Metamaterial Absorber And Spring (pp. 942)
Wei Zhi Weng, Tsung-Yu Huang

Simultaneous Photonic And Phononic Topological Interface States In A Si-based Membrane Crystal (pp. 944)
Nouh Krai, Gaëtan Lévêque, Bahram Djafari-rouhani, Yan Pennec

Phononic Quantum State Preparation And Ultrafast Coherent Control Via Pulsed Excitation Of Quantum Emitters (pp. 946)
Seán Ffrench, Daniel D.A. Clarke, Daniel Wigger, Ortwin Hess

Study of the Scattering of Elastic Surface Waves by Nano-Resonators (pp. 948)
S. C. Baltogiannis, Olga Boyko, B. Tallon

Metamaterial-based Dielectric Elastomers for Enhanced Energy Harvesting (pp. 950)
Arnob Dutta, Yan Pennec, Gaëtan Lévêque, Bahram Djafari-Rouhani, Marco Miniaci

Advanced Techniques for Computational Electromagnetics

Variational Optical Processors (pp. 953)
Charles Roques-Carmes, Aviv Karnieli, David A. B. Miller, Shanhui Fan

A Gain Route To Reversed Cherenkov Radiation (pp. 955)
Ruoxi Chen, Xiao Lin

Near-field shaping by ray-caustic synthesis at microwaves and millimeter waves (pp. 957)
Federica Anfuso, Ahsan Ullah Khan, Gino Sorbello, Santi Concetto Pavone

Silicon-based metasurface polarizer supporting quasi-bound states in the continuum (pp. 959)

Maria Antonietta Vincenti, Sonia Freddi, Alfonso Nardi, Agostino Di Francescantonio, Johann Osmond, Attilio Zilli, Michele Gherardi, Domenico de Ceglia, Michele Celebrano, Marco Finazzi, Monica Bollani

Retrieving Optical Properties of Biological Multilayers using Symbolic Regression (pp. 961)

Julian Sierra-Velez, Alexandre Vial, Marco A. Giraldo, Demetrio Macias

Near-field Optoelectronic Heat Engines And Thermal Emission Of Subwavelength Objects (pp. 963)

Julien Legendre, Thomas Chatelet, Kyriaki Kontou, Jose Sojo-Gordillo, Ahmed Alwakil, Azeddine Tellal, Taha Benyattou, Olivier Merchiers, P-Olivier Chapuis

The Effective Refractive Index Of Resonant Particulate Media Depends On The Shape Of The Particule Arrangement (pp. 965)

Cédric Blanchard, Timothée Guerra, Jean-Paul Hugonin, Christophe Sauvan

Beam Dynamics Induced By The Quantum Metric Of Exceptional Rings (pp. 967)

Z. Zhang, I. Septembre, Z. Liu, P. Kokhanchik, S. Liang, F. Liu, C. Li, H. Wang, M. Liu, Y. Zhang, M. Xiao, G. Malpuech, Dmitry Solnyshkov

Scattering-matrix-based Optical Property Analysis And Simulation Acceleration For Periodic Photonic Structures And Metasurfaces (pp. 969)

Yijia Cheng, Chengnian Huang, Wei Sha

Directional Near Fields Generated By Small Particles (pp. 971)

Shubo Wang

Exploiting Radially Polarized Beams To Excite Bound States In The Continuum In Periodic Arrays Of Dipoles (pp. 973)

Luis Cerdán, Juan Ramón Deop-Ruano, Miguel Angel Martín, Rosario Martínez-Herrero, Alejandro Manjavacas

Resonances In Doubly Anisotropic, High-index Nanoplatelets (pp. 975)

Bingying You, Tom Sistermans, Alberto Curto

Analysis Of A Tunable Terahertz Waveguide Using The Frequency-dependent Hie-fdtd Method (pp. 977)

Jun Shibayama, Hiroto Miyao

Coupling Quantum Mechanical Molecular Excitations With Localized Surface Plasmons Using Boundary Element Methods In The Time-domain (pp. 979)

Stefano Corni

The Fourier Modal Method, Equipped With Adaptive Spatial Resolution, Simplified For Shallow Gratings (pp. 981)

Brahim Guizal

Photothermal Engineering In Graphene Nanoplasmonics (pp. 983)

Joel Cox

Multiphysics Topology Optimization For Optimal Photon-electron Interaction In Geometrically Tailored Quantum-well Environments (pp. 985)

Rasmus Christiansen, Ole Sigmund

Metasurfaces With Integrated Mems Structures As Tunable Elements For Spoof Surface Plasmon Polaritons (pp. 987)

Lars Franke, Steffen Klingel, Marco Rahm

Gstcs: A Connection To Exact Spherical Multipoles (pp. 989)

Hossein Allahverdizadeh, Karim Achouri

Physics Informed Bayesian Optimization For Efficient Solution Of Inverse Problems In Nanophotonics (pp. 991)

Ivan Sekulic, Philipp-Immanuel Schneider, Martin Hammerschmidt, Sven Burger

Free-electron Optical Nonlinearities In Heavily Doped Semiconductors: From Fundamentals To Integrated Photonics (pp. 993)

Gonzalo Alvarez-Perez, Huatian Hu, Michele Ortolani, Cristian Ciracì

Tunable Plasmonic Metasurfaces With Epsilon-near-zero Semiconductors: The Case For A Quantum Carrier Model (pp. 995)
Masoud Shahbaninezhad, Lora Ramunno, Pierre Berini

An FFT-Accelerated PML-BIE Method For 3d Acoustic Scattering Problems In Layered Media (pp. 997)
Hangya Wang, Wangtao Lu

Inverse Design Of Large And Complex Metaoptics Systems (pp. 999)
Bryan Stone, Evan Heller, Li-Ce Hu, Rob Scarmozzino, Mayank Bahl, Ziwei Zhu, Maryvonne Chalony, Yijun Ding, Chenglin Xu

Recent Progress In The Design And Simulation Of Large-scale Metalenses (pp. 1001)
Jens Niegemann, Dan-Nha Huynh, Han-Hsiang (Michael) Cheng, Thibault Leportier, Dylan McGuire

Study Of The Radiative Properties Of Quasi-bound States In The Continuum In Dimer Gratings Using The Quasi-normal Mode Method (pp. 1003)
Emmanuel Centeno, Victor Kalt, Rafik Smalli, Antoine Moreau

Effect Of Top Metallic Contacts On Energy Conversion Performances For Near-field Thermophotovoltaics (pp. 1005)
Mauro Antezza

The Technology And Commercialization Strategy Of Next-generation Computational Electrodynamics (pp. 1006)
Zongfu Yu, Shanhui Fan, Jianming Jin

Inverse Design And Knowledge Discovery In Nanophotonics Through Integration Of Shape Optimization And Machine Learning Algorithms (pp. 1007)
Reza Marzban, Ali Adibi

Adiabatic Time Modulations Vs. Photonic Time Interfaces (pp. 1008)
Mariya Antyufeyeva, Victor Pacheco-Peña

Spin-mediated Radiative Caloritronics (pp. 1010)
Philippe Ben Abdallah

Predictive Modeling For Ultrafast Photothermal Effects In Nanophotonic Systems (pp. 1011)
Alessandro Alabastri

Terahertz Parametric Detection: High Sensitivity And Applications In Nondestructive Testing (pp. 1013)
Kosuke Murate, Sota Mine, Kodo Kawase

Understanding Collective Excitations In Finite-Sized Arrays Using Discrete-Dipole Approximation (pp. 1015)
Jussi Kelavuori, Ali Panahpour, Mikko Huttunen

Super-Bound States In The Continuum In One-Dimensional Gratings On a Substrate (pp. 1017)
Nan Zhang, Ya Yan Lu

Inferring Structure From Fundamental Limits (pp. 1019)
Sean Molesky, Pengning Chao, Alessio Amaolo, Alejandro W. Rodriguez

Stokes Solitons And Pt-Symmetric Coupled Cavities: Two Paths To Mode-Locking Without Saturable Absorbers (pp. 1021)
Takasumi Tanabe, Ryo Otake, Riku Imamura, Heng Wang

Quantum Effects And Ultrafast Thermoelectric Phenomena In Nanoplasmonics (pp. 1023)
P. André Gonçalves

Advances In Topology Optimization For Nanophotonics (pp. 1024)
Antonio Calà Lesina

Graphene-based Optoelectronics: Simulations And Design (pp. 1026)
Spyros Doukas, Ioannis Katsantonis, Eleftherios Lidorikis, Anna Tasolamprou

Focusing of Heat Flux Radiated by Magneto-Optical Nanoemitters in the Presence of a Magnetic-Field (pp. 1028)

Louis Rihouey, Philippe Ben-Abdallah, Riccardo Messina

Bounds as Blueprints: Towards Optimal and Accelerated Photonic Inverse Design (pp. 1030)
Pengning Chao, Alessio Amaolo, Sean Molesky, Alejandro Rodriguez

Nonlinear-Nonlocal Flat Optics for Space-Time Image Processing (pp. 1032)
Costantino De Angelis

Deep Learning Based inverse Design Approach for Infrared Phonon-Polariton Microstructures: a SiC-Array Toy Model (pp. 1034)
Emmanuele Cannavò, Oscar K. C. Jackson, Davide Baiocco, Ecem Bozdogan, Simone De Liberato, Alessandro Tredicucci

Nanophotonic Design for Augmented Reality Displays: Opportunities and Challenges (pp. 1036)
Christina Spaegele

Hybrid Silicon Metamaterial Combining Microstructured Siliconsurface With Silicon / Silicon Dioxide Multilayer As A Selectiveemitter For Thermophotovoltaic Applications (pp. 1037)
Karam Choukri, Maha Ben Rhouma, Armande Hervé, Elodie Richalot-Taisne, Elyes Nefzaoui

Accelerating Proximity-field Nanopatterning: Gpu-optimized Electromagnetic Solvers For Complex 3d Nanostructure Design (pp. 1039)
Dohyeon Lee, Moosung Lee, Bakytgul Yerenzhep, Myungjoon Kim, Hugonnet Herve, Seokwoo Jeon, Jonghwa Shin, Yongkeun Park

Tailoring The Design Space Of Structurally Colored Stretchable Materials (pp. 1041)
Bilel Abdennadher, Matthias Saba, Ullrich Steiner, Mathias Kolle

Efficient Lookup Table Computation For The Design Of Metalenses Leveraging Propagation Phase (pp. 1043)
Andrea Locatelli, Marco Gandolfi, Davide Rocco, Olga Sergaeva, Costantino De Angelis

Modeling Microstructured Optical Fibers Using Boundary Element Method (pp. 1045)
Marc Amour Ayela, Jean-René Poirier, Frederic Surre, Han Cheng Seat

Cosine Beams For Near-field Space Division Multiple Access In 6g Communications And Beyond (pp. 1047)
Sotiris Droulias, Giorgos Stratidakis, Angeliki Alexiou

Impact Of Disorder On The Radiative Efficiency Of Bound States In The Continuum In Dimer Gratings (pp. 1049)
Victor Kalt, Emmanuel Centeno, Rafik Smaali, Antoine Moreau

Metamaterials: novel trends and applications

Dynamic In-Situ Photoluminescence Lifetime Imaging of Halide Anion Exchange in CsPbBr3 Nanocrystals (pp. 1052)
Petr Liška, Pavel Klok, Jan Král, Tomáš Musálek, Rebeka Kuželová, Petr Viewegh, Tomáš Šikola

Anisotropic Response Of Hybridized Collective Plasmon Modes Of 2d-metal Nanoparticle Arrays Assembled On Periodically Corrugated Sapphire Substrates. (pp. 1054)
Maciej Wiesner, Ephraim Thomas Matthew, Andriy Serebryannikov, Jacek Jenczyk, Igor Iatsunskyi, Szymon Murawka, Mikolaj Lewandowski

Etching-free Rare Earth Doped Meta-surfaces Made By Pulsed Laser Deposition (pp. 1056)
Antoine Bernard, Antonio Pereira, Hai-Son Nguyen, Sébastien Cueff, Tam-Trong Nguyen, Christian Seassal, Etienne Cleyet-merle, Yannick Guyot, Alban Gassenq

Lattice Resonances In Bipartite Arrays Of Nanostructures For Tailored Optical Responses (pp. 1058)
Juan Jose Alvarez Serrano, Juan R. Deop-Ruano, Luis Cerdán, V. Aglieri, A. Toma, Alejandro Manjavacas

Design Of Complex Liquid Crystal Photonic Devices (pp. 1060)
Peter Ropač, Yu-Tung Hsiao, Žiga Černe, Brecht Berteloot, Yera Ussembayev, Inge Nys, Jeroen Beeckman, Kristiaan Neyts, Miha Ravnik

Meta-cracks In Thin Films For Ultrasensitive Strain Monitoring (pp. 1062)
Jae-Hwan Lee, Seung-Kyun Kang

Strong Field Tunable Light-generating Metasurfaces (pp. 1064)
Euclides Almeida, Matthew Feinstein, George Trivizas

An all Al Terahertz Metasurface with Friedrich-Wintgen Bound States in the Continuum (pp. 1066)
Tenyu Aikawa, Gustavo Rodriguez Barrios, Zairui Li, Andrey Baydin, Junichiro Kono, Wesley Sims, Pai-Yen Chen, Thomas Searles, Zizwe Chase

300-GHz-band metasurface technology for wireless communication and sensing (pp. 1068)
Adam Pander, Hibiki Kagami, Daisuke Kitayama, Haruka Matsunaga, Hiroyuki Takahashi

Tunable beamsplitter based on continuous transition between a planar metasurface and a Brewster metafilm (pp. 1070)
Yasuhiro Tamayama, Yugo Shibata

Plasmonic Enhanced Si-based Hot Electron Photodetector For Swir Range (pp. 1072)
Dana Cristea, Roxana Tomescu, Gabriel Craciun, Adrian Dinescu

Tailoring The Rf Fields In Mri: A New Compact Multi-layer Metamaterial Design Combining A Hexagonally-structured Artificial Dielectric With Electric And/or Magnetic Dipoles (pp. 1074)
Rita Schmidt

Breaking The Diffraction Limit: Far-field Super-resolution Imaging Via Metasurfaces And Holography (pp. 1076)
Pooria Salami, Leila Yousefi

Terahertz Collimating Metalens Antenna Based On Polarization-independent Isotropic Metasurface With High Refractive Index And Low Reflectance Mounted On A Resonant Tunneling Diode (pp. 1078)
Yuki Saito, Kento Sato, Kazuisao Tsuruda, Takehito Suzuki

Hybrid Gold--vanadium-dioxide Tunable Plasmonic Devices (pp. 1080)
Vlastimil Křápek, Rostislav Řepa, Jiří Liška, Peter Kepič, Jiří Kabát, Michal Horák, Tomáš Šikola

Van Der Waals Metamaterials For Photonics Enabled By Fib Lithography (pp. 1082)
Andreas Liapis, Xiaoqi Cui, Nianze Shang, Henri Kaaripuuro, Juan Camilo Arias-Muñoz, Xu Cheng, Zhipei Sun

Nir To Visible Upconversion Luminescence From Single Rare-earth Doped Nanoparticles On Self-assembled Chiral Metasurfaces (pp. 1084)
A. Ahmed, K. Y. Chiok, S. May, A. Baride, R. B. Anderson, S. Zhou, Steve Smith

Relative Illumination Of Metalens (pp. 1085)
Qiu-Chun Zeng, Chen-Yi Yu, Wei-Lun Hsu, Che-Chin Chen, Chih-Ming Wang

Emerging Fabrication Technologies For All-Dielectric Periodic Metastructures (pp. 1087)
Lina Grineviciute, Julianija Nikitina, Lukas Ramalis, Simonas Indrisiunas, Kestutis Staliunas

Aluminum Nanoparticles For Photobleaching Resistance Of Quantum Dots In Solution (pp. 1089)
Jérôme Plain, Théo Duarte, Silvère Schuermans, Thomas Lerond, Jérôme Martin, Davy Gérard, Thomas Maurer, Julien Proust

Chalcopyrite - Noble Metal Hybrids As Catalytic Nanoscale Metamaterials With Enhanced Interfacial Excitation Transfer (pp. 1091)
Bjoern Reinhard

Narrow Conducting Polymer Plasmonics via Collective Lattice Resonance (pp. 1093)
Dongqing Lin, Yulong Duan, Pravallika Bandaru, Magnus Jonsson

Bound-state-in-the-continuum Dielectric Bowtie Metasurfaces For Strongly Enhanced Light-matter Interaction (pp. 1095)
Sergei Lepeshov, Nikolaj Balslev Hougs, Søren Stobbe

Plasmonic Multilayers Metamaterials Combining Nitrides, Oxynitrides And Transparent Conductors With Novel, Broad And Tunable Properties (pp. 1097)
Cristina Mancarella, Claudia Pernilla Hallqvist, Simone Bossetti, Ludovica Tovaglieri, Gianluigi Baiardi, Alessio Lamperti, Demosthenes Koutsogeorgis, Nikolaos Kalfagiannis, Vincenzo Caligiuri, Antonio De Luca, Andrea Li Bassi

Geometric Approach Based On Optimal Toric Packings For Photonic Crystals And Metamaterials Design. (pp. 1099)

Alexander Itin

Germanium Metalenses for Long-Wavelength Infrared Spectroscopy Applications (pp. 1104)
Jesus Hernan Mendoza Castro, Giovanni Piscopo, Vorobev Artem, Tomasz Piwonski, Antonella D'orazio, Giovanni Magno, Bernhard Lendl, Liam O'Faolain

Study Of Active And Bleached Tdbc Dye Devices For Photonics Applications (pp. 1106)
Bienlo-Flora Zerbo, Komlan S. Gadedjisso-Tossou, Jean-Michel Benoit, Clementine Symonds, Joel Bellessa, Alban Gassenq

Quasi Three Dimensional Gold Plasmonic Metasurfaces For Enhanced Harmonic generation And Light Conversion To Uv (pp. 1108)
Shroddha Mukhopadhyay, Ana Conde-Rubio, Agustín Mihi, Jose Trull, Maria Antonietta Vincenti, Michael Scalora, Crina Cojocaru

Technology Of Formation And New Areas Of Application Of Composite Metastructures Based On Aluminum Oxide (pp. 1110)
Ekaterina Muratova, Dmitry Kozodaev, Anton Bobkov, Maxim Mesh, Vyacheslav Moshnikov

Parity-Time and quasi-normal modes in Photonics, Plasmonics, Acoustics

Fermi Arcs In Dielectric Resonators (pp. 1116)
Nikolay Solodovchenko, Mikhail Bochkarev, Kirill Samusev, Andrey Bogdanov, Mikhail Limonov

Bright And Dark Soliton Blending Stabilized By Non-hermitian Potentials In Kerr Ring Cavities (pp. 1118)
Salim Benadouda Ivars, Muriel Botey, Kestutis Staliunas, Ramon Herrero

Active Parabolic Waveguide Amplifiers With Non-hermitian Mode Control (pp. 1120)
Nayeem Akhter, Ramon Herrero, Kestutis Staliunas, Muriel Botey

Exceptional Points And Large Chirality In Coupled Photonic Waveguides (pp. 1122)
Alice De Corte, Stefanos Koufidis, Martin McCall, Bjorn Maes

Exceptional Points In Open Quantum Systems: A Quantum Channel Approach (pp. 1124)
Jensen Li, Wai Chun Wong, Bei Zeng

Resonant States Of Photonic Time Crystals (pp. 1126)
Adria Canos Valero, Sergei Gladyshev, David Globosits, Stefan Rotter, Egor Muljarov, Thomas Weiss

Trapping Light At An Exceptional Point (pp. 1128)
Adria Canos Valero, Zoltan Sztranyovszky, Egor A. Muljarov, Andrey Bogdanov, Thomas Weiss

Spherical Representation Of (anti-)parity-time States Of Bragg Gratings (pp. 1130)
Tianyi Hao, Pavel Cheben, Jens Schmid, Pierre Berini

Field Localization Metamaterial For Stable Pseudo Parity-time Symmetrical Wireless Power Transfer System. (pp. 1132)
Abdulrahman Alsaadi, Inki Kim

New Advances in Metamaterials and Their Functional Applications

Dynamical Manipulation of Terahertz Waves based on Moiré Metamaterials (pp. 1135)
Jin Zhang, Zhipei Sun

Dual-band acoustic topological metalaterials with valley-locked waveguide sates (pp. 1136)
Changlin Ding, Yang Sun

Optical near-field enhancement by metal particles at higher-order plasmon resonances (pp. 1138)
Sagar Sehrawat, Andriy Shevchenko

One-time Pad Encryption With Optical Metasurface Ciphertext And Dynamic Visual Keys (pp. 1140)
Zhenfei Li, K. Song, W. R. Zhu

Chirality Nonlinear Optics With Two-dimensional Materials (pp. 1142)
Yi Zhang

Relaxing Symmetry Constraints And Enhancing Robustness Of Photonic Bound States In The Continuum (pp. 1143)
Huayu Bai, Andriy Shevchenko, Radoslaw Kolkowski

Anomalous Reflection Multifunctional Metagrating (pp. 1145)
Yahong Liu, Wenyu Gao, Xin Zhou, Peng Li

Electric Field Reconfigurable Mechanical Metamaterials (pp. 1147)
Haoming Pang, Jianbo Yin

Optimization Of Symmetric Disordered Metastructures For Near-perfect Broadband Transmission (pp. 1148)
Zhazira Zhumabay, Clement Ferise, Vincent Pagneux, Stefan Rotter, Matthieu Davy

Single-pixel Matrix Imaging In Reflection (pp. 1150)
Antton Goicoechea, Theodosios Karamanos, François Sarrazin, Mathias Fink, Fabrice Lemoult, Matthieu Davy

Mid-infrared Spectroscopy Enhanced By Means Of Surface Electromagnetic States On One-dimensional Photonic Crystals (pp. 1152)
Agostino Occhicone, Marialilia Pea, Raffaella Polito, Valeria Giliberti, Alberto Sinibaldi, Francesco Mattioli, Sara Cibella, Andrea Notargiacomo, Alessandro Nucara, Michele Ortolani, Leonetta Baldassarre, Francesco Michelotti

Inherent Spin-Orbit Locking In Topological Bound State In The Continuum Lasing (pp. 1154)
Jiajun Wang, Xinhao Wang, Lei Shi, Yuri Kivshar, Jian Zi

Spectrum And Polarization-Resolved Nonlinear Optical Near-Field Imaging Of Plasmonic Nano-Antennas (pp. 1156)
Yaxin Liu, Jiajun Wang, Lei Shi, Zhensheng Tao

Chiral fields and ultrafast chiral spectroscopy

Utilization Of Strong Chiro-optical Field Near Chiral And Achiral Plasmonic Nanostructure: Chiral Emission And Photofabrication (pp. 1159)
Hyo-Yong Ahn, Junsuke Yamanishi, Hiromi Okamoto

Chiral Stark shift - tweezing molecules in enantiofashion (pp. 1161)
Robert M Jones, Nicola Mayer, Serguei Patchkovskii, Emilio Pisanty, Margarita Khokhlova

Knotted topologies in the polarization state of bichromatic light (pp. 1163)
Emilio Pisanty

Deep Learning and Nano-optics: Designing nanoscale polaritonic effects in twisted chiral multilayers of vdW materials (pp. 1164)
Lucia Álvarez-Tomillo

Chiral Far-field Signature Of Single Achiral Gold Nano-antennas (pp. 1166)
Annika Mildner, Andreas Horrer, Patrizia Weiss, Simon Dickreuter, Christian Simo, Davy Gérard, Dieter P. Kern, Monika Fleischer

Enantiosensitive Exceptional Points For Exceptional Detection Of Molecular Chirality (pp. 1168)
Nicola Mayer, Alexander Löhr, Nimrod Moiseyev, Misha Ivanov, Olga Smirnova

Ultrafast Light-Matter Interaction in Photocatalytic Systems

X-ray Techniques For Probing And Inducing Ultrafast Dynamics At Nanoscale (pp. 1171)
Naman Agarwal

Sensitizing Diamond To Visible Light To Increase Electron Emission Under Solar Radiation (pp. 1172)
Patrick O'Keeffe, Giuseppe Ammirati, Bellucci Alessandro, Daniele Catone, Faustino Martelli, Matteo Mastellone, Silvia Orlanducci, Alessandra Paladini, Riccardo Polini, Raffaella Salerno, Francesco Toschi, Daniele M. Trucchi, Stefano Trucchi, Veronica Valentini

Time-Resolved Raman Spectroscopy In Photoexcited Mos2: Transient Doping, Resonance Effects And Electron-phonon Coupling (pp. 1174)

Claudia Fasolato, A. M. Finardi, M. Capeccia, A. Giugni, R. Cucini, E. Cappelluti, G. Panaccione, F. Sacchetti, P. Postorino, C. Petrillo, G. Ross

Ultrafast Chiral Spectroscopy For Stereocontrolled Photochemistry (pp. 1176)

Malte Oppermann

Elucidating Charge Transfer Processes In Plasmonic And Semiconductor Photocatalysts (pp. 1177)

Giulia Tagliabue

Quantum Light Emitters and Photonic Heterogeneous Integration

Room-temperature Quantum Emission From Interface Excitons In Mixed-dimensional Heterostructures (pp. 1179)

Nan Fang, Yih-Ren Chang, Shun Fujii, Daiki Yamashita, Mina Maruyama, Yanlin Gao, Chee Fai Fong, Daichi Kozawa, Keigo Otsuka, Kosuke Nagashio, Susumu Okada, Yuichiro K. Kato

Designer Van Der Waals Materials For Quantum Optical Emission (pp. 1181)

Shengxi Huang

Spatial resolution enhancement by quantum entanglement (pp. 1183)

Zhe He

Towards top-down integrated quantum photonics based on color centers in hBN (pp. 1185)

Aymeric Delteil

Deterministic Formation Of Single Organic Color Centers In Single-walled Carbon Nanotubes (pp. 1187)

Daichi Kozawa, Yuto Shiota, Yuichiro K. Kato

Lattice Symmetry Guided Spin Dynamics In Supramolecular Assemblies (pp. 1189)

Xuedan Ma

Nanoscale Magnetic Field Imaging Based On Nv Center In Diamond: Instruments And Applications (pp. 1190)

Pengfei Wang

Cavity Quantum Electrodynamics With Single Photon Emitters In 2d Crystals (pp. 1192)

Carlos Antón Solanas

Exciton, Charge And Spin Lattices In Moiré Heterostructures (pp. 1194)

Alexander Högele

Electrical Control Of Quantum Emitters In Van Der Waals Crystals (pp. 1195)

Jieun Lee

Atomically Thin Near Infrared Quantum Light Emitters (pp. 1197)

Han Htoon

Strained Two-dimensional Semiconductors Toward Straintronics (pp. 1199)

Jin Myung Kim, Soyeong Kwon, SungWoo Nam

Fundamental Limits Of Boron-vacancy Spin Dynamics In Hexagonal Boron Nitride (pp. 1201)

Benjamin Lawrie, Yueh-Chun Wu, Abhishek Solanki, Ian Gallagher, Hamza Ather, Aravindh Shankar, Priyo Adhikary, Owen Matthiessen, Xingyu Gao, Demid Sychev, Alexei Lagoutchev, Tongcang Li, Yong Chen, Vladimir Shalaev, Pramey Upadhyaya, Huan Zhao, Ivan Vlassiouk

Diamond Color Center For In-memory Computing (pp. 1203)

Xiaodong Yan

A Colloidal Quantum Dot On A Hybrid Nanoantenna As An Ultrafast And Efficient Single Structured Photon Source For Room Temperature High Dimensional Quantum Communications (pp. 1204)

Ronen Rapaport

Quantum Light In A Moiré Heterostructure (pp. 1206)
Mauro Brotons-Gisbert

Increased Formation Of Silicon-vacancies In Diamond By Sub-bandgap Light Irradiation During Annealing (pp. 1208)
Coleman Cariker, Yifan Yao, Andre Schleife, Michael Titze

Quantum Transport And Spin-valley Control In Monolayer $MoTe_2$ For Photonic Integration (pp. 1210)
M. A. Campbell, T. J. McSorley, J. Liu, Luis Jauregui

From Light To Matter: Controlling Excitons For Quantum Innovation (pp. 1212)
Libai Huang

Quantum Optical Description Of Nanophotonic Systems (pp. 1213)
Johannes Feist

Thin Film Materials and Device Platforms for Quantum Photonics and Sensing Applications (pp. 1214)
Yong P. Chen

Enhanced Quantum Emission Via Epsilon Near Zero Materials (pp. 1215)
Sven Stengel, Abhishek Solanki, Hamza Ather, Pei-Gang Chen, Jae Ik Choi, Brandon M. Triplett, Mustafa Ozlu, Kyu Ri Choi, Alexander Senichev, Wallace Jaffray, Alexei S. Lagoutchev, Marcello Ferrera, Alexandra Boltasseva, Vladimir M. Shalaev

Integration Of Single-defect Carbon Nanotube Photon Sources Into Waveguide Circuits For Quantum Applications (pp. 1217)
Clement Deleau, Chee Fai Fong, Finn L. Sebastian, Jana Zaumseil, Yuichiro Kato

High-Q microresonators unveil quantum rare events (pp. 1219)
Arghadip Koner, Sricharan Raghavan-Chitra, Joel-Yuen Zhou

Functional materials for tunable and reconfigurable photonics

VO2 Nanoparticles: Phase-transition Properties and Optical Memory Demonstration (pp. 1222)
Filip Ligmajer, Peter Kepič, Michal Horák, Jiří Kabát, Martin Hájek, Andrea Konečná, Tomáš Šikola

Deep Learning Enabled Programmable Silicon Photonics Using Low-Loss Phase Change Material Sb2Se3 (pp. 1224)
Otto Muskens, Sophie Blundell, Thomas Radford, Daniel Lawson, Idris Ajia, Latif Rozaqi, Priya Deoli, Daniel-Iosif Trubacs, Peter Wiecha, Alberto Politi, David Thomson, Ioannis Zeimpekis

Tunable Conducting Polymer Mid-ir Plasmonic Microantenna Arrays (pp. 1226)
Pravallika Bandaru, Mohammad Shaad Ansari, Aleksandr Poliakov, Suraya Kazi, Magnus Jonsson

Programmable Polariton Nanophotonics With Phase-change Materials (pp. 1227)
Lukas Conrads, Thomas Taubner

Zero-static-power Photonics Using Chalcogenide Metacoatings With Engineered Volatile And Non-volatile Transitions (pp. 1229)
Behrad Gholipour, Avik Mandal, Joshua Perkins, Mahirah Zaini, Abbas SheikhAnsari, Yihao Cui, Kwanghyun Kim

Reconfigurable Nonlocal Metasurfaces (pp. 1231)
Andrea Alu

Metasurface Tuning Based On Carrier Manipulation (pp. 1232)
Andrea Tognazzi

Dynamic Optical Control with VO2 Metasurfaces (pp. 1234)
Rocio Camacho-Morales

Hybrid Integration of Ferroelectric Oxides in Silicon Photonics Platform (pp. 1236)
Ana-Maria Statie, Pablo Bedoya-Ríos, Clément Ben Braham, Alicia Ruiz-Caridad, Ali El Boutaybi, Roy Prosopio, Sebastian Alvarez Ortega, Jonathan Peltier, Daniele Melati, Etienne Herth, Samson Edmond, Ali Belarouci, Eric Cassan, Delphine Marris-Morini, Panagiotis Karamanis, Michel Rérat, Guy Aubin, Regis Orobtchouk, Léopold Virot, Yohan Désière

Phase Change Material Programmed Photonics: Plasmonic, Dielectric, and Interband Resonances (pp. 1238)
Robert Edward Simpson, Eleanor Gaggs, Daniel Chambers-Sims, Nur Qalishah Adanan, Simon Wredh, Ting Yu Teo, Li Lu, Liu Yan, Zhaogang Dong, Joel Yang

Scalable Architectures for Photonic Compute-In-Memory Using Nonvolatile Optical Materials (pp. 1240)
Sadra Rahimi Kari, Paolo Pintus, Nathan Youngblood

Multifunctional materials for plasmonics in extreme conditions (pp. 1242)
Arrigo Calzolari

Semimetal-based nanostructured thin films for sustainable reconfigurable plasmonics and photonics (pp. 1244)
Fernando Chacon-Sanchez, Marina Garcia-Pardo, Johann Toudert, Rosalía Serna

Combining Phase Change Materials With Soft-nil Dielectric Metasurfaces For Large-scale Tunable Optics (pp. 1246)
Magali Putero, Oumaïma Meskini, Yudha Ramanda, Jacopo Remondina, Victor Malgras, Beniamino Sciacca, Florian Schenk, Maksym Yarema, David Grosso

Programmable Infrared Geometric Phase Metasurfaces with the Plasmonic Phase-Change Material In3SbTe2 (pp. 1248)
Lukas Conrads, Thomas Taubner

Physics of Low-loss Phase Change Material (Sb2Se3) Enabled Nanophotonic Metasurface (pp. 1250)
Priya Deoli, Otto Muskens, Ioannis Zeimpekis, Kai Sun

Development Of A New Reconfigurable Nanophotonic Platform Based On Spin Modulation (pp. 1252)
Lucas Mascaro-Burguera, Jorge Parra, Ramon Torres-Cavanillas, Teresa Mengual, Luis Manuel Mañez-Espina, Pablo Sanchis, Ana Díaz-Rubio, Elena Pinilla-Cienfuegos

Dynamic Local Strain Engineering In Suspended 2d Materials (pp. 1254)
Eric Herrmann, Sai Rahul Sitaram, Ke Ma, S M Jahadun Nobi, Xi Wang

META Quantum Nanophotonics Workshop

Polarization-entangled photon pair generation from an epsilon-near-zero metasurface (pp. 1257)
Wenhe Jia Yang, Grégoire Saerens Yang, Ülle-Linda Talts Yang, Helena Weigand Yang, Robert J. Chapman Yang, Liu Li, Rachel Grange, Yuanmu Yang

Lighting The Future: Advancing Quantum Nanophotonics With Forward And Inverse Designs (pp. 1258)
Lin Wu

Superresolution For Nanometer-scale Optical Imaging (pp. 1260)
Robert Boyd

Nanophotonic Interfaces For Integrated Quantum Technologies (pp. 1261)
Hamidreza Siampour

Nanoscale Gap-Plasmon-Enhanced Superconducting Photon Detectors at Single-Photon Level (pp. 1263)
Yu-Jung Lu

Quantum Radar with Undetected Photons (pp. 1264)
Diego Dalvit

Controlling Multiple Quantum Dots using Structured Light (pp. 1265)
Suraj Goel, Sheena Shaji, Julian Wiercinski, Antoine Borel, Natalia H. Valencia, Moritz Cygorek, Erik Gauger, Brian Gerardot, Mehul Malik

Multimode And Collective Strong Coupling In Plasmonic Nanocavities (pp. 1267)
Angus Crookes, Ben Yuen, Angela Demetriadou

Colored Quantum Random Walks As A Route To Floquet States In Plasmonic Systems (pp. 1269)
Zahra Jalali-Mola, Ortwin Hess

Quantum metaphotonics

Broadband And Bright Photon Pairs From Periodically Poled Triple-resonance Metasurface (pp. 1272)
Jihua Zhang, Chaoxin Shi, Jinyong Ma, Frank Setzpfandt, Thomas Pertsch, Chunxiong Bao, Jianjun Zhang, Andrey Sukhorukov

Highly Directional Photon-emitter Interactions In Slow-light Waveguides (pp. 1274)
Hamidreza Siampour

Quantum metasurfaces of quantum emitters arrays (pp. 1276)
Uri Israeli, Ada Krasnovski, Itai David, Shahar Levi, Rivka Bekenstein

Shaping the emission directivity of single quantum dots in dielectric nanodisks exploiting Mie resonances (pp. 1277)
Armando Genco, Cristina Cruciano, Davide Rocco, Andrea Tognazzi, Andrea Locatelli, Luca Carletti, Alexey Fedorov, Chiara Trovatello, Giuseppe Di Blasio, Ilaria Bargigia, Charalambos Louca, Paolo Gubian, Giulio Tavani, Luca Lovisolo, Artur Tuktamyshev, Lucio C. Andreani, Matteo Galli, Giulio Cerullo, Giuseppe Leo, Stefano Sanguinetti

Metamaterials for Sustainable Energy and Environmental Solutions

Computational Design Of Crystalline Chalcogenides For Intermediate-band Solar Cells (pp. 1280)
Matteo Cagnoni

Radiative Cooling and Metalens for Advanced Micro-Concentrating Photovoltaic Systems (pp. 1282)
Pietro Testa, Matteo Cagnoni, David Osuna-Ruiz, Alicia Elena Torres-Garcia, Miguel Beruete, Federica Cappelluti

Advanced Light-Scattering Control For High-performance Radiative Cooling Surfaces (pp. 1284)
Rainer Bravo-Pino, Alicia Elena Torres García, Jorge Sanchez Dolado, Miguel Beruete, Íñigo Liberal

Making The Miracle Possible: Concrete As A Radiative Cooling Material (pp. 1286)
Jorge Dolado, Guido Goracci, Ghizlane Moutaoukil, Ridwan Agbaoye, Miguel Beruete, Alicia Elena Torres-García, Laura Carlosena, Iñigo Liberal, Achutha Prabhu, José Antonio Ibañez, Nick Adams, Nicole van Lipzig, Karen Allacker

Manipulation Of Silver Thicknesses Of Patterned Metal By Nanosphere Lithography And Electroplating For A Smart Window (pp. 1288)
Cheng-Yuan Xiao, Tsung-Yu Huang

Ito-based Heterostructures Toward Tunable Windows And Radiative Cooling (pp. 1290)
Ermes Peci, Marangi Fabio, Emma Spotorno, Scotognella Francesco, Maurizio Canepa, Francesco Bisio, Michele Magnozzi

Optical antennas and metasurfaces: fundamentals and applications of enhanced light-matter interactions

Chiral Symmetry Breaking In Chiral Crystallization On Mie-resonant Metasurface (pp. 1293)
Hiromasa Niinomi, Kazuhiro Gotoh, Naoki Takano, Miho Tagawa, Iori Morita, Akiko Onuma, Hiroshi Y. Yoshikawa, Ryuzo Kawamura, Tomoya Oshikiri, Masaru Nakagawa

Purcell Broadening And Lamb Shift For Dna-assembled Near-infrared Quantum Emitters (pp. 1295)
Sachin Verlekar, Maria Sanz-Paz, Mario Zapata-Harrera, Mauricio Pilo-Pais, Karol Kolataj, Ruben Esteban, Javier Aizpurua, Guillermo Acuna, Christophe Galland

Mechanically Tunable Optical Responses In Silicon Nanospheres Square Lattice Array Metasurface Fabricated Via Bottom-up Process (pp. 1297)
Yongan Hu, Patrick Probst, Mojtaba Karimi Habil, Hiroshi Sugimoto, Minoru Fujii

Enhanced Linear And Nonlinear Single-particle Spectroscopy Within Plasmonic Nanocavities (pp. 1299)
Femi Ojambati

Dna Origami-based Rhodium Dimers As A New Type Of Uv-plasmonic Nanoantennas (pp. 1300)
Karol Kolataj, Nicco Corduri, Guillermo Acuna

Solving Maxwell Equations Using Polarimetry Alone (pp. 1302)
Jorge Olmos-Trigo

Multivalency Studied At The Single Molecule Level Via Plasmon Enhanced Fluorescence (pp. 1303)
Kasper Okholm, Sjoerd Nooteboom, Peter Zijlstra, Duncan Sutherland

Controlling The Light Emission Of Quantum Emitters Using Plasmonic Nanoantennas (pp. 1305)
Mario Zapata-Herrera, José Luis Montaño-Priede, Nerea Zabala, Rubén Esteban, Javier Aizpurua

Plasmonic Nanoparticles And Wgm Single-Molecule Sensing (pp. 1307)
Frank Vollmer

Fluorescence Color-routing And Steering With A Single Dielectric Nanoparticle (pp. 1308)
Maria Sanz-Paz, Nicole Siegel, Guillermo Serrera, Javier Gonzalez-Colsa, Fangjia Zhu, Hiroshi Sugimoto, Pablo Albella, Guillermo Acuna

Fabrication of Plasmonic Lattices through Optical Printing (pp. 1310)
Abril Julieta Pereyra, Maria Cristina Mina Villarreal, Alejandro Manjavacas, Juan Jose Alvarez-Serrano, Fernando Daniel Stefani, Julian Gargiulo, Ianina Lucila Violi

Cooperative electron-vibron interactions in Surface-Enhanced Raman Scattering (SERS) (pp. 1312)
Miguel A. Martínez García, Diego Martin-Cano

High-refractive-index And Flexible Sic Nanoantenna Stickers (pp. 1314)
Shunsuke Murai, Hiroya Maruyama, Joshua Tse, Hongjie Gao, Katsuhisa Tanaka

Chiral Sensing With Degenerate Quasi-bound States In The Continuum (pp. 1315)
Diana Shakirova, Adrià Canós Valero, Andrey Bogdanov, Thomas Weiss

Full-stokes Polarimetric Microscopy Using Cross-grating Wavefront Microscopy (polar-cgm) (pp. 1317)
Baptiste Marthy, Khosro Z. Kamali, Mikael Käll, Guillaume Baffou

Au Core/Nanoporous Shell Sers Nanoprobe For Ultrasensitive Detection Of Small Pesticide Molecule (pp. 1318)
Ryeong Myeong Kim, Afsana Mimi, Eun-Ah You

Advanced Theoretical Methods for Nanoplasmonics and Molecular Plasmonics

Emission Quenching In Plasmonics - Understanding And Countering It (pp. 1320)
Jacob Khurgin

Modeling Plasmonics And Molecular Plasmonics From An Atomistic Perspective (pp. 1321)
Chiara Cappelli

A computational Maxwell solver for nonlocal Feibelman parameters in Plasmonics (pp. 1323)
Lorenz Huber, Ulrich Hohenester

Time-dependent quantum/continuum modeling of plasmon-enhanced electronic circular dichroism (pp. 1325)
L. Biancorosso, P. D'Antoni, S. Corni, M. Stener, Emanuele Coccia

Modelling hot carrier generation, relaxation and extraction in large metallic nanoparticles (pp. 1327)
Johannes Lischner

Theory Of Imaging Molecules Using Light In A Scanning Tunneling Microscope (pp. 1328)
Tomas Neuman

Multiscale Modelling Insights On Plasmon-assisted Hot-carrier Injection Driving Carbon Dioxide Reduction On Rhodium Nanocubes (pp. 1330)
Margherita Marsili, Giulia Dall'Osto, Mirko Vanzan, Daniele Toffoli, Mauro Stener, Stefano Corni, Emanuele Coccia

Active Control Of Smith-purcell Radiation Emission Using 2d Nanoribbons (pp. 1332)
Eduardo Dias, Theis Rasmussen, Álvaro Rodríguez Echarri, Javier García de Abajo, Joel Cox

Nonadiabatic Dynamics Of Plasmon-mediated Photochemistry (pp. 1334)
Yu Zhang

Polaritonic Index: A Computational Tool For Classifying Hybrid Light-matter Excitations In Metal-molecule Systems (pp. 1336)
Lucia Cascino, Roberto Messina, Stefano Corni, Stefania D'Agostino

Optical Properties Of Au-based Nanoparticles (pp. 1338)
Mirko Vanzan, Giacomo Becatti, Sofia Zinzani, Rilinda Plakaj, Mauro Stener, Francesca Baletto

Ultrafast Thermodynamics In Srtio3: Beyond Perturbation (pp. 1340)
Fredrik Eriksson, Yulong Qiao, Erik Fransson, Matthias Geilfhufe, Paul Erhart

Mechanisms Of Plasmon-molecule Energy And Charge Transfer (pp. 1341)
Andrei Stefancu, Emiliano Cortes

Multiscale Models Integrating Different Physical Mechanisms Of Plasmonic Photocatalysis (pp. 1343)
Lucas Vazquez Besteiro

Atomistic multiscale modeling of surface-enhanced IR absorption (pp. 1344)
Sveva Sodomaco, Piero Lafiosca, Tommaso Giovannini, Chiara Cappelli

Far-field Patterns Of Second-harmonic Generation In Plasmonic Nanostructures:differentiating Surface And Bulk Contributions (pp. 1346)
Ebru Buhara, Sergejs Boroviks, Olivier J. F. Martin

Higher-order Effects In Extended Conjugated Molecular Emitters Near Plasmonic Nanostructures (pp. 1348)
Mhamad Hantro, Gilles Rosolen, Bjorn Maes, Colin Van Dyck

Light-matter interaction on a chip

Dynamically reconfigurable topological routing in nonlinear photonic systems (pp. 1351)
Stephan Wong, Simon Betzold, Sven Hofling, Alexander Cerjan

Transformation And Amplification Of Light In Optical Resonators Modulated By A Relatively Slow Travelling Wave (pp. 1352)
Misha Sumetsky

Tunable On-chip Meta-waveguides (pp. 1353)
Atefeh Habibpourmoghadam, Wenyong Xie, Antonio Calà Lesina

Telecom Wavelength Quantum Dot Single Photon Sources For Photonic Quantum Technologies (pp. 1354)
Andreas Pfenning, Tobias Huber-Loyola, Sven Hoefling

On The Shapes Of The Rogue Waves In Optical Fibers (pp. 1356)
Stanislav Derevyanko, S. K. Turitsyn

Microscopic Theory Of Collimated Light Propagation In Dipolar Arrays With Emergent Epsilon-Near-Zero Responses (pp. 1358)
Lewis Ruks, Janne Ruostekoski

Anapole Response With Polarization-independent Properties Of A Trimer-based dielectric Metasurface (pp. 1360)
Andrey Evlyukhin, Vladimir Tuz

Cascade Enhancement Of Magnetic Purcell Effect And Efficient Collection Of Photons In Hybrid Topological Structure (pp. 1361)
Zihan Mo, Yali Jia, Zhaohua Tian, Qi Liu, Zhengyang Mou, Yu Tian, Qihuang Gong, Ying Gu

Bottom-up approaches, new fabrication routes and ENSEMBLE3

Mie Resonant Silicon Particles Via Bottom-up Synthetic Routes And Assembled Into 2d Metasurfaces (pp. 1364)

Glenna L. Drisko, Megan A. Parker, Lucien Roach, Maria Letizia De Marco, Mathieu Gonidec, Patrick Rosa, Brian A. Korgel, Virginie Ponsinet, Peter R. Wiecha, Alexander Grigorenko, Philippe Barois

Resonant hybrid nanostructures based on 2D semiconductors for advanced optoelectronics (pp. 1366)

Isabelle Staude, Zlata Fedorova

Metal oxide metasurfaces elaborated by nanoimprint and derived methods (pp. 1367)

David Grosso, B. Kerzabi, M. Abbarchi, M. Putero, A. Gourdin, M. Bouabdellaoui, E. Daher, L. Weber

Template-assisted Self-assembly Of Functional Metasurfaces For Advanced Photonic Applications (pp. 1369)

Sezer Seçkin, Tobias König

Multi-oriented Self-assembled Hexagonal Arrays For Isotropic Plasmonic Reflectors (pp. 1371)

Gil Cardoso, Frédéric Hamouda, Vy Yam, Béatrice Dagens

Multifunctional Composite Materials Based On Nanoparticles-doped Blue-phase Liquid Crystals For Advanced Tunable Photonic Devices (pp. 1373)

Kamil Orzechowski, Chun-Ta Wang, Olga Strzeżysz, Wiktor Lewandowski, Tomasz Ryszard Woliński

Numerical Modelling Of Controlled Light Amplification in Liquid Crystal Micro-structures (pp. 1375)

Jaka Zaplotnik, Urban Mur, Igor Muševič, Miha Ravnik

A Scalable Fabrication Method For High-efficiency Photocatalytic Metasurfaces (pp. 1377)

Parvaneh Mokarian-Tabari

Harnessing Plasmonic Phenomena In Glass Composites Obtained By Crystal Growth Techniques (pp. 1379)

Piotr Piotrowski, Govindan Vadivel, Krzysztof Wyrwas, Piotr Paszke, Rafal Nowaczyński, Barbara Surma, Nuttawut Kongsuwan, Johann Toudert, Ortwin Hess, Dorota A. Pawlak

Bottom-up Wet-chemical Synthesis Of Nanometals Assisted By Ultrafast Irradiation (pp. 1380)

Andrés Guerrero-Martínez

Tailored Photonic Bandgap In Liquid Crystalline Cellulose Ether Mesophases: Harnessing Self-assembly Kinetics And Polymer Chain Mobility (pp. 1382)

Cecile Chazot, Simona Fine, Charmaine Guo

3d Topological Insulator-based Eutectic Heterostructures: Fabrication And Potential Applications (pp. 1384)

Kingshuk Bandopadhyay, Krzysztof Markus, Andrzej Materna, Federico Mazzola, Craig Polley, Masayoshi Tonouchi, Rainer Hillenbrand, Dorota A Pawlak

Bottom-up Design Of Isotropic Auxetic Metamaterials Via Kolmogorov-arnold Networks (pp. 1386)

Heyuan Huang

Grow With The Flow: Bottom-up Synthesis Of Anisotropic Plasmonic Nanoparticles Within Microfluidic Channels (pp. 1388)

Martina Lonza, Gail Vinnacombe-Willson, Francisco Bevilacqua, Leonardo Scarabelli, Luis Liz-Marzán, Gail Vinnacombe-Willson

Beyond Threshold: Geometry Matrix Modeling Of Active Plasmonic Nanoparticles (pp. 1390)

Nicole Recalde, Karen Caicedo, Milena Mora, Ashod Aradian, Melissa Infusino, Maria Antonia Iatì, Rosalba Saija, Onofrio Maragò, Alessandro Veltri

Deterministic Bottom-up Fabrication Of Plasmonic Nanostructures On Tapered Optical Nanofibers Via Blurred Electron Beam Deposition (pp. 1392)

Antonio Balena, Marianna D'Amato, Muhammad Fayyaz Kashif, Chengjie Ding, Massimo De Vittorio, Ferruccio Pisanello, Alberto Bramati

Helicity Preserving Metasurface Mirrors For Thz Applications (pp. 1394)

J. Yan, I. Katsantonis, S. Papamakarios, P. Konstantakis, M. Loulakis, Th. Koschny, M. Farsari, M. Kafesaki, Stelios Tzortzakis

Composite Plasmonic Nanoparticles With Extraordinary Optical Properties: Nanolasing, Artificial Magnetism, And Spatial Dispersion (pp. 1396)

Ashod Aradian, Karen Caicedo, Ranjeet Dwivedi, Andres Cathey, Nicole Recalde, Melina Mora, Melissa Infusino, Kevin Vynck, Alessandro Veltri, Alexandre Baron

Light Scattering Of Hyperuniform-Disordered Metasurfaces (pp. 1398)
Alexander Sprafke, Peter Piechulla, Davy Tesch, Prerak Dhawan, Carsten Rockstuhl, Ralf Wehrspohn

Tailoring The Spontaneous Emission Of Magnetic Dipole Transitions With Plasmonic Multipods (pp. 1400)
Joshua Davis, Sébastien Bidault, Mathieu Mivelle, Mona Tréguer-Delapierre, Alexandre Baron

Integration of Plasmonic Metamaterials in Sensing and Photocatalytic Technologies via Scalable Fabrication Techniques (pp. 1402)
Anastasiia Zaleska

Intriguing Electromagnetic Coupling In Eutectic ZnO-ZnWO4 From Visible To Medium Infrared Range (pp. 1403)
Emilija Petronijevic, Alessandro Belardini, Maria Cristina Larciprete, Marco Centini, Grigore Leahu, Roberto Li Voti, Monica Tomczyk, Pawel Osewski, Piotr Piotrowski, Dorota Anna Pawlak, Concita Sibilia

Non-Hermitian Photonics: Topological, Disordered and Quantum systems

Emission Of Emitters Into The Bulk Or Photonic Graphene (pp. 1406)
Francesco Ciccarello

Enhanced Sensing Using Hysteresis Loops Near Exceptional Points (pp. 1407)
Arunn Suntharalingam, Lucas Fernandez-Alcazar, Pablo Wagner-Boian, Mattis Reisner, Urlich Kuhl, Tsampikos Kottos

Light Trapping By Non-hermitian Thin Films (pp. 1408)
Lina Grineviciute, Ignas Lukosiunas, Julianija Nikitina, Indre Meskelaite, Darius Gailevicius, Kestutis Staliunas

Disordered Gain-loss Coupled Systems Investigated By Tracking Petermann Factors Upon Applying Continuous Gradients (pp. 1410)
Hajar Amyar, Mondher Besbes, Henri Benisty

Causal Structure Of Interacting Weyl Points In Acoustic Crystals (pp. 1412)
Hau Tian Teo, Gui-Geng Liu, Yong Ge, Hong-yu Zou, Wei-Chi Chiu, Hongyu Chen, Yang Long, Shou-qi Yuan, Arun Bansil, Hong-xiang Sun, Guoqing Chang, Baile Zhang

Intrinsic Non-Hermiticity In Photonic Floquet Topological Insulators With Genuine Temporal Modulation (pp. 1414)
Junda Wang, Haoye Qin, Zhe Zhang, Romain Fleury

Geometrical Phase Resonators (pp. 1416)
Yuma Kawaguchi, Daria Smirnova, Filipp Komissarenko, Daria Kafeeva, Svetlana Kiriushechkina, Anton Vakulenko, Jeffery Allen, Monica Allen, Alexander B. Khanikaev

Are Lasing Zero Modes Always Topological? (pp. 1418)
M. Alizadeh, S. K. Ozdemir, A. M. Yacomotti, Ramy ElGanainy

Non-Hermitian Topology Solely from Optical Loss Modulation (pp. 1420)
Amin Hashemi, Elizabeth L. Pereira, Hongwei Li, Jose L. Lado, Andrea Blanco-Redondo

Use of Complex Time Delay to Control Propagation Through Generic Non-Hermitian Scattering Systems (pp. 1422)
Isabella Giovannelli, Nadav Shaibe, Jared Erb, Thomas M. Antonsen, Steven Anlage

Fock space skin effects in many body systems (pp. 1424)
Masatoshi Sato

Quantum Walks Of Correlated Photons In Non-hermitian Photonic Lattices (pp. 1425)
Chong Sheng, H. Liu, S. N. Zhu

Algebraic Skin Effect In Higher-dimensional Non-hermitian Metamaterials (pp. 1427)
Mingyang Li, Jing Lin, Kun Ding

Reflectionless Transient Excitation in Complex Media (pp. 1428)
Clément Ferise, Philipp del Hougne, Matthieu Davy

Optimal Focusing On Non-linear Targets Embedded Within Complex Media (pp. 1430)
Antton Goicoechea, Jakob Hupfl, Stefan Rotter, François Sarrazin, Matthieu Davy

Correlation Between Topological Effects In Photonic Crystal Slabs: A Theoretical And Experimental Exploration Of Bic, Weyl Points And Fermi Arcs (pp. 1432)
Karen Caicedo, Sivia Romano, Gianluigi Zito, Ivo Rendina, Vito Mocella

Multi-Order Exceptional Points In Higher Dimensions (pp. 1434)
Athanasios Athanasopoulos, Dimitrios Kaltsas, Konstantinos Makris

Lasing And Coherent Perfect Absorption Beyond Canonical Pt-Symmetry Using Electrically-Injected Dfb Lasers With Complex-Coupled Bragg Grating (pp. 1436)
Yaoyao Liang, Yara El Droubi, Jean-René Coudevylle, Laurence Ferlazzo, Xavier Lafosse, Francois Maillard, Alexandre Garreau, Arnaud Wilk, Olivier Delorme, Henri Benisty, Abderrahim Ramdane, Anatole Lupu

Chiral And Non-chiral Swift Mode Conversion Through Adiabaticity Engineering (pp. 1438)
Dong Wang, Wen-Xi Huang, Bo Zhou, Wenduo Yu, Pei-Chao Cao, Yu-Gui Peng, Zheng-Yang Zhou, Hongsheng Chen, Xue-Feng Zhu, Ying Li

Complex Continuation Exceptional Point And Its Role In Eigenvalue Knots For Open Boundary Lattices (pp. 1440)
Yuancheng Zhao, Kun Ding

Nano-Lasers, Spasers, and Nanostructures with Quantum Elements

Geometric Antibunching And Directional Shaping Of Photon Anticorrelations (pp. 1442)
Blas Durá-Azorín, Alejandro Manjavacas, Antonio I. Fernández-Domínguez

Exploring Extreme Dielectric Confinement For Nano-lasers (pp. 1444)
Yi Yu, M. Xiong, Y. Berdnikov, S. K. Borregaard, A. H. Dubré, E. Semenova, K. Yvind, J. Mørk

Light Goes Nano: The T-Matrix Method In Nanoplasmonics with Active Gain Media (pp. 1446)
Maria Antonia Iatì, Rosalba Saija

Emission Landscape And Spectrum Of Plasmonic Nanoshell Lasers (pp. 1448)
Karen Gabriela Caicedo Santamaria, Melissa Infusino, Ashod Aradian, Alessandro Veltri

Interface Engineering In Surface Plasmon Polariton Nanolasers For Integrated Photonic Applications (pp. 1450)
Yu-Hsun Chou

Enhancement Of Lasing And Spasing Phenomena Via Individual, Periodic And Complex Plasmonic Resonators (pp. 1452)
Dávid Vass, András Szenes, Miklós Waldhauser, Emese Tóth, Olivér Fekete, Balázs Bánhelyi, Mária Csete

Plasmonic slot waveguides: a quantum leap in nonlinear nanophotonics (pp. 1454)
L. Rojas Yanez, H. Hu, C. Ciracì, J. A. Scott, L. Sortino, M. Toth, P. G. Zotev, A. I. Tartakovski, Stefano Palomba

Round Table: Nanolasers: prospects and challenges (pp. 1456)
Ashod Aradian

Laser Cooling Of Hybrid Nanoparticles (pp. 1457)
Onofrio Marago, Alessandro Veltri, Melissa Infusino, Rosalba Saija, Maria Antonia Iati

Electrically-biased Surface Plasmon Nanolaser With A Hyperbolic Metasurface (pp. 1458)
Jun-Yu Wu, Tsung-Yu Huang

Optical Tweezers: A Powerful And Versatile Micro- And Nano Manipulation Tool With Applications From Space To Spaser (pp. 1460)
Melissa Infusino, Karen Caicedo, Maria Antonia Iatí, Onofrio Maragó, Maria Grazia Donato, Alessandro Veltri

Plasmonics and Nanophotonics: Fundamentals and Applications

Quantum Beam Splitting On Metasurfaces: Principles And Applications (pp. 1463)
Yu Tian, Qi Liu, Xuan Liu, Zhaohua Tian, Shuyun Su, Guixin Li, Xifeng Ren, Qihuang Gong, Ying Gu

Birefringence-Driven Chiral Resonances in Lithium Niobate Metasurfaces (pp. 1465)
Bo Wang, Tingyue Zhu, Junjie Li

Exploring Mesoscopic Plasmonics by Integrating Transformation Optics and Feibelman d Parameters (pp. 1467)
Fan Yang

Near-field Spacetime Imaging of THz Surface Plasmon Polaritons in Graphene (pp. 1469)
Simon Anglhuber, Martin Zizlsperger, Eva A. A. Pogna, Yaroslav A. Gerasimenko, Anastasios D. Koulouklidis, Imke Gronwald, Svenja Nerreter, Leonardo Viti, Miriam S. Vitiello, Rupert Huber, Markus A. Huber

Plasmonic Effects On The Crystal Transformation And Emission Control Of Luminescence Particles (pp. 1471)
Hairong Zheng, Huan Chen, Chengyun Zhang, Zhenglun Fu, Zhenglong Zhang

Memristive Nanogaps With Biophoton-like Properties As A Building Block For Advanced Nanophotonic Applications (pp. 1473)
Maciej Ćwierzona, Diana Singh, Konstantin Malchow, Sarah Hamdad, Alexandre Bouhelier

Electrically Driven Functional Plasmonic Nanocavities (pp. 1475)
Pan Wang

Particle-in-cell (pic) Simulations For Next-gen Nanoscopic Photonics And Plasmonics (pp. 1476)
Lin Wu

Hyperbolic Photonic Topological Insulators And Quantum Sources (pp. 1478)
Lu He, Xiangdong Zhang

Chiral Plasmonic Nanoparticle-molecule Hybrids For Circularly Polarized Oleds (pp. 1480)
Lei Shao

Strong Coupling With Excitons And One-dimensional Photonic Crystal Modulated Plasmonic Nanocavities (pp. 1481)
Xiulai Xu

Control Of Polaritons In Low-dimensional Nanomaterials (pp. 1483)
Qing Dai

Thermal Emission Control And Applications Of Metasurfaces (pp. 1485)
Xiaohe Shang, Ye Zhang, Fan Zhong, Shining Zhu, Hui Liu

Plasmon-Modified Light Emission from Monolayer Semiconductors (pp. 1487)
Hong Wei

High-Contrast Ratio Optical Switching in multilayer Fabry-Perot Cavities with Phase Change Materials (pp. 1488)
Ruhao Pan, Bo Wang, Zhiyang Tang, Junjie Li

Monte Carlo Simulation For Dense Nanoparticle Dispersion With Rigorous Treatment Of Particle Types And Distributions (pp. 1490)
Changgyun Noh, Seokhwan Min, Jonghwa Shin

Strong Near-field Enhancement Through Sphp And Lsp Coupling On Cdo Gratings (pp. 1492)
Pablo Ibáñez Romero, Maria Villanueva Blanco, Eduardo Martinez Castellano, Javier Yeste, Fernando Gonzalez-Posada, Vicente Muñoz-Sanjosé, Thierry Taliercio, Miguel Montes Bajo, Adrian Hierro

Energy And Momentum Distribution Of Surface Plasmon-induced Hot Carriers (pp. 1494)
Christopher Weiß, Tobias Eul, Eva Prinz, Benjamin Stadtmüller, Martin Aeschlimann

Electromagnetically Induced Transparency And Lasing Without Inversion In Chiral Molecules (pp. 1495)

Somasree Pal, Ambaresh Sahoo, Raju Adhikary, Matteo Venturi, Giovanna Salvitti, Carino Ferrante, Davide Tedeschi, Paola Benassi, Massimiliano Aschi, Andrea Marini

Influence Of The Plasmonic Lattice Kerker Effect On Second-harmonic Generation (pp. 1497)

Sergejs Boroviks, Benjamin Syriam Garcia, Olivier Martin

Plasmon-enhanced Vibrational Circular Dichroism In Plasmonic Nanostructures Incorporating Chiral Drugs (pp. 1499)

Raju Adhikary, Matteo Venturi, Giovanna Salvitti, Ambaresh Sahoo, Carino Ferrante, Paola Benassi, Francesco Di Stasio, Andrea Toma, Hatice Altug, Massimiliano Aschi, Andrea Marini

Modeling Of The Zno/ag Related Lspr Peak Shift Due To Zinc Oxide Refractive Index Changing (pp. 1501)

Svitlana Redko, Grigorii Milenin, Vitaliy Shvalagin, Olga Kapush, Artem Fedorenko, Roman Redko

Quantum Quasinormal Mode Theory For Dissipative Nano-optics And Magnetodielectric Cavity Quantum Electrodynamics (pp. 1503)

Lars Meschede, Daniel Clarke, Ortwin Hess

Large Purcell Enhancement With High-Quality Factor In Dielectric Nanoantenna-Microtoroid Structure (pp. 1505)

Zihan Mo, Yali Jia, Xinchen Zhang, Yu Tian, Ying Gu

New Materials for Photonics (Graphene, MoS2, WS2, etc

On-chip Refractive Index Sensors In 200 Mm Wafer Silicon Technology (pp. 1508)

Sebastian Reiter, Akant Sengül, Christian Mai, Carlos Alvarado Chavarin, Christian Wenger, Inga Anita Fischer

Tunable Impedance Matching Layer Based On Piezoelectric Materials With External Circuits (pp. 1510)

Han Jia, Yuzhen Yang

Side-coupled Fabry-perot Based On Multi-slot Subwavelength Grating Metamaterials For Sensing Applications (pp. 1512)

Seyedhadi Badri, Artem S. Vorobev, Liam O'Faolain

On-chip Lasers On Waveguides: A Meta-morphosis In Waveguide Imaging (pp. 1514)

Scattering-based microscopy with an evanescent field enhances signal-to-noise by suppressing background. Waveguides generate evanescent waves, but edge-coupling of light is difficult to use. Bonding a VCSEL to a waveguide platform enables an easy coupling via a grating coupler. Integrating a metasurface into the VCSEL tilts emission, improving waveguide excitation. Oliver, ooliver@chalmers.se Khosro, khosro.zangeneh@chalmers.se Erik Strandberg, erik.strandberg@chalmers.se Hana, hana.jungova@chalmers.se Mikael

Excitation Of Multiple Fano Resonances Through Broadband Oblique-wire-bundle Metamaterial Absorbers And Targeted Molecules (pp. 1516)

Kai Lin Hsiao, Tsung-Yu Huang

Slanted Anisotropic Metasurfaces for Enhanced Reflectance Minimization in CMOS Image Sensors (pp. 1518)

Mingwan Cho, Jonghwa Shin

Analysis of the temperature sensitivity of split ring resonator metamaterials (pp. 1520)

Michael Töfferl, Alexander Schossmann, Alexander Bergmann

All-Optical Phase Modulation of mm-waves for Beam Steering Applications (pp. 1522)

George Neville White, Ian Hooper, Fraser Burton, Dave Phillips, Euan Hendry

Optimized bilayer meta-substrate for hyper-sensitive strain monitoring (pp. 1524)

Jae-Hwan Lee, Junsang Lee, Seung-Kyun Kang

A Broadband Artificial Magnetic Conductor Utilising Magnetodielectric Substrate And Multilayered Metasurface (pp. 1526)

Cameron Gallagher, Simon Berry, Chris Lawrence, Alastair Hibbins

A Simplified Approach To 3d Spherical Cloaking Using Shell Based Dielectric Metamaterials (pp. 1528)

Guan Wen Chen, Jing-Hao Huang, He-Jun Ren, Tsung-Yu Huang

Water-based Cylindrical Metamaterials With Radial Anisotropy For Electric Field Enhancement And Suppression (pp. 1530)

Julia Brandt, Hagen Renner, Dominik Langer, Manfred Eich, Alexander Koelpin, Alexander Petrov

On-chip Angle-scanning Scattering Microscopy With All-dielectric Metasurfaces And Surface-emitting Lasers (pp. 1532)
Khosro Zangeneh Kamali, Oliver Olsson, Erik Strandberg, Hana Jungová, Mikael Käll

Design And Fabrication Of Parity-time Symmetric Optical Waveguides For Unidirectional Propagation Of Light (pp. 1534)
Indre Meskelaite, Kestutis Staliunas, Darius Gailevicius

Towards An Inverse-designed Low-cost Waveguide Absorber (pp. 1536)
Christoph Schmidt, Alexander Schossmann, Alexander Bergmann

Terahertz Liquid Crystal Transmissive Metasurface With In-plane Switching Structure (pp. 1538)
Wei Zhu, Sheng Wang, Hangbing Guo, Jingbo Wu, Kebin Fan, Caihong Zhang, Biaobing Jin, Huabing Wang, Jian Chen, Peiheng Wu

Calculating Analogue Solutions To Pdes With Waves (pp. 1540)
Ross Glyn Macdonald, Alex Yakovlev, Victor Pacheco-Peña

A Metamaterial Coherent Detector for mmWave Operation (pp. 1542)
Natalie Rozman, O. Khatib, W. J. Padilla

Tunable Nanostructured Metamaterial With Epsilon-near-zero Transition Layer (pp. 1544)
Tatjana Gric, Edik Rafailov

Optical Characterization Of Barium Titanate From The Visible To Mid-infrared Range By Using Mueller-matrix Spectroscopic Ellipsometry (pp. 1546)
Jiwon Kang, Nina Hong, Martin Thomaschewski, Prachi Thureja, Sangjun Han, Harry Atwater, Min Seok Jang

Optical Characterization Of Periodic Subwavelength Structures Composed Of Polycyclic Aromatic Hydrocarbons (pp. 1548)
Ken Morita, Hiromi Okamoto, Kohei Imura

Spatio-spectral Fission Through Time-varying Layers (pp. 1550)
Wallace Jaffray, Sven Stengel, Fabio Biancalana, Colton Fruhling, Mustafa Ozlu, Michael Scalora, Alexandra Boltasseva, Vladimir Shalaev, Marcello Ferrera

Circularly Polarized Photoluminiscence In Tmig/tmds Heterostructures (pp. 1552)
María Teresa López Carrasco, Daniel Vaquero Monte, Maxen Natanael Colin Ganesh Cosset-Chéneau, Cao Van Phuoc, Jeong Jong-Ryul, Marcos H.D. Guimarães

Electrical Control Of Light Emission Process Of Two-Dimensional Materials On The Nanoscale (pp. 1554)
Elysé Laurent, Elizabeth Boer-Duchemin, Séverine Le Moal, Guillaume Schull, Stéphane Berciaud, Eric Le Moal

TMDCs' Monolayer PL Enhancement Using h-BN and SiO2 Gratings (pp. 1556)
Mahan Bakhshikhah, C. Palekar, Y. Yang, M. Podhorský, B. Sankar Sahoo, S. Machchhar, I. Limame, M. Ries, M. Hrtoň, J. Liška, T. Šikola, S. Reitzenstein

Nanophotonics and Plasmonics Applications

Transfer Learning For The Design Of A Composite Metasurface Unit Cell In The Ka-band (pp. 1559)
Alexander Wolff, Lukas Mueller, Steffen Klingel, Marco Rahm

Broadband Field Prediction Via Parameter-efficient Electromagnetic Surrogate Solver (pp. 1561)
Chanik Kang, Joonhyuk Seo, Changkyun Lee, Haejun Chung

Superscatterers For Tailoring Electromagnetic Interactions: Radar Visibility And Scattering Suppression (pp. 1563)
Pavel Ginzburg

Neural Network Surrogate For Monte Carlo Prediction Of Radiative Properties In Nanoparticle-embedded Layers (pp. 1565)
Fahime Seyedheydari, Kevin Conley, Simo Särkkä

Optical Polarization Modulation Based On Metasurfaces (pp. 1571)

Chen Chen

All-optical Ultrafast Polarization Switching With Nonlinear Plasmonic Metasurfaces (pp. 1572)
Heng Wang, Guixin Li

Chaos-based Communication In Synthetic Temporal Lattices (pp. 1573)
Chenyu Liu, Bing Wang, Peixiang Lu

Enhancement Of Light-matter Interaction In Topological Waveguides And Resonators (pp. 1575)
Michael Brauckmann, E. Narvaez Castaneda, D. Siebert, B. Brecht, J. Forstner, T. Zentgraf

Pixelated plasmonic metasurfaces as a platform for sensing applications in mid-IR (pp. 1577)
Amirmostafa Amirjani, Ewald Janssens

A phenomenon of noise avalanche in bosonic chains with random off-diagonal disorder and its quantum quenching (pp. 1579)
Vladislav Stefanov, André Stefanov, Lea Sirota, Gregory Slepyan, Dmitri Mogilevtsev

Peem Based Near-field Imaging Of Plasmonic Topological Harper Nanochains (pp. 1581)
Qiuchen Yan, Boheng Zhao, Xiaoyong Hu, Qihuang Gong

Slot Mode Optomechanical System For Mass Sensing (pp. 1582)
Cheeru Thrideep, Miroslav Belov, Wayne K. Hiebert

Incoherent Dielectric Tensor Tomography For Robust 3d Birefringence Imaging Using Non-interferometric System (pp. 1584)
Juheon Lee, Herve Hugonnet, Chulmin Oh, YongKeun Park

3d Strain Tensor Analysis In Micro-indented Glass Via Dielectric Tensor Tomogram (pp. 1586)
Juheon Lee, YongKeun Park

Generation of high-efficiency bi-functional holography with metasurfaces (pp. 1588)
Changhong Dai, Tong Liu, Dongyi Wang, Lei Zhou

Theoretical Analysis Of Recoil Force Generated By Stimulated Emission Of Higher-order Optical Vortices (pp. 1590)
Yoshiki Umekawa, Takao Horai, Masaaki Ashida, Hajime Ishihara

Computing Metalens Array For Programmable Quantum Algorithms And Complex-to-complex Discrete Fourier Transform (pp. 1592)
Randy Stefan Tanuwijaya, So Lap, Wai Chun Wong, Tailin An, Wing Yim Tam, Jensen Li

Single-shot Optical Imaging Of Plasmonic Nanoparticles: Orientation, Polarization Anisotropy, Aspect Ratio (pp. 1594)
Petr Bouchal, P. Dvorak, Martin Hrtoň, Katarína Rovenská, Vlastimil Křápek, Radim Chmelík, Tomáš Šikola, Zdeněk Bouchal

Investigation of Structural and Optical Properties of Tungsten Doped VO2-Au Plasmonic Switchable Material (pp. 1596)
Shraddha Shukla, Urvashi Solanki, Abhishek Prasad, P. Mandal

Strong Coupling Of Chiral Light With Chiral Matter: A Macroscopic Study (pp. 1599)
Natalia Salakhova, S. A. Dyakov, I. A. Smagin, I. M. Fradkin, N. A. Gippius

Integrated Spectral Sensitivity As Physics-based Figure Of Merit For Spectral Transducers In Optical Sensing (pp. 1601)
Felix McCluskey, Anne van Klinken, Andrea Fiore

Fabrication Of Porous Au Nanowires On Flexible Substratesfeaturing High- Density Nanogaps Via Nanotransfer Printing For Sers (pp. 1603)
Hyojin An, Byeong-Kwon Ju, Joo-Yun Jung

Metasurface-enabled Dynamic Focusing Arrays For Transport Of Multiple Particles (pp. 1605)
Hyeonhee Kim, Taeyong Chang, Joonkyo Jung, Jonghwa Shin

Spectrally Tailored Surface-Enhanced Raman Spectroscopy (sers) With Polarization-Sensitive Metasurface (pp. 1607)
Julia Lövgren, Angelos Xomalis

Strong Light-matter Coupling Of Photosynthetic Chlorophyll-a Molecules On Plasmonic Arrays (pp. 1609)
Yadav Rohit Umashankar, Parinda Vasa

Ultrastrong Coupling of Si(1−x) Gex Parabolic Quantum Wells to Terahertz Microcavities (pp. 1613)
Sara Cibella, Maria Gambelli, Leonetta Baldassarre, Tommaso Venanzi, Fritz Berkmann, Enrico Talamas Simola, Luciana Di Gaspare, Elena Campagna, Cedric Corley, Giovanni Capellini, Michele Virgilio, Giacomo Scalari, Michele Ortolani, Monica De Seta

Nanoscale Time-Resolved Photoluminescence Mapping of CsPbBr3 Nanocrystals via Near-Field Optical Microscopy (pp. 1615)
Pavel Klok, Petr Viewegh, Petr Liška, Vlastimil Křápek, Zdeněk Nováček, Matouš Kratochvíl, Filip Ulč, Jan Čecháček, Jiří Spousta, Tomáš Šikola

Super-resolution Imaging Using Photonic Nanojet Generated By A Cylinder (pp. 1617)
Maya Shor Peled, Alina Karabchevsky

Plasmon-enhanced photovoltaics, photocatalysis, and solar fuels

Randomness In Self-assembled Photonic Crystals (pp. 1620)
Duanduan Wan

Impact of Realistic 3D Hole Shapes on Photonic Crystal Surface Emitting Laser (PCSEL) Performance (pp. 1621)
Ana Vukovic, Phillip Sewell, Ben Lang, Karl Boyan, Samir Rihani, David Moodie, Nannicha Hattasan, Graham Berry

From Photonic Time-Crystals to Gravitational Waves (pp. 1623)
Martin McCall, Stefanos Koufidis

Multiple Unidirectional Chiral Zero Modes Arising From A Large Chern Number In 2d Photonic Crystals (pp. 1625)
Weiyuan Tang, Hsun-Chi Chan, Shaojie Ma, Chuang Tan, Biye Xie, Kazuki Hasebe, Nicholas X. Fang, Shuang Zhang

Demonstration Of A Broadband Polarization Control Device For Terahertz Waves Using Silicon Photonic Crystals (pp. 1626)
Hidemasa Yamane, Yoshiharu Yamada, Yusuke Kondo, Takuya Ehiro, Masayuki Fujita, Shuichi Murakami

Topological Line Singularities In Scattering Matrix And Bound States In The Continuum (pp. 1628)
Wenzhe Liu, Yuan-Song Zeng, Geng-Bo Wu, C. T. Chan

Harnessing Anisotropic Photonic Crystals for Advanced Chiral Mirrors (pp. 1630)
Andrea Alessandrini, Leone di Mauro Villari, Luca Assogna, Matteo Silvestri, Matteo Venturi, Carino Ferrante, Paola Benassi, Davide Tedeschi, Andrea Marini

Thermal Dissipation In Pillar-based Optomechanical Resonators: Comparing Monolithic Silicon And Hybrid Silicon-silicon Dioxide Nanopillars (pp. 1632)
Víctor González Morote, David Alonso-Tomás, Martín Poblet, Néstor Eduardo Capuj, Albert Romano-Rodriguez, Daniel Navarro-Urrios

Mechanism And Demonstration Of Interference And Multi-port Switching In Silicon Topological Photonics (pp. 1634)
Xing-Xiang Wang, Sho Okada, Towa Maekawa, Liyan Hu, Xiao Hu, Tomohiro Amemiya

Spin Valley Topological Photonics (pp. 1636)
Ekta -, Brijesh Kumar, Abhishek Kumar, Anshuman Kumar

Emitting Properties Of A-si:c:h- Coated 2d-opaline Photonic Crystals (pp. 1638)
Mikhail Bochkarev, Sergey Dyakov, Valery Golubev, Sergey Grudinkin, Sergey Pavlov, Alexander Pevtsov

Interplay Of Two Structures Of Nano-modulated Thin Films (pp. 1640)
Lucciano Antonio Letelier Carreño, Julianija Nikitina, Lina Grineviciute, Kestutis Staliunas

Calculation Of Density Of States In A One-dimensional Photonic Biosensor (pp. 1642)
Francis Segovia-Chaves

Confined Mode Shift In A Photonic Crystal With A Cavity Infiltrated By Chikv Cells (pp. 1644)

Francis Segovia-Chaves

Photonic Routing In A Multiple-input Valley Photonic Crystal Junction (pp. 1646)
Christian Johnson-Richards, Ross Glyn MacDonald, Alex Yakovlev, Victor Pacheco-Peña

Near-unity Index Meta-surfaces and Design of Thermally Emitting Meta-surfaces for Catalysis (pp. 1648)
Joel Yi Yang Loh

Polarization-dependent Au Nanopillar Array For Resonance-driven Photocatalysis (pp. 1650)
Ning Lyu, Anjalie Edirisooriya, Zelio Fusco, Fiona Beck, Christin David

Cofactor Regeneration In Enzyme Membrane Reactors By Photoenzymatic Methods: A Biomimetic Light-harvesting Platform With Ionic Porphyrins For Co_2 Reduction (pp. 1652)
Zhibo Zhang, Manuel Pinelo

Plasmonically Enhanced Solar Water Splitting with TiO2/Au/Pt Nanoparticles in three-dimensional porous PDMS Substrates (pp. 1654)
Nicolas Albenge, F. Laible, S. Glocker, M. Fleischer

Plasmonic Metasurfaces As Solar Absorption Enhancers For The Perovskite Thin Film Solar Cells (pp. 1656)
Sergii Mamykin, Iryna Mamontova, Roman Redko, Olexandr Shtykalo, Tetiana Lunko, Igor Dmytruk, Oleg Yeshchenko, Oles Fedotov, Natalia Berezovska, Anatoliy Pinchuk

Plasmonic Gold Nano-dendrites For Efficient Co_2 Reduction: Tailored Architectures And Enhanced Multi-electron Pathways (pp. 1658)
Anjalie Edirisooriya, Ning Lyu, Zelio Fusco, Fiona Beck

Theoretical Comparison Of Longitudinal And Transverse Interactions Between Plasmon And Electron-Hole Pairs In Ag Thin Film (pp. 1660)
Soshun Inoue, Takeshi Inaoka, Hajime Ishihara

Laser Cavities, Photovoltaic, and Light-Emitting Technologies

Enhancing Anti-reflective Coating Performance Through Binary Optimization Of structural Parameters With Concurrent Material Selection And Thickness optimization (pp. 1663)
Serang Jung, Eungkyu Lee

High Purcell Values From Inverse Design Of Bullseye Cavities By Machine Learning (pp. 1665)
F. M. Sanchez, C. Everly, L. M. Weituschat, L. N. Goduguluri, P. K. Anwla, Pablo A. Postigo

High-efficiency Metasurface Color Routers Inverse-designed Via Accelerated Genetic Algorithms (pp. 1666)
Hyoseok Park, Samuel Kim, Yeonsang Park, Myungjae Lee

Experimental Realization Of Convolution Processing In Photonic Synthetic Dimensions (pp. 1668)
Xinyuan Hu, Bing Wang, Chenzhi Qin, Peixiang Lu

Learning Higher-order Interactions With Factorization Machine For Material Design (pp. 1670)
Sanghyo Hwang, Chaeyoung Park, Seongmin Kim, Tengfei Luo, Eungkyu Lee

Deep Learning and Nano-Optics: Designing nanoscale polariton propagations in twisted van der Waals multilayers (pp. 1672)
Lucia F. Alvarez-Tomillo, José Álvarez-Cuervo, Pablo Calvo-Barlés, Sergio Gutierrez Rodrigo, Enrique Terán García, Aitana Taragaza Martín-Luengo, Kirill Voronin, Alexey Y. Nikitin, Luis Martín Moreno, Pablo Alonso-González

Laser Generation With Metal-free Carbogenic Quantum Dots (pp. 1674)
David Hernández Pinilla, Barun Kumar Barman, Tadaaki Nagao

Semiconductor Microcavity Lasers For Unidirectional And Single Mode Lasing (pp. 1676)
Youling Chen

Fabrication Of Bound States In The Continuum Laser Cavity Compatible With Standard Semiconductor Technology (pp.

1678)

Karolina Bogdanowicz, Laura Stanco, Weronika Glowadzka, Tomasz Fas, Jan Suffczynski, Marek Ekielski, Jan Muszalski, Tomasz Czyszanowski, Anna Szerling

Multicolor Scintillators Coupled With Physics-aware Postprocessing Allows Energy-resolved X-ray Imaging Of Medical Contrast Agents (pp. 1680)

Seokhwan Min, Seou Choi, Simo Pajovic, Sachin Vaidya, Nicholas Rivera, Shanhui Fan, Marin Soljacic, Charles Roques-Carmes

Versatile Design Approach Of Switchable On-chip Emitter-coupled Meta-optics Photon Source (pp. 1682)

Sören im Sande, Torgom Yezekyan, Yinhui Kan, Danylo Komisar, Cuo Wu, Shailesh Kumar, Nur Qalishah Adanan, Golnoush Zamiri, Joel Yang, Sergey Bozhevolnyi, Fei Ding

Micro/Nano Fabrication and Characterization Techniques

Phononic Hyperbolic Metamaterial With Zno/(zn,mg)o Heterostructures (pp. 1685)

Julia Inglés Cerrillo, Pablo Ibáñez Romero, Rajveer Fandan, Jorge Pedrós, Nolwenn Le Biavan, Denis Lefebvre, Maxime Hugues, Jean-Michel Chauveau, Miguel Montes, Adrián Hierro

Uapo Diffracted Field By A Pec-backed Chiral Half-sheet (pp. 1687)

Giovanni Riccio, Flaminio Ferrara, Gianluca Gennarelli, Rocco Guerriero, Francesco Chiadini

Enhanced Chiral Sensing In Epsilon-near-zero metamaterials (pp. 1689)

Ashis Paul, Matteo Venturi, Raju Adhikary, Leone di Mauro Villari, Giovanna Salvitti, Carino Ferrante, Davide Tedeschi, Francesco Di Stasio, Andrea Toma, Hatice Altug, Andrea Marini

Enhanced Frequency Conversion By Plasmonic-Dielectric Metasurfaces With High-Q Quasi-bics In The Visible Spectral Range (pp. 1691)

Timo Stolt, Huayu Bai, Andriy Shevchenko, Radoslaw Kolkowski

Phase-Matched Second-Harmonic Generation from Metasurfaces Inside Multipass Cells (pp. 1693)

Madona Mekhael, Timo Stolt, Anna Vesala, Heikki Rekola, Tommi Hakala, Robert Fickler, Mikko Huttunen

Nonlinear Enhancement From Epsilon-near-zero Material-based Metasurface structure (pp. 1695)

Shakti Mahato, Vipul Rastogi

Polarization-dependent Anapole States In Elliptical Nanodisks For Nonlinear And Filtering Applications (pp. 1697)

Mikko Kjellberg, Hanna Kylhammar, Anand Srinivasan

Deep and vertical etching technique using hydrogen fluoride gas for glass-based metasurfaces (pp. 1699)

Yoshitaka Ono, Kohei Sano, Akira Ueno, Yasuo Hayashi

Gold nanostructure gratings produced using direct laser writing with pulse energy-dependent morphology for SERS substrates (pp. 1701)

Kernius Vilkevicius, Ilja Ignatjev, Gediminas Niaura, Evaldas Stankevicius

Comparative Study of Nanocrystalline Dy2O3 Thin Films deposited on Sapphire and Silicon Wafers by Means of Electron Beam (pp. 1703)

Faisal Alresheedi

Metrology Of Singular Metasurfaces (pp. 1704)

Yanel Tahmi, Matthieu Ansquer, Pierre-Marie Coulon, Sébastien Chenot, Virginie Brandli, Benoit Wattellier, Patrice Genevet, Samira Khadir

Thermal-Mechanical Coupling Performance of the Printable Al-Si Alloy Antisymmetric Lattice Metastructure (pp. 1706)

Jiaqi Yan, Youdao Gao, Heyuan Huang

Large area metalenses for the generation of vector beams (pp. 1708)

Daniele Bonaldo, Andrea Vogliardi, Gianluca Ruffato, Simone Dal Zilio, Vittorio Apolloni, Filippo Romanato

Application of micro-CT technology in performance characterization of composite materials under extreme temperatures (pp. 1710)

Xiaoyang Ren, Yaguang Dai, Meiying Zhao, Heyuan Huang

Submicron Periodic Structures In Metal Oxide Thin Film Via Laser Ablation And Thermal Oxidation (pp. 1712)
Julianija Nikitina, Simonas Indrišiūnas, Tomas Tolenis, Mindaugas Andrulevičius, Lukas Ramalis, Lina Grinevičiūtė

Optical Biosensor For Rapid Detection Of Medical Biomarkers Based On Bound States In The Continuum (pp. 1714)
Magdalena Zadura, Weronika Glowadzka, Karolina Bogdanowicz, Piotr Polak, Joanna Jankowska-Śliwińska, Kamil Kosiel, Krzysztof Piskorski, Marek Ekielski, Tomasz Czyszanowski, Anna Szerling

Broadband Anti-reflectance By Disordered Si Nanodisks For Thin-film Solar Cells (pp. 1718)
Hanna Kylhammar, Sarah Zayouna, Ada Dumitrescu, Mikko Kjellberg, Srinivasan Anand

Cryogenic Bistable Current-voltage Dependence In A Silicon Pn-junction Formed By Wafer-bonding (pp. 1720)
Sung Hoon Cho, Petr Moroshkin, Damir Kulzhanov, Jimmy Xu, Ki Tae Nam

Cost-effective And Mass Production Of Meta-hologram Using Photolithography And Nanoimprint Lithography (pp. 1721)
Chanwoong Park, Seungyeon Lee, Hansang Sung, Jaein Park, Heon Lee

Mass Production of Metasurfaces Using BaTiO3 Nanoparticle-Embedded Resin (nano-PER) (pp. 1723)
Seungyeon Lee, Chanwoong Park, Hansang Sung, Heon Lee

Fabrication And Study Of Nd-doped Bct-based Dielectric Ceramics For Functional Metamaterial Applications (pp. 1725)
Jolanta Makowska, Kamil Feliksik, Malgorzata Adamczyk-Habrajska, Beata Wodecka-Dus

Synthesis And Characterization Of Dielectric Metamaterials Based On Bltf Ceramics (pp. 1727)
Beata Wodecka-Dus, Malgorzata Adamczyk-Habrajska, Jolanta Makowska

Fabrication Of Optical Phase Elements In Bulk Sapphire By Ultrashort Pulses (pp. 1729)
Edvinas Aleksandravičius, Gabrielius Kontenis, Indrė Meskelaite, Darius Gailevičius

Acoustic, Seismic, and Thermal Metamaterials

Dual-directional Acoustic Metamaterial Absorber For Noise Reduction (pp. 1732)
Tzu-Hsuan Chan, Tsung-Yu Huang

Bound states in the continuum of underwater phononic crystals (pp. 1734)
Yuzhen Yang, Han Jia

Tunable curved piezoelectric metasurface for flexural wave manipulation in cylindrical shells (pp. 1736)
Jie Xu, Youqi Zhang, Weihan Wang, Zheng Li

Design Of Tunable Bound States In The Continuum For Flexural Waves In Elastic Waveguide (pp. 1738)
Weihan Wang, Shixuan Shao, Rongyu Xia, Zheng Li

Real-time Manipulation Of Spoof Surface Acoustic Waves Via A Reconfigurable Coding Metasurface (pp. 1740)
Haoxiang Li, Jie Hu

A Surface Integral Equation With Bianisotropic Impedance Boundary Conditions For Simulation Of Acoustic Metasurfaces (pp. 1742)
Junze Shao, Rui Chen, Hakan Bagci

Metamaterial Two-Sphere Newton's Cradle (pp. 1744)
Simon Pope, Oliver Wright

Basic Performance Test Results Of A 3d Underwater Acoustic Metalens Using A Sensor Positioning Device In A Water Tank (pp. 1746)
Sea-Moon Kim, Beomseok Oh, Yeon-Seong Choo, Jeong-Bin Jang, Dongwoo Lee, Junsuk Rho, Sung-Hoon Byun

Programmable Sound Wave Transmission By Active Acoustic Meta-layers (pp. 1748)
Shoubo Dai, Hao Gao, Yegao Qu

An ultrasonic metamaterial based on Lieb lattice structures (pp. 1750)
Anusha Rehman, David A. Hutchins, Peter J. Thomas, Rudolph Römer, Katarzyna Sopińska, Jisun Im, Phillip Sheffield, Stefano Laureti

Plasmonics and Nano-Optics

Highly-efficient meta-surface for vectorial holography generation (pp. 1753)
Tong Liu, Changhong Dai, Dongyi Wang, C. T. Chan, Lei Zhou

Designing Temperature Invariant All-dielectric Photothermal Metasurfaces (pp. 1755)
Gopal Narmada Naidu, Can O. Karaman, Giulia Tagliabue

Quantum Two-photon Density-matrix Holography With Metasurfaces (pp. 1758)
Qinmiao Chen, Guangzhou Geng, Hong Liang, Tailin An, Wai Chun Wong, Junjie Li, Jensen Li

A Dual Bound States In The Continuum Mid-ir Metasurface (pp. 1760)
Giovanni Piscopo, Artem Vorobev, Jesus Hernan Mendoza Castro, Giovanni Magno, William Whelan-Curtin

Dispersive Meta-lens Temperature Detector (pp. 1762)
Yulun He, Mu Ku Chen, Mingrui Huang, Yifei Zhang, Shengxian Shi

Green Metasurface for Wearable ETA Radar Antenna Protection (pp. 1764)
Maria Elena de Cos Gómez, Alicia Flórez Berdasco, Fernando Las-Heras Andrés

Meta-DRA Array for Mm-Wave Wearable ETA Radar Applications (pp. 1766)
Lara Prendes Suarez, Maria Elena de Cos Gómez, Fernando Las-Heras Andrés

Aperiodic tiling-based metasurface design for angle- and polarization-tolerant structural color (pp. 1768)
Minyeul Lee, Suwan Jeon, Jonghwa Shin

Liquid Crystal-Based Asterisk-Shaped Millimeter-Wave Reflectarray for Reconfigurable Intelligent Surfaces (pp. 1770)
Junaid Ahmed Uqaili, Dayan Perez-Quintana, David Osuna Ruiz, Miguel Beruete

Polarization-Independent Huygens' Metasurfaces based on Split Ring Resonator for Highly Efficient Wavefront Formation at sub-THz bands (pp. 1773)
Hibiki Kagami, Daisuke Kitayama, Adam Pander, Haruka Matsunaga, Hiroyuki Takahashi

Designing Impedances Surfaces For Simultaneous Anomalous Reflection And Polarisation Conversion (pp. 1775)
Jonathon Smith, Calvin Hooper, Nathan Clow, Alastair Hibbins, Ian Hooper, Simon Horsley

Topology Optimization Of Blazed Metasurfaces For High-efficiency Spectrographs (pp. 1778)
Simon Ans, Frédéric Zamkotsian, Guillaume Demésy, Quentin Tanguy, Roland Salut, Andrei Mursa, Nicolas Passilly

Discrete Multilevel Metasurfaces For Absorbers And Antireflective Layers (pp. 1780)
Mihai Kusko, Cristian Kusko

Incoherent Digital Holography Using Multilayer Metasurfaces For Zeroth-order-light-free Recording (pp. 1782)
Teruyoshi Nobukawa, Ryo Higashida, Koki Imamura, Yasutaka Maeda, Kei Hagiwara

Angle Independent Enhancing And Diminishing Metasurface With Susceptibility-driven Inverse Design (pp. 1784)
Sandeep Yadav Golla, Jian Cao, Sarah Salhi, Paula Nuño Ruano, Carlso Alonso-Ramos, Daniele Melati

Ring Distributed Metamaterial With Phase Cancellation For Rcs Reduction (pp. 1786)
Oscar Fernandez, Rodrigo Gonzalez, Alvaro Gomez, Ismael Barba

Numerical Investigation Of Transverse-mode Theory For Strongly Coupled Periodic All-dielectric Metasurfaces (pp. 1788)
Pooja Uday Naik, Massimiliano Guasoni

Polarization-multiplexed Vectorial Oam Holography Based On Dielectric Metasurfaces (pp. 1790)
Joonkyo Jung, Hyeonhee Kim, Jonghwa Shin

Characterization Of Flat Optical Devices In A Transformation Optics Context (pp. 1792)
Mircea Giloan

Resistive Metamaterial Based Ultrathin Broadband Microwave Absorber (pp. 1793)
Jyoti Yadav, Kumar Vaibhav Srivastava, J. Ramkumar

Tunable Terahertz Polarization Converter Based On Liquid Crystal (pp. 1795)
Sheng Wang, Wei Zhu, Jingbo Wu, Hangbing Guo, Caihong Zhang, Kebin Fan, Biaobing Jin, Jian Chen, Peiheng Wu

Complete Asymmetric Polarization Conversion Through Zero-eigenvalued Exceptional Points Of Non-Hermitian Metasurfaces (pp. 1797)
Donghak Oh, Soojeong Baek, Sangha Lee, Kyungmin Lee, Jagang Park, Zhaowei Liu, Teun-Teun Kim, Bumki Min

Singular Flat Band In Metallic Kagomé Lattice (pp. 1799)
Dongho Lee, Hyeon Gi Park, Donghak Oh, Yung Kim, Soojeong Baek, Bumki Min

Design Of A Metasurface Deflector Integrated With A Grating Coupler To Collimate A gaussian Beam From An Optical Fiber For Vertical Coupling (pp. 1801)
Suhee Shin, Jaewon Jang, Minsu Park, Yeonsang Park

Dual-Functional Metalenses For The Generation Of 2d And 3d Structured Beams (pp. 1803)
Andrea Vogliardi, Gianluca Ruffato, Daniele Bonaldo, Simone Dal Zilio, Filippo Romanato

Flat Optics For Hybrid Grafted Vortex Beams And Azimuthally Tailored Multispectral Oam Combs (pp. 1805)
Hammad Ahmed, Xianzhong Chen

Tamm Plasmon for the enhancement of Light Matter Interaction (pp. 1806)
Andrea Rossini, F. Marangi, C. Florindi, A. Pianetti, F. Lodola, F. Scotognella, G. Lanzani, Giuseppe Maria Paternò

Acoustically Driven Soft Metasurfaces (pp. 1807)
Skyler P. Selvin, Johan D. Carlstrom, Mohammad Taghinejad, Mark L. Brongersma

Surface Enhanced Raman Spectroscopy (sers) Based On A Polarization-insensitive Nanoparticle-on-a-slit Cavity With Dielectric Waveguide. (pp. 1808)
Daniel Arenas Ortega, Javier Redolat, Ángela Barreda, Amadeu Griol, Elena Pinilla Cienfuegos, Alejandro Martínez

Experimental Observation Of Bound States In The Continuum In Fully Semiconductor Subwavelength Gratings (pp. 1810)
Weronika Glowadzka, Tomasz Fas, Kartik Gaur, Floriana Laudani, Sarthak Tripathi, Niels Heermeier, Jan Suffczyński, Stephan Reitzenstein, Tomasz Czyszanowski

Mems-Tunable Multifunctional Optical Metasurfaces For Advanced Imaging (pp. 1812)
Zhihao Zhu, Chao Meng, Mingwei Tang, Sergey I. Bozhevolnyi, K. Wei

Evolution Of Quantum Plasmonics In Relatively Large Doped Quantum Dots (pp. 1814)
D. Subedi, D. Dada, Mogus Mochena

Rainbow Trapping with Graded Triangular Grooves for Enhanced Raman Spectroscopy of Biomolecules (pp. 1817)
Yi Loh

Magnetic Field Induced Shift In Lspr Of Photochemical Synthesized Zno/ag Nanocomposites (pp. 1819)
Roman Redko, Vitaliy Shvalagin, Grigorii Milenin, Svitlana Redko

Sequential Deposition of Silver Nanoparticles on Silicon Ripples for LSPR Anisotropy minimization and SERS Applications (pp. 1821)
Tarundeep Kaur Lamba, Sebin Augustine, K. P. Sooraj, Mukesh Ranjan

Plasmon-enhanced Circular Dichroism For Chiral Drugs Enantiomeric Discrimination (pp. 1824)
Matteo Venturi, Raju Adhikary, Ambaresh Sahoo, Carino Ferrante, Matteo Silvestri, Giovanna Salvitti, Davide Tedeschi, Isabella Daidone, Francesco Di Stasio, Andrea Toma, Francesco Tani, Hatice Altug, Antonio Mecozzi, Massimiliano Aschi, Andrea Marini

Multiphysics Calculation Of Plasmonic Photothermal Effects In Gold Nanorod Dimers: Influence Of Size Mismatch (pp. 1825)

Tong Zhou, Maria Vanessa Balois-Oguchi, Kotaro Kajikawa

Canalized Light Creates Directional And Switchable Surface Structures In Vanadium Dioxide (pp. 1827)
Daniel Kazenwadel, Noel Neathery, Peter Baum

Modelling, Fabrication And Characterization Of Tunable Plasmonic Substrates For Designer Ultra-thin Optical Filters (pp. 1829)
Arka Jyoti Roy, Sai Rama Krishna Malladi, Shourya Dutta Gupta

Thermal Radiation Forces On Nanostructures With Reduced Symmetry (pp. 1833)
Juan R. Deop-Ruano, Alejandro Manjavacas

Fourier Modal Method For Calculating Two-dimensional Periodic Photonic Crystals With Chiral Inclusions (pp. 1835)
Ilia Smagin, Sergey Dyakov

Interaction Between Ag Nanoparticles And Excitons In Organic Light Emitting Diode: Plasmonic Enhancement And Quenching (pp. 1836)
Amadou Tierno Diallo, Nabil Khiri, Mahmoud Chakaroun, Azzedine Boudrioua

Enhanced Light Harvesting And Photothermal Conversion With Anisotropic Gold nanoparticles (pp. 1838)
Runpeng Miao, M. Bissoli, V. Amendola

Self-assembly Of High-quality Single Crystals Of Dna-functionalized Gold Nanoparticle Superlattices For In-vivo Sers Detection (pp. 1840)
Taito Ikeuchi, Lidong Zhang, Saki Kozawa, Shoko Kojima, Hiromasa Niinomi, Makoto Kuwahara, Kotaro Hiramatsu, Miho Tagawa

Frozen Plasmons On Uniformly Moving Surface (pp. 1842)
Stephane Azar, Francisco J. Rodríguez-Fortuño

Optical writing Of Stable Single-atom Features In Plasmonic Nanogaps (pp. 1844)
Paul Kerner, Rakesh Arul, Damien Thompson, Jeremy Baumberg, Bart de Nijs

Resonant Optical Metasurfaces for Eye-Tracking Applications (pp. 1846)
Vittorio Bonino, Filippo Coviello, Pietro Baldin, Alberto Sivera, Rafael Bellei de Carvalho, Paolo Biagioni, Giuseppe Della Valle, Giovanni Isella, Roman Sordan, Gianluca Valentini, Giulio Cerullo, Anna Cesaratto, Tommaso Ongarello, Jacopo Stefano Pelli Cresi

Single Molecule Detection in hBN metasurfaces (pp. 1848)
Saeid Izadshenas Jahromi, Karolina Slowik

Infrared Spectroscopy Of Heavily Doped Germanium Crystals (pp. 1850)
Sergey Pavlov, Aravind N. Subramanian, R. Radhakrishnan Sumathi, S. Bin Anooz, Nikolay V. Abrosimov, Mariia Sidorova, Heinz-Wilhelm Hübers

Theoretical study and experimental validation of nonlocal metasurfaces for Augmented Reality (pp. 1853)
Pietro Baldin, Alberto Sivera, Rafael Bellei de Carvalho, Filippo Coviello, Vittorio Bonino, Jacopo Stefano Pelli Cresi, Anna Cesaratto, Tommaso Ongarello, Paolo Biagioni, Roman Sordan, Giovanni Isella, Gianluca Valentini, Giulio Cerullo, Giuseppe Della Valle

Suppressing Photobleaching Of J-aggregates Via Strong Light-matter Coupling (pp. 1855)
Yadav Rohit Umashankar, Parinda Vasa

Nanostructures meet Perovskites: Advanced Applications and Future Challenges

Tailoring The Metal-insulator Transition Of Rare Earth Nickelates Thin Films Towards Optical Applications (pp. 1860)
Luigi Matera, Julian Peiro, Laurent Divay, Christophe Galindo, Paolo Bortolotti, Manuel Bibes, Lucia Iglesias Bernardo

Electrically And Optically Driven Exciton-polaritons In All-perovskite Metasurfaces (pp. 1862)
Andrea Zacheo, Yutao Wang, Giorgio Adamo, Cesare Soci

Controllable Suppression of Non-Hermitian Skin Effects (pp. 1863)
Chao Xu, Zhiqiang Guan, Hongxing Xu

Indoor Energy Harvesting Enhancement With Nanostructured Grating Contact (pp. 1865)
Daniel Sarcanean, Ángela Barreda, Braulio Garcia-Camara, Eduardo Lopez-Fraguas, Ricardo Vergaz Benito, Iván M. Mora-Seró

Strong Light-Matter Coupling in Perovskite Quantum Dot Solids (pp. 1867)
F. J. Coto-Ruiz, R. Tao, C. Bujalance, L. Caliò, D. N. Dirin, M. V. Kovalenko, Hernán Ruy Míguez García

Plenary presentations

Applications of highly nonlinear epsilon-near-zero materials in photonics

Robert W. Boyd

Department of Physics and School of Electrical Engineering and Computer Science
University of Ottawa, Ottawa, ON Canada

The Institute of Optics and Department of Physics and Astronomy
University of Rochester
Rochester, NY USA

Abstract: Optical materials display extremely large nonlinear response in a spectral band around their plasma frequency. This presentation reviews the origin of this behavior and provides examples of such materials and of applications enabled by this response.

Research reported in 2016 [1] showed that materials such as indium tin oxide (ITO) display an unprecedentedly large nonlinear refractive index when excited at a frequency where the dielectric permittivity is nearly vanishing. The large nonlinear response of these epsilon-near-zero (ENZ) materials, some million times larger than that of silica glass, suggest that these materials would prove extremely useful in the development of new classes of photonic devices. In this contribution, we review the history of the understanding of nature of the nonlinear response of ENZ materials and the development of ENZ-based photonic devices. Specific investigations over the past eight years have led to increased understanding of topics including (1) the origin of the enhancement of the nonlinear optical response, (2) the possibility of using nanofabrication methods to create ENZ behavior at any specified wavelength, and (3) the exploration of what interactions and devices are enabled through use of ENZ materials. In this contribution, we review the recent history of the development of the field of ENZ science and of the development of ENZ applications.

[1] M. Z. Alam, I. D. Leon, and R. W. Boyd, Large Optical Nonlinearity of Indium Tin Oxide in its Epsilon-Near-Zero Region, Science 352, 795 (2016).

Nanoplasmonic Quantum Photonics

Ortwin Hess[1]

[1]School of Physics and CRANN Institute, Trinity College Dublin, The University of Dublin, Dublin 2, Ireland
*corresponding author: ortwin.hess@tcd.ie

Abstract: Nanoplasmonic quantum photonics revolutionizes quantum information technologies by enabling room-temperature quantum operations through extreme nanoscale field confinement and strong photon-emitter coupling. This facilitates ultrafast single-photon emission, multipartite entanglement, near-field coupling, and quantum sensing, enhanced by quantum nanoplasmonic coherent perfect absorption, paving the way for practical quantum devices operable at ambient conditions.

Nanoplasmonic quantum photonics represents a groundbreaking advancement, bridging nanotechnology and quantum information processing to overcome fundamental limitations of conventional quantum devices. This approach enables quantum operations at room temperature, achieving significant miniaturization, enhanced speed, and practicality by leveraging cavity quantum electrodynamics (cQED) in the strong coupling regime, where coherent photon-emitter interactions produce polariton states [1,2] while previously, single quantum emitter strong coupling required complex and costly cryogenic setups, severely restricting broad applicability.

Nanoplasmonic cavities offer a transformative solution by confining electromagnetic fields to scales far below the diffraction limit. Nanoparticle-on-mirror (NPoM) architectures enable sub-nanometric confinement and intense electromagnetic field enhancement, allowing unprecedented room-temperature strong coupling at the single-molecule level [3]. Chikkaraddy et al. demonstrated practical room-temperature strong coupling within these cavities, significantly impacting quantum photonic device development [3]. Additionally, near-field coupling techniques have been shown to strongly couple single quantum dots at room temperature, further illustrating the power of nanoplasmonics in achieving robust quantum interactions at ambient conditions [4].

Recent advances underscore the capability of nanoplasmonics for ultrafast single-photon generation, multipartite entanglement, and quantum sensing. Near-field transducers (NFTs), originally designed for data storage applications, now enable highly efficient optical field focusing into nanoscale volumes, significantly increasing quantum dot emission rates and facilitating precise control over quantum states. Xiong et al. emphasized the significance of room-temperature plexcitonic strong coupling and associated ultrafast quantum dynamics, essential for efficient quantum state manipulation and entanglement [5]. NFTs have successfully supported both bipartite and tripartite entanglement under ambient conditions, paving the way for scalable quantum information processing systems [6,7]. Quantum sensing has also benefited from nanoplasmonic platforms, where quantum plasmonic immunoassays have demonstrated extraordinary sensitivity and specificity at the single-molecule detection limit, highlighting their potential in biomedical and diagnostic applications [8]. Continued refinement of these technologies addresses existing challenges, such as fidelity enhancement and improved coherence control.

Addressing the pivotal challenge of coherence preservation, quantum nanoplasmonic coherent perfect absorption (qnCPA) introduces an innovative solution [9]. qnCPA exploits directional energy transfer from plasmonic waveguides to selectively excite and maintain polaritonic states, effectively mitigating dissipation effects. Jalali-Mola et al. highlighted the potential of slow-wave nanoplasmonic waveguides to mediate coherent

interactions among distant quantum emitters, an essential step toward robust quantum networks and chip-scale quantum technologies [10].

These developments position nanoplasmonic quantum photonics as a key driver in revolutionizing practical quantum device implementation, significantly enhancing scalability, coherence, and ambient operational viability for next-generation quantum technologies

Acknowledgement: Support by Research Ireland (formerly Scieince Foundation Ireland) via Grants no. 18/RP/6236 and 22/QERA/3821 is gratefully acknowledged.

References

1. Mabuchi, H. and A. C. Doherty, "Cavity Quantum Electrodynamics: Coherence in Context," Science, Vol. 298, No. 5597, 1372–1377, 2002.
2. Walls, D. F. and G. J. Milburn, Quantum Optics, Springer-Verlag, Berlin, 2008.
3. Chikkaraddy, R., B. de Nijs, F. Benz, S. J. Barrow, O. A. Scherman, E. Rosta, A. Demetriadou, P. Fox, O. Hess and J. J. Baumberg, "Single-Molecule Strong Coupling at Room Temperature in Plasmonic Nanocavities," Nature, Vol. 535, No. 7610, 127–130, 2016.
4. Groß, H., J. M. Hamm, T. Tufarelli, O. Hess and B. Hecht, "Near-Field Strong Coupling of Single Quantum Dots," Sci. Adv., Vol. 4, No. 3, eaar4906, 2018.
5. Xiong, X., N. Kongsuwan, Y. Lai, C. E. Png, L. Wu and O. Hess, "Room-Temperature Plexcitonic Strong Coupling: Ultrafast Dynamics for Quantum Applications," Appl. Phys. Lett., Vol. 118, No. 13, 130501, 2021.
6. Bello, F., N. Kongsuwan, J. F. Donegan and O. Hess, "Controlled Single-Photon Emission and Multipartite Entanglement Using Plasmonic Nanocavities," Nano Lett., Vol. 20, No. 8, 5830–5836, 2020.
7. Bello, F., N. Kongsuwan and O. Hess, "Dynamic Modulation of Three-Qubit Entanglement Using Plasmonic Nanostructures," Nano Lett., Vol. 22, No. 7, 2801–2808, 2022.
8. Kongsuwan, N., X. Xiong, P. Bai, J.-B. You, C. E. Png, L. Wu and O. Hess, "Quantum Plasmonic Immunoassay Sensing," Nano Lett., Vol. 19, 5853–5861, 2019.
9. Lai, Y., D. D. A. Clarke, P. Grimm, A. Devi, D. Wigger, T. Helbig, T. Hofmann, R. Thomale, J.-S. Huang, B. Hecht and O. Hess, "Quantum Nanoplasmonic Coherent Perfect Absorption," Nat. Commun., Vol. 15, 6324, 2024.
10. Jalali-Mola, Z., S. Asgarnezhad-Zorgabad and O. Hess, "Collective Quantum Dynamics with Distant Quantum Emitters in Slow-Wave Nanoplasmonic Waveguides," APL Quantum, Vol. 1, No. 4, 046104, 2024.

Robust Edge States in Topological Lattices for Quantum information Transfer

J. Zurita[1], C.E. Creffield[2]and G. Platero[1*]

[1] *Materials Science Institute of Madrid (CSIC) , Spain*
[2]*Department of Physics of Materials, Complutense University of Madrid, Spain* [2]
[*]gplatero@icmm.csic.es

Abstract: This talk will deal with the transfer of quantum information using protected topological edge states. I will discuss the long-range transfer in a dimer chain, a 1D topological insulator, and in the Creutz-Ladder lattice and the role of topological domain walls to speed up the particle transfer.

META 2025, MALAGA - SPAIN, JULY 22 – 25, 2025

Routes for integrated photonics and meta-optics in quantum technologies and precision experiments

S. Kroker[1,2,3*], M. Gaedtke[1,2], S. Häfner[1,2], L. Shelling Neto[1,2], S. Sauer[1,2], M. Schittenhelm[1,2], A. Sorokina[1,2], and N. Wagner[1,2]

[1]TU Braunschweig, Institute for Semiconductor Technology, Hans-Sommer-Str. 66, 38106 Braunschweig, Germany

[2]TU Braunschweig, LENA Laboratory for Emerging Nanometrology, Langer Kamp 6 a/b, 38106 Braunschweig, Germany

[3]Physikalisch-Technische Bundesanstalt, Bundesallee 100, 38116 Braunschweig, Germany

[*]corresponding author: s.kroker@tu-braunschweig.de

Abstract:

Integrated photonics and meta-optics enable compact, precise light control, advancing optical metrology in applications like atomic clocks and gravitational wave detectors. This work explores nanophotonic devices for precision experiments and atom chips, focusing on light-matter interactions and the impact of material properties on performance and precision.

Metastructures That Compute and Optimize

N. Engheta

University of Pennsylvania, USA
engheta@seas.upenn.edu

Abstract: I will present some of the most recent results of our ongoing research projects on nonlocal metasurfaces and metastructures that perform ultrafast analog computation, such as vector-matrix multiplication, matrix inversion, constrained optimization, equation solving, etc. Time permitting, I will also discuss how incoherent light can be used for certain analog computations.

What I Wish I Had Known, as I Searched for the First 3d Photonic Bandgap

Eli Yablonovitch

Electrical Engineering and Computer Sciences Dept.,
UCLA/University of California, Berkeley, USA
eliy@eecs.berkeley.edu

Abstract: The first 3-dimensional Photonic Bandgap was found by Edison-ian search, trial-and-error, guided by physical intuition. The 4-year search was beset by pseudo-gaps, and required deep physical insights to find the right geometry (diamond unit cell in a face-centered-cubic lattice). Nonetheless, there do exist mathematical techniques for 3d geometry optimization that could have led to the right structure more quickly.

Summary:

The optimization problem is exacerbated by the reality that any geometrical design could have millions of design parameters that define a desirable shape. With a particular goal in mind, the adjustment of any one design parameter, requires a revision of all the other parameters, making it hard, or impossible to converge on a good design. Essentially this is a problem in multi-variable calculus: How to co-optimize the millions of parameters that are implicit in any geometrical shape? It might be called “Shape Calculus”.

Fortunately there are elegant mathematical methods that have emerged that permit the co-optimization of millions of variables, but requiring only two solutions of Maxwell’s Equations [1]. The mathematical approach is sometimes called the “Adjoint Method”, and it is a merger the chain rule of calculus, with linear algebra [2].

The earliest application of the adjoint method was for military logistics in the 1950’s, and called Operations Research. Indeed the mathematics has been rediscovered numerous times in the past 70 years, within various fields, wherever some optimization over many variables is needed. This has many names. For example, in neural networks this is called “Back-Propagation”, in photolithography it’s called Inverse Lithography Technology, (ILT), but it is also used in Control Theory, mechanical design, etc.

One of the first electromagnetic applications of the “Adjoint Method” was toward the design of lithographic masks for the photographic process by which electronic chips are manufactured. These masks consist of thin-film Chromium on glass, intricately patterned, to photographically project out the sub-wavelength shapes of transistors, wires, and other components on an integrated circuit. These metal film masks, so heavily used in electronics manufacturing, can be regarded as the original “meta-surface” [3].

Sub-wavelength transistor images were desired, but it was not at all clear what the mask pattern should be, that would produce those desired sub-wavelength images. The first company founded to employ the “Adjoint Method” for photo-lithography was Luminescent Inc., (2002). Luminescent introduced the slogan ILT “Inverse Lithography Technology” to be understood as a sub-category of Inverse Electromagnetic Design. Today, almost all memory chips and micro-processors use thin-film chromium masks and ILT software in their design and manufacture, meta-surfaces indeed [4].

Whether it's a meta-lens or any other type of electromagnetic function, there is no need to slavishly follow a periodicity constraint. Mathematical methods have been developed, to efficiently optimize any type of electromagnetic function. I will provide some examples: "Silicon Photonics" couplers, optical antennas, solar cell surface textures, etc

References

1. Burger, M., Osher, S., Yablonovitch, E., "Inverse Problem Techniques for the Design of Photonic Crystals," IEICE Transactions on Electronics, vol E87-C, no. 3, pp. 258-265, March 2004.
2. Kao C.Y., Osher S., Yablonovitch E., "Maximizing band gaps in two-dimensional photonic crystals by using level set methods," Applied Physics B-Lasers & Optics, vol. B81, no.2-3, July 2005, pp.235-44.
3. Daniel S. Abrams, Linyong Pang, "Fast inverse lithography technology," Proc. SPIE 6154, Optical Microlithography XIX, 61541J (15 March 2006); doi: 10.1117/12.658876
4. T. Cecil, D.P, Peng, D. Abrams, S. Osher, & E. Yablonovitch, "Advances in Inverse Lithography" ACS Photonics, (2022). https://doi.org10.1021/acsphotonics.2c01026

Keynote presentations

Modulating Optical Properties in Time Using Plasmonic Resonances

John Pendry[1]

[1]Imperial College London, UK
*corresponding author: j.pendry@imperial.ac.uk

Abstract: Plasmonic effects in Indium Tin Oxide enable rapid switching of transparency which can be exploited to modulate THz radiation on a fs time scale.

Short Abstract: Plasmonic effects in Indium Tin Oxide enable rapid switching of transparency which can be exploited to modulate THz radiation on a fs time scale.

With the growing interest in extreme time modulation of material properties attention has turned to materials such as Indium Tin Oxide which is commonly doped to give a Fermi energy of around 1eV and plasma frequency, ω_p, of similar magnitude. Thin films of ITO are transparent to visible light with frequency well above ω_p. It is well known that heating the electrons with a fast laser pump pulse lowers ω_p and hence switches between opaque and transparent for near IR radiation [1]. Along with extremely rapid switching times of the order of the few cycles, contrast levels of the order of 50% are commonly observed.

Basics of the mechanism are understood: rapid heating of electrons followed by slow equilibration with lattice phonons. Controversy over details remains, but recent experiments shed light on the time scales of the several processes taking place. Experiments in Sapienza's group at Imperial College revealed the existence of extremely fast processes by generating Young's fringes in frequency [2]. It was evident from these experiments that switching happened faster than any of the known time scales: 100fs pulse width for the pump and probe, 300fs electron-electron scattering time. The origin of the fast event will remain a mystery until the excitation process can be probed with single cycle pulse widths.

My talk will speculate about possible mechanisms at play and suggest experiments that will help further our understanding. Time permitting I shall discuss the theoretical challenges awaiting for the new ultrafast material experiments.

References

1. Alam, M. Z., De Leon, I. & Boyd, R. W., 2016, *Science* 352, 795–797.
2. Tirole, R., Vezzoli, S., Galiffi, E., Robertson, I., Maurice, D., Tilmann, B., Maier, S.A., Pendry, J.B., Sapienza, R., 2023, *Nature Physics*, 19, 999-1002.

Quantum Aspects of Light Propagation in Time-Varying Media

John Pendry[1]

[1]Imperial College London, UK
[*]corresponding author: j.pendry@imperial.ac.uk

Abstract: Recent experiments demonstrate ultra-fast modulation of refractive indices opening up the field of space-time modulation [1-3]. Breaking time invariance presents new challenges to theory with the removal of conservation of energy/frequency. New conservation laws are emerging which deepen our understanding of these systems. A recent review can be found here [4].

Typically space -time structures involve no physical movement of material meaning that movement at any speed can happen without violating causality. This removes many theoretical obstacles to theoretical treatment. Many new phenomena are being found such as novel amplification mechanisms that work by squeezing lines of force together. Some systems can be regarded as reversible heat engines capable of heating or cooling radiation incident upon them.

Quantum aspects of 4D systems are rich field of study particularly for systems in uniform motion which obey PT symmetry and therefore have some elements in common with traditional QED but with the difference that frequency is not conserved. In particular transitions between positive and negative frequencies can be induced and are associated with spontaneous emission of radiation as photon pairs. By analogy between a refractive index and gravitational metrics, systems have been found which model the Schwarzschild singularity and emit Hawking-like radiation. Other systems that make travelling-wave modulations of a medium's impedance but leave the speed of light a constant, are analogous to the interaction of gravitational waves with electromagnetic fields.

Acknowledgements, if any, including all funding information, should be gathered into a brief statement at the end.

References

1. Large optical nonlinearity of indium tin oxide in its epsilon-near-zero region. Alam, M. Z., De Leon, I. & Boyd, R. W. Science 352, 795–797 (2016).
2. Near-zero-index materials for photonics. Kinsey, N., DeVault, C., Boltasseva, A. & Shalaev, V. M., Nat. Rev. Mater. 4, 742–760 (2019).
3. Double-slit time diffraction at optical frequencies R Tirole, S Vezzoli, E Galiffi, I Robertson, D Maurice, B Tilmann, SA Maier, John B. Pendry, Riccardo Sapienza, Nature Physics, 19, 999-1002 (2023).
4. Photonics of Time-Varying Media, E Galiffi, et al., Advanced Photonics 4, 014002 (2022).

Chemically Functionalized Two-Dimensional Materials for Quantum Photonic Science and Technology

Mark C. Hersam[1*]

[1]Northwestern University, Evanston, IL 60208, USA
[*]Corresponding author: m-hersam@northwestern.edu

Abstract: Chemical functionalization allows tailoring of the properties of 2D materials and the degree of coupling across heterointerfaces. In this talk, the prospects of 2D materials for quantum photonic science and technology will be discussed with a focus on how chemical functionalization can enhance quantum emission in 2D transition metal dichalcogenides.

Layered two-dimensional (2D) materials interact primarily via van der Waals (vdW) bonding, which has created opportunities for heterostructures that are not constrained by epitaxial lattice matching [1]. However, since any passivated surface interacts with another via non-covalent forces, vdW heterostructures are not limited to 2D materials alone. In particular, 2D materials can be integrated with a diverse range of other materials, including those of different dimensionality, to form mixed-dimensional vdW heterostructures [2]. Furthermore, chemical functionalization allows tailoring of the properties of 2D materials and the degree of coupling across heterointerfaces [3]. In this talk, the prospects of mixed-dimensional heterostructures for quantum photonic science and technology will be discussed with a focus on how chemical functionalization can manipulate and enhance quantum emission in 2D transition metal dichalcogenides [4]. In addition to technological implications, this talk will explore fundamental issues including band alignment, doping, trap states, and charge/energy transfer across heterointerfaces [5].

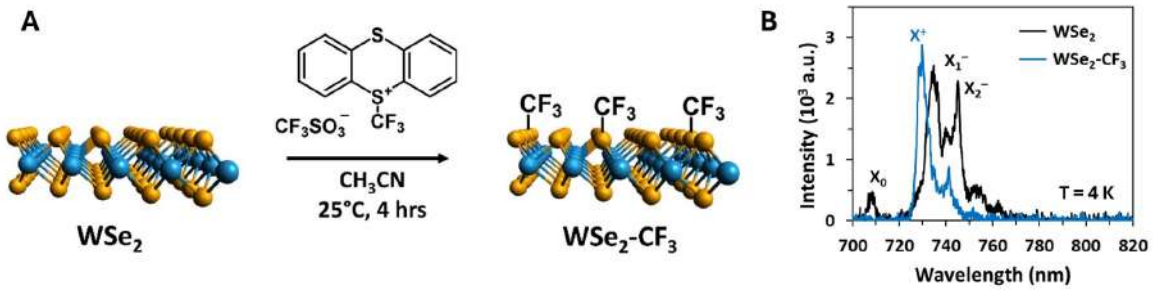


Figure 1. (A) Covalent trifluoromethylation of monolayer WSe_2 is achieved via reaction with trifluoromethyl thianthrenium triflate. (B) The resulting p-type doping enhances low temperature photoluminescence from the positively charged trion at the expense of neutral and negatively charged trions. Figure adapted from Ref. 5.

References

1. S. Hadke, *et al.*, *Chemical Reviews*, **125**, 835 (2025).
2. M. I. B. Utama, *et al.*, *MRS Bulletin*, **48**, 905 (2023).
3. J. T. Gish, *et al.*, *Nature Electronics*, **7**, 336 (2024).
4. M. I. B. Utama, *et al.*, *Nature Communications*, **14**, 2193 (2023).
5. B. Kerwin, *et al., Angew. Chem. Int. Ed.*, **63**, e202403494 (2024).

Empowering chiral metamaterials with gain materials

I. Katsantonis[1,2], A. Tasolamprou[1,3], M. Kafesaki[1,2*,]

[1]Institute of Electronic Structure and Laser, Foundation for Research and Technology Hellas (FORTH), Heraklion, Crete, Greece
[2]Dept. of Materials Science and Engineering, Univ. of Crete, Greece
[3]Dept. of Physics, National and Kapodistrian University of Athens, Athens, Greece
[*]corresponding author: kafesaki@iesl.forth.gr

Abstract: We will review our recent works on chiral metamaterials involving gain materials and on chiral metamaterials combining gain and loss. Special attention will be given to parity-time symmetric chiral metamaterials and to chiral metamaterials for circularly polarized laser emission.

Chiral metamaterials, i.e. metamaterials lacking any mirror symmetry plane, constitute one of the most fascinating metamaterial categories, as they enable interesting polarization-related effects, allowing different polarization control properties and capabilities. Such capabilities include, among others, giant polarization rotation and giant circular dichroism, enabled by ultra-subwavelength structures (see, e.g,. Fig. 1).

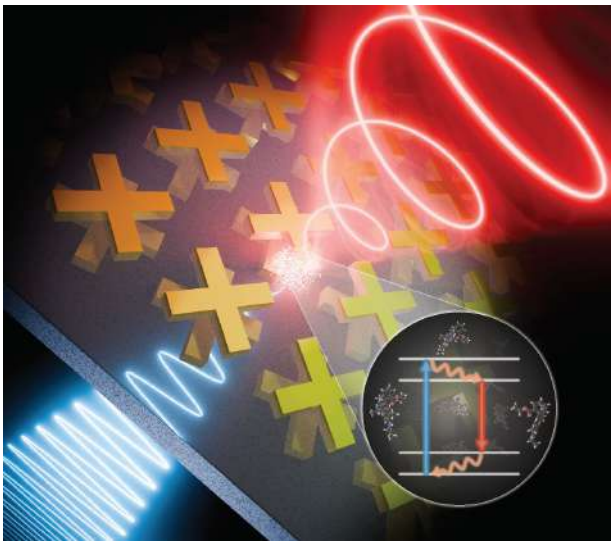


Fig. 1. Artistic demonstration of circularly polarized wave emission by an ultrathin plana chiral structure embedding a gain material. The basic structure-building-block is a pair of mutually twisted metallic crosses. The structure can give almost pure circularly polarized laser emission if excited by a pump wave of linear polarization. The laser emission can be switched from left- to right-handed by tuning the pump wave polarization. Picture reprinted from [1].

Adding gain media into chiral metamaterials and exploiting the chiral resonant electromagnetic fields in such media, one can not only greatly enhance the chiral response, but also enable novel and important for applications wave phenomena. Among such phenomena of particular interest are the ones enabled by Parity-Time (PT) symmetric chiral metamaterials, i.e. chiral metamaterials that combine gain and loss in a balanced way as to respect combined parity and time reversal symmetry. As we will show in this talk such media enable unidirectional perfect reflection, highly asymmetric wave absorption, simultaneous coherent-prefect absorption (CPA) and lasing, CPA-lasing of elliptically and circularly polarized waves, multiple and highly controllable exceptional points and PT-related phases, and dynamically controllable optical rotation and circular dichroism [2-4]. Some of those phenomena remain to a large degree intact if one departs from the strict PT-symmetry as to enable practically realizable metamaterial configurations.

Another category of important chiral-gain phenomena are related with electromagnetic wave emission and lasing. As we will show in the talk, properly designed chiral metamaterials can give not only circularly polarized emission lasing but also lasing of dynamically controllable polarization, able to be switched between left- and right-handed [1].

All these results highlight the rich response of the chiral-gain media and their importance in current and future polarization-related phenomena and applications.

We acknowledge funding by the EU-MSCA project CHARTIS, Project No. 101007896.

References

1. I. Katsantonis, A. Tasolamprou, E.N. Economou, Th. Koschny, and M. Kafesaki, "Ultrathin, dynamically controllable circularly polarized emission laser enabled by resonant chiral metasurfaces", ACS Photon., Vol, 12, 71, 2024.
2. S. Droulias, I. Katsantonis, M. Kafesaki, C. M. Soukoulis and E. N. Economou, "Chiral metamaterials with PT symmetry and beyond", Phys. Rev. Lett., Vol. 122, 213201, 2019.
3. I. Katsantonis, S. Droulias, C. M. Soukoulis, E. N. Economou, M. Kafesaki, "Scattering properties of PT-symmetric chiral metamaterials", Photonics, Vol. 7, 43, 2020.
4. I. Katsantonis, S. Droulias, C. M. Soukoulis, E. N. Economou, M. Kafesaki, "PT-symmetric chiral metamaterials: Asymmetric effects and PT-phase control", Phys. Rev. B, Vol. 101, 214109, 2020.

Photonic Metamaterial Time Crystals and Timetronics

Nikolay I. Zheludev[1,2]

[1)]Optoelectronics Research Center, University of Southampton, UK
[2)]Institute for Advanced Study, Texas A&M University, USA
zheludev@soton.ac.uk

Abstract: We discuss recent developments in understanding functionalities and developing applications of time crystals - a new state of matter, a many-body interacting system that exhibits a spontaneous mobilization transition to the robust state of oscillation, breaking time translation symmetry under an infinitely small change of the external driving force.

Light-driven nonreciprocal forces in an array of nano-opto-mechanical oscillators (e.g. metamaterial) can underpin the functionality of Time Crystal, a many-body interacting system that exhibits a spontaneous mobilization transition to the robust state of oscillation under an infinitely small change of the external driving force. Such time crystals are a form of Active Matter with life-mimicking dynamics accompanied by the breaking of time translation symmetry, ergodicity, and local entropy decrease. This is of interest to optical "timetronics" – a data processing and communications technology relying on the unique functionalities of time crystals.

Computational Models of Light Management in Photovoltaics and LEDs

V. E. Ferry[1*]

[1]Department of Chemical Engineering and Materials Science, University of Minnesota-Twin Cities, Minneapolis MN 55455 USA

[*]corresponding author: veferry@umn.edu

Abstract: This talk will discuss the computational models for light management strategies in photovoltaics, including systems that integrate luminescent solar concentrators in greenhouses and reduce the temperature of outdoor panels.

This talk will discuss a few case studies where computational models provide insight into energy systems, and determine the design rules that guide experimental work. One example is in agrivoltaics, the dual use of land for agricultural production and electricity generation. One strategy is to create a greenhouse with a luminescent solar concentrator (LSC) roof and sidewalls. The LSC simultaneously generates electricity on site and filters transmitted sunlight, and it is possible to tune the properties of the LSC (light emitting material, concentration, and architecture) to promote both electricity generation and crop yield. The system is complex, since integrating the LSC into the greenhouse also changes the heating and cooling needs. By developing models that account for these factors, we can identify the optimal characteristics of the light-emitting materials, which in turn informs experimental development.

A second example is the design of structures that increase energy yield of a photovoltaic panel installed outdoors through a combination of anti-reflection of above-bandgap radiation and below-bandgap reflection to mitigate performance losses due to heating. Our computational models first determine the characteristics that are necessary in these dual-purpose photonic structures, then find the materials and structures to realize those refined performance goals. These models are validated with outdoor experimental measurements.

References

1. Loh, K. Q., K. Harbick, N. J. Eylands, U. R. Kortshagen, and V. E. Ferry, “Design guidelines for luminescent solar concentrator greenhouses in the United States,” Adv. Sustain. Syst.., Vol. 9, No. 2, 2400749, 2024.
2. Slauch, I. M., M. G. Deceglie, T. J Silverman, and V. E. Ferry, “Optical approaches for passive thermal management in c-Si photovoltaic modules,” *Cell Reports Phys. Sci.,* Vol 2, 100430, 2021.

Rethinking Linking – Topology in Magnetism, and Plasmonics

M. Azhar[1], R. Knapman[1], P. Gessler[1], A. Neuhaus[1], P. Dreher[1], F. Meyer zu Heringdorf[1] and K. Everschor-Sitte[1*]

[1]Faculty of Physics and CENIDE, University of Duisburg-Essen, 47057 Duisburg, Germany
[*]corresponding author: karin.everschor-sitte@uni-due.de

Abstract: Topology in physics explores robust, fault-tolerant states of matter aiming at practical applications. Similar topological structures arise in magnetism, optics, and plasmonics despite differing physics. A challenge is understanding them when traditional mathematical topological frameworks are not necessarily applicable. Linking and geometry offer intuitive ways to describe these complex textures.

The field of topology and topological excitations in physics is spurred by the key idea of robust and fault-tolerant states of matter for technological applications. In recent years, many topological field configurations observed and predicted in magnetism[1] have been emulated in optics[2] and plasmonics[3], despite the fundamentally different underlying physics. While magnetic systems host topological field configurations as (meta-)stable states, plasmonic textures require an out-of-equilibrium system to sustain the collective dynamical redistribution of charge density in a solid. Unlike the typically non-volatile, vector fields of constant amplitude studied in magnetism, topological electromagnetic excitations are more complex and highly tunable. Their increased complexity arises from two key aspects: (i) both electric and magnetic fields – or their combinations – can form topologically non-trivial configurations, and (ii) these vector fields may have time-varying or even vanishing amplitudes. The high degree of tunability stems from the ability to tailor geometry and external drives to generate specific topological electromagnetic excitations. Thus, rather than relying on intricate material engineering to shape energy landscapes for stabilizing magnetic topological states, plasmonics requires engineering of excitation geometries and drive mechanisms.

In terms of topological characterization, the fields share similar challenges. Homotopy theory comprises topological indices, such as the Skyrmion winding number in two dimensions and the Hopf index in three dimensions – which can be expressed as integral expressions to be calculated for vector fields. However, these indices rely on certain prerequisites that real-world textures may violate. One of these prerequisites is that the field configuration is uniform at the boundary (or at infinity). This, however, does not apply to three-dimensional structures that are effectively "two plus one" dimensional – those consisting of two-dimensional textures extending periodically along a third direction. Notable examples include (twisted) Skyrmion tubes, screw dislocations, and space-time Hopfions[4].

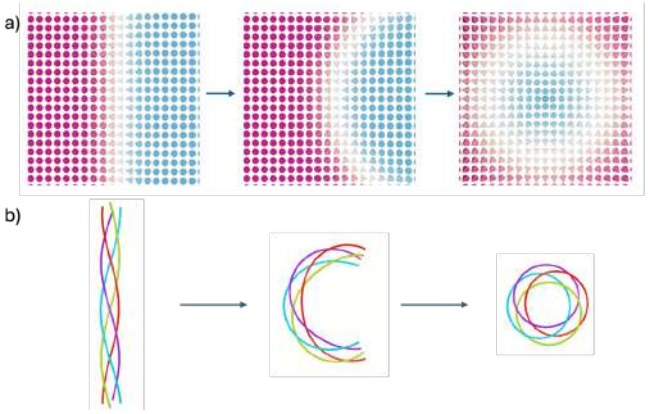


Figure 1: Connection of linking and topology. a) connecting the ends of a domain wall to a Skyrmion; b) linking the ends of a Skyrmion tube to obtain a Hopfion.

Rather than computing the integral expression of the topological index for field configurations, the concept of linking provides deeper insight into their nature, as illustrated in Figure 1. For instance, Skyrmions can be

regarded as extended domain walls whose ends are connected to each other, while Hopfions can be interpreted as linked or braided Skyrmion tubes.

By employing a discrete geometric definition of the Hopf index, a general framework for the description of three-dimensional textures beyond the constraints of homotopy theory is established[5]. This approach overcomes the pitfalls and limitations of using the conventional Whitehead integral formula to compute the Hopf index in finite volumes[6]. Furthermore, it naturally provides a foundation for space-time Hopfions and explains the emergence of topological textures with arbitrary Hopf indices. In particular, it enables the interpretation of non-integer Hopf values as states of "mixed topology," capable of continuously transitioning between multiple topological sectors. This is exemplified in Figure 2 with the "Twiston", a peculiar topological texture which possesses a fractional Hopf index and can evolve into either a Hopfion (Hopf index 1) or a Skyrmion tube (Hopf index 0), both of which have integer Hopf indices.

This framework not only enhances our understanding of magnetic topological field configurations but also reveals their fundamental connections across diverse physical systems.

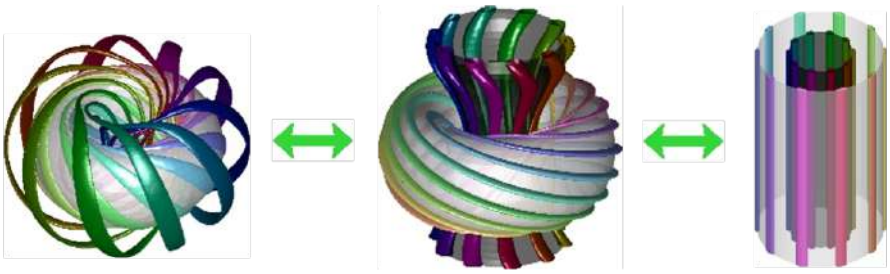


Figure 2: A Twiston with a fractional Hopf index (middle panel) can transform into a Hopfion with Hopf index 1 (left) or Skyrmion tube which has a Hopf index of 0 (right).

We acknowledge funding from the Deutsche Forschungsgemeinschaft (DFG, German Research Foundation) Project No. 403233384 (SPP Skyrmionics), Project No. 278162697-SFB 1242 (project B10 and B06) and Project No. 505561633 which is part of the TOROID project co-funded by the French National Research Agency (ANR) under Contract No. ANR-22-CE92-0032.

References

1. Everschor-Sitte, K., Masell, J., Reeve, R. M., and Kläui, M. "Perspective: Magnetic skyrmions—Overview of recent progress in an active research field," J. Appl. Phys. 124, 240901 (2018).
2. Shen, Y., Zhang, Q., Shi, P., Du, L., Yuan, X., and Zayats, A. V. "Optical skyrmions and other topological quasiparticles of light," Nat. Photon. 18, 15–25 (2024).
3. Davis T. J, Janoschka, D. Dreher, P., Frank, B., Meyer zu Heringdorf, F., and Giessen, H. "Ultrafast vector imaging of plasmonic skyrmion dynamics with deep subwavelength resolution," Science 368, eaba6415 (2020).
4. Knapman, R., Tausendpfund, T., Díaz S. and Everschor-Sitte, K. "Spacetime magnetic hopfions: from internal excitations and braiding of skyrmions," Commun. Phys. 7, 151 (2024).
5. Azhar, M., Shaju, S. C., Knapman, R., Pignedoli, A. and Everschor-Sitte, K., "3D Magnetic Textures with Mixed Topology: Unlocking the Tunable Hopf Index," arXiv:2411.06929.
6. Knapman, R., Azhar, M., Pignedoli, A., Gallard, L., Hertel, R., Leliaert, J. and Everschor-Sitte, K. "Numerical Calculation of the Hopf Index for 3D Magnetic Textures," arXiv:2410.22058.

Space-Time Metamaterials

A. Alù[1,2]

[1]Photonics Initiative, Advanced Science Research Center, City University of New York, New York, NY 10031, USA
[2] Physics Program, Graduate Center, City University of New York, New York, NY 10016, USA
[*]corresponding author: aalu@gc.cuny.edu

Abstract: In this talk, I will discuss my group's recent work in the area of space-time metamaterials, with an emphasis on the use of abrupt time switching and spatio-temporal modulation patterns for efficient frequency translation and energy manipulation.

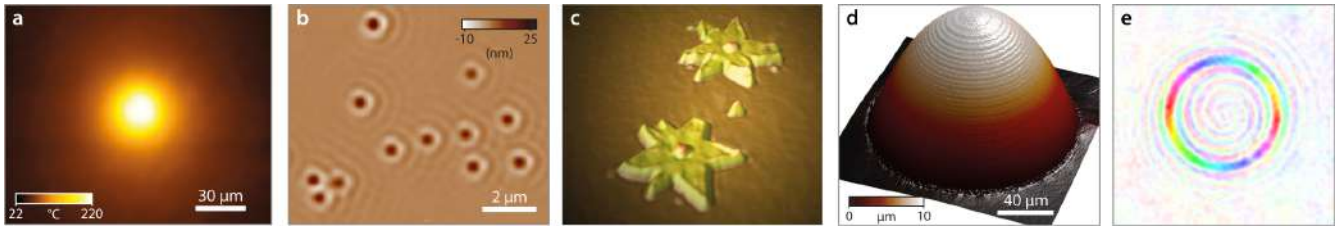
Wavefront microscopy for nanophotonics

Guillaume Baffou

[1]Institut Fresnel, CNRS, Aix Marseille University, Centrale Med, Marseille, France
[*]corresponding author: guillaume.baffou@fresnel.fr

Abstract: Cross-grating wavefront microscopy (CGM) consists of the association of a 4-wave diffraction grating and a camera separated by millimeter distance. We show how CGM can be used to measure the optical properties of nanoparticles, 2D material a metasurfaces, such as the complex optical polarizability, conductivity, refractive indices, and cross-sections.

Cross-grating wavefront microscopy (CGM) is a high-resolution, high-sensitivity wavefront imaging technique [1,2]. It consists of the association of a 4-wave diffraction grating and a camera separated by millimeter distance. Mostly used in biology this last decade, it is now becoming popular in nanophotonics applications as well. This contribution is aimed to explain (i) how we turned CGM into a thermal microscopy technique to map the temperature of gold nanoparticles under illumination [3], enabling applications in physics [4], chemistry [5] and biology [6] at the nano/microscale; (ii) how CGM can map all the optical properties of 2D materials and nanoparticle arrays [7] (namely the complex optical conductivity, complex refractive index, transmittance, reflectance, absorbance) from a single image acquisition; (iii) how CGM can retrieve the complex optical polarizability of nanoparticles, along with the extinction, scattering and absorption cross sections from a single image acquisition [8,9], and finally (iv) how CGM can fully characterize metasurfaces [10].



CGM images. (a) Temperature distribution around laser-heated gold nanoparticles. (b) Wavefront distortion image of 100-nm gold nanoparticles used to compute their optical cross sections. (c) Wavefront distortion imagex of MoS2 structures, used to map their complex refractive index. (d) Wavefront distortion created by a metalens. (e) Polarization resolved image of a plasmonic corral.

References

1. G. Baffou. “Wavefront microscopy using quadriwave lateral shearing interferometry: from bioimaging to nanophotonics”, ACS Photonics 10, 322-339, 2023
2. G Baffou. “Quantitative phase microscopy using quadriwave lateral shearing interferometry (QLSI): principle, terminology, algorithm and grating shadow description”. J. Phys. D: Appl. Phys., (54): 294002, 2021.
3. G. Baffou, P. Bon, J. Savatier, J. Polleux, M. Zhu, M. Merlin, H. Rigneault and S. Monneret. “Thermal Imaging of Nanostructures by Quantitative Optical Phase Analysis”. ACS Nano, (6): 2452-2458, 2012.
4. G. Baffou, P. Berto, E. Bermúdez Ureña, R. Quidant, S. Monneret, J. Polleux, H. Rigneault. “Photo-induced heating of

nanoparticle arrays". ACS Nano (7): 6478-6488, 2013.

5. H. Robert, F. Kundrat, E. Bermudez-Urena, H. Rigneault, S. Monneret, R. Quidant, J. Polleux, G. Baffou. "Light-Assisted Solvothermal Chemistry Using Plasmonic Nanoparticles". ACS Omega (1): 2-8, 2016.
6. H. Robert, J., Savatier, S. Vial, J., Verghese, B. Wattelier, H. Rigneault, S. Monneret, S., J. Polleux, G. Baffou. "Photothermal control of heat-shock protein expression at the single cell level". Small (14): 1801910, 2018.
7. S. Khadir, P. Bon, D. Vignaud, E. Galopin, N. McEvoy, D. McCloskey, S. Monneret, G. Baffou. "Optical imaging and characterization of graphene and other 2D materials using quantitative phase microscopy". ACS Photonics (4): 3130-3139, 2017.
8. S. Khadir, P. Chaumet, G. Baffou, A. Sentenac. "Quantitative model of the image of a radiating dipole through a microscope". J. Opt. Soc. Am. A 36, 478-484, 2019.
9. S. Khadir, D. Andrén, P. Chaumet, S. Monneret, N. Bonod, M. Käll. A. Sentenac, G. Baffou. "Full optical characterization of single nanoparticles using quantitative phase imaging". Optica (7): 243-248, 2020.
10. [10] S. Khadir, D. Andrén, R. Verre, Q. Song, S. Monneret, P. Genevet, M. Käll, G. Baffou. "Metasurface optical characterization using quadriwave lateral shearing interferometry". ACS Photonics (8): 603-613, 2021.

Vortices, Skyrmions, Möbius Strips: From Nanooptics to Ocean Waves

Konstantin Y. Bliokh[1,2,3*]

[1]Donostia International Physics Center (DIPC), Donostia-San Sebastián 20018, Spain
[2]IKERBASQUE, Basque Foundation for Science, Bilbao 48009, Spain
[3]Centre of Excellence ENSEMBLE3 Sp. z o.o., 01-919 Warsaw, Poland

[*]corresponding author: konstantin.bliokh@dipc.org

Abstract: I will present recent theoretical and experimental results on: (i) subwavelength high-intensity vortices around 'holes' in 2D wave systems: from polaritons to ocean waves, (ii) Bessel-type vortices, displacement-field skyrmions, and polarization Möbius strips in sound and water waves, and (iii) manipulation of floating particles using topologically structured water waves.

50 years ago, Nye and Berry published a seminal work [1] introducing phase singularities, also known as wave vortices. This initiated a surge of interest in topological structures in linear waves [2]. Since then, a variety of topological wave structures has been discovered, such as polarization singularities [3], polarization Möbius strips [4,5], and skyrmions [6]. Although topological wave forms were mostly studied for optical fields, these can equally appear in any linear waves, from water waves to quantum mater waves.

Here, I will provide an overview of recent theoretical and experimental works describing new type of wave vortices which appear around subwavelength 'holes' in 2D planes [7], polarization singularities and Möbius strips in sound and water waves [8,9], wave vortices and skyrmions in water waves [10–12]. Furthermore, I will show that structured water waves have the dynamical momentum and angular-momentum properties entirely similar to those in optical and acoustic fields [10], which enables trapping and manipulation of floating particles [13], similar to optical and acoustic tweezers [14].

I acknowledge support from support from Marie Skłodowska-Curie COFUND Programme of the European Commission (project HORIZON-MSCA-2022-COFUND-101126600-SmartBRAIN3), ENSEMBLE3 Project (MAB/2020/14) which is carried out within the International Research Agendas Programme (IRAP) of the Foundation for Polish Science co-financed by the European Union under the European Regional Development Fund and Teaming Horizon 2020 programme (GA. No. 857543) of the European Commission and the project of the Minister of Science and Higher Education "Support for the activities of Centers of Excellence established in Poland under the Horizon 2020 program" (contract MEiN/2023/DIR/3797).

References

1. Nye, J. F. and M. V. Berry, "Dislocations in wave trains," Proc. R. Soc. Lond. A, Vol. 336, 165–190, 1974.
2. Dennis, M. R. and K. Y. Bliokh, "Wave vortices 50 years on," Newton, Vol. 1, 100005, 2025.
3. Nye, J. F. and J. V. Hajnal, "The wave structure of monochromatic electromagnetic radiation," Proc. R. Soc. Lond. A, Vol. 409, 21–36, 1987.

4. Freund, I., “Optical Möbius strips in three-dimensional ellipse fields: I. Lines of circular polarization,” Opt. Commun., Vol. 283, 1–15, 2010.
5. Bauer, T., P. Banzer, E. Karimi, S. Orlov, A. Rubano, L. Marrucci, E. Santamato, R. W. Boyd and G. Leuchs, “Observation of optical polarization Möbius strips,” Science, Vol. 347, 964–966, 2015.
6. Tsesses, S., E. Ostrovsky, K. Cohen, B. Gjonaj, N. H. Lindner and G. Bartal, “Optical skyrmion lattice in evanescent electromagnetic fields,” Science, Vol. 361, 993–996, 2018.
7. Domina, K., P. Alonso-González, A. Bylinkin, M. Barra-Burillo, A. I. F. Tresguerres-Mata, F. J. Alfaro-Mozaz, S. Vélez, F. Casanova, L. E. Hueso, R. Hillenbrand, K. Y. Bliokh and A. Y. Nikitin, “High-intensity wave vortices around subwavelength holes: from ocean tides to nanooptics,” arXiv:2501.13860, 2025.
8. Bliokh, K. Y., M. A. Alonso, D. Sugic, M. Perrin, F. Nori and E. Brasselet, “Polarization singularities and Möbius strips in sound and water-surface waves,” Phys. Fluids, Vol. 33, 077122, 2021.
9. Muelas-Hurtado, R. D., K. Volke-Sepúlveda, J. L. Ealo, F. Nori, M. A. Alonso, K. Y. Bliokh and E. Brasselet, “Observation of Polarization Singularities and Topological Textures in Sound Waves,” Phys. Rev. Lett., Vol. 129, 204301, 2022.
10. Bliokh, K. Y., H. Punzmann, H. Xia, F. Nori and M. Shats, “Field theory spin and momentum in water waves,” Sci. Adv., Vol. 8, eabm1295, 2022.
11. Smirnova, D. A., F. Nori and K. Y. Bliokh, “Water-Wave Vortices and Skyrmions,” Phys. Rev. Lett., Vol. 132, 054003, 2024.
12. Wang, B., Z. Che, C. Cheng, C. Tong, L. Shi, Y. Shen, K. Y. Bliokh and J. Zi, “Topological water-wave structures manipulating particles,” Nature, Vol. 638, 394–400, 2025.
13. Toftul, I., S. Golat, F. J. Rodriguez-Fortuno, F. Nori, Y. Kivshar and K. Y. Bliokh, “Radiation forces and torques in optics and acoustics,” arXiv:2410.23670, 2024.

Hybrid plasmonic nanosystems based on weak and strong coupling

M. Chen[1,2], Y. Zhao[1,2], S. Marguet[3], S. Jradi[1,2], A. Issa[1,2], A. L. Baudrion[1,2], J. Plain[1,2], C. Couteau[1,2], C. Dang[4], A. Govorov[5], R. Bachelot*[1,2,4]

[1]Light, Nanomaterials & Nanotechnologies Laboratory, CNRS UMR 7076. University of Technology of Troyes, France
[2]European University of Technology Institute of Nanomaterials and Nanotechnologies (EUTINN), European University of Technology, European Union
[3] Université Paris Saclay, CEA, CNRS, NIMBE, Gif sur Yvette, France
[4] IRL 3288 CINTRA, CNRS-NTU-Thales, Nanyang Technological University, Singapore
[5] Department of Physics and Astronomy, Ohio University, Athens, OH, 45701 USA
*corresponding author: renaud.bachelot@utt.fr

Abstract: Hybrid plasmonic nanosystems based on weak or strong coupling are discussed in terms of controlling the spatial distribution, and associated symmetry, of the active medium in the vicinity of the metallic nanocavities.

Over the past 20 years, hybrid plasmonic light nano-emitters or nano-absorbers, based on weak or strong coupling between metallic nanocavities and quantum nano-emitters/absorbers, have given rise to major research efforts.[1,2]

One of the main current challenges is to control the spatial distribution on the nanometric scale, and the associated symmetry, of the active medium (emitting or absorbing entities) in the vicinity of the metal nanoparticles.[3,4]

We describe the main principles of weak and strong coupling and present examples of achievements demonstrating weak or strong coupling on hybrid nanosystems.

In particular, through selected examples, we show that controlling the spatial distribution of the active medium has opened up new avenues, such as polarization-sensitive photoluminescence[1,3,4], lifetime engineering[5], local spatial symmetry group control[1], controlled donor-acceptor energy transfer[3,6], polarization-driven single-photon switching[4], and chiral nano-emitters (see illustration of this last case in Fig. 1).

Some future challenges will be discussed in more detail.

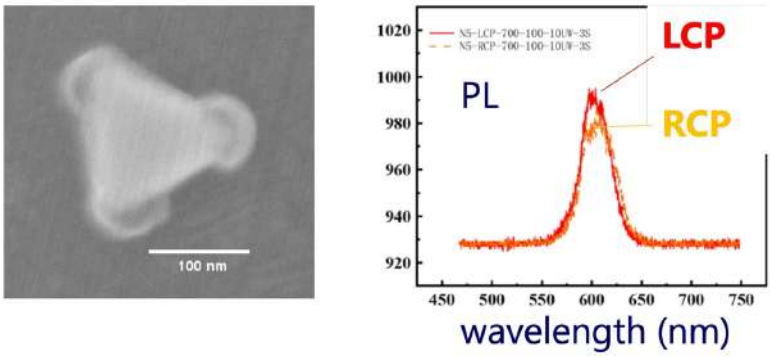


Figure 1. Chiral hybrid nanosource of light. Left: SEM image of a gold nanotriangle surrounded by a nano-emitters-containing medium presenting 2-D chirality. Right: Photoluminescence (PL) from the hybrid nanosystem excited at 405 nm by two kinds of polarization: left-hand circular polarization (LCP) and right-hand circular polarization (RCP). Not published data.

References

1. Chen, M. et al. “Approaches for Positioning the Active Medium in Hybrid Nanoplasmonics. Focus on Plasmon-Assisted Photopolymerization”, ACS Photon., Vol. 11, 3933, 2024.

2. Bitton, O. et al. “Quantum dot plasmonics: from weak to strong coupling”, Nanophotonics, Vol. 8 (4), 559−57, 2019

3. Zhou, X. et al. “Two-Color Single Hybrid Plasmonic Nanoemitters with Real Time Switchable Dominant Emission Wavelength”, Nano Lett., Vol. 15, 7458, 2015.

4. Ge, D. et al. “Hybrid plasmonic nano-emitters with controlled single quantum emitter positioning on the local excitation field”, Nat. Commun., Vol. 11, 3414, 2020.

5. Ge, D. et al. “Advanced hybrid plasmonic nano-emitters using smart photopolymer” Photon. Res. Vol. 10, 1552, 2022.

6. Broussier, A. et al. “Unidirectional frequency conversion of surface plasmon polaritons on metal nanowires”, Micro and Nano Engineering, Vo. 19, 100193, 2023.

Certain intersections of AI and Photonics

Marin Soljacic

Physics Department, MIT, Cambridge, MA 02139, USA
soljacic@mit.edu

Abstract: This talk will explore how photonics can enhance AI hardware and how AI can accelerate photonics research. Topics will include large language models for scientific discovery and robotics for photonics experiments, highlighting key opportunities and challenges at this intersection.

Spectral Frequency Response of Hypersonic Phonons in a Non-Trivial Topological Waveguide

O.R. Ranjbar-Naeini[1], O. Florez[2], M.D. Koijam[3], B. Djafari-Rouhani[3], Y. Pennec[3], T. Makkonen[4], O.M.E. Ylivaara[4], S. Pourjamal[4], J. Ahopelto[4] and C.M. Sotomayor Torres*[1]

[1] INL-International Iberian Nanotechnology Laboratory, 4715-330 Braga, Portugal

[2] Catalan Institute of Nanoscience and Nanotechnology- ICN2, Barcelona, Spain and now Columbia University, US

[3] IEMN (UMR CNRS 8520), University of Lille, Lille 59650, France.

[4] VTT Technical Research Centre of Finland Ltd, P.O. Box 1000, FI-02044 VTT, Espoo, Finland

*Contact: clivia.sotomayor@inl.int

Abstract: The spectral frequency response of a hypersonic phononic wave propagating along a non-trivial topological waveguide is obtained by laser Doppler vibrometry. The guided mode at 2.115 GHz is shown to propagate with minimal loss.

The topological nanoelectromechanical structure in this work is based on the phononic analogue of the valley Hall effect (VHE). The valley pseudospin characterizes degenerate energy extrema in momentum space, with its topological nature arising from the nontrivial Berry curvature localized at k points in the reciprocal space. An interface waveguide 18.84 µm long was designed to exhibit a full phononic gap between 2.058 and 2.198 GHz and to support a topologically protected edge mode. The scanning electron microscopy (SEM) image of the fabricated device and the simulations are depicted in Fig.1(b). The waveguide is fabricated in a membrane nanocrystalline Si (nc-Si) [1] 220 nm thick and characterized using laser Doppler vibrometry. The device features aluminum (Al) interdigitated transducers (IDTs) on an aluminum nitride (AlN) layer deposited on the nc-Si film in order to launch the acoustic excitation focused at the entrance of the topological waveguide. The phonon propagation was studied by swiping the frequency of the surface acoustic waves (SAW) from 1.9 to 2.4 GHz.

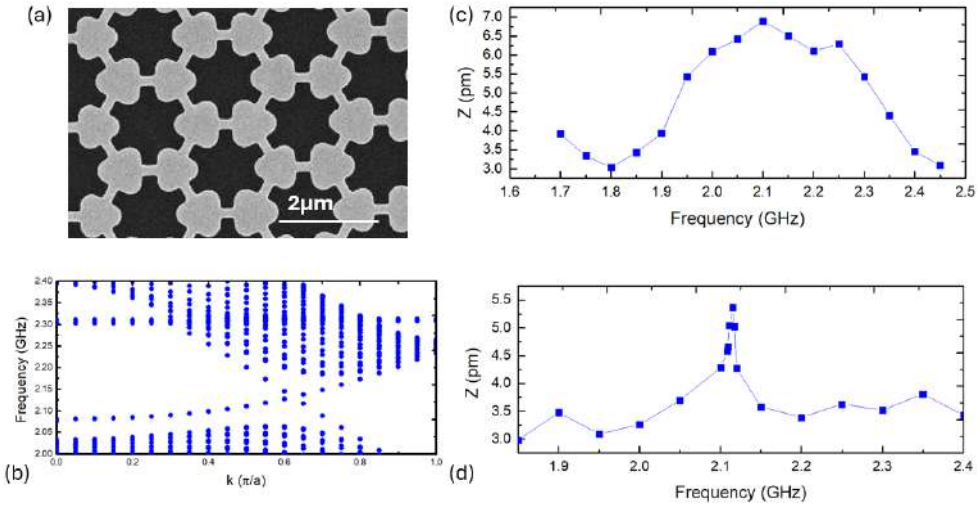


Figure. 1 (a). SEM image of the fabricated structure. (b) Simulated phononic bandgap and topological edge modes. (c, d) Out-of-plane displacement magnitude versus frequency at the entrance and exit of the interface waveguide, respectively.

Frequency specific SAWs were generated by a vector network analyzer from 1.90 GHz to 2.40 GHz in steps of 50 MHz. This signal was transfer to Al electrodes via electrical probes. The full width at half maximum of each input signal was 10 KHz. The out-of-plane displacements were measured at the entrance and exit of the waveguide as shown in Fig.1(c) and (d). Fig.1(c). shows the broad band envelope of the SAWs generated by the IDTs. The displacement field at the exit of the waveguide in Fig.1(d) shows that within the bandgap, phonos at 2.115 GHz are guided with minimal loss, whereas other frequencies experience a strong attenuation.
We suggest that our results constitute a demonstration of phonon propagation with low attenuation (-2.1dB) in a topological phononic waveguide.

We acknowledge the support from the project LEIT funded by the European Research Council, H2020 Grant Agreement No. 885689.

References

1. Maire J, Chávez-Ángel E, Arregui G, Colombano MF, Capuj NE, Griol A, Martínez A, Navarro-Urrios D, Ahopelto J and Sotomayor-Torres CM, Advanced Functional Materials, **32(4)**, p.2105767 (2022).
2. Florez O, Arregui G, Albrechtsen M, Ng RC, Gomis-Bresco J, Stobbe S, Sotomayor-Torres CM, García PD, Nature Nanotechnology, **17(9)**, 947-51 (2022).
3. Zhang Q, Lee D, Zheng L, Ma X, Meyer SI, He L, Ye H, Gong Z, Zhen B, Lai K, Johnson AC. Gigahertz topological valley Hall effect in nanoelectromechanical phononic crystals. Nature Electronics. 2022 Mar;5(3):157-63.

AI to Discover and Synthesize Sub-terahertz Chips beyond Human Intuition

Kaushik Sengupta

Princeton University, Princeton, NJ, USA
*corresponding author: kaushiks@princeton.edu

Abstract: Traditionally, chip-scale high-frequency system design has been in the domain of the expert, dominated by thumb rules and trial and error techniques. With AI, not only designs can emerge orders of magnitude faster, but it can lead to new design spaces previously unexplored resulting in circuits that are beyond human intuition and insights---circuits that can break through many of the traditional trade-offs and performance limits. We demonstrate here for the first time how AI can not only allow design times that are orders of magnitude faster, but also unearth new architectures that are beyond human intuition.

Bio: Dr. Sengupta received his Ph.D. in Electrical Engineering from Caltech in 2012. Dr. Sengupta joined the Department of Electrical and Computer Engineering at Princeton University, Princeton, NJ, as a Faculty Member in 2013, where he is currently a Professor. His research interests include novel chip-scale architectures for intelligent sensing and communication for a wide range of emerging applications.

Dr. Sengupta is an IEEE Fellow. He received the DARPA Young Faculty Award in 2018, the Bell Labs Prize in 2017, the Young Investigator Program Award from the ONR in 2017, the 2015 Microwave Prize, and multiple best paper awards in IEEE IMS and RFIC. He served as a Distinguished Lecturer for the IEEE Solid-State Circuits Society from 2019 to 2020 and for the IEEE Microwave Theory and Technology Society from 2021 to 2023. He is a recipient of the 2021 IEEE Microwave Theory and Technology Outstanding Young Engineer Award and the 2022 IEEE Solid-state Circuits New Frontier Award. He currently serves as the co-chair of the IEEE Solid-state Directions Sub-committee and as a technical advisor for the wireless start-up company, GuRu, based in Pasadena, CA. His group received IEEE Journal of Solid-State Circuits Best Paper of the Year in 2023.

Tailoring the visual appearance with correlated-disorder metasurfaces

M. Chen[1], T. Wu[1], A. Agreda[1*], M. Tréguer-Delapierre[2], K. Vynck[3], R. Pacanowski[4], and P. Lalanne[1]

[1]LP2N, CNRS, Institut d'Optique Graduate School, Univ. Bordeaux, F-33400 Talence, France
2Institut de Chimie de la Matière Condensée de Bordeaux, CNRS, Pessac, France
[3]Institut Lumière Matière, CNRS, Université Claude Bernard Lyon 1, Villeurbanne, France
[4]INRIA Bordeaux Sud-Ouest, Talence, France
[*]corresponding author: philippe.lalanne@institutoptique.fr

Abstract: We will review our current effort to model the resonance of individual resonators and collections of them with various theories, including quasinormal modes expansion and multiple scattering.

Disordered metasurfaces, comprising non-periodic arrangements of meta-atoms, have recently emerged as a versatile platform for harnessing both near- and far-field scattered light in a wide range of applications [1].

Quantitatively predicting the scattering properties of disordered metasurfaces requires advanced knowledge of the nanoscale resonances, mesoscale interferences and macroscale light transport to compute the bidirectional reflectance distribution function (BRDF). Understanding the link between appearance and morphology represents a fantastic challenge because metasurfaces offer a multitude of degrees of freedom to harness the diffuse and specular light

Despite this difficulty, some of the authors have recently succeeded in designing the very first simulation tool to predict the appearance of disordered metasurfaces [2]. The modelling platform may find use in several branches of visual arts, to predict the appearance of augmented reality devices using metasurfaces, design unusual effects for counterfeiting applications… Importantly, the tool predicts the possibility to create fancy appearances, unseen so far with the nanostructures available in nature, see the Supplementary Videos 1 & 2 in [2,3] for a rapid glance.

At the conference, we will review our recent efforts to model and understand the optical properties of disordered metasurfaces with various theories: independent scattering approximation [1], multiple scattering, quasinormal mode analysis [4], and ray-tracing rendering.

We will also present striking visual appearances created by the metasurfaces designed with these theories.

Acknowledgements

This work has received financial support from the GPR Light of the University of Bordeaux and the European Research Council Advanced grant (Project UNSEEN No. 101097856).

References

1. P. Lalanne, M. Chen, C. Rockstuhl, A. Sprafke, A. Dmitriev and K. Vynck, "Disordered optical

metasurfaces: basics, properties and applications," Adv. Opt. Photon. **17**, 45-112 (2025).

2. K. Vynck, R. Pacanowski, A. Dufay, X. Granier, and P. Lalanne, "The visual appearances of disordered metasurfaces," Nat. Materials **21**, 1035-41 (2022).
3. A. Agreda, T. Wu, A. Hereu, M. Treguer-Delapierre, G.L. Drisko, K. Vynck, P. Lalanne, "Tailoring Iridescent Visual Appearance with Disordered Resonant Metasurfaces," ACS Nano **17**, 6362-72 (2023).
4. T. Wu and P. Lalanne, "Dissipative Coupling in Photonic and Plasmonic Resonators," Advanced Photonics (2025).

Silicon Quantum Photonics

Vladimir M. Shalaev[1,2]

[1]School of Electrical and Computer Engineering, Birck Nanotechnology Center and Purdue Quantum Science and Engineering Institute, Purdue University, West Lafayette, IN 47906, USA

[2]The Quantum Science Center (QSC), a National Quantum Information Science Research Center of the U.S. Department of Energy (DOE), Oak Ridge, TN 37931, USA

Corresponding author: shalaev@purdue.edu

Abstract: We discuss scalable quantum photonics circuitry based on room-temperature single-photon emitters in silicon nitride that we recently discovered in this technologically important material platform. We also consider integration of SiN single-photon emitters with waveguides as well as the quantum emission enhancement through integration with resonant cavities and plasmonic nanostructures. This hybrid dielectric-plasmonic design paves the way for advanced quantum photonic systems by leveraging the benefits of both cavity confinement and plasmonic enhancement. Furthermore, we discuss a new approach for all-optical modulation using silicon avalanche photodiode, where the avalanche multiplication produces significant refractive index changes at ultra-low, single-photon intensities, enabling record-high nonlinearity in a telecom-compatible platform with a potential for integrated silicon quantum photonics.

Quasi-2D Materials: From Tailorable Photonics to New Physics

Alexandra Boltasseva

Elmore Family School of Electrical and Computer Engineering, School of Materials Engineering, Birck Nanotechnology Center and Purdue Quantum Science and Engineering Institute, Purdue University, West Lafayette, IN 47906, USA
and
The Quantum Science Center (QSC), a National Quantum Information Science Research Center of the U.S. Department of Energy (DOE), Oak Ridge, TN 37931

*corresponding author: aeb@purdue.edu

Abstract: The recent advent of tailorable, quasi-two-dimensional (2D) materials such as 2D transition-metal carbides and nitrides (MXenes) and transdimensional (TD) plasmonic ceramics, including several atomic layers thin titanium-, zirconium-, and hafnium nitrides, as well as ultra-thin transparent conducting oxides (TCOs) is currently driving the development of new concepts and devices for on-chip circuitry, communication, sustainable energy and quantum technologies. These materials exhibit great tailorability of their linear and nonlinear optical properties, remarkable dynamic tunability under external electric, optical, mechanical and other stimuli, strong plasmonic behavior, and high optical nonlinearities. These platforms also offer pathways to uncovering new optical and quantum phenomena ranging from epsilon-near-zero (ENZ) behavior to strongly correlated electronic systems. In this talk, we discuss the designer-like characteristics of MXenes, achievable with the choice of transition metal and control of stoichiometry, remarkable tailorability of properties of TD materials with the thickness, and ultra-fast TCOs response. We also explore new device concepts for flat optics/metasurfaces, all-optical switching, high-harmonic-based XUV generation that utilize ENZ regime and extremely strong light confinement. Finally, we analyze physical effects in atomically thin TD plasmonic films enabling metal-to-insulator transitions. Our work paves the way to novel device designs with tailorable optical materials.

A Large Language Model Agent for Autonomous Inverse Metamaterial Design

W. J. Padilla[1*], D. Lu[1], and J. M. Malof[2]

[1]Departement of Electrical and Computer Engineering, Duke University, USA
[2]Department of Electrical Engineering and Computer Science, University of Missouri, USA
[*]corresponding author: willie.padilla@duke.edu

Abstract: An agentic framework consists of large language models coordinating the completion of complex tasks and have recently shown novel results. We propose and demonstrate an agentic system capable of the inverse design of a material which achieves a desired spectra. The future of this rapidly growing field is discussed.

Recent progress in the integration of multiple Large Language Models (LLMs) has enabled such systems to carry out complex tasks that are difficult to achieve with single LLMs. Such an assembly of coordinated LLMs is termed an Agentic Framework and they have also demonstrated the capability for autonomous novel scientific research. We discuss the development of an Agentic framework which is capable of understanding a natural language input, developing a deep learning forward model, optimizing model parameters, carrying out numerical simulations in CST, utilizing short term and long term memory, and realizes a final metamaterial design using a deep inverse model. The Agent achieves a forward deep learning model with an accuracy on par with the best models developed by human deep learning experts. We demonstrate the effectiveness of our Agentic Framework through a comparison on three photonic benchmark problems, and highlight the future of this fascinating field.

Exotic exciton phases in two-dimensional quantum materials

W. K. Lou, Kai Chang*

Center for Quantum Matter, Zhejiang University, Hangzhou, P. R. China
*Corresponding author: kchang@zju.edu.cn

Abstract: Exciton insulator phases has attracted intensive interests in 2D systems. We demonstrated the existence of topological exciton insulating phases in InAs/GaSb semiconductor quantum wells. For InAs/GaSb quantum wells, which can even survive under intense in-plane magnetic fields [1]. In van der Waals systems, we identify not only conventional exciton insulator phases but also a novel topological exciton density wave state [2]. Recently, we propose a scheme to realize exciton supersolidity in 2D heterostructures through light-engineered artificial gauge fields [3].

Summary: Excitons, light-induced quasiparticles in two-dimensional systems, have garnered significant attention owing to their distinctive electronic configurations and promising electro-optical device applications. Through BCS-like theoretical frameworks, we establish the existence of topological exciton insulating phases in 2D semiconductor systems. The coupled BCS-like equations can be expressed as:

$$\Delta\left(\vec{k}\right)=\sum_{k'}V^{ab}_{k-k'}\frac{\Delta\left(\vec{k'}\right)}{E\left(k'\right)}\left[1-f\left(\frac{E\left(k'\right)-\eta\left(k'\right)}{2}\right)-f\left(\frac{E\left(k'\right)+\eta\left(k'\right)}{2}\right)\right] \quad (1)$$

$$\xi\left(\vec{k}\right)=\varepsilon\left(\vec{k}\right)-\mu-\sum_{k'}V^{ab}_{k-k'}\left[1-\frac{\xi\left(\vec{k'}\right)}{E\left(k'\right)}\right]\left[1-f\left(\frac{E\left(k'\right)-\eta\left(k'\right)}{2}\right)-f\left(\frac{E\left(k'\right)+\eta\left(k'\right)}{2}\right)\right] \quad (2)$$

$$\eta\left(\vec{k}\right)=\varepsilon_M\left(\vec{k}\right)-\mu-\sum_{k'}V^{ab}_{k-k'}\left[1-f\left(\frac{E\left(k'\right)-\eta\left(k'\right)}{2}\right)+f\left(\frac{E\left(k'\right)+\eta\left(k'\right)}{2}\right)\right] \quad (3)$$

where $\epsilon_P(\boldsymbol{k})$ and $\epsilon_M(\boldsymbol{k})$ are defined as $\epsilon_P(\boldsymbol{k}) = \epsilon_b(\boldsymbol{k}) + \epsilon_a(\boldsymbol{k})$ and $\epsilon_P(k) = \epsilon_b(\boldsymbol{k}) - \epsilon_a(\boldsymbol{k})$, respectively, and $f(x)=1/(e^x+1)$ is the Fermi distribution function. $E(\boldsymbol{k})$ is the pair-breaking excitation spectrum. From the relation $\Delta^2(\boldsymbol{k}) = E^2(\boldsymbol{k}) - \xi^2(\boldsymbol{k})$, we can obtain the gap function $\Delta(\boldsymbol{k})$ by solving the above coupled equations self-consistently. Focusing on two representative systems - InAs/GaSb quantum wells and van der Waals heterostructures - we reveal critical phase transitions.

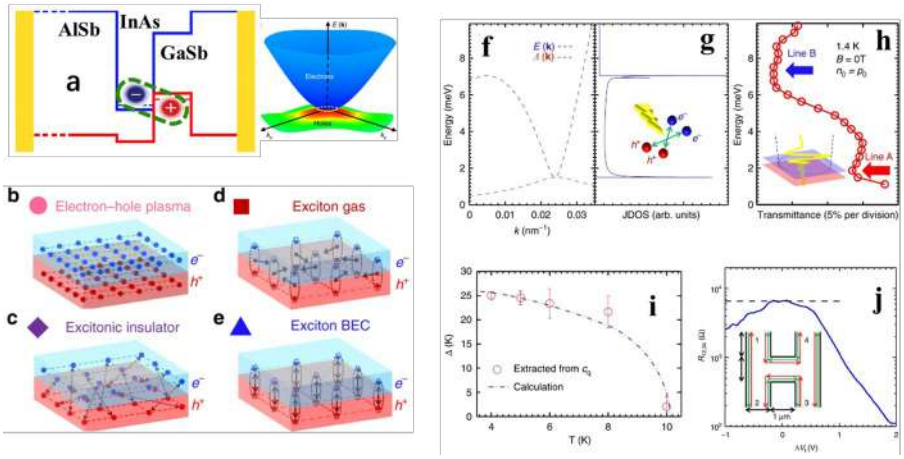


Figure 1. Evidence for a topological excitonic insulator in InAs/GaSb bilayers

For InAs/GaSb quantum wells (intrinsic 2D topological insulators), incorporation of electron-hole Coulomb interactions fundamentally alters the ground state, transforming it into a topological exciton insulator that persists under intense in-plane magnetic fields [1]. It possesses a unique band structure that allows for the spontaneous formation of spatially separated electron layers (InAs layer) and hole layers (GaSb layer) in intrinsic samples [see Fig. 1(a)], even without optical excitation. The model (see Eqs. (1)-(3)) predicted the emergence of an exciton insulator phase in the system and suggested the use of terahertz transmission spectra to verify its existence. The terahertz transmission spectrum exhibits two absorption peaks, and experimental measurements of the terahertz absorption peak positions aligned with theoretical predictions, resolving the long-standing issue of optically observing exciton insulator phases [see Fig. 1(f)-(h)]. Furthermore, electrical transport measurements revealed that the gap is independent of in-plane magnetic field strength but significantly depends on electron-hole density and system temperature [see Fig. 1(i)]. Additionally, the system exhibits conductive behavior of helical edge states [see Fig. 1(j)], further supporting the idea that the system enters a two-dimensional topological exciton insulator state.

In van der Waals systems, we identify not only spin-triplet exciton insulator phases [2] but also a novel topological exciton density wave state [3]. Based on the first-principles calculations coupled with the Bethe-Salpeter equation, the topological exciton density wave is investigated in two-dimensional monolayer WSe_2. We find that the topological excitonic insulator phase can exist in monolayer WSe_2(Fig. 2(b)), and it is robust against in-plane strain. In this system, the energy minimum of exciton bands is shifted to a finite in-plane momentum, forming a Fulde-Ferrell-Larkin-Ovchinnikov-like state. Using the Gross-Pitaevskii equations, stripe-patterned exciton density waves with a nonzero velocity emerge in monolayer WSe_2(Fig. 2(g)-(i)). Our findings pave a new way for exploring the interplay between electron correlation and nontrivial topology.

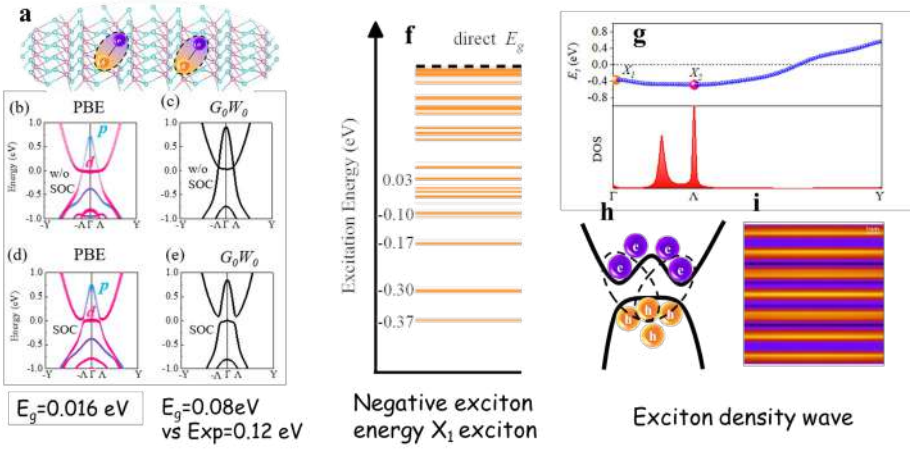


Figure 2.Topological Exciton Density Wave in Monolayer WSe2

Furthermore, we present an interesting scheme for realizing exciton supersolidity in 2D heterostructures through light-engineered artificial gauge fields [4].

References

1. L. J. Du, X. W. Li, W. -K. Lou, G. Sullivan, Kai Chang*, J. Kono*, and R.-R. Du*, Nature Commun. 8, 1971 (2017).
2. Z. Jiang, W. Lou, Y. Liu, Y. Li*, H. Song, Kai Chang, W.H Duan, and S.B Zhang, Phys. Rev. Lett. 124, 166401(2020).
3. S. Dong, Y. -D Chen, H. W. Qu, W. -K. Lou*, and Kai Chang*, Phys. Rev. Lett. 134, 066602(2025).
4. R. P. Luo, D. Zhang, W. K. Lou, and Kai Chang*, submitted.

AI-Driven Photonics: From Metaphotonics to Silicon Photonics Integration

S. Yun*

Samsung Advanced Institute of Technology, Suwon, 16678, Korea
*corresponding author: seok.h.yun@samsung.com

Abstract: As we enter the AI era, photonics is evolving beyond boundaries. This keynote explores advances in metaphotonics and silicon photonics—enabling next-generation image sensors, LiDAR, micro-LED displays, and optical interconnects. Their convergence opens new pathways to compact, power-efficient, and high-performance devices that elevate the capabilities of future optical systems.

Beyond the Voigt lineshapes: Efficient statistics-convolved approximants in the time domain

L. J. Prokopeva[1], **and A. V. Kildishev**[1*]

[1]Purdue University, West Lafayette, IN 47907, USA
[*]corresponding author: kildishev@purdue.edu

Abstract: We present a minimax-based approach for efficient time-domain modeling of optical responses from materials with disorder. The utility of our approach, generally applicable to symmetric and non-symmetric disorder statistics, is demonstrated by the non-classical oscillator, relaxation, and conductivity models, achieving the shortest possible numerical stencil for a given controlled accuracy.

Non-normality, Pseudospectra and Exponential sensitivity in non-Hermitian Photonics

K. G. Makris[1,2*]

[1]ITCP-Department of Physics, University of Crete, 70013, Heraklion, Greece

[2]Institute of Electronic Structure and Laser (IESL),FORTH, 71110, Heraklion, Greece

[*]corresponding author: makris@physics.uoc.gr

Abstract: In the context of non-Hermitian photonics, we present recent results regarding non-normal optical waveguides. We investigate photonic lattices with gain/loss, as well as, asymmetric couplings and study their spectral and dynamical response based on pseudospectra theory. The recent notions of exponential sensitivity, and power eigenchannels will be also discussed.

Active Metastructures – Tailoring Space-Time and Breaking Reciprocity

Harry Atwater

California Institute of Technology, USA

Abstract: In this talk, I will discuss approaches to spatiotemporal wavefront control in active metastructures that can modify energy and momentum states of light, break reciprocity via space-time modulation, and break Kirchhoff's radiation law via action of external or internal magnetic fields.

Functional “Meta”-Optical Fibers for Advanced Imaging and Endoscopy

Ho Wai Howard Lee[1,2,3*], Andrew Palmer, [1,2,3] Yucheng Jin, [1,2,3] Jin Yan, [1,2,3] Beyonce Hu,[1,2] Harvey Lin,[1,2] Stuart Love, [1,2,3] David Dang, [1,2,3] M. Father, [1,2,3] L. Liu, [1,2,3], A. Teoh [1,2,3]

[1] *Department of Physics & Astronomy, University of California, Irvine, United States*

[2] *Beckman Laser Institute and Medical Clinic, University of California, Irvine, United States*

[3] *Eddleman Quantum Institute, University of California, Irvine, United States*

Howardhw.lee@uci.edu

Abstract: Optical metasurfaces represent an important avenue towards novel optical functionality and innovative applications, thanks to their exceptional capability to manipulate the phase, amplitude, and polarization of transmitted, reflected, and diffracted light. Since their first integration onto the optical fiber endfaces a decade ago, the resulting “meta”-optical fiber platform has demonstrated immense potential, both in exploiting the strengths of optical fibers and overcoming their limitations, enabling revolutionary next-generation photonic devices.

In this talk, I will review the various material platforms (metallic, dielectric, and compound structures) and geometric platforms which have been utilized in “meta”-fiber devices to date. I will present our recent development of “Meta”-optical fiber, an advanced optical fiber integrated with emerging metasurface concepts. I will present the development of ultrathin optical metalens which is cascaded on the facet of optical fiber that enables advanced optical functions via wavefront shaping such as light focusing. I will also discuss the ability to develop tunable meta-optical fiber for advanced beam steering and dynamic focusing, and their potential application for biomedical imaging. These advanced “meta”-optical fibers open a pathway to revolutionary in-fiber optical imaging/endoscopy, biomedical imaging, lasers/spectroscopies, and optical/quantum communication devices.

Bio-inspired hierarchical phononic crystals and metamaterials

Marco Miniaci

IEMN - Université de Lille, France

Abstract: Phononic crystals and elastic metamaterials are traditionally regarded as artificially engineered materials designed to exhibit wave manipulation capabilities not typically found in natural systems. However, recent pioneering research has revealed that many biological structures—characterized by complex, often hierarchical organizations with periodic or gradient arrangements across multiple length scales—naturally demonstrate remarkable wave control functionalities. In this talk, I will explore the potential and limitations of bio-inspired phononic crystals and metamaterials. Particular emphasis will be placed on their dynamic behavior, analyzed through both numerical simulations and experimental investigations.

Transition waves in multistable mechanical metamaterials

V. Tournat[1*]

[1] Laboratoire d'Acoustique de l'Université du Mans (LAUM), UMR 6613, Institut d'Acoustique - Graduate School (IA-GS), CNRS, Le Mans Université, France
[*]corresponding author: vtournat@univ-lemans.fr

Abstract: Multistable metamaterials, composed for example of bistable mechanical units elastically coupled to their nearest neighbors, have recently been conceived in diverse ways, particularly within the family of flexible mechanical metamaterial architectures. Such multistable metamaterials can support progressive fronts, also called transition waves, switching sequentially its multistable units front one equilibrium to another, and resulting in the local or global reconfiguration of the medium. In addition, these nonlinear metamaterials are also known to support a rich variety of nonlinear waves, as vector solitons, breathers, cnoidal waves, among others. In this presentation, I will highlight the fundamentals and a selection of recent results on transition waves triggering, propagation, and discuss some of their potential applications. In general, these reconfiguration fronts obey nonlinear reaction-diffusion equations and show specific properties not necessarily found in other waves supported by periodic and/or nonlinear media, e.g., strong nonreciprocity, robustness, extreme amplitude dependent behavior… They can consequently be implemented for applications involving local or global reconfiguration of a medium, manipulating mechanical memory, controlling waves in space and time, mechanical computing or be the vector for material embedded intelligence.

Empowering Topological Photonics for OAM Manipulation

Zhigang Chen
The MOE Key Laboratory of Weak-Light Nonlinear Photonics,
TEDA Applied Physics Institute and School of Physics,
Nankai University, Tianjin, China
zgchen@nankai.edu.cn

Abstract: In this talk, we present a few demonstrated examples of topology-driven photonic applications based on the simplest topological model. Building on these foundations, we introduce our design and implementation of more advanced photonic structures that enable robust optical vortex transport and effective manipulation of orbital angular momentum (OAM).

Tutorial

Nonlocal metasurfaces

Andrea Alù

[1]City University of New York, USA
[*]corresponding author: aalu@gc.cuny.edu

Abstract: The use of engineered nonlocal responses in metasurfaces has been recently unveiled as a paradigm for extreme wave control, enabling rational control over space, time, frequency and momentum of the incoming signals, as well as analog-based image processing and computing. Several recent demonstrations of metasurfaces performing edge-detection and image-processing using engineered spatial nonlocality have shown a path towards ultrafast, efficient, massively parallel analog image processing based on passive devices, which holds the promise for being extended towards general analog computing platforms. Space-time nonlocal metasurfaces performing the space- and time-derivatives of the incoming signal were also envisioned by tailoring their frequency and momentum dispersion. In this tutorial, I will discuss the basics of nonlocality engineering in metasurfaces and their various implementations and opportunities for this field of research, showcasing compact meta-structures with reconfigurable properties that can perform mathematical operations, solve compact mathematical problems and address the issues of reprogrammability and cascaded responses. I will discuss how these findings may open exciting opportunities for applications in imaging, automotive vehicles, sensing and computing, and serve as a pre-processing tool for simplifying complex computing architectures.

New trends in nanophotonics and advanced materials

Photonic Crystal Information Processing Chips

Xiaoyong Hu[1*], and Kun Liao[1]

[1] Department of Physics, Peking University, China
[*]corresponding author: xiaoyonghu@pku.edu.cn

Abstract: Several topological photonic crystal chips are realized and used to photonic information processing applications. Silicon-based optical neural network chip is fabricated to perform topological state simulation functions.

Topological photonic crystal provides an excellent platform for the photonic information processing chips owing to the unique properties of topological photonic states. However it is still a great challenge to construct topological photonic information processing chips. Several topological photonic crystal chips are realized and used to photonic information processing applications, including silicon-based topological photonic crystal chips and surface plasmonic topological photonic chips. Silicon-based optical neural network chip is fabricated to perform topological state simulation functions.

References

1. Zhuochen Du[†], Kun Liao[†], Tianxiang Dai[†], Yufei Wang[†], Jinze Gao[†], Haiqi Huang, Huixin Qi, Yandong Li, Xiaoxiao Wang, Xinran Su, Xingyuan Wang, Yan Yang*, Cuicui Lu*, Xiaoyong Hu*, Qihuang Gong, “Ultracompact and multifunctional integrated photonic platform”, Science Advances, Vol. 10, No. 25, eadm7569 (2024).
2. Huixin Qi, Yandong Li, Xiaoxiao Wang, Yaolong Li, Xuyang Li, Xingyuan Wang,* Xiaoyong Hu,* Qihuang Gong,“Dynamically Encircling Exceptional Points in Different Riemann Sheets for Orbital Angular Momentum Topological Charge Conversion”, Physical Review Letters, Vol. 132, No. 24, 243802 (2024).

Advanced Self-Powered Room-Temperature NIR Plasmonic Photodetection and Reconstructive Spectroscopy

Eslam Abubakr [1, 2*], Shiro Saito [3], Hironori Suzuki [3], Tetsuo Kan [1]**

[1] *Graduate School of Informatics and Engineering, The University of Electro-Communications, Tokyo, 182-8585, Japan*

[2] *Department of Electrical Engineering, Faculty of Engineering, Aswan University, Aswan 81542, Egypt*

[3] *IMRA JAPAN CO., LTD., Kariya, Aichi 448- 8650, Japan*

[*] abubakr_eslam@kyudai.jp, [**] tetsuokan@uec.ac.jp

Abstract: Combining metal's plasmonic properties with the interface characteristics of a Schottky junction, we demonstrated effective broadband filter-free NIR spectroscopy. A single tunable device delivers excellent responsivity, wavelength-specific detection(up to 2.3μm), and enhanced spatial resolution. We emphasize extending the spectral range for reconstructive spectroscopy while scaling down infrared-spectroscopy to chip level.

Introduction

The development of plasmonic photodetectors, especially in the near-infrared (NIR) region, has gained significant attention due to their non-destructive nature. Schottky plasmonic spectrometers can effectively detect NIR light, providing a compact and simplified approach to optical sensing [1]. Accurate and reliable detection of NIR with high sensitivity is crucial; however, it presents challenges due to the inherently low energy. Prior studies have laid a solid foundation for NIR detection [2]. However, responsivity was limited to a few tens of μA/W, and spectroscopy of the longer wavelength range beyond 1400 nm is not yet clearly demonstrated while maintaining detection selectivity [3]. In addition, typical Au/Si photodetectors exhibit unstable interface properties, reliability issues, and plasmonic shifts. This work demonstrates a low Schottky-barrier photodetector with a plasmonic assist that receives NIR light at room temperature, enhancing device adhesion and modifying charge carrier generation and transport processes.

Description of the New Method or System

The study meticulously engineered an embedded grating structure. Device geometry is designed through extensive experimental and modeling results, ensuring wavelength-specific plasmonic photodetection with a one-to-one correspondence between absorption angles/wavelengths for guaranteed selectivity. This allows for unique determination and inverse calculation of multiple parallel incident spectrums. While maintaining gold as a plasmonic antenna, interface properties are modified by incorporating an interfacial layer acting as a Schottky interlayer metal, a diffusion barrier, an adhesion promoter, and to suppress the formation of intermetallic compounds or plasmonic resonance shifts.

Experimental Results

Combining different metals in the plasmonic structure can potentially broaden the device operation range, considering the modification of junction barrier height and interface properties. This produced the highest responsivity of ten times compared to previous reports [4], due to the lowered barrier height, facilitating the transport of low-energy photogenerated carriers at room temperature and zero biasing conditions while maintaining high linearity and sensitivity to low light intensities (less than 25 μW at 1900 nm) (Fig. 1). It further demonstrated clear SPR peaks even with parallel exposure to visible light. It maintained higher stability with

neither hysteresis nor deterioration in photocurrent measurements over 380 days so far. The sharp and selective SPR peaks facilitated the expansion of the spectral range for reconstructive spectroscopy to longer wavelengths. Since the degree of surface sensitivity can be controlled by collecting photoelectrons emitted at different emission angles to the surface plane by changing the incident photon energy, the reconstruction of multiple parallel incident wavelengths could be successfully demonstrated (Fig. 2). Making it a powerful technique for investigating the electronic and chemical structures of various nanolayers and devices for green chemistry. With further incorporation of a refractory diffusion barrier/interfacial layer to our structure (as confirmed by XPS), long-term stability and durability testing demonstrated less than a 5% decline in responsivity with no observable plasmonic shift. Meanwhile, conventional Au/Si devices exhibited a plasmonic shift in SPR peaks of 1.5° per SPR peak and a responsivity reduction exceeding 30%.

This research represents a significant leap in NIR photodetection and spectroscopy, with far-reaching implications across applications for various scenarios such as gas sensing and environmental monitoring.

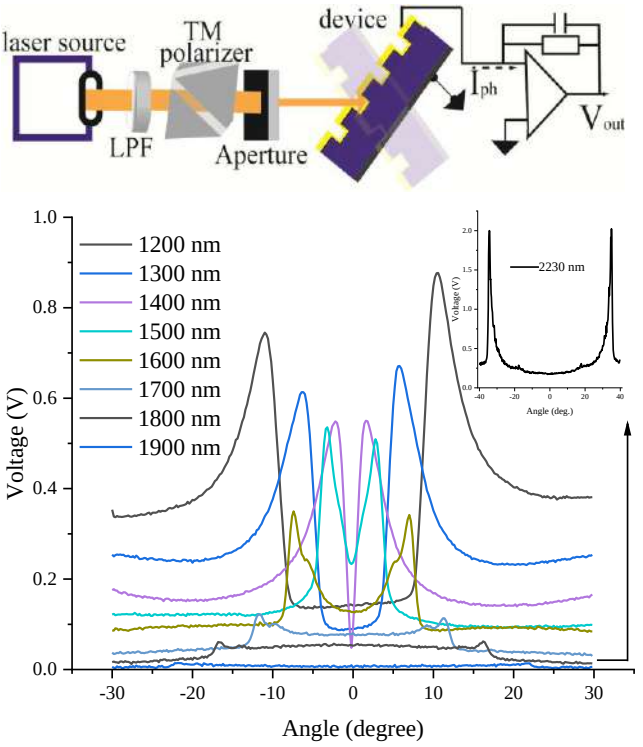


Figure 3: High linearity and selectivity of output photocurrent signal. The upper inset shows the experimental setup.

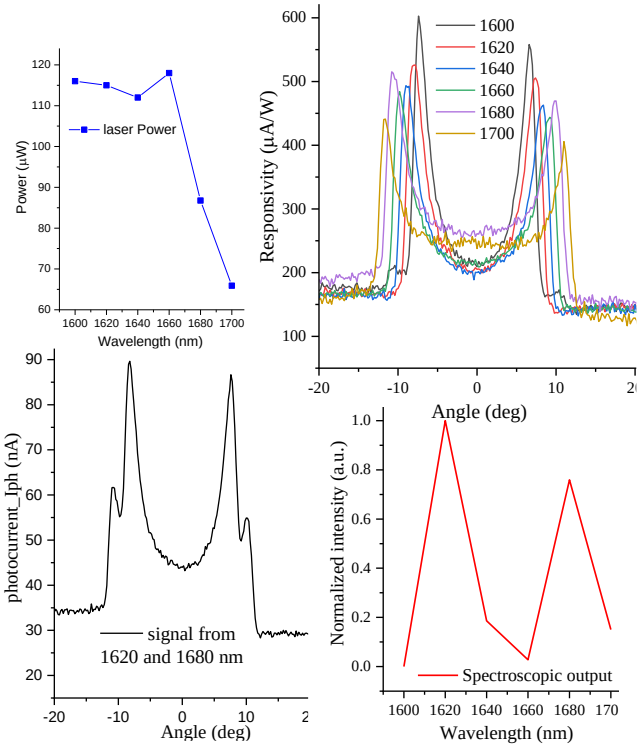


Figure 4: (a)Input laser power. (b) Responsivity for each wavelength (c) is the photocurrent at multiple parallel wavelengths (λ = 1620 and 1680)(I_{ph}). (d) Accurate deduction/reconstruction of input light spectrum

References

1. E. Abubakr, et al., “Optimizing geometry and metal-dependent performance of Si-based Schottky plasmonic photodetectors,” Opt. Mater., vol. 150, 2024, doi: 10.1016/j.optmat.2024.115175.
2. Tetsuo Kan et al., “Electromechanically reconfigurable plasmonic photodetector with a distinct shift in resonant wavelength,” Microsystems Nanoeng.,9,2023, doi: 10.1038/s41378-023-00504-4.
3. E. Abubakr, et al., "Advanced Room-Temperature NIR Plasmonic Photodetection and Reconstructive Spectroscopy," in IEEE Trans. Electron Devices, doi: 10.1109/TED.2024.3509385.
4. Y. Yamamoto, et al., “Near-Infrared Spectroscopic Gas Detection Using a Surface Plasmon Resonance Photodetector with 20 nm Resolution,” *ACS Appl. Nano Mater.*, vol. 4, no. 12, pp. 13405–13412, 2021, doi: 10.1021/acsanm.1c02925.

Holotomography in optics and X-ray: advancing the study of metamaterials

Y.K. Park[1*]

[1] Physics Department, KAIST, South Korea
[2]Tomocube Inc. South Korea
[*]corresponding author: yk.park@kaist.ac.kr

Abstract: Holotomography reconstructs 3D refractive index distributions of unlabeled samples with high resolution. This talk covers advancements in visible-light and X-ray techniques, machine learning integration, and dielectric tensor tomography, emphasizing applications in cell biology and industrial fields like semiconductors and display technologies.

Holotomography (HT) is an imaging technology that enables label-free, three-dimensional visualization of refractive index (RI) distributions in biological and material specimens. By combining high-resolution optical and X-ray modalities, HT addresses limitations inherent in traditional microscopy methods. Through quantitative reconstruction of RI distributions, HT serves as a powerful tool for uncovering structural details and dynamic processes in a variety of samples ranging from living cells to complex materials.

HT reconstructs 3D RI maps by capturing multiple 2D images of the sample under varying illumination conditions. Optical HT operates using coherent or low-coherence light sources, while X-ray HT extends the methodology to denser and larger samples by leveraging higher penetration depth. Reconstruction relies on advanced phase retrieval algorithms and the integration of machine learning techniques to enhance image quality and address challenges such as noise and missing cone artifacts.

Key advances include the introduction of dielectric tensor tomography (DTT), which expands HT capabilities to measure 3D anisotropic properties such as birefringence and molecular alignment. DTT uses polarized illumination and vectorial field measurements to reconstruct 3D dielectric tensor distributions, enabling detailed characterization of optically anisotropic materials. This is particularly valuable for applications in liquid crystals, biomolecular structures, and soft matter physics

The following applications of HT will be discussed:

Biology and Medicine: HT is widely applied in cell biology for non-invasive imaging of live cells and tissues. Its ability to visualize subcellular structures, such as lipid droplets, mitochondria, and nuclei, without labeling is transformative. HT supports long-term studies of cellular dynamics and phase-separated biomolecular condensates, critical for understanding pathophysiological states and drug interactions

Material Science: The combination of HT and DTT enables precise visualization of 3D molecular orientations and phase distributions in liquid crystals and other anisotropic materials. This capability is crucial for studying the properties and dynamics of soft materials, enabling the design of advanced functional composites

Industrial Applications: In semiconductor and display technology, HT offers detailed defect analysis and quality inspection by identifying variations in material properties at micro and nano scales. Its X-ray implementation provides insight into thicker and denser materials where optical techniques face limitations.

HT's fusion with artificial intelligence (AI) significantly enhances its capabilities. AI-driven algorithms address noise reduction, segmentation, and automated analysis, improving the accuracy of RI reconstruction and facilitating real-time imaging. Furthermore, combining HT with complementary modalities such as Raman spectroscopy and fluorescence microscopy adds chemical specificity to its imaging, unlocking new possibilities in biomedical and industrial research.

The ongoing development of HT focuses on improving imaging speed, resolution, and depth penetration. The integration of high-speed sensors and adaptive optics aims to push the boundaries of temporal resolution, enabling the capture of fast dynamic processes. Expanding HT's application to organoid and tissue imaging, regenerative medicine, and high-throughput drug screening holds promise for addressing critical challenges in healthcare and technology.

In conclusion, holotomography stands at the forefront of imaging innovation, offering unparalleled insights into the microanatomy and material properties of diverse samples. Its versatile applications across disciplines make it a pivotal tool in both fundamental research and practical applications.

References

1. G. Kim et al., *Nature Reviews Methods Primers*, 4(1) 51, (2024)
2. Y. Park, C. Depeursinge and G. Popescu, *Nature Photonics* 12 (10), 578-589 (2018).
3. Y. Baek and Y. Park, *Nature Photonics* 15 (5), 354-360 (2021).
4. S. Shin and Y. Park, *Nature Materials* 21(3), 317-324, (2022)
5. J. Park et al., *Nature Methods* 20(11),1645-1660 (2023)
6. K. Lee et al., *Light: Science and Applications*, 12, 88 (2023)
7. K. Lee et al., *Optica*, 10(3), 407-414 (2023)
8. K. Lee et al., *Optica*, 10(3), 393-400 (2023)

Momentum-direct infrared interlayer exciton and photodetection in WSe_2/InSe heterostructures

Jiong Yang[1,2*] **and Chao Zhang**[1,2]

[1]School of Optoelectronic Science and Engineering & Collaborative Innovation Center of Suzhou Nano Science and Technology, Soochow University, Suzhou 215006, China
[2]Author Affiliation, Country Key Lab of Advanced Optical Manufacturing Technologies of Jiangsu Province & Key Lab of Modern Optical Technologies of Education Ministry of China, Soochow University, Suzhou 215006, China
[*]corresponding author: jiongyang@suda.edu.cn

Abstract: Momentum-direct interlayer excitons (IX) in the infrared are crucial for excitonic devices but remain underexplored. We construct a WSe_2/InSe heterostructure that hosts momentum-direct IX and manifests near-infrared interlayer absorptions at room temperature, realizing photodetection at 1150 nm with an optimal photoresponsivity and response time of 33 A/W and 3.7 μs.

When layered semiconductors form van der Waals heterostructures (vdWH) with type-II band alignment, interlayer charge transfer facilitates the accumulation of electrons in the layer with lower conduction band minimum (CBM) and holes in the layer with higher valence band maximum (VBM).[1, 2] Those electrons and holes interact strongly *via* the Coulomb force due to the sub-nanometer interlayer spacing and form spatially separated electron-hole pair quasi-particles, namely interlayer excitons (IX). To date, IX have been detected or predicted, mainly in the visible range, in hetero- and homo-bilayers among transition metal dichalcogenides (TMD), metal chalcogenides, black phosphorus, and other layered semiconductors.[3-6] One of the challenges for IX-based excitonic devices is the severely reduced luminescence quantum yield of momentum-indirect IX recombinations that could result from the lattice mismatch and stacking misalignment in vdWH.

Layer engineering of vdWH that host IX has attracted widespread attentions to realize direct bandgap transitions.[7-9] One of its advantages is that IX emission energies can be precisely tuned as band structures of layered semiconductors gradually evolve with the layer number. Besides, for vdWH consisting of TMD monolayers, the typical and most widely studied IX platforms, the CBM and VBM are located at different positions in the reciprocal space (*k*-space), even though TMD monolayers possess direct bandgaps at the K point in *k*-space. Such momentum mismatch of carriers hinders photoexcitation and IX recombination in vdWH.

In addition to intralayer absorptions followed by ultrafast interlayer charge transfer in vdWH, IX can be formed by excited electrons and holes from one-step interlayer absorptions.[10, 11] Because of the staggered band alignment in type-II vdWH, interlayer absorptions occur at longer wavelengths compared to intralayer absorptions, and thus can be readily applied to infrared photodetections. Such IX-driven infrared photodetectors have been demonstrated to realize a trade-off between the low dark current and the detection of long wavelength.[12]

In this work, we report the observation and manipulation of momentum-direct near-infrared (NIR) IX at room temperature in a vertical type-II vdWH consisting of bilayer (2L) WSe_2 and five-layer (5L) InSe. First-principles density functional theory (DFT) calculations indicate that, in the 2L-WSe_2/5L-InSe vdWH, the CBM and VBM both locate at the Γ point of the first Brillouin zone, thus forming a direct bandgap and facilitating interlayer carrier photoexcitation and recombination. Raman and photoluminescence (PL) spectroscopies were utilized to characterize the efficient interlayer coupling. Specifically, a NIR IX emission peak at 1130 nm was detected and manipulated by temperature, excitation power, electric field, and the layer

number. By conducting absorption spectroscopy, we observed intralayer absorption peaks of 2L WSe_2 and 5L InSe, as well as the vdWH interlayer absorption at ~1110 nm. The binding energy of the IX was extracted to be 43 ± 5 meV, well above the thermal energy at room temperature (26 meV), indicating its stable existence at room temperature. As the IX owns a permanent out-of-plane dipole moment, we further demonstrated its electrical tunability by applying a vertical electrical field, and the IX emission energy was linearly tuned from 1.04 to 1.22 eV. By taking advantage of the direct interlayer absorption, we fabricated a photoconductive NIR photodetector modulated by strong photogating effect based on the 2L-WSe_2/5L-InSe vdWH, achieving a responsivity of 33 A/W, a specific detectivity of 1.8×10^{10} Jones, and a fast response time of 3.7 μs at 1150 nm.

We acknowledge financial supports from the National Natural Science Foundation of China (62120106001, 62205227), the National Key Research and Development Program of China (2021YFB3502200), the Natural Science Foundation of Jiangsu Province (BK20210713), the Natural Science Research of Jiangsu Higher Education Institutions of China (22KJB140005, 22KJA510011, 23KJA510008), and the Suzhou Science and Technology Plan Projects (SYG202124, SYG202304). Jiong Yang acknowledges the financial support from the Distinguished Professor Award of Jiangsu Province (SR15900124).

References

1. X. Hong, J. Kim, S.-F. Shi, Y. Zhang, C. Jin, Y. Sun, S. Tongay, J. Wu, Y. Zhang, F. Wang, *Nat. Nanotechnol* 2014, **9**, 682—686.
2. A. Sood, J.B. Haber, J. Carlström, E.A. Peterson, E. Barre, J.D. Georgaras, A.H. Reid, X. Shen, M.E. Zajac, E.C. Regan, *Nat. Nanotechnol* 2023, **18**, 29—35.
3. E.C. Regan, D. Wang, E.Y. Paik, Y. Zeng, L. Zhang, J. Zhu, A.H. MacDonald, H. Deng, F. Wang, *Nat. Rev. Mater* 2022, **7**, 778—795.
4. V. Villafañe, M. Kremser, R. Hübner, M.M. Petrić, N.P. Wilson, A.V. Stier, K. Müller, M. Florian, A. Steinhoff, J.J. Finley, *Phys. Rev. Lett* 2023, **130**, 026901.
5. X. Sun, Y. Zhu, H. Qin, B. Liu, Y. Tang, T. Lü, S. Rahman, T. Yildirim, Y. Lu, *Nature* 2022, **610**, 478—484.
6. K.-Q. Lin, P.E. Faria Junior, R. Hübner, J.D. Ziegler, J.M. Bauer, F. Buchner, M. Florian, F. Hofmann, K. Watanabe, T. Taniguchi, *Nat. Nanotechnol* 2024, **19**, 196—201.
7. Q. Tan, A. Rasmita, S. Li, S. Liu, Z. Huang, Q. Xiong, S.A. Yang, K. Novoselov, W.-b. Gao, *Sci. Adv* 2021, **7**, eabh0863.
8. Y. Zhang, C. Xiao, D. Ovchinnikov, J. Zhu, X. Wang, T. Taniguchi, K. Watanabe, J. Yan, W. Yao, X. Xu, *Nat. Nanotechnol* 2023, **18**, 501—506.
9. N. Ubrig, E. Ponomarev, J. Zultak, D. Domaretskiy, V. Zólyomi, D. Terry, J. Howarth, I. Gutiérrez-Lezama, A. Zhukov, Z.R. Kudrynskyi, *Nat. Mater* 2020, **19**, 299—304.
10. E. Barré, O. Karni, E. Liu, A.L. O'Beirne, X. Chen, H.B. Ribeiro, L. Yu, B. Kim, K. Watanabe, T. Taniguchi, *Science* 2022, **376**, 406—410.
11. C. Jin, E.C. Regan, D. Wang, M. Iqbal Bakti Utama, C.-S. Yang, J. Cain, Y. Qin, Y. Shen, Z. Zheng, K. Watanabe, *Nat. Phys* 2019, **15**, 1140—1144.
12. S. Lukman, L. Ding, L. Xu, Y. Tao, A.C. Riis-Jensen, G. Zhang, Q.Y.S. Wu, M. Yang, S. Luo, C. Hsu, *Nat. Nanotechnol* 2020, **15**, 675—682.

Accelerating topological pumps on integrated photonic chips

Wange Song

National Laboratory of Solid State Microstructures, Key Laboratory of Intelligent Optical Sensing and Manipulations, Jiangsu Key Laboratory of Artificial Functional Materials, College of Engineering and Applied Sciences, Nanjing University, Nanjing, 210093, China.

*corresponding author: songwange@nju.edu.cn

Abstract: We demonstrated the acceleration of adiabatic evolutions by leveraging the concepts of the quantum metric, adiabatic infimum, and shortcut to adiabaticity (STA), respectively. Specifically, we achieved fast topological pumping and non-Abelian braiding in integrated photonic waveguides, significantly enhancing on-chip functionality and efficiency within high-density integrations.

Topological photonics has paved the way for robust optical transport and light manipulation through the emergence of edge states in topologically distinct systems. Topological pumps, originally proposed by Thouless, have gained considerable attention for their ability to facilitate robust excitation transfer in systems with topological edge states, showing great potential for on-chip functional devices like quantum state transfer and reliable integrated photonic interconnects. However, their on-chip applicability is limited by the need for slow evolution speeds to satisfy adiabaticity requirements. In this talk, I will discuss our recent efforts to overcome this challenge.

Firstly, we have identified a direct link between adiabaticity and the quantum metric, an underexplored aspect of quantum geometry compared to the Berry curvature. By reducing the quantum metric through long-range coupling in the Rice-Mele model, we increased the evolution speed of topological pumps between nontrivial edge states without affecting bulk state evolution. We validated our findings experimentally using bilayer integrated silicon waveguides at telecommunication wavelengths [1]. Additionally, we propose and demonstrate the adiabatic infimum of topological pumps using on-chip lithium niobate on insulator (LNOI) waveguides. Our systematic investigation of the adiabatic criterion reveals its dependence on the effective Berry connection between modes and modulation speed. By minimizing the effective Berry connection along the loop, we achieve fast parameter modulation and realize the infimum pump in the shortest possible length [2]. More recently, employing a shortcut to adiabatic (STA) strategy, we demonstrated compact trilayer 3D silicon photonic chips capable of performing non-Abelian braiding and photonic quantum gates, significantly reducing the size of the braiding apparatus and making it CMOS-compatible [3]. These advancements accelerate adiabatic evolutions, paving the way for more compact and efficient photonic integration.

References

1. Song, W. et al. “Fast topological pumps via quantum metric engineering on photonic chips,” Sci. Adv. 10, 30, eadn5028, 2024.
2. Wu, S. et al. “Approaching the adiabatic infimum of topological pumps on thin-film lithium niobate waveguides,” Nat. Commun. 15, 1, 9805, 2024.
3. Song, W. et al. “Shortcuts to adiabatic non-Abelian braiding on silicon photonic chips,” Sci. Adv. Accepted.

Enhancing brightness and directional control of dark excitons via all-dielectric metasurfaces

A. Barreda[1*], S, Klimmer[2,3], G. Soavi[2,4] and I. Staude[2,4,5]

[1]Group of Displays and Photonics Applications, Carlos III University of Madrid, Avda. de la Universidad, 30, Leganés, 28911 Madrid, Spain
[2]Institute of Solid State Physics, Friedrich Schiller University Jena, 07743 Jena, Germany
[3]ARC Centre of Excellence for Transformative Meta-Optical Systems, Department of Electronic Materials Engineering, Research School of Physics, The Australian National University, Canberra, ACT 2601, Australia
[4]Abbe Center of Photonics, Friedrich Schiller University Jena, 07745 Jena, Germany
[5]Institute of Applied Physics, Friedrich Schiller University Jena, 07745 Jena, Germany

[*]corresponding author: abarreda@ing.uc3m.es

Abstract: We investigate an all-dielectric metasurface featuring two symmetrically protected quasi-bound states in the continuum, designed to enhance both the excitation and emission of dark excitons in a tungsten diselenide monolayer. Simulations reveal a significant photoluminescence signal enhancement (∼520) accompanied by directional emission, presenting clear advantages for optoelectronic and valleytronic applications.

Efficient quantum emitters are crucial for the development of quantum photonic technologies based on single-photon sources. These sources need to produce single photons on demand with high efficiency, purity, and indistinguishability [1]. In this sense, different quantum emitters have been explored in the last years, such as nitrogen vacancy centers, quantum dots or excitons in 2D materials (transition metal dichalcogenides (TMDs), hexagonal boron nitride, phosphorene…) [2,3]. In particular, monolayer TMDs are highly promising due to their significant exciton binding energy arising from two-dimensional confinement and diminished dielectric screening, and their direct band gap leading to intense photoluminescence (PL) [4]. However, in order to fulfil the requirements for practical applications, efficiency and purity must still be improved. With this objective, the coupling of TMDs with metallic or dielectric nanostructures has been proposed [5-7]. The excitation of localized surface plasmons or Mie modes in metallic or dielectric nanostructures, respectively, can increase the local density of optical states (LDOS), promoting the spontaneous emission in TMDs according to the Purcell effect [8].

In recent years, significant progress has been made in the study of quasi-bound states in the continuum (quasi-BIC) within symmetry-broken all-dielectric metasurfaces. The exceptionally high Q-factors associated with quasi-BIC resonances have made them highly attractive for enhancing light-matter interaction [9].

In this work, we analyze the excitation and emission enhancement of dark excitons in a tungsten diselenide monolayer under normal light incidence. Our study focuses on the coupling of the TMD material with an all-dielectric metasurface showing two symmetrically protected quasi-bound states in the continuum (q-BIC) at the excitation and emission wavelengths, respectively [10].

Our findings reveal a significant enhancement in the photoluminescence signal (approximately 520-fold), achieved through the combined effects of excitation and emission amplification. These results hold promising implications for the experimental investigation of spin-forbidden dark excitons with possible applications in valleytronics and opto-electronics.

Acknowledgements

This work was funded by the Deutsche Forschungsgemeinschaft (DFG, German Research Foundation)—IRTG 2675 (Meta-Active), project number 437527638. AB gratefully acknowledges financial support from Spanish national project No. PID2022-137857NA-I00. AB thanks MICINN for the Ramon y Cajal Fellowship (grant No. RYC2021-030880-I).

References

1. Esmann, M., S. C. Wein and C. Antón-Solanas, "Solid-State Single-Photon Sources: Recent Advances for Novel Quantum Materials," Adv. Funct. Mater., Vol. 34, 2315936, 1-27, 2024.
2. Senellart, P., G. Solomon and A. White, "High-performance semiconductor quantum-dot single-photon sources," Nature Nanotech, Vol. 12, 1026–1039, 2017.
3. Chakraborty, C., N. Vamivakas and D. Englund, "Advances in quantum light emission from 2D materials," Nanophotonics, Vol. 8, No. 11, 2017-2032, 2019.
4. Wang, Q. H., K. Kalantar-Zadeh, A. Kis, J. N. Coleman and M. S. Strano, "Electronics and optoelectronics of two-dimensional transition metal dichalcogenides," Nature Nanotech., Vol. 7, 699–712, 2012.
5. B. N. Tugchin et al., "Photoluminescence Enhancement of Monolayer WS_2 by n-Doping with an Optically Excited Gold Disk," Nano Lett., Vol. 23, 10848−10855, 2023.
6. Gao, W., Y. H. Lee, R. Jiang, J. Wang, T. Liu and X. Y. Ling, "Localized and Continuous Tuning of Monolayer MoS_2 Photoluminescence Using a Single Shape-Controlled Ag Nanoantenna," Adv. Mater., Vol. 28, 701–706, 2016.
7. L. Sortino et al. "Enhanced light-matter interaction in an atomically thin semiconductor coupled with dielectric nano-antennas," Nat. Commun., Vol. 10, 5119, 2019.
8. E. M. Purcell, "Spontaneous Emission Probabilities at Radio Frequencies," Phys. Rev., Vol. 69, 681, 1946.
9. Hsu, C. W., B. Zhen, A. D. Stone, J. D. Joannopoulos and M. Soljačić, "Bound states in the continuum," Nat. Rev. Mater., Vol. 1, 1-13, 2016.
10. Klimmer, S., G. Soavi, I. Staude and A. Barreda, "Brightening and Directionality Control of Dark Excitons through Quasi-Bound States in the Continuum," Nanomaterials, Vol. 13, 3028, 2023.

DNA identification using surface-enhanced Raman spectroscopy (SERS) and surface plasmon resonance (SPR) sensors: Identification of BRCA1 gene mutation variants in clinical samples

A. Kowalczyk[1], A. M. Nowicka[1], A. Michałowska[1], M. Duszczyk[1], M. Sikorska[1], J. L. Weyher[2], S. Zięba[3], A. Kowalik[3,4], and A. Kudelski[1*]

[1]Faculty of Chemistry, University of Warsaw, Poland
[2]Institute of High Pressure Physics of the Polish Academy of Science, Poland
[3]Holy Cross Cancer Center, Poland
[4]Institute of Biology, Jan Kochanowski University, Poland
[*]corresponding author: akudel@chem.uw.edu.pl

Abstract: Surface-enhanced Raman scattering (SERS) spectroscopy and surface plasmon resonance (SPR) are promising methods for detection of specific DNA fragments. In this contribution, we describe construction and tests with clinical samples of SERS and SPR sensors for the identification of six the most popular in Poland variants of *BRCA1* gene mutations.

The deoxyribonucleic acid (DNA) is the carrier of genetic information for all living organisms. Even a small mutation in DNA sentence can cause many diseases. Therefore, developing sensitive, fast and precise methods for detection of DNA mutations is very important from a practical point of view. Promising methods for detection of specific DNA fragments are surface-enhanced Raman scattering (SERS) spectroscopy [1-4] and surface plasmon resonance (SPR) [5,6]. In this contribution we describe construction and tests with clinical samples of SERS and SPR sensors for the identification of six the most popular in Poland variants of *BRCA1* gene mutations (5370C>T, 300T>G, 5382insC, 4154delA, 185delAG, and 3819delGTAAA). Both sensors were based on the selective hybridization of target DNA with the capture DNA immobilized on plasmonic substrates (see Figure 1). Moreover, in both sensors the same thiolated capture DNA was used.

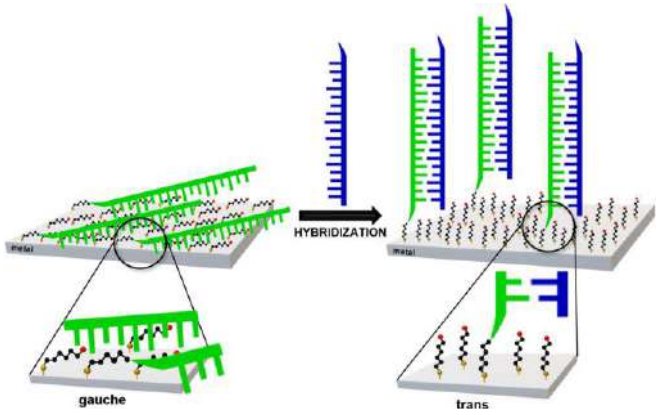


Figure 1. Scheme of the SERS DNA sensor based on rearrangement of the alkanethiol chains (alkanethiolate linking moiety of single stranded DNA and 6−mercaptohexan−1−ol). Reprinted from ref. [3]. CC BY license.

The mutation identification process using SPR detector relied on the shape of the SPR sensorgrams, whereas for the SERS sensors, the intensity of the Raman band at about 715-735 cm^{-1} (this band is due to the superimposition of mainly the band due to the ν(C−S) vibration of the alkanethiol chain in the *trans*

conformation and the band due to the breathing vibration of adenine) was used as an analytical signal (see Figure 2). The demonstrated biosensors are characterized by the low detection limit at the level of pg·μL^{-1}, wide analytical range and high selectivity. It was found that for different DNA sequences, a SPR or SERS sensor achieves greater detection sensitivity, which means that the selection of the optimal sensor type depends on the sequence of the target DNA. The proposed analytical approaches demonstrated completely new capabilities of SPR and SERS techniques and new insights into gene mutation detection.

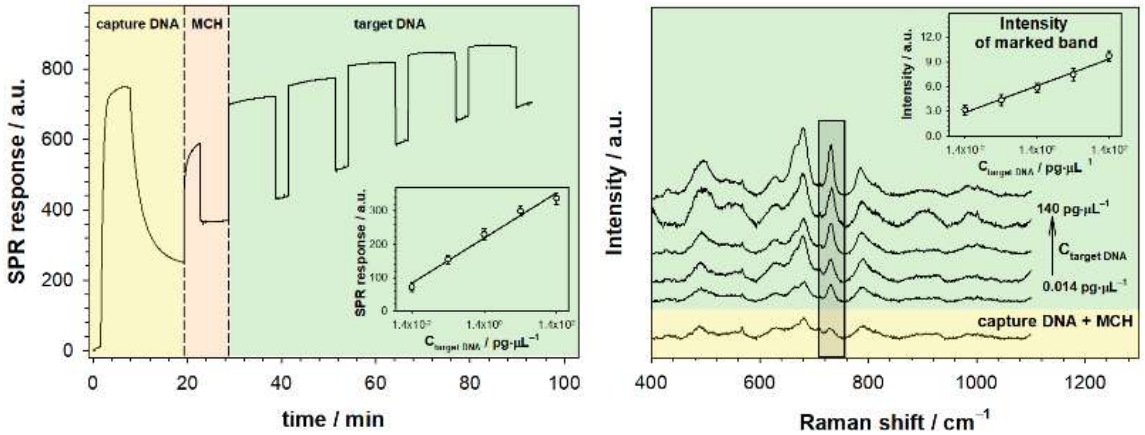


Figure 1. Example SPR curve and SERS spectra obtained before and after hybridization process with synthetic target DNA characteristic for the 4154delA mutation of the *BRCA1* gene. Insets: calibration curves. Experimental conditions: $C_{\text{capture DNA}}$ = 1.35 – 1.50 ng·μL^{-1} and $C_{\text{target DNA}}$ = 0.014; 0.14; 1.4; 14; 140 pg·μL^{-1}.

Acknowledgments

This work was financed by the National Science Centre, Poland, project No. 2019/35/B/ST4/02752.

References

1. He, Y., Su, S., Xu, T., Zhong, Y., Zapien, J. A., Li, J., Fan, C. and Lee, S.-T., "Silicon nanowires-based highly-efficient SERS-active platform for ultrasensitive DNA detection," Nano Today, Vol. 6, No. 2, 122–130, 2011.
2. He, S., Liu, K.-K., Su, S., Yan, J., Mao, X., Wang, D., He, Y., Li, L.-J., Song, S. and Fan, C., "Graphene-based high-efficiency surface-enhanced Raman scattering-active platform for sensitive and multiplex DNA detection," Anal. Chem., Vol. 84, No. 10, 4622–4627, 2012.
3. Michałowska, A., Gajda, A., Kowalczyk, A., Weyher, J. L., Nowicka, A. M. and Kudelski, A., "Surface-enhanced Raman scattering used to study the structure of layers formed on metal surfaces from single-stranded DNA and 6-mercaptohexan-1-ol: influence of hybridization with the complementary DNA and influence of the metal substrate," RSC Adv., Vol. 12, No. 54, 35192–35198, 2022.
4. Kowalczyk, A., Krajczewski, J., Kowalik, A., Weyher, J. L., Dzięcielewski, I., Chłopek, M., Góźdź, S., Nowicka, A. M. and Kudelski, A., "New strategy for the gene mutation identification using surface enhanced Raman spectroscopy (SERS)," Biosens. Bioelectron., Vol. 132, 326–332, 2019.
5. Gajda-Walczak, A., Potęga, A., Kowalczyk, A., Sęk, S., Kowalik, A., Zięba, S., Kudelski, A. and Nowicka, A. M., "New, fast and cheap prediction tests for BRCA1 gene mutations identification in clinical samples," Sci. Rep., Vol. 13, 7316, 2023.
6. Carrascosa, L. G., Calle, A. and Lechuga, L. M., "Label-free detection of DNA mutations by SPR: application to the early detection of inherited breast cancer," Anal. Bioanal. Chem., Vol. 393, No. 4, 1173–1182, 2009.

Topological photonic devices based on artificial gauge fields

Cuicui Lu[1]

[1]Beijing Institute of Technology, China
*corresponding author: cuicuilu@bit.edu.cn

Abstract: We realize on-chip topological rainbow nanophotonic devices by constructing synthetic dimensional photonic crystal. Recently, we further realize artificial gauge fields of both magnetic field and electric field, and observe different frequencies of Landau modes are localized at different positions of the photonic crystal, so we term this phenomenon “Landau rainbow”.

Topological photonics provides a robust platform for the realization of nanophotonic devices. We propose to construct synthetic dimensional topological photonic crystal by piecing a perfect photonic crystal and a deformed one to realize topological rainbow, where multiple topological photonic states spanning the whole bandgap can be realized at the interface. Figure 1a shows the fabricated photonic crystal sample. Multi-frequencies with different group velocities can be obtained and localized at different positions accompanied by multiple topological states (Fig.1b). Therefore, this contributes to the realization of topological rainbow device and slow-light devices.

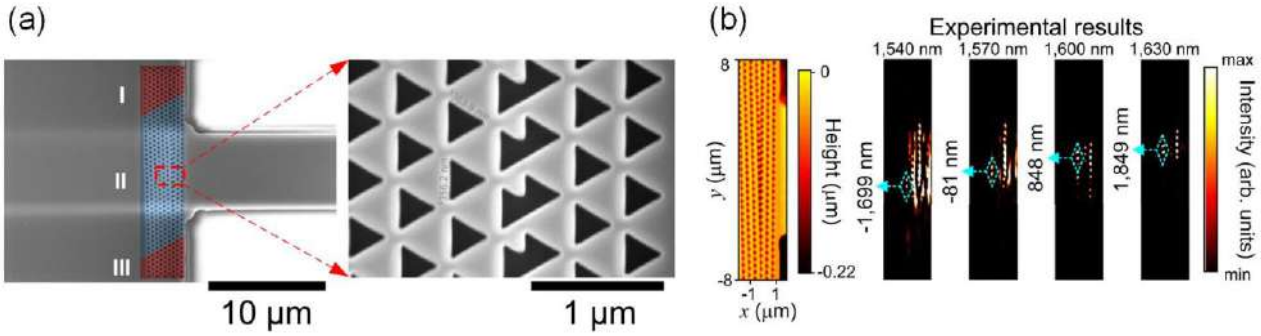


Fig. 1 On-chip topological rainbow. (a) SEM image of the topological photonic crystal. (b)Measured surface intensity of the electric field of the whole photonic crystal for incident different wavelengths using near-field scanning optical microscope system.

Recently, we simultaneously realize pseudo magnetic field (PMF) and pseudo-electric field (PEF) on a photonic crystal (PC) platform and observe a rainbow effect of the Landau zeroth modes. While PMF induces a series of discretized Landau levels of photons in a similar way as the quantum Hall effect for electrons (left figure of Fig.2a), PEF breaks the degeneracy of the flat band of Landau levels over a broad range (right figure of Fig.2a), thus different frequencies of the Landau modes can be dispersed into different spatial positions, leading us to term this phenomenon “Landau rainbow” (Fig.2b). The Landau rainbow, induced by the joint action of PMF and PEF, features robustness, broadband, and scalability, and may find applications in slow-light effect, multi-frequency divider, and optical information multiplexing.

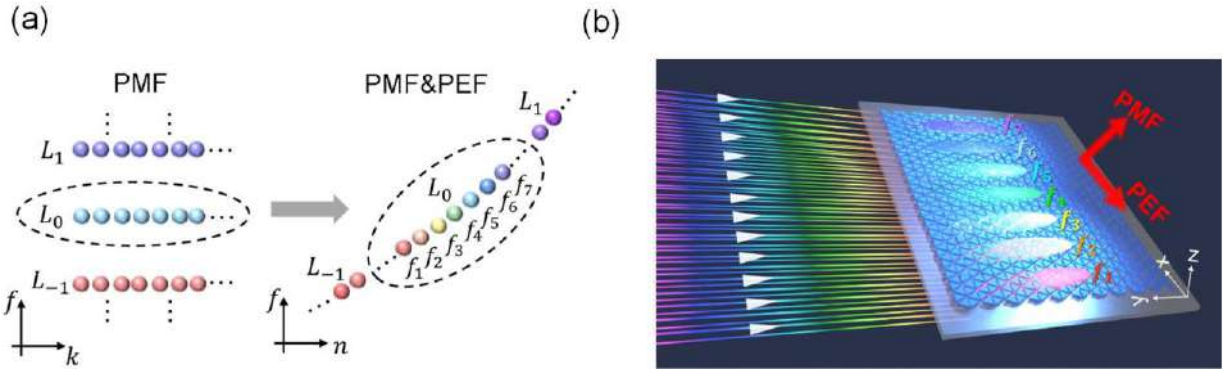


Fig. 2 Sketch of the Landau rainbow induced by pseudo-magnetic field (PMF) and pseudo-electric field (PEF). (a) The Landau levels are induced by PMF in *k* space, and the degeneracy of Landau levels is broken by the introduction of PEF in an aperiodic system. "*f*" denotes frequency and "*n*" represents the solution number. (b) The formed Landau rainbow effect, which can endow the zeroth Landau mode with different frequencies to be separated into different positions.

References

1. Cuicui Lu,*† Yi-Zhi Sun,† Chenyang Wang,† Hongyu Zhang, Wen Zhao, Xiaoyong Hu,* Meng Xiao, Wei Ding,* Yong-Chun Liu, C. T. Chan, "On-chip nanophotonic topological rainbow", Nature Communications vol. 13, 2586 (2022).
2. Wen Zhao†, Yanji Zheng†, Cuicui Lu†*, Zhihao Wang, Yong-Chun Liu, Shuang Zhang*, "Landau Rainbow Induced by Artificial Gauge Fields," Physical Review Letters, vol. 133, No. 23, 233801 (2024).

Engineering complex structured beams with flat optics

Xianzhong Chen, Hammad Ahmed, Chunmei Zhang*

School of Engineering and Physical Sciences, Heriot-Watt University, Edinburgh, UK
*corresponding author: x.chen@hw.ac.uk

Abstract: We experimentally demonstrated novel compact optical devices to generate complex structured beams such as new vector vortex beams and 3D polarization structures without relying on the complicated optical setup and realize their multifaceted control. The unprecedented design degree of freedom of optical metasurfaces has provided a compact platform to develop ultrathin optical devices for generating complex structured beams.

Vector vortex beams (VVBs) and 3D polarization structures represent typical complex structured beams. VVBs carry both orbital angular momentum (OAM) and polarisation information, allowing for high-dimensional information encoding. VVBs play a crucial role in singular optics and quantum optics and have been applied in many fields ranging from particle trapping to quantum entanglement. Polarization control has been used to record, process and store information. Light beams with 3D polarization distributions have received great attention owing to their peculiar optical features and practical applications such as higher resolution lithography and patterning of lyotropic chromonic liquid crystals by photoalignment.

Driven by device miniaturization and system integration, there is huge interest in developing ultrathin (light wavelength scale) and lightweight planar optical devices with novel functionalities that cannot be obtained with conventional optical elements. Optical metasurfaces are planar nanostructured interfaces and have recently attracted tremendous interests due to their unprecedented capability in the manipulation of the amplitude, phase and polarization at subwavelength scale. Optical metasurface have revolutionized design concepts in photonics, providing a new platform to develop unusual ultrathin optical devices. Optical metasurfaces have shown much promise for generating and manipulating complex structured beams. We have experimentally demonstrated grafted VVBs [1], multispectral grafted VVBs [2], superimposed Ince-Gaussian beams [3], cascaded multispectral polarization structures [4], and orbital angular momentum combs.

Multispectral manipulation will add more degrees of freedom. Furthermore, multifunctional optical devices have profound implications for research fields where light weight and integrated optical systems are highly desirable. There is an urgent need to develop multifunctional ultrathin devices that can simultaneously encode color and intensity information into 3D polarization profiles. A compact platform to generate and manipulate these beams is fundamentally challenging and technically impossible with conventional optics.

An innovative metasurface approach was proposed to break the current bottleneck. Many sophisticated optical tasks for grafted VVBs manipulation were completed for the first time. Grafted VVBs with multiple colours can realise asymmetric singularity modulation and colour selective functionalities, providing more degrees of freedom for multiplexing modulation and further increasing the capacity in optical communications and quantum information. The unique properties of the invented ultrathin devices will allow us to explore new phenomena in singular optics, nonlinear optics and quantum science, e.g., colour selective grafted VVBs, dynamic control of multispectral grafted VVBs and 3D polarization structures. The small volume, light weight, and color selective functionality bring 3D engineering capabilities closer to the real world and wearable devices

with smaller footprints. The flexible and controllable generation with customized complex structured beams of different colors (wavelengths) may be of interest to many practical applications such as vector beam generation, virtual reality, color displays, information security, and quantum science.

Acknowledgements

This work is supported by Engineering and Physical Sciences Research Council of the United Kingdom (Grant Ref: EP/P029892/1) and the Leverhulme Trust (RPG-2023-283 and RPG-2021-145).

References

1. H. Ahmed, M.A. Ansari, Y. Li, T. Zentgraf, M.Q. Mehmood, X. Chen, Dynamic control of hybrid grafted perfect vector vortex beams, Nature Communications, 14, 3915, 2023.
2. G. Wang, H. Ahmed, M.A. Ansari, Y. Li, C. Zhang, H. Tian, L. Li, X. Chen, Creating Multispectral Grafted Perfect Vector Vortex Beams in a Queue, Laser & Photonics Reviews, 240032, 2024.
3. H. Ahmed, M.A. Ansari, L. Paterson, J. Li, X. Chen, Metasurface for Engineering Superimposed Ince-Gaussian Beams Advanced Materials, 2312853, 2024.
4. Y. Li, Q. Yu, S. Zhao, Q. Yuan, F. Zhong, X. Chen, S. Wang, Metasurface-Enabled Cascaded Multispectral Polarization Structures Along the Longitudinal Direction, Advanced Optical Materials, 2403093, 2024.

Conducting polymer-cellulose devices for tunable infrared and THz optics

C. Y. Kuang[1*], S. Z. Chen[2], and M. P. Jonsson[1]

[1] Laboratory of Organic Electronics (LOE), Department of Science and Technology (ITN), Linköping University, Campus Norrköping, SE 601 74, Sweden

[2] School of Electronic Science and Engineering, State Key Laboratory of Electronic Thin Film and Integrated Devices, University of Electronic Science and Technology of China, Chengdu, Sichuan, 610 054, P. R. China

[*]corresponding author: Chaoyang.kuang@liu.se

Abstract: Conducting polymers possess excellent reversible tunability for optical and electrical properties, enabling their various applications ranging from organic (opto)electronics to nanophotonics. In this talk, I will present our latest studies on conducting polymer devices for terahertz and infrared photonic applications.

Conducting polymers possess redox-tunable optical and electronic properties and have been explored in various areas, including electrochemical transistors, electronic skins, and thermoelectric generators. Recently, we reported their applications for plasmonic nanoantennas for near infrared applications, showing promising redox-state tunability towards spatiotemporally dynamic metasurfaces. In this study, we combined conducting polymers with sustainable cellulose nanofibrils (CNF) to form optoelectronic devices for tunable terahertz (THz) and infrared (IR) photonic applications.

The tunable electrical and optical properties of conducting polymers originate from the difference of their redox states, where at the oxidized state the polymers possess a high charge carrier density, while the charges are neutralized at the reduced state. Such redox state modulation can be realized by various ways, and in this talk, we chose both chemical and electrical switching approaches.

I will first present a conducting polymer-cellulose aerogel and demonstrate that it can provide broadband reversible tuning of THz transmission between 13% and 91% through chemical approach, while maintaining specular reflection loss below -30 dB in both states. We associate the exceptional THz modulation with the anomalous optical conductivity peak of conducting polymers, which enhances the THz absorption in its oxidized state while it decreases the reflection in its reduced state. We believe that such switchable THz materials provide a promising route towards large and broadband THz modulation for next-generation intelligent THz devices.[1]

By structural modification, we obtained a flexible conducting polymer-cellulose paper with highly suitable properties for electrically controlled IR devices. Both the specular reflection and emissivity could be modulated with large amplitudes (more than 40%) via the polymer redox state. This enabled various new application scenarios, where we focused on tunable radiative coolers, dynamic thermal camouflage, infrared anti-counterfeiting tags, and infrared dynamic displays. The devices are sustainable, cheap, flexible and mechanically robust, providing a versatile materials platform for active and adaptive IR optoelectronic devices.[2]

Acknowledgements: C.K. and C.S. contributed equally to this work. The authors acknowledge support from the Swedish Research Council (VR, 2020-00287, 2022-00211, and 2022-06214), the Swedish Foundation for Strategic Research (SSF), the Stellenbosch Institute for Advanced Study (STIAS), the Swedish Foundation for

International Cooperation in Research and Higher Education (STINT), the Knut and Alice Wallenberg Foundation, the Swedish Government Strategic Research Area in Materials Science on Functional Materials at Linköping University (Faculty Grant SFO-Mat-LiU No. 2009 00971), Wallenberg Wood Science Center, the National Natural Science Foundation of China (NFSC, 62311530115, 62235004, 61831012, 62131006, and 52003202), the Sichuan Province Science & Technology Support Program (2021JDTD0026), and the Guangdong Science and Technology Major Special Fund (2019-252). M.P.J. is a Wallenberg Academy Fellow.

References

1. C. Kuang, S. Chen, M. Luo, Q. Zhang, Q. Wang, S. Han, X. Sun, M. J. Jafari, V. Stanishev, V. Darakchieva, T. Ederth, X. Crispin, M. Fahlman, Q. Wen, and M. P. Jonsson. “Tunable broadband terahertz absorbers based on sustainable conducting polymer aerogels,” Adv. Sci., Vol. 11, 2305898, 2024.
2. C. Kuang, S. Chen, M. Liao, A. Rahmanudin, D. Banerjee, J. Edberg, K. Tybrandt, D. Zhao, and M. P. Jonsson. “Electrically tunable infrared optics enabled by flexible ion-permeable conducting polymer-cellulose paper,” npj Flex Electron, Vol. 8, 55,2024.

Spectroscopy of single metal nanoparticles for single-molecule biosensing

Peter Zijlstra[1]

[1]Eindhoven University of Technology, Department of Applied Physics, The Netherlands

[*]corresponding author: p.zijlstra@tue.nl

Abstract: In this talk I will discuss two biosensing platforms that exploit plasmon-enhanced single-molecule detection. The first platform enables fluorescence-free sensing for hours, and is based on reversible nanoparticle-on-film coupling. The second platform enables the study of multivalent single-molecule interactions with microsecond temporal resolution.

Accurately quantifying kinetic processes such as protein interactions is essential for advancing our understanding of disease mechanisms and for the development of future diagnostic technologies. I will introduce two plasmon-enhanced single-molecule sensing platforms designed to investigate biomolecular processes across a broad range of timescales, from microseconds to hours. First, I will discuss a dynamic nanoparticle-on-film sensor that utilizes resonant coupling between localized and propagating plasmons for single-molecule detection [1,2,3]. This platform enables continuous monitoring of fluctuating biomolecular concentrations over extended periods by exploiting low-affinity (reversible) interactions [4]. Next, I will present an innovative platform based on plasmon-enhanced fluorescence, capable of probing single-molecule dynamics at microsecond timescales [5,6]. I will explore the underlying signal generation mechanisms and demonstrate the platform's potential to quantify both mono- and multivalent interactions in real-time. Accurately quantifying such kinetic processes across a wide temporal range is essential for advancing our understanding of disease mechanisms and for the development of future diagnostic technologies.

References

1. RE Armstrong, M Horáček, P Zijlstra, “Plasmonic assemblies for real-time single-molecule sensing,” Small **16,** 2003934 (2020).
2. A. Saateh, S. Ansaryan, J. Gao, L. Oliveira de Miranda, P. Zijlstra, H. Altug, “Long‐term and Continuous Plasmonic Oligonucleotide Monitoring Enabled by Regeneration Approach,” Angew. Chem. Int. Ed. **63,** e202410076 (2024).
3. L. Oliveira de Miranda, M. Dolci, K. Sergelen, C. Scarpellini, A. Dillen, A. Saateh, J. Lammertyn, H. Altug, P. Zijlstra, “Reversible Nanoparticle-on-film coupling for highly sensitive and continuous biosensing,” *in preparation.*
4. V. Lamberti, M. Dolci, P. Zijlstra, “Continuous monitoring biosensing mediated by single-molecule plasmon-enhanced fluorescence in complex matrices,” ACS Nano **18,** 5805-5813 (2024).
5. S.W. Nooteboom, K.R. Okholm, V. Lamberti, B. Oomen, D.S. Sutherland, P. Zijlstra, “Rate-Engineered Plasmon-Enhanced Fluorescence for Real-Time Microsecond Dynamics of Single Biomolecules,” Nano Lett. **24,** 11641-11647 (2024).
6. K.R. Okholm, S.W. Nooteboom, V. Lamberti, S. Dey, P. Zijlstra, D.S. Sutherland, “Kinetics and dynamics of single-molecule multivalent interactions revealed by plasmon-enhanced fluorescence,” ACS Nano **18,** 35429–35442 (2024).

Arbitrarily configurable nonlinear topological modes

K. Bai[1], **D. D. Wan**[1], **M. Xiao**[1*]

[1] Key Laboratory of Artificial Micro- and Nano-structures of Ministry of Education and School of Physics and Technology, Wuhan University, Wuhan 430072, China

[*]Corresponding author: phmxiao@whu.edu.cn

Abstract: We utilize nonlinearity to deform, reshape, and design topological mode (TM) wave functions, enabling dynamically tunable, arbitrarily shaped nonlinear topological modes controlled by external intensity. The nonlinear spectral localizer is employed to characterize the topological origin of these modes.

Topological modes (TMs) are typically localized at boundaries, interfaces and dislocations, and exponentially decay into the bulk of a large enough lattice. Recently, the non-Hermitian skin effect has been leveraged to delocalize the wavefunctions of TMs from the boundary and thus to increase the capacity of TMs dramatically. Here, we explore the capability of nonlinearity in designing and reconfiguring the wavefunctions of TMs. With growing intensity, wavefunctions of these in-gap nonlinear TMs undergo an initial deviation from exponential decay, gradually merge into arbitrarily designable plateaus, then encompass the entire nonlinear domain, and eventually concentrate at the nonlinear boundary. Intriguingly, such extended nonlinear TMs are still robust against defects and disorders, and stable in dynamics under external excitation. Advancing the conceptual understanding of the nonlinear TMs, our results open new avenues for increasing the capacity of TMs and developing compact and reconfigurable topological devices.

References

1. Bai, K. *et al.* “Arbitrarily Configurable Nonlinear Topological Modes”. Phys. Rev. Lett. **133**, 116602, 2024.

MEMS-tunable Metasurfaces for Dynamic Vortex Beam Generation

Chuanshuo Wang[1,2], Chao Meng[2,*], Lili Gui[1,*], Paul C. V. Thrane[2,3], Xianglong Mei[1], Hao Chen[1], Fei Ding[2], Kun Xu[1], and Sergey I. Bozhevolnyi[2]

[1]State Key Laboratory of Information Photonics and Optical Communications, Beijing University of Posts and Telecommunications, Beijing, 100876, China
[2]SDU Nano Optics, University of Southern Denmark, Campusvej 55, DK-5230 Odense, Denmark
[3]SINTEF Microsystems and Nanotechnology, Gaustadalleen 23C, 0737 Oslo, Norway
[*]Corresponding author: liligui@bupt.edu.cn; chao@mci.sdu.dk

Abstract: We present two electrically-driven MEMS-tunable metasurfaces for dynamic vortex beam generation: a single-layer optical metasurface for mode-switchable vortex lasers, and a double-layer metasurface for dynamic vortex wave plates, showcasing high mode purity and fast response at 1030 nm wavelength.

Optical metasurfaces (OMSs) have revolutionized light manipulation by offering compact and flexible optical devices. However, most OMSs are typically designed with well-defined optical responses, limiting their use in smart and adaptive photonic systems. Micro-electro-mechanical system (MEMS) provides a promising solution by supporting real-time reconfiguration of optical responses.[1,2] Here, we propose and demonstrate two MEMS-tunable metasurface platforms: (1) MEMS-OMS (single-layer OMS): integrated into a fiber laser, enabling rapid Gaussian-to-vortex mode switching.[3] (2) MEMS-BMS (bilayer OMS): functions as a dynamic vortex wave plate, toggling topological charges between $l = 2$ and $l = -1$ vortex modes. Both platforms leverage MEMS-actuated Fabry-Pérot (FP) resonance tuning, offering a novel solution for dynamic light manipulation.

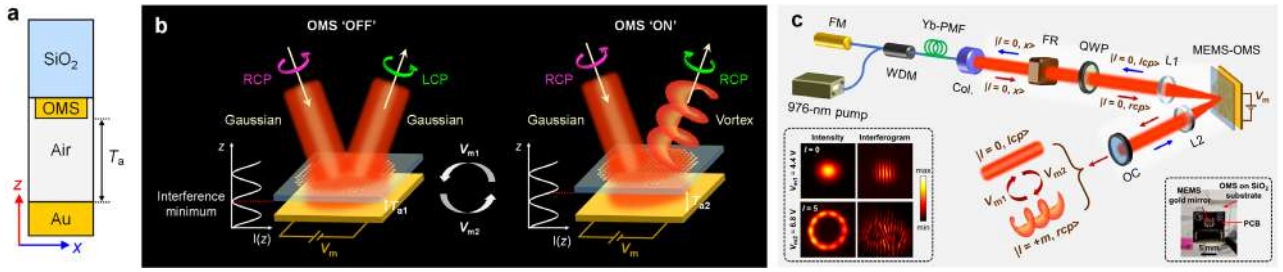


Fig. 1. (a) Schematic of the MEMS-OMS unit cell. (b) Working principle of the dynamic MEMS-OMS. (c) Schematic of the dynamic V-shaped vortex fiber laser. Bottom right inset: typical photo of the assembled MEMS-OMS component. Bottom left inset: measured intensity distributions and self-interference patterns of emitted Gaussian ($l = 0$, $V_{m1} = 4.4$ V) and vortex beams ($l = 5$, $V_{m2} = 6.8$ V).

The MEMS-OMS unit cell consists of a SiO_2 substrate, a gold (Au) nanobrick, and a movable MEMS Au mirror (Fig. 1a). The separation T_a between MEMS mirror and OMS can be precisely controlled by applying the voltage (V_m) to MEMS mirror. The MEMS-OMS operates in the periodic FP regime, with its optical response governed by the interplay of plasmonic and FP resonances. As shown in Fig. 1b, when the OMS layer is located at the interference minimum ('OFF' state, $T_{a1} = \sim k \times \lambda/2$, k is non-negative integers) induced by the incident and reflected fields, the MEMS-OMS functions as a standard mirror, reflecting left-handed circularly polarized (LCP) Gaussian beams ($l = 0$). When positioned away from the interference minimum ('ON' state) under a different V_m, the MEMS-OMS acts as a half-wave plate, imprinting a Pancharatnam-Berry (PB) phase to generate right-handed circularly polarized (RCP) vortex beams ($l = +m$). The MEMS-OMS component is assembled from an OMS fabricated on a SiO_2 substrate, a MEMS mirror, and a printed circuit board (PCB) for electrical connections (Fig.

1c, bottom right inset). The V-shaped laser cavity is formed between a fiber mirror (FM), a MEMS-OMS, and an output coupler (OC), with the intracavity beam evolution following a self-consistent polarization and mode transformation process (Fig.1c). This allows for controllable laser emission between Gaussian ($l = 0$, $V_{m1} = 4.4$ V) and vortex ($l = 5$, $V_{m2} = 6.8$V) modes (Fig. 1c, bottom left inset), featuring high mode purities (>95%) and fast response (100 μs).

The MEMS-BMS extends the dynamic functionality of metasurfaces by incorporating a BMS, consisting of MS1 and MS2 layers separated by an SU8 spacer, positioned above a MEMS-actuated Au mirror (Fig. 2a). This configuration allows independent phase modulation at two different separations, facilitating controlled mode switching between vortex beams with $l = 2$ and $l = -1$ under RCP light excitation (Fig. 2b). When the MS2 layer is in the 'OFF' state (interference minimum), the functionality of the MEMS-BMS is determined solely by the MS1 layer. Upon transitioning the MS2 layer to the 'ON' state (enhanced interference), the MEMS-BMS is jointly modulated by both MS1 and MS2 layers, enabling dynamic reconfiguration of the reflected vortex profiles. Scanning electron microscope (SEM) images of the fabricated BMS demonstrate good alignment between MS1 and MS2 layers (Fig. 2c). The detailed optical micrographs of the assembled MEMS-BMS component clearly show the piezoelectric material lead zirconate titanate (PZT) membrane cantilevers supporting a MEMS Au mirror, above which the circular BMS is fully covered (Fig. 2d, front view). Electrical connections were established by wire-bonding the MEMS mirror to the electrodes on the PCB (Fig. 2d, back view). The intensity and self-interference patterns of the reflected vortex beams with $l = 2$ ($V_{m1} = 4.8$ V) and $l = -1$ ($V_{m2} = 1.6$ V) confirm the dynamic mode-switching process (Fig. 2e). The faster response time (9 μs) is attributed to the intrinsic oscillation frequency, which is improved by the miniaturization of the MEMS mirror.

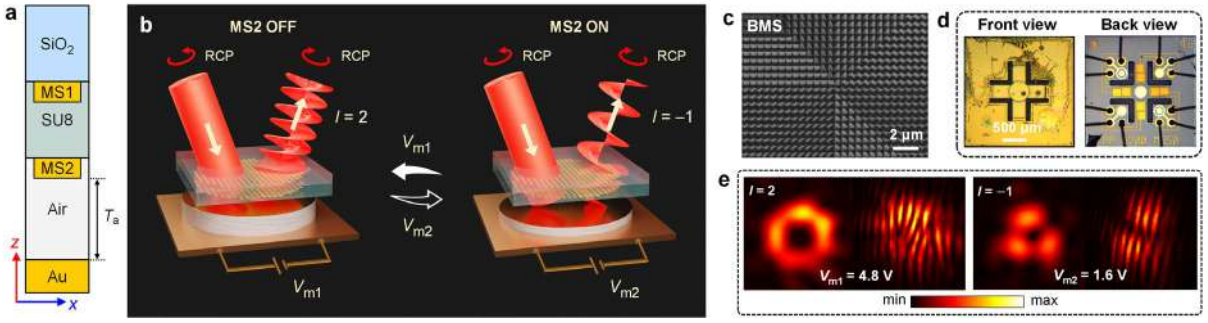


Fig. 2. (a) Schematic of the MEMS-BMS unit cell. (b) Working principle of the dynamic MEMS-BMS-based vortex wave plates. (c) SEM image of the fabricated BMS nanostructures. (d) Detailed optical micrographs of the assembled MEMS-BMS component. (e) Measured intensity distributions and self-interference patterns of reflected vortex beams with $l = 2$ ($V_{m1} = 4.8$ V) and $l = -1$ ($V_{m2} = 1.6$ V).

Our proposed MEMS-tunable metasurface platforms bridge static optics and adaptive systems, providing enhanced flexibility for dynamic light manipulation and paving the way for the next-generation photonic systems.

Acknowledgements This work was supported by National Natural Science Foundation of China (61905018), Fundamental Research Funds for the Central Universities (ZDYY202102), Fund of State Key Laboratory of Information Photonics and Optical Communications (Beijing University of Posts and Telecommunications) of China (IPOC2021ZR02), the Villum Fonden (Award in Technical and Natural Sciences 2019, Grant No. 37372 and 50343), and Attract Programme funded by the European Union's Horizon 2020 Research and Innovation Programme (101004462).

References

1. Meng, C., Thrane, P., Ding, F., Gjessing, J., Thomaschewski, M., Wu, C., Dirdal, C., and S. I. Bozhevolnyi, "Dynamic piezoelectric MEMS-based optical metasurfaces," Sci. Adv., Vol. 7, No. 26, eabg5639, 2021.
2. Meng, C, Thrane, P., Wang, C., Ding, F., and S. I. Bozhevolnyi, "MEMS-tunable topological bilayer metasurfaces for reconfigurable dual-state phase control," Optica, Vol. 11, No. 11, 1556-1566, 2024.
3. Wang, C., Meng, C., Mei, X., Gui, L., Thrane, P., Chen, H., Ding, F., Xu, K., and S. I. Bozhevolnyi, "MEMS-metasurface–enabled mode-switchable vortex lasers," Sci. Adv., Vol. 10, No. 47, eadq6299, 2024.

Edge bound state in the continuum on silicon pillar photonic crystal

R. Sato[1], C. Vinther Bertelsen[2], M. Nikitin[1], E. Lopez Aymerich[3], R. Malureanu[1], W. E. Svendsen[2], A. V. Lavrinenko[1], and O. Takayama[1,*]

[1]DTU Electro, Technical University of Denmark, Ørsteds Plads, Building 343, DK-2800, Kgs. Lyngby, Denmark

[2]DTU Bioengineering, Technical University of Denmark, Søltofts Plads, Building 221, DK-2800, Kgs. Lyngby, Denmark

[3]DTU Nanolab, Technical University of Denmark, Ørsteds Plads, Building 347, DK-2800, Kgs. Lyngby, Denmark
[*]corresponding author: otak@dtu.dk

Abstract: We report the first observation of bound states in the continuum mode supported at the edge of truncated photonic crystal where the terminating row of silicon pillars has different diameter from the rest of photonic crystal. Additionally we demonstrate the tuning of resonance by depositing nanometer thick alumina film.

A bound state in the continuum (BIC) is a highly localized optical mode trapped in radiative region of dispersion, which occurs at a certain special point of the dispersion diagram due to destructive interference in the structure that suppresses the radiative mode [1]. Regardless of the presence of leakage radiation, BIC modes exhibit extremely high quality (Q) factors and narrow resonances. In a realistic experimental system with a finite number of periodic elements and imperfections of structure, such as surface roughness and absorption loss, a BIC is called a quasi-BIC, which still possesses a finite high Q-factor. High Q-factors and highly confined electric fields of BIC modes have been studied for various potential applications, such as lasing [2], light modulation [3], biochemical sensing [4 - 6].

A unique type of BIC modes supported at the edge of truncated two-dimensional photonic crystal (2DPhC), a periodic arrangement of dielectric or metallic elements with a period typically smaller than the wavelength of light, was predicted a decade ago [7]. In such systems, surface waves or edge states supported at the edge of 2DPhC become a BIC mode under certain condition, depending on the pillar diameter. As a result, the BIC propagates along the terminating array of dielectric pillars, being highly localized at their vicinity.

Here we report the first experimental demonstration of such edge bound states in the continuum supported at the terminating row of silicon (Si) pillars which diameter is bigger than that of the rest of a Si-pillar square lattice two-dimensional photonic crystal, as illustrated in Fig. 1(a) [8]. The Q-factor and resonance wavelength of the edge BIC modes can be significantly controlled by the diameter of Si pillars in the terminating row diameter and there is an optimum diameter to support edge BIC. Furthermore, we show that their Q-factor and resonance position also are sensitive to a presence of a few nanometer-thick dielectric layer conformally deposited around Si pillars, as shown in Fig. 1(b). We conformally deposited 2.5, 4.7, and 7.3 nm thick aluminium oxide (alumina) films by atomic layer deposition (ALD). A slight change of the dielectric environment induced by the dielectric nanofilm results in over 60% improvement of the Q-factor from 237 to 396 for the deposited alumina film thickness of 2.5 nm, which can serve as post-fabrication tuning of edge BIC. Meanwhile, the resonance wavelength shifts 1.1 nm per 1 nm increase of the film thickness (Fig. 1(b) inset). This shows the surface sensitivity to detect the presence of a dielectric nanofilm and a potential sensing application to detect biomarkers.

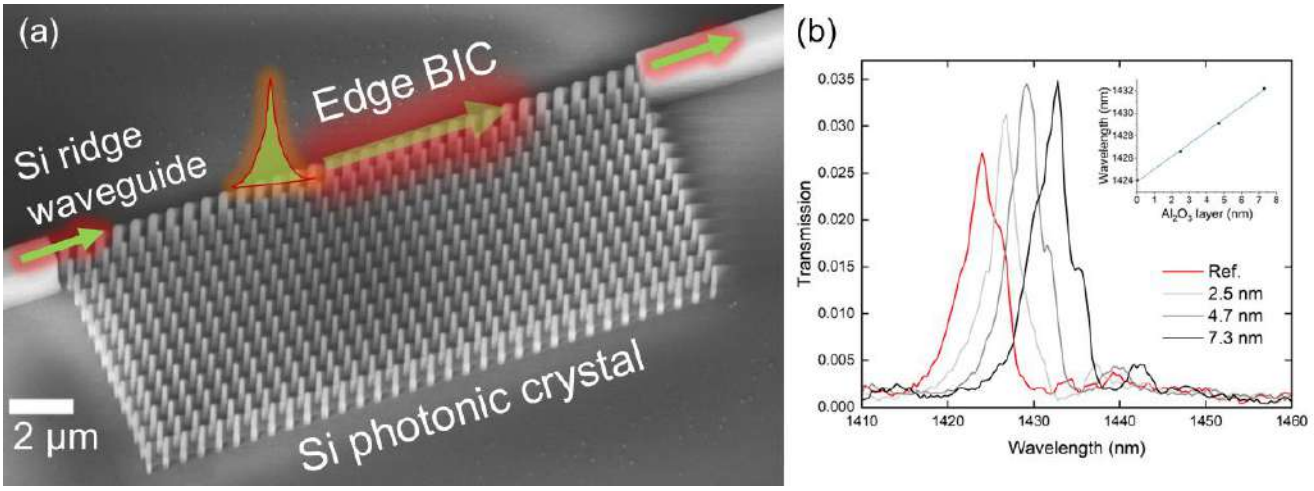


Figure 1: (a) Scanning electron microscope (SEM) image (birds-eye-view) of fabricated Si pillar photonic crystal structures connected with Si ridge waveguides. (b) Measured transmission spectra for different thickness of aluminum layer deposited. The inset shows the peak wavelength in terms of alumina layer thickness.

This research was supported by the European Union's Horizon 2020 research and innovation programme under the FETOPEN (grant number: 964808) "Continuous two-dimensional Stretch monitoring of fresh tissue Biopsies (StretchBio)", the Danish National Research Foundation through NanoPhoton - Center for Nanophotonics (grant number: DNRF147), and Villum Fonden, Villum Investigator Project (grant number: 00037822) "Table-Top Synchrotrons". The authors would like to acknowledge the support from the Danish National Center for Micro- and Nanofabrication (DTU Nanolab).

References

1. Hsu, C. W., B. Zhen, A. D. Stone, J. D. Joannopoulos and M. Soljacic, "Bound states in the continuum," Nat. Rev. Mater. Vol. 1, 16048, 2016.
2. Kodigala, A., T. Lepetit, Q. Gu, B. Bahari, Y. Fainman and B. Kanté, "Lasing action from photonic bound states in continuum," Nature Vol. 541, 196–199 2017.
3. Sun, X., J. Sun, Z. Wang, L. Wang, F. Qiu and L. Wen, "Manipulating Dual Bound States in the Continuum for Efficient Spatial Light Modulator," Nano Lett. Vol. 22, 9982–9989, 2022.
4. Romano, S., G. Zito, S. Torino, G. Calafiore, E. Penzo, G. Coppola, S. Cabrini, I. Rendina and V. Mocella, "Label-free sensing of ultralow-weight molecules with all-dielectric metasurfaces supporting bound states in the continuum," Photonics Res. Vol. 6, 726, 2018.
5. Tittl, A., A. Leitis, M. Liu, F. Yesilkoy, D.-Y. Choi, D. N. Neshev, Y. S. Kivshar and H. Altug, "Imaging-based molecular barcoding with pixelated dielectric metasurfaces," Science Vol. 360, 1105–1109, 2018.
6. Beliaev, L., O. Takayama and S. Xiao, "Effectively detecting cardiac myoglobin by use of bound states in the continuum in silicon nitride gratings," J. Appl. Phys. Vol. 135, 223101, 2024.
7. Wei Hsu, C., B. Zhen, S.-L. Chua, S. G. Johnson, J. D. Joannopoulos and M. Soljačić, "Bloch surface eigenstates within the radiation continuum," Light. Sci. Appl. Vol. 2, 84, 2013.
8. Sato, R., C. V. Bertelsen, M. Nikitin, E. L. Aymerich, R. Malureanu, W. E. Svendsen, A. V. Lavrinenko and O. Takayama, "Observation of edge bound states in the continuum at truncated silicon pillar photonic crystal," Nature Communications, Vol. 15, 10544, 2024.

Sub-wavelength optical lattice in 2D materials

S. Sarkar[1*], M. J. Mehrabad[1], D. G. Suárez-Forero[1], L. Gu[2], Y. Zhou[2], and M. Hafezi[1]
[1]Joint Quantum Institute, University of Maryland, College Park, USA
[2]Materials Science and Engineering, University of Maryland, College Park, USA
*sarkar@umd.edu (corresponding author)

Abstract

Conventional schemes for exploring light-induced phenomena rely on uniform and diffraction-limited free-space optics, which limits spatial resolution and efficiency of light-matter interaction. We overcome these challenges using metasurface plasmon polaritons to form a sub-wavelength optical lattice which allows efficient near-field modulation of excitons with on-chip pump rejection and thermal management.

1 Introduction

Recently, light-matter interaction has been expanded as a control tool for inducing and enhancing emergent non-equilibrium phenomena [1]. However, conventional schemes for exploring such light-induced phenomena rely on uniform and diffraction-limited free-space optics, which limits the spatial resolution and the efficiency of light-matter interaction. Here, we overcome these challenges using metasurface plasmon polaritons (MPPs) proposed in Ref. [2] to form a sub-wavelength optical lattice [3, 4]. Specifically, we report a "nonlocal" pump-probe scheme where MPPs are excited to induce a spatially modulated AC Stark shift for excitons in a monolayer of $MoSe_2$, several microns away from the illumination spot.

Figure 1(a) illustrates our scheme. The metasurface device consists of a 1D array of silver nano-grooves and is designed to support a 1D lattice of MPPs with negligible diffraction around wavelengths close to the excitonic resonance. A pump laser (marked in red) is coupled into the MPP modes through the top coupler. The traveling MPPs form a sub-diffraction periodic potential for the $MoSe_2$ monolayer, whose exciton resonance lies at a wavelength $\sim$750 nm. A broadband beam (marked in white) probes the modulation of the transition metal dichalcogenide (TMD) excitons at a spot distant from the top coupler. Figure 1(c) shows the normalized electric field intensity $|E|^2$ in the x-z plane at 800 nm. The red curve in Fig. 1(b) shows the electric field intensity $|E|^2$ at the position of the TMD. Importantly, due to this sub-diffraction variation of $|E|^2$, the excitons experience a position-dependent AC stark shift: those located at the local maxima of $|E|^2$ experience a larger blue shift compared to other excitons.

2 Results

To demonstrate the sub-diffraction nonlocal AC Stark shift scheme, we excite the MPP modes using a 150 fs pulsed laser at 800 nm wavelength. Remarkably, we identify nearly two orders of magnitude reduction for the required modulation power compared to the free-space optical illumination counterpart for the same amount of AC Stark shift (Fig. 1f-g). Moreover, we demonstrate a broadening of the excitons' linewidth as a robust signature of MPP-induced periodic sub-diffraction modulation of the electric field (Fig. 1h-i). Additionally, our scheme provides protection from parasitic thermal and pump-induced noise ubiquitous in traditional "local" pump-probe spectroscopy. Our results open new avenues for exploring power-efficient

light-induced lattice phenomena below the diffraction limit in active chip-compatible MPP architectures.

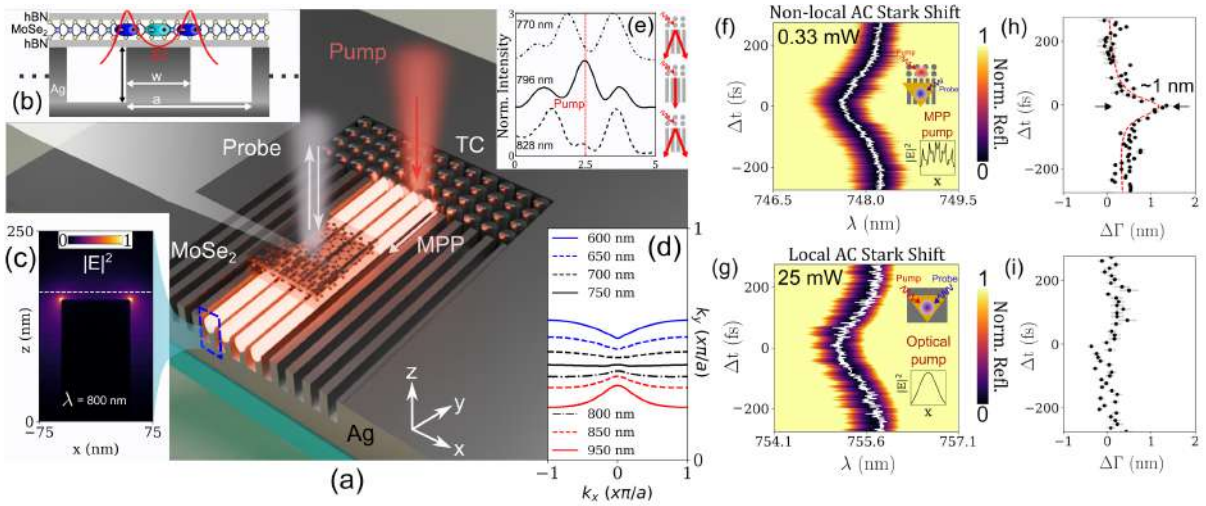


Figure 1: **Sub-wavelength optical lattice in 2D materials.** (a) Scheme for inducing AC Stark shift on a $MoSe_2$ monolayer using MPPs in a 1D lattice of silver grooves. The periodically modulated MPP modes are excited with a pump laser (red beam) at the top coupler (TC). The MPP device is designed to strongly confine the plasmonic modes, which propagate in the y-direction of the lattice with negligible diffraction within $700 \in 800$ nm, which is close to the excitonic resonance of ~ 750 nm in $MoSe_2$. A secondary broadband laser (white beam) probes the $MoSe_2$ excitons. (b) Schematic of the device cross-section. The red curve shows the strong $|E|^2$ modulation at the position of the $MoSe_2$ monolayer for a pump of 800 nm. (c) Normalized $|E|^2$ at the x-z cross-section of the device. The position of the TMD is marked by the dashed horizontal line. (d) Iso-frequency contours of the MPP device for different wavelengths of MPPs showing suppressed diffraction in the range 700-800 nm. (e) Experimentally measured spatial pattern of the emission from the output coupler for three different wavelengths: 770 nm, 796 nm and 828 nm. The red dashed line shows the position of the pump laser. (f-g) Measured nonlocal and local AC Stark shifts respectively. The white lines show the extracted exciton peak wavelength. The insets show the experimental schematic. (h-i) The change in linewidth $\Delta\Gamma$ of the exciton extracted from the numerical fitting of the nonlocal and local AC Stark shift data respectively.

References

[1] Bloch, J., A. Cavalleri, V. Galitski, M. Hafezi, and A. Rubio, "Strongly correlated electron–photon systems," *Nature*, 606(7912), pp.41-48, 2022.

[2] High, A.A., R.C. Devlin, A. Dibos, M. Polking, D.S. Wild, J. Perczel, N.P. De Leon, M.D. Lukin, and H. Park, "Visible-frequency hyperbolic metasurface." *Nature*, 522(7555), pp.192-196, 2015.

[3] Sarkar, S., M.J. Mehrabad, D.G. Suárez-Forero, L. Gu, C.J. Flower, L. Xu, K. Watanabe, T. Taniguchi, S. Park, H. Jang, Y. Zhou, and M. Hafezi, "Sub-wavelength optical lattice in 2D materials," *arXiv:2406.00464*, 2024.

[4] Kim, H., H. Dehghani, H. Aoki, I. Martin, and M. Hafezi, "Optical imprinting of superlattices in two-dimensional materials." *Physical Review Research*, 2(4), p.043004, 2020.

Metasurface-Enhanced Single-Shot 3D Imaging for High-Precision Biological and Industrial Applications

Huijie Hao[1], Jian Liu[1], and Xumin Ding[1*]

[1] Advanced Microscopy and Instrumentation Research Center, School of Instrumentation Science and Engineering, Harbin Institute of Technology, Harbin 150080, China
[*]corresponding author: xuminding@hit.edu.cn

Abstract: We present a metasurface-enabled microscope for single-shot three-dimensional (3D) imaging, leveraging double-helix point spread function (DH-PSF) to achieve high axial localization accuracies in both 4*f* and 2*f* systems. This compact system facilitates rapid, high-precision 3D reconstruction of biological specimens and industrial samples, advancing meta-microscopy for bioimaging and semiconductor inspection.

3D imaging plays a critical role in biological research and industrial quality control. However, conventional techniques such as confocal and light-sheet microscopy often depend on bulky optical components and mechanical scanning mechanisms, which hinder operational efficiency [1, 2]. PSF engineering, particularly the DH-PSF, enables single-shot 3D imaging with high precision, which is suitable for multiple applications [3]. Metasurfaces, with their ability to manipulate light at subwavelength scales, present a promising avenue for the miniaturization of optical systems [4, 5]. Here, we integrate DH-PSF engineering with metasurfaces to develop a compact meta-microscope, achieving efficient, single-shot 3D imaging with exceptional precision and resolution.

Our meta-microscope is realized in two configurations: a 4*f* imaging system (Fig. 1a) and a 2*f* imaging system (Fig. 1b). The 4*f*-DH meta-microscope, with an NA of 0.7, achieves an axial localization accuracy of 0.12 μm over a 15.47 μm range. The 2*f*-DH meta-microscope, with an NA of 0.3, extends the detection range to 227.33 μm with an accuracy of 1.12 μm. Both systems utilize an all-dielectric metasurface to generate the DH-PSF, enabling rapid and precise 3D imaging without mechanical scanning.

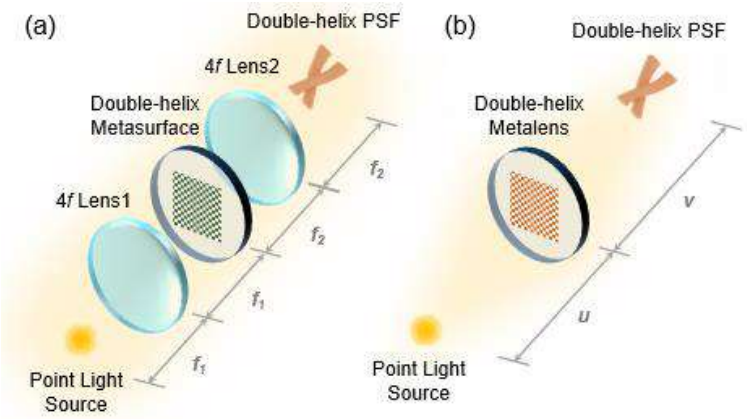


Fig. 1. Schematic of DH meta-microscope. (a) Sketch for the imaging process of 4*f*-DH meta-microscope, which is composed of a DH metasurface placed in the Fourier plane of the 4*f* system, where f_1 and f_2 are the focal lengths of two 4*f* lenses. (b) Mechanism of 3D-meta-imager composed of an integrated DH metalens. *u* and *v* represent the object distance and image distance respectively, which are related to the axial detection range and localization accuracy.

Figure 2 presents the 3D imaging and reconstruction capabilities of the DH meta-microscope. Three letter-shaped apertures—H, I, and T (Fig. 2a)—are positioned along the optical axis of the 2*f*-DH meta-microscope. Fig. 2b displays the raw image and reconstruction result of modulated objects recorded through the DH metalens, with the letters placed at the front focal, focal plane, and back focal plane. To further validate the 3D imaging performance of biological samples, peach anther particles (10–20 μm in size) were positioned on either side of a 170 μm thick cover glass. The raw data and reconstruction results are depicted in Fig. 2c and 2d. The results demonstrate the system's ability to simultaneously capture transverse intensity and axial depth information. This metasurface-enabled meta-microscope offers a compact, high-speed, and high-precision solution for single-shot 3D reconstruction.

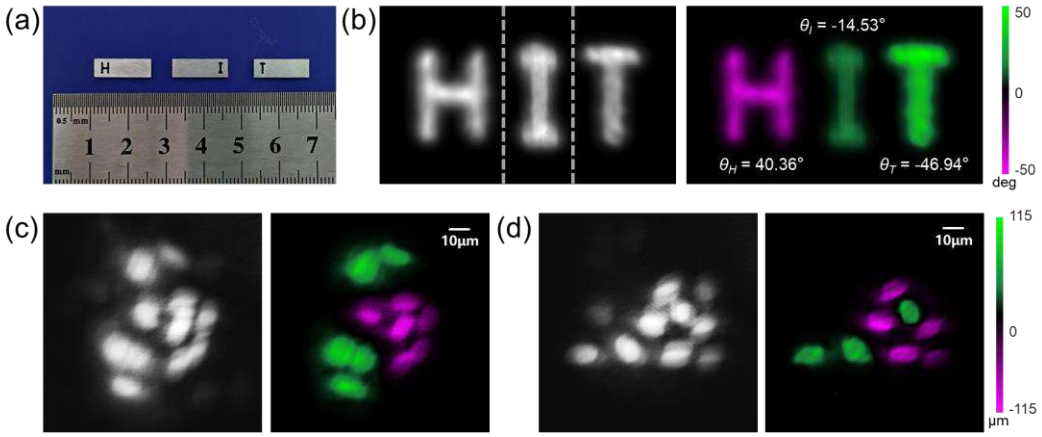


Fig. 2. 3D imaging results of DH meta-microscope. (a) Schematic diagram of the fabricated letter samples. The line width of the letters is 0.4 mm. (b) The reconstruction image of letters, where the rotation angles of H, I, and T are shown in the colored image. (c, d) Biological imaging demonstration of peach anthers.

Acknowledgments

This work was supported by National Key R&D Program of China (2021YFF0603500), and National Natural Science Foundation of China (62275063).

References

1. Wilson, T. "Confocal microscopy," Academic Press London, 1990.
2. Chen, B. C., Legant, W. R., Wang, K., et al. "Lattice light-sheet microscopy: imaging molecules to embryos at high spatiotemporal resolution," Science, Vol. 346, No. 6208, 1257998, 2014.
3. Pavani, S. R., Piestun, R. "High-efficiency rotating point spread functions," Opt. Express, Vol. 16, No. 5, 3484-3489, 2008.
4. Yu, N., Genevet, P., Kats, M. A., et al. "Light propagation with phase discontinuities: generalized laws of reflection and refraction," Science, Vol. 334, No. 6054, 333-337, 2011.
5. Shen, Z., Zhao, F., Jin, C., et al. "Monocular metasurface camera for passive single-shot 4D imaging," Nat. Commun., Vol. 14, No. 1, 1035, 2023.

All-optical control and detection of broken time-reversal symmetry and topological nonlinear optics

G. Soavi[1]

[1]Institute of Solid State Physics, Friedrich Schiller University Jena, Germany
[*]corresponding author: giancarlo.soavi@uni-jena.de

Abstract: I will discuss our recent experimental and theoretical efforts in the field of all-optical control and detection of broken time-reversal symmetry and topological nonlinear optics.

Layered materials, such as graphene and transition metal dichalcogenides (TMDs), possess unique nonlinear optical (NLO) properties [1], which allow a full control over the intensity [2,3], polarization [4] and orbital angular momentum [5] of the light emitted *via* perturbative harmonic generation processes.

Furthermore, TMDs have emerged as the ideal platform to study the interplay between space-inversion and time-reversal symmetries, which can be independently engineered in these layered materials by tuning the number of layers (space-inversion) and *via* excitation with circularly polarized light (time-reversal). In this talk, I will discuss our recently developed approaches to modulate the bandgap in TMDs using ultrafast and off-resonant excitation, and the possibility to subsequently detect broken time-reversal symmetry using second [6,7] and third harmonic generation. In particular, all-optical bandgap modulation can be achieved *via* the coherent optical Stark and Bloch-Siegert effects, with the additional degree of freedom to create either a symmetric or asymmetric bandgap opening in the ±K valleys, depending on the polarization state of the excitation beam. In monolayer TMDs, asymmetric bandgap modulation effectively corresponds to breaking of time-reversal symmetry. Subsequently, both symmetric and asymmetric all-optical bandgap modulation can be probed *via* polarization and intensity dependent measurements of perturbative NLO (**Figure 1**).

Finally, I will discuss our recent theoretical efforts to establish the background for the field of topological nonlinear optics [8]. I will show that the derivatives of the Berry curvature can be readily linked to the properties of specific crystal classes *via* a simple expression that involves the second order nonlinear susceptibility tensor. From this, we find features that are unique of chiral and polar crystal classes, and we discuss a possible and novel geometrical interpretation of circular dichroism and spontaneous polarization.

This work was funded by the German Research Foundation (DFG) (CRC 1375 NOA), project number 398816777 (subproject C4); the International Research Training Group (IRTG) 2675 ‘Meta-Active’, project number 437527638 (subproject A4); and the Federal Ministry for Education and Research (BMBF) project number 16KIS1792 SiNNER.

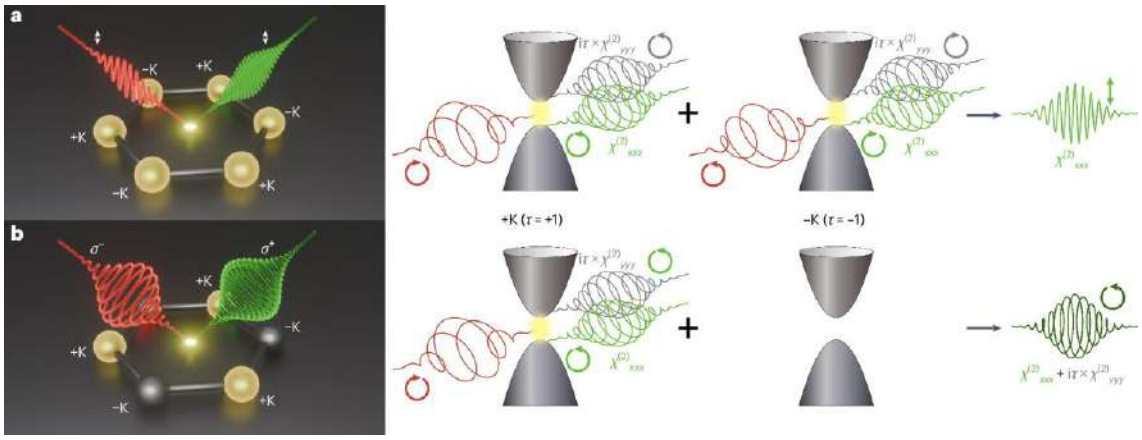


Figure 1. a, A linearly polarized FB (left, red) can be decomposed into right- and left-circular components that interact with both the ±K valleys in a symmetric way **b**, A right-circularly polarized FB (left, red) interacts only with the +K valley. This creates and probes an asymmetric bandgap modulation in the valleys, which corresponds to a situation where time-reversal symmetry is broken. Reprinted with permission from Ref. [6].

References

1. Dogadov, O. *et al.*, "Parametric Nonlinear Optics with Layered Materials and Related Heterostructures", Laser & Photon. Rev., Vol. 16, No. 9, 2100726, 2022
2. Soavi, G. *et al.*, "Broadband, electrically tunable third-harmonic generation in graphene", Nat. Nanotechnol., Vol. 13, 583-588, 2018
3. Ghaebi, O. *et al.*, "Ultrafast Opto-Electronic and Thermal Tuning of Third-Harmonic Generation in a Graphene Field Effect Transistor", Adv. Science, Vol. 11, No. 31, 2401840, 2024
4. Klimmer, S. *et al.*, "All-optical polarization and amplitude modulation of second-harmonic generation in atomically thin semiconductors", Nat. Photon., Vol. 15, 837-842, 2021
5. Sinelnik, A. et al., "Ultrafast all-optical second harmonic wavefront shaping", Nat. Comms., Vol. 15, 2507, 2024
6. Herrmann, P. *et al.*, "Nonlinear valley selection rules and all-optical probe of broken time-reversal symmetry in monolayer WSe_2", Nat. Photon., *published online*, 2025.
7. Herrmann, P. *et al.*, "Nonlinear All-Optical Coherent Generation and Read-Out of Valleys in Atomically Thin Semiconductors", Small, Vol. 19, No.37, 2301126, 2023
8. Soavi, G. and Wilhelm, J., "The signature of topology in polar and chiral non-magnetic crystal classes", arXiv:2501.03684 [cond-mat.mes-hall], 2025

Creation of Novel Scattering Singularities in Generic Non-Hermitian Systems Probed Through Complex Time Delay

Jared Erb[1], Nadav Shaibe[1], Thomas M. Antonsen[1], and Steven M. Anlage[1*]

[1] Physics Department, University of Maryland, College Park, MD 20742-4111 USA
[*]corresponding author: anlage@umd.edu, website: https://anlage.umd.edu

Abstract: We utilize continuously tunable metasurfaces to find conditions for divergent complex time delay to create and identify numerous types of scattering singularities in generic complex microwave resonant systems in 1, 2, and 3-dimensions. We demonstrate novel properties of several composite scattering singularities in two- and three-dimensional parameter spaces.

The complete control of wave scattering in complex non-Hermitian settings is of interest for communications applications in indoor environments, among other things. This requires the ability to engineer the resonant spectrum of the underlying physical structures which is conventionally accomplished by carefully imposing geometrical and/or dynamical symmetries. In contrast, by taking active control over the boundary conditions in complex scattering environments which lack artificially-imposed geometric symmetries, we demonstrate via microwave experiments the ability to manipulate the spectrum of the scattering operator [1]. We utilize measurements of the scattering matrix to determine the complex time delay for wave propagation through the system [2-4]. Divergences of the complex time delay reveal the location of many different types of scattering singularities [5]. For example, by means of active control of the boundary conditions we can create, destroy and re-position exceptional point degeneracies (EPD's) in a two-dimensional (2D) parameter space [6]. The presence of EPD's signifies a coalescence of the scattering eigenmodes, which dramatically affects transport. The scattering EPD's are partitioned in domains characterized by a binary charge, as well as an integer winding number, are topologically stable in the two-dimensional parameter space, and obey winding number-conservation laws upon interactions with each other, even in cases where Lorentz reciprocity is violated; in this case the topological domains are destroyed. Ramifications of this understanding is the proposition for a unique input-magnitude and phase-insensitive 50:50 in-phase/quadrature (I/Q) power splitter for EPDs combined with conditions that enable Coherent Perfect Absorption (CPA) [7]. We also discovered a new way in which the CPA condition creates a novel type of splitter with fixed but arbitrary values for relative output and phase. We show that this condition can be tuned in frequency and in output power/phase ratio by means of the system metasurfaces. Our study establishes an important step towards complete control of scattering processes in complex non-Hermitian settings.

We thank David Shrekenhamer and Timothy Sleasman of JHU APL for the design and fabrication of the metasurfaces used in this work. This work was supported by NSF/RINGS under grant No. ECCS-2148318, ONR under grant N000142312507, DARPA WARDEN under grant HR00112120021.

References

1. Jared Erb, David Shrekenhamer, Timothy Sleasman, Thomas M. Antonsen, and Steven M. Anlage, "Control of the Scattering Properties of Complex Systems By Means of Tunable Metasurfaces," Acta Physica Polonica A **144** (6), 421-428 (2023).

2. Lei Chen, Steven M. Anlage, and Yan V. Fyodorov. Generalization of Wigner time delay to subunitary scattering systems. Phys. Rev. E, **103**, L050203, (2021).
3. Lei Chen, Steven M. Anlage, Yan V. Fyodorov, "Statistics of Complex Wigner Time Delays as a counter of S-matrix poles: Theory and Experiment," Phys. Rev. Lett. **127**, 204101 (2021).
4. Lei Chen and Steven M. Anlage, "Use of Transmission and Reflection Complex Time Delays to Reveal Scattering Matrix Poles and Zeros: Example of the Ring Graph," Phys. Rev. E **105**, 054210 (2022).
5. Nadav Shaibe, Jared M. Erb, and Steven M. Anlage, "Superuniversal Statistics of Complex Time-Delays in Non-Hermitian Scattering Systems," arXiv:2408.05343 (2024).
6. Jared M. Erb, Nadav Shaibe, Robert Calvo, Daniel Lathrop, Thomas Antonsen, Tsampikos Kottos, Steven M. Anlage, "Novel Topology and Manipulation of Scattering Singularities in Complex non-Hermitian Systems." arXiv:2411.01069 (2024).
7. Lei Chen, Tsampikos Kottos, and Steven M. Anlage, "Perfect Absorption in Complex Scattering Systems with or without Hidden Symmetries," Nature Communications **11**, 5826 (2020).

Non-noble metal plasmonic nanostructures

M. Horák[1*], M. Foltýn[1], and T. Šikola[1]

[1]Brno University of Technology, Brno, Czech Republic
[*]corresponding author: michal.horak2@ceitec.vutbr.cz

Abstract: We present an investigation of localized surface plasmon resonances in nanostructured non-noble metals at a single particle level, with a focus on their spectral tunability. The study specifically examines silver amalgam, gallium, and bismuth while the latter has been identified as a viable substitute for gold.

In metallic nanostructures, collective oscillations of free electrons are strongly coupled to the electromagnetic field, forming excitations known as localized surface plasmons. These excitations are characterized by a significant enhancement of the electromagnetic field within the surrounding dielectric, along with its confinement on the subwavelength scale. This property can be utilized to control various optical processes, even below the free space diffraction limit. Despite the considerable promise exhibited by gold-based plasmonic applications, their widespread utilization is impeded by two significant challenges. Firstly, the high fabrication costs associated with these applications pose a substantial obstacle, and secondly, the plasmon energy range is constrained by interband transitions, which limits their effectiveness. These challenges can be addressed by exploring alternative metals such as gallium, bismuth, lead, and tin. Theoretical predictions indicate that these metals could offer comparable plasmonic performance while providing a broader plasmon energy range [1]. In this contribution, we present an experimental investigation of the plasmonic properties of silver amalgam [2] and gallium nanoparticles [3] as well as bismuth plasmonic antennas [4] using scanning transmission electron microscopy (STEM) combined with electron energy loss spectroscopy (EELS) [5,6], which allows for single particle analysis.

Silver amalgam is one of the most suitable solid electrode materials in electroanalysis. An exploration of the plasmonic nature of its nanoparticles has been conducted, resulting in the observation of strong plasmon resonances spanning the ultraviolet to mid-infrared regions for sizes ranging from nano- to micro-scale [2]. These findings establish silver amalgam nanoparticles as promising candidates for applications within photochemistry and spectroelectrochemistry, where the synergy between their plasmonic and electrochemical qualities can be fully utilized.

Gallium is a plasmonic material offering facile and scalable preparation and good stability of nanoparticles. We have grown lens-shaped gallium nanoparticles directly on a silicon nitride membrane using an effusion cell and experimentally proven that their dipole mode can be tuned through their size from the ultraviolet to near-infrared spectral region [3].

Finally, to investigate the plasmonic potential of bismuth, thin polycrystalline bismuth films were sputtered onto silicon nitride membranes. Thereafter, bowtie and bar plasmonic antennas of varying sizes were fabricated using focused ion beam lithography [7,8]. While the fabricated bismuth antennas exhibit lower plasmon resonance intensity than gold ones, the nearly identical plasmon energies across the entire range of tested antenna sizes demonstrate bismuth's potential as a viable alternative in plasmonic applications (see Figure 1). Moreover, the experimentally verified wider interval of bismuth plasmon energies allows applications at shorter wavelengths as well. The plasmonic performance of bismuth antennas has been validated, highlighting their potential as a viable substitute for gold [4].

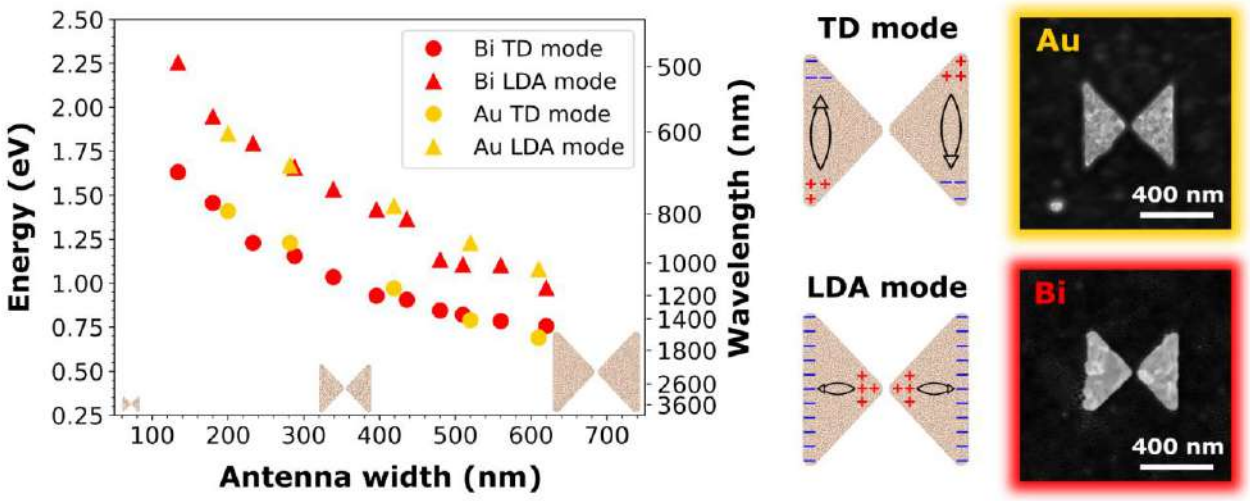


Figure 1: Energy of transverse dipole (TD) and longitudinal antibonding dipole (LDA) mode as a function of the reciprocal antenna width for bismuth and gold antennas. Based on the observed overlap of the two dependencies, bismuth can serve as a cheaper plasmonic alternative to gold. The data for gold bowtie antennas originates from Ref. [9].

This work is supported by the project QM4ST (project No. CZ.02.01.01/00/22_008/0004572) by OP JAK, call Excellent Research. M.F. acknowledges the support of the Brno Ph.D. talent scholarship.

References

1. Sanz, J. M., D. Ortiz, R. Alcaraz de la Osa, J. M. Saiz, F. González, A. S. Brown, M. Losurdo, H. O. Everitt and F. Moreno, "UV Plasmonic Behavior of Various Metal Nanoparticles in the Near- and Far-Field Regimes: Geometry and Substrate Effects," J. Phys. Chem. C, Vol. 117, No. 38, 19606–19615, 2013.
2. Ligmajer, F., M. Horák, T. Šikola, M. Fojta and A. Daňhel, "Silver Amalgam Nanoparticles and Microparticles: A Novel Plasmonic Platform for Spectroelectrochemistry," J. Phys. Chem. C, Vol. 123, No. 27, 16957−16964, 2019.
3. Horák, M., V. Čalkovský, J. Mach, V. Křápek and T. Šikola, "Plasmonic Properties of Individual Gallium Nanoparticles," J. Phys. Chem. Lett., Vol. 14, No. 8, 2012–2019, 2013.
4. Foltýn, M., T. Šikola and M. Horák, "Bismuth plasmonic antennas," *in preparation*, 2025.
5. Horák, M. and T. Šikola, "Influence of experimental conditions on localized surface plasmon resonances measurement by electron energy loss spectroscopy," Ultramicroscopy, Vol. 216, 113044, 2020.
6. Horák, M., A. Konečná, T. Šikola and V. Křápek, "Spatio-spectral metrics in electron energy loss spectroscopy as a tool to resolve nearly degenerate plasmon modes in dimer plasmonic antennas," Nanophotonics, Vol. 12, No. 15, 3089–3098, 2023.
7. Horák, M., K. Bukvišová, V. Švarc, J. Jaskowiec, V. Křápek and T. Šikola, "Comparative study of plasmonic antennas fabricated by electron beam and focused ion beam lithography," Sci. Rep., Vol. 8, No. 1, 9640, 2018.
8. Foltýn, M., M. Patočka, R. Řepa, T. Šikola and M. Horák, "Influence of Deposition Parameters on the Plasmonic Properties of Gold Nanoantennas Fabricated by Focused Ion Beam Lithography," ACS Omega, Vol. 9, No. 35, 37408−37416, 2024.
9. Křápek, V., A. Konečná, M. Horák, F. Ligmajer, M. Stöger-Pollach, M. Hrtoň, J. Babocký and T. Šikola "Independent engineering of individual plasmon modes in plasmonic dimers with conductive and capacitive coupling," Nanophotonics, Vol. 9, No. 3, 623–632, 2020.

Characterizing the mechanical properties of single bacteria in air by multimode tracking nanomechanical resonators

A. Aparicio-Millán*, E. Sentre-Arribas, J. J. Ruz, S. García-López, P. M. Kosaka, M. Calleja, J. Tamayo and E. Gil-Santos

Instituto de Micro y Nanotecnología (IMN-CNM, CSIC), C/Isaac Newton 8 (PTM, Tres Cantos), 28060, Madrid, Spain
*alicia.aparicio@csic.es

Abstract: Nanomechanical resonators are powerful biosensing tools. While the mass and mechanical properties of individual human cells have been characterized in liquid, smaller entities, including bacteria, viruses, and proteins, have only been reliably analysed in vacuum. We demonstrate the characterization of single bacterial cells' mass and mechanical properties under ambient conditions.

In recent decades, nanomechanical resonators have become powerful tools for developing innovative biosensing technologies. Researchers have successfully characterized the mass and mechanical properties of individual human cells in liquid environment, as well as single bacteria, viruses and even proteins in vacuum [1]. This work presents a new technique for characterizing the mass and mechanical properties of single bacterial cells (*Staphylococcus epidermidis* and *Escherichia coli*) under ambient conditions. We deposit individual bacterial cells onto the sensor surface (100 nm-thick squared shaped microcantilevers made of silicon nitride, 40 μm side) with micrometric precision using an injection micropipette system. We monitor the frequency response of multiple mechanical modes of the sensor simultaneously, specifically, 1st and 2nd flexural modes, and 1st and 2nd torsional modes (Figure 1), to the adsorption of an individual bacterial cell. This enables disentangling the mass and stiffness effects induced by analyte adsorption, while also providing information about its morphology [2]. Finally, we demonstrate that our technique allows to distinguish between the two bacterial species, based on their mass, stiffness and morphology [3].

In the near future, we want evaluate this technique through its application to many other bacterial cell species and other microbiological entities, such as human cells or viruses. Additionally, we plan to extend this technique to liquid operation, the natural medium for biology. Our technique will provide new insights into the inherent properties of different microbiological entities and their biological processes, significantly impacting the biomedicine and clinical diagnosis.

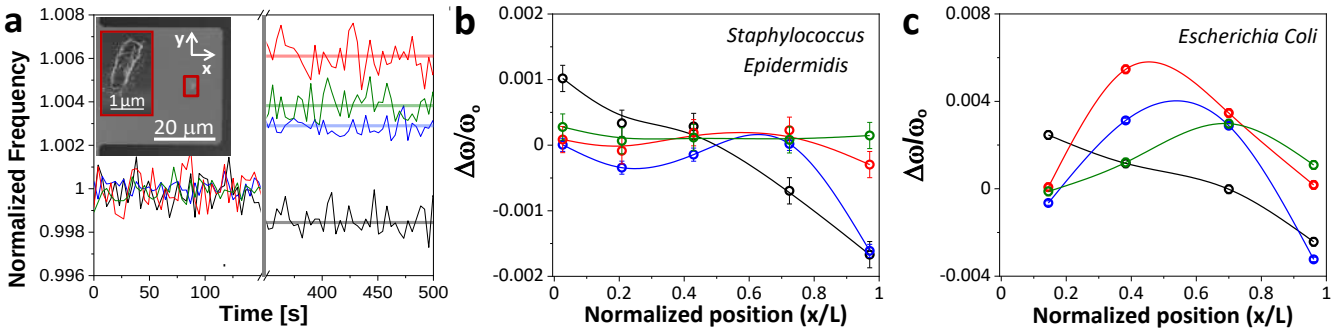


***Figure 1. a**. Normalized frequencies (ω/ω_o) of the sensor's 1st flexural (black), 1st torsional (red), 2nd flexural (blue) and 2nd torsional (green) modes before and after the adsorption of an individual Escherichia coli cell. The*

inset shows a scanning electron microscope image of a sensor after bacterium adsorption. Solid lines indicate the averaged normalized frequencies before and after the adsorption. ***b.*** *Relative frequency shifts of the sensor's mechanical modes induced by the adsorption of individual Staphylococcus epidermidis cells, adsorbed at positions centered along the y-axis and distributed along the longitudinal direction.* ***c.*** *Relative frequency shifts of the sensor's mechanical modes induced by the adsorption of individual Escherichia coli cells, adsorbed at positions centered along the y-axis and distributed along the longitudinal direction. Solid lines serve as visual guides.*

Acknowledgments: This work was supported by the Spanish Science, Innovation and Universities Ministry through the projects CNS2022-135367, PDC2023-145867-I00 and PID2023-1511160B-I00. We acknowledge Jesús Mingorance for guidance and for providing the bacterial samples. All the authors acknowledge service from the IMN X-SEM Laboratory, which is funded by MCIU (project CSIC13-4E-1794) and the EU (FEDER, FSE).

References

1. J. Tamayo, P. M. Kosaka, J. J. Ruz, Á. San Paulo and M. Calleja, "Biosensors based on nanomechanical systems," Chem. Soc. Rev., **42**, 1287–1311, 2013.
2. J. J. Ruz, Ó. Malvar, E. Gil-Santos, M. Calleja and J. Tamayo, "Effect of particle adsorption on the eigenfrequencies of nano-mechanical resonators," J. Appl. Phys., **128**, 104503, 2020.
3. A. Aparicio-Millán, et al. In preparation.

High-resolution photothermal imaging using mid-infrared photo-induced force microscopy - modeling and experiment

M. Ali[1,2], S. T. Anindo[3,4], R. Schneider[2,5], C. David[3,6], and D. Täuber[1,2*]

[1]Institute of Physical Chemistry, Friedrich Schiller University Jena, Germany
[2]Leibniz Institute of Photonic Technology, Germany
[3]Institute of Condensed Matter Theory and Optics, Friedrich Schiller University Jena, Germany
[4]Abbe Center of Photonics, Friedrich Schiller University Jena, Germany
[5]Aalen University of Applied Sciences, Germany
[6]University of Applied Sciences Landshut, Germany
[*]corresponding author: daniela.taeuber@uni-jena.de

Abstract: Mid-IR photo-induced force microscopy (PiF-IR) provides unprecedented spatial and high spectral resolution of the chemical composition in surfaces in the Materials and Life Sciences. We model the near-field-enhanced interaction of nanostructured materials with metallic atomic force microscopy tips enabling a qualitative evaluation of experimental results in PiF-IR and related methods.

The development of powerful mid-infrared (mid-IR) lasers in combination with sophisticated approaches in signal detection has opened the avenue for chemical characterization on the nanoscale complementing structural information provided by other methods, as for example, electron and fluorescence microscopy. In mid-IR photo-induced force microscopy (PiF-IR, also named mid-IR PiFM) tunable and pulsed quantum cascade lasers (QCLs) illuminate the region between a sharp metallic atomic force microscopy probe (AFM-tip) and the sample of interest. The conservative component $F_c(z)$ of the static tip-sample interaction force $F_{ts}(z)$ in the non-contact regime is the attractive van der Waals interaction force [1–3]. The near-field enhanced absorption in the tip-sample region induces a thermal expansion of the materials at their resonant IR frequencies resulting in a modulation of the van der Waals interaction due to material density reduction. PiF-IR is operated in dynamic non-contact AFM mode at small oscillation amplitudes of 1-2 nm, which enables to detect the force gradient $\partial F_{ts}/\partial z$ by employing a heterodyne detection scheme (sideband mode) [1, 3]. This sideband detection scheme provides access to the characterization of the chemical composition of materials surfaces with an unprecedented spatial resolution of ≈ 5 nm [4].

In a study applying PiF-IR to differently polarized F-Actin, a major structural protein in vertebrate cells, nanoscale chemical variations associated with the protein organization were found and compared to the significant local variations obtained from PiF-IR scans of mouse liver tissue at three different IR frequencies [4]. Our preliminary results from the investigation of *Bacillus subtilis* cells incubated with a β-Lactam antibiotic affecting the cell wall reveal the heterogeneous response of individual bacteria cells to the antibiotics by showing variations in the protein and glycan content of the cell surfaces (Figure 1a). For fully exploiting the potential of PiF-IR and related tip-enhanced infrared spectroscopic imaging methods for applications in the Life and Materials Sciences, further understanding of the signal generation in nanostructured samples is required.

In a comprehensive approach, we modeled the non-linear impact of material characteristics and surface shape on the tip-sample interaction, the photo-induced electric field (the schematics for our setup are depicted in the 3D topography image of the bacteria cells in Figure 1b), the heat generation and the associated thermal expansion under different illumination conditions including light polarization, as well as, the feedback to the dynamic tip

motion due to the expansion [3]. The comparison of the results from a simulated setup with our experimental investigation of a spherical polymer nanoparticle (NP, see Figure 1c, d) shows good agreement [3] contributing new insights into the understanding of PiF-IR contrasts obtained from nanostructured materials. In the here studied case of isotropically absorbing materials, an enhanced signal is found on the nanostructure perpendicular to the propagation vector k_0 of the illuminating field E_0, which oscillates in-plane with the oblique incidence onto the tip-sample region [3], see the enhanced signal on the NP in the experimentally obtained PiF contrast in respect to the illuminating field depicted by red arrows in Figure 1d).

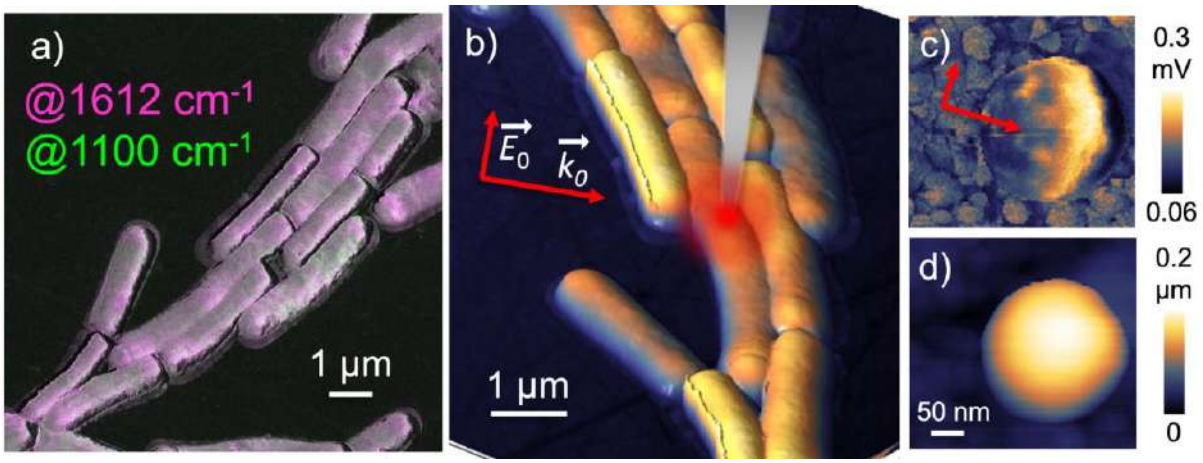


Figure 1. Photo-induced for microscopy: a) Merged RGB image PiF contrast of Bacillus subtilis cells succeedingly scanned @1100 cm^{-1} (green, glycans) and @16120 cm^{-1} (pink, peptides); b) schematics of near-field enhancement in our setup on 3D image of simultaneously acquired topography; c) PiF contrast of a spherical PMMA nanoparticle with radius 50 nm and d) simultaneously acquired height image.

Such signal enhancement parallel to the field oscillation vector is also visible in a study applying peak force infrared (PFIR) on grains of an isotropically absorbing material [5], which confirms the relevance of our results for a qualitative interpretation of data obtained using tip-enhanced infrared illumination on nanostructured materials. Further work, including other geometries and also anisotropically absorbing materials is required for a quantitative analysis of such contrasts obtained on nanostructured materials.

Funding by the Friedrich Schiller University, Profile line LIGHT, project pintXum and by the German Research Foundation (439139881) is acknowledged.

References

1. Sifat, A.A., Jahng, J., Potma, E.O. “Photo-induced force microscopy (PiFM) – principles and implementations,” Chem. Soc. Rev. 4208–4222, 2022.
2. Wang, L., Wang, H., Vezenov, D., Xu, X.G. “Direct Measurement of Photoinduced Force for Nanoscale Infrared Spectroscopy and Chemical-Sensitive Imaging,” J. Phys. Chem. C, Vol. 122, 23808–23813, 2018.
3. Anindo, S.T., Täuber, D., David, C. “Photothermal Expansion of Nanostructures in Photo-induced Force Microscopy,” J. Phys. Chem. C, doi: 10.1021/acs.jpcc.4c08305, 2025.
4. Joseph, J., Spantzel, L., Ali, M., Moonnukandathil Joseph, D., Unger, S., Reglinski, K., Krafft, C., Müller, A.-D., Eggeling, C., Heintzmann, R., Börsch, M., Press, A.T., Täuber, D. “Nanoscale chemical characterization of secondary protein structure of F-Actin using mid-infrared photoinduced force microscopy (PiF-IR),” Spectrochimica Acta A, Vol. 306, 123612, 2024.
5. Xie, Q., Wang, H., Xu, X.G. “Dual-Frequency Peak Force Photothermal Microscopy for Simultaneously Spatial Mapping Chemical Distributions and Energy Dissipation.” J. Phys. Chem. C., Vol. 126, 8393–8399, 2022.

Hyperuniform Disordered Materials for Solar and Solar-Thermal Absorbers

M. Florescu[1*]

[1]Optoelectronics Research Centre, University of Southampton, Southampton SO17 1BJ, United Kingdom

[*]corresponding author: m.florescu@soton.ac.uk

Abstract: Hyperuniform disordered structures demonstrate great potential to enhance light absorption in solar cell and solar-thermal absorber architectures and due to unique light trapping mechanisms capable of attaining absorption enhancements up 85% over the visible spectrum and record solar cell efficiency in ultra-thin film solar cells.

Keywords: hyperuniform disorder, correlated disorder, solar cell, solar-thermal absorbers

In recent decades, advancements in nanoscience and nanotechnology have enabled precise control over nanostructures, playing a crucial role in enhancing solar energy capture, conversion, and storage. State-of-the-art fabrication techniques now offer extensive design flexibility, facilitating the development of complex and aperiodic geometries, such as hyperuniform, quasi-periodic, fractal, and seemingly random patterns. When appropriately designed, these structures can outperform conventional approaches while demonstrating increased resilience to fabrication imperfections. However, the absence of simple and systematic design methodologies has thus far hindered their full exploitation.

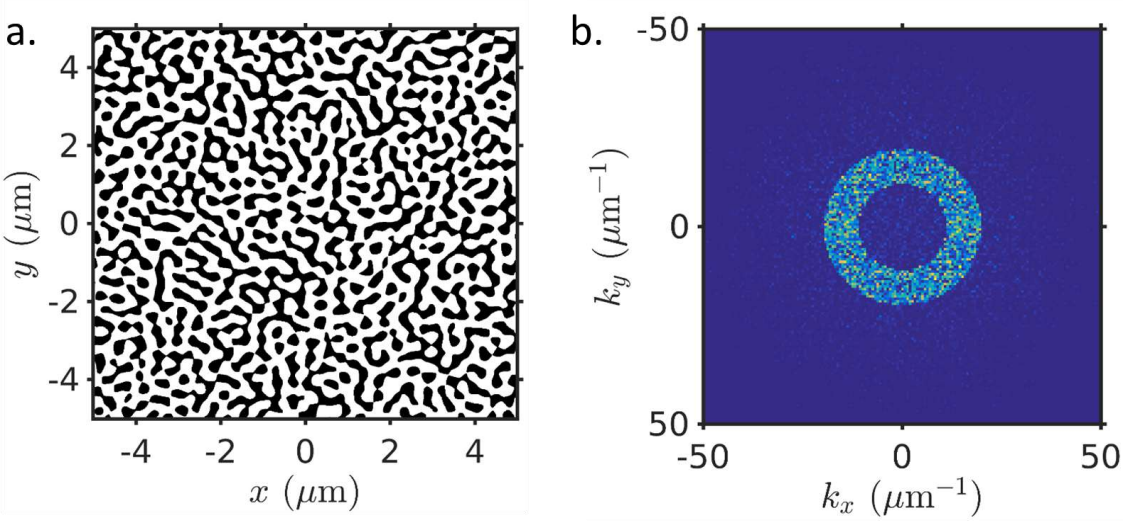


Figure 1. (a) Nearly-hyperuniform distribution of dielectric material generated under periodic boundary conditions. (b) Diffraction spectrum of the structure in (a) with most of the diffraction power concentrated in a circular shell of predefined boundaries.

Here, we employ novel hyperuniform and nearly-hyperuniform disordered architectures [1], [2], [3], [4] for selective absorbers to achieve an optimal control over the absorption of the solar spectrum. Utilizing an inverse Fourier-space design approach, we identify optimal absorber designs based on their Fourier components to achieve two key objectives: enhancing the efficiency and angular acceptance of solar cell absorbers while optimizing the trade-off between undesirable out-of-plane scattering losses and beneficial in-plane light trapping.

This approach aims to push absorption performance toward its ultimate theoretical limit.

The hyperuniform patterning is implemented as a textured layer atop a 1-micron-thick silicon slab, designed to optimize the coupling of incident solar radiation to the slab's supported optical modes [5]. Within the targeted spectral range of 400 to 1050 nm, silicon exhibits strong dispersion, leading to significant curvature of the silicon light cone and substantial variations in absorption. At shorter wavelengths, absorption remains high even with suboptimal coupling to incident radiation. However, at longer wavelengths, efficient coupling to the quasi-waveguided modes of the silicon slab becomes critical to counteract the inherently lower absorption of silicon. Our focus is on optimizing coupling to modes with wavevectors in the range of [10, 20] μm^{-1}, which facilitate access to the spectral region where silicon absorption is weaker [6]. The absorption spectra of hyperuniform disordered structures exhibit several notable characteristics. Most significantly, the spinodal structure achieves the highest overall absorption efficiency, reaching 85%, representing a substantial improvement over the untextured anti-reflective coating. Notably, despite their differing morphologies, the optimized structures share a common feature: filling fractions consistently within the 50–60% range. Additionally, the oscillations observed in the absorption spectrum of the unpatterned silicon slab are attributed to Fabry-Pérot resonances, which have previously been leveraged to enhance absorption in thin-film solar cells.

In conclusion, we have investigated the application of hyperuniform disordered texturing to enhance solar radiation absorption. The efficiency of solar energy harvesting is governed by key physical mechanisms, including diffraction induced by surface patterning and coupling to the relevant guided modes of the crystalline silicon (c-Si) slab. Our findings demonstrate that an absorption enhancement of up to 85% of incident solar radiation can be achieved within the broadband range of 400–1050 nm on a 1 μm-thick silicon membrane. This approach can be extended to other solar energy harvesting applications, such as solar-thermal absorbers for solar thermionic systems [6–9], where concentrated sunlight is utilized to generate electricity with high efficiency and minimal cost. In this context, solar radiation absorption would occur within a specially designed metasurface, composed of optimally engineered metal-dielectric-metal resonators arranged in a hyperuniform pattern to enhance coupling to the resonant modes.

Acknowledgements. This work was supported by the EPSRC (United Kingdom) Strategic Equipment under grant No. EP/Y016440/1 and EP/M027791/1 awards.

References

1. Florescu, M., Torquato, S., and Steinhardt, P. , Proceedings of the National Academy of Sciences 106, 20658 (2009);
2. G. Gkantzounis, T. Amoah and M. Florescu, Phys. Rev. B, 95, 094120 (2017);
3. T. Amoah and M. Florescu, Phys. Rev. B 91, 020201(R) (2015).
4. M. M Milosevic, W. Man, G. Nahal, P. J Steinhardt, S. Torquato, P. M Chaikin, T. Amoah, B. Yu, R. A. Mullen, and M. Florescu , Scientific Reports 9, 20338 (2019)
5. N. Tavakoli, R. Spalding, A. Lambertz, P. Koppejan, G. Gkantzounis, C. Wan, R. Rohrich, E. Kontoleta, A. F. Koenderink, R. Sapienza, M. Florescu and E. Alarcon-Llado, ACS Photonics 9, 2102565 (2022);
6. Nunez-Sanchez, S. et al., Micro Nano Lett., 13: 1325 (2018); https://doi.org/10.1049/mnl.2018.0156
7. Croot, A. et al., Diam. Relat. Mater. 109, 108011 (2020); https://doi.org/10.1016/j.diamond.2020.108011
8. Croot, A. et al., Front. Mech. Eng. 3, 17 (2017). https://doi.org/10.3389/fmech.2017.00017
9. Wan, G. et al., Carbon 185, 376-38(2021); https://doi.org/10.1016/j.carbon.2021.09.045

Developing quantitative multiscale models for nonlinear molecular plasmonics

M. Sukharev

Arizona State University, USA
maxim.sukharev@asu.edu

Abstract: The research program established in my group integrates computational electrodynamics in the nonlinear optical regime with the quantum dynamics of large molecular systems. This talk overviews our recent advances in the field of nonlinear nano-optics and molecular plasmonics highlighting newly developed computational method, namely molecular mapping technique.

Nonlinear plasmonics has been a subject of increasing interest in the past few decades. With significant advancements in experimental capabilities enabling the localization of light into sub-diffraction volumes, numerous nonlinear optical phenomena, once predominantly studied in macroscopic systems, are now being explored at the nanoscale. A wide variety of metal nanoparticles (MNPs) shapes and arrays of nanoholes have been employed to investigate phenomena such as second harmonic generation, four-wave mixing, and many other nonlinear processes. For instance, we have recently demonstrated that the second harmonic generation can be used as a very sensitive optical tool for detecting spatial variations in MNPs shapes at the nanoscale level.

While significant attention has been paid to the harmonic generation using plasmonic nanostructures, reports on the reverse process of difference frequency generation (DFG) have been limited. With the help of a theoretical model and FDTD simulations based on the hydrodynamic-Maxwell model, we examine the effect of DFG in an array of L-shaped MNPs characterized by intrinsic plasmonic nonlinearity. The outcomes of the calculations reveal the spectral interplay of the gain and loss in the vicinity of the fundamental frequency of the localized surface-plasmon resonances. Our results suggest that the parametric amplification regime becomes feasible on a scale of hundreds of nanometers and parametric downconversion on the scale of tens of nanometers, opening exciting new opportunities for developing building blocks of photonic metasurfaces.

I will discuss the effect of resonant optical cavities on nonlinear multiphoton transitions in molecules. Our self-consistent quantum model provides fundamental insights into the complex dynamics of strongly coupled molecule-cavity systems. The observed modifications in molecular relaxation pathways, particularly the persistent alignment and collective dephasing effects, demonstrate the profound influence of cavity coupling on molecular quantum states. The cavity-induced rotational pumping mechanism represents a novel approach for controlling molecular orientation, with potential applications in ultrafast molecular switches and Schrödinger–Maxwell information processing. The discovery of relaxation stabilization through collective dephasing suggests new strategies for preserving quantum coherence in molecular systems. Furthermore, the predicted alterations in circular dichroism spectra of chiral metasurfaces under strong coupling open avenues for engineering enhanced light-matter interactions in nanophotonic devices and chiral sensing applications. These findings advance our understanding of molecular polaritonics and provide a theoretical framework for designing next-generation quantum optical devices and molecular control techniques.

M.S. research is supported by the Air Force Office of Scientific Research under Grant No.

FA9550-22-1-0175 and by the Office of Naval Research, Grant No. N000142512090.

References

1.ω Sukharev, M., J. Subotnik, A. Nitzan, “Unveiling the Dance of Molecules: Ro-Vibrational Dynamics of Molecules under Intense Illumination at Complex Plasmonic Interfaces”, J. Chem. Theory Comput, ASAP (2025). DOI: 10.1021/acs.jctc.4c01652

2.ω Shah, S., M. R. Clark, J. Zyss, M. Sukharev and A. Piryatinski, “Interplay of gain and loss in arrays of nonlinear plasmonic nanoparticles: toward parametric down-conversion and amplification”, Opt. Let.., Vol. 49, 104107 (2024).

3.ω Clark, M. R., S. A. Shah, A. Piryatinski and M. Sukharev, “Harnessing complexity: nonlinear optical phenomena in L-shapes, nanocrescents, and split-ring resonators”, J. Chem. Phys., Vol. 161, 104107 (2024).

4.ω Sukharev, M, “Efficient parallel strategy for molecular plasmonics – a numerical tool for integrating Maxwell-Schrödinger equations in three dimensions”, J. Comp. Phys., Vol 477, 111920 (2023).

5.ω Ngo, H. M., E. Drobnyh, M. Sukharev, Q. K. Vo, J. Zyss and I. Ledoux-Rak, “High yield synthesis and quadratic nonlinearities of gold nanoprisms in solution: the role of corner sharpness”, Isr. J. Chem. e202200009 (2022).

6.ω Li, C., X. Lu, A. Srivastava, S. D. Storm, R. Gelfand, M. Pelton, M. Sukharev and H. Harutyunyan, “Second harmonic generation from a single plasmonic nanorod strongly coupled to a WSe_2 monolayer”, Nano Lett., Vol. 21, 1599 (2020).

7.ω Maekawa, H., E. Drobnyh, C. A. Lancaster, N. Large, G. C. Schatz, J. S. Shumaker-Parry, M. Sukharev and N.-H. Ge, “Wavelength and polarization dependence of second harmonic responses from gold nanocrescent arrays” J. Phys. Chem. C, Vol. 124, 20424 (2020).

Metasurface with gap and collective surface plasmon modes

A.O. Pinchuk[1*], and O.A. Yeshchenko[2]

[1]Center for Plasmonics, Nanophotonics, and Metamaterials, University of Colorado Colorado Springs, CO, 80918 USA, [2]Physics Department, Taras Shevchenko National University of Kyiv, Kyiv, 01601, Ukraine

*corresponding author: apinchuk@uccs.edu

A tunable metasurface, constructed from a monolayer of gold nanoparticles on a glass substrate positioned in close proximity to a thin aluminum film, was studied both numerically and experimentally. Three distinct peaks, dependent on angle and polarization, were observed in the metasurface's extinction spectra. Using the Finite-Difference Time-Domain (FDTD) method, we confirmed the positions of both the collective surface plasmon and the gap modes. We found that changing the polarization of the incident light results in a wavelength shift of these spectral peaks.

A strong coupling between gap and collective surface plasmon polariton modes was recently reported in a system consisting of a monolayer of gold nanoparticles on a glass substrate, separated from a thin aluminum film by a shellac polymer spacer of varying thickness. [1-3] Two optical extinction bands were identified: a long-wavelength gap mode and a short-wavelength collective surface plasmon mode. Both modes' positions and amplitudes strongly depend on the shellac dielectric spacer thickness. Changing this thickness shifts the two modes, eventually causing them to degenerate into a single mode as the spacer thickness increases. [1-3] These findings revealed a complex interplay between the gap and collective surface plasmon polariton modes. Although detailed numerical and experimental studies were conducted for various plasmonic metasurface geometries, all these investigations were performed with normal incidence of the probing light beam. No reports have examined the polarization dependence of extinction spectra for monolayers of gold nanoparticles in close proximity to a thin metal film.

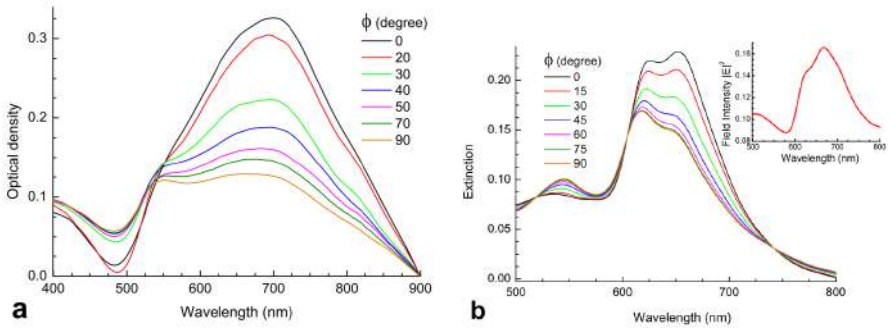


Figure 1. Experimental (a) and numerical (b) extinction spectra of the metasurface as a function of polarization angle φ of the incident probe beam for a sample with a shellac thickness of 10 nm. The angle of incidence of the light beam relative to the normal of the surface is $\theta = 60°$. The polarization angle of the incident light beam is gradually changed from 0° (s-polarization) to 90° (p-polarization). The inset picture (b) shows the results of the FDTD calculations of the intensity of the electric field in the middle of the shellac spacer as a function of the wavelength.

Here we examine a plasmonic metasurface composed of a monolayer of gold nanoparticles in close proximity to a thin aluminum film. A shellac dielectric spacer controls the distance (gap size) between the gold nanoparticles and the aluminum thin film. A similar structure, consisting of gold nanoparticle monolayers separated from an aluminum film by shellac spacers of varying thickness, was

recently studied under normal incidence of the probing beam.[1] Two modes were identified under this normal excitation: a gap mode and a collective SPR (Surface Plasmon Resonance) mode. Both the collective surface plasmon and the gap mode were excited when the spacer thickness was less than 30 nm. For spacer thicknesses larger than 30 nm, the two modes degenerated into one hybrid surface plasmon-gap mode.[1-3]

In the present work, we study the effects of different polarizations and incident angles of the probe beam on similar metasurfaces. Figure 1 shows both the experimental results (a) and FDTD numerical calculations (b) of the metasurface's extinction spectrum as a function of probe beam polarization when the angle of incidence relative to the surface normal is $\theta = 60°$. The polarization angle of the incident beam gradually changes from $\varphi = 0°$ for s-polarization to $\varphi = 90°$ for p-polarization. The experimental results for s-polarized incident light ($\varphi = 0°$) exhibit three peaks around 550 nm, 620 nm, and 650 nm. We attribute the peak near 550 nm to the collective SPR in the monolayer of gold nanoparticles. This collective SPR wavelength is close to the localized SPR wavelength in individual spherical gold nanoparticles (90 nm size) embedded in a dielectric with refractive index n=1.5. The broader gap mode peak is located around 700 nm. The FDTD calculations reveal a SPR collective mode near 550 nm and narrower two-peak gap modes near 610-650 nm, as seen in Fig.1(b). As the incident beam polarization gradually changes from $\varphi = 0°$ to $\varphi = 90°$, the collective SPR peak position remains around 550 nm. Simultaneously, the low-energy gap modes decrease in amplitude and exhibit a distinct two-peak structure.

The FDTD numerical calculations show a two-peak structure of gap modes with narrower bandwidth peaks for the p-polarized light beam. The broader bandwidth of the collective SPR and gap modes observed experimentally may be explained by the relatively large size distribution of gold nanoparticles in the sample. The inset in Fig.1(b) shows the numerically calculated electric field intensity at the shellac level in the gap. Maximum intensity is observed at ~650 nm, corresponding to the optical density maximum where the gap mode is excited (Fig. 1(a,b)). This confirms that the peak at ~650 nm is attributable to the gap mode. While the collective SPR peak wavelength doesn't change significantly as polarization shifts from s-polarization to p-polarization, the gap mode amplitude decreases. This effect is more pronounced experimentally than in numerical calculations. The gap mode bandwidth increases as polarization changes from 0° to 90°. The wavelengths of both the collective SPR mode and gap modes are similar to those observed with normal incidence of the probing beam.

Acknowledgements: This work was supported in part by NATO SPS (G-6197) grant.

References:

1. Yeshchenko, O.A., Kozachenko, V.V., Tomchuk, A.V., Haftel, M., Knize, R.J., and Pinchuk, A.O. "Plasmonic metasurfaces with tunable gap and collective surface plasmon resonance modes," The Journal of Phys. Chem. C, Vol. 123, No. 20, 13057-13062, 2019.
2. Yeshchenko, O.A., Tomchuk, A.V., Kozachenko, V.V., Naumenko, A.P., Slominskii, Y.L., Knize, R.J., Haftel, M., Pinchuk A.O., "Planar plasmonic nanocavity for efficient enhancement of photoluminescence of molecular emitters," Optical Materials, Vol. 7, No.11, 3885-3893, 2017.
3. Yeshchenko, O.A., Kozachenko, V.V., Naumenko, A.P., Berezovska, N.I., Kutsevol, N.V., Chumachenko, V.A., Haftel, M., Pinchuk, A.O., "Gold nanoparticle plasmon resonance in near-field coupled Au NPs layer/Al film nanostructure: Dependence on metal film thickness," Photonics and Nanostructures- Fundamentals and Applications, Vol.29, 1-7, 2018.

Nonlocal metasurfaces and thin film devices for all-optical image processing and phase contrast imaging

A. Roberts[1*]

[1] ARC Centre of Excellence for Transformative Meta-Optical Systems, School of Physics, University of Melbourne, Victoria 3010, Australia

[*]Corresponding author: ann.roberts@unimelb.edu.au

Abstract: Metasurfaces and tailored thin film devices can manipulate images and extract information from optical fields in the object plane, leading to a significant reduction in size compared to other optical approaches. Here recent progress in extending and utilizing the range of information obtainable using these devices will be presented.

It is well-known that optical systems can perform image processing in the Fourier plane, but currently computational methods are more commonly employed for tasks such as edge detection, object identification, and image enhancement. The latter approaches, however, rely on the capture of information with a digital camera discarding phase information, and the resources required scale as the amount of information being processed. Hence, there is an ongoing interest in being able to perform operations directly at the sensor level. Furthermore, Frits Zernike demonstrated that the inclusion of phase plates as spatial filters using Fourier methods permitted visualization of essentially transparent objects such as unstained biological cells [1]. While there are advanced computational methods to extract phase information from intensity images, these methods can be slow and computationally intensive and are orthogonal to the drive to the sensor-level processing. Well-established all-optical Fourier and other image processing and phase contrast imaging methods, however, usually require large and sometimes costly optics. With the push for more compact optical components and advances in nanooptics, there is an emerging interest in all-optical image processing taking advantage of the unique capabilities of metasurfaces [1-4] and thin film devices [5-6].

Traditional spatial frequency filtering involves introducing a mask into the focal plane of a lens taking advantage of its Fourier transforming property to independently manipulate contributions to the angular spectrum of the optical wavefield. This approach places a lower bound on the axial extent of the system due to the introduction of lenses and propagation distances. Nonlocal approaches, on the other hand, involve the direct manipulation of the spatial frequency content of the field by using a device that has a reflectance or transmittance sensitive to the angle of incidence of a plane wave. This directly modifies the amplitude and/or phase of a given angular spectrum component of the field. Not only does this present a more compact optical system but permits flexibility in positioning the device [7]. Concepts leveraging known light-matter interactions or inverse design methods can be used to develop metasurfaces with a tailored angular dispersion and, hence, perform a particular operation [2,3]. Specifically, there is considerable scope for the development of compact devices that can generate enhanced contrast images of transparent objects. Indeed, we have previously shown that an off-the-shelf notch filter [8] or a metal-insulator-metal Salisbury screen [9] can perform edge detection and phase contrast imaging of unstained biological samples in, respectively, transmission and reflection. We also used a resonant waveguide grating in transmission [10, 11] to generate phase contrast images of unstained HeLa

cells. Our recent research has focused on dynamically modifying the imaging modality without removing the metasurface by changing the polarization of the incident field [12] or using phase change materials [13].

This presentation will focus on recent results utilizing inverse design strategies [14] to produce spatial frequency selective metasurfaces, tailored thin film devices and the introduction of tunable materials to modify image processing operations. Wavelength and polarization multiplexed information extraction from an optical wavefield will also be discussed and applications to quantitative phase imaging presented.

This research was funded by the Australian Government through the Australian Research Council Centre of Excellence grant (CE200100010). The contributions of members of my group and collaborators who have contributed to the articles below are also gratefully acknowledged.

References

1. Zernike, F. “Phase contrast, a new method for the microscopic observation of transparent objects,” Physica Vol. 9, No. 7, pp. 686– 698, 1942.
2. Zangeneh-Nejad, Sounas, D.L., Alù, A. and Fleury, R, “Analogue computing with metamaterials,”, Nature Reviews Materials, Vol. 6, 207-225, 2021
3. Wesemann, L., Davis, T. J. and Roberts, A. “Meta-optical and thin film devices for all-optical information processing,” Applied Physics Reviews, Vol. 8 No. 3, 031309, 2021.
4. Priscilla, N., Sulejman, S., Roberts, A. and Wesemann, L., “New Avenues for Phase Imaging: Optical Metasurfaces,” ACS Photonics, Vol. 11, No. 8, pp. 2843-2859, 2024.
5. S.B. Sulejman, N. Priscilla, L. Wesemann, W. S. L. Lee, J. Lou, E. Hinde, T. J. Davis and A. Roberts, “Thin film notch filters as platforms for biological image processing,” Sci. Rep., Vol. 13, 4494, 2023.
6. Wesemann, L., Panchenko, E., Singh, K. Della Gaspera, E., Gómez, D.E., Davis, T.J. and Roberts, A. “Selective near-perfect absorbing mirror as a spatial frequency filter for optical image processing,” APL Photonics, Vol. 4, 100801, 2019.
7. Case, S.K. “Fourier processing in the object plane”, Opt. Lett. Vol. 4, No. 9, 286-288, 1979.
8. Roberts, A., Gómez, D.E. and Davis, T.J., “Optical image processing with metasurface dark modes,” J. Opt. Soc. Am. A, Vol. 35, No. 9, 1575-1584, 2018
9. Davis, T.J., Eftekhari, F., Gómez, D.E. and Roberts, A. “Metasurfaces with asymmetric optical transfer functions for optical signal processing,” Phys. Rev. Lett. Vol. 123, 013901, 2019.
10. Wesemann, L., Rickett, J., Song, J., Lou, J., Hinde, E., Davis, T.J. and Roberts, A. "Nanophotonics enhanced coverslip for phase imaging in biology" Light Sci. Appl., Vol. 10, No. 1, 98, 2021.
11. Wesemann, L., Rickett, J., Davis, T.J. and Roberts, A., “Real-time phase imaging with an asymmetric transfer function metasurface,”, ACS Photonics, Vol. 9, No. 5, 1803-1807, 2022.
12. Sulejman, S. B., Wesemann, L., McCormack, M., et al., “Metasurfaces for infrared multi-modal microscopy: phase contrast and bright field”, ACS Photonics, DOI: 10.1021/acsphotonics.4c02097, 2025.
13. Cotrufo, M., Sulejman, S. B., Wesemann, L., Rahman, Md. A., Bhaskaran, M., Roberts, A. and Alù, A., “Reconfigurable image processing metasurfaces with phase-change materials”, Nat. Commun., Vol. 15, 4483 2024.
14. Priscilla, N., Li, N., Wesemann, L., Sulejman, S., et al., “High resolution bio-imaging via inverse design of metasurfaces,” SPIE Proceedings Volume 12895, Quantum Sensing and Nano Electronics and Photonics XX; 128950P 2024.

Chern insulators: nonlinearity and switching

Justin T. Cole[1]
[1]University of Colorado, Colorado Springs, USA
jcole13@uccs.edu

Abstract

Most results on Chern insulators are based on linear theories. Here nonlinear Chern insulator models and the states they support are examined. Solitons and traveling waves are investigated. A secondary agenda examines switching within Chern insulator models. Namely, mechanisms for controlling the flow of light are to be discussed.

Active Conducting Polymer Plasmonics and Metasurfaces

M. P. Jonsson

[1] Laboratory of Organic Electronics, Department of Science and Technology (ITN), Linköping University, Norrköping, SE-60174, Sweden
[*]corresponding author: magnus.jonsson@liu.se

Abstract

Our group recently introduced conducting polymers as a new type of active plasmonic materials, enabling chemically and electrically controlled metasurfaces.[1-3] I will present the background to this emerging area and discuss challenges and recent advances, including exploration of different polymers,[4,5] narrowing of resonances through nonlocal coupling,[6] and new possibilities based on hyperbolic polymers.[7,8]

References

1. Chen *et al.* "Conductive polymer nanoantennas for dynamic organic plasmonics," *Nature Nanotech.* 15, 35-40 (2020)
2. Karki *et al.* "Electrical Tuning of Plasmonic Conducting Polymer Nanoantennas" *Adv. Mater.* 34, 2107172, (2022)
3. Chen et al. "Dynamic conducting polymer plasmonics and metasurfaces" *ACS Phot.* 10, 3, 571–581, (2023)
4. Karki et al. "Doped Semiconducting Polymer Nanoantennas for Tunable Organic Plasmonics" *Comm. Mat.* 3, 48 (2022)
5. Kazi et al. "n-Type redox-tuneable conducting polymer optical nanoantennas" *JMCC* 12, 17469–17474 (2024)
6. Lin et al. "Switchable Narrow Nonlocal Conducting Polymer Plasmonics" doi: 10.21203/rs.3.rs-6016363/v1 (2025)
7. Duan et al. "Tuneable anisotropic plasmonics with shape-symmetric conducting polymer nanoantennas" *Advanced Materials* 35, 51, 2303949 (2023)
8. Duan et al. "Broadband chiroptics with twist-stacked hyperbolic conducting polymer thin films" *In review* (2025)

Microenvironment Responsive Bio-Acoustic Metamaterials for Precision Medicine

Hanchuan Tang[1*]

[1] School of Integrated Circuits, Huazhong University of Science and Technology, Wuhan 430074, China.
[*]corresponding author: hctang1@hust.edu.cn

Abstract: This study develops injectable ultrasonic sensors using bio-acoustic metamaterials, enabling wireless monitoring of pressure, temperature, and pH via wearable ultrasound devices. These biodegradable sensors eliminate surgical removal needs, offering minimally invasive implantation and multi-signal detection capabilities for advanced healthcare monitoring.

The seamless integration of humans and machines lies at the heart of the next technological frontier, enabling transformative applications capable of enhancing our sensory capabilities, health monitoring, and overall quality of life. I have cultivated a multidisciplinary approach, delving into the design theory, manufacturing, and biomedical engineering applications of acoustic bio-metamaterials. Drawing upon foundational research, bio-acoustic metamaterials aimed at tackling the challenges inherent in transmitting information and energy across the skin barrier, with a specific focus on healthcare and sensory augmentation. For example, addressing the need for non-invasive, wireless monitoring solutions, I have pioneered the development of metagel-ultrasonic sensors (Figure 1). These sensors can be injected into the body via a needle, eliminating the need for open surgery. Compatible with handheld or wearable ultrasound devices, they facilitate precise, continuous, and wireless monitoring of various internal signals, including pressure, temperature, and pH. After the intended monitoring period, the metagel sensor naturally degrades, obviating the requirement for surgical removal. Offering advantages in implantation size, multi-signal decoupling, and biodegradability over existing wireless implantable sensors, this research holds promise for driving the development of safe, compact, wireless implantable sensors. It stands to inspire further investigations and potentially supplant the current paradigm of percutaneous wired sensors in clinical settings.

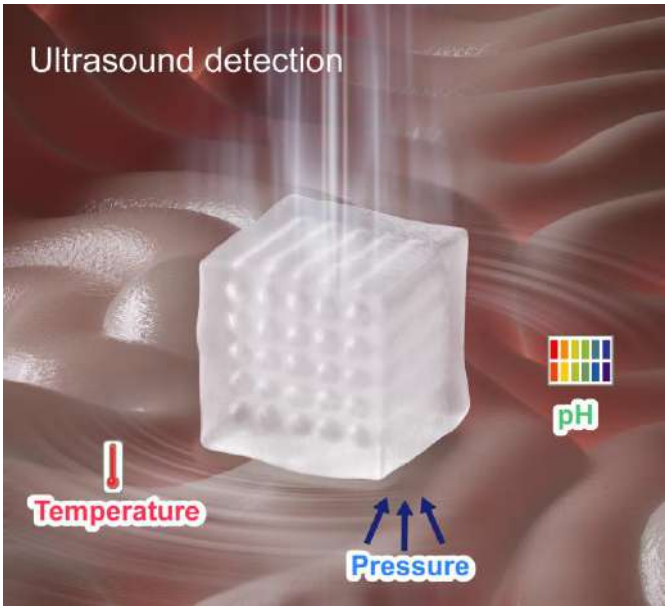


Figure 1. Schematic of injectable ultrasonic sensors using bio-acoustic metamaterials.

References

1. **Tang, H.**, Y. Yang, Z. Liu, W. Li, Y. Zhang, T. Kang, Y. Yu, N. Li, Y. Tian, X. Liu, Y. Cheng, Z. Yin, X. Jiang, X. Chen, J. Zang, Injectable metagel-ultrasonic sensor for wireless monitoring of intracranial signals, *Nature*, Vol. 630, pp. 84–90, 2024.
2. **Tang, H.**, S. Zhang, Y. Tian, T. Kang, C. Zhou, S. Yang, Y. Liu, X. Liu, Q. Chen, H. Xiao, W. Chen, J. Zang, Bioinspired Soft Elastic Metamaterials for Reconstruction of Natural Hearing. *Advanced Science*, Vol. 10, pp. 2207273, 2023.
3. **Tang, H.**, Z. Hao, Y. Liu, Y. Tian, H. Niu, J. Zang. Soft and disordered hyperuniform elastic metamaterials for highly efficient vibration concentration, *National Science Review*, Vol. 9, pp. nwab133, 2022.
4. **Tang, H.**, Z. Chen, N. Tang, S. Li, Y. Shen, Y. Peng, X. Zhu, and J. Zang, Hollow-out patterning ultrathin acoustic metasurfaces for multi-functionalities using soft fiber/rigid bead network, *Advanced Functional Materials*, Vol. 28, pp. 1801127, 2018.

Tailored Resonant Metasurfaces for Enhanced Third-order Nonlinear Optics

Hailun Xie, Lili Gui*, and Kun Xu

State Key Laboratory of Information Photonics and Optical Communications, Beijing University of Posts and Telecommunications, Beijing, 100876, China
*Corresponding author: liligui@bupt.edu.cn

Abstract: We demonstrate two tailored resonant metasurfaces for enhancing third-order nonlinear optics, namely, a surface lattice resonance aluminum metasurface for wavelength-tunable Q-switched fiber laser, and a quasi-bound state in the continuum amorphous silicon metasurface to amplify two-photon absorption effect.

Resonant metasurfaces provide promising solutions to overcome the limitations of conventional nonlinear materials by enhancing the interaction between light and matter and amplifying optical nonlinearity. Here, we propose and demonstrate two tailored-resonant metasurface platforms: (1) a surface lattice resonance (SLR) aluminum (Al) metasurface, functioning as a saturable absorber (SA) integrated within a fiber laser cavity, which enables wavelength-tunable (1020-1048 nm) Q-switched pulse generation.[1] (2) a quasi-bound state in the continuum (q-BIC) amorphous silicon (a-Si) metasurface, featuring a theoretical Q-factor up to 930, which exhibits a giant nonlinear two-photon absorption (TPA) effect with nonsaturation TPA coefficient β_0= 173.2 cm/MW and TPA saturation intensity I_{sat}= 93.0 MW/cm^2.[2] Both platforms enhance third-order nonlinear absorption responses, offering significant potential applications in nonlinear optics and ultrafast optics.

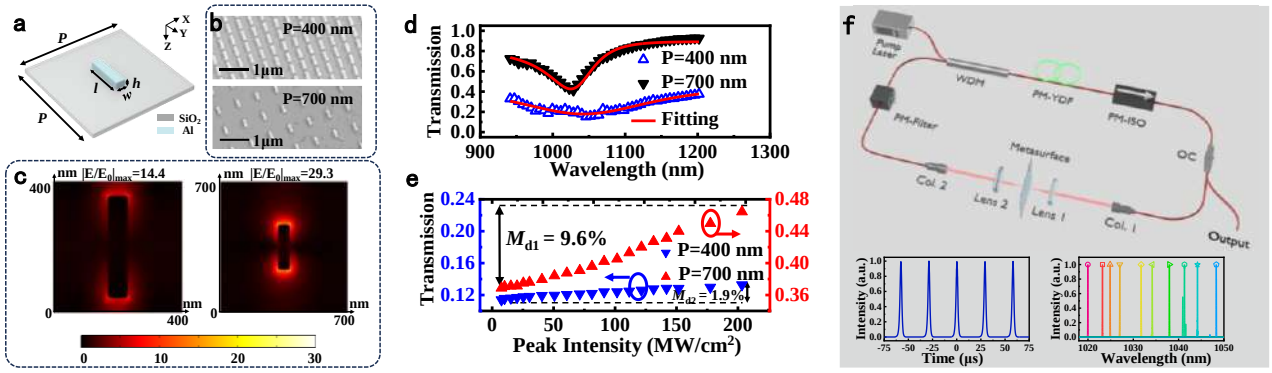


Fig. 1. The SLR aluminum metasurface and its application in a pulse fiber laser. (a) Schematic of the Al unit cell. (b) SEM images of the fabricated metasurfaces. (c) Electric near-field distributions at resonance wavelength 1035 nm at the X-Y plane of the half height of Al nanostructures. (d) Linear transmission spectra and (e) Nonlinear transmission measurements that exhibit the considerable saturation absorption of Al metasurfaces in experiment. 1035 nm fs laser is used for nonlinear measurement. (f) Setup of the Q-switched ytterbium-doped polarization-maintaining fiber laser. Typical pulse train (bottom right inset) and tunable spectra (bottom left inset) of Q-switching operation.

We fabricated two Al metasurfaces with different periods *P*, each consisting of periodic single-nanorod arrays. The unit cell and SEM images are shown in Fig. 1a and 1b, respectively. In order to achieve resonance within the desired wavelength range (~ 1 μm), metasurfaces are excited by Y-polarized normal incidence. As displayed in Fig. 1c and 1d, due to the coupling between the Rayleigh anomaly (RA, $\lambda_{RA}=n_{sub} \times P$) and localized surface plasmon resonance (LSPR), the metasurface with *P*=700 nm (supporting SLR mode) exhibits a narrower linewidth and a more prominent near-field enhancement compared to the metasurface with *P*=400 nm (supporting LSPR mode). This indicates a greater ability to amplify nonlinear optical responses. As a result, the SLR metasurface

(modulation depth M_d=9.6%) shows a more significant saturation absorption than the LSPR metasurface (M_d=1.89%) under a low incident fluence (25 μJ/cm^2) (Fig. 1e). Then, we have further achieved wavelength-tunable (1020-1048nm) Q-switched pulse generation by incorporating the SLR-based Al metasurface as a passive SA in a polarization-maintaining ytterbium-doped fiber laser (Fig. 1f).

The q-BIC metasurface consists of Π-like a-Si nanostructures with symmetric defects that trigger the transition from BIC to the q-BIC mode (Fig. 2a and the set of Fig. 2b). As shown in Fig. 2b, the Q-factor of the q-BIC mode increases as the asymmetry parameter α decreases. However, too small α will bring challenges to practical nanofabrication. Fig. 2c depicts the simulated (top panel) and experimental (bottom panel) transmission spectra, respectively. The metasurface exhibits a sharp q-BIC resonance (Q about 930 theoretically) with asymmetric Fano line shape and excellent near-field enhancement when are excited by X-polarized normal incidence. In contrast, when excited by Y-polarized normal incidence, the metasurface does not exhibit any resonance behavior in this wavelength range. As illustrated in Fig. 2d (black dots), the metasurface demonstrates a typical TPA response by X-polarized incident light. We fit the experimental data using the homogeneously broadened model of TPA saturation theory, which indicates a nonsaturation TPA coefficient β=173.2 cm/MW and a TPA saturation intensity I_{sat}=93.0 MW/cm^2. As a comparison, the TPA almost vanishes at Y-polarized incidence, confirming that the noticeable nonlinear response originates from the strong local near-field enabled by the excited q-BIC resonance.

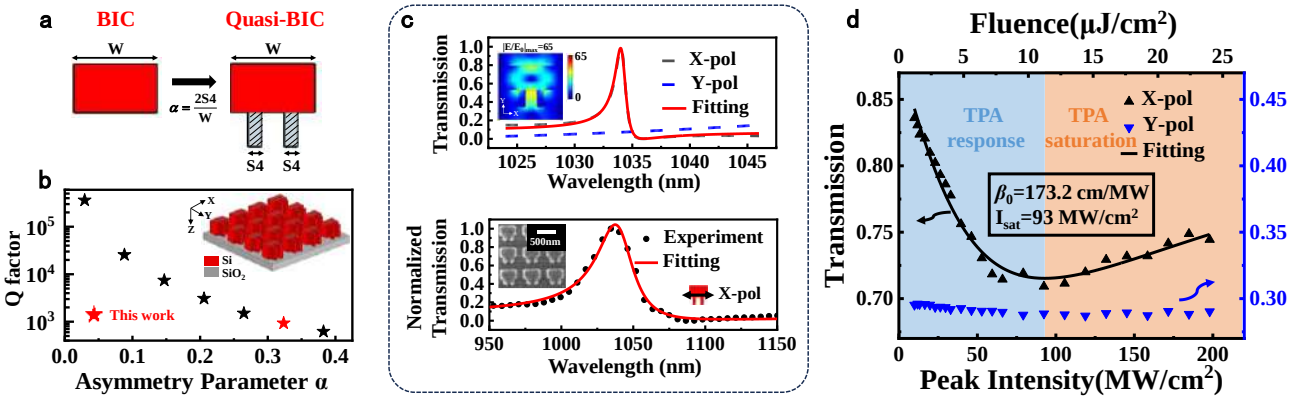


Fig. 2. The q-BIC silicon metasurface and its giant TPA effect. (a) Diagram of the meta-atom for transition from the BIC mode to the q-BIC mode. (b) Dependence of the Q factor on the asymmetry parameter α. The α is about 0.32 in experiment. Inset: schematic of the q-BIC metasurface. (c) Linear transmission spectra in simulation (top) and in experiment (bottom), respectively. Inset: electric near-field distributions for incident X-pol light (top panel) at 1035 nm wavelength and SEM image of the fabricated q-BIC metasurface (bottom panel). (d) Nonlinear experimental results using 1035 nm fs laser. The black solid curve is the fitting of the TPA saturation.

Our proposed resonant metasurface platforms are committed to achieving high Q-factor and low losses, offering exciting and flexible methods to enhance nonlinear optical effects.

Acknowledgements This work was supported by National Natural Science Foundation of China (61905018), Fundamental Research Funds for the Central Universities (ZDYY202102), Fund of State Key Laboratory of Information Photonics and Optical Communications (Beijing University of Posts and Telecommunications) of China (IPOC2021ZR02), BUPT Excellent Ph.D. Students Foundation (CX20241034).

References

1. Xie, H., Gui, L., Zhou, X., et al, "Less is more: surface-lattice-resonance-enhanced aluminum metasurface with giant saturable absorption for a wavelength-tunable Q-switched Yb-doped fiber laser," Photonics Res., Vol. 12, No. 10, 2198-2206, 2024.
2. Xie, H., Gui, L., Liu, Y., et al, "Giant two-photon absorption response from a silicon quasi-BIC metasurface," Appl. Phys. Lett., Vol. 123, 211704, 2023.

Structurally engineered phosphors for high color-conversion efficiency

Tae-Yun Lee[1,2], Hansol Lee[1,2], and Heonsu Jeon[1,2,3*]

[1]Department of Physics and Astronomy, Seoul National University, Seoul 08826, Korea
[2]Inter-university Semiconductor Research Center, Seoul National University, Seoul 08826, Korea
[3]Institute of Applied Physics, Seoul National University, Seoul 08826, Korea
[*]Corresponding author: hsjeon@snu.ac.kr

Abstract: Phosphors have enabled modern full-color display technologies as well as solid-state lighting. In this talk, a paradigm-shifting novel approach is introduced to improve the color-conversion efficiency of phosphor: *structural engineering* under the principles of nanophotonics. Two structural platforms to be discussed are lateral photonic crystal and vertical resonant cavity.

The importance of phosphor has been revived ever since it enabled solid-state lighting in conjunction with blue LEDs. Phosphors are now playing a key role in full color display devices and systems as well. Conventionally, phosphor development has been mainly accomplished via developing new materials, which is culminated by the emergence of colloidal quantum dots (CQDs). Yet another possible route, which has been proposed and demonstrated by the author's group, is to reconfigure phosphor material into a nanophotonic structure such that its resonance is tuned to excitation wavelength for the phosphor material, resulting in a great improvement in color-conversion efficiency due to resonant absorption of excitation photons.

So far, we have successfully demonstrated two nanophotonic platforms in this purpose: lateral photonic crystal (PhC) and vertical resonant cavity (RC). The PhC phosphor, which utilizes a Γ-point band-edge mode, consists of a passive PhC platform and a phosphor material (such as CQDs) incorporated into the PhC backbone structure. In the RC phosphor, on the other hand, a thin CQD film is inserted in a cavity layer sandwiched between two distributed Bragg reflectors. Although amply different in structures, the both platforms exhibit a significantly enhanced CQD fluorescence when compared with reference phosphor having an equal amount of CQDs but no resonant structure. Continuous efforts are being exerted to improve the fabrication, performance, and functions of the structurally engineered phosphors.

References

1. Lee, H., et al., "Structurally engineered colloidal quantum dot phosphor using TiO2 photonic crystal backbone", Light Sci. Appl. 11, 318, 2022.
2. Lee, T.-Y., et al., "Resonant cavity phosphor", Nat. Commun. 14:6661, 2023.

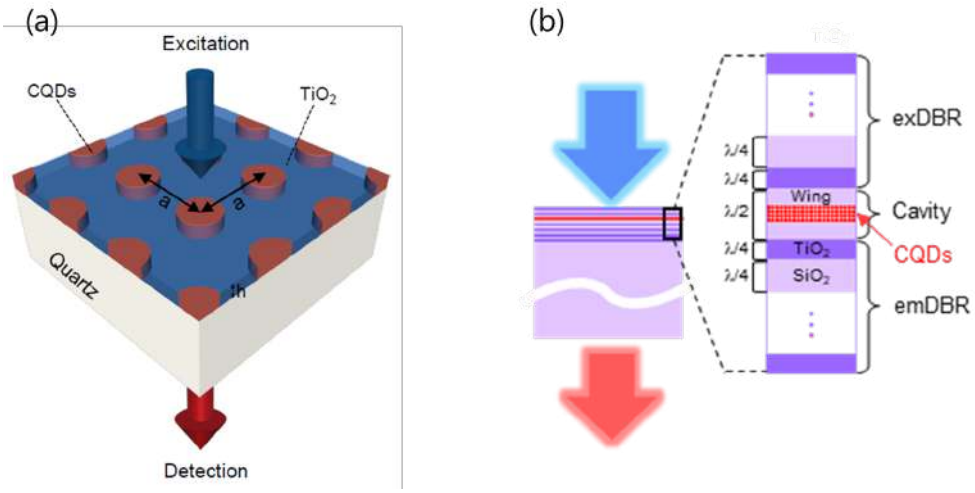


Fig. 1. Schematics of the structurally engineered phosphors. (a) PhC phosphor based on a 2D square-lattice photonic crystal and (b) RC phosphor based on a vertical resonant cavity.

Investigate the growth of (multi)metallic nanoparticles synthesized by physical vapor deposition.

J.Ramade[1], M.Costes[1], S. Camelio[1], S. Rousselet[1], F. Pailloux[1], M.Marteau[1], K.Dusaillant[1], D. Babonneau[1]

[1]Institut PPRIME, France
[*]julien.ramade@univ-poitiers.fr, david.babonneau@univ-poitiers.fr

Abstract: We investigate the growth dynamics of AuPd nanoparticles produced by electron evaporation through *in situ* optical spectroscopy. Our results shows that the optical response is dominated by the plasmonic properties of gold and is greatly influenced by the buffer structuring, the deposition angle and the amount of Pd in NPs.

For several decades, bimetallic nanoparticles (NPs), also called nanoalloys, have been the subject of unceasing investigations as they combine specific characteristics of the matter at the nanoscale with interesting properties of alloys as compared to their constituents. Such a combination can induce remarkable physical and chemical properties far different from their bulk counterpart, thereby leading to various applications in optics, magnetism or catalysis.[1]

In addition to size and shape effects, the relative composition of both species as the chemical arrangement are supplemental parameters allowing the tailoring of novel properties that may develop in such systems. However, their (chemical, geometric, electronic) structure may evolve under specific environments, especially under oxidizing or reducing conditions.[2] Among properties emerging in the nanometer range, the Localized Plasmon Resonance (LSPR) is an optical resonance leading to a strong absorption band and a local field amplification, which features are fully dependent on the structural parameters (size, morphology, chemical configuration) and the surrounding medium (nature and composition) of the NPs. In other words, the LSPR can be used as a probe of both the chemical structure and the composition of the local environment of plasmonic nanostructures.[3,4]

We recently developed an experimental setup for the physical vapor deposition (electron evaporation) of one to five different metals at various incidence angles. The uniqueness of this setup lies in the possibility of monitoring in real time the growth of the nanostructures through the measurement of their optical transmittance or reflectance. This allows probing the evolution of their chemical structure through the analysis of their optical response, and then access to their growth dynamics.

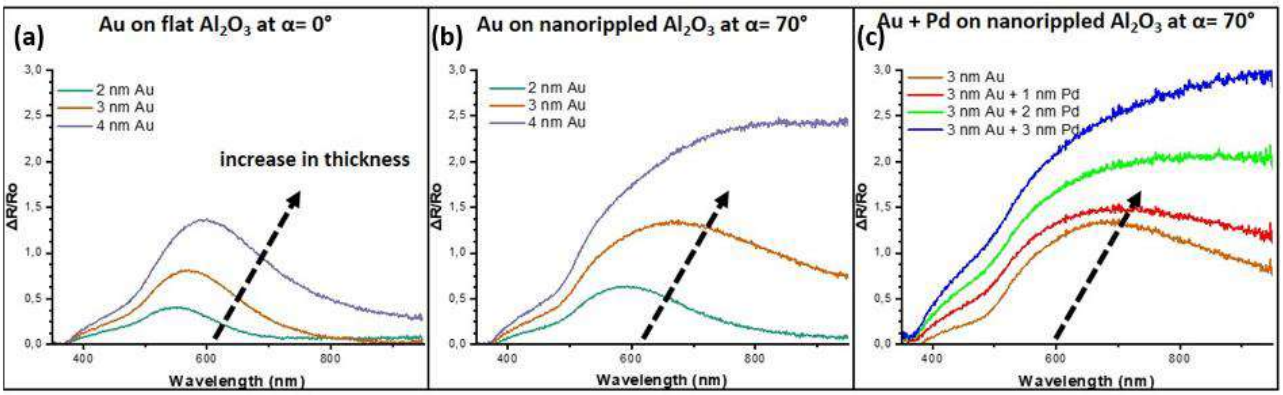


Figure 1: Optical reflectance of thin films measured in situ during their growth. (a) gold deposited at normal incidence (α=0°) on Al_2O_3 buffer. (b) gold deposited at oblique incidence (α=70°) on nanorippled Al_20_3 buffer. (c). 3 nm of gold followed by 3 nm of Palladium deposited on nanorippled Al_2O_3 buffer.

Here, we investigate the structure and the optical properties of Au_XPd_{1-X} bimetallic NPs. Au present a LSPR in the visible spectral range, while Pd NPs are very efficient catalysts, in particular for the rapid dissociation of hydrogen. Combining Au LSPR to Pd reactivity might then lead to a new generation of optical hydrogen sensors.[5,6] We synthesized AuPd NPs through a sequential deposition (gold followed by palladium) at normal and oblique angles (denoted as α) on flat and nanorippled Al_2O_3 surfaces. The optical response acquired during the growth of Au nanoparticles is dominated by its LSPR, which broadens and shifts towards near-IR range as the amount of Au increases, traducing deep structural modifications during the growth (fig 1.a). These LSPR changes are more pronounced when the flat buffer is replaced by nanoripples (fig 1.b) and when Pd is deposited onto Au NPs (fig. 1.c). The i*n situ* optical characterization of large assembly of NPs is supported by Transmission Electron Microscopy (TEM) observations. These results stress the importance of the deposition conditions on the adopted configurations. It also shows the promising perspective of monitoring the growth and the evolution of the optical response to tune the LSPR features (especially its spectral position) for specific applications by adjusting the quantity of deposited elements and the growth parameters.

This work pertains to the French Government programs “Investissements d’Avenir” (EUR INTREE, reference ANR-18-EURE-0010) and LABEX INTERACTIFS (reference ANR-11-LABX-0017-01). The authors also acknowledge financial support from Excellence UP-SQUARED program.

References

1 R. Ferrando, J. Jellinek and R. L. Johnston, *Chem. Rev.*, 2008, **108**, 845–910.
2 J. Ramade, C. Langlois, M. Pellarin, L. Piccolo, M.-A. Lebeault, T. Epicier, M. Aouine and E. Cottancin, *Nanoscale*, 2017, **9**, 13563–13574.
3 J. Ramade, E. Cottancin, M.-A. Lebeault, C. Langlois, L. Piccolo, M. Hillenkamp, J. Lermé, F. Calvo and M. Pellarin, *The Journal of Physical Chemistry C, paper accepted*.
4 E. Cottancin, C. Langlois, J. Lermé, M. Broyer, M.-A. Lebeault and M. Pellarin, *Phys. Chem. Chem. Phys.*, 2014, **16**, 5763–5773.
5 L. J. Bannenberg, F. A. A. Nugroho, H. Schreuders, B. Norder, T. T. Trinh, N.-J. Steinke, A. A. van Well, C. Langhammer and B. Dam, *ACS Appl. Mater. Interfaces*, 2019, **11**, 15489–15497.
6 C. Wadell, F. A. A. Nugroho, E. Lidström, B. Iandolo, J. B. Wagner and C. Langhammer, *Nano Lett.*, 2015, **15**, 3563–3570.

Time-Resolved Vector Polarimetry for Identifying Topological Features of Surface Plasmon Polaritons

P. Dreher[1], A. Neuhaus[1], T. Davis[1,2,3], B. Frank[2], H. Gießen[2], and F. Meyer zu Heringdorf[1*]

[1] University of Duisburg-Essen, Lotharstraße 1, 47057 Duisburg, Germany
[2] 4-th Physics Institute and Research Center SCoPE, University of Stuttgart, 70569 Stuttgart, Germany
[3] School of Physics, University of Melbourne, Parkville Victoria 3010, Australia
[*]corresponding author: meyerzh@uni-due.de

Abstract: Determining the electric field vectors of surface plasmon polaritons (SPPs) in space and time is a challenging endeavor. It is accomplished with nanometer resolution in a time-resolved photoemission microscopy experiment. After reconstruction of the time-dependent electromagnetic field vectors, local topological properties of the SPPs are derived.

During the last years, the experimental determination of the electromagnetic vector fields of surface plasmon polaritons (SPPs) has become possible, and fundamental properties like the spin-momentum locking of SPPs have been demonstrated.[1] To investigate more complicated SPP field configurations that require a particular polarization for excitation, the concepts of these early vector reconstruction concepts had to be extended. By now, the experimental reconstruction of SPP fields with particular properties is possible.[2] This 'vector polarimetry' is based on the combination of nonlinear photoemission microscopy with femtosecond laser pulses in a time-resolved interferometric pump-probe experiment. The experimental concept is as follows: Femtosecond laser pulses from a Ti:Sapphire oscillator are separated into two pulses at the first beam-splitter of a Pancharatnam's phase stabilized Mach-Zehnder Interferometer. In both arms of the interferometer the polarization can be adjusted independently using $\lambda/2$ waveplates. Moreover, the polarization of both arms can jointly be adjusted by a combination of a $\lambda/2$ and a $\lambda/4$ waveplate that are placed behind the exit of the interferometer. The fs laser pulses are guided into the photoemission microscope (PEEM) where they impinge on the sample in a normal incidence geometry. A complete description of the contrast mechanism was provided by Dreher et al.[3] In brief, a SPP is excited by the pump pulse at a groove where the necessary momentum for an optical excitation is provided. The specific spatiotemporal structure of the excited SPP is controlled by the shape of the groove and the polarization of the pump pulse. The propagating SPP is then subsequently probed several times at different temporal delays with probe pulses of different polarization. The pump-probe contrast in the PEEM images depends predominantly on the longitudinal field component of the SPP, and using Fourier-techniques, the longitudinal electric field vector of the SPP can be triangulated.[1] The transverse component of the electric field vector can be calculated from the divergence-free nature of the evanescent SPP field in the vacuum: $\boldsymbol{\nabla} \cdot \mathbf{E}(\mathbf{r}, \mathrm{t}) = 0$. Since the temporal dependence of the electric field vectors is known after this calculation, the magnetic field vectors can be derived using the induction law where $\mathbf{H}(\mathbf{r}, \mathrm{t}) = -\int dt\, \boldsymbol{\nabla} \times \mathbf{E}(\mathbf{r}, \mathrm{t})$.

Figure 1 shows examples from a benchmarking experiment, building on the work by Dai et al.[4] An Archimedean spiral was cut into a single-crystalline Au island on a SiO_2 support using a focused ion beam. The gap in the spiral equals to two SPP wavelengths, i.e., with circularly polarized pump pulses, SPPs with an orbital angular momentum of J=1 or J=3 could be excited, depending on the handedness of the polarization.[5] Exciting this structure with linearly polarized light thus leads to an interference between the two possible orbital angular momentum modes. Panel b of Fig. 1 shows the experimentally determined electric field vectors at a pump-probe

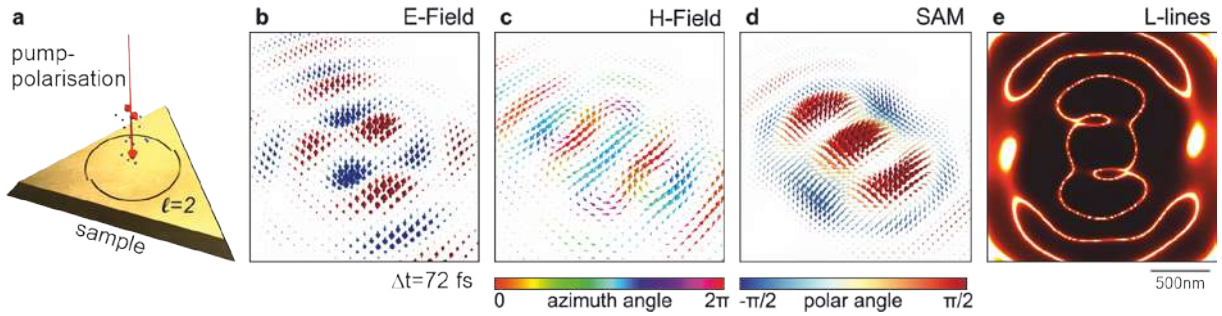


Figure 1: Results from a polarimetric reconstruction. (a) Sample design and excitation. (b) experimentally determined electric field vectors at delay time of 72 fs, (c) derived magnetic field vectors, (d) spin angular momentum vectors, (e) L-line plot, marking the regions where the transverse component of the spin angular momentum vanishes.

delay of 72 fs. The red arrows indicate electric field vectors in the vacuum that point away from the surface, blue arrows indicate regions that point into the surface. The field configuration rotates as a function of delay-time with optical frequencies.[5] Figure 1c shows the derived magnetic field for this delay-time that lies entirely in the surface plane and rotates as well. Since both the electric and magnetic field vectors are known, it is possible to calculate further field properties, such as the spin angular momentum (SAM) $\mathbf{S}(\mathbf{r},t) = \mathrm{Im}(\varepsilon\mathbf{E}^*(\mathbf{r},t) \times \mathbf{E}(\mathbf{r},t) + \mu\mathbf{H}(\mathbf{r},t)^* \times \mathbf{H}(\mathbf{r},t))/2\omega$ which does not rotate any longer, but is stable in time. The SAM for the excitation situation in Fig. 1a is shown in Fig. 1d. The prominent three red maxima are isolated regions where $\mathbf{S}$ is pointing away from the surface, that are surrounded by a region where $\mathbf{S}$ is pointing toward the surface. For infinitely long laser pulses this alternating behavior of red and blue regions would become an infinite series, however, the duration of the used laser pulses of $\approx$15 fs limits the observable region to the center of the spiral. As $\mathbf{S}$ must lie in the surface plane (or vanish altogether) for a transition between spin-upwards and spin-downwards regions, it is interesting to mark the regions where $\mathbf{S}_z = 0$. These regions form closed bands (L-lines). The experimentally determined L-lines are shown in Fig. 1e. The central L-line encircles the three red areas of $\mathbf{S}$ and allows identification of three Merons in the inner region of the spin structure.

In conclusion, we have developed a novel PEEM based technique, 'vector polarimetry' that allows to determine electric and magnetic field vectors of SPPs with thus far unprecedented temporal and spatial resolution. The accuracy of the reconstruction enables the experimental determination of topological properties, such as the SAM landscape, L-lines and Chern densities. The method is applicable to a wide range of SPP field configurations, including situations that are truly not periodic in space.[6] Vector polarimetry is thus clearly expected to play an important role in the future analysis of topological plasmonic structures.

References

1. Davis T.J. et al., "Ultrafast vector imaging of plasmonic skyrmion dynamics with deep subwavelength resolution", Science 368, eaba6145, 2020
2. Dreher P. et al., "Spatiotemporal topology of plasmonic spin meron pairs revealed by polarimetric photo-emission microscopy". Adv. Photon. 6, 066007, 2024
3. Dreher P. et al. "Momentum space separation of quantum path interferences between photons and surface plasmon polaritons in nonlinear photoemission microscopy", Nanophotonics 13, 1593, 2024
4. Dai Y. et al., "Plasmonic topological quasiparticle on the nanometre and femtosecond scales", Nature 588, 616, 2020
5. Spektor G. et al, "Revealing the subfemtosecond dynamics of orbital angular momentum in nanoplasmonic vortices", Science 355, 1187, 2017
6. Tsesses S. et al., "Four-dimensional conserved topological charge vectors in plasmonic quasicrystals", Science 387, 644, 2025

Single Crystals of Two-Dimensional Layered Perovskite Heterostructures

Alexander Schleusener[1], Mehrdad Faraji[1], Martina Borreani[1], Linhan Li[2], Miao-Ling Lin[2], Ping-Heng Tan[2], Sirous Khabbaz Abkenar[1], Giorgio Divitini[1], and Roman Krahne[1*]

[1] Italian Institute of Technology (IIT), Via Morego 30, Genova, Italy

[2] State Key Laboratory of Superlattices and Microstructures, Institute of Semiconductors, Chinese Academy of Sciences, Beijing, China

[*]corresponding author: roman.krahne@iit.it

Abstract: Two-dimensional metal-halide perovskite microcrystals with homogeneous and regular rectangular shape are fabricated by a solution-based process. These light-emitting semiconductor crystals can act as photonic cavities and feature strong light-matter interaction. Extending the solution growth employing various materials allows to obtain heterostructures defining regions with different band gap.

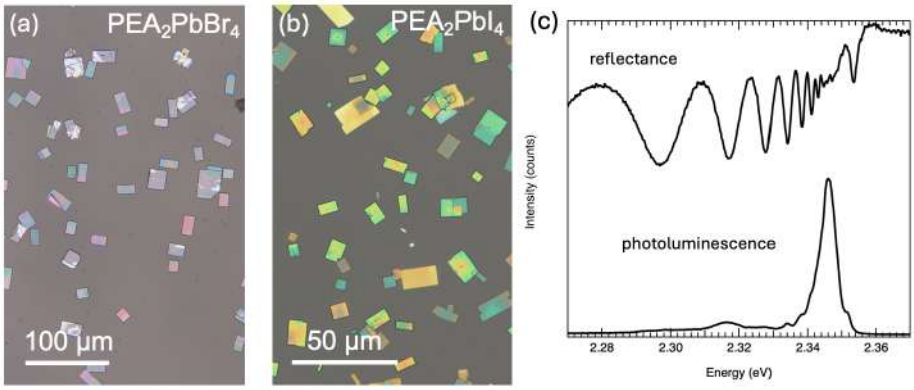


Figure 1. (a-b) Optical microscope images of 2D perovskite single crystals. (c) Reflectance and emission recorded from a single crystal, with evidence of Fabry-Perot resonances in reflection.

Two-dimensional organic/inorganic metal-halide perovskites (2DLHPs) are currently in the spotlight for their appealing optical properties and large structural and functional variety. Their layered structure in which a semiconducting octahedra lattice is sandwiched between dielectric organic layers renders them as natural quantum wells with strong quantum and dielectric confinement.[1] The possibility to tailor their properties via composition and architecture makes these materials highly promising for photonic and optoelectronic applications. Currently, 2DLHPs are mainly fabricated as powders, thin films or crystals with low control on their shape, thickness, and homogeneity on a larger scale.

We first demonstrate a solvent-antisolvent recrystallization method to fabricate 2DLHPs microcrystals (MCs) with highly regular rectangular shape, flat and nearly step-free surfaces (Figure 1a-b). We achieve this by dissolving pre-synthesized 2DLHP powders[2] and fine-tuning of the recrystallization parameters in terms of solvent/antisolvent choice, temperature, and concentration of the different components. With this we obtain single crystals with sizes in the tens and hundreds of µm range and good control on their lateral dimensions and thickness. [3] Our approach can be applied to various substrates, including glass, silicon oxide, and gold, as well as on functionalized or pre-patterned areas. The high crystalline quality and high refractive index of the resulting MCs is appealing for optical resonators where the crystal itself can act as the cavity (Figure 1c).

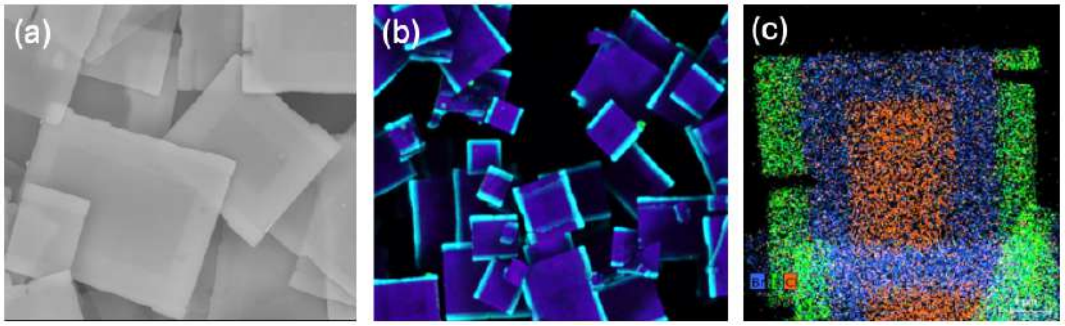


Figure 2. Triple-halide heterostructures in 2D perovskite single crystals. (a) Scanning electron microscopy image, (b) emission recorded with a confocal fluorescence microscope (λ_{ex}=400 nm), (c) overlay of the elemental mapping via energy-dispersive X-ray spectroscopy (EDX) showing Cl as orange, Br as blue, and I as green color.

Lateral heterostructures in semiconductor materials, and the ability to tailor the band gap in different regions of single crystals, are highly interesting for optoelectronics since they provide control on charge localisation and diffusion. Heterostructures have been fabricated by a solution-based sequential crystallization approach,[4] and by anion exchange processes in solid-gas phase processes with HBr or butylammonium halide vapor.[5, 6] We recently developed a solution-based anion exchange synthesis of lateral heterostructures with bromide and iodide as different halides.[3] We extended our solution based approach to grow heterostructures with high-quality crystalline interfaces, and phases of up to three different halides in a single microcrystal (Figure 2).

References:

1. R. Krahne, *Two-Dimensional Layered Perovskites for Photonic Devices*, in *Halide Perovskites for Photonics*. 2021, AIP Publishing LLC. p. 9-1-9-32.
2. B. Dhanabalan, et al., "Simple fabrication of layered halide perovskite platelets and enhanced photoluminescence from mechanically exfoliated flakes". *Nanoscale,* 11, 8334-8342, (2019).
3. A. Schleusener, et al., "Heterostructures via a Solution-Based Anion Exchange in Microcrystalline 2D Layered Metal-Halide Perovskites". *Adv. Mater.,* 36, 2402924, (2024).
4. E. Shi, et al., "Two-dimensional halide perovskite lateral epitaxial heterostructures". *Nature,* 580, 614-620, (2020).
5. C.R. Roy, et al., "Anion Exchange of Ruddlesden–Popper Lead Halide Perovskites Produces Stable Lateral Heterostructures". *J. Am. Chem. Soc.,* 143, 5212-5221, (2021).
6. C. He, et al., "Robust Heterostructures in Two-Dimensional Perovskites by Threshold-Dominating Anion Exchange". *Small,* 18, 2203036, (2022).

Development of three-dimensional bulk metamaterials suppliable as meta-atomic grains

Yoshiaki Kanamori[1*]

[1] Department of Robotics, Graduate School of Engineering, Tohoku University, Japan
[*]corresponding author: ykanamori@tohoku.ac.jp

Abstract: With the aim of realizing terahertz optical elements that can be formed into any shapes and have arbitrary refractive indices, our group has succeeded in developing a technology to manufacture grains containing meta-atoms and in putting them into a mold to produce three-dimensional bulk metamaterials.

In the terahertz region, the choice of optical materials is limited, making it difficult to realize a wide variety of optical elements. Therefore, the development of new materials that are easy to process and have a wide range of refractive index characteristics is awaited. Metamaterials are artificial optical materials composed of ultrafine structures, and are attracting attention as innovative artificial structures that break the limits of conventional electromagnetic wave manipulation technology. So far, our research group has aimed to realize terahertz optical elements that can be formed into any shape and have arbitrary refractive indices. We have succeeded in controlling the refractive index around a frequency of 0.7 THz by implementing a three-dimensional bulk metamaterial using a meta-atomic grain with a side length of 100 μm that contains a single-layered split-ring resonator as the unit structure of the metamaterial [1].

Recently, we have developed a three-dimensional bulk metamaterial in which double-layered split-ring resonators are irregularly arranged three-dimensionally based on the amorphous structure of a solid, as shown in Fig.1 [2]. By using meta-atomic grains containing double-layered split-ring resonators shown in Fig.2, the density of the resonators per unit volume is increased compared to a single-layer structure, and we have confirmed that the refractive index changes by 2.314 per terahertz at a frequency of around 0.34 THz. This refractive index change rate is 1.25 times larger than that of the previously reported three-dimensional bulk metamaterial, and it was also demonstrated that it can be adjusted by the density of the arrangement of the meta-atomic grains.

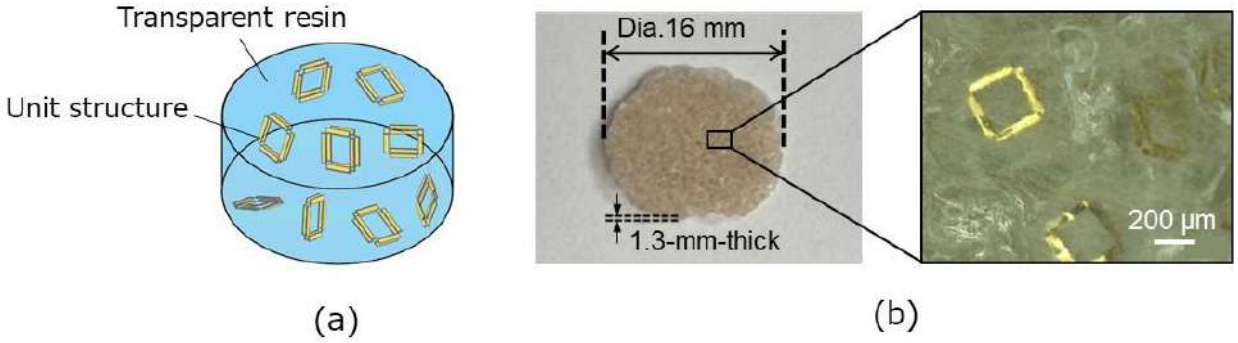


Figure 1: A three-dimensional bulk metamaterial. (a) Conceptual diagram and (b) fabricated three-dimensional bulk metamaterial.

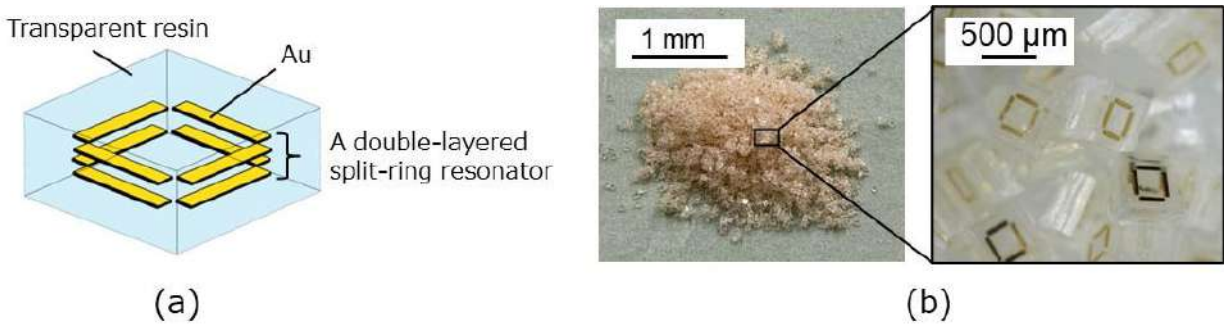


Figure 2: Meta-atomic grains. (a) Conceptual diagram and (b) fabricated meta-atomic grains.

Furthermore, we developed a dielectric three-dimensional bulk metamaterial (Si microparticle dispersion) [3]. The structure is such that Si microparticles are uniformly dispersed in a transparent resin with three-dimensional random orientation, achieving isotropic optical properties. We achieved an effective refractive index in the range of 1.53 to 1.96 at frequencies of 0.1 to 0.2 THz, which includes the 6G communication band. This effective refractive index can be freely controlled by the Si concentration in the Si microparticle dispersion.

Acknowledgements

Part of this work was supported by JSPS Grants-in-Aid for Scientific Research (KAKENHI) 21H04659 and JST Program for co-creating startup ecosystem, Grant Number JPMJSF2312, Japan. Some of this work was performed at the Micro/Nano-Machining Research and Education Center, Tohoku University, Japan.

References

1. Taiyu Okatani, Yuto Sunada, Kazuhiro Hane, and Yoshiaki Kanamori, “Terahertz 3D bulk metamaterials with randomly dispersed split-ring resonators,” Nanophotonics, Vol. 11, No. 9, 2065–2074, 2022.
2. Ying Huang, Takanori Kida, Shun Wakiuchi, Taiyu Okatani, Naoki Inomata, and Yoshiaki Kanamori, “3D Bulk Metamaterials with Engineered Optical Dispersion at Terahertz Frequencies Utilizing Amorphous Multilayered Split-Ring Resonators,” Advanced Science, Vol. 11, No. 34, 2405378, 2024.
3. Shun Wakiuchi, Taiyu Okatani, Naoki Inomata, and Yoshiaki Kanamori, “Fabrication of silicon microparticle dispersion as terahertz wave refractive index control material,” Optics and Laser Technology, Vol. 181, No. Part C, 112051, 2024.

Large-diameter Infrared Si Metalenses through Deep-UV Lithography

K. Sun[1*], X. Yan[2], J. Scott[1], J. N. Monks[3], J. Y. Ou[1] and O. L. Muskens[1]

[1]Physics and Astronomy, University of Southampton, UK
[2]Optoelectronics Research Center, University of Southampton, UK
[3]Teledyne Qioptiq ltd, UK
[*]corresponding author: k.sun@soton.ac.uk

Abstract: We report our latest works on large-diameter infrared silicon metalenses manufactured using production-ready Deep UV scanning lithography.

With the adoption of artificial metasurfaces, the metalenses are developed through phase-shifts control by different nano-features [1]. Although metalenses have been widely demonstrated through e-beam lithography as a lab solution, it is still challenging to use Deep UV lithography to make metalenses with suitability of mass production. Recently, we have demonstrated that large-area and wafer-scale metal oxide metasurface can be reliably manufactured using DUV lithography [2]. In this work, we demonstrate large-diameter Si-based metalenses, based on our novel designs and fabrication. With full CMOS compatibility, these metalens were fabricated using DUV lithography on 8-inch silicon substrates with individual metalens diameters ranging from 12 mm to above 25 mm (over a single DUV exposure field). Figure 1 shows the photo of a wafer with large-diameter metalenses over a 200 mm substrate (a), micrograph of the metalens center (b) and Zoom-in SEM image of the exact center with four exposure stitching. We will demonstrate the novel capabilities of our metalenses, which have been developed in the past years, and their real-world IR imaging capability with their integration into IR cameras.

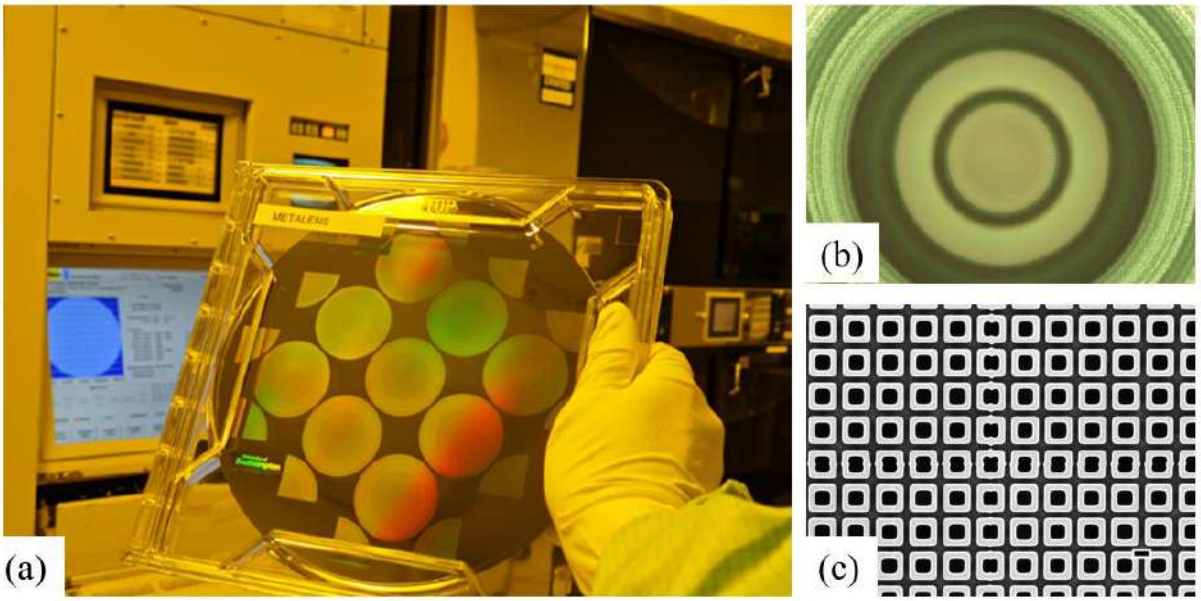


Figure 1. (a) a typical photograph of metalens on a 200 mm Si substrate with Deep UV scanner and Track at the background, (b) micrograph of an infrared metalens center and (c) SEM image showing the metalens center with multi-exposure stitching. SEM bar is 1 µm scale.

References

1. Brongersma, M. L., Pala, R. A., Altug, H., Capasso, F., Chen, W. T., Majumdar, A. and Atwater, H. A. “The second optical metasurface revolution: moving from science to technology,” Nature Reviews Electrical Engineering, Vol. 2, 125–143, 2025.
2. Sun, K., Vassos, E., Yan, X., Wheeler, C., Churm, J., Wiecha, P.R., Gregory, S. A., Freresidis, A., de Groot, C.H. and Muskens, O.L., “Wafer-Scale 200 mm Metal Oxide Infrared Metasurface with Tailored Differential Emissivity Response in the Atmospheric Windows,” Ad. Optical Mater., 2200452, 2022.

Plasmonic nanohole array for tumor cell and tissue biosensing

A. Franco[1*], D. Ortiz[1], C. Velásquez[2,4], V. García-Milán[2], S. Marcos[3], R. Martin-Laez[2], F. Moreno[1], J. L. Fernández-Luna[5]

[1]Applied Physics Department, University of Cantabria, Spain
[2]Neurological Surgery and Spine Unit, Hospital Universitario Marqués de Valdecilla, Spain
[3]Pathology Unit, Hospital Universitario Marqués de Valdecilla, Spain
[4]Anatomy and Cell Biology Department, University of Cantabria, Spain
[5]Genetics Unit, Hospital Universitario Marqués de Valdecilla, Spain
[*]corresponding author: alfredo.franco@unican.es

Abstract: Accurate detection of single tumor cells in liquid biopsies and tumor tissues in brain is crucial for diagnostics and surgery, respectively. We present a label-free plasmonic biosensor for tumor discrimination in complex biological samples, based on the extraordinary optical transmission from nanoholes arrays in gold films.

The identification of single live tumor cells in liquid biopsies is essential for developing personalized treatments[1], while accurate identification of tumor margins in the brain is critical for effective glioblastoma surgery[2]. A simple, fast, and label-free optical technique to distinguish tumor cells and tissues from healthy ones would be highly valuable in clinical practice. This work presents a nanostructured plasmonic-based optical biosensor designed to meet these requirements in a minimally invasive way.

As a proof of concept, we applied nanohole arrays for optical label-free biosensing, based on the extraordinary optical transmission phenomenon. This biosensor offers a promising platform for developing fast, sensitive, and reliable detection systems suitable for both biomedical research and potential clinical applications.

We have used an optical microscopy setup to measure extraordinary optical transmission through the plasmonic biosensor after contact with biological samples[3]. The biosensor features nanoholes (diameter: 220 nm) arranged in a square array (periodicity: 550 nm) within a gold film (thickness: 60 nm). Spectral shifts in the transmission response correlate with changes in refractive index when cells or tissues interact with the sensor surface. We have observed refractive index differences between tumor and healthy cells and tissues, ranging from 0.002 to 0.3 RIU[1,2,4].

We first applied the label-free plasmonic biosensor to discriminate between single live cancer cells and normal cells. The optical setup isolates the spectral response of single cells in contact with the nanohole array, exploiting the localized interaction between the cell membrane and the plasmonic field. This approach demonstrated high sensitivity and specificity (80% to 100%) in distinguishing colorectal cancer cells from normal peripheral blood mononuclear cells and fibroblasts[1]. Notably, the system identified the actin cortex, a cytoskeletal structure located just beneath the cell membrane, as the main factor influencing the spectral response[1]. This highlights the biosensor's ability to detect physical and biochemical alterations at the cell surface.

The plasmonic biosensor was further used to monitor two dynamic cancer hallmarks: cell-matrix adhesion and cell division. Spectral shifts induced by interactions between cancer cells and extracellular matrix proteins were detected in real time, allowing the monitoring of cell adhesion processes during their first hour of contact with the biosensor[4]. Furthermore, by synchronizing colorectal cancer cells at different stages of the cell cycle, the biosensor successfully discriminated resting cells (G0/G1) from dividing cells (G2)[4]. These results highlight how changes in the actin cortex during adhesion and division directly influence the spectral response, demonstrating the biosensor's versatility in studying diverse cancer-related processes.

The label-free plasmonic biosensor was also tested in a pre-clinical context, using ex-vivo surgical specimens to discriminate glioblastoma tissue from peritumoral brain tissue. By comparing extraordinary optical transmission spectral shifts induced by tumor and non-tumor tissues in contact with the nanohole array, the biosensor achieved 81% sensitivity and 80% specificity[2]. These results demonstrate the biosensor's potential as a rapid, label-free intraoperative tool for neurosurgeons to improve tumor margin identification during surgery.

Overall, this work illustrates how nanohole array biosensing based on the extraordinary optical transmission phenomenon can enable label-free detection of cancer cells and tissues[1,2]. Key advantages include simplicity, speed, and versatility, making this approach a strong candidate for clinical translation. Beyond its diagnostic potential, this biosensor has proven valuable for studying cancer cell processes, from adhesion and migration to proliferation[4], further reinforcing its role as a powerful tool for both biomedical research and clinical applications.

Acknowledgements: This work is supported by the Ministerio de Ciencia e Innovación grant PID2021-128220NB-I00, the Instituto de Salud Carlos III through grant DTS18/00141, co-funded by the European Regional Development Fund/European Social Fund, "A way to make Europe/Investing in your future", and the Instituto de Investigación Valdecilla (IDIVAL) (APG/03).

References

1. Franco, A., V. Vidal, M. Gómez, O. Gutiérrez, M. Martino, F. González, F. Moreno, J. L. Fernández Luna, "A label-free optical system with a nanohole array biosensor for discriminating live single cancer cells from normal cells", Nanophotonics, Vol. 11, 315-328, 2022.
2. García-Milán, V., A. Franco, M. E. Zvezdanova, S. Marcos, R. Martín-Laez, F. Moreno, C. Velasquez, J. L. Fernández-Luna, "Discriminating glioblastoma from peritumoral tissue by a nanohole array-based optical and label-free biosensor", Biosensors, Vol. 13, 591, 2023.
3. Franco, A., D. Otaduy, A. I. Barreda, J. L. Fernández-Luna, S. Merino, F. González, F. Moreno, "Optical inspection of manufactured nanohole arrays to bridge the lab-industry gap", Optics & Laser Technology, Vol. 116, 48-57, 2019.
4. Carcelen, M., V. Vidal, A. Franco, M. Gómez, F. Moreno, J. L. Fernández-Luna, "Plasmonic biosensing for label-free detection of two hallmarks of cancer cells: cell-matrix interaction and cell division", Biosensors, Vol. 12, 674, 2022.

Near-Infrared Photodetector Enhancement via Plasmonic Diffraction

Soh Uenoyama

[1]Central Research Laboratory, Hamamatsu Photonics K.K.,

5000, Hirakuchi, Hamana-ku, Hamamatsu City, 434-8601, Japan
[*]Corresponding author: so.uenoyama@crl.hpk.co.jp

Abstract: Near-infrared photodetectors have gained attention due to their attractive applications. However, the photo-absorption efficiency of Si-based photodetectors is relatively weak. In this talk, we demonstrate a plasmonic-diffraction approach that increases the effective photo-absorption length, resulting in a 2.0× enhancement in photocurrent at a specific wavelength and polarization.

Near-infrared (NIR) photodetectors have gained significant attention due to their attractive applications in Light Detection and Ranging (LiDAR), gas sensing, and facial recognition. However, compared to the visible range, the photo-absorption length at NIR wavelengths is considerably longer, resulting in poor photodetection efficiency.

A common approach to enhance photo-sensitivity is to increase the epitaxial layer thickness to absorb as many photons as possible. However, electrons excited near the bottom of the layer have difficulty reaching the photocurrent, resulted in the degrade of the photodetection efficiency.

Recently, nanophotonic approaches such as metalenses [1,2], nano-hole arrays [3], and black silicon [4] have gained significant attention for enhancing the photosensitivity of photodetectors. In this study, we focus on plasmonic diffraction phenomena [5,6]. In this approach, the period of the metal nano-grating is carefully designed to diffract incident light with a large diffraction angle toward the Si substrate at the target wavelength. Furthermore, optimizing the geometry of the metal nano-grating allows selective transmission at a specific wavelength and polarization, making it highly effective for active-sensing applications such as LiDAR. For this study, considering LiDAR applications, we selected 905 nm as the target wavelength.

Figure. 1 shows the photocurrent enhancement as a function of the incident wavelength (λ = 650 – 1000 nm). The red and black line plots correspond to TM-polarization and TE-polarization, respectively. Note that TM-polarization and TE-polarization refer to light polarized parallel and perpendicular to the period direction of the gold nano-grating, respectively. Photocurrent enhancement was defined as the ratio of photocurrent values with and without the gold nano-grating. As a result, gold nano-grating demonstrated a significant photocurrent enhancement (2.0×) under TM-polarization, particularly at a limited wavelength around the target wavelength (λ = 905 nm). In contrast, under TE-polarization, the photocurrent enhancement was suppressed.

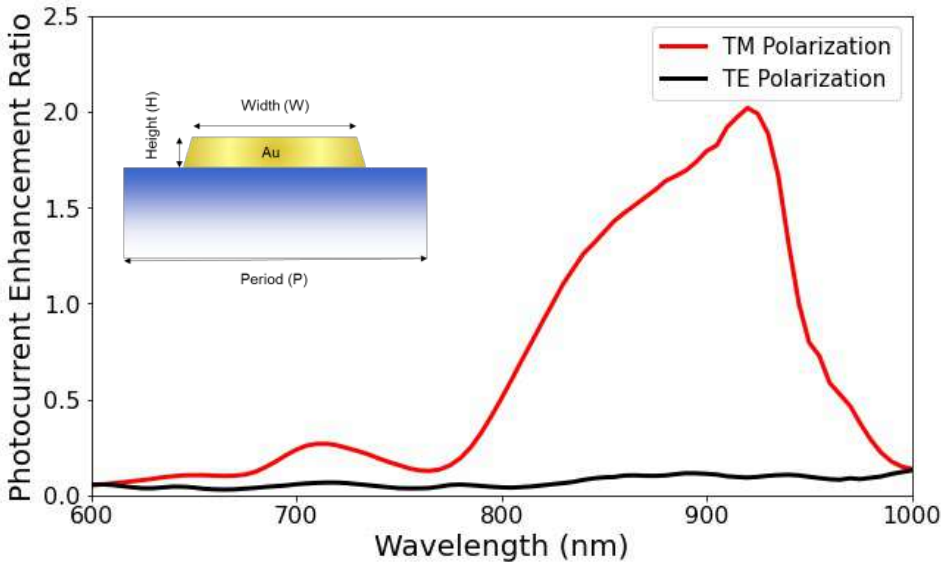


Figure.1. Photocurrent enhancement ratio as a function of the incident wavelength (**λ = 600 – 1000 nm**). The inset illustrates the geometry of the gold nano-grating, where the period (**P**), height (**H**), and width (**W**) are **520 nm, 200 nm, and 440 nm**, respectively.

References

1. Uenoyama, S. and R. Ota, "40 × 40 Metalens Array for Improved Silicon Photomultiplier Performance" ACS Photonics, Vol. 8, No. 6, 1548–1555, 2021.
2. Uenoyama, S. and R. Ota, "Monolithic integration of Metalens in Silicon Photomultiplier for Improved Photodetection efficiency" Advanced Optical Materials, Vol. 10, No. 9, 202102707, 2022.
3. Gao, Y.; Cansizoglu, H.; Polat, K.; et al. "Photon-Trapping Microstructures Enable High-Speed High-Efficiency Silicon Photodiodes" Nat. Photonics, Vol. 11, No. 5, 301–308, 2017.
4. Savin, H.; Repo, P.; von Gastrow, G.; Ortega, P.; Calle, E.; Garín, M.; Alcubilla, R. "Black Silicon Solar Cells with Interdigitated Back-Contacts Achieve 22.1% Efficiency" Nat. Nanotechnol., Vol. 10, No. 7, 624–628, 2015.
5. Ono, A.; Hashimoto, K.; Teranishi, N. "Near-Infrared Sensitivity Improvement by Plasmonic Diffraction for a Silicon Image Sensor with Deep Trench Isolation Filled with Highly Reflective Metal" Opt. Express, Vol. 29, No. 14, 21313, 2021. https://doi.org/10.1364/oe.428314.
6. Uenoyama, S.; Tanaka, K.; Fujiwara, H.; Watanabe, A.; Ono, A. "Experimental Demonstration of Improvement in Near-Infrared Photodetection Efficiency by Plasmonic Diffraction" *ACS Appl. Electron. Mater.*, Vol. 6, No. 9, 7046–7054, 2024.

Reconfigurable Plasmonics Enabled by Phase Change Materials

Yael Gutierrez[1], Gonzalo Santos[1], Capucine Laprais[2], Lofti Berguiga[2], Saul Vázquez-Miranda[3], Mateusz Rebarz[3], Shirly Espinoza[3], Sebastien Cueff[2] and Maria Losurdo[4]

[1]Universidad de Cantabria, Spain

[2]Université Lyon, France

[3]ELI Beamlines, Czech Republic

[4]CNR-ICMATE, Italy

[*]corresponding author: gvelay@unican.es

Abstract: The dynamic tunability of the optical response in plasmonic systems through optical, mechanical, and electrical stimuli is pivotal for advancing reconfigurable nanophotonic applications. In this work, we present an innovative approach to achieve tunable plasmonic properties using ultrafast laser pulses by integrating phase-change materials (PCMs) with plasmonic nanostructures.

Plasmonic systems traditionally rely on fixed geometries and material properties, limiting post-fabrication tunability.[1] In this talk, we present active heterostructures where metallic nanoparticles (Au and Ga) are coupled to low-loss phase-change materials (PCMs), enabling dynamic control over the localized surface plasmon resonance (LSPR). By leveraging the reversible phase transitions of the PCM layer, we demonstrate spectral tuning of the optical response through low-energy thermal and laser-induced switching between amorphous and crystalline states.[2,3]

In the second part, we extend this concept to a metamaterial composed of VO_2 nanocrystals,[4] where we demonstrate ultrafast switching of plasmonic modes. Using pump-probe spectroscopic techniques, we reveal how light-driven phase transitions in VO_2 can modulate plasmonic excitations on picosecond timescales. These results highlight the potential of phase-change materials in reconfigurable nanophotonics and active plasmonic devices.

References

[1] Y. Gutiérrez, A. S. Brown, F. Moreno, M. Losurdo, *J. Appl. Phys.* **2020**, *128*, 080901.

[2] C. Laprais, C. Zrounba, J. Bouvier, N. Blanchard, M. Bugnet, A. Gassenq, Y. Gutiérrez, S. Vazquez-Miranda, S. Espinoza, P. Thiesen, R. Bourrellier, A. Benamrouche, N. Baboux, G. Saint-Girons, L. Berguiga, S. Cueff, *Adv. Opt. Mater.* **2024**, *12*, DOI 10.1002/adom.202401214.

[3] J. Resl, K. Hingerl, Y. Gutierrez, M. Losurdo, C. Cobet, *J. Appl. Phys.* **2024**, *136*, DOI 10.1063/5.0224152.

[4] J. John, Y. Gutierrez, Z. Zhang, H. Karl, S. Ramanathan, R. Orobtchouk, F. Moreno, S. Cueff, *Phys. Rev. Appl.* **2020**, *13*, 044053.

META 2025, MALAGA - SPAIN, JULY 22 – 25, 2025

Recognition of Shiga Toxins by Plasmonic SERS Metasurface PCA Assisted

M. Rippa[1]*, A. Milano[1], V. Marchesano[1], D. Sagnelli[1], B. Guilcapi[1], A. D'Avino[1], M. Brigotti[2,1], S. Morabito[3,1], J. Zyss[4] and L. Petti[1]

[1]Institute of Applied Sciences and Intelligent Systems "E. Caianiello" CNR, Pozzuoli, Italy
[2]Dipartimento di Scienze Mediche e Chirurgiche, Sede di Patologia Generale, Università di Bologna, Bologna, Italy
[3]Department of Food Safety, Nutrition and Veterinary Public Health, Istituto Superiore di Sanitá, Rome, Italy
[4]Lumière, Matière et Interfaces (LUMIN) Laboratory, Institut d'Alembert, Ecole Normale Supérieure Paris-Saclay, Université Paris Saclay, Gif sur Yvette, France

*Corresponding author: massimo.rippa@isasi.cnr.it

Abstract: A plasmonic biosensor based on a nanopatterned metasurface is presented for the recognition and differentiation of Shiga toxins (Stx1a, Stx2a, Stx2a-cl). Using Surface-Enhanced Raman Spectroscopy (SERS) and principal component analysis (PCA), the system enables highly sensitive, label-free identification, offering a promising tool for improved diagnostics of STEC infections.

Shiga toxin-producing Escherichia coli (STEC) are zoonotic pathogens causing severe diseases, including hemolytic uremic syndrome (HUS), the leading cause of acute renal failure in children, which can be fatal in some cases [1]. The primary virulence factors of STEC that contribute to HUS onset are two main types of cytotoxins: Shiga toxins 1 (Stx1) and 2 (Stx2). Currently, no effective therapies exist for STEC infection, and available diagnostic methods are often complex and sometimes inconclusive. Plasmonic biosensors are powerful platforms for detecting various types of analytes. Surface-Enhanced Raman spectroscopy (SERS) enables label-free, highly sensitive, and selective detection [2]. In this study, we designed, characterized, and tested SERS substrates based on a novel nanopattern fabricated using a top-down approach for the recognition and differentiation of Stx1, Stx2, and a cleaved version of the latter (Stx2a-cl). The sensors consist of an engineered planar plasmonic metasurface that we previously developed, studied and characterized [3, 4]. It features a hexagonal array of asymmetric nanocavities (NCs) fabricated on a gold thin film via electron beam lithography. The NCs are formed by the fusion of three equilateral triangles: two aligned on one side and the third centered on the opposite side, with an overall size of approximately 450 × 430 μm^2. A scanning electron microscopy (SEM) image of the metasurface is shown in Figure 1a. The plasmonic metasurface was tested to define the SERS fingerprint spectra of the three Stx variants under investigation. Equal concentrations of the three toxins (45 nM in water) were deposited onto three identical nanopatterned metasurfaces by direct adsorption. Measurements were performed on each nanopattern, yielding repeatable spectra with well-resolved peaks. Figure 1b shows the average, normalized SERS spectra obtained for Stx1a (blue line), Stx2a (red line) and its cleaved form Stx2a-cl (green line). The three spectra exhibit a complex distribution of vibrational modes corresponding to the molecular structures of the toxins. Overall, the three fingerprints appear highly similar, with only subtle differences. To further analyze these spectral variations, principal component analysis (PCA) was employed to extract key spectral features.

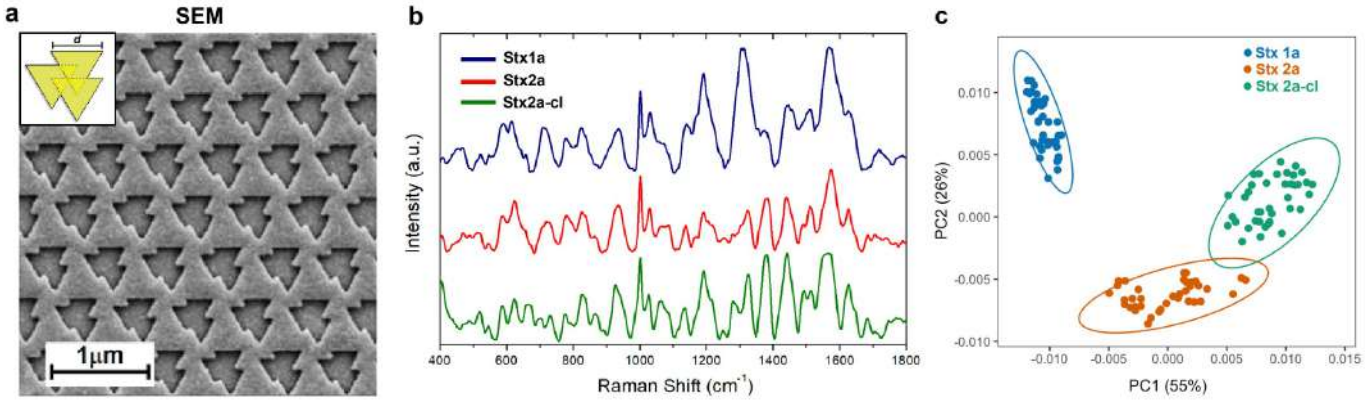


Figure 1. SERS analysis of the three Stx taken into consideration: (a) SEM image of the plasmonic metasurface employed, (b) average SERS fingerprint of the Stx1a (blue line), Stx2a (red line) and Stx2a-cl (green line), and (c) PCA analysis associated with the SERS measurements of the Stx1a (blue points), Stx2a (red points) and Stx2a-cl (green points).

Figure 2b shows the data projected in a two-dimensional space defined by the first two principal components (PC1 and PC2), with Stx1a (blue points), Stx2a (red points), and Stx2a-cl (green points) corresponding to the SERS measurements. As shown in the plot, the three toxins are clearly distinguishable, forming well-separated clusters. Notably, the relative distances between the clusters reflect the actual chemical differences among the toxins: the distinction between Stx1a and Stx2a is pronounced, while Stx2a and Stx2a-cl show only subtle differences, with partial overlap. This successful separation can be attributed to the variance explained by PC1 (55%) and PC2 (26%), which together account for over 80% of the total variance, a threshold commonly used for adequate differentiation of analytes. These findings demonstrate that SERS, combined with PCA, is a valuable tool for distinguishing different Stx variants in water, enabling specific analyte recognition without the need for antibody probes.

Acknowledgements

The authors gratefully acknowledge the support for this work from European Union - NextGenerationEU Call PRIN2022 Development of a plasmonic nanobiosensor for the rapid diagnosis of Shiga toxin producing E. coli human infections at the point of care - SENSOSTEC (CUP B53D23019990006).

References

1. Altug, H., Oh, S.H., Maier, S.A. and Homola, J., “Advances and applications of nanophotonic biosensors,” Nat. Nanotechnol., Vol. 17, 5–16, 2022.
2. Freedman, S.B., van de Kar, N.C.A.J., and Tarr, P.I., “Shiga Toxin–Producing Escherichia coli and the Hemolytic–Uremic Syndrome,” N. Eng. J. Med., vol. 389, No. 15, pp. 1402–1414, 2023.
3. Palermo, G., Rippa, M., Aceti, D.M., Guglielmelli, A., Valente, L., Sgnelli, D., D’avino, A., Guilcapi, B., Maccaferri, N., Petti, L., Strangi, G., “Intrinsic Superchirality in Planar Plasmonic Metasurfaces,” Nano Lett, vol. 24, no. 33, 10202–10209, 2024.
4. Rippa, M., Castagna, R., Kolkowski, R., Zyss, J., Zhou, J., and Petti, L., “Novel supra-molecular arrangements with plasmonic functionalities for fipronil pesticide detection,” Proc. SPIE 11345, Nanophotonics VIII, 1134510, 2020.

Boosting the magnetic response of a composite nanostructure in the near-visible region with a Fano resonance

Maximilian Grimmer[1*] and Monika Fleischer[1]

[1] Institute for Applied Physics and Center LISA[+], Eberhard Karls University of Tübingen, Auf der Morgenstelle 10, 72076 Tübingen, Germany

[*]maximilian-karl.grimmer@student.uni-tuebingen.de

Abstract: We investigate the optical properties of a plasmonic nanostructure, focusing on its magnetic response. Using the geometry of a composite split-ring resonator, it is possible to create a magnetic response at wavelengths close to the visible regime, which can be increased by modifying the geometry and enabling a Fano resonance.

Metallic nanostructures have optical properties that greatly differ from those of their respective bulk materials. At the nanoscale, the electric field component of light can affect the entire volume of the structure, as well as its conducting electrons. These electrons move in response to the electric field, leading to a charge separation within the nanostructure that oscillates with the frequency of the incident light. Plasmonics is the corresponding research field that investigates these oscillations. Nanoparticles made from (noble) metals can have a plasmonic resonance in the visible and the near-infrared range, causing a high scattering cross-section and strong electric near-field enhancement at the surface of the nanoparticle [1].

Plasmonics offer an easy way to create a structure with a strong electric response to light at optical frequencies. It is, however, more difficult to create a structure that shows a *magnetic* response to light at optical frequencies as well. The magnetic response of all natural materials decreases towards higher frequencies, dropping off in the GHz range for most materials. Landau and Lifschitz have shown that the magnetization and the magnetic permeability become irrelevant towards higher frequencies, with the relative magnetic permeability μ_r of all natural materials being 1 at optical frequencies [2]. It is nevertheless possible to engineer a material with a magnetic response at higher frequencies by utilizing not the magnetic but the electric response of the material. By designing the nanostructure so that the plasmonic current flows in a circular loop, a magnetic dipole is induced. The split-ring resonator (SRR) is a commonly used geometry to achieve such a magnetic response. It consists of a single nanoring with a gap. This structure with its resonance can be modeled as a coil with the inductance L (the nanoring) and a capacitor with the capacitance C (the nanogap), with a resonance frequency

$$\omega_0 = 1/\sqrt{L * C} \quad (1)$$

SRRs and their magnetic resonance have already been investigated for many applications, such as metamaterials, cloaking, sensing, and super-chiral near fields. However, saturation effects limit the maximum resonance frequency to the near-infrared range [3].

The purpose of our work is to shift the magnetic resonance towards higher frequencies and to increase the magnetic response to enable applications at such higher frequencies. For this aim, we propose a variation of the SRR geometry with two additional gaps. These gaps serve as additional capacitors connected in series, lowering the total capacitance and blue-shifting the magnetic resonance towards the visible range by more than 350 nm. We also demonstrate a novel way to boost the magnetic response of the structure by adding a nanorod below the central element of the SRR. The ensuing mode coupling leads to an interference phenomenon known as Fano resonance [4], resulting in a spectral dip that leads to an additional scattering peak. The new magnetic resonance shows a higher magnetic near-field enhancement than the resonance of the SRR; its excitation is calculated to boost the overall magnetic response of this structure by 70%. Such an increase in the magnetic response may improve the

performance of many applications of the SRRs at higher frequencies.
Both structures are investigated using numerical simulations as well as experimental fabrication and optical measurements. The two proposed nanostructures have both a geometry consisting of multiple elements that are separated by a gap of 10 nm and lower. Fabrication of these composite nanostructures is challenging and was done with a two-step process, where the basic structure is created using electron beam lithography, while the small gaps were milled into the structure using focused Helium-ion beam milling [5]. This approach is well-suited to create challenging nanostructures with small gap sizes, which can hardly be achieved with conventional electron beam lithography.

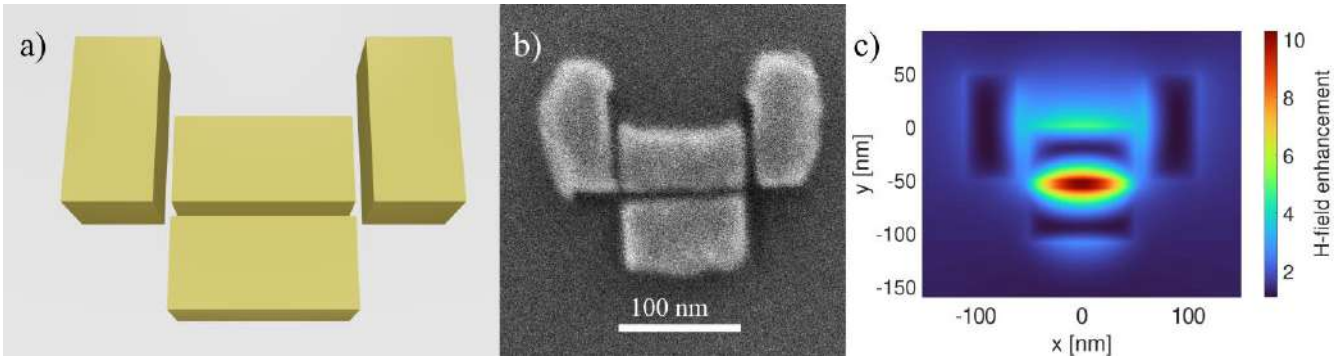


Figure 1: (a) Scheme of the proposed extended split-ring resonator (ESRR), (b) image of a fabricated ESRR after the milling step was performed, (c) simulated magnetic near-field enhancement of the ESRR at a wavelength of 876 nm.

Acknowledgments: This work was supported by Deutsche Forschungsgemeinschaft DFG under Grant INST 37/959-1 FUGG. Maximilian Grimmer gratefully acknowledges financial support by the Landes-graduiertenförderung of the Ministry of Science, Research and the Arts Baden-Württemberg.

References:

1. S. Maier, Plasmonics: Fundamentals and applications (Springer, 2007)
2. F. Monticone et al., “The quest for optical magnetism: from split-ring resonators to plasmonic nanoparticles and nanoclusters,” J. Mater. Chem. C 2, Vol. 2, No. 43, 9059–9072, 2014
3. E. Calandrini, et al., “Magnetic hot-spot generation at optical frequencies: from plasmonic metamolecules to all-dielectric nanoclusters,” Nanophotonics Vol. 8, No. 1, 45–62, 2018
4. M. Grimmer et al., “Enhancing Fano resonances through coupling of dark modes in a dual-ring nanostructure,” Opt. Express, Vol. 32, No. 2, 1926-1940, 2024
5. S. He et al., “Helium-ion-beam nanofabrication: extreme processes and applications,” Int. J. Extrem. Manuf., Vol. 3, No.1, 012001, 2021

Electric field induced second order nonlinearity in amorphous As_2S_3, SiO_x and SiN_x

L. Wardenberg[1], K.K. Upadhyayula[1], G. von Freymann[2], V. Talalaev[1], M. Hanke[3], A. Kühling[1] and J. Schilling[1]

[1]Department of Physics, Martin-Luther-Universität Halle-Wittenberg,06120 Halle, Germany
[2]Department of Physics and Research Center OPTIMAS, RPTU Kaiserslautern-Landau, 67663 Kaiserslautern, Germany
[3]Paul-Drude-Institut für Festkörperelektronik, 10117 Berlin, Germany
*corresponding author: joerg.schilling@physik.uni-halle.de

Abstract: Applying an electric field to As_2S_3, and silicon rich SiO_x and SiN_x leads to the formation of a field dependent quasi-$\chi^{(2)}$ and field induced second harmonic generation in transmission. Both PECVD-grown SiO_x and SiN_x also exhibit a field free $\chi^{(2)}$ leading to enhanced SHG by a waveguide surface grating.

When a strong static electric field E_{DC} is applied to a material and an intense Light wave ($E(\omega)$) is incident at the same time, the third order dipolar contribution is calculated via: $P^{(3)} \sim \chi^{(3)} \cdot \left(E_{DC} + E(\omega)\right)^3$. Multiplying out the cubic bracket gives then rise to the different third order nonlinear phenomena like third harmonic generation or intensity dependent refractive index. One term, which is usually overlooked is the generation of a frequency doubled polarization – the so called electric field induced second harmonic generation (EFISH) [1]:

$$P_{EFISH}^{2\omega} = \underbrace{\chi^{(3)}\, E_{dc}(0)}_{\text{quasi-}\chi^{(2)}} E(\omega)\, E(\omega) \qquad (1)$$

In this the product $\chi^{(3)} \cdot E_{DC}$ can be considered as a quasi-$\chi^{(2)}$. This means, that by applying a strong electric field on any material symmetry breaking occurs and an electric field induced quasi-$\chi^{(2)}$ can be generated, allowing the usual second order nonlinear processes like sum- or difference frequency generation. To observe this process and determine the achievable quasi-$\chi^{(2)}$ values we performed EFISH-measurements in transmission, first, using thin films of the chalcogenide glass As_2S_3 sandwiched between two semitransparent Cr-electrodes, which could be used to apply voltages up to 1000V across the As_2S_3-film (Fig. 1a) [2]. The observed parabolic relationship between

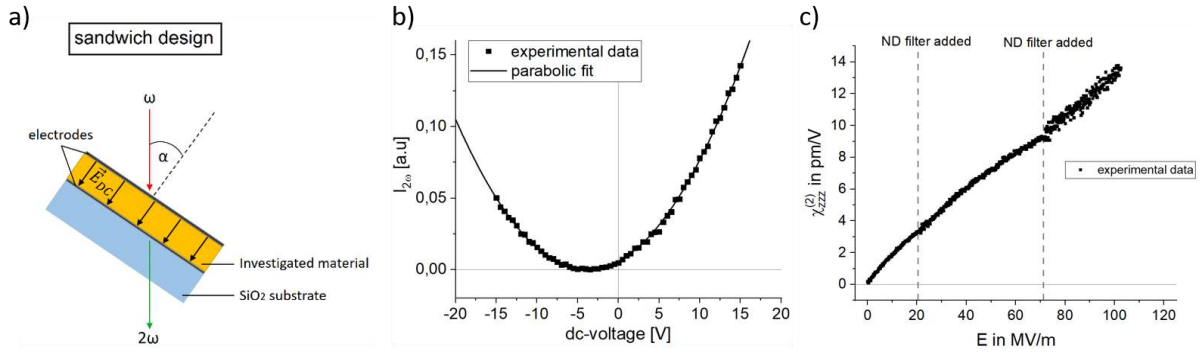


Fig. 1: EFISH-measurement in transmission a) Experimental setup applying TM (p-)-polarised light b) observed parabolic dependence between SHG-intensity and applied DC-voltage, c) Deduced field dependent quasi-$\chi^{(2)}$

the detected SHG and the applied DC-voltage confirms the assumed EFISH effect (Fig. 1b), since the detected

SHG-intensity depends on the squared second order polarization from (1). Applying DC-fields up to the break-down field of 100 MV/m resulted in quasi-$\chi^{(2)}$ values of about 13pm/V exceeding the $\chi^{(2)}$-values of classic nonlinear crystals like KDP or BBO. Furthermore, this field induced quasi- $\chi^{(2)}$ is not bound to a specific crystallographic direction but follows from the tensor product $\chi^{(3)} \cdot E_{DC}$. In amorphous films with isotropic $\chi^{(3)}$ we determined the $\chi^{(2)}_{zzz}$ component to be the strongest $\chi^{(2)}$ component generated by the z-oriented DC-field.

Besides As_2S_3-films we also investigated amorphous silicon rich SiO_x and SiN_x-films and measured their EFISH signals. For part of the films the measurement geometry was changed and lateral contacts were applied (Fig. 2a). This induced a strong in-plane quasi-$\chi^{(2)}_{xxx}$ component, so that also for TE (s-) polarized light EFISH could be measured (Fig. 2b). The measured $\chi^{(2)}$-values profited from the large $\chi^{(3)}$ which occurs in silicon rich SiNx. Surprisingly this was also the case for silicon rich Oxide (SiO_x), whose $\chi^{(3)}$ reached values of $10^{-18} m^2/V^2$ and was therefore comparable to the known high third order susceptibilities in ultra-Si-rich SiNx [2].

Finally, we could also observe a sizeable built-in (field-free) bulk -$\chi^{(2)}$ normal to the surface for the PECVD-grown SiN_x and SiO_x-films. In an attempt to further boost the impact of this field-free bulk -$\chi^{(2)}$ we etched a grating on top of a SiNx-waveguide and measured the SHG in transmission at near normal incidence. The period of the grating was adjusted in such a way that summetry and polarization protected bound states in continuum (BIC) appear at normal incidence giving still rise to increased Q-factors at small lateral k-vectors (small incidence angles.) Overall this geometry resulted in a 4 order of magnitude increase of the SHG-signal compared to unstructured films.

These results demonstrate, that the field induced quasi-$\chi^{(2)}$ can be introduced in photonic circuits based on dielectric/insulating materials. The possibility to switch the quasi-$\chi^{(2)}$ on or off- or modulating its strength just by changing the applied static electric field, allows for a large degree of flexibility and design freedom.

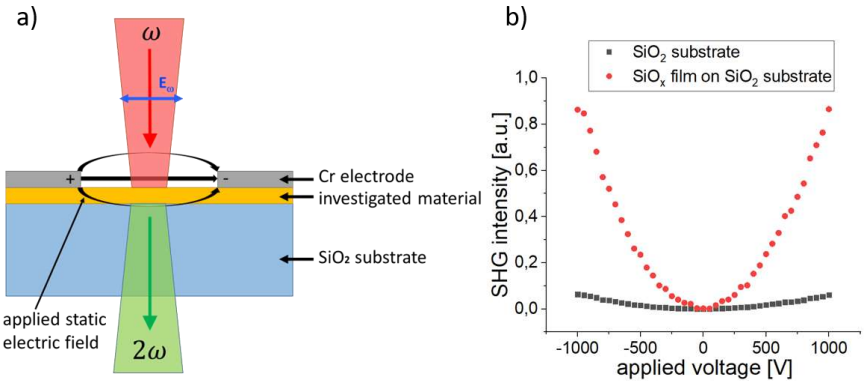


Fig. 2: EFISH measurements with lateral electric contacts and in-plane DC-field a) measurement geometry, b) Observed large EFISH-Signal for amorphous silicon rich SiO_x. [4]

References

1. Boyd, R.W. “Nonlinear Optics”, Academic Press, 3. Ed. (2008)
2. Wardenberg, L., B. Bunk, G.von Freymann and J. Schilling, “Electric field induced second harmonic generation in arsenic sulfide deposited by thermal evaporation”, Opt. Express **32**, 23856-23864 (2024)
3. Wardenberg, L. A. Kühling and J. Schilling, “Optical Second- and Third-Order Nonlinearities in Plasma-Enhanced Chemical Vapor Deposition-Grown Silicon Oxides and Silicon Nitrides”, Adv. Photonics Res. 2400142. (2025)
4. Wardenberg, L., K.K. Upadhyayula, V. Talalaev, M. Hanke, A. Kühling and J. Schilling, “Electric field-induced second-harmonic generation in silicon nanocrystals embedded in a SiOx matrix”, Optics express (accepted)

Superconducting Nanowire Single Photon Detectors for photon counting applications in the mid-infrared.

Dmitry Morozov[1], Daniel Kuznesof[1], Ciaran Lennon[2], Umberto Nasti[3], Robert H. Hadfield[1]

[1]James Watt School of Engineering, University of Glasgow, Glasgow, United Kingdom

[2]Oxford Instruments Plasma Technology, Bristol, United Kingdom

[3]School of Engineering and Physical Sciences, Heriot-Watt University, Edinburgh, United Kingdom

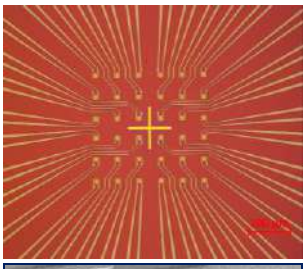
*corresponding author: Dmitry.Morozov@glasgow.ac.uk

Abstract: This study focuses on developing mid-infrared superconducting nanowire single-photon detector (SNSPD) arrays. Using optimised NbN films, the research analyses electrical, optical, and temporal performance, alongside pixel performance uniformity. The study explores potential applications in the single-photon regime, including imaging, laser ranging, medical imaging, and astronomy.

Counting individual photons in the mid-infrared range is crucial for applications in quantum optics, quantum-enhanced imaging, depth sensing, and astronomy. Superconducting nanowire single-photon detectors (SNSPDs) are efficient, low-noise devices ideal for detecting low photon levels [1]. These detectors offer near-perfect quantum efficiency at telecom wavelengths, can detect photons up to 29 µm in the mid-IR range [2], and have a timing jitter as low as 3 ps. Advances in superconducting materials and manufacturing processes have enabled scaling from single pixels to multiplexed SNSPD arrays.

This study focuses on developing 36-pixel mid-infrared SNSPD arrays. The core element of the SNSPDs is the ultrathin superconducting film patterned into the nano-strip 30 to 200 nm wide. Figure 1(a) shows the optical image of the array, while Figure 1(b) presents a Scanning Electron Microscope (SEM) image of a single pixel. The SNSPD is cooled to cryogenic temperatures (typically below 2K) and biased just below its critical current value. When a photon is absorbed in the nanowire, it creates a resistive domain in the film, generating a voltage pulse in the read-out circuit. After a brief recovery period, the superconductivity is restored, allowing the detector to register another photon. Magnetron sputtering, commonly used for deposition of thin superconducting films of NbN, has limitations in uniformity, hindering large-area device development. However, multi-pixel SNSPDs require films with spatially uniform parameters such as thickness, superconducting transition temperature, and critical current density. A newer technique, Atomic Layer Deposition (ALD), enables the production of high-quality thin films of NbN, TiN, and NbTiN [3]. The ALD method offers greater uniformity in pixel performance compared to sputtering, making it ideal for SNSPD arrays. The devices in this study are based on optimised ultrathin NbN films grown using both sputtering

a)



b)

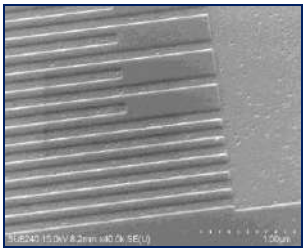


Figure 1: (a) Photograph of the 36-pixel SNSPD chip. (b) SEM image of the SNSPD pixel.

and ALD techniques.

This study presents a thorough analysis of the electrical, optical, and temporal performance of individual pixels, along with an assessment of pixel uniformity across arrays with varying pixel spacing. Figure 2 shows the uniformity of superconducting critical current values across the SNSPD array based on 8 nm thick sputtered NbN film. To characterise the devices, a setup using tunable optical parametric oscillator (OPO) sources was employed, delivering picosecond pulses in the 1.5 – 10 μm spectral range. Additionally, proof-of-concept tests for ranging and imaging are included to showcase the potential applications of SNSPD arrays. The present study is aimed towards the prospective applications such as detecting of faint mid-infrared sources, long-range communication, laser ranging, medical imaging and astronomy.

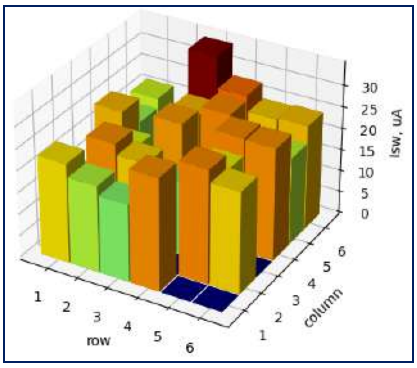


Figure 2: Critical current value of 36-pixel SNSPD array.

The authors would like to acknowledge support from EPSRC SPEX programme grant and QuantIC QT hub.

References

1. Morozov, D. V., Casaburi, A., & Hadfield, R. H., “Superconducting photon detectors”. Contemporary Physics, 62(2), 69–91, 2021
2. G. G. Taylor, A. B. Walter, B. Korzh, B. Bumble, S. R. Patel, J. P. Allmaras, A. D. Beyer, R. O’Brient, M. D. Shaw, and E. E. Wollman, "Low-noise single-photon counting superconducting nanowire detectors at infrared wavelengths up to 29 μm," Optica, 10, 1672-1678, 2023
3. C. T. Lennon, Y. Shu, J. C. Brennan, D. K. Namburi, V. Varghese, D. T. Hemakumara, L. A. Longchar, S. Srinath and R. H. Hadfield, "High-uniformity atomic layer deposition of superconducting niobium nitride thin films for quantum photonic integration", Mater. Quantum. Technol., 3, 045401, 2023

Freestanding ultra-thin BIC membrane metasurface for high-Q surface emission in the visible

C. Z. Deng, Y. L. Ho*
Research Center for Electronic and Optical Materials, National Institute for Materials Science (NIMS),
1-1 Namiki, Tsukuba, Ibaraki 305-0044, Japan
E-mail: HO.Ya-Lun@nims.go.jp

Abstract: The freestanding dielectric membrane metasurface, with a thickness of 36 nm, has been demonstrated to achieve a bound state in the continuum (BIC) mode, exhibiting spontaneous emission with a high Q-factor over 2037 in the visible regime.

Embedded within the radiation continuum, photonic bound states in continuum (BICs) represent exceptional nonradiative states where modes become fully trapped through destructive interference or symmetry protection mechanisms. This trapping phenomenon enhances light-matter interactions and can generate impressive Q factors[1]. Freestanding membrane structures offer ideal platforms for BIC implementation, confining light without substrate field leakage. These characteristics significantly amplify spontaneous emission rates and optical absorption, creating structures perfectly suited for applications demanding robust optical confinement and elevated Q-factors[2,3]. The thickness of a freestanding membrane plays a critical role in optimizing light-matter interactions, particularly when interfacing with atomically thin materials where even nanoscale dimensional changes can dramatically alter coupling efficiency and field confinement. The reduced thickness of the membranes decreases mode volume and positions the resonant mode field in closer proximity to atomically thin materials like monolayer transition metal dichalcogenides. This proximity substantially improves coupling efficiency between the photonic structure and these ultra-thin materials[3], a critical factor for maximizing light-matter interaction and enhancing spontaneous emission efficiency.

Figure 1(a) and (b) present simulated reflection spectra for two configurations: a SiN metasurface on a SiO_2 substrate and a free-standing SiN membrane metasurface, respectively. These metasurfaces featured triangular lattices of air holes (period P = 600 nm, hole diameter D = 300 nm). In both configurations, all modes exhibited a blueshift with decreasing thickness, attributable to reduced effective optical path. Figure 1(a) displays simulation results across varying thicknesses, as the thickness approaches 100 nm, coupling between the modes and substrate radiation channels becomes dominant, resulting in weakened field confinement that barely sustains the modes. Electric field distribution simulations were analyzed for distinguishing between BICs and GMs. Figure 1(b) presents reflectance spectra identifying specific BICs and GMs in the SiN membrane metasurface. Due to vertical symmetry and minimal leakage, all TE modes remained observable even as thickness approached zero, while only two TM modes disappeared below approximately 75 nm thickness due to their vertical resonance characteristics.

Spontaneous emission spectra for 163 nm and 36 nm thick SiN membrane metasurfaces (Figure 1(c)) demonstrate significantly enhanced emission peaks. As thickness decreased, a blueshift in peaks occurred, aligning with simulation data from Figure 1(b). The 36 nm device exhibited two sharp peaks corresponding to BIC modes at 561 nm and 572 nm with enhanced intensity and narrower linewidths. Notably, the BIC_4 peak at 598.44 nm achieved an exceptional Q-factor of 2037 in the visible spectrum.

In this work, we have successfully demonstrated the realization of BIC modes in ultra-thin free-standing SiN hole-array membrane with thicknesses down to 36 nm. Through systematic investigation of thickness-dependent optical properties, we observed that both TE- and TM-BIC modes persist in these ultra-thin photonic structures, maintaining high Q-factors as thickness decreases. Notably, we achieved an exceptional Q-factor of 9632 for a TE-BIC mode at a thickness of 163 nm, with substantial Q-factors of 2037 preserved even at thicknesses down to 36 nm. Our comparative study between free-standing membranes and substrate-supported structures revealed the critical role of substrate-induced field leakage in mode sustainability. The spectral positions of these modes exhibited predictable blue-shifts with decreasing thickness, allowing for precise wavelength tuning. This tunability, combined with the enhancement of spontaneous emission (up to 130-fold compared to plain SiN thin-film on Si), demonstrates the potential of these structures for various photonic applications. The achievement of high-Q BIC modes in ultra-thin hole-array membrane is particularly significant for sensing applications and applications involving atomically thin 2D materials.

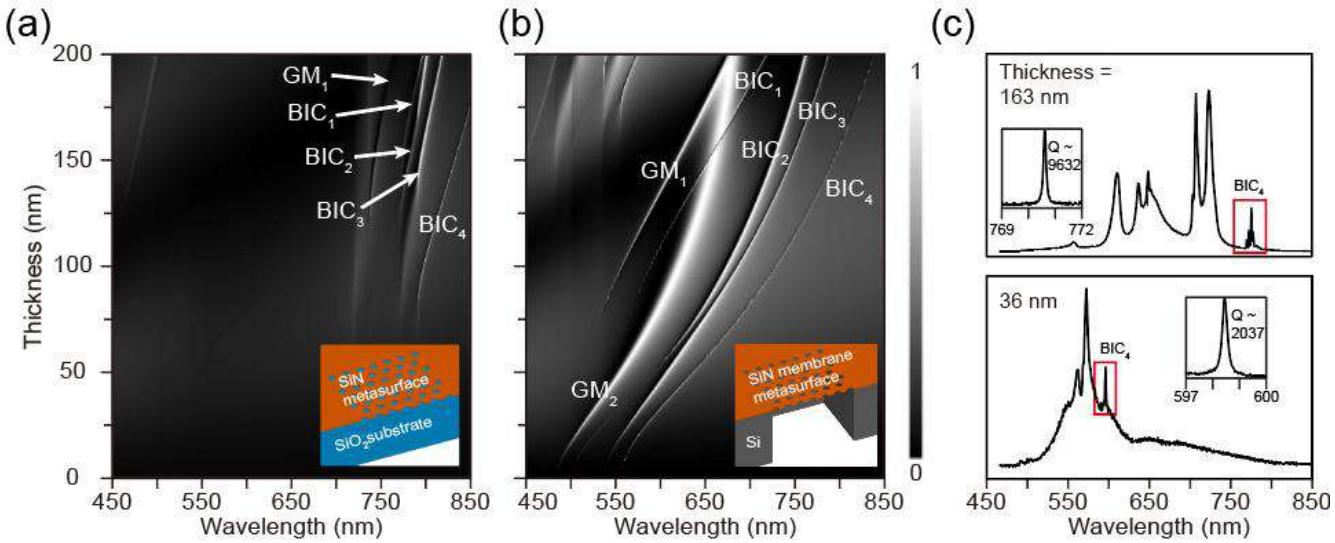


Fig. 1 Simulated reflection spectral variation to the thickness of (a) the SiO_2 substrate-based SiN metasurface and (b) the SiN membrane metasurface. The light incident angle is 4˚. (c) Spontaneous emission spectra of the 163 nm and 36 nm-thick freestanding SiN membrane metasurface.

References

1. Hsu, C. W., Zhen, B., Stone, A. D., Joannopoulos, J. D., Soljacic, M. "Bound states in the continuum," Nat. Rev. Mater, 1, 1–13, 2016.
2. Zhang, X., Choi, S., Wang, D., Naylor, C. H., Johnson, A. T. C., Cubukcu, E, M. "Unidirectional Doubly Enhanced MoS2 Emission via Photonic Fano Resonances," Nano Lett., 17, 6715–6720, 2017.
3. Ho, Y. L., Fong, C. F., Wu, Y. J., Konishi, K., Deng, C. Z., Fu, J. H., Kato, Y. K., Tsukagoshi, K., Tung, V., Chen, C. W. "Finite-Area Membrane Metasurfaces for Enhancing Light-Matter Coupling in Monolayer Transition Metal Dichalcogenides," ACS Nano, 18, 24173–24181, 2024.

Steering plasmonic optical losses using alkali metals

Jie Liang, Yuhan Yang, Lin Zhou*

College of Engineering and Applied Sciences, Nanjing University, China
*corresponding author: linzhou@nju.edu.cn

Abstract: Plasmonic losses has been regarded as one of the most crucial issues for nanophotonics and integrated optics. In this talk, the authors will present the recent advancements on a variety of material and/or meta-structure strategies on steering the optical losses based on alkali metals, from the fundamental optical properties to the potential applications.

Alkali metals, with their simple electronic structure, low free carrier density, and weak interband optical transition, are promising plasmonic materials expected to exhibit lower optical damping rates than conventional noble metals. Additionally, their potential as negative electrode materials in high-capacity, high-energy-density batteries offers a natural platform for low-powered dynamic plasmonics control.

I will first present the fundamental physical mechanisms behind the optical low-loss nature in alkali metals, along with new fabrication techniques aimed at further reducing these losses and advanced experimental methods for measuring the optical loss in alkali metals. Based on these foundational studies, I will then introduce the diverse applications enabled by low-loss alkali metal plasmonics, including plasmonic nanolasers, waveguides, optical filters, strong coupling applications such as optical sensing, and low-powered dynamic plasmonics leveraging battery energy storage properties.

A notable study based on high-performance sodium-based metasurfaces for optical filtration in the visible range is shown in Figure 1. By using a unique design with spatially decoupled concave surfaces and precise fabrication, the sodium based metasurfaces achieve narrow linewidths (~15 nm), high optical contrast (~93%), and a strong spectral match ratio. This work marks the first extension of sodium-based plasmonic devices from infrared to visible wavelengths, filling a gap in commercial optical filters.

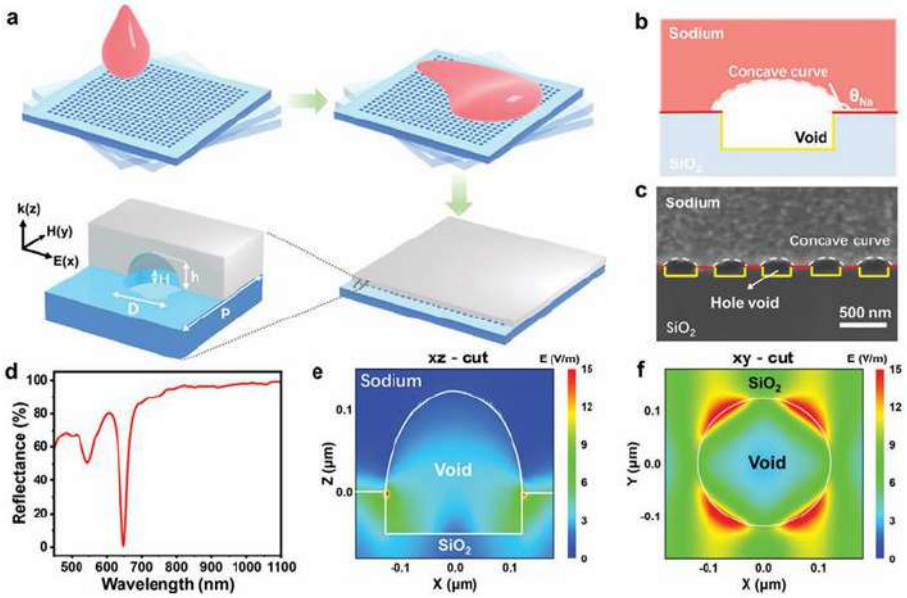


Figure 1. The low-loss sodium anti-dome metasurface. (a) Schematic of the templated spin-on-sodiophobic-glass fabrication process. (b) Schematic diagram of a single anti-dome curve patterned structure. (c) The cross-sectional SEM image of a representative sodium-based concave metasurface. (d-f) Representative simulated reflectance spectrum and electric field of an arbitrary sodium-based concave metasurface.

Another most representative example, the electric-driven dynamic plasmonics for low-powered display, is shown in Figure 2. It is well known that, display and power supply have been two essential and independent cornerstones of modern electronics. A low power or even self-powered display devices are highly desired but rather challenging thus far. Our recent work reported a lithium plasmon based low-powered dynamic color display with inherited dual functionalities, the plasmonic display and energy recycling unit (see Figure 2a), through electric-driven transformation of nanostructured lithium metals. In such an intriguing operation configuration, each display pixel can work as a micro-battery cell and most excitingly, each micro-pixel (micro-battery) can be powered by its adjacent counterpart, making the manipulation of dual functionalities (information and energy) more flexible (Figure 2b).

We acknowledge the financial supports from the National Key Research and Development Program of China (Nos. 2022YFA1404300, 2021YFA1400700).

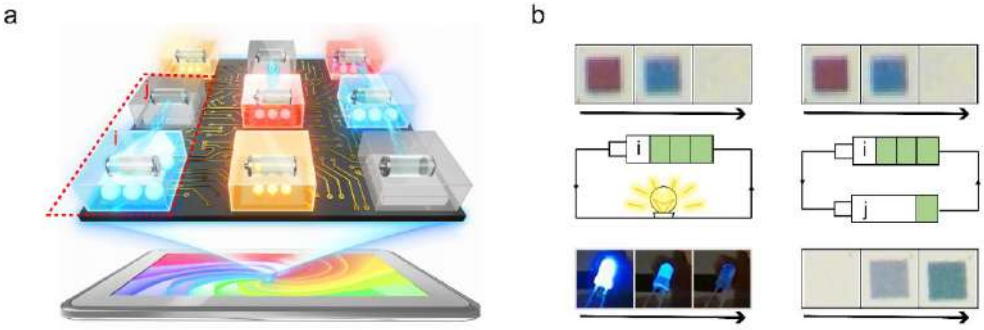


Figure 2. Low-powered dynamic plasmonic color display. (a) The operation schematic of the low-powered dynamic plasmonic color display. (b) The dual functionalities of the power supplier and information display of the device.

References

1. Yang Wang, Jianyu Yu, Yifei Mao, Ji Chen, Suo Wang, Huazhou Chen, Yi Zhang, Siyi Wang, Xinjie Chen, Tao Li, Lin Zhou*, Renmin Ma*, Shining Zhu*, Wenshan Cai, Jia Zhu*, Stable and high-performing sodium-based plasmonic devices in the near-infrared, ***Nature*** 581, 401-405 (2020)
2. Yuhan Yang, Hanyu Fu, Huanhuan Su, Shuying Chen, Shan Wu, Jie Liang, Tianqi Wei, Yang Wang, Shining Zhu, Jia Zhu*, Lin Zhou*, Sodium-based concave metasurfaces for high performing plasmonic optical filters by templated spin-on-sodiophobic-glass, ***Advanced Materials*** 35 (25), 2300272 (2023)
3. Jie Liang, Yan Jin, Huiling Yu, Xinjie Chen, Lin Zhou*, Pengcheng Huo, Ye Zhang, Haiyang Ma, Yi Jiang, Bin Zhu, Ting Xu, Hui Liu, Shining Zhu, Jia Zhu*. Lithium-plasmon-based low-powered dynamic color display, ***National Science Review*** nwac120, (2023)
4. Jie Liang, Yurui Qu, Lin Zhou*, Angle-robust plasmonic color printing of deep subwavelength nanopixelated sodium metasurfaces, ***Advanced Photonics Nexus*** 4, 016006 (2025)
5. Yurui Qu, Jie Liang, Wei Yan, Qile Wu, Jia Zhu*, Lin Zhou*. Low loss plasmonics based on alkali metals: from fundamentals to applications. ***Advances in Optics and Photonics*** 17, 1-44 (2025)

Manipulation of light propagation in photonic crystals via non-Hermitian photonic band engineering

T. Inoue, M. Yoshida, and S. Noda

Kyoto University, Japan
*corresponding author: t_inoue@qoe.kuee.kyoto-u.ac.jp

Abstract: Non-Hermitian photonic systems are known to exhibit unique light propagation phenomena, where non-Hermiticity is typically introduced by material loss or gain. Here, we propose and experimentally demonstrate manipulation of light propagation solely based on radiation loss via non-Hermitian photonic band engineering of photonic crystals.

Non-Hermitian photonic systems are known to exhibit various unique optical phenomena near the exceptional point (EP) such as unidirectional reflectionless light propagation and enhanced sensing. Photonic crystal slabs are ideal platforms to embody such unique phenomena because they inherently involve non-Hermiticity caused by radiation loss even when material loss nor gain is introduced. Here, we demonstrate flexible manipulation of light propagation solely based on radiation loss via non-Hermitian photonic band engineering of photonic crystals. We first show that various types of non-Hermitian photonic band structures such as a conical dispersion with a single EP and multiple exceptional rings can be realized by controlling both Hermitian and non-Hermitian couplings inside the photonic crystal [1,2]. Then we experimentally demonstrate several unique light propagations using such non-Hermitian band engineering, including unidirectional radiation/reflection phenomena and arbitrary manipulation of vertical radiation profiles.

Figures 1(a) and 1(b) shows the schematic diagram of Hermitian and non-Hermitian wave couplings inside double-lattice photonic crystals [1,3]. Figure 1(a) denotes the Hermitian couplings without accompanying energy loss, which includes ±180° diffractions (κ_{1D}) and ±90° diffractions ($\kappa_{2D\pm}$), while Fig. 1(b) shows the non-Hermitian couplings via radiative waves, which accompany energy loss. Using these coupling coefficients, complex eigenfrequencies ($\delta + i\alpha$) at an in-plane wavevector (k_x, k_y) near the second-order Γ-point can be derived by solving the following coupled-wave equation [1]:

$$\left(\delta + \mathrm{i}\frac{\alpha}{2}\right)\begin{pmatrix} R_x \\ S_x \\ R_y \\ S_y \end{pmatrix} = \begin{pmatrix} \kappa_{11} + \mathrm{i}\mu + k_x & \kappa_{1\mathrm{D}} + \mathrm{i}\mu e^{\mathrm{i}\theta_{\mathrm{pc}}} & \kappa_{2\mathrm{D}+} & \kappa_{2\mathrm{D}-} \\ \kappa_{1\mathrm{D}}^* + \mathrm{i}\mu e^{-\mathrm{i}\theta_{\mathrm{pc}}} & \kappa_{11} + \mathrm{i}\mu - k_x & \kappa_{2\mathrm{D}-}^* & \kappa_{2\mathrm{D}+} \\ \kappa_{2\mathrm{D}+} & \kappa_{2\mathrm{D}-} & \kappa_{11} + \mathrm{i}\mu + k_y & \kappa_{1\mathrm{D}} + \mathrm{i}\mu e^{\mathrm{i}\theta_{\mathrm{pc}}} \\ \kappa_{2\mathrm{D}-}^* & \kappa_{2\mathrm{D}+} & \kappa_{1\mathrm{D}}^* + \mathrm{i}\mu e^{-\mathrm{i}\theta_{\mathrm{pc}}} & \kappa_{11} + \mathrm{i}\mu - k_y \end{pmatrix}\begin{pmatrix} R_x \\ S_x \\ R_y \\ S_y \end{pmatrix} \quad (1)$$

Figures 1(c)-1(f) show several examples of the calculated non-Hermitian photonic band structures, where two out of four bands (band A, C) are plotted for simplicity. Type I dispersion [Fig. 1(c)] has a small photonic band gap between the two bands while radiation loss of the lower band rapidly increases away from the Γ point, which is suitable for the realization of ultra-large-area photonic-crystal surface-emitting lasers [1,4]. When the 180° and 90° couplings are effectively cancelled out (more rigorously, $\mathrm{Re}[(\kappa_{1\mathrm{D}} + \kappa_{2\mathrm{D}-})e^{-\mathrm{i}\theta_{\mathrm{pc}}}]=0$), Type II dispersion [Fig. 1(d)] or Type III dispersion [Fig. 1(e)] appears, where the former has a degenerate flat band surrounded by EPs, while the latter has a conical dispersion with a single EP [2]. In a more specific case where there is a large anisotropy in ±90° couplings, Type IV dispersion with multiple exceptional rings can be also realized.

Using these non-Hermitian photonic band structures, we can realize various counterintuitive light propagation phenomena in photonic crystals. Figures 2(a) and 2(b) show two such examples in one-dimensional photonic-

crystal waveguides, where ±90° diffractions do not occur ($\kappa_{2D\pm}$=0). In Fig. 2(a), we employ photonic crystals with Type III dispersion, and demonstrate a unidirectional waveguide which shows perfect radiation when light is incident from the left side, and shows perfect reflection when light is incident from the other side [2]. In Fig. 2(b), we employ photonic crystals with Type II dispersion, and demonstrate vertically radiative waveguides that have arbitrary radiation profiles (e.g. uniform or step-like profiles) with suppressed backward reflection. The details of these experiments and other possible applications will be reported at the conference.

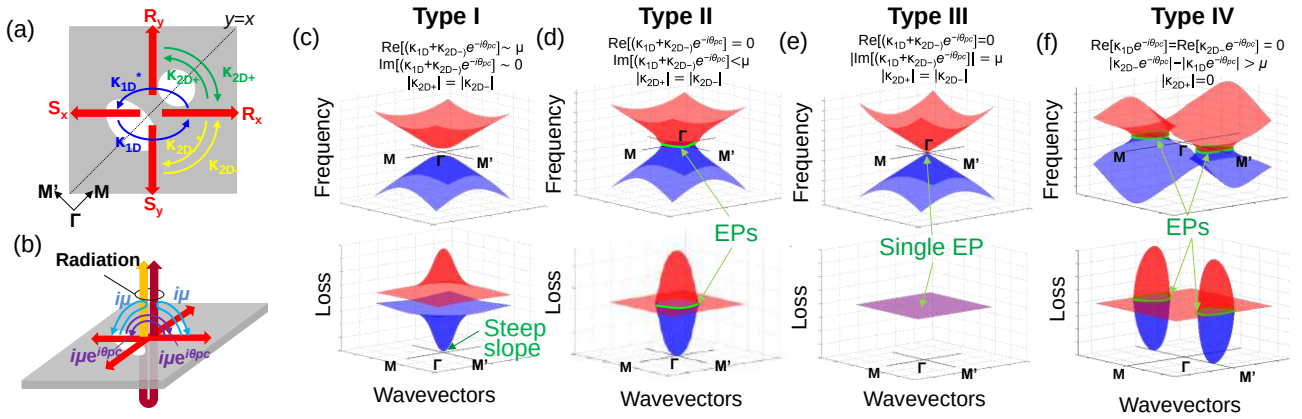


Fig. 1. (a)(b) Hermitian and non-Hermitian mutual couplings inside double-lattice photonic crystals. (c)-(f) Four types of non-Hermitian photonic band structures realized by the control of Hermitian and non-Hermitian couplings.

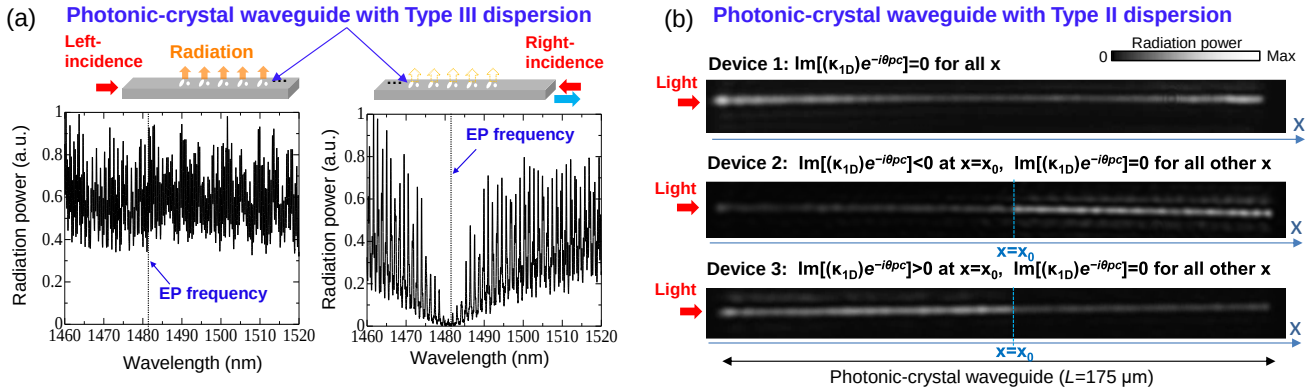


Fig. 2. Experimental demonstrations of unique light propagation phenomena in non-Hermitian photonic crystals. (a) Unidirectional radiation and reflection. (b) Arbitrary manipulation of vertical radiation profiles.

Acknowledgements: This work was partially supported by a Grant-in-Aid for Scientific Research (22H04915, 24H00430) from the Japan Society for the Promotion of Science (JSPS).

References

1. Inoue, T. *et al.*, "General recipe to realize photonic-crystal surface-emitting lasers with 100-W-to-1-kW single-mode operation," Nat. Commun., Vol. 13, 3262, 2022.
2. Inoue, T. *et al.*, "Unidirectional perfect reflection and radiation in double-lattice photonic crystals," Phys. Rev. Appl., Vol. 20, No. 1, L011001, 2023.
3. Yoshida, M. *et al.*, "Double-lattice photonic-crystal resonators enabling high-brightness semiconductor lasers with symmetric narrow-divergence beams," Nat. Mater., Vol. 18, No. 2, 121–128, 2019.
4. Yoshida, M. *et al.*, "High-brightness scalable continuous-wave single-mode photonic-crystal laser," Nature, Vol. 618, No. 7966, 727–732, 2023.

Exploration of Optical Chirality Based on the Orbital Angular Momentum of Light Using a Single Chiral Metallic Nanostructure as a Probe

S. Hashiyada[1*], A. Wu[2], and Y. Y. Tanaka[1,2]

[1]Research Institute for Electronic Science, Hokkaido University, Japan
[2]Institute of Industrial Science, The University of Tokyo, Japan

[*]corresponding author: shun.hashiyada@es.hokudai.ac.jp

Abstract: Optical chirality (OC) is traditionally linked to spin angular momentum of light. Recent studies suggest that chiral dichroism (ChD) in chiral materials may also be governed by an alternative form of chirality associated with orbital angular momentum of light (orbital OC). We investigate ChD in a single twisted gold nanorod dimer using circularly polarized optical vortex beams, revealing wavelength-dependent ChD behavior at the beam center, indicative of orbital OC.

The chirality of a material can only be identified through asymmetric interactions with other chiral objects or chiral fields [1]. Circularly polarized (CP) lights, carrying spin angular momentum (SAM: $s = \pm 1$), are well-known chiral optical fields, and their interaction with chiral materials have been extensively studied. Chiral materials exhibit circular dichroism (CD), where their absorption differs between left- and right-handed CP light. This effect primarily arises from lower-order excitation modes, such as electric and magnetic dipole modes. In 2010, it was revealed that the magnitude of CD arising from lower-order excitation modes of isotropic chiral materials depends on a physical parameter known as optical chirality (OC), or spin OC, which characterizes the chirality of the excitation light based on its optical SAM [2]. This discovery opened up new research directions, enabling the control of chiral light-matter interactions through the design of tailored optical fields.

Recently, optical vortices (OVs), carrying orbital angular momentum (OAM: $l = 0, \pm 1, \pm 2, \ldots$), have gained attention as another form of chiral optical field. The chirality of materials has also been detected using OVs through vortex dichroism (VD), where they exhibit different optical responses to left- and right-handed linearly polarized OVs [3]. Since OVs can excite higher-order modes such as electric quadrupole modes [4], VD signals are suggested to reflect the geometric characteristics of chiral materials more strongly than CD. If the analogy between spin OC and CD extends to VD resulting from higher-order chiral excitations, this suggests the existence of a new physical parameter, orbital OC, which characterizes chirality based on optical OAM. However, in most previous studies, chiral materials larger than the wavelength of excitation light were used, leading to the simultaneous excitation of multiple modes. This spectral overlap has made it challenging to determine which specific modes contribute to the VD signal, preventing the establishment of a definitive link between VD and orbital OC.

To address this issue, we employ a subwavelength-scale twisted gold nanorod dimer (TND) (Figure 1, left) as a nanoscale chiral probe, which enables clear spectral separation of electric dipole and quadrupole modes. This minimizes mode overlap and allows for a more precise analysis of the relationship between excitation modes and optical SAM and OAM of the excitation light in its chiral optical response. To systematically investigate the contributions of optical SAM and OAM in chiral optical responses of the TND, we utilize CP OVs as excitation light. CP OVs inherently carry both optical SAM and OAM, making them well-suited for distinguishing the respective roles of these angular momentum components in chiral light-matter interactions. However, the dichroic

response of chiral materials to CP OVs does not fit conventional CD or VD classifications. To address this, we introduce chiral dichroism (ChD) as a generalized framework that encompasses both CD and VD. Here, $g_{\mathrm{ChD}}(s, l) \equiv 2(I_{+s,+l} - I_{-s,-l})/(I_{+s,+l} + I_{-s,-l})$ defines the ChD signal, where $I_{\pm s,\pm l}$ denotes the transmission intensities for CP OVs with $(\pm s, \pm l)$.

We developed a ChD microscopic spectroscopy system to measure ChD in the TND. Since OVs exhibit a doughnut-shaped intensity profile, the relative position between the beam and the sample is critical for analyzing ChD signals, necessitating microscopic imaging. Additionally, spectral acquisition is required to understand the relationship between ChD and excitation modes. Our system integrates a high-speed CP OV modulation optical setup [5] within an optical microscope, enabling rapid switching of CP OV handedness at ~50 kHz while also allowing wavelength tuning of the excitation light. This setup facilitates precise spatially resolved ChD imaging while simultaneously acquiring spectral data, enabling a comprehensive analysis of structured light interactions with chiral materials.

To systematically examine ChD under different excitation conditions, we conduct two sets of experiments. The first employs a CP Gaussian beam ($s = \pm 1$, $l = 0$) as a baseline measurement to establish a reference ChD (CD) response. Under this condition, a wavelength-independent positive ChD signal is observed, reflecting the spatial structure of the Gaussian beam (Figure 1, top right). In contrast, when using a CP OV beam ($s = \pm 1$, $l = \pm 1$), the ChD signal exhibits two distinct characteristics (Figure 1, bottom right). First, a wavelength-independent positive ChD signal is observed, mirroring the doughnut-shaped intensity profile of the OV beam. Second, at the beam center, where spin OC is expected to be zero, the ChD signal displays a wavelength-dependent sign reversal. Specifically, at 800 nm, the ChD signal is positive; at 825 nm, it vanishes; and at 850 nm, it becomes negative. The observed wavelength-dependent sign reversal at the beam center suggests that ChD in OVs cannot be fully explained by spin OC alone, indicating the necessity of an alternative physical parameter, orbital OC. This finding highlights the importance of OAM in chiral light-matter interactions and demonstrates the potential of structured light as a tool for enhancing and tailoring chiral optical responses in nanophotonic systems.

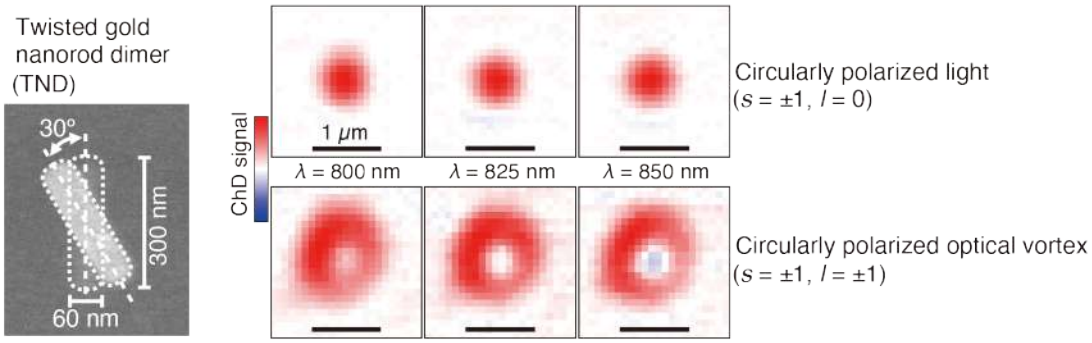


Figure 1. (left) Scanning electron micrograph of a single twisted gold nanorod dimer (TND). (Right) Experimentally obtained chiral dichroism (ChD) images of a single TND.

References

1. J. Larmor, *Nature* **143,** 240–241 (1939).
2. Y. Tang, and A. E. Cohen, *Phys. Rev. Lett.* **104,** 163901 (2010).
3. J. R. Rouxel *et al, Nat. Photonics* **16,** 570–574 (2022).
4. K. Sakai, K. Nomura, T. Yamamoto, and K. Sasaki, *Sci. Rep.* **5,** 8431 (2015).
5. S. Hashiyada, and Y. Y. Tanaka, *Rev. Sci. Instrum.* **95,** 053101 (2024).

Susceptibility invariance and disorder-induced statistical properties in time-varying media

Bo Zhou[1], Enzong Wu[1] and Zuojia Wang[1*]

[1] Zhejiang University, China
[*]corresponding author: zuojiawang@zju.edu.cn

Abstract: We present theoretical and analytical frameworks for perpendicular-moving metasurfaces, where susceptibility invariance and duality-matching conditions are derived via generalized sheet transition conditions and Lorentz transformations. We also discuss the emergent wave dynamics in disordered time-varying cavities, where temporal reflections lead to non-normal electromagnetic field distributions, contrasting classical spatial localization.

Space-time systems (space-time media, usually focus on space-time metamaterials), whose physical parameters change over time, are becoming extremely attractive, as they may allow complete control of electromagnetic waves in time and space. They are categorized into two main types: modulated systems (by time-varying media) and moving systems (by space-varying media). Here, we present some progression in understanding wave-matter interactions within time-varying systems, combining insights from two interconnected studies on relativistic electrodynamics and statistical electrodynamics in time-varying systems.

First, we present theoretical and analytical frameworks for perpendicular-moving metasurfaces, where susceptibility invariance and duality-matching conditions are derived via generalized sheet transition conditions and Lorentz transformations [1]. Under these frameworks, we derive the boundary conditions of moving metasurface and reveal the relativistic constraints for the intriguing invariant phenomenon of susceptibility parameters (specific susceptibility parameters remain invariant during motion). We further verify the effectiveness of invariance phenomenon in bianisotropic media. These findings could provide foundational guidance for the analysis and design of space-time metasurface.

Second, we develop a model to analyze the statistical properties of the transient electric field strengths in one-dimensional locally disordered time-varying cavities [2]. We demonstrate that temporal disorders within the cavity can lead to an approximate normal distribution of the field strengths at any spatial point. But over extended temporal scales, this approximate normal distribution will disappear. By incorporating the framework of disordered space-time crystals and invoking Lyapunov's theorem, we identify that the time-varying nature of the cavity triggers an exponential surge in energy over extended periods, thereby resulting in a deviation from the normal distribution. Then we employ the generalized central limit theorem to prove that the field strength will ultimately evolve into a non-normal Lévy skew alpha-stable distribution. These statistical characteristics offer insights into the spatiotemporal dynamics of wave phenomena and hold potential implications for predicting extreme events occurring within enclosed spaces.

By unifying these perspectives, the report underscores the unique opportunities and challenges of time-

varying systems, including unavoidable reflections in parameter-discontinuous media and the role of temporal symmetry breaking in hyperbolic propagation. These findings provide foundational guidance for developing advanced nanophotonic devices, such as dynamically reconfigurable metasurfaces and temporal disorder-engineered sensors.

References

1. Zhou, B., Feng, X., Wu, E., Gao, F., Chen, H. and Wang, Z., "Susceptibility Invariance and Duality-Matching Condition for Perpendicular-Motion Metasurface," Advanced Physics Research, Vol. 3, No. 10, 2400073, 2024.
2. Zhou, B., Feng, X., Guo, X., Gao, F., Chen, H., and Wang, Z., "Transition from normal to non-normal distributions of an electromagnetic field in a disordered time-varying cavity," Physical Review A, Vol. 110, No. 21, 063524, 2024.

Scalable integration of multiple single-photon sources for fiber quantum network

W. B. Jeon[1], D. H. Park[1], J. S. Moon[1,2], K.-Y. Kim[1], M. Benyoucef[3], J.-H. Kim[1*]

[1]Department of Physics, Ulsan National Institute of Science and Technology (UNIST), Ulsan 44919, Republic of Korea
[2]Quantum Technology Research Division, Electronics and Telecommunications Research Institute (ETRI), Daejeon, 34129, Republic of Korea

[3]Institute of Physics, INA, University of Kassel, Heinrich-Plett-Str. 40, Kassel, 34132, Germany
[*]corresponding author: jehyungkim@unist.ac.kr,

Abstract: We present a novel approach to a tunable array of fiber-integrated single-photon sources. By developing a versatile fiber platform that integrates multiple cavity-coupled quantum dot devices using a pick-and-place technique, we achieve high-efficiency, scalable, and tunable quantum light sources for telecom-based quantum networks and protocols.

Single-photon sources serve as a fundamental building block for a wide range of quantum technologies that rely on photonic qubits, including photonic quantum simulators, secure quantum communication, and large-scale quantum networks. Beyond single-photon sources, the ability to generate highly indistinguishable single photons arrays is crucial for advancing quantum protocols and increasing the capacity of quantum channels. While significant progress has been made in developing solid-state quantum emitters with high performance, integrating these sources into scalable and practical optical platforms remains a key challenge in realizing real-world quantum applications.

In this work, we present a novel approach to developing a tunable array of fiber-integrated single-photon sources, offering a scalable and reliable solution for multi-channel quantum light generation. Our system is based on a hole-based circular Bragg grating cavity, which enables efficient vertical beaming of single photons that match the mode profile of a single-mode optical fiber [1]. This ensures optimal photon collection efficiency and enhances the practicality of fiber-based quantum photonic systems. To achieve high scalability and precision, we employ a pick-and-place technique to selectively integrate multiple quantum dot (QD) devices onto a V-groove fiber platform. This method allows for the precise alignment and positioning of quantum emitters, overcoming fabrication constraints associated with conventional approaches. Furthermore, our uniquely designed etched fiber ensures that the membrane cavity remains air-suspended, preserving its optical characteristics before and after integrationTherefore, this post-characterization and selective integration allows us the high-yield of multi-channel devices.

For cryogenic operation of multi-channel fiber-integrated systems, we developed metal patterning on the fiber platform, which serves a dual purpose. First, it facilitates efficient cooling of the integrated quantum dot devices to cryogenic temperatures, ensuring stable and high-purity single-photon emission. Second, it enables the application of electric fields to the quantum dots, allowing for tunable emission wavelengths and controlled operation of the photon sources [2]. These integrated functionalities significantly enhance the versatility of our platform, making it a promising candidate for on-demand, reconfigurable quantum light sources.

Our fiber-integrated quantum platform exhibits key advantages, including high single-photon coupling efficiency, scalability, and tunability. By leveraging these features, we demonstrate the potential for realizing compact, high-yield

single-photon arrays directly on fiber-based chips, specifically at telecom wavelengths. This advancement paves the way for the practical deployment of quantum photonic systems in fiber networks, facilitating their integration into future quantum communication and computing architectures.

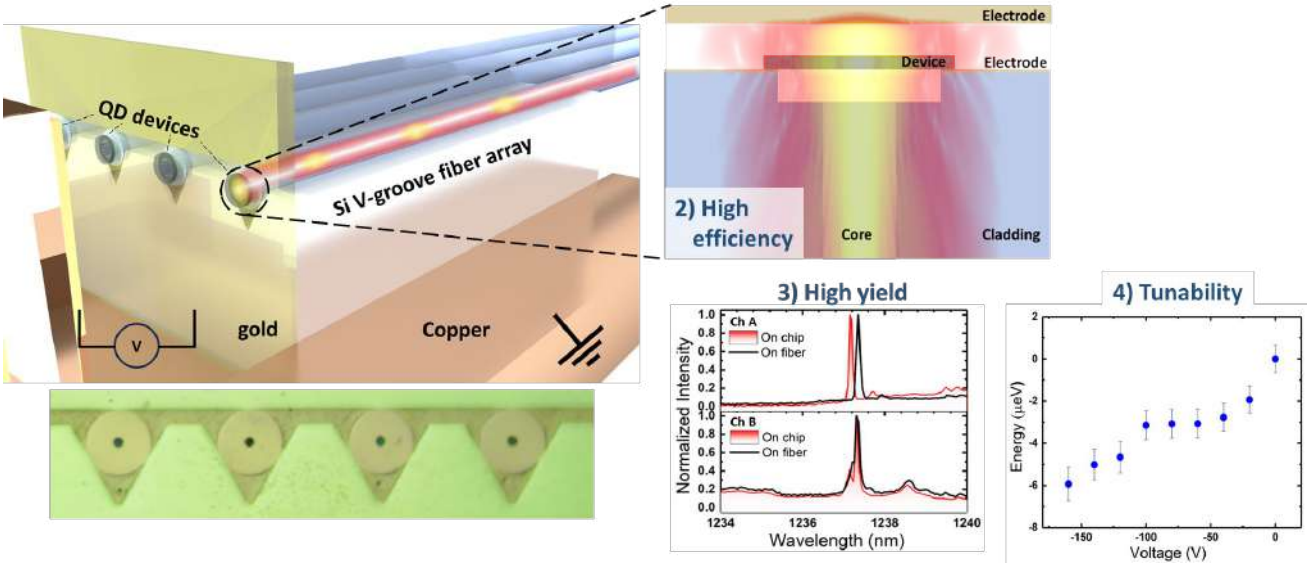


Fig. 1. Schematic illustration of the multi-functional fiber-integrated platform. The insets display a photo of cavity-coupled quantum dots integrated onto a V-groove fiber facet, a numerical simulation of field propagation from the integrated cavity, the emission spectrum before and after integration, and wavelength tuning by applying voltage.

References

1. W. B. Jeon, J. S. Moon, K.-Y. Kim, Y.-H. Ko, C. J. K. Richardson, E. Waks, J.-H. Kim, “Plug-and-play single-photon devices with efficient fiber-quantum dot interface”, Adv. Quantum. Technol. 2200022 (2022)
2. W. B. Jeon, D. H. Park, J. S. Moon, K.-Y. Kim, M. Benyoucef, and J.-H. Kim. Multi-channel, tunable quantum photonic devices on fiber-integrated platforms", arXiv:2410.14976 (2024)

Second-order coherence of Bose-Einstein condensation in plasmonic lattices

E. A. Mamonov[1*], S. Eyvazi[1], L. Freter[1], and P. Törmä[1]
[1]Department of Applied Physics, Aalto University School of Science, Espoo, Finland
Corresponding author: evgeny.mamonov@aalto.fi

Abstract: Plasmonic lattices accompanied with active media are versatile platform for many applications such as lasing or Bose-Einstein condensation (BEC). Here we present our studies of second-order coherence of BEC in plasmonic lattices. We analyze the behavior of $g^{(2)}(\tau = 0)$ function in the three stages of emission: lasing, incomplete thermalization and condensation.

Plasmonic lattices of different configurations combined with emissive materials offer unique opportunities to study fascinating phenomena such as lasing with topologically nontrivial properties [1, 2] and Bose-Einstein condensation (BEC) [3, 4]. BEC in strong coupling regime in plasmonic lattices undergoes three consecutive stages as the pump fluence increases: polariton lasing, incomplete stimulated thermalization and condensation, making it distinctive from many other systems both in strong and weak coupling regimes [5].

Unlike second-order coherence, first-order coherence properties of different types of BE condensates have already been studied more extensively [6,7] although the former highly depends on a quantum state of an emitter and can bring additional information on the processes occurring before and during the condensation.

Here we study BEC in a plasmonic lattice of gold nanocylinders with a diameter of 100 nm and a periodicity of 570 nm supporting surface lattice resonance (SLR) excitation; its frequency at Γ point is a band edge for BEC. As an active media IR-792 dye was used which provided BEC in strong coupling regime.

To study second-order coherence properties of BEC, we measured pulse-to-pulse intensity fluctuation resolving it spectrally and in momentum space. Under certain assumptions about emission's spatial and temporal modes structure, this measurement gives the value of the second-order correlation function $g^{(2)}(\tau = 0)$.We show that the $g^{(2)}$ values decrease with increasing pump fluence and discuss the peculiarities of the function's behavior during the transition to BEC.

This work was supported by the Jane and Aatos Erkko Foundation and the Technology Industries of Finland Centennial Foundation as part of the Future Makers funding program.

References

1. Arjas, K., Taskinen, J.M., Heilmann, R. et al. "High topological charge lasing in quasicrystals," *Nat Commun*, 15, 9544, 2024.

2. Hwang, MS., Lee, HC., Kim, KH. et al. "Ultralow-threshold laser using super-bound states in the continuum," *Nat Commun*, 12, 4135, 2021.

3. Hakala, T.K., Moilanen, A.J., Väkeväinen, A.I. et al. "Bose–Einstein condensation in a plasmonic lattice," *Nature Phys* 14, 739–744, 2018.

4. Väkeväinen, A.I., Moilanen, A.J., Nečada, M. et al. "Sub-picosecond thermalization dynamics in condensation of strongly coupled lattice plasmons," *Nat Commun* 11, 3139, 2020.

5. Bloch, J., Carusotto, I., and Wouters, M. "Non-equilibrium Bose–Einstein condensation in photonic systems," *Nat Rev Phys* 4, 470–488, 2022.

6. Moilanen, A. J., Daskalakis, K. S., Taskinen, J. M., and Törmä, P. "Spatial and temporal coherence in strongly coupled plasmonic Bose-Einstein condensates," *Phys Rev Lett*, 127(25), 255301, 2021.

7. Daskalakis, K. S., Maier, S. A., and Kéna-Cohen, S, "Spatial coherence and stability in a disordered organic polariton condensate," *Phys Rev Lett*, 115(3), 035301, 2015.

META 2025, MALAGA - SPAIN, JULY 22 – 25, 2025

Optical Picometrology

K. F. MacDonald[1], T. A. Grant[1], C.-H. Chi[1], H. Zhou[1], A. Vetlugin[2], E. Plum[1], S. Rotter[3], and N. I. Zheludev[1,4]

[1]Optoelectronics Research Centre, University of Southampton, Highfield, Southampton, SO17 1BJ, UK
[2]Centre for Disruptive Photonic Technologies, TPI, SPMS, Nanyang Technological University, Singapore 637371
[3]Institute for Theoretical Physics, Vienna University of Technology (TU Wien), A-1040 Vienna, Austria
[4]Hagler Institute for Advanced Study, Texas A&M University, College Station, Texas, 77843, USA
[*]corresponding author: kfm@orc.soton.ac.uk

Abstract: The information content of a scattered field increases orders of magnitude with topologically structured (as opposed to unstructured) light, and plasmonic effects can enhance/redirect information flow. On this basis, picometric precision and accuracy can be achieved in optical metrology and imaging.

Complex optical fields can contain structure at deeply subwavelength scales – including point-like singularities, zones of energy back-flow, and strong phase and intensity gradients. The scattering of light from an object can thus depend strongly on exactly where its features are located within such a field. On this basis, precision and accuracy reaching the atomic scale (100-200 pm; $<\lambda/5000$) have recently been demonstrated in single-shot optical measurements of nano-object positions and dimensions, based on deep-learning analyses of their far-field diffraction patterns in topologically structured light (doi: 10.1038/s41563-023-01543-y).

Here, we explain how such performance – reaching far beyond the conventional diffraction limit – is possible, through a Fisher Information analysis of the technique, showing that the scattered field from an object located near a singularity can have information content orders of magnitude higher than the scattered field from a plane wave. We further show how plasmonic effects can resonantly enhance and redirect the flow of Fisher information (very differently from the flow of energy), directly impacting the limits of measurement precision and accuracy; and we illustrate how the concepts can be extended from the constrained problem of retrieving single/few dimensional parameter measurements to the greater challenge of imaging arbitrary nano-objects.

Negative frequency generation and temporal diffraction in graphene at THz frequencies

E. Hendry

School of Physics and Astronomy, University of Exeter, Stocker Road, Exeter, EX4 4QL, UK
e.hendry@exeter.ac.uk

Abstract: Temporal modulation of graphene using ultrafast pulses can be incredibly fast compared to the period of a transmitted THz field. We demonstrate that this gives rise to distinct signatures in the transmission spectrum arising from generation of negative frequency components. We then discuss several temporal diffraction experiments using graphene modulation.

Fast modulation of the optical properties of materials has recently been shown to produce strikingly different electrodynamics from passive materials, giving rise to effects such as temporal diffraction and associated generation of new frequency components of a field. In the first demonstrations of this concept in [1], new frequencies were generated using ITO modulators at optical frequencies, where the modulation time (the time taken to switch the optical transmission) was considerably slower than the characteristic period of the electromagnetic wave. Here, we show that graphene, a highly efficient modulator for THz fields, is capable of modulating transmission on a timescale that is substantially faster than the period of the THz wave. This leads to an extremely large bandwidth for the generated frequencies covering the entire THz spectral band, even crossing the origin to generate negative frequencies. We see in experiment distinct oscillatory features (see figure) in transmission spectra of a modulated narrow band THz source (centred at 0.5 THz) arising from interference with negative frequency components of the field. Finally, we present our first experimental results displaying temporal diffraction arising from stimulation using multiple pulses, starting with the traditional temporal analogue of a Youngs double slit experiment [1], which give diffraction fringes covering the entire THz spectral band from 0 to 2 THz.

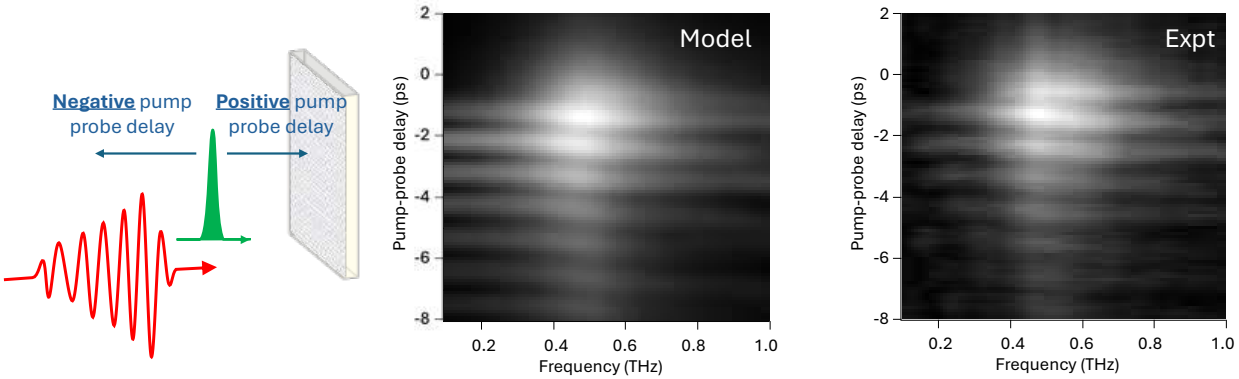


Figure: Modelling and experiment showing spectra of the change in transmission in a temporal diffraction experiment using a single stimulation pulse and a narrow band THz source centred at 0.5 THz. We observe new frequencies in transmission, which are not present in the incident field, spanning the entire THz band. Moreover, the oscillatory features in both model and experiment arise from interference with generated negative frequency components of the field.

References

[1] Romain Tirole, Stefano Vezzoli, Emanuele Galiffi, Iain Robertson, Dries Maurice, Benjamin Tilmann, Stefan A. Maier, John B. Pendry & Riccardo Sapienza
Nature Physics volume 19, pages 999-1002 (2023)

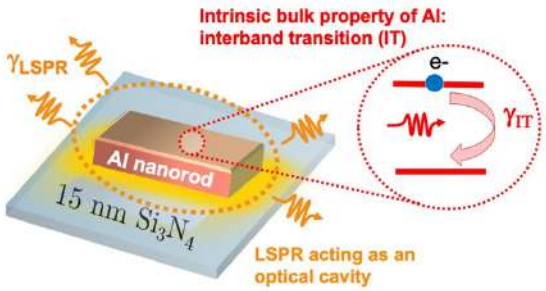
Self-hydridized plasmonic excitations and hot electron generation in aluminum nanorods

J. Martin[1], O. Avalos-Ovando[2], T. Simon[1], G. Arditi[3], F. Lamaze[1], J. Proust[1], L. Tizei[3], M. Kociak[3], A. Govorov[2], O. Stéphan[3], and D. Gérard[1*]

[1]Light, nanomaterials, nanotechnologies, CNRS UMR 7076, Université de Technologie de Troyes, France
[2]Department of Physics and Astronomy & Nanoscale and Quantum Phenomena Institute, Ohio University, United States
[2]Laboratoire de Physique des Solides, UMR CNRS 8502, Université Paris-Saclay, France
[*]corresponding author: davy.gerard@utt.fr

Abstract: We evidence a phenomenon of self-hybridization of the resonances sustained by aluminum nanorods, owing to the strong coupling of the localized plasmonic resonances with interband transitions occurring within the metal. Anomalously high rates of hot electron generation are associated with these hybridized states.

Strong coupling is typically observed between two distinct entities or between an entity and its environment (e.g., an atom and a cavity). However, it can also occur between two distinct excitations within the same object, a phenomenon that has been less extensively investigated. In this work, we present evidence of strong coupling between localized surface plasmon resonances and the interband transition in aluminum nanorods. This coupling is evidenced by optical spectroscopy and electron energy loss spectroscopy (EELS), supported by numerical simulations. The strong coupling involves multiple orders of plasmon modes, including dark modes. The corresponding Rabi energy, which defines the energy splitting between the two polaritonic branches, is determined in each case. Notably, the use of EELS allowed us to experimentally map the hybrid modes with nanoscale resolution, giving further evidence of the strong coupling.



Furthermore, a dedicated numerical model [1] is employed to demonstrate that strong coupling in the near-infrared region facilitates efficient hot electron generation, exploiting the hybrid nature of the modes. The plasmonic component provides a high absorption cross-section, while the interband transition ensures efficient hot electron generation. The associated interband HE efficiency is predicted to reach about 40%. Importantly, this phenomenon is triggered by red and near infrared light, a spectral range that is particularly well suited to solar light-based applications, such as hot carrier-based photodetection.

References

1. A. Muravitskaya, A. Movsesyan, O. Avalos-Ovando, V.A. Bahamondes Lorca, M. Correa-Duarte, L.V. Besteiro, T. Liedl, P. Yu, Z. Wang, G. Markovich, and A.O. Govorov. “Hot Electrons and Electromagnetic Effects in the Broadband Au, Ag, and Ag–Au Nanocrystals: The UV, visible, and NIR Plasmons,” ACS Photonics, Vol. 11, 68–84, 2023.

Enhancing Thermoplasmonic Sensing *via* Plasmonic Nanoplatforms

A. Campu [1,2*], **S. Astilean**[1,3], **and M. Focsan** [1,3]

[1] Nanobiophotonics and Laser Microspectroscopy Center, Interdisciplinary Research Institute in Bio-Nano-Sciences, Babes-Bolyai University, Treboniu Laurian No. 42, 400271 Cluj-Napoca, Romania.
[2] Research Center for Complex Physical Systems, Faculty of Sciences, Lucian Blaga University, Doctor Ion Rațiu No. 5-7, 550012 Sibiu, Romania.
[3] Biomolecular Physics Department, Faculty of Physics, Babes-Bolyai University, Mihail Kogalniceanu No. 1, 400084 Cluj-Napoca, Romania.

[*]Corresponding author: andreea.campu@ulbsibiu.ro/andreea.campu@ubbcluj.ro

Abstract: Thermoplasmonic detection is an emerging application within the rapidly expanding and promising field of thermoplasmonics. While the heat generated by gold nanoparticles has been utilized in biomedical applications such as photothermal therapy, the impact of nanoscale photothermal processes remains a topic of ongoing discussion.

In this context, this work aims to provide a better understanding on the thermoplasmonic mechanism leading to efficient and sensitive detection by evaluating the performances as thermoplasmonic generators of colloidal gold nanobipyramids (AuBPs) in solution and immobilized onto a paper nanoplatform. For this purpose, firstly AuBPs with different aspect ratios were synthesized in aqueous solution and their intrinsic light-to-heat performances were assessed by their exposure to the 808 nm laser line. Thus, photothermal efficiencies (η) up to 64 % were determined for the colloidal nanoparticles close to the resonance condition related to the excitation wavelength. Next, 4-mercaptobenzoic acid was grafted onto their surface through its thiol group. As a consequence of the 4-MBA functionalization, η was decreased by 5 to 8 %. Additionally, after their immobilization of Whatman No. 1 filter paper through immersion, their optical properties and intrinsic thermoplasmonic activity were preserved. As 4-MBA – a small molecule, was added onto the plasmonic paper, the photothermal conversion performances were significantly decreased causing an increase in the cooling time constant. Furthermore, a more complex molecule was tested, specifically thiol-polyethylene glycol-amine – as a thermo-sensitive polymer, proving temperature-induced phase transitions in materials can be also highlighted by modifications is the light-to-heat conversion performances of the immobilized nanoparticles. Thus, the obtained results contribute to the consolidation of the versatile thermoplasmonic detection technique and represent a steppingstone in the development of simple plasmonic nanoplatforms for thermoplasmonic-driven applications.

Acknowledgements: This work was supported by the Babes-Bolyai University, through the Starting Research Grant (SRG-UBB), contract no. 32984/ 23.06.2023 and the project "Plasmon mediated biology: Exploitation of plasmonics to investigate and enhance biological processes and application to biomedical issues (acronym: BioPlasmonics)" funded by European Union – NextgenerationEU and Romanian Government, under National Recovery and Resilience Plan for Romania, contract no 760037/23.05.2023, cod PNRR-C9-I8-CF-199/28.11.2023, through the Romanian Ministry of Research, Innovation and Digitalization, within Component 9, Investment I8.

Low-loss resonant nonlinear nanophotonics in the visible spectral range using wafer-bonded crystalline AlInP

R. Kolkowski[1*], S. A. Shahahmadi[2], S. Novikov[2], J. Oksanen[2], A. C. Liapis[3], H. Bai[1], T. Stolt[1], M. Kaivola[1], and A. Shevchenko[1]

[1] Department of Applied Physics, Aalto University, Espoo, Finland
[2] Engineered Nanosystems Group, Aalto University, Espoo, Finland
[3] Department of Electronics and Nanoengineering, Aalto University, Espoo, Finland
[*]corresponding author: radoslaw.kolkowski@aalto.fi

Abstract: We present AlInP as an attractive alternative to common nonlinear materials used in nanophotonic structures and devices, especially in the visible spectral range. As a demonstration, we show enhanced second-harmonic generation from nanodisks fabricated in a wafer-bonded crystalline AlInP layer.

Resonant nanophotonic systems with enhanced second-order optical nonlinearity ($\chi^{(2)}$) are desired for many applications, including electro-optic modulation, generation of entangled photons, and frequency conversion.[1] Achieving a high quality (Q) factor and strong light confinement in a nanoresonator requires a material with high refractive index (n) and low absorption loss (k). On the other hand, efficient $\chi^{(2)}$ nonlinearity is usually provided by noncentrosymmetric crystalline materials. The choice of a suitable material is often dictated by a trade-off between n, k, $\chi^{(2)}$, and fabrication feasibility. For example, in the visible spectral range, some materials (e.g., GaAs) have high n and $\chi^{(2)}$, but are strongly absorbing, while other materials (e.g., $LiNbO_3$) are transparent, but show moderate n and $\chi^{(2)}$. There are also materials offering a decent combination of n, k, and $\chi^{(2)}$, like GaP, but nanofabrication involving these materials is not easy.[2] Therefore, there is a need for alternative $\chi^{(2)}$ materials that would enable efficient fabrication of high-Q resonant nanostructures, especially for operation in the visible spectral range. In search for such a material, we turned our attention to aluminum indium phosphide (AlInP).

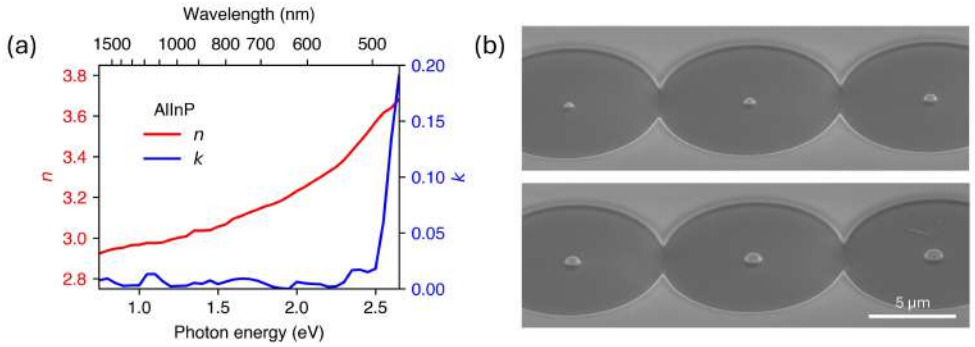


Figure 1. Demonstration of AlInP as an attractive material for resonant nanophotonics. (a) Real and imaginary parts of the refractive index (n and k, respectively) measured ellipsometrically for a 400 nm thick AlInP layer bonded to glass. (b) Scanning electron microscope (SEM) images of a AlInP layer patterned using FIB.

Despite extensive use of AlInP in solar cells, transistors, and light-emitting diodes, its potential for nonlinear nanophotonics has so far been largely overlooked.[3] Since AlInP is lattice-matched to GaAs, it can be grown on relatively inexpensive GaAs wafers, and then transferred onto a low-refractive-index substrate. Here, we used metal-organic vapor-phase epitaxy (MOVPE) and wafer bonding to obtain a thin crystalline AlInP layer on glass. The optical constants of this layer, measured by ellipsometry, are shown in Fig. 1(a), demonstrating $n > 3$ across

the visible and most of the near-infrared spectral range and high transparency down to the wavelength of 500 nm. The layer can easily be patterned with a focused ion beam (FIB), as presented in Fig. 1(b). Already these properties make AlInP an attractive alternative to GaP. We are currently developing a process based on electron-beam lithography (EBL) to enable high-throughput fabrication of AlInP nanostructures.

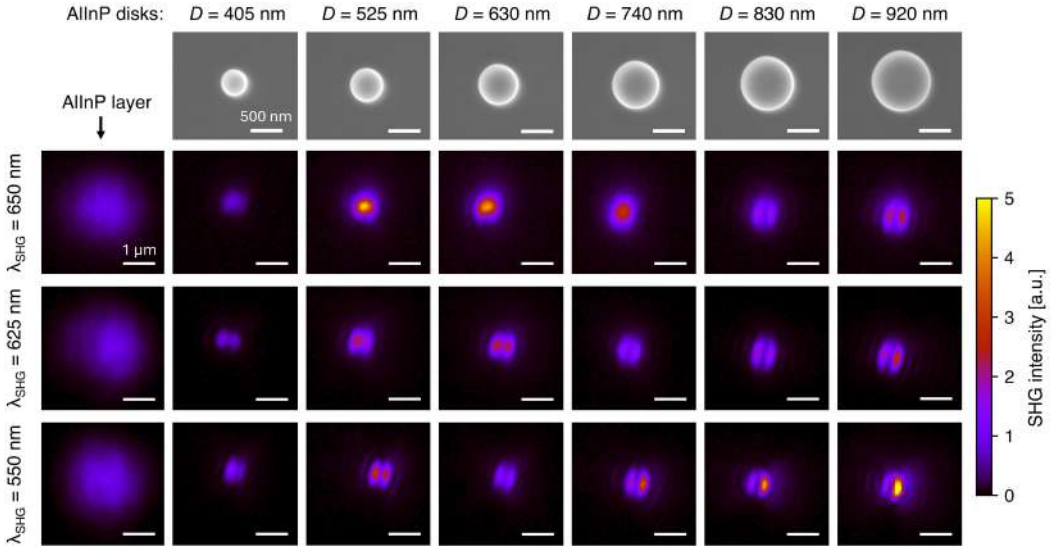


Figure 2. SEM images (top row) and optical microscopy images of SHG excited at different fundamental wavelengths in the range 1100-1300 nm (SHG wavelength 550-650 nm) from AlInP nanodisks of various diameters (*D* from 405 to 920 nm). The scale bars correspond to 500 nm in all the SEM images, and to 1 μm in all the SHG images. The incident beam is polarized horizontally (along the scale bars) with a possible out-of-plane component due to the tight focusing.

To showcase the potential of AlInP for nonlinear nanophotonics, we studied second-harmonic generation (SHG) in AlInP nanodisks excited by a focused femtosecond laser beam, as shown in Fig. 2. At the fundamental wavelength of 1300 nm (λ_{SHG} = 650 nm), nanodisks of diameters D = 525 and 630 nm provide a 5-fold resonant enhancement of SHG compared to a bare AlInP layer. A resonant enhancement is visible also in the largest disks at a shorter wavelength. The observed SHG patterns result from an interplay between the incident beam polarization, the $\chi^{(2)}$-tensor symmetry, and shaping the incident and SHG fields by Mie resonances. Further demonstrations of enhanced $\chi^{(2)}$ phenomena in AlInP-based Mie resonators, anapoles, and periodic metasurfaces supporting bound states in the continuum are a target of our ongoing research.

The authors acknowledge support of the Research Council of Finland (Grants No. 347449 and 353758). R. K. has received funding from the European Union's Horizon Europe programme for research and innovation under the Marie Skłodowska-Curie Grant Agreement No. 101060306 (NExIA). The authors acknowledge the provision of facilities and technical support by Aalto University OtaNano – Nanofabrication Centre for sample fabrication.

References

1. Bogdanov, A. A., S. Makarov, and Y. Kivshar, "New frontiers in nonlinear nanophotonics," *Nanophotonics*, Vol. 13, No. 18, 3175–3179, 2024.
2. Yang, M., *et al.*, "Second harmonic generation in monolithic gallium phosphide metasurfaces," *Nanophotonics*, Vol. 13, No. 18, 3311–3319, 2024.
3. Vermeulen, N., *et al.*, "Post-2000 nonlinear optical materials and measurements: data tables and best practices," *J. Phys. Photonics*, Vol. 5, No. 3, 035001, 2023.

Fluorescence-based chiral sensing with silicon metasurfaces

Tom T. C Sistermans[1,2], Artemijs Krimovs[3], Robert Pal[3] and Alberto G. Curto[1,2*]

[1] Photonics Research Group, Ghent University-imec, Ghent, Belgium
[2] Center for Nano- and Biophotonics, Ghent University, Ghent, Belgium
[3] Department of Chemistry, Durham University, Durham, UK
[*]corresponding author: Alberto.Curto@UGent.be

Abstract: Chiral molecules with opposite handedness can have strongly different biological functionalities. Identifying chirality is, however, limited by low sensitivity, restricting detection to high concentrations and large volumes. We propose a silicon nanophotonics-based sensing technique to enhance the sensitivity of chiral molecular detection.

Detecting the handedness of chiral molecules is critical in biochemistry, where the functionality of biomolecules such as proteins, amino acids, and carbohydrates can strongly differ between enantiomers. Circularly polarized light is commonly used to distinguish enantiomers based on their differential absorption for the two circular polarizations, *i.e.*, circular dichroism (CD). This transmission-based method requires measuring very small changes in absorption, which is inherently difficult due to the large background caused by negligible absorption at low concentrations. As a result, the sensitivity is reduced, requiring a high density of molecules and long measurement times. This makes the conventional method unsuitable for critical applications like detecting protein aggregates linked to various diseases.

Fluorescence-based chiral sensing bypasses some of the difficulties of CD by shifting the wavelength of the light that interacted with the chiral molecules, allowing for separating this signal from the background of the excitation source. However, fluorescence is weak and its polarization very low. Nanophotonics provides routes for enhancing chiral sensitivity [1], [2], [3]. Optical resonators function as antennas, facilitating a more efficient light-matter interaction between the analyte and the excitation light. This effect can be amplified by arranging the resonators in arrays with an appropriate pitch [4]. In addition to excitation enhancement, the fluorescence of the analytes can also be increased thanks to Purcell enhancement, which increases the radiative rate. Furthermore, the resonator array can improve the directionality, enabling more efficient detection of the emitted fluorescence. These combined enhancement processes significantly boost the detected fluorescence of chiral molecules. Additionally, for chiral sensing, the polarization component is also critical. Utilizing resonators made from high-refractive-index dielectrics allows for tuning of electric and magnetic resonances, enabling control over optical chirality density, which can even generate local super-chiral fields, enabling a CD greater than that produced by of a circularly polarized plane wave.

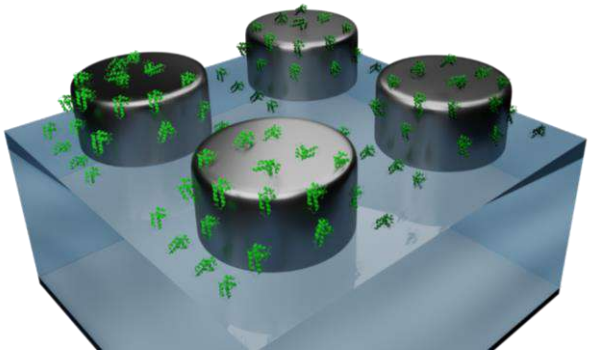


Figure 1. Chiral molecules on a silicon metasurface.

In this presentation, we introduce our recent experimental results on enhancing fluorescence-based chiral sensing using silicon metasurfaces. We fabricate crystalline silicon nanostructures displaying optical resonances in the visible. By combining them with chiral materials, we demonstrate enhanced circularly polarized fluorescence. To this end, we developed a custom-built polarization-sensitive microscope with polarization-modulation and photon-counting capabilities. Our microscope can measure smaller chiral analyte volumes than commercial systems.

Acknowledgements. This work was financially supported by the European Research Council (ERC) under the European Union's Horizon 2020 research and innovation program (grant agreement 948804, CHANSON).

References

[1] E. Mohammadi, A. Tittl, K. L. Tsakmakidis, T. V. Raziman, and A. G. Curto, "Dual Nanoresonators for Ultrasensitive Chiral Detection," *ACS Photonics*, vol. 8, no. 6, 2021, doi: 10.1021/acsphotonics.1c00311.

[2] T. V. Raziman, R. H. Godiksen, M. A. Müller, and A. G. Curto, "Conditions for Enhancing Chiral Nanophotonics near Achiral Nanoparticles," *ACS Photonics*, vol. 6, no. 10, 2019, doi: 10.1021/acsphotonics.9b01200.

[3] E. Mohammadi, T. V. Raziman, and A. G. Curto, "Nanophotonic Chirality Transfer to Dielectric Mie Resonators," *Nano Lett*, vol. 23, no. 9, 2023, doi: 10.1021/acs.nanolett.3c00739.

[4] S. Murai, G. W. Castellanos, T. V. Raziman, A. G. Curto, and J. G. Rivas, "Enhanced Light Emission by Magnetic and Electric Resonances in Dielectric Metasurfaces," *Adv Opt Mater*, vol. 8, no. 16, 2020, doi: 10.1002/adom.201902024.

Nanophotonics for integrated chiroptical sensing of drug solutions

R. Adhikary[1], A. Sahoo[1], M. Aschi[1], I. Daidone[1], M. Silvestri[1], M. Venturi[1], G. Salvitti[1], C. Ferrante[2], P. Benassi[1,2], D. Tedeschi[1*] and A. Marini[1,2]

[1]Department of Physical and Chemical Sciences, University of L'Aquila, Via Vetoio, 67100 L'Aquila, Italy
[2]Consiglio Nazionale delle Ricerche, CNR-SPIN, Via Vetoio 10, 67100 L'Aquila, Italy
[*]corresponding author: davide.tedeschi@univaq.it

Abstract: We theoretically investigate new chiroptical sensing techniques in nano-scale drug volumes by modelling the bi-anisotropic linear response of reparixin, ladarixin and levodropropizine solutions through molecular dynamics, time-dependent density functional theory and Perturbed Matrix Method, and by obtaining an analytical expression for the macroscopic optical parameters from first principles.

Enantiomers play a central role in pharmaceutics since they affect drug functionality, as in particular in pharmacodynamics, pharmacokinetics and toxicity [1]. Moreover, chiral sensing is essential for optimizing biological tissue penetration and to gain enhanced control of contrast agents, detection markers and biosensors.
Currently, optical sensing techniques, e.g., polarimetry and vibrational circular dichroism (VCD), offer the advantage of real-time analysis capabilities and potential lab-on-a-chip integration and wider nanomedicine applications.

Here, we explore the potential of nanophotonics-based devices for chiroptical sensing of drug solutions. We model drug solutions using molecular dynamics (MD) to find the conformational states of the molecules, time-dependent density functional theory (TD-DFT) to obtain the unperturbed eigenvalues of the vibrational and electronic molecular states, and, finally, Perturbed Matrix Method (PMM) to consider the perturbation due to the solvent to find the perturbed eigenvalues and their static and transition electric/magnetic dipole moments.
Moreover, we obtain the macroscopic optical parameters by perturbatively solving the density matrix equations within the dipole approximation and by averaging the obtained first/second-order hyper-polarizability tensors over the random molecular orientation through the Euler rotation matrix approach. Specifically, in Fig.1 one can see the dielectric permittivity ε_r, the magnetic permeability μ_r and the chiral parameter κ of three different chiral mixtures: reparixin (solid curves in Figs. 1a,b), that is an inhibitor of the CXCR2 function attenuating inflammatory responses [2,3] that has been adopted in clinical trials for the treatment of hospitalized patients with COVID-19 pneumonia [4], dissolved in $CH_3CN + H_2O$ (50:50 volume ratio), levodropropizine (dashed curves in Figs. 1a,b) dissolved in $C_6H_{14} + C_2H_5OH$ (40:60 volume ratio), and ladarixin (dotted curves in Figs. 1a,b) dissolved in water.
In all cases we study the chiral parameter κ (Figs. 1c-h) as a function of the wavelength and the relative concentration $\Delta n_{mol}/n_{mol} = [n^{(S)}_{mol} - n^{(R)}_{mol}]/n_{mol}$), where $n^{(R,S)}_{mol}$ indicate the number densities of R and S enantiomers, respectively and the number molecular density is $n_{mol}=n^{(R)}_{mol}+n^{(S)}_{mol} \approx 10^{-2}$ nm^{-3} (corresponding to a concentration of 5 mg/ml).
Finally, our results are relevant for the development of innovative integrated schemes for chiroptical sensing of drug solutions, such as plasmon-enhanced circular dichroism spectroscopy [5].

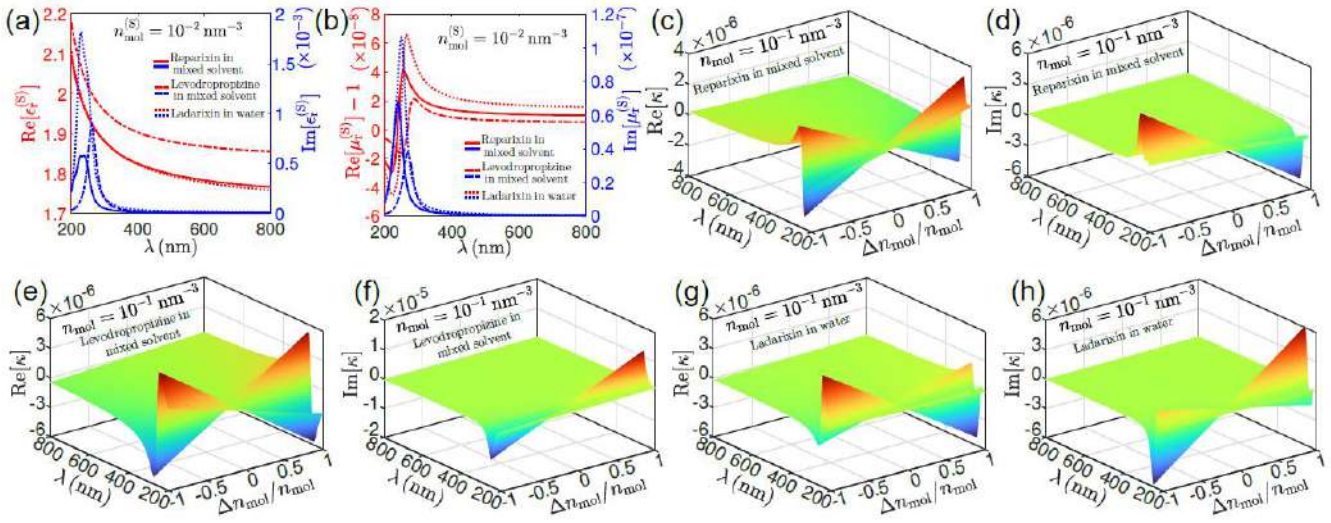


Fig. 1 Real (red curves) and imaginary (blue curves) parts of the **(a)** relative permittivity ϵ_r and **(b)** permeability μ_r of the S-type chiral enantiomer of the three pharmaceutical molecules (with concentration $n_{mol} = 10^{-2}$ nm^{-3}) in different solvents. Here, the left (red) and right (blue) axes represent the real and imaginary parts of ϵ_r and μ_r. The solid curves correspond to reparixin dissolved in $CH_3CN + H_2O$ (50:50 volume ratio), the dashed curves indicate levodropropizine dissolved in $C_6H_{14} + C_2H_5OH$ (40:60 volume ratio), and the dotted curves correspond to ladarixin dissolved in water. **(c,e,g)** Real and **(d,f,h)** imaginary parts of κ as a function of wavelength (λ) for relative concentration ($\Delta n_{mol}/n_{mol} = [n^{(S)}_{mol} - n^{(R)}_{mol}]/n_{mol}$) of an enantiomeric mixture of R and S enantiomers.

References

1. Nguyen, L. A., He, H. and Pham-Huy, C. "Chiral drugs: an overview," Int J Biomed Sci. Vol. 2, 85 – 100, 2006.
2. Bertini R. et al. "Noncompetitive allosteric inhibitors of the inflammatory chemokine receptors CXCR1 and CXCR2: Prevention of reperfusion injury," PNAS Vol. 101, 11791 - 11796, 2004.
3. Bertini R. et al. "Receptor binding mode and pharmacological characterization of a potent and selective dual CXCR1/CXCR2 non-competitive allosteric inhibitor," British Journal of Pharmacology Vol. 165, 436 – 454, 2012.
4. Landoni, G., Piemonti, L., d'Arminio Monforte, A., Grossi, P., Zangrillo, A., Bucci, E., Allegretti, M., Goisis, G., Gavioli, E. M., Patel, N., De Pizzol, M., Pasedis, G. and Mantelli, F. "A multicenter phase 2 randomized controlled study on the efficacy and safety of reparixin in the treatment of hospitalized patients with COVID-19 pneumonia," Infect Dis Ther. Vol. 11,1559 – 1574, 2022.
5. Venturi, M., Adhikary, R., Sahoo, S., Ferrante, C., Daidone, I., Di Stasio, F., Toma, A., Tani, F., Altug, H., Mecozzi, A., Aschi, M. and Marini, A. "Plasmon-enhanced circular dichroism spectroscopy of chiral drug solutions," The Journal of Chemical Physics Vol. 151 ,154703, 2023.

Large-area Nanohelices as Chiral Metasurface for Engineering Optical Chirality

Thu H. H. Le[1*], H. Sato[2], and T. Tanaka[3]

[1]National Institute of Advanced Industrial Science and Technology (AIST), Japan
[2]Graduate School of Science and Engineering, Ehime University, Japan
[3] RIKEN Center for Advanced Photonics, Japan
[*]corresponding author: thu.le@aist.go.jp

Abstract: This study presents a wafer-scale, self-assembly fabrication method of metallic helices by engineering the residual stresses and gradient strains in thin films to induce spontaneous folding and twisting. The fabricated nanohelices of sub-micrometer radii exhibit strong chiroptical responses in the infrared regime, enabling practical applications in chiroptical spectroscopies and chiral chemistry.

Chiral metasurface has emerged as a promising candidate to enhance the chiroptical activity towards spectroscopic and chiral chemistry applications. Recent theoretical and experimental works show that the chiroptical signals of chiral molecules are significantly amplified when they couple with chiral metastructures. Among various chiral metastructures reported so far, helices are particularly well-studied due to their intrinsic optical chirality, arising from their geometric configuration.[1-2] They are particularly valuable in maximizing light-matter interactions in applications such as chiral sensing or stereochemical reactions. However, despite their potential, the fabrication and optical characterization of metallic helices remain underexplored due to substantial technical challenges, particularly the tradeoff between precise structural control and process efficiency.

In this study, we present a self-assembly fabrication technique for nanohelices that offers precise feature control, wafer-scale production capability, and broad material compatibility. Our method involves the single-step transformation of metallic strips composed of multilayered thin films into helical geometries once released from the substrate. This transformation is driven by the nanoscale control of the residual stresses and gradient strains within the metallic strips, which spontaneously generate the necessary forces for folding and twisting. This technique facilitates the efficient fabrication of centimeter-scale samples, allowing for chiroptical characterization using standard commercial spectrometers. Experimental measurements and numerical simulations confirm strong chiroptical responses in the infrared (IR) region for helices with radii on the order of hundreds of nanometers.

The fabrication process begins with the preparation of micrometer-scale strips of multilayered metallic thin films on a Si substrate, using ultraviolet (UV) lithography, electron-beam evaporation, and lift-off techniques. The substrate is then coated with the electron-beam lithography (EBL) resist, and uniform nanoscale line-and-space patterns are written at a specific angle θ relative to the strip's axis. After development, selective wet etching is performed to partially remove the top metal layer. Upon removal of the EBL resist, microstrips with nanogroove patterns are formed. The substrate then undergoes isotropic reactive ion etching to eliminate the underlying silicon. As the Si beneath the strips is fully removed, the strips detach from the substrate. Residual stresses in the nanogrooves create a periodic strain gradient, causing the strips to fold and twist spontaneously into nanohelices.

Figure 1(a-b) shows the scanning electron microscope (SEM) images of nanohelices aligned in parallel to the Si substrate fabricated from aluminum (Al)/titanium (Ti)/aluminum (Al) and gold (Au)/nickel (Ni)/aluminum (Al)

trilayer films, respectively. We have succeeded in fabricating helices with diameter ranging from 800 nm to several μms. Based on the helical geometry, the pitch P between adjacent rings is related to radius R of helix by $P = \frac{2\pi R}{\tan\theta}$. The radius R can be expressed as $R \approx \frac{l}{|\alpha|}$, where l is the periodicity of the nanogroove patterns and α is the folding angle induced at each nanogroove. These relationships indicate that structural parameters such as R and P can be precisely tuned by adjusting the nanogroove periodicity l, the folding angle α, and the alignment angle θ of the groove patterns.

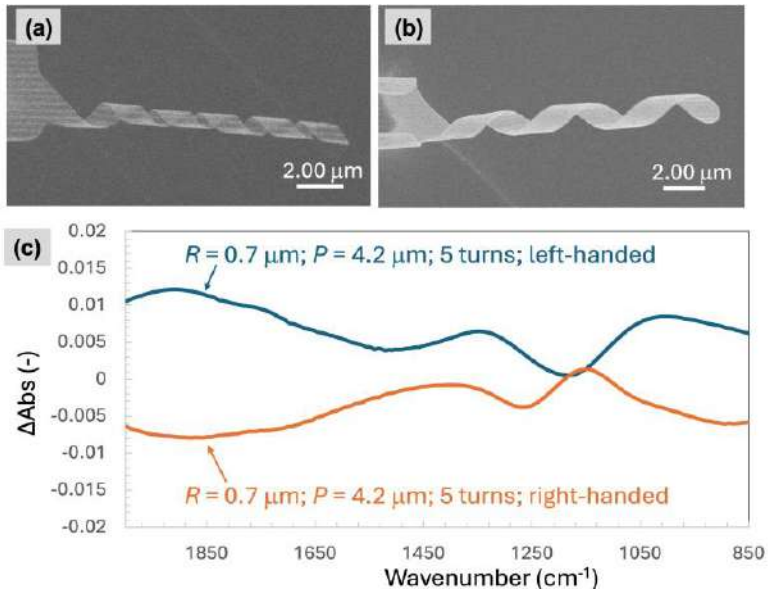


Figure 1. SEM images of helices fabricated from (a) Al/Ti/Al and (b) Ni/Au/Al thin films. (c) IR-CD spectra of pairs of helices.

A key advancement of this technique is its ability to achieve wafer-scale fabrication within a relatively short processing time. The realization of cm²-sized samples has enabled the characterization of the chiroptical properties of metallic helices using standard spectrometers, eliminating the need for previously required microscope-based setups. To verify the chiral responses of the fabricated helices, we measured the extinction spectrum differences for incident circularly polarized light of opposite handedness in the IR range of 850 – 2000 cm^{-1}, using a standard Fourier transform-based IR circular dichroism (IR-CD) spectrometer. The resulting IR-CD spectra, shown in Fig. 1(c) for two Al helices with opposite handedness, reveal distinct circular dichroism (CD) peaks and dips at identical frequencies. The right- and left-handed structures exhibit opposite signs with nearly equal amplitudes, demonstrating the mirror-symmetric behavior characteristic of chiral systems, which arises from the chiral eigenmodes of their intrinsic geometry.

We have developed a robust method for fabricating submicrometer metallic helices by engineering the stress and strain in metallic thin films through conventional lithography techniques. The ability to fabricate helical structures at the wafer scale, combined with tunable structural parameters and tailored optical properties, establishes this technique as a transformative chiral metasurface platform. It holds promise for practical applications in photonics, chiroptical spectroscopy, and stereochemistry, including chiral sensing, IR inspection, stereostructural characterization, and enantioselective chemical reactions.

Acknowledgements

This study was supported by Fusion Oriented Research for disruptive Science and Technology (JPMJFR203Z) from The Japan Science and Technology Agency and Grant-in-Aid for Early-Career Scientists (19K15454). The authors gratefully acknowledge the Nanotechnology Hub of Kyoto University, Japan for the support in nanofabrication processes.

References

1. Gansel, J. K., Wegener, M, et al. “Gold helix photonic metamaterial as broadband circular polarizer”, Science 325, 1513-1515, 2009.
2. Schäferling, M., Yin, X., Engheta, N., and Giessen, H. “Helical plasmonic nanostructures as prototypical chiral

near-field sources", ACS Photon. 6, 530-537, 2014.

Transition Metal Dichalcogenide lateral heterostructure-based excitonic platform for photonics and optoelectronics

H. Lamsaadi[1], A. Cuche[1], G. Agez[1], I. Paradisanos[2], D. Beret[3], L. Lombez[3], P. Renucci[3], D. Lagarde[3], X. Marie[3], Z. Gan[4], A. George[4,5], K. Watanabe[6], T. Taniguchi[7], A. Turchanin[4,5], N. Combe[1], B. Urbaszek[8], J-M. Poumirol[1], and V. Paillard[1*]

[1]CEMES-CNRS, Université de Toulouse, 29 Rue Jeanne Marvig, Toulouse 31055, France
[2]Institute of Electronic Structure and Laser, Foundation for Research and Technology-Hellas, Heraklion 70013, Greece
[3]LPCNO, Université de Toulouse, INSA, CNRS, 135 Avenue Rangueil, Toulouse 31077, France
[4]Friedrich Schiller University Jena, Institute of Physical Chemistry, 07743 Jena, Germany
[5]Abbe Centre of Photonics, 07745 Jena, Germany
[6]Research Center for Functional Materials National, Institute for Materials Science1-1 Namiki, Tsukuba 305-0044, Japan
[7]International Center for Materials Nanoarchitectonics, National Institute for Materials Science 1-1 Namiki, Tsukuba 305-0044, Japan
[8]Institute of Condensed Matter Physics, Technische Universität Darmstadt, 64289 Darmstadt, Germany

[*]Corresponding author: vincent.paillard@cemes.fr

Abstract: Lateral heterostructures of different Transition Metal Dichalcogenide monolayers provide new architectures leading to a wide range of novel photonic and optoelectronic applications. In recent studies, we have shown that such lateral heterostructures can be used to filter, focus, collimate, or trap neutral excitons, giving a base for excitonic devices.

Transition Metal Dichalcogenide monolayers (TMD-ML) have been the focus of extensive research in recent years thanks to their strong light-matter coupling and intriguing optical and excitonic properties.[1-2] A particular emphasis has been placed on the manipulation of neutral excitons at room temperature (RT) in these materials, which is a direct consequence of their tight binding energies and notably high mobilities.[3-4] Indeed, controlling the spatial motion of these quasi-particles has the potential to yield significant advancements in excitonic circuits, photonics, and optoelectronics. However, the neutral charge nature of the main excitons in TMD-MLs limits their interaction with external electric or magnetic fields, making their manipulation a challenging task. Several studies have focused on spatially manipulating excitons while localizing their emission using local strain gradient engineering of TMD-MLs deposited on nanoantennas.[5-6] Furthermore, combining two or more TMD-MLs with different optical properties for designing innovative vertical heterojunctions (VHs)[7-8] or lateral heterojunctions (LHs)[9-11] have been paying increasing attention, thanks to their unique excitonic properties, such as Moiré interlayer excitons and charge transfer excitons.

Recently, we demonstrated efficient unidirectional transport of excitonic flux from a higher bandgap TMD-ML to a lower gap TMD-ML at RT in high-quality type-II band alignment CVD-grown LHs[12]. Near-field optical spectroscopies based on tip-enhanced Raman scattering and photoluminescence (PL), providing a spatial resolution of about 30 nm, were performed on high-quality WSe_2-$MoSe_2$ LH, exhibiting an excitonic diode-like effect. Indeed, neutral excitons generated inside WSe_2 (large gap) were able to pass through the junction before recombining inside $MoSe_2$ (narrow gap), while the reverse case was not allowed. This phenomenon gives rise to a Kapitza resistance-like effect,[13] which manifests as a strong discontinuity in the excitonic density at the interface between both materials. As a result, the high-gap material-related PL is quenched, while the low-gap material-related PL is enhanced near the junction. Furthermore, by using μ-PL imaging combined with numerical simulations based on statistical approach of randomly moving excitons through specific geometries of sharp WSe_2-

$MoSe_2$ LHs, we showed that various shapes formed by those interfaces enable advanced in-plane control of both excitonic distribution and fluxes over large distances[14]. Thus, a triangular shape LH allows both exciton focalization and flux collimation, consisting in the formation of parallel current lines extending a few micrometers away from the source. We also proved that sub-wavelength $MoSe_2$ triangles embedded in a WSe_2 matrix provide efficient systems for trapping and confining excitons in adjustable size spaces[14]. Our finding about sharp TMD-LHs opens new perspectives for the manipulation of neutral excitons in flat semiconducting 2D materials, hence for the design and production of new excitonic devices.

References

1. M. Koperski et al. “Optical properties of atomically thin transition metal dichalcogenides: observations and puzzles,” Nanophotonics 6, 1289–1308 (2017).
2. T. Mueller et al. “Exciton physics and device application of twodimensional transition metal dichalcogenide semiconductors. npj 2d materials and applications 2018, 2, 29,” (2018).
3. S. Zhang et al. “Two-dimensional heterostructures and their device applications: progress, challenges and opportunities,” Journal of Physics D: Applied Physics 54, 433001 (2021).
4. G. Wang et al. “Colloquium: Excitons in atomically thin transition metal dichalcogenides,” Reviews of Modern Physics 90, 021001 (2018).
5. F. Dirnberger et al. “Quasi-1D exciton channels in strain-engineered 2D materials”, Science Advances 7 (2021).
6. J.-M. Poumirol et al. “Unveiling the Optical Emission Channels of Monolayer Semiconductors Coupled to Silicon Nanoantennas” *ACS Photonics* **2020**, *7* (11) , 3106-3115
7. W. Li et al. “Robust growth of 2d transition metal dichalcogenide vertical heterostructures via ammonium-assisted cvd strategy,” Advanced Materials 36, 2408367 (2024).
8. J. Zhu et al. “One-pot selective epitaxial growth of large WS2/MoS2 lateral and vertical heterostructures,” Journal of the American Chemical Society 142, 16276–16284 (2020).
9. S. Zhang et al. “Lateral layered semiconductor multijunctions for novel electronic devices,” Chemical Society Reviews 51, 4000–4022 (2022).
10. S. Zhang et al. “Two-dimensional heterostructures and their device applications: progress, challenges and opportunities,” Journal of Physics D: Applied Physics 54, 433001 (2021).
11. S. Zhang et al. “Lateral layered semiconductor multijunctions for novel electronic devices,” Chemical Society Reviews 51, 4000–4022 (2022).
12. D. Beret, I. Paradisanos, H.Lamsaadi, et al. “Exciton spectroscopy and 3 unidirectional transport in $MoSe_2$-WSe_2 lateral heterostructures encapsulated in hexagonal boron nitride”. npj 2D Materials and Applications, 6(1):84, 2022.
13. H. Lamsaadi et al. Kapitza-resistance-like in flat $MoSe_2$-WSe_2 lateral heterjunction. Nature communications, 5881(1):84, 2023.
14. H. Lamsaadi et al. “Exciton Collimation, Focusing and Trapping Using Complex Transition Metal Dichalcogenide Lateral Heterojunctions” Adv. Optical Mater. 2024, 2403009.

Wavefront engineering of microcavity-empowered multi-resonant metasurfaces

Shih-Hsiu Huang[1], Hsiu-Ping Su[1], Zijin Yang[2], Yuzhi Shi[3], Qinghua Song[2], and Pin Chieh Wu[*1]

[1]Department of Photonics, National Cheng Kung University, Tainan, Taiwan
[2]Tsinghua Shenzhen International Graduate School, Tsinghua University, Shenzhen, China
[3]Institute of Precision Optical Engineering, School of Physics Science and Engineering, Tongji University, Shanghai, China
[*]corresponding author: pcwu@gs.ncku.edu.tw

Abstract: We report a microcavity-assisted metasurface with a gradient-thickness DBR substrate that achieves 15 high-Q resonances across the visible to NIR spectrum, enabling efficient amplitude and phase modulation for advanced optical control.

Metasurfaces have revolutionized optical modulation at subwavelength scales, yet their performance has largely been confined to single-wavelength or narrowband operation. This work introduces a novel microcavity-assisted metasurface [1, 2] that enables multi-wavelength wavefront control by incorporating a distributed Bragg reflector (DBR) substrate with precisely engineered meta-atoms. The proposed design supports multiple high-Q resonances spanning from the visible to near-infrared spectrum, achieving remarkable efficiency and uniformity across different wavelengths. Our experimental results confirm the generation of up to 15 resonant peaks with enhanced optical performance, enabling flexible amplitude and phase manipulation. Additionally, we demonstrate the integration of this metasurface into advanced optical applications such as structured color generation, holographic imaging, and hyperspectral imaging. These findings offer new possibilities for the development of multifunctional metasurfaces, paving the way for applications in imaging, sensing, and next-generation display technologies.

References

1. C.-H. Lin, S.-H. Huang, T.-H. Lin et al., "Metasurface-empowered snapshot hyperspectral imaging with convex/deep (CODE) small-data learning theory," *Nature Communications* **14**, 6979 (2023).
2. S.-H. Huang, H.-P. Su, C.-Y. Chen et al., "Microcavity-assisted multi-resonant metasurfaces enabling versatile wavefront engineering," *Nature Communications* **15**, 9658 (2024).

Photonics and AI for Next-Generation Smart Applications

L. Di Lauro[1*], A. Aadhi[1], I. Alamgir[1], P. Dmitriev[1], B. Fischer[1,2], C. Mazoukh[1], N. Perron[1], E.A. Viktorov[3], A.V. Kovalev[3], A. Eshaghi[4], M. Chemnitz[1,2], P. Roztocki[1,5], S. Vakili[1], B.E. Little[6], S.T. Chu[7], D.J. Moss[8], and R. Morandotti[1]

[1]Institut National de la Recherche Scientifique - Énergie Matériaux Télécommunications (INRS-EMT), Varennes, QC J3X 1P7, Canada
[2]Leibniz Institute of Photonic Technology, Jena, 07745, Germany
[3]ITMO University, St. Petersburg, 199034, Russia
[4]Huawei Technologies, Markham, ON L3R 5A4, Canada
[5]Ki3 Photonics Technologies, Montreal, QC H1V 2Y8, Canada
[6]QXP Technology Inc., Xi'an, 710119, China
[7]City University of Hong Kong, Hong Kong, China
[8]ARC Centre of Excellence in Optical Microcombs for Breakthrough Science (COMBS), Swinburne University of Technology, Hawthorn, VIC 3122, Australia
[*]corresponding author: Luigi.DiLauro@inrs.ca

Abstract: We demonstrate an all-optical reservoir computing device with a nonlinear amplifying loop mirror for high-speed ML tasks and optimization algorithms for microcomb design. These advancements enhance AI, telecommunications, and smart photonic optimization.

Introduction

Machine learning (ML) has emerged as a transformative tool for tackling complex computational tasks with minimal human intervention, driving the need for faster and more efficient processing. Conventional electronic processors struggle with speed and energy limitations when handling large neural networks, prompting the exploration of photonic computing as an alternative[1-2]. By leveraging the inherent parallelism, bandwidth, and speed of light, photonic artificial intelligence (AI) hardware—such as optical neural networks and reservoir computing systems—promises to overcome these bottlenecks, reducing power consumption, increasing processing speed, and minimizing latency beyond electronic limits. At the same time, photonic technologies are advancing rapidly, enabling new possibilities for AI-driven optimization. For instance, chip-scale frequency combs ("microcombs") generated in nonlinear microring resonators provide vast potential for applications in metrology, communications, and sensing. Meanwhile, ML techniques are reshaping photonic system design, offering robust solutions for optimizing experimental parameters in nonlinear optical systems. The synergy between photonics and AI is thus paving the way for next-generation computing platforms that integrate light-based computation with intelligent data processing. Here, first, we show an all-optical reservoir computing[3] (RC) device based on a nonlinear amplifying loop mirror (NALM), capable of executing multiple ML tasks in parallel via wavelength-division multiplexing (WDM). This device exhibits high accuracy in chaotic time-series prediction while minimizing latency, addressing the limitations of traditional electronic AI accelerators. Second, we demonstrate an ML-based optimization framework employing genetic algorithms (GAs) for stable microcomb generation within microring resonators (MRRs). By optimizing pump parameters, laser detuning, and system feedback, this approach enables repeatable microcomb formation with long-term stability and high spectral coherence.

NALM-based photonic reservoir computing

Optical time-delayed reservoir computing (RC) emerges among others for its ability to form a recurrent network with fading memory while maintaining a minimal hardware footprint. Our proposed photonic RC system consists of a Sagnac interferometer with a NALM as the processing unit, with tunable gain and transmission. This architecture supports a wide range of coherent nonlinear dynamics, both with and without continuous-wave (CW)

injection. By leveraging a wide range of coherent nonlinear dynamics, the processing unit classifies continuous-valued input signals, even when they exhibit significant complexity and nonlinearity. By leveraging WDM, multiple input channels are injected into the system, enabling parallel execution of Mackey-Glass chaotic time-series prediction. As a result, we reach a processing speed of approximately 27 MHz, achieving an error rate of 1%, as shown in Fig.1 (a), after applying a ML training algorithm, i.e., the ridge regression. This scalable approach significantly enhances AI processing capabilities for new photonic intelligent applications.

Optimization algorithms for microcomb designing

Microcombs, generated in microring resonators (MRRs), arise due to the nonlinear interactions of the injected optical field with the material composing their structure. When pumped with enough power, Kerr-induced parametric effects, such as four-wave mixing, allow the generation of broadband microcombs covering the entire telecom C-Band. However, their spectral properties are highly sensitive to pump conditions and detuning, making stable generation challenging. To address this, we implement an optimization scheme based on a genetic algorithm (GA), which performs in a manner analogous to natural selection in evolutionary theory and autonomously identifies optimal experimental parameters for microcomb formation. The fitness function considers key spectral features such as comb line spacing, intracavity power, and spectral envelope uniformity. Through iterative evolution, the GA minimizes spectral deviations, as shown in Fig. 1 (b), achieving power-per-line stability exceeding one day and coherence values of ~86% for three-photon lifetimes. This model-free approach ensures robustness across different microcomb generation regimes, facilitating practical applications in high-capacity optical communications, neuromorphic computing, and quantum photonics.

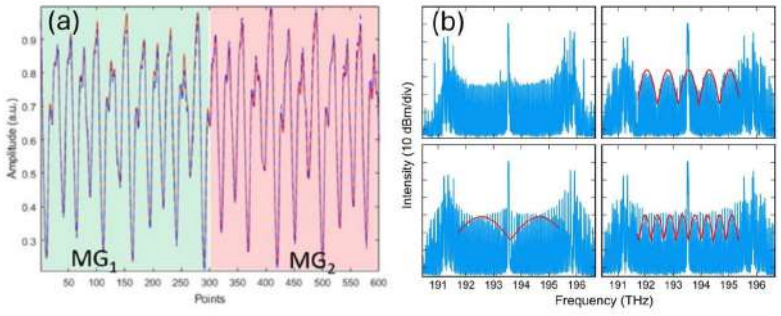


Figure 1. Experimental results. (a) Optical machine learning classification of two MG time series signals using the NALM-based processing unit. (b) Microcombs' spectral design using our GA[4].

Conclusions

Our work underscores the bidirectional synergy between photonics and ML. Optical RC offers a high-speed, energy-efficient solution for AI tasks, while ML-driven optimization enables robust and stable photonic applications design. These advancements pave the way for next-generation photonic processors and intelligent optical systems, driving new possibilities in AI, telecommunications, and beyond.

References

1. Xu, X. et al. “11 TOPS photonic convolutional accelerator for optical neural networks,” Nature, Vol. 589, 44–51, 2021.
2. Xia, S. et al. “Deep-learning-empowered synthetic dimension dynamics: morphing of light into topological modes,” AP Vol. 6, No. 026005, 2024.
3. Brunner, D. et al. “Roadmap on neuromorphic photonics,” Preprint at https://doi.org/10.48550/arXiv.2501.07917, 2025.
4. Mazoukh, C. et al. “Genetic algorithm-enhanced microcomb state generation,” Commun. Phys., Vol. 7, 1–11, 2024.

Optical pulling forces for 3-dimensional motion control in plasmonic nanomotors

G. Serrera[1*], Y. Y. Tanaka[2], and P. Albella[1]

[1]Department of Applied Physics, University of Cantabria, Avda. Los Castros, s/n, 39005 Santander, Spain.
[2]Research Institute for Electronic Science, Hokkaido University, N21W10, Kita, Sapporo, Hokkaido 001-0021, Japan.
[*]corresponding author: guillermo.serrera@unican.es

Abstract: We present a novel nanomotor design that enables 3-dimensional control of motion. A moderate cone angle Bessel beam with azimuthal polarization, acting on a glass chassis, allows for stable optical pulling; while asymmetric plasmonic dimers embedded within this chassis provide lateral movements upon plane wave illumination.

Momentum transfer in light-matter interactions generates optical forces, which play a crucial role in advancing micro- and nanotechnology, particularly in lab-on-a-chip devices [1]. Traditionally, gradient optical forces from optical tweezers have been employed to drive components such as pumps and valves, but these forces are limited by the size, shape, and material properties of the actuated objects. To overcome these limitations, recent research has proposed nanomotors utilizing scattering forces from asymmetric plasmonic nanoantennas or dielectric metasurfaces [2,3]. While showing successful results in enabling movement within two-dimensional planes, controlling longitudinal motion has remained a persistent challenge [4]. In contrast to the relatively trivial and well-known pushing effect obtained from scattering, optical pulling forces, first recognized in the last decade, require precise illuminating and scattering conditions [5].

This optical pulling effect has been theoretically achieved by the exploitation of several schemes, such as large cone angle Bessel beams, plane wave pairs, hyperbolic materials or chiral light-matter interactions [6]. However, most of these strategies propose unrealistic experimental conditions, making the practical realization of the effect challenging. A promising solution to this problem was proposed by Li et al. in 2019, using a dielectric cylinder that collimates Bessel beams by acting as a waveguide, allowing optical pulling effects across long distances with low cone angle Bessel beams [7].

In this work, we present a novel nanomotor design that enables control over both transversal and longitudinal motion. The system utilizes a coupling mechanism between an azimuthally polarized Bessel beam and a dielectric glass cylinder, which serves also as a chassis for the nanomotor (Figure 1a). Asymmetric plasmonic dimers are embedded within the cylinder in a way that minimizes their interaction with the pulling beam. This scheme allows for lateral motion, driven by the scattering forces from the plasmonic dimers under plane wave illumination (Figure 1b,d), while Bessel beam incidence enables longitudinal motion through optical pulling forces on the cylinder. Our design unlocks a new degree of freedom in motion control, allowing for pulling, pushing, and lateral movement by adjusting the polarization or switching between plane waves and Bessel beams. Furthermore, the optical pulling force in our system is robust against rotational and translational disturbances (Figure 1c), including Brownian motion, enhancing its practical applicability for advanced optical manipulation applications.

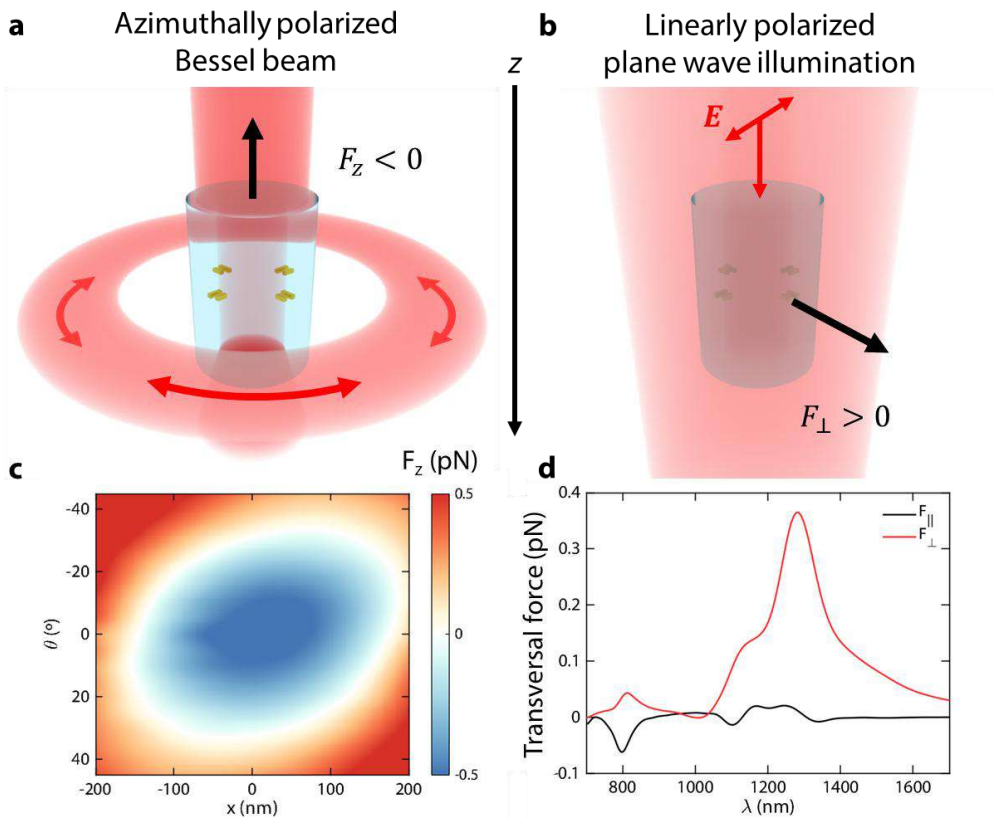


Figure 1. Depiction of the nanomotor design, acting in its optical pulling (a) and lateral movement (b) configurations. c) Longitudinal optical force with respect to angle and position. d) Lateral force components with respect to incident wavelength.

G. S. acknowledges funding from the Spanish government for his predoctoral contract grant (FPU21/02296). This work was funded by the MOPHOSYS Project (PID2022-139560NB-I00) from Proyectos de Generación de Conocimiento provided by the Spanish Agencia Estatal de Investigación.

References

1. Glückstad, J. “Sorting particles with light”, Nat Mater, Vol. 3, 9-10, 2004.
2. Tanaka, Y. Y., et al., “Plasmonic linear nanomotor using lateral optical forces”, Sci Adv, Vol. 6, No. 45, 2020.
3. Ardrén, D., et al., “Microscopic metavehicles powered and steered by embedded optical metasurfaces”, Nat Nanotechnol, Vol. 16, No. 9, 970-974, 2021.
4. Wu X. et al., “Light-driven microdrones”, Nat Nanotechnol, Vol. 17, No. 5, 477-484, 2022.
5. Chen, J., et al., “Optical pulling force”, Nat Photonics, Vol 5., No. 9, 531–534, 2011.
6. Li, H., et al., “Optical pulling forces and their applications”, Adv Opt Photonics, Vol. 12, No. 2, 288-366, 2020.
7. Li, X., et al., “Optical pulling at macroscopic distances”, Sci Adv, Vol. 5, No. 3, 2019.

Nonlinear optics in the XUV spectral range

L. Assogna[1*], E. Principi[2], M. Silvestri[1], A. Sahoo[1], G. Batignani[3,4], G. Fumero[3,5,6], L. Foglia[2], R. Mincigrucci[2], D. Tedeschi[1], C. Masciovecchio[2], T. Scopigno[3,4], A. Marini[1,7], and C. Ferrante[7]

[1]Department of Physical and Chemical Sciences, University of L'Aquila, Via Vetoio, 67100 L'Aquila, Italy.

[2]Elettra-Sincrotrone Trieste S.C.p.A., SS 14-km 163.5, 34149 Basovizza, Trieste, Italy.

[3]Dipartimento di Fisica, Università di Roma "La Sapienza", Piazzale Aldo Moro 5, 00185 Roma, Italy.

[4]Center for Life Nano Science @Sapienza, Istituto Italiano di Tecnologia, Viale Regina Elena 291, I-00161 Roma, Italy.

[5]Department of Physics and Astronomy, West Virginia University, Morgantown, WV 26506, USA.

[6]Associate, Nanoscale Device Characterization Division, National Institute of Standards and Technology, USA.

[7]Consiglio Nazionale delle Ricerche, CNR-SPIN, Via Vetoio 10, 67100 L'Aquila, Italy.

[*]corresponding author: luca.assogna@graduate.univaq.it

Abstract: Nonlinear effects are fundamental in spectroscopy and ultrafast physics but are limited in the XUV regime due to weak radiation-matter interaction. By means of femtosecond free-electron laser radiation, we report the first observation of the ENZ enhancement of self-action nonlinear effects in a the extreme ultraviolet.

The extreme ultraviolet (XUV) spectral range, thanks to the advent of pulsed sources, provides a window to a plethora of phenomena that cannot be observed in other spectral ranges, opening novel avenues for our understanding of ultrafast relaxation and non-equilibrium processes. Indeed, with the development of high harmonic generation (HHG) table-top sources, new spectroscopy schemes have enabled experimental implementations, such as nonlinear spectroscopy, coherent multidimensional spectroscopy, and time-resolved XUV transient absorption. The limited power of such sources hampers the observation of extreme nonlinear effects in a table-top framework, restricting their application mainly to spectroscopic techniques. However, by means of femtosecond free electron laser (FEL) pulses, it is possible to reach enough power to probe NL effects in the XUV regime (peak intensity > 200 TW/cm^2) [1]. Moreover, such NL effects can be enhanced owing to the tremendous field enhancement that epsilon-near-zero (ENZ) materials can provide.

Here, we report the first experimental observation of the ENZ enhancement of a third order nonlinear effect, namely self-phase modulation (SPM), in the XUV range. Specifically, the femtosecond FEL pulse [2] is characterized by a wavelength λ=44nm, and impinges on a 300nm tick Al foil. The near-zero effective-index (NZI) condition (eq. 1),

$$\mathrm{Re}\sqrt{\epsilon_{\mathrm{Al}}(\lambda) - \sin^2\theta_{\mathrm{NZI}}(\lambda)} = 0 \quad , \tag{1}$$

can be reach by tuning the impinging angle θ. In this regime, broadband Ferrell-Berreman (FB) modes in the Al thin foils occurs, leading to an enhancement of SPM. Particularly, during the ultrafast interaction between the femtosecond FEL pulse, the electron in Al undergoes ultrafast heating, followed by a relaxation process via electron-phonon collisions. This complex dynamics is theoretically taken into account by modeling a spatio-temporal electronic temperature, which causes a modulation of the refractive index.

In conclusion, we report the first observation of ENZ enhancement of self-induced spectral modulation in the XUV spectral range. In our extended theoretical model [3], we describe the enhancement of nonlinear effects that can occur at the epsilon-near-zero (ENZ) wavelength for a nanometric bilayer of poor metal, where plasmons play a crucial role in light-matter interaction.

References

1. Ferrante, C., et al, “Non-linear self-driven spectral tuning of Extreme Ultraviolet Femtosecond Pulses in monoatomic materials” Light: Science & Applications 10, 92, 2021.
2. Masciovecchio, C. et al. “EIS: the scattering beamline at FERMI. ” J. Synchrotron Radiat. 22, 553-564, 2015.
3. Silvestri, M. et al “Resonant third-harmonic generation driven by out-of-equilibrium electron dynamics in sodium-based near-zero index thin films,” Nanophotonics, Vol. 13, No. 11, pp. 2003-2013, 2024.

Labyrinthine Magnetic Domains in Epitaxial Magnetooptical Garnet Films for Synchrotron Analysis and Optical Modulator Applications

Taichi Goto[1]

[1]Research Institute of Electrical Communication, Tohoku University, Japan
*corresponding author: taichi.goto.a6@tohoku.ac.jp

Abstract: Ce-substituted yttrium iron garnet grown epitaxially on garnet substrates exhibits labyrinthine magnetic domains. We analyzed these domains in detail using synchrotron radiation facilities and applied them to modulation devices utilizing magneto-optical effects.

Magnetooptical devices including Q-switched lasers [1], spatial light modulators, optical isolators, and magnetic holographic memory systems have attracted considerable attention due to their unique operational characteristics. The dynamic manipulation of magnetic domains offers promising approaches for next-generation optical modulation technologies with advantages in switching speed and energy efficiency.

In this study, we investigate cerium-substituted yttrium iron garnet (Ce:YIG) films epitaxially grown on gadolinium gallium garnet (GGG) and substituted GGG (SGGG) substrates using RF ion beam sputtering [2]. The deposition process was optimized with substrates maintained at 810°C and rotated at 4.3 rpm for uniform film growth across 10 mm × 10 mm substrates. The resulting Ce:YIG films measured ~130 nm in thickness, characterized through stylus profilometry and cross-sectional transmission electron microscopy. Compositional analysis via energy-dispersive spectroscopy revealed a stoichiometry of $Ce_{0.9}Y_{2.1}Fe_5O_{12-\delta}$, where δ represents oxygen deficiency.

We employed synchrotron radiation facilities to visualize magnetic domain structures with exceptional clarity, revealing distinct labyrinthine patterns with well-defined boundaries suitable for detailed quantitative analysis. The relationship between film thickness, magnetooptical response, perpendicular magnetic anisotropy, and magnetic domain width presents significant engineering challenges. Specifically, while increased film thickness enhances magnetooptical effects, it simultaneously reduces perpendicular magnetic anisotropy due to strain relaxation at the film-substrate interface, causing magnetization to reorient toward an in-plane configuration and resulting in the disappearance of desirable domain structures.

To understand domain dynamics, we conducted micromagnetic simulations using a 20 × 20 × 2 mm model discretized into 80 × 80 × 80 nm cells (4.77×10^6 total cells). Material parameters included 40 mT saturation magnetization, 7 pJ/m exchange coupling constant, and 2.5×10^4 A/m anisotropic field. These calculations were executed using Fujitsu's EXAMAG software on a high-performance system with Intel Xeon Gold 6132 processors (128 cores, 960 GB memory), completing in approximately 30 minutes.

Simulation results provided critical insights into magnetization dynamics and domain wall motion under various applied fields, revealing rapid domain reconfiguration in response to external magnetic fields—a characteristic essential for high-speed modulation devices. The agreement between experimental observations and simulation results validates both our material synthesis approach and computational methodology.

This work provides foundational knowledge regarding the growth, characterization, and theoretical understanding of Ce:YIG films with labyrinthine magnetic domains, contributing to the development of high-performance magnetooptical devices for optical communication systems, information processing

technologies, and specialized photonic applications requiring rapid light modulation capabilities.

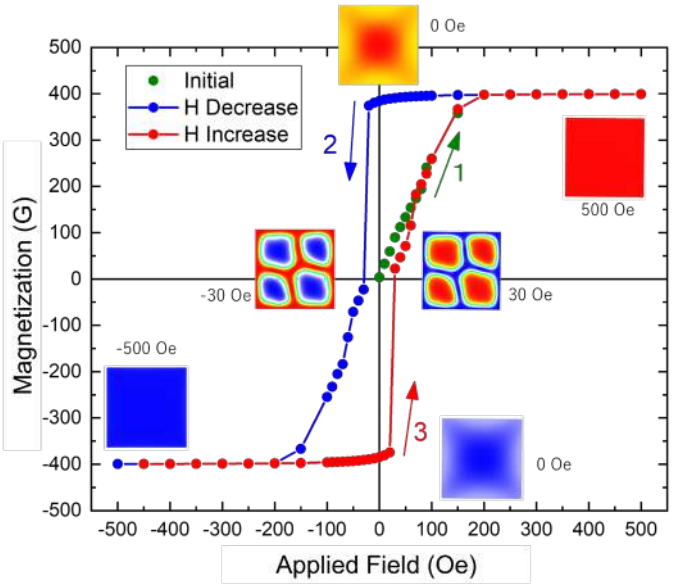


Figure 1. Calculated magnetic domain state in a magnetic garnet film. Magnetic domains were erased by applying magnetic field.

This work was partly supported by the Japan Society for the Promotion of Science (JSPS) KAKENHI Grants No. 20H02593, No. 23H01439, and No. 23K17758; the New Energy and Industrial Technology Development Organization (NEDO) Grants No. 23200047, the Inamori Foundation, and the Amada Foundation. T.G. thanks for the TI-FRIS fellowship, and the shared facilities of CINTS, LNS, GIMRT, and FTCTU.

References

1. T. Goto, M. C. Onbasli, D. H. Kim, V. Singh, M. Inoue, L. C. Kimerling, and C. A. Ross, "A nonreciprocal racetrack resonator based on vacuum-annealed magnetooptical cerium-substituted yttrium iron garnet," Opt. Express 22, 19047-19054 (2014).
2. Y. Yoshihara, K. Ishiyama, T. Watanabe, P. B. Lim, M. Inoue, C. A. Ross, and T. Goto, "Growth of magnetooptical cerium-substituted yttrium iron garnet on yttrium aluminum garnet using ion beam sputtering," Appl. Phys. Lett. 123, 112404 (2023).

Quasi-Babinet principle in dielectric resonators and Mie voids

M. Hamidi[1], K. Koshelev[2*], S. Gladyshev[1], A. C. Valero[1], M. Hentschel[3]
H. Giessen[3], Y. Kivshar[2], and T. Weiss[1*]
[1]Institute of Physics, University of Graz, Austria
[2]Nonlinear Physics Center, Research School of Physics, Australian National University, Australia
[3]4th Physics Institute and SCoPE, University of Stuttgart, Germany
Corresponding author: kirill.koshelev@anu.edu.au, thomas.weiss@uni-graz.at

Abstract: We establish a quasi-Babinet principle for dielectric systems, linking dielectric Mie voids and their complementary structures. Among its various implications, this principle notably connects their resonant properties, and our work establishes simple design rules for constructing dielectric resonators with complex functionalities from their complementary counterparts.

Advancing resonant nanophotonics requires novel building blocks. Recently, cavities in high-index dielectrics have been shown to resonantly confine light inside a lower-index region [1]. These so-called Mie voids represent a counterpart to solid high-index dielectric Mie resonators, offering novel functionality such as resonant behavior in the ultraviolet spectral region [1]. In the simplest case, this structure can be assumed to be a spherical void in a high-index surrounding, which can be filled with a high-index particle. Such an analogy is shown in Fig. 1.

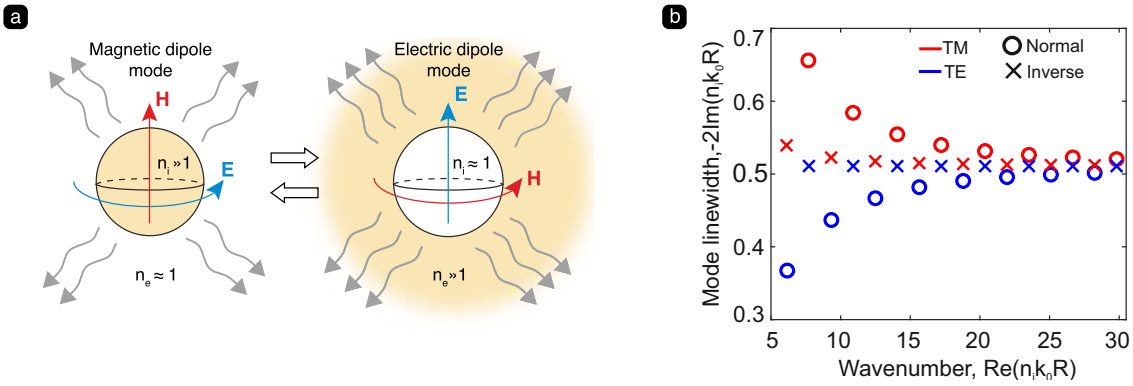


Figure 1: (a) High-index dielectric structure and low-index void in high-index dielectric host medium as its inverse system (b) Demonstration of the quasi-Babinet principle for a high-index dielectric sphere with $n_\mathrm{i} = 4$, $n_\mathrm{e} = 1$ and a spherical low-index void with $n_\mathrm{i} = 1$, $n_\mathrm{e} = 4$.

Looking at these two complementary structures reminds us of the well-known and highly useful Babinet's principle, a fundamental concept in electromagnetism that relates the scattering properties of thin perfect metallic conductors to complementary apertures in metal sheets [2]. Up to some extent, it applies as well to diffraction patterns from radiation passing through complementary metallic screens, exchanging transmission and reflection spectra [3]. However, it is not strictly applicable to dielectrics and volumetric systems. Here, we show that within certain boundaries, Babinet's principle can be generalized to dielectric and magnetodielectric systems, which we refer to as the quasi-Babinet principle and demonstrated for spherical and more generically shaped Mie resonators [4]. We reveal that for spherical nanoparticles, even

an analytic form of the quasi-Babinet principle can be established, connecting the electric and magnetic fields of a structure and its complementary counterpart, as well as their resonant frequencies and quality factors. The new principle holds quantitatively for voids (nanoparticles) with size larger than the wavelength, and approximately for subwavelength voids (nanoparticles). The quasi-Babinet principle remains approximately valid for nonspherical geometries, while it breaks down in the regions of high absorption and high dispersion.

Our work not only offers deeper physical insight into the working mechanism of these systems but also establishes simple design rules for constructing dielectric resonators with complex functionalities from their complementary counterparts. We anticipate the developed principle to pave the way toward smart engineering of nanoscale metadevices comprising applications in strong light-matter interaction, biosensing, and quantum information processing.

References

1. M. Hentschel et al., "Dielectric Mie voids: confining light in air," Light Sci. Appl. **12**, 3 (2023).

2. J. Meixner, "Das Babinetsche Prinzip der Optik," Z. Naturfors. A **1**, 496 (1946).

3. T. Zentgraf et al., "Babinet's principle for optical frequency metamaterials and nanoantennas," Phys. Rev. B **76**, 033407 (2007).

4. M. Hamidi et al., "Quasi-Babinet principle in dielectric resonators and Mie voids," Phys. Rev. Res. **7**, 013136 (2025).

Chiral semiconductor nanophotonics

Alberto G. Curto[1,2*]

[1] Photonics Research Group, Ghent University-imec, Ghent, Belgium
[2] Center for Nano- and Biophotonics, Ghent University, Ghent, Belgium

[*]corresponding author: Alberto.Curto@UGent.be

Abstract: Atomically thin semiconductors such as WS_2 can sustain spin-valley polarization and emit circularly polarized light. Using few-layer WS_2, we investigate the electrodynamic nature of valley-polarized emission using back focal plane imaging. We also demonstrate a Drexhage experiment to enhance and control valley-polarized emission.

Two-dimensional semiconductors hold great promise for nanoscale photonics and optoelectronics. Based on robust excitons at room temperature, they exhibit strong light absorption and emission, and they are easy to integrate into nanophotonic structures. One of their most promising properties is spin-valley polarization. In atomically thin semiconductors such as monolayer MoS_2 or WS_2, the spin and momentum direction of carriers can be locked. As a result, using circularly polarized light, we can populate carriers with a momentum direction that depends on the handedness of the optical excitation.[1] This degree of freedom, known as valley polarization, could be exploited to add a new dimension to information processing and optoelectronics. To fully take advantage of valley polarization for nanophotonics, it is necessary to better understand the conditions for it to occur, its electrodynamic nature, and the possibilities for enhancing it through optical means.

In this presentation, we characterize the microscopic electrodynamic character of valley polarization and valley coherence in few-layer WS_2 at room temperature. We employ back focal plane (BFP) imaging to record polarization-resolved angular radiation patterns. By analyzing the spin of the evanescent part of the angular spectrum, we identify circular and linear electric dipole characteristics in WS_2 excitons under circularly and linearly polarized excitations, respectively. Such evanescent optical spin is transferable to the far field using a glass substrate and has peculiar characteristics. Our investigation compares theory and experimental results for a dipolar source of photoluminescence in few-layer WS_2 semiconductors on a glass substrate. Utilizing polarization-resolved BFP imaging, we attribute valley-polarized emission to circularly polarized electric dipoles and valley-coherent emission to linearly polarized dipoles. Interestingly, it is possible to observe emission with linear polarization under certain angles for valley-polarized emission, and radiation with circular polarization for valley-coherent emission.

The ideal valley-polarized material should exhibit high emission quantum efficiency together with high polarization. However, currently available transition metal dichalcogenides suffer from either low efficiency or low polarization. In the second part of this presentation, we follow a nanophotonic route to enhance circularly polarized emission capable of enhancing both the emission intensity and the degree of polarization. We introduce a Drexhage experiment for valley polarization, where we control the distance between a WS_2 bilayer and a mirror using dielectric spacers. Our experiment achieves nearly complete control over valley-polarized emission at room temperature, with a degree of circular polarization varying from 0.1 to 0.75 at different distances. We characterize the lifetime of the polarized emitted photons and the angular radiation patterns. We interpret the results using a rate equation model and highlight the impact of distance and power-dependent polarization on valley dynamics, providing a new path to control valley polarization. Unlike complex arrays of nanostructures,[2] our Drexhage

experiment is a simple yet effective method to exert robust control over valley polarization by exploiting exciton dynamics. Our findings elucidate the spin-valley dynamics influenced by exciton-exciton annihilation.

Our results offer valuable insights into the dipolar nature of exciton emitters with valley polarization and their intrinsic evanescent fields. By understanding, controlling, and enhancing the circular polarization of light emitted by WS_2, our results open up new possibilities for spin-based nanophotonic and optoelectronic devices. Our findings have implications for applications such as polarization-controlled light on-chip and the development of valley-based technologies and integrated photonic devices.

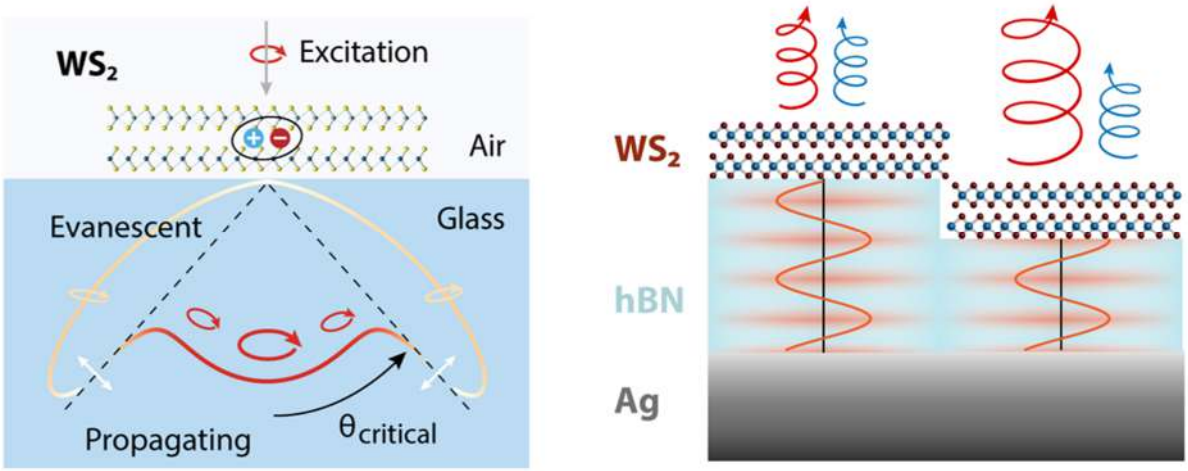


Figure 1. Polarization-resolved angular radiation patterns of few-layer WS_2 and enhanced valley-polarized emission near a mirror.

References

1. Godiksen, R. H., Wang, S. Raziman, T. V., Gómez Rivas, J., Curto, A. G. Impact of indirect transitions on valley polarization in WS_2 and WSe_2, *Nanoscale* 14, 17761 (2022).
2. Raziman, T. V., Godiksen, R. H. , Müller, M. , Curto, A. G.. Conditions for enhancing chiral nanophotonics near achiral nanoparticles, *ACS Photonics* 6, 2583 (2019).

Resonant Light Absorption Driving by Bound States in the Continuum in Hybrid Metasurfaces

A. B. Evlyukhin[1,2*], **M. A. Poleva**[3], **C. Rockstuhl**[3,4]
[1]Institute of Quantum Optics, Leibniz University Hannover, Welfengarten 1, Hannover 30167, Germany
[2]Cluster of Excellence PhoenixD, Leibniz University Hannover, Hannover 30167, Germany
[3]Karlsruhe Institute of Technology, Kaiserstr. 12, 76131, Karlsruhe, Germany
*corresponding author:evlyukhin@iqo.uni-hannover.de

Abstract: We study how material-induced bianisotropy of hybrid nanostructures leads to resonant features in the optical response of both individual hybrid particles and metasurfaces composed of them. The excitation of quasi-bound states in the continuum in hybrid metasurfaces leading to spectral absorption bands is discussed.

Hybrid nanostructures promise to combine the beneficial properties of metallic nanostructures, such as strong confinement of electromagnetic energy, and dielectric nanostructures, such as high scattering directivity and low losses. Hybrid nanostructures, including their periodic arrays (metasurfaces), have already been extensively studied theoretically and experimentally [1]. The use of hybrid metasurfaces for refractive index sensing with high sensitivity was proposed in [2]. Reconfigurable hybrid metasurfaces incorporating phase transition material into meta-atoms [3] and hybrid metasurfaces with broken out-of-plane symmetry [4] have been recently proposed for efficient control of light properties.

In this work the features of optical properties of hybrid silicon-gold nanodisks are studied, demonstrating that internal material inhomogeneity can lead to a strong bianisotropic response of the particles associated with the distortion of their inversion symmetry. A method for obtaining information on the structure of the dipole polarizability tensor of hybrid particles based on the analysis of symmetry properties and the multipole composition of their eigenmodes is discussed. The spectral response of metasurfaces composed of such particles, in turn, can have narrow resonance features associated with resonant multipole coupling and excitation of quasi-bound states in the continuum (BICs). It is shown that these resonance features strongly depend on the polarization of incident waves and are accompanied by an increase in absorption and field enhancement in the plane of the metasurface. It is also shown that, using a special procedure for determining (tuning) the period of the metasurface, it is possible to implement switching control of the excitation of quasi-BICs of magnetic and electric types by changing the only polarization of the incident wave.

Thus, it was found that, unlike purely dielectric metasurfaces, quasi-BIC excitation in hybrid metasurfaces leads to the resonant absorption of light. Under the resonant absorption, strong electromagnetic fields are concentrated in the dielectric part of the hybrid metasurface particles, providing contribution into transmission and reflection. Multipole analysis of reflection showed that, depending on the polarization of the incident wave, its suppression can be associated with the anapole effect and the Kerker effect. In the case of hybrid structures, information about the distribution of near electromagnetic fields is of particular importance, as it reveals new possibilities for manipulating light energy on subwavelength scales by combining resonances of the plasmonic and dielectric parts. For the practical implementation of hybrid structures, it should be possible to use several methods specially developed for obtaining hybrid particles of various shapes [5,6].

References

1. A. Barreda, F. Vitale, A. E. Minovich, C. Ronning, and I. Staude, “Applications of Hybrid Metal-Dielectric

Nanostructures: State of the Art", Adv. Photonics Res. Vol. 3, 2100286, 2022.

2. D. Ray, T. V. Raziman, C. Santschi, D. Etezadi, H. Altug, and O. J. F. Martin, "Hybrid Metal-Dielectric Metasurfaces for Refractive Index Sensing", Nano Lett. Vol. 20, 8752, 2020.
3. S. Abdollahramezani, O. Hemmatyar, M. Taghinejad, H. Taghinejad, Y. Kiarashinejad, M. Zandehshahvar,. . Fan, S. Deshmukh, A. A. Eftekhar, W. Cai, et al., "Dynamic hybrid metasurfaces", Nano Lett. Vol. 21, 1238, 2021.
4. J. Wohlwend, A. Hilti, C. Polinari, R. Spolenak, and H. Galinski, Hybrid resonant metasurfaces with configurable structural colors, Adv. Opt. Mater. Vol. 12, 2401501, 2024.
5. J. Hu, S. Zhou, Y. Sun, X. Fang, and L. Wu, "Fabrication, properties and applications of janus particles", Chem. Soc. Rev. Vol. 41, 4356, 2012.
6. X. Pang, C. Wan, M. Wang, and Z. Lin, "Strictly biphasicsoft and hard janus structures: synthesis, properties, and applications", Angewandte Chemie International Edition Vol. 53, 5524, 2014.

Multilayer and microbead structures for ultraviolet to near infrared spectroscopic applications based on metal-free phosphors

D. Hernandez-Pinilla[1], B. K. Barman[1], K. Watanabe[1], H. Yamada, D. Thien Ngo[1], T. Nagao[*,1,2]

[*]corresponding author: NAGAO.Tadaaki@nims.go.jp

[1]Research Center for Materials Nanoarchitectonics, National Institute for Materials Science, Tsukuba-city, Japan.

[2]Department of Condensed Matter Physics, Hokkaido University, Sapporo, Hokkaido, Japan.

Abstract:

Wavelength-selective light absorbers, emitters, or spectroscopic energy transducers for light, are widely utilized in our society by providing wide variety of applications in lighting, solar energy harvesting, remote sensing, and label free bio-sensing. With the combination of novel and efficient phosphor materials and simple micro- and nano-architectures, such as Fabri-Perot resonator[1,2] and whispering gallery resonatores[3], and polaritonic grating absorbers[4], one can engineer spectroscopic feature in wavelength conversion and light amplification which will be useful for lighting application and photonic encryption.

Fluorescent carbon dots/carbonized polymer dots (CDs/ CPDs) are promising materials that exhibit unique luminescence in the visible-to near-infrared wavelength region. These metal-free novel phosphor materials have gained significant interest because of their unique optical properties, photo stability, low cost, and low toxicity, thus being utilized in widespread applications in various fields, including optoelectronic devices. Owing to the limitations of rare-earth elements and heavy toxic effects of chalcogenides and perovskite quantum dots on the environment and biological systems, researchers have started focusing on CDs/CPDs to overcome the drawbacks of conventional phosphor materials.

In this talk, we introduce some of our recently developed light-emitting devices combining metal-free carbogenic phosphors and DBR based microcavity as well as microbeads for controlling the sharp resonant emission and chromaticity via wavelength-selective photoluminescence as well as lasing and infrared emission. By adopting Fabri-Perot structure with two dielectric multilayer-photonic mirrors, we could realize light amplification in the blue wavelength region. We could also observe whispering gallery mode from the CPDs in the visible to the red and finally in the near infrared region. These proposed devices in this study will open a new avenue for potential applications in chromaticity-tunable white light emitters, lasers[5], spectroscopic authentication, and single-microparticle-based chemical/bio sensing.

References:

1. B. K. Barman, D. Hernández-Pinilla *et al.*, *Advanced Science* 2407090 (2024).
2. A. T. Doan *et al., Optics Express* **27** (12), pp. A725-A737 (2019).
3. B. K. Barman, H. Yamada, K. Watanabe *et al.*, *Advanced Science*, 2400693 (2024).
4. T. D. Dao *et al., Advanced Science* **6** (20), 1900579 pp. 1-9 (2019).

5. B. K. Barman, D. Hernández-Pinilla *et al.*, *ACS Sustainable Chemistry and Engineering* **11**, 12291-12303(2023).

Exfoliation of Millimeter-Sized Flakes of 2D Transition Metal Dichalcogenides on Arbitrary Substrates

E. Peci[1*], R. Galafassi[2,3], V. Venturino[1], E. Spotorno[1], F. Telesio[1], M. Magnozzi[1], M. Canepa[1], F. Bisio[2]

[1]Dipartimento di Fisica, Università degli Studi di Genova, via Dodecaneso 33, 16146 Genova, Italy
[2]CNR-SPIN, corso Perrone 24, Genova, Italy
[3]RAISE Ecosystem, Genova, Italy
[*]Corresponding author: ermes.peci@edu.unige.it

Abstract: gold-assisted exfoliation techniques yield large-area monolayers of 2D materials on gold films, but transferring them to final substrates remains challenging. This innovative approach enables the effortless exfoliation of millimeter-sized 2D materials onto arbitrary substrates, providing an efficient and refined solution for large-area transition metal dichalcogenide exfoliation.

Semiconducting transition metal dichalcogenides (TMDCs), such as MoS_2 and WS_2, have emerged as promising candidates for next-generation optoelectronic devices, owing to their remarkable electronic and optical properties. They exhibit room-temperature excitonic effects and, when thinned down to a three-atom-thick monolayer, exhibit direct-gap semiconducting band structure, making them an excellent playground for exploiting light-matter interaction at the nanoscale.

Many methods have been developed to fabricate monolayer flakes of TMDCs. Scotch-tape exfoliation from bulk crystals yields high-quality monolayers flakes, but their lateral size rarely exceeds few micrometers. Chemical vapor deposition techniques can yield large-area flakes, but they often suffer from homogeneity issues, and it is difficult to reproduce the same recipe on different deposition furnaces.

Recently, gold-assisted exfoliation has emerged as a reliable technique for peeling off large-area TMDC monolayers from bulk crystals. Indeed, the strong affinity between gold and chalcogens overcomes the van der Waals interlayer attraction, thus peeling off the outermost layer from the bulk TMDC. However, the use of a conducting substrate like gold often limits the subsequent application of the 2D semiconductor. Therefore, several strategies have been developed so far to eventually transfer the gold-exfoliated monolayer to another substrate [1]. These methods, however, require lengthy and complex procedures, involving multiple chemical treatments and strict substrate compatibility constraints.

Our work represents a significant improvement of the technique proposed by Liu et al. [2] and refined by Petrini et al. [3]. We adopt from these works the use of thermal release tape to pick up the gold film and bring it into contact with the bulk crystal. We simplify the process and extend its applicability, enabling both exfoliation and deterministic transfer of large-area monolayer TMDCs onto virtually any substrate. The key innovation in our method is the introduction of a sacrificial, mechanically constraining layer during the critical tape-release step. This enhancement enables controlled exfoliation, yielding high-quality flakes with minimal defects and large lateral dimensions, while requiring limited experimental effort and using common consumables.

In our work, we show the applicability of our novel exfoliation method to the production of millimeter-size MoS_2 monolayers on SiO_2/Si, fused silica, and PDMS substrates. We assess sample quality and morphology using XPS, Raman, and photoluminescence spectroscopy, and imaging spectroscopic ellipsometry. Figure 1 shows the thickness maps obtained by means of imaging spectroscopic ellipsometry, displaying large-area

monolayer flakes on various substrates. Finally, using samples produced on PDMS substrates, we demonstrate the possibility of systematically transferring the produced samples onto a desired target with micrometer control of the sample positioning. The deterministic transfer process allows us to achieve large-area even on fragile substrates, such as silicon nitride membranes for transmission electron microscopy.

This optimized gold-assisted method provides a simple and reproducible pathway to produce large-area 2D TMDs, opening new possibilities for their integration into advanced nanoelectronic and photonic systems.

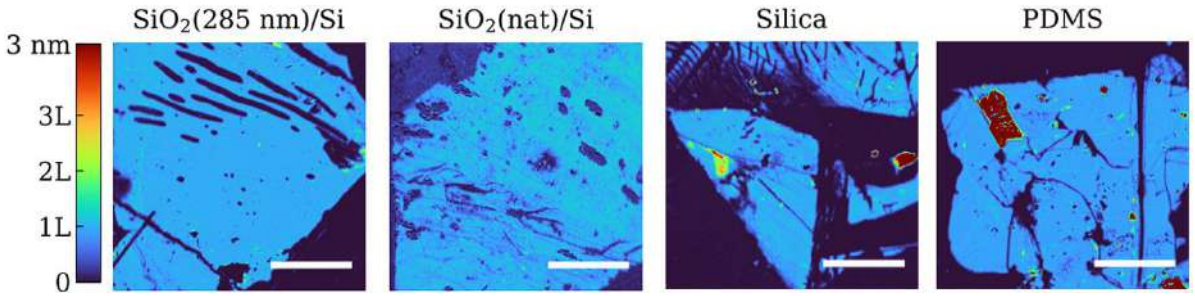


Figure 1. Thickness mapping by means of imaging spectroscopic ellipsometry of the exfoliated samples on various substrates. Large-area monolayer (1L) MoS_2 covers most of the image area. Scale bar: 300 μm.

We acknowledge support from Ministero dell'Istruzione, dell'Università e della Ricerca, Dipartimenti di Eccellenza 2018-2022, PRIN 2017 no. 2017KFY7XF, the National Recovery and Resilience Plan (NRRP), Mission 4, Component 2, Investment 1.1, Call for tender no. 104 PRIN 2022 published on 2.2.2022 by the Italian Ministry of University and Research (MUR), funded by the European Union – NextGenerationEU – Project Title ERACLITO – CUP B53D2300904006, Robotics and AI for Socio-economic Empowerment (RAISE), Piano Nazionale di Ripresa e Resilienza (PNRR).

References

1. Panasci, S. E., Schilirò, E., Roccaforte, F., and Giannazzo, F., "Gold-Assisted Exfoliation of Large-Area Monolayer Transition Metal Dichalcogenides: From Interface Properties to Device Applications". *Adv. Fuct. Mater.*, Vol. 35, No.5, 2414532, 2025.
2. Liu, F., Wu, W., Bai, Y., Chae, S. H., Li, Q., Wang, J., Hone, J, and Zhu, X. Y., "Disassembling 2D van der Waals crystals into macroscopic monolayers and reassembling into artificial lattices". *Science*, Vol. 367, No. 6480, 903-906, 2020.
3. Petrini, N., Peci, E., Curreli, N., Spotorno, E., Kazemi Tofighi, N., Magnozzi, M., Scotognella F., Bisio F., and Kriegel, I., "Optimizing Gold-Assisted Exfoliation of Layered Transition Metal Dichalcogenides with (3-Aminopropyl)triethoxysilane (APTES): A Promising Approach for Large-Area Monolayers". *Adv. Opt. Mater.*, Vol. 12, No. 7, 2303228, 2024.

Design of Broadband Multilayer Metamaterials Based on Genetic Algorithm and Neural Network

Kotaro Kajikawa
Institute of Science Tokyo, Japan
Corresponding author: kajikawa@ee.e.titech.ac.jp

Abstract: I report on the design of broadband multilayer metamaterials based on genetic algorithms (GA) or a combination of GA and neural networks (NN). With many unknown parameters, preparing a dataset for NN is impossible within a realistic time scale. Thus, GA is a good choice for the design.

It is essential to design metamaterials with the desired functions. Using machine learning, it is possible to find such structures. Machine learning is relatively accurate and fast when we use it for metamaterial design. Our research group has conducted structure searches using genetic algorithms (GA) and optical response calculations using neural networks (NN) [1]. Once a dataset is constructed, fast calculations using NN are possible, and inverse design becomes possible by combining it with methods for solving linear programming problems, such as the simplex method. On the other hand, it has been found that combining GA and NN makes it possible to perform fast GA calculations.

In my talk, I will discuss the design of broadband multilayer metamaterials. These metamaterials include optical cloaking, millimeter-wave absorbers, and sky radiators. We have found a cloaking structure covering the visible light region [2]. Most cloaking reported so far has operated in relatively narrow bands, but we have achieved this by appropriately designing a multilayer structure with around 30 layers. Similar broadband metamaterials also proved effective in the design of millimeter-wave absorbers, and we designed a thin (less than 0.5 mm-thick) with a simple metamaterial structure that covers the entire W-band (75-110 GHz) [3]. These methods can also be applied to the design of radiative cooling materials, and we designed highly efficient multilayer metamaterials.

This work was partly supported by JST CREST (MJCR22B4).

References

1. Akashi, N., Toma, M., and Kajikawa, K. "Design by neural network of concentric multilayered cylindrical metamaterials," *Appl. Phys. Express*, Vol. 13, pp. 042003, 2020.

2. Momose, M. Toma, M., and Kajikawa, K., "Ultrabroadband invisibility cloaking design of a concentric multilayered cylindrical metamaterial," *J. Opt. Soc. Am. B*, Vol. 41, No. 8, pp. 1815–1820, 2024.

3. Momose, M., Kondo, H., Haemori, M., and Kajikawa, K., "Design of thin multilayer absorbers of graphite/polymer composites for W-band millimeter waves," *Jpn. J. Appl. Phys.*, Vol. 64, 022003, 2025.

Surface Acoustic Wave Stimulated Brillouin Scattering

Moritz Merklein

The University of Sydney, Australia

Abstract: Stimulated Brillouin scattering (SBS) is a third-order nonlinear optical effect that describes the coherent coupling between acoustic and optical modes. SBS has a linewidth in the Megahertz to tens of Megahertz, is optically induced and frequency tunable, and hence ideal for optical signal processing applications such as filter, phase-shifter and delay schemes. Furthermore, the ability to generate strong SBS in integrated photonic circuits opens a pathway toward all-optical signal processing in a small footprint. Inducing SBS on a photonic chip comes with its own challenges, however, as the integrated waveguides need to guide optical and acoustic modes simultaneously to enable strong interaction. In this talk, I will introduce a new type of on-chip SBS interaction that harnesses surface acoustic waves (SAWs). Those acoustic waves are travelling along the surface of the waveguide rather than in the waveguide core. Surface acoustic wave stimulated Brillouin scattering (SAW-SBS) opens a path toward exploring new material platforms and applications arising from the exposure of the SAWs to the surroundings of the waveguide.

Permittivity-driven ultrafast photonic bound states in the continuum

A. Tittl[1]

[1]Nanoinstitute Munich, Faculty of Physics, Ludwig-Maximilians-Universität München, 80539 Munich, Germany
*corresponding author: Andreas.Tittl@physik.uni-muenchen.de

Abstract: Permittivity-driven bound states in the continuum enable all-dielectric metasurfaces that overcome geometrical symmetry-breaking limits. Recent demonstrations reveal high-Q resonances with exceptional spectral control, dynamic tunability with electro-optical polymers, and all-optical generation via ultrafast pulses, enabling promising applications in adaptive photonics and high-speed modulators.

All-dielectric metasurfaces supporting photonic bound states in the continuum (BICs) have emerged as a transformative platform for manipulating light-matter interactions at the nanoscale. They are able to confine light with exceptionally high quality (Q) factors and significant near-field enhancements, enabling a diverse array of applications, including ultrasensitive biospectroscopy, catalytic detection, enhanced photon emission, and strong polaritonic coupling, all of which benefit from the precise control over resonance properties that BICs provide. Traditionally, BIC-driven metasurfaces have achieved tailored resonance characteristics by breaking the geometrical symmetry of their unit cells, transitioning symmetry-protected BICs into quasi-BIC (qBIC) modes that couple to the far field. While effective, this method is constrained by challenges such as the precision required in nanofabrication, the smallest achievable asymmetry limited by atomic scales, and the inherent difficulties in achieving dynamic tunability post-fabrication.

Here, I will present our recent advancements in realizing permittivity-asymmetric BICs (ε-qBICs), an innovative approach that introduces permittivity variations within geometrically symmetric unit cells. This strategy overcomes the limitations of geometrical symmetry breaking, offering enhanced flexibility and new degrees of freedom for resonance control and nanoscale light manipulation. I will begin with the fundamentals of ε-qBICs, establishing that symmetry-protected qBICs can be induced by breaking the in-plane permittivity symmetry of a metasurface's unit cell, rather than its geometry [1]. Using theoretical analysis and eigenmode expansion, we derive a Fano-shaped transmittance formula, revealing that ε-qBICs emerge when permittivity asymmetry disrupts the conditions sustaining a true BIC. A key finding is the inverse-square dependence of the radiative Q-factor on the permittivity asymmetry parameter ($\Delta\varepsilon/\varepsilon$), validated through numerical simulations of a metasurface with paired resonators of differing permittivities. These findings highlight the complete equivalence of ε-qBICs to geometrically asymmetric qBICs in their optical response, near-field distributions, and Q-factor tunability. Importantly, permittivity modulations (which can be achieved, e.g., through minute refractive index changes via carrier doping or electro-optical effects) can access asymmetry regimes beyond the reach of geometrical fabrication limits, where angstrom-level accuracy would be needed to reach asymmetries below 10^{-4}. ε-qBICs in the near-infrared were demonstrated using a multi-material metasurface, where the unit cell consists of geometrically identical resonators with a give permittivity contrast between Si and TiO_2.

Building on static ε-qBICs, I will present their dynamic tunability using an electro-optically active polymer [2]. This study introduces environmental symmetry breaking by embedding identical TiO_2 nanorods in contrasting refractive index media: one in PMMA ($n \approx 1.5$) and the other in air or polyaniline (PANI). The integration of PANI, grown in-situ via electrochemical polymerization, enables electrically reconfigurable ε-qBICs. By applying voltages from -0.2 V to +0.6 V, the refractive index of PANI can be precisely tuned,

modulating the asymmetry parameter (Δn) and thus the resonance properties. Experimental results show a pronounced ON/OFF switching capability in transmittance spectra, as well as rapid switching speeds (rise time 12.2 ms, fall time 18 ms) and exceptional durability over 1000 cycles, attributed to PANI's stable electron redistribution properties. This approach enhances the metasurface's responsiveness to environmental perturbations, offering millisecond-timescale control over resonance position and linewidth, applicable to adaptive optical devices.

Subsequently, I will showcase the all-optical generation of ε-qBICs using ultrashort laser pulses [3]. We demonstrate the creation of transient ε-qBICs in an unstructured 45 nm amorphous silicon (a-Si) thin film by interfering two 180 fs laser pulses at an angle, creating a periodic permittivity modulation via carrier excitation in the bright fringes. Pump-probe experiments revealed a Fano-shaped resonance with >30% transmittance modulation, tunable across the near-infrared by varying the pump wavelength and interference angle. Resonances with high Q factors up to 80 and decay times in the ps range could be generated, and additional control over the resonance properties could be obtained via the pump power. Furthermore, we show that all-optical ε-qBICs can carry out photonic functionalities by demonstrating a >200% enhancement of third-harmonic generation (THG) at around 345 nm when the fundamental beam at 1020 nm aligns the ε-qBIC resonance wavelength. This lithography-free method provides spectral, linewidth, and temporal control, extending to ultrafast near-field enhancement applications.

Finally, I will present our latest research on the realization of temporal symmetry-breaking in BIC-driven metasurfaces via ultrafast optical pumping [4]. We introduce the new concept restored of symmetry-protected bound states in the continuum, which arise in metasurfaces with *geometrically asymmetric* unit cells, where the total dipole moment (composed of two antisymmetric dipoles) is precisely engineered to cancel out, effectively restoring photonic symmetry despite the structural asymmetry. Mie-resonant optical absorption within specific regions of the unit cell locally modifies the refractive index, disrupting the balance between the two dipole moments, which provides ultrafast control over the radiative loss channel of the metasurface and allows precise adjustment of the resonance linewidth, near-field enhancement, and resonance amplitude. We experimentally demonstrated resonance broadening (ΔQ = 100, a change of 25%), resonance sharpening (ΔQ = 150, a change of 150%), and resonance creation and annihilation on 300 fs timescales. These advancements significantly enhance the dynamic tunability of ε-qBICs and pave the way for transformative applications, such as high-speed optical modulators, ultrafast optical switches, and next-generation devices for optical computing and communication.

Overall, ε-qBICs provide a promising new paradigm for the design and functionality of all-dielectric metasurfaces and unlock new possibilities for static and dynamic light manipulation, with profound implications for next-generation photonic technologies.

References

1. R. Berté, T. Weber, L. S. Menezes, L. Kühner, A. Aigner, M. Barkey, F. J. Wendisch, Y. Kivshar, A. Tittl, S. A. Maier, "Permittivity-Asymmetric Quasi-Bound States in the Continuum", Nano Lett. 23, 2651-2658 (2023).
2. H. Hu, W. Lu, R. Berté, S. A. Maier, A. Tittl, "Environmental permittivity-asymmetric BIC metasurfaces with electrical reconfigurability", Nat. Commun. 15, 7050 (2024).
3. R. Berté, T. Possmayer, A. Tittl, L. S. Menezes, S. A. Maier, "Emergent resonances in a thin film tailored by optically-induced small permittivity asymmetries", arXiv:2403.05730 (2024).
4. A. Aigner, T. Possmayer, T. Weber, L. S. Menezes, S. A. Maier, A. Tittl, "Temporally symmetry-broken metasurfaces for ultrafast resonance creation and annihilation", arXiv:2501.12879 (2025).

Enhanced Sensing with Ultrastrong Coupling Condition

Wen-Hui (Sophia) Cheng[1,*], Alexis Angelo R. Garcia[1], Cheng-An Mao[1]
[1] National Cheng Kung University, Taiwan
[*]corresponding author: wcheng@gs.ncku.edu.tw

Abstract: Raman spectroscopy can detect molecules through their vibrational modes, and its efficiency is enhanced by localized electric field. The proposed ANA heterostructure, combining gold nanoparticles and nickel oxide, achieves ultrastrong coupling and significantly improves Raman sensing, demonstrating over 20-fold enhancement for tetracycline detection.

Raman spectroscopy has been effectively employed to detect molecules based on their specific vibrational modes. However, the efficiency of this process is often limited and significantly influenced by the local electric field. In confined metallic nanostructures, oscillations in the electric field can induce localized surface plasmon resonances (LSPR), which can substantially enhance the electric field. This enhancement results in a stronger Raman signal, a phenomenon known as surface-enhanced Raman scattering (SERS). To further improve light-matter interactions, we aim to achieve electromagnetic coupling between the LSPR in metals and the cavity modes in dielectric materials. We propose a heterostructure consisting of gold nanoparticles (Au-NPs), p-type nickel oxide (p-NiO), and an Au film—collectively referred to as the ANA structure. This design intends to establish strong coupling effects to enhance Raman sensing capabilities. We have designed and simulated this structure to optimize its optical benefits. The heterostructure has been experimentally realized through air-liquid interface self-assembly, successfully achieving the conditions for ultrastrong coupling with a Rabi splitting energy surpassing 650 meV. The emonstration of tetracycline molecules sensing using the ANA structure showed more than 20-fold improvement compared to the bare substrate. These findings underscore the promising potential of plasmonic hybrid platforms, which can be further refined for enhanced sensing applications.

References

1. Garcia, A. A. R., Mao, C.-A. Cheng and W.-H. “Realization of ultrastrong coupling between LSPR and Fabry–Pérot mode via self-assembly of Au-NPs on p-NiO/Au film,” Nanophotonics, Vol. 13, No. 14, 2501–2512, 2024.

Self-illuminated Plasmonic Biosensor Enabled by Inelastic Tunneling Luminescence

J. Lee[1, †], Y. Wu[2, †], I. Sinev[1, †], M. Masharin[1], S. Papadopoulos[3], E. J. C. Dias[2], L. Wang[3], M. L. Tseng[4], S. Moon[5,6], J.-S. Yeo[5,6], L. Novotny[3], F. J. García de Abajo[2,7], and H. Altug[1*].

[1] Institute of Bioengineering, École Polytechnique Fédérale de Lausanne (EPFL), Switzerland

[2] ICFO-Institut de Ciencies Fotoniques, The Barcelona Institute of Science and Technology, Spain

[3] Photonics Laboratory, ETH Zürich, Switzerland

[4] Institute of Electronics, National Yang Ming Chiao Tung University, Taiwan

[5] School of Integrated Technology, Yonsei University, Republic of Korea

[6] BK21 Graduate Program in Intelligent Semiconductor Technology, Yonsei University, Republic of Korea

[7] ICREA-Institució Catalana de Recerca i Estudis Avançats, Spain

† Contributed equally

[*]corresponding author: hatice.altug@epfl.ch

Abstract: We present a self-illuminating plasmonic biosensor using quantum tunneling-driven light emission for label-free biomolecule detection. Integrating a plasmonic metasurface with a metal-insulator-metal tunnel junction removes the need for an external light source. Experiments confirm detection of nanoscale organic and biological coatings via refractive index changes, advancing compact biosensing platforms.

Introduction. Plasmonic nanostructures have gained substantial attention in optical sensing due to their ability to generate strong optical field enhancements and confine light at the subwavelength scale [1]. These properties have led to the development of biosensors with significantly improved detection capabilities compared to conventional optical sensors [2]. Traditional surface plasmon resonance (SPR) sensors rely on external light sources, requiring bulky optical components that limit their portability and ease of integration into miniaturized platforms.

To address these limitations, we propose a self-illuminating plasmonic biosensor that eliminates the need for external light sources. Our device utilizes a metal-insulator-metal (MIM) tunnel junction integrated with a plasmonic metasurface, enabling intrinsic light generation through inelastic electron tunneling [3-6]. The emitted light is coupled to plasmonic modes, resulting in enhanced sensitivity for biosensing applications.

Results. The plasmonic metasurface layer acts as a transducer, outcoupling plasmons excited by inelastic electron tunneling to far-field light emission. In addition to supporting optical plasmonic resonances, the conductive metasurface serves as electrical contact layer for charge transport. We optimized the sensor design and fabrication process to provide uniform emission over a large area under an applied voltage of 2.4 V, producing a total collected optical power of 40 pW, making it feasible for practical sensing applications. Angle-resolved spectroscopy revealed the presence of plasmonic lattice modes that strongly influence electroluminescence emission spectra. These modes convert plasmon-polaritons, excited through inelastic

electron tunneling, into photons at specific wavelengths and angles, dictated by their dispersion characteristics. Notably, the electric fields of these lattice modes are highly localized at the tops of the gold resonators, providing optical sensing capabilities. To evaluate the biosensing capability, we tested with several analytes including thin polymer layer and biofilms and showed its performance is already comparable to state-of-the-art passive nanoplasmonic biosensors.

Conclusion. By leveraging quantum tunneling and plasmonic nanoantennas, our sensor provides a compact and efficient platform for biochemical detection. This approach enables label-free biosensing with high spatial resolution, offering significant potential for integration into next-generation diagnostic devices. The demonstrated high sensitivity and stability make it a promising candidate for real-world applications in medical diagnostics and environmental monitoring.

References

1. Maier, Stefan A. Plasmonics: Fundamentals and Applications. Springer US, 2007,
2. Altug, H.; Oh, S.-H.; Maier, S. A.; Homola, J. Advances and applications of nanophotonic biosensors. Nat. Nanotechnol. 17, 5–16, 2022.
3. Lambe, J.; McCarthy, S. L. Light Emission from Inelastic Electron Tunneling. Phys. Rev. Lett. 37, 923–925, 1976
4. Parzefall, M.; Bharadwaj, P.; Jain, A.; Taniguchi, T.; Watanabe, K.; Novotny, L. Antenna-coupled photon emission from hexagonal boron nitride tunnel junctions. Nat. Nanotechnol. 10, 1058–1063, 2015.
5. Namgung, S.; Mohr, D. A.; Yoo, D.; Bharadwaj, P.; Koester, S. J.; Oh, S.-H. Ultrasmall plasmonic single nanoparticle light source driven by a graphene tunnel junction. ACS nano, 12, 2780–2788, 2018.
6. Zhang, C.; Hugonin, J.-P.; Coutrot, A.-L.; Sauvan, C.; Marquier, F.; Greffet, J.-J. Antenna surface plasmon emission by inelastic tunneling. Nat. Commun. 10, 1–7, 2019.

Characteristics of optical chiral fields around nanostructures revealed by scanning near-field optical microscopy

Kohei Imura[1*]
[1]Department of Chemistry and Biochemistry, School of Advanced Science and Engineering, Waseda University, Japan
[*]corresponding author: imura@waseda.jp

Abstract: Optical chiral density is amplified near the gold and dielectric nanostructures. We investigate the optical chiral field near the nanostructure by using apertured near-field optical microscope and reveal that the unique spatial characteristics of the optical chiral field are induced depending on the elementary mode excited.

Nanomaterials exhibits unique optical properties due to light confinement capability. Optical fields are enhanced in the vicinity of the nanomaterials. For metal and dielectric nanoparticles, plasmons and Mie resonances are excited, respectively, and optical field is confined near the particle. These resonances provide strong light-matter interaction. Recently, localized near-fields induced in these materials are utilized for enhancement of chiral responses. Chiral signal of molecules is detected by the difference in absorbance between left- and right-circularly polarized light and is in general very small compared to the absorption signal. This originates partly from the fact that the spatial scale of the molecules is much smaller than that of the light. Spatial scale of the near-field in the nanomaterials becomes comparable to that of light, and therefore scale mismatch between the material and light is compensated. Since the optical near-field is enhanced in these materials, the plasmon and Mie resonances are promising for enhancing the optical chiral responses.

In order to amplify the chiral responses, understanding of the near-field is essential. Spatial scale of the localized field is smaller than the diffraction of light, nanoimaging techniques are indispensable for visualization. Near-field imaging technique overcome the diffraction limit and utilize for this purpose. We have been developing various near-field imaging techniques to visualize plasmon modes and plasmonic optical fields in gold nanoparticles.[1] For instance, by combining the aperture near-field apparatus with phase stepping method, near-field reflection spectroscopy is demonstrated.[2] This imaging technique is applicable to transparent sample as well as opaque one. By analyzing the transmission and reflection signals, absorption and scattering properties are able to be obtained at the same time.[3] These properties are crucial for deeper understanding control of the optical properties.[4,5] We also developed three-dimensional near-field imaging technique to visualize spatial extension of the near-field signal and revealed that the light confinement capability depends on the plasmon mode excited.[6,7] In this study, we have investigated the optical chirality near gold and Si nanostructures by using the three-dimensional near-field imaging. We also performed electromagnetic field simulation to reveal the physical origin of the observed near-field properties.

Gold nanoparticles were synthesized chemically. Si nanoparticles were prepared by laser ablation of the Si substrate. The particles were dispersed onto glass substrate for near-field imaging. Aperture near-field optical microscope is used for locally illuminating sample, and transmitted light was detected. For three-dimensional imaging, distance between the near-field probe tip to sample surface was regulated from 10 to several hundred nm. For chiral optical imaging, incident light is adjusted to be linearly polarized at the aperture of the near-field probe, and circularly polarized components in the transmission light are detected by using a quarter waveplate and a polarizer.

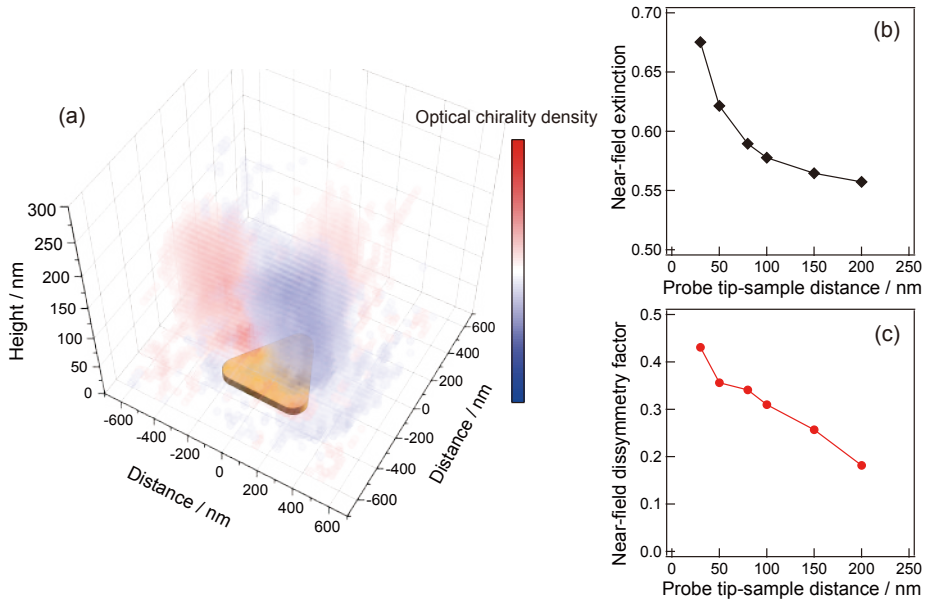


Figure 1. (a) Reconstructed three-dimensional chiral optical fields near the gold nanoplate. (b,c) Near-field probe tip-sample distance dependence of the near-field extinction and dissymmetry factor, respectively.

Figure 1(a) shows the three-dimensional chiral optical field near single gold nanoplate.[8] We found that the sign of the chiral signals varies at the left and right side of the plate. We also examine steric extension of the near-field extinction signal in Fig. 1(b) and the chiral signal in Fig. 1(c) and found that the spatial extension of the near-field extinction decays faster than that of the chiral signal. To revel the physical origin of the difference, we performed electromagnetic field calculation of the chiral field by assuming the reciprocity of light propagation. Simulated distance dependencies of the near-field signal are well reproduced. We also examine spatial distributions of the electric and magnetic field. Near-field extinction is well correlated to the local electric field, while the chiral field is correlated to both the magnetic and electric field. We reveal from these simulations that the difference originates from the calm distribution of the magnetic field compared to those of the electric field. We have studied the near-field properties of the Si nanoparticle and found unique near-field characteristics. We will discuss the details at the conference.

The author is grateful to the collaborators who contributed to this study, in particular, Dr. S. Hasegawa, Dr. K. Imaeda, Dr. H. Mizobata, and Mr. Matsuura. This work was supported in part by JSPS KAKENHI (grant nos. 22K19013, 23H04604, 23H01927) from the Japan Society for the Promotion of Science.

References

1. Imaeda, K., Hasegawa, S., K. Imura, K. *J. Phys. Chem. Lett.* 9, 4075 (2018).
2. Mizobata, H., Hasegawa, S., Imura, K. *J. Phys. Chem. C 121,* 11733 (2017).
3. Mizobata, H., Hasegawa, S., Tamura, M., Iida, T., Imura, K. *J. Chem. Phys.* 153, 144703 (2020).
4. Imaeda, K., Hasegawa, S., Imura, K. *J. Chem. Phys.* 156, 044702 (2022).
5. Hasegawa, S., Ichikawa, H., Imura, K. *J. Phys. Chem. C*. 128, 2536 (2024).
6. Matsuura, T., Imaeda, K., Hasegawa, S., Suzuki, H., Imura, K. *J. Phys. Chem. Lett.* 10, 819 (2019).
7. Suzuki, H., Imaeda, K., Mizobata, H., Imura, K. *J. Chem. Phys*. 152, 014708 (2020).
8. Hasegawa, S., Imura, K. *Nano Lett.* 25, 376-382 (2025).

Hybrid photoresists in multi-photon lithography: optical properties and post-processing strategies

D. Ladika[1], M. Stavrou[2], G. Zyla[1], A. Harnik[1], F. Dumur[5], M. Vengris[1], M. Kafesaki[2], D. Gray[2], S. Juodkazis[1,3,4], M. Malinauskas[1] and M. Farsari[2]

[1]Laser Research Center, Physics Faculty, Vilnius University, Vilnius, LT-10223 Lithuania

[2] Institute of Electronic Structure and Laser, Foundation for Research and Technology-Hellas, Heraklion, Crete, Greece

[3] Optical Sciences Centre and ARC Training Centre in Surface Engineering for Advanced Materials (SEAM), School of Science, Swinburne University of Technology, Melbourne, Australia

[4] WRH Program International Research Frontiers Initiative (IRFI) Tokyo Institute of Technology, Nagatsuta-cho, Midori-ku, Yokohama, Japan

[5] UMR 7273, Aix Marseille Univ., CNRS, ICR, 13397 Marseille, France

[*]Corresponding author: dimitra.ladika@ff.vu.lt

Abstract: Multi-photon lithography (MPL) enables high-resolution 3D structuring using hybrid photoresists. The presence or absence of photoinitiators affects fabrication and application. Post-processing techniques, including selective coatings and heat treatments, enhance functionality without altering the material's chemistry. This work explores material characterization and post-processing strategies for advancing MPL.

The interaction between light and matter has driven significant advancements in manufacturing, particularly through femtosecond laser-based techniques [3]. Among these, MPL has emerged as a powerful tool for fabricating intricate 3D micro- and nanostructures with sub-micron resolution. MPL relies on multi-photon absorption (MPA), where two or more photons are simultaneously absorbed to induce polymerization or chemical transformations in a photoresist. The success of this process depends on the careful design of materials that exhibit high optical sensitivity, efficient cross-linking mechanisms, and precise control over photopolymerization [2].

Hybrid photoresists, consisting of both organic and inorganic components, are widely used in MPL due to their low shrinkage when processed with ultrafast laser radiation. However, their potential extends far beyond this advantage. The presence or absence of a photoinitiator (PI) in the photoresist—a molecule that generates reactive species upon photon absorption—significantly influences fabrication thresholds, resolution, processing speed, and the ultimate functionality of the 3D-printed structures [5]. While conventional PIs enhance polymerization efficiency, they often introduce challenges such as high fluorescence, and coloration, limiting their use in biomedicine and micro-optics. On the other hand, these properties can be beneficial for applications such as fluorescent microscopy and bio-imaging. Understanding the linear and nonlinear optical properties of hybrid materials and PIs is therefore essential for optimizing their performance [6]. These insights can guide the selection of appropriate MPL wavelengths beyond the conventional ~800 nm, potentially improving excitation efficiency through higher two-photon cross-sections.

Furthermore, the inclusion or exclusion of a PI alters the chemical composition of the hybrid photoresist, introducing constraints during both the MPL process and the final 3D printed object. To address such limitations, post-processing techniques have expanded the versatility of MPL, enabling functionalization of fabricated structures. For instance, selective coatings have unlocked new applications in optics, biosensing, and photonic

devices. Additionally, integrating MPL with metamaterials offers exciting opportunities for nanophotonics, sensing, and tunable optical components [4].

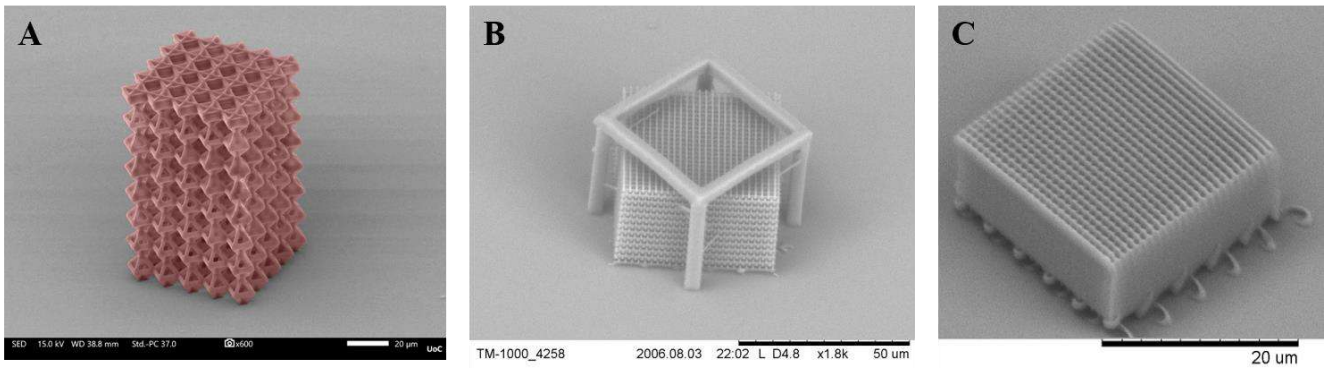


Figure 1 3D microstructures fabricated via MPL with **A.** a new-lab-made low-fluorescent PI, with red intrinsic coloration, onto the hybrid SZ2080^{TM}, **B.** hybrid SZ2080^{TM} dopped with Ytterbium and calcinated in 1200^{o} and **C.** hybrid SZ2080^{TM} without PI using 1035nm laser source

Emerging post-processing methods, such as heat treatments, further extend MPL's capabilities [1]. Calcination—a process that removes the organic fraction of a structure—and pyrolysis—the heating of organic material in the absence of oxygen—enable the fabrication of purely inorganic materials at micro- and nano-scales. These techniques provide a means to enhance the functionality of MPL-fabricated structures without chemically altering the hybrid photoresist itself.

This work highlights the versatility and suitability of hybrid photoresists in MPL, emphasizing the importance of material characterization in optimizing process parameters for diverse applications. Additionally, it explores post-processing pathways that enable functionalization of 3D-printed structures while preserving the fundamental properties of the hybrid photoresist.

References

1. Balčas, G., Malinauskas, M., Farsari, M. and Juodkazis, S., "Fabrication of Glass-Ceramic 3D Micro-Optics by Combining Laser Lithography and Calcination". Adv. Funct. Mater. **33**, 2215230, 2023
2. G. Zyla, M. Farsari, "Frontiers of Laser-Based 3D Printing: A Perspective on Multi-Photon Lithography". Laser Photonics Rev 2024, 18, 2301312, 2024
3. H. Wang, W. Zhang, D. Ladika, H. Yu, et.al., "Two-Photon Polymerization Lithography for Optics and Photonics: Fundamentals, Materials, Technologies, and Applications". Adv. Funct. Mater., **33**, 2214211, 2023
4. G. Zyla, S. Papamakarios, D. C. Zografopoulos, A. Christoforidou, et.al., "Film-Based Multi-Photon Lithography for Efficient Printing of Electromagnetic Surface Structures". Adv. Mater. Technol., 2402137, 2025
5. D. Ladika, A. Butkus, V. Melissinaki, E. Skliutas, et.al., "X-photon 3D lithography by fs-oscillators: wavelength-independent and photoinitiator-free". Light: Advanced Manufacturing **5**, 48, 2024
6. M. Stavrou, G. Zyla, D. Ladika, F. Dumur, M. Farsari, and D. Gray, "Push–Pull Carbazole-Based Dyes: Synthesis, Strong Ultrafast Nonlinear Optical Response, and Effective Photoinitiation for Multiphoton Lithography", ACS Applied Optical Materials 2 (8), 1653-1666, 2024

Exploring Channelrhodopsin-2 and Gold Nanoparticle Interaction for Optogenetics

R. Messina[1,2], L. Bellucci[3], S. Corni[4,5], L. Cascino[1,2], S. D'Agostino[*,1,2,6], and L. Zanetti-Polzi[*,5]

[1]Mathematics and Physics Department "E. De Giorgi", University of Salento, Lecce, 73100, Italy
[2]Institute of Nanotechnology, National Research Council (CNR-NANOTEC), Lecce, 73100, Italy
[3]NEST-SNS, CNR Institute of Nanoscience, Piazza San Silvestro 12, Pisa, 5612, Italy
[4] Department of Chemical Sciences, University of Padova, via Marzolo 1, Padova, 35100, Italy
[5] Center S3, CNR-Institute of Nanoscience, Via Campi 213/A, Modena, 41125, Italy
[6] Center for Biomolecular Nanotechnologies, Istituto Italiano di Tecnologia (IIT), Arnesano, Lecce, 73100, Italy
[*]Corresponding author: stefania.dagostino@nanotec.cnr.it

Abstract: A molecular dynamics study revealed that functionalized gold nanoparticles are able to form stable complexes with Channelrhodopsin-2, without disturbing the protein structure and dynamics. The results pave the way for exploiting the polaritonic properties of nanoparticles to tune the photoactivity of light-gated ion channels in a controlled way.

Optogenetics, using light-sensitive proteins like Channelrhodopsin-2 (ChR2), is a powerful tool for manipulating neural activity [1]. ChR2's function relies on light-induced retinal isomerization, triggering ion channel opening [2]. Metal nanoparticles (MNPs), particularly gold nanoparticles, have been explored in optogenetics to enhance light penetration, to increase specificity, and to improve photothermal effects [3]. Interestingly, MNPs also have the potential to influence the photochemistry of photo-reactive systems like ChR2 through polaritonic effects, where strong coupling between molecular electronic excitations and localized surface plasmons on the MNPs creates polaritonic potential energy surfaces [4]. This work uses molecular dynamics (MD) simulations to investigate the interaction between ChR2 and a small hydrophobic-coated Au25 nanoparticle (NP) as a first step towards identifying configurations suitable for strong coupling and future quantum mechanical investigations of the NP-ChR2 system's response to electromagnetic excitation. The goal is to develop plasmon-mediated optogenetic tools with enhanced capabilities through the exploitation of computation-based polaritonic chemistry [5]. In this study, MD simulations are performed to investigate the dark state of a ChR2 dimer (with all-trans retinal), both alone and interacting with a hydrophobic thiol-protected gold NP.

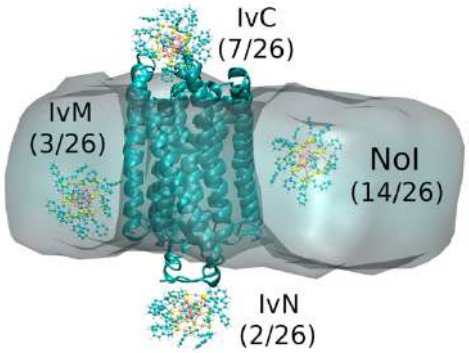


Figure 1. Representation of NP-ChR2 interaction sites: IvC, interacting via C-terminal; IvN, interacting via N-terminal; IvM, interacting via membrane; NoI, non-interacting. The numbers in parentheses indicate the fraction of MDs exhibiting the specific interaction.

By varying the initial relative positions of the protein and the NP, the spontaneous formation of a stable NP-ChR2 complex is observed at different protein sites in about 50% of the simulations (Fig. 1).
Importantly, the interaction with the NP does not significantly perturb the protein: the analyses performed indicate that the structural stability, the conformational dynamics, the content of water in the protein interior as well as crucial interactions inside the retinal binding cavity are not significantly affected by the presence of the nanoparticle. However, more subtle changes in the retinal binding cavity are observed, suggesting that NPs can be able to affect ChR2 photochemistry. These results open the way for the development of novel optogenetic tools that exploit direct effects such as a plasmon-mediated tuning of the photoactive protein activity.

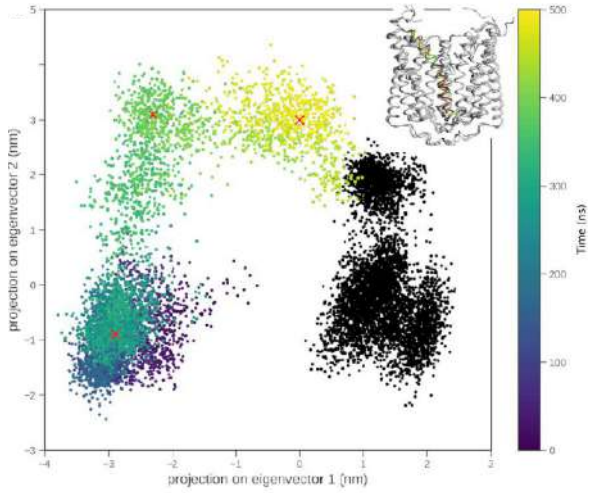


Figure 2. Projection of the trajectories without NP (black) and IvM2 (colored according to time) on the plane of the first two eigenvectors of the alfa-carbon covariance matrix. The red crosses mark densely populated regions from which representative structures are extracted.

Acknowledgements: S. D'Agostino thanks the Project PNRR I-PHOQS of CNR-NANOTEC.

References

1. Pastrana, É. "Optogenetics: controlling cell function with light", Nat. Methods, 8, 24-25, 2011.
2. Kandori, H. "Biophysics of rhodopsins and optogenetics." Biophys. Rev., Vol. 12,2, 355-361, 2020.
3. Sardoiwala, M. N., Srivastava, A. K., Karmakar, S., & Roy Choudhury, S., "Nanostructure Endows Neurotherapeutic Potential in Optogenetics: Current Development and Future Prospects", ACS Chem. Neurosci., 10(8), 3375–3385, 2019.
4. Cascino, L., Corni, S. and D'Agostino, S. "Revealing the Interplay between Hybrid and Charge-Transfer States in Polariton Chemistry", J. Phys. Chem. C, 128 (7), 2917-2927, 2024.
5. D'Agostino, S., Rinaldi, R., Cuniberti, G., and Della Sala, F., "Density Functional Tight Binding for Quantum Plasmonics", J. Phys. Chem. C, Vol. 122, 19756-19766, 2018.

Neural Network-Optimized Multifunctional Metasurfaces for Adaptive High-Frequency Wireless Communication

M. Beruete[1,2], Damián Rodríguez-Trujillo[1], Alicia E. Torres-García[1], Mikel Aldea[3], Jorge Teniente[1,2], Asier Marzo-Pérez[3]

[1]Department of Electrical, Electronic and Communications Engineering, Public University of Navarre (UPNA); Pamplona, 31006, Spain.

[3]Institute of Smart Cities (ISC), Public University of Navarre (UPNA); Pamplona, 31006 Spain

[2]Author Affiliation, Country

[3]Department of Statistics, Computer Science, and Mathematics, Public University of Navarre (UPNA); Pamplona, 31006, Spain.

[*]corresponding author: miguel.beruete@unavarra.es

Abstract: This paper introduces a novel design for passive, multifunctional metasurfaces that enable dynamic functionalities like beam steering and holographic imaging. Using neural network-driven optimization, these metasurfaces provide adaptable solutions for high-frequency wireless communication systems without the need for active components, offering a scalable, cost-effective approach for next-generation networks.

The rapid and unprecedented growth of wireless communication technologies has led to a significant increase in the number of connected devices. Projections suggest that next-generation wireless systems (6G and beyond) will achieve ultimate connectivity by integrating humans and machines, giving rise to a new “Internet of Everything” era, with an expected number of connected devices near 500 billion by 2030—far surpassing the projected world population of 8.5 billion by that time. Additionally, the increasing demand for data and higher speeds is driving the need for more bandwidth, pushing the limits of the microwave spectrum traditionally used for wireless communications. As a result, the microwave range's limited bandwidth struggles to meet both current and future demands effectively [1], [2].

To overcome these constraints, there is a shift toward higher frequencies such as millimeter-waves and terahertz, which naturally offer broader bandwidths for high-speed data transmission and are already integrated into next-generation communication systems [1], [2]. In this context, metasurfaces are emerging as a transformative solution for wireless communication devices, thanks to their ability to manipulate electromagnetic waves at subwavelength scales. This capability enables the development of compact, highly efficient, and adaptable devices that can address the challenges posed by future communication systems [3].

The integration of metasurfaces into wireless communication systems has led to the concept of Smart Walls, which are closely related to Reconfigurable Intelligent Surfaces (RIS) [4]. These Smart Walls turn passive surfaces into active components that manipulate electromagnetic waves to optimize signal propagation, enhance coverage, and improve overall system performance. By embedding intelligent metasurfaces into building walls or other structures, Smart Walls become integral to communication systems, enabling them to steer, focus, and modulate signals to meet the demands of modern wireless networks.

Current research is heavily focused on implementing RIS with dynamic responses, often relying on active components like PIN diodes, MEMs, liquid crystals, and varactors [4]. While these devices can be reconfigured in real time, they face significant challenges when operating at higher frequencies, particularly in millimeter-wave and terahertz ranges. These challenges include high insertion losses and limited availability, which hinder the practical implementation of RIS-based Smart Walls at these frequencies.

In response to these issues, we propose a novel approach that leverages non-reconfigurable metasurfaces with multifunctional capabilities. These passive metasurfaces exploit parameters such as polarization, angle of incidence, and frequency to achieve dynamic functionalities without the need for active components or complex control systems. By manipulating one or more parameters of a single illumination source, these passive metasurfaces can provide responses such as beam steering, focusing, and holographic imaging, simplifying the design and implementation of adaptable communication systems for high-frequency applications.

In this communication, we introduce a multifunctional metasurface design that can produce different outputs depending on illumination conditions. The required phase distribution for each response is calculated using a combination of established analytical methods and optimization techniques driven by neural networks. Neural networks optimize the metasurface design, enabling it to integrate multiple functionalities within a compact structure while maintaining high efficiency, low losses, and reliable performance across diverse conditions.

Ultimately, we show that by incorporating intelligence into the illumination system instead of the metasurface itself, we can create passive, adaptive smart walls with the potential to revolutionize wireless communication. This strategy provides a scalable, cost-effective solution while redefining the future of wireless infrastructure and reshaping our approach to next-generation networks.

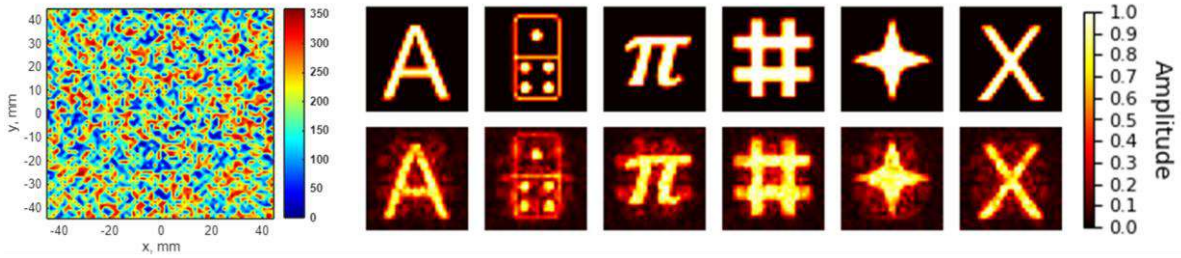


Fig. 1. (a) Phase distribution of the metasurface designed using the proposed neural network architecture. The design exhibits significant phase variability, enabling up to six distinct responses by modifying the illumination conditions. (b) Model convergence and performance after 10,000 epochs. The first row presents the original dataset, while the second row shows the predicted outcomes generated by the trained neural network, exhibiting minimal deviation and high precision.

Acknowledgements

This work has received financial support from Project No. PID2022-137845NB-C21, funded by MCIN/AEI/10.13039/501100011033 and by FEDER Una manera de hacer Europa.

References

1. "6G. Spectrum Expanding the Frontier," [Online]. Available: https://cdn.codeground.org/nsr/downloads/researchareas/2022May_6G_Spectrum.pdf.
2. "6G. The Next Hyper Connected Experience for All," [Online]. Available: https://cdn.codeground.org/nsr/downloads/researchareas/20201201_6G_Vision_web.pdf.
3. Hu, J., Bandyopadhyay, S., Liu, Y., and Shao, L., "A Review on Metasurface: From Principle to Smart Metadevices," Front. Phys., Vol. 8, p. 586087, Jan. 2021, doi: 10.3389/fphy.2020.586087.
4. Yang, F., Pitchappa, P., and Wang, N., "Terahertz Reconfigurable Intelligent Surfaces (RISs) for 6G Communication Links," Micromachines, Vol. 13, No. 2, Art. no. 2, Feb. 2022, doi: 10.3390/mi13020285.

Temporal Topological Aharonov-Bhom Phase in Quantum-Systems under Electric and Gravitational Scalar Potentials

M. E. Tobar[1*], M. T. Hatzon[1], G. R. Flower[1], M. Goryachev[1], J. F. Bourhill[1], R. Y. Chiao[2], N. A. Inan[2,3,4], M. Scheibner[2], J. Sharping[2], D. A. Singleton[3]

[1]Quantum Technologies and Dark Matter Labs, Department of Physics, University of Western Australia, Crawley, 6009, WA, Australia
[2]University of California, Merced, School of Natural Sciences, Merced, California 95344, USA
[3]Department of Physics, California State University Fresno, Fresno, California, USA
[4]Clovis Community College, Fresno, California 93730 USA
[*]corresponding author: michael.tobar@uwa.edu.au

Abstract: We present results that shed light on a quantum system's scalar Aharonov-Bohm (AB) phase and how the effect can be measured. We show that the electric-scalar effect is the temporal dual of the vector-magnetic effect and propose a setup using a Faraday cage, where the observable is the modification of a quantum system's energy levels. For the scalar gravitational potential, we propose a quantum system in an eccentric orbit, which manifests as a temporal generalization of the gravitational redshift.

The Aharonov-Bohm (AB) effect is a quantum mechanical phenomenon where potentials, rather than classical fields, produce observable effects on a quantum system. The original electromagnetic version included both electric-scalar and magnetic-vector potentials[1]. While the magnetic-vector AB effect has been extensively tested due to the relative simplicity of its experimental setup, the scalar-electric AB effect remains elusive. The electric AB effect involves a geometric phase created over time by a time-dependent scalar potential without spatial variation. Despite its theoretical importance, a clean experimental realization of the this effect has yet to be achieved.

Recently, we proposed a novel temporal experiment, which uses a Faraday cage as shown in Fig. 1[2], offering a promising path toward the first clean measurement of the scalar-electric AB effect on a quantum system, such as an atomic clock or a qubit. The observable to determine the effect is the generation of sidebands in a manner similar to the AC Stark effect[2].

More recently, we developed for the first time a resonant microwave Faraday cage[3], capable of use for this experiment. The Faraday cage consisted of a cylindrical microwave cavity resonator, operating in the capacitor-like $TM_{0,1,0}$ mode, and excited

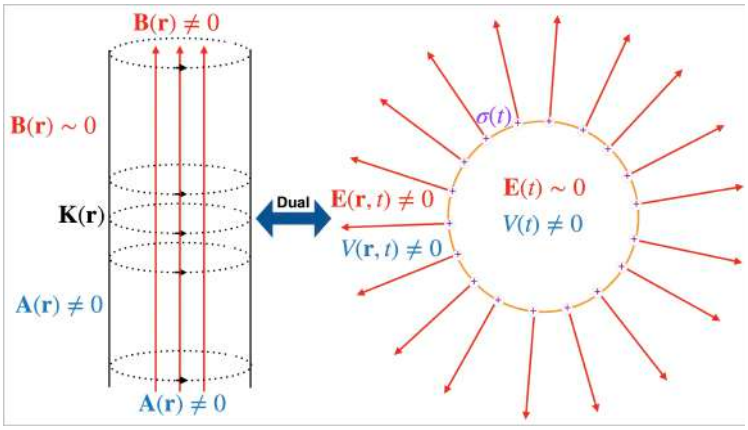


Fig 1. Comparison of magnetic AB setup (left) with the dual-electric AB setup (right). The former has been experimental proven to create a geometric phase shift on a quantum system due to the vector potential, **A**(**r**), while the magnetic field, **B**(**r**), is suppressed. In contrast, the latter has been predicted to create a temporal effect similar to the AC Stark effect due to the scalar potential, V(t), being non-zero inside a Faraday cage where the electric filed, **E**(t), is suppressed. The static magnetic AB effect has a azimuthal surface current density, K(r), at the solenoid boundary, compared to the electric AB effect which has a time-varying surface charge density, σ(t), at the Faraday cage boundary.

using an interferometric setup[3]. This novel design allowed precise manipulation of the electric field and potential within the resonator by adjusting the phase and amplitude in the two interferometer arms driving the system. Through fine tuning, a 25 dB suppression of the electric field at the resonance frequency was achieved, while simultaneously enhancing the time-varying electric-scalar potential. Under these conditions, the system exhibited a phenomenon analogous to electromagnetically induced absorption, caused by the cancellation of the electric field at resonance. This effect, may be regarded as a form of extreme dispersion, and has led to an order of magnitude increase in the cavity's phase response. This experimental setup is an example of a system that could be used to verify the electric-scalar AB effect.

More recently, the AB effect has been observed in the context of gravitational interactions using atom interferometry[4]. Additionally, recent predictions suggest that temporal variations in the phase of an electron wave function will induce modulation sidebands in the energy levels of a quantum-system, similar to the electric-scalar effect, solely driven by a time-varying scalar gravitational potential[5]. In this study, we considered an atomic clock as a quantum two-level system undergoing continuous Rabi oscillations between the electron's ground and excited state[6]. We assume that the photons driving the transition are precisely frequency-stabilized to match the transition, enabling accurate clock comparisons. Our analysis takes into account, that when an atom transitions from its ground state to an excited state, it absorbs energy, increasing its mass according to the mass-energy equivalence principle. Due to the mass difference between the two energy levels, we predict that an atomic clock in an eccentric orbit will exhibit a constant frequency shift relative to a ground clock corresponding to the orbit's average gravitational redshift, with additional modulation sidebands due to the time-varying gravitational potential. This type of experiment may be thought of as a temporal Pound-Rebka experiment[7].

Acknowledgements

This work was funded by the Australian Research Council Centre of Excellence for Engineered Quantum Systems, CE170100009 and the Centre of Excellence for Dark Matter Particle Physics, CE200100008.

References

1. Y. Aharonov, D. Bohm, “Significance of electromagnetic potentials in the quantum theory,” Phys. Rev. Vol. 115, 485, 1959.
2. R. Y. Chiao, H. Hart, N. A. Inan, M. Scheibner, J. Sharping, D. A. Singleton, M. E. Tobar, “Energy level shift of quantum systems via the electric Aharonov-Bohm effect,” Phys. Rev. A, Vol. 107, 042209, 2023.
3. MT Hatzon, GR Flower, M Goryachev, JF Bourhill, ME Tobar, “Sharp electromagnetically induced absorption via balanced interferometric excitation in a microwave resonator,” Phys. Rev. Applied, Vol. 23, 024058, 2025.
4. C. Overstreet, P. Asenbaum, J. Curti, M. Kim, M. A. Kasevich, “Observation of a gravitational Aharonov-Bohm effect,” Science, Vol. 375, No. 6577, 226-229, 2022.
5. RY Chiao, NA Inan, M Scheibner, J Sharping, DA Singleton, ME Tobar, “Gravitational Aharonov-Bohm effect,” Phys. Rev. D, Vol. 109, 064073, 2024.
6. ME Tobar, MT Hatzon, GR Flower, M Goryachev, Scalar gravitational Aharonov–Bohm effect: Generalization of the gravitational redshift, Appl. Phys. Lett. 125, 094002, 2024.
7. RY Chiao, NA Inan, DA Singleton, ME Tobar, “Temporal Pound-Rebka experiment as gravitational Aharonov-Bohm effect,” Int. J. Mod. Phys. D, Vol. 33, no. 15, 2441021, 2024. SPECIAL ISSUE: Selected Essays from the Annual Essays Competition of the Gravity Research Foundation 2024.

Two-Dimensional Semiconductors for On-Chip Polarization-Sensitive Photodetectors

Marcos H. D. Guimarães[1]

[1]Zernike Institute for Advanced Materials, University of Groningen, The Netherlands
*corresponding author: m.h.guimaraes@rug.nl

Abstract: Optical communication of information through light polarization provides a viable route to overcome the interconnect problem in modern ICT architecture. In this talk I will show how atomically-thin semiconductors can be used for photodetectors with sensitivity to light polarization.

The continuous advancement of faster, smaller, and more energy-efficient electronic devices hinges on addressing two critical challenges: the energy inefficiency of interconnects, and the degradation of device properties at nanoscale dimensions. As the dimensions of front-end-of-line devices continue to decrease, the interconnects between them are also reducing in size, leading to smaller cross-sectional areas, leading to lower bandwidths and higher heat dissipation. While CPU and GPU performance is increasing by a factor of around 3 every two years, interconnect bandwidth is only increasing by a factor of 1.4. This is further aggravated by the constant need for information transfer between the data processing and storage units in a computer, a problem known as the von Neumann bottleneck. With this, energy demand is skyrocketing, with ICT projected to consume over 20% of the global energy by 2030. Additionally, the miniaturization of devices, now reaching feature sizes in the order of a few nanometers, leads to a steep decline in device properties due to small material imperfections, element interdiffusion, and relatively rough interfaces between two different materials.

In this talk I show how we can use 2D semiconductors as polarization-sensitive light detectors[1]. These atomically-thin devices can be used to read light information at fast time-scales and with high sensitivity. I will show how the Schottky barriers arising from the metal-semiconductor interfaces can play an important role in the response time and polarization sensitivity of 2D materials photodetectors. Additionally I will demonstrate how we can be fabricate lateral 2D heterostructures by laser writing, allowing for the design of all-2D circuitry for opto-electronics[2]. These $MoTe_2$-based photodetectors show significant improvement on the response time and responsivity, making this method a viable alternative for atomically-thin optoelectronic circuitry. Finally, I will discuss how strong crystalline anisotropy can be used to enhance the polarization contrast in the photocurrent response. In such crystals, we are able to achieve much stronger dichroic responses in photocurrent measurements than on optical reflectivity alone, indicating that the conductivity anisotropy plays an important role. Our works pave the way for the use of 2D materials in future photonic technologies.

References

1. Quereda, J. et al., “The role of device asymmetries and Schottky barriers on the helicity-dependent photoresponse of 2D phototransistors” NPJ 2D Mater. and Appl. 5, 13 (2021).
2. Hidding, J. et al., “Locally Phase-Engineered MoTe2 for Near-Infrared Photodetectors” ACS Photonics 11, 4083 (2024).
3. Cordero-Silis, C.A. et al., “Photoelectronic control of transport in antiferromagnetic semiconductor $CrPS_4$” *in preparation.*

Controlled Synthesis of Silver-Coated Gold Nanostars for Tunable Optical Properties

N. Pazos-Perez[1*]

[1]Department of Physical and Inorganic Chemistry, Universitat Rovira i Virgili, Tarragona, Spain
[*]corresponding author: nicolas.pazos@urv.cat

Abstract: This study explores the controlled epitaxial deposition of silver onto gold nanostars (NSts), enhancing their SERS properties while maintaining their branched morphology. The silver coating enables plasmon resonance tuning and boosts SERS brightness by an order of magnitude. These findings present silver-coated NSts as promising substrates for advanced plasmonic sensing applications.

Over the past decades, substantial research efforts have been dedicated to the development of plasmonic nanoparticles capable of delivering the highest possible surface-enhanced Raman scattering (SERS) intensities. Spherical gold and silver colloids have been extensively employed in SERS applications, but their inherent limitations often necessitate aggregation to generate localized electromagnetic field "hotspots," which are essential for achieving high SERS enhancement. While aggregation-based approaches can lead to exceptionally low detection limits, they suffer from inherent reproducibility issues, making them less reliable for practical applications. To address this challenge, strategies involving the controlled aggregation or assembly of nanoparticles into well-defined superstructures, such as core-satellite configurations,[1-4] have been widely explored. However, a key limitation of these constructs is that the hotspots formed between the plasmonic nanoparticles are often buried within the nanostructure, reducing accessibility to analytes and thus compromising their sensing efficiency.

An alternative approach to overcome this limitation is the use of individual nanoparticles that possess intrinsic hotspots, such as gold nanorods and nanostars (NSts).[5-7] Among these, Au NSts exhibit superior SERS properties due to their multiple sharp branches, each capable of sustaining highly localized and significantly enhanced electromagnetic fields at their tips. This unique structural feature provides multiple accessible hotspots directly at the nanostructure surface, ensuring both high SERS enhancement and efficient analyte interaction.

While gold nanostructures offer excellent chemical stability and tunability, silver nanoparticles are known to be optically more efficient due to their higher plasmonic activity. However, the controlled synthesis of anisotropic silver nanostructures remains challenging, limiting their widespread application in SERS-based detection. To overcome this issue, a well-established strategy involving the silver deposition onto preformed gold nanoparticles is commonly used.[8] This process not only preserves the high monodispersity and well-defined morphology of gold nanoparticles but also enhances their plasmonic response by exploiting the superior optical properties of silver. Although silver coating has been successfully applied to various gold nanoparticle morphologies, relatively few studies have focused on the deposition of silver onto gold NSts. Moreover, in most of the reported cases, silver growth occurs preferentially at the core of the NSts,[9] leading to morphological alterations that compromise the specific NSts features responsible for their exceptional SERS activity.

Beyond the enhancement of SERS intensities, silver nanoparticles exhibit plasmon resonances at shorter wavelengths, within the ultraviolet (UV) region. Consequently, the deposition of silver onto gold nanostructures has been widely employed as a means to systematically blue-shift their plasmon resonances, allowing for tunable optical properties across the visible to near-infrared (Vis-NIR) spectrum.[8]

In this study, we present a strategy for the controlled epitaxial deposition of silver onto gold NSts, achieving precise modulation of their optical properties while preserving their characteristic branched morphology. By fine-tuning the silver deposition process, we successfully obtained silver-coated gold NSts with varying degrees of silver coverage, enabling the systematic blue-shifting of their plasmon resonances within the Vis-NIR range. Importantly, this approach retains the distinctive multiple sharp branches of the NSts, ensuring the preservation of their intrinsic hotspots. In terms of SERS performance, our results demonstrate that the silver-coated NSts exhibit a one-order-of-magnitude increase in SERS brightness compared to their uncoated gold counterparts. These findings highlight the potential of silver-coated NSts as highly efficient SERS substrates with precisely tailored optical properties, offering new opportunities for advanced plasmonic sensing and molecular detection applications.

References

1. Pazos-Perez, N., Fitgerald, J. M., Giannini, V., Guerrini, L., Alvarez-Puebla, R., "Modular assembly of plasmonic core–satellite structures as highly brilliant SERS-encoded nanoparticles," Nanoscale Advances 1 (1), 122-131.
2. Tebbe, M., Lenzt, S., Guerrini, L. Fery, A. Alvarez-Puebla, R., Pazos-Perez, N., "Fabrication and optical enhancing properties of discrete supercrystals," Nanoscale 8 (25), 12702-12709.
3. Blanco-Formoso, M., Pazos-Perez, N., Alvarez-Puebla, R., "Fabrication of Plasmonic Supercrystals and Their SERS Enhancing Properties," ACS omega 5 (40), 25485-25492.
4. Terrones-Morey, G., Xiao, X., Giannini, V., Fragoso, A., Guerrini, L., Pazos-Perez, N., "Comparative SERS Activity of Homometallic and Bimetallic Core–Satellite Assemblies," Nanomaterials 14 (18), 1506.
5. Tebbe, M., Maennel, M., Fery, A., Pazos-Perez, N., Alvarez-Puebla, R., "Organized Solid Thin Films of Gold Nanorods with Different Sizes for Surface-Enhanced Raman Scattering Applications," The Journal of Physical Chemistry C 118 (48), 28095-28100.
6. Pazos-Perez, N., Guerrini, L., Alvarez-Puebla, R., "Plasmon Tunability of Gold Nanostars at the Tip Apexes," ACS omega 3 (12), 17173-17179.
7. Morla-Folch, J., Guerrini, L., Pazos-Perez, N., Arenal, R., Alvarez-Puebla, R., "Synthesis and Optical Properties of Homogeneous Nanoshurikens," ACS Photonics 1 (11), 1237-1244.
8. Tebbe, T., Kuttner, C., Mayer, M., Maennel, M., Pazos-Perez, N., König, T.A.F., Fery, A., "Silver-Overgrowth-Induced Changes in Intrinsic Optical Properties of Gold Nanorods: From Noninvasive Monitoring of Growth Kinetics to Tailoring Internal Mirror Charges," The Journal of Physical Chemistry C 119 (17), 9513-9523.
9. Fales, A.M., Yuan, H., Vo-Dinh, T., "Development of Hybrid Silver-Coated Gold Nanostars for Nonaggregated Surface-Enhanced Raman Scattering," J. Phys. Chem. C 2014, 118, 7, 3708–3715.

Tailoring the emission and the photodynamics of quantum emitters with simple and optimized high-index dielectric nanostructures

Swaroop Palai[1,2], Mélodie Humbert[1,2], Romain Hernandez[1,2], Peter R. Wiecha[3], Jonas Muller[3], Etienne Palleau[2], Frank Fournel[4], Vincent Larrey[4], Aurélie Lecestre[3], Guilhem Larrieu[3], Christian Girard[1], Vincent Paillard[1], Laurence Ressier[2], and Aurélien Cuche[1,*]

[1]CEMES-CNRS, Université de Toulouse, CNRS, UPS, Toulouse, France

[2]LPCNO, Université de Toulouse, CNRS, INSA, UPS, 135 Avenue de Rangueil, 31077 Toulouse, France

[3]LAAS-CNRS, Université de Toulouse, CNRS, INP, Toulouse, France

[4]Université Grenoble Alpes, CNRS, CEA-Leti Minatec, Grenoble, France

*corresponding author, E-mail: aurelien.cuche@cemes.fr

Abstract: Through experimental and theoretical methods, we demonstrate the controllable photodynamics of quantum emitters (NV colored centers in nanodiamonds) precisely positioned near silicon dimer nanoantennas. Then, by designing specific geometries with an evolutionary optimization algorithm, we explore enhancing the directional emission of these quantum sources numerically.

Introduction

Improving the brightness and efficiency of single photon sources by the mean of optically resonant nanostructures is a major stake for the development of efficient nanodevices for quantum communications.

For a couple of decades, these resonant nanostructures have mainly been made of noble metal that sustain strong localized resonances that can be used to manipulate, concentrate or redirect visible light. Such properties have led to numerous actual or potential applications in integrated optics, sensors, nonlinear optics, field-enhanced spectroscopies, or photovoltaics. Recently, an alternative emerged with high refractive index dielectric nanostructures, which offer the same range of applications as plasmonics by manipulating Mie optical resonances [1].

These resonances can be efficiently tuned by modifying the size, shape, and material of those nanostructures (e.g. silicon, n ~ 4) [2]. Furthermore, high index dielectric nanostructures offer several key advantages when compared to their metallic counterparts: absorption losses are far weaker for wavelengths longer than the direct band gap, access to semiconductor (CMOS) technology for nanostructure fabrication, and presence of intrinsic strong magnetic and electric resonances, providing an unique opportunity to spatially separate and redistribute the energy of the magnetic and electric parts of the electromagnetic field in the near field, otherwise inextricably connected in the far field [3].

Discussion

We discuss here the effect of simple high index dielectric nanoantennas on the spontaneous emission of model quantum emitters. First, we accurately positioned arrays of nanodiamonds hosting NV colored centers in the gap

of silicon dimer nanoantennas, using atomic force microscopy (AFM – [4]) nanoxerography [5]. The NV center is an ideal model system exhibiting single photon emission properties at room temperature, which is well adapted for proof of concept experiments in quantum nano-optics. Since the emission rate of the emitters, and therefore the local density of photonic states (LDOS), are modified by the nanostructure, we show by the mean of time-resolved photoluminescence acquisitions that the photodynamics of these emitters can be enhanced by the coupling to the nanoantenna down to the single photon emission regime [5]. Our experimental results are in good agreement with multipolar analysis and numerical simulations based on the Green Dyadic Method - GDM.

Next, to go a step further, we numerically investigate controlling the directional emission of quantum dipolar sources using complex Si antennas. These antennas, composed of specific numbers of building blocks, are optimized via an Evolutionary Algorithm (EA). The resulting geometries enable precise tailoring of emission direction, enhancing light intensity within defined solid angles. Our numerical experiments demonstrate the effectiveness of these EA-optimized antennas [6].

Acknowledgements

This work was supported by Programme Investissements d'Avenir under the program ANR-11-IDEX-0002-02, reference ANR-10-LABX-0037-NEXT, by the HiLight ANR project ANR-19-CE24-0026, by LAAS-CNRS micro and nanotechnologies platform member of the French Renatech network, by the CNRS and INSA (M.H. PhD grant), by the Région Midi-Pyrénées via the Institute for Quantum technologies in Occitanie (IQO), and by the computing facility center CALMIP of the University of Toulouse under grants P12167 and P1107.

References

1. Kallel, H., Arbouet, A., Benassayag, G., Chehaidar, A., Poti, A., Salem, B., Baron, T., Paillard, V., "Tunable enhancement of light absorption and scattering in Si1xGex nanowires", Phys. Rev. B 12, 085318, 2012.

2. Wiecha, P.R., Cuche, A., Arbouet, A., Girard, C., Colas des Francs, G., Lecestre, A., Larrieu, G., Fournel, F., Larrey, V., Baron, T., Paillard, V., "Strongly directional scattering from dielectric nanowires", ACS Photonics 4, 2036, 2017.

3. Wiecha, P.R., Majorel, C., Girard, C., Arbouet, A., Masenelli, B., Boisron, O., Lecestre, A., Larrieu, G., Paillard, V., Cuche, A., "Enhancement of electric and magnetic dipole transition of rare-earth-doped thin films tailored by high-index dielectric nanostructures", Appl. Opt. 58, 1682, 2019.

4. Humbert, M., Hallez, Y., Larrey, V., Fournel, F., Palleau, E., Paillard, V., Cuche, A., Ressier, L., "Versatile, rapid and robust nanopositioning of single-photon emitters by AFM-nanoxerography", Nanotechnology 33, 215301, 2022.

5. Humbert, M., Hernandez, R., Mallet, N., Larrieu, G., Larrey, V., Fournel, F., Guérin, F., Palleau, E., Paillard, V., Cuche, A., Ressier, L., "Large-scale controlled coupling of single-photon emitters to high index dielectric nanoantennas using AFM nanoxerography", Nanoscale 15, 599, 2023.

6. Hernandez, R., Wiecha, P. R., Poumirol, J.-M., Agez, G., Arbouet, A., Ressier, L., Paillard, V., Cuche, A., "Directional silicon nano-antennas for quantum emitter control designed by evolutionary optimization" JOSA B 41 (2), A108-A115, 2024.

Optimising Cross-Polarisation Conversion of Ghost Hyperbolic Polaritons with a Twist

Mark C. Cunningham[1*] and Rair Macêdo[1]

[1]James Watt School of Engineering, Electronics and Nanoscale Engineering Division, University of Glasgow, Glasgow, G12 8QQ United Kingdom

[*]Corresponding author: m.cunningham.2@research.gla.ac.uk

Abstract: We demonstrate tuning and optimisation of cross-polarisation conversion in multilayered hyperbolic systems by introducing a twist angle between layers (i.e. their anisotropy orientations). Using a 4×4 transfer matrix method, we show significant enhancement of polarisation conversion efficiency due to Ghost Hyperbolic Polaritons. This could influence next-generation, direction-dependent infrared optical devices.

Manipulating polarisation of electromagnetic waves is a key aspect of a broad range of technologies including wireless communication [1] and sensing [2]. In the infrared, birefringence is the main mechanism behind optical components that convert polarisation [3], but their large form-factor limits their use in practical applications. To circumvent this, the development of thin metasurfaces - with respect to the device's operating wavelength - has received much attention [4]. However, manufacturing these metasurfaces can be a sophisticated and expensive process. An emerging alternative to this is using naturally occurring anisotropic crystals which display hyperbolic behaviour across the far-infrared range [5]. That is because, along with exotic effects such as surface polaritons [5], negative refraction [6] and subwavelength confinement [6], hyperbolic materials have been shown to support cross-polarisation conversion upon reflection at their interface, depending on the orientation of their anisotropy axis with respect to both incidence angle and incidence plane [7].

An example of such natural hyperbolic materials is low-symmetry crystals, such as calcite. This is due to anisotropic, infrared-active phonon resonances which, in turn, lead to the principal elements of its diagonal permittivity tensor possessing opposite signs [5] and consequently display a 'hyperbolic dispersion'. Hyperbolic dispersion is commonly referred to as type I when a single extraordinary component of the dielectric tensor is negative while the two ordinaries are positive, creating a two-sheet hyperboloid isofrequency contour. Conversely, when the extraordinary component is positive while the two ordinary components are negative, an open-sheet hyperbolic isofrequency contour forms, known as type II dispersion [6].

More recently, these materials have been shown to support ghost hyperbolic polaritons (GHP). For example, GHPs have previously been observed in bulk calcite at $1430\text{-}1500\ \mathrm{cm}^{-1}$ [8], corresponding to a free space wavelength of $6.6 - 7\mu m$. Supported in type II dispersion [8], GHPs possess slanted phase wavefronts into the bulk of the crystal, parallel Poynting vectors to the surface, and exponential decay away from the surface. In addition to long-range, directional, and diffraction-less polariton propagation [8] in s-NOM studies, the reflectance of the GHP has also been studied in-depth [9], showing direction-dependent cross-polarisation conversion.

In this study, we investigate how multiple layers of natural hyperbolic media - using calcite as the example material - can exhibit enhanced cross-polarisation conversion through introduction of a twist-angle γ to misalign their anisotropy axes with respect to each other. We consider the geometry shown in Fig. 1. (a) where a prism is placed close to the sample surface of our layered structure, separated by a thin air gap, i.e. using the Otto configuration [10]. P-polarised incident waves undergo total internal reflection at the prism-air interface, allowing for the excitation of the GHP on the sample surface. In this configuration, the top calcite layer (of thickness $4\mu m$) is rotated relative to the bottom semi-infinite calcite crystal by an angle γ. This has been analysed in depth in the

context of hyperbolic shear polaritons and their application in metasurfaces [11]. Here, we use this method to assess its effect on cross-polarisation conversion. For this, we model reflectance using a 4×4 transfer matrix method [12].

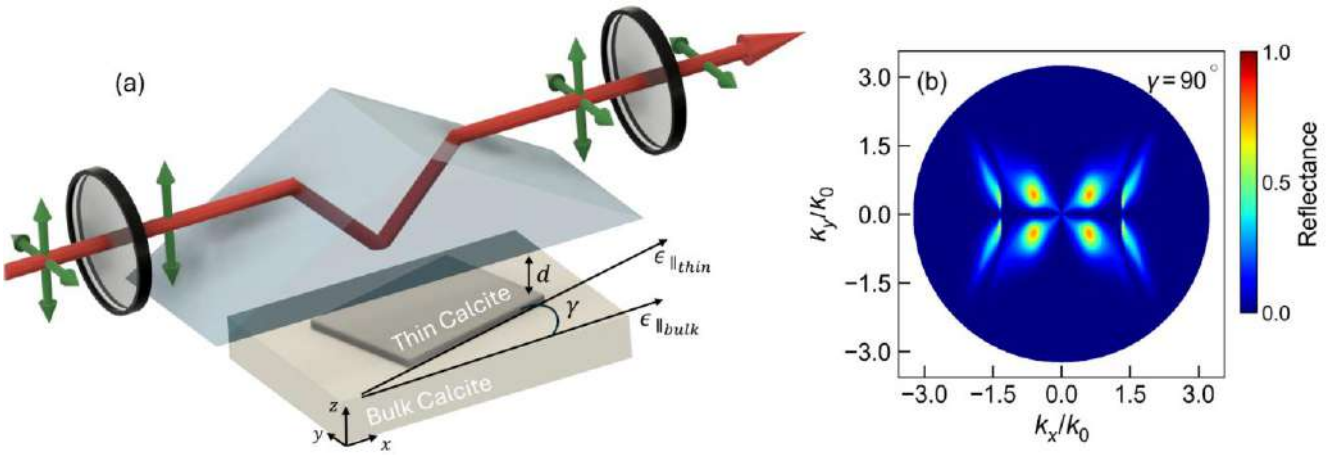


Fig. 1. (a) Setup Geometry, where a polariser is used to generate a TM-polarised beam which is incident at the surface of the calcite multilayer at an incident angle greater than that of the critical angle of the prism/air interface, creating evanescent decay to couple with the GHP on the thin calcite surface. After reflection, another polariser is used to capture the converted TE-polarised component of the beam. (b) The cross-polarisation conversion reflectance induced by the twisted GHP in the calcite multilayer at a twist angle of $\gamma = 90°$. This quantity is the amount of TE-polarised light reflected off the surface from the incident TM-polarised radiation.

With their anisotropy orientations aligned ($\gamma = 0°$), the maximum cross-polarisation conversion value $R_{ps} = 0.3$ at 1460 cm^{-1}. We find that polarisation conversion of the twisted GHP increases to $R_{ps} = 0.7$ when $\gamma = 90°$, as shown in Fig.1. (b). We can see four emission lobes corresponding to the GHP beyond k_x/k_0=1.4, with 4 enhanced sources of polarisation conversion at the boundary of the prism/air critical angle k_x/k_0=1.

Our results show that tailoring the twist angle can maximise polarisation conversion. These findings demonstrate the potential of twist-engineered interfaces in hyperbolic materials as a versatile tool in photonic design. By harnessing the sensitivity of cross-polarisation conversion to the twist angle, an optical device could dynamically manipulate light based on orientation and the polarisation state.

MCC acknowledges funding from the Engineering and Physical Sciences Research Council (EPSRC) under grant number EP/S023321/1.

References

1. Y. Wang, C. Yang, Y. Wang, and N. Chi, ‘Gigabit polarization division multiplexing in visible light communication’, Opt. Lett., OL, vol. 39, no. 7, pp. 1823–1826, Apr. 2014, doi: 10.1364/OL.39.001823.
2. H. Yu and Z. Qin, ‘Multifunctional plasmonic metamaterial absorber in the middle infrared range for polarization detection’, Optics Communications, vol. 574, p. 131124, Jan. 2025, doi: 10.1016/j.optcom.2024.131124.
3. D. R. Solli, C. F. McCormick, R. Y. Chiao, and J. M. Hickmann, ‘Birefringence in two-dimensional bulk photonic crystals applied to the construction of quarter waveplates’, Opt. Express, OE, vol. 11, no. 2, pp. 125–133, Jan. 2003, doi: 10.1364/OE.11.000125.
4. Z. Zhou, R. Zhang, Z. Chen, R. Nie, Z. Pan, and Z. Song, ‘Terahertz generation of Airy beam with polarization

conversion in a reflective vanadium dioxide metasurface', Phys. Scr., 2024, doi: 10.1088/1402-4896/ad3ee8.

5. T. Dumelow, 'Chapter Two - Negative Refraction and Imaging from Natural Crystals with Hyperbolic Dispersion', in Solid State Physics, vol. 67, R. E. Camley and R. L. Stamps, Eds., Academic Press, 2016, pp. 103–182. doi: 10.1016/bs.ssp.2016.06.001.
6. Macêdo, R., Dumelow, T., Camley, R. E. & Stamps, R. L. Oriented Asymmetric Wave Propagation and Refraction Bending in Hyperbolic Media. ACS Photonics 5, 5086–5094 (2018).
7. Wu, X., McEleney, C. A., Shi, Z., González-Jiménez, M. & Macêdo, R. Asymmetric Reflection Induced in Reciprocal Hyperbolic Materials. ACS Photonics 9, 2774–2782 (2022).
8. W. Ma et al., 'Ghost hyperbolic surface polaritons in bulk anisotropic crystals', Nature, vol. 596, no. 7872, Art. no. 7872, Aug. 2021, doi: 10.1038/s41586-021-03755-1.
9. M. Cunningham, A. L. Lafferty, M. González-Jiménez, and R. Macêdo, 'Optical Footprint of Ghost and Leaky Hyperbolic Polaritons', Jan. 30, 2025, arXiv: arXiv:2501.18354. doi: 10.48550/arXiv.2501.18354.
10. H. J. Falge and A. Otto, 'Dispersion of Phonon-Like Surface Polaritons on Quartz Observed by Attenuated Total Reflection', physica status solidi (b), vol. 56, no. 2, pp. 523–534, 1973, doi: 10.1002/pssb.2220560213.
11. S. Yves, E. Galiffi, X. Ni, E. M. Renzi, and A. Alù, 'Twist-Induced Hyperbolic Shear Metasurfaces', Phys. Rev. X, vol. 14, no. 2, p. 021031, May 2024, doi: 10.1103/PhysRevX.14.021031.
12. N. C. Passler and A. Paarmann, 'Generalized 4 × 4 matrix formalism for light propagation in anisotropic stratified media: study of surface phonon polaritons in polar dielectric heterostructures', J. Opt. Soc. Am. B, JOSAB, vol. 34, no. 10, pp. 2128–2139, Oct. 2017, doi: 10.1364/JOSAB.34.002128.

Broadband third harmonic generation through strong coupling between all-dielectric metasurfaces and epsilon-near-zero materials

Hui-Hsin Hsiao[1*]

[1]Department of Engineering Science and Ocean Engineering, National Taiwan University, Taipei 10617, Taiwan

[*]corresponding author: hhhsiao@ntu.edu.tw

Abstract: A hybrid metasurface, consisting of amorphous silicon nanocubes with a drilled hole on an ultrathin indium tin oxide film, is designed to explore the coupling among Mie resonance, quasi-bound states in the continuum, and the bulk-plasma mode, as well as their impact on third-harmonic generation.

Epsilon-near-zero (ENZ) materials such as Indium Tin Oxide (ITO), featured by a vanishing real part of the dielectric function at near infrared, possess a remarkable intrinsic nonlinear susceptibility and meanwhile sustain a significant field enhancement at bulk-plasma resonance [1]. However, the excitation of bulk-plasma mode requires transverse-magnetic polarized light under oblique incidence, and the effective nonlinearity is constrained to a narrow spectral range close to the zero-permittivity wavelength. To further enhance nonlinear conversion efficiency and broaden the spectral range of nonlinear response, the integration of ENZ materials with plasmonic or dielectric metasurfaces have been demonstrated as a promising platform for the enhancement of second harmonic generation (SHG) [2] and Kerr effect [3, 4].

In this work, we designed a hybrid metasurface to investigate the coupling between Mie resonances, quasi-BICs, and bulk-plasma modes. As displayed in Fig. 1(a) and 1(b), the hybrid metasurface consists of nanocube arrays drilled with a detuned square hole on an ITO film. Via the analysis of coupled mode theory (CMT) and near-field features of the hybridized modes, a more efficient strong coupling was found to take place between the Mie resonance and the bulk-plasma mode owing to their comparable resonant linewidths, resulting in a large measured Rabi-splitting energy of 190 meV. While the excited quasi-BIC resonances achieve stronger near-field enhancement than Mie resonance, they exhibit shallower resonant depths in the spectra and lower field intensity in the ITO layer within the hybrid metasurface (Fig. 1(c)). The hybrid metasurface exhibits at least 5 orders of magnitude THG enhancement in the wavelength (λ) range of 1100 to 1600 nm when compared to the planar Si/ITO film in simulations. The measured THG conversion efficiency shows a value beyond 10^{-7} from λ = 1340 nm to 1600 nm for nanocube arrays in the absent of ITO layer and further extends to the range of λ = 1230 nm to 1600 nm for the hybrid metasurface (Fig. 1(d)). Our findings provide promising advancements for broadband nonlinear optics and photonics applications.

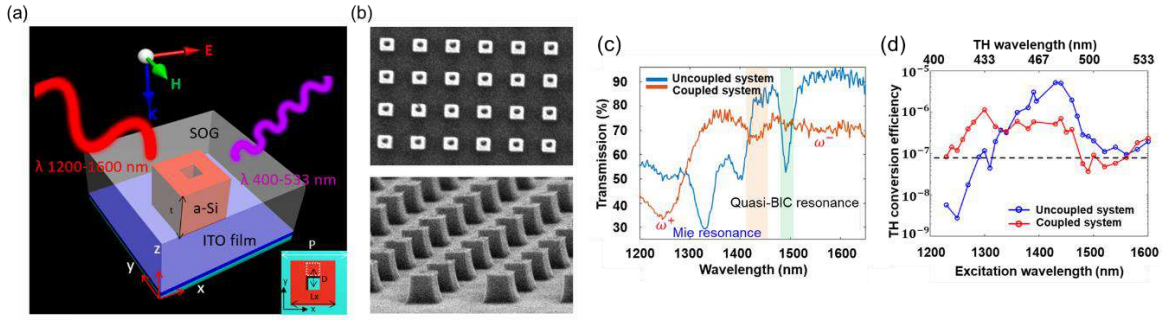


Fig. 1 (a) Schematic view of the nonlinear hybrid metasurfaces. (b) The SEM images of the fabricated sample at the top (upper) and lateral views (bottom). (c) Measured transmission spectra for the uncoupled (blue curve) and coupled (red curve) systems. The orange and green regions indicate the spectral position of the quasi-BIC mode in the coupled and uncoupled systems, respectively. (d) Measured TH conversion efficiency spectra for the uncoupled (blue dots) and coupled (red dots) systems.

The authors acknowledge financial support from the National Science and Technology Council (NSTC) of Taiwan (grant no. NSTC 113-2628-M-002-015-MY3, NSTC 113-2112-M-006-031, and NSTC 112-2221-E-002-203) and from the National Taiwan University (NTU) (grant no. NTU-114L7844).

References

1. I. Liberal and N. Engheta, "Near-zero refractive index photonics," *Nature Photonics*, vol. 11, no. 3, pp. 149-158, 2017.
2. J. Deng, Y. Tang, S. Chen, K. Li, A. V. Zayats, and G. Li, "Giant enhancement of second-order nonlinearity of epsilon-near-zero medium by a plasmonic metasurface," *Nano Letters*, vol. 20, no. 7, pp. 5421-5427, 2020.
3. M. Z. Alam, S. A. Schulz, J. Upham, I. De Leon, and R. W. Boyd, "Large optical nonlinearity of nanoantennas coupled to an epsilon-near-zero material," *Nature Photonics*, vol. 12, no. 2, pp. 79-83, 2018.
4. K. Wang, A.-Y. Liu, H.-H. Hsiao, C. Genet, and T. Ebbesen, "Large optical nonlinearity of dielectric nanocavity-assisted mie resonances strongly coupled to an epsilon-near-zero mode," *Nano Letters*, vol. 22, no. 2, pp. 702-709, 2022.

Efficient modeling of particle acceleration in structured dielectric waveguides driven by short-pulse laser excitation

A. Locatelli[1*], G. Sorbello[2], D. Guarnera[2], R. Palmeri[3], G. Mauro[4], G. Torrisi[4], N. Salerno[2], D. Rocco[1], and L. Vincetti[5]

[1]Department of Information Engineering, University of Brescia, Italy
[2]Department of Electric, Electronics, and Computer Engineering, University of Catania, Italy
[3]DIIES, University Mediterranea of Reggio Calabria, Italy
[4]Southern National Laboratories – National Institute for Nuclear Physics, Italy
[5]Department of Engineering "Enzo Ferrari", University of Modena and Reggio Emilia, Italy
[*]corresponding author: andrea.locatelli@unibs.it

Abstract: We present an optimization technique for sub-relativistic acceleration in guided-wave dielectric accelerators. Our approach exploits fast modal analysis of the guiding structure to explore geometric dependencies. Laser pulse propagation is then simulated using the Beam Propagation Method, while single-particle beam dynamics calculations are used to determine energy gain.

The miniaturization of particle sources has been attracting increasing interest worldwide. Indeed, laser-driven dielectric accelerators operating in the near infrared are potentially characterized by an increase in the accelerating gradient and a reduction of size and cost with respect to RF devices typically used in applications [1]. It is well known that dielectrics are characterized by a higher damage threshold compared to metals, and photonic crystals can suppress the propagation of higher-order modes, further enhancing the potential of dielectric accelerators. In this context, Dielectric Laser Accelerators (DLAs) have been studied by focusing mainly on side-pumped geometries [2]. However, this approach inherently puts an upper bound on the accelerator length and the energy gain. An alternative approach is based on a guided mode which is copropagating along the particle beam to achieve acceleration. In this scenario, particle and phase velocity need synchronization to guarantee net acceleration, therefore the guiding structure must be tapered by engineering its cross-section [3, 4]. Moreover, the temporal evolution of the pulses should be taken into account, since the interaction length in a waveguide can be large.

In this work we present an efficient numerical technique for the analysis of sub-relativistic acceleration in guided-wave dielectric accelerators. The proposed methodology is characterized by good accuracy and strongly improved computational efficiency with respect to cumbersome 3D FDTD simulations. The approach is based on a fast modal analysis of the waveguide cross-section as a function of the taper parameter, for instance the width a of the silicon strips in a tapered slot waveguide [3, 4]. The outcomes of this preliminary study are lookup tables with the modal properties of the waveguide, which can be summarized by propagation constant β_0, group velocity $v_g = 1/\beta_1$, second- and third-order dispersion β_2 and β_3 as a function of a. The optimal taper profile that

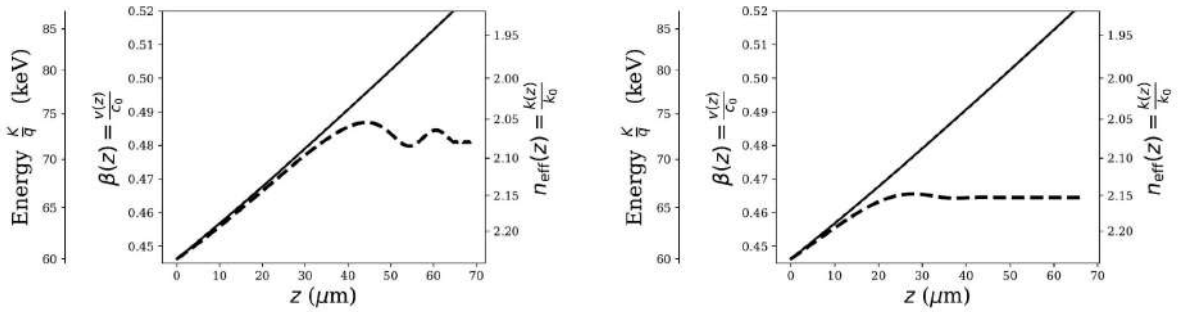


Figure 1. Acceleration profile in terms of energy and particle velocity (dashed lines) and waveguide effective index (solid lines) as a function of the propagation direction z. (Left) Pulse FWHM is 2 ps. (Right) Pulse FWHM is 0.25 ps.

guarantees synchronization between accelerating field and particles is obtained by solving single-particle beam dynamics (BD) and imposing that particle and phase velocity match along the propagation direction z. Next, the evolution $A(z,t)$ of the input pulse, which is governed by the linear Schrödinger equation (see Eq. 1), is determined by using the Beam Propagation Method (BPM) as commonly done in optical fibers. It should be noted that the BPM algorithm was implemented by exploiting the split-step technique, and at each step the correct values of the parameters β_0, β_1, β_2 and β_3 are taken from the lookup tables according to the taper geometry.

$$\frac{\partial A}{\partial z} = -\beta_1 \frac{\partial A}{\partial t} - j\frac{\beta_2}{2}\frac{\partial^2 A}{\partial t^2} - \frac{\beta_3}{6}\frac{\partial^3 A}{\partial t^3} \tag{1}$$

The proposed technique is quite general and can be applied to any kind of tapered waveguide geometry once a modal analysis is available. We studied both tapered slot waveguides and photonic crystal waveguides for sub-relativistic particle acceleration under pulse excitation, with the goal of identifying the main limitations imposed by the short-pulsed regime. As an example, in Fig. 1 we report the BPM-BD analysis of acceleration in a tapered slot waveguide [3, 4]. Design of the taper has been performed by assuming CW excitation, therefore a monotonic increase of particle and phase velocity is expected. Nevertheless, the behavior of the DLA is strongly affected by pulse duration when input energy and pulse amplitude are fixed. In fact, group velocity cannot be matched with particle velocity thus the effective interaction length is limited by pulse-particle walkoff. Furthermore, this detrimental effect is emphasized for short pulses, as it is possible to notice by analyzing the simulations reported in Fig. 1. Comparison between different scenarios wherein we vary pulse duration by modifying at the same time its amplitude to guarantee constant energy is underway, for the purpose of identifying an optimal pulse duration.

The authors acknowledge financial support from the Italian Ministry for University and Research and the European Union – Next Generation EU Mission 4 Component 1, as part of PRIN 2022 project DOSE (CUP D53D23001350006) and PRIN 2022 PNRR project IDEAS (CUP E53D23014520001).

References

1. England, R.J., et al., “Dielectric laser accelerators,” Rev. Mod. Phys., Vol. 86, No. 4, pp. 1337-1389, 2014.
2. Broaddus, P., T. Egenolf, D. Black, M. Murillo, C. Woodahl, Y. Miao, U. Niedermayer, R. Byer, K. Leedle, and O. Solgaard, “Subrelativistic alternating phase focusing Dielectric Laser Accelerators,” Phys. Rev. Lett., Vol. 132, No. 8, 085001, 2024.
3. Zhao, Z., T. W. Hughes, S. Tan, H. Deng, N. Sapra, R. J. England, J. Vuckovic, J. S. Harris, R. L. Byer, and S. Fan, “Design of a tapered slot waveguide dielectric laser accelerator for sub-relativistic electrons,” Opt. Express, Vol. 26, No. 18, pp. 22801–22815, 2018.
4. Palmeri, R., N. Salerno, G. S. Mauro, D. Rocco, A. Locatelli, G. Torrisi, and G. Sorbello, “Optimization of sub-relativistic co-propagating accelerating structures,” Opt. Express, Vol. 31, No. 23, pp. 38891-38909, 2023.

Nonlinear Photonics in Low-Index Time-Varying Systems

M. Ferrera[1,*], W. Jaffray[1], and S. Stengel[1]

[1] Institute of Photonics and Quantum Sciences, Heriot-Watt University, EH14 4AS, United Kingdom
[*]corresponding author: m.ferrera@hw.ac.uk

Abstract: Over the past decade, transparent conductive oxides (TCOs) have attracted interest due to their electro-optical properties. Operating near their cross-over wavelength, these materials have emerged as the most nonlinear solid-state platform for all-optical integrated devices. These systems closely approximate ideal time-varying systems, with potential applications extending into the quantum domain.

Summary: In recent years, there has been a resurgence of interest in transparent conducting oxides (TCOs) within the optics and photonics community. Historically, TCOs have been employed for over two decades as transparent electrodes in applications such as photovoltaics and touchscreens. This renewed attention was initially driven by their promise as low-loss metal substitutes in the design of highly compact plasmonic devices, and more recently by their extraordinary optical nonlinearities near the crossover wavelength [1].

TCOs are also notable for their epsilon-near-zero (ENZ) characteristics across a wide range of the near infrared spectrum, encompassing the entire telecommunications window. Within this spectral region, TCOs facilitate the realization of unique electromagnetic effects, such as super-coupling, wavefront freezing, and photon doping [2]. A distinctive feature of TCOs, in contrast to other ENZ materials, is their extremely low real refractive index ($n < 0.2$) near the ENZ wavelength, which is associated with relaxed phase matching conditions. The peculiar dispersion properties of TCOs have also been linked to a slow-light effect that further enhances the nonlinear optical responses [3-7]. Furthermore, it is important to note that these giant low-index nonlinearities come with an extremely broad bandwidth capable of accommodating optical pulses of just a few cycles in duration [8,9].

The fast-paced development of nonlinear optics with TCOs is fueled by experimental breakthroughs demonstrating extraordinary optical phenomena, including unitary refractive index changes, broad frequency shifts, and highly efficient on-chip nonlinear frequency conversion [10-12]. In this talk, I will discuss the evolving role of TCOs—from their origins in industrial applications as transparent electrodes to their emergence as a key solution for low-loss plasmonics and, most recently, as a pivotal enabler of advanced integrated nonlinear systems.

While providing a general overview of our latest findings, I will explore how evanescent coupling between a low-loss optical channel and an indium tin oxide layer enables the creation of novel nonlinear waveguides with unmatched nonlinear figures of merit over propagation distances spanning hundreds of microns (see Fig. 1-a). Furthermore, I will discuss how extreme modulation of the complex refractive index within a low-index thin film leads to a complete spatio-spectral fission of an incident pulse (see Fig. 1-b).

Finally, I will conclude by addressing the need for advanced material modeling and by offering some future perspectives for the use of these compounds in integrated quantum optics [13-14].

M.F. acknowledges economic support from EPSRC project ID: EP/X035158/1 and AFOSR (EOARD) under Award No.FA8655-23-1- 7254.

References

1. W. Jaffray, et al., "Transparent conducting oxides: from all-dielectric plasmonics to a new paradigm in integrated photonics" Adv. Opt. Phot. 14 (2), 148-208 (2022)
2. I. Liberal, N Engheta "Near-zero refractive index photonics" Nat. Photonics 11 (3), 149-158 (2017)
3. N Kinsey, et al., "Near-zero-index materials for photonics" Nat. Rev. Mater. 4 (12), 742-760 (2019)
4. O. Reshef, et al. "Beyond the perturbative description of nonlinear response of low-index materials" Opt. Lett. 42, 16, 3225-3228 (2017)
5. W. Jaffray, et al., "Nonlinear Loss Engineering in Near,ÄêZero,ÄêIndex Bulk Materials" Adv. Opt. Mater. 12 (1), 2301232 (2023)
6. M. Clerici, et al. "Controlling hybrid nonlinearities in conducting oxides via two-colour excitation" Nat. Commun. 8 (1), 1-7 (2017)
7. J.B. Khurgin, et al. "Adiabatic frequency shifting in epsilon-near-zero materials: the role of group velocity" Optica 7 (3), 226-231 (2020)
8. W. Jaffray, et al. "Near-zero-index ultra-fast pulse characterization" Nature Commun. 13 (1), 1-8 (2022)
9. E Lustig, et al., "Time-refraction optics with single cycle modulation", Nanophotonics 12 (12), 2221-2230 (2023)
10. E. G. Carnemolla, et al., "Visible photon generation via four-wave mixing in near-infrared near-zero-index thin films" Optics Letters 46 (21), 5433-5436 (2021)
11. M. Z. Alam, et al., "Large optical nonlinearity of nanoantennas coupled to an epsilon-near-zero material" Nature Photonics 12 (2), 79-83 (2018)
12. W Jaffray, et al., "High-Order Nonlinear Frequency Conversion in Transparent Conducting Oxide Thin Films" Advanced Optical Materials 12 (28), 2401249 (2024)
13. I. Liberal, A. Al√π, N. Engheta "Zero-index metamaterials for classical and quantum light" Appl. Phys. Lett. 120, 260401 (2022)
14. L. Vertchenko, N. Akopian, & A. V. Lavrinenko, "Epsilon-Near-Zero Grids for On-chip Quantum Networks". Scientific Reports 9, 6053 (2019).

Continuous translational symmetry breaking metamaterial design for photonic integrated circuits to free space outcouplers

A. Azarov[1,2*], D. Maurya[1,3], D. Westly[1] and V.A. Aksyuk[1]

[1] Physical Measurement Laboratory, National Institute of Standards and Technology, USA

[2] Theiss Research, USA

[3] Department of Chemistry and Biochemistry, University of Maryland, USA

[*] corresponding author: alexei.azarov@nist.gov

Abstract: Simulated and experimentally demonstrated photonic metamaterial antennas capable of emitting one or multiple ≈300μm diameter optical beams with customizable direction, intensity, phase, and polarization state (new result) at 460nm. Single transverse electric (TE) slab mode scatters from weak continuous perturbations superimposed on translationally-symmetric slab metamaterial.

Photonic integrated circuits (PICs) enable cost-efficient, large-scale fabrication of advanced photonic systems. PIC functionality can be further enhanced by direct coupling with photonic modes in free space, such as wide, collimated Gaussian beams [1]. We have previously demonstrated a fish-bone grating large beam emitter design based on breaking a continuous translational symmetry [2]. It allowed control over direction, intensity (shape), and phase of a TE, s-polarized output beam generated from an incident TE slab mode.

Heqing, et. al. [3] demonstrated precise and flexible control of the emitted intensity, wavefront and polarization at 1550 nm through discrete translation symmetry-breaking in 2D planar metamaterials. Such designs require accurate fabrication of dense 2D arrays of very small structural elements, which is particularly challenging for shorter wavelengths in the blue and even ultraviolet necessary for coupling PICs to miniature atomic systems.

In this work we demonstrate full polarization control with the continuous translation symmetry breaking which uses much larger minimum features and gaps, than its discrete counterpart [3]. The ability to create weak modulation without making very small features enables broad and smooth beam profiles while retaining ≈100 nm lines and spaces, compatible with 193 nm photolithography.

We introduce a mirror-anti-symmetric “wiggle” modulation along the walls (Fig.1(b)). Wiggle modulation emits transverse magnetic (TM) (p-polarized) light from the TE slab mode, while suppressing the TE (s-polarized) emission by symmetry. Fish-bone and wiggle modulations produce orthogonal linear polarizations. They can be superimposed with the appropriate relative amplitudes and phase to create any output polarization state. Different modulations and corresponding output polarizations are shown on Figure 1 (a-d). Light is outcoupled into wide collimated free-space beams emitted at near normal incidence. Polarization is measured by imaging through a rotating linear polarizer (Figure 1 (e,f)). Since modulation period controls the emitted beam angle, by superimposing modulations with different periods we simultaneously produce multiple beams with distinct polarizations and emission directions (Figure 2). Furthermore, by spatially varying the modulation across the device surface, it is possible to achieve complex, user-defined spatial distributions of phase, intensity, and polarization in the output.

To summarize, metamaterials with continuous translational symmetry breaking enable large-area, flat photonic beam emitters that can operate anywhere from the blue to infrared and generate a wide range of custom spatial profiles for polarization, intensity, and phase. Furthermore, the devices created from these metamaterials

are fully compatible with foundry-scale fabrication techniques, including photolithography, making them scalable and suitable for mass production.

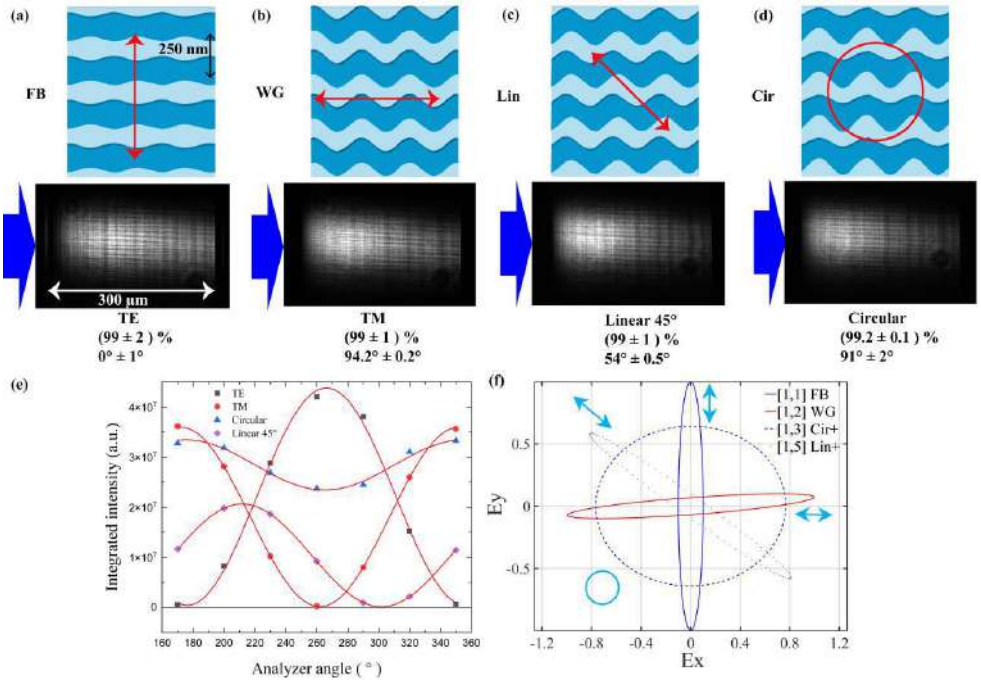


Fig. 1. (a) Fish-bone grating (FB) emitting TE polarization, (b) wiggle grating (WG) emitting TM polarization, (c-d) combination grating designs (45º linear and circular). The etched regions of 100 nm thick SiNx are depicted in dark blue, showing maximum modulations, located at the right-hand side of the spatially apodised gratings. Images show light emission from the corresponding gratings, with the slab mode light at 460nm incident from the left (indicated by the blue arrow). The numerical values below indicate the estimated fraction of the power emitted into the dominant linear/circular polarizations and polarization major axis orientation. (e) Integrated optical intensity through a linear polarization analyzer (symbols) with sinusoidal fits (f) Reconstructed field ellipses showing the electric field vector trajectory.

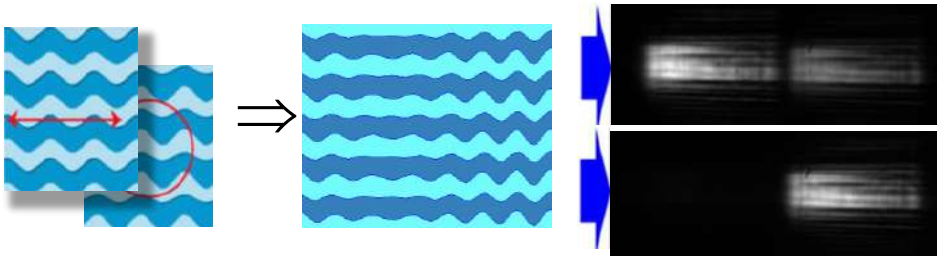


Fig. 2. A grating emitting two beams with the nominally circular and TM polarizations at different emission angles, which become spatially separated in the image plane ≈ 1.3 mm above the chip surface. The two images are taken at the same location with the orthogonal linear polarizer directions showing high extinction for the linear polarization.

This work was performed under financial assistance award 70NANB23H108 from the National Institute of Standards and Technology, U.S. Department of Commerce. The statements, findings, conclusions, and recommendations are those of the author(s) and do not necessarily reflect the views of the National Institute of Standards and Technology or the U.S. Department of Commerce.

References

1. Ropp, C., A. Yulaev, D. Westly, G. Simelgor and V. Aksyuk, "Meta-grating outcouplers for optimized beam shaping in the visible," Opt. Express 29, 14789-14798, 2021.
2. Ropp, C., D. Maurya, A. Yulaev, D. Westly, G. Simelgor and V. Aksyuk. “Scalable and Robust Beam Shaping Using Apodized Fish-bone Grating Couplers.” Optics Express, Vol 31, No. 24, pp. 40792-40802, 2023.
3. Heqing, H., A. C. Overvig, Y. Xu, S. C. Malek, C-C. Tsai, A. Alù and N. Yu. “Leaky-wave metasurfaces for integrated photonics,” Nature nanotechnology Vol. 18, 580-588, 2023.

META 2025, MALAGA - SPAIN, JULY 22 – 25, 2025

Optical Fresnel zone plate lenses fabricated entirely of colored photoresist with i-line stepper

K. Konishi[1]
[1]Institute for Photon Science and Technology, Japan
*corresponding author: kkonishi@ipst.s.u-tokyo.ac.jp

Abstract: This study presents a method for fabricating optical Fresnel zone plate lenses using color photoresist, requiring only spin-coating, i-line stepper exposure, and development. The lenses achieved 1.1 μm resolution with 7.2% focusing efficiency. This approach, utilizing resist as a metasurface material, enables mass production and significantly reduces fabrication costs.

The demand for compact and high-performance optical lenses has led to increased interest in flat lens technologies, particularly metalenses. However, fabricating metalenses operating in the visible region requires high-resolution lithography and dry etching, making large-scale production challenging. As an alternative, Fresnel zone plates (FZPs) provide a diffractive optical solution that does not require high-aspect-ratio structures, making them more compatible with mass production techniques. However, conventional FZPs still require additional fabrication steps such as thin-film deposition and dry etching, increasing costs.

In this study, we demonstrate a simplified fabrication method for visible-light FZP lenses using color photoresist1. The process involves only spin-coating, exposure with an i-line stepper (widely used in semiconductor microfabrication), and development—without the need for etching or post-processing as show in Fig.1. The color photoresist exhibits high absorption at specific wavelengths, enabling the creation of amplitude-type diffractive optical elements. This method was successfully used to mass-fabricate FZP lenses on 8-inch silica glass wafers for different visible wavelengths.

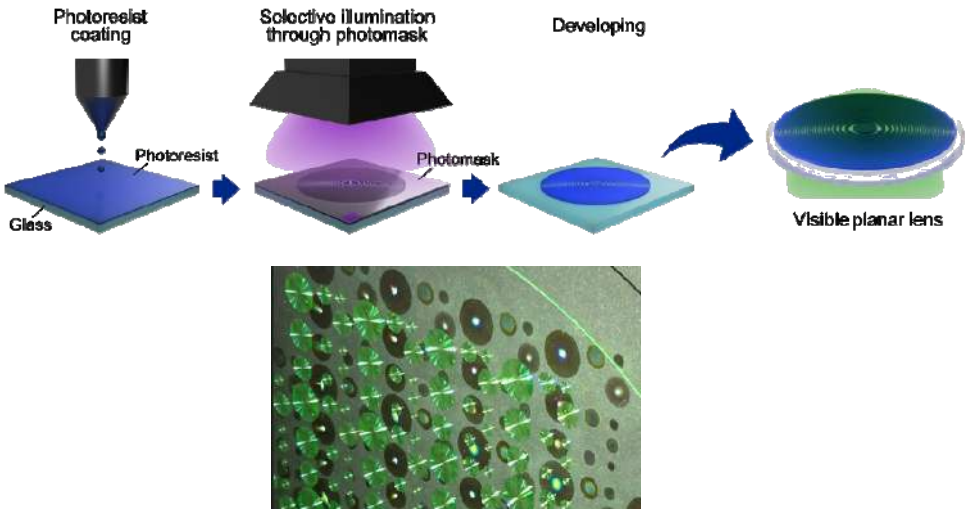


Fig. 1 Schematic diagram of the Fresnel zone plate lens fabrication method developed in this study and photograph of actual samples.

The FZP lenses were designed with a 0.8 μm minimum feature size, determining the outer radius and maximum numerical aperture. Fabrication involved spin-coating color resist, exposure via an i-line stepper, and development, using resists opaque at 450 nm, 550 nm, and 650 nm. Focusing tests showed a clean beam profile with FWHM of about 1.1 μm, with experimental results matching FDTD simulations. The focusing efficiency was 7.2%. Imaging tests using a USAF resolution chart demonstrated the ability to resolve 1.1 μm features, confirming the effectiveness of the FZP lenses for high-resolution imaging applications. The results of this research are innovative in that the resist itself is used as a metasurface material, which has the potential to reduce the cost of flat lenses significantly.

References

1. R. Yamada et al., "Optical Fresnel zone plate flat lenses made entirely of colored photoresist through an i-line stepper," Light Sci. Appl. Vol. 14, 43, 2025.

META 2025, MALAGA - SPAIN, JULY 22–25, 2025

Integrating superconductors with silicon photonic circuits for high-performance quantum optic applications

Jeff F. Young[1,3*], M. Khalifa[2,3], P. S. Kirwin[2,3], and J. Salfi[2,3]
[1]Department of Physics and Astronomy, University of British Columbia, Canada
[2]Department of Electrical and Computer Engineering, University of British Columbia, Canada
[3]Quantum Matter Institute, University of British Columbia, Canada
Corresponding author: young@phas.ubc.ca

Abstract: Quantum information can be processed in the microwave or optical frequency domains, but can only be transported via optical or infrared photons. We propose and quantitatively model a novel microwave-optical quantum transducer that relies on intimate coupling of superconducting microwave and semiconducting optical cavities with an ensemble of color centers.

The past decade has seen major advances in chip-based quantum information processing solutions implemented on various platforms [1]. Superconducting circuits based on Josephson junction technologies, and spin qubit circuits process all of the information in the microwave domain, and operate at millikelvin temperatures [2], [3]. Photonic circuits operating at ambient temperatures can perform complex unitary operations on quantum information encoded at near-infrared frequencies, but the requirement for high-efficiency, discrete photon detection currently requires the use of superconductor-based detectors operating at cryogenic temperatures [4], [5]. Even spin qubit circuits often rely on passive and/or active components made of superconducting material. The anticipated scaling challenges associated with any of these technologies suggests that an efficient means of exchanging quantum information encoded at microwave and near-infrared frequencies will be required, thus driving research on hybrid circuits that co-locate superconducting and photonic components.

Experimental reports of chip-based parametric microwave-optical transduction via electro- and magneto-optic mechanisms have yet to demonstrate high efficiency conversion [6]–[8]. We recently proposed a transducer (see Fig. 1) based on co-integrated silicon photonic and Nb superconducting microwave resonators [9] wherein an ensemble of color centers embedded within the silicon provide a $\chi^{(2)}$ magneto-optic parametric coupling between signal microwave/near-infrared photons at $\quad_{\mu} \quad _{o}$. The color centers have a Λ energy level configuration wherein two spin-split states in the ground state manifold are resonantly coupled to the magnetic field of the surrounding microwave cavity, and each is dipole-coupled via the racetrack mode(s) to the high energy color center state. The strength of the nonlinear response is controlled by the vacuum Rabi strength of a classical pump field oscillating at frequency $\quad_{p} = \quad _{o} - \quad _{\mu}$.

Our work extends previous treatments in two important ways. First, it generalizes the transduction model to the regime where the cavity mode(s) are on resonance with, and can be strongly coupled/hybridized to the relevant ensemble transitions. Second, it quantitatively accounts for linear and nonlinear optical, microwave, and optically-induced microwave losses, in the presence of realistic inhomogeneous broadening of the ensemble transitions. A counter-intuitive operating regime is identified that is robust to these imperfections, allowing a predicted $\sim 95\%$

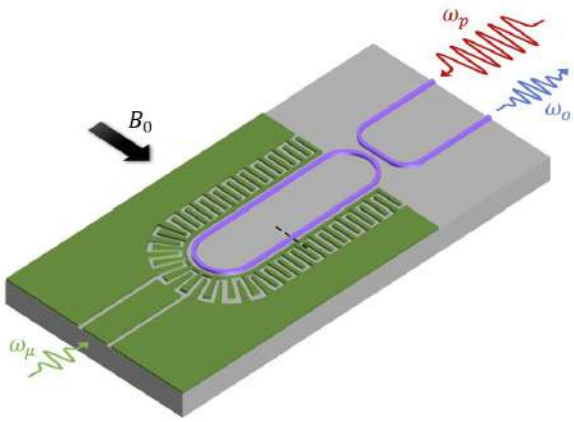


Figure 1: Device schematic comprising an optical racetrack cavity and a distributed superconducting microwave cavity loaded with an interdigitated capacitor, with applied magnetic field.

total conversion efficiency with added noise $\ll 1$ quanta possible at low (µW) pump powers for both Er- and T-centers in Si. This occurs when the signal photons are tuned *on resonance with the bare atomic transitions*, a situation that previous model assumptions precluded.

Acknowledgements: Financial assistance provided by the Quantum Matter Institute, the Natural Sciences and Engineering Research Council, the Canadian Foundation for Innovation, the National Research Council, and from Defence Canada.

References

[1] N. P. de Leon, K. M. Itoh, D. Kim, *et al.*, "Materials challenges and opportunities for quantum computing hardware," *Science*, vol. 372, no. 6539, eabb2823, 2021.

[2] M. Kjaergaard, M. E. Schwartz, J. Braumüller, *et al.*, "Superconducting Qubits: Current State of Play," *Annu. Rev. Condens. Matter Phys.*, vol. 11, no. 1, pp. 369–395, 2020.

[3] G. Burkard, T. D. Ladd, A. Pan, J. M. Nichol, and J. R. Petta, "Semiconductor spin qubits," *Rev. Mod. Phys.*, vol. 95, no. 2, p. 025 003, 2023.

[4] H. Aghaee Rad, T. Ainsworth, R. N. Alexander, *et al.*, "Scaling and networking a modular photonic quantum computer," *Nature*, vol. 638, no. 8052, pp. 912–919, 2025.

[5] K. Alexander, A. Benyamini, D. Black, *et al.*, "A manufacturable platform for photonic quantum computing," *Nature*, 2025.

[6] L. Fan, C.-L. Zou, R. Cheng, *et al.*, "Superconducting cavity electro-optics: A platform for coherent photon conversion between superconducting and photonic circuits," *Sci. Adv.*, vol. 4, no. 8, eaar4994, 2018.

[7] J. Rochman, T. Xie, J. G. Bartholomew, K. C. Schwab, and A. Faraon, "Microwave-to-optical transduction with erbium ions coupled to planar photonic and superconducting resonators," *Nat. Commun.*, vol. 14, no. 1, p. 1153, 2023.

[8] M. J. Weaver, P. Duivestein, A. C. Bernasconi, *et al.*, "An integrated microwave-to-optics interface for scalable quantum computing," *Nat. Nanotechnol.*, vol. 19, no. 2, pp. 166–172, 2024.

[9] M. Khalifa, P. S. Kirwin, J. F. Young, and J. Salfi. "Robust Microwave-Optical Photon Conversion Using Cavity Modes Strongly Hybridized with a Color Center Ensemble." arXiv: `2502.16775 [quant-ph]`. (2025).

META 2025, MALAGA - SPAIN, JULY 22 – 25, 2025

Recent progress in metasurface fluorescence biosensors: Expansion of the targets to next-generation nucleic acid biomarkers

Masanobu Iwanaga

National Institute for Materials Science (NIMS), Japan
*corresponding author: iwanaga.masanobu@nims.go.jp

Abstract: Metasurface fluorescence (FL) biosensors are a powerful biosensing tool that has been applicable for diverse biomolecules across DNA and antigen/antibody, exhibiting outstanding biosensing performance. We address a recent progress in the metasurface FL biosensors—extremely high sensitivity detection of next-generation biomarker of microRNA.

Metasurfaces are rapidly developing towards diverse optical and photonic applications. In addition to purely optical applications such as metalens, efficient interplay of metasurfaces with molecules enables us to conduct molecular sensing [1].

Resonant wavelength shift is used for small molecule sensing; the working principle is similar to surface plasmon resonance method. This type of sensors has been tested in various configurations [1].

Another type of metasurface biosensors is based on fluorescence (FL) detection [1]. In bioscience and biotechnology, FL detection is a major and established technique to identify and observe biomolecules and tissues. Recently, metasurface FL biosensors have been exploited to detect antigen/antibody [2–4] and DNA [5–7]. Especially, cell-free DNA (cfDNA) was detected in an ultimate high-sensitivity with discriminating one cfDNA from zero [6]. The detection signals representing target biomolecule concentrations are transduced to FL intensity, being quantified explicitly. This feature can contribute to huge numbers of bio-inspections and yield big data that would be the base for artificial intelligence use for healthcare services [8], as illustrated in Figure 1.

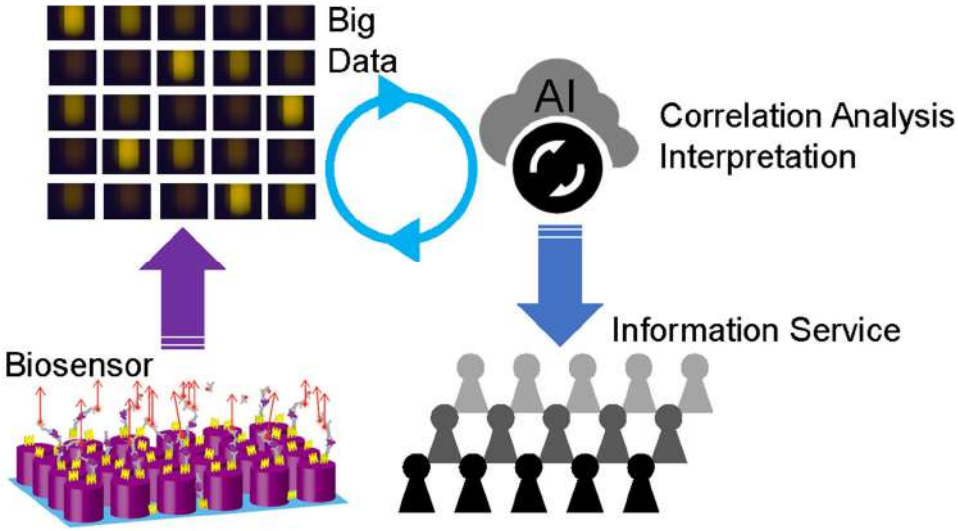


Figure 1. Illustration of all-dielectric metasurface FL biosensor to contribute to big data taking, which is the base for artificial intelligence (AI)-driven healthcare information service in the future. Cited from [8] under a CC BY license.

We address recent progress in the metasurface FL biosensors. In particular, extremely high-sensitivity detection of next-generation microRNA biomarkers has been attained employing the metasurface FL biosensors. A simplified protocol to detect the nucleic acid targets is described.

This study was partially supported by JSPS KAKENHI Grant number JP24K01389 and NIMS project "Biomaterials". Nanofabrication was conducted at "Advanced Research Infrastructure for Materials and Nanotechnology in Japan (ARIM)" of the MEXT, Japan (Proposal Number JPMXP1224NM5096).

References

1. Iwanaga, M. Q. Hu and Y. Tang, "Metasurface biosensors: Status and prospects," Appl. Phys. Rev. (accepted).
2. Iwanaga, M. "All-Dielectric Metasurface Fluorescence Biosensors for High-Sensitivity Antibody/Antigen Detection," ACS Nano, Vol. 14, No. 12, 17458–17467, 2020.
3. Iwanaga, M., "Highly sensitive wide-range target fluorescence biosensors of high-emittance metasurfaces," Biosens. Bioelectron., Vol. 190, No. 1, 113423, 2021.
4. Iwanaga, M. "Robust Detection of Cancer Markers in Human Serums Using All-Dielectric Metasurface Biosensors," Biosensors, Vol. 13, No. 3, 377, 2023.
5. Iwanaga, M. "High-Sensitivity High-Throughput Detection of Nucleic-Acid Targets on Metasurface Fluorescence Biosensors," Biosensors, Vol. 11, No. 2, 32, 2021.
6. Iwanaga, M. "Rapid Detection of Attomolar SARS-CoV-2 Nucleic Acids in All-Dielectric Metasurface Biosensors," Biosensors, Vol. 12, No. 11, 987, 2022.
7. Iwanaga, M. T. Hironaka, N. Ikeda, T. Sugasawa and K. Takekoshi, "Metasurface Biosensors Enabling Single-Molecule Sensing of Cell-Free DNA," Nano Lett. Vol. 23, No. 12, 5755–5761, 2023.
8. Iwanaga, M. "Productive biosensing techniques empowered by all-dielectric metasurfaces," Front. Bioeng. Biotechnol., Vol. 12, No. 1, 1484638, 2025.

Anisotropic nonlinearities in crystalline gold and how to exploit them

S. Boroviks[1*], and O. J. F. Martin[1]

[1] Nanophotonics and Metrology Laboratory, École Polytechnique Fédérale de Lausanne (EPFL), Switzerland
[*]corresponding author: sergejs.boroviks@epfl.ch

Abstract: We demonstrate a monocrystalline plasmonic metasurface which takes advantage of the anisotropic second-harmonic generation from {111}-type gold surface. Furthermore, we provide a comprehensive description of this anisotropic nonlinearity that is rooted in the microscopic symmetries of the crystal, and validate experimental results with numerical simulations, which show excellent agreement.

Second-order nonlinear processes, such as second-harmonic generation (SHG) typically do not occur in bulk metals due to their centrosymmetric crystal structure. Nevertheless, SHG does occur at metal surfaces, since centrosymmetry is naturally broken at the interfaces. Albeit being small, these surface nonlinearities can be substantially enhanced by virtue of surface plasmon resonances, which is the central topic of research in the field of nonlinear plasmonics [1, 2].

Furthermore, in the case of monocrystalline metals, the second-order nonlinear response becomes more complex and manifold, as compared with conventional polycrystalline films. In particular, {111} gold surfaces possess C_{3v} symmetry (Fig. 1a), giving rise to a characteristic six-fold pattern of the SHG signal, that can be co- or cross-polarized, depending on the sample orientation angle (Fig. 1a). The SHG signal contains two contributions: isotropic (stemming from broken centrosymmetry in surface-normal direction) and anisotropic (due to centrosymmetry broken along $\langle 11\bar{2} \rangle$ crystal axis) [3].

In this work, we investigate the possibilities to control the anisotropic SHG by fabricating metasurfaces on the large {111}-type surfaces of chemically synthesized monocrystalline gold flakes [4,5]. The metasurface is comprised of V-shaped grooves with subwavelength periodicity, that are fabricated using focused ion beam (FIB) milling (Fig. 1 c and d). Intriguingly, FIB fabrication does not diminish the crystal structure and yields structures with outstanding quality. Tailoring the geometric dimensions of the grooves allows to tune the spectral position of the localized plasmonic resonance, which allows to considerably enhance the SHG signal [6]. Remarkably, isotropic and anisotropic SHG contributions are extremely sensitive to the near-field distribution at the resonance (Fig. 1 g and h), which allows to selectively amplify or reduce co- or cross-polarized SHG signals. We substantiate our results with numerical simulations, which show excellent agreement with the experiment (Fig. 1 e and f).

We anticipate that these results will serve as a guide for exploiting the tensorial nature of nonlinear susceptibility in gold and the development of compact nonlinear devices that operate in reflection mode.

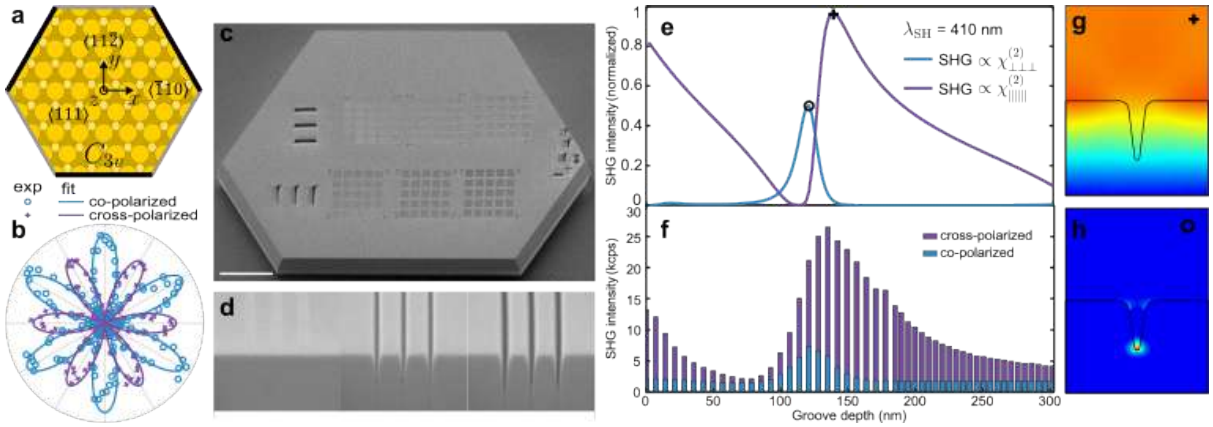


Figure 1

References

1. Kauranen, M., Zayats, A.V. , "Nonlinear plasmonics", Nat. Photon 6, 737 (2012).
2. Butet, J., et al. "Optical Second Harmonic Generation in Plasmonic Nanostructures: From Fundamental Principles to Advanced Applications", ACS Nano 9, 11, 10545 (2015).
3. Boroviks, S., et al. "Anisotropic second-harmonic generation from monocrystalline gold flakes", Opt. Lett. 46, 4, 833 (2021).
4. Huang, J.-S., et al., "Atomically flat single-crystalline gold nanostructures for plasmonic nanocircuitry" Nat. Commun. 1, 1, 150 (2010).
5. Boroviks, S., et al. "Interference in edge-scattering from monocrystalline gold flakes", Opt. Mater. Express 8, 12, 3688 (2018).
6. Boroviks, S., Martin, O. J. F. "Monocrystalline Gold Metasurface to Control Anisotropic Second Harmonic Generation", Adv. Opt. Mater. 2402525 (2025).

Fabrication of polymer structures in the sub-micron range as potential landscapes for photon Bose-Einstein condensates via Direct Laser Writing

S. Enns[1*], J. Schulz[1], K. Karkihalli Umesh[2], F. Vewinger[2] and G. von Freymann[1,3]

[1]Physics Department and Research Center OPTIMAS, RPTU Kaiserslautern-Landau, 67663 Kaiserslautern, Germany

[2]Institute of Applied Physics, University of Bonn, 53115 Bonn, Germany

[3]Fraunhofer Institute for Industrial Mathematics ITWM, 67663 Kaiserslautern, Germany

Corresponding author: enns@rptu.de

Abstract: Using the technology of Direct Laser Writing, we fabricate sub-micron polymer structures on top of a cavity mirror, serving as potential landscapes to experimentally investigate the properties of photon gases, such as the 2D to 1D crossover of a photon Bose-Einstein condensate or topological edge states in a SSH-chain.

In this talk we will discuss the realization and basic principles of photon Bose-Einstein condensates (PBEC) in a harmonic microcavity. Showing recent measurements, the polarization properties of PBECs are demonstrated in good agreement to theoretical simulations. While simple potentials such as harmonic confinement can be achieved using curved mirrors, the technology of Direct Laser Writing (DLW) allows the microcavity to be modified by printing polymer structures onto one of the cavity mirrors, creating more complex potentials. Tailoring specific potentials enables the investigation of thermodynamic properties in different dimensions. Furthermore, the possibilty to create and study the characteristics of coupled photon gases is emphasised.

Bose-Einstein condensation is a quantum phase transition of a Bose gas in thermal equilibrium, leading to a macroscopic occupation of the system's ground state above a critical phase-space density. Especially for photon Bose-Einstein condensates, a crucial aspect of this process is thermalization. To achieve this, the photon gas is coupled to a dye solution, which serves as both a particle and heat reservoir [1]. A microcavity consisting of two Bragg mirrors with a reflectivity above 99,998% is used to increase the lifetime of the photons and obtain the required conservation of the average photon number. Within the cavity, photons can undergo several absorption and emission cycles, leading to a coupling of the photon energy distribution to the rovibrational energy levels of the dye. The free spectral range of the resonator is tuned by the distance of the cavity mirrors and is chosen such that the dye can only emit into one longitudinal resonator mode q. Hence, the photon gas is effectively two-dimensional and has a well-defined ground mode TEM_{q00}. The transversal modes are occupied according to the Bose-Einstein statistics. Increasing the pumping power leads to a saturation of the excited modes and results in the condensation into the ground mode [2].

To understand the nature of the PBEC, we experimentally investigate its polarization properties and show good agreement with previous theoretical predictions [3]. While the gas below the condensation threshold is unpolarized, a strong increase of the polarization strength can be measured for the condensate. Thereby it follows the polarization of the pump in case of

linear polarization. However, circular polarization cannot be imprinted onto the condensate due to the achiral nature of the dye. Additionally, the pump polarization influences the condensation threshold: linear polarization results in more efficient dye excitation and thus requires lower pump power to reach condensation compared to circular polarization.

The ability to create potential landscapes enhances the control over the experimental setup and more properties can be analyzed. Methods as heat induced delamination to structure the mirror and usage of the non-lineaer Kerr effect already exist to form such potentials. However, using the technology of Direct Laser Writing is offering advantages especially with regard to higher resolution and fabrication of structures with steep edges. DLW is a 3D laser lithography technology that enables the fabrication of nearly arbitrary three-dimensional polymer structures at the sub-micron scale. Therefore, a photosensitive material, also called photoresist, is deposited on a substrate and exposed to a focused femtosecond pulsed laser. Only in the focal area of the laser beam, the intensity is sufficient for two-(multiple-) photon absorption to occur, which then induces a polymerization process. The volume in which the polymerization takes place is called a voxel. By generating a relative movement between the voxel and the photoresist while controlling speed and laser power, crosslinked polymerized areas are created. A following development process to remove the unpolymerized resist delivers the final structure. By printing these structures onto one of the cavity mirrors, the refractive index contrast between the dye solution and the polymer creates a potential landscape for the photon gas.

Quantum mechanical phenomena such as quantized energy levels in a box potential can be visualized in this setup and confirm the general suitability of the method. But more important, it also enlarges the possibilities to investigate new phenomena. Due to the higher resolution of the DLW 1D and even 0D potentials are fabricated. Since the dimensionality of a system influences its properties, we investigate thermodynamic properties during the transition from two- to one-dimensional photon gases. This transition is realized by performing and comparing measurements on isotropic harmonic potential to anisotropic potentials of higher aspect ratios and stronger confinements. The results confirm theoretical expectations and show a second-order phase transition in 2D, while a crossover behavior is observed in 1D [4]. Recent measurements even show the possibility to investigate characteristics of coupled photon gases. This is demonstrated by observing the band structure of an SSH chain, including the topological trivial and the non-trivial case with its corresponding edge states.

We acknowledge support by the Deutsche Forschungsgemeinschaft (DFG) through CRC/ Transregio 185 OSCAR B06 (project No. 277625399) and by the Max Planck Graduate Center with the Johannes Gutenberg University of Mainz (MPGC).

References

1. Klaers, J., F. Vewinger and M. Weitz, "Thermalization of a two-dimensional photonic gas in a 'white-wall' photon box," *Nature Physics*, Vol. 6, pp. 512–515, 2010.

2. Klaers, J., J. Schmitt, F. Vewinger and M. Weitz, "Bose-Einstein condensation of photons in an optical microcavity," *Nature*, Vol. 468, pp. 545–548, 2010.

3. Moodie, R. I., P. Kirton, and J. Keeling, "Polarization dynamics in a photon Bose-Einstein condensate," *Phys. Rev. A*, Vol. 96, 043844, 2017.

4. Karkihalli Umesh, K., J. Schulz, J. Schmitt, M. Weitz, G. von Freymann and F. Vewinger, "Dimensional Crossover in a Quantum Gas of Light," *Nature Physics* , Vol. 20, pp. 1810–1815, 2024.

Scanning Near-Field Optical Microscopy on Hyperuniform Disordered photonic materials

N. Granchi[1*], G. Calusi[1], K. Stokkereit[2], M. Lodde[3], C. Gonzini[1], A. Fiore[3], M. Florescu[4] and F. Intonti[1]

[1]Department of Physics and Astronomy and LENS, University of Florence, Italy

[2] Advanced Technology Institute and Department of Physics, University of Surrey, UK

[3]Department of Applied Physics and Institute for Photonic Integration, Eindhoven University of Technology, NL

[4] Optoelectronics Research Centre, University of Southampton, UK

[*]corresponding author: nicoletta.granchi@unifi.it

Abstract: A special class of disordered photonic heterostructures, hyperuniform disordered (HuD) photonic structures, allows to deterministically tailor Anderson localization and diffusive transport. Here, we detect for the first time the presence of level repulsion between delocalized states in a HuD photonic platform, by means of the Scanning Near-field Optical Microscopy technique.

Disordered photonic nanostructures have attracted tremendous interest in the past three decades, not only due to the fascinating and complex physics of light transport in random media, but also for peculiar functionalities in a wealth of interesting applications. Recently, the interest in dielectric disordered systems has received new inputs by exploiting the role of short and long-range spatial correlations within scatterer configurations. Hyperuniform disordered (HuD) photonic materials [1], that share features of photonic crystals and random systems, are an example of engineered disorder to control, through short range-order, both spectral and momentum responses of light.

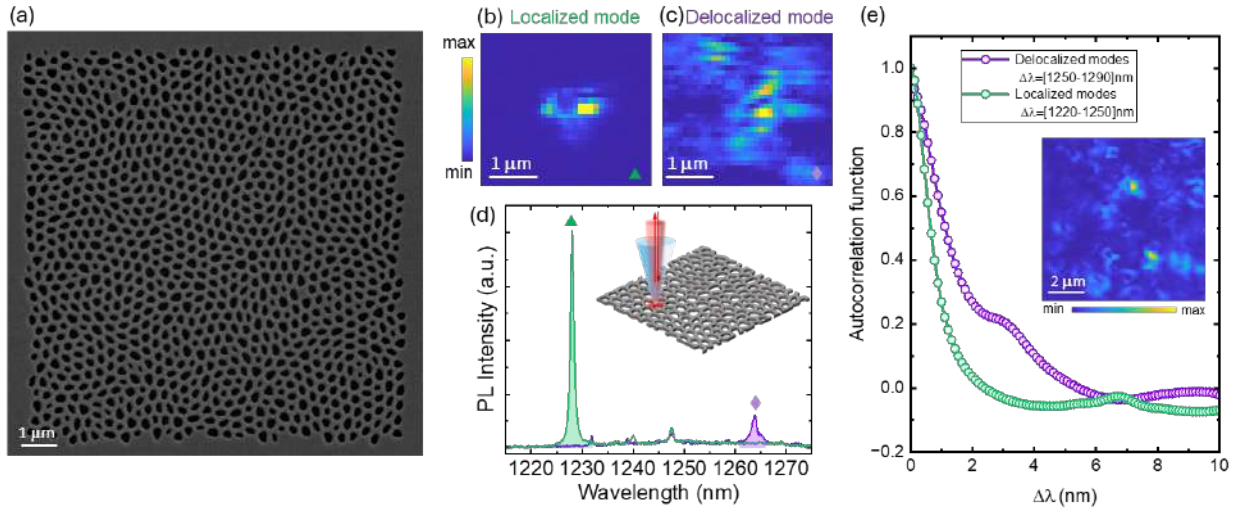
Recently, an experimental study has revealed the transition from light localization to diffusive transport in an optically active platform with a HuD design [2], showing that this type of correlated disorder system hosts Anderson-like modes very promising for fundamental studies but also for technological applications in the field of light-matter interactions. The presence of deterministically tailored localized and diffusive transport within the same photonic platform has raised novel and exciting questions.

Quantum mechanical level repulsion in complex and disordered quantum systems has first been modeled by Wigner and Dyson's random matrix theory [3], and thanks to the many experimental verifications in various branches of physics, became a most valuable criterion for the study of the Anderson transition [4,5].

Here, taking advantage of the Scanning Near-field Optical Microscopy (SNOM) technique, we present the first experimental evidence of level repulsion in HuD systems in a tailored diffusive regime.

The studied samples consist in 200nm thick GaAs slabs patterned with a HuD design (Fig.1a); embedded in the middle of the slab are InAs quantum dots that act as optically active medium. The room temperature SNOM, capable of subwavelength spatial resolution in the near-IR range, is employed in illumination/collection configuration, meaning that the sample is excited with light from a diode laser (785 nm) coupled into a chemically etched optical fiber. Photoluminescence (PL) spectra from the sample are collected at each tip position through the same probe. Fig.1b-d report the results of a SNOM measurement performed on the sample; the PL SNOM maps of a typical Anderson localized mode (b) and of a delocalized one (c), along with their relative spectra acquired in the positions of maximum intensity (d).

The method employed to detect the level repulsion phenomenon is based on the evaluation of the autocorrelation function [4,6], which allows for a statistical description of the systems in terms of energy level distribution of the optical modes sustained by the system. Within a single SNOM scan performed on the entire sample (as shown in the inset of Fig.1e) we have access to all the modes within a large spectral range. We selectively evaluate the autocorrelation function in the two spectral ranges corresponding to localized and delocalized modes, and the results are plotted in Fig.1e. The presence of a pronounced shoulder at short spectral distances in the purple curve is a clear indication of level repulsion between delocalized modes, differently, from what is observed in the autocorrelation function of localized modes. Moreover, through the evaluation of the spectral width of the autocorrelation peak, our spatially resolved spectroscopy technique gives direct insights on the typical hallmark of light localization regimes, like for example the smaller (larger) spectral width of localized (delocalized) modes.



References

1. Florescu, M., Torquato, S., Steinhardt, and P.J., Designer disorderd materials with large, complete photonic band gaps PNAS 106, 20658–20663, 2009.
2. Granchi, N., Spalding, R., Lodde, M., Petruzzella, M., W. Otten, F., Fiore, A., Intonti, F., Sapienza, R., Florescu, M. and Gurioli, M., Near-Field Investigation of Luminescent Hyperuniform Disordered Materials, Advanced Optical Materials, 2102565, 2022.
3. Kramer, B. and MacKinnon, A., Rep. Prog. Phys. 56, 1469, 1993.
4. Intonti, F., Emiliani, V., Lienau, C., Elsaesser, T., Savona, V., Runge, E., and Zimmermann, R., Quantum Mechanical Repulsion of Exciton Levels in a Disordered Quantum Well, Phys. Rev. Lett., **87**, 076801, 2001.
5. Escalante, J.M., Skipetrov, S.E. Level spacing statistics for light in two-dimensional disordered photonic crystals. *Sci Rep* **8**, 11569 (2018).
6. von Freymann, G., Kurtz, E., Klingshirn, C., Wegener, M., Statistical analysis of near-field photoluminescence spectra of single ultrathin layers of CdSe/ZnSe, Appl. Phys. Lett. 77 (3) 394–396, 2000.

Spectroscopic proof of the non-thermal reactant activation in plasmon-photocatalysis

Z. H. Kim*

Department of Chemistry, Seoul National University, Seoul 08826, Korea
*corresponding author: zhkim@snu.ac.kr

Abstract: Recent studies on plasmon photocatalysis suggest that the hot-electrons generated by plasmon-excited nanostructures may induce non-thermal vibrational activation of metal-bound reactants. However, this postulate has not been fully validated. Here, we provide direct and quantitative evidence that such activation occurs on plasmon-excited nanostructures.

Using anti-Stokes surface-enhanced Raman scattering (SERS) spectroscopy, we mapped the vibrational state population distributions of reactants on plasmon-excited nanostructures (Fig. 1a). The vibrational quantum state distributions reveal that a specific vibrational mode of the reactant is selectively excited (Fig. 1b), with the reactants exhibiting >10 times more energy in this mode than expected for fully thermalized molecules at the given local temperature [1]. Furthermore, a significant portion (>20%) of the excited reactant is in multi-quantum excited vibrational states ($v \geq 2$, Fig 1c). This mode-specific and multi-quantum vibrational excitation cannot be explained by photothermal heating of the reactant or direct optical transitions of the metal-molecule complex [2]. Instead, the observation can be modeled by hot electron-molecule energy transfer mediated by the transient negative ions. This establishes links between non-thermal reactant activation, plasmon-induced hot electrons, and negative ion resonances. Our findings validate the mechanism of plasmon photocatalysis and introduce a new method to explore the vibrational reaction control on metal surfaces.

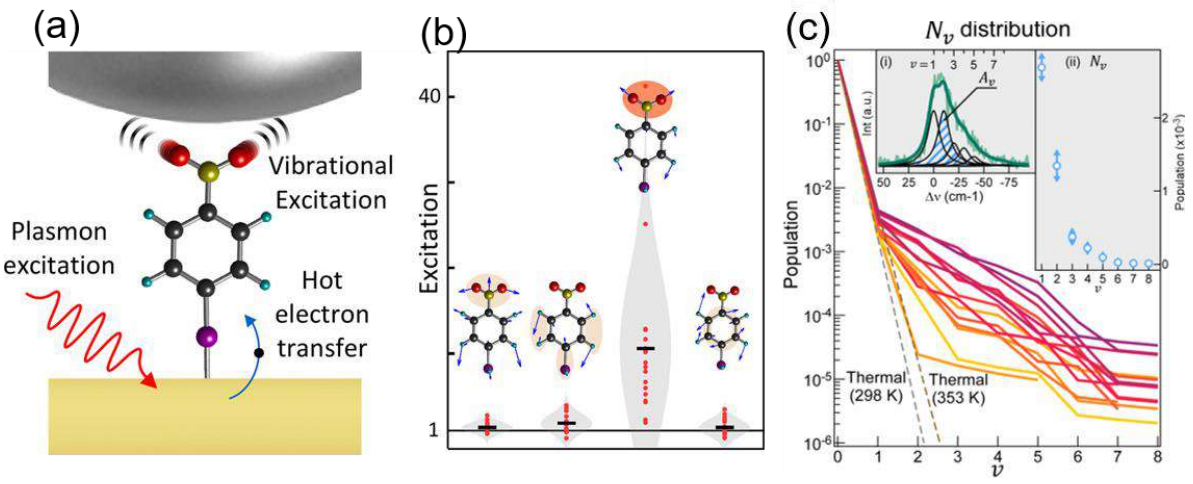


Fig. 1 (a) Schematic of the hot-electron induced vibrational excitation. (b) Mode-selective vibrational excitation of 4-nitrobenzenethiol (4-NBT) in a plasmonic hotspot. The y-axis of the graph denote the vibrational occupation number in reference to the thermal occupation number [1]. (c) Vibrational quantum number distributions (N_v) of NO-symmetric stretching mode of the 4-NBT, plotted as a function of vibrational quantum number (v). Dashed lines denote the expected thermal populations. The inset graphs display the (i) asymmetrically broadened lineshape of the anti-Stokes vibrational peak of 4-NBT and (i) the resulting population in linear scale [2]

References

1. Shin, H-. H.; Jeong; J.; Nam, Y.; Lee, K. S.; Yeon, G. J.; Lee, H.; Lee, S. Y.; Park, S.; Park., H.; Lee, J. Y.; Kim, Z. H. 2023. *J. Am. Chem. Soc.* 145, 12264-12274.
2. Jeong; J.; Shin, H-. H.; Kim, Z. H. 2024. *ACS Nano* 18, 25290-25301.

Active modulation of optical response in transparent conducting oxide films

S. Benedetti,[1*] A. di Bona,[1] S. D'Addato,[1,2] A. Y. Petrov,[3] P. Torelli,[3] M. Magnozzi,[4] S. Colace,[4] M. Canepa,[4] Francesco Bisio[5]

[1] CNR–Istituto Nanoscienze, Modena, Italy.
[2] Dipartimento di Scienze Fisiche, Informatiche, Matematiche, Universita` di Modena e Reggio Emilia, Modena, Italy
[3] CNR-IOM, Laboratorio TASC, AREA Science Park, Basovizza, 34149 Trieste, Italy
[4] OptMatLab, Dipartimento di Fisica, Universita` di Genova, Italy
[5] CNR-SPIN, Genova, Italy
[*]corresponding author: stefania.benedetti@nano.cnr.it

Abstract: We investigated the room temperature, low-voltage-enabled modulation of the optical response of a Al:ZnO film with controlled structural quality (from crystalline to amorphous) coupled with $BaTiO_3$ film by means of in-operando spectroscopic ellipsometry, ascribed to a combination of charge accumulation/depletion at the interface and Pockels effect in the $BaTiO_3$ layer.

Transparent conductive oxides (TCOs) show the ability to adjust the free carrier concentration through the doping level and allow epsilon-near-zero conditions to be tuned in visible light communications and infrared telecommunication windows. While the tuning of the optoelectronic properties of TCO by modulating their intrinsic properties is extensively exploited, a great challenge is their control by external stimuli, which would pave the way for intriguing applications in photonic devices. The most flexible and appealing method to perform optical modulation is to exploit the field effect (FE) by applying an external bias to TCO thin films within a suitable metal–oxide–semiconductor (MOS) device and inducing an ultrathin accumulation/depletion layer at the dielectric/conducting oxide interface.

In this work we have investigated the room temperature, low-voltage-enabled modulation of the optical response of hybrid transparent-conductive-oxide/ferroelectric multilayers. We have shown that Al-doped ZnO (AZO) films in a plane capacitor configuration have been optically modulated through FE gating and a 100 V bias at 4.2 K determines a sizable charge displacement and a variation of the refractive index in the infrared range up to value of more than 0.1.[1] Reducing the insulator thickness by exploiting a high-k-dielectric $BaTiO_3$ (BTO) film allows boosting the charge-density modulation by increasing the capacitance of the system, allowing lower bias and room temperature operation, with relevant applicative consequences. For this purpose, we have fabricated an optical multilayer consisting of AZO and BTO films deposited on a Nb-doped $SrTiO_3$(110) (NSTO) substrate. We have exploited AZO films prepared with different structural order by magnetron sputtering.[2] Epitaxially grown films on STO(110) substrates have been compared with polycrystalline films grown in the same conditions on SiO_2/Si. Epitaxial films with larger crystalline grains retain their optimal properties down to low thickness, limited mostly by ionized impurity scattering, while polycrystalline films, where grain boundary scattering is dominant, are considerably more resistive. Optical properties do not show significant differences, confirming that the intrinsic properties of the material are not affected by crystal quality. Amorphization, on the contrary, induces an increase in carrier density but a strong reduction in mobility.

We have then fabricated AZO/BTO/NSTO capacitors of about 100 μm lateral size by EBL. We have detected a sizable variation of the optical response at an applied bias of 0.2 V at room temperature that we have

ascribed to the combined effect of exponentially graded charge accumulation/depletion at the AZO/BTO and BTO/NSTO interfaces, accompanied by the voltage-induced Pockels effect in the BTO layer through the development of a complex optical model.[3] Despite the complexity of the system and the variety of the physical effects concurring to its FE-induced variation of the optical response, we have succeeded in modeling the optical response of each layer involved and in introducing the main bias-induced mechanisms that lie underneath the FE-induced variation of the refractive index in the infrared range up to value of more than 0.1. This work therefore provides important clues to model and understand in detail the behavior and the working mechanisms of optically active systems, with relevant applications in the field of active photonics.

Authors acknowledge financial support under the National Recovery and Resilience Plan (NRRP), Mission 4, Component 2, Investment 1.1, Call for tender no. 104 PRIN 2022 published on 2.2.2022 by the Italian Ministry of University and Research (MUR), funded by the European Union – NextGenerationEU AMONIX – CUP B53D23004060006, ERACLITO – CUP B53D2300904006, PRIN PNRR 2022 ARCO – CUP B53D23027690001.

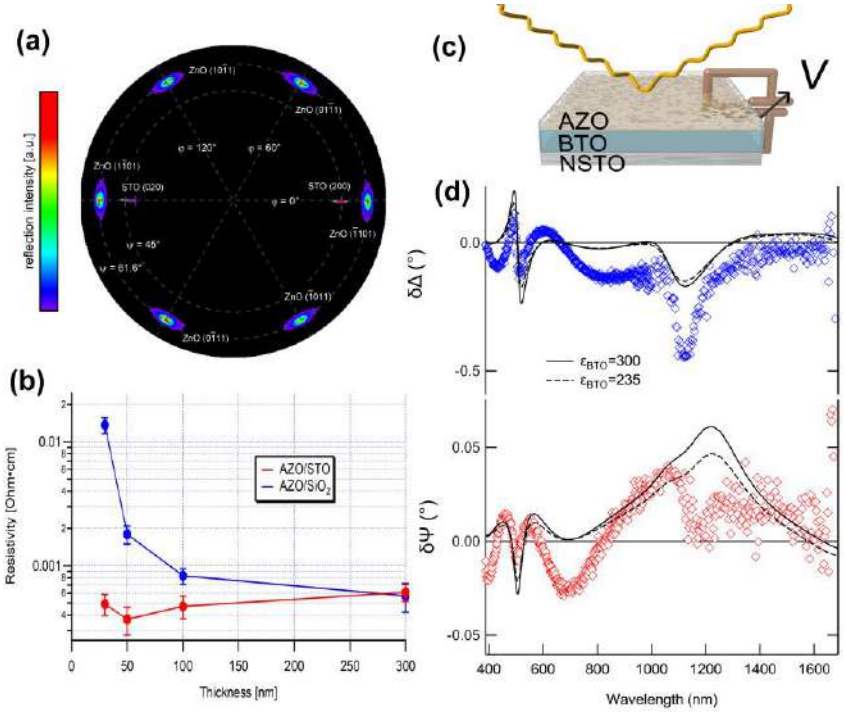


Figure 1: (a) XRD pole figure of AZO on STO(110) and (b) resistivity of AZO on STO and on SiO2/Si [1]; (c) sketch of the AZO/BTO capacitor stack and (d) measured and modelled differentials δΔ and δΨ of the ellipsometric angles with a +0.2 V bias applied.[3]

References

1. Sygletou, M., S. Benedetti, A. di Bona, M. Canepa, F. Bisio and E. Bellingeri, "In-Operando Optical Spectroscopy of Field-Effect-Gated Al-Doped ZnO" ACS Appl. Mater. Interfaces, Vol. 15, 3112−3118, 2023.
2. Magrin Maffei, R., A. di Bona, M. Sygletou, F. Bisio, S. D'Addato and S. Benedetti, "Suppression of grain boundary contributions on carrier mobility in thin Al-doped ZnO epitaxial films", Appl. Surf. Sci., Vol. 624, 157133, 2023.
3. Magrin Maffei, R., M. Magnozzi, M. Sygletou, S. Colace, S. D'Addato, A. Yu. Petrov, M. Canepa, P. Torelli, A. di Bona, S. Benedetti and F. Bisio, "Active optical modulation in hybrid transparent-conductive oxide/electro-optic multilayers", J. Mater. Chem. C, 2025, doi: 10.1039/d4tc04748f.

Photonic force microscopy in front of Epsilon-near-zero (ENZ) surfaces

M. G. Donato[1, *], M. Hinczewski[2], T. Letsou[2], M. El Kabbash[2], R. Saija[1, 3], P. G. Gucciardi[1], N. Engheta[4], G. Strangi[2, 5], O. M. Maragò[1]

[1]CNR-IPCF, Istituto per i Processi Chimico-Fisici, I-98158 Messina, Italy.

[2]Dept. of Physics, Case Western Reserve University, 10600 Euclid Avenue, 44106, Cleveland, Ohio, USA

[3]Dip. di Scienze Matematiche e Informatiche, Scienze Fisiche e Scienze della Terra, Università di Messina, I-98166 Messina, Italy

[4]Dept. of Electrical and Systems Engineering, University of Pennsylvania, Philadelphia, PA 19104, USA

[5]CNR-NANOTEC, Istituto di Nanotecnologia and Department of Physics, University of Calabria, Via Pietro Bucci 87036, Rende, Italy

[*]corresponding author: maria.donato@cnr.it

Abstract: Photonic force microscopy has been used to highlight a pN range levitation force on a 1 μm polarizable particle trapped in proximity of an Epsilon-near-zero (ENZ) surface.

Photonic force microscopy uses optically trapped micro and nanoparticles to probe the interactions with a surface [1-3]. Short-range repulsive or attractive forces between the probe and the surface, due to electrostatic and Van der Waals interactions or Casimir effect, or even the limitation of the particle hydrodynamic due to the presence of the wall may be considered for the correct evaluation of the total force on the trapped particle. A careful calibration of the trap is necessary to precisely measure dynamic axial forces and surface force gradients [4, 5]. Moreover, some peculiarities of the surface itself may introduce additional forces that must be taken into account. As an example, a repulsive near field force is expected [6] when a point dipole is in front of an Epsilon-near-zero (ENZ) surface which is illuminated at its ENZ wavelength. In this talk, we will discuss, both theoretically and experimentally, the possibility of using photonic force microscopy to investigate if such an ENZ-related force could be observed on a trapped particle with size larger than a point dipole. By using different theoretical methods (dipole approximation, finite elements calculation, transition (T-)matrix) we will show [7] that particle optomechanics depends on surface and particle characteristics, such as particle size, particle-surface edge-to-edge distance, surface nature (dielectric, metallic, ENZ). Moreover, we devise an experimental procedure in which a 1 μm radius dielectric bead is optically trapped in front of a surface with ENZ properties at 547 nm. The trap equilibrium point of the particle is perturbed by a square-wave pulsed beam, exciting the surface at wavelengths ranging between 480 nm and 620 nm. A repulsive force in the pN range, having a maximum close to the ENZ wavelength of the surface, has been measured on the trapped particle; on the contrary, an attractive force is observed when trapping in front of dielectric or metallic surfaces. We attribute this repulsive-attractive optomechanics to ENZ-related repulsion and thermal effects.

Acknowledgement. Funding by European Union (NextGeneration EU), through the project PRIN2022 "EnantioSelex – Mapping and controlling nanoscale optomechanical forces for separation of chiral analytes" (grant number 2022P9F79R) is gratefully acknowledged.

References

1. A. Ashkin, “Acceleration and trapping of particles by radiation pressure,” *Phys. Rev. Lett.,* vol. 24, pp. 156, 1970.
2. O. M. Maragò, P. H. Jones, P. G. Gucciardi, G. Volpe, and A. C. Ferrari, “Optical trapping and manipulation of nanostructures,” Nature Nanotechnol., vol. 8, pp. 807, 2013.
3. L. P. Ghislain and W. W. Webb, “Scanning–force microscope based on an optical trap,” Opt. Lett., vol. 18, pp. 1678–1680, 1993
4. E. Schaeffer, S. F. Norrelykke, and J. Howard, “Surface forces and drag coefficients of microspheres near a plane surface measured with optical tweezers,” Langmuir, vol. 23, pp. 3654–3665, 2007.
5. S. F. Tolic-Nørrelykke, E. Schäffer, J. Howard, F. S. Pavone, F. Jülicher, and H. Flyvbjerg, “Calibration of optical tweezers with positional detection in the back focal plane,” Rev. Sci. Instrum., vol. 77, no. 10, p. 103101, 2006.
6. F. J. Rodríguez-Fortuño, A. Vakil, and N. Engheta, “Electric levitation using epsilon-near-zero metamaterials,” Physical Review Letters, vol. 112, no. 3, p. 033902, 2014.
7. Y. Kiasat, M. G. Donato, M. Hinczewski, M. ElKabbash, T. Letsou, R. Saija, O. M. Maragò, G. Strangi, and N. Engheta, “Epsilon-near-zero (ENZ)-based optomechanics,” Communications Physics, vol. 6, no. 1, p. 69, 2023.

Extracting resonances in nanophotonic systems from light scattering simulations

F.Binkowski[1], F. Betz[1], L. Zschiedrich[1,2], S.Burger[1,2] and M. Hammerschmidt[1,2]
[1]Zuse Institute Berlin, Germany
[2]JCMwave GmbH, Germany
Corresponding author: martin.hammerschmidt@jcmwave.com

Abstract: In this contribution, we present a rigorous method for calculating resonance modes from scattering solutions of nanophotonic systems. We demonstrate its application in computing resonant states in periodic nanostructures such as metasurfaces, nanostructured waveguides, and other photonic systems.

In this contribution, we review a recently introduced approach for the calculation of resonance modes based on the rational approximation of optical response functions [1]. The rational approximation of the optical response is calculated by the AAA algorithm [3], where scattering solutions are computed at selected sampling points and superposed based on the poles and weights of the rational approximation. These are used to determine the resonance modes, the solutions of the nonlinear, non-hermitian eigenmode problems that would be otherwise difficult to calculate for most nanophotonic systems with state-of-the-art solvers like the Arnoldi method.

We demonstrate the method, explain the solution approach, and show accuracy and convergence in selected examples. For a chiral metasurface, we show that the chiroptical response on parameter variations can be accurately modeled in the vicinity of the relevant resonance frequencies [1]. We demonstrate that we can obtain parameter sensitivities in addition to the fields of the resonance modes.

Furthermore, we report on an application of the approach to microstructured photonic waveguides recently presented in [2]. Special light sources for solving the scattering problems are used to calculate only the fundamental resonance modes of the waveguides. Other types of modes, such as modes localized in the cladding of the waveguides or higher-order modes, are filtered out directly. We compare the AAA-based approach with a standard approach from the field of computational photonics and discuss corresponding numerical convergence studies.

We acknowledge funding by the Deutsche Forschungsgemeinschaft (DFG, German Research Foundation) under Germany's Excellence Strategy - The Berlin Mathematics Research Center MATH+ (EXC-2046/1, project ID: 390685689) and by the German Federal Ministry of Education and Research (BMBF Forschungscampus MODAL, project 05M20ZBM).

References

1. Fridtjof Betz, Martin Hammerschmidt, Lin Zschiedrich, Sven Burger, and Felix Binkowski. Efficient rational approximation of optical response functions with the aaa algorithm. *Laser Photonics Rev.*, 18(11):2400584, 2024.

2. Felix Binkowski, Fridtjof Betz, Martin Hammerschmidt, Lin Zschiedrich, and Sven Burger. Resonance modes in microstructured photonic waveguides: Efficient and accurate computation based on AAA rational approximation. *preprint arXiv:2412.13826*, 2024.

3. Yuji Nakatsukasa, Olivier Sète, and Lloyd N. Trefethen. The AAA algorithm for rational approximation. *SIAM J. Sci. Comput.*, 40(3):A1494–A1522, 2018.

Towards photonic orbitronics: exploiting the orbital angular momentum of light

M. Weber[1], J. Schulz[1], I. Heil[1], C. Jörg[1], and G. von Freymann[1,2*]
[1]Department of physics and research center OPTIMAS,
RPTU University of Kaiserslautern-Landau, Germany
[2]Fraunhofer Institute for Industrial Mathematics ITWM, Kaiserslautern, Germany
georg.freymann@rptu.de (corresponding author)

Abstract

Combining higher order modes in coupled waveguide systems with light possessing orbital angular momentum allows for preparing and studying interesting solid-state-phenomena like the orbital-Hall-effect in a photonic model system. We report on several recent experimental realizations.

Coupled waveguide arrays have long been established as photonic model systems to explore solid state physics described by the 2D time-dependent Schrödinger equation. The mathematical analogy between the Schrödinger equation and the paraxial Helmholtz equation allows to visualize quantum mechanical effects like topological protection in quantum-Hall systems, thus providing visual insights into complex condensed matter physics effects not easily imaged in electronic solid state systems. The most prominent example being photonic graphene, demonstrating the existence of topologically protected edge states under the influence of an artificial magnetic field. [1]

However, most of the work along this line of photonic quantum simulation has been limited to waveguides supporting only the fundamental mode of the waveguides, thus simulating the s-orbital of the corresponding atoms.

Higher orbitals can be addressed using higher order modes of the waveguides, either by changing the size and/or shape of the waveguide or by adjusting the wavelength. Along these lines we could recently demonstrate a quadrupole topological insulator, [2] realizing the required artificial magnetic π-flux in one plaquette of the structure via a combination of s- and p-orbitals.

Besides hard-wiring the orbitals in the sample, another degree of freedom is achieved externally with the help of a spatial light modulator, which allows shaping the exciting light between Gaussian modes and modes with orbital angular momentum. Switching between modes without and with orbital angular momentum leads to switchable gauge fields and thus to either localization or propagation of light inside the structure. [3]

Combining both approaches, i.e. using higher orbitals of the waveguide system and light with orbital angular momentum, allows for the realization of photonic orbitronics, following the recent development in solid-state physics, [4] where realizing the orbital-Hall-effect is especially difficult due to the omnipresent spin-orbit-coupling and orbital quenching.

Coupled waveguide arrays are fabricated using direct laser writing via two-photon polymerization using a commercial device (Nanoscribe Photonic Professional GT). In a first step, hollow waveguide arrays are written in the commercial resin IP-Dip (Nanoscribe), which are subsequently infiltrated with SU8-10 (Microresist technology) and baked to remove remaining solvents. Dimensions and separation of the individual waveguides are optimized using beam propagation simulations. The waveguides are arranged to emulate a polarized SnTe lattice, found in solid-state physics under application of an external electric field. The distortion breaks the mirror symmetry and thus lifts the orbital quenching.

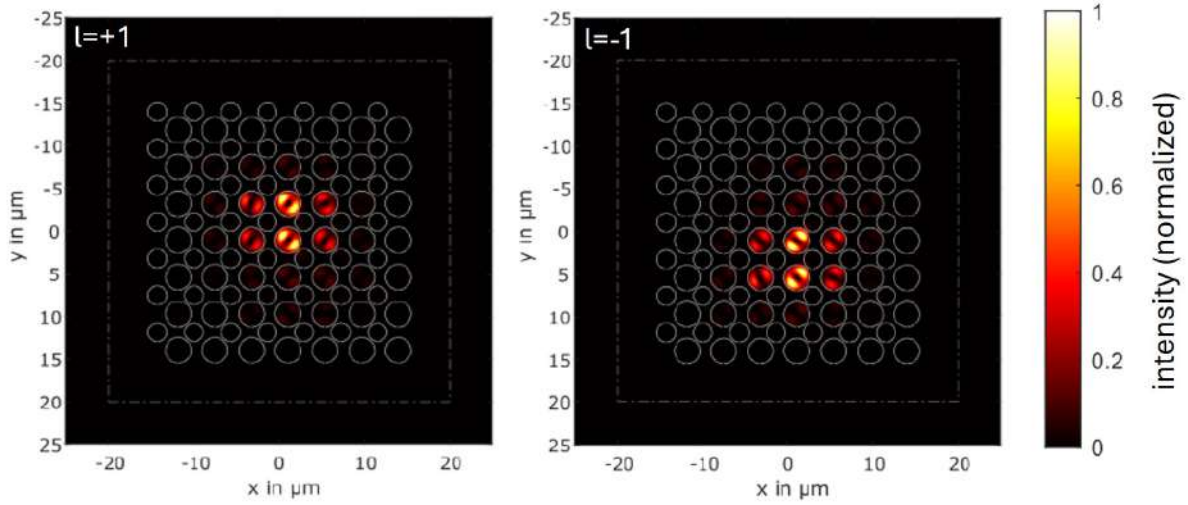


Figure 1: Numerical simulation: Light with orbital angular momentum with different handedness is coupled into the waveguide structure highlighted by the gray circles. Depending on the orbital angular momentum the wave package either moves up (left hand side) or down (right hand side), demonstrating the realization of the orbital Hall effect.

Light from a HeNe-laser is sent to a spatial light modulator (Hamamatsu) to prepare a wavepacket of modes with orbital angular momentum either with $l = +1$ or $l = \in 1$ and with a separation in phase to address certain k-vectors of the Brillouin-zone. These modes are coupled into the waveguide array at the entrance facet.

Observation at the output facet after a propagation length of 700 µm shows transport either up or down in good correspondence with the respective orbital angular momentum of light and in accordance with numerical simulations shown in Figure 1.

In conclusion we could demonstrate a first realization of the orbital Hall effect in a polarized photonic SnTe lattice by combining proper waveguide design with orbital angular momentum of the light propagating inside the structure.

We acknowledge support by the Deutsche Forschungsgemeinschaft (DFG) through CRC/ Transregio 185 OSCAR B06 (project No. 277625399).

References

[1] M. Rechtsman, J. Zeuner, Y. Plotnik, et al. "Photonic Floquet topological insulators", *Nature* **496**, 196 (2013).

[2] J. Schulz, J. Noh, W. A. Benalcazar, G. Bahl, and G. von Freymann "Photonic quadrupole topological insulator using orbital-induced synthetic flux", *Nature Communications* **13**, 6597 (2022).

[3] C. Jörg, G. Queraltó, M. Kremer, G. Pelegrí, J. Schulz, A. Szameit, G. von Freymann, J. Mompart, V. Ahufinger "Artificial gauge field switching using orbital angular momentum modes in optical waveguides", *Light: Science&Applications* **9**, 150 (2020).

[4] D. Go, D. Jo, H.-W. Lee, M. Kläui, and Y. Mokrousov "Orbitronics: orbital currents in solids", *EPL* **135**, 37001 (2021).

Direct Determination of Carrier Parameters in Plasmonic Indium Tin Oxide Nanocrystals Exploiting Magnetoplasmonic Modulation

A. Gabbani[1,2*] E. Della Latta,[2] X. Li,[3] A. Scarperi,[2] F. Martini,[2] F. Biccari,[4] M. Kociak,[3] M. Geppi,[2] S. Borsacchi,[5] F. Pineider,[2,4]

[1]Department of Chemistry "Ugo Schiff", University of Florence, Italy

[2]Department of Chemistry and Industrial Chemistry, University of Pisa, Italy

[3]Université Paris-Saclay, CNRS, Laboratoire de Physique des Solides, Orsay, France

[4]Department of Physics and Astronomy, Università degli Studi di Firenze, via Sansone 1, Sesto Fiorentino, FI, Italy

[5]Institute of Chemistry of Organometallic Compounds, Italian National Research Council (ICCOM-CNR), via G. Moruzzi 1, 56124 Pisa, Italy

*corresponding author: alessio.gabbani@unifi.it

Abstract: Tin-doped indium oxide nanocrystals are promising candidates for optoelectronics and active plasmonics in the NIR. Here, an integrated approach was developed involving magneto-optics and single particle spectroscopy to directly determine experimentally the carrier parameters as a function of tin doping, which is challenging in such small nanosystems.

Indium Tin Oxide (ITO) is the prototype conductive oxide, which has recently gathered interest in nano-optics,[1] owing to the excellent plasmonic properties displayed by ITO nanocrystals (NCs) in the infrared spectral region. Unlike noble metals, the plasmonic resonance frequency in spherical ITO NCs can be tuned synthetically by controlling the tin content.[2] Nanostructuration typically introduces several challenges in the characterization of electronic parameters in NCs, hampering advanced material design. Indeed, while films of doped oxides are routinely studied through electrical experiments, these cannot be reliably applied to NCs, since the insulating ligand layer forces charge hopping and results in a complex (albeit interesting) behaviour. Moreover, the surface potential creates a depletion region near the surface, which typically requires core@shell models with a purely dielectric shell to fit the extinction spectrum.[3]

In this work,[4] we present an integrated approach (Figure 1) based on magneto-optics, single-particle Electron Energy Loss (EELS) spectroscopy and ^{119}Sn Solid State Nuclear Magnetic Resonance (SSNMR) spectroscopy to extract the fundamental electronic parameters of a series of ITO NCs with variable tin doping. Our methodology overcomes the limitations of standard fitting approaches based on extinction spectroscopy, which can only determine the ratio between carrier density and mass. Conversely, exploiting concepts from magnetoplasmonics[5,6] we determined the carrier effective mass directly on the NCs, discarding the use of literature values. We found that mass values depart appreciably from those measured on thin films; consequently, we found carrier density values that are different from reported literature values for similar systems. The effective mass was found to deviate from the parabolic approximation at high carrier density. This approach can be generalized to other plasmonic heavily-doped semiconductor nanostructures and represents, to the best of our knowledge, the only method to date to characterize the full Drude parameter space of 0-D nanosystems.

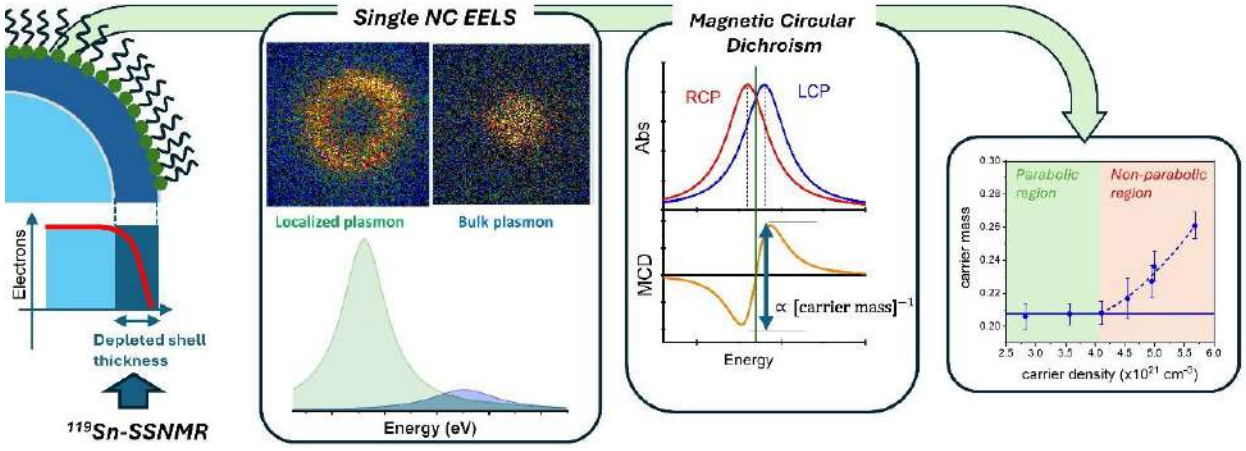


Figure 1: Scheme of the multitechnique approach employed in this work to extract the relation between carrier mass and carrier density in a series of chemically prepared ITO NCs with variable Sn content.

Italian MUR is acknowledged through PRIN 2022 PNRR project P20229723Z (CUP: B53D23025560001).

References

1. A. Agrawal, *et al.*, Chem. Rev. 2018, 118 (6), 3121–3207.
2. A. Mazzotta, *et al.*, ACS Appl. Mater. Interfaces 2022, 14 (30), 35276–35286.
3. S. L. Gibbs, *et al.*, Acc. Chem. Res. 2019, 52 (9), 2516–2524.
4. A. Gabbani, *et al.*, ACS Nano 2024, 18, 15139−15153.
5. A. Gabbani, *et al.*, Nano Lett. 2022, 22 (22), 9036–9044.
6. A. Gabbani, *et al.*, J. Appl. Phys. 2021, 129 (21), 211101.

Chiral Metasurface Photodetectors for Circular-Polarization-Selective Phase Contrast Imaging

A. M. Erturan, J. Liu, M. A. Roueini, N. Malamug, L. Tian, and R. Paiella*

Department of Electrical and Computer Engineering and Photonics Center,
Boston University, 8 St. Mary's St., Boston, MA 02215, USA
*corresponding author: rpaiella@bu.edu

Abstract: We report metasurface photodetectors that can selectively measure the local phase gradient of only one circular polarization component of any incident wave, in a single shot and with standard imaging optics. Pixel arrays of these devices may enable new functionalities for applications in chemical sensing, biomedical microscopy, and machine vision.

Light waves possess multiple degrees of freedom besides intensity, including phase and polarization, that can contain important information of interest but require complex and bulky systems for their measurement. As a result, recently there has been growing interest in the development of miniaturized multifunctional photodetectors that can provide direct access to the same information [1]. Within this general context, the present work introduces an entirely new functionality for an integrated device – the ability to selectively measure the local phase gradient of only one circular polarization component of the incident light [2].

These devices consist of planar photodetectors stacked with a plasmonic gradient metasurface that introduces a strong dependence of responsivity on illumination angle and polarization. Specifically, the metasurface is designed to couple light incident at the desired detection angles and polarization into surface plasmon polaritons (SPPs) supported by an underlying metal film, which are then scattered into the photodetector active layer by a set of subwavelength slits perforated through the metal film [Fig. 1(a)]. A similar architecture (with a periodic diffraction grating instead of a gradient metasurface) has been used in our prior work focused on lensless compound-eye vision [3] and linearly polarized phase contrast imaging [4]. For phase imaging, the target detection angle θ_p should be small enough so that the resulting peak in the angular response overlaps asymmetrically with normal incidence, leading to large variations in responsivity with illumination angle around $\theta = 0$. The resulting devices can therefore be used to measure any deflection in the local direction of light propagation away from normal incidence, which in turn is proportional to the local transverse phase gradient of the incident light.

For the angle- and circular-polarization-selective excitation of SPPs, here we rely on the combined use of the plasmonic resonance and Pancharatnam-Berry (PB) phase of the individual meta-units, which consist of rectangular Au nanoparticles (NPs) of different size and orientation [Fig. 1(b)]. The NP array is designed so that, for one circular polarization component, the resonance and PB scattering phase profiles cancel each other, leading to specular reflection. At the same time, for the other circular polarization, these two phase profiles add up to each other to match the incident-light wavevector at the target detection angle to that of an SPP on the Au film. Using this design strategy, we have developed two devices (labeled R and L) providing angle-sensitive photodetection peaked at $\theta_p \approx -2°$ for right and left circularly polarized (RCP and LCP) light, respectively.

Figures 1(c)-(e) show the measured responsivity data of device R, illustrating the expected angle and polarization dependence. For circular-polarization-selective phase imaging, the key feature of these data is the large versus near-zero responsivity slope $d\mathscr{R}/d\theta$ at normal incidence ($\theta = 0$) for RCP and LCP light, respectively

[see Fig. 1(e), where the shaded region indicates the range of angles incident on the sensor array in a typical microscope]. In particular, our measurements show that the ratio $|d\mathscr{R}_{RCP}/d\theta|/|d\mathscr{R}_{LCP}/d\theta|$ is 37× on average over a bandwidth of ~70 nm around the 1.55-μm design wavelength, which provides a measure of the polarization selectivity of this device with respect to phase gradient. Similar results with the two states of circular polarization interchanged were obtained with device L. A detailed analysis of these data also provides a direct illustration of spin-momentum locking in SPPs and the role of spin conservation in photon/plasmon interactions.

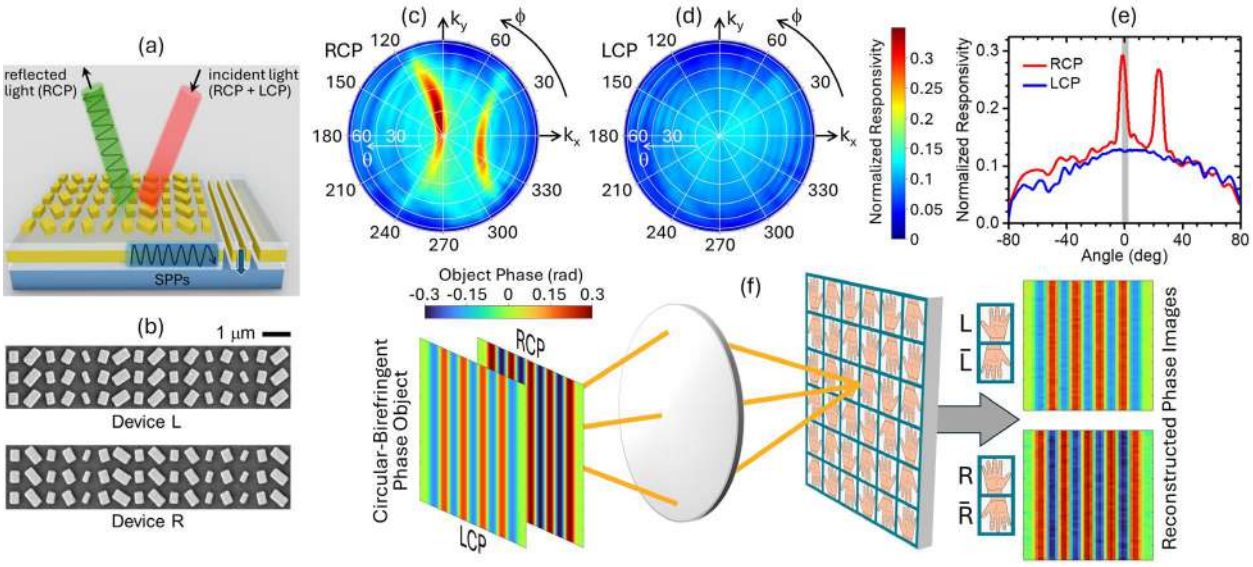


Fig. 1. (a) Schematic device structure. (b) SEM images of the metasurfaces of devices L and R. (c), (d) Measured responsivity of device R versus illumination angles under RCP (c) and LCP (d) illumination. (e) Horizontal line cuts of the color maps of (c) and (d). (f) Computational imaging results for a pixel array combining both types of devices.

Finally, we have conducted computational imaging simulations based on the measured angular response maps to show how these devices can be combined in a pixel array that allows for the simultaneous separate mapping of the RCP and LCP incident wavefronts [Fig. 1(f)]. This capability could benefit multiple imaging applications involving chiral matter, e.g., for drug development, studies of live cells, and biomedical diagnostics. Furthermore, these devices provide a key enabling ingredient for the development of a sensor array that could directly measure, in a single shot and with standard imaging optics, the spatial distribution of the incident optical intensity, phase, and polarization. In turn, such a system could dramatically improve our ability to sense visual information in low-contrast environments, with broad applicability in machine vision and image processing.

This work was supported by NSF under Grant ECCS 2139451.

References

1. Yuan, S., C. Ma, E. Fetaya, T. Mueller, D. Naveh, F. Zhang, and F. Xia, "Geometric deep optical sensing," Science, vol. 379, eade1220 (2023).
2. Erturan, A. M., J. Liu, M. A. Roueini, N. Malamug, L. Tian, and R. Paiella, "Chiral phase-imaging meta-sensors," arXiv:2412.16084, 2024.
3. Kogos, L. C., Y. Li, J. Liu, Y. Li, L. Tian, and R. Paiella, "Plasmonic ommatidia for lensless compound-eye vision," Nat. Commun., vol. 11, 1637, 2020.
4. Liu, J., H. Wang, Y. Li, L. Tian, and R. Paiella, "Asymmetric metasurface photodetectors for single-shot quantitative phase imaging," Nanophotonics, vol. 12, 3519-3528, 2023.

Harmonic generation from aluminium and gold nanolayers and nanogratings: bound and hot electron contributions

S. Mukhopadhyay[1]*, C. Cojocaru[1], M. A. Vincenti[2], K. Hallman[3], M. Scalora[4], and J. Trull[1]
[1]Department of Physics, Universitat Politècnica de Catalunya, Rambla Sant Nebridi 22, 08222 Terrassa (Barcelona), Spain [2] Department of Information Engineering – University of Brescia, Via Branze 38, 25123 Brescia, Italy
[3] PeopleTec, Inc. 4901-I Corporate Dr., Huntsville, AL 35805, USA
[4] Aviation and Missile Center, US Army CCDC, Redstone Arsenal, AL 35898-5000, USA
*corresponding author: shroddha.mukhopadhyay@upc.edu

Abstract: We report a combined experimental-theoretical investigation on the second and third harmonic generation from aluminium and gold nanolayers and nanostructures, with specific focus on bound and hot electron contributions. Our experimental results are validated by our unique microscopic, hydrodynamic model for linear and nonlinear interactions in metal surfaces.

In the last few decades, both experimental and theoretical nonlinear (NL) optical studies have not considered the use of metals as potential materials for harmonic generation due to its large absorption. However, despite their high absorption in the visible and near infrared spectral ranges, metals are highly NL materials and the study of NL optics from metal surfaces combined with plasmonics is a very active field of research with important applications in the fabrication of functional nano-photonic devices.

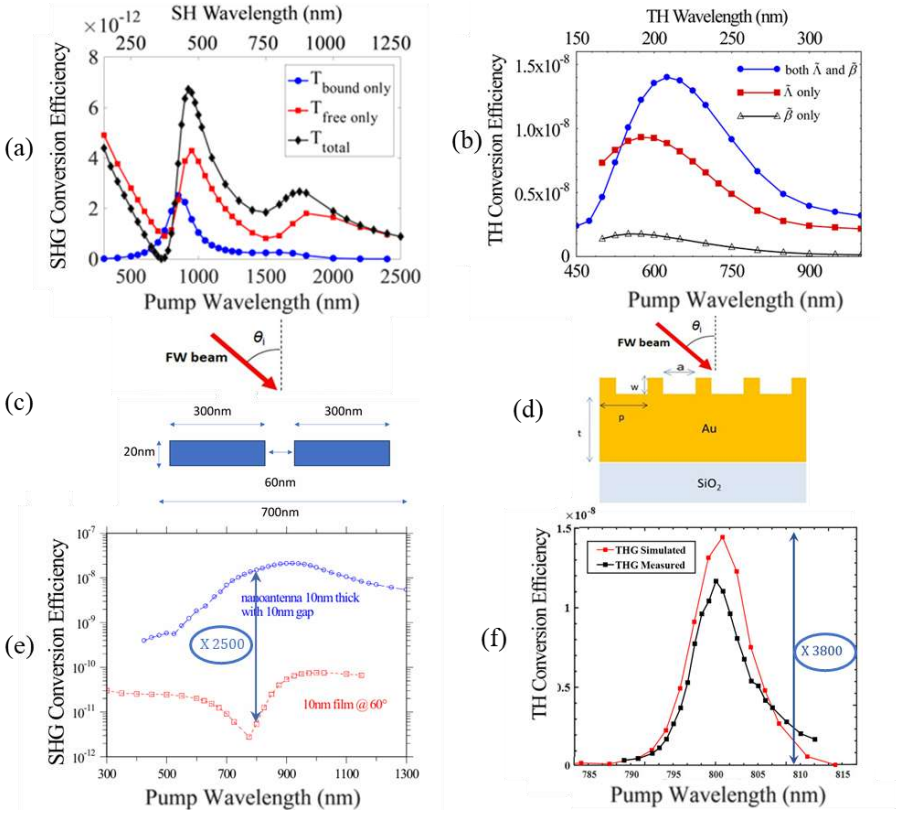
Most of the experimental results presented in literature often show only qualitative aspects of NL generation from metal surfaces and metallic nanostructure. Also, the theoretical models rely on assigning effective surface and volume $\chi^{(2)}$ and $\chi^{(3)}$ to describe second harmonic generation (SHG) and third harmonic generation (THG) respectively, that generally lack a detailed, microscopic, dynamical description of light propagation and light-matter interactions. Our approach consists in formulating a microscopic, hydrodynamic model in order to understand linear and NL optical properties of metals by accounting for competing surface, magnetic, and bulk nonlinearities arising from both free (conduction) and bound (valence) electrons. Just as importantly, our model preserves linear and NL material dispersions, nonlocal effects, and the influence of hot electrons, i.e. electrons that may be temporarily excited from the valence into the conduction band, thus causing a transient increase of the free electron density [1].

Here, we present experimental measurements of the spectral dependence of SHG from Aluminium (Al) nanolayers that display Lorentz-like behavior and interband transitions centered near 810 nm. Detailed analysis of the results reveal that bound charges play a previously unknown role in SHG, pointing to the fact that predictions based solely on the free electron model do not adequately describe light-matter interactions in these materials, and that the absorption resonance plays a pivotal role well beyond pre-supposed limits [2].

On the other hand, third harmonic generation from 20 nm- and 70 nm-thick gold (Au) layers, described by combined Drude and Lorentz electrons illuminated by a pulsed pump laser source has at least two main THG sources: interband transitions (Lorentz resonances, with NL interactions governed by the bulk nonlinearity) and hot electrons, whose relative strength is determined by temperature-dependent effective mass (Fig. 1(b)) [3].

Heading towards structured nanomaterials, hence the grating, we take advantage of strong plasmonic resonances that significantly enhance light-matter interaction in the metal-dielectric interface, and generate very large surface nonlinearities promising more practical applications such as sensors, photonic circuits etc. Our sophisticated detection system and precision calibration enables us to detect and quantify SH/TH efficiencies,

and corroborate our theoretical and experimental observations of shape, spectral width, and amplitude of the spectral response. Fig. 1(c) and (d) shows the Al and Au grating simulated and experimentally measured. Fig. 1(e) and (f) shows the SHG from the Al grating and the THG from the Au grating being enhanced by three



orders of magnitudes, compared to the SH/TH signal from the unpatterned metal [4].

Fig. 1(a) Reflected SH conversion efficiencies from a free-standing 20nm-thick Al membrane. 100fs pulses are incident at 60°, Conversion efficiency has been calculated assuming NL sources reside only in: (i) bound electrons (blue curve), (ii) free electrons (red curve) [2] (b) Prediction of reflected THG conversion efficiency vs. wavelength for pump pulses incident at 55° [3]. (c) Al grating and (d) Au grating investigated. (e) SHG from Al grating and (f) THG from Au grating, showing the corresponding enhancement factors when the pump is tuned around the resonant frequency of the structure [4].

Acknowledgement

SM, JT, and CC acknowledge Spanish Agencia Estatal de Investigación (project no. PID2023-148620NB-I00) and US Army Research Laboratory Cooperative Agreement N◦ W911NF-22-2-0236 issued by US ARMY ACC-APG-RTP.

References

1. Scalora, M. and Vincenti, M. and de Ceglia, D. et al, "Nonlinear Duffing oscillator model for third harmonic generation," J. Opt. Soc. Am. B, Vol. 32, 2129-2138, 2015.
2. Scalora, M. and Hallman, K. and Mukhopadhyay, S. et al; “Below the surface: Unraveling the intricacies of the nonlinear optical properties of aluminum through bound electrons,” APL Photonics, Vol. 9, 086108, 2024.
3. Rodriguez-Suñé, L. and Trull, J. and Cojocaru, C. et al, “Harmonic generation from gold nanolayers: bound and hot electron contributions to nonlinear dispersion,” Optics Express, Vol. 29, 8581, 2021.
4. Mukhopadhyay, S. and Rodriguez-Suné, L. and Cojocaru, C. et al, “Three orders of magnitude enhancement of second and third harmonic generation in the visible and ultraviolet ranges from plasmonic gold nanogratings,” APL Photonics, Vol. 8, 046108, 2023.

Hyperbolic Plasmon Polaritons in van a der Waals Crystal at Visible Frequencies

A. Mancini[1*], G. Venturi[1], N. Melchioni[1], S. Chiodini[1], and A. Ambrosio[1]

[1]Centre for Nano Science and Technology, Fondazione Istituto Italiano di Tecnologia, Via Rubattino 81, Milan 20134, Italy
[*]corresponding author: andrea.mancini@iit.it

Abstract: We demonstrate low-loss, in-plane hyperbolic plasmon polaritons in $MoOCl_2$ thin films at visible and near-infrared frequencies. Predicted using biaxial media theory and confirmed via nano-imaging, $MoOCl_2$ hyperbolic plasmons enable extreme light confinement in the visible for applications like hyperlensing and super-resolution imaging, overcoming the losses and limitations of traditional metamaterials.

Polaritons—hybrid light-matter states formed by coupling photons with material excitations—enable subwavelength light control for a range of applications, including in optical sensing, nanoscale heat management, photocatalysis, and nonlinear optics. The associated light confinement is determined by the material dielectric permittivity setting specific isofrequency contours (IFCs), which can have different shapes in k-space. Media where the permittivity elements all have the same sign yield closed IFCs and elliptical wavefronts, whereas strongly anisotropic materials with mixed sign permittivity support hyperbolic polaritons with unbounded wavevectors. The unboundedness of the IFCs results in extreme subwavelength light confinement over a broadband range. Van der Waals (vdW) materials like hBN[1] and α-MoO_3[2] have demonstrated hyperbolic phonon polaritons in the mid-infrared. However, many applications—such as hyperlensing, super-resolution imaging, and high-resolution photolithography—require visible-frequency operation. While nanostructured metamaterials can be tailored to host visible hyperbolic plasmon polaritons, they face challenges including complex nanofabrication and high ohmic losses. We report the discovery of low-loss in-plane hyperbolic plasmon polaritons in thin films of the vdW molybdenum oxide dichloride ($MoOCl_2$) at visible and near-infrared frequencies[3]. Using the theoretical framework of biaxial media, we identify hyperbolic plasmon polaritons alongside directional ghost modes with damped propagation even in lossless conditions. $MoOCl_2$ exhibits a broad hyperbolic region spanning visible and near-infrared frequencies. We confirm $MoOCl_2$'s optical anisotropy via reflectivity measurements on exfoliated flakes. The axis orientation with respect to the flakes geometry is probed by atomic force microscopy with atomic resolution, enabling reconstruction of the unit cell shape. Finally, real-space polariton nanoimaging $MoOCl_2$ demonstrates the presence of hyperbolic plasmon polaritons as launched by a gold scattered fabricated on top of a flake. Our findings introduce MoOCl2 as a the first material supporting low-loss visible-frequency hyperbolic polaritons, enabling applications envisioned for hyperbolic metamaterials but without the need for nanofabrication and reduced ohmic losses.

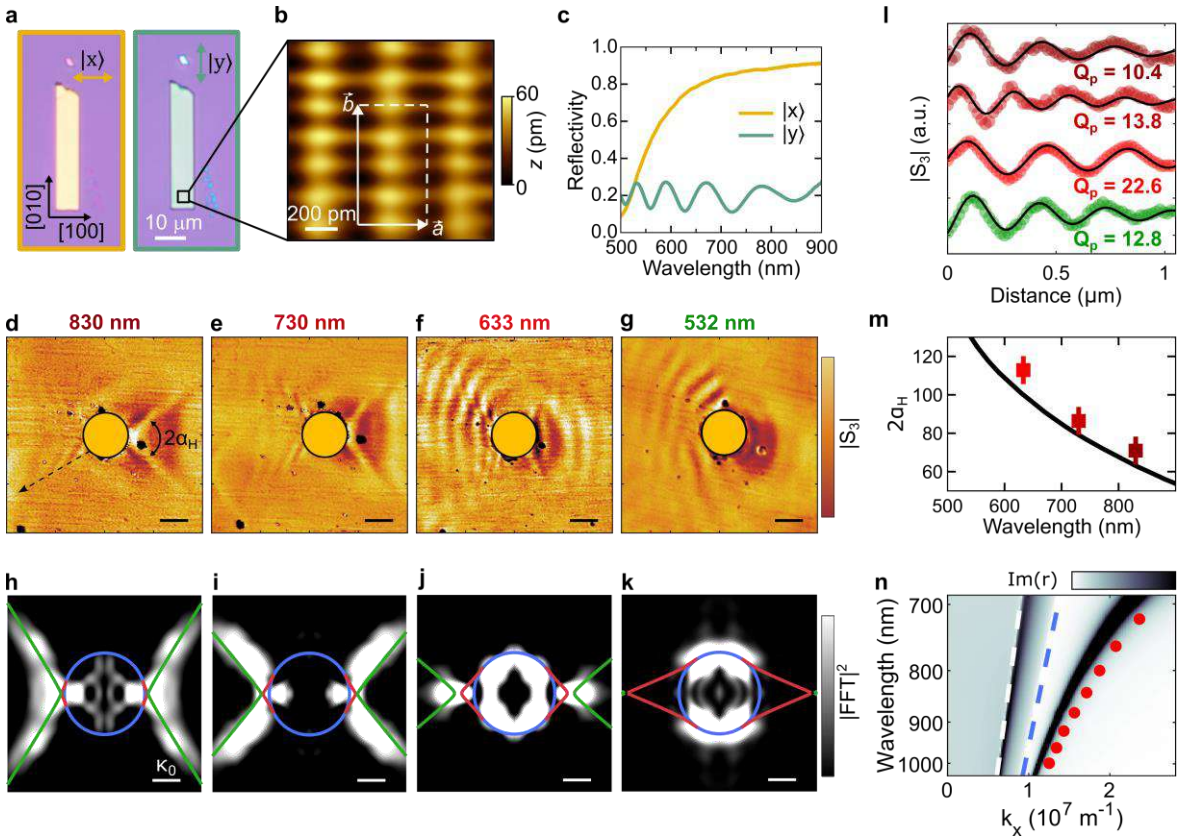


Figure 1. **a** Optical images of an exfoliated flake under polarized illumination along the x (left) and y (right) directions. **b** High-resolution AFM of the flake surface. **c** Reflectivity spectra along orthogonal axes for a 560 nm-thick flake. **d–g** s-SNOM amplitude maps of polaritons launched by a gold disk on a 42 nm flake (scale bars: 500 nm). θ denotes the hyperbolic PPs opening angle. **h–k** Corresponding FFT maps with superimposed analytical PPs dispersion (blue: SiO_2 light-cone, red: lenticular modes, green: hyperbolic modes). **l** Polariton decay profiles (along dashed line in **d**) with best-fit curves for decay length and quality factor Q_p. **m** Extracted hyperbolic aperture angle from panels in **d** with theoretical predictions (black curve). **n** Experimental PPs dispersion along the metallic axis of a 20 nm flake (red dots) overlaid with transfer matrix calculations. White (blue) dashed lines indicate the air (SiO_2) light-line.

References

1. Ambrosio, A., et al. "Selective excitation and imaging of ultraslow phonon polaritons in thin hexagonal boron nitride crystals.", Light Sci. Appl., Vol. 7.1, No. 27, 2018.
2. Ma, W., et al. "In-plane anisotropic and ultra-low-loss polaritons in a natural van der Waals crystal." Nature, Vol. 562, No. 7728, 557-562, 2018.
3. Venturi, G., Mancini, A., Melchioni, N., Chiodini, S., & Ambrosio, A. "Visible-frequency hyperbolic plasmon polaritons in a natural van der Waals crystal. ", Nature Comm., Vol. 15, No.1, 2024.

Femtosecond laser delamination cavities and their applications

P. Varlamov[1], A. Barros[1], A. Swaminathan[1], J. Marx[2], A. Ostendorf[2], A. Semisalova[3], D. Makarov[4], A. M. Lomonosov[5], P. Vavassori[6,7], Y. Laplace[1], M. Raynaud[1], and V. V. Temnov[1*]

[1]LSI, Ecole Polytechnique, CEA/DRF/IRAMIS, CNRS, IP Paris, 91128 Palaiseau, France
[2]Applied Laser Technologies, Ruhr University Bochum, 44801 Bochum, Germany
[3]Faculty of Physics and CENIDE, University of Duisburg-Essen, 47057 Duisburg, Germany
[4]Helmholtz-Zentrum Dresden-Rossendorf e.V., 01328 Dresden, Germany
[5]B+W Department, Offenburg University of Applied Sciences, 77652 Offenburg, Germany
[6]CIC nanoGUNE—BRTA, Donostia—San Sebastian, 20018 Donostia, Spain
[7]IKERBASQUE, Basque Foundation for Science, 48009 Bilbao, Spain
Corresponding author: `vasily.temnov@cnrs.fr`

Abstract: Nano-to-micrometer size single-shot *femtosecond laser delamination* (FLD) membranes or cavities of ferromagnetic thin films and multilayers are quantified using the Abbe-limited interferometric, ultrafast scanning photo-acoustic and magneto-plasmonic microscopies. Cavity formation mechanisms as well as their applications for ultrafast GHz-to-THz frequency acoustics and magneto-plasmonics in the Otto configuration are discussed.

Femtosecond laser pulses are commonly used both to produce and investigate new structures for a wide range of applications in nanotechnology, chemistry, solid-state physics, life sciences, and today in industrial processes (e.g. micromachining). At low energies, these ultrashort pulses can excite ultrafast dynamics in the samples under study, or, at higher intensities, induce permanent modifications creating new nanostructures with unique physical properties. For example, closed FLD cavities can be produced from thin-film or multilayer samples by delamination, i.e. local film separation from the substrate.

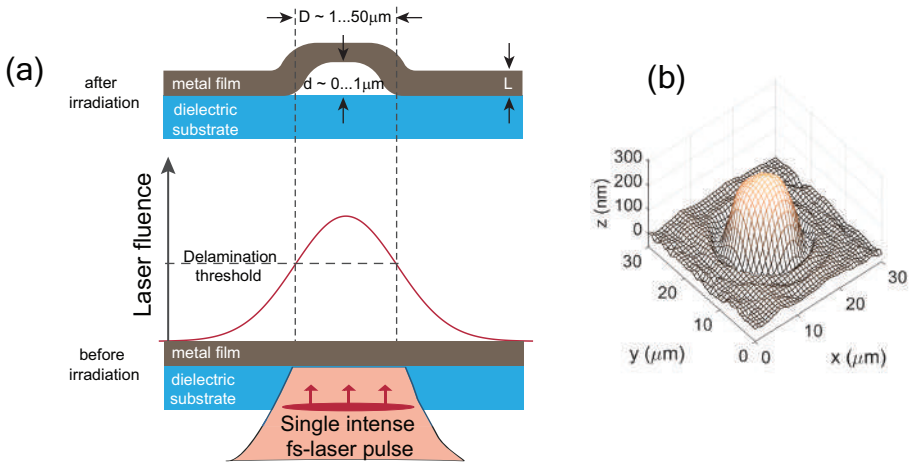


Figure 1: (a) A single high-energy femtosecond laser pulse with peak fluence >0.1 J/cm^2 focused on a thin metal film (or multi-layer structure) produces a closed FLD-cavity. (b) The resulting cavity shapes can be observed by in-situ optical interferometric microscopy.

The principle of femtosecond laser delamination (FLD) is quite simple: single laser pulses are focused onto the thin film or multilayer through an optically transparent substrate [1]. The film thickness and laser focusing conditions are chosen so that only the central part of the excited film separates from the substrate, forming closed cavities. Depending on laser focusing and fluence (incident laser energy per unit surface area, measured in J/cm^2), their lateral size D ranges from a few hundred nanometers to several tens of microns (Fig. 1). The film-substrate separation d can be further quantified with nm-precision by optical interference microscopy during the laser nanofabrication process.

Physical properties of the cavities obtained by FLD are noteworthy: the delaminated part of the membrane forms a high-quality "acoustic" cavity. Time-resolved photoacoustic microscopy using low-energy laser pulses (<1/100th of the high-energy pulses creating the structure) allows to record pulses of coherent acoustic phonons propagating in the membrane (Fig. 2). The analysis of acoustic pump-probe dynamics provides access to the properties of these ultra-high-frequency (>100 GHz) phonon modes and evidence some modes with a high quality factor Q>40 [2].

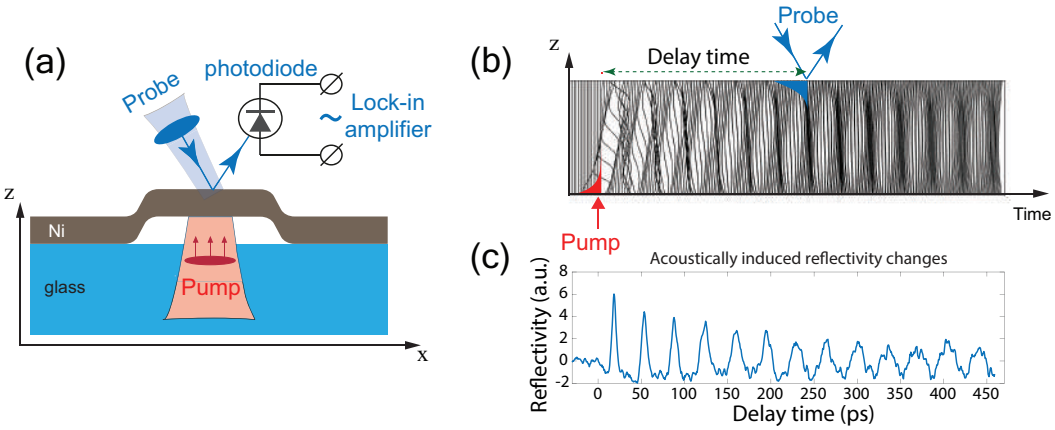


Figure 2: Using low-energy pulses, time-resolved pump-probe microscopy can be used to measure the ultrafast dynamics in FLD cavities, obtained by laser delamination of a thin layer of nickel on a glass substrate. (b) Elastic vibrations evidence long-lived oscillations of FLD cavity/membrane, as shown in (c) by multiple peaks in the time-resolved reflectivity signal.

Another system based on cobalt-gold bilayers on sapphire [2] shows that FLD cavities with a large separation $d \sim \lambda$ can be used for plasmonic measurements in the Otto-configuration, which is otherwise different to achieve experimentally. FLD structures with smaller gap $d \ll \lambda$ could be used to measure the theoretically predicted nanogap resonances [3]. The results of all-optical fabrication and characterization of magnetic FLD cavities uncover the potential of single femtosecond laser pulses for the controlled nanofabrication of new architectures for acousto-magneto-plasmonic and nanophotonic applications.

References

1. Varlamov, P. et al., "Femtosecond Laser Ablation and Delamination of Functional Magnetic Multilayers at the Nanoscale," *Nanomaterials*, Vol. 14, No. 1488, pp. 1–13, 2024.

2. Varlamov, P. et al., "Tunable nanoscaled architectures produced by single femtosecond laser pulses," *Phys. Rev. Lett.*, (in review) 2025.

3. Varlamov, P. et al., "Grazing incidence nanogap resonance in the prism-gap-ferromagnet magneto-plasmonic Otto configuration," *Opt. Lett.*, Vol. 50, No. 1, pp. 109–112, 2025.

UV upconversion in lanthanides-doped thin films assisted by photonic crystals.

D. Rinnert[1,2*], E. Drouard[1], A. Pereira[2], C. Chevalier[1], A. Benamrouche[1], B. Fornacciari[1], H.S. Nguyen[1], G. Ledoux[2], and C. Seassal[1]

[1]CNRS, INSA Lyon, Ecole Centrale Lyon, Université Claude Bernard Lyon 1, CPE Lyon, INL, UMR 5270, F-69622, Villeurbanne, France

[2]Univ Lyon, Université Claude Bernard Lyon 1, CNRS, Institut Lumière Matière, UMR 5306, F-69622, Villeurbanne, France

[*]Corresponding author: damien.rinnert@ec-lyon.fr

Abstract: Upconverting the solar spectrum to ultra-violet using lanthanides is of major interest for photocatalysis applications, but limited by their low absorption cross-sections. We have designed, fabricated and characterized two dimensional photonic crystals enhancing multisolar upconversion process from near infra-red and visible to ultra-violet in Yb^{3+}, Tm^{3+}.

UV upconversion is a lever for improving the efficiency of photocatalysis processes [1]. Harvesting the long-wavelength part of the solar spectrum requires substantial anti-Stokes conversion, which can be achieved with lanthanides [2,3]. The co-doped system Yb^{3+}, Tm^{3+} is used to ensure UV emission from part of the visible and IR solar spectrum absorption. However, the energy conversion efficiency is limited by lanthanides low absorption cross-section [4, 5]. So far, two-dimensional photonic crystals (2D PC) have been designed to assist the NIR to visible upconversion [6, 7], but not to UV upconversion. Here we present a design composed of a non-stochiometric silicon nitride (SiN_x) 2D PC and a Y_2O_3:Yb^{3+}(7,5%),Tm^{3+}(0,5%) thin film on a fused silica wafer, enhancing the UV emission from NIR and visible upconversion with guided mode resonances on excited state absorption (ESA) and emission transitions. SiN_x, deposited by plasma-enhanced chemical vapor deposition, has been optimized to be transparent from the UV to the NIR range, and exhibits a refractive index close to the Y_2O_3:Yb^{3+},Tm^{3+} thin film one. Doping rates of the Y_2O_3:Yb^{3+},Tm^{3+} thin film, deposited by pulsed laser deposition, have been studied to find the best compromise to foster the energy transfer upconversion while avoiding concentration quenching. 2D PC structure has been investigated with rigorous coupled-wave analysis simulations, then fabricated using electron-beam lithography and inductively coupled plasma - reactive ion etching.

The 2D PC illustrated Figure 1a is designed in order to promote ESA in Tm^{3+} from the metastable excited-state $^3F_4$ to $^1D_2$ ($\sim$ 450 nm), which emits UV while relaxing to the ground-state $^3H_6$ ($\sim$ 365 nm). $^3F_4$ being sensitized by Yb^{3+} in the NIR ($\sim$ 980 nm), it is a multisolar absorption process [3]. The nanophotonic structure consists of a Y_2O_3:Yb^{3+},Tm^{3+} thin film and a SiN_x layer with hole patterns in a square lattice, whose lattice parameter is standing in the 240-280 nm range. In this way, the visible guided mode resonance is confined in the lanthanide doped thin film according to our simulations. The experimental measurement of ΓX dispersion-band diagram of the 2D PC (Figure 1b) confirms a guided mode resonance increasing the photonic density of states on the ESA transition for a normal incidence ($\theta = 0°$). It also shows modes on the emission range, whose impact on the emission directionality is still under study. UV emission spectra measurement under visible and NIR excitation (Figure 1c)

finally demonstrates that these modes assist the multisolar absorption process: the fabricated 2D PC shows a ×6 4 enhancement of the UV emission compared to an unpatterned reference.

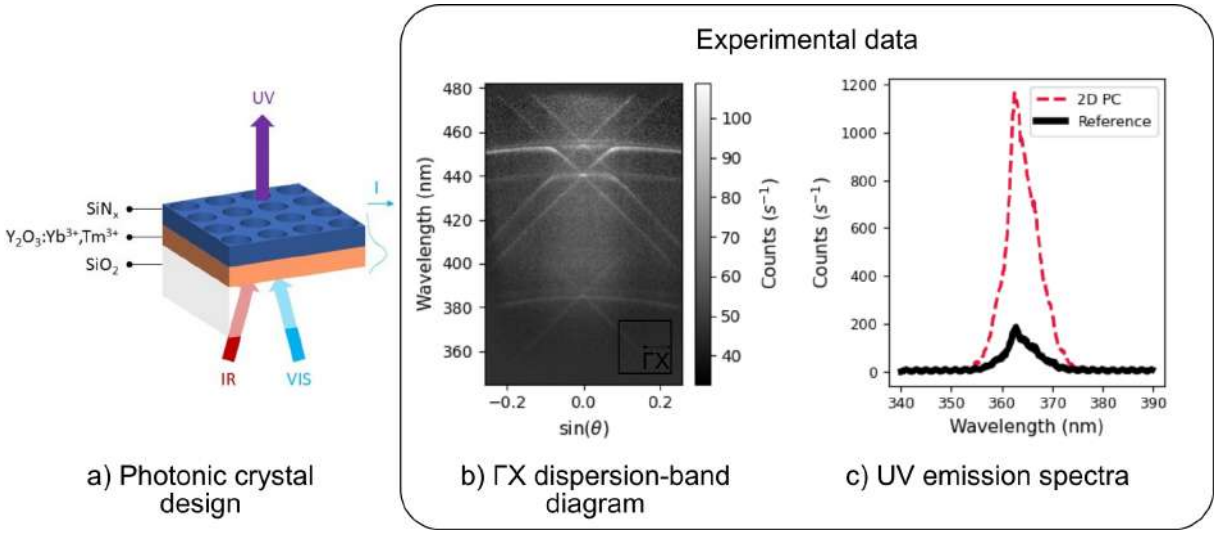


Figure 1: a - Schematic of the 2D PC combined with lanthanide-doped thin film. b - ΓX dispersion-band diagram of the 2D PC measured by angle-resolved reflectance, θ referring to the incidence angle. c - The 2D Photonic Crystal UV emission (red dashed line) is compared to the unpatterned reference one (black continuous line), under the following excitation conditions: 447 nm (58.5 kW/cm^2) + 995 nm (228.4 kW/cm^2).

We acknowledge the funding from Agence Nationale de la Recherche through the grant number ANR-22-CE09-0036. We acknowledge support from the CNRS/IN2P3 Computing Center (Lyon - France) for providing computing and data-processing resources needed for this work. Photonic crystals have been realized on the Nanolyon plaform, member of the CNRS-RENATECH+ national network.

References

1. Bryce S. Richards et al. *ACS Chemical Reviews*, 2021, vol. 121, no. 15, p. 9165-9195.

2. Feng Wang et al. *Nature materials*, 2011, vol. 10, no 12, p. 968-973.

3. Bhagyesh Purohit et al. *ACS photonics*, 2019, vol. 6, no 12, p. 3126-3131.

4. Alexandre S. Pinheiro et al. *Chemical Physics Letters*, 2014, vol. 592, p. 164-169.

5. Richard Moncorgé et al. *Journal of Luminescence*, 2022, vol. 241, p. 118537.

6. Duc Tu Vu et al. *Crystals*, 2021, vol. 11, no. 10, p. 1187.

7. Yen-Ta Tseng et al. *ACS Sensor*, 2024, vol. 9, no. 1, p. 445-463.

Miniaturized Microfluidic Plasmonic Chip for Enhanced Biosensing

A. Campu[1], Daria Stoia[1,2], D. Maniu[1,2], S. Astilean[1,2], Marc Lamy de la Chapelle[1] and M. Focsan[1,2*]

[1]Nanobiophotonics and Laser Microspectroscopy Center, Interdisciplinary Research Institute in Bio-Nano-Sciences, Babes-Bolyai University, Treboniu Laurian No. 42, 400271 Cluj-Napoca, Romania

[6] Biomolecular Physics Department, Faculty of Physics, Babes-Bolyai University, Mihail Kogalniceanu No. 1, 400084 Cluj-Napoca, Romania

[*]corresponding author: monica.iosin@ubbcluj.ro

Abstract: Acute myocardial infarction is one of the most severe cardiovascular diseases. As a result, considerable efforts are being made to develop biosensing technologies that can efficiently detect cardiac troponin biomarkers. Therefore, we developed a microfluidic plasmonic chip for the fast and real-time detection of the cardiac troponin I biomarker.

The fabrication of a plasmonic nanoplatform is based on immobilized gold nanobipyramids, which exhibits optical and thermoplasmonic properties that favour a multimodal localized surface plasmon resonance (LSPR) & surface enhanced Raman spectroscopy (SERS) & thermal detection of the cTnI biomarker. The plasmonic nanoplatform is characterized in terms of LSPR and SERS sensitivity and the thermoplasmonic performance is evaluated. Based on a sandwich-like immunoassay, the “proof-of-concept” LSPR-SERS-thermal detection of the cTnI in simulated conditions is evidenced. Furthermore, after the integration of the plasmonic nanoplatform in a microfluidic channel, the determination of the cTnI in real plasma samples is successfully realized and compared with a conventional high-sensitivity clinical assay proving good correlation. Thus, the proposed portable and miniaturized microfluidic plasmonic chip is validated for clinical applications supporting the further transfer to clinical settings for the early diagnosis of cardiac diseases and progress of personalized medicine.

Natural hyperbolic Van der Waals materials towards low-loss near unity linear dichroism

N. Melchioni[1,*], A. Mancini[1], L. Nan[1], A. Efimova[1,2], G. Venturi[1], A. Ambrosio[1]

[1]Centre for Nano Science and Technology, Fondazione Istituto Italiano di Tecnologia, Via Rubattino 81, Milano 20134, Italy

[2]Physics Department, Politecnico di Milano, Piazza Leonardo da Vinci 32, Milano 20134, Italy

[*]corresponding author: nicola.melchioni@iit.it

Abstract: In-plane hyperbolic crystals, enable nearly perfect linear dichroism by exhibiting metallic behavior in one direction and dielectric in the orthogonal. $MoOCl_2$ achieves strong polarization control with low loss, making it promising for miniaturized photonic devices, including direct integration into optical fibers.

Control over light polarization is essential for various optical technologies, including optical fiber communication[1], quantum cryptography[2], and display technologies[3]. Achieving polarization control requires materials with strong optical anisotropy that produces distinct transmission or reflection coefficients along orthogonal axes. Traditional approaches, such as wire-grid polarizers and metasurfaces, offer broadband polarization control but often suffer from high losses and complex fabrication processes[4]. As a result, there is a growing interest in natural anisotropic materials for low-loss, integrated photonic applications[5].

An ideal polarization control material should achieve "perfect linear dichroism," where one polarization is completely transmitted while the orthogonal one is fully reflected. This scenario is characterized by a high contrast between reflection and transmission coefficients without introducing optical losses, and can be quantified by the parameter

$$\Delta_{LD} = \frac{(R_x - R_y) - (T_x - T_y)}{2}$$

Perfect linear dichroism can be realized in bulky polarizing beam splitters or wire-grid polarizers in the IR low-loss region but a natural, versatile and miniaturizable platform is yet to be found.

The best configuration to achieve this effect in a natural material requires a combination of metallic and dielectric behavior along different crystallographic axes, which is the defining characteristic of hyperbolic materials. Hyperbolic materials possess a permittivity tensor where one principal component is negative while the other is positive, leading to strongly anisotropic light-matter interactions. While hyperbolic behavior has been observed in materials like MoO_3[6] and $CaCO_3$[7] in the mid-infrared, few materials exhibit hyperbolicity in the visible and near-infrared ranges, with only few reported materials mostly working in the UV region[8,9].

In this contribution, we demonstrate that van der Waals crystal $MoOCl_2$ exhibits a broad hyperbolic region spanning the visible and near-infrared spectrum by extracting the dielectric permittivity tensor experimentally. The in-plane hyperbolicity in the visible spectrum makes $MoOCl_2$ an excellent candidate for achieving perfect linear dichroism. Indeed, experimental results reveal that $MoOCl_2$ exhibits strong optical anisotropy in reflection and transmission simultaneously across the visible spectrum above 550 nm. This remarkable anisotropy enables nanometer-scale $MoOCl_2$ flakes to achieve record-high value of $\Delta LD \sim 0.8$, surpassing even the previous record-holder $NbOCl_2$[10]. To demonstrate the ready integrability of MoOCl2 nanocrystals in working optical elements, we fabricated a broadband polarizing fiber by transferring a flake of MoOCl2 onto the core of a commercially

available optical fiber.

Our findings highlight the potential of hyperbolic vdW crystals as excellent candidates for developing low-loss, compact optical components for advanced polarization control in integrated photonic systems

References

1. Khonina, S. N.; Kazanskiy, N. L.; Butt, M. A.; Karpeev, S. V. *Opto-Electronic Advances* 2022, 5, 210127–1.
2. Hamel, D. R.; Shalm, L. K.; Hübel, H.; Miller, A. J.; Marsili, F.; Verma, V. B.; Mirin, R. P.; Nam, S. W.; Resch, K. J.; Jennewein, T. *Nature Photonics* 2014, 8, 801–807.
3. Yang, D.-K.; Wu, S.-T., *Fundamentals of liquid crystal devices*; John Wiley & Sons: 2014
4. Schirato, A.; Maiuri, M.; Toma, A.; Fugattini, S.; Proietti Zaccaria, R.; Laporta, P.; Nordlander, P.; Cerullo, G.; Alabastri, A.; Della Valle, G. *Nature Photonics* 2020, 14, 723–727
5. Zhang, Y.; Wu, J.; Jia, L.; Jin, D.; Jia, B.; Hu, X.; Moss, D.; Gong, Q. *npj Nanophotonics* 2024, 1, 28
6. Zheng, Z.; Xu, N.; Oscurato, S. L.; Tamagnone, M.; Sun, F.; Jiang, Y.; Ke, Y.; Chen, J.; Huang, W.; Wilson, W. L., et al. *Science advances* 2019, 5, eaav8690
7. Ma, W.; Hu, G.; Hu, D.; Chen, R.; Sun, T.; Zhang, X.; Dai, Q.; Zeng, Y.; Alù, A.; Qiu, C.- W., et al. *Nature* 2021, 596, 362–366
8. Zhou, Y.; Guo, Z.; Gu, H.; Li, Y.; Song, Y.; Liu, S.; Hong, M.; Zhao, S.; Luo, J. *Nature Photonics* 2024, 1–6
9. Kang, B.; Shin, J.; Kang, M.; Choi, U.; Seo, U.; Chung, K.; Ok, J. M.; Jin, H.; Sohn, C. *arXiv preprint arXiv:2412.12697*, 2024.
10. Guo, Q.; Zhang, Q.; Zhang, T.; Zhou, J.; Xiao, S.; Wang, S.; Feng, Y. P.; Qiu, C. - W. *Nature Photonics* 2024, 1–6

Two-dimensional gold flakes for nonlinear and low-loss plasmonics

A. V. Krasavin[1*], C. Pan[2], L. Liu[2], Z. Wang[2], A. V. Zayats[1], L. Tong[2], and P. Wang[2]

[1]Department of Physics and London Centre for Nanotechnology, King's College London, Strand, London WC2R 2LS, UK
[2]State Key Laboratory of Extreme Photonics and Instrumentation, College of Optical Science and Engineering, Zhejiang University
[*]corresponding author: alexey.krasavin@kcl.ac.uk

Abstract: In this report, we will discuss exquisite optical properties of single-crystal two-dimensional gold flakes (2DGFs). The ultrathin thickness of the 2DGFs leads to the onset of quantum confinement effects, which create new pathways for gold photoluminescence and nonlinear harmonic generation, leading to their enhancement by orders of magnitude.

In this report, we will discuss exquisite optical properties of single-crystal two-dimensional gold flakes (2DGFs) having a large area together with a thickness down to few nanometres, which are synthesised via a chemical etching approach providing atomic-level precision [1,2]. The ultrathin thickness of the 2DGFs leads to the onset of quantum confinement effects, which create a new pathway for gold photoluminescence, increasing its magnitude manyfold [3]. Furthermore, the quantisation boosts optical nonlinearity of the 2DGFs and provides over two orders of magnitude enhancement in harmonic generation compared to thicker polycrystalline counterparts. The single-crystal quality and atomically smooth surfaces also makes 2DGFs highly attractive for low-loss nanoscale plasmonics. For example, nanoribbon arrays produced from them exhibit strongly confined near-infrared plasmonic resonances with high quality factors. These findings establish two-dimensional gold as a versatile platform for nanophotonic research, with promising applications in ultrathin plasmonics, optoelectronics, and quantum devices.

References

1. L. Liu, A. V. Krasavin, J. Zheng, Y. Tong, P. Wang, X. Wu, B. Hecht, C. Pan, J. Li, L. Li, X. Guo, A. V. Zayats, and L. Tong, "Atomically smooth single-crystalline platform for low-loss plasmonic nanocavities," Nano Lett., Vol. 22, No. 4, 1786–1794, 2022.
2. Z. Wang, L. Liu, D. Zhang, A. V. Krasavin, J. Zheng, C. Pan, E. He, Z. Wang, S. Zhong, Z. Li, M. Ren, X. Guo, A. V. Zayats, L. Tong, and P. Wang, "Effect of mirror quality on optical response of nanoparticle-on-mirror plasmonic nanocavities," Adv. Opt. Mat., Vol. 11, No. 3, 2201914, 2023.
3. C. Pan, Y. Tong, H. Qian, A. V. Krasavin, J. Li, J. Zhu, Y. Zhang, B. Cui, Z. Li, C. Wu, L. Liu, L. Li, X. Guo, A. V. Zayats, L. Tong, and P. Wang, "Large area single crystal gold of single nanometer thickness for nanophotonics," Nat. Commun., Vol. 15, 2840, 2024.

Infrared electroluminescence and energy transfer in hBN-encapsulated graphene devices under high bias voltage

Y. De Wilde[1*]

[1] Institut Langevin, ESPCI Paris, Université PSL, 1 rue Jussieu, 75005 Paris, France

[*]corresponding author: yannick.dewilde@espci.fr

Abstract: We detect mid-infrared radiation from high-mobility graphene devices encapsulated in hexagonal boron nitride (hBN) under large bias voltage, and demonstrate that it results from the electroluminescence of hyperbolic phonon-polaritons. We show that the effect is concomitant with the onset of a highly efficient out-of-plane energy transfer process.

Electroluminescence corresponds to the emission of electromagnetic radiation beyond incandescence. It is usually known to occur at visible wavelengths in light emitting devices made of doped semiconductors. However, electroluminescence of hyperbolic phonon-polaritons (HPhPs) has been proposed by Baudin's group at LPENS as an explanation for the peculiar radiative energy transfer within hexagonal boron nitride (hBN)-encapsulated graphene transistors [1][2]. The first indication of electroluminescence was based on electrical transport measurements using noise thermometry, which gave only indirect evidence of the existence of the effect.

We recently collaborated with the LPENS group to help them search for direct evidence of electroluminescence in hBN-encapsulated graphene transistors [3]. The structure of the investigated devices is shown in figure 1a. Infrared microscopy combined with high sensitivity modulation spectroscopy [4][5] has been used to investigate the radiation produced by high quality hBN-encapsulated graphene transistors with a mobility of tens of thousands of $cm^2 . V^{-1} . s^{-1}$. When a sufficiently large bias voltage is applied between the source and the drain, electron-hole pair injection occurs as a result of interband Zener-Klein tunneling [1][2]. We observe then a substantial mid-infrared emission from the device channel, as shown in Figure 1b. It appears above the threshold voltage of the Zener-Klein tunneling effect.

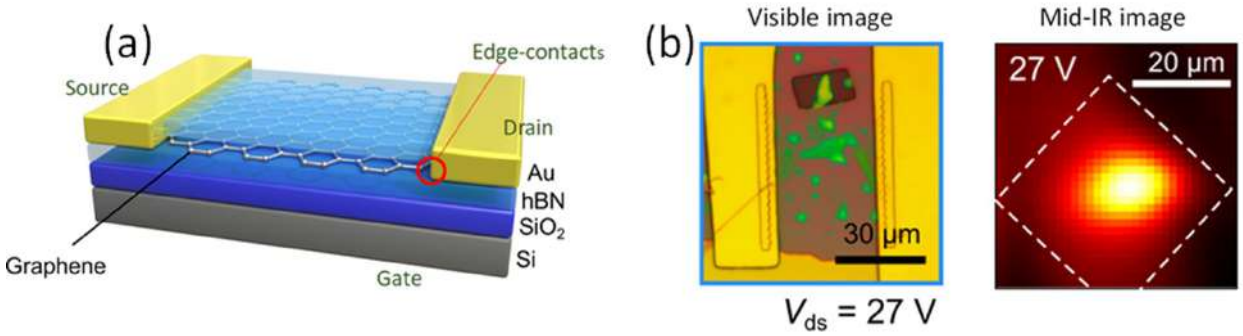


Figure 1: (a) Sketch of the hBN-encapsulated graphene transistors; (b) Visible microscopy image and spatial scan of the spectrally integrated mid-IR emission of the device biased above the Zener Klein threshold voltage.

Indeed, as hBN is a hyperbolic material, interband electron-hole recombination in graphene gives rise to the emission of HPhPs in hBN. Based on far-field mid-IR spectroscopy and electromagnetic simulations, we show

that electroluminescence is due to propagating small-wavevector HPhPs scattered elastically at discontinuities in the Van der Waals heterostructure. This produces a spectral peak at ~ 190 meV beyond incandescence. Large wavevector HPhPs are also produced by electron-hole recombination above the Zener-Klein threshold voltage. Their dissipation occurs over nanometric length scales near the graphene layer, producing a heating of hBN and out-of-plane energy transfer through the silica layer at the gate of the device. Incandescent emission results from the hot silica, whose intensity makes it possible to quantify the energy transfer.

This work is the result of a project whose principal investigator is Prof. Emmanuel Baudin (LPENS). It involves collaboration [3] between groups from LPENS, Institut Langevin, ONERA, MATEIS, Laboratoire des Multimatériaux et Interfaces, Laboratoire Charles Fabry-IOGS, Advanced Materials Laboratory, IEMN, Tim Taylor Department of Chemical Engineering. The research leading to these results has received partial funding from the European Union Horizon 2020 research and innovation program under grant agreement No.881603 "Graphene Core 3", and from the French ANR-21-CE24-0025-01 "ELuSeM". This work has received support under the program “Investissements d’Avenir” launched by the French Government.

References

1. Yang, W., Berthou, S., Lu, X., Wilmart, Q., Denis, A., Rosticher, M., Taniguchi, T., Watanabe, K., Fève, G., Berroir, JM., Zhang, G., Voisin, C., Baudin, E., and Plaçais. B. "A graphene Zener–Klein transistor cooled by a hyperbolic substrate.", Nat. Nanotechnol., 13, 47–52, 2018.
2. Baudin, E ., Voisin, C. and Plaçais, B. "Hyperbolic phonon polariton electroluminescence as an electronic cooling pathway," Adv. Funct. Mater., 30, 1904783, 2020.
3. Abou-Hamdan, L., Schmitt, A., Bretel, R., Rossetti, S., Tharrault, M., Mele, D., Pierret, A., Rosticher, M., Taniguchi, T., Watanabe, K., Maestre, C., Journet, C., Toury, B., Garnier, V., Steyer, P., Edgar, J. H., Janzen, E., Berroir, J-M., Fève, G., Ménard, G., Plaçais, B., Voisin, C., Hugonin, J-P., Bailly, E., Vest, B., Greffet, J-J., Bouchon, P., De Wilde, Y., and Baudin, E. " Electroluminescence and Energy Transfer Mediated by Hyperbolic Polaritons", Nature, in press, 2025. arXiv:2310.08351v5 [cond-mat.mes-hall]
4. Abou-Hamdan, L., Li, C., Haidar, R., Krachmalnicoff, V., Bouchon, P. and De Wilde, Y. "Hybrid modes in a single thermally excited asymmetric dimer antenna", Optics Letters, 46, 981-984, 2021.
5. Abou-Hamdan, L., Coudrat, L., Bidault, S., Krachmalnicoff, V., Haïdar, R. Bouchon, P., De Wilde, Y. " Transition from phononic to geometrical Mie modes measured in single subwavelength polar dielectric spheres ", ACS Photonics, 9, 2295–2303, 2022.

Unified Framework for Enhancing Chiral Light-Matter Interactions

C. F. Doiron[1]
[1]Center for Integrated Nanotechnologies, Sandia National Laboratories, USA
Corresponding author: cfdoiro@sandia.gov

Abstract: While nanophotonics can enhance, typically weak, chiral light-matter interactions, the absence of a unified theory for understanding the flow of energy and chirality prevents a complete understanding of ultimate performance limits and requirements. Here, we present a unified framework for simultaneously understanding energy and chirality flows in resonant nanophotonic systems.

Over the past 20 years, significant advances have been made in harnessing chirality with experimental demonstrations of circularly polarized lasers, chirality-sensitive emission, and chiral molecular sorting. Understanding the role of chirality in nanophotonics traces back to Lipkin's discovery of the conserved "00-zilch" quantity, which is carried solely by circularly polarized waves [1]. Subsequent works [2, 3] established 1) this conserved quantity directly relates to chirality and 2) the conservation of such a quantity allows the formulation of a chiral continuity equation analogous to the energy conservation continuity equation (Eqs. 1-8), where the optical chirality ($\bar{\chi}$) parallels the electromagnetic energy ($\bar{u}$) comprised of electric ($\bar{\chi}_e$ and $\bar{u}_e$) and magnetic ($\bar{\chi}_m$ and $\bar{u}_m$) contributions. The generation and dissipation of chirality ($\mathrm{Im}(\bar{\chi}_e \in \bar{\chi}_m)$) is linked to a chiral flux ($\mathbf{F}$) through a continuity equation similar to how the generation and dissipation of energy ($\mathrm{Im}(\bar{u}_e \in \bar{u}_m)$) is related to the Poynting vector ($\mathbf{S}$).

Energy		**Chirality**	
$\bar{u} = \bar{u_e} + \bar{u_m}$	(1)	$\bar{\chi} = \bar{\chi_e} + \bar{\chi_m}$	(5)
$\bar{u}_e = \frac{1}{4}\mathbf{E}\cdot\mathbf{D}^*$	(2)	$\bar{\chi}_e = \frac{1}{8}\left[\mathbf{D}^*\cdot(\nabla\times\mathbf{E}) + \mathbf{E}\cdot(\nabla\times\mathbf{D}^*)\right]$	(6)
$\bar{u}_m = \frac{1}{4}\mathbf{H}\cdot\mathbf{B}^*$	(3)	$\bar{\chi}_m = \frac{1}{8}\left[\mathbf{H}^*\cdot(\nabla\times\mathbf{B}) + \mathbf{B}\cdot(\nabla\times\mathbf{H}^*)\right]$	(7)
$0 = -2\omega\int_V \mathrm{Im}(\bar{u}_e - \bar{u}_m)\,dV + \int_V \mathrm{Re}(\nabla\cdot\mathbf{S})\,dV$	(4)	$0 = -2\omega\int_V \mathrm{Im}(\bar{\chi}_e - \bar{\chi}_m)\,dV + \int_V \mathrm{Re}(\nabla\cdot\mathbf{F})\,dV$	(8)

Such a continuity equation not only allows the flow of chirality to be accounted for, but also provides near-field definitions for the spatial distribution of chirality storage and generation. As these definitions have been applied to resonant photonic systems, the physical mechanisms behind chirality have attracted a long list of adjectives including "extrinsic," "intrinsic," "false," "true," and "super." To date, there is no unified framework for combining the near-field distribution and conservation of chirality with the conservation of energy in resonant systems. Moreover, the absence of such a framework obscures the roles that geometric and material asymmetries play in generating chirality in resonant systems. Consequently, there are numerous claims regarding the features of chirality needed or preferred for chiral emission (both direct and through

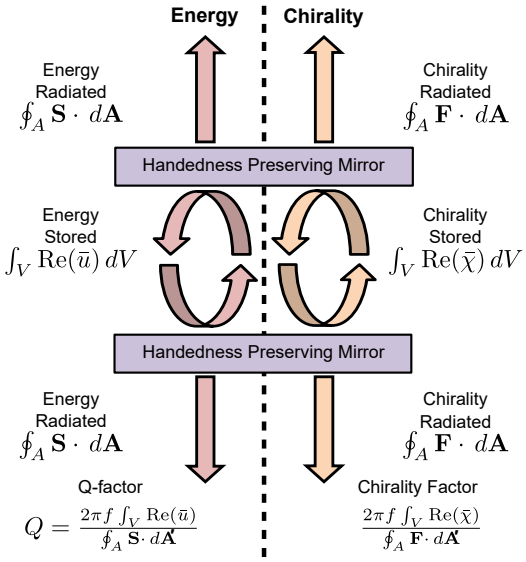


Figure 1: Schematic diagram of energy and chirality flow in a lossless, single-handed cavity where there is no chirality creation or destruction.

non-linear optical effects), molecular sensing, and trapping. The lack of a unified framework for combining chirality and energy prevents a thorough understanding of how chirality needs to be controlled for a specific situation, hindering the design of metasurfaces for enhancing chiral light-matter interactions.

Here, we present a unified framework centered around a chirality analogue of temporal coupled mode theory for simultaneously understanding chirality and energy flows in resonant systems to enhance light-matter interactions. By applying this framework to non-resonant interference systems with bi-isotropic materials, resonant cavities, chiral quasi-bound states in the continuum, and systems with geometric and material asymmetry, we demonstrate the necessity of considering chirality and energy to maximize chiral light-matter interactions. Moreover, we use this unified framework to reveal the definitions and roles of "extrinsic," "intrinsic," "false," "true," and "super" chirality when designing metasurfaces for lasing, single-photon source emission, non-linear mixing, and chiral sensing and separation.

Acknowledgments: This work was performed, in part, at the Center for Integrated Nanotechnologies, an Office of Science User Facility operated for the U.S. Department of Energy (DOE) Office of Science. Sandia National Laboratories is a multimission laboratory managed and operated by National Technology and Engineering Solutions of Sandia, LLC, a wholly owned subsidiary of Honeywell International Inc., for the U.S. Department of Energy's National Nuclear Security Administration under contract DE-NA0003525.

References

1. Lipkin, D. M.,"Existence of a New Conservation Law in Electromagnetic Theory" Journal of Mathematical Physics 1964, 5 (5), 696–700.

2. Tang, Y., Cohen, A. E., "Optical Chirality and Its Interaction with Matter." Phys. Rev. Lett. 2010, 104 (16), 163901.

3. Bliokh, K. Y., Nori, F. "Characterizing Optical Chirality," Phys. Rev. A 2011, 83 (2), 021803.

Fabrication of plasmonic transition metal nitride thin films and nano-arrays

R. Bower,[1*] E. Muir,[2] G. Kerherve,[1] B. Rente,[1] A. Ehiasarian,[2] and P. K. Petrov[1]

[1]Department of Materials, Imperial College London, Royal School of Mines, Exhibition Road, London, SW7 2AZ, U.K.
[2]National HIPIMS Technology Centre, Materials and Engineering Research Institute, Sheffield Hallam University, Sheffield S1 1WB, UK
[*]corresponding author: r.bower16@imperial.ac.uk

Abstract: Transition metal nitrides (TMNs), have emerged as promising alternative plasmonic materials, displaying spectral tunability, thermal stability and mechanical stability. This work reports the CMOS compatible deposition of plasmonic TMN films at low temperature. We also describe dry etching methods for the scalable production of TMN metamaterial nano-arrays.

TMNs such as titanium nitride (TiN) have emerged as promising alternatives to gold and silver for tailored plasmonic applications. TiN has potential applications for plasmonics and optoelectronics in the visible and near-IR spectral ranges including sensing, catalysis, and thermophotovoltaics.[1-3] However, the realization of these applications has been limited by the high deposition temperatures (> 800 °C). required for the production of TMN thin films with suitable optical properties. For example, such deposition temperatures are a barrier to the integration of plasmonic TMN components in CMOS fabrication processes.

In this paper, we report the deposition of binary, ternary, and layered TMN thin films at low (< 300 °C) temperatures using High-Power Impulse Magnetron Sputtering (HIPIMS). The optical, structural, and morphological properties of the thin films are characterized via spectroscopic ellipsometry, XRD, AFM, and XPS. We demonstrate that the thin film properties obtained using this low temperature deposition method are comparable to those reported in the literature.[4]

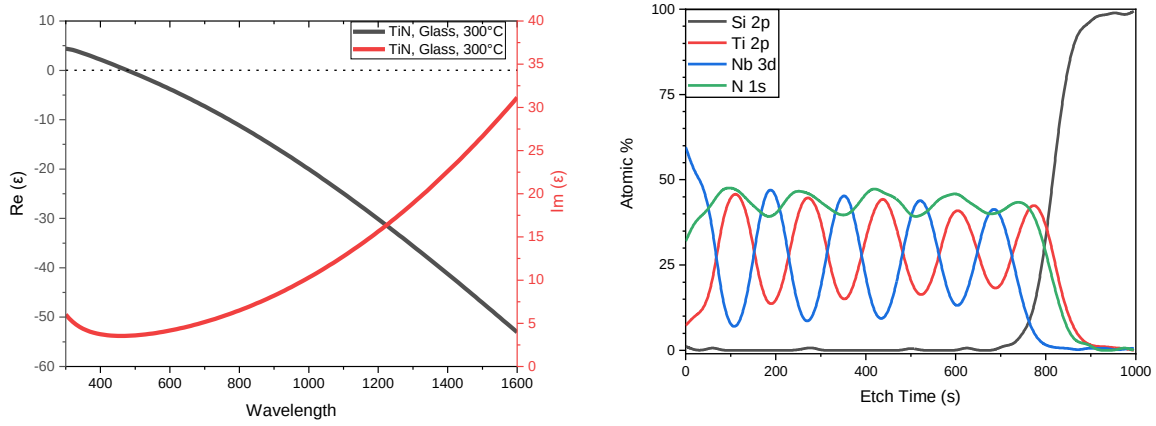


Figure 1: (Left) Spectroscopic ellipsometry data for TiN thin films deposited at 300 °C. (Right) XPS depth profiling data of multilayered TiN/NbN thin films.

In addition to low temperature deposition methods for plasmonic TMNs, we report the fabrication and characterization of plasmonic nano-arrays and meta-surfaces. Dry-etching methods including Reactive Ion Etching (RIE) and Chemically Assisted Ion Beam Etching (CAIBE) are used to fabricate plasmonic nanofeatures. We also discuss scalable fabrication methods for the large area (cm-scale) production of TMN metamaterial arrays.

Acknowledgements

This work was partially supported by the Henry Royce Institute through the EPSRC grant EP/R00661X/1; EPSRC grant EP/W009501/1; and EPSRC grant EP/V001914/1.

References

1. Doiron, B. et al "Quantifying Figures of Merit for Localized Surface Plasmon Resonance Applications: A Materials Survey" ACS Photonics 2019 6 (2), 240-259
2. Mascaretti, L. et al "Designing Metasurfaces for Efficient Solar Energy Conversion" ACS Photonics 2023 10 (12), 4079-4103
3. Patsalas, P. et al "Conductive nitrides: Growth principles, optical and electronic properties, and their perspectives in photonics and plasmonics" Materials Science and Engineering R Volume 123, January 2018, Pages 1-55
4. Bower, R. et al "Complementary Metal–Oxide–Semiconductor Compatible Deposition of Nanoscale Transition-Metal Nitride Thin Films for Plasmonic Applications" ACS Applied Materials & Interfaces 2020 12 (40), 45444-45452

Multilayer structures for broadband switchable absorption and switchable radiative cooling based on phase-change materials

G. Veronis[1*], Md T. Emrose[1], M. Zhou[2], and S. Fan[2]

[1]Louisiana State University, USA
[2]Stanford University, USA
[*]corresponding author: gveronis@lsu.edu

Abstract: We introduce multilayer structures with the phase-change material germanium-antimony-tellurium (GST) for use as broadband switchable absorbers in the infrared wavelength range. We also introduce multilayer structures with GST for switchable radiative cooling.

We introduce multilayer structures with the phase-change material germanium-antimony-tellurium (GST) for use as broadband switchable absorbers in the infrared wavelength range. In many cases, multilayer structures can provide absorption spectra similar to that of more complex and harder-to-fabricate three-dimensional structures. We use a memetic optimization algorithm coupled with the impedance method to optimize both the material composition and the layer thicknesses of the multilayer structures. We maximize the difference between the absorption for GST in its crystalline phase and the absorption for GST in its amorphous phase in the wavelength range of interest. We show that in the optimized structures near perfect absorption can be switched to very low absorption in a broad wavelength range by switching GST from its crystalline to its amorphous phase. We find that our approach of simultaneously optimizing the material composition as well as the layer thicknesses leads to structures which achieve better performance with smaller number of layers. Our results could pave the way to a new class of broadband switchable absorbers and thermal sources in the infrared wavelength range.

In addition, we introduce multilayer structures with GST for switchable radiative cooling. Our system is based on two components: a wavelength-selective filter on the top and a radiative cooler at the bottom, separated by a large air gap. We calculate the net cooling power of our system, which depends on the emissivity of the radiative cooler in the presence of the top filter, by solving the heat balance equation. We use the memetic optimization algorithm to optimize the multilayer filter and cooler structures. We show that our optimized system can achieve a very high net cooling power when the GST layers in the cooler are in their crystalline phase. By switching the GST layers in the cooler to their amorphous phase, our system can achieve a near zero net cooling power. Our proposed switchable radiative cooling system could advance the thermal management of buildings, smart windows, vehicles, and textiles.

Detection of Ammonia in Water Using Self-Assembled Plasmonic Colorimetric Sensor

M. Soudi[1,2,3], P. Cencillo-Abad[1,2,3], S. Ghimire[4], D. Chanda[1,2,3], and K. Mukhopadhyay[4,5,6*]

[1]Department of Physics, University of Central Florida, Orlando, Florida 32816, United States

[2]CREOL, The College of Optics and Photonics, University of Central Florida, Orlando, Florida 32816, United States

[3]NanoScience Technology Center, University of Central Florida, Orlando, Florida 32826, United States

[4]Department of Materials Science and Engineering, University of Central Florida, Orlando, Florida 32816, United States

[5]Advanced Materials Processing and Analysis Centre, University of Central Florida, Orlando, Florida 32816, United States

[6]Biomedical Engineering, University of Central Florida, Orlando, Florida 32816, United States

[*]Corresponding author: kausik@ucf.edu

Abstract: Monitoring chemicals, such as elevated ammonia levels, is crucial for safeguarding public health and the environment. Elevated ammonia indicates contamination from agriculture, industry, or sewage. We have developed a plasmonic sensor to detect ammonia by correlating changes in optical response to analyte concentration, developing a portable, high-resolution, and affordable solution.

Summary:

Conventional methods for detecting ammonia in water are classified as electrochemical, biological, and optical[1]. Electrochemical sensors for ammonia detection use ion-selective electrodes sensitive to the presence of ammonia. These sensors translate changes in electrical properties such as voltage, conductivity, or current flow into ammonia concentrations. In contrast, biological methods excel in ammonia detection when high specificity is required. However, despite delivering precision, these methods necessitate intricate sample preparation and entail higher costs[2]. Alternatively, optical detection methods harness the optical attributes of substances to conduct chemical analyses, demonstrating portability, cost-effectiveness, and high resolution. Recently, Surface-enhanced Raman scattering has drawn attention among all optical detection methods due to its low detection limit (1 ppm), high response time (within a few seconds), and high sensitivity. In addition, colorimetric or fluorescent reagents are introduced into the target solutions to interact with ammonia, inducing alterations in color or fluorescence that are directly correlated to the ammonia concentration. Among these, the prevailing methods are the Indophenol Blue (IPB) method, a colorant-based approach, and the o-phthalaldehyde (a fluorant-based approach). Past decades have observed the widespread use of nanofabrication techniques that have enabled the development of plasmonic structures for chemical sensing. When light of a specific wavelength illuminates a metallic nanostructure, it induces a collective and coherent oscillation of the free electrons within the metal, a phenomenon known as plasmon resonance. However, all these techniques lack portability and user-friendliness, as they still rely on reagents or expensive optical equipment like spectrometers, which prohibits their potential for widespread adoption.

Herein, we present a low-cost, easy-to-use, and label-free plasmonic colorimetric sensor that detects ammonia in water by correlating the color change in the sensor with the concentration of the target solution[3]. The plasmonic structure consists of a self-assembled layer of aluminum nanoparticles on an aluminum backplane coated with a thin transparent oxide supporting gap plasmons at visible wavelengths. Hence, when illuminated by surrounding

white light, the nanostructure absorbs certain spectral bands and reflects the rest, resulting in a specific color appearance. Interestingly, when the aluminum nanoparticles interact with ammonia in water, the nanoparticles oxidize, leading to a loss of color. Thus, by analyzing this color transformation, the ammonia concentration can be determined directly from the solution without additional reactants. Significantly, this colorimetric platform relies on a self-assembling technique for producing large-scale and low-cost structural color fully compatible with industrial standards, thus allowing for a cost-effective and high-volume production method for the sensors, essential for commercial success. We present a simple algorithm using a smartphone camera, and image recognition can eliminate the need for traditional bulky and expensive spectroscopic systems, simplifying color-reading[3]. Our colorimetric plasmonic platform only requires a sensor and a smartphone to determine ammonia levels as low as 8.5 ppm in water[3], eliminating the need for additional chemicals. This makes the sensor suitable for use in contexts where low cost and portability are required.

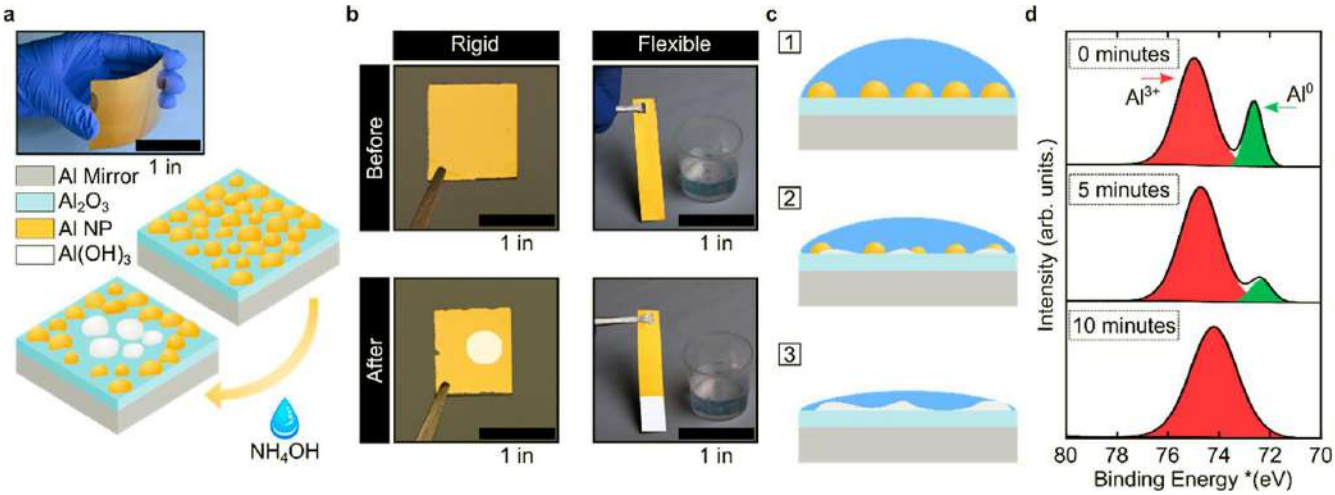


Figure 1. Chemical reaction-induced color change in nanosensor. (a) The plasmonic colorimetric sensor consists of an aluminum self-assembled layer over a thin Al_2O_3 layer over a back mirror on rigid (glass) and flexible (PET) substrates. (b) Nanoislands structural change causes observable color shifts before/after exposure to dissolved ammonia in water. (c) Al_2O_3 transforms to $Al(OH)_3$ after reaction with dissolved ammonia in water. Subsequent exposure to water cyclically prompts Al_2O_3 layer formation. (d) XPS measurements of the top surface of the sensor at different time intervals indicate aluminum nanoparticles oxidize during the reaction with aqueous ammonia.

Acknowledgments: K.M. and D.C. acknowledge the National Science Foundation Grant #ECCS-1920840, Department of Homeland Security FEMA Grant #EMW-2018-FP00329, and NSF MRI Grant# ECCS-1726636.

References

1. Ryer-Powder, J. E. "Health Effects of Ammonia," Plant Oper. Prog. Vol. 10, No. 4, 228–232, 1991.
2. Smith, A. F., X. Liu, T. L. Woodard, T. Fu, T. Emrick, J. M. Jiménez, D. R. Lovley, J. Yao, "Bioelectronic Protein Nanowire Sensors for Ammonia Detection," Nano Res. Vol. 13, No. 5, 2020, 1479–1484, 2020.
3. Soudi, M., P. Cencillo-Abad, J. Patel, S. Ghimire, J. Dillon, A. Biswas, K. Mukhopadhyay, D. Chanda, "Self-Assembled Plasmonic Structural Color Colorimetric Sensor for Smartphone-Based Point-Of-Care Ammonia Detection in Water," ACS Appl. Mater. Interfaces, Vol. 16, No. 34, 45632–45639, 2024.

Visualization of Thermal Extraction Process Achieved by Metamaterial Absorber

Wakana KUBO
Tokyo University of Agriculture and Technology (TUAT)
*corresponding author: w-kubo@cc.tuat.ac.jp

Abstract: We visualized how a metamaterial absorber extracts heat from surrounding objects for the first time. After a certain period of heating, we observed that the temperature of the Cu plate placed on the metamaterial substrate attached to the thermoelectric device decreased faster than that of the Cu plate placed on the control substrate.

The development of technologies to recycle waste heat is essential for establishing a decarbonized society. Thermoelectric conversion is a promising technology for recycling waste heat. However, due to its inherent limitations, power generation is impossible in an environment with uniform thermal radiation, meaning that conventional thermoelectric devices cannot collect and recycle the waste heat diffused in environments. To address this issue, we proposed and demonstrated metamaterial thermoelectric conversion capable of power generation even in an environment with uniform thermal radiation.[1-3] In this mechanism, a metamaterial absorber (MA) installed on one end of the thermoelectric element absorbs thermal radiation emitted from the surrounding environment, which is then converted into electricity by the thermoelectric element.

In previous studies, the ability of MA to absorb thermal radiation has been demonstrated through measurements of its absorption and emission spectra in far-fields and through direct observation of localized heat generation. Furthermore, we previously demonstrated that MA induces nonradiative cooling, reducing the air temperature in its vicinity.[4] However, the nonradiative cooling has been evaluated using thermistors, which measure the average temperature drop of the surrounding air in the vicinity of the MA electrode. Moreover, no prior study has visualized the process of MA extracting heat from surrounding materials. Therefore, we attempted to observe how MA extracts heat from surrounding objects using an infrared camera.

We fabricated a metamaterial thermoelectric device by attaching a MA substrate, composed of Ag disks, a calcium fluoride (CaF_2) layer, and a Ag layer, to one side of a thermoelectric element (Fig. 1(a-c)). The MA substrate is electrically isolated from the thermoelectric device using polymer double-side tape. The MA thermoelectric device and control device (with Cu electrodes only) were placed on a cooler maintained at 303 K, and a Cu plate bonded with polyimide (PI) was placed on the top electrodes of the devices.

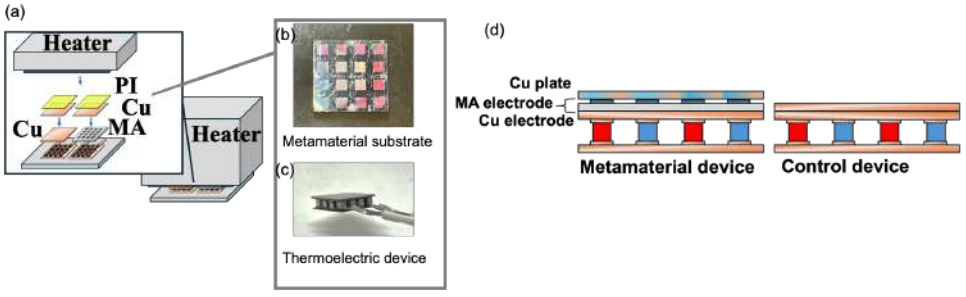


Figure 1. (a) Schematic of experimental setup. Photographs of (b) the metamaterial substrate and (c) thermoelectric device. (d) Cross-sectional experimental schematics of the metamaterial (left side) and control (right side) thermoelectric devices.

The PI film on the Cu plate is used to reduce reflectivity, leading to more accurate temperature measurements using an IR camera. The upper surfaces of the Cu plates were heated for 1 minute by a heater set to be 373 K. After removing the heater, we observed the natural cooling process of the upper Cu plate. The temperature reduction on the Cu substrate was measured using an infrared camera and thermistors, and the voltage and current of the thermoelectric devices were recorded.

Fig. 1(d) presents the expected mechanism that the MA extracted heat from the upper Cu substrate and gave it to the thermoelectric device. This caused the faster temperature reduction of the Cu substrate on the MA device than that of the Cu plate on the control device, leading to an increase in the output voltage generated by the MA device.

Figure 2(a) shows the time dependence of the output voltage generated by the MA and control thermoelectric devices. Figure 2(b) displays the voltage difference of the MA and control devices after 320 s, demonstrating that the MA device exhibited a higher output voltage. The absolute value of the temperature difference between the Cu plates on the MA and control devices is shown as red plots in Fig. 2(b), indicating that the temperature reduction of the Cu plate on the MA device occurred after the MA exhibited higher output voltage. Figure 2(c) presents the infrared camera images of the Cu plates on the MA and control devices. At 16 s after heating stopped, the temperature of the Cu substrate placed on the MA device was visually confirmed to be lower than that on the control device, indicating that the MA extracted heat from the Cu plate. This trend is also supported by the output voltage difference profile. These results support the cooling mechanism observed for the Cu plate placed on the MA device. In conclusion, we successfully visualized the process of MA extracting heat from the surrounding objects.

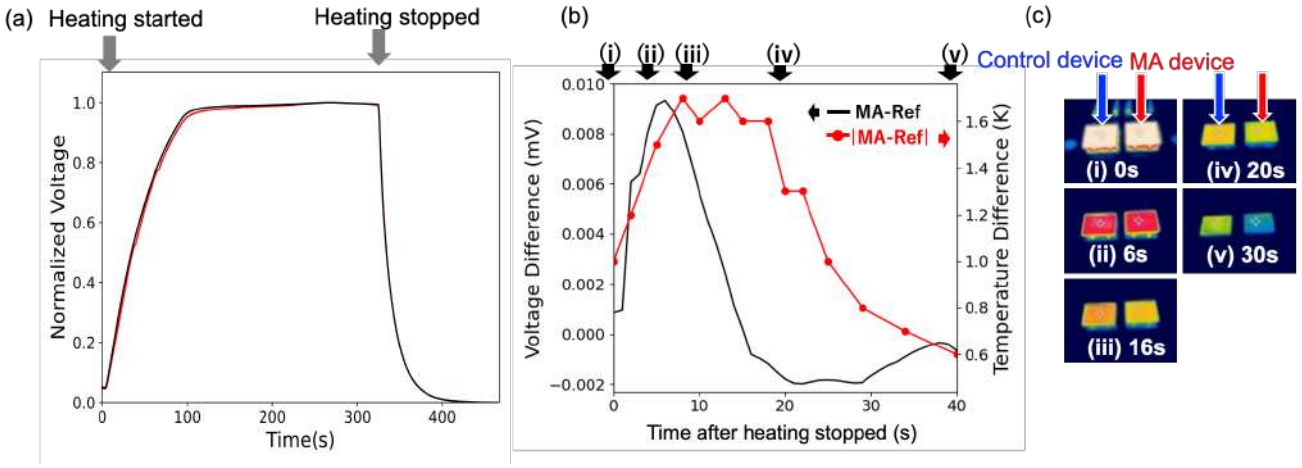


Figure 2(a) Normalized output voltage profile of the metamaterial (red line) and control (black line) thermoelectric devices. Heating was stopped at a time of 320 s. (b) Comparison of the voltage differences of the metamaterial and control devices, and the absolute value of temperature difference between the Cu plates on the metamaterial and control devices. (c) IR camera photographs of the Cu plates placed on the MA and control devices at (i) 0 s, (ii) 6 s, (iii) 16 s, (iv) 20 s, and (v) 30 s, respectively.

References

1 Katsumata, S., Tanaka, T. & Kubo, W. Metamaterial perfect absorber simulations for intensifying the thermal gradient across a thermoelectric device. *Opt. Express* **29**, 16396-16405 (2021).

2 Nakayama, R., Saito, S., Tanaka, T. & Kubo, W. Metasurface absorber enhanced thermoelectric conversion. *Nanophotonics* **13**, 1361-1368 (2024).

3 Saito, S., Yamamoto, A., Lu, Y.-J., Tanaka, T. & Kubo, W. Artificial thermal flow control on thermoelectric device by tuning electrode absorptivity. *Discover Nano* **20**, 44 (2025).

4 Kawamura, N., Tanaka, T. & Kubo, W. Nonradiative Cooling. *ACS Photonics* **11**, 1221–1227 (2024).

Twisted Moiré Metasurfaces with Emissive Gap Layers Enabling Giant and Tunable Chiral Emission

Zijie Jiang[1], Sun Zhao[1], Zhuofei Gan[1], and Wen-Di Li[1*]

[1]Department of Mechanical Engineering, The University of Hong Kong, Pokfulam, Hong Kong S.A.R., China
[*]corresponding author: liwd@hku.hk

Abstract: We present twisted moiré chiral metasurfaces (TMCMs) with tunable chiral emission using cost-effective and large-area fabrication combining nanoimprint and interference lithography. TMCMs achieve luminescence dissymmetry factor (g_{lum}) of −1.21. Chirality is tuned via twist angles and gaps, validated by reciprocity-based simulations. Compatibility with quantum dots and perovskites enables versatile chiral light sources.

Chiral light sources with direct circularly polarized emission are critical for sensing, imaging, and quantum technologies [1]. Conventional chiral metasurfaces rely on complex meta-atoms and costly electron-beam lithography, limiting their manufacturability and scalability. Twisted moiré metasurfaces [2,3] offer intrinsic chirality through lattice-level symmetry breaking but face challenges in emission performance and fabrication efficiency. Here, we demonstrate emissive TMCMs with a dye-doped polymer gap layer between reusable structural layers, fabricated via nanoimprint (NIL) and laser interference lithography (LIL). This method enables centimeter-scale production while maintaining high tunability and cost-effectiveness.

The TMCM design comprises two twisted gold nanopillar arrays separated by an emissive gap. The moiré lattice, dictated by the twist angle (α), breaks symmetry without intricate meta-atoms. A key innovation in our work is the reusable structural layers, fabricated using high-throughput and scalable techniques like interference lithography, UV-curable and thermal NIL, and electrochemical deposition. The thickness (g) of the emissive gap layer in the TMCM structure is controlled via spin-coating, enabling precise modulation of interlayer coupling.

Emission chirality was quantified by the g_{lum} factor, defined as $g_{lum} = 2\frac{I_{LCP}-I_{RCP}}{I_{LCP}+I_{RCP}}$, with the maximal value achieved to be −1.21 at 719 nm. Chirality tuning was demonstrated by varying α from 0° to 165° and g from 35 to 210 nm. For instance, reversing α beyond 90° inverted g_{lum}, while adjusting g shifted resonance wavelengths and flipped chirality. We also carried out reciprocity-based simulations, which revealed that the emission asymmetry correlates with field enhancement contrasts.

Notably, the TMCM platform supports diverse emissive materials. Replacing dye molecules with CdSe quantum dots or $CsPbI_3$ perovskites in the gap layer yielded comparable g_{lum} values. This versatility, combined with dynamic tunability, positions TMCMs as ideal candidates for applications like encryption, 3D displays, and spin-photonics.

In conclusion, our work addresses critical barriers in chiral metasurface fabrication and performance. The scalable fabrication method, high g_{lum}, and tunability via geometric parameters establish TMCMs as a promising platform for practical chiral light sources.

References

1. Q. Song et al., Moiré Perovskite Photodetector toward High-Sensitive Digital Polarization Imaging, Adv. Energy Mater. **11**, 2100742 (2021)
2. M. Cen et al., Chirally Selective and Switchable Luminescence from Achiral Quantum Emitters on Suspended Twisted Stacking Metasurfaces, ACS Nano (2024)
3. Z. Wu, Y. Liu, E. H. Hill, and Y. Zheng, Chiral metamaterials via Moiré stacking, Nanoscale **10**, 18096 (2018)

Optimization of Photonic Structures for CMOS Image Sensors using Adjoint Sensitivity

Rishad Arfin[1], Jeongwoo Son[2], Jens Niegemann[3], Dylan McGuire[3], Mohamed H. Bakr[1*]

[1]Department of Electrical & Computer Engineering (ECE), McMaster University, Hamilton, ON L8S 4K1, Canada
[2]Ansys Korea, Republic of Korea
[3]Ansys Canada Ltd.,1700 – 1095 West Pender Street, Vancouver, BC V6E 2M6, Canada

[*]corresponding author: mbakr@mcmaster.ca

Abstract: This work presents a systematic optimization approach to develop efficient photonic structures with enhanced optical performance for CMOS image sensors. Adjoint sensitivity analysis (ASA) is used to optimize the structure for improved focusing and collection of light. The adjoint-optimized structure demonstrates enhanced performance compared to the conventional designs.

In recent years, there has been a great interest in advancing CMOS image sensors to achieve high resolution sensing and imaging. The broad integration of CMOS image sensors in various imaging and sensing technologies is largely driven by their miniaturized feature size, resulting in reduced pixel size. This reduced pixel size affects the light collection in the photoactive region, which degrades the intensity, angular response, and overall performance. Efficient photonic designs such as microlenses [1] or dielectric metasurfaces [2] can significantly improve the light collection and optical efficiency of CMOS image sensors. We use adjoint-driven optimization techniques to accelerate the development of efficient design of microlenses and metasurfaces to enhance the overall optical efficiency of CMOS image sensors.

In our study, we carried out shape optimization of CMOS microlenses using ASA [1, 3]. We utilize an optical stack for CMOS image sensor that includes conventional microlenses as initial design. The derivative-based optimizer perturbs the shape (or design parameters) of the microlenses to improve the figure of merit (FOM). The FOM sensitivities information is used during perturbation to determine the optimal design parameters. The FOM sensitivities with respect to all the design parameters are efficiently computed through only two simulations using ASA. We used Ansys Lumerical FDTD to carry out electromagnetic simulations. LumOpt [4], an open-source package, is utilized to perform adjoint-based optimization. We have substantially modified and extended the LumOpt framework, significantly enhancing its ability to integrate adjoint formulation for free-space photonic problems and incorporate FOM for new classes of photonic devices, such as microlenses [1] and dielectric metasurfaces [2].

In our work, the front-side illuminated (FSI) optical stack for CMOS image sensor is represented using an Si substrate with metallic interconnect embedded in a dielectric layer of SiO_2. The optimizable microlenses are positioned above the Bayer color filters. Each color pixel is 2 μm wide and a fill factor of 25% is used during the optimization. We aim to maximize the absorption of light at the Si surface for the central RGB wavelengths, i.e. 650 nm, 550 nm, and 450 nm, by defining a novel FOM for adjoint field formulation as follows:

$$FOM = \sum_{\lambda} w_{\lambda} \left| E(x,\lambda) \right|^2 , \tag{1}$$

where $E(x,\lambda)$ is the electric field at location x for wavelength λ and w_{λ} is the assigned weight for each λ .

Our study demonstrates significant improvement in the FOM and angular response (AR) through adjoint-assisted shape optimization of CMOS microlenses and outperforms the conventional microlenses, as shown in Fig 1. This work further accelerates the development of nonintuitive yet highly efficient 3D CMOS microlens for practical applications.

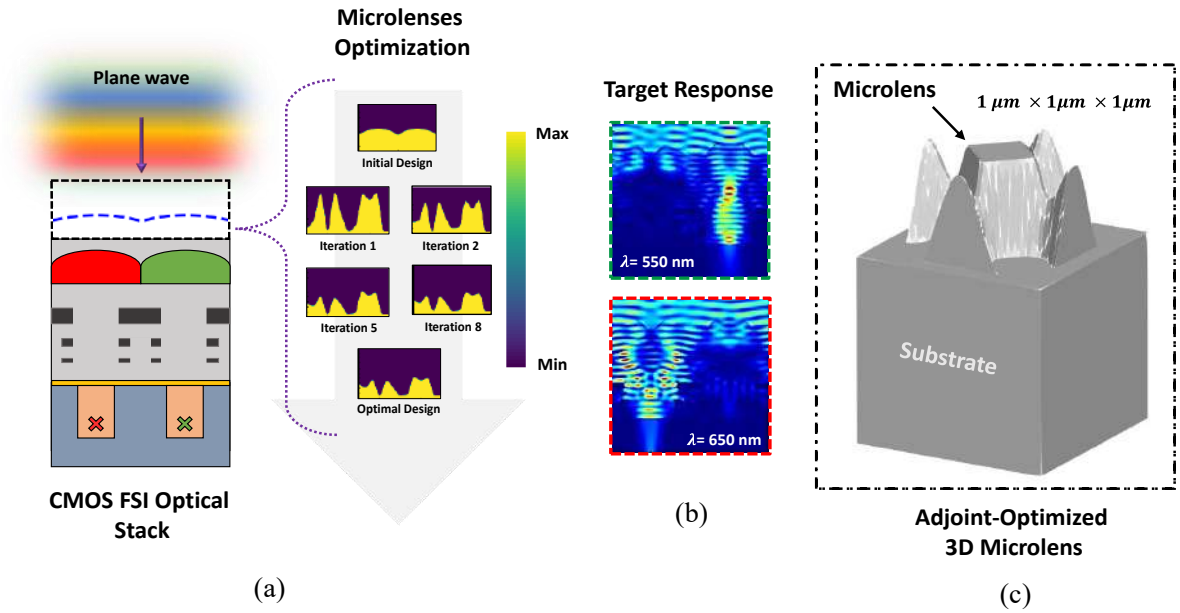


Figure 1. (a) Evolution of optimal microlenses for CMOS FSI optical stack during optimization process. (b) Intensity of incoming light at target wavelengths. (c) Optimization of 3D microlens for a quarter-unit cell on a substrate to maximize the light intensity at a target wavelength.

The contribution of our work is not only limited to the development of efficient designs of CMOS microlenses. The novel FOM developed in this work, supported by adjoint-driven optimization, enables the development of efficient optical devices to address the free-space photonic problems, presented in [2]. In [2], the adjoint-optimized dielectric metasurface (TiO_2–Si_3N_4), employed as color router, demonstrated improved optical efficiency (OE) over the visible spectrum and addressed the drawbacks associated with conventional color filters.

References

1. Arfin, R., Niegemann, J., McGuire, D., and Bakr, M. H., "Adjoint-Assisted Shape Optimization of Microlenses for CMOS Image Sensors," Sensors, Vol. 24, No. 23, 7693, 2024.
2. Son, J., Arfin, R., Bakr, M. H., and Niegemann, J., "Designing a metasurface color router via photonic inverse design," The 14th International Conference on Metamaterials, Photonic Crystals, and Plasmonics, META 2024, Toyama – Japan, July 16 – 19, 2024.
3. Bakr, M. H., Elsherbeni, A., and Demir, V., "Adjoint Sensitivity Analysis of High Frequency Structures with MATLAB," Institution of Engineering and Technology (IET), SciTech Publishing Inc., London, UK, 2017.
4. Lalau-Keraly, C.M., Bhargava, S., Miller, O.D., and Yablonovitch, E., "Adjoint shape optimization applied to electromagnetic design," Opt. Express, Vol. 21, No. 18, pp. 21693-21701, 2013.

Modulation and amplification of waves by metasurfaces

I. V. Shadrivov
Research School of Physics and Australian Research Council Centre of Excellence for Transformative Meta-Optical Systems, The Australian National University, Canberra ACT 2601, Australia
ilya.shadrivov@anu.edu.au

Abstract: In this presentation I will overview our approaches to creating tunable metasurfaces for controlling amplitude, phase and polarization of electromagnetic waves. I will further discuss the parametric processes that allow amplification and up-conversion of electromagnetic waves.

First, we explore tunable polarization conversion in metasurface-assisted anisotropic slab waveguides using electro-optic modulation. We show that by an appropriate choice of the crystal axis, quasi-TE and quasi-TM modes in lithium niobate (LN) waveguide can be made degenerate. Using grating excitation of such modes and coupling between the modes, we enable efficient linear polarization conversion. The achieved broadband polarization conversion is demonstrated for varying crystal angles. Furthermore, voltage-induced refractive index changes in LN allow dynamic tuning of the conversion efficiency and phase. The study highlights the potential for versatile and tunable polarization conversion of light by a 1 micron thick structure.

In the second part of the presentation, we will focus on developing reconfigurable and time-varying metasurfaces, which can dynamically adjust their behaviour in response to external signals. This ability to change over time opens up exciting possibilities for new functionalities, such as real-time beam steering, enhanced signal processing, and advanced wave control mechanisms. Metasurfaces that change their properties with time are often referred to as time-varying or parametric metasurfaces. Unlike passive surfaces, which only redirect or filter incoming waves, parametric metasurfaces can actively amplify and convert the frequency of electromagnetic waves, enabling entirely new applications in signal processing and wireless communications. Recent studies have explored how time-varying metasurfaces can be used for nonreciprocal wave transmission (allowing waves to travel differently in opposite directions), the creation of so-called "time crystals," and the up-conversion of electromagnetic waves to higher frequencies.

Despite these exciting developments, most studies on time-varying metasurfaces have focused on either frequency conversion or wave amplification, but not both simultaneously. Only a few theoretical works have suggested that metasurfaces could achieve both amplification and frequency up-conversion at the same time, and even in those cases, the reported conversion efficiency was relatively low. Furthermore, previous designs often relied on reflective structures, making them bulky and less practical for integration into compact systems.

In this study, we propose a new type of parametric metasurface that overcomes these limitations. Our design is based on a dual-resonance structure consisting of two coupled split-ring resonators (SRRs), with an embedded varactor diode. By modulating the capacitance of this varactor, our metasurface can simultaneously amplify and up-convert incident electromagnetic waves. Through theoretical modeling, we demonstrate that our metasurface achieves an up-conversion efficiency exceeding 20 dB, surpassing conventional limitations set by the Manley-Rowe relations. Moreover, by tuning the phase of the external modulation, we gain precise control over the phase of the up-converted waves, offering additional possibilities for advanced wave manipulation.

This research was supported by the Australian Research Council Centre of Excellence for Transformative Meta-Optical Systems (Project ID CE200100010).

Negative refraction of light using atoms instead of metamaterials

L. Ruks[1], K. E. Ballantine[2], and J. Ruostekoski[2]
[1]NTT Basic Research Laboratories, NTT Corporation, Kanagawa, 243-0198, Japan
[2]Department of Physics, Lancaster University, Lancaster, LA1 4YB, United Kingdom
Corresponding author: j.ruostekoski@lancaster.ac.uk

Abstract: Negative refraction has driven the development of metamaterials. However, due to material characteristics, the applications of this phenomenon, such as perfect lensing, have been constrained. Here, we demonstrate negative refraction of light in an atomic array without the use of artificial metamaterials, employing essentially exact simulations of light propagation.

Atoms primarily interact with light through electric dipole transitions, while magnetic dipole and electric quadrupole transitions are significantly weaker. Although atomic systems with well-developed quantum technologies otherwise provide a pristine optical medium where each atom possesses a precise resonance frequency, free from manufacturing imperfections or non-radiative absorption losses, these inherent constraints in the optical transitions have hampered any efforts to achieve unusual optical properties, such as negative refraction of light, in a natural medium. While negative refraction has driven the development of metamaterials, material characteristics of artificially engineered media have constrained the applications of this phenomenon, such as lensing that surpasses the diffraction limit.

Here we show that negative refraction of light can be obtained in atomic media without the use of artificially fabricated resonators [1]. This is made possible by harnessing and utilising cooperative, non-local atom responses that arise from strong light-mediated interactions at high densities. We achieve this controlled response by considering subwavelength atomic arrays [2] with unit filling, which can be experimentally realised in system sizes up to tens of wavelengths. Cooperative optical interactions in atomic arrays have recently been confirmed in transmitted light, as evidenced, e.g, by the spectral resonance narrowing below the fundamental quantum limit dictated by a single atom [3].

We demonstrate the negative refraction of light through microscopic, atom-by-atom simulations that exactly incorporate all recurrent scattering processes between stationary atoms in the low light intensity limit which accurately describes experimental conditions. The simulations uncover a distinct deflection of propagating light beams in the opposite direction to what normally occurs. This enables us to extract from microscopic simulations the negative value of refractive index. We demonstrate high-transmission negative refraction that is resilient to lattice imperfections, such as missing atoms and position uncertainty, over a range of laser frequencies, incident angles, and lattice constants by modelling 3D atom arrays as stacked infinite 2D planar layers when in each layer the scattering problem is represented in momentum space. Our findings, confirmed for finite-sized arrays in a few-layer scenario through large-scale simulations, reveal that such refraction aligns with the simple phenomenology of transverse Bloch band collective resonances. Notably, negative refraction can be realised by engineering and exciting such resonance bands whose in-plane group velocities are antiparallel to the excitation quasimomenta – which are a common occurrence in moderately subwavelength arrays. Intriguingly, the effective refractive index can be significantly enhanced through coupling with more subradiant

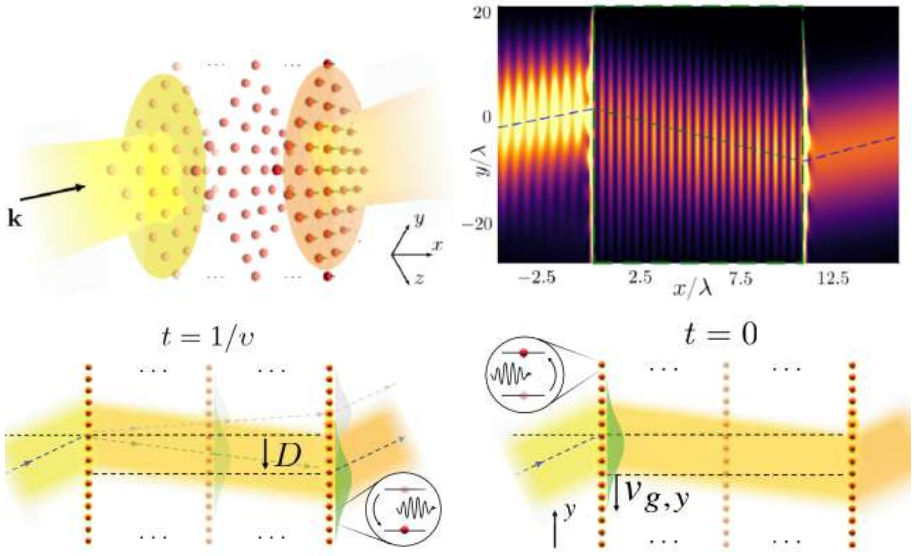


Figure 1: **Negative refraction and transmission of light through an atomic medium.** Top left: Light transmission through a cubic atom array, stacked in infinite planar lattices along the x axis. The transmitted beam undergoes lateral displacement D along the y axis. Top right: Negative refraction of a beam incident with the angle $\theta = 0.2 \times \pi$ and laser detuning $\Delta/\gamma = 0.73$ from the atomic resonance, in units of single-atom linewidth γ, through a 25-layer atomic lattice. Bottom row: Microscopic origin of negative refraction. An atomic polarisation wavepacket, excited by the incident beam, propagates along the y-axis over its lifetime $t = 1/\upsilon$, where $\upsilon = \upsilon^{(j)}(q_y, q_z = 0)$ is the collective linewidth, accumulating a transverse displacement of $D \simeq v_{g,y} \times 1/\upsilon$. The transverse group velocity component $v_{g,y} = \in \partial\delta^{(j)}(q_y, q_z = 0)/\partial q_y$ is derived from the collective line shifts $\delta^{(j)}(q_y, q_z = 0)$ for phase-matched quasimomenta q_y in resonant band j. Green and grey wavepackets illustrate cases of negative and positive displacement, respectively.

excitations.

In Fig. 1, we demonstrate cooperative negative refraction of light through a 25-infinite-layer atomic medium based on atom-by-atom simulations for the propagating beam incident at angle $\theta = 0.2 \times \pi$ relative to the array normal. The illustration also describes the microscopic origin of the negative refraction in this system in terms of lifetimes of the collective excitations. Targeting a resonance energy band with subradiant features can considerably enhance negative refraction.

References

1. Ruks L., Ballantine, K. E., and Ruostekoski, J. "Negative refraction of light in an atomic medium," *Nature Comm.* Vol. 16, 1433 (2025).

2. Ruostekoski, J. "Cooperative quantum-optical planar arrays of atoms," *Phys. Rev. A* Vol. 108, 030101 (2023).

3. Rui, J. *et al.* "A subradiant optical mirror formed by a single structured atomic layer," *Nature* Vol. 583, 369–374 (2020).

Development of a Silicon Nitride Platform for Next Photonic Integrated Circuits

B. Ahammou[1], N. Dalvand[2], B. Le Drogoff[1], Y. Ouldhnini[1], A. Radi[1], M. Taghavi[1], K. Ghuman[1], J. Margot[3], M. Ménard[2], and M. Chaker[1*]

[1]INRS-EMT, Canada
[2]ETS, Canada
[2]Université de Montréal, Canada
[*]corresponding author: Mohamed.chaker@inrs.ca

Abstract: As an ideal platform for photonic integrated circuits, silicon nitride material is explored. In particular, we investigate residual stress and cracking limits in SiN_x films through experimental and computational approaches, as well as plasma-based SiN_x nanopatterning.

Silicon nitride (SiN_x) has become a key material for photonic integrated circuits (PICs) due to its ultra-low optical losses, broad spectral transparency, and compatibility with standard semiconductor processes. It plays a crucial role in telecommunications, nonlinear optics, quantum photonics, and biosensing. However, its widespread adoption remains limited by stress-induced cracking in thick SiN_x films and the challenges associated with precise nanopatterning and etch fidelity in plasma etching.

Our research group addresses these challenges by integrating experimental fabrication with computational modeling to advance SiN_x photonics. We investigate SiN_x deposition, stress control, and nanofabrication using a combination of low-pressure chemical vapor deposition (LPCVD) experiments and molecular dynamics (MD) simulations. Our experimental findings reveal that while LPCVD produces ultra-smooth (~0.16 nm roughness) and highly uniform SiN_x films, it also induces high tensile stress (>1 GPa), leading to crack formation in stochiometric compositions. To understand this, we use MD simulations to explore how deposition conditions—substrate temperature, deposition power, and precursor composition—affect intrinsic stress. We also investigate alternative deposition methods such as reactive sputtering to produce thick, low-stress, hydrogen-free SiN_x films, offering promising solutions for high-performance photonics.

Beyond stress control, our group develops advanced SiN_x etching techniques to improve fabrication precision. By optimizing fluorine-based plasma etching and investigating lithographic densification, we enhance etching selectivity, uniformity, and sidewall smoothness and angles. We systematically compare different mask materials, including SiO_2 and metal hard masks, to assess their impact on etch fidelity and feature resolution. Using inductively coupled plasma etching, we achieve precise, anisotropic patterning of SiN_x structures, enabling high-resolution, low-loss photonic devices with improved reproducibility. Our optimized process allows for the fabrication of square SiN_x waveguides with optical losses below 1 dB/cm and minimal birefringence, validating the platform's suitability for scalable, low-loss photonic integration.

Vectorial metasurface for polarization encoding and imaging

Fengjun Li[1], Zilan Deng[1], and Xiangping Li[1*]

[1]College of Physics and Optoelectronic Engineering, Jinan University, P.R.China
[*]corresponding author: xiangpingli@jnu.edu.cn

Abstract: With powerful wavefront manipulations metasurfaces emerge as a transformative platform for multifarious and ultra-compact optical devices. In this talk, we present the vectorial metasurface design that enables polarization encoding in the 2D parametric space of polarizations including both polarization rotation angle and ellipticity. In addition, we show the monolithic metasurface design by fusing vectorial grating and lens functions to enable ultra-compact polarization camera with large field-of-view of 14 degrees and full stokes polarization imaging capability.

Metasurfaces, composed of arrays of subwavelength meta-atoms with exquisitely tailored geometries, have offered unprecedented prospects for light management and wavefront shaping [1,2]. The upsurge in metasurfaces based on various meta-atom designs has impelled marvelous developments such as lenses, holograms, illusionary optics and color prints, which have demonstrated potentials as a transformative platform for lightweight, ultra-compact and multi-furious miniaturized optical devices. In this talk, we present the vectorial metasurface design that empowers full parametric control of diverse polarization states across the full Poincare sphere. Leveraging this polarization manipulation freedom, we introduce a method for polarization encoding information along trajectories on the Poincaré sphere using metasurfaces, based on a generalized Malus' law (GML) [3]. This generalized law facilitates universal 2D projections among any pair of elliptical polarizations over the entire PS. By custom-designing PS trajectories through either specific analytic functions or strategically aligned modulation grids, we enable a diverse set of polarization-based image transformation capabilities. In addition, we demonstrate a meta-grating-lens (MGL) based monolithic polarization camera that fuses polarization analysis, beam-splitting, and imaging functionalities within a singlet metasurface in a fine-grained pixel level [4]. The optimized MGL exhibits >80% diffraction efficiency with <0.1% zeroth-order noise for high performance polarization imaging. We envision that the vectorial metasurface approach provides an ultra-compact and miniaturized paradigm underpinning diverse polarization-dependent applications ranging from autonomous anti-spoofing imaging, 3D imaging, information encoding and defogging imaging.

References

1. Yu, N., et al. Light Propagation with Phase Discontinuities: Generalized Laws of Reflection and Refraction. Science 334, 333-337 (2011).
2. Khorasaninejad, M. & Capasso, F. Metalenses: Versatile multifunctional photonic components. Science 358, 1146 (2017).
3. Zi-Lan Deng, Meng-Xia Hu, Shanfeng Qiu, Xianfeng Wu, Adam Overvig, Xiangping Li & Andrea Alù, Poincaré sphere trajectory encoding metasurfaces based on generalized Malus' law, Nature Communications. 15, 2350, (2024)
4. Fengjun Li, Ziwei Feng, Tan Shi, Zi-Lan Deng, & Xiangping Li, Meta-grating-lens based monolithic polarization camera. To be submitted

Highly Sensitive CMOS Image Sensor Integrating Color-routing Nanostructures

C. Cho, S. Lee, S. Roh, S. Ahn, S. Lee, J. Lee, S. Song, S. Yun*

Samsung Advanced Institute of Technology, Korea
*corresponding author: seok.h.yun@samsung.com

Abstract: We present CMOS image sensor with tailored color-routing nanostructures, which significantly enhances sensitivity while preserving most of its spatial resolution as well. Furthermore, adjusting the arrangement of nanostructures based on relative position, enables mitigating oblique light incidence, enabling commercial CMOS image sensors.

With the recent advancements in CMOS image sensors, the demand for high-quality image resolution has led to smaller pixel sizes. As pixel downsizing results in an increased number of pixels in the same form factor, it suffers from low sensitivity, especially in low-light environments, as its light-receiving region becomes smaller [1]. To this end, image sensors employing color-routing nanostructures have been suggested [2-4]. While two third of light are dissipated in color filter in conventional image sensors, image sensors featuring color-routing structure enable separating lights by colors and then filter, thereby improve quantum efficiency (QE). Although color-routing nanostructures achieves high sensitivity or even color filter free image sensors, the diffraction mechanism dilute spatial resolution and corrupt the image quality. While image could be refined by running reconstruction algorithm, it consumes high power resources which is undesirable in real cases.

Here we present highly sensitive image sensor featuring color-routing nanostructure, preserving most of its spatial resolution compared to conventional microlens based image sensor. As illustrated in Fig.1, the color-routing structure consist of TiO_2 pillars embedded in a SiO_2 bilayer, which separates and focuses incoming light onto different locations based on wavelength. It achieves 15% improvement in average QE for RGB channels compared to conventional microlens image sensors in a 0.7um pixel-sized, 4-pixel binning configuration. Additionally the autofocus contrast ratio at a 10° incident angle reaches as high as 2.2 at the center of sensor. By adjusting the arrangement of TiO_2 pillars and shift of two layers with respect to the center of sensor, relative to the chief ray angle (CRA), performance is maintained in the high CRA. Furthermore, by arranging the pillars tightly, the sensors preserve more spatial resolution information by restricting uncontrolled light transmission through the layer. Under slanted edge illumination simulation, it shows MTF of 94.9% with respect to reference at 1/2 Nyquist frequency.

In summary, we developed a CMOS image sensor incorporating tailored color-routing nanostructures that significantly enhance sensitivity while maintaining most of its spatial resolution. Additionally, by optimizing the nanostructure arrangement relative to position, we effectively mitigate the impact of oblique light incidence, making color-routing nanostructure feasible for commercial CMOS image sensors.

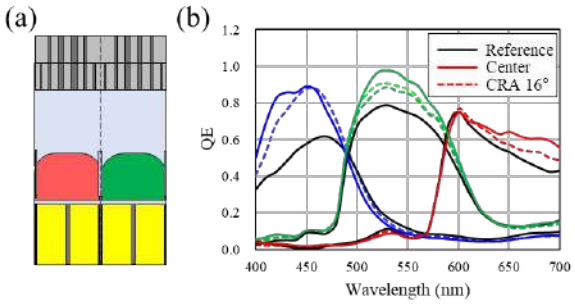


Figure 1. (a) Schematic of bilayer color-routing nanostructures on CMOS image sensor. (b) Relative QE spectrum of reference (black solid line) and color-routing image sensor at center (colored solid line) and CRA 16° (colored dashed line)

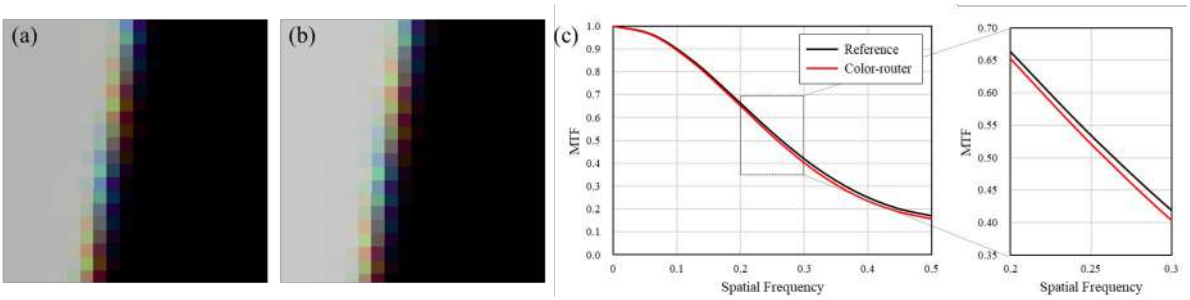


Figure 2. Simulation image of slated-edge illumination for (a) a conventional microlens (reference) and (b) a color-routing image sensor. (c) MTF of reference and color-router structures, calculated from images in (a) and (b) at wavelengths of 450nm, 540nm, and 630nm using white balance and bilinear algorithm.

References

1. P. Catrysse and B. Wandell, “Roadmap for CMOS image sensors: Moore meets Planck and Sommerfeld,” SPIE 5678, 2005.
2. S. Yun et al, “Highly Efficient Color Separation and Focusing in the Sub-micron CMOS Image Sensor,” 2021 IEDM, 641-644, 2021.
3. Miyata, M. et al. “Full-color-sorting metalenses for high-sensitivity image sensors,” Optica 8, 1596–1604, 2021.
4. C. Choi et al., "Optical design of dispersive metasurface nano-prism structure for high sensitivity CMOS image sensor," 2023 IEDM, 1-4, 2023.

Non-Lorentzian effects for exciton-plasmon systems at strong coupling

Tigran V. Shahbazyan

Department of Physics, Jackson State University, Jackson, MS 39217 USA
shahbazyan@jsums.edu

Abstract: We study non-Lorentzian effects in the scattering spectrum of quantum emitters strongly coupled to surface plasmons in metal nanoparticles. We develop a semiclassical approach incorporating optical dispersion and losses in the metal to show that non-Lorentzian effects cause a shift of the spectral weight towards the lower energy polaritonic band.

The shape of scattering spectra of quantum emitters (QE) resonantly coupled to localized surface plasmons (LSP) in metal nanoparticles (NP) as the system transitions to the strong coupling regime has been an actively debated issue as the relative spectral weight of polaritonic bands is determined by several competing processes. In general, the scattering spectrum of a hybrid system characterized by a broad spectral band is enhanced on the higher frequency side due to a faster radiation rate of upper-energy states, implying that, in the strong coupling regime, the spectral band associated with the upper-energy polaritonic state should be relatively enhanced. Such a spectral profile is consistent with the classical model of two coupled oscillators (CO), in which one of the oscillators (LSP) couples much stronger to the electromagnetic (EM) field due to a much smaller QE optical dipole moment [1]. However, recent experiments for excitons resonantly coupled to LSP in metal-dielectric structures [2,3] reveal the opposite asymmetry pattern characterized by enhanced lower polaritonic band. In this paper, we demonstrate that non-Lorentzian effects originating from the material optical dispersion and losses strongly affect the optical spectra of hybrid QE-LSP systems and, in the strong coupling regime, results in a shift of the spectral weight towards the lower-energy polaritonic band, consistent with the experiment. Using the non-Lorentzian LSP Green function for NP of arbitrary shape [4], we set up non-Lorentzian Maxwell-Bloch equations which include complex dielectric function of the metal rather than Lorentzian approximation for the LSP resonance. We show that the non-Lorentzian effects show up prominently in the optical spectra of plasmonic systems due to an interplay between the real and imaginary part of the metal dielectric function which define, respectively, the plasmon coupling to the EM field and the broad plasmon optical band. Specifically, the temporal dispersion of its real part, which originates from free-electron absorption is metals, leads to a spectral weight shift towards the lower frequency side of the spectra. In the strong coupling regime characterized by well-separated polaritonic bands, such non-Lorentzian effects result in an inversion of spectral asymmetry as compared to the CO model predictions.

In Fig. 1 we show the scattering spectra for a QE near an Au NP calculated using non-Lorentzian model for three different LSP frequencies. As the QE-LSP coupling increases, the system undergoes transition to strong coupling regime signaled by the emergence of Rabi splitting between polaritonic bands. In the higher-energy region, the spectrum exhibits enhancement of the lower-energy polaritonic band, consistent with the experiment [2,3], while for lower energies, the spectral weight shifts towards the upper energy band. In contrast, for scattering spectra calculated in the Lorentzian approximation shown in Fig. 2, the upper energy polaritonic band is enhanced in the entire energy range, as predicted by the CO model. This difference can be traced to the effect of metal temporal dispersion on the LSP optical dipole moment which results in a suppression of the LSP radiation efficiency for higher energies.

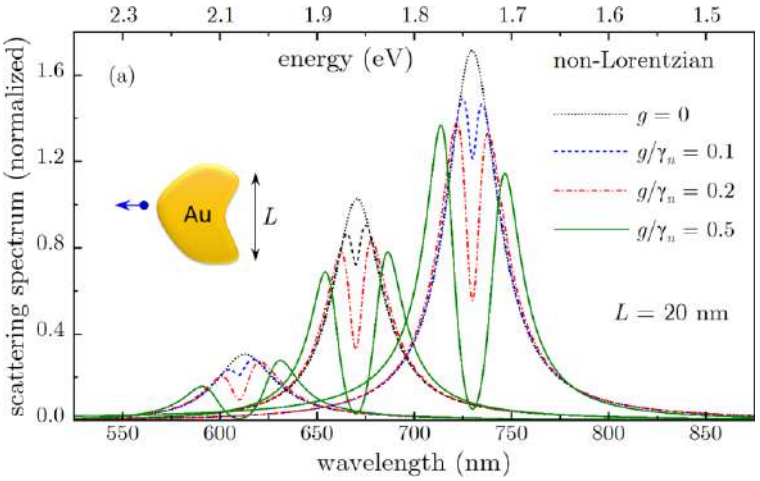


Figure 1. Scattering spectra for an Au NP coupled to a QE calculated using non-Lorentzian model.

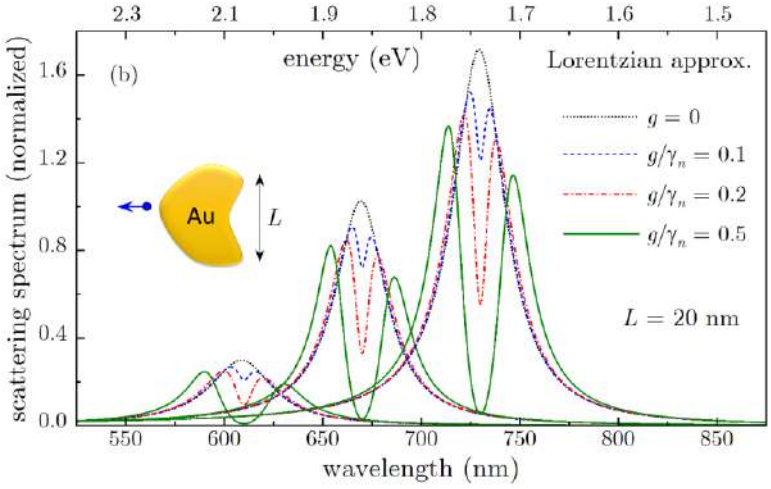


Figure 2. Scattering spectra for an Au NP coupled to a QE calculated using Lorentzian approximation.

This work was supported in part by the National Science Foundation grants DMR-2000170, DMR-2301350, and NSF-PREM-2423854.

References

1. H. Leng, B. Szychowski, M.-C. Daniel, and M. Pelton, “Strong coupling and induced transparency at room temperature with single quantum dots and gap plasmons”, Nat. Commun. Vol. 9, 4012, 2018.
2. M. Wersall, *et al.*, “Correlative Dark-Field and Photoluminescence Spectroscopy of Individual Plasmon–Molecule Hybrid Nanostructures in a Strong Coupling Regime”, ACS Photonics Vol. 6, 2570–2576, 2019.
3. K.-D. Park, *et al.*, “Tip-enhanced strong coupling spectroscopy, imaging, and control of a single quantum emitter”, Sci. Adv. Vol. 5, eaav5931, 2019.
4. T. V. Shahbazyan, “Universal optical polarizability for plasmonic nanostructures”, Phys. Rev. A 107, L061503, 2023.

Sub-1-volt, reconfigurable Gires-Tournois resonators for full-colour monopixel array

Young Min Song

[1]Electrical Engineering and Computer Science, Gwangju Institute of Science and Technology, Gwangju 61005, Korea
[*]corresponding author: ymsong@gist.ac.kr

Abstract: We present an electrically reconfigurable Gires-Tournois resonator integrated with polyaniline for full-colour, energy-efficient modulation at CMOS-compatible voltages. This system achieves vibrant colour shifts across the visible spectrum within a sub-1V range, supporting ultrahigh pixel densities and wafer-scale fabrication, with bistable memory-in-pixel functionality for low-power passive matrix addressing in display applications.

Ensuring uniform colouration and efficiency across pixel scales remains a key challenge in modern display technology, particularly for near-eye applications where micrometre-scale pixel precision is essential. Conventional approaches such as liquid crystal on silicon (LCoS) displays offer high spatial resolution and precise pixel control but require high operating voltages (~6 V) and suffer from sub-pixel configurations, light loss, and scalability issues due to crosstalk. Monopixel reflective displays, which integrate optically active materials within photonic architectures, have emerged as a promising alternative by enabling colour generation directly within the pixel. For instance, phase-change materials (PCMs) like Ge-Sb-Te enable sub-micrometre pixelation but face challenges related to heat dissipation, response-time fluctuations, and limited electrical addressability. Meanwhile, electro-optic (EO) materials provide high-speed modulation but require operating voltages exceeding 30 V and exhibit limited refractive index variation, constraining their colour modulation capacity. Conductive polymers such as polyaniline (PANI) and PEDOT:PSS offer a low-power solution (<1 V, <0.3 mW/cm²) with a significant refractive index change in the visible spectrum, yet their standalone implementation lacks the necessary light-matter interaction for achieving vibrant, broad-spectrum colour modulation. Plasmonic and Mie resonators have been investigated to enhance colour performance but introduce absorption-related losses and fabrication complexity, limiting practical scalability.

To overcome these challenges, we introduce an electrically reconfigurable Gires-Tournois (r-GT) resonator integrated with PANI, enabling full-colour modulation with ultra-low energy consumption (90 μW/cm²) at CMOS-compatible voltages (-0.2 V to 0.8 V). The r-GT resonator exploits sharp and strong resonance effects from impedance matching, achieving colour shifts that exceed complementary hue changes. By stabilizing the resonator interfaces during redox reactions, we mitigate chromatic degradation and scalability constraints, allowing operation across a wide range of pixel scales, from high-density micro-pixels (1.5 μm, ~16,900 PPI) to centimetre-scale image printing. Furthermore, PANI's bistable memory properties enable the memory-in-pixel feature, significantly reducing energy consumption compared to emissive-type displays, with energy savings up to 7.2 times greater. We demonstrate the feasibility of this technology with a passive matrix addressing system, validating its potential for scalable, high-performance reflective displays and other photonic applications requiring energy-efficient, high-resolution dynamic colour control.

Acknowledgements: This work was supported by the GIST Research Institute (GRI) RISE and GIST-MIT Research Collaboration through a grant funded by the GIST and National Research Foundation of Korea (NRF) funded by the Ministry of Science and ICT (2023R1A2C3004531, 2021M3H4A1A04086357). This work is also partly based upon work supported by the International Technology Center Indo-Pacific (ITC IPAC) and Army Research Office, under Contract No. FA5209-22-P-0162 and supported by the Technology Innovation Program (RS-2024-00467230) funded by the Ministry of Trade Industry & Energy (MOTIE, Korea).

References

1. Ko, J.H. et al. Electrochromic nanopixels with optical duality for optical encryption applications. Nanophotonics 13, 1119-1129 (2024).
2. Ko, J.H., Seo, D.H., Jeong, H.H., Kim, S. & Song, Y.M. Sub 1 volt electrically programmable optical modulator based on active Tamm plasmon. Adv. Mater. 36, 2310556 (2024).

Single-shot weak measurement for spin Hall effect of light using a metasurface

M. Kim[1*]

[1]School of Mechanical and Robotics Engineering, Gwangju Institute of Science and Technology (GIST), Republic of Korea
[*]corresponding author: m.kim@gist.ac.kr

Abstract: A metasurface-enabled weak measurement is devised for a single-shot observation of the spin Hall effect of light. By using a polarization beamsplitting metasurface, we achieve a real-time tracking of the spin Hall shift, thereby enabling high-precision optical sensing in dynamic environments.

The spin Hall effect of light (SHEL) manifests as a spin-dependent transverse shift when light undergoes refraction or reflection at an interface. When paired with a signal amplification method known as weak measurement [1], it offers nondestructive, high-precision metrology. However, conventional weak measurements require a multistep process, thus limiting their applicability in dynamic scenarios. Here, we introduce a metasurface-enabled single-shot weak measurement approach that allows real-time detection of the SHEL without the need for calibration [2].

Our method replaces the postselection polarizer, a component in the weak measurement, with a polarization beamsplitting metasurface. It functions as a beam splitter and two polarizers simultaneously and thus squeezes the two snapshots from traditional methods into a single capture. Two postselected beams with orthogonal polarizations reach the camera simultaneously at different positions, from which the transverse distance between them is extracted as a weak value. The spin Hall shift follows a linear relation with the weak value as $Y = 2\delta F/\sin 2\alpha$ where α is the postselection angle. The amplification factor of our setup corresponds to $1/\cos^2\alpha$ of that of the previous setup, which indicates that the amplification is even higher compared to the conventional method.

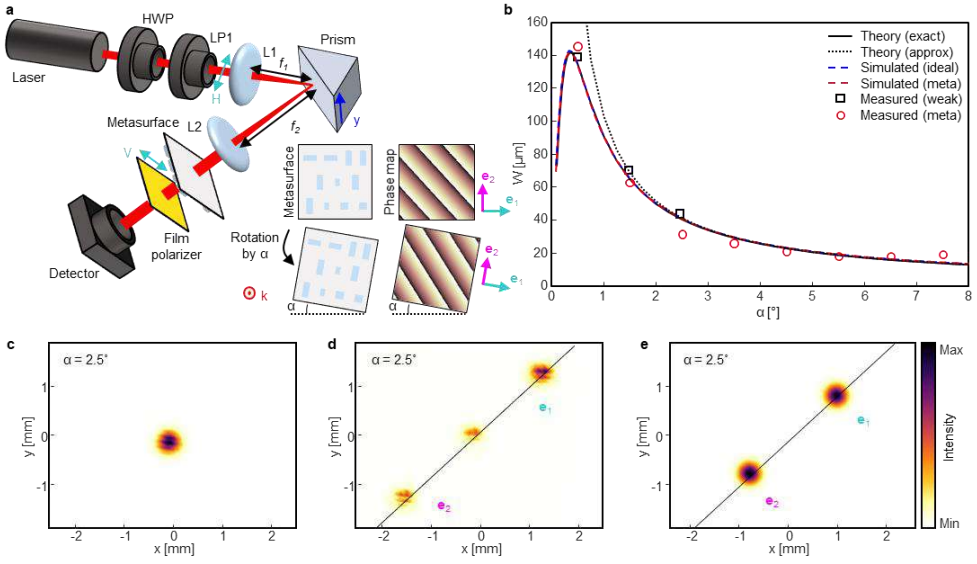


Figure 1. Comparison between conventional weak measurement and metasurface-enabled single-shot weak measurement. (a) Schematic of the experimental setup. (b) Measured weak values for various postselection angles. (c-e) Captured intensity distributions from conventional and single-shot measurements at the postselection angle is 2.5°.

This new measurement scheme simplifies the measurement process and enables a single-shot measurement of the SHEL even when the beam position fluctuates over time. It is tested for two cases, one static and the other dynamic. We first measure the SHEL at a static air-prism interface using both methods and compare them (Fig. 1). Our new method shows excellent agreement in comparison to the conventional one, even with a single capture. In a dynamic scenario, we track the SHEL in real time by continuously varying the tilt angle of an anisotropic interface over a range of 30° to 40°. Our setup provides measured weak values closely matching theoretical and simulation results.

The metasurface-assisted single-shot weak measurement technique enhances the feasibility of SHEL-based precision metrology in time-varying environments. Its potential applications include high-sensitivity optical sensing for biomedical diagnostics, chemical analysis, and environmental monitoring. By eliminating the constraints of conventional weak measurement techniques, our approach paves the way for real-time, high-precision optical measurements in a wide range of scientific and technological fields.

Acknowledgements: This work was financially supported by the National Research Foundation grants (NRF-2022R1C1C2004662) funded by the Ministry of Science and ICT of the Korean government

References

1. Hosten, O. and Kwiat, P. “Observation of the spin Hall effect of light via weak measurements,” Science Vol. 319, 787-790, 2008
2. Lee, J., Kim, J., Shim, S., Yang, Y., Choi, J., Rho, J., Lee, D. and Kim, M. “Real-time observation of the spin Hall effect of light using metasurface-enabled single-shot weak measurements,” Nature Comm. in press, 2025

Laser color printing on disordered metal-dielectric multilayer structures

P. Nyga[1*], M. P. Nowak[1], M. Woszto[1], T. Wojciechowski[2], B. Bartosewicz[1], and P. Wachulak[1]

[1]Institute of Optoelectronic, Military University of Technology, Poland
[2]International Research Centre MagTop, Institute of Physics, Polish Academy of Sciences, Poland
[*]corresponding author: piotr.nyga@wat.edu.pl

Abstract: We report plasmonic color printing through a femtosecond laser-induced modification of disordered metal-dielectric multilayer structures. The structures are fabricated by sequential deposition of subwavelength-thick dielectric layers and island-type layers of disordered metal nanoparticles. Colors are controlled by parameters of femtosecond laser pulses, e.g., fluence, polarization, repetition, and scanning parameters.

Disordered plasmonic nanostructures have been explored in plasmonic color [1–5] and other photonic applications [6]. Nano-island type or semicontinuous films can be deposited using industry-proven physical vapor deposition (PVD) processes [1,4]. They form through self-organization when a thin film of metal is deposited on a non-wetting substrate. Laser post-fabrication processing of disordered structures allows material modification at the nanoscale and local control of sample color, polarization selective response, diffractive structures formation, and diffuse reflectance component control [1–5].

Herein, we report a direct femtosecond laser modification of disordered metal-dielectric multilayer structures. These structures are composed of metallic nanoparticles embedded in a dielectric matrix. We fabricated these composites using the electron-beam PVD technique. In a single process, without breaking the vacuum, we sequentially deposited subwavelength-thick dielectric layers and island-type films composed of disordered metal nanoparticles. Such composites have been explored in the past, as their transmittance, reflectance, and absorption can be controlled by details of the fabrication process, number of layers and their thickness, and choice of constituent materials [7,8]. Next, we studied how laser modification parameters influence the optical properties of composites. We used a femtosecond laser with the following characteristics: pulse duration of 215 fs, wavelength of 1030 nm, fluence range of 1 - 100 mJ cm^{-2}. The laser pulses induce polarization selective color changes in modified regions of the metal-dielectric multilayer structure.

This technique allows high throughput and high-resolution color printing. It could be used in anti-counterfeiting, information encryption, hidden marking, and data storage applications.

This research was funded by the National Science Centre, Poland under grant no 2024/53/B/ST11/04193.

References

1. A. S. Roberts, S. M. Novikov, Y. Yang, Y. Chen, S. Boroviks, J. Beermann, N. A. Mortensen, and S. I. Bozhevolnyi, “Laser Writing of Bright Colors on Near-Percolation Plasmonic Reflector Arrays, “ACS Nano, Vol. 13, No. 1, 71–77, 2019.
2. S. N. Chowdhury, P. Nyga, Z. A. Kudyshev, E. Garcia Bravo, A. S. Lagutchev, A. V. Kildishev, V. M. Shalaev, and A. Boltasseva, “Lithography-Free Plasmonic Color Printing with Femtosecond Laser on Semicontinuous Silver Films,“ ACS Photonics, Vol. 8, No. 2, 521–530, 2021.
3. S. N. Chowdhury, J. Simon, M. P. Nowak, K. Pagadala, P. Nyga, C. Fruhling, E. G. Bravo, S. Maćkowski, V. M.

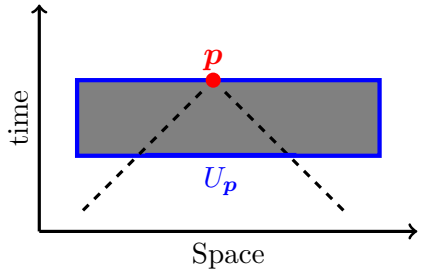
Shalaev, Substrates, “hev, and A. Boltasseva, “Wide-Range Angle-Sensitive Plasmonic Color Printing on Lossy-Resonator Substrates,“ Adv. Opt. Mater., Vol. 12, No. 4, 2301678, 2023.

4. M. P. Nowak, B. St˛ Epak, M. Pielach, Y. Stepanenko, T. Wojciechowski, B. Bartosewicz, U. Chodorow, M. Jakubaszek, P. Wachulak, and P. Nyga, “Laser Control of Specular and Diffuse Reflectance of Thin Aluminum Film-Isolator-Metal Structures for Anti-Counterfeiting and Plasmonic Color Applications,“ Coatings, Vol. 14, No. 10, 1298, 2024.
5. N. Dalloz, V. D. Le, M. Hebert, B. Eles, M. A. Flores Figueroa, C. Hubert, H. Ma, N. Sharma, F. Vocanson, S. Ayala, N. Destouches, N. Dalloz, V. D. Le, M. Hebert, B. Eles, M. A. F. Figueroa, C. Hubert, H. Ma, F. Vocanson, N. Destouches, and N. Sharma, “Anti-Counterfeiting White Light Printed Image Multiplexing by Fast Nanosecond Laser Processing,“ Adv. Mater., Vol. 34, No. 2, 2104054, 2022.
6. X. Zhu, J. Engelberg, S. Remennik, B. Zhou, J. N. Pedersen, P. Uhd Jepsen, U. Levy, and A. Kristensen, “Resonant Laser Printing of Optical Metasurfaces, “ Nano Lett., Vol. 22, No. 7, 2786–2792, 2022.
7. M. D. Thoreson, J. Fang, A. V. Kildishev, L. J. Prokopeva, P. Nyga, U. K. Chettiar, V. M. Shalaev, and V. P. Drachev “Fabrication and realistic modeling of three-dimensional metal-dielectric composites, “ J. Nanophotonics, Vol. 5, No. 1, 051513, 2011.
8. P. Nyga, S. Chmiel, M. Szczurek, M. Liszewska, M. Stefaniak, J. Firak, M. Michalska-Domanska, J. Mierczyk, and M. Norek, “Silver nanoparticles in titanium dioxide host plasmonic absorbers,” in 2016 18th International Conference on Transparent Optical Networks (ICTON), Trento, Italy, 2016.

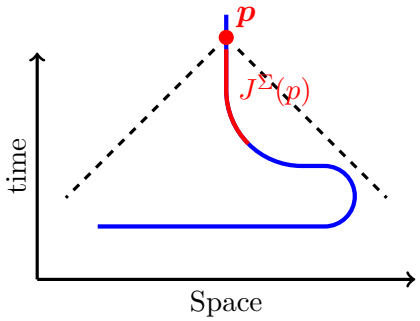
The General Boundary Conditions for all interfaces, including arbitrary moving metasurfaces and instantaneous changes in constitutive relations.

J. Gratus[1,2*]2, S. A. R. Horsley[3], and M. W. McCall[2]
[1]Physics Department, Lancaster University, Lancaster LA1 4YB, UK
[2]The Cockcroft Institute, Sci-Tech Daresbury, Warrington WA4 4AD, UK
[3]School of Physics and Astronomy, Stocker Road, University of Exeter, Exeter EX4 4QL, UK
[4]Blackett Laboratory, Imperial College, London SW7 2BZ, UK
*Corresponding author: `j.gratus@lancaster.ac.uk`

Abstract: We present the most general boundary conditions, which satisfy basic physical constraints: linearity, causality and local to the boundary. Using relativity they are valid for all motions of the interface, including arbitrary moving metasurfaces and superluminal motion. We discuss the nature of causality for boundaries.



(a) An initially uniform homogeneous medium simultaneously changes its constitutive relations within a bounded region (indicated as a gray rectangle), before the constitutive relations revert back to their original form. The boundary of the gray region (blue) consists of the two spacelike hypersurfaces arising from the temporal change, plus the spatial boundary of the finite region. Note that, the region $U_{\boldsymbol{p}}$ which is both in Σ *and* in the past lightcone of $\boldsymbol{p}$, cannot influence $\boldsymbol{p}$ via the boundary conditions.



(b) Here the boundary initially is superluminal, it then becomes subluminal. Even though a lot of the boundary depicted lies in the past light cone of $\boldsymbol{p}$, only the red part is connected to $\boldsymbol{p}$ via curves which remain subluminal.

Figure 1: **Causality and spacetime boundaries:** In these two spacetime diagrams, there are places where the boundary (blue and red) moves instantaneously or superluminal and others where it is stationary or subluminal. The region of the boundary which can communicate with the event $\boldsymbol{p}$ is given in red.

As soon as one wishes to consider electromagnetic fields passing from one medium in one region of space-time to another, once has to consider what are the correct boundary conditions to impose. The natural boundary conditions for a static interface: continuity of perpendicular components of $\boldsymbol{E}$ and $\boldsymbol{H}$ and the tangential components of $\boldsymbol{B}$ and $\boldsymbol{D}$, have served us

well. However these are insufficient when one or both of the regions are spatially dispersive, when additional boundary conditions are required. Superluminal and instantaneous boundary conditions [1, 2] are required when an entire region of space suddenly changes its constitutive relations. Furthermore, metasurfaces can be modelled using more exotic boundary conditions. Thus similar to constitutive relations, the range of potential boundary conditions is limited only by the imagination of the researchers: the experimentalist's ability to manufacture them and the theorist's ability to model them. Instead of coming up with ever more complicated boundary conditions, in this talk, we present a general formula for all boundary conditions which satisfy a small number of conditions: linearity, causality and local to the boundary.

The result can be succinctly expressed as a number of integrals over the 3–dimensional spacetime hypersuface which represents the interface. The kernel within the integral may include δ–functions. The reason for the integral is that the boundary condition allow for temporal and spatial dispersion at the interface.

Many additional boundary conditions are considered, including all the standard boundary conditions both on a spatial boundary and on a temporal boundary. We also consider dispersive boundaries where polaritons propagate inside the boundary. Since these polaritons carry information, and boundaries can move subluminally, luminally and superluminally, there is a discussion of the nature of causality for boundary conditions. Since polaritons involve the actual movement of charges, they can only move subluminally (or luminally). As a result the integral for the boundary conditions at the point $\boldsymbol{p}$ can only be over regions of the spacetime boundary that lie in the past of a point and are causally connected to $\boldsymbol{p}$ via luminal paths that lie in the boundary. This can be visualised on a spacetime diagram, as in figure 1.

Acknowledgements

JG would like to thank the STFC and the Cockcroft Institute (ST/V001612/1). This work is a result of discussions at META2023.

References

1. Gratus, R. Seviour, P. Kinsler, and D. A. Jaroszynski, "Temporal boundaries in electromagnetic materials", New Journal of Physics 23, 083032 (2021)

2. A. C. Harwood, S. Vezzoli, T. V. Raziman, C. Hooper, R. Tirole, F. Wu, S. Maier, J. B. Pendry, S. A. R. Horsley, and R. Sapienza, "Super-luminal synthetic motion with a spacetime" optical metasurface, arXiv:2407.10809 (2024).

Harnessing the power of mid-infrared metasurfaces for ultrafast and high-efficiency all-optical modulation

The Linh Pham,[1,*] Amirmostafa Amirjani,[1] Kacper Pilarczyk,[1] Nils Deßmann,[2] Thanh Tung Nguyen,[3] and Ewald Janssens[1]

[1] *Quantum Solid State Physics, Department of Physics and Astronomy, KU Leuven, 3001 Leuven, Belgium*

[2] *Institute for Molecules and Materials, FELIX Laboratory, Radboud University, 6525 ED, Nijmegen, Netherlands*

[3] *Institute of Materials Science, Vietnam Academy of Science and Technology, Hanoi, Vietnam*

[*]corresponding author: thelinh.pham@kuleuven.be

Abstract: In this study, we propose a comprehensive platform to harness the localized surface plasmon resonance of metasurfaces for achieving ultrafast all-optical modulation via carrier multiplication in the silicon substrate. Transmission changes in the picosecond time scale are demonstrated via single-color time-resolved pump-probe experiments using an infrared free electron laser, along with an impact ionization model and full-wave simulation. The findings can lead to high-speed optical modulation using low-photon energy light sources.

Plasmonic metasurfaces represent a fascinating frontier in nanotechnology, merging the principles of plasmonics with engineered surface structures to manipulate light at unprecedented scales [1]. These planar nanostructures exploit the unique properties of surface plasmons—collective oscillations of electrons at the interface of metal and dielectric—to achieve extraordinary optical phenomena. The ability to control light on the subwavelength scale opens up numerous potential applications, ranging from high-resolution imaging and biosensing to enhanced photovoltaics [1].

In this study, we explore the potential of plasmonic resonance in metasurfaces for ultrafast all-optical modulation applications. The most common method to modulate the optical characteristics of materials is via optical pumping through the semiconductor bandgap, which requires high photon energy and introduces additional losses into the system [2]. Our approach leverages on field enhancement that is localized at the subwavelength scale, efficiently accelerating free electrons to a sufficiently high kinetic energy to cause carrier multiplication [3, 4]. Carrier concentrations in certain regions of silicon change within picoseconds, leading to a strong modulation of optically transmitted signals. The crucial role of localized surface plasmon resonance in achieving ultrafast all-optical modulation is established, with a modulation depth that is on-resonance higher than 125%, which is unprecedentedly high considering the photon energy employed. These phenomena are further validated through an analytical model and numerical simulations, which clarify the roles of plasmonic field enhancement and impact ionization in shaping carrier dynamics. Our findings provide a comprehensive and robust understanding of carrier dynamics in plasmonic metasurface platforms occurring over several to a few hundred picoseconds, forming a foundation for developing time-variant media with potential applications in low-photon energy ultrafast all-optical modulators.

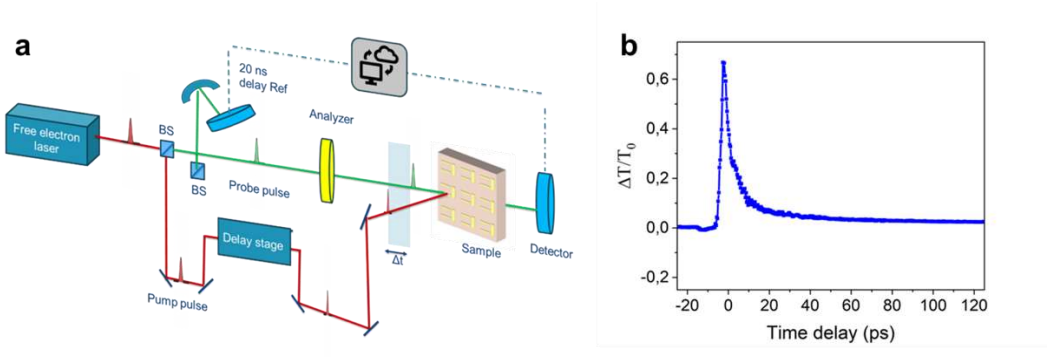


Figure 1: (a) Scheme of time-resolved pump-probe experiment in FELIX and (b) example of an obtained transient transmission change spectrum at 10.5 μm excitation with a laser fluence of 0.6 J/m².

Acknowledgment: This research has been funded by a joint research project between the Research Foundation Flanders (FWO) under Grant No. G0DAX23N and the Vietnam National Foundation for Science and Technology Development (NAFOSTED) under Grant No. FWO.103-2022.01. TLP thanks the KU Leuven Research Council for an IRO Fellowship.

References

1. Meinzer, N., Barnes, W. & Hooper, I. “Plasmonic meta-atoms and metasurfaces”, Nature Photon. 8, 889–898, 2014.
2. M. Maiuri, A. Schirato, G. Cerullo & G. D. Valle, “Ultrafast All-Optical Metasurfaces: Challenges and New Frontiers”, ACS Photonics, 11, 8, 2888–2905 2024.
3. Cartier, E., Fischetti, M. V., Eklund, E. A. & McFeely, F. R. “Impact ionization in silicon”, Appl. Phys. Lett. 62, 3339–3341, 1993.
4. M. Bejide, T. L. Pham, A. Amirjani, G. Libeert, N. Dessmann, T. T. Nguyen & E. Janssens, “Picosecond dynamics of hot carriers in infrared plasmonic metasurfaces”, submitted, 2025.

META 2025, MALAGA - SPAIN, JULY 22 – 25, 2025

Injecting Physics Knowledge in Neural Networks for a Wide Range of Photonic Devices: QNM-Net

V. A. Lilja, A. J. Svärdsby, T. Gahlmann, and P. Tassin
Chalmers University of Technology, Department of Physics, Göteborg, Sweden

Abstract: We will present our work on QNM-Net, a physics-informed neural network for electromagnetic scattering. Our network incorporates physics knowledge through the quasi-normal-mode framework, which means it can model a vast range of (nano)photonic devices. By incorporating physics knowledge, we can achieve a tenfold reduction of training data needed.

In recent years, machine learning has been shown to be a powerful tool for the design of optical devices. Typically, a neural-network model is constructed to act as a fast surrogate for full-wave electrodynamics solvers, which is then used to search the design landscape through iterative optimization or through the training of inverse models such as tandem or generative-adversarial networks [1]. Indeed, since a neural network prediction is typically many orders of magnitude faster than a full-wave simulation, a trained neural network makes it possible to explore the design space efficiently.

However, obtaining a neural network that is accurate enough across the entire design space normally requires a very large training dataset, typically requiring thousands of full-wave simulations. This is a large computational cost, but is possible on high-performance computing clusters, because all the training data samples are independent and can be generated concurrently. Nevertheless, to advance the field, we need to reduce the need for training data.

One way to make neural networks modelling physical devices more data efficient is to incorporate physics knowledge into the network [2], significantly restraining the relationship between design parameters and device response. We show that this can be done for a large range of electromagnetic scattering devices using quasi-normal-mode theory. The resulting network, called QNM-net, contains a physics layer that calculates the scattering response of an optical device from the resonances of the system, preceded by a neural network that relates the properties of the resonances to the design parameters. This allows for a neural network with much fewer hyperparameters.

We will demonstrate the power of QNM-Net with two examples, a photonic crystal with free-form holes and a metasurface with free-form nanopillars on a substrate. QNM-Net let us incorporate a priori physical principles such as energy conservation and mirror symmetry. In comparison with standard neural network architectures directly modeling the relationship between the design parameters and the scattering response, QNM-Net requires an order of magnitude less training data and trainable parameters to achieve the same validation loss. This brings the data generation problem to the realm of the practical, with data generation times of days instead on months.

We acknowledge financial support from Chalmers' area of advance Nano (Excellence Grant) and from the Swedish Research Council under Grant No. 2020-05284. The training data generation and neural network training were performed on resources provided by the Swedish National Infrastructure for Computing (NAISS), at the Chalmers/C3SE and KTH/PDC sites, partially funded by the Swedish Research Council under Grant No. 2022-06725.

References

1. T. Gahlmann and P. Tassin “Deep neural networks for the prediction of the optical properties and the free-form inverse design of metamaterials,” Phys. Rev. B, Vol. 106, 085408, 2022.
2. L. von Rueden, *et al.*, “Informed Machine Learning – A Taxonomy and Survey of Integrating Prior Knowledge into Learning Systems,” IEEE Trans. Knowl. Data Eng., Vol. 35, 614–633, 2023.
3. V. A. Lilja, A. J. Svärdsby, T. Gahlmann, and P. Tassin, “A general framework for knowledge integration in machine learning for electromagnetic scattering using quasinormal modes,” under review, 2025.
4. M. Benzaouia, J. D. Joannopoulos, S. G. Johnson, and A. Karalis, “Quasi-normal mode theory of the scattering matrix, enforcing fundamental constraints for truncated expansions”, Phys. Rev. Research, Vol. 3, 033228, 2021.

Suspended AlGaAs Integrated Nonlinear Photonics

Changzheng Sun*, Yuqian Zhang, Bing Xiong, Jian Wang, Zhibiao Hao, Lai Wang, Yanjun Han, Hongtao Li, Lin Gan, and Yi Luo

Beijing National Research Centre for Information Science and Technology (BNRist), State Key Laboratory of Space Network and Communications, Department of Electronic Engineering, Tsinghua University, Beijing 100084, China
*corresponding author: czsun@tsinghua.edu.cn

Abstract: We present our recent work on nonlinear optics in suspended AlGaAs waveguides/micoresonators, including fabrication of high-Q suspended AlGaAs microring resonators, microcomb generation in near and mid-infrared regime, and octave-spanning supercontinuum generation.

1. Introduction

Aluminum gallium arsenide (AlGaAs) is a promising nonlinear optical material with an enormous intrinsic third order Kerr nonlinearity $n_2 \sim 10^{-17}$ m^2/W [1], and its bandgap can be tailored by varying the Al content to avoid two photon absorption (TPA) at telecom wavelengths. However, to date, the fabrication of low-loss AlGaAs waveguides is mainly based on bonding process [2,3]. In this talk, we present our recent work on nonlinear optics in suspended AlGaAs waveguides/microresonators formed directly on GaAs substrate. Suspended AlGaAs microrings with intrinsic Q factor exceeding 10^6 have been fabricated with optimized plasma dry-etching and surface treatment, allowing efficient Kerr comb generation in the near- and mid-infrared regime. Furthermore, octave-spanning supercontinuum is demonstrated in a 2-mm-long suspended AlGaAs waveguide.

2. High-Q Suspended AlGaAs Microring Resonator for Kerr Comb Generation

Figure 1(a) depicts the schematic of our suspended AlGaAs microring, which is formed on the $Al_{0.2}Ga_{0.8}As$ waveguide layer by plasma dry etching based on BCl_3 and Ar mixture [4]. The underlying $Al_{0.8}Ga_{0.2}As$ sacrificial layer is selectively removed by chemical wet etching in diluted HF solution. After surface treatment in HCl, NH_4OH, and *N*-methyl-pyrrolidone solutions to ensure complete removal of residual etching products, the microring is encapsuled with 10-nm-thick Al_2O_3 by atomic layer deposition (ALD). The intrinsic Q-factor of the fabricated 50-μm-radius, 1800-nm-wide microring is measured to be 1.3×10^6 for TM_{00} mode, as shown in Fig. 1(b). Near-infrared Kerr comb generation with milliwatt-level pump power is recorded in Fig. 1(c).

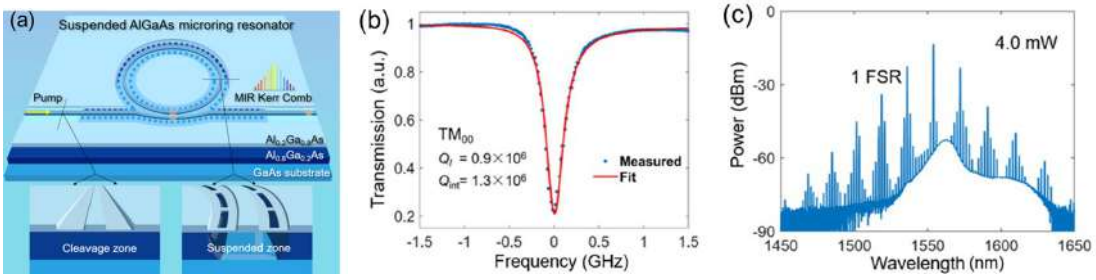


Fig. 1. (a) Schematic of the suspended AlGaAs microring. (b) TM_{00} mode resonance around 1550 nm. (c) Kerr comb lines generated with a TM polarized pump at 1550 nm.

The air-clad suspended AlGaAs microring is particularly suitable for mid-infrared (MIR) frequency comb generation. With the experimental setup shown in Fig. 2(a), MIR frequency combs covering from 1250 to 5450 nm are generated in an 80-μm-radius, 1800-nm-wide microring with a TE-polarized pump at 2.7 μm.

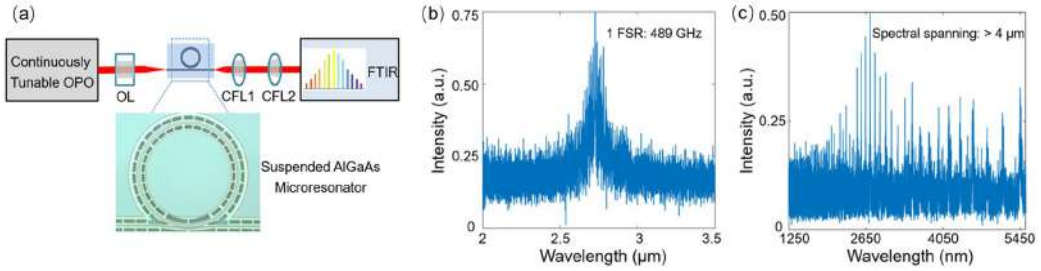


Fig. 2. (a) MIR frequency comb generation. (b) and (c) MIR frequency combs generated with a 2.7 μm pump.

3. Octave-spanning Supercontinuum Generation in Suspended AlGaAs Waveguides

The experimental setup for supercontinuum generation (SCG) in a 2-mm-long suspended AlGaAs waveguide is shown in Fig. 3(a), where an erbium-fiber-based femtosecond laser (pulse duration ~70 fs) acts as the pump. The evolution of output spectra with varying pump pulse energy is plotted in Fig. 3(b). The onset of SCG occurs near 7.9 pJ, and octave-spanning supercontinuum covering 1000-2250 nm is recorded with a pulse energy of 20 pJ, corresponding to an average waveguide-coupled power of 2 mW.

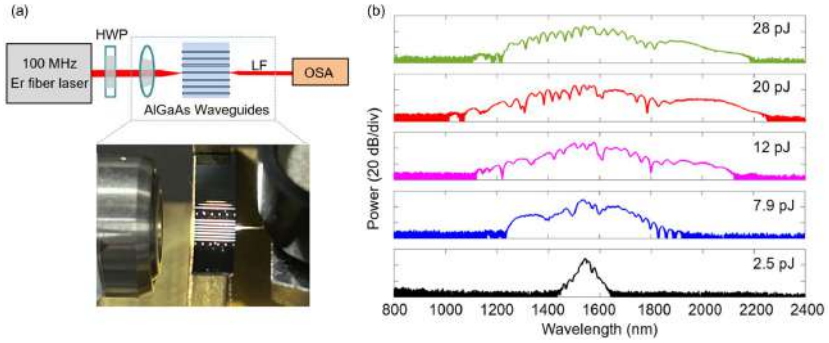


Fig. 3. (a) Experimental setup for SCG in suspended AlGaAs waveguides. (b) Output spectra for different pulse energies.

4. Conclusions

We have investigated nonlinear optics in low loss suspended AlGaAs microresonators/waveguides. Our demonstration opens up a new prospect for employing AlGaAs devices in integrated nonlinear photonics.

Acknowledgements

This work was supported in part by National Key R&D Program of China (2022YFB2803002); National Natural Science Foundation of China (62235005, 62127814, 62225405 and 62475130).

References

1. J. S. Aitchison, D. C. Hutchings, J. U. Kang, G. I. Stegeman, A. Villeneuve, “The nonlinear optical properties of AlGaAs at the half band gap,” IEEE J. Quantum Electron., Vol. 33, No. 3, 341-348, 1997.
2. M. Pu, L. Ottaviano, E. Semenova, and K. Yvind, “Efficient frequency comb generation in AlGaAs-on-insulator,” Optica, Vol. 3, No. 8, 823–826, 2016.
3. L. Chang, W. Xie, H. Shu, Q. F. Yang, B. Shen, A. Boes, J. E. Bowers, “Ultra-efficient frequency comb generation in AlGaAs-on-insulator microresonators,” Nat. Commun., Vol. 11, 1331, 2020.
4. Y. Zhang, C. Sun, B. Xiong, J. Wang, Z. Hao, L. Wang, Y. Han, H. Li, Y. Luo, “Fabrication of high-Q suspended AlGaAs microresonators for efficient Kerr comb generation,” App. Phys. Lett., Vol. 125, 091110, 2024.

Far-field Petahertz Sampling of Plasmonic Fields

K. F. Wong[1,2*], W. Li[3,4], Z. Wang[3,4], V. Wanie[2], E. Månsson[2], D. Hoeing[1], J. Blöchl[3,4], T. Nubbemeyer[3,4], A. Azzeer[5], A. Trabattoni[2,6], H. Lange[1,7], F. Calegari[1,2], and M. F. Kling[3,4,8,9]

[1]The Hamburg Centre for Ultrafast Imaging, Luruper Chaussee 149, 22761 Hamburg, Germany
[2]Center for Free-Electron Science CFEL, Deutsches Elektronen-Synchroton DESY, Notkestr. 85, 22607 Hamburg, Germany
[3]Max Planck Institute of Quantum Optics, Hans-Kopfermann-Str. 1, 85478 Garching, Germany
[4]Physics Department, Ludwig-Maximilians-Universität Munich, Am Coulombwall 1, 85478 Garching, Germany
[5]Attosecond Science Laboratory, Physics and Astronomy Department, King-Saud University, P.O. Box 2455, Riyadh 11451, Saudi-Arabia
[6]Institute of Quantum Optics, Leibniz Universität Hannover, Welfengarten 1, 30167 Hannover, Germany
[7]Institute of Physics and Astronomy, Universität Potsdam, Karl-Liebknecht-Str. 24, 14476 Potsdam, Germany
[8]Stanford PULSE Institute, SLAC National Accelerator Laboratory, 2575 Sand Hill Rd, Menlo Park, CA 94025, USA
[9]Applied Physics Department, Stanford University, 348 Via Pueblo, Stanford, CA 94305, USA
[*]corresponding author: kai-fu.wong@cfel.de

Abstract: We demonstrate the realtime observation of linear plasmonic fields by optical field sampling. Our findings also demonstrate the ability to manipulate the spectral properties of ultrashort laser pulses by plasmonic samples.

Plasmon excitation in nanosystems allows for extreme light confinement beyond the diffraction limit, therefore enabling a number of new applications in photonics, energy harvesting and biology. In this context, it is key to obtain a realtime characterization of the onset from plasmonic field and its ultrafast dephasing dynamics. Tunnel ionization with a perturbation for the time-domain observation of an electric field, short TIPTOE, is a recent established technique allowing for the optical sampling of ultrashort laser pulses based on strong field ionization. Subsequently, this ionization is modulated by a weaker pulse to be sampled. With this method it is possible to characterize arbitrary electric fields as long as ionization by the weak pulse itself does not occur. [1,2] Here, we implement TIPTOE for the optical sampling of linear plasmonic fields measured in the far-field regime.

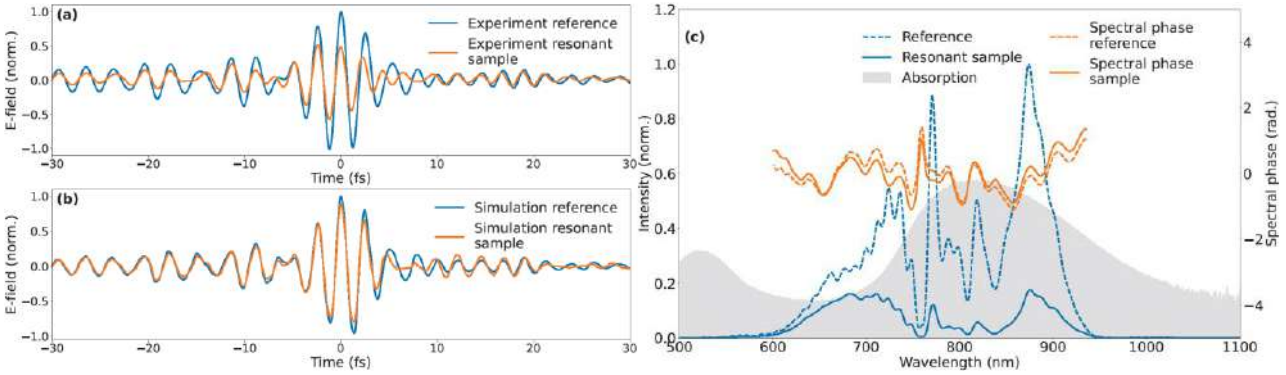


Fig. 1 Normalized (a) measured TIPTOE traces and (b) simulated traces for the electric field after interaction with the plasmonic sample. As reference the input field is depicted in blue, which was also used as the input for the FDTD simulation. (c) Retrieved spectrum (blue) and spectral phase (orange) via FFT for the plasmonic sample. The retrieved spectra were normalized to the reference. The dashed lines display the retrieved spectra and spectral phase of the input field respectively. The shaded area displays the absorption spectra of the plasmonic nanorods.

In our experiment, sub 5 fs pulses with a central wavelength of 780 nm are exciting plasmonic gold nanoparticles embedded on a fused silica substrate, the transmitted beam is then sent into a TIPTOE setup for the optical field sampling. While the latter sample displays a broadband plasmonic resonance, i.e. the longitudinal localized surface plasmon resonance (L-LSPR), covering a major part of the few-cycle spectrum, the plasmonic resonance of the spherical particles is located outside the exciting broadband pulse bandwidth.

The measured traces for the resonantly excited plasmonic samples strongly differ from the few-cycle input field, with a large deviation window in the trailing edge of the laser pulse and within a 15 fs decay range. The retrieved spectrum exhibits the expected strong reduction in intensity due to large absorption induced by the L-LSPR and remarkable effects in the spectral phase, which displays a crossing in the region of the plasmon resonance. These effects are not observed with the non-resonantly excited particles, therefore confirming that a strong signature of the resonant excitation persist in the far-field. The obtained results were compared with theory using finite difference time domain (FDTD) simulations, where the detection of the electric field is performed after the plasmonic sample to mimic the far-field conditions of the experiment. The simulations reproduce the same deviations observed in the experiment well, therefore confirming that a measurement in the far-field still carries crucial information on the excited plasmonic field. These results not only pave the way to realtime observation of plasmonic fields from arbitrary samples on the petahertz scale, but also opens interesting perspectives in the engineering of the spectral phase of ultrashort laser pulses using plasmonic metasurfaces.

References

1. Park, S. B. *et al.*, “Direct sampling of a light wave in air”. Optica, 5, 402-408, 2018.
2. Bionta, M. R. and Ritzkowsky, F. and Turchetti, M. *et al.*, “On-Chip sampling with attosecond resolution”, Nature Photonics, 15, 456-460 , 2021.

Degenerate Metasurface Eigenstates: Coupling and Interfering for Maximum-Chiral Optics

M.V. Gorkunov[1]*, A.A. Antonov[2], and Y.S. Kivshar[3]

[1] Shubnikov Institute of Crystallography, NRC "Kurchatov Institute", Moscow 119333, Russia
[2] Chair in Hybrid Nanosystems, Ludwig-Maximilians-University of Munich, Munich 80539, Germany
[3] Nonlinear Physics Centre, Research School of Physics, Australian National University, Canberra ACT 2601, Australia
*corresponding author: gorkunov@crys.ras.ru

Abstract: Maximum-chiral metasurfaces, selectively interacting with circularly polarized light, are designed by optimizing their photonic eigenstates. The design constraints are relaxed by employing uncoupled interfering and coupled hybridized eigenstates. Then freestanding planar structures become helicity-preserving chiral mirrors, while those stacked upon substrates perform as chiral filters, absorbers and reflectors.

Metasurfaces with strong and eventually maximum optical chirality facilitate emission and detection of chiral light, perform versatile nonlinear chiral light transformations and generally enhance chiral light-matter coupling. Maximum chirality can be achieved by tuning a specific photonic eigenstate to selective coupling with circularly polarized light of a particular handedness [1,2]. Depending on the metastructure symmetry (the presence of rotation axes and in- and out-of-plane mirror planes), different functionalities including chiral absorbers, reflecting filters and helicity-preserving mirrors can be realized [3]. Strong extrinsic chirality in oblique directions is available in structures with the in-plane mirror symmetry lacking optical chirality for normal incidence [4]. The origin of maximum-chiral properties allowed by the symmetry is conveniently explained by the phenomenological coupled-mode theory (CMT) and by the semi-analytical resonant state expansion (RSE) both treating the metasurface response as determined by the spectrum and spatial structure of its eigenstates.

Technologically convenient planar metastructures are photonic crystal slabs (PCSs) and arrays of particles of the same height. Their out-of-plane mirror symmetry determines spatial parity of the eigenstates which are denoted as even and odd according to the parity of their in-plane electric field components and resemble in-plane electric and magnetic dipoles respectively. Such states on their own have linearly polarized far field and provide achiral individual contributions to the metasurface response. Neglecting dissipation losses in CMT, the parameters of their coupling to free-space plane waves are expressed by the in-plane vectors [3]:

$$\mathbf{m}_{\mathrm{even}} = \mathbf{m'}_{\mathrm{even}} = \mathbf{e}_{\mathrm{even}} i\sqrt{\gamma_{\mathrm{even}}} e^{i\frac{(\alpha+\beta)}{2}} \quad , \quad \mathbf{m}_{\mathrm{odd}} = -\mathbf{m'}_{\mathrm{odd}} = \mathbf{e}_{\mathrm{odd}} \sqrt{\gamma_{\mathrm{odd}}} e^{i\frac{(\alpha-\beta)}{2}} \quad , \qquad (1)$$

where the unit vectors $\mathbf{e}_{\mathrm{even}}$ and $\mathbf{e}_{\mathrm{odd}}$ are the far-field polarization directions, and γ_{even} and γ_{odd} are the decay rates of the corresponding states. The primes denote coupling with light on the back metasurface side. The phases α and β characterize the background metasurface phase shift and transparency correspondingly ($\beta = 0$ for a transparent and $\beta = \pi/2$ for a fully reflective non-resonant response).

In a free-standing PCS, even and odd states are uncoupled, but their individual contributions to reflected and transmitted waves can peculiarly interfere. This interference is similar to that giving rise to the generalized Kerker effect [5], but here the state far field polarization is of key importance. Thus a pair of degenerate orthogonally polarized states with $\omega_{\mathrm{even}} = \omega_{\mathrm{odd}}$ and $\mathbf{e}_{\mathrm{even}} \cdot \mathbf{e}_{\mathrm{odd}} = 0$ and a transparent background with $\beta = 0$ build up an achiral mirror which resonantly reflects circularly polarized light preserving its helicity regardless of the handedness. Alternatively, a pair with the unit vectors $\mathbf{e}_{\mathrm{even}}$ and $\mathbf{e}_{\mathrm{odd}}$ building an angle of

$\pi/4$ combined with a semi-transparent background with $\beta = \pi/4$ constitutes a helicity preserving chiral mirror reflecting waves of one circular polarization and transmitting others inverting their handedness [6].

Placing a metasurface with degenerate eigenstates of different parity on a substrate induces their direct near-field coupling. The arising observable effects are truly remarkable, as a rotation-symmetric PCS can exhibit a pair of close maximum-chiral transmission resonances of the opposite handedness. The underlying mechanism of state coupling is quantitatively well explained by the RSE which explicitly shows the importance of the initial state degeneracy as well as of the state coupling through their twisted near-fields [7]. It is also possible to couple the states of different parity with $\mathbf{e}_{\mathrm{even}} \cdot \mathbf{e}_{\mathrm{odd}} \neq 0$ through their far field. Placing such a metasurface above a mirror establishes symmetry-breaking far-field coupling merging the states into chiral hybrids with the quality factor controlled by the distance to the mirror.

Structures with the in-plane mirror symmetry lack optical chirality for normally incident light but can exhibit remarkably strong extrinsic chirality in oblique directions. Here, for the normal incidence, one can establish degenerate states, even and odd with respect to the vertical symmetry plane. Tilting the direction of incidence breaks this symmetry and merges the states into rotating dipole combinations selectively coupled to circularly polarized light. This can be realized in meta-atoms of simple shapes, such as triangles, and their arrays exhibit remarkable chiral selectivity of resonant transmission in oblique directions. Combining such arrays with mirrors allows building extrinsically chiral metacavities. Filled with functional optoelectronic materials, the cavities become efficient electroluminescent sources of chiral light emitted in the opposite oblique directions [4].

Altogether, controlled interference and coupling of degenerate photonic eigenstates substantially broadens the palette of chiral optical properties available in planar metasurfaces convenient for fabrication by standard nanolithographic techniques.

Support from the Russian Science Foundation (project 23-42-00091) is gratefully acknowledged.

References

1. Gorkunov, M. V., A. A. Antonov, and Y. S. Kivshar, “Metasurfaces with maximum chirality empowered by bound states in the continuum,” *Phys. Rev. Lett.,* Vol. 125, No. 9, p. 093903, 2020.
2. Kühner, L., F. J. Wendisch, A. A. Antonov, J. Bürger, L. Hüttenhofer, L. de S. Menezes, S. A. Maier, M. V. Gorkunov, Y.S. Kivshar, and A. Tittl, “Unlocking the out-of-plane dimension for photonic bound states in the continuum to achieve maximum optical chirality,” *Light Sci. Appl.* Vol. 12, No. 1, p. 250, 2023.
3. Gorkunov, M. V. & Antonov, A. A. Rational design of maximum chiral dielectric metasurfaces. in *All-Dielectric Nanophotonics* 243–286 (Elsevier, 2024).
4. Kim, S., S.-C. An, Y. Kim, Y.S. Shin, A.A. Antonov, I.C. Seo, B.H. Woo, Y. Lim, M.V. Gorkunov, Y.S. Kivshar, J.Y. Kim, Y.C. Jun, “Chiral electroluminescence from thin-film perovskite metacavities”, *Sci. Adv*., Vol. 9, p. eadh0414, 2023.
5. Liu, W., Kivshar, Y. S. Generalized Kerker effects in nanophotonics and meta-optics [Invited]. *Opt. Express* Vol. 26, p. 13085, 2018.
6. Voronin, K, A. S. Taradin, M. V. Gorkunov, and D. G. Baranov, “Single-handedness chiral optical cavities,” *ACS Photonics*, Vol. 9, No. 8, pp. 2652–2659, 2022.
7. Gorkunov, M. V., A. A. Antonov, A. V. Mamonova, E. A. Muljarov, Y. Kivshar, “Substrate-Induced Maximum Optical Chirality of Planar Dielectric Structures,” *Adv. Opt. Mater.* Vol. 13, p. 2402133, 2025.

Non-Hermitian Skin Effect in Lossy Anisotropic Nanophotonic systems

Yuto Moritake[1 *], Nozomi Ogawa[1,2], Issei Takeda[1,2], and Masaya Notomi[1,2,3]

[1]Institute of Science Tokyo, Japan
[2]NTT Basic Research Laboratories, NTT Corporation, Japan
[3]Nanophotonics Center, NTT Corporation, Japan
[*]corresponding author: moritake@phys.titech.ac.jp

Abstract: We experimentally demonstrated a non-Hermitian (NH) point gap in complex frequency space using NH photonic crystals. Furthermore, we propose unique light transport and the generation of orbital angular momentum enabled by the NH skin effect in nanophotonic systems.

In recent years, systems governed by non-Hermitian (NH) Hamiltonians have garnered considerable research attention. Studies exploring exceptional points in NH systems with parity-time (PT) symmetry have led to the discovery of various novel optical phenomena that do not appear in conventional nanophotonics [1-3]. Another key characteristic of NH systems is the presence of point gaps and the non-Hermitian skin effect (NHSE) [4-9]. A point gap arises when complex energy values encircle a specific reference point, forming a loop in complex energy space. This concept is fundamental to understanding the topological properties of NH systems and NHSE, where bulk states become localized at the system's boundaries.

In this presentation, we report the experimental observation of NH point gaps in nanophotonic systems [10] and the optical functionalities enabled by the skin effect [11]. In photonic crystals, point gaps and NHSE emerge when both anisotropy and material loss are present [7-9]. While NHSE has been experimentally observed, point gaps have remained elusive. To address this, we directly observed point gaps in complex frequency space. In the process, we discovered that point gaps and NHSE can be realized not through material loss but through radiation loss. In other words, a conventional silicon photonic crystal can be employed, and our band measurements [12] and analysis enabled the first successful observation of point gaps. Furthermore, we propose that the skin effect can arise even in uniform systems [9]. By leveraging the unidirectional propagation behavior of skin modes in two-dimensional systems, we demonstrate that skin modes facilitate anomalous light propagation and the generation of optical orbital angular momentum (OAM).

We acknowledge E. Kuramochi, M. Ono, K. Takata, H. Sumikura, T. Yoda, and T. Uemura for invaluable contribution. This work was supported by KAKENHI JP20H05641, JP21K14551, 24K01377, 24H02232 and 24H00400.

References

1. L. Feng, R. El-Ganainy, and L. Ge, "Non-Hermitian photonics based on parity–time symmetry," *Nat. Photon.* **11**, 752 (2017).
2. Ş. K. Özdemir, S. Rotter, F. Nori, and L. Yang, "Parity–time symmetry and exceptional points in photonics," *Nat. Mater.* **18**, 783 (2019).
3. M. -A. Miri and A. Alù, "Exceptional points in optics and photonics," *Science* **363**, 6422 (2019).
4. Z. Gong, Y. Ashida, K. Kawabata, K. Takasan, S. Higashikawa, and M. Ueda, "Topological Phases of Non-Hermitian

Systems," *Phys. Rev. X* **8**, 031079 (2018).

5. K. Kawabata, K. Shiozaki, M. Ueda, and M. Sato, "Symmetry and Topology in Non-Hermitian Physics," *Phys. Rev. X* **9**, 041015 (2019).
6. S. Yao and Z. Wang, "Edge States and Topological Invariants of Non-Hermitian Systems," *Phys. Rev. Lett.* **121**, 086803 (2018).
7. J. Zhong, K. Wang, Y. Park, V. Asadchy, C. C. Wojcik, A. Dutt, and S. Fan, "Nontrivial point-gap topology and non-Hermitian skin effect in photonic crystals," *Phys. Rev. B* **104**, 125416 (2021).
8. K. Yokomizo, T. Yoda, and S. Murakami, "Non-Hermitian waves in a continuous periodic model and application to photonic crystals," *Phys. Rev. Research* **4**, 023089 (2022).
9. T. Yoda, Y. Moritake, K. Takata, K. Yokomizo, S. Murakami, and M. Notomi, "Optical non-Hermitian skin effect in two-dimensional uniform media," arXiv:2303.05185
10. N. Ogawa, Y. Moritake, T. Uemura, T. Yoda, K. Takata, E. Kuramochi, H. Sumikura, and M. Notomi, "Experimental observation of non-Hermitian point-gap using photonic crystals with radiation loss," CLEO2025, 2025.
11. I. Takeda, T. Yoda, Y. Moritake, K. Takata, and M. Notomi, "Generation of OAM by optical non-Hermitian skin effect in MT symmetric media," META2024, 2024.
12. T. Uemura, Y. Moritake, T. Yoda, H. Chiba, Y. Tanaka, M. Ono, E. Kuramochi, and M. Notomi, "Photonic topological phase transition induced by material phase transition," *Sci. Adv.* **10**, eadp7779 (2024).

Electrically tunable free-electron nonlinearity in heavily-doped InGaAs

V. Giliberti[1]*, T. Venanzi[1], A. Rossetti[2], H. Hu[3], R. Polito[4], A. Notargiacomo[4], A. Valletta[5], F. Mattioli[4], A. Bousseksou[6], G. Beaudoin[6], I. Sagnes[6], R. Colombelli[6], M. Ludwig[2], D. Brida[2], M. Pea[4], C. Ciracì[3], M. Ortolani[1,4,7]

[1]Center for Life Nano- and Neuro-Science, IIT, Roma, Italy
[2]Department of Physics and Materials Science, University of Luxembourg, Luxembourg, Luxembourg.
[3]Center for Biomolecular Nanotechnologies, IIT, Arnesano, Italy
[4] Istituto di Fotonica e Nanotecnologie, CNR, Roma, Italy
[5]Istituto per la microelettronica e microsistemi, CNR, Roma, Italy
[6] Centre de Nanosciences et de Nanotechnologies, CNRS, University of Paris-Saclay, Palaiseau, France
[7] Dipartimento di Fisica, Sapienza Università di Roma, Roma, Italy

*corresponding author: valeria.giliberti@iit.it

Abstract: We report on the experimental investigation of the electrically tunable third harmonic generation of mid-infrared pulses from grating-gate field effect devices fabricated on n-doped InGaAs/InP heterostructure. Our findings pave the way for future exploitation of free-electron nonlinearities in all-semiconductor photonic integrated circuits.

Photonic integrated circuits with implementation of nonlinear functions hold promises as future hardware for neuromorphic information processes. However, the development of nanoscale nonlinear elements in photonic integrated circuits is hindered by the physical limits to the nonlinear optical response of dielectrics [1]. Recently, we have shown that optical nonlinearities in heavily-doped semiconductors due to nonlinear collective behavior of free-electrons can exceed by several orders of magnitude the efficiency of conventional dielectric nonlinearities [2]. We measured third-harmonic generation (THG) of mid-infrared (mid-IR) pulses from plasmonic nanoantenna arrays made of heavily n-doped InGaAs with increasing levels of free-carrier density. A further distinctive advantage of using semiconductors is the possibility to tune nonlinearity by means of field effect. In this work, to demonstrate the electrical reconfigurability of optical nonlinearity by means of an applied DC bias, we measured THG of mid-IR pulses from heavily doped InGaAs layer with gold antenna gratings on top (sketch in Figure 1a), investigating the effect of the applied bias on the emission intensity.

Plasmonic metal grating-gates have been fabricated by electron beam lithography starting from a HfO_2/n-doped InGaAs/InP multiplayer. The 750 nm-thick n-doped InGaAs layer ($n = 8.8\times10^{18}$ cm^{-3}) has been grown by metal organic chemical vapor deposition (MOCVD) on a lightly doped InP substrate, and the 35 nm-thick HfO_2 layer has been evaporated by atomic layer deposition on the n-doped InGaAs to work as gate dielectric material. Plasmonic metal gratings consist of arrays of rectangular gold electrodes with equal pitch (2 μm) and varying electrode width from around 300 nm to around 900 nm. All gratings are connected to the same electrical pad, while on the bottom of the lightly-doped InP substrate a metal back contact was fabricated by depositing a 50nm-thick Ni/50nm-thick Au layer. Electrical characterization of the plasmonic grating-gates confirmed efficient InGaAs carrier density modulation. The grating-gates have been then characterized by linear mid-IR Fourier transform IR micro-spectroscopy, confirming that plasmonic resonances shift towards higher energies by decreasing the gate width (see extinction curves in Figure 1b), in agreement with computational results.

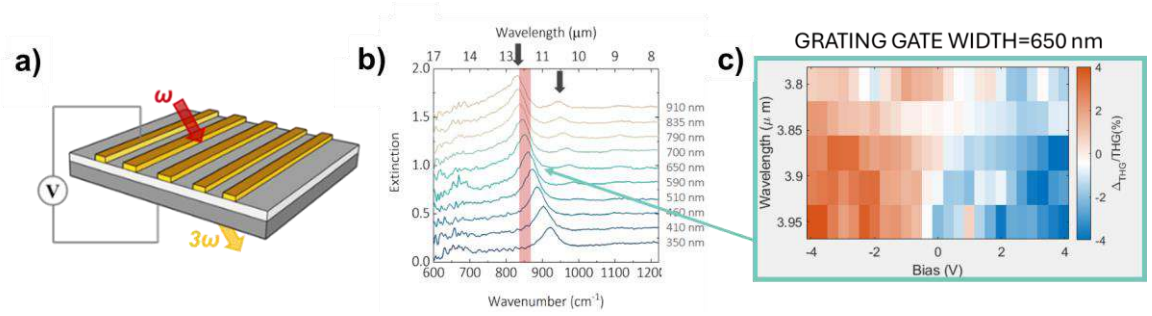


Figure 1 (a) Schematic of THG experiment with applied voltage bias on the n-doped InGaAs layer with gold antennas on top spaced with 35 nm HfO_2. (b) Extinction curves obtained by measuring both the reflection and the transmission of each grating (E=1-T-R). The red vertical band represents the optical pump spectrum used for the THG experiments. (b) Colormaps of the variation of THG emission intensity as a function of applied voltage bias for the grating with gate electrode width of 650 nm.

Finally, to assess the electrical reconfigurability of optical nonlinearity, we measured THG from the grating-gates with a mid-IR optical pump at approximately 12 μm, which corresponds with the main plasmonic resonance of many of the grating-gates (see Figure 1b), while varying the applied gate bias. We calculated the variation of THG spectrum ($\Delta_{THG}/THG_{0V} = (THG_V - THG_0)/ THG_0$) as a function of applied bias for the different grating structures. In all cases, we observe a change of the THG emission intensity depending on the applied bias. When the mid-IR radiation is resonant with the grating (grating width 650 nm, Figure 1c), which is the condition of optimal spatial overlap between gated semiconductor and plasmonic near-field, we observe an increase of the THG emission for negative bias, i.e. towards the depletion region of the n-doped InGaAs layer. Our results demonstrate that it is possible to modulate optical nonlinearity with an applied voltage bias by controlling the semiconductor carrier density. Having employed the common material platform InGaAs/InP that supports integrated waveguides, these findings pave the way for future exploitation of free-electron nonlinearities in all-semiconductor photonic integrated circuits.

Acknowledgements: We acknowledge funding by the European Innovation Council (NEHO, 101046329). Views and opinions expressed are, however, those of the authors only and do not necessarily reflect those of the European Union. Neither the European Union nor the granting authority can be held responsible for them.

References

1. Ferreira De Lima, T.; Shastri, B. J.; Tait, A. N.; Nahmias, M. A.; Prucnal, P. R. “Progress in neuromorphic photonics”. *Nanophotonics, 6(3), 577-599*, 2017.
2. Rossetti, A.; Hu, H.; Venanzi, T.; Bousseksou, A.; De Luca, F.; Deckert, T.; Giliberti, V.; Pea, M.; Sagnes, I.; Beaudoin, G.; Biagioni, P.; Baù, E.; Maier, S. A.; Tittl, A.; Brida, D.; Colombelli, R.; Ortolani, M.; Ciracì, C. “Control and enhancement of optical nonlinearities in plasmonic semiconductor nanostructures”. *Light Science and Applications*, just accepted

Material aspects for ultra-stable laser interferometers

N. Wagner[1,2*], B. Fang[4], S. Häfner[1,2], M. T. Hartman[4], M. Jetter[5], T. Legero[6], M. Narożnik[3], M. Zimmer[5], and S. Kroker[1,2,6]

[1]Institut für Halbleitertechnik, Technische Universität Braunschweig, Hans-Sommer-Str. 66, Braunschweig, 38106 Germany

[2]Laboratory for Emerging Nanometrology, Langer Kamp 6a-b, Braunschweig, 38106 Germany

[3]Institute of Physics, Faculty of Physics, Astronomy and Informatics, Nicolaus Copernicus University, Grudziądzka 5, PL-87-100 Toruń, Poland

[4]LNE-SYRTE, Observatoire de Paris, Université PSL, CNRS, Sorbonne Université - Paris, France

[5]Institut für Halbleiteroptik und Funktionelle Grenzflächen (IHFG), Center for Integrated Quantum Science and Technology (IQ^{ST}) and SCoPE, University of Stuttgart, Allmandring 3, 70569 Stuttgart, Germany

[6]Physikalisch-Technische Bundesanstalt, Bundesallee 100, 38116 Braunschweig, Germany

Corresponding author: nico.wagner@tu-braunschweig.de

Abstract: We present an overview of state-of-the-art materials for ultra-stable laser interferometers, focusing on thermal noise in various components. Investigated materials include NEXCERA for spacers, GaAs for highly reflective mirrors, metamirrors for ultra-low noise mirrors, and Eu^{3+}:Y_2SiO_5 for spectral-hole burning experiments.

Ultra-stable laser interferometers are key instruments in optical metrology, e.g., finding application in gravitational wave detectors [1] or optical lattice clocks [2]. The high precision is achieved through a laser source with ultra-stable frequency stability, typically ensured by stabilizing the laser to a high-finesse optical reference cavity [3]. A fundamental limitation of frequency stability arises from the reference cavity itself, or more specifically, from the thermal noise of its components—two high-reflectivity mirrors and a spacer [4]. An essential material parameter for quantifying Brownian thermal noise is the mechanical loss factor, which is linked to the intrinsic energy dissipation of a material.

In this study, we employ the mechanical ringdown technique to determine the mechanical loss factor of different materials, providing key insights into the reduction of thermal noise. Beyond conventional mirror technologies, we also investigate metamirrors, which offer an ultra-low noise performance and hold great potential for improving the frequency stability of next-generation ultra-stable lasers.

A material that has recently gained interest for use as a spacer in optical cavities is NEXCERA™, a ceramic-based composition. Its key feature is a coefficient of thermal expansion that crosses zero around room temperature, making it an ideal candidate for room-temperature cavities, as frequency fluctuations due to temperature variations are negligible. However, its thermal noise performance remains uncertain and could be a limiting factor if the Brownian noise level is high, even though thermo-optic noise is negligible. To address this, we measured the mechanical loss factor of NEXCERA and estimated the thermal noise for different spacer geometries and complete cavity configurations [5]. Our results indicate that NEXCERA exhibits lower Brownian thermal noise than ULE, the material currently used in the most stable optical cavity [6].

While the spacer plays a crucial role in stabilizing the optical cavity, the performance of the mirrors is also essential. For this purpose, a material currently under investigation is GaAs, combined with AlGaAs to form a stack of alternating layers, creating a highly reflective

crystalline Bragg mirror for ultra-high-finesse cavities [7]. Crystalline coatings offer a significant advantage: the mechanical loss factor is much lower than that of conventional amorphous coatings, resulting in a substantially reduced thermal noise limit. However, unexplained excess noise has been observed in these coatings, likely due to photoinduced effects, preventing them from outperforming traditional coatings [8]. In this work, we present our latest findings on photoinduced effects in elasticity and mechanical loss in GaAs. Our results indicate that laser illumination modifies both mechanical loss and elasticity, with effects persisting over timescales ranging from seconds to minutes [9].

While conventional Bragg mirrors achieve outstanding reflectivity through alternating layers, their main drawback is that increasing the number of layers also increases the overall thermal noise. Metamirrors provide a promising alternative by significantly reducing thermal noise while maintaining high reflectivity [10]. Unlike multilayer coatings, where each interface contributes to thermal noise, metamirrors rely on a single reflective surface, minimizing noise contributions and offering a highly stable solution for next-generation optical cavities.

Furthermore, in addition to cavity-referenced laser stabilization, the spectral-hole burning technique has emerged as a promising method. Here the stabilizing laser is locked to an ultra-narrow optical transition in an optical crystal, such as Eu^{3+}:Y_2SiO_5. Previous experiments have demonstrated significant potential for high-precision optical metrology, achieving frequency stability comparable to the most stable cavity-referenced lasers [11]. However, since the mechanical loss factor of Eu^{3+}:Y_2SiO_5 remains unknown, the fundamental thermal noise limitation in spectral-hole burning experiments is not yet well defined. In this work, we present cryogenic mechanical loss measurements, allowing us to estimate an upper limit for the Brownian thermal noise [12]. Our findings indicate that Eu^{3+}:Y_2SiO_5 could be a promising candidate for future ultra-stable laser applications.

In conclusion, our results highlight promising pathways for improving the frequency stability of next-generation laser cavities through the use of novel materials.

References

1. B. P. Abbott *et al.*, "Observation of gravitational waves from a binary black hole merger," *Phys. Rev. Lett.*, Vol. 116, No. 6, pp. 061102, 2016.
2. A. D. Ludlow *et al.*, "Optical atomic clocks," *Rev. Mod. Phys.*, Vol. 87, No. 2, pp. 637–701, 2015.
3. T. Kessler *et al.*, "A sub-40-mHz-linewidth laser based on a silicon single-crystal optical cavity," *Nat. Photon.*, Vol. 6, No. 10, pp. 687–692, 2012.
4. D. G. Matei *et al.*, "1.5 μm Lasers with Sub-10 mHz Linewidth," *Phys. Rev. Lett.*, Vol. 118, No. 26, pp. 263202, 2017.
5. N. Wagner *et al.*, "Mechanical losses and stability performance of NEXCERA in ultra-stable laser cavities," *arXiv:2409.14120*, 2024.
6. S. Häfner *et al.*, "8×10^{-17} fractional laser frequency instability with a long room-temperature cavity," *Opt. Lett.*, Vol. 40, No. 9, pp. 2112, 2015.
7. G. D. Cole *et al.*, "Tenfold reduction of Brownian noise in high-reflectivity optical coatings," *Nat. Photon.*, Vol. 7, No. 8, pp. 644–650, 2013.
8. J. Yu *et al.*, "Excess Noise and Photoinduced Effects in Highly Reflective Crystalline Mirror Coatings," *Phys. Rev. X*, Vol. 13, No. 4, pp. 041002, 2023.
9. N. Wagner and S. Kroker, "Room-temperature photoinduced effects in elasticity and mechanical loss of GaAs for applications in high-precision optical metrology," *EPJ Web of Conferences*, Vol. 309, pp. 06020, 2024.
10. J. Dickmann and S. Kroker, "Highly reflective low-noise etalon-based meta-mirror," *Phys. Rev. D*, Vol. 98, No. 8, pp. 082003, 2018.
11. M. J. Thorpe *et al.*, "Frequency stabilization to 6×10^{-16} via spectral-hole burning," *Nat. Photon.*, Vol. 5, No. 11, pp. 688–693, 2011.
12. N. Wagner *et al.*, "Temperature-dependent mechanical losses of Eu^{3+}:Y_2SiO_5 for spectral hole burning laser stabilization," *arXiv:2409.14126*, 2024.

Ultrafast plasmonic hot carriers: from light generation to pulsed photocatalysis

A. Schirato[1,2], Y. Luo[3], S. Sheng[3], G. Cerullo[1,4], A. Alabastri[5,6], M. Garg[3], P. Nordlander[2,6], G. Della Valle[1,4]

[1]Department of Physics, Politecnico di Milano, Piazza L. Da Vinci 32, 20133 Milano, Italy
[2]Department of Physics and Astronomy, Rice University, 6100 Main Street, Houston, TX 77005, USA
[3]Max Planck Institute for Solid State Research, Heisenbergstr. 1, 70569 Stuttgart, Germany
[4]Istituto di Fotonica e Nanotecnologie - CNR, Piazza Leonardo da Vinci 32, 20133, Milan, Italy
[7]Departiment of Electrical and Computer Engineering, Rice University, 6100 Main Street, Houston, TX 77005, USA
[8]Smalley Curle Institute & Laboratory for Nanophotonics, Rice University, 6100 Main Street, Houston, TX 77005, USA
[*]corresponding author: andrea.schirato@polimi.it

Abstract: Photoexcited plasmonic hot carriers unlock opportunities in applications ranging from nonlinear optics to photocatalysis. Here, we combine simulations and experiments to track these nonequilibrium carriers with spatial (sub-nm), temporal (few fs), and energy (meV) resolution, and then discuss an example of photocatalytic reaction leveraging hot carriers under ultrafast pulse illumination.

Plasmonic hot carriers – highly energetic electron-hole pairs with energy distributions far from equilibrium – photoexcited in metallic nanostructures hold great promise for a wide range of applications[1,2]. Their intrinsic spatial (a few nanometers), temporal (femto- to picoseconds), and energy (up to a few eV) scales offer unparalleled degrees of freedom for manipulating light-matter interactions. Effectively harnessing the large excess energy of these nonequilibrium carriers within their ultrafast lifetime has unlocked new opportunities for nanophotonic systems, with implications in fields ranging from nonlinear optics[5] to photocatalysis[6]. In this talk, we will first introduce an advanced technique for the real-time tracking of hot carries, and then discuss a photocatalytic reaction whose rate is modified by photoinduced nonlinearities under pulsed illumination.

When considering the ultimate limits of atomic-length scale structures, the ability to directly investigating hot carrier dynamics has remained out of reach until now, primarily due to the challenge of attaining simultaneous resolution in all the three domains – space, time and energy. Here, by combining time-dependent semi-classical modelling and two-colour femtosecond pump-probe microscopy, we present the real-time tracking of hot carriers in a well-defined plasmonic picocavity, formed in the tunnel junction of a scanning tunneling microscope (STM, sketched in Fig. 1a). The photoexcitation of hot carriers in the picocavity enables the ultrafast all-optical control over the broadband anti-Stokes (aS) electronic resonance Raman scattering (ERRS), and subsequent aS emission at the sub-nm scale. By leveraging the unique spatial confinement within the picocavity and ensuing spatio-temporal dynamics of hot carriers, the aS signal is generated in an active volume as small as 11 nm x 11 nm x 4 nm, and modulated with a sub-150-fs full recovery time, well before hot carrier relaxation.

The picocavity in unperturbed conditions emits aS photons over a broad spectrum (Fig. 1b, blue) following the illumination with a probe pulse (green in Fig. 1a) and excitation of its LSP (Fig. 1b, red), which decays to generate hot carriers. Finite element method-based simulations of the picocavity local density of photonic states (Fig. 1b, green), correlating with both the aS signal and the LSP, exhibit good agreement with measurements.

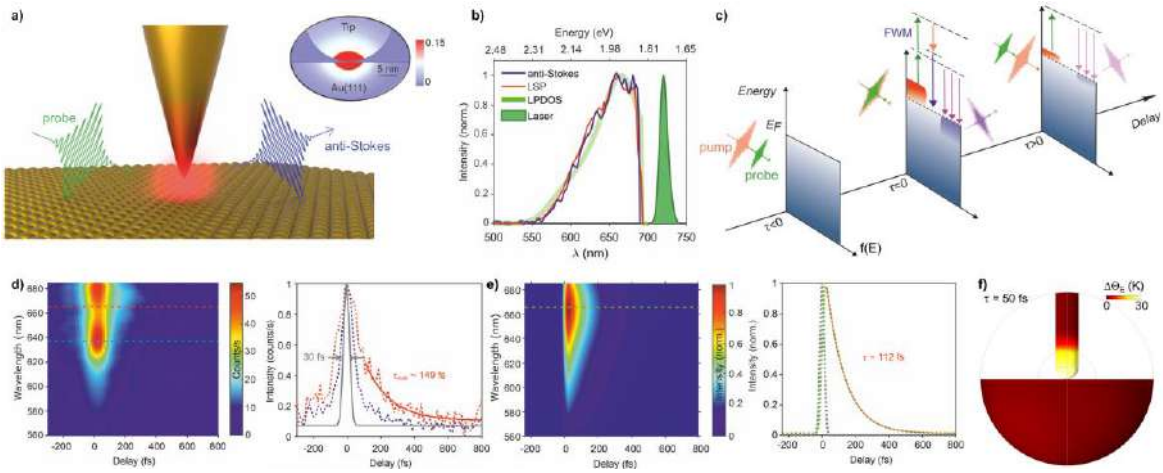


Fig. 1. a) Sketch of the picocavity excited by an ultrashort pulse (green) and generating aS photons (blue). Inset: simulated spatial distribution of the electromagnetic dissipated power. **b)** Measured aS spectrum (blue), local LSP (red), and the calculated local density of photonic states (green). **c)** Sketch of the temporal evolution of the hot carrier energy distribution as a function of the pump-probe delay τ. **d)** Experimental map (left) of the aS signal and ultrafast dynamics (right) of the signal at ~ 665 nm (red) and 640 nm (blue). **e)** Simulations for (d). **f)** Simulated spatial distribution of the electronic temperature across the metallic regions (tip and substrate), at 50 fs after the pump pulse arrival.

To dynamically modulate the aS emission, we conduct and model a pump-probe experiment, where the pump controls the hot carrier density, and the probe gives rise to aS ERRS (Fig. 1c). The recorded map of the aS signal is shown in Fig. 1d, with a section at 665 nm (red line), where the signal due to hot carriers is the strongest. Experiments are well explained by our simulations (Fig. 1e), reproducing both the spectral shape and temporal evolution of the measured aS modulation. The model combines a formulation of the ERRS cross-section with a rate-equation description of the hot carrier dynamics incorporating the ultrafast spatial carrier diffusion (Fig. 1f). Our time-resolved calculations indicate that the aS emission modulation is dominated by nonthermal hot carriers, while thermalised hot carriers (i.e., closer to the Fermi level) are drastically reduced by their spatial diffusion.

To conclude with an example of application exploiting the energy of hot carriers, we discuss the effects of pulsed illumination in driving a photocatalytic reaction (ammonia decomposition using CuRu antenna-reactors). By combining photothermal models and time-resolved measurements, we report a 20-fold increase in the reaction rate upon doubling the pulse repetition rate, for the same pulse energy and steady-state temperature. The effect is rationalised by light-driven transient nonlinearities modulating the reaction effective activation energy.

We acknowledge the EU's Horizon Europe research and innovation programme under the MSCA PATHWAYS HORIZON-MSCA-2023-PF-GF no. 101153856, and the METAFAST project (no. 899673) funded by the EU H2020.

References

1. Brongersma, M., et al. "Plasmon-induced hot carrier science and technology", Nat. Nanotech., 10, 25-34, 2015.
2. Schirato, A., Maiuri, M., Cerullo, G., Della Valle, G. "Ultrafast hot electron dynamics in plasmonic nanostructures: experiments, modelling, design", Nanophot., 12, 1, 2023.
3. Davidson, R.B., et al., "Ultrafast plasmonic control of second harmonic generation", ACS Photon. 3, 1477-1481, 2016.
4. Linic, S., et al., "Photochemical transformations on plasmonic metal nanoparticles", Nat. Mater. 14 (6), 567-576, 2015.

Chiral photoacoustic spectroscopy on plasmonic materials

C. Skubisz[*,1], E. Petronijevic[1], G. Leahu[1], Teemu Hakkarainenb[2], Eero Koivusalob[2], Mircea Guina[2], R. Li Voti[1], C. Sibilia[1] and A. Belardini[1]

1.Sapienza Università di Roma, SBAI Department, Italy

2. Optoelectronics Research Centre, Tampere University of Technology, Finland

[*]corresponding author: claudia.skubisz@uniroma1.it

Abstract: The Photoacoustic spectroscopy is a technique that allow to study the local absorption of the sample. The new set-up allows for spatial and spectral mapping of absorption enabling the study of extrinsic chirality in nanostructured metasurfaces and the homogeneity of the nanostructures.

Circularly polarized light is conventionally used to probe the chirality of the sample , left and right circular polarization are absorbed differently, and this difference is defined as Circular Dichroism (CD). The chirality can be induced by combining the asymmetry of the sample and the optical set-up. This property is called extrinsic chirality and it is obtained by breaking the symmetry of the light-sample interaction by forming a non-planar triad of vectors between the light wave-vector, the normal of the sample's surface, and the vector of the sample's asymmetry. Previously, the chirality was studied by conventional techniques only for a single laser [1] wavelengths, however to measure the directly absorption response we can use unconventional photo-thermal techniques. Photo-acoustic spectroscopy (PAS) is a photothermal technique that exploits the interaction between an incident light beam and matter, inducing a non-radiative de-excitation process that generates heat. The fluctuations produce an acoustic signal, converted into an electrical signal and this approach enables direct measurement of local absorption, thereby detecting effects that might otherwise be obscured by other scattering-dependent techniques.

The PAS set-up, Fig. 1., used for the measurement consists of a widely tunable near-infrared laser, covering a wavelength range from 680 nm to 1080 nm. The light is modulated by a mechanical chopper at different frequencies. Before reaching the sample housed within the photoacoustic cell, the light beam, passes through a polarizer, a quarter-wave plate and the light can be focused on the sample in a closed PAS cell. The photoacoustic cell is equipped with a rotating stage, that enables examination of the sample at different angles of incidence relative to the surface normal, and a translation stage that allows the scanning of the sample in different areas.
This methodology allows us to study the homogeneity of the sample even on very small areas.

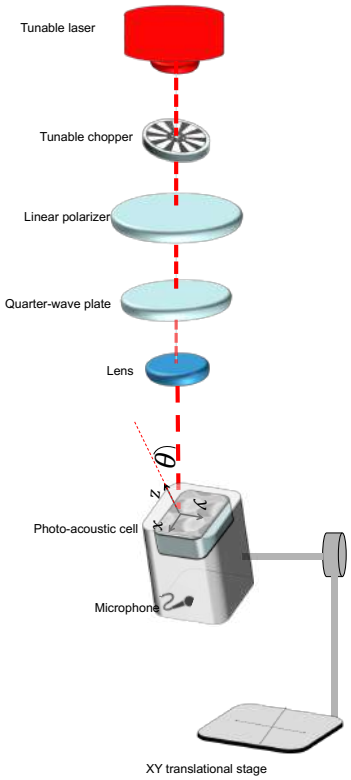


Figure 1- Photo-acoustic set-up positioned on rotational and translation stages allows for multiple tunable parameters

References

1. Leahu, G., Petronijevic, E., Belardini, A., Centini, M., Sibilia, C., Hakkarainen, T., Koivusalo, E., Piton, M.R., Suomalainen, S., and Guina, M. (2017). Evidence of Optical Circular Dichroism in GaAs-Based Nanowires Partially Covered with Gold. *Advanced Optical Materials*, *5*(16), 1601063.

META 2025, MALAGA - SPAIN, JULY 22 – 25, 2025

Next-generation implantable neural probes: advanced photonics on the tip of multimode optical fibers for enhanced endoscopic sensing

L. Piscopo[1,2,*], M.S. Andriani[1,2], L. Algieri [2], L. Collard[1,3], D. Zheng[1,4], M. F. Kashif[1,5], C. Montinaro[1], M. Kazemzadeh[1], S. Aslanoglou[1], F. Pisano[6], A. Balena [1,7], M. Bianco [1], M. Pisanello [8], B. Spagnolo [1], M. Scaraggi [1,2] , T. Fellin [9] ,M. De Vittorio[1,2,10,&], F. Pisanello[1,&]

[1]Istituto Italiano di Tecnologia, Center for Biomolecular Nanotechnologies, Arnesano, Italy
[2]Dipartimento di Ingegneria dell'Innovazione, Università del Salento, Lecce, Italy
[3] Comprehensive Cancer Centre, School of Cancer and Pharmaceutical Sciences, King' s College London, London, UK
[4] State Key Laboratory of Radio Frequency Heterogeneous Integration, Shenzhen University, Shenzhen 518060, China
[5] Dipartimento di Ingegneria Elettrica e delle Tecnologie dell'Informazione, Università Degli Studi di Napoli Federico II, 80125 Napoli, Italy
[6] Department of Physics and Astronomy "G. Galilei", University of Padova, Via Marzolo 8, 35131, Padova, Italy
[7] Laboratoire Kastler Brossel, Sorbonne University, CNRS, ENS-PSL University, Collège de France, Paris, 75005, France
[8] OptogeniX s.r.l., Arnesano, Lecce,73010,Italy
[9] Optical Approaches to Brain Function Laboratory, Istituto Italiano di Tecnologia, Genova, Italy
[10]IDUN section, Department of Health Technology, Technical University of Denmark, DK-2800 Kgs. Lyngby, Denmark
[*]corresponding author: linda.piscopo@iit.it, & co-last authors

Abstract: Integrating photonic elements on multimode optical fibers combined with traditional wavefront shaping systems can enhance neural endoscope sensing. Here, we present our approaches to fabricating nano- and micro-photonic and plasmonic structures at the output of the fiber and achieve precise control over their coupling with thousands of guided modes.

Over the past 15 years, optical techniques have revolutionized the study of neuronal activity and connections within the brain, enabling all-optical observation of neuronal dynamics through electrical and chemical sensing[1,2]. The integration of endoscopic methods to excite and collect functional fluorescence has emerged as a promising approach for investigating local microcircuits[3] and mapping neural activity[4] in deep brain regions in a minimally invasive fashion. In this framework, multimode optical fibers (MMFs) represent an excellent platform for endoscopic sensing, thanks to the small cross-section, their inherently light-couple nature, and the possibility to shape the multimode fiber to engineer the emission and collection volume. This presentation will describe our approach to improving and extending the detection capabilities of MMFs for neural endoscopy applications, based on the use of photonic structures at the fiber output to exploit light-matter interactions to better interface with brain tissue[5]. To fully access the potential of this approach, we developed a set of methods to optimize and dynamically control the coupling of thousands of guided modes in the MMF of either dielectric elements or plasmonic systems.

Firstly, we will describe how wavefront shaping offers a dynamic solution to optimize the incident phase profile on a system composed by a MMF hosting at the output a meta-lens fabricated by two-photon lithography. By iteratively refining the wavefront, the optical response of the photonic structures can be maximized, enabling sub-diffraction spatial confinement by tailoring the near field, and selecting a working point of the coupled system's dispersion diagram by acting on the far field reciprocal plane[6]. By designing a diverging meta-lens that increases the numerical aperture of the fiber, it was possible to generate a scanning focused spot beyond the diffraction limit while simultaneously improving the collection volume of the probe. The same concepts were also applied to plasmonic MMFs, featuring gold nanoslit arrays or nanoparticles to integrate molecular sensing capability through spatial-resolved surface-enhanced Raman spectroscopy (SERS).

An alternative method to control the coupling between guided modes and plasmonic resonances on MMFs is to operate directly onto the shape of the fiber optic and the geometry of the plasmonic structures. The second part of the presentation will describe how this approach enhances the performance of a SERS probe. SERS offers significant advantages

to the neuroscience community by providing a label-free alternative for molecular sensing[7,8] and complements genetically encoded indicators which have been pivotal in neuroscience but are limited to animal models. To increase the probe sensitivity, we explored two complementary strategies: modifying the fiber itself and tailoring the design of the plasmonic structures. Tapered optical fibers (TFs) offer a unique advantage in SERS-based biosensing due to their modal demultiplexing properties and the co-existence of both radiative and evanescent field on the output surface[9], which enhance the coupling with plasmonic structures and the collection of the generated vibrational signal. To integrate plasmonic structures on TFs we employed physical vapor deposition, enabling the spontaneous nucleation of gold nanoparticles on the highly curved surface. This process leads to a transition from a rough gold nanofilm to a uniform layer of spherical nanoparticles with inter-particle gaps of less than 5 nm. The resulting plasmonic sensor exhibits remarkable detection capabilities, enabling the detection of serotonin dispersed in an aqueous solution at the physiological resting concentration (10^{-9} M) even in a through-fiber measurement scheme. Additionally, repeated measurements at varying concentrations reveal the detection of different stereoisomeric forms of serotonin.

Acknowledgments

M.D.V. and F.P. acknowledge funding by European Union's Horizon Europe under grant agreement 101125498, project MINING - "Multifunctional nano-bio interfaces with deep brain regions". D.Z., M.F.K., Li.C., M.D.V., and F.P. acknowledge funding from the European Union's Horizon 2020 Research and Innovation Program under Grant Agreement No. 828972. Li.C., C.M., M.D.V., and F.P. acknowledge funding from the Project "RAISE (Robotics and AI for Socio-economic Empowerment)" code ECS00000035 funded by European Union – NextGenerationEU PNRR MUR - M4C2 – Investimento 1.5 - Avviso "Ecosistemi dell'Innovazione" CUP J33C22001220001. S.A, Fi.P., M.D.V. and F.P. acknowledge funding from the European Union's Horizon 2020 Research and Innovation Program under Grant Agreement No. 101016787. M.D.V and F.P acknowledge financial support under the National Recovery and Resilience Plan (NRRP), Mission 4 "Education and Research" – Component 2 "From Research to Business" – Investment 1.3, funded by the European Union – NextGenerationEU, within the framework of the cascade funding call of Spoke 3 – Extended Partnerships among Universities, Research Centers, and Enterprises for Research Project Funding, "Mnesys" (PE00000006). This work is part of the project "Correlating multifunctional signals in 3D printed neurochips for next generation studies on neural degeneration, via spectroscopy and electrophysiological recordings" (acronym: COMBO) – CUP: E63C22002170007

References

1. Patriarchi, T. *et al.* Imaging neuromodulators with high spatiotemporal resolution using genetically encoded indicators. *Nat. Protoc.* **14**, 3471–3505 (2019).

2. Shen, Y., Nasu, Y., Shkolnikov, I., Kim, A. & Campbell, R. E. Engineering genetically encoded fluorescent indicators for imaging of neuronal activity: Progress and prospects. *Neurosci. Res.* **152**, 3–14 (2020).

3. Turtaev, S. *et al.* High-fidelity multimode fibre-based endoscopy for deep brain in vivo imaging. *Light Sci. Appl.* **7**, 92 (2018).

4. Hayashi, Y., Tagawa, Y., Yawata, S., Nakanishi, S. & Funabiki, K. Spatio-temporal control of neural activity *in vivo* using fluorescence microendoscopy. *Eur. J. Neurosci.* **36**, 2722–2732 (2012).

5. Pisano, F. *et al.* Plasmonics on a Neural Implant: Engineering Light–Matter Interactions on the Nonplanar Surface of Tapered Optical Fibers. *Adv. Opt. Mater.* **10**, 2101649 (2022).

6. Collard, L. *et al.* Holographic Manipulation of Nanostructured Fiber Optics Enables Spatially-Resolved, Reconfigurable Optical Control of Plasmonic Local Field Enhancement and SERS. *Small* **18**, 2200975 (2022).

7. Zheng, D. *et al.* Tunable Nanoislands Decorated Tapered Optical Fibers Reveal Concurrent Contributions in Through-Fiber SERS Detection. *ACS Photonics* **11**, 3774–3783 (2024).

8. Fortuni, B. *et al.* SERS Endoscopy for Monitoring Intracellular Drug Dynamics. *ACS Sens.* **8**, 2340–2347 (2023).

9. Pisano, F. *et al.* Depth-resolved fiber photometry with a single tapered optical fiber implant. *Nat. Methods* **16**, 1185–1192 (2019).

Incident light selective metasurfaces

K. Y. Yang[1*]

[1]BrightEST Technology, Taiwan
[*]corresponding author: piano77814@gmail.com

Abstract: Photonic nanostructures can tailor the scattering phase from various polarizability induced by incident light. By introducing subwavelength meta-atoms with selective response of incident light, we have demonstrated additional design freedom to engineering dispersion, birefringence, wavevector selection and enhancement of second harmonic generation beyond arbitrary wavefront shaping for metasurfaces.

The development of nanophotonics has enabled tailoring the optical scattering phase in subwavelength photonics elements, so called meta-atoms. Thanks to the enrichment of mode and near-field coupling, meta-atoms can generate varying electromagnetic polarizability for different incident wavelength, polarization and illumination angle.

In this talk, we will first demonstrate the design of meta-atoms that can support independent scattering phase for horizontal and vertical linear polarizations. The meta-hologram arranged the polarization-selective meta-atoms as the building block of computer-generated meta-hologram, which can provide distinguish wavefront reconstruction and thus holographic images with different incident polarizations.

Besides the incident polarization, we have also realized the wavelength-selective metasurface which supports diffraction-free beam steering within 100 nm operation bandwidth at 750 nm central wavelength. To achieve optical phase engineering without introducing unwanted inhomogeneous broadening, plasmonic dark mode in meta-atoms supported Fano resonance plays a key role. This work demonstrates the color-routing metasurface can provide diffraction-free wavefront shaping beyond conventional bandpass filtering or grating with a subwavelength device thickness.

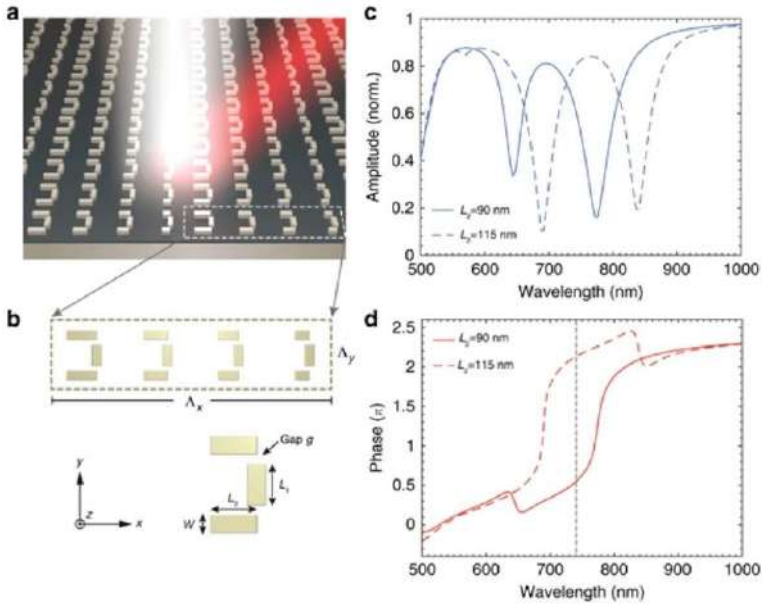


Figure 1. Design principle of a narrowband metasurfaces composed of plasmonic Fano resonators.

In the following, we will present our 2 works to achieve the selective response of incident angle for second harmonic (SH) generation (SHG). For SHG in plasmonic nanostructures, the second-harmonic dipole is enhanced by spatially overlapping fundamental hot spot to the area where centro-symmetric is broken. The unique 3D gold nanopillars with different tilted angles can support fundament plasmonic resonance only when incident angle is such that the polarization is paralleled to the nanopillars. Therefore, allows the subwavelength-thickness metasurface exhibits wavevector-selective SH enhancement.

Furthermore, we demonstrate a reflective type metasurfaces that can efficiently couple incident planewave to a hybrid plasmonic mode propagating along the interface of gold backplate of metasurfaces. A pronounced SH enhancement can be detected when the hybrid mode is excited by corresponding incident angle. Importantly, the SHG is at least 230 times higher than other angles that only localized plasmonic mode is excited at fundamental wavelength. These results underline the fascinating physics of SHG in the symmetry of fundamental plasmonic mode. The wavevector-selective nonlinear response in metasurfaces can find applications in the field of vacuum ultra-violet (VUV) super-resolution imaging, silicon photonics, etc.

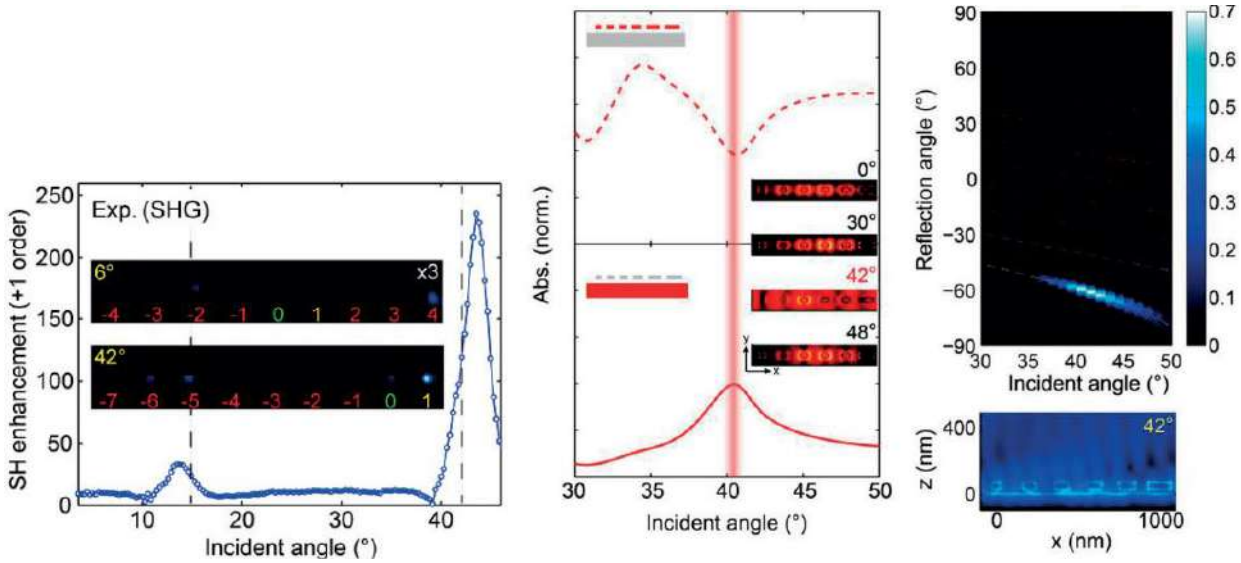


Figure 2. The experiment and simulation of SH enhancement from a hybrid plasmonic mode propagating along silver backplate of reflective metasurfaces with specific incident angle at fundamental wavelength.

Finally, I would like to acknowledge my Ph.D. advisor Prof. Olivier Martin, Dr. Jeremy Butet in EPFL and M.Sc. advisor Prof. Din Ping Tsai in National Taiwan University who provide endless support in completing the research of this talk.

References

1. Chen Y., K.-Y. Yang and O. J. F. Martin, “Fano-resonance-assisted metasurface for color routing,” Light: Science & Applications, Vol. 6, e17017, 2017.
2. Yang, K.-Y., R. Verre, J. Butet, C. Yan, T. J. Antosiewicz, M. Kall and O. J. F. Martin, “Wavevector-Selective Nonlinear Plasmonic Metasurfaces,” Nano Lett., Vol. 17, 5258–5263, 2017.
3. Yang, K.-Y., “Plasmonic metasurfaces to tailor second harmonic generation,” EPFL thesis, No. 8309, 2018.

Precision Fabrication of Nanoscopic Europium Emitters Utilizing Electron Beam Lithography

M. Rikers[1,2,3,*], A. Bashiri[1,2], Á. Barreda[1,2,4], M. Steinert[2],
D.-Y. Choi[3], T. Pertsch[2,5,6] and I. Staude[1,2,6]
[1]Institute of Solid State Physics, Friedrich Schiller University Jena,
Max-Wien-Platz 1, 07743 Jena, Germany
[2]Institute of Applied Physics, Abbe Center of Photonics,
Friedrich Schiller University Jena, Albert-Einstein-Str. 15, 07745 Jena, Germany
[3]Department of Quantum Science and Technology,
Research School of Physics, Australian National University,
60 Mills Rd., Canberra, ACT 2601, Australia
[4]Department of Electronic Engineering, University Carlos III of Madrid,
Avda. de la Universidad 30, 28911 Leganés, Spain
[5]Fraunhofer-Institute for Applied Optics and Precision Engineering IOF,
Albert-Einstein-Str. 7, 07745 Jena, Germany
[6]Max Planck School of Photonics, Hans-Knöll-Str. 1, 07745 Jena, Germany
marijn.rikers@uni-jena.de (corresponding author)

Abstract

A new method for fabricating fluorescent nanostructures with defined magnetic dipolar transitions is presented. Electron beam lithography exposes a negative tone resist embedded with Europium complexes, achieving emitter diameters as small as 80 nm, which facilitates investigations of magnetic local density of optical states in nanophotonics.

1 Introduction

In studies of spontaneous emission modification, the magnetic component of light is often neglected in light-matter interactions due to its amplitude being 10^{-5} times smaller than that of the electric component. However, this is not the case when we engineer nanostructures with strong magnetic field localization [1]. To study the magnetic-field mediated light-matter interactions a magnetic emitter is utilized. Magnetic dipolar (MD) transition dominates when because of selection rules, the electric dipolar transitions are forbidden. These types of transitions occur primarily in lanthanides such as Europium; specifically we consider the $Eu^{3+}(^5D_0) \rightarrow Eu^{3+}(^7F_1)$ transition. Therefore, a Europium-based emitter enables us to study the often neglected magnetic component of light.

Previous works show that high refractive-index dielectric nano-antennas have great potential for the modification of magnetic transitions. However, the magnetic field localizations are much sub-wavelength, thus; we need a localization method for the magnetic emitters with nanometer precision. We introduces a fabrication method to deterministically create nanoscopic europium emitters which can be used to probe nanoscopic photonic environments [2]. The method utilizes electron beam lithography (EBL), and provides nanometer precision for the deterministic placement of magnetic emitters.

To create the nanoscopic emitters, we embed metal-organic complexes $Eu(TTA)_3$ into negative-tone electron beam resist series ma-N at a mass percentage of 0.1%. The mixture is filtered with a 0.2 μm filter and rested for 24 hours before spin-coating onto the substrate. To investigate

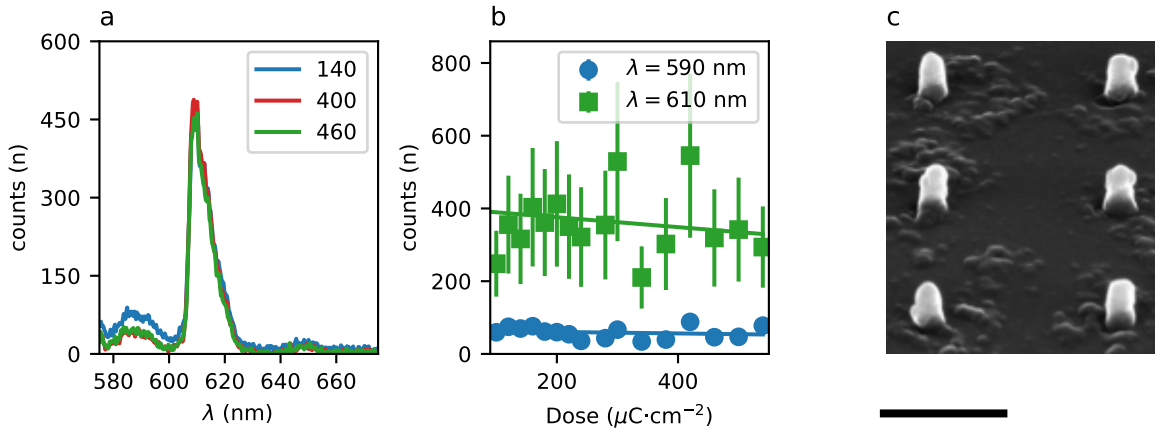


Figure 1: (**a**) Fluorescence spectra taken form exposed resist: Blue, red, and green lines correspond to doses of 140, 400, and 460 $\mu C \cdot cm^{-2}$, respectively. (**b**) Intensities of the $\lambda = 590\,nm$ transition (blue circles) and the $\lambda = 610\,nm$ transition (green squares) for different exposure doses. The solid lines are linear fits to the data. (**c**) Tilted electron microscope image showing the nanodot array. The scale bar is 400 nm.

the exposure properties, it is exposed to doses ranging from 100 $\mu C \cdot cm^{-2}$ to 540 $\mu C \cdot cm^{-2}$ in steps of 20 $\mu C \cdot cm^{-2}$, and after development, the fluorescence properties of the nanostructure are examined. In Figure 1a, some representative spectra are shown, and Figure 1b displays the intensity of the $\lambda = 590\,nm$ and $\lambda = 610\,nm$ transitions versus the exposure dose. We find that the fluorescence of the europium emitters is not altered by exposure to the electron beam. Additionally, we demonstrate the creation of fluorescent nanodots with a diameter of 80 nm using point exposures with a dose of 5 fC, see Figure 1c.

In conclusion, a new negative-tone fluorescent EBL resist ma-N : $Eu(TTA)_3$ with a mass percentage of 0.1% is demonstrated. The resist has good exposure properties and exhibits the fluorescence characteristics of Eu^{3+}. Considering the high flexibility of EBL, with multi-layer alignment, the new resist allows for the creation of hybrid photonics devices where the precise placement of emitters showing magnetic dipolar is critical.

2 Acknowledgements

This research was funded by the Deutsche Forschungsgemeinschaft (DFG), IRTG 2675 Meta-Active, 437527638. A.B. gratefully acknowledges financial support from the Spanish national project No. PID2022-137857NA-I00. A.B. thanks MICINN for the Ramon y Cajal Fellowship (grant No. RYC2021-030880-I).

References

[1] Bashiri, A., et. al., "Color Routing of the Emission from Magnetic and Electric Dipole Transitions of Eu^{3+} by Broken-Symmetry TiO_2 Metasurfaces," *ACS Nano*, Vol. 18, No. 1, pp. 506-514, 2024.

[2] Rikers, M., et. al., "Deterministic Fabrication of Fluorescent Nanostructures Featuring Distinct Optical Transitions," *Nanomaterial*, Vol. 15, No. 3, pp. 219-231, 2025.

Controlled electrophoretic deposition of nanoparticle films and their applications in light emitting diodes

N. Liu[1*], A. Mullen[1], L. Lyu[1], Y-L. Zhang[1], N. Biswas[1] and K. M. Ryan[2]

[1]Department of Physics and Bernal Institute, University of Limerick, Republic of Ireland

[2]Department of Chemical Sciences and Bernal Institute, University of Limerick, Republic of Ireland

[*]corresponding author: ning.liu@ul.ie

Abstract: Electrophoretic deposition provides a feasible route to form closely packed, crack-free nanoparticle thin films as the emissive layer in a LED device. Herein, we present a method to monitor the film growth in real time and obtain information on film thickness and morphology without resorting to advanced microscopy techniques.

Electrophoretic deposition (EPD) is a method to form particle films on a solid substrate from a charged particle solution assisted by an external electric field. EPD has been widely used in industrial applications such as forming protective coatings on flat surfaces,[1] or inner surfaces of tubes that are otherwise difficult to have access to.[2] More recently, EPD was used to form various structured nanomaterials and films that can still take advantage of the unique properties of individual nanoparticles (NPs).[3,4] In this work, we propose a EPD model considering the finite volume of the NP solution and the dissolution of the NPs back to its solution. The mass of deposited NP film and the concentration change of the NP solution can be described by the following coupled equations:

$$\begin{cases} \dfrac{dw}{dt} = R_{dep} - R_{dis} & (1) \\ c_c = c_0 - \dfrac{\int R_{dep}\,dt}{V} & (2) \\ c_n = \dfrac{\int R_{dis}\,dt}{V} & (3) \\ c = c_c + c_n & (4) \end{cases}$$

where w is the deposited mass on the substrate, R_{dep} the deposition rate, R_{dis} the dissolution rate, c_c and c_n the concentrations of charged and neutral particles in solution respectively, V the volume of the solution and c_0 the initial concentration of charged particles. The plots below show how deposition current, charged particle concentration and deposited mass vary with time when a limited volume of particle solution is used.

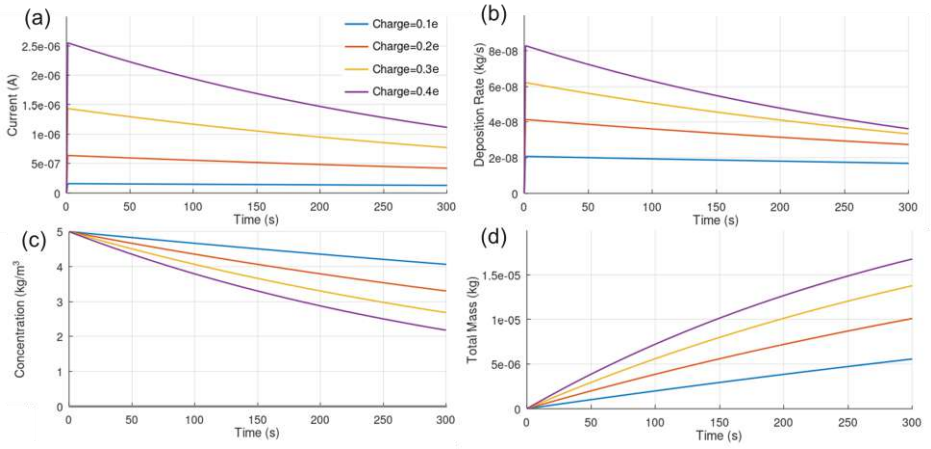


Figure 1: Modelling of I, R_{dep}, c_c and w vs. time with an initial charged NP concentration c_0= 5 mg/ml

We show that with appropriate assumptions, analytical solutions to the coupled equations can also be obtained. By measuring the deposition current vs. time trace, we can predict the single particle charge in solution and the deposition thickness of NP film as a function of time.

We employed this EPD method to form closely packed, vertically aligned CdSe/CdS core/shell nanorods (NRs) as the emissive layer in an inverted light emitting diode. Following an organic-inorganic architecture, the device fabricated yields an external quantum efficiency (EQE) of 6.3 % and a maximum luminance of 4320 cd/m^2 at 11 V.[5] This good performance can be attributed to the vertically aligned NR layer enhancing the charge transport through the long axis of NRs as it requires less hopping from NR to NR compared to a QD film of the same thickness. Achieving vertically aligned NR-LEDs can therefore maintain high current density. The EPD technique may prove useful to the development of a vast class of nanocrystal-based optoelectronics, including solar cells and laser devices.

Acknowledgements

This work was supported by the Research Ireland career development award RI 17/CDA/4733, RI 12/RC/2276_P2, 18/EPSRC-CDT/3585 and IRCLA/2017/285.

References

1. *Electrophoretic deposition: fundamentals and applications III*; Trans Tech Publications: Stafa-Zurich, Switzerland; Enfield, NH, 2009.
2. Dickerson, J. H. and A. R. Boccaccini, *Electrophoretic Deposition of Nanomaterials*; Springer, 2011.
3. Zhang, H., Y. Liu, Y. Dong, A. Ashokan, A. Widmer-Cooper, Ju. Köhler, and P. Mulvaney, "Electrophoretic Deposition of Single Nanoparticles", Langmuir, Vol. 40, 2783−2791, 2024.
4. Liu, P., S. Singh, Y. Guo, J.-J. Wang, H. X. Xu, C. Silien, N. Liu, K. M. Ryan, "Assembling ordered nanorod superstructures and their application as microcavity lasers", Sci. Rep. Vol 7, 43884. 2017.
5. Zhang, Y., X.-M. Pham, T. Keating, N. Jia, A. Mullen, D. Laishram, M.-Y. Gao, B. Corbett, P. Liu, X. W. Sun, T. Soulimane, C. Silien, K. M. Ryan, Z. Ma, and N. Liu, "Highly Efficient Inverted Light-Emitting Diodes Based on Vertically Aligned CdSe/CdS Nanorod Layers Fabricated by Electrophoretic Deposition", ACS Appl. Mater. Interfaces Vol. 16, 10459–10467, 2024.

Classical–quantum correspondence in photonic temporal crystals

Bumki Min

Department of Physics, KAIST, Daejeon 34141, Republic of Korea
*corresponding author: bmin@kaist.ac.kr

Abstract: We present a quantum electrodynamics model of photonic temporal crystals (PTCs) that connects classical and quantum pictures. A localization–delocalization phase transition takes place in a Floquet-photonic synthetic lattice, causing a two-level atom's Rabi oscillations to irreversibly decay into a mixed state, driven by photonic delocalization.

In this work, we develop a quantum electrodynamical framework for photonic temporal crystals (PTCs), bridging classical momentum gaps and fully quantum phenomena within a single theoretical model. Building on previous studies of non-Hermitian band structures in time-periodically modulated media [1-4], we show that a PTC can be quantized through a Floquet Hamiltonian where the photonic modes form a synthetic lattice in momentum–Floquet space. A key insight is that the exponential field growth seen in classical PTCs corresponds, quantum-mechanically, to a localization–delocalization transition of photon wavefunctions. At critical momenta (i.e., the edges of the momentum gap), photon number states become delocalized, triggering exponential increases in photonic energy.

Notably, when a two-level atom couples to these modes in a single-frequency cavity, conventional Rabi oscillations can be dramatically altered by the large continuum of Floquet–photonic states. Rather than exhibiting recurrent population exchange, the atomic state irreversibly decays into a half-and-half mixed state, even though there is only one nominal cavity resonance, illustrating how time-periodic modulation effectively expands the available photonic Hilbert space [4]. These results highlight that, despite the overall Hamiltonian being Hermitian, classical pseudo-Hermitian features emerge through Floquet band folding and interplay with quantum light–matter interactions. Beyond clarifying the classical–quantum correspondence of PTCs, this framework opens avenues for exploring photon pair creation, squeezing, and tailored non-equilibrium light-matter interactions [4, 5].

References

1. M. Lyubarov et al., “Amplified emission and lasing in photonic time crystals”, Science 377, 425 (2022)
2. N. Wang et al., “Photonic Floquet media with a complex time-periodic permittivity”, Phys. Rev. B 98, 085142 (2018)
3. J. Park et al., “Revealing non-Hermitian band structure of photonic Floquet media”, Science Advances 8, eabo6220 (2022)
4. J. Park et al., “Spontaneous emission decay and excitation in photonic temporal crystals”, arXiv:2404.13287 (2024)
5. J. Bae et al., “Cavity quantum electrodynamics of photonic temporal crystals”, arXiv:2501.03106 (2025)

Harnessing Plasmonic Nanostructures for Selective Light-Driven CO_2 Reduction

Anjalie Edirisooriya[1], Zelio Fusco, Ning Lyu[1,2], Christin David[3], Fiona Beck[1*]
[1]School of Engineering, Australian National University, Canberra ACT2600, Australia
[2]IFTO, Friedrich-Schiller-Universität Jena, 07743 Jena, Germany
[3]University of Applied Sciences Landshut, Am Lurzenhof 1, 84036 Landshut, Germany
[*]corresponding author: Fiona.beck@anu.edu.au

Abstract: Plasmonic nanostructures offer a powerful strategy for selective CO_2 reduction, overcoming challenges in conventional catalysis. By leveraging dendritic morphologies to enhance plasmonic effects, we drive efficient C-C coupling under light excitation. This talk explores our integrated approach combining simulations, spectroscopy, and nanoscale modelling to advance scalable, energy-efficient CO_2 conversion into valuable multi-carbon products.

Reducing CO_2 is essential for tackling climate change, but capturing it is only part of the solution. Transforming CO_2 into valuable chemicals offers a pathway to carbon-neutral fuels and essential industrial products. In particular, converting CO_2 into C_2+ products, such as ethylene and ethanol, is highly desirable due to their energy density, versatility, and economic significance. However, achieving high selectivity for these products remains a major challenge. The CO_2 molecule is highly stable, requiring multiple electron and proton transfers for reduction, and competing side reactions such as hydrogen evolution or CO formation often lower efficiency[1]. Traditional catalytic methods struggle with selectivity and require substantial energy input, limiting their scalability.

Plasmonic photocatalysis offers a promising alternative by using light to drive chemical reactions in a more controlled. When light interacts with plasmonic nanostructures, it excites localized surface plasmons, generating strong electromagnetic fields and energetic charge carriers. These effects can be harnessed to influence reaction pathways, steering CO_2 reduction toward multi-carbon products with greater precision. Unlike conventional approaches that rely solely on thermal or electrochemical activation, plasmonic excitation has the potential selective energy transfer to key reaction intermediates, modifying adsorption dynamics and enhancing reaction rates[2]. By tuning the optical and electronic properties of plasmonic nanostructures, we aim to improve both the efficiency and selectivity of CO_2 reduction, unlocking new possibilities for sustainable chemical production.

In this talk, I will give an overview of our investigations into plasmonic light-matter coupling and how it can be used to modify photocatalytic (PC) and photo-electrochemical (PEC) reactions. Our approach combines insights from nanoscale characterization and modeling of plasmonic resonances (BEM, FEM), and in situ monitoring of chemical reactions using surface-enhanced Raman spectroscopy (SERS) to probe underlying mechanisms. In addition, I will discuss how insights from atomistic studies and model molecule-nanoparticle systems can be leveraged to design practical photoelectrodes and photocatalysts for large-scale CO_2 reduction based on self-assembled dendritic structures.

Building on this foundation, we present a strategy using plasmonic dendritic nanostructures to drive selective CO_2 reduction. These self-assembled dendrites, fabricated via a scalable electrodeposition

process, exhibit sharp tips and intricate morphologies that amplify plasmonic effects[3]. By tuning their structure, we seek to optimize hot carrier generation, near-field localization, and local reaction conditions, which could provide a platform for C-C coupling. We will examine how these properties influence the reaction landscape and whether they enable new pathways for multi-carbon product formation with improved selectivity under light-driven conditions. This work contributes to the development of more efficient and scalable approaches to CO_2 utilization, with potential implications for sustainable chemical production.

References

1. Z. Fusco and F. J. Beck, "Advances in fundamentals and application of plasmon-assisted CO2 photoreduction," *Nanophotonics,* vol. 13, no. 4, pp. 387-417, 2024.
2. Z. Fusco, K. Catchpole, and F. J. Beck, "Investigation of the mechanisms of plasmon-mediated photocatalysis: synergistic contribution of near-field and charge transfer effects," *Journal of Materials Chemistry C,* vol. 10, no. 19, pp. 7511-7524, 2022.
3. Z. Fusco, A. Riaz, C. David, and F. J. Beck, "Cathodoluminescence Spectroscopy of Complex Dendritic Au Architectures for Application in Plasmon□Mediated Photocatalysis and as SERS Substrates," *Advanced Materials Interfaces,* vol. 10, no. 3, p. 2202236, 2023.

Complex modulation of light in polarization and space using laser-written multi-plane light conversion

Oussama Korichi[1], Markus Hiekkamäki[1], and Robert Fickler[1]

[1] Photonics Laboratory, Physics Unit, Tampere University, Tampere FI-33720, Finland

[*]Corresponding author: oussama.korichi@tuni.fi

Multi-plane Light Conversion (MPLC) [1-3] is a technique for performing complex transformations of a set of light modes by propagating them through multiple phase modulations thereby transforming them into desired set of output modes. The phase modulation profiles are optimized using a wavefront matching algorithm [4] and are typically implemented with a spatial light modulator. However, practical limitations of MPLC - such as losses and lack of polarization control - necessitate new implementation approaches.

Recent studies have demonstrated that full-vectorial mode conversion can be achieved using the MPLC concept by replacing phase masks with locally varying birefringent metasurfaces, which a fabricated using demanding nanofabrication methods [5]. Hence, having more compact designs with similarly high efficiency, great flexibility in polarization control and no need for cleanroom facilities are desirable.

In this work, we present a novel method for MPLC systems based on low-loss, transmissive silica slides, which locally modulate the polarization of light with high resolution resulting in a global modulation of the full vectorial light field, i.e. its polarization, phase, and amplitude. The design of the required modulation planes is found via a numerical optimization algorithm based on Jones formalism, wavefront matching, and gradient descent. The modulations are physically implemented as waveplates with a fixed retardance but locally varying orientation angles of the optical axis.

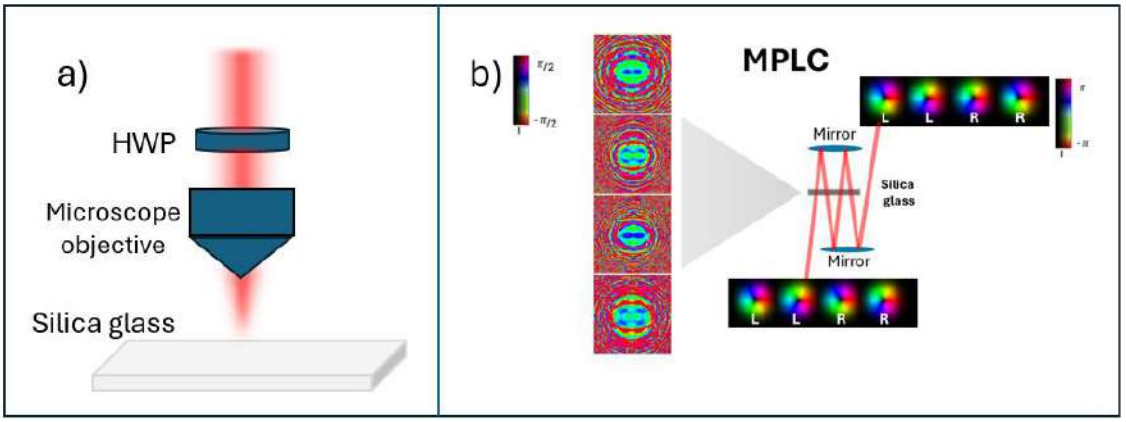


Fig. 1: (a) Simplified sketch of the laser direct writing technique used to fabricate waveplates with self-assembled nanogratings in silica glass. (b) Sketch of the MPLC implementation of 4 half waveplates with locally varying orientation angles of the optical axis. An example of a Single-photon CNOT gate is illustrated using circular polarization as a control qubit for the manipulation of OAM modes with masks

To fabricate the desired spatially varying waveplates with high resolution and low loss, we utilized the technique of direct laser writing of self-assembled nanogratings in silica glass [6], see Fig. 1 a). Through optimizing the

fabrication parameters such as writing speed, laser power, and repetition rate, we obtained a spatial resolution of around 1-2 μm per pixel and a efficiency of around 90% transmission per plane, which in principle can be as high as 99% [7]. Instead of realizing the MPLC system along a straight beam line with individual consecutive silica slides, we implement the scheme in a compact multi-pass design. A sketch of the setup can be found in Fig. 1b). In this scheme, all modulations are laser-written into one slide, with each modulation plane being 2x2 mm in size and separated from adjacent modulations by 2 mm. We note that owing to the high modulation resolution of our polarization modulation technique the sizes of the modulation can be further downscaled in future implementations enabling a smaller footprint of the MPLC system.

In our experimental demonstrations, we use an 808 nm laser beam that is simultaneously shaped in polarization and spatial structure through four modulations planes each acting as a complex structured half-waveplate (retardance of π). As a first test, we demonstrate the ability of our scheme in advanced full-field modulations and implement a mode de-multiplexer capable of decomposing the input light field into its spatial modes as well as polarization components. We further show that our scheme allows a unitary operation between sets of orthogonal spatial vector beams, i.e. spatial modes with transversely varying polarizations structure, and leverage this to demonstrate high-dimensional quantum gates. Finally, we show the ability of a polarization dependent spatial mode manipulation, which can be utilized as a single-photon controlled-NOT operation in which the two qubits are encoded in the two degrees of freedom of polarization and spatial structure.

In summary, our laser-written realization of an MPLC system shows great promise in advanced modulations of the full vectorial transverse spatial structure of light, thanks to it high-resolution and high-efficiency. I also enable increasingly complex modulation tasks possibly also including the modulation of the light's frequency components, which would result in the modulation of all degrees of freedom of light using an efficient single modulation scheme. As such, we are confident that using laser-written MPLC modulation schemes, will be a beneficial tool in various fields such as optical communications, imaging, sensing, and laser processing.

References

1. Labroille, G., Denolle, B., Jian, P., Genevaux, P., Treps, N., & Morizur, J. F. (2014). Efficient and mode selective spatial mode multiplexer based on multi-plane light conversion. Optics express, 22(13), 15599-15607.
2. Fontaine, N. K., Ryf, R., Chen, H., Neilson, D. T., Kim, K., & Carpenter, J. (2019). Laguerre-Gaussian mode sorter. Nature communications, 10(1), 1865.
3. Brandt, F., Hiekkamäki, M., Bouchard, F., Huber, M., & Fickler, R. (2020). High-dimensional quantum gates using full-field spatial modes of photons. Optica, 7(2), 98-107.
4. Sakamaki, Y., Saida, T., Hashimoto, T., & Takahashi, H. (2007). New optical waveguide design based on wavefront matching method. Journal of lightwave technology, 25(11), 3511-3518.
5. Soma, G., Komatsu, K., Nakano, Y., & Tanemura, T. (2024). Complete vectorial optical mode converter using multi-layer metasurface. *arXiv preprint arXiv:2401.05127*.
6. Beresna, M., Gecevičius, M., & Kazansky, P. G. (2014). Ultrafast laser direct writing and nanostructuring in transparent materials. Advances in Optics and Photonics, 6(3), 293-339.
7. Sakakura, M., Lei, Y., Wang, L., Yu, Y. H., & Kazansky, P. G. (2020). Ultralow-loss geometric phase and polarization shaping by ultrafast laser writing in silica glass. Light: Science & Applications, 9(1), 15.

Integration technique of micro- and nano-lasers on Si by epitaxial growth using III-V-on-Si wafer

T. Fujii, K. Takeda, E. Kanno, T. Tsurugaya, T. Sato, and S. Matsuo

NTT Device Technology Labs, NTT Corporation, Atsugi-shi, Kanagawa, Japan
*corresponding author: takuro.fujii@ntt.com

Abstract: We present our integration technique of low-power-consumption III-V lasers on Si. We use a directly bonded III-V membrane on SiO_2 as an integration platform and perform epitaxial growth to fabricate a buried-heterostructure. Based on this technique, direct modulation of membrane lasers and photonic crystal lasers with low-power consumption are reported.

The explosive increase in traffic within data centers requires the micro- and nano-lasers that are suitable for short-range optical transmission. A key to achieving high speed and low power consumption is the use of directly modulated lasers (DMLs) with strong optical confinement in a small active region. The power consumption of the laser is proportional to the volume of the active region, and the modulation speed of the DML is limited by a relaxation oscillation frequency determined by the optical confinement factor. To satisfy both, we have developed a heterogeneous integration technique of III-V nanostructure on SiO_2/Si platform using epitaxial growth after direct bonding of III-V membrane structure on Si with SiO_2 interlayer [1]. The III-V membrane structure (typically 250 nm thick) sandwiched between low-index materials provides strong vertical (*y*-direction) optical confinement. The active region is buried with InP by epitaxial regrowth to provide high lateral (*x*-direction) optical confinement. We have fabricated the lateral p-i-n structure by ion implantation of Si and thermal diffusion of Zn into the InP layer, allowing the lasers to be driven by lateral current injection.

Figure 1 shows the schematic drawings of the membrane lasers on Si. Longitudinal (*z*-direction) optical confinement was achieved by a surface grating fabricated by etching InP channel waveguides. For data transmission over a few kilometers, we developed a distributed feedback (DFB) laser with an active region of ~100 μm long, as mW-class optical output power is required. The membrane laser array demonstrated 2 km transmission of 56 Gbps (28 Gbaud) PAM-4 signals at 50°C with an energy cost of ~645 fJ/bit [2]. On the other hand, the energy cost required for chip-to-chip optical communication is much lower, while the optical output power required is lower. Therefore, we have also developed distributed Bragg reflector (DBR) membrane lasers. A high reflectivity of the DBR mirror enabled us to reduce the active region length to 5-μm. The laser was directly modulated by a 25.8 Gbit/s non-return-to-zero (NRZ) signal with a bias current of 600 μA and a bias voltage of 1.63 V, resulting in an energy cost of 38 fJ/bit [3].

To further reduce power consumption, we have also developed photonic crystal lasers that provide ultra-high optical confinement in an active region. Figure 2 shows a schematic drawing of the two types of photonic crystal lasers. The two-dimensional (2D) photonic crystal laser uses photonic crystals to increase both *z*- and *x*-directional optical confinement. The size of the buried heterostructure was only $2.5 \times 0.3 \times 0.15$ μm^3. We achieved 10 Gbit/s NRZ direct modulation with a bias current of 60 μA and a bias voltage of 1.71 V, corresponding to an energy cost of 10.3 fJ/bit. An on-chip optical link between a 2D photonic crystal laser and a membrane photodiode via the integrated Si waveguide has been demonstrated [4]. We have also demonstrated a 1D photonic crystal laser. The laser uses the photonic crystal only for *z*-direction confinement, and a deep-etched rib waveguide structure provides very high *x*-direction optical confinement. The optical output can be obtained

from the InP channel waveguide, which is directly butt-jointed to the active region. Thanks to the high optical confinement factor, we have achieved 40 Gbit/s NRZ direct modulation with a bias current of 180 μA [5]. We believe that these micro- and nano-lasers and their integration technology will pave the way for the fabrication of short-range optical links for the data centers of the future.

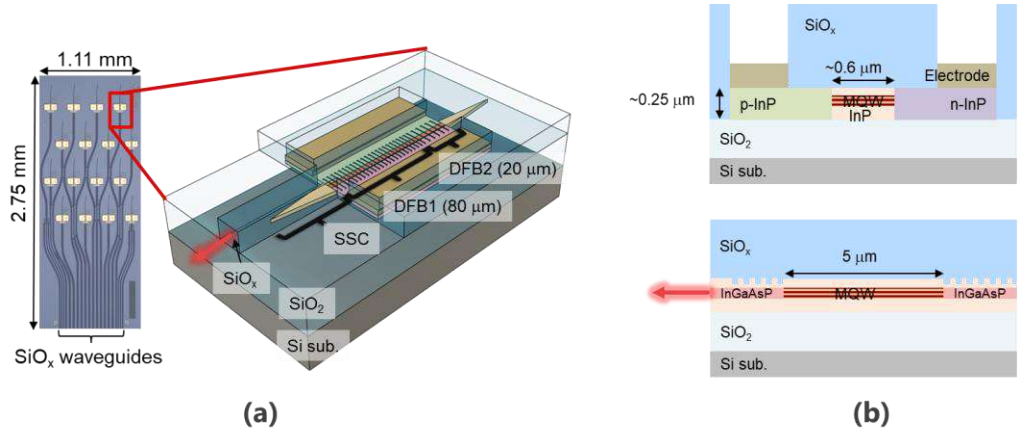


Fig. 1 Schematic drawing of 16-ch membrane DFB lasers (a), and short-cavity membrane DBR laser on Si

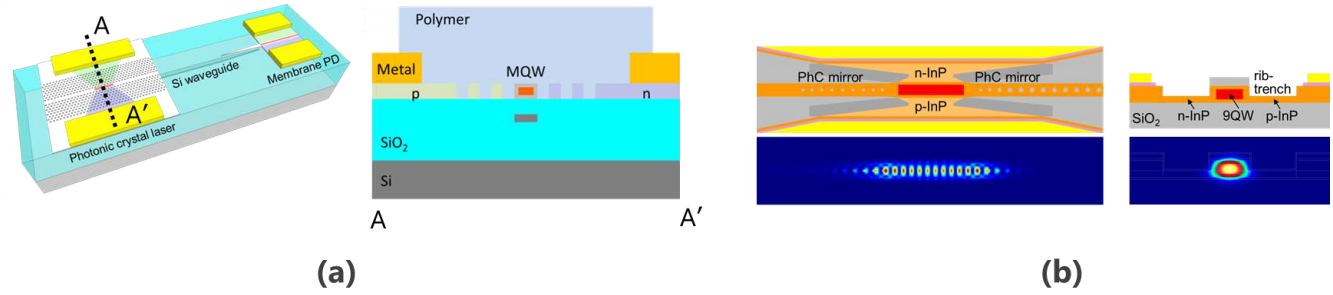


Fig. 2 Schematic drawing of 2D photonics crystal laser and optical link via Si waveguide (a), and 1D photonic crystal laser.

References

1. T. Fujii et al, “Epitaxial growth of InP to bury directly bonded thin active layer on SiO_2/Si substrate for fabricating distributed feedback lasers on silicon”, IET Optoelectronics, Vol. 9, No. 4, 151–157, 2014.
2. T. Fujii et al, “16 × 112 Gbps directly modulated membrane laser array for co-packaged interconnects”, Optics Express, Vol. 32, No. 16, 27614–27623, 2024.
3. E. Kannno et al, “Low-power-consumption modulation of short-cavity DBR laser on SiO_2/Si substrate”, Optics Express, Vol. 32, No. 8, 14746–14754, 2024.
4. K. Takeda et al., “Optical links on silicon photonic chips using ultralow-power consumption photonic-crystal lasers” Optics Express, Vol. 29, No. 16, 26082–26092, 2021.
5. T. Tsurugaya et al, “40-Gbps direct modulation of electrically driven 1D photonic-crystal nanolaser on SiO_2/Si”, in CLEO 2024, SW3H.6.

New materials for metaoptics from infrared (IR) to deep-ultraviolet (DUV)

Zeng Wang[1]

[1] Institute of Materials Research and Engineering (IMRE), Agency for Science, Technology and Research (A*STAR), Singapore
Corresponding author: wang_zeng@imre.a-star.edu.sg

Abstract: Our study investigates novel materials for metaoptics applications across a broad spectral range, from infrared (IR) to deep-ultraviolet (DUV). We focus on cavity-enhanced excitonic metaoptics utilizing two-dimensional transition metal dichalcogenides (TMDCs) for visible and IR applications, showcasing significant advancements in tunability, absorption enhancement, and excitonic effect control. These findings underscore the potential of TMDCs as a transformative platform for optoelectronic devices. Additionally, we demonstrate the use of aluminum nitride (AlN) for DUV metaoptics, highlighting its suitability for applications in this challenging spectral regime. Together, these developments pave the way for next-generation metaoptical systems with enhanced performance across diverse wavelengths.

Excitons in two-dimensional transition metal dichalcogenides (TMDCs) are quasiparticles formed by electron-hole pairs, exhibiting strong binding energies due to reduced dielectric screening and enhanced Coulomb interactions within their atomically thin layers, which give rise to exceptional optical characteristics for advanced optoelectronic devices[1]. Leveraging these unique excitonic properties, we first demonstrate atomically thin metaoptics operating in the visible spectrum by harnessing the robust excitonic resonances in MoS_2 multilayers[2]. Next, we extend the utility of MoS_2 to the infrared (IR) range by implementing cavity enhancement and subtle doping for band engineering, enabling strong absorption in the IR spectrum and broadening the scope of MoS_2-based metaoptical applications. Furthermore, we achieve a significant enhancement in exciton-trion conversion in atomically thin WS_2, facilitated by an optical cavity and electrical modulation. This results in a 40% modulation in reflectivity for excitons and 7% for trions at room temperature, paving the way for tunable, ultra-compact optical devices based on two-dimensional materials[3]. Finally, we report a breakthrough in metalens technology using aluminum nitride (AlN), achieving sub-200 nm resolution in the deep-ultraviolet (DUV) range. This advancement highlights the potential of AlN-based metalenses for high-resolution DUV applications, such as lithography and bio-spectroscopy, where precision at the nanoscale is critical. Collectively, these findings underscore the versatility of TMDCs and AlN in advancing metaoptics across a wide spectral range, from visible to DUV, with significant implications for next-generation optical technologies.

References

1. Mak, K. F., & Shan, J. (2016). Photonics and optoelectronics of 2D semiconductor transition metal dichalcogenides. Nature Photonics, 10(4), 216-226.
2. Wang, Z., Yuan, G., Yang, M., Chai, J., Steve Wu, Q. Y., Wang, T., ... & Teng, J. (2020). Exciton-enabled meta-optics in two-dimensional transition metal dichalcogenides. Nano Letters, 20(11), 7964-7972.
3. Wang, Z., Sebek, M., Liang, X., Elbanna, A., Nemati, A., Zhang, N., ... & Teng, J. (2023). Greatly Enhanced Resonant Exciton‐trion Conversion in Electrically Modulated Atomically Thin WS2 at Room Temperature. Advanced Materials, 2302248.

Probing nanoscale light-matter interactions with fast electrons and near-field optical probes

C. Maciel-Escudero[1*], E. Malic[1], R. Hillenbrand[2,3], and J. Aizpurua[3,4]

[1]Department of Physics, Philipps-Universität Marburg, Germany
[2]CIC nanoGUNE BRTA, Tolosa Hiribidea, 20018, Donostia-San Sebastián, Spain
[3]IKERBASQUE, Basque Foundation for Science, Bilbao, 48011, Spain
[4]Donostia International Physics Center (DIPC), Paseo Manuel de Lardizabal 4, 20018 Donostia-San Sebastián, Spain
[*]corresponding author: macieles@uni-marburg.de

Abstract: We investigate the excitation and probing of hybrid light-matter electromagnetic modes (polaritons) using a fast electron beam and a metallic tip. By employing these localized probes, we are able to excite and spatially map strongly coupled systems that are challenging to access using conventional far-field optical spectroscopy techniques.

Polaritons are hybrid light-matter electromagnetic waves that arise from the coupling between photons and dipolar excitations in matter, such as phonons in polar materials, plasmons in metals, or excitons in semiconductors [1]. The strong field confinement induced by polaritons can produce electromagnetic fields that are orders of magnitude more intense than the incident field, leading to a variety of applications. A major challenge of polariton physics, however, stems from their large momentum mismatch with free-space photons, thus preventing their excitation using conventional far-field optical techniques. Among the variety of techniques to circumvent this limitation, scattering-type scanning near-field optical microscopy (s-SNOM) and electron energy-loss spectroscopy (EELS) in scanning transmission electron microscopy (STEM) are unique techniques for probing polaritons due to their ability to access their near field and provide information not accessible in the far field [2,3].

In this work, we present a numerical and experimental analysis of the excitation of polaritons in the near field using a fast electron beam or a metallic tip. Specifically, we analyze the near-field spectra of various polaritonic systems being excited by the localized probes (Fig. 1). We demonstrate that a metallic tip is capable of probing the hybrid polaritonic modes of single hexagonal boron nitride (h-BN) nanorods partially covered with a molecular layer [4]. Additionally, we theoretically describe how fast electrons couple to polaritonic modes in h-BN and the metallic delafossite oxide $PdCoO_2$ by analyzing their electron energy-loss spectra. Due to the optical anisotropy of h-BN and $PdCoO_2$, we show that the excitation of the polariton modes is strongly related to the electron velocity and highly dependent on the angle between the electron beam trajectory and the anisotropy axis [5]. Finally, we discuss the excitation of optical anapoles and anapole-exciton hybrids in transition metal dichalcogenides (TMDCs) tungsten disulfide (WS_2) nanodisks using EELS. We identify prominent dips in the electron energy loss (EEL) spectra of the WS_2 disks and demonstrate that they are associated with the excitation of various optical anapoles supported in the nanodisk [6].

The optical properties of semiconducting TMDC are dominated by excitons, which are electron-hole pairs that are tightly bound by Coulomb interactions. Excitons exhibit a large oscillator strength making TMDCs appealing for exploring exciton-polaritons. Thus, in the final section of the presentation, we briefly discuss recent findings on excitons in TMDC coupled to both photons and phonons, leading to the formation of a

three-body quasiparticle known as phonoritons [7].

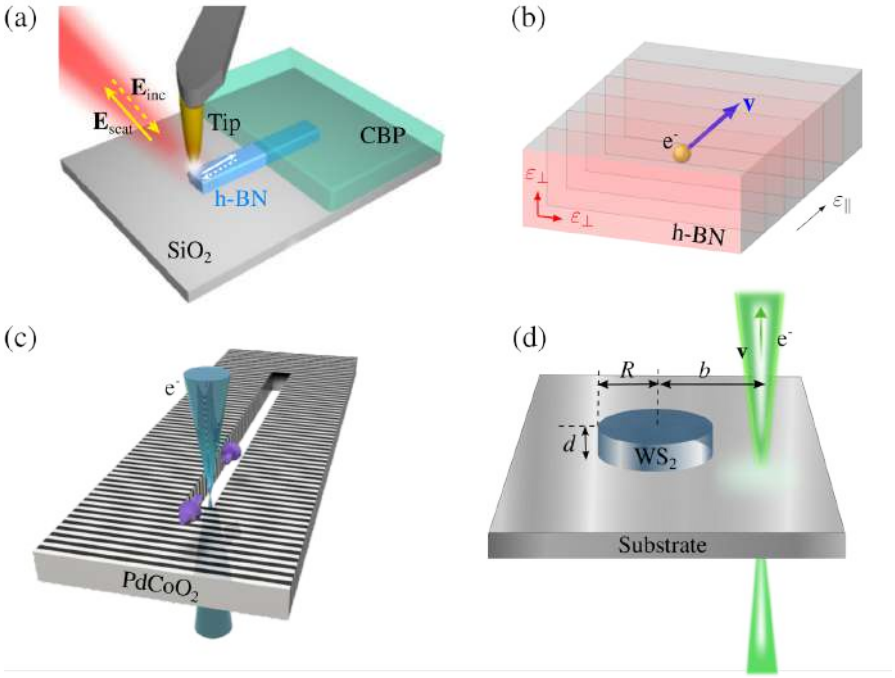


Figure 1: Sketch of the systems under study. (a) A s-SNOM tip (yellow conical structure) is positioned on top of the molecules-free part of an h-BN antenna (blue rod) half-covered by a molecular layer (green structure). (b) A fast electron traveling through h-BN. The red planes illustrate the stacking of single h-BN layers along the optical axis. (c) A fast electron passing through a $PdCoO_2$ slit, close to one of the sidewalls. (d) A WS_2 nanodisk (blue cylinder) excited by a focused electron beam (green ray) traveling along the vertical direction at a distance *b* with respect to the nanodisk center.

In summary, our results offer insights into the use of near-field spectroscopic techniques for exciting, probing, and mapping strongly coupled systems that cannot be easily accessed by far-field optical spectroscopy techniques.

References

1. Basov, D. N., et al. “Polaritons in van der Waals materials”, Science, Vol. 354, 2016.
2. Hillenbrand, R., et al. “Visible-to-THz near-field nanoscopy”, Nat. Rev. Mater., 2025.
3. García de Abajo, F. J. “Optical excitations in electron microscopy”, Rev. Mod. Phys., Vol. 82, No. 1, 209–275, 2010.
4. Dolado, I., et al. “Remote near-field spectroscopy of vibrational strong coupling between organic molecules and phononic nanoresonators”, Nat. Commun., Vol. 13, No. 1, 6850, 2022.
5. Maciel-Escudero, C., et al. “Probing and steering bulk and surface phonon polaritons in uniaxial materials using fast electrons: Hexagonal boron nitride”, Phys. Rev. B, Vol. 102, No. 11, 2020.
6. Maciel-Escudero, C., et al. “Probing optical anapoles with fast electron beams”, Nat. Commun., Vol. 14, No. 1, 8478, 2023.
7. Li, D., et al. “Hybridized exciton-photon-phonon states in a transition metal dichalcogenide van der Waals heterostructure microcavity”. Phys. Re. Lett., Vol. 128, No. 8, 087401, 2022.

Automated Design of One-dimensional Photonic Crystals for Surface Wave Enhanced Chiroptical Spectroscopy

Jonathan Barolak[1*], Francesco Michelotti[2], Agostino Occhicone[2], Marco Finazzi[3], Paolo Biagioni[3], and Giovanni Pellegrini[1]

[1]Dipartimento di Fisica, Via Bassi 6, Università di Degli Studi di Pavia, Pavia, Italy
[2]Dipartimento di Scienze di Base ed Applicate per l'Ingegneria, SAPIENZA Università di Roma, Via A. Scarpa 16, 00161 Roma, Italy
[3]Dipartimento di Fisica, Politecnico di Milano, Piazza Leonardo Da Vinci 32, 20133, Milano, Italy
[*]corresponding author: jonathanjames.barolak@unipv.it

Abstract:
In this work, a multi-objective, automated design process is presented to optimize one-dimensional photonic crystals for the purpose of exciting planar fields with enhanced optical chirality over a range of wavelengths. Using this procedure, we show the surprising result that designs composed of polymeric materials offer significantly superior performance.

Summary:

Chiral molecules are abundantly found in natural and engineered materials. Biomolecules ranging from DNA to synthetically engineered drugs are well known for having a chiroptical property where a molecule and its mirror image are non-superimposable. Despite having identical chemical composition, the effects of different handed chiral biomolecules (called enantiomers) can differ drastically, making the determination of the handedness crucial [1]. Optical sensors are prolifically used to determine the handedness of enantiomers, through circular dichroism with circularly polarized light, due to their non-invasive behavior and rapid detection schemes. However, due to the small size of typical biomolecules and the relatively large diffraction-limited focal spot of lasers in the optical regime, standard circular dichroism measurements require measuring a relatively large density of chiral biomolecules limiting its applicability. To match the increased demand by the pharmaceutical industry for improved chiroptical sensors, scientists have turned to the field of nanophotonics.

Optical sensors with enhanced chirality rely on the idea that confined light improves the interaction of circularly polarized light with chiral matter. That is to say that confining light containing both vertical and horizontal polarization states simultaneously with the appropriate phase offset will increase the optical chirality coefficient and thus improve the sensitivity of the optical sensor to the presence of chiral matter. A plethora of nanophotonic solutions have proposed such sensors which utilize different physical mechanisms to achieve the increased optical chirality such as SPP, metasurfaces, Bloch Surface Waves (BSWs), etc. [2]. However, it remains a challenge to produce a sensor with an enhanced optical chirality that is uniform over a large surface area which can be easily switched from left- to right- hand circularly polarized light. Additionally, to move from chiral sensing to chiral spectroscopy, the sensor must have a large and relatively even optical chirality enhancement over a significant operating wavelength range. In the past few years, exciting BSW inside specially designed one-dimensional photonic crystals (1DPCs) has shown a route towards developing such a nanophotonic solution [3]. However, designs remain elusive which allow for large, uniform chiroptical enhancements over extended wavelength ranges. To accommodate for these challenging design criteria, in this work we propose the use of an automated design process to optimize the structure of a 1DPC which can generate broadband, superchiral light. We use this optimization method to investigate the effect of using polymeric materials on the sensor's performance.

To generate superchiral light in 1DPCs, one must design structures to excited BSW which confine light to the surface of the 1DPC due to the presence of a photonic band gap and being in total internal reflection. While previous methods have generated such structures by hand tuning a 'defect' layer at the termination of a 1DPC, to support the superchiral enhancement over a large wavelength range an automated design can be very beneficial.

For our automated design, we used a multi-objective genetic optimizer, specifically a two-objective genetic optimization algorithm called “non-dominant sorting genetic algorithm”. In this optimization scheme, we have the freedom to choose the parameters to optimize and the evaluation functions to evaluate the individuals of the population. One example optimization is shown in figure 1, where the parameters of the evaluation were the thicknesses of each layer in the multi-layer dielectric stack for both a standard design, using SiO_2 and Ta_2O_5 for the layers, and a polymeric platform that used polystyrene and cellulose as the materials for the layers. The criteria used to evaluate the individuals were the maximum optical chirality calculated at 400 nm and 500 nm. As can be seen in figure 1b, a Pareto front forms at the end of the optimization, representing all the optimal designs and possible tradeoffs between the two evaluation criteria.

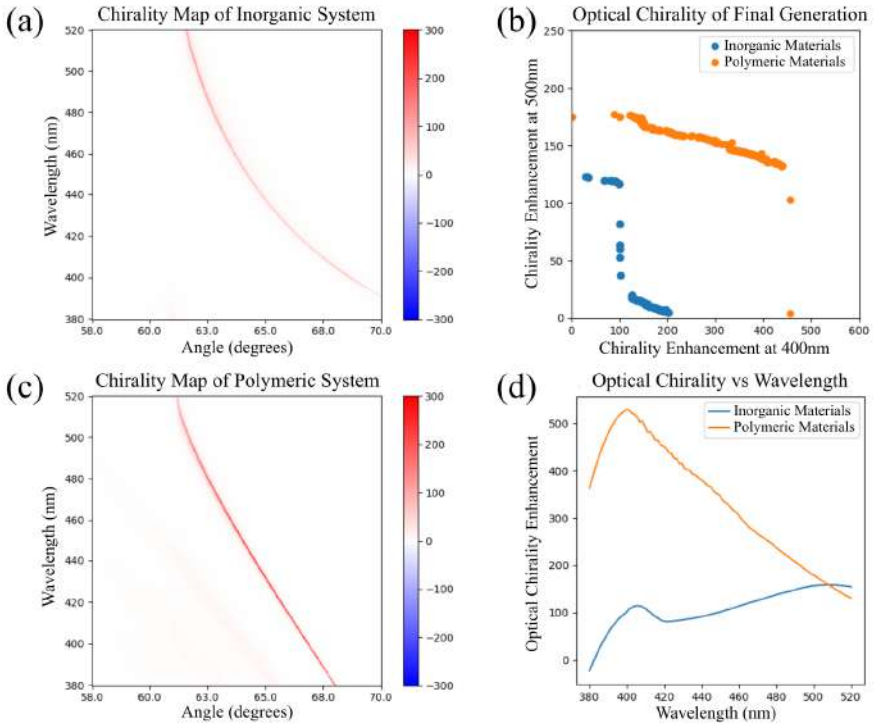


Figure 1: a) and c) show the optical chirality enhancement as a function of wavelength and incident angle for an optimized 1DPC design with inorganic and polymeric materials, respectively. b) shows the Pareto front from the last geneation of the optimizations. d) shows the optical chirality enhancement as a function of wavelength to visually compare the results of the inorganic and polymeric designs.

The optical chirality enhancement factor was calculated as a function of wavelength and incident angle to compare the two designs, as shown in figure 1a and 1c. The demonstrated possibility to employ low-index polymeric platforms without compromising but rather improving the performance of the device in terms of optical chirality enhancement paves the way to a class of low-cost and recyclable chips for optical chiral sensing.

Acknowledgments: This work was partially funded by the European Union-Next Generation EU-PNRR-M4C2, investimento 1.1- “Fondo PRIN 2022”-“SPIRAL – Lossless surface waves for chiral spectroscopy” – id 2022WFM5MZ – CUP F53D23001140001.

References:

1. P.-H. Chuong, L. A. Nguyen, Hua He., “Chiral Drugs. An Overview,” *Int. J Biomed Sci.*, vol. 2, no. 2, pp. 85–100, Sep. 2006
2. M. L. Solomon, A. A. E. Saleh, L. V. Poulikakos, J. M. Abendroth, L. F. Tadesse, and J. A. Dionne, “Nanophotonic Platforms for Chiral Sensing and Separation,” *Acc. Chem. Res.*, vol. 53, no. 3, pp. 588–598, Mar. 2020
3. G. Pellegrini, M. Finazzi, M. Celebrano, L. Duò, and P. Biagioni, “Chiral surface waves for enhanced circular dichroism,” *Phys. Rev. B*, vol. 95, no. 24, p. 241402, Jun. 2017

Exponentially Sensitive Lattices: Pseudospectral Scalings

Ioannis Kiorpelidis[1*] and Konstantinos G. Makris[1,2]
[1]Institute of Electronic Structure and Laser (IESL), FORTH, Heraklion 71110, Greece
[2]ITCP, Department of Physics, University of Crete, Heraklion 71003, Greece
Corresponding author: gkiorpelidis@iesl.forth.gr

Abstract: We examine the sensitivity of non-Hermitian photonic lattices with asymmetric couplings by exploring the underlying pseudospectral scalings. We show that the extreme lattice nonnormality leads to exponentially sensitive eigenvalue spectra and power growth, suggesting a route for designing ultrasensitive systems without relying on exceptional points.

A key characteristic of non-Hermitian Hamiltonians $\mathbf{H}$ is the presence of exceptional points (EPs), unique singularities where both eigenvalues and eigenvectors coalesce [1]. Systems operating near an EP exhibit strong sensitivity to perturbations [2], enabling applications such as microresonators [3] and gyroscopes [4], to name a few. Alternatively, ultrasensitivity appears in lattices with asymmetric couplings, which typically display the non-Hermitian skin effect (NHSE) [5], i.e., the localization of all eigenstates at one lattice end. It has been shown that the spectra of such asymmetric lattices exhibit exponential sensitivity with respect to the lattice size when the boundary conditions are varied, and this sensitivity has been linked to the lattice's topological properties [6]. In this work, we analyze the exponential sensitivity of asymmetric lattices by applying the pseudospectra theory [7]. We show that not only the spectra, but also the growth of an initial state exhibit exponential variations with N, and that this effect is due to the extreme lattice nonnormality [8].

Our results are schematically illustrated in Fig. 1. We investigate the Hatano-Nelson model [see Fig. 1(a1)], where the Hamiltonian matrix is given by $\mathbf{H} = \sum_{j=1}^{N-1} \left(t_L |j\rangle\langle j+1| + t_R |j+1\rangle\langle j|\right)$, with $|j\rangle$ denoting the state localized at lattice site j, t_R as the hopping amplitude for transitions from site $j+1$ to j, and t_L as the hopping amplitude in the reverse direction. We note here that $\mathbf{H}$ is a nonnormal matrix, meaning that $[\mathbf{H}, \mathbf{H}^\dagger] \neq 0$, which leads to nontrivial amplification effects as discussed in the following. The evolution of the amplitude ψ_n at each lattice site $n = 1, \ldots, N$ is

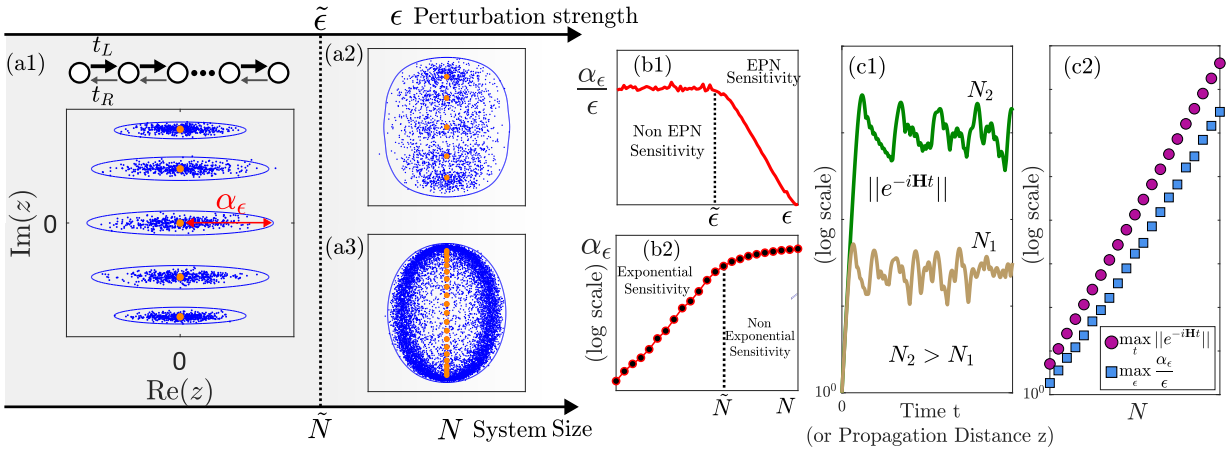


Figure 1: Spectrum (orange dots) and pseudospectrum (blue dots) of $\mathbf{A} = \in i\mathbf{H}$, for (a1) small N and ϵ, (a2) large ϵ and moderate N, and (a3) large N and moderate ϵ. (b1), (b2) Variation of the pseudospectral abscissa α_ϵ with (b1) ϵ and (b2) N. (c1) Time (or spatial) growth dynamics for light propagation through cavities (or waveguides) and for two lattice sizes $N_2 > N_1$. (c2) Power growth and Kreiss constant scaling with N.

described by $\dot{\boldsymbol{\psi}} = \mathbf{H}\boldsymbol{\psi}$, where dot denotes differentiation with respect to time t (distance z) for light propagation in cavities (in waveguides) and $\boldsymbol{\psi} = [\psi_1, ..., \psi_N]^T$. Figure 1(a1) shows the spectrum σ (orange dots) and the pseudospectrum σ_ϵ (blue dots) of the matrix $\mathbf{A} = \in i\mathbf{H}$. The pseudospectrum [7] is defined as the set with the eigenvalues of perturbed matrices $\mathbf{A}+\mathbf{E}$, with $\mathbf{E}$ being a complex random matrix with 2-norm less than ϵ. Note that for small N and ϵ, the pseudospectrum consists of N disks centered at the N eigenvalues of $\mathbf{A}$ [Fig. 1(a1)]. As the perturbation strength ϵ [Fig. 1(a2)] or lattice size N [Fig. 1(a3)] increases, the pseudospectrum extends into the complex plane. The variation of the pseudospectrum size — measured by the pseudospectral abscissa $\alpha_\epsilon = \max \Re[\sigma_\epsilon(\mathbf{A})]$ — with ϵ and N is shown in Figs. 1(b1) and 1(b2) respectively. We observe that α_ϵ scales as a power law (exponentially) beyond a (up to a) critical perturbation strength $\tilde{\epsilon}$ (critical lattice size $\tilde{N}$). These results show the extreme sensitivity of the spectrum to perturbations of the Hamiltonian.

We will now illustrate the sensitivity of the HN model in relation to power growth dynamics. We note first that the evolution of an initial state $\boldsymbol{\psi}_0$ is given by $\boldsymbol{\psi}(t) = e^{-i\mathbf{H}t}\boldsymbol{\psi}_0$, where the matrix $e^{-i\mathbf{H}t}$ is refereed as the propagator or evolution matrix [7]. A measure of the power dynamics is the maximum growth at any given time t, defined as $\max_{\boldsymbol{\psi}_0} \frac{||\boldsymbol{\psi}(t)||}{||\boldsymbol{\psi}_0||}$, which corresponds to the 2-norm of the propagator matrix $||e^{-i\mathbf{H}t}||$. Figure 1(c1) shows the time evolution of the propagator norm for two lattice sizes $N_{1,2}$. Amplification is observed ($||e^{-i\mathbf{H}t}|| > 1$), which results from the nonnormality of $\mathbf{H}$. Additionally, the maximum amplification $\max_t ||e^{-i\mathbf{H}t}||$ increases with N. Specifically, $\max_t ||e^{-i\mathbf{H}t}||$ scales exponentially with N, as illustrated in Fig. 1(c2), highlighting the exponential sensitivity of the growth. Furthermore, the pseudospectrum offers an estimate of this growth through the Kreiss matrix theorem, which states that $\max_t \left\|e^{-i\mathbf{H}t}\right\| \geq \max_{\epsilon>0} \frac{\alpha_\epsilon}{\epsilon}$. The right-hand side of this inequality, known as the Kreiss constant, is shown in Fig. 1(c2) to also increase exponentially with N.

In conclusion, we have conducted a scaling analysis of pseudospectra in exponentially sensitive lattices. Considering recent experimental realizations of such asymmetric optical lattices in non-Hermitian photonics [5], our results could facilitate the efficient design of ultrasensitive devices without the need for higher-order exceptional points.

This project was funded by the European Research Council (ERC-Consolidator) under grant agreement No. 101045135 (Beyond Anderson).

References

1. Berry, M. V., "Physics of Nonhermitian Degeneracies," *Czech. J. Phys.*, Vol. 54, No. 10, pp. 1039–1047, 2004.

2. Wiersig, J., "Sensors operating at exceptional points: General theory," *Phys. Rev. A*, Vol. 93, No. 3, pp. 033809, 2016.

3. Hodaei, H., Hassan, A.U., Wittek, S., Garcia-Gracia, H., El-Ganainy, R., Christodoulides, D.N. and Khajavikhan, M., "Enhanced sensitivity at higher-order exceptional points," *Nature*, Vol. 548, No. 7666, pp. 187-191, 2017.

4. Hokmabadi, M. P., Schumer, A., Christodoulides, D. N., and Khajavikhan, M., "Non-Hermitian ring laser gyroscopes with enhanced Sagnac sensitivity," *Nature*, Vol. 576, No. 7785, pp. 70-74, 2019.

5. Weidemann, S., et al. "Topological funneling of light," *Science*, Vol. 368, No. 6488, pp. 311-314,, 2020.

6. Budich, J. C. and Bergholtz, E. J., "Non-Hermitian topological sensors," *Phys. Rev. Lett.*, Vol. 125, No. 18, pp. 180403, 2020.

7. Trefethen, L. N. and Embree, M., *Spectra and Pseudospectra*, Princeton University Press, 2005.

8. Kiorpelidis, I. and Makris, K. G., "Scaling of pseudospectra in exponentially sensitive lattices", arXiv:2409.12036 (2024).

Subwavelength Metamaterials for High-Performance Power and Modal Control in Silicon Photonics

R. Fernández de Cabo[1], A. Sánchez-Sánchez[2], Y. Yang[3], D. Melati[3], C. Alonso-Ramos[3], P. Cheben[4], A. V. Velasco[5], and D. González-Andrade[2*]

[1]Institute of Photonic Sciences (ICFO), Castelldefels 08860, Spain
[2]Telecommunication Research Institute (TELMA), Universidad de Málaga, E.T.S.I. Telecomunicación, Málaga 29010, Spain
[3]Centre de Nanosciences et de Nanotechnologies, CNRS, Université Paris-Saclay, Palaiseau 91120, France
[4]National Research Council Canada, 1200 Montreal Road, Bldg. M50, Ottawa K1A 0R6, Canada
[5]Instituto de Óptica Daza de Valdés, Consejo Superior de Investigaciones Científicas (CSIC), Madrid 28004, Spain
[*]corresponding author: dga@ic.uma.es

Abstract: Subwavelength metamaterials have significantly driven silicon photonic integrated circuits since their inception in 2006. In this invited talk, we will provide an overview of our latest findings, with particular emphasis on the development of high-performance building blocks engineered for highly-efficient modal manipulation and power distribution.

Patterning of a subwavelength grating (SWG) onto a silicon wire with periods between 100–150 nm provides unprecedented control of the flow of light in photonic chips [1]. Such periodic structures suppress diffractive effects and behave as homogeneous metamaterials whose optical properties (refractive index, dispersion profile and anisotropy) can be tailored by modifying geometrical design parameters [2]. This versatility has enabled the demonstration of several ground-breaking devices as well as the enhancement of nonlinear effects in silicon nanophotonic waveguides [3-5], exhibiting remarkable prospects for overcoming the prevailing challenges of photonic integration, including suboptimal performance of key building blocks such as power splitters and mode converters. In this invited contribution, we will review our recent advances in the development of subwavelength-engineered metamaterial devices for high-performance power and modal control.

Firstly, we present two distinct architectures based on symmetric Y-junctions and SWG metamaterials for efficient power division: i) a Y-junction with SWG nanostructured stem and arms [6], and ii) a Y-junction assisted by SWG metamaterials between the arms [7]. The first power splitter has been optimized for two different lithographic resolutions, namely 50 and 100 nm. Experimental measurements demonstrated excess loss <0.3 dB for the fundamental transverse-electric (TE_0) mode considering the high-resolution process (i.e., 50 nm) and <0.5 dB for the 100 nm resolution scenario. The device is also robust against fabrication errors of up to ±10 nm. The second power splitter (i.e., SWG-assisted Y-junction) achieves one of the broadest operating bandwidths reported to date. Full 3D finite-difference time-domain (FDTD) simulations predict excess losses <0.2 dB for TE_0 and TE_1 modes over an ultra-broad bandwidth of 700 nm, while the TM_0 power splitting also yields a remarkably broad bandwidth of 500 nm. Experimental results confirm the broadband operation of the device for all three modes within a bandwidth of 250 nm (limited by our measurement setup).

Regarding modal management, we propose a novel mode converter based on two symmetric Y-junctions that are connected in a back-to-back arrangement through their arms. These arms include SWG metamaterials, enabling precise control of mode exchange to broaden the operating bandwidth [8]. The device was rigorously

simulated using a 3D FDTD solver, predicting insertion loss (IL) <0.3 dB and extinction ratio (ER) >20 dB over the wavelength range of 1472 – 1622 nm. The fabricated device shows an excellent agreement with simulation results, showcasing IL <0.5 dB and ER >18 dB over 150 nm bandwidth. To the best of our knowledge, this device achieves one of the broadest experimentally demonstrated bandwidths for TE_0-TE_2 conversion.

These devices underscore the significant potential of SWG metamaterials in advancing the next generation of high-performance functional building blocks. Notably, the power splitters and mode converter presented in this work are particularly suited for state-of-the-art on-chip applications, including programmable photonics, multi-target spectroscopy, nonlinear photonics, and quantum computing.

Acknowledgements: This work has been funded by the Spanish Ministry of Science and Innovation (PID2020-115353RA-I00); the Spanish State Research Agency and the European Social Fund Plus under grant PRE2021-096954, and the European Union's Horizon Europe research and innovation program under Grant Agreement No. 101135523 (SYMPHONY) and Marie Sklodowska-Curie grant No. 101062518. This publication is part of the grant RYC2023-045670-I funded by MICIU/AEI/10.13039/501100011033 and by ESF+. Views and opinions expressed are however those of the authors only and do not necessarily reflect those of the EU. The EU cannot be held responsible for them. This work was done in part within the C2N micro nanotechnologies platforms and partly supported by the RENATECH network and the General Council of Essonne.

References

1. Cheben, P., Halir, R., Schmid, J. H., Atwater, H. A. and Smith, D. "Subwavelength integrated photonics," Nature, Vol. 560, No. 7720, 565–572, 2018.
2. Cheben, P., Schmid, J. H., Halir, R., Luque-González, J. M., Wangüemert-Pérez, J. G., Melati, D. and Alonso-Ramos, C., "Recent advances in metamaterial integrated photonics," Adv. Opt. Photonics, Vol. 15, No. 4, 1033–1105, 2023.
3. Luque-González, J. M., Sánchez-Postigo, A., Hadij-ElHouati, A., Ortega-Moñux, A., Wangüemert-Pérez, J. G., Schmid, J. H., Cheben, P., Molina-Fernández, I. and Halir, R., "A review of silicon subwavelength gratings: building break-through devices with anisotropic metamaterials," Nanophotonics, Vol. 10, No. 11, 2765–2797, 2021.
4. González-Andrade, D., Nuño-Ruano, P., Zhang, J., Cassan, E., Marris-Morini, D., Vivien, L., Lanzillotti-Kimura, N. D. and Alonso-Ramos, C., "Enhancing stimulated Brillouin scattering in suspended silicon waveguides through subwavelength nanostructuration," Opt. Mater. Express, Vol. 14, No. 11, 2562–2577, 2024.
5. Dinh, T. T. D., Le Roux, X., Montesinos-Ballester, M., Lafforgue, C., Zhang, J., González-Andrade, D., Melati, D., Bouville, D., Benedikovic, D., Cheben, P., Cassan, E., Marris-Morini, D., Vivien, L. and Alonso-Ramos, C., "Dispersive wave control enable by silicon metamaterial waveguides," arXiv:2201.06516, 2022.
6. Fernández de Cabo, R., Vilas, J., Cheben, P., V. Velasco, A. and González-Andrade, D., "Experimental characterization of an ultra-broadband dual-mode symmetric Y-junction based on metamaterial waveguides," Opt. Laser Technol., Vol. 157, 108742, 2023.
7. Fernández de Cabo, R., González-Andrade, D., Cheben, P. and V. Velasco, A., "Extending the spectral operation of multimode and polarization-independent power spitters through subwavelength nanotechnology," Opt. Laser Technol., Vol. 181, 111921, 2025.
8. Fernández de Cabo, R., Sánchez-Sánchez, A., Yang, Y., Melati, D., Alonso-Ramos, C., V. Velasco, A. and González-Andrade, D., "Broadband mode exchanger based on subwavelength Y-junctions," Nanophotonics, Vol. 13, No. 21, 4037–4045, 2024.

Unconventional Phenomena from Space-Time Modulation of Dispersive Media

C. Rizza[1*], A. Contestabile[1], M. A. Vincenti[2], G. Castaldi[3], M. Scalora[4], and V. Galdi[3]

[1]University of L'Aquila, Department of Physical and Chemical Sciences, I-67100 L'Aquila, Italy

[2]University of Brescia, Department of Information Engineering, I-25123 Brescia, Italy

[3]University of Sannio, Department of Engineering, Fields & Waves Lab, Benevento, I-82100, Italy

[4]Aviation and Missile Center, U.S. Army CCDC, Redstone Arsenal, Alabama 35898-5000, USA

Corresponding author: carlo.rizza@univaq.it

Abstract: We investigate a time-vaying dispersive interface. We discuss unconventional effects supported by this system: the generation of frequencies at the system's natural resonances, the direct excitation of confined wave modes, and unusual spin-dependent effects.

We investigate a time-varying, dispersive interface that features Lorentzian dispersion, whose parameters are modulated in time. Specifically, we consider a time-varying interface, i.e., a dispersive dielectric layer of thickness L (with $L << \lambda$, and λ denoting a characteristic wavelength) sandwiched between two homogeneous, stationary and non-dispersive half-spaces (see Fig.1(a)). We investigate transverse-electric (TE) modes of the kind $Re[E(z,t)e^{ik_x x}]\hat{e}_y$, where k_x is the conserved transverse wavenumber, $\hat{e}_y$ is an y-directed unit vector. The interface lies on the plane $z = 0$, and its response can be modeled in terms of sheet transition conditions, i.e., $\Delta E = 0, \quad \Delta H = \frac{dP(t)}{dt}$, with $\Delta G = G(z = 0^+, t) \in G(z = 0^-, t)$ $(G = E, H)$ and where H, and P denote the z-component of magnetic field and the y-component of the surface polarization, respectively. We assume that any field component G is of the form $Re[G(z,t)e^{ik_x x}]$. The dynamics of the surface polarization is governed by

$$\frac{d^2P(t)}{dt^2} + \gamma\frac{dP(t)}{dt} + \omega_0^2 P(t) = \varepsilon_0 L\omega_p^2(t)E(0,t), \tag{1}$$

where ε_0 is the vacuum permittivity, ω_0 and γ are the resonance frequency and damping parameter, respectively (constant over time), whereas ω_p is the time-varying plasma frequency. In the scenario where the system exhibits a temporal boundary (i.e., the plasma frequency undergoes a sudden switch), we derive analytical solutions (see [1] for details). In the stationary scenario (constant plasma frequency), the metasurface can support discrete bound modes that propagate along the x-axis and exhibit evanescent decay along the z-axis. In the standard scenario, these bound modes cannot be directly excited by a propagating wave, whereas the temporal boundary activates the natural resonance modes supported by the interface when interacting with an incident wave packet.

As a relevant example, we consider a scenario where a wave packet impinges at oblique incidence on the time-varying interface. Specifically, we assume that the incident electric field is $E_i = E_0 e^{-(t-t_0)^2/\sigma^2 - i\omega_i(t-t_0)}$ at a reference plane $z = \in L_1 \simeq \in 35c/\omega_0$, with $t_0 \simeq 53/\omega_0$, $\sigma = 4/\omega_0$, $\omega_i = 2.5\omega_0$, and $k_x \simeq 1.44\omega_0/c$ (corresponding to an incidence angle of 24° from the z-axis at the carrier angular frequency ω_i). Moreover, we set $\omega_p^2 = \omega_0^2 A(t)$, where $A(t) = A_1 + (A_2 \in A_1)U(t)$ [$U(t)$ is the standard unit step function] with $A_2 = 1.2$, $A_1 = 1$, $L = 0.16c/\omega_0$, $\varepsilon_L = 2$, $\varepsilon_R = 1$, and $\gamma = 5 \cdot 10^{-3}\omega_0$. Results are reported in Fig.1. Fig.1(b) shows the normalized electric-field map associated with bound resonant modes excited through a propagating wave

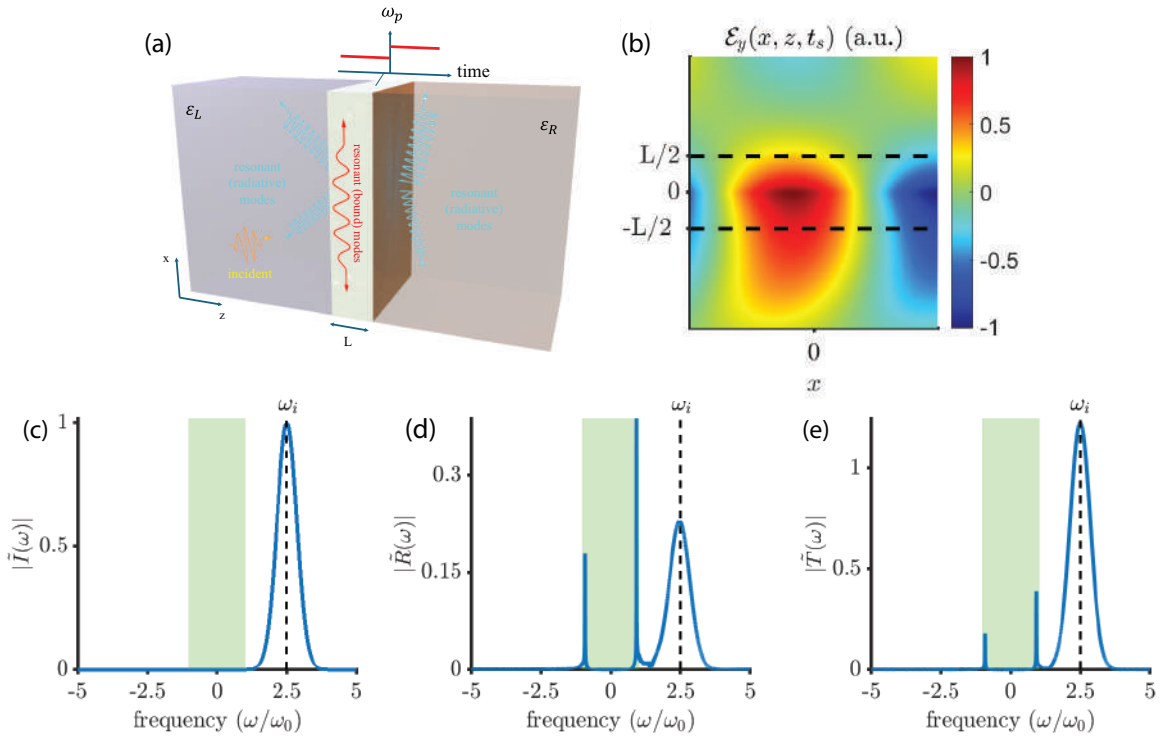


Figure 1: (a) A time-varying dispersive interface is represented as a thin dielectric layer between two homogeneous, stationary half-spaces with relative permittivities ε_L and ε_R. (b) Normalized electric-field map at time $t_s \simeq 61/\omega_0$, showing the excitation of a bound resonant mode (surface wave). The horizontal dashed lines delimit the thin layer interfaces at $z = \pm L/2$. Normalized spectra of the incident (c), reflected (d), and transmitted (e) wave packets; the dashed vertical lines represent the carrier frequency of the incident field. All spectra are normalized with respect to the peak value of incident one.

packet. Figures 1(c), 1(d) and 1(e) display the incident, reflected and transmitted spectra, respectively. For the chosen parameters, the resonant modes are bound since their eigenfrequencies lie within the evanescent spectral range (highlighted with green shading in Fig.1). Therefore, the excitation of the natural resonance modes induced by the temporal boundary enables the coupling of a propagating wave packet with bound modes (surface waves), without the need for any spatial subwavelength structuring or extended time-periodic modulations. The occurrence of this phenomenon is also confirmed through full-wave simulations (see [1] for additional details).

Finally, we note that a time-varying spatial interface can support other intriguing effects due to the unconventional interaction of the electromagnetic field with both temporal and spatial boundaries. In our presentation, we will also discuss these effects, highlighting their unexpected polarization dependence.

Research was supported by the European Union - NextGenerationEU under the Italian Ministry of University and Research (MUR) National Innovation Ecosystem grant ECS00000041 - VITALITY - CUP E13C22001060006.

References

1. C. Rizza, M. A. Vincenti, G. Castaldi, A. Contestabile, V. Galdi and M. Scalora, “Harnessing the natural resonances of time-varying dispersive interfaces”, *Phys. Rev. Lett.* 133(18), 186902, 2024.

Engineered Single-Photon Emitters in Materials for Integrated Quantum Photonics

A. Senichev[1,2*], Z. O. Martin[1,2], S. Peana[1,2], P. Maan[1,2], A. Kryvobok[1,2], D. Sychev[1,2], A. S. Lagutchev[1,2], A. Boltasseva[1,2], and V. M. Shalaev[1,2]

[1]School of Electrical and Computer Engineering, Birck Nanotechnology Center and Purdue Quantum Science and Engineering Institute, Purdue University, West Lafayette, IN 47906, USA
[2]The Quantum Science Center (QSC), a National Quantum Information Science Research Center of the U.S. Department of Energy (DOE), Oak Ridge, TN 37931, USA
[*]corresponding author: senichev@purdue.edu

Abstract: We report our progress on single-photon emitters in materials for integrated quantum photonics, focusing on silicon nitride (SiN) and aluminum nitride (AlN) photonic platforms. We study emitter characteristics, defect origins, and site-controlled fabrication. We also discuss coupling emitters with resonant nanostructures to enhance emission efficiency.

Quantum photonic technologies rely on scalable and coherent single-photon sources integrated into photonic circuits. Silicon photonics, including SiN, enables photonic integrated circuits (PICs) compatible with CMOS processes. SiN is particularly advantageous, offering ultralow-loss waveguides, broad spectral transparency, and fabrication processes compatible with standard semiconductor foundries.

Our work demonstrated single-photon emitters in silicon nitride (SiN) fabricated via high-density plasma chemical vapor deposition (HDPCVD) [1] and plasma-enhanced chemical vapor deposition (PECVD), followed by thermal annealing. Emitters form primarily at interfaces between SiN and silicon dioxide (SiO_2), exhibiting stable room-temperature emission with high brightness, single-photon purity, and linear polarization [1]. These characteristics of single-photon sources are suitable for quantum key distribution protocols employing polarization encoding [2]. At cryogenic temperatures, emitters exhibit distinct zero-phonon lines (ZPL) around 548 nm [3]. Current research involves resonant excitation studies aimed at achieving lifetime-limited linewidths of ZPL essential for indistinguishable photon generation.

We integrated single-photon emitters into SiN waveguides [4] and proposed a scalable, site-controlled fabrication method compatible with semiconductor foundry processes [5]. Comprehensive materials characterization and modeling were used to identify potential defect complexes responsible for single-photon emission. Metasurfaces and resonant nanostructures enhance emission rates and enable efficient generation and control of quantum states of light [6]. We recently demonstrated bullseye cavity-enhanced single-photon emission in SiN, achieving improved emission rates and directionality. Future studies will focus on further optimizing bullseye and other resonant cavity structures to enhance the performance and integration potential of SiN-based single-photon emitters.

We also explored single-photon emitters in AlN, a promising platform for integrated quantum photonics, using heavy-ion irradiation followed by thermal annealing [7]. The emitter density showed a direct correlation with ion fluence. Zirconium (Zr) ions were used to generate theoretically predicted optically addressable spin defects. Ongoing studies aim to experimentally verify their spin-related optical properties.

In summary, our work highlights the capabilities of SiN and AlN with single-photon emitters for integrated quantum photonics, addressing emitter formation, defect origins, and scalable integration with photonic circuits and resonant nanostructures. Future research will focus on deepening our understanding of emitter photophysical properties and improving integration methods with nanophotonic components.

This work was supported in part by the U.S. Department of Energy (DOE), Office of Science through the Quantum Science Center (QSC), a National Quantum Information Science Research Center and Air Force Office of Scientific Research AFOSR under award FA9550-22-1-0372. The sample preparation, material, and optical characterization were supported by National Science Foundation (NSF) grant 2015025-ECCS and Purdue's Elmore ECE Emerging Frontiers Center "The Crossroads of Quantum and AI."

References

[1] A. Senichev, Z. O. Martin, S. Peana, D. Sychev, X. Xu, A. S. Lagutchev, A. Boltasseva, and V. M. Shalaev, Room-temperature single-photon emitters in silicon nitride, Sci Adv **7**, FW4I.6 (2021).

[2] A. Senichev et al., Single-Photon Source in Silicon Nitride Photonics for Quantum Key Distribution, Frontiers in Optics + Laser Science 2024 (FiO, LS) (2024), Paper LW6F.4 LW6F.4 (2024).

[3] Z. O. Martin, A. Senichev, S. Peana, B. J. Lawrie, A. S. Lagutchev, A. Boltasseva, and V. M. Shalaev, Photophysics of Intrinsic Single-Photon Emitters in Silicon Nitride at Low Temperatures, Adv Quantum Technol. 2300099, 2300099 (2023).

[4] A. Senichev, S. Peana, Z. O. Martin, O. Yesilyurt, D. Sychev, A. S. Lagutchev, A. Boltasseva, and V. M. Shalaev, Silicon Nitride Waveguides with Intrinsic Single-Photon Emitters for Integrated Quantum Photonics, ACS Photonics 9, 3357 (2022).

[5] S. Peana et al., Site-Controlled SiN/SiO2 Single Photon Sources Coupled to Silicon Nitride Integrated Photonics, CLEO: Fundamental Science FM2F.3 (2024).

[6] A. I. Kuznetsov et al., Roadmap for Optical Metasurfaces, ACS Photonics 11, 816 (2024).

[7] A. Senichev, Z. O. Martin, Y. Wang, O. M. Matthiessen, A. Lagutchev, H. Htoon, A. Boltasseva, and V. M. Shalaev, Quantum emitters in aluminum nitride induced by heavy ion irradiation, APL Quantum 1, 36103 (2024).

Optical fiber microstructure devices inscribed by femtosecond laser and their sensing applications

Xuewen Shu[1] (Invited)

[1]Wuhan National Laboratory for Optoelectronics, Huazhong University of Science and Technology, Wuhan, 430074, China
*corresponding author: xshu@hust.edu.cn

Abstract: We hereby report our recent progress in the fabrication of various in-fiber microstructures, such as interferometers and gratings, by using femtosecond laser, and then discuss their sensing applications.

Optical fiber-based devices have witnessed remarkable advancements in recent decades, driven by their extensive applications in diverse fields such as optical communication, environmental monitoring, and biomedical sensing. Among the various techniques for fabricating fiber-optic devices, femtosecond laser inscription has emerged as a powerful and versatile approach. Femtosecond lasers, characterized by ultra-short pulse durations and high peak powers, enable precise and minimally invasive modification of the fiber's internal structure. This unique property allows for the creation of in-fiber microstructures, including interferometers and gratings. Fiber interferometers are crucial for measuring physical parameters such as temperature, strain, and pressure with high sensitivity. Fiber gratings, on the other hand, have revolutionized the field of fiber-optic sensing by providing wavelength-selective reflection or transmission. Despite the significant progress made in this area, there remains a continuous need to develop novel fabrication methods and explore new applications. In this context, our research focuses on leveraging femtosecond laser inscription to create a variety of in-fiber microstructures. We hereby report our recent progress in the fabrication of these microstructures and then discuss their potential sensing applications. This work not only contributes to the fundamental understanding of femtosecond laser-fiber interactions but also holds great promise for the development of next-generation fiber-optic sensing technologies.

Figure 1 shows a specific example of a complex fiber grating structure fabricated by femtosecond laser. The fabricated grating is a kind of small-period long-period fiber gratings (SP-LPFGs) [1-3]. We use a femtosecond laser to inscribe a series of annuli inside the fiber, forming the grating. The annuli grating structure enables flexible adjustment of the transverse refractive index (RI) modulation region and the duty cycle along the axial direction. Additionally, the annular tracks effectively enlarge the scale of the RI modulation region. As a result, greater resonance intensity can be achieved with fewer cycles. Therefore, the gratings produced using this method can be relatively short, with a length of around 3 mm. By inscribing multiple adjacent annuli in each period, we can improve the axial duty cycle of the grating. We studied the effects of different annuli radii and the number of annuli in each period on the transmission spectrum. It was found that the SP-LPFG with annuli radii of 3μm and 4 annuli in each period exhibits distinct Bragg resonance dips and cladding mode resonance dips in its transmission spectrum. We also tested the RI and temperature sensing performances of the grating. The results show that the cladding mode resonances are sensitive to both RI and temperature, while the Bragg resonances are only sensitive to temperature. This indicates that the annular SP-LPFGs can be used for the simultaneous sensing of RI and temperature.

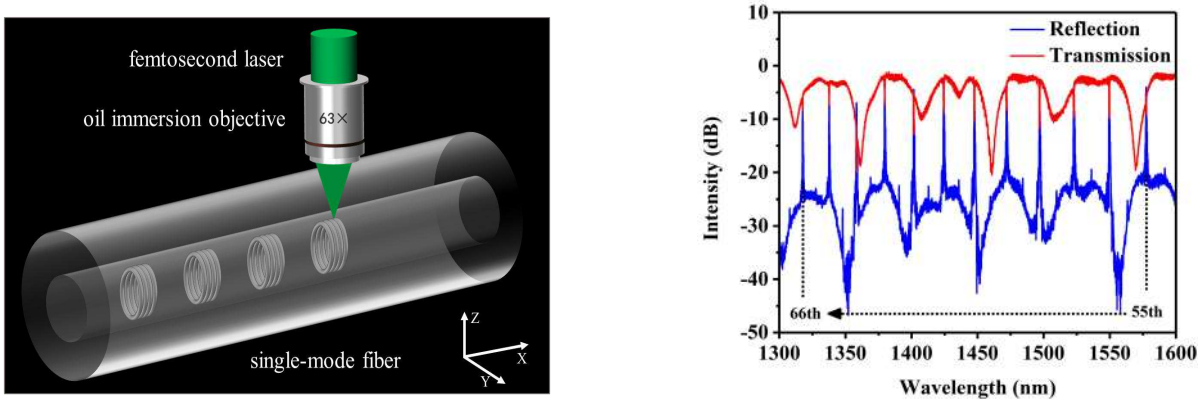


Fig. 1. (a) Schematic diagram of the annular SP-LPFG fabrication, (b) Reflection and transmission spectra of the annular SP-LPFG with annuli radii of 3μm and 4 annuli in each period.

Acknowledgments: This work was supported by the National Key Research and Development Program of China (2023YFE0105800) and National Natural Science Foundation of China (62275093).

References

1. Liu, Y., J. Cai, H. Liu and X. Shu, "Femtosecond laser direct writing annular small-period long-period fiber gratings for simultaneous refractive index and temperature sensing," Opt. Lett., Vol. 49, 4194 – 4197, 2024.
2. Kong, Y., X. Shu and Z. Xu, "A novel in-fiber helical long period grating with small period inscribed by femtosecond laser for twist sensing with comprehensive performance," IEEE Trans. Instrum. Meas., Vol. 73, 9507015, 1 - 15, 2024.
3. Liu, H., J. Cai, L. Zhang and X. Shu, “Femtosecond laser inscribed small-period long-period fiber grating coated with a nano-assembled polyelectrolyte film for independent sensing of ammonia gas and temperature”, Sens. Actuators B - Chem., Vol. 423, 136860, 2025.

Multi-temperature modeling of hot-carrier dynamics in photonic metastructures

A. Schirato[1,2], G. Crotti[1] and G. Della Valle[1*]

[1]Politecnico di Milano - Dipartimento di Fisica, Milan, Italy
[2]Rice University - Department of Physics and Astronomy, Houston, Texas, USA
[*]corresponding author: giuseppe.dellavalle@polimi.it

Abstract: Photonic metastructures can be made reconfigurable and switchable via hot carriers photogenerated by fs-laser pulses. Here we show how multi-temperature modeling of hot-carrier dynamics can be exploited to design active metastructures made of plasmonic or dielectric media for a variety of applications, including ultrafast all-optical modulation and pulsed photocatalysis.

Hot carriers represent an unparalleled channel for manipulating photoinduced phenomena on the picosecond timescale [1]. When combined with the flexibility of photonic metastructures in moulding electromagnetic fields [2], the control of light-matter interactions can be achieved in subwavelength regions and at unprecedented speed, offering renewed degrees of freedom for ultrafast nanophotonics. An open challenge remains the active reconfiguration of the optical response of metasurfaces, whose properties are most often irreversibly fixed at the fabrication stage.

Here, we review our recent results in the field of dynamic metaphotonics. In particular, we show how multi-temperature modeling of the hot carrier dynamics combined with a semiclassical description of light-matter interactions at the nanoscale offers a versatile tool for the study and design of reconfigurable and switchable photonic metastructures based on noble metals, degenerate semiconductors and even all-dielectric media. Our modeling, based on a rate-equation approach, is validated by quantitative comparison with transient absorption spectroscopy measurements in a variety of configurations and for different functionalities, including ultrafast giant light amplitude modulation, dichroism and birefringence modulation [3], ultrafast diffraction management, and the tailoring of the modulation dynamics [4].

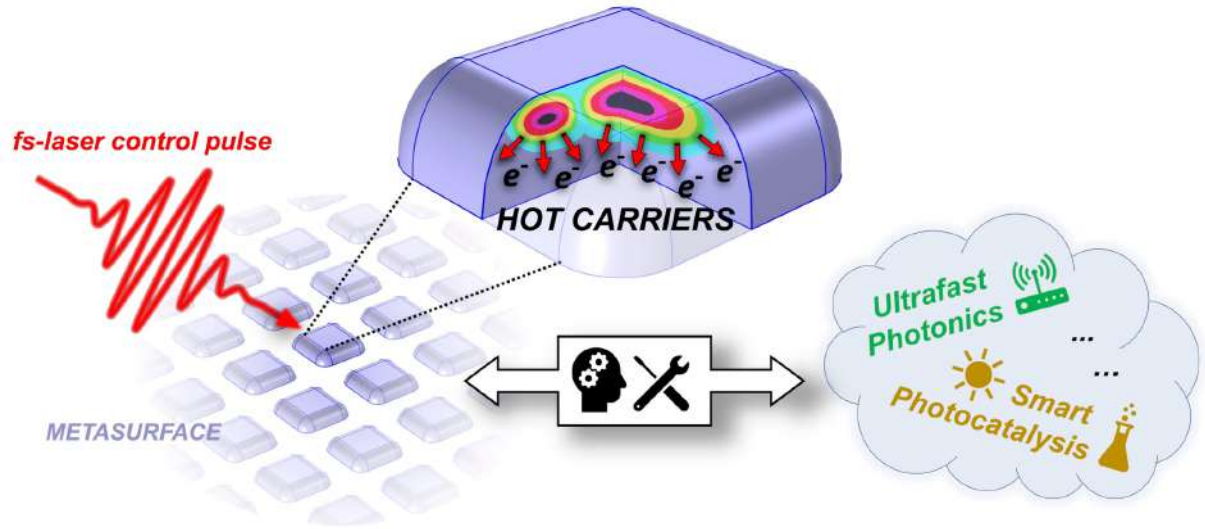


Figure 1: Sketch of the photoinduced hot-carrier spatial inhomogeneities at the metaatom level to be engineered for novel advanced functionalities, with applications ranging from ultrafast photonics to pulsed photocatalysis.

Moreover, shaping at the deep sub-wavelength scale the spatio-temporal evolution of nonequilibrium carriers can be crucial to disclose unprecedented possibilities for ultrafast all-optical modulation of light [5] and even to envisage new advanced functionalities (Fig. 1). For example, when carrier injection takes place besides internal relaxation, metallic metastructures provide the energy needed for photocatalytic conversion, and photoexcited nanoparticles can promote/alter chemical reactions, both through thermal and non-thermal pathways. In this context, we propose an original approach extending the model previously introduced, to investigate numerically with spatial, temporal, and energy resolution the ultrafast dynamics and ensuing effects of hot carriers across plasmonic nanostructures in the presence of adsorbed molecules resonantly accepting energy from photoexcited electrons [6].

This work is part of the Italian MUR-PRIN2022 HOTMETA project funded by the European Union - Next Generation EU, Mission 4 Component 1 CUP D53D2300229 0006. We also acknowledge the EU's Horizon 2020 METAFAST project under grant agreement no. 899673, and EU's Horizon Europe research and innovation programme under the MSCA PATHWAYS HORIZON-MSCA-2023-PF-GF no. 101153856.

References

1. Brongersma, M., Halas, N. J., Nordlander, P. "Plasmon-induced hot carrier science and technology," Nat. Nanotech., Vol. 10, 25-34, 2015.
2. Yu, N., Capasso, F. "Flat optics with designer metasurfaces," Nat. Mater., Vol. 13, 139, 2014.
3. Crotti, G., Akturk, M., Schirato, A., Vinel, V., Trifonov, A.A., Buchvarov, I.C., Neshev, D.N., Proietti Zaccaria, R., Laporta, P., Lemaître, A., Leo, G., Cerullo, G., Maiuri, M., and Della Valle, G. "Giant ultrafast dichroism and birefringence with active nonlocal metasurfaces," Light: Science & Applications, Vol. 13, 204, 2024.
4. Schirato, A., Maiuri, M., Cerullo, G., and Della Valle, G. "Ultrafast hot electron dynamics in plasmonic nanostructures: experiments, modelling, design," Nanophotonics, Vol. 12, No. 1, 1-28, 2023.
5. Crotti, G., Schirato, A., Pashina, O., Sergaeva, O., Petrov, M., De Angelis, C., and Della Valle, G. "Ultrafast switching of a metasurface quasi-bound state in the continuum via transient optical symmetry breaking," Light: Science & Applications, *just accepted*.
6. Schirato, A., Sanders, S., Proietti Zaccaria, R., Nordlander, P., Della Valle, G., and Alabastri, A. "Quantifying ultrafast energy transfer from plasmonic hot carriers for pulsed photocatalysis on nanostructures," ACS Nano, Vol. 18, 18933−18947, 2024.

F. Hemmann[1,2], V. Glauser[1], U. Steiner[1,2], and M. Saba[1,2*]
[1]Adolphe Merkle Institute, University of Fribourg, CH-1700 Fribourg, Switzerland
[1]NCCR Bio-inspired Materials, University of Fribourg, CH-1700 Fribourg, Switzerland
Corresponding author: matthias.saba@unifr.ch

Abstract: Complete photonic band gaps are frequency domains where light cannot enter a material from any angle. Here, we generate network-like photonic crystals with varying coordination numbers and correlate their photonic density of states to local and global statistical quantifiers that characterize the structural variantions.

Photonic band gap (PBG) materials have attracted attention for the past decades thanks to their ability to control the scattering and localization of light. A (complete) PBG is a frequency domain where destructive interference prevents propagating light states inside a photonic material [1]. Incident light within the PBG is totally reflected. Inside the material, PBGs can lead to light localization and altered spontaneous emission properties [2], [3]. These stunning phenomena have driven past research to understand and tailor the emergence of PBGs. For periodic photonic materials, so-called photonic crystals, the mechanism giving rise to a PBG can be understood using Bloch theory. In analogy to electronic crystals' valence and conduction bands, the Bloch modes in the *dielectric* bands below a gap concentrate light in the dielectric region, in contrast to the *air* bands above, giving rise to a frequency separation [1]. Several properties facilitate this separation, such as interpenetrating network topologies of high and low index and if the product of the fill fraction and the refractive index is the same in both domains.

While these general rules also apply to disordered materials [4], [5], the emergence of PBGs becomes more challenging to model and interpret. Nevertheless, some general theoretical observations have been made. Large PBGs are favored by a high statistical homogeneity on large length scales, which is maximal for so-called stealthy-hyperuniform systems [6]–[9]. In a hyperuniform medium, density fluctuations are absent in the limit of infinite-length scales, and thus long wavelength scattering is suppressed. Furthermore, tetravalent and trivalent networks of diamond-like and gyroid-like simplices create the most significant known PBGs. This superiority is traced back to the equality of all bond angles and lengths through the concept of local self-uniformity [10].

Here, we investigate the isolated effects of different kinds of disorders on the PBG of 3D photonic networks. We generate a statistical population of disordered networks with a well-established WWW Metropolis Monte Carlo algorithm [11], [12]. We vary the character and strength of the disorder by varying the initial network configuration, the weight of the bending energy β compared to the bond length energy in the associated Keating energy, and the temperature profile governing the network's evolution. We correlate the isolated effects of disorder in bond angles and lengths to the networks' PBG using a principle component analysis. Disorder in the photonic networks can be quantified using a plethora of order metrics that measure primarily short- or long-range order. The bond angle and bond length standard deviations σ_{angle} and σ_{length} of 420 networks generated at seven different values of β are presented in fig. 1. We additionally use the networks' pore size distribution [13], clustering, anisotropy, and local bond order [14]. We study the influence of the different order metrics on the photonic density of states simulated for rod-connected networks.

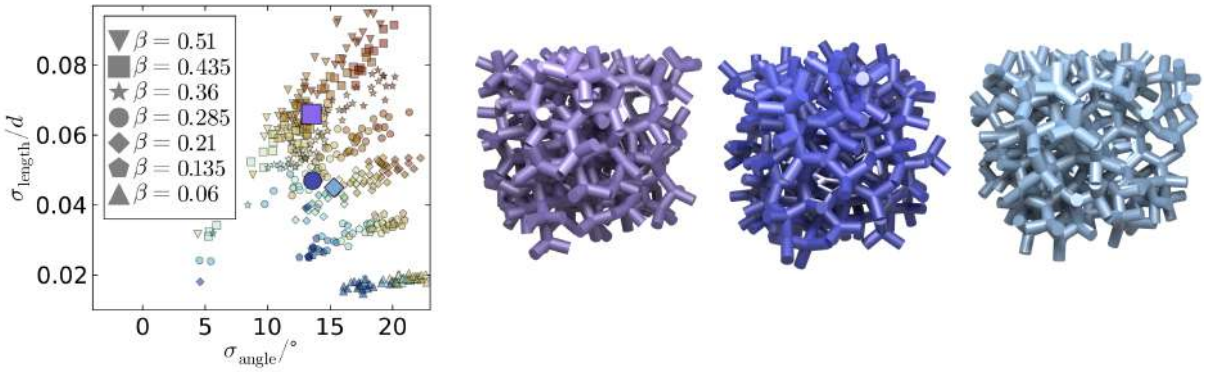


Figure 1: Bond length standard deviation σ_{length} as a function of the bond angle σ_{angle} for disordered networks generated at different values of the β parameter that tunes the bending energy contribution to the Keating energy. The color indicates the maximal temperature of the temperature profile to generate the disordered networks, ranging from $T_{\text{max}} = 0.06$ (dark blue) to $T_{\text{max}} = 0.27$ (dark red). Three exemplary networks are highlighted and depicted on the right.

References

[1] J. Joannopoulos, S. Johnson, J. Winn, and R. Meade, *Photonic crystals: Molding the flow of light (Second Edition)*, English (US). United States: Princeton University Press, Oct. 2011.

[2] E. Yablonovitch, "Inhibited Spontaneous Emission in Solid-State Physics and Electronics," en, *Physical Review Letters*, vol. 58, no. 20, pp. 2059–2062, May 1987.

[3] S. John, "Strong localization of photons in certain disordered dielectric superlattices," *Physical Review Letters*, vol. 58, no. 23, pp. 2486–2489, Jun. 1987.

[4] K. Edagawa, S. Kanoko, and M. Notomi, "Photonic amorphous diamond structure with a 3d photonic band gap," *Phys. Rev. Lett.*, vol. 100, p. 013 901, 1 Jan. 2008.

[5] S. F. Liew, J.-K. Yang, H. Noh, C. F. Schreck, E. R. Dufresne, C. S. O'Hern, and H. Cao, "Photonic band gaps in three-dimensional network structures with short-range order," *Physical Review A*, vol. 84, no. 6, p. 063 818, Dec. 7, 2011, Publisher: American Physical Society.

[6] S. Torquato and F. H. Stillinger, "Local density fluctuations, hyperuniformity, and order metrics," *Phys. Rev. E*, vol. 68, p. 041 113, 4 Oct. 2003.

[7] M. Florescu, S. Torquato, and P. J. Steinhardt, "Designer disordered materials with large, complete photonic band gaps," *Proceedings of the National Academy of Sciences*, vol. 106, no. 49, pp. 20 658–20 663, Dec. 8, 2009.

[8] S. Torquato, "Hyperuniform states of matter," *Physics Reports*, vol. 745, pp. 1–95, 2018, Hyperuniform States of Matter.

[9] L. Siedentop, G. Lui, G. Maret, P. M. Chaikin, P. J. Steinhardt, S. Torquato, P. Keim, and M. Florescu, "Stealthy and hyperuniform isotropic photonic band gap structure in 3d," *PNAS Nexus*, vol. 3, no. 9, pgae383, Sep. 1, 2024.

[10] S. R. Sellers, W. Man, S. Sahba, and M. Florescu, "Local self-uniformity in photonic networks," *Nature Communications*, vol. 8, no. 1, p. 14 439, Feb. 17, 2017.

[11] F. Wooten, K. Winer, and D. Weaire, "Computer generation of structural models of amorphous si and ge," *Physical Review Letters*, vol. 54, no. 13, pp. 1392–1395, Apr. 1, 1985, Publisher: American Physical Society.

[12] G. T. Barkema and N. Mousseau, "High-quality continuous random networks," *Physical Review B*, vol. 62, no. 8, pp. 4985–4990, Aug. 15, 2000.

[13] S. Song, Q. Ding, and J. Wei, "Improved algorithm for estimating pore size distribution from pore space images of porous media," *Physical Review E*, vol. 100, no. 5, p. 053 314, Nov. 21, 2019, Publisher: American Physical Society.

[14] P. J. Steinhardt, D. R. Nelson, and M. Ronchetti, "Bond-orientational order in liquids and glasses," *Physical Review B*, vol. 28, no. 2, pp. 784–805, Jul. 15, 1983, Publisher: American Physical Society.

Nano-optomechanical disk resonators: operating principles and sensing applications

E. Sentre-Arribas[1*], A. Aparicio-Millán[1], I. Favero[2], A. Lemaître[3], O. Malvar[1], J. J. Ruz[1], M. Calleja[1], J. Tamayo[1] and E. Gil-Santos[1]

[1]Instituto de Micro y Nanotecnología, IMN-CNM (CSIC), Isaac Newton 8 (PTM), 28760, Tres Cantos, Madrid, Spain.
[2]Matériaux et Phénomènes Quantiques, CNRS, Université Paris-Cité, 10 rue Alice Domon et Léonie Duquet, 75015, Paris, France.
[3]Centre de Nonocsciences et Nonotechnologies, CNRS, Université Paris-Saclay, 10 boulevard Thomas Gobert, 91129, Palaiseau, France.
[*] e.sentre.arribas@csic.es

Abstract: Nano-optomechanical disks are great candidates for sensing applications due to their capacity of simultaneously support very high quality optical and mechanical modes. In the last decade, different applications have been proposed. In this talk, we will review these applications, explain their operating principles, and discuss their future potential.

In the recent years, optomechanical systems stand out among nanomechanical resonators for their high sensitivity to displacement due to the strong interaction between optical and mechanical vibration modes. As a consequence, they provide high sensitivity to adsorbed particles even when operating in air and liquid [1], which is ideal for sensing of biological analytes.

Here we will talk about nano-optomechanical disk resonators (Figure 1(a,b)), a specific optomechanical device that optically supports whispering gallery modes. These optical modes strongly couple with mechanical radial breathing modes. We will review the operating principle of this kind of resonators, focusing on their potential for sensing applications. Particularly, we will talk about environmental monitoring [2], nanoparticle and pathogen detection and characterization [3, 4] (Figure 1c), and finally we will consider the future potential of these devices as biological sensors [5].

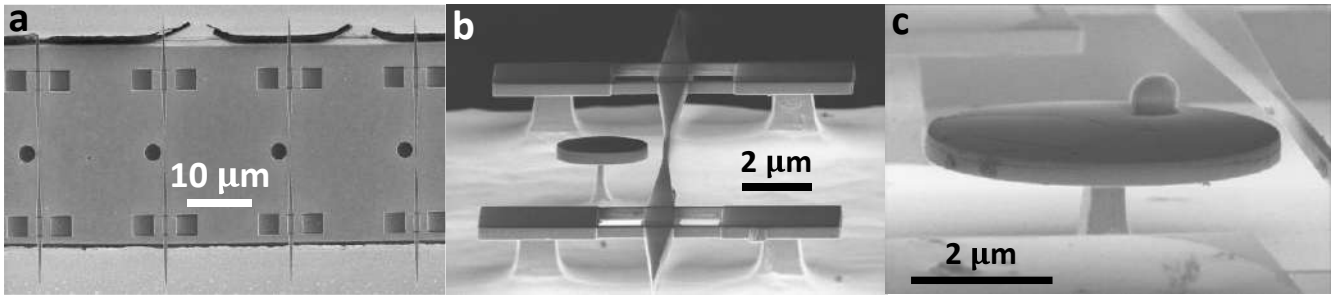


Figure 1. a. Scanning electron microscope (SEM) image (top view) of an array of GaAs nano-optomechanical disks (1 mm in radius) and their integrated optical waveguides. **b.** SEM image (side view) of a disk, its waveguide, and the pedestal that holds the disk. **c.** SEM image of a disk and a *S. epidermidis* bacterial cell adsorbed on its top surface.

Acknowledgments: We acknowledge the service from the Micro and Nanofabrication Laboratory and the X-SEM laboratory at IMN-CNM funded by the "Comunidad de Madrid" (project S2018/NMT-4291 TEC2SPACE) and by MINECO (project CSIC13-4 × 10–1794 with support from FEDER, FSE). Work partially supported by the European Union's Horizon 2020 Research and Innovation Program under grant agreement no. 731868-VIRUSCAN. Also acknowledge the financial support by the Spanish Science, Innovation and Universities Ministry through the projects CNS2022-135367, PDC2023-145867-I00 and PID2023-1511160B-I00.

References

1. Gil-Santos, E., Baker, C., Nguyen, D.T., Hease, W., Gomez, C., Lemaître, A., Ducci, S., Leo, G. & Favero, I. (2015) High-frequency nano-optomechanical disk resonators in liquids. Nature nanotechnology 10 (9), 810-816.
2. Sentre-Arribas, E., Aparicio-Millán, A., Lemaître, A., Favero, I., Tamayo, J., Calleja, M. & Gil-Santos, E. (2023) Simultaneous optical and mechanical sensing based on optomechanical resonators. ACS sensors 9 (1), 371-378.
3. Gil-Santos, E., Ruz, J. J., Malvar, O., Favero, I., Lemaître, A., Kosaka, P. M., García-López, S., Calleja, M. & Tamayo, J. (2020) Optomechanical detection of vibration modes of a single bacterium. Nature Nanotechnology, 15 (6), 469-474.
4. O. Malvar *et al*., "Multifrequency Nanomechanical Mass Spectrometer Prototype for Measuring Viral Particles Using Optomechanical Disk Resonators," *2023 IEEE 36th International Conference on Micro Electro Mechanical Systems (MEMS)*, Munich, Germany, 2023, pp. 153-156.
5. Gil-Santos, E. (2023) Listening to microorganisms with light. Nature Photonics 17 (11), 931-932.

Ab initio simulation of nonlinear optical response in periodic semiconducting nanostructures

M. Uemoto[1]

[1]Graduate School of Engineering, Kobe University, JAPAN
*corresponding author: uemoto@eedept.kobe-u.ac.jp

Abstract: First-principles electron dynamics simulation has become a practical approach to describing light-matter interactions, including linear and nonlinear optical phenomena. We use a multiscale method that combines electron dynamics simulation with electromagnetics to predict harmonic generation enhancement in an all-dielectric, periodically structured nanostructure array and analyze the influence on geometric parameters.

In the field of nanophononics, the artificial nanoscale structures, particularly semiconductor-based all-dielectric nanoparticles and metasurfaces, have been intensively studied as a new platform for nonlinear optics, such as optical wavelength conversion, waveform shaping, second harmonic generations (SHGs) and high harmonic generations (HHGs). For the design of such nanophotonic devices above, the computational electromagnetics simulations based on Maxwell's equations, such as the time-domain finite difference (FDTD) method, have been utilized as an powerful tool. However, the conventional method requires empirical optical constants of media and is limited to light intensity with linear and low-order perturbative nonlinear optical responses. To overcome the limitations, we investigate a theoretical and computational method of electron dynamics based on time-dependent density functional theory (TDDFT) [1] and apply it to various material systems [2-3], such as atoms, molecules, and bulk solids. The TDDFT can successfully predict linear dielectric function [3], low-order nonlinear susceptibilities [4], and non-perturbative nonlinear phenomena such as tunnel ionization, saturable absorption, and HHGs. In addition, we also developed the coupled method, the first-principles TDDFT, and the electromagnetic simulation, the so-called "Maxwell+TDDFT multiscale method," which enables us to simulate light–matter interaction in nanoscale materials self-consistently [5]. We couple Maxwell's wave equation involving the current density J in this electron system and calculate the time evolution.

$$\nabla \times \nabla \times \mathbf{A}(\mathbf{r},t) + \frac{1}{c^2}\frac{\partial^2}{\partial t^2}\mathbf{A}(\mathbf{r},t) = \frac{4\pi}{c}\mathbf{J}(\mathbf{r},t)$$

where the current J is given by the microscopic electron dynamics. At each grid point R, the individual electron dynamics governed by time-dependent Kohn-Sham (TDKS) equation:

$$i\frac{\partial}{\partial t}u_{b\mathbf{kR}}(\mathbf{r},t) = \left\{\frac{1}{2}\left[-i\nabla_{\mathbf{r}} + \mathbf{k} + \frac{1}{c}\mathbf{A}_{\mathbf{R}}(t)\right]^2 + V_{\mathbf{R}}(\mathbf{r},t)\right\}u_{b\mathbf{kR}}(\mathbf{r},t)$$

where u_{bkR} are the Bloch orbitals of electrons and V_R is the effective potentials including the ionic, Hartree and exchange-correlation terms. Figure 1 illustrates the conceptual framework of the Maxwell+TDDFT multiscale coupling method.

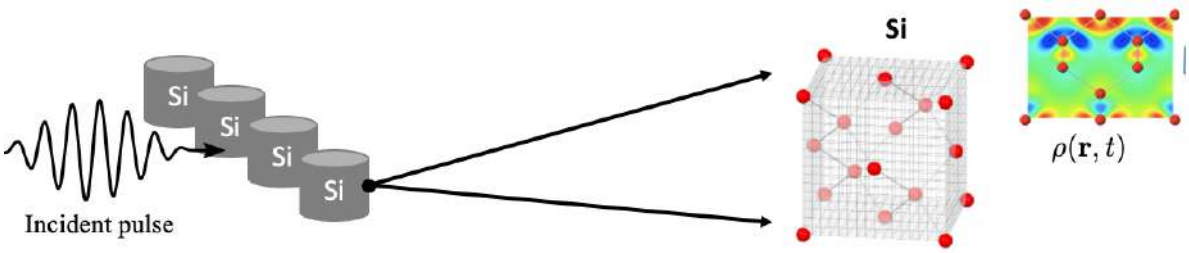


Figure 1: illustration of multiscale coupling between macroscopic nanostructure and microscopic electronic system

Besides, it is possible to improve the electrodynamics calculation to semiconducting Bloch equation:

$$\mathrm{i}\frac{\partial}{\partial t}\rho_{ij}^{(\mathbf{k})}(t) = \frac{1}{c}\mathbf{A}(t)\cdot\left[\sum_l \mathbf{p}_{il}^{(\mathbf{k})}(t)\,\rho_{lj}^{(\mathbf{k})}(t) - \sum_l \rho_{il}^{(\mathbf{k})}(t)\,\mathbf{p}_{lj}^{(\mathbf{k})}(t)\right]$$

,

where ρ is the density matrix, p is the transition dipole moment, and A is the vector potential. The calculation result by Maxwell+SBE agrees well with that by Maxwell+TDDFT because ρ and p are given by first-principles calculations using DFT in both methods. Owing to SBE's less computational cost than TDDFT, the Maxwell+SBE is capable of large-scale device models.

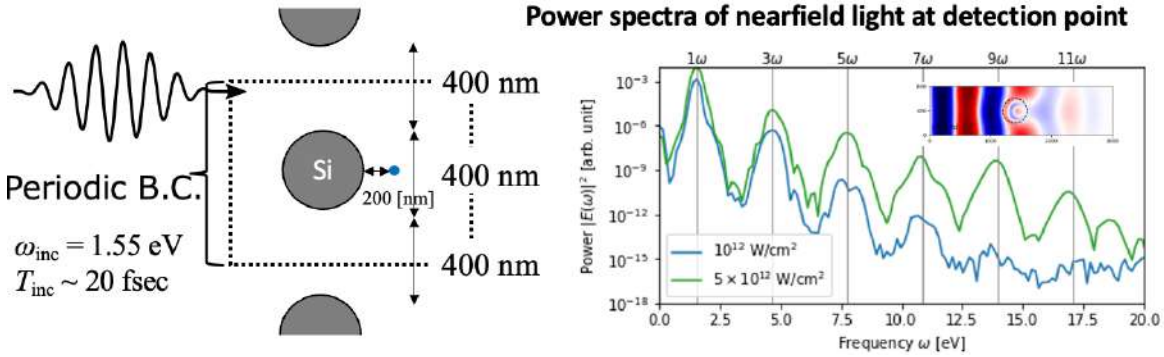


Figure 2: Result of harmonic generation spectra from semiconductor nanocylinder array.

Figure 2 shows the power spectrum of the near-field light in a silicon nanocylinder array under high-intensity laser excitation pulse. We observe higher-order harmonic components enhanced by light confinement and Mie resonances. The simulation also shows that cylinder geometry significantly affects the field intensity and harmonic generation efficiency. Besides, we also analyzed the influence on field amplitude which represents the drastic change of scattering filed distribution by nonlinear change of dielectric properties. These results pave the way for designing advanced nanophotonic devices that exploit nonlinear optical effects at the nanoscale.

References

1. E. Runge, E. K. U. Gross, Phys. Rev. Lett. **52**, 997 (1984)
2. K. Yabana, G. F. Bertsch, Phys. Rev. B **54**, 4484 (1996)
3. G. F. Bertsch, J. -I. Iwata,A.Rubio,K. Yabana, Phys. Rev. B **62**, 7998 (2000)
4. M. Uemoto,Y. Kuwabara,S. A. Sato, K. Yabana, J. Chem. Phys. **150**, 094101 (2019)
5. K. Yabana,T. Sugiyama,Y. Shinohara,T. Otobe, G. F. Bertsch, Phys. Rev. B **85**, 045134 (2012)

Lasing emission from guided mode-assisted quasi-bound states in the continuum in all-dielectric metasurfaces

A. Bashiri[1,2*], A. Vaskin[2], M. Yang[1,2,4], K. Tanaka[1,2,4], M. Rikers[1,2,5], T. Pertsch[2,3,4], I. Staude[1,2,4]

[1]*Institute of Solid-State Physics, Friedrich Schiller University Jena, Germany*
[2]*Abbe Center of Photonics, Institute of Applied Physics, Friedrich Schiller University Jena, Germany*
[3]*Fraunhofer-Institute of Applied Optics and Precision Engineering IOF, Germany*
[4]*Max Planck School of Photonics, Germany*
[5]*Research School of Physics, Australian National University, Australia*
[*]corresponding author: Ayesheh.bashiri@uni-jena.de

Abstract: We demonstrated lasing action in quasi-BIC all-dielectric metasurfaces integrated with a slab waveguide containing laser dyes. Our system offers both single and multimode lasing emission directed toward true zeroth-order and oblique angles with the ability for passive tunability of the emission wavelength within the spectral range of the gain medium.

The precise control over the laser emission properties, such as wavelength and directionality, is crucial for numerous applications, including quantum sensing, biomedicine, and optical communication. Achieving efficient coherent light emission necessitates strong light-matter interaction, which can be realized through high-quality-factor (Q-factor) optical cavities that enhance localized electromagnetic fields within the gain medium.

One promising approach to achieve high-Q resonances involves the integration of symmetry-broken all-dielectric metasurfaces with slab waveguides [1]. This configuration supports quasi-bound states in the continuum (quasi-BIC) and guided mode resonances, enabling the engineering of lasing modes within the spectral range of the gain material. In addition, all-dielectric metasurfaces provide an excellent platform for nanoscale lasing due to their low absorption losses and compatibility with a variety of gain media [2]. By carefully designing the geometrical parameters of these metasurfaces, specific resonant modes can be tailored, allowing for precise spectral and directional control of lasing emission.

Recent studies [3] have demonstrated multimode lasing emission in dielectric nanocylinder arrays, predominantly propagating in the near-normal direction. Here, we present both single and multimode lasing emission directed toward true zeroth-order and oblique angles, with the additional capability of passive wavelength tunability within the spectral range of the gain medium. This is achieved through the integration of symmetry-broken all-dielectric metasurfaces with slab waveguides, which exhibit high-Q resonances essential for generating coherent light emission.

To this end, we designed and fabricated broken symmetry titanium dioxide (TiO_2) metasurfaces supporting high Q-factor resonances in the visible range and covered the metasurfaces with a Rh6G doped SU8 film using spin-coating. Figure 1A shows the focused-ion beam (FIB) cross-section of one of the fabricated metasurfaces after spin coating. Next, we characterized the power-dependent behavior of the fluorescent emission as well as its directionality using momentum-resolved fluorescence spectroscopy. Varying the metasurface geometry parameters and leveraging both quasi-BIC and guided mode resonances within this configuration, we achieved lasing emission over the broad spectral range of the gain medium from 550 nm to 600 nm, emitting into both normal direction and oblique angles.

Figure 1B and 1C represent the momentum-resolved spectra of a metasurface with a lattice constant of 380

nm below and above the lasing threshold, respectively, featuring a triple-mode lasing emitted normally out of the plane of the metasurface. The spectral positions of the three lasing peaks are marked with green arrows and numbers.

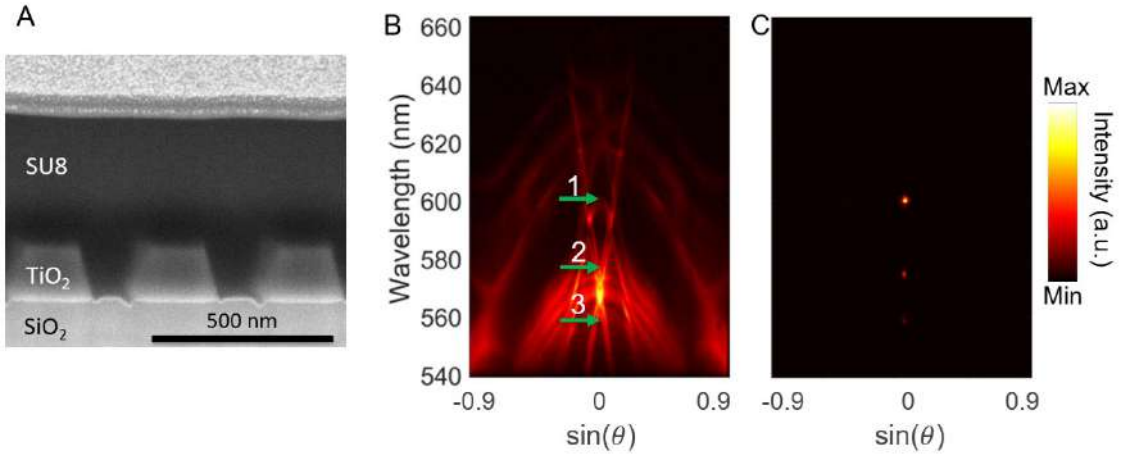


Figure 1: (A) The FIB cross-section of the fabricated metasurface coated with dye-doped SU8 film. (B) The measured momentum-resolved spectra of the metasurface below lasing threshold. The spectral positions of the three lasing modes are marked with green arrows and numbers. (C) The measured momentum-resolved spectra of the metasurface above lasing threshold, showing a triple-mode lasing emitted normally out of the plane of the metasurface, at: 1. 600 nm, 2. 580 nm, and 3. 560 nm.

Our experimental results demonstrate passively tunable single and multimode lasing across a broad spectral range, with emission directed both normally and at oblique angles, highlighting the potential of this approach for advanced on-chip laser applications.

Acknowledgements:
This work was funded by the Deutsche Forschungsgemeinschaft (DFG, German Research Foundation) through the International Research Training Group (IRTG) 2675 “Meta-ACTIVE”, project number 437527638, and through the Emmy Noether Program, project number STA 1426/2-1.

References

1. Wu, M. et al., “Bound State in the Continuum in Nanoantenna-Coupled Slab Waveguide Enables Low-Threshold Quantum-Dot Lasing,” Nano Lett, Vol. 21, No. 22, 9754–9760, 2021.
2. Staude, I. and Schilling, J., “Metamaterial-inspired silicon nanophotonics,” Nat. Photonics, Vol. 11, No. 5, 274-284, 2017.
3. Shaimaa I, A. et al., “Single and Multi-Mode Directional Lasing from Arrays of Dielectric Nanoresonators,” Laser Photonics Rev, Vol. 15, No. 3, 2021.

Real-space Renormalization Group on Topological Scattering under Strong Disorder

Z. Zhang[1] and R. Fleury[1]

1 École Polytechnique Fédérale de Lausanne (EPFL), LWE, CH-1015, Lausanne, Switzerland

Abstract: Strong disorder typically induces trivial Anderson insulating phases. We introduce a real-space renormalization group approach for unitary scattering networks, uncovering robust scattering attractors that distinguish trivial from anomalous Floquet Anderson insulators hosting chiral edge states. Numerical and microwave experiments confirm our method, enabling prediction and design of topologically resilient photonics.

Anomalous Floquet topological phases uniquely host chiral edge states spanning all quasienergy gaps, exhibiting remarkable resilience against strong disorder[1-5]. While disorder typically induces trivial Anderson insulating states by localizing all modes, certain unitary scattering networks sustain robust, delocalized edge states, which are of anomalous Floquet Anderson insulating (AFAI) phase. Traditional band and scattering invariants fail to characterize these strongly disordered topological regimes. To overcome this, we introduce a real-space renormalization group (RG) scheme utilizing iterative block-scattering transformations. Our RG framework identifies stable scattering attractors distinguishing trivial and AFAI phases, significantly advancing theoretical understanding and enabling efficient prediction and engineering of disorder-resilient Floquet topological states.

Our real-space RG procedure systematically analyzes topological scattering networks under strong disorder via iterative block-scattering transformations. Unlike traditional momentum-space or Hamiltonian-based approaches, our method directly manipulates real-space scattering matrices, naturally accommodating strong disorder and real-space topological physics. The RG approach contains three key steps (Fig. 1a). First, for an arbitrary scattering network composed of unitary scatterers $S_0(\xi,\eta)$ interconnected by reciprocal phase-delay links, we partition it into triangular subnetworks (left panel). Second, we perform block-scattering transformation: Each triangular block is replaced by an effective three-port scatterer described by a smaller, 3×3 unitary matrix S'. Crucially, this transformation preserves three essential physical features: flux conservation, reflection, and chirality, ensuring macroscopic scattering characteristics are accurately captured. Newly simplified scatterers are reconnected, producing a progressively coarse-grained network (middle panel). Finally, by iterating this RG procedure, the network's size shrinks systematically, ultimately converging to a single three-port unitary scattering matrix called the scattering attractor S_F (right panel). Upon successful convergence, S_F encodes the macroscopic topological nature of the original network[5]. Specifically, two distinct attractors emerge: (i) **Trivial Anderson insulating attractor** S_F, which is a fully reflective unitary scattering matrix, signifying complete localization with no edge transport; and (ii), **Anomalous Floquet Anderson insulating attractors** S_{CW} or S_{CCW} which are perfectly chiral circulator matrices, revealing robust unidirectional edge transport immune to disorder-induced localization.

Applying our RG scheme extensively over the parameter space defined by the microscopic scatterers $S_0(\xi,\eta)$, we systematically derive the RG topological phase diagram (Fig. 1b). This diagram categorizes disordered scattering networks with strong, distributed phase-delay disorder into distinct topological regimes according to the corresponding attractor they approach[5]. The resulting phase diagram clarifies the critical boundaries between trivial

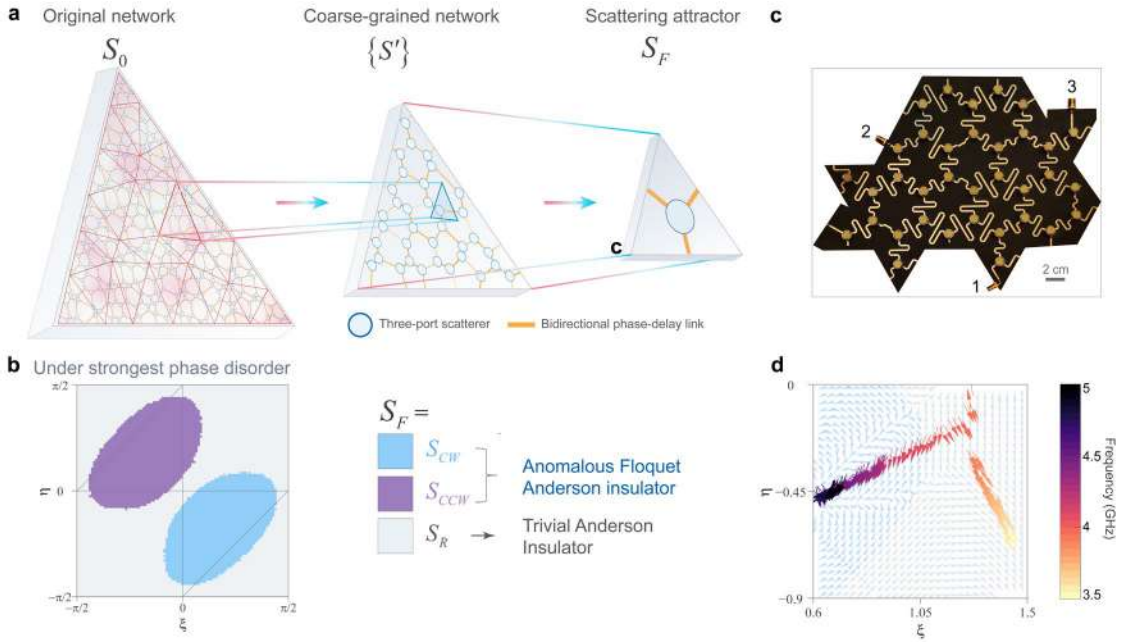


Fig. 1. Real-space renormalization group (RG) of a unitary scattering network with phase-link disorder[5]. a, RG scheme. Starting from a scattering network composed of three-port unitary scatterers (S_0, left), iterative block-scattering transformations simplify triangular subnetworks into three-port scatterers S′ (center), eventually yielding a single scattering attractor S_F (right). The attractor classifies the network as either trivial (trivial Anderson insulator) or topological (anomalous Floquet Anderson). **b,** RG topological phase diagram by summarizing scattering attractors for networks built from $S_0(\xi,\eta)$ with fully random phase-delay links. Attractors S_{CW} or S_{CCW} indicate anomalous Floquet Anderson insulating phases, while attractor S_R indicates trivial Anderson insulators. **c, d,** Experimental validation of RG flow.

Anderson phase and AFAI. These results underscore the remarkable ability of certain strongly disordered systems to preserve topological robustness despite the complete destruction of crystalline order. Independent validations through localization-length scaling analysis confirmed the accuracy of our RG predictions[5]. Additionally, experimental validations using microwave scattering networks closely matched theoretical results, further validating the RG scheme as shown in Figs. 1c and d.

We introduce a real-space renormalization group for strongly disordered topological scattering networks using iterative block-scattering transformations, independent of Hamiltonian methods. Our numerical analyses yield a clear RG phase diagram differentiating trivial Anderson insulators from anomalous Floquet Anderson insulating phases, offering a powerful tool for predicting and engineering disorder-resilient topological waves.

References

1. Titum, P., Berg, E., Rudner, M. S., Refael, G. & Lindner, N. H. Anomalous Floquet-Anderson Insulator as a Nonadiabatic Quantized Charge Pump. Phys. Rev. X 6, 021013 (2016).
2. Zhang, Z., Delplace, P. & Fleury, R. Superior robustness of anomalous non-reciprocal topological edge states. Nature 598, 293–297 (2021).
3. Zhang, Z., Delplace, P. & Fleury, R. Anomalous topological waves in strongly amorphous scattering networks. Sci. Adv. 9, eadg3186 (2023).
4. Zhang, Z., Wang, J., Qin, H. & Fleury, R. Floquet topological physics in photonics. Optical Materials Express (2025).
5. Zhang, Z. et al. Renormalization group of topological scattering networks. arXiv (2024).

Photodegradation of dyes using Fe_3O_4-Au-Pd hybrid nanoparticles synthesized liquid-phase

Y. Yokota[1*], T. Uehara[1] and Mao. Takeda[1]

[1] Department of Materials and Life Sciences, Faculty of Science and Technology, Sophia University, 7-1Kioicho, Chioyoda, Tokyo 102-8554, Japan
[*]corresponding author: y_yokota@sophia.ac.jp

Abstract: We focused on iron oxide nanoparticles that can be recovered using magnets. and synthesized Iron oxide-gold-palladium nanoparticles (Fe_3O_4-Au-Pd hybrid nanoparticles) were prepared in the liquid phase under different synthesis conditions. The catalytic activity of these hybrid nanoparticles was investigated in dye degradation reactions.

The fabrication of metasurfaces and metamaterials using visible and near-infrared light requires precise control of the 2D or 3D alignment of noble metal nanoparticles. We focused on magnetic iron oxide with magnetic properties to enable controllable aggregation and arrangement. We are also pursuing chemical applications and expect that iron oxide can be used as a plasmonic catalyst for simple collection with magnets and reuse. Composite nanoparticles combining gold nanoparticle surfaces, which induce localized surface plasmon resonance, with palladium nanoparticles as an auxiliary catalyst are expected to be used as visible and near-infrared photocatalysts to promote organic chemical reactions and other applications. We have already synthesized Fe_3O_4-Au-Pd hybrid nanoparticles (hybrid nanoparticles), which can be recovered by a magnet. [1] In this study, the synthesized hybrid nanoparticles were used as catalysts for photochemical decolorization reactions.

Based on a previous study [1], iron oxide nanoparticles were synthesized by liquid phase co-precipitation. Then, iron oxide-gold core-shell nanoparticles were synthesized by adding sodium gold chloride. The core-shell nanoparticles were then covered with palladium by adding palladium chloride solution, and hybrid nanoparticles were synthesized and collected with a magnet. The synthesized nanoparticles were collected with a magnet, measured for absorbance, and observed for shape by scanning electron microscopy (SEM) and transmission electron microscopy (TEM). For the degradation reaction, the synthesized hybrid nanoparticles were added to an aqueous solution of methyl violet (MV) as a dye, and the mixture was stirred in the dark, under 300 W Xe lamp (wavelength 440 nm-740 nm) and under table-top white LED irradiation, respectively, and the absorbance was measured at regular intervals.

The synthesized hybrid nanoparticles had an average particle size of 220 nm. The shape was a sphere with an uneven surface. When the synthesized hybrid nanoparticles were added to the aqueous MV solution and reacted in the dark, the peak intensity at an absorption wavelength of 580 nm derived from MV remained unchanged after 72 hours, and the solution also remained purple and did not decolorize. Under Xe lamp irradiation, decolorization progressed with a decrease in the value of the absorbance peak at 580 nm wavelength. The color of the solution became clear after 6 hours. Under LED irradiation, a slight decrease in the peak was observed with time. From these results, the synthesized hybrid nanoparticles acted as a photocatalyst under visible light irradiation. Since the photodegradation was promoted even under weak light sources such as household tabletop white LEDs, the hybrid nanoparticles are expected to be applied as visible light

photocatalysts.

Acknowledgements

This work was supported by “Advanced Research Infrastructure for Materials and Nanotechnology in Japan (ARIM)” of the Ministry of Education, Culture, Sports, Science and Technology (MEXT), Grant Number JPMXP1224UT0193 and JSPS KAKENHI “Grant-in-Aid for Scientific Research (C)”, Grant Numbers 23K04823.

References

1. Yokota, Y, Takeda, M. “Synthesis and plasmonic properties of Fe_3O_4-Au-Pd hybrid nanoparticles,” META2024, 2024.

Photonic Antiferromagnetic Topological Insulator with a Single Surface Dirac Cone

Yihao Yang[1]

[1]Zhejiang University, Hangzhou 310027, China.

*corresponding author: yangyihao@zju.edu.cn

Abstract: We report on the realization of a three-dimensional (3D) photonic antiferromagnetic topological insulator (AF TI) configured as a *z*-directional stack of two-dimensional (2D) Chern insulators. This photonic AF TI features symmetry-protected single-Dirac-cone surface states, which have been demonstrated to be resilient against random disorder of any type on the surface.

Topological metamaterials/photonic crystals have provided a revolutionary platform for manipulating the flow of light. Among them, Chern photonic crystal with time-reversal symmetry broken have been extensively studied due to their chiral edge states (CESs) located at the boundary of structure which are completely immune to the disorders or defects existing in the propagation channel thus considered as an ideal candidate for realizing broadband slow light. On the other hand, stacking two-dimensional (2D) Chern photonic crystals along the third direction to construct three-dimensional (3D) structure has also been demonstrated exhibiting fantastic phenomena such as torus knots or links of topological surface states. Here, in this report, I will introduce some achievement with Chern photonic crystal.

Specifically, in 2D Chern photonic crystal, we have experimentally demonstrated the multiple Brillouin zone winding of topological CESs to slow down light over a relatively wide range of frequencies [1]. We experimentally show that by coupling to the resonance-induced nearly-flat bands, the CESs can wrap many times around the BZ. Thus, their group velocity can be significantly slowed down, and the fractional bandwidth with a reduction of the group velocity of more than 50% relative to the original CESs is 5.7%. Impressively, the winding number can be up to five in experiments and has no strict limit in theory. Finally, we demonstrate the robustness of such broadband topological slow light against obstacles and defects, as well as the smooth transport through slow-light regions with different group velocities.

Further, we stack the 2D Chern photonic crystals with opposite Chern number alternatively along z direction to construct a 3D photonic antiferromagnetic topological insulator (AF TI) featuring a single gapless *S*-protected Dirac surface state [2]. The nontrivial $\mathbb{Z}_2$ bulk topological invariant is numerically confirmed by tracking the evolution of Wannier centres in first-principles simulations. By directly mapping out both bulk and surface band structures, we have unambiguously verified the existence of a single symmetry-protected surface Dirac cone at the $k_z = \pi/a_z$ plane, the defining characteristic of bosonic AF TIs. Our photonic AF TI can also be regarded as the first realization of a 3D strong photonic TI in terms of the odd number of surface Dirac cones. Additionally, our experiments have demonstrated the remarkable resilience of the single-Dirac-cone surface state against random magnetic disorders that, on

average, respect the *S* symmetry. Our findings pave the way for further realizing and engineering novel magnetic topological phenomena in photonic systems, which are inaccessible in electronic systems.

References

1. Chen, F. J., Han, N., and Yang, Y. H.* et al., “Multiple Brillouin zone winding of topological chiral edge states for slow light applications”. *Phys. Rev. Lett.*, 132, 15, 156602, 2024.
2. Chen, F. J., Han, N., and Yang, Y. H.* et al., “Photonic antiferromagnetic topological insulator with a single surface Dirac cone”. arXiv:2501.07424.

Spin-Orbit Coupling and Tunable Lasing in Liquid-Crystal-Based Photonic 1D Crystals

Jacek Szczytko,[1] Marcin Muszyński,[1] Pavel Kokhanchik,[2] Przemysław Oliwa,[1] Piotr Kapuściński,[1] Daniil Bobylev,[2] Eva Oton,[3] Rafał Mazur,[3] Przemysław Morawiak,[3] Wiktor Piecek,[3] Przemysław Kula,[3] Witold Bardyszewski,[1] Barbara Piętka,[1] Dmitry Solnyshkov,[2,4] Guillaume Malpuech,[2]

[1]Faculty of Physics, University of Warsaw, Poland;
[2] Université Clermont Auvergne, CNRS, Institut Pascal, Clermont-Ferrand, France;
[3]Military University of Technology, Warsaw, Poland;
[4]Institut Universitaire de France, Paris, France
*corresponding author Jacek.Szczytko@fuw.edu.pl

Abstract: We created a tunable one-dimensional photonic crystal with strong polarization dependence by embedding a uniform lying helix (ULH) structure in a planar optical microcavity. The voltage-controlled orientation of liquid crystal molecules modifies the photonic band gaps and induces spin-orbit coupling, which can be interpreted as a synthetic non-Abelian gauge potential. Additionally, doping with dyes enables tunable polarized lasing.

Unlike spin-orbit coupling (SOC) in solid-state materials, which is inherently difficult to manipulate, liquid-crystal (LC) optical cavities offer significant tunability of photonic modes. The behavior of polarized electromagnetic waves propagating through one- or two-dimensional structures can be effectively described using a two-mode Hamiltonian, representing a massive spin-½ particle via Pauli matrices. By employing Green's function techniques and k·p perturbation theory from semiconductor physics, we obtained results interpretable as effective cavity-mode spin-orbit coupling and non-Hermitian Hamiltonians [1].

To further develop this analogy, we engineered a one-dimensional photonic crystal with strong polarization dependence, tunable via an applied electric field. This was realized by embedding a cholesteric liquid crystal into a planar optical microcavity, which spontaneously formed a uniform lying helix (ULH) structure (Figure). The orientation of LC molecules was controlled electrically, allowing us to tune the strength of a polarization-dependent periodic potential. This voltage-induced control resulted in the opening and closing of photonic bandgaps in the dispersion of massive photons within the microcavity.

Furthermore, when the ULH structure possessed a molecular tilt, it induced interband spin-orbit coupling (ISOC) between lattice bands of different parity. This ISOC is analogous to optical activity and can be interpreted as a synthetic non-Abelian gauge potential. Finally, we demonstrated that doping the LC with dyes enabled lasing, which inherited all the tunable features of the LC microcavity – including dual and circularly polarized emission [2].

Beyond traditional lithographic methods, our approach enables the self-organization of macromolecular photonic structures, with geometry controlled by temperature or applied electric fields. These periodic architectures allow for precise manipulation of optical modes, offering new possibilities for photonic device engineering.

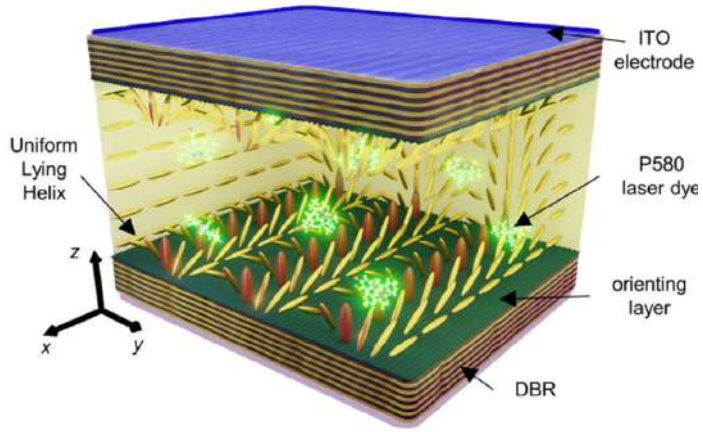


Figure. ULH texture inside optical microcavity. Schematic of the dye-doped optical microcavity with an embedded, stabilized ULH structure. Rows of molecules whose directors are oriented vertically are colored red to indicate the periodicity of the lattice.

Acknowledgements, National Science Centre Poland 2021/43/I/ST5/02632, 2023/51/B/ST3/03025 and Horizon2020 FET Open research and innovation action under the grant agreements No. 964770 (TopoLight).

References

1. P. Oliwa et al, Phys. Rev. Research 6, 013324 (2024).
2. M. Muszynski, et al., Laser & Phot. Rev. DOI 10.1002/lpor.202400794 (2024)

Room-temperature Exciton-polariton Condensation in Prism-shaped GaN Microcavity Structures

Yong-Hoon Cho

Department of Physics and KI for the NanoCentury,
Korea Advanced Institute of Science and Technology (KAIST), Daejeon, Republic of Korea
*corresponding author: yhc@kaist.ac.kr

Abstract: We fabricated GaN-based hexagonal and triangular microcavity structures by using selective area growth. We formed room-temperature exciton-polariton condensation with whispering gallery mode and superscar mode in the hexagonal and triangular microcavities, respectively. Angle-resolved micro-photoluminescence experiments with varying excitation power were conducted to investigate the processes of polariton formation and condensation.

Group III-nitride semiconductors are promising materials for studying exciton-polaritons at room temperature due to their large exciton binding energy and high oscillator strength. It has been reported that exciton-polaritons can be observed in hexagonal-shaped GaN microrod structures at room temperature using whispering gallery mode cavities [1, 2]. However, the whispering gallery mode shows a relatively lower quality factor, which is a major obstacle for the room-temperature polariton devices. The superscar mode is an optical cavity mode found in polygonal structures, which has higher quality factors and a longer optical path compared to the whispering gallery mode. Here, we successfully fabricated prism-shaped GaN structures by selective area growth method and metal-organic chemical vapor deposition [3]. From the prims-shaped cavity structures, the superscar mode polaritons are observed at room temperature. Spatially-resolved and angle-resolved micro-photoluminescence experiments are performed with varying excitation beam spot sizes and excitation power densities. The detailed emission characteristics are analyzed and compared in real and momentum spaces. We could adjust the dominant mode between whispering gallery mode and superscar mode for the condensation by changing the opening shape on the GaN template for the selective area growth.

References

1. H. G. Song, S. Choi, C. H. Park, S. H. Gong, C. Lee, M. S. Kwon, D. G. Choi, K. Y. Woo, and Y. H. Cho*, Optica Vol. 6, 1313, 2019.
2. H. G. Song, M. Choi, K. Y. Woo, C. H. Park, and Y. H. Cho*, Nature Photonics Vol. 15, 582, 2021.
3. C. Y. Seong, et al., (in preparation)

High-Temperature Superfluorescence in Perovskites

K. Gundogdu

[1]Physics Department, NC State University, USA
*corresponding author: kgundog@ncsu.edu

Abstract: In this presentation, I will introduce the superradiance mechanism that leads quantum coherence in lead-halide perovskites and its implications for designing new materials that exhibit macroscopic quantum coherence at high temperatures.

The formation of coherent macroscopic states and the manipulation of their entanglement using external stimuli are essential for emerging quantum applications. However, the observation of collective quantum phenomena such as Bose–Einstein condensation, superconductivity, superfluidity and superradiance has been limited to extremely low temperatures to suppress dephasing due to random thermal agitations. In this presentation I will talk about room-temperature superfluorescence (SF) in hybrid perovskite thin films [1,2]. In SF an optically excited population of incoherent dipoles develops collective coherence spontaneously. This emergent collective state forms a giant dipole and radiates a burst of photons. Because electronic transitions dephase extremely fast, observation of SF in semiconductors is extremely rare and under high magnetic fields and at very low temperatures. Therefore, the discovery of room temperature SF in perovskites is very surprising and shows that in this material platform, there exists an extremely strong immunity to electronic dephasing due to thermal processes. To explain this observation, we propose that the formation of large polarons in hybrid perovskites provides a quantum analogue of vibration isolation to electronic excitation and protects it against dephasing even at room temperature. Understanding the origins of sustained quantum coherence and the superfluorescence phase transition at high temperatures can provide guidance to design systems for emerging quantum information technologies and to realize similar high-temperature macroscopic quantum phenomena in tailored materials.

References

[1] M. Biliroglu et.al., Room Temperature Superfluorescence in Hybrid Perovskites and Its Origins, Nature Photonics **16**, pages324–329 (2022)
[2] G. Findik et.al., High Temperature Superfluorescence in MethylAmmonium Lead Iodide **15**, pages 676–680 (2021)
* Acknowledgement(s) : authors acknowledge support from DOE DE-SC0024396

Multipartite Light-Matter Interactions in High-Q 2D-Material Nanophotonic Cavities

C. Qian[1,2,3], V. Villafañe[3], P. Soubelet[3], A. V. Stier[3], J. J. Finley[3]

[1]Institute of Physics, Chinese Academy of Sciences, Beijing 100190, China
[2]School of Physical Sciences, University of Chinese Academy of Sciences, Beijing 100049, China
[3]Technische Universität München, Am Coulombwall 4, 85748 Garching, Germany
[*]corresponding author: chenjiang.qian@iphy.ac.cn

Abstract: We fabricated hybrid nanobeam cavities with high Q-factor and integrate the pristine hBN-encapsulated 2D materials with controllable cavity-material overlap. This allows the observation of novel light-matter interactions for the unique quantum emitters in 2D materials

2D materials such as monolayer transition metal dichalcogenides host a variety of excitonic transitions with rich exciton-photophysics, and thereby, are ideally suited as the active emitters for nanophotonic cavities. Moreover, 2D materials can be assembled into heterostructures via van der Waals bonding, and the atomical thickness of material results in the sensitivity and strong coupling to the multi-physics local environment. Therefore, 2D-material nanophotonic cavity paves the way to the coupling between different physical degrees of freedom. However, the common pick-and-place method introduces disorders that perturb the excitonic quality in 2D materials. Meanwhile, perforating nanophotonic structures in 2D flakes results in complex effects and limits the cavity Q-factor ~10^3. We fabricated hybrid nanobeam cavities with high Q-factor (>10^4) and integrate the pristine hBN-encapsulated 2D materials with controllable cavity-material overlap [1]. Based on this platform, we observed novel light-matter interactions for the unique quantum emitters in 2D materials [2]. Moreover, the photonic crystal is also phononic crystal, and thereby, the nanophotonic cavity also hosts the nanomechanical modes with phonon vibrations. We observe the phononic hybridization between the atomic lattice phonons and cavity nanomechanical phonons in the light-matter interaction [3]. Such multi-modal couplings provide novel methods to interface emitters, photons, and phonons as a hybrid solid-state quantum system [4].

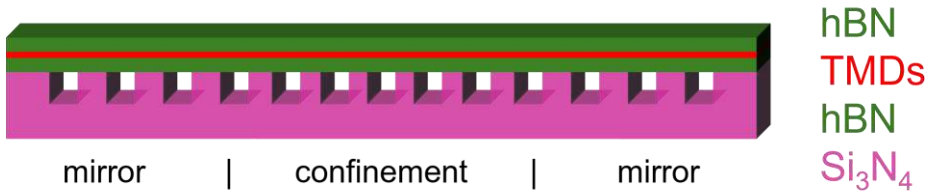


Figure 1: Schematic of the hybrid 2D-material nanophotonic cavity, including hBN-encapsulated TMDs and photonic crystal nanoholes for the cavity photonic mode.

References

1. C. Qian et al., Phys. Rev. Lett. 128, 237403 (2022).
2. C. Qian et al., Sci. Adv. 10, eadk6359 (2024).
3. C. Qian et al., Phys. Rev. Lett. 130, 126901 (2023).
4. C. Qian et al., Phys. Rev. Lett. 133, 086902 (2024).

META 2025, MALAGA - SPAIN, JULY 22 – 25, 2025

From exceptional point to bound states in the continuum and from lasing to coherent perfect absorption, or there and back again using non-Hermitian metasurfaces

Y. Liang[1], Y. El Droubi[1], L. Ivzhenko[2], M. Krawczyk[2], A. E. Serebryannikov, and A. Lupu[1,*]

[1] Centre de Nanosciences et de Nanotechnologies, CNRS, Université Paris-Saclay, Palaiseau, 91120, France
[2]Institute of Spintronics and Quantum Information, Faculty of Physics, Adam Mickiewicz University, Poland
[*]corresponding author: anatole.lupu@c2n.upsaclay.fr

Abstract: The objective is to provide guidelines for the engineering of Fano resonances and metasurfaces composed of coupled antenna-like resonators, possibly integrating gain and loss. The large number of degrees of freedom of these systems allows for great design versatility, allowing to tailor on demand spectral properties.

The objective of this work is to address the spectral response engineering of Fano resonances and metasurfaces, placing it in the general context of non-Hermitian open systems composed of the coupled antenna-like resonators possibly incorporating gain and loss. Following this approach, we have shown in our recent study that the natural frequency solutions obtained for a particular case of scattering matrix are rather general and valid for arbitrary values of the antenna radiative rates, thanks to an appropriate transformation of the coupling-detuning parametric space by simple linear expansion and rotation [1]. The universality of the obtained solutions thus provides a general recipe for an infinite diversity of optimal metasurface designs, meeting the requirements of tailor-made sensors with target spectral responses.

Specifically, the control of the asymmetry and sharpness of the Fano resonance achieved by navigating between the Parity-Time symmetry phase transition path and the Bound State in Continuum (BIC) path representing the natural hidden axis of universal scattering matrix solutions in the parametric coupling-detuning plane has been demonstrated. The validity of the analytical model has been confirmed by comparison with experimental and full 3D numerical simulation results reported in the literature for a metasurface with a unit cell composed of two asymmetrically split ring resonators operating in the THz domain [2].

Furthermore, the conditions required to achieve the superscattering regime corresponding to a passive metasurface, such as the one shown in Figure 1a, have also been established. The obtained solutions are then extended to the case where one resonator experiences a gain and another a loss. The superscattering regime in this case corresponds to the onset of laser emission. It is shown that modulation of the medium gain and loss level within realistic parameters is an efficient approach for implementation of tunability. This two-antenna configuration can serve as inspiration for the implementation of high-contrast resonance tunable metasurfaces.

The large amount of degrees of freedom offered by a coupled resonator system: near field coupling strength - κ, detuning of the resonance frequency - δ, the resonators' radiative decay rates- γ_i, the resonators gain and/or absorption losses - χ_i, opens the way to a great versatility of designs with the possibility of adjusting the spectral properties of this type of metasurface on demand.

Additional features can be obtained by introducing the third dimension into the system by considering a Fabry-Perot cavity formed by metasurfaces A and B with detuned resonance frequencies that exhibit absorption losses. Generally, their presence results in a decrease in the Fano resonance contrast and is considered detrimental. Figure 1b shows an example where the intentional introduction of absorption losses can result in a

high-contrast narrowband $S_{11\,A}$ reflection dip associated with a narrowband X_A absorption peak close to 100% for an electromagnetic wave incident on this Fabry-Perot cavity from the side of metasurface A. This coherent perfect absorption (CPA) results from a combination of interference and dissipation. The portion of the incident beam reflected by metasurface B destructively interferes with that transmitted through metasurface A, and vice versa, so that the radiation is trapped in an interference pattern in the cavity and entirely suppressed by dissipation. This CPA mechanism is reciprocal but substantially asymmetric. As shown in Figure 1b, the $S_{11\,B}$ reflection and X_B absorption spectral responses are completely different for a beam incident on the metasurface B side. It is worth noting that, as expected, the $S_{12\,A}$ and $S_{12\,B}$ transmissions on both sides are perfectly identical. This type of structures, exhibiting narrowband spectral characteristics despite absorption losses, is also of great interest for sensing applications. In turn, narrowband CPA can be used to suppress the transmission of a given wavelength in diverse applications.

The power of the developed analytical approach lies in its ability to provide, on the basis of a mathematical formalism, the prediction of the spectral behavior of the system without going through more complex and time-consuming full-wave 3D numerical simulations which are still necessary, but rather at next stages, when translating the mathematical model into a practical design.

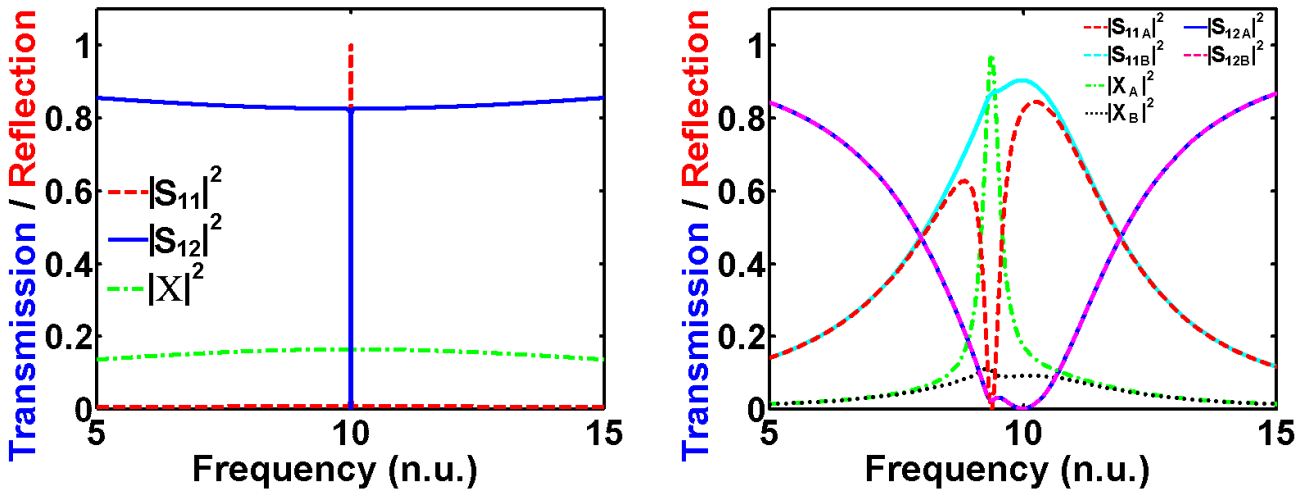


Figure 1: a) Spectral response of a single-layer metasurface composed of unit cells comprising two resonators with different absorption and radiative losses. b) Spectral response of a bilayer metasurface with the same radiative losses but different resonance frequencies and in the presence of absorption losses.

Acknowledgements

This work was partially funded by the French Agence Nationale pour la Recherche (project "PARTISYMO", contract number N° ANR-18-CE24-0024) and by PHC POLONIUM grant (project "DYNAMET" contract numbers 49324QA and BPN/BFR/2022/1/00023/U/00001). Funding by the China Scholarship Council is acknowledged by Y. L (grant number 201906750021).

References

1. Y. Liang, *et al*, "Engineering of the Fano resonance spectral response with non-Hermitian metasurfaces by navigating between exceptional point and bound states in the continuum conditions," Opt. Express 32, 7158-7170 (2024).
2. W. Cao, *et al*, "Low-loss ultra-high-Q dark mode plasmonic Fano metamaterials," Opt. Lett. 37(16), 3366-3368 (2012).

Chirality Transfer in Silicon Nanoparticles with Chiral Molecules

H. Sugimoto[1*], H. Kasai, K. Shintani, S. Ghamari, F. Vollmer, M. Fujii[1]

[1]Department of Electrical and Electronic Engineering, Graduate School of Engineering at Kobe University, Japan
[2]Department of Physics and Astronomy, Living Systems Institute, University of Exeter, Exeter, EX4 4QD, UK

[*]corresponding author: sugimoto@eedept.kobe-u.ac.jp

Abstract: Chiral molecular sensing plays a crucial role in biomedical and pharmacological applications. However, the sensitivity of existing methods for chiral discrimination is limited by the weak interaction between light and molecules. In this study, we introduce a novel platform that enhances chiral light-matter interactions using Mie-resonant silicon nanospheres, ranging in size from 100 to 200 nm, which can be dispersed in solution.

The bioactivity of chiral molecules varies significantly between enantiomers, making highly sensitive detection techniques essential. Although circular dichroism (CD) spectroscopy can distinguish between enantiomers, detecting small amounts of chiral molecules (<μM) remains challenging due to the extremely weak interaction between chiral molecules and circularly polarized light. Recently, approaches to enhance CD signals through optical chirality amplification or chirality transfer via optical nanoantennas have been proposed.[1] Among the nanoantennas, high index dielectric nanoparticles exhibit electric and magnetic Mie resonances and provide opportunities for manipulating and enhancing the light-matter interactions. In addition, several theoretical studies have predicted significant CD enhancement using resonant nanostructures. Dielectric nanoantennas are typically fabricated using electron beam lithography on solid substrates, which limits the applicability of solution-based assembly techniques compared to their plasmonic counterparts, as commercially available gold and silver colloids are widely used.

In this work, we experimentally investigate chirality transfer in silicon nanoparticle antennas with chiral molecule-doped polymer shells, utilizing colloidal silicon nanospheres developed in our group.[2-4] We also discuss the mechanism behind the enhanced signals and the contributions of optical chirality and chirality transfer.

Colloidal suspension of perfectly spherical silicon nanoparticles dispersible in alcohol by thermal disproportionation of silicon monoxide at very high temperature (>1450°C) followed by chemical etching. We also developed monodisperse silicon nanoparticles by applying density gradient centrifugation process for the size separation.[2-4] Figure 1a shows the solution in which different sized silicon nanoparticles are dispersed. The solutions exhibit bright scattering colors depending on

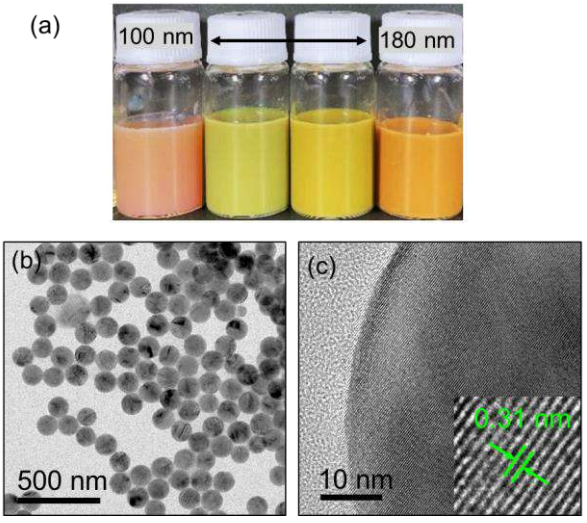


Figure 1. (a) Photo of colloidal suspension of Si nanoparticles with different average diameters. (b, c) TEM and HRTEM images of Si nanoparticles, respectively.

nanoparticles sizes. TEM image in Fig. 1b shows the monodisperse silicon nanoparticles with highly spherical shapes. In addition, HRTEM image in Figure 1c demonstrates high crystallinity of the particle.

We calculate the differential extinction spectra[5] under right- and left-handed circularly polarized light assuming a chiral medium shell with a refractive index n = 1.33 and Pasteur parameter κ = -10^{-5}–$10^{-7}i$. The upper panel compares the extinction spectra of a 150 nm silicon nanosphere with (red) and without (black) a 10 nm chiral medium shell. A slight shift in the spectrum can be observed due to the shell coating. The lower panel shows the differential extinction (ΔC_{ext}) spectra of a silicon nanosphere with a 10 nm chiral shell under right- and left-handed circularly polarized light. ΔC_{ext} shows peaks at the wavelengths of ED and MD resonances for a silicon nanosphere. It should be noted here that these signals are absent in a bare silicon nanosphere, as it is an achiral structure. These results suggest that chirality transfer occurs from the chiral shell to the Mie-resonant silicon nanosphere. In the presentation, we will also show the experimental results on silicon nanospheres with chiral molecule-doped polymer shells.

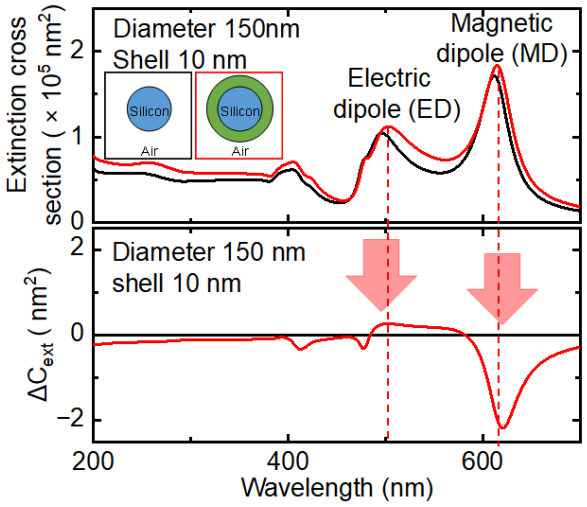


Figure 2. (Upper panel) Calculated extinction spectra of 150 nm silicon nanosphere with (red) and without (black) a 10 nm chiral medium shell (n = 1.33 and κ = -10^{-5}–$10^{-7}i$) (upper panel). (Lower panel) Calculated ΔC_{ext} spectra of 150 nm silicon nanosphere with a 10 nm chiral medium shell under right and left handed circularly polarized light.

References

1. Mohammadi, E, *et al.*, "Nanophotonic Chirality Transfer to Dielectric Mie Resonators", Nano Letters, Vol. 23, Issue 9, pp. 3978-3984, 2023.
2. Sugimoto, H. *et al.*, "Mie Resonator Color Inks of Monodispersed and Perfectly Spherical Crystalline Silicon Nanoparticles", Advanced Optical Materials, Vol. 8, Issue 12, 2000033, 2020.
3. Hinamoto, T. *et al.*, "Colloidal Solutions of Silicon Nanospheres toward All-Dielectric Optical Metafluids", Nano Letters, Vol. 20, Issue 10, 7737-7743, 2020.
4. Negoro, H. Sugimoto. H, Fujii, M. "Helicity-Preserving Optical Metafluids", Nano Letters, Vol. 23, Issue 11, pp.5101-5107, 2023.
5. Kim, T, *et al.*, "Molecular chirality detection using plasmonic and dielectric nanoparticles", Nanophotonics, Vol. 11, Issue 9, pp. 1897-1904, 2022.

META 2025, MALAGA - SPAIN, JULY 22 – 25, 2025

Imaging method of the photodegradation mechanism at the nanoscale over a gold metasurface

Marlo Vega[1,2,3], Paul-Ludovic Karsenti [1,3], Paul G. Charette[1,3], Julien Moreau[2], Michael Canva[1,3], Jean-François Bryche[1,3]

[1] Laboratoire Nanotechnologies Nanosystèmes (LN2) - IRL3463, CNRS, Université de Sherbrooke, UGA, ECL, INSA Lyon, Canada.

[2] Laboratoire Charles Fabry - UMR 8501, Université Paris-Saclay, IOGS, CNRS, France.

[3] Département de Physique, Université de Sherbrooke, Sherbrooke, Canada
*corresponding author: jean-francois.bryche@cnrs.fr

Abstract: This study explores the photothermal heating of asymmetric gold nano-crosses using ultrashort light pulses. We demonstrate the control at the nanoscale of thermal energy via polarization and then introduce a new method for nanoscale surface chemistry imaging that relies on photothermal degradation.

META 2025, MALAGA - SPAIN, JULY 22 – 25, 2025

Symposium II: New trends in nanophotonics and advanced materials:

Non-Hermitian dynamics in bosonic systems: classical and quantum realizations.

Y. N. Joglekar[1]

[1]Indiana University Indianapolis, United States
[*]corresponding author: yojoglek@iu.edu

Abstract: Open systems governed by a non-Hermitian Hamiltonian, called Parity-Time (PT) symmetric systems, have been deeply investigated over the past decade. Although most of their realizations are with waves, in recent years, these ideas have been extended to the quantum domain. With a photonic Floquet topological insulator and number-resolved phonon dynamics as examples, I will present salient properties of such systems in the classical and quantum domains respectively. (Work done in collaboration with Alexander Szameit's group (University of Rostock, Germany), Anthony Laing's group (University of Bristol, UK), and David Allcock's group (University of Oregon, US)).

PAST, PRESENT AND FUTURE OF MASS DIFFUSION METAMATERIALS

J.M Restrepo-Florez

[1]University of Florida, United States of America
[*]corresponding author: restrepoflorezj@ufl.edu

Abstract: Precise control of mass diffusion is vital in separations, reactions, and sensors. Metamaterials theory has recently advanced our understanding of mass diffusion in these systems. This talk explores how metamaterials can transform separations, outlining the current state of the art, key challenges, and promising future research directions.

Enhanced photo-excitation of spin-forbidden gray exciton in 2D materials by using spin-orbit-coupled vector vortex beams

Shun-Jen Cheng*

Department of Electrophysics, National Yang Ming Chiao Tung University, Hsinchu 300, Taiwan

*corresponding author: sjcheng@nycu.edu.tw

Abstract: We present a comprehensive theoretical investigation, implemented on the first-principles base, of the light-matter interaction between excitons in WSe2 monolayers and vector vortex beams. Through the optical spin-orbit interaction, vector vortex beams are shown to enable the photo-generation of gray excitons, a type of spin-forbidden dark exciton.

Superimposing two scalar optical vortex beams produces a vector vortex beam (VVB) in non-separable states where not only complex amplitude but also polarization are spatially structured and entangled with each other. Hence, a VVB can be encoded with entangled degrees of freedom of angular momentum (AM), both spin angular momenta (SAM) and orbital ones (OAM). In addition to the non-separability, the SAM and OAM in a VVB are intrinsically coupled by optical spin-orbit interaction (SOI), which has recently drawn a great deal of attention because of the profound underlying physics and potential photonic applications.[1] In this work, we present a comprehensive theoretical investigation, implemented on the first-principles base, of the intriguing light-matter interaction between spin-orbit-coupled VVBs and exciton complexes in transition-metal dichalcogenide monolayers (TMD-MLs) monolayers, being one of the best-promising two-dimensional (2D) materials in optoelectronics.

Theoretically, we have established the theory of the light-matter interaction between a 2D exciton and structured light carrying OAMs, i.e. a scalar vortex beam, by using the time-dependent perturbation theory.[2,3] Accordingly, we calculate the energy band structures and the microscopic wave functions of structured-light-excited exciton complexes in 2D materials by solving the Bethe Salpeter equation (BSE) established on the base of first principles.[4] We show that an incident structured OAM-light photo-generates an exciton wave packet that is formed by the coherent superposition of finite momentum exciton states and whose spatial structures are encode with the optical information of the structured light. The experimental signature of those photo-generation of finite momentum exciton states by structured OAM-light is the spectral blue shift in photo-luminescence spectroscopy that is increased with increasing the optical OAM, and was for the first time observed in Ref.[2].

Furthermore, the theory of structured-light-exciton interaction has been extended for the study of the intriguing interaction between 2D exciton and VVB, a superposition of multiple scalar vortex beams.[5] As one of the key findings, we show that, via the optical SOI, a VVB enables the photo-excitation of the one of

the spin-forbidden dark exciton doublet, i.e. gray exciton. Moreover, the spatial structure of the wave function of a VVB-generated gray exciton is imprinted by the entangled SAM and OAM encoded in the exciting VVB. Those findings unveil the indispensable role of gray excitons in the desired conversion of optical information to solid-state optoelectronic systems.

References

1. Shen, Y., Wang, X., Xie, Z., Min, C., Fu, X., Liu, Q., Gong, M., Yuan, X. ‘Optical Vortices 30 Years On: OAM Manipulation from Topological Charge to Multiple Singularities”, Light: Sci. Vol. 8 No.1, 90, 2019.
2. Simbulan, K.B., Huang, T.D., Peng, G.H., Li, F., Gomez Sanchez, O.J., Lin, J.D., Lu, C.I., Yang, C.S., Qi, J., Cheng, S.J., Lu, T.H., Lan, Y. W., "Selective Photoexcitation of Finite- Momentum Excitons in Monolayer MoS2 by Twisted Light", ACS Nano Vol. 15 No.2, 3481-3489, 2021.
3. Peng, G.-H., Sanchez, O. J. G., Li, W.-H., Lo, P.-Y., Cheng, S.J. "Tailoring the superposition of finite-momentum valley exciton states in transition-metal dichalcogenide monolayers by using polarized twisted light", Phys. Rev. B Vol. 106 No. 15, 155304, 2022.
4. Peng, G.H., Lo, P.Y., Li, W.H., Huang, Y.C., Chen, Y.H., Lee, C.H., Yang, C.K. Cheng, S.J., "Distinctive Signatures of the Spin- and Momentum-Forbidden Dark Exciton States in the Photoluminescence of Strained WSe2 Monolayers under Thermalization", Nano Lett. Vol. 19, 2299, 2019
5. Sanchez, O. J. G., Peng, G. H., Li, W. H., Shih, C. H., Chien, C. H. Cheng, S. J., Enhanced Photo-excitation and Angular-Momentum Imprint of Gray Excitons in WSe2 Monolayers by Spin–Orbit-Coupled Vector Vortex Beams, ACS Nano, 18, 17, 11425, 2024.

.

Higher-order Mie resonant metasurfaces for ultrafast all-optical light manipulation

C.U. Hail[1,2*], L. Michaeli[1], and H.A. Atwater[1]

[1]California Institute of Technology, United States
[2]University of California, Berkeley, United States
[*]corresponding author: cuhail@berkeley.edu

Abstract: We report on high-Q dielectric optical metasurfaces for ultrafast spatiotemporal light manipulation leveraging the optical Kerr effect and free-carrier effects from two-photon absorption.

Local modulations in refractive index due to ultrafast nonlinear effects present a promising route for realizing space-time-varying optical materials. However, the typically small changes in refractive index prohibit their application for spatial wavefront patterning. In this talk, we will introduce dielectric higher-order Mie resonant metasurfaces and show how these surfaces enable space-time light modulation using local ultrafast all-optical changes of the refractive index due to the optical Kerr effect and free-carrier effects. We present experimental results of strong pump self-modulation, space-time diffraction using a transient ultrafast grating, and time-dependent pump-probe measurements.

Snapshot Polarimetric Stereoscopic Imaging and On-Chip High Dynamic Range Correction System

Shuming Wang[1]

[1]Department of Physics, Nanjing University, China
[*]corresponding author: wangshuming@nju.edu.cn

Abstract: Capturing 3D objects in 2D images leads to significant information loss. While time-of-flight (ToF) and structured light techniques reconstruct 3D morphology, they require active excitation and are highly sensitive to environmental conditions. Polarization stereo-imaging passively collects reflected light, avoiding these limitations, but conventional methods rely on multiple polarizers, restricting single-shot imaging. We present a snapshot polarimetric stereoscopic imaging (SPSIM) system based on a polarimetric metalens that decouples and focuses six distinct polarizations, enabling high-resolution 3D reconstruction with a neural network-mediated algorithm (Fig. a & b). The system achieves an average extinction ratio of 25 dB and a central wavelength efficiency of 65%, surpassing conventional polarization cameras. With the ability to capture full Stokes parameters (FSPs), our approach reconstructs complete 3D textures with sub-millimeter precision, significantly enhancing surface normal recovery.

Beyond 3D imaging, high dynamic range (HDR) correction is essential for accurate visual representation under complex lighting conditions. Traditional HDR methods suffer from ghosting, computational intensity, or increased system complexity, making them impractical for compact and dynamic imaging applications. To address these challenges, we introduce an on-chip metasurface-based non-uniform transmittance array for single-exposure HDR imaging. This system achieves multi-exposure-equivalent performance while eliminating motion artifacts and temporal delays. Experimental validation (Fig. b & c) confirms its broadband response and ability to capture high-contrast scenes, preserving details in both bright and dark regions. By integrating optical and computational strategies, the system employs ultrathin metasurface films directly fabricated onto chips for on-chip light field modulation (Fig. d & e). This highly integrated solution provides a compact, high-performance HDR imaging approach, particularly suited for dynamic video applications, advancing next-generation imaging technologies.

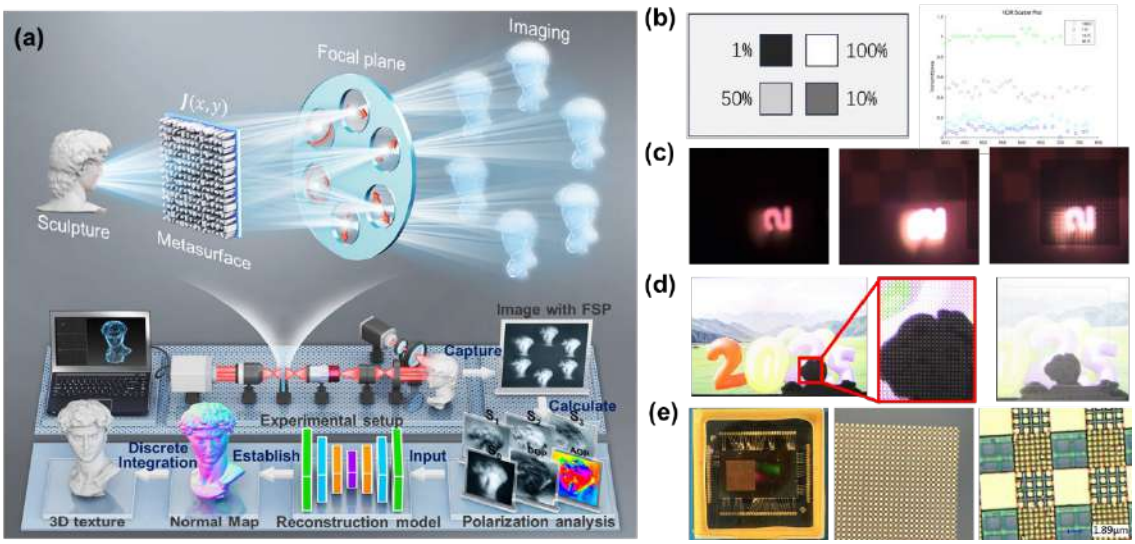


Fig. (a) The schematic diagram of miniaturized snapshot polarimetric stereoscopic imaging with an individual metalens. (b) Numerical amplitude modulation of a single unit in the non-uniform transmittance metasurface and corresponding experimental measurements. (c) Imaging results under low exposure, high exposure, and HDR achieved by the metasurface-based system. (d) Imaging results of the metasurface-based system and optimization through computational processing. (e) Photographic image of the on-chip integrated fabrication, along with optical and electron microscope images.

Building complex nanophotonic device with self-assembled colloidal particles

Weihua Zhang

College of Engineering and Applied Sciences, Nanjing University, Nanjing, Jiangsu 210023, China
*corresponding author: zwh@nju.edu.cn

Abstract: Deterministic self-assembly techniques were developed for functional colloidal nanomaterials, including semiconductor, dielectric, plasmonic, and magnetic micro-/nanoparticles, with single-particle, nanometer precision. Using these techniques, novel devices such as subwavelength non-replicable QR codes and unidirectional optical antennas were demonstrated, presenting a new approach for fabricating complex nanophotonic devices.

Van Der Waals Polaritonic Crystals and Their Applications in THz Detection

Huanjun Chen*, Ximiao Wang, Shaojing Liu, Hongjia Zhu, and Shaozhi Deng

[1]State Key Laboratory of Optoelectronic Materials and Technologies, Guangdong Province Key Laboratory of Display Materials and Technologies, School of Electronics and Information Technology, Sun Yat-sen University, Guangzhou 510275, China

*corresponding author: chenhj8@mail.sysu.edu.cn

Abstract: Polaritons are hybrid modes formed through the coupling of the electromagnetic field with the charged collective excitations in materials [1]. They exhibit a remarkable ability to confine the electromagnetic field within or at the surface of a material, thereby significantly enhancing the interaction between electromagnetic fields and matter at the nanoscale. This unique property positions polaritons as highly advantageous for the development of nanophotonic and optoelectronic devices. Noble metals, doped semiconductors, and their nanostructures excel at supporting polaritons in the visible and near-infrared regime. However, their field confinement capabilities degrade significantly as the operational frequency shifts into the mid-infrared and terahertz region. This limitation makes them unsuitable for developing high-performance and miniaturized photonic and optoelectronic devices in the specified frequency domain. Recent studies have uncovered the remarkable capability of van der Waals (vdW) two-dimensional atomic crystals and their nanostructures to sustain diverse polaritonic modes across the mid-infrared to terahertz spectral range [2,3]. In this presentation, we will briefly review the roadmap of polaritonic van der Waals crystals. Subsequently, we will introduce our recent work on the plasmon polariton properties of graphene and its nanostructures. Following that, we will share our recent results on multiparameter THz detection using these graphene plasmonic nanostructures [4,5].

References:

1. Michaels, A. M.; Nirmal, M.; Brus, L. E. *J. Am. Chem. Soc.* **1999**, *121*, 9932.

2. Raether, H. *Surface Plasmons on Smooth and Rough Surfaces and on Gratings* (Springer, New York, **1988**).

1. Huang, K. *Nature* **1951**, *167*, 779–780.

2. Basov, D. N.; Fogler, M. M.; García de Abajo F. J. *Science* **2016**, *354*, aag1992.

3. Low, T.; Chaves, A.; Caldwell, J. D.; Kumar, A.; Fang, N. X.; Avouris P.; Heinz, T. F.; Guinea, F.; Martin-Moreno, L.; Koppens F. *Nat. Mater.* **2017**, *16*, 182–194.

4. Chen, H. J.; Wang, X. M.; Liu, S. J.; Cao, Z. L.; Li, J. Y.; Zhu, H. J.; Li, S. D.; Xu, N. S.; Deng, S. Z. *Adv. Mater.* **2025**, *37*, 2410946.

5. Liu, S. J.; Wang, X. M.; Xu, N. S.; Li, R. L.; Ou, H.; Li, S. D.; Zhu, Y. S.; Ke, Y. L.; Zhan, R. Z.; Chen, H. J.; Deng, S. Z. *Adv. Sci.* **2024**, *11*, 2401631.

Plasmonic sensing on nanofibers for in vivo protein measurement in the brain

J.F. Masson[1*], **M.H. Jodaylami**[1]

[1]Département de chimie, Institut Courtois, Centre interdisciplinaire de recherche sur le cerveau et l'apprentissage, Quebec Center for Advanced Materials, R1egroupement québécois sur les matériaux de pointe, Université de Montréal, Complexe des sciences, C.P. 6128 succursale Centre-Ville, Montréal, QC, H3C 3J7, Canada
[*]corresponding author: jf.masson@umontreal.ca

Abstract: The optical properties of nanofibers show a combination of resonator modes and lensing effect that enhances plasmonic enhancement. This presentation will detail these optical effects and show the application of nanofibers for monitoring proteins in brain tissue using surface-enhanced Raman scattering and its translation to in vivo measurement.

Ultrafast manipulation of collective modes via chiral fermions in a charge density wave Weyl semimetal

L. Cheng[1], Z. X. Wei[1], Y. G. Yao[2] and J. Qi[1*]

[1] State Key Laboratory of Electronic Thin Films and Integrated Devices, University of Electronic Science and Technology of China, Chengdu 610054, China

[2]School of Physics, Beijing Institute of Technology, Beijing 100081, China

[*]corresponding author: jbqi@uestc.edu.cn

Abstract: In Weyl semimetal $(TaSe_4)_2I$, excitation of femtosecond optical pulses induces terahertz emission in the CDW state, arising from contributions of ultrafast photocurrent and various collective modes. Due to topologically non-trivial linear bands, we discover that properties of the collective modes at low temperatures can be manipulated with an ultrafast manner.

Charge density wave (CDW) is widely present in various quantum materials[1], where investigation and control of its associated collective modes have been a subject of great interest[2]. Here, the terahertz (THz) emission spectroscopy has been used to study the collective excitations in the typical quasi-one-dimensional CDW Weyl semimetal $(TaSe_4)_2I$. Upon excitation of femtosecond optical pulses, we observe broadband THz radiation including the contribution from the ultrafast photocurrent and multiple collective modes related to CDW at low temperature. We discover that properties of the collective modes can be controlled by tuning the circular polarization state of the incident light (see Figure1). Essentially, the Weyl fermions play the key role in switching the phase of collective modes. Our findings have significant implications for manipulating CDW, provide novel insights into control of charge ordering parameters in quantum materials.

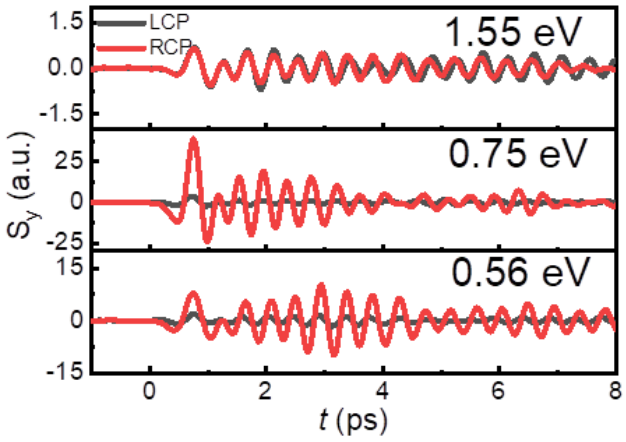


Figure1. Typical THz emission signal measured for left-handed (black) and right-handed (blue) circularly polarized pump light at 78 K with various photon energies.

Reference

[1] P. Monceau. "Electronic crystals: an experimental overview." Adv. Phys **61** 325 (2012).

[2] A. Tomeljak, H. Schäfer, D. Städter, et al. "Dynamics of photoinduced charge-density-wave to metal phase transition in $K_{0.3}MoO_3$. " Phys. Rev. lett. **102** 066404 (2009).

Coexisting and Cooperating Light-Matter Interaction Regimes in a Polaritonic Photovoltaic System

Roberto Termine[1], Vincenzo Caligiuri[1,2], Svetlana Siprova[1], Attilio Golemme[1,2,3], Aniket Patra [2,4], Giuseppe E. Lio[5], and Antonio De Luca[1,2]

[1] Institute of Nanotechnology CNR-NANOTEC, SS di Rende, Italy
[2] Department of Physics, University of Calabria, via P. Bucci, 31C, 87036, Rende (CS), Italy
[3]LPM (Laboratorio Preparazione Materiali), Materia-Star, Polo Tecnologico, 87036 Rende (CS), Italy
[4]Istituto Italiano di Tecnologia, via Morego 30, 16163 Genova (GE), Italy
[5]CNR-INO and European Laboratory for Non Linear Spectroscopy (LENS), Via Nello Carrara, 1 - 50019, Sesto Fiorentino, Firenze (FI), Italy

[*]corresponding author: roberto.termine@cnr.it

Abstract:
We studied the properties of a perovskite photovoltaic cell engineered to behave as an optical cavity tuned to the excitonic transition of the embedded active material to study how the cooperation of the strong coupling regime and the photovoltaic effect can enhance the photovoltaic properties of the cell.

.

Nanostructured Surfaces for Enhanced Spectroscopy and Nonlinear Optics

L. Razzari*

Institut National de la Recherche Scientifique, Centre Énergie Matériaux Télécommunications (INRS-EMT), Canada
*luca.razzari@inrs.ca

Abstract: In this talk, I will present our results regarding the exploitation of a nanostructured metallic surface to enhance terahertz spectroscopy of monolayer WSe_2 [1], as well as the use of dielectric metasurfaces to artificially engineer nonlinear wavelength conversion.

References

[1] X. Jin et al., Enhanced Terahertz Spectroscopy of a Monolayer Transition Metal Dichalcogenide, *Adv. Funct. Mater.* 2419841, 2025.

Configurable Quantum Simulator for Few Atoms in a Super-Resolved Optical Tweezers

V. Mancois[1,2], K. Lim[1], H. Wu[3], Y. Shen[1,4] and D. Wilkowski[1,2,5]

[1]Centre for Disruptive Photonic Technologies, SPMS, Nanyang Technological University, Singapore

[2]Majulab, International Joint Research Unit IRL 3654, CNRS, Universite Cote d'Azur, Sorbonne Universite, National University of Singapore, Nanyang Technological University, Singapore

[3]Wang Da-Heng Center, Heilongjiang Key Laboratory of Quantum Control, Harbin University of Science and Technology, Harbin, China

[4]School of Electrical and Electronic Engineering, Nanyang Technological University, Singapore

[5]Centre for Quantum Technologies, National University of Singapore, Singapore

*Corresponding author: vincent.mancois@ntu.edu.sg

Abstract: Many fields of research rely on optical trapping, whose limits are dictated by diffraction. We report the trapping of multiple cold atoms in four super-resolved traps and demonstrated the control of the reshuffling of atoms among traps. We also provide a simple and quantitative modelling of the atom dynamics.

Over the past few years, tremendous efforts have been made to realize digital and analog quantum computation using cold atoms trapped in optical tweezer arrays. This technique offers versatility in trapping geometry and atom arrangement. However, the inter-trap distance remains typically large, limiting the interaction strength between atoms and preventing tunneling. Here, we address this important limitation by creating an ensemble of four traps super-resolved in size and separation [1].

To realize our super-resolved light structures, we use an original approach consisting of a superoscillatory field [2] in combination with phase control of the traps. We benchmark the system by transferring atoms into the super-resolved traps with an efficiency close to one. In addition, by analyzing the atom-pair losses, we are able to precisely characterize the reshuffling mechanisms of the atoms among the traps. This is an important figure of merit for future quantum simulation experiments. Finally, the compact arrangement of the tweezers can be used to strongly enhance energy scales in quantum simulation and computing experiments. Thanks to its promising spatial and temporal control, super-resolution has the potential to initiate a paradigm shift in the field of atom trapping.

References

1. Lim, K., Mancois V., Wu H., Shen Y and Wilkowski D. "Super-resolution optical trapping of multiple cold atoms" Arxiv, 2502.07177 (2025).
2. Rivy H. M., Aljunid S. A., Lassalle E., Zheludev N. I., and Wilkowski D., "Single atom in a superoscillatory optical trap", Commun. Phys. 6, 155 (2023).

Optical skyrmions from metamaterials

Yijie Shen and Nilo Mata-Cervera

Nanyang Technological University, Singapore

Abstract: Optical meta-materials and the topologies of light are two emerging hot topics in the photonics community. In this article, we perspective a very emerging direction – Meta-devices for generation, manipulation and detection of diverse novel topologies of light – which will be rapidly growing interdisciplinary field across the studies in electromagnetic metamaterials and structured light. We will provide a bird's-eye view of the roadmap outlining how recent metasurface technologies enable integrated optical skyrmion generators and the future trends in meta-devices for generating more complex light topologies, which will help turning these novel structures from abstract concepts into practical applications.

1. Introduction: Many novel particle-like topologies were recently created in light [Nat. Photon. 18, 15–25 (2024)]. Generation of such topologies requires precise spatial control over phase, amplitude and polarization of light, which has been traditionally addressed with spatial light modulator setups, making it bulky and hindering applications. Metasurfaces and metamaterials [Science 376, eabi6860 (2022)] provide practical solutions for synthetizing the generation stage in a single device. Up to date, basic topological textures have been generated with metasurfaces, but the generation of higher dimensional particle-like topologies is still an intriguing direction to explore.

2. Recent advances of topological optical skyrmions: We summarize optical topologies in a zoological way. Singular points (phase, polarization singularities), then topological textures from basic cylindrical vector beams, 2D baby skyrmions, 3D and 4D knots, links, and particle-like topologies.

3. Meta-generators of topological light: Optical vortices with phase and polarization singularities is one of the main applications of meta-generators [Science368,707-708(2020), Science357,645-645(2017), Science374, eabj0039 (2021), Nanophotonics 10, no.5, 1469-1486 (2021)]. Here we focus on topologies beyond 2D (skyrmions, merons, hopfions), the emerging meta-designs for skyrmions [Nat Commun 15, 10141 (2024), J. Opt. 26 09LT01, Optica11 (11), 1588-1594 (2024), Nanophotonics (2025)] optical knots [Adv Opt Mat, 7(10), 1900263 (2019), ACS Photonics 11(10), 4380-4389 (2024)]. The next challenge is tunability, there is tunable OAM vector solution [Science 368, 760-763 (2020); Nature 612, 246–251 (2022)] and recent designs with tunable knotted fields [arXiv:2410.16756 (2024)], but how to achieve tunable control of polarization-inhomogeneous beams with topological features is still a direction to explore.

4. Perspectives of meta-detectors of topological light: We review the meta-devices for OAM sorting [Laser & Photonics Reviews, 18(9), 2400113, ACS Photonics 9(9), 3043-3051 (2022)] and meta-detectors of OAM [Science 368, 763–767 (2020)] and SAM-OAM [Nat Commun 15, 5396 (2024)] with detection of the higher-order Poincaré sphere. However, currently there are no compact meta-devices for detection of skyrmion number or other higher-order topological structures of light. We will propose the potential solutions and perspective the future trend of the meta-detectors for topologies of light.

Thermal Photonics for Advanced Energy Conversion Systems

A. Sakurai[1,2,3*]

[1] Department of Mechanical and Production Engineering, Niigata University, Japan
[2] Graduate School of Science and Technology, Niigata University, Japan
[3] Interdisciplinary Research Center for Carbon-Neutral Technologies, Niigata University, Japan
[*]corresponding author: sakurai@eng.niigata-u.ac.jp

Abstract: We investigate thermal photonics strategies for improving energy conversion efficiency. Emphasis is placed on near-field radiation, spectral control of emission, and carbon-based films. These approaches demonstrate the potential to surpass classical thermal limits, offering scalable routes to high-performance energy harvesting.

Thermal photonics offers a powerful framework for manipulating radiative and photonic heat transport to enhance energy conversion performance [1-3]. In this work, we present a set of studies focused on nanoscale control of thermal processes relevant to advanced energy systems. The first study explores near-field thermal radiation, where engineered photonic structures facilitate radiative heat transfer well beyond the blackbody limit. This enhancement is crucial for compact energy harvesting and thermal management applications under high energy density conditions. The second study examines a thermophotonic system optimized for low-grade waste heat utilization. By tailoring the spectral properties of emitters and filters, the system achieves far-field emission control that allows for efficient energy recovery even from sub-ambient sources [4]. This concept is particularly promising for applications where conventional thermodynamic cycles underperform due to temperature constraints. Lastly, we investigate carbon nanotube (CNT) films exhibiting strong anisotropic emission and wavelength-selective absorption. These films serve as robust platforms for directional radiative control, with implications for solar thermal conversion and thermally-driven photonic devices. Their unique spectral and thermal stability make them attractive candidates for scalable and tunable energy technologies.

Together, these results highlight the critical role of material design and spectral engineering in thermal photonics. The presented approaches offer practical routes to overcome classical efficiency barriers and pave the way toward next-generation sustainable energy solutions.

Acknowledgement

This research was supported by JSPS KAKENHI Grant Number JP23K26048.

References

1. S. Fan, “Thermal Photonics and Energy Applications,” Joule, Vol. 1, pp. 264–273, 2017.
2. S. Basu, Z. M. Zhang, and C. J. Fu, “Review of near-field thermal radiation and its application to energy conversion,” International Journal of Energy Research, Vol. 33, No. 13, pp. 1203–1232, 2009.
3. A. Fiorino, D. Thompson, L. Zhu, T. Reddy, P. Ben-Abdallah, and E. Meyhofer, “Thermal radiation and energy conversion in the near field,” Nature Nanotechnology, Vol. 13, pp. 806–811, 2018.
4. Y. Matsuno, N. Nagumo, M. Araki, K. Yada, K. Yamaga, and A. Sakurai, “Non-equilibrium mid-infrared black phosphorus light emitter and absorber for thermophotonic applications,” Journal of Quantitative Spectroscopy and Radiative Transfer, Vol. 288, 108271, 2022.

Quadrupole Topological Phase Constructed by Gyromagnetic Photonic Crystal

Peiheng Zhou[1*], Gui-Geng Liu[2], Qindong Xie[1], Longjiang Deng[1], and Baile Zhang[2,3]

[1]National Engineering Research Center of Electromagnetic Radiation Control Materials, Key Laboratory of Multi-spectral Absorbing Materials and Structures of Ministry of Education, University of Electronic Science and Technology of China, Chengdu 611731, China

[2]Division of Physics and Applied Physics, School of Physical and Mathematical Sciences, Nanyang Technological University, 21 Nanyang Link, Singapore 637371, Singapore

[3]Centre for Disruptive Photonic Technologies, The Photonics Institute, Nanyang Technological University, 50 Nanyang Avenue, Singapore 639798, Singapore

[*]corresponding author: phzhou@uestc.edu.cn

Abstract: Here we report the study of a quadrupole topological states in a gyromagnetic PhC, and verify its topological phase transition from the Chern insulator phase, as well as the formation of topological bound states in the continuum. This work thus expands the scope of higher-order topological physics, and integrates topologically protected propagating and localized modes in a same platform.

Polarization optics using nonlocal dielectric metasurfaces

Yu Geun Ki[1], Changhyun Lee[1], SeokJae Yoo[2] and Soo Jin Kim[1*]

[1]School of Electrical Engineering, Korea University, Seoul 02841, Republic of Korea
[2]Department of Physics, Inha University, Incheon 22212, Republic of Korea
[*]corresponding author: kimsjku@korea.ac.kr

Abstract: In this work, we exploit nonlocal resonances, including guided mode resonances (GMR), to realize ultrathin polarization optics which exhibit spin-selective responses with near-unity efficiency. We experimentally demonstrate chiroptical behavior induced by symmetry-breaking in nanostructures, facilitating precise manipulation of polarization states and effective detection of Stokes parameters at the nanoscale.

The field of nanophotonics has attracted significant technological interest over the past decade due to its potential to enable ultrathin optical components and next-generation optoelectronic devices. However, a key challenge remains in addressing the mismatch between electronic and photonic length scales: while CMOS technology has successfully scaled electronics to the nanoscale, photonic components are still predominantly limited to the microscale.

Metasurfaces—ultrathin layers composed of subwavelength nanostructures—have emerged as a promising solution to overcome these limitations and drive advances in nano-optics development. More recently, designing metasurfaces with the geometry of symmetry-breaking have enabled the effective manipulation and detection of spin states of light [1-3]. Such metasurfaces, typically defined as chiral metasurfaces, open up new opportunities in spin-selective light–matter interactions and chiroptical applications including molecular sensing, optical communications, and advanced imaging.

In this work, we explore effective light manipulation with spin-selective fashion using nonlocal dielectric metasurfaces engineered with symmetry-breaking in nanostructures. We optimize the design parameters of such nanostructures for a dynamically reconfigurable metasurface capable of controlling phase, wavefront, and polarization states of light with near unity efficiency at the nanoscale. We further reveal that the chiroptical behavior of the designed metasurface could be maximized by judiciously combining nonlocal and local resonances, such as GMR and Mie resonances.

In addition, we analyze various symmetry-breaking configurations—both in-plane and out-of-plane—to distinguish between intrinsic and extrinsic types of chiral metasurfaces. In particular, ultrathin and planar type of intrinsic chiral properties without three-dimensional structures are demonstrated by designing a metasurface with substrate induced out-of-plane symmetry breaking. It is found that the hybrid resonance mode caused by the chiral resonance interacting with the substrate breaks the out-of-plane mirror symmetry of the optical near fields and mimics the resonances which typically occur in helicity structures. The operational principles of these metasurfaces are evalusted using coupled-mode theory, which offers a robust framework for their design by relating the co-polarized and cross-polarized components of transmitted light in terms of their phase and amplitude.

In summary, the proposed work demonstrates the potential of nonlocal dielectric metasurfaces as polarization optics and effective platform for compact and nanoscaled photonic systems. By strategically integrating nanostructures with symmetry-breaking and leveraging hybrid resonances, we demonstrate versatile control over multiple optical degrees of freedom at the nanoscale including the detection of Stokes parameters

and manipulation of polarization conversions. The designing rules of polarization metasurface can be applicable to the development of tunable, multifunctional metasurfaces tailored for applications in integrated optics, chiral light detection, and next-generation polarization-based nanoscaled photonics.

Acknowledgements: This research was supported by National Research Foundation of Korea (NRF) grant funded by the Korea government (MSIT) (No. RS-2023-00254920) and by the Technology Innovation Program (korea-led for K-sensor technology for market leadership) (No. RS-2023-00256247) funded by the Ministry of Trade, Industry and Energy (MOTIE, Korea) and by Korea University grant.

References

1. Tanaka, K.; Arslan, D.; Fasold, S.; Steinert, M.; Sautter, J. r.; Falkner, M.; Pertsch, T.; Decker, M.; Staude, I. “Chiral Bilayer All-dielectric Metasurfaces” ACS Nano,14, 15926, (2020)
2. Zhao, Y.; Belkin, M.; Alù, A. “Twisted Optical Metamaterials for Planarized Ultrathin Broadband Circular Polarizers”, Nat. Communi. 3, 870 (2012)
3. Ki, Y. G.; Jeon, B. J.; Song, I. H.; Kim, S. J.; Jeon, S.; Kim, S. J. “Realizing Minimally Perturbed, Nonlocal Chiral Metasurfaces for Direct Stokes Parameter Detection, ACS Nano, Vol 18, No. 9, 7064-7073, 2024

Extreme-ultraviolet spatiotemporal optical vortices

Rodrigo Martín-Hernández[1,2], Guan Gui[3], Luis Plaja[1,2], Henry K. Kapteyn[3], Margaret M. Murnane[3], Miguel A. Porras[4], Chen-Ting Liao[3,5] and Carlos Hernández-García[1,2*]

[1]Grupo de Investigación en Aplicaciones del Láser y Fotónica, Departamento de Física Aplicada, Universidad de Salamanca, 37008, Salamanca, Spain
[2]Unidad de Excelencia en Luz y Materia Estructuradas (LUMES), Universidad de Salamanca, Salamanca, Spain
[3]JILA and Department of Physics, University of Colorado and NIST, Boulder, CO 80309, USA
[4]Grupo de Sistemas Complejos, ETSIME, Universidad Politécnica de Madrid, 28003 Madrid, Spain
[5]Department of Physics, Indiana University, Bloomington, IN 47405, USA
[*]corresponding author: carloshergar@usal.es

Abstract: We demonstrate the first generation of spatiotemporal optical vortices (STOVs) in the extreme ultraviolet via high harmonic generation. This highly nonlinear process enables attosecond-scale spatiotemporal coupling, paving the way for novel probes of ultrafast light-matter interactions with structured light carrying high topological charge in space and time.

In recent years, the ability to tailor structured light pulses has attracted growing interest due to the emergence of novel light-matter interaction schemes. For instance, vector beams with spatially varying polarization states enable interactions where the magnetic field can dominate over the electric field [1, 2]. More recently, spatiotemporal optical vortices (STOVs)—light pulses carrying angular momentum coupled in space and time—have gained attention. Unlike conventional longitudinal optical vortices with spiral phase profiles in the transverse plane, STOVs exhibit twisted phase structures in the spatiotemporal domain. Defined by their topological charge—the number of 2πpi phase windings across space and time—STOVs have been successfully generated in the near-infrared (IR) spectrum, as well as in the visible range through perturbative harmonic generation [3,4]. However, generating STOVs in the extreme ultraviolet (EUV) or even soft x-ray range, where attosecond temporal resolution is achievable, has remained challenging due to the inefficiency of conventional optics at such high frequencies.

In this work, we build on a successful strategy that has enabled during the last decade the generation of highly coherent structured light beams in the EUV and even attosecond regime. Exploiting the nonlinear process of high-order harmonic generation (HHG) we demonstrate that STOVs can be upconverted from the near-IR into the EUV. This approach has proven highly effective in generating longitudinal high-frequency vortices [5], among other structured light beams. Recent theoretical advancements have also outlined the feasibility of producing high-frequency STOVs through HHG [6]. Notably, focused STOVs introduce additional degrees of control over the HHG process, particularly with respect to the target's position, as these vortices do not constitute propagating eigenmodes [7]. We demonstrate both theoretically and experimentally that EUV high-order harmonic STOVs can be generated through HHG [8]. Our research opens the pathway for using STOVs with controlled high topological charges in the EUV/soft x-ray spectral regime, offering unique tools to probe ultrafast electronic and magnetic dynamics near absorption edges. The spatiotemporal characterization of EUV STOVs and SSOVs is addressed, aiming to motivate the development of complete spatiotemporal characterization techniques of HHG pulses with tailored angular momentum [9-10].

ACKNOWLEDGEMENTS

This project has received funding from the European Research Council (ERC) under the European Union's Horizon 2020 research and innovation programme (grant agreement No 851201). C.H.-G. and L.P. acknowledge funding from Ministerio de Ciencia e Innovación (Grant PID2022-142340NB-I00) and Junta de Castilla y León and Fondo Europeo de Desarrollo Regional (FEDER), under grant No. SA108P24. Financial support of the Department of Education of the Junta de Castilla y León and FEDER Funds is gratefully acknowledged (Escalera de Excelencia CLU-2023-1-02). C.T.L. acknowledges support from AFOSR YIP (FA9550-23-1-0234) and partial support by DOE BER (DE-SC0023314). M.A.P. acknowledges funding from Ministerio de Ciencia e Innovación (Grant PID2021-122711NB-C21). M.M.M. and H.C.K. gratefully acknowledge support from the Department of Energy Basic Energy Sciences Award No. DE-FG02-99ER14982 for the experiments, which were done at JILA, and the US National Science Foundation through JILA Physics Frontiers Center PHY-2317149 for the experimental facilities. R.M.-H., L.P. and C.H.-G. thankfully acknowledge RES resources provided by BSC in MareNostrum 5, and CESGA in Finisterrae3 to FI-2024-2-0010 and FI-2024-3-0035.

REFERENCES

[1] M. Blanco, F. Cambronero, M. T. Flores-Arias, E. Conejero Jarque, L. Plaja, C. Hernández-García, Ultraintense femtosecond magnetic nanoprobes induced by azimuthally polarized laser beams, ACS Photonics 6, 38–42 (2019).

[2] L. Sánchez-Tejerina, R. Martín-Hernández, R. Yanes, L. Plaja, L. López-Díaz, and C. Hernández-García, All-optical non-linear chiral ultrafast magnetization dynamics driven by circularly polarized magnetic fields. High Power Laser Science and Engineering 11, e82 (2023).

[3] G. Gui, N. J. Brooks, et al. Second-harmonic generation and the conservation of spatiotemporal orbital angular momentum of light. Nat. Photon. 15, 608–613 (2021).

[4] S. W. Hancock, S. Zahedpour, and H. M. Milchberg, "Second-harmonic generation of spatiotemporal optical vortices and conservation of orbital angular momentum," Optica 8, 594-597 (2021)

[5] C. Hernández-García, A. Picón, J. San Román, and L. Plaja "Attosecond extreme ultraviolet vortices from high-order harmonic generation" Phys. Rev. Lett., 111:083602, 2013.

[6] Fang, Y., Lu, S., & Liu, Y. Controlling photon transverse orbital angular momentum in high harmonic generation. Physical Review Letters, 127(27), 273901 (2021).

[7] M.A. Porras and S.W. Jolly "Procedure for imparting transverse orbital angular momentum by focusing spatiotemporally coupled ultrashort pulses", Phys. Rev. A 109, 033514 (2024).

[8] R. Martín-Hernández, G. Gui, L. Plaja, H. C. Kapteyn, M. M. Murnane, C.-T. Liao, M. A. Porras and C. Hernández-García. arXiv:2412.01716, Nature Photonics, in press (2025).

[9] Y. Esashi, C.-T. Liao, et al., "Ptychographic amplitude and phase reconstruction of bichromatic vortex beams," Opt. Express 26, 34007-34015 (2018).

[10] A. K. Pandey, et al., ACS Photonics *9* (3), 944-951 (2022).

Optical properties of nanoporous gold and their change upon electrochemical oxidation

Maurice Pfeiffer[1], Xinyan Wu[1], Manfred Eich[1,2], Alexander Yu. Petrov[1,2*]
[1]Institute of Optical and Electronic Materials, Hamburg University of Technology, Hamburg, Germany
[2]Institute of Functional Materials for Sustainability, Helmholtz Zentrum Hereon, Geesthacht, Germany
[*]corresponding author: a.petrov@tuhh.de

Abstract: Nanoporous gold shows a strong change of color upon electrochemical oxidation. This can result from a reduced volume of plasmonic gold, dielectric coating on the gold surface or an increase of electron collision frequency. Using brute-force simulations we identify the contribution of these effects.

Nanoporous gold (npAu) is a sponge-like material obtained by dealloying. The dealloying procedure typically leads to a porous sponge-like structure with gold ligament diameter in the order of 10 nm. The thin films of npAu usually have brown appearance as radiation can enter the network structure and is strongly absorbed. This absorption has two origins: ligaments parallel to applied electric field and resonances between dangling ligaments at the surface of npAu. Upon electrochemical oxidation the npAu color changes to black which is attributed to increased absorption and transmission. Several explanations for the observed optical effect are possible:

1. Oxidation results in a smaller volume of gold in the porous structure, changing its effective dielectric constant. Also, the gap between two gold surfaces of the dangling ligaments is increasing.
2. The dielectric coating produced by oxidation changes the effective dielectric constant of npAu and increases the dielectric constant in the gap between two dangling ligaments.
3. The change of gold surface leads to the increase of the electron collision frequency, so-called Chemical Interface Damping (CID) [1]. CID changes the effective medium parameters, but also the damping of resonances at dangling ligaments.

We have implemented a 3D leveled-wave model for the structure of npAu similar to Ref. [2] and simulated its optical response. Implementing all of these free effects sequentially, we have identified that gold volume reduction and dielectric coating both define the change of color in the visible range. Whereas CID effect becomes dominant only in the IR range.

This study shows the complexity of the random plasmonic network and its response to surface oxidation. Further reduction of the ligament size can be used to increase the modulation by electrochemical oxidation and can lead to even stronger modulation of the reflection and transmission.

References

1. M. Pfeiffer, X. Wu, F. Ebrahimi, N. Mameka, M. Eich, and A. Yu. Petrov, “Chemical Interface Damping by Electrochemical Gold Oxidation,” J. Phys. Chem. C, vol. 128, no. 37, pp. 15686–15693, 2024
2. Y. Li, B. N. Dinh Ngô, J. Markmann, and J. Weissmüller, “Topology evolution during coarsening of nanoscale metal network structures,” Phys. Rev. Mater., vol. 3, no. 7, p. 76001, 2019

Low-Loss Phase Change Materials for integrated photonics

I. Zeimpekis[1,2*], A. Shoaa[2], Q. Luo[2], I. Johnson[2], D. Lawson[3], L. Rozaqi[3], P. Deoli[3], D. Trubacs[3], S. Blundell[2], O. L. Muskens[3], and F. Gardes[2]

[1]Electronics and Computer Science, Faculty of Engineering and Physical Sciences, University of Southampton, UK
[2]Optoelectronics Research Centre, Faculty of Engineering and Physical Sciences, University of Southampton, UK
[3]Physics and Astronomy, Faculty of Engineering and Physical Sciences, University of Southampton, UK

[*]corresponding author: izk@soton.ac.uk

Abstract: Optical phase change materials (PCMs), such as Sb_2Se_3 and Sb_2S_3, have created a paradigm shift for integrated photonics. Ought to the decoupling of phase and amplitude they enable more complex functions and lower losses. This talk will discuss the development of low-loss PCMs for higher transparency and longer switching durability.

Optical response in twisted bilayer graphene

M. Sánchez Sánchez[1], J. González[2], and T. Stauber[1*]
[1]Instituto de Ciencia de Materiales de Madrid, CSIC, E-28049 Madrid, Spain
[2]Instituto de Estructura de la Materia, CSIC, E-28006 Madrid, Spain
Corresponding author: tobias.stauber@csic.es

Abstract: We report on the optical response of twisted bilayer graphene obtained from an atomistic tight-binding model. Within the Hartree-Fock approximation, the Drude response increases due to the renormalization of the Fermi velocity. We will also calculate the chiral response and the shift current related to the Berry curvature dipole.

Twisted bilayer graphene (TBG) has attracted much attention mainly due to the discovery of superconductivity [1]. Assuming the weak-coupling regime such that the one-particle band-structure of the normal and superconducting state only differs by the one-particle gap, the transverse superfluid density can be discussed by the longitudinal Drude weight that can be measured e.g. via scattering-type scanning near-field optical microscopy. Calculating the optical response of the TBG can thus complement the discussion of the electronic properties.

Here, we will investigate the optical properties of TBG employing the tight-binding model using the Slater-Koster parametrization proposed by Koshino and Moon [2]. Also lattice relaxation shall be included, but more importantly, Coulomb interaction is approximated by a self-consistent Hartree-Fock scheme [3]. By this, we are able to discuss the renormalization of the Drude weight shown in Fig. 1 for a twist-angle of 1.3°.

Apart from that, not only the charge response characterizes TBG, also the huge paramagnetic counterflow and chiral response give important insights in the electronic structure of TBG. Together with the charge response, they are defined by the following expressions:

$$D_{tot}(\mu) = \frac{1}{2A} \sum_{\mathbf{k},n} \int \mathbf{k},n|j_x|\ \mathbf{k},n\ |^2 + |\ \mathbf{k},n|j_y|\mathbf{k},n\ |^2\big)\, f_F(\epsilon_{\mathbf{k},n} \in \mu) \tag{1}$$

$$D_{mag}(\mu) = \frac{1}{2A} \sum_{\mathbf{k},n} \int \mathbf{k},n|j_x^1 \in j_x^2|\mathbf{k},n\ |^2 + |\ \mathbf{k},n|j_y^1 \in j_y^2|\mathbf{k},n\ |^2\big)\, f_F(\epsilon_{\mathbf{k},n} \in \mu) \tag{2}$$

$$D_{chi}(\mu) = \frac{1}{2A} \sum_{\mathbf{k},n} \int \mathbf{k},n|\mathbf{j}^1|\mathbf{k},n\ |\times|\ \mathbf{k},n|\mathbf{j}|\mathbf{k},n\ |^2\big)\, f_F(\epsilon_{\mathbf{k},n} \in \mu) \tag{3}$$

In the above equations, we introduced the eigenenergies $\epsilon_{\mathbf{k},n}$ and eigenstates $|\mathbf{k},n\ $ of the tight-binding Hamiltonian as well as $\mathbf{j}^\ell$, the sheet-currents of layer ℓ, and $\mathbf{j}$, the total current. Furthermore, $f_F(x) = (e^{\beta x}+1)^{-1}$ denotes the Fermi function with $\beta = (k_B T)^{-1}$.

Finally, we will also comment on non-linear response and discuss shift current. Special attention shall be placed on the quantum response due to a Berry curvature dipole, present in TBG samples with uniaxial heterostrain.

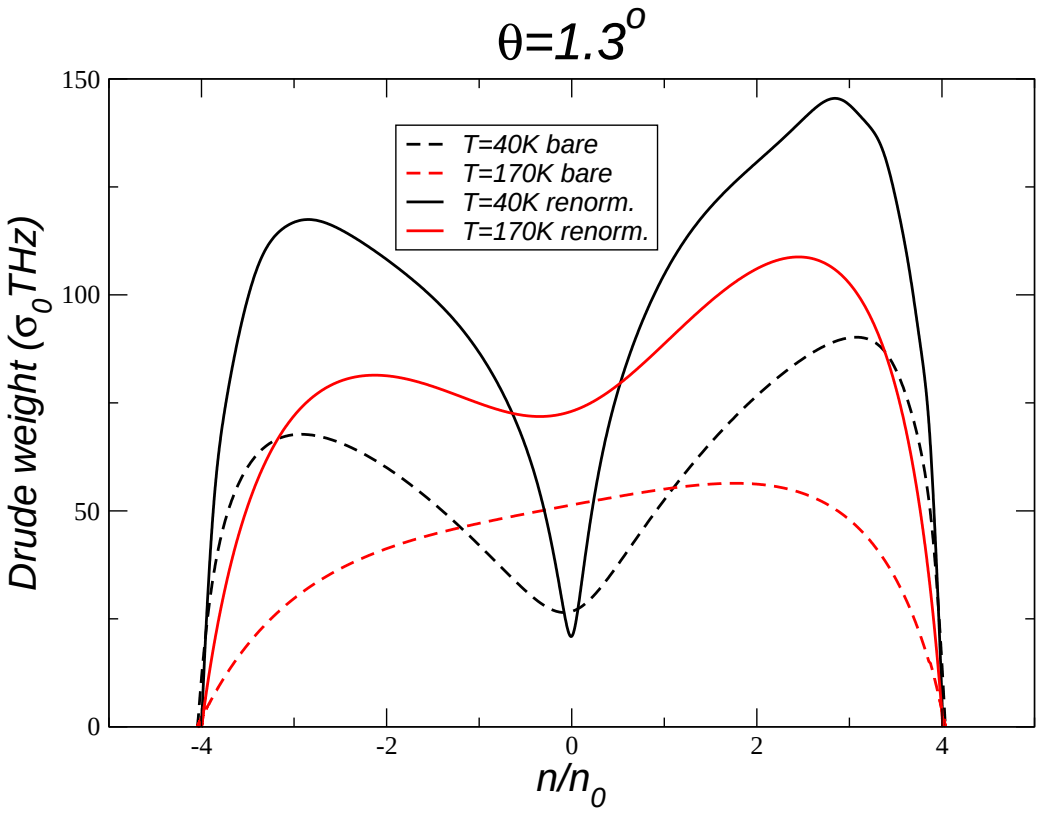


Figure 1: The Drude weight at temperatures $T = 40, 170$K as function of the carrier density n of the flat bands with n_0 being the density of one particle per moiré unit cell. The dashed lines are the bare quantities whereas the solid lines denote the renormalized Drude weights due to Coulomb interaction, in units of the conductance quantum $\sigma_0 = e^2/h$.

Acknowledgements. The work was supported by grant PID2023-146461NB-I00 funded by Ministerio de Ciencia, Innovación y Universidades as well as by the CSIC Research Platform on Quantum Technologies PTI-001. The access to computational resources of CESGA (Centro de Supercomputación de Galicia) is also gratefully acknowledged.

References

1. Cao,Y., V. Fatemi, S. Fang, K. Watanabe, T. Taniguchi, E. Kaxiras, and P. Jarillo-Herrero, "Unconventional superconductivity in magic-angle graphene superlattices," *Nature*, Vol. 556, pp. 43–50, 2018.

2. Moon, P. and M. Koshino, "Optical absorption in twisted bilayer graphene," *Phys. Rev. B*, Vol. 87, 205404, 2013.

3. Sánchez Sánchez, M., J. González, and T. Stauber, "Nonflat bands and chiral symmetry in magic-angle twisted bilayer graphene", *arXiv:2501.09197*, 2025

Heterostrucutred Photonic Media for PHz Optoelectronics Applications

Václav Hanus[1], Beatrix Fehér[1*] and Péter Dombi[1,2,*]

[1] HUN-REN Wigner Research Centre for Physics, 1121 Budapest, Hungary
[2] ELI ALPS Research Institute, ELI ERIC, 6728 Szeged, Hungary
[*]Corresponding author: dombi.peter@wigner.hu, dombi.peter@eli-alps.hu

Abstract: We demonstrate an optical chip with which one can induce the transient metallization of dielectrics with pJ-level femtosecond laser pulses in micron-sized gaps between electrodes. Because of the ultrafast and reversible nature of the current generation process, our device paves the way toward PHz optoelectronics applications.

Ultrafast current control in dielectric media was demonstrated some 12 years ago with amplified femtosecond laser pulses [1]. By the use of few-optical-cycle pulses as short as 5 fs, one can even steer the direction of the generated current with the carrier-envelope phase of the pulse, enabling ultrafast switching applications.

Based on this phenomenon, we developed an optical chip with which we realized light-field-driven current control in homogeneous dielectric media with pJ-level laser pulses at 80 MHz repetition rate, i.e. the full repetition rate of a femtosecond laser oscillator for the first time [2]. As a first application, we used this device for building a 3D carrier-envelope phase scanner tool [3].

We will also feature very recent results on how to use dielectric-metal heterostructures to enhance CEP dependent signal levels significantly, also relevant for the strong-field nano-optics research direction [4]. In addition, our new experiments on revealing the mechanisms of the ultrafast current generation process will also be presented.

In summary, our demonstration of a robust optical-to-electrical readout of light waveforms using an engineered heterostructured material represents an important cornerstone for the development of few-cycle beam diagnostics and PHz devices.

References

[1] A. Schiffrin et al., “Optical-field-induced current in dielectrics,” Nature **493**, 70 (2013).
[2] V. Hanus et al., „Light-field-driven current control in solids with pJ-level laser pulses at 80 MHz repetition rate” Optica **8,** 570-576 (2021).
[3] V. Hanus et al., “Carrier-envelope phase on-chip scanner and control of laser beams,” Nature Commun. **14**, 5068 (2023).
[4] P. Dombi et al., “Strong-field nano-optics,” Rev. Mod. Phys. **92**, 025003 (2020).

Modifying perovskite solar cell architecture to limit the effective radiative recombination to enhance the open circuit voltage

M. D'Andrea[1,*], R. Runjun[1], F. Bernal-Texca[1], and Jordi Martorell[1,2]

[1]ICFO-The Institute of Photonic Sciences, The Barcelona Institute of Science and Technology, 08860 Castelldefels, Barcelona Spain.
[2]Departament de Física, Universitat Politécnica de Catalunya, Terrassa 08222, Spain.

[*]Corresponding author: Martina.Dandrea@icfo.eu

Abstract: We provide experimental evidence that an effective radiative recombination of complete perovskite cells can be larger than 10% of the total direct recombination. The design and fabrication of nano-structures which are effective in limiting radiative recombination and raising the open circuit voltage without significantly altering sunlight absorption will be discussed.

Summary:

Single junction semiconductor non-concentrator solar cell devices can convert sunlight into electrical energy with a relatively low upper limit efficiency established by Shockley and Queisser many years ago. Different intrinsic energy loss mechanisms such as thermalization, below bandgap transmission or Boltzmann losses limit the power conversion efficiency of such photovoltaic devices to about 33 %. Overcoming thermalization or below bandgap losses has been explored following different strategies. Among them, the tandem or multiple junction approach are, probably, the most successful ones. However, Boltzmann losses, which are linked to the large mismatch between the cell light absorption and emission cones, have been largely overlooked for several different reasons which partially relate to a low external fluorescence quantum yield in the majority of the photovoltaic configurations used and the challenge to obtain cell architectures simultaneously effective in trapping photons emitted by the photovoltaic material but also in capturing sun photons.

It has been shown that an adequate nano-structuration of the solar cell architecture may lead to an upper limit conversion efficiencies slightly higher than 43%. In here, we will provide experimental measurements based on a $Cs_{0.05}FA_{0.95}PbI_3$ perovskite cell indicating that the effective radiative recombination of completed cells can be larger than 10% of the total direct recombination. We will also discuss the design and fabrication of nano-structures which are effective in limiting radiative recombination without significantly altering sun photon absorption in perovskite solar cells.

Active IR and THz light modulators based on epsilon-near zero InAs and GaSb semiconductor frequency-selective surfaces

J. Guise[1], F. Gonzalez-Posada Flores[1*], S. Blin[1] and T. Taliercio[1]

[1]Institute for Electronic and Systems, University of Montpellier, France
[*]corresponding author: fernando.gonzalez-posada-flores@umontpellier.fr

Abstract: Our research explores light-matter interaction applications, focusing on surface field-enhanced optical filters and transducers in the mid-infrared (MIR) and terahertz (THz) spectral ranges using plasmonic effects. We present thermal and optical activation of epsilon-near-zero (ENZ) materials based on epitaxial InAs and GaSb semiconductors, with emphasis on THz and IR frequency-selective surface optical devices.

The terahertz (THz) and mid-infrared (MIR) ranges are critical for the development of efficient, tunable, and integrable detection and filtering devices. Our approach leverages plasmonic light-matter interactions in heavily doped semiconductors to address these challenges. In particular, we demonstrate how semiconductor-based plasmonic epsilon-near-zero (ENZ) platforms enable high-sensitivity detection and lay the foundation for reconfigurable IR filters. These advances have significant implications for healthcare diagnostics, environmental monitoring, spectroscopic imaging, and telecommunications.

Our work focuses on enhancing plasmonic filtering and transduction mechanisms in the THz and MIR domains using semiconductor-based metal-insulator-metal (MIM) structures, in which the insulating layer is replaced by an ENZ material. The development of such structures, featuring tunable absorption and resonance behavior through surface patterning, enables frequency-selective filtering. Ultimately, our goal is to dynamically control the activation of these metasurfaces to realize IR and THz filters integrated into photodetectors or spectrometers.

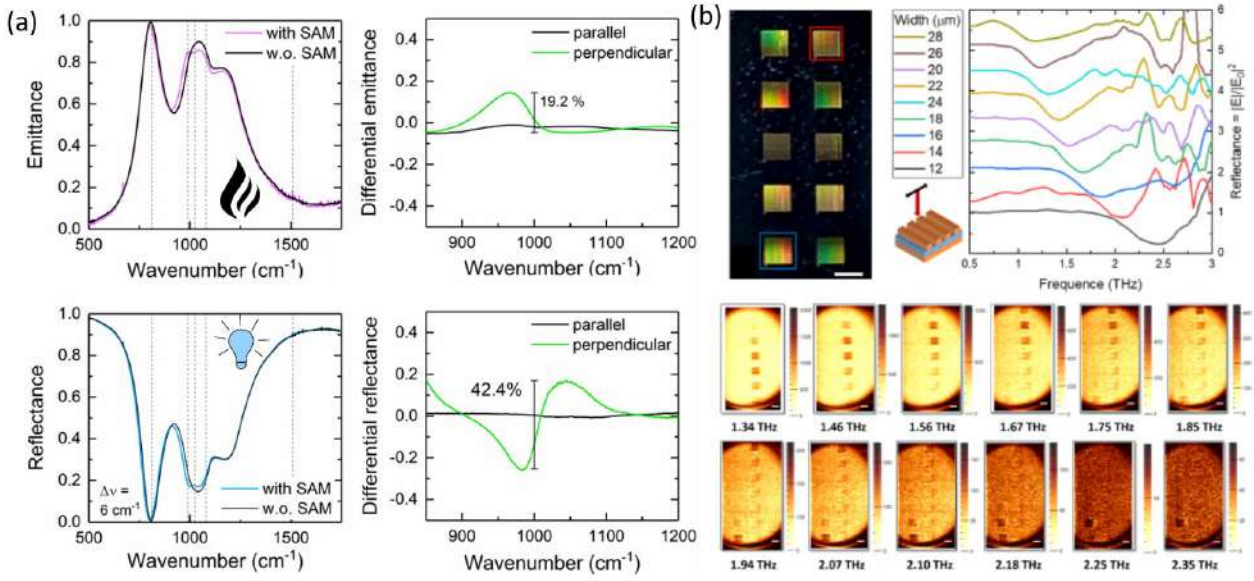


Figure 1: (a) Surface-enhanced thermal emission spectroscopy (SETES); (b) Frequency-selective THz surface measured via time-domain spectroscopy (TDS).

We adopt a systematic and modular approach, beginning with electromagnetic simulations (FDTD and RCWA) to design semiconductor-based plasmonic architectures tailored to MIR and THz operation. We present

a perfect absorber model based on a semiconductor MIM-like configuration that enables full absorption in the IR and THz ranges. This design supports surface enhanced thermal emission-based spectroscopy (SETES) and allows for the selective detection of surface-adsorbed molecules, such as self-assembled monolayers (SAMs).

The fabrication of the layered transducers and surface antennas is based on epitaxial GaSb and InAs. Precise doping allows us to target specific plasma frequencies and achieve ENZ behavior. Surface patterning is performed via e-beam lithography to create ribbon-shaped antennas that act as frequency-selective elements in both the MIR and THz regions. These platforms support scalable, on-chip THz sensing with both material and geometric tunability.

A major focus of our current work is the activation and dynamic control of metasurfaces for tunable IR and THz filters. Starting from monolayer and absorber models, we have engineered metasurfaces capable of thermal, optical, and electrical modulation. By tuning carrier density or integrating localized heaters and electrical contacts, we achieve real-time dynamic control of plasmonic resonances, enabling selective filtering on demand. This strategy opens the path toward reconfigurable IR filters directly integrated onto photodetectors, overcoming the inherent limitations of static designs.

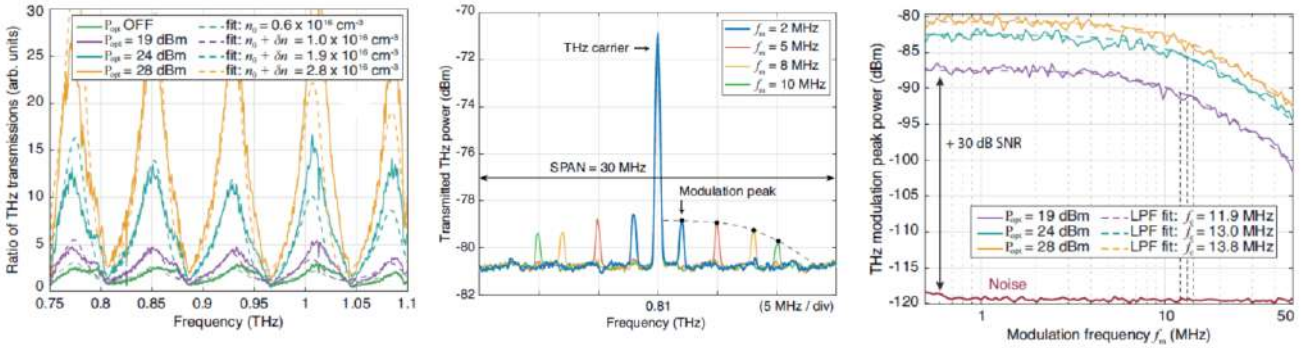


Figure 2: Optical modulation of THz signals under varying excitation power and frequencies.

Our results demonstrate that semiconductor-based plasmonics unlock new capabilities in THz sensing and dynamic IR filtering. We have established proof-of-concept platforms for surface-enhanced thermal molecular detection and tunable optical filtering in both the IR and THz domains using microstructured surfaces. Future research will focus on the development of fully integrated IR chips that combine sources, detectors, transducers, and reconfigurable metasurfaces. These systems have wide-ranging potential applications in on-chip spectroscopy, smart sensing, and telecommunications.

Acknowledgements: The authors acknowledged technical support from Aurelie Combres, Delphine Jourdain, Ariane Meguekan, Guilhem Boissier, and Jean-Marc Aniel. The authors acknowledged the technical work of the cleanroom staff, Frédéric Pichot, Jean-Marie Peiris, and Renaud Felix at Montpellier Technological Center (CTM). Funding from SEA (Occitanie French region-ESR-PREMAT-238), EXTRA (ANR 11-EQPX-0016, 2012 – 2019), NanoElastir (ASTRID 2020 – 2023), ENVIRODISORDERS (MUSE UM 2021– 2023), HYBAT (ANR 21-ESRE-0026, 2021 – 2029).

References

1. F. B. Barho, F. Gonzalez-Posada, L. Cerutti, T. Taliercio, “Heavily Doped Semiconductor Metamaterials for Mid-Infrared Multispectral Perfect Absorption and Thermal Emission”, Advanced Optical Materials, 2020, 8, 1901502.
2. F. Gonzalez-Posada, D. Coquillat, M. Najem, T. Taliercio, “THz time-domain spectroscopy modulated with semiconductor plasmonic perfect absorber”, Optics Express 2023, 31, 32152 – 32161.
3. J. Guise et al., “Measuring low doping level and short carrier lifetime in indium arsenide with a contactless terahertz technique at room temperature”, J. Appl. Phys. 2023,134, 165701

High-Speed Self-biased 2D InS Photodetector

S. R. Tamalampudi[1], Ghada Dushaq[1], and M. S. Rasras[1*]

[2] Electrical Engineering Program, Engineering Division, New York University Abu Dhabi, UAE
[*]corresponding author: mr5098@nyu.edu

Abstract: We demonstrate a high-speed, self-powered InSe Schottky photodetector featuring a 2.5 MHz response time at 785 nm. Through integration with a SiN platform and the application of strain modulation, we extend its detection capability to 1550 nm and attain an ultrafast response time of 4.5 ns under 974 nm excitation.

Indium selenide (InSe), a layered 2D semiconductor, has attracted considerable interest for optoelectronic applications due to its high optical absorption, direct bandgap, and tunable photoresponse across visible to near-infrared (NIR) wavelengths. InSe photodetectors have demonstrated outstanding responsivities up to ~10^5 A/W, with performance further enhanced by engineering strategies such as the use of graphene electrodes and h-BN encapsulation [1]. However, vertically illuminated InSe devices often suffer from slow response times in the millisecond-to-microsecond range, limiting their use in high-speed applications. Recent efforts have focused on self-driven photodetectors using heterojunctions (e.g., graphene/InSe/MoS_2, InSe/SnS_2) or Schottky junctions with engineered contacts to minimize interface doping [2].

Here, we report a self-powered, high-speed InSe photodetector based on an asymmetric Au-InSe-Gr/Au Schottky junction. Fabricated on a Si/SiO_2 substrate, the device exploits the work function difference between Au (~5.1 eV) and graphene (~4.7 eV), generating a built-in electric field for efficient photocarrier separation [3].

Device fabrication began on a Si/SiO_2 substrate, where Cr/Au metal contacts were first patterned via standard lithography. A multilayer graphene flake was mechanically transferred onto one of the Au pads. Following this, an exfoliated InSe flake was laminated to form an asymmetric Au-InSe-Gr/Au Schottky junction (Fig. 1a). This architecture leverages the work function disparity between gold (~5.1 eV) and graphene (~4.7 eV) to create a built-in electric field via an asymmetric Schottky barrier [3].

Electrical characterization was conducted under dark and 785 nm illumination (Fig. 1b). Even at 0 V bias, a photocurrent of 0.5 μA was observed due to the internal field effectively separating photogenerated carriers without the need for external power. Frequency response measurements under the same illumination revealed a 3-dB cutoff frequency of 2.5 MHz, equating to a response time (τ_a = 0.35/f_{3dB}) of 0.12 μs (Fig. 1c), outperforming previously reported self-driven InSe photodetectors [2].

To further enhance speed, InSe was integrated onto a silicon nitride (SiN) photonic waveguide platform. Figure 2a presents an SEM image of the integrated structure. I-V measurements across a broad spectral range (520–1550 nm) showed that waveguide-induced strain modified InSe's band structure, improving light absorption and carrier mobility (Figs. 2b–d). Speed performance significantly improved, with the 3-dB cutoff frequency rising to 77 MHz under 974 nm illumination and 5 MHz at 1310 nm (Fig. 2e) [4].

These findings emphasize the potential of combining InSe with photonic platforms for ultrafast, self-powered detection.

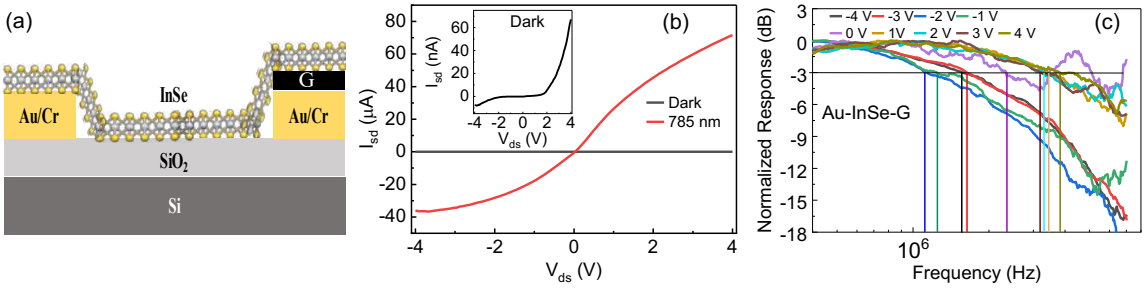


Fig. 1. (a) Schematic representation of the device. (b) I-V characteristics under dark and illuminated conditions at 785 nm. (c) Measured 3-dB cut-off frequency.

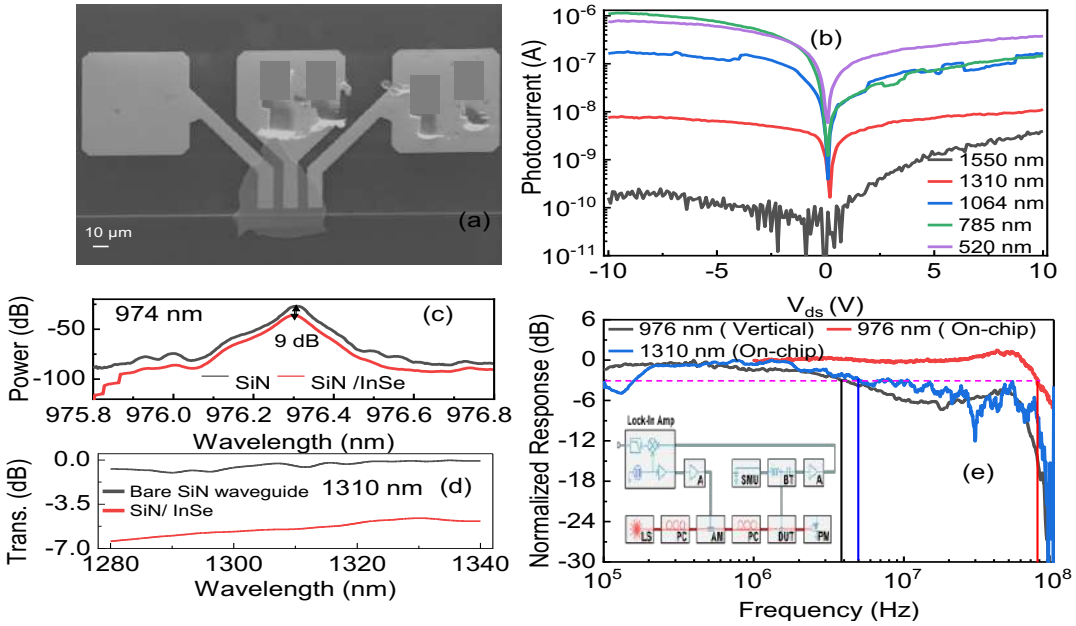


Fig. 2. (a) SiN waveguide integrated with an InSe photodetector. (b) Photocurrent characteristics of the SiN-integrated InSe device. (c) Measured optical propagation losses (d) SiN waveguide transmission before and after multilayer InSe transfer. (e) 3-dB RF cutoff.

Acknowledgements, this work was supported by Tamkeen under NYUAD RRC Grant No. CG011.

References

1. [1] D. Bandurin, "High electron mobility, quantum Hall effect and anomalous optical response in atomically thin InSe.," *Nature nanotechnology*, *12*(3), 223-227 (2017).
2. [2] H. Qiao, "Self-powered photodetectors based on 2D materials," *Advanced optical materials*,*8*(1), 1900765 (2020).
3. [3] D. Chen, "A dual-band multilayer InSe self-powered photodetector with high performance induced by surface plasmon resonance and asymmetric Schottky junction," *ACS nano*, *12*(8), 8739-8747 (2018).
4. [4] S. R. Tamalampudi, "High-Speed Waveguide-Integrated InSe Photodetector on SiN Photonics for Near-Infrared Applications," *Advanced Photonics Research*, *4*(11), 2300162 (2023).

Integrated photonic platforms for nonlinear light generation in the ultraviolet and visible regions

Natale G. Pruiti[1*], Elissa McKay[1], Eugenio Di Gaetano[1], Cosmin Suciu[1], Daniel Kelly[1], Stuart May[1], Marc Sorel[1,2]

[1] University of Glasgow, Glasgow, United Kingdom
[2] Istituto di Tecnologie della Comunicazione, dell'Informazione e della Percezione (TeCIP), Pisa, Italy
[*]corresponding author: natale.pruiti@glasgow.ac.uk

Abstract: We report on integrated photonic platforms for visible-range nonlinear optics using alumina, silicon nitride, and lithium niobate waveguides. Efficient supercontinuum generation and nonlinear wavelength conversion are demonstrated in ultra-low-loss, dispersion-engineered waveguides fabricated via multi-pass lithography and heterogeneous material integration.

Colloidal Self-Assembly as Templating for 3D Second-Harmonic Photonic Crystals

T. Kainz[1*], H. Weigand[2], Ü.-L. Talts[2], R. Grange[2], U. Steiner[1], and V. V. Vogler-Neuling[1]

[1]Adolphe Merkle Institute and NCCR Bio-inspired Materials, University of Fribourg, Switzerland

[2]Optical Nanomaterials Group, Department of Physics, ETH Zürich, Switzerland

Corresponding author: thomas.kainz@unifr.ch

Abstract: We present fully 3D scalable $\chi^{(2)}$ photonic crystals with unprecedented domain sizes (>100 unit cells), overcoming previous z-direction limitations. We combine colloidal self-assembly of polystyrene opals for templating and sol-gel barium titanate chemistry for replication. These nonlinear crystals facilitate controlled second harmonic generation within a fabrication-tunable photonic bandgap.

Three-dimensional nonlinear (second-harmonic) photonic crystals can simultaneously generate different nonlinear processes such as second-harmonic generation, optical parametric amplification, or other sum- and difference-frequency processes along different photonic crystalline directions. [1] Laser-poling and laser-erasing have been utilized in materials like lithium niobate, and barium-calcium titanate. [2] With the first bottom-up fabricated 3D second-harmonic woodpile photonic crystal, we introduced the later used sol-gel chemistry in combination with soft-nanoimprint lithography. [3] However, creating large crystals in all three dimensions, mainly in the z-direction, presents a considerable challenge, primarily due to the chemical inertness of metal oxides. [4]

This study shows the first demonstration of colloidal-crystal-templating for a second-order optical material. We selectively synthesized monodisperse nanospheres with tunable unit sizes to self-assemble polystyrene opals with different band gaps (Figure 1 a-d). These serve as templates for infiltration with barium titanate sol-gel. After a calcination step, we obtained an inverse fcc network of tetragonal barium titanate (Figure 1 e,f). We fabricated samples with unprecedented sizes for single domains: >3000 unit cells in x y directions and >100 in z (Figure 1 g). The achieved optical reflectivity values are above 80 % throughout the fabrication. We can engineer the final photonic band gap over the entire optical range, matching it both to material and setup requirements (Figure 1 h).

We successfully replicated the photonic network into a second-order material and demonstrated, for the first time, a linear photonic band gap from a fully scalable three-dimensional photonic crystal made of a $\chi^{(2)}$ optical material. With our approach, we overcame previous limitations, especially stacking in the z-direction, while obtaining full tunability of the initial unit cell. With reverse engineering of the final band gap wavelength we can both avoid the materials absorption regime and match the available laser setups. This enables the experimental investigation of SHG generated within a band gap, such as inhibited spontaneous emission. [5] Configurations for probing enhanced nonlinearities at the band edges and inhibited excitation can be fabricated with the same technique. [6] In addition, we are planning to replace the colloidal fcc template with a photonically superior, larger bandgap colloidal diamond structure. [7]

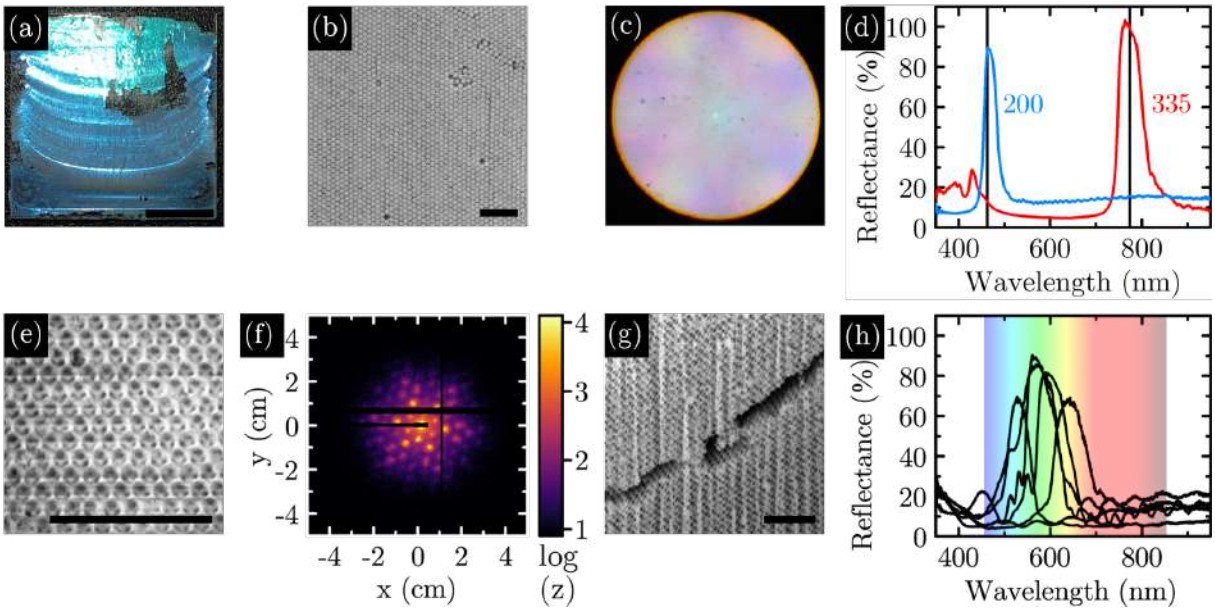


Figure 1. Polystyrene face-centered cubic opal: (a) Image of opals on whole fused silica chip, (b) Scanning electron microscopy in (111) direction, (c) Optical microscope k-space image, (d) Reflectance spectra with calculated bandgap positions (vertical lines) for different initial PS bead diameters;
Barium titanate inverse fcc crystal: (e) SEM in (111) direction, (f) Ultra-small angle X-ray spectroscopy 2D diffraction pattern, (g) Focused ion beam-SEM cross-section, (h) Reflectance spectra of inverse Barium Titanate opals for different inclinations with optical range color coding; Scale bars: a: 500 µm, others: 2 µm.

References

1. Slusher, R. E., and Eggleton, B. J., "Nonlinear Photonic Crystals" (*Springer Berlin Heidelberg*, Berlin, Heidelberg, 2003).

2. Zhang, Y., Sheng, Y., Zhu, S., Xiao, M., and Krolikowski, W. "Nonlinear photonic crystals: from 2D to 3D", *Optica*, Vol.8, pp. 372-381, 2021.

3. Vogler-Neuling, V. V., Talts, Ü.-L., Ferraro, R., Weigand, H., Finco, G., Winiger, J., Benedek, P., Kusch, J., Karvounis, A., Wood, V., Leuthold, J., and Grange, R., "Large-Scale Bottom-Up Fabricated 3D Nonlinear Photonic Crystals", *Advanced Photonics Research* , Vol. 5,Vo. 12, p. 2400058, 2024.

4. Vogler-Neuling,V. V., Karvounis, A., Morandi, A., Weigand, H., Dénervaud, E., and Grange, R., "Photonic Assemblies of Randomly Oriented Nanocrystals for Engineered Nonlinear and Electro-Optic Effects", *ACS Photonics*, Vol. 9, 2193-2203 (2022).

5. Yablonovitch, E., "Inhibited Spontaneous Emission in Solid-State Physics and Electronics", *Phys. Rev. Lett.*, Vol.58, No. 20, pp. 2059–2062, 1987.

6. Soljačić, M., Johnson, S. G., Fan, S., Ibanescu, M., Ippen, E., Joannopoulos, J. D., "Photonic-crystal slow-light enhancement of nonlinear phase sensitivity", *J. Opt. Soc. Am. B*, Vol. 19, No. 9, 2002.

7. He, M., Gales, J.P., Ducrot, É, Gong, Z., Yi, G.-R., Sacanna, S., and Pine, D. J., "Colloidal Diamond", *Nature*, Vol. 585 No. 7826, pp. 524-529, 2020.

Multi-photon lithography for advanced micro-optics and large-area metasurfaces

G. Zyla[1*], D. Ladika[1], V. Melissinaki[2], M. Stavrou[2], I. Kassamakov[3], Savvas Papamakarios[2], Dimitrios C. Zografopoulos[4], Anna Christoforidou[5], George Kenanakis[2], Odysseas Tsilipakos[6], Mangirdas Malinauskas[1] and Maria Farsari[2]

[1] Laser Research Center, Physics Faculty, Vilnius University, Vilnius, LT-10223 Lithuania
[2] Institute of Electronic Structure and Laser, Foundation for Research and Technology-Hellas, Heraklion, GR-70013 Greece
[3] Electronics Research Laboratory, Department of Physics, University of Helsinki, Helsinki, FIN-00170 Finland
[4] School of Electrical and Computer Engineering, Aristotle University of Thessaloniki, Thessaloniki, GR-54124 Greece
[5] Lund University, Faculty of Engineering, Lund, SE-22100 Sweden
[6] Theoretical and Physical Chemistry Institute, National Hellenic Research Foundation, Athens, GR-11635 Greece
[*]corresponding author: gordon.zyla@ff.vu.lt

Abstract: This work demonstrates the flexibility of micro- and nanoscale 3D printing via multi-photon lithography for the realization of advanced micro-optics in the field of photonic nanojets, the fabrication of flat optical components for wavefront manipulation in the visible range, and the production of large-area metasurfaces for the mid-infrared and terahertz regimes.

META 2025, MALAGA - SPAIN, JULY 22 – 25, 2025

Strong light-matter interaction in dielectric hybrid metasurfaces

G. Adamo[1,2*], M. Marangi[1,2], A. M. Dubrovkin,[1,2] A. Zacheo,[1,2] and C. Soci[1,2,3]

[1] Centre for Disruptive Photonic Technologies, TPI, Nanyang Technological University, Singapore 637371

[2] Division of Physics and Applied Physics, School of Physical and Mathematical Sciences, Nanyang Technological University, Singapore 637371

[3] National Centre for Advanced Integrated Photonics, Nanyang Technological University, Singapore 639798

[*]corresponding author: g.adamo@ntu.edu.sg

Abstract: Low-loss, high-Q dielectric metasurfaces are versatile platforms to manipulate strong light-matter interaction. By using silicon metasurfaces, we are able to realize strong-coupling-induced enhancement and phase-transition in molecular J-aggregates superradiance and exciton-polariton condensation and lasing in polycrystalline perovskite films. These works establish scalable pathways for polaritonic devices compatible with silicon photonics.

Rapid, Full-wafer Fabrication of All-inorganic, High-Efficiency Metaoptics and AR Waveguides via Additive Nanoimprint Lithography

J. J. Watkins

University of Massachusetts and Myrias Optics, Inc. USA

watkins@umass.edu, watkins@myriasoptics.com

Abstract: We fabricate all-inorganic, high-efficiency, metalenses, metasurfaces, DOEs and waveguides on full-wafer platforms with cycle times of less than 5 minutes/wafer via additive nanoimprint lithography using TiO_2 nanoparticle dispersion inks for applications in the visible and near IR.

Monolithic integration for Silicon photonics

Frederic Gardes[1], Ilias Skandalos[1], Xingshi Yu[1], Afrooz Shoaa[1], Qianbin Luo[1], Thalia Dominguez Bucio[1], Ipsita Chakrabort[1], Michele Paparella[1], Ioannis Zeimpekis[1], Huiyun Liu[2], Alwyn Seeds[2],

[1]University of Southampton , UK

[2] University College London , UK

[*]corresponding author: F.Gardes@Soton.ac.uk

Abstract: We report recent advancements in silicon nitride monolithic integration schemes, highlighting progress in integrated broadband nonlinear structures, non-volatile photonic memories, and precise device trimming techniques. These developments underscore significant strides in the field, paving the way for enhanced photonic device functionality and integration.

Controlling and applying the loss of electromagnetic metasurface based on machine learning

Peng Fu, Yang Guo, and Changzhi Gu*

[1]Institute of Physics, Chinese Academy of Sciences, Beijing 100190, China
*corresponding author: czgu@iphy.ac.cn

Abstract: By integrating the non-Hermitian optical theory and machine learning methods, we promoted the design of metasurfaces from traditional experience-driven to data-driven, and from single function to multi-functional collaboration.

As an artificial optical material with a subwavelength structure, metasurfaces can accurately manipulate multiple degrees of freedom of electromagnetic waves at a very small scale and are widely used in cutting-edge fields such as meta-lenses, polarization control, holographic imaging and electromagnetic stealth. However, metasurfaces inevitably introduce material loss and radiation loss in practical applications, which are regarded as the main obstacles to performance degradation in traditional design concepts. In recent years, the development of non-Hermitian physics has subverted this traditional cognition and proposed a new paradigm that takes loss as a design dimension rather than a constraint, providing theoretical support for the realization of novel optical effects such as singularity point (EP)-induced unidirectional transmission, loss-induced laser recovery and transparency. At the same time, machine learning methods such as deep learning have performed well in high-dimensional space modeling and optimization, providing powerful tools for the precise design of metasurface structures under non-Hermitian conditions.

In this work, we systematically explored the modeling, design and experimental implementation of non-Hermitian metasurface systems around the two core concepts of "loss control" and "intelligent optimization". First, Starting from non-Hermitian optics, a theoretical model suitable for metasurface design is established to sort out the advantages of singular point-related topological effects in light regulation; then, A bidirectional deep learning framework is constructed to realize the design of multifunctional devices based on scattering EP, solving the difficulties of traditional methods in high Q value prediction and dimensional matching; finally, A coupled multi-layer non-Hermitian THz metasurface system is proposed, combined with machine learning optimization methods to achieve accurate construction and positioning of EP3.

This study not only promotes the practical application of non-Hermitian optical theory in metasurface device design, but also provides methodological support for the design of future intelligent photonic devices.

Key Words:
Loss, machine learning, metasurfaces, non-Hermitian physics

Development of plasmonic components for artificial neural networks

M. Aeschlimann
RPTU Kaiserslautern-Landau, 67663 Kaiserslautern, Germany
ma@physik.uni-kl.de

Abstract: We present a neuromorphic architecture based entirely on surface plasmon polariton interactions. A concept for a plasmonic network node (PLNN) is introduced, utilizing an optical angular momentum sorter for input encoding. Dynamic weighting is achieved through controlled excitation of plasmonic edge modes via directed optical waves.

DNA Origami Self-assembled Diamond Lattice Photonic Crystals

Xin Yin[1*], Gregor Posnjak[1], Paul Butler[2], Oliver Bienek[2], Mihir Dass[1], Seungwoo Lee[3], Ian Sharp[2], and Tim Liedl[1]

[1]Ludwig-Maximilian-Universität München, Germany
[2]Walter Schottky Institute, Technical University Munich, Germany
[3]Department of Integrative Energy Engineering (College of Engineering), KU-KIST Graduate School of Converging Science and Technology, Department of Biomicrosystem Technology, KU Photonics Center, Korea University, Seoul 02841, Republic of Korea
[*]corresponding author: xin.yin@physik.uni-muenchen.de

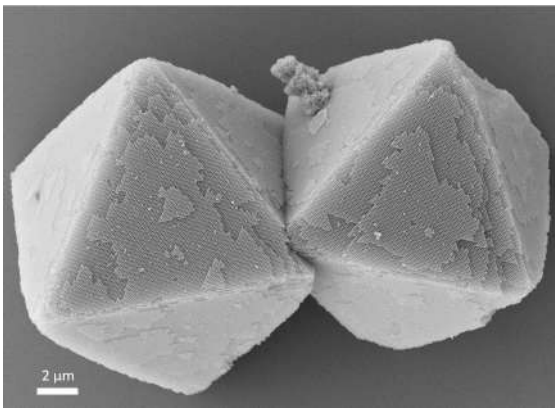
Abstract: We present a DNA-origami-assembled diamond lattice photonic crystal with 170 nm periodicity. Silicification and TiO_2 coating yield mechanically robust, high-index structures supporting UV-range photonic bandgaps. Optical measurements and simulations confirm tunable bandgap behavior. This bottom-up approach offers a scalable route toward programmable 3D photonic metamaterials with subwavelength precision.

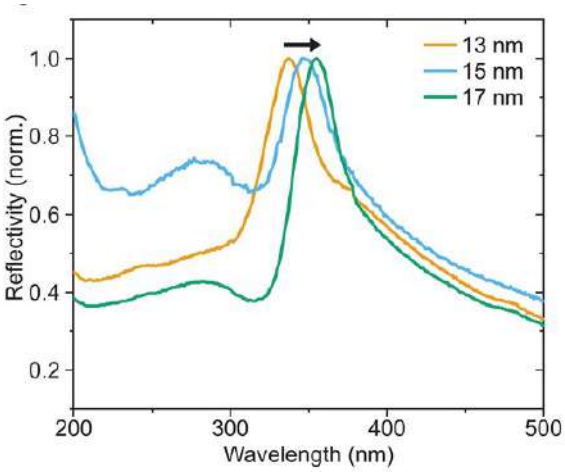
Photonic crystals are periodic dielectric structures that manipulate light propagation via Bragg scattering, giving rise to photonic bandgaps—spectral ranges where light cannot propagate through the crystal. Among 3D photonic crystal geometries, the diamond lattice is particularly attractive for its potential to support a wide and complete photonic bandgap even at relatively low refractive index contrasts [1,2]. Despite significant theoretical interest, experimental realization of diamond lattice photonic crystals at the submicron scale has remained a challenge, especially with the degree of precision required for optical applications.

Here, we demonstrate a bottom-up approach using DNA origami to self-assemble a direct rod-connected diamond lattice with a periodicity of 170 nm. DNA origami enables the programmable folding of single-stranded DNA into rigid, well-defined nanostructures, which can be functionalized with high spatial precision [3]. In our system, we design tetrapod-shaped DNA origami monomers that mimic the tetrahedral coordination found in diamond crystals. Each monomer features four arms extending at 109.5° angles, with programmable "sticky" ends for directional binding and "fuzzy" ends to discourage non-specific aggregation. The resulting interactions enable assembly into a 3D diamond lattice with the desired cubic symmetry.

Post-assembly, the lattice is silicified to enhance mechanical stability [4] and coated with TiO_2 via atomic layer deposition (ALD) to increase refractive index contrast [5]. To characterize its optical response, we measure the reflectance spectrum using UV-Vis spectroscopy. The resulting data reveal a distinct reflection band in the ultraviolet, which red-shifts with increasing TiO_2 thickness. This observation is in agreement with photonic band simulations performed using the MIT Photonic Bands (MPB) software, which predicts a bandgap in the UV range for a diamond lattice with the measured structural parameters. The ability to tune the optical properties via ALD thickness offers additional flexibility in photonic device design. [6]

This work demonstrates the potential of DNA-origami-driven self-assembly for constructing scalable, functional 3D photonic architectures and offers a versatile platform for future metamaterial design.





References:

[1] E. Yablonovitch. Scientific American. 2001, 285.6: 46.

[2] R. K. Cersonsky, J. Antonaglia, B. D. Dice, & S. C. Glotzer. Nature communications, 12(1), 2543. (2021).

[3] P. W. Rothemund. Nature, 440(7082), 297-302. (2006).

[4] L.Nguyen, M.Döblinger, T. Liedl, & A. Heuer□Jungemann. Angewandte Chemie International Edition, 58(3), 912-916. (2019).

[5] A. Ermatov, M. Kost, X. Yin, P. Butler, M. Dass, I. D. Sharp, ... & G. Posnjak. Journal of the American Chemical Society. (2025).

[6] G. Posnjak, X. Yin, P. Butler, O. Bienek, M. Dass, S. Lee, ... & T. Liedl. Science, 384(6697), 781-785. (2024).

Photon Manipulation with the Interface of Synthetic Temporal Photonic Lattices

Bing Wang[1*]

[1]School of Physics and Wuhan National Laboratory for Optoelectronics and, Huazhong University of Science and Technology, Wuhan 430074, China.

[*]corresponding author: wangbing@hust.edu.cn

Abstract: We experimentally constructed a synthetic dimensional temporal photonic lattice based on dual-loop coupled fiber architecture, and demonstrated its versatile applications in gauge potential modulation and nonlinear photonics. By tailoring the distribution of scalar and vector potentials, we demonstrate reconfigurable temporal interfaces enabling phenomena such as refraction, total internal reflection, and perfect imaging. We further observe a temporal Goos–Hänchen shift arising from total internal reflection, jointly governed by scalar and vector potentials. Finally, by introducing optoelectronic Kerr nonlinearity, we realize nonlinear non-Hermitian skin effects and demonstrate robust skin solitons enabled by the interplay between nonlinearity and non-Hermitian transport.

Main results:

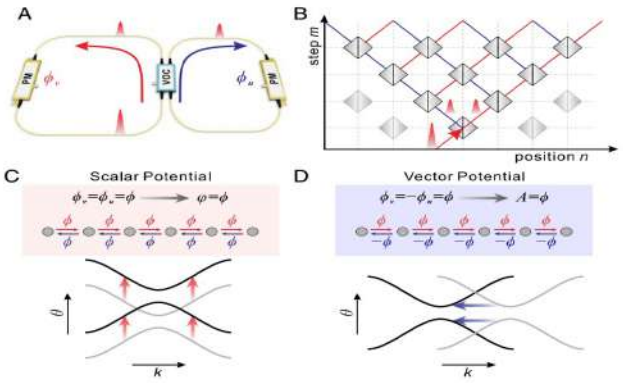


Fig. 1. A. Schematic sketch of the experimental setup used for implementing synthetic temporal lattice. **B.** Synthetic temporal lattice mapping from the pulse evolutions in A. **C,D** Effective scalar and vector potentials and their influence on the band structure.

As illustrated in Fig. 1, applying identical phase modulations to the long and short fiber loops induces an effective scalar potential in the synthetic temporal lattice, leading to a vertical shift of the Floquet band structure. In contrast, opposite phase modulations generate an effective vector potential, resulting in a horizontal displacement of the bands.

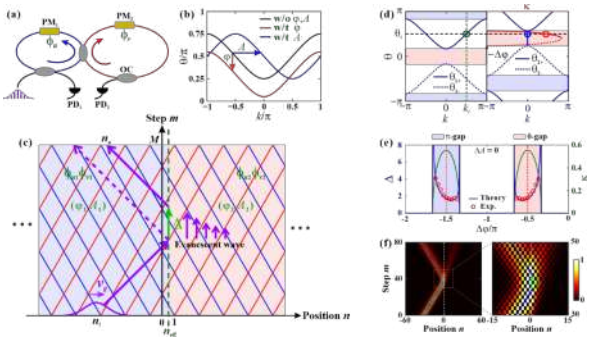


Fig. 2. (a). Schematic of two coupled fiber loops for realizing the synthetic temporal lattice. (**b)** Illustration of the effects of scalar and vector potentials: inducing vertical and horizontal shifts of the band structure, respectively. (**c)**

Diagram of a temporal heterolattice with a gauge-potential interface; the green arrow indicates the Goos–Hänchen shift along the interface due to temporal total internal reflection. (**d)** Band structure matching between the left and right regions across the interface. (**e)** Dependence of the Goos–Hänchen shift on the relative scalar potential difference. (**f)** Temporal evolution of the reflected wave packet; the green arrow marks the Goos–Hänchen shift.

We propose the construction of photonic gauge-potential heterointerfaces using synthetic temporal lattices, and experimentally confirm the existence of temporal Goos–Hänchen shifts (GHS) in discrete-time reflections. The physical connection between GHS induced by single-interface total internal reflection and by finite-width potential barriers is revealed. Moreover, we introduce an accumulation-based reflection scheme to enhance the precision for detecting small GHS values.

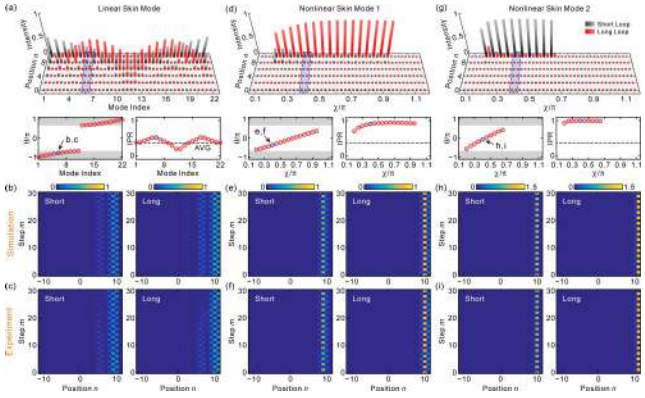


Fig. 3. (a) Mode profiles, eigenvalue spectrum, and IPR of linear skin modes. The black and red bars in mode profile subplot correspond to short and long loops, respectively. The gray zones in spectrum indicate the real parts of bulk band structure, and the circles correspond to the skin modes. The dashed line in the IPR subplot represents the IPR of the averaging intensity of all skin modes. **(b),(c)** Simulated and measured intensity evolutions of the 6th linear skin mode. **(d)** Mode profiles, eigenvalue spectrum, and IPR of nonlinear skin mode 1 versus Kerr coefficient χ. **(e),(f)** Simulated and measured intensity evolutions of nonlinear skin mode 1 for $\chi = 0.4\pi$. **(g)-(i)** correspond to the nonlinear skin mode 2.

We experimentally demonstrate the nonlinear non-Hermitian skin effect (NHSE) in a Kerr-like temporal photonic lattice, where opto-electronic feedforward provides tunable artificial nonlinearity without requiring high optical power. Kerr self-trapping enhances localization and robustness at the boundary, and can suppress NHSE transport to form stable skin solitons. Leveraging this effect, we design a nonlinear optical router with tunable output. These results hold promise for robust signal transmission and photonic routing.

Acknowledgements: This work is supported by the National Natural Science Foundation of China (No. 12374305, No. 12021004, No. 12147151, No. 62305122 and No. 12204185).

References

1. Han Ye *et al*., "Reconfigurable refraction manipulation at synthetic temporal interfaces with scalar and vector gauge potentials," *Proceedings of the National Academy of Sciences*, 2023, 120(20): 1-8.
2. Chengzhi Qin *et al*., "Temporal Goos-Hänchen Shift in Synthetic Discrete-Time Heterolattices," *Physical Review Letters*, 2024, 133(8): 1-6.

Nonlinear and optomechanical applications harnessing silicon nanostructures

P. Nuño Ruano[1], J. Zhang[1,2], D. González-Andrade[1], H. E. B. Ferhart[1], T. T. D. Dinh[1], D. Medina-Quiroz[1], S. Edmond[1], P. Cheben[3], D. Marris-Morini[1], E. Cassan[1], L. Vivien[1], N. D. Lanzillotti-Kimura[1] and C. Alonso-Ramos[1,*]

[1]Université Paris-Saclay, CNRS, Centre de Nanosciences et de Nanotechnologies, 91120 Palaiseau, France
[2]National Research Council Canada, 1200 Montreal Road, Bldg. M50, Ottawa, Ontario K1A 0R6, Canada
[3]Center for Research in Photonics, University of Ottawa, Ottawa, Ontario K1N 6N5, Canada
[*]Corresponding author: carlos.ramos@c2n.upsaclay.fr

Abstract: Subwavelength silicon nanostructures provide unprecedented flexibility in the control of optomechanical effects. Here, we review our recent results on the use of nanostructures for the optimization of Brillouin interactions in suspended and non-suspended optomechanical cavities.

Cavity-induced attractive interactions in Van der Waals Quantum Materials

F. Helmrich[1,†], T. F. Nova[1,2,†], H. S. Adlong[1,3], I. Khanonkin[1], E. Jöchl[1], M. Kroner[1], G. Scalari[1], J. Faist[1], and A. Imamoglu[1,*]

[1]Institue for Quantum Electronics, ETH Zürich, Switzerland
[2]Department of Quantum Matter Physics, Université de Genève, Switzerland
[3]Institute of Theoretical Physics, ETH Zürich, Switzerland
[*]corresponding author: imamoglu@phys.ethz.ch
[†]These authors contributed equally.

Abstract: We present the creation of a cavity-induced excitonic bound state in a dual-gated hBN-encapsulated Bernal bilayer graphene device coupled to a meta-material-inspired THz cavity. The bound state originates solely from ultrastrong coupling of a continuum of interband transitions to the cavity, and not from standard Coulomb interactions.

BICs and *quasi*-BICs in unpatterned media

R. Berté[1*], T. Possmayer[1], A. Tittl[1], L. de S. Menezes[1,2] and S. A. Maier[3,4]

[1] Chair in Hybrid Nanosystems, Nanoinstitut München, Fakultät fur Physik,
Ludwig-Maximilians-Universität München, 80799 München, Germany
[2] Departamento de Física, Universidade Federal de Pernambuco, Recife, Pernambuco 50670-901, Brazil
[3] School of Physics and Astronomy, Monash University, Clayton, Victoria 3800, Australia
[4] The Blackett Laboratory, Department of Physics,
Imperial College London, London SW7 2AZ, United Kingdom

[*]corresponding author: R.Berte@physik.uni-muenchen.de, berte.rodrigo@gmail.com

Abstract: All-optical permittivity symmetry breaking leads to tailored ultrafast resonances in a Si thin film.

Photonic bound states in the continuum (BICs) are among the most versatile tools in optics and nanophotonics. Yet, as for most of the nano-optics toolkit, they require samples to be patterned at the nanoscale. In this talk we discuss an addition to this toolkit, where permittivity symmetry breaking via optical means is used for the excitation of photonic BICs in an unpatterned medium. Tailored ultrafast resonances and spectrally-selective third harmonic generation are demonstrated in an amorphous Si thin film. This method circumvents the optical bandwidth constraints imposed by sample patterning and allows a whole set of materials with small electro-optical coefficients to be exploited in light manipulation.

Flat band finetuning and its photonic applications

S. Flach[1*]

[1]Institute for Basic Science, South Korea
[*]corresponding author: sflach@ibs.re.kr

Abstract: Flat bands – single-particle energy bands – in tight-binding lattices, aka networks, have attracted attention due to the presence of macroscopic degeneracies and their sensitivity to perturbations. They support compact localized eigenstates protected by destructive interference. This makes them natural candidates for emerging exotic phases and unconventional orders. In this talk we consider the recently proposed systematic ways to construct flat band networks based on symmetries or fine-tuning [1]. We then discuss how the construction methods can be further extended, adapted or exploited in presence of perturbations, both single-particle and many-body. This strategy has lead to the discovery of non-perturbative metal-insulator transitions, fractal phases, nonlinear and quantum caging and many-body nonergodic quantum models. We discuss what implications these results may have for the design of fine-tuned nanophotonic systems including photonic crystals, nanocavities, and metasurfaces.

[1] Carlo Danieli, Alexei Andreanov, Daniel Leykam, Sergej Flach, Nanophotonics **13**, 3925 (2024).

Programmable Nanophotonic Devices with Low-Loss Phase-Change Materials

Fouad Bentata,[1,2] Capucine Laprais,[1] Stéphane Monfray,[2] Nicolas Baboux,[1] Xavier Letartre,[1] Guillaume Saint-Girons,[1] Patrice Genevet,[3] Lotfi Berguiga,[1] and Sébastien Cueff[1,*]

[1] CNRS, Ecole Centrale de Lyon, INSA Lyon, Universite Claude Bernard Lyon 1, CPE Lyon, INL, UMR5270, 69130 Ecully, France
[2]STMicroelectronics, 850 Rue Jean Monnet, Crolles, 38920, France
[*]corresponding author: sebastien.cueff@ec-lyon.fr

Abstract: We exploit low-loss phase-change materials such as Sb_2S_3 to propose and demonstrate integrated photonic devices with original programmable functionalities.

Phase change materials (PCMs) are currently revolutionizing nanophotonics by providing ways to tune and reconfigure optical functionalities without any moving parts. Building on this phenomenon, the last decade has witnessed many exciting reports of novel devices exploiting PCMs such as for example beam-steering, tunable light emission, reflection and absorption, programmable metasurfaces and reconfigurable neural networks [1-3]. A large majority of the first studies were using standard PCMs such as GeSbTe as simple binary on-off switches, in which the ON state is the amorphous phase and the OFF state the fully crystalline phase. However, PCMs present another degree of freedom for tunability: the possibility to encode multilevel non-volatile states via partial change of phase. Furthermore, recently a new class of low-loss PCMs emerged (e.g. Sb2S3 and Sb2Se3), with negligible optical absorption in the near-infrared [4,6].

In this talk, we will present recent results on the physics and properties of PCMs and on original methods to program PCMs into various multilevel states of crystallization. We will then present nanophotonic devices leveraging this multilevel programming and conclude on the perspectives for this technology.

We acknowledge fundings from the French National Research Agency (ANR) under the project MetaOnDemand (ANR-20-CE24-0013).

References

1. E. Mikheeva, et al. "Space and time modulations of light with metasurfaces: recent progress and future prospects." in ACS photonics 9 (2022).
2. S. Cueff et al. "VO_2 nanophotonics." APL Photonics 5.11 (2020).
3. B. J. Shastri, et al. "Photonics for artificial intelligence and neuromorphic computing." Nature Photonics 15, 102 (2021).
4. W. Dong et al. "Wide bandgap phase change material tuned visible photonics." Advanced Functional Materials 29 1806181 (2019)
5. M. Delaney, et al. "A new family of ultralow loss reversible phase-change materials for photonic integrated circuits: Sb_2S_3 and Sb_2Se_3." Advanced Functional Materials 30, 2002447 (2020)
6. A. Taute, et al., “Programming multilevel crystallization states in phase-change-material thin films,” Optical Materials Express 13, 3113–3120 (2023).

Near-unity absorption in semiconductor nanowire metasurfaces

Michael. E. Reimer[1*]

[1]Department of Electrical and Computer Engineering and Institute for Quantum Computing, University of Waterloo, Ontario N2L 3G1, Canada
[*]Corresponding author: mreimer@uwaterloo.ca

Abstract: Semiconductor nanowire metasurfaces can be engineered for realizing near-unity absorption efficiency to enhance the performance of photodetectors. We demonstrate ~95% absorption efficiency by controlling the nanowire geometry and spacing. This also improves the photodetector response time by significantly reducing device capacitance and controlling the spatial location of the absorption profile.

The ability to detect light with high speed and near-unity efficiency is desirable in photodetection-based applications. However, photodetectors have limited detection efficiency in the 850 nm – 1100 nm wavelength range, known as the 'valley of death'. In this talk, novel semiconductor nanowire metasurfaces will be presented that absorb light with near-unity efficiency in this 'valley of death' wavelength region. By controlling the nanowire geometry and pitch, we show enhanced absorption efficiency with an average of 94% absorptance over the wavelength range from 900-1600 nm [1]. We also designed multimode nanostructure resonators that generate Kerker interference at the target wavelength of 920 nm. For such metasurface absorbers, we demonstrate a peak absorptance of ~95%. By modifying the dimensions and pitch of the resonators, the Kerker resonance peak can be controllably shifted. We also show that our design enables spatial control of the absorption profile within the resonators, which is promising for a novel class of photodetectors with improved timing response without sacrificing detection efficiency. Finally, we will present our most recent work where we show photodetector devices with a fast time response (~100 ps) and high external quantum efficiency (> 90%), and progress in enhancing the performance of single-photon detectors with semiconductor nanowire metasurfaces.

[1] B. Tekcan, B. van Kasteren, S.V. Grayli, D. Shen. M.C. Tam, D. Ban, Z. Wasilewski, A.W. Tsen, and M.E. Reimer, Semiconductor nanowire metamaterial for broadband near-unity absorption. *Scientific Reports* **12**:9663 (2022).

Switching of topological edge transmission in Si photonics platform

T. Amemiya[1*], S. Okada[2], L. Hu[1], Q. Wang[1], X.-X. Wang[1] and X. Hu[3]

[1] Institute of Science Tokyo, Tokyo 152-8552, Japan
[2] National Institute of Information and Communications Technology, Tokyo 184-8795, Japan
[3] Shanghai University, Shanghai 200444, China
[*]Corresponding author: amemiya.t.e262@m.isct.ac.jp

Abstract: Topological photonics allows us to systematically handle information derived from the topology of light, such as optical spin and orbital angular momentum. In this talk, we focus on an ultra-compact and low-power-consumption optical switch by manipulating the interference effect of orbital angular momentum using topological photonics.

Topological electronic properties have attracted a great deal of attention in recent years, and there are growing expectations for the discovery of novel physical phenomena associated with topologically protected surface states and the development of devices based on such phenomena. Inspired by this, research centered on "topological photonics," in which the topology of an electronic system is traced to a photon system, has been flourishing in recent years [1-3].

Topological photonics has a particularly strong affinity with optical circuits, and is characterized by its ability to control optical signals with specific internal degrees of freedom (optical spin and orbital angular momentum) within a circuit. Optical circuits integrate various functions essential for optical communications on a single chip to achieve high processing speed and energy efficiency, but current optical circuits cannot handle even the internal degrees of freedom of photons themselves. In such a situation, if these can be controlled, it will be possible to make significant progress on various issues that are reaching their limits in the field of photonics.

Since optical switches are indispensable for ultrafast optical information processing and are also important as pass gates for optical computing, it is essential to increase speed and downsize them. However, current optical switches based on Mach-Zehnder interferometers tend to have large device sizes, and more innovative operating principles are required for future photonics-electronics convergence. In this situation, we have realized an ultra-compact and low-power-consumption optical switch by manipulating the interference effect of orbital angular momentum using topological photonics [4, 5]. Since the interference effect of orbital angular momentum occurs within the unit cell of a topological photonic crystal, it can ultimately be downsized to the size level of the unit cell. In this talk, we will mention the details.

References

[1] A. B. Khanikaev *et al.*, "Photonic topological insulators," *Nat. Mater.* **12**, 233 (2013).
[2] T. Ozawa *et al.*, "Topological photonics," *Rev. Mod. Phys.* **91**, 015006 (2019).
[3] L.-H. Wu and X. Hu, Scheme for achieving a topological photonic crystal by using dielectric material," *Phys. Rev. Lett.* **114**, 223901 (2015).
[4] S. Okada *et al.*, "Port switching of topological edge transmission using phase interference on Si-topological waveguide," Proc. *2023 International Conference on Solid State Devices and Materials,* H-7-03 (2023).
[5] X.-X. Wang *et al.*, "Interference and switching effect of topological interfacial modes with geometric phase," *Phys. Rev. Research* **7**, 023067 (2025).

Second harmonic generation of high-coherence light in Si_3N_4 microresonators

K. Vahala[1], Z. Yuan[1], B. Li[1], J. Ge[1], P. Liu[1], M. Li[2], J.-Y. Liu[1], Y. Yu[1], H.-J. Chen[1], J. Bowers[2]

[1] Applied Physics, California Institute of Technology, Pasadena, CA 91125, USA.
[2] ECE Department, University of California Santa Barbara, Santa Barbara, CA 93106, USA
*corresponding author: vahala@caltech.edu

Abstract: High-coherence visible and near-visible light is generated by combining second-harmonic generation (SHG) with self-injection locking (SIL) of a pump laser. Both SIL and SHG processes occur within high-Q Si_3N_4 microresonators. SHG is enabled by the photogalvanic effect together with all-optical poling, which induces a second-order nonlinearity in the Si_3N_4 microresonator.

Very Large-Scale Integration for Fibers (VLSI-Fi): Assembling Fiber-Embedded Photonics and Optoelectronics by Melt-Shaping Multimaterial Cores

Alexander Gumennik[1*]

[1]Indiana University Bloomington, Indiana, United States of America
[*]corresponding author: gumennik@iu.edu

Abstract: Fiber optics interconnecting the post–Moore's law Internet is likely to embed photonics with data processing capabilities. Inspired by the VLSI design of modern microprocessors, we melt-shape multimaterial fiber cores into architectures typical of integrated circuitry to realize fiber-embedded photonics. We dubbed this fabrication approach the "VLSI for Fibers."

The information medium of the 20th century was revolutionized twice: first with the invention of the integrated circuit, boosting data processing, and second with the demonstration of low-loss fibre optics, bringing data communication up to speed. Those two components lay the basis of the Internet in its current form: a global-scale network of data-processing nodes interconnected by high-throughput communication links.

Similarly, in the 21st century, we find ourselves on the verge of a transformative leap in the hardware used for data processing and distribution. With modern lithography reaching the ability to define features so minute they are only a few tens of atoms in cross-section, Moore's law – the necessity of doubling the areal density of transistors on a microprocessor every two years – has factually reached its physical limit driving the emergence of a whole plethora of alternative computation schemes. From spintronic and photonic to neuromorphic and quantum, the novel computational hardware platforms differ from one another in terms of the protocols used for data processing and even employ physically disparate forms and degrees of freedom in which the data itself is encoded.

Yet, fibre optics – the workhorse of digital communication - still awaits the transformation that would enable it to interconnect those diverse platforms into one harmonized network. The fibre of tomorrow will need to translate the data across those platforms. Integrating on-the-fly data transformation capabilities into fiber optics is likely to require combining photonic and optoelectronic devices and systems directly within the fiber itself.

At least one example of a comparable technological leap occurred in integrated microelectronics in the 1970s with the invention of the Very Large-Scale Integration (VLSI) approach to microprocessor design and fabrication. VLSI enabled a complete restructuring of the microelectronics industry, allowing one to think about microprocessors in terms of circuit design software, hiding the device physics "under the hood."

In fabricating a microprocessor designed using VLSI, the photoresist is deposited on the silicon wafer, which is then selectively exposed through photolithography. Exposed areas are then functionalized by a series of chemical and thermal treatments. This defines a single layer **2D** cross-section of the microchip. The process is repeated, layer by layer, resulting in a "pie" of connectorized layers stacked perpendicularly to the wafer surface in an additional **1D**. Ion implantation into the semiconducting substrate and annealing of dopants functionalize each device electronically, providing a **0D** structural and functional control on the level of an individual device. The result is the microprocessor's **3D** (or, rather, **2D+1D+0D**) structure.

Would it be possible to formulate a similar toolbox for architectural patterning of fibre-embedded structures? We develop such a toolbox, demonstrated in Figure 1. We call it the "VLSI for Fibers" [1] (or "VLSI-Fi"), and it combines several patterning approaches to control in-fiber multimaterial architecture in all three dimensions:

- **(2D)** In the fiber cross-sectional plane, the structure is defined by 3D printing the preform cladding, filling its voids with functional materials, such as metals and semiconductors, and scaling the cross-section geometry down by a thermal draw of the preform into a fiber.
- **(+1D)** Along the fiber axis, we pattern the initially continuous functional-material cores into periodic arrays of spheres using a material-selective spatially coherent capillary breakup, yielding self-assembly of electronic and photonic devices and structures in fibers, with tight dimensional control on multiple scales, from submicron to millimetric. We have recently discovered [2] that a typically chaotic capillary instability becomes predictable, and thus engineerable, in a wide yet well-defined range of processing regimes.
- **(+0D)** Internally to an individual active-material sphere, we control the crystallinity and electronic properties, forcing it to solidify from a melt along the externally imposed temperature profile. This will result in segregation-driven dopant redistribution and crystallinity defined by the stability of the solidification front.

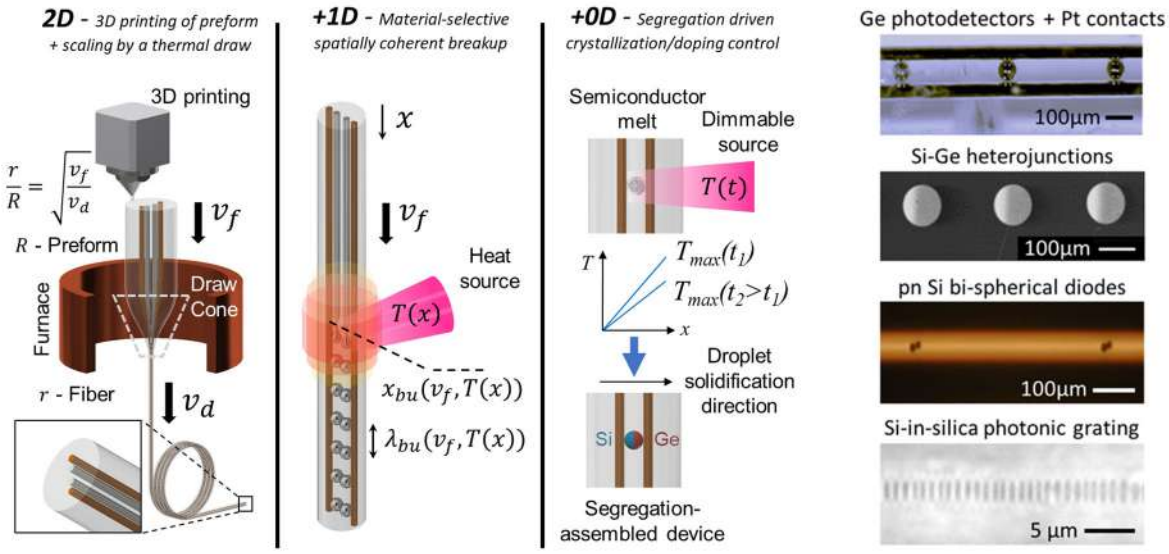


Figure 1. VLSI-Fi and the library of fiber-embedded structures realized by it [from Ref. [1]]. The manufacturing approach includes (from left to right) thermal draw of 3D printed preforms, system assembly by a spatially coherent material-selective capillary breakup (for instance, of an array of bi-spherical pn Si diodes), controlled recrystallization, and dopants redistribution (for example, of Ge mixed into Si) in an externally induced time-varying temperature gradient, due to higher solubility of the dopant in a liquid than in solid phase of the solvent material. **Notations:** R-preform radius, r-fibre radius, R/r-draw scaling factor, v_f-feed speed, v_d-draw speed, x_{bu}-breakup location, λ_{bu}-breakup period, T(t,x)-spatiotemporal temperature profile.

The authors acknowledge the partial support for this research work from the US National Science Foundation [award numbers CMMI-2143467 and ECCS-2240227].

References

1. Gumennik, A., Coulter, J., van der Elst, L. A., Leffel, T. A., Levi, E. C., Faccini de Lima, C., Miller, T., Zheng, M.., "Very-large-scale Integration for Fibers," Chapter 9 in Optical and Electronic Fibers: Emerging Applications and Technological Innovations (Wiley-VCH GmbH), Edited by Wei, L., 197-224, 2024.
2. Faccini de Lima, C., Wang, F., Leffel, T. A., Miller, T., Johnson, S. G., and Gumennik A., "Multimaterial fiber as a physical simulator of a capillary instability," Nature Communications, Vol. 14. No. 1, 5816 1-17, 2023.

Bulk Embedded Laue type Photonic Crystals

D. Gailevicius[1*], E. Aleksandravicius[1], G. Tamošauskas[1], G. Kontenis[1], A. Dubietis[1] and K. Staliūnas[1,2,3]

[1]Vilnius University, Faculty of Physics, Laser Research Center, Saulėtekio ave. 10, LT-10223 Vilnius, Lithuania
[2]ICREA, Passeig Lluís Companys 23, 08010, Barcelona, Spain
[3]UPC, Dep. de Fisica, Rambla Sant Nebridi 22, 08222, Terrassa (Barcelona) Spain

[*]corresponding author: darius.gailevicius@ff.vu.lt

Abstract: Traditionally, photonic crystals are associated with the Bragg condition requiring subwavelength periods. However, over the resent years we developed direct laser written long period photonic crystals based on the Laue diffraction condition, as spatial filters. Development of such bulk structures evolving into spatial dispersion shaping for nonlinearity control.

Typically, photonic crystals (PhCs) are associated with a periodic distribution of refractive index with lattice constants on a subwavelength scale. Smart engineering allows smart light manipulation, for instance, having omnidirectional reflectors[1], switching devices[2], advanced sensors[3] etc. In terms of optical modes of operation, associated with the visible or sometimes the near-infrared range the lattice constants are achievable either by planar lithography (single or multi-layer), laser additive manufacturing, self-assembly, deposition-based methods, which in their own way provide superb resolutions, but either limit the dimensionality of the structure, the lattice geometry or are high resolution along limited dimensions (e.g. planar). However, with a shift in paradigm moving from the Bragg-like conditions (sub) to the Laue diffraction (sup-wavelength), one can achieve both transmittance and dispersion control with lower constraints in resolution and added benefit of moving in the realm of bulk processing and optical grade materials. This is important for high intensity laser applications, where optically induced damage can be an issue[4] and the technological steps to have resilient photonics are more complicated.[5] This Laue PhC concept is presented here.

The unique application that can make use of these structures is spatial filtering, mainly in laser cavities. By employing a multiphoton femtosecond direct laser wright approach interlaced phased gratings can be arranged in the bulk of an optical grade substrate (Fig. 1a). By engineering consecutive interlaced phase gratings one can produce a spatially resonant structure that has quasi-stop gaps only at preset incidence angles. If such a structure is placed inside a laser cavity it can even result in higher transverse mode suppression improving both the M^2 and Brightness output beam values per pump unit[6,7] (Fig. 1b). This led to the discovery that the principle is even applicable to gain patterns on the active media[8]. This is the simplest implementation and application of such PhCs.

However, most recently, we discovered that one can engineer the spatial dispersion curves not in terms of limited nodes, but their curvature itself[9]. This is important for a target application of counteracting the Kerr nonlinearity and suppressing destructive filamentation in cases, where one wants the propagation of high intensity beams for supercontinuum generation or other self-modulation effects (Fig. 1c). If the intensity is too high or propagation distances not controlled, one might lose the coherence of the generated beam. We demonstrate that smart engineering of the geometry allows us the manipulate the effective spatial dispersion enough to observe something alike to “antidifraction”, which is discussed in this paper in more detail.

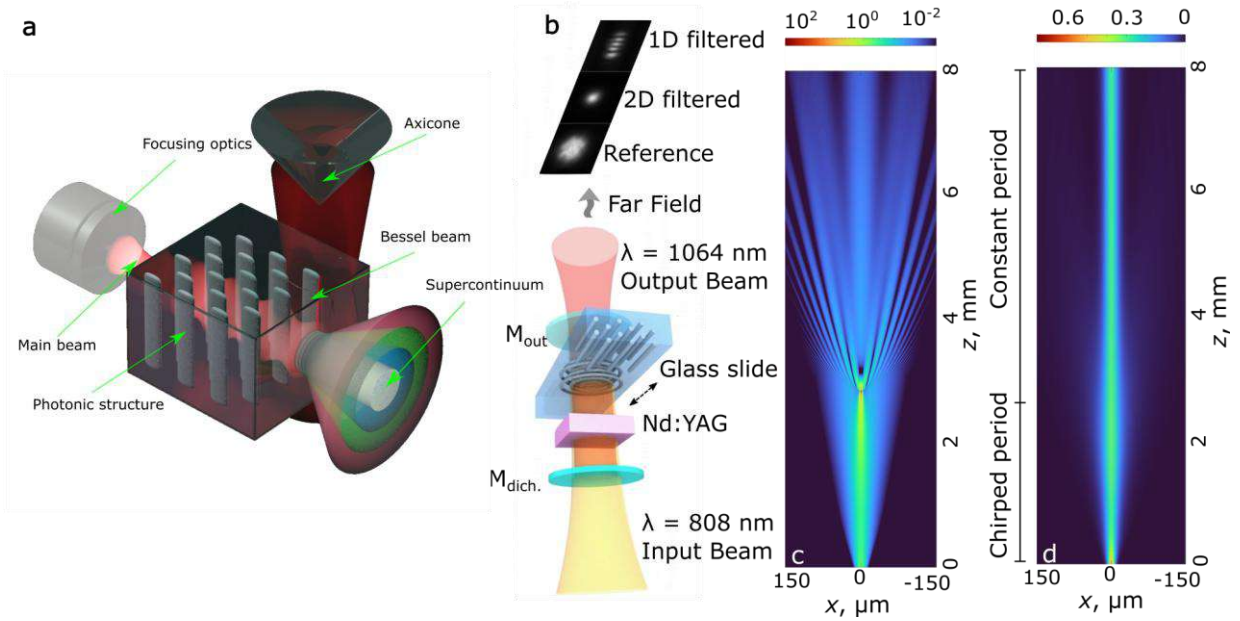


Fig. 1 a-the concept of in bulk fabricated structure; b-spatial filtering in cavity; c-example of how beam propagation can be controlled with dispersion compensation (left-collapse, right-compensated propagation).

References

1. 1. W. Zhang, J. Min, H. Wang, H. Wang, X. L. Li, S. T. Ha, B. Zhang, C.-F. Pan, H. Li, H. Liu, H. Yin, X. Yang, S. Liu, X. Xu, C. He, H. Y. Yang, and J. K. W. Yang, "Printing of 3D photonic crystals in titania with complete bandgap across the visible spectrum," Nat. Nanotechnol. 19(12), 1813–1820 (2024).
2. J. Peng, J. Brandt, M. Pfeiffer, L. G. Maragno, T. Krekeler, N. T. James, J. Henf, C. Heyn, M. Ritter, M. Eich, A. Y. Petrov, K. P. Furlan, R. H. Blick, and R. Zierold, "Switchable 3D Photonic Crystals Based on the Insulator-to-Metal Transition in VO2," ACS Appl. Mater. Interfaces (2024).
3. J. W. Goessling, P. Martínez-Pérez, L. Rodriguez-Lorenzo, P. Braga-Fernandes, B. Espiña, and M. Lopez-Garcia, "Natural Slab Photonic Crystals as Biogenic, Customizable Nanomaterial for Label-Free Detection," ACS Appl. Nano Mater. 8(16), 7911–7919 (2025).
4. T. A. Laurence, D. A. Alessi, E. Feigenbaum, R. A. Negres, S. R. Qiu, C. W. Siders, T. M. Spinka, and C. J. Stolz, "Mirrors for petawatt lasers: Design principles, limitations, and solutions," J. Appl. Phys. **128**(7), (2020).
5. D. Gailevicius, R. Zvirblis, K. Galvanauskas, G. Bataviciute, and M. Malinauskas, "Calcination-Enhanced Laser-Induced Damage Threshold of 3D Micro-Optics Made with Laser Multi-Photon Lithography," Photonics **10**(5), 597 (2023). 1.
6. D. Gailevicius, V. Koliadenko, V. Purlys, M. Peckus, V. Taranenko, and K. Staliunas, "Photonic Crystal Microchip Laser," Sci. Rep. 6(1), 34173 (2016). 1.
7. S. Gawali, D. Gailevičius, G. Garre-Werner, V. Purlys, C. Cojocaru, J. Trull, J. Montiel-Ponsoda, and K. Staliunas, "Photonic crystal spatial filtering in broad aperture diode laser," Appl. Phys. Lett. 115(14), 1–5 (2019).
8. G. Kontenis, D. Gailevicius, V. Taranenko, and K. Staliunas, "Spatially Structured Optical Pump for Laser Generation Tuning," Nanomaterials 14(1), 49 (2023). 1.
9. E. Aleksandravičius, D. Gailevičius, A. Dubietis, and K. Staliūnas, "Suppression of filamentation in refraction index modulated Kerr media," Opt. Laser Technol. 169(September 2023), 109973 (2024).

Overcoming Integration Challenges in Photonic AI Accelerators

A. Ortega-Gomez[1*], N. Farmakidis[1], Håvard Hem Toftevaag[1] , Yi Zhang[1] and Harish Bhaskaran[1]

[1] Department of Materials, University of Oxford, Parks Road, Oxford OX1 3PH, UK

[*]corresponding author: angel.ortegagomez@materials.ox.ac.uk

Abstract:

How can we overcome the current challenges hindering the implementation of photonic accelerators in complex AI workloads? We explore an integrated all-optical neural architecture comprising: i) a high-speed and nonlinear photonic integrator as a neuron block, ii) an ultra-low loss photonic mesh with reconfigurable interconnections.

Artificial intelligence (AI) is reshaping modern computing, but its growing demand for data throughput and energy efficiency is pushing electronic platforms to their limits. Integrated photonics, and particularly Photonic Integrated Circuits (PICs), are promising alternatives due to their high bandwidth and low-power capabilities. However, despite demonstrating impressive performance in small-scale systems with fewer than 100 devices, fully optical AI accelerators have struggled to achieve widespread adoption due to fundamental challenges in scalability, nonlinearity implementation, and programmability. Contemporary photonic platforms remain constrained by their dependence on slow electro-optic conversions and electronic interfaces, while also lacking the flexibility needed for versatile connectivity and functionality [1]. In this work, we present a unified approach toward all-optical neuromorphic computing by combining two key building blocks: i) PHIL (Photonic-Heater-In-Lightpath) [2], which acts as a fully optical neuron unit, enabling high-speed temporal integration and reconfigurable nonlinear activation and ii) FPCA (Field-Programmable Coupler Array), which provides programmable, non-volatile interconnection between photonic neurons. By integrating both technologies, we outline a conceptual architecture where PHILs are interconnected via FPCAs, enabling cascadable and reconfigurable optical neural networks that operate without electro-optic conversion, paving the way for efficient photonic AI accelerators.

We present the first operation of an FPCA (see Fig 1a), providing programmable and reconfigurable interconnections between optical neurons. Our implementation is based on non-volatile units' cells using the low-loss phase-change material Sb_2Se_3 as the core tuning element, routing light by tuning the couplers implemented as 2×2 Mach-Zehnder interferometers. This allows compact π-phase shift in a compact footprint ($L\pi$ = 16.7 μm) with minimal insertion losses (~0.3 dB), thus enabling efficient and compact photonic meshes. We set a 4-coupler FPCA unit cell in a square mesh, achieving high extinction ratio switching (~20 dB) and programmable light routing via non-volatile states. We also demonstrate the reconfiguration of the FPCA as synapsis in a fully optical neuronal computing mimicking a functional ring resonator by selectively programming the coupling state of individual couplers, represented in Fig. 1a. Resonance wavelength tuning and coupling strength control are achieved by adjusting the PCM refractive index. Switching energy ranges from 0.15 μJ (amorphization) to ~1 mJ (crystallization), after which no static power is required.

We subsequently introduce the concept of the PHIL which performs two key neural operations: signal integration and nonlinear activation, entirely in the optical domain. Specifically, counter-propagating standing waves create high-field antinodes aligned with titanium nano-antennas in a ring resonator, enabling wavelength-selective absorption and localized thermal accumulation (see Fig 1b). This induces a controlled

thermo-optic phase shift on a low-loss probe signal. Crucially, PHIL achieves signal integration at 50 GHz over a ~130 ns thermal window, allowing the accumulation of up to 6,500 signals per wavelength, mirroring the integration function of biological neurons. Beyond integration, PHIL also enables fully photonic nonlinear activation, analogous to neuronal firing. This is achieved by exploiting the Lorentzian lineshape of the microring resonance. By tuning the probe wavelength (λ_PS) relative to the resonance peak, the thermal response from control signals (λ_cs-a and λ_cs-b) produces different nonlinear transfer characteristics. Varying the spectral position of the probe along the resonance slope leads to distinct output behaviors, ranging from quasi-linear to strongly nonlinear responses. We experimentally validate this behavior by injecting a continuous-wave control signal and measuring the transmission at different probe, confirming the tunable shape-dependent modulation.

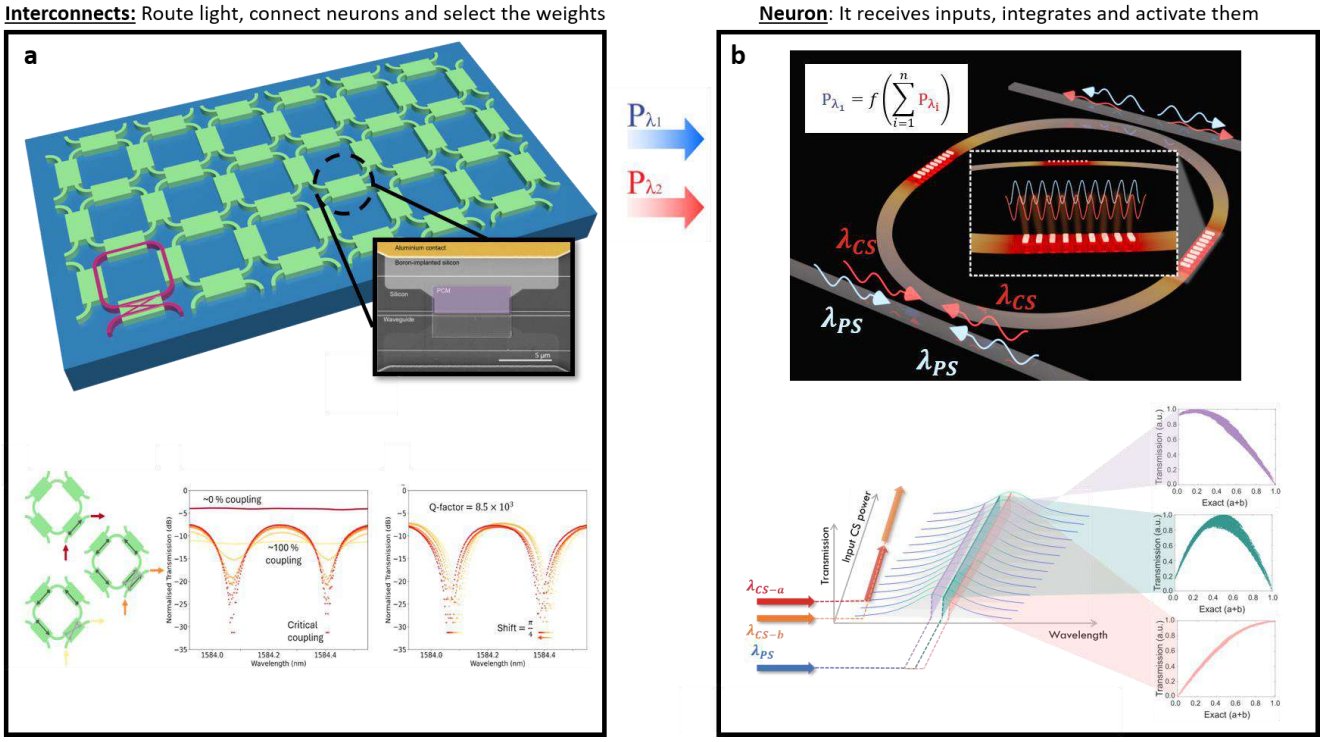


Figure 1. a) Interconnections block based on FPCA, implemented by unit cells with low-loss and non-volatile phase change material. b) Neuron block based on PHIL implementation based on standing wave activating the titaniu nano-heaters located on the top of the ring.

In summary, we present a unified neuromorphic photonic platform composed of two complementary modules, the neuron block (PHIL), with an approach that enables fully optical temporal integration and nonlinear activation functions, and the programable mesh (FPCA), with a compact, non-volatile and programmable photonic mesh. Combined, these building blocks establish a scalable, cascadable and energy-efficient architecture for AI acceleration, offering full programmability and functionality in the optical domain.

References

1. Farmakidis, N., Dong, B. & Bhaskaran, H. “Integrated photonic neuromorphic computing: opportunities and challenges”. Nat Rev Electr Eng 1, 358–373 (2024).
2. Shastri, B.J., Tait, A.N., Ferreira de Lima, T. et al. “Photonics for artificial intelligence and neuromorphic computing”. Nat. Photonics 15, 102–114 (2021).
3. Yi Zhang et al. “High-speed multiwavelength photonic temporal integration using silicon photonics” ArXiv (2025).

Strong Coupling of Surface Plasmons and Excitons in a Semiconductor Organic Material

Zouheir Sekkat

[1]Department of Chemistry, Faculty of Sciences, University Mohammed V, Rabat, Morocco.
[2]Optics and Photonics Center, Moroccan Foundation for Advanced Science and Innovation and Research, Mohammed VI Polytechnic, Benguerir, Morocco.
* Corresponding author: z.sekkat@mascir.ma

Abstract: We report on strong coupling between surface plasmons and excitons in an optically nonmetallic excitonic dye-polymer material of different thicknesses. We carried experiments of angular scans of reflectivity from silver and dye-polymer layers in a Kretshmann-Raether configuration, and we obtained the dispersive dielectric constant of the dye solutions for different dye concentrations using Lorentz model. Reflectometry theoretical experiments yielded dispersion relations of hybrid modes of propagating surface plasmons and excitons. The latter exhibit anticrossing which is the signature of strong coupling. The energy of Rabi splitting, E_{Rabi}, is sample dependent, and is in the 173-215 meV range. Strong coupling between surface plasmons and excitons is due to the field localization and enhancement as well as the sharp transition in the absorption spectrum of the excitonic material.

Interfacing the brain by photonic technologies

Massimo De Vittorio, F. Pisanello

[1]Center for Biomolecular Nanotechnologies, Istituto Italiano di Tecnologia, Via Barsanti, Arnesano (LE), Italy
[2]Dip. Ingegneria dell'Innovazione, Università del Salento, Via Monteroni, 73100 Lecce (LE), Italy
*

Abstract: In this talk, new technological and methodological approaches for interfacing the brain by tapered optical fibers (TOFs) will be shown. TOFs are nanomachined to produce optical probes and optrodes for accessing deep brain regions in animal models with spatial and temporal resolution for both recording and controlling neural activity.

Modeling Electromagnetic Wave Interactions with Ferroelectric Vortex Lattices in the Sub-THz Regime

M. Degen[1], R. Khomeriki[2], V. Jandieri[1], J. T. Svejda[1], P. L. Werner[3], D. H. Werner[3], J. Berakdar[4], and D. Erni[1]

[1]General and Theoretical Electrical Engineering (ATE), University of Duisburg-Essen (UDE), and Center for Nanointegration Duisburg-Essen (CENIDE), D-47048 Duisburg, Germany

[2]Physics Department, Tbilisi State University, 3 Chavchavadze, 0128 Tbilisi, Georgia

[3]Department of Electrical Engineering, The Pennsylvania State University, University Park, PA 16802, USA

[4]Institute of Physics, Martin-Luther-University Halle-Wittenberg, D-06120 Halle, Germany

marvin.degen@uni-due.de (corresponding author)

Abstract

A frequency response in the sub-THz regime of strained ferroelectric materials forming chiral polar ferroelectric vortex-antivortex lattices (FVL) in a meta-stable state has been observed experimentally. In this contribution, we discuss the physics of the interactions in the sub-THz regime and aim at a corresponding numerical full-wave model.

1 Introduction

Conventional bulk ferroelectric materials have been used in electronic and optical devices for decades. The recent discovery of strained ferroelectric materials forming chiral polar ferroelectric vortex-antivortex lattices (FVL) in a meta-stable state and the experimental observation of a frequency response in the sub-THz regime [1] point to the potential of such materials to be used in electronic devices operating in the sub-THz regime. However, to understand the underlaying physics and to exploit the full potential of these materials, analytical and numerical models of their electromagnetic wave interaction are required but have yet to be developed.

2 Modeling

A schematical view of a FVL is shown in Fig. 1. The structure is invariant along the z-direction and the distance between the (anti-) periodic polar vortices is d and $2d$ in the x and y direction, respectively. One prominent candidate of such a strucutre consists of alternating perovskite layers of strontium titanate (STO) and lead titanate (PTO) grown on a dysprosium scandium oxide (DSO) substrate [not shown in the figure], where d is on the order of 10 nm [1]. Based on these size parameters in conjunction with Bloch's theorem, one assumes a frequency response in the optical regime. However, although counterintuitive, the experimental observation of a frequency response in the sub-THz regime, where the wavelength is on the order of 1 mm and thus drastically exceeds the size parameters of the FVL, has been reported [1]. The reason for this is a coupling of the electromagnetic wave with the polarization vortices, as given by the Maxwell equations

$$\nabla \times \mathbf{E} = -\mu_0 \frac{\partial \mathbf{H}}{\partial t}, \qquad \text{(1a)} \qquad\qquad \nabla \times \mathbf{H} = \varepsilon_0 \frac{\partial \mathbf{E}}{\partial t} + \frac{\partial \mathbf{P}}{\partial t}, \qquad \text{(1b)}$$

where $\mathbf{E}$, $\mathbf{H}$, and $\mathbf{P}$ are the electric field, magnetic field, and polarization density, respectively, and ε_0 and μ_0 are the vacuum permittivity and permeability. It should be noted that the polarization density $\mathbf{P}$ is a superposition of dielectric polarization density $\mathbf{P}_\mathrm{d}$ and spontaneous polarization density $\mathbf{P}_\mathrm{s}$ where the former describes the dielectric response of the material (usually

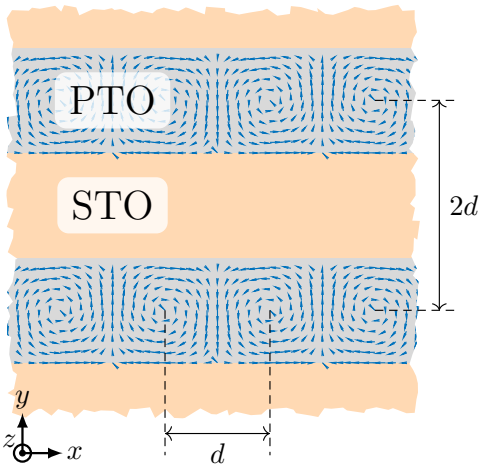


Figure 1: Cross-sectional view of a ferroelectric vortex lattice composed of alternating layers of PTO and STO. The spontaneous polarization $\mathbf{P}_\mathrm{s}$ is indicated by the arrows and evolves predominantly in the PTO material. The distance between the polar vortices is d and $2d$ in x and y direction, respectively. The structure is assumed to be invariant along the z-direction.

taken into account via a relative permittivity ε_r) and the latter refers to the vortex lattice structure. Microscopically, the spontaneous polarization density is caused by discrete dipoles, indicated by the arrows in Fig. 1. Once an electromagnetic wave interacts [cf. (1a) and (1b)] with a FVL, the dipoles' steady state is slightly perturbed yielding a restoring force towards the steady state and subsequently an oscillation. This is the case for a transversal electric (with the axis of invariance) polarized wave, when the electric field lies in the same plane as the polarisation vortices. As experimental [1] and numerical [2] observations show, the eigenfrequency of these oscillations is in the sub-THz regime explaining the frequency response in this spectral regime. Contrary, in the case of a transversal magnetic wave, the electric field is perpendicular to the polarisation vortices, and hence no first-order (linear) interaction occurs [2].

To further investigate these interactions, rigorous numerical models are required. The core of these models is the description of the dipole dynamics in the FVL based on a second-order time-dependent Landau-Ginzburg-Devonshire (LGD) equation [3] minimizing the free energy of the system

$$\alpha_\mathrm{k}\ddot{P}_i + \frac{1}{L}\dot{P}_i = -\frac{\delta F}{\delta P_i}, \tag{2}$$

where α_k and L are kinetic coefficients, index i indicates the directional components of a vector and F is the free energy functional of the system taking into account strain, depolarization, gradient energy effects and mechanical displacement.

The interaction with the electromagnetic wave in a full-wave manner is then described by solving the system of coupled differential equations (1a), (1b), and (2).

Acknowledgements

This work was supported by the Deutsche Forschungsgemeinschaft (DFG) through CRC/TRR 196 MARIE (287022738) under project M03.

References

[1] Li, Q., *et al.*, "Subterahertz collective dynamics of polar vortices," *Nature*, Vol. 592, No. 7854, pp. 376-380, 2021.

[2] Khomeriki, R., Jandieri, V., Watanabe, K., Erni, D., Marin, A., and Berakdar, J., "Photonic ferroelectric vortex lattice," *Phys. Rev. B*, Vol. 109, No. 4, pp. 4528-1–4528-10, 2024.

[3] Yang, T., Wang, B., Hu, J.-M., and Chen, L.-Q., "Domain dynamics under ultrafast electric-field pulses," *Phys. Rev. Lett.*, Vol. 124, No. 10, pp. 107601-1-107601-6, 2020.

Metamaterial grating Distributed Feedback laser Spatial Coupled-mode modelling

H. Benisty[1*], Y. Liang[2], A. Ramdane[2] and A. Lupu[2]

[1]Laboratoire Charles-Fabry (LCF), Institut d'Optique Graduate School, Univ. Paris-Saclay, Palaiseau, France
[2]Centre de Nanoscience et de Nanotechnologies (C2N), CNRS, Univ. Paris-Saclay, Palaiseau, France
[*]corresponding author: henri.benisty@institutoptique.fr

Abstract: A metamaterial grating based on arrays of cut-wires interacts with a laser ridge to provide resonant distributed feedback. We describe the device operation by a four-modes coupled-mode model. With proper parameters, it reproduces well the electromagnetically-induced-transparency type feature of the spectrum.

The concept of resonant units is central in metamaterials. The concept was recently applied to the grating that provide the feedback, wavelength selective mechanism, in ubiquitous distributed feedback (DFB) laser diodes. Usually, the grating is dielectric, and its units are as small as $\lambda/4n$ (about 250 nm in telecom DFB laser diodes), and cannot become resonant themselves. Careful interaction with metallic system can be used to implement the concept of resonant grating units. We describe here the approach followed in the recent publication [1] to model the corresponding device.

The device principle is shown in Fig.1. The cut-wire array is the grating (typical period Λ=250 nm) that acts as a metamaterial as well. The inner gold wire is made as adjacent to the active ridge as possible, in order to provide interaction with the ridge mode. If there were only one such element, we would have a DFB with a metallic grating, which typically behaves as a modulated loss device, with in general thresholds that are degraded due to metal losses, compared to dielectric feedback (refractive index modulation thanks to various flavours of ridge etching and regrowth).

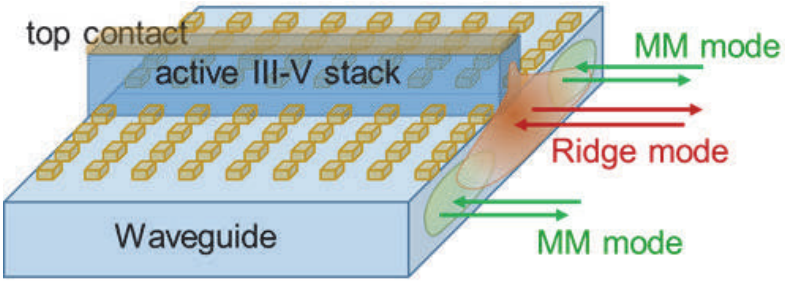


Figure 1: Scheme of a DFB laser diode with feedback provided on both sides by identical cut-wire arrays, made of gold "atoms". Each gold "atom" is a nanowire coupled to its neighbor.

By employing cut-arrays of wire, we favour a resonant behavior of the ensemble, and we get closer to the operation as a resonant metamaterial grating. However, attempts to model the cut-wires as separate resonators did not provide a good description of the observed spectra. Instead we found that the remaining dielectric guide under the cut-array should be considered as giving birth to the "MM modes" described in green in Fig.1, hence with slightly different effective indices in the ridge and for the "MM". Actually, both sides act together into a

single “supermode” of even parity. Also, the MM still has large losses, at least compared to the standard of good DFB values, but tuned in such a way that the impact is modest on the laser.

We will describe the coupled-mode theory modelling of this system. Due to the role of the grating, both modes (Ridge and MM) first interact with its counter-propagative partner. Then, we couple them together by a block matrix with two coefficients acting over the four modes. At the present stage, and for reasons that we believe to be similar to the dominance of loss over reflection in metallic DFB lasers, we do not introduce “cross-DFB” coupling with the ridge mode. Furthermore, in a Hermitian setting, we would select a rotation matrix, essentially. But here, given the various losses, we slightly modify the setting to go to a slightly non-Hermitian block matrix. As a result, we get the following dispersion relations, using five gradual sets of parameters to obtain a large modulation of the electromagnetically induced transparency (EIT) peak:

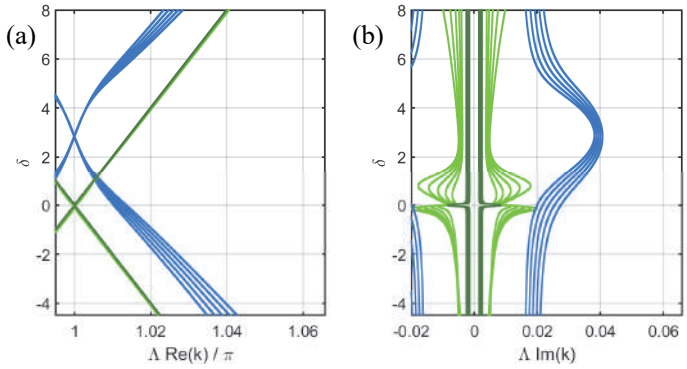


Figure 2: Dispersion relations of the system four modes given as frequency detuning δ around the Bragg frequency of the laser mode as a function of real (a) and imaginary (b) normalized wavevectors for a representative parameter span. Green are the hybridized laser modes and blue the MM modes. The dark-green line is the case of DFB only, without any MM interaction, i.e. not hybridized. It only has the small narrow dip at the Brag condition. The landscape around the Bragg peak is heavily affected by the coupling to the MM.

Essentially, the green lines of Fig.2(b) resemble closely the laser output spectra, which we analyse as an EIT feature (it is even sometimes above the background level by a couple of dB in experimental data).

We will discuss how 3D electromagnetic calculation of systems with much less periods than the actual lasers can be made to critically support (or critically question) this modelling approach.

This work was partially funded by the Labex NanoSaclay project DISYPTE, the CNRS INSIS prematuration project LACOMETA and BpiFrance IPCEI-CIS project METAGRAAL (LS 262296).

References

1. Dubrovina, N., Y.Liang, Q. Gaimard, V. Brac de la Perrière, K. Merghem, H. Benisty, A. de Lustrac, and A. Ramdane, “Electrically Injected Metamaterial Grating DFB Laser Exploiting an Ultra-High Q Electromagnetic Induced Transparency Resonance for Spectral Selection,” Adv. Func. Mater. 2405912 (1-10) 2024.

Discretization effects in topological plasmonics

A. Neuhaus[1*], P. Dreher[1], and F.-J. Meyer zu Heringdorf[1]
[1]University of Duisburg-Essen, Faculty of Physics and CENIDE, Duisburg-Essen, Germany
Corresponding author: alexander.neuhaus@uni-due.de

Abstract: Determining the full electric field of surface plasmon polaritons (SPPs) is experimentally challenging. Therefore, experimental data often needs to be compared to numerical simulations. We use a Hankel-wavelet based simulation to address why Chern numbers, invariant in topologic plasmonic systems, are systematically smaller than the theoretical expectation.

The experimental determination of the vectorial electric fields of SPPs on the nano-femto scale has become possible in recent years by means of polarimetric photoemission electron microscopy (PEEM) [1]. This allows direct access to topological properties of these fields. Using this method, topological quasiparticles such as skyrmions [2] or merons [1] have been observed in the electric field or the spin angular momentum (SAM). The SAM is not subject to the diffraction limit and can thus exhibit deep sub-wavelength features [3]. To understand the effect of such deep sub-wavelength features on the derived topological quantities, efficient simulations are needed that include the effects of the finite resolution of the polarimetric PEEM experiment.

In a polarimetric PEEM experiment, SPPs are excited at a shaped excitation groove on a Au(111) platelet by a normally-incident pump laser pulse, as shown in Fig. 1a. To simulate the electric field of the SPPs we follow the approach by Davis et al. [4] and describe the SPPs by Hankel wavelets originating from the groove with an excitation wavelength of 800 nm. To create a meron pair topology within the SAM of the excited SPPs an Archimedean spiral groove with a gap of one SPP wavelength is illuminated with linearly polarized pump laser pulses. The simulated electric field vectors $\mathbf{E}_{\mathrm{spp}}$ in the center of the spiral are shown in Fig. 1b. The electric field vectors rotate in space with the SPP frequency due to the orbital angular momentum provided by the spiral. The magnetic field vectors $\mathbf{H}_{\mathrm{spp}}$ can be calculated from the electric field vectors using Faraday's law. Assuming time-harmonic fields with frequency ω_{spp}, the SAM can than be calculated from the electric and magnetic fields using the relation

$$\mathbf{s}(\mathbf{r},t) = \mathrm{Im}\int_{\mathcal{A}} \left(\mathbf{E}^*_{\mathrm{spp}} \times \mathbf{E}_{\mathrm{spp}} + \mu \mathbf{H}^*_{\mathrm{spp}} \times \mathbf{H}_{\mathrm{spp}}\right)/2\omega \tag{1}$$

and the result is shown in Fig. 1c. The two red-shaded SAM maxima in the center correspond to the two merons that form the meron pair. Such as skyrmions, merons are classified by their Chern number

$$C = \frac{1}{4\pi} \int_{A} \hat{\mathbf{s}} \cdot (\partial_x \hat{\mathbf{s}} \times \partial_y \hat{\mathbf{s}})\, dA, \tag{2}$$

which can be calculated from the normalized SAM vectors $\hat{\mathbf{s}} = \mathbf{s}/|\mathbf{s}|$. The integrand of eq. 2 is the Chern density, which describes the enclosed solid angle density between neighboring SAM vectors. The Chern density is shown in Fig. 1d for the simulated meron pair. Integrating the Chern density over the marked area in Fig. 1d should yield a Chern number of $C = 1 = 1/2+1/2$ given by the two individual merons within the meron pair. However, there is a true zero of the SAM field with $S_x = S_y = S_z = 0$ in between the two adjacent merons as visible in the center of Fig. 1c, that is called an amplitude vortex. As the Chern density is determined from normalized SAM vectors, the amplitude vortex acts as a point singularity. A point singularity should not contribute to the surface integral over the Chern density. In a discretized case however, such

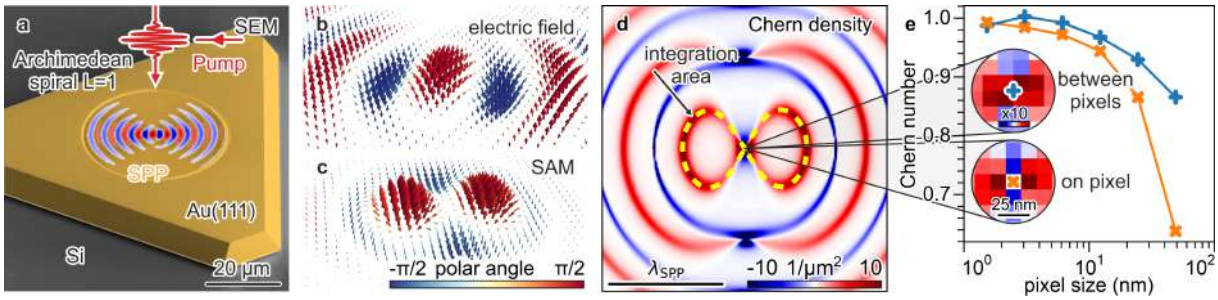


Figure 1: Excitation and analysis of a plasmonic spin meron pair. a) scanning electron microscope image of a structured Au(111) platelet excited by a linearly polarized pump laser pulse. b) simulated electric field configuration in the center of the spiral. c) simulated SAM texture in the center of the spiral. d) calculated chern density from the SAM texture. e) integrated Chern number as function of amplitude vortex position relative to pixel grid and pixel size.

point singularities are mapped onto pixels of finite size and thus can dramatically contribute to the integral. Therefore, the relative alignment of the vortex to the pixel grid and the pixel size are of great importance when analyzing SAM textures carrying point singularities. Figure 1 shows the expected Chern number for the meron pair as a function of pixel size and relative position of the amplitude vortex and the pixel grid. With decreasing pixel size, both relative alignments converge towards $C = 1$. For typical discretizations using polarimetric PEEM (approx. 10 nm) however, the Chern number is always strongly underestimated and heavily depends on the relative alignment.

The strong dependence of the numerically calculated Chern number on the pixel grid highlights the need for high resolution data and careful analysis of the topological SAM textures. The singularities occuring within the Chern density can significantly change the Chern number when analyzing experimental data. Numerical simulations of the SPPs can help to disentangle real topological features from contributions caused by the pixelation of the data itself. Generally one needs to be careful when analyzing topological SAM textures as these can contain all types of singularities in the Chern density, significantly contributing to the overall Chern number.

The authors acknowledge support from the DFG via CRC 1242 “Non-Equilibrium Dynamics of Condensed Matter in the Time Domain” Grant Nos. 278162697-SFB 1242.

References

1. Dreher, P., A. Neuhaus, D. Janoschka, A. Rödl, T. C. Meiler, B. Frank, T. J. Davis, H. Giessen, and F. Meyer zu Heringdorf, ”Spatiotemporal Topology of Plasmonic Spin Meron Pairs Revealed by Polarimetric Photo-Emission Microscopy,” *Advanced Photonics*, Vol. 6, No. 6, 066007, 2024.

2. Davis, T. J., D. Janoschka, P. Dreher, B. Frank, F.-J. Meyer zu Heringdorf, and H. Giessen, ”Ultrafast Vector Imaging of Plasmonic Skyrmion Dynamics with Deep Subwavelength Resolution,” *Science*, Vol. 368, No. 6489, eaba6415, 2020.

3. Du, L., A. Yang, A. V. Zayats, and X. Yuan, ”Deep-Subwavelength Features of Photonic Skyrmions in a Confined Electromagnetic Field with Orbital Angular Momentum,” *Nat Phys*, Vol. 15, No. 7, pp. 650-654, 2019.

4. Davis, T. J., B. Frank, D. Podbiel, P. Kahl, F.-J. Meyer zu Heringdorf, and H. Giessen, ”Subfemtosecond and Nanometer Plasmon Dynamics with Photoelectron Microscopy: Theory and Efficient Simulations,” *ACS Photonics*, Vol. 4, No. 10, pp. 2461-2469, 2017.

Terahertz metasurface for realizing high-Q chiral BICs

Xinyue Liang[1], Jian Liu[1], and Xumin Ding[1*]

[1] Advanced Microscopy and Instrumentation Research Center, School of Instrumentation Science and Engineering, Harbin Institute of Technology, Harbin 150080, China
[*]corresponding author: xuminding@hit.edu.cn

Abstract: We propose a metal metasurface design for terahertz chiral sensing systems, leveraging symmetry-protected bound states in the continuum (BICs) to realize high Q-factor transmissive terahertz (THz) chiral response. This provides new perspectives into the creation of novel BICs in terahertz, advancing terahertz spectroscopy, polarization optics, and biochemical sensing applications.

Chiral research plays a pivotal role in analytical chemistry, pharmaceutics, and related disciplines. However, detection sensitivity has long been constrained by intrinsic physical limitations of natural materials, posing signal-to-noise ratio challenges for detection devices [1, 2]. Metasurfaces can induce strong interactions between chiral fields and chiral substances, enabling chiral effects far surpassing those of natural materials which are versatile applications [3,4]. The bound states in the continuum (BICs), characterized by theoretically infinite quality factors(Q), has opened new avenues for achieving high-Q chiral optical responses [5,6]. Here, we integrate metasurfaces with BICs physics to design a chiral BICs metasurface, achieving chiroptical responses with high-Q factors and enhanced sensitivity.

Our chiral BIC metasurface utilizes dual Z-shaped configurations (Fig. 1a) with in-plane inversion C_4 symmetry but lacking in-plane mirror symmetry to establish quasi-bound states in the continuum (q-BICs). Intrinsic planar chirality is achieved under normal incidence, demonstrating maximum circular dichroism (CD) values of 0.41 (theoretical) at 0.81 THz and 0.36 (experimental) at 0.79 THz. The q-BICs state maintains a strongly enhanced local field within structural gaps, exhibiting up to 432.0-fold enhancement (Fig. 1c).

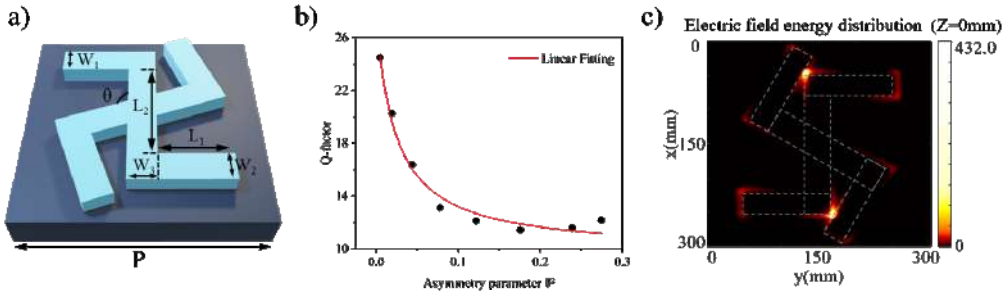


Figure 1. a) Schematic of the unit cell of a planar chiral q-BICs meta-surface formed by an aluminum dual Z-shaped configurations on a SiO_2 substrate. b) Dependence of the Q-factors of the planar chiral q-BICs mode on the relative asymmetry parameter θ^2 around the chiral q-BICs state. The curve shows a quadratic fitting. c) Electric field energy distribution of the planar chiral q-BICs meta-surface with circular eigen-polarization.

Figure 2 demonstrates the sensing performance metrics of the metasurface as a sensor. Fig. 2a illustrates that the chiral resonance peak undergoes a redshift with increasing refractive index of the analyte material, while maintaining a consistently above 0.3. The sensor sensitivity reaches S = 200.239 GHz/RIU (Fig. 2b). The

Q-factor of the resonance peak exhibits minor fluctuations around 13 with increasing refractive index (Fig. 2c), while the FOM value oscillates slightly above and below 4.5 (Fig. 2d). This highly sensitive chiral sensing system provides a viable solution for identifying chiral biomolecules with diverse refractive indices.

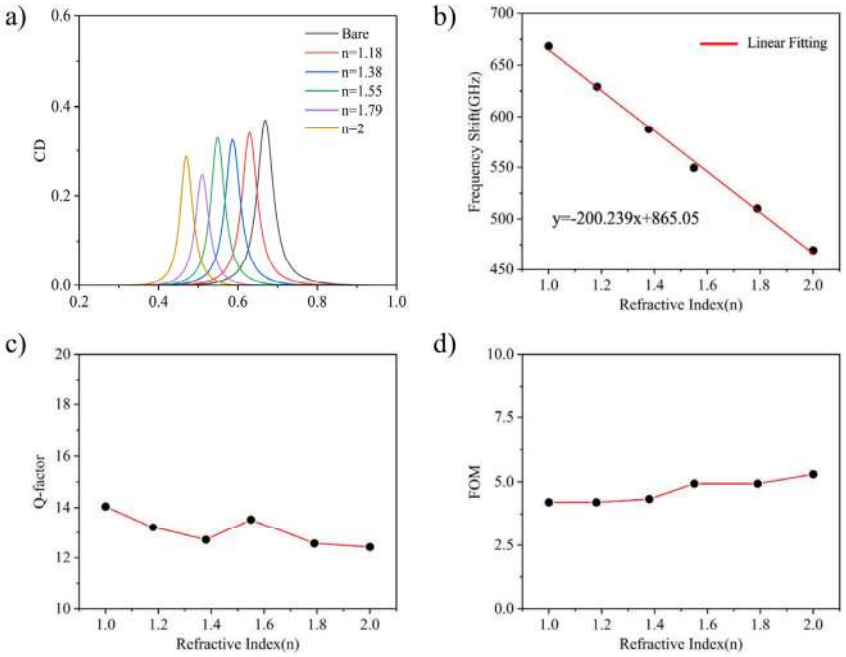


Figure 2. Indicators of sensor performance. a) Simulated CD spectra with different refractive indices. b) CD sensitivity fitting curve. c) Effect of analytes refractive indices on Q-factor. d) Effect of analytes refractive indices on FOM.

References

1. Choi, W.J., Cheng, G., Huang, Z. et al. “Terahertz circular dichroism spectroscopy of biomaterials enabled by kirigami polarization modulators,” Nature Materials, vol. 18, No. 8, 820–826, 2019.
2. Fedotov, V.A., Mladyonov, P.L., Prosvirnin, S.L., et al. “Asymmetric propagation of electromagnetic waves through a planar chiral structure,” Physical Review Letters, vol. 97, No. 16, 167401, 2006.
3. Gansel, J.K., Thiel, M., Rill, M.S., et al. “Gold helix photonic metamaterial as broadband circular polarizer,” Science, vol. 325, No. 5947, 1513–1515, 2009.
4. Hsu, C.W., Zhen, B., et al. Stone, A.D., “Bound states in the continuum,” Nature Reviews Materials, vol. 1, No. 9, 16048, 2016.
5. Azzam, S.I., Kildishev, A.V. “Photonic bound states in the continuum: from basics to applications,” Advanced Optical Materials, vol. 1, No. 1, 2001469, 2021.

Transport properties of coupled-resonator phononic graphene ribbons

R. A. Méndez-Sánchez[1], Y. Hernández-Espinosa[1], E. G. Sotelo-Parra[1], and A. M. Martínez-Argüello[2]
[1]Instituto de Ciencias Físicas, Universidad Autónoma de México, México
[2]Instituto de Física, Benemérita Universidad Autónoma de Puebla, México
mendez@icf.unam.mx (corresponding author)

Abstract

We study the transport properties of honeycomb-like elastic ribbons composed of resonators and finite phononic crystals called coupled resonator phononic waveguides. Spectra for ribbons with zigzag and armchair edges were obtained for various ribbon widths. Although zigzag ribbons are gapless, armchair ribbons display a gap depending on the ribbon width.

1 Introduction

Coupled-resonator phononic metamaterials (CRPnMs), recently introduced by our group, can replicate the electronic transport properties of condensed matter systems. The study of several phenomena that are hardly or impossible to study in that area is now possible with CRPnMs. Inspired by the coupled-resonator optical waveguides [1], CRPnMs allow for the precise engineering of higher-order couplings and satisfy a phononic tight-binding model similar to that of condensed-matter physics [2, 3]. Here we study the phononic transport of coupled-resonator phononic ribbons that mimic the behavior of graphene nanoribbons. The coupled-resonator phononic ribbons are composed of resonators coupled by finite phononic crystals arranged in a honeycomb lattice as seen in Fig. 1. When a normal-mode frequency of the resonator falls within the bandgap of the finite phononic crystal the wave amplitude associated with the normal-mode frequency localize within the resonator and decay evanescelty through the finite phononic crystal. When two or more resonators are coupled, the localized modes couple to each other yielding a set of modes that satisfy a phononic version of the tight-binding model.

2 Engineering of the coupled-resonator phononic ribbons

The graphene nanoribbons are graphene strips of width w and infinite length. They can have armchair or zigzag borders. The unit cell of the coupled-resonator phononic ribbons, that mimic the graphene nanoribbons, are depicted in Figs. 1 (a) and (b); these ribbons are repeated infinitely in the vertical direction. The resonators are hexagonal plates of side L_h and thickness e and are interconnected via finite phononic crystals. The unit cell of the connectors is formed by a square plate of $L \times L \times e$ and two cuboids of $h_c \times e \times L_c/2$. The resonators are located in the vertices of a honeycomb ribbon whereas

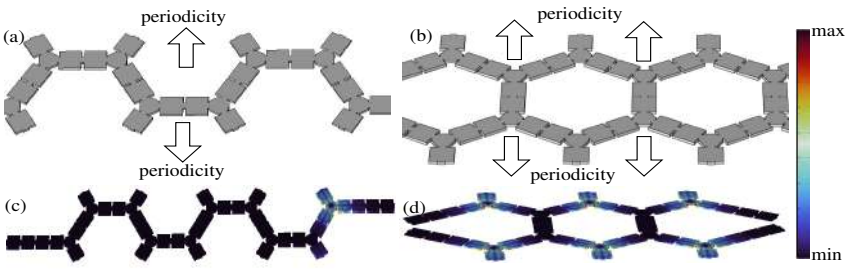


Figure 1: Unit cell of the coupled-resonator phononic ribbons: (a) zigzag and (b) armchair. (c) Localized edge wave amplitude and (d) dimeric wave amplitude.

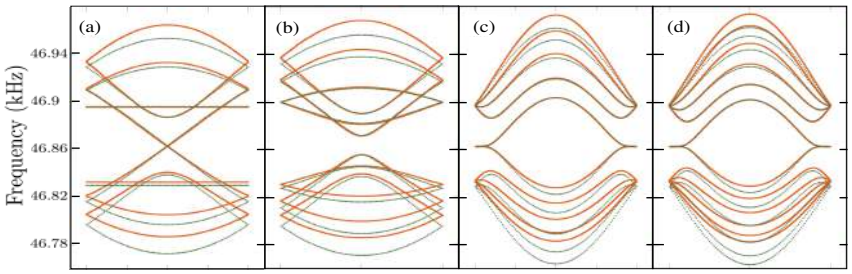


Figure 2: Band structure of the coupled-resonator phononic ribbons: (a) and (b) armchair ribbons of widths 5 and 6. (c) and (d) zigzag ribbons of widths 5 and 6. The continuous lines correspond to the finite element simulations and the continuous lines to the tight-binding model.

the finite phononic crystals connect them over the edges of the grid. The phononic crystal is designed to present a frequency bandgap between 38 kHz and 48 kHz whereas the resonant frequency of the hexagonal plate is above 40 kHz. All numerical calculations were performed using COMSOL Multiphysics.

3 Transport properties of the phononic graphene ribbons

Due to Bloch's theorem, the properties of the vibrations of the periodic (infinite) structures can be obtained by studying only a unit cell of the ribbons (See Figs. 1 (a) and (b)). The frequency spectrum will consist of bands and gaps in which vibrations can or cannot travel through the structure. In Fig. 2 the obtained band structures for the armchair –(a) and (b)– and zigzag –(c) and (d)– ribbons, are presented. As can be seen, the armchair ribbons could present a frequency bandgap, depending on the ribbon width, whereas the zigzag ribbons do not present such a bandgap and always transmit the vibrations independently of the ribbon width. Some wave amplitudes of the ribbons are given in Figs. 1 (c) and (d). In the zigzag case (c) one can observe a wave amplitude localized at the border of the ribbon. The armchair case (d) shows a wave amplitude localized in some dimers of the ribbon.

4 Conclusions

We obtained the vibration transport properties of phononic-crystal graphene ribbons. The obtained band structures show that armchair ribbons can present a frequency bandgap or a Dirac cone depending on the ribbon width, whereas zigzag ribbons do not present either a bandgap or a Dirac cone. As expected, the calculated wave amplitudes are localized on the resonators and connect through evanescent waves in the couplers.

5 Acknowledgements

This work was supported by CONAHCYT, now SECIHTI, under Grant No. CF-2023-G-763 and by DGAPA-UNAM under project IN108825. Y.H.E. and A.M.M.-A were supported by UNAM Posdoctoral Program (POSDOC).

References

[1] Yariv, A., Y. Xu, R. K. Lee and A. Scherer "Coupled-resonator optical waveguide: a proposal and analysis," *Opt. Lett.*, Vol. 24, No. 11, pp. 711–713, 1999.

[2] Ramírez-Ramírez, F., E. Flores-Olmedo, G. Báez, E. Sadurí and R. A. Méndez-Sánchez "Emulating tightly bound electrons in crystalline solids using mechanical waves," *Sci. Rep.*, Vol. 10:10229, pp. 1-7, 2020.

[3] Betancur-Ocampo, Y., Manjarrez-Montañez, B., Martínez-Argüello, A. M., and Méndez-Sánchez, R. A. (2024). "Twofold topological phase transitions induced by third-nearest-neighbor hoppings in one-dimensional chains." Physical Review B, 109(10), 104111.

Orienting fluorophores with the DNA origami for highly efficient plasmonic nanoantennas

Karol Kołątaj[1*], Aleksandra Adamczyk[1], Guillermo Acuna[1*]

[1] Department of Physics, University of Fribourg, Chemin du Musée 3, Fribourg CH 1700, Switzerland

[*]corresponding authors: guillermo.acuna@unifr.ch, karol.kolataj@unifr.ch

Abstract: Here, we use the DNA origami technique to assemble an optical antenna and position a single fluorophore at the antenna gap with controlled, parallel and perpendicular orientation. We study the coupling for both conditions revealing a 5-fold higher fluorescence intensity when the emitter is aligned with the antenna's main axis.

For more than a decade, the DNA origami technique has been one of the most successful strategies in nanofabrication. Initially, due to its high addressability and specificity, DNA origami was extensively used as a nanometric platform to accommodate nanoparticles, biomolecules, and small molecules with nanometer precision. Moreover, DNA origami structures can be easily modified to arrange a predefined number of entities with stoichiometric control. Finally, just recently, the orientation of covalently bound molecules has been achieved by stretching the fluorophores incorporated into DNA origami structures.[1] Specifically, the orientation of a dye molecule can be varied from almost parallel to almost perpendicular relative to the dsDNA by linking the fluorophores to both sides with ssDNA while leaving some unpaired bases in the scaffold, as shown in Figure 1a.

Here, we present applications of this orientation scheme to produce highly efficient plasmonic systems. The investigated photonic nanoantennas were composed of two gold nanoparticles with a single fluorophore at the hotspot, oriented either parallel or perpendicular to the dimer's main axis (see Figure 1b).[2] We observed a remarkable 250-fold fluorescence enhancement when the dye was oriented along this axis - five times higher than the other orientation. Interestingly, despite orienting the dyes along the DNA origami structures, the performance of the nanoantennas remained rather inhomogeneous, with high signal dispersion. Therefore, we further investigated the dispersion of fluorescence enhancement for both configurations using superspherical NPs, comparing the distributions of enhancement factors to realistic simulations. We concluded that the dispersion of results arises from variations in molecular orientations and gap sizes.

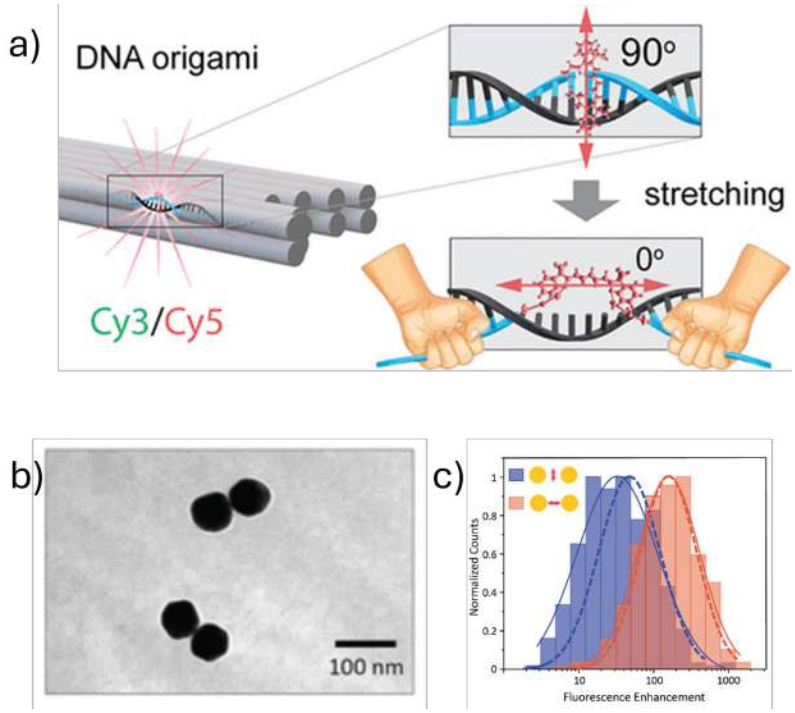


Figure 1. (a) Orienting fluorophores by applying a stretching force in the DNA origami structures (b) TEM image of the obtained optical nanoantennas (c) Fluorescence enhancement of the dye with a different relative orientation in the nanostructures.

This project has received funding from the European Union's Horizon 2020 Research and Innovation Program under the Marie Skłodowska–Curie Grant Agreement No. 860914.

References

1. Adamczyk et al. "DNA Self-Assembly of Single Molecules with Deterministic Position and Orientation", ACS Nano. 16: 16924-16931, 2022
2. Adamczyk et al. "Coupling Single Molecules to DNA-Based Optical Antennas with Position and Orientation Control", ACS Photonics 2024, 11, 12, 5267–5272, 2024

Mechanically Machinable, Printable Photonic Materials

Jong G. Ok[1*], Minwook Kim[1], and Kwangjun Kim[1]

[1]Department of Mechanical and Automotive Engineering, Seoul National University of Science and Technology, Seoul 01811, Korea

[*]corresponding author: jgok@seoultech.ac.kr

Abstract: We demonstrate recently developed approaches for creating photonic structures and materials by mechanical machining and printing methods. The printable nanophotonic structures fabricable by imprinting and printing of metallic ink, the mechanically inscribed microtrenches with solution-processable metallic wires embedded therein, and the direct machining of metallic micrograting will be mainly presented.

We present several novel methodologies for facile, scalable, and cost-effective manufacturing of photonic structures and materials particularly by utilizing mechanical machining, printing, and imprinting techniques. First, we describe a rapid and simple method to create photonic Ag nanostructures through direct mechanical patterning – either imprinting or printing – of ionic Ag ink coating by using a soft elastomer patterning mold [1]. Then, we demonstrate the facile fabrication of metal wire-embedded microtrenches interconnected with semiconducting nanowires via continuous mechanical machining of micrograting trenches, mechanical embedding of solution-processable metal wires therein, and hydrothermal nanowire growth thereto [2]. Last, we demonstrate the highly scalable precision machining of metal micrograting structures by continuous mechanical scribing of the sawtooth-patterned cemented carbide edge tool over a metal workpiece [3]. We also discuss the excellent scalability, high productivity, and broad applicability of these methods along with their specific applications into the practical fabrication of diverse photonic materials and devices including but not limited to color filters, light sensors, and diffractive optical elements.

Acknowledgements: This research was supported by grants from the National Research Foundation of Korea (NRF-2021M3H4A3A02099204, NRF-2022M3C1A3081178, RS-2024-00413607, and RS-2024-00449882 (Ministry of Science and ICT), and NRF-2022R1I1A2073224 (Ministry of Education)) funded by the Korean Government.

References

1. Ok, J. G. et al., “Facile fabrication of stretchable photonic Ag nanostructures by soft-contact patterning of ionic Ag solution coatings”, Nanophotonics, Vol. 11, No. 11, 2693-2700, 2022.
2. Ok, J. G. et al., “Mechanically processed, vacuum- and etch-free fabrication of metal-wire-embedded microtrenches interconnected by semiconductor nanowires for flexible bending-sensitive optoelectronic sensors”, Nanophotonics, Vol. 13, No. 7, 1141-1148, 2024.
3. Ok, J. G. et al., “Direct continuous scribing of scalable micrograting structures on metal surfaces by using a sawtooth-patterned cemented carbide edge”, Journal of Manufacturing Processes, under review.

Linear logic operations in a quasi-digital system

R. G. MacDonald[1], A. Yakovlev[2], and V. Pacheco-Peña[1*]

[1] School of Mathematics, Statistics and Physics, Newcastle University, Newcastle Upon Tyne, NE1 7RU, United Kingdom

[2] School of Engineering, Newcastle University, Newcastle Upon Tyne, NE1 7RU, United Kingdom
[*]corresponding author: victor.pacheco-pena@newcastle.ac.uk

Abstract: Electromagnetic (EM) wave-based quasi-digital logic operations are realized by carefully controlling the superposition of incident signals in a network of waveguides. Information is encoded into the wave characteristics of the incident signals (amplitude, phase or both). The encoding scheme is carefully selected to maximize the distinguishability of the operations.

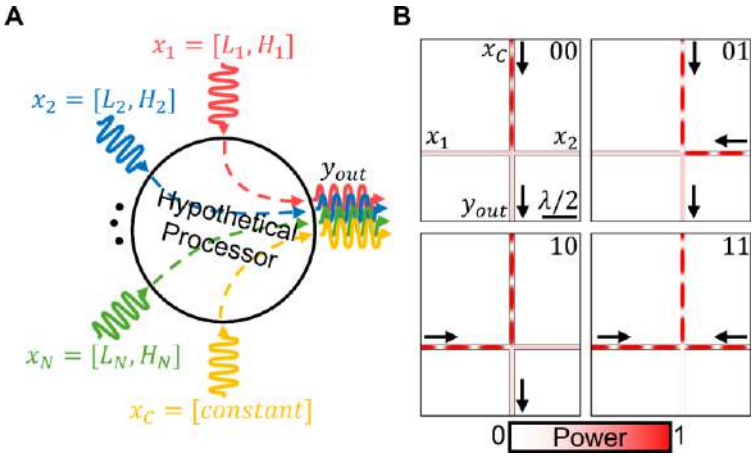


Figure 1. A. Schematic representation of a hypothetical quasi-digital processor based on the superposition of EM waves. **B.**, **C.** Numerical simulation results for the power distribution of a quasi-digital linear NAND operation.

Electromagnetic (EM) wave-based computing is an emerging paradigm which aims to harness the potential of waves[1] (high speed as an example). EM wave-based structures have been used in various computing tasks such as differentiation[2–4], integration[5], solving differential equations[6,7] and decision-making processes[8–11]. Conventional digital (or quasi-digital) computing operations including elementary logic operations have also been demonstrated[12–17]. Within this domain, a distinction exists between techniques exploiting structures with non-linearities[12–14] and those using a purely linear system. Using purely linear structures poses a challenge as output signals cannot be independently controlled[18]. This means there are a wide range of potential output signals, as opposed to a typically two-level system. Hence the adoption of the term, quasi-digital. Our work is focused on this challenge. In this work we will discuss the design of a linear system which can be used to produce distinguishable high and low output signals. i.e. where the contrast ratio $C_R = |20\log_{10}(Th_H/Th_L)|$ is maximized (Th_H and Th_L are the threshold values of the high and low output classification regions).

As will be presented in the conference, to address this, the information is encoded into the wave characteristics of input EM signals x_a (amplitude, phase or both), where $a = [1,2,\dots,N]$ is the input bit being represented. These signals, x_a, adopt one of two distinct values, L_a or H_a when a is low or high, respectively. Quasi-digital operations are then realized by carefully selecting these values such that the superposition of signals at the output y_{out}, resembles the desired logic operation, while maximizing C_R. This scenario is depicted in Fig. 1A. As an example, numerical simulation results (obtained using CST Studio Suite®) of a quasi-digital linear

NAND operation are presented in Fig. 1B, respectively. As it can be seen, the high output signal is clearly distinguishable from the low output signals indicating the linear structure is indeed emulating the NAND operation. During the conference, the core principles used to design quasi-digital logic gates will be presented along with further examples including the remaining elementary operations, many-to-one operations (*N*-input AND) and many-to-many operations (adders).

This work was supported by the Leverhulme Trust under the Leverhulme Trust Research Project Grant scheme (No. RPG-2020-316 and RPG-2023-024).

References

1. Rajabalipanah, H., Momeni, A., Rahmanzadeh, M., Abdolali, A. & Fleury, R. Parallel wave-based analog computing using metagratings. *Nanophotonics* **11**, 1561–1571 (2022).
2. MacDonald, R. G., Yakovlev, A. & Pacheco-Peña, V. Time derivatives via interconnected waveguides. *Sci Rep* **13**, 13126 (2023).
3. Knightley, T., Yakovlev, A. & Pacheco-Peña, V. Neural Network Design of Multilayer Metamaterial for Temporal Differentiation. *Adv Opt Mater* **11**, 2202351 (2023).
4. Sol, J., Smith, D. R. & del Hougne, P. Meta-programmable analog differentiator. *Nat Commun* **13**, 1713 (2022).
5. Silva, A. *et al.* Performing Mathematical Operations with Metamaterials. *Science (1979)* **343**, 160–163 (2014).
6. MacDonald, R. G., Yakovlev, A. & Pacheco-Peña, V. Solving partial differential equations with waveguide-based metatronic networks. *Advanced Photonics Nexus* **3**, (2024).
7. Sun, S. *et al.* Induced homomorphism: Kirchhoff's law in photonics. *Nanophotonics* **10**, 1711–1721 (2021).
8. MacDonald, R. G., Yakovlev, A. & Pacheco-Peña, V. Amplitude controlled electromagnetic pulse switching using waveguide junctions for high-speed computing processes. *arXiv:2205.04814* (2022) doi:10.1002/aisy.202200137.
9. Yakovlev, A. & Pacheco-Peña, V. Enabling High-Speed Computing with Electromagnetic Pulse Switching. *Adv Mater Technol* **5**, 2000796 (2020).
10. Pacheco-Peña, V. & Yakovlev, A. Computing with Square Electromagnetic Pulses. in *Handbook of Unconventional Computing,* (ed. Adamatzky, A.) 465–492 (World Scientific, London, 2021). doi:10.1142/9789811235740_0016.
11. Rogers, W., Johnson-Richards, C., Yakovlev, A. & Pacheco-Peña, V. Perfect splitting in rectangular-waveguide junctions for analog computing. *Phys Rev Appl* **21**, 054054 (2024).
12. Chattopadhyay, T. All-optical simultaneous XOR-AND operation using 1-D periodic nonlinear material. *Journal of Optical Communications* **45**, 183–190 (2024).
13. Fagotto, E. A. M. & Abbade, M. L. F. All-optical demultiplexing of 4-ASK optical signals with four-wave mixing optical gates. *Opt Commun* **283**, 1102–1109 (2010).
14. Stubkjaer, K. E. Semiconductor optical amplifier-based all-optical gates for high-speed optical processing. *IEEE Journal of Selected Topics in Quantum Electronics* **6**, 1428–1435 (2000).
15. Peng, C. *et al.* Universal Linear-Optical Logic Gate with Maximal Intensity Contrast Ratios. *ACS Photonics* **5**, 1137–1143 (2018).
16. Qian, L. & Caulfield, H. J. What can we do with a linear optical logic gate? *Inf Sci (N Y)* **176**, 3379–3392 (2006).
17. MacDonald, R. G., Yakovlev, A. & Pacheco-Peña, V. Quasi-digital linear logic gates. *In Prep* (2025).
18. Zhang, W. *et al.* Performing photonic nonlinear computations by linear operations in a high-dimensional space. *Nanophotonics* **12**, 3189–3197 (2023).

Emitting properties of a-Si:C:H-coated 2D-opaline photonic crystals

S. I. Pavlov[1*]. M. E. Bochkarev[2], S. A. Dyakov[3], V.G. Golubev[1], S.A. Grudinkin[1], M. F. Limonov[2] and A. B. Pevtsov[1]
[1]Ioffe Institute, Russia
[2]ITMO University, Russia
[3]Skolkovo Institute of Science and Technology, Russia
Pavlov_Sergey@mail.ioffe.ru (corresponding author)

Abstract

Two-dimensional (2D) photonic crystals (PhC) are fabricated from opal slabs coated with an a-Si:C:H emitting layer. The optical response of the emitting 2D PhC's near Γ-point of the Brillouin zone have been studied. A significant increase in the luminescence intensity in the visible spectral range has been demonstrated in the synthesized structures.

1 Introduction

2D PhC's are currently as considered one of the most promising dielectric media for achieving enhance light emission by increasing the probability of radiative recombination, described by the Purcell factor [1]. In this work, we studied the possibility of increasing the photoluminescence (PL) intensity of an a-Si:C:H emitting layer, resulted from interaction with the modes of a 2D PhC fabricated on the basis of an opal slab. Such interaction can be realized if the a-Si:C:H emission is located above the photonic band gap, where various radiative modes of the photonic crystal can exist within the light cone [2]. The spectral position of the PL contour can be easily varied by changing the content of carbon in the a-Si:C:H film. The full width at the half-maximum (FWHM) of the PL contour of a-Si:C:H reaches a value of 0.6-0.7 eV.

2 Results

The samples of the opal slabs being studied include opal films [2-3 monolayers (ML) of a-SiO_2 spheres of diameter 520 nm with a spread in diameter smaller than 3] grown on fused silica substrates. The a-Si_{1-x}:C_x:H layer with a thickness of 250 nm was deposited on opal film by the plasma-enhanced chemical vapor deposition (PECVD) technique in a capacitive reactor at various relative flows of silane (SiH_4) and methane (CH_4). The optical thickness of the layers was monitored in-situ by the laser beam interference pattern. Carbon content in the film is x = 0.58, which corresponds to PL peak at 1.7 eV and refractive index n = 2.2 [3].

Angle-resolved optical spectra were measured using a Fourier imaging spectroscopy technique. For PL measurements, a 405 nm laser diode illuminates the sample by the from the backside. The spectral resolution of the setup is 0.17 nm, whereas the angular resolution is not less than 0.4° [4]. Theoretical analysis of the optical response of the structure included numerical calculations of the structure's eigenmodes and angle-resolved spectra performed by a Fourier modal method in the scattering matrix form.

The experimental and theoretical angle-resolved PL spectra are presented in Fig. 2(a, b) Due to a broad PL band in the range of 500–1000 nm, the PL spectra contain many peaks resulted from interaction processes of the a-Si:C:H emitting clusters with PhC modes near Γ-point of

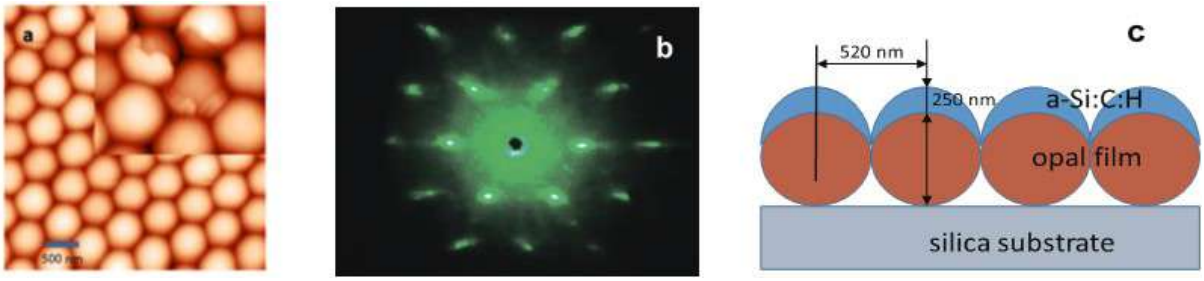


Figure 1: AFM image of the a-Si:C:H/opal slab (a). Insert: a fragment of the structure where the aSi:C:H film is partially absent and SiO2 spheres are exposed. Laser diffraction pattern of an a-Si:C:H/opal slab (b). Schematic view of the structure used in scattering matrix method calculations. Only one monolayer of SiO2 spheres is shown for simplicity (c).

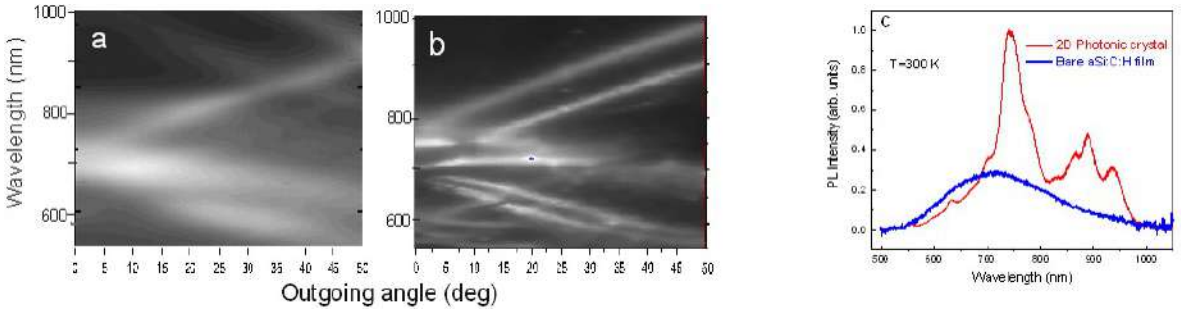


Figure 2: Experimental (a) and theoretical (b) angle-resolved photoluminescence spectra measured in p-polarization. Comparison of PL spectrum of the PhC with PL spectrum of the a-Si:C:H bare film (c).

the Brillouin zone. Figure 2c shows PL spectra from PhC slab coated with a-Si:C:H layer (a) and bare a-Si:C:H film (b) measured near Γ-point of the Brillouin zone. It is seen remarkable increasing PL intensity from PhC slab.

Finally, we have studied the angle-resolved PL spectra of 2D opal coated with a thin luminescent a-Si:C:H film. Since the measurements were carried out near the Γ-point of the Brillouin zone of the PhC, it can be assumed that the observed PL lines of different widths correspond to the interaction of the radiation of a-Si:C:H nanoclusters with PhC modes of different nature. The calculations of the PhC band diagram showed that in such structures it is possible to observe radiative modes located inside the light cone and characterized by a small group velocity, which appear in the PL spectra in the form of relatively broad, intense lines.

References

[1] M. Pelton, Modified spontaneous emission in nanophotonic structures," Nature Photonics, Vol. 9, pp. 427-435, 2015.

[2] A. Mahdavi, G. Sarau, J. Xavier et al, "Maximizing photoluminescence extraction in silicon photonic crystal slabs", Sci. Rep., Vol. 6, pp. 25135, 2016.

[3] R. Carius, "Optical gap and photoluminescence properties of amorphous silicon alloys", JPhilos. Mag., Vol. B 804, No. 4, pp. 741-753, 2000.

[4] S.I Pavlov, I. M. Fradkin, S. A. Dyakov et al, "Bound states in the continuum in a waveguide structure covered by a two-dimensional square array of gold nanodisks", Phys. Rev., B, Vol. 108, pp. 205425, 2023.

Hybrid Nanomaterials and Metastructures for Photonics, Sensing and Energy

Rhodium Nanospheres for Expanding Plasmonic Applications with UV and Visible Light

V. Amendola[1]

[1] Department of Chemical Sciences, University of Padova, Padova

[*]vincenzo.amendola@unipd.it

Abstract: Rhodium nanospheres synthesized via laser ablation in liquid address the UV plasmonic gap left by gold and silver and can be easily functionalized with thiols. The spherical morphology enables UV-visible optical sensing and benchmarking with classical electrodynamic models. Rh stability at high temperature and against acids outperforms Au and Ag.

Plasmonics has penetrated fields ranging from energy conversion to catalysis, biomedical analysis, nanomedicine, light management, and quantum phenomena. However, gold and silver nanostructures do not support plasmons in the ultraviolet (UV) region, while other UV-plasmonic compounds are not chemically stable and cannot be coated with functional molecules. Rh, on the other hand, has favorable characteristics for UV plasmonics, but its high cohesive energy leads to anisotropic nanocrystals with red-shifted plasmon resonance when their size exceeds 7–10 nm, which is the critical threshold for optimal performance.

To address this issue, in this study[1] we show the synthesis of Rh nanospheres (20–45 nm) via laser ablation in liquid (LAL). Unlike chemical routes, LAL avoids the formation of anisotropic shapes, preserving the spherical morphology critical for the plasmonic optical properties. The rapid cooling of Rh vapors in LAL prevents reshaping, and, while excess Rh oxide is formed, it is recoverable, promoting sustainability.

These nanospheres exhibit plasmonic behaviors modeled using classical electrodynamics, achieving a close match with experimental data. The extinction spectra, predicted via the Mie model, align Rh NPs with Ag and Au in terms of performance but uniquely extend functionality to UV ranges. In particular, Rh nanospheres display extinction cross-sections comparable to Ag and Au. While Rh's plasmonic quality factor is lower in the visible range due to interband transitions, it excels in the UV spectrum. Larger nanospheres exhibit pronounced red shifts (73 nm) in their LSP compared to Ag (24 nm) and Au (7 nm), indicating stronger size-dependent retardation effects. Moreover, Rh demonstrates balanced scattering and absorption cross-sections, making it suitable for near-field and nanolensing phenomena.

Joining the easy surface chemistry with thiolated molecules to the optical properties, functionalized Rh NPs detected toxic ions in aqueous solutions. Besides, the Rh NPs showcased stability in harsh environments (e.g., aqua regia, high temperatures) surpassing Au and Ag counterparts.

Rh nanospheres were evaluated also for surface-Enhanced Raman Spectroscopy (SERS) applications with UV and visible light, achieving calculated enhancement factors (G_{SERS}) up to 10^7 at 350 nm excitation. Numerical simulations confirmed optimal enhancement in dimers with 40 nm NPs at short wavelengths.

Although the LAL synthesis can still be optimized in terms of yield and size control, the versatility of Rh nanospheres for diverse applications emerged clearly, as well as the potential of the laser synthetic method for achieving this category of plasmonic tools.

Rhodium nanospheres bridge the gap in UV plasmonics, combining superior stability with optical performance comparable to traditional plasmonic metals. Their scalability, sustainability, and unique attributes herald innovative solutions across UV-visible plasmonic applications, including UV-visible nanosensing, catalysis, chiroplasmonics, and photodegradation of organic compounds.

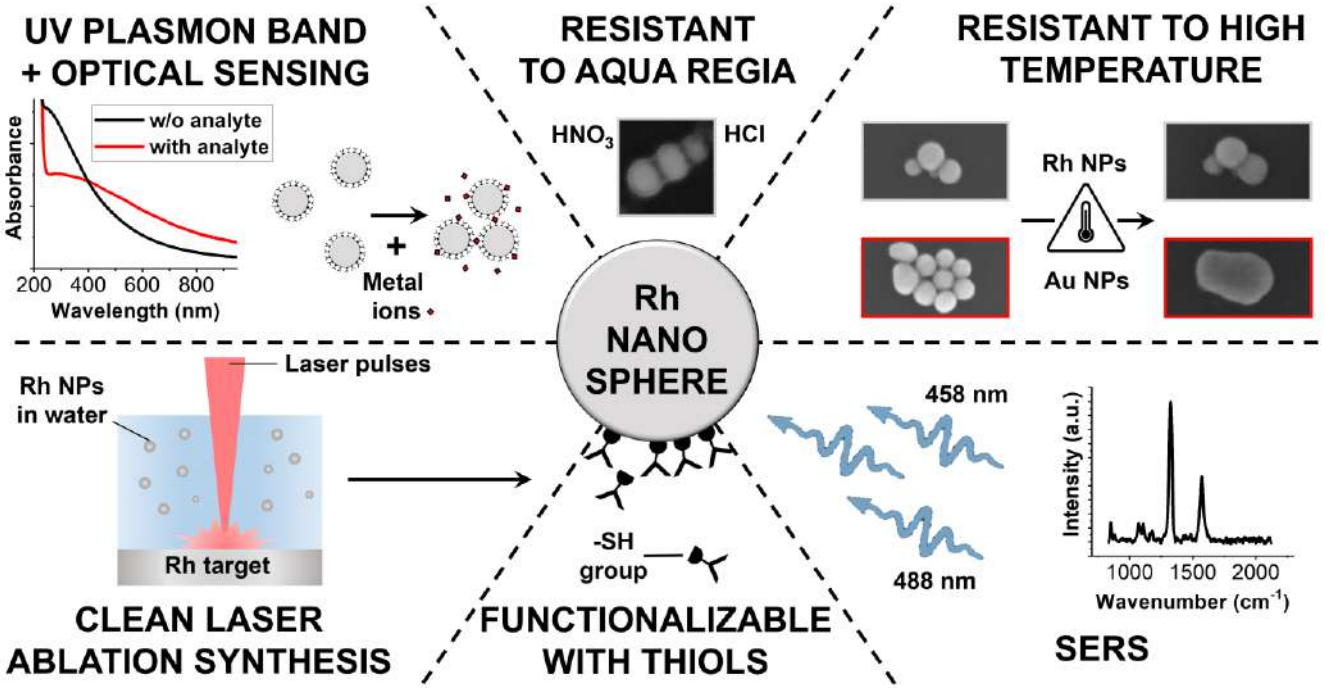


Figure 1. Sketch of the features brought by rhodium nanospheres. From Ref. 1.

References

1. Muñeton Arboleda, D.; Coviello, V.; Palumbo, A.; Pilot, R.; Amendola, V. "Rhodium nanospheres for ultraviolet and visible plasmonics," Nanoscale Horiz., 2025, Advance Article.

Multiplexed, label-free biosensing with plasmonic nanoparticles

S. Kastner, A. Heewig, F. Seier, A. Csaki*, and W. Fritzsche[2]

Leibniz Institute of Photonic Technology (IPHT), Germany
*corresponding author: wolfgang.fritzsche@leibniz-ipht.de

Abstract: A biosensing platform using gold nanoparticle sensors immobilized in an array of spots is described, allowing after biofunctionalization to detect the respective target analyte molecules in a multiplexed assay. For detection, the shift in localized surface plasmon resonance (LSRP) peak due to the change in refractive index is utilized.

A biosensing platform based on the localized surface plasmon resonance (LSPR) principle has been developed: Gold nanoparticles (80 nm diameter) are thereby used as sensor: any change in refractive index around the particles induces a change in resonance frequency, which is monitored using UV/VIS imaging spectrometry. By modification of the nanoparticles with highly specific receptors molecules (such as DNA, proteins or aptamers), a molecular specificity can be achieved for the respective target molecules. In the case of DNA targets, a single-stranded (ss) DNA molecule with a sequence complementary to the target DNA is utilized, for detection of proteins and small molecules either antibodies or aptamers. The principle was demonstrated for both DNA [1,2] as well as protein detection [3]. Compared to fluorescence array formats, the chosen principle does not require labels, resulting in a more streamlined assay, and reducing time as well as costs. The platform is capable of multiplex sensing, by using an array of immobilized nanoparticle spots all incubated simultaneously in a flow chamber with the analyte solution, which can (by utilizing different receptors) detect the presence of multiple target molecules simultaneously in one assay [4,5]. Therefore, a gold nanoparticle solution is spotted by a piezoelectric tool in an array pattern with dimensions of about 300 µm spot diameter and similar scales of spot-to-spot distance. Biofunctionalization is by subsequently spotting thiolated molecules, which bind via a sulfur-gold bond to the sensor surface.

For readout of the LSPR peak shift, a spectroscopic monitoring of all spots is needed. Instead of a scanning approach (where the spots are subsequentially measured by a spectrometer) with the required mechanical movement of beam and/or sample, imaging spectrometry is utilized. This allows for a quasi-simultaneous spectroscopic readout of all spots (all pixels of the viewing field). Different approaches with spectrally filtered light have been compared: One method is using liquid crystal tunable filter (LCTF), which is quite flexible (the resolution of the reconstructed spectrum can be chosen, but higher resolution results in longer measurement times) but still complex and requiring costly equipment; the other one uses just a series of LEDs of different wavelength to reconstruct a spectrum [6], allowing for a very simple and cost-efficient detection.

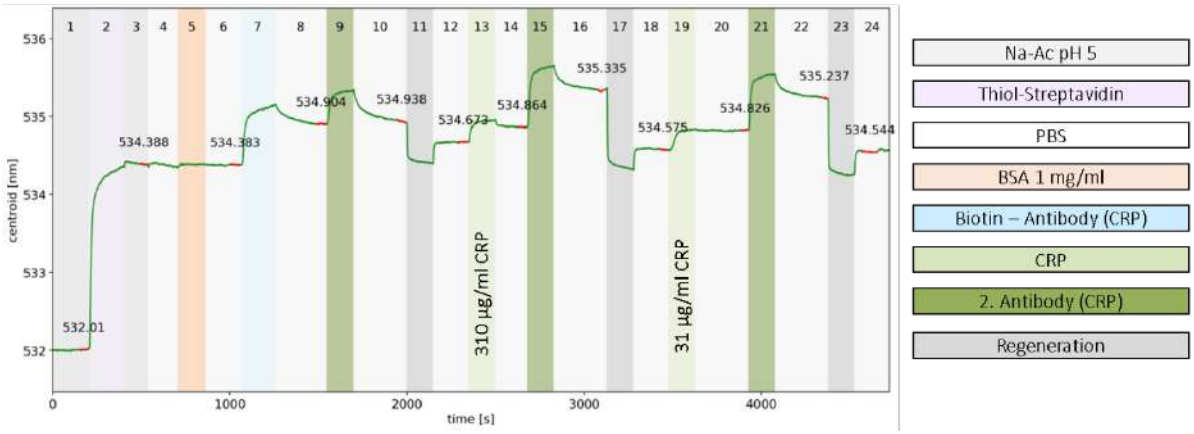


Figure 1. Sensogramm (LSPR peak wavelength centroid plotted over time) of the various steps (including sensor functionalization and control experiments) of a CRP protein detection assay. Different colors mean different (buffer/analyte) solutions. (From [3])

References

1. T. Schneider et al., *J Nanopart Res* 15 (2013), 1531
2. S. Kastner et al., *Small* 202207953 (2023)
3. S. Kastner et al., *Scientific Reports* 12 (2022), 836
4. D. Zopf et al., *ACS Sensors* 4 (2019), 335-343
5. A. Pittner et al., *Analytical and Bioanalytical Chemistry* 411 (2019), 1537-1547
6. S. Kastner et al., *Advanced Photonics Research* 2200252 (2023)

Plasmonic Nanostructures on Paper Lateral Flow Assays for Point-of-Care Testing

Nianqiang Wu[1*]

[1]Department of Chemical Engineering, University of Massachusetts Amherst, Amherst, MA 01003-9303, USA
[*]corresponding author: nianqiangwu@umass.edu

Abstract: This talk will introduce three types of plasmonic probes used in paper lateral flow assays. It will show how to utilize plasmonic nanostructures to amplify fluorescence and surface-enhanced Raman scattering signals. It will also demonstrate our effort to incorporate plasmonic nanostructure into paper lateral flow assays.

Plasmonic nanostructures exhibit color to human eyes due to surface plasmonic resonance (SPR) in the visible-light spectral range. As a result, plasmonic gold nanoparticles can serve as colorimetric probes,[1,2] which are extensively used in paper lateral flow strips (PLFS). However, such colorimetric PLFS suffer low sensitivity and poor resistance to interference in complex human fluidic samples, especially blood samples. In contrast, near-infrared (NIR) fluorescence and surface-enhanced Raman scattering (SERS) probes exhibit much higher signal-to-noise ration and much better interference resistance, but the sensitivity is still insufficient.[1,2] Therefore, we strived to couple plasmon with fluorescence or SERS to amplify signal. We also gained insight into the mechanisms of plasmonic enhancement of fluorescence or SERS. We optimized the structure of plasmonic nanostructure, and the overall architecture of optical probes based on the plasmonic enhancement mechanisms. We integrated the plasmonic fluorescence probes and SERS probes into PLFS, which show high sensitivity and good resistance to interference.[3,2] These plasmon-enhanced PLFS have been used to detect acute diseases such as traumatic brain injury, COVID-19, and HIV at point-of-care settings, such as home, schools, clinics and emergency departments. These efforts have paved new avenues for point-of-care testing.

Acknowledgements: This work was partially supported by the National Institute of Neurological Disorders and Stroke (NINDS) of the National Institutes of Health (1U01NS119647-01), the National Institute of Allergy and Infectious Diseases (NIAID) and the National Institute on Drug Abuse (NIDA) with a grant number (1R61AI181019-01). The content is solely the responsibility of the authors and does not necessarily represent the official views of the National Institutes of Health. We also appreciate the support from Armstrong-Siadat Chair Professorship Endowment.

References

1. Hang, Y., Boryczka, J., Wang, A., Wu N. Q. “Visible-light and near-infrared fluorescence and surface-enhanced Raman scattering point-of-care sensing and bio-imaging: A Review”, Chem Soc Rev, Vol. 51, 329-375, 2022.
2. Hang, Y., Wang, A., Wu N. Q. “Plasmonic silver and gold nanoparticles: shape- and structure-modulated plasmonic functionality for point-of-caring sensing, bio-imaging and medical therapy”, Chem Soc Rev, Vol. 53, 2932-2971, 2024.
3. Gao, X., Boryczka, J., Zheng, P., Kasani, S., Yang, F., Engler-Chiurazzi, E. B., Simpkins, J. W., Wigginton, J. G., Wu, N. Q. “A “hot spot”-enhanced paper lateral flow assay for ultrasensitive detection of traumatic brain injury biomarker S-100β in blood plasma”, Biosens Bioelectron, VOL.177, 112967, 2021.
4. Gao, X., Boryczka, J., Kasani, S., Wu, N. Q. “Enabling direct protein detection in a drop of whole blood with an “on-strip” plasma separation unit in a paper-based lateral flow strip”, Analy Chem, voL.93, 1326-1332, 2021.

5. Hang, Y., Wang, A., Tan, W., Bess, K., Eaton, A., Wu N. Q. “A plasmon-enhanced fluorescence paper lateral flow strip for point-of-care testing of SARS-CoV-2 antigens”, Anal Chem, doi.org/10.1021/acs.analchem.4c04697, 2025.

Colloidal Synthesis of Chiral Plasmonic Nanocomposites via Circularly Polarized Light Irradiation

K. Saito[1*], Y. Nemoto[2], and Y. Ishikawa[1]

[1]National Institute of Advanced Industrial Science and Technology (AIST), Japan
[2]National Institute for Materials Science, Japan
[*]corresponding author: koichiro.saito@aist.go.jp

Abstract: The synthesis of chiral plasmonic nanoparticles using circularly polarized light as a chiral source has attracted attention because it does not require any chiral molecules. In this presentation, we will report a novel method for colloidal synthesis of chiral plasmonic nanocomposites including AuNR@MnOx.

[Introduction] Nanoparticles of gold and silver with chiral shapes are called chiral plasmonic nanoparticles, and are expected to be applied to chiral sensing, asymmetric catalysis, etc. The synthesis method of chiral plasmonic nanoparticles using circularly polarized light as a chiral source has the advantage that it does not require chiral molecules [1]. For mass synthesis, it is desirable to synthesize chiral plasmonic nanoparticles in a state dispersed in solution, but the nanoparticles must be fixed on a solid substrate during the synthesis process, which has been a major challenge. We have succeeded in synthesizing rod-shaped chiral plasmonic nanoparticles that exhibit circular dichroism for the first time by driving a photochemical reaction that precipitates silver on the surface of gold nanorods (AuNRs) dispersed in solution with circularly polarized light [2]. At present, it is not clear how the chiral growth behavior changes depending on reaction conditions such as temperature. In addition, there have been no reports of the preparation of chiral plasmonic nanocomposites using materials other than gold and silver [3]. In this study, we investigated the effect of reaction temperature on chiral growth under circularly polarized light irradiation. Furthermore, we also succeeded in preparing chiral plasmonic nanocomposite by photo-induced deposition of manganese oxide on AuNRs.

[Experiment] AuNRs covered with silver (AuNR@Ag) were synthesized by irradiating left- or right-handed circularly polarized light (CPL) from a red LED (λ ~ 630 nm) on a dispersion of AuNRs containingcitrate and silver ion (**Figure 1**). CPL irradiation experiments at reaction temperatures of 5°C, 35°C, and 65°C were carried out using a water bath. We also tried to synthesize chiral AuNR@MnOx by adding permanganate reagent in the reaction solution. The synthesized nanoparticles were observed with a scanning electron microscope (SEM). The absorbance and circular dichroism (CD) of the dispersion were measured by using UV-vis and CD spectrometer. Because the CD signals depends on the absorbance of the dispersions, we calculated the g_{CD}-factors using the following equation (1) to compare between different samples:

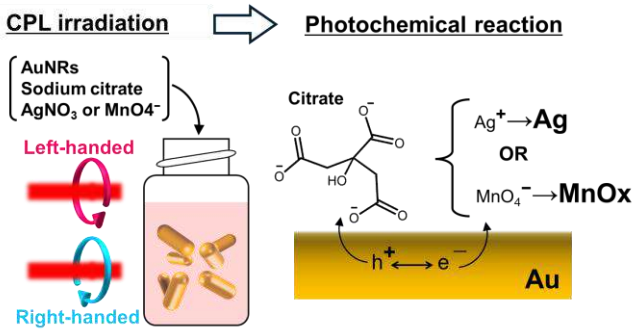


Figure 1. Schematic illustration of photodeposition of Ag or MnOx on AuNRs driven by CPL irradiation.

$$g_{CD} = \frac{4\pi \log_{10} e}{180} \frac{\text{CD Intensity (deg)}}{\text{Absorbance}} \quad (1)$$

[Results and Discussion] The absorbance peak wavelength of the AuNRs dispersion shifted to shorter wavelengths due to the silver deposition by circularly polarized light irradiation (**Figure 2a, c, e**). The peak wavelength shifted depending on the reaction temperature, and the absorbance at a wavelength of 400 nm increased. While silver deposition was accelerated at higher temperatures, the reaction was also driven at lower temperatures. As shown in Figure 2b, d, and f, CD signals were observed at all reaction temperatures. However, the CD spectra clearly changed depending on the reaction temperature. Interestingly, Interestingly, the g_{CD} values were larger at 35°C than at other temperatures. Temperature-driven silver deposition should not contribute to chiral growth. Therefore, we expected that a lower reaction temperature would be favorable for chiral growth, but the results were different from our expectation. When the reaction rate is too slow, silver deposition on AuNRs may be uniform. It was indicated that the rate of silver deposition can affect chiral growth behavior under CPL irradiation.

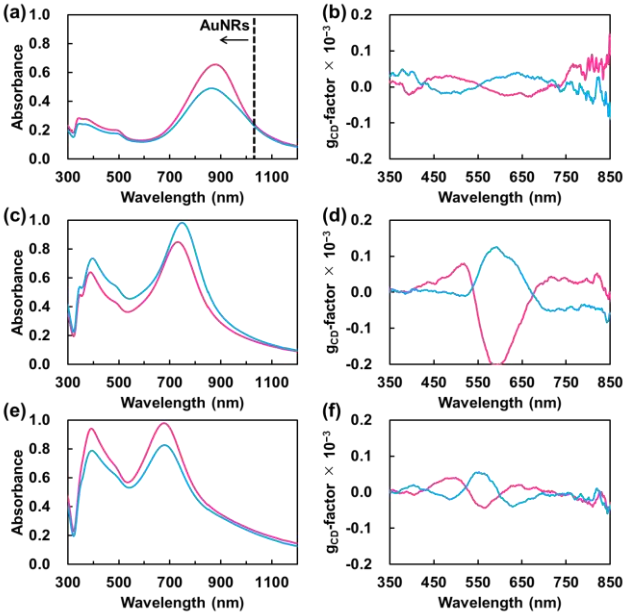


Figure 2. Absorbance and CD spectra of the AuNRs irradiated with LCP (pink) or RCP (blue) light at reaction temperatures of (a,b) 5°C, (c,d) 35°C, and (e,f) 65°C.

Figure 3a shows the absorbance spectra after CPL irradiation on colloidal AuNRs with permanganate. Unlike the case of silver deposition, the absorbance peaks were red-shifted. This result indicates that the refractive index around the AuNRs increased due to the deposition of MnOx. Indeed, several needle-like structures were observed around the AuNRs in the SEM image (Figure 3b). As shown in Figure 3c, the CD spectra clearly showed peaks and dips according to the handedness of the CPL. Although the composition and morphology of MnOx need to be investigated in detail in the future, we have succeeded in colloidal synthesis of chiral plasmonic nanocomposites of AuNRs and metal oxides via CPL irradiation for the first time. Because MnOx is useful as a catalyst, this study may contribute to the development of asymmetric catalysts.

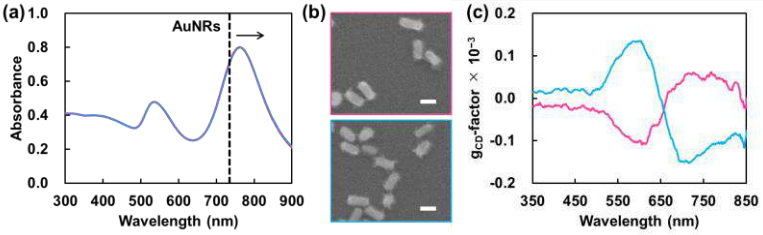


Figure 3. (a) Absorbance amd (c) CD spectra of the AuNRs with permanganate irradiated with LCP (pink) or RCP (blue) light (b) SEM images of the samples synthesized by LCP or RCP light.

Acknowledgement: This work has been funded by the JSPS, KAKENHI (JP23H04610).

References

1. Saito, K. and Tastuma, T, "Chiral Plasmonic Nanostructures Fabricated by Circularly Polarized Light," Nano Lett., Vol. 18, No. 5, 3209–3212, 2018.
2. Saito, K., Nemoto, Y. and Ishikawa, Y., "Circularly Polarized Light-Induced Chiral Growth of Achiral Plasmonic Nanoparticles Dispersed in a Solution.," Nano Lett., Vol. 24, No. 41, 12840–12848, 2024.
3. Ghalawat, M., Feferman, D., Besteiro, L.V., He, W., Movsesyan, A., Muravitskaya, A., Valdez, J., Moores, A., Wang, Z., Ma, D., Govorov, A. O. and Markovich, G., "Chiral Symmetry Breaking in Colloidal Metal Nanoparticle Solutions by Circularly Polarized Light," ACS Nano, Vol. 18, No. 41, 28279–28291, 2024.

Magnetic micro- and nanorods for viscosity imaging using heterodyne holography

C. Gentner[1], Z. Zhang[1], J.-F. Berret[2], P. Berto[1,3], H.Robert[1], R. Kuszelewicz[1], G.Tessier [1]*

[1] Sorbonne Université, INSERM, CNRS, Institut de la Vision, 17 rue Moreau, F-75012, Paris, France

[2] Université Paris Cité, CNRS, Matière et systèmes complexes, 75013 Paris, France

[3] Université de Paris Cité, 45 Rue des saints Pères, F-75006 Paris, France
*corresponding author: gilles.tessier@sorbonne-universite.fr

Abstract: An external magnetic field forces the oscillation of superparamagnetic iron oxide nanorods, which cease to rotate above a frequency related to the local viscosity. The blinking of the scattered light is analyzed at high frequencies by heterodyne holography, and 3D rod superlocalization provides high resolution viscosity imaging.

In microfluidics and biology, many processes are driven or affected by viscosity. Mechanonsensing is indeed an essential signal pathway in the regulation of cell growth, proliferation or apoptosis, and this field of studies is now reaching out to other fields, including materials science and chemistry (e.g. polymers, soft and complex matter), clinical research (mechanical properties are crucial to cancer cells) and physics. Several methods can measure this parameter globally, but very few can provide high resolution viscosity images.

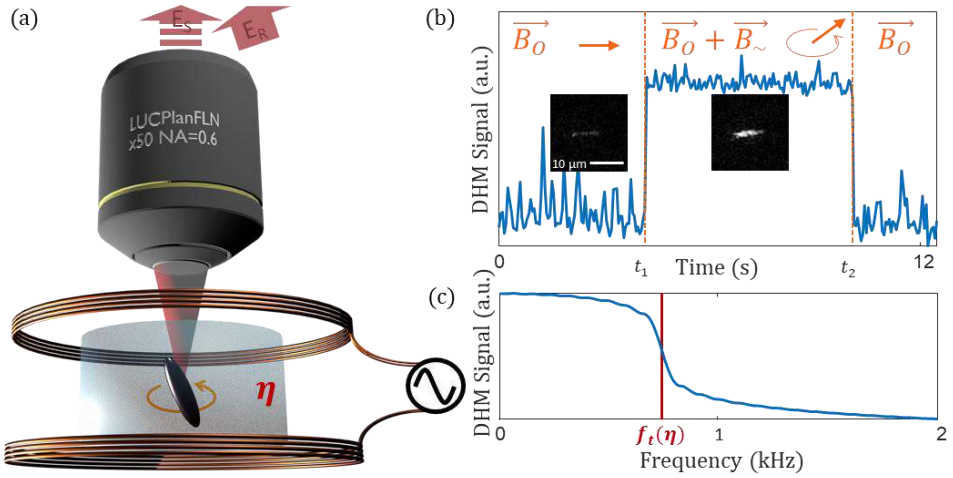


Figure 1 : a) Principle of the measurement. b) Holographic images (insets) and holographic intensity at the rotation frequency with a magnetic field turned off and on. c) Frequency dependence of the holographic signal. The cutoff frequency provides a measurement of the viscosity η.

To measure and understand the role of intracellular mechanical properties, we propose to use sub-micrometer magnetic rods to perform high resolution viscosity imaging. An external magnetic field forces the oscillation of superparamagnetic iron oxide nanorods (Fig. 1a). Under linearly polarized illumination, the rotation of these highly anisotropic optical scatterers induces a blinking which is analyzed by heterodyne holography (Fig. 1b). Rods can follow the slow rotation of an external magnetic field, but stop oscillating beyond a cutoff frequency due to the viscosity of the liquid (Fig. 1c). The local viscosity is therefore deduced from a spectral analysis of the rotation dynamics.

We have shown that 3D superlocalization with holography allows nm-range precision of nanoparticles as small as 30 nm, and that stochastic movements of the particle can be used to explore the environment and obtain a dense 3D super-resolved map. When using stochastic probes, however, Brownian diffusion affects the locality of the measurement. Optimizing the locality of viscosity measurements demands smaller probes but also shorter lateral diffusion lengths and measurement times. Indeed, during the measurement time τ_{acq}, Brownian probes travel stochastically over $\sqrt{D\tau_{acq}}$ (where D is the viscosity-dependent diffusion coefficient).

A calibration performed in model media (glycerol-water mixtures with variable concentrations) allows to validate the quantitative measurement of viscosity. We will show viscosity images obtained in various media and contexts, and show that holographic detection can reduce τ_{acq}, allowing to probe a volume of (0.5 μm^3). This time can be pushed further by increasing the magnetic field, frequency, and optical intensity. Coupled to 3D superlocalization by holography, this provides ultralocal (0.5 μm^3) viscosity measurements, paving the way for high resolution intracellular viscosity measurements.

References

1. C.Gentner, J-F Berret, P.Berto, S.Reichman, R.Kuszelewicz and G.Tessier*, “Magnetic sub-micron rods for quantitative viscosity imaging using heterodyne holography”, ACS Photonics 11, 7, 2561–2569, 2024.

Chiral photogrowth on plasmonic nanostructures under circularly polarized light

L. V. Besteiro[1*]

[1]CINBIO, University of Vigo, Campus Universitario de Vigo, Lagoas Marcosende, 36310 Vigo, Spain

[*]corresponding author: lucas.v.besteiro@uvigo.es

Abstract: With adequate conditions, achiral plasmonic structures under circularly polarized light can develop chiral shapes by photocatalytically imprinting on them the reduced symmetry of the local fields. Experimental realizations of this strategy can exploit different energy-transfer mechanisms. We will discuss the fundamentals of such light-to-matter chirality transfer and recent experimental demonstrations.

Plasmonic nanostructures offer strong resonant responses in the UV-to-IR spectral range, which has led to their use in many optical and energy-related applications. Plasmonic photocatalysis stands as a prominent example of the latter, with plasmonic nanostructures serving as nanoscale antennas funneling radiant energy into their local environment. This talk will cover a particular subset of plasmonic photocatalytic setups with two defining characteristics: (i) the light-driven process modifies the geometry of the plasmonic nanoparticle or the optical properties of its immediate environment, and (ii) does so preserving local asymmetries induced by impinging circularly polarized light (CPL). This creates chiral features in initially achiral shapes, hence transferring chirality from light to the nanostructures, and contrasting with common strategies yielding chiral plasmonic systems, where chirality is seeded from molecules or introduced through top-down fabrication methods. The presentation will cover theoretical considerations underpinning light-to-matter chirality transfer in plasmonics,[1] a discussion about the physical energy-transfer mechanisms driving this phenomenon,[2,3] as well an overview of experimental work going from pioneering examples[4,5] to recent progress.[6,7]

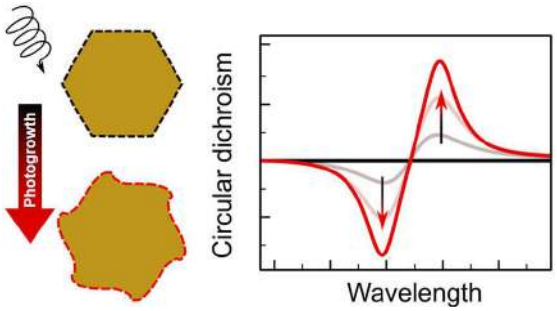


Figure 1. Diagram representing chiral growth of an achiral plasmonic nanostructure under CPL.[1]

References

1. L. V. Besteiro *et al.*, "Local Growth Mediated by Plasmonic Hot Carriers: Chirality from Achiral Nanocrystals Using Circularly Polarized Light," *Nano Lett.*, vol. 21, no. 24, pp. 10315–10324, 2021.

2. A. Movsesyan *et al.*, "Creating Chiral Plasmonic Nanostructures Using Chiral Light in a Solution and on a Substrate: The Near-Field and Hot-Electron Routes," *Adv. Opt. Mat.*, vol. 11, no. 18, p. 2300013, 2023.

3. O. Ávalos-Ovando *et al.*, "Universal imprinting of chirality with chiral light by employing plasmonic metastructures," *Appl. Phys. Rev.*, vol. 10, no. 3, p. 031412, 2023.

4. K. Saito and T. Tatsuma, "Chiral Plasmonic Nanostructures Fabricated by Circularly Polarized Light," *Nano Lett.*, vol. 18, no. 5, pp. 3209–3212, 2018.

5. A. Horrer *et al.*, "Local Optical Chirality Induced by Near-Field Mode Interference in Achiral Plasmonic Metamolecules," *Nano Lett.*, vol. 20, no. 1, pp. 509–516, 2020.

6. S. Lee *et al.*, "Unraveling the Chirality Transfer from Circularly Polarized Light to Single Plasmonic Nanoparticles," *Angew. Chem. Int. Ed*, p. e202319920, 2024.

7. M. Ghalawat *et al.*, "Chiral Symmetry Breaking in Colloidal Metal Nanoparticle Solutions by Circularly Polarized Light," *ACS Nano*, vol. 18, no. 41, pp. 28279–28291, 2024.

Directional light scattering in Mie-resonant Si particles with ultra-thin plasmonic shells

Emmanuel O Idowu,[1] Kevin O'Connor,[2] Jonathan GC Veinot,[2] Sabrina Lacomme,[3] Julien Proust,[4] Jérôme Plain,[4] Xiaoyan Li,[5] Mathieu Kociak,[5] Alexandre Baron,[6] Virginie Ponsinet,[6] Lucien Roach[1,7,*], Peter R Wiecha,[8] and Glenna L Drisko[1]

[1] Univ. Bordeaux, CNRS, Bordeaux INP, ICMCB, UMR 5026, 33600 Pessac, France.
[2] Department of Chemistry, University of Alberta, Edmonton, AB, Canada.
[3] Univ. Bordeaux, CNRS, INSERM, Bordeaux Imaging Center, UAR3420, 33600 Pessac, France.
[4] L2n, CNRS UMR 7076, Univ. of Technology Troyes, 10004 Troyes, France.
[5] Université Paris-Saclay, CNRS, Laboratoire de Physique des Solides, 91405 Orsay, France
[6] Univ. Bordeaux, CNRS, CRPP, UMR 5031, 33600 Pessac, France
[7] Laboratoire de Chimie de l'Ecole Normale Supérieure de Lyon, Lyon, France.
[8] LAAS, Université de Toulouse, CNRS, 31000 Toulouse, France.
[*]corresponding author: lucien.roach@ens-lyon.fr

Abstract: We present the synthesis and characterization of Au-decorated Si core-shells as candidate meta-atoms. We found a damped magnetic dipole (MD) for smaller Si cores (100 – 130 nm) and an enhanced MD for larger cores (150 – 200 nm). Continuous plasmonic shells of ~12 nm are needed to significantly improve forward scattering.

Subwavelength-sized Si particles interact strongly with visible (vis) and near-infrared (NIR) light to produce strong electric and magnetic resonances. These can combine to produce interesting optical effects, such as pure forward scattering. A requirement for this to occur efficiently is that the electric dipole (ED) and magnetic dipole (MD) modes must be of similar amplitude and phase. At wavelengths where this occurs, the particles act analogously to the forward-propagating point sources of light used in Huygens' constructions. This directional scattered light has a range of potential applications in the creation of metamaterials.

We have investigated dielectric@metal core-shell architectures comprised of both resonant cores and resonant shells as candidate particles in which the spectral overlap of the electric and magnetic dipoles might be controlled to create strong directional scattering. There are currently two reports of the synthesis and characterization of Au shells around Si cores, both thicker than desirable. [1,2] Chaâbani *et al*. presented Si@Au particles, with non-uniform shells composed of Au particle diameters between 10 and 25 nm, which presented enhanced electric field and Fano-resonances due to the coupling of the Mie modes of the Si core and the localized surface plasmon resonance (LSPR) of the Au shell. [1] Sugimoto *et al.* similarly presented Si@Au particles with a rough ~25 nm Au shell. [2] In both of these reports of Si@Au core-shell particles, the experimental data could not be accurately fit by simulations due to non-spherical cores and inhomogeneous shells. Ultrathin and homogeneous coatings have not yet been achieved around spherical Si particles.

In this study, we present a two-step aqueous approach to prepare Si@Au core-shell particles with controllable shell thickness below 10 nm. The Au nanoparticle (AuNP) density around the Si particles can be increased by performing a second functionalization/deposition step. We studied the electromagnetic response of the particles using single-particle scatter spectroscopy and electron energy loss spectroscopy (EELS). Our results were

compared with reference Si spheres and SiO_2@Au core-shell particles, to allow us to establish the contribution from the Au decoration to the optical response of the hybrid particles. To further elucidate the nature of the electromagnetic response of the particles, these observations were supported by T-matrix simulations which replicated our experimental findings, and showed the importance of controlling the shell/core dimensions and the need for a continuous shell to maximize forward scattering. We found that continuous plasmonic shells of ~12 nm thickness are needed to significantly improve forward scattering intensity.

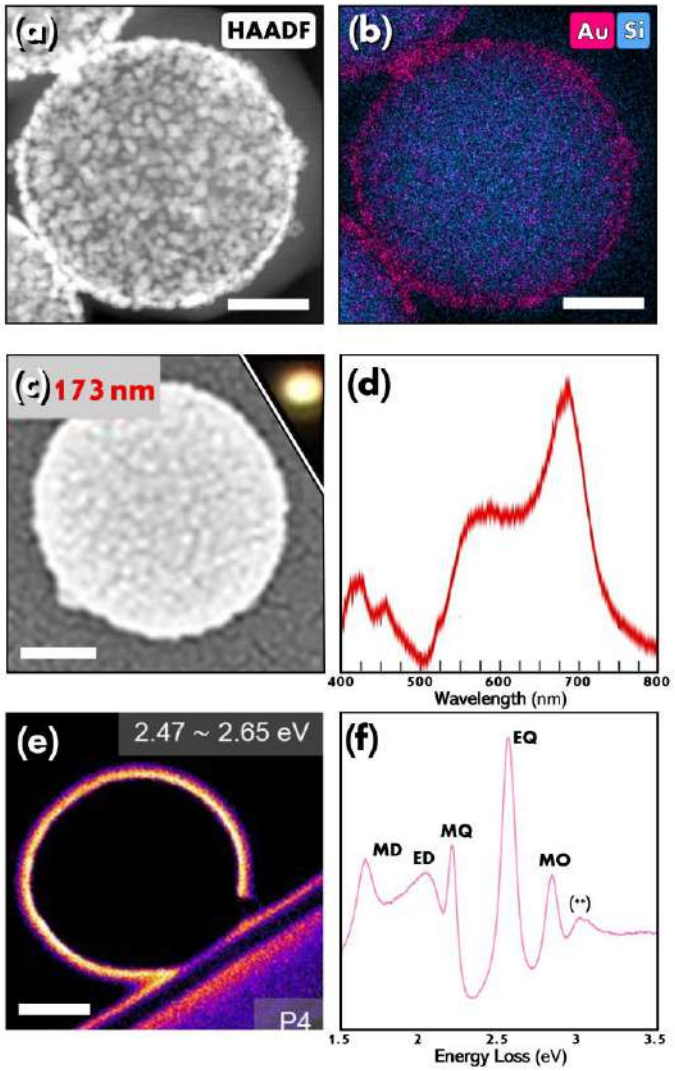


Figure. a) High-angle annular darkfield TEM micrograph and b) EDX map showing the position of the Si core (blue) and Au shell (pink). c) SEM micrograph and inset, optical darkfield images of a Si@Au core-shell. d) Single particle scattering spectra of a Si@Au core-shell (blue), alongside T-matrix–simulated spectrum for bare Si (green) and Si@Au core-shell (red). e) EELS intensity maps for the (iii) magnetic dipole (MD) in a Si@Au core-shell. f) Experimental EELS spectrum for a Si@Au core-shell, showing the various multipolar modes. All scale bars represent 50 nm.

References

1. Chaâbani, W, J Proust, S Ouellet, A Movsesyan, J Béal, R Bachelot, T Xu, A-L Baudrion, PA Adam, D Boudreau, A Chehaidar, and J Plain, "Si@Au core–shell nanostructures: Toward a new platform for controlling optical properties at the nanoscale." *J Phys Chem C*, Vol. 125, 20606. 2021. DOI: 10.1021/acs.jpcc.1c06182
2. Sugimoto, H., T Hinamoto, Y Kazuoka, A Assadillayev, S Raza, and M Fujii. "Mode hybridization in silicon core–gold shell nanosphere." *Small* Vol. 18, 2204890, 2022. DOI: 10.1002/smll.202204890

Chiral Silicon Meta Biosensors.

Dominic J.P. Koyroytsaltis-McQuire[1*], Rahul Kumar[1], Tamas Javorfi[2], Giuliano Siligardi[2], Adiran Lapthorn[1], Nikolaj Gadegaard[3], Malcolm Kadodwala[1*]

[1] School of Chemistry, University of Glasgow, Glasgow, G12 8QQ, UK
[2] Diamond Light Source Ltd., Harwell Science and Innovation Campus, Didcot, United Kingdom
[3]School of Engineering, Rankine Building, University of Glasgow, Glasgow G12 8LT, UK
* Corresponding Authors
E-mail: Malcolm.kadodwala@glasgow.ac.uk
E-mail: d.koyroytsaltis-mcquire.1@research.gla.ac.uk

Abstract

Chiral molecules exhibit optical activity, helicity-dependent interactions with circularly polarized light, a key for rapidly characterizing biological and pharmaceutical molecules via spectroscopy. However, the intrinsic weakness of optical activity restricts its applications. In contrast, our study introduces an innovative chirally sensitive spectroscopic phenomenon that liberates itself from reliance on weak optical activity. This novel approach capitalizes on the substantial chirally sensitive birefringent response, monitored through the linear dichroism of complexes formed between charged biomolecules electrostatically coupled to enantiomorphic pairs of silicon nanostructures. Termed "meta-diastereomers," these complexes are symmetry-inequivalent diastereomers with differing birefringent properties, enabling biomolecule chirality detection. This effect is nine orders of magnitude larger than the optical active response of proteins in conventional measurements, allowing the detection of femtomole quantities. Serving as an electromagnetic analogue to the chemical strategy of leveraging diastereomers' different properties for stereostructure determination, this phenomenon is specifically applicable to charged chiral biomacromolecules and insensitive to non-charged chiral/achiral environments. It presents an ideal candidate for biosensing technologies, with charge sensitivity offering a novel discrimination mechanism to minimize off-target detection and ensure ultrasensitivity.

Chiro-optical microscopy of plasmonic materials and chiral near-field interaction with molecules and materials

H. Okamoto*, S. Hashiyada, H.-Y. Ahn, and J. Yamanishi

Institute for Molecular Science, National Institutes of Natural Sciences, Okazaki, Japan
*corresponding author: aho@ims.ac.jp

Abstract: We demonstrate here microscopic and nanoscopic imaging of chiral optical fields with far-field CD microscopy, near-field polarimetry, and chiro-photoinduced force microscopy for plasmonic materials, and near-field chiral plasmon-matter interaction phenomena.

Chirality is a broad concept that characterizes structures in wide hierarchy of materials and systems. It is of fundamental importance to investigate geometrical structures of chiro-optical responses in nanomaterials, to design chiral features and functions of the nanomaterials. We developed novel optical activity imaging methods with a few of optical measurement methods, which allow us to visualize local structures of optical activity in nanomaterials. The methods were applied to observe and control chiral plasmonic fields for gold nanostructures. We found very different characteristic features of local chiro-optical effects as compared with macroscopic chiro-optical spectroscopic characteristics. The local chiral fields that interact with molecules and materials in the peripheries of the nanomaterials provide characteristic chiro-optical properties the molecules.

For chiro-optical imaging beyond the diffraction limit, we developed a near-field polarimetry microscope using aperture-type optical fiber probe and a chiro-photoinduced force microscope. In the former one, the sample is illuminated with a linearly polarized optical near-field through the probe, and the forward scattered field in the far-field is analyzed for its ellipticity (η, corresponding to CD) and polarization rotation. Figure 1 shows a near-field ellipticity image of a gold nanorectangle.[1] In this image, the ellipticity of the scattered optical field from the sample upon near-field linearly polarized excitation parallel to the long axis of the rectangle was mapped as a function of the position of the excitation. The results suggest that strongly twisted plasmonic local fields are generated in the vicinities of metal nanostructures.

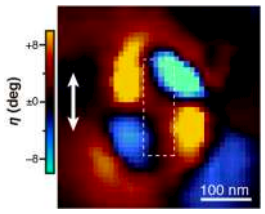
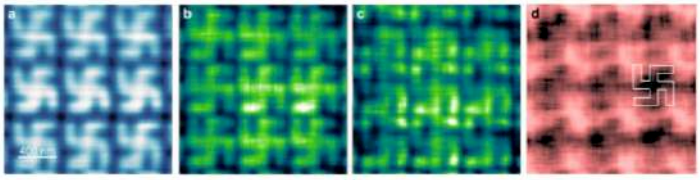


Figure 1. Near-field η image (at 800 nm) of a gold nanorod.[1]


Figure 2. (From left to right) AFM image, photoinduced force images under right- and left-circularly polarized light at 785 nm, and the differential image between the two photoinduced force images. The unit cell size is 540 nm.[2]

In the chiro-photoinduced force microscope, the local chiro-optical effect is detected through optical force measurements with an atomic force microscope. By detecting difference between the force under left- and right-handed circularly polarized illumination with the photoinduced force microscopy, we can visualize the chiral optical fields on the sample under irradiation of light. We developed an experimental system for nanoscopic observation of chiro-optical force and imaging of chiral optical fields on the samples, based on photo-induced force microscope. The photoinduced force images under illumination of left- and right-circularly polarized light were recorded, and the chiro-optical image was obtained as the difference between the two. As the test sample, we fabricated left- and right-handed gold gammadion structure arrays by

electron-beam lithography method. The result of chiro-optical image of the sample is demonstrated in Fig. 2.[2] We succeeded in visualizing nanoscale chiral optical fields in the vicinity of the nanostructures. It is seen that the local chiro-optical effect is prominent at the corners of each gammadion.

The strong local chiro-optical activity associated with the chiral plasmons indicates existence of highly chiral local fields, which may induce strong chiral near-field interaction between the plasmons and the materials in the vicinity of the nanostructures. We can thus expect near-field interaction between dye molecules and chiral plasmons, which yields highly circularly polarized luminescence from the dye coexisting with the chiral plasmonic material. In fact, we found that the luminescence from achiral dye molecules combined with chiral plasmonic nanostructure was highly circularly polarized (dissymmetry factor $g > 0.1$) as compared with luminescence from dyes with chiral molecular structures ($g \approx 10^{-3}$-10^{-2}).[3] Furthermore, the generation of circularly polarized two-photon-induced photoluminescence (TPI-PL) from chiral gold helicoid nanoparticles was demonstrated. Measurements of TPI-PL show that it has a strong dissymmetry factor of ≈0.7 for a single chiral Au nanoparticle (Fig. 3).[4] A theoretical simulation study showed that a local chiral electromagnetic field confined to the chiral gap structures contributes to the high degree of circular polarization.

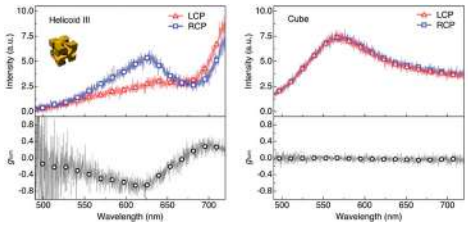


Figure 3. TPI-PL intensity and *g*-factor spectra for chiral helicoid (left) and cubic (right) gold nanoparticles.[4]

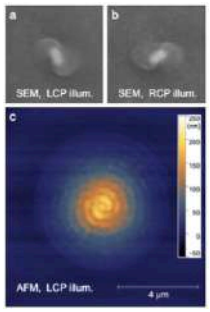


Figure 4. (a,b) SEM images of photopolymerized structure formed around the cuboid nanoparticle under the (a) LCP and (b) RCP illumination. (c) AFM image of chiral double spiral structure.[6]

When an achiral nanostructure is illuminated by circularly polarized light, chiral optical field distribution is induced, which has a potential to create materials with chiral assymmetry through photochemical reactions. This idea was reported to be achieved with metal nanocuboid, on which photoproduct was deposited at two of diagonal apexes.[5] The result was attributed to the plasmonic mode structure induced on the cuboid when excited by circularly polarized light. We report experimental results that an additional mechanism of chiral field generation due to interaction between the symmetric nanoparticle and circularly polarized light provides a further complex spiral structure of the photoproduct (Fig. 4).[6]

The authors thank Drs. T. Narushima and K. Q. Le, for their contributions. This work was supported by Grants-in-Aid for Scientific Research (KAKENHI Nos. JP21H04641, JP21K18884, and JP22H05135).

References

1. S. Hashiyada, T. Narushima, H. Okamoto, ACS Photon. Vol. 5, 1486–1492, 2018.
2. J. Yamanishi, H.-Y. Ahn, H. Okamoto, Nano Lett. Vol. 23, 9347–9352, 2023.
3. K. Q. Le, S. Hashiyada, M. Kondo, H. Okamoto, J. Phys. Chem. C Vol. 122, 24924–24932, 2018.
4. H.-Y. Ahn, K. Q. Le, T. Narushima, J. Yamanishi, R. Myeong Kim, K. T. Nam, H. Okamoto, Adv. Optical Mater. Vol.12, 2400699, 2024.
5. K. Saito and T. Tatsuma, Nano Lett. Vol. 18, 3209–3212, 2018.
6. H.-Y. Ahn, T. Narushima, H. Okamoto, J. Phys. Chem. C Vol. 128, 7159−7168, 2024.

Chiral Photochemical Amplification in Mesoporous Plasmonic Shurikens Demonstrating Asymmetric Catalysis

Olga Guselnikova[a,b,c*], Pavel Postnikov[b,d], Markus Valtiner[c], Jonathan P. Hill[a], Joel Henzie[a], Daniel T. Payne[a], Martin Kartau[e], Iliyana Samardzhieva[e], George Lefroy Brookes,[e] Malcolm Kadodwala[e], Alexander O. Govorov[f], Affar S. Karimullah[e*], Yusuke Yamauchi[g,h,i*]

a Research Center for Materials Nanoarchitectonics, National Institute for Materials Science (NIMS), Namiki 1-1 Tsukuba, Ibaraki 305-0044, Japan

b Research School of Chemistry and Applied Biomedical Sciences, Tomsk Polytechnic University, Tomsk, Russian Federation

c Institute of Applied Physics, Vienna University of Technology, 1040 Vienna, Austria

d Department of Solid-State Engineering, University of Chemistry and Technology, Prague, Czech Republic

e School of Chemistry, Joseph Black Building, University of Glasgow, Glasgow, G12 8QQ, UK

f Department of Physics and Astronomy, Ohio University, Athens, OH, 45701 USA

g Department of Materials Process Engineering, Graduate School of Engineering, Nagoya University, Nagoya 464−8603, Japan

h Department of Chemical and Biomolecular Engineering, Yonsei University, 50 Yonsei-ro, Seodaemun-gu, Seoul 03722, South Korea

i Australian Institute for Bioengineering and Nanotechnology (AIBN) and School of Chemical Engineering, The University of Queensland, Brisbane, Queensland 4072, Australia

*corresponding author: olga.guselnikova@tuwien.ac.at

Abstract: We demonstrate enantioselective photocleavage exceeding circularly polarized light using chiral plasmonic shurikens with mesoporous gold. Optimized chiral near-fields enhance interactions for spectroscopy and catalysis, achieving 2–3× higher R/S-metalaxyl photolysis rates and >25% enantiomeric excess, marking the first proof of chiral plasmonic catalysis via superchiral fields.

Interactions between light and molecules present a foundation for the development of optical and spectroscopic technologies, where the modulation and control of molecular chirality is critical [1–4]. Although light is a promising stimulus for the management of enantiomers, the scale mismatch between the wavelength of light and the molecular wavefunction prevents effective interactions between molecules and the chirality of applied light [5]. Light-matter interactions involving plasmonic excitation at nanomaterials allows redirection of energy from nonradiative decay pathways for purposes of molecular transformation[6,7]. Despite the active development of chiral self-assembled nanomaterials for plasmon catalysis[8], for example, involving Au and TiO_2 NPs on chiral SiO_2 nanoribbons[9], dumbbell-like chiral Au NRs[10,11], or gold-gap-silver nanostructures with cysteine[12], the direct enantiospecific transformation of molecules has not been demonstrated. These structures exhibit catalytic activity in chemical reactions not involving chirality, including water splitting, dye degradation and reduction.

With the aim to generate evidence for chiral plasmonic catalysis, we have used a chiral plasmonic system with excitation using linearly polarized light (LPL) for interactions either with individual enantiomers or a racemic mixture of a photo-cleavable molecular entity. More specifically, we have used arrays of chiral shuriken indentations, which exhibit extraordinarily homogeneous chiroptical properties over large areas[13,14]. The chiral shurikens of our array also show high sensitivity to local interactions with chiral molecules[15–17]. The superchiral field generated by shuriken shaped nanostructures is a promising candidate for the enhancement of light-matter interactions for chiral catalysis. In this work, the superchiral plasmonic field in the resulting mesoporous chiral shuriken metafilms (MCSMs) shows enhanced surface area with increased interactions between chiral molecules and the excited superchiral near-field for enantiospecific recognition and enantioselective photocleavage of the fungicide R/S-metalaxyl.

We have adapted this strategy for preparation of a chiral metamaterial by using micelle-assisted deposition of porous gold on sub-micron-sized shurikens arranged in a square lattice (Fig. 1a). For electrodeposition, shuriken arrays were placed in a solution of polyethylene oxide block polystyrene (PEO-*b*-PS) micelles and $HAuCl_4$ prior to electrochemical reduction (0-250 seconds) leading to the further formation of mesoporous Au structures (Fig. 1a). The optimization of deposition via morphological changes (Fig. 1b), optical rotation measurements, enhancement factor in surface-enhanced Raman spectroscopy using R/S-metalaxyl revealed 150 seconds as optimal deposition time for the strongest chiral response.

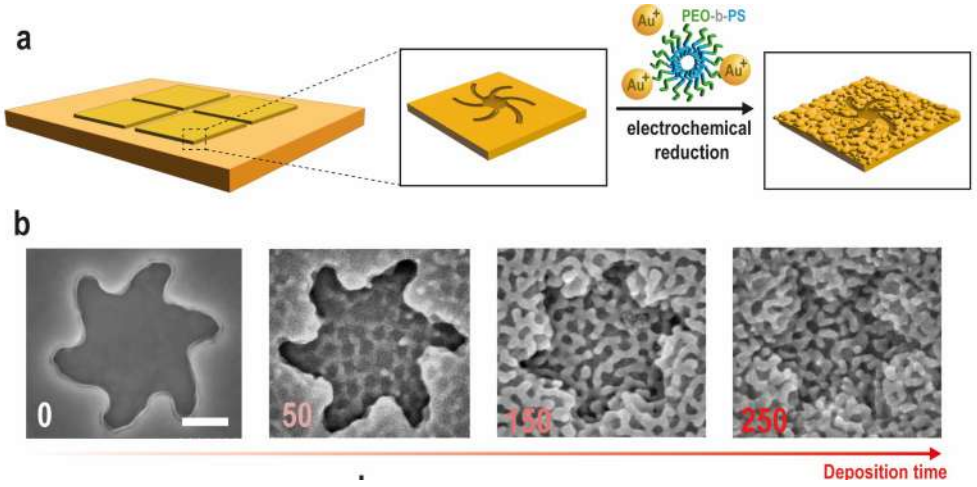


Figure 1. Synthesis and characteristics of shuriken arrays. **a**, Shuriken array (0.5 × 0.5 cm^2) is coated by electrodeposition using PSS-*b*-PEO block copolymer micelles and $HAuCl_4$ precursor to create MCSM. **b**, SEM images of MCSMs (scale bar – 150 nm) with increasing deposition time (time in s given bottom left

Subsequently, optimized mesoporous shurikens were tested to compare photocleavage efficacy towards R- and S-metalaxyl. Progress of photocleavage was monitored by precalibrated HPLC measurement using a chiral column over 48 h. We found that in the case where the enantiomer and MCSMs handedness is matched (R-metalxyl and RH, or S-metalaxyl and LH), photocleavage proceeded 2–3 times more rapidly than in case of the unmatched combinations (Fig. 2a, b). Similar differences in chiral plasmonic activity have been reported for Au and TiO_2 NPs on chiral SiO_2 nanoribbons during RhB degradation[9] and gold-gap-silver nanostructures with cysteine in nitrophenol reduction[12].

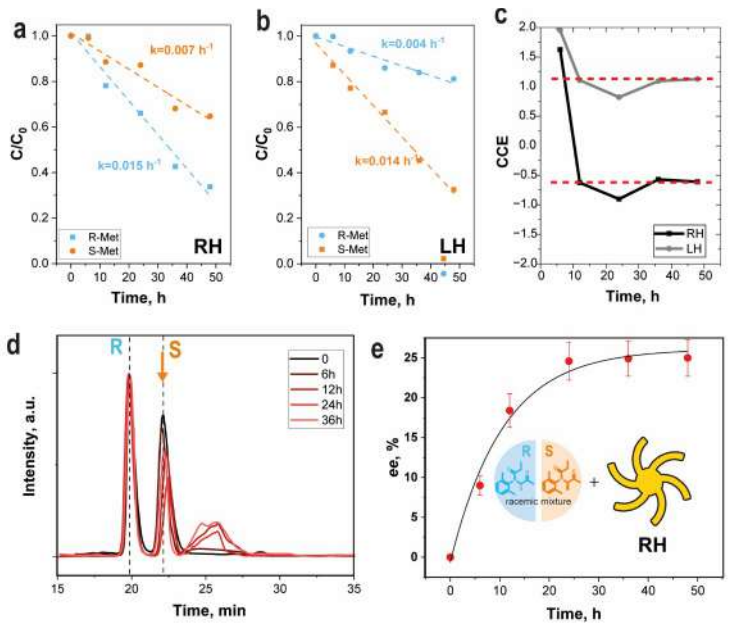


Figure 2. Plasmonic performance of MCSMs. **a**, RH and **b**, LH MCSMs for photocleavage of the individual enantiomers of R and S-metalaxyl (10^{-4} M). **c**, Related chiral catalytic efficiency (CCE). **d**, HPLC chromatograms 6, 12, 24, and 36 h after illumination with 780 nm LPL. **e**, Evaluation of enantiomeric excess obtained by exposure of racemic metalaxyl mixture.

Enantioselective transformations must also be demonstrated on a racemic mixture (Fig. 2d,e) where competing reactivity might take place, and is one of the most challenging tasks. The action of enantioselectivity during reaction leads to an emergence of *ee*, which is a measure of the ratio of one enantiomer over the other (Fig. 2e). We tested RH/LH-MCSMs under similar experimental conditions using a racemic mixture instead of pure enantiomers. The occurrence of chiral photocleavage was evaluated using *ee* as a standard descriptor for chiral catalysis. In the case of both RH and LH-MCSMs, *ee* ≈26 % was achieved.

Herein, we report enhanced light-matter interactions between R/S-metalaxyl, as a chiral subject molecule, and porous metamaterials affording enantioselective cleavage. This is made possible through the generation of a superchiral near-field achieved by the modification of shurikens with a plasmonic mesoporous Au layer. In contrast to previously published CPL-guided plasmonic activity of achiral molecules, the enantioselectivity in a racemic mixture reached >25 % based on coincidence of molecule chirality and MCSM handedness under excitation by LPL. Our work will enable new research directions in chiral systems. First, further refinement of chiral nanostructures by tuning of size, shape, and distribution of mesopores to maximize the chiral near-field effects could lead to even greater enantioselectivity generating larger enantiomeric excesses. Second, the versatility of focused superchiral plasmonic fields as an enantioselectivity source could be studied by broadening the range of target molecules especially high value targets in pharmaceuticals, agrochemicals, and materials science.

This research was supported by the JST-ERATO Yamauchi Materials SpaceTectonics Project (JPMJER2003) and the Japan Society for the Promotion of Science (JSPS) Grants-in-Aid for Scientific Research Kakenhi Program (20K05453).). OG acknowledges the JSPS Postdoctoral Fellowship program. PS and OG acknowledge RSF 23–73-00117 (evaluation of catalytic activity of plasmonic structure for organic transformations). AK

would also like to acknowledge support from EPSRC through grants EP/S001514/1, EP/S029168/1 and EP/X525716/1.

References

1. Wang, P. *et al.* Molecular Plasmonics with Metamaterials. *Chem. Rev.* **122**, 15031–15081 (2022).
2. Zhang, L. *et al.* Microfluidics for chiral separation of biomolecules. *TrAC Trends Anal. Chem.* **158**, 116842 (2023).
3. Teng, Y. *et al.* Advances and applications of chiral resolution in pharmaceutical field. *Chirality* **34**, 1094–1119 (2022).
4. Buser, H. R., Müller, M. D., Poiger, T. & Balmer, M. E. Environmental behavior of the chiral acetamide pesticide metalaxyl: Enantioselective degradation and chiral stability in soil. *Environ. Sci. Technol.* **36**, 221–226 (2002).
5. Okamoto, H. Local optical activity of nano- to microscale materials and plasmons. *J. Mater. Chem. C* **7**, 14771–14787 (2019).
6. Zhang, Z., Zhang, C., Zheng, H. & Xu, H. Plasmon-Driven Catalysis on Molecules and Nanomaterials. *Acc. Chem. Res.* **52**, 2506–2515 (2019).
7. Votkina, D. *et al.* Uncovering the Role of Chemical and Electronic Structures in Plasmonic Catalysis: The Case of Homolysis of Alkoxyamines. *ACS Catal.* **13**, 2822–2833 (2023).
8. Fu, W., Tan, L. & Wang, P. P. Chiral Inorganic Nanomaterials for Photo(electro)catalytic Conversion. *ACS Nano* **17**, 16326–16347 (2023).
9. Negrin-Montecelo, Y. *et al.* Chiral Generation of Hot Carriers for Polarization-Sensitive Plasmonic Photocatalysis. *J. Am. Chem. Soc.* **144**, 1663–1671 (2022).
10. Tan, L., Yu, S. J., Jin, Y., Li, J. & Wang, P. peng. Inorganic Chiral Hybrid Nanostructures for Tailored Chiroptics and Chirality-Dependent Photocatalysis. *Angew. Chemie Int. Ed.* **61**, e202112400 (2022).
11. Bainova, P. *et al.* Plasmon-Assisted Chemistry Using Chiral Gold Helicoids: Toward Asymmetric Organic Catalysis. *ACS Catal.* **13**, 12859–12867 (2023).
12. Hao, C. *et al.* Unusual Circularly Polarized Photocatalytic Activity in Nanogapped Gold–Silver Chiroplasmonic Nanostructures. *Adv. Funct. Mater.* **25**, 5816–5822 (2015).
13. Chen, Y. *et al.* Multidimensional nanoscopic chiroptics. *Nat. Rev. Phys. 2021 42* **4**, 113–124 (2021).
14. Lee, Y. Y., Kim, R. M., Im, S. W., Balamurugan, M. & Nam, K. T. Plasmonic metamaterials for chiral sensing applications. *Nanoscale* **12**, 58–66 (2019).
15. Tullius, R. *et al.* Superchiral Plasmonic Phase Sensitivity for Fingerprinting of Protein Interface Structure. *ACS Nano* **11**, 12049–12056 (2017).
16. Karimullah, A. S. *et al.* Disposable Plasmonics: Plastic Templated Plasmonic Metamaterials with Tunable Chirality. *Adv. Mater.* **27**, 5610–5616 (2015).
17. Guselnikova, O. *et al.* Coupling of plasmonic hot spots with shurikens for superchiral SERS-based enantiomer recognition. *Nanoscale Horizons* **8**, 499–508 (2023).

Photocatalytic hydrogen evolution with plasmonic and photonic nanomaterials

A. Naldoni[1]

[1]Department of Chemistry and NIS Centre, University of Turin, 10125 Turin, Italy
[*]corresponding author: alberto.naldoni@unito.it

Abstract: Plasmonic and photonic nanomaterials have emerged as promising platforms for transducing solar into chemical energy. In this contribution, I will present our research on hydrogen evolution driven by plasmonic and photonic photocatalysts. These catalysts leverage heat, hot electrons, or nanoscale coupling effects to drive chemical reactions relevant to energy applications.

The commitment to achieving a net-zero-emission society by 2050 necessitates the decarbonization of industry, a sector responsible for nearly 40% of global greenhouse gas emissions. Since most industrial processes involve chemicals (e.g., hydrogen, ammonia, plastics, and solvents), developing alternatives to heat and fossil fuels for driving chemical production is crucial for the future of energy and industry. Plasmonic and photonic nanomaterials have emerged as promising platforms for enabling solar energy conversion and storage in value-added molecules. Their enhanced light-matter interaction and unique non-equilibrium, non-linear effects are opening new avenues in photocatalysis. In this contribution, I will present our recent findings on clean hydrogen evolution driven by plasmonic and photonic photocatalysts. These catalysts leverage heat, hot electrons, or nanoscale coupling effects to drive chemical reactions relevant to energy applications.

From Symmetry to Chirality: Near-Field Optical Activity in Achiral Gold Nanoparticles

Minyu Chen[1,2], Thinhinane Aoudjit[1], Baozhong Deng[2], Yuqing Zhao[1], Ali Issa[1], Sylvie Marguet[3], Davy Gerard[1], Lucas Vázquez Besteiro[4], Safi Jradi[1], Bin Wei[2], Alexander Govorov[5], Tao Xu[2*], Renaud Bachelot[1*]

[1] Light, Nanomaterials & Nanotechnologies (L2n) Laboratory, CNRS UMR 7076. University of Technology of Troyes, France
[2] School of Mechatronic Engineering and Automation and School of Microelectronics, Shanghai University, Shanghai, China
[3] Université Paris Saclay, CEA, CNRS, France
[4] CINBIO, University of Vigo, Campus Universitario de Vigo, Spain
[5] Department of Physics and Astronomy, Ohio University, USA
[*]corresponding author: renaud.bachelot@utt.fr, xtld@shu.edu.cn

Abstract: Chirality plays a crucial role in light-matter interactions, with traditional research focusing on chiral structures interacting with chiral light. This study reveals that achiral gold nanotriangles with C3v symmetry can exhibit chiral near-field distributions when excited by linearly polarized light. This emergent chirality arises from the anisotropic near-field response of the plasmonic structure. By employing near-field-assisted two-photon polymerization, we further translate these optical near-field distributions into chiral-symmetric plasmonic structures, enabling direct visualization and structural manifestation of near-field chirality. We systematically investigate the wavelength-dependent behavior of these chiral optical fields under both resonant and off-resonant conditions.

Chirality plays a fundamental role in light-matter interactions, traditionally associated with the interplay between chiral structures and circularly polarized light. However, recent research has demonstrated that achiral plasmonic nanostructures can also exhibit chiral optical responses when excited by linearly polarized light.[1, 2] In this study, we demonstrate that achiral gold nanotriangles (NTs) with C_{3v} symmetry can exhibit chiral near-field distributions under linearly polarized excitation. Using near-field-assisted two-photon polymerization (NF-TPP), we translate these optical near-field patterns into chiral plasmonic polymerized structures, allowing direct visualization of near-field chirality. The SEM image of a pristine NT (Figure a) and its modified structure after 780 nm polarized irradiation (Figure b) highlight polarization-dependent polymerization effects. Additionally, AFM difference mapping (Figure c) and simulated field dissymmetry maps (Figure d) reveal asymmetry in the plasmonic response.

To quantify this emergent chirality, we compute the chirality density enhancement factor (C_{enh}), defined as the local chirality density normalized to free-space circularly polarized light. Figures e and f illustrate the spatial distribution of C_{enh} under LH (45°) and RH (-45°) polarization, showing sign reversal at key structural points. Our results indicate that plasmonic chirality arises from the anisotropic near-field response, where the incident electric field aligns differently with the nanotriangle's edges and corners, leading to local chirality inversion. Furthermore, by varying wavelengths and polarization, we investigate resonant and off-resonant chiral responses, confirming that plasmon-induced chirality is highly tunable.

These findings provide a new approach to engineering chiral plasmonic structures without the need for

inherently chiral materials. The ability to control and visualize near-field chirality using polarization and plasmonic polymerization offers potential applications in chiral light manipulation, optical sensing, and nanophotonic device fabrication. This study highlights the significance of anisotropic plasmonic interactions in shaping and controlling chiral optical

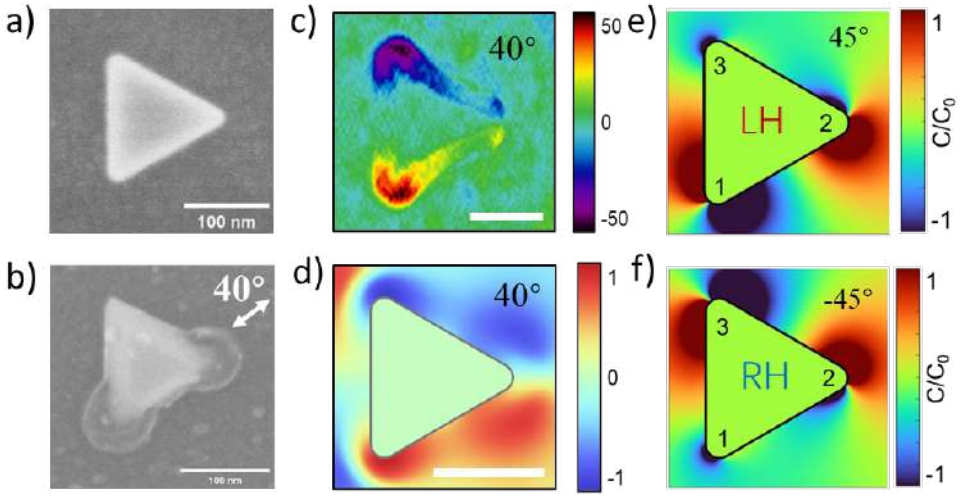


Figure a) SEM image of single gold nanoprism. b) SEM image of single gold nanoprism after irradiation with linearly polarized optical light at 780 nm. c) AFM difference map derived from the LH (40°) AFM map and RH (-40°) AFM map. d) Field dissymmetry map obtained from simulation calculations. e) Spatial distribution of chirality density across the triangular nanostructure under excitation at 45° and f) −45° polarization angles.

f

Acknowledgments: This work was supported by the National Natural Science Foundation of China (Grant No. 12174244), the French Research Agency (ANR) projects STRONG-NANO (Grant No. ANR-22-CE24−0025), POPCORN (Grant No. ANR-21-CE09−0035), and ADVANSPEC (Grant No. ANR-21-CE42−0006). Minyu Chen's doctoral scholarship was funded by Conseil Régional Grand Est and FEDER. The P2PP approach was developed under the Graduate School "NANO-PHOT" (Grant No. ANR-18-EURE-0013).

References

1. Cui, L.; Yang, X.; Reynier, B.; Schwob, C.; Bidault, S.; Gallas, B.; Mivelle, M., Achiral Magnetic Photonic Antenna as a Tunable Nanosource of Chiral Light. *ACS Photonics* **2023,** *10* (11), 3850-3857.

2. Hashiyada, S.; Narushima, T.; Okamoto, H., Imaging Chirality of Optical Fields near Achiral Metal Nanostructures Excited with Linearly Polarized Light. *ACS Photonics* **2018,** *5* (4), 1486-1492.

Plasmonic Materials for Healthcare and Solar Energy Harvesting Applications

Fang Xie

Department of Materials, Imperial College London, UK
*Corresponding author: f.xie@imperial.ac.uk

Abstract:

Novel plasmonic nanostructures developed in our group can serve as powerful fluorescence enhancers and boost solar energy harvesting. In this talk, I will present plasmonic materials for healthcare applications using Metal-Enhanced Fluorescence. Additionally, the role of plasmonic nanoparticles in enhancing photoelectrochemical water splitting will be discussed.

Pancake Meta-Photonics: Stacking Layers to Prepare Quasi-3D Metasurfaces

S. Murai[1]

[1] *Department of Material Chemistry, Graduate School of Engineering, Kyoto University, Nishikyo-ku, Kyoto,615-8510 Japan*
*corresponding author: murai@dipole7.kuic.kyoto-u.ac.jp

Abstract: A general approach to prepare 3D metasurfaces by stacking metasurface layers will be proposed. Bilayer metasurfaces prepared by nanoantenna stickers on another nanoantenna are exhibited as preliminary examples.

Three-dimensional (3D) metasurfaces allow light manipulation with a higher degree of freedom in comparison to 2D counterparts, but it is generally a challenge to fabricate them. Here we propose a concise and reproduceable way of constructing such 3D metasurfaces by stacking 2D metasurface layers. For this we utilize nanoantenna stickers, which is the nanoparticle array embedded in the flexible polymer[1,2]. They are self-adhesive to any clean surfaces to work as nanoantenna. As preliminary examples, we show bilayer systems by combining nanoantenna sticker and the nanoantenna on the substrate [Fig. 1]. By placing light emitters in between, we can tune the photoluminescence from the emitter modulated by both top and bottom metasurfaces[3]. Another example is the induced chirality from twist or moiré metasufaces[4]. We believe these works will lead to future construction of multiple-layered metasurfaces, like a pancake, with multiple functionalities.

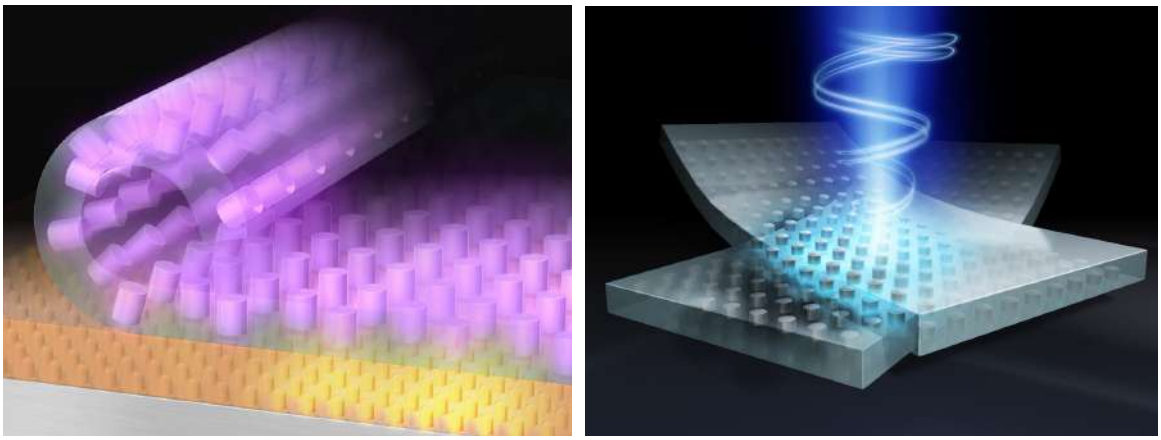


Fig.1: Sketch of bilayer metasurfaces. (left) Nanoantenna layers with an optical emitter in between to photoluminescence control. (right) Nanoantenna layers with a twist angle in between to induce chirality.

References

1. K Agata, et al., ***Appl. Phys. Lett***. **118**, 021110 (2021).
2. TY Lo, et al., ***ACS Appl. Opt. Mater.*** 1, 4, 870-877 (2023).
3. S. Murai, et al., ***J. Appl. Phys.*** **129**, 183101 (2021)
4. J. He et al., to be submitted

Acknowledgments

We acknowledge financial support from Kakenhi & Bilateral programs, Japan.

Sensing mechanical resonances of living human cells using nanomechanical resonators

J. J. Ruz[1*], V. Puerto-Belda[1], C. Millá[1], A. Cano[1], M. L. Yubero[1], S. García[1], P. M. Kosaka[1], M. Calleja[1] and J. Tamayo[1]

[1]Instituto de Micro y Nanotecnología, IMN-CNM, CSIC, Spain
[*]corresponding author: jose.ruz@csic.es

Abstract: A mechanical resonance is a very specific way of energy absorption. The question of whether human living cells exhibit mechanical resonances has remained unresolved for more than 70 years. In this work, we have finally proved the existence of these resonances exploring the frequency response of a nanomechanical resonator.

The cell, the basic unit of life, is an extremely complex structure whose behavior is governed by numerous biochemical processes constantly occurring within it. All these processes give the cell its identity and provide it with certain properties as a complex mechanical structure. Diseases alter these processes, which in turn affect the mechanical properties of cells. Therefore, the mechanical properties of cells can be considered an excellent indicator of disease or cellular malfunction[1,2]. One of the main parameters that might be considered as a mechanical fingerprint of a structure is its resonance frequency. Moreover, a mechanical resonance constitutes a highly specific way of energy absorption, meaning that a structure will not absorb energy if the signal from the source is not close to its resonance frequency. This has motivated the search for mechanical resonances of human cells in their natural environment for more than 70 years[3]. However, due to the high dissipation in such an environment, this question has remained unresolved all these years. In this work, we have finally demonstrated the existence of these resonances using nanometric-thickness cantilevers[4]. The cell is placed near the free end of the cantilever, and the frequency response is measured by searching for anomalies in the cantilever's flexural and torsional spectra (Figure 1).

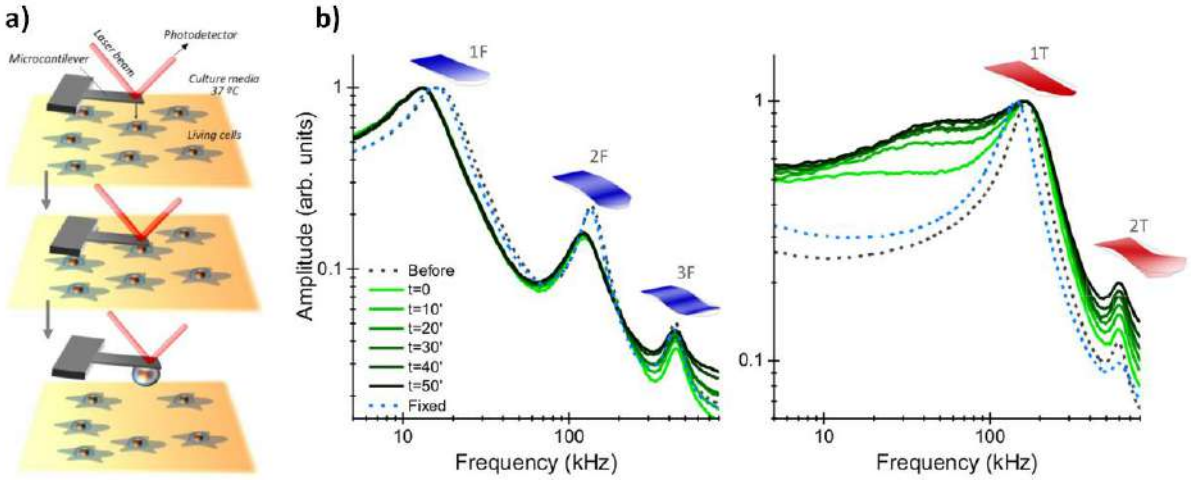


Figure 1. a) Schematic depiction of the process of capturing the cell with the cantilever resonator and b) flexural and torsional spectra measured before and after the cell attachment for different times.

Both spectra are monitored in real time using the optical laser beam deflection technique. With this method, we have found clear evidence of coupling between the mechanical resonances of the cantilever and those of the cell itself. Finally, through a theoretical model that explains the experimental observations, we have been able to extract valuable real-time information about the cell, such as its resonance frequency, intrinsic dissipation, elasticity modulus, and contact area with the cantilever surface (Figure 2).

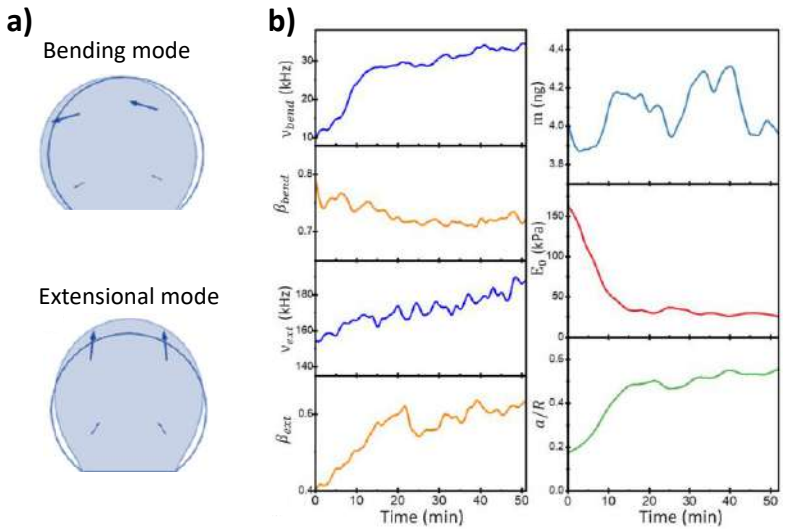


Figure 2. a) Schematic of the bending and extensional vibration modes of the cell and b) different mechanical properties of the cell as a function of time: resonance frequencies and power-law exponent of bending and extensional modes, total mass, Young's modulus and relative radius of contact.

This discovery paves the way for new techniques to study and measure the mechanical properties of human cells in their natural environment, as well as new therapies for diseases such as cancer.

Acknowledgements

This work was supported by the European Union through Project "VIRUSONG" (HORIZON-EIC-2022-PATHFINDEROPEN-01) and the Spanish Science and Innovation Ministry through Projects No. RTI2018-099369-B-I00 [related Doctoral Fellowship No. (FPI) PRE2019-087448], No. AES (DTS21/00136)/ISCIII/EU/FEDER, No. "CELLBIOPHYS" (PID2021-126993OB-I00/MCIN/AEI/10.13039/501100011033/FEDER, UE), "ONCOLIGHT" (No. PDC2022-133503-I00/MCIN/AEI/10.13039/501100011033/European Union/Next Generation EU/PRTR), "ONCODEEPLASM" (No. PLEC2021- 007892/MCIN/AEI/10.13039/501100011033/European Uni- on/Next Generation EU/PRTR). It has also been supported by the private FERO Foundation and Elena Torres Cancer Association funding.

References

1. Cano, A. et al. "Rapid mechanical phenotyping of breast cancer cells based on stochastic intracellular fluctuations". iScience, vol. 27, no 11, 2024.
2. Di, X. et al. "Cellular mechanotransduction in health and diseases: from molecular mechanism to therapeutic targets". Sig Transduct. Target. Ther. 8, 282, 2023.
3. Ackerman, E. "Resonances of biological cells at audible frequencies", Bull. Math. Biophys. 13, 93, 1951.
4. Puerto-Belda, V. et al. "Measuring vibrational modes in living human cells." PRX Life 2.1, 013003, 2024.

Organic optoelectronic devices and biofunctionalized nanoplasmonic gratings: integration into miniaturized optical biosensors

M. Bolognesi[1*], M. Prosa[1], and S. Toffanin[1]

[1] *Institute of Nanostructured Materials (ISMN) – National Research Council (CNR), Via P. Gobetti 101, Bologna 40129, Italy*

[*]corresponding author: margherita.bolognesi@cnr.it

Abstract: We present the design approaches, characterization and demonstration of miniaturized optical biosensors relying on the combination of: i) miniaturized and monolithically integrated organic light-emitting diodes or transistors, and organic photodiodes as the optical transduction elements; ii) antibody-based immunoassays as recognition elements; iii) nanoplasmonic gratings for surface plasmon resonance (SPR) sensing.

Optical sensors demonstrate the largest potential for Lab-on-a-chip (LOC) systems to perform sensitive, quantitative, and fast sensing for food quality and safety monitoring, but also for environmental monitoring or healthcare. Among all options, biosensors based on optical plasmonic sensing schemes combine high sensitivity with label-free detection. However, most of them still have not yet been miniaturized in LOC devices for sensing or analysis in situ of real samples.[1]

We present here the chemical, physical and engineering design approaches,[2] the full characterization, and the detection performance of miniaturized optical SPR sensors and biosensors, that enable quantitative detection of analytes of interest from different food chain production systems. The sensors rely on the combination of: i) miniaturized, monolithically integrated, and cost-effective optical transduction elements based on organic optoelectronic devices, such as organic light-emitting diodes and transistors,[3] and organic photodiodes; ii) direct and competitive immunoassay-based bio-recognition elements; iii) nanostructured plasmonic gratings for SPR based detection.

Quantitative or semi-quantitative analyte-specific detection is demonstrated for different targets, each one representing a different class of analytes: a high molecular weight protein (lactoferrin) is detected at a sensitivity as low as 9 ug/mL;[4] an antiparasitic small molecule (albendazole) is detected at the ppb level; a heavy metal (Cadmium) is detected at the ppb level.

The presented work opens the way for the universal application of optical plasmonic biosensors in LOC devices, for on-site food analysis, environmental or health monitoring, among others.

This work has received funding from the European Union's Horizon Europe research and innovation programme under grant agreement 101157922 (E-SPFdigit) and from the PNRR MUR Project ECS_00000033_ECOSISTER within the FARM project.

References

1. Prosa M, Bolognesi M, Fornasari L, Grasso G, Lopez-Sanchez L, Marabelli F and Toffanin S., "Nanostructured Organic/Hybrid Materials and Components in Miniaturized Optical and Chemical Sensors", Nanomaterials, Vol. 10 No. 3, 480, 2020.

2. Benvenuti E., Moschetto S., Angelini M., Marabelli F., Natali M., Pellacani P., Bolognesi M., Prosa M., Toffanin S. “Design of an optical sensor based on organic optoelectronics and nanoplasmonics for multiplex and multimodal detection”, Org. Electron., Vol. 128, 107023, 2024.
3. Prosa M., Benvenuti E., Kallweit D., Pellacani P., Toerker M., Bolognesi M., Lopez-Sanchez L., Ragona V., Marabelli F. and Toffanin S., “Organic Light-Emitting Transistors in a Smart-Integrated System for Plasmonic-Based Sensing”, Adv. Funct. Mater., Vol. 31, 2104927, 2021.
4. Bolognesi M., Prosa M., Toerker M., Lopez Sanchez L., Wieczorek M., Giacomelli C., Benvenuti E., Pellacani P., Elferink A., Morschhauser A., Sola L., Damin F., Chiari M., Whatton M., Haenni E., Kallweit D., Marabelli F., Peters J. and Toffanin S., “A Fully Integrated Miniaturized Optical Biosensor for Fast and Multiplexing Plasmonic Detection of High- and Low-Molecular-Weight Analytes, Adv. Mater., Vol. 35, 2208719, 2023.

DNA ORIGAMI SELF-ASSEMBLED OPTICAL ANTENNAS FOR SINGLE-PHOTON CHIRAL EMISSION

Fangjia Zhu[1], Maximilian Lengauer[2], Maria Sanz-Paz[1], Karol Kolataj[1], Sophie Brasselet[2], Guillermo P. Acuna[1*]

[1]Department of Physics, University of Fribourg, Fribourg CH-1700, Switzerland
[2]Aix Marseille Univ, CNRS, Centrale Marseille, Institut Fresnel, F-13013 Marseille, France
[*]corresponding author: guillermo.acuna@unifr.ch

Abstract: In the realm of chirality, the helicity of photons, akin to the spins of electrons, holds promise for encoding information swiftly through the polarization of light in both classical and quantum computing. However, the development of a chiral single photon source remains a significant challenge due to the degeneracy of magnetic sublevels in achiral emitters. Here, we demonstrate the achievement of chiral single-photon sources made by a DNA templated trimer antenna (Figure 1) with C2v symmetry group, excited by an asymmetrically positioned achiral emitter without vector beam excitation. In this 2D configuration without inherent structural chirality, the antenna still exhibits chiral emission with a high degree of circular polarization (DCP), attributed to the presence of excited rotating orthogonal electric dipoles inside the structure.

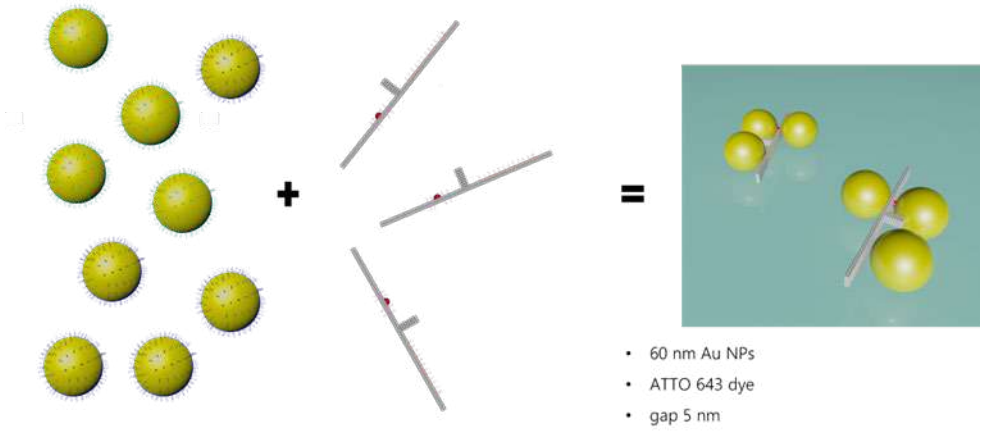


Fig. 1: Au NPs assembly onto DNA origami to form a chiral trimer optical antenna.

Experimental femtosecond pulse trains for time-modulation metamaterials in the terahertz spectral band

W. P. Wardley[1], C. M. Hooper[1], I. R. Hooper[1], S. A. R. Horsley[1], E. Hendry[1]

[1]University of Exeter, UK
[*]corresponding author: w.wardley@exeter.ac.uk

Abstract: Time-modulated metamaterials are investigated using femtosecond pulses for modulation of THz absorption in graphene-based materials. To do this, we describe a new multi-cavity optic which generates pulse-trains from a single femtosecond pulse. We demonstrate the use of this tool for temporal diffraction experiments, including temporal double-slit experiments and constant-amplitude pulse-trains.

Time-modulated metamaterials offer a mostly unexplored route to elaboration and innovation within the field of metamaterials. Traditionally, metamaterial design has, for the most part, been based on repeating structural units in space. However, there is nothing preventing metamaterials using variation in time instead. For instance, a temporally periodic variation of material properties (such as by high energy laser excitation) in an otherwise spatially homogenous medium can equally be used to form novel and otherwise unobtainable properties when the magnitude of the modulation is large enough.

One such means of modulation is based on generating frequency shifts via temporal diffraction effects that are larger than the resonant frequency of a system, allowing experimental demonstration of negative frequencies and the ramifications of interference between them and positive frequencies. In many spectral regimes this is challenging to achieve due to the large frequencies and modulation speeds required, but for terahertz (THz) based systems it is not only achievable via excitation with optical frequencies, but can take advantage of the need for ultrafast laser light for optical rectification for the generation of terahertz radiation, meaning that a femtosecond laser is a key part of many THz systems already. Therefore, simply adding another beamsplitter and beam-path to reroute enough energy to include an additional pump-probe scan can produce a route to the coherent and high-frequency modulation of THz interactions required for the generation of negative frequencies in THz-active materials.

To investigate this time-varying behaviour, a system is required where the modulation behaviour is both rapid and large in extent. For the THz regime, graphene and similar materials make excellent candidates due to their significant change in THz transmissivity, due to the large change in the permittivity when charge carriers are photoexcited.

In particular, we focus on an experimental scheme based around our design of an optic to produce pulse trains of femtosecond laser light of near-constant amplitude to rapidly modulate resonances in the terahertz spectral region, demonstrated by pump-probe measurements of graphene-based materials. These include double-pulse experiments, analogous to Young's double slit experiment, and multiple pulse experiments that offer a route to amplification of terahertz radiation. The double-slit interference measurements show strong evidence for interference between positive and negative frequencies, a key indication of the presence of negative frequencies in our system and a useful tool for investigating time-varying phenomena. In addition to the experimental results, simulations showing the possible extent of negative frequency effects are presented alongside future plans for experimental demonstrations of more novel and exotic temporally modulated effects. This will include discussion of the route to designing and producing the means to generate pulse trains and the technical problems therein, the analysis of the THz measurements from a range of

graphene-based systems and routes to applications based on the results generated.

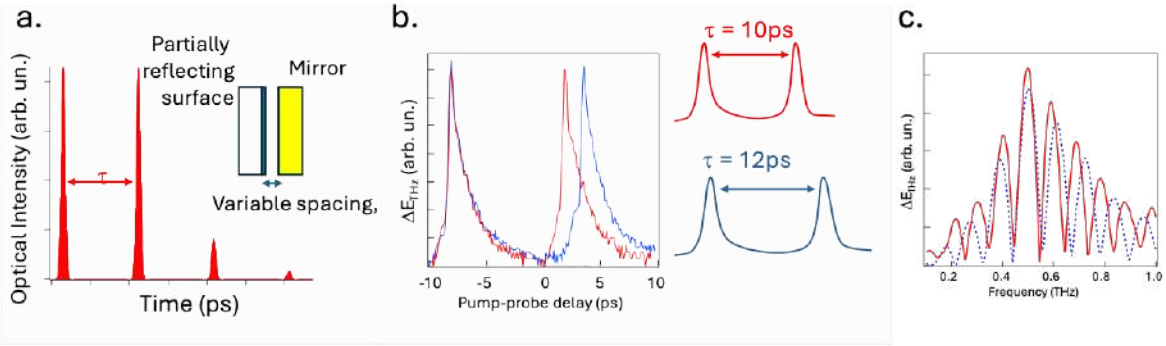


Figure 1a. Intensity versus delay for the generation of pulse pairs with a variably spaced cavity, as shown in top right. 1b. Change in the THz field versus delay time for a pair of pulses with a delay time of 10 and 12 ps. 1c. Change in the THz field versus frequency, derived from the cross-section plot from the interference between the two pulses.

Attomolar sensing of cancer markers using a novel plasmonic nanocomposite thin film for early stage disease diagnosis

M. Gireau[1], F. Du[2], J. Youssef[3,4], G. Humbert[3], S. Zeng[2], C. Champeaux[1] and F. Dumas-Bouchiat[1]

[1]Univ. Limoges, CNRS, IRCER, UMR 7315, F-87000 Limoges, France
[2]Univ. Troyes, CNRS, L2N, UMR 7076, F-10300 Troyes, France
[3]Univ. Limoges, CNRS, XLIM, UMR 7252, F-87000 Limoges, France
[4]ALPhANOV, Optics & Lasers Technology Ctr., Institut d'optique d'Aquitaine, France
[*]corresponding author: manon.gireau@unilim.fr

Abstract: A plasmonic device with a complex design has been developed. The nanocomposite, consisting of an ultra-thin aluminum oxide matrix with tiny embedded silver nanoparticles and a gold film, is fabricated in a single reactor using dual laser ablation. It enables sub-attomolar cancer markers detection, offering promise for early disease diagnosis.

This communication presents the development of a specific highly sensitive plasmonic device for rapid and early-stage disease diagnosis. Surface plasmons are collective oscillations of free electrons waves that exist at the interface between a thin metallic layer, and a dielectric environment. Surface Plasmon Resonance (SPR) is generated when a *p*-polarized incident light interacts with these oscillating electrons under specific conditions, leading to a resonance effect. This unique property of thin metallic films is highly sensitive to changes in the surrounding environment, and can be particularly useful for sensing applications to detect biological molecules in fields of medical diagnosis, biochemical research, and environmental monitoring. Even if plasmonic sensors provide label-free and real-time detection, most classical SPR-based sensors (angle or intensity-interrogating devices) often exhibit limited sensitivity regarding cancer markers, hormones or antibiotic detection. To overcome this issue, the development of a specific sensing setup based on lateral position shift, known as Goos-Hänchen (GH) effect, together with a highly-sensitive plasmonic material was achieved.

SPR occurs when attenuated total reflection (ATR) conditions are met, typically using a prism in Kretschmann configuration. At the resonant angle, the phase of the reflected p-polarized wave undergoes a drastic change due to its coupling with surface plasmons, while the *s*-polarized wave remains unaffected and serves as the incident point reference. This phase variation leads to a giant differential GH shift, where the lateral displacement of the reflected wave is significantly enhanced for the *p*-polarized component. The magnitude of this shift is directly linked to the derivative of the reflection phase change and can be expressed as,

$$\Delta GH = -\frac{\lambda}{2\pi n}\left(\frac{\partial\Phi_p - \partial\Phi_s}{\partial\theta}\right) \quad (1)$$

where λ and n are the wavelength of incident light and the refractive index of the prism respectively, θ is the incident angle and Φ is the phase shift of reflection [1].

Gold (Au) and silver (Ag) are well known for their excellent plasmonic properties in the visible range, mostly due to their high conduction electron density and low energy losses. Gold has been more used for its stability, chemical inertness and biocompatibility, while silver suffers from oxidation and toxicity against living entities, even if it has better plasmonic capabilities. The ability to reach high sensitivities by the association of Au and Ag in a single device was demonstrated by simulations based on Transfer Matrix Method coupled with Maxwell-Garnett theory. The nanocomposite material is made of an ultra-thin (12 nm) aluminum oxide (Al_2O_3) matrix, with embedded 2.3 nm sized Ag nanoparticles (NPs). The characteristic of this layer is to support localized SPR, with

electromagnetic field amplification in the vicinity of the NPs. An upper 48 nm gold film is finishing the architecture. The combination of localized SPR in NPs with propagating SPR in the Au layer provides high resonance performances, highlighted by the simulations of attenuated total reflectance spectrum that describes reflected intensity as a function of incident angle of light on the sample surface. For this architecture, calculations of the minimum reflectivity in water at $\lambda = 785$ nm, was estimated to 10^{-6}, while standard 50 nm gold film was estimated at 0.07, considering the normalized power of the reflected wave.

The fabrication of this challenged complex architecture is achieved using a specific reactor developed by our group [2], which combines pulsed laser deposition (PLD) coupled with a free cluster generator. PLD allows the deposition of films with nanometer-scale controlled thicknesses, with high quality in terms of density and crystallinity. The associated free cluster generator leads to controlled NPs synthesis, with a diameter chosen in the range 1-10 nm and a quasi-monodisperse size distribution. This coupled setup enables the synthesis of the nanocomposite thin film architecture presented in Figure 1, showing dense films free from porosity and well-defined contamination-free interfaces, respecting the desired ultra-low thicknesses for each layer.

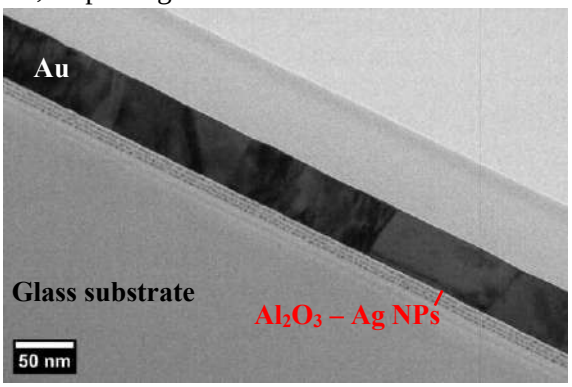


Figure 1 - High-resolution Transmission Electron Microscope cross-section image presenting the architecture of the nanocomposite: Ag-NPs in aluminum oxide covered by Au thin film on glass substrate, 50000× magnification.

The GH shift measurements are performed at $\lambda = 785$ nm with a specialized setup that allows direct changes of the biological environment in contact with the sensor. The ratio between GH shift and refractive index unit (RIU) indicating the sensitivity of the material for our nanocomposite achieved of 3.3×10^{-8} nm.RIU^{-1}. Significant GH shift of 10 µm to 1 aM concentration for a specific cancer marker, namely Tumor Necrosis factor-α was obtained. To the best of our knowledge, this represents the highest detection level ever reached [1]. Furthermore, those sensors are biocompatible and do not require any functionalization before detection tests, making them easier to use compared to other platforms. Given these detection capabilities, our materials have excellent potentials as biosensors for the ultra-early-stage detection of cancers.

This work was partially supported by the LabEx SigmaLim ANR-10-LBX-0074-01, laboratory of excellence launched by the French Ministry of Higher Education and Research (https://www.unilim.fr/labex-sigma-lim) between the IRCER (https://www.ircer.fr) and XLIM (https://www.xlim.fr) Research Institutes.

References

1. S. Zhu, R. Jaffiol, A. Crunteanu, C. Vézy, S.T. Chan, W. Yuan, H.P. Ho, and S. Zeng, “Label-free biosensing with singular-phase-enhanced lateral position shift based on atomically thin plasmonic nanomaterials”, Light Sci. Appl., Vol. 13, No. 1, 2, 2024.
2. M. Gaudin, P. Carles, E. Laborde, C. Champeaux, and F. Dumas-Bouchiat, “A dual nanosecond-pulsed laser setup for nanocomposite synthesis-Ag nanoparticles in Al2O3/VO2 matrix”, J. Appl. Phys., Vol. 125, No. 5, 054301, 2019.

Topological Thermal Emitters

Said Ergoktas

Department of Physics, University of Bath, UK
mse38@bath.ac.uk

Abstract: The ability to control thermal emission has scientific and technological importance and profound implications for thermal management. We introduce a new concept that offers unconventional manipulation of thermal emission by controlling the reflection topology of a surface, achieving the near unit emissivity at the boundary of two topologically distinct surfaces.

Controlling the thermal emission by conventional methods have been limited by the spatial resolution of the engineered material structures and materials' absorption in the infrared regime. In this work, we implement a new route to control light emission from thermal sources based on the concept of topology. We used a lossy optical cavity with one mirror being a thin metal film to tailor the thermal emission at well defined frequency. Precise tuning of the thin metal layer enables a continuous transition from trivial to non-trivial reflection topology, leading to topologically protected zero reflection at a critical thickness. Transition regions from sub critical to super critical domains support topological states that exhibit localized near unit emissivity. Our experimental results illustrate that topological concept would enable new tools for infrared optics and thermal management.

References

1. Ergoktas, M. Said, Ali Kecebas, Konstantinos Despotelis, Sina Soleymani, Gokhan Bakan, Askin Kocabas, Alessandro Principi, Stefan Rotter, Sahin K. Ozdemir, and Coskun Kocabas. "Localized thermal emission from topological interfaces." Science 384, no. 6700 (2024): 1122-1126.

DNA Sensing with Whispering Gallery Mode Microlasers

Soraya Caixeiro[1,2*], Robert Dörrenhaus[3], Anna Popczyk[1], Marcel Schubert[1], Stephanie Kath-Schorr[3], and Malte C. Gather[1,4]

[1]Department of Chemistry and Biochemistry, Humboldt Centre for Nano- and Biophotonics, Institute for Light and Matter, Greinstr. 4-6, 50939 Cologne, Germany
[2]Centre for Photonics and Photonic Materials, Department of Physics, University of Bath, Bath BA2 7AY, United Kingdom
[3]Department of Chemistry and Biochemistry, Institute of Organic Chemistry, Greinstr. 4, 50939 Cologne, Germany
[4]Centre of Biophotonics, SUPA School of Physics and Astronomy, University of St Andrews, St Andrews KY16 9SS, United Kingdom
[*]corresponding author: scc201@bath.ac.uk

Abstract: We present a DNA-functionalized whispering gallery mode microlaser for DNA hybridization detection via spectral shifts. Gold nanoparticles enhance sensitivity without secondary labelling, and we introduce a hairpin-based system as a dual-purpose sensor and controlled release mechanism for potential drug delivery. This novel platform advances sequence-specific detection and in vivo applications.

(Photo-)catalytic activity of sub-5nm gold nanoparticles limited by Coulomb repulsion

M. Garai[1] and T.A. Klar[1*]

[1]Institute of Applied Physics, Johannes Kepler University Linz, 4040 Linz, Austria
[*]corresponding author: thomas.klar@jku.at

Abstract: Gold nanoparticles can serve as (photo-)catalytic agents promoting reductions. Frequently, it is assumed that the smaller the particles, the better they serve as catalysts. However, when storage of electrons takes place between the oxidative and reductive half-reactions, Coulomb blockade hampers the activity for nanoparticles with diameters ≤ 4 nm.

Noble metal nanoparticles can act as redox catalysts in reactions including water splitting, nitrogen fixation, or CO_2 reduction.[1] In case their diameter falls below about 10 nm, literature is split between, on the one hand, reports of ever-increasing catalytic activity with decreasing diameter[2-4] or, on the other hand, reports about an optimal diameter of about 5 nm, below which the catalytic activity decreases rapidly.[5, 6] In our study, we use the model reduction of ferricyanide to ferrocyanide[7] catalyzed by gold nanoparticles of diameters between 2 and 13 nm and determine the reduction rates and the activation energies to demonstrate that it actually depends on the oxidative counter reaction whether the decrease of the diameter below 5 nm leads to an increased or a decreased catalytic activity.

If no intermediate charge storage takes place on the nanoparticles, the catalytic activity increases monotonically roughly with the inverse of the diameter, down to 2 nm. If, however, the strong reductant triethanolamine (TEOA)[8] is present, the nanoparticles act as an intermediate storages of electrons, so called nano-cathodes. [2, 7, 9] We now find that such electron storage is compromised by Coulomb repulsion.[10, 11] This leads to an optimal diameter of 4-5 nm. In our study,[11] exactly the same batches of gold nanoparticles and the same model reduction were used, so that the parameter space for the different size dependencies of the catalytic activity is restricted to the differences in oxidative counter-reactions. Besides, the two qualitatively distinct dependencies of the catalytic activity on diminishing particle diameter are independent form the use of the gold nanoparticles as catalyst in the dark or as photocatalysts. Although illumination increases the overall catalytic activity, there is still an optimal diameter of about 4 nm if intermediate cathodic charging takes place, while the activity monotonously increases with shrinking diameter if no such intermediate charging takes place.

The fact that the Coulomb repulsion is detrimental rather than helpful (as sometimes assumed)[3] when using sub–5 nm AuNPs should have even more impact in case of multi-electron redox-reactions catalyzed by AuNPs. We also note that the Coulomb blockade is symmetric in adding or removing electrons from a gold nanoparticle. Therefore, in an alternative scenario where an oxidant is used to positively charge gold nanoparticles in order to render them oxidative agents, the problem that the Coulomb repulsion compromises the (positive) charging of the AuNP will equally hold.

Acknowledgements

We acknowledge experimental support by Sebastian Diethör, Felix Mayr and Günter Hesser as well as fruitful discussions with Markus Scharber and Serdar Sariciftci. This work was funded by the Austrian Klima und Energiefonds, handled by the Austrian Research Promotion Agency (FFG), project number FO999888408.

References

1. Camargo, P. H. C.; Cortes, E., *Plasmonic Catalysis*. Wiley-VCH: Weinheim, Germany, 2021.
2. Kiwi, J.; Grätzel, M., Projection, size factors, and reaction dynamics of colloidal redox catalysts mediating light induced hydrogen evolution from water. *J. Am. Chem. Soc.* **1979,** *101* (24), 7214-7217.
3. Stewart, S.; Wei, Q.-H.; Sun, Y., Surface chemistry of quantum-sized metal nanoparticles under light illumination *Chemical Science* **2021,** *12*, 1227-1239.
4. Mao, Z.; Vang, H.; Garcia, A.; Tohti, A.; Stokes, B. J.; Nguyen, S. C., Carrier Diffusion—The Main Contribution to Size-Dependent Photocatalytic Activity of Colloidal Gold Nanoparticles. *ACS Catalysis* **2019,** *9*, 4211-4217.
5. Deng, J.-P.; Shih, W.-C.; Mou, C.-Y., Hydrogenation of Anthracene Catalyzed by Surfactant-Protected Gold Nanoparticles in Aqueous Solution: Size Dependence. *ChemPhysChem* **2005,** *6*, 2021-2025.
6. Lin, C.; Tao, K.; Hua, Z.; Zhou, S., Size Effect of Gold Nanoparticles in Catalytic Reduction of p-Nitrophenol with $NaBH_4$. *Molecules* **2013,** *18*, 12609-12620.
7. Carregal-Romero, S.; Perez-Juste, J.; Herves, P.; Liz-Marzan, L. M.; Mulvaney, P., Colloidal Gold-Catalyzed Reduction of Ferrocyanate (III) by Borohydride Ions: A Model System for Redox Catalysis. *Langmuir* **2010,** *26* (2), 1271-1277.
8. Pellegrin, Y.; Odobel, F., Sacrificial electron donor reagents for solar fuel production. *Comptes Rendus Chimie* **2017,** *20*, 283-295.
9. Miller, D. S.; Bard, A. J.; McLendon, G.; Ferguson, J., Catalytic water reduction at colloidal metal "microelectrodes". 2. Theory and experiment. *J. Am. Chem. Soc.* **1981,** *103* (18), 5336-5341.
10. Ingram, R. S.; Hostetler, M. J.; Murray, R. W.; Schaaff, T. G.; Khoury, J. T.; Whetten, R. L.; Bigioni, T. P.; Guthrie, D. K.; First, P. N., 28 kDa Alkanethiolate-Protected Au Clusters Give Analogous Solution Electrochemistry and STM Coulomb Staircases. *J. Am. Chem. Soc.* **1997,** *119*, 9279-9280.
11. Garai, M.; Diethör, S.; Mayr, F.; Scharber, M. C.; Sariciftci, N. S.; Klar, T. A., Redox-Chemical Electron Storage on Sub-5nm Gold Nanoparticles Compromised by Coulomb Repulsion. *Journal of Physical Chemistry C* **2025,** *in press*.

Collective behavior of a plasmonic particle array with a chiral arrangement under modal coupling regime

T. Oshikiri[1*]
[1]Institute of Multidisciplinary Research for Advanced Materials, Tohoku University, Sendai, Miyagi 980-8577, Japan
[*]corresponding author: tomoya.oshikiri.c1@tohoku.ac.jp

Abstract: We fabricated a cluster of isotropic gold nanodisks with a chiral arrangement on the Fabry–Pérot (FP) nanocavities of TiO_2/Au film. We demonstrate that collective mode formation under modal coupling regime between localized surface plasmon resonances with a chiral arrangement and Fabry–Pérot (FP) nanocavity modes can induce chiroptical responses.

Introduction

Chiral systems, that are noncongruent with their mirror images, have attracted much attention due to their unique properties and applications. Generally, the interactions between circularly polarized light (CPL) and chiral molecules are not strong because of the size difference between the light wavelength and the molecule[1, 2]. Localized surface plasmon resonances (LSPRs), which is the collective oscillation of surface electrons in metal nanostructures, harvest incident light and enhance local electric fields in the near field. The interaction of incident light with chiral metal nanostructures induces helical near fields around these structures[3, 4]. Additionally, metal nanostructures irradiated with light possessing angular momentum, such as CPL and optical vortices, show asymmetric near field distributions[5-7]. The configuration and arrangement of plasmonic particles also play important roles in determining their chiroptical response[8, 9]. This study aimed to induce chiroptical responses in a cluster of isotropic plasmonic particles with a chiral arrangement based on collective mode formation under modal coupling between the LSPRs and FP nanocavity modes.[10] We designed a cluster of isotropic Au nanodisks (Au-NDs) with a chiral arrangement (Au nanowindmill, Au-NW) on an FP nanocavity. We evaluated the contribution of modal coupling to the chiroptical responses by comparing the spectral properties of the identical cluster in the presence and absence of the FP nanocavity.

Experimental

Au NWs were fabricated on a substrate by electron beam exposure and lift-off techniques. The substrates were fabricated by coating with the titanium oxide (TiO_2) onto indium-thin oxide (ITO)-coated SiO_2 (ITO/SiO_2) and coating TiO_2 onto Au-coated SiO_2 (Au/SiO_2). We deposited TiO_2 thin films having thickness of 60 nm using an atomic layer deposition equipment at 300°C. The morphologies of the nanostructures were observed using field-emission scanning electron microscopy. The transmission and reflection spectral properties were investigated at room temperature using a W-halogen lamp as an irradiation source, a microscope with an objective lens (40×/NA0.75), a spectrometer, and a charge-coupled device camera detector electronically cooled to -80°C. Left- or right- CPL (LCPL or RCPL) was generated by a linear polarizer module, half-wave module, and quarter-wave module with a retardance of $0.25\pm0.03\pi$. T

Results and Discussion

We designed Au-NWs, as shown in Figures 1. Au-NW was a cluster of Au-NDs with a two-dimensional chiral arrangement bearing three-fold or five-fold rotational symmetry on TiO_2/Au (Au-NWs on TiO_2/Au). TiO_2/Au works as an FP nanocavity whose resonant wavelength was approximately 700 nm. The FP nanocavity couples with multiple plasmonic particle modes. In this situation, the interparticle interaction between plasmonic particles is also enhanced through the FP nanocavity as reported[11]. Consequently, the formation of collective mode and corresponding near-field can be expected based on the

arrangement of the cluster of Au-NDs under modal coupling conditions. Au-NWs in the absence FP nanocavities were also fabricated on TiO_2-coated ITO/SiO_2 under the same conditions as the control samples (Au-NWs on TiO_2).

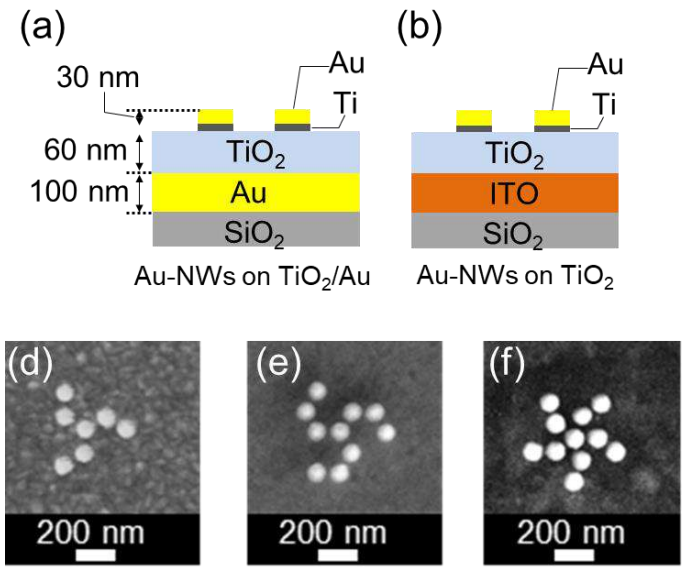


Figure 1. (a,b) Cross-sectional view of Au-NWs on TiO_2/Au (a) and TiO_2 (b). (c-e) FE-SEM images of Au-NWs on TiO_2/Au with different geometries. Scale bars indicate 200 nm.

We measured the differential absorption spectra of the LCPL and RCPL irradiations. The differential absorption spectrum of TiO_2/Au did not show a significant signal, indicating that the FP nanocavity alone did not exhibit a chiroptical response. In contrast, the differential absorption spectra of the Au-NWs on the TiO_2/Au-film show clear negative signals. These results suggest that the modal coupling between the LSPR and FP nanocavity modes induces chiroptical responses in Au-NWs having a chiral arrangement.

References

1. Inoue, Y.; Tsuneishi, H.; Hakushi, T.; Yagi, K.; Awazu, K.; Onuki, H. *Chem. Commun.* **1996,** , 2627-2628.
2. Kuhn, A.; Fischer, P., *Angew. Chem. Int. Ed.* **2009,** *48*, 6857-6860.
3. Hendry, E.; Mikhaylovskiy, R. V.; Barron, L. D.; Kadodwala, M.; Davis, T. J. *Nano Lett.* **2012,** *12*, 3640-3644.
4. Paterson, G. W.; Karimullah, A. S.; Smith, S. G.; Kadodwala, M.; Maclaren, D. A. *J. Phys. Chem. C* **2018,** *122*, 5049-5056.
5. Hashiyada, S.; Narushima, T.; Okamoto, H. *J. Phys. Chem. C* **2014,** *118*, 22229-22233.
6. Arikawa, T.; Hiraoka, T.; Morimoto, S.; Blanchard, F.; Tani, S.; Tanaka, T.; Sakai, K.; Kitajima, H.; Sasaki, K.; Tanaka, K. *Sci. Adv.* **2020,** *6*, eaay1977.
7. Oshikiri, T.; Sun, Q.; Yamada, H.; Zu, S.; Sasaki, K.; Misawa, H. *ACS Nano* **2021,** *15*, 16802-16810.
8. Zu, S.; Bao, Y.; Fang, Z. *Nanoscale* **2016,** *8*, 3900-3905.
9. Wang, F.; Harutyunyan, H. *Adv. Opt. Mater.* **2019,** *7*, 1900744.
10. Oshikiri, T.; Matsuo, Y.; Niinomi, H.; Nakagawa, M., *Photochem. Photobiol. Sci.* **2024,** *24*, 13-21.
11. Liu, Y.-E.; Shi, X.; Yokoyama, T.; Inoue, S.; Sunaba, Y.; Oshikiri, T.; Sun, Q.; Tamura, M.; Ishihara, H.; Sasaki, K.; Misawa, H. *ACS Nano* **2023,** *17*, 8315-8323.

Photocatalysis and Local Growth Driven by Plasmonic Hot Electrons

E. Y. Santiago[1*]

[1]CINBIO, Universidade de Vigo, Spain
[*]corresponding author: evayazmin.santiago@uvigo.gal

Abstract: This study explains a phenomenon intrinsic to plasmonic nanomaterials: the efficient generation of hot carriers on their surface that drive secondary processes, such as photocatalysis. This can lead to a photogrowth process that constructs nanostructures with a controlled and asymmetric optical response that depends on the incident light polarization.

Summary

The study of plasmonic nanomaterials is a fundamental part of modern nanoscience and nanotechnology. These systems exhibit strong and tunable absorption and scattering of electromagnetic radiation due to their strong localized surface plasmon resonances (LSPRs) excited by light, dependent on the nanostructure shape and composition. A phenomenon intrinsic to plasmonic nanomaterials that currently elicit great research interest is the efficient generation of hot carriers[1], which are electrons and holes that can leave the metal due to their large kinetic energies and drive secondary processes such as photocatalysis. By taking advantage of non-uniform distribution of these excited carriers on the metal surface, we can create an asymmetrical optical response by building nanostructures in a controlled manner through a photogrowth process[2].

This occurs when electromagnetic radiation is absorbed and the LSPRs relax. Depending on the geometry, size, material and surrounding medium of the nanoparticle, hot carriers are generated on its surface. They can then drive surface chemistry, which in adequate conditions can lead to a nonlinear and inhomogeneous photogrowth process. Such photogrowth can be exploited in combination with sources of light to break the symmetry of an initially symmetric nanoparticle. This study explains our deepened understanding of the light-matter interaction through plasmonics, which allows us to explore new avenues to develop a fine control over nanoparticle morphology. This is done through theoretical and computational methodologies to explain the response of nanoparticles under light of different polarizations.

References

1. Santiago, E. Y., L. V. Besteiro, X. T. Kong, M. A. Correa-Duarte, Z. Wang, A. O. Govorov, “Efficiency of Hot-Electron Generation in Plasmonic Nanocrystals with Complex Shapes: Surface-Induced Scattering, Hot Spots, and Interband Transitions,” ACS Photonics, Vol. 7, No. 10, 2807-2824, 2020.
2. Besteiro, L. V., A. Movsesyan, O. Ávalos-Ovando, S. Lee, E. Cortés, M. A. Correa-Duarte, Z. M. Wang, and A. O. Govorov, “Local Growth Mediated by Plasmonic Hot Carriers: Chirality from Achiral Nanocrystals Using Circularly Polarized Light,” Nano Letters, Vol. 21, No. 24, 10315–10324, 2021.

Hybrid TMDC/plasmonic systems

E. Peci[1], E. Spotorno[1], M. Magnozzi[1], L. Ramò[1], V. Venturino[1], , M. C. Giordano[1], M. Canepa[1], F. Bisio[2*]

[1]Dipartimento di Fisica, Università degli Studi di Genova, Via Dodecaneso 33, 16146 Genova (Italy)
[2]CNR-SPIN, C.so Perrone 24, 16152 Genova (I)
[*]corresponding author: francesco.bisio@spin.cnr.it

Abstract: We discuss the fabrication and the exploitation of hybrid systems composed by plasmonic optical resonators coupled with 2D materials. We provide examples of TMDC transfer onto plasmonic nanostructures and of nanofabrication of plasmonic systems on top of TMDC layers. Different applications are discussed.

Semiconducting transition metal dichalcogenides (TMDCs), such as MoS_2 and WS_2, have emerged as promising candidates for next-generation optoelectronic devices, owing to their remarkable electronic and optical properties. They exhibit room-temperature excitonic effects and, when thinned down to a three-atom-thick monolayer, exhibit direct-gap semiconducting band structure, making them an excellent playground for exploiting light-matter interaction at the nanoscale.

By coupling a TMDC monolayer with metallic nanostructures exhibiting localized surface plasmon resonances (LSPR) it becomes possible to realize hybrid photonic systems for fundamental studies and novel applications. Within this framework, the excitons of the TMDC and the LSPR are viewed as optical resonators whose spatial coupling and spectral overlap can be freely tuned by engineering their nanoscale characteristics. Additionally, hybrid TMDC/plasmonic systems can be exploited as novel platforms to investigate the heat dynamics at the nanoscale, exploiting the thermoplasmonic effect of the plasmonic counterparts for locally generating heat, and the temperature dependence of the PL energy to act as a nano-thermometer.

Realizing these hybrid structures is by all means a complex task, that typically combines nanolithography approaches to deterministically fabricate the plasmonic counterpart with delicate growth-and-transfer methods to introduce the TMDC in the system. The issue with the realization of these systems is that the direct fabrication of plasmonic structures onto TMDCs with energetic particles (electrons, ions) is prone to damage these materials, whereas the transfer of TMDCs onto fabricated structures tends to be a non-deterministic process. In this contribution, we report results from two different approaches. In the former case, we achieve a deterministic transfer of TMDC layers onto existing plasmonic resonators, while in the latter, we succeed in fabricating plasmonic nanostructures onto monolayer 2D materials.

The common denominator of both approaches is the achievement of large-area TMDC-monolayer flakes, that allow to have large spatial extensions for transfer or fabrication. In detail, we exploited gold-assisted exfoliation as a reliable technique for peeling off large-area TMDC monolayers from bulk crystals. The strong affinity between gold and chalcogens overcomes the van der Waals interlayer attraction, thus peeling off the outermost layer from the bulk TMDC, and allowing in some cases to transfer such a layer onto another substrate [1]. We recently demonstrated a large-scale exfoliation-and-transfer procedure based on the technique proposed by Liu et al. [2], and refined by Petrini et al. [3], where Au films are adopted to exfoliate large-area monolayer TMDCs. Subsequent treatments then allow the deterministic transfer of large-area monolayer TMDCs onto virtually any substrate, yielding high-quality flakes with minimal defects and large lateral dimensions, while requiring limited experimental effort and using common consumables.

Using samples produced on PDMS substrates, we demonstrate the possibility of systematically transferring the produced samples onto a desired target with micrometer control of the sample positioning. Examples of MoS_2 transfer onto previously-fabricated plasmonic nanostructures are reported and discussed, including nanosystems for measuring the thermoplasmonics heating of metallic nanodisks.

For the latter approach, we exploit thermal scanning-probe lithography (t-SPL) as a viable alternative to electron-beam lithography or focused-ion-beam etching to directly write plasmonic nanostructures onto previously-fabricated large-scale exfoliated 2D materials [1,2]. t-SPL works similarly to an atomic force microscope (AFM) with a heating tip; the desired pattern is written on a thermosensitive resist while acquiring a topological image of the sample. After gold deposition and resist lift-off, we are left with gold nanostructures over our TMDC. We demonstrated the appeal of this technique, fabricating regular, evenly spaced, 15 nm-thick plasmonic nanodisks (NDs) on square lattices onto monolayer- and bilayer-thick regions of TMDCs. We show that delicate photonic functionalities, such as TMDC photoluminescence, are preserved after the fabrication [4].

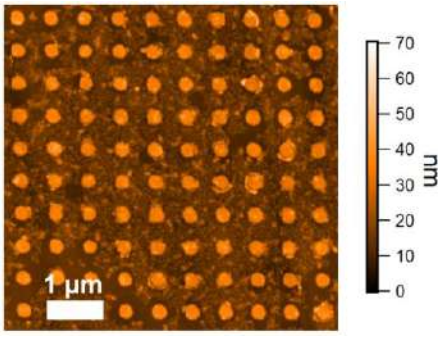


Figure 1: AFM image of Au NDs on MoS_2 monolayer.

We acknowledge support from Ministero dell'Istruzione, dell'Università e della Ricerca, Dipartimenti di Eccellenza 2018-2022, PRIN 2017 no. 2017KFY7XF, the National Recovery and Resilience Plan (NRRP), Mission 4, Component 2, Investment 1.1, Call for tender no. 104 PRIN 2022 published on 2.2.2022 by the Italian Ministry of University and Research (MUR), funded by the European Union – NextGenerationEU –Project Title ERACLITO – CUP B53D2300904006, Robotics and AI for Socio-economic Empowerment (RAISE), Piano Nazionale di Ripresa e Resilienza (PNRR).

References

1. Panasci, S. E. et al., "Gold-Assisted Exfoliation of Large-Area Monolayer Transition Metal Dichalcogenides: From Interface Properties to Device Applications". Adv. Fuct. Mater., Vol. 35, No.5, 2414532, 2025.
2. Liu, F. et al., "Disassembling 2D van der Waals crystals into macroscopic monolayers and reassembling into artificial lattices". Science, Vol. 367, No. 6480, 903-906, 2020.
3. Petrini, N., Peci, E. et al., "Optimizing Gold-Assisted Exfoliation of Layered Transition Metal Dichalcogenides with (3-Aminopropyl)triethoxysilane (APTES): A Promising Approach for Large-Area Monolayers". Adv. Optical Mater., Vol. 12, No. 7, 2303228, 2024.
4. Ramò L. *et al.* "Thermal Scanning-Probe Lithography for Broad-Band On-Demand Plasmonic Nanostructures on Transparent Substrates" ACS Appl. Nano Mater. 6, 19, 18623–18631, 2023.

Statistical Evaluation and Dipole Determination by Polarimetric Spectroscopy Yielding the Orientation of Gold Nanorods

P. C. Simo[1*], A. Mildner[1], D. P. Kern[1], M. Zbytovska[1], and M. Fleischer[1]
[1]University of Tübingen, Institute for Applied Physics and Center LISA$^+$, Germany
Corresponding author: christian.simo@uni-tuebingen.de

Abstract: Within just four measurements the presented technique acquires the azimuthal orientation of gold nanorods of various aspect ratios. An analytical dipole model in tandem with dark-field spectroscopy enables the extraction of phase shift information to determine the azimuthal orientations.

The polarization and spatial orientation of a plasmonic emitter, such as a gold nanorod (AuNR), are required for the investigation of optically active hybrid compounds through applications such as chiroptical spectroscopy in the pharmaceutical and biomedical research fields [1]. Similarly, quality control of meta-atom constituents of metasurfaces would benefit from a reliable non-contaminating method that determines an accurate azimuthal orientation to pass a set error margin. Simple structures like AuNRs are known to exhibit a longitudinal resonance (LR) mode that naturally coincides with their azimuthal orientation, and can be extracted by conventional excitation polarization sweep measurements [2]. Advanced optical setups that benefit from image analysis with deep-learning algorithms allow pioneering high-throughput single-shot techniques [3,4]. Nevertheless, the orientation prediction is limited to AuNR aspect ratios (ARs) of under 1.6 and reaches standard deviations of below 5°.

In this work, we present an alternative all-spectroscopic method that yields angular information of single AuNRs within four measurements [5]. A regular dark-field spectroscopy setup, two polarizing filters, and a cross-shaped aperture realize this technique with an accuracy of ±2.4° for a range of ARs. An analytical dipole model is applied to coherently fit the measurements obtained by varying the planar orientation of the analyzing filter [6]. The additional elements, such as a piezo-electric rotational mount for the positioning of the analyzing polarizer filter, offer enhanced automation possibilities.

With a fixed excitation angle $\Phi = 45°$ and randomly varying analyzer angles (here $\Theta = [9°, 106°, 155°]$), one can use the model to fit the data coherently and extract γ_{fit} (Figure 1a)). Compared to γ_{fit}, the SEM-extracted angle γ_{SEM} shows a standard deviation of only ±2.4° for a set of multiple AuNRs of diverse ARs [5]. An SEM micrograph with the drawn-in γ_{fit} and γ_{SEM} can be seen in Figure 1b) and shows good concordance. This approach proves to be reliable and has a low sensitivity to AR. To statistically evaluate the choice of the analyzer angles used for the coherent fitting, a range of discretized analyzer angles Θ from 0° to 180° in 15° steps were used, and the results for any three-angle combination were compared (Figure 1c)). Nearly all fitted azimuthal orientation angles γ_{fit} are within one standard deviation of the real physical orientation γ_{SEM} throughout the possible combinations of three analyzer angles.

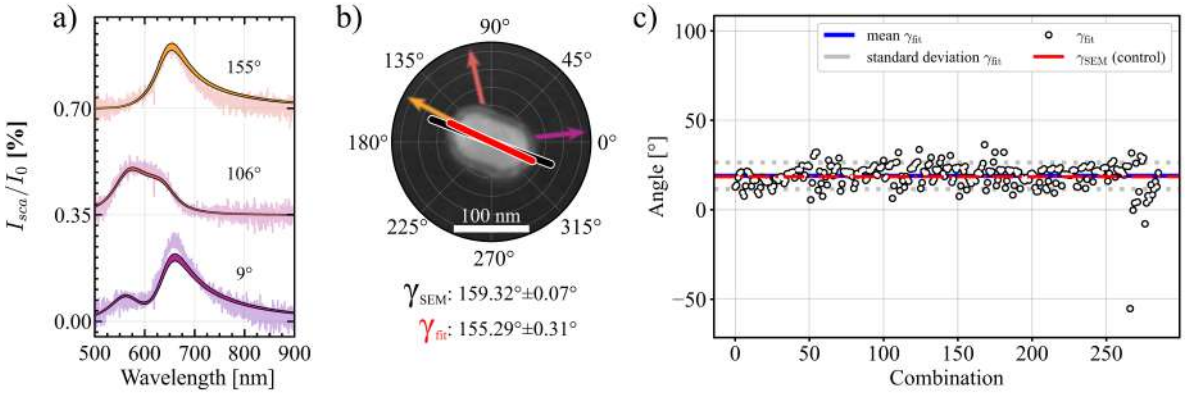


Figure 1: **a)** Polarimetric spectra at a fixed polarization angle Φ and three separate random analyzer angles Θ. The corresponding fitting curves of the analytical model are overlayed with the data. **b)** SEM micrograph of particle which exhibited the spectra shown in b), overlayed with the physical (black) and fitted (red) orientation. **c)** Statistical evaluation of the fitted angle γ_{fit} for all 286 possible combinations. The obtained angle γ_{fit} for the respective combination is shown versus the physical orientation γ_{SEM} of an arbitrary AuNR. Graphs a) and b) taken from [5] with permission.

References

1. Sachs, J., J.-P. Günther, A. G. Mark, and P. Fischer, "Chiroptical spectroscopy of a freely diffusing single nanoparticle", *Nat. Commun.*, Vol. 11, No. 10, 4513, 2020.

2. Chang, W.-S., J. W. Ha, L. S. Slaughter, and S. Link, "Plasmonic nanorod absorbers as orientation sensors", *PNAS*, Vol. 107, No. 7, pp. 2781-2786, 2010.

3. Bouchal, P., P. Dvořák, M. Hrtoň, K. Rovenská, R. Chmelík, T. Šikola, and Z. Bouchal, "Single-Shot Aspect Ratio and Orientation Imaging of Nanoparticles", *ACS Photonics*, Vol. 10, No. 9, pp. 3331-3341, 2023.

4. Hu, J., T. Liu, P. Choo, S. Wang, T. Reese, A. D. Sample, and T. W. Odom, "Single-Nanoparticle Orientation Sensing by Deep Learning", *ACS Cent. Sci.*, Vol. 6, No. 12, pp. 2339-2346, 2020.

5. Simo, P. C., A. Mildner, D. P. Kern, and M. Fleischer, "Dipole Determination by Polarimetric Spectroscopy Yielding the Orientation of Gold Nanorods", *Small Science*, pp. 2400340, 2025.

6. Mildner, A., A. Horrer, P. Weiss, S. Dickreuter, P. C. Simo, D. Gérard, D. P. Kern, and M. Fleischer, "Decoding Polarization in a Single Achiral Gold Nanostructure from Emitted Far-Field Radiation", *ACS Nano*, Vol. 17, No. 24, pp. 25656-25666, 2023.

Single-Particle Chiral Optical Microscope with High Precision

Wei-Shun Chang[1*], Angel Rose Thomas[1], Vidhi Singla[1], Oscar Avalos Ovando[2], Trang Nguyen[1], Tamie Vo[1], Alexander O Govorov[2]

[1]Department of Chemistry and Biochemistry, University of Massachusetts Dartmouth, North Dartmouth, Massachusetts, 02747, United States

[2]Department of Physics and Astronomy, Ohio University, Athens, OH, 45701, United States

[*]corresponding author: wchang2@umassd.edu

Abstract: Characterizing the chirality of nanostructure at the single-particle level is essential for understanding the relationship between morphology and chirality. Here, we present our recent development of a single-particle chiral optical microscope, which enables high-precision and high-throughput characterization of chiral nanostructures.

Engineering the chirality of the plasmonic nanostructures is crucial for various applications, including biosensing, chiral catalysis, and chiral separation. As the chirality of the nanostructures is regulated by their morphologies, understanding the relationship between morphology and chirality remains very challenging. Conventional circular dichroism spectroscopy, which measures the average chiral signal from a sample with a heterogeneous geometry distribution, often fails to provide this insight. Therefore, quantifying the chirality of a single nanostructure is important to overcome this limitation.

To address this challenge, several single-particle techniques have been developed to measure the chirality of plasmonic nanostructures. Dark-field scattering (DFS) microscopy is widely used because of its ease of implementation and the ability to acquire circular differential scattering (CDS) spectra, which quantify the chirality of plasmonic nanostructures. While DFS microscopy has demonstrated success in characterizing single-particle chirality, it is often prone to false CDS signals, introducing uncertainties in chiral characterization.

In this presentation, we introduce a novel DFS microscope designed to measure CDS spectra of single plasmonic nanostructures with high accuracy and throughput. We pinpoint the source of artifact CDS signals, attributing them to linear dichroism and the imperfect retardance of polarization optics. Moreover, we have developed a robust method to identify and completely eliminate these artifact signals, ensuring reliable chiral characterization.

Acknowledgments: This work is supported by the National Science Foundation (CHE-2247710, CAT) and by UMass Dartmouth's Marine and Undersea Technology (MUST) Program funded by the Office of Naval Research (N00014-23-1-2141). The electron microscopy images in this work were obtained using a scanning electron microscope supported by the National Science Foundation under Grant No. 1726239.

Photoluminescence-based polarization conversion in quantum rods aggregate-containing hybrid polymer system

Y. Okazaki[1*], Y. Kawahara[1], S. Kimura[1], H. Shimizu[1], K. Hachiya[1], and T. Sagawa[1]

[1]Graduate School of Energy Science, Kyoto University, Japan
[*]corresponding author: okazaki.yutaka.8c@kyoto-u.ac.jp

Abstract: We fabricated various hybrid linearly polarized luminescent films containing different aggregation states of quantum rods in dilute condition. In this presentation, we discuss about the correlation between aggregation states of QRs and polarization converting properties.

Polarization converting materials have attracted attention because of its intrinsic property to utilize incoming light energy effectively. In particular, photoluminescence (PL)-based polarization converting materials have advantage including spectral conversion function, and material formability. For the fabrication of PL-based polarization converting materials, several approaches such as donor-molecule/acceptor-polymer composite system[1] and quantum-dot/quantum-rod system[2] have been reported. However, little is known about the correlation between aggregation formation of luminogens in dilute system and resulting polarization converting property. We recently found that CdSe/CdS core/shell quantum rods (QR) form nano to micrometric aggregates in polymer media in a diluted condition, resulting clear polarization conversion phenomenon based on excitation energy transfer. In this study, we investigate the effect of aggregation forms of QRs in polymer media on the polarization conversion.

QR was synthesized by hot-injection method based on the previous report[3]. The obtained QR/toluene solution showed yellow-colored emission under 365 nm UV light irradiation. Transmission electron microscope (TEM) observation of the dried sample showed a clear rod-like structure with over 90 nm average length and 5.0 nm average width. The width (5.0 nm) is smaller enough than the exciton size of CdSe (10.6-10.8 nm) calculated from the previously reported exciton Bohr radius (5.3-5.4 nm)[4-5], indicating that the obtained QR can show linearly polarized luminescence (LPL). Photoluminescence excitation (PLE) spectra of the QR/toluene solution showed clear PL peak shift by changing the excitation wavelength. Time resolved PL spectral measurements of the QR/toluene solution showed no significant peak shift by time. These results indicate that QRs are well dispersed in the liquid toluene media. Next, the QR/toluene solution was mixed with polymer/toluene solutions, and the mixtures were casted on the substrate to obtain QR/polymer films. The QR/polymer films were uniaxially stretched to obtained $LPL_{QR/polymer}$ films. We first selected poly(ethylene-*co*-vinyl acetate) (EVA) as a media polymer. In contrast to the solution system, PLE spectra of $LPL_{QR/EVA}$ film showed no significant excitation wavelength dependence on PL peak. In addition, PL peak shift was observed in time resolved PL spectral measurements. These results evident that the excitation energy transfer occurred in the $LPL_{QR/EVA}$ film system, indicating aggregation formation of QRs in the EVA media. Aggregation of QRs can also be formed in the liquid media by adding a bad solvent for QRs. When a certain volume of ethanol (EtOH) was added into the QR/toluene solution, no significant excitation wavelength dependence in PLE spectra was confirmed. Using this approach, we fabricated various hybrid LPL films containing different aggregation states of QRs. In this presentation, we will discuss about the correlation between aggregation states of QRs and polarization

converting properties.

References

1. A. Montali, C. Bastiaansen, P. Smith and C. Weder, “Polarizing energy transfer in photoluminescent materials for display applications”, Nature, Vol. 392, 361–264, 1998.
2. P. T. K. Chin, R. A. M. Hikmet, S. C. J. Meskers and R. A. J. Janseen, “Energy Transfer and Polarized Emission in Cadmium Selenide Nanocrystal Solids with Mixed Dimensionality”, Advanced Functional Materials, Vol. 17, 3829–3835, 2007.
3. L. Carbone, C. Nobile, M. De Giorgi, F. Della Sala, G. Morello, P. Pompa, M. Hytch, E. Snoeck, A. Fiore, I. R. Franchini, M. Nadasan, A. F. Silvestre, L. Chiodo, S. Kudera, R. Cingolani, R. Krahne and L. Manna, “Synthesis and Micrometer-Scale Assembly of Colloidal CdSe/CdS Nanorods Prepared by a Seeded Growth Approach”, Nano Letters, Vol. 7, 2942–2950, 2007.
4. K. Kyhm, J.H. Kim, S.M. Kim and H.-S. Yang, “Gain dynamics and excitonic transition in CdSe colloidal quantum dots”, Optical Materials, Vol. 30, 158–160, 2007.
5. V. Babentsov and F. Sizov, “Defects in quantum dots of IIB-VI semiconductors”, Opto-Electronics Review, Vol. 16, 208–225, 2008.

Meta-Atoms Based on Self-Assembly of Gold Nanoparticle on Polymer Microspheres

H. Yabu[1*]

[1]Advanced Institute for Materials Research (WPI-AIMR), Tohoku University, Japan
[*]corresponding author: hiroshi.yabu.d5@tohoku.ac.jp

Abstract: Fabrication of gold nanoparticle decorated polymer microspheres and their applications as sensors and metamaterials will be shown.

Particles that accumulate noble metal nanoparticles on the surface of dielectric particles can become 'meta-atoms', the building blocks of metamaterials that utilize plasmon absorption with independent of incident angle of light. Efforts have been made to realize such meta-atoms by electroless plating of silver on the surface of dielectric particles like silica or polymer microspheres, or by adsorbing noble metal nanoparticles such as gold. However, challenges existed in controlling nanoparticle size, as well as their arrangement and density.

We have reported a method for fabricating polymer microspheres with nanostructures mixing various types of polymers, using the Self-ORganized Precipitation (SORP) method, which involves adding a poor solvent to a polymer solution and removing the good solvent by evaporation to obtain a dispersion of polymer microspheres. We have applied the method to fabricate metal nanoparticles-polymer composite particles for various applications (Figure 1). When polystyrene (PS) and amino-terminated polybutadiene (PB-NH2) were mixed and fabricated using the SORP method, core-shell type microspheres were obtained[1], with positively charged PS as the core and PB-NH2 as the shell[2]. Subsequently, by mixing a dispersion of uniformly sized gold nanoparticles, composite microspheres were obtained, where the gold nanoparticles were densely arranged on the surface due to electrostatic interactions.

The resulting composite microspheres have been demonstrated to be applicable as dispersed surface-enhanced Raman scattering (SERS) substrates[3] for analyzing adsorbed molecules, as meta-atoms in the visible to near-infrared region[4], and as probes for antigen-antibody reactions with high optical density[5].

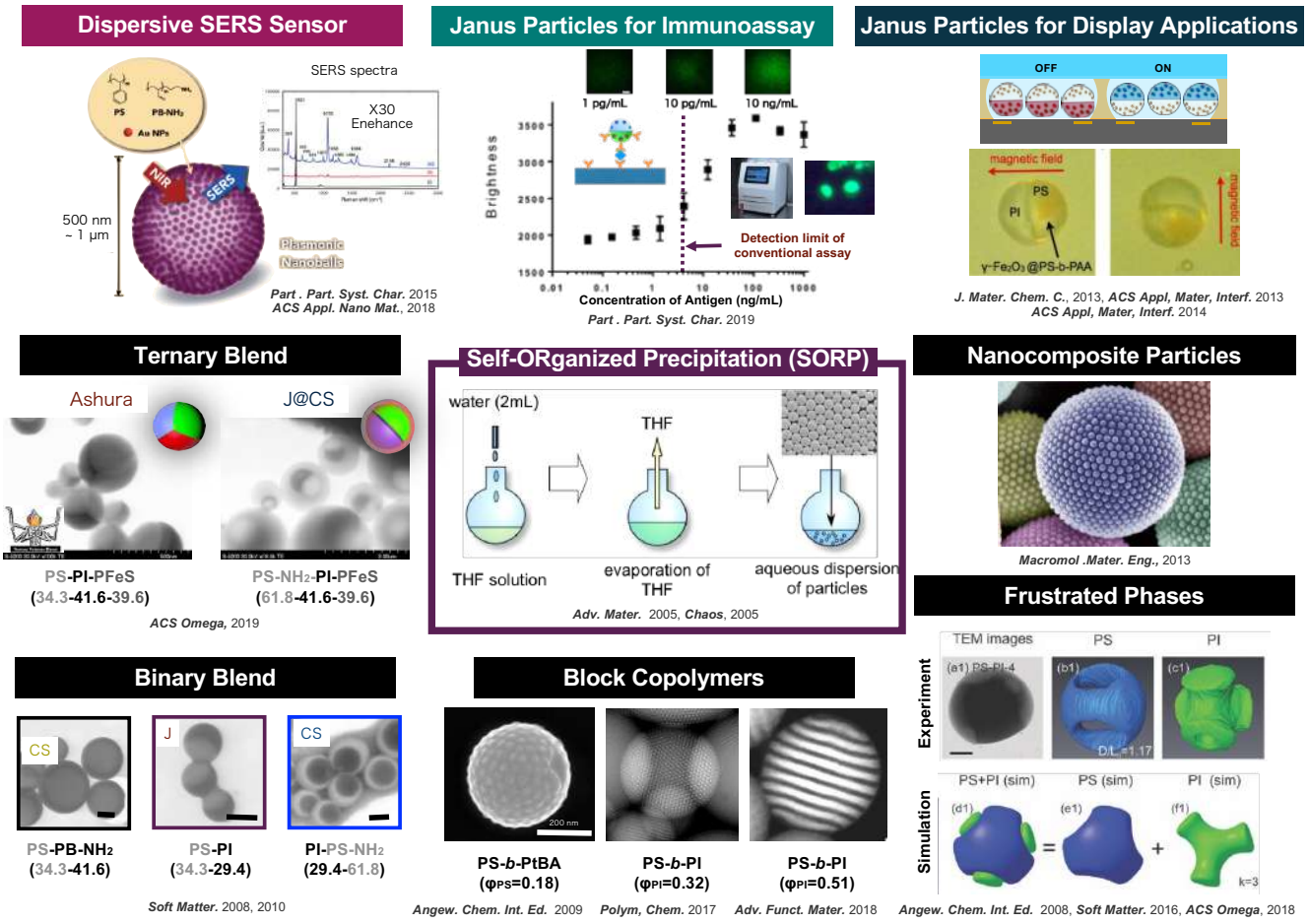


Figure 1. SORP method and their applications.

References

References

1 Hirai, Y.; Avalos, E.; Teramoto, T.; Nishiura, Y.; Yabu, H. Ashura Particles: Experimental and Theoretical Approaches for Creating Phase-Separated Structures of Ternary Blended Polymers in Three-Dimensionally Confined Spaces. *ACS Omega* **2019**, *4* (8), 13106–13113.

2 Kanahara, M.; Satoh, H.; Higuchi, T.; Takahara, A.; Jinnai, H.; Harano, K.; Okada, S.; Nakamura, E.; Matsuo, Y.; Yabu, H. Fabrication of NIR-Excitable SERS-Active Composite Particles Composed of Densely Packed Au Nanoparticles on Polymer Microparticles. *Part. Part. Syst. Charact.* **2015**, *32* (4), 441–447.

3 Hirai, Y.; Matsuo, Y.; Yabu, H. Near-Infrared-Excitable SERS Measurement Using Magneto-Responsive Metafluids for in Situ Molecular Analysis. *ACS Appl. Nano Mater.* **2018**, *1* (9), 4980–4987.

4 Deng, T. S.; Parker, J.; Hirai, Y.; Shepherd, N.; Yabu, H.; Scherer, N. F. Designing “Metamolecules” for Photonic Function: Reduced Backscattering. *Phys. Status Solidi Basic Res.* **2020**, *257* (12), 1–11.

5 Yabu, H.; Yokokura, S.; Shimizu, S. Gold Nanoparticle-Decorated Polymer Particles for High-Optical-Density Immunoassay Probes. *Langmuir* **2024**, web released.

Hot-electron dynamics and speciality optical fibres for quantum applications

Kristina R. Rusimova[1]
[1]Department of Physics, University of Bath, BA2 7AY, UK
Email - K.R.Rusimova@bath.ac.uk

I will discuss two experimental systems – the first uses a scanning tunnelling microscope (STM) to capture the ultrafast dynamics of hot electrons that are relevant to energy applications [1]; the second integrates atomic vapors within speciality optical fibres for quantum technologies [2].

1. STM induced hot-electron dynamics. Hot electrons are central to the operation of important electronic devices like transistors and solar cells. However, accessing and understanding their dynamics is challenging (with only a few experimental techniques capable of such a measurement so far) due to their ultrashort lifetimes (~100s of fs) and corresponding nanometre transport length scales. The tip of a scanning tunnelling microscope is a local tunable source of hot electrons and can be used to excite and manipulate matter right down to the single chemical bond limit. Recently, molecular nanoprobe experiments, where the target molecule is a few nanometres away from the STM tip, have come in the spotlight as viable tool for studying the dynamics of hot electrons in real space. In molecular nanoprobe experiments, charge injected from the STM tip is transported across the surface causing the apparent-simultaneous manipulation of hundreds of molecules with a single pulse of charge carriers. The manipulation process is in effect parallelised and completely decoupled from the STM tip.

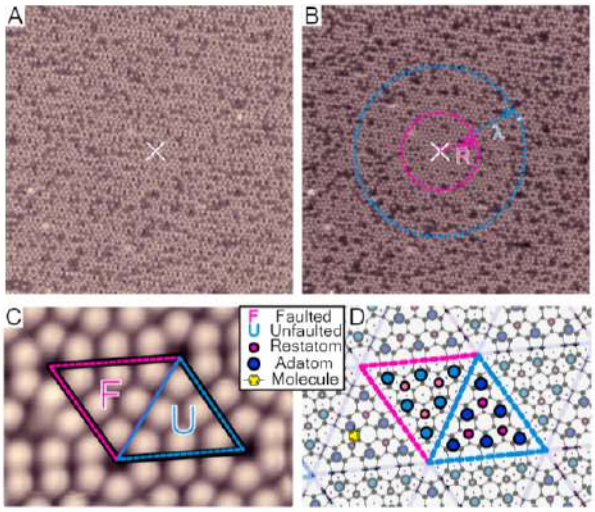


Figure 1 A,B Nonlocal manipulation of toluene molecules on Si(111)-7x7. C,D STM image and corresponding schematic of the Si(111)-7x7 surface reconstruction.

Here we quantitatively link the voltage dependence of the nonlocal manipulation probability to the integrated local density of surface states of the Si(111)–7×7 surface. Our results further corroborate the previously proposed ballistic-diffusive transport model.[3] We show that the measured increase in the probability of nonlocal manipulation with injection bias voltage is not due to an energy dependence of the molecular manipulation process. Instead, it is caused by an increase in the fraction of the tunnelling current that is captured by the surface state mediating nonlocal manipulation. This result is an important breakthrough in the understanding of hot electron dynamics and should allow us to tailor the energy band structures of catalytic systems.

2. Speciality optical fibres for quantum technologies. Alkali metal vapors enable access to single electron systems, suitable for demonstrating fundamental light-matter interactions and promising for quantum logic operations, storage and sensing. However, challenges remain in achieving low-loss, high bandwidth storage and multiplexing that is required for quantum schemes. Moreover, demonstrations of optical quantum memories and switches which address these challenges have been predominantly done with bulk optical components, which require free space alignment and result in high losses when integrated with optical fibres. One way of mitigating loss resulting from the coupling between free space and optical fibres is by integrating the atomic vapours directly inside the core of a hollow-core optical fibre. Here, we demonstrate a low-loss, fibre-integrated cell which once filled with an atomic vapour, can be used to realise an in-fibre quantum memory. We also discuss progress towards filling optical fibres with warm alkali vapours and ensuring high vapour density while at the same time preventing decoherence of the atomic states upon collisions with the walls of the fibres. One way of achieving this condition is

by using plasmonic nanoparticles to convert light into localized thermal energy and to achieve optical depths in warm vapors, corresponding to a ~16 times increase in vapor pressure in less than 20 ms, with possible reload times much shorter than an hour. Our results enable robust and compact light-matter devices, such as efficient quantum memories and photon-photon logic gates, in which strong optical nonlinearities are crucial.

Experimental measurement of nanoscale circular dichroism in plasmonic chiral structures using electron beams

M. Bézard[1], S. Garrigou[2*], Y. Auad[1], J. Béal[3], H. Lourenço-Martins[2*], D. Gérard[3*] and M. Kociak[1*]

[1]Université Paris-Saclay, CNRS, Laboratoire de Physique des Solides, 91405, Orsay, France
[2]CEMES-CNRS, Université de Toulouse, CNRS, Toulouse, France
[3]Light, nanomaterials and nanotechnologies (L2n), CNRS-ERL 7004, Université de Technologie de Troyes, Troyes, France
[*]corresponding authors: hugo.lourenco-martins@cnrs.fr, davy.gerard@utt.fr, mathieu.kociak@universite-paris-saclay.fr

Abstract: Measuring and understanding optical polarization at the nanometer scale is usually a complex problem. Here, we present recent nanometer-scale measurements using cathodoluminescence, demonstrating highly localized circular dichroism in canonical 3D plasmonic chiral objects. The relationship between local dichroism and global chirality is discussed.

Measuring and understanding unpolarized optical properties at the nanometer scale is now commonplace with various spectroscopy techniques. However, addressing optical polarization at this scale remains a much more challenging problem.

In this presentation, we will present recent results on nanometer-scale circular dichroism in canonical 3D chiral objects and their interpretation. More specifically, these results concern a series of nanoscale, circularly polarized cathodoluminescence (CL) experiments performed in a scanning transmission electron microscope on plasmonic Born-Kuhn systems (BKS, see Figure 1, left).

Using a novel detection scheme, we demonstrated a highly localized and strongly circularly dichroic signal (Figure 1, center), which can be reproduced by simulations (Figure 1, right). While this strong dichroic signal could have been naively interpreted as a signature of the well-known large chirality of BKS, a systematic experimental and simulation analysis as a function of the BKS geometrical parameters reveals a surprisingly small effect of this chirality in the emergence of strong local circular dichroism.

A theoretical analysis, ongoing at the time of writing, will be discussed during the presentation to explain this unexpected observation.

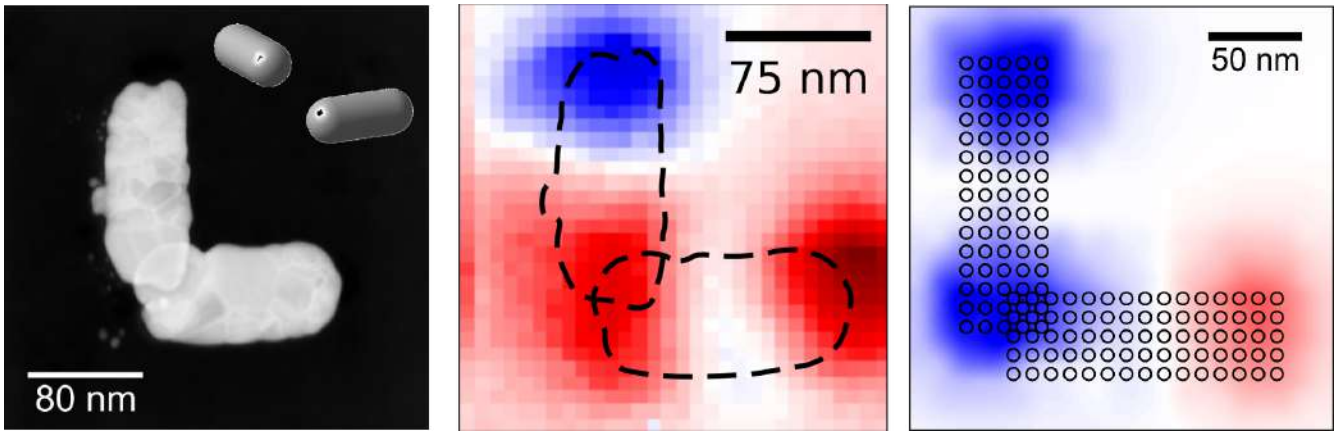


Figure 1: Circular dichroic measurement of a plasmonic BKS structure by spatially resolved cathodoluminescence in a STEM. Left: High angle annular dark field image of a BKS with a schematic of the BKS structure in the inset. Middle: Experimental and Right: simulated circular dichroic cathodoluminescence maps filtered at ~ 1.38 eV.

This project has been funded in part by the European Union through the Horizon 2020 Research and Innovation Program (Grant 101017720 (EBEAM)), the French National Agency for Research under the program of future investment TEMPOS- CHROMATEM (Reference ANR-10-EQPX-50) and QUENOT (ANR-20-CE30-0033).

Highly efficient and reversible chirality transfer between protein and achiral plasmonic assemblies

Ziwei Zhou[1]*, Ningwei Sun[1], Nina Tverdokhleb[1,2,3], Artur Movsesyan[4], Anja Maria Steiner[1], Patrick T. Probst[1], Vaibhav Gupta[1], Bo Yin[5], Nicolás Pazos-Peréz[6], Ramón A. Álvarez-Puebla[6,7], Mirjam Hofmaier[1], Martin Müller[1], Holger Merlitz[1], Olga Guskova[1,2], Yaroslava G. Yingling[8], Franziska Lissel[1,9], Tobias A. F. König[1,2], Zhiming Wang[4], Alexander O. Govorov[10], Nicholas A. Kotov[11,12,13]*, and Andreas Fery[1,14,15]*

[1]Leibniz-Institut für Polymerforschung Dresden e.V., Dresden, Germany.
[2]Technische Universität Dresden, Dresden Center for Computational Materials Science (DCMS), Dresden, Germany.
[3]Dresden Center for Computational Materials Science (DCMS), TU Dresden, Dresden, Germany.
[4]Institute of Fundamental and Frontier Sciences, University of Electronic Science and Technology of China, China.
[5]Ansys Inc., 2600 Ansys Dr. Canonsburg, PA 15317, USA.
[6] Department of Physical and Inorganic Chemistry Universitat Rovira i Virgili, Tarragona, Spain.
[7]ICREA, Passeig Lluís Companys 23, Barcelona, Spain.
[8]Department of Materials Science and Engineering, North Carolina State University, Raleigh, North Carolina 27695, USA.
[9]Faculty of Chemistry and Food Chemistry, Technische Universität Dresden, Dresden, Germany.
[10]Department of Physics and Astronomy, Ohio University, Athens, Ohio 45701, USA.
[11]Department of Chemical Engineering, University of Michigan, Ann Arbor, MI, USA.
[12]Biointerfaces Institute, University of Michigan, Ann Arbor, MI, USA.
[13]Department of Materials Science and Engineering, University of Michigan, Ann Arbor, MI, USA.
[14]Center for Advancing Electronics Dresden (cfaed), Technische Universität Dresden, Dresden, Germany.
[15]Department of Physical Chemistry of Polymeric Materials, Technische Universität Dresden, Dresden, Germany.

*corresponding author: zhou@ipfdd.de, kotov@umich.edu, fery@ipfdd.de

Abstract: Based on the assembly of Au@protein nanoparticles, we enhance and modulate plasmon-coupled circular dichroism (PCCD) by in-situ stretching of biomolecules between plasmonic nanoparticles, achieving a 1.18-degree circular dichroism and 0.2 dissymmetry factor. Unlike hotspot-based methods, our approach enables reversible PCCD switching over 100+ cycles with significant amplitude changes.

Traditional plasmon-coupled circular dichroism (PCCD) suffers from inherently weak signals due to the size mismatch between chiral molecules and achiral nanoparticles[1,2]. Consequently, researchers have long attempted to enhance PCCD via the creation of strong plasmonic hotspots; however, such approaches have yielded limited improvements, and PCCD intensity still remains far below that of structural circular dichroism (CD)[3-6]. In our work, we shift the focus from engineering plasmonic hotspots to investigating the conformation of chiral molecules. By applying a simple yet effective strategy—namely, the in-situ stretching of biomolecules anchored to plasmonic nanoparticles—we achieve a substantial enhancement of PCCD, with a circular dichroism of 1.18 degree and a dissymmetry factor of 0.2. This lever-effect not only amplifies the PCCD signal to levels comparable to structural CD but also introduces a reversible switching capability over more than 100 cycles. Our approach harnesses dynamic modulation of asymmetric electrostatic fields, enabling real-time tunable chiroptical activity through various stimuli such as pH, light, electric fields, and temperature.

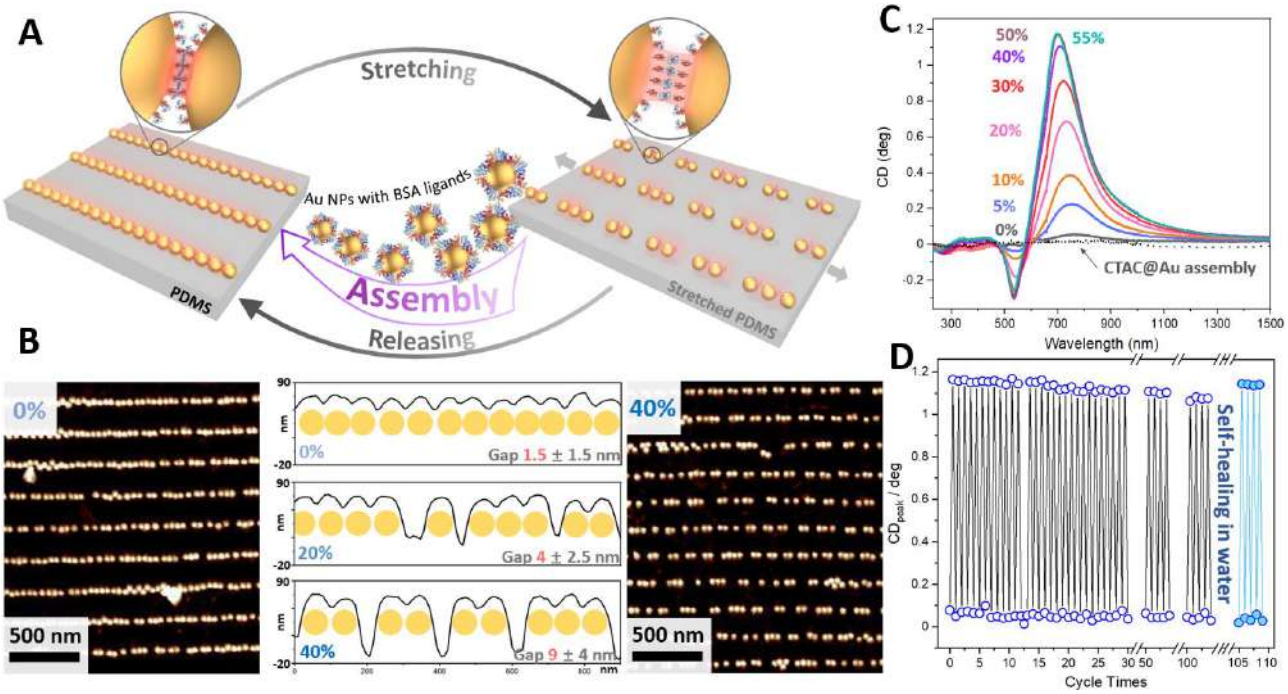


Figure 1. Novel 1D chiral assembly of Au nanoparticles coated with BSA protein, which can be stretched due to the elastic PDMS substrate (A). During stretching the distance between nanoparticles increased gradually (B), triggering sharply increased CD signals (C) together with super cyclic stability (D).

References

1 Govorov, A. O. Plasmon-Induced Circular Dichroism of a Chiral Molecule in the Vicinity of Metal Nanocrystals. Application to Various Geometries. *The Journal of Physical Chemistry C* **115**, 7914-7923, doi:10.1021/jp1121432 (2011).

2 Zhang, Q. *et al.* Unraveling the origin of chirality from plasmonic nanoparticle-protein complexes. *Science* **365**, 1475-1478, doi:10.1126/science.aax5415 (2019).

3 Kneer, L. M. *et al.* Circular Dichroism of Chiral Molecules in DNA-Assembled Plasmonic Hotspots. *ACS Nano* **12**, 9110-9115, doi:10.1021/acsnano.8b03146 (2018).

4 Hao, C. *et al.* Chirality on Hierarchical Self-Assembly of Au@AuAg Yolk-Shell Nanorods into Core-Satellite Superstructures for Biosensing in Human Cells. *Advanced Functional Materials* **28**, doi:10.1002/adfm.201802372 (2018).

5 Cao, Z. *et al.* Chirality Transfer from Sub-Nanometer Biochemical Molecules to Sub-Micrometer Plasmonic Metastructures: Physiochemical Mechanisms, Biosensing, and Bioimaging Opportunities. *Adv Mater* **32**, e1907151, doi:10.1002/adma.201907151 (2020).

6 Lan, X. *et al.* DNA-Enabled Chiral Gold Nanoparticle-Chromophore Hybrid Structure with Resonant Plasmon-Exciton Coupling Gives Unusual and Strong Circular Dichroism. *J Am Chem Soc* **141**, 19336-19341, doi:10.1021/jacs.9b08797 (2019).

Surface Plasmon Enhanced Photocatalysis

D. Ma[1]

[1]Institut national de la recherche scientifique (INRS), Canada

[*]corresponding author: dongling.ma@inrs.ca

Abstract: Plasmonic nanostructures can enhance photon harvesting of semiconductor materials via hot carrier injection, near-field effects and/or enhanced scattering, which has significant implications for the realization of cost-effective high-performance solar utilization technologies. In this talk, I will overview some of our recent progress on the development of plasmonic nanostructures for photocatalysis.

With unique surface plasmon resonance properties and high potential for many important applications, plasmonic nanostructures are attracting more and more attention in the past decades. In addition to consistent research interest in realizing precise control over their structure (such as size, shape, aspect ratio and uniformity), plasmon enhanced photocatalysis represent a highly promising and important research area. In this context, I will present some of our development in plasmonic nanostructures, such as Cu nanoparticles, CuS nanocrytstals and Ag nanoparticles as well as their contributions to solar fuel production and photocatalytic degradation of pollutants [1-4].

One example is about Ag nanoparticle (NP)-enhanced metal-organic matrix (MOM) with interface-engineering for efficient photocatalytic hydrogen evolution. We developed a facile one-step approach to construct a hybrid structure of in situ synthesized plasmonic AgNPs and Ag-porphyrin MOM, denoted as Ag–AgMOMs. The in-situ growth strategy enables the AgNPs and AgMOM to share the Ag atoms at the interface, which appears essential for an intimate interface between the two compounds (Fig. 1a). A“clean” metal-MOM interface with few surfactants is demonstrated by surface-enhanced Raman spectroscopy (SERS) and related control experiments. The lack of surfactants (polyvinylpyrrolidone, PVP) at the inner NP/MOM interface allows the ef cient interfacial charge transfer, while PVP on the outer surface of Ag–AgMOMs imparts the excellent dispersibility and stability of the latter in aqueous solution. Electron energy loss spectroscopy (EELS) spectra and mapping offer the observation of the plasmonic effect of AgNPs on the AgMOM. The plasmonic AgNPs signicantly enhance the photocatalytic hydrogen evolution of the AgMOM, reaching high values of 1025 and 3153 μmol h−1 g−1 under visible-light and full-spectrum light irradiation, respectively. These values are comparable with those of the state-of-the-art metal-organic-based photocatalytic systems. The underlying charge transfer from the plasmonic AgNPs to AgMOM, exciton- plasmon coupling and associated dynamics under light irradiation are further revealed by in-situ X-ray photoelectron spectroscopy (XPS) and ultrafast transient absorption (TA) spectroscopy. This work may guide the design of plasmonic nanoparticles coupled with organic semiconductors for effective electronic and energy communication.

In another case, we achieved efficient hot hole collection via interfacing plasmonic CuS nanoplatelets with a suitable p-type semiconductor for the first time [2]. The approach we applied was to rationally select a semiconductor (herein, BiOCl) such that it has a suitable band structure to prevent the hole loss from CuS in the dark, while allowing the hot hole injection from the plasmon-excited CuS under illumination. The resultant, efficient hot hole injection was then verified by our systematic measurements along with theoretical modelling. We showed that the transversal mode dominates the hot hole generation and has a greater contribution to photocatalysis than the longitudinal mode. We then elaborated on an optimal CuS/BiOCl composite configuration allowing for efficient hot hole collection in near-infrared photocatalysis. This work demonstrates

the feasibility of harvesting hot holes from plasmonic semiconductors and opens a new route for the rational design of broadband and cost-effective plasmonic photo catalysts.

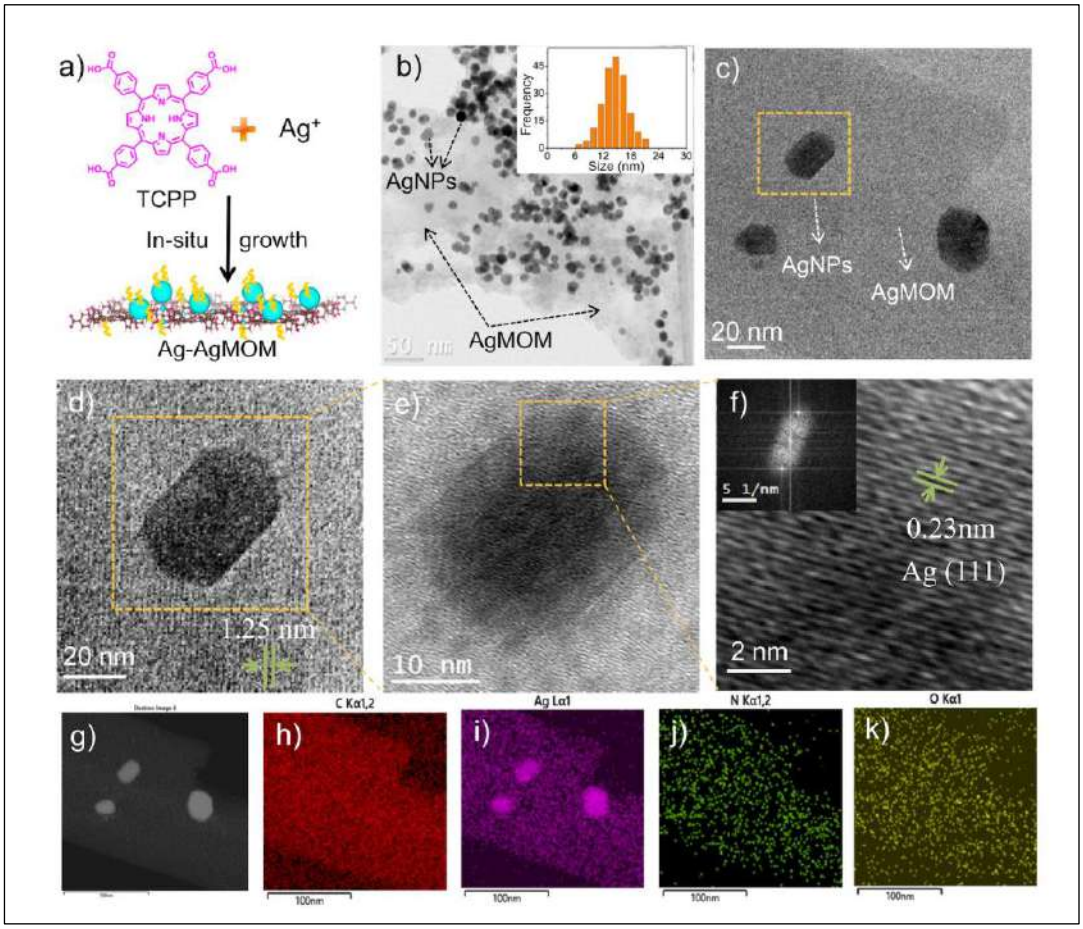


Figure 1. Morphology characterizations of Ag–AgMOM. **a** Schematic diagram of the one-step synthesis of Ag–AgMOM using in-situ solvothermal method. **b** Typical low magnified TEM image of Ag–AgMOM with reaction time 28 h. Inset is the statistical size distribution of Ag nanoparticles (AgNPs). **c, d** Enlarged TEM images of Ag–AgMOM; the lattice of AgMOM was observed. **e, f** HR-TEM images and crystal lattice of a single Ag nanoparticle (AgNP) on AgMOM in (d) (inset is the FFT image of the AgNP). **g** High-angle annular dark- eld (HAADF) image of Ag–AgMOM. h–k Mapping of carbon (C), silver (Ag), nitrogen (N) and oxygen (O) elements in Ag–AgMOM, respectively.

Acknowledgements: The author would like to acknowledge financial support from the Natural Sciences and Engineering Research Council of Canada, Fonds de la recherche sur la nature et les technologies and CQMF. The author sincerely thanks all co-authors shown below for their contributions

References

[1] Y. Liu, C. Liu, T, Debnath, Y. Wang, D. Pohl, L. V. Besteiro, D. M. Meira, S. Huang, F. Yang, B. Rellinghaus, M. Chaker, D. F. Perepichka and D. Ma, "Silver nanoparticle enhanced metal-organic matrix with interface-engineering for efficient photocatalytic hydrogen evolution," *Nat. Commun.*, 2023, 14:541.

[2] Q. Zhang, A. Mirzaei, Y. Wang, G. Song, C. Wang, L. V. Besteiro, A. O. Govorov, M. Chaker and D. Ma, "Extracting hot holes from plasmonic semiconductors for photocatalysis," *Apply. Catal. B: Environ.* 2022, 317: 121792.

[3] Z. Xu, M. Quintanilla, F. Vetrone, A. O. Govorov, M. Chaker and D. Ma, "Harvesting lost photons: plasmon and upconversion enhanced broadband photocatalytic activity in core@shell microspheres based on lanthanide-doped $NaYF_4$, TiO_2 and Au," *Adv. Funct. Mater*. 25: 2950–2960, 2015 (Front Cover).

[4] W. He, C. Chen, Y. Liu, A. Tomasino, S. S. M. Masouleh, J. Valdez, T. Guner, R. Morandotti, A. Moores, G. A.Botton, Y. Zhou, A. Yurtsever and D. Ma, "Imaging photon-induced near-field distributions of a plasmonic, self-assembled vesicle by a laser-integrated electron microscope," *Nano Lett.*, 2023, 23, 5842.

Sensing 3D Electromagnetic Landscapes with Enhanced Quantum Light-Matter Interaction at the Single-Molecule and Nanometer Resolution

R. M. Córdova-Castro[1,2]
[1] Institut Langevin, ESPCI Paris, Université PSL, CNRS, France.
[2] Department of Physics, University of Ottawa, Canada
[*]corresponding author: rcordova@uottawa.ca

Abstract: We apply single molecule super-resolved measurements to observe the fine details of quantum light-matter interaction at the nanoscale, simultaneously mapping the position of the emitters and its spontaneous emission decay rate modified by the enhanced density of photonic states in unique engineered material platforms.

Understanding how to control the spontaneous emission of light, which determines how likely, how quickly, and where an excited emitter will release a photon, is a necessary part for exploiting the quantum behavior of light for new or advancing existing quantum technologies. The rate at which an emitter can convert its excited-state energy into a photon increases as more photon states are available to radiate into, which is quantified by the local density of states (LDOS) and the Purcell factor. The efficiency with which a single quantum emitter can generate photons in a prescribed optical mode depends on a number of factors: efficiency of excitation (absorption cross-section of the system), the quantum yield of emitted fluorescence and overall collection efficiency. Coupling single emitters to nanostructures that support very small mode volumes can enhance and control the interaction. By acceleration of the spontaneous emission process diminishing the probability of other vibrational transitions, the number of photons per second can significantly increase achieving a bright single photon source with a well-defined two-level system transition decay rate, yielding quantum light behavior at room temperature. When light illuminates a nanostructure, the electromagnetic field is concentrated extremely close to the nanoparticle by resonant optical modes. Quantum emitter's spontaneous emission will dramatically depend on its position near these modes. This makes the single-photon emission rate a precise measure of location, far more accurate than the optical resolution from the same photon. We present three system with engineered LDOS enhancement; GaP nanodimers, 3D hollow plasmonic nanocones and hyperbolic nanorod metamaterial, the engineered materials can drastically modify the photon emission rate of single molecules observed at the nanometer scale. We compared numerical calculations of Purcell factors with the detected enhancements, finding accuracy in the variation of the nanoposition along the 3D fields inside the material. These properties make it an exceptionally sensitive platform for molecular sensing applications and variations of small vectorial fields detections.

Far-Field Single-Molecule Super Localization Microscopy (SMLM) allows the detection of single- emitter position and emission rate modification without disrupting the local environment with metallic probes. The single-photon emission lifetime is measured by a single-photon avalanche diode connected to a time correlating single photon counter (TCSPC) with picoseconds resolution, and correlated with SMLM to image the Purcell factor enhancement below the diffraction limit. Single-molecule nanophotonics is an emerging sub-field with many possibilities to explore new phenomena at the super resolution level of light-matter interaction. Opening up solutions for applications in technologies limited by the resolution, the efficiency of emission of single

photons, the detection of small changes of small fields, the sensing for early diagnostics for low density detections, and many more.

We show that molecular quantum emitters hold promise to play a key role in sensing at the super-resolution level with nanoscale resolution when interaction with nanostructures that supports a high local density of photonic states, with ultra-high enhancement of the spontaneous emission lifetime till picoseconds with extremely position dependence at the nanoscale level. While bringing the possibility of controlling fast single-photons sources on demand at room temperature, the extreme variation of decay rate with the position and dipolar moment, enabled by the metamaterials, creates substantial nanoscale variations in the density of photonic states throughout the structure. These properties provide an exceptionally sensitive platform for applications in molecular sensing and detection of small vectorial fields variations, suggesting potential applications in developing quantum nanophononics technologies.

References

1. Córdova-Castro, R. M., van Dam, B., Lauri, A., Maier, S. A., Sapienza, R., De Wilde, Y., Izeddin, I., Krachmalnicoff, V.. "Single- emitter super resolved imaging of radiative decay rate enhancement in dielectric gap nanoantennas", *Light: Science & Applications*, 13, 2024.

2. Jonker, D., Jafari, Z., Winczewski, J., Eyovge, C., Berenschot, J. W., Tas N. R., Gardeniers J. G. E., De Leon, I., and Susarrey-Arce, A., "A wafer-scale fabrication method for three dimensional plasmonic hollow nanopillars," Nanoscale Adv., 3, 2021.

Reconfigurable Integrated Photonics for Next-Generation Optical Computing and Quantum Technologies

A. Karabchevsky

Ben-Gurion University of the Negev, Beer-Sheva, IL
Lancaster University, Lancaster, UK
a.karabchevsky@lancaster.ac.uk
alinak@bgu.ac.il

Abstract:
The rapid advancement of nanophotonics and integrated optics is driving the transition toward reconfigurable and adaptive photonic systems capable of operating at the speed of light [1-2]. My talk will overview recent breakthroughs in reconfigurable integrated photonics, focusing on the development of dynamically tunable optical components that enable ultra-fast signal processing, optical memory storage, and quantum photonic applications[3-6]. I will introduce novel material platforms with high optical nonlinearity and phase-change properties, facilitating real-time reconfigurability in compact photonic circuits. Special emphasis will be placed on the integration of photochromic materials, metasurfaces, and Fabry-Pérot resonators to achieve adaptive optical functionality. Additionally, the role of AI-driven optimization for self-learning photonic systems will be discussed, paving the way for autonomous, high-performance optical computing and secure quantum communications. These advancements hold significant promise for applications in next-generation telecommunication networks, quantum information processing, and energy-efficient data centers [1].

References:
[1] Karabchevsky, A, Choudhary, A, On-Chip Photonics: Principles, Technology and Applications, Elsevier, (2024).
[2] Karabchevsky, A., Ultra-broadband spectrometer on a chip of picometer scale resolution, *Nature Light: Science & Applications*, 12, (2023).
[3] Karabchevsky, A., Perovskite beyond solar: toward novel developments of lasers and detectors for photonic circuits, Nature Light: Science & Applications, 12, (2023)
[4] Hazan, A.,..,Gogotsi, Y., Karabchevsky, A., MXene Nanoflakes Enabled All-Optical Nonlinear Activation Function for On-Chip Photonic Deep Neural Networks, *Advanced Materials*, 35(11), 2210216, (2023).
[5] Sun, …, Karabchevsky, A. and Booth, M. J., On-chip beam rotators, adiabatic mode converters, and waveplates through low-loss waveguides with variable cross-sections. *Nature Light: Science & Applications*, 11(1), 1-15, (2022).
[6] Karabchevsky, A, Katiyi, A., Ang, A. S., Hazan, A. On-chip nanophotonics and future challenges. Nanophotonics, Invited Review, 9(12), 3733-3753, *Invited Review* (2020)

Colloidal Quantum Optoelectronics

H. V. Demir

NTU Singapore – Nanyang Technological University, School of Electrical and Electronic Engineering, School of Physical and Mathematical Sciences, School of Materials Science and Engineering, Singapore

Bilkent University UNAM, Department of Electrical and Electronics Engineering, Department of Physics, Institute of Materials Science and Nanotechnology, Ankara, Turkey

hvdemir@ntu.edu.sg, volkan@bilkent.edu.tr

Colloidal semiconductor nanocrystals enable enriched color conversion essential to superior lighting and displays. These colloids span different types and heterostructures of semiconductors from colloidal quantum dots to wells. In this talk, we will focus on atomically flat, tightly confined, quasi-2-dimensional quantum wells for use in lighting and displays [1-14].

Also, we will present a powerful, large-area, orientation-controlled self-assembly technique for orienting these quantum wells either all face down or all edge up and demonstrate three-dimensional constructs of their oriented self-assemblies with monolayer precision [8,9].

Among their extraordinary features important to applications in lighting and displays, we will show record high efficiency from their colloidal LEDs [10,11] and record high gain coefficients and record low lasing thresholds from their colloidal laser media [1,12,13] using a variety of their heterostructures [2-6,10] and/or oriented assemblies [8,9,11]. We will finally discuss our recent work for the use of colloidal quantum wells intimately integrated into metasurfaces to make a new class of colloidal meta-devices [14].

References

[1] B. Guzelturk et al., Nano Letters 19, 277 (2019)
[2] Y. Altıntas et al., ACS Nano 13, 10662 (2019)
[3] N. Taghipour et al., Nature Communications 11, 3305 (2020)
[4] F. Shabani et al., Small 18, 2106115 (2022)
[5] X. Liang et al., ACS Nano 17, 19981 (2023)
[6] S. Delikanli et al., JACS 145, 12033 (2023)
[7] Y. Junhong, et al., Nature Communications 16, 823 (2025)
[8] O. Erdem et al., Nano Letters 19, 4297 (2019)
[9] O. Erdem et al., Nano Letters 20, 6459 (2020)
[10] B. Liu et al., Advanced Materials 32, 1905824 (2020)
[11] H. D. Baruj et al., Small 19, 2206582 (2023)
[12] J. Maskoun et al., Advanced Materials 33, 2007131 (2021)
[13] F. Isik et al., Small 20, 2309494 (2024)
[14] S. T. Ha et al., Science 386, eadm7442 (2024)

From hairy particles to particle-based metamaterials

Andreas Fery

Institut für Polymerforschung Dresden e.V. and Technical University Dresden, Germany

Metallic nanoparticles offer a number of interesting optical and electronic effects. A prominent example is the localized surface plasmon resonance (LSPR), which is due to resonance excitations of the particle's free electron cloud vibrations by light. Consequently plasmonic nanoparticles provide excellent opportunities for controlling electromagnetic near-fields at optical frequencies, which has led to a wide range of applications in various fields such as surface-enhanced spectroscopy, light harvesting, or photonics.

While much of the research has been devoted to understanding nanoparticle synthesis and tailoring their LSPR at the single-particle level, novel perspectives arise from combining plasmonic nanoparticles with a functional polymeric shell which does not only allow controlling inter-particle distances but as well tailor transport / electronic couping. [1,2,3]

Increasing the level of complexity, the ordering of particles at different length scales opens another powerful routes to optical and electronic functionality due to novel collective plasmonic excitations arising from plasmonic coupling effects. We focus on achieving such ordered particle arrays through self-assembly approaches. Colloidal self-assembly can indeed yield well-defined colloidal clusters and surface arrays [4] in which coupling effects can be controlled. In particular, large-scale assemblies are possible in combination with biomimetic surface patterning like controlled wrinkling. We discuss the underlying physicochemical principles of the structure formation process and the resulting plasmonic coupling effects including chiroplasmonic metamaterial effects [5, 6]. Finally, we present perspectives on how these assembly principles can be relevant for developing circular economy approaches for advanced materials.

1. Rossner, C.; König, T. A. F.; Fery, A., Hairy Plasmonic Nanoparticles. In Hairy Nanoparticles: From Synthesis to Applications, 1 ed.; Lin, Z.; Liu, Y., Eds. WILEY-VCH GmbH: Weinheim, 2023; pp 351-374.2.

2. Sun, N.; Singh, S.; Zhang, H.; Hermes, I.; Zhou, Z., .; Schlicke, H.; Vaynzof, Y.; Lissel*, F.; Fery, A., Gold Nanoparticles with N-Heterocyclic Carbene/Triphenylamine Surface Ligands: Stable and Electrochromically Active Hybrid Materials with Potential for Optoelectronics Cells. Advanced Science 2024, 11 (2400752), 1-8.

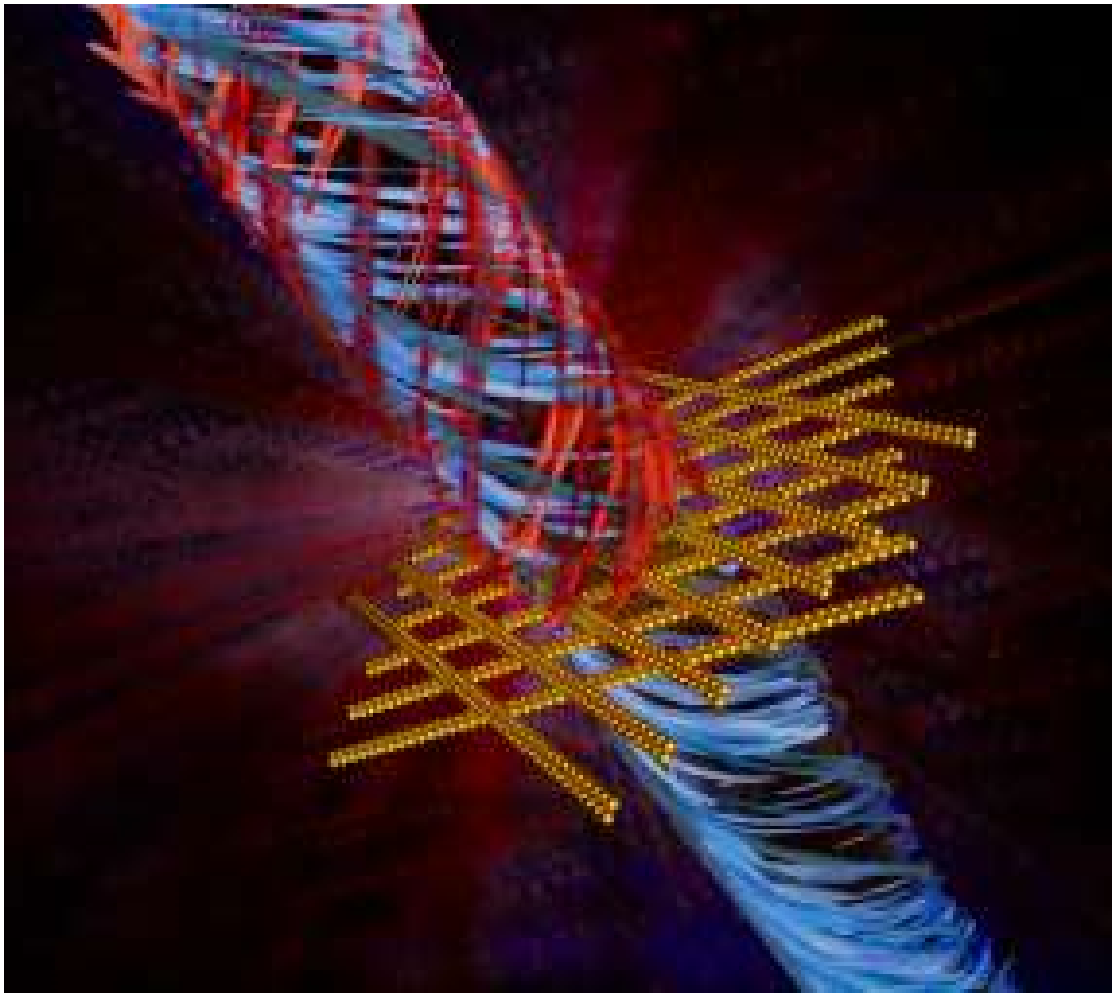
3. Jones, A.; Searles, E. K.; Mayer, M.; Hoffmann, M.; Gross, N.; Oh, H.; Fery, A.; Link, S.; Landes, C. F., Active Control of Energy Transfer in Plasmonic Nanorod−Polyaniline Hybrids. J. Phys. Chem. Lett. 2023, 14, 8235−8243.

4. Rossner, C.; Koenig, T. A. F.; Fery, A., Plasmonic properties of colloidal assemblies. Advanced Optical Materials 2021, 2001869 (https://doi.org/10.1002/adom.202001869).

5. Probst, P. T.; Mayer, M.; Gupta, V.; Steiner, A. M.; Zhou, Z.; Auernhammer, G. K.; König, T. A. F.;

Fery, A., Mechano-tunable chiral metasurfaces via colloidal assembly. Nature Materials 2021, 20, 1024–1028.
6. Probst, P. T.; Dong, Y.; Zhou, Z.; Aftenieva, O.; Fery, A., Bottom-Up Assembly of Inorganic Particle-Based Chiroptical Materials. Advanced Optical Materials 2024, 12 (5), 2301834.

Figure:



Schematic of a giant circular dichroitic metamaterial, adopted from [5]

Hyperdoped silicon nanocrystals embedded in a silica matrix for infrared plasmonics

Clavel Berclis Kengne[1], Xavier Devaux[1], Mathieu Stoffel[1],
Michel Vergnat[1] and Hervé Rinnert[1,*]

[1]Université de Lorraine, CNRS, Institut Jean Lamour, F-54000 Nancy, France
*Corresponding author: herve.rinnert@univ-lorraine.fr

Due to their potential use in a wide range of applications such as nanophotonics, light harvesting, sensing, photothermal therapies, nanocrystals (NCs) exhibiting localized surface plasmon resonance (LSPR) have induced a strong research activity. Highly doped semiconductors NCs have recently gained a significant attention in particular for sensing because the LSPR frequency is expected to be tuned by controlling the free carrier concentration and to be redshifted as compared to metals. Indeed, in metal nanoparticles such as Au or Ag, the high charge carrier concentration leads to resonance frequencies for LSPR in the visible spectrum. As the resonance frequency strongly depends on the dielectric constant of the environment, targeted molecules can be sensed by measuring the spectral shift of the plasmon resonance. Another sensing approach consists of coupling the molecular vibrational mode, characterized by a low cross section, with the near field around plasmonic nanoparticles. A high vibrational signal enhancement is expected if the overlap between LSPR and molecular vibrations is strong. With metals, micrometer sized particles or even more complex structures are usually required to reach an optical resonance in the near-infrared or mid-infrared range. To overcome the limitation of plasmonic metal nanoparticles, highly doped semiconductors NCs are interesting alternative plasmonic particles.

As a low cost, non-toxic and CMOS compatible material, silicon has emerged as a promising material for plasmonic application. The existence of LSPR in semiconductor nanostructures especially in silicon nanocrystals (Si-NC) embedded in silica as well as the role of dopant concentration on the plasmon resonance have been demonstrated [1,2,3]. In our group, phosphorus-doped Si-NCs were obtained by thermal evaporation of phosphorus-doped SiO/SiO_2 multilayers in ultrahigh vacuum. As-deposited multilayers were amorphous. Samples were then post-growth-annealed in a rapid thermal annealing furnace at 1100 °C for 15 minutes under a constant nitrogen flow. As a result, the SiO layers is destabilized leading to the formation of Si-NCs embedded in a silica matrix, as shown in Figure 1. The multilayer architecture hence enables accurate tuning of the Si-NCs size, controlled by the SiO thickness. The SiO_2 layer thickness was kept around 12 nm and that of SiO can be varied from 3 nm to around 20 nm. Phosphorus atoms were incorporated in both SiO and SiO_2 layers by a heated GaP decomposition source held at 800 °C during the whole deposition for all samples. The fixed GaP cell temperature allows us to keep a constant phosphorus content in the multilayers as well as in the Si-NCs regardless of their size. The nanocrystal size and the dopants localization were studied at the nanoscale by scanning transmission electron microscopy.

Here, the size dependence of the LSPR is investigated for a P content in the layer close 1 at.% and for a NC diameter varying from 7 to 16 nm. The LSPR is located at around 5 µm (2000 cm^{-1}). Infrared absorption spectroscopy revealed that both the energy of the resonance and the mobility of the charge carriers are increasing functions of Si-NCs size. The plasmonic response is modeled in the framework of the Mie theory, using the Drude model to describe the dielectric function of Si and a size-dependent scattering of free carriers at the NC/SiO_2 interface [4]. The temperature dependence of the plasmonic response, from 10 to 350 K, is in good

agreement with the metal-like behavior of the heavily doped nanocrystals and the carrier transport can be modeled taking into account electron-lattice and electron-defects interactions.

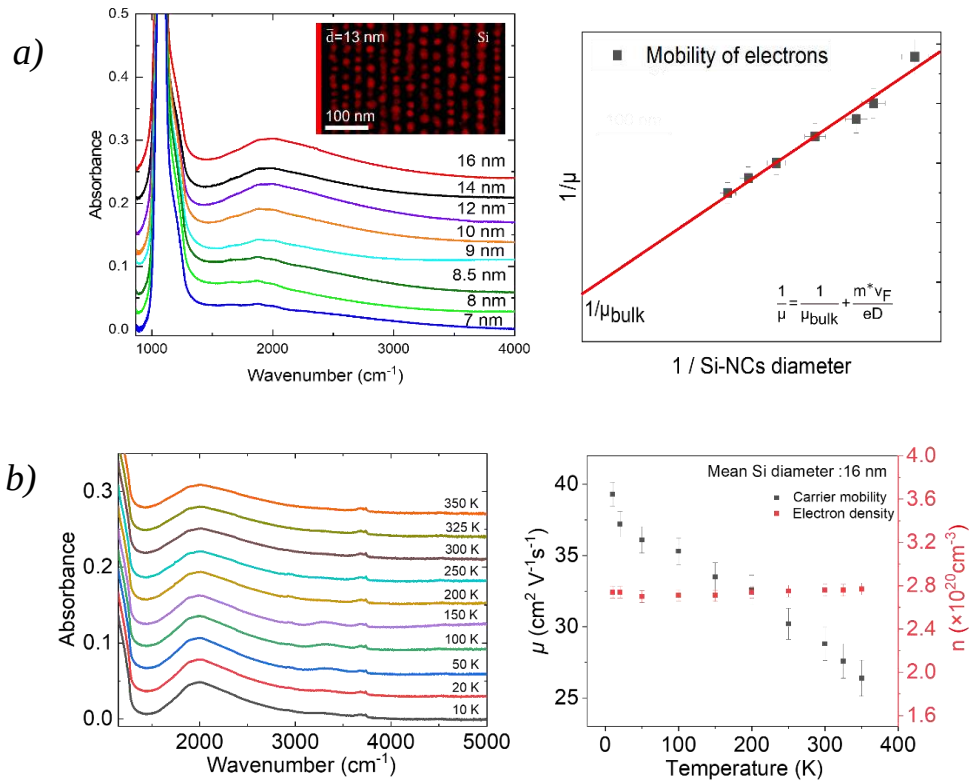


Figure 1: a) Size dependence of the LSPR of P-doped Si-NCs (left) and of the carrier mobility (right); b) Temperature dependence of the LSPR response (left) and of the mobility and free carrier density (right) for Si-NCs with a diameter equal to16 nm.

[1] Phosphorus doped Si nanocrystals exhibiting mid-infrared localized surface plasmon resonance, D. J. Rowe, J. S. Jeong, K. A. Mkhoyan, and U. R. Kortshagen, Nano Lett. 13, 1317-1322, 2013.

[2] Infrared nanoplasmonic properties of hyperdoped embedded Si nanocrystals in the few electrons regime, M. Zhang, J. M. Poumirol, N. Chery, C. Majorel, R. Demoulin, E. Talbot, H. Rinnert, C. Girard, F. Cristiano, P. R. Wiecha, T. Hungria, V. Paillard, A. Arbouet, B. Pécassou, F. Gourbilleau and C. Bonafos, Nanophotonics 11, 3487-3493, 2022.

[3] Heavily Doped Si Nanocrystals Formed in P-(SiO/SiO2) Multilayers: A Promising Route for Si-Based Infrared Plasmonics, A. Valdenaire, A. E. Giba, M. Stoffel, X. Devaux, L. Foussat, J.-M. Poumirol, C. Bonafos, S. Guehairia, R. Demoulin, E. Talbot, M. Vergnat, and H. Rinnert, ACS Appl. Nano Mater. 6, 3312-3320, 2023.

[4] Size Dependence of Plasmonic Response in Phosphorus-Doped Si Nanocrystals: Implication for Infrared Plasmonics, C. B. Kengne, X. Devaux, M. Stoffel, M. Vergnat and H. Rinnert, ACS Appl. Nano Mater. 7, 28612-28618, 2024.

Controlled Self-Assembly of Polymer-Grafted Nanoparticles Toward Hyperuniform Materials

Kyoungweon Park,[1,2] Derek Huang, [1,2] Kenya Hazell, [1,2] Anesia Auguste, [1] Andrew Gillman, [1] Rich Vaia[1], Larry Drummy[1]

[1] Materials & Manufacturing Directorate, Air Force Research Laboratory, Wright-Patterson Air Force Base, Ohio 45433-7750
[2] Bluehalo, Dayton Ohio, 45432

Hyperuniform materials combine local disorder with long-range uniformity, enabling control over wave propagation. Here we developed a synthetic protocol for highly concentrated, monodispersed gold nanoparticles (AuNPs) with tunable size and shape. Using bimodal size distributions, we fabricated thin films of polymer-grafted AuNP assemblies, achieving macroscale packing and statistically verified hyperuniformity.

The interplay of order and disorder across length scales has long fascinated materials scientists. Recently, hyperuniform materials—exotic disordered systems that exhibit local randomness alongside globally suppressed density fluctuations—have garnered significant interest. In two-phase materials, hyperuniformity combines the short-range disorder of amorphous systems with the long-range uniformity of crystals. In nanocomposites, particle packing is a critical parameter for tuning material properties, and hyperuniform packings enable precise control of electromagnetic and mechanical wave propagation.

Polymer-grafted nanoparticles (PGNs) represent a novel class of materials that are compatible with polymer additive manufacturing techniques and offer diverse functionality through their tunable nanoparticle (NP) cores—ranging from plasmonic and semiconducting to magnetic NPs. PGNs offer a level of structural control beyond traditional composites, with tunability stemming from core size/shape and polymer grafting parameters such as density and molecular weight.

Gold nanoparticles (AuNPs) are particularly attractive NP cores due to their tunable size, versatile surface chemistry, and strong interactions with optical fields. Despite advances in synthesis, producing highly monodisperse AuNPs larger than 10 nm in high yield remains a challenge. Here, we present a robust, scalable synthesis of concentrated, monodisperse AuNPs with tunable diameters from 10 to 50 nm via optimized seed-mediated growth and strategic regrowth techniques.

Using these AuNPs, we fabricated PGN assemblies with bimodal core size distributions, demonstrating macroscale packing and confirming large-area hyperuniformity through statistical analysis. Furthermore, we show that the degree of hyperuniformity correlates with the composite's mechanical properties, as measured by Brillouin light scattering.

These concepts offer a pathway to multifunctional materials capable of manipulating propagating energy—such as light, sound, and heat—and are expected to guide the design of next-generation structural and component-level materials.

A Platform for Single-Crystal Nanomaterials and Metasurfaces with Application in Nanophotonics, Sensing and Energy Harvesting

S. V.-Grayli[1], A. Adserias[2], F. MacNab[2] and G. W. Leach[2*]

[1]Institute for Quantum Computing, University of Waterloo, Canada
[2]Department of Chemistry, Simon Fraser University, Canada
[*]corresponding author: gleach@sfu.ca

Abstract: We describe a versatile platform for single-crystal (SC) plasmonic nanomaterials and metasurfaces. Au(100) metasurfaces provide tailored fields that produce large surface enhanced Raman scattering yields for sensing. Metasurfaces of single-crystal split ring resonators provide flat optics for polarization manipulation, and hybrid SC plasmonic alloys provide improved electrocatalysts for energy harvesting.

Material quality plays a critical role in the performance of nanometer-scale plasmonic structures and represents a significant hurdle to large-scale device integration. Progress has been hindered by the challenges of realizing scalable, high quality, metal deposition strategies, and by poor pattern transfer and device fabrication yields characteristic of most metal deposition approaches, which yield polycrystalline metal structure. Here we highlight a novel, scalable and versatile platform to deposit ultrasmooth, single-crystal (SC) gold films ideal for subtractive patterning of nanostructures through ion beam milling, and high definition, sub-wavelength SC nanostructures through lithographic patterning methods to yield SC metasurfaces.[1,2]

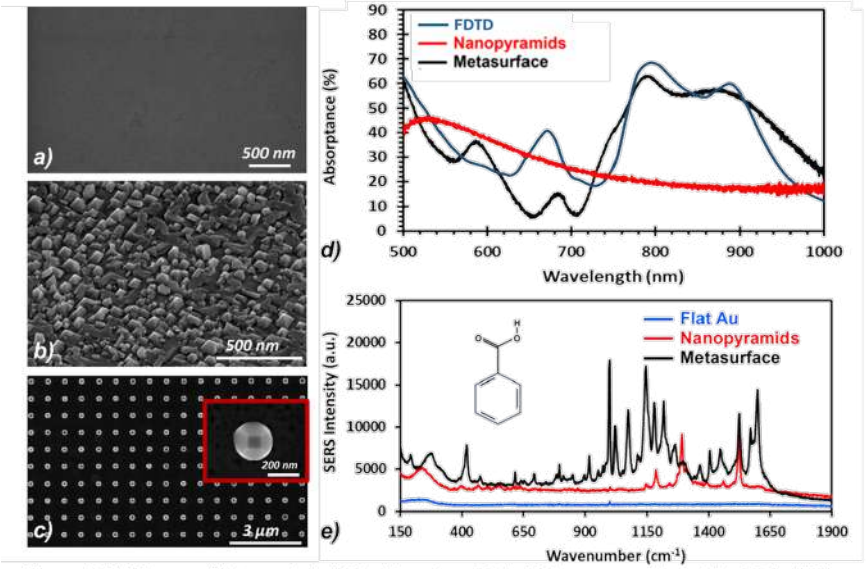


Figure 1. SEM images of (a) smooth Au(100), (b) random SC Au(100) nanopyramids and (c) SC-Au(100) metasurface. (d) Experimental absorptance spectrum of random nanopyramids (red), SC Au(100) metasurface (blue) and FDTD spectrum (black) of the BA-covered metasurface. (e) SERS spectra of BA-coated surfaces (a)-(c); flat gold (blue), random nanopyramids (red) and SC Au(100) metasurface (black).

SC Au(100) metasurfaces comprised of square pyramidal nanostructures with dominant Au(111) facets have been fabricated to tailor the local plasmonic fields to provide resonant enhancement of the surface enhanced Raman scattering (SERS) spectra. Finite Difference Time Domain (FDTD) simulations guide the design of the metasurfaces through nanostructure size and periodicity to provide local field enhancement resonant with the 785 nm laser employed for SERS measurements. This resonant enhancement provides significantly larger SERS response from Raman marker molecules such as benzoic acid (BA), compared to the SERS response from BA-covered SC gold surfaces comprised of SC square pyramids of random disposition.[3]

Metasurfaces comprised of SC gold split ring resonators (SC-SRRs) provide an example of the fabrication of more complex nanostructures and of the high-fidelity pattern transfer that can be achieved. Large area arrays of

SC-SRRs provide a path toward scalable, reflective “flat optics” (Figure 2). The structures are variants of more traditional SRRs and have been designed to impart broadband polarization control. The diffracted reflection of incident white light shows 2-D structure with each diffraction order comprised of different spectral components having similar polarization characteristics.

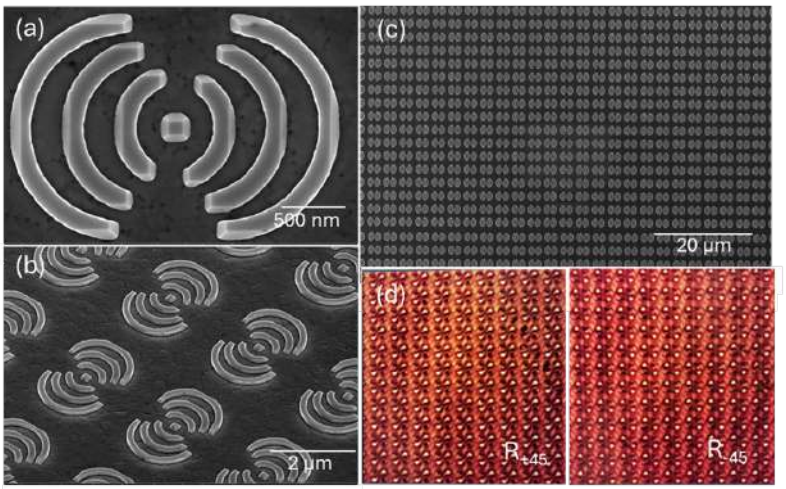


Figure 2. (a) top-view SEM of an individual SC-SRR, (b) angle-view SEM of several SC-SRRs, (c) large area-view SEM of the SC Au(100) SC-SRR metasurface array, (d) polarized reflectivity images of 800 nm light from the SC-SRR metasurface.

The polarization characteristics of the SC-SRR metasurface have been analyzed through control of both the linear incident polarization and the polarized output. Our results indicate that the metasurface imparts circular polarization to the diffracted output, providing broadband polarization control.

Current strategies for renewable energy harvesting necessitate the storage of intermittent electricity sources and typically employ batteries, or the production of “solar fuels” such as hydrogen, as a means of intermediate energy storage. We have investigated the use of plasmonic surfaces and nanostructures to improve the electrocatalytic production of hydrogen and other small hydrocarbons through the deposition of new SC plasmonic alloy materials of controlled composition. When deposited in smooth single-crystal form, the electrocatalytic production of solar fuels can be characterized as a function of alloy composition to define improved electrocatalysts with common electroactive surface areas (ECSAs). Here we describe the fabrication of SC alloy catalysts for the hydrogen evolution reaction (HER) and for the electrocatalytic CO_2 reduction reaction (CO2RR) in alkaline environments. We show that Pt:Ag and Pt:Au HER electrocatalysts provide lower overpotentials and activation barriers than the benchmark Pt. Likewise, the formation of new SC Au:Cu alloys help to define electrocatalyst compositions that provide small hydrocarbon product selectivity. We also describe our recent efforts to control surface texture to form high surface area nanostructures of controlled composition to generate improved electrocatalysts with high activity and photocatalytic response.

We acknowledge the financial support from the Natural Sciences and Engineering Research Council of Canada, the Canada Foundation for Innovation, the British Columbia Knowledge Development Fund, and CMC Microsystems.

References

1. V. Grayli, S., Zhang, X., MacNab, F. C., Kamal, S., Star, D. and Leach, G. W.*, “Scalable, Green Fabrication of Single-Crystal Noble Metal Films and Nanostructures for Low-Loss Nanotechnology Applications,” ACS Nano. **14,** 7581–7592, 2020.
2. V. Grayli, S., Kamal. S. and Leach, G. W.*, “High performance, single crystal gold bowtie nanoantennas fabricated via epitaxial electroless deposition,” Scientific Reports, **13,** 12745, 2023.
3. V. Grayli, S., Zhang, X., Star, D. and Leach, G. W.*, “Tailoring Plasmonic Fields with Shape-Controlled Single-Crystal Gold Metasurfaces,” ACS Appl. Mat. and Interfaces, **16**, 35410−35420, 2024.

Photopolymerized Molecularly Imprinted Polymers for Plasmonic Sensing Platforms

A. Khitous, C. Molinaro, O. Soppera

[1]Université de Haute Alsace, CNRS, IS2M UMR 7361, F-68100 Mulhouse, France
[2] Université de Strasbourg, France
*corresponding author: olivier.soppera@uha.fr

Abstract: We present plasmonic sensors functionalized with photopolymerized molecularly imprinted polymers (MIPs) for selective detection of small molecules and enantiomers. Controlled MIP growth on metallic substrates preserves plasmonic properties and enables highly selective recognition in SPR and SERS configurations. Applications include pollutants, pharmaceuticals, and chiral analytes.

Molecularly Imprinted Polymers (MIPs) are synthetic recognition materials with tailor-made selectivity toward specific analytes (also called « plastic antibodies »), including small molecules, biomarkers, and even enantiomers. Coupling MIPs with plasmonic nanostructures opens promising avenues for enhancing the selectivity, sensitivity, and stability of surface-based detection techniques such as Surface Plasmon Resonance (SPR) and Surface-Enhanced Raman Scattering (SERS).

In this work, we present the use of photopolymerization to fabricate and pattern MIP layers directly on metallic surfaces or nanostructures. Light-assisted processes allow precise spatial control over the polymer growth, enabling nanoscale patterning and conformal coating of complex plasmonic architectures. These strategies are compatible with various SPR configurations, including Kretschmann geometry and optical fiber-based sensors.

The resulting hybrid systems combine the molecular selectivity of MIPs with the near-field enhancement of plasmonic substrates. We demonstrate their performance for the selective detection of pollutants (such as PFAS), pharmaceutical residues, and chiral compounds, including enantiomer-specific recognition. Spatial localization of polymerization is shown to correlate with plasmonic field distribution, supporting the use of these hybrid structures for high-performance, miniaturized sensing platforms..

References

1. Khitous, A.; Lartigue, L.; Moreau, J.; Soppera, O. Insights into Photopolymerization at the Nanoscale Using Surface Plasmon Resonance Imaging. *SMALL* **2024**. DOI: 10.1002/smll.202401885.
2. Khitous, A.; Molinaro, C.; Abdallah, S.; Chen, M. Y.; Marguet, S.; Laurent, G.; Vidal, L.; Malval, J. P.; Fiorini-Debuisschert, C.; Adam, P. M.; et al. Spatial Distribution of the Photopolymerization Induced by Localized Surface Plasmons: Impact of the Morphology of the Au Nanoparticles. *J Phys Chem C* **2024**, *128* (31), 13097-13107. DOI: 10.1021/acs.jpcc.4c03148
3. Khitous, A.; Molinaro, C.; Gree, S.; Haupt, K.; Soppera, O. Plasmon-Induced Photopolymerization of Molecularly Imprinted Polymers for Nanosensor Applications. *Advanced Materials Interfaces* **2023**, *10* (7), 2201651, https://doi.org/10.1002/admi.202201651. DOI: https://doi.org/10.1002/admi.202201651.
4. Arcadio, F.; Noël, L.; Del Prete, D.; Maniglio, D.; Seggio, M.; Soppera, O.; Cennamo, N.; Bossi, A. M.; Zeni, L. Soft molecularly imprinted nanoparticles with simultaneous lossy mode and surface plasmon multi-resonances for

femtomolar sensing of serum transferrin protein. *SCIENTIFIC REPORTS* **2023**, *13* (1). DOI: 10.1038/s41598-023-38262-y.

5. Khitous, A.; Molinaro, C.; Thomas, C.; Haupt, K.; Soppera, O. Synthesis and Integration of Hybrid Metal Nanoparticles Covered with a Molecularly Imprinted Polymer Nanolayer by Photopolymerization. In *Sensors*, 2023; Vol. 23.

Finite Element Analysis of Light Scattering in Resonant Multi-Dielectric Coverslips for Enhanced Total Internal Reflection Fluorescence Microscopy

Y. Toumi[1], R. Gurram[1,2], F. Lemarchand[1], A. Moreau, C. Favard[2], J. Lumeau[1], G. Demesy[1,*] and A. L. Lereu[1,*]

[1]Aix Marseille Univ, CNRS, Centrale Med, Institut Fresnel, Marseille, France

[2] Institut de Recherche en Infectiologie de Montpellier, CNRS, Univ of Montpellier France

[*]Corresponding authors: guillaume.demesy@fresnel.fr, aude.lereu@fresnel.fr

Abstract: We investigate the optimization and implementation of resonant dielectric multilayers (DM) coverslips to enhance total internal reflection fluorescence microscopy contrast. These DM can support surface waves resulting in amplifying the local excitation field, directly acting on fluorescence enhancement. However, scattering from substrate roughness can degrade performances that will be discussed.

Total Internal Reflection Fluorescence (TIRF) microscopy is a powerful imaging technique that enables selective excitation of fluorophores in a thin region near the interface between a coverslip and a biological sample. This is achieved using evanescent waves generated under conditions of total internal reflection. However, TIRF microscopy suffers from several limitations, such as uneven illumination due to beam divergence and a trade-off between excitation angle and evanescent field intensity, which can reduce image quality. Enhancing the local excitation field without compromising angular tolerance is thus critical for improving image contrast and sensitivity.

Dielectric multilayer (DM) thin films, when properly engineered, provide an effective approach to enhance the evanescent field at the sample interface. These multilayers can be designed to create optical resonances at specific wavelengths and incident angles [1-4], thereby increasing field confinement without requiring alterations to standard TIRF microscope optics. Such stacks can also provide spectral and angular tunability, crucial for achieving optimal fluorescence enhancement. We demonstrated up to a 4-fold fluorescence signal enhancement using such resonant stacks compared to a standard glass coverslip [5-6]. However, discrepancies between numerical predictions and experimental measurements prompted a deeper investigation and especially into light scattering effects that become significant under resonant conditions [2-3].

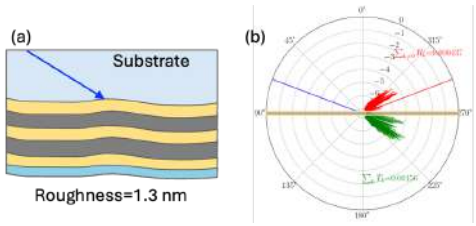


Figure 1: (a) Schematic of the multilayer structure with alternating high/low materials layers with roughness (b) Calculated radiation pattern showing scattering response caused by surface roughness under resonance conditions.

To understand the mismatch between simulations and experimental results, we investigated light scattering due to surface roughness, which becomes more significant under resonance. Rough surfaces in multilayer stacks act like diffraction gratings, modifying both field distribution and angular emission patterns (see Figure 1). We used atomic force microscopy to measure the substrate and free surface roughness's of the fabricated samples and incorporated these features into a Finite Element Method (FEM) model [7]. The roughness, often inherited across layers from the

substrate, was assumed to be periodic, allowing for a computationally efficient truncated simulation domain. By FEM, we calculated the diffraction efficiencies and angles of each diffracted order under resonant excitation. These results revealed additional scattering channels and angular redistribution of the emission, which main explain the higher background noise observed in experiments.

Resonant multi-dielectric coverslips represent a viable route to enhance the sensitivity of TIRF microscopy through tailored field enhancement. However, practical implementation requires careful balance between field amplification and scattering enhancement. Our combined experimental and FEM-based numerical approach shows that scattering from surface roughness is influencing the system's optical response, especially under resonant conditions. By incorporating realistic surface features into the simulations, we achieved a better match with experimental observations, paving the way for more accurate design and interpretation of enhanced TIRF systems for biological studies, particularly pathogen dynamics at cell membranes.

The authors acknowledge the CNRS for financial supports through the 80|PRIME2019 interdisciplinary program and the French research agency through the ANR NIS.

References

1. Ndiaye, C. et al, "Optimal design for 100% absorption and maximum field enhancement in thin-film multilayers at resonances under total reflection," Appl. Opt. 50(9), C382, 2011.
2. Lereu, A. L. et al, "Multi-dielectric stacks as a platform for giant optical field," Proc. SPIE 9162, 916219, 2014.
3. Lereu, A. L. et al, "Scattering losses in multidielectric structures designed for giant optical field enhancement," Appl. Opt. 53(4), A412, 2014.
4. Zerrad, M. et al, "Bandwidths limitations of giant optical field enhancements in dielectric multi-layers," Opt.Exp. 25, 14883, 2017.
5. Mouttou, A. et al, "Resonant dielectric multilayer with controlled absorption for enhanced total internal reflection fluorescence microscopy", Opt. Exp. 30, 15365, 2022.
6. Mouttou, A. et al, "Optimization of resonant dielectric multilayer for enhanced fluorescence imaging," Optical Materials: X, 17:100223, 2023.
7. Demesy, G. et al, "The finite element method as applied to the diffraction by an anisotropic grating," Opt. Exp. 15, 18089, 2007.

Metasurfaces by Two-Photon Polymerization Gray Scale Lithography

'Dewa Ade-Onojobi,[1,2] Kiernan E. Arledge, [1,2] Xitlali G. Juarez,[3] Nazli Rasouli,[2,4] Chase T. Ellis,[3] Joseph G. Tischler[1,2]*

[1]Department of Physics, University of Oklahoma, Norman, USA[2]Author Affiliation, Country
[2]Center for Quantum Research and Technology, University of Oklahoma, Norman, USA
[3]U.S. Naval Research Laboratory, DC, USA
[4]Electrical and Computer Engineering, University of Oklahoma, Norman, USA
*corresponding author: tischler@ou.edu

Abstract: Traditionally, nanostructuring is accomplished through etching of films and substrates using standard photolithography or electron beam lithography (EBL) which limit these structures to flat two-dimensions or fixed height. To overcome these challenges, we developed fabrication of gray scale masks using two-photon polymerization using a Photonic Professional GT2 Nanoscribe 3D printer.

Dielectric nanostructures are used in photonic applications, such as sensing, wavefront manipulation, light detection, and quantum computing. Traditionally, two-dimensional structures are fabricated by patterning and etching a dielectric substrate using standard photolithography or electron beam lithography (EBL) methods. While these well-established methods are powerful, limitations such as their mask requirement, resolution limit, and limitations to create beyond two-dimensional patterns hinders their use. To overcome these challenges, we explore fabrication of gray scale masks using two-photon polymerization using a Photonic Professional GT2 Nanoscribe 3D printer. We combine this digital laser writing (DLW) technology, and reactive ion etching (RIE). Using this maskless laser-writing technique, the Nanoscribe is capable of writing 2.5-dimensional polymer structures which are etched to the substrate to create metasurfaces of different shape, several lateral sizes, and varied heights. This fabrication technique enables the production of one dimensional and two dimensional periodic and aperiodic gratings. The quality of these structures is explored optically through infrared reflectivity using a Fourier Transform infrared (FTIR) spectrometer equipped with an infrared microscope as well as Raman scattering mapping. Our results are compared to COMSOL models of the achieved nanostructures.

To demonstrate the power of this fabrication technique, we cover several examples of the structures fabricated as well as the novel physics of these 2.5D nanophotonic structures. In particular, we present the first observation of traveling surface phonon polariton modes on a nanostructured surface of an isotropic ionic crystal (i.e., SiC). This achievement represents a development towards utilizing SPhPs in novel nanophotonic devices such as metatronics , waveguides and nanoscale optoelectronic devices. Surface phonon polaritons (SPhPs) are a low-loss alternative to surface plasmon polaritons with the potential for mid-infrared to terahertz nanophotonic devices. One requirement for the development of nanophotonic circuitry is the transport of information (i.e., polaritons) from one circuit component to the next. Traveling surface phonon polaritons in isotropic media presents a potential mechanism to achieve the desired interconnects. While localized surface phonon polaritons have been widely implemented, no traveling surface phonon polaritons in nanostructured isotropic ionic crystals have been demonstrated or explored up to date. In this study, we experimentally and theoretically demonstrate traveling surface phonon polaritons in one-dimensional grating. Furthermore, Raman mapping, when compared with phonon distribution based on selection rules, provided additional evidence for the presence of both traveling and localized modes. We provide mechanisms to control the group velocity, propagation length, and confinement of the traveling modes by engineering the geometric parameters of the gratings. Our results show that the group velocity can be slowed down at least to 4% speed of light in the vacuum, while achieving propagation lengths higher than 150 μm and confinement below 2μm.

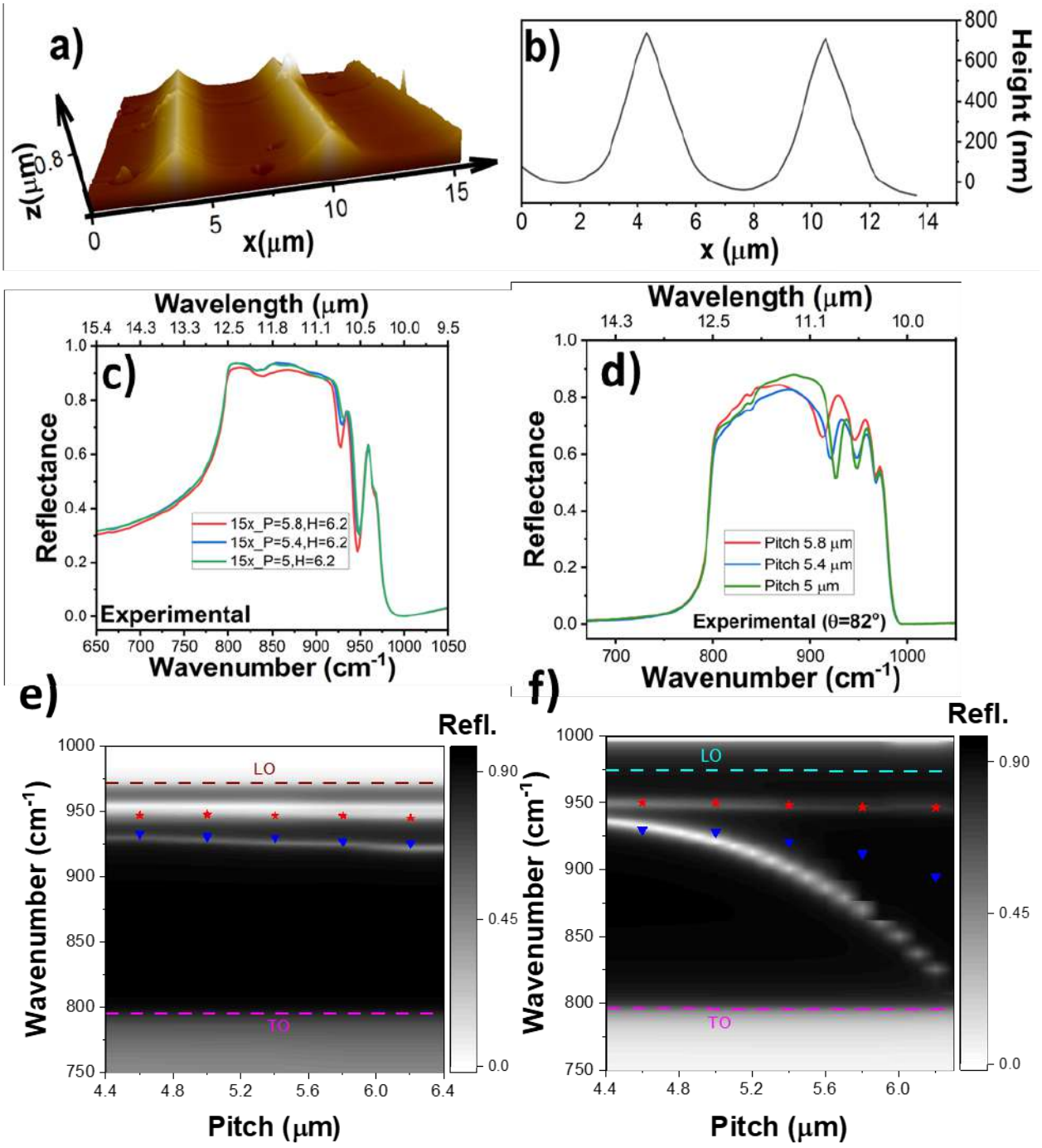


Figure 1(a) AFM image of a 1D grating made of 4H SiC, displaying the surface morphology of the sample. (b) Cross-sectional view of the surface grating. (c-d) Experimental reflection spectrum with p-polarized light at (c) a 15° angle of incidence and (d) a 75° angle of incidence, for a fixed height (0.8 μm), demonstrating resonance position shifts with varying pitches for the lower energy mode. (e-f) Simulated reflection spectra for varying pitches with a fixed height of 0.8 μm at (e) 15° and (f) 75° angles of incidence. Experimental traveling and localized modes are marked by triangular and star symbols, respectively. Dotted lines illustrate the LO and TO modes, depicting the Reststrahlen band.

Hybrid Self-Assembled Plasmonic Metasurfaces for Applications in Photonics

T. Tamulevičius[1,2,3,*], K. Midveris[1], G. Klyvis[1], T. Klinavičius[1], A. Tamulevičienė[1,3], M. Juodėnas[1], D. Peckus[1,2], J. Henzie[4], S. Tamulevičius[1,2]

[1]Institute of Materials Science, Kaunas University of Technology, Kaunas 51423, Lithuania
[2]Physics Department, Kaunas University of Technology, Kaunas 51368, Lithuania
[3]UAB Nanoversa, Kaunas 51423, Lithuania
[4]International Center for Materials Nanoarchitectonics, National Institute for Materials Science, Tsukuba 305-0044, Japan
[*]corresponding author: tomas.tamulevicius@ktu.lt

Abstract: Chemically synthesized monodisperse plasmonic nanoparticle colloids self-assembled into soft lithography replicated elastomer templates and transferred onto desired surfaces serve as macroscopic scale metasurfaces. Regular noble metal nanoparticle arrays in organic dyes or semiconductor layers couple the scattered localized plasmon light into high-Q surface lattice resonances serving in nanolasing and photocatalysis.

Precise average size, high monodispersity, shape control, and reproducibility of wet-chemically synthesized plasmonic nanoparticles (NPs) [1-2] enable their applications for photonic devices which are originally made employing top-down methods [3-4]. Template-defined nanoparticle self-assembly from concentrated nanoparticle colloids is an established method for the manipulation and deposition of NPs into lithography-defined positions originating desired photonic coupling and controlled local field enhancements [3-6]. Regular sub-wavelength spaced noble metal NP arrays can diffractively couple the scattered light from broad localized surface plasmons (LSPs) into narrow and high-Q resonances termed plasmonic lattices or surface lattice resonances (SLRs) [3-7]. The wavelength taylorability of SLR positions rises from the size-dependent LSPR coupling with the pitch-determined Rayleigh's anomaly [3-7]. The laterally confined light can act as an optical resonator for a dye nanolaser [7], can confine the electromagnetic radiation for desired wavelength Raman enhancement [5,6], and can contribute to efficient solar water splitting by metasurface photoelectrodes [8]. Electron beam lithography defined master replication with soft lithography into Polydimethylsiloxane elastomer deposition templates act as plasmonic metasurface for direct application or as a transfer carrier for integration into more complex photonic structures. Regular plasmonic hybrid structures in wide band gap semiconductor layers serve as efficient hot carrier injectors while NP arrays in organic days sustain resonance modes amplifying the stimulated emission.

The work was supported by the European Economic Recovery and Resilience Plan "New Generation Lithuania" and the budget of the Republic of Lithuania, Project No. 02-002-P-0001.

References

1. Khinevich N., *et al.* "Size and Crystallinity Effect on the Ultrafast Optical Response of Chemically Synthesized Silver Nanoparticles" J. Materiomics, Vol. 10, 3, 594-6002023, 2024.
2. Klinavičius T. *et al.* "Deep Learning Methods for Colloidal Silver Nanoparticle Concentration and Size Distribution Determination from UV–Vis Extinction Spectra" J. Phys. Chem. C Vol. 128, 23, 9662–9675, 2024.
3. Juodėnas M., *et al.* "Surface Lattice Resonances in Self-Assembled Arrays of Monodisperse Ag Cuboctahedra," ACS Nano, Vol., 13, No. 8, 9038–9047, 2019.

4. Juodėnas M., *et al.* “Effect of Ag Nanocube Optomechanical Modes on Plasmonic Surface Lattice Resonances,” ACS Photonics, Vol. 7, No. 11, 3130–3140, 2020.
5. Khinevich N., *et al.* “Wavelength-tailored Enhancement of Raman Scattering on a Resonant Plasmonic Lattice,” Sens. Actuator B-Chem., Vol. 394, 134418, 2023.
6. W. Andrzejewska, *et al.* “Towards ultrasensitive biosensors based on virus-like particles and plasmonic surface lattice resonance,” Biosensors and Bioelectronics, Vol. 274, 117143, 2025
7. M. Juodėnas, *et al.* “Lasing in an assembled array of silver nanocubes,” Nanoscale Horiz., Vol. 10, 142-149, 2025
8. Hüttenhofer L., *et al.* “Metasurface Photoelectrodes for Enhanced Solar Fuel Generation,” Adv. Energy Mater., Vol. 11, No. 46, 2102877, 2021.

Environmental permittivity-asymmetric BIC metasurfaces with electrical reconfigurability

Haiyang Hu[1,4], Wenzheng Lu[1,4], Alexander Antonov[1], Rodrigo Berté[1], Stefan A Maier[2,3], and Andreas Tittl[1*]

[1]Chair in Hybrid Nanosystems, Nanoinstitute Munich, Faculty of Physics, Ludwig-Maximilians-Universität München, Königinstraße 10, 80539 München, Germany.

[2]School of Physics and Astronomy, Monash University Clayton Campus, Melbourne, Victoria 3800, Australia.

[3]The Blackett Laboratory, Department of Physics, Imperial College London, London SW7 2AZ, United Kingdom.

[4]These authors contributed equally

[*]corresponding author: Andreas.Tittl@physik.uni-muenchen.de

Abstract: In nanophotonics, we introduce permittivity-driven quasi-BICs (ε-qBICs), achieved by embedding identical resonators in a refractive index-contrasting medium. Integrating electro-optic polyaniline enables electrically reconfigurable ε-qBICs with rapid switching and durability, advancing tunable metasurfaces for on-chip optics, sensing, and adaptive photonic applications without modifying resonator geometry.

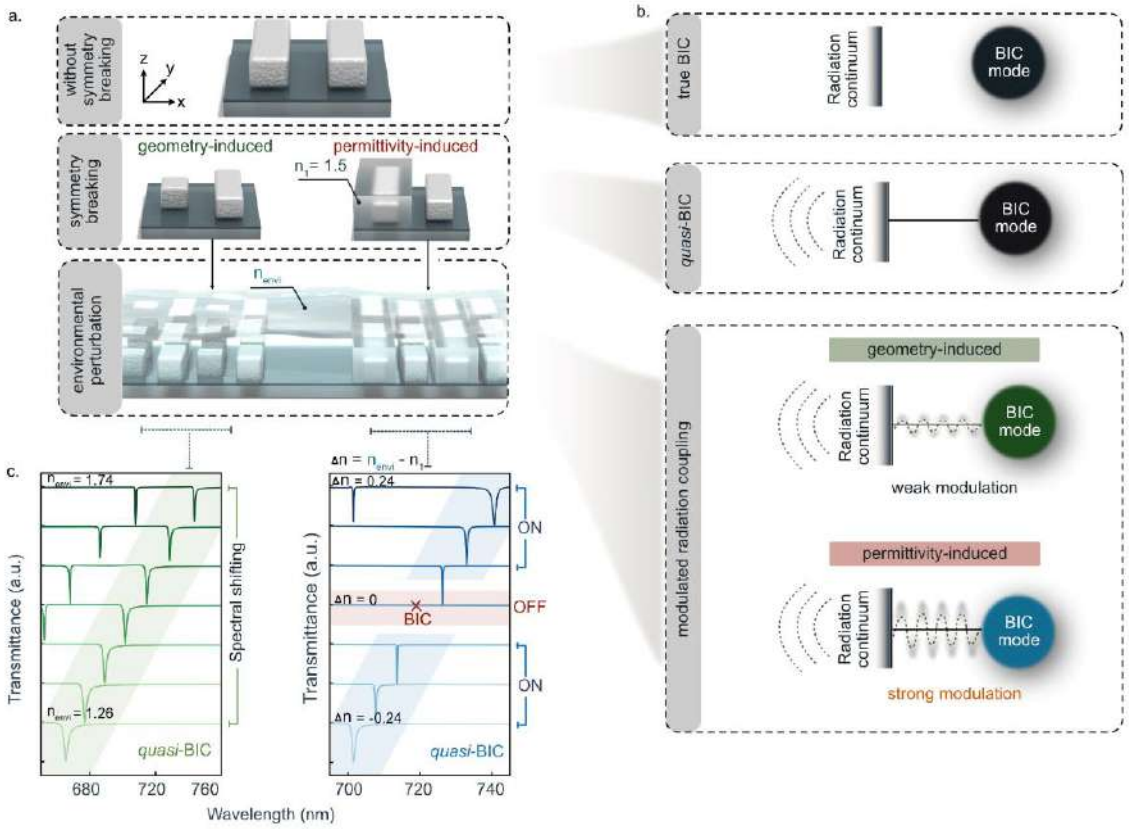


Figure 1. Modulation of radiation coupling in permittivity-asymmetric quasi-BIC metasurfaces under environmental perturbation. (a) Illustration of transition from symmetry-protected BICs to *q*BICs via

geometry- and permittivity-based symmetry breaking. (b) Schematic illustration of the BIC coupling mechanism. (c) Simulated transmittance spectra reveal that the geometry-induced *q*BICs only present spectral shifts when environmental RI changes, while permittivity-induced *q*BICs respond dynamically and present a transition between the 'ON' and 'OFF' states. Adapted from Ref. [1]

Photonic bound states in the continuum (BICs) have emerged as a powerful means of controlling light [2], their common reliance on geometrical symmetry breaking for obtaining tailored resonances makes them highly susceptible to fabrication imperfections and the fixed asymmetry factor fundamentally limits their application in reconfigurable metasurfaces [3].

Our research introduces a new approach for engineering BIC metasurfaces via permittivity-induced symmetry breaking in the surrounding environment of the resonators, a significant departure from traditional, geometry-reliant methods. This strategy not only overcomes the inherent constraints of geometric asymmetry manipulation but also unlocks the flexibility of post-fabrication control over the coupling to the radiation continuum, a governing aspect of BIC physics.

Additionally, our ε-qBICs metasurface design showcases enhanced optical response to the refractive index perturbations of the surrounding medium. In contrast to straightforward spectral shifts, our ε-qBICs metasurface concept opens possibilities to finely modulate between quasi and true BIC states.

We have experimentally demonstrated the generation of the ε-qBICs from specifically designed metasurfaces, where the coupling channel of BIC to continuum radiation is established by the embedding of two identical TiO_2 nano-rods into surrounding media with different permittivity (such as PMMA and air). The ε-qBICs concept is further exploited for realizing electrically reconfigurable BICs by integrating a conductive polymer into our metasurfaces.

The advantageous electro-optical properties of PANI endow the ε-qBICs with excellent electrical reconfigurability. By tuning the optical properties of PANI, the ε-qBICs can be dynamically switchable, exhibiting fully reconfigurable qBICs with high modulation contrast. Additionally, we have demonstrated the electrical switching performance of the reconfigurable ε-qBICs, with fast switching speed (12.2 ms and 18 ms for switch-on and switch-off processes, respectively), and excellent switching durability even after 1000 cycles. Our design is compatible with a range of active materials beyond PANI, including liquid crystals, phase change materials, and transparent conducting oxides.

The permittivity-induced BIC metasurfaces unlock an additional degree of freedom for manipulating and engineering BIC states. Thereby laying the groundwork for the on-demand integrated electro-optical devices.

References

1. Hu, H., Lu, W., Antonov, A., Berté, R., Maier, S. A., & Tittl, A. "Environmental permittivity-asymmetric BIC metasurfaces with electrical reconfigurability," Nat. Commun., Vol. 15, No. 1, 7050, 2024.
2. Hsu, C. W., Zhen, B., Stone, A. D., Joannopoulos, J. D., & Soljačić, M. "Bound states in the continuum," Nat. Rev. Mater., Vol. 1, No. 1, 1–13, 2016.
3. Koshelev, K., Lepeshov, S., Liu, M., Bogdanov, A., & Kivshar, Y. "Asymmetric metasurfaces with high-Q resonances governed by bound states in the continuum," Phys. Rev. Lett., Vol. 121, No. 19, 193903, 2018.

High-Resolution and Broadband Metafiber Refraction Index Sensors

J. Wang[1*], L. Zhang[2,3], and M. Qiu[2,3]

[1]Ministry of Education Engineering Research Center of Smart Microsensors and Microsystems, School of Electronics and Information, Hangzhou Dianzi University, Hangzhou 310018, China
[2]Key Laboratory of 3D Micro/Nano Fabrication and Characterization of Zhejiang Province, School of Engineering, Westlake University, 18 Shilongshan Road, Zhejiang Province, Hangzhou 310024, China
[3]Institute of Advanced Technology, Westlake Institute for Advanced Study, 18 Shilongshan Road, Zhejiang Province, Hangzhou 310024, China
[*]corresponding author: jiyongwang@hdu.edu.cn

Abstract: An all-fiber optical sensor with high resolution (2664 RIU^{-1}) and broad linear range (refraction index 1.330–1.430) is realized by coupling resonances from the Fabry–Perot cavity and plasmonic metasurfaces. The whole device is integrated on the fiber tip to enable in-situ liquid monitoring.

Summary:

Refractive index (RI) sensors play an important role in various applications including biomedical analysis and food processing industries. However, developing RI sensors with both high resolution and wide linear range remains a great challenge due to the tradeoff between quality (Q) factor and free spectral range (FSR) of resonance mode. Here, we address this challenge by coupling resonances from the Fabry–Perot (FP) cavity and metasurface, integrated in a hybrid configuration form on the end facet of optical fibers. Specifically, the FP resonance offers high resolution while the plasmonic resonance provides a wide linear range. Featuring asymmetric Fano spectrum due to modal coupling between these two resonances, a high Q value (~ 3829 in liquid) and a sensing resolution of 2664 RIU−1 are experimentally demonstrated. Meanwhile, a wide RI sensing range (1.330–1.430 in the simulation and 1.3403–1.3757 in the experiment) is realized, corresponding to a spectral shift across several FSRs (four and two FSRs in the simulation and experiment, respectively). The proposed steelyard RI sensing strategy is promising in versatile monitoring applications, e.g., water salinity/turbidity and biomedical reaction process, and could be extended to other types of sensors calling for both high resolution and wide linear range.

The authors gratefully acknowledge the support from the National Natural Science Foundation of China (Fund No. 62475065,62275221).

References

1. Zhang, L., Shang, X., Cao, S., Jia, Q., Wang, J., Yan, W., Qiu, M.. Optical steelyard: high-resolution and wide-range refractive index sensing by synergizing Fabry–Perot interferometer with metafibers. PhotoniX, 5, 24, 2024.
2. Zhang, C., Zhang, L., Zhang, H., Fu, B., Wang, J., Qiu M. Pulsed polarized vortex beam enabled by metafiber lasers. PhotoniX, 5, 36, 2024.
3. Zhang, L., Sun, X., Yu, H., Deng, N., Qiu, F., Wang, J., Qiu, M.. Plasmonic metafibers electro-optic modulators . Light: Science & Applications, 12, 198, 2023.

N-Heterocyclic Carbene as Robust and Conductive Linkages to Couple Gold Nanoparticles and Conductive Polymers

Ningwei Sun[1], Franziska Lissel [1, 2]*

[1]Leibniz-Institut für Polymerforschung Dresden, Hohe Straße 6, 01069 Dresden. Germany

[2]Hamburg University of Technology: Hamburg, Germany

*corresponding author: lissel@ipfdd.de

Abstract: N-heterocyclic carbene (NHC) anchors enable electron delocalization over the gold/conductive polymer (CP) interface, resulting in an improved conductivity. Here we developed a new class of real hybrid nanocomposites using NHC to coupling AuNPs and CPs, including small Au NP@NHC-CP by bottom-up methods and large Au NP@NHC-CP by top-down methods.

Due to their excellent stability and conductivity, *N*-heterocyclic carbenes (NHCs) have attracted great attention as versatile ligands for the functionalization of gold surface and gold nanoparticles (Au NPs) [1-3]. Yet so far, these efforts are confined to non-conjugated ligands – i.e. focused on exploiting the stability aspect. Using NHCs to link Au NPs and electronically active organic components, e.g. conjugated polymers (CPs), will allow to capitalize on the stability as well as the inherent conductivity of the NHC anchors. Here, we developed several types of real hybrid nanocomposites using NHC to coupling Au NPs and CPs, including small Au NPs by directly reduction from the precursor of poly(3-hexylthiophenes)-NHC-Au (P3HTs-NHC-Au) and large Au NPs with NHC-based initiators to grow CPs (polyaniline). The corresponding NPs show excellent thermal as well as redox stability. The NHC anchors enable electron delocalization over the gold/CP interface, resulting in an improved conductivity. This work demonstrates for the first time that CPs functionalized with NHCs can serve as ligands for the stabilization of Au NPs, paving a way for potential (opto-)electronical applications of Au NP@NHC-CP nanomaterials.

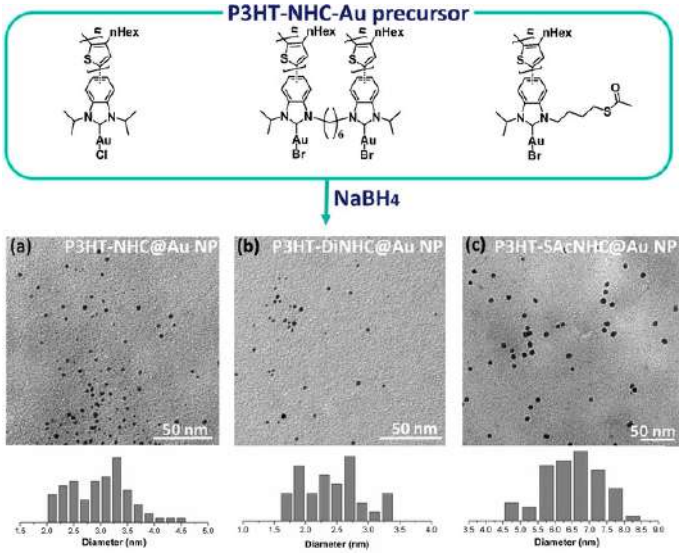


Figure 1 Bottom-up method for synthesis of small Au NP@NHC-P3HT by using P3HT-NHC-Au precursors.

For the bottom-up method to synthesize small Au NPs, a series of P3HT using NHC-Au as end functional group were synthesized by Kumada polymerization (Figure 1). The resulting polymers can be readily reduced to form Au NPs, leading the Au NP@NHC-P3HT architecture. TEM images of all Au NPs revealed small spherical particles with

average diameters of 2-6 nm. NHCs are highly conductive linkages, and one can assume that binding the polymer to Au NPs via a conductive NHC anchor group will increase the electrochromic response speed, allowing to estimate the organic/inorganic electron transfer of Au NP@NHC-P3HT. The response time, was found to be 1.21/1.05 s for neat P3HT-NHC-Au and 0.79/0.52 s for the composite containing 10 % Au NP@NHC-P3HT. indicating that the NHC promote the electron transfer in the electrochromic films.

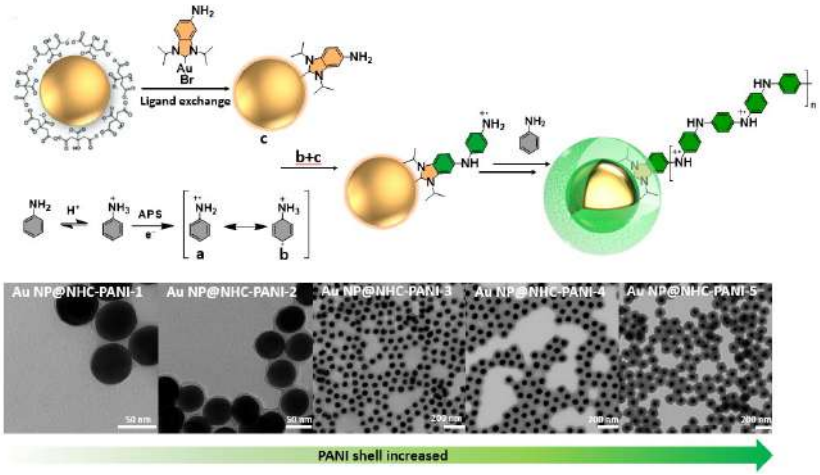


Figure 2 Top-down method to synthesize large Au NP@NHC-PANI.

For the top-down method to synthesize large Au NPs, an amino-substituted NHC–Au(I) complex was synthesized and grafted onto citrate-stabilized AuNPs, where the amino group serves as a nucleation site for oxidative polymerization of polyaniline (PANI) to form an Au NP@NHC-PANI composite (Figure 2). By assembling these hybrids into SAMs, we have, for the first time, experimentally demonstrated the conductive role of NHC as a linker at the metal-polymer interface. Compared to conventional Au NP@PANI hybrids, the incorporation of NHCs significantly improves electrical conductivity. Conductive atomic force microscopy (C-AFM) measurements revealed that at 300 mV bias, the contact current increased from 14.6 pA (Au NP@PANI) to 99.4 pA (Au NP@NHC-PANI). Similarly, four-probe lateral conductance measurements showed a remarkable enhancement from 0.17 nS to 3.5 nS upon NHC modification.

Acknowledgments

This work has received funding from the European Innovation Council (EIC) under the project ESiM (grant agreement No. 101046364) and from the DFG Project 545984433.

References

1. Sun, N., Zhang, S.-T., Simon, F., Steiner, A. M., Schubert, J., Du, Y., Qiao, Z., Fery, A., & Lissel, F. “Poly (3‐hexylthiophene)s Functionalized with N‐Heterocyclic Carbenes as Robust and Conductive Ligands for the Stabilization of Gold Nanoparticles,” Angew. Chem. Int. Ed., Vol. 60, No. 8, 3912–3917, 2021.
2. Sun, N., Singh, S., Zhang, H., Hermes, I., Zhou, Z., Schlicke, H., Vaynzof, Y., Lissel, F., & Fery, A. “Gold Nanoparticles with N‐Heterocyclic Carbene/Triphenylamine Surface Ligands: Stable and Electrochromically Active Hybrid Materials for Optoelectronics,” Adv. Sci., Vol. 11, No. 29, 2400752, 2024.
3. Khera, N., Sun, N., Park, S., Das, P., Au‐Yeung, K. H., Sarkar, S., Plate, F., Robles, R., Lorente, N., Lissel, F. S.-C., & Moresco, F. “N‐Heterocyclic Carbene vs. Thiophene – Chiral Adsorption and Unidirectional Rotation on Au(111),” Angew. Chem. Int. Ed., e202424715, 2025.

Biocompatible Plasmonic Nanoparticle-Doped Hydrogel for Facile Optical Detection of Cortisol

A. Nicolae-Maranciuc [1,2,3], D. Chicea [2] and A. Campu [1,2,4*]

[1] Academy of Romanian Scientists, Ilfov No. 3, 050044 Bucharest, Romania.
[2] Research Center for Complex Physical Systems, Faculty of Sciences, Lucian Blaga University, Doctor Ion Rațiu No. 5-7, 550012 Sibiu, Romania.
[3] Institute for Interdisciplinary Studies and Research (ISCI), Lucian Blaga University of Sibiu, Victoriei Blvd. No. 10, 550024 Sibiu, Romania.
[4] Nanobiophotonics and Laser Microspectroscopy Center, Interdisciplinary Research Institute in Bio-Nano-Sciences, Babes-Bolyai University, Treboniu Laurian No. 42, 400271 Cluj-Napoca, Romania.

[*]Corresponding author: andreea.campu@ulbsibiu.ro/andreea.campu@ubbcluj.ro

Abstract: Nowadays, the population is subject to a lot of stress, being one of society's most encountered problems affecting people worldwide. Cortisol is one of the main indicators of stress, long-term exposure to cortisol can lead to severe medical conditions, thus its rapid, facile and effective real-time monitorization is highly desired.

Being under a lot of stress for prolonged periods of time impacts the physical and mental health of the individuals, leading to severe medical conditions such as heart disease, lung issues, obesity, anxiety, depression, etc. In this context, the current work focuses on the development of a biocompatible, flexible hybrid plasmonic sensor for the non-invasive Localized Surface Plasmon Resonance (LSPR) detection of cortisol levels with high accuracy. To achieve this goal, firstly, silver nanospheres (AgNPs) and gold nanobipyramids (AuBPs) were chemically synthesized and optically and morphologically characterized. Additionally, their bulk sensitivity– AuBPs proving superior sensing capabilities, as well as their antibacterial effects were assessed. Further, biocompatible hydrogel matrices were prepared and doped with cortisol monoclonal antibody-functionalized plasmonic nanoparticles. To confirm the successful integration of the plasmonic nanoparticles, the optical and morphological properties were monitored along with their antibacterial activity. Finally, the developed hybrid plasmonic hydrogel was exposed to the cortisol hormone at medically relevant concentrations in order to evaluate the LSPR detection capabilities of the hybrid biocompatible plasmonic hydrogel, proving its versatility and high potential for cortisol monitoring while ensuring a facile utilization by the patients in the comfort of their home with a view to providing personalized medicine and improved health care.

Acknowledgements: This work was supported by Academy of Romanian Scientists, under the AOSR-Teams III-2023-2024 programme and by the Lucian Blaga University of Sibiu through the research grant LBUS-IRG-2024.

Nanocomposite materials for biosensors made by a dual pulsed laser source

M. Gireau[1], F. Du[2], J. Youssef[3,4], G. Humbert[3], S. Zeng[2], C. Champeaux[1] and F. Dumas-Bouchiat[1]

[1]Univ. Limoges, CNRS, IRCER, UMR 7315, F-87000 Limoges, France
[2]Univ. Troyes, CNRS, L2N, UMR 7076, F-10300 Troyes, France
[3]Univ. Limoges, CNRS, XLIM, UMR 7252, F-87000 Limoges, France
[4]ALPhANOV, Optics & Lasers Technology Ctr., Institut d'optique d'Aquitaine, France
[*]corresponding author: manon.gireau@unilim.fr

Abstract: Nanomaterials with complex architectures were engineered using a dual pulsed laser source. Silver nanoparticles embedded in aluminum oxide thin films exhibit concentration-dependent maximum absorption, shifting from 432 nm at 2% vol. to 465 nm at 8% vol. Their integration with gold unlocks promising applications for sensing.

This communication lies on the development and synthesis of nanometer-scale complex materials made of gold (Au), silver (Ag) and aluminum oxide (Al_2O_3). The association of noble metals with a dielectric at nanometric dimensions, in the form of thin films or nanoparticles, can yield new materials with exotic physical and chemical properties, finding a wide range of applications such as photonic, optoelectronic, plasmonic devices, nonlinear optics and catalysis fields.

Synthetize well-controlled architectures integrating nanoparticles and thin film remains challenging.

Nanocomposites are fabricated using Pulsed nanosecond-Laser Deposition (PLD) combined with a free cluster generator. PLD, known for its ability to provide congruent transfer of the species, enables the deposition of Ag, Au and Al_2O_3 thin films with nanometer-scale thicknesses control, high density and crystallinity. The synthesis of metallic Ag nanoparticles (NPs) is achieved using a cluster generator developed by our group, based on Smalley's source principle [1]. The pulsed plasma plume generated by focusing a YAG (2ω) laser on the Ag target is strongly quenched by a synchronized helium (He) puff delivered in a specific nucleation chamber through a controlled pulsed valve. The opening date and the duration of the valve aperture are key-parameters to monitor the size of the nanoparticles. These formed NPs flowed through a nozzle designed to maintain the size and shape of NPs, from the nucleation site to the PLD chamber. In this ambient temperature process, the synthesized NPs with a diameter in the range 1-10 nm, present a quasi-monodisperse size distribution. The setup coupling PLD and cluster generator enables the synthesis of nanomaterials with exotic properties by using each technique separately, simultaneously or sequentially—resulting NP-stacks, nanocomposite thin films with embedded NPs or multilayers NPs/thin films respectively [2].

The aim of our study is the development of thin nanocomposite devices for biosensing applications based on plasmonic effect. It includes Ag NPs embedded in aluminum oxide thin film matrix and gold upper layer. Single continuous 50 nm Au films deposited on glass, with a low Root Mean Square (RMS) roughness below 1 nm provide an ultra-smooth surface, making them highly suitable for plasmonic applications such as waveguides, where minimizing scattering losses is essential for efficient light propagation. Additionally, four-probe measurements confirm that these films exhibit an electrical conductivity of 2.5×10^7 $S.m^{-1}$, close to bulk gold, even at such very low thickness. These films are therefore ideal for high-performance electrical contacts in nano and optoelectronic devices, ensuring efficient charge transport while maintaining excellent plasmonic behavior.

The synthesis of small Ag NPs with a diameter of 2.3 ± 0.8 nm was successfully achieved. The quasi-monodispersed size distribution makes this approach suitable for finely tune and control optical properties, as these

properties strongly depend on the size and shape of the particles. The incorporation of metallic NPs inside a dielectric film leads to a nanocomposite with novel electrical and optical properties. The stoichiometry of the Al_2O_3 matrix was verified through X-ray Photoelectron Spectroscopy (XPS). Atomic Force Microscopy (AFM) was used to analyze the roughness and thickness of the films. The Ag NPs randomly embedded in an amorphous Al_2O_3 matrix using the dual pulsed laser source described before, exhibit specific optical absorption at a wavelength of 432 nm, consistent with Mie theory. The amount of NPs embedded in the matrix influences the localized surface plasmon resonance, leading to a shift in the maximum absorption wavelength, from 432 nm for 2 %Vol., to 465 nm for 8 %Vol. The resonance position can thus be tuned by modifying the NPs concentration inside the Al_2O_3 matrix, making it an effective material for optical modulation applications. The dielectric function of the material is also modified, resulting in significant changes in electrical properties, such as increased conductivity, tunable permittivity and enhanced charge storage capabilities.

The ability to design a composite nanomaterial including Au thin film and Ag NPs surrounded by an Al_2O_3 matrix without contamination interfaces, is confirmed by Transmission Electron Microscopy (TEM) cross section analysis. These analyses show the capability of our laser ablation process to monitor, in one-way, complex materials with desired thickness, ensuring optimal nanocomposites properties. As a result, the association of a 12 nm Al_2O_3 matrix with embedded Ag NPs, covered by a 48 nm Au film already demonstrated excellent performances as a Surface Plasmon Resonance (SPR)-based biosensor. The detection of a specific cancer marker, namely Tumor Necrosis factor-α, was achieved at a concentration below the attomolar level, making it, to the best of our knowledge, one of the most sensitive SPR biosensors reported to date [3].

This work was partially supported by the LabEx SigmaLim ANR-10-LBX-0074-01, laboratory of excellence launched by the French Ministry of Higher Education and Research (https://www.unilim.fr/labex-sigma-lim) between the IRCER (https://www.ircer.fr) and XLIM (https://www.xlim.fr) Research Institutes.

References

1. M. Gaudin, P. Carles, E. Laborde, C. Champeaux, and F. Dumas-Bouchiat, “A dual nanosecond-pulsed laser setup for nanocomposite synthesis-Ag nanoparticles in Al2O3/VO2 matrix”, J. Appl. Phys., Vol. 125, No. 5, 054301, 2019.
2. F. Dumas-Bouchiat, M. Gaudin, I.A. Alonzo Zapata, C. Champeaux, “VO2 thin films: various microstructures for hysteresis manipulations,” Vacuum, Vol. 227, 113408, 2024.
3. S. Zhu, R. Jaffiol, A. Crunteanu, C. Vézy, S.T. Chan, W. Yuan, H.P. Ho, and S. Zeng, “Label-free biosensing with singular-phase-enhanced lateral position shift based on atomically thin plasmonic nanomaterials”, Light Sci. Appl., Vol. 13, No. 1, 2, 2024.

Silicon nanoparticle arrays for studies on colloidal WS_2 nanosheets

M. Sommer[1*], M. Fröhlich[2], L. Lang[1], P. C. Simo[1], J. Lauth[2], M. Fleischer[1]
[1]Institute for Applied Physics and Center LISA$^+$, University of Tübingen, Germany
[2]Institute of Physical and Theoretical Chemistry, University of Tübingen, Germany
Corresponding author: melanie.sommer@uni-tuebingen.de

Abstract: Silicon nanoantennas have gathered a lot of interest in recent years because of their ability to manipulate light on the nanoscale with simultaneous excellent CMOS compatibility. Here we investigate their properties aiming to enhance the photoluminescence of colloidal WS_2 nanosheets, fabricated by a wet-chemical synthesis.

Nanoantennas give us the ability to manipulate light on the nanoscale. Made from a high index material, like silicon, these antennas can support Mie-like modes, manifesting as electric and magnetic resonances in their optical spectra [1]. These resonances lead to field enhancement around the particles. This confinement of light can be further applied in combination with other optical emitters to manipulate their properties.

Transition metal dichalcogenides (TMDCs) for example are known for their photoluminescence when appearing in mono- or few-layer form. The two-dimensional TMDCs are commonly realized by exfoliation methods or chemical vapor deposition (CVD). They can, however, also be prepared with a wet-chemical synthesis [2]. This synthesis generates colloidal monolayer nanosheets with sizes of a few to several ten nanometers. The photoluminescent properties of these TMDCs are not yet as strong as the ones of TMDCs gained from exfoliation or CVD. Therefore, the colloidal TMDC nanosheets can benefit greatly from silicon nanoantennas, as their high near fields and the Purcell effect can enhance the photoluminescence intensity.

In our study we combine colloidal semiconducting WS_2 nanosheets with truncated silicon cones. The cones can be fabricated in different sizes, tuning their resonance wavelengths over the whole optical spectrum, as can be seen in Figure 1 a). Figure 1 b) shows a scanning electron microscope image of the cones, fabricated with electron beam lithography. The nanosheets are dispersed around the nanoantennas by drop casting, placing them randomly around the cones. A sketch of the system can be seen in Figure 2 a). Depending on the size of the silicon nanoantennas, the enhancement of the photoluminescence changes. The radiation enhancement can also be theoretically approached with simulations, by approximating the TMDC's excitons as dipoles and taking into account the field enhancement around the nanoantennas and Purcell factors [3] (Figure 2 b)).

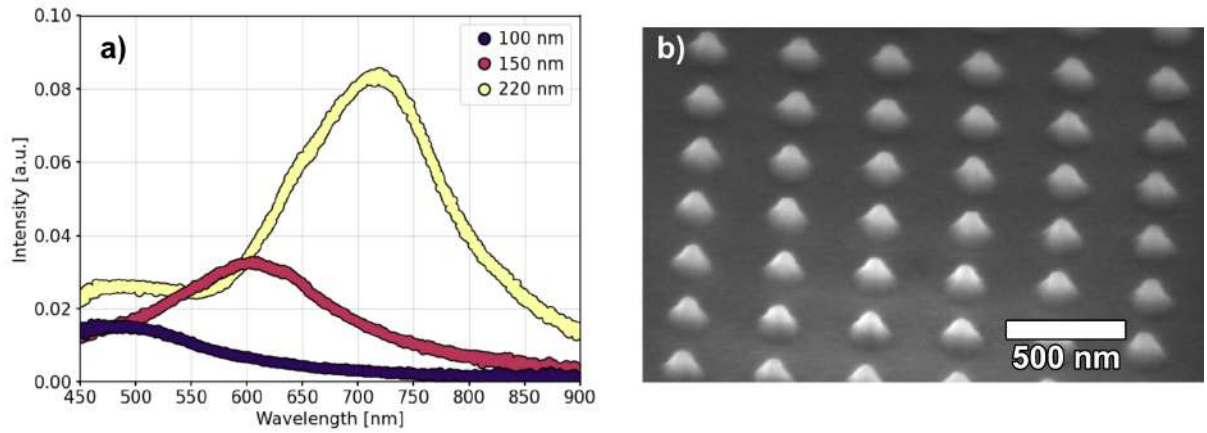


Figure 1: a) Dark-field scattering spectra of silicon nanoantennas with different diameters. For bigger particles the resonances appear at longer wavelengths. b) Micrograph of silicon nanoantennas arranged in a square lattice.

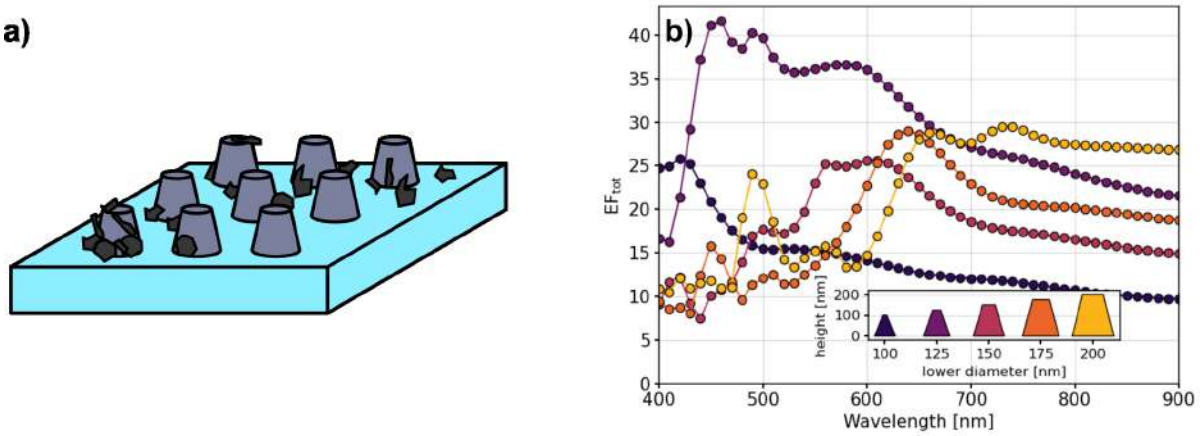


Figure 2: a) Sketch of the system of dropcast colloidal WS_2 nanosheets around truncated nanocones. b) Simulation of the photoluminescence enhancement factors for silicon nanoantennas of different sizes.

References

1. Staude, I., T. Pertsch, Y. S. Kivshar, "All-dielectric resonant meta-optics lightens up," *ACS Photonics*, Vol. 6, No. 4, pp. 802-814, 2019.

2. Frauendorf, A. P., A. Niebur, L. Harms, S. Shree, B. Urbaszek, M. Oestreich, J. Hübner, J. Lauth, "Room temperature micro-photoluminescence studies of colloidal WS_2 nanosheets," *J. Phys. Chem. C*, Vol. 125, No. 34, pp. 18841-18848, 2021.

3. Lepeshov, S., A. Krasnok, A. Alù, "Enhanced excitation and emission from 2D transition metal dichalcogenides with all-dielectric nanoantennas," *Nanotechnology*, Vol. 30, No. 25, pp. 254004, 2019.

Silver nanocubes decorated silicon nanostructures used as 3D active SERS platforms for detection of microplastics

A. Boldeiu[1*], P. Varasteanu[1], O. Brancoveanu[1], G. Craciun[1], R. Pascu[1], A. Avram[1], C. Romanitan[1], I. Mihalache[1] and M. Kusko[1*]

[1] National Institute for Research and Development in Microtechnologies (IMT-Bucharest), 126A Erou Iancu Nicolae Street, 077190, Voluntari, Romania

[*]corresponding author: adina.boldeiu@imt.ro, mihaela.kusko@imt.ro

Abstract: In this work, 3D hybrid architectures on silicon substrate have been fabricated and employed to detect plastic particles using surface-enhanced Raman spectroscopy (SERS). The novel SERS platforms were obtained by embedding silver nanocubes synthesized using an eco-friendly route in two types of silicon nanostructures substrates, Si nanotrees and nanopillars, respectively.

Surface-Enhanced Raman Spectroscopy (SERS) is a non-destructive, fast, and label-free analytical method, with high sensitivity towards molecules containing polar/nonpolar functional groups, which has been used in recent years for the detection of microplastics [1]. In this field, there is still work to be done, in order to develop efficient SERS platforms towards small concentrations of these nanomaterials types and to understand the involved enhancement mechanisms.

Fabrication of the hybrid nano-assemblies started with the nanopaternation of the Si substrate. Thus, black silicon like nanostructures were fabricated using the cost effective Deep Reaction Ion Etching method. Adjusting the process parameters, both Si based nanotrees (SiNT) and nanopillars (SiNP) were obtained, having around 2 μm in heights, the walls of which were later decorated with synthesized AgNC, having the mean edge lengths of 42.7 ± 3.5 nm.

First, crystal violet (CV) was used as analyte molecule to evaluate the SERS performances and the enhancement given by the two novel platforms. Thus, 20 μl CV of concentrations ranging from 10^{-6} to 10^{-12} M were dropped onto the SERS substrates and left it to dry. Remarkable is that we were able to detect concentrations of 10^{-11}M, the SERS spectra being more intense for AgNC@SiNT platform. The average values of the enhancement factors are EFs were estimated [2] as 4.2×10^{9} for AgNC@SiNT and 1.9×10^{8} AgNC@SiNP,respectively. The higher enhancement of the AgNC@SiNT platform might be caused by, on the one hand, their morphology and, on the other hand, by the presence of more hot spots available on top of nanotrees, while numerous small nanocubes can be observed fallen down into the pores of the nanopillars.

The SERS substrates' sensitivity towards the plastics nanobeads was investigated using different concentrations of polystyrene nanoparticles (PS) having 500 nm in diameter, and both substrates were able to detect PS concentrations as low as 50 μg/ml. Moreover, we tested the substrates' reproducibility, which showed excellent relative standard deviation (RSD) values, about 8% for AgNC@SiNT, and even better, ~ 1% for AgNC@SiNP.

Acknowledgements: This work was funded from two projects: 1. "National Platform for Semiconductor Technologies", contract no. G 2024-85828/390008/27.11.2024, SMIS code 304244, co-funded by the European Regional Development Fund under the Program for Intelligent Growth, Digitization, and Financial Instruments. 2. Romanian Core Program PNCDI 2022-2027 "Advanced research in micro-nano-electronics, photonics,

sensors and microsystems devices for societal applications- μNanoEl", 2307/29.12.2022 (2023-2026), financed by the Ministry of Research, Innovation and Digitalization.

References

1. Xu G., Cheng H., Jones R., Feng Y., Gong K., Li K., Fang X., Tahir M. A., Valev V. K. and Zhang L. "Surface-Enhanced Raman Spectroscopy Facilitates the Detection of Microplastics <1 μm in the Environment", Environ. Sci. Technol. Vol. 54, No. 24, 15594–15603, 2020.
2. Ben-Jaber S., Peveler W. J., Quesada-Cabrera R., Sol C.W. O., Papakonstantinou I., Parkin I. P., "Sensitive and specific detection of explosives in solution and vapour by surface-enhanced Raman spectroscopy on silver nanocubes", Nanoscale Vol. 9 16459–16466, 2017.

Angularly resolved optical response of organic molecules in single and collective plasmonic gold nanosphere systems

F. Schneider[1,*], D. Schäfer[2], S. Schlücker[2], A.J. Meixner[1], and D. Zhang[1]

[1]Institute for Physical and Theoretical Chemistry and LISA[+], Eberhard Karls University Tübingen, Germany

[2]Physical Chemistry I, Department of Chemistry and Center of Nanointegration Duisburg-Essen, and Center of Medical Biochenology, University of Duisburg-Essen, Germany

[*]corresponding author: felix.schneider@uni-tuebingen.de

Abstract: Plasmon-based nanosphere systems are used for surface enhanced Raman scattering (SERS) of organic molecules. Angular excitation effects are investigated by varying the electric field distribution and incidence angle of the excitation radiation. We excite different plasmonic coupled or collective resonances to analyze the spatial emission behavior in the *k*-space.

Surface enhanced Raman scattering (SERS) has taken its firm place as a fundamental spectroscopy method to allow the observation of Raman scattering despite low scattering cross sections. Popular substrates consist of metallic nanostructures with strong plasmon resonances that provide electromagnetic enhancement in their vicinity. For single gold nanosphere-on-mirror systems, multiple resonances have been identified that show excitation-specific behavior[1]. Due to their different plasmonic resonances, the emission behavior of multiple resonances is expected to differ. Part of our work focuses on elucidating the spatial distribution of Raman scattering by angle-resolved spectroscopy in the *k*-space for varying electric field distributions in the focal field when exciting two different coupled gap-mode resonances. Furthermore, we will investigate angle of incidence excitation effects for SERS in hybridized collective resonances found on grating waveguide-structures assembled of nanospheres[2]. The collective resonance strongly depends on the angle of incidence that is used for excitation, which manifests a powerful tool for multiple applications in the same metasurface.

The single gold nanosphere-on-mirror samples were fabricated by deposition of super-spherical gold nanospheres[3] with 100 nm nominal diameter on a two-layer film of cobalt(II)-phthalocyanine (CoPc) on an ultrasmooth gold film. The nanosphere density was controlled to achieve single particle dispersion on the sample. The coupled system of nanosphere and film shows multiple resonances, with one resonance found about 600 nm and one found about 800 nm[1]. We excite both resonances using 633 nm and 785 nm continuous-wave lasers. The laser polarizations are varied between radial and azimuthal polarization to excite the system with purely in-plane (i.e., parallel to the gold surface) electric fields or dominantly out-of-plane (i.e., perpendicular to the gold surface) electric fields at both resonances. The back focal plane is sectioned into multiple angular ranges, of which the spectral information is collected to access the spatially distributed Raman scattering signal. Preliminary results indicate that the Raman scattering of CoPc is indeed linked to the radiation behavior of the plasmonic resonances, and that the excitation with different electric field directions in the focal field leads to strong intensity variations in the angular Raman scattering behavior of the system.

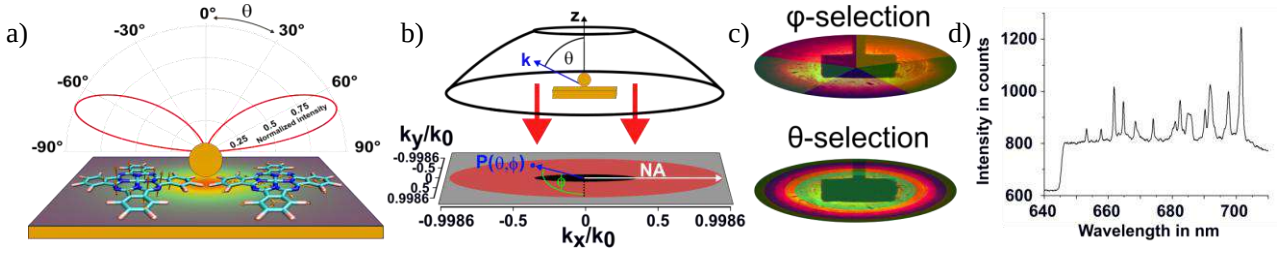


Figure 1: Angularly resolved Raman scattering of a single gold nanosphere-on-mirror configuration. a) Experimental setup with single gold nanosphere on CoPc. The simulated emission is shown as θ-plot above. b) Parabolic mirror collection scheme to access angular information. c) Sketch of the angular sectioning in the k-space to obtain angularly resolved spectral information in φ- and θ-sections. d) Exemplary Raman scattering spectrum obtained in one angular section.

We will extend the study of nanospheres by investigating guided mode resonances on waveguide-structures assembled from gold nanospheres. We expect the absorption to strongly depend on the angle of incidence[2], because the collective resonance gradually shifts, also depending on the waveguide periodicity. Thus, excitation with in-plane and out-of-plane electric field excitation are expected to yield significant differences in the Raman enhancement and due to a shift in the resonance energy depending on the angle of incidence. This will be confirmed by the plasmonic spectral shaping effect[4]. We will excite the guided mode resonances using 532 nm, 633 nm and 785 nm continuous-wave lasers while systematically blocking parts of the incoming radiation angles used for excitation. We will compare gradual changes of the angle of incidence and discuss its influence on the collective resonance, as the resonance energy is expected to shift across the wavelength-range we use for excitation. Successfully demonstrating this expected behavior will allow us to provide more insight into collective resonances commonly employed in metasurfaces.

Acknowledgement: This work was financially supported by the German Research Foundation (Nos. ZH 279/13-1, ZH 279/15-1, ZH 279/16-1, ME 1600/21-1, ME 1600/23-1).

References

1. Schneider, F., L. Lang, L. Wang, J. Gierschner, A.J. Meixner, M. Fleischer., and D. Zhang, “Higher Order Cavity Modes for SERS in a Gold Nanosphere-on-Mirror Configuration”, JPCC, Vol. 128, No. 44, 18807-18819, 2024.
2. Seçkin, S., P. Singh, A. Jaiswal, and T.A.F. König, “Super-Radiant SERS Enhancement by Plasmonic Particle Gratings”, ACS Appl. Mater. Interfaces, Vol. 15, No. 36, 43124-43134, 2023.
3. Jose, J., L. Schumacher, M. Jalali, G. Haberfehlner, J.T. Svejda, D. Erni, and S. Schlücker, „Particle Size-Dependent Onset of the Tunneling Regime in Ideal Dimers of Gold Nanospheres”, ACS Nano, Vol. 16, No. 12, 21377-21387.
4. Lin, K.-Q., J. Yi, J.-H. Zhong, S. Hu, B.-J. Liu, J.-Y. Liu, C. Zong, Z.-C. Lei, X. Wang, J. Aizpurua, R. Esteban, and B. Ren, „Plasmonic photoluminescence for recovering native chemical information from surface-enhanced Raman scattering”, Nat Commun, Vol. 8, 14891, 2017.

Synthesis of silver and gold nanoparticles with tunable plasmonic properties for light-assisted anticancer therapy

A. Panáček[1*], L. Válková[1], L. Hochvaldová[1], A. Pedan[1], H. Kolářová[2], and L. Kvítek[1]

[1]Department of Physical Chemistry, Faculty of Science, Palacký University, Olomouc, Czech Republic

[2]Department of Biophysics, Faculty of Medicine and Dentistry, Palacký University, Olomouc, Czech Republic
[*]corresponding author: ales.panacek@upol.cz

Abstract: Noble metal NPs with tunable plasmonic properties were synthesized using two step reduction process and applied for *in vitro* anticancer photothermal efficacy. The highest photothermal anticancer effect with cell viability decreasing under 20% was induced using AuNPs irradiated by 660 nm laser at irradiation energy of 20 J.

Light-based phototherapy is a promising technique used in anticancer approaches and, in combination with noble metal nanoparticles (NPs), represents an effective way to treat cancer diseases[1]. In this work, noble metal NPs with tunable plasmonic properties were synthesized using two step reduction process and applied for *in vitro* anticancer photothermal efficacy. Water dispersion of anisotropic silver NPs stabilized by citrate was synthesized by two-step reduction process, involving partial reduction of the $[Ag(NH_3)_2]^+$ complex cation by sodium borohydride in the first step resulting in the formation of the silver nuclei, which were subsequently in the second step grown up to anisotropic NPs by the reduction using hydrazine (Fig. 1a). In the case of gold plasmonic NPs stabilized by citrate, the first step involved synthesis of silver nuclei by reduction of $AgNO_3$ via sodium borohydride followed by addition of $HAuCl_4$ solution and subsequent reduction by ascorbic acid producing star-shaped AuNPs (Fig. 1b).

For the anticancer determinations, silver and gold NPs were deposited on a 96-well plate (Fig. 2a) using the layer-by-layer technique to evaluate *in vitro* photothermal anticancer efficacy to human cervical carcinoma cells (HeLa). To induce the photothermal effect, laser sources of different powers and wavelengths corresponding to the plasmon band of the metal NPs were used. A significant decrease in cell viability was observed in HeLa cells cultivated on both Ag and AuNPs-coated plates subjected to irradiation of various irradiation energy doses. The highest photothermal anticancer effect with cell viability decreasing under 20% was induced using AuNPs-coated plates irradiated by 660 nm laser (100 mW) at irradiation energy of 20 J (Fig. 2b). Viability of the cells cultivated on normal plates and subjected to the same energy doses remained unchanged. Based on the obtained results we can conclude that this relatively non-invasive and novel technique based on physicochemical properties of plasmonic materials is offered as an effective and promising tool to fight against cancer diseases.

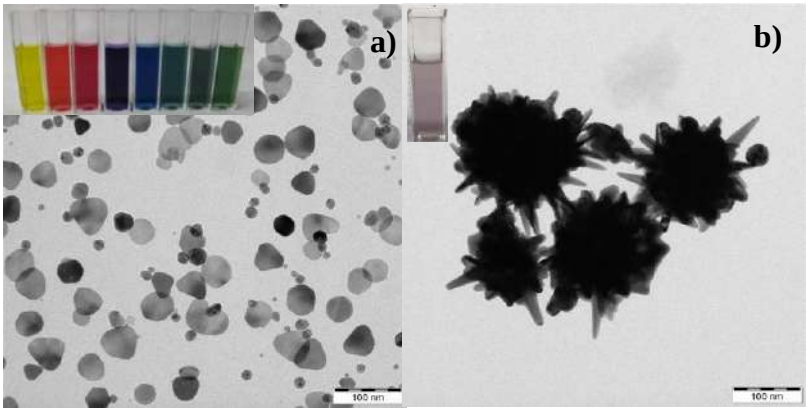


Figure 1. Dispersions and electron microscopy images of (a) silver NPs and (b) gold NPs.

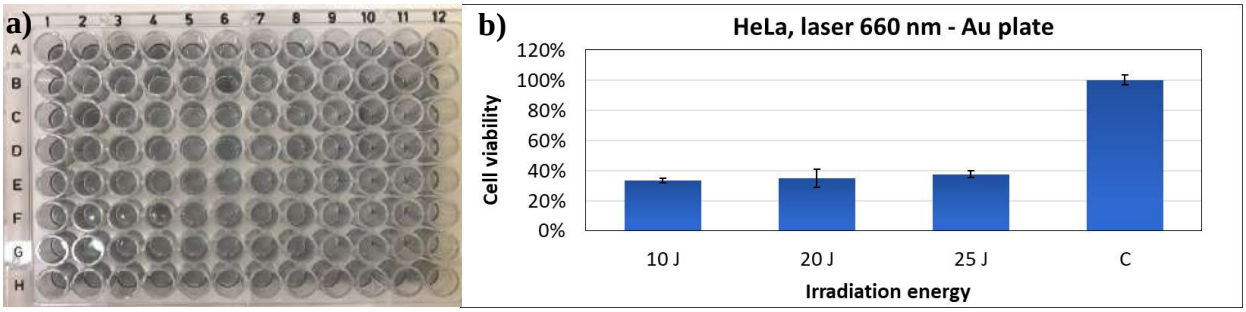


Figure 2. (a) Gold NPs layer deposited on a 96-well plate and (b) viability of cells irradiated using a 660 nm laser at different energies.

This research was funded by Palacký University in Olomouc, Czech Republic, grunt number IGA_PrF_2025_022.

References

1. Kim M. et al. Plasmonic Photothermal Nanoparticles for Biomedical Applications, Adv. Sci. 6, 2019.

Advanced passive and active metasurfaces and zero-index materials

Nonlocal metalens for far-field label-free super-resolution imaging

Bohan Zhang, Yuanmu Yang[1*]

[1] Department of Precision Instrument, Tsinghua University, China
[*]corresponding author: ymyang@tsinghua.edu.cn

Abstract: We introduce an alternative approach to far-field, label-free super-resolution imaging that surpasses the diffraction limit by breaking the fundamental shift-invariance assumption of conventional imaging systems.

The resolution of imaging systems has long been limited by the Abbe-Rayleigh diffraction limit. Although substantial advancements have been made in far-field super-resolution techniques, many methods depend on fluorescence labeling, multi-frame measurements, or involve compromises between field-of-view, energy efficiency, and resolution. Here, we present a novel far-field, label-free super-resolution imaging approach using a topology-optimized 3D metalens. By leveraging the nonlocal (angle-dependent) response of the metalens, we overcome the fundamental spatial shift-invariance of conventional imaging systems. This effectively increases the equivalent aperture and achieves resolution beyond the Rayleigh criterion without sidebands in the image plane, through a phenomenon we call momentum-space superoscillation. Prototype experiments conducted at microwave frequencies show a two-fold resolution enhancement over the diffraction limit, without the need for post-processing.

Room-Temperature, Tunable Lasing from Quasi-2D Perovskites Integrated with Plasmonic Lattices

Yu-Jung Lu[1,2]*

*E-mail: yujunglu@gate.sinica.edu.tw

[1]Research Center for Applied Sciences, Academia Sinica, Taipei 11529, Taiwan
[2]Department of Physics, National Taiwan University, Taipei 10617, Taiwan

We presented a stable, wavelength-tunable, room-temperature single-mode laser based on quasi-2D perovskites coupled with a waveguide-hybridized surface lattice resonance mode composed of aluminum nanoparticle arrays.

Abstract:
Room-temperature plasmonic nanolasers are crucial for advancing optical communication and quantum technologies. However, they face significant challenges, including material instability and high lasing thresholds. To address these issues, we leverage the unique properties of quasi-2D perovskites [1] and high-Q plasmonic nanostructures to enhance both optical gain and coupling strength. In this study, we introduce a stable, wavelength-tunable, room-temperature single-mode laser based on $PEA_2Cs_{n-1}Pb_nBr_{3n+1}$ quasi-2D perovskites coupled with a waveguide-hybridized surface lattice resonance (SLR) mode composed of aluminum nanoparticle arrays. This configuration leverages the enhanced light-matter interaction of the SLR cavity, tailored *via* finite-difference time-domain (FDTD) simulations. Additionally, amplified spontaneous emission (ASE) from trap states in the quasi-2D perovskite significantly boosts optical gain in the system. The results confirm the laser's performance and operational stability in an atmospheric environment; the gain medium maintained stable emission intensity up to 1.8×10^6 excitation pulses. By adjusting the periodicity of the surface lattice resonance (SLR) nanostructures, we achieved a tunable lasing wavelength across a 20 nm spectral range. Our findings establish a low-cost, energy-efficient approach for scalable plasmonic lasing. This advancement not only broadens the understanding of plasmonic systems [2, 3] but also unlocks potential in next-generation photonic applications such as sensing, optical communication, and computation. Finally, we will discuss the detailed working mechanisms of the room-temperature plasmonic nanolasers.

Keywords:
Plasmonic nanolasers, quasi-2D perovskite, surface lattice resonances, room-temperature, tunable lasing

References:

[1] Yu-Kuan Lin, Chiung-Han Chen, Yen-Yu Wang, Ming-Hsuan Yu, Jing-Wei Yang, I-Chih Ni, Bi-Hsuan Lin, Ivan S. Zhidkov, Ernst Z. Kurmaev, **Yu-Jung Lu*** and Chu-Chen Chueh*. Realizing High Brightness Quasi-2D Perovskite Light-Emitting Diodes with Reduced Efficiency Roll-Off via Multifunctional Interface Engineering. **2023,** *Advanced Science* 2302232.

[2] **Yu-Jung Lu***, Teng Lam Shen, Kang-Ning Peng, Pi-Ju Cheng, Shu-Wei Chang, Ming-Yen Lu, Chih Wei Chu, Tzung-Fang Guo, Harry Atwater*, Upconversion Plasmonic Lasing from an Organolead Trihalide Perovskite Nanocrystal with Low Threshold. **2021,** *ACS Photonics* 8,335–342.

[3] Yu-Hung Hsieh, Bo-Wei Hsu, Kang-Ning Peng, Kuan-Wei Lee, Chih Wei Chu, Shu-Wei Chang, Hao-Wu Lin*, Ta-Jen Yen*, and **Yu-Jung Lu***, Perovskite Quantum Dot Lasing in a Gap-Plasmon Nanocavity with Ultralow Threshold, *ACS Nano* **2020**, 14, 11670–11676.

Symmetry-Breaking and Disorder-Assisted Bound States in the Continuum

Qinghua Song[1*]

[1]Tsinghua Shenzhen International Graduate School, Tsinghua University, Shenzhen, 518055
[*]corresponding author: song.qinghua@sz.tsinghua.edu.cn

Abstract: In this talk, we discuss recent advances in metasurface singularities based on bound states in the continuum (BICs). We show that BICs with arbitrary polarization can be achieved using a bilayer twisted metasurface. Introducing magnetic materials enables robust circular polarization generation, and structural disorders facilitate real-momentum duality control.

BICs have been demonstrated to be associated with topological charge and vortex polarization singularities in momentum space. However, conventional BICs rely on symmetric and periodic structures. Here, we demonstrate that symmetry-breaking and disorder can be used as additional degrees of freedom to control light, while preserving the topology of the BIC.

Figure 1a shows the design of a structural symmetry-breaking using a bilayer photonic crystal (PhC) with a relative angle between the two layers. When the relative angle is non-zero, the symmetry is broken along the propagation direction, results in intrinsic chirality. However, the BIC is maintained regardless of the symmetry-breaking (Fig. 1b). This approach allows for the manipulation of the polarization, while keeping the BIC topology [1].

Figure 2a shows the design of a magnetic PhC that employs magnetic material to break the time-reversal symmetry. As a results, robust C points are generated at the center of the Brillouin zone (Fig. 2b), enabling unique chiral wave manipulations.

Figure 3 demonstrates that by designing special eigenmodes protected by a singularity, the structural perturbations will not alter the BIC topology. This allows the disorder to be used for encoding the useful information for wavefront modulation at BIC. Our findings may open up new avenues for applications in structured light, quantum optics and twistronics for photons.

References

1. Qin, H., Su, Z., Liu, M., Zeng, Y., Tang, M.-C., Li, M., Shi, Y., Huang, W., Qiu, C.-W. and Song, Q., “Aibitrarily polarized bound states in the continuum with twisted photonic crystal slabs,” Light: Science & Applications, Vol. 12, 66, 2023.
2. W. Lv, H. Qin, Z. Su, C. Zhang, J. Huang, Y. Shi, B. Li, Genevet, P. and Song, Q., “Robust generation of intrinsic C points with magneto-optical bound states in the continuum,” Science Advances, Vol. 10, eads0157, 2024.
3. H. Qin, Z. Su, Z. Zhang, W. Lv, Z. Yang, W. Chen, X. Gao, H. Wei, Y. Shi, B. Li, J. Zhou, R. Fleury, C. W. Qiu, Q. Song, “Disorder-assisted real-momentum topological photonics crystal,” Nature, 2025. (DOI: 10.1038/s41586-025-08632-9)

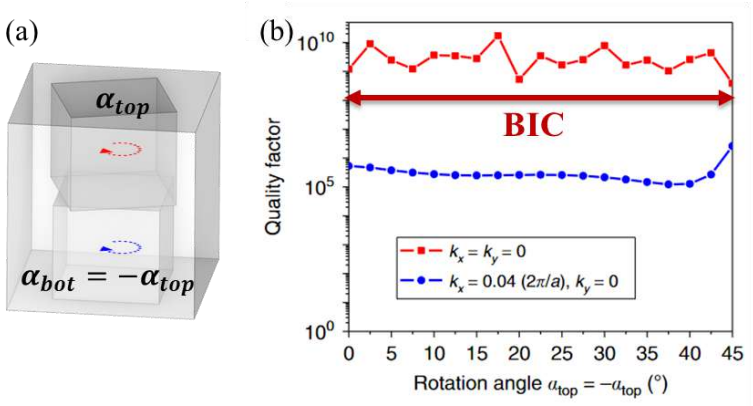


Fig. 1 Design of bilayer PhCS. (a) Schematic of the bilayer PhCS with structural symmetry-breaking in the propagation direction. (b) The BIC is maintained regardless of the rotation angle.

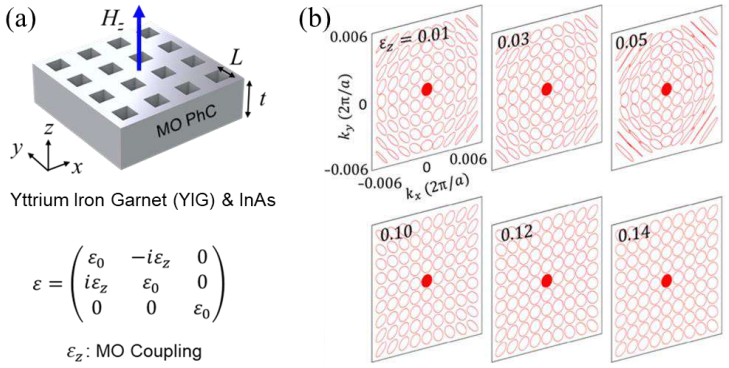


Fig. 2 Design of magnetic-optical PhC. (a) Schematic of MO PhC. (b) Simulated results of robust C points generation.

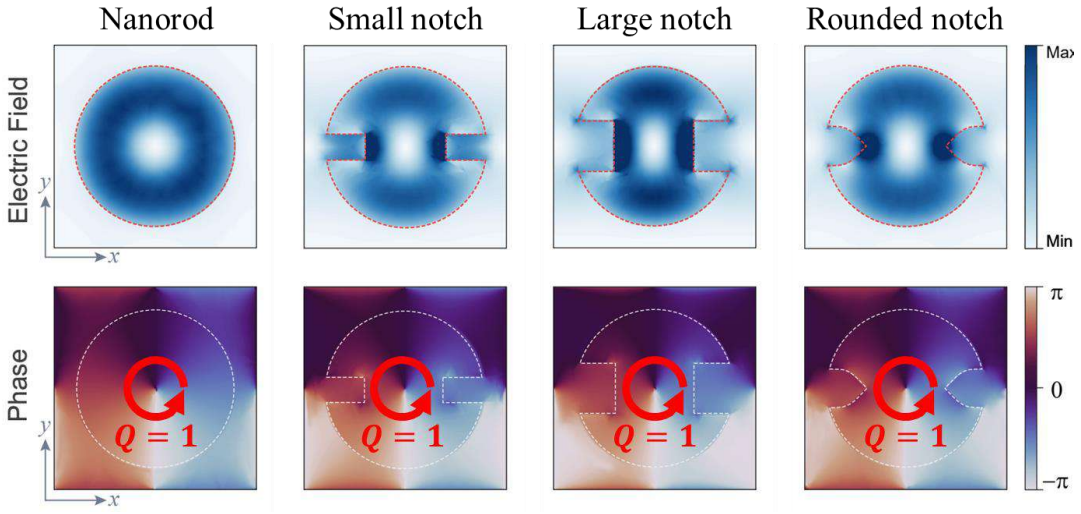


Fig. 3 Design principle of disorder-assisted topological PhC.

Shaping photon emission with emitter-coupled metasurfaces

F. Ding

Centre for Nano Optics, University of Southern Denmark, Campusvej 55, DK-5230 Odense, Denmark

School of Electronic Science and Technology, Eastern Institute of Technology, Ningbo, China

*corresponding author: feid@mci.sdu.dk

Abstract: We propose general approaches to designing versatile photon sources using on-chip QE-coupled meta-optics that enable direct transformations of QE-excited surface plasmon polaritons into spatially propagating photon streams with arbitrary polarization states, directionality, and amplitudes *via* designed metasurfaces.

Optical metasurfaces, i.e., subwavelength planar nanostructures, have attracted increasing attention due to their unprecedented capabilities of molding classical light and revolutionized conventional optics by replacing bulky optical components [1]. In addition to controlling classical light, metasurfaces demonstrate the potential to efficiently manipulate nonclassical light and start to enter the realm of quantum photonics [2]. In this talk, I will discuss how to shape the directionality, polarization state, and amplitude of photon emission by using emitter-coupled metasurfaces [3-5].

References

1. F. Ding, A. Pors, and S. I. Bozhevolnyi, “Gradient metasurfaces: a review of fundamentals and applications,” Rep Prog Phys. 81,026401 (2018).
2. F. Ding and S. I. Bozhevolnyi, “Advances in quantum meta-optics”, Mater. Today 71, 63−72 (2023).
3. X. Liu, Y. Kan, S. Kumar, L. F. Kulikova, V. A. Davydov, V. N. Agafonov, F. Ding, and S. I. Bozhevolnyi, “Off-normal polarized single-photon emission with anisotropic holography metasurfaces”, Nano Lett. 24, 13867−13873 (2024).
4. X. Liu, Y. Kan, S. Kumar, L. F. Kulikova, V. A. Davydov, V. N. Agafonov, F. Ding, and S. I. Bozhevolnyi, “Single-photon emission into arbitrary polarization states with emitter integrated anisotropic metasurfaces”, submitted.
5. S. im Sande, Y. Kan, D. Komisar, C. Wu, S. Kumar, S. I. Bozhevolnyi, and F. Ding, “On-Chip Emitter-Coupled Meta-Optics for Versatile Photon Sources”, Preprint on arXiv 2501.15840.

Nonlinear optics driven by out-of-equilibrium electron dynamics in epsilon-near-zero media

M. Silvestri[1], A. Sahoo[1], L. Assogna[1], M. Venturi[1], R. Adhikary[1], P. Benassi[1,2], C. Ferrante[2], D. Tedeschi[1], A. Ciattoni[2], and A. Marini[1,2*]

[1]Department of Physical and Chemical Sciences, University of L'Aquila, Via Vetoio, 67100 L'Aquila, Italy
[2]Consiglio Nazionale delle Ricerche, CNR-SPIN, Via Vetoio 10, 67100 L'Aquila, Italy
[*]corresponding author: andrea.marini@univaq.it

Abstract: We theoretically model nonlinear optical effects produced by collision-driven electron dynamics in epsilon-near-zero heterogeneous nanostructures. We explore the potential of several setups based on poor metals for the development of compact extreme ultraviolet radiation sources and for integrated spectroscopy schemes.

Harnessing nonlinear (NL) effects in nanoscaled photonic systems is crucial for several applications including frequency conversion as in particular high-harmonic generation (HHG), but in standard bulk materials the NL effects are small, and nonlinearity acts as a perturbation. To amplify the NL effects, typically, one enhances the intensity by confining light under the wavelength scale to develop plasmonic nano-devices, by using noble metals or oxide-based transparent conductors in the middle-infrared (IR) range. Moreover, to obtain plasmonic functionalities in the extreme-ultraviolet (XUV) one can use poor metals, such as Aluminum (Al), Sodium (Na), Titanium (Ti), Tungsten (W), and Vanadium (V), that show marked epsilon-near-zero (ENZ) feature in this spectral region. Indeed, these materials are promising for guidance [1], for resonant third-harmonic generation (THG) in thin films [2], and for manipulation and guidance of XUV radiation.

Here, by considering that, for poor metals, the linear and NL response derives completely from free electron dynamics due to the lack of interband transitions, we model this NL response through a hydrodynamical model [3]. Indeed, by considering the Fokker-Planck-Landau (FPL) theoretical framework, we obtain a set of hydrodynamical equations (HDEs) by solving the Landau collisional integral in the weak coupling limit. In turn, thanks to a perturbative approach, we derive an analytical expression for the collision-driven NL-susceptibility and for the forward (FW) and backward (BW) THG intensity by both transverse electric (TE) and transverse magnetic (TM) pump polarisation for three different setups: the first one involves a Na – based thin film [2], the second one a Na/Al-based nanosphere [4], and the third one a Na-Al bilayer [5], all with nanometer-size thicknesses. In Fig. 1a, where we depict the dependence of the FW intensity of the THG signal over the pump wavelength λ and incidence angle θ for the latter configuration, one can see that the THG process exhibits a double resonance for TM pump excitation $\lambda_{THG} = \lambda/3$ in the ENZ regime due to the coupling of the pump field enhancement and the radiation of the microscopic dipoles. Moreover, in the ENZ regime of Na it's possible to excite surface plasmon polaritons (SPPs) at the Na-Al interface, because in this regime this setup is analogous to an Otto configuration, achieving a THG enhancement factor of three orders of magnitude greater than the single thin film [2]. Finally, Al/Na-based nanoparticles sustain localized surface plasmon excitations enabling enhanced functionalities in nanoscale environments [4]. These results suggest the potential of ENZ heterogeneous nanostructure devices in the development of integrated XUV sources.

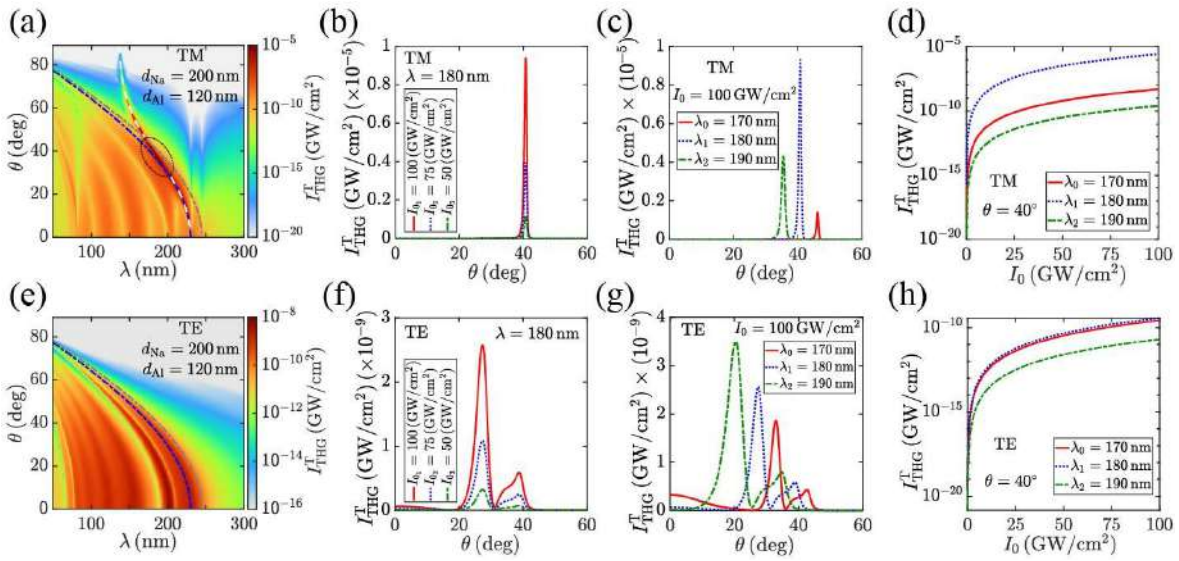


Fig. 1. **(a,e)** Dependence of the FW intensitiy of the THG signal I^T_{THG} over the pump wavelength λ and incidence angle θ for fixed pump intensity $I_0 = 100$ GW/cm^2. The dashed white curve in **(a)** indicates the SPP dispersion curve, while the dot-dashed grey and blue curves indicate the Al and Na NZI dispersion curves, respectively for λ_{THG} and λ. **(b,c,f,g)** Dependence of I^T_{THG} over the pump incidence angle for **(b,f)** fixed pump wavelength λ =180 nm and several intensities $I_0 = 50$, 75, 100 GW/cm^2, and **(c,g)** fixed pump intensities $I_0 = 100$ GW/cm^2 and several wavelengths λ = 170, 180, 190 nm [highlighted by the black circled area in (a)]. **(d,h)** Dependence of I^T_{THG} over the pump intensity I_0 for fixed incidence angle and several wavelengths λ = 170, 180, 190 nm. All plots are obtained for $d_{Na} = 200$ nm and $d_{Al} = 120$ nm and refer to either **(a-d)** TM or **(e-h)** TE polarisation of the impinging pump field.

References

1. Assogna, L., C. Ferrante, A. Ciattoni and A. Marini, "XUV plasmonic waveguides by near-zero index heterostructures," J. Phys. Photonics Vol. 5, 045001, 2023.
2. Silvestri, M., A. Sahoo, L. Assogna, P. Benassi, C. Ferrante, A. Ciattoni, and A. Marini, "Resonant third-harmonic generation driven by out-of-equilibrium electron dynamics in sodium-based near-zero index thin films," Nanophotonics, Vol. 13, No. 11, pp. 2003-2013, 2024.
3. Marini, A., A. Ciattoni, and C. Conti, "Out-of-equilibrium electron dynamics of silver driven by ultrafast electromagnetic fields – a novel hydrodynamical approach," Faraday Discuss., Vol. 214, 235-243, 2019.
4. Silvestri, M., A. Sahoo, C. Ferrante, P. Benassi, A. Ciattoni, and A. Marini, "Doubly resonant third-harmonic generation in near-zero-index heterogeneous nanostructures", Phys. Rev. A, Vol. 110, No.2, 023524, 2024.
5. Silvestri, M., M. Venturi, M. Di Muzio, R. Adhikary, C. Ferrante, P. Benassi, and A. Marini, "Harnessing collisional nonlinearity for enhanced harmonic generation by ultraviolet plasmonic nanoparticles", J. Chem. Phys., Vol. 161, No. 5, 054111, 2024.

Terahertz Modulators Enabled by Vanadium Dioxide: From Materials Optimization to Devices

Xi Wang

Department of Materials Science and Engineering, University of Delaware, Newark, DE 19716, USA
corresponding author: wangxi@udel.edu

Abstract: This talk focuses on optimizing the deposition techniques to produce high-quality, large-area vanadium dioxide (VO_2) thin films with precisely controlled phase transitions. Additionally, it introduces novel metasurface design concepts that may improve the scalability, performance, and tunability for various applications of VO_2-based terahertz (THz) devices.

Among the various approaches explored for Terahertz (THz) modulation, phase-transition materials have emerged as one of the most promising solutions. These materials undergo reversible transitions between distinct electronic and structural states under external stimuli, such as temperature, electric fields, or optical excitation, leading to substantial changes in their optical and electrical properties. In particular, vanadium dioxide (VO_2) has attracted significant attention due to its insulator-to-metal transition (IMT) near 68°C. VO_2-based THz modulators offer several advantages over traditional approaches, including low power consumption, broadband tunability, and compact device integration.

However, despite its promising properties, the practical implementation of VO_2-based THz modulation faces significant challenges. One of the most critical limitations is the synthesis of high-quality, large-area VO_2 thin films with precisely controlled phase-transition characteristics. The properties of VO_2 films, including transition temperature, hysteresis width, and optical contrast, are highly dependent on factors such as crystallinity, stoichiometry, and film thickness. Achieving large-scale VO_2 thin film with high uniformity and consistency while maintaining versatile growth capability remains an area of active research.

Beyond material synthesis, the design and optimization of device architectures play a crucial role in maximizing the performance of VO_2-based THz modulators. Metasurfaces, composed of subwavelength resonant structures, can significantly amplify the phase-transition response of VO_2 by locally engineering the electromagnetic field distribution. By integrating VO_2 with carefully designed metasurfaces, researchers have demonstrated tunable THz absorbers, beam deflectors, and spatial light modulators with improved performance[1].

Given the growing demand for dynamic and efficient THz modulation, it is vital to advance both material synthesis techniques and device engineering strategies. The development of high-quality VO_2 thin films with controlled phase-transition properties and the integration of novel metamaterial-based design architectures will be crucial for achieving high-performance THz modulators. These advancements will not only improve the efficiency, modulation depth, and response speed of THz devices but will also enable their widespread adoption in applications such as ultra-fast THz communication networks, adaptive THz imaging systems, and tunable THz spectroscopy platforms.

In this talk, I will focus on the fabrication of high-quality VO_2 thin films using pulsed laser deposition, emphasizing their uniformity and phase-transition characteristics. I will show VO_2 thin films deposited on 4-inch substrates with the resistance changes of 4 orders of magnitude and a thickness variation of less than 2%. The developed deposition recipe has shown consistency and stability over a two-year period. I will then introduce the

design, fabrication, and characterization of a VO_2-based THz beam steering metasurface. It highlights the metasurface's nearly 100% transmission in the 'OFF' state and its potential for broadband beam steering. I will also introduce the integration of VO_2 with MEMS-based actuators for dynamically tunable chiral THz metamaterials, demonstrating their ability to achieve tunable amplitude, phase, and polarization modulation [2].

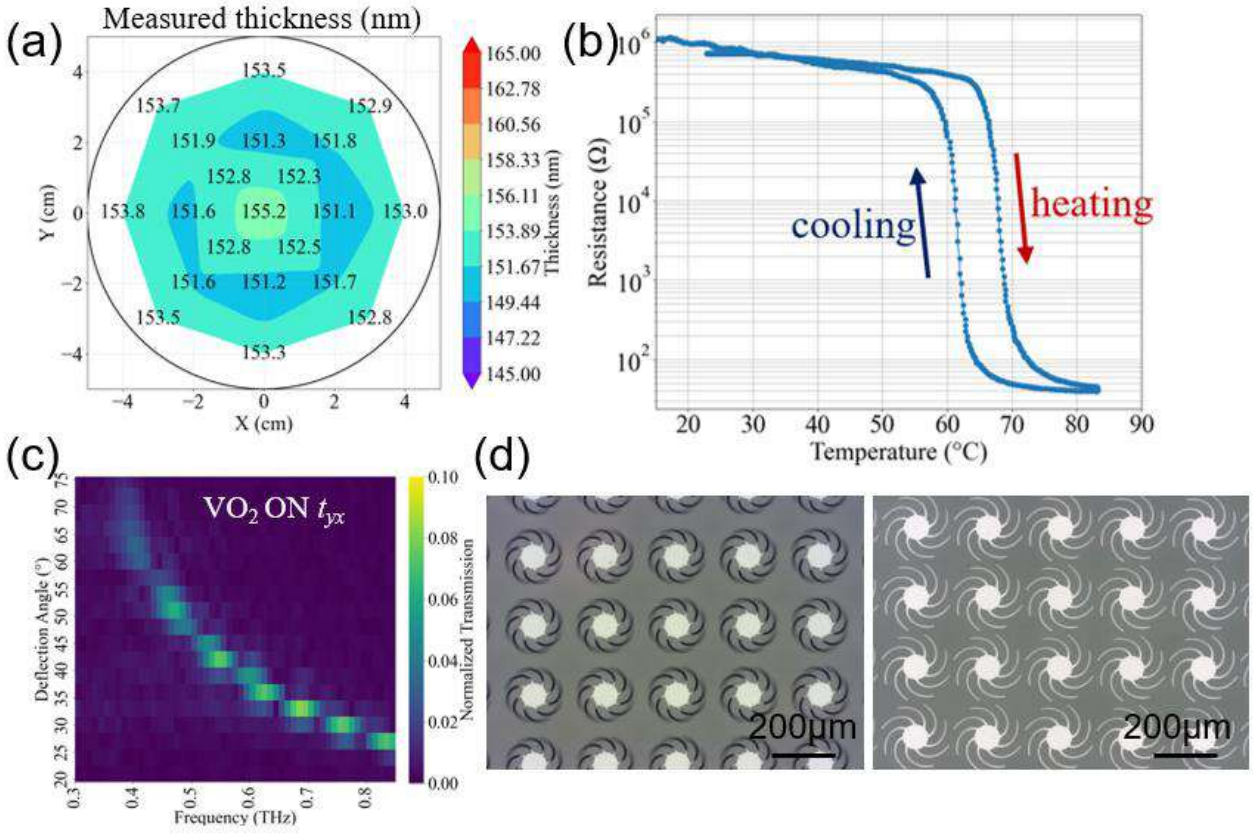


Figure 1 (a) Thickness distribution of a VO_2 thin film on sapphire wafer measured by ellipsometry. (b) The resistance-temperature measurement on the (4cm,0) point of the thin film in (a). (c) Normalized cross-polarized angle-dependent transmission plot of the VO_2 metasurface in 'ON' state showing beam steering. (d) Optical microscope images of the VO_2 MEMS-based actuators curve up at 30 °C (left) and are fully flat at 90 °C (right).

Acknowledgements. This research was primarily supported by NSF through the University of Delaware Materials Research Science and Engineering Center, DMR-2011824. Additional support was received from NASA Grant Number 80NSSC23M0076.

References

1. Herrmann, E., Gao, H., Huang, Z., Sitaram, S. R., Ma, K. and Wang, X. "Modulators for mid-infrared and terahertz light," J. Appl. Phys., Vol. 128, No. 14, 140903, 2020.
2. Huang, Z., Wu, W., Herrmann, E., Ma, K., Chase, Z. A., Searles, T. A., Jungfleisch, M.B. and Wang, X, "MEMS-actuated terahertz metamaterials driven by phase-transition materials," Front. Optoelectron., Vol. 17, No. 1, 13, 2024.

Electrochemically-tunable oxide materials for metasurfaces

V. E. Ferry[1*]

[1]Department of Chemical Engineering and Materials Science, University of Minnesota-Twin Cities, Minneapolis MN 55455 USA

[*]corresponding author: veferry@umn.edu

Abstract: This talk will discuss the use of electrolyte gating to control the optical properties of materials, focusing on $La_{1-x}Sr_xCoO_{3-d}$ (LSCO) as an exemplary case. We create electric double layer transistors of LSCO, and show that on application of gate voltage there is sustained cycling between metallic and dielectric states.

Alternative materials for metasurfaces enable new properties and lay the foundation for advanced applications. Electrochemical phase-change materials that change optical properties in response to an applied stimulus, such as voltage, are highly attractive for the development of tunable and switchable metamaterials.

One convenient method to drive these transformations is to create electric double layer transistors, where the gate dielectric is replaced by an ion gel. This talk will focus mainly on $La_{1-x}Sr_xCoO_{3-\delta}$ (LSCO), one of the premier examples of an electrochemical phase change material. $Sr_xCoO_{3-\delta}$ (SCO) has attracted considerable attention recently as a voltage-tunable materials system; $La_{1-x}Sr_xCoO_{3-\delta}$ (LSCO) offers similar advantages, but with additional advantages in stability. As deposited, LSCO has a perovskite structure, but upon application of the positive gate voltage, oxygen vacancies are formed that drive a phase transformation to a brownmillerite crystal structure. This is accompanied by substantial change in magnetic, electrical, thermal, and optical properties.

This talk will discuss two key aspects of this work. First, we will demonstrate using spectroscopic ellipsometry measurements that LSCO is a versatile materials system for switchable metasurface systems. At $x < 0.18$, we measure $\Delta n > 0.6$ upon application of the gate voltage. For $x > 0.18$, as-grown LSCO has a perovskite structure and is a lossy metal. Application of the gate voltage transforms LSCO to an oxygen-vacancy-ordered brownmillerite crystal structure with high-index ($n > 2.5$) and low-loss. The talk will then discuss endurance in LSCO. Using operando FTIR measurements, we uncover mechanistic information about the transformation, and use this insight to increase the endurance of metal-insulator cycling in LSCO. The talk will conclude with perspectives on electrochemically tunable oxides for metasurfaces.

Acknowledgements. This work was supported primarily by the National Science Foundation through the University of Minnesota MRSEC under Award Number DMR-2011401. Parts of this work were performed in the Characterization Facility at the University of Minnesota, which receives partial support from NSF through the MRSEC program. Portions of this work were also conducted in the Minnesota Nano Center, which is supported by NSF through the National Nano Coordinated Infrastructure (NNCI) under Award Number ECCS-2025124.

References

1. Chakraborty, R. D. , W. Postligione, S. Ghosh, K. A. Mkhoyan, C. Leighton, and V. E. Ferry, “Optical properties of electrochemically gated $La_{1-x}Sr_xCoO_{3-\delta}$ as a topotactic phase change material,” Adv. Opt. Mater., Vol. 11, No. 16,

2300098, 2023.

2. Chakraborty, R. D. , J. Liang, T. Fasasi, K. A. Stoerzinger, C. Leighton, and V. E. Ferry, “High metal-insulator topotactic cycling endurance in electrochemically gated LSCO probed by humidity-dependent operando FTIR spectroscopy,” *Submitted*.

Electrochemically active mid-IR metasurfaces based on conjugated polymers

P.-C. Hsu[1*]

[1]Pritzker School of Molecular Engineering, University of Chicago, USA
[*]corresponding author: pochunhsu@uchicago.edu

Abstract: Electrochemistry can introduce substantial optical property change reversibly and efficiently, making it a promising tool for active metasurfaces. This talk will discuss our recent progress in co-designing hierarchical structures, charge transport properties, and optical cavities of conjugated polymers for mid-IR active metasurface with high performance and functionality.

An active metasurface's performances and functionalities hinge on rational designs of materials with largely and reversibly tunable optical property and strong light-matter interaction. Electrochemical reactions are powerful approaches that enable electrical controllability on chemical reactions by decoupling the electron and ion pathways to ensure charge neutrality, so they can avoid the limitations of Coulombic repulsion and drastically vary the carrier density or even trigger a phase transformation. Although (electro)chemical reactions are inherently slower than electrostatic phenomena, their large tunable range and non-volatility are ideal for certain applications such as building thermoregulation, display, and spacecraft thermal engineering. Meanwhile, employing antenna and cavity design provide strong light-matter interaction and additional degrees of freedom to boost performance and achieve multifunctional control. To tap the full potential of electrochemically active metasurfaces, a systematic study of both fundamental materials science and optical engineering is needed.

In this talk, I will introduce our recent progress on conjugated polymer-based active metasurfaces in mid-IR frequency, particularly for dynamic radiative thermoregulation. We used solid-liquid interfacial polymerization to synthesize high molecular weight polyaniline with both decent crystallinity and electrochemical activity, allowing significant tunability between the metallic and the dielectric states. Complex permittivities at both doped and dedoped states were measured by mid-IR ellipsometry, followed by metasurface design to maximize the thermal emissivity contrast in both spectral and angular domains. We will also elaborate on polyaniline's unique structure-property relationship and the anisotropic polaronic transport.

Acknowledgements: We thank funding support from the National Science Foundation (ECCS Award No. 2324286) and the Pritzker School of Molecular Engineering at the University of Chicago.

References

1. T.-H. Chen, Y. Hong, C.-T. Fu, A. Nandi, W. Xie, J. Yin, P.-C. Hsu, A kirigami-enabled electrochromic wearable variable-emittance device for energy-efficient adaptive personal thermoregulation. *PNAS Nexus* **2**, pgad165 (2023).
2. T.-H. Chen, Q. Li, X. Wu, K. Hulle, P.-J. Hung, Q. Fan, C.-T. Fu, P.-C. Hsu, Active Metasurface Thermal Emitters by Metallic Polymers. https://doi.org/10.26434/chemrxiv-2025-m586z.
3. P.-J. Hung, Q. Li, T.-H. Chen, C.-T. Fu, Y. Han, R. Wu, G. Yan, Q. Fan, J. Liu, P.-R. Huang, Y. Chen, C. Sui, G. Higueros, A. Flores, F. Shi, P.-C. Hsu, All-Solution-Processed Mid-Infrared Electrochromics (ASPIRE) for Thermoregulation with Arbitrary Curvatures. https://doi.org/10.26434/chemrxiv-2025-g97zs.
4. Q. Li, T.-H. Chen, P.-C. Hsu, Use electrochemistry to charge the next dynamic thermal metamaterials. *Energy* **3**, 100108 (2024).

5. T.-H. Chen, P.-C. Hsu, Wearable variable-emittance devices—The future of dynamic personal thermoregulation. *Appl. Phys. Lett.* **125**, 180501 (2024).

Thermo-optical Effects in Nanoantennas and Metasurfaces

G. Tagliabue[1]

[1]Laboratory of Nanoscience for Energy Technologies (LNET), EPFL, 1015 Lausanne, Switzerland

[*]corresponding author: giulia.tagliabue@epfl.ch

Abstract: The combination of photothermal and thermo-optical effects in dielectric nanoresonators open new opportunities for contactless manipulation of metasurfaces.

In the last decade, optical nanoantennas have revolutionized light manipulation and control at the nanoscale. Light absorption was initially considered a purely detrimental process, reducing the efficiency of optoelectronic devices. Recently, however, it has attracted growing interest, enabling novel light-energy conversion pathways and offering intriguing opportunities for reconfigurable systems.

In this talk, I will discuss self-induced optical heating effects in highly absorbing dielectric nanoresonators, with a special focus on Silicon ones. In particular, I will show recent calculations demonstrating that, due to thermo-optical effects, self-heating can give rise to a complex, non-linear relationship between illumination intensity and temperature, even for moderate illumination intensities relevant for applications such as Raman scattering [1]. Subsequently, I will discuss how self-induced optical heating could be employed for thermally reconfigurable optical devices and metasurfaces [2]. Concurrently, I will discuss our recent effort in controlling the temperature field in multi-dimensional arrays of nanoantennas, highlighting the importance and opportunities offered by thermo-optical effects [3]. Then, I will discuss how the non-linearity introduced in the system by thermo-optical effects can be leveraged to achieve fast (MHz) transmission modulation with a decoupling of the thermal and optical characteristic times [4]. Finally, I will show how thermal effects can be leveraged for chirality detection [5] and conclude with a perspective on emerging opportunities of applications for photo-thermo-optical effects.

References

1. T. V. Tsoulos, G. Tagliabue, Self-induced thermo-optical effects in silicon and germanium dielectric nanoresonators, Nanophotonics 9 (12), 3849-3861, 2020.
2. A. Archetti, RJ Lin, N. Restori, F. Kiani, T. V. Tsoulos, G. Tagliabue, Thermally Reconfigurable Metalens, Nanophotonics 2022.
3. A. Naef, E. Mohammadi, T. V. Tsoulos, G. Tagliabue, Light‐Driven Thermo‐Optical Effects in Nanoresonator Arrays, Advanced Optical Materials 11 (20), 2023.
4. C Karaman, G N Naidu, A R Bowman, E NDayi, G Tagliabue, Decoupling Optical and Thermal Responses: Thermo-optical Nonlinearities Unlock MHz Transmission Modulation in Dielectric Metasurfaces, arXiv:2412.00996
5. E Mohammadi, G Tagliabue, Nanophotonic-Enhanced Thermal Circular Dichroism for Chiral Sensing, ACS Photonics 2025 12 (1), 152-158

Heterogeneous high-entropy alloy (HEA) plasmonics for superior and low-cost photocatalytic hydrogen evolution Reaction (HER)

Chun-Yen Chen[1], Yu-Hsuan Cheng[1], Alex Sam[1], Arya Pilakunnath[1], Ta-Jen Yen[1,*]

[1]Department of Material Sciences and Engineering, National Tsing Hua University, Hsinchu Taiwan.
[*]corresponding author: tjyen@mx.nthu.edu.tw

Abstract: A heterogeneous system has been designed in the form of gold or high-entropy alloy (HEA) nanoparticles, as well as silicon nanowires (SiNW) and molybdenum disulfide (MoS_2) nanofilms (PNP/SiNW/MoS_2), which exhibits excellent photocatalytic hydrogen evolution reactions (PC-HER) up to 477.5 mmol g^{-1} h^{-1}.

Plasmonic nanoparticles (PNP) can hybridize with atomically thin transition metal dichalcogenides (TMD), to dramatically intensify the weak light–matter interaction of those functional semiconductors. Herein, such a heterogeneous system has been designed in the form of gold or high-entropy alloy (HEA) nanoparticles, as well as silicon nanowires (SiNW) and molybdenum disulfide (MoS_2) nanofilms (PNP/SiNW/MoS_2), which exhibits excellent photocatalytic hydrogen evolution reactions (PC-HER). The resonance frequency of the 0D-PNP, the antireflection frequency of 1D-SiNW and the absorption frequency of 2D-MoS_2, match with the visible range simultaneously, for effectively harvesting the free solar energy. In addition, to enable superior efficiency and low cost of PC-HER, there present the following synergetic mechanisms. First, PNP not only show strong electromagnetic enhancement, but also offer photochemical to be a powerful co-catalyst. Next, the SiNW substrate exhibits high antireflection of 95% within the visible light absorption. Besides, an optimal MoS_2 structure that is a hybrid of both 1T and 2H phases was prepared by using reproducible and facile pyrolysis. Moreover, a p–n junction formed at the MoS_2/SiNW interface, facilitates charge separation to further boost the efficiency. In the end, our Au and HEA heterogeneous plasmonics demonstrate exceptional H_2 hydrogen generation rates of 246 and 477.5 mmol g^{-1} h^{-1}, respectively.

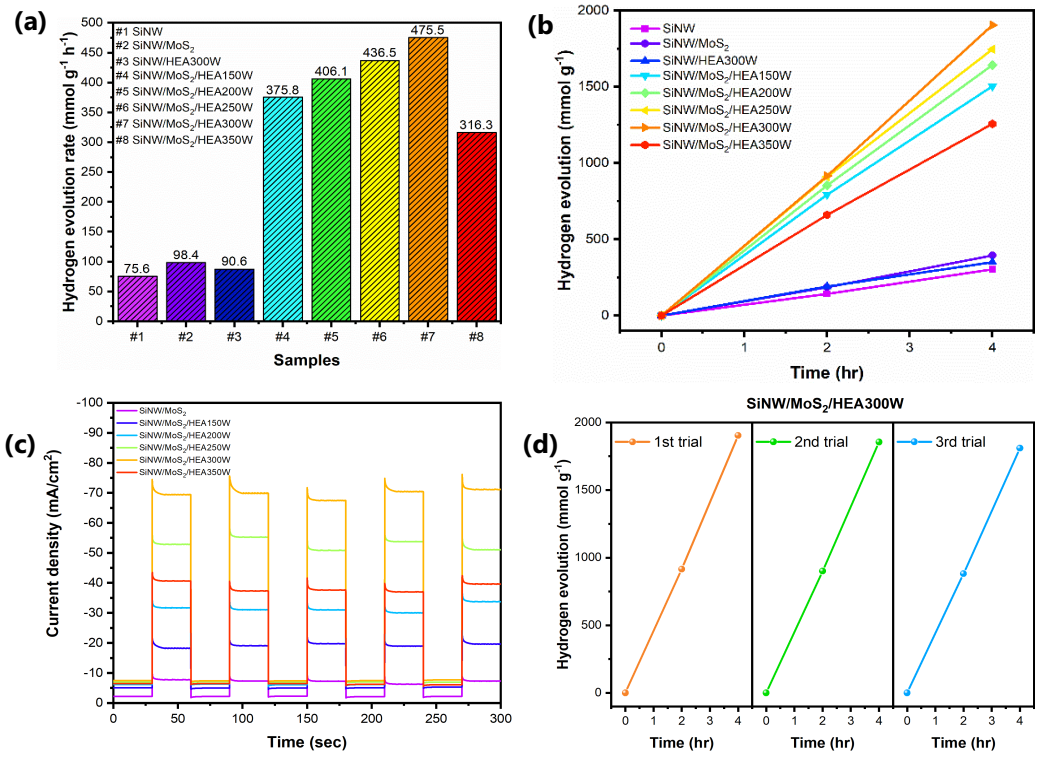


Fig. 1 Photocatalytic HER performance. (a-b) Hydrogen evolution rate & Time dependent hydrogen production graphs of the different samples (c) Transient photocurrent response of the photocatalyst showing its photoelectrochemical activity (d) Cycling stability for the constant photocatalytic H_2 production.

Accelerating the Design of Photonic Metamaterials with Artificial Intelligence

Yongmin Liu[1*]

[1]Department of Mechanical and Industrial Engineering, Northeastern University, Boston, MA, USA

[2]Department of Electrical and Computer Engineering, Northeastern University, Boston, MA, USA

[*]corresponding author: y.liu@northeastern.edu

Abstract: I will discuss how to accelerate the design of novel metamaterials by deep learning. Different from the conventional approaches, deep learning can produce fast and accurate designs without the need of case-by-case and time-consuming numerical calculations, helping to push the function capacity of metamaterials towards their physical limits.

Over the past decades, we have witnessed tremendous progress and success of photonic metamaterials. By tailoring the geometry of the building blocks of metamaterials and engineering their spatial distribution, we can control the amplitude, polarization state, phase and trajectory of light in an almost arbitrary manner.[1-2] The design process of metamaterials can benefit from physics-inspired methods, resorting to human knowledge such as physical insights revealed by simplified analytical modeling, similar experience transferred from previous practice, and intuition obtained by scientific reasoning. Very often, we rely on electromagnetic modeling based on finite-difference time-domain method, finite-element method, finite integration technique, the method of moments and other numerical simulation methods either with or without optimization algorithms. However, theses physics- or rule-based approaches are insufficient for designing multi-functional and multi-dimensional metamaterials, since the degrees of freedom in the design space become extremely large.

Deep learning (DL) could potentially accelerate the development of complex metamaterials with high efficiency, accuracy and fidelity. As a very powerful tool, DL has been applied to many other research fields such as material science, chemistry, laser physics, particle physics, quantum mechanics and microscopy, showing great potential to circumvent the drawbacks of traditional methods in these areas. The application of DL in the design of photonic structures and metamterials has also emerged as an exciting direction over the past a few years.[3-4] Advanced model architectures, such as convolutional neural network (CNN), recurrent neural network (RNN), recurrent neural network (RNN), generative adversarial network (GAN) and variational autoencoder (VAE), are employed to solve various tasks in photonic design.[5-9]

We propose to embed machine-learning models in both gradient-based and nongradient optimization loops for the automatic implementation of multifunctional metasurfaces.[10] The proposed end-to-end framework facilitates full exploitation of the prescribed design space and pushes the multifunctional design capacity to its physical limit. With a single-layer structure that can be readily fabricated, metasurface focusing lenses and holograms are experimentally demonstrated in the near-infrared region. They show up to eight controllable responses subjected to different combinations of working frequencies and linear polarization states, which are unachievable by the conventional physics-guided approaches. These results manifest the superior capability of the data-driven scheme for photonic design, and will accelerate the development of complex devices and systems for optical display, communication, and computing.

We also demonstrate multiwavelength infrared image sensors based on dielectric freeform metasurfaces, which are designed by the deep learning approach.[11] The metasurfaces can separate the mixed near-infrared light

into distinct wavelengths. To effectively modulate the complex amplitude of the transmitted light at three distinct near-infrared wavelengths (1150, 1350, and 1550 nm), we utilize high-index silicon freeform nanostructures supporting pronounced resonant modes. An inverse design model based on deep learning is employed to generate individual freeform nanostructures pixel by pixel, satisfying the complex amplitude requirement for a multiplexed metalens design. Both the simulated and experimental results show that the wavelength-multiplexing effect of the devices is in good agreement with the target with negligible crosstalk. Finally, a metasurface is employed to realize near-infrared multispectral imaging, which allows for the distinct detection and decoding of images at the three target wavelengths. The proposed technology has a wide range of applications in clinical medicine, biological tissue imaging, and deep-space exploration.

The concept of deep learning has far exceeded a computational analogy of biological neural systems, and emerged as a powerful tool that solves extremely complex problems, such as photonic metamaterials in arbitrary shape with prescribed optical responses, by building up multilevel abstraction of massive data. For photonics community, deep learning and other AI techniques are currently transforming the areas of optical design, integration and measurements. Using the developed novel photonic structures, in return we may implement all-optical platforms to perform deep learning and other AI algorithms at the speed of light.

Acknowledgements

Y. Liu acknowledges financial support from the National Science Foundation (DMR-2323908 and DMR-2202268).

References

1. Liu, Y.; Zhang, X., Metamaterials: a new frontier of science and technology. *Chemical Society Reviews* **2011,** *40* (5), 2494-2507.

2. Soukoulis, C. M.; Wegener, M., Past achievements and future challenges in the development of three-dimensional photonic metamaterials. *Nature Photonics* **2011,** *5* (9), 523-530.

3. Ma, W.; Liu, Z.; Kudyshev, Z. A.; Boltasseva, A.; Cai, W.; Liu, Y., Deep learning for the design of photonic structures. *Nature Photonics* **2021,** *15*, 77-90.

4. Jiang, J.; Chen, M.; Fan, J. A., Deep neural networks for the evaluation and design of photonic devices. *Nature Reviews Materials* **2021,** *6* (8), 679-700.

5. Ma, W.; Cheng, F.; Liu, Y., Deep-Learning Enabled On-Demand Design of Chiral Metamaterials. *ACS nano* **2018,** *12*, 6326-6334.

6. Malkiel, I.; Mrejen, M.; Nagler, A.; Arieli, U.; Wolf, L.; Suchowski, H., Plasmonic nanostructure design and characterization via Deep Learning. *Light: Science & Applications* **2018,** *7* (1), 60.

7. Liu, Z.; Zhu, D.; Rodrigues, S. P.; Lee, K.-T.; Cai, W., Generative model for the inverse design of metasurfaces. *Nano letters* **2018,** *18* (10), 6570-6576.

8. Ma, W.; Cheng, F.; Xu, Y.; Wen, Q.; Liu, Y., Probabilistic Representation and Inverse Design of Metamaterials Based on a Deep Generative Model with Semi‐Supervised Learning Strategy. *Advanced Materials* **2019,** *31* (35), 1901111.

9. Wu, Q.; Xu, Y.; Zhao, J.; Liu, Y.; Liu, Z., Localized Plasmonic Structured Illumination Microscopy Using Hybrid Inverse Design. *Nano Letters* **2024,** *24* (37), 11581-11589.

10. Ma, W.; Xu, Y.; Xiong, B.; Deng, L.; Peng, R. W.; Wang, M.; Liu, Y., Pushing the limits of functionality‐multiplexing capability in metasurface design based on statistical machine learning. *Advanced Materials* **2022,** *34* (16), 2110022.

11. Xiong, B.; Xu, Y.; Li, W.; Ma, W.; Chu, T.; Liu, Y., Deep Learning Design for Multiwavelength Infrared Image Sensors Based on Dielectric Freeform Metasurface. *Advanced Optical Materials* **2024,** *12* (10), 2302200.

Dynamic IR Beam Steering and Switching with Active Metasurfaces

M. S. Jang[1*]

[1] School of Electrical Engineering, Korea Advanced Institute of Science and Technology (KAIST), Korea
[*]corresponding author: jang.minseok@kaist.ac.kr

Abstract: This presentation reports our recent works on dynamic infrared beam steering and switching based on active metasurfaces. Full 2π phase-only transmission modulation, single-gate beam switching, and thermal emission steering will be discussed.

The growing demand for ultra-fast telecommunications, autonomous driving, and futuristic technologies highlights the crucial role of active beam steering at the nanoscale. In most studies, such devices rely on gate arrays composed of a large number of independently-controllable local gate electrodes that address local scattering response of individual metaatoms. While this approach in principle enables arbitrary wavefront control, the complicated driving mechanism and low optical efficiency have been hindering its practical applications. In this presentation, we experimentally demonstrate an active beam switching device that provides high directivity, consistent efficiency across diffraction orders, and a wide field of view while operating with only a single-gate bias. We then theoretically expand the idea of single-gate beam switching from two-level to multi-level configurations by utilizing a low-loss dielectric metasurface platform with freeform inverse-design approaches. Finally, we present that active metasurfaces can steer not only the input beam with high spatial coherence, but also incoherent thermal emissions by employing a laterally delocalized optical mode.

Towards tunable metamaterial-based torque sensing

M. Töfferl[1,3*], A. Schossmann[1,3], M. Saiko[1], P. Banzer[2,3], and A. Bergmann[1,3]
[1]Graz University of Technology, Austria.
[2]University of Graz, Austria.
[3]Christian Doppler Laboratory Structured Matter Based Sensing, Austria.
m.toefferl@tugraz.at (corresponding authors)

Abstract

We show the potential application of tunable metamaterials in torque sensing systems. Our concept comprises broad-side coupled split-ring resonators as passive sensor components and state-of-the-art millimeter wave transceiver for read-out. We provide a proof-of-concept demonstration for torque measurements on a fixed shaft.

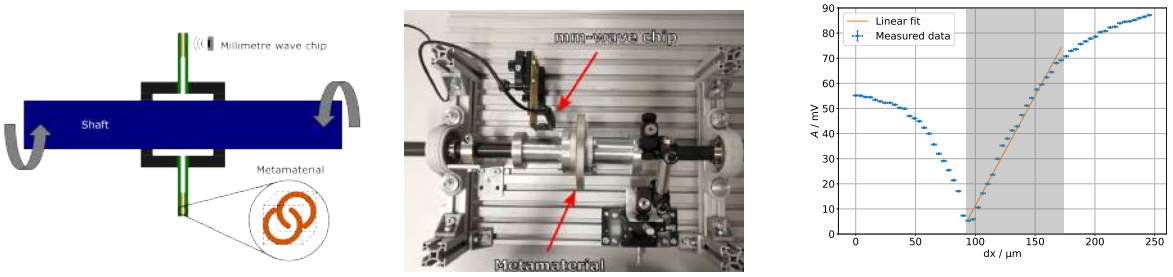
1 Tunable millimeter wave metamaterials

Tunable metamaterials are an emerging field of research in the context of novel sensor technologies [1]. Their unique properties, going beyond the capabilities of natural materials, derive from the structuring and the arrangement of resonant building-blocks on a sub-wavelength scale. Particularly in the millimeter wave regime, the requirements for structuring these building-blocks are already met with low-cost state-of-the-art technologies, such as printed circuit board (PCB) manufacturing. Tunable metamaterials in this work are characterized by two distinct properties: first, their resonant behavior is highly sensitive to the smallest structural changes in their building-blocks [2]. Second, their resonant behavior is measurable telemetrically as a change of reflection signals. These two properties are the basis for our concept of measuring torque on rotating drivetrain components.

2 Metamaterial-based torque sensor concept

Our approach is based on a circular array of broadside-coupled split-ring resonators. Two disks with one split-ring layer each are separately fixed to a shaft, as shown in fig. 1. Torque along the shaft leads to a shift in the relative angular arrangement between the discs and the coupled split-rings and thus changes their resonant behavior. This finally changes amplitude and phase at frequencies within the bandwidth of the metamaterial resonance. We designed the metamaterial to show a characteristic resonance at 60 GHz and, thus, a distinct minimum in the reflection spectra. The design was achieved by adjusting only the geometrical parameters of the split-rings within the capabilities of PCB manufacturing, using finite element calculations. We studied the sensor concept with a demonstrator as depicted in fig. 1b. We used a state-of-the-art millimeter wave chip transceiver for read-out and implemented a quadrature continuous wave radar architecture as it is used for vital sign detection [3]. In contrast to the latter, the amplitude of the quadrature signal was evaluated. The idea is that the metamaterial modifies both the amplitude and phase of the reflection signals, whereas small changes in distance to the antenna mainly affect the phase. We used a micrometer stage to precisely adjust the shift between the metamaterial discs in the demonstrator. The raw data of the millimeter wave chip was read out with a digital oscilloscope connected to a PC. Figure 1c shows the measured quadrature amplitude as a function of the shift dx between the metamaterial elements. To study the sensor

concept, we chose the data in the grey-shaded area in fig. 1c. A linear fit gives a sensitivity of $(0.88 \pm 0.02)\,\mathrm{mV\,\mu m^{-1}}$. The shift is related to an applied torque M by the linear relationship $M = \alpha \cdot dx$, with α determined by the stiffness and dimensions of the shaft. Our demonstrator showed a sensitivity of $(15.7 \pm 0.4)\,\mathrm{mV\,N^{-1}\,m^{-1}}$, which is comparable to state-of-the-art E-bike sensors [4].



(a) (b) (c)

Figure 1: Metamaterial-based torque sensor concept: (a) Sectional drawing of setup. (b) Demonstrator setup. (c) Measurement data of quadrature amplitude as a function of shift dx.

3 Challenges towards a torque sensor system

To realize a driveshaft torque sensor, measuring with rotating metamaterial is crucial. This requires that the resonance shift of the metamaterial is constant and known when rotated and no torque is applied. The underlying sensor effect, the tuning of the characteristic resonance, is also sensitive to variations in the distance between the discs and variations in the permittivity of the materials. This requires calibration, particularly for the sensing of starting torque. Our ongoing work focuses on the study of calibration requirements and possible migitation strategies based on anisotropic metamaterial designs, which comprises characterizing the rotating metamaterial in a laboratory setup.

4 Acknowledgements

The financial support by the Austrian Federal Ministry of Labour and Economy, the National Foundation for Research, Technology and Development and the Christian Doppler Research Association is gratefully acknowledged.

References

[1] Zheludev, N. I. and Kivshar, Y. S., "From metamaterials to metadevices" *Nature Materials*, Vol. 11, No. 11, pp. 917–924, 2012.

[2] Powell D. et al., "Metamaterial tuning by manipulation of near-field interaction" *Physical Review B*, Vol. 82, No. 15, 2010.

[3] Lin J.C., "Noninvasive Microwave Measurement of Respiration" *Proceedings of the IEEE*, Vol. 63, No 10 pp. 1530-1530, 1975

[4] NCTE, "Electric Bicycle Sensors", https://ncte.com/en/e-bikes/#series-portfolio, (accessed March 17, 2025)

[5] Schossmann, A., Hammerschmidt, D., Michenthaler, C. and Bergmann, A., "Torque measurement with tunable metamaterial and a modified Doppler radar" *2022 IEEE International Instrumentation and Measurement Technology Conference (I2MTC)* pp. 1-6, 2020

Active and dynamic optical phase gradient metasurfaces enabled by resonant nanophotonics and electro-optic materials

D. Barton[1*], S. Dagli[2], S. Abedini Dereshgi[1], and J. Dionne[2]

[1]Materials Science and Engineering, Northwestern University, USA

[2]Materials Science and Engineering, Stanford University University, USA
[*]corresponding author: dbarton@northwestern.edu

Abstract: Tunable subwavelength metasurfaces will enable low energy consumption and compact computing, communications, and sensing devices. Towards this, we will discuss our work leveraging electro-optics and high quality factor nanoantennas to demonstrate high efficiency phase gradient modulators operating at GHz speeds.

The ability to sculpt electromagnetic radiation with subwavelength optical antennas has enabled fundamental advances in small form-factor and high performance optical devices[1]. Reconfigurable metasurfaces can advance key optical technologies[2,3] including light detection and ranging[4], optical communications[5], and augmented or virtual reality. However, it remains a fundamental challenge to create dynamical optical devices that have simultaneously high efficiency, contrast, low switching voltages, and high modulation bandwidths, as either the optical properties or geometry much change by a significant amount to modify the optical transfer function.

Demonstrations of dynamic devices based on phase change materials[6], liquid crystals[7], and doped semiconductors[8] have shown promise in this space. In addition, electro-optic materials provide a platform for high speed and low-loss modulation[9-12], but are limited in the refractive index difference because of the second order nonlinearity being used. Indeed, the electro-optic coefficient of commonly available lithium niobate is approximately 31 pm/V, requiring integrated photonic modulators to be much longer (~1 cm) than metasurface devices can allow for significant optical phase shifts.

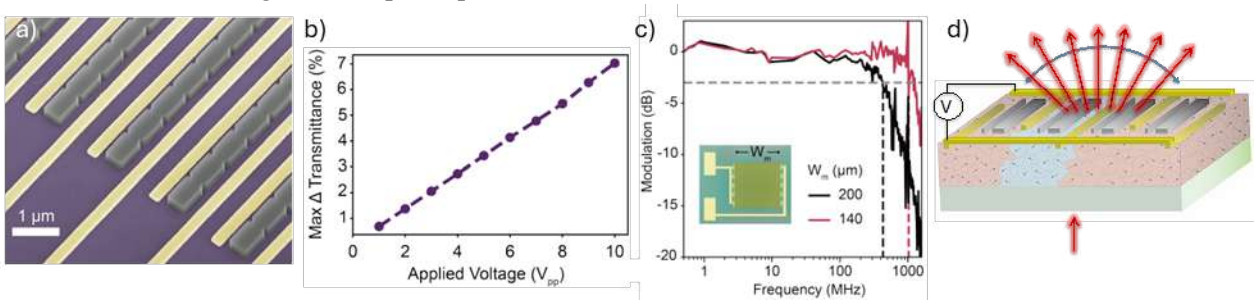


Figure 1: Electro-optic metasurfaces. a) Silicon on lithium niobate metasurface. Scale bar: 1 um. b) Ffficient modulation tuning with >7% modulation within 10 Vpp. c) >GHz bandwidth beamsplitting metasurfaces, limited by device size. d) Future materials integrated with high-Q antennas will enable efficient reconfigurable metasurface elements.

Here[13], we will show how rational design of nanoantennas in conjunction with transparent electro-optic materials can enable high efficiency and GHz-speed modulation of metasurfaces. Utilizing electro-optic materials like Lithium Niobate on Insulator can guarantee high efficiency devices without significant absorption at the cost of low refractive index tuning through the Pockel's effect. We show that this can be overcome using resonant nanoantennas based on guided mode resonances (GMRs)[14, 15] (fig. 1a). An optical resonance in the transmission profile leads to significant variation in transmitted amplitude and phase when an electric field is

applied through the electro-optic material. We demonstrate that guided mode resonant silicon nanoantennas 300 nm tall on top of a thin film of lithium niobate can be used to create electro-optically tunable optical devices. Using this as a prototype device, we demonstrate >0.7%/V shifting efficiency and 7.1% absolute transmission modulation with ±5 V applied to the metasurfaces. We then show how beamsplitting metasurfaces can be designed and demonstrate GHz- bandwidth modulation between a beamsplitting state and a transmissive state (fig. 1b). The bandwidth is limited by the RC delay of the electrodes, as shrinking the devices down increases the 3 dB bandwidth (fig. 1c).

Finally, we will discuss our further work developing electro-optic material platforms that leverage resonant optical modes for spatially programmable metasurfaces. Developing nanofabrication techniques and new integrated electro-optic materials will enable advances towards broadband and low energy consumption metasurface modulators. Together this work demonstrates the value of wide bandgap nonlinear materials for electrically-controllable wavefront shaping devices, and further demonstrates that combined electronic-photonic interfaces for control of free-space light is a meaningful platform for future photonic systems.

Acknowledgements: The authors acknowledge support from the Office of Naval Research under the Multi University Research Initiative (MURI) program (award N00014-231-2567); and the U.S. Department of Energy Office of Science National Quantum Information Science Research Centers as part of the Q-NEXT center; and the National Defense Science and Engineering Graduate (NDSEG) Fellowship Program. Work was performed in part at the Stanford Nanofabrication Facility (SNF) and the Stanford Nano Shared Facilities (SNSF), supported by the National Science Foundation (awards ECCS-1542152 and ECCS-2026822, respectively).

References

1. Kuznetsov, A.I., Brongersma, et al. Roadmap for optical metasurfaces. ACS Photonics 11, 816–865 (2024)
2. Liu, K., Ye, C.R., Khan, S., Sorger, V.J. “Review and perspective on ultrafast wavelength-size electro-optic modulators,” Laser & Photonics Reviews 9, 172–194 (2015)
3. Jung, C., Lee, E., Rho, J.: The rise of electrically tunable metasurfaces. Science Advances 10 (2024)
4. Kim, I., Martins, R.J., et al. Nanophotonics for light detection and ranging technology. Nature Nanotechnology (2021)
5. Thureja, P., Sokhoyan, et al. Toward a universal metasurface for optical imaging, communication, and computation. Nanophotonics 11, 3745–3768 (2022)
6. Li, S.-Q., Xu, X., Veetil, R.M., Valuckas, V., Paniagua-Dom´ınguez, R., Kuznetsov, A.I.: Phase-only transmissive spatial light modulator based on tunable dielectric metasurface. Science 364, 1087–1090 (2019)
7. Zhang, Y., Fowler, et al. Electrically reconfigurable non-volatile metasurface using low-loss optical phase-change material. Nature Nanotechnology 16(6), 661–666 (2021)
8. Huang, Y.-W., Lee, H.W.H., et al. Gate-tunable conducting oxide metasurfaces. Nano Letters 16, 5319–5325 (2016)
9. Benea-Chelmus, I.-C., Mason, S., Meretska, M.L., Elder, D.L., Kazakov, D., Shams-Ansari, A., Dalton, L.R., Capasso, F.: Gigahertz free-space electro-optic modulators based on mie resonances. Nature Communications 13, 3170 (2022)
10. Weigand, H., Vogler-Neuling, V.V., Escal´ e, M.R., Pohl, D., Richter, F.U., Karvounis, A., Timpu, F., Grange, R.: Enhanced electro-optic modulation in resonant metasurfaces of lithium niobate. ACS Photonics 8, 3004–3009 (2021)
11. Weiss, A., Frydendahl, C., Bar-David, J., Zektzer, R., Edrei, E., Engelberg, J., Mazurski, N., Desiatov, B., Levy, U.: Tunable metasurface using thin-film lithium niobate in the telecom regime. ACS Photonics 9, 605–612 (2022)
12. Damgaard-Carstensen, C., Yezekyan, T., Brongersma, M.L., Bozhevolnyi, S.I.: Highly efficient, tunable, electro-optic metasurfaces based on quasi-bound states in the continuum. ACS Photonics (2025)
13. Dagli, S, Shim, J., […] Barton, D.*, and Dionne, J*, GHz-speed wavefront shaping metasurface modulators enabled by resonant electro-optic nanoantennas, *under review* https://arxiv.org/abs/2503.08853 (2025)
14. Lawrence, M., Barton, D.R., Dixon, J., Song, J.-H., Groep, J., Brongersma, M.L., Dionne, J.A.: High quality factor phase gradient metasurfaces. Nature Nanotechnology 15, 956–961 (2020)
15. Barton, D., Lawrence, M., Dionne, J.: Wavefront shaping and modulation with resonant electro-optic phase gradient metasurfaces. Applied Physics Letters 118, 071104 (2021)

Metasurface for multi-functional edge imaging and quantitative phase imaging

Zhaowei Liu*
Department of Electrical and Computer Engineering, University of California, San Diego
9500 Gilman Drive, La Jolla, California, USA
*Corresponding author: zhaowei@ucsd.edu

Abstract: Metasurfaces have been proved to be a promising approach for various optical imaging techniques with advanced functionalities. In this talk, I will summarize some of our recent progresses in the field and showcasing quantitative phase imaging and edge detection imaging using metasurfaces.

Edge detection is of fundamental importance in optical imaging analysis since it preserves important geometric boundaries and significantly reduces the amount of data to be process. We demonstrated the effectiveness to perform optical edge detection using dielectric metasurface with high optical efficiency[1-3]. Combined with nonlinear materials, metasurface can be used for power dependent edge detection or performing complex optical transformation [4,5]. The quantum edge imaging has also been demonstrated if entangled photon source is used [6]. Compared to the classical cases, quantum edge imaging scheme comprises significantly improved signal to noise ratio. Switchable edge imaging has also been studied by incorporating the phase changing materials into the edge detection metasurface [7].

Quantitative phase imaging (QPI) and microscopy is another field with extensive explorations by using metasurfaces. We proposed a QPI methodology named Fourier optical spin splitting microscopy (FOSSM) by placing a single metasurface at the back focal plane [8]. A pair of metasurface can be placed at any place in the optical path for single-shot QPI imaging by using a polarized camera [9]. Single-shot QPI without polarized camera was achieved by combining deep learning with the transport-of-intensity equation [10]. The metasurface fabricated directly inside a traditional lens was used to showcase its advanced QPI capability for bioimaging [11].

References

1. Zhou, J., et. al., “Optical edge detection based on high-efficiency dielectric metasurface,” PNAS 116, 11137-40, 2019.
2. Zhou, J., et. al., “Two-dimensional optical spatial differentiation and high-contrast imaging,” Natl Sci. Rev. 8, nwaa176, 2021.
3. Cui, T. J., et., al., “Roadmap on electromagnetic metamaterials and metasurfaces,” J. Phys. Photonics, 6, 032502, 2024.
4. Zhou, J., et. al., “Kerr metasurface enabled by metallic quantum wells,” Nano Lett. Vol, 21, No. 1, 330-336, 2020.
5. Zhou, J., et. al., “Nonlinear computational edge detection metalens,” Adv. Funct. Mater. Vol. 32, No. 34, 2204734, 2022.
6. Zhou, J., et. al., “Metasurface enabled quantum edge detection,” Sci. Adv. Vol, 6, No. 51, eabc4385, 2020.
7. Chen, G., et. al., “Visible and near-infrared dual band switchable metasurface edge imaging,” Opt. Lett. Vol 47, No. 16, 4040-4043, 2022.
8. Zhou, J., et. al., “Fourier optical spin splitting microscopy,” Phys. Rev. Lett. 129, 020801, 2022.
9. Wu, Q., et. al., “Single-shot quantitative amplitude and phase imaging based on a pair of all-dielectric metasurfaces,” Optica, Vol. 10, No. 5, 619, 2023.
10. Zhou, J., et. al., “Advanced quantitative phase microscopy achieved with spatial multiplexing and a metasurface,” Nano Letters Vol. 25, No. 5, 2034-2040, 2025.
11. Zhou, J., et. al., “Eagle-eye inspired meta-device for phase imaging,” Adv. Mat. Vol. 36, No. 32, 2402751, 2024.

Highly confined, low-loss infrared phonon polaritons in perovskite oxide membranes

Yin Liu

1. Department of Materials Science and Engineering, North Carolina State University, Raleigh, NC 27695, United States

*corresponding author: yliu292@ncsu.edu

Abstract: Phonon polaritons (PhPs), excitations arising from the coupling of light with lattice vibrations, enable light confinement and local field enhancement, which is essential for various photonic and thermal applications. To date, PhPs with high confinement and low loss have been mainly observed in the mid-infrared regime and mostly in manually exfoliated flakes of van der Waals (vdW) materials. In this work, we demonstrate the existence of low-loss, thickness-tunable phonon polaritons in the far-infrared regime within transferable free-standing $SrTiO_3$ membranes synthesized through a scalable approach, achieving high figures of merit, which are comparable to the previous record values from the vdW materials. Leveraging atomic precision in thickness control, large dimensions, and compatibility with mature oxide electronics, functional oxide membranes present a promising large-scale two-dimensional (2D) platform beyond vdW materials for on-chip polaritonic technologies in the far-infrared regime.

Acknowledgements: Y.L. acknowledge the support by the National Science Foundation under Award No. DMR-2340751.

References

1. Koons K., Bechtel H. A., Taboada-Gutiérrez J., Ghanbari R., Wang Y., Gilbert Corder S.N., Kuzmenko A.B., Xu R. and Liu Y, “Low-loss far-infrared surface phonon polaritons in suspended $SrTiO_3$ nanomembranes,” submitted.
2. Xu R., Crassee I., Bechtel H.A., Zhou Y., Bercher H. A., Korosec L., Rischau C. W., Teyssier J., Crust K. J., Lee Y., Gilbert Corder S. N., Li J., Dionne J. A., Hwang H. Y., Kuzmenko A. B. and Liu Y., “Highly confined epsilon-near-zero and surface-phonon polaritons in $SrTiO_3$ membranes”, Nature Communications, 15,4743 (2024).

Liquid-Metal-Based Reconfigurable Metasurfaces for Display and Sensing Applications

Peter Qiang Liu

Department of Electrical Engineering, State University of New York at Buffalo, Buffalo, NY 14260, USA

Email: pqliu@buffalo.edu

Abstract

The flexibility, conformability and transformability of room-temperature gallium-based liquid metals are unique advantages over widely used solid metals [1]. In this talk, I will discuss our recent explorations into using such liquid metals to realize dynamically reconfigurable metasurfaces for different spectral regions and various applications, such as display and molecular sensing [2-4].

Reference

[1] P.Q. Liu, X. Miao, S. Datta, “Recent Advances in Liquid Metal Photonics: Technologies and Applications”, *Optical Materials Express* **13**, 699 (2023).

[2] X. Miao, T.S. Luk, P.Q. Liu, “Liquid-metal-based nanophotonic structures for high-performance SEIRA sensing”, *Advanced Materials* **34**, 2107950 (2022).

[3] S. Datta, S. Vasini, X. Miao, P.Q. Liu, “Surface-Enhanced Raman Scattering Sensors Employing a Nanoparticle-On-Liquid-Mirror (NPoLM) Architecture”, *Small Methods* **8**, 2400119 (2024).

[4] M.A.K. Khan, Y. Zhao, S. Datta, P. Paul, S. Vasini, T. Thundat, P.Q. Liu, "Deterministic Fabrication of Liquid Metal Nanopatterns for Nanophotonics Applications", *Small*, 2403722 (2024).

Metasurface-Based Optical Elements for Biomedical Applications

S. Vyas[1], C. H. Chu[2], J. A. Yeh[3], and Y. Luo[1,2,4,5]

[1]Institute of Medical Device and Imaging, National Taiwan University, Taipei, 10051, Taiwan, R.O.C.
[2] YongLin Institute of Health, National Taiwan University, Taipei, 10087, Taiwan, R. O. C
[3]Institute of Nano Engineering and Micro-systems, National Tsing Hua University, Hsinchu, 30013, Taiwan, R.O.C.
[4]Program for Precision Health and Intelligent Medicine, National Taiwan University; Taipei, 106319, Taiwan, R.O.C.
[5]Department of Biomedical Engineering, National Taiwan University, Taipei, 10051, Taiwan, R.O.C
[6]Taiwan International Bio Research Center, National Taiwan University, Taipei, 10051, Taiwan, R.O.C.
[*]corresponding author: yuanluo@ntu.edu.tw

Abstract: Metasurfaces are vital for creating flat optical components with tailored functionalities. By manipulating light properties such as amplitude, phase, and polarization, metasurface-based optical elements enhance biomedical imaging system' performance. This work explores recent advancements in our laboratory applying metasurface optical components in biomedical instruments.

Optical sectioning microscopy is vital for biomedical imaging. We integrated metalenses into multiple imaging modalities.

Biophotonics applications require precise optical energy delivery to specific sites without affecting surrounding areas. Metasurfaces integrated in light sheet fluorescence microscopy enables compact, and high-resolution imaging of biological samples. We also show the benefits of using a variable focus metalens in a telecentric design with HiLo imaging for high-resolution optically sectioned images. The varifocal dielectric Moiré metalens delivers promising fluorescence imaging performance with standard test targets and biological samples. In addition, abrupt autofocusing (AAF) beams are ideal for laser-tissue interactions due to high energy contrast between the input and focal plane. We present the design and implementation of a metasurface optical element for the AAF beam. Experimental demonstrations show fluorescence-guided laser micro-profiling of mice heart tissues and photocoagulation in skin tissue using the AAF beam. These experiments highlight AAF beams' unique propagation and focusing properties, such as ballistic dynamics, high-intensity contrast, and self-reconstruction. Traditional bulky spatial light modulators can be replaced with metasurface optical elements in optical tweezers. We developed a two-dimensional Airy beam in the visible region for lateral shifting and guiding particles along the axial direction. Quantitative measurements for optical trap characterization demonstrate the potential of metasurface optical elements in miniaturizing optical tweezer setups. Implementing ultrathin optical devices in biomedical instruments opens new avenues for creating compact and high-performance systems. Our work has important applications in interdisciplinary research, including metasurface, optical microscopy, and biomedical optical instrumentation.

References

1. S. A. Suresh, S. Vyas, C. H. Chu, T. Yamaguchi, T. Tanaka, J. A. Yeh, D. P. Tsai, Y. Luo, “All-Dielectric Meta-Microlens-Array Confocal Fluorescence Microscopy”. Laser Photonics Rev, 2401314, 2024.
2. Y.H. Chia, W.H. Liao, S. Vyas, C.H. Chu, T. Yamaguchi, X. Liu, T. Tanaka, Y.Y. Huang, M.K. Chen, W.S. Chen, D.P. Tsai, and Yuan Luo, "In vivo intelligent fluorescence endo-microscopy by varifocal meta-device and deep learning," Advanced Science, doi.org/10.1002/advs.202307837. 2024.
3. Cheng Hung Chu, Sunil Vyas, Yuan Luo*, Pan-Chyr Yang, Din Ping Tsai, "Recent developments in biomedical

applications of metasurface optics," APL Photonics, 9, 030901, 2024.

4. S. Vyas, C. H. Chu, J. A. Yeh, Yuan Luo*, “Abrupt autofocusing beam from a phase-only mask,” JOSA A, 41 (3), A40-A46, 2024.
5. Cheng Hung Chu, Yu-Hsin Chia, Hung-Chuan Hsu, Sunil Vyas, Chen-Ming Tsai, Takeshi Yamaguchi, Takuo Tanaka, Huei-Wen Chen, Yuan Luo*, Pan-Chyr Yang, and Din Ping Tsai, "Intelligent phase contrast meta-microscope system", Nano Letters, 23(24), 11630-11637, 2023.
6. Yuan Luo*, M.L. Tseng, S. Vyas, H. Y. Kuo, C.H.Chu, M.K.Chen, H.C.Lee, W.P.Chen, V.C.Su, X.Shi, H.Misawa, D.P.Tsai, and P.C.Yan, “Metasurface based abrupt autofocusing beam for biomedical applications, ” Small methods, vol. 6, pp. 2101228, 2022.
7. Yuan Luo, M.L.Tseng, S. Vyas, T.Y. Hsieh, J.C. Wu, S.Y. Chen,H.F. Peng, V.C. Su, T.T.Huang, H. Y. Kuo, C.H. Chu, M.K.Chen,J.W. Chen, Y.C. Chen, K.Y.Huang, C.H. Kuan, X.Shi, H. Misawa and D. P. Tsai, “Meta-lens light-sheet fluorescence microscopy for in vivo imaging, ”Nanophotonics, vol.11,pp.1949-1959, 2022.
8. Yuan Luo, Cheng Hung Chu, Sunil Vyas, Hsin Yu Kuo, Yu Hsin Chia, Mu Ku Chen, Xu Shi, Takuo Tanaka, Hiroaki Misawa, Yi-You Huang, Din Ping Tsai, "Varifocal metalens for optical sectioning fluorescence microscopy," Nano Letters, vol.21, pp.5133–5142, 2021.

Confinement-Induced Nonlocality, Topological Darkness, and Goos-Hänchen Effect Enhancement in Transdimensional Plasmonic Film Systems

I. V. Bondarev[1*] and S.-A. Biehs[2]

[1]Department of Mathematics and Physics, North Carolina Central University, Durham, NC 27707, USA
[2]Institut für Physik, Carl von Ossietzky Universität, Oldenburg, 26111, GERMANY
[*]Corresponding author: ibondarev@nccu.edu

Abstract: We classify topologically protected singularities for the reflection coefficient of transdimensional plasmonic films. Originating from their nonlocal electromagnetic response due to vertical electron confinement, these singularities lead to lateral (angular) Goos-Hänchen shifts on the millimeter (milliradian) scale in the visible range, greatly exceeding those reported previously for artificially designed metasurfaces.

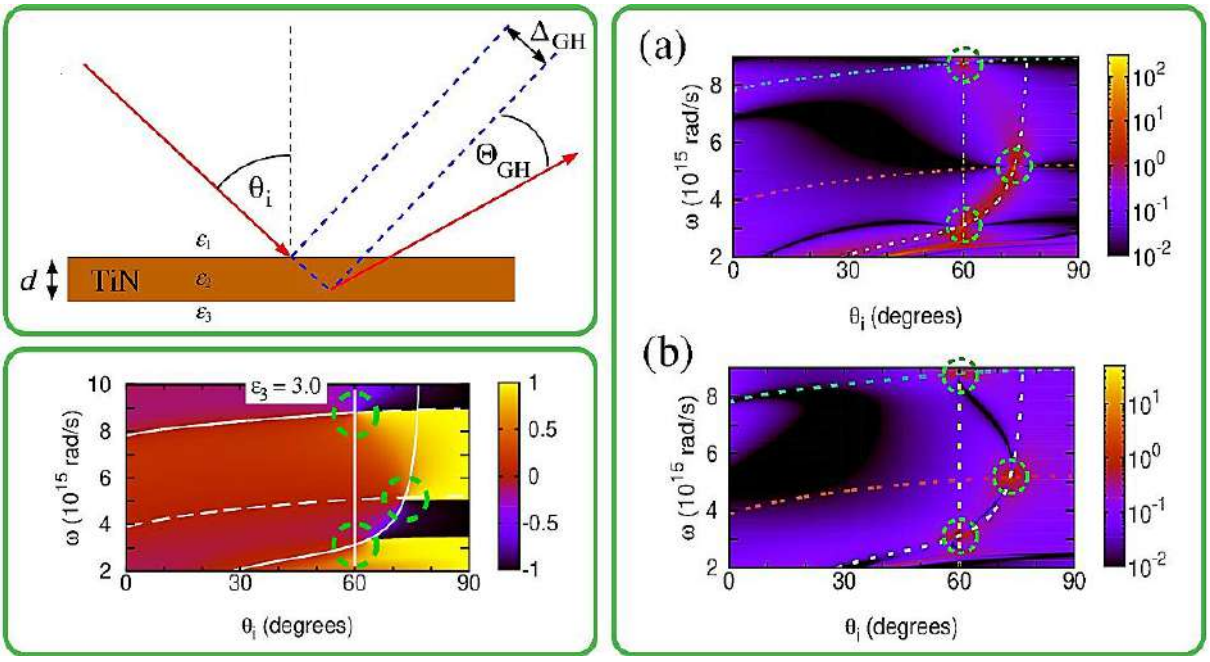


Figure 1. *Top left*: Sketch of the lateral and angular GH shifts for finite cross-section light beam incident on a TiN plasmonic slab of broken in-plane reflection symmetry. *Bottom left & Right*: Reflection phase φ_p/π and absolute values of the lateral/angular GH shifts (a)/(b) in mm/mrad, calculated for a 40 nm thick TiN slab with ε_1=1 and ε_3=3 (MgO) neglecting dissipation. Lines show the EM eigen modes of the system. Circles indicate the topological singularity points at the eigen-mode intersections. See Ref. [5].

Plasmonic transdimensional (TD) materials are atomically thin metal, semimetal or doped semiconductor films of precisely controlled countable number of monolayers [1]. Due to current progress in nanofabrication techniques [2–4], such materials can be reproducibly grown and offer high tailorability of their optoelectronic properties not only by altering their chemical and/or electronic composition (stoichiometry, doping), or strain, but also by varying their thickness. Here we show theoretically [5] that the in-plane electromagnetic (EM) response nonlocality induced by the vertical electron confinement in the ultrathin TD films leads to topologically protected singularities of their nonlocal reflection coefficient (Fig.1). These singularities result in the giant lateral and angular Goos-Hänchen (GH) shifts in the millimeter and milliradian ranges, respectively, exceeding greatly those reported for light beams of finite

transverse extent with no material-induced nonlocality [6,7]. The singularities appear in the plasmonic TD film systems with broken in-plane reflection symmetry (substrate and superstrate of unequal permittivities) where the EM eigenmode degeneracy is lifted to create the points of topological darkness in the visible range, which do not exist in local (Drude-like) plasmonic materials. The topological darkness points are intersection points of the non-degenerate EM eigenmodes of the TD film system. We demonstrate by direct calculations (Fig.1) that they can lead to the lateral and angular GH shifts as large as ~0.4 mm and ~40 mrad, respectively, for typical 40 nm thick TD plasmonic TiN films, which can be observed by using for example the conventional He-Ne laser light. The remarkable opportunity to bring the giant GH effect to the visible range comes from the fact that the nonlocal plasma frequency of the TD plasmonic films can be red-shifted not only by decreasing their thickness [2–4] but also by in-plane momentum reduction through the incident angle change [5].

This work was supported in part by grant NSF PHY-2309135 to the Kavli Institute for Theoretical Physics. I.V.B. gratefully acknowledges support from the U.S. Army Research Office under award # W911NF2310206.

References

1. Boltasseva, A. and Shalaev, V. M. “Transdimensional photonics,” ACS Photonics, Vol. 6, 1–3, 2019.
2. Shah, D., et. al. “Thickness-dependent Drude plasma frequency in transdimensional plasmonic TiN,” Nano Lett., Vol. 22, 4622–4629, 2022.
3. Salihoglu, H., et al. “Nonlocal near-field radiative heat transfer by transdimensional plasmonics,” Phys. Rev. Lett., Vol. 131, 086901, 2023.
4. Das, P., et al. “Electron confinement-induced plasmonic breakdown in metals,” Science Adv., Vol. 10, eadr2596, 2024.
5. Biehs, S.-A. and Bondarev, I. V. “Goos-Hänchen effect singularities in transdimensional plasmonic films,” arXiv:2410.09308 (*submitted to Optica*).
6. Shadrivov, I. V., Zharov, A. A., and Kivshar, Yu. S. “Giant Goos-Hänchen effect at the reflection from left-handed metamaterials,” Appl. Phys. Lett., Vol. 83, 2713–2715, 2003.
7. Bliokh, K. Y. and Aiello, A. “Goos-Hänchen and Imbert-Fedorov beam shifts: an overview,” J. Opt. Vol. 15, 014001, 2013.

Ultra-sensitive infrared gas molecular measurement using three-dimensional broadband metasurface absorber

Takuo Tanaka[1,2]

[1]RIKEN Center for Advanced Photonics, Japan
[2] Institute of Post-LED Photonics, Tokushima University, Japan
[*]t-tanaka@riken.jp

Abstract: A broadband metasurface absorber featuring three-dimensional metal double-cylinder structures was fabricated and applied to an ultra-sensitive infrared spectroscopic gas measurement technique. Owing to its strong and broadband resonant absorption, the signal-to-background ratio has been improved, enabling the measurement of IR spectroscopic signals from different gas molecules.

Ultra-sensitive biomolecular sensing technologies are becoming increasingly crucial in modern life. Among the various available techniques, infrared (IR) absorption spectroscopy is highly promising due to its label-free and noninvasive detection capabilities. However, practical applications are often hindered by weak signals, due to the intrinsically low IR absorption of natural substances and substantial background noise. To address these challenges, we introduced metamaterial absorbers to enhance the sensitivity of infrared spectroscopy by suppressing parasitic background signals. Through the use of plasmon-enhanced electromagnetic fields and plasmon-molecular coupling within the metamaterial absorbers, we achieved molecular sensitivity down to the attomolar level (10^{-18} mol). This was demonstrated using self-assembled monolayers of 16-Mercaptohexadecanoic acid, which formed a complete monolayer on the device surface [1].

We extended this sensing mechanism to liquid samples by successfully developing a three-dimensional metal-insulator-metal (MIM) metasurface absorber, which integrates a nanofluidic channel, several tens of nanometers in depth, as the insulating layer [2, 3, 4]. In this hybrid metamaterial-nanofluidic device, analyte molecules are precisely delivered to the metamaterial's hot-spot region. Owing to the strong interaction between the analyte molecules and the metamaterial, we attained molecular sensitivity at an approximate density of 10^{-4} molecules/Å^2, representing a two-order-of-magnitude improvement over previous plasmonic-enhanced IR detection methods.

We further applied this advanced sensing mechanism to gas-phase samples. Since the molecular signal strength is highly dependent on the density of hot spots in the metamaterial, we designed and fabricated a vertically aligned MIM (v-MIM) structure featuring a 25 nm nanogap, designed as a small footprint MIM configuration to enhance hot spot density [5].

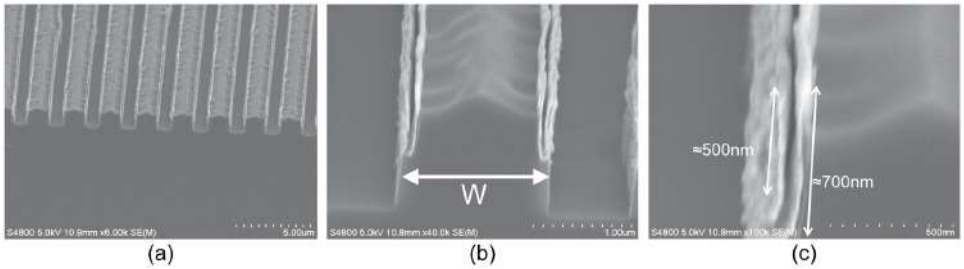


Figure 1. Scanning electron micrographs of 3D vertically aligned MIM structure.

This v-MIM metamaterial absorber was applied to carbon dioxide and butane detection, designed to exhibit resonances at 4033 cm^{-1} and 2945 cm^{-1}, which spectrally overlap with the C=O and $–CH_2$ vibrational modes, respectively. The coupling between these two resonant modes induces a Fano resonance, with their distinct peaks clearly observed as corresponding transmission dips.

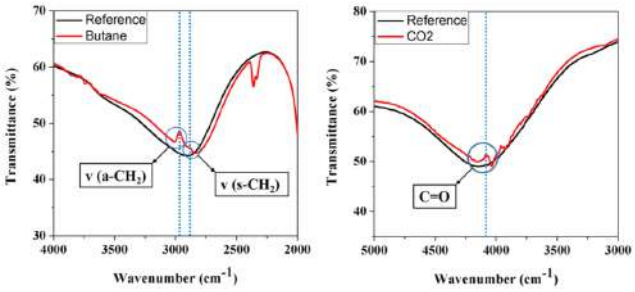


Figure 2. Experimental results of butane and carbon dioxide gas detection.

To achieve a more durable and optically efficient structure, we propose a three-dimensional coaxial double-cylinder metamaterial, as shown in Figure 3(a). This 3D metamaterial absorber exhibits a broad absorption band ranging from 2.5 μm to 7 μm, as shown in Figure 3(b). Owing to the broad absorption band of this coaxial double-cylinder metamaterial, we clearly observed absorption peaks of multiple gases. Figure 3(c) presents the absorption spectra of methane, butane, and carbon dioxide gases, while Figure 3(d) displays the absorption spectrum when a dimethyl ether and carbon dioxide gas mixture was introduced into the gas chamber.

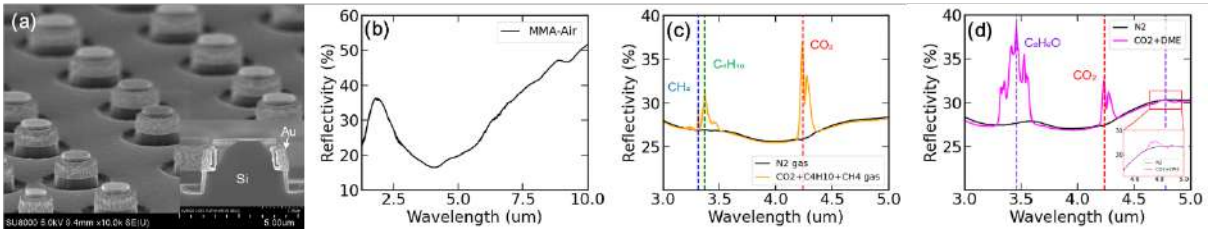


Figure 3. Three-dimensional coaxial double-cylinder metamaterial absorber and its experimental results of multiple gas sensing. (a) SEM image of a three-dimensional coaxial double-cylinder metamaterial, (b) its reflection spectrum showing broad absorption band, (c) experimental results with methane, butane, and carbon dioxide, and (d) experimental result with dimethyl ether and carbon dioxide gases.

Acknowledgements

This work was financially supported by JST CREST under Grant No. JPMJCR1904, Japan.

References

[1] A. Ishikawa and T. Tanaka, Scientific Reports **5**, 12570 (2015).

[2] T. H. H Le and T. Tanaka, ACS Nano **11**, 9780-9788 (2017).

[3] T. Le, A. Morita, K. Mawatari, T. Kitamori, and T. Tanaka, ACS Photonics **5**, 3179 (2018).

[4] T. H. H. Le, A. Morita, and T. Tanaka, Nanoscale Horiz. **5**, 1016 (2020).

[5] D.-S. Su, D. P. Tsai, T.-J. Yen, and T. Tanaka, ACS Sensors **4**, 2900-2907 (2019).

Nonreciprocal and directional control of infrared emissivity in semiconductor ENZ systems

A. P. Raman[1*]

[1]Department of Materials Science and Engineering, University of California, Los Angeles, Los Angeles, CA 90095 USA
[*]corresponding author: aaswath@ucla.edu

Abstract: Controlling the spectral and directional characteristics of thermal emission is of fundamental interest for sensing and energy applications. I will introduce our recent work on controlling spectral and directional emissivity in III-V semiconductor-based photonic structures and metasurfaces, and exploiting the magneto-optic response of these architectures to break Lorentz reciprocity.

1.

Multi-Layer Flat Optics: Challenges & Opportunities

Ahmed H. Dorrah[1,*]

[1]Department of Applied Physics & Science Education, Eindhoven University of Technology, The Netherlands
a.h.dorrah@tue.nl

Abstract: Metasurfaces have enabled advanced imaging, sensing and communications due to their CMOS compatibility, versatility, and compactness. However, challenges in diffraction efficiency, bandwidth, scalability, and limited polarization control persist. Multi-layer metasurfaces address these issues, enabling high-efficiency devices with full polarization control, achromatic response, and improved performance for many applications.

Introduction: Optical metasurfaces are planar nano-optics patterned with sub-wavelength resolution to control light's phase, intensity, and polarization over a compact thickness [1]. A single lithography step enables tailoring a variety of meta-atoms, offering versatile functionalities within the same planar form factor. Metasurfaces have enabled numerous applications, including diffraction-limited focusing, computational imaging, holography, and polarization imaging, and has inspired multifunctional and reconfigurable devices [2]. While metasurfaces have simplified fabrication compared to 3D metamaterials, their limited thickness poses fundamental challenges in wavefront shaping, particularly at high numerical apertures (NA). As a result, new multi-layer, cascaded, and 3D meta-optic architectures have gained attention, driven by advancements in multi-level nanofabrication.

Motivation: Compound meta-optics have emerged due to limitations in single-layer metasurfaces, which often result in trade-offs between diffraction efficiency, bandwidth, field of view, high NA, and complex amplitude modulation. For example, ultrathin metasurfaces, such as plasmonic nano-antennas, require balanced loss and gain to achieve unitary efficiency, due to impedance mismatch between the input and target fields [3]. This limits the range of phase control and causes undesired reflections. Stacking multi-layer metasurfaces can enhance transmission without sacrificing phase control [4-5]. Furthermore, using high-index contrast dielectrics or nonlocal metasurfaces can relax these constraints. Nevertheless, complex amplitude modulation still requires compound or cascaded architectures [6-7]. Additional challenges remain in achieving achromatic response at high NA due to the thin form factor and delay-bandwidth product, necessitating thicker or multi-layer metasurfaces [8]. Distributing wavefront transformations across multiple layers introduces additional degrees of freedom, offering redundancy and enabling multifunctional devices with high diffraction efficiency, broadband performance, wide field of view, and controllable dispersion. To this end, we highlight our free-standing bilayer metasurface platform and focus on the advances in polarization optics and dispersion control that it brings [9].

Advances in Polarization Optics: Shape-birefringent dielectric nanofins function like waveplates, with their transmission behavior described by a 2x2 unitary and symmetric Jones matrix. While this enables technologies like single-shot Stokes and Mueller imaging, and vectorial holograms, it has limitations for more complex functionalities as depicted in Fig. 1(a) [10]. For example, a single-layer non-chiral nanofin cannot serve as a circular analyzer, as this requires decoupling the off-diagonal components of the Jones matrix. Rectangular non-chiral nanofins only provide linear shape-birefringence with a symmetric Jones matrix. This limitation arises from the 2D symmetry of single-layer metasurfaces and cannot be overcome with topology optimization. Bilayer metasurfaces, Fig. 1(b-c), allow for more general polarization transformations by decoupling all elements of the Jones matrix, enabling arbitrary, non-symmetric polarization control [11]. This not only allows the most general polarization transformations but also inspires a new class of directional metasurfaces with asymmetric focusing.

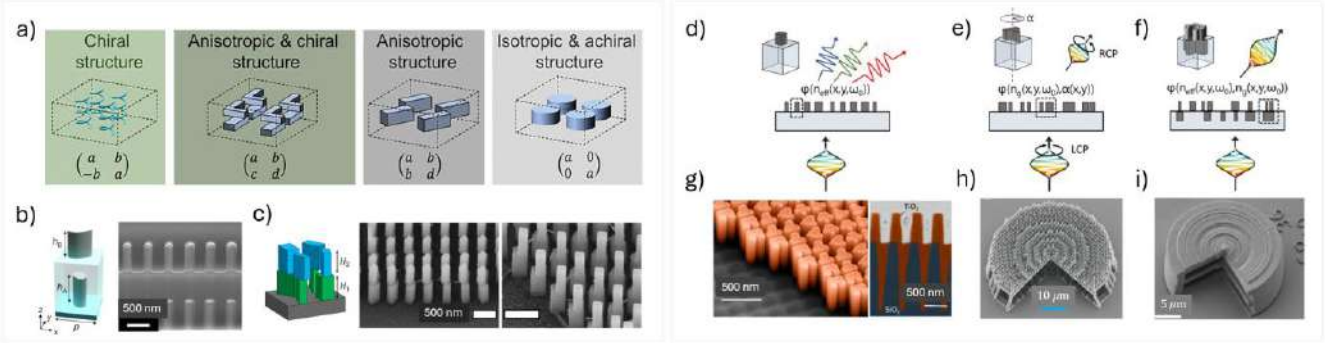


Figure 1: Multi-layer metasurfaces for polarization control and dispersion engineering. (a) Schematic of metasurface nanostructures and the corresponding Jones matrices that can be implemented. The letters a, b, c, and d represent complex numbers [11]. **(b)** Left: Schematic of bilayer metasurface unit cell composed of 790 nm tall amorphous silicon nano posts. The bottom layer is encapsulated in SU-8. Right: SEM image of the fabricated metasurface [11]. **(c)** Left: Schematic of a free-standing bilayer meta-atom made of 600 nm titanium dioxide nanofins. Right: SEM images of the fabricated device [9]. **(d-f)** Comparison of three metasurface platforms [12]. **(d)** A single-layer metasurface made of meta-atoms with simple geometries, exemplified by a square pillar-shaped meta-atom typically suffer from dispersion. **(e)** Single-layer achromatic metasurface featuring rotated meta-atoms with varying geometries, illustrated by a double-fin meta-atom with a rotation angle, yet remains polarization-sensitive. **(f)** Achromatic, polarization-insensitive, bilayer metasurface created by stacking heterogeneous freeform meta-atoms. The unit cell diagram shows a freeform meta-atom stacked on top of a cross-shaped meta-atom embedded in the substrate [12]. **(g)** SEM image of a fabricated metalens. The cross section of the stack is taken by using focused ion beam. **(h)** A hybrid achromatic metalens combines a phase plate and a metalens to simultaneously correct for chromatic aberration and improve focusing efficiency. SEM images of air-spaced (0.32 NA) metalens fabricated with multi-photon lithography on fused silica substrate [13]. **(i)** 3D-printed multilayer achromatic metalens made from a low-index material. SEM images of the fabricated metalens operating in the visible range, 400 to 800 nm, with 0.5 NA [14]. Panels (a-b) adapted with permission from [11], panels (d-g) adapted with permission from [12], panels (h) and (i) adapted with permission from [13] and [14], respectively.

Advances in Dispersion Engineering: Controlling phase and group delay independently is limited by the delay-bandwidth product, influenced by the geometry, height, and composition of the meta-atom [8]. This results in dielectric metalenses with inadequate phase coverage, restricting performance, Fig. 1(d-e). Additionally, inverse design for larger devices is computationally intensive, and adjoint methods may encounter local minima. New metasurface designs are needed to achieve high transmission, broadband, and polarization-insensitive responses without these limitations. Multi-layer meta-optics address these drawbacks (Fig. 1(f)). In first-order approximation, the phase and group delays of a bilayer meta-atom are the sum of the individual layers. By stacking materials like titanium dioxide and silica (Fig. 1(g)), phase and group delays can be independently controlled, pixel-by-pixel. Precise freeform design further enhances this decoupling, enabling the development of advanced dispersion-engineered metasurfaces with up to 80% efficiency from 420 nm to NIR wavelengths [12]. These devices are fabricated using two-step nanolithography, atomic layer deposition, and plasma etching.

Outlook: We envision the future of flat optics being driven by 3D techniques (Fig. 1(h-i)), supported by recent advancements in multi-step lithography, nanoimprint lithography, two-photon polymerization, and thermal scanning probe lithography. With these tools, a new generation of high-performance metasurfaces will be capable of meeting the strict performance requirements of many emerging classical and quantum applications.

References

1. Yu, N. et al. “Light propagation with phase discontinuities: Generalized laws of reflection and refract.,” *Science* **334**, 333–337, 2011.
2. Dorrah, A. H & Capasso, F. “Tunable structured light with flat optics,” *Science* **376**, eabi6860, 2022.
3. Mohammadi Estakhri, N. & Alù, A. “Wave-front transformation with gradient metasurfaces,” *Phys. Rev. X* **6**, 04100840, 2016.
4. Zheng, G. et al. “Metasurface holograms reaching 80% efficiency,” *Nature Nanotechnology* **10**, 308–312, 2015.
5. Malek, S. et al. “Multifunctional resonant wavefront-shaping meta-optics…,” *Light: Science & Applications* **11**, 246, 2022.
6. Mirzapourbeinekalaye, B. et al. “General lossless polarization and phase…,”. *Advanced Optical Materials* **10**, 2102591, 2022.
7. Raeker, B. et al. “All-dielectric meta-optics for high-efficiency independent…,” *Advanced Photonics Research* **3**, 2100285, 2022.
8. Presutti, F. & Monticone, F. “Focusing on bandwidth: achromatic metalens limits,” *Optica* **7**, 624–631, 2020.
9. Dorrah, A. H., Park, J.-S., Palmieri, A. & Capasso, F. “Free-standing bilayer metasurfaces in the vis,” *Nat Commun* **16**, 3126, 2025.
10. Rubin, N. A., Shi, Z. & Capasso, F. “Polarization in diffractive optics and metasurfaces,” *Adv. Opt. Photon.* **13**, 836–970, 2021.
11. Chang, T. et al. “Universal metasurfaces for complete linear control of coherent light…,” *Advanced Materials* **34**, 2204085, 2022.
12. Li, Z. et al. “Heterogeneous freeform metasurfaces: A platform for advanced broadband dispersion…,” *arXiv* 2412.12028, 2024.
13. Balli, F., Sultan, M., Lami, S. K. & Hastings, J. T. “A hybrid achromatic metalens,” *Nat Commun* **11**, 3892, 2020.
14. Pan, C.-F. et al. “3D-printed multilayer structures for high–numerical aperture achromatic…,” *Science Advances* **9**, eadj9262, 2023.

Far-Field Radiation and Polarization Engineering using Luminescent Metasurfaces

E. Bailly[1], A. Nguyen, J.-P. Hugonin[1], J.-J. Greffet[1] and B. Vest[1]

1[1]Université Paris-Saclay, Institut d'Optique Graduate School, CNRS, Laboratoire Charles Fabry, 91127, Palaiseau, France.

*corresponding author: benjamin.vest@institutoptique.fr

Abstract: Intrinsically incoherent luminescent emitters can be coupled to metasurfaces to establish some coherence in emission and therefore to enable structuration of the emitted field. We present here light-emitting metasurfaces designed using a Kirchhoff's law approach demonstrating a control of the polarization and of the angular radiation pattern.

Designing a light-emitting system means shaping light emission so that it matches requirements in terms of radiation pattern, polarization, or spectrum. However, non-lasing sources rely on spontaneous emission processes: the intrinsic randomness of emission prevents the structuration of a light beam by interference effects and most often results in isotropic and unpolarized emission. This has a straightforward solution: optical components such as lenses, filters or polarizers. However, components increase the bulkiness of light-emitting devices, affecting their total energy footprint, introducing losses and limiting integration and miniaturization.

We exploit the concept of Light-Emitting Metasurfaces (LEMs): devices consisting typically of a substrate covered with arrays of nanoresonators in interaction with luminescent emitters, distributed over the surface of the device. LEM support extended electromagnetic modes which play the role of a resonator. Although emitters are incoherent, their decay into the surface modes establishes a non-zero degree of coherence at long range. Besides, the surface modes can be coupled to the far-field. Light emission engineering is achieved by tailoring the properties of this leaky mode. At this end, we use a Kirchhoff's approach. Here, the power emitted for a polarization (l) in a solid angle dΩ around the direction u at wavelength λ is given by [1] :

$$\mathrm{d}^2 P_e^{(l)}(\mathbf{u},\lambda,\mu) = d\lambda d\Omega \int_V d^3\mathrm{r}' \alpha^{(l)}(-\mathbf{u},\mathrm{r}',\lambda,\mu)\frac{hc^2}{\lambda^5}\frac{1}{\exp(\frac{hc}{\lambda k_B T}-\frac{\mu}{k_B T})-1} \qquad (1)$$

where α is the local absorption rate, computed by considering the system illuminated by a plane wave at wavelength λ, from the direction u and with polarization state (l). The second factor is the blackbody radiance evaluated at hc/λ-μ, where μ is the photon chemical potential. This relation shows that the local absorption rate is the key to tailor quantitatively the spectral, angular, and polarization dependence of the emission. We use the Kirchhoff's approach to design and fabricate a LEM consisting of a 2D silver grating covered with nanoplatelets emitting around 610 nm. Most of the light is emitted within 20° from the normal direction (Fig. 1), therefore establishing directional emission out of an ensemble of incoherent emitters [2].

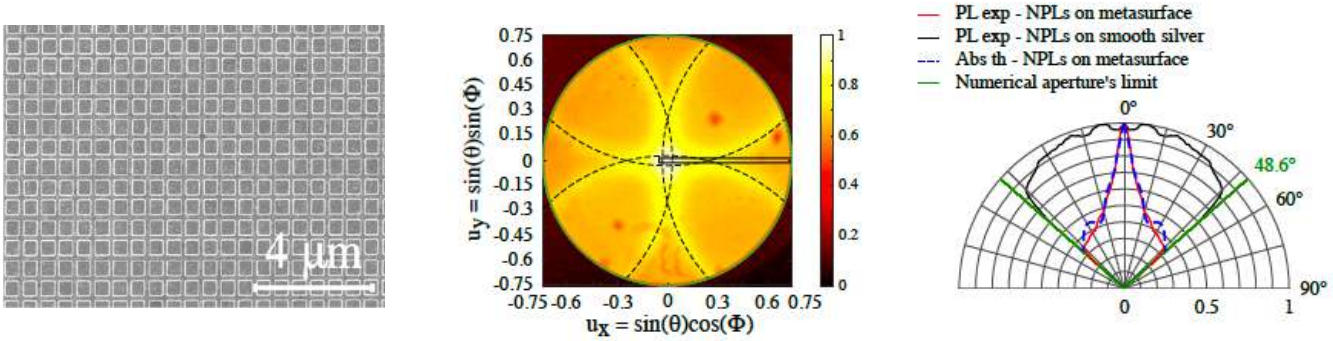


Fig. 1 2D Photoluminescent LEM for directional emission [2]. (Left) SEM image of the 2D silver grating forming the base of the LEM (Center) Fourier plane image of the photoluminescent emission **(**Right) Experimental angular radiation pattern (solid red) compared to simulated absorption using the Kirchhoff's formalism (blue dotted). Emission occurs within a 20° FWDH angular cone. Emission from unstructured emitter layer is isotropic (solid black)

The same Kirchhoff's law approach can by used to design **incandescent LEM** providing chiral emission in the MWIR (see Fig. 2) [3]. It consists of an array of thin metallic wires, heated by Joule effect on top of a transparent substrate. While the whole wire is heated at once, only the central fraction of the pattern, where inversion symmetry is broken, contributes to dichroism.

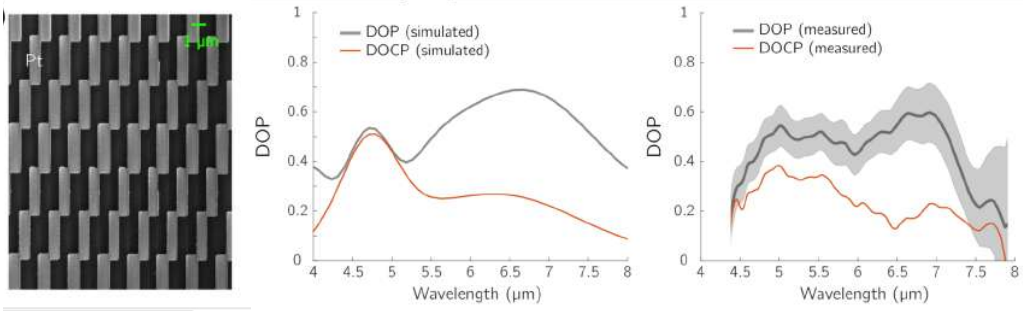


Fig. 2 Incandescent LEM for chiral emission [3] (a) SEM picture of the fabricated device. (b) Simulated and measured degree of polarization (DOP) and degree of circular polarization (DOCP). Shaded areas represent one-sigma error bars.

We will further discuss approaches to move towards a more advanced control of far-field radiation over several degrees of freedom combining previous design ideas. We will highlight the advantages of a Kirchhoff's approach in the perspective of providing an engineering toolbox able to provide quantitative and reliable prediction of the performances as well as a way to compare different metasurface architectures.

Acknowledgements. This work is supported by the French National Agency (ANR) (ANR-17-CE24-0046 and ANR-17-CE24-016).

References

[1] J. J. Greffet, P. Bouchon, G. Brucoli, and F. Marquier, *Light Emission by Nonequilibrium Bodies: Local Kirchhoff Law*, Phys. Rev. X **8**, 21008 (2018).

[2] E. Bailly, J.-P. Hugonin, J.-R. Coudevylle, C. Dabard, S. Ithurria, B. Vest, and J.-J. Greffet, *2D Silver-Nanoplatelets Metasurface for Bright Directional Photoluminescence, Designed with the Local Kirchhoff's Law*, ACS Nano **18**, 4903 (2024).

[3] A. Nguyen, J.-P. Hugonin, A.-L. Coutrot, E. Garcia-Caurel, B. Vest, and J.-J. Greffet, *Large Circular Dichroism in the Emission from an Incandescent Metasurface*, Optica **10**, 232 (2023).

Multi-polar high quality factor metasurfaces

Mark Lawrence, Bo Zhao, Shuqin Dai, Samuel Ameyaw, and Lin Lin

Department of Electrical and Systems Engineering, Washington University in St. Louis, St. Louis, Missouri 63130, USA

Email: markl@wustl.edu

Abstract: Highly resonant phase gradient metasurfaces represent an exciting development for nonlinear and programmable wave shaping, but simultaneous access to spatial, spectral and polarization multiplexing remains limited. Here, we introduce multi-mode high-Q metasurfaces for multi-functional image processing, including multiband and cross-color image thresholding, polarization independent narrowband wave-shaping, and high dimensional color-polarizers.

Nanofocusing of the orbital angular momentum laser beam for nanoimaging

Zhenrong Zhang

Department of Physics, Baylor University, Waco, Texas, United States

Optical vortex beam has been used in many applications such as nanoscale imaging, telecommunication, sensing, and so on due to its unique azimuthal phase distribution. In this talk, I present the development of plasmonic fiber probes for nanoscale chirality imaging. The vortex beam carrying an orbital angular momentum (OAM) has a phase singularity that can be used to distinguish the enantiomers of the chiral molecule. I will present the design, simulation, fabrication, and characterization of plasmonic OAM probes. The vortex beam was generated in free space and propagated through a polarization-maintaining ring core vortex fiber, making the setup easier and less optically sensitive. Simulations showed the nano-focusing of the OAM beam when plasmonic nanostructures are incorporated on the vortex fiber facet. The experimental helicity measurement showed stable transmission of the circularly polarized -OAM beam through the nanostructures fabricated on the straight-cleaved vortex fiber facet.

Metasurface for Bioimaging and Thermal Radiation Management

Guangwei Hu[1]

[1]School of Electrical & Electronic Engineering, Nanyang Technological University Affiliation, Singapore

[*]corresponding author: guangwei.hu@ntu.edu.sg

Abstract: Metasurface with full control of wave properties can be integrated into an optical system, thus unlocking new opportunities to customize the multidimensional transfer function of the system. In this talk, I will discuss our efforts along this path for two applications: passive metasurface with advanced bio-imaging that can simultaneously capture and process the bioimages and active metasurface for the thermal camouflage compatible with radiative dissipation channels.

Metasurface with full control of wave properties can be integrated into an optical system, thus unlocking new opportunities to customize the multidimensional transfer function of the system. With this, I will present our recent findings of optical computation for bio-imaging based on passive metasurface [1-4] and thermal radiation manipulation for camouflage capable of thermal dissipation channels with phase change active metasurface.

Specifically, I will show how a single-layer metasurface with 2f system could be exploited to implement various transfer functions in conventional 4f system. This includes the first-order derivation and cross-correlation operation [1], the differential contrast with dual-polarization channels for the isotropic and miniaturized differential interference contrast (DIC) microscope [2], the 3D double-helix point spread functions for 3D imaging and depth measurement [3] and others [4]. Our work here enables the advanced engineering of optical systems for simultaneous capturing and processing the biological sample [4].

I will also show the active metasurface could be harnessed for advanced thermal radiation manipulation. Particularly, I will discuss the camouflage application based on emerging non-volatile phase change materials, In_3SbTe_2 (IST). I will discuss how to realize the programmable modulation of thermal emissivity with IST nanostructures, thus enabling the colored camouflage [5,6]. More importantly, the camouflage actually perturbs thermal radiation channels and hence the thermal equilibrium. Using the multifunctional active metasurface, we further develop the camouflage-dissipation compatible metadevices, which can compensate the camouflage-induced thermal emissivity perturbations.

Our work will be important to unlock various applications of metasurface for bio-imaging, thermal management and others.

Acknowledgements: Nanyang Assistant Professorship; A*STAR AME IRG No. M24N7c0081 and M24N7c0087.

References

1. Z. Wang, G. Hu, X. Wang, X. Ding, K. Zhang, H. Li, S. N. Burokur, Q. Wu, J. Liu, J. Tan, C.-W. Qiu, "Single-layer spatial analog meta-processor for imaging processing", Nature Communications, Vol. 13, No. 2188, 2022.
2. X. Wang, H. Wang, J. Wang, X. Liu, H. Hao, Y. S. Tan, Y. Zhang, H. Zhang, X. Ding, W. Zhao, Y. Wang, Z. Lu, J.

Liu, H. Li, J. K.W. Yang, J. Tan, C.-W. Qiu, G. Hu, X. Ding, “Single-shot Isotropic Differential Interference Contrast Microscopy”, Nature Communications, Vol. 14, No. 2063, 2023.

3. X. Ding, H. Hao, H. Wang, X. Wang, S. Zhang, C.-F. Pan, M. A. Rahman, T. Ling, H. Li, J. Tan, J. K.W. Yang, W. Lu, J. Liu, G. Hu, "Single-Shot 3D Imaging Meta-Microscope", Nano Letters, Volume 24, Issue 42, p.p. 13364-13373, 2024.
4. X. Wang, H. Hao, X. He, P. Xie, J. Liu, J. Tan, H. Li, H. Wang, P. Genevet, Y. Luo, X. Ding, G. Hu, “Advances in information processing and biological imaging using flat optics”, Nature Reviews Electrical Engineering, Volume 1, p.p. 391-411, 2024.
5. S. Zhou, S. Dong, Y. Guo, Y. Shuai, H.-X. Xu, G. Hu, “Colored Thermal Camouflage and Anti-Counterfeiting with Programmable In3SbTe2 Platform”, Nanophotonics, Volume 13, Issue 6, p.p. 945-954, 2024.
6. S. Zhou, Y. Guo, L. Zhu, Y. Liu, Q. Pan, Y. Shuai, G. Hu, “A Continuous Programmable Mid-Infrared Thermal Emitter and Camouflage Based on In3SbTe2 Phase-Change Material”, Optics Letters Vol. 48, Issue 16, p.p. 4388-4391, 2023.

Merging nanophotonics and optical fibers for flexible beam control using 3D nanoprinting

M. A. Schmidt[1,2,3*], B. Fischer[1], M. Zeisberger[1], M. Khosravi[1], S. Hosseinabadia[1] and O. Yermakov[1,4]

[1]Leibniz Institute of Photonic Technology, Albert-Einstein-Str. 9, 07745 Jena, Germany
[2]Abbe Center of Photonics and Faculty of Physics, Friedrich-Schiller-Universität Jena, Germany
[3]Otto Schott Institute of Materials Research (OSIM), Friedrich-Schiller-Universität Jena, Germany
[4]V. N. Karazin Kharkiv National University, Kharkiv, Ukraine
[*]corresponding author: markus.schmidt@ipht-jena.de

Abstract: We show that combining optical fibers with 3D nanoprinted nanostructures creates a new category of fiber-integrated devices - metafibers - that enable novel applications, including high-NA holographic meta-lenses on fibers for trapping and flexible light focussing, on-fiber achromatic metasurface-based lenses and beam shapers, and ring-like gratings to boost coupling efficiency.

High Contrast Nanoscale Chirality Imaging

Seongmin Im[1], Gayatri Chandran[1], and Y. Zhao[1,*]

[1]Department of Electrical and Computer Engineering, Grainger College of Engineering, University of Illinois Urbana Champaign, Urbana, IL 61801, USA
[*]corresponding author: yzhaoui@illinois.edu

Abstract: Near-field optical force imaging reveals nanoscale light-matter interactions but suffers from overlapping effects. I will present our recent advances in Decoupled optical force nanoscopy (Dofn), a technique that isolates optical forces to enable high-contrast, nanometer-resolution imaging of nanoscale light-matter interactions, in particular, chiral light-matter interactions in nanoparticle systems.

Summary:

Near-field scanning optical microscopy, including both aperture-type[1] and apertureless[2] configurations, provides near-field distribution with spatial resolution that surpasses the diffraction limit. However, the resolution of aperture-type near-field scanning optical microscopy is typically in the order of several tens of nanometers, which corresponds to the size of the aperture. In contrast, apertureless near-field scanning optical microscopy is limited by the fact that it inevitably incorporates far-field information while measuring the near-field scattering signal via the tip. On the other hand, electron energy loss spectroscopy[3] and photoemission electron microscopy[4], which utilize electron microscope systems, are also capable of measuring the near-field. However, these techniques require a high-vacuum environment, and controlling the incident light is not as straightforward as it is with optical microscope systems. Namely, despite advancements in nanophotonics using the near-field, achieving a near-field distribution of less than 10 nm with an optical microscope system remains challenging.

The acquisition of a high-resolution image by utilizing multiple low-resolution images is widely used in the fields of image processing and computational imaging[5]. In particular, structured illumination microscopy[6] and Fourier ptychography[7] are major examples, which enable the acquisition of low-numerical-aperture images into a high-numerical-aperture image through known illumination incidence. The multiple low-resolution images recorded under different illuminations are computationally merged to reconstruct high-frequency information about the object, producing a high-resolution image. Meanwhile, multiple scans of atomic force microscopic images with local maxima probability algorithm provide the unprecedented resolution[8]. However, to our

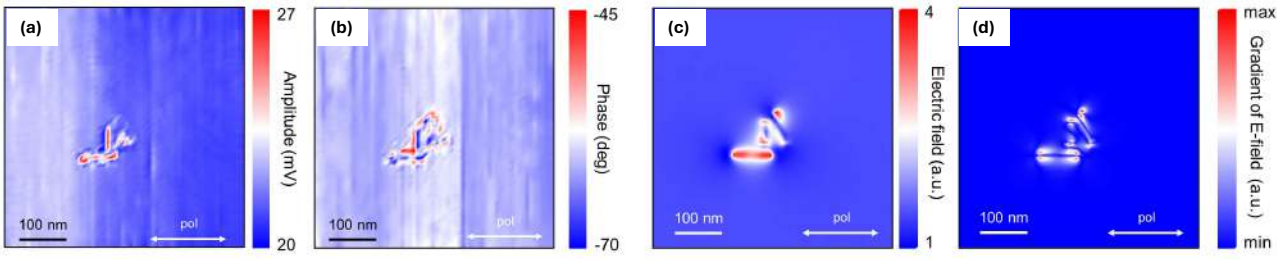


Figure 1. (a) Amplitude and (b) phase of experimentally measured optical force map. (c) Simulated electric field distribution of the trimer. (d) The gradient of electric field distribution.

knowledge, such super-resolution imaging algorithms have never been applied to near-field imaging or optical force mapping.

In this talk, I will discuss imaging of nanoscale chirality with Dofn. The resolution of Dofn is often limited by the radius of curvature of the atomic force microscopy (AFM) probes used in the scan. Chiral nanostructures, such as asymmetric trimers with gaps that are smaller than the radius of curvature of the probe, often miss important information during the scan. To further suppress the background noise and enhance imaging contrast, particularly optical forces at these gaps, I will introduce a Fourier-filling method. By combining multi-directional scanning and the Fourier-filling method to reconstruct high-frequency information, we identified optical forces induced by near-field at the gap between the nanostructures that are unavailable with regular optical force scans. Reliable near-field chirality near these gaps has been imaged with greater detail. Our method provides a high signal-to-noise ratio, which is essential for lock-in measurements, and thereby enables measurement of optical forces under a variety of illumination conditions, which were previously challenging to observe.

References

1. Lee, H. et al. Probing Temperature-Induced Plasmonic Nonlinearity: Unveiling Opto-Thermal Effects on Light Absorption and Near-Field Enhancement. *Nano Lett* **24**, 3598-3605 (2024).
2. Hu, X.T., Zhou, L., Wu, X. & Peng, Y. Review on near-field detection technology in the biomedical field. *Adv Photon Nexus* **2**, 044002 (2023).
3. Nelayah, J. et al. Mapping surface plasmons on a single metallic nanoparticle. *Nat Phys* **3**, 348-353 (2007).
4. Sun, Q. et al. Direct imaging of the near field and dynamics of surface plasmon resonance on gold nanostructures using photoemission electron microscopy. *Light-Sci Appl* **2**, e118 (2013).
5. Mait, J.N., Euliss, G.W. & Athale, R.A. Computational imaging. *Adv Opt Photonics* **10**, 409-483 (2018).
6. Heintzmann, R. & Huser, T. Super-Resolution Structured Illumination Microscopy. *Chem Rev* **117**, 13890-13908 (2017).
7. Zheng, G., Shen, C., Jiang, S., Song, P. & Yang, C. Concept, implementations and applications of Fourier ptychography. *Nature Reviews Physics* **3**, 207-223 (2021).
8. Heath, G.R. et al. Localization atomic force microscopy. *Nature* **594**, 385-390 (2021).

Bright and Dark Lasing in Nanoplasmonic Metasurfaces

Ortwin Hess[1]

[1]School of Physics and CRANN Institute, Trinity College Dublin, The University of Dublin, Dublin 2, Ireland
[*]corresponding author: ortwin.hess@tcd.ie

Abstract: We investigate the dynamic competition between bright (radiation-coupled) and dark (non-radiative) lasing modes in nanoplasmonic double-fishnet metasurfaces. Employing advanced Maxwell-Bloch Langevin simulations, we demonstrate methods for selectively enhancing bright mode lasing despite significant competition from dark modes, offering pathways toward controlled nanoscale coherent emission.

Nanoplasmonic metasurfaces offer revolutionary prospects in photonics, enabling unprecedented control of electromagnetic fields far below the diffraction limit. However, the intrinsic metal losses within these metasurfaces pose a significant challenge for their practical application. By integrating optical gain into nanoplasmonic structures, coherent amplification and lasing at deeply subwavelength scales become achievable, essential for applications in integrated photonic circuits, sensing, quantum optics, and communications.

In nanoplasmonic systems, lasing modes can broadly be categorized as bright or dark modes. Bright modes efficiently couple to radiation, providing strong emission to the far field, while dark modes remain localized and non-radiative, typically exhibiting significantly higher quality factors due to reduced radiative losses. However, despite the superior intrinsic quality of dark modes, experimental observations often highlight bright-mode lasing as the predominant emission. Understanding the mechanisms that facilitate bright-mode dominance and controlling mode competition dynamics is thus critically important for the future design and optimization of nanoplasmonic laser devices.

In this work, we focus on double-fishnet plasmonic metasurfaces, well-known for their negative refractive index properties and strong field localization capabilities. Employing rigorous, full-vectorial time-domain simulations coupled with Maxwell-Bloch Langevin equations, we explore the nonlinear dynamics of bright and dark lasing states. Our computational framework captures complex phenomena such as gain saturation, spatial hole burning, and ultra-fast transient dynamics, providing detailed insight into the competition between modes.

Through comprehensive simulations, we demonstrate that bright modes, despite having inherently lower quality factors due to their radiative nature, can dominate the lasing output under specific conditions. We attribute this dominance to two primary factors: spatial overlap and spectral alignment. Bright modes typically exhibit a superior spatial overlap with regions of high gain inversion, which allows them to effectively deplete the available population inversion, limiting the growth of competing dark modes. Additionally, spectral alignment between the gain emission profile and bright-mode resonances significantly enhances their effective gain.

Our simulations reveal complex temporal dynamics, including relaxation oscillations arising from the competitive interplay between bright and dark modes. These oscillations occur due to the mutual depletion of available gain, as bright and dark modes alternately experience growth and suppression in a dynamically balanced environment.

Understanding these transient dynamics is crucial, as they directly impact the stability and coherence properties of the resulting lasing emission.

To systematically investigate these dynamics, we introduce the concept of "local gain," combining spectral characteristics, spatial population inversion distributions, and mode profiles. Local gain analysis provides deep insights into the spatial and spectral conditions necessary for selective bright-mode enhancement. By precisely engineering the spectral overlap between the gain material's emission line and the metasurfaces's resonant modes, we establish conditions under which bright modes are strongly favoured. This strategy effectively suppresses dark-mode excitation, optimizing bright-mode lasing efficiency and coherence.

We further explore the role of spatial inversion profile management through polarization control of the pumping laser. Adjusting the pump polarization state influences the spatial deposition of gain within the metasurface. We demonstrate that, due to geometry-dependent field enhancements in the double-fishnet structure, polarization adjustments can drastically change local gain distributions, significantly affecting mode competition dynamics. By selecting appropriate polarization states, it becomes possible to further promote bright-mode lasing, offering another practical avenue for mode control.

The implications of these findings extend significantly into practical device applications. Controlling mode competition and enhancing bright-mode dominance improves emission coherence, spectral purity, and output stability, characteristics vital for advanced integrated photonic devices, nanoscale sensing technologies, quantum optics experiments, and next-generation communications platforms.

Our results highlight the importance of mode engineering in nanoplasmonic systems, providing clear pathways for designing and optimizing future metasurface-based lasers. Specifically, the capability to selectively suppress or enhance particular modes through spectral and spatial gain engineering allows unprecedented flexibility and efficiency in nanoscale photonic device design.

In conclusion, this comprehensive study elucidates the fundamental dynamics of bright and dark lasing modes in nanoplasmonic double-fishnet metasurfaces, identifies critical factors underpinning bright-mode dominance, and presents effective strategies for selective mode control. Our findings significantly advance the understanding and practical capabilities of nanoscale lasing, promising substantial impacts on future nanophotonics and integrated device applications.

Acknowledgement: Support by Research Ireland (formerly Scieince Foundation Ireland) via Grants no. 18/RP/6236 and 22/QERA/3821 is gratefully acknowledged.

Tunable focus manipulation in multicore meta-fibers through 3D nanoprinted phase-only holograms

Mohammadhossein Khosravi[1,2], Torsten Wieduwilt[1], Matthias Zeisberger[1], Adrian Lorenz[1], Markus A. Schmidt[1,2,3,*]

[1]Leibniz Institute of Photonic Technology, Jena, Germany

[2]Abbe Center of Photonics and Faculty of Physics, FSU Jena, Jena, Germany

[3]Otto Schott Institute of Material Research, FSU Jena, Jena, Germany

[*]Corresponding author: markus-alexander.schmidt@uni-jena.de

Abstract: This study presents a novel method for remote focus control in multicore meta-fibers using 3D nanoprinted phase-only holograms. By integrating computationally designed holograms onto single-mode multicore fibers, we achieve precise, crosstalk-free focus manipulation at visible wavelengths. This innovation enhances applications in optics, telecommunications, laser micromachining, and biomedical imaging.

Remote focus manipulation is a critical capability in modern photonics, with applications spanning biological imaging [1], laser micromachining [2], telecommunications [3], and laser surgery [4]. Conventional optical systems rely on bulky components, limiting flexibility and scalability. Recent advances in photonic integration have highlighted the potential of optical fibers as compact platforms for precise light delivery and beam shaping [5]. However, existing on-fiber optical elements often suffer from static focusing limitations, lack of reconfigurability, and modal crosstalk.

In this study, we introduce a novel method for advanced remote focus control by integrating computationally designed 3D nanoprinted phase-only holograms onto the end face of single-mode multicore fibers (SM-MCFs). This approach enables precise, tunable light focusing within a monolithic metafiber device, overcoming the constraints of conventional lenses and static optical systems. The proposed SM-MCFs feature 37 cores arranged in a hexagonal lattice, designed to suppress modal crosstalk, ensuring independent light propagation at visible wavelengths. The phase-only holograms were computationally optimized using a modified Gerchberg-Saxton Algorithm (GSA) in conjunction with the Angular Spectrum Method (ASM) to accurately map input wavefronts to predefined focal positions. Fabrication was performed using femtosecond direct laser writing (fs-DLW), a high-resolution 3D nanoprinting technique that allows precise structuring of polymeric phase elements directly on the fiber surface (Fig. 1a).

The functionality of this metafiber device was experimentally validated across three distinct focusing configurations: cross-axis focusing, same-side focusing, and line-array focusing. Figure 1 (b-e) presents the experimental realization of the line-array focusing configuration, demonstrating robust agreement between computational design, simulations, and measured intensity distributions. The generated focal spots exhibit high localization with minimal background noise, while inter-core crosstalk is effectively suppressed, ensuring reliable and independent operation of each core.

This research represents the first successful implementation of nanostructured holograms for remote focus control in SM-MCFs, with significant implications for a wide range of applications. Potential uses include biological microscopy, high-speed laser micromachining, optical tweezers, and next-generation fiber-optic

telecommunications. Future advancements could leverage adaptive holograms, machine-learning-based design optimization, and dynamic reconfiguration via spatial light modulators (SLMs) to further enhance tunable focus control [6]. The results of this study establish a foundation for the development of next generation metafiber devices with superior optical performance, paving the way for transformative progress in nanophotonics, integrated optics, and reconfigurable photonic systems.

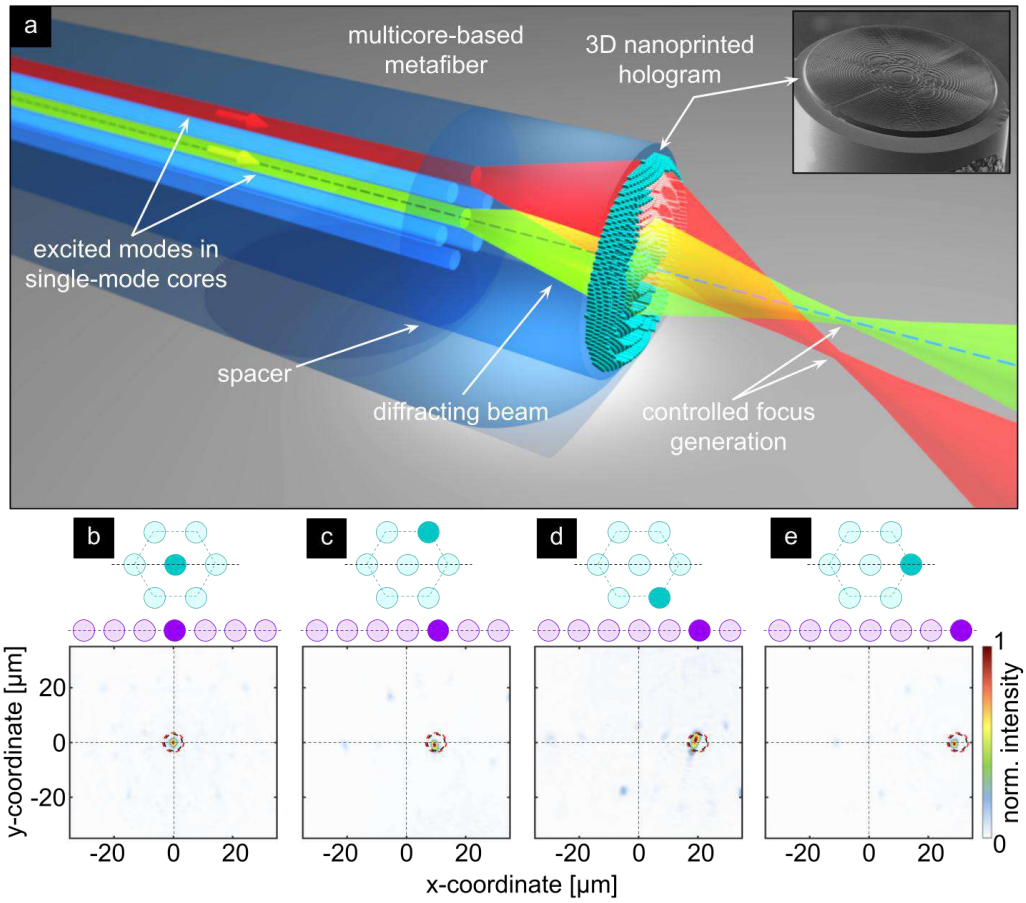


Fig. 1: Tunable focus manipulation using a multicore fiber with a phase-only hologram: (a) schematic illustration showing two cores excited, producing two focal points at different image plane locations. The top-right inset shows a realized hologram on the fiber. (b-e) show examples of measured intensity distributions of the line-array focusing configuration. Each plot corresponds to a combination of addressed core and foci in the SM-MCF.

References

1. Emiliani, V. et al. Optogenetics for light control of biological systems. Nat. Rev. Methods Prim. 2, 55 (2022).
2. Cheng, J. et al. A review of ultrafast laser materials micromachining. Opt. Laser Technol. 46, 88–102 (2013).
3. Huang, J. et al. Implementation of on-chip multi-channel focusing wavelength demultiplexer with regularized digital metamaterials. Nanophotonics 9, 159–166 (2020).
4. Vogel, A. et al. Mechanisms of pulsed laser ablation of biological tissues. Chem. Rev. 103, 577–644 (2003).
5. Khosravi, M. et al. "Interfacing high numerical aperture metalenses with thermally expanded core fibers via 3D nanoprinting for advanced meta-fiber operation," Opt. Express 32, 28206-28214 (2024)
6. Khosravi, M. et al. Advanced remote focus control in multicore meta-fibers through 3D nanoprinted phase-only holograms. Nat Commun 16, 507 (2025).

Transient optical symmetry breaking for the ultrafast switching of a metasurface quasi-BIC

G. Crotti[1*], A. Schirato[1,2], O. Pashina[3,4], O. Sergaeva[4],
M. Petrov[3], C. De Angelis[4,5] and G. Della Valle[1,6*]
[1] Politecnico di Milano, Milan, Italy
[2] Rice University, Houston, Texas, USA
[3] ITMO University, Saint Petersburg, Russia
[4] University of Brescia, Brescia, Italy
[5] Istituto Nazionale di Ottica - CNR, Brescia, Italy
[6] Istituto Nazionale di Fisica Nucleare, Milan, Italy
[*]giulia1.crotti@polimi.it, giuseppe.dellavalle@polimi.it

Abstract

We theoretically propose an innovative strategy to obtain an ultrafast, fully reversible switch from a photonic bound state in the continuum (BIC) to a quasi-BIC leaky mode in a semiconductor metasurface via transient optical symmetry breaking, by exploiting inhomogeneities of the photo-induced free carriers population at the nanoscale.

1 Introduction

Electromagnetic bound states in the continuum (BICs) are of interest both for their fundamental properties and their potential for applications in photonic systems. They correspond to solutions of Maxwell equations which are spatially confined and completely decoupled from radiation, albeit having the same energy of propagative waves [1].

If coupling channels are opened, the bound state transforms into a "quasi-BIC" leaky mode, which can be excited in scattering and manifests as an ultra-sharp resonance in the transmission or reflection spectrum. In photonic metasurfaces, this mechanism has been exploited for the particular class of symmetry-protected BICs, by modifying the unit-cell geometry to slightly break the in-plane rotation or reflection symmetry of the electromagnetic problem. This makes it possible to control the quasi-BIC quality factor, which scales as the squared inverse of a properly defined asymmetry parameter [2]. This strategy allows to tailor the optical response of the system for various applications, from filtering and modulating light to obtaining high-sensitivity sensors. However, a dynamical control is often desirable, which cannot be achieved once geometrical parameters are fixed with fabrication.

In this direction, we propose an innovative approach for achieving an ultrafast switch between a BIC and a quasi-BIC state, by actively inducing symmetry-breaking in semiconductor metasurfaces (Fig. 1a), designed to work in the near-infrared region of the electromagnetic spectrum. This is obtained by relying on the spatial inhomogeneities of the electron-hole population, generated in the dielectric medium upon the absorption of an intense fs-laser pump (left part of Fig. 1b). We present a theoretical model of the ultrafast photoexcitation, including a description of (i) the spatio-temporal transients of the free carriers, which are distributed non-uniformly at the meta-atom scale and undergo diffusion and recombination (see the middle panel in Fig. 1b), and (ii) the lattice temperature, which gradually increases as a result of phonon emission from the nonradiative recombination of the electron-hole pairs.

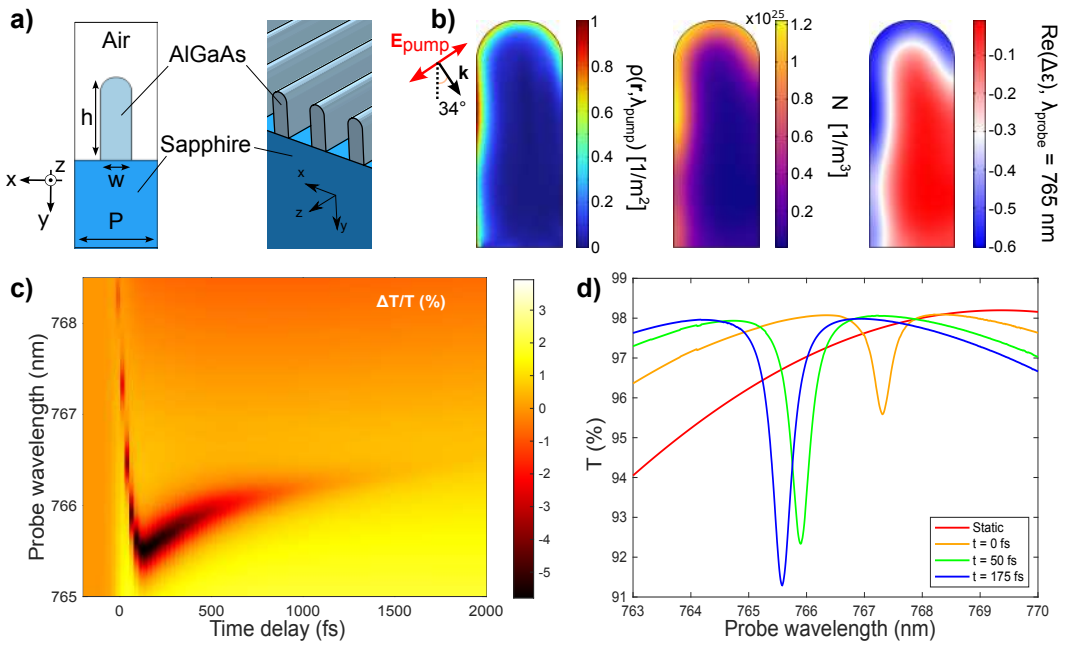


Figure 1: a) Metasurface design. The geometrical parameters are $w = 150\,\text{nm}$, $P = 400\,\text{nm}$, $h = 400\,\text{nm}$. b) Inhomogeneous photoexcitation. From left to right: normalized pump absorption pattern $\rho(\mathbf{r}, \lambda_{\text{pump}})$; spatial distribution of the electron-hole pair population at 100 fs after the pump peak; real part of the permittivity variation at 100 fs, for a probe wavelength of $\lambda_{\text{probe}} = 765\,\text{nm}$. c) Simulated pump-probe transmission map $\Delta T/T$. d) Transmission spectra at selected time delays.

We demonstrate that the ensuing (spatially inhomogeneous) third-order nonlinearity entails an almost instantaneous breaking of the in-plane left-right symmetry, as shown in the right part of Fig. 1b. In turn, this translates into the switching from a steady-state, symmetry-protected BIC (i.e., a non-resonant state) to a quasi-BIC leaky mode, which is revealed in full-wave scattering simulations as an extremely sharp resonance, appearing in the transmission spectrum of the structure (see Fig. 1c-d). The recovery of the symmetry, which is regulated by diffusion of the photogenerated carriers, marks the disappearance of the narrow resonant feature in $\sim 2\,\text{ps}$. This ultrafast process allows to overcome the intrinsic time limit of carriers relaxation towards the lattice, which is the usual bottleneck for the design of reconfigurable optical devices.

2 Acknowledgements

This work is part of the METAFAST project that received funding from the European Union Horizon 2020 Research and Innovation program under grant agreement no. 899673. G.C. acknowledges financial support from the ERC-StG ULYSSES grant agreement no. 101077181 funded by the European Union.

References

[1] Hsu, C. W. *et al.*, "Bound states in the continuum," *Nat. Rev. Mater.*, Vol. 1, No. 16048, 2016.

[2] Koshelev, K. *et al.*, "Asymmetric Metasurfaces with High-Q Resonances Governed by Bound States in the Continuum," *Phys. Rev. Lett.*, Vol. 121, No. 193903, 2018.

Addressing the Challenge of Phase-only Dynamic Modulation of Transmissive Metasurfaces

J. Y. Kim[1,2,†], R. Sokhoyan[1,†], H. A. Atwater[1*], M. S. Jang[1,2*]

[1]Thomas J. Watson Laboratories of Applied Physics, California Institute of Technology, USA
[2]School of Electrical Engineering, Korea Advanced Institute of Science and Technology, South Korea
[†]Equal Contribution
[*]corresponding author: haa@caltech.edu (H.A.A), jang.minseok@kaist.ac.kr (M.S.J)

Abstract: Dynamic phase-only modulation in transmissive metasurfaces is instrumental to on-chip photonic applications, but has been elusive due to zero transmission near the resonance frequency in two-port, single-resonance systems. We show that by introducing extra diffraction ports in reflection we are able to evade this issue, and demonstrate a proof-of-concept metasurface with around 300° phase modulation while keeping the transmission amplitude nearly constant.

The ability to manipulate wavefronts in real-time is the centerpiece technology in nanophotonic applications. To achieve this, actively modulating the scattered phase while keeping the amplitude uniform is one important aspect, and for compact, on-chip integration purposes, enabling this in a transmissive setup is highly sought-after. However, due to the phenomenon of zero transmission near the resonance frequency in two-port, single-resonance systems (*1*), it has been difficult to: 1) span the full 2π scattered phase range due to the π phase jump, and 2) modulate the phase independently from the transmission amplitude, as they tend to be highly coupled to one another. Many research teams have therefore utilized the Huygens metasurface condition by engineering two specific resonances (such as the electric dipole and the magnetic dipole) and overlapping them spectrally, thereby cancelling reflection through destructive interference between the two resonances and allowing for a smooth 2π phase change (*2*). For active tuning purposes, however, this method has been problematic due to the fact that the two resonances spectrally shift at different rates with the tuning parameter change, breaking the Kerker condition required for the full 2π phase modulation. There have been efforts to use two different tuning mechanisms such as voltage and temperature to compensate for the differences in the spectral shifting (*3*), but this complicates the device architecture and is also susceptible to thermal fluctuations.

In this paper we propose a methodology to enable full 2π phase-only modulation utilizing a single resonance. Our idea utilizes additional ports, namely diffraction ports, and we illustrate the theory behind achieving 2π phase-only modulation using temporal coupled-mode theory (TCMT). If we have a single resonance system, the complex transmission amplitude according to TCMT is given by:

$$\mathrm{t} = t + \frac{id_1 d_2}{(\omega - \omega_0) + i\gamma} \tag{1}$$

The first term on the right-hand side refers to the direct transmission scattering parameter and the second term refers the resonance interaction term. The above complex transmission amplitude draws a circle on the

complex plane as frequency is evolves around the resonance frequency, and for a two-port system the circle goes through the origin with zero losses with the circle becoming even smaller for finite losses, preventing 2π phase-only modulation. We then demonstrate that adding diffraction ports allows us to engineer the complex transmission amplitude circle to be more centered, enabling 2π phase-only modulation, with the theoretical upper bound being a perfectly centered, phase-only varying circle with a complex transmission amplitude radius being 0.5, or 25% transmission efficiency.

To realize this theory on a feasible metasurface setup, we showcase a proof-of-example metasurface that achieves a near-centered complex transmission amplitude circle using full-wave simulations. This is accomplished by integrating an electro-optically tunable lithium niobate (LNO) layer into the high-Q resonant metasurface structure (*4*). The resonant metasurface structure is based on germanium (Ge) resonators that support higher-order Mie modes. These high-Q Mie modes exhibit quality factors as high as 10,000. Our full-wave electromagnetic simulations show that we can achieve a dynamically tunable phase shift of 300° while maintaining a nearly constant transmission efficiency of around 22% as the refractive index of the LNO layer varies from 2.114 to 2.126, nearing the theoretical upper bound.

References

1. Wang, K. X., Yu, Z., Sandhu, S., and Fan, S. “Fundamental bounds on decay rates in asymmetric single-mode optical resonators,” Optics letters, 38(2), 100-102, 2013
2. Epstein, A., and Eleftheriades, G. V. “Huygens’ metasurfaces via the equivalence principle: design and applications,” Journal of the Optical Society of America B, 33(2), A31-A50, 2016
3. Yang, Z., Liu, M., Komar, A., Xu, L., and Neshev, D. N. “Phase-only tuning of extreme Huygens metasurfaces enabled by optical anisotropy,” Advanced Optical Materials, 10(2), 2101893, 2022
4. Sokhoyan, R., Hail, C. U., Foley, M., Grajower, M. Y., and Atwater, H. A. “All-Dielectric High-Q Dynamically Tunable Transmissive Metasurfaces,” Laser & Photonics Reviews, 18(6), 2300980, 2024

All-dielectric electrically-tunable metasurface for efficient beam steering

Junghyun Park*, Byung Gil Jeong, Sun Il Kim, Minkyung Lee, Young Kim, Jang-Woo You, Wontaek Seo, Byung-Hoon Ko, and Seokho Yun

Samsung Advanced Institute of Technology, Samsung Electronics, Suwon, Gyeonggi-do, 16678, Republic of Korea
*corresponding author: jhy.park@samsung.com

Abstract: We present an all-dielectric phase-modulating metasurface composed of Si and SiO_2, at 940 nm with high efficiency and directivity. By tuning the resonance between the top high contrast grating and the bottom distributed Bragg reflector via thermal control, we achieve over 20%-efficiency and 12 dB-directivity for 1-D beam steering.

Optical metasurfaces are component that manipulate the amplitude, phase, polarization, and angular momentum of transmitted, reflected, or scattered light at subwavelength scales by arranging sub-wavelength-sized optical structures in periodic or aperiodic patterns on a planar surface. This enables diverse unprecedented applications, including ultrathin lenses, wide-angle holograms, and high-sensitivity sensors [1]. Notably, tunable metasurfaces with post-fabrication tuning capabilities can dynamically alter their functions in response to input control signals. These properties make them promising for real-time displays, free-space optical communications, and light detection and ranging (LiDAR) applications [2]. Over the years, various material platforms have been employed to develop tunable metasurfaces, including gate-tunable transparent conducting oxides, liquid crystals, phase change materials. However, exiting phase modulation-based metasurfaces often suffer from low efficiency, defined as the ratio of the desired beam intensity to the incident beam intensity, and limited directivity, as undesired beam directions exhibit intensities comparable to those of the desired direction [3]. In this study, we present a phase-modulating metasurface composed solely of Si and SiO2, aiming to reduce optical losses. By employing localized thermal control, we achieve high efficiency and directivity in phase modulation in the near-infrared regime (940 nm).

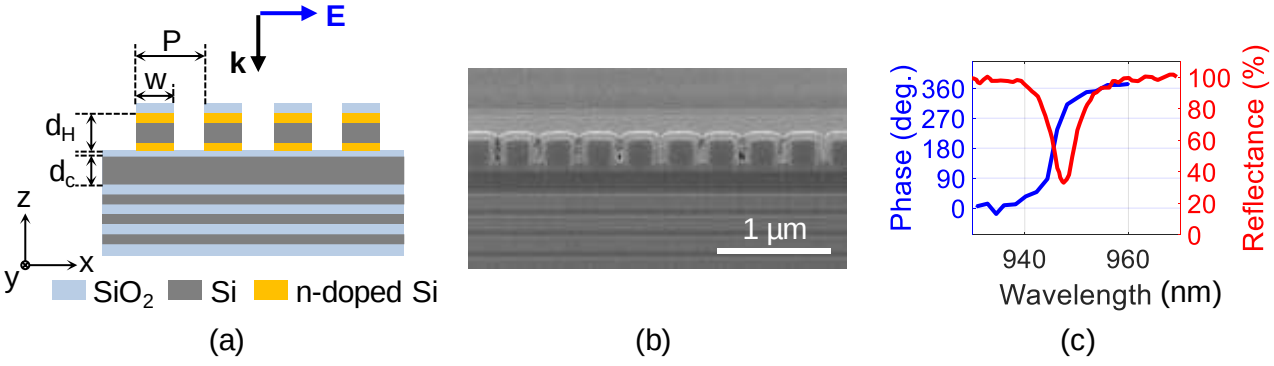


Figure 1. (a) Schematic diagram of the proposed Si-based tunable metasurface. (b) Scanning electron microscopy image of the fabricated sample. (c) Experimentally measured reflection phase and reflectance

Figure 1(a) shows the schematic diagram, where the Si cavity with the thickness d_c is located between the top high contrast grating (HCG) with the thickness d_H and the bottom 3-pair distributed Bragg reflector (DBR) of Si and SiO_2. The thicknesses d_{Si} and d_{SiO2} of Si and SiO2 are chosen as $\lambda_0/(4n_{Si})$ and $\lambda_0/(4n_{SiO2})$, respectively, where λ_0 denotes the operating wavelength (940 nm) in free space, while n_{Si} and n_{SiO2} correspond to the real part

of the refractive index of Si and SiO2, respectively. The period P, height d_H, and the width W of the HCG are designed as 330 nm, 205 nm, and 210 nm, respectively so as to contribute to the partial reflection 60% of light from cavity to air. This enables the over-coupling operation, which is advantageous for the high reflectance. By applying electrical bias between the upper and lower n-doped Si layers in the HCG, the thermal heat is generated, resulting in the refractive index increase and the phase change of light in reflection. We conduct the optical reflectance and phase measurement of the fabricated device (Fig. 1(b)) and show the data in Fig. 1(c), where the phase spans around 360° as a function of the wavelength and the reflection dip around 940 nm.

To analyze the beam steering characteristics, we apply spatially-varying two voltage signals across the 1-dimensional array of the proposed unit device (Fig. 2(a)). One voltage is to invoke the 0°-phase in reflection (off-state, $V_{0°}$), whereas the other one is for 180°-phase (on-state $V_{180°}$). As we manipulate the spatial period of two alternating voltages, denoted by Λ, we can control the angle $\theta = \pm\sin^{-1}(\lambda_0/\Lambda)$. Since the tuning mechanism is based on the thermal heating, we employ thermal isolation trenches between neighboring unit cells with the width of 500 nm as well as 5 μm-thick-SiO_2 block below the DBR. The design effectively prevents thermal leakage from the on-state cell to its adjacent off-state cell. By making the thermal path to the highly thermally conductive Si as long as possible, heat transfer to adjacent cells can be effectively blocked. As a result, we could obtain the stark contrast of 12 dB between the intensities between weakest intended beam and the strongest unintended beam as shown in Fig. 2(c). In addition, the absolute efficiency, defined by the ratio the sum of the intensities of the two intended beams over the input beam intensity, is measured around 20%.

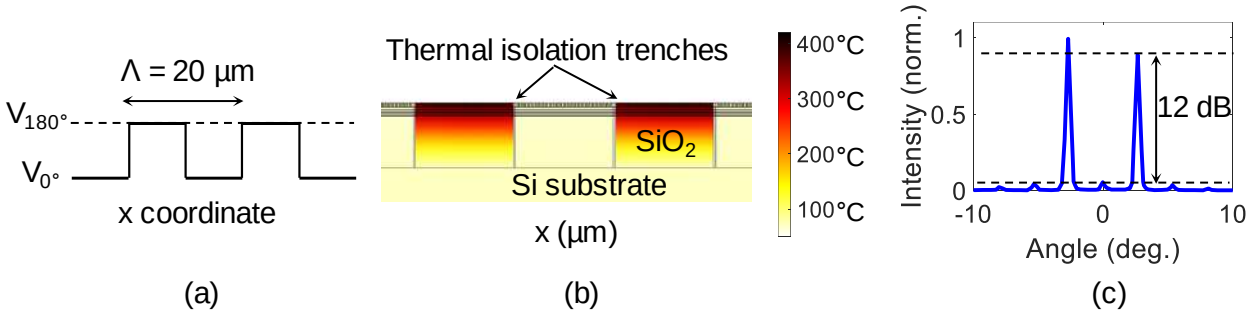


Figure 2 (a) Schematic diagram of the distribution of the applied bias, showing alternatively switching between one voltage for 0° in the reflection phase ($V_{0°}$) and another voltage for 180° in the reflection phase ($V_{180°}$) with the super cell period (Λ) of 20 μm. (b) Thermal simulation results of the device with the isolation trenches preventing the thermal crosstalk between neighboring cells. (c) Experimentally measured far-field distribution as a function of the angle under the binary phase grating (BPG) operation

In conclusion, we have demonstrated the all-dielectric electrically-tunable phase metasurface by using thermo-optic effect with carefully designed thermal isolation, which exhibits the efficiency of 20% and the directivity over 12 dB at the near-infrared regime. We believe the proposed device may shed light to the further research and development for various applications.

References

1. Kuznetsov, A. I. *et al.* "Roadmap for Optical Metasurfaces," ACS Photon. Vol. 11, 816–865, 2024.
2. Jung, C., Lee, E., and Rho, J. "The rise of electrically tunable metasurfaces," Sci. Adv. Vol 10, eado8964, 2024.
3. Park, J. *et al.* "All-solid-state spatial light modulator with independent phase and amplitude control for three-dimensional LiDAR applications," Nat. Nanotechnol. Vol. 16, 69–76, 2021.

Optical Charge Trap Memory Based on Graphene/ZnO Heterostructures for Long-Term Retention and Adaptive Learning

Junhyung Kim[†,1], Seungmin Shin[†,2], Hyeongdoh Lee[2], Min Seok Jang[*,1], Himchan Cho[*,1,2]

[1]School of Electrical Engineering, Korea Advanced Institute of Science and Technology (KAIST), Daejeon, 34141, Republic of Korea

[2]Department of Materials Science and Engineering, Korea Advanced Institute of Science and Technology (KAIST), Daejeon, 34141, Republic of Korea

[*]corresponding authors: jang.minseok@kaist.ac.kr, himchan@kaist.ac.kr

Abstract

Graphene/ZnO optical charge trap memory exhibits long retention via charge transfer quenching and electron trapping. Photodoping analysis confirms rapid charge transfer, with a high energy barrier preventing recombination. Adaptive learning reduces pulses needed for memory restoration. ANN simulations show fast convergence, making charge trap memory promising for energy-efficient neuromorphic applications.

Introduction

Neuromorphic on-device computing enables real-time biometric data processing while reducing the computational cost and energy consumption of traditional AI[1]. Optoelectronic neuromorphic devices, which modulate conductance via light exposure, offer advantages such as wider bandwidth, wavelength-dependent tunability, and lower computational power consumption[2]. However, challenges in biocompatibility, scalability, and long retention remain[3]. In this study, we present a graphene/ZnO (GZO) optical charge trap memory (CTM), demonstrating retention exceeding 54 hours, enabled by electron trapping at ZnO defect states and a high Schottky barrier, preventing charge recombination and sustaining photodoping effects. This retention enhances relearning efficiency, requiring fewer pulses for memory restoration. Artificial neural network (ANN) simulations validate its potential, demonstrating rapid convergence and near-unity accuracy within 20 epochs.

Results and Discussion

The GZO optical CTM exhibits a current increase in response to ultraviolet light, driven by electron doping from ZnO nanoparticles (NPs) into graphene. This effect is confirmed in transfer curve, where the leftward shift of the Dirac point with increasing irradiation time indicates progressive electron doping. The electron doping concentration can be calculated using capacitance model, reaching up to $1.38*10^{12}$ cm^{-2} after 30 seconds at an intensity of 1.131 mW cm^{-2}. Addtionally, higher UV power enhances both the drain current and retention time, due to a stronger temporal carrier concentration gradient, which drives charge transfer to graphene. However, at higher carrier densities, recombination processes become dominant, leading to saturation of the doping rate rather than a linear increase, as described by a multi-body recombination model.

The charge transfer quenching process in the GZO optical CTM is investigated using transient absorption (TA) spectroscopy, confirming rapid electron transfer from ZnO to graphene. The rapid absorption decay in GZO compared to ZnO highlights efficient charge dissociation. Retention analysis using stretched exponential fitting revealed a retention time exceeding 54 hours at 1.131 mW cm^{-2} optical stimulus, demonstrating the stability of the photodoped electrons and the effectiveness of the energy barrier in maintaining the excitation. Interaction between transferred electrons in graphene and trapped holes in ZnO further enhances charge retention. The Schottky barrier at the GZO interface, quantified as 2.02 eV, further hinders carrier recombination, enabling

long-term memory. Gate bias modulation experiments confirmed that increasing gate bias reduces the energy barrier, accelerating the recovery rate and demonstrating the Schottky barrier's crucial role in charge retention.

For the effective implementation of ANNs, the process of weight updating and validation are essential, typically performed iteratively over several epochs to optimize the network's performance. We examined the conductance increase behavior under different optical stimuli. System learns more rapidly when stimuli are applied more freuquently, over longer durations, and with higher intensity. The device exhibits enhanced relearning efficiency, requiring fewer pulses after memory loss, reducing power consumption. ANN simulations with the MNIST dataset validate the device's neuromorphic capabilities, showing rapid accuracy improvement despite its non-linearity. After 20 epochs, recognition accuracy reaches 93.75 %, comparable to 94.49 % in the ideal case.

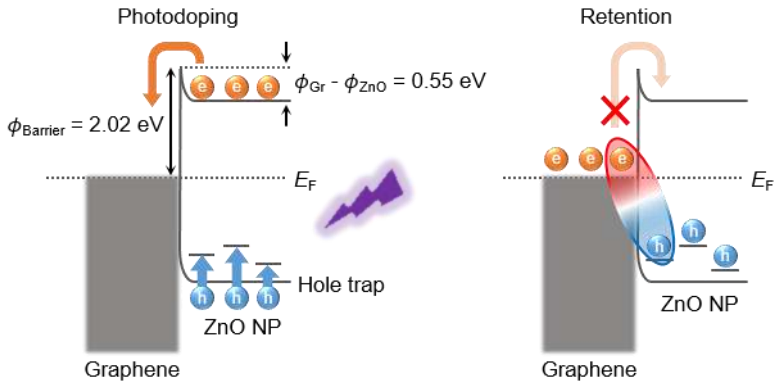


Figure. Schematic mechanism of photodoping (left); retention (right)

Conclusion

We demonstrated the neuromorphic capabilities of the GZO optical CTM, highlighting its potential for efficient ANN applications. The GZO optical CTM demonstrates long retention, high adaptability, and energy-efficient learning, making it a promising candidate for next-generation neuromorphic computing. The biocompatibility of graphene and ZnO further supports its application in bio-sensing and brain-computer interfaces.

Acknowledgments

This research was supported by the National Research Foundation of Korea (NRF) grants funded by the Ministry of Science and ICT (RS-2022-NR070476, RS-2024-00416583, RS-2024-00414119, and RS-2023-00216992). This research was also supported by Culture, Sports and Tourism R&D Program through the Korea Creative Content Agency grant funded by the Ministry of Culture, Sports and Tourism in 2024 (RS-2024-00332210).

References

[1] H. Park, "An Analysis of Components and Enhancement Strategies for Advancing Memristive Neural Networks", *Adv. Mater.* Vol. 37, No. 8, 2025.

[2] Y. Yang, "Light Stimulated IGZO-Based Electric-Double-Layer Transistors for Photoelectric Neuromorphic Devices", *IEEE Electron Device Lett.* Vol. 39, No. 6, 2018.

[3] S. Ham, "Photonic Organolead Halide Perovskite Artificial Synapse Capable of Accelerated Learning at Low Power Inspired by Dopamine-Facilitated Synaptic Activity", *Adv. Funct. Mater.* Vol. 29, No. 5, 2019.

Dynamic Multi-Wavelength Coded Aperture Imaging Using Reconfigurable Metasurfaces

[1]Reza Marzban, [1]Hamed Abiri, [1]Ali Adibi

[1]School of Electrical and Computer Engineering, Georgia Institute of Technology

Abstract

We present a reconfigurable coded-aperture imaging platform that harnesses the phase-transition properties of vanadium dioxide (VO_2) integrated with wavelength-selective metasurfaces in the near-infrared (NIR) range (1.1–1.6 μm). Each pixel in the metasurface array is designed for a specific resonant wavelength, allowing the device to generate a spatio-temporal "code" by switching individual pixels on or off. This on/off actuation is powered by the rapid insulator–metal transition of VO_2, triggered on millisecond timescales. In contrast to static coded-mask approaches, the dynamic system can be reconfigured to any desired pattern in real time, thus enabling high-resolution image reconstruction and enhanced signal throughput. Furthermore, the strong wavelength sensitivity provided by each pixel's metasurface design improves spectral control for applications ranging from telescope imaging to remote sensing. By combining programmable aperture coding with computationally efficient reconstruction algorithms, this platform offers a compact, tunable, and power-efficient solution for NIR imaging applications.

1. Introduction

Coded-aperture systems are widely used for imaging in energy regimes or wavelength bands where refractive or reflective optics are limited or impractical. Traditional coded apertures consist of patterned masks that modulate incoming light to produce an intensity distribution—a "shadow"—on a detector. The original scene or source distribution is then reconstructed from this shadow using computational algorithms. Such masks, however, are typically passive and fixed in their geometry, limiting their usability across broad wavelength ranges and restricting the ability to adapt the aperture pattern in real time. Here, we demonstrate a dynamic coded-aperture device in the short-wave infrared (SWIR) domain, specifically 1.1–1.6 μm, that leverages the unique properties of the phase-change material, vanadium dioxide (VO_2) integrated with metasurface nanoresonators. VO_2 undergoes a thermally driven phase transition near 68 °C, switching from an insulating to a metallic state and thereby changing its optical properties. By using transparent indium-tin-oxide (ITO) electrodes to deliver localized current for Joule heating, each pixel can be addressed individually and switched on sub-millisecond timescales. Figure 1 illustrates a conceptual rendering of the multi-wavelength metasurface array on a silicon dioxide (SiO_2) substrate, where each metasurface tile is designed to interact strongly at a different wavelength (λ_1–λ_5). In this manner, the array can serve as a spatio-spectral coded aperture that is reconfigurable on demand.

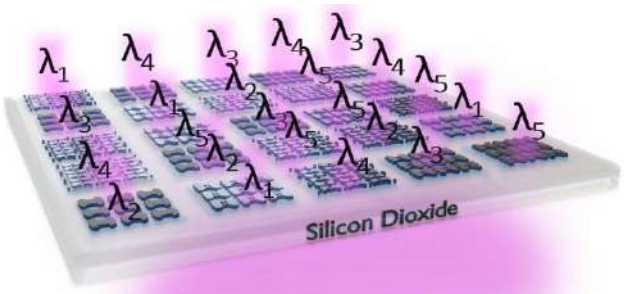


Figure 1. *Conceptual rendering of the multi-wavelength metasurface array fabricated on a SiO_2 substrate. Each metasurface tile is engineered to resonate at one of five distinct near-infrared wavelengths (λ_1–λ_5) to enable spatio-spectral modulation of incident light. By using VO_2 phase transition for rapid pixel switching, the array can be dynamically reconfigured into various coded patterns, facilitating high-resolution IR imaging in the 1.1–1.6 μm range.*

Device Architecture and Operation

Each pixel consists of a lower (negative) ITO backplane, an insulating alumina (Al_2O_3) pattern to define the active areas, and upper (positive) ITO lines arranged so that localized electrical current can be driven into specific pixels (Figure 2). A VO_2 layer and a metasurface—tuned for the desired resonant wavelength—are fabricated atop these electrodes. When voltage is applied, VO_2 rapidly heats past its transition temperature, changing from a low-loss insulating state to a more metallic state with high reflectivity and altered resonance behavior. By carefully designing the metasurface geometry for each pixel, the on/off optical contrast can be optimized at the target wavelength. Unlike static coded apertures that feature a single fixed pattern, the present approach allows each pixel to be toggled independently. This means the aperture can be reconfigured in real time, creating a new coded pattern whenever needed. The rapid phase transition of VO_2 allows the device to switch patterns on the order of milliseconds, which can be synchronized with computational imaging algorithms. Multiple patterns can be displayed sequentially, and each detector measurement captures a different coded projection of the scene. By fusing these snapshots, one obtains an improved reconstruction over what would otherwise be possible with a single static code. Since each pixel is tailored to a distinct resonant wavelength, the same device can encode and discriminate spectral information without bulky dispersive optics.

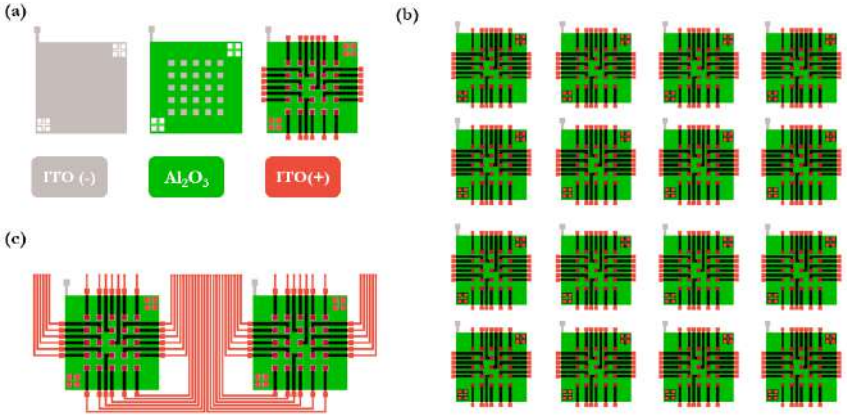


Figure 2. *(a) Each device layer comprises a large negative (–) ITO electrode (gray), patterned insulating Al_2O_3 squares (green), and positive (+) ITO lines (red) for individual pixel addressing. (b) An example 4 × 4 array of these addressable devices. (c) Expanded view illustrating how multiple devices are wired in parallel, enabling independent actuation of each pixel.*

The millisecond VO_2 switching capability, combined with independently addressable pixels, supports flexible spatio-temporal coding and higher signal-to-noise ratios than a simple pinhole configuration. Each pixel's wavelength selectivity provides built-in spectral discrimination, making the system well-suited to SWIR imaging for astronomy, remote sensing, or portable instruments. The dynamic aperture also enables advanced computational imaging strategies, such as compressed sensing or multi-pattern acquisition, enhancing resolution and speed. Details of the pixel design as well as the experimental demonstration of individual pixels and a small array will be presented.

Dynamic control of bound states in the continuum by MEMS-enabled hybridization of 1D and 2D metasurfaces

F. V. Kovalev[1,4*], M. Martyniuk[2,4], A. E. Miroshnichenko[3] and I. V. Shadrivov[1,4]

[1]Research School of Physics, The Australian National University, Canberra ACT 2601, Australia
[2]School of Engineering, The University of Western Australia, Perth, WA 6009, Australia
[3]School of Engineering and Technology, University of New South Wales Canberra, Canberra ACT 2612, Australia
[4]Australian Research Council Centre of Excellence for Transformative Meta-Optical Systems, Australia
[*]corresponding author: fedor.kovalev@anu.edu.au

Abstract: We propose a tunable metasurface composed of coupled 1D and 2D metasurfaces. Our study demonstrates that this hybrid structure supports an ultranarrow quasi-BIC resonance, which can be tuned over 60 nm while maintaining a constant quality factor. This tuning is achieved through MEMS-enabled horizontal and vertical displacements within the structure.

The concept of Bound States in the Continuum (BICs) represents a fascinating phenomenon in modern physics, where certain states remain localized within a system despite existing at energies or frequencies that typically allow for radiation[1]. Originating from quantum mechanics, BICs have found significant applications in photonics and metamaterials, enabling strong confinement of electromagnetic waves and leading to the formation of extremely high-Q resonances[2,3]. Recent advancements have focused on the active control of BICs, where external stimuli, such as electric fields, temperature variations, or material phase transitions, are used to dynamically tune their properties[4]. The precise manipulation of quasi-BIC resonances in real-time could revolutionize photonic systems, enhancing device performance and functionality.

In this work, we propose a new approach to controlling quasi-BIC resonances in transmission within all-dielectric metasurfaces, enabled by microelectromechanical systems (MEMS). The quasi-BIC resonance is achieved via breaking the out-of-plane symmetry by introducing a 2D MEMS membrane that moves near a 1D metasurface. We demonstrate that the resonance quality factor approaches infinity as a MEMS structure moves farther from a 1D metasurface, thereby reducing the asymmetry, a defining characteristic of quasi-BIC resonances. Furthermore, the vertical movement of a MEMS membrane combined with horizontal displacement within a 1D metasurface enables the central wavelength of the quasi-BIC resonance to be shifted by more than 60 nm while maintaining consistent resonance bandwidth and Q-factor. The proposed all-dielectric metasurfaces achieve an ultranarrow resonance linewidth with dynamic tunability in the infrared range, making them promising candidates for advanced tunable filtering applications highly relevant for spectroscopy, remote sensing, and imaging.

Figure 1a depicts the tunable metasurface design consisting of silicon ridge pairs that can move horizontally relative to each other, while the 2D membrane moves vertically above the ridges. The polarization of the incident plane wave is shown using a triple of vectors. Two independent orthogonal tuning mechanisms enable precise control of both the central wavelength and bandwidth (or Q-factor) of the quasi-BIC resonance. Figure 1b presents the transmission characteristics for various distances between the ridges (d) when the distance between two layers (a) is equal to 900 nm. The horizontal movement of the ridges allows the resonance wavelength to shift by approximately 65 nm. By combining two independent orthogonal tuning mechanisms, complete control over the quasi-BIC resonance characteristics can be realized. Figures 1c and 1d illustrate the

dependence of the resonance central wavelength and Q-factor on two parameters: the distance between two layers (*a*) and the distance between the ridges (*d*). By precisely adjusting both parameters, as indicated by the black lines in Figure 1d, it is possible to maintain a constant Q-factor while tuning the central wavelength by more than 60 nm.

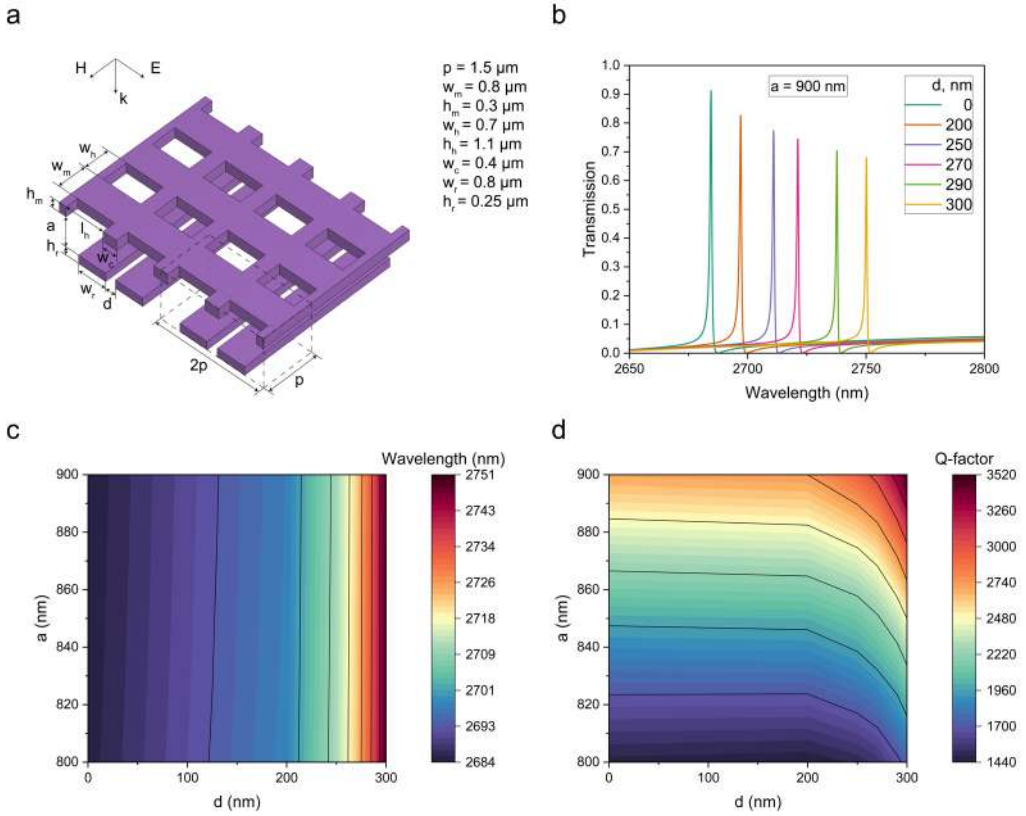


Figure 1. a) Schematic of the tunable metasurface design consisting of pairs of silicon ridges and an overlying MEMS membrane, depicting the unit cell indicated by the dashed lines; b) Transmission characteristics for varying distances between the ridges (*d*), with the distance between two layers (*a*) fixed at 900 nm; c, d) Dependence of the resonance central wavelength and Q-factor on two parameters: the distance between two layers (*a*) and the distance between the ridges (*d*). The black lines indicate examples of curves with constant wavelength and Q-factor, respectively.

This research was supported by the Australian Research Council Centre of Excellence for Transformative Meta-Optical Systems (Project ID CE200100010).

References

1. Hsu, C. W., Zhen, B., Stone, A. D., Joannopoulos, J. D. & Soljačić, M. Bound states in the continuum. *Nat Rev Mater* **1**, 16048 (2016).
2. Koshelev, K., Bogdanov, A. & Kivshar, Y. Meta-optics and bound states in the continuum. *Science Bulletin* **64**, 836–842 (2019).
3. Azzam, S. I. & Kildishev, A. V. Photonic Bound States in the Continuum: From Basics to Applications. *Advanced Optical Materials* **9**, 2001469 (2021).
4. Zeng, Y. *et al.* Manipulating Light with Bound States in the Continuum: from Passive to Active Systems. *Advanced Optical Materials* **12**, 2400296 (2024).

Chirality, magnetism, and magnetoelectricity: Separate phenomena and joint effects in metamaterial structures

A QED Theory of Discriminatory RET Mediated by One or Two Polarisable Molecules

A. Salam

Department of Chemistry, Wake Forest University, Winston-Salem, NC 27109, USA
salama@wfu.edu

Abstract: QED theory is employed to study the influence of one or two mediator particles on the resonance energy transfer rate between a pair of chiral molecules. It is found that direct and relayed rates are discriminatory, maximised for collinear geometry, and require the bridging species to be multi-levelled systems.

An especially attractive aspect of non-relativistic or molecular quantum electrodynamics (QED) is that the interaction between light and matter, and between material particles, may be treated within a single theoretical framework [1,2]. A signature feature of this theory is that electromagnetic radiation, as well as atoms and molecules, obey quantum mechanical principles [3]. Thus, photons arise naturally because of quantisation of the electromagnetic field. They are classified as belonging to two types, real or virtual photons [4]. The former are associated with a change in the state of the radiation field as occurs in numerous linear and nonlinear spectroscopic and parametric processes. Virtual photons, on the other hand, are unobservable but their existence is allowed by time-energy uncertainty and manifests in processes in which the state of the radiation field remains the same, giving rise to an energy shift or transfer rate. It is the exchange of virtual photons between particles of matter that accounts for the coupling between them.

Perhaps the best-known example of a molecular process that involves the propagation of a single virtual photon between two centres is resonance energy transfer (RET) [5] in which typically electronic excitation is exchanged between an initially excited donor species and an acceptor particle that is in its ground state. A QED calculation of the probability amplitude shows that the tensor coupling the electric dipoles of the emitter and absorber is properly retarded, with the subsequent Fermi golden rule rate formula exhibiting an inverse square dependence on separation distance at long-range that is indicative of radiative transfer of energy. At the other extreme in the near-zone, the well-known Förster exchange rate is found to apply. Transfer of energy is radiationless, originating from inter-particle coupling that is static in origin.

When both molecules exchanging energy are chiral, there is an additional contribution to the transfer rate that is discriminatory, changing sign when one enantiomer of the pair is replaced by its isomer of opposite handedness [6,7]. Spectroscopic selection rules in such species are less restrictive relative to non-chiral substances enabling multipole moments higher than the leading electric dipole term to contribute to the transfer probability. In the dipolar approximation the interaction Hamiltonian is given by

$$H_{int}(\xi) = -\varepsilon_0^{-1}\vec{\mu}(\xi)\cdot\vec{d}(\vec{R}_\xi) - \vec{m}(\xi)\cdot\vec{b}(\vec{R}_\xi), \tag{1}$$

where $\vec{\mu}(\xi)$ and $\vec{m}(\xi)$ are electric and magnetic dipole moment operators of the donor or acceptor molecule, ξ, positioned at $\vec{R}_\xi$, and $\vec{d}(\vec{r})$ and $\vec{b}(\vec{r})$ are microscopic electric displacement and magnetic field operators, respectively. To leading order, the interference of electric and magnetic dipole coupling terms yields a

discriminatory rate, with purely electric and purely magnetic dipole contributions independent of handedness.

The modification of the migration rate between two optically active molecules is investigated when one [8] or two [9] identical, neutral, passive, electric dipole polarisable mediator particles are introduced. Their role is to relay energy from the chiral emitter to the chiral acceptor, remaining in the ground state before and after transfer. In the case of one bridging molecule, twenty-four time-ordered diagrams have to be evaluated and summed at fourth-order of perturbation theory when using an interaction Hamiltonian that is linear in the electric displacement field. To ensure a manageable number of time-ordered sequences occurs when two mediators are present, it is convenient to employ an interaction Hamiltonian that is quadratic in the electric displacement field and proportional to the ground state dynamic polarisability of each mediator. It has the form

$$H_{int}(M_i) = -\varepsilon_0^{-2}\alpha_{ij}(M_i)d_i(\vec{R}_{M_i})d_j(\vec{R}_{M_i}),\ i = 1,2, \tag{2}$$

where $\alpha_{ij}(M_i)$ is the ground state dynamic electric dipole polarisability of mediator M_i, i = 1, 2. Twenty-four diagrams again contribute to the matrix element at fourth-order of perturbation theory.

In both cases, the isotropic mediated Fermi golden rule rate is discriminatory, depending on the chirality of the species exchanging energy. Maximum rates are achieved when all three or four bodies are arranged in a collinear configuration. Interestingly, the energy transfer probability vanishes if each mediator is modelled as a two-level system. In the case of one bridging particle, the rate is found to be retarded at *all* separation distances and vanishes when the three molecules are oriented at right angles to one another.

As a result of this work, considerable insight is gained into the conveyance of excitation energy between chiral entities in a dielectric medium [10].

References

1. Craig, D. P. and T. Thirunamachandran, Molecular Quantum Electrodynamics, Dover, 1998.

2. Woolley, R. G. Foundations of Molecular Quantum Electrodynamics, Cambridge University Press, 2022.

3. Andrews, D. L., G. A. Jones, A. Salam and R. G. Woolley, "Perspective: Quantum Hamiltonians for Optical Interactions", J. Chem. Phys., Vol. 148, No. 4, 040901 1-10, 2018.

4. Andrews, D. L., D. S. Bradshaw, K. A. Forbes and A. Salam, "Quantum Electrodynamics in Modern Optics and Photonics: Tutorial", J. Opt. Soc. Am. B, Vol. 37, No. 4, 1153-1172, 2020.

5. Salam, A. "The Unified Theory of Resonance Energy Transfer According to Molecular Quantum Electrodynamics", Atoms, Vol. 6, No. 4, 56 1-20, 2018.

6. Craig, D. P. and T. Thirunamachandran, "Chiral Discrimination in Molecular Excitation Transfer", J. Chem. Phys., Vol. 109, No. 4, 1259-1263, 1998.

7. Salam, A. Molecular Quantum Electrodynamics, Wiley, 2010.

8. Salam, A. "Discriminatory Resonance Energy Transfer Mediated by a Third Molecule", J. Phys. Chem. A, Vol. 125, No. 17, 3549-3555, 2021.

9. Salam, A. "Two Bridge-Particle-Mediated RET Between Chiral Molecules", J. Chem. Phys., Vol. 157, No. 10, 104110 1-14, 2022.

10. Franz, J. C., S. Y. Buhmann and A. Salam, "Macroscopic Quantum Electrodynamics Theory of Resonance Energy Transfer Involving Chiral Molecules", Phys. Rev. A, Vol. 107, No. 3, 032809 1-11, 2023.

Theory of Unidirectional Magnetoresistance in Nanoscale Bilayers

X. R. Wang[1,2*]
[1]School of Science and Engineering, Chinese University of Hong Kong (Shenzhen), Shenzhen 51817, China
[2]The Hong Kong University of Science and Technology, Clear Water Bay, Kowloon, Hong Kong
phxwan@cuhk.edu.cn (corresponding author)

Abstract

Unidirectional magnetoresistance (UMR) of bilayers arises from the influences of magnetization present in the magnetic material and the interfacial potential inherent in heterostructures. This theory explains unifiedly universal UMR and unusual anisotropic magnetoresistance and capture all experimental features such as dependence on current direction, film thickness, and magnetic field strength.

1 Introduction

The study of magnetoresistance (MR) in nanoscale multilayers has gained significant attention due to its fundamental interest and important applications in spintronic devices. Recent studies have given birth to many new concepts and phenomena, such as spin Hall MR (SMR) [1, 2]—termed as unusual anisotropic MR (UAMR) in this study—and unidirectional MR (UMR) [3]. UAMR and UMR have emerged as key phenomena that reflect the intricate interplay between charge transport and magnetism.

UAMR is the MR of bilayers at low current density. For a current density $\vec{j} \parallel \hat{x}$, flowing in the plane of a ferromagnet-nonmagnet (FM/NM) bilayer, the longitudinal and transverse resistivity depends on the direction of magnetization $\vec{m}$ as: $\rho_{xx} = \rho_0 + \rho_1 m_x^2 + \rho_2 m_z^2 + \rho_3 m_z^4 + \rho_4 m_x^2 m_z^2$ and $\rho_{xy} = \rho_5 m_z + \rho_6 m_z^3 + \rho_1 m_x m_y + \rho_4 m_x m_y m_z^2$. This is in contrast to the conventional anisotropic MR (AMR), which is given by $\rho_{xx} = \rho_0 + \rho_1 m_x^2$ and $\rho_{xy} = \rho_5 m_z + \rho_1 m_x m_y$. Here, the parameters ρ_i (where $i = 0, 1, \ldots, 6$) are independent of the magnetization direction. UAMR has stimulated the development of the SMR theory [1, 2], which attributes UAMR to the spin Hall effect and its inverse effect via the absorption/reflection of spin current at the magnetic interface. SMR theory predicts $\rho_{xx} = \rho_0 + \rho_1 m_x^2 + \rho_2 m_y^2$ and has been widely used to interpret UAMR ubiquitously observed in all kinds of nanoscale multilayers. Clearly, the original SMR theory cannot apply to this wide range of multilayers. As a result, alternative spin-current-related MR models have been proposed to explain the universal nature of UAMR. A natural question arises: Why does the same UAMR emerge from so many different microscopic origins? Why do so many different microscopic interactions exhibit the same angular dependence? Wouldn't it be more natural to expect a unified origin for UAMR? Indeed, a recent two-vector theory predicts exactly the observed ρ_{xx} and ρ_{xy} of UAMR [4–6]. In this two-vector theory, the key components are magnetization of ferromagnetic (FM) layers and the effective internal interfacial electric field arising at the interface between ferromagnetic (FM) and non-magnetic (NM) materials. These two ingredients result in the universal behaviors of UAMR in FM/NM bilayers and FM single layers, independent of the details of microscopic interactions among electrons, lattices, spins, and magnons.

UMR is the nonlinear part of MR of bilayers at high current density [above $10^{10}\mathrm{A/m^2}$] [3]. Different from UAMR whose resistivity does not depend on the current and follows $\rho_{xx} = \rho_0 + \rho_1 m_x^2$ when $\vec{m}$ rotates in the xy-plane, ρ_{xx} in UMR is linear in current density and is odd in m_y. Both ρ_{xx} and ρ_{xy} are sensitive to the magnetic field, film thickness, and temperature. Under an alternating current of frequency ω, single harmonic resistivity of ρ_{xx}^{ω} and ρ_{xy}^{ω} follow the behaviour of UAMR while the second harmonic resistivity of $\rho_{xx}^{2\omega}$ and $\rho_{xy}^{2\omega}$ reverses sign with the directions of current and transverse field, and has a strong 3-fold symmetry at low magnetic field and only a 1-fold symmetry of $\rho_{xx}^{2\omega} \propto m_y$ and $\rho_{xy}^{2\omega} \propto m_x$ at high magnetic field. The same behaviour is observed in a wide range of systems, including FM/NM, FM/semiconductor, FM/topological insulator bilayers, and 2D materialsits. To date, UMR is attributed to multiple origins including giant MR effect, spin Hall effect and inverse spin Hall effect, the Rashba-Edelstein effect, magnon effect, spin-flip and spin-dependent scatterings, and thermal effects. From the coexistence of UAMR and UMR in vast different systems, it is natural to ask whether two-vector theory can also explain the universal features of UMR.

We consider the electric field response $\vec{E}$ to an applied current density $\vec{j}$ flowing along the x-direction of a bilayer in the xy-plane under the influence of magnetization ($\vec{M} = M\vec{m}$) of the FM layer and an interfacial field ($\vec{n} \parallel \hat{z}$). Under a high $\vec{j}$, a thermal gradient $\nabla T = aj^2\hat{z}$ perpendicular to the bilayer is generated due to Joule heating [3], where a is a device parameter. The most general expression for $\vec{E}$, which is linear in both $\vec{j}$ and ∇T, is given by [4–6]

$$\vec{E} = C_0 \nabla T + C_1 \vec{m} \times \nabla T + \rho_{\vec{m},\vec{n}} \vec{j}, \tag{1}$$

where C_0 is the Seebeck coefficient and C_1 measures the anomalous Nernst effect. $\rho_{\vec{m},\vec{n}}$ is the rank-2 resisitivty tensor which can only be constructed from $\vec{m}$ and $\vec{n}$. It is straight to show

$$\begin{aligned} \rho_{xx} &= \rho_0 + \rho_1 m_x^2 + \rho_2 m_z^2 + \rho_3 m_z^4 + \rho_4 m_x^2 m_z^2 + C j m_y \\ \rho_{xy} &= \rho_5 m_z + \rho_6 m_z^3 + \rho_1 m_x m_y + \rho_4 m_x m_y m_z^2 - C j m_x, \end{aligned} \tag{2}$$

where ρ_i and C are angular-independent parameters. Eq. 2 is exactly the widly observed UAMR.

Under an alternating current (AC) of frequency ω, $\vec{j} = j\cos(\omega t)\hat{x}$, one can obtain, after some algebra,

$$\begin{aligned} &\rho_{xx}^{2\omega}(\alpha) = (C + c_1) j \sin\alpha - c_1 j \sin 3\alpha, \quad \rho_{xy}^{2\omega}(\alpha) = -(C + c_1) j \cos\alpha + c_1 j \cos 3\alpha, \\ &\rho_{xx}^{2\omega}(\beta) = (C + c_2) j \sin\beta + (c_3 - c_2) j \sin 3\beta - c_3 j \sin 5\beta, \quad \rho_{xy}^{2\omega}(\beta) = c_4 j \sin 2\beta + c_5 j \sin 4\beta, \\ &\rho_{xx}^{2\omega}(\gamma) = 0, \quad \rho_{xy}^{2\omega}(\gamma) = c_1 + c_6 - C j \sin\gamma - c_1 \cos 2\gamma - c_6 \cos 4\gamma, \end{aligned} \tag{3}$$

where C and c_i are material parameters. $\rho_{xx}^{2\omega}(\alpha)$ and $\rho_{xy}^{2\omega}(\alpha)$ are exactly what were observed in UMR. The dierction dependences of $\rho_{xx}^{2\omega}$ and $\rho_{xy}^{2\omega}$ can be used for future experiments to test.

In conclusion, we have presented a novel theoretical approach to understanding UAMR and UMR. According to this theory, UAMR and UMR do not depend on microscopic interactions and do not require the interconversion between spin current and charge current. In principle, materials with any spin-electron scattering under the influence of an interfacial potential should exhibit the universal UAMR and UMR discussed herein. Several predictions are new. Some of them are supported by existing experiments while the others are awaited for experimental confirmation.

2 Acknowledgements

This work is supported by the University Development Fund of the Chinese University of Hong Kong, Shenzhen, the NKRDPC grant (No. 2020YFA0309600), the NSFC Grant (No. 12374122), and HK RGC Grants (No. 16300523 and 16300522).

References

[1] Y. T. Chen et. al., Phys. Rev. B 87, 144411 (2013).

[2] H. Nakayama et. al., Phys. Rev. Lett. 110, 206601 (2013).

[3] C. O. Avci et. al., Nat. Phys. 11, 570 (2015).

[4] X.R. Wang, Commun. Phys. 4, 55 (2021); Chin. Phys. Lett. 39, 027301 (2022).

[5] X.R. Wang et. al., Sci. Rep. 13, 309 (2023).

[6] Y. Zhang, H. W. Zhang, and X. R. Wang, Europhys. Lett. 113, 47003 (2016).

New Topological Magnetic Photonic Crystals

C. T. Chan[1*]

[1]Hong Kong University of Science and Technology, Hong Kong SAR, China

[*]corresponding author: phchan@ust.hk

Abstract: We introduces several new types of magnetic photonic crystals, specifically photonic alloys and gyromagnetic double-zero-index materials. Photonic alloys can support topological edge states even at very low concentrations of magnetic components. The gyromagnetic double-zero-index photonic crystal exhibits special non-trivial topological characteristics in both near-field and far-field contexts.

We present the concept of some new magnetic photonic crystals that exhibit intriguing topological features. First, we explore “photonic alloys” [1], which are disordered, non-periodic topological materials. This new class of materials consists of two-dimensional (2D) photonic crystals made up of a mixed lattice of non-magnetized and magnetized components occupying randomly chosen lattice sites. These materials demonstrate non-trivial topology even at very low concentration of magnetic components, characterized by the winding of the reflection phase. Notably, we experimentally observe non-reciprocal chiral edge states resulting from a local breakdown of time-reversal symmetry, rather than a global one. The concentration of magnetic components required to induce non-trivial topological depends on the lattice structure. Interestingly, in certain lattice configurations, non-trivial topology and chiral edge states can be identified even at minimal concentrations of magnetic components.

Additionally, we introduce gyromagnetic double-zero-index materials (GDZIM) [2], a type of magnetic photonic crystal characterized by zero scalar permittivity and unique tensorial magnetic permeability with non-zero components, yet possessing a zero determinant. This is achieved by constructing a magnetized 2D photonic crystal that displays a spin-1/2 Dirac cone at the Brillouin center. This configuration is at the critical point of a topological transition between two Chern insulator phases. A key topological feature of GDZIMs is the presence of an unpaired spin-1/2 Dirac point at the center of momentum space. Through both theoretical and experimental validation, we demonstrate that the spin-1/2 Dirac topology of GDZIMs provides an intrinsic pathway for generating optical spatiotemporal vortex pulses (STVPs) with remarkable robustness. The central frequency and wavevector of the generated STVPs remain firmly anchored to those of the bulk Dirac point at the zone center, independent of material thickness or background medium. We show that this exceptional robustness arises from a novel form of topological correspondence—bulk-spatiotemporal reflection correspondence—which links the quantized jump of topological invariants at the phase transition point to the vortex charge of the generated STVPs. Our findings illuminate the connections between zero-refractive-index photonics, topological photonics, and singular optics.

This work is supported by the Hong Kong RGC.

References

1. Qu, T. et al., “Topological photonic alloy,” Phys. Rev. Lett., 132 (22), 223802 (2024).
2. Zhang R.Y. et al., "Bulk-spatiotemporal vortex correspondence in gyromagnetic double-zero-index media" arXiv:2408.06182 (2024).

META 2025, MALAGA - SPAIN, JULY 22 – 25, 2025

Development of Carbon Fiber Composites with Ferromagnetic Microwire Inclusions for Free Space Microwave Sensing

V. Zhukova[1], J. Malm[2], C. Johansson[2], R. B. Garcia-Etxabe[3,4], F. J.Vallejo[5], P. Olaskoaga[5] and A. Zhukov[1,6]

[1] Dept. Polymers and Advanced Materials, and Dept. Appl. Phys. University of Basque Country, UPV/EHU, 20018 San Sebastian

[2]RISE Research Institutes of Sweden, Digital Systems, Göteborg, Sweden

[3]GAIKER Technology Centre, Basque Research and Technology Alliance (BRTA), Spain

[4]Department of Electricity and Electronics, University of Basque Country, UPV/EHU, 48940 Leioa, Spain

[5] Ideko Technology Centre, Basque Research and Technology Alliance (BRTA), Elgoibar, Spain

[6]IKERBASQUE, Basque Foundation for Science, 48011 Bilbao, Spain

[*]corresponding author: arkadi.joukov@ehu.es

Abstract: We provide free space microwave measurements of composites made from carbon fibers and ferromagnetic microwires inclusion focusing on the electromagnetic properties. We observed that a low frequency modulating AC magnetic field allows to distinguish the microwave signals originated by ferromagnetic microwires inclusions from that generated by the carbon fibers.

Glass-coated microwires prepared by the Taylor-Ulitovsky technique with diameters between 0.5 and 100 μm covered with thin, insulating, biocompatible and flexible glass-coating can present excellent magnetic softness, superior mechanical properties. Such features of glass-coated microwires allow development of new exciting applications in various magnetic sensors, as well as in smart composites with tunable magnetic permittivity [1,2].

One common challenge in composite materials is monitoring of stresses and temperature. Recently, stress dependencies of hysteresis loops and GMI effect have been proposed for the mechanical stresses monitoring in composites containing microwires inclusions [2].

In this paper, we present our latest results on studies of magnetic properties of glass-coated microwires and on our attempts to wireless health monitoring of composites containing both carbon fibers and ferromagnetic glass-coated microwires.

The composites containing both carbon fibers and Co-rich ferromagnetic glass-coated microwires were manufactured in the INFINITE EU project (Horizon Europe) at IDEKO's facilities (see Figure 1). For wireless measurements we used a free space microwave measurement setup (see Figure 1b) consisting of two broadband horn antennas (1-17 GHz) fixed to the anechoic chamber and a vector network analyzer, previously employed for the characterization of the composites with magnetic wire inclusions [2]. Such setup allows to characterize composites of dimensions 20 x 20 cm^2. $Co_{64.6}Fe_{5.0}B_{16.0}Si_{11.0}Cr_{3.4}$ microwires (metallic nucleus diameter d=38 μm) microwires with better MI effect have been selected for the carbon fiber composite preparation. The expected problem with composites containing electrical conductive carbon fibers is that they can substantially interfere with the microwave signal from the magnetic microwire inclusions.

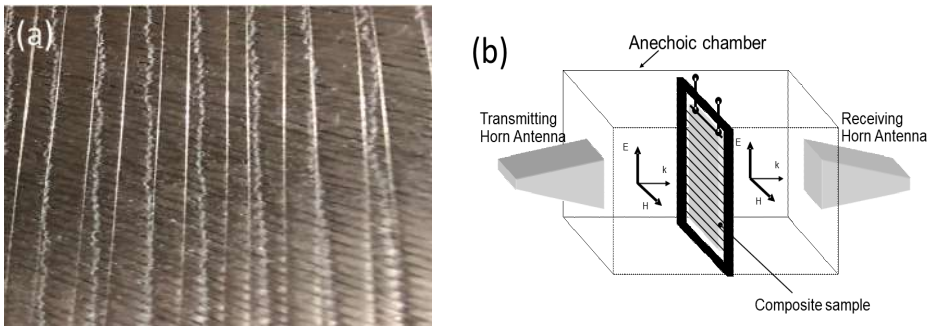


Figure 1. Image of the carbon fiber composite with magnetic microwire inclusions (the vertical lighter fibres) with 5 mm spacing (a) and the free-space setup sketch (b).

We proposed several solutions. Thus, in order to separate the microwave signal from ferromagnetic microwires, we used an external low frequency modulated magnetic field [2].

The other possibility is to separate the conductive carbon fibers from the magnetic microwires. Finally, use of magnetic microwires with better GMI performance can further increase the microwave response.

In Figure 2a,b the microwave signals (S_{11} parameters, reflection) measured at 2 GHz with no separation and with a separation between magnetic microwires and carbon fibers are shown. As illustrated, the position of carbon fibers in the vicinity of magnetic microwires critically affect the response signals obtained from such composites.

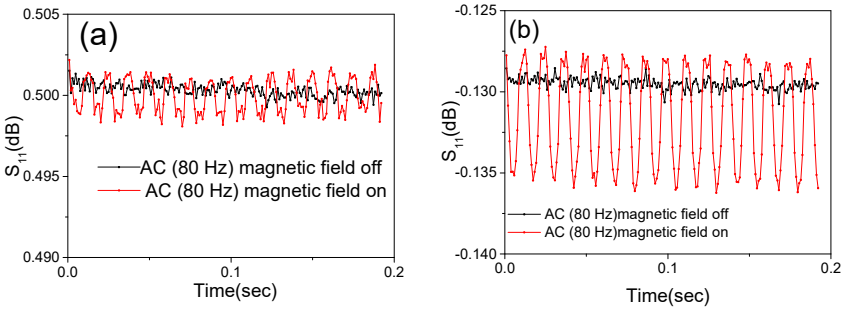


Figure 2. Effect of introducing an insulating plastic layer between the microwires and carbon fibre composite on the S_{11} parameter. Measurements without plastic layer (a) and with plastic layer (b).

Thus, the presence of a thin insulating plastic layer (30 μm thick) between the ordered microwires and carbon fiber composite can further increase the S_{11} parameters (see Figure 2b).

The aforementioned examples provide the routes for development of the composites made from the carbon fibers and magnetically soft amorphous glass-coated microwires inclusions.

References

1. Makhnovskiy, D., A. Zhukov, A., V. Zhukova, V., J. Gonzalez, J. “Tunable and self-sensing microwave composite materials incorporating ferromagnetic microwires,” Advances in Science and Technology, Vol.54 pp. 201-210, 2008.
2. Panina, L.V., Ipatov, M., Zhukova, V., Zhukov, A., Gonzalez, J. Appl. Phys. Vol. 109, 053901, 2011.
3. Zhukova, V., Ipatov, M., Corte-Leon, P., Gonzalez, A., García- Gómez, A., Vallejo, F. J., P. Olaskoaga, P., Garcia-Etxabe, R., Malm, J., Johansson, C., Zhukov, A. "Free Space Microwave Sensing of Carbon Fiber Composites With Ferromagnetic Microwire Inclusions," IEEE Sens. Lett., Vol. 8(1), 2500104, 2024.

Spin current generation due to differential rotation

M. Matsuo[1]
[1]Kavli Institute for Theoretical Sciences, University of Chinese Academy of Sciences, China
mamoru@ucas.ac.cn (corresponding author)

Abstract

We theoretically investigate nonequilibrium spin dynamics in differentially rotating systems, deriving an effective Hamiltonian for conduction electrons in the comoving frame. In contrast to conventional spin current generation mechanisms that rely on vorticity, our theory reveals spins and spin currents arising from differentially rotating systems regardless of vorticity-gradient.

1 Introduction

In this talk, we consider a novel mechanism of spin current generation from non-uniform rotational motion without relying on vorticity[1]. To date, theoretical descriptions of the interaction between spatially non-uniform rotational motion and spin have been primarily framed as an extension of the gyromagnetic effect, originally identified by Einstein and others[2,3]. The conventional approach was limited to introducing spin-vorticity coupling by replacing the rigid rotation with vorticity associated with non-uniform rotation[4,5]. We formulate an effective Hamiltonian for the conduction electrons in differentially rotating systems, demonstrating the emergence of effective gauge fields. We also derive microscopic expressions for the spin current driven by the emergent gauge fields and apply them to two examples of differentially rotating systems, such as a liquid metal and a non-magnetic metallic cantilever. Our estimation of the generated spin currents indicates that they are realistically measurable in experiments.

2 Acknowledgements

This work is done in collaboration with T. Funato, S. Kinoshita, N. Tanahashi, and S. Nakamura. The author was supported by the National Natural Science Foundation of China (NSFC) under Grant No. 12374126. We also thank RIKEN iTHEMS NEW working group for providing the genesis of this collaboration.

References

[1] T. Funato, S. Kinoshita, N. Tanahashi, S. Nakamura, and M. Matsuo, "Spin current generation due to differential rotation," *Phys. Rev. B* 111, 0451231 (2025).

[2] S. J. Barnett, "Magnetization by rotation," *Phys. Rev.* 6, 239 (1915).

[3] A. Einstein and W. J. de Haas, "Experimental proof of Ampere' s molecular currents," KNAW, 18, 696, 1915.

[4] R. Takahashi et al., "Spin hydrodynamic generation," *Nat. Phys.* 12, 52-56 (2016).

[5] D. Kobayashi et al., "Spin current generation using a surface acoustic wave generated via spin-rotation coupling," *Phys. Rev. Lett.* 119, 077202 (2017).

Experimentally testing the spontaneous disentanglement hypothesis using a ferri–magnetic resonator

Eyal Buks[1]
[1]Andrew and Erna Viterbi Department of Electrical Engineering, Technion, Haifa 32000 Israel
eyal@ee.technion.ac.il (corresponding author)

Abstract

The spontaneous disentanglement hypothesis makes the collapse postulate of quantum mechanics redundant, and enables meta-stability in finite quantum systems, which is otherwise excluded. We report on an experiment performed using a ferri–magnetic resonator, which indirectly supports the spontaneous disentanglement hypothesis.

1 Introduction

The spontaneous disentanglement hypothesis [1] is motivated by two outstanding issues in the foundations of quantum mechanics (QM). The first one originates from the collapse postulate. This postulate arguably gives rise to an internal inconsistency in QM [2], which was first introduced in 1935 by Schrödinger [3], and which is commonly known as the problem of quantum measurement. Moreover, the spontaneous disentanglement hypothesis is relevant to an apparent conflict between linearity of dynamics in standard QM , and experimental observations of multi–stabilities and phase transitions in quantum systems [4].

2 Experimentally testing the hypothesis

Here, the hypothesis that disentanglement spontaneously occurs in quantum systems is experimentally tested using a ferri–magnetic resonator. According to this hypothesis, time evolution is governed by a modified master equation having an added nonlinear term, which deterministically generates disentanglement [1]. The added term can give rise to multistabilities, which are otherwise theoretically excluded. Bistability is experimentally observed in the resonator's response to an externally applied monochromatic driving [5]. Experimental results are compared with predictions derived from the disentanglement–based model, and an alternative model, which is based on the method of Bosonization and the Holstein–Primakoff transformation. It is found that better agreement with data is obtained from the disentanglement–based model (see Fig. 1). This finding, together with a difficulty to justify the Bosonization–based model, indirectly support the spontaneous disentanglement hypothesis.

References

[1] Eyal Buks, "Spontaneous disentanglement and thermalization", *Advanced Quantum Technologies*, p. 2400036, 2024.

[2] Roger Penrose, "Uncertainty in quantum mechanics: faith or fantasy?", *Philosophical Transactions of the Royal Society A: Mathematical, Physical and Engineering Sciences*, vol. 369, no. 1956, pp. 4864–4890, 2011.

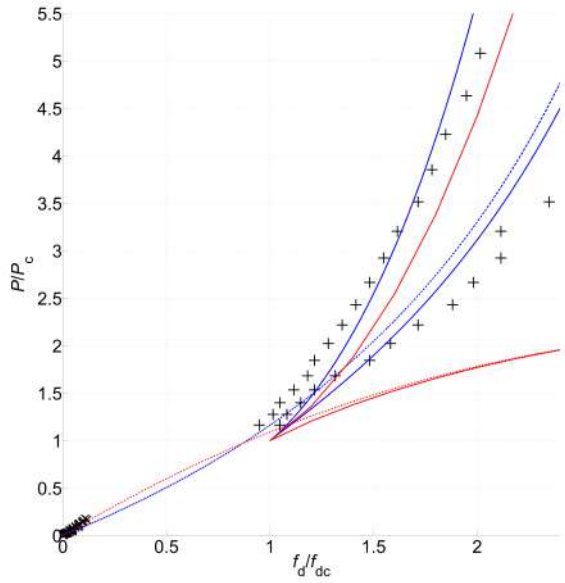


Figure 1: Comparison with experimental results (see [5] for details). Measured jump points are labeled by the symbol +, whereas the symbol × is used for measured peak points. The blue and red curves represent theoretical predictions based on the disentanglement–based and the Bosonization–based models, respectively. Calculated jump points are represented by solid lines, whereas dashed lines label calculated peak points.

[3] E. Schrodinger, "Die gegenwartige situation in der quantenmechanik", *Naturwissenschaften*, vol. 23, pp. 807, 1935.

[4] Eyal Buks, "Disentanglement-induced multistability", *Physical Review A*, vol. 110, no. 1, pp. 012439, 2024.

[5] Eyal Buks, "Disentanglement–induced bistability in a magnetic resonator", *Advanced Quantum Technologies*, p. 2400587, 2025.

Optical quasiparticles induced structured materials

Takshige Omatsu[1,2,3,4,5*]

[1]Molecular Chirality Research Center, Chiba University, Japan
[2]National Yang Ming Chiao Tung University, Taiwan
[3]Tianjin University, China
[4]Fujian Normal University, China
[5]Ajou University, Republic of Korea

[*]corresponding author: omatsu@faculty.chiba-u.jp

Abstract: Optical quasiparticle carries topologically protected polarization textures in a two- or three-dimensional space. We here demonstrate the direct imprint of polarization textures of optical quasiparticles onto a material. This demonstrates a modern approach for materials manipulation, such as the optically induced direct creation and annihilation of skyrmion textures in materials.

Structured light, such as an optical vortex and vector beam, carries a unique physical property, including an annular spatial form and an orbital angular momentum (OAM), associated with its on-axis phase/polarization singularity, and it has been widely utilized in versatile applications across optical manipulation, optical communication, and high spatial resolution optical microscopy. Furthermore, it twists the irradiated materials to fabricate chiral surface structures at a nano/micron scale. Thus, structured light opens new avenues towards advanced materials manipulation.

To date, structured light involves a new class of optical waveforms, such as a particle-like optical waveform with spatially inhomogeneous polarization structures in space, referred herein to as optical quasiparticle.

Optical skyrmion, most commonly studied as optical quasiparticle, encompasses all polarization states mapped on a Poincaré sphere, and it has been experimentally demonstrated by the coherent superposition of orthogonally oriented, circularly polarized fundamental Gaussian and Laguerre–Gaussian (LG) modes with the appropriate relative phase. Interestingly, it exhibits space-invariant characteristics under propagation even through turbulent media (topologically protected polarization textures), and thus, it is rapidly finding ability in advanced applications, such as free-space communications, and polarization nanoscale-metrology. However, in contrast to more conventional optical vortex, the optical quasiparticle is still in its infancy.

In this presentation, we review the fundamentals and applications of optical quasiparticles and also address the demonstration of microfabrication of exotic structures with optical quasiparticles (direct imprint of optical quasiparticles) onto a material. Intriguingly, the fabricated structures possess sub-wavelength-scale periodical ripples and knots, manifesting the polarization textures of optical quasiparticles. This demonstration gives rise to a new and modern approach to microfabrication and materials processing.

References

1. Padgett, M.J., “Orbital angular momentum 25 years on,” Opt. Express 25, 11265-11274 (2017).
2. Omatsu, T., *et al.*, “A new twist for materials science: the formation of chiral structures using the angular momentum of light,” Adv. Opt. Mater. 7, 1801672 (2019).
3. Omatsu, T., *et al.*, “Twisted mass transport enabled by the angular momentum of light,” J. Nanophotonics 14, 010901 (2020).
4. Shen, Y., *et al.*, “Generation of optical skyrmions with tunable topological textures,” ACS Photon. 9, 296–303 (2022).
5. Allam, S. R., *et al.*, “Optical quasiparticles: skyrmions, bimerons and skyrmionic hopfions in paraxial laser beams,” arXiv:2501.10760 (2025).

6. Kerridge-Johns, W.R., “Optical skyrmion laser using a wedged output coupler,” Optica 11, 769-775 (2024).
7. Yoneda, Y., *et al.*, “Multicolor optical quasiparticle laser source formed of a Pr^{3+} doped fiber laser with a dual output coupling geometry,” Las. Photon. Rev. 2401403 (2024).
8. Tamura, R., *et al.*, “Direct imprint of optical skyrmions in azopolymers as photoinduced relief structures,” APL Photon. 9, 010901 (2024).
9. Tamura, R., *et al*., “Three-dimensional projection of optical hopfion textures in a material,” ACS Photon. 11, 4958-4965 (2024).

Topological magneto-optical effect in skyrmion-hosting Mott insulator

Y. Okamura[1*], R. Shimizu[1], K. Okigami[1], S. Okumura[1],
N. Kanazawa[2], Y. Tokura[1,3,4], T. Morimoto[1], and Y. Takahashi[1]

[1]Department of Applied Physics and Quantum Phase Electronics Center, University of Tokyo, Japan
[2]Institute of Industrial Science, University of Tokyo, Japan
[3]RIKEN Center for Emergent Matter Science, Japan
[4]Tokyo College, University of Tokyo, Japan
[*]corresponding author: okamura@ap.t.u-tokyo.ac.jp

Abstract: We demonstrate the magneto-optical Kerr effect (MOKE) induced by the skyrmion formation, i.e., topological MOKE, in insulating GaV_4Se_8. The observed optical rotation is comparable to the that reported for itinerant systems, which establishes the significant impact of emergent magnetic field even on the Mott insulator driven by strong electron correlation.

Magnetic skyrmions are nanometric whirlpools of spins, where the directions of the constituent spins wrap the unit sphere [1], attracting enormous attention as potential information carriers in next-generation memory/logic devices. Due to their non-coplanar spin arrangement, the resultant scalar spin chirality gives rise to the fictious magnetic field (emergent magnetic field) acting on the conduction electrons, which leads to unique electromagnetic phenomena, as represented by the topological Hall effect (THE). Recently, some of us discover the novel magneto-optical effect by the emergent field, which we call the topological magneto-optical effect, in the skyrmion-hosting itinerant magnet Gd_2PdSi_3 [2]. The magneto-optical Kerr effect (MOKE) is remarkably enhanced by the skyrmion formation, being similar to the THE. This topological MOKE should be universal even for the system where the emergent field effect is not explicitly observed in the dc electrical transport measurement, which has remained elusive.

In this presentation, I show the observation of topological magneto-optical effect in the skyrmion-hosting Mott insulator GaV_4Se_8. While the THE is never observed because of insulating nature, we find that the MOKE is substantially enhanced by the skyrmion lattice (SkL) formation, as is the case for the THE in itinerant systems. This topological magneto-optical effect is observed at the particular photon energy, which directly demonstrates the resonantly enhanced THE in the optical region. The spectral characteristics are well captured by a minimal theoretical model, revealing the crucial role of momentum-space Berry curvature induced by band reconstruction through SkL formation. The observed Hall angle at the resonance energy is comparable to the THE reported for itinerant systems, which establishes the robust and significant impact of the emergent magnetic field even on the Mott insulating state driven by strong electron correlation. These findings demonstrate the universal light-skyrmion interaction mediated by the emergent field in the optical region, potentially enabling the functional operation of skyrmion-based devices integrated with the versatile laser technology.

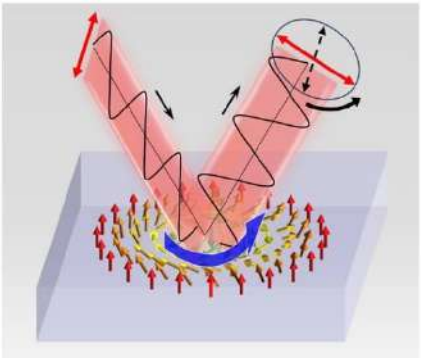


Fig.1. Schematic illustration of topological magneto-optical effect by skyrmion formation.

References

[1] Back, C. *et al.,* J. Phys. D: Appl. Phys. **53**, 363001 (2020).
[2] Kato, Y. D., Okamura, Y. *et al.,* Nat. Commun. **14,** 5416 (2023).

Listening to nanostructures' absorption and chirality: widely tunable photo-acoustic spectroscopy

E. Petronijevic[1*], C. Skubisz[1], G. Leahu[1], C. Sibilia[1], R. Li Voti[1] and A. Belardini[1]

[1]Sapienza Università di Roma, SBAI Department, Italy
[*]corresponding author: emilija.petronijevic@uniroma1.it

Abstract: Photo-acoustic spectroscopy (PAS) is a low-cost, scattering-free and non-destructive method of measuring material absorption. Here, we enrich PAS with many degrees of freedom: laser wavelength, polarization, direction, focus, and the possibility of spatial and frequency mapping. We show its potential in characterizing both commercial and specially designed nanostructures.

Sensing chirality by direct absorption characterization is of great interest in the fields of plasmonics and nanophotonics, where the nanomaterials are specially designed to enhance otherwise weak chiro-optical light-matter interaction. Circular dichroism (CD) is a differential absorption of circular polarizations of opposite handedness, which defines the chirality of a material. Besides intrinsically chiral nanostructures[1], chirality can be induced in asymmetric samples by exciting them at oblique incidence, obtaining CD via extrinsic chirality[2]. We previously showed that unconventional, photo-thermal methods can be used to directly reveal absorption and chirality in nanostructures[3]. Specifically, in photo-acoustic spectroscopy (PAS), periodically modulated light absorption creates pressure changes in the vicinity of the sample closed in the photo-acoustic cell: these changes correspond to an acoustic signal, caught by a microphone. PAS is scattering-free, low-cost, non-destructive and sensitive. We applied it to measure absorption in asymmetric plasmonic-dielectric metasurfaces[4] and GaAs nanowires asymmetrically covered by gold[5]; however, to precisely measure extrinsic chirality, the photo-acoustic response was obtained at single laser wavelengths.

Here, we enrich the PAS set-up with new degrees of freedom, overcoming previous limitations such as low power and inability to precisely tune the polarization. The set-up is shown in Fig. 1(a). We use a widely tunable laser, covering the near-infrared (680-1080 nm) and visible (340-540 nm) ranges, and modulate its output with a tunable mechanical chopper. The laser polarization is defined by a linear polarizer and a quarter-wave plate, and the laser can be focused before impinging on the sample in a closed PAS cell. Moreover, the cell is attached to rotation and translation stages, which allows for incidence angle control, and surface absorption scanning, respectively.

In Fig. 1(b), we show the possibility to map extrinsic CD in metasurfaces asymmetrically covered by Ag[4]; as such samples are large areas of self-assembled nanospheres (with plasmonic semi-shells), no focusing was required. As expected, CD signal, defined as normalized differential absorption of left and right circular polarizations (LCP and RCP, respectively), falls to zero at normal incidence, and changes sign for the opposite angles of incidence. In Fig. 1(c), we show spatial mapping on commercial nanostructures covered by Ag, conventionally used in Surface Enhanced Raman Spectroscopy (SERS) and purchased from Silmeco. We set the laser wavelength to 800 nm and focus it to 70 μm beam diameter at normal incidence; the chopper frequency is 81 Hz, and the maps are scanned with 100 μm step in both planar directions. In the upper part of the absorption maps, the local absorption increase is due to the vicinity of the sample border. Finally, the overall CD of the

zone goes to zero, as the sample is intrinsically achiral.

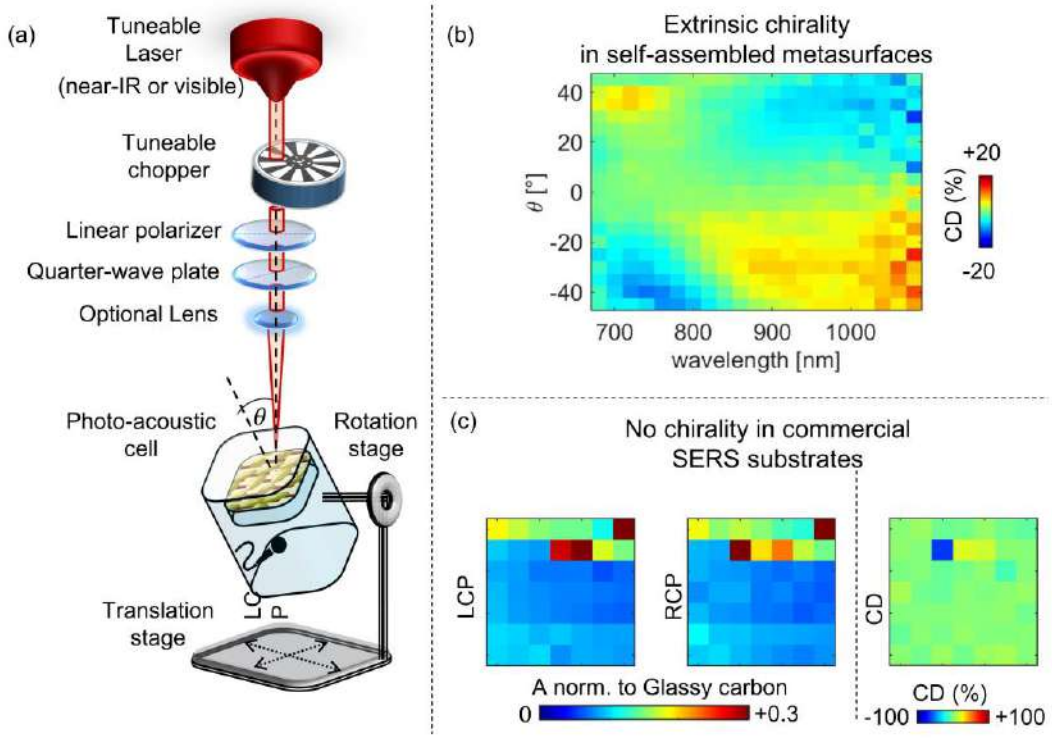


Figure 1 (a) Photo-acoustic set-up positioned on rotational and translation stages allows for multiple tuneable parameters: laser wavelength, chopper frequency, polarization, beam-waist, angle of incidence. (b) Detection of extrinsic chirality: example of circular dichroism (CD) characterization of asymmetric, self-assembled metasurfaces (without lens). (c) Spatial mapping of commercial achiral nanostructures (Silmeco Ag SERS substrates); uniformity and CD mapping is obtained by exciting the sample with 800 nm laser beam, focused to 70 μm beam-diameter; chopper frequency is set to 81 Hz. Top parts of the spatial map show the local absorption increase due to the vicinity to the sample's border.

We strongly believe that such enriched boosted PAS can be used to sensitively map absorption and chirality of nanostructured media in a broad wavelength range and with many degrees of freedom.

References

1. B. J. Olohan et al, "Chiroptical Second-Harmonic Tyndall Scattering from Silicon Nanohelices", ACS Nano 18(26), 16766–16775 (2024).
2. E. Petronijevic et al, "Extrinsic chirality tailors Stokes parameters in simple asymmetric metasurfaces", Nanoscale 16, 16477 – 16484 (2024).
3. E. Petronijevic et al, "Nanostructured materials for circular dichroism and chirality at the nanoscale: towards unconventional characterization [Invited]", Opt. Mater. Express 12, 2724-2746 (2022).
4. E. Petronijevic et al, "Photo-acoustic detection of chirality in metal-polystyrene metasurfaces", Appl. Phys. Lett. 114, 053101 (2019).
5. G. Leahu et al, "Evidence of Optical Circular Dichroism in GaAs-Based Nanowires Partially Covered with Gold", Adv. Opt. Mater. 5(16), 1601063 (2017).

Optical Force Nanoscopy of Circular Dichroism in Photoinduced Force Microscopy

J. Yamanishi[1, 2*], H.-Y. Ahn[1], and H. Okamoto[1]

[1]Instutute for Molecular Science, National Institutes of Natural Science, Okazaki, Japan
[2]Graduate School of Engineering Science, Osaka University, Toyonaka, Japan
[*]corresponding author: yamanishi@ims.ac.jp

Abstract: We conducted imaging of nanoscale local chiro-optical effects utilizing photoinduced force microscopy, a force imaging technique. This study successfully achieved enantio-selective chiro-optical force nanoscopy of individual nanostructures.

Microscopic analysis of nanomaterials using circularly polarized light is crucial in materials science, chemistry, and biology. It determines structural characteristics like chirality and local magnetic properties such as magnetic circular dichroism (MCD). Novel applications include interactions between chiral molecules and high refractive index nanomaterials. Historically examined through macroscopic spectroscopy, there is a demand for nanoscopic observation of circular dichroism, which is challenging due to weak signals and limited spatial resolution.[1] Breakthroughs in microscopy techniques are needed, with photoinduced force microscopy (PiFM) being a promising method.[2, 3] PiFM leverages optical forces on tips to enhance detection and analysis of chiral materials at the nanoscale, advancing pharmaceutical and biological sciences. The present study focuses on imaging chiro-optical forces around individual chiral nanoparticles using CD-PiFM.

We synthesized three-dimensional chiral gold nanoparticles and recorded CD-PiFM images of them on a quartz substrate using CD-PiFM by irradiating left and right circularly polarized light at a wavelength of 785 nm. The chiral gold nanoparticles, as illustrated in the SEM images (insets of Figs. 1a and e), exhibit helicoidal structures, and the D- and L-forms display opposite CD activities in the visible wavelength range.[4] The results for the D-form nanoparticles are presented in Figs. 1a-d. A significant feature, namely the strong attractive and repulsive forces (positive and negative PiFM signals, respectively) around the gold nanoparticles, was observed in the PiFM images (Figs. 1b, c; refer to Fig. 1a for nanoparticle positions). When the probe is positioned below the gold nanoparticles (negative y-direction in the figure), the attractive interaction (positive PiFM signals) increases substantially due to the sharpened tip apex of the cantilever orienting toward the direction of the gold nanoparticles, resulting in a strong attractive interaction. Conversely, when the tip is directly above the gold nanoparticles, where the dipoles of the tip and the nanoparticle are aligned parallel due to illumination from the bottom side of the substrate, a strong repulsive force is observed. The images under left and right circularly polarized illumination (Figs. 1b and c, respectively) appear nearly identical. However, in the differential image (Fig. 1d), differential PiFM signals are observed around a single particle, particularly below (negative y side) the nanoparticles, as indicated by arrows. Similar but inverted image features were observed in the L-form nanoparticles (Figs. 1e-h). This finding demonstrates that the current CD-PiFM technology enables the determination of the handedness of individual particles and the enantio-selective nanoscopy of chiro-optical effects.

It is apparent from the magnified image of a D-form nanoparticle in Figs. 2a-d that a negative signal is present in the lower (negative y) part of the differential image (Fig. 2d). Based on the imaging features

demonstrated, we conclude that enantio-selective chiro-optical force nanoscopy has been achieved with CD-PiFM.

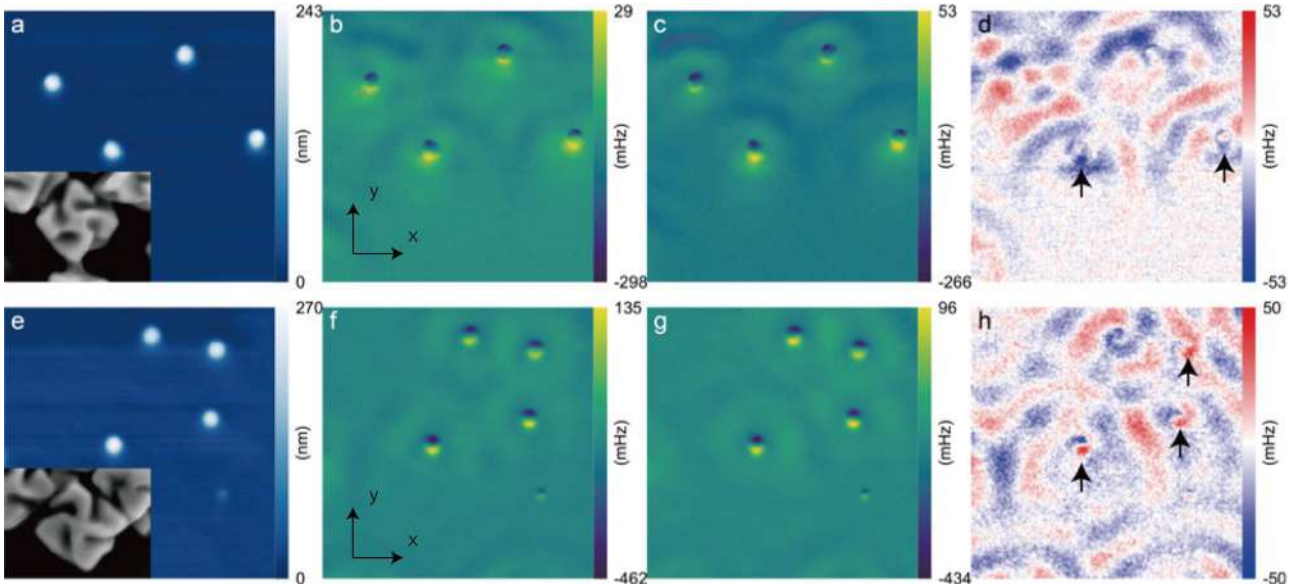


Figure 1. CD-PiFM measurements of D- and L-form nanoparticles. (a-d) AFM image, PiFM image with left-circularly polarized light illumination, that with right-circularly polarized light illumination, and the differential image of D-form nanoparticles. (e-h) the images of L-form. Scan sizes are (a-d) 6.5 μm x 6.5 μm and (e-h) 5.65 μm x 5.65 μm.

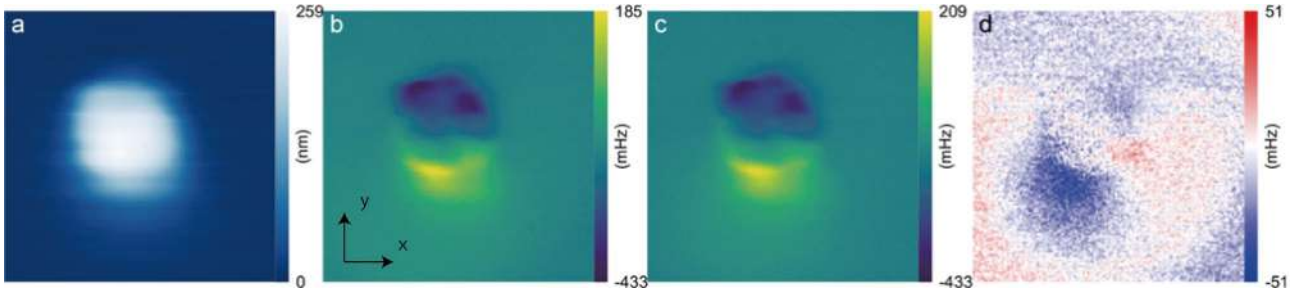


Figure 2. CD-PiFM measurement of a D-form nanoparticle (magnified). (a-d) AFM image, PiFM image with left-circularly polarized light illumination, PiFM image with right-circularly polarized light illumination, and the differential image. Scan size is 1.0 μm x 1.0 μm (a-d).

This work was supported by Grants-in-Aid for Scientific Research (grant nos. JP22H05131, JP22H05135, JP21H04641, and JP22H01901).

References

1. Narushima, T. and Okamoto, H., "Circular dichroism microscopy free from commingling linear dichroism via discretely modulated circular polarization," Sci. Rep., Vol. 6, No. 1, 35731, 2016.
2. Yamanishi, J., Yamane, H., Naitoh, Y., Li, Y. J., Yokoshi, N., Kameyama, T., Koyama, S., Torimoto, T., Ishihara, H., and Sugawara, Y., "Optical force mapping at the single-nanometre scale," Nat. Commun., Vol. 12, No. 1, 3865, 2021.
3. Yamanishi, J., Ahn, H.-Y., and Okamoto, H., "Nanoscopic observation of chiro-optical force," Nano Lett., Vol. 23, No. 20, 9347-9352, 2023.
4. Lee, H.-E., Ahn, H.-Y., Mun, J., Lee, Y., Kim, M., Cho, N. H., Chang, K., Kim, W. S., Rho, J., and Nam, K. T., "Amino-acid and peptide-directed synthesis of chiral plasmonic gold nanoparticles," Nature, Vol. 556, No. 7701, 360-365, 2018.

Two-color laser driven novel phenomena in solids: Detection of symmetries and control of photocurrent

Masahiro Sato*, Minoru Kanega, and Mina Udono

[1]Department of Physics, Chiba University, Japan
*corresponding author: sato.phys@chiba-u.jp

Abstract: We theoretically explore novel nonlinear responses of materials to two-color lasers, mixed waves of two different lasers. We show that (a) two-color-laser driven harmonic generation is useful to detect symmetries in quantum magnets and (b) the photocurrent in graphene can be controlled by tuning the laser intensity, ellipticity, and phase.

Two-color lasers, namely, electromagnetic waves consisting of two laser beams with different frequencies, have been studied since the end of the last century [1]. However, its application to material science has been less developed. In recent years, we have predicted novel optical responses that are realized by applying two-color laser to materials. In this conference, we would like to report the following two results (I) and (II) in our recent studies.

(I) Control of photocurrent and high harmonic generation (HHG) in graphene by two-color laser [2]: We theoretically consider the control of two-color-laser driven HHG spectra in graphene. The HHG stands for the laser-driven phenomenon that when a laser pulse with frequency ω is applied to gases or materials, a mixed radiation pulse including multiple lasers with frequencies $n\omega$ $(n = 0, 1, 2, 3, ,,)$ is generated through the nonlinear light-matter interaction. The 0^{th} order harmonic corresponds to the photocurrent (photovoltaic effect). In electron systems in solids, it is known that even-order harmonics are all forbidden if the system is inversion symmetric. Using the quantum master (GKSL) equation approach that takes the inevitable dissipation effect into account, we numerically calculate the two-color-laser driven HHG spectra of inversion-symmetric graphene. We find that the nth order HHGs are drastically changed by tuning frequencies and ellipticities of the laser (as shown

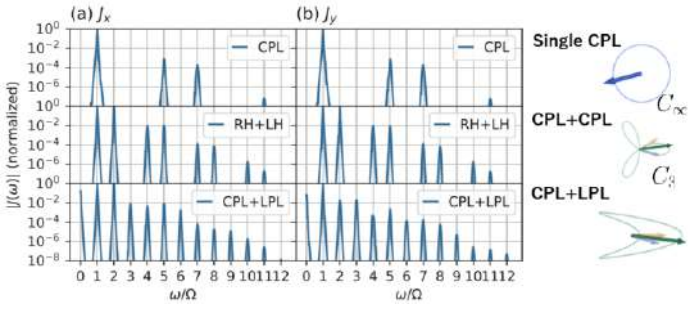


Fig. 1: Two-color-laser driven HHG spectra of graphene; HHG intensity vs radiation-wave frequency. Left and right panels, (a) and (b), respectively correspond to the HHG by the x and y components of current. First, second and third lines are respectively the results of single circularly polarized laser (CPL), two CPLs with different frequencies and combination of a CPL and a linearly polarized laser (LPL). The closed curves denote trajectories of three kinds of laser fields.

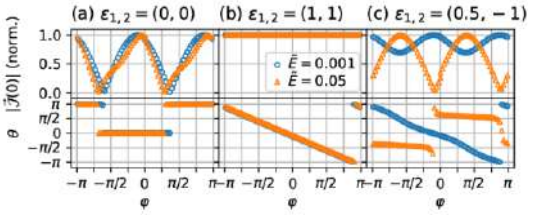


Fig. 2: Relative phase $\varphi = \phi_2 - \phi_1$ dependence of the photocurrent driven by tow-color laser. ϕ_1 and ϕ_2 are respectively the initial phases of first and second beam in the two-color laser. Blue and orange mean the results of weak and strong lasers, respectively. Panels (a), (b) and (c) are the results with different ellipticities of two-color lasers. The first line shows the photocurrent intensity, and the second line is its direction (angle θ).

in Fig. 1) and such features of the HHG spectra can be captured by the dynamical symmetry argument. Moreover, the photocurrent (0^{th} order harmonics) is shown to be controlled by varying the intensity, ellipticities, and relativistic phase of two beams in the two-color laser (see Fig. 2). Remarkably, any single-color laser cannot create photocurrent as graphene is inversion symmetric, while two-color laser enables us to create a finite photocurrent depending on the shape of two-color laser wave. We will report some important results of these two-color laser driven responses in graphene.

(II) Detection of symmetries or symmetry breakings in magnets with two-color laser [3]: Laser is useful to generate new optical phenomena, whereas observing laser-driven optical responses in materials is also efficient to detect new information about them. We theoretically argue what information can be detected from the two-color-laser driven HHG spectra in the Shastry-Sutherland (SS) magnet. This model is a typical two-dimensional (2D) frustrated spin model consisting of orthogonally coupled spin-dimers as shown in Fig. 3. The ground state is in the dimer-singlet phase, where spin-singlet pairs reside on all the strong bonds. As a result, the ground state has no magnetization, and it possesses unusual elementary excitations; spin-1 triply degenerate magnetic modes called triplons and two-triplon bound states (triplon molecules). The SS model with small perturbations can describe the magnetism of the quasi-2D magnet $SrCu_2(BO_3)_2$, which has been actively studied. In frustrated magnets including SS models, disordered or complex equilibrium states often appear, and it is generally difficult to experimentally observe characteristics of such featureless many-spin states. Moreover, if we slightly perturb such a disordered state by changing external parameters (temperature, magnetic field, electric field, pressure, etc.), a phase transition often occurs, i.e., frustrated systems are instable against perturbations and many ordered states are competing each other. Therefore, it is important to propose different methods of measuring various physical quantities to understand such less visible or unstable states. We compute the HHG spectra of the SS model by using an unbiased numerical diagonalization method for finite-size SS models. From the numerical result, we find that the existence or absence of even-order harmonics (i.e., selection rule) strongly depends on the trajectory of the applied two-color laser (see Fig. 4), and this selection rule can be explained by the dynamical symmetry argument. This clearly indicates that one can obtain information about symmetries or symmetry breakings in magnets from the observation of the two-color-laser driven HHG spectra. We will report this symmetry argument in detail.

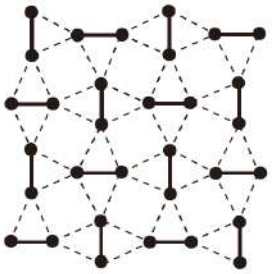


Fig. 3: Crystal structure of the SS model. Black and dotted lines respectively denote strong and weak antiferromagnetic exchange interactions. Spin singlet pair resides on the strong bond.

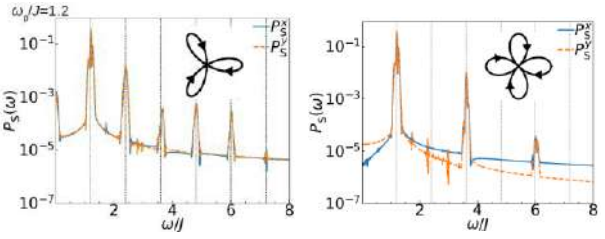


Fig. 4: HHG spectra of the SS model under the applications of three- and four-leaves shaped two-color lasers. Polarization intensity vs frequency.

References

1. For example, see H. Eichmann, *et al*, Phys. Rev. A **51**, R3414 (1995); A. Hach´e, *et al*, Phys. Rev. Lett. **78**, 306 (1997); A. Fleischer, *et al*, Nature Photon **8**, 543 (2014); O. Kfir, *et al*, Nature Photon **9**, 99 (2015); K. Ogawa, *et al*, Nat Commun **15**, 6310 (2024).
2. M. Kanega and M. Sato, arXiv:2410.07767.
3. M. Udono and M. Sato, Phys. Rev. B (2024).

UV-Plasmonics for Surface-Enhanced Spectroscopies

B. M. Reinhard[1,*]

[1]Department of Chemistry and The Photonics Center, Boston University, Boston, Massachusetts, United States

[*]corresponding author: bmr@bu.edu

Abstract: Aluminum (Al) nanostructures provide tunable plasmon resonances in the UV, which makes Al nanostructures interesting antennas for applications in surface-enhanced chiroptical spectroscopies. In this presentation scalable fabrication strategies for Al nanoparticles are investigated and the wavelength-dependent circular dichroism signal of Al nanostructures embedded in a chiral molecular film is examined.

Al nanostructures provide tunable plasmon resonances in the ultraviolet (UV) where the absorption bands of most biomolecules lie. This energetic overlap makes Al nanostructures interesting antennas for surface-enhanced chiroptical spectroscopies. In this presentation, we will investigate the circular dichroism (CD) signal of different Al nanoantenna geometries embedded in a chiral molecular film and compare with Ag nanoantennas of similar morphology that lack resonances in the UV. We place an emphasis on nanostructures accessible through scalable fabrication strategies. Hole mask colloidal lithography methods were applied to generate nanoparticles whose plasmon resonances could be tuned through variation of the morphology. It is demonstrated that the fabricated Al nanostructures provide distinct plasmon modes in the UV. The fabrication of metal nanoparticles using polystyrene nanoparticles of different diameters as mask is discussed and the fabricated nanoparticles are characterized by optical spectroscopy and scanning electron microscopy (SEM).

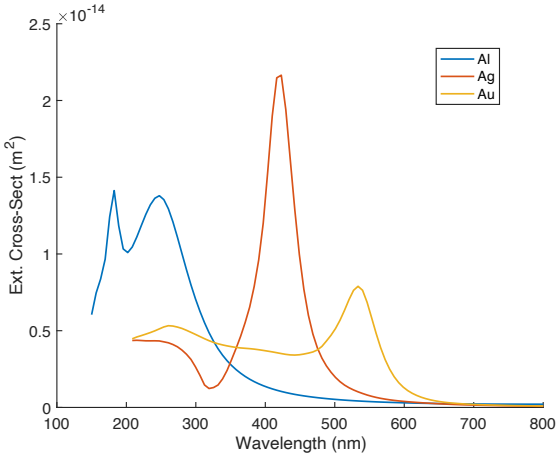


Figure 1: Simulated extinction cross-sections for 50 nm diameter Al, Ag, Au nanospheres in an ambient refractive index of $n_r = 1.333$.

Chiral test analytes with molecular absorption bands in the UV were spincoated on optimized Al nanoparticles and Ag nanoparticle “controls”, and CD spectra were recorded. Collecting CD spectra for the same analyte with achiral Al and Ag nanoparticle substrates facilitated data acquisition in the presence and absence of UV plasmon resonances. The wavelength-dependent CD signal under both conditions is examined and analyzed with a particular focus on the role of the nanoparticles under both conditions.

A second group of UV-resonant substrates to be discussed is that of nanoholes in an Al film generated by scalable bead lithography methods. The spectral properties of the nanoholes are characterized through combination of experimental spectroscopy and electromagnetic simulations. The performance of the substrates is evaluated by characterizing the limit of detection of the CD signal for selected probe molecules.

The spectral properties and performance of nanoparticle and nanohole substrate are compared, and a general

framework for the design of UV-resonant nanoparticles for surface-enhanced spectroscopies in a wavelength range not accessible with conventional Au and Ag plasmonic antennas is developed and presented.

Helicity-dependent optical control of the magnetization emerging from the Zeeman energy

A. Capua[1]

[1]The Hebrew University of Jerusalem, Israel

[*]corresponding author: amir.capua@mail.huji.ac.il

Abstract: Typically, the magnetic component of the optical radiation is neglected when considering light-matter interactions. Here, we show that by simply accounting for the Zeeman energy of the magnetic component of the EM radiation, an optically induced torque emerges, influencing the magnetization state.

The ferromagnetic resonance (FMR) experiment is pivotal for developing Spintronics technology. It occurs on Gigahertz timescales due the relatively slow relaxation time of the spins in ferromagnets. In contrast, optical fields oscillate much faster, at $\sim 400-800$ THz. Therefore, it seems unlikely that such fast-oscillating fields may interact with magnetic moments. However, by combining principles from quantum optics, we have recently [1] realized that the equations governing the FMR experiment are even relevant for magnetic fields that oscillate much faster, at optical frequencies. Namely, the interaction between optical beams and the magnetization is made possible merely by considering the optical magnetic field and its interaction with the magnetization which is determined by the Zeeman energy. We find that the strength of the interaction can be expressed by an elementary efficiency parameter $\eta=\alpha\gamma H/f_{opt}$, where H is the amplitude of the optical magnetic field, α is the dissipation rate of spin angular momentum to the lattice, and f_{opt} and γ are the optical frequency and gyromagnetic ratio. Our results shed light on a variety of highly debated experimental observations on the interaction between optical fields and ferromagnets that have been reported in the last 25 years.

References

1. Assouline, B. and Capua, A. “Helicity-dependent optical control of the magnetization state emerging from the Landau-Lifshitz-Gilbert equation” Phys. Rev. Res. 6, 013012, 2024.

Observation of large nonreciprocal propagation constants in zero-index magneto-optical meta-waveguides

Y. Yang[1,2], Y. Liu[3], Y. Li[3] and L. Bi[1,2*]

[1]National Engineering Research Centre of Electromagnetic Radiation Control Materials, University of Electronic Science and Technology of China, China

2Key Laboratory of Multi-spectral Absorbing Materials and Structures of Ministry of Education, University of Electronic Science and Technology of China, China

[3]State Key Laboratory of Precision Measurement Technology and Instrument, Department of Precision Instrument, Tsinghua University, China

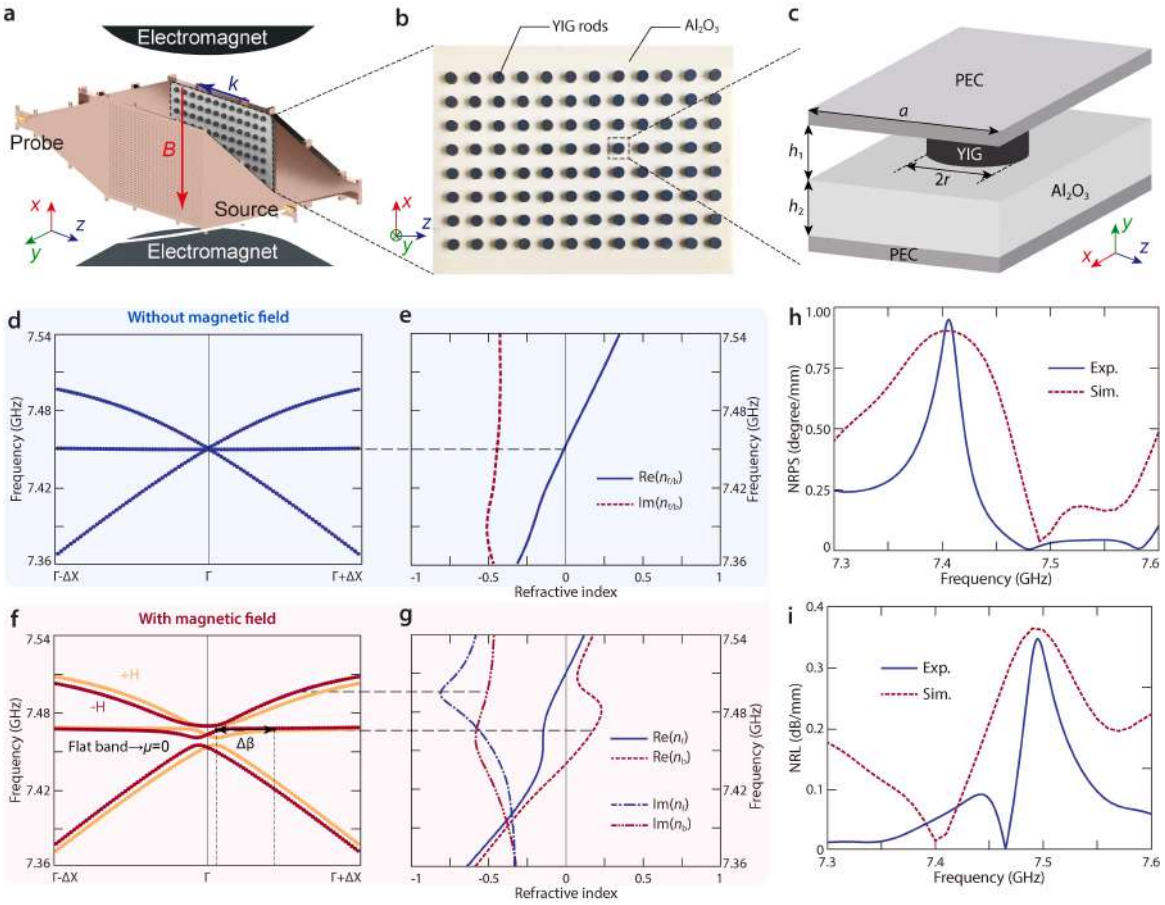
[*]corresponding author: bilei@uestc.edu.cn

Abstract: We report observation of giant nonreciprocal phase shift (NRPS) and nonreciprocal loss (NRL) effects in magneto-optical(MO) zero-index metawaveguides (MZIMs). One order of magnitude enhancement of NRPS and NRL in MZIMs is observed at both microwave and optical frequencies, which agree well with both effective medium and photonic band theories.

Magneto-optical waveguides are widely used as nonreciprocal phase shifters for wireless communication, optical communication and sensing applications. Thanks to the weak gyromagnetic or gyroelectric property of magnetic materials, such devices are usually much larger compared to other components in the system. A general way to reduce the device footprint is to engineer the magnetic material with large off-diagonal component of its permittivity or permeability tensor by element doping or fabrication process improvement. However, the ratio of the off-diagonal component of μ to its diagonal part is smaller than 1 for microwave frequency. This number is even smaller down to 10^{-2} for optical frequencies. Another method to enhance the magneto-optical effect is to develop magnetic materials or metamaterials with near zero index. Giant magneto-optical Kerr effect(MOKE) and nonreciprocal absorption were observed in semiconductor materials such as indium tin oxide or InAs films at the epsilon near zero frequencies.[1,2] However, such materials are diamagnetic with weak MO effect. Recently, MZIMs emerge as a fascinating playground for the discovery of new MO phenomena. [3,4] However, it is unclear how the nonreciprocal effect is influenced in MZIMs.

In this paper, we report observation of large nonreciprocal phase shift (NRPS) and nonreciprocal loss (NRL) in MZIM metawaveguides. We studied a microwave ferrite phase shifter consisted of a square array of gyromagnetic yttrium iron garnet (YIG) pillars above an Al_2O_3 slab in a parallel-plate aluminum waveguide. (Fig. 1a-c) Under zero applied magnetic field, this metamaterial shows a Dirac-like cone dispersion at the center of the Brillouin zone (Fig. 1d), corresponding to an impedance-matched zero index at 7.45 GHz (Fig. 1e). Due to the gyromagnetic property of YIG, the metamaterial shows distinct band structures for forward and backward propagation of microwave (Figure. 1f). At 7.46 GHz to 7.48 GHz where $n_{eff} \rightarrow 0$, the magnetic field causes a distortion of the flat band, introducing a giant NRPS near the center of the Brillouin zone, as shown by $\Delta\beta$ in Figure 1f. Moreover, the magnetic field tilted and shifted the band between 7.48 GHz to 7.52 GHz, causing distinct bandgap sizes between the forward and backward propagation. A large NRL, that is the imaginary part of $\Delta\beta$, is observed as indicated by the imaginary part of n_{eff} in Fig. 1g. Experimentally, we observed giant NRPS and NRL of this device by measuring the waveguide transmittance as shown in Fig. 1h and 1i. The results agree well with simulations. Analytical calculation of the wave propagation by approximating the device to a MO two-layer slab waveguide with near zero effective index showed good agreement with experiments, indicating

such devices can be also be accurately depicted by the effective medium theory.



The authors are grateful for the support by the National Natural Science Foundation of China (NSFC) (Grant Nos. U22A20148, 52450018, 52021001 and 52102357), Sichuan Provincial Science and Technology Department (Grant No. 2025ZNSFSC0040).

References

1. Ikeda K, Liu T, Ota Y, Kobayashi N, Iwamoto S. “Enhanced magneto-optical effects in epsilon-near-zero indium tin oxide at telecommunication wavelengths.” Adv. Opt. Mater. 12, 2301320, 2023
2. Liu M, Xia S, Wan W, Qin J, Li H, Zhao C, et al. “Broadband mid-infrared non-reciprocal absorption using magnetized gradient epsilon-near-zero thin films.” Nature Mater. 22, 1196-202, 2023
3. Yang Y, Liu Y, Qin J, Cai S, Su J, Zhou P, et al. “Magnetically tunable zero-index metamaterials.” Photon. Res., 11, 1613-1626, 2023
4. Zhang R, Cui X, Zeng Y, Chen J, Liu W, Wang M, Wang D, Zhang Z, Wang N, Wu G, Chan C. T., “Bulk-spatiotemporal vortex correspondence in gyromagnetic double-zero-index media”, arXiv:2408.06182, 2024

Attosecond magnetism: ultrafast control of magnetic phases and novel probes

O. Neufeld[1,*]

[1]Techinon Israel Institute of Technology, Faculty of Chemistry, Haifa, Israel.
[*]corresponding author: ofern@technion.ac.il

Abstract: Magnetism can be coherently controlled by light *via* mechanisms that allow transfer of spin and orbital moments from electric fields to matter at varying timescales, down to femtoseconds. I will present our recent works towards controlling magnetism at even faster attosecond timescales, and developing novel ultrafast spectroscopies for detecting it.

It is commonly established that by irradiating intense laser pulses onto magnets, their magnetization can be manipulated on ultrafast timescales, e.g. causing magnetization flip or demagnetization[1,2]. I will discuss our recent predictions that have established a highly nonlinear optical regime where attosecond magnetization dynamics can occur *via* strong-field driving[3]. Here the solid can be transformed into a magnet within several femtoseconds due to intense circularly-polarized laser driving (see Fig. 1(a)), which is enabled by ultrafast and coherent spin flip processes that build-up from cycle-to-cycle. By driving the system with linearly-polarized lasers that are polarized along non-high-symmetry axes, an oscillating attosecond magnetic response can be generated, forming the prediction for the fastest magnetization dynamics to date (Fig. 1(b)).

In principle, such generation of either persistent magnetic states (i.e. which are long-lived up to several tens to hundreds of femtoseconds), or transient magnetic states that only exist while the laser field is on, both relies on an inherent time-reversal symmetry (TRS) breaking by the laser. This is typically enabled by circularly-polarized light that also carries angular momentum, or in the case of transient magnetism driven by linearly-polarized driving, by a time-local breaking of symmetry that only arises for individual laser half-cycles. I will present our recent work that establishes a new magneto-optical effect by which linearly-polarized driving can generate a persistent magnetic state, which is enabled by few-cycle pulsed driving. In that case, TRS can be broken intrinsically by the carrier envelope phase (CEP)-stable short laser pulse, depending on the value of the CEP (see Fig. 1(c))[4]. This marks the first scheme that allows to coherently turn-on, as well as off, persistent magnetic states, with linearly-polarized lasers.

Besides using light to control magnetism, I will also discuss our recent efforts to measure such extremely fast phenomena. Femtosecond magnetism has been previously measured by circular dichroism (CD) in attosecond transient absorption spectroscopy (ATAS)[2]. However, this approach is very challenging to implement in the attosecond domain, and also leads to XUV light that better probes magnetism in higher energies, far from the Fermi surface. Our recent work proposed to use strong-field induced helical ring currents in order to gate generation of Tesla-scale attosecond magnetic pulses (see Fig. 1(d))[5]. This is the first scheme that can generate attosecond magnetic pulses, which should be usable in down-the-line experiments of ultrafast magnetization. It also permits a tunable control over synthesizing tailored isolated magnetic pulses in the atto- to- femtosecond duration window.

Lastly, I will discuss our recent approach for detecting magnetization based on symmetry-breaking spectroscopy[6] of ultrafast photocurrent measurements[7,8]. By engineering tailored driving fields that break, or exhibit, TRS, and using them to drive photogalvanic currents, we can sense magnetism – photocurrents can only be generated if the sample breaks TRS, which generates a background free signal. We demonstrate this scheme with *ab-initio* simulations and show that it also applies to other phases with broken TRS such as Chern insulators. This is the first scheme capable of probing magnetism in the absence of magnetic or circularly-polarized electric fields.

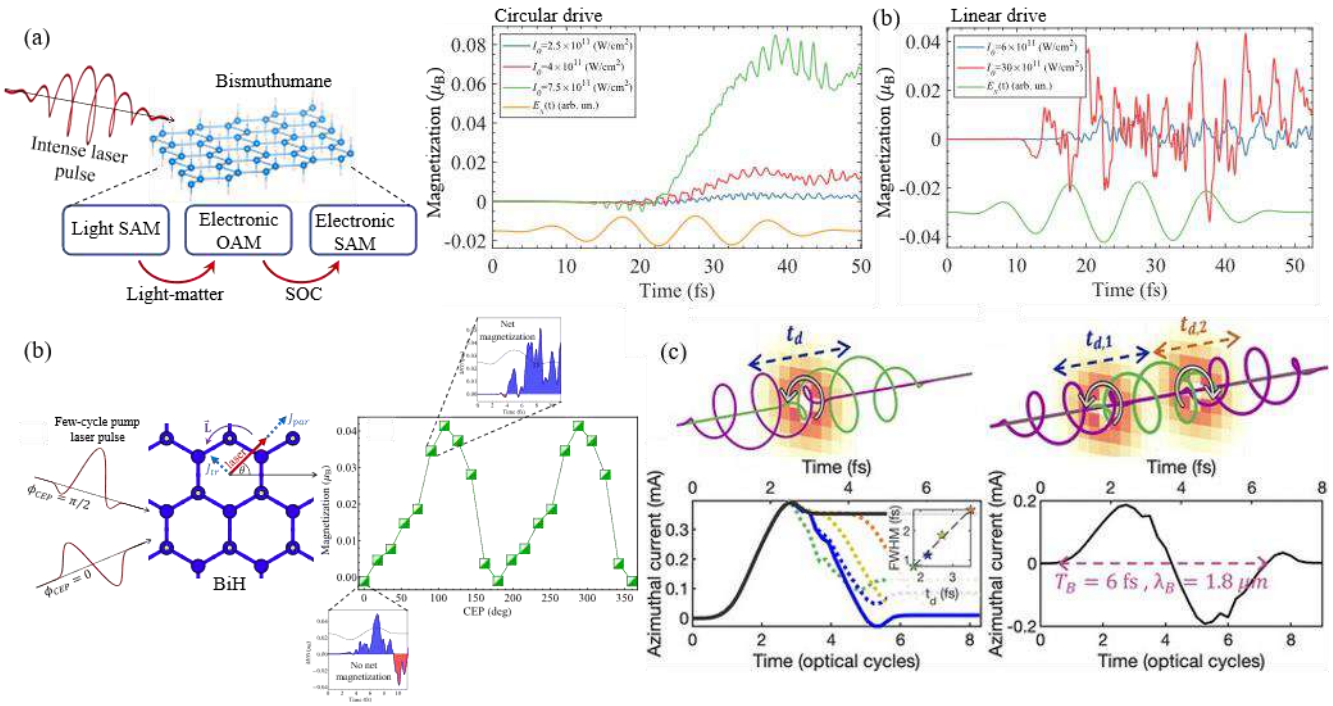


Figure 1. (a) Illustration of ultrafast turn-on of magnetization in monolayer Bismuth – circularly-polarized light transfers angular momentum to the electronic system, which subsequently induces spin-flips through spin-orbit coupling (SOC). The induced magnetic response takes several femtoseconds to build-up (right panel), and is highly-nonlinear and non-perturbative. (b) For linearly-polarized driving magnetism can only be induced transiently while the laser pulse is on (because the laser pulse overall respects TRS, but breaks it locally in time), which allows accessing pure attosecond magnetization dynamics. (c) Few-cycle linearly-polarized pulses can also break TRS if the CEP is properly chosen. Even though such pulses do not carry angular momentum, this is enough to induce a transient magnetic state within few femtoseconds. (d) Sets of counter-rotating circularly-polarized laser pulses irradiate an atomic gas, generating helical ring currents in the medium. By gating the current in time, attosecond magnetic pulses can be generated down to ~800 attosecond durations, and with potentially synthesizable properties such as wavelength and temporal envelope.

References

[1] M. Hofherr *et al.*, "Ultrafast optically induced spin transfer in ferromagnetic alloys," *Sci. Adv.*, vol. 6, no. 3, p. eaay8717, 2024.

[2] F. Siegrist *et al.*, "Light-wave dynamic control of magnetism," *Nature*, vol. 571, no. 7764, pp. 240–244, 2019.

[3] O. Neufeld, N. Tancogne-Dejean, U. De Giovannini, H. Hübener, and A. Rubio, "Attosecond magnetization dynamics in non-magnetic materials driven by intense femtosecond lasers," *npj Comput. Mater.*, vol. 9, no. 1, p. 39, 2023.

[4] O. Neufeld, "Linearly-polarized few-cycle pulses drive carrier envelope phase-sensitive coherent magnetization injection," *submitted*.

[5] A. de las Heras, F. P. Bonafé, C. Hernández-García, A. Rubio, and O. Neufeld, "Tunable Tesla-Scale Magnetic Attosecond Pulses through Ring-Current Gating," *J. Phys. Chem. Lett.*, vol. 14, no. 49, pp. 11160–11167, 2023.

[6] O. Neufeld, D. Ayuso, P. Decleva, M. Y. Ivanov, O. Smirnova, and O. Cohen, "Ultrasensitive Chiral Spectroscopy by Dynamical Symmetry Breaking in High Harmonic Generation," *Phys. Rev. X*, vol. 9, no. 3, p. 031002, 2019.

[7] O. Neufeld, N. Tancogne-Dejean, U. De Giovannini, H. Hübener, and A. Rubio, "Light-Driven Extremely Nonlinear Bulk Photogalvanic Currents," *Phys. Rev. Lett.*, vol. 127, no. 12, p. 126601, Sep. 2021.

[8] T. Weitz *et al.*, "Lightwave-driven electrons in a Floquet topological insulator," *arXiv2407.17917*, 2024.

Extreme light manipulation: Hyperbolic Plasmon Polaritons and Subcycle Orbital Angular Momentum Control

A. Ambrosio[1]

[1]Istituto Italiano di Tecnologia, Via Rubattino 81, 20134 – Milano, Italy

[*]corresponding author: antonio.ambrosio@iit.it

Abstract: This research explores two extreme light manipulation phenomena: hyperbolic plasmon polaritons in van der Waals materials and ultrafast modulations with subcycle control of orbital angular momentum. By confining light beyond the diffraction limit and dynamically modulating its properties on femtosecond timescales, we enable new frontiers in nanophotonics.

Extreme light confinement and ultrafast modulation, this research investigates hyperbolic plasmon polaritons in natural van der Waals materials and femtosecond-scale control of structured light. Hyperbolic plasmon polaritons allow for unparalleled spatial confinement of light, breaking the diffraction limit by supporting highly anisotropic wave propagation in the visible and near-infrared range; Novel approaches to orbital angular momentum (OAM) modulation enable subcycle temporal control of light, dynamically shaping its properties at femtosecond speeds. We achieve unprecedented control over light–matter interactions, where tightly confined optical fields can be rapidly modulated to influence ultrafast processes in nanostructures. This dual approach has far-reaching implications for applications such as ultrafast optical switching, next-generation quantum photonics, and high-resolution imaging, unlocking new possibilities at the intersection of extreme spatial and temporal light manipulation.

References

1. Venturi, G., Mancini, A., Melchioni, M., Chiodini, S. and Ambrosio, A. “Visible-frequency hyperbolic plasmon polaritons in a natural van der Waals crystal”, Nat. Comm. 15:9727, 2024.
2. De Oliveira, M., and Ambrosio, A. “Subcycle modulation of light’s orbital angular momentum via Fourier space-time transformation”, Sci. Adv. 11:eadr6678, 2025.

Tailoring Broadband Large Chiral Response in All-Dielectric Twisted L-shape Metamaterial Platforms

Ufuk Kilic[1,*], Eva Schubert[1], Christos Argyropoulos[2] and Mathias Schubert[1,3]

[1]Department of Electrical and Computer Engineering, University of Nebraska-Lincoln, Lincoln, NE 68588, USA

[2] Department of Electrical Engineering, The Pennsylvania State University, University Park, PA 16803, USA

[3] Solid State Physics and NanoLund, Lund University, P.O. Box 118, 22100, Lund, Sweden

[*]corresponding author: ufukkilic@unl.edu

Abstract: This study presents the fabrication of all-dielectric silicon-based twisted L-shape metamaterials using a two-step electron-beam glancing angle deposition approach. Systematic chiroptical characterization and optimization are performed through Mueller matrix generalized spectroscopic ellipsometry and finite element modeling, demonstrating tunable, broadband chirality response with potential applications in chiral-chemistry, quantum optics, and nanophotonics.

Introduction: Metamaterials with subwavelength-scale periodic structures exhibit unique material properties that are not found in nature, enabling a broad range of advanced functionalities [1-3]. Among these properties, chirality or handedness is particularly intriguing due to its relevance in various disciplines such as physics, chemistry, and biology. Chirality refers to systems where the structure and its mirror image (enantiomer) cannot be superimposed. The optical manifestation of chirality, known as circular dichroism (CD), is the differential absorbance (A) of left (L)- and right(R)-circularly polarized (CP) light and is given as $CD = A_{LCP} - A_{RCP}$. The chiroptical response is quantified using Kuhn's dissymmetry factor (g-factor), given by $g\text{-factor} = 2CD/(A_{LCP} + A_{RCP})$ [1,2]. In this study, we present the fabrication, characterization, and optimization of all-dielectric silicon-based broken L-shape metamaterials using a two-step electron-beam glancing angle deposition (GLAD) approach.

Figure 1 Spectral evolution of g-factor as a function of distortion angle of second columnar segment in broken L-shape metamaterial design. (b) The schematic illustration of conceptual definition of chiral light-proposed metamaterial design interaction. Mueller matrix generalized spectroscopic ellipsometry based experimentally measured (c) circular dichroism (CD) and (d) linear dichroism (LD) as a function of full in plane rotation from 0^{o} to 36^{o} by 15^{o} steps.

During fabrication, the sample stage is rotated before the deposition of the second columnar segment (see the schematic representation in Fig. 1). Depending on the rotation direction, we theoretically verify and experimentally demonstrate both handedness of our proposed metamaterial design (see Fig 1 (a)). By utilizing Mueller matrix generalized spectroscopic ellipsometry, we analyze the chiroptical response of these metamaterials, extracting circular dichroism as well as other optical properties such as linear dichroism, circular birefringence, and linear birefringence (see Fig. 1(c)). We further explore the optical properties of the metamaterials through finite element simulations which employs the structural and optical properties extracted from the anisotropic Bruggeman effective medium model approach-based Mueller matrix generalized spectroscopic ellipsometry data analysis. This enables a more robust understanding of the chiral near- and far- field optical response of proposed metamaterial design. Additionally, we will also discuss that when the structure is dispersed in a liquid environment i.e., the random orientation of the metamaterials eliminates other optical anisotropies, revealing the average chiral response of individual structure design.

In conclusion, this work presents a straightforward yet effective approach to fabricating tunable, broadband chiral metamaterials, offering control over their chiroptical response. These metamaterials have promising applications in areas such as chiral chemistry, quantum optics, and on-chip nanophotonics, with potential for further development in advanced optical devices.

Acknowledgements: Support is acknowledged by the National Science Foundation under awards CMMI 2211858, DMR 2224456, ECCS 2329940, DMR 2423277, and OIA-2044049 Emergent Quantum Materials and Technologies (EQUATE), by Air Force Office of Scientific Research under awards FA9550-18-1-0360, FA9550-19-S-0003, FA9550-21-1-0259, and FA9550-23-1-0574 DEF, and by the University of Nebraska Foundation. M.S. acknowledges support from the J.~A.~Woollam Foundation.

References

1. Kilic, U., *et al.,* ”Broadband enhanced chirality with tunable response in hybrid plasmonic helical metamaterials.” Advanced Functional Materials 31, no. 20: 2010329, (2021).
2. Kilic, U., *et al.,* Controlling the broadband enhanced light chirality with L-shaped dielectric metamaterials. Nat Commun 15, 3757 (2024).
3. A. Kuzyk,*et al.,* “DNA-based self-assembly of chiral plasmonic nanostructures with tailored optical response,” Nature 483, 311–314 (2012).

Spin-Charge Dynamics of Topological Magnetic Textures in Kondo-Lattice Magnets

Masahito Mochizuki
Department of Applied Physics, Waseda University, Japan
masa_mochizuki@waseda.jp (corresponding author)

Abstract

Kondo-lattice models describe spin-charge coupled magnets with localized spins and itinerant electrons coupled via exchange interactions. Spin-charge dynamics of topological magnetism in these models are investigated using large-scale spin-dynamics simulations. We will discuss magnetic topology switching and nontrivial spin-wave excitations in skyrmion crystals and hedgehog lattices under microwave irradiation.

The Hamiltonian of the Kondo-lattice model is given by [see also Fig. 1(a)],

$$\mathcal{H}_{\rm KLM} = \sum_{i,j,\sigma} t_{ij} \hat{c}^{\dagger}_{i\sigma} \hat{c}_{j\sigma} - \frac{J_{\rm K}}{2} \sum_{i,\sigma,\sigma'} \hat{c}^{\dagger}_{i\sigma} \boldsymbol{\sigma}_{\sigma\sigma'} \hat{c}_{i\sigma'} \cdot \boldsymbol{S}_i - \sum_i \left[\boldsymbol{H}_{\rm ext} + \boldsymbol{H}(t) \right] \cdot \boldsymbol{S}_i \tag{1}$$

The first term describes kinetic energies of itinerant electrons. The second term describes the Kondo exchange coupling between the itinerant electron spins and the localized classical spins $\boldsymbol{S}_i$ ($|\boldsymbol{S}_i| = 1$). The last term describes the Zeeman coupling where $\boldsymbol{H}_{\rm ext} = (0, 0, H_z)$ is a static magnetic field, and $\boldsymbol{H}(t)$ is a time-dependent magnetic field.

Time evolutions of the localized spins are numerically simulated using the Landau-Lifshitz-Gilbert (LLG) equation,

$$\frac{d\boldsymbol{S}_i}{dt} = -\boldsymbol{S}_i \times \boldsymbol{H}_i^{\rm eff} + \frac{\alpha_{\rm G}}{S} \boldsymbol{S}_i \times \frac{d\boldsymbol{S}_i}{dt}. \tag{2}$$

The equation is composed of two contributions. The first term describes precession of localized spins around the effective local magnetic field $\boldsymbol{H}_i^{\rm eff}$. The second term phenomenologically describes a dissipation effect where $\alpha_{\rm G}$ is the dimensionless Gilbert-damping coefficient. The effective field $\boldsymbol{H}_i^{\rm eff}$ is calculated by,

$$\boldsymbol{H}_i^{\rm eff} = -\frac{\partial \Omega}{\partial \boldsymbol{S}_i} + \boldsymbol{H}_{\rm ext} + \boldsymbol{H}(t). \tag{3}$$

The thermodynamic potential Ω for $\mathcal{H}_{\rm KLM}$ is given by,

$$\Omega = \int \rho(\varepsilon, \{\boldsymbol{S}_i\})\ f(\varepsilon - \mu)\ d\varepsilon, \tag{4}$$

with

$$\rho(\varepsilon, \{\boldsymbol{S}_i\}) = \frac{1}{2N} \sum_{\nu=1}^{2N} \delta(\varepsilon - \varepsilon_\nu(\{\boldsymbol{S}_i\})), \qquad f(\varepsilon - \mu) = -\frac{1}{\beta} \ln \left[1 + e^{-\beta(\varepsilon - \mu)} \right], \tag{5}$$

where $\rho(\varepsilon, \{\boldsymbol{S}_i\})$ is the density of states of the itinerant electrons for a given set of the localized spins $\{\boldsymbol{S}_i\}$, and $f(\varepsilon - \mu)$ is the free energy density of the system. We use the kernel polynomial method based on the Chebyshev polynomial expansion to calculate Ω and the automatic differentiation technique to calculate its magnetization-derivative $\partial\Omega/\partial\boldsymbol{S}_i$ [?, ?]. We solve the LLG

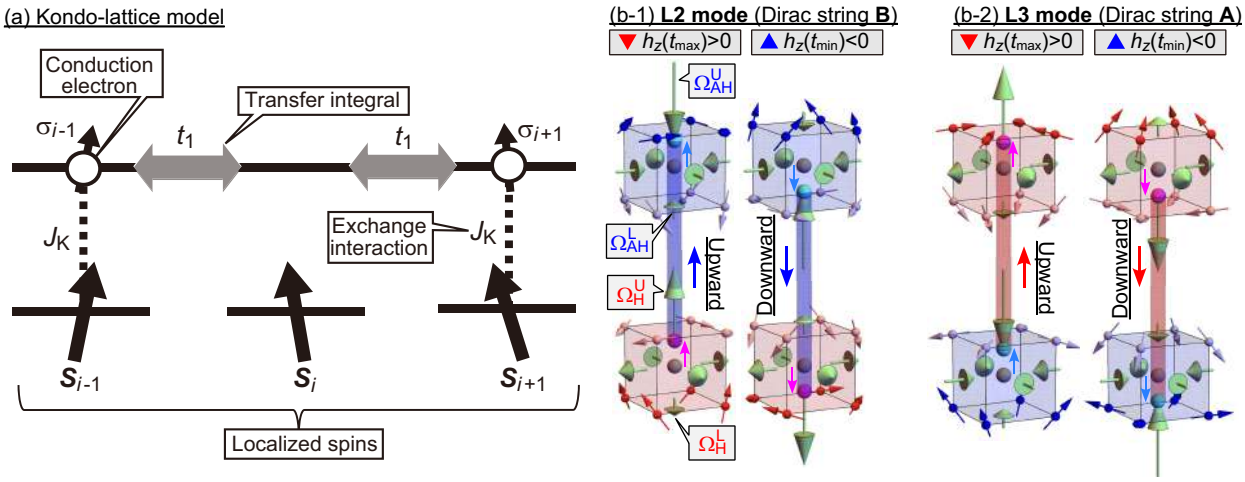


Figure 1: (a) Schematics of the Kondo-lattice model. Itinerant electrons and localized spins are coupled via the Kondo exchange coupling $J_{\rm K}$. The localized spins are not necessarily interacting directly, but indirect interactions mediated by the itinerant electrons exist, which realize long-range ordering of the localized spins. (b) Schematics of the translational oscillations of (b-1) the Dirac string B in the L2 mode and (b-2) the Dirac string A in the L3 mode.

equation using the fourth-order Runge-Kutta method to obtain the spatiotemporal profiles of the dynamics of localized spins.

In this paper, we review the following three topics associated with recent theoretical works studied using the above models and methods.

(1) Microwave-induced magnetic topology switching [1]: It is discovered that application of circularly polarized microwave magnetic field can switch the magnetic topology among three topological magnetic phases characterized by different topological numbers ($|N_{\rm sk}|$=0, 1, and 2) in a triangular Kondo-lattice model.

(2) Low-energy excitation modes and spin-charge segregation [2]: It is discovered that a zero-field skyrmion crystal phase in a triangular Kondo-lattice model has three linearly dispersive Goldstone modes associated with spin excitations and one quadratically dispersive pseudo-Goldstone mode associated with charge excitations. Surprisingly they turn out to be perfectly decoupled in contrast to our naive expectation of strong spin-charge coupling in the Kondo-lattice model.

(3) Spin-wave modes associated in the quadratic hedgehog lattices [3]: It is discovered that quadratic hedgehog lattice phases in the cubic Kondo-lattice model have collective excitation modes associated with translational oscillation of Dirac strings connecting a hedgehog and an antihedgehog [Figs. 1(b-1) and (b-2)]. One of the two modes turn out to vanish upon a field-induced topological phase transition where one of the two types of Dirac-string sublattices undergoes pair annihilations and disappears.

References

[1] R. Eto and M. Mochizuki, Phys. Rev. B **104**, 104425 (2021).

[2] R. Eto, R. Pohle, and M. Mochizuki, Phys. Rev. Lett. **129**, 017201 (2022).

[3] R. Eto, and M. Mochizuki, Phys. Rev. Lett. **132**, 226705 (2024).

Microwave-modulated optomagnet as a tunable nanosource of spin-waves

V. Karakhanyan[1], M. Suarez[1], M. Raschetti[1] and T. Grosjean[1]
[1]*FEMTO-ST Institute, UMR 6174, CNRS, University of Franche Comté, 25000 Besançon, France*
A. Duvakina[2], M. Xu[2],M. A. Deenen[2], A. Mucchietto[2] and D. Grundler[2,3]
[2]*Institute of Materials, Laboratory of Nanoscale Magnetic Materials and Magnonics (LMGN), École Polytechnique Fédérale de Lausanne (EPFL), 1015 Lausanne, Switzerland*
[3]Institute of Electrical and Micro Engineering, EPFL, 1015 Lausanne
dirk.grundler@epfl.ch (Dirk Grundler)
thierry.grosjean@univ-fcomte.fr (Thierry Grosjean)

Abstract

We demonstrate the tunable excitation of spin waves using nanoscale a modulated optomagnet. The modulated optomagnet is a plasmonic nanoantenna coupled to a modulated continuous wave (CW) infrared laser source. We experimentally demonstrate the conversion of different sinusoidal microwave signals into monochromatic spin waves belonging to different allowed magnon bands in the GHz frequency regime.

Introduction

Optics has enabled efficient and compact sources of propagating magnons by use of femtosecond optical pulses[1, 2], based on the Inverse Faraday effect (IFE) produced with single or periodic light pulses[3, 4]. However, being diffraction limited, the resulting excitation spots have not allowed for ultracompact magnon emitters. Recently, subwavelength gratings have been successfully used to locally excite spin waves beyond the diffraction limit[5]. However, the tightly confined light spots were obtained through coherent scattering across a large array of subwavelength grooves, and the development of a truly nanometer-scale optical source of spin waves has not yet been presented.

Recent studies on IFE report that illumination with circularly polarized light turns the plasmonic nanoantenna into a nanoscale optomagnet i.e generates a static magnetic field around the disk [6–10]. Our approach is to use these optomagnets to generate spin-waves from a compact tunable nanosource. In this approach a microwave-modulated CW laser beam excites spin-waves trough optomagnet vie resonant IFE. The modulation can be fine tuned which makes optomagnet highly tunable source of spin waves. Here, we report the experimental demonstration of a nanometer-scale optical source of spin waves by coupling a microwave-modulated CW laser to a resonant plasmonic nanoantenna.

Results and discussion

We positioned a 50nm thick gold nanodisk on top of a transparent thin-film yttrium iron garnet (YIG) in a presence of an external static magnetic field ($\mu_0 H$) of 20mT (Fig. 1, (**a**) blue arrow). The diameter of the nanodisk is set to 130 nm to match its electromagnetic resonance with the frequency of the illuminating modulated infrared (IR) laser (λ=808nm). When illuminated with a circularly polarized CW IR laser, the nanodisk generates a static magnetic field around itself, known as the optomagnetic field (Fig. 1, (**a**) black arrows). The idea now is to illuminate

the nanodisk with a microwave-modulated CW laser source, thereby enabling the modulation of the optomagnetic field around the nanodisk as evidenced in [11, 12]. This way we create a microwave-modulated optomagnet on YIG via resonant IFE. The modulated optomagnetic field couples to the spin-waves in YIG (Fig. 1 (**a**) red arrows) which are detected by means of inelastic/Brillouin light scattering (BLS) (Fig. 1 (**a**) green arrows).

Fig. 1 (**b**) shows that when the modulation is removed spin-waves are not excited. Moreover, in Fig. 1 (**c**) one can see that the acquired BLS spectra show the enhancement of spin-wave signals at the frequencies corresponding exactly to the modulation frequencies of the IR CW laser: 3.6 GHz (red), 4.5 GHz (green), and 7.4 GHz (blue). The small peak at 6.2 GHz (indicated with a cross) did not depend on H and was attributed to a parasitic line of the green laser.

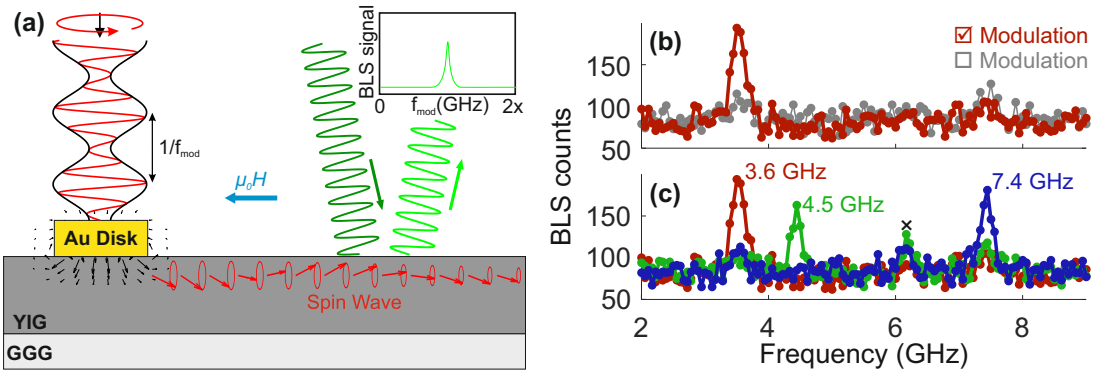


Figure 1: **Excitation of monochromatic spin waves by an optomagnetic nanoemitter.** (**a**) Experiment depiction. (**b**) BLS spectra of the probe beam with/without modulation (3.6 GHz) of the IR laser. (**c**) BLS spectra of the probe beam with different modulations of the IR laser that are indicated in the legend.

Our results show that plasmonic nanoantennas are nanoscale emitters capable of tunably transduce a microwave signal into short-wavelength spin-waves, while avoiding physical and technical constraints inherent to microwave antennas. Particularly, our approach offers a broad spin-wave-frequency bandwidth from MHz to sub-THz depending only on the light-modulation methodology. Spin waves, in turn, serve as a novel probe for investigating plasmon-induced optomagnetic effects a the nanoscale.

References

[1] D. M. Wang et al. In: *Phys. Rev. B* 75 (23 June 2007), p. 233308.

[2] Y Au et al. In: *Phys. Rev. Lett.* 110.9 (2013), p. 097201.

[3] M Jäckl et al. In: *Phys. Rev. X* 7.2 (2017), p. 021009.

[4] IV Savochkin et al. In: *Sci. Rep.* 7.1 (2017), pp. 1–10.

[5] Alexander I Chernov et al. In: *Nano Lett.* 20.7 (2020), pp. 5259–5266.

[6] A. Nadarajah and MT Sheldon. In: *Opt. Express* 25.11 (2017), pp. 12753–12764.

[7] Jérôme Hurst et al. In: *Phys. Rev. B* 98.13 (2018), p. 134439.

[8] SM Hamidi et al. In: *Opt. Commun.* 338 (2015), pp. 240–245.

[9] Vage Karakhanyan et al. In: *Optics Letters* 46.3 (2021), pp. 613–616.

[10] Vage Karakhanyan et al. In: *OSA Continuum* 4.5 (2021), pp. 1598–1608.

[11] Oscar Hsu-Cheng Cheng et al. In: *Nat. Photon.* 14.6 (2020), pp. 365–368.

[12] Oscar Hsu-Cheng Cheng et al. In: *Nano Lett.* 22.13 (2022), pp. 5120–5126.

Inverse Design of Chiral Structures for Giant Helical Dichroism

Munseong Bae[1,*], Chia-Chun Pan[2,*], Hongtao Wang[3], Jaesung Lim[1],
Ranjith R. Unnithan[2], Joel Yang[3], Sejeong Kim[2,†], and Haejun Chung[1,†]
[1]Department of Electronic Engineering
Hanyang University, Seoul, Korea
[2]Department of Electrical and Electronic Engineering
University of Melbourne, VIC, Australia
[3]Engineering Product Development
Singapore University of Technology and Design, Singapore
haejun@hanyang.ac.kr, sejeong.kim@unimelb.edu.au (co-corresponding author)

Abstract

An inverse design framework optimizes a chiral nanostructure for maximal helical dichroism (HD), achieving 107 % HD at 800 nm for orbital angular momentum beams. This approach significantly enhances differential absorption of the OAM beams with opposite signs of topological charges.

1 Introduction

Chiral light-matter interactions are essential for applications in sensing, imaging, and pharmaceutical development [1]. However, the weak chiroptical response in natural chiral molecules limits practical use. Recent advances have explored the use of light with orbital angular momentum (OAM) [3,4], characterized by a helical phase front and topological charge (l), to probe chirality more effectively. This approach introduces helical dichroism (HD), which measures the difference in absorbance between opposite-helicity OAM beams. This work uses inverse design to create a chiral structure that maximizes HD, achieving a record-breaking response.

The inverse design framework aims to optimize the geometry of a chiral structure to maximize HD, where HD quantifies the differential absorption of opposite OAM beams. Using adjoint-based topology optimization [2], we formulated this as a design problem to maximize HD through iterative adjustments of the material layout. The HD objective function is based on the difference in absorbance between two OAM beams with opposite charges ($\pm l$). The chiral structure is parameterized so that its shape or material distribution can be adjusted during optimization. We used adjoint simulations to compute the gradient of the HD with respect to design parameters, guiding the gradual evolution of the design parameters toward maximizing the differential absorbance between opposite OAM helicities. The design is iterated until the HD reaches a maximum, at which point the geometry is optimized for the largest possible chiroptical effect. This method allows for non-intuitive, complex designs that significantly enhance the HD response, surpassing conventional designs based on heuristic or spiral geometries.

The optimized structure achieves a giant HD of 107% for OAM beams with $l = \pm 3$ at 800 nm. This represents a significant improvement over previous studies, where HD rarely exceeded 20%. The optimized chiral structure exhibits a strong dichroic effect, with a 107% HD response at 800 nm for OAM beams with $l = \pm 3$, far surpassing conventional designs. The structure absorbs the one-handedness of the light more strongly than the opposite, producing a marked difference in reflectance between the two OAM helicities. The HD achieved in our design is an order of magnitude greater than the best previously reported results. The inverse design approach is flexible, allowing for modifications such as different wavelengths or topological

charges (l), making it suitable for various applications. The physical mechanism behind the giant HD response lies in the geometry of the chiral structure, which interacts differently with OAM beams depending on their handedness. The design selectively enhances absorption for one handedness while minimizing it for the other, leading to a large difference in reflectance. This demonstrates the potential for custom-tailored chiroptical responses using inverse design.

We demonstrated that inverse design can be used to create a chiral nanostructure with a giant HD response of 107%, significantly larger than previously reported values. This achievement marks an important step in the development of high-performance chiroptical devices, opening new possibilities for chiral sensing, advanced spectroscopic techniques, and other applications where chirality plays a crucial role.

By combining OAM light with inverse-designed structures, we were able to enhance chiroptical effects to a degree previously unachievable. This work not only advances the field of chiral photonics but also illustrates the power of computational design in unlocking new optical phenomena. Future work may explore extending this framework to 3D structures or broader spectral ranges, further enhancing the versatility and application of such devices.

2 Acknowledgements

This work was supported by the National Research Foundation of Korea (NRF) grant funded by the Korean government (MSIT) under the following grant numbers: (RS-2024-00338048), and (RS-2024-00414119). It was also supported by the Global Research Support Program in the Digital Field (RS-2024-00412644) under the supervision of the Institute of Information and Communications Technology Planning & Evaluation (IITP), and by the Artificial Intelligence Graduate School Program (RS-2020-II201373, Hanyang University), also supervised by the IITP. Additionally, this research was supported by the Artificial Intelligence Semiconductor Support Program (RS-2023-00253914), funded by the IITP, and by the Korea government (MSIT) grant (RS-2023-00261368). This work received support from the Culture, Sports, and Tourism R&D Program through a grant from the Korea Creative Content Agency, funded by the Ministry of Culture, Sports and Tourism (RS-2024-00332210).

References

[1] Nam Heon Cho, Andrés Guerrero-Martínez, Jessica Ma, Sara Bals, Nicholas A Kotov, Luis M Liz-Marzán, and Ki Tae Nam. Bioinspired chiral inorganic nanomaterials. *Nature Reviews Bioengineering*, 1(2):88–106, 2023.

[2] Haejun Chung and Owen D Miller. High-na achromatic metalenses by inverse design. *Optics express*, 28(5):6945–6965, 2020.

[3] Yae-Chan Lim, Ryeong Myeong Kim, Jeong Hyun Han, Igor Aharonovich, Ki Tae Nam, and Sejeong Kim. Strong chiral response of chiral plasmonic nanoparticles to photonic orbital angular momentum. *Advanced Optical Materials*, page 2402268.

[4] Yijie Shen, Xuejiao Wang, Zhenwei Xie, Changjun Min, Xing Fu, Qiang Liu, Mali Gong, and Xiaocong Yuan. Optical vortices 30 years on: Oam manipulation from topological charge to multiple singularities. *Light: Science & Applications*, 8(1):90, 2019.

Magnonic ϕ Josephson junctions and synchronized precession

Kouki Nakata[1], Ji Zou[2], Jelena Klinovaja[2], and Daniel Loss[2]
[1]Advanced Science Research Center, Japan Atomic Energy Agency, Tokai, Ibaraki 319-1195, Japan
[2]Department of Physics, University of Basel, Klingelbergstrasse 82, 4056 Basel, Switzerland
[3]Center for Emergent Matter Science, RIKEN, 2-1 Hirosawa, Wako-shi, Saitama 351-0198, Japan

Abstract

We uncover theoretically that a surprisingly rich dynamics can emerge in magnetic junctions due to intrinsic nonlocal damping, using analytical and numerical methods. In particular, under microwave pumping, we show that coherent spin precession in the right and left insulating ferromagnet of the junction becomes synchronized by nonlocal damping.

1 Introduction

Recently, non-Hermitian physics has been attracting growing interest from both fundamental science and applications such as energy-efficient devices. One of its main themes is to engineer dissipation and to explore the resulting functionality. Since magnons are intrinsically damped in magnetic systems, the goal of non-Hermitian physics aligns well with magnonics, which aims at efficient transmission and processing of information for computing and communication technologies using magnons as its carrier in units of the Bohr magneton μ_B. To this end, establishing methods for the control and manipulation of magnon transport subjected to dissipation is crucial. In magnonics, the effect of dissipation due to local (Gilbert) damping on magnon transport, such as the magnonic analog of the Josephson effect, has been explored, where the macroscopic coherent magnon state, the key ingredient for the magnonic Josephson effect, realizes an oscillating behavior of magnon transport. However, the effect of non-local damping on the magnonic Josephson effect and the resulting functionality remain missing, despite that non-local damping is inevitable and has been playing a central role in non- Hermitian magnonics.

2 Results

We find that the inherent non-local damping leads to rich dynamics, and, interestingly, can be utilized to realize a magnonic analog of the φ Josephson junction [1]. Under microwave pumping, coherent spin precession in each insulating ferromagnet (FM) of the magnetic junction (see Fig. 1) is synchronized by non-local damping as time advances and gives rise of a magnonic φ Josephson junction, where φ stands for the stationary value of the relative precession phase of the left and right FMs. Interestingly, we find that φ decreases monotonically from π to $\pi/2$ as the magnon-magnon interaction, arising from spin anisotropies across the junction, increases. Applying microwaves to each FM continuously, the junction reaches the nonequilibrium steady state where the loss of magnons due to dissipation is precisely balanced by the injection of magnons. Hence, spins in each FM continue to precess coherently, and the synchronized precession of the left and the right magnetization remains stable even at room temperature. Finally, we show that the magnetic junction exhibits rectification and acts as a diode for the magnon current.

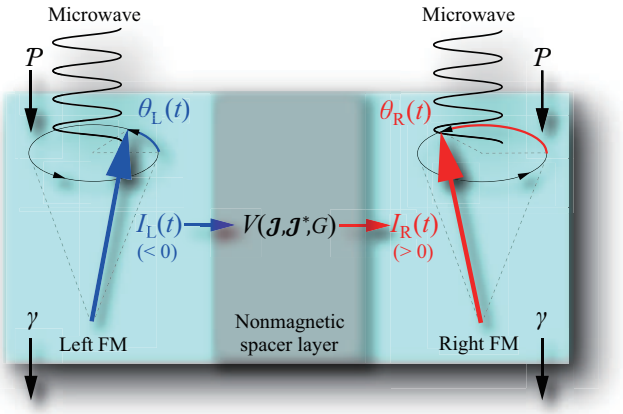


Figure 1: Magnonic φ Josephson junction, formed by a ferromagnetic bilayer coupled by a non-magnetic spacer. Magnons are subjected to local damping at rate $\gamma > 0$. The spacer layer-mediated interaction V between the two FMs consists of coherent coupling ($\mathcal{J}$) and non-local damping (G). Under microwave pumping, the spatially uniform mode of magnons is injected into each FM at rate $\mathcal{P}$, generating coherent spin precessions. The loss of magnons due to dissipation is exactly balanced by the injection of magnons. In the steady state, the spin precessions in each FM get synchronized due to non-local damping and a relative precession angle emerges $\varphi = \lim_{t\to\infty}[\theta_{\rm R}(t) \in \theta_{\rm L}(t)]$ that depends on the magnon-magnon interaction. The associated magnon currents $I_{\rm L/R}$ get rectified when $G = 0$.

3 Acknowledgements

This work was supported by the Georg H. Endress Foundation and by the Swiss National Science Foundation, and NCCR SPIN (grant number 51NF40-180604). K.N. acknowledges support by JSPS KAKENHI Grants No. JP22K03519.

References

[1] Kouki Nakata, Ji Zou, Jelena Klinovaja, and Daniel Loss, *Magnonic ϕ Josephson junctions and synchronized precession* Phys. Rev. Research **6**, 033207 (2024).

Classifying Fragile Topology Using Matrix Homotopy

A. Cerjan[1*]

[1]Center for Integrated Nanotechnologies, Sandia National Laboratories, Albuquerque, New Mexico 87185, USA
[*]corresponding author: awcerja@sandia.gov

Abstract: We develop a Z_2 energy-resolved topological marker for classifying fragile phases using a system's position-space description, enabling the direct classification of finite, disordered, and aperiodic materials, and illustrate this marker's application in both material and photonic crystal systems.

The moiré flat bands in twisted materials have attracted considerable attention not only because of the emergence of correlated phases but also due to their ability to manifest nontrivial topology. Specifically, they can exhibit a new class of topology that can be nullified by the addition of trivial bands, termed fragile topology, which has required an expansion of existing classification schemes. Here, we develop a Z_2 energy-resolved topological marker for classifying fragile phases using a system's position-space description, enabling the direct classification of finite, disordered, and aperiodic materials. Specifically, by translating the physical symmetries protecting the system's fragile topological phase into matrix symmetries of the system's Hamiltonian and position operators, we are to use results from matrix homotopy to construct our topological marker while simultaneously yielding a quantitative measure of topological robustness. We demonstrate our framework's effectiveness using a C_2T-symmetric twisted bilayer graphene model and photonic crystal as a continuum example. Our findings reveal that fragile topology can persist under strong disorder and in heterostructures lacking a bulk spectral gap. Moreover, we find an example of disorder-induced re-entrant topology. Overall, the proposed scheme serves as an effective tool for elucidating aspects of fragile topology, offering guidance for potential applications across a variety of experimental platforms from topological photonics to correlated phases in materials.

Acknowledgements: This work is part-funded by Sandia National Laboratories (SNL). SNL is managed and operated by NTESS under DOE NNSA contract DE-NA0003525.

References

1. A. Cerjan and T. A. Loring, "Classifying photonic topology using the spectral localizer and numerical K-theory," APL Photonics 9, 111102 (2024).
2. K. Y. Lee, S. Wong, S. Vaidya, T. A. Loring, and A. Cerjan, in submission.

Electromagnetic Helicity in Twisted Cavity Resonators

J. Bourhill[1*], E. C. Paterson[1], M. Goryachev[1], and M. E. Tobar[1]
[1]The University of Western Australia, Australia
jeremy.bourhill@uwa.edu.au (corresponding author)

Abstract

Twisting the conducting boundary conditions of an electromagnetic cavity with an equilateral triangle cross-section generates eigenmodes with electromagnetic helicity – a result of the coupling of previously degenerate TE and TM modes. This can be interpreted as an emergence of magnetoelectricity, which produces a confirmable shift in resonant mode frequency.

The unique light-matter interactions exhibited by helical radiation have garnered significant interest across various fields, including material science, nanophotonics, spectroscopy, and quantum information processing. These interactions offer numerous applications, from probing molecular chirality to advancing optical communication technologies and sensitivity to dark matter candidates [1]. Electromagnetic helicity typically only occurs in surface states, at optical frequencies, or due to complex meta-structures.

We present evidence of resonant electromagnetic modes with non-zero helicity produced in vacuo. We investigate a cavity with an equilateral triangular cross-section and electrically conducting boundary conditions at the end faces. The mirror symmetry of this resonator can be broken by introducing an arbitrary twist angle around the central axis of the cavity, resulting in a chiral geometry.

Electromagnetic helicity is intrinsically linked to the dual transformation of the electromagnetic state, effectively rotating the electric and magnetic properties of the medium. This results in the effective mixing of electric and magnetic fields and so electromagnetic helicity will necessarily produce a magnetoelectric coupling. Electromagnetic helicity can be quantified by the following normalised parameter:

$$h_p(\vec{r}) = 2\mathrm{Im}\left[\vec{\mathbf{e}}(\vec{r})\cdot\vec{\mathbf{h}}^*(\vec{r})\right] = \frac{2\mathrm{Im}\left[\vec{\mathbf{E}}_p(\vec{r})\cdot\vec{\mathbf{H}}_p^*(\vec{r})\right]}{\mathcal{E}\mathcal{H}}, \tag{1}$$

where $\mathcal{E}$ and $\mathcal{H}$ are real constants, $\vec{\mathbf{E}}_p(\vec{r}) = \mathcal{E}\vec{\mathbf{e}}(\vec{r})$ and $\vec{\mathbf{H}}_p(\vec{r}) = \mathcal{H}\vec{\mathbf{h}}(\vec{r})$ are the time-dependent electric and magnetic vector fields of some mode p, respectively, and $\vec{\mathbf{e}}(\vec{r})$ and $\vec{\mathbf{h}}(\vec{r})$ are the normalised position dependent eigenvectors such that $\int \vec{\mathbf{e}}(\vec{r})^*\cdot\vec{\mathbf{e}}(\vec{r})dV = \int \vec{\mathbf{h}}(\vec{r})^*\cdot\vec{\mathbf{h}}(\vec{r})dV = 1$. The total helicity for a given mode, $\mathscr{H}_p$ can then be written as the integral of (1) over the cavity volume:

$$\mathscr{H}_p = \int h_p dV. \tag{2}$$

It is observed that the frequency of certain resonant modes in the cavities of interest can be shifted as the boundary conditions are twisted. An eigenmode analysis conducted using finite element modelling (FEM) software reveals that by breaking the mirror symmetry, near degenerate transverse electric (TE) and transverse magnetic (TM) modes are coupled together producing to a non-zero $\mathscr{H}_p$. This effect is detailed in Fig. 1, where the various field components are plotted for the $\phi = 0$ case and the $\phi = 2\pi$ case. We observe a new orthogonality basis generated in the twisted case, appearing as either in-phase mixing of the form TM_{11p}+$\mathrm{TE}_{11(p+1)}$ (labelled ψ^+_{p+1})

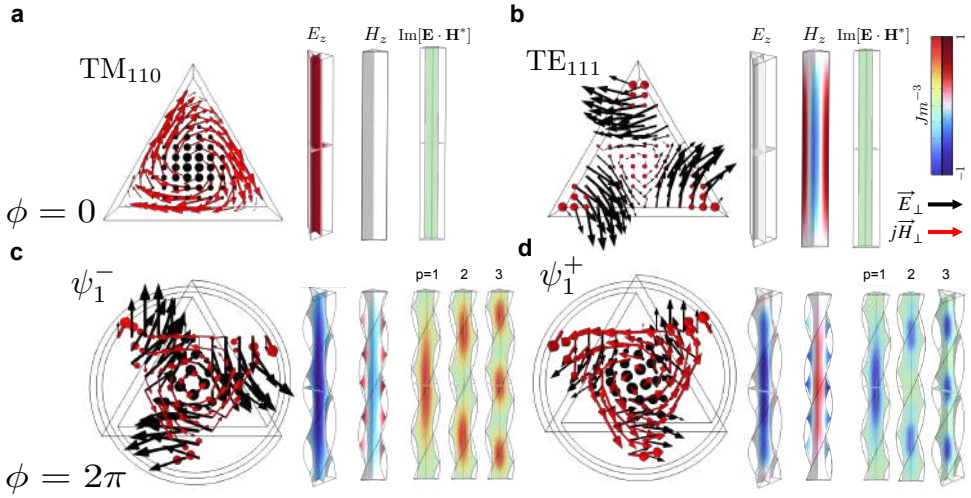


Figure 1: The perpendicular $\vec{E}_\perp$ (black) and imaginary $\vec{H}_\perp$ (red) fields plotted in the cross-section and the normalised densities of the axial fields E_z, H_z & $\mathrm{Im}\,[\mathbf{E}\cdot\mathbf{H}^*]$ for the (a) TM_{110} mode, (b) TE_{111} mode, and the twisted ($\phi = 2\pi$) (c) ψ^- mode, and (d) ψ^+ mode.

or out-of-phase mixing of the form TM_{11p}−$\mathrm{TE}_{11(p+1)}$ (ψ^-_{p+1}). The mixing of previously orthogonal mode solutions can only be explained by a magnetoelectric coupling emerging, resulting in normal mode splitting. Indeed, evaluating the imaginary component of the $\vec{\mathbf{E}}\cdot\vec{\mathbf{H}}$ product in the twisted case reveals the existence of non-zero $\mathscr{H}_p$ which represents the new basis in which mode numbers (such as p) can be counted. From perturbation theory [2], it can be shown that there is a fundamental relationship between $\mathscr{H}_p$ and a resonant mode's frequency shift, $\delta\omega$, given by:

$$\left(\frac{\delta\omega}{\omega_p}\right)_{\kappa\ll 1} = \frac{\delta\kappa\mathscr{H}_p}{2\mu_r\epsilon_r}, \tag{3}$$

where ω_p is the unperturbed cavity frequency, μ_r and ϵ_r the media's relative permeability and permittivity, respectively, and κ is the so-called material "chirality parameter", which acts to mix $\vec{\mathbf{E}}$ and $\vec{\mathbf{H}}$ fields according to:

$$\begin{aligned}\vec{\mathbf{D}} &= \epsilon\vec{\mathbf{E}} - j\kappa\sqrt{\mu_0\epsilon_0}\vec{\mathbf{H}},\\ \vec{\mathbf{B}} &= \mu\vec{\mathbf{H}} + j\kappa\sqrt{\mu_0\epsilon_0}\vec{\mathbf{E}}.\end{aligned} \tag{4}$$

Whilst κ is typically considered a material parameter, it can be shown that there is an empirical equivalence to cavity twist angle ϕ and hence frequency shifts as a function of twist angle can be predicted from (3). Indeed, frequency spectral response measurements of 3D-printed cavities with $\phi = 0$ and $\phi = \pm 10\pi/9$ confirm the predicted frequency shifts from FEM and (3), indicating the generation of electromagnetic helicity in a hollow, free-space volume.

This work was funded by the Australian Research Council Centre of Excellences for Engineered Quantum Systems and Dark Matter Particle Physics.

References

[1] Bourhill, J. F., E. C. I. Paterson, M. Goryachev, and M. E. Tobar, "Searching for ultralight axions with twisted cavity resonators of anyon rotational symmetry with bulk modes of nonzero helicity," *Phys. Rev. D*, Vol. 108, 052014, 2023.

[2] Tretyakov, S. A., and A. J. Viitanen, "Perturbation theory of a cavityy resonator with a bi-isotropic sample: applications to measurement techniques," *Mic. and Opt. Tech. Lett.*, Vol. 5, pp. 174–177, 1992.

Electrical control of ultrastrong coupling of 2-dimensional electronic systems to single meta-atoms

E. Jöchl[1], F. Helmrich[1], A-L.Vieli[1], L. Hale[1], D. Turan,[2]
M. Jarrahi,[2] M. Beck[1], A. Imamoglu[1], J. Faist[1], T. Nova[1], G. Scalari[1,*]
[1] Institute for Quantum Electronics, Department of Physics, ETH Zürich, Switzerland
[2] Department of Electrical & Computer Engineering, UCLA, Los Angeles, CA, USA
[*]corresponding author: gscalari@ethz.ch

Abstract: We demonstrate electrical control of ultrastrong light-matter coupling regime in high mobility III-V 2DEG and bilayer graphene at THz and sub-THz frequencies. The meta-atom surface is of the order of 10 μm^2 , allowing the THz (0.05-10 THz) study of exfoliated bilayer graphene devices and other 2D systems.

Strong light-matter coupling has been recently successfully explored in the GHz and THz range with on-chip platforms, where metallic resonators with small cavity volumes are combined with high electron density materials to exploit the collective enhancement of the coupling Ω. New and intriguing quantum optical phenomena have been predicted in the ultrastrong coupling regime, when the coupling strength Ω becomes comparable to the unperturbed frequency of the system ω [1][2]. The use of extremely small cavity volumes ($V/\lambda^3 \simeq 10^{-6}$), attainable with circuit-like resonators, has allowed the study of ultrastrong light-matter coupling at THz frequencies[3][4][5] While sub-wavelength localization of terahertz fields can be efficiently achieved using micro-structured metallic resonators, conventional approaches rely on metamaterials of repeating resonators placed atop the material of interest.[3] [6] This method is incompatible with exfoliated 2D materials, which are usually limited to in-plane dimensions of just a few microns, and with the study of few-electron systems requiring an active mode surface of a few micrometer squared.

We will discuss experimental results where a single strongly subwavelength resonator is coupled to single GaAs/AlGaAs 2 DEG and, in a second experiment, to a dual-gated Bernal stacked bilayer graphene.

In the first experiment, we use the Landau polariton platform that has been extensively exploited to investigate the physics of ultrastrong light-matter coupling both in optical and transport experiments [3][7]. We employ a system of immersion lenses [8](Fig.1(a)) to spectroscopically investigate the single resonator. The resonator features an electrical gate in order to modulate the electron density ρ_{2deg} and, as a consequence, the Rabi frequency Ω. In this case the tuning of the coupling strength happens through the tuning of the dipole that is proportional to the square root of the 2DEG filling factor $\nu = 2\pi\hbar\rho_{2deg}/eB$ [9]. In Fig.1(b) are visible transmission spectra taken for different values of the applied gate voltage. It is evident the closing of the polariton splitting and the progressive disappearance of the diamagnetic shift as the resonator is depleted from electrons and the upper branch at B=0 converges to the empty cavity value of 270 GHz (horizontal dashed line). The gate voltage allows the tuning of the normalized coupling ratio from $\Omega/\omega=0.5$ to $\Omega/\omega= 0.12$, so from ultrastrong coupling to strong coupling.

In the second experiment, we couple a Bernal stacked bilayer graphene (BLG) to a bow-tie antenna resonator (Fig. 1(c)). The presence of a dual gate system allows to independently tune the carrier density and the displacement field, with which we tune the BLG gap in the range 0-6 THz [10]. As visible in Fig.1(d), the measured THz transmission as a function of the displacement field reveals an anticrossing behavior, and the estimated coupling strength, defined by the ratio between the vacuum Rabi (Ω) and the cavity (ω) frequencies, is $\eta= \Omega/\omega \approx 0.43$, which places our system well into the ultrastrong coupling regime.

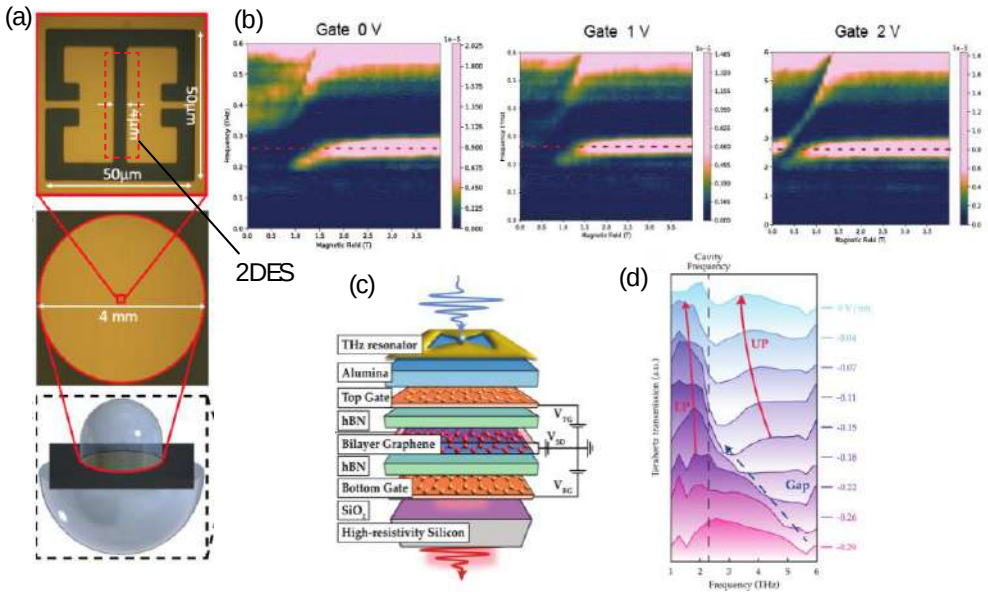


Figure 1. (a): schematic of the immersion lenses arrangement together with the single-meta atom sample. (b):Transmission spectra as a function of gate bias for an electrically-gated, single SRR coupled to a single quantum well. (c): Lateral view of the sample structure. The heterostructure consists of Bernal bilayer graphene, few-layer graphite gates and hbN dielectrics placed on a high-resistivity Si/SiO2 substrate. The heterostructures is insulated from the bow-tie resonator with alumina dielectric. (d): BLG transmission spectra atvarious displacement fields under zero doping (n = 0) measured at 5 K.. The cavity resonance frequency is indicated by a dashed line. A black dashed arrow points to the closing band gap edge, while redarrows highlight the lower and upper polariton branches.

References

[1] C. Ciuti, G. Bastard, and I. Carusotto, “Quantum vacuum properties of the intersubband cavity polariton field,” vol. 72, no. 11, p. 115303, Sep. 2005.

[2] P. Forn-Díaz, L. Lamata, E. Rico, J. Kono, and E. Solano, “Ultrastrong coupling regimes of light-matter interaction,” *Rev. Mod. Phys.*, vol. 91, no. 2, p. 025005, Jun. 2019.

[3] G. Scalari *et al.*, “Ultrastrong Coupling of the Cyclotron Transition of a 2D Electron Gas to a THz Metamaterial,” *Science*, vol. 335, no. 6074, pp. 1323–1326, Mar. 2012.

[4] Y. Todorov *et al.*, “Ultrastrong Light-Matter Coupling Regime with Polariton Dots,” *Phys. Rev. Lett.*, vol. 105, no. 19, p. 196402, Nov. 2010.

[5] A. Bayer *et al.*, “Terahertz Light–Matter Interaction beyond Unity Coupling Strength,” *Nano Lett.*, p. acs.nanolett.7b03103-5, Sep. 2017.

[6] X. Jin *et al.*, “Enhanced Terahertz Spectroscopy of a Monolayer Transition Metal Dichalcogenide,” *Adv. Funct. Mater.*, vol. n/a, no. n/a, p. 2419841, Jan. 2025, doi: 10.1002/adfm.202419841.

[7] F. Appugliese *et al.*, “Breakdown of topological protection by cavity vacuum fields in the integer quantum Hall effect,” *Science*, vol. 375, no. 6584, pp. 1030–1034, Mar. 2022, doi: 10.1126/science.abl5818.

[8] S. Rajabali *et al.*, “An ultrastrongly coupled single terahertz meta-atom,” *Nat. Commun.*, vol. 13, no. 1, p. 2528, May 2022, doi: 10.1038/s41467-022-29974-2.

[9] D. Hagenmüller, S. De Liberato, and C. Ciuti, “Ultrastrong coupling between a cavity resonator and the cyclotron transition of a two-dimensional electron gas in the case of an integer filling factor,” vol. 81, no. 23, p. 235303, Jun. 2010.

[10] Helmrich,Felix, Khanonkin, Igor, Kroner, Martin, Scalari, Giacomo, Faist, Jerome, and A. Imamoglu, Atac, “Ultrastrong Terahertz Coupling in a van der Waals Heterostructure,” *arXiv:2408.00189*.

Chiral Polaritons in Bulk van der Waals Metasurfaces

A. A. Antonov[1*], C. Heimig[1], M. V. Gorkunov[2], Y. S. Kivshar[3] and A. Tittl[1]

[1]Chair in Hybrid Nanosystems, Nanoinstitute Munich, Faculty of Physics, Ludwig-Maximilians-Universität München, Munich, Germany
[2]Shubnikov Institute of Crystallography, NRC "Kurchatov Institute", 119333, Moscow, Russia
[3]Nonlinear Physics Centre, Research School of Physics, Australian National University, Canberra, ACT 2601, Australia
[*]corresponding author: a.antonov@lmu.de

Abstract:
We analyze a maximally chiral metasurface composed of van der Waals (vdW) material within the strong light-matter coupling regime. We demonstrate that, due to specific photonic eigenstates – chiral quasi-bound state in the continuum (quasi-BIC) uncoupled from light of specific circular polarization, chiral self-hybridized exciton-polaritons of certain handedness are formed.

Exciton-polaritons, as eigenstates of systems exhibiting strong light-matter interaction, inherit properties from both massless photons and massive excitons. This makes them promising candidates for novel applications based on polaritonic lasing [1], controlled electronic transport [2] and modified chemical kinetics [3]. Special attention is paid to chiral polaritons, which are crucial for chiral molecular sensing [4] and quantum materials engineering [5].

Metasurfaces with chiral photonic quasi-BICs [6], whose polarization and Q-factor depend on structural asymmetry, offer a convenient platform for creating chiral polaritons. Here we analyze a metasurface composed of dielectric rods of different heights (Fig. 1(a)) arranged to sustain a quasi-BIC uncoupled from normally incident light of right circular polarization (RCP) while resonantly interacting with left circular polarized (LCP) light (Fig. 1(b)). The rods are made of bulk vdW material WS_2, which has stable excitons at room temperature (Fig. 1(c)). As illustrated in Fig. 1(d), the hybridization of the chiral photonic quasi-BIC and achiral excitons results in the formation of two chiral polaritons, resonantly interacting only with LCP light (Fig. 1(e)). To demonstrate chiral polaritonic branches with corresponding Rabi splitting we introduce an in-plane scaling factor S and tune the quasi-BIC resonance wavelength. The resulting transmittance difference between RCP and LCP waves exhibits a characteristic anticrossing pattern around the exciton position at 629 nm (Fig. 1(f)).

To assess the polariton chirality, we perform a multipole decomposition of the coupling coefficients between the metasurface eigenstate displacement current $\mathbf{J}(\mathbf{r})$, which predominantly flows in the *xy*-plane ($J_z(\mathbf{r}) \approx 0$), and free-space plane waves with a wave number $k = \omega/c$ and circular polarizations along the unit vectors $\mathbf{e}_\pm = (\mathbf{e}_x \pm i\mathbf{e}_y)/\sqrt{2}$:

$$m_\pm \propto \int_V \mathbf{J}(\mathbf{r}) \cdot \mathbf{e}_\pm \, e^{i\mathbf{k}\cdot\mathbf{r}} dV \approx \int_V \mathbf{J}(\mathbf{r}) \cdot \mathbf{e}_\pm \, (1 + i\mathbf{k}\cdot\mathbf{r}) dV \approx -i\omega \left(\left[P_x \pm i\frac{2}{c} M_x \right] + i \left[\pm P_y + i\frac{2}{c} M_y \right] \right). \quad (1)$$

The electric and magnetic dipole moments components are given by $P_{x,y} = i/\omega \int_V J_{x,y}(\mathbf{r})\, dV$ and $M_{x,y} = \mp \int_V z J_{y,x}(\mathbf{r})\, dV/2$, respectively. The condition of maximum chirality $m_\pm = 0$ is satisfied when $\mathbf{M} = \pm ic\mathbf{P}/2$, which is analogous to the condition of an ideal chiral point emitter (with an extra factor of 2), where electric $\mathbf{P}$ and magnetic $\mathbf{M}$ dipoles are collinear with a $\pm\pi/2$ phase difference. Next, we numerically analyze the multipole composintion of hybrid eigenstates of metasurfaces with fixed scaling factors (capital letter marks in Fig.1(f)). The calculated dipole moments of polaritons, presented in Fig.1(g), closely match the condition of maximum chirality. To quantify this, we evaluate the dissymmetry factor *g* as the ratio of the rotational strength *R* [7] to the dipole strength *D*:

$$g = 4\frac{R}{D} = 4\frac{\mathrm{Im}(2\mathbf{M}\cdot c\mathbf{P})}{|2\mathbf{M}|^2 + |c\mathbf{P}|^2}. \quad (2)$$

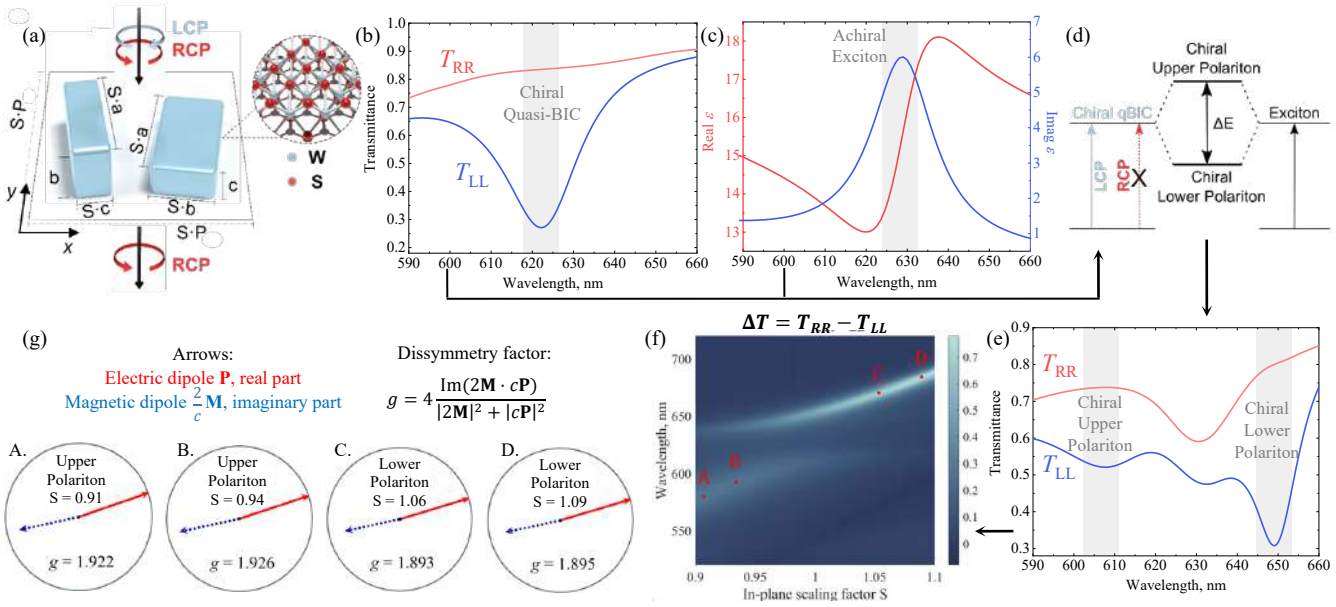


Figure 1. (a) Maximally chiral metasurface made of WS_2 rods with dimensions: a = 225 nm, b = 115 nm, c = 45 nm. The unit cell has a periodicity of P = 375 nm, each rod is rotated in-plane by 12°. (b) Transmittance spectra of the metasurface, showing the photonic chiral quasi-BIC in the absence of excitons. (c) Tabulated dispersion of bulk WS_2. (d) Simplified energy-level diagram of self-hybridization of an exciton and a quasi-BIC into a pair of chiral polaritons. (e) Transmittance spectra of the metasurface with self-hybridized chiral polaritons. (f) Transmittance difference $\Delta T = T_{RR} - T_{LL}$ of the metasurface for different in-plane scaling factors S. Capital letter marks indicate metasurfaces whose eigenstates are analyzed by the multipole decomposition in (g).

The calculated g values approach the theoretical limit of the dissymmetry factor $g = 2$, making our metasurface with polaritons a perspective platform for chiral linear and nonlinear polaritonics [8].

Acknowledgement. The work of A.A.A., C.H. and A.T. is funded by the European Union* (EIC, OMICSENS, 101129734, ERC, METANEXT, 101078018). The work of M.V.G. is supported by the Russian Science Foundation (project 23-42-00091, https://rscf.ru/project/23-42-00091/). Y.K. acknowledges the support of the Australian Research Council (Grant No. DP210101292) and the International Technology Center Indo-Pacific (ITC IPAC) via the Army Research Office (contract FA520923C0023). *Views and opinions expressed are however those of the author(s) only and do not necessarily reflect those of the European Union or the European Research Council Executive Agency. Neither the European Union nor the granting authority can be held responsible for them.

References

1. Jiaxin Zhao et al., “Ultralow Threshold Polariton Condensate in a Monolayer Semiconductor Microcavity at Room Temperature”, Nano Lett., Vol. 21, № 7, 3331–3339, 2021.
2. F. Pisani et al., “Electronic transport driven by collective light-matter coupled states in a quantum device”, “Electronic transport driven by collective light-matter coupled states in a quantum device”, Nat. Commun., Vol. 14, 3914, 2023.
3. B. Munkhbat et al., “Suppression of photo-oxidation of organic chromophores by strong coupling to plasmonic nanoantennas”, Sci. Adv., Vol 4, 7, 2018.
4. E. Hendry et al., "Ultrasensitive detection and characterization of biomolecules using superchiral fields", Nat. Nanotechnol., Vol. 5, 11, 783-787, 2010.
5. H. Hübener et al., "Engineering quantum materials with chiral optical cavities", Nat. Mat. 20(4), 438-442, 2021.
6. L. Kühner et al., “Unlocking the out-of-plane dimension for photonic bound states in the continuum to achieve maximum optical chirality”, Light Sci. Appl, 12, 250, 2023.
7. E. U. Condon., “Theories of Optical Rotatory Power”, Rev. Mod. Phys. 9, 432, 1937.
8. C. Heimig et al., “Chiral nonlinear polaritonics with van der Waals metasurfaces”, arXiv:2410.18760, 2024.

META 2025, MALAGA - SPAIN, JULY 22 – 25, 2025

Fluctuation-Driven Phenomena in Chiral and Indefinite-Gain Systems

Daigo Oue[1,2] **Mário G. Silveirinha**[1*]

[1] Instituto Superior Técnico-University of Lisbon and Instituto de Telecomunicacações, Lisbon 1049-001, Portugal

[2]RIKEN Center for Advanced Photonics, Saitama 351-0198, Japan

Abstract: We explore fluctuation-induced effects in indefinite-gain systems, where gain and dissipation depend on the polarization or momentum of the wave. We examine their impact on optical forces, quantum friction, and energy flow in steady-state regimes. Additionally, we analyze how quantum fluctuations in such media modify a qubit's ground state, revealing new opportunities for nonreciprocal quantum engineering.

Over the past decade, there has been significant interest in nonreciprocal effects in quantum systems. Nonreciprocity can be achieved through various means, such as preparing the system in a chiral quantum state, utilizing nonlinearities, or using an external magnetic field. When a quantum system is prepared in a state that favors specific circularly polarized (chiral) optical transitions, it exhibits remarkable directional properties [1].

Recently, we investigated the light-matter interactions between an atom with Kramers degeneracy and a reciprocal environment in the absence of any external bias [2]. Our analysis showed that the combined influence of the electron's intrinsic spin magnetic moment and the chiral atomic dipolar transitions could lead to the spontaneous breaking of time-reversal symmetry or the emergence of time-crystal-like states, characterized by notably long relaxation times. These findings present a compelling opportunity to engineer nonreciprocal responses at the nanoscale, driven solely by quantum vacuum fluctuations.

In this talk, we will discuss how material gain can foster more robust nonreciprocal interactions. Specifically, we extend our analysis to environments exhibiting "chiral gain" [3-6]. Such environments can be realized in electrically-biased two-dimensional materials with broken inversion symmetry and significant Berry curvature dipole. It has been demonstrated that these systems facilitate non-Hermitian responses, with the gain dependent on the polarization handedness [3-6].

We will examine various fluctuation-induced effects in systems with chiral gain and, more broadly, in indefinite-gain systems. These systems can be characterized by either gain or dissipative interactions, typically governed by wave polarization [3-6] or wave momentum [7-8]. Our discussion will focus on how indefinite gain can be leveraged to tailor optical forces, induce quantum friction and optical instabilities, and control the flow of fluctuation-induced energy in a steady-state regime. Additionally, we will analyze the interaction between a qubit and a chiral-gain medium, demonstrating that it can give rise to unique nonreciprocal responses. These results underscore the vast potential of chiral gain in manipulating quantum system behavior.

Acknowledgments: This work was partially funded by the Institution of Engineering and Technology (IET), by the Simons Foundation (Award 733700) and by FCT/MECI through national funds and when applicable cofunded EU funds under UID/50008: Instituto de Telecomunicações.

References

1. Lodahl, P., Mahmoodian, S., Stobbe, S., Rauschenbeutel, A., Schneeweiss, P., Volz, J., Pichler, H., and Zoller, P. "Chiral quantum optics," *Nature*, Vol. 541, No. 7638, 473–476, 2017.
2. Silveirinha, M. G., Terças, H., and Antezza, M. "Spontaneous symmetry breaking of time-reversal symmetry and time-crystal states in chiral atomic systems," *Phys. Rev. B*, Vol. 108, No. 23, 235154, 2023.
3. Rappoport, T. G., Morgado, T. A., Lannebère, S., and Silveirinha, M. G. "Engineering transistor-like optical gain in two-dimensional materials with Berry curvature dipoles," *Phys. Rev. Lett.*, Vol. 130, No. 7, 076901, 2023.
4. Lannebère, S., Fernandes, D. E., Morgado, T. A., and Silveirinha, M. G. "Chiral-gain photonics," *Laser Photonics Rev.*, Vol. 2400881, No. 1, 1–17, 2025.
5. Hakimi, A., Rouhi, K., Rappoport, T. G., Silveirinha, M. G., and Capolino, F. "Chiral terahertz lasing with Berry curvature dipoles," *Phys. Rev. Appl.*, Vol. 22, No. 4, L041003, 2024.
6. Morgado, T. A., Rappoport, T. G., Tsirkin, S. S., Lannebère, S., Souza, I., and Silveirinha, M. G. "Non-Hermitian linear electrooptic effect in 3D materials," *Phys. Rev. B*, Vol. 109, No. 24, 245126, 2024.
7. Oue, D., Shapiro, B., and Silveirinha, M. G. "Quantum friction near the instability threshold," *Phys. Rev. B*, Vol. 111, No. 7, 075403, 2025.
8. Oue, D., Pendry, J. B., and Silveirinha, M. G. "Stable-to-unstable transition in quantum friction," *Phys. Rev. Res.*, Vol. 6, No. 4, 043074, 2024.

Unified Dipolar Interactions in Bispinor Formalism and the Energy Symmetry Sphere

Sebastian Golat[1*], Alex J. Vernon[1], and Francisco J. Rodríguez-Fortuño[1]
[1]Department of Physics and London Centre for Nanotechnology,
King's College London, Strand, London WC2R 2LS, UK
[*]sebastian.1.golat@kcl.ac.uk (corresponding author)

Abstract

We present a unified bispinor framework that simplifies dipolar interaction expressions. Our approach leads to the concept of an energy symmetry sphere, which captures how broken parity and time-reversal symmetry give rise to chiroptical and magnetoelectric effects and offers new insights into light-matter interactions.

1 Bispinor Formalism and Dipolar Interactions

Conventionally, the electric field ($\boldsymbol{E}$) and magnetic field ($\boldsymbol{B}$) are treated as separate entities. Nonetheless, according to the theory of relativity, both fields must hold equal significance since an electric phenomenon perceived by one observer could manifest as a magnetic effect to another. This duality symmetry is fundamental to the form of Maxwell's equations in free space. It is only broken in the presence of matter: typically, the dynamics of the electric field are more strongly engaged with by atoms, molecules, and particles, and as a result, it is commonplace in optics to measure only electric quantities like energy, momentum, and angular momentum densities. However, light's more exotic mechanical capabilities and physical significance become obscured without considering the combined behaviour of electric and magnetic fields over space and their interaction with matter. By combining $\boldsymbol{E}$ and $\boldsymbol{B}$ into a single six-component bispinor,

$$\boldsymbol{\psi}(\boldsymbol{r}) = \frac{1}{2\sqrt{\mu_0}} \begin{pmatrix} \boldsymbol{E}(\boldsymbol{r})/c \\ \boldsymbol{B}(\boldsymbol{r}) \end{pmatrix}, \tag{1}$$

we recast the electromagnetic description into a compact form where both fields are treated on equal footing. This bispinor can be understood as a phasor representation of the electromagnetic field tensor up to the prefactor chosen such that the norm squared is the total energy density

$$W(\boldsymbol{r}) = \|\boldsymbol{\psi}\|^2 = \boldsymbol{\psi}^\dagger\boldsymbol{\psi} = \frac{1}{4}\left(\varepsilon_0|\boldsymbol{E}|^2 + |\boldsymbol{B}|^2/\mu_0\right) = W_\mathrm{e}(\boldsymbol{r}) + W_\mathrm{m}(\boldsymbol{r})\,. \tag{2}$$

Instead of considering eq. (1) to be a six-component complex vector ($\mathbb{C}^6$), we can consider it a complex two-component vector ($\mathbb{C}^2$) whose components are three-component vectors ($\mathbb{C}^3$) [1]. A key advantage of this interpretation of bispinor representation is its inherent basis flexibility in the $\mathbb{C}^2$ space. Since the $\mathbb{C}^2$ space is isomorphic to the space of Jones vectors that describe electric field polarisation in a plane wave, it has a very similar mathematical structure. We know that Jones vectors can be expressed not only in a horizontal/vertical basis but also in diagonal/antidiagonal and right/left-handed circular bases. In the case of bispinor, the standard electromagnetic (EM) basis plays the role of horizontal/vertical basis, and we can define alternative bases—such as the parallel–antiparallel (PA) and right–left-handed (RL) bases—which are analogous to the diagonal and circular bases for Jones vectors.

2 The Energy Symmetry Sphere

For Jones vectors, we can define Stokes parameters that describe the polarisation, where S_0 is the sum of squares of the two components in any basis while S_1, S_2, S_3 are their differences in each of the three bases. Any polarisation state can then be mapped to a point (S_1, S_2, S_3) which lies on or inside of the Poincaré sphere of radius S_0. Similarly, for the bispinor the total energy density $W_0 = W_\mathrm{e} + W_\mathrm{m} = W_\mathrm{p} + W_\mathrm{a} = W_\mathrm{R} + W_\mathrm{L}$ (eq. (2)) plays the role of S_0 and then the remaining parameters are analogous to $W_1 = W_\mathrm{e} \in W_\mathrm{m}$ (associated with the reactive power), $W_2 = W_\mathrm{a} \in W_\mathrm{p}$ (linked to the concept of reactive helicity density or magnetoelectric energy), and $W_3 = W_\mathrm{R} \in W_\mathrm{L}$ (proportional to the helicity density) which correspond to energy imbalances in the EM, PA, and RL bases. Any field can then be mapped to a point (W_1, W_2, W_3) which has to be inside the *energy symmetry sphere*. Much like the Poincaré or Bloch sphere visualises polarisation states, the energy symmetry sphere provides a geometric representation of how energy is distributed among various symmetry channels.

Crucially, the coordinates (W_1, W_2, W_3) transform characteristically under symmetry operations. Under parity inversion, components associated with mirror asymmetry (W_2 and W_3) change sign, while time reversal distinctly changes sign of only W_2. The discreet duality transformation changes the sign of reactive quantities (W_1 and W_2), which are only nonzero for non-paraxial light. For symmetric fields such as linearly polarized plane waves, the energy point lies at the centre of the sphere. In contrast, fields exhibiting broken symmetry—whether due to breaking parity, duality, or time-reversal symmetry—result in an off-centre displacement. This displacement can be directly linked to the emergence of chiral, magnetic and magnetoelectric interactions. For example, one can use the bispinor formalism to show that the power absorbed (or similarly scattered and extinguished) by an electromagnetic dipole can be written in terms of the absorption (scattering/extinction) cross-section σ_0 and its asymmetries (σ_1, σ_2, σ_3)—which form their own symmetry sphere—as a simple sum of four terms

$$P = \underbrace{\sigma_0 c W_0}_{\text{active}} + \underbrace{\sigma_1 c W_1}_{\text{reactive}} + \overbrace{\underbrace{\sigma_2 c W_2}_{\text{reactive}} + \underbrace{\sigma_3 c W_3}_{\text{active}}}^{\text{chiral}}, \tag{3}$$

where the first term is well-known as it is the only term that will appear even if no symmetries are broken. The remaining three terms can only appear if both the field and the particle break corresponding symmetries (parity for chiral terms and duality for reactive terms). Similar simplification can be shown for the dipolar force [2] and for the torque by introducing asymmetries in other quantities, such as momentum and angular momentum densities.

3 Acknowledgements

SG and FJRF acknowledge support from EIC-Pathfinder-CHIRALFORCE (101046961) which is funded by Innovate UK Horizon Europe Guarantee (UKRI project 10045438). AJV is supported by EPSRC Grant EP/R513064/1.

References

[1] Sebastian Golat, Alex J. Vernon, and Francisco J. Rodríguez-Fortuño. *The electromagnetic symmetry sphere: a framework for energy, momentum, spin and other electromagnetic quantities*. 2024. arXiv: 2405.15718 [physics.optics].

[2] Sebastian Golat et al. "Optical dipolar chiral sorting forces and their manifestation in evanescent waves and nanofibers". In: *Phys. Rev. Res.* 6.2 (Apr. 2024), p. 023079. ISSN: 2643-1564. DOI: 10.1103/PhysRevResearch.6.023079.

Topological and geometric effects in magnetic nanowires

Oleksandr V. Pylypovskyi[1,2]
[1]Helmholtz-Zentrum Dresden-Rossendorf e.V.,
Institute of Ion Beam Physics and Materials Research, 01328 Dresden, Germany
[2]Kyiv Academic University, Kyiv 03142, Ukraine
Corresponding author: o.pylypovskyi@hzdr.de

Abstract: We analyze the relation between the magnetic state in low-dimensional curvilinear magnets and global characteristics of geometry, such as topology and knotting. It is shown that (i) ferromagnetic wireframes support the topologically-protected high-order negative vorticity states, and (ii) sharp knots in antiferromagnetic spin chains allow tailoring signatures of geometric frustration.

Vector fields defined on a particular manifold necessarily acquire intrinsic characteristics of the manifold, related to its topology [1]. In the particular case of magnetism, the diversity of magnetic responses driven by geometry and distinction from other types of ordered media like nematic crystals is given by the finite out-of-surface component of the order parameter (magnetization m or Néel vector n). Namely, the local values of anisotropy and Dzyaloshinskii–Moriya interaction (DMI) are changed, which leads to the modification of the topologically non-trivial textures like domain walls or skyrmions and their pinning [2, 3]. Still, the relation between the magnetic state and global characteristics of the geometry is under exploration.

Here, we consider magnetic states in 3D nanowires. On the mesoscopic scale, 3D magnetic systems can be designed via additive nanotechologies like focused electron beam deposition (FEBID). Surfaces of magnetically soft ferromagnetic wireframes with segment's diameters of several hundredths of nanometers can be considered as compact manifolds hosting merons (vortices and antivortices). The total vorticity of the manifold allowed by its topology is determined by the Euler characteristic, counting the minimal number of closed cycles formed in the wireframe. While the local geometric shape of the wireframe favors formation of either vortex or antivortex with opposite vorticities, any wireframe homeomorphic to a sphere contains two more vortices than antivortices. Wireframes homeomorphic to N-toruses with $N > 1$ may host the only antivortices being the special case of the geometry with tunable large negative vorticity of magnetic texture [4].

Small enough diameters of the nanowire do not allow the appearance of meron textures in favour of domain walls. There are intensive studies of such effectively 1D systems for plane geometries and high-symmetry space curves like helices with the constant curvature and torsion [5], while lower symmetries haven't been systematically studied with the same details yet. In addition, ultrathin nanowires open a possibility to consider antiferromagnetic systems, where, unlike ferromagnets, the dipolar interaction leads to the hard-axis anisotropy. An exemplary closed curve of a constant torsion (spherical epicycle) can be obtained by the Bäcklund transformation of a spherical curve with M knots [6]. The resulting spin chain possesses the same M-fold symmetry axis of the M-knotted spherical curve, and, as such, its curvature is periodically distributed along the chain. The important signature of this geometry is that the curvature is strongly inhomgeneously distributed along the curve, with sharp peaks near the knots and with almost zero value within the epicycle's segments.

In addition to geometry itself, antiferromagnetic spin chains built along closed space curves provide an additional degree of freedom in the total number of spins because of the presence (absence) of pure geometric frustration for the case of even (odd) spins along the curve. The geometry-driven DMI together with the dominating hard-axis anisotropy lead to the rotation of n by 180° on each segment of the epicycle. For the 4-fold epicycle with an even number of spins, the segment's state fits the periodic boundary conditions on n. This is not the case of the 3-fold epicycle, where fitting of the boundary conditions leads to the dominating weak geometry-induced easy-anisotropy over DMI in one of the segments. These characteristic signatures of the global states in 4- and 3-fold epicycles are opposite in the case of the spin chain with the odd number of spins, where the boundary conditions on n are antiperiodic. The latter opens a possibility to tailor the signature of geometric frustration in antiferromagnetic systems by geometric features [7].

References

1. Turner, A. M., Vitelli, V. and Nelson, D. R. "Vortices on curved surfaces," *Rev. Mod. Phys.* Vol. 82, pp. 1301 2010.

2. Makarov, D., Volkov, O. M., Kákay, A., et al. "New dimension in magnetism and superconductivity: 3D and curvilinear nanoarchitectures," *Adv. Mater.*, Vol. 34, p. 2101758, 2022; Gentile, P., Cuoco, M., Volkov, O. M., et al. "Electronic materials with nanoscale curved geometries," *Nat. Electron.*, Vol. 5, pp. 551-563, 2022; Raftrey, D., Hierro-Rodriguez, A., Fernandez-Pacheco, A., and Fischer, P. "The road to 3-dim nanomagnetism: Steep curves and architectured crosswalks,", *J. Magn. Magn. Mater.*, Vol. 563, p. 169899, 2022.

3. "Curvilinear Micromagnetism, " Ed. by D. Makarov and D. D. Sheka, Springer International Publishing, 2022.

4. Volkov, O. M., Pylypovskyi, O. V., Porrati, F., et al. "Three-dimensional magnetic nanotextures with high-order vorticity in soft magnetic wireframes," *Nat. Commun.*, Vol. 15, p. 2193, 2024.

5. Sheka, D. D., Pylypovskyi, O. V., Volkov, O. M., et al., "Fundamentals of Curvilinear Ferromagnetism: Statics and Dynamics of Geometrically Curved Wires and Narrow Ribbons," *SMALL*, Vol. 18, p. 2105219, 2022.

6. Bates, L. M. and Melko, O. M., "On curves of constant torsion I," *J. of Geom.*, Vol. 104, p. 213, 2013.

7. Pylypovskyi, O. V., Di Benedetto, E., Ortix, C. and Makarov, D. "Manipulation by magnetic frustration in ferrotoroidal spin chains via curvature and torsion, " *Phys. Rev. Research*, Vol. 7, p. 013088, 2025.

Terahertz pulse shaping and chirality control using magnetic heterostructures

Weipeng Wu[1], Wilder Acuna[2], Zhixiang Huang[2], Xi Wang[2], Lars Gundlach[1,3], Matthew F. Doty[2], Joshua M. O. Zide[2], and M. Benjamin Jungfleisch[1,*]

[1]Department of Physics and Astronomy, University of Delaware, Newark, Delaware 19716, USA
[2]Department of Materials Science and Engineering, University of Delaware, Newark, Delaware 19716, USA
[3]Department of Chemistry and Biochemistry, University of Delaware, Newark, Delaware 19716, USA

[*]mbj@udel.edu

Abstract: We demonstrate a hybrid THz source with pulse shaping capability and chirality control of the emitted radiation without external components. This hybrid THz source integrates a spintronic emitter and a semiconductor photoconductive antenna into one single device in which each of the two emitters respond independently to external parameters.

Terahertz (THz) radiation, spanning from 0.3 - 30 THz, fills the crucial gap between the microwave and infrared spectral range. THz technology has applications in various fields, from imaging and sensing to telecommunication and biosensing. However, the full potential of these applications is often hindered by the need for precise control and manipulation of the frequency and polarization state, which typically requires external THz modulators [1].

Here, we demonstrate a hybrid THz source that overcomes this limitation by integrating two THz emitters into a single device to enable pulse shaping and chirality control of the emitted radiation without external components [2], see Figure. The two sources are a spintronic emitter (SE) [3] and a semiconductor photoconductive antenna (PCA) [4]. The two emitters respond independently to external parameters: the PCA is controlled by the applied bias voltage, while the SE is controlled by the applied magnetic field or the internal magnetic field distribution [5,6]. Moreover, a dual-wavelength excitation scheme at 780 nm and 1560 nm allows for control of the relative time delay between the THz emission from each constituent. These properties of the hybrid emitter enable precise control of the mixing of the two signals to control the frequency, polarization, and chirality of the overall THz radiation. This on-chip hybrid emitter thus provides a powerful platform for engineered THz radiation with wide-ranging potential applications.

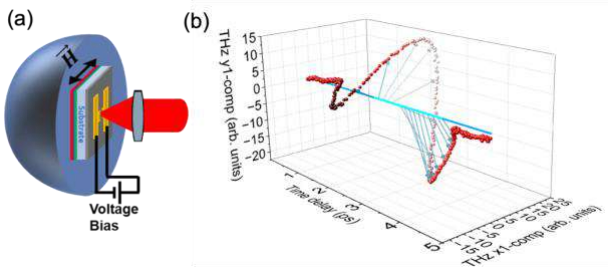


Figure: (a) Schematic diagram of the hybrid emitter integrating a PCA with a SE into a single device. (b) Representative THz waveforms with left-handed elliptical polarization. Adapted from Ref. [2].

This research was supported by NSF through the University of Delaware Materials Research Science and Engineering Center, DMR-2011824.

References

1. Z. Huang, W. Wu, E. Herrmann, K. Ma, Z. A. Chase, T. A. Searles, M. B. Jungfleisch, and X. Wang, Front. Optoelectron.

17, 13 (2024).

2. W. Wu, W. Acuna, Z. Huang, X. Wang, L. Gundlach, M. F. Doty, J. M. O. Zide, and M. B. Jungfleisch, Adv. Opt. Mater. 2402374 (2024).
3. W. Wu, C. Y. Ameyaw, M. F. Doty, and M. B. Jungfleisch, J. Appl. Phys. **130**, 091101 (2021).
4. W. Acuna, W. Wu, J. Bork, M. F. Doty, M. B. Jungfleisch, L. Gundlach, and J. M. O. Zide, Adv. Funct. Mater. 2401853 (2024).
5. W. Wu, S. Lendinez, M. T. Kaffash, R. D. Schaller, H. Wen, and M. B. Jungfleisch, J. Appl. Phys. **128**, 103902 (2020).
6. W. Wu, S. Lendinez, M. T. Kaffash, R. D. Schaller, H. Wen, and M. B. Jungfleisch, Appl. Phys. Lett. **121**, 052401 (2022).

Enantioselective molecular sensing by chiral gold helicoid nanoparticles

Jeong Hyun Han[1], and Ki Tae Nam[1*]

[1]Department of Materials Science and Engineering, Seoul National University, Seoul 08826, Republic of Korea
[*]corresponding author: nkitae@snu.ac.kr

Abstract: Colloidally synthesized chiral plasmonic gold nanoparticles, helicoids, offer enhanced and non-vanishing chiral light-matter interaction and thereby great potential for ultrasensitive enantioselective molecular sensing. We demonstrate experimental realization and relevant theory of spectroscopic molecular chirality detection based on circular dichroism and SERS from systematically integrated helicoids platform.

Considering the significance of molecular chirality in various fields including biochemistry, pharmacology, and diagnostics, the ability to accurately detect molecular chirality with ultrahigh sensitivity is of paramount importance. Spectroscopic detection based on the chiral light–matter interactions between circularly polarized light and molecules offers a non-destructive and highly precise approach. In particular, plasmonic metamaterials compress and enhance electromagnetic fields into deep-subwavelength scales, comparable to molecular dimensions, thereby selectively and significantly amplifying chiral interactions in localized nanoscale regions and magnifying the signal from molecular chirality. However, bulk spectroscopic detection from multiple molecules inevitably encounters signal cancellation due to the intrinsic dipolar nature of electromagnetic fields. The counteracting signals originating from oppositely handed local fields near the nanostructure lead to a net signal that, at the ensemble level, is much weaker than that obtainable from single molecules. In this context, helicoid nanoparticles with three-dimensional chiral morphology, synthesized via a seed-mediated colloidal method directed by chiral organothiols, is especially advantageous providing a nearly isotropic, highly chiroptical environment. Their high circular dichroism (g-value upto 0.3) and high symmetry of 432 enhance the chiral interaction between molecules and electromagnetic fields in a consistent handedness. We demonstrate the detection of chiral molecules using helicoid-based platforms in two distinct systems. First, by implanting helicoids in a two-dimensional periodic nanoholes, a photonic crystal is formed that exhibits large-area, strong, and uniform optical helicity density induced by collective resonances of helicoids. In this system, the resonant energy of the helicoid crystal is perturbed by chiral molecules in both its dielectric and chiral energy terms, enabling high-performance, multidimensional sensing that simultaneously captures information on both concentration and chirality via circular dichroism measurement. This approach supports multimodal sensing via transmission, reflection, and conjugation chemistry-based methods. Secondly, the grating-directed self-assembly of helicoids induces extraordinary optical helicity density within their nanogaps, which in turn selectively and dramatically enhances enantioselective molecular excitation. This enhancement facilitates the realization of an enantioselective surface-enhanced Raman scattering (SERS) system. We further envision that the wide synthetic tunability of nanoparticle properties (e.g., shape and size) paves the way for chiroptical molecular detection in a variety of optical systems beyond the two discussed.

References

1. Kim, R. M., Han, J. H., ..., Nam, K. T. “Chiral plasmonic sensing: From the perspective of light–matter interaction,” The Journal of Chemical Physics, Vol. 160, No. 6, 2024.

2. Kim, R. M., ..., Nam, K. T, “Enantioselective sensing by collective circular dichroism,” Nature, Vol. 612, No. 7940, 470-476, 2022.
3. Skvortsova, A., Han, J. H., ..., Nam, K. T., Lyutakov, O., “Enantioselective Molecular Detection by Surface Enhanced Raman Scattering at Chiral Gold Helicoids on Grating Surfaces,” ACS Applied Materials & Interfaces, Vol. 16, No. 36, 48526–48535, 2024.

Dynamics of softened spin waves in thin films with perpendicular anisotropy at temporal interfaces

K. Sobucki[1], N. Leśniewski[2,1], and P. Gruszecki[1*]

[1] ISIQ, Adam Mickiewicz University in Poznań
[2] CNRS, Lab-STICC, UMR 6285, ENIB, Brest, France
[*]corresponding author: gruszecki@amu.edu.pl

Abstract: Spin wave dynamics in thin ferromagnetic films with perpendicular anisotropy and Dzyaloshinskii-Moriya interaction is studied near the phase transition between uniform and stripe-domain phases. Micromagnetic simulations show spin-wave reflection, refraction, and amplification at temporal interfaces introduced by modulating the external magnetic field, offering a novel method for spin-wave control.

Spin waves are propagating precessional disturbances of magnetic moments in magnetic materials, offering promising applications in beyond-CMOS computing, including artificial neural networks [1]. However, efficient methods for spin-wave amplification and control remain critical for their full integration into devices. Time-varying media, along with phenomena such as time reflection and refraction, present new opportunities for magnonics in this regard [2,3].

The dynamics of spin waves and static magnetic configuration strictly result from the mutual competition between various energies present in magnetic systems. For instance, perpendicular Magnetic Anisotropy (PMA) in thin ferromagnetic films at low magnetic fields enables the formation of periodic stripe domain patterns, with well-defined periodicities down to 100 nm [4]. PMA not only modifies the magnetic texture but also significantly influences spin-wave dynamics [4, 5]. This effect arises both from the inhomogeneous magnetic configuration and the intrinsic impact of PMA on spin-wave precession, leading to surprising consequences. Using micromagnetic simulations [6], we show that the effect of PMA on dispersion is most pronounced at low fields near the phase transition to the stripe domain pattern. This leads to novel effects such as bi-reflection and negative reflection of an obliquely incident spin-wave beam at a uniform interface (see Figure. 1(b)) [5].

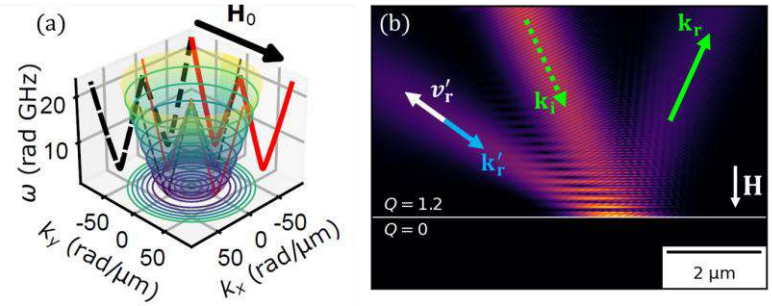


Figure 1. (a) Dispersion relation of spin waves in 2-nm-thick CoFeB film with reduced anisotropy constant Q=1.2. The system is uniformly magnetized by the in-plane applied bias magnetic field of value 220 mT. *(b)* Micromagnetic simulation of the reflection of an SW beam in a 2 nm CoFeB film, incident at a *25°* angle on an interface separating regions with different values of PMA defined a *Q*.

Another important interaction in magnetic systems is the Dzyaloshinskii-Moriya interaction (DMI), which prefers the chiral rotation of neighboring magnetic moments. This causes the dispersion relation in magnetic layers with DMI to be nonreciprocal (different wavelengths for opposite propagation directions). In the next part of the paper, we consider an ultrathin ferromagnetic film with PMA and DMI and we exploit the connection between magnetic texture for fields below the critical field and softened spin wave modes in a uniformly magnetized system, leading to spin wave

freezing[7]. We show how temporal modulations of the magnetic field influence spin-wave propagation near the critical bias field, where a phase transition occurs between high-symmetry (uniform in-plane magnetization) and low-symmetry (aligned stripe domains) phases [7]. Micromagnetic simulations demonstrate phenomena such as spin-wave reflection and refraction at temporal interfaces. Notably, the temporal profile of the bias field modulates time refraction and reflection, leading to spin-wave amplification (Fig. 2). These findings present a practical and easily implementable method for controlling spin waves using external magnetic fields, which can be adjusted via coplanar antennas.

Acknowledgements: The research leading to these results has received funding from the National Science Centre of Poland, projects no. PRELUDIUM 2022/45/N/ST3/01844, and SONATA-15 2019/35/D/ST3/03729

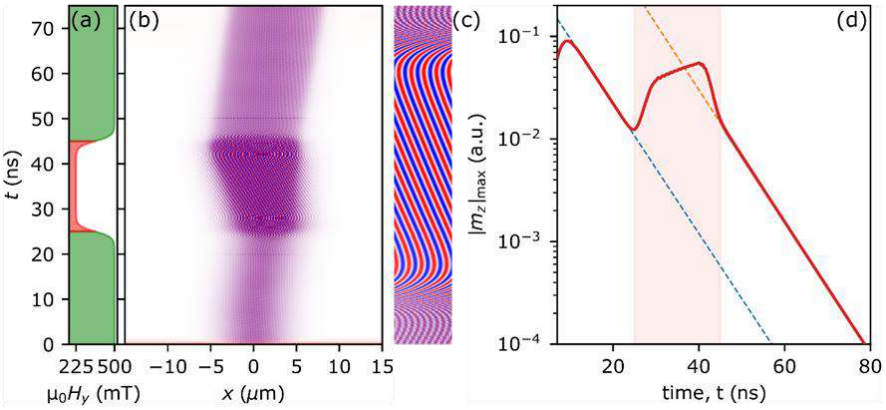


Figure 2. (a) Time dependence of the spatially uniform bias magnetic field value. (b) Space- and time-dependence of the out-of-plane component of magnetization (m_z). (c) Enlarged region in (b) showing the space and time dependence of m_z as the bias field changes are introduced. (d) maximal value of m_z magnitude as a function of simulation time with the time of lowered external magnetic field indicated with red area in the plot. The blue dashed line in (b) indicates calculated decrease of excited SW wavepacket amplitude in time without lowering of the external magnetic field. In the simulated case lowering of the magnetic field causes amplification of spin waves amplitude by the factor of 20, indicated with a green arrow.

References

1. Chumak, A. et al., “Advances in Magnetics Roadmap on Spin-Wave Computing,” IEEE Trans. Magn., Vol. 58, 1-72, 2022.
2. Toedt, Jan-Niklas, and Wolfgang Hansen. "Dynamic control of spin-wave propagation." Scientific Reports, Vol. 11, 7821, 2021.
3. Schultheiss, K., et al. "Time refraction of spin waves." Phys. Rev. Lett., Vol. 126,137201, 2021.
4. Banerjee, C., et al. “Magnonic band structure in a Co/Pd stripe domain system investigated by Brillouin light scattering and micromagnetic simulations,” Phys. Rev. B, Vol. 96, 024421, 2017.
5. Leśniewski, N., et al. “Softened Spin Waves in Films with Perpendicular Magnetic Anisotropy: Sombrero-Like Dispersion, Negative Reflection, Bi-, and Trireflection”, arXiv:2502.10085 (2025)
6. Vansteenkiste, A., et al. "The design and verification of MuMax3." AIP advances 4.10 (2014).
7. Kisielewski, J, et al. "Between waves and patterns: Spin wave freezing in films with Dzyaloshinskii-Moriya interaction." Phys. Rev. B, Vol. 107, 134416, 2023.

A Multiscale Approach to Molecular Nanoplasmonics: From SERS to Chiroptical Spectroscopies

T. Giovannini[1]

[1]Department of Physics, University of Rome Tor Vergata, Rome, Italy

[*]corresponding author: tommaso.giovannini@uniroma2.it

Abstract: We present a multiscale approach combining a fully atomistic approach to nanoplasmonics and quantum mechanics to model plasmon-enhanced spectroscopies, from SERS to chiroptical response.

The interaction between molecular systems and plasmonic substrates, such as noble metal nanoparticles and graphene, leads to peculiar electromagnetic responses. Among them, Surface-Enhanced Raman Scattering (SERS) has emerged as a widely used analytical technique that exploits the large enhancement of the Raman signal when a target molecule is adsorbed on metallic nanostructures [1]. This enhancement can reach factors up to 10^{10}, even enabling single-molecule detection [1].

In this contribution, we present a novel theoretical framework for surface-enhanced spectroscopies, extending our previous fully atomistic classical electromagnetic models [2-5] to describe the plasmon-mediated chiroptical response [6]. Specifically, we introduce a new methodology for describing Surface-Enhanced Raman Optical Activity (SEROA), which is the chiral analog of Raman signal. Such a mixed electric/magnetic/vibrational spectroscopy provides key insights into chiral molecular responses as modulated by plasmonic environments. Our multiscale method couples an atomistic electrodynamics treatment of the plasmonic nanostructure with a quantum mechanical (QM) description of the adsorbed molecular system. This hybrid integrated strategy is capable of describing metallic nanoparticles [2,3,5] and graphene-based materials [4,7] at the same level of accuracy.

The method is highly scalable, allowing large-scale nanoplasmonic simulations involving more than one million atoms, while also capturing critical quantum effects, such as subnanometer plasmonic junctions [2,5] and geometrical defects [7,8]. The robustness of our approach is demonstrated through selected test cases, including SERS and SEROA spectra [6,9].

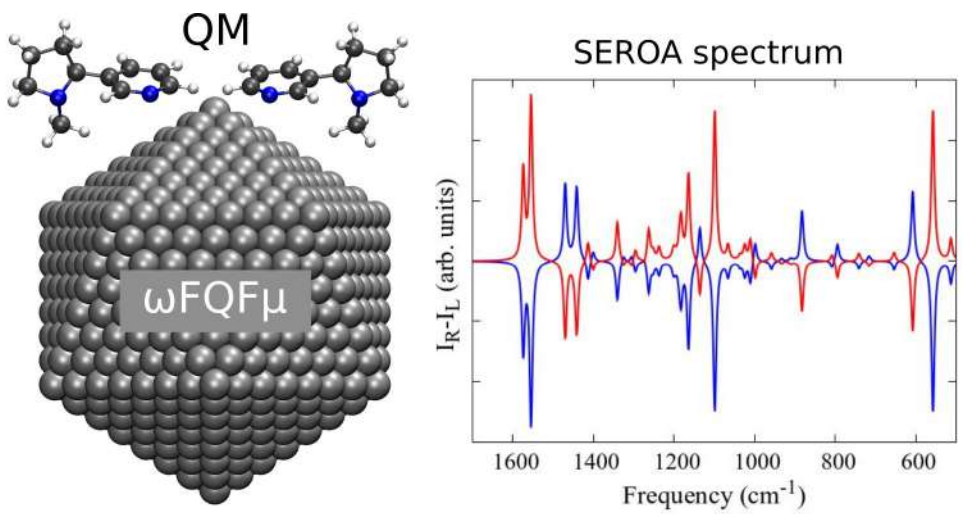


Fig. 1 Graphical depiction of (S)- and (R)-nicotine adsorbed on a silver icosahedral nanoparticle (left) and the corresponding calculated chiroptical Surface Enhanced Raman Optical Activity (SEROA) spectrum (right).

References

1. Langer, J. et al. "Present and future of surface-enhanced Raman scattering", ACS Nano, Vol. 14, 28–117, 2019.
2. Giovannini, T., M. Rosa, S. Corni and C. Cappelli, "A classical picture of subnanometer junctions: an atomistic Drude approach to nanoplasmonics", Nanoscale, Vol. 11, 6004–6015, 2019.
3. Bonatti, L., G. Gil, T. Giovannini, S. Corni and C. Cappelli, "Plasmonic resonances of metal nanoparticles: Atomistic vs. continuum approaches", Front. Chem., Vol. 8, 340, 2020.
4. Giovannini, T., L. Bonatti, M. Polini and C. Cappelli, "Graphene plasmonics: Fully atomistic approach for realistic structures", J. Phys. Chem. Lett., Vol. 11, 7595–7602, 2020.
5. Giovannini, T., L. Bonatti, P. Lafiosca, L. Nicoli, M. Castagnola, P. Grobas Illobre, S. Corni and C. Cappelli, "Do we really need quantum mechanics to describe plasmonic properties of metal nanostructures?", ACS Photonics, Vol. 9, 3025–3034, 2022.
6. Grobas Illobre, P., T. Giovannini, and C. Cappelli, in preparation.
7. Bonatti, L., L. Nicoli, T. Giovannini and C. Cappelli, "In silico design of graphene plasmonic hot-spots", Nanoscale Adv., Vol. 4, 2294–2302, 2022.
8. Zanotto, S., L. Bonatti, M. F. Pantano, V. Miseikis, G. Speranza, T. Giovannini, C. Coletti, C. Cappelli, A. Tredicucci and A. Toncelli, "Strain-Induced Plasmon Confinement in Polycrystalline Graphene", ACS Photonics, Vol. 10, 394–400, 2023.
9. Lafiosca, P., L. Nicoli, L. Bonatti, T. Giovannini, S. Corni and C. Cappelli, "QM/Classical Modeling of Surface Enhanced Raman Scattering Based on Atomistic Electromagnetic Models", J. Chem. Theory Comput. Vol. 19, 3616–3633, 2023.

Chiral modes in photonic integrated waveguides

I. Diez[1*], **D. Arenas-Ortega**[1], **J. Martínez-Romeu**[1] **and A. Martínez**[1]

[1]Nanophotonics Technology Center, Universitat Politècnica de Valencia, Camino de Vera, s/n Building 8F, 46022, Valencia, Spain

[*]corresponding author: iroddie@upv.edu.es

Abstract: A key requirement for chiral separation using integrated waveguides and chiral optical forces is the support of a guided chiral mode. We present an experimental method, based on analyzing the spectral response of Mach-Zehnder interferometers, to determine the optimal waveguide width that satisfies this requirement.

Enantiomeric separation, crucial in chemistry and pharmaceuticals, is traditionally performed using techniques like chiral High-Performance Liquid Chromatography. However, these methods are often slow, expensive, and molecule-specific. Optical chiral forces offer a compelling alternative, and while recent research has primarily focused on separating particles with free-space beams [1,2], utilizing guided light in integrated dielectric waveguides presents a promising new avenue. Apart from facilitating large-scale integration, this approach enhances chiroptical interactions, essential for sorting particles of small size and low chirality.

Our recent theoretical work has investigated the chiral forces exerted by guided optical modes on chiral nanoparticles, demonstrating the potential of silicon nitride waveguides for rapid enantiomeric separation within photonic integrated circuits operating at wavelengths of 1310 nm and 633 nm [3,4,5]. A particularly promising configuration leverages the differential chiral pressure force experienced by opposite enantiomers. This results in distinct propulsion speeds along the waveguide, leading to the enantiomeric longitudinal separation [5].

This separation method requires a quasi-circularly polarized mode within the waveguide, created by superimposing the quasi-TE_0 and the quasi-TM_0 modes with a $\pi/2$ phase difference. Crucially, these modes must share the same effective index to maintain the phase delay and prevent polarization oscillation, i.e. to preserve the helicity (or chirality) of the mode. This degeneracy of the TE and TM modes is achieved at a specific waveguide width (given a fixed wafer layer thickness) [5].

In this work, we present an experimental method for determining the effective indices of the quasi-TE_0 and quasi-TM_0 waveguide modes. We fabricated an array of integrated asymmetric Mach-Zehnder Interferometers with varying waveguide widths. Analyzing their transmitted optical power across a spectral range allowed us to calculate the effective indices and pinpoint the waveguide width at which degeneracy occurs.

The authors acknowledge funding from the European Commission under the CHIRALFORCE Pathfinder project (grant no. 101046961).

References

1. Tkachenko, G.; Brasselet, E. *Nat. Commun., 5*, 1– 7, **2014.**
2. Zhang T.; Mahdy, M. R. C.; Liu Y.; Teng, J. H. Lim C. T.; Wang, Z. and Qiu C-W. ACS Nano, 11, 4, 4292–4300, **2017**
3. S. Golat, J.J. Kingsley-Smith, I. Diez, J. Martinez-Romeu, A. Martínez, F.J. Rodríguez-Fortuño, Phys. Rev. Res. 6,

023079, **2024.**

4. J Martínez-Romeu, I Diez, S Golat, FJ Rodríguez-Fortuño, A Martínez. Photonics Research 12 (3), 431-443, **2024.**
5. J Martínez-Romeu, I Diez, S Golat, FJ Rodríguez-Fortuño, A Martínez. Nanophotonics 13 (23), 4275-4289, **2024**

Magneto nanophotonics platform based on monocrystalline yttrium iron garnets

Y. Ota[1*], S. Gao[1], K. Taniguchi[1], T. Yambe[1] Y. Tanimura[1] and S. Iwamoto[2]

[1]Department of Applied Physics and Physico-Informatics, Keio University, Japan
[2]Research Center for Advanced Science and Technology, The University of Tokyo, Japan
[*]corresponding author: ota@appi.keio.ac.jp

Abstract: Monocrystalline yttrium iron garnets (YIGs) are an outstanding material for magneto-optics. However, their application to nanophotonics has been limited due to the difficulty of fine nanopatterning. Here, we report a platform of magneto-nanophotonics based on YIG realized by the development of high-quality YIG membranes and their nanopatterning using dry etching.

Magneto optical (MO) effects are essential to break the reciprocity of light traveling through an unmodulated transparent optical structure with a linear response, which is vital to realize handy nonreciprocal photonic devices. In general, MO responses in any natural materials are weak in the optical regime and hence the devices tend to be bulky, hindering many applications in particular in integrated photonics. To enhance MO effects, optical confinement is promising as it effectively increases MO interactions. In this context, high quality photonic structures based on high quality MO materials will be a key development to realize compact but functional MO devices. In the telecom band wavelengths at room temperature, the choice of transparent MO material is not many and is virtually limited to the family of yttrium iron garnets (YIGs) in particular in the form of monocrystal. However, there has been no monocrystalline YIG thin film detachable from the mother substrate and furthermore the nanopatterning of YIG is notoriously difficult due to e.g. the chemical inactivity of the material. These obvious obstacles have hampered the progress of YIG-based magneto nanophotonics in the telecom wavelength band.

In this contribution, we report our effort to develop a magneto nanophotonics platform based on monocrystalline YIG. We are developing YIG thin films on glass using a bonding-and-grinding approach. The large refractive index difference between YIG and glass will enable tight light confinement in the YIG layer, facilitating the design of high confinement photonic structures. Furthermore, the glass layer can be selectively etched out to form a freestanding YIG membrane, which will provide an extra refractive index difference between YIG and the cladding material. We are also working on nanopatterning of YIG using dry etching. Perforating airholes in the YIG membranes with diameters of a few hundreds will be required to realize photonic crystals and metasurfaces operating in the telecom wavelength bands. The key requirements will be the faithful patterning of the designed structures and the realization of vertical etched sidewalls. Such a technology for fine nanopatterning of the monocrystalline YIG thin films will entail a variety of magneto nanophotonic devices including MO metasurfaces for giant Faraday rotation[1], hybrid metasurfaces[2] and nonreciprocal slow light waveguides based on the bound states in the continuum[3]. Figure 1 illustrates how the development of the YIG-based nanophotonic platform will lead to the realization of various magneto nanophotonic devices. Such a platform will also advance magnonics since YIG is also known as one of the best magnetic materials with the lowest magnon damping.

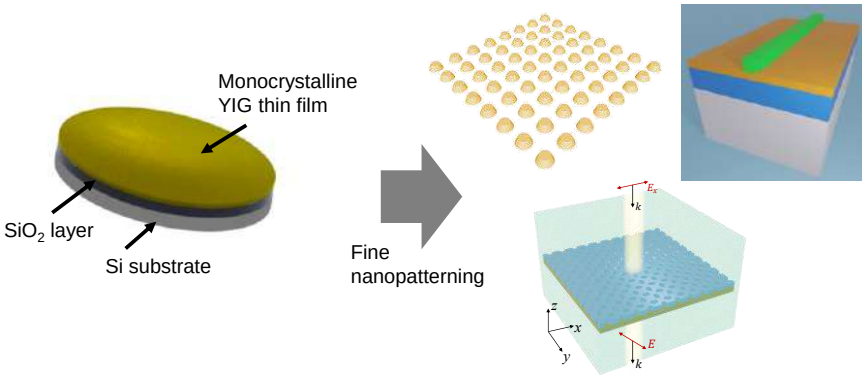


Figure 1. High quality monocrystalline YIG thin films will lead to a variety of magneto nanophotonic devices

Acknowledgements: We thank T. Liu, F. Tian, S. Ishida, H. Matsukiyo, H. Otsuki, and D. Sato for their technical support and fruitful discussions. This work was supported by KAKENHI (17H06138, 19K05300, 22H00298, 22H01994, 22K18989), JST CREST(JPMJCR19T1), JST FOREST Program (JPMJFR213F), Nippon Sheet Glass Foundation.

References

1. Gao, S., Ota, Y., Tian, F., Liu, T. & Iwamoto, S. Optimizing the optical and magneto-optical response of all-dielectric metasurfaces with tilted side walls. *Opt. Express* **31**, 13672–13682 (2023).

2. Gao, S., Ota, Y., Liu, T., Tian, F. & Iwamoto, S. Faraday rotator based on a silicon photonic crystal slab on a bismuth-substituted yttrium iron garnet thin film. *Appl. Phys. Express* **16**, 072003 (2023).

3. Tanimura, Y., Ota Y., *et al*., Slow Light Waveguides Based on Bound States in the Continuum, Opt. Lett. Accepted.

Microwave-to-Optical Quantum Transduction Mediated by Antiferromagnetic Magnons in Antiferromagnets

Akihiko Sekine*, **Ryo Murakami, and Yoshiyasu Doi**
Fujitsu Research, Fujitsu Limited, Kawasaki 211-8588, Japan
akihiko.sekine@fujitsu.com (corresponding author)

Abstract

While earlier studies regarding the magnon-mediated quantum transduction have so far utilized ferromagnetic magnons in ferromagnets, here we formulate a theory for the microwave-to-optical quantum transduction mediated by antiferromagnetic magnons in antiferromagnets. We find that the quantum transduction can occur even in the absence of an external static magnetic field.

The quantum transduction, or equivalently quantum frequency conversion, between microwave and optical photons is a quantum technology that enables the interconnects between quantum devices such as quantum memories and quantum processors. It is also essential for realizing large-scale quantum computers with superconducting qubits. Due to the large frequency difference between microwave and optical ranges, the quantum transduction needs to be done via the interactions between photons and intermediate bosonic modes or via the nonlinear interaction between photons [1].

In this study, we focus on the quantum transduction mediated by magnons. Such a quantum transduction mediated by magnons can have a wide bandwidth and can be operated even at room temperature. While earlier studies have so far utilized ferromagnetic magnons in ferromagnets [2, 3], here we formulate a theory for the microwave-to-optical quantum transduction mediated by antiferromagnetic magnons in antiferromagnets. We derive analytical expressions for the transduction efficiency in the cases with and without an optical cavity (where a microwave cavity is used in both cases) [4]. In contrast to the case of ferromagnets, we find that the quantum transduction can occur even in the absence of an external static magnetic field. We also find that, in the case with an optical cavity, there exists an optimal value of the thickness d_{AFM} of the antiferromagnets at which the transduction efficiency takes a maximum value. This results from a competitive behavior between the microwave-magnon interaction $\propto \sqrt{d_{\mathrm{AFM}}}$ and the light-magnon interaction $\propto 1/\sqrt{d_{\mathrm{AFM}}}$. On the other hand, in the case without an optical cavity, the transduction efficiency is an monotonically increasing function of the thickness d_{AFM}, which comes from a cooperative behavior between the microwave-magnon interaction $\propto \sqrt{d_{\mathrm{AFM}}}$ and the light-magnon interaction $\propto d_{\mathrm{AFM}}$.

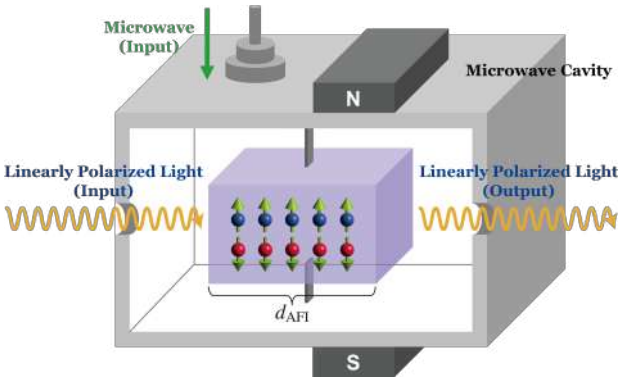


Figure 1: Schematic illustration of our experimental setup for the microwave-to-optical quantum transduction without an optical cavity.

References

[1] X. Han, W. Fu, C.-L. Zou, L. Jiang, and H. X. Tang, Optica **8**, 1050 (2021).

[2] R. Hisatomi, A. Osada, Y. Tabuchi, T. Ishikawa, A. Noguchi, R. Yamazaki, K. Usami, and Y. Nakamura, Phys. Rev. B **93**, 174427 (2016).

[3] N. Zhu, X. Zhang, X. Han, C.-L. Zou, C. Zhong, C.-H. Wang, L. Jiang, and H. X. Tang, Optica **7**, 1291 (2020).

[4] A. Sekine, R. Murakami, and Y. Doi, arXiv:2412.12907.

Excitations and light-matter interactions in polar topologies

S. Rijal, Y. Nahas[1], S. Prokhorenko[1*], and L. Bellaiche[2]

[1]Smart Ferroic Materials Center, Physics Department and Institute for Nanoscience and Engineering, University of Arkansas, Fayetteville, Arkansas, USA

[*]corresponding author: sprokhor@uark.edu

Abstract: Polar topological textures such as polar vortices, bubbles and skyrmions, are swirling patterns of electric polarization spontaneously emerging in ultra-thin ferroelectrics. Here, we explore lattice excitations giving rise to polar textures and novel phenomena entailed by non-linear interactions of such excitations with IR light in ultra-thin $Pb(Zr,Ti)O_3$ films.

Polar topological textures are swirling patterns of electric polarization that can spontaneously form in ultra-thin ferroelectrics due to strong depolarizing fields[1]. A prototypical example of polar topologies is given by the so-called vortex crystals[2]. These structures can be described as vortex tubes formed by local electric dipoles that are periodically arranged within the plane of an ultra-thin ferroelectric film such as $Pb(Zr_{0.4},Ti_{0.6})O_3$ (Fig. 1a). In some cases, polar vortex tubes are also known to develop spontaneous polarization along their axis rendering the structure chiral on the local scale[1] (Fig. 1b).

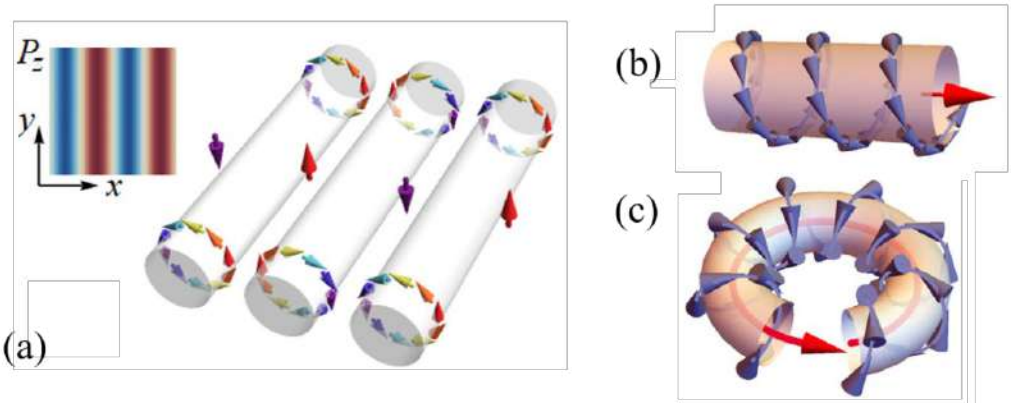


Figure 1. (a) Schematical structure of polar vortex crystals consisting of alternating clockwise/anti-clockwise vortex tubes formed by local electric dipoles and periodically arranged within the plane of an ultra-thin ferroelectric film. Inset shows the distribution of out-of-plane polarization in the mid-point horizontal cross-section of the film. (from Ref. 4) (b) Structure of a vhiral vortex tube with non-zero polarization component along the vortex tube axis. (from Ref. 5) (c) Structure of a chiral electric bubble obtained by closing a chiral vortex tube into a vortex ring. (from Ref. 5)

Here, we use first principles based effective Hamiltonian simulations to show that the formation of polar vortex patterns in ultra-thin $Pb(Zr_{0.4},Ti_{0.6})O_3$ is intrinsically linked to vortex-like lattice excitations that soften upon cooling[2] and, depending on external conditions, can give rise to ordered vortex crystals[2], glass-like vortex labyrinth[3] or arrays of electric bubbles[3,4] (Fig. 1c). By analyzing the calculated finite-temperature phonon dispersions and mode eigenvectors, we show that the vortex modes induce precession of local electric dipoles and discuss possible implications of such dynamics for magnetoelectric coupling. Additionally, we show that changing

PZT composition can lead to emergent chirality on the local scale and identify lattice excitation responsible for the transition from non-chiral (Fig. 1a) to locally chiral structures (Figs. 1b-c).

Finally, we will discuss non-linear interactions of the vortex modes in ultra-thin ferroelectrics and the dynamical phenomena it entails2. Based on the analysis of the effective Hamiltonian model and symmetry arguments, we show that the finite wave-vector vortex modes (γ) are non-linearly coupled to zone-center phonons (ϕ). The corresponding fourth-order interactions $\phi\,\gamma^3$ and $\phi^2\,\gamma^2$ induce non-trivial dynamical phenomena that can be used to operate e.g. resonant switching of the vortex tube orientation with far-infrared light.

Our results provide insight into the dynamics of the formation of polar topologies and open new routes for functionalizing ultrathin ferroelectrics.

This work is supported by the Vannevar Bush Faculty Fellowship (VBFF) Grant No. N00014-20-1–2834 from the Department of Defense and the MonArk NSF Quantum Foundry supported by the National Science Foundation Q-AMASE-i Program under NSF Award No. DMR-1906383.

References

1. Junquera, J., Nahas, Y., Prokhorenko, S., Bellaiche, L., Iniguez, J., Schlom, D. G., Chen, L.-Q., Salahuddin, S., Muller, D. A. *et al.,* "Topological phases in polar oxide nanostructures," Rev. Mod. Phys., Vol. 95, 025001, 2023.
2. Rijal, S., Nahas, Y., Prokhorenko, S. and Bellaiche, L. "Dynamics of Polar Vortex Crystallization," Phys. Rev. Lett., Vol. 133, 096801, 2024.
3. Nahas, Y., Prokhorenko, S., Zhang, Q., Govinden, V., Valanoor, N. and Bellaiche, L., "Topology and control of self-assembled domain patterns in low-dimensional ferroelectrics," Nat. Commun., Vol. 11, 5779, 2020.
4. Govinden, V., Rijal, S., Zhang, Q., Nahas, Y., Bellaiche, L., Valanoor, N. and Prokhorenko, S., "Stability of ferroelectric bubble domains," Phys. Rev. Materials, Vol. 7, L011401, 2023.
5. Govinden, V., Prokhorenko, S., Zhang, Q., Rijal, S., Nahas, Y., Bellaiche, L. and Valanoor, N., "Spherical ferroelectric solitons," Nat. Mater., Vol. 22, 553–561, 2023.

Quantum theory of polarization in inhomogeneous crystals and its relation to orbital magnetoelectric effect

Nobuhiro Arai[1], Yang Gao[2], Di Xiao[3,4], Shuichi Murakami[1,5,6*]

[1] Department of Physics, Institute of Science Tokyo, Tokyo 152-8551, Japan
[2] University of Science and Technology of China, Hefei, Anhui 230026, China
[3] Department of Materials Science & Engineering, University of Washington, Seattle WA 98915, USA
[4] Department of Physics, University of Washington, Seattle WA 98915, USA
[5] International Institute for Sustainability with Knotted Chiral Meta Matter (WPI-SKCM^2), Hiroshima University, Hiroshima 739-8526, Japan
[6] Department of Applied Physics, University of Tokyo, Tokyo 113-8656, Japan
[*] corresponding author: murakami@stat.phys.titech.ac.jp

Abstract: We derive a formula for the polarization in a crystal induced by a perturbation linear in the coordinates. We use the linear response theory, and found that there appears an additional correction term to the previous work on the semiclassical theory. We confirm this result in a model calculation.

In crystals with certain symmetries such as inversion or *PT* symmetries, the polarization is identically zero in the bulk. If we introduce some perturbation linear in the coordinates, the symmetry that prohibits polarization will be broken, and the polarization is expected to appear. In Refs. 1 and 2, this problem is studied by the semiclassical theory, and a polarization formula has been obtained for an arbitrary perturbation linear in the coordinates. This class of perturbations includes the uniform electric field and the uniform orbital magnetic field, and the results reproduce the known formulae for the dielectric constant and the magnetoelectric tensor.

In the present talk, we study this problem by the linear response theory. We add a general perturbation linear in the spatial coordinates to the system, and calculate the induced polarization[3]. To calculate the polarization, we need a special treatment; we first make the perturbation to have a wavenumber q and a frequency ω, and calculate the current response. By dividing the response by $q\omega$ and take the limits of q and ω going to zero, we obtain the formula for the polarization[3]. The result is almost the same as that in the semiclassical theory[1,2], but we find an additional correction term to the polarization. We show the validity of our result by numerical calculation on a two-dimensional tight-binding model[3].

Y.G. acknowledges the support of the Fundamental Research Funds for the Central Universities, China (Grant No. WK2340000102). D.X. is supported by DOE Award No. DE-SC0012509. S. M is supported by JSPS KAKENHI Grant Numbers JP22K18687, JP22H00108 and JP24H02231, and by MEXT Initiative to Establish Next-generation Novel Integrated Circuits Centers (X-NICS) Grant Number JPJ011438.

References

1. Xiao, D., J. Shi, D. P. Clougherty, and Q. Niu, “Polarization and Adiabatic Pumping in Inhomogeneous Crystals”, Phys. Rev. Lett. 102, 087602 (2009).
2. Zhao, Y., Y. Gao, and D. Xiao, “Electric polarization in inhomogeneous crystals”, Phys. Rev. B 98, 060402(R) (2018).
3. Arai, N., Y. Gao, D. Xiao, and S. Murakami, in preparation (2025)

Optical response of periodic arrays of graphene nanostructures under static magnetic fields

J. R. Deop-Ruano[1*], M. H. Eriksen[2], J. J. Alvarez-Serrano[1], J. D. Cox[2,3], A. Manjavacas[1]

[1]Instituto de Química Física Blas Cabrera (IQF), CSIC, Spain
[2]POLIMA-Center for Polariton-driven Light–Matter Interactions, Denmark
[3]Danish Institute for Advanced Study, University of Southern Denmark

[*]corresponding author: juan.deop@csic.es

Abstract: We study the optical properties of periodic arrays of graphene nanostructures under static magnetic fields. We demonstrate the magnetic-field-controlled activation and deactivation of collective modes, offering new possibilities for tunable graphene-based photonic devices. Furthermore, our findings reveal magneto-optic phenomena such as chiral response and Faraday rotation.

Doped graphene nanostructures support electromagnetic resonances known as plasmons, which exhibit strong optical responses in the infrared and terahertz regimes [1]. When subjected to a static magnetic field, the conductivity tensor of graphene acquires a Hall component, leading to the emergence of magnetoplasmons—hybrid modes that retain the strong confinement and tunability of plasmons while introducing novel magneto-optic effects. These effects include nonreciprocal wave propagation, circular dichroism, and polarization rotation, making magnetoplasmons highly attractive for a plethora of applications.

To fully exploit the unique properties of graphene nanostructures, they are often arranged in periodic arrays. This approach has been leveraged to achieve giant Faraday rotation in metasurfaces composed of graphene ribbons under a static magnetic field [2]. Furthermore, periodic arrays of graphene disks can sustain collective modes driven by coherent interactions among their constituents [3]. Due to their collective nature, these resonances exhibit exceptionally high quality factors and a strong electric field enhancement across a significant area of the unit cell. However, previous studies on collective resonances have primarily focused on scenarios without an external magnetic field. The interplay between coherent interactions and magneto-optic effects remains unexplored and holds the potential to unlock new avenues to control light-matter interactions.

In this work, we investigate the optical properties of periodic graphene nanostructures subjected to static magnetic fields. We show that the external magnetic field provides a powerful means of modulating collective modes, effectively allowing for their selective activation and deactivation [4]. Moreover, we explore the magneto-optic phenomena induced by the magnetoplasmons, including perfect chiral absorption and perfect chiral emission [5]. These findings underscore the potential of graphene-based photonic systems for the active manipulation of the optical response and the development of tunable magneto-optic devices.

.

References

1. Yu R., Cox J. D., Saavedra J. R. M., García de Abajo F. J., “Analytical Modeling of Graphene Plasmons,” ACS Photonics, Vol. 4, No. 12, 3106–3114, 2017.
2. M. Tymchenko, A. Nikitin, Martin-Moreno L., “Faraday Rotation Due to Excitation of Magnetoplasmons in Graphene Microribbons,” ACS Nano, Vol. 7, No. 11, 9780–9787, 2013.
3. Deop-Ruano J. R., Sanders S., Alabastri A., Kort-Kamp W. J. M., Dalvit D. A. R., Manjavacas A.,“Optical Response of Periodic Arrays of Graphene Nanodisks,” Phys. Rev. Lett. Vol. 18, 044071, 2022
4. Deop-Ruano J. R., Eriksen M. H, Alvarez-Serrano J. J., Manjavacas A., and Cox J. D., “Magnetically activated collective modes in arrays of graphene nanostructures” In preparation, 2025
5. Eriksen M. H., Deop-Ruano J. R., Cox J. D., and Manjavacas A., “Chiral Light–Matter Interactions with Thermal Magnetoplasmons in Graphene Nanodisks” Nano Lett., Vol. 25, No. 1, 313–320, 2025.

Nonlinear response of truly chiral phonons: light-induced phonon angular momentum and Peltier effect

Hiroaki Ishizuka[1] **and Masahiro Sato**[2]
[1]Institute of Science Tokyo, Japan
[2]Chiba University, Japan
Corresponding author: ishizuka@phys.sci.isct.ac.jp

Abstract: The nonlinear response of chiral phonons to electromagnetic waves is theoretically studied. We show that chiral phonons give rise to large angular momentum compared to ordinary phonons. In addition, we show that the Peltier effect by chiral phonons occurs from a mechanism distinct from those proposed recently.

The chiral phonon is a phonon mode whose angular momentum and the wavenumber couple, $\mathbf{L}\cdot\mathbf{k}\neq 0$, where $\mathbf{L}$ is the crystal angular momentum and $\mathbf{k}$ is the phonon momentum, respectively. In centrosymmetric materials, these phonons appear in a pair of right-handed and left-handed modes, which are degenerate. In contrast, in chiral crystals [Fig. 1(a)], non-degenerate chiral phonons emerge, which are called truly chiral phonons; such phonon modes have recently been observed in α-HgS [1]. These truly chiral phonons are characterized by a non-zero group velocity at the symmetric points in the Brillouin zone, and hence, they may possess unique properties such as the efficient energy and angular momentum transport. However, the functionality arising from the truly chiral phonons has not been fully explored.

In this work, we theoretically studied the nonlinear responses of truly chiral phonons to electromagnetic waves. We consider a general phonon model whose Hamiltonian reads,

$$\hat{H}=\sum_{ia\mu}\frac{\hat{p}_{ia\mu}^2}{2m_a}+\frac{1}{2}\sum_{ia\mu,jb\nu}(\hat{u}_{ia\mu}-\hat{u}_{jb\mu})D_{ia\mu,jb\nu}(\hat{u}_{ia\nu}-\hat{u}_{jb\nu}), \tag{1}$$

where $D_{ia\mu,jb\nu}$ is the dynamical matrix, $\hat{u}_{ia\mu}$ is the displacement along the μ axis of $a\,(=1,2,3)$ sublattice atom in ith unit cell, and $p_{ia\mu}$ is the conjugate momentum of $\hat{u}_{ia\mu}$ satisfying $[\hat{u}_{ia\mu},\hat{p}_{jb\nu}]=\mathrm{i}\delta_{ij}\delta_{ab}\delta_{\mu\nu}$. The second-order nonlinear response of $\hat{H}$ to electromagnetic waves is studied using the nonlinear response theory [2, 3]. Using this theory, we show that a series of nonlinear responses reflects the unique properties of truly chiral phonons, such as phonon angular-momentum generation, the Peltier effect of phonons, and the photo-induced phonon orbital current. In addition, we consider a three-ion model of the chiral crystal in Fig. 1(a) as a demonstration.

Firstly, we studied the generation of angular momentum of phonons. We find that the angular momentum of the phonon is generated by both chiral and non-chiral phonons. However, a unique feature of chiral phonons is that there is a polarization-dependent contribution with τ^2 dependence on the lifetime of the phonon τ. This behavior is in contrast to the contribution of non-chiral phonons whose nonlinear conductivity increases as τ^1. This result implies that a significantly larger angular momentum may be induced by chiral phonons, especially in a clean system with a long phonon lifetime.

In addition to selectively exciting phonons, such as in the case of angular-momentum generation, recent theoretical studies pointed out that a nonlinear response of phonons can be

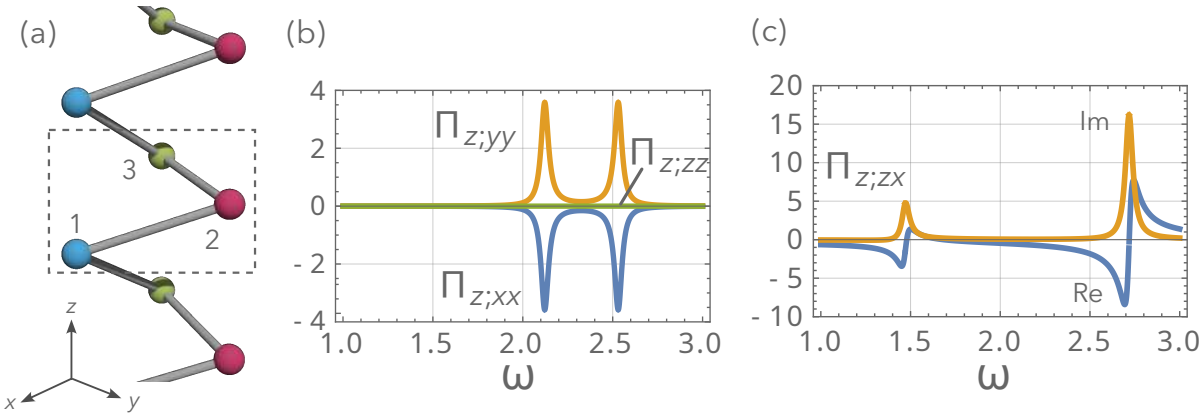


Figure 1: (a) A schematic of a chiral crystal with truly chiral phonon modes. The fequency dependence of nonlinear Peltier coefficient for (b) the linearly polarized electromagnetic wave and (c) circularily polarized electromagnetic wave. The results are for phonon current along the z axis.

used to control the flow of phonons and other charge-neutral excitations through a mechanism similar to the bulk photovoltaic effect [4–7]. One such phenomenon is the Peltier effect of phonons, in which a steady current of phonons is generated by the electromagnetic wave [2]. By analyzing the Peltier effect of chiral phonons, we find that, in addition to the shift-current-like effect studied in a previous work [2], the energy current of phonons occurs through a mechanism similar to the injection current. Moreover, for chiral phonons whose bands are doubly degenerate at $\mathbf{k} = \mathbf{0}$, we show that the phonon current is related to the asymmetric excitation of phonons with opposite angular momentum.

This work is supported by JSPS KAKENHI (Grants No. JP19K14649, No. JP23K03275, No. JP20H01830, and No. JP20H01849), JST PRESTO (Grant No. JPMJPR2452), Grant-in-Aid for Scientific Research on Innovative Areas "Quantum Liquid Crystals" (Grant No. JP19H05825), and "Evolution of Chiral Materials Science using Helical Light Fields" (Grants No. JP22H05131 and No. JP23H04576) from JSPS of Japan.

References

1. Ishito, Y., H. Mao, Y. Kousaka, Y. Togawa, S. Iwasaki, T. Zhang, S. Murakami, J.-I. Kishine, and T. Satoh, "Truly chiral phonons in α-HgS," *Nat. Phys.*, Vol. 19, pp. 35-–39, 2023.

2. Ishizuka, H. and M. Sato, "Peltier effect of phonons driven by electromagnetic waves," *Phys. Rev. B*, Vol. 110, pp. L020303-1–6, 2024.

3. Ishizuka, H. and M. Sato, *in preparation.*

4. Proskurin, I., A. S. Ovchinnikov, J.-I. Kishine, and R. L. Stamps, "Excitation of magnon spin photocurrents in antiferromagnetic insulators," *Phys. Rev. B*, Vol. 98, 134422, 2018.

5. Ishizuka, H. and M. Sato, "Theory for shift current of bosons: Photogalvanic spin current in ferrimagnetic and antiferromagnetic insulators," *Phys. Rev. B*, Vol. 100, 224411, 2019.

6. Ishizuka, H. and M. Sato, "Large photogalvanic spin current by magnetic resonance in bilayer Cr trihalides," *Phys. Rev. Lett.*, Vol. 129, 107201, 2022.

7. Ishizuka, H. and M. Sato, "Rectification of Spin Current in Inversion-Asymmetric Magnets with Linearly Polarized Electromagnetic Waves," *Phys. Rev. Lett.*, Vol. 122, 197702, 2019.

Nano-Squeezing of Optical Chirality via Topology-Optimized 3D Nanogap Antennas

A. Taguchi[1*]
[1]Research Institute for Electronic Science, Hokkaido University, Japan
taguchi@es.hokudai.ac.jp (corresponding author)

Abstract

We numerically investigated optical chirality flowing in a topology-optimized 3D chiral dielectric nanostructure. From the near-field analysis, we observed that chirality flux concentrates and eventually leads to a local enhancement of chirality density at the nanogap. This finding has important implications for better controlling chiral light-matter interactions at the nanoscale.

1 Introduction

Circularly polarized light (CPL) not only carries energy but also transports a physical quantity known as optical chirality, which is vital for the enantioselective excitation of chiral molecules. Despite its importance, enhancing optical chirality at the nanoscale remains challenging. This difficulty partly arises from the inherently complex behavior of near-fields involving the spin angular momentum (SAM) of light. In this work, we demonstrate that rationally designed nanostructures can guide the flow of optical chirality, enabling its confinement into subwavelength spaces while simultaneously enhancing its density. These findings provide novel insights into controlling optical chirality using nanostructures, paving the way for enhanced chiral light-matter interactions at the nanoscale.

2 Chiral Structure Design using Topology Optimization

To design a 3D chiral nanostructure for enhancing optical chirality at the nanoscale, we employ topology optimization (TO), a machine-aided design methodology that enables the creation of complex nanostructures with desired physical properties constrained by Maxwell's equations. As shown in Fig. 1(a), our optimization model comprises an antenna region made of TiO_2, which receives counter-propagating right-handed CPL (r-CPL) with a wavelength of 532 nm. The counter-propagating CPL creates a polarization standing wave, where the electric and magnetic

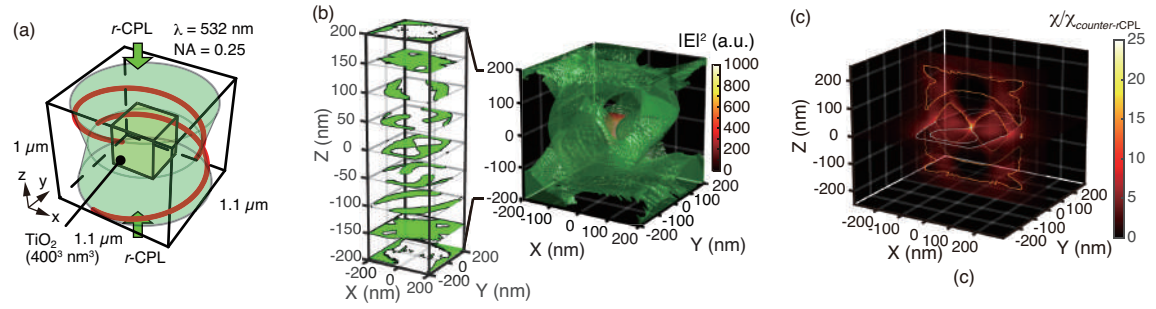


Figure 1: Topology-designed gap antenna for counter-propagating r-CPL. (a) Schematic of boundary conditions. (b) 3D model of the antenna with Z-sliced sections, overlaid with electric field intensity distribution. (c) Optical chirality density, χ, normalized to structure-free, displayed at planes $Z = 0$ nm and $Y = 0$ nm under counter-propagating r-CPL excitation.

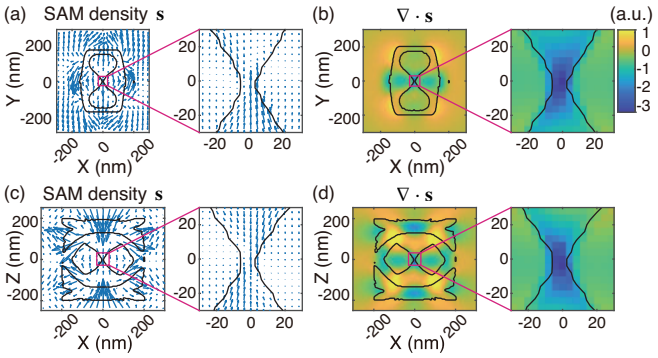


Figure 2: (a) SAM density vector in X-Y plane at $Z = 0$ nm and (b) the corresponding SAM divergence. (c,d) Same as (a,d) but X-Z plane at $Y = 0$ nm.

fields are aligned in parallel and $\pi/2$ out of phase, with the azimuthal orientation spiraling along the propagation axis. This configuration establishes the optimal conditions for maximizing optical chirality. TO is then applied to determine the optimal material distribution, maximizing the field intensity at the center while preserving the conditions for chirality enhancement.

Figure 1(b) shows the resulting structure, which features a nanogap as narrow as 8 nm at the center ($Z = 0$ nm), where the electric field intensity is significantly enhanced. We observe an enhancement factor of 1,250 for counter-propagating r-CPL. Figure 1(c) illustrates the distribution of optical chirality, which peaks within the gap with an enhancement factor of 24.5. The spatial width of the chiral field at full width at half maximum (FWHM) is 10.4 nm, indicating subwavelength confinement.

3 Chirality Flux within the Chiral Nanostructure

Figure 2 illustrates how the spin angular momentum (SAM) density, or equivalently, the chirality flux of the incident CPL, flows into the nanogap. The SAM converges into the nanogap and cancels out, creating a distinct negative divergence of SAM. This leads to an increase in the local optical chirality density, as dictated by the conservation laws of optical chirality. This illustration demonstrates how the optimized 3D chiral structure "squeezes" the optical chirality inherent in the incoming CPL into the nanoscale region.

4 Conclusion

This work demonstrates that topology-optimized 3D dielectric nanogap antennas can effectively enhance and confine optical chirality within a subwavelength mode volume, representing a valuable step toward chiral light control at the nanoscale. These findings pave the way for applications in chiral light-based technologies, including chiral molecular sensing, quantum spin optics, and other nanoscale photonic systems exhibiting chirality.

References

[1] Taguchi, A, Y. Fukui, and K. Sasaki, "Nanoscale chirality enhancement using topology-designed three-dimensional dielectric nanogap antennas," *Phys. Rev. Applied.*, Vol. 23, L021002 (2025).

[2] Tang, Y., Cohen, A.E. "Optical chirality and its interaction with matter," *Phys. Rev. Lett.* Vol. 104, 163901 (2010).

[3] Jensen, J. and Sigmund, O. "Topology optimization for nanophotonics," *Laser Photon. Rev.* Vol. 5, pp. 308–321 (2011).

Magnetoelectric effect in antiferromagnetic Chern insulators

T. Hirosawa, D. Komine, and N. Furukawa

Aoyama Gakuin University, Japan
*corresponding author: hirosawa@phys.aoyama.ac.jp

Abstract: The magnetoelectric effect is a cross-correlation phenomenon between electric and magnetic dipole moments, which occurs when both the time-reversal and inversion symmetries are broken. In this work, we discuss the magnetoelectric effect in antiferromagnetic Chern insulators, which support spin-polarized chiral edge states.

The magnetoelectric effect occurs when the electric and magnetic dipole moments are strongly coupled. It is characterized by a higher-order multipole moment, such as the magnetic toroidal moment [1]. Since the magnetic toroidal moment is induced by a pair of localized spins with opposite polarization, antiferromagnetic materials provide an ideal platform for the magnetoelectric effect. However, the linear magnetoelectric effect is generally very small in antiferromagnetic materials.

Here, we investigate the magnetoelectric effect in antiferromagnetic Chern insulators. Chern insulators are time-reversal-symmetry broken topological phases of matter. When they are in proximity to the antiferromagnetic order, both the time-reversal and inversion symmetries are broken, allowing the magnetoelectric effect. Furthermore, the bulk-boundary correspondence guarantees the emergence of chiral edge states, partially spin-polarized due to the coupling with the antiferromagnetic order. We discuss the magnetoelectric effect of spin-polarized chiral edge modes and propose tight-binding models for their realization.

References

1. Spaldin, N. A., Fiebig, M., and Mostovoy, M., “The toroidal moment in condensed-matter physics and its relation to the magnetoelectric effect”, J. Phys.: Condens. Matter 20, 434203 (2008).

Enhanced chiral sensing and unambiguous enantiomer differentiation with achiral anisotropic photonic metasurfaces

S. Droulias

Department of Digital Systems, University of Piraeus, Piraeus 18534, Greece

corresponding author: sdroulias@unipi.gr

Abstract: Achiral anisotropic photonic metasurfaces can provide enhanced sensing and unambiguous enantiomer differentiation of weak chiralities at the nanoscale. In this work it is demonstrated how the additional degrees of freedom offered by anisotropic metasurfaces with respect to their isotropic counterparts can enable chiroptical signals with unprecedented enhancement.

Sensing molecular chirality at the nanoscale has been a long-standing challenge, due to the inherently weak nature of the associated chiroptical signals. Recently, circular dichroism (CD) measurements of chiral media embedded in nanophotonic platforms have granted access to weak chiralities at the nanoscale [1,2]. However, because in such measurements the incident wave probes the chiral medium together with the metasurface, chiroptical signals result from the dispersion of both. As a result, although CD measurements are intuitively expected to be sensitive only to the imaginary part of the chirality parameter κ, Im(κ), they are sensitive to both Re(κ) and Im(κ) [3]. Therefore, it is crucial to be able to isolate the metasurface's contribution from the total chiroptical signal, in order to deconvolve and unambiguously determine the unknown chirality. While several chiral sensing schemes based on CD measurements have been proposed for the detection and differentiation of enantiomers, a scheme that is able to distinguish Re(κ), Im(κ) is still missing.

Recently it was shown how, with the aid of achiral isotropic metasurfaces, it is possible to deconvolve the unknown chirality from the background dispersion of the metasurface [3]. The idea is based on probing the metasurface, in which the chiral inclusion is embedded, with linearly polarized waves, and measuring changes in the transmitted polarization, which is characterized in terms of the rotation θ and ellipticity η of the polarization vector. Because the metasurface is achiral, any changes in the transmitted polarization are solely due to the embedded chirality. In this scheme, the unknown κ_A is expressed in terms of the reference κ_B, as

$$\kappa_A = \kappa_B \frac{\theta_A + i\eta_A}{\theta_B + i\eta_B} \tag{1}$$

where θ_A, η_A and θ_B, η_B are the chiroptical signals from simulations or experiments with chiral inclusions A and B, respectively.

In this work, achiral anisotropic metasurfaces are studied as a vehicle for the detection of a chiral inclusion and the unambiguous retrieval of its unknown chirality parameter κ with unprecedented enhancement. Anisotropic metasurfaces offer additional degrees of freedom with respect to their isotropic counterparts and can thus enable detection schemes, beyond probing with linearly polarized beams [4,5]. An example is shown in Fig. 1, in which a realistic anisotropic metasurface is used. The metasurface supports resonant conductivities along the y-axis, similar to the one examined in [4] for chiral sensing in the near infrared. In this example, the metasurface is composed of a 100 nm thin dielectric slab on which a 50 nm chiral layer with refractive index $n = 1.5 - 0.001i$ and chirality parameter κ is placed.

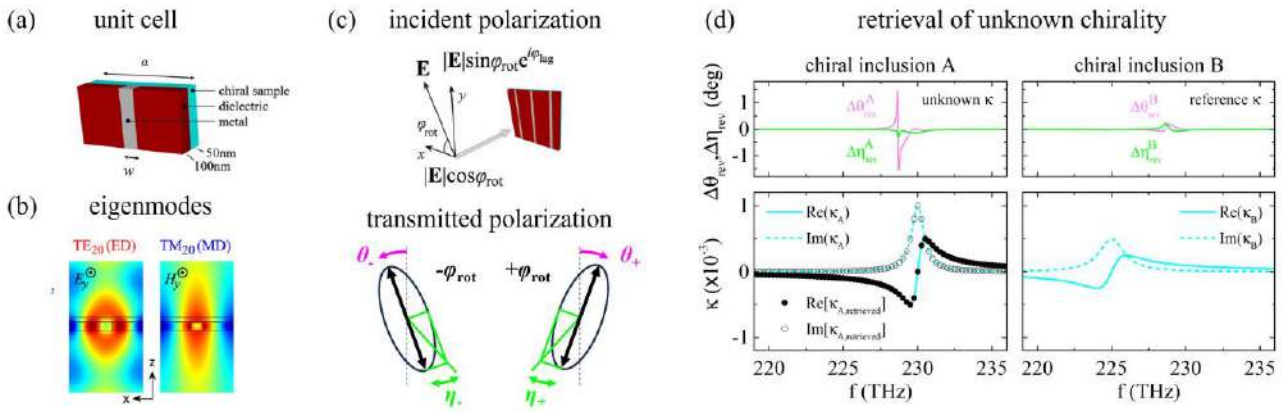


Figure 1. Achiral anisotropic photonic metasurface for enhanced chiral sensing and unambiguous enantiomer differentiation. (a) Schematic illustration of unit cell. The periodicity is α = 840 nm and the silver wire has thickness w = 140 nm. (b) Field distribution of the electric type (TE_{20}) and magnetic type (TM_{20}) modes that are utilized for sensing. (c) Excitation with elliptically polarized wave, and polarization state of the transmitted wave, analyzed in terms of its rotation θ and ellipticity η, for excitation with $\pm\varphi_{rot}$ orientation. (d) Retrieval of the unknown chirality parameter κ_A of inclusion A, with reference chirality parameter κ_B of inclusion B, using the averaged chiroptical signals $2\Delta\theta_{rev} = \theta_+ + \theta_-$, $2\Delta\eta_{rev} = \eta_+ + \eta_-$ in transmission. *Top row*: numerically calculated chiroptical signals of the transmitted wave. *Bottom row:* chirality parameters κ_A, κ_B of the two inclusions (cyan lines) and retrieved κ_A (black lines) of inclusion A.

The dielectric slab has refractive index n = 3.4 and supports TE (components H_x, E_y, H_z) and TM (components E_x, H_y, E_z) waveguide modes, which are used to implement the electric/magnetic moment pair. The slab is periodically interrupted by silver wires with periodicity α = 840 nm and the whole system is placed on a glass substrate of refractive index n = 1.5. The space on the opposite side (adjacent to the chiral layer) is index-matched with the substrate.

It is demonstrated how anisotropic metasurfaces, like the one presented in the above example, can be used to (i) achieve enhanced chiroptical signals by more than two orders of magnitude, (ii) perform complete measurements of the total chirality (magnitude and sign of both its real and imaginary parts) and (iii) enable chirality measurements in an absolute manner, i.e. without the need for sample removal, using a crucial signal reversal (excitation with reversed polarization). Analytical formulas that provide insight into the sensing mechanism are derived and numerically verified, generalizing Eq.(1) to detection with elliptically polarized beams.

References

1. Zhao, Y., Askarpour, A. N, Sun, L., Shi, J., Li, X., and Alù, A., "Chirality detection of enantiomers using twisted optical metamaterials", Nat. Commun. 8, 14180, 2017.
2. García-Guirado, J., Svedendahl, M., Puigdollers, J., and Quidant, R., "Enhanced Chiral Sensing with Dielectric Nanoresonators", Nano Lett. 20, 585-591, 2020.
3. Droulias, S., "Chiral sensing with achiral isotropic metasurfaces", Phys. Rev. B 102, 075119, 2020.
4. Droulias, S. and Bougas, L, "Chiral sensing with achiral anisotropic metasurfaces", Phys. Rev. B 104, 075412, 2020.
5. Droulias, S., "Enhanced chiral sensing with achiral photonic metasurfaces", Chapter 9 in Ordered and Disordered Metamaterials - Design and applications, pp. 9-1 to 9-41 , IOP Publishing Ltd 2024.

What is and what is not a good measure for enhanced chiroptical response?

T.Weiss[1*]

[1]University of Graz and NAWI Graz, Universitätsplatz 5, 8010 Graz, Austria

Corresponding author: thomas.weiss@uni-graz.at

Abstract: Enhancing chiral light-matter interaction by nanophotonic resonators has attracted a lot of interest in recent years. However, various theories and measures exist to understand and quantify this enhancement. We are going to compare these approaches and discuss their advantages and disadvantages.

Detecting the handedness of chiral molecules is of utmost importance for chemical, biological, and pharmaceutical applications, since the handedness of a molecule determines its interaction with the environment. This includes chemical interactions as well as the interaction with light. Hence, it is possible to determine the handedness of chiral molecules by optical measurements, but the chiroptical response of such molecules is usually rather weak. Therefore, conventional approaches require using large numbers of chiral molecules.

Nanophotonic resonators such as plasmonic and dielectric nanoantennas can enhance the chiroptical response. However, two questions naturally arise: What are the dominant mechanisms of this enhancement and how can we actually quantify it?

A widespread approach to address these questions is to consider the local optical chirality $C \quad \mathbf{E}^* \cdot \mathbf{H}$ (prefactor depends on unit system), which has been shown to quantify the absorption difference between left- and right-handed circularly polarized light by single molecules [1]. This quantity can be easily calculated and optimized for arbitrarily complex electromagnetic environments [2], see figure 1. However, it does not account for the backaction of chiral molecules on the nanophotonic resonator, thus excluding possible effects such as resonant shifts.

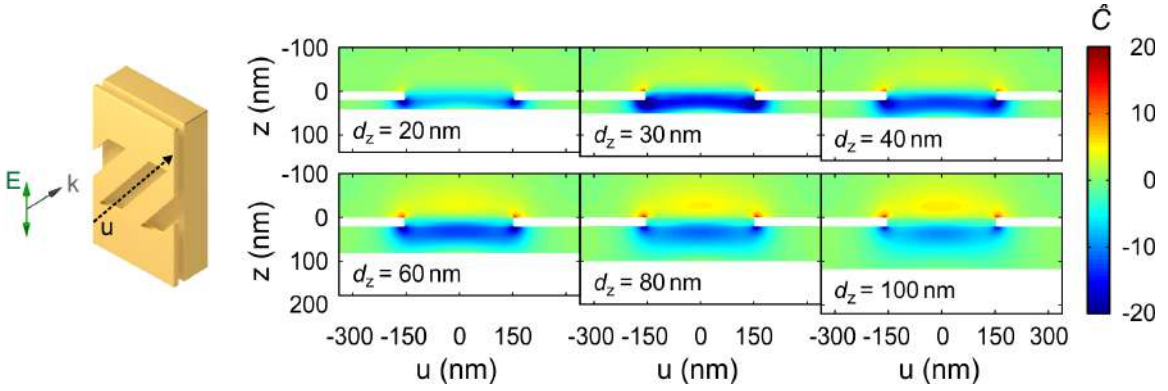


Figure 1: Local optical chirality C for inclined two-dimensional periodic arrays of slits in a gold film that is located at a distance d_z on top of a gold mirror. Figure taken from reference [2]

While full-wave simulations account for such backaction [3], they provide little insight into the underlying physics, and one needs to somehow quantify the enhanced chiral light-matter interaction. Regarding the physical insight, we have developed a first-order perturbation

theory [4] that allows us to approximate the near- and far-field response and indentify several contributions to enhance chiral light-matter interaction by nanophotonic resonators. The first one is a change in the excitation and emission efficiencies of the resonant states, which requires a coplanarity of the incident field and the dominant field components at the location of the chiral medium. The second one is a chirality-induced resonance shift, which surprisingly only occurs in chiral spatial arrangements of the resonator and the chiral medium. The third contribution is based on an interplay of nearly degenerate resonant states.

Playing with these contributions provides different strategies to enhance chiral light-matter interaction. Yet, we might ask what is the connection to the local optical chirality. Indeed, it turns out that the resonance shift can be brought into a form of an integral with the integrand being proportional to the local optical chirality for high-quality resonant states [4]. However, this intgrand is calculated for the resonant contributions alone, while the local optical chirality is usually derived by accounting for resonant and incident field. Thus, the local optical chirality is not a universal quanitity of the nanophononic resonator, since it depends on the underlying experimental conditions, while the resonant contributions are universal. We will analyze the connections and differences in detail.

Finally, we are going to address the question of measures for the enhancement of chiroptical response. Here, we focus on the far-field response. Experimentally accessible quantities are the transmission, reflection, and possible diffraction. From those, it is possible to calculate the circular dichroism as the absorption difference between left- and right-handed circularly polarized incident light. Since not all necessary terms to calculate circular dicroism are experimentally accessible, often only the difference in reflection or transmission is considered. Finally, a normalization or a conversion from intensities to degrees can be carried out. To quanitify the enhancement, these measures are then often normalized by expressions attributed to the system in the absence of resonant contributions. We are going to compare these various approaches and discuss under which circumstances they are equivalent and what are potential pitfalls, particularly when postprocessing experimentally accessible quantities and renormalizing them by some reference value. As it turns out, not all claims of huge enhancement factors actually rely on enormous resonant enhancement but are partially a consequence of how this enhancement is quanitified.

References

1. Y. Tang and A. E. Cohen, "Optical chirality and its interaction with matter," Phys. Rev. Lett. **104**, 163901 (2010).

2. M. Schäferling, N. Engheta, H. Giessen, and T. Weiss, "Reducing the complexity: Enantioselective chiral near fields by diagonal slit and mirror configuration," ACS Photonics **3**, 1076–1084 (2016).

3. M. L. Nesterov, X. Yin, M. Schäferling, H. Giessen, and T. Weiss, "The role of plasmon-generated near fields for enhanced circular dichroism spectroscopy," ACS Photonics **4**, 578–583 (2016).

4. S. Both, M. Schäferling, F. Sterl, E. A. Muljarov, H. Giessen, and T. Weiss, "Nanophotonic chiral sensing: How does it actually work?," ACS Nano **16**, 2822–2832 (2022).

Emergent chirality, antiskyrmions and Bloch skyrmions in ferroelectrics

J. Hlinka[1]

[1]Institute of Physics, Czech Acad. Sci, Prauge, Czech Republic
*corresponding author: hlinka@fzu.cz

Abstract: The talk is summarizing symmetry aspects of magnetic and structural skyrmion defects and phases in ferroelectric crystals and relationships to the species of macroscopic chiral symmetry breaking.

In this talk, I would like to provide summary of our recent results and open questions related to magnetic and structural skyrmion and antiskyrmion topological defects, and ordered skyrmion and antiskyrmion phases in ferroelectric crystals. It concerns both chiral and nonchiral structures, and we shall discuss the relationships to the concept Aizu species of macroscopic chiral symmetry breaking[1-3]. Potentially, I would also like to discuss some unresolved challenges related to the interaction of crystals with skyrmion textures with the light as well as with the exotic light beams carrying a nonzero orbital angular momentum.

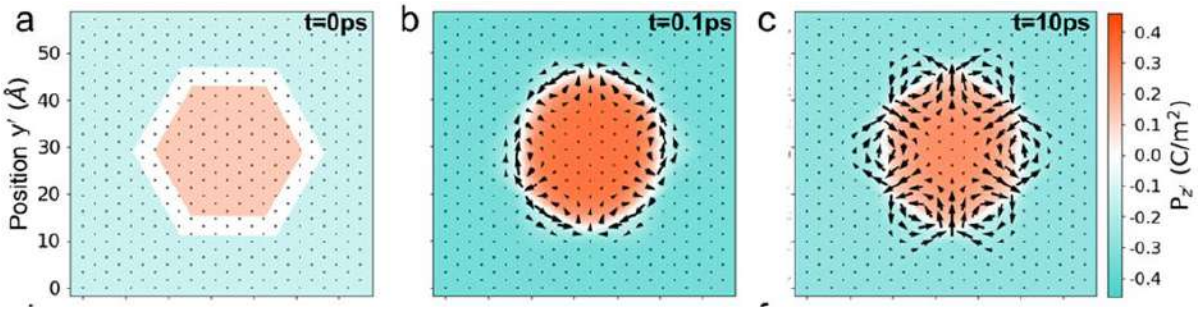


Figure 1. Results of atomistic shell-model based computational experiment with barium titanate showing spontaneous formation of the of-axis polarization pattern, responsible for the conversion of the topologically trivial ferroelectric bubble domain into a topological antiskyrmion[1].

This work was supported by the Czech Science Foundation (project no. 19-28594X) and by the European Union's Horizon 2020 research and innovation programme under grant agreement no. 964931 (TSAR).

References

1. M. Gonçalves, M. Paściak, J. Hlinka, "Antiskyrmions in ferroelectric barium titanate," *Phys. Rev. Lett.*, Vol. 133, 066802, 2024.
2. K. C. Erb and J. Hlinka, "Vector, bidirector, and Bloch skyrmion phases induced by structural crystallographic symmetry breaking," *Phys. Rev.* B 102, 024110 (2020).
3. J. Hlinka, "Eight Types of Symmetrically Distinct Vectorlike Physical Quantities," *Phys. Rev. Lett.*, Vol. 113, 165502, 2014.

Ultrafast TACOS

J. Terentjevas[1,2], P. Vindel-Zandbergen[3], L. Rego[2,4,5,6], F. Morales[1], A. Ordóñez[2,7], O. Smirnova[1,8,9] and D. Ayuso[1,2,7,10,*]

[1]Max-Born-Institut, 12489 Berlin, Germany
[2]Department of Physics, Imperial College London, SW7 2BW London, United Kingdom
[3]Department of Chemistry, New York University, New York 10003, New York, USA
[4]Instituto Madrileño de Estudios Avanzados en Nanociencia (IMDEA Nano), Cantoblanco 28049, Madrid, Spain
[5]Departamento de Química, Universidad Autónoma de Madrid, 28049 Madrid, Spain
[6]Instituto de Ciencia de Materiales de Madrid (ICMM-CSIC), Madrid, 28000, Spain
[7]Department of Chemistry, School of Physical and Chemical Sciences, Queen Mary University of London, E1 4NS, UK
[8]Technische Universität Berlin, Berlin, Germany
[9]Technion – Israel Institute of Technology, 3200003 Haifa, Israel
[10]Department of Chemistry, Molecular Sciences Research Hub, Imperial College London, W12 0BZ London, UK
[*]d@ayuso@imperial.ac.uk

Abstract: We bring together the advantages of terahertz and optical spectroscopies to introduce TACOS (Terahertz-Assisted Chiro-Optical Spectroscopy), a novel approach for ultrafast and highly efficient imaging of molecular chirality. TACOS relies on driving nonlinear electronic dynamics with terahertz and few-cycle optical pulses, but it does not require optical carrier-envelope phase stability.

Like our hands, opposite versions of the same chiral molecule (enantiomers) behave identically unless they interact with another chiral entity. Telling them apart is vital, but also challenging. Traditional optical methods rely on the weak magnetic coupling between light and matter, yielding weak enantiosensitivity. The electric-dipole "revolution" [1] is transforming the landscape of molecular chiral discrimination with a new generation of chiro-optical methods offering orders-of-magnitude greater enantiosensitivity. Different "streams" of this revolution rely on analyzing different observables, but share one common ingredient: the chiro-optical response is driven by purely electric-dipole interactions – weak magnetic effects are not needed.

Locally chiral light [2-4], where the tip of the electric-field vector draws a chiral 3D Lissajous figure in time, can drive highly enantiosensitive *electronic* dynamics within the electric-dipole response. Such light can be created by overlapping two laser beams that propagate in different directions and carry several frequencies. However, non-collinear configurations lead to spatial modulations of the field's properties, such as amplitude, phase or polarization gratings, with spatial periodicities on the order of the wavelengths. In the case of optical frequencies, these are significantly smaller than typical interaction regions. Thus, one needs to carefully design the optical setup so that such gratings do not wash out enantiosensitive effects in the macroscopic response of the medium.

Locally chiral fields are not limited to optical frequencies. As shown by S. Eibenberger [5-7] and co-workers, one can drive highly enantiosensitive *rotational* dynamics by combining microwave fields with different frequencies propagating in different directions. Thanks to their longer wavelengths, these arrangements of microwave fields maintain their properties over spatial regions that can cover the size of typical molecular samples. This means that, in contrast with the optical domain, here one does not need to worry about a potential cancelation of the enantiosensitive response in the macroscopic response of the medium. However, microwaves are not well suited for *attochemistry*, an emerging field which aims to image and control chemical reactions by manipulating *electronic* motion in molecules on the attosecond timescale.

TACOS [8] brings the advantages of both approaches together and creates an opportunity for imaging and controlling molecular chirality at the level of electrons over large spatial regions. Our approach involves cross-polarized and cross-propagating THz and optical pulses interacting with a medium of randomly oriented chiral molecules, see Fig 1. Without the THz field, the local response of the medium to the optical pulse would be linearly polarised and insensitive to its handedness. The linear response to the THz field breaks this symmetry by transiently orienting the electronic clouds of the molecules. As a result, the non-linear response to the optical pulse acquires an enantiosensitive polarization component that is orthogonal to both driving fields and enables efficient chiral recognition: it leads to emission of harmonic light which has opposite polarizations in opposite enantiomers.

The multiphoton pathways giving rise to the enantiosensitive response are depicted in Fig. 1. Because both pathways involve absorption of the same number of optical photons, their relative amplitude and phase are not sensitive to the intensity and phase of the optical field. As a result, the polarization of the nonlinear optical response is not sensitive to the carrier-envelope phase of the optical pulse. In contrast, only the chiral pathway is sensitive to the THz field, and thus we can control the enantiosensitive response by adjusting the properties of the THz pulse.

Using the linear response to a THz pulse to electronically orient the molecules ensures that they maintain the same orientation over a spatial region on the order of half the THz wavelength and that the orientation persists during half the THz period. Thus, if the optical beam, the medium, or a substantial part of them is smaller than half the THz wavelength, the enantiosensitive response can be maintained across the interaction region, creating exciting opportunities for chiral attochemistry.

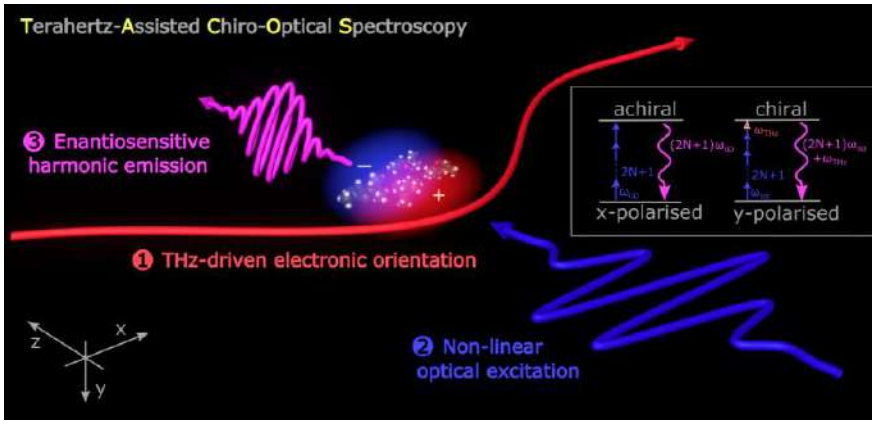


Figure 1. Step 1: a linearly polarized THz field (red) orients the electronic density of the medium via linear response, inducing anisotropy. **Step 2:** the non-linear response to an ultrashort optical pulse (blue) becomes twisted. **Step 3:** the medium radiates at new optical frequencies (magenta) with enantiosensitive elliptical polarization. The relevant multiphoton pathways are depicted in the inset (achiral and chiral).

References

1. D. Ayuso et al, *Phys. Chem. Chem. Phys* **24**, 26962 (2022)
2. D. Ayuso et al, *Nature Photonics* **13**, 866 (2019)
3. D. Ayuso et al, *Nature* Communications **12**, 3951 (2021)
4. N. Mayer et al, *Nature Photonics* **18**, 1155–1160 (2024)
5. S. Eibenberger et al, *Physical Review Letters* **118**, 123002 (2017)
6. J. Lee et al, *Physical Review Letters* **128**, 173001 (2022)
7. J. Lee et al, *Nature* Communications **15**, 7441 (2024)
8. J. Terentjevas et al, ArXiv:2406.14258 (2024)

Coherent dynamics of a magnon Bose–Einstein condensate – temporal coherence and correlation characteristics

A. A. Serha[1*]

[1]Fachbereich Physik and Landesforschungszentrum OPTIMAS,
Rheinland-Pfälzische Technische Universität Kaiserslautern-Landau, 67663 Kaiserslautern, Germany
[*]corresponding author: serha@rptu.de

Abstract: Nonlinear interactions in externally excited magnetic media can lead to Bose–Einstein condensation of spin-wave quanta—magnons. Using frequency- and time-resolved microwave detection techniques, we have observed the spontaneous formation of a coherent magnon BEC phase at the ferromagnetic resonance frequency in a perpendicularly magnetized magnetic film.

Bose–Einstein condensation (BEC) is the spontaneous accumulation of bosonic particles or quasiparticles at the minimum frequency of their spectrum. This can be achieved by a reduction in temperature or an increase in particle density. The second method is also relevant for systems with a temperature-dependent population, such as magnons, photons, polaritons, and excitons [1-3]. In an artificially overpopulated magnon gas in single-crystal ferromagnetic samples of yttrium iron garnet (YIG), BEC of magnons can be observed even at room temperature [4]. The spontaneous appearance of coherence is a key feature of BEC [5, 6] and determines effects such as supercurrents and Josephson oscillations [7]. Here, I present direct measurements of a magnon condensate's time and phase coherence by detecting microwave radiation from a parametrically pumped perpendicularly magnetized YIG film. In particular, I report the spontaneous narrowing of the spectrum line associated with this magnon state and demonstrate the appearance of a randomly coherent BEC phase in every single measurement.

This study was funded by the Deutsche Forschungsgemeinschaft (DFG, German Research Foundation) – TRR 173 – Grant No. 268565370 Spin+X.

References

1. Snoke, D. “Spontaneous Bose coherence of excitons and polaritons,” Science, Vol. 298, No. 5597, 1368–1372, 2002.
2. Bunkov, Y. M. and G. E. Volovik, “Bose–Einstein condensation of magnons in superfluid ^{3}He,” J. Low Temp. Phys., Vol. 150, 135–144, 2008.
3. Klaers, J., J. Schmitt, F. Vewinger and M. Weitz, “Bose–Einstein condensation of photons in an optical microcavity,” Nature, Vol. 468, 545–548, 2010.
4. Demokritov, S. O., V. E. Demidov, O. Dzyapko, G. A. Melkov, A. A. Serga, B. Hillebrands and A. N. Slavin, “Bose–Einstein condensation of quasi-equilibrium magnons at room temperature under pumping,” Nature, Vol. 443, 430–433, 2006.
5. Snoke, D. “Coherent questions,” Nature, Vol. 443, 403–404, 2006.
6. Noack, T. B., V. I. Vasyuchka, A. Pomyalov, V. S. L’vov, A. A. Serga and B. Hillebrands, “Evolution of room-temperature magnon gas: Toward a coherent Bose–Einstein condensate,” Phys. Rev. B, Vol. 104, L100410, 2021.
7. Schweizer, M. R., F. Kühn, V. S. L’vov, A. Pomyalov, G. von Freymann, B. Hillebrands and A. A. Serga, “Local temperature control of magnon frequency and direction of supercurrents in a magnon Bose–Einstein condensate,” App. Phys. Lett., Vol. 124, 092402, 2024.

Electron-phonon interaction in chiral crystal: Angular momentum and phonon chirality

J. Kishine,[1] T. Tateishi,[1] A. Kato[2]

[1]The Open University of Japan, Japan

[2]Osaka Metropolitan University, Japan

Abstract: Chiral phonons in helical crystals enable angular momentum transfer in quantum materials. We establish a framework incorporating conserved crystal momentum and crystal angular momentum, deriving electron-phonon interactions. Examining Lipkin's Zilch and macroscopic angular momentum, we reveal insights into chiral systems, impacting optoelectronic, thermoelectric, and spintronic material design.

Chiral phonons in crystals with helical symmetry [Fig. (a)] play a crucial role in angular momentum transfer in quantum materials. In this work, we construct the wavefunction of chiral phonons in a chiral helical crystal, establishing a theoretical framework that rigorously incorporates both the crystal momentum (CM) and the crystal angular momentum (CAM) as conserved quantities. Based on this formulation, we derive the electron-chiral phonon interaction using the tight-binding scheme [Fig. (b)], ensuring explicit conservation of these quantities. A hallmark of chiral phonons is the mixing of longitudinal and transverse modes, which distinguishes them from conventional phonons. Unlike conventional electron-phonon interactions, where electrons couple only to longitudinal phonons, chiral helical crystals permit coupling to left- and right-handed chiral rotational modes, with the interaction vertex carrying CAM.

Furthermore, we analyze the phononic analogue of Lipkin's Zilch, a time-even pseudoscalar originally introduced in electromagnetism as

$$Z^{\mu} = \epsilon^{\mu\nu\rho\sigma}\partial_{\nu}\left(F_{\rho\lambda}\tilde{F}^{\lambda}{}_{\sigma}\right)$$

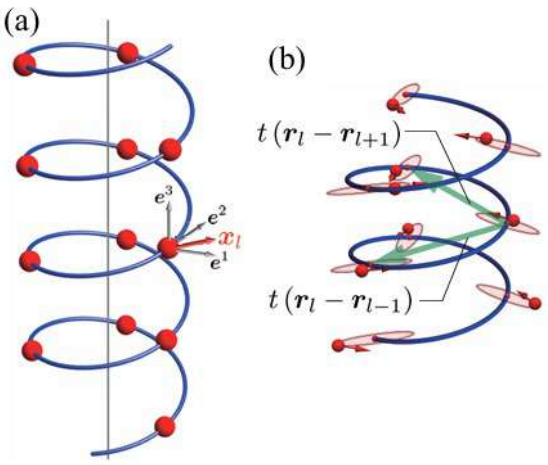
where $F_{\mu\nu}$ is the electromagnetic field tensor and $\tilde{F}_{\mu\nu}$ is its dual. In the context of chiral phonons, we extend this concept to phononic fields, providing a chirality measure analogous to circularly polarized light. By examining the interrelations between macroscopic angular momentum (MAM) and Zilch, we offer complementary perspectives on angular momentum dynamics in chiral materials. Our analysis shows that while CAM governs the interactions of chiral phonons with electrons, Zilch provides a global measure of phononic chirality, revealing novel conservation laws in vibrational dynamics.

These findings uncover intricate interactions between electronic and vibrational degrees of freedom, offering deeper insight into chiral quantum systems. The proposed framework, when combined with realistic electronic band structures incorporating spin-orbit coupling and first-principles phonon calculations, provides a powerful approach to elucidating angular momentum transfer mediated by phonons in chiral crystals. These insights hold significant implications for the understanding and design of chiral quantum materials with novel optoelectronic, thermoelectric, and spintronic functionalities, paving the way for advanced applications in quantum technologies.

JK acknowledges support from JSPS KAKENHI, under Grant Nos. 23K20825 and 23H00091, the grant of OML Project by the National Institutes of Natural Sciences (NINS program No. OML012301).

References

1. J.Kishine, A.S.Ovchinnikov,andA.A.Tereshchenko:Phys.Rev.Lett. 125(2020)245302.
2. A.Kato and J.Kishine:J.Phys.Soc.Jpn.92(2023)075002.



(a) Helical crystal with symmetry of the line group $L3_1$. (b) Schematic illustration of atomic motion (red spheres) and electron hopping paths (green arrows) for electrons localized at atoms.

Spin polarization induced by nonequilibrium fluctuation near the surface in chiral metals

Y. Kato[1,2*]
[1]Department of Basic Science, The University of Tokyo, Japan
[2]QuaRC, Institute of Molecular Science, Japan
Corresponding author: yusuke@phys.c.u-tokyo.ac.jp

Abstract: We theoretically address spin polarization induced by the fluctuating electric fields, i.e., noises in chiral metals, with the Boltzmann transport theory. Based on these results, we discuss chirality-induced spin selectivity (CISS) without biased inputs and the enantio-selective interaction between chiral materials and a magnetic substrate.

Recently, magnetic properties inherent to nonmagnetic chiral molecules [1,2], chiral metals [3,4] and chiral superconductors [5], which have been dubbed chirality-induced spin selectivity (CISS), have attracted much attention from chemists and physicists [6]. The term CISS now describes a general correlation between electron spin polarization and handedness of chiral materials [6]. Among various phenomena related CISS, the spin polarization near the edges in chiral molecules without intentional inputs is one of the issues to be addressed. This phenomenon has been inferred in experiments of enantio-specific adsorption of chiral molecules by a magnetic substrate [2].

In this presentation, we argue spin polarization near the surface in chiral metals subject to the fluctuating electric fields [7], as a theoretical basis for an analogous phenomenon observed in [2]. We consider the simplest model for chiral metals. The Hamiltonian is given by

$$\mathcal{H} = \frac{k^2}{2m} + \alpha \boldsymbol{\sigma} \cdot \boldsymbol{k}, \tag{1}$$

with $k = |\boldsymbol{k}|$ and a coupling constant α of the hedge-hog type antisymmetric spin-orbit interaction. The sign of α represents the chirality of the system and determines whether the wave vector $\boldsymbol{k}$ and the spin are parallel or antiparallel for a given spin-splitting band. We solve the Boltzmann equation for the chiral metal within the relaxation time approximation in the presence of fluctuating electric fields

$$E_\mu(t, \boldsymbol{r}) = \int_{-\infty}^{\infty} \frac{\mathrm{d}\omega}{2\pi} E_\mu(\omega, \boldsymbol{r}) e^{-\mathrm{i}\omega t} \tag{2}$$

that satisfies

$$\langle E_\mu(\omega, \boldsymbol{r}) \rangle = 0, \quad \langle E_\mu(\omega, \boldsymbol{r}) E_\nu(\omega', \boldsymbol{r}') \rangle = 2\pi \delta_{\mu\nu} S_E^{\mathrm{w}} \delta(\omega + \omega') g(|\boldsymbol{r} - \boldsymbol{r}'|), \tag{3a}$$

with a power spectrum S_E^{w} of the white noise and the spatial correlation of the fluctuating electric field as $g(|\boldsymbol{r} - \boldsymbol{r'}|) = \frac{e^{-|\boldsymbol{r}-\boldsymbol{r}'|/\lambda_E}}{8\pi\lambda_E^3}$,with a correlation length λ_E.

Figure 1 (a) shows the profile of the spin polarization in the presence of fluctuating electric fields (2) obeying Eq. (3) , near the surface in the chiral metal occupying a semi-infinite region with $z > 0$. The boundary $z = 0$ with the vacuum $z < 0$ is perfectly rough. This result is schematically drawn in Fig. 1(b), where the red arrows represent spin polarization when $\alpha > 0$. The sign of spin is the opposite when $\alpha < 0$

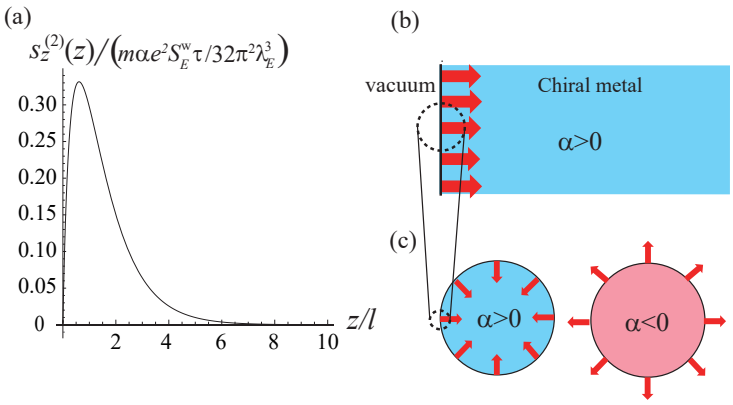


Figure 1: (a) Spin density induced by the fluctuating electric field. m, α, e, τ denote electron mass, the coupling constant of the spin-orbit interaction, and the relaxation time. The coordinate z is scaled by the mean free path ell. (b) Schematics of the spin polarization represented by the red arrows in the chiral metal with $\alpha > 0$. (c) The hedge-hog type spin polarization at the surface of the chiral metal with a spherical shape.

Our results also imply the hedge-hog type spin polarization in the sphere of the chiral metals, as shown in Fig. 1(c), where the radius of the nano-particle is assumed to be much larger than the mean free path. By Fig. 1(c), we emphasize that the spin polarization is chirality-dependent (enantio-selective in the terminology of chemistry [2]). This result is analogous to the antiparallel spin polarization at the edges in chiral molecules discussed in [2]

As an implication to experiments, the radial spin polarization shown in Fig. 1(c) in chiral metals could be used to separate the nanoparticle of chiral metals by a magnetic substrate, similarly to enantio-separation of chiral molecules [2].

This presentation is based on a recent collaboration with Suzuki, Y., Sato, T., Yamamoto, H. M., Togawa, Y., Kusunose, H., Kishine, J-i. [7]. This work was supported by JSPS KAKENHI Grants No. JP20K03855, No. JP21H01032, Joint Research by the Institute for Molecular Science (IMS program No. 23IMS1101), and the grant of OML Project by the National Institutes of Natural Sciences (NINS program No, OML012301).

References

1. Ray, K. et al., "Asymmetric Scattering of Polarized Electrons by Organized Organic Films of Chiral Molecules", *Science*, Vol. 284, pp. 814–816,1999.

2. Banerjee-Ghosh, K. et al. "Separation of enantiomers by their enantiospecific interaction with achiral magnetic substrates" *Science*, Vol. 360, pp. 1331–1334, 2018.

3. Inui, A. et al. "Chirality-induced spin-polarized state of a chiral crystal $CrNb_3S_6$," *Phys. Rev. Lett.*, Vol. 124, pp. 166602, 2020.

4. Shiota, K. et al. "Chirality-induced spin polarization over macroscopic distances in chiral disilicide crystals," *Phys. Rev. Lett.*, Vol. 127, pp. 126602, 2021 .

5. Nakajima, R, et al. "Giant spin polarization and a pair of antiparallel spins in a chiral superconductor," *Nature*, Vol. 613, pp. 479–484, 2023.

6. Bloom, B. P. et al. ,"Chiral Induced Spin Selectivity", *Chem. Rev.*, Vol. 124, pp. 1950, 2024.

7. Kato, Y. , Suzuki, Y., Sato, T., Yamamoto, H. M., Togawa, Y., Kusunose, H., Kishine, J-i., "Chirality-dependent spin polarization in diffusive metals: linear and quadratic responses", *arXiv*, 2408.04450, 2024.

Sensing and generating structured and twisted light through photonic integrated circuits

M. Šimić[1,2], J. Bütow[1,2], V. Sharma[1,2,3], D. Brandmüller[1,2], J. S. Eismann[1,2], and P. Banzer[1,2,*]

[1]Institute of Physics, University of Graz, NAWI Graz, Universitätsplatz 5, A-8010 Graz, Austria
[2]Christian Doppler Laboratory for Structured Matter Based Sensing, Institute of Physics, Universitätsplatz 5, A-8010 Graz, Austria
[3]School of Applied and Engineering Physics, Cornell University, Ithaca, New York 14853, USA
[*]Corresponding author: peter.banzer@uni-graz.at

Abstract: Advances in photonics enable precise control of structured light for imaging, sensing, and quantum applications. While bulky optics limit scalability, photonic integrated circuits (PICs) offer compact solutions. Here we present a reconfigurable PIC to measure and generate structured and twisted light, enhancing applications in imaging, sensing, and manipulation.

Advances in optics and photonics have led to unprecedented control of the spatial and temporal properties of light fields, with applications ranging from optical imaging and sensing to communication and quantum technologies [1]. Central to these developments is the strong demand for precise and scalable tools to measure, manipulate, and generate structured light. Traditional approaches often rely on bulky free-space optics, which limit integration and scalability in real-world applications. Photonic integrated circuits (PICs) offer a promising solution, enabling compact, robust, and highly flexible platforms for structured light applications [2–4].

In this paper we present a PIC designed for the measurement and generation of structured and twisted modes of light, implemented on a silicon-on-insulator platform [2, 3]. Our photonic chip consists of a mesh of Mach-Zehnder interferometers in combination with carefully arranged grating couplers acting as a free-space interface (see Fig. 1). By actively controlling the interferometers, we guide light across the photonic circuit, enabling the characterization and generation of various structured light fields sampled by an application-tailored array of grating couplers.

We analyze the sampled light using a theoretical framework based on transmission matrices to obtain information about intensity, phase, and polarization. We discuss the basic physical principles underlying our measurement scheme [4] and demonstrate its applicability as a photonic sensor by processing fundamental Gaussian modes and higher-order light modes such as Laguerre-Gaussian (LG) and Hermite-Gaussian modes, as well as combinations thereof. We demonstrate on the example of LG modes the distinction and sensing of orbital angular momentum (OAM) states of light as well as the handedness of their twisted phase fronts [2].

By operating the chip in reverse, with a single injection waveguide (see Fig. 2) combined with the interferometric on-chip control, this configuration also enables the fast and precise generation of complex structured light fields in free space with well-defined amplitude and phase distributions [3]. Our results prove that the presented photonic chip provides a flexible workbench for numerous applications as well as developments towards future applications in imaging, sensing, or manipulation in nanooptics [5].

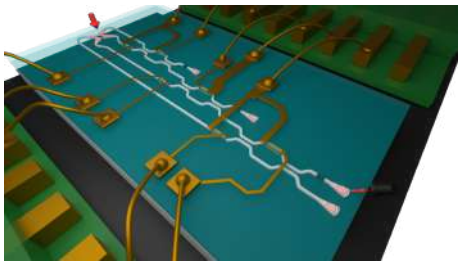


Figure 1: Simplified schematics of the photonic integrated circuit for light processing. Light is coupled into the chip through an application-tailored array of grating couplers, serving as a free-space interface. On-chip processing of the incoming light is performed by a mesh of actively controlled Mach-Zehnder interferometers, ultimately allowing for the extraction of information about its intensity, phase, and polarization through intensity measurements at the terminating waveguides through a correspondingly developed theoretical model.

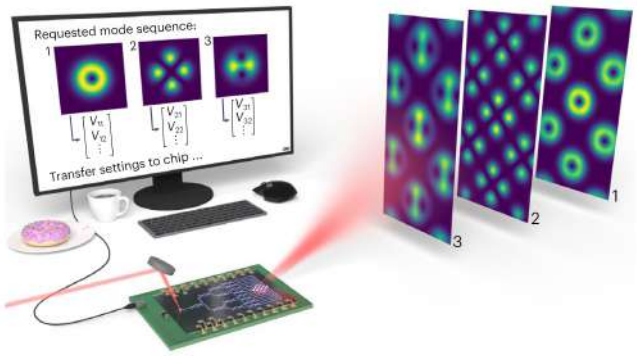


Figure 2: Overview of the light generation process using the photonic chip. A desired target field distribution or sequence is defined on a computer, upon which the required mesh configuration is calculated based on a corresponding theoretical model and transferred onto the chip. This allows distributing light from an injection waveguide in such a way that the chip re-emits it at terminating waveguides with tailored amplitude and phase, resulting in the desired far-field patterns, as exemplarily shown on the right. Reproduced with permission from Ref. [3].

Acknowledgments: Financial support from the Austrian Federal Ministry of Labour and Economy, the National Foundation for Research, Technology and Development, and the Christian Doppler Research Association is gratefully acknowledged.

References

1. Rubinsztein-Dunlop et al., "Roadmap on structured light", *Journal of Optics*, Vol. 19, No. 1, pp. 013001, 2016.

2. Bütow, J. et al., "Photonic integrated processor for structured light detection and distinction", *Communication Physics*, Vol. 6, No. 1, pp. 369, 2023.

3. Bütow, J. et al., "Generating free-space structured light with programmable integrated photonics", *Nature Photonics*, Vol. 18, No. 3, pp. 243–249, 2024.

4. Bütow, J. et al., "Spatially resolving amplitude and phase of light with a reconfigurable photonic integrated circuit", *Optica*, Vol. 9, No. 8, pp. 939–946, 2022.

5. Šimić, M. et al., In preparation.

THz metastructures using spintronic THz emitters

Christian Bohley[1], Ramaz Khomeriki[2], Vakhtang Jandieri[3], Dominik Schulz[1], Benjamin Schwager[1], Björn Niedzielski[1], and Jamal Berakdar[1,*]

[1]Martin-Luther University, Halle-Wittenberg, 06099 Halle, Germany
[2]Physics Department, Tbilisi State University, 3 Chavchavadze, 0128 Tbilisi, Georgia
[3]Faculty of Engineering, Center for Nanointegration Duisburg-Essen, 47048 Duisburg, Germany
[*]corresponding author: jamal.berakdar@physik.uni-halle.de

Abstract: We show that textured spintronic emitters can be used as THz metamaterials for molding the vectorial distribution and the topological properties of the emitted fields. The proposed metastructures are shown to control the sub-wavelength characteristics of propagating modes with the possibility for novel applications, as demonstrated for the non-destructive supercurrent generation in Type-II superconductors.

In layered heterostructures hosting a ferromagnetic layer interfaced with a normal metal with strong spin-orbit coupling, heating with an infrared laser leads to a buildup of a spin-polarized current emanating from the magnetic layer. The current diffuses into the normal layer where it is converted into a swiftly decaying charge current pulse due to spin-orbital scattering. The resulting coherent broadband THz radiation [1] can be well enhanced by material compositions. This element for producing THz radiation is called spintronic THz emitter (STE) [2].

Here, we propose to exploit intrinsic interactions in the magnetic/normal metal system for generating metastructures of such spintronic THz emitters [3,4,5]. By performing analytical and numerical micromagnetic/electromagnetic simulations, we demonstrate that appropriately engineered STE metastructures are capable of producing broadband, strong THz radiation with a predefined polarization, orbital, chiral, and topological properties. An example is shown in Fig.1. To demonstrate the usefulness of the emitted fields we quantified the action of these fields on the order parameter of a Type-II superconducting micron-size Niobium disc (Fig.1). Using time-dependent Landau-Ginzburg equations, we show how the topology of the THz fields results in a texturing of the superconducting phase while the superconducting density remains almost constant leading to a superconducting current only (Fig.1). Further numerical simulations evidence that the structured THz fields are utilizable for generating and steering on the nanoscale Abrikosov vortices, which can be useful for a *ps*-control of the transport properties of nanoscale superconductors. Further examples including driving non-collinear magnetic texture will be discussed.

The results point to a new way for the generation of structured broadband THz fields with possible applications in the fields of optoelectronics, ultrafast magnetism, and superconductivity.

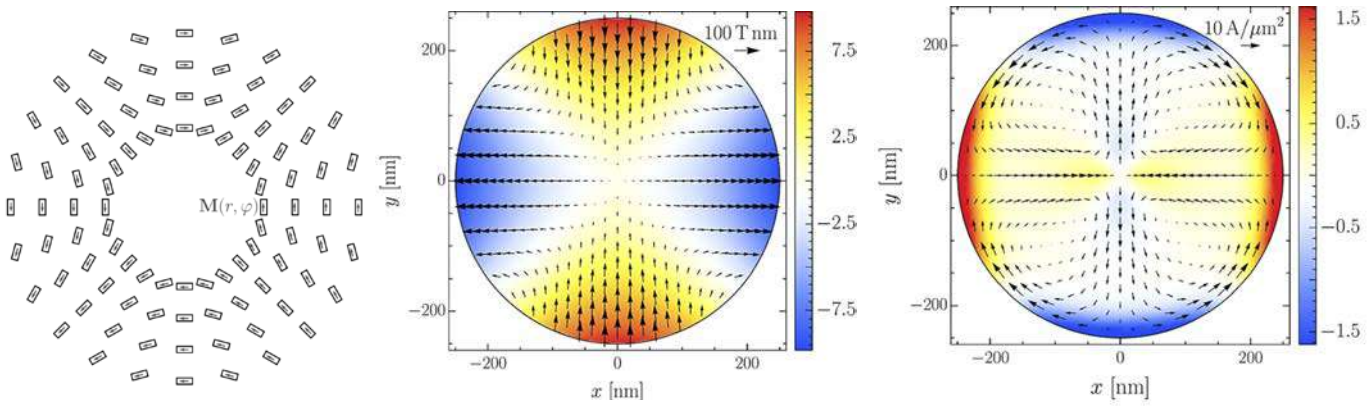


Figure 1: Left: Top view of the magnetization direction (arrows) **M** in the individual STEs leading to the THz emission of topological propagating fields. *Middle*: Typical vector potential of emitted radiation in a plane $5\mu m$ above the STEs. *Right:* $5\mu m$ above the STEs, the emitted fields are applied to a type-II superconducting Nb disc (with a 80 *nm* height, and a 250 *nm* radius) resulting in the depicted supercurrent density, while the superconducting density is basically preserved.

Acknowledgement: This research is supported financially by the Deutsche Forschungsgemeinschaft under SFB-TRR227 B06.

References

[1] Papaioannou, Th. E., and Beigang, R. "THz spintronic emitters: a review on achievements and future challenges" Nanophotonics, **10**, 1243-1257, (2021).

[2] Seifert, T. *et al.* "efficient metallic spintronic emitters of ultrabroadband terahertz radiation" Nat. Photonics **10**, 483–488 (2016).

[3] Schulz, D., Schwager, B., and Berakdar, J. "Nanostructured Spintronic Emitters for Polarization-Textured and Chiral Broadband THz Fields" ACS Photonics, **9**, 1248–1255 (2022).

[4] Niedzielski, B., Schulz, D., and Berakdar, J. "Spatio-temporal superconducting dynamics driven by THz fields

from topological spintronic terahertz emitters" Scientific Reports, **12**, 15610 (2022).

[5] Bohley, Ch. *et al.* "Subwavelength focused propagating broadband helical fields using spintronic THz emitters" *to appear*.

Tunable of Universal Quantum States at Weyl Semimetal Interstitial Interfaces with Magnetic Textures

E. Thareja[1], G. Pantano[1], I. Vekhter[2], and J. Gayles[1*]

[1]Department of Physics, University of South Florida, Tampa, FL 33620
[2]A
[*]corresponding author: gayles@usf.edu

Abstract: Magnetic multilayers combining Weyl and skyrmionic topologies enable tunable electronic states with novel functionalities. We model Fermi-arc-like bound states at interfaces, demonstrating tunability via magnetic and electrostatic potentials. Using CoGe/FeGe interfaces, we show enhanced spin-orbit coupling and transport phenomena, optimizing Weyl-skyrmion interactions for next-generation spintronic devices.

Magnetic multilayers of alternating Weyl and Skyrmionic topologies are highly sought for novel device technology due to the possibility of efficiently manipulating magnetic textures and realizing phenomena such as the quantum anomalous Hall effect. In magnetic Weyl semimetals, the electronic band structure features pairs of Weyl nodes with opposite chirality charges, and the momentum space position of these nodes can reverse across a planar interface, giving rise to Fermi-arc-like bound states. We use a low-energy approximation to show that a magnetic interstitial layer can tune these states in three distinct ways: the electrostatic potential and in-plane magnetic potential components control the shape of the bound-state Fermi-arcs, with moderate in-plane magnetic potentials spin-filtering electrons a chirality-reversed planar interface (CRPI)[1].

$$H_{CRPI}(\boldsymbol{q}, x) = \mathrm{sgn}(x) ta(n\tau_z q_z \sin k_0 a) + (U_0\tau_0 + \boldsymbol{U}\cdot\boldsymbol{\tau})\delta(x) + \tau_y q_y + \tau_x \hat{q}_x \quad (1)$$

Additionally, both in-plane magnetic components and electrostatic potentials regulate electron transmission, while the ratio of in-plane to out-of-plane magnetic components modulates magnetic potential effects. This tunability stems from spin-momentum locking and chirality reversal at the interface, allowing for a material-dependent interchange of states. Some of our seminal results are summarized in Figure 1. Our model can be universally extended to investigate 2D planar twinning interfaces in B20 compounds using first-principles calculations, focusing on the Weyl semimetal CoGe[2] with a FeGe[3] interstitial. By employing supercell calculations that restrict the interface to the primitive cell, we demonstrate that the spin and anomalous Hall effects are significantly enhanced due to increased spin-orbit coupling and atomic potential variations at the interface. We explore the interplay between nonmagnetic Weyl semimetals and magnetic skyrmion-hosting systems in heterostructures across two thickness regimes: one with a semi-infinite Weyl system and a thin skyrmion-hosting film and the other with a semi-infinite skyrmion system and a thin Weyl film. This work defines the physical bounds of skyrmion-Weyl interactions and determines methods to maximize the synergy of these two systems

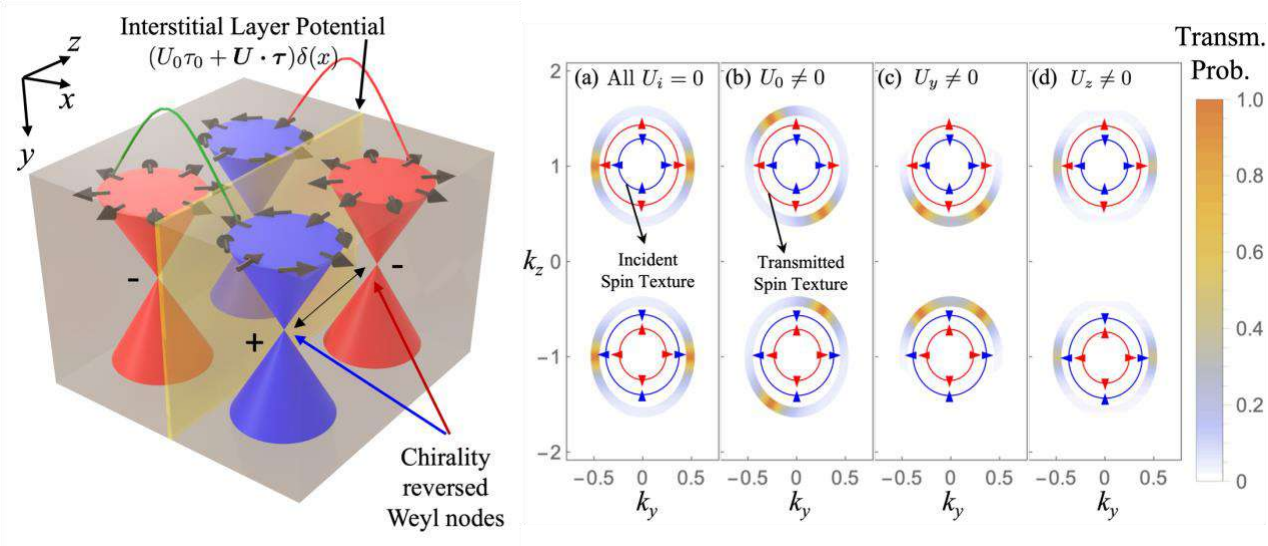


Figure 1. On the left is a schematic of the chirality-reversed planar interface (CRPI) which Weyl chirality denoted by red and blue. The interface is detailed by the yellow plane which consist of a δ electrostatic and magnetic potential. On the right are transport results of the transmission probability of electrons through the CRPI with variation of the inplane momenta. Inner (outer) circle arrows represent spin texture of the incident (transmitted) electron. The incident momentum component perpendicular to the interface kx = 0.1, energy E = 0.5t, and interface potentials (b) U_0 = t, (c) Uy = t and (d) Uz = t.

This material is based upon work supported by the Air Force Office of Scientific Research under award number FA9550-23-1-0132. J.G. and G.P. acknowledges support from the Max Planck Society through the Max Planck Partner Group Programme. Work was also supported by Research Corporation for Science Advancement under the grant number CS-CSA-2024-106.

References

1. Thareja, E., Pantano, G., Vekhter, I. & Gayles, J. Tuning Quantum States at Chirality-Reversed Planar Interface in Weyl Semimetals using an Interstitial Layer. (2025).
2. Spencer, C. S. et al. Helical magnetic structure and the anomalous and topological Hall effects in epitaxial B20 Fe1−*y*Co*y*Ge films. Phys. Rev. B 97, 214406 (2018).
3. Gayles, J. et al. Dzyaloshinskii-Moriya Interaction and Hall Effects in the Skyrmion Phase of Mn1−*x*Fe*x*Ge. Phys. Rev. Lett. 115, 036602 (2015).

Nonlinear chiral quantum photonics

N. Rotenberg[1]

[1] Centre for Nanophotonics, Department of Physics, Engineering Physics & Astronomy, Queen's University, Kingston, Canada

[*]corresponding author: nir.rotenberg@queensu.ca

Abstract: This talk explores the physics that emerge when different coloured photons simultaneously and coherently interact with a chirally-coupled single quantum emitter. We focus on the strength with which these interactions can be used to control the phase and amplitude of the scattered photons, showing that surprising trends emerge when compared to the more standard symmetric (i.e., not chiral) or single-beam configurations.

Two fundamental aspects of quantum optics that have benefited tremendously from the maturation of nanophotonic platforms are chiral and coherent nonlinear optics. This is due to the ability of nanophotonic systems to control the flow and structure of light at the same nanoscale dimensions that characterize quantum emitters such as atoms or quantum dots. For chiral quantum optics, the ability to shape complex vector light-fields results in directional interactions, where photons only interact with an emitter if they flow in one direction down a waveguide [1]. In this ideal case, the presence of the quantum emitter is imprinted only on the phase of the scattered photons, and not their amplitude (as is more usual). For nonlinear quantum optics, nanophotonic structures can enhance the efficiency of light-matter interactions to the point where strong coherent nonlinearities can be observed at the few-photon level. For a single molecule and two colors of photons, for example, this has enabled the observation of efficient nonlinearities originally predicted by Mollow for atomic clouds, including the AC Stark shift (a tuning of the emitter resonance) an energy exchange between the photon beams, and even a coherent amplification [2].

Here, I discuss our recent work to understand the physics that emerges at the union of these two aspects: that is, the coherent optical nonlinearities that emerge in chiral quantum systems. I show how such a system may be modeled, and then use this model to explore the nonlinear signatures on the spectra of the scattered photons. Although this (chiral) system is very similar to the more symmetric scenario considered by Mollow, surprising differences emerge. These will be highlighted, as will the way in which they could enable all-optical control of quantum optical states. Finally, I will touch on the structures that support and enable few-photon chiral nonlinear optics.

References

1. Lodahl, P, *et al.,* "Chiral quantum opitcs," Nature, Vol. 541, 473–480, 2017.
2. Tuerschmann, P., *et al.*, "Chip-based all-optical control of single molecules coherently coupled to a waveguide," Nano Lett., Vol. 17, 4941–4945, 2017.

Symmetry in magnetoelectric electromagnetism

E. O. Kamenetskii *

Ben Gurion University of the Negev, Israel
*corresponding author: kmntsk@bgu.ac.il

Abstract: When studying the relationship between electromagnetism and magnetoelectricity, one of the main questions is how to unite these two entities of different symmetry properties. There are claims that quantum vacuum can asymmetrically transfer momentum to ME structures. Conversely, dynamic processes in ME structures cause asymmetric transfer of momentum to vacuum.

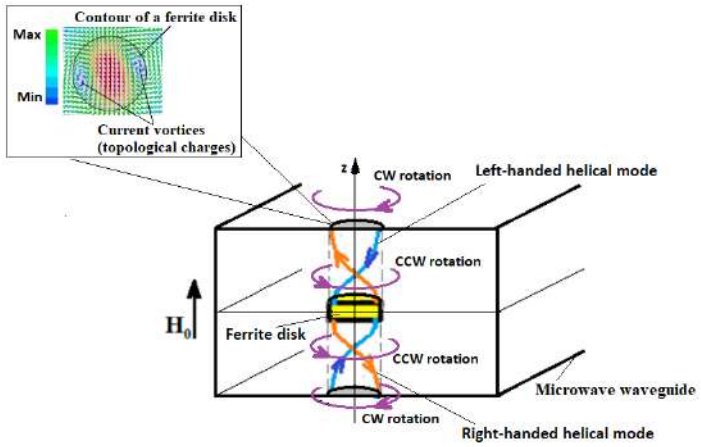
When studying the relationship between electromagnetism and magnetoelectricity, one of the main questions whether is it even possible to unite these two entities. This seems to be the cornerstone of magnetoelectric (ME) QED. While in electromagnetism we have space-time symmetry, ME processes are characterized by space-time symmetry breakings. The propagation of an EM wave is considered as a process of coupling between polar (e.g., E-field) and axial (e.g., H-field) vectors in a region the size of a wavelength. In the ME meta-atom, we observe the coupling between polar and axial vectors in the subwavelength region. There are claims that the vacuum can impart momentum asymmetrically on ME structures. Asymmetric momentum transfer arises from the ME structure since it breaks the temporal and spatial symmetries of electromagnetic modes.

In a 3D-confined structure of a magnetic insulator with magnetodipolar mode (MDM) oscillations, an orbital angular momentum (OAM) as well as a spin angular momentum (SAM) can be observed along a static magnetic field. In such a confined structure as quasi-2D ferrite disk, energy levels of MDM oscillations are quantized. Quantum confinement is characterized by a half-integer internal OAM, which is also associated with a circulating energy flow. The ME effect can be realized through magnetic modes that break both space-inversion and time-reversal symmetries. We consider ME magnon-photon coupling in cavities hosting ferrite ME meta-atoms. In this structure, quantum vacuum field fluctuations of the photons confined in the cavity are ME fields.

In the Figure, we show a structure in which a small ferrite disk is placed in a rectangular waveguide in close proximity to the waveguide walls. There are quasistatic solutions for helical modes. Rotation of the electric field in a ferrite disk is in the angular momentum balance with the rotation of electric currents and topological charges induced on the metal walls. We can observe *braided fields in vacuum* cylinders above and below a ferrite disk. The insertion shows the topology of surface electric currents on the upper wall of a waveguide. The whole picture of this topological structure rotates clockwise.

Inside a ferrite disk, the total angular momenta of CW and CCW modes do not eliminate each other. The CW – CCW asymmetry in a ferrite disk would give the vacuum an angular momentum in one azimuth direction, and the metal wall of the cavity would have to gain momentum in the opposite direction to compensate. The spin and orbital angular momentum of vacuum zero fluctuations contribute to the motion of electrons on the metal walls of the cavity. The possibility of extracting momentum from vacuum was discussed by Feigel [1]. Feigel argued that the momentum of vacuum zero fluctuations can occur only in a structure with PT-symmetry breakings. The main idea is to suggest a new quantum mechanical effect, namely the extraction of momentum from the electromagnetic vacuum oscillations. In the proposed effect, momentum is extracted from a vacuum field. This is different from the case of the Casimir

effect, in which energy is extracted from a vacuum field [2]. In Ref. [3], Feigel argued that rotating ME particles can generate changes in momentum of zero-point fluctuations, which result in the self-propulsion in quantum vacuum. The self-propulsion requires mechanical back-action from ME particle. To provide this ME particle should be a propellor-like device. In our case, we see that, while keeping the solid body motionless, the rotating fields of ME particles modify the momentum of quantum vacuum



[1] A. Feigel, “Quantum vacuum contribution to the momentum of dielectric media”, Phys. Rev. Lett. 92, 020404 (2004).

[2] O. J. Birkeland, I. Brevik, “Feigel effect: Extraction of momentum from vacuum?”, Phys. Rev. E 76, 066605 (2007).

[3] A. Feigel, “A magneto-electric quantum wheel”,arXiv:0912.1031 (2009).

One-way transparency at custom wavelengths via a layered magnetoelectric window

A. M. Kuzmenko[1], A. A. Mukhin[1], A. Shuvaev[2], A. Pimenov[2] and D. Szaller[2,3*]

[1]Prokhorov General Physics Institute, Russian Academy of Sciences, 119991 Moscow, Russia

[2]Institute of Solid State Physics, TU Wien, 1040 Vienna, Austria

[3]HUN-REN–BME Condensed Matter Physics Research Group, 1111 Budapest, Hungary

Corresponding author: szaller.david@ttk.bme.hu

Abstract: We demonstrate one-way transparency in a tunable artificial structure of split-ring metamaterial and magnetic substrate, overcoming the temperature and resonance frequency limitations of multiferroic crystals. This dynamic interaction enables controllable non-reciprocal light propagation, paving the way for practical applications.

The study of controllable non-reciprocal light propagation is driven by both fundamental interest and telecommunication applications. So far, polarization-independent, switchable one-way transparency has only been achieved in multiferroic crystals under cryogenic temperatures and high magnetic fields, limiting its practical use. Here [1], we present an alternative approach using an artificial layered structure composed of split-ring metamaterial and magnetic substrate layers interacting in the dynamic regime. Our quasi-optical experiments in the GHz range show that this system breaks both time-reversal and spatial inversion symmetries under a moderate external magnetic field. The ability to tune its dynamic response and achieve controllable one-way transparency makes this method highly promising for real-world applications.

The proposed one-way transparent structure consists of a paramagnetic gadolinium gallium garnet ($Gd_3Ga_5O_{12}$, GGG) layer coupled to a two-dimensional periodic array of split-ring resonators. [**?**] In contrast to most of the experimental studies of non-reciprocity in multiferroics (e.g. [2, 3]), our sample possesses no spontaneous magnetic or ferroelectric ordering, and the magnetoelectric interaction is manifested only in the dynamic regime. The presence of both the paramagnetic and the split-ring layers and their electromagnetic coupling by the close vicinity are essential to the realization of the non-reciprocal propagation of light.

The physical mechanism behind the proposed effect can be understood through a simple argument. A linearly polarized electromagnetic wave propagating along the z-axis, with oscillating (ac) field components e_x and h_y, excites the split rings lying in the xy-plane via the electric channel when their gaps are aligned along the x-axis. Due to induction, currents in the rings generate a secondary ac magnetic field along the z-direction. When combined with the wave's h_y component, this results in an elliptically polarized magnetic field with a rotational axis along x. This field interacts with the paramagnetic moments in the GGG layer, which are aligned by the static external magnetic field.

The precession direction of the magnetic moments is dictated by the external field's sign, while the rotation sense of the ac-field h_{yz} is determined by the experimental geometry. Consequently, the two can either rotate in the same direction or in opposite directions. Ideally, in the first case, strong magnetic absorption occurs, whereas in the latter, absorption is suppressed.

In a our experiments, we observed a strongly asymmetric transmission of the structure with respect to the applied field direction. In a similar structure, where centrosymmetry is restored,

the light propagation was reciprocal. The results are interpreted in a phenomenological model consisting of coupled magnetic and electric oscillators.

We acknowledge enlightening discussions with R. Pisarev. This work was supported by the Russian Science Foundation (16-12-10531) and by the Austrian Science Funds (W1243, I 2816-N27, I 1648-N27, TAI 334-N). D.S. acknowledges the support of the Hungarian Academy of Sciences via the János Bolyai Research Grant (BO-00580/22/11) and that of the National Research, Development and Innovation Office of Hungary (STARTING 150230, 2023-1.2.4-TÉT-2023-00051).

References

1. Kuzmenko, A. M., A. A. Mukhin, A. Shuvaev, A. Pimenov and D. Szaller, "One-way transparency at custom wavelengths via a layered magnetoelectric window", submitted to *Phys. Rev. B*, 2024.

2. Schneider, A., A. Shuvaev, S. Engelbrecht, S. O. Demokritov, and A. Pimenov, "Electrically Excited Inverse Electron-Spin-Resonance", *Phys. Rev. Lett.*, Vol. 103, pp. 103907, 2009.

3. Kézsmárki, I., D. Szaller, S. Bordács, V. Kocsis, Y. Tokunaga, Y. Taguchi, H. Murakawa, Y. Tokura, H. Engelkamp, T. Rõõmm and U. Nagel, "One-way transparency of four-coloured spin-wave excitations in multiferroic materials", *Nat. Commun.*, Vol. 5, pp. 3203, 2014.

4. Kuzmenko, A. M., V. Dziom, A. Shuvaev, Anna Pimenov, M. Schiebl, A. A. Mukhin, V. Yu. Ivanov, I. A. Gudim, L. N. Bezmaternykh, and A. Pimenov, "Giant directional birefringence in multiferroic ferroborate", *Phys. Rev. B*, Vol. 92, pp. 184409, 2015.

Skyrmion Hall effect in altermagnets

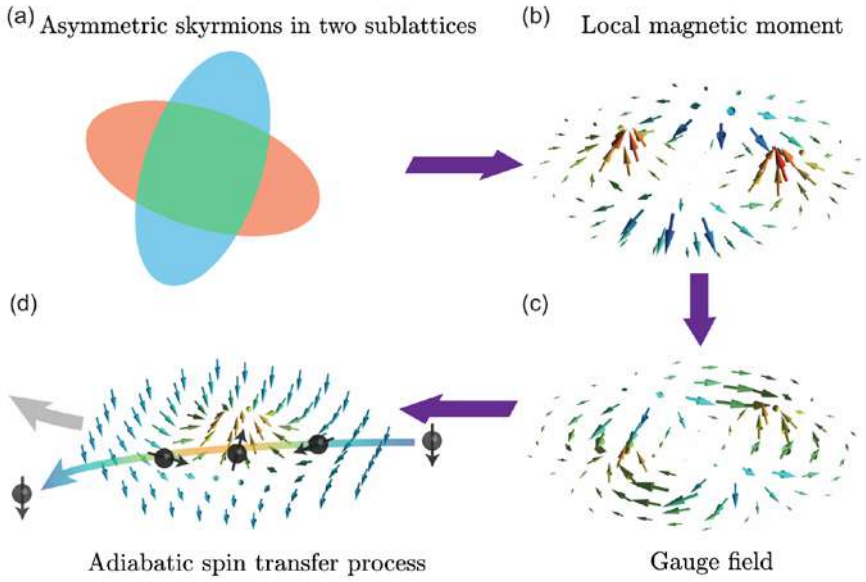
Z. Jin[1], Z. Zeng[1], Y. Cao[1], and P. Yan[1*]

[1]School of Physics and State Key Laboratory of Electronic Thin Films and Integrated Devices,

University of Electronic Science and Technology of China, Chengdu 610054, China

[*]corresponding author: yan@uestc.edu.cn

Abstract: It is widely believed that the skyrmion Hall effect is absent in antiferromagnets because of the vanishing topological charge. However, the Aharonov-Casher theory indicates the possibility of topological effects for neutral particles. Here, we predict the skyrmion Hall effect in emerging altermagnets with zero net magnetization and zero skyrmion charge.



We first show that the neutral skyrmion manifests as a magnetic quadrupole in altermagnets.We reveal a hidden gauge field from the magnetic quadrupole, which induces the skyrmion Hall effect when driven by spin transfer torque. Interestingly, we identify a sign change of the Hall angle when one swaps the anisotropic exchange couplings in altermagnets. Furthermore, we demonstrate that both the velocity and Hall angle of altermagnetic skyrmions sensitively depend on the current direction. Our findings real the critical role of magnetic quadrupole in driving the skyrmion Hall effect with vanishing charge, and pave theway to discovering new Hall effect of neutral quasiparticles beyond magnetic skyrmions.

This work was funded by the National Key R&D Program under Contract No. 2022YFA1402802, and the National Natural Science Foundation of China (NSFC) (Grants No. 12434003, No. 12374103, and No. 12074057). Z. J. acknowledges the financial support from NSFC (Grant No. 12404125) and the China Postdoctoral Science Foundation (Grant No. 2024M750337).

Reference

1. Jin, Z., Zeng, Z., Cao, Y., Yan, P., “Skyrmion Hall effect in altermagnets,” PRL, Vol. 133, No. 19, 196701, 2024.

Optically and Magnetically Responsive Metamaterial Capsules for Drug Delivery

P. Ginzburg[1,*]

and H. Barhom, A. Machnev, A. Ushkov, D. Kolchanov, P. Bezrukov

T. Salgals, V. Bobrovs

[1]Department of Electrical Engineering, Tel Aviv University, Ramat Aviv, Tel Aviv, 69978 Israel
[2]Institute of Telecommunications Riga Technical University, Azenes Street 12, Riga, 1048 Latvia
[*]corresponding author: pginzburg@tauex.tau.ac.il

Abstract: Nanoparticles, with their ability to integrate multiple biomedical modalities, are among the most promising candidates for developing electromagnetically-responsive theranostic carriers. We present the concept of a metamaterial drug delivery capsule based on golden and magnetized vaterite, highlighting its distinct advantages in the emerging field of light-activated theranostics.

The presentation is based on our recent works [1], [2], [3], [4], [5], [6], [7], [8] and on a large set of new data. On top of our published results, we will demonstrate novel light-driven functions, including release, uptake acceleration, and cell treatment, underlying 'golden', 'gilded', and magnetized' vaterite advantages.

The fast-changing and evolving landscape of biomedical challenges motivates the continuous development of new functional platforms. Implantable devices made from biocompatible materials, capable of responding to optical signals and tailoring propagation of light waves, can be employed in health monitoring applications and therapeutics. The incorporation of such elements into living organisms can boost light-tissue interactions and shift conventional approaches toward precision medicine by opening new opportunities in sensing, photothermal therapy, photoacoustic tomography, and bioimaging. One of the grand challenges on those pathways is the miniaturization of biocompatible photonic structures along with providing multiple functionalities, such as monitoring of vital biological processes, light-responsive drug release, or local heating of a nanoscale area with the simultaneous measurement of its temperature.

The vaterite polymorph of calcium carbonate ($CaCO_3$) has a wide scope of potential applications in biology and medicine due to its outstanding combination of chemical, morphological, and physical properties. Being a fully biocompatible, FDA-approved material, it possesses a sponge-like morphology that effectively entraps a variety of functional materials. In addition, vaterite synthesis is a cheap, simple yet flexible process, yielding particles of different shapes depending on the chemicals used. As cargo release from vaterite particles is associated with structural transformations, an understanding of particle−fluid interactions is required for the future advancement of this material platform toward targeted drug delivery needs. Furthermore, the propulsion and diffusion of capsules are also dependent on interaction with a fluid environment, further motivating the performance of detailed studies with full control over parameters. Figure 1 is our executive summary. The panels on the left demonstrate the different shapes of fabricated particles. The shapes are not only responsible for optical properties but have a crucial impact on particle-cell interaction dynamics, as we will demonstrate. The right panel is 'golden' vaterite' – small 3nm size gold nanoparticles are diffused into the mesoporous matrix, thus creating a new metamaterial – this structure possesses an artificial localized plasmon resonance at the infrared spectral range, matching the biological transparency window. The bottom part is the imaging.

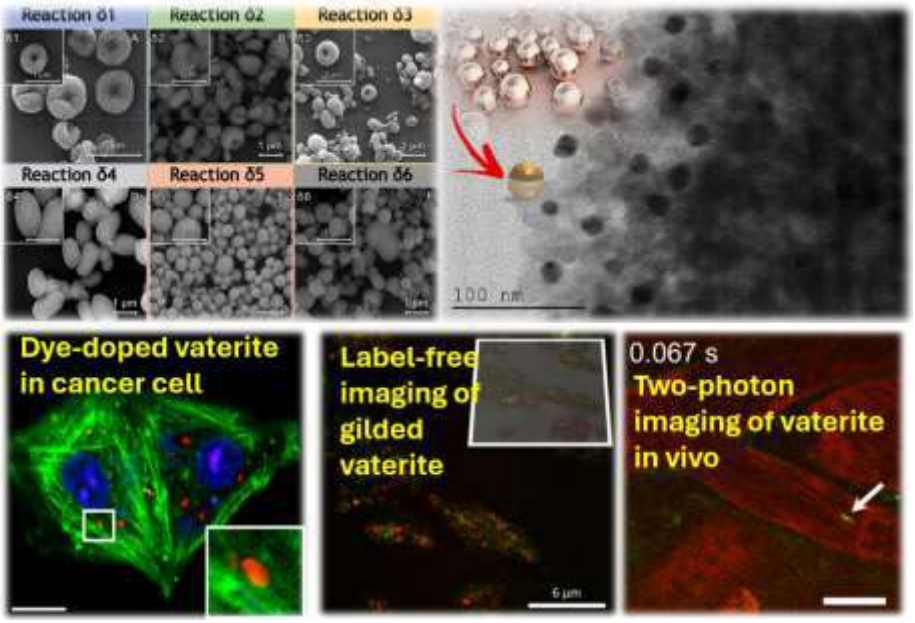


Fig. 1: Vaterite. (Left) Particles of different shapes to tailor both optical properties and particle-cell interaction dynamics. (Right) 'Golden' Vaterite – TEM image of CaCO3 matrix, loaded with gold nanoparticles. Bottom: Imaging of capsules in vitro and in vivo.

We demonstrated a new mesoscopic approach to on-demand engineering of electric and magnetic resonances in submicron low-index vaterite spherulites by filling them with gold nano inclusions. This makes it possible to increase the effective permittivity of the structure and provide efficient light trapping. The controllable variations in the volumetric gold filling factor allow tuning the spectral positions of both Mie resonances from the dipole to octupole order within the visible and near-infrared ranges. As an example of a potential thermal therapy application, we demonstrate an efficient laser heating of golden spherulites. Both water suspensions and individual spherulites, being illuminated with near-infrared light were investigated via time-resolved fluorometry and fluorescence-lifetime imaging microscopy (FLIM) and demonstrated an efficient local temperature elevation. The combination of various Mie resonances, high payload capacity for drugs, and the submicron size offer golden vaterite as a unique platform for multifunctional biomedical nanophotonic devices. The fabrication of the samples is made with the aid of colloidal chemistry.

References

1. R. E. Noskov, I. I. Shishkin, H. Barhom, and P. Ginzburg, "Non-Mie optical resonances in anisotropic biomineral nanoparticles," Nanoscale, vol. 10, no. 45, pp. 21031–21040, Dec. 2018,
2. R. E. Noskov et al., "Golden Vaterite as a Mesoscopic Metamaterial for Biophotonic Applications," Advanced Materials, vol. 33, no. 25, p. 2008484, Jun. 2021, doi: 10.1002/ADMA.202008484.
3. H. Barhom et al., "Biological Kerker Effect Boosts Light Collection Efficiency in Plants," Nano Lett, vol. 19, no. 10, pp. 7062–7071, Oct. 2019, doi: 10.1021/acs.nanolett.9b02540.
4. H. Bahrom et al., "Controllable Synthesis of Calcium Carbonate with Different Geometry: Comprehensive Analysis of Particle Formation, Cellular Uptake, and Biocompatibility," ACS Sustain Chem Eng, vol. 7, no. 23, 19142, 2019.
5. D. Harpaz, H. Barhom, B. Veltman, P. Ginzburg, and E. Eltzov, "Biocompatibility characterization of vaterite with a bacterial whole-cell biosensor," Colloids Surf B Biointerfaces, vol. 222, p. 113104, 2023
6. H. Gilad et al., "Gilded vaterite optothermal transport in a bubble," Scientific Reports 2023 13:1, vol. 13, no. 1, pp. 1–11, Jul. 2023, doi: 10.1038/s41598-023-39068-8.
7. A. Ushkov, A. Machnev, and P. Ginzburg, "Controllable switch of dissolution kinetics mechanism in drug microcapsules," Apr. 2023, Accessed: Jun. 02, 2023.
8. D. Kislov et al., "Optothermal Needle-Free Injection of Vaterite Nanocapsules," Advanced Science, vol. 11, no. 5, p. 2305202, Feb. 2024, doi: 10.1002/ADVS.202305202.

Microwave coherent storage based on the long lifetime cavity electromechanical system

Tiefu Li[1*]

[1]Tsinghua University, China
[*]corresponding author: litf@tsinghua.edu.cn

Abstract: We demonstrate coherent microwave signal storage in a cavity electromechanical system. 55ms storage time has been experimentally realized. This result shows potential of cavity electromechanical systems with high-quality factors for the application in quantum storage devices for quantum computers.

Cavity optomechanical system holds potential for applications in ultrasensitive detection and serves as a fundamental element in the development of general quantum networks. Here we demonstrate the coherent storage of microwave signals in the gigahertz range using a cavity electromechanical system consisting of a high-quality SiN membrane resonator and a superconducting cavity. The membrane resonator was first cooled to its quantum ground state, where the phonon occupation number is 0.79. Subsequently, through the operations of writing, storing, and restoring, we demonstrate the coherent storage of microwave signals, which is manifested in the precise reproduction of the amplitude and phase of the written signal. The experimental results show a coherent storage time of 55 milliseconds, which means that less one thermal noise phonon is thermalized during this interval. This suggests that cavity electromechanical systems with high-quality factors hold significant potential for application in quantum storage devices for quantum computers.

References

1. Liu, Y. L., Liu, Q. C., Sun, H. Y., Chen, M., Wang, S. P., and Li, T. F., “Coherent memory for microwave photons based on long-lived mechanical excitations,” npj Quantum Inf., Vol. 9, 80, 2023.
2. Liu, Y. L., Liu, Q. C., Wang, S. P., Chen, Z., Sillanpää, M. A., and Li, T. F., “Optomechanical Anti-Lasing with Infinite Group Delay at a Phase Singularity,” Phys. Rev. Lett., Vol. 127, 273603, 2023.

Can the spinterface model explain all different CISS related effects?

A. Sharoni[1]*, S. Alwan[2] and Y. Dubi[2]

[1] Department of Physics & Institue of Nanosciene, Bar Ilan University, Ramat Gan 590002, Israel

[2] Department of Chemistry, Ben Gurion University of the Negev, Beer Sheva, Israel
*corresponding author: amos.sharoni@biu.ac.il

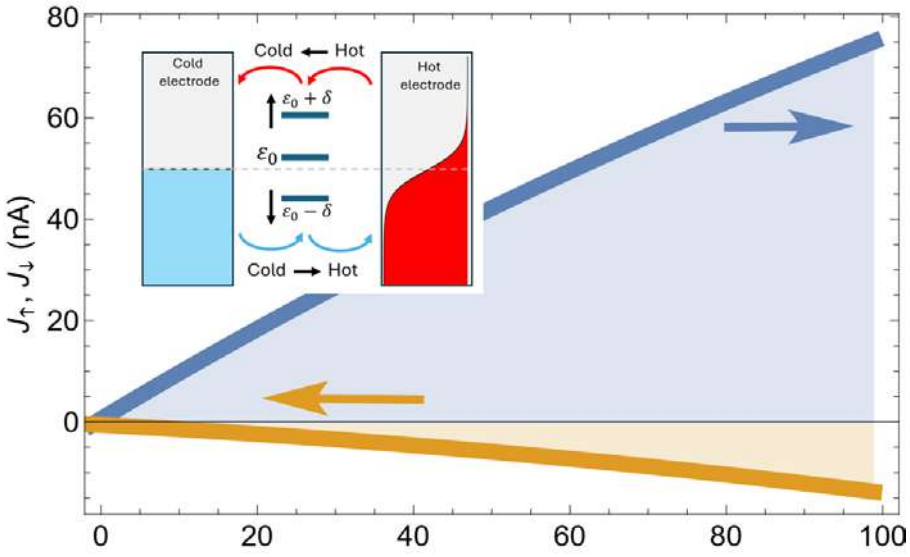
Abstract:
The CISS effect, where chiral materials cause magnetic like behavior has different manifestations, including in electron transport, photoelectric effect, magnetic switching, and others. But can these effects be understood from one underlying theory? We show our spinterface model explains many of the effects. However, there is still work to be done.

The chirality-induced spin selectivity (CISS) effect was reported a quarter of a century ago and relates to a number of different observational findings that reveal that chiral layers (usually of molecules) can preferentially transmit electrons with specific spin orientations. This can influence transport properties, optical properties, enantioselectivity and more. The effect is clearly rising from the chirality of the layers, since the preferred spin orientation is reversed when the chirality is reversed.

Interest in the CISS effect has increased in the past decade due to being potentially useful for a variety of applications, including spintronic devices (chiral-based magnetic memory devices and non-magnetic efficient spin sources for spin logic devices), chiral semiconductors and semimetals for displays, spintronics and sensors, and even quantum technologies (quantum spin-state preparation and manipulation, and chiral-based qubits and quantum gates).

Interestingly, there is still no agreement on the origin of this effect. W number of theoretical explanations have been put forward to explain the CISS effect, yet to date, there is no agreement to the underlying physical mechanism. Moreover, it is not clear if the same mechanism is common to all the various experimental observation that were all clumped under the CISS umbrella, and even on what constitutes the CISS effect and its signatures.

In this talk we will show our approach, referred to as the spinterface model, as a plausible explanation for the CISS effect. We will present its strong suits in capturing quantitatively many of the experimental observations, but also critically discuss where it (and other theories) is still lacking. We will also describe a series of old and new predictions which arise from the spinterface model, which we invite the experimental CISS community to test and the theory community to challenge.



In this figure we exemplify the spinterface predication for the thermoelectric effect, showing current as a function of temperature-difference for different electrode magnetizations (parallel and antiparallel to the current flow, blue and orange lines respectively). For the relevant junction parameters (which will be discussed), the current can change direction when the electrode magnetization is reversed (or equivalently the molecular chirality), a signature of the spinterface mechanism. Inset: schematic of the thermo-electric CISS effect.

References

1. Alwan, S. and Y. Dubi, Spinterface Origin for the Chirality-Induced Spin-Selectivity Effect. Journal of the American Chemical Society, 143, 14235 (2021).

2. Alwan, S., Sharoni, A. and Y. Dubi, The role of electrode polarization in the electron transport chirality-induced spin-selectivity effect. The Journal of Physical Chemistry C 128, 6438 (2024).

3. Alwan, S., Sarkar, S., Sharoni and Y. Dubi, Temperature-dependence of the chirality-induced spin selectivity effect—Experiments and theory. The Journal of Chemical Physics, 159 014106 (2023).

4. Monti, O. L. A. and Y. Dubi. *Surface Magnetic Stabilization and the Photoemission Chiral-Induced Spin-Selectivity Effect*. Journal of the American Chemical Society **146**, 32795 (2024).

Plasmonic Nanocrystals for Hot Electron Generation and Chiral Photochemistry

Alexander Govorov

Ohio University, Athens, USA
govorov@ohio.edu

Abstract: Plasmonic nanostructures with hot spots exhibit significantly amplified optical and energy-related effects, including the hot-electron generation via plasmonic hot spots for photochemistry and photodetection, chiro-optical plasmonic phenomena for sensing chiral biomolecules and asymmetric photochemistry, and more.

Plasmonic nanostructures with hot spots exhibit significantly amplified optical and energy-related effects. This talk will cover the following phenomena:

(1) Plasmonic hot spots efficiently generate energetic electrons, which can be applied in photochemistry and photodetection.

(2) Nanostructures with small interparticle gaps enhance optical heat generation and confine high photo-temperatures to small volumes.

(3) Colloidal nanocrystal assemblies and metastructures with plasmon resonances significantly amplify biomolecules' chiral optical responses (circular dichroism) and induce chiral photochemical effects.

Manipulating Light-Driven Nanoscale Vectorial Currents

Hou-Tong Chen[1*]

[1]Los Alamos National Laboratory, USA
[*]corresponding author: chenht@lanl.gov

Abstract: By breaking the inversion symmetry in a class of optoelectronic metasurfaces, nanoscale vectorial photocurrents and terahertz cylindrical vector beams have been successfully demonstrated through integrating raindrop-shaped plasmonic nanoantennas on graphene as a model system. Appropriate symmetry designs further enable the control of the photocurrent direction utilizing the incident light polarization.

The generation directional photocurrent generally requires breaking the spatial inversion symmetry or time reverse symmetry. This could be accomplished by applying electric and/or magnetic fields, using materials without a centrosymmetric crystal structure, or extrinsically by nanostructure patterning. Here we show that in a class of optoelectronic metasurfaces, the inversion symmetry-broken plasmonic nanoantennas can lead to a preference of direction for the flow of the excited hot electron near the plasmonic hotspot, and generation of ultrafast terahertz radiation and vector beams when excited by femtosecond lasers.

More specifically, we integrate arrays of teardrop-shaped gold nanoantennas designed to resonate at near-infrared wavelengths (800 nm and 1550 nm) on top of large-area CVD graphene. The plasmonic hotspot concentrates the incident light and enhances the light absorption in graphene near the sharp tip of the nanoantenna. The excited hot electrons see a broken inversion symmetry environment: a fixed Fermi energy level for graphene underneath the gold nanoantenna and a tunable and different Fermi energy level for the bare graphene outside the gold nanoantenna. This leads to a difference in graphene Seebeck coefficient when hot electrons look toward left (i.e., gold nanoantenna) and right (i.e., bare graphene) directions, resulting in a net directional flow of charge carriers. We investigated such a light-driven directional current generation by varying the nanoantenna size, excitation fluence, wavelength and polarization, nanoantenna orientation patterning, and graphene Fermi energy level (by back gating).

We further investigated the generation of ultrafast terahertz radiation and cylindrical vector beams arising from the transient nanoscale vectorial photocurrents upon femtosecond laser excitations. We found that appropriate designs of nanoantenna symmetry allow us to control the direction of the nanoscale current by tuning the polarization direction of the linearly polarized incident light. The demonstrated optoelectronic metasurface platform can impact many research fields such as ultrafast terahertz generation, photodetection, microscopic magnetism, ultrafast spintronics, etc.

We acknowledge the partial support provided by the Los Alamos National Laboratory Laboratory Directed Research and Development (LDRD) program. This work was primarily performed at the Center for Integrated Nanotechnologies, an Office of Science User Facility operated for the U.S. DOE Office of Science. Los Alamos National Laboratory is managed by Triad National Security, LLC for the US DOE NNSA, under contract no. 89233218CNA000001.

References

1. Pettine, J., P. Padmanabhan, T. Shi, L. Gingras, L. McClintock, C.-C. Chang, K. W. C. Kwock, L. Yuan, Y. Huang, J. Nogan, J. K. Baldwin, P. Adel, R. Holzwarth, A. K. Azad, F. Ronning, A. J. Taylor, R. P. Prasankumar, S.-Z. Lin, and H.-T. Chen, “Light-driven nanoscale vectorial currents,” Nature Vol. 626, No. 8001, 984–989, 2024.

Planar Dielectric Structures with Mirror Symmetry Broken by Substrate as Versatile Sources of Chiral Light

A. V. Mamonova[1*], P. M. Kovaleva[2], A. A. Antonov[3] and M. V. Gorkunov[1]

[1]Shubnikov Institute of Crystallography, NRC "Kurchatov Institute", Russia

[2]Faculty of Physics, Lomonosov Moscow State University, Russia

[3]Chair in Hybrid Nanosystems, Faculty of Physics Ludwig-Maximilians-University, Germany

* Corresponding author: alen.mamon@yandex.ru

Abstract: Planar dielectric structures with mirror symmetry broken by substrate exhibit strong circular dichroism for normally and obliquely incident light. We demonstrate that these structures implemented on different material platforms, such as perovskites or noncentrosymmetric semiconductors, perform as efficient luminescent and second harmonic sources of circularly polarized light.

Chiral metasurfaces are capable of maximum optical chirality – selective interaction with light of particular helicity. The fundamental requirement for this is the absence of mirror symmetry planes. In practice, fabrication of structures with such symmetry demands complicated technological capabilities, as it involves assembling meta-atoms with different tilts or heights [1, 2]. The most straightforward method to break the mirror symmetry is to use a substrate [3]. Apart from applying such chiral metasurfaces as chiral mirrors or polarization filters, they can be used as efficient sources of chiral light. In this study, we demonstrate that a planar dielectric structure with mirror symmetry broken by a substrate can perform strongly chiral luminescence and second harmonic generation (SHG).

We consider a C_{4h}-symmetric photonic crystal slab (PCS), see Figure 1a), which does not convert polarization of normally incident waves. Without substrate, the PCS is optically non-chiral. Upon a substrate, the PCS exhibits a pair of near-maximum chiral transmission resonances for left circularly polarized (LCP) and right circularly polarized (RCP) light, Figure 1b). Note that the transmission chirality is maintained when the light is incident at a small angle from the normal [3]. To analyze chiral luminescence capabilities of such PCS made of perovskite semiconductor $MAPbBr_3$, we model the spectra and the degree of circular polarization (DCP) of emitted light in COMSOL Multiphysics using the reciprocity principle. We obtain that the metasurface emits into a narrow cone between $\pm 5^\circ$ along the side and $\pm 2^\circ$ along the diagonal of the PCS unit cell. The DCP achieves the values of ± 0.8 within this directions, see Figure 1c).

We also model in COMSOL Multiphysics SHG by a metasurface of similar design with the PCS made of noncentrosymmetric semiconductor AlGaAs with the normal directed along the [101] crystallographic axis. Pumping wavelength is varied in order to generate second harmonic (SH) in the range covering the chiral linear transmission resonances, see Figure 1b). If the metasurface is pumped by RCP or LCP light, the SH intensity spectra manifest Fano-type resonances, see Figure 1d). Almost full conversion of circular polarization during SHG is observed, similarly to the performance of a homogeneous layer of AlGaAs of the same crystal orientation. In the case of linearly polarized pumping, strong dependence on the pumping polarization direction relatively to the AlGaAs crystal axis is observed. When the direction of the pumping polarization coincides with the crystal axis, i.e., $\alpha = 0^\circ$ on Figure 1e), Lorentz-type resonances are observed. When the direction of the pumping polarization is perpendicular to the crystal axis, i.e., $\alpha = \pm 90^\circ$ on Figure 1e), Fano-type resonances are observed.

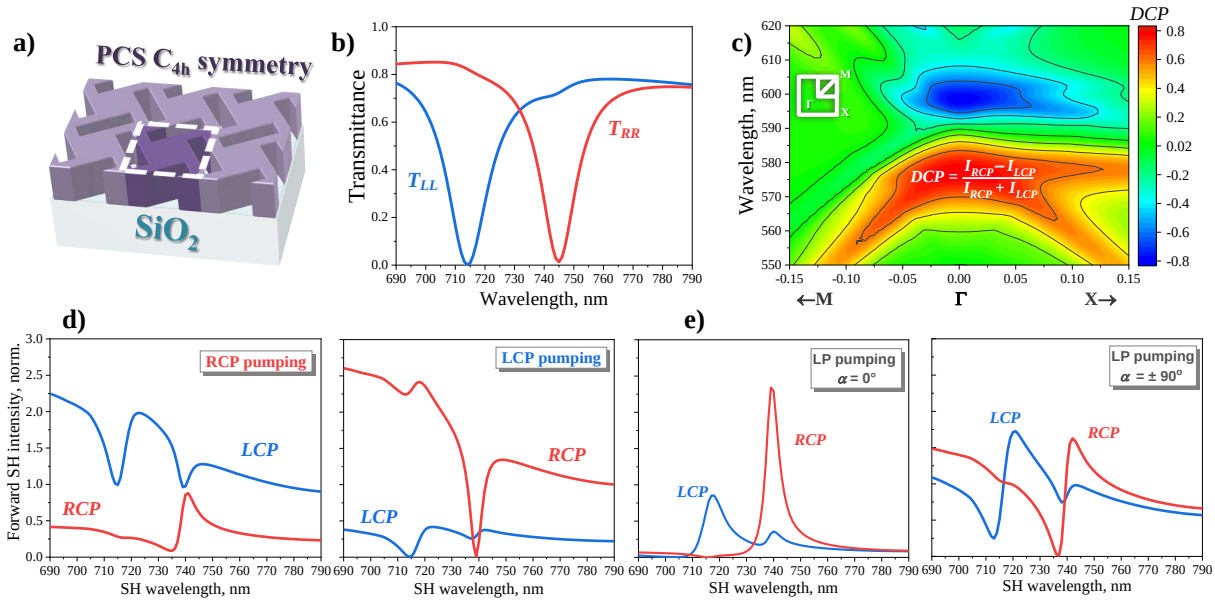


Figure 1: a) Scheme of the planar chiral structure: C_{4h}-symmetric PCS on a SiO_2 substrate with the unit cell marked by white dashed square. b) Simulated transmission spectra of LCP and RCP light of an AlGaAs PCS on glass. c) Colormap of luminescence DCP of a $MAPbBr_3$ PCS on glass in the axes of the in-plane wavenumber and wavelength. Spectra of SH intensity generated by circularly polarized (d) and linearly polarized (e) pumping of an AlGaAs PCS on glass. Different angles α between the pumping polarization and the AlGaAs crystal axis are shown in e).

In this study, we consider rotational symmetric PCSs on substrates that exhibit maximum optical chirality in linear transmission. We demonstrate the versatility of such structures for applications in chiral optics as luminescent emitters of circularly polarized light of either handedness at very close wavelengths. We also show that they can perform as nonlinear sources of chiral light of either handedness depending on the pumping field polarization and wavelength.

The work of A.V. and M.V. is supported by the Russian Science Foundation (project 23-42-00091, https://rscf.ru/project/42-00091/). The work of A.A. is funded by the European Union* (EIC, OMICSENS, 101129734).
*Views and opinions expressed are however those of the author(s) only and do not necessarily reflect those of the European Union or the European Innovation Council and SMEs Executive Agency (EISMEA). Neither the European Union nor the granting authority can be held responsible for them.

References

1. Kühner, L., et al. “Unlocking the out-of-plane dimension for photonic bound states in the continuum to achieve maximum optical chirality,” *Light Sci Appl*, Vol. 12, pp. 250, 2023

2. Antonov, A. A., et. al., “Chiral Harmonic Generation by Quasi-Bound States in the Continuum,” *Seventeenth International Congress on Artificial Materials for Novel Wave Phenomena (Metamaterials), Chania, Greece*, pp. X-013-X-015, 2023.

3. Gorkunov, M. V., et.al., “Substrate-Induced Maximum Optical Chirality of Planar Dielectric Structures,” *Adv. Optical Mater.*, Vol. 13, pp. 2402133, 2025.

Band structure evolution of quaternary magnetic semiconductors for photonic and spintronic application

O. Yastrubchak[1*], N. Tataryn[1], S. Mamykin[1], V. Romanyuk[1], O. Kondratenko[1], L. Borkovska[1], L. Khomenkova[1], X. Liu[2], B. A. Assaf[2], J. Furdyna[2], Y. Ichiyanagi[3], M. Sawicki[4], J. Sadowski[4]

[1]V.E. Lashkaryov Institute of Semiconductor Physics, National Academy of Sciences of Ukraine, Kyiv, Ukraine
[2]Department of Physics and Astronomy, University of Notre Dame, IN 46556, USA
[3]Department of Physics, Graduate School of Engineering Science, Yokohama National University, Yokohama, Kanagawa 240-8501, Japan
[4]Institute of Physics, Polish Academy of Sciences, Aleja Lotnikow 32/46, 02668 Warsaw, Poland
[*]corresponding author: plazmonoki@gmail.com

Abstract: Impact of Bi, P and Mn incorporation into GaAs layers on their electronic and band structures as well as magnetic and structural properties has been studied. A set of the homogenous (Ga,Mn)(P,As) layers with 8% of Mn and 32% of P contents and (Ga,Mn)(Bi,As) layers with 4% of Mn and 0.3% of Bi contents of high structural perfection have been grown by low-temperature molecular-beam epitaxy. Embedding P ions into the GaAs crystal lattice leads to an increase in the band gap, while Bi and Mn impurities lead to its decrease. A significant impact of Mn interstitial impurities on the structural and magnetic properties of the films was observed. We observe an enhancement of charge density in the presence of Mn. The schematic energy band diagrams for the LT-GaAs, (Ga,Mn)(Bi,As) and (Ga,Mn) (P,As) were proposed.

Dilute quaternary III-V semiconductors such as (Ga,Mn)(Bi,As) and (Ga,Mn)(P,As) offer a unique platform to explore spintronic functionalities by combining semiconducting behavior with ferromagnetism [1]. In these materials, Mn atoms act as acceptors, increasing hole concentration and mediating ferromagnetic exchange, while Bi and P substitute for As, modifying the band structure and spin–orbit interactions [2–4]. Bi narrows the band gap and enhances spin–orbit coupling, enabling phenomena such as anisotropic magnetoresistance and spin–orbit torque [5]. P doping, on the other hand, introduces tensile strain and promotes perpendicular magnetic anisotropy and anomalous Hall effect [6]. In this study, we investigate the structural, magnetic, and optical properties of (Ga,Mn)(Bi,As) and (Ga,Mn)(P,As) nanofilms using HRXRD, micro-Raman spectroscopy, FTIR, spectroscopic ellipsometry, and SQUID magnetometry [5–7]. Our results provide critical insights into band structure evolution, magnetic anisotropy, Curie temperature, and spin-related effects, contributing to the development of next-generation spintronic devices.

HRXRD confirmed high crystalline quality, pseudomorphic growth, and strain variations due to Bi (compressive) and P (tensile) incorporation [8, 9]. Annealing led to partial strain relaxation in all samples. SQUID magnetometry revealed ferromagnetic ordering at low temperatures in all systems. (Ga,Mn)(Bi,As) films exhibited easy-plane magnetic anisotropy with in-plane 〈100〉 axes, while tensile-strained (Ga,Mn)(P,As)

showed perpendicular magnetic anisotropy. Micro-Raman data also confirmed enhanced and more uniform hole distribution after annealing, leading to increased Curie temperatures (Tc), consistent with SQUID results.

The optical properties of the epitaxial films were investigated using spectroscopic ellipsometry (SE) [10, 11]. From SE measurements the spectral dependences of the ellipsometric angles $\Psi(\lambda)$ and $\Delta(\lambda)$ are obtained, allowing us to calculate the effective complex dielectric function $\varepsilon(E) = \varepsilon_1(E) + i\varepsilon_2(E)$. The analysis of the optical transition energies enables elucidation of the behavior of the Fermi level in *p*-type samples depending on the acceptor-doping level.

Summarizing all the experimental results, we propose the schematic model of the energy band diagrams for LT-GaAs, (Ga,Mn)(Bi,As) and (Ga,Mn)(P,As) layers. For the LT-GaAs the transitions originating from heavy-, light-hole and spin-orbit split off sub-bands (denoted by HH, LH and SO, respectively) to the conduction band at the critical point of the Brillouin zone are indicated. The Fermi level (red dashed line) is located within the band gap due to a large amount of arsenic antisite (As_{Ga}) double donor defects originating from the low-temperature growth conditions. For the disordered-valence-band regime in high-Mn-doped epitaxial layers of (Ga,Mn)(Bi,As) the impurity band and the host valence band merge into one inseparable band, whose tail may still contain localized states (shaded parabolas) depending on the free carrier concentration and disorder. The Fermi levels lie within the strongly disturbed valence band, which, in turn, is extended into the band gap as a result of the carrier-induced many-body effects. For the (Ga,Mn)(P,As) the Fermi level is located in-gap Mn impurity states – possibly hybridized with the valence band.

This research is supported by the IEEE "2025Magnetism in Ukraine Initiative."

References

1. Furdyna, J. K. “Diluted magnetic semiconductors,” Journal of Applied Physics, Vol. 64, No. 4, R29-R64, 1988.

2. Yastrubchak, O. *et al*., “Influence of Bi doping on the electronic structure of (Ga,Mn)As epitaxial layers,“ Scientific Reports, Vol. 13, No. 1, 17278, 2023.

3. Tataryn, N. *et al*., “Valence Band Dispersion in Bi Doped (Ga,Mn)As Epitaxial Layers,“ IEEE Transactions on Magnetics, Vol. 59, No. 11, 4100405, 2023.

4. Yastrubchak, O. *et al*., “Band engineering of magnetic (Ga,Mn)As semiconductors by phosphorus doping,“ IEEE Transactions on Magnetics, Vol. 59, No. 11, 1600106, 2023.

5. Wosinski, T. “Bismuth Doping-Induced Enhancement of the Spin–Orbit Coupling Strength in the Prototype Dilute Ferromagnetic Semiconductor (Ga, Mn) As: A Review.“ Journal of Electronic Materials, 1-12, 2025.

6. Lemaître, A. et al., “Strain control of the magneticanisotropy in (Ga,Mn)(As,P) ferromagnetic semiconductor layers,” Applied Physics Letters, Vol. 93, No. 2, 021123, 2008.

7. Gluba, L. *et al.* “On the nature of the Mn-related states in the band structure of (Ga, Mn) As alloys via probing the E_1 and $E_1+\Delta_1$ optical transitions,“ Appl. Phys. Lett., Vol. 105, No. 3, 032408, 2014.

8. Yastrubchak, O. et al., “Anisotropic strain relaxation in lattice-mismatched III–V epitaxial layers,“ Physica Status Solidi (c), Vol. **2**, No. 6, 1943–1947, 2005.

9. Yastrubchak, O. *et al*., “Strain release in InGaAs/InxAl1−xAs/InP heterostructures,” Physica B: Condensed Matter., Vol. 340–342, 1082–1085, 2003.

10. N.L. Dmitruk, M. Klopfleisch, O.I. Mayeva, S.V. Mamykin, E.F.Venger, O.B. Yastrubchak, “Multilayer diffraction gratings Al/GaAs as polaritonic photodetectors” , Phys. Stat. Sol. (a), 184, 165–174 (2001).

11. N.L. Dmitruk, O.Yu. Borkovskaya, I.B. Mamontova, O.I. Mayeva, O.B. Yastrubchak, “Ultraviolet responsivity control in Schottky barrier heterostructures with textured interface,” Thin Solid Films, 364, 280–283, (2000).

Novel Sensing Technique for Non-destructive Composites Monitoring

V. Zhukova[1,2,3], P. Corte-León[1,2,3,4], A. Allue[5], K. Gondra[5], J. M. Blanco[2,3] and A. Zhukov[1,2,3,6]

[1]Dept. Polymers and Advanced Materials: Physics, University of Basque Country, UPV/EHU, 20018 San Sebastian, Spain

[2]Dpto. de Física Aplicada, EIG, UPV/EHU, San Sebastian, Europa Plaza, 1,20018, Spain

[3]EHU Quantum Center, University of the Basque Country, UPV/EHU, San Sebastian, Spain

[4]Dept. Mater. Science & Metallurgy, Univ. Cambridge, Cambridge CB3 0FS, UK

[5]Gaiker Technological Centre, 48170, Zamudio, Spain

[6]IKERBASQUE, Basque Foundation for Science, Bilbao, 48011, Spain

*corresponding author: valentina.zhukova@ehu.es

Abstract: Using free space setup we observed a remarkable change of the reflection and transmission at frequencies of 4-7 GHz upon the matrix polymerization with embedded magnetic microwire inclusions. Observed dependencies are attributed to the influence of heating and stresses variation on magnetic properties of magnetic microwires during the matrix polymerization.

One of the common problems in the composite materials is the contactless stresses and temperature monitoring. One of the promising solutions addressing the problem of non-destructive fiber reinforced composites, FRC, monitoring is a novel sensing technique involving free space microwave spectroscopy utilizing ferromagnetic microwire inclusions presenting the high frequency impedance quite sensitive to tensile stress and magnetic field [1,2]. Recently several successful attempts for non-destructive FRC monitoring have been reported [2,3].

In this paper, we present our last results on studies of magnetic properties of glass-coated Co-rich microwires and on in-situ polymerization process monitoring of the FRC with Co-rich glass-coated microwires inclusions.

We used inclusions of Co-rich glass-coated $Co_{65.4}Fe_{3.8}Ni_1B_{13.8}Si_{13}Mo_{1.35}C_{1.65}$ (metallic nucleus diameter, d=18.8 μm, total diameter, D=22.2 μm) microwires with low negative magnetostriction coefficients, λ_s, prepared by Taylor-Ulitovsky technique described elsewhere [3].

Studied microwires present good (coercivity of about 10 A/m), high giant magnetoimpedance GMI effect (GMI ratio about 100%).

For the composite matrix we used a vinylester resin (DERAKANE 8084) resin, accelerated with Cobalt Octoate (0,3 pph) and catalyzed with Methyl Ethyl Ketona (MEK 60%, 1,5 pph).

We used the free space measurement system consisting of two broadband horn antennas fixed at the anechoic chamber and a vector network analyzer for the in-situ experiments on polymerization of the composite placed inside the anechoic chamber, as previously described in details in [1]. The reflection (R) and transmission (T) coefficients were measured in free-space. As recently reported [3], the matrix polymerization produces a heating of the composite up to 80 ºC. On the other hand, when a resin polymerizes, it shrinks, since the solid obtained will have a smaller volume than the monomer from which it started. The volume shrinkage is of about 8.2 %. The cured resin presents the following mechanical properties: a tensile strength of 76 MPa, a tensile modulus of 2.9 GPa, and a tensile elongation of 8-10%.

As shown in Figure 1, significant variation in the T parameter is observed in the frequency range, *f*, of 4-7

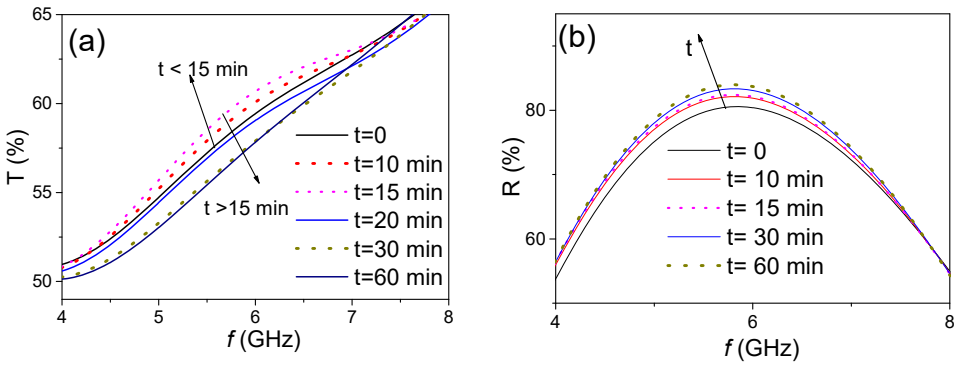


Figure 1. The Transmission, T (a) and reflection, R (b) parameters measured using free-space system during the composite polymerization.

GHz during thermoset matrix polymerization. Additionally, some changes in the R-parameter are also observed over a wide frequency range (Figure 1b).

The observed *T(f)* dependencies with are non- monotonic (see Figure 1a): there is an initial increase in T up to t=15 min (at f≈4-7 GHz), followed by a decrease in T for t>15 min. Previously, heating to 80° C and subsequent cooling of FRC during polymerization was experimentally demonstrated. Additionally, the matrix generally shrinks during cooling. Therefore, we can assume that the matrix shrinkage produces compressive stresses in magnetic nucleus of glass-coated microwires.

These experimental findings are crucial for the development of a new sensing technique that enables non-destructive and contactless monitoring of the composites with tunable magnetic permittivity sensitive to applied stress and temperature with ferromagnetic glass-coated microwire inclusions with magnetic properties sensitive to applied stress and temperature variations.

References

1. Makhnovskiy, D., A. Zhukov, A., V. Zhukova, V., J. Gonzalez, J. "Tunable and self-sensing microwave composite materials incorporating ferromagnetic microwires," Advances in Science and Technology, Vol.54 pp. 201-210, 2008.
2. Ipatov, M., Aranda, G.R. V. Zhukova, V., Panina, L.V., González J., Zhukov,A. "Tunable effective permittivity of composites based on ferromagnetic microwires with high magneto-impedance effect," Appl. Phys. A, Vol. 103(3), 693-697, 2011.
3. Zhukova, V., Corte-Leon, P., Allue, A., Gondra, K., Ipatov, M., Blanco, J. M., Olivera, J., & Zhukov, A. "Magnetic Properties and Applications of Glass-coated Ferromagnetic Microwires. Advanced Electromagnetics," Vol. 12(3), 69–74. 2023, https://doi.org/10.7716/aem.v12i3.2240

The Generation of Two Distinct Berry Phases on the Surface of a Twisted Triangular Möbius Cavity Resonator

E. C. I. Paterson[1], M. E. Tobar[1*], M. Goryachev[1*] and J. F. Bourhill[2]
[1]Department of Physics, University of Western Australia, Australia
22734222@student.uwa.edu.au (E. C. I. Paterson)

We present the experimental observation of two distinct Berry phases ($\Pi = \pm\frac{2\pi}{3}$) on the surface of a microwave Möbius cavity resonator supporting the TE_{10} mode. These phases arise from self-interference-induced helicity $\mathscr{H}$. This resonator consists of a twisted, hollow equilateral triangular prism with mirror asymmetry, bent around on itself to form a ring.

The Berry phase (Π) is a topologically protected phase factor generated in both quantum and classical systems undergoing cyclical evolution. The accumulation of a π spin-redirection Berry phase has been experimentally observed in optical Möbius strip cavities. This Berry phase is an example of a holonomy, where due to the curved surface of the Möbius resonator the wave vector undergoes a change in it's angular momentum as it travels the closed loop and returns to it's initial position, accumulating a phase shift. Here, we investigate its topological generation on an equilaterial triangular cross-section microwave Möbius resonator.

The Möbius resonator consists of a twisted equilateral triangular hollow prism bent into a ring, as shown in the subplot of Fig. 1(a). If the twist is reversed halfway along its length, the angular momentum of the wave vector returns to its initial orientation after a full circulation. This configuration, along with the homeomorphic torus resonator with zero net twist ($\phi = 0$), as seen in Fig. 1(b), is referred to as the *mirror-symmetric cavity*. In this configuration, the wave vector interferes in phase, accumulating no Berry phase and forming a standing wave pattern with integer azimuthal mode numbers n. In contrast, the Möbius configurations form standing wave patterns with mode numbers of the form $n \pm \frac{1}{3}$, where n is an integer, due to the wave vector requiring three round trips of the cavity before interfering with itself in-phase.

To confirm the expected mode number behavior, we simulated the Möbius resonator with three different twist angles, $\phi = \frac{2\pi}{3}$, $\frac{4\pi}{3}$, and 2π, along with the torus resonator, using the finite element method (FEM). Because the modes in the bulk of the resonator can be fully determined by its surface according to the holographic principle [2], we determined n by counting the number of anti-nodes in the azimuthal tangential surface current density ($\mathbf{K}_{\beta\perp}$) over one loop of the resonator and dividing by the number of windings.

As shown in Fig. 1(a), the TE_{10} mode frequencies in both the Möbius and torus resonators follow the same dispersion relationship, with the fractional ($\mathbb{Z} \pm \frac{1}{3}$) TE_{10} modes in the Möbius resonator lying inbetween the integer TE_{10} modes in the torus resonator.

The Berry phase Π is related to the frequency shift (Δf_i) required to align the fractional modes in the Möbius resonator with the integer modes in the mirror-symmetric resonator. This relationship is given by

$$\Pi = \Delta f_i 4\pi^2 R/c \quad \overline{1 \in \left(\frac{2c}{3v f_i^c}\right)^2} \tag{1}$$

where $\Delta f_i = f^m_{i+\Delta n} \in f^c_i$ is the frequency difference between the $TE_{10(i+\Delta n)}$ mode in the Möbius cavity ($f^m_{i+\Delta n}$) and the TE_{10i} mode in the mirror-symmetric cavity (f^c_i). Here, v is the vertex length of the triangular cross-section, R is the radius of both cavities, and c is the speed of light.

The TE_{10} modes in the Möbius resonator generate electromagnetic helicity $\mathscr{H}$ [3] due to self-interference as they travel the closed loop of the resonator. For the $\phi = \frac{2\pi}{3}$ twisted Möbius

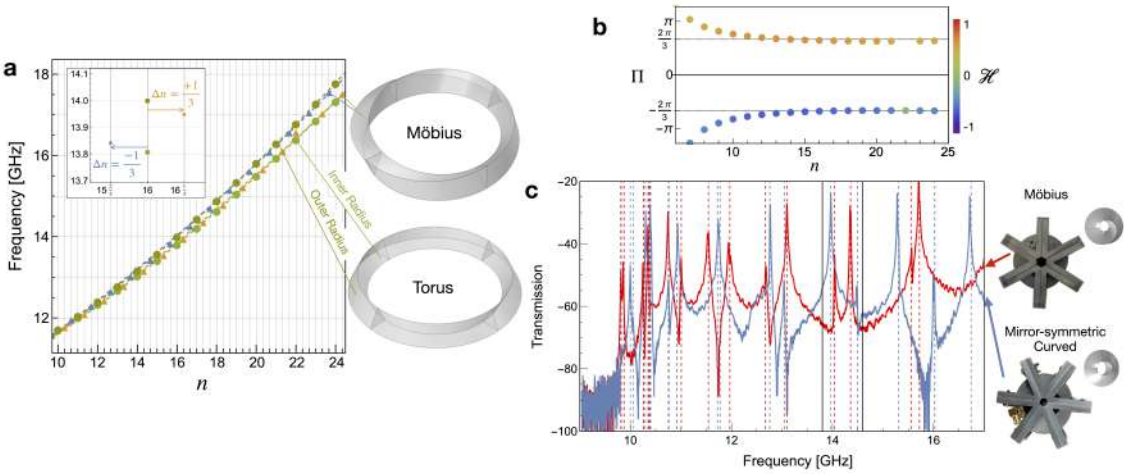


Figure 1: (a) The eigenfrequencies of the TE_{10n} modes as a function of azimuthal mode number n for the trinagular Möbius resonator with a twist of $\phi = \frac{2\pi}{3}$ and torus resonator. (b) Berry phase Π as a function of n with associated $\mathscr{H}$ of the mode depicted by colour, where the asymptotic limits are illustrated as black dashed gridlines. (c) The experimental S_{21} transmission measurements were performed on two resonators: a 3D-printed mirror-symmetric resonator (blue); and a Möbius resonator (red). Both resonators have an absolute twist angle of $\phi = \frac{2\pi}{3}$.

resonator, the positive and negative $\mathscr{H}$ modes have mode numbers adjusted by $\Delta n = +\frac{1}{3}$ or $\Delta n = \in \frac{1}{3}$, respectively, compared to the two radii modes of the mirror-symmetric resonator. Consequently, the sign of the mode's $\mathscr{H}$ corresponds to the sign of the accumulated Π, as demonstrated in Fig. 1(b). In the case of the $\phi = 2\pi$ twisted Möbius resonator, the mode numbers remain constrained to integer values, indicating no Berry phase accumulation, as would be expected.

To validate the expected frequency shift in the mirror-symmetric and Möbius resonators, we 3D-printed aluminum prototypes. The measured transmission spectra are compared with the eigenfrequencies obtained from FEM, as shown by the gridlines in Fig. 1(c). Strong agreement between the transmission peaks and simulation results confirms the presence of two distinct Berry phases ($\Pi = \pm\frac{2\pi}{3}$).

The topologically protected nature of the Berry phase renders it resilient to dynamic perturbations, such as environmental noise, ensuring gauge invariance throughout its evolution and hence the potential to be exploited to encode information via prime factorisation [1] or pack information more densely.

This work was funded by the Australian Research Council Centre of Excellence for Engineered Quantum Systems and Centre of Excellence for Dark Matter Particle Physics.

References

[1] Larocque, H., D. D'Errico, M.F. Ferrer-Garcia, et. al. "Optical framed knots as information carriers," *Nat. Comm.*, 11, 5119 2020.

[2] Fields, C., J. F. Glazebrook, A. Marciano, "The physical meaning of the holographic principle," *arXiv e-prints*, 10.48550/arXiv.2210.16021, 2022.

[3] Bourhill, J. F., E. C. I. Paterson, et. al., "Searching for ultralight axions with twisted cavity resonators of anyon rotational symmetry with bulk modes of nonzero helicity," *Phys. Rev. D*, Vol. 108, No. 5, pp. 052014, 2023.

Architectured Elastic and Acoustic Metamaterials & Phononic Crystals

A template-aided versatile approach for creating metamaterials

R. Xu[1], and D. Makarov[1*]

[1] Helmholtz-Zentrum Dresden-Rossendorf e.V., Institute of Ion Beam Physics and Materials Research, Bautzner Landstrasse 400, 01328, Dresden, Germany

[*]corresponding author: r.xu@hzdr.de

Abstract: By employing customizable anodic aluminum oxide templates, we achieve precise geometrical control of nanostructures, including their sizes, in-plane/out-of-plane shapes, and spatial arrangements. This approach offers a cost-effective, scalable method for fabricating metamaterials.

Structural engineering of metamaterials provides a versatile platform to adjust their macroscopic properties [1]. Controlling the geometrical parameters (i.e., size, shape, and spatial arrangement) of nanostructured metamaterials have been the central aspects of scientific investigations and practical applications. Low-cost high-yield template-guided techniques have been a workhorse for the fabrication of such metamaterials. Here we report designable anodic aluminum oxide templates with well-defined pore features within templates in terms of in-plane and out-of-plane shape, size, spatial configuration, and pore combination [2]. By using designable anodic aluminum oxide template, we realize geometrical controlling of nanostructured metamaterials over their sizes, in-plane/out-of-plane shapes, and spatial arrangements. Integrating geometrically designable metamaterials into optoelectronic devices [3-4] and magnetic devices [5], the resulting performance can be obviously enhanced.

References

1. R. Xu, L. Du, D. Adekoya, G. Zhang, S. Zhang, S. Sun, and Y. Lei, Well-defined nanostructures for electrochemical energy conversion and storage, Adv. Energy Mater. 11, 2001537, 2021.
2. R. Xu, Z. Zeng, Y. Lei, Well-defined nanostructuring with designable anodic aluminum oxide template, Nat. Commun. 13, 2435, 2022.
3. R Xu, L Wen, Z Wang, H Zhao, G Mu, Z Zeng, M Zhou, S Bohm, H Zhang, Y. Wu, R. Erich, and Y. Lei, Programmable multiple plasmonic resonances of nanoparticle superlattice for enhancing photoelectrochemical activity, Adv. Funct. Mater. 30, 2005170, 2020.
4. R. Xu, H. Zhao, H. Jin, Z. Wang, Z. Zhang, S. Xu, Z. Zeng, S. Wang, and Y. Lei., Nano Energy 58, 543, 2019.
5. O Bezsmertna, R Xu, O Pylypovskyi, D Raftrey, A Sorrentino, J. A. Fernandez-Roldan, I. Soldatov, D. Wolf, A. Lubk, R. Schäfer, P. Fischer, and D. Makarov, Magnetic Solitons in Hierarchical 3D Magnetic Nanoarchitectures of Nanoflower Shape, Nano Lett. 24, 15774, 2024.

Acoustic lattice resonances and generalised Rayleigh–Bloch waves

M. A. Peter[1*], L. G. Bennetts[2], G. J. Chaplain[3], S. C. Hawkins[4], K. Matsushima[5], T. A. Starkey[3]

[1]University of Augsburg, Germany
[2]University of Adelaide, Australia
[3]University of Exeter, UK
[4]Macquarie University, Australia
[5]University of Tokyo, Japan
[*]corresponding author: malte.peter@math.uni-augsburg.de

Abstract: Rayleigh–Bloch waves are modes localised to periodic arrays of scatterers with unbounded unit cells. We study them for line arrays of sound-hard scatterers embedded in an acoustic medium above the cut-off, both theoretically and experimentally, in which we observe the first generalised Rayleigh–Bloch waves in the radiative regime.

One-dimensionally periodic lattices (with appropriate boundary conditions on the scatterers) support surface waves that propagate along and exponentially decay away from the lattice. These exist under many guises for both scalar and vector wave regimes from acoustics and electromagnetism to linear water waves and elasticity. Distinct from naturally occurring interfacial surface waves (e.g. Rayleigh, Stonely and Scholte waves, or surface plasmon polaritons), the waves we allude to owe their existence to the underlying embedded periodic lattice and are thus commonly termed Rayleigh–Bloch (RB) waves; they exist on infinite lattices, with the criterion for their existence having been analysed in the context of functional analysis for some time [1]. In particular, they differ from pure Bloch waves that exist in cells which are bounded (e.g. an infinite 2D phononic crystal), as RB waves exist in 1D lattices with an unbounded unit cell, resembling a strip or ribbon, and they are known to have a large influence on the response of the corresponding semi-infinite or finite structures with equally spaced bodies.

Here, we study RB waves for line arrays of sound-hard circular scatterers embedded in a two-dimensional acoustic medium, for which it has recently been shown that they exist for higher frequencies than previously thought. Moreover, it was shown that RB waves can cut off (disappear) and cut on (reappear), and additional Rayleigh–Bloch waves can cut on and interact with the existing ones [2]. These complicated behaviours are reconsidered using a family of quasi-periodic Green's functions that allow particular plane-wave components to become unbounded away from the array so as to trace the trajectories of the Rayleigh–Bloch wavenumbers as they swap between Riemann sheets that are categorized according to the unbounded plane wave(s) and provide new understanding of RB waves around the critical frequency intervals where they cut on/cut off/interact [3].

More specifically, to find acoustic RB waves, we seek solutions ϕ of the 2D Helmholtz equation

$$(\Delta + k^2)\,\phi = 0, \tag{1}$$

in the (x,y)-plane with sound-hard (Neumann) boundary conditions applied on periodically spaced circular scatterers with boundary Γ and separation a, that satisfy both radiation and Bloch conditions, i.e.

$$\partial_{\boldsymbol{n}}\phi = 0 \qquad \text{on } \Gamma, \tag{2a}$$

$$\phi \to 0 \qquad \text{as } |y| \to \infty, \tag{2b}$$

$$\phi_R = \mathrm{e}^{\mathrm{i}R\beta}\,\phi_0, \tag{2c}$$

$$\partial_x\phi_R = \mathrm{e}^{\mathrm{i}R\beta}\,\partial_x\phi_0, \tag{2d}$$

where $\boldsymbol{n}$ is the outward surface normal, ϕ_0 is the solution in the fundamental cell and ϕ_R is the solution in the R^{th} cell at a distance $R = n\,a$ for $n \in Z$. Solutions to this problem are known as pure RB surface waves [1] with the prescribed values of k^2, at which they occur, being eigenvalues of the operator $-\Delta$ subject to (2). As is often the case, a non-dimensional form is adopted and, as such, k is a wavenumber that acts as a proxy for a prescribed angular frequency. With this, β represents the RB wavenumber, i.e. the component of the wavevector parallel to the array.

The unboundedness of the periodicity cell and the associated existence of a continuous spectrum make it difficult to compute RB wavenumbers above the first cut-off induced by the Bloch conditions (2c–d). We present a method for solving this problem by introducing a family of quasi-periodic Green's functions that allow particular plane-wave components to become unbounded away from the array [3]. The Green's function formulation is combined with the block Sakurai–Sugiura method to trace the trajectories of the RB wavenumbers as they swap between Riemann sheets that are categorized according to the unbounded plane wave(s). The Green's function approach allows the point spectrum to be calculated separately from the continuous spectrum, which facilitates analysis of critical points where RB waves cut on or cut off. The Green's function solution method also gives a convenient ansatz for the far-field of the eigenmodes, which allows the modes to be identified as decaying away from the grating (thus, in the point spectrum, and embedded if the eigenvalue lies on a branch cut) or bounded but non-decaying (thus, in the continuous spectrum). Moreover, the Green's function approach allows the eigenpairs to be generalised to unbounded solutions that grow away from the array, which allows RB waves to be tracked in frequency space after they cut off or before they cut on.

These theoretical investigations are complemented by experimental results in airborne acoustics, in which we experimentally observe the first generalised RB waves above the first cut-off, i.e., in the radiative regime. We consider radiative acoustic lattice resonances along a diffraction grating and connect them to generalised RB waves by considering both short and long arrays of non-resonant 2D cylindrical Neumann scatterers embedded in air, forming both small and large-scale acoustic gratings for airborne sound in the audible frequency range. On short arrays, we observe finite-lattice resonances under continuous wave excitation, and on long arrays, we observe propagating Rayleigh–Bloch waves under pulsed excitation [3]. The first generalised RB mode is shown to exist over a range of frequencies for an example aspect ratio predicted by [2]. In airborne acoustics, we are able to achieve both continuous wave and pulsed excitations that permit the excitation of collective acoustic lattice resonances on short arrays and propagating generalised RB waves on long arrays, respectively. In doing so, we demonstrate that they are one and the same and that their interpretation is unified through the analogue of polarisability of the scatterers and the gaps between them.

References

1. Linton, C. M. and McIver M., "The existence of Rayleigh–Bloch surface waves". Journal of Fluid Mechanics, Vol. 470, 85–90, 2002, https://doi.org/10.1017/S0022112002002227
2. Bennetts, L. G. and M. A. Peter, "Rayleigh–Bloch waves above the cutoff", Journal of Fluid Mechanics, Vol. 940, A35, 2022, https://doi.org/10.1017/jfm.2022.247
3. Matsushima, K., L. G. Bennetts, and M. A. Peter, "Tracking Rayleigh–Bloch waves swapping between Riemann sheets", Proceeding Royal Society A, Vol. 480, 2301, 2024, https://doi.org/10.1098/rspa.2024.0211
4. Chaplain, G. J., S. C. Hawkins, M. A. Peter, L. G. Bennetts, T. A. Starkey, "Acoustic Lattice Resonances and Generalised Rayleigh–Bloch Waves", arXiv:2409.10074, 2024, https://arxiv.org/abs/2409.10074

Reconfigurable Topological Insulators and Acoustic Devices Based on an Electroacoustic Material Platform

M. J. Leamy[1*]

[1]Woodruff Endowed Professor, George W. Woodruff School of Mechanical Engineering, Georgia Tech, USA
[*]corresponding author: michael.leamy@me.gatech.edu

Abstract: We present recent work on reconfigurable, electroacoustic topological insulators as a platform for enabling acoustic devices such as multiplexers/demultiplexers, transistors, logic gates, and single-bit memory. The theoretical underpinnings of the reconfigurable topological insulator will be discussed together with experimental results confirming multiple device operation.

Topological insulators (TIs), exhibiting topologically-protected edge and interface waves, have recently emerged in phononic systems [1]. Reconfigurabilty is essential for enabling TI-based applications [2]. To address this need, we employ shunted piezoelectric (PZT) disks with negative capacitance circuits to dynamically alter a unit cell's mechanical impedance [3-5], thus breaking inversion symmetry and realizing topological states. Dynamic reconfigurability and programmability of such material platforms can then be obtained through simple on/off switching.

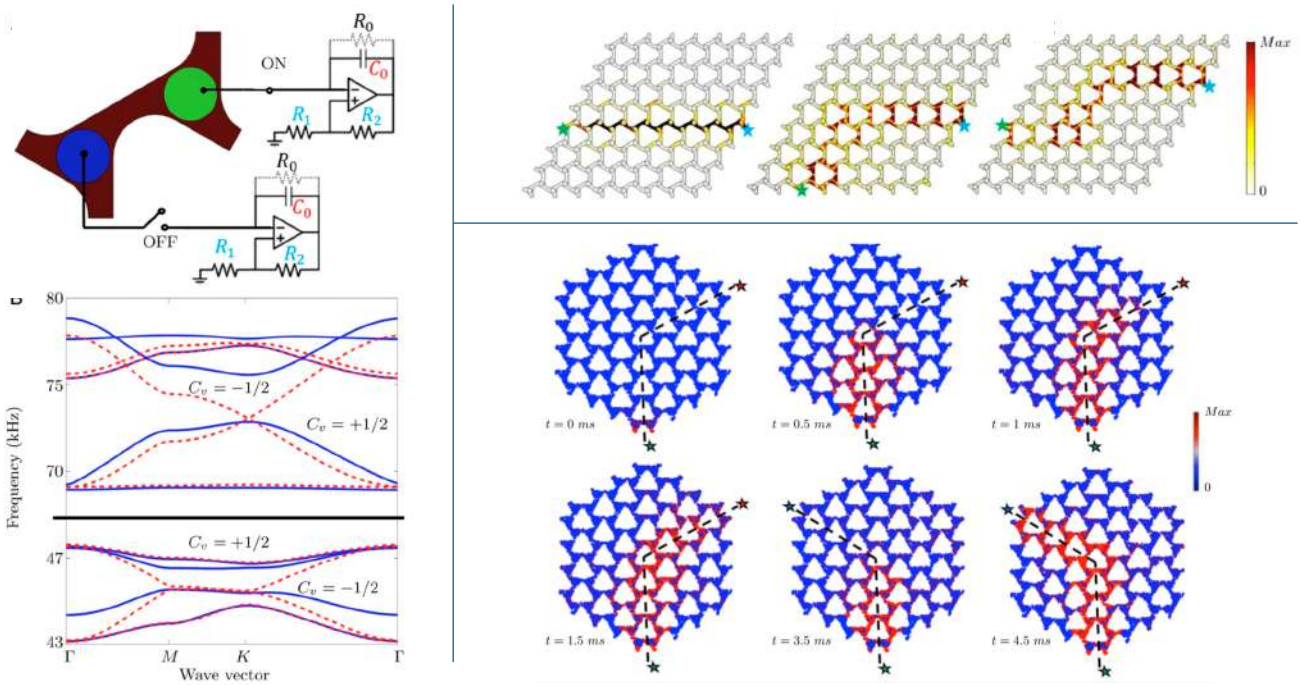


Figure 1: (left) Electroacoustic unit cell depicting two PZT disks, shunted circuits, and associated band structure where red dashed curves correspond to all shunted circuits open, while blue solid curves correspond to one open and one closed shunted circuit. (top-right) Numerically-computed interface waves along reconfigurable domain walls. (bottom-right) Experimentally characterized operation of an electroacoustic demultiplexer.

Figure 1 documents an electroacoustic unit cell (left subfigure) exhibiting programmable topologically protected interface states useful for acoustic multiplexers, demultiplexers, transistors, and single-bit memory [6-8]. The reconfigurable structure is composed of an elastic hexagonal lattice whose unit cell contains two shunted PZT disks, each connected to a negative capacitance circuit by an on/off switch. Closing one or the other circuit results in the breaking of mirror symmetry and yields mechanical behavior analogous to the quantum valley Hall effect. By interfacing two topologically-distinct materials (i.e., differing switches closed), a reconfigurable domain wall is introduced exhibiting a localized interface state topologically-protected from backscattering at defects and sharp edges (top-right subfigure). Through the use of programmable time-division, in which topological domain walls appear and disappear in time, we have experimentally demonstrated multiplexing and demultiplexing (bottom-right subfigure). Specifically, for demultiplexing, two channels of information enter at the input located at the bottom of the lattice spaced in time with a known period. When Channel A is present at the input, a topological domain wall connects the input to Channel A's output at the top-right of the lattice; similarly, when Channel B is present at the input, a topological domain wall connects the input to Channel B's output at the top-left of the lattice. Multiplexing is achieved using reverse operation. We have also demonstrated an acoustic transistor using the same programmable platform, and a memory device for storing a single bit using a single electroacoustic unit cell with a shunted defect. Details will be provided during the talk.

We would like to acknowledge the U.S. National Science Foundation for support of this research under grant numbers 1929849 and 2424345.

References

1. Alu, A., Daraio, C., Deymier, P.A., Ruzzene, M., "Topological Acoustics," *Acoustics Today*, Vol. 17, No. 3, 1-9, 2021.
2. Darabi, A., Leamy, M.J., "Reconfigurable Topological Insulator for Elastic Waves," *Journal of the Acoustical Society of America*, Vol. 146, No. 1, 773-781, 2019.
3. Darabi, A., Collet, M., Leamy, M.J., "Experimental Realization of a Reconfigurable Electroacoustic Topological Insulator," *Proceedings of the National Academy of Sciences*, Vol. 114, No. 28, 16138-16142, 2020.
4. Darabi, A., Ni, X., Leamy, M.J., Alu, A., "Reconfigurable Floquet Elastodynamic Topological Insulators Based on Synthetic Angular Momentum Bias," *Science Advances*, Vol. 6, eaba8656, 1-5, 2020.
5. Kuchibhatla, S.A.R., Leamy, M.J., "Nonadiabatic Shifting of a Topological Interface in an Electroacoustic Su-Schrieffer-Heeger Lattice," *Physical Review Applied*, Vol. 18, No. 5, 054058, 1-7, 2022.
6. Darabi, A., Kliewer, E., Leamy, M.J., "Reconfigurable Acoustic Multiplexer/Demultiplexer Using Time Division," *Applied Physics Letters*, Vol. 119, 113501, 1-6, 2021
7. Kuchibhatla, S.A.R., Leamy, M.J., "Numerical Demonstration of a Topologically-Protected Electroacoustic Transistor," *Frontiers in Acoustics*, Vol. 1**,** 1251215, 1-11, 2023.
8. Kuchibhatla, S.A.R., Leamy, M.J., "Experimental Demonstration of an Electroacoustic Transistor," *Applied Physics Letters*, Vol. 124, 244102, 1-7, 2024.

Elastic spin angular momentum in continuum and metamaterials rod structures

Jinfeng Zhao[1*], Yuxuan Zhang[1], Yongdong Pan[1]
[1]School of Aerospace Engineering and Applied Mechanics, Tongji University, 100 Zhangwu Road, 200092, Shanghai, China
[*]corresponding author: jinfeng.zhao@tongji.edu.cn

Abstract: Elastic spin angular momentum is reported for all three basic modes in continuum rods. Elastic spin controlled unidirectional wave routing is observed in experiment. Similar phenomena are observed for guided modes in rods made of metameterials.

Bosonic-like waves in topological metamaterials and/or phononic crystals have raised wide interest owing to their exotic features. The chirality of topological edge states (TES), known as pseudo-spin, is an important feature for performing robust wave manipulation. Unlike the mathematical concept of pseudo-spin, the spin angular momentum (SAM) of elastic waves describes their local but intrinsic chirality. The SAM of some guided modes locks to the wave direction, which leads to unidirectional routing in both metamaterials and classical structures.

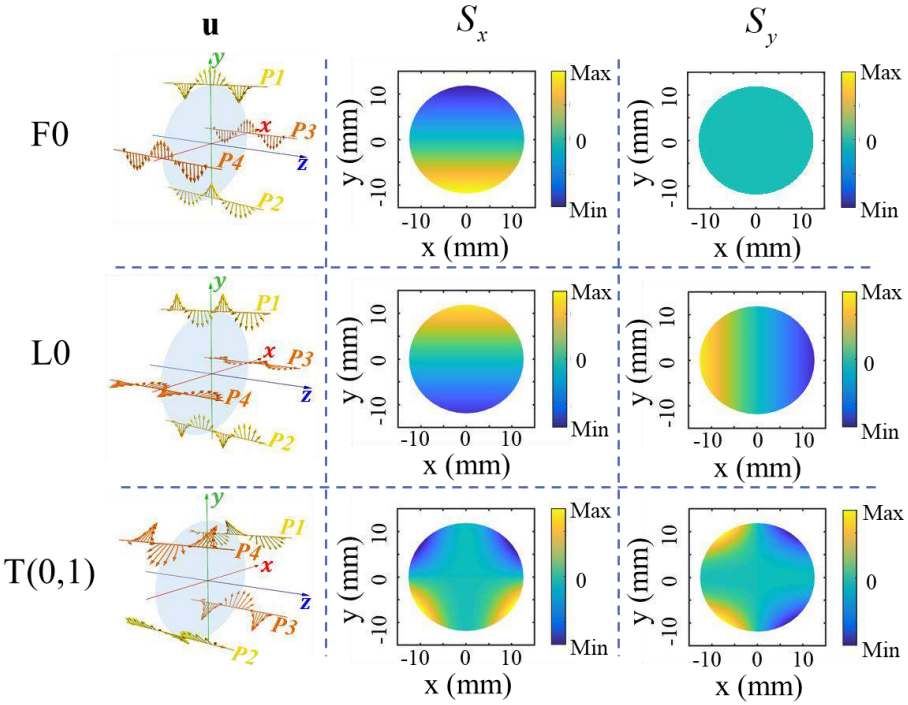


Fig. 1. Displacement field and SAM distribution [5]. First column shows the real part of displacements for F0, L0 and T(0,1) modes at 25 kHz, second and third columns present the relevant distribution of S_x and S_y.

For example, the elastic spin has been charactered for in Lamb-Rayleigh waves along different directions, and demonstrate spin-wavenumber locking over a broad frequency range [1, 2]. Interestingly, we extend elastic SAM to topological metamaterials. We observe the previously overlooked elastic spin-valley locking mechanism [3] and the elastic SAM texture in topological metamaterials based on *p*/*d* symmetry inversion [4]. The chiral,

spatial, and frequency controlling of wave routing is shown in phononic circuits.

In this work, we report the elastic spin for guided modes in continuum rods, including the zero-order flexural (F0) mode, zero-order longitudinal (L0) mode, and zero-order tortional (T(0,1)) mode [5]. Figure 1 shows the displacement polarization and spin component S_x and S_y, for all three guided modes in continuum rods with ellipse cross section. Basically, F0 and L0 modes show some similarity with Lamb modes, i.e. the zero-order antisymmetric plate (A0) mode and zero-order symmetric plate (S0) modes. Yet, F0 and L0 modes demonstrate more elastic spin, along other spatial direction, due to their three-dimensional polarized displacement field. A further study is shown for guided modes in rod structures composed by metamaterials.

References

1. Yuan, W., Yang, C., Zhang, D., Long, Y., Pan, Y., Zhong, Z., Chen, H., Zhao, J., and Ren, J., "Observation of elastic spin with chiral meta-sources", Nature Communications, Vol. 12, 6594, 2021.
2. Yang, C., Zhang, D., Zhao, J., Gao, W., Yuan, W., Long, Y., Pan, Y., Chen, H., Nori, F., Bliokh, K.Y., Zhong, Z., and Ren, J., "Hybrid spin and anomalous spin-momentum locking in chiral surface elastic waves", Physical Review Letters, Vol. 131, No. 13, 136102, 2023.
3. Zhao, J., Yang, C., Yuan, W., Zhang, D., Long, Y., Pan, Y., Chen, H., Zhong, Z., and Ren, J., "Elastic valley spin controlled chiral coupling in topological valley phononic crystals", Physical Review Letters, Vol. 129, No. 27, 275501, 2022.
4. Huang, Y., Yang, C., Yuan W., Zhang, Y., Pan, Y., Yang, F., Zhong Z., Zhao, J., Wright, O. B., and Ren, J., "Parity-frequency-space elastic spin control of wave routing in topological phononic circuits", Advanced Science, Vol. 11, 2404839, 2024.
5. Zhang, Y., Zhao, J., Huang, Y., Yang, C., Yuan, W., Zhong, Z., Ren, J., Pan, Y., "Elastic wave spin and unidirectional routing in thin rod systems", International Journal of Mechanical Sciences, Vol. 277, 109512, 2024.

Periodic infilled trench barriers for Rayleigh wave attenuation in saturated soil

Z. F. Shi[1*], S.Y. Cai[1] and A. Chen[1]

[1] School of Civil Engineering, Beijing Jiaotong University, Beijing, 100044, PR China

[*]corresponding author: zfshi178@bjtu.edu.cn

Abstract

This paper designed periodic infilled trench barriers for attenuating Rayleigh waves with frequencies between 10 to 30 Hz. The saturated soil model is adopted and the waste rubber tire is used as filling material. Both the dispersion curves and the performance of some periodic infilled trench barriers are obtained.

1 Introduction

Ambient vibration results in an adverse impact on the surrounding sensitive buildings and people's daily live. To reduce these undesirable vibrations, the suppression of Rayleigh wave propagation plays a key role due to Rayleigh wave carries a major amount of energy. Till now, a variety of vibration mitigating methods have been developed, among which periodic wave barriers have been received much attention by many researches[1,2]. However, there are a lot of issues still need to be considered in studying periodic wave barriers. First, some ambient vibrations concentrate in the low-frequency range between 10 to 30 Hz[3]. How to design a periodic surface wave barrier to attenuate this vibration is still open. Second, most of the achievements related to periodic surface wave barriers are under the assumption of single-phase soil. The results suitable to the scenario of saturated soil can be countable[4,5]. Third, there is few study on the performance of periodic wave barriers using waste rubber tire as fillers.

In the present study, some combined periodic infilled trenches as wave barriers for Rayleigh wave attenuation in saturated soil are developed. The dispersion curves and the performance of the combined periodic infilled trenches are obtained. The numerical simulation results show that the barriers proposed by the present study could effectively manipulate the propagation of Rayleigh waves with frequencies between 10 to 30 Hz.

2 Equations

The wave equations of saturated soil in **u**-***p*** form can be expressed as follows[6]:

$$\begin{cases} -\omega^2(\rho-\dfrac{\rho_f}{\rho_c})\mathbf{u}-\nabla(\sigma(\mathbf{u})-\alpha\mathbf{p}\mathbf{I})=\dfrac{\rho_f}{\rho_c}\nabla\mathbf{p} \\ -\dfrac{\omega^2}{M}\mathbf{p}-\nabla\bullet\dfrac{1}{\rho_c}(\nabla\mathbf{p}-\omega^2\rho_f\mathbf{u})=\omega^2\alpha\zeta_{vol} \end{cases} \tag{1}$$

In addition, the criterion based on strain energy is introduced in order to distinguish the surface wave modes, which is expressed as[7]:

$$\xi=\frac{1}{H}\frac{\int_0^H z\cdot E_p dV}{\int_0^H E_p dV} \tag{2}$$

The symbols shown in Eq.(1) and Eq.(2) have the same meanings as those as in the papers [6,7], respectively.

3 Figures and Tables

For the saturated soil[8], we designed a periodic infilled trench barrier. The periodic constant and the width of the trench are chosen as 2 m and 0.6 m, respectively. The trench is filled with foam and waste rubber with the same thickness 0.3 m. The Young modulus, Poisson ratio and the density of the two filling materials are 37 and 4.5 MPa, 0.32 and 0.48, 60 and 1480 kg/m^3, respectively. The depth of the barrier is 4 m. Figure 1 gives the dispersion curves of the combined periodic trenches for Rayleigh waves. It is found that the barrier has the first two attenuations 13.8 ~21.1 Hz and 21.2 ~27.7 Hz. Figure 2 shows the vibration models of points A and B in the dispersion curves. The surface wave models of the two points are obvious.

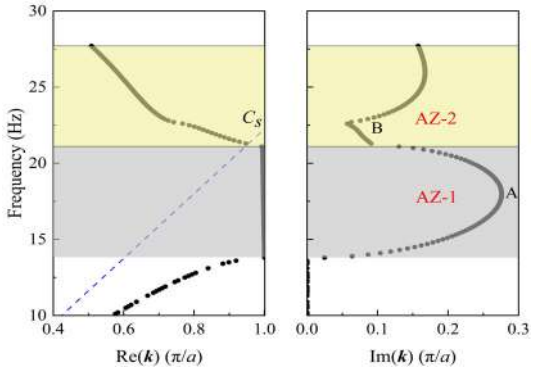


Fig.1 Dispersion curves of the combined periodic barrier for Rayleigh waves

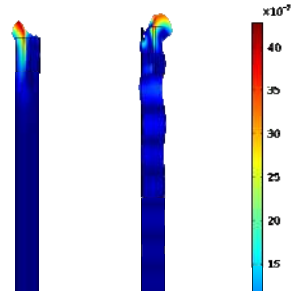


Fig.2 2D-vibration modes of single-cell model

4 Acknowledgements

This study is supported by the National Natural Science Foundation of China (52178269).

References

[1] Huang J.K. and Shi Z.F. “Attenuation zones of periodic pile barriers and its application in vibration reduction for plane waves,” J Sound Vib, 332:4423-4439, 2013.

[2] Brûlé S., et al. “Experiments on seismic metamaterials: molding surface waves,” Phys Rev Lett, 112:133901, 2014.

[3] Shi Z.F., et al. “Periodic structures: theory and applications to seismic isolation and vibration reduction,” Beijing, Science Press Ltd, 2017.

[4] Shi Z.F., et al. “Propagation attenuation of plane waves in saturated soil by pile barriers,” Int J Geomech, 17(9): 04017053, 2017.

[5] Amanat S., et al. “Plane waves mitigation in saturated porous media using optimal periodic wave barriers,” Appl Acoust, 200:109085, 2022.

[6] Atalla N., et al. “A mixed displacement-pressure formulation for poroelastic materials,” J Acoust Soc AM, 104(03): 1444-1452, 1998.

[7] Pu X.B. and Shi Z.F. “Broadband surface wave attenuation in periodic trench barriers,” J Sound Vib, 468: 115130, 2020.

[8] Gao G.Y., et al. “Investigation of ground vibration due to trains moving on saturated multi-layered ground by 2.5D finite element method,” Soil Dynam Earthq Eng, 40: 87-98, 2012.

Simulation of Acoustic Metamaterial Lens Imaging under Complex-Frequency Excitation in a Real-Frequency Solver

Tuo Liu[1*]

[1]Institute of Acoustics, Chinese Academy of Sciences, China
[*]corresponding author: liutuo@mail.ioa.ac.cn

Abstract: This summary presents a method for complex-frequency acoustic simulation implementable in real-frequency solvers based on a conversion of the imaginary frequency component into effective material properties. The method is subsequently applied to evaluating the complex-frequency subwavelength imaging of an acoustic holey-structured metamaterial lens with inherent thermal-viscous loss.

Complex frequency excitation (CFE) corresponds to temporally decaying or growing oscillatory signals that supply virtual gain or loss in space, under which wave systems can exhibit interesting response behaviors or propagation properties. Recent works have shown that the inherent material loss, which has long been a problem that superlensing systems suffer from, can be overcome via CFE so that the overall imaging performance is recovered as if in an ideal lossless scenario [1,2]. While the theoretical analyses in those works are straightforward together with readily available experimental realizations, the associated full-wave simulations are rather resource-consuming and indirect, commonly performed by utilizing truncated transient signals either in the time domain or synthesized at a series of discrete frequencies since most numerical solvers do not support computations at complex-valued frequencies. This summary reports on a simple and general method compatible with real-frequency solvers for complex-frequency calculation [3] and shows its effectiveness in the simulation of an acoustic holey-structured metamaterial lens under CFE with realistic thermo-viscous effect included.

To implement the full-wave simulation at a complex angular frequency, $\omega^* = \omega_r + i\omega_i$, the inhomogeneous acoustic Helmholtz equation with time dependence $e^{i\omega^* t}$ is re-written into the form of

$$\nabla \cdot \left(-\frac{1}{-\rho} (\nabla p - \mathbf{q}_d) \right) - \frac{\omega_r^2 p}{\rho c_{\mathrm{eq}}^2} = Q_m, \tag{1}$$

where $c_{\mathrm{eq}} = \omega_r c / \omega^*$ is a mathematical treatment to the original equation [3]. Here p, ρ, c, and $\mathbf{q}_d$ and Q_m are the acoustic pressure, density, speed of sound, and dipole and monopole domain sources, respectively. They are generally all functions of the position vector $\mathbf{r}$ and real-valued angular frequency ω_r, *viz.*, $p = p(\mathbf{r}, \omega_r)$, etc. After a conversion of the imaginary part, ω_i, into the equivalent speed of sound, c_{eq}, as an additional background parameter variation, Eq. (1) only contains real frequency, ω_r, and can thus be solved by any real-frequency numerical solvers to mimic the response under CFE at ω^*, as depicted in Fig. 1(a).

Next the above method is applied to the frequency-domain finite-element simulation of the super-resolution imaging of a lossy acoustic superlens under CFE [2] in the commercial software COMSOL Multiphysics. As presented in Fig. 1(b), the acoustic superlens is a holey-structured metamaterial [4] immersed in air with thermo-viscous effect considered through the acoustic boundary layer impedance boundaries (no slip, isothermal) inside the narrow holes, and the object to be imaged is a letter "A" of deep subwavelength dimensions. The simulation results at the image plane are given by Figs. 1(c) and 1(d). The metamaterial lens produces sub-diffraction-limited

image at its Fabry-Perot resonance (~1705 Hz) in the ideal lossless case. The presence of thermo-viscous effect leads to not only a red shift of the resonance frequency (~1614 Hz) but also non-negligible dissipative losses that attenuate the evanescent waves and consequently result in degraded performance under real-frequency excitation. As expected, CFE provides virtual gain effect to compensate the loss, and the image is almost fully recovered at $1614 + i88$ Hz. The results therefore confirm the effectiveness of the proposed method in performing complex-frequency simulations in a more straightforward and efficient way as compared to existing methods [1,2].

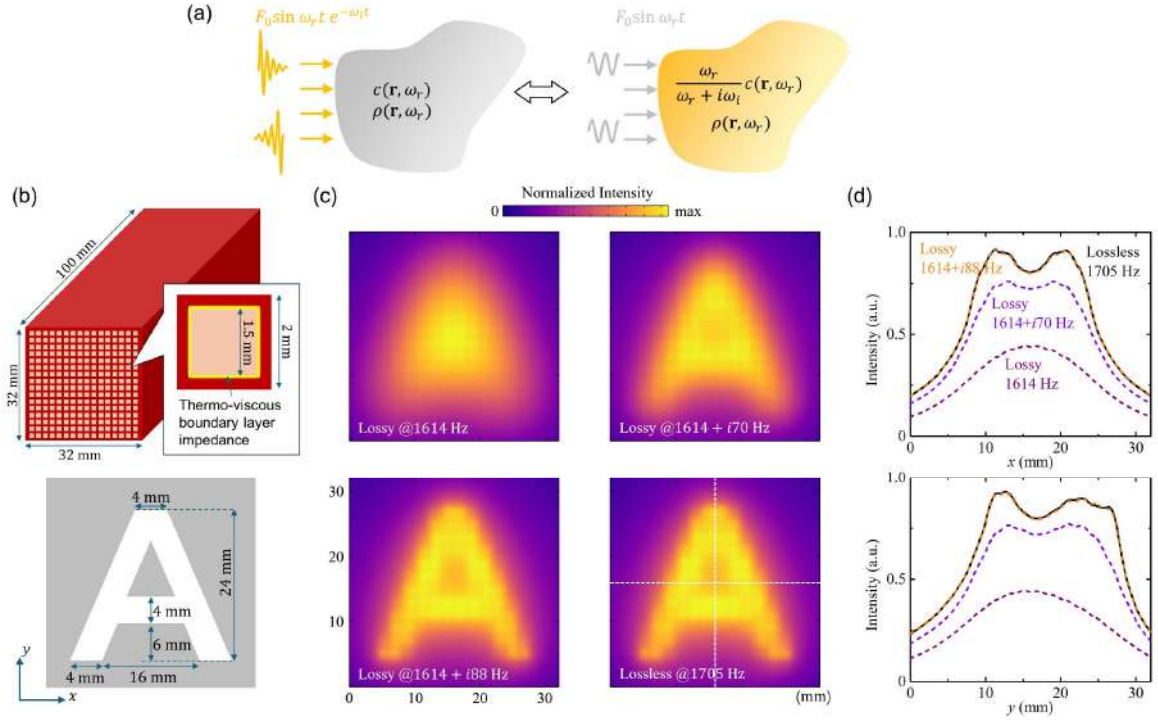


Fig. 1. Complex-frequency simulation of a lossy acoustic superlens. (a) Conceptual illustration of the method for complex-frequency calculation. (b) Schematics of the holey-structured metamaterial lens and object to be imaged. The object/image plane is 0.5 mm away from the lens inlet/outlet. (c) Simulated sound fields at the image plane. (d) Intensity magnitude distributions along the dashed lines in (c). Properties of air in the simulation: density $1.21\ \mathrm{kg/m^3}$, speed of sound 343 m/s, heat capacity at constant pressure $1.005 \times 10^3\ \mathrm{J/(kg \cdot K)}$, ratio of specific heats 1.4, thermal conductivity $0.0258\ \mathrm{W/(m \cdot K)}$, and dynamic viscosity $1.81 \times 10^{-5}\ \mathrm{Pa \cdot s}$.

This work was supported by the National Natural Science Foundation of China (Grant No. 12104383) and the Basic and Frontier Exploration Project Independently Deployed by Institute of Acoustics, Chinese Academy of Sciences (Grant No. JCQY202403).

References

1. Guan, F. *et al.*, "Overcoming losses in superlenses with synthetic waves of complex frequency," *Science,* Vol. 381, No. 6659, 766-771, 2023.
2. Kim, S., Peng, Y.-G., Yves, S., and Alù, A., "Loss Compensation and Superresolution in Metamaterials with Excitations at Complex Frequencies," *Physical Review X,* Vol. 13, No. 4, 041024, 2023.
3. An, S., Liu, T., Zhu, J., and Cheng, L., "Complex-frequency calculation in acoustics with real-frequency solvers," *Physical Review B,* Vol. 111, No. 2, L020301, 2025.
4. Zhu, J. *et al.*, "A holey-structured metamaterial for acoustic deep-subwavelength imaging," *Nature Physics,* Vol. 7, No. 1, 52-55, 2010.

Vibrational dynamics of single supported plasmonic nanodisks

N. Berrit[1], C. Panais[1], N. Lascoux[1], S. Marguet[2], N. Del Fatti[1,3], and A. Crut[1*]

[1] Université de Lyon, CNRS-UCBL, Institut Lumière Matière, 69622 Villeurbanne, France
[2] Université Paris-Saclay, CEA, CNRS, NIMBE, 91191 Gif-sur-Yvette, France
[3] Institut Universitaire de France (IUF), France
[*]corresponding author: aurelien.crut@univ-lyon1.fr

Abstract: The vibrational dynamics of single substrate-supported gold nanodisks were investigated using optical methods and numerical simulations, allowing to address the dependence of vibrational frequencies and quality factors on both nanodisk and substrate characteristics. The transient optical response caused by nanodisk vibrations was also studied.

Metal nanoparticles constitute mechanical resonators with many potential advantages, including high vibrational frequencies (f in the GHz-THz range), small mass and developed chemical synthesis and optical probing methods. However, their vibrational quality factors Q are typically low, resulting in fQ values too low for ultrasensitive mass sensing applications or for quantum phononics experiments at room temperature.[1] It is therefore desirable to achieve a deeper understanding and minimization of vibrational mode damping, which arises from both internal processes and acoustic emission in the environment, as done for larger size resonators.[2]

In this context, we present here investigations of the vibrational dynamics of gold nanodisks based on the combination of single-particle optical experiments with finite-element numerical investigations. Optical experiments were performed by combining spatial modulation spectroscopy, a tool allowing the localization and extinction spectroscopy of single nano-objects randomly deposited on a solid substrate, and single-particle pump-probe spectroscopy, which provides access to the ultrafast electronic, acoustic and thermal dynamics of the investigated nano-objects.

Previous work in our group had demonstrated that the vibrational quality factors of supported nanodisks are highly morphology-dependent, and show largely enhanced values for specific values of their diameter/thickness ratios.[3] These observations could later be ascribed to the radiative coupling of two distinct nanodisk modes.[4] We present here new experimental studies on this theme, addressing the roles played by both the nanodisk and substrate properties. The nanodisks considered here were synthesized using colloidal chemistry rather than electron beam lithography, which is expected to reduce the density of crystalline defects in the nanoparticles. They were deposited on various solid substrates, differing by their composition and thicknesses. Comparison of the measured frequencies with finite-element simulations allowed the identification of the detected vibrational modes. Moreover, our experiments confirmed the strong dependence of vibrational quality factors on the nanodisk diameter/thickness ratio.

We also investigated the transient optical response induced by nanodisk vibrations, which was quantitatively addressed by tuning the wavelength of the probe beam used for transducing the vibrations of the nanodisks into an optical signal. This transient response dramatically differ from that, also measurable in our experiments, induced by nanodisk heating. Indeed, while the latter primarily reflects a broadening of the nanodisk surface

plasmon resonance, vibrations appear to mostly spectrally shift the resonance. Our measurements open the way to precise tests of the numerical models recently introduced in the literature to describe acousto-plasmonic coupling in metal nanoparticles.[5]

This work was supported by the French National Research Agency (ANR) under the reference ANR-20-CE30-0016 (ULTRASINGLE project).

References

1. Boggiano, H. D., T. Possmayer, L. Morguet, L. Nan, L. Sortino, S. A. Maier, E. Cortès, G. Grinblat, A. V. Bragas and L. de S. Menezes, "Coherent Acoustic Phonons in Plasmonic Nanoparticles: Elastic Properties and Dissipation at Low Temperatures", ACS Nano, Vol. 18, No. 46, 31903–31911, 2024.
2. Nguyen, D. T., C. Baker, W. Hease, S. Sejil, P. Senellart, A. Lemaître, S. Ducci, G. Leo and I. Favero, "Ultrahigh Q-frequency product for optomechanical disk resonators with a mechanical shield", *Appl. Phys. Lett.* Vol. 103, No. 24, 241112, 2013.
3. Medeghini, F., A. Crut, M. Gandolfi, F. Rossella, P. Maioli, F. Vallée, F. Banfi and N. Del Fatti, "Controlling the Quality Factor of a Single Acoustic Nanoresonator by Tuning its Morphology", Nano Lett., Vol. 18, No. 8, 5159–5166, 2018.
4. Crut, A., "Substrate-supported nano-objects with high vibrational quality factors", J. Appl. Phys. Vol. 131, No. 24, 244301, 2022.
5. Ahmed, A., M. Pelton and J. R. Guest, "Understanding How Acoustic Vibrations Modulate the Optical Response of Plasmonic Metal Nanoparticles", ACS Nano, Vol. 11, No. 9, 9360–9369, 2017.

Mechanically time-modulated 2D phononic crystal

D. Shymkiv[1], M. Li[1], Ying Wu[2], and A. Krokhin[1*]
[1]University of North Texas, USA
[2]King Abdullah University of Science and Technology, Saudi Arabia
arkady@unt.edu (corresponding author)

Abstract

A periodic arrangement of bimetallic rods in solid matrix is proposed as time-modulated phononic crystal. The rods oscillate along their axes. High elastic contrast between the components of the rods provides deep time modulation. A band structure with mixed gaps formed from coalescence of energy and momentum gaps is calculated and analyzed.

Formal symmetry between time and space variables in the wave equation opens new possibilities for active manipulation of sound by periodic temporal modulation of elastic properties of the constituents of phononic crystals. Spatial periodicity gives rise to frequency band gaps (ω-gaps) in spectrum, provided the elastic contrast between the inclusions and the background material is sufficiently high. For frequencies within ω-gap the Bloch vector $\mathbf{k}$ is pure imaginary and the eigenfunctions decay exponentially with coordinates. Periodicity over time may generate momentum gaps, i.e., regions in $\mathbf{k}$-space within Brillouin zone where solutions of the eigenvalue problem for ω are complex with increasing and decaying eigenfunctions. For the momentum gaps to appear, time modulation must be sufficiently deep. This requirement is not easy to satisfy since elastic properties are robust against external perturbations. Electrical modulation of piezoelectric constituent of a phononic crystal may be not sufficiently deep to generate experimentally resolvable $\mathbf{k}$-gap. Here we propose pure mechanical temporal modulation of elastic properties of 2D phononic crystal of bimetallic cylindrical rods. Temporal modulation occurs not due to weak variation of elastic modulus of a given material but due to sharp temporal alternations of the material of the scatterers. This method, as well as other mechanical methods [1–3] lead to deep level of modulation and relatively wide momentum band gaps.

The phononic crystal structure is shown in Fig. 1. The scatterers are bimetallic, Cu-Al, rods of radius$R = 6$ cm distributed in a square lattice in the $x \in y$ plane with period $a = 15$ cm. The rods vertically oscillate in phase with frequency f_{vib} along axis z. The background matrix is epoxy. Sound wave propagates perpendicular to the rods. The dispersion relation is obtained from the solution of the eigenvalue problem for the displacement vector $\mathbf{u}(\mathbf{r}, t) = (u_x, u_y)$, which satisfies the wave equation. Due to spatiotemporal periodicity the wave equation can be reduced to an infinite set of linear equations for the Fourier components of the displacement vector

$$\mathbf{u}(\mathbf{r}, t) = e^{i(\mathbf{k}\cdot\mathbf{r}-\omega t)} \sum_{\mathbf{G},\Omega} \mathbf{u}(\mathbf{G}, \Omega) e^{i(\mathbf{G}\cdot\mathbf{r}-\Omega t)}, \tag{1}$$

where $\mathbf{G} = (G_x, G_y)$ are the reciprocal lattice vectors and $\Omega = 2\pi f_{\text{vib}}$.

In a temporally modulated medium the eigenvalue problem for $\mathbf{u}(\mathbf{G}, \Omega)$ is quadratic, i.e., there are matrix terms proportional to ω^0, ω and ω^2. The spectrum of the eigenfrequencies $\omega(\mathbf{k}, f_{\text{vib}})$ for the quadratic eigenvalue problem can be calculated by the method of linearization [4]. Three lowest bands of the numerically calculated dispersion relation for $f_{\text{vib}} = 4$ kHz are plotted in Fig. 1b. There are several relatively wide momentum band gaps. Inside these gaps, highlighted in red dots, the eigenfrequency acquires an imaginary part. Here a propagating sound wave can be amplified by gaining energy from the vibrating rods. The

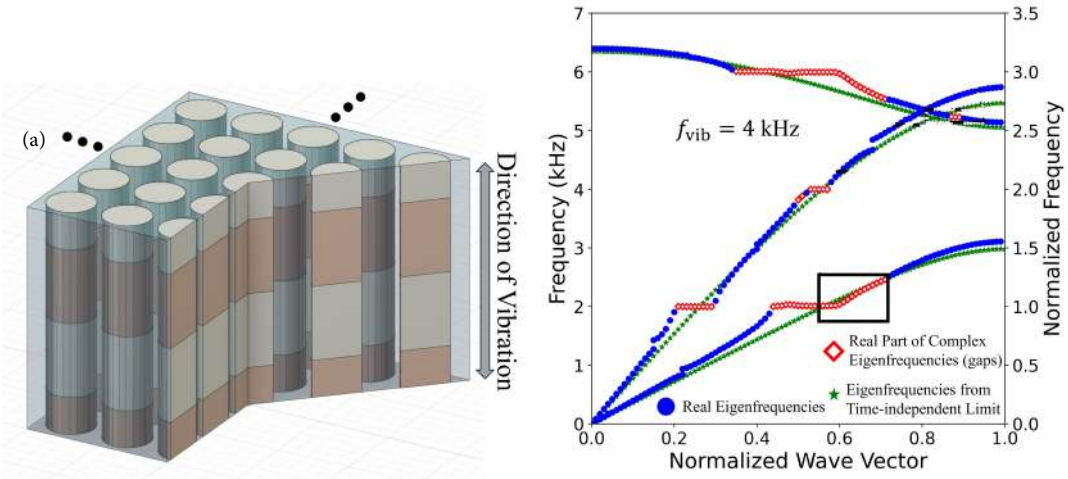


Figure 1: (a) Geometrical scheme for experimentally feasible spatiotemporal 2D phononic crystal consisting of oscillating bimetallic rods arranged in a square lattice and imbedded in an elastic background. (b) Unfolded band structures along the ΓX direction. The band structure for the time-independent crystal, where $f_{vib} = 0$, is shown in green dots. The region of the mixed band gap inside the black rectangle is zoomed in Fig. 2.

band structure in Fig. 1b exhibits a new type of band gap – a mixed band gap where ω and k become complex, $\omega = \omega_0(k_0) \pm i\Omega(k_0)$ and $k = k_0 + \delta'(\omega_0) + i\delta''(\omega_0)$. The region of the mixed band gap inside a black rectangle is zoomed in Fig. 2. The eigenfunctions inside a mixed band gap may exponentially decrease or increase with time and coordinate. The imaginary part, $\pm\Omega_0(k)$, is represented by the vertical distance between each green and red dot for every real Bloch vector k_0. Numerically calculated corrections δ' and δ'' for $k_0 = 0.65$ are shown by multicolored dots, where the color gradient represents the imaginary part δ'' of k.

This work is supported by the NSF and AFORS grants No. 1741677 and FA9550-23-1-0630.

References

[1] Goldsberry, B. M., S. P. Wallen, and M. R. Haberman, "Non-reciprocal wave propagation in mechanically-modulated continuous elastic metamaterials," *J. Acoust. Soc. Am.*, Vol. 146, pp. 782–788, 2019.

[2] Xu, X., Q. Wu, H. Chen, H. Nassar, et al., "Physical observation of a robust acoustic pumping in waveguides with dynamic boundary," *Phys. Rev. Lett.*, Vol. 125, p. 253901, 2020.

[3] Wang, Q., Y. Yang, X. Ni, et al., "Acoustic asymmetric transmission based on time-dependent dynamical scattering," *Sci. Rep.*, Vol. 5, p. 10880, 2015.

[4] Tisseur, F. and K. Meerbergen, "The quadratic eigenvalue problem," *SIAM Review*, Vol. 43, issue 2, 2001.

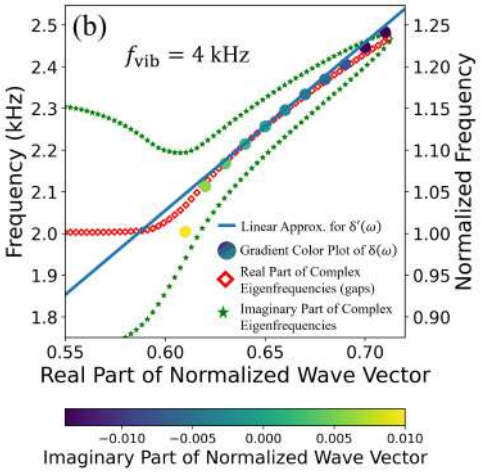


Figure 2: Mixed bandgap. The red diamonds and green dots contain information about the real and imaginary part of each eigenfrequency. The real part of the complex Bloch vectors calculated from the quadratic eigenvalue problem are plotted as multicolored dots, where the color represents the imaginary part (δ'') of each k_0.

Enhanced ultrasound focusing through dense barrier

Zhongming Gu, Jie Zhu[1*]
[1]Institute of Acoustics, School of Physics Science and Engineering, Tongji University, Shanghai 200092, People's Republic of China
[*]corresponding author: jiezhu@tongji.edu.cn

Abstract: The substantial impedance mismatch between dense materials and the surrounding medium poses a challenge to the transmission of ultrasound waves through dense barriers. To address this challenge, we propose an inverse design scheme aimed at achieving ultrasound focusing through dense layers with multiple foci, resulting in significantly enhanced transmission efficiency.

Ultrasound waves are essential in a wide range of practical applications across various fields, including diagnostic imaging, nondestructive testing, and medical treatment, due to their unique properties. However, the presence of dense objects (such as tissue in biomedical applications) in the ultrasound propagation path can lead to significant reflection and reduced transmission. This occurs because the dense materials have a much higher acoustic impedance compared to the surrounding medium. Additionally, dense layers can cause scattering of ultrasound waves, which disperses energy and diminishes focusing capability, further complicating effective imaging or therapeutic applications.

Recent advancements in acoustic metamaterials offer promising strategies to enhance ultrasonic focusing, thereby improving the accuracy and effectiveness of ultrasound applications. Metamaterial lenses have been successfully designed to enhance transmission through impedance-mismatched layers. For instance, complementary acoustic metamaterials have been theoretically proposed to achieve enhanced noninvasive transmission through such layers, utilizing doubly negative acoustic properties. However, experimental demonstrations of complementary acoustic metamaterials have been limited due to the challenges of precisely prototyping either the membranes or complex metallic meta-atoms. Very recently, a metamaterial lens featuring a simple structure made from commonly used materials has demonstrated enhanced focusing and transmission through impedance-mismatched layers [1, 2], albeit limited to a single focus.

In this work, we have designed a meta-lens that focuses ultrasound through a dense layer with multiple foci, thereby enhancing the effectiveness and versatility of ultrasound technologies in both medical and industrial applications. A hemispherical structure made of brass (Young's modulus: 110 GPa; density: 8960 kg/m^3; Poisson's ratio: 0.35) is considered to act as a dense barrier, mimicking the human skull. Due to the significant impedance mismatch between brass and water, a considerable portion of the ultrasound wave is reflected, as shown in Fig. 1(a). Given that the structure is immersed in water, the acoustic-solid interactions must be taken into account. Therefore, we propose utilizing an inverse design method to fabricate a metamaterial lens that allows the ultrasound wave to transmit efficiently through this dense layer. This inverse design approach combines the Non-Superiority Sorting Genetic Algorithm II with the Finite Element Method, circumventing the challenges of deriving analytical solutions. The meta-lens consists of ten concentric rings, with a periodicity of 5 mm. The width (d) and height (h) of each ring are the parameters to be optimized, with the goal of maximizing the ultrasound intensity at the designated positions. The output of the meta-lens demonstrating optimal performance is illustrated in Fig. 1(f). When this lens is positioned on the upper side of the dense layer, the

ultrasound wave can effectively transmit through the barrier and be focused at specific locations, as demonstrated in Fig. 1(b).

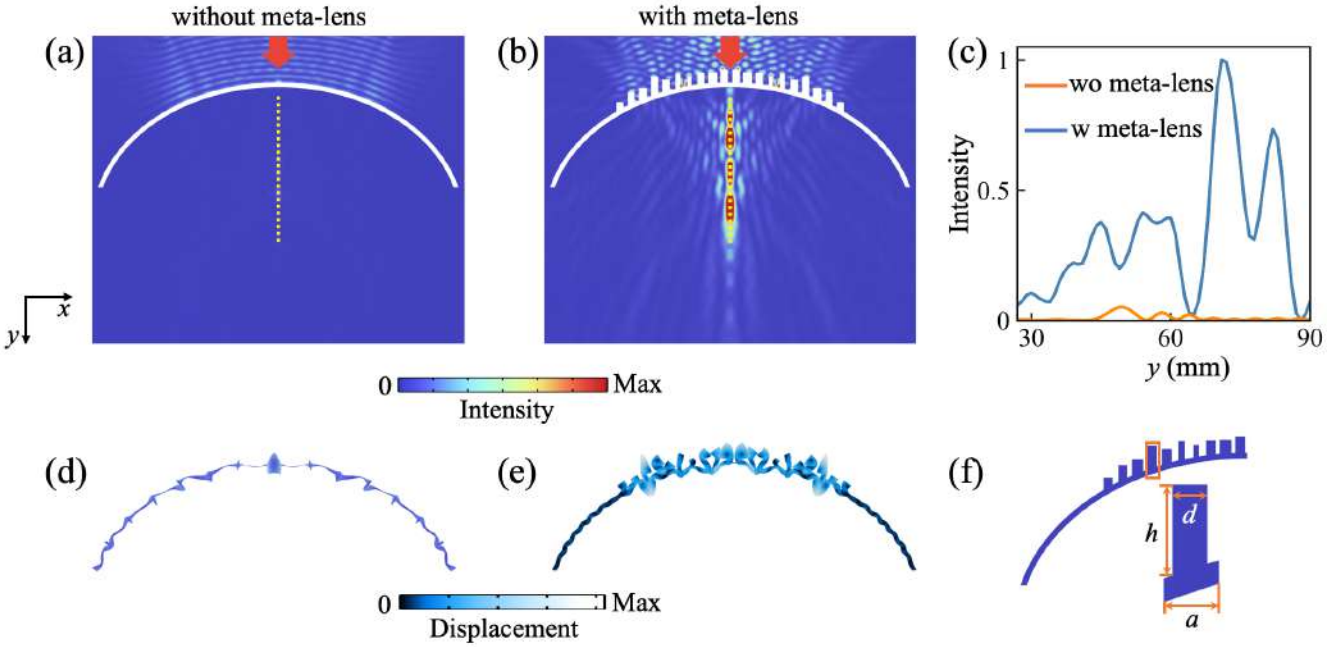


Figure 1. Numerically calculated ultrasound field distributions for the dense barrier: (a) without the optimized meta-lens and (b) with the optimized meta-lens. (c) Intensity profiles along the white dashed lines in (a) and (b), respectively. Simulated total displacement for the dense barrier: (d) without the optimized meta-lens and (e) with the optimized meta-lens. (f) Detailed cross-sectional view of the patterned barrier. In (a), (b), (d), (e), the results represent the fields in the central *xy* plane.

To clearly compare the transmission enhancement and multi-foci focusing effect, we calculated the intensity profiles along the white dashed lines in Figs. 1(a) and 1(b). The ultrasound power for the dense layer patterned with the optimized meta-lens [blue line in Fig. 1(c)] is significantly higher than that of the bare dense layer [orange line in Fig. 1(c)]. Moreover, four distinct foci are observed behind the patterned dense layer, confirming the multi-foci focusing capability of the designed meta-lens. Additionally, we numerically calculated the total displacement of both the bare dense layer and the patterned dense layer, as depicted in Figs. 1(d) and 1(e), respectively. It is evident that the layer equipped with the meta-lens exhibits much higher vibrational displacement, allowing more ultrasound waves to pass through. The proposed scheme to achieve enhanced ultrasound focusing with multi-foci demonstrates a significant ability to precisely target multiple locations simultaneously, facilitating complex manipulations of ultrasound waves and paving the way for breakthroughs in medical treatment and industrial processes.

References

1. Gao, H., Gu, Z., Liang, S., Liu, T., Zhu, J., & Su, Z. “Enhancing ultrasound transmission and focusing through a stiff plate with inversely optimized auxiliary meta-lens,” Applied Physics Letters, Vol. 120, No. 11, 111701, 2022.
2. Ma, M., Gao, H., Guo, X., & Su, Z. “Reconfigurable ultrasound focusing effect through acoustic barriers,” Ultrasonics, Vol. 145, 107470, 2025.

Optomechanical Photonic Crystal Cavities Based on Silicon and Hybrid Nanopillars for Integrated Force Sensing

D. Navarro-Urrios[1,2*]

[1] MIND, Departament d'Enginyeria Electrònica i Biomèdica, Universitat de Barcelona, 08028 Barcelona, Spain

[2] Institute of Nanoscience and Nanotechnology (IN2UB), Universitat de Barcelona, 08028 Barcelona, Spain

[*]corresponding author: dnavarro@ub.edu

Abstract: We present novel optomechanical (OM) photonic crystal cavity geometries based on either monolithic silicon or hybrid silicon/silicon oxide nanopillars integrated with adjacent waveguides. These structures enable optical transduction of cantilever-like modes with OM coupling rates exceeding 1 MHz. We also demonstrate sensitivity to local forces by tracking mechanical resonance shifts.

One-dimensional photonic crystal (1D-PhC) pillar cavities provide a compelling platform for integrated optomechanics, offering enhanced mechanical transduction and nanoscale force sensing. In this work, we present two complementary approaches: (i) full-silicon 1D-PhC cavities with high optical and mechanical Q-factors (Figure 1a), [1] and (ii) hybrid silicon/silicon oxide pillar cavities (Figure 1b) optimized for integration with adjacent waveguides. [2] These structures enable strong light-matter interaction, efficient optical transduction of cantilever-like mechanical modes, and seamless on-chip integration for photonic applications.

We demonstrate 1D-PhC cavities where each nanopillar acts as an independent mechanical resonator that can modulate the optical cavity resonance. By engineering the pillar geometry, we achieve vertical light confinement and a photonic bandgap in the near-infrared regime for transverse-magnetic (TM) polarization. Optical characterization reveals high-quality factors greater of about $2x10^3$ in the case of monolithic silicon pillars and $4x10^3$ in the case of the hybrid geometry. Mechanical transduction of flexural modes up to the fourth order is achieved, with optomechanical coupling rates exceeding 1 MHz.

The hybrid architecture facilitates integration with photonic circuits, indeed enabling efficient evanescent coupling with adjacent waveguides that have been accessed using a butt coupling technique with lensed fibers. Experimental measurements validate the feasibility of transducing thermally activated mechanical modes in the MHz frequency range via the integrated waveguide, eliminating the need for external tapered fiber coupling. By varying the waveguide-cavity distance, we optimize optical coupling for enhanced mechanical transduction.

The sensitivity of 1D-PhC pillar cavities to external forces has been studied by bringing a tapered fiber into contact with the pillars and tracking RF spectral shifts. Mechanical damping caused linewidth broadening, while fiber contact increased oscillation frequencies in relation to an effective elastic constant increase. Peaks stabilized upon detachment, indicating mechanical resonance recovery.

Our work advances the field of optomechanical photonic crystals by demonstrating high-performance silicon and hybrid silicon/silicon oxide pillar cavities. The combination of strong optomechanical interactions, high Q-factors, and waveguide integration paves the way for practical implementations in force sensing, biosensing, and nanoscale optomechanics.

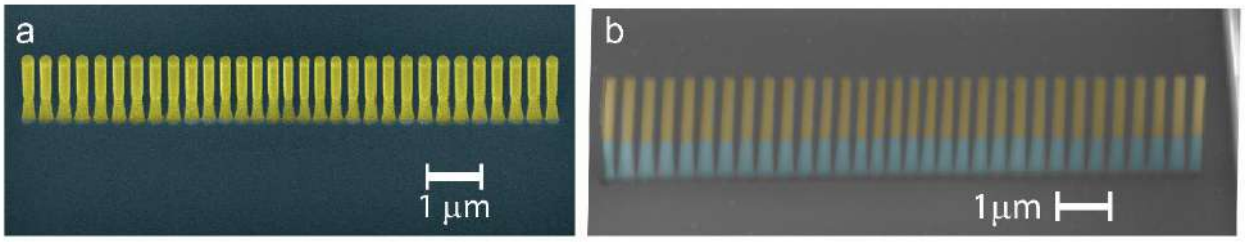


Figure 1. Scanning electron microscope (SEM) tilted view (30°) of representative fabricated pillar-based optomechanical crystal (OMC) designs. *(a) Fully silicon-based OMC. (b) Hybrid Si/SiO_2 OMC, with the silicon top portion highlighted in yellow and the SiO_2 bottom portion in blue.*

This work has been financially supported by the European Union's H2020 FET-OPEN project STRETCHBIO (GA 964808) and MICINN projects ALLEGRO (Grants Nos. PID2021-124618NB-C22 and PID2021-124618NB-C21) and MOCCASIN-2D (Grant No. TED2021-132040B-C21).

References

1. Jaramillo-Fernandez J., Poblet M., Alonso-Tomás D., Vinther Bertelsen C., López-Aymerich E., Arenas-Ortega D., Svendsen W. E., Capuj N. E., Romano-Rodríguez A., Navarro-Urrios D., "Strong Cavity-Optomechanical Transduction of Nanopillar Motion", ACS Nano 18 (35), 24550-24557, 2024.
2. Poblet M., Vinther Bertelsen C., Alonso-Tomás D., López-Aymerich E., Goldschmidt J., Svendsen W. E., Romano-Rodríguez A., Navarro-Urrios D., Hybrid Si/SiO_2 Pillar-Based Optomechanical Crystals for On-Chip Photonic Integration, to be submitted.

Time-resolved two-dimensional imaging of GHz acoustic waves in phononic crystals and metamaterials

Osamu Matsuda
Division of Applied Physics, Faculty of Engineering, Hokkaido University, Japan
omatsuda@eng.hokudai.ac.jp

Abstract

The all optical time-resolved two-dimensional imaging of GHz surface acoustic waves is efficient to study the GHz acoustic properties of media. Here the principle of the technique is explained briefly, and some applications of the technique to micron-scale phononic crystals and metamaterials are shown.

1 Introduction

Surface acoustic waves in MHz-GHz frequency region have been exploited in filter devices in microwave communications, sensor devices for gas molecules, various data-processing devices, etc. For developing these applications as well as understanding the fundamental physics of acoustic waves, the spatiotemporal observation of the waves is quite efficient.

We have been developing an all optical time-resolved two-dimensional imaging technique for MHz-GHz surface acoustic waves or vibrations. [1–3] In this paper, the principles of the above-mentioned imaging technique is overviewed, and some representative results for the imaging of acoustic waves on phononic crystals and phononic metamaterials are presented.

2 Principle

The imaging technique is based on the optical pump-probe method which utilizes periodic light pulses of sub-picosecond temporal widths. We use a mode-locked Ti-sapphire laser generating light pulses at the repetition frequency around 80 MHz. The light pulses are focused onto the sample to be imaged using a microscope objective to a small spot of diameter around 1 μm. These are named "pump light pulses" and are used to generate acoustic waves mostly through the thermal expansion caused by the light absorption. The same light pulses are delayed and focused onto the sample surface to detect the acoustic field at the moment of the light pulse arrival to the sample surface. These are named "probe light pulses". The small surface-normal displacement ($<$ nm) is detected using an optical interferometer. To achieve the two-dimensional imaging, the probe light focusing position is scanned across the sample surface typically in a rectangular region with the edge length of several hundreds microns at a fixed delay time. To achieve the time-resolved measurement, the delay time is varied from 0 to 13 ns (period of pulse repetition) using an optical variable delay line (the optical path length varies from 0 to 4 m). Taking the "snap-shot" images with varying the delay time, the spatiotemporal variation of the acoustic field is obtained as a movie. [1, 2].

3 Results

Figure 1 shows an example of the measurement for a two-dimensional phononic crystal. [4] Circular holes of diameter 2.8 μm and depth 1.3 μm are aligned in a square lattice of period 5.6 μm in a square region of 110×110 μm^2 on a crystalline Si (100) surface. The acoustic waves are generated by focusing the pump light around the center of the phononic crystal region, and the area 200×200 μm^2 including the surrounding pristine Si substrate is imaged. Though the raw obtained data is a set of acoustic fields as a function of delay time and probing position, and involving several frequency components, the shown is a real-part of temporal Fourier transform of the raw data, corresponding to a snapshot of the acoustic field at 884 MHz. A plus-sign-shaped phonon collimation pattern (phonon focusing) is seen in the phononic crystal, and each collimated beam is split into two when it goes out from the phononic crystal region to the surrounding pristine silicon substrate. Further detailed analysis clarifies the dispersion relation of the phononic crystal.

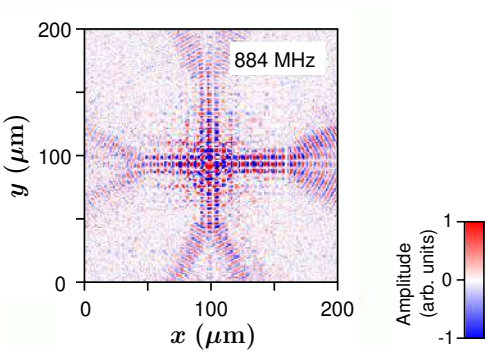


Figure 1: Snapshot image of the acoustic field strength of a square lattice phononic crystal on a Si (100) substrate at 884 MHz.

Figure 2 shows an example of the measurement for a phononic metamaterial which consists of a monolayer of silica spheres of diameter 1.08 μm and density 2.0 g cm^{-3} on a float glass substrate coated with a 100 nm Al film. The shown is the dispersion relation of the acoustic waves: it is obtained by the spatiotemporal Fourier transform of the raw time-resolved data. To have the frequency resolution much finer than the laser repetition frequency, a special frequency controling technique is used. [3] The coupling of the propagating modes and the localized modes are clearly seen around 250–300 MHz.

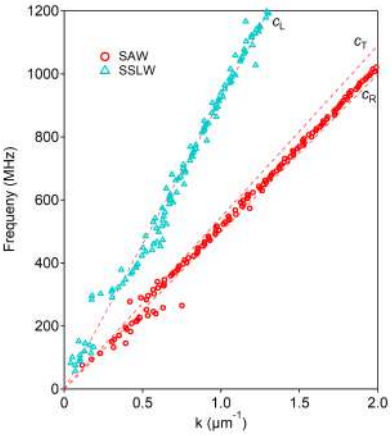


Figure 2: Dispersion relation of the acoustic waves of a phononic metamaterial.

4 Conclusion

The all optical time-resolved two-dimensional acoustic wave imaging technique has been developed and utilized to clarify the acoustic properties of medium. It can be utilized for detailed study of phononic crystals and phononic metamaterials up to GHz frequency region, and would be useful for developing functional devices based on them.

References

[1] Y. Sugawara, O. B. Wright, O. Matsuda, M. Takigahira, Y. Tanaka, S. Tamura, and V. E. Gusev, Phys. Rev. Lett. **88**, 185504 (2002).

[2] T. Tachizaki, T. Muroya, O. Matsuda, Y. Sugawara, D. H. Hurley, and O. B. Wright, Rev. Sci. Instrum. **77**, 043713 (2006).

[3] O. Matsuda, S. Kaneko, O. B. Wright, and M. Tomoda, IEEE Trans. Ultrason. Ferroelectr. Freq. Control **62**, 584 (2015).

[4] O. Matsuda, H. Koga, H. Nishita, M. Tomoda, P. H. Otsuka, and O. B. Wright, Photoacoustics **30**, 100471 (2023).

Surface acoustic waves-driven magnon spin Hall effect in atomically thin van der Waals antiferromagnets

R. Sano[1*], Y. Ominato[2], and M. Matsuo[3]

[1]Kyoto University, Japan
[2]Waseda University, Japan
[3]University of Chinese Academy of Sciences, China
[*]corresponding author: sano.ryotaro.m07@kyoto-u.jp

Abstract: Van der Waals antiferromagnets have lacked comprehensive tools for probing their intricate magnetic properties. We propose using surface acoustic wave-driven intrinsic magnon spin Hall currents to mechanically detect and manipulate magnetic order in two-dimensional antiferromagnets. This innovative method overcomes weak magnetic responses, offering a promising foundation for future antiferromagnetic spintronics.

Intrinsic magnetism in two-dimensional (2D) materials had long been believed to hardly survive due to the enhanced thermal fluctuations. However, the recent discovery of exfoliated van der Waals (vdW) magnets has opened up a new avenue for 2D magnetism at finite temperatures [1,2]. Especially, transition metal phosphorus trichalcogenides $MPX3$ (M = Fe, Ni, Mn; X = S, Se) are a family of easily exfoliatable vdW antiferromagnets [3]. These materials share the same honeycomb lattice structure, but the bulk antiferromagnetic (AFM) phase varies depending on the magnetic elements [4]. It therefore provides an ideal platform to investigate magnetism and magnetic excitations in the 2D limit. Furthermore, compared to ferromagnets, antiferromagnets exhibit ultrafast dynamics in the terahertz regime, null stray field, and robustness against the external magnetic field perturbation. Therefore, the investigation of these materials paves the way towards not only the fundamental understanding of 2D magnetism, but also the possibility of high-speed and compact AFM spintronics.

Standard methods such as magnetization measurements and neutron diffraction, which could only access macroscopic magnetic properties, are not suitable for the study of atomically thin magnets. Especially, antiferromagnets do not have net magnetization, direct measurement of AFM ordering using the magneto-optical Kerr effect is not available either. Although recent studies have focused on the Raman spectroscopy [5,6] and the second-harmonic generation [7,8] to detect the crystal symmetry lowering associated with the AFM transition, these signals often do not provide clear identification of the AFM order in the monolayer limit. Therefore, a comprehensive method which suits for exploring the magnetic properties of 2D antiferromagnets is highly desired.

Here, we propose an ac intrinsic magnon spin Hall current mechanically driven by surface-acoustic waves (SAWs) as a novel method to probe the magnetic structures of such 2D honeycomb antiferromagnets [9]. Owing to extremely large mechanical flexibility of 2D materials, SAWs are ideally suited for fundamental research of them [10]. When an inhomogeneous strain is applied to 2D honeycomb magnets, a spatial modulation of exchange energies mimics the role of artificial gauge fields for magnons. These strain gauge fields work at two valley points of the Brillouin zone in the opposite direction, which in turn activate the valley degrees of freedom (DOF). Therefore, the valley DOF with the use of SAWs is a promising concept for mechanical detection and

manipulation of the magnetic order in 2D vdW antiferromagnets. Furthermore, our mechanically driven magnon spin Hall effect will overcome the difficulties with weak magnetic responses inherent in the use of antiferromagnets and hence provide a building block for more sophisticated AFM spintronics.

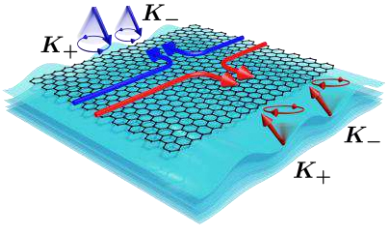


Fig. 1. Schematics of the acoustomagnonic spin Hall effect. A spatial modulation of the exchange energies due to strain mimics the role of artificial gauge fields for magnons in a honeycomb lattice. Both the strain-induced electric fields and the magnon Berry curvature work at the two valley points in the opposite direction, leading to a net spin Hall current.

This work was supported by the Priority Program of Chinese Academy of Sciences under Grant No. XDB28000000, and by JSPS KAKENHI (Grants No. 20H01863, No. 21H04565, No. JP22J20221, No. 22KJ1937, and No. 23H01839) from MEXT, Japan.

References

1. C. Gong *et al*., "Discovery of intrinsic ferromagnetism in two-dimensional van der Waals crystals." Nature **546**, 265 (2017)
2. B. Huang *et al*., "Layer-dependent ferromagnetism in a van der Waals crystal down to the monolayer limit.", Nature **546**, 270 (2017)
3. K. Du *et al*., "Weak Van der Waals Stacking, Wide-Range Band Gap, and Raman Study on Ultrathin Layers of Metal Phosphorus Trichalcogenides." ACS Nano **10**, 1738 (2016)
4. P. Joy and S. Vasudevan, "Magnetism in the layered transition-metal thiophosphates *M*PS3 (*M* = Mn, Fe, and Ni)." Phys. Rev. B **46**, 5425 (1992)
5. J. Lee *et al*., "Ising-Type Magnetic Ordering in Atomically Thin FePS3." Nano Lett. **16**, 7433 (2016)
6. K. Kim *et al*., "Suppression of magnetic ordering in XXZ-type antiferromagnetic monolayer NiPS3." Nat. Commun. **10**, 345 (2019)
7. H. Chu *et al*., "Linear Magnetoelectric Phase in Ultrathin MnPS3 Probed by Optical Second Harmonic Generation." Phys. Rev. Lett. **124**, 027601 (2020)
8. Z. Ni *et al*., "Imaging the Néel vector switching in the monolayer antiferromagnet MnPSe3 with strain-controlled Ising order." Nat. Nanotechnol. **16**, 782 (2021)
9. R. Sano, Y. Ominato, and M. Matsuo, "Acoustomagnonic spin Hall effect in honeycomb antiferromagnets." Phys. Rev. Lett. **132**, 236302 (2024)
10. X. Nie *et al*., "Surface acoustic wave induced phenomena in two-dimensional materials." Nanoscale Horiz. **8**, 158 (2023)

Acoustic trapping, emission enhancement, and harvesting from bound states in the continuum

Sibo Huang[1], Yong Li[2], Jie Zhu[2], and Din Ping Tsai[1*]

[1]Department of Electrical Engineering, City University of Hong Kong, Hong Kong SAR 999077, China
[2]Institute of Acoustics, School of Physics Science and Engineering, Tongji University, Shanghai 200092, China
[*]corresponding author: dptsai@cityu.edu.hk

Abstract: Acoustic bound states in the continuum (BICs) are special modes characterized by high quality factors and strong localization. By constructing a series of coupled Friedrich-Wintgen BICs and appropriately tuning their radiation and intrinsic losses, we achieved novel and efficient acoustic trapping, emission enhancement, and energy harvesting.

Acoustic Bound States in the Continuum (BICs) demonstrate infinite Q-factors and complete isolation, facilitating high Q-factors and external radiation access when transformed into quasi-BICs. These quasi-BICs enable tunable, minimal radiation losses, enhancing various high-quality and high-performance acoustic devices for sound trapping [1,2,3], emission [4,5], and harvesting [6].

In Figures (a)-(d), we introduce a BIC-supporting system composed of two closely-coupled cavities. This configuration achieves BIC when the cavities satisfy the condition of $\kappa(\gamma_A-\gamma_B)=\sqrt{\gamma_A\gamma_B}(\omega_A-\omega_B)$. Here, $\omega_{A(B)}$ is the angular resonant frequency of cavity A(B), $\gamma_{A(B)}$ and $\Gamma_{A(B)}$ indicate the radiation loss and the intrinsic loss of cavity A(B), respectievly. κ and $\sqrt{\gamma_A\gamma_B}$ indicate the near-field and the far-field coupling among cavity A and cavity B. Additionally, radiation losses can be modulated freely by adjusting the depth difference between the cavities, while intrinsic losses are tuned by altering the cavities' cross-sectional sizes. This simple architecture facilitates effective modulation of radiative and intrinsic losses, beneficial for acoustic devices requiring high Q-factors.

Figures (e)-(f) display the acoustic trapping phenomenon enabled by BICs. When intrinsic losses in our two-cavity system are minimized and further adjusted along with the cavities' height differences to match radiative losses, the system captures all incident sound waves, resulting in zero reflection as shown in Figure (e). Moreover, due to the system's low intrinsic losses, sound waves persist for extended periods, leading to extreme acoustic trapping as depicted in Figure (f).

Figures (g)-(i) manifest the acoustic emission enhancement achieved by BICs. We establish a theoretical framework considering both radiative and dissipative losses and systematically investigate the acoustic Purcell effect. Our results reveal that the acoustic Purcell factor is governed by the system’s radiative and dissipative factors, necessitating a simultaneous reduction in both to achieve significant emission enhancement. Initially demonstrated in a dual-cavity system supporting a quasi-BIC with a Purcell factor of 84.7, we further employ collective BICs in multi-resonator systems to achieve broadband emission enhancement.

Figures (j)-(k) illustrate enhanced acoustic harvesting with BICs. Sound, an ubiquitous, clean, and renewable energy source, is often underutilized due to its low energy density. Our study introduces a two-state system supporting a Friedrich-Wintgen BIC, achieving an unprecedented enhancement in sound energy density—up to 1849 times the incident intensity. Integrating this BIC-supporting system with energy conversion mechanisms, such as piezoelectric films, we realize high-performance acoustic energy harvesting.

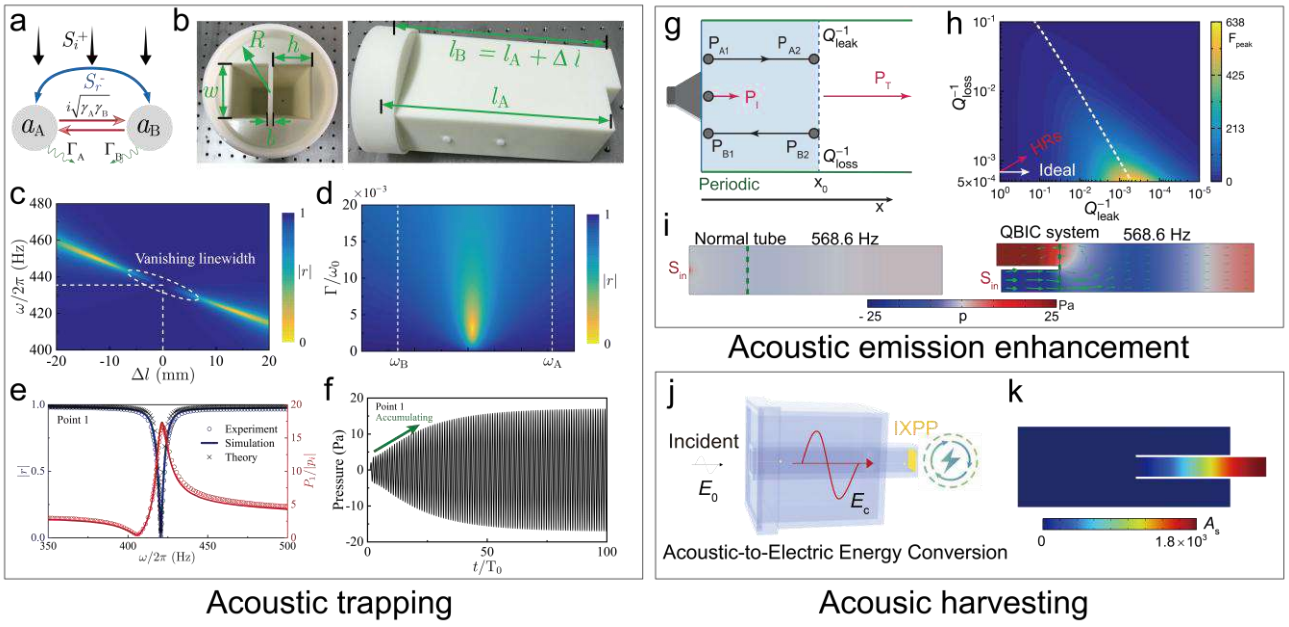


Figure 1. Acoustic trapping, emission enhancement and harvesting based on BICs. (a) Typical mode interaction among two resonances with radiation coupling. (b) A BIC-supporting system consisting two acoustic cavities. (c)-(d) Reflection properties of the two-cavity BIC-supporting system by modulating radiation loss (c) and intrinsic loss (d). (e) Zero reflection of the BIC-supporting system. (f) Acoustic field enhancement at the bottom of the system. (g) Schematic of an acoustic source influenced by a resonant system treating as an effective medium. (h) Achieving great Purcell factors by modulating the intrinsic and radiation losses. (i) Acoustic emission properties of an identical acoustic sources within in a normal tube and a QBIC system, respectively. (j) Schematic of an BIC-supporting acoustic harvester. (k) Pressure-field enhancement at the system's bottom.

Acknowledgements

This work is supported by the University Grants Committee/Research Grants Council of the Hong Kong Special Administrative Region, China (Project No. AoE/P-502/20, CRF Project: C5031-22G, GRF Project: CityU15303521; CityU11305223; CityU11300224), City University of Hong Kong (Project Nos. 9380131, and 7005867), and National Natural Science Foundation of China (Project Nos. 62375232, and 92263208), the Science and Technology Commission of Shanghai Municipality (Project Nos. 21JC1405600, and 22JC1404100),

References

1. S. Huang, T. Liu, Z., Zhou, et al, "Extreme sound confinement from quasibound states in the continuum," Phys. Rev. Applied, 14.2, 021001, 2020.
2. L. Huang, Y. Chiang, S. Huang, et al, "Sound trapping in an open resonator," Nat. Common., 12.1, 4819, 2021.
3. Y. Liang, D.P. Tsai, Y. Kivsharm, "From local to nonlocal high-plasmonic metasurfaces," Phys. Rev. Lett., 133.5, 053801, 2024.
4. S. Huang, S. Xie, H. Gao, et al, "Acoustic Purcell effect induced by quasibound state in the continuum," Fundam. Res., 4.1, 57-62, 2024.
5. S. Huang, S. Xie, T. Liu, T. Hao, et al, "Broadband Acoustic Purcell Effect from Collective Bound States in the Continuum," Adv. Sci. 11.48, 2414627, 2025.
6. C. Song, S. Huang, H. Ma, et al, "Self-powered frequency-selective acoustic sensor based on bound states in the continuum," Adv. Sci. 11.48, 2410379, 2025.

Maximizing the modal effective mass of metamaterial resonators through topology optimization

V. Cool[1,2*], W. Jaspers[1,3], B. Biçer[1,2], C. Claeys[1,2] and E. Deckers[2,4]

[1] KU Leuven, Department of Mechanical Engineering, Celestijnenlaan 300, Heverlee, Belgium
[2] Flanders Make@KU Leuven, B-3001 Heverlee, Belgium
[3] Flanders Make, Core Lab CodesignS, B-3001 Heverlee, Belgium
[4] KU Leuven Campus Diepenbeek, Department of Mechanical Engineering, Wetenschapspark 27, 3590 Diepenbeek, Belgium
[*]corresponding author: vanessa.cool@kuleuven.be

Abstract: The lightweight nature of locally resonance-based metamaterial solutions is a key design factor. A topology optimization framework is proposed to maximize the modal effective mass (MEM) of structural resonators. A novel design achieving a MEM of 96.2% is presented and validated through vibration attenuation evaluation for a finite metamaterial structure.

Introduction: Vibroacoustic metamaterials are known to be lightweight structures achieving exceptional vibrational or acoustic attenuation. Although mass is an important design aspect, the modal effective mass (MEM) of typical resonance-based metamaterial designs varies between 40-90% [1,2]. This work presents a topology optimization routine to maximize the modal effective mass of a resonator at a specified frequency under both connectivity and mass constraints. The paper first elaborates on the applied optimization framework, after which the results are discussed for a specified case study.

Methodology: The MEM describes the amount of mass in motion in a specific direction for a given modeshape ϕ_p. In this work, the translational MEM normal to a base plate is of interest. Assuming mass-normalized modeshapes, the normal MEM of mode p reads [3]:

$$MEM_{z,p} = \left(\phi_p^H \mathbf{M}\boldsymbol{\tau}\right)^2 \quad \text{with} \quad \left(\mathbf{K} - \omega_p^2 \mathbf{M}\right)\phi_p = 0 \tag{1}$$

with $\mathbf{K}, \mathbf{M}$ the stiffness and mass system matrices of the clamped-based resonator, ω and ϕ, respectively the p[th] eigenfrequency and eigenmode, $\boldsymbol{\tau}$ the normal-translational selection vector and the superscript H the Hermitian transpose. The optimization routines aims at obtaining a resonator design with the highest possible MEM at a targeted frequency ($\bar{f}$). A density-based topology optimization is applied. The envisaged design space is divided into finite elements while each element contains a design variable ξ_i which varies between 0 and 1, representing the void and solid phase. To alleviate numerical instabilities and force the design towards black and white, both a density-filtering and Heaviside projection are applied [4]. The topology optimization problem is given as:

$$\begin{cases} \max\limits_{\xi} & \sum_1^{N_m} \exp\left(-\frac{1}{2}\left(\frac{f_p - \bar{f}}{\sigma_f}\right)^2\right) MEM_{z,p} \\ st. & v \geq V_{min} \\ & v \leq V_{max} \\ & \theta_{sw} \leq \mu\, \bar{\theta}_{sw} \\ & 0 \leq \xi_i \leq 1 \end{cases} \tag{2}$$

in which the objective function is defined as the weighted MEM_z sum of the first N_m modes considered using a Gaussian frequency window, while σ_f is a parameter to control the relative penalty for eigenfrequencies away from $\bar{f}$. This parameter is decreased during the optimization. The optimization is subjected to both a minimum and maximum volume constraint, a connectivity constraint and box constraints. The connectivity constraint is required to diminish the presence of solid islands of materials. A self-weight compliance constraint is used in which the resonator is subjected to self-weight loading, while the corresponding compliance energy (θ_{sw}) is limited with respect to the compliance energy of a full design domain ($\bar{\theta}_{sw}$). In order to ensure well-connected, black and white designs, the self-weight force is considered from the design itself while it is subjected to an eroded version of the design of interest. Since a gradient-based optimization solver is applied, the sensitivities are required which are analytically derived using the adjoint method.

Result: The proposed optimization framework is applied on a design space of 4 x 40 x 40 mm, while a discretization of 80 x 80 linear shell elements is used. The material is PMMA with Young's modulus 4850 MPa, density of 1188.38 kg/m^3, Poisson's ratio of 0.31 and structural damping of 5%. The targeted frequency is set to $\bar{f} = 1500$ Hz, while the volume is restricted between 40-50% and μ equals 100. The resonator is added in post-processing on a base plate of 6 mm PMMA while the unit cell spacing is 45 x 45 mm leading to Bragg frequency of the base plate of 2855 Hz.

Figure 1a shows the resulting optimized resonator. The fourth mode of the resonator consist of a near-perfect vertical translation of the mass, achieving a MEM of 96.2% at 1500 Hz. The leg design of the resonator makes a perfect trade-off in minimizing material usage while obtaining adequate stiffness and frequency tuning. The corresponding dispersion curves (Figure 1b) of the resonator on the 45 x 45 mm unit cell show a bandgap around the tuned frequency (1448-1667 Hz). A vibration transmission is computed on the finite plate with 6 x 3 resonators (Figure 1c). The resulting vibration transmission (Figure 1d) shows a large attenuation of the structural waves at the targeted frequency of 1500 Hz.

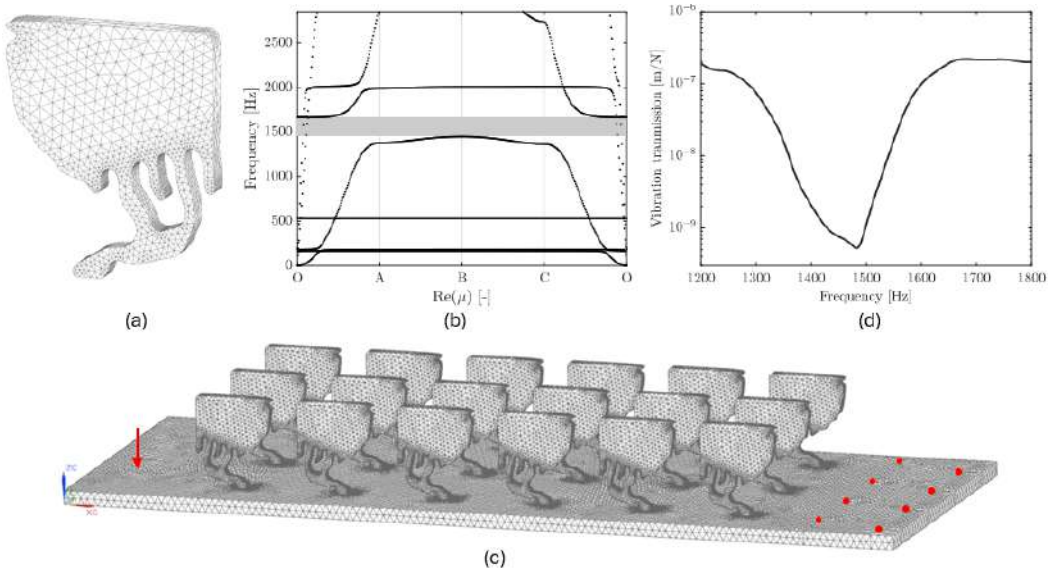


Figure 1. Result of the optimization. a) Optimized resonator, b) corresponding dispersion curves, c) problem set-up to compute the vibration transmission and d) resulting vibration transmission.

Conclusion: This work introduces a density-based topology optimization framework for the maximization of the translational modal effective mass of metamaterial resonators. A novel resonator design with effective mass of 96.2% is presented while an investigation on the resulting vibration transmission shows high attenuation levels at the targeted frequency.

Acknowledgements: The research of V. Cool (no. 1213925N) is funded by a grant from the Research Foundation - Flanders (FWO). The Research Fund KU Leuven is gratefully acknowledged for its support. The European Union is gratefully acknowledged for their support of the METRAMAT research project (GA 101119917). Views and opinions expressed are however those of the authors only and do not necessarily reflect those of the European Union. The European Union cannot be held responsible for them.

References

1. Janssen, S., Van Belle, L., et al. (2023). Improving the noise insulation performance of vibro-acoustic metamaterial panels through multi-resonant design. *Applied Acoustics*, *213*, 109622.
2. Pires, F. A., Boukadia, R. F., et al. "Novel resonator concept for improved performance of locally resonant based metamaterials." *Thin-Walled Structures* (2024): 112866.
3. J. J. Wijker. "Spacecraft Structures". 1st ed. Springer Berlin Heidelberg, 2008, pp. 247–263.
4. Bendsoe, M. P., and Sigmund, O. "Topology optimization: theory, methods, and applications". *Springer Science & Business Media*, 2013.

Spectral methods for designing quasiperiodic metamaterials

B. Davies
Mathematics Institute, University of Warwick, Coventry, UK
bryn.davies@warwick.ac.uk (corresponding author)

Abstract

Quasiperiodic metamaterials hold significant potential to unlock novel phenomena. We present convergence analyses of popular methods to approximate their spectra (superspace and supercell methods) and show how they can be used to design new metamaterials.

1 Introduction

Quasiperiodic metamaterials have been the subject of significant recent excitement, thanks to their ability to support spectra with exotic properties. This exciting class of new materials use non-periodic arrangements of meta-atoms to unlock spectra with fractal, dense patterns of spectral gaps, giving engineers the ability to build devices with novel, broadband properties.

Although using non-periodic geometries can unlock some exciting properties, removing the assumption of periodicity means that standard analytic techniques (based on Bloch's theorem) are no longer directly applicable. In practice, the spectral properties of a quasicrystal are typically approximated by methods that replace the quasicrystal with a periodic version of the geometry (meaning that calculating the spectrum is then straightforward). There are two main variants of this in the literature, the *supercell method* and the *superspace method*. We summarise these here and show how the resulting Bloch spectra converge to the spectrum of the quasiperiodic metamaterial.

2 Approximating spectra

Quasicrystals are a special class of non-periodic geometries that can be obtained by taking a projection from a higher-dimensional periodic function. For example, a function $f : \mathbb{R}^n \to \mathbb{R}$ is said to be quasiperiodic if there exists some $m > n$ and some $g : \mathbb{R}^m \to \mathbb{R}$ such that

$$f(x) = g(Rx), \tag{1}$$

for all $x \quad \mathbb{R}^n$, where R is a rectangular m-by-n matrix that "lifts" the vector $x \quad \mathbb{R}^n$ up to Rx in the higher-dimensional space $\mathbb{R}^m$. An example is given in Fig. 1. This means that, although quasiperiodic functions are not generally periodic, they have underlying periodicity that is responsible for their exotic properties and can be exploited to yield efficient methods to compute spectra of systems with quasiperiodic coefficients.

The most widely used approach in the physical literature is a so-called *supercell* method, whereby a non-periodic material is approximated by a periodic one by taking a large piece of the non-periodic material and using it as the periodic unit cell for Bloch spectral calculations (depicted on the right in Fig 1). The intuition is that, if the supercell is sufficiently large, then you will get a reasonable approximation of the desired spectrum. In [1, 2] convergence in the limit of large unit cell size is proved. This means that any features that are common to all the spectra in the sequence (such as the *super band gaps* established for Fibonacci tilings [3]) will exist in the limiting spectrum also.

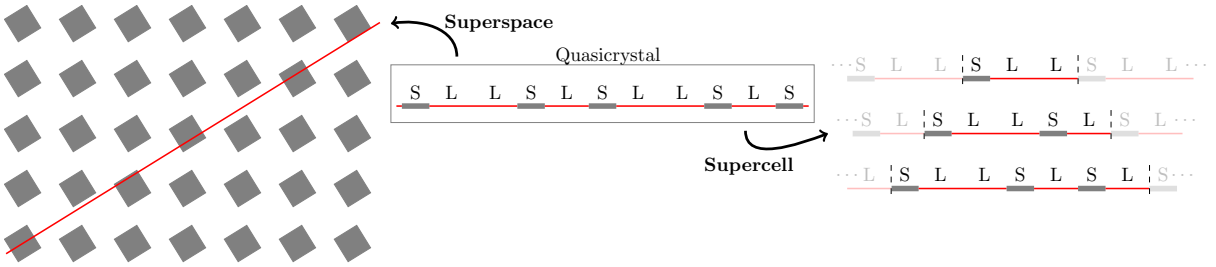


Figure 1: A quasiperiodic crystal can be approximated by a periodic geometry either by lifting into the higher-dimensional *superspace* (left) or by choosing sections to use as a *supercell* (right).

The other promising method is to take advantage of the higher-dimensional periodicity from 1 and solve the differential problem in the higher-dimensional periodic superspace. The challenge here is that the resulting differential operator is somewhat difficult to handle, so it is important to choose the right numerical method to solve the superspace problem. For example, the plane wave expansion method leads to spurious modes appearing [4] (since the operator is not elliptic so we can't expect decay of the Fourier coefficients). However, methods such as finite differences and finite elements give convergent approximations [1].

Given these methods for approximating the spectra of quasicrystals, we can use them to design novel metamaterials. For example, it is possible induce strong wave localisation by introducing an artificial axis of reflectional symmetry, see [5] and references therein. Similarly, graded metamaterials can be created by slowly modulating the projection angle from the superspace. In the framework illustrated in Fig 1, for example, this corresponds to projecting onto a curve instead of a straight line. In [6] it was shown that projecting onto a quadratic givels a *fractal rainbow effect* whereby broadband signals are sorted according to their frequency (a fractal version of the rainbow effects observed in classical graded metamaterials).

3 Acknowledgements

This work was partly supported by the EPSRC under grant number EP/X027422/1.

References

[1] Davies, B. and Thalhammer, C. "Convergence of supercell and superspace methods for computing spectra of quasiperiodic operators," *arXiv pre-print*, arXiv:2411.15906, 2024.

[2] Shubin, M. A., "Almost periodic functions and partial differential operators," Russ. Math. Surv., Vol. 33, No. 2, p. 1, 1978.

[3] Davies, B. and Morini, L., "Super band gaps and periodic approximants of generalised Fibonacci tilings," *Proc. R. Soc. A*, Vol. 480, No. 2285, p. 20230663, 2024.

[4] Rodriguez, A. W., McCauley, A. P., Avniel, Y., and Johnson, S. G. "Computation and visualization of photonic quasicrystal spectra via Bloch's theorem," *Phys. Rev. B*, Vol. 77, No. 10, p. 104201, 2008.

[5] Davies, B. and Craster, R. V., "Symmetry-induced quasicrystalling waveguides," *Wave Motion*, Vol. 115, p. 103068, 2022.

[6] Davies, B., Chaplain, G. J., Starkey, T. A. and Craster R. V., "Graded quasiperiodic metamaterials perform fractal rainbow trapping," *Phys. Rev. Lett.*, Vol. 131, No. 17, p. 177001, 2023.

Tunable Phonon-Electron Fano Resonance in Si Nanoparticles via Electromagnetic Confinement and Anharmonic Decay in Engineered Media

Michel Kazan

Department of Physics, American University of Beirut, P.O. Box 11-0236, Riad El-Solh, Beirut, 1107-2020, Lebanon
Email: mk140@aub.edu.lb

Abstract: We introduce strategies for modulating phonon-electron Fano resonance in silicon nanoparticles through a designed nanoparticle environment. By leveraging prolonged laser irradiation and electromagnetic field confinement, the resonance can be enhanced, whereas anharmonic phonon decay provides a mechanism for its attenuation. These findings offer new opportunities in photonics and phononics.

The phonon-electron Fano effect, a quantum interference phenomenon between discrete phonon modes and an electronic continuum, plays a pivotal role in nanoscale light-matter interactions [1, 2]. Controlling this resonance is essential for applications in quantum technologies, photonics, phononics, and energy conversion [3-8]. Conventional modulation techniques primarily rely on laser intensity variations [9-11], yet achieving fine-tuned control remains challenging.

This study introduces a dual-approach strategy that integrates external perturbations (laser exposure) and structural modifications (nanoparticle embedding) to achieve precise resonance modulation. Silicon (Si) nanoparticles were embedded within granular matrices composed of zinc oxide (ZnO), monoclinic gallium oxide (β-Ga_2O_3), and graphite (C), and their phonon-electron interactions were investigated via Raman spectroscopy. The analysis focused on the effects of laser-induced electronic transitions, electromagnetic field confinement, and anharmonic phonon decay on the Fano resonance.

Prolonged laser irradiation increased electronic transitions, thereby enhancing phonon-continuum coupling. Raman spectral analysis revealed increased asymmetry and coupling strength over time, signifying an intensification of the Fano effect. Embedding Si nanoparticles within ZnO and β-Ga_2O_3 resulted in multiple light-scattering events that confined the electromagnetic field around the Si nanoparticles. This confinement significantly enhanced the local electric field, strengthening phonon-electron interactions.

In contrast, when Si nanoparticles were embedded in ZnO, laser heating induced a redshift in their phonon resonance frequencies, aligning them with a key feature of the ZnO two-phonon density of states. This alignment facilitated strong anharmonic decay, effectively shortening the phonon lifetime and attenuating the Fano resonance.

The study demonstrates that laser exposure time serves as a crucial parameter for tuning phonon-electron coupling strength, providing a new degree of control beyond conventional laser intensity modulation. Additionally, multiple light scattering in ZnO and β-Ga_2O_3 offers a scalable approach to field confinement and resonance enhancement without requiring intricate nanostructuring. Furthermore, coupling Si phonons with the vibrational modes of the surrounding medium enables controlled attenuation of the Fano resonance, a critical capability for applications requiring selective suppression of phonon-electron interactions.

These modulation strategies unlock new possibilities for optimizing Fano-based sensing, photonic devices, and phononic metamaterials for thermoelectric applications, enabling precise, scalable control over phonon-electron interactions.

In conclusion, this work advances the understanding of phonon-electron Fano resonance in Si nanoparticles, experimentally validating methods for both enhancing and suppressing the effect. By leveraging laser-induced electronic transitions, electromagnetic field confinement, and anharmonic phonon interactions, this study introduces a versatile, cost-effective platform for fine-tuning nanoscale interactions across a wide range of technological applications.

References

1. M. Tanwar, L. Bansal , C. Rani, S. Rani, S. Kandpal, T. Ghosh, D. K. Pathak, I. Sameera, R. Bhatia, R. Kumar, Fano-type wavelength-dependent asymmetric Raman line shapes from MoS2 nanoflakes, ACS Phys. Chem. Au, 2, 417, 2022.
2. S. J. Chang, P. C. Huang, J. S. Su , Y. W. Hsieh, C. J. Quiroz Reyes, T. H. Fan, H. S. Sun, A. P. Nguyem, T. I. Liu, H. W. Cheng, C. W. Lin, Optically Tunable Many‐Body Exciton‐Phonon Quantum Interference, Adv. Sci. 11, 2404741, 2024.
3. K. L. Lee, J. B. Huang, J. W. Chang, S. H. Wu, P. K. Wei, Ultrasensitive biosensors using enhanced Fano resonances in capped gold nanoslit arrays, Sci. Rep. 5, 8547, 2015.
4. Y. Li, Y. Yuan, X. Peng, J. Song, J. Liu, J. Qu, An ultrasensitive Fano resonance biosensor using two dimensional hexagonal boron nitride nanosheets: theoretical analysis, RSC Adv. 9, 29805, 2019.
5. B. Ruan, J. Guo, L. Wu, J. Zhu, Q. You, X. Dai, Y. Xiang, Ultrasensitive terahertz biosensors based on Fano resonance of a graphene/waveguide hybrid structure, Sensors, 17, 1924, 2017.
6. M. Yamaguchi, A. Lyasota, T. Yuge, Theory of Fano effect in cavity quantum electrodynamics, Phys. Rev. Res. 3, 013037, 2021.
7. A. Lyasota , C. Jarlov, M. Nyman, A. Miranda, M. Calic, B. Dwir, A. Rudra , A. Shevchenko, E. Kapon, Mode interference effect in optical emission of quantum dots in photonic crystal cavities, Phys. Rev. X, 12, 021042, 2022.
8. C. L. Dreeßen, C. Ouellet-Plamondon, P. Tighineanu, X. Zhou, L. Midolo, A. S. Sørensen, P. Lodahl, Suppressing phonon decoherence of high performance single-photon sources in nanophotonic waveguides, Quantum Sci. Technol. 4, 015003, 2018.
9. M. Riesner, R. Fainblat, A. K. Budniak, Y. Amouyal, E. Lifshitz, G. Bacher, Temperature dependence of Fano resonances in CrPS4, J. Chem. Phys. 156, 054707, 2022.
10. J. A. Briones-Torres, I. Rodríguez-Vargas, Fano resonances in bilayer graphene superlattices, Sci. Rep. 7, 16708, 2017.
11. D. K. Mishra, V. G. Sathe, Evidence of the Fano resonance in a temperature dependent Raman study of CaCu3Ti4O12 and SrCu3Ti4O12. J. Phys. Condens. Matter, 24, 252202, 2012.

Distinct Exceptional Points in Hermitian Phononic Laminates

A. Fishman, B. Lustig, G. Elbaz, A. Muhafra, V. Varma and G. Shmuel*
Technion – Israel Institute of Technology, Israel
Corresponding author: meshmuel@technion.ac.il

Abstract: Breaking Hermitian symmetry creates degenerate states called exceptional points, typically requiring a challenging gain-loss material design. We exploit the unique nature of elastodynamics to obviate the need for gain or loss, enabling access to distinct exceptional points and excitation of anomalous frozen modes and negative refraction in conservative phononic laminates.

Open systems, which are described by non-Hermitian operators, can exhibit degeneracies where two or more of their eigenmodes coalesce. These degeneracies, termed *exceptional points* (EPs), present exotic wave phenomena, such as anisotropic transmission and negative refraction, and thus serve as a tool for metamaterial design.

Most studies focus on temporal EPs, which form when two (or more) resonance frequencies coalesce. These works incorporate gain and loss that are often balanced to form parity-time symmetry for temporal stability.

Spatial EPs, which form in the complex wavevector space at real frequencies, have received less attention, particularly in elastodynamics, despite their robustness against imperfections. However, elastic waves exhibit features not found in sound and light waves that can be leveraged to design spatial EPs. To appreciate this, consider the ubiquitous scenario of isotropic media, where acoustic waves are longitudinal, electromagnetic waves are transverse, while only elastic waves exhibit both polarizations.

Here, we present a framework that eliminates the need for material gain or loss by breaking spatial Hermitian symmetry using the aforementioned features of elastodynamics. The analysis considers a conservative solid with open boundaries and a sustained driving source. More specifically, we revisit a canonical scattering problem of monochromatic plane waves impinging on a semi-infinite periodic laminate made of two conservative materials. By designing the composition of a unit cell with two isotropic materials, we tuned the energy transfer between the two elastic polarizations at the material interfaces such that two of the forward quasi-transverse and quasi-longitudinal Bloch modes coalesce inside the Brillouin zone [1] (Fig. 1a), forming a second-order EP (EP2). This is in sharp contrast with the well-known scenario of degeneracies at the band edges between forward- and backward Bloch modes of the same polarization. These non-resonant EPs are surrounded by a self-intersecting Riemann surface whose curvature is related to the energy flow, and therefore, the unique topology of these surfaces can be leveraged for anomalous energy transport. We showed that these spatial EPs give rise to negative refraction (Fig. 1b), as they are the crossing of branches of opposite slopes [1].

We extended our design beyond EP2 to achieve the coalescence of three Bloch modes (EP3) by replacing one of the isotropic materials in the unit cell with an anisotropic one [Fig. 1(c)]. This higher-order, non-resonant degeneracy further expands the toolbox for elastic wave shaping by forming waves with zero axial group velocity and finite transmittance (known as 'axially frozen modes' [3]), which can even reach unity [Fig. 1(d)]. Notably, these modes, previously discovered in 3D dielectric laminates [3], are now accessible in simpler, planar settings in elastodynamics, thanks to the distinct tensorial properties of elastodynamics.

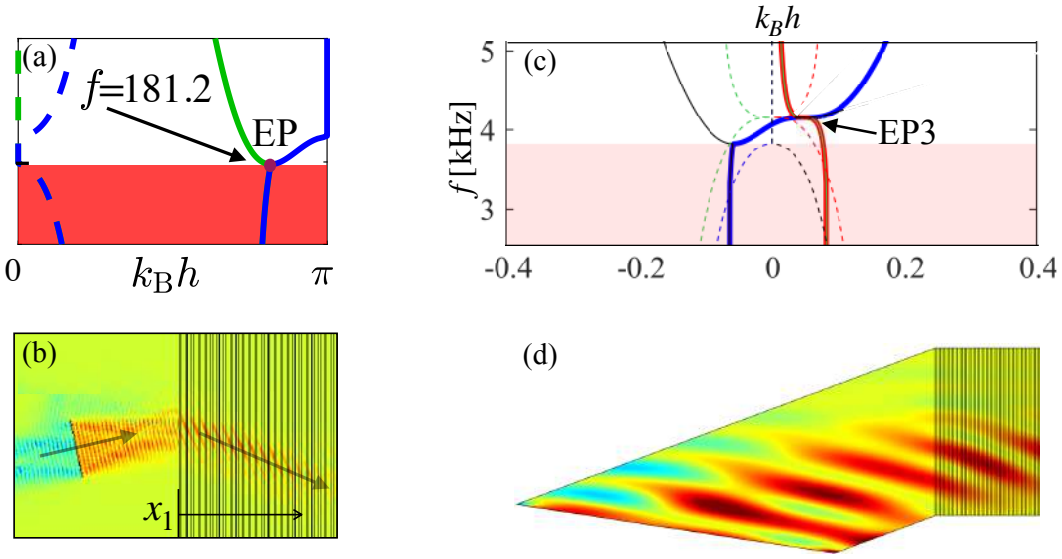


Figure 1: (a) The coalescence of two Bloch modes of the exemplary conservative laminate considered by Lustig et al. [1]. The EPs are shown in a cut in the frequency-Bloch wavenumber (f, k_B) diagram for specific vertical wavenumber about 181.2 kHz. $\mathrm{Re}\, k_B$ and $\mathrm{Im}\, k_B$ are shown in solid and dashed curves, respectively. The real and imaginary parts of a certain branch are plotted using the same color. (b) Full-wave finite element simulations of the axial energy flux in the pertinent scattering problem near the EP. The energy flux is preserved in the laminate and exhibits negative refraction. (c) Coalescence of three Bloch modes of the exemplary conservative laminate considered by Fishman et al. [2]. This EP3 is shown in a cut in the (f, k_B) diagram for certain vertical wavenumber about 4.15 kHz. (d) Full-wave finite element simulations of the axial energy flux in the pertinent scattering problem near the EP, giving rise to axially frozen modes with unity transmittance.

We acknowledge funding by the European Union (ERC, EXCEPTIONAL, Project No. 101045494). Funded by the European Union. Views and opinions expressed are however those of the authors only and do not necessarily reflect those of the European Union or the European Research Council Executive Agency. Neither the European Union nor the granting authority can be held responsible for them.

References

1. B. Lustig, G. Elbaz, A. Muhafra, and G. Shmuel, "Anomalous energy transport in laminates with exceptional points," *J Mech Phys Solids*, 133, 103719, 2019.

2. A. Fishman, G. Elbaz, T. V. Varma and G. Shmuel, "Third-order exceptional points and frozen modes in planar elastic laminates," *J Mech Phys Solids*, 186, 105590, 2024.

3. A. Figotin and I. Vitebskiy, "Oblique frozen modes in periodic layered media," *Phys Rev E*, 68, 036609, 2003.

Band structure engineering in artificial phononic trans-polyamynoborane with first and second-nearest neighbors.

R. A. Méndez-Sánchez[1*], Y. Betancur-Ocampo[2], B. Manjarrez-Montañez[1], and A. M. Martínez-Argüello[3]

[1]Instituto de Ciencias Físicas, Universidad Nacional Autónoma de México, Cuernavaca, Mexico
[2]Instituto de Física, Universidad Nacional Autónoma de México, Ciudad de México, Mexico
[3]Instituto de Física, Benemérita Universidad Autónoma de Puebla, C. P. 72570 Puebla, Puebla, Mexico
[*]corresponding author: mendez@icf.unam.mx

Abstract: An artificial phononic molecule that emulates the electronic properties of trans-polyaminoborane with second-nearest-neighbor hoppings is studied. The numerical band structures obtained with COMSOL Multiphysics agree with tight-binding calculations of the κ-deformed Dirac equation. Topologically protected states are obtained in a 1D finite chain.

Trans-polyaminoborane, a molecule quite similar to trans-polyacetylene, is a polymeric molecule with fundamental properties from an electronic point of view. Being a polymer with high conductivity, it became a cornerstone in organic semiconductors. Its atoms, boron and nitrogen, are located instead of the two carbon atoms composing trans-polyacetylene. We study this molecule with first- and second-nearest neighbors and, in a certain regime, it satisfies the κ-deformed Dirac equation. Although a photonic realization was proposed earlier [1], a fine-tuning of higher couplings is very difficult or almost impossible in that area [1]. As we will show, the engineering of first- and second-nearest neighbors in the coupled-resonator phononic version of these molecules is straightforward. Fig. 1 shows the molecular and artificial representation of the trans-polyaminoborane.

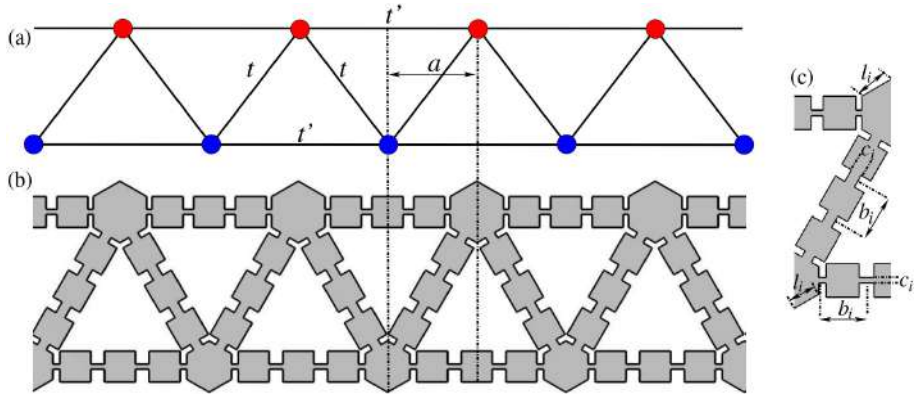


Figure 1: (a) Schematic representation of trans-polyamynoborane with first (t) and second-nearest-neighbors (t´) hoppings. (b) Coupled-resonator phononic molecule of trans-polyamynoborane. (c) Unit cell of length a and l_i is the size of hexagon resonator and b_i the size of connector between resonators and c_i control the detuning hopping parameter. For i = 1, 2 that represent first and second-nearest-neighbors.

The coupled-resonator phononic metamaterials (CRPnMs) [2,3,4] are inspired by the coupled-resonator optical waveguides [5]. In the CRPnMs, resonators are coupled through finite phononic crystals. To build a CRPnM, the following condition is needed: When a normal-mode frequency of the resonator falls within the bandgap of the phononic crystal, the modes of the resonators couple to each other through evanescent waves. In

this case, a phononic tight-binding (TB) regime similar to the TB regime of condensed-matter physics emerges. Additionally, a fine-tuning of the hopping parameters in the CRPnMs opens the opportunity to explore phenomena predicted in solid-state physics and molecular physics that are difficult to observe in those areas.

The band structure of the TB Hamiltonian given in the Eq 1 agrees with finite element simulations. Also, the TB model with second-nearest-neighbor hoppings follows a κ-deformed Dirac equation; the bands are shown in Fig 2. The Dirac cone in one case and the deformation of the bands confirm the theoretical predictions for different hopping values of the second nearest-neighbor hopping.

$$H(ka) = \begin{pmatrix} f_A + 2t_2\cos(ka) & t_1 + t_1' e^{-ika} \\ t_1 + t_1' e^{ika} & f_B + 2t_2'\cos(ka) \end{pmatrix} \quad \textbf{(Eq 1)}$$

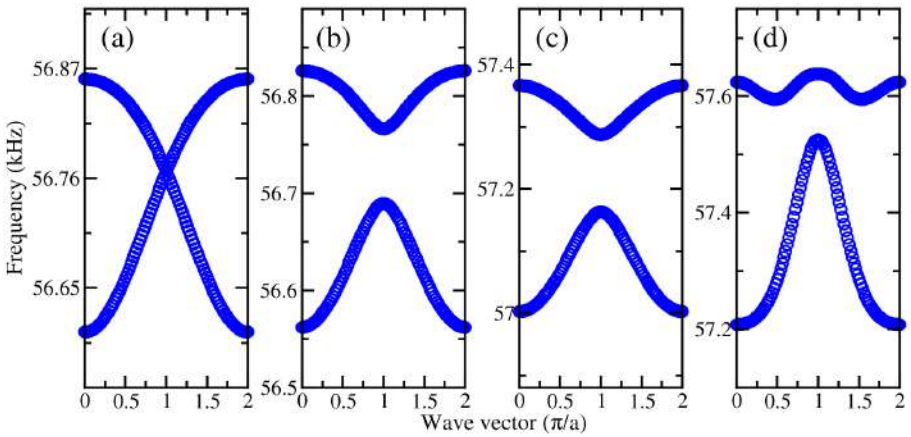


Figure 2: Band structure of the artificial trans-polyamynoborane calculated using finite-element. (a) $f_A = f_B$ and t = 1 and t′ = 0. (b) $f_A \neq f_B$ and t=1 and t′ = 0.1 (c) $f_A \neq f_B$ and t = 1 and t′ = 0.2. (d) $f_A \neq f_B$ and t = 1 and t′ = 0.5.

RAMS and YBO were supported by PAPIIT-UNAM under projects IN108825 and IA106223, respectively. BMM is grateful to CONAHCYT for financial support through a Ph. D. fellowship.

References

1. Majari, P., Sadurni, E., Setare, M. R., Franco-Villafane, J. A., & Seligman, T. H. (2021). Photonic realization of the κ-deformed Dirac equation. *Physical Review A*, *104*(1), 013522.
2. Ramírez-Ramírez F., Flores-Olmedo E., Báez G., Sadurní E., and Méndez-Sánchez R.A., "Emulating tightly bound electrons in crystalline solids using mechanical waves", Sci. Rep. 10, 10229 (2020)
3. López-Toledo J.A., Báez G. and Méndez-Sánchez R.A, "Tight-binding model for torsional and compressional waves in high-quality coupled-resonator phononic metamaterials," Mech. Adv. Mater. Struct. (2021).
4. Betancur-Ocampo, Y., Manjarrez-Montañez, B., Martínez-Argüello, A. M., & Méndez-Sánchez, R. A. (2024). Twofold topological phase transitions induced by third-nearest-neighbor hoppings in one-dimensional chains. *Physical Review B*, *109*(10), 104111.
5. Yariv, A., Xu. Y., Lee R. K. and Scherer A. "Coupled-resonator optical waveguide: a proposal and analysis," Opt. Lett. 24, 711 (1999).

Realizations of acoustic and elastic meta-structures to reduce noise and vibration

W. Jeon[1*]

[1]Korea Advanced Institute of Science and Technology (KAIST), Republic of Korea
[*]corresponding author: wonju.jeon@kaist.ac.kr

Abstract: We present three meta-structures with audiovisual demonstrations aiming at real-world applications. The first is an ultra-light soundproofing meta-panel to insulate broadband noise from electric vehicles. The second is a meta-liner to insulate noise in ducts while allowing flow. The third is a modified acoustic black hole to suppress structural vibrations.

Acoustic and elastic meta-structures have garnered significant attention as a new technology capable of overcoming the limitations of traditional materials for sound and vibration control. We propose three meta-structures to reduce noise and vibration. The first one is the lightweight soundproofing meta-panel. This light-weight panel efficiently blocks two separate broadband noises simultaneously, offering a solution for isolating and mitigating diverse noise sources. The second one is an acoustic meta-liner. This structure allows airflow while blocking noise, striking a balance that enables the passage of air while impeding the transmission of unwanted sounds. The last one is the meta-damper, and this structure is a waveguide absorber designed based on a spiral acoustic black hole (ABH). The meta-damper absorbs and dissipates elastic waves, effectively reducing vibrations and minimizing their impact.

Our meta-structures for controlling wave energy initially stemmed from conceptualization and theory- and simulation-based examination. The pivotal aspect of the present work lies in the advancement of these conceptualization into realization, marking a breakthrough in wave (e.g. noise/vibration) control technologies.

Acoustic and elastic metamaterials are proposed in this study, showcasing extraordinary performance as wave absorbers and insulators. These characteristics are revealed through fabrication and experimental realization of metamaterials.

1. Meta-panel: “ultra-light soundproofing meta-structure”

The proposed meta-structure consists of membranes and a multi-scale lattice structure and achieves high sound isolation with the aid of negative effective material properties of the meta-panel in each target band [1]. The soundproof performance was experimentally tested in an anechoic chamber using the fabricated meta-panel for practical applications in electric cars. The experimental results show that the meta-panel having area density 1.51 exhibits better insulation performance with a 1/20 times lighter weight compared to a steel plate. We are attempting to utilize the meta-panel to reduce road noise in the low-frequency band and motor noise in the high-frequency band of electric vehicles.

2. Meta-liner: “noise insulator without flow resistance in a duct”

Traditional methods for noise reduction in dusts, such as acoustic mufflers, often impede airflow, compromising system, and exhibit poor performance at low frequencies. To overcome these limitations, a meta-liner is proposed that can attenuate noise for various grazing flow speeds, considering the effect of flow, with little flow resistance. The proposed meta-liner attenuates noise in ducts while allowing airflow. The meta-liner consists of two different sub-wavelength Helmholtz resonators in order to induce hybrid-resonance,

leading to high absorption in upstream direction as well as high transmission loss in downstream direction. The meta-liner is designed using a theoretical model established in a recent study [2] and simulation, which demonstrates high transmission loss per unit length of more than 45 dB/m with a bandwidth of 10% of the target frequency for various flow speeds of 0, 17, and 34 m/s.

3. Meta-damper: "waveguide absorber based on spiral acoustic black holes"

An ABH is a structure with a wedge-shaped geometry, where the thickness decreases according to a specific power law [3]. It concentrates elastic wave energy near the tip of the wedge, utilizing a small amount of damping material to absorb and dissipate the concentrated energy as heat. While such acoustic black holes can significantly attenuate vibrational energy within a structure, they have been limited by their large occupying space due to the long wedge-shaped structure. We address this limitation by proposing a spiral ABH [4]. Its wave absorption performance is validated through fabrication and experiment [5]. Recent advancements include the application of spiral ABH to plate or box-type structures by modifying the spiral ABH into a waveguide absorber [6]. The surface-averaged mobility of the host plate with and without meta-dampers are compared and the results show that reductions in peaks up to 20 dB could be obtained using the meta-dampers. Compared to the traditional material to dampen vibrations, the meta-damper is more light-weight and could achieve superior damping performance by absorbing elastic waves propagating in the plate.

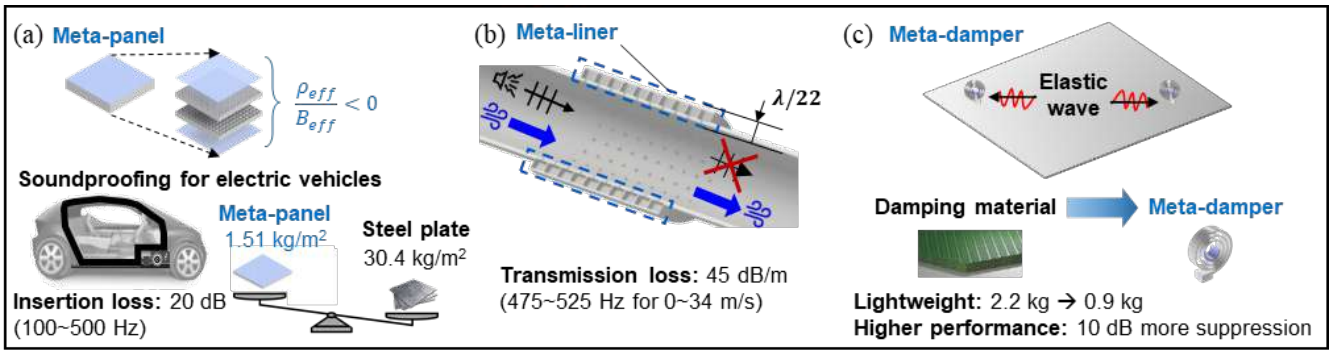


Figure 1. Conceptual schematics of three meta-structures. (a) Meta-panel. (b) Meta-liner. (c) Meta-damper.

References

1. J. Kim, E. Choi and W. Jeon "Lightweight soundproofing meta-panel for separate wide frequency bands," Mech. Syst. Signal Process., Vol. 184, 109647, 2023.
2. T.S. Oh and W. Jeon, "Acoustic metaliners for sound insulation in a duct with little flow resistance," Appl. Phys. Lett., Vol. 120, 044103, 2022.
3. M. A. Mironov, "Propagation of a flexural wave in a plate whose thickness decrease smoothly to zero in a finite interval," Sov. Phys. Acoust., Vol. 34, 318–319, 1988.
4. J.Y. Lee and W. Jeon, "Vibration damping using a spiral acoustic black hole," J. Acoust. Soc. Am., Vol. 141, 1437–1445, 2017.
5. S. Park, M. Kim and W. Jeon, "Experimental validation of vibration damping using an Archimedean spiral acoustic black hole," J. Sound Vib., Vol. 459, 114838, 2019.
6. S. Park, J.Y. Lee and W. Jeon, "Vibration damping of plates using waveguide absorbers based on spiral acoustic black holes," J. Sound Vib., Vol. 521, 116685, 2022.

Locally Resonant Mosaic Meta-Plate

Nan Gao[1,*], Vicente Romero-García[1], Jean-Philippe Groby[2] and Ping Sheng[3,4]

[1]Instituto Universitario de Matemática Pura y Aplicada, Departamento de Matemática Aplicada, Universitat Politècnica de València, Camino de Vera, València, 46022, Spain
[2] *Laboratoire d'Acoustique de l'Université du Mans (LAUM), UMR 6613, Institutd'Acoustique—Graduate School (IA-GS), CNRS, Le Mans Université, Le Mans, France*
[3] *The Hong Kong University of Science and Technology, Hong Kong, China*
[4]*Associate of Clare Hall College, Cambridge University, Cambridge, CB3 9AL, the United Kingdom*

[*]Presenting author: ngao@upvnet.upv.es

Abstract: This work proposes and realizes a mosaic plate system with a zero-frequency bandgap extending from 0+ up to 6800 Hz, while maintaining translational degrees of freedom. Simulation and experimental results show that this structure exhibits significant vibration cancellation in the 50-6800 Hz range and offers notable sound insulation advantages over a homogeneous plate with the same mass density.

In this work, we propose a mosaic design strategy to achieve a broadband zero-frequency bandgap for flexural modes of a structured plate. By linking finite-sized tile pieces (TPs), we form a mosaic plate (MPt). Multilayered corner joiner pieces (JPs) connect adjacent TPs (Fig.1a and b), enabling the desired zero-frequency bandgap while maintaining TPs' locally resonant modes. This approach effectively disables low-frequency bending wave excitations in the linked system.

The overall MPt structure exhibits static rigidity while displaying an absence of modes at frequencies between 0+ and the locally resonant mode at 6.8 kHz, which can be reflected in the simulated dispersion (Fig. 1c). The vibrational transmission spectrum referenced to a point harmonic vibrator source, obtained by laser vibrometer test, can also support the above conclusion. The experimental results also agree well with the Green function fitting. Compared to a homogeneous plate with the same mass density, the vibration transmission of the MPt shows a significant reduction of amplitude in the 50-6800 Hz range (Fig. 1d to f).

Furthermore, the application of the MPt in sound insulation was analyzed through both simulations and experiments, showing an excellent sound insulation effect that exceeds the performance predicted by the mass density law (Fig. 1g). Our results provide valuable insights into the design and application of acoustic and mechanical metamaterials, especially in the low-frequency regime.

Acknowledgements
This project has received funding from the European Union's Horizon 2020 research and innovation program under the Marie Skłodowska-Curie grant agreement No. 101106904 - MDS-APP-UAF. V.R.-G. is grateful for the partial support under Grant No. PID2023-146237NB-I00 funded by MICIU/AEI/10.13039/501100011033.

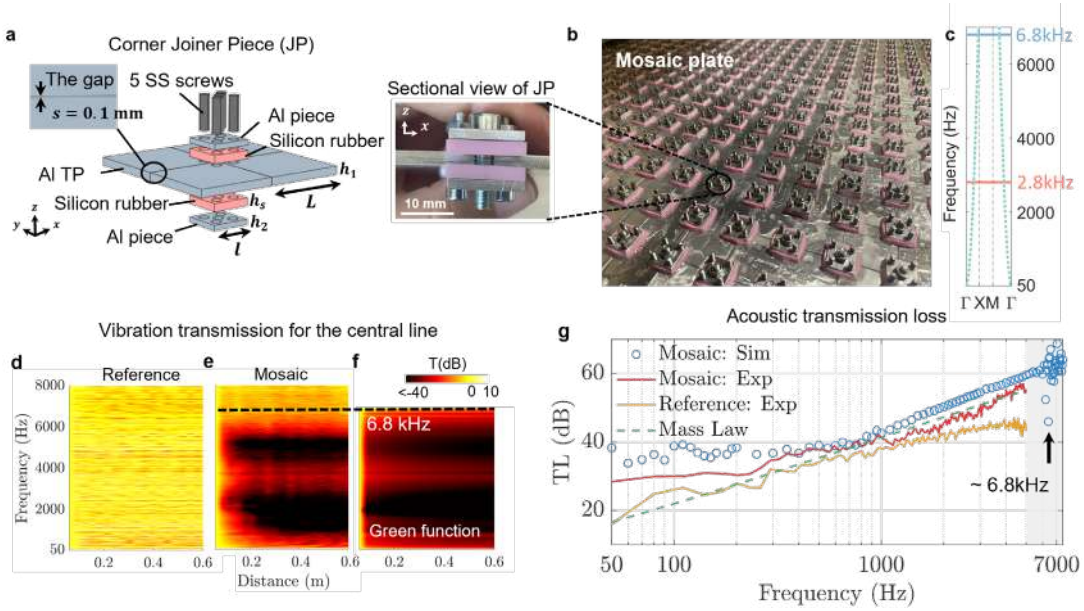


Fig.1 (a) Corner joiner piece (JP) design: (left) Illustration of the JP with screws. A JP comprises alternating hard and soft layers set at the four corners of each TP (L = 30 mm, h_1 = 3 mm). Every JP has two aluminum alloy pieces, each with side length l =15 mm thickness h_2 = 2 mm Two silicone rubber layers with side length l =15 mm and thickness h_s = 3 mm, are sandwiched symmetrically between the TP and the aluminum pieces. The whole assembly is tightly connected by five stainless steel screws. The central screw, 4 mm in diameter, runs through each of the four TPs' corners. The other four screws are 3 mm in diameter. (right) A photo of the JP and its components. **(b)** A photo of mosaic plate (MPt) sample. **(c)** Simulated dispersion relation of the MPt. The flat dispersion (red line) indicates localized soft layer modes at 2.8 kHz. The localized mode at 6.8 kHz (the flat blue line) is that of a single TP with four corners clamped. The green dotted line is the bending mode dispersion relation of a homogeneous aluminum plate with a thickness of 3 mm. **(d)-(f)** Vibration transmission for the central line of 2 mm stainless steel reference plate, the MPt and fitting results based on Green function, respectively. **(g)** Acoustic transmission loss for the mosaic plate sample and the reference plate. Comparison of mass density law (green dashed line) with simulation result (hollow blue dot). Here the yellow line delineates the measured results for the reference plate, and the red line is that for the MPt. The experimental test frequency range is 50 Hz to 5 kHz, but the simulation results extend to 7.5 kHz.

References

1. Liu, Z., Zhang, X., Mao, Y., Zhu, Y.Y., Yang, Z., Chan, C.T. and Sheng, P., 2000. "Locally resonant sonic materials." science, 289(5485), pp.1734-1736.
2. Poulton, C.G., Movchan, A.B., Movchan, N.V. and McPhedran, R.C., 2012. "Analytic theory of defects in periodically structured elastic plates." *Proceedings of the Royal Society A: Mathematical, Physical and Engineering Sciences*, *468*(2140), pp.1196-1216.
3. Oh, J.H. and Assouar, B., 2016. "Quasi-static stop band with flexural metamaterial having zero rotational stiffness." Scientific Reports, 6(1), p.33410.

Conditions for Weak Scattering in Flexural Waves

M. Lázaro[1*], V. Romero-García[1], and L.M. García-Raffi[1]

[1]Universitat Politècnica de València, Spain
[*]corresponding author: malana@upv.es

Abstract: This work examines wave propagation in continuous media with weakly coupled scatterers. We rigorously analyze the quantification of weak scattering and the applicability of the Born approximation to elastic waves. The eigenvalues of the scattering matrix are evaluated, and the spectral radius is selected as a representative parameter of scattering behavior.

Metamaterials are structured composites with engineered wave propagation properties. In elasticity, they offer advanced control over flexural waves, with applications in vibration isolation, energy harvesting, and cloaking. The wave response in such systems is influenced by multiple scattering interactions between discrete resonators. When these interactions are weak, simplified models, such as the Born approximation, provide accurate solutions. However, a rigorous criterion for weak scattering in flexural wave systems is necessary. We consider a thin elastic plate governed by the Kirchhoff-Love equation and analyze the scattering induced by a collection of point-like resonators. The total wave field is expressed as:

$$w(\boldsymbol{r}) = \psi_0(\boldsymbol{r}) + \sum_{\alpha=1}^{N} G(\boldsymbol{r} - \boldsymbol{R}_\alpha) T_\alpha \, w(\boldsymbol{R}_\alpha)$$

where $G(r)$ is the Green's function of the plate, T_α characterizes the local response of the scatterers, and $\psi_0(\boldsymbol{r})$ is the incident wavefield. The scattering coefficients satisfy a matrix equation:

$$\boldsymbol{\Psi} = (I - \boldsymbol{g})^{-1} \boldsymbol{\Psi}_0$$

where $\boldsymbol{g} = \boldsymbol{GT}$ encapsulates the interaction between scatterers. If the spectral radius $\rho(\boldsymbol{g}) < 1$, the solution can be approximated by the Neumann series expansion, leading to the Born approximation. To assess the validity of the weak scattering assumption, we analyze periodic and random distributions of resonators. The spectral radius $\rho(\boldsymbol{g})$ is found to depend on both the spatial arrangement of the scatterers and their local mechanical properties. For periodic structures, strong scattering occurs at Bragg frequencies, whereas for random distributions, scattering is governed by the spectral properties of **g**. The solution can be expanded in terms of the Neuman series of the above expression as

$$\boldsymbol{\Psi} = \boldsymbol{\Psi}_0 + \boldsymbol{g}\,\boldsymbol{\Psi}_0 + \boldsymbol{g}^2\boldsymbol{\Psi}_0 + \cdots \equiv \boldsymbol{\Psi}_0 + \boldsymbol{\Psi}_1 + \boldsymbol{\Psi}_2 + \boldsymbol{\Psi}_3 + \cdots$$

Which constitutes the evaluation of the different orders of the scattering problem. Mathematically, this series converges provided that the spectral radius of the matrix is less than the unity. Numerical examples confirm that the Born approximation provides accurate results when $\rho(\mathbf{g}) < 1$.

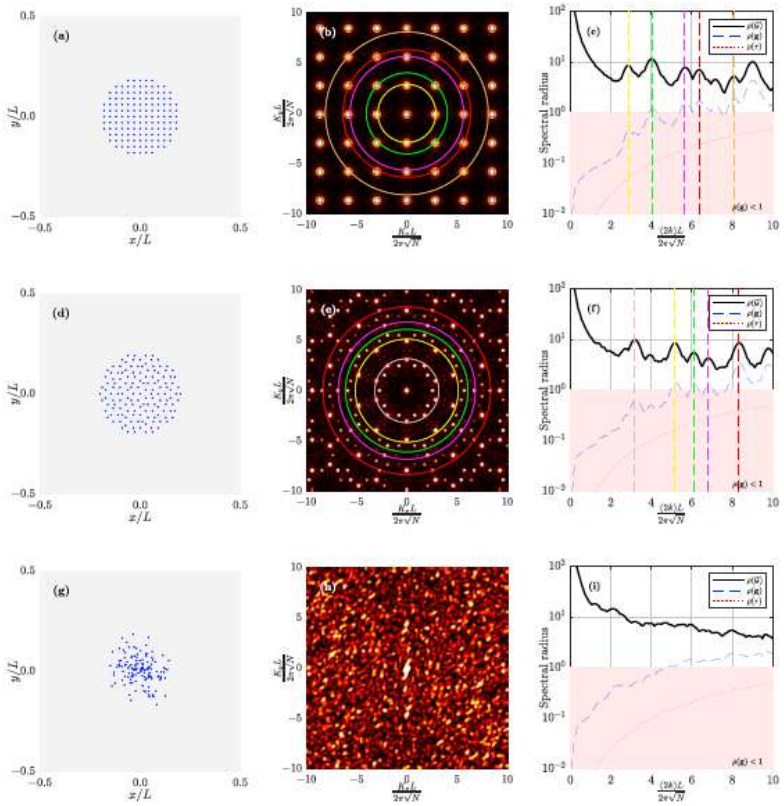


Figure 1. Three mass clusters with different geometric distributions confined within a circle of 80 cm centered on the 2 mm thick aluminum plate. Point distribution patterns: (a) periodic, (d) quasiperiodic (Penrose crystal), and (g) random. The graphs in the central column show the intensity of the structure factor in reciprocal space for each distribution. The right column reproduces the spectral radius of the scattering matrix g and its components, G and, as a function of the plate wavenumber k. The circles centered at the origin of graphs (b) and (e) have radii corresponding to the abscissas of graphs (c) and (f), respectively (same color).

Acknowledgments

M.L. L.M.G.R and V.R.-G.. are grateful for the partial support under Grant No. PID2020-112759GB-I00 366 funded by MCIN/AEI/10.13039/501100011033, and also for the partial support under Grant No. PID2023-367 146237NB-I00 funded by MCIU/AEI. L.M.G.-R. acknowledge support from Grant No. CIAICO/2022/052 368 of the "Programa para la promoción de la investigación científica, el desarrollo tecnológico y la innovación 369 en la Comunitat Valenciana" funded by Generalitat Valenciana. M.L is grateful for support under the 370 "Programa de Recualificaci´on del Sistema Universitario Español para 2021-2023", funded by "Instrumento 371 Europeo de Recuperación (Next Generation EU) en el marco del Plan de Recuperación, Transformación y 372 Resiliencia de España", a través del Ministerio de Universidades.

References

1. M. Born, "Quantenmechanik der Stoßvorgänge," Zeitschrift für Physik, 38, 803–827 (1926)..
2. J. Gubernatis et al., "The Born approximation in elastic wave scattering," J. Appl. Phys., 48(7), 2812–2819.
3. D. Torrent, J. Sánchez-Dehesa, "Dirac cones in acoustic surface waves," Phys. Rev. Lett., 108, 174301 (2012).

Towards a generalized theory for aeroacoustic metacontinua

U. Iemma[1*] and G. Colombo[1]

[1]Department of Civil, Computer Science and Aeronautical Technologies Engineering, Roma Tre University, Italy
[*]corresponding author: umberto.iemma@uniroma3.it

Abstract: Acoustic metamaterials enable unconventional wave manipulation but lose efficiency in a moving medium, if designed for static conditions. This work encloses the past decade's progress toward a generalized theory for acoustic metacontinua modelling, incorporating convective effects and integrating spacetime differential geometry into enhanced formulations of existing methodologies for aeroacoustic analysis.

Acoustic metamaterials have become one of the research fields that experienced remarkable growth in the last 20 years. This interest is due to their versatility, originating from the possibility of manipulating incoming wavefronts in unconventional ways. Each application requires a specific distribution of parameters that imparts the desired deformation to the incoming wavefronts. Aim of the present work is to present a summary of the recent findings and main achievements attained in the last decade in the development of aeroacoustics noise abatement strategies using metamaterials. One of the outcomes of the European project AERIALIST (H2020, 2017-2020) is the assessment of the substantial increase in the efficiency of the design process when an analytical model of a generic acoustic metacontinuum is used to define the characteristics of the desired meta-device, with the additional advantage of an easier integration in any existing multidisciplinary optimization framework. Indeed, the availability of a model based on unconventional constitutive equations makes possible the achievement of a wide range of targeted wave manipulations, independently of the specific architecture of the device, by simply interpreting it as a black box characterized by the equivalent parameters' distribution. However, in aeroacoustic applications, the performance of acoustic meta-devices deteriorates due to the non-quiescence of the medium in which they operate. This undesired behaviour arises from the underlying physics of the convection phenomenon which, in the mathematical perspective, is represented by the mixed space and time derivatives in the differential operator.In 2013 Garcia-Meca et al. proposed the Analogue Transformations Acoustics (ATA) where, through the reinterpretation of the equations into the spacetime, they circumvent the problematics associated with the background flow presence and create a link between isotropic propagations and convective ones by introducing spacetime coordinate transformations. The methodology relies on the modification of the characteristic of the propagating medium preserving the formal invariance of the governing equation under spacetime coordinate change, with the limitation of not being able to account for anisotropic distributions of its parameters.

Taking inspiration from this work, the authors proposed a similar approach, where the spacetime reinterpretation is integrated into the acoustic metacontinuum modelling procedure: in this fashion, spacetime mappings are used to fictitiously induce convective–like propagation patterns within exotic devices. Since then, the research efforts were directed toward the validation of the spacetime framework and into the analysis of the intimate relationship between the propagation mechanism and the curvature to which the spacetime is subject. So far, the spacetime framework has been validated through the implementation of specific spacetime coordinate transformations associated with specific flow conditions typical of aeronautical applications. Specifically, the methodology's performances rely on the convective effect that the spacetime mapping used is inducing in the acoustic metacontinuum and, therefore, it has been proven that whenever the convective-like propagation

patterns are introduced through a spacetime transformation non-comprehensive of generic flow conditions, analytical errors are inevitably introduced in the model. This effect takes the form of an incomplete performance recovery, which has been demonstrated to be independent of the specific acoustic mirage aimed at, being only related to the properties of the spacetime coordinate transformation used. In fact, the use of an approximate spacetime coordinate change introduces a mismatch between the convective behaviour induced in the metacontinuum and the external conventional flowing medium with which it is communicating. This aspect becomes more relevant the higher the intensity of the background flow, as the relevance of the convection effects that have been neglected is accentuated and, therefore, the difference between the differential operators involved. Consequently, the adapted meta-device reveals a sensitivity to the variations of the background flow intensity and the relative position of the treated zone and the acoustic source: these two aspects represent determining factors in minimizing the residual correction defect and must therefore be considered during the design process of engineering applications. Nevertheless, if one can provide a spacetime mapping fully comprehensive of the characteristics of general flow conditions, then the total recovery of acoustic metacontinua performances can be feasible for any operative condition. The ultimate goal of the present research is to define a generalized theory for the design of aeroacoustic metacontinua that foresees the integration of the mathematical tools of the spacetime differential geometry into the already existing methodologies for aeroacoustic analysis. In particular, one of the objectives of the work is the derivation of an extended, generalised boundary/field integral formulation based on an event-dependent Green function, comprising both anisotropic features and spacetime curvature.

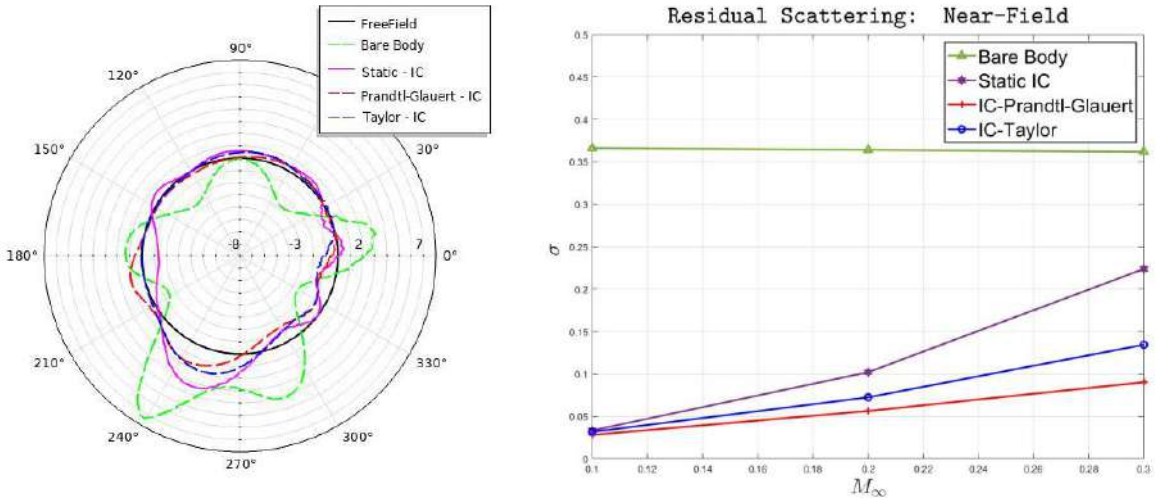


Figure 1: On the left, the near-field Insertion Loss (IL) of the bare obstacle compared with those of the cloaked object. Inertial cloaking (IC) convective correction at $M_\infty = 0.3$. On the right, the overall IL sensitivity to the M_∞ variations.

References

1. Iemma, U. and Palma, G. "Design of metacontinua in the aeroacoustic spacetime", *Sci. Rep*., Vol. 10, No. 18192, pp. 1-10, 2020.
2. Colombo, G., Palma, G., and Iemma, U., "Numerical aeroacoustic assessment of a metacontinuum device impinged by a laser-generated sound source", *Journal of Engineering*, Vol. 2024, No. 1, 1-11, 2024.
3. Colombo, G. and Iemma, U., "Assessment of the performances and limitations of spacetime convective corrections for acoustic metacontinua design,", *In press to Scientific Reports*

Acoustic and Mechanical Features of Polymer Colloidal Crystals – Brillouin Spectroscopy Studies

Bartlomiej Graczykowski[1]

[1]Adam Mickiewicz University Poznan, Faculty of Physics and Astronomy,

Uniwersytetu Poznańskiego 2, 61-614 Poznań, POLAND

[*]corresponding author: bartlomiej.graczykowski@amu.edu.pl

Abstract: Colloidal crystals (CCs) of polymer nanoparticles exhibit tunable acoustic and mechanical properties but are often brittle. Using Brillouin light scattering, we study GHz sound filtering and elasticity mapping in 2D and 3D CCs. We also demonstrate a supercritical fluid-based cold soldering method to enhance CCs robustness while preserving periodicity.

Colloidal crystals (CCs) made of polymer particles are low-cost and low-effort volumetric structures that serve as promising metamaterials for surface coatings and light and sound manipulation. Colloidal crystals composed of sub-micrometer particles can host features typical for photonic (PhCs) and phononic crystals (PNCs), operating in the visible light and hypersound regimes, respectively.

Typically, CCs are formed through the self-assembly of nanoparticles (NPs) into 1D (chains), 2D (monolayers), or 3D (bulk) structures. The mechanical and acoustic properties of CCs are mostly fixed and predetermined during fabrication and depend on particle size, elasticity, and interfacial forces. However, due to the weak van der Waals forces binding the constituent particles, self-assembled CCs are often brittle, which may limit their applications and performance.

This work presents results of experimental studies utilizing Brillouin light scattering spectroscopy (BLS) to investigate the acoustic and mechanical properties of 2D and 3D CCs made from self-assembled polymer (polystyrene and PMMA) nanoparticles. Specifically, we demonstrate multiband GHz sound filtering in 2D colloidal PnCs) attributed to three distinct types of acoustic band gaps that can be tuned by particle size and are influenced by adhesion and unavoidable fabrication impurities at contact interfaces.

Additionally, we introduce upgraded BLS capabilities by integrating it with a microscope and a scanning sample stage for elasticity mapping of colloidal mesostructures with micrometer spatial resolution. Our focus includes CCs and colloidal glasses (CGs) with varying spatial distributions of particle sizes and degrees of order. These include CGs with monodisperse systems, binary mixtures, bilayer structures, continuous size-gradient structures, and size-gradient mixtures.

Finally, we demonstrate how CCs can be mechanically reinforced into robust systems using a non-chemical treatment with supercritical fluids at temperatures well below the glass transition. This method, termed solid soldering, leverages two key effects: plasticization of the particle surface and compressive hydrostatic pressure. This process results in permanent physical contact between nanoparticles while preserving the periodic arrangement of the colloidal crystal. Using BLS, we determined the optimal pressure, particle size, temperature, and time range for effective soldering.

Acknowledgements: The research was supported by the National Science Center of Poland (NCN) by OPUS Grant Number UMO-2021/41/B/ST5/03038.

References

1. 4. Graczykowski, B. et al. Multiband Hypersound Filtering in Two-Dimensional Colloidal Crystals: Adhesion, Resonances, and Periodicity. Nano Lett. Nano Lett., 20, 3, 1883–1889 (**2020**)
2. Varghese, J. et al. Size-dependent nanoscale soldering of polystyrene colloidal crystals by supercritical fluids. Journal of Colloid and Interface Science 633, 314–322 (**2023**).
3. Babacic, V. et al. Mechanical reinforcement of polymer colloidal crystals by supercritical fluids. Journal of Colloid and Interface Science 579, 786–793 (**2020**).
4. Vasileiadis, T. et al. Elasticity Mapping of Colloidal Glasses Reveals the Interplay between Mesoscopic Order and Granular Mechanics. Small Methods, 2400855, (**2024**)

Locally Resonant Elastic Metagratings: Theory, Experiment, and Applications

L. Cao[1*], Y. -F. Wang[1], B. Assouar[2] and Y. -S. Wang[1]
[1]Department of Mechanics, School of Mechanical Engineering, Tianjin University, China
[2]Institut Jean Lamour, CNRS, Université de Lorraine, France
Corresponding author: liyun_cao@tju.edu.cn

Abstract: This report introduces the concept of Locally Resonant Elastic Metagrating (LREM), a new paradigm for efficient, compact, and lightweight wave manipulation in elastic wave systems. By combining elastic impedance modulation and hybridization of evanescent waves, LREM overcomes size limitations and challenges posed by vibration modes in traditional metastructures.

Metamaterials and metasurfaces have revolutionized the manipulation of waves, enabling new control over electromagnetic, acoustic, and elastic waves. However, these technologies have been limited by challenges such as low efficiency and complex fabrication processes. Optical and acoustic metagratings have helped address some of these issues, but challenges remain, especially in the context of elastic wave manipulation. This research presents a new type of metagrating called the Locally Resonant Elastic Metagrating (LREM), which combines the benefits of both locally resonant materials and metagrating principles to overcome limitations in size, efficiency, and real-world application hurdles.

The concept of the LREM is based on the idea of elastic impedance modulation and the hybridization of intrinsic evanescent waves, which leads to highly efficient and compact wave manipulation. By adjusting local resonance properties, the LREM structure can achieve performance characteristics that are difficult or impossible for conventional elastic metagratings and metasurfaces to replicate. The LREM overcomes some of the most significant challenges posed by traditional metastructures, particularly the issue of vibration modes in finite structures, which often hinder their practical implementation in real-world applications.

To demonstrate the effectiveness of the LREM, we conducted both theoretical analyses and experimental validations. The LREM can achieve wide-angle perfect absorption, direct wavefront reflection with unitary efficiency, and other complex wave-manipulation behaviors. These results indicate that LREM structures are not only efficient but also versatile in their ability to control wave propagation in elastic systems.

The potential applications of the LREM are vast. The ability to control elastic wave propagation with high efficiency, compactness, and minimal mass makes it a promising candidate for integration into micro-electromechanical systems (MEMS). MEMS-based sensors and signal processors could benefit significantly from the integration of LREM structures, allowing for more efficient, smaller, and more functional devices.

Moreover, the LREM's ability to enable advanced wave transformations, such as focusing and holography, makes it ideal for cutting-edge applications in fields like medical imaging and

wave-based computing. The unique properties of LREM could also lead to further innovations in the design of elastic wave systems, opening the door for future investigations into impedance-engineered wave manipulation across a range of physical wave systems.

This work is supported by the National Natural Science Foundation of China (No. 12402072).

References

1. Cao, L. et. al., "Observation of phononic skyrmions based on hybrid spin of elastic waves," *Sci. Adv.*, 9, eadf3652, 2023.

2. Cao, L. et. al., "Elastic bound state in the continuum with perfect mode conversion," *J. Mech. Phys. Solids*, 154, 104502. 2021.

3. Cao, L. et. al., "On the design of non-Hermitian elastic metamaterial for broadband perfect absorbers," *Int. J. Eng. Sci.*, 181, 103768, 2022.

4. Cao, L. et. al., "Locally Resonant Metagrating by Elastic Impedance Modulation," *Adv. Mater.*, Accepted, 2025.

Applications of mechanical metamaterials in microsystems: challenges and perspectives

V. Zega[1,*]

[1]Politecnico di Milano, Italy
[*]corresponding author: valentina.zega@polimi.it

Abstract: Mechanical metamaterials, thanks to their exceptional properties, are entering the world of microsystems as valid solutions for the increasing request of better performances at reduced power-consumption, footprint and costs. Here, an overview of the main results achieved on the topic are reported together with the main challenges and perspectives.

Mechanical metamaterials are artificial materials designed with specific geometric structures to achieve unique mechanical properties and/or to control wave propagation in unconventional ways [1].

Among different examples of mechanical metamaterials available in the literature, here the ones that find a direct application in the Micro-Electro-Mechanical Systems (MEMS) world are identified and described. A special focus will be addressed to the recent research activity carried out in the Civil and Environmental Engineering Department of Politecnico di Milano on the integration of metamaterials on microsystems.

MEMS, because of the large variety of their possible applications spanning from the consumer electronics, to the automotive industry up to the aerospace field, are indeed asking for innovative solutions in terms of mechanical design and working principles to satisfy the increasing request for better performance, reduced footprints, low power consumption and low costs. To date, mechanical metamaterials represent a valid candidate for achieving such goal.

Auxetic materials, i.e. mechanical structures exhibiting a negative Poisson's ratio, have been demonstrated at the small scale exploiting the typical capacitive MEMS actuation/readout mechanism [2]. The auxetic unit cell has been optimized to obtain a negative Poisson's ratio and at the same time to represent a valid alternative to motion coupling mechanisms needed in MEMS devices like e.g. gyroscopes.

The bandgap property of a periodic arrangement of properly shaped unit cell has been then exploited to design, fabricate and test an innovative vibration isolation platform to be installed between the MEMS device and the external package [3]-[4]. The unit cell, fully compatible with standard MEMS fabrication processes, has been optimized to provide a total isolation of the MEMS resonant device from the external unwanted vibrations that could compromise the correct functioning of the sensor/actuator. The proposed solution has been firstly validated at a bigger scale by considering a manual assembly of the vibration isolation platform with the MEMS device under test [3] and then designed to be fabricated in a fully-integrated system through the Thelma-Double fabrication process developed by STMicroelectronics [4]. Fabrication of the last device is currently in progress.

The bandgap property of a properly designed unit cell has been also optimized for applications in MEMS resonators for clocks applications. In such devices, indeed, it is crucial to minimize damping sources. The bandgap property of a phononic crystal surrounding the MEMS mechanical structure has been demonstrated to strongly reduce anchor losses, which is one of the dominant dissipation mechanisms in MEMS resonators packaged in near-vacuum conditions [5].

The last two results summarized in the present review contribution, regards the elastic waves manipulation through metamaterials. In particular, a MEMS waveguide has been designed, fabricated and tested by

introducing a defect line in a periodic matrix disposition of properly shaped unit cells [6]. The waveguide, fully compatible to standard MEMS fabrication processes, is able to transfer energy from one resonator to another one located far apart in the silicon wafer. Finally, aware of the promising results achieved at the macroscale [7], a MEMS lens has been designed and fabricated to amplify and focus elastic waves on a specific point where a piezoelectric patch is able to acquire the signal and, in principle, harvest energy. Experimental testing is currently ongoing.

Despite some applications of metamaterials in MEMS have been demonstrated in the literature, there is still a lot of work to do to bring such technology in the industrial practice. Main limitations are at the moment related to the lack of knowledge in terms of reliability, but also to the not negligible encumbrance with respect to standard MEMS requirements.

Part of the research activity is funded by the European Union's EU Framework Programme for Research and Innovation Europe Horizon under Grant Agreement No 101119917.

Part of the research is funded by STMicroelectronics through the Joint Research Platform STEAM.

The Author greatly acknowledge Raffaele Ardito, Lingzhi Chen, Alberto Corigliano, Claudia Comi, David Faraci, Marco Ferrari, Vittorio Ferrari, Attilio Frangi, Matteo Furlan, Chiara Gazzola, Mohamadjavad Ghoudjani, Alessandro Nastro, Yan Su, Xiuqi Yang, Zhichao Yao for their precious scientific contributions on the topic.

References

[1] Jiao, P., Mueller, J., Raney, J.R. et al. “Mechanical metamaterials and beyond”, *Nat. Commun.*, vol. 14, p. 6004, 2023.

[2] V. Zega, A. Nastro, M. Ferrari, R. Ardito, V. Ferrari, A. Corigliano ‘Design, fabrication and experimental validation of a MEMS periodic auxetic structure’ *Smart Mater. Struct*., vol. 28, p. 095011, 2019.

[3] Z. Yao, V. Zega, Y. Su, J. Ren, J. Zhang, A. Corigliano ‘Design, fabrication and experimental validation of a metaplate for vibration isolation in MEMS’ *J. Microelectromech. Syst*., vol. 29, n. 5, pp. 1401-1410, 2020.

[4] D. Faraci, V. Zega, G. Gattere, C. Comi ‘A MEMS device integrating a metaplate for vibration absorption’ Eccomas 2024, Lisboa, Portugal, June3-8, 2024.

[5] A. Frangi, M. Cremonesi, “Semi-analytical and numerical estimates of anchor losses in bistable MEMS” *Intern. J. of Solids and Structures,* vol. 92-93, pp. 141-148, 2016.

[6] V. Zega, C. Gazzola, A. Buffoli, L. G. Falorni, G. Langfelder, A. Frangi ‘A defect-based MEMS phononic crystal slab waveguide in electronic circuits’ *J. Microelectromech. Syst*., vol. 32, n. 5, pp. 494-504, 2023.

[7] M. Antonacci, E. Riva, A. Frangi, A. Corigliano, V. Zega ‘Planar GRIN lenses: numerical modelling and experimental validation’ *J. Sound and Vibr*., vol.537, p. 117217, 2022.

META 2025, MALAGA - SPAIN, JULY 22 – 25, 2025

Developing active acoustic metamaterials using magneto-rheological fluids

R. L. Watson[1*]

[1]University of Warwick, United Kingdom
[*]corresponding author: r.watson.2@warwick.ac.uk

Abstract: Active acoustic metamaterials are being developed through incorporation of magneto-rheological fluids to allow control of fluid/ metamaterial structure interactions and provide active control of metamaterial systems. Investigation of Magneto-rheological fluids, non-magnetic phononic crystals and their acoustic properties has been undertaken with locally manufactured magnetic field generation systems.

Acoustic metamaterials are formed through the construction of structures which show metamaterial properties. These structures are typically fixed and unable to be varied resulting in desired properties only at specific fixed frequencies[1,2]. The ability to vary the performance of metamaterials both in action and frequency of operation would widen the possible applications in acoustics and ultrasonics. These vary from sound absorption (minimising unwanted industrial or road noise), and filtering of specific ultrasonic frequencies for NDT and medical applications[3].

The operation principles for acoustic metamaterials are dependent on the dimensions of the acoustic metamaterial and the acoustic impedance difference between the metamaterial structure and the surrounding fluid. Acoustic impedance difference controls the fraction of the total energy of the acoustic waves passing into the metamaterial structure[4]. A large difference also results in greater surface reflection and minimizes sound wave energy entering the metamaterial structure. Control of acoustic impedance between the metamaterial substrate and the fluid with its structure is also essential for the operation of both phononic crystals and metamaterials with resonant cavity structures.

Magneto-rheological Fluids (MRFs) are fluids which change their properties due to an applied external magnetic field. MRFs are composed of a carrier fluid (typically mineral or silicone oils) and micron sized magnetic (typically iron) particles. When a magnetic field is applied, the particles align and form chains along the magnetic field. These chains alter the rheological properties of the fluid, and hence the application of an external field to an active fluid enables external control of metamaterial properties[5]. MRFs are widely used in adaptive suspension systems in cars due to this behaviour. The ability to change the rheological properties of the fluid allows the possibility of changing the acoustic impedance of the metamaterial fluid interaction, and hence to allow the development of active acoustic metamaterials. This would allow alteration of frequency of operation for the metamaterial system without changing the structure of the metamaterial.

MRFs have been prepared and their acoustic and ultrasonic properties have been studied in different magnetic fields, with further investigation of non-magnetic phononic crystal structures. Manufacturing of the required apparatus has been undertaken at Warwick to allow the control of the applied magnetic fields, shown in Figure 1.



Figure 1: Double coil magnetic field generation system manufactured at the University of Warwick.

Acknowledgements: Funding from the University of Warwick, School of Engineering. Adil Bhatti, Nathan Jossa, William Mennear, and the University of Warwick Engineering Build Space for their assistance with design and manufacture of apparatus used in this work

References

1. Montgomery S. M., Wu S., Kuang X., Armstrong C. D., Zemelka, C., Ze, Q., Zhang, R., Zhao, R. , Qi, H. J., "Magneto-Mechanical Metamaterials with Widely Tunable Mechanical Properties and Acoustic Bandgaps". Adv. Funct. Mater., 31, 2005319, 2021. doi 10.1002/adfm.202005319,
2. Liao, G. Luan, C. Wang, Z., Liu, J., Yao, X. Fu, J., "Acoustic Metamaterials: A Review of Theories, Structures, Fabrication Approaches, and Applications". Adv. Mater. Technol., 6, 2000787, 2021, doi: 10.1002/admt.202000787
3. Lu, Q., Li, X., Zhang, X., Lu, M., Chen, Y., "Perspective: Acoustic Metamaterials in Future Engineering", Engineering, 17, 22-30, 2022, doi: 10.1016/j.eng.2022.04.020
4. Laureti, S., Hutchins, D.A., Astolfi, L. et al. "Trapped air metamaterial concept for ultrasonic sub-wavelength imaging in water". Sci Rep 10, 10601, 2020. doi: 10.1038/s41598-020-67454-z
5. Dong, E., Cao, P., Zhang, J., Zhang, S, Fang, N. X., Zhang, Y., "Underwater acoustic metamaterials", *National Science Review*, 10, nwac246, 2023, doi: 10.1093/nsr/nwac246

META 2025, MALAGA - SPAIN, JULY 22 – 25, 2025

Accurate FEM investigation of acoustic properties in aerospace sandwich structures with metamaterial core

M. Cinefra[1*], M. C. Moruzzi[2], M. Petrolo[3], M. Filippi[3] and G. Petrone[4]

[1]Politecnico di Bari, Italy
[2]Università di Bologna, Italy
[3]Politecnico di Torino, Italy
[4]Università degli Studi di Napoli Federico II, Italy

[*]corresponding author: maria.cinefra@poliba.it

Abstract: It is well known that, to compete in the global market, the design of modern aircraft is driven by the continuous improvement of the safety and cabin comfort. The surrounding environment and particularly noise and vibration (N&V) can deeply affect passengers and pilots in cabin and cockpit, especially during long haul flights. On the other hand, spacecraft and its payload are subjected to high structural vibrations, during launch phase, that are crucial in view of the overall success of a spacecraft's mission. In this sense, reducing the acoustic loads plays a significant role in cost optimization of the mission. A possible solution to the problem of noise is the conception of high-performance acoustic treatments for the trim panels of aerospace vehicle.

An overarching challenge is the design of 2D structures capable of providing exceptional sound insulation on a wide frequency range, especially in the aerospace field where the materials are required to obey several criteria that usually clash with the acoustic one, such as lightness, thinness, mechanical strength, fire-resistance, etc. Low frequencies are especially difficult to absorb with conventional materials, as the order of magnitude of the wavelength is much greater than the reasonable thickness of trim panels. Therefore, a new research field has emerged to study acoustic metamaterials (AMM).

Aircraft noise is due to the combination of different sources such as powerful propulsion systems, high-speed aerodynamic flow over vehicle surfaces and operation of on-board systems, as air conditioners, pressurization system, etc. In order to evaluate noise levels and vibration transfer paths in the whole frequency range, there are various methods to consider, because none of them has shown a complete reliability, but can be used only in a limited frequency region. In the low frequency range, the behavior of a structure is deterministic and the basic tool applied for the analysis of vibration problems is the finite element analysis on the numerical side [101].

The Finite Element Method (FEM) is well-established and yields accurate results for the structural analysis of any geometrical shapes. However, the metamaterials require a mesh of all the details of the constituent unit cells, so this method can become very costly in computational time when large components are analyzed. Efficient FEM models have been recently implemented on the basis of Carrera Unified Formulation (CUF) to perform the vibro-acoustic analysis of advanced materials coupled with fluid [2] and the dynamic characterization of composite metamaterials [3].

Applying these innovative models, the present work aims to analyze the transmission loss properties of sandwich structures with metamaterial core. The metamaterial configurations considered are inspired to the work

[4]. The results demonstrate that a new concept of sandwich light-weight structures can be conceived by taking into account the acoustic requirement in the design of aerospace trim panels. The Figure 1 shows an example of metamaterial core considered and some curves of transmission loss computed with the advanced FEM models employed in this work.

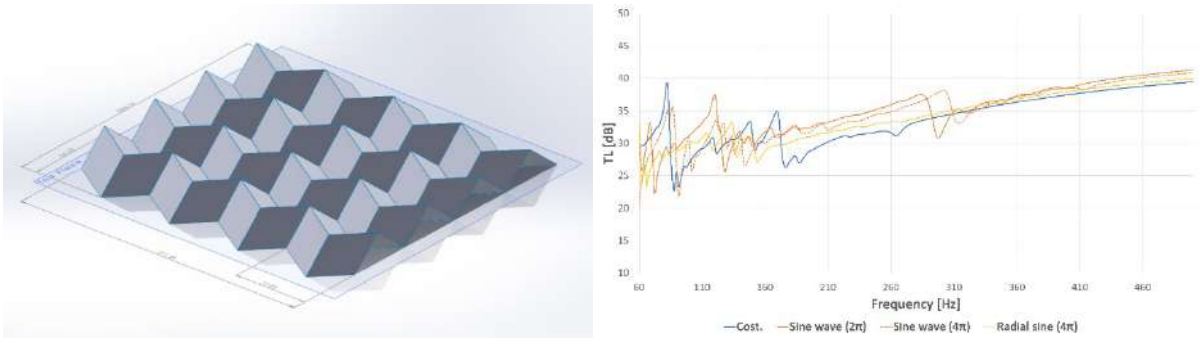


Figure 1: Miura-ori phononic structure and transmission loss curves computed for different AMM configurations.

References

1. V.N. Koukounian and C.K. Mechefske,"Computational modelling and experimental verification of the vibro-acoustic behavior of aircraft fuselage sections," App Acous, Vol. 132, 8–18, 2018.
2. M. Cinefra, M.C. Moruzzi, S. Bagassi, E. Zappino and E. Carrera, "Vibro-acoustic analysis of composite plate-cavity systems via CUF finite elements," Comp Struc, Vol. 259, 113428, 2020.
3. A. Garcia De Miguel, M. Cinefra, M. Filippi, A. Pagani and E. Carrera, "Validation of FEM models based on Carrera Unified Formulation for the parametric characterization of composite metamaterials," J Sound Vibr, Vol. 498, 115979, 2021.
4. X. Zhang, X. Huang and G. Lu, "Tunable bandgaps and acoustic characteristics of perforated Miura-ori phononic structures," Int J Mech Scie, Vol. 253, 108389, 2023

Acknowledgements

The authors acknowledge the support of the Italian Ministry of Education, University and Research (MIUR) through the project DAMA, funded under the scheme PRIN-2022 – grant agreement No. 20229PLCAC.

Hypersonic Surface Acoustic Wave in a Nanomembrane

O. R. Ranjbar Naeini[1] *, T. Makkonen[2], O.M.E. Ylivaara[2], J. Ahopelto[2], and C. M. Sotomayor Torres[1]

[1]INL – International Iberian Nanotechnology Laboratory, Portugal
[2]VTT – Technical Research Centre of Finland Ltd, Finland
*Corresponding author: omid.ranjbar@inl.int

Abstract: Hypersonic surface acoustic wave (SAW) propagation was experimentally studied by laser Doppler vibrometry. The SAW was measured along different regions of nanocrystalline silicon devices at excitation frequencies from 2-2.3 GHz. The data reveals wavelength variations, phase velocity differences and acoustic impedance mismatches which contribute to the dissipation of mechanical energy.

The study of hypersonic surface acoustic waves (SAW) propagation and its interaction with nanostructures enriches our understanding of elastic energy coupling and dissipation in micro and nano scale phononic circuits [1-3]. This is relevant for acousto-electric interactions [4], phononic waveguiding, and quantum applications [5].

We report the propagation of hypersonic SAWs along a 220 nm thick nanocrystalline silicon (nc-Si) supported by silicon dioxide (SiO_2) and free-standing nc-Si nanomembrane. The geometrical parameters are depicted in Fig.1(a). Showing the structure studied from the bottom to the top: silicon substrate, 1000 nm silicon dioxide (SiO_2), 220 nm nc-Si, 550 nm thick aluminum nitride (AlN) film, and 100 nm thick aluminum (Al). The interdigitated transducer (IDT) was patterned on the Al layer by optical lithography with about 500 nm spacing between the electrodes and 500 nm in width. Optical microscopy image of the fabricated device is shown in Fig.1(b).

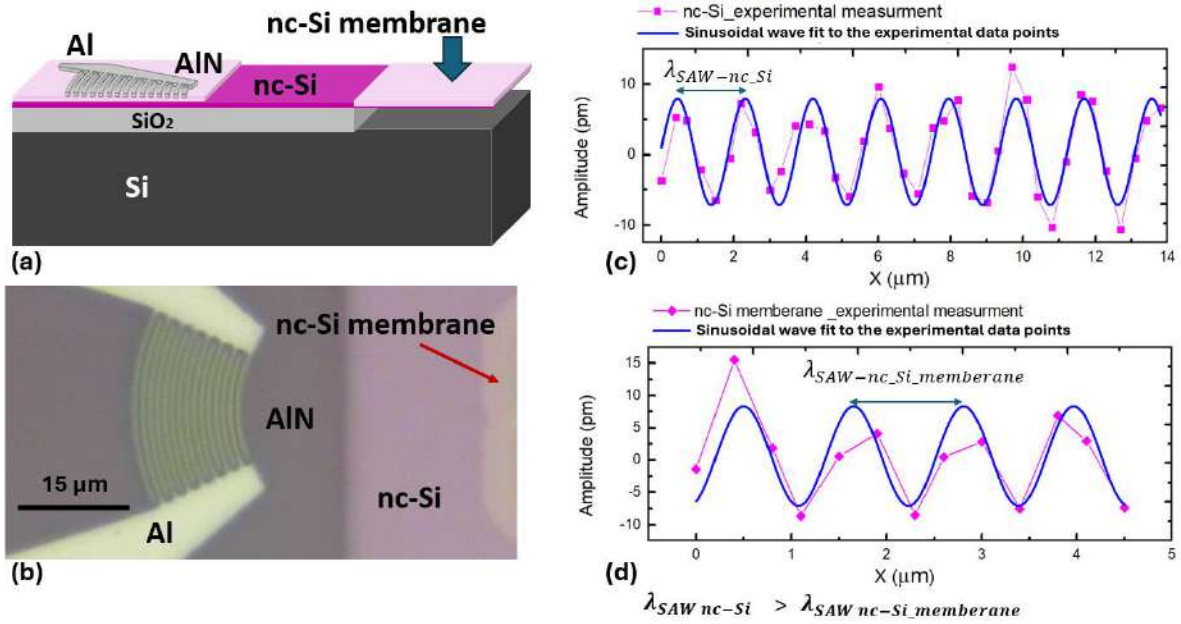


Figure. 1 (a). Schematics of the device. (b). Its optical microscopy image. (c). Out-of-plane displacement amplitude as a function of position (x) along the supported nc-Si, and (d). along the nc-Si membrane.

We measure the out-of-plane SAW displacement over nc-Si and the nc-Si membrane at frequencies range

from 2.0 to 2.3 GHz with a 50 MHz resolution by laser Doppler vibrometry. The SAW was excited by a coherent electrical signal generated by a vector network analyzer and delivered to the Al electrodes via electrical probes. The out-of-plane displacement amplitude as a function of position (x) is shown in Fig.1(c). and Fig.1(d). for the supported nc-Si and the free-standing nc-Si membrane, respectively. A sinusoidal wave fits the experimental data is shown by the blue line in Fig.1(c, d).

Fig.1(c, d). reveal the variations in the SAW wavelength along the supported nc-Si and nc-Si membrane, respectively. The SAW propagates at different phase velocities based on the variation of its wavelength along *x*. This indicates changes in phase velocity and acoustic impedance. The impedance mismatch at the interface leads to partial wave reflection, mode conversion, and energy dissipation, contributing to attenuation. In other words, due to the change in phase velocity at the interface and consequently, the acoustic impedance mismatch, a portion of the energy does not couple to the membrane and is dissipated within the multilayer structure. These effects influence the acousto-electric interactions, the phononic waveguiding, coupling, and signal transmission.

The study in [6] discusses various factors contributing to mechanical energy dissipation, including clamping losses, air /surrounding medium friction, body radiation and material properties. By analyzing SAW propagation and its phase velocity, our data suggests that the acoustic impedance mismatch contributes to the dissipation. This observation will improve the understanding of the coupling efficiency of acoustic waves to membrane-based devices [7].

We acknowledge the support from the project LEIT funded by the European Research Council, H2020 Grant Agreement No. 885689.

References

1. Iyer, A., Kandel, Y.P., Xu, W., Nichol, J.M. and Renninger, W.H., “Coherent optical coupling to surface acoustic wave devices”. Nat. Commun, 15(1), p.3993, 2024
2. Hendrik, K., Platz, D. and Silvan, S, “Surface acoustic wave coupling between micromechanical resonators”. Commun. Phys., 5(1), 2022.
3. Glushkov, E., Glushkova, N. and Zhang, C., “Surface and pseudo-surface acoustic waves piezoelectrically excited in diamond-based structures”. J. Appl. Phys., 112(6), 2012.
4. Navarro-Urrios, D., Colombano, M.F., Arregui, G., Madiot, G., Pitanti, A., Griol, A., Makkonen, T., Ahopelto, J., Sotomayor-Torres, C.M. and Martínez, A., “Room-temperature silicon platform for GHz-frequency nanoelectro-opto-mechanical systems”. ACS photonics, 9(2), pp.413-419, 2022.
5. Delsing, P, et al. “The 2019 surface acoustic waves roadmap.” J. Phys. D Appl. Phys. 52 (35), 353001, 2019.
6. Li, Y., Cui, K., Feng, X., Huang, Y., Huang, Z., Liu, F. and Zhang, W. “Optomechanical crystal nanobeam cavity with high optomechanical coupling rate”. J. Opt, 17(4), p.045001,2015.
7. Korovin, A.V., Pennec, Y., Stocchi, M., Mencarelli, D., Pierantoni, L., Makkonen, T., Ahopelto, J. and Rouhani, B.D., “Conversion between surface acoustic waves and guided modes of a quasi-periodic structured nanobeam”. J. Phys. D Appl. Phys., 52(32), p.32LT01, 2019.

Metastructures: New Approaches to Enhancing Disaster Resilience and Reduced Embodied Carbon

O. S. Bursi[1], T. Guner[1]

[1] University of Trento, Dept. of Civil, Environmental and Mechanical Eng., Via Mesiano, 38123, Trento, Italy
*corresponding author: oreste.bursi@unitn.it

"Symposium V: Architectured Elastic and Acoustic Metamaterials & Phononic Crystals."

Abstract: Locally resonant linear and nonlinear metafoundations have been conceived for seismic isolation of small modular reactors also for significant vertical components of earthquakes. Along the same lines, metastructures have been introduced into typical steel frames enhanced with locally resonant metastructures in view of weight reduction and, hence, reduced embodied carbon.

Differently from the word metamaterials, the word metastructure denotes concepts and applications for which a performance is defined not only by the configuration of atoms or molecules that influence material bulk properties, but also by overall dimensions, i.e. geometry and boundary conditions imposed on an assembly consisting of a finite number of units – a finite lattice -. Along these lines, some researchers proposed the seismic isolation of nuclear power plants by means of metastructures with massive solutions [1]. Conversely, we study the seismic mitigation of a typical nuclear small modular reactor (SMR) where extreme loading conditions are considered by the safe shutdown earthquake (SSE). For this purpose, to reproduce the main dynamic properties of the reactor's reinforced concrete system, a detailed structural model was synthesized, also taking into account the presence of the reactor pools, as shown in Fig. 1. Thus, to protect the reactor from strong earthquakes, finite locally resonant multiple degrees of freedom metafoundations were developed; and resonator parameters were optimized by means of an improved frequency domain multivariate and multiobjective optimization procedure [2]. Also, the stochastic nature of the seismic input was taken into account. It is then proposed: i) a linear metafoundation endowed with multiple cells, linear springs and linear viscous dampers as shown in Fig. 2.; and ii) a foundation equipped with additional nonlinear vertical quasi-zero stiffness (QZS) cells. QZS cells were obtained by horizontally precompressed springs in an unstable state with vertical springs in parallel. With this arrangement, additional flexibility and dissipation against non-symmetrical modes of the SMR and vertical seismic loadings are proposed.

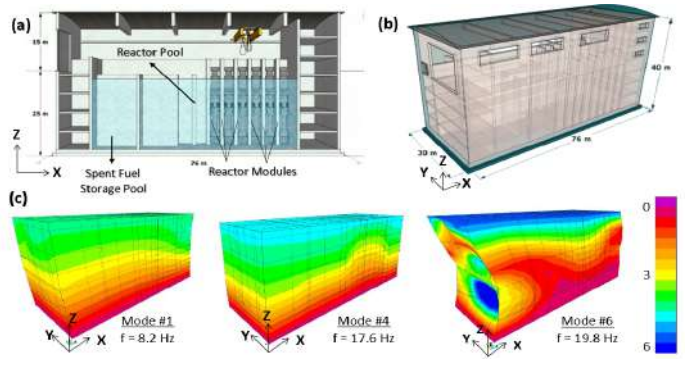
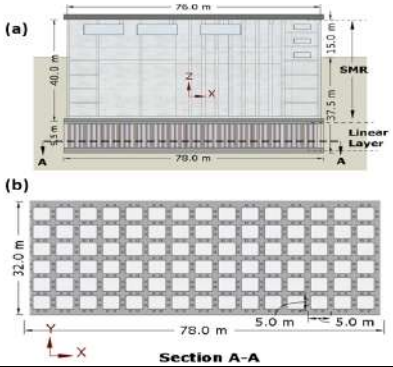


Fig. 1 Schematic of the SMR and FE modal analysis results: (a) inner view; (b) outer view; (c) deformed shapes relevant to Modes 1,4 and 6.



Linear Metafoundation (LM) layout: (a) Section view of coupled LM-SMR, (b) Plan view of the linear layer.

Thus, the performance of the optimized metafoundations was assessed by means of frequency and time history analyses, and finally, results were compared with an SMR endowed with both rigid foundation and conventional base-isolation solutions.

In 2021, the construction sector accounted for 37 per cent of worldwide carbon emissions and 36 per cent of the global primary energy supply [3]. Thus, the issues of sustainability and embodied carbon are important [4]. In this respect, we introduce controlled steel buildings endowed with novel locally resonant metastructures inspired by metamaterial concepts. A major limitation of finite locally resonant metastructures in low-frequency vibration control is the requirement for large additional masses. Conversely, properly designed periodic structures inside a main structure can function as locally resonant metastructures with limited extra mass and proper damping. By incorporating locally resonant metamaterials, this study advances the potential of seismic steel frames, to enhance seismic performance while reducing material usage, thus addressing both structural efficiency and sustainability. Therefore, our research covers both the elastic and the inelastic range, where frames are optimally designed to meet both immediate occupancy and life safety performance limit states. In particular, to demonstrate the efficacy of the proposed approach two case studies, one involving a 25-story moment resisting steel frame, see Fig. 3 and 4, and the other focusing on a 20-story eccentrically braced steel frame structure, are analysed. A multi-objective optimisation methodology is employed to illustrate the trade-off between metastructure inherent damping ratio and material usage, i.e. embodied carbon emissions, highlighting the environmental benefits alongside structural performance improvements. The results demonstrated that optimal mass reduction for the proposed metastructures in both lateral-resisting systems was feasible, with reduction rates of at least 11.3 per cent and 13.7 per cent without additional damping in the metastructures compared to the original configurations. Finally, the reduction in embodied carbon was analyzed based on the material usage in the framed structures.

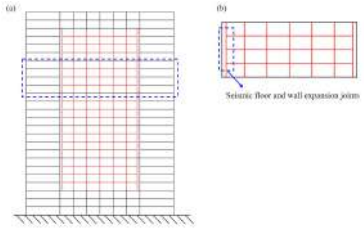


Fig. 3. Coupled MRF structure: (a) Lateral view; (b) Internal metastructure layout

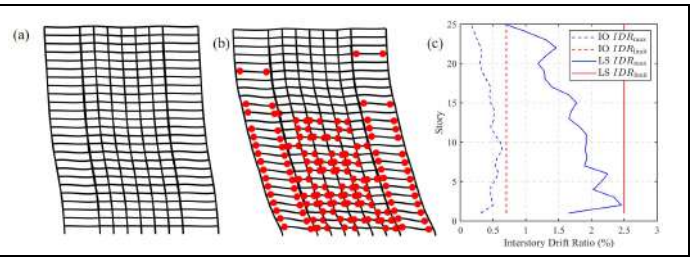


Fig. 4. Coupled MRF structure results: (a) Maximum deformation at the Immediate Occupancy limit state; (b) Max. deformation at the Life Safety limit state; (c) Max. Interstorey Drift values for each storey

References

1. Witarto, W., Wang, S. J., Yang, C. Y., Wang, J., Mo, Y. L., Chang, K. C., & Tang, Y. (2019). Three-dimensional periodic materials as seismic base isolator for nuclear infrastructure. AIP Advances, 9(4).
2. Guner, T., Bursi, O. S., & Erlicher, S. (2022). Optimization and performance of metafoundations for seismic isolation of small modular reactors. Computer-Aided Civil and Infrastructure Engineering, 1–25, 2022
3. United Nations Environment Programme, 2022, global status report for buildings and constructions
4. Di Filippo, R., Maracchini, G., Albatici, R., Di Maggio, R., Bursi, O.S., "A novel prescriptive approach for buildings' insulation design considering embodied carbon., Renewable and Sustainable Energy Reviews, 212 (2025) 115369.

On the practical use of wooden logs sonic crystals as road traffic noise barriers

P. Amado-Mendes[1*], and L. Godinho[1]

[1] University of Coimbra, ISISE, ARISE, Department of Civil Engineering, Portugal
[*]corresponding author: pamendes@dec.uc.pt

Abstract: The concept of sonic crystals for road traffic noise mitigation has been explored, making use of a highly sustainable solution made of wooden logs. Complementary approaches have been adopted, with extensive numerical analyses, concept validation in laboratory conditions and in situ prototype acoustic characterization.

Since the mid-twentieth century, the developed world has been aware of the harmful effects of noise caused by road and rail circulation on users near the communication pathways. Recent studies by the World Health Organization point to the annual loss of 1 million years of healthy life, only in Western Europe as a consequence of exposure to environmental noise and, in particular, traffic noise. A widely implemented mitigation solution has been that of physical sound attenuation systems, positioned in the vicinity of the pathways, designated by noise barriers. Currently, there are several solutions on the market for noise attenuation from road and rail traffic, the vast majority of them based on a vertical and continuous, usually with opaque structure, solutions that are already widely studied, thus being known their behavior and performance limits.

In order to overcome some disadvantages of traditional noise barriers, in the last two decades, investigations have addressed the concept of noise barriers based on sonic crystals. These are manmade periodic structures, created with scatterers periodically arranged in regular configurations with a constant lattice and exhibiting contrasting properties to the host acoustic medium where they are embedded [1]. Because of the periodicity effect, this arrangement of scatterers generates a well-defined frequency range (usually called bandgap), where significant sound attenuation occurs. In fact, sonic crystals are considered a promising solution, especially for the selective attenuation of sounds, e.g. as road traffic noise barriers [2]. The idea developed in the scope of a recent research project corresponds to a highly sustainable solution, with the scatterers being made up of wooden logs collected from forest cleaning operations and only requiring very low processing of the timber logs. Thus, a contribution to the state of the art of sonic crystal barriers is proposed, with data registered from experimental tests and compared to numerical results computed through different numerical and simulation methods [3,4,5].

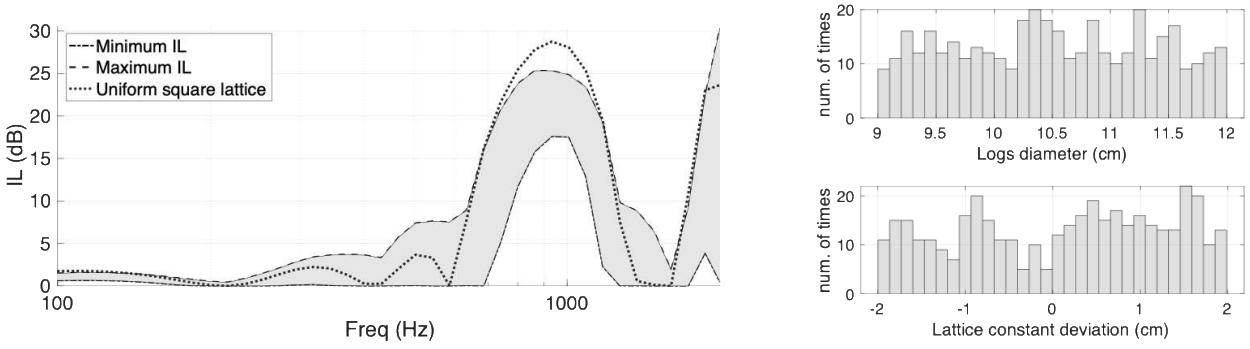


Figure 1. Left: Insertion Loss variation range resulting from randomization of both scatterer position and diameter; Right: histograms accounting for the lattice constant deviation and logs diameter change.

The noise barriers' behavior and obtained insertion loss values have been studied for different scatterer arrangements and shapes, as well as the effect of variations in the regular arrangement of the logs (Figure 1) [6].

In a further step, a wooden sonic crystal noise barrier prototype has been proposed and designed, man crafted and installed along a roadway, giving the opportunity to fully characterize the in situ acoustic behavior of this sustainable and innovative noise mitigation device [7]. Both the in situ airborne sound insulation under direct sound field conditions, in accordance to EN 1793-6 standard, and the in situ Insertion Loss of the outdoor noise barriers, following the ISO 10847 standard, have been evaluated, and the corresponding global acoustic indices have also been computed, demonstrating very interesting attenuation values in practical real context.

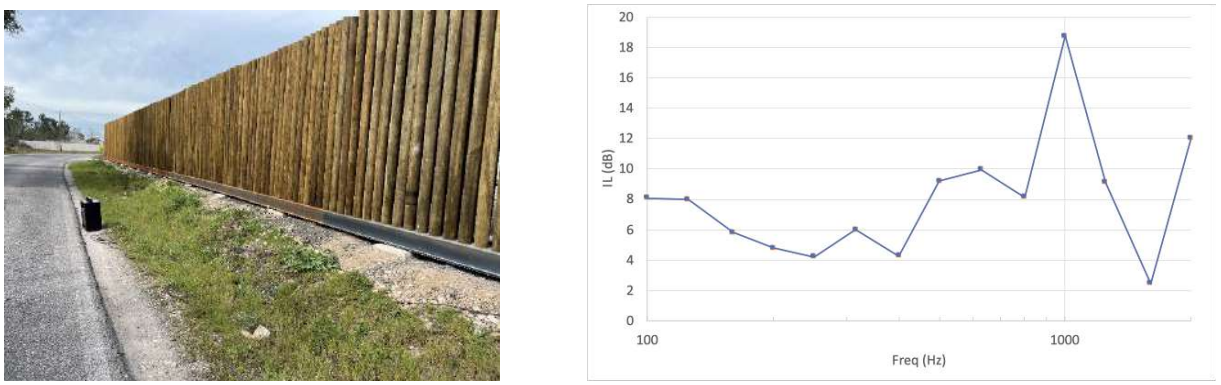


Figure 2. In situ Insertion Loss measurement. Left: Setup for wooden sonic crystal noise barrier prototype characterization; Right: Insertion Loss measured data in 1/3 octave frequency band, following ISO 10847.

This work was developed within the scope of the projects with references POCI-01-0247-FEDER-033691 "HLS—Hybrid Log Shield" and PTDC/ECI-EGC/3352/2021 "IntRAIL". This work was partly financed by FCT / MCTES through national funds (PIDDAC) under the R&D Unit Institute for Sustainability and Innovation in Structural Engineering (ISISE), reference UIDB / 04029/2020 (doi.org/10.54499/UIDB/04029/2020), and under the Associate Laboratory Advanced Production and Intelligent Systems ARISE reference LA/P/0112/2020.

References

1. Gupta, A. "A review on sonic crystal, its applications and numerical analysis techniques", Acoust. Phys., Vol. 60, 223–234, 2014.
2. Fredianelli, L., A. Del Pizzo, G. Licitra, "Recent Developments in Sonic Crystals as Barriers for Road Traffic Noise Mitigation", Environments, Vol. 6, 14, 2019.
3. Godinho, L., J. Redondo and P. Amado-Mendes, "The method of fundamental solutions for the analysis of infinite 3D sonic crystals", Eng. Anal. Bound. Elem., Vol. 98, 172–183, 2019.
4. Peiró-Torres, M.P., M. Ferri, L. Godinho, P. Amado-Mendes, F.J.V. Folch, J. Redondo, "Normal incidence sound insulation provided by Sonic Crystal Acoustic Screens made from rigid scatterers – assessment of different simulation methods", Acta Acustica, Vol. 5, 28 1-10, 2021.
5. Atalla, N., F. Sgard, Finite Element and Boundary Methods in Structural Acoustics and Vibration, CRC Press, 2015.
6. D'Orazio, T., F. Asdrubali, L. Godinho, M. Veloso, P. Amado-Mendes, "Experimental and Numerical Analysis of Wooden Sonic Crystals Applied as Noise Barriers", Environments, Vol. 10, 116 1-21, 2023.
7. Morandi, F., M. Miniaci, A. Marzani, L. Barbaresi, M. Garai, "Standardised acoustic characterisation of sonic crystals noise barriers: Sound insulation and reflection properties", Appl. Acoust., Vol. 114, 294–306, 2016.

Topological modes in phononic waveguide interfaces

K. Monika Devi[1*], Clivia M. Sotomayor Torres[2], Y. Pennec[1] and B. Djafari-Rouhani[1]

[1] Institut d'Electronique, de Microélectonique et de Nanotechnologie, UMR CNRS 8520, Université de Lille, 59650 Villeneuve d'Ascq, France

[2]INL International Iberian Nanotechnology Laboratory, Avenida Mestre José Veiga s/n, 4715-330, Braga, Portugal

[*]corresponding author: koijamm@univ-lille.fr

Abstract: We report phononic waveguide interfaces capable of supporting topological edge modes. We investigate the topological properties of the edge modes in different waveguide interfaces, revealing robust propagation with negligible backscattering. Our results provide valuable insights for the design of low-loss phononic components for device applications.

Topological waveguide systems have recently emerged as one of the important platforms for the control of electromagnetic and elastic waves due to their unique properties like unidirectionality, robustness, backscattering-free propagation in the presence of structural defects/disorders, etc. [1-4]. Here, we investigate different topological waveguide interfaces using hypersonic phononic crystal structure consisting of patterned plates and exhibiting Dirac gaps in the range of 13-14 GHz. The design of the proposed topological phononic waveguide is illustrated in Fig. 1.

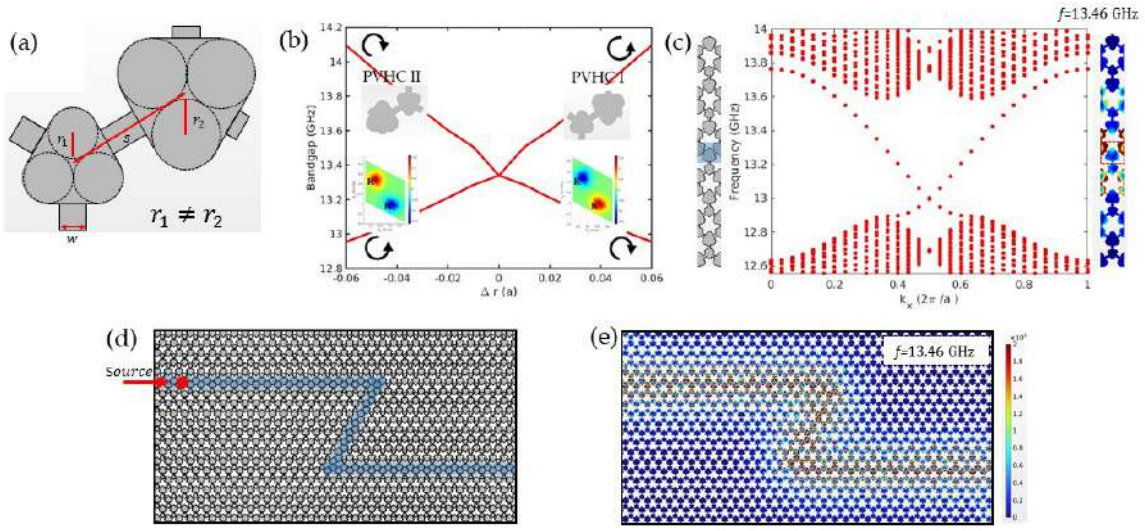


Figure 1. (a) Unit cell for PVHC. (b) Bandgap variation as a function of asymmetry (Δr); Inset shows the unit cell and corresponding Berry curvature distributions. (c) Dispersion plot for the Zigzag interface with a periodicity of a = 381 nm, r_1= 0.11a and r_2= 0.15a; Right: shows the supercell along with the displacement field. (d) Z-path topological waveguide, and (e) Robust topological wave propagation through a Z-path waveguide.

The waveguide structure is formed by using two topologically different phononic valley Hall crystals (PVHCs), whose unit cell comprises of two rounded triangles made of silicon. When $r_1 = r_2$, a degeneracy exists at $f \sim$ 13.3 GHz, which is lifted when $r_1 \neq r_2$. Topological invariants such as the Berry curvature (inset of Fig.1(b))

and Valley Chern number exhibit non-zero and opposite values around the K-points for the PVHC-I and PVHC-II structures confirming their nontrivial and distinct topological nature. The topological waveguide is then engineered by interfacing these two PVHC structures.

The supercell for the topological Zigzag type waveguide is shown in the left panel of Fig. 1(c). By examining the dispersion plot (Fig. 1(c)), it is observed that topological edge modes are excited within the band gap. The displacement field distributions (right panel of Fig. 1(c)) indicate that the field is primarily confined to the larger triangles forming the interface. To assess the robustness of the proposed topological waveguide, we probe the transmission through a Z-path waveguide, as shown in Fig. 1(d). For this, a point source is introduced at the waveguide's input and the transmission is examined along the Z-path. The displacement field distributions (Fig. 1(e)), reveal stronger confinement of field close to the interface. A detailed inspection of the transmission before and after the sharp bends of the Z-path waveguide shows that displacement field amplitudes remain nearly unchanged thus, confirming the robust nature of the excited edge modes. Further studies are performed for different cases of asymmetry as well as waveguide configurations. Our results demonstrate backscattering immune robust propagation of elastic waves paving the way for low-loss phononic device applications [5,6].

Acknowledgements

The authors acknowledge the support from the project LEIT funded by the European Research Council (ERC) under the European Union's Horizon 2020 research and innovation programme (Grant Agreement No. 885689).

References

1. Price, H., Y. Chong, A. Khanikaev, H. Schomerus, L. J. Maczewsky, M. Kremer, M. Heinrich et al. "Roadmap on topological photonics." Journal of Physics: Photonics, Vol. 4, No. 3, 032501, 2022.
2. Wang W., B. Bonello, Y. Pennec and B. Djafari-Rouhani, "Topological valley, pseudospin and pseudospin-valley protected edges states in symmetric pillared phononic crystals." Phys. Rev. B, Vol. 100, 140101, 2019.
3. Miniaci, M., R.K. Pal, R. Manna, and M. Ruzzene, "Valley-based splitting of topologically protected helical waves in elastic plates," Phys. Rev. B, Vol. 100, No. 2, 024304, 2019.
4. Zhang, Q., D. Lee, L. Zheng, X. Ma, S. I. Meyer, L. He, H. Ye, Z. Gong, B. Zhen, K. Lai, and A.C. Johnson, "Gigahertz topological valley Hall effect in nanoelectromechanical phononic crystals," Nat. Electronics, Vol. 5, No. 3, 157-163, 2022.
5. Pirie, H., S. Sadhuka, J. Wang, R. Andrei, and J. E. Hoffman. "Topological phononic logic." Phys. Rev. Lett., Vol. 128, No. 1, 015501, 2022.
6. Bahrami, E. and A. Bahrami, "Topological phononic switch based on reconfigurable symmetry-broken crystals with rotatable scatterers," *Sci. Rep.*, Vol. *15, No.* 1, 6521, 2025.

When acoustic artificial materials meet artificial intelligence: AI-empowered metamaterials and their applications

Bin Liang*, Jingjing Liu, Jing Yang, and Jianchun Cheng

Key Laboratory of Modern Acoustics, MOE, Institute of Acoustics, Department of Physics, Nanjing University, Nanjing 210093, P. R. China
*corresponding author: liangbin@nju.edu.cn

Abstract: This talk will focus on the novel discoveries emerging from the integration of artificial intelligence and artificial structures, and explore how this synergy has led to groundbreaking advancements in relevant application fields including such as acoustic imaging and noise reduction.

The recent emergence of acoustic metamaterials has overcome the limitations of acoustical properties of naturally available materials and enabled novel wave-steering phenomena, opening up new applications in a wide range of scenarios. Meanwhile, artificial intelligence is already making a significant impact in many other scientific disciplines and research fields. In this talk, I will first briefly review some of our recent advances obtained by coalescing acoustic metamaterial and artificial intelligence. To go beyond the limitation in current acoustic metamaterials that can only manipulate the sound fields in a predetermined way, we build an acoustic "neuromorphic system" based on artificial structures, and proved that an array of unit cells following deep-learning-assisted design of parameters is endowed with the 'intelligence' to solve various complicated tasks in a simple, precise, fast and passive manner. Additionally, a new imaging mechanism based on synthetic frequency codec, achieved by integrating disordered metamaterials with artificial intelligence, will also be introduced, which enables reducing the imaging system's dimension in both space and time simultaneously and thereby allows real-time imaging from only a single signal. On the other hand, based on the unconventional wave-steering functionality and high design flexibility, we propose to inversely design acoustic metamaterials with the aid of machine learning technique and realize a series of acoustic functional devices with superb performance, whose applications in various scenarios such as absorption and isolation of low-frequency sound are also demonstrated.

References

1. J. Weng, Y. Ding, C. Hu, X.-F. Zhu, B. Liang, J. Yang, and J. Cheng, Meta-neural-network for real-time and passive deep-learning-based object recognition, Nature Communications, 11, 6309, 2020.
2. B. Assouar, B. Liang, Y. Wu, Y. Li, J. C. Cheng, and Y. Jing, Acoustic metasurfaces, Nature Reviews Materials, 3, 460, 2018.
3. W. Wang, J. Hu, J. Liu, Y. Tan, J. Yang, B. Liang, J. Christensen, and J. Cheng, Single-sensor and real-time ultrasonic imaging using an AI-driven disordered metasurface, arXiv preprint arXiv:2307.07364, 2023.
4. Z. X. Xu, B. Zheng, J. Yang, B. Liang, and J. C. Cheng, Machine-Learning-Assisted Acoustic Consecutive Fano Resonances: Application to a Tunable Broadband Low-Frequency Metasilencer, Physical Review Applied 16, 044020, 2021.

5. A. Chen, Z. X. Xu, B. Zheng, J. Yang, B. Liang, and J. C. Cheng, Machine learning-assisted low-frequency and broadband sound absorber with coherently coupled weak resonances, Applied Physics Letters, 120, 033501, 2022.

META 2025, MALAGA - SPAIN, JULY 22 – 25, 2025

Sound-absorbing Metasurface using Hybrid Resonators with Embeded Necks and Micro-perforations

Hyeonbin Ryoo[1*], Ki Yong Lee[2], and Wonju Jeon[2]

[1]Korea Institute of Machinery and Materials, Republic of Korea

[2]Korea Advanced Institute of Science and Technology, Republic of Korea
[*]corresponding author: hbryoo@kimm.re.kr

Abstract: This study introduces a hybrid resonator combining Helmholtz resonators with micro-perforations to achieve perfect sound absorption with a low Q-factor. Based on a theoretical model to outline the effective impedance, an acoustic metasurface is designed to achieve the 90%-absorption bandwidth from 380 to 790 Hz with a compact thickness (λ/15).

Mitigating noise from mechanical systems remains a critical challenge, particularly in developing sound absorbers with strong performance in targeted frequency ranges. Conventional approaches to acoustic absorption have primarily utilized porous or fibrous materials, where sound energy is dissipated through viscous and thermal boundary layers in their microstructures, as well as through internal heat conduction.[1,2] Numerous researchers[3-7] have attempted to design absorbers with subwavelength scales, as alternatives to conventional acoustic materials, by using such resonance-based structures as Helmholtz resonators (HRs). Acoustic metasurfaces (AMS) based on hybrid resonance between coupled HRs have emerged as promising solutions due to their compatibility with cost-effective 3D printing techniques. In 2016, a metasurface achieved perfect absorption at a specific frequency through hybrid resonance between adjacent HRs.[5] However, their numerical simulations accounted for losses only within limited frequency and geometric conditions. More recent studies have advanced AMS designs using hybrid resonance mechanisms to create thin absorbers with broader bandwidths, guided by theory-based, tunable design methods[6,7].

This study proposes a novel sound-absorbing metasurface whose unit cell consists of a hybrid resonator (HybR). As shown in Fig. 1(a), each HybR contains a parallel array of an embedded neck and a front panel with multiple micro-perforations, designed to achieve perfect absorption with a low Q-factor at a target frequency via hybrid resonance.[4] This resonance arises from strong near-field interactions between the neck and perforations and destructive interference in the far field. To predict performance and enable rapid design, the frequency-dependent effective impedance of the HybRs is analytically derived, taking into account visco-thermal losses and end corrections due to radiation impedance at discontinuities of surface areas. These derivations yield optimal geometrical parameters for impedance matching with ambient air at the target frequency, facilitating wider high-absorption bands (over 0.9) compared to traditional absorbers.

We explore how broader absorption can be realized by arraying multiple HybRs with distinct geometrical configurations for multiple target frequencies. Unlike conventional arrays using coupled Helmholtz resonators (HRs) that require 2N resonators for N frequencies, the proposed HybR-based array needs only N, offering a more spatially efficient broadband absorber. As shown in Fig. 1(b), supercells with N = 4 HybRs are fabricated via 3D printing and validated through impedance tube experiments.

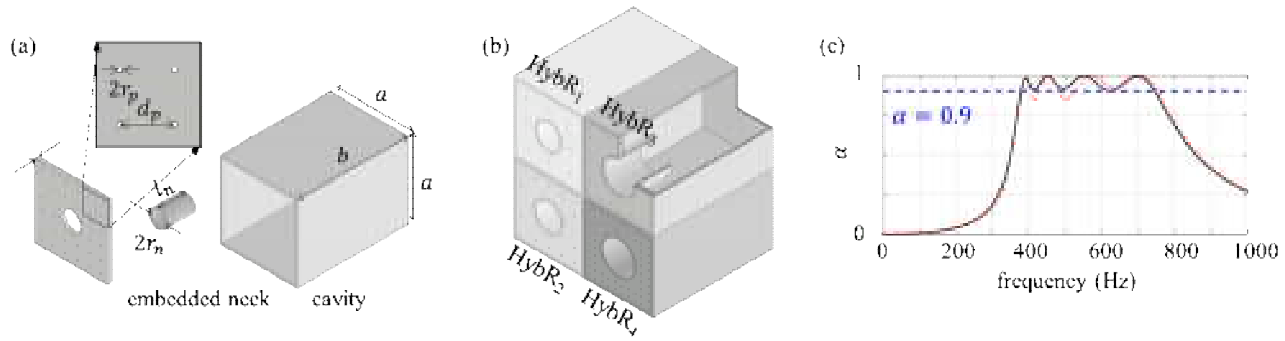


Fig. 1. (a) Geometrical configurations of a HybR that consists of three components: a front panel, a neck, and a cavity. (b) Geometry of the supercell composed of four types of $HybR_1$, $HybR_2$, $HybR_3$, and $HybR_4$. (c) Absorption spectrum of designed supercell, which shows over 90% of energy absorption in frequency range of 380 to 790 Hz with the blue dashed line.

As shown in Fig. 1(c), the trained model predicts geometrical configurations that optimize the figure of merit (FOM) and average absorption coefficient (α_{avg}). As the dataset size increases, the FOM converges to 9.18. The final design achieves over 90% absorption in the 380–790 Hz range. Theoretical predictions and finite element (FE) simulations closely align, confirming the model's validity.

Overall, this work demonstrates that combining HybR-based metasurfaces with machine learning enables efficient, compact, and high-performance acoustic designs, achieving significantly improved absorption bandwidths within limited space.

References

1. M.A. Biot, "Theory of Propagation of Elastic Waves in a Fluid-Saturated Porous Solid. I. Low-Frequency Range," J. Acoust. Soc. Am. Vol. 28, 168-178, 1956.
2. G. Ji, Y. Fang, J. Zhou, "Porous acoustic metamaterials in an inverted wedge shape," Extreme Mech. Lett. Vol. 36 100648, 2020.
3. N. Jiménez, W. Huang, V. Romero-García, V. Pagneux, J.-P. Groby, "Ultra-thin metamaterial for perfect and quasi-omnidirectional sound absorption," Appl. Phys. Lett. Vol. 109, 121902, 2016.
4. M. Yang, S. Chen, C. Fu and P. Sheng, "Optimal sound-absorbing structures," Mater. Horiz. Vol. 4, 673-680, 2017.
5. J. Li, W. Wang, Y. Xie, B. I. Popa and S. A. Cummer, "A sound absorbing metasurface with coupled resonators," Appl. Phys. Lett. Vol. 109, 091908, 2016.
6. H. Ryoo, W. Jeon, "Broadband sound absorption using multiple hybrid resonances of acoustic metasurfaces," Int. J. Mech. Sci. Vol. 229, 107508, 2022.
7. H. Ryoo, K.Y. Lee W. Jeon, "Broadband sound absorption using hybrid resonators with embedded necks and micro-perforations in parallel," Mech. Syst. Signal Process. Vol. 211, 111205, 2024.

META 2025, MALAGA - SPAIN, JULY 22 – 25, 2025

Unlocking Large-Scale Metasurface Fabrication with Electron Beam Lithography through Algorithmic Patterning

M. Kahl[1*], F. Nouvertné[1], R. Schmid[2] and V. Boegli[1]

[1]Raith GmbH Dortmund, Germany
[2]Raith America Inc., USA
[*]corresponding author: michael.kahl@raith.com

Abstract: Algorithmic patterning enhances electron beam lithography (EBL) by reducing data overhead, enabling large-scale metasurface fabrication and intricate photonic designs. By adding new shapes and tailored design data formats at the pattern generator level, it streamlines workflows, accelerates exposures, and expands design possibilities for next-generation photonic devices.

Electron beam lithography (EBL) has been instrumental in fabricating electronic and photonic devices, traditionally relying on the GDSII format for pattern definition. However, the Manhattan-style layouts inherent to GDSII pose challenges for complex geometries, particularly in photonics applications such as metasurfaces, photonic integrated circuits (PICs), and augmented reality/virtual reality (AR/VR) devices. The demand for diverse patterns, including circles, ellipses, and other non-polygonal features, has exposed the inefficiencies of conventional data handling, leading to excessive file sizes and impractical exposure times.

To address these challenges, we present an advanced algorithmic patterning methodology that enables the direct integration of user-defined algorithms into the pattern generator software via custom C# code [1]. This approach allows real-time generation of complex geometries, bypassing traditional file-based limitations. By embedding a userhook.dll, operators can add user-defined shapes and dynamically compute complete exposure patterns [2], significantly reducing data transfer overhead. Illustrating the power of algorithmic patterning, we showcase the generation of intricate patterns, including the iconic Mandelbrot set and associated Julia sets, with seamless efficiency. Notably, these patterns are produced on the fly, with the pattern generator computing a pixel stream of over 800 million pixels without the need for data transfer from external files (see figure 1).

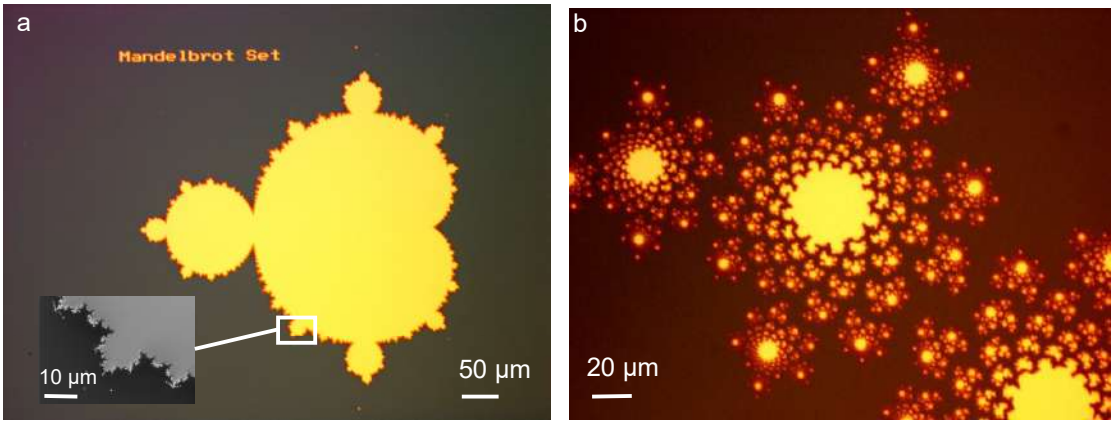


Figure 1. Optical microscope images of patterns exposed as user-defined shapes in PMMA resist, without data transfer from external files: a) Mandelbrot Set (20×), with SEM image inlet, b) Julia set for c= -0.4 + 0.6 i, (50×).

We demonstrate the efficacy of this method in an illustrative example with large-scale metasurface fabrication, where conventional polygon-based approaches generate impractically large files. For instance, a circular, 1 mm diameter metasurface featuring a 2D array of randomly sized circles with a fixed pitch of 500 nm results in a 1.92 GB GDSII file, escalating to an infeasible 4.8 TB for a 50 mm design. Through algorithmic patterning on the Raith VOYAGER system, we have optimized this process by exporting parametric data to 5 MB large ASC files, one per write field, dynamically generating the required structures in real-time during exposure. This enables patterning of a 50 mm metasurface in under two days at a beam current of 13.4 nA (see figure 2 and table 1).

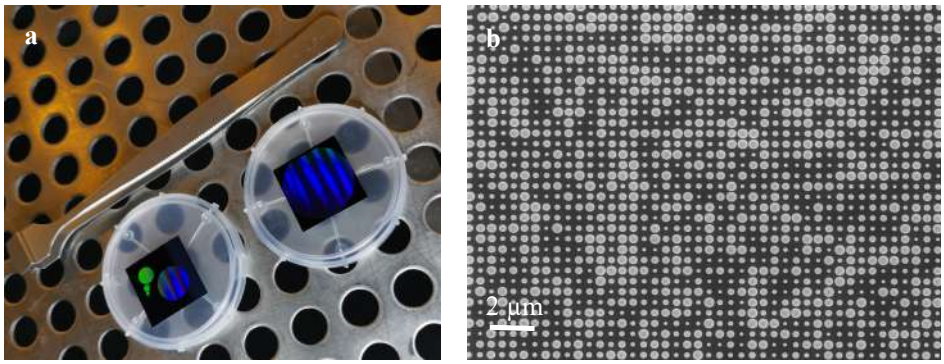


Figure 2. a) Photo of 20 mm large silicon samples with metasurfaces with different diameters, exposed in PMMA resist with algorithmic patterning, b) SEM image of metasurface (5,000×)

Diameter	GDSII file	No. of circles	No. of asc files	Data volume	Exposure time
0.2 mm	80 MB	0.13×10^6	1	4 MB	2 s
1 mm	1.92 GB	3.14×10^6	4	20 MB	1 min 4 s
2 mm		12.57×10^6	16	84 MB	4 min 20 s
5 mm		78.54×10^6	100	506 MB	26 min 35 s
10 mm		314.16×10^6	400	1.97 GB	1 h 46 min
20 mm		$1{,}257\times10^6$	1,600	7.91 GB	7 h 5 min
50 mm	~ 4.8 TB	$7{,}853\times10^6$	8,024	42.1 GB	44 h 12 min

Table 1. Pattern data of metasurfaces with different diameters

Beyond metasurfaces, our approach extends to aperiodic layouts, rotated gratings, and other complex photonic structures, including proximity effect corrections. By overcoming the limitations of GDSII and unlocking new design possibilities, algorithmic patterning empowers researchers and engineers to push the frontiers of photonic device fabrication, paving the way for next-generation optical technologies.

References

1. M. Kahl, F. Nouvertné, R. Schmid and V. Boegli, “Tailoring Electron Beam Lithography with User-defined Shapes and Design Data Formats,” in 50th International Micro and Nano Engineering Conference, 2024, conference booklet, p. 156
2. F. Nouvertné, C. Aulbach, G. Piaszenski, J. Münchenberger and V. Boegli , “Enabling and perfectioning advanced large Area Metalens Nanofabrication by Electron Beam Lithography (EBL),” in META 2023 Proceedings, Paris, July 18 – 21, 2023, 1593-1594

A Non-diffracting Resonant Angular Filter

T. M. Lawrie[1*], G. Tanner[1], and G. J. Chaplain[2]

[1]University of Nottingham, United Kingdom
[2]University of Exeter, United Kingdom

[*]corresponding author: tristan.lawrie@nottingham.ac.uk

Abstract: We conceptualize and numerically simulate a resonant metamaterial interface incorporating non local, or beyond nearest neighbor, coupling that acts as a discrete angular filter. It can be designed to yield perfect transmission at customizable angles of incidence, without diffraction, allowing for tailored transmission in arbitrarily narrow wavenumber windows.

In recent years the scattering language of quantum graph theory has been successfully applied to the study of metamaterials, both theoretically [1] and experimentally [2]. The simple formulation allows for wave transport in complex network like systems to be studied (semi-)analytically, allowing for simple expressions that can be written in a closed form [3]. Following this successful formulation we study wave transport of an acoustic pressure field, with wave number k, across a filter formed of a network of thin tubes [4]. The network forms a grating with period ℓ that couples two semi-infinite slab waveguides, as shown in Figure 1 (a). Atop the grating are additional tubes of length ℓ_μ that form a helix that couple μ^{th} nearest neighbor grating channels. In the quantum graph formulation, it is trivial to show that the transmission coefficient t_μ across the filter is given analytically by:

$$t_\mu = \frac{i\sin(k\ell_\mu)}{\cos(\kappa_y \mu\ell) - \cos(k\ell_\mu) + i\sin(k\ell_\mu)} = \begin{cases} 1, & \text{if } k\ell_\mu = p\pi \text{ and } \kappa_y = \kappa_y^{(q)} = q\pi/\mu\ell \\ 0, & \text{if } k\ell_\mu = p\pi \text{ and } \kappa_y \neq \kappa_y^{(q)}. \end{cases} \quad (1)$$

Where κ_y is the wave vector tangential to the interface that defines the angle of incidence. The filter effectively acts as a Kronecker-delta function at resonance where transmission is forbidden accept for at unique angles of incident, as shown in Figure 1 (b) and (c).

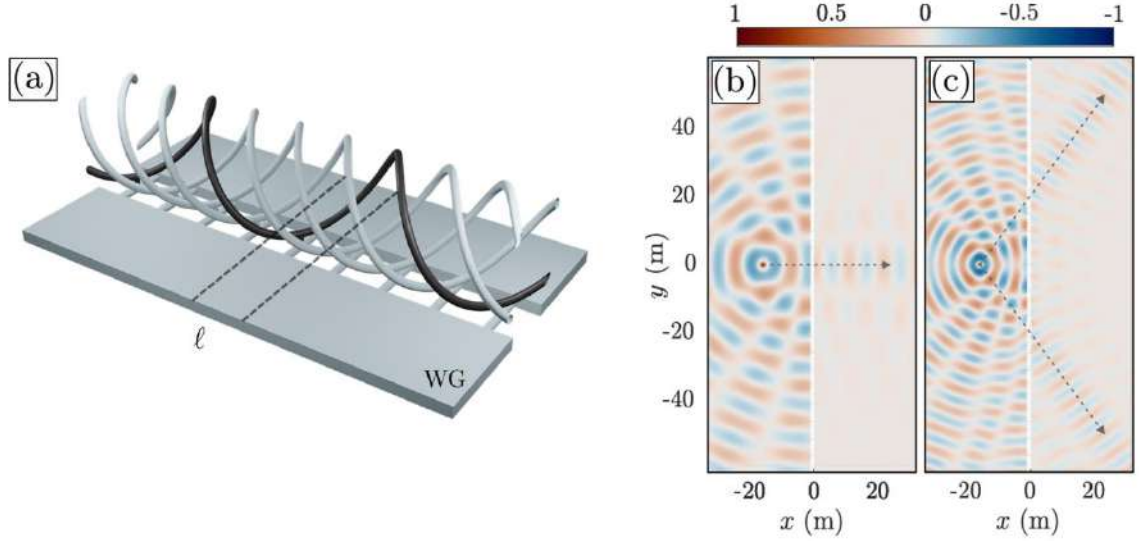


Figure1: (a) shows two semi-infinite slab waveguides connected by a grating of thin tubes, ontop of the grating are additional thin tubes that form beyond nearest neighbour connections that yeild the unit tranmission filtering effect. (b) shows the resulting pressure field from finite element simulation with unit transmission at zero angle, while (c) shows unit transmission at non-zeros angles.

Acknowledgements

T.M.L acknowledges the financial support by the EPSRC in the form of the Postdoctoral Prize Fellowship. G.J.C acknowledges the financial support by the EPSRC (grant no EP/Y015673/1). All data created during this research are available upon reasonable request to the corresponding author.

References

1. Lawrie, T., Tanner, G. and Chronopoulos, D., 2022. A quantum graph approach to metamaterial design. *Scientific Reports*, *12*(1), p.18006.
2. Lawrie, T.M., Starkey, T.A., Tanner, G., Moore, D.B., Savage, P. and Chaplain, G.J., 2024. Application of quantum graph theory to metamaterial design: Negative refraction of acoustic waveguide modes. *Physical Review Materials*, *8*(10), p.105201.
3. Lawrie, T., Gnutzmann, S. and Tanner, G., 2023. Closed form expressions for the Green's function of a quantum graph—a scattering approach. *Journal of Physics A: Mathematical and Theoretical*, *56*(47), p.475202.
4. Lawrie, T., Tanner, G. and Chaplain, G., 2024. A Non-diffracting Resonant Angular Filter. *arXiv preprint arXiv:2410.17329*.

Phase-Matching holographic metasurfaces for accurate acoustic image generation

V. Vegas-Luque[1*], D. Andrés[1], A. Eroles-Simó[1], J. J. Rodríguez-García[1], F. Camarena[1] and N. Jiménez[1]

[1]Instituto de Instrumentación para Imagen Molecular (i3M), Universitat Politècnica de València (UPV) – Consejo Superior de Investigaciones Científicas (CSIC), València, Spain

Corresponding author: vvegluq@i3m.upv.es

Abstract: Holographic metasurfaces can tailor acoustic wavefronts to produce arbitrary acoustic images; however, current methods are not able to accurately encode the target phase distribution. We propose a novel technique for designing the metasurface by matching the phase at the lens exit with the target phase over a whole volume.

Acoustic holograms are complex lenses that encode customized phase distributions in their structure, allowing the creation of specific acoustic pressure patterns within a medium [1]. The underlying principles of this technology are based on interference and diffraction, much like optical holograms, but applied to sound waves. This technology has proven to be highly adaptable, with a wide range of applications in areas, mainly using ultrasound [2–7]. Between them, a promising application of acoustic holograms is therapeutic ultrasound and in particular transcranial ultrasound, where holograms can compensate for phase aberrations produced by the skull and generate sharp focal spots or arbitrary acoustic images inside the human brain [2].

In current hologram design techniques, the target field is defined along a transverse plane, and the lenses are designed to match the phase of the field in this plane. This approach is ideal when the lens is a perfect flat metasurface. However, its implementation using phase plate lenses often fails to reproduce the desired phase as a result of nonplane wave propagation, refraction, and diffraction effects.

In this work, we propose a novel approach called *phase matching*, where the field is acquired in a volume rather than a plane, and the phase at the lens exit is aligned with the target phase throughout the volume. The proposed method is validated through analytical solutions, simulations, and experiments. First, a single focal lens is designed using a 1.1-MHz circular 50-mm aperture source and various 3D printing materials and a parametric study of its focusing performance is conducted. Second, several complex acoustic images at different depths are generated, with their structural similarity index measure (SSIM) evaluated.

For simple focused beams, our method produces sharper focal spots with greater focusing gain. These focal spots are closer to the diffraction-limited estimations. For materials with a refractive index lower than one, both methods produce hyperbolic phase profiles, but only the phase-matching approach provides the optimal solution as seen in Fig. 1(a-b). For low f-numbers, phase matching outperforms classical methods, while for moderately focused beams, both approaches converge. Furthermore, we observe that the structural similarity index measure (SSIM) of complex acoustic images generated at shorter distances is higher with the proposed method, particularly for short focal lengths as shown in Fig. 1(c).

Phase-matching holograms enable precise synthesis of the target field's phase at the lens exit, surpassing traditional acoustic hologram design methods. This approach is particularly suited for emerging therapeutic ultrasound applications that require precise acoustic beam control, especially in cases where full-wave simulations are computationally intensive to be used for optimization methods.

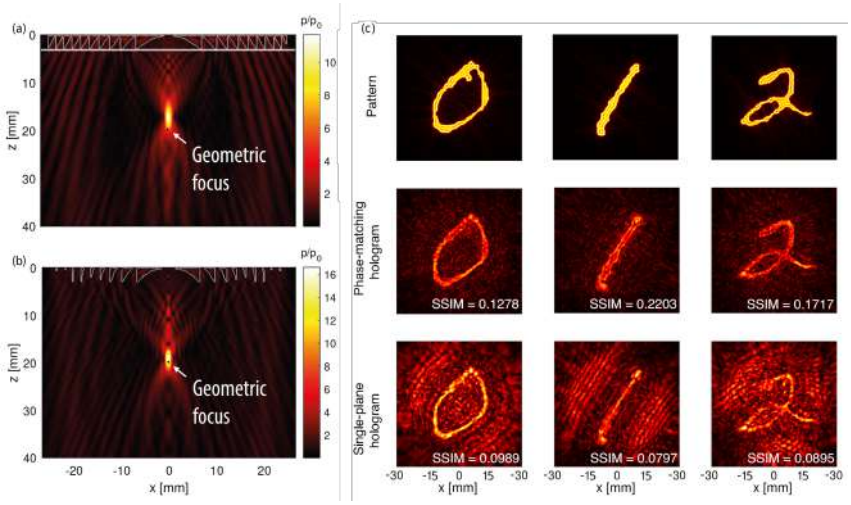


Figure 1: (a) Focal lens obtained through traditional methods. (b) Focal Lens obtained through phase-matching approach. (c) Acoustic patterns obtained using phase-matching and traditional (single-plane) methods

Acknowledgments

This research has been supported grants RYC2021-034920-I, PID2022-142719OB-C21, and CNS2023-145707 funded by MCIN/AEI/10.13039/ 501100011033; Agencia Valenciana de la Innovació grants INNVA2/2022/11, INNVA1/2022/37, INNEST/2022/345, Generalitat Valenciana grant INVEST/2023/553 and Universitat Politècnica de València PAID-01-24.

References

1. K. Melde, A. G. Mark, T. Qiu, and P. Fischer, "Holograms for acoustics," *Nature*, vol. 537, pp. 518–522, 9 2016.

2. S. Jiménez-Gambín, N. Jiménez, J. M. Benlloch, and F. Camarena, "Holograms to focus arbitrary ultrasonic fields through the skull," *Physical Review Applied*, vol. 12, 7 2019.

3. Y. Xie, C. Shen, W. Wang, J. Li, D. Suo, B. I. Popa, Y. Jing, and S. A. Cummer, "Acoustic holographic rendering with two-dimensional metamaterial-based passive phased array," *Scientific Reports*, vol. 6, 10 2016.

4. S. Jimenez-Gambin, N. Jimenez, A. Pouliopoulos, J. M. Benlloch, E. Konofagou, and F. Camarena, "Acoustic holograms for bilateral blood-brain barrier opening in a mouse model," *IEEE Transactions on Biomedical Engineering*, vol. 69, pp. 1359–1368, 4 2022.

5. D. Andrés, J. Vappou, N. Jiménez, and F. Camarena, "Thermal holographic patterns for ultrasound hyperthermia," *Applied Physics Letters*, vol. 120, 2 2022.

6. D. Andrés, I. Rivens, P. Mouratidis, N. Jiménez, F. Camarena, and G. ter Haar, "Holographic focused ultrasound hyperthermia system for uniform simultaneous thermal exposure of multiple tumor spheroids," *Cancers*, vol. 15, 5 2023.

7. K. Melde, H. Kremer, M. Shi, S. Seneca, C. Frey, I. Platzman, C. Degel, D. Schmitt, B. Schölkopf, and P. Fischer, "Compact holographic sound fields enable rapid one-step assembly of matter in 3d," *Science Advances*, vol. 9, 2 2023.

Visualization of topological edge and boundary modes in mechanical metamaterials

M. Tomoda[1,2*], K. Yamaguchi[2], G. Yoon[2], H. Takeda[2], R. Minami[2], O. Matsuda[2], and O. B. Wright[2,3]

[1]Oita University, Japan
[2]Hokkaido University, Japan
[3]Osaka University, Japan
[*]corresponding author: mtomoda@eng.hokudai.ac.jp

Abstract: We developed two types of two-dimensional mechanical wave machines to investigate topologically protected edge and boundary vibration modes. One system simulates quantum Hall effects by breaking time-reversal symmetry through the Coriolis force. The other replicates quantum valley Hall effects, where vibrations propagate along a topological interface.

The topological phases that emerged from the discovery of the quantum Hall effect have garnered significant attention for their applications in classical wave phenomena, particularly in artificial periodic structures such as photonic [1,2] and phononic crystals [3]. Topological waveguides in these crystals exhibit inherent robustness against bends and defects, effectively preventing backscattering. In the case of phononics, this holds promise for the realization of more efficient waveguides and non-reciprocal acoustic devices.

Breaking time-reversal (*T*) symmetry is essential for realizing a phononic analog of quantum Hall (QH) systems. Most electronic QH systems achieve this by utilizing magnetic fields and Lorentz forces; however, phononic and acoustic systems generally do not interact with magnetic fields. Initially theoretical methods involving rotating fluids [4] or gyroscopes [5] were proposed and later validated experimentally [6,7]. A more direct approach involves introducing uniform rotational motion into the system instead of a uniform magnetic field. In a rotating reference frame, a mass experiences a Coriolis force perpendicular to its velocity, thereby breaking *T* symmetry in a manner analogous to how an electron experiences the Lorentz forces in a magnetic field. In prior research, a structure called “mechanical graphene,” consisting of masses and springs in a hexagonal lattice, was proposed [8]. Numerical calculations demonstrated that unidirectional vibration propagation along fixed boundaries could be achieved when vibrational excitation was applied to this system. However, in practical experiments, the presence of centrifugal forces disrupted the translational symmetry of the system, preventing its realization.



Fig. 1 (a) Photograph of the rotating wave machine.

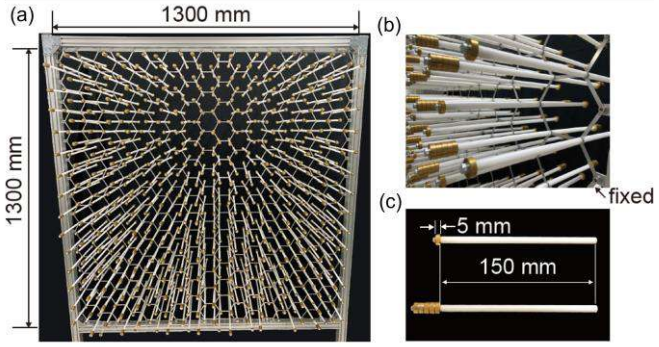


Fig. 2 (a) Photograph of the flexural wave machine. (b) Close-up view. (c) The plastic rods.

On the other hand, quantum valley Hall (QVH) systems can be realized by connecting two regions that break the spatial inversion (*P*) symmetry of the unit cells. QVH phononic crystals have been extensively studied from kilohertz to gigahertz frequencies, but observing the motion of mechanical vibrational modes with small displacements remains challenging, as conventional cameras cannot capture them. Although a low-frequency experimental study on a mechanical QVH system at ~10 Hz, based on magnetically coupled spinners, has been reported [9]. Since this system has only a single degree of freedom per lattice point, it cannot effectively capture modes with high degrees of freedom, such as chiral phonons.

Here, we realize and visualize both QH topological edge modes and QVH topological boundary modes [10] using mechanical metamaterials as two-dimensional extensions of the Shive wave machine. To realize a QH system, we constructed a wave machine with a honeycomb mass-spring lattice supported by spherical bearings embedded in a plastic board (Fig. 1). This design maintains equilibrium despite rotation due to centrifugal forces. In this system, the centrifugal and gravitational forces acting on the front and back surfaces on the plate cancel each other out, while the Coriolis forces remain uncompensated.

To realize a QVH system, we developed a suspended honeycomb lattice flexural wave machine, composed of a stainless-steel thin plate and plastic rods with brass weights (Fig. 2). The rods and weights enhance the moment of inertia, lowering the eigenfrequencies of the topological modes to approximately 5 Hz. To break P-symmetry and induce valley polarization, we adjust the brass weights within each unit cell [10].

The motions of each cell of both mechanical metamaterials were monitored with a motion capture system. In the QH system, a unidirectional topological edge state was observed when the system was rotated. In QVH system, topologically protected vibration modes along a bearded boundary were identified. The measured vibrations of these systems were compared with theoretical and simulation results.

We are also developing a mechanical analog of quantum spin Hall (QSH) system based on a suspended flexural wave machine. Our approach should be applicable to mechanical metamaterials, including reconfigurable and active systems.

Acknowledgements: This work was supported by the Japan Society for the Promotion of Science KAKENHI Grant Numbers 21H05020 and 22H01930.

References

1. L. Lu, J.D. Joannopoulos, and M. Soljacic, “Topological photonics,” Nat. Photon., Vol. 8, 821, 2014.
2. T. Ozawa *et al.*, “Topological photonics,” Rev. Mod. Phys. Vol. 91, 015006, 2019.
3. G. Ma, M. Xiao and C.T. Chan, “Topological phases in acoustic and mechanical systems,” Nat. Rev. Phys., Vol. 1. 281, 2019.
4. Z. Yang *et al,*. “Topological Acoustics,” Phys. Rev. Lett., Vol. 114, 114301, 2015.
5. P. Wang, L. Lu, and K. Bertoldi, “Topological Phononic Crystals with One-Way Elastic Edge Waves,” Phys. Rev. Lett., Vol. 115, 104302, 2015.
6. Y. Ding *et al.*, “Experimental Demonstration of Acoustic Chern Insulators,” Phys. Rev. Lett., Vol. 122, 014302, 2019.
7. L. M. Nash *et al.*, “Topological mechanics of gyroscopic metamaterials,” Proc. Natl. Acad. Sci. U.S.A., Vol. 112, 14495-500., 2015.
8. T. Kariyado and Y. Hatsugai, “Manipulation of Dirac Cones in Mechanical Graphene,” Sci. Rep., Vol. 5, 18107, 2016.
9. K. Qian *et al.*, “Topology of the valley-Chern effect,” Phys. Rev. B, Vol. 98, 144138, 2018.
10. H. Takeda *et al.*, “Phononic band calculations and experimental imaging of topological boundary modes in a hexagonal flexural wave machine,” Appl. Phys. Express, Vol.17, 017004, 2024.

Compact elastic plate for bound state in the continuum

Zhihui Wen[1], **Marc Marti-Sabaté**[2], **Yabin Jin**[3], **Daniel Torrent** [4] **and Yegao Qu**[1,*]

1 State Key Laboratory of Mechanical System and Vibration, Shanghai Jiao Tong University, Shanghai 200240, China
2 Department of Mathematics, Imperial College London, 180 Queen's Gate, London SW7 2AZ, United Kingdom
3 Shanghai Key Laboratory of Intelligent Sensing and Detection Technology, School of Mechanical and Power Engineering, East China University of Science and Technology, Shanghai 200237, China
4 GROC-UJI, Institut de Noves Tecnologies de la Imatge, Universitat Jaume I, 12080 Castello, Spain

*corresponding author: quyegao@sjtu.edu.cn (Yegao Qu)

Abstract: We demonstrate high-quality flexural wave localization mechanism in symmetric scatterer clusters, where resonance quality (Q) escalates with energy density, approaching bound states in the continuum (BICs) with infinite Q. High-multipole modes form whispering galleries. A cylindrical-shelled metaplate achieves symmetry-protected BICs, enabling compact, high-efficiency wave control for on-chip applications.

Realizing elastic wave modulation with high energy density in small-sized spaces has always been a huge challenge for elastic wave functional devices to move towards engineering applications [1]. Pillared plates composed of pure cylindrical scatterers embedded in a homogeneous material provide a practical and efficient platform for designing bound states in the continuum (BIC). Their simplicity and homogeneity offer significant advantages in fabrication and engineering applications.

Based on the symmetry protection of the bound state of the continuum (BIC), we proposed the reverse numerical design method for achieving compact bound states. The three-dimensional model of the pillared plates in the left panel of Fig. 1(a). In the right panel of Fig. 1(a) is the arrangement of circular clusters, where N is the number of pillars of the cluster, R_{cluster} is the radius of the cluster, and θ defines the angular position of the pillars within the cluster. Finally，the BIC is the real-eigenmodes of scattering matrix [2, 3], which's polarization mode is defined by the order of the Bessel function l [4].

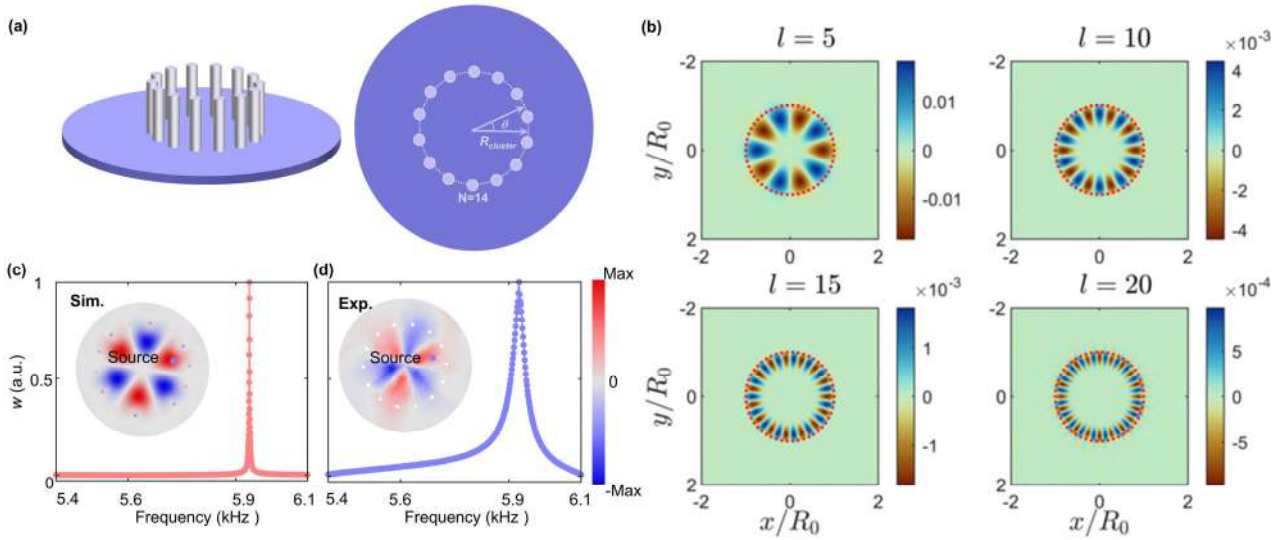


Figure 1. (a) The three-dimensional model of the pillared plates in the left panel. Arrangement of circular clusters, with the number of pillars of the cluster N, the radius of the cluster R_{cluster}, and the angular position of the pillars

θ in the right panel. (b) Real part of the eigenfunction for different resonant index l. The clusters have the same number of scatterers (N = 50) [5]. (c) Normalized response curves of the out-of-plane displacement w(a.u.) from the simulation and (d) the experiment at the maximum displacement of the hexapole mode with the design parameter l = 3 [4]. Insets in panels (c) and (d) show the out-of-plane displacements for the simulation and the experiment, respectively, with the blue points indicating the excitation sources of sine waves.

High-index modes typically localize near scattering structures, forming whispering gallery modes. This method enables the systematic engineering of high-quality whispering gallery modes. Figure 1(b) illustrates such modes for a cluster of 50 scatterers with refractive indices of 5, 10, 15, and 20. As the index increases, the plots clearly show enhanced field confinement near the cluster's perimeter [5].

The normalized response curves of bound states in the continuum (BICs) are presented in Figs. 1(c) and 1(d). The simulated BIC frequency is 5937.8 Hz, while the experimental value is 5926.2 Hz, demonstrating strong agreement with an error $\delta = \left| f_{\text{sim}} - f_{\text{exp}} \right| / f_{\text{sim}}$ of less than 0.2%. The experimental quality factor is Q = 137.8. Minor deviations align with expectations due to damping and fabrication imperfections. Insets in Figs. 3(a) and 3(b) depict out-of-plane displacement fields from simulation and experiment, respectively, which reveal weakly coupled leakage modes [4].

Acknowledgements

This work was supported by the National Key R&D Program (Grant No. 2022YFB3902702), the National Natural Science Foundation of China (Grant Nos. U2141244, 11932011, 12393781, 12121002, 12202267, 12402021), Shanghai Pujiang Program (Grant No. 22PJ1405300), the Oceanic Interdisciplinary Program of Shanghai Jiao Tong University (Grant No. SL2021ZD104), the Science and Technology Cooperation project of Shanghai Jiao Tong University & Inner Mongolia Autonomous Region-Action Plan of Shanghai Jiao Tong University for "Science and Technology Prosperity" (Grant No.2022XYJG0001-01-08), the Industry-university-research Cooperation Fund of Shanghai Academy of Spaceflight Technology (No. USCAST2021-11), and the China Postdoctoral Science Foundation (Grant No. 2023M742268). This publication is part of the project PID2021-124814NB C22, funded by MCIN/AEI/10.13039/501100011033/ "FEDER A way of making Europe", project Grant CIPROM/2023/44 funded by Generalitat Valenciana. We thank Project No. CNS2023-145510 funded by MCIN/AEI/10.13039/501100011033, "European Union Next Generation EU/PRTR".

References

[1] Zhihui Wen, Wan Wang, A. Khelif, B. Djafari-Rouhani, Y. Jin, A perspective on elastic metastructures for energy harvesting, Applied Physics Letters, 120 (2022) 020501.

[2] Zhihui Wen, Y. Jin, Penglin Gao, Xiaoying Zhuang, Timon Rabczuk, Bahram Djafari-Rouhani, Topological cavities in phononic plates for robust energy harvesting, Mechanical Systems and Signal Processing, 162 (2022) 108047.

[3] Marc Martí-Sabaté, Daniel Torrent, Dipolar localization of waves in twisted phononic crystal plates, PHYSICAL REVIEW APPLIED, 15 (2021) L011001.

[4] Zhihui Wen, Penglin Gao, Jiawei Mao, Shoubo Dai, Marc Marti-Sabaté, Yabin Jin, Yegao Qu and Dani Torrent, Compact metaplate with bound state in the continuum: from quasi-symmetry to symmetry, 2025.

[5] Marc Martí-Sabaté, B. Djafari-Rouhani, Dani Torrent, Bound states in the continuum in circular clusters of scatterers, Physical Review Research, 5 (2023) 013131.

Topological phase transitions and edge states in SSH-type elastic systems with periodic and disordered non-Hermitian modulations

R. Cai[1,2], Y. Jin[3], Y. Pennec[1], X. Zhuang[2] and B. Djafari-Rouhani[1*]

[1]Institut d'Electronique, de Microélectonique et de Nanotechnologie, UMR CNRS 8520, Département de Physique, Université de Lille, 59650 Villeneuve d'Ascq, France

[2]Department of Geotechnical Engineering, College of Civil Engineering, Tongji University, 200092 Shanghai, China

[3] Shanghai Key Laboratory of Intelligent Sensing and Detection Technology, School of Mechanical and Power Engineering, East China University of Science and Technology, Shanghai 200237, China.

[*]corresponding author: bahram.djafari-rouhani@univ-lille.fr

Abstract: Based on a generalized Su–Schrieffer–Heeger model, we design a non-Hermitian periodic or disordered elastic platform with feedback control where we theoretically study the topological phase diagrams and edge states. Considering both one and two-dimensional structures, we demonstrate in theory and simulations the relative effects of non-Hermiticity and disorder.

Topological states have been receiving a great deal of interest in various wave problems and have been used to design novel artificial structured materials to manipulate acoustic and elastic waves robustly. However, most studies have focused on periodic and Hermitian systems characterized by real-valued eigenfrequencies and orthogonal eigenvectors, while the role of non-Hermiticity and disorder in topological properties needs to be further explored. Recently, it was shown that novel topological phase transitions can be driven by non-Hermiticity and disorder. Inspired by these models, we study in this work the topological phase transitions induced by periodic and disordered on-site non-Hermitian modulations in one-dimensional (1D) and two-dimensional (2D) systems.

We first develop a theoretical approach, based on a generalization of the Su-Schrieffer-Heeger (SSH) model, to investigate the full topological phase diagram as a function of the physical parameters and non-Hermitian strengths. To characterize the topological phase transitions of the system, the polarization P_x in real space for a system is defined as [1-3]:

$$P_x = \frac{1}{2\pi}\,\mathrm{Im}\left\{\log\left[\det(U_l^{\dagger}\,\hat{Q}\,U_r)\sqrt{\det(\hat{Q}^{\dagger})}\right]\right\}, \tag{1}$$

where $\hat{Q}$ is the coordinate operator represented by a diagonal matrix with $\hat{Q}(j,j) = e^{i2\pi j/N}$. U_l and U_r are the matrices constituted by the normalized and occupied left and right eigenstates of the Hamiltonian matrix H, respectively. For the system with pseudo-anti-Hermiticity symmetry, P_x becomes a quantity taking the values of 0 (corresponding to a trivial system) or 0.5 (corresponding to a nontrivial system).

We find that an initially trivial system can become nontrivial under periodic or moderately disordered non-Hermitian modulations for 1D systems. The 2D systems are more sensitive to disorder and trivial-nontrivial phase transitions only survive under periodic and weak disordered non-Hermitian modulations.

Besides, it is shown that similar phase diagrams as in disordered structures can also be reproduced in some super-periodic structures exhibiting the same average of the non-Hemiticity strength. Therefore, the relative roles of non-hermiticity and disorders in the creation of the various phase diagrams are discussed.

We construct an elastic analog of the SSH model consisting of elastic square plates with thin connecting

beams, where the non-Hermitian modulations are introduced by attached piezoelectric patches with a feedback control loop. The trivial-nontrivial phase transitions as well as topological edge/corner modes driven by non-Hermitian modulations are demonstrated in elastic structures.

Our study provides a novel way to explore topological states based on periodic/disordered non-Hermitian modulations. The proposed elastic platform has the advantage of active tunability and intelligent control, which presents a versatile platform for studying disordered and non-Hermitian metamaterials and has potential applications in vibration control, energy harvesting, and sensing.

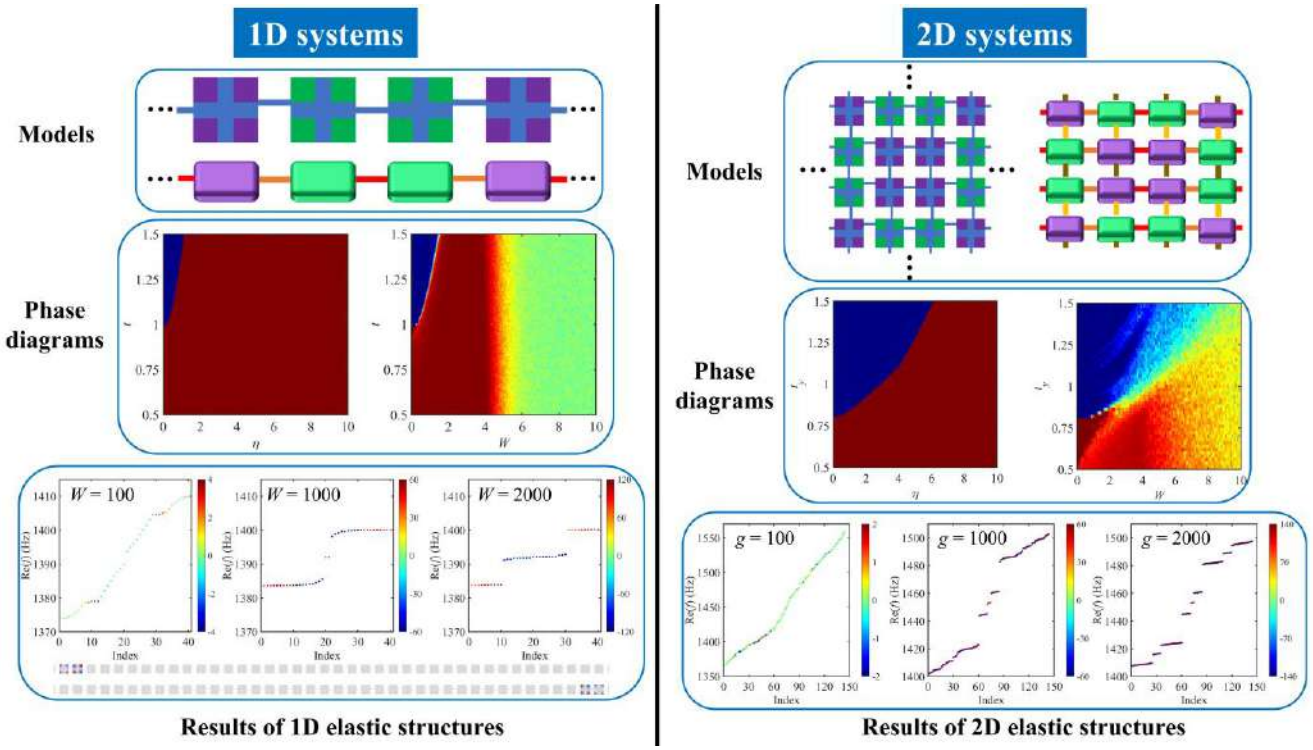


Figure 1. Graphical abstract of this work. The left panel shows, for 1D systems, from top to bottom: the elastic and analytical models, the topological phase diagrams as a function of non-Hermiticity strength and the eigenfunctions of elastic structures. The right panel shows similar results for 2D systems.

Acknowledgments: This work is part of the project MAGNIFIC of the European Union's Horizon Europe research and innovation program under grant agreement No 101091968 and the CHIST-ERA Call 2021 under grant agreement No CHIST-ERA-20-NOEMS-003.

References

1. Li, C.-A., B. Fu, Z.-A. Hu, J. Li and S.-Q. Shen, "Topological phase transitions in disordered electric quadrupole insulators," Phys. Rev. Lett., Vol. 125, No. 16, 166801, 2020.
2. Gu, Z., H. Gao, H. Xue, D. Wang, J. Guo, Z. Su, B. Zhang and J. Zhu, "Observation of an acoustic non-Hermitian topological Anderson insulator," Sci. China-Phys. Mech. Astron., Vol. 66, No. 9, 294311, 2023.
3. Liu, H., J.-K. Zhou, B.-L. Wu, Z.-Q. Zhang and H. Jiang, "Real-space topological invariant and higher-order topological Anderson insulator in two-dimensional non-Hermitian systems," Phys. Rev. B, Vol. 103, No. 22, 224203, 2021.

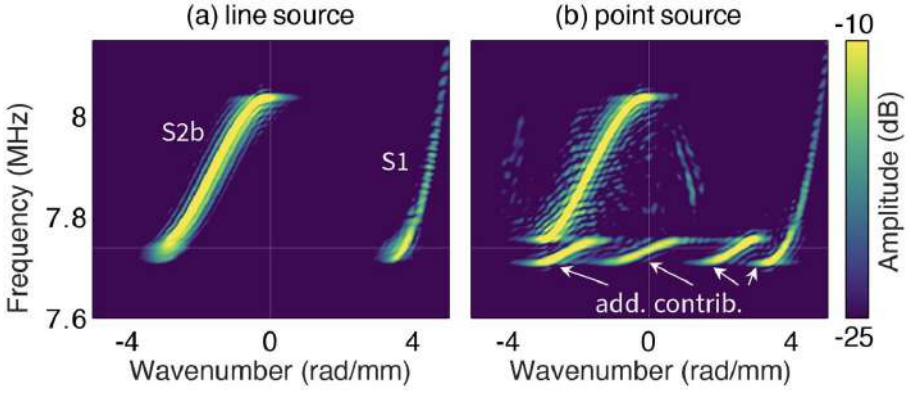
Skewing of guided waves in anisotropic plates close to zero-group-velocity points

D. A. Kiefer*, S. Mezil, and C. Prada
Institut Langevin, ESPCI Paris, Université PSL, CNRS
Corresponding author: daniel.kiefer@espci.fr

Abstract: In anisotropic media the power flux of waves is usually skewed, i.e., it is not collinear to the wave vector. We describe how this effect impacts the measurable dispersion spectrum of guided elastic waves in plates. The theory is generally applicable to linear wave propagation in anisotropic media.

Guided waves in plates [1] are often measured on a line away from the source. A spatio-temporal Fourier transform yields the dispersion spectrum in the frequency-wavenumber domain. We performed such measurements on a 525-µm thick, [001]-cut, monocrystalline silicon wafer of cubic anisotropy and the results are depicted in Fig. 1. It is striking that the spectrum excited with a point source contains additional contributions compared to that of the line source. The multiple contributions are all due to the same mode. This effect can be explained with the wave's skew angle, i.e., the angle between the wave vector and the power flux [2].

We show that guided waves close to zero-group-velocity resonances are particular in that they exhibit skew angles between 0° and 360°. As a consequence, the modal multiplicity always exists–independent of the measurement direction. To illustrate this, we study the particular case of *transverse-group-velocity waves*, whose power flux is orthogonal to the wave vector [3]. We have measured this wave on the same sample and the resulting spatio-temporal intensity field is shown in Fig. 2. This wave packet is radiated along the line source instead of orthogonally away from it. This behavior affects the measured dispersion spectra and needs to be accounted for in the corresponding model. A point on the dispersion surface where the power flux is along the measurement direction is called a *stationary phase point*. The ensemble of stationary phase points precisely models the observed point-source spectrum, including the "additional



;

Figure 1: Dispersion spectra obtained by scanning a line at [110]+22.5° away from (a) a line source and (b) a point source. The thermoelastic excitation is performed with a pulsed laser. The normal surface displacement is measured with a laser interferometer. From Ref. [2].

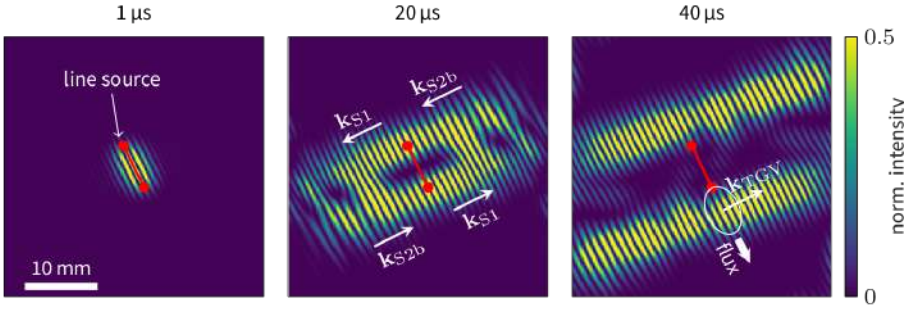


Figure 2: Transverse-group-velocity wave radiated from a synthesized line source. The experimental setup is as before. Frequency-wavenumber filtering has been applied to isolate the mode. From Ref. [3].

contributions" [2]. Since the power flux of waves is not known in advance, the computation of stationary phase points is particularly challenging. We have done so by computing the dispersion surface on a dense grid of about two million points and selecting the waves whose power flux is in the desired direction within a fixed tolerance. Our open source software `GEWtool` [4] achieves this in one to two minutes on eight cores of an Apple M1 Pro processor.

The extreme skewing yields multi-directional information on the material behavior even when performing only a single line scan. Hence, it is highly valuable for anisotropic material characterization.

References

1. B. A. Auld *Acoustic Fields and Waves in Solids*, Vol. 2, 2nd ed., Malabar FL: Krieger Publishing Company, 1990.

2. D. A. Kiefer, S. Mezil, and C. Prada. "Extreme wave skewing and dispersion spectra of anisotropic elastic plates," *Physical Review Research* Vol. 7, No. 1, p. L012043, 2025. doi: 10.1103/PhysRevResearch.7.L012043

3. D. A. Kiefer, S. Mezil, and C. Prada. "Beating resonance patterns and extreme power flux skewing in anisotropic elastic plates," *Science Advances*, Vol. 9, No. 51, p. eadk6846, 2023. doi: 10.1126/sciadv.adk6846

4. D. A. Kiefer. GEWtool. 2023. doi: 10.5281/zenodo.10114243. (`https://github.com/dakiefer/GEWtool`).

Elastic-wave control based on non-Hermitian metasurfaces

Bing Li[1*], Bochen Ren[1], and Jiali Cheng[1]

[1] School of Aeronautics, Northwestern Polytechnical University, Xi'an, Shaanxi, 710072, China
*corresponding author: bingli@nwpu.edu.cn

Abstract: Beyond the traditional paradigm of Hermitian physics, the concept of non-Hermiticity has recently inspired a surge of nontrivial principles and applications. In this work, we propose several active and passive non-Hermitian metasurfaces that enable unprecedented elastic-wave manipulations, including skin-like effects, asymmetric wave propagation, and perfect absorption.

The past decades have witnessed the remarkable development and explosive implications of meta-structures in elastic-wave steering under the Hermitian systems that disregard material loss. However, the reality of practical applications is inevitably intertwined with loss, leading to the dissipation of elastic wave energy. Traditionally, such losses were viewed as detrimental, potentially compromising the performance of elastic wave devices. Yet, a paradigm shift has emerged from recent groundbreaking research, which has uncovered the potential of strategically engineered loss/gain within non-Hermitian systems to facilitate remarkable wave steering phenomena[1-3]. In this work, we achieve highly flexible and precise non-Hermitian modulation by integrating a piezoelectric sheet-shunt circuit system with a metasurface. The transmittance curves of piezoelectric metasurface units were calculated across a broad frequency range, and the effects of loss and gain induced by positive and negative resistances in the shunt circuit were analyzed. We present various non-Hermitian piezoelectric supercells, as shown in Fig. 1, which enable the enhancement or attenuation of energy in higher-order diffraction waveguides across different modes. In the experimental phase, we designed and fabricated a negative-resistance and tunable inductor synthesis circuit, which allowed for precise tuning of phase delay and energy transmission characteristics of the piezoelectric metasurface. Our study provides new methods and insights for the manipulation and stable implementation of energy gain, offering valuable technical references for the active control of guided waves and precise non-Hermitian modulation.

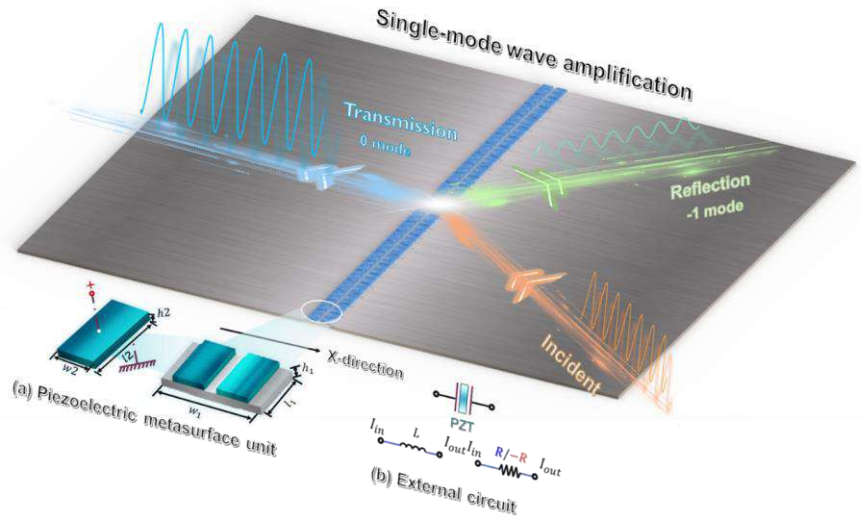


Fig. 1 Single mode wave amplification in a non-Hermitian piezoelectric metasurface

The authors gratefully acknowledge the support from the National Natural Science Foundation of China (NSFC) (Grant No. 12272298).

References

1. Zhu, W., Fang, X., Li, D., Sun, Y., Li, Y., Jing, Y., & Chen, H. “Simultaneous observation of a topological edge state and exceptional point in an open and non-Hermitian acoustic system,” Physical Review Letters, 121(12), 124501, 2018.
2. Li, B., Hu, Y., Chen, J., Su, G., Liu, Y., Zhao, M., & Li, Z. “Efficient asymmetric transmission of elastic waves in thin plates with lossless metasurfaces,” Physical Review Applied, 14(5), 054029, 2020.
3. Cheng, J., Hu, Y., Li, B. “Non-Hermitian metagrating for perfect absorption of elastic waves,” Materials Horizons, Advance Article, 2024.

Acoustic Metasurfaces for High-Resolution Imaging of Additively Manufactured Metals

Hrishikesh Danawe[1] , Raguez A. Taha[2], Talha Khan[2], Didem Ozevin[2], and Serife Tol[1*]

[1]Department of Mechanical Engineering, University of Michigan, Ann Arbor, MI, USA 48109

[2]Department of Civil and Materials Engineering, University of Illinois Chicago, Chicago, IL, USA 60607

[*]corresponding author: stol@umich.edu

Abstract: This study explores a 3D-printed Helmholtz resonator (HR)-based metasurface lens for high-resolution imaging microscale defects in 4mm metal plates. Enhancing resolution over twofold with MHz-frequency acoustic transducers, the lens improves defect detection in extreme applications like nuclear reactors, advancing scanning acoustic microscopy for early fault identification.

Metasurface lenses are gaining attention for manipulating acoustic waves in applications like wave focusing. These lenses use subwavelength units to create a gradient phase distribution, functioning as point sources with engineered phase and amplitude. They are classified as space-coiling (path-length engineering) or resonance-based (localized resonance), with Helmholtz resonators (HR) demonstrating the latter through strong acoustic confinement for complete 2π phase control and excellent impedance matching [1-3]. By engineering the spherical phase gradient, HR metasurface lenses focus sound waves with minimal aberrations, achieving superior resolution. However, microscale fabrication for MHz operation faces challenges, and current acoustic metasurface demonstrations are limited to kilohertz frequencies with millimeter-scale resolution. In critical settings like nuclear reactors, micron-sized defects can cause catastrophic failures. Traditional acoustic transducers struggle with resolution and rely on high-frequency, power-intensive systems for detecting small defects. Also, higher-frequency ultrasonic imaging may not be feasible due to scattering and surface conditions.

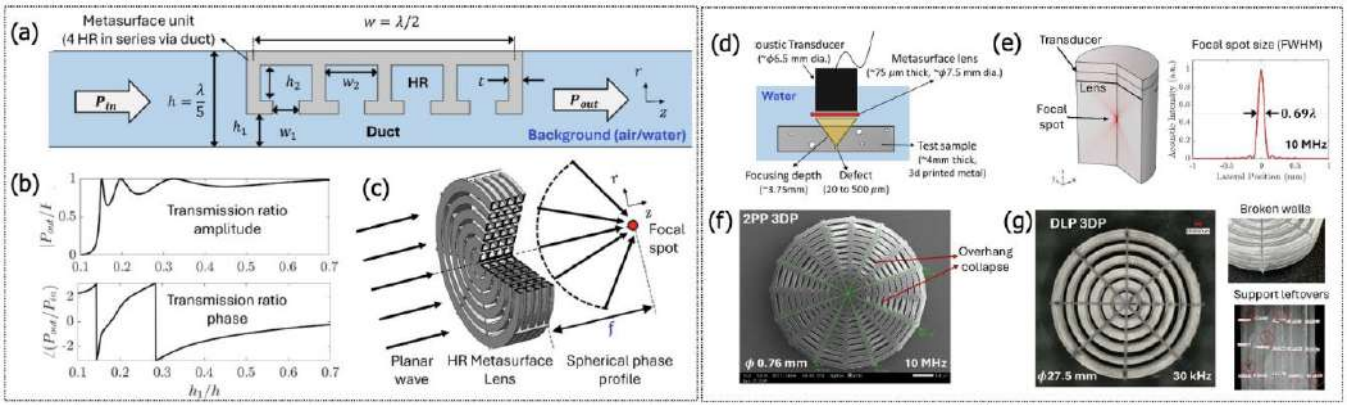


Figure 1 A Helmholtz resonator-based acoustic metasurface lens for wave focusing. **(a)** A transmission study utilizing a waveguide comprising of four Helmholtz resonators in series, connected through a common duct within a background acoustic medium. **(b)** Transmission amplitude and phase plots obtained for varying duct heights. **(c)** An axisymmetric metasurface lens formed using 4HR metasurface units stacked in the radial direction for focusing of planar waves using a spherical phase profile. Acoustic imaging using HR metasurface lens and practical considerations. **(d)** Underwater acoustic imaging microscopy setup. **(e)** Numerical simulation of wave focusing using a 10 MHz water-coupled HR metasurface lens. **(f)** A small 3D printed sample of 10 MHz water-coupled HR metasurface lens (only 13 units of total 125 units) showing collapse of overhangs. 2PP stands for two-photon lithography. **(g)** A 3D printed sample of 30 kHz air-coupled metasurface lens showing broken wall and deformities induced by printing support. DLP stands for digital light processing.

Recent advances in additive manufacturing, particularly two-photon lithography, enable intricate nanostructures for subwavelength metasurfaces. Our goal is to develop an HR metasurface lens that detects microscale defects at several millimeters within a sample, integrating metasurface lenses with planar acoustic transducers at low frequencies to improve resolution from conventional ultrasound imaging (over 1.5λ) to subwavelength resolution (less than λ). We examine a metasurface featuring a subwavelength unit cell that integrates four Helmholtz resonators arranged in series, interconnected via a common duct, as illustrated in Fig. 1(a). The resonator's geometry is defined by the wall thickness (t), the width of the resonator cavity (w_2), cavity height (h_2), neck width (w_1), and duct height (h_1). The overall height of the unit (h) is limited to λ/5. At the same time, the total width (w) is set at λ/2 to maintain the subwavelength condition critical for sub-diffraction focusing through these units. This design is particularly effective for achieving a highly efficient frequency-selective transmission response. Adjusting the duct height controls variations in the transmitted output phase and amplitude; a complete 2π phase shift can be achieved by modifying the duct height, while the amplitude of the transmission ratio remains relatively stable and close to one across all duct height values, as demonstrated in Fig. 1(b). A metasurface lens consists of multiple such units stacked radially. It creates an asymmetric lens design that focuses a planar wavefront on the input side to a focal point along its axis on the output side, as depicted in Fig. 1(c). The duct height profile along the radial direction of the Helmholtz resonator metasurface lens is engineered to correspond to a spherical transmission phase profile, with f representing the focal length, indicating the distance from the lens at which focusing occurs. The lens design has been iteratively optimized for 3D printing. The application of a metasurface lens for acoustic imaging is illustrated in Figs. 1(d)-(e). Figure 1(d) shows an underwater ultrasonic setup that integrates a conventional planar acoustic transducer with a metasurface lens designed to detect micro-sized defects in 4-mm thick 3D printed metal plates. We validated the wave-focusing capabilities by designing the HR metasurface for 10 MHz underwater operation through numerical simulations, achieving a focal spot size of 0.69λ, as illustrated in Fig. 1(e). This performance significantly surpasses the 1.7λ spot size of a standard 10 MHz focusing acoustic transducer. Currently, we are working on fabricating this design, which has a wall thickness of 4 microns, using a two-photon polymerization (2PP) Nanoscribe 3D printer that offers a printing resolution of 100 nanometers. We are addressing several challenges related to the HR metasurface lens design, including the collapse of overhangs and scaling the design to full size. To date, a small sample containing 13 out of 125 units has been printed in 3D using 2PP, as shown in Fig. 1(f), which is under evaluation. Concurrently, we are exploring an air-coupled HR metasurface lens for concept validation at 30 kHz, which features a wall thickness of 300 microns, utilizing digital light processing (DLP) 3D printing with a precision of 27 microns, as the lens design is scalable (Fig. 1(g)). This research has significant implications for non-destructive evaluation, which is crucial for numerous applications, particularly in critical environments where early detection of small-scale defects facilitated by the metasurface lens can prevent catastrophic failure.

References

1. Y. Xie, W. Wang, H. Chen, A. Konneker, B. Popa and S. A. Cummer, *Nat. Commun.* **5**, 5553 (2014).
2. Y. Li, X. Jiang, B. Liang, J. Cheng, and L. Zhang, *Phys. Rev. Appl.* **4**, 024003 (2015).
3. J. Hyun, Kim, Y.T., Doh, I. et al. Realization of an ultrathin acoustic lens for subwavelength focusing in the megasonic range. Sci Rep 8, 9131 (2018). https://doi.org/10.1038/s41598-018-27312-5

Electromechanical Excitation of Nanostructures by Bulk Acoustic Wave Transducers

T. Makkonen[1], O. Ylivaara[1], S. Pourjamal[1], and J. Ahopelto[1*]

[1] VTT Technical Research Centre of Finland Ltd, Finland
[*]corresponding author: jouni.ahopelto@vtt.fi

Abstract: An efficient broadband bulk acoustic wave electromechanical transducer at GHz range is demonstrated. The free-standing transducer with a small footprint can be integrated directly into nanostructures to guarantee efficient coupling. The potential applications include optomechanics and topological phononics.

Surface acoustic waves (SAW) generated by an interdigitated transducer (IDT) are usually used to excite nanoscale mechanical structures [1-3]. IDTs can provide a narrow bandwidth excitation at desired frequency range, but to achieve high coupling efficiency can be challenging [4]. Furthermore, the surface area required by the IDTs can, in some cases, prevent integration of nanoelectromechanical devices.

Integration of a miniaturized bulk acoustic wave (BAW) transducer directly to the nanodevice provides high efficiency coupling, broad bandwidth and a small footprint. In Figure 1(a), the transducer integrated to a nanobeam is depicted schematically, and the Figure 1(b) shows an SEM image of a test device. The transducer itself is a very small BAW resonator with aluminum nitride (AlN) or aluminum scandium nitride (AlScN) piezo layer sandwiched between the top and bottom electrodes. The transducer is free-standing and isolated from the surroundings by narrow supporting beams. The main loss mechanisms reducing the energy flow only to the nanobeam are the viscous dissipation in the piezoelectric film and the anchor losses to the surroundings.

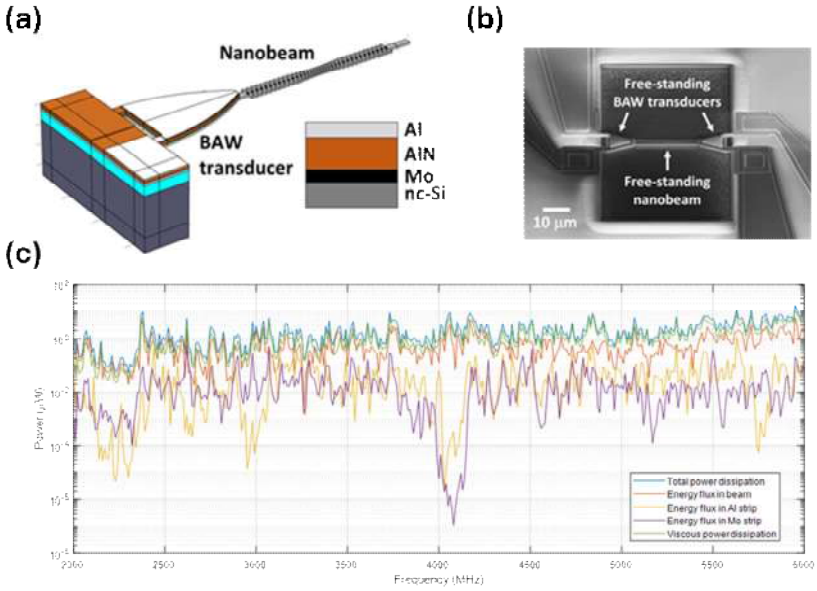


Figure 1. (a) BeamBAW concept shown schematically. A small free-standing BAW transducer is integrated directly to a nanobeam to enhance the coupling efficiency. (b) SEM image of a test structure. (c) Simulation of

the flow of energy in a device with 1D phononic crystal supports as a function of frequency in logarithmic scale. The green line is the total power dissipated, and the red is the flow of energy to the nanobeam. The yellow and purple lines show the leakage to the substrate via the supporting beams. The phononic band gaps of the supporting beams were designed to be at around 4 GHz. The difference between the yellow and purple lines arises from the different designs of the phononic crystals due to the different electrode metals, the bottom being molybdenum and top aluminum.

The leak to the substrate can be minimized by making the supporting beams 1-dimensional phononic crystals with the gap at desired frequency. Figure 1(c) shows the simulated very broad bandwidth of the BeamBAW transducer with a gap at around 4 GHz with 1D phononic crystal supports.

In this presentation, we will describe in more detail the BeamBAW concept and the device properties.

This work has been partially funded by the Research Council of Finland through ERA-NET CHISTERA Program, project MUSICIAN, Grant # 357745, and by the European Commission, project MAGNIFIC, Grant # 101091968.

References

1. Navarro-Urrios D., M. F. Colombano, G. Arregui, G. Madiot, A. Pitanti, A. Griol, T. Makkonen, J. Ahopelto, C. M. Sotomayor-Torres, and A. Martínez, “Room-Temperature Silicon Platform for GHz-Frequency Nanoelectro-Opto-Mechanical Systems,” ACS Photonics, Vol. 9, 413−419, 2022.
2. Mirhosseini M., A. Sipahigil, M. Kalaee, and O. Painter, ”Superconducting qubit to optical photon transduction,” Nature, Vol.588, 599-603, 2020.
3. Pitanti, A., T. Makkonen, M. Colombano, S. Zanotto, L. Vicarelli, M. Cecchini, A. Griol, D. Navarro-Urrios, C. Sotomayor-Torres, A. Martinez, and J. Ahopelto, “High-Frequency Mechanical Excitation of a Silicon Nanostring with Piezoelectric Aluminum Nitride Layers,” Phys. Rev. Appl. Vol 14, 014054, 2020.
4. Korovin A. V., Y. Pennec, M. Stocchi, D. Mencarelli, L. Pierantoni, T. Makkonen, J. Ahopelto, and B. Djafari Rouhani, ”Conversion between surface acoustic waves and guided modes of a quasiperiodic structured nanobeam,” J. Phys. D: Appl. Phys., Vol. 52, 32LT01, 2019.

Nanocrystalline Silicon for Optomechanical Metamaterials

G. Conte[1*], O. R. Ranjbar Naeini[1], C. Alves[1], O. Schraidt[1], O. Ylivaara[2], S. Pourjamal[2], J. Ahopelto[2], and C. M. Sotomayor Torres[1]

[1]INL – International Iberian Nanotechnology Laboratory, Portugal
[2]VTT – Technical Research Centre of Finland Ltd, Finland
[*]corresponding author: gloria.conte@inl.int

Abstract: Nanocrystalline silicon is a promising material for nano-opto-electro-mechanical metamaterials to be integrated into information and communication technology. The fabrication of nanocrystalline silicon has an impact on properties associated to grain sizes and grain boundaries, which influence the mechanical quality factor of one-dimensional nanoresonators.

Nanocrystalline silicon (nc-Si) is a novel material consisting of randomly oriented Si grains, so that it has an isotropic behavior. Developed for MEMS applications in the 1980's [1], it has been recently considered as a possible material for optomechanical devices and circuits.

Nc-Si is produced by low pressure chemical vapour deposition (LPCVD) and consequent annealing of 220 nm of amorphous silicon on a 500-nm-thick silicon dioxide layer, which in turn is on a crystalline silicon (c-Si) substrate. The annealing temperature ranges from 650°C to 1050°C. During the annealing, nucleation and growth of nanocrystallites take place, until obtaining a material as the one reported in Figure 1(a). The thermal annealing process determines the electronic, optical and mechanical properties of nc-Si, which can be tuned by varying the annealing parameters [2]. In particular, the annealing temperature affects the grain size distribution and the grain boundaries [2], which impact the thermal transport [3] and, consequently, the performance of the devices [4]. The structural information is one example of characterisation needed to unravel the high mechanical quality factors of optomechanical nc-Si metamaterial devices compared to similar devices fabricated in silicon-on-insulator (SOI) [5]. The size of the nanocrystallites have been investigated by dark-field TEM images acquired at different diffraction areas through the hollow-cone technique [6], so that nanocrystallites with different orientations could be revealed. The resulting average grain size is larger for higher annealing temperatures (57.5 nm and 53.4 nm for 950°C and 1050°C, respectively) rather than the lowest annealing temperature (33.5 nm for 650°C). The different average grain size determines a different volume of grain boundaries, which is crucial to understand electron and phonon transport in the material. The grain boundaries play a key role because they are expected to host a relatively high number of electronic gap states, which affect the optical absorption, in particular the efficiency of one- versus two-photon absorption. In some cases, the grain boundaries appear amorphous. In other cases, the grain boundaries exhibit 3-5 atomic planes.

The devices under investigation consist of suspended nanobeams, which act as both photonic and phononic one-dimensional metamaterials working at hypersonic frequencies. In such devices photons and phonons are confined in a small region, leading to the optomechanical interaction. The performance of these devices is determined not only by the material properties, but also by the device design. Two examples of nc-Si nanobeams are shown in Figures 1(b) and 1(c).

Structural and future optical analysis of nc-Si will shed light on the interplay among electrons, photons and phonons in the material, specifically regarding the role of nanocrystallites and grain boundaries in absorption and dissipation mechanisms at the nanoscale. This knowledge, combined with the structural analysis, will be crucial

for a much improved understanding of the device performance, particularly about losses, variability and device integration technology.

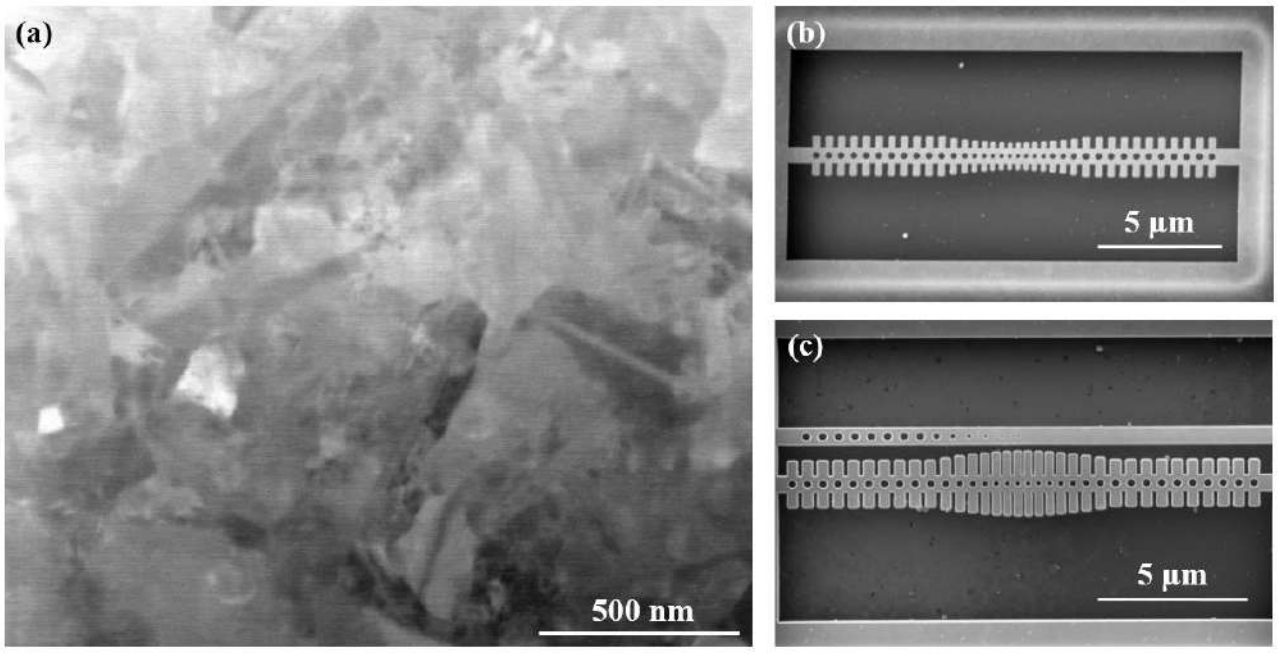


Figure 1 (a) TEM image of nc-Si annealed at 950°C. (b) SEM image of a nc-Si nanobeam operating at a mechanical frequency of 4 GHz. (c) SEM image of a nc-Si nanobeam operating at a mechanical frequency of 2 GHz and coupled to a waveguide.

The authors acknowledge funding from the project MAGNIFIC (HORIZON-CL4-2022-RESILIENCE-01, Grant Agreement No. 101091968) and thank the Electron Microscopy and X-Rays (EMX) facility at INL.

References

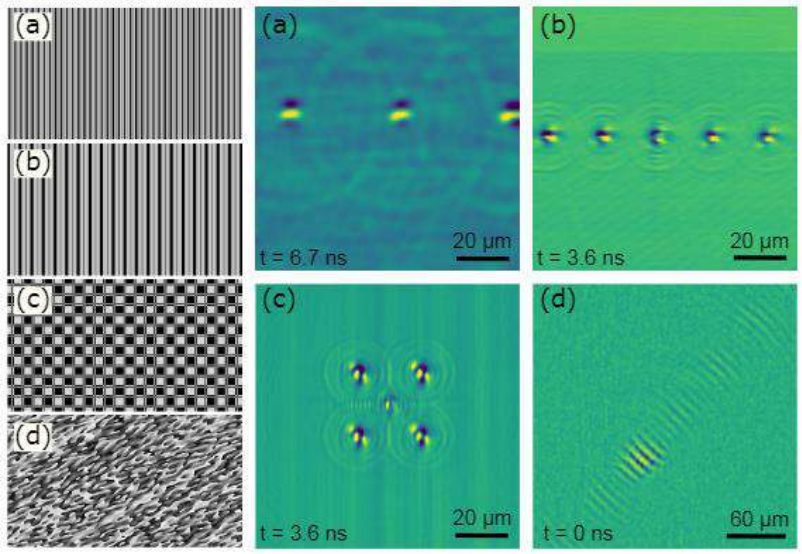
1. G. Harbeke, L. Krausbauer, E. F. Steigmaier, A. E. Widmer, H. F. Kappert and G. Neugebauer, "Growth and physical properties of LPCVD polycrystalline silicon films," J. Electrochem. Soc., Vol. 131, 675-682, 1984.
2. D. Navarro-Urrios, M. F. Colombano, J. Maire, E. Chávez-Ángel, G. Arregui, N. E. Capuj, A. Devos, A. Griol, L. Belleries, A. Martínez, K. Grigoras, T. Häkkinen, J. Saarilahti, T. Makkonen, C. M. Sotomayor Torres and J. Ahopelto, "Properties of nanocrystalline silicon probed by optomechanics" Nanophotonics, Vol. 9, No. 16, 4819-4829, 2020.
3. E. Isotta, S. Jiang, R. Bueno-Villoro, R. Nagahiro, K. Maeda, D. A. Mattlat, A. R. Odufisan, A. Zevalkink, J. Shiomi, S. Zhang, C. Scheu, G. J. Snyder and O. Balogun, "Heat transport at silicon grain boundaries", Adv. Funct. Mater., Vol. 34, No. 2405413, 1-12, 2024.
4. J. Maire, E. Chávez-Ángel, G. Arregui, M. F. Colombano, N. E. Capuj, A. Griol, A. Martínez, D. Navarro-Urrios, J. Ahopelto and C. M. Sotomayor Torres, "Thermal properties of nanocrystalline silicon nanobeams", Adv. Funct. Mater., Vol. 32, No. 2105767, 1-9, 2022.
5. D. Navarro-Urrios, N. E. Capuj, J. Maire, M. Colombano, J. Jaramillo-Fernandez, E. Chávez-Ángel, L. L. Martin, L. Mercadé, A. Griol, A. Martínez, C. M. Sotomayor Torres and J. Ahopelto, "Nanocrystalline silicon optomechanical cavities", Opt. Express, Vol. 26, No. 8, 9829-9839, 2018.
6. B. Yao, T. Sun, A. Warren, H. Heinrich, K. Barmak and K. R. Coffey, "High contrast hollow-cone dark field transmission electron microscopy for nanocrystalline grain size quantification", Micron, Vol. 41, 177-182, 2010.

Tailoring GHz Surface Acoustic Waves by Spatial Modulation of Ultrashort Light Pulses

O. Boyko *, F. Soldevila, V. Bochkarev, L. Belliard
Sorbonne Université, CNRS, Institut des Nanosciences de Paris, INSP, F-75005 Paris, France
Olga.Boyko@insp.jussieu.fr

Abstract: We demonstrate the spatial and spectral manipulation of GHz surface acoustic waves (SAWs) using an ultrafast laser setup integrated with a Spatial Light Modulator. Arbitrary acoustic wavefronts and point-source distributions are dynamically created on flat substrates, providing versatile, non-invasive control critical for acoustic signal processing and phononic circuits.

Miniaturization in electro-acoustic technologies and high-speed communications necessitate advanced control of elastic waves at GHz frequencies [1]. Current phononic systems rely predominantly on fabricated nanostructures that limit flexibility due to fixed geometry, posing significant experimental challenges [2,3].



Here, we present a flexible, optical method for generating GHz-range SAWs by integrating a Spatial Light Modulator (SLM) into a picosecond ultrasonics setup. By modulating the spatial phase profile of ultrashort (140 fs) laser pulses at 800 nm, we non-invasively excite complex acoustic wavefronts on flat surfaces without custom-fabricated nanostructures. The SLM-generated patterns control both spatial distribution and spectral characteristics of the acoustic waves, enabling on-demand reconfigurability.

Figure 1. Generation of multiple source distributions with an SLM. Four different configurations are shown, each consisting of a phase mask codified on the SLM (left, grayscale images) and a snapshot of the surface displacement at different times after the arrival of the pump beam (right, false-color images):

(a) Three point-like sources;
(b) Five point-like sources;
(c) Four point-like sources, arranged in a square array;
(d) Excitation with a linear grating with a well-defined period and oriented at 45°.
Field of view (FoV): (a), (b), and (c) – 100×100 µm²; (d) – 290×290 µm².

Through this approach, we generate precise point-source acoustic arrays and directional wavefronts (Fig. 1), demonstrating significant improvements in acoustic wave engineering capabilities. We further exploit controlled

wavevectors from spatial gratings to measure dispersion relations, validating the method's applicability for material characterization and phononic device optimization. This programmable acoustic source distribution significantly enhances phononic system versatility, paving the way for new developments in high-frequency acoustic signal processing, phonon spectrometry, and non-destructive testing techniques [4,5].

References

1. Zhu, Topological Phononic Metamaterials, J. Phys., 2023.
2. Zhang et al., Gigahertz Topological Valley, Nat. Phys., 2022.
3. Yan et al., Launching Directional Hypersonic Waves, Phys. Rev., 2023.
4. Matsukawa et al., Ultrasonics: Physics and Applications, Wiley, 2022.
5. Rogers et al., Optical Generation and Characterization of SAWs, J. Appl. Phys., 2000.

Temperonic metamaterials: shaping wave-like temperature oscillations on the ultrafast time scale

G. Benetti[1], M. Gandolfi[2,3], R. Rurali[4], C. Giannetti[5], F. Banfi[6,*]

[1]Dipartimento di Fisica Medica, San Bortolo Hospital, viale Rodolfi 37, Vicenza, Italy
[2]Istituto Nazionale di Ottica - Consiglio Nazionale delle Ricerche (INO-CNR), Via Branze 45, Brescia, 25123, Italy
[3]Dipartimento di Ingegneria dell'Informazione, Università degli Studi di Brescia, Via Branze 38, Brescia, 25123, Italy
[4]Institut de Ciència de Materials de Barcelona, ICMAB-CSIC, Campus UAB, 08193 Bellaterra, Spain
[5]Interdisciplinary Laboratories for Advanced Materials Physics (I-LAMP) and Dipartimento di Matematica e Fisica, Università Cattolica del Sacro Cuore, Via Garzetta 48, Brescia, 25133, Italy
[6]Université Claude Bernard Lyon1, CNRS, Institut Lumière Matière, F-69622 Villeurbanne, France
[*]corresponding author: francesco.banfi@univ-lyon1.fr

Abstract: At small spatial and temporal scales, in specific materials addressed as temperonic, temperature propagates in a wave-like fashion. The talk covers a finite size temperonic crystal, a superlattice composed of alternating temperonic materials, hallowing coherent control of temperature waves, similarly to the case of phononic crystal for the displacement field.

At small spatial and temporal scales, and in specific types of materials, addressed as temperonic materials, heat transfer can transition into a hydrodynamic regime [1-4]. Within this regime, the temperature scalar field exhibits wave-like behavior, propagating in a coherent manner that resembles the characteristics of acoustic and electromagnetic waves, rather than dispersing through diffusion.

We will first review advances in temperonic materials, which have been marked by important developments in phononic and electronic systems, paving the way for new research opportunities and applications. Specifically, graphene has been shown to exhibit the ability to support phononic temperature waves under cryogenic conditions and ultrafast timescales [5]. Furthermore, layered materials with strong electronic correlations have been found to accommodate a diverse range of electronic heat transport regimes, including ballistic, hydrodynamic, and diffusive regimes, offering a high degree of flexibility and control [6].

We will then cover the concept of a temperonic crystal, a specially designed superlattice composed of alternating temperonic materials, which enables the manipulation of temperature waves on extremely short timescales [7]. This concept is analogous to phononic crystals in solid mechanics and photonic crystals in electromagnetism, and offers a new paradigm for temperature wave control.

The validity of the temperonic crystal concept will be verified through numerical simulations, focusing on a finite structure composed of graphene slabs at varying temperatures, as opposed to an idealized infinite system. The simulations will track the spatio-temporal evolution of a temperature pulse interacting with the temperonic crystal, considering different constitutive equations, including the Fourier law (FL), Cattaneo-Vernotte (CV) equation, and Dual-Phase Lag (DPL) model. These equations yield distinct mathematical formulations, ranging from the traditional diffusive equation to hyperbolic and parabolic equations, which solutions can exhibit wave-like behavior under certain conditions. To characterize the temperature pulse's interaction with the temperonic crystal, concepts analogous to transmission and reflection coefficients will be introduced. The impact of the number of slabs and the presence of disorder on the crystal's behavior will also be examined, providing insight into the finite temperonic crystal's performance.

The present talk widens the concepts of acoustic and electromagnetic wave propagation in metamerials to the realm of thermal transport in solid state systems, paving the way to new paradigms in heat transport. [8-10].

References

1. Huberman, S., R. A. Duncan, K. Chen, B. Song, V. Chiloyan, Z. Ding, A. A. Maznev, G. Chen, and K. A. Nelson, "Observation of second sound in graphite at temperatures above 100K," Science, Vol. 364, 375, 2019.
2. Zhang, Y., X. Shi, Wenjing You, Z. Tao, Y. Zhong, F. Cheenicode Kabeer, P. Maldonado, P. M. Oppeneer, M. Bauer, K. Rossnagel, H. Kapteyn, and M. Murnane, "Coherent modulation of the electron temperature and electron-phonon couplings in a 2D material," PNAS, Vol. 117, 16, 8788–8793, 2020.
3. Gandolfi, M., G. L. Celardo, F. Borgonovi, G. Ferrini, A. Avella, F. Banfi, and C. Giannetti, "Emergent ultrafast phenomena in correlated oxides and heterostructures," Phys. Scr., Vol. 92, 034004, 2017.
4. Beardo A., López-Suárez M., Pérez L. A., Sendra L., Alonso M. I., Melis C., Bafaluy J., Camacho J., Colombo L., Rurali R., Alvarez F. X., Reparaz J. S., "Observation of second sound in a rapidly varying temperature field in Ge", Science advances, Vol. 7, 7, 2021.
5. Gandolfi, M., G. Benetti, C. Glorieux, C. Giannetti, and F. Banfi, "Accessing temperature waves: A dispersion relation perspective," Int. J. Heat Mass Transfer, Vol. 143, 118553, 2019.
6. Mazza, G., M. Gandolfi, M. Capone, F. Banfi, and C. Giannetti, "Thermal dynamics and electronic temperature waves in layered correlated materials," Nat. Com., Vol. 12, 6904, 2021.
7. Gandolfi, M., C. Giannetti, and F. Banfi, "Temperonic crystal: A superlattice for temperature waves in graphene," Phys. Rev. Lett., Vol. 125, 265901, 2020.
8. Sobolev, S. L. and W. Dai, "Heat transport on ultrashort time and space scales in nanosized systems: Diffusive or wave-like?," Materials, Vol. 15, 4287, 2022.
9. Li, Z.Y., Mellmann, M., Wang, Y., Ma, T.X., Yan, D., Golub, M.V., Hosseini, S.M., Liu, D., Wei, P. and Zhang, C., 2024. Non-Fourier heat conduction in 2D thermal metamaterials. Materials Today Communications, Vol. 38, 107828, 2024.
10. Kovács R., "Heat equations beyond Fourier: From heat waves to thermal metamaterials", Physics Reports, Vol. 1048, 1, 2024.

Interaction of sloshing water waves with a vertically oscillating plate

M. Koukouraki[1*], P. Petitjeans[1], A. Maurel[2] and V. Pagneux[3]
[1]Laboratoire de Physique et Mécanique des Milieux Hétérogènes, ESPCI-Paris, France
[2]Institut Langevin, ESPCI-Paris, France
[3]Laboratoire d'Acoustique de l'Université du Mans, Le Mans Université, France
Corresponding author: magdalini.koukouraki@espci.fr

Abstract: We theoretically investigate the interaction of a surface sloshing wave with a vertically oscillating plate inside a water tank, reporting on the stability of the surface elevation with respect to the plate oscillation amplitude and frequency. Using conformal mapping and then a Floquet stability analysis, we identify parametric amplification windows.

Periodically time-varying media can lead to wave phenomena such as parametric or transient amplification [1]- [2], with Mathieu equation governing the dynamics in various periodically forced systems. This work explores wave amplification for water waves by using an infinitely thin plate that is vertically oscillating at the fluid bottom. First, the 2D problem in the linearised water wave theory framework is schematically represented in Figure 1a, where $\Phi(x,z,t)$ denotes the velocity potential and $\mu(t)$ the dimensionless plate height. Because of the complexity of the moving bottom boundary condition, it is convenient to map the problem into a new domain where the plate is absent (see Figure 1b). For a family of bathymetric profiles, including vertical plates, there exists a conformal transformation in explicit form which maps the initial domain in the (x,z,t) plane into a rectangular domain of constant depth in the (ξ,χ,τ) plane with $t=\tau$. We denote the transformation as $w=F(\zeta,t)$ with $w=x+iz$ and $\zeta=\xi+i\chi$ and its illustration at $\chi=0$ is shown in Figure 1c. Thus, the modified set of equations in the transformed domain is written as

$$\partial_\xi^2\Phi+\partial_\chi^2\Phi=0, \quad \Omega(\tau), \tag{1a}$$

$$\partial_\chi\Phi=0, \quad \chi=-1, \tag{1b}$$

$$\partial_\chi\Phi=-r(\xi,\tau)\mathcal{L}_{(\tau,\xi)}\Phi, \quad \chi=0, \tag{1c}$$

$$\partial_\xi\Phi=0, \quad \xi=\pm L(\tau), \tag{1d}$$

where $\mathcal{L}_{(\xi,\tau)}=\partial_\tau^2+\left(\frac{\partial\xi}{\partial t}\right)^2\partial_\xi^2+2\left(\frac{\partial\xi}{\partial t}\right)\partial_{\tau\xi}+\frac{\partial^2\xi}{\partial t^2}\partial_\xi$ and $r(\xi,\tau)=\left.\frac{dF(\zeta,\tau)}{d\zeta}\right|_{\chi=0}$. The oscillation of the wall position $x=\pm L(\tau)$ is linked to $\mu(t)$ which in turn translates into the blockage coefficient time variation $B_\mu(t)$ from the expression $\mu=1-\frac{2}{\pi}\arcsin\left[\exp\left(-\frac{\pi}{2}B_\mu\right)\right]$. In this study we set $B_\mu(t)=B_{\mu,0}+B_{\mu,1}\cos(\Omega_p t)$ with Ω_p the dimensionless frequency of oscillation.

In order to solve system (1), we consider a solution in the form of a Fourier series: $\Phi(\xi,\chi,\tau)=\sum_n\alpha_n(\tau)\cosh\left(\frac{n\pi(\chi+1)}{2L(\tau)}\right)\gamma_n(\xi,\tau)$, $\gamma_n(\xi,\tau)=\sqrt{\frac{2-\delta_{0n}}{2L(\tau)}}\cos\left(\frac{n\pi(\xi+L(\tau))}{2L(\tau)}\right)$, with $n\in\mathrm{N}$. This solution satisfies directly Equations (1a), (1b) and (1d) and its substitution on the surface condition (1c) yields after projecting on the γ_n an ordinary differential equation for the coefficients α_n:

$$\ddot{a}_m+2A_{mn}(\tau)\dot{a}_n+B_{mn}(\tau)a_n=0, \tag{2}$$

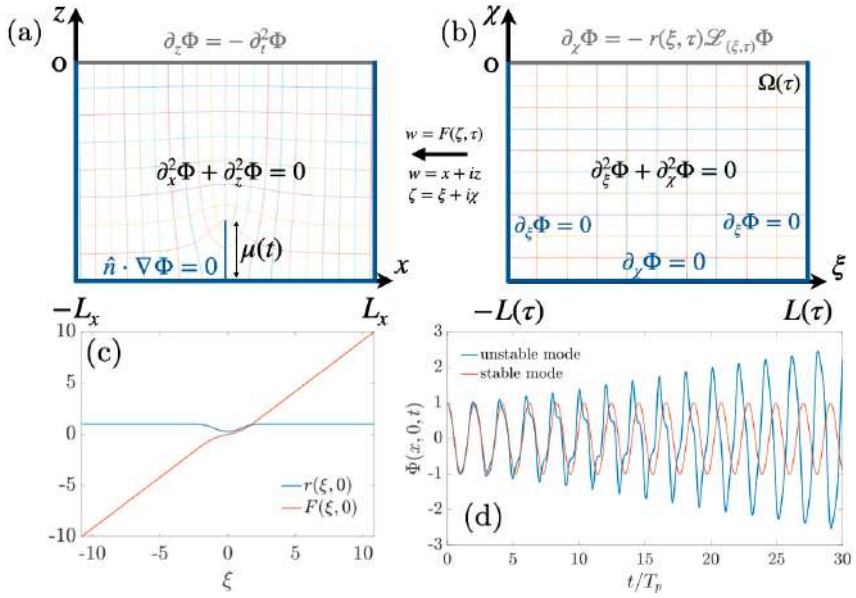


Figure 1: The time-varying sloshing problem in (a) and its transformation in the (ξ, χ, τ) plane in (b). (c) Variation of $F(\xi, 0)$ and $r(\xi, 0)$ with ξ at $\chi = 0$ when $\mu = 0.82$. (d) Evolution of the surface elevation at the wall position $x = L_x$ for parameters $(\epsilon, \Omega) = (0.1, 2.08)$ (stable case) and $(0.6, 2.08)$ (unstable case).

where $A_{mn}(\tau)$ and $B_{mn}(\tau)$ are time-dependent coefficients. In order to characterise the stability of Equation (2), and as an extension the stability of the full system, we need to follow a Floquet stability analysis [3]. We proceed by rewriting Equation (2) in the form

$$\frac{dX}{d\tau} = \mathrm{C}(\tau)X, \text{ with } \mathrm{C}(\tau) = \begin{pmatrix} \mathrm{O} & \mathrm{I} \\ -\mathrm{B}(\tau) & -2\mathrm{A}(\tau) \end{pmatrix}, \; X = \begin{pmatrix} \mathbf{a} \\ \dot{\mathbf{a}} \end{pmatrix}. \tag{3}$$

Here the matrices A and B have elements $(\mathrm{A})_{mn} = A_{mn}$, $(\mathrm{B})_{mn} = B_{mn}$, I is the identity matrix and $\mathbf{a}, \dot{\mathbf{a}}$ vectors containing $a_n, \dot{a}_n$. Then, by applying Floquet theorem, an independent solution of the system (3) is written as $X_j(t) = e^{\lambda_j t}U_j(t)$, with $U_j(t + T_p) = U_j(t)$ and T_p the period of plate oscillation. Hence, instability occurs if $\Re\{\lambda_j\} > 0$. A more detailed analysis then follows where we study the eigenvalues of the propagator L(t) defined as $X(t) = \mathrm{L(t)}X(0)$ over one period T_p, which are linked to λ_j. This leads to recovering the unstable windows in the (ϵ, Ω) plane, where $\epsilon = B_{\mu,1}/B_{\mu,0}$ and $\Omega = \Omega_p/\Omega_0$, with Ω_0 the dimensionless frequency of the first antisymmetric sloshing mode. Figure 1d shows the evolution of the first antisymmetric mode in time at the wall boundary $x = L_x$ for a plate oscillation that corresponds to either a stable or an unstable case. Finally, in the perspectives part of this work, experiments are in progress with the aim to experimentally observe the parametric amplification and characterise it.

References

1. Galiffi, E. et al., "Photonics of time-varying media", *Adv. Photonics*, Vol. 4, pp. 014002, 2022.

2. Kiorpelidis, I. et al., "Transient amplification in stable Floquet media", *Phys. Rev. B*, Vol. 110, pp. 134315, 2024.

3. Yakubovich, V. and V. Starzhinskii, Linear Differential Equations with Periodic Coefficients, John Wiley Sons, New York, 1975.

Perfect absorption of flexural waves in vibration transmission problems via coupled monopolar-dipolar resonant scatterers

D. Giannini[1*], J.-P. Groby[2]

[1]Department of Civil Engineering, KU Leuven, Leuven, Belgium

[2]Laboratoire d'Acoustique de l'Université du Mans (LAUM), UMR 6613, Institut d'Acoustique - Graduate School (IA-GS), CNRS, Le Mans Université, France

Corresponding author: daniele.giannini@kuleuven.be

Abstract: We propose a strategy to achieve perfect absorption of flexural waves in transmission problems using coupled monopolar-dipolar resonant scatterers. By enforcing vanishing transmission and reflection, we analytically derive the required scatterer impedance. A perfect absorber design, based on two cantilever beam-mass structures, is proposed and validated through full-wave simulations.

Recent studies have explored low-frequency perfect absorption of acoustic and elastic waves using subwavelength locally resonant metamaterials and scatterers. Achieving perfect absorption requires fulfilling the critical coupling condition, ensuring that the energy leakage of the system is precisely balanced by its intrinsic losses.

Perfect absorption furthermore corresponds to a condition where the eigenvalues of the scattering matrix become zero. In reflection problems (one-port systems), the scattering matrix reduces to the reflection coefficient, and critical coupling can be obtained by tuning the losses of the scatterer at resonance. In transmission problems (two-port systems with one-sided excitation), the scattering matrix has two distinct eigenvalues. Achieving perfect absorption becomes more challenging, since both eigenvalues must vanish at the same exact frequency. To achieve this, a symmetric (monopolar) and an antisymmetric (dipolar) resonance must be activated at the same frequency (degenerate resonances). Furthermore, the symmetry of the scatterer plays a crucial role. For mirror-symmetric scatterers, perfect absorption occurs on both sides of the system, whereas for non-mirror-symmetric scatterers, absorption varies on each side, enabling unidirectional perfect absorption by fulfilling critical coupling only on one side.

The study of critical coupling conditions has been exploited to design various classes of perfect absorbers for acoustic waves in both reflection and transmission problems [1, 2]. This concept is also highly relevant for vibrations, due to the growing industrial demand for low-frequency damping materials. Traditional solutions, such as viscoelastic coatings and tuned vibration absorbers, primarily suppress flexural wave transmission but not reflection in two-port problems. Recent works have explored using open lossy resonators to maximize flexural wave absorption by simultaneously reducing both transmission and reflection, identifying the achievable performance limits [3]. It has been demonstrated that conventional transverse resonant scatterers can achieve perfect absorption only in reflection problems, whereas in transmission problems, maximum absorption is inherently limited to 0.5, as monopolar resonances can critically couple only one of the two eigenvalues of the scattering matrix.

In this work, we address these limitations by introducing scatterers that support both monopolar transverse and dipolar rotational resonances, enabling perfect absorption of flexural waves through the critical coupling of both scattering modes. The scattering behavour is analyzed through an analytical model that accounts for both propagating and evanescent waves in the host medium, as well as for transverse and rotational scatterer impedances. Notably,

mirror asymmetries in the scatterer are captured by cross-coupling terms appearing between the transverse and the rotational impedances. Leveraging this model, we analytically derive the required scatterer impedances for symmetric and asymmetric perfect absorption, by imposing vanishing transmission and (unidirectional) reflection.

Using these theoretical insights, we propose the design of an asymmetric perfect absorber. The scatterer consists of a horizontal cantilever beam-mass structure exhibiting a coupled monopolar-dipolar resonance and a vertical cantilever beam-mass structure exhibiting a pure dipolar resonance. The impedances of the scatterer are expressed as a function of its modal effective masses, which are determined through a fixed-base modal analysis. The geometrical parameters of the scatterer are optimized to match the required impedances and achieve one-sided perfect absorption. Finally, the peformance of the proposed design is validated through full-wave numerical simulations, showing agreement with analytical predictions.

The results of this work demonstrate the feasibility of designing perfect absorbers for flexural wave in vibration transmission problems, representing a significant advancement in wave absorption mechanisms.

Acknowledgements. Daniele Giannini gratefully acknowledges the financial support of the Research Foundation - Flanders (FWO), Belgium, through the postdoctoral fellowship 12A3Q24N and the travel grant V409625N to visit LAUM.

References

1. A. Merkel, G. Theocharis, O. Richoux, V. Romero-García, V. Pagneux, "Control of acoustic absorption in one-dimensional scattering by resonant scatterers", *Appl. Phys. Lett.*, Vo. 107, No. 24, 244102, 2015.

2. V. Romero-García, N. Jiménez, J.-P. Groby, A. Merkel, V. Tournat, G. Theocharis, O. Richoux, V. Pagneux, "Perfect Absorption in Mirror-Symmetric Acoustic Metascreens", *Phys. Rev. Appl.*, Vo. 14, No. 5, 054055, 2020.

3. J. Leng, F. Gautier, A. Pelat, R. Picó, J.-P. Groby, V. Romero-García, "Limits of flexural wave absorption by open lossy resonators: reflection and transmission problems", *New J. Phys.*, Vo. 21, No. 5, 053003, 2019.

Ultrafast Phononic Manipulation of Magnetization

C. S. Davies
HFML-FELIX, Radboud University, Nijmegen, The Netherlands
*corresponding author: carl.davies@ru.nl

Abstract: Upon driving doubly-degenerate optical phonons at resonance within a paramagnetic substrate, we demonstrate that magnetization can be created on an ultrafast timescale. Further, this transient magnetization can remotely switch magnetic ordering in an overlayer. This application of the ultrafast Barnett effect offers a potentially universal method for controlling magnetization.

Over the last few decades, breakthrough experiments have demonstrated that ultrashort laser pulses have the capacity to both temporarily manipulate and permanently switch magnetic ordering [1]. A variety of different mechanisms can facilitate all-optical switching of magnetization, relying for example on ultrafast exchange-driven demagnetization [2] or the excitation of electronic transitions at resonance in dielectric iron-garnet films [3].

Spin-lattice coupling plays a central role in the research fields of magnetism and spintronics. Very recently, it has been demonstrated that ultrafast demagnetization involves the transfer of angular momentum from the spins to the lattice [4]. Reciprocally, it is also feasible for vibrations of the lattice (phonons) to modulate magnetic interactions such as exchange [5]. Going further, it is even possible for one to drive at resonance circularly-polarized optical phonons – the angular momentum of the latter can give rise to emergent magnetization [6] and large effective magnetic fields [7].

Here, I will discuss our experimental measurements studying how we can create and manipulate magnetization by selectively driving optical phonons at resonance. To achieve this, we use ultra-narrowband optical pulses in the infrared spectral range as delivered by the free-electron lasers at the FELIX facility. Upon, for example, irradiating paramagnetic rare-earth trihalide substrates, we find (using a two-color pump-probe scheme) that a magnetization emerges on an ultrafast timescale, consistent with recent measurements published in Ref. [7]. The spectral dependence of the transient magnetic moment scales reasonably well with the population of doubly-degenerate optical phonons. Further, upon pumping magnetic heterostructures mounted atop paramagnetic substrates with circularly-polarized infrared pulses, we find that the magnetic ordering can be switched only when the pulse drives at resonance doubly-degenerate optical phonons within the substrate [8]. The direction of switching can be controlled by adjusting the helicity of the incident pulses. So far, we have identified this mechanism in structures grown on glass-ceramic, c-cut sapphire and zinc oxide substrates.

We thank all technical staff at FELIX for technical support. We gratefully acknowledge the Nederlandse Organisatie voor Wetenschappelijk Onderzoek (NWO-I) for their financial contribution, including the support of the FELIX Laboratory. C.S.D. acknowledges support from the European Research Council ERC Grant Agreement No. 101115234 (HandShake).

References

1. Kirilyuk, A. V. Kimel and Th. Rasing, “Ultrafast optical manipulation of magnetic order.” Rev. Mod. Phys., Vol. 82, 2731 (2010).
2. C. S. Davies et al, “Helicity-independent all-optical switching of magnetization in ferrimagnetic alloys.” J. Magn. Magn.

Mater., Vol. 563, 169851 (2022).
3. A. Stupakiewicz, K. Szerenos, D. Afanasiev, A. Kirilyuk and A. V. Kimel, “Ultrafast nonthermal photo-magnetic recording in a transparent medium.” Nature, Vol. 542, 71 (2017).
4. S. R. Tauchert et al, “Polarized phonons carry angular momentum in ultrafast demagnetization.” Nature, Vol. 602, 73 (2022).
5. D. Afanasiev et al, “Ultrafast control of magnetic interactions via light-driven phonons.” Nature Materials, Vol. 20, 607 (2021).
6. M. Basini et al, “Terahertz electric-field-driven dynamical multiferroicity in $SrTiO_3$.” Nature, Vol. 628, 534 (2024).
7. J. Luo et al, “Large effective magnetic fields from chiral phonons in rare-earth halides.” Science, Vol. 382, 698 (2023).
8. C. S. Davies et al, “Phononic switching of magnetization by the ultrafast Barnett effect.” Nature, Vol. 628, 540 (2024).

Controlling the propagation of 20 GHz coherent acoustic phonons in an optophononic waveguide

E. R. Cardozo de Oliveira[1*], C. Xiang[1], S. Sandeep[1], K. Papatryfonos[1], M. Morassi[1], L. Le Gratiet[1], A. Harouri[1], I. Sagnes[1], A. Lemaitre[1], O. Ortiz[1], M. Esmann[1,2] and N. D. Lanzillotti-Kimura[1]

[1]Université Paris-Saclay, CNRS, Centre de Nanosciences et de Nanotechnologies, 10 Boulevard Thomas Gobert, 91120 Palaiseau, France
[2]Carl von Ossietzky Universität Oldenburg, 26129 Oldenburg, Germany
[*]corresponding author: edson.cardozo@universite-paris-saclay.fr

Abstract: We studied the propagation of ultrahigh frequency coherent acoustic phonons in a ridge waveguide based on multilayered GaAs/AlAs optophononic Fabry-Perot resonator. Additionally, by optically generating two distant phonon sources, we demonstrated the interference of the propagating coherent phonons in such system.

Acoustic phonons at ultrahigh frequencies can be employed as information carriers in the solid state, being an asset for signal processing and quantum technologies. [1-3] During the past decade, confinement of ultrahigh-frequency acoustic phonons in planar structures and micropillars has been achieved. [4, 5] However, coherent manipulation of propagation and dynamics of ultrahigh frequency phonons remains challenging. This study focuses in characterizing the propagation of coherent acoustic phonons in a phononic waveguide system based on multilayered GaAs/AlAs microcavity optophononic resonators confining acoustic phonons at ~20 GHz and light at ~840 nm [6-8], as shown in Figure 1(a).

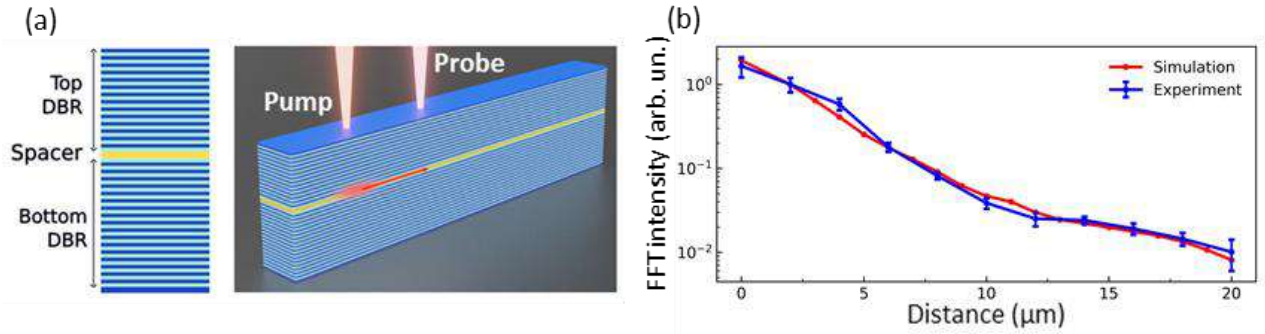


Figure 1. (a) Schematic of the GaAs/AlAs optophononic Fabry-Pérot resonator. The left panel illustrates the vertical structure designed to confine 20 GHz acoustic phonons and ~840 nm photons. The top and bottom distributed Bragg reflectors (DBRs) create a stop-band around 20 GHz, while the GaAs spacer serves as a cavity for phonon confinement. The right panel presents a schematic of the waveguide, showing the pump and probe optical beams. (b) Intensity of the 20 GHz resonance as a function of the separation distance between the generation and detection.

We used a reflection-type pump-probe technique to generate and detect the coherent acoustic phonons via photoelastic interaction. [9] A strong and short pump pulse generates coherent acoustic phonons via photoinduced stress, which modulate the material refractive index. A delayed probe pulse senses the transient reflectivity changes induced by the acoustic phonons. To evaluate the phonon propagation, we performed the

pump-probe measurements in two configurations: local, when pump and probe beams are overlapped, and remote, by spatially separating both beams. The later configuration allows us to observe the contribution of propagating acoustic phonons at different positions in the waveguide. We demonstrated a quasi-continuous and coherent source of acoustic phonons propagating up to 20 µm from the source, as displayed in Figure 1(b). Additionally, we confirmed the coherence of the propagating acoustic phonons through spatio-temporal interference between two distant sources.

These results constitute a promising avenue for revealing the fundamental properties of phonon dynamics and manipulating phonon propagation in more complex structures. They also correspond to a significant step forward in the development of phononic networks for telecommunications and quantum applications.

The authors acknowledge funding from European Research Council Consolidator Grant No.101045089 (T-Recs) and through a public grant overseen by the ANR as part of the "Investissements d'Avenir" Program (Labex NanoSaclay Grant No. ANR-10-LABX-0035). This work was done within the C2N micro nanotechnologies platforms and partly supported by the RENATECH network and General Council of Essonne. M.E. acknowledges funding by University of Oldenburg through a Carl von Ossietzky Young Researchers' Fellowship.

References

[1] A. H. Safavi-Naeini, D. Van Thourhout, R. Baets, and R. Van Laer, "Controlling phonons and photons at the wavelength scale: integrated photonics meets integrated phononics," *Optica*, vol. 6, no. 2, p. 213, 2019.

[2] Y. Chu, P. Kharel, W. H. Renninger, L. D. Burkhart, L. Frunzio, P. T. Rakich, and R. J. Schoelkopf, "Quantum acoustics with superconducting qubits," *Science*, vol. 358, no. 6360, pp. 199–202, 2017.

[3] Priya, E. R. Cardozo de Oliveira, and N. D. Lanzillotti-Kimura, "Perspectives on high-frequency nanomechanics, nanoacoustics, and nanophononics," *Appl. Phys. Lett.*, vol. 122, no. 14, p. 140501, 2023.

[4] A. Fainstein, N. D. Lanzillotti-Kimura, B. Jusserand, and B. Perrin, "Strong Optical-Mechanical Coupling in a Vertical GaAs/AlAs Microcavity for Subterahertz Phonons and Near-Infrared Light," *Phys.Rev.Lett.*, vol.110, no.3, 037403, 2013.

[5] S. Anguiano, A. E. Bruchhausen, B. Jusserand, I. Favero, F. R. Lamberti, L. Lanco, I. Sagnes, A. Lemaître, N. D. Lanzillotti-Kimura, P. Senellart, and A. Fainstein, "Micropillar Resonators for Optomechanics in the Extremely High 19–95-GHz Frequency Range," *Phys. Rev. Lett.*, vol. 118, no. 26, p. 263901, 2017.

[6] C. Xiang, A. Rodriguez, E. R. Cardozo De Oliveira, L. Le Gratiet, I. Sagnes, M. Morassi, A. Lemaître, and N. D. Lanzillotti-Kimura, "Elliptical micropillars for efficient generation and detection of coherent acoustic phonons," *Phys. Rev. Appl.*, vol. 22, no. 1, p. 014069, 2024.

[7] O. Ortiz, P. Priya, A. Rodriguez, A. Lemaitre, M. Esmann, and N. D. Lanzillotti-Kimura, "Topological optical and phononic interface mode by simultaneous band inversion," *Optica*, vol. 8, no. 5, p. 598, 2021.

[8] C. Xiang, K. Papatryfonos, M. Morassi, L. L. Gratiet, A. Harouri, I. Sagnes, A. Lemaitre, O. Ortiz, M. Esmann, and N. D. Lanzillotti-Kimura, "Interference of ultrahigh frequency acoustic phonons from distant quasi-continuous sources", arXiv:2407.06821 [cond-mat.mes-hall].

[9] C. Thomsen, J. Strait, Z. Vardeny, H. J. Maris, J. Tauc, and J. J. Hauser, "Coherent Phonon Generation and Detection by Picosecond Light Pulses," *Phys. Rev. Lett.*, vol. 53, no. 10, 989–992, 1984.

Wave locking in periodically folded beams: influence of modelling choices on complete band gap prediction

E. Manconi[1*], F. Tatar[1]
[1]University of Parma, Italy
Corresponding author: elisabetta.manconi@unipr.it

Abstract: This work presents a study on the formation of complete band gaps in periodically folded one-dimensional waveguides. The effects of modelling choices on the coupling of contradirectional Bloch waves and the formation of the first band gap are investigated. Numerical examples and a parametric analysis are provided.

Folded waveguides are fundamental elements in numerous structural systems, widely utilised in engineering due to their high strength-to-weight ratio and structural efficiency. The periodic nature of many folded structures, such as origami-based configurations, enables the emergence of unique mechanical and dynamic properties. An interesting phenomenon in periodically folded structures is the formation of complete band gaps. These band gaps significantly affect vibration isolation, acoustic filtering performance, and mechanical energy redirection in engineered structures.

Although many previous studies have investigated wave propagation in conventional thin plates and lattice structures, the effects of fold geometry, plate thickness, and fold modelling on wave behaviour in folded structures have rarely been examined. Traditional modelling approaches frequently treat folds as idealised creases with zeroth-order geometric continuity. However, including finite fold thickness and higher-order continuity at folds can alter the predictions of mechanical response and dynamic behaviour of these structures, as shown, for example, in [1]. The aim of this work is to study periodically folded one-dimensional waveguides, investigating

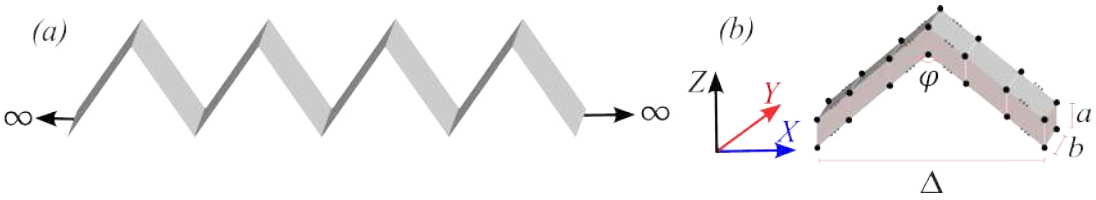


Figure 1: (a) 1D periodic waveguide. (b) model of the unit cell: φ folding angle, Δ periodic length, a and b cross-section dimensions.

the characteristics of wave propagation and explicitly considering the effects of the structure's thickness and modelling of the fold on wave behaviour. The study applies the exact dynamic stiffness method (DSM) with the Floquet-Bloch theorem to predict wave propagation and band gaps in idealised zero-thickness models. Results are compared with those obtained by applying a Wave Finite Element (WFE) method to consider full 1D, 2D and 3D models, [2]. See Figure 1.

As an example, Fig. 2 shows the comparison between the dispersion curves of a folded beam modelled using the exact DSM formulation for an Euler-Bernoulli beam and the WFE method applied to a full 3D FE model of the unit cell using 8-noded brick elements (three degrees of freedom per node: displacements u_x, u_y, u_z in the X, Y, Z directions). Waves propagating

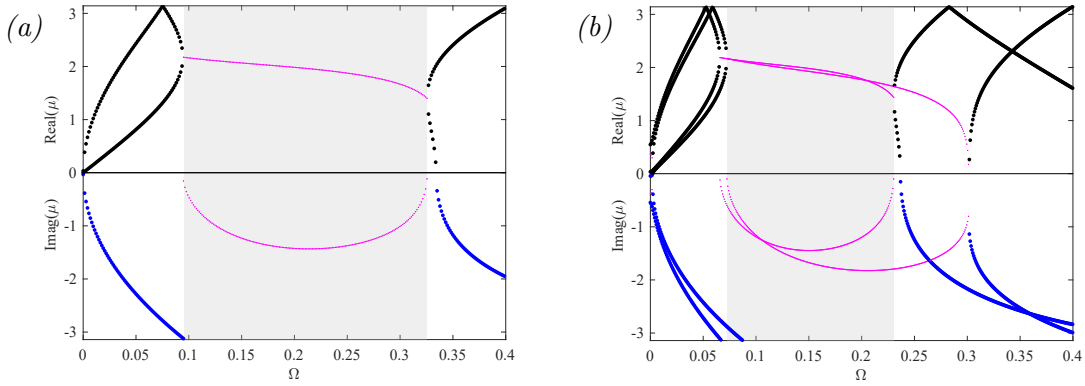


Figure 2: Complex dispersion curves for waves propagating in the positive X direction in two models of the same folded 1D waveguides: (a) exact beam formulation (DSM formulation); (b) 3D FE model using 8-nodes solid elements (WFE method). Black solid lines: pure propagating Bloch waves; blue lines: evanescent waves; magenta lines: complex propagation constants. The grey area shows the first complete band gap.

in the positive direction are assumed. In this figure, the dimensionless frequency $\Omega = \frac{\omega\Delta}{c_L}$ is introduced, where $c_L = \sqrt{\frac{E}{\rho}}$ is the propagation velocity of longitudinal waves in the material, while μ is the propagation constant (real μ representing the propagating waves). The grey area shows the complete stop band formation, where the propagation constants are complex conjugate solutions. In this area, no real branches corresponding to propagating waves are allowed. For finite structures, this implies that all types of vibrations are attenuated in this zone. It can be seen that this first complete band gap starts at the frequency where contradirection coupling (locking) of two propagating Bloch waves occurs, viz. where two pure-real propagation constants intersect, becoming a complex conjugate pair. [3]. The figure also indicates the effect of the modelling choices on wave dispersion and band gap edge frequencies.

Conclusions.

Wave propagation and band gap formation in periodically folded waveguides were studied. Wave coupling due to folding was investigated, and the effects of changes in fold thickness and modelling were analysed. The results showed that incorporating fold thickness and smooth modelling affects both wave propagation and band gap predictions.

Acknowledgements. Research supported by PNRR MISSION 4 COMPONENT 2 INVESTMENT 1.3 – Funded by NEXTGENERATION EU – Research program PE00000004 "Made in Italy Circolare e Sostenibile - MICS" funded by DD n.1551, 11.10.2022 on PNRR MUR – M4C2 – Investment 1.3 –"Partenariati estesi alle università, ai centri di ricerca, alle aziende per il finanziamento di progetti di ricerca di base" - D.D. n. 341, 15 marzo 2022. CUP D43C22003120001

References

1. Peraza-Hernandez, E. A., Hartl, D. J., Lagoudas, D. C. (2017). Design and simulation of origami structures with smooth folds. *Proc Roy Soc A*, Vol. 473.

2. Mace, B., Duhamel, D., Brennan, M. J, Hinke, L. Finite element prediction of wave motion in structural waveguides. *J Acoust Soc Am*, Vol. 117, pp. 2835–2843, 2005.

3. Mace, B. R., Manconi, E., Wave motion and dispersion phenomena: veering, locking and strong coupling effects, *J Acoust Soc Am*, Vol. 229, pp 1015–1028, 2012.

Sensitivity and nonlinear effects in non-Hermitian quasi-periodic lattices

Ananya Ghatak[1] , Dimitrios H. Kaltsas[2], Manas Kulkarni[3],and Konstantinos G. Makris[1,2]

[1]Institute of Electronic Structure and Laser (IESL) – FORTH, Heraklion, 71110, Greece
[2]ITCP-Physics Department, University of Crete, Heraklion, 71003, Greece
[3]International Centre for Theoretical Sciences, TIFR, Bangalore, 560089, India
Corresponding author: gananya@iesl.forth.gr

Abstract: We study the sensitivity of non-Hermitian quasiperiodic lattices in terms of their corresponding pseudospectra. In particular, we investigate $\mathcal{PT}$-symmetry transitions, and the dependence of the spectral sensitivity around the underlying multiple exceptional points. Nonlinear effects that stem from the gain saturation, are also examined.

Localization arises from inherent randomness, making disordered systems difficult, if not impossible, to study them analytically. The Aubry-André-Harper (AAH) model [1–3] provides a framework for analyzing one-dimensional quasicrystals with a metal-insulator transition [2, 3]. We extend this model to a non-Hermitian quasiperiodic AAH lattice with onsite gain and loss (NHAAH) [4–6], revealing $\mathcal{PT}$-symmetry transitions and multiple exceptional points (EPs). Using pseudospectra [7, 8], we investigate the spectral properties and the sensitivity of the corresponding even and odd lattices. More over, we explore the linear diffraction dynamics, that exhibits quantized jumps [9–11] between non-orthogonal eigenstates and examine the impact of the saturable nonlinearity of the optical gain.

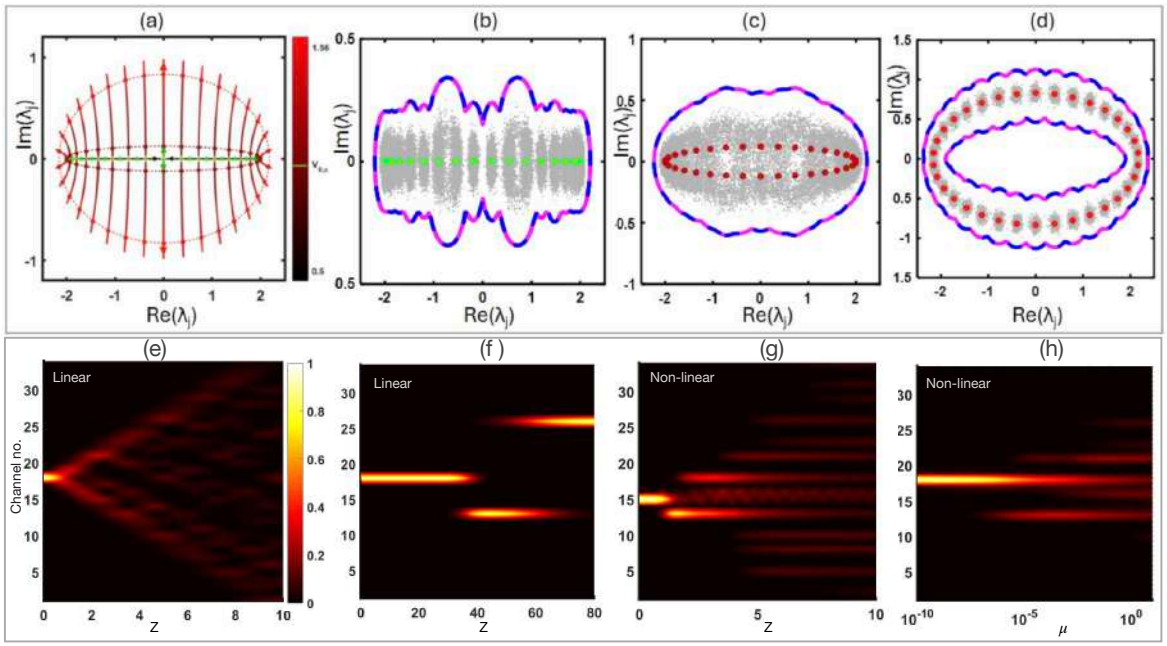


Fig. 1 (a) Spectral flows of the system ($N = 34$) in the complex plane as potential strength V_0

varies for coupling strength $J = 1$ (see colorbar). Green, maroon, and red dots represent spectra before, near, and after the $\mathcal{PT}$-phase transition, with arrows indicating eigenvalue trajectories. (b)-(d) Pseudospectra before, at, and after the $\mathcal{PT}$-phase transition, using three different methods (gray dots, blue, and pink lines). Eigenspectra from (a) are marked in green, maroon, and red. (e), (f) Dynamical evolution under single-channel excitation in the linear case, where (f) highlights three modes involved in sudden jumps. (g) Nonlinearity prevents jumps despite loalized eigenstates, in contrast to the linear case. (h) Increasing nonlinearity induces an insulator-to-metallic transition.

Our results are shown in Fig. 1. In particular, the spectral flows of the associated eigenvalues are presented, along with the corresponding pseudospectra in the complex plane (by using three different methods). The bottom panel shows how the waves diffracts in terms of quantized jumps due to eigenstate localization. The last two figures (g), (h) demonstrate the effect of saturable gain, namely that nonlinearity suppress the jumps. On other words, unbroken $\mathcal{PT}$-symmetry enables wavepacket spreading, whereas broken $\mathcal{PT}$-symmetry induces localization.

In conclusion, we have analyzed the $\mathcal{PT}$-symmetric NHAAH model's sensitivity using pseudospectra, and determined the conditions under which quantized jumps occur. The detrimnetla role of gain saturation was also examined.

This project was funded by HFRI (4th Call for PhD Fellowships, Fellowship No. 10638) and the European Research Council (ERC-Consolidator, Grant No. 101045135).

References

1. S. Aubry, and G. André, "Analyticity breaking and Anderson localization in incommensurate lattices", *Ann. Israel Phys. Soc*, 3, 18 (1980).

2. J. B. Sokoloff, "Band structure and localization in incommensurate lattice potentials", *Phys. Rev. B*, 23, 6422 (1981).

3. J. B. Sokoloff, "Unusual band structure, wave function and electrical conductance in crystals with incommensurate periodic potentials", *Phys. Rep.*, 126, 189 (1984).

4. S. Longhi, "Metal-insulator phase transition in a non-Hermitian Aubry-André-Harper model", *Phys. Rev. B* , 100, 125157 (2019).

5. Y. Liu, X. P. Jiang, J. Cao, and S. Chen, " Non-Hermitian mobility edges in one-dimensional quasicrystals with parity-time symmetry", *Phys. Rev. B* , 101, 174205 (2020).

6. S. Weidemann, M. Kremer, S. Longhi, and A. Szameit, " Topological triple phase transition in non-Hermitian Floquet quasicrystals", *Nature*, 601, 354 (2022).

7. L. N. Trefethen and M. Embree, "Spectra and Pseudospectra", (Princeton University Press, Princeton, NJ, 2005).

8. K. G. Makris, "Transient amplification due to non-Hermitian interference of dissipative supermodes", *Appl. Phys. Lett.*, 125, 011102 (2024).

9. A.F. Tzortzakakis, K.G. Makris, A. Szameit, and E.N. Economou,"Transport and spectral features in non-Hermitian open systems", *Phys. Rev. Research*, 3, 013208 (2021).

10. A. Leventis, K. G. Makris , and E. N. Economou, "Non-Hermitian jumps in disordered lattices", *Phys. Rev. B*, 106, 064205 (2022).

11. A. Ghatak, D. H. Kaltsas, M. Kulkarni, K. G. Makris, "Diffraction and pseudospectra in non-Hermitian quasiperiodic lattices", *Phys. Rev. E*, 110, 064228 (2024).

Luneburg lens for surface water waves

S. M. Kuznetsova[1], V. F. dal Poggetto [1], M. Mazzotti[1], M. Onorato[2], V. Pagneux[3] and M. Miniaci[1*]

[1]Univ. Lille, CNRS, Centrale Lille, Junia, Univ. Polytechnique Hauts-de-France, UMR 8520 -IEMN – Institut d'Electronique de Microélectronique et de Nanotechnologie F-59000 Lille, France

[2]Dipartimento di Fisica, Università degli Studi di Torino, Via Pietro Giuria 1, 10125 Torino, Italy; INFN, Sezione di Torino, Via Pietro Giuria 1, 10125 Torino, Italy

[3]Laboratoire d'Acoustique de l'Université du Mans, Unite Mixte de Recherche 6613 Centre National de la Recherche Scientifique, Avenue O. Messiaen, F-72085 Le Mans Cedex 9, France

Corresponding author: marco.miniaci@gmail.com, marco.miniaci@univ-lille.fr

Abstract: Focusing of surface water waves is investigated using an analog of a Luneburg lens constructed by submerged pillars. Efficient focusing is observed on a wide range of frequencies. The results may find application in the ocean-human interaction, such as coastal protection.

In recent years, advances in acoustic metamaterials and photonic/phononic crystals have spurred growing interest in the manipulation of surface water waves (SWWs). Among the various phenomena studied, wave focusing has received considerable attention, particularly through the use of artificial structures with gradient refractive indices [1]. One notable example is the Luneburg lens, originally developed for electromagnetic waves and later adapted for acoustic applications [2]. Its refractive index varies with the radial distance r from the center according to $n_L = \sqrt{2 - r^2/R^2}$, where R is the radius of the lens.

The primary objective of this work is to demonstrate the feasibility of extending the Luneburg lens concept to the realm of surface water waves, a direction that, to the best of our knowledge, has not yet been explored. The analogue of a Luneburg lens is constructed using submerged pillars with varying radii r_c and equal height h. We first study the periodic arrangement of the pillars of the same radii (with period $L = 25$ mm) and retrieve their dispersion relation $f(k_x)$. Taking into account that $kh << 1$ we introduce the wavenumber by $f = \sqrt{gH}k/2\pi$, where H is the depth of the water. Then in the linear part of the curve the Bloch wave vector is $k_b = nk$ with n being the refractive index [3].

Assuming that water is an inviscid and incompressible fluid, the velocity potential satisfies the Laplace equation $\Delta\phi = 0$ subject to the following boundary conditions: on the free surface at $z = 0$, $\frac{\partial\phi}{\partial z} = \frac{\omega^2}{g}\phi$ and on the non-flat bottom $\nabla\phi \cdot \vec{n} = 0$ [4]. The corresponding dispersion curves are presented in Fig. 1(a) for the maximum and minimum filling fraction ($r_c = 0$ and $r_c = 0.5L$), while the recovered refractive index is reported in Fig. 1(b) for different heights as a function of r_c.

We construct the lens by placing the pillars of different radii in the form of a square lattice approximating n_L. We choose the radius of the lens to be $R = 10L$ and divide its area into circles with a step equal to L as shown in Fig. 2. From the function $n_L(r)$ we define the refractive index at every circumference $r_i = i \cdot a$ and calculate the filling fraction ff_i of the corresponding square lattice utilizing the Fig. 1(b). Then we fill the circles in such a way that if the coordinates of the pillar satisfy $x^2 + y^2 \in [r_i, r_{i+1})$, then the pillar has the radius $r_i = a\sqrt{ff_i/\pi}$. This allows us to gradually change n from the maximum $\sqrt{2}$ in the center to the minimum 1 in the corner

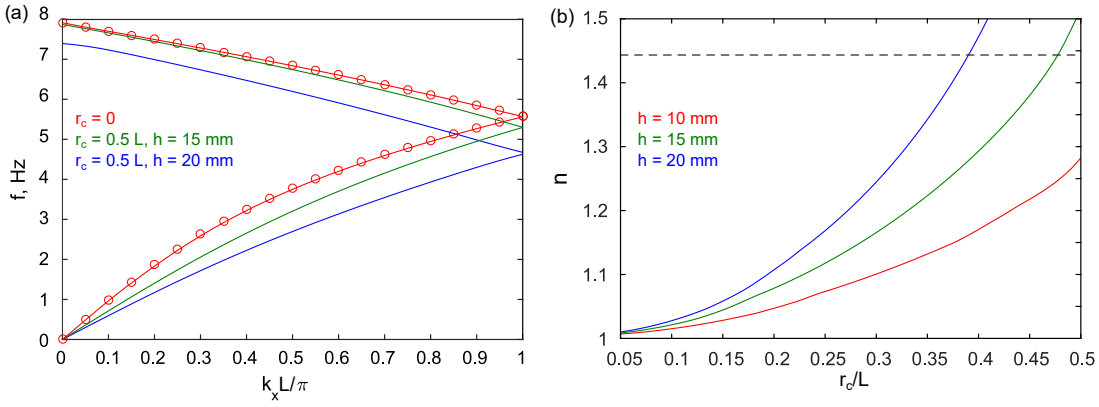


Figure 1: **Dispersion diagram and refractive index**. Dispersion diagram for minimal and maximal filling fraction (a) and refractive index as a function of r_c for different heights (b).

of the lens. The resulting structure is sketched in Fig. 2.

The perspective of this study is to consider focusing in terms of the full equation for the velocity potential in order to take into account the near-field effects occurring between the interacting pillar.

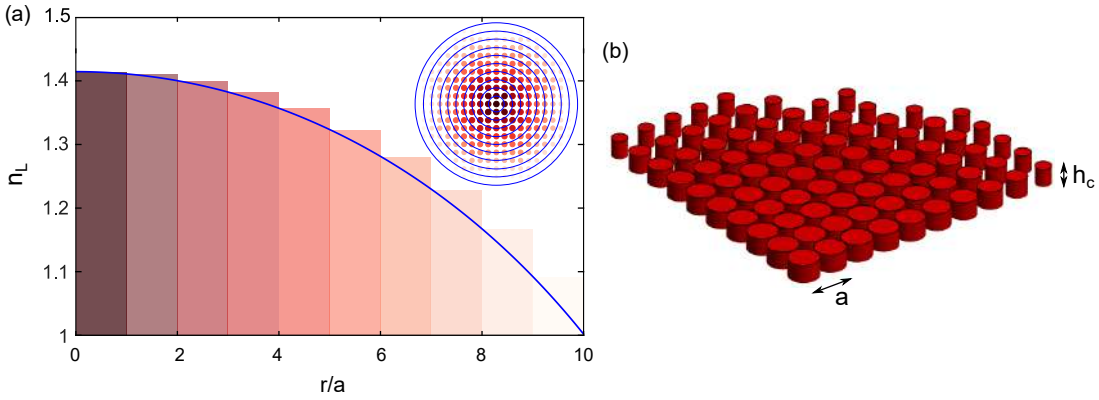


Figure 2: **Construction of the lens**. Refractive index of the Luneburg lens as a function of the distance r from its center and with colored areas corresponding to its discretization (a) and a quarter of a lens (b).

References

1. Wang Z. et al. "Focusing of liquid surface waves by gradient index lens," *Europhysics Let.*, Vol. 108, No. 2, pp. 24003, 2014.

2. Zhao L. et al. "A review of acoustic Luneburg lens: Physics and applications," *Mechanical Systems and Signal Processing*,Vol. 199, pp. 110468, 2023.

3. Hu X., Chan C. T. "Refraction of water waves by periodic cylinder arrays," *Phys. rev. let.*, Vol. 95, No. 15, pp. 154501, 2005.

4. Maurel A. et. al. "Revisiting the anisotropy of metamaterials for water waves," *Phys. Rev. B*, Vol. 96, No. 12, pp. 134310, 2017.

META 2025, MALAGA - SPAIN, JULY 22–25, 2025

Design of underwater noise reduction ultra-thin metabarriers

V. F. Dal Poggetto [1] and M. Miniaci[1*]

[1]Univ. Lille, CNRS, Centrale Lille, Junia, Univ. Polytechnique Hauts-de-France,
UMR 8520 -IEMN – Institut d'Electronique de Microélectronique et de Nanotechnologie, F-59000 Lille, France
Corresponding authors: vinicius.fonseca-dal-poggetto@univ-lille.fr, marco.miniaci@gmail.com

Abstract: In this work, we propose a metabarrier with a tailored elastic anisotropy for efficient underwater noise reduction. The constitutive unit cell of the metabarrier is optimized to enhance wave mode coupling to effectively operate in the sub-wavelength regime and also exhibit high sound transmission loss at higher frequencies.

Effective noise reduction at low frequencies with structures much thinner than the wavelength of incident waves (sub-wavelength behavior) remains a significant scientific and technological challenge. This is particularly true in underwater acoustics, where wavelengths are much longer than in air, and solid-structure interactions play a crucial role. Mitigation strategies typically involve a careful adjustment of the impedance match or mismatch between barriers and water, resulting in (i) absorptive or (ii) reflective behavior [1]. However, reducing underwater noise at very low frequencies (below 1000 Hz) and over a broadband frequency range remains a challenge.

We address this problem by introducing a periodic metamaterial with an optimized unit cell designed to facilitate coupled normal-shear behavior along predefined directions. An initially homogeneous two-dimensional structure is considered whose constitutive matrix $\mathbf{C}$ presents components so that the ratio $C_{33}/C_{11} = 0.9$ is satisfied. We also assume the relationship between the speed of the acoustic waves and the mass densities in the fluid (subscript $_0$) and the solid (without subscripts) to be $c_0/\sqrt{C_{11}/\rho} = 0.9$ and $\rho_0/\rho = 0.9$, respectively. The effect of the dimensionless coupling factor $\delta = C_{13}/\sqrt{C_{11}C_{33}}$ on STL curves is then investigated numerically by considering, as an illustrative example, the following material properties for the metabarrier: density $\rho = 1000$ kg/m^3, stiffness coefficient $C_{11} = 1$ GPa, and thickness $\overline{h} = 10^{-2}$ m. Figure 1**a** (top panel) reports STL curves computed using a transfer matrix method, adopting a thickness $h = \overline{h}$ and $\delta = \{0.9, 0.95, 0.995\}$. The results indicate that increasing δ leads to (i) a five-fold amplification of the first STL peak and (ii) a reduction of 80% in its corresponding frequency. Alternatively, for $\delta = 0.999$ and $h/\overline{h} \in [10^{-2}, 10^{0}]$, Fig. 1**a** (bottom panel) indicates (i) a monotonic behavior for $h/\overline{h} < 10^{-2}$ and (ii) a red shift of STL peaks for increasing h, suggesting that the first STL peak can be tuned using the thickness of the metabarrier. These results are used to design the metabarrier unit cell through topology optimization as follows: (i) we divide a square unit cell into $2q \times 2q$ pixels (Fig. 1**b**, top panel), with matching boundaries to ensure continuity and $\pi/2$-rotational interior symmetry to ensure $\delta \neq 0$; (ii) we set an optimization objective to maximize $|\delta|$ while ensuring connectivity. The unit cell obtained is reported in Fig. 1**b** (bottom panel), with a geometry smoothed for manufacturing reasons, resulting in $\delta = 0.9582$. The dispersion curves of this unit cell in the ΓX direction are reported in Fig. 1**c**, adopting a unit cell length $a = 10$ mm and material properties $E = 3$ GPa, $\nu = 0.3$, $\rho = 1150$ kg/m^3.

Dispersion curves are reported following the polarization metric: $p = \int_S |u_y|^2 \, dS / \int_S |u_x|^2 + |u_y|^2 \, dS$, where u_x (u_y) is the displacement in the x- (y)-direction and S the unit cell domain. This polarization implies that $p = 0$ ($p = 1$) indicates a purely longitudinal (transverse) motion. The band diagram is shown for $[0, 5]$ kHz using continuous lines, with dashed lines representing the dispersion diagram for the equivalent homogeneous medium. The polarization factor of the first branch ranges from 0.403 to 0.414, suggesting a high degree of hybridization of the mode, with a slight tendency toward longitudinal polarization of the deformation. The wave mode at point X at 2.67 kHz is reported for the sake of clarity. The second branch presents $p \in [0.585, 0.589]$, also suggesting a high degree of hybridization, although this time with a slight tendency toward transverse polarization of the deformation. The wave mode shown at 5 kHz (wavenumber $k \approx 0.14\pi/a$) displays a rigid body-like transverse motion. Although the coupling

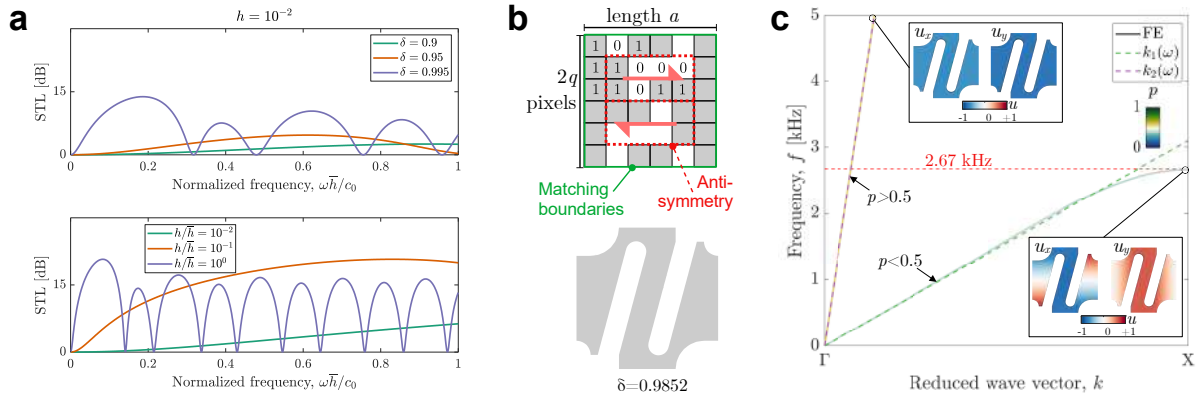


Figure 1: Metabarrier design strategy. **a**. STL curves for non-dimensional thickness $h = 10^0$ and coupling factor $\delta = \{0.9, 0.95, 0.995\}$ (top panel); $\delta = 0.999$ and $h = \{10^{-2}, 10^{-1}, 10^0\}$ (bottom panel). **b**. Unit cell ($2q \times 2q$ pixels) with internal $\pi/2$-rotational symmetry (top panel). Result of optimization procedure after smoothing (bottom panel). **c**. Dispersion diagram (continuous lines) with polarization values p. Dashed lines represent dispersion curves with effective homogenized properties.

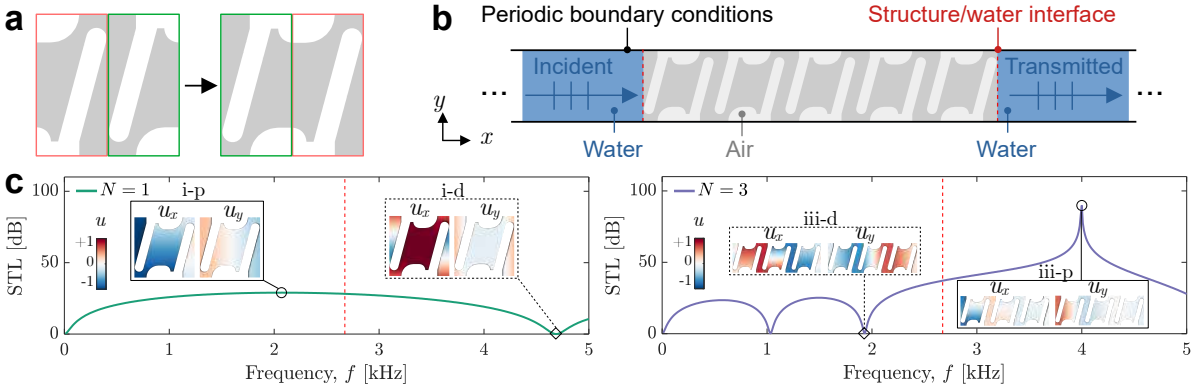


Figure 2: Finite metabarrier and STL curves. **a**. Swapping left/right halves to obtain unit cells without gaps at edges. **b**. Arrangement of unit cells filled with air and submerged into water. The medium is periodic in the y-direction. **c**. STL curves obtained for $N = 1$ and $N = 3$ unit cells.

between normal/shear stresses/strains was optimized in the static regime (ie, $\omega = 0$), dynamic coupling in longitudinal-transverse motion has been observed.

To evaluate the STL properties of a metabarrier made up of a finite number of unit cells, the left and right halves of the optimized unit cell have been swapped (Fig. 2**a**). This operation maintains the periodicity of the system. The unit cell is then repeated along the x-direction using N unit cells, obtaining finite structures with thickness $h = Na$. The STL curve of this structure immersed in water (Fig. 2**b**) considers a periodic medium in the y direction, and is calculated using a FE-based method [2]. These results are shown considering $N = 1$ and $N = 3$ unit cells (Fig. 2**c**). When $N = 1$, the metabarrier presents a maximum STL of 29.0 dB at 2.07 kHz (inset i-p) with deep sub-wavelength performance ($h/\lambda \approx 1/70$). The STL curve reaches a dip at 4.7 kHz, with a symmetric displacement profile (inset i-d). When $N = 3$, three STL peaks are found: attenuation of 23.5, 25.2, and 89.8 dB at 0.57, 1.49, and 4.00 kHz, respectively.

Acknowledgments. This project is funded by the European Union's Horizon Europe programme under the ERC StG POSEIDON (GA no. 101039576).

References

1. Dong, J., Tian, P., "Review of underwater sound absorption materials," *Iop C. Ser. Earth. Env.*, Vol. 508, No. 1, pp. 012182, 2020.

2. Yang, Y. et al., "Prediction of sound transmission through, and radiation from, panels using a wave and finite element method," *J. Acoust. Soc. Am.*, Vol. 141, No. 4, pp. 2452–2460, 2017.

Ultrathin architected plates and their applications

Igor Bargatin

[1]University of Pennsylvania, USA
[*]corresponding author: bargatin@seas.upenn.edu

Abstract: Ultralight architected plates, like nanocardboard, offer unprecedented stiffness-to-weight ratios and shape recovery. Made from nanometer-thick films, these metamaterials enable macroscopic photophoretic levitation via thermal transpiration. They also inform designs for relativistic lightsails, where high bending stiffness and engineered curvature (billowing) are crucial for managing intense photon pressure stresses.

For centuries, engineers have sought plates that are simultaneously lightweight and stiff. Traditional approaches often involve solid materials or macroscale composites like corrugated cardboard or honeycomb panels, with applications ranging from doors to aerospace structures. However, fundamental limits in material density and manufacturing constraints cap the achievable performance, especially when extreme lightness is paramount. Recent advances in nanofabrication have unlocked a new approach: plate mechanical metamaterials, where carefully designed micro- and nano-architectures, rather than just material composition, dictate mechanical properties. This overview focuses on a class of *plate* mechanical metamaterials—ultrathin, architected films—and explores their potential to revolutionize two disparate propulsion concepts: photophoretic levitation and extreme laser-driven acceleration for relativistic lightsails.

We began by creating continuous, free-standing corrugated plates from ultrathin (~25-100 nm) films of materials like alumina using atomic layer deposition (ALD) on patterned silicon molds [1]. Initial designs, using honeycomb patterns, demonstrated that microscale 3D architecture could impart significant bending stiffness and flatness to films otherwise prone to warping, enabling centimeter-scale plates weighing as little as 0.1g/cm^{-2}. We also developed nanoscale analogs of sandwich plates, initially demonstrating ultrathin corrugated plates and later "nanocardboard," a monolithic material composed of nanometer-thick (25-400 nm) face sheets connected by micrometer-height tubular webbing, *i.e.* microchannels [2]. A remarkable property emerged: these brittle

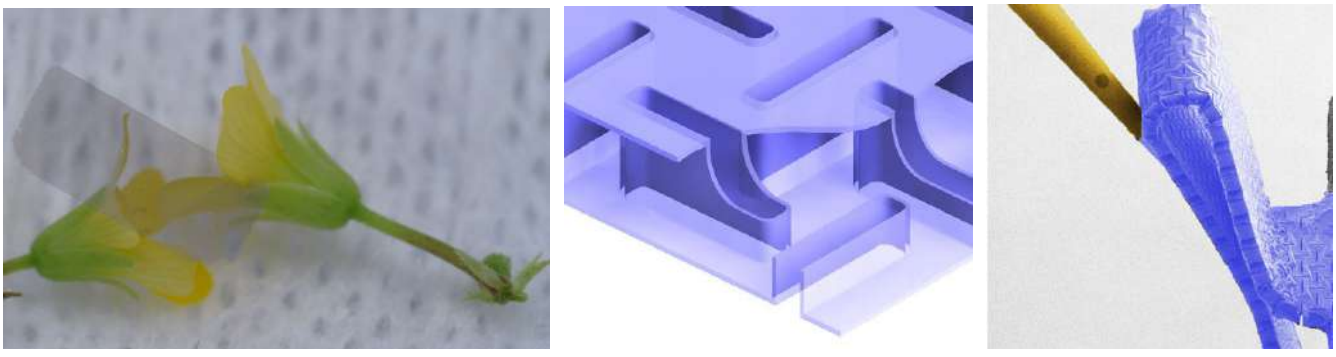


Fig. 1: (left) An architected plate with 50-nm-thickness and cm-scale lateral dimensions resting upon a flower. (center) A schematic of the hollow structure of nanocardboard, a nanoscale analog of sandwich plates. (right) Artificially colored scanning electron micrograph showing the sharp bending of nanocardboard with a micromanipulator probe, which surprisingly does not damage the structure, leading to full shape recovery.

ceramic plates could undergo sharp bends, folding over 90 degrees, yet recovering their original shape without damage (Fig. 1), a feat we attributed to the nanoscale thickness limiting strain to less than ~1% during sharp bending and local buckling.

The unique combination of ultralow mass and low thermal conductivity in nanocardboard enables macroscopic **photophoretic levitation**. Photophoresis, the force exerted on an object immersed in a gas due to light-induced temperature gradients, is typically significant only for micrometer-sized particles but can also be maximized for carefully engineered architected plates. By coating the bottom side of the nanocardboard with an absorbing layer (e.g., carbon nanotubes), incident light creates a temperature difference across the plate thickness. This drives thermal transpiration flow through the internal microchannels. At atmospheric pressure, this flow creates an air cushion beneath the plate, allowing it to hover stably at heights of ≈ 0.5 mm above a substrate [3]. At low pressures (10-200 Pa, relevant to Mars or Earth's mesosphere), the enhanced flow generates a jet enabling mid-air levitation and payload carriage (e.g., 0.33 mg payload on a 0.1 mg plate) [3]. Extending this idea, we proposed meter-scale, 3D hollow structures using Knudsen pumping through porous walls to create high-speed jets, potentially enabling kilogram-scale payloads at mesospheric altitudes (55-80 km) [4].

The extreme lightness and potential for high-temperature resistance make nanostructured plates candidates for **relativistic lightsails**, envisioned for interstellar missions like Breakthrough Starshot. Such sails require acceleration to a significant fraction of the speed of light (e.g., 0.2c) using high-power lasers. However, the intense photon pressure required poses a significant mechanical challenge. Our analysis shows flat sails would likely tear; sails must billow (curve significantly) to reduce stress can also benefit from architected plate geometry to maintain this shape. Optimal meter-scale designs balance curvature, thickness, optical properties, and thermo-mechanical limits. Sufficient laser power allows curved architected sails to achieve shorter acceleration distances, highlighting the necessity of curvature for both integrity and potential performance.

Architected plates therefore represent a class of ultralight metamaterials with unique mechanical properties enabling novel flight via photophoresis and offering structural solutions for relativistic lightsails, paving the way for exploration in previously inaccessible regimes of gas flow and related applications.

References

1. Davami, K., Zhao, L., Lu, E., Cortes, J., Lin, C., Lilley, D. E., Purohit, P. K. & Bargatin, I. “Ultralight shape-recovering plate mechanical metamaterials,” Nat. Commun. 6, 10019, 2015. https://doi.org/10.1038/ncomms10019
2. Lin, C., Nicaise, S. M., Lilley, D. E., Cortes, J., Jiao, P., Singh, J., Azadi, M., Lopez, G. G., Metzler, M., Purohit, P. K. & Bargatin, I. “Nanocardboard as a nanoscale analog of hollow sandwich plates,” Nat. Commun. 9, 4442, 2018. https://doi.org/10.1038/s41467-018-06818-6
3. Cortes, J., Stanczak, C., Azadi, M., Narula, M., Nicaise, S. M., Hu, H. & Bargatin, I. “Photophoretic Levitation of Macroscopic Nanocardboard Plates,” Adv. Mater. 32, 1906878, 2020. https://doi.org/10.1002/adma.201906878
4. Celenza, T, A. Eskenazi, I. Bargatin, “Three-dimensional photophoretic aircraft made from ultralight porous materials can carry kilogram-scale payloads in the mesosphere,” Physical Review Applied 22, 054081, 2024. https://doi.org/10.1103/PhysRevApplied.22.054081
5. Campbell, M. F., Brewer, J., Jariwala, D., Raman, A. P. & Bargatin, I. “Relativistic Light Sails Need to Billow,” Nano Lett. 22, 90–96, 2022. https://doi.org/10.1021/acs.nanolett.1c03272

Optomechanical Su-Schrieffer–Heeger States in a Nanobeam Cavity

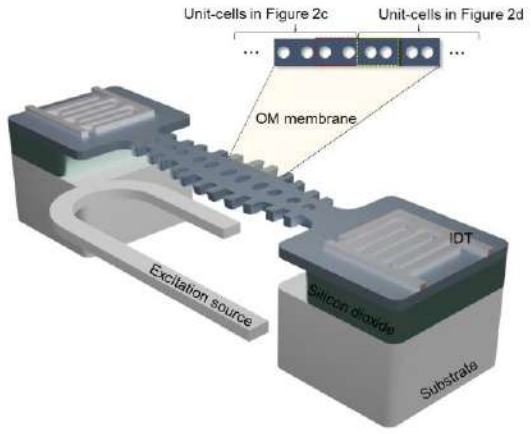
Hicham Mangach[1,*], Abdellatif Gueddida[1], Ricardo Alcorta-Galvan[1], Gaëtan Lévêque[1], Marco Miniaci[1], Yan Pennec[1], and Bahram Djafari-Rouhani[1]

[1] *Univ. Lille, CNRS, UMR 8520 - IEMN, Avenue Poincaré, Cité Scientifique, F-59652 Villeneuve d'AScq, France,*

[*]corresponding author: hicham.mangach@univ-lille.fr

Abstract: We design an optomechanical nanobeam cavity based on the Su–Schrieffer–Heeger (SSH) model, created via alternating two mechanical/optical domains at the interface through controlled holes and stubs spacing. The system provides topologically protected photon–phonon coupling ($g/2\pi$ = 782 KHz) and a high optical quality factor ($Q = 3.77\times10^5$).

Phoxonic crystals offer a compelling platform for controlling light and sound at the nanoscale, enabling coherent photon–phonon interactions through the simultaneous confinement of optical and mechanical modes. While substantial progress has been made in one-dimensional (1D) optomechanical systems—most notably nanobeam cavities—recent advances point to the possibility of achieving vacuum coupling rates on the order of $g/2\pi\sim1$ MHz in more complex geometries[1]. These structures not only allow precise control over phonon-mediated photon dynamics but also open new avenues for integrated quantum transduction, nonreciprocal photonics, and ultra-sensitive metrology[2].



cavity. The silicon nanobeam is anchored at both ends to a thick substrate via an intermediate SiO_2 layer. Optical excitation is provided by a telecom-frequency waveguide coupled to the SSH-cavity, while paired interdigital transducers (IDTs) enable mechanical actuation and elastic energy detection.

Here, we present a 1D phoxonic nanobeam cavity inspired by the Su–Schrieffer–Heeger (SSH) model, designed to host topological modes in both the photonic and phononic domains. Figure 2 (a,b) illustrate the dimerized unit cell designs, with symmetrically placed holes and stubs that give rise to Dirac-like dispersion at $k_y = \pi/2a_y$. By systematically breaking this symmetry—displacing holes and stubs either inward or outward from the center—we induce topological phase transitions in both the optical and acoustic spectra, as shown in Figure 2(g–j).

To analyze the system, we simulate a finite nanobeam composed of 40 unit cells—20 on each side of a central interface—using finite element analysis. The left half of the beam features unit cells with a larger separation between holes and stubs, while the right half contains a more compact configuration. The topological gaps are preserved across the structure by finely tuning an anti-symmetric design parameter σ. Mode profiles in Figure 2 (marked by letters A-H) show the topological transition resulting from the unit cell changes at the interface, analogous to the behavior observed in mechanical SSH chains composed of identical masses connected by alternating spring constants. The resulting cavity exhibits strong electromagnetic field confinement within a single optical cycle—comparable to that observed in higher-dimensional phoxonic crystals (Figure 3a)—and achieves high photon-phonon coupling rate of $g/2\pi$ =782 KHz in air.

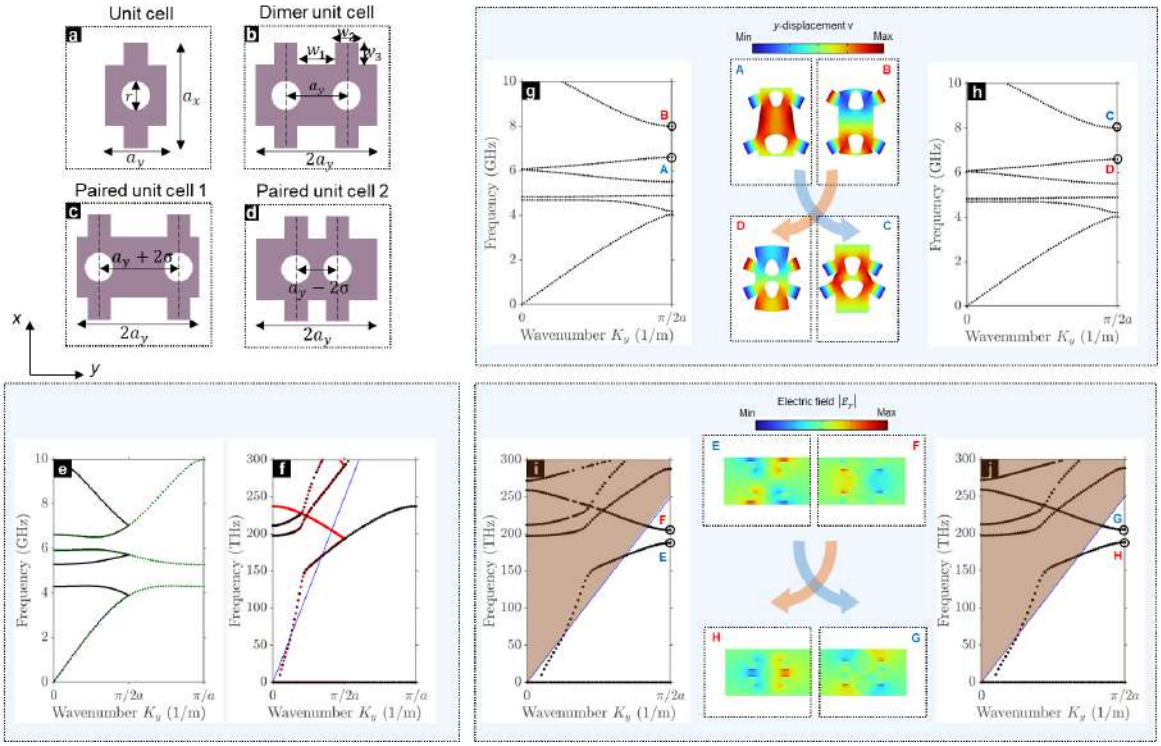


Figure 2 **Unit cell configurations and Energy bands**. (a-b) Single and double unit cell(s) with centered holes and stubs. (c-d) Asymmetric variants with holes and stubs shifts (σ∈[-100, 100] nm), used to build the graded nanobeam. All designs maintain fixed periodicity ($a_x = a_y$ 300 nm), nanobeam thickness (220 nm) and stub lengths ($w_1 = w_2$ = 100 nm). (e-f) Phononic and photonic dispersion bands for (a) and (b), showing Dirac points at ky = $\pi/2a_y$ for symmetric cases. (g-j) Topological gaps (σ≠0) with edge modes (A-H) demonstrating topological band inversion.

This coupling strength is comparable to that reported in more complex two-dimensional phoxonic systems, yet it is realized here with significantly reduced fabrication complexity. These findings highlight the potential of SSH-inspired optomechanical nanobeams as a scalable and robust architecture for advancing next-generation integrated photonic and phononic technologies.

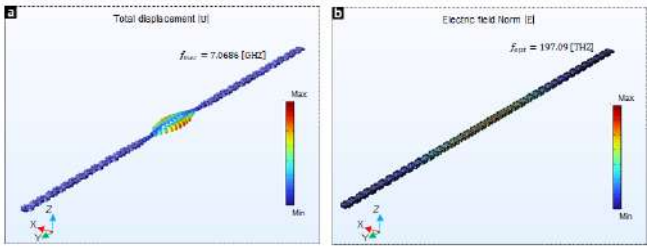


Figure 3 **Phononic and photonic interfacial modes**. (a–b) A non-trivial optomechanical interface featuring a smooth transition, demonstrating a high-quality photonic Q-factor of 3.77×10^5 and an optimized coupling rate $g/2\pi$ = 782 KHz. Normalized displacement is shown in false color, with exaggerated deformation for clarity.

Acknowledgments

This project has received funding from the European Union's Horizon Europe research and innovation programme under grant agreement MAGNIFIC (GA No 101091968). This work is part of the MUSICIAN CHIST-ERA Call 2021 under GA No CHIST-ERA-20-NOEMS-003.

References

1. Ren, H., Shah, T., Pfeifer, H., Brendel, C., Peano, V., Marquardt F., Painter, O., Nat. Commun. Vol. 13, No. 1, 3476, 2022.
2. Gomis-Bresco, J., Navarro-Urrios, D., Oudich, M., El-Jallal, S., Griol, A., Puerto, D., Chavez, E., Pennec, Y., Djafari-Rouhani, B., Alzina, F., Nat Commun, Vol. 5, No. 1, 4452, 2014.

Springtronics: Towards advanced information processing in elastic metamaterials

F. Bohte, S. Zahedi Fard*, P. Omidvar, T. Louvet, S. Zohoori and M. Serra-Garcia[2]

[1]AMOLF, Netherlands
*corresponding author: m.serragarcia@amolf.nl

Abstract: We introduce a design framework for information-processing phononic metamaterials. The key idea consists in encoding the desired functionality as a mass-spring network, that is then translated into a metamaterial geometry and, eventually, into an experimental realization. The talk will discuss mass-spring and geometry design strategies, as well as example applications.

Elastic systems are an exciting platform for information processing. They can, for example, compute with very low power dissipation [1], directly process mechanical signals such as speech [2], steps [3] or building vibrations without transducers, and embody intelligence in robotic structures [4]—thus, they present the tantalizing prospect of having internet-of-things devices powered by speech, and soft robots that are agile and safe to interact with. However, designing an elastic metamaterial that performs a desired computation is challenging: It means solving an elastic inverse problem—that can be potentially high-dimensional, nonlinear, and transient.

Our approach to the design of intelligent elastic systems draws inspiration from electrical engineering. In this field, it is customary to start the design process by drawing a lumped model—a circuit schematic—that performs the required task. During this initial phase, little attention is placed on the specific geometry and materials that will define the final system. The circuit schematic is subsequently converted into a device geometry (such as a printed circuit board or integrated circuit) either manually or via automated software tools, and eventually fabricated. This stands in contrast with the geometry-first approach that is usually taken in the design of metamaterials, highly focused on specific realizations, and dominated by tools such as topological and parametric optimization. In analogy with electrical engineering, we refer to our approach as *springtronics* [5].

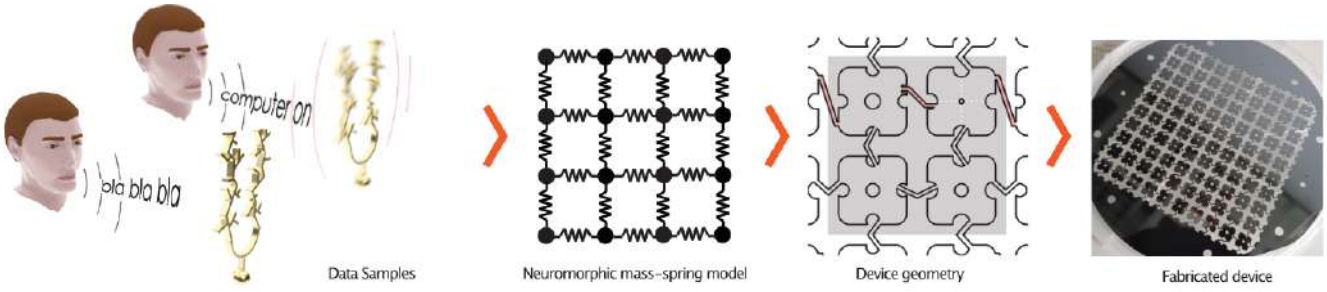


Figure 1. In *springtronics*, functionalities such as speech recognition are first encoded in a mass-spring model, that is then translated into a geometry, and, eventually, fabricated.

In this talk, I will start by discussing our fundamental building blocks. Remarkably, we conclude that a small number of interactions (three types of conservative springs, plus a local damper) suffice to express an extreme variety of tasks, from digital computers that perform operations on signals encoded either as static displacements or as amplitudes [6], to nonvolatile memories, and including speech-recognizing mass-spring networks [5], that

achieve accuracy comparable to low-power electronic alternatives. I will show a few examples of springtronic models that perform interesting tasks.

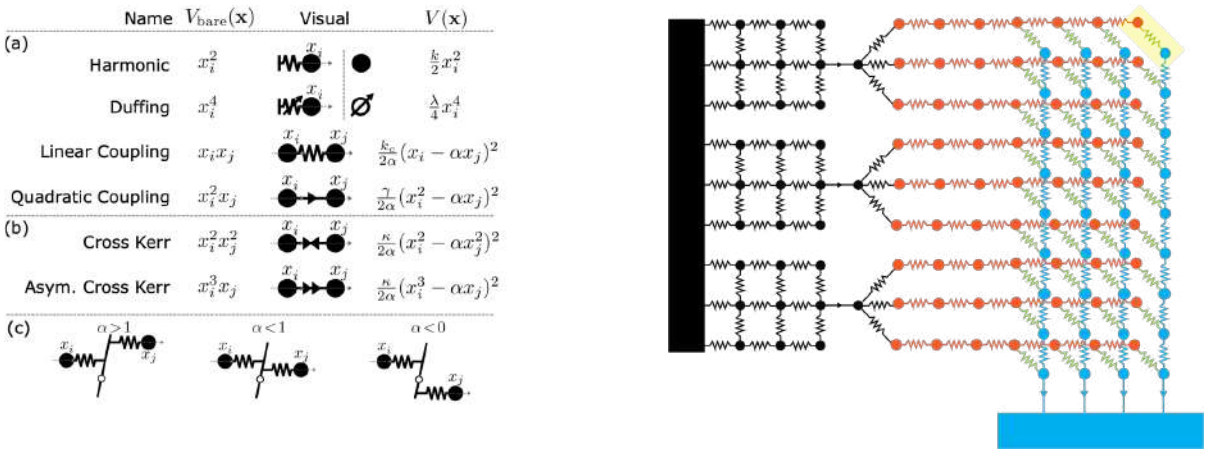


Figure 2. Springtronic models are constructed by combining elementary potentials (left). These potentials can be combined into complex functionalities, such as speech-classifying systems (right).

Then, I will discuss how these mass-spring models can be translated into geometries. We do so within the perturbative metamaterial framework [7], where the masses correspond to degrees of freedom localized at each metamaterial site, and interaction potentials are constructed as geometric perturbations to the design. Although the original perturbative metamaterial work was only applicable to linear systems, we have developed a nonlinear coordinate transformation that allows for a similar principle to be applied to the design of nonlinear metamaterials. Finally, I will show some examples of experimental realizations of springtronic systems.

This work is supported by the ERC grant 101040117 (INFOPASS).

References

1. Masmanidis, S. C., et al. “Multifunctional Nanomechanical Systems via Tunably Coupled Piezoelectric Actuation,” Science, Vol. 317, No. 5839, 780–783, 2007.
2. Dubček, T. et al., “In-Sensor Passive Speech Classification with Phononic Metamaterials,” Adv. Func. Matter., Vol. 34, No. 17, 2311877, 2024.
3. V. Barazani et al., “Microfabricated Neuroaccelerometer: Integrating Sensing and Reservoir Computing in MEMS,” J. Microelectromechanical Syst., Vol. 29, No. 3, 338-347, 2020.
4. Howard, D. et al., “Evolving embodied intelligence from materials to machines,” Nat. Mach. Intell., Vol. 1, No. 12-19, 2019.
5. Bohte, F., T. Louvet, V. Maillou and M. Serra-Garcia, “Mass-Spring Models for Passive Keyword Spotting: A Springtronics Approach,” arXiv: 2504.05802, 2025.
6. Serra-Garcia, M., “Turing-complete mechanical processor via automated nonlinear system design,” Phys. Rev. B, Vol. 100, No. 4, 042202, 2019.
7. Matlack, K. H., M. Serra-Garcia, A. Palermo, S. D. Huber and C. Daraio, “Designing perturbative metamaterials from discrete models,” Nat. Mater., Vol. 17, No. 4, 323-328, 2018.

Wave dispersion analysis of frame-shear wall building structures based on the periodic structure theory

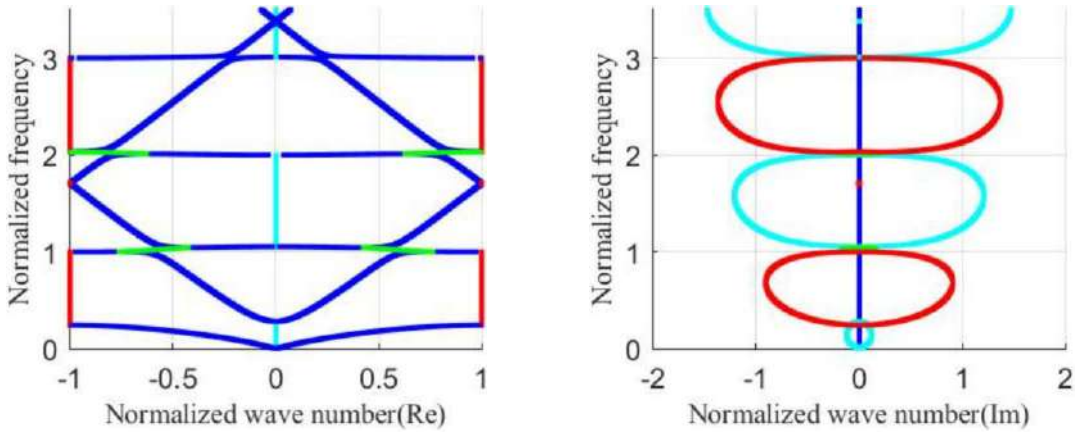
Z. B. Cheng[1*], J. M. Li[1], P. Pan[1], and J. Sun[1]

[1] School of Civil Engineering, Beijing Jiaotong University, China
[*]corresponding author: chengzb@bjtu.edu.cn

Abstract: Introducing the periodic structure theory developed in the field of solid-state physics into the field of civil engineering, this paper investigates the wave dispersion properties of frame-shear wall building structure, a typical structural system for high-rise building structure, through theoretical and numerical analysis.

The frame-shear wall structure is widely recognized as a typical design for high-rise buildings. In the vertical direction, these structures can be seen as periodic systems created by the repetitive arrangement of standard floors. As a result, similar to phononic crystals, this periodic arrangement affects certain dispersion characteristics of frame-shear wall structures. Although many researchers have applied periodic structure theory to civil engineering, there is limited research specifically focused on high-rise building structures.

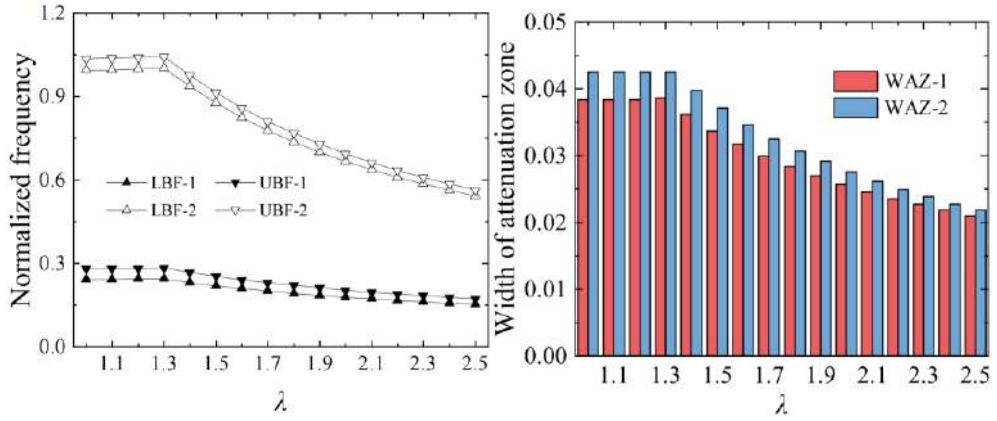
In this work, we first propose a theoretical infinite periodic model suitable for frame-shear wall structures. Using this model, we solve the dispersion equation of the infinite periodic system by combining the Bloch-Floquet theorem with the state space transfer matrix method (SSTMM). We investigate the dispersion curve of a reinforced concrete frame-shear wall building structure by solving the dispersion equation. It is important to note that the dispersion curve includes a region of complex solutions, which represents the attenuation domain, even though the wave vector in this region has a real component.



(a) (b)

Figure 1. Dispersion curve (a) X-Z plane (b) Y-Z plane.

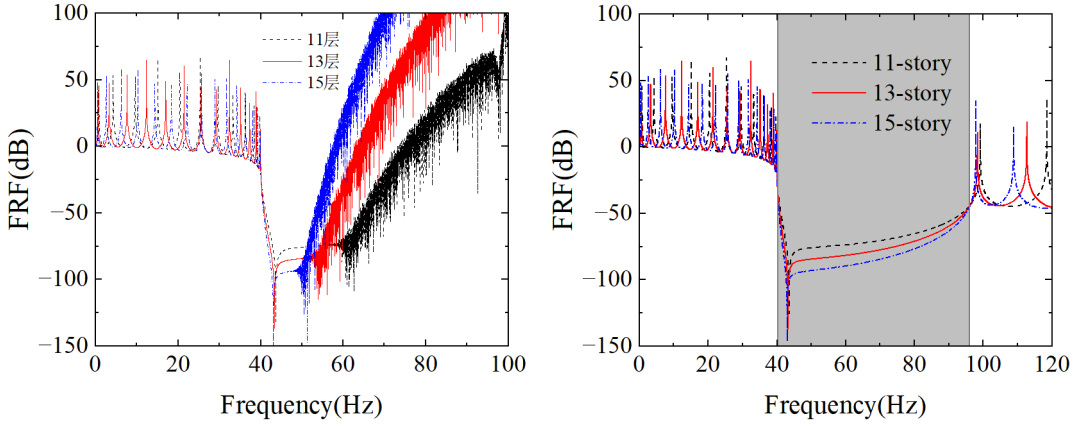
Further, a parametric analysis is conducted on the influences of the anti-lateral stiffness, stiffness characteristic values, material parameters, theoretical simplified parameters and damping parameter of the frame-shear wall building structures on the dispersion properties.



(a) (b)

Figure 2. Stiffness characteristic values versus the first two attenuation zones (a) edge frequency (b) width.

A numerical analysis is conducted on the frame-shear wall structure. The results of the numerical analysis indicate that when the frequency of external excitation is within the passband, the dynamic response of the frame-shear wall structure will experience amplification. However, when the frequency of external excitation is within the attenuation zones, the dynamic response will significantly decrease.



(a) (b)

Figure 3. Displacement FRFs of the frame-shear wall structures (a) SS-TMM (b) Riccati SS-TMM

Acknowledgment

This work is supported by the Beijing Natural Science Foundation, China (8232010).

References

1. Cheng, Z. B., W. K. Lin and Z. F. Shi, “Wave dispersion analysis of multi-story frame building structures using the periodic structure theory,” Soil Dynamics and Earthquake Engineering, Vol. 106, No. 10, 215–230, 2018.
2. Zhibao Cheng, Zhifei Shi, Antonio Palermo, Hongjun Xiang, Wei Guo, Alessandro Marzani. “Seismic Vibrations Attenuation Via Damped Layered Periodic Foundations,” Engineering Structures, Vol. 211, 110427, 2020,
3. Cheng, Z. B. and Z. F. Shi, “Composite periodic foundation and its application for seismic isolation,” Earthquake Engineering & Structural Dynamic, Vol. 47, No. 4, 925-944, 2018.

Transforming room acoustics with causality-driven dual-function passive metamaterials

E. Ballestero[1], Y. Meng[1], P. Sheng[2], V. Tournat[1],
V. Romero-García [3], and J.-P. Groby[1*]
[1]Laboratoire d'Acoustique de l'Université du Mans (LAUM),
Institut d'Acoustique - Graduate School (IA-GS), UMR CNRS 6613, Le Mans, France.
[2]Institute for Advanced Study, Hong Kong University of Science and Technology,
Clear Water Bay, Kowloon, Hong Kong, China.
[3]Instituto Universitario de Matemática Pura y Aplicada (IUMPA),
Universitat Politècnica de València, Spain.
Jean-Philippe.Groby@univ-lemans.fr (corresponding author)

Abstract

A dual-function passive acoustic metamaterial is proposed that effectively balances absorption and diffusion within the same structure by leveraging causality principle.

1 Introduction

Most existing acoustic metamaterial solutions remain configuration-dependent, addressing either sound absorption or diffusion, but rarely both. Hybrid solutions attempting to integrate these functions have often been constrained by physical and spatial trade-offs, leading to suboptimal performance.

In this work, we adopt a causality-driven approach to design a Dual-Function Passive Acoustic Metamaterial (DFPAM) that optimizes both absorption and diffusion within a single structure.

2 Design principle

Absorption and diffusion of acoustic waves are contrastive effects as the former needs to dissipate the acoustic energy and the latter needs to scatter the waves with minimal dissipation. In the present case, we intend to use a strategy based on rigidly-backed slits loaded by an array of Helmholtz resonators as shown in Fig. 1(a).

By analyzing the sum rule given by the passivity/causality conditions of the acoustic system accounted for in this work, it is possible to evaluate the optimal value of the absorption-to-diffusion surface area ratio, $\phi_{\alpha|\delta}$, with a given target absorption spectrum. A depth of 12 cm is chosen in order to provide a solution that fits within dimensions similar to other metamaterial designs reported in the literature. It follows that $\min\left(\phi_{\alpha|\delta}\right) \approx 0.33$. Starting from a 3×3 square grid for the quarter of unit-cell with a combinatorial ratio of absorption cells to overall cells $\phi_\alpha = 1/3$, there are a total of 84 possible combinations. Due to mirror symmetries and further physical considerations regarding the choice of tesselation pattern and diffusion optimality, the rhombus depicted in Fig. 1(a) happens to be one of the best candidates available for sound diffusion. We finally make use of non-linear constrained minimization algorithms for maximizing both absorption and diffusion as well as determining their respective geometries. Figures 1(b-c) display the analytical, numerical and experimental sound diffusion and absorption coefficients obtained throughout this study. The DFPAM achieves high broadband sound absorption (<

$\alpha >\approx 0.85$) and diffusion ($< \delta >\approx 0.8$), covering more than one octave in each configuration. For more details, the reader can refer to [1].

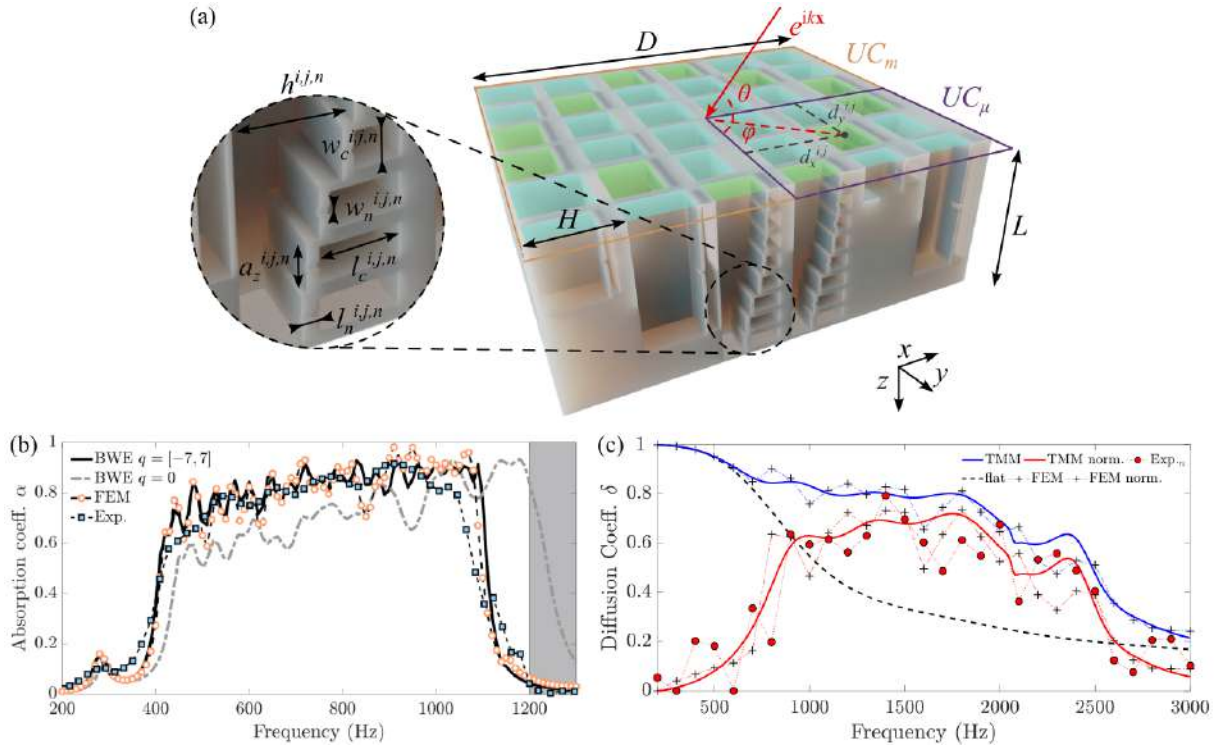


Figure 1: (a) 3D visualization of the DFPAM of side width $D = 30$ cm and depth $L = 12$ cm, with highlights on the micro unit cell (violet), used for absorption measurement in a square impedance tube and the overall macro unit cell (orange), which is formed by two-fold mirror symmetry. (inset) Geometrical parameters of the $(x, y) \to (i, j)$ slit for the n-th slit resonator section of height h and depth a_z. (b) Analytical, numerical and experimental absorption coefficients overlayed with those of each individual slits. (c) Analytical, numerical and experimental frequency-dependent diffusion coefficient $\delta(\omega)$.

3 Acknowledgements

The authors gratefully acknowledge the ANR-RGC METARoom (No. ANR-18-CE08-0021) project. E.B. acknowledges N. Pajusco and B. Hamilton for their great help in the numerical room simulations.

References

[1] Ballestero E., Meng Y., Sheng P., Tournat V., Romero-García V., and Groby J.-P., "Transforming Room Acoustics with Causality-Driven Dual-Function Passive Metamaterials," *Adv. Mater. Technol.*, 2402082, 2025.

Nonreciprocal Acoustic Wave Control with Field-Transforming Metasurface

Xinhua Wen[1*], Choonlae Cho[2], Xinghong Zhu[1], Namkyoo Park[2] and Jensen Li [1*]

[1] Department of Physics, The Hong Kong University of Science and Technology, Clear Water Bay, Hong Kong, China
[2] Photonic Systems Laboratory, Department of Electrical and Computer Engineering, Seoul National University, Seoul 08826, South Korea
[*]corresponding author: xwenai@connect.ust.hk; jensenli@ust.hk

Abstract: Manipulating nonreciprocal wave propagation using the transformation approach is highly desirable for important applications like nonreciprocal cloaking and sensing. However, the conventional framework of transformation optics based on coordinate transformation poses substantial challenges to practical experimental realization [1,2]. Field transformation, as an extension of the transformation optics, provides a possible means for nonreciprocal field manipulation [3]. Nonetheless, due to the stringent constraint on material parameters for this approach, the experimental realization of nonreciprocal field transformation is still elusive. Here we experimentally realize a field-transforming acoustic metasurface, which enables tailor-made field distribution manipulation and nonreciprocal wave control.

Field-transforming metasurface: Firstly, we discuss the design of the field-transforming acoustic metasurface. We start from the desired field distribution using a ring-shaped field-transforming metasurface with inner and outer radii R_1 and R_2, as illustrated in Fig. 1**A**. For an external incident wave outside the metasurface, the metasurface transforms the pressure field by a transformation function $f(\boldsymbol{r})$, resulting that the pressure field within the region enclosed by the metasurface (dark blue region) is amplified by a factor of $1+s$, i.e., $p(\boldsymbol{r}) = (1+s)p_0(\boldsymbol{r})$, where $p_0(\boldsymbol{r})$ represents the propagating pressure field in the background, and a positive s denotes field amplification. Outside the metasurface (cyan region), the pressure field remains unaffected, i.e. $p(\boldsymbol{r}) = p_0(\boldsymbol{r})$, by eliminating the scattered field outside the metasurface. To achieve such a field manipulation, we design a metasurface based on field transformation approach, in which the pressure and velocity fields are transformed by

$$p = f(r)p_0, \qquad v_{\mathrm{r}} = f(r)v_{\mathrm{r0}}, \qquad v_{\theta} = f(r)v_{\theta 0} \tag{1}$$

where v_{r} and v_{θ} are the radial and azimuthal components of the velocity field in the cylindrical coordinates (r,θ). $f(r)$ is a transformation function (only in terms) of r to relate the original (without the presence of the field-transforming metasurface) and the transformed fields. By substituting Eq. (1) into the acoustic wave equation and performing the necessary calculations, we can get the required compressibility and density $\beta = \rho = 1$ and the Willis couplings in the radius direction $\tau = \tau' = -f'(r)/\big(k_0 f(r)\big)$. By choosing a transformation function $\ln f(r)$ to be linear in r, nonreciprocal Willis coupling τ can be a constant value (facilitating the experimental implementation):

$$\tau = -\frac{f'(r)}{k_0 f(r)} = -\frac{\ln f_2 - \ln f_1}{k_0(R_2 - R_1)} \tag{2}$$

where $f_1 = f(R_1)$ and $f_2 = f(R_2)$ are different scaling factors at inner and outer boundaries, respectively. Therefore, the local field amplification ratio can be expressed as

$$f_1/f_2 = e^{\tau k_0 (R_2 - R_1)} = 1 + s \tag{3}$$

Therefore, a constant positive real nonreciprocal Willis coupling τ enables filed amplitude amplification, as illustrated in the lower panel in Fig.1 (**A**).

To implement the field-transforming metasurface with required material parameters, we use 24 active meta-atoms to construct the ring-shaped metasurface, as shown in Fig. 1(**B**). The active meta-atom (shown in Fig. 1(**C**)), enables to independently control all constitutive parameters by controlling the convolution kernels relating the microphones signals

(denoted as D_1, D_2) to speaker signals (denoted as S_1, S_2) [4]. Particularly, the meta-atom enables the realization of purely nonreciprocal Willis coupling, overcoming the limitations inherent in conventional metamaterials [5,6].

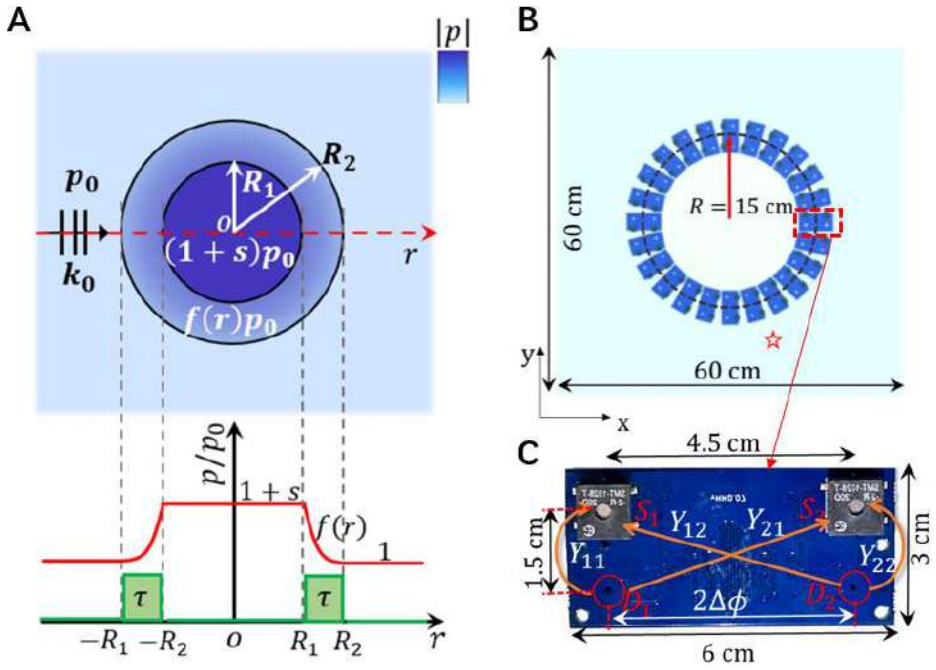


Figure 1: (**A**) Schematic of the localized field amplification by a ring-shaped metasurface with inner and outer radii R_1 and R_2 (upper panel). Lower panel: the line mapping of the pressure field along the red dashed line, in which the transformation function is associated with the Willis coupling τ (green line). (**B**) The constructed metasurface using 24 active meta-atoms. (**C**) A photograph of the meta-atom.

The field-transforming metasurface enables nonreciprocal wave manipulation. As shown in Fig. 2(**A**), when sound comes from outside at point source A, the metasurface increases the sound pressure inside by a factor of 1.5 times, but the sound pressure outside stays the same. On the other hand, when sound comes from inside at point source B, the sound pressure outside is reduced by the same factor, while the inside sound pressure stays the same (shown in Fig. 2(**B**)). Therefore, the active metasurface works like a one-way diode for sound now in two dimensions: people inside hear louder, amplified sounds coming from outside, but people outside hear quieter, attenuated sounds from inside. In addition, the metasurface demonstrates the self-adaptive capability, allowing to automatically adjust to different sound excitations without needing any changes to the metasurface itself.

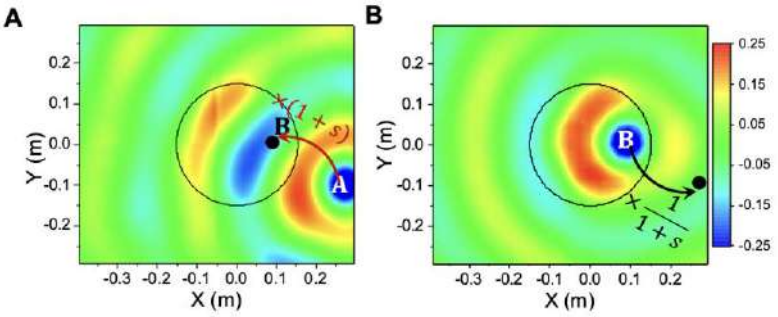


Figure 2: The measured field patterns for (**A**) an external excitation at location A and (**B**) an internal excitation at location B. The transmission wave for A → B (B → A) is scaled by a ratio of 1.5 (1/1.5). The experimental results presented herein exemplify a scenario of $s = 0.5$.

Conclusions: We have developed and demonstrated nonreciprocal field transformation in a 2D acoustic system. The field-transforming metasurface, constructed using active meta-atoms, enables tailor-made field manipulation and nonreciprocal wave control. The nonreciprocal field transformation significantly extends the framework of TO toward nonreciprocal wave manipulation, and is expected to trigger further design of nonreciprocal devices using transformation approaches, such as nonreciprocal cloaking.

Acknowledgements: This work was supported by Research Grants Council (RGC) of Hong Kong through projects no. 16303019, 16307522, and AoE/P-502/20 and the Croucher Foundation (CF23SC01); and Korea National Research Foundation grant 2014M3A6B3063708.

References

1. He, C., Zhang, X. L., Feng, L., Lu, M. H., & Chen, Y. F. One-way cloak based on nonreciprocal photonic crystal. Appl. Phys. Lett. 99, 151112 (2011).
2. Zhang, Y., Shi, L., Chan, C. T., Fung, K. H., & Chang, K. Geometrical Theory of Electromagnetic Nonreciprocity. Phys. Rev. Lett. 130, 203801 (2023).
3. Tretyakov, S. A., Nefedov, I. S., & Alitalo, P. Generalized field-transforming metamaterials. New J. Phys. 10, 115028 (2008).
4. Cho, C., Wen, X., Park, N., & Li, J. Digitally virtualized atoms for acoustic metamaterials. Nat. Commun. 11, 251 (2020).
5. Cho, C., Wen, X., Park, N., & Li, J. Acoustic Willis meta-atom beyond the bounds of passivity and reciprocity. Commun. Phys. 4, 82 (2021).
6. Wen, X., Yip, H. K., Cho, C., Li, J., & Park, N. Acoustic Amplifying Diode Using Nonreciprocal Willis Coupling. Phys. Rev. Lett. 130, 176101 (2023).

Momentum-resolved Studies of Plasmon – Acoustic Phonon Interactions in an Acoustoplasmonic Metamaterial

A. K. Dhiman[1] , H. Dongre[1], K. Zaleski[2], P. Graczyk[1], B. Graczykowski[1], T. Vasileiadis[1]*

[1] Faculty of Physics and Astronomy, Adam Mickiewicz University, Poznan, Poland

[2] NanoBioMedical Centre, Adam Mickiewicz University, Poznan, Poland

* thomas.vasileiadis@amu.edu.pl

Abstract: We perform momentum-resolved studies of acoustic phonons in an acoustoplasmonic metamaterial (APM) using Brillouin light scattering and finite-element-method calculations. The APM is a square lattice of nanoholes on a gold-covered SiO_2-on-Si wafer. For certain modes, the acoustic and plasmonic fields are localized in the nanoholes leading to plasmon-enhanced optomechanical interactions.

Various signal-processing operations require the transduction of electromagnetic waves (light) to mechanical vibrations (acoustic phonons) and vice versa. The transport properties of acoustic phonons can be controlled with the so-called phononic metamaterials[1]. For many modern applications, the acoustic phonons need to couple to electromagnetic radiation at optical frequencies[2]. Potentially, the coupling between acoustic phonons and optical radiation can be enhanced with plasmonic nanostructures[3]. The relevant artificial structures combining phononic and plasmonic functionalities are termed acoustoplasmonic metamaterials (APM). So far, the bulk of studies on plasmon-enhanced optomechanics were devoted to Surface Enhanced Raman Scattering (SERS), while recent works demonstrated plasmon-enhanced Brillouin Light Scattering (BLS) by acoustic vibrations in metallic nanoparticles[3]. Here, we explore the interactions of plasmons with propagating acoustic phonons in an APM structure using BLS spectroscopy and finite-element-method (FEM) calculations. Following a top-down approach, we prepared a square lattice of nanoholes on a gold-covered thermal-oxide-on-silicon wafer (30 nm Au / 300 nm SiO_2 / bulk Si).

The BLS measurements were performed in the backscattering geometry using two continuous wave (CW) lasers with wavelengths 532 nm or 660 nm. The angle of incidence (θ) of light is used to select the wavevector of the probed phonons parallel to the surface ($k_{\parallel}$) through the relationship: $k_{\parallel} = 4\pi \sin\theta / \lambda$. In this way, we recorded the phononic band structure, while the vibrational density of states (VDOS) was found by averaging the spectra for different $k_{\parallel}$-values. The obtained VDOS was of course modulated by the mode-dependent optomechanical coupling that gives rise to the BLS signal. In the presence of nanoholes, the Rayleigh and Sezawa modes of the homogenous flat film transformed into a rich phononic band structure. The distribution of the BLS intensity in reciprocal space varied strongly with the used wavelength of light (532 or 660 nm). On the one hand, the 532 nm radiation gave strong BLS for low-frequency modes (~2-4 GHz range) and revealed phenomena like avoided crossing and partial Bragg gaps. On the other hand, the 660 nm radiation gave the strongest BLS signal for high-frequency modes at ≥7 GHz. The photon-energy dependent optomechanical coupling strength is evident in the VDOS spectra of **Figure 1a**. The FEM calculations revealed that as the wavelength of light increases, the electromagnetic field is enhanced near the nanoholes (**Figure 1b**). The displacement fields and the elastic energy density of high-frequency modes (≥7 GHz) are also localized near the nanoholes (**Figure 1c**) leading to enhanced BLS signal for 660 nm light. Generally, the optomechanical interactions between photons (/plasmons) and acoustic phonons are mediated by two mechanisms: the photoelastic (PE) effect in the volume and the moving interface (MI) effect on the surface of materials[3]. The FEM calculations of the PE and MI effects were

used to visualize the coupling strength between plasmons and acoustic phonons in reciprocal space (**Figure 1d**). Our work paves the way for tailoring plasmon-enhanced optomechanics in the GHz range using acoustoplasmonic metamaterials and metasurfaces.

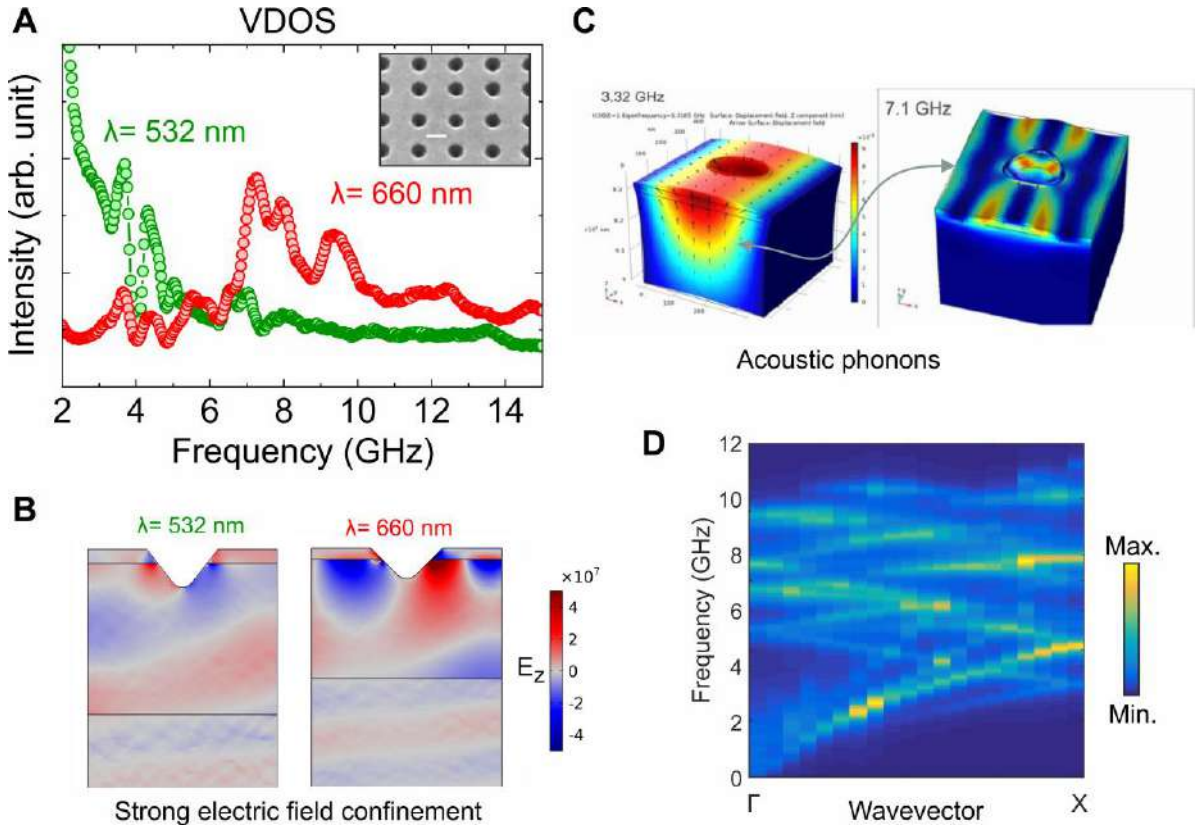


Figure 1. A) VDOS of nanohole arrays measured with BLS using 532 nm wavelength of light (green) or 660 nm wavelength of light (red). The inset shows an SEM image of the nanohole array. The white bar is 200 nm. **B)** The electromagnetic fields for 532 nm (left) and 660 nm (right). **C)** The displacement fields of acoustic modes at 3.3 GHz (left) and 7.1 GHz (right) at the X-point of the band structure. The grey arrow indicates the spatial confinement of the elastic energy within the gold film and around the nanoholes at higher frequencies. **D)** The calculated coupling between plasmons and acoustic phonons at different parts of the acoustic band structure for 660 nm wavelength.

Acknowledgements: This project received funding from the National Science Center of Poland (NCN) with the Sonata Grant UMO-2021/43/D/ST3/02526.

References

[1] T. Vasileiadis, J. Varghese, V. Babacic, J. Gomis-Bresco, D. N. Urrios, B. Graczykowski, *J. Appl. Phys.* 129, 160901 (2021).

[2] T. C. van Thiel, M. J. Weaver, F. Berto, P. Duivestein, M. Lemang, K. L. Schuurman, M. Žemlička, F. Hijazi, A. C. Bernasconi, C. Ferrer, E. Cataldo, E. Lachman, M. Field, Y. Mohan, F. K. de Vries, C. C. Bultink, J. C. van Oven, J. Y. Mutus, R. Stockill, S. Gröblacher, *Nature Physics*, 3237 (2025).

[3] T. Vasileiadis, A. Noual, Y. Wang, B. Graczykowski, B. Djafari-Rouhani, S. Yang, G. Fytas, *ACS Nano* 16(12), 20419–20429 (2022).

Customized inverse design of quasi-zero-stiffness metamaterials by topology optimization

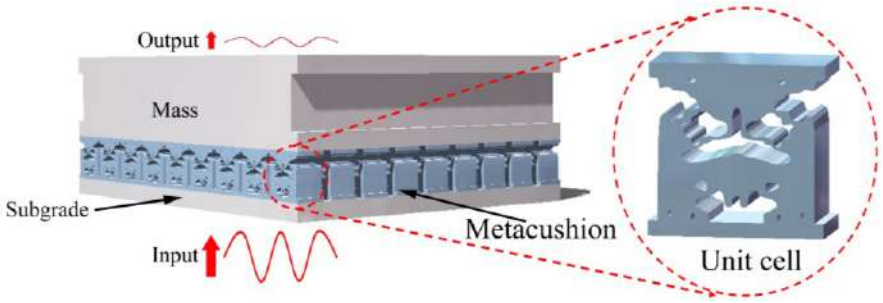
Chao Ma1[1], Kun Wu2[1*]

[1]Tianjin University, China
[*]corresponding author: kunwu@tju.edu.cn

Abstract: This work presents an inverse design approach for metamaterials with customized quasi-zero-stiffness property. Finite element simulations and experiments are performed on the optimized topological configuration to validate the QZS feature. The proposed inverse-design methodology may pave a new way for low-frequency vibration isolation using compact single-phase solid structure without assembly.

This study develops an approach for inverse design of periodic QZS metacushion on the basis of topology optimization, as shown in Figure 1. The combination of coded modelling and finite element method is employed in iterative calculations so as to obtain periodic QZS metamaterials with objective static properties. Customized QZS metacushions with different porosity values and sizes are investigated on terms of weight and space arrangement, as shown respectively in Figure 2. In terms of dynamics, QZS metacushion exhibits excellent performance in low-frequency vibration isolation with confirmation by both experiments and simulations. The selection of payload has significant influence on the vibration responses which is necessary to approach the restoring force for a better performance of low-frequency vibration isolation.

(a)



(b)

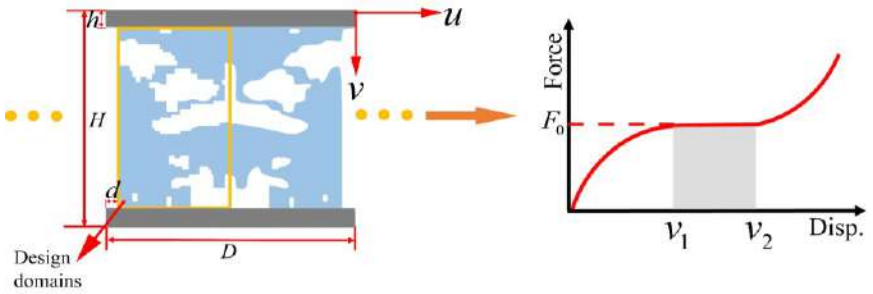


Figure 1. Schematic of the topology design: (a) QZS metacushion consisting of multiple cells; (b) representative cell design and target force-displacement curve

(a)

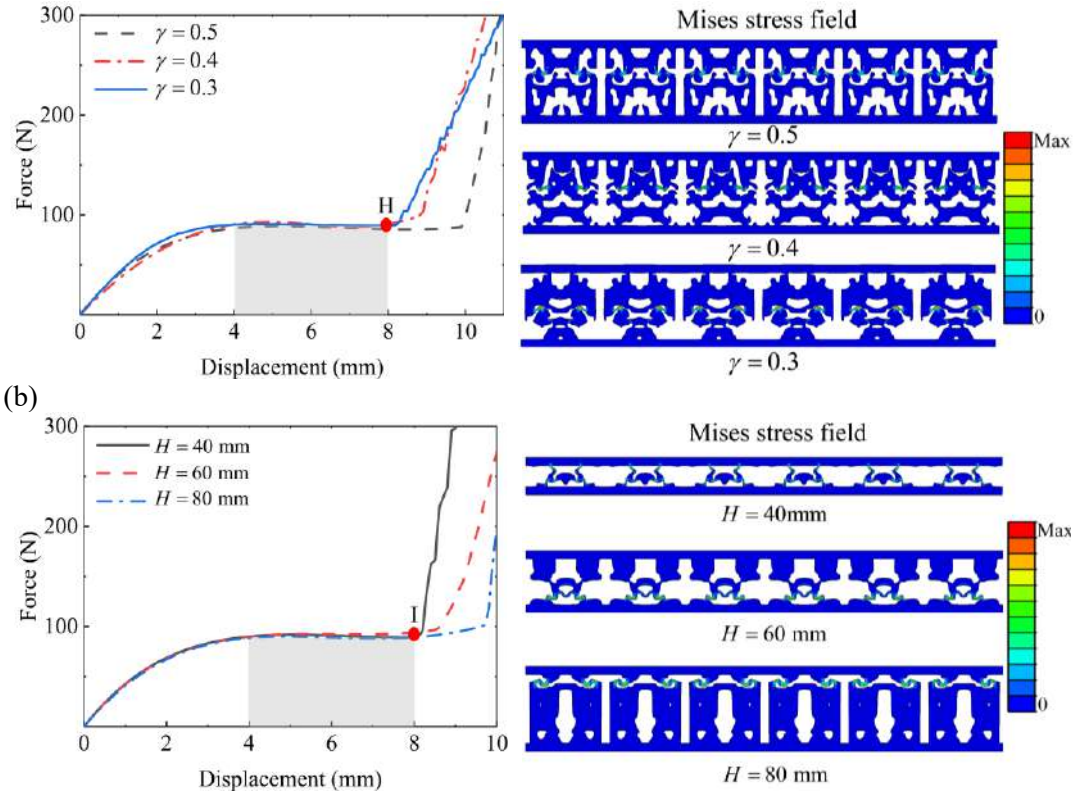


Figure 2. Static behavior of finite periodic QZS metacushion with (a) different porosity values and (b) height sizes.

References

1. Y. Xu, H.-W. Dong, Y.-S. Wang, Topology optimization of programable quasi-zero-stiffness metastructures for low-frequency vibration isolation, International Journal of Mechanical Sciences **280**, 109557 (2024).
2. M. Jia, N. Dai, T. Wang, Q. Cao, L. Yan, H. Dai, A compact quasi-zero stiffness metamaterial for energy absorption and impact protection, Thin-Walled Structures **205**, 112360(2024).

Realization of Weyl elastic metamaterials with spin skyrmions

Yuang Pan[1], **Yihao Yang**[*]

[1]Zhejiang University, China

[2] Zhejiang University, China

[*]corresponding author: yangyihao@zju.edu.cn

Abstract: Topological elastic metamaterials provide a topologically robust way to manipulate the phononic energy and information beyond the conventional approaches. Among various topological elastic metamaterials, Weyl elastic metamaterials stand out. Here, we realize an ideal, 3D printed, all-metallic Weyl elastic metamaterial with low dissipation losses.

Topological elastic metamaterials provide a topologically robust way to manipulate the phononic energy and information beyond the conventional approaches. Among various topological elastic metamaterials, Weyl elastic metamaterials stand out, as they are unique to three dimensions and exhibit numerous intriguing phenomena and potential applications. To date, however, the realization of Weyl elastic metamaterials remains elusive, primarily due to the full-vectoral nature of elastic waves and the complicated couplings between polarizations, leading to complicated and tangled three-dimensional (3D) bandstructures that unfavorable for experimental demonstration. Here, we overcome the challenge and realize an ideal, 3D printed, all-metallic Weyl elastic metamaterial with low dissipation losses. Notably, the elastic spin of the excitations around the Weyl points exhibits skyrmion textures, a topologically stable structure in real space. Utilizing 3D laser vibrometry, we reveal the projection of the Weyl points, the Fermi arcs and the unique spin characteristics of the topological surface states. Our work extends the Weyl metamaterials to elastic waves and paves a topological way to robust manipulation of elastic waves in 3D space.

Numerical and Experimental Investigation of Multi-Stable Metastructures Endowed with Free-Standing Bistable Locally Resonant Unit Cells

Tugberk Guner[1*], Oreste S. Bursi[1] and Hasan N. Olmez [1]

[1]University of Trento, Dept. of Civil, Environmental and Mechanical Eng., Via Mesiano, 38123, Trento, Italy
*corresponding author, E-mail: tugberk.guner@unitn.it

Abstract

We have conceived new multi-stable metastructures endowed with free-standing bistable locally resonant unit cells for passive vibration attenuation. Notably, bistability is introduced into each main cell, using novel slender pre-buckled beams. It is demonstrated how the presence of resonators can enhance the elastodynamic response of metastructures both numerically and experimentally.

1. Introduction

Multi-stable systems exhibit rich static and dynamic behaviours, driven by transitions between discrete equilibrium states [1]. This results in rich dynamics and underscores the importance of further research to harness their potential. A frequently studied category of multi-stable systems, bistability is attracting attention, due to the potential revealed by recent research [2]. The rich and advantageous functionalities inherent in bistable mechanisms make them viable candidates for applications spanning diverse fields such as engineering, physics, biology, materials science, and beyond [3]. Bistable mechanisms are increasingly used in vibration and impact protection devices such as isolators [4] and structural dampers [5]. In energy harvesting, bistability enhances power output by leveraging large-amplitude, high-velocity snap-through motions and generating subharmonic responses, thus overcoming the limitations of resonance-based systems [6; 7].

Recent advances have also integrated bistability into metamaterials, giving rise to novel functionalities such as chirality [8], deployability [9], foldability [10], and so on. More specifically, [11], investigated the dynamics of the locally resonant (LR) metamaterial beam with bistable attachments and produced an attenuation frequency range that is 350% wider than the corresponding linear LR bandgap. Several studies have investigated the nonlinear dynamics of 1D bistable lattices. Nadkarni et al. [12] analyzed snap-through instabilities and provided closed-form analytical solutions. Frazier et al. [13] demonstrated supratransmission with dual amplitude thresholds, enabling energy transmission through band gaps. Deng et al. [14] explored the behaviour of transition waves considering the nearest-neighbour spring interactions. A simple and effective way to realize multi-stable systems is by connecting bistable springs in series. This concept underlies free-standing bistable lattices, where unit cells are interconnected through bistable elements, forming a multi-stable metastructure (Fig. 1). These lattices have been shown to either trap input energy or transmit it as solitary waves, depending on the system's dynamic response [15]. Advances in additive manufacturing have further enabled the rapid and precise fabrication of such complex metastructures, facilitating experimental validation. Based upon the gap in the literature, this study undertakes a numerical and experimental investigation of multi-stable 1D metastructures made up of locally resonant bistable unit cells. Notably, bistability is introduced into the main springs as elastodynamic slender beams under buckling, as illustrated in Fig. 1. Consequently, metastructures consisting of six cells were experimentally tested and compared against numerical results.

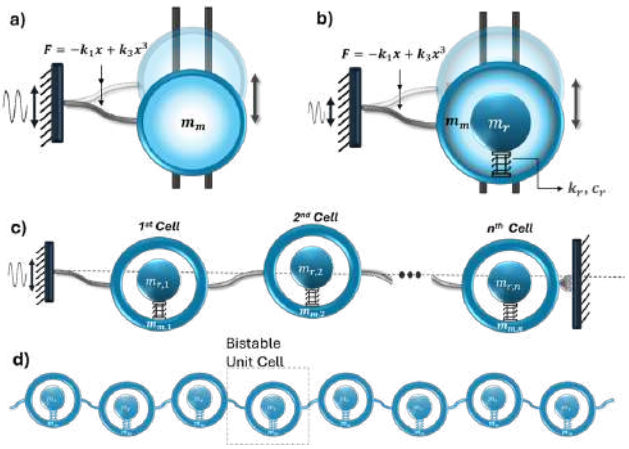


Figure 1: A bistable oscillator (a) standalone, (b) coupled with a resonator, (c) a multistable metastructure composed of locally resonant unit cells (MLRM), (d) metamaterial made up of locally resonant bistable unit cells (BLRM)

2. Dynamics of Bistable LR Metamaterials

In basics, metamaterials can be constructed by arranging unit cells in a repeating pattern; importantly, their properties are also influenced by their designed structure. Accordingly, herein, two metamaterials that were made of a periodic arrangement of: (i) bistable oscillators; and (ii) bistable oscillators coupled with linear resonators were examined. Respectively, these metastructures are called bistable metamaterials (BM) and bistable locally resonant metamaterials (BLRM). Here, the locally resonant (LR) property governs from the anti-resonance of attached resonators in a periodic medium. The schematic representations of these metamaterials are given in Fig. 1(d), where i represents the i-th cell in the lattice. The non-dimensionalised EoMs of the i-th cell of the BLRM can be written as follows:

$$\begin{aligned}&\hat{x}''_{m,n}+\eta(2\hat{x}'_{m,n} \in \hat{x}'_{m,n-1} \in \hat{x}'_{m,n+1})\\ &\quad \in (2\hat{x}_{m,n} \in \hat{x}_{m,n-1} \in \hat{x}_{m,n+1})\\ &\quad +\varepsilon(\hat{x}_{m,n} \in \hat{x}_{m,n-1})^3+\varepsilon(\hat{x}_{m,n} \in \hat{x}_{m,n+1})^3 \quad (1a)\\ &\quad +\varphi\eta_r(\hat{x}'_{m,n} \in \hat{x}'_{r,n})+\varphi\lambda^2(\hat{x}_{m,n} \in \hat{x}_{r,n})\\ &\quad =f_{ext}(\alpha,\Omega,\tau)\\ &\hat{x}''_{r,n}+\eta_{r,n}(\hat{x}'_{r,n} \in \hat{x}'_{m,n})+\lambda^2(\hat{x}_{r,n} \in \hat{x}_{m,n})=0 \quad (1b)\end{aligned}$$

where $\hat{x}=x/\delta_s$, $\tau=t\omega_n$, $\omega_n=\sqrt{k_1/m_m}$, $\eta=c(m_m\omega_n)^{-1}$, $\varepsilon=k_3\delta_s^2(m_m\omega_n^2)^{-1}$, $\Omega=\omega_0/\omega_n$, $\alpha=A_0/\delta_s$, $\eta_r=c_r(m_r\omega_n)^{-1}$, $\omega_r=\sqrt{k_r/m_r}=\lambda\omega_n$ and $m_r=m_m\varphi$

The dispersion relation and wave solutions of the system can be obtained analytically or numerically under the assumption of periodic response. However, as highlighted by Van Belle [16] and Aloschi et al. [17], the presence of damping introduces amplitude-dependent effects due to nonlinearity, causing the dispersion characteristics of each unit cell to differ. This variation breaks the fundamental assumption of uniform periodicity required by Floquet-Bloch theory. Despite numerical methods remaining effective in approximating *band-gap-like behaviours* and capturing key wave propagation characteristics. Following the methodology of [18], a BLRM composed of 500 bistable unit cells was modelled, with an additional 1000 perfectly matched layer (PML) cells at the free end to eliminate reflections. The system was subjected to sinusoidal excitation with varying amplitudes ($0<\alpha<5$) and frequencies up to 3Ω. Each simulation was run for 500 seconds to ensure steady-state behaviour, with a smooth ramp-up over the first 20 seconds to suppress transient impact effects. The resulting wave field was analysed using a 2D Fast Fourier Transform (FFT), and the dispersion characteristics are shown in Fig. 2. In Fig. 2, it is evident that at each frequency, a peak point emerges, corresponding to the wavenumber

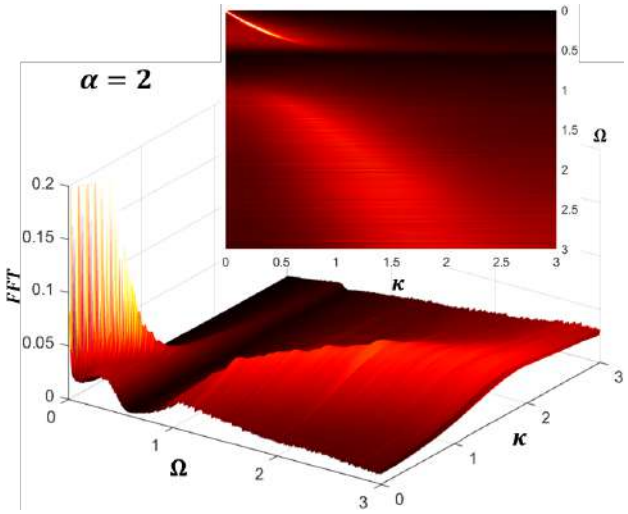


Figure 2: Frequency–wavenumber relation obtained using 2D Fast Fourier Transform (FFT) for $\alpha=1.0$.

of the predominant wave propagating through the chain. Consequently, at each frequency, the peak can be isolated, and the dispersion relation can be plotted. For comparison, the results of the BM were also examined and plotted alongside the BLRM results in Fig. 3. Moreover, as illustrated in Fig. 4, the wave amplitude varies across the cells of the BLRM. When the input amplitude α is small, the long-wavelength waves propagate over a longer distance, reaching up to the 100th cell. In contrast, for higher input amplitudes, wave attenuation becomes significant, with noticeable energy confinement within the first 10 cells. At high amplitudes and shorter wavelengths, the initial cells exhibit higher displacement ratios, followed by a rapid decay, indicating that the wave energy is effectively trapped within the first few cells.

3. Dynamics of Multi-stable Metastructures

In practical applications of low-frequency metamaterials, implementing structures with as many as 500 unit cells is often infeasible due to physical size and spatial limitations. The experimental study presented in the following sections demonstrates that even assembling six cells posed significant challenges. Consequently, this research also focusses on finite lattice metastructures with a limited number of cells, where periodicity is inherently constrained and boundary effects, such as wave reflections, must be carefully considered.

To investigate these effects, numerical simulations were conducted on finite BM and BLRM, composed of 3, 6, and 9 unit cells. These correspond to multi-stable metastructures (MM) and their locally resonant counterparts

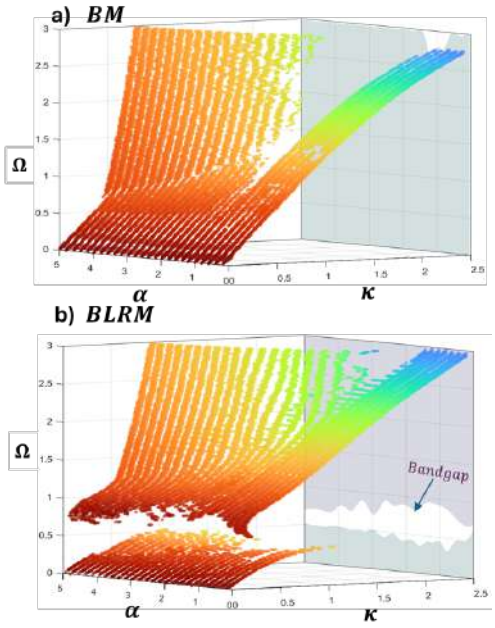


Figure 3: Dispersion relations obtained for varying input amplitudes, highlighting the influence of excitation magnitude on wave propagation characteristics.

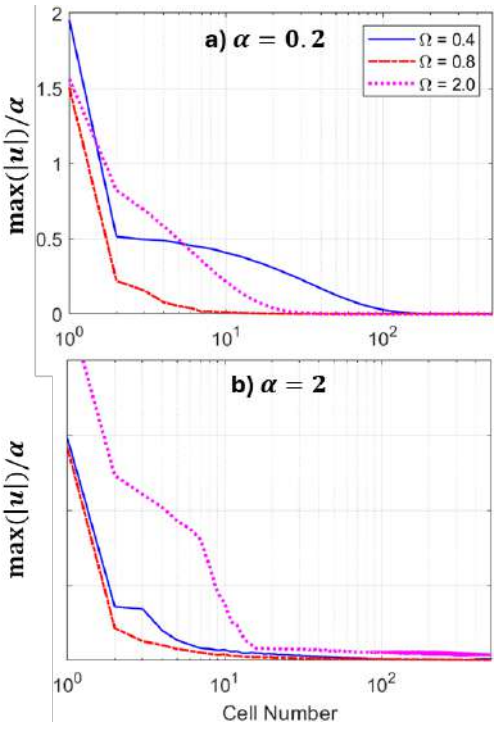


Figure 4: Variation of peak steady-state displacement amplitudes across the unit cells of the BLRM under sinusoidal excitation with amplitude: (a) $\alpha = 0.2$ and (b) $\alpha = 2.0$

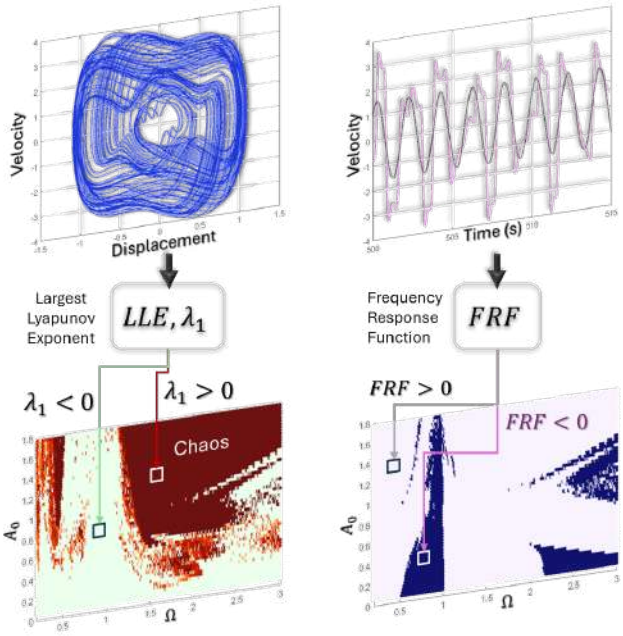


Figure 5: Numerical tools adopted and typical outcomes to characterise the response of MMs and MLRMs

(MLRM), respectively. The analysis methodology is illustrated in Fig. 5. Specifically, regions of chaotic response were identified using Lyapunov exponent analysis, with the largest Lyapunov exponent (LLE) computed via the algorithm proposed by Rosenstein et al.[19]. Additionally, the frequency response function (FRF) was calculated as:

$$FRF(\omega_0) = 20log_{10}\left(\frac{max|\dot{x}_{out}|}{max|\dot{x}_{in}|}\right) \tag{2}$$

where velocities are used instead of displacements, as they are more reliable in capturing inter-well motions. The FRF characterises the regions of amplification (FRF > 0) or attenuation (FRF < 0). Simulations were performed for a range of input amplitudes $\alpha \leq 3$ and excitation frequencies, i.e. $\Omega \leq 3$.

For MMs, as shown in Fig. 6, increasing the number of cells enhances the presence of chaotic behavior, particularly in the low-amplitude regime. However, more cells also extend the range of amplitude and frequency where attenuation occurs. In contrast, the behavior of MLRMs, depicted in Fig. 7, reveals the influence of local resonances. As the number of cells increases, the band gap widens, suppressing chaotic responses not only within the attenuation band but also in surrounding propagation zones. Furthermore, larger cell counts allow for attenuation of higher-amplitude excitations.

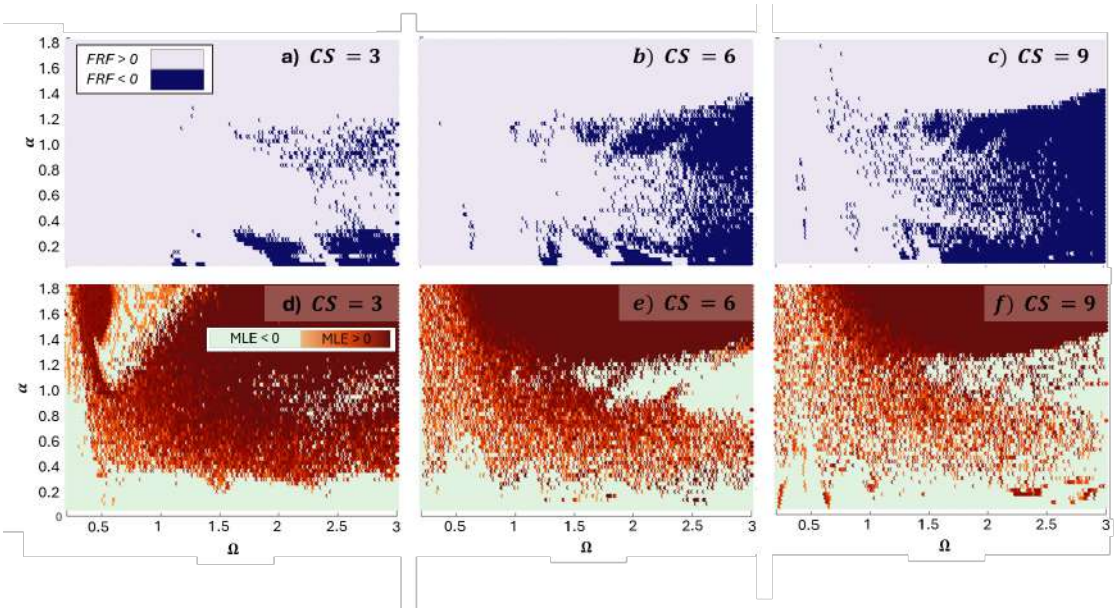


Figure 6: The effect of increasing the number of cells in the MM. The top row presents attenuation/propagation zones, whilst the bottom row presents chaotic behaviour.

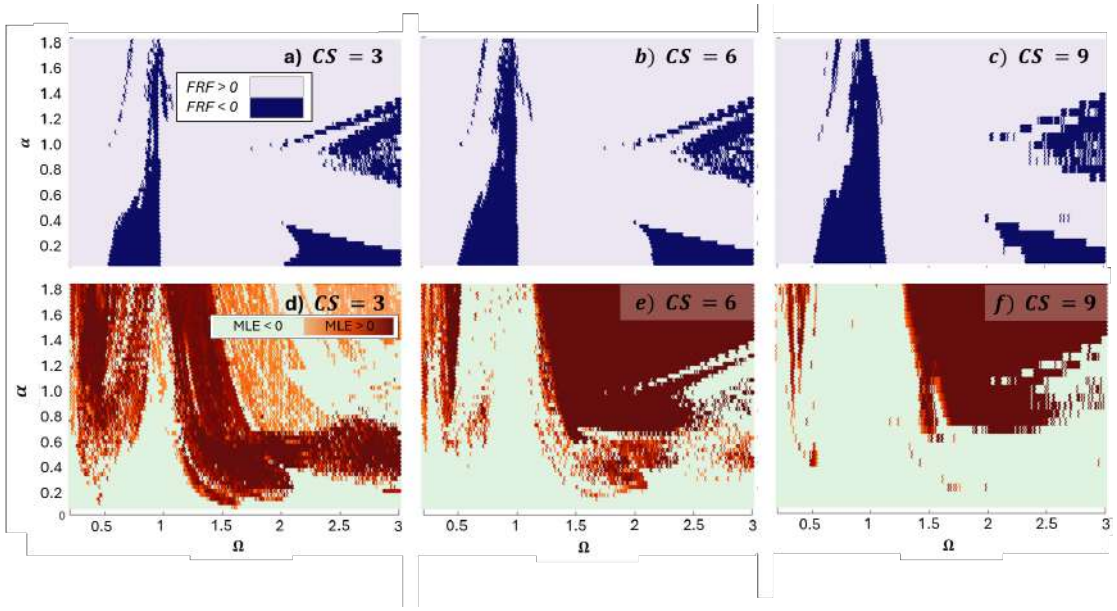


Figure 7: The effect of increasing the number of cells in the MLRM. The top row presents attenuation/propagation zones, whilst the bottom row presents chaotic behaviour.

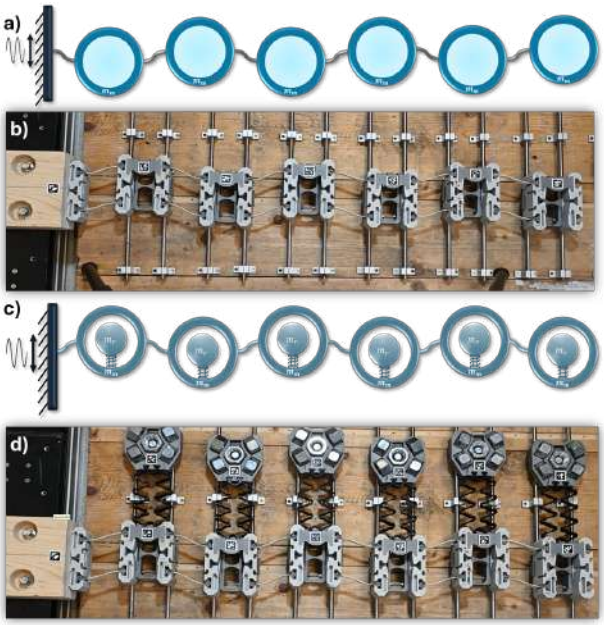


Figure 8: MM and MLRM configurations with six unit cells: (a, c) equivalent spring–mass–damper models; (b, d) corresponding realizations using 3D-printed experimental setups.

Table 1: Properties of materials used for 3D FFF printing

Material	Components	Density kg/m^3	Elastic Modulus MPa	Tensile Strength MPa
ABS+PC	Main beams	1.02	2100	40
TPU	Res. beams	1.16	150	50
ABS	Others	1.10	2030	43.6

4. Experimental Setup and Unit Cell Design

For the experiment, six cell MM and MLRM were created using bistable unit cells as depicted in Fig. 8. The input was provided as a driven boundary that is given a compact shake table with a maximum velocity of 0.5m/s and 2g under 50 kgf payload. Overall, in connection with previous studies, the objective was to create a metastructure aiming band gap in the low-frequency range, i.e. 1-5 Hz, also within the limits of the shake table. Consequently, the unit cells were manufactured using, Fused Filament Fabrication (FFF) 3D printing. As a result, commonly available filaments, such as ABS, TPU, were used, and their technical details provided by the manufacturer are given in the Table 1.

A schematic illustrating the correspondence between the LR unit cell and its 3D-printable counterpart is shown in Fig. 9. In this design, beams subjected to shear are modelled as spring-damper elements. When unloaded axially, these beams behave as mono-stable spring-dampers, with damping arising from internal deformation and material viscosity. However, when an axial load exceeding the critical buckling threshold is applied, the beams buckle (Fig. 10), and their lateral force–displacement behaviour exhibits bistability. This enables the creation of simple, easily manufactured bistable springs. To ensure repeatable performance, the beam ends were designed with rotational constraints and each unit cell was guided by circular aluminium rails.

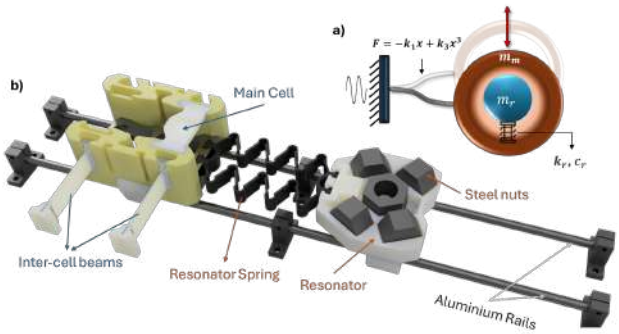


Figure 9: Schematic of the unit cell design and its equivalent spring–mass–damper model.

For experimental data acquisition, Digital Image Correlation (DIC) was employed. High-speed videos (1920×1080 pixels at 120 fps) were captured and processed in MATLAB. Multi-object tracking was achieved using AprilTags [20].

5. Experimental Results

Six-cell MM and MLRM configurations were initially analyzed through separate frequency sweeps with two input amplitudes: $A_0 = 8\,\text{mm}$ with ω ranging from 0 to 10 Hz, and $A_0 = 15\,\text{mm}$ with ω_0 spanning from 0 to 5 Hz. The displacement responses of the cell farthest from the shake table are illustrated in Fig. 11. For both scenarios, the attenuation effect caused by the locally resonant resonators is notably apparent. Under low-amplitude input, MM exhibited propagation peaks at 2.5 Hz and 8.4 Hz, with noticeable attenuation between the 4.3-7 Hz range. In contrast, MLRM showed a complete attenuation range starting from 0 Hz and extending up to 8.5 Hz. With $A_0 = 15\,\text{mm}$, MM displayed an aperiodic response with a pronounced amplification at 1 Hz, whereas MLRM's response remained below 10 mm and non-chaotic throughout the range considered, validating the numerical predictions.

For a more detailed examination, Fig. 12 displays the displacement responses of the MLRM resonators under the condition of $A_0 = 15\,\text{mm}$. The greatest displacement was

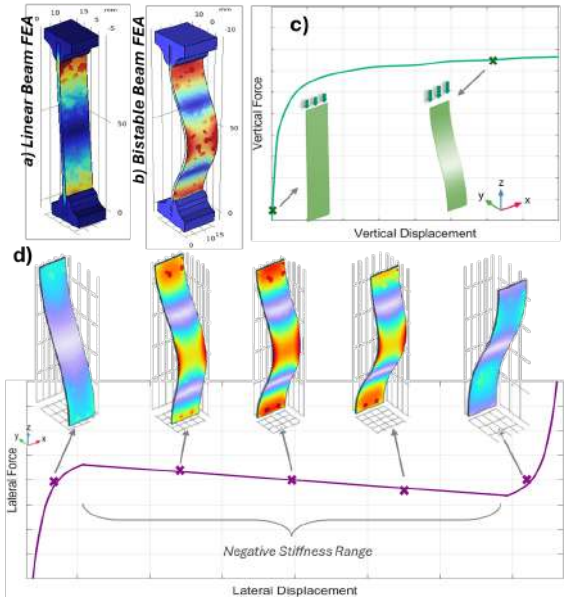


Figure 10: Stress distribution in a beam under axial load; (a) below and (b) exceeding the critical buckling load; (c) vertical force–vertical displacement response; (d) lateral force–displacement response under sustained axial load greater than the critical buckling load.

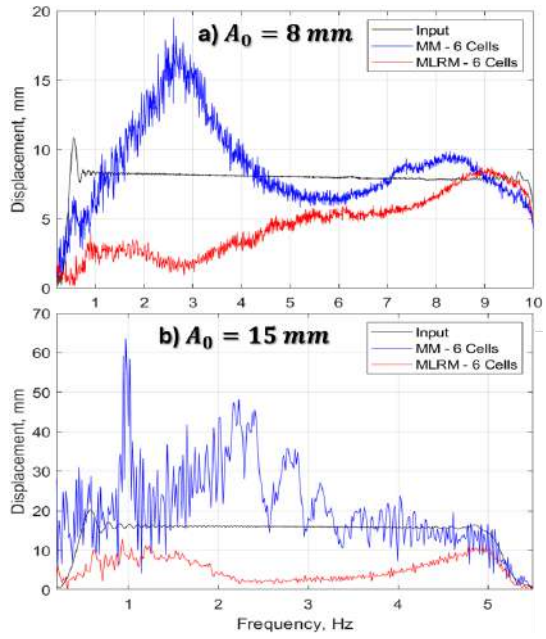


Figure 11: Six-cell MM and MLRM tested for frequency sweeps with: (a) $A_0 = 8\,\text{mm}, \omega = 0 \in 10Hz$, and (b)$A_0 = 15\,\text{mm}, \omega_0 = 0 \in 5Hz$. The displacement responses of the cells farthest from the shake table are presented.

found in the resonator nearest to the input source, namely the shake table, occurring at 2.2 Hz. As the distance from the input increases, both the displacement and the resonant frequency of the resonators diminish. Notably, the resonator furthest from the input showed an equivalent displacement to that of the main mass. Finally, configurations with three cells and six cells were evaluated under a high input amplitude of $A_0 = 20\,\text{mm}$, with the results presented in Fig. 13. For MMs, using fewer cells led to an aperiodic amplified response within the 1-2.5 Hz range, followed by an attenuation zone beyond 2.6 Hz. With a six-cell setup, the amplified response was diminished, but the attenuation zone also vanished. In the case of MLRMs, a three-cell configuration produced chaotic responses below the 1 Hz range, which is beyond the resonators' operating range. With six cells, there was a marked reduction in performance above 1 Hz. Thus, in MLRMs, increasing the number of cells improved dynamic responses and enhanced vibration isolation. However, when the number of cells is restricted, it is essential to focus on the lower frequency ranges and non-periodic reactions. Displacement responses of the MLRM resonators. The MRLM is subjected to frequency sweep with $A_0 = 15\,\text{mm}$

6. Conclusions and Future Perspectives

This study investigated the dynamic behaviour of periodic metamaterials composed of bistable locally resonant unit cells, BLRM, and finite lattice metastructures, specifically multi-stable metastructures (MM) and their locally resonant counterparts (MLRM) with a limited number of unit cells. Through numerical simulations, the propagation characteristics of the waves in the BLRMs were investigated. In finite MM and MLRMs, using Lyapunov exponent analysis and frequency response functions, we identified regions of chaotic response and assessed the influence of unit cell count and excitation amplitude. Experimental results demonstrate that increasing the number of unit cells generally enhances vibration attenuation and reduces chaotic behaviour, particularly in MLRMs, as a result of the widening of the locally resonant band gap. MMs, while capable of attenuation, were more prone to chaotic amplification under high excitation. MLRMs exhibited superior performance in mitigating vibrations in a broader frequency range, even with high input amplitudes. However, when constrained to fewer cells, MLRMs showed sensitivity to excitation frequencies outside the resonator's effective range, resulting in diminished isolation capability.

These findings emphasise the importance of finite boundaries, unit cell count, input amplitude, and frequency in the design of finite nonlinear metastructures, especially when aiming for robust performance in compact systems. Future work may focus on optimising the placement and

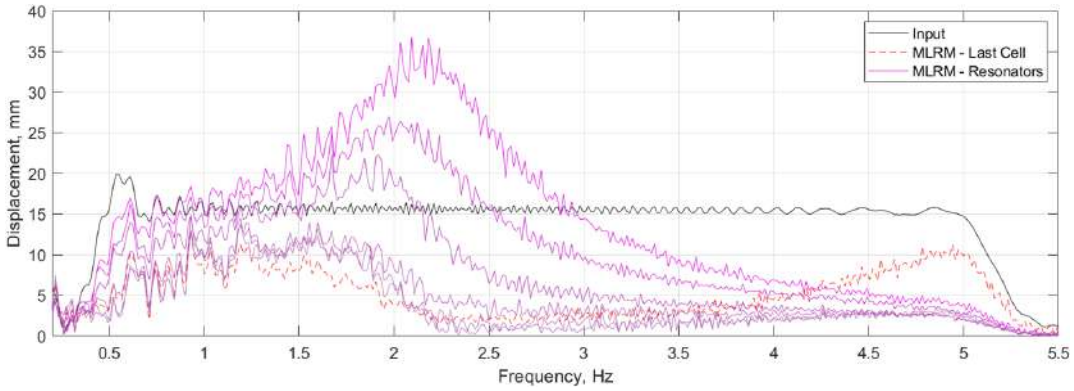


Figure 12: Displacement responses of the resonators. The MRLM is subjected to frequency sweep with $A_0 = 15\,\text{mm}$

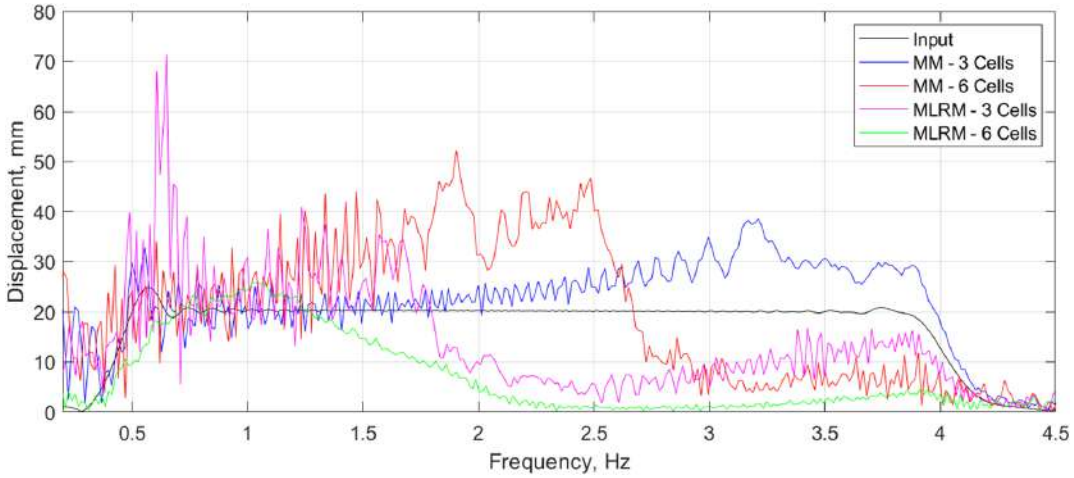


Figure 13: Furthest cell displacement results for configurations with three cells and six cells, which were evaluated under a high input amplitude of $A_0 = 20\,\text{mm}$

tuning strategies of the resonator with varying frequencies to further improve energy absorption in short, finite configurations.

Acknowledgement

This work is carried out within the DPC-ReLUIS 2024-2026 project, WP9, funded by the Department of Civil Protection of Italy. The authors also acknowledge the Italian Ministry of Education, Universities, and Research (MUR) in the framework of the DICAM-EXC project (Departments of Excellence 2023–2027, grant L232/2016) for the use of the M3 Laboratory.

References

[1] S. Fang, S. Zhou, D. Yurchenko, T. Yang, and W.-H. Liao, "Multistability phenomenon in signal processing, energy harvesting, composite structures, and metamaterials: A review," *Mechanical Systems and Signal Processing*, vol. 166, p. 108419, Mar. 2022.

[2] Y. Cao, M. Derakhshani, Y. Fang, G. Huang, and C. Cao, "Bistable Structures for Advanced Functional Systems," *Advanced Functional Materials*, vol. 31, no. 45, p. 2106231, 2021.

[3] R. L. Harne and K.-W. Wang, *Harnessing bistable structural dynamics: for vibration control, energy harvesting and sensing*. John Wiley & Sons, 2017.

[4] M. Friswell and E. Saavedra Flores, "Dynamic isolation systems using tunable nonlinear stiffness beams," *The European Physical Journal Special Topics*, vol. 222, no. 7, pp. 1563–1573, Sep. 2013.

[5] L. Fan, C. Huang, and L. Huo, "Development of a Negative Stiffness Bistable Damper for Structural Vi-

bration Control," *Shock and Vibration*, vol. 2022, p. e6397602, Nov. 2022, publisher: Hindawi.

[6] S. P. Pellegrini, N. Tolou, M. Schenk, and J. L. Herder, "Bistable vibration energy harvesters: A review," *Journal of Intelligent Material Systems and Structures*, vol. 24, no. 11, pp. 1303–1312, Jul. 2013, publisher: SAGE Publications Ltd STM.

[7] M. F. Daqaq, R. Masana, A. Erturk, and D. Dane Quinn, "On the Role of Nonlinearities in Vibratory Energy Harvesting: A Critical Review and Discussion," *Applied Mechanics Reviews*, vol. 66, no. 4, p. 040801, Jul. 2014.

[8] Y. Liu, F. Pan, F. Xiong, Y. Wei, Y. Ruan, B. Ding, K. Yang, and Y. Chen, "Ultrafast Shape-Reconfigurable Chiral Mechanical Metamaterial based on Prestressed Bistable Shells," *Advanced Functional Materials*, vol. 33, no. 25, p. 2300433, 2023.

[9] Y. Liu, F. Pan, B. Ding, Y. Zhu, K. Yang, and Y. Chen, "Multistable shape-reconfigurable metawire in 3D space," *Extreme Mechanics Letters*, vol. 50, p. 101535, Jan. 2022.

[10] Z. Meng, W. Chen, T. Mei, Y. Lai, Y. Li, and C. Q. Chen, "Bistability-based foldable origami mechanical logic gates," *Extreme Mechanics Letters*, vol. 43, p. 101180, Feb. 2021.

[11] Y. Xia, M. Ruzzene, and A. Erturk, "Bistable attachments for wideband nonlinear vibration attenuation in a metamaterial beam," *Nonlinear Dynamics*, vol. 102, no. 3, pp. 1285–1296, Nov. 2020.

[12] N. Nadkarni, C. Daraio, and D. M. Kochmann, "Dynamics of periodic mechanical structures containing bistable elastic elements: From elastic to solitary wave propagation," *Physical Review E*, vol. 90, no. 2, p. 023204, Aug. 2014, publisher: American Physical Society.

[13] M. J. Frazier and D. M. Kochmann, "Band gap transmission in periodic bistable mechanical systems," *Journal of Sound and Vibration*, vol. 388, pp. 315–326, Feb. 2017.

[14] B. Deng, P. Wang, V. Tournat, and K. Bertoldi, "Nonlinear transition waves in free-standing bistable chains," *Journal of the Mechanics and Physics of Solids*, vol. 136, p. 103661, Mar. 2020.

[15] S. Katz and S. Givli, "Solitary waves in a bistable lattice," *Extreme Mechanics Letters*, vol. 22, pp. 106–111, Jul. 2018.

[16] L. Van Belle, C. Claeys, E. Deckers, and W. Desmet, "On the impact of damping on the dispersion curves of a locally resonant metamaterial: Modelling and experimental validation," *Journal of Sound and Vibration*, vol. 409, pp. 1–23, Nov. 2017.

[17] F. Aloschi, O. S. Bursi, A. Palermo, and A. Marzani, "A time domain procedure for the identification of periodic structures," *International Journal of Mechanical Sciences*, vol. 269, p. 109054, 2024.

[18] T. Guner, O. S. Bursi, and M. Broccardo, "Seismic vibration mitigation of steel storage tanks by metafoundations endowed with linear and bistable columns," *Bulletin of Earthquake Engineering*, vol. 22, no. 1, pp. 29–54, Jan. 2024.

[19] M. T. Rosenstein, J. J. Collins, and C. J. De Luca, "A practical method for calculating largest Lyapunov exponents from small data sets," *Physica D: Nonlinear Phenomena*, vol. 65, no. 1, pp. 117–134, May 1993.

[20] "AprilTag — april.eecs.umich.edu," https://april.eecs.umich.edu/software/apriltag, 2024, [Accessed 22-05-2024].

Multimode phonon lasing in a self-modulated silicon optomechanical crystal cavity

D. Alonso-Tomás[1,*], **C. Mas-Arabí**[2], **C. Milián**[2], **N. E. Capuj**[3], **A. Martínez**[4], **D. Navarro-Urrios**[1]

[1] MIND-IN2UB, Departament d'Enginyeria Electrónica i Biomédica, Facultat de Física, Universitat de Barcelona, Martí i Franquès 1, Barcelona 08028, Spain

[2]Institut Universitari de Matemàtica Pura i Aplicada, Universitat Politècnica de València, 46022 (Val`encia), Spain

[3]Depto. Física, Universidad de La Laguna, 38200 San Cristóbal de La Laguna, Spain

[4]Nanophotonics Technology Center, Universitat Politècnica de València, Camino de Vera s/n, 46022 Valencia, Spain
[*]corresponding author: david.alonso@ub.edu

Abstract: We theoretically and experimentally investigate an optically self-modulated multimode optomechanical platform. The self-induced modulation adapts to optomechanical feedback from multiple modes, enabling synchronous pumping and driving them into high-amplitude coherent mechanical motion despite strong mode competition. These findings advance the generation of multi-phonon coherent sources in chip-integrated silicon platforms.

Cavity optomechanics [1] has enabled the realization of coherent phonon sources ("phonon lasers"), but extending this phenomenon to multimode systems remains challenging due to mode competition, which typically suppresses simultaneous oscillations in multiple mechanical modes [2]. Previous approaches rely on externally modulated laser inputs to induce parametric coupling [3] or use widely separated mechanical frequencies to mitigate competition [4], both of which constrain scalability and integration.

Here, we experimentally demonstrate a stable multimode phonon lasing regime in a silicon nanobeam optomechanical cavity, where two flexural mechanical modes achieve high-amplitude, self-sustained oscillations despite strong mode competition.

Using a simple setup (Fig. 1a), we characterize the optical (Fig. 1b) and mechanical (Fig. 1c) modes of the structure. Under strong blue-detuned optical drives (sweeping from lower to higher laser wavelengths), the interplay between thermo-optic (TO) and free-carrier dispersion (FCD) effects induces cyclic modulation of the refractive index (Fig. 1d), known as self-pulsing (SP). This SP cycle [5] features a tunable repetition rate in the 10–100 MHz range, where several flexural modes of the nanobeam exhibit large optomechanical coupling.

Counterintuitively, we demonstrate that the adaptive capabilities of SP enable simultaneous, synchronous, radiation-pressure-driven amplification of oscillations in two strongly competing mechanical modes. This adaptation persists even when the mechanical frequencies are incommensurable, leading to transitions between periodic (Fig. 1e), quasi-periodic (Fig. 1f), and chaotic intra-cavity power dynamics, while maintaining coherent, high-amplitude mechanical oscillations.

Supported by a predictive macroscopic model, these findings provide a novel strategy for engineering coherent multimode phonon sources and pave the way for optomechanical frequency comb generation with low repetition rates and advanced nonlinear phononic systems.

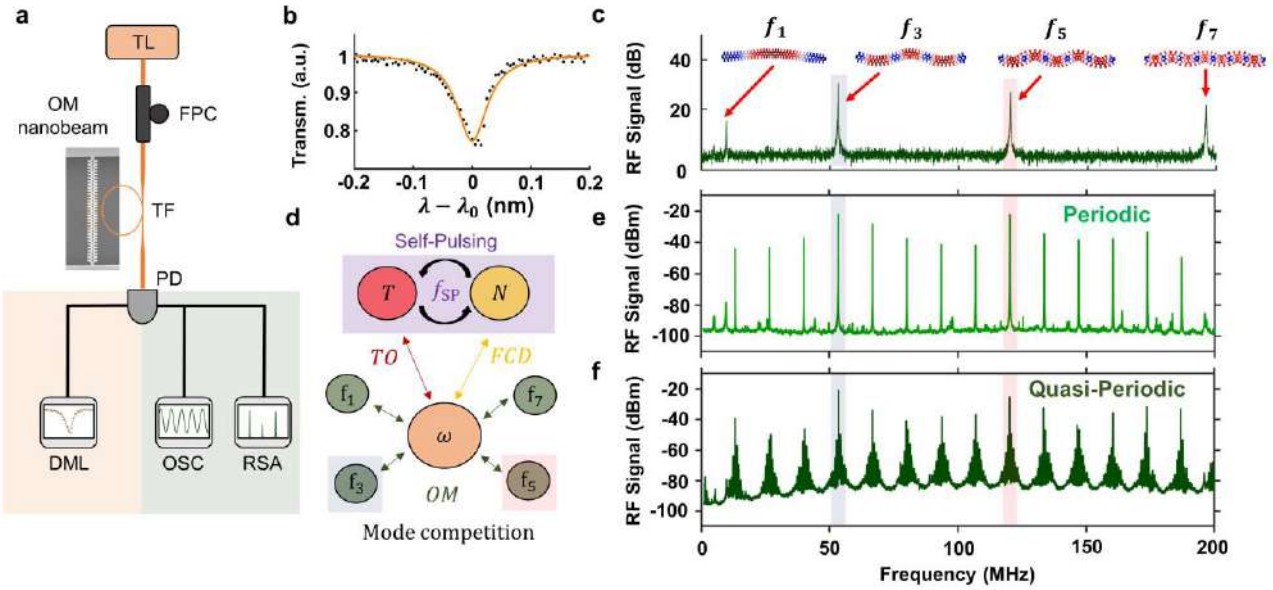


Fig. 1: (a) Experimental setup. A tunable laser (TL) couples light to an optomechanical nanobeam via a tapered fiber (TF). Polarization is optimized using a fiber polarization controller (FPC). Transmitted light is detected by a photodetector (PD) and analyzed with a digital multimeter (DML), radio-frequency spectrum analyzer (RSA), and oscilloscope (OSC). **(b)** The DML records normalized transmission as the TL wavelength is swept across the optical resonance at low input power. **(c)** The RSA measures the RF signal after background subtraction. Arrows connect FEM simulations of mechanical displacement for various in-plane odd antinode flexural modes to their corresponding RF peaks. **(d)** Schematic representation of key magnitudes and interactions in the system. A self-induced cycle of increases in temperature (T) and free carrier density (N) influences the cavity mode through the thermo-optic (TO) and free-carrier dispersion (FCD) effects. **(e-f)** RF signal detected at the RSA where the modes 3 and 5 overcome mode competition and the system exhibits multimode phonon lasing in periodic and quasi-periodic regimes, respectively.

Acknowledgements

This work was supported by the MICINN projects ALLEGRO (Grants No. PID2021-124618NB-C22 and PID2021-124618NB-C21) and MOCCASIN-2D (Grant No. TED2021-132040B-C21)

References

1. Aspelmeyer, M., T. J. Kippenberg and F. Marquardt, “Cavit optomechanics”, Rev. Mod. Phys, Vol 86, 1391 (2014).
2. Kemiktarak, U., M. Durand, M. Metcalfe and J. Lawall, “Mode competition and anomalous cooling in a multimode phonon laser”, Phys. Rev. Lett, Vol 113, 030802 (2014).
3. Mercadé, L., K. Pelka, R. Burgwal, A. Xuereb, A. Martínez and E. Verhagen, “Floquet phonon lasing in multimode optomechanical systems”, Phys. Rev. Lett. Vol 127, 073601 (2021).
4. Ng, R. C., P. Nizet, D. Navarro-Urrios et al, “Intermodulation of optical frequency combs in a multimode optomechanical system”, Phys. Rev. Res, Vol 5, L032028 (2023).
5. Navarro-Urrios, D., N. Capuj, J. Gomis-Bresco et al, “A self-stabilized coherent phonon source driven by optical forces”, Sci. Rep. Vol 5, 15733 (2015).

A reconfigurable coding acoustic metasurface based on coiling units

Jie Hu *, Hao Zhou, Haoxiang Li

Nanjing Forestry University, China
*corresponding author: hujie@njfu.edu.cn

Abstract: In this paper we design a reconfigurable coding metasurface comprising two types of encoding coiling units that can manipulates the acoustic waves arbitrarily over a certain frequency. The multi-functional performance of our scheme is numerically verified via the demonstration of two distinctive examples of beam splitting and acoustic focusing.

The key to constructing a binary encoding metasurface lies in selecting two coding units with a consistent transmission amplitude and a relative phase difference of π. To achieve this, we employ a coiling unit that effectively manipulates the phase modulation of acoustic waves. Through the adjustment of the internal crossbars, the output acoustic phase difference of units changes by π and the units can be encoded as "0" and "1" in digital format. Figure 1(a, b) illustrates a schematic of the 1-bit encoding units representing "1" and "0", allowing for various functionalities through the combination of these units. Here we select 2 kHz as the operational frequency, and the relationship between the unit phase and the length of the movable crossbar is plotted in Fig. 1(c). The length *l* of "0" and "1" coding units are chosen as 7 mm and 19 mm respectively to ensure the phase and amplitude requirements for the "0" and "1" units being simultaneously satisfied at 2kHz.

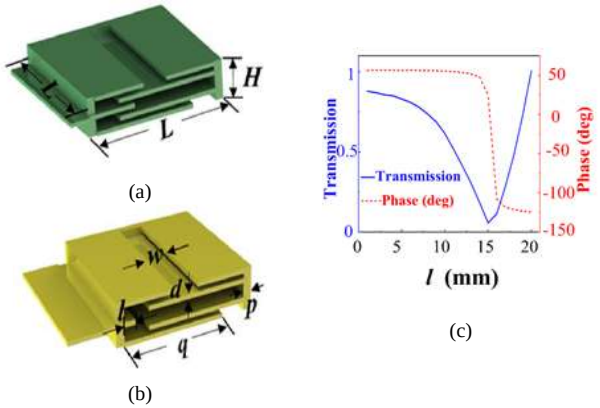


Figure 1 Schematic diagram of "1" coding unit (a) and "0" coding unit(b); (c) Relationship between unit phase, amplitude, and movable plate *l* at a frequency of 2 kHz

In this study, we exhibit two examples to verify the outstanding performance of multi-functional manipulation of our structure: beam splitting and acoustic focusing.

When incident plane waves penetrate perpendicularly into a programmable metasurface composed of *M*×*N* "0" or "1" units, the far-field function can be expressed as follows[1]:

$$f(\theta,\beta)=f_e(\theta,\beta)\sum_{m=1}^{M}\sum_{n=1}^{N}\exp\left\{-i\left\{\varphi(m,n)+kL\sin\theta\left[\left(m-\frac{1}{2}\right)\cos\beta+\left(n-\frac{1}{2}\right)\sin\beta\right]\right\}\right\} \quad (1)$$

where θ and β are the elevation and azimuth angles, respectively, and $f_e(\theta, \beta)$ is the pattern function of a unit; k is the wave number; $\varphi(m, n)$ is the scattering phase of the unit at (m, n), which is either 0 or π. From Eq. (1), it can be concluded how to achieve maximum scattering in different directions by adjusting θ and β.

For simplicity but without losing generality, we construct a programmable metasurface using a 2×2 units configuration for illustration purpose. Simulations are conducted at 2kHz to investigate the beamforming effect with single beam, binary beam and quad-beam in the transmitted field.

Additionally, we conduct further research by utilizing 12 tunable units to create a reconfigurable acoustic encoding lens which not only demonstrates excellent focusing capabilities but also allows for arbitrary control of the focal point's position.

The diagram of our design and simulation results of beam splitting with different encoding sequences are shown in Figs. 2(a-c). Figs. 2(d) illustrates the principle of adjustable acoustic focusing via acoustic waves passing through the encoded metasurface lens and Figs. 2(e) display the focusing performance at different spots.

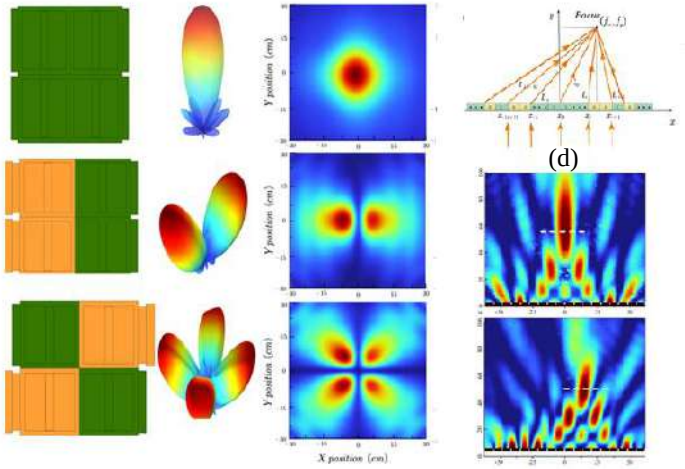


Figure 2. (a) diagram of the 2×2 structure with different arrangement 00/00, 01/01, 01/10. (b)3D structure and far-field sound pressure distribution of the 00/00, 01/01, 01/10 coded metasurface, respectively. (c) Simulation of the sound pressure distribution with 00/00, 01/01, 01/10 coded metasurface, respectively. (d) Schematic diagram of tunable focusing. (e) Simulated acoustic pressure distribution with arbitrary focusing

Here we design a reconfigurable coding acoustic metasurface that comprises the minimized types of building blocks with compactness and manipulates the transmitting waves arbitrarily. In our design, each individual unit cell of metasurface has a coiled configuration that can be divided into two types of encoding units: 0 and 1. The multi-functional performance of our scheme is numerically verified via the demonstration of beam splitting and acoustic focusing. The simulated results agree well with the theoretical predictions, showing the designed coding metasurface efficiently and flexibly manipulates the wavefront of the outcoming waves to form the desired specific patterns. With advantages in terms of easy fabrication, ultrathin thickness, our design opens route to the design of novel acoustic functional devices based on active space-coiling metasurfaces and holds significant application potential in diverse fields such as acoustic imaging and communication, etc.

Acknowledgements: This work is supported by the National Natural Science Foundation of China (grant no. 12374416) and the Natural Science Foundation of Jiangsu Province (grant no. BK20240659).

References

1. Cui, T. J., Qi, M. Q., Wan, X., Zhao, J. & Cheng, Q. Coding metamaterials, digital metamaterials and programmable metamaterials. Light-Sci Appl ,99 (2014).

Observation of oriented Landau levels and helical zero modes in Berry dipole acoustic crystals

Qingyang Mo[1], Riyi Zheng[3], Cuicui Lu[1,2§], Xueqin Huang[3‡], Zhengyou Liu[4], Shuang Zhang[1,5,6†]

[1] New Cornerstone Science Laboratory, Department of Physics, University of Hong Kong; 999077, Hong Kong, China
[2] Key Laboratory of Advanced Optoelectronic Quantum Architecture and Measurements of Ministry of Education, Beijing Key Laboratory of Nanophotonics and Ultrafine Optoelectronic Systems, Center for Interdisciplinary Science of Optical Quantum and NEMS Integration, School of Physics, School of Physics, Beijing Institute of Technology, Beijing 100081, China
[3] School of Physics and Optoelectronics, South China University of Technology, Guangzhou, Guangdong 510640, China
[4] Key Laboratory of Artificial Micro- and Nanostructures of Ministry of Education and School of Physics and Technology, Wuhan University, Wuhan 430072, China
[5] Department of Electrical & Electronic Engineering, University of Hong Kong; 999077, Hong Kong, China
[6] Quantum Science Center of Guangdong-Hong Kong-Macao Great Bay Area, 3 Binlang Road, Shenzhen, China

§cuicuilu@bit.edu.cn
‡phxqhuang@scut.edu.cn
†shuzhang@hku.hk

Abstract: We experimentally demonstrate unconventional oriented Landau levels in acoustic Berry dipole systems, wherein by reversing the orientation of the pseudomagnetic field, the system exhibits distinct Landau spectra. Remarkably, we observe a new type of helical zero modes whose existence critically depends on the magnetic field's orientation.

Band crossing plays an important role in condensed matter theory, serving as the origin for various topological semimetals and insulators [1,2]. A well-known example is Weyl point, which can be regarded as a source or sink of Berry curvature field in the momentum space, characterized by integer Chern numbers [3–7]. When a magnetic field couples with a Weyl point, resulting in isotropic discrete Landau levels independent of the orientation of the magnetic field and a chiral zero mode unidirectionally propagating along the direction of the magnetic field [8–11].

Very recently, band crossing beyond the above paradigm was predicted and studied theoretically [12-14]. These band crossing points, referred to as “Berry dipoles”, carry a dipolar Berry curvature field, resulting in zero Chern number but nonzero Berry dipole moment. Interestingly, it was recently proposed that oriented Landau levels are formed when a Berry dipole is subject to an external magnetic field [15-17].

In this work, we experimentally realize oriented Landau levels and helical zero modes in Berry dipole semimetals constructed by engineering an inhomogeneous acoustic crystal to introduce pseudomagnetic fields. We demonstrate dramatically different Landau level spectra when the pseudomagnetic field is parallel or antiparallel to the Berry dipole moment. Specifically, when the pseudomagnetic field is parallel to the Berry dipole moment, there exist a pair of helical zero modes propagating respectively along and opposite to the pseudomagnetic field. Remarkably, the helical zero modes vanish and Landau levels are gapped when the pseudomagnetic field is reversed. Our work offers a platform to study topological matter beyond Chern class, such as Berry multipoles, four-dimensional tensor monopoles.

References

[1] M. Z. Hasan and C. L. Kane, *Colloquium: Topological Insulators*, Rev Mod Phys **82**, 3045 (2010).
[2] X.-L. Qi and S.-C. Zhang, *Topological Insulators and Superconductors*, Rev Mod Phys **83**, 1057 (2011).

[3] L. Lu, L. Fu, J. D. Joannopoulos, and M. Soljačić, *Weyl Points and Line Nodes in Gyroid Photonic Crystals*, Nat Photonics **7**, 294 (2013).
[4] S.-Y. Xu et al., *Discovery of a Weyl Fermion Semimetal and Topological Fermi Arcs*, Science **349**, 613 (2015).
[5] L. Lu, Z. Wang, D. Ye, L. Ran, L. Fu, J. D. Joannopoulos, and M. Soljačić, *Experimental Observation of Weyl Points*, Science **349**, 622 (2015).
[6] B. Q. Lv et al., *Experimental Discovery of Weyl Semimetal TaAs*, Phys Rev X **5**, 31013 (2015).
[7] B. Yang et al., *Ideal Weyl Points and Helicoid Surface States in Artificial Photonic Crystal Structures*, Science **359**, 1013 (2018).
[8] E. McCann and V. I. Fal'ko, *Landau-Level Degeneracy and Quantum Hall Effect in a Graphite Bilayer*, Phys Rev Lett **96**, 86805 (2006).
[9] N. Schine, A. Ryou, A. Gromov, A. Sommer, and J. Simon, *Synthetic Landau Levels for Photons*, Nature **534**, 671 (2016).
[10] Z. Yang, F. Gao, Y. Yang, and B. Zhang, *Strain-Induced Gauge Field and Landau Levels in Acoustic Structures*, Phys Rev Lett **118**, 194301 (2017).
[11] X. Wen, C. Qiu, Y. Qi, L. Ye, M. Ke, F. Zhang, and Z. Liu, *Acoustic Landau Quantization and Quantum-Hall-like Edge States*, Nat Phys **15**, 352 (2019).
[12] A. Nelson, T. Neupert, T. Bzdušek, and A. Alexandradinata, *Multicellularity of Delicate Topological Insulators*, Phys Rev Lett **126**, 216404 (2021).
[13] A. Nelson, T. Neupert, A. Alexandradinata, and T. Bzdušek, *Delicate Topology Protected by Rotation Symmetry: Crystalline Hopf Insulators and Beyond*, Phys Rev B **106**, 75124 (2022).
[14] P. Zhu, J. Noh, Y. Liu, and T. L. Hughes, *Scattering Theory of Delicate Topological Insulators*, Phys Rev B **107**, 195110 (2023).
[15] A. Graf and F. Piéchon, *Massless Multifold Hopf Semimetals*, Phys Rev B **108**, 115105 (2023).
[16] Z.-Y. Zhuang, C. Zhang, X.-J. Wang, and Z. Yan, *Berry-Dipole Semimetals*, (2024).
[17] A. C. Tyner and S. Sur, *Dipolar Weyl Semimetals*, Phys Rev B **109**, L081101 (2024).

Design Principle and Application Exploration of Water-to-Air Vibroacoustic Metasurfaces

H.-T. Zhou[1*], Y.-F. Wang[1], and Y.-S. Wang[1, 2]

[1]Department of Mechanics, Tianjin University, Tianjin 300350, China
[2]Department of Mechanics, Beijing Jiaotong University, Beijing 100044, China
[*]corresponding author: zhouhongtao@tju.edu.cn

Abstract: We propose and experimentally validate the concept of a vibroacoustic metasurface to enhance sound transmission across the water-air interface. Furthermore, we explore the potential application of encapsulating airborne loudspeakers with optimized vibroacoustic metasurfaces to function as sound sources underwater.

Modulation of waves for cross-media transmission has garnered widespread attention due to its extensive applications in various engineering fields [1]. However, the transmission efficiency at the interface is rather low due to impedance mismatch between different media. A prominent example is the transmission of sound through the water-air interface [2]. Given the substantial contrast in acoustic impedance (approximately 3600 times), only 0.1% of sound energy naturally propagates between water and air [3]. Here, we propose a vibroacoustic metasurface to enhance water-to-air sound transmission and further explore its potential applications [4].

The photograph of the fabricated sample of vibroacoustic metasurface with a partially enlarged view of the cross-section is shown in Figure 1A. By taking advantage of fluid-solid interaction, specific vibration modes are induced for the inverse-design solid metasurface. Figure 1B plots the measured transmission enhancement of the sample varying with frequency compared with the bare water-air interface. It can be observed that the sample exhibits above 20 dB (ten times) amplitude enhancement from 9.84 to 11.53 kHz. The measured peak frequency is found to be around 10.45 kHz with approximately 25.9 dB (nearly 20 times) transmission enhancement, close to the perfect transmission of 30 dB. The measured time-domain sound signals at a test point are presented in Figure 1C. The sharp contrast between sound pressure amplitudes transmitted by the sample and the bare water-air interface further confirms the excellent performance of the sample of vibroacoustic metasurface for sound transmission enhancement through the water-air interface.

In addition, we measure the sound pressure fields transmitted through the sample and bare water–air interface at the peak frequency, as shown in Figure 1D and 1E, respectively. It can be clearly observed that the sound waves emitted from underwater transducer are converted into uniform plane waves after passing through the sample, and the transmission amplitudes through the sample over the entire measurement area are greatly improved compared to the bare water-air interface.

To reveal the mechanism of enhanced sound transmission, we performed the vibration test for the fabricated sample. Figure 1F shows the experimental setup. The normal displacement component was measured by using the PSV scanning vibrometer. Figure 1G presents the measured vibrations of sample at different frequencies, and the corresponding simulated results of a single unit cell are given for comparison. Vibrations at the notch are more pronounced than on both sides when the frequency is close to the peak one. An anti-phase vibration mode is clearly observed. In contrast, when the incident frequency is away from the peak one, the collaborative vibration at the notch becomes unapparent. The enhanced water-to-air sound transmission is mainly attributed to the unique flexural vibrations of the solid unit cell, which gives rise to the required sound impedance by inducing compression and expansion of the inner air cavity. More details can be seen in reference [4].

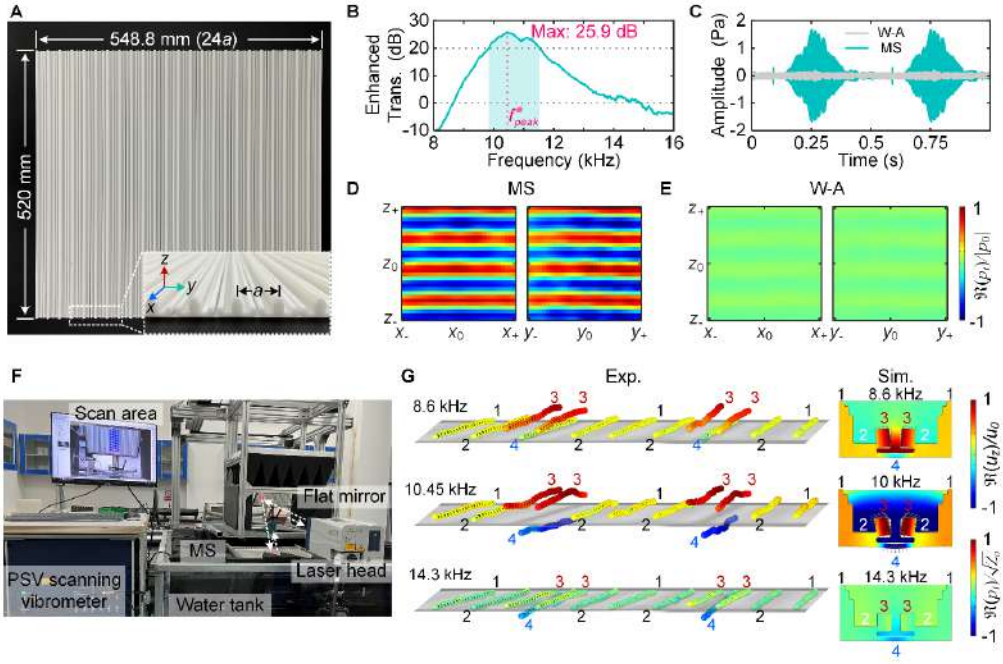


Figure 1: Vibroacoustic metasurface for sound transmission enhancement through the water-air interface [4]. (A) Photograph of sample of vibroacoustic metasurface. (B) Measured sound amplitude enhancement (dB) of sample compared to the bare water–air interface. (C) Measured time-domain sound signals from water to air through the sample and water–air interface. (D) Measured real parts of transmitted sound fields through the sample and (E) water–air interface. (F) Photograph of the experimental set-up for vibration measurements of sample. (G) Measured vibration at different locations of sample for different frequencies, and the corresponding simulated results are given for comparison.

Furthermore, we explore the application scenario by encapsulating airborne loudspeakers with optimized vibroacoustic metasurfaces, using them as a sound source underwater. In this configuration, the vibroacoustic metasurfaces function as a sealed shell, enclosing the airborne loudspeakers inside. Numerical simulations were conducted to evaluate the air-to-water sound transmission performance. The results show that the designed sound source significantly outperforms a solid cavity without the metasurface in terms of sound emission. Furthermore, effective air-to-water transmission was maintained, even when accounting for solid viscosity losses. Overall, the proposed vibroacoustic metasurfaces not only opens a new avenue for realizing water-air communication but also holds promise for applications in high signal-to-noise ratio sensing devices.

References

1. Chen, A.-L., Wang, Y.-S., Wang, Y.-F., Zhou, H.-T., Yuan, S.-M., "Design of Acoustic/Elastic Phase Gradient Metasurfaces: Principles, Functional Elements, Tunability, and Coding," Appl. Mech. Rev., Vol. 74, No. 2, 2022.
2. Zhang, S.-C., Zhou, H.-T., Gong, X.-T., Wang, Y.-F., Wang, Y.-S., "Discrete metasurface for extreme sound transmission through water-air interface," J. Sound Vib., Vol. 575, No. 118269, 2024.
3. Gong, X.-T., Zhou, H.-T., Zhang, S.-C., Wang, Y.-F., Wang, Y.-S., "Tunable sound transmission through water-air interface by membrane-sealed bubble metasurface," Appl. Phys. Lett., Vol. 123, No. 23, 2023.
4. Zhou, H.-T., Zhang, S.-C., Zhu, T., Tian, Y.-Z., Wang, Y.-F., Wang, Y.-S., "Hybrid metasurfaces for perfect transmission and customized manipulation of sound across water-air interface," Adv. Sci., Vol. 10, No. 2207181, 2023.

Vibration and sound radiation reduction in broadband by meta-plate with rainbow reflection effect

Feng Liu[1*], Yan-Feng Wang[1], and Yue-Sheng Wang[1,2]

[1]Department of Mechanics, Tianjin University, China
[2]Department of Mechanics, Beijing Jiaotong University, China
[*]corresponding author: liu_feng@tju.edu.cn

Abstract: A meta-plate with a rainbow reflection effect is proposed to suppress vibration and sound radiation. Results show significant broadband suppression with extremely low structural damping. The suppression mechanism is attributed to vibration redistribution and systematic reduction, driven by the slowing-down velocity and energy enhancement effects of the rainbow reflection phenomenon.

In this work, we propose a meta-plate with radial trapping effect [1], which is realized by sixteen rings with gradient heights, attached on the host plate with a side length a and thickness h_0, as shown in Figure 1. Here, the rings are made of photosensitive resin by utilizing its extreme-low inherent loss instead of introducing additional damping materials.

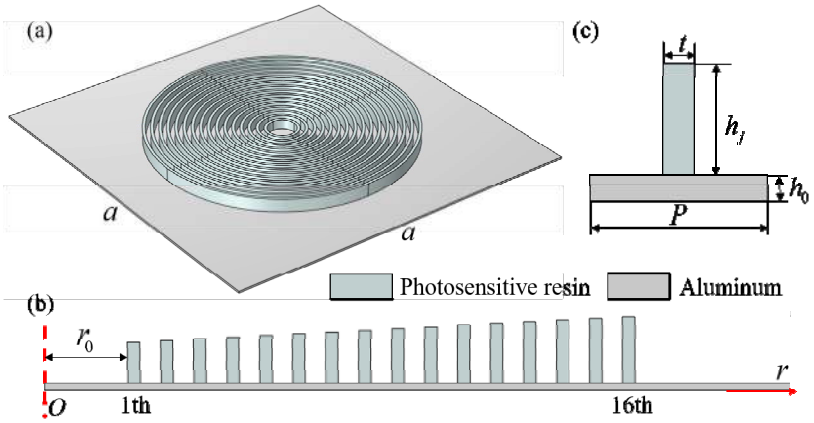


Figure 1 (a) Sketch of square meta-plate with unit-cells of gradient rings; (b) Sketch of two-dimensional axis-symmetrical rainbow reflection structure; (c) Sketch of the unit-cell.

To demonstrate the rainbow reflection effect of the designed meta-plate, the wave propagation for the infinite two-dimensional meta-plate under a point load applied at the center is analyzed without considering the reflection from the outmost boundary. The wavefields at different frequencies are shown in Figure 2. The incident flexural waves are stopped at corresponding unit-cell and cannot propagate into the host plate. The wave energy within the rings where the wave stopped is obviously lager than other regions, demonstrating the energy enhancement of the rainbow reflection effect.

The normal mean square velocities of the bare plate and meta-plate are shown in Figure 3(a). For frequency larger than 1880 Hz (marked by the dashed line), near the first-order locally resonant frequency 1920 Hz of the 16th unit-cell, the rainbow reflection effect is emerged. Therefore, for most of the frequencies from 1880 Hz to 3500 Hz, the mean square velocity of the meta-plate is reduced compared with that of the bare plate, leading to a

substantial reduction of sound power (reference: 10^{-12} W) at these frequencies, as shown in Figure 3(b). The significantly reduction of mean square velocity and sound power is owing to the slowing-down of the wave velocity and energy enhancement of the rainbow effect, profited from which, the waves can be effectively absorbed only relying on an extreme-low inherent loss of the gradient rings. As further evidence, the modal loss factor of the lossy meta-plate is calculated, as shown in Figure 3(c). The modal loss factors of the meta-plate suddenly increase significantly when the frequency is larger than 1880 Hz. The results of modal loss factors further demonstrate that the substantial reduction of mean square velocity and sound power of the lossy meta-plate is attributed to the bandgap and slowing-down wave effects simultaneously possessed by rainbow trapping structures, which is quite different from previous studies based only on bandgaps.

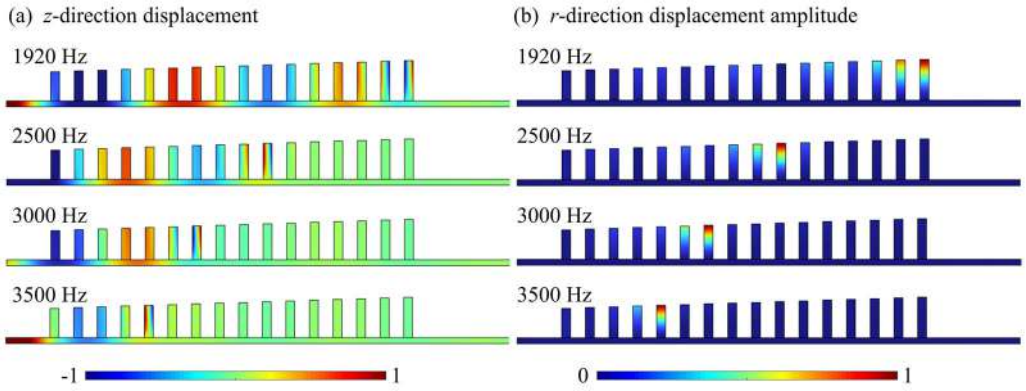


Figure 2 (a) *z*-direction displacement and (b) *r*-direction displacement amplitude of the meta-plate at different frequencies to demonstrate rainbow reflection effect.

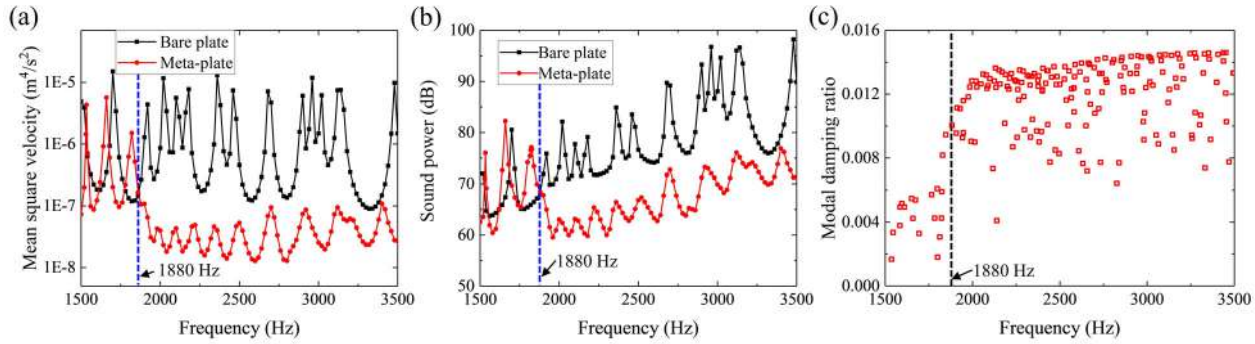


Figure 3 (a) Mean square velocity and (b) sound power for meta-plate and bare plate. (c) Modal loss factor of meta-plate.

The proposed meta-plate is similar to a plate with several circular reinforcement ribs, which enhances the structural stiffness while significantly suppressing the vibration and sound radiation in broadband without additional damping materials. The present design provides a novel approach for vibration and noise reduction in engineering, such as for the cabins of high-speed trains and aircraft.

References

1. Liu F., Xu Y.L., Peng P., et al., "A meta-plate with radial rainbow reflection effect for broadband suppression of vibration and sound radiation," J. Sound Vib., Vol. 585, No. 118428, 2024.
2. Liu F. Shi. P., Shen Y., et al., F. M. Lastname, "Advances in suppression of structural vibration and sound radiation by flexural wave manipulation," Thin Wall. Struct., Vol. 200, No. 111936, 2024.

Quadratic Weyl semimetal and topological double negative refraction in phononic crystals

Y. T. Yang[1*]

[1]Beijing University of Chemical Technology, China
[*]corresponding author: yangyating@buct.edu

Abstract: We report the realization of an acoustic quadratic Weyl semimetal, which hosts a pair of quadratic Weyl points with opposite charges ±2. Nonzero charges of the quadrative Weyl points give rise to the Fermi-arc boundary states. We further achieve the double negative refraction of the boundary acoustic waves without reflection.

Weyl semimetals, featured with nontrivial band crossing in three-dimensional momentum space dubbed as the Weyl point (WP), have been studied extensively [1-4]. We design a bilayer PC with chiral interlayer interactions to realize a quadratic Weyl semimetal, which hosts only a pair of quadratic WPs at the M and A points. D4 and time-reversal symmetries protect the existence of the quadratic WPs, which carry topological charges ±2, and possess quadratic dispersions along the kx and ky directions and linear one along the kz direction. Interestingly, we construct an interface formed by two different Weyl semimetals with opposite chirality of the interlayer interactions. Double negative refraction is observed in experiment. Different from the conventional negative refraction, which means that only one transmitted wave and the incident wave are located on the same side of the interface normal, double negative refraction manifests that two transmitted waves satisfy the negative refraction condition at the same time. Moreover, the refraction fields are distributed in two separate planes, which will facilitate wave manipulation.

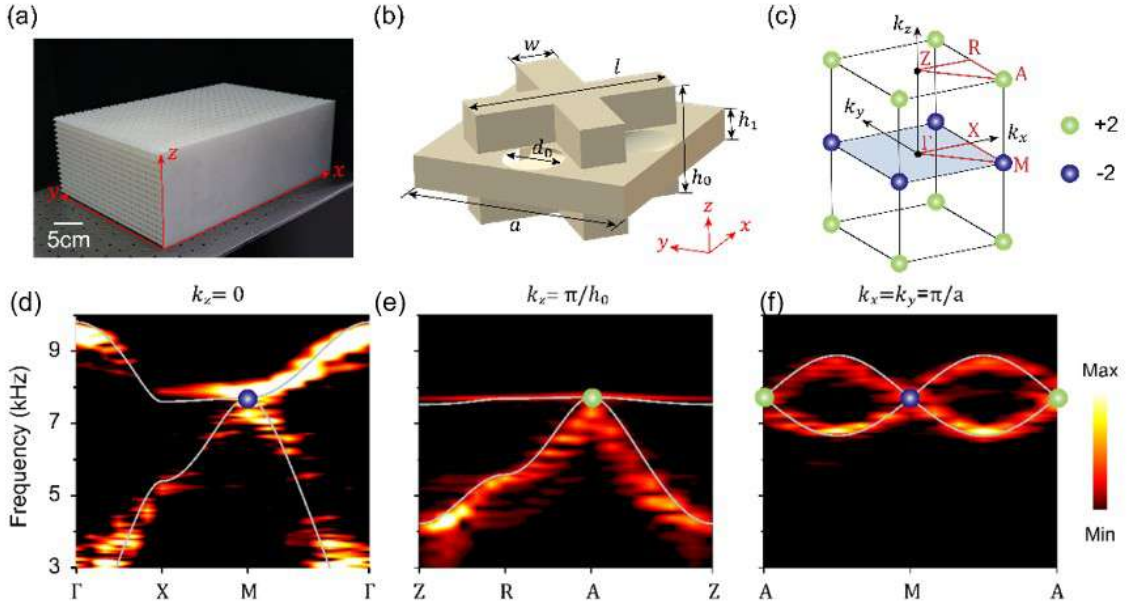


FIG. 1. PC with a pair of quadratic WPs and the bulk band dispersions. (a) Photo of the sample fabricated by 3D printing technology. (b) Unit cell of the PC, composed of vertical crossed scatterers in each layer and four chiral tubes connecting the two layers. (c) First Brillouin zone with quadratic WPs labelled by green (topological charge of +2) and blue (topological charge of -2) spheres. (d) and (e) for kz=0 and kz=π/h0. (f) Along the kz direction for kx=ky=π/a. Color maps and gray lines denote the experimental and simulated results, respectively.

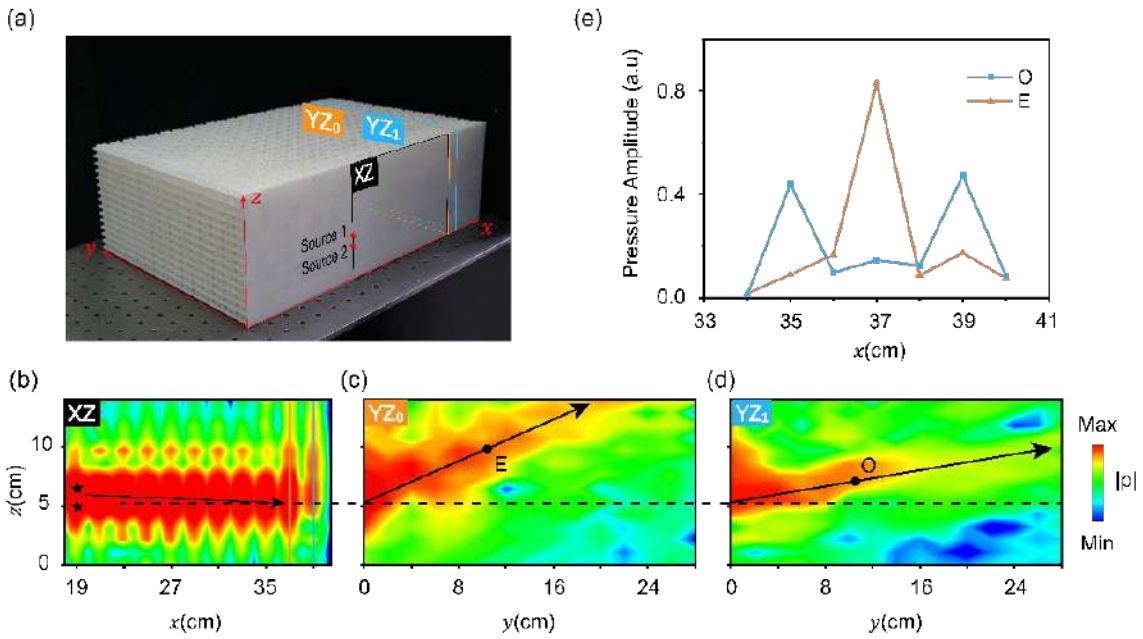


FIG. 2. Observation of topological double negative refraction. (a) Side view of the sample. Two point sources are placed on the XZ plane with a vertical distance h_0. The phase difference of them is 0.4π. (b)-(d) Measured pressure field distributions on the XZ, YZ0 and YZ1 planes, respectively. Two stars label the positions of the point sources, black arrows represent the directions of wave propagation. (e) Measured pressure fields along the x direction at the E (marked in (c)) and O (marked in (d)) points.

This work is supported by the National Key R&D Program of China (Nos. 2022YFA1404500, 2022YFA1404900, 2018YFA0305800), National Natural Science Foundation of China (Nos. 11890701, 11974120, 11974005, 12074128, 12222405, 12247169), and Guangdong Basic and Applied Basic Research Foundation (Nos. 2019B151502012, 2021B1515020086, 2022B1515020102).

References

1. N. P. Armitage, E. J. Mele, and A. Vishwanath, “Weyl and Dirac semimetals in three-dimensional solids”, Rev. Mod. Phys. Vol. 90, No. 01, 5001, 2018.
2. X. Wan, A. M. Turner, A. Vishwanath, and S. Y. Savrasov, Topological semimetal and Fermi-arc surface states in the electronic structure of pyrochlore iridates, Phys. Rev. B Vol. 83, No. 20, 5101 2011.
3. B. Q. Lv, H. M. Weng, B. B. Fu, X. P. Wang, H. Miao, J. Ma, P. Richard, X. C. Huang, L. X. Zhao, G. F. Chen, Z. Fang, X. Dai, T. Qian, and H. Ding, Experimental discovery of Weyl semimetal TaAs, Phys. Rev. X Vol. 5, No. 03, 1013, 2015.

High-Performance Nanotriboelectric Generator Integrating an Acoustic Metamaterial Absorber and Spring

Wei-Zhi Weng[1] and Tsung-Yu Huang[1,*]

[1]Department of Materials Science and Engineering, Ming Chi University of Technology, New Taipei City, Taiwan, 243303

[*]corresponding author: huang.tsungyu@mail.mcut.edu.tw

Abstract: This study integrates an acoustic metamaterial absorber, springs, and triboelectric nanogenerators to convert urban noise into electricity. By tuning absorber and spring resonance, the system achieves maximum displacement, enabling effective energy harvesting for low-power devices, offering a sustainable solution for noise pollution and green energy.

Noise pollution, particularly low-frequency noise, poses a significant challenge as traditional sound-absorbing materials struggle to attenuate it effectively. Helmholtz resonators (HRs) have emerged as a promising solution due to their local resonance effect, enabling efficient low-frequency absorption within a compact structure. However, a single HR typically produces only one absorption peak, limiting its effectiveness in multi-frequency noise reduction. To address this limitation, researchers have developed multi-layer Helmholtz resonator (MHR) structures, which combine multiple resonator units to achieve multiple absorption peaks across different frequencies.The design of MHRs leverages several key strategies. By tuning the geometric parameters of multiple HR units, researchers have successfully introduced multiple narrowband absorption peaks. Additionally, stacking multiple HR layers further expands the absorption bandwidth, while embedded aperture modifications allow for precise control over resonance frequencies and impedance matching. Studies have demonstrated that even with a thickness as small as 1/30th of the working wavelength, MHRs can achieve near-perfect absorption at specific low-frequency targets, such as 100 Hz and 400 Hz. Experimental results from 3D-printed samples, validated against finite element simulations, confirm the effectiveness of these structures in multi-frequency noise mitigation.Future research directions could explore adaptive MHR designs with tunable properties, advanced material optimization, and large-scale implementations in architectural acoustics, transportation, and defense applications. This study addresses the current energy shortage and growing environmental awareness by proposing an innovative solution to convert urban noise into electrical energy. As green energy research progresses, researchers worldwide are striving to find eco-friendly and sustainable power generation devices. Among them, the triboelectric nanogenerator, which can convert weak mechanical energy into electrical energy, has garnered significant attention. This technology offers advantages such as simplicity, high energy density, and low cost, making it an ideal candidate for alternative energy sources. However, urban areas face increasing noise pollution, leading to irritability and health issues among residents. To address this problem, the introduction of acoustic metamaterials has enabled researchers to design an absorber that can perfectly absorb incident sound waves with sub-wavelength thickness. In this study, we integrate an acoustic metamaterial absorber, springs, and triboelectric nanogenerators to design a system that converts noise pollution into electrical energy to power low-energy devices. As shown in Fig. 1(a), we designed a quasi-Helmholtz resonator as the acoustic metamaterial absorber, incorporating a spring within it. Both the absorber and spring are made from 3D-printed resin. Considering that general traffic noise has a frequency of about 2000 Hz and a decibel level of approximately 90 dB, we set the sound pressure of the incident sound wave to 1×10^{6}. Next, we

placed two different materials for triboelectric generation at the position of maximum displacement between the spring and the sidewalls of the absorber. As shown in Fig. 1(b), the absorption spectrum and spring displacement diagram demonstrated that by fine-tuning the dimensions of the absorber and spring, we align the absorption frequency with the spring's resonance frequency to achieve maximum displacement. In the simulation, the relative displacement between the spring and absorber is approximately 1.8 mm. This system shows potential for converting noise into energy, providing a new direction for green energy development in urban environments.

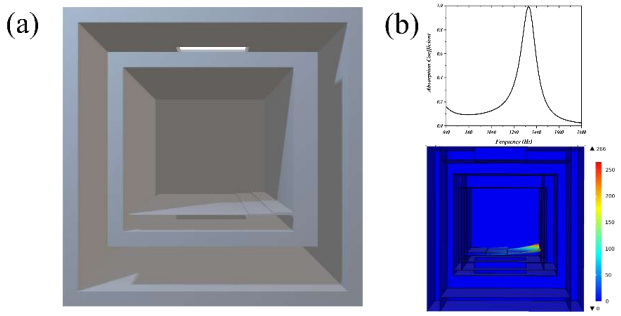


Fig. 1. (a) Scheme of an acoustic metamaterial absorber and an spring and (b) its displacement and absorption/reflection spectrum.

References

1. The Journal of the Acoustical Society of America, 2019, 145.1: 254-262.
2. Nano Energy, 2015, 15: 321-328.
3. DEGRAEVE, Sebastien; OCLEE-BROWN, Jack. Metamaterial absorber for loudspeaker enclosures. In: Audio Engineering Society Convention 148. Audio Engineering Society, 2020.
4. DUAN, Haiqin, et al. Acoustic multi-layer Helmholtz resonance metamaterials with multiple adjustable absorption peaks. Applied Physics Letters, 2021, 118.24.

Simultaneous Photonic and Phononic Topological Interface States in a Si-based Membrane Crystal

Nouh Krai[1*], Gaëtan Lévêque[1], Bahram Djafari-Rouhani[1], Yan Pennec[1]

[1]Institut d'Electronique, de Microélectronique et de Nanotechnologies, UMR CNRS 8520, Université de Lille, 59650 Villeneuve d'Ascq, France

[*]nouh.krai@univ-lille.fr

Abstract: We investigate the emergence of topological interface states in a silicon-based crystal supporting both photonic and phononic modes. Our results demonstrate that these modes are robust and immune to certain defects, such as bends, ensuring stable wave propagation.

Topological insulators exhibit exceptional properties that enable low-loss wave transport along topological waveguides, even in the presence of impurities. Originally associated with the Quantum Hall Effect (QHE) in condensed matter physics, this phenomenon has been extended to photonic and phononic regimes, leading to the development of topological photonic [1, 2] and phononic crystals [4, 5].

Designing a single crystal that simultaneously supports topological photonic and phononic modes is particularly challenging due to the intrinsic differences between electromagnetic (photonic) and mechanical (phononic) waves. Achieving such a structure could unlock promising applications in optomechanics and telecommunications. In this work, we propose a periodic silicon-based two-dimensional membrane to realize an analog of the quantum valley Hall effect (QVHE) [3, 6] (Fig. 1 (a)). Careful optimization of the geometric parameters leads to the emergence of two isolated Dirac cones in both photonic and phononic band diagrams. Breaking spatial inversion symmetry lifts these degeneracies, opening two Dirac gaps at approximately 0.332

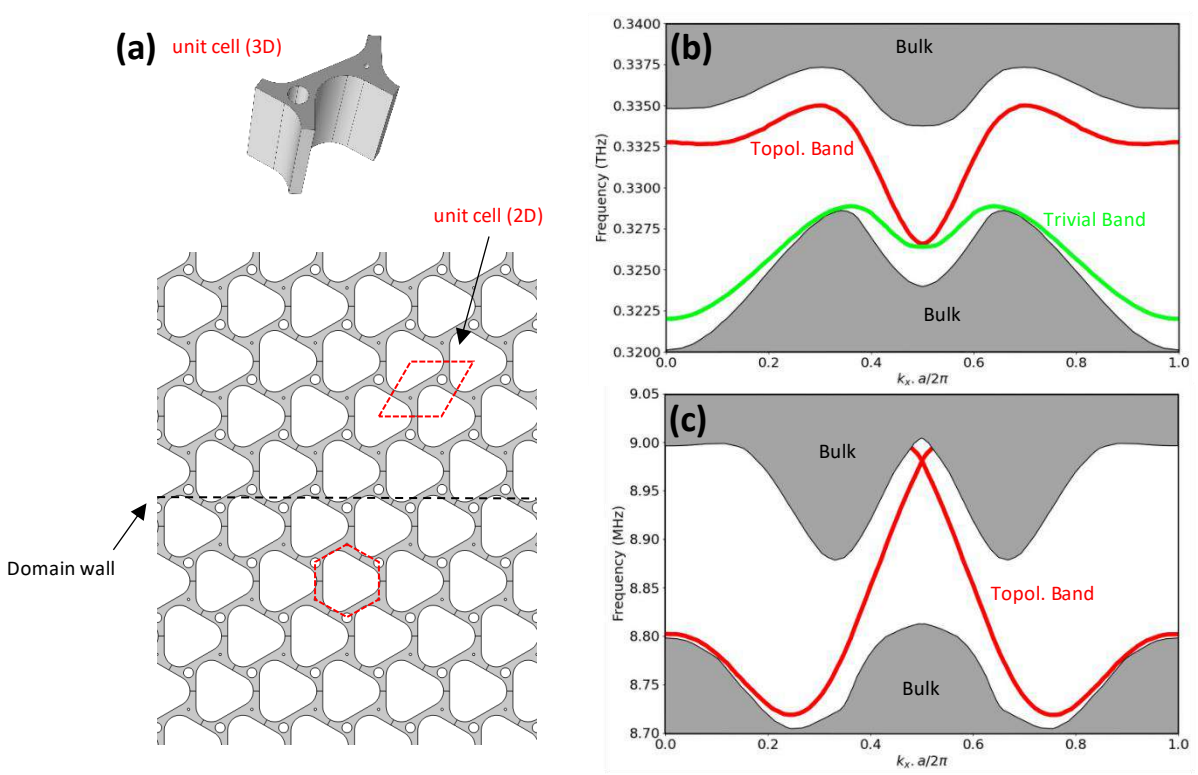


Fig. 1 (a) Unit cell of the honeycomb phononic crystal (top) and representation of the interface between two topologically distinct crystals (bottom). **(b)** and **(c)** show the photonic and phononic band diagrams for supercells, respectively, where topological branches are highlighted in red (Topol. Band). In the photonic case, a non-topological (Trivial) branch is also present, shown in green.

THz and 8.85 MHz for TE-polarized photonic and symmetric phononic modes, respectively. Introducing a domain wall with a zigzag interface results in the emergence of two topological branches in both the photonic and phononic regimes (Fig. 1 (b) and Fig. 1 (c)).

Figures 2 (a) and 2 (b) illustrate the magnetic field and the z-component of the displacement field amplitudes of topological interface modes propagating through a Z-shaped waveguide at frequencies of 0.3318 THz and 8.86 MHz for photonic and phononic crystals, respectively. The slight intensity decay observed in the photonic case after the bending is due to the radiative nature of these modes in the air medium, as the band diagram lies above the light cone. This is confirmed by our analysis techniques, such as Laplace transform, and is clearly visible in Fig. 2 (a), where the field remains uniform along the entire path, with no visible standing wave.

Those results highlight the robustness and immunity of these topological interface modes (both optical and mechanical) while maintaining the same structural characteristics. These insights pave the way for significant advancements in optomechanical and telecommunication technologies.

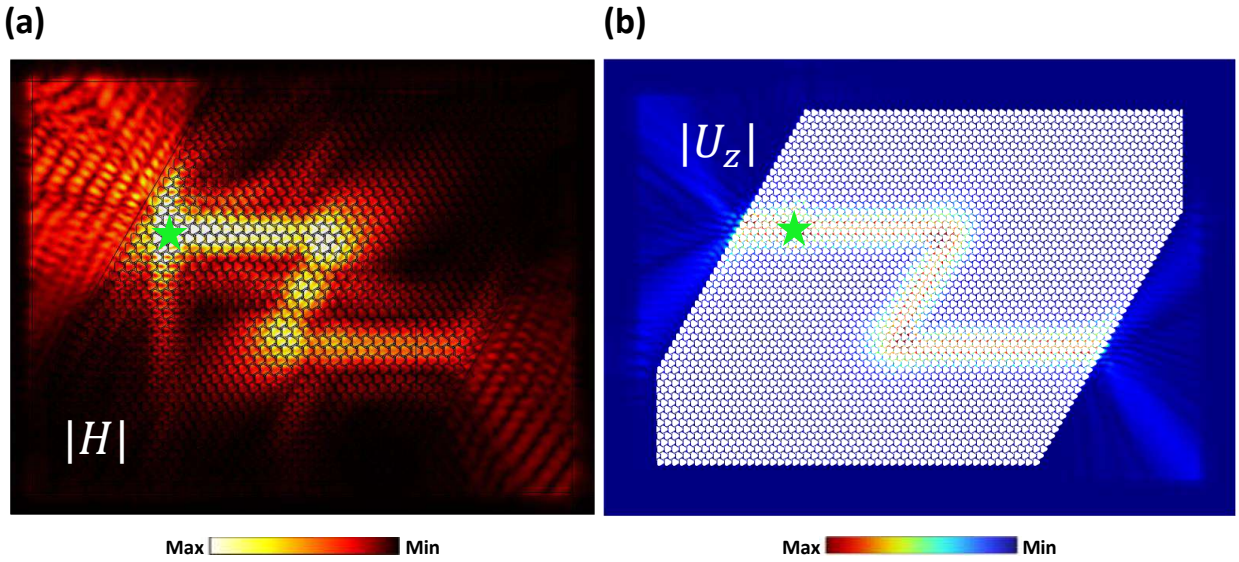


Fig. 2. (a) Photonic topological interface mode propagating along a zigzag path. **(b)** Same as **(a)** for the phononic interface mode. The green stars in **(a)** and **(b)** indicate the positions of the photonic/phononic sources.

References

1. T. Ozawa *et al.*, « Topological photonics », *Reviews of Modern Physics*, vol. 91, nº 1, March 2019.
2. J.-K. Yang, Y. Hwang and S. S. Oh, « Evolution of topological edge modes from honeycomb photonic crystals to triangular-lattice photonic crystals », *Phys. Rev. Research*, vol. 3, nº 2, L022025, 2021.
3. G. Lévêque, P. Szriftgiser, A. Amo and Y. Pennec, "Relation between interface symmetry and propagation robustness along domain walls based on valley topological photonic crystals.", APL Photonics 9, 126107, 2024.
4. M. Miniaci, R. K. Pal, B. Morvan and M. Ruzzene, « Experimental Observation of Topologically Protected Helical Edge Modes in Patterned Elastic Plates », *Phys. Rev. X*, vol. 8, nº 3, 031074, Sept. 2018.
5. S. H. Mousavi, A. B. Khanikaev and Z. Wang, « Topologically protected elastic waves in phononic metamaterials », *Nat Commun*, vol. 6, nº 1, 8682, Nov. 2015.
6. W. Wang, B. Bonello, Y. Pennec and B. Djafari-Rouhani, "Topological valley, pseudospin and pseudospin-valley protected edges states in symmetric pillared phononic crystals." Phys. Rev. B100, 140101, 2019.

Phononic Quantum State Preparation and Ultrafast Coherent Control via Pulsed Excitation of Quantum Emitters

S. S. Ffrench[1], D. D. A. Clarke[1], D. Wigger[1] and O. Hess[1*]
[1]School of Physics and CRANN Institute, Trinity College Dublin, College Green, Dublin 2, Ireland
Corresponding author: ortwin.hess@tcd.ie

Abstract: Phonons are quintessential for emerging solid-state quantum technologies, yet coherent control is challenging. Using the independent boson model, we derive the pulse area condition for selective phononic quantum state preparation via optical excitation of quantum emitters. Optimized ultrashort pulses enable high-fidelity multiphonon generation despite dephasing and phonon decay.

Introduction: As ubiquitous quasiparticle excitations in crystalline solids, phonons are poised to play a vital role in emerging solid-state quantum technologies, with prospective applications extending from the coherent manipulation of spin qubits and modulating the photonic performance of quantum emitters (QEs) to the realization of universal quantum interfaces at the nanoscale. Nevertheless, achieving the full potential of phononic quantum information science relies on extending concepts and strategies for ultrafast, coherent quantum control to systems of interacting QEs and lattice vibrational modes [1]. Whilst the preparation of phononic coherent and Schrödinger cat states via optical excitation of QEs has been reported, few studies have emerged surrounding the selective preparation of single- and multiphonon Fock states, despite their fundamental and quantum technological importance.

In this contribution, we explore the practical limits of schemes for selective multiphonon quantum state preparation via ultrafast optical excitation of solid-state QEs. Adopting the example of color centers in two-dimensional hexagonal boron nitride (hBN), we explore via time-dependent density matrix techniques the relative performance and intricacies of single- and multipulse excitation protocols, demonstrating that suitably optimized, ultrashort pulse sequences enable high-fidelity multiphonon generation despite dephasing and phonon decay.

Phononic quantum state preparation: Our analysis is based on the optically-driven independent boson model (IBM) for a two-level QE coupled to a phonon mode in the presence of a laser field [2, 3]. Analytical diagonalization of the field-free IBM Hamiltonian via a polaron transformation yields the spectrum shown in Fig. 1(a). Assuming that the system is prepared in some initial state $|n\rangle_G$ at time $t = 0$, an exact treatment of the time evolution operator establishes that the requisite pulse area for a total population inversion to the excited state $|m\rangle_X$ is given by $\Theta^n_{m,k} = (2k + 1)\pi R^n_m$, where k is a non-negative integer, $R^n_m = 1/|M^n_m|$ and M^n_m is the Franck-Condon factor pertaining to the specific vibrational transition of interest.

Adopting parameters appropriate to visible region color centers and longitudinal optical phonon modes in hBN [3], Fig. 1(b) demonstrates the achievable population inversion. Assuming the coupled system to be prepared initially in the ground state $|0\rangle_G$, irradiation by an ultrashort, resonant Gaussian pulse with appropriate area excites the system to the target state $|0\rangle_X$ (upper) or $|1\rangle_X$ (lower). To circumvent the requirement of exponentially scaling pulse areas for populating higher multiphonon states (stemming from the Franck-Condon factors), we also explore optimized sequences of ultrashort laser pulses, whereby the coupled system is driven to

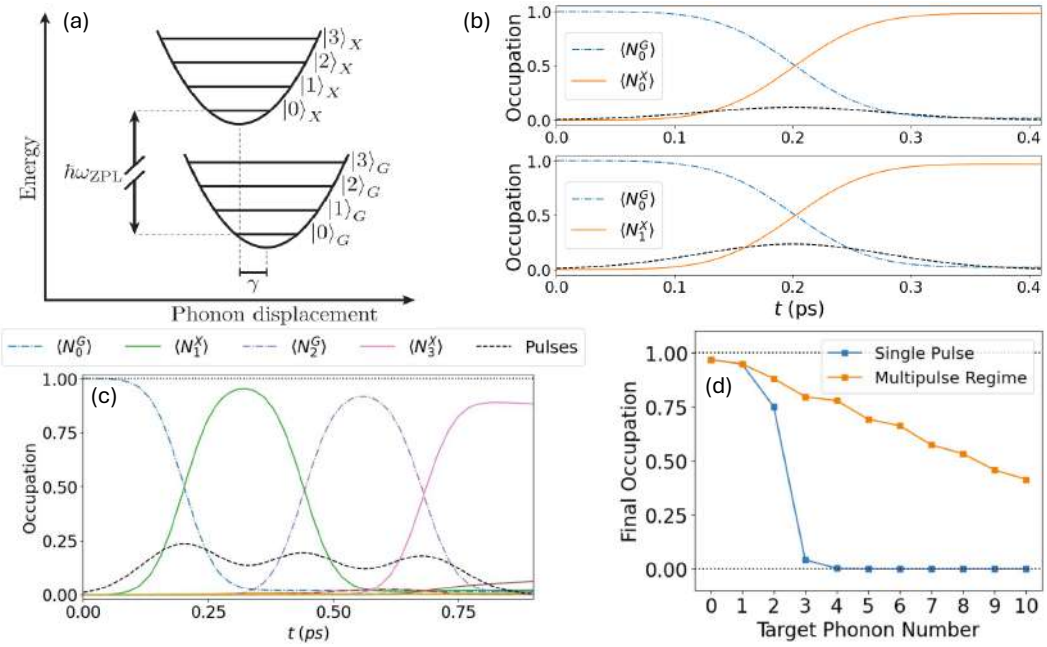


Figure 1: (a) Schematic representation of the spectrum of the IBM Hamiltonian, comprising two harmonic oscillator spectra displaced in energy according to the zero phonon line energy $\hbar\omega_{\mathrm{ZPL}}$ and in configuration coordinate by the polaron shift γ (adapted from Ref. [2]). (b) Time-dependent populations of the initial (ground) state $|0\rangle_G$ and the target excited states $|0\rangle_X$ (upper) and $|1\rangle_X$ (lower), under resonant excitation by Gaussian laser pulses with renormalized pulse area and width $\sigma = 80$ fs. (c) Optimized three-pulse sequence to populate $|3\rangle_X$ via intermediate states. (d) Comparison of the attainable populations in the n-phonon states $|n\rangle_{G/X}$ via single-pulse and optimized multipulse excitation schemes. Occupations are recorded 2σ after the peak of the final pulse in the sequence. See Ref. [3] for numerical parameters.

some target phononic state along a transition pathway that minimizes the total required pulse area. Such a scheme is exemplified for the three-phonon state $|3\rangle_X$ in Fig. 1(c), where an occupation probability exceeding 85% is attained in spite of phonon decay and QE pure dephasing. Finally, Fig. 1(d) compares the achievable population transfers from the ground state $|0\rangle_G$ to various n-phonon states $|n\rangle_{G/X}$ under both renormalized single-pulse and optimized multipulse excitation. Notably, while the single-pulse approach already fails beyond $n = 2$, the use of multiple pulses allows the generation of states with up to $n = 6$ phonons at occupation probabilities above 75%, and even up to $n = 8$ phonons with occupation probabilities above 50%.

Acknowledgements: The authors gratefully acknowledge funding from Research Ireland (formerly Science Foundation Ireland) via Grants No. 18/RP/6236 and 22/QERA/3821.

References

[1] Preuss, J. A. *et al.*, "Resonant and phonon-assisted ultrafast coherent control of a single hBN color center", *Optica*, Vol. 9, No. 5, pp. 522–531, 2022.

[2] Groll, D. *et al.*, "How to Read Out the Phonon Number Statistics via Resonance Fluorescence Spectroscopy of a Single-Photon Emitter", *Adv. Quantum Technol.*, Vol. 8, 2300153, 2025.

[3] Groll, D. *et al.*, "Controlling photoluminescence spectra of hBN color centers by selective phonon-assisted excitation: a theoretical proposal", *Mater. Quantum Technol.*, Vol. 1, 015004, 2021.

Study of the scattering of elastic surface waves by nano-resonators.

S. C. Baltogiannis[1], O. Boyko[1*], and B. Tallon[2]

[1]Institut des nanosciences de Paris, Paris, France
[2]Institut d'Alembert, Paris, France
[*]corresponding author: stavrosbaltogiannis@etu.sorbonne-universite.fr

Abstract: Investigation of the interaction between elastic surface waves and nano-cylinder scatterers to identify resonant regimes and thereby extract crucial transport parameters in multiple scattering experiments aimed at exploring two-dimensional sub-diffusive Anderson localization. Using a Ti:Sapphire pump-probe setup we recorded spatial maps of the displacement.

1) Introduction

Understanding scattering resonances by a single object is essential for calculating scattering cross sections σ_s and, consequently, the key transport parameters in disordered media -the mean free path l_s and the diffusion constant D. Single-scatterer measurements also enable exploration of two-dimensional localized sub-diffusive states where the power spread $\langle r^2 \rangle \propto t^{\alpha}$ with $0 < \alpha < 1$, and Anderson localization where elastic waves remain trapped in a region of the medium. Pump-probe interferometry has long been used to image surface elastic waves and give the advantage of non-contact methods. Previous observations of localized, multiple scattering states observed on nano-structures have left open whether confinement arises from weak-localization (reciprocal-path interference) or from volume-wave leakage into the substrate. Here the scattered displacement field of (A_0,S_0) Lamb waves by Au discs of 2μm diameter and variable heights of 50-100nm placed over a 50nm Au film over Si_3N_4 membrane and the scattered displacement field of Rayleigh waves by the same discs on 50nm Au film on Si_3N_4, Si substrate, were measured.

2) Experimental setup

We employ a Coherent Chameleon Ultra II Ti:Sapphire laser delivering >3 W average power at 800 nm in ~140 fs pulses at an 80 MHz repetition rate. A half-wave plate (λ/2) and polarizing beamsplitter (PBS) split the beam into pump and probe arms. The pump arm is amplitude-modulated at 1.5 MHz using an acousto-optic modulator (AOM) and only the first diffracted order is selected for excitation. To reduce optical penetration depth and generate higher-frequency acoustic components, the 800 nm pump is frequency-doubled to 400 nm via second-harmonic generation in a β-BaB_2O_4 (BBO) crystal.

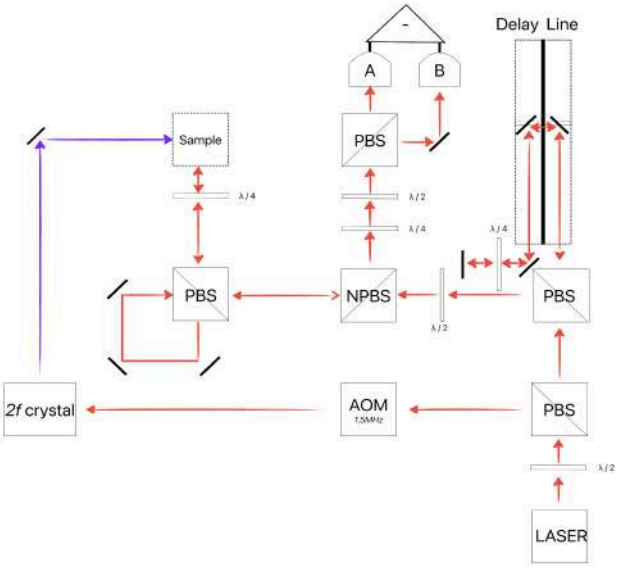


Figure 1: Pump probe setup

The probe arm traverses a 12.5 ns optical delay line before entering a Sagnac interferometer, which splits it into two counter-propagating pulses that interrogate the sample at times t and $t+\Delta t$. Upon reflection, the complex reflection coefficient

$$r(t) = |r|e^{i\varphi(t)} \qquad (1)$$

is modulated by both the strain-induced refractive index change (photoelastic effect) and the surface displacement Δz(t). After recombination, the two probe pulses interfere at photodiodes A and B; subtracting their outputs yields

$$I \propto \varphi(t + \Delta t) - \varphi(t) \qquad (2)$$

which, when demodulated at 1.5 MHz by a Stanford Research Systems SR830 lock-in amplifier, provides sensitivity to surface displacements in the 100 MHz–5 GHz band.

3) **Results**

We conducted spatial mappings on the substrates and obtained

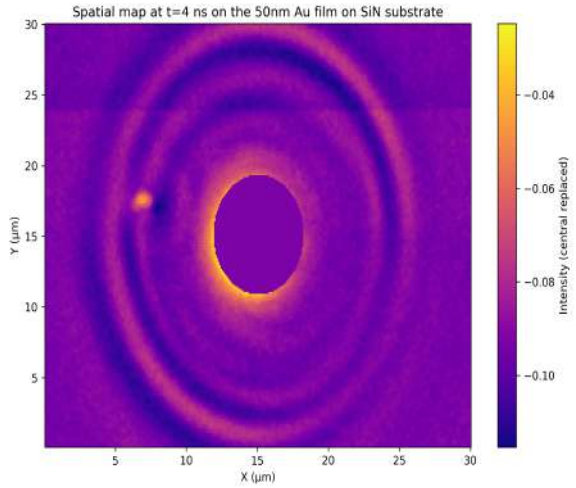


Figure 2*: A (30 by 30µm) spatial scan of a Rayleigh wave with a lateral precision of 125nm at t= 4ns.*

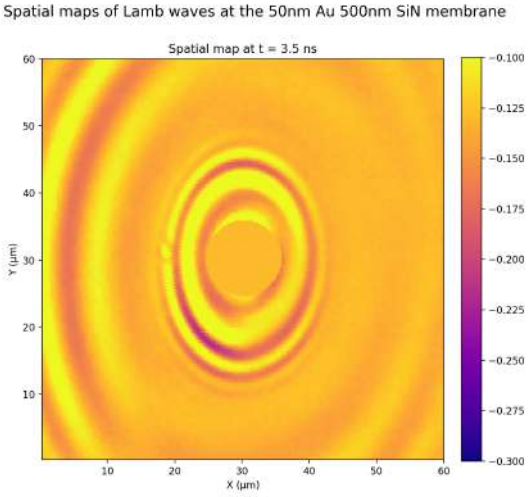


Figure 3*: A 60 by 60 µn spatial scan of Lamb waves with a lateral precision of 250nm at different t.*

Figure 2 shows the spatial map of the out-of-plane displacement on the Si_3N_4/Si substrate. The gold cylinder appears as a bright yellow spot on the left, due to its locally enhanced reflectivity. From that point, a circular scattered wave-front propagates outward. To improve visibility of the weak scattered signal, we digitally masked the central specular reflection (static background) using a mean-value subtraction, which enhances the contrast of the propagating wave. In contrast, the membrane sample (Figure 3) supports highly dispersive Lamb modes (A_0 and S_0), therefore the scattered wave is difficult to spot in the spatial scan. Quantitative analysis of the scattered field was done with frequency-filtered reconstructions.

4) Conclusion

We have demonstrated that spatially resolved pump–probe interferometry can quantitatively map the scattering of surface and guided elastic waves by isolated Au nano-cylinders. On rigid Si_3N_4/Si substrates, Rayleigh-wave scattering produces clear circular wave fronts, enabling direct extraction of the angular cross-section and hence the elastic mean free path ls. In contrast, on freestanding Si_3N_4 membranes the dispersive Lamb modes (A_0, S_0) smear out the scattered field, reducing peak amplitudes of the incident wave and necessitating frequency-filtered analysis. Future work will extend this approach to denser scatterer arrays and to time-resolved studies of sub-diffusive transport.

References

Takehiro Tachizaki, Toshihiro Muroya "Scanning ultrafast Sagnac interferometry for imaging two dimensional surface wave propagation" Rev. Sci. Instrum. , Vol. 77, 043713, 2006.

A Tourin, A Derode, A Peyre, and M Fink. Transport parameters for an ultrasonic pulsed wave propagating in a multiple scattering medium. J. Acoust. Soc. Am., 108:503–512, 2000.

H Hu, A Strybulevych, J H Page, S E Skipetrov, and B A Van Tiggelen. Localization of ultrasound in a three-dimensional elastique network. Nature Physics, 4:945–948, 2008.

Perrin, Bernard, et al. "Interferometric detection in picosecond ultrasonics." *Physica B: Condensed Matter* 263 (1999): 571-573

Metamaterial-based Dielectric Elastomers for Enhanced Energy Harvesting

A. Dutta[1*], Y. Pennec[1], G. Leveque[1], B. Djafari-Rouhani[1], M. Miniaci[1]**

[1] Univ. Lille, CNRS, Centrale Lille, Junia, Univ. Polytechnique Hauts-de-France, UMR 8520 - IEMN - Institut d'Electronique de Microélectronique et de Nanotechnologie, F-59000 Lille, France
[*] arnob.dutta@univ-lille.fr
[**] marco.miniaci@gmail.com, marco.miniaci@univ-lille.fr

Abstract: This work investigates the integration of mechanical metamaterials into dielectric elastomer generators (DEGs) to enhance energy harvesting performance. By introducing auxetic and multi-stable geometries in both two-dimensional (2D) and three-dimensional (3D) DEGs, we demonstrate enhanced capacitance variation and broadband response, leveraging metamaterial-induced nonlinearities and deformations to improve energy conversion efficiency.

Introduction: Dielectric elastomers (DEs) are a class of soft electroactive materials capable of converting mechanical deformation into electrical energy, and vice versa. Often referred to as stretchable capacitors, their performance is strongly influenced by their geometric and topological properties [1].
Mechanical metamaterials are artificially engineered structures designed to exhibit unusual quasi-static (and dynamic) behaviors, including auxeticity, multi-stability, frequency band gaps, which make them promising candidates for enhancing energy harvesting performances of DEs.
While the operation of DEs in actuator mode (DEA) has been extensively studied, especially in soft robotics [2], their application in generator mode for energy harvesting remains comparatively underexplored [3], [4].
In this work, we aim to exploit the unique mechanical properties of metamaterials to enhance the performance of DEGs. As a demonstration, we integrate metamaterial architectures into both 2D and 3D DEGs [3] [5], and investigate how their distinctive behaviors affect energy harvesting efficiency.

Modeling: A DE consists of an elastomer sandwiched between two compliant electrodes. When mechanical input, usually tensile force, is applied, the elastomer's area increases while its thickness decreases, resulting in a change in capacitance [3]. As illustrated in Fig 1., if the structure is electrically charged in a low-capacitance state and then stretched, the stored electrical energy increases as mechanical work is done on the system. When the elastomer returns to its original, unstretched state, this energy can be recovered as electrical output in the form of current.

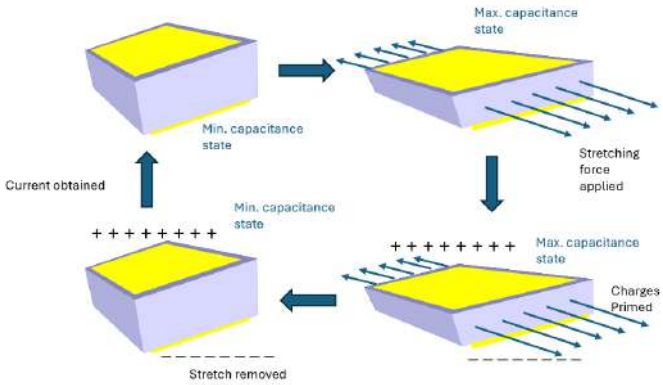


Figure 1: Typical energy harvesting cycle with a DEG.

Moretti et al. [3] investigated the effects of different strain modes on the capacitance variation of DEs. While uniform biaxial strain yields the highest capacitance change, real-world applications involve a wide range of non-uniform and complex deformation inputs. To accommodate such conditions, alternative configurations have been proposed, such as the diamond configuration in 2D [6], and the conical and bubble configurations in 3D.

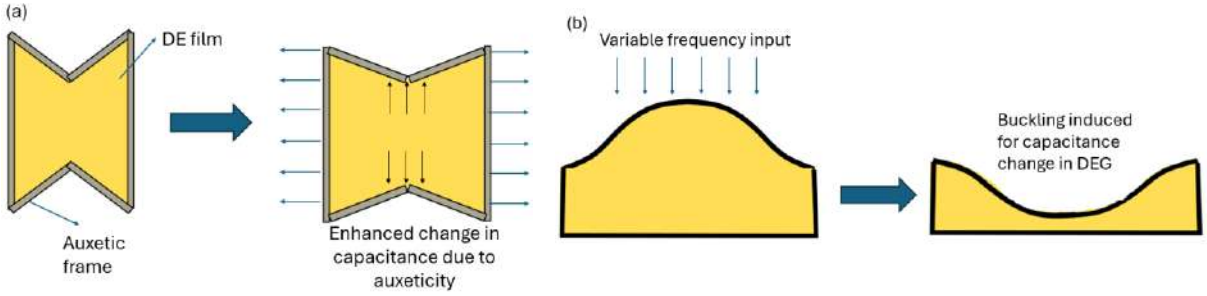


Figure 2: (a) Auxetic frame DEG, (b) buckling frame DEG.

In this work, we first modify the geometry of 2D DEs to include auxetic behavior upon deformation [7], as shown in Fig 2 (a), building upon the approach introduced in [5]. We then compare the change in capacitance with the base geometry. Next we extend the 2D metamaterial design to incorporate snap-through buckling – Fig. 2 (b), and investigate its response under variable-frequency excitation to demonstrate broadband energy harvesting behavior. Finally, we explore more complex 3D metamaterial architectures, including origami-inspired structures, to assess their potential for enhanced energy conversion.

Acknowledgments: This project has received funding from the European Union's Horizon Europe research and innovation programme under grant agreement MetacMed (GA No 101119738).

References

[1] T. Lu, C. Ma, and T. Wang, “Mechanics of dielectric elastomer structures: A review,” Extreme Mech Lett, vol. 38, p. 100752, Jul. 2020, doi: 10.1016/J.EML.2020.100752.

[2] J. H. Youn et al., “Dielectric Elastomer Actuator for Soft Robotics Applications and Challenges,” Applied Sciences 2020, Vol. 10, Page 640, vol. 10, no. 2, p. 640, Jan. 2020, doi: 10.3390/APP10020640.

[3] G. Moretti, S. Rosset, R. Vertechy, I. Anderson, and M. Fontana, “A Review of Dielectric Elastomer Generator Systems,” Advanced Intelligent Systems, vol. 2, no. 10, Oct. 2020, doi: 10.1002/aisy.202000125.

[4] S. J. A. Koh, C. Keplinger, T. Li, S. Bauer, and Z. Suo, “Dielectric elastomer generators: How much energy can be converted?,” IEEE/ASME Transactions on Mechatronics, vol. 16, no. 1, pp. 33–41, Feb. 2011, doi: 10.1109/TMECH.2010.2089635.

[5] W. Wu et al., “Largely Enhanced Energy Harvesting Performance of Silicone-Based Dielectric Elastomer Generators through Controlling the Uniaxial Device Structure,” ACS Sustain Chem Eng, vol. 12, no. 14, pp. 5447–5458, Apr. 2024, doi: 10.1021/acssuschemeng.3c07155.

[6] G. Moretti, M. Fontana, and R. Vertechy, “Parallelogram-shaped dielectric elastomer generators: Analytical model and experimental validation,” J Intell Mater Syst Struct, vol. 26, no. 6, pp. 740–751, Apr. 2015, doi: 10.1177/1045389X14563861.

[7] X. Li *et al.*, “Auxetic metamaterials and structures: a review,” *Smart Mater Struct*, vol. 27, no. 2, p. 023001, Jan. 2018, doi: 10.1088/1361-665X/AAA61C.

Advanced Techniques for Computational Electromagnetics

Variational Optical Processors

C. Roques-Carmes[1*], A. Karnieli[1*], D. A. B. Miller[1], and S. Fan[1]

[1]E.L. Ginzton Laboratory, Stanford University, CA, USA
[*]corresponding author: chrc@stanford.edu, karnieli@stanford.edu

Abstract: We introduce "variational optical processors," self-configuring photonic networks that learn modal representations of partially coherent or quantum optical fields through optimization, applicable to diverse classical and quantum optical processing tasks.

Classical and quantum light fields can be described in terms of modes. Modal decompositions play a central role in our understanding of multimode light field generation, propagation, and measurement. Some important examples include the decomposition of partially coherent light into so-called "natural modes" (a form of Karhunen-Loeve expansion [1]), coherency and density matrix eigendecomposition [1, 2], Schmidt decomposition of pure quantum bipartite states [2], and the Bloch-Messiah decomposition of multimode Gaussian states [3]. Methods relying on tomographic projection of the fields onto an *ad hoc* basis, usually requiring prior knowledge of the modes' geometry, have been realized to perform modal decomposition of multimode quantum and classical fields [4, 5].

Networks of Mach-Zehnder interferometers (MZIs) have proven highly effective in manipulating [6] and measuring [7] coherent multimode light. We now propose that these self-configuring meshes can be used to measure, process, and generate multimode light fields that exhibit some degree of partial (classical or quantum) coherence.

Here, we introduce a general framework for modal decomposition of partially coherent or quantum multimode light fields using a new class of optical devices coined "variational optical processors (VOP)." These networks consist of self-configuring MZI arrays whose parameters are optimized sequentially to e.g., maximize a function of the detected output signal. We find that in various cases – including Karhunen-Loeve expansions of classical and quantum light, Schmidt decomposition of bipartite states, and Bloch-Messiah decomposition of multimode squeezed vacuum – the modal decomposition can be mapped to a sequential output optimization by variational principles. Once trained, the resulting device physically separates the input light fields into mutually orthogonal components that have the properties of the modal decomposition of interest (e.g., mutually incoherent, separable quantum states, supermodes, etc.). Furthermore, by sequentially learning the modes associated with the largest eigenvalues or singular values, our framework achieves favorable scaling in both physical hardware and required measurements compared to traditional tomographic techniques. Our method therefore paves the way to full characterization of multimode classical and quantum light fields in various use cases such as spatially partially coherent light [8], single photon mixtures [8], entangled photon pairs [9], and multimode squeezed vacuum [10].

Acknowledgements. C. R.-C. is supported by a Stanford Science Fellowship. A.K. is supported by the VATAT-Quantum fellowship by the Israel Council for Higher Education; the Urbanek-Chodorow postdoctoral fellowship by the Department of Applied Physics at Stanford University; the Zuckerman STEM leadership

postdoctoral program; and the Viterbi fellowship by the Technion. S.F. and D.A.B.M. acknowledge support by the Air Force Office of Scientific Research (AFOSR, grant FA9550-21-1-0312). D.A.B.M. also acknowledges support by the Air Force Office of Scientific Research (AFOSR, grant FA9550-23-1-0307).

References

1. E. Wolf, "Unified theory of coherence and polarization of random electromagnetic beams," *Physics letters A*, 312 (5-6), 2003.
2. M. A. Nielsen, I. L. Chuang, "Quantum computation and quantum information," *Cambridge university press*, 2010
3. C. Fabre and N. Treps, "Modes and states in quantum optics," *Reviews of Modern Physics*, vol. 92, no. 3, p. 035005, 2020.
4. V. A. Averchenko, G. Frascella, M. Kalash, A. Cavanna, and M. V. Chekhova, "Reconstructing two-dimensional spatial modes for classical and quantum light," *Physical Review A*, vol. 102, no. 5, p. 053725, 2020.
5. K. H. Kagalwala, H. E. Kondakci, A. F. Abouraddy, and B. E. A. Saleh, "Optical coherency matrix tomography," *Scientific Reports*, 5 (1), 15333, 2015.
6. M. Milanizadeh, F. Toso, G. Ferrari, T. Jonuzi, D. A. B. Miller, A. Melloni, and F. Morichetti, "Coherent self-control of free-space optical beams with integrated silicon photonic meshes," *Photonics Research*, 9 (11), 2196-2204, 2021.
7. D. A. B. Miller, "Analyzing and generating multimode optical fields using self-configuring networks," *Optica* 7, 794-801 (2020)
8. C. Roques-Carmes, S. Fan, and D. A. B. Miller, "Measuring, processing, and generating partially coherent light with self-configuring optics," *Light: Science & Applications*, vol. 13, no. 1, p. 260, 2024.
9. C. Roques-Carmes, A. Karnieli, D. A. B. Miller, and S. Fan, "Automated modal analysis of entanglement with bipartite self-configuring optics," *arXiv preprint*, arXiv:2407.16849
10. A. Karnieli, C. Roques-Carmes, P. A. Mor, E. Lustig, J. Sloan, J. Vuckovic, D.A.B. Miller, and S. Fan, "Continuous-variable quantum information processing in real and synthetic dimensions with self-configuring optics", *in preparation* (submitted to CLEO:2025)

A gain route to reversed Cherenkov radiation

Ruoxi Chen[1,2] **and Xiao Lin** [1,2*]

[1] Interdisciplinary Center for Quantum Information, State Key Laboratory of Extreme Photonics and Instrumentation, Zhejiang Key Laboratory of Intelligent Electromagnetic Control and Advanced Electronic Integration, College of Information Science & Electronic Engineering, Zhejiang University, Hangzhou 310027, China.

[2]International Joint Innovation Center, The Electromagnetics Academy at Zhejiang University, Zhejiang University, Haining 314400, China.

[*]corresponding author: xiaolinzju@zju.edu.cn (X. Lin)

Abstract: We find precise conditions to enable reversed Cherenkov radiation from a positive-index gain isotropic slab under which the backward-propagating Cherenkov radiation is maintained while the forward-propagating one is suppressed. Counterintuitively, the intensity and the angular spread of reversed Cherenkov radiation can be made robust to the slab thickness.

When a charged particle moves with a velocity larger than the phase velocity of light in a surrounding material, that particle emits light into a highly directional cone. This exotic light emission process, known as Cherenkov radiation [1], was experimentally observed by Cherenkov under the guidance of Vavilov and later theoretically explained by Frank and Tamm. The many variants of Cherenkov radiation phenomena are now a common sight in modern physics (e.g. the bluish glow of an underwater nuclear reactor). According to the famous Frank-Tamm formula $cos\theta = \frac{c}{nv}$, the angle θ of light emission (also known as the Cherenkov angle) is related in a unique way to the particle velocity $v = |\bar{v}|$, where n is the refractive index of the surrounding material and c is the speed of light in vacuum. Enabled by this unique feature, the Cherenkov radiation is crucial to many practical applications, ranging from particle detectors/counters and light sources to bio-medical imaging and photodynamic therapy.

Upon close inspection of the Frank-Tamm formula, the Cherenkov angle inside the conventional material with $n > 0$ has $\theta < 90°$. That is, conventional Cherenkov radiation in positive-index materials is emitted in the forward direction relative to the direction of the particle motion. The forward direction is often undesirable. For example, Cherenkov detectors that rely on measuring Cherenkov radiation must cope with the energetic charged particles that cause radiation damage. This radiation damage limits the performance of particle identification and counting. Radiation emission in the backward direction is desired for both practical applications that rely on the Cherenkov effect (e.g. the development of advanced Cherenkov detectors with improved performance) and for fundamental reasons that relate to the nature of radiation emission in optical materials.

The most famous way to create such unconventional Cherenkov radiation is using exotic materials with $n < 0$, for which $\theta > 90°$ in the Frank-Tamm formula. In this case, the emitted photons and the emitting charged particles are spatially well-separated in opposite directions. This unconventional phenomenon, as first proposed by Veselago in 1968 [2], is the so-called reversed Cherenkov radiation [3]. In addition to negative-index materials, people later found that reversed Cherenkov radiation could also occur in anisotropic materials (e.g. hyperbolic materials) and photonic crystals. Essentially, the occurrence of reversed Cherenkov radiation requires the surrounding material — such as negative-index materials, hyperbolic materials, and photonic crystals — to support a judiciously-designed photonic eigenmodes, whose group velocity $\bar{v}_g$ has the antiparallel component with respect to the particle velocity $\bar{v}$, namely $\bar{v} \cdot \bar{v}_g < 0$. In contrast, conventional Cherenkov radiation inside any isotropic positive-index material has $\bar{v} \cdot \bar{v}_g > 0$. Whether reversed

Cherenkov radiation can emerge for $\bar{v} \cdot \bar{v}_g > 0$ remains elusive.

Here we reveal a mechanism for creating the effective reversed Cherenkov radiation from a positive-index isotropic slab, by exploiting the optical gain. This finding breaks the long-standing belief that the reversed Cherenkov radiation occurs only under the scenario of $\bar{v} \cdot \bar{v}_g < 0$. We show in Fig. 1 that a judiciously-designed gain medium can not only maintain backward-propagating radiation emission, but even suppress the forward-propagating emission. This way, while the initially-induced Cherenkov radiation inside the gain material still has $\bar{v} \cdot \bar{v}_g > 0$, the modified Cherenkov radiation after the interaction with the gain slab could transmit only into the backward vacuum region, leading to effective reversed Cherenkov radiation. We highlight that the connection between the reversed Cherenkov radiation and the optical gain has never been explored before, despite the long research history of free-electron radiation and optical gain. Meanwhile, whereas the pseudo-Brewster effect of gain materials was recently reported possible to simultaneously enhance the radiation intensity and directionality of transition radiation [4] (another typical type of free-electron radiation that occurs when an electron moves across an optical interface), the influence of optical gain on the performance of Cherenkov radiation remains under-explored.

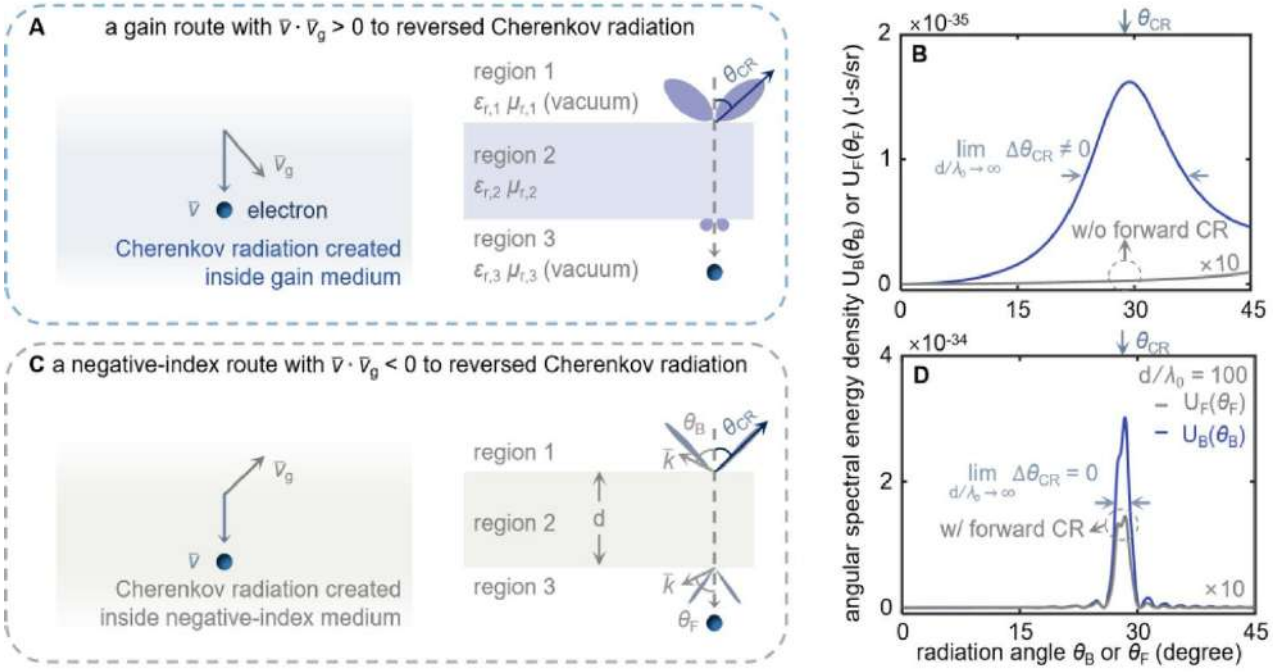


Fig. 1 Conceptual demonstration of a gain route to reversed Cherenkov radiation.

References

1. C. Luo, et al "Cerenkov radiation in photonic crystals". **Science**, Vol. 299, 368-371, 2003.

2. Veselago, V. G. "The electrodynamics of substances with simultaneously negative values of ε and μ." **Sov. Phys. Usp.**, Vol. 10, 509-514, 1968.

3. Skryabin, D. V., et al "Backward Cherenkov radiation emitted by polariton solitons in a microcavity wire." Nat. Commun., Vol. 8, 1554, 2017.

4. Chen, R., et al "Free-electron Brewster-transition radiation." **Sci. Adv.**, Vol. 9, eadh8098, 2023.

Near-field shaping by ray-caustic synthesis at microwaves and millimeter waves

Federica Anfuso[1], Ahsan Ullah Khan[1], Gino Sorbello[1] and Santi C. Pavone[1*]
[1]DIEEI, University of Catania, Via S. Sofia 64, 95123 Catania, Italy.
santi.pavone@unict.it (corresponding author)

Abstract

We present a method for synthesizing focused electromagnetic beams by manipulating ray caustics at microwave and millimeter wave frequencies. In ray optics, caustics are high-intensity ray trajectories where rays converge, allowing for precise near-field beam focusing. This approach has significant potential for advanced communication systems and near-field launcher design.

1 Introduction

Caustic theory finds applications in optics [1, 2] and electrical engineering, especially for near-field focusing. In the context of ray optics, caustics represent the envelope of the tangents to rays, which are adopted – under the high-frequency approximation – to describe the propagation of electromagnetic waves through a general medium. In this sense, caustics result in localized increase in field intensity. By controlling the position and shape of a target ray-caustic, it is possible to manipulate the radiated beam along specific trajectories in the near-field region. This contribution aims at introducing at microwaves and millimeter waves a useful near-field shaping technique based on ray-caustic synthesis [1], thus proving a physics-based approach that surpasses, in principle, more conventional non-diffractive beams, thanks to the interesting possibility to radiate almost-arbitrary curved beams in space.

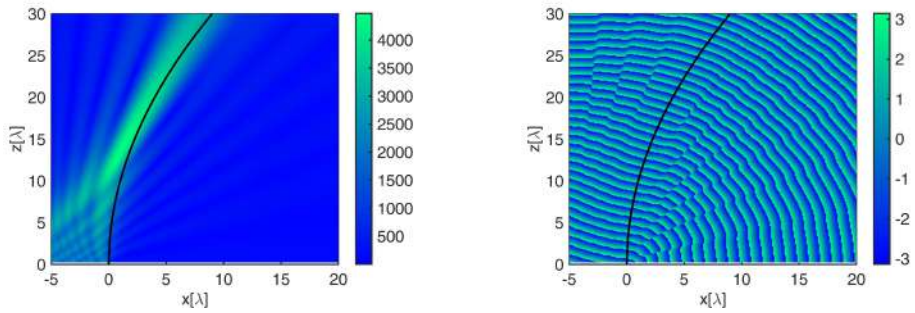
2 Formulation and Numerical Results

For simplicity, we consider a 2-D environment, where a phase gradient surface along the x-axis is designed to synthesize a phase function $\phi = \phi(x)$. Ray-caustic shaping in such an equivalent 2-D environment has been proven to be effective, as shown in [3–6]. This concept is based on the determination of a spatial phase profile $\phi(x)$ at the plane $z = 0$, which enables the synthesis of the desired curved caustic. The trajectory of the target ray is defined by the curve $z = f(x)$, with the tangent slope $\theta_t(x) = \frac{df(x)}{dx}$, which enables direct computation of the phase function. By appropriately designing $\phi(x)$, the electric field can be focused to follow the prescribed ray-caustic path. The 2-D radiated electric field by the n-th elementary radiator, placed at $x = x_n$ and phased as $e^{j\phi(x_n)}$, can be evaluated as

$$\mathbf{E}_n(\mathbf{r}) = -\hat{\mathbf{y}} e^{-j\phi(x_n)} G_{2D}(|\mathbf{r} - \mathbf{r}_n|), \tag{1}$$

where $G_{2D}(|\mathbf{r} - \mathbf{r}_n|)$ is the 2-D scalar Green's function of an unbounded medium, and $\mathbf{r}$ is the observation vector.

A numerical example has been developed, based on a caustic described by the function $f(x) = \gamma\sqrt{x}$, with $\gamma = 10$, extending over a prescribed length $L = 10\lambda$ at $z = 0$, being $\lambda = 1$ m. The objective is to demonstrate that the radiated electric field follows the trajectory defined by $f(x)$. The numerical result, shown in Fig. 1, validates the theoretical model by confirming that the field aligns with the intended caustic trajectories. It is important to note that the phase plot in Fig. 1(b) shows the local wave-fronts close to the desired caustic are planar and orthogonal to the caustic trajectory, as dictated by geometrical optics.



(a) (b)

Figure 1: (**a**) Amplitude and (**b**) phase of the radiated field generated by the phase profile described by $\phi(x)$.

3 Conclusions

We presented a new method for near-field curved-beam shaping using caustic synthesis, for innovative applications and microwaves and millimeter waves. Caustics, which are the envelope of tangents to reflected or refracted rays, naturally concentrate field intensity on arbitrary trajectories, making them ideal for focusing beams along curved trajectories. The proposed approach offers additional design parameters for innovative near-field launchers, beyond more traditional non-diffractive beams.

4 Acknowledgements

The work of Federica Anfuso and Ahsan Ullah Khan was partially supported by the European Union under the Italian National Recovery and Resilience Plan (NRRP) of NextGenerationEU, partnership on "Telecommunications of the Future" (PE0000001 - program "RESTART"). Santi C. Pavone and Gino Sorbello would like to thank the project PRIN 2022 DOSE (2022MANFK5), granted by the Ministero dell'Università e della Ricerca (MUR), and the project PIA.CE.RI. "Temistocle", granted by the University of Catania.

References

[1] L. Zhu, A. Wang, and J. Wang, "Free-space data-carrying bendable light communications," *Sci. Rep.*, vol. 9, no. 1, p. 14969, 2019.

[2] X. Zhou, H. Wang, S. Liu, H. Wang, J. Y. E. Chan, C.-F. Pan, D. Zhao, J. K. Yang, and C.-W. Qiu, "Arbitrary engineering of spatial caustics with 3d-printed metasurfaces," *Nature Communications*, vol. 15, no. 1, p. 3719, 2024.

[3] S. C. Pavone, G. Sorbello, and L. Di Donato, "On the orbital angular momentum incident fields in linearized microwave imaging," *Sensors*, vol. 20, no. 7, p. 1905, 2020.

[4] ——, "Improving Physical Optics approximation through Bessel beam scattering," *IEEE Antennas Wireless Propag. Lett.*, vol. 20, no. 6, pp. 993–997, 2021.

[5] ——, "Forward and inverse scattering of metallic objects through focused Bessel-shaped fields," *IEEE Open Journ. Antennas Propag.*, vol. 3, pp. 911–916, 2022.

[6] S. C. Pavone and G. Sorbello, "Near-field power efficiency maximization of a Bessel-shaped beam through planar layered media," *IEEE Trans. Antennas Propag.*, vol. 72, no. 4, pp. 3783–3788, 2024.

Silicon-based metasurface polarizer supporting quasi-bound states in the continuum

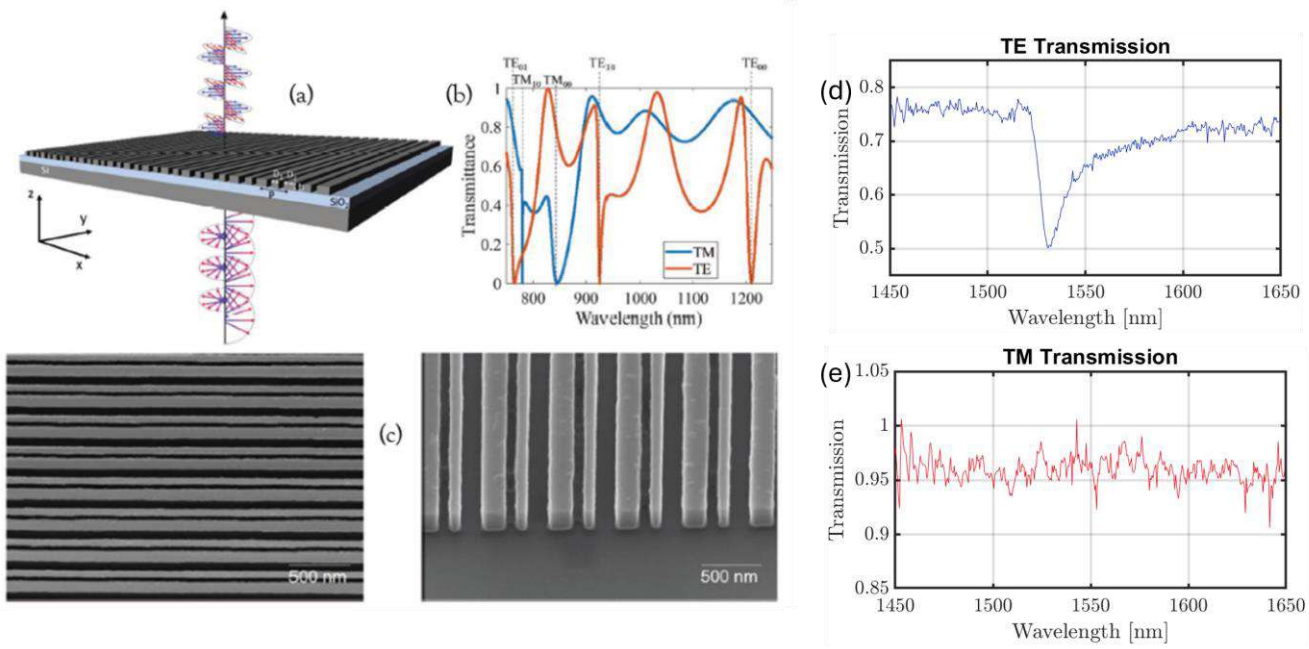
Maria Antonietta Vincenti[1], Sonia Freddi[2], Alfonso Nardi[3], Agostino Di Francescantonio[3], Johann Osmond[4], Attilio Zilli[3], Michele Gherardi[3], Domenico de Ceglia[1], Michele Celebrano[3], Marco Finazzi[3], Monica Bollani[1*]

[1]Department of Information Engineering, University of Brescia, Brescia, Italy
[2]Institute of Photonics and Nanotechnology (IFN) – CNR, LNESS, Como, Italy
[3]Physic Department of Milano Politecnico, Milano, Italy
ICFO-Institut de Ciencies Fotoniques, Barcelona, Spain
[*]corresponding author: monica.bollani@ifn.cnr.it

Abstract: (limited to 50 words max) The study reports the theoretical and experimental demonstration of an ultra-compact dielectric metasurface that leverages the topological features of symmetry protected quasi-bound states in the continuum supported by a silicon-based nanostructure. The dual-mode operating regime allows you to select the transmitted polarization without modifying the device orientation.

Manipulation of light polarization is crucial for a variety of applications including quantum communications, sensing, imaging, and material characterization, to name a few[1]. Since resorting to traditional approaches, such as cascading waveplates, is not effective in chip-scale environments, the quest for more compact, integrable solutions has been steadfast and has led to different answers, all aimed at reducing the size of the polarization devices. Some examples are devices based on photonic crystals, metallic gratings and nanoparticles or epsilon-near-zero materials [1,2]. Metasurfaces have emerged as a solution for polarization detection and engineering at the nanoscale. However, current metasurface-based polarizers can convert the incoming light into a single linear polarization state with some degree of flexibility in terms of spectral tunability [3,4]. Here we present two ultracompact all-dielectric metasurfaces that can convert any incoming polarization into either horizontal or vertical polarization without pre-determination of the incoming state of light [5]. This is achieved through the excitation of symmetry-protected quasi-bound states in the continuum (q-BICs) in a properly designed metasurfaces. Our optical modulators are based on silicon, specifically on silicon on insulator (SOI) and amorphous silicon (a-Si) on glass. Silicon has gained a foothold in nonlinear nanoscale photonics thanks to its well-established fabrication processes, high refractive index and strong third-order optical susceptibility. In these metasurfaces the symmetry is broken by changing the width of every other silicon nanobar in the array, supporting several quasi-bound states in the continuum modes (q-BICs), which are otherwise dark bound modes (BIC) in its symmetric counterpart. More specifically, in the SOI metasurface composed of a set of silicon nanobars with periodicity p = 600 nm, widths D1 = 150 nm and D2 = 90 nm (corresponding to an asymmetry factor $\alpha = 0.4$) and height h = 145 nm, placed on top of 1 μm SiO2 substrate we can identify five q-BICs in the near-IR frequency range. Each mode possesses a very high electric field enhancement and topological features that are typical of q-BIC modes. The presence of a finite SiO_2 layer in the fabricated samples introduces some additional Fabry-Perot resonances in the spectra that do not alter the spectral position of the q-BICs. On the contrary, for a-Si metasurface we optimize the following parameters: periodicity p = 650 nm, widths D1 = 130 nm and D2 = 91 nm (corresponding to an asymmetry factor $\alpha = 0.3$) and height h = 140 nm, placed on top of glass substrate. The metasurfaces are fabricated through a top-down process performed by a combination of e-beam lithography and reactive ion etching, paying particular attention to the correct definition of the gap and

to the vertical shape of the nanorods. Transmission spectra from the metasurface have been simulated and experimentally measured for normal incidence conditions and two orthogonally polarized linear waves for different structural asymmetry. The experimental results are in excellent agreement with the predicted spectra and show how the incoming linear polarization can be selectively suppressed whenever a q-BIC resonance is excited. In figure 1 we summarize the results.



(a) Working principle of the frequency selective polarization controller: a silicon-based nanostructure supporting q-BICs converts arbitrarily polarized incoming light into linearly polarized light; b) Transmission spectra for incoming TE (red line – electric field oriented along y) and TM (blue line – electric field oriented along x) polarizations. (c) SEM characterization in top-view of the crystalline and amorphous nanostructures. (d) TE and (e) TM transmission measurements, showing a resonance at $\lambda_{exp} = 1529$ *nm*

We acknowledge partial funding from NATO SPS Grant no. G5984, from Ministero dell'Istruzione, dell'Università e della Ricerca (Grant nos. PNRR PE0000023 NQSTI and PRIN Grant no.2022YJ5AZH).

References

1. Guo, Y., Xiao, M., Zhou, Y., Fanet, S., "Arbitrary Polarization Conversion with a Photonic Crystal Slab", Advanced Optical Materials 7, 1801453, 2019.
2. Okhlopkov, K.I., et al., "Tailoring Third-Harmonic Diffraction Efficiency by Hybrid Modes in High-Q Metasurfaces", Nano Letters, 21, 24, 10438–10445, 2021.
3. Yu, N. and Capasso, F. "Nature Materials" 13, 139-150, 2014.
4. A. Tognazzi, A. et al., "Third-harmonic light polarization control in magnetically resonant silicon metasurfaces", Optics Express Vol. 29, Issue 8, 11605, 2021.
5. Fagiani, L. et al., "Dual-Mode Polarization Control with Quasi-Bound States in the Continuum", Adv. Optical Mater., 2301456, 2023.

Retrieving Optical Properties of Biological Multilayers using Symbolic Regression

J. Sierra-Velez[1], A. Vial[1], M.A. Giraldo[2], and D. Macias[1*]
[1]Laboratory Light, nanomaterials & nanotechnologies - L2n, University of Technology of Troyes & CNRS EMR 7004,12 rue Marie Curie, Troyes-France
[2]Biophysics Group - Institute of Physics, University of Antioquia, Calle 70 52-21 A.A. 1226, Medellin, Colombia
demetrio.macias@utt.fr (corresponding author)

Abstract

We use Symbolic Regression to recover a closed-form expression that models the dielectric function of one of the materials that make up the wing of the *Morpho helenor* butterfly. This scheme provides a reliable alternative for characterizing the properties of materials from experimentally measured spectral data.

Symbolic Regression (SR) has regained popularity as a powerful tool, for discovering analytical expressions that model a given dataset, without requiring any prior assumptions about the algebraic form of the solution. This capability makes SR particularly valuable for applications in biomimetics [1], where retrieving the optical properties of materials remains an open challenge. In this work, we used SR to retrieve the dielectric function of the high-index layer in the multilayer system of the *Morpho helenor's* wing scale, from its experimentally measured reflectance spectra.

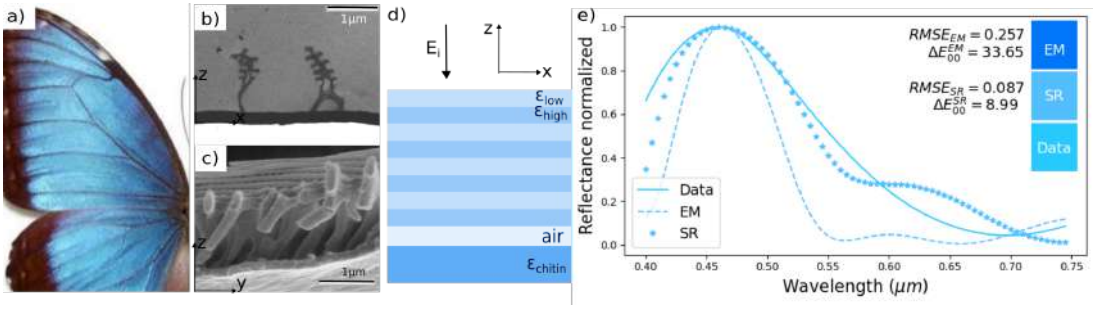


Figure 1: a) Part of a *Morpho helenor's* butterfly wing (adapted from [2]). b,c) TEM front view and SEM side view of a cover scale, revealing its ridge-lamellar multilayer structure and the lower chitin lamina. d) Multilayer system considered in this work. e) Normalized reflectance of the experimentally measured Data, the effective medium EM model, and the SR prediction, with their corresponding RMSE accuracy metric, and their ΔE^*_{00} color difference.

The *Morpho helenor* butterfly Fig. 1-(a), is widely recognized for its brilliant blue structural coloration. In the TEM and SEM images in Fig. 1-(b,c) we can see the two distinct structures responsible for its optical response. The first is a lower lamina of chitin that acts as a thin film, whose reflectance defines the overall spectral shape of the reflectance and is the dominant contributor to the coloration. The second is the ridge-lamellar multilayer configuration, whose geometric parameters are well-tuned with the thin film, enhancing reflectance in the blue wavelength range and intensifying the characteristic brilliant blue appearance [2].

Previous research has modeled the general structure of *Morpho* butterflies using an effective medium (EM) approach [3]. In *Morpho helenor*, the presence of large open windows introduces significant air gaps between consecutive ridges, resulting in at least 75% of air in each effective layer and reducing the accuraccy of the model. In this work, we used SR to model the *Morpho helenor* without the EM approach. We consider the simplified geometry depicted in Fig. 1-(d), a multilayer system composed of alternating high- and low-refractive-index layers. The incident and substrate medium are air, while the low-index layer is approximated as a homogeneous medium with a dielectric function of $\epsilon_l = 1.1$. The final two layers consist of an air layer and a 220 nm chitin film, respectively.

The butterfly's reflectance spectrum $R(\lambda)$ was experimentally measured using a bifurcated optical fiber probe at normal incidence. We used $R(\lambda)$ as input for the SR, and predicted the dielectric function of the high-index material ϵ_h^{SR}. We used the Berreman 4x4 method to compute the reflectance $R^{SR}(\lambda, \epsilon_h^{SR})$ of the multilayer considered in Fig. 1-(d), incorporating the prediction. We used the RMSE metric to quantify the accuracy of R^{SR} to reproduce the input $R(\lambda)$. To provide insights into the stability of the retrieved models, we performed 50 realizations of the SR corresponding to different initialization random seeds. Each realization yields a list of dimensionally homogeneous expressions. To assess the model's reliability we implemented two additional metrics: Presence, which quantifies the number of realizations where the model is retrieved, and Occurrence, which measures the relative frequency of the model compared to all retrieved expressions. The results are summarized in Table 1.

Table 1: Top four models retrieved by SR. Each one is presented with a Presence and Occurrence metric across realizations, and its response accuracy $RMSE$ metric.

Expressions	**Presence**	**Occurrence**	**RMSE**$_R$
$\epsilon_{h1} = \frac{A}{B-\lambda}$	50	59%	0.087
$\epsilon_{h2} = A$	21	11%	0.095
$\epsilon_{h3} = \frac{(A+B\lambda)}{(C-D\lambda)}$	16	8%	0.087
$\epsilon_{h4} = A\lambda$	14	9%	0.080

The best model retrieved by SR is $\epsilon_h^{SR} = \epsilon_{h1}$ of Table 1, with $A = 1.124\mu m$ and $B = 1.124\mu m$. This model is present in the results of all realizations, and it corresponds to 59% of all retrieved expressions. In Fig. 1-(e) we show that the retrieved SR model outperforms the EM model in accuracy, exhibiting a lower $RMSE_R$ value and a lower ΔE_{00}^* color difference when compared to the experimentally measured data. The metrics suggest that this model represents the best approximation for the dielectric function of the high-index layer under the assumed geometry, likely representing a local optimum of the problem. This approach can be extended to cases where the optical properties of the materials are unknown, or to more complex configurations, paving the way for biomimetic photonics applications.

References

[1] Sierra-Velez, J., M. Inchaussandague, D. Skigin, A. Vial, H. Hölscher, D. Macias, "Symbolic regression: an alternative method to model the optical response of photonic biological and bio-inspired structures," *Opt. Lett.*, Vol. 49, No. 23, pp. 6753–6756, Dec. 2024.

[2] Giraldo, M. A., D. G. Stavenga, "Brilliant iridescence of Morpho butterfly wing scales is due to both a thin film lower lamina and a multilayered upper lamina," *J. Comp. Physiol. A*, Vol. 202, No. 5, pp. 381–388, 2016.

[3] Berthier, S., E. Charron, A. Silva, "Determination of the cuticle index of the scales of the iridescent butterfly Morpho menelaus," *Opt. Commun.*, Vol. 228, No. 4–6, pp. 349–356, 2003.

Near-field optoelectronic heat engines and thermal emission of subwavelength objects

J. Legendre[1], T. Châtelet[1*], K. Kontou[1], J. Sojo-Gordillo[2,3], A. Alwakil[1], A. Tellal[4], T. Benyattou[4], O. Merchiers[1], and P.-O. Chapuis[1*]

[1]Centre for Energy and Thermal Sciences of Lyon (CETHIL), CNRS – INSA Lyon, Villeurbanne (Lyon), France
[2]Catalonia Institute for Energy Research (IREC), Barcelona, Spain
[3]Departement of Physics, University of Basel, Switzerland
[4]Institut des Nanotechnologies de Lyon, France
[*]corresponding author: olivier.chapuis@insa-lyon.fr

Abstract: First, a novel class of heat engines based on the radiative exchange between hot and cold pin junctions is studied by coupling the drift-diffusion equations for heterostructures to fluctuational electrodynamics. Then we address thermal emission of objects of size smaller than the wavelength, including spheres, nanowires and discs on surface.

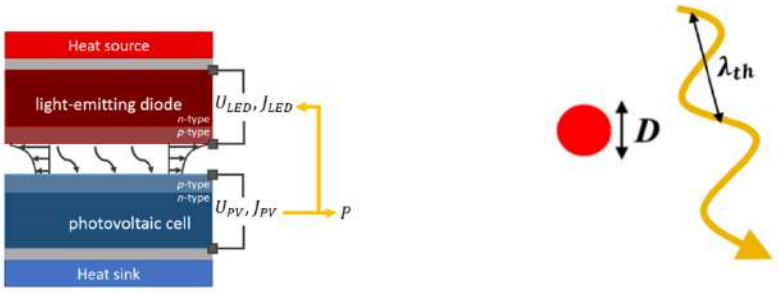


Figure 1. (a) Schematic of a thermophotonic energy harvester, highlighting the LED heat pump and the PV cell heat engine as elements of the dual radiative heat engine. (b) Schematic of an object of subwavelength size.
We report on two different works.

First, we study heat engines based on the radiative exchange between hot and cold bodies. The surface of one or each of the two bodies is covered with a pin junction, leading to electroluminescence (EL) and/or photovoltaic (PV) conversion [1]. For instance, when a passive hot body faces one room-temperature pin junction, thermophotovoltaic energy conversion happens. A device with both hot and cold pin junctions can be termed a dual radiative engine. Interestingly, such configuration allows for exchanging radiation above the Planck blackbody limit in far field since EL is not bounded. Bringing the two bodies in close proximity further allows to increase the radiative exchange by means of near-field tunneling. Thermal-to-electrical conversion or refrigeration by such devices can therefore compete with current state-of-the-art ones such as thermoelectrics [2].

Most of the analyses of these devices performed to date are based on accurate optical computations with fluctuational electrodynamics, i.e. the combination of electromagnetism and statistical physics describing thermal radiation at the wavelength scale. However, electrical charge transport is usually treated with a detail-balance approach [3-4], which does not include the local variation of chemical potential and therefore is unable to capture the fine interplay between the electrical quantities and the light emission. To predict more accurately the effects, we have developed a combined solver of the drift-diffusion equations for charge transport

in heterostructures and the radiation emission and absorption, called CRESCENT-1D [5], available on GitHub [6]. We will report on its capabilities with the example in the case of a near-field thermophotonic converter, which is made of a hot light-emitting diode (LED) and a room-temperature PV cell in the case of waste-heat harvester. If one wants a refrigerating device, the LED is cold and the PV cell is place to the room-temperature side of the device. We discuss also the issues associated with photon recycling and spatial dispersion in these computations.

In a second part, we address thermal radiation involving objects of sub-wavelength size [7]. For these objects, the usual concept of emissivity assumed to be size independent breaks down. An apparent emissivity can be defined based on the absorption cross section, well studied for nanoparticles or antennas. For isolated objects, such as spheres [8] or nanowires, it was found that the apparent emissivity can strongly surpass unity. The results depend on the permittivity of the material and some interplay with the geometry. Interestingly, the power law deviates from the Stefan-Boltzmann law with an exponent that can be way larger than 4. We extend the study to more complex objects, such as disks on surfaces. In [9], the emission of a blackbody by a diffracting hole was computed and found to scale as T^8 following the Bethe-Bouwkamp results. We analyze how this prediction evolves for real materials, in particular those supporting surface polaritons.

We acknowledge funding from EU projects FETProactive TPX-Power (GA951976), FETOpen OPTAGON (GA 964698), and French ANR project STORE (21-CE42-0032).

References

1. Legendre, J. and P.-O. Chapuis, “Operating conditions and thermodynamic bounds of dual radiative heat engines”, Phys. Rev. App., in press, 2025. arXiv:2402.07527
2. Legendre, J. and P.-O. Chapuis, “Overcoming non-radiative losses in near-field thermophotonics with AlGaAs PIN junctions”, Appl. Phys. Lett., Vol. 121, 193902, 2022.
3. Zhao, B., *et al*., “Near-Field Thermophotonic Systems for Low-Grade Waste-Heat Recovery”, Nano Lett., Vol. 18, 8, 5224, 2018.
4. Legendre, J. and P.-O. Chapuis, “GaAs-based near-field thermophotonic devices: approaching the idealized case with one-dimensional pn junctions”, Sol. Energy Mater Sol. Cells, Vol. 238, 111594, 2022.
5. Legendre, J., and P.-O. Chapuis, “CRESCENT-1D: A 1-D Solver of Coupled Charge and Light Transport in Heterostructures for the Design of Near-Field Thermophotonic Engines”, IEEE Trans. Elec. Dev., in press 2025. DOI: 10.1109/TED.2025.3528870
6. https://github.com/JulienLegendre/CRESCENT-1D/
7. Chapuis, P.-O., B.-J. Lee and A. Rodriguez, “Thermal radiation at the nanoscale and applications”, Appl. Phys. Lett., Vol. 123, 220401, 2023.
8. Nguyen, K.L., *et al*., “Temperature-dependent and optimized thermal emission by spheres”, Appl. Phys. Lett., Vol. 112, 111906, 2018.
9. Joulain, K., *et al.,* “Thermal emission by a subwavelength aperture”, J. Quant. Spectr. Rad. Transf., Vol. 173, 1, 2016.

The effective refractive index of resonant particulate media depends on the shape of the particule arrangement

C. Blanchard[1*], T. Guerra[2], J. P. Hugonin[3], and C. Sauvan[3]

[1]CNRS, CEMHTI UPR3079, Université d'Orléans, Orléans, France
[2]CEA/LETI, University Grenoble Alps, Grenoble, France
[3]Université Paris-Saclay, IOGS, CNRS, Laboratoire Charles Fabry, Palaiseau, France
cedric.blanchard@cnrs-orleans.fr (corresponding author)

Abstract

The effective properties of random particulate media must be extracted on volumes large enough to include all kind of interactions between the scatterers. We show that for resonant interactions, this so-called representative volume element may also depend on the shape of the geometrical boundary of the particle suspensions.

1 Results

The smallest unit of a microstructure that exhibits the same effective refractive index n_{eff} as the entire microstructure sample is referred to as representative volume element (RVE). By performing numerical simulations of RVE one may save considerable computational ressources, in opposition to larger domains. Therefore, it is worth having a hint of the expected RVE before launching numerical simulations.

Usually, the strategy to determine the RVE is to gradually increase the size of the computed unit, until the extracted effective value converges toward a constant value, which is therefore considered as the actual n_{eff} [1,2] of the microstructure at a given wavelength λ. In this context, a legitimate question is whether other parameters than the size can be used to reduce further the computational ressources. For example, the shape of the unit in which the inhomogeneities are arranged may well affect how quickly the extracted value approaches the n_{eff} limit.

In this contribution, we do not address this precise question – which would desserve a study not performed so far in the literature – but a related one, encompassing the cooperative scattering of light in random particulate media. We show that there exist regimes of resonant interactions between the particles where the extracted effective value is biased by the shape of the computed unit. To be specific, while the extracted effective value no longer evolves when the size of the computed unit is increased, it turns out to reach different values when the shape is varied.

We also show that this effect is totally decorrelated from electromagnetic field fluctuations between computed units differing only in the location of the particles (i.e., the different microstates of a statistical ensemble, see section 2). There exist regimes where these fluctuations may be quite large and strongly conditioned by the shape of the computed units while, simultaneously, the same n_{eff} is found irrespective of the shape.

These intriguing phenomena are examined from the vantage point of the eigenmodes of the computed units. Since the systems of particles are absorptive and open, such eigenmodes are actually quasinormal modes (QNMs) and their eigenfrequencies are complex. The analysis of the dispersion of the QNMs in the complex λ-plane reveals striking different behaviors depending

on the permittivity of the particles. We are therefore able to discriminate two types of resonant regimes that we will referred to as (i) the scattering and (ii) the fluctuating regimes. While the modes exhibit a clear tendency to gather in certain regions of the complex plane for the former, the modes are spread out in the whole complex plane for the latter. Another big difference between these two regimes lies in the field structure of the modes. The QNMs of the former are Mie-type modes, while for the latter they are localized modes in the sense that the associated fields are concentrated in specific regions of the particulate medium.

2 Methodogy

The effective refractive index n_{eff} of the random particulate material is extracted from the mean field $\mathbf{E}_{\text{sc}}$ scattered by the computed units, in agreement with the wave equation

$$\nabla \times \nabla \times \langle \mathbf{E}_{\text{sc}} \rangle - n_{\text{eff}}^2 \frac{\omega^2}{c^2} \langle \mathbf{E}_{\text{sc}} \rangle = 0 \tag{1}$$

which links these two quantities [3]. In other words, the computed units can be considered as the constitutive configurations of a statistical ensemble, and they differ from one to another in the position of the particles, all other parameters (fill-factor, size of particles, etc.) being kept constant. The mean field is obtained by averaging the field scattered by all the computed units of the ensemble. Such a mean field is then compared to the field scattered by an homogenous domain of refractive index n_{hmg} (i.e., a closed-form problem), having same size and shape as the computed unit. When the field scattered by the homogeneous domain fits the numerical data, then $n_{\text{eff}} = n_{\text{hmg}}$.

In a nutshell, we operate here on the shape of the ensemble's microstates to investigate the impact on the extracted n_{eff} and, in addtion to that, we study the corresponding evolution of the eigenmodes of these microstates.

Acknowledgements

This work was performed in the frame of the OUTWARDS project (ID: ANR 19-CE05-0021), led by C. Blanchard and funded by the Agence Nationale de la Recherche (ANR).

References

[1] T. Kanit, S. Forest, I. Galliet, V. Mounoury, and D. Jeulin. Determination of the size of the representative volume element for random composites: statistical and numerical approach. *International Journal of Solids and Structures*, 40(13):3647–3679, 2003.

[2] C. Blanchard, J.-P. Hugonin, A. Nzie, and D. De Sousa Meneses. Multipolar scattering of subwavelength interacting particles: Extraction of effective properties between transverse and longitudinal optical modes. *Phys. Rev. B*, 102:064209, 2020.

[3] N. J. Schilder, C. Sauvan, Y. R. P. Sortais, A. Browaeys, and J.-J. Greffet. Homogenization of an ensemble of interacting resonant scatterers. *Physical Review A*, 96:013825, 2017.

Beam dynamics induced by the quantum metric of exceptional rings

Z. Zhang[1], I. Septembre[2,3], Z. Liu[1], P. Kokhanchik[2], S. Liang[1], F. Liu[1], C. Li[1], H. Wang[1], M. Liu[4], Y. Zhang[1], M. Xiao[5], G. Malpuech[2] and D. Solnyshkov[2,6*]

[1]Xi'an Jiaotong University, Xi'an, China
[2]Institut Pascal, CNRS/University Clermont Auvergne, France
[3]Universität Siegen, Siegen, Germany
[4]International Research Center for Renewable Energy, Xi'an Jiaotong University, China
[5]University of Arkansas, Fayetteville, Arkansas, USA
[6]Institut Universitaire de France (IUF), Paris, France
[*]corresponding author: dmitry.solnyshkov@uca.fr

Abstract: We study experimentally and theoretically the dynamics of wave packets at exceptional rings stemming from Dirac points in a photonic honeycomb lattice. We demonstrate a new effect: the transverse non-Hermitian drift in the reciprocal space, useful for beam steering. Its description is based on biorthogonal quantum metric.

The control of non-Hermiticity opens new opportunities in photonics. Non-Hermitian systems often exhibit exceptional points, characterized by the coalescence of the eigenvectors and the reduction of the number of eigenvalues. These points have been extensively studied in the past few years, especially in photonics [1]. The square root behavior of the eigenvalues leads to high sensitivity [2]. It can be traced back to the quantum metric, which diverges close to exceptional points [3]. While the properties of the dispersion and the group velocity were analyzed quite extensively [4,5], the dynamic behavior of wavepackets at the exceptional rings has not been deeply studied yet. This dynamics provides a better microscopic understanding of the macroscopic transport phenomena (as for the anomalous Hall effect), and because of the possible practical applications. It is often influenced by the quantum geometric tensor that includes the Berry curvature and the quantum metric [6]. This led to an important question of the choice of the quantum metric for the description of non-Hermitian systems [7]. Despite the hot debate, the question is still open [8].

In this work, we use a honeycomb photonic lattice in rubidium atomic vapors in the regime of electromagnetically-induced transparency (EIT) to unveil the role of the quantum metric. We introduce non-Hermiticity by inducing different losses on A and B lattice sites, which results in the transformation of Dirac points into exceptional rings. This transition is evidenced by the qualitative change in the probe dynamics: we observe a transition from conical diffraction to non-Hermitian spatial broadening. The scaling of the size of the wave packet with the non-Hermiticity magnitude is quantitatively determined by the quantum metric. Next, we demonstrate both experimentally and theoretically the presence of a non-Hermitian counterpart of the anomalous Hall effect. We observe a drift of the probe wavepacket in the reciprocal space. This drift occurs not only in the direction of the gradient of the imaginary part of the energy, but more surprisingly, also in the transverse direction. We call this effect the transverse non-Hermitian drift and demonstrate that it is entirely due to the non-orthogonality of the eigenstates and requires the biorthogonal quantum metric for its description [9]. The resulting non-Hermitian reciprocal-space dynamics can be applicable to beam steering.

This work was supported by National Natural Science Foundation of China (No.52488201, and No.12074306) and European Union's Horizon 2020 program, through a FET Open grant No. 964770 (TopoLight). Additional support was provided by the ANR Labex GaNext (ANR-11-LABX-0014), the ANR program "Investissements d'Avenir" through the IDEX-ISITE initiative 16-IDEX-0001 (CAP 20-25), the ANR project MoirePlusPlus, and the ANR project "NEWAVE" (ANR-21-CE24-0019). IS acknowledges support from the Deutsche Forschungsgemeinschaft (DFG, German Research Foundation, project numbers 447948357 and 440958198), the Sino-German Center for Research Promotion (Project M-0294), the ERC (Consolidator Grant 683107/TempoQ), the German Ministry of Education and Research (Project QuKuK, BMBF Grant No. 16KIS1618K) and the Stiftung der Deutschen Wirtschaft.

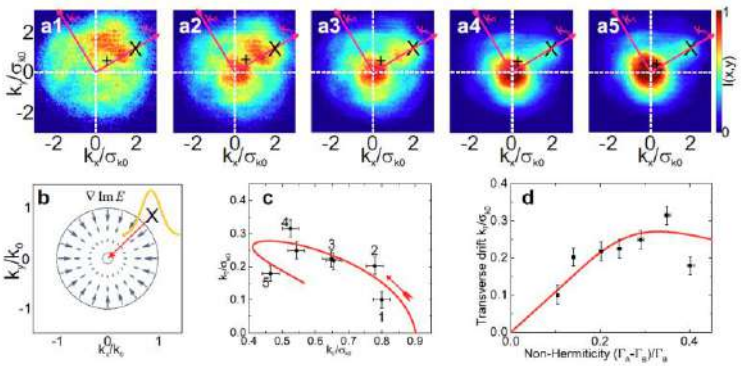


Figure 1. a1-a5) Images of the output wave packet in the reciprocal space with increasing non-Hermiticity (experiment), "X" marks the initial position of the wave packet and "+" marks the center of mass of the snapshot; b) Sketch of the gradient of the imaginary part of the energy (blue arrows), responsible for the longitudinal drift (red arrow); c) Position of the center of mass in the reciprocal space at fixed *t* for different non-Hermiticity (numbers correspond to panels a1-a5, arrow marks the non-Hermiticity increase); d) Transverse (anomalous) non-Hermitian drift as a function of non-Hermiticity. In c,d): black dots -- experiment, red curve -- theory.

References

1. M. A. Miri and A. Alù, "Exceptional points in optics and photonics", *Science* 363, 10.1126/science.aar7709, 2019.
2. J. Wiersig, "Enhancing the sensitivity of frequency and energy splitting detection by using exceptional points Application to microcavity sensors for single-particle detection", *Phys. Rev. Lett.* 112, 203901, 2014.
3. Q. Liao, C. Leblanc, J. Ren, F. Li, Y. Li, D. Solnyshkov, G. Malpuech, J. Yao, and H. Fu, "Experimental measurement of the divergent quantum metric of an exceptional point", *Phys. Rev. Lett.* 127, 107402, 2021.
4. A. Cerjan, S. Huang, M. Wang, K. P. Chen, Y. Chong, and M. C. Rechtsman, "Experimental realization of a Weyl exceptional ring", *Nat. Photonics* 13, 623, 2019.
5. J.-J. Liu, Z.-W. Li, Z.-G. Chen, W. Tang, A. Chen, B. Liang, G. Ma, and J.-C. Cheng, "Experimental realization of Weyl exceptional rings in a synthetic three-dimensional non-Hermitian phononic crystal", *PRL* 129, 084301, 2022.
6. A. Gianfrate, O. Bleu, L. Dominici, V. Ardizzone, M. De Giorgi, D. Ballarini, G. Lerario, K. West, L. Pfeiffer, D. Solnyshkov, D. Sanvitto, and G. Malpuech, "Measurement of the quantum geometric tensor and of the anomalous Hall drift", *Nature* 578, 381, 2020.
7. D. C. Brody and E. M. Graefe, "Information geometry of complex Hamiltonians and exceptional points", *Entropy* 15, 3361, 2013.
8. Y.-M. R. Hu, E. A. Ostrovskaya, and E. Estrecho, "Generalized quantum geometric tensor in a non-Hermitian exciton-polariton system", *Opt. Mater. Express* 14, 664, 2024.
9. Z. Zhang et al, "Beam dynamics induced by the quantum metric of exceptional rings" *arXiv*:2410.14428, 2024.

Scattering-Matrix-Based Optical Property Analysis and Simulation Acceleration for Periodic Photonic Structures and Metasurfaces

Yijia Cheng[1], Chengnian Huang[1], and Wei E. I. Sha[1*]

[1]College of Information Science and Electronic Engineering, Zhejiang University, Hangzhou 310027, China
[*]corresponding author: 12131036@zju.edu.cn (Y. Cheng); weisha@zju.edu.cn (W. E. I. Sha)

Abstract: The scattering matrix method (SMM) enables spectral/field analysis of periodic photonic structures. Leveraging S-matrix physical properties, finite-difference matrix differentiation accelerates complex pole extraction in band-structure eigenvalue solutions. By decomposing non-periodic metasurfaces into coupled quasi-periodic subunits with parallel computation, SMM extends to large-scale aperiodic simulations bypassing full-wave modeling.

As a widely-used mode matching method as well as a semi-analytical model, scattering matrix (S-matrix) method not only provides excitation solution to accurately predict the behavior of light in photonic structures but also allows for corresponding eigenvalue analysis and band diagram calculation, which makes it an effective solver for some novel photonic structures.

Regarding periodic photonic structures, the S-matrix of a whole structure can be obtained by the Bloch mode expansion and layer-by-layer analysis for generating and cascading S-matrices in all layers, respectively. By giving the input vector, the reflection, transmission, and absorption coefficients can be calculated. Furthermore, the eigenvalue analysis can be implemented through finding poles of the determinant of inverse of S-matrix. To find the complex poles, we calculate the derivatives of complex S-matrix with iterative Newton-like method

$$\omega_{n+1} = \omega_n + 2\frac{\max \operatorname{eig} S'(\omega_n)}{\max \operatorname{eig} S''(\omega_n)} \tag{1}$$

by using the numerical FD stencils [1] instead of matrix decomposition and inverse, which avoids complex matrix operations and is free from the ill-conditioned inverse of large-dimensional S-matrix. A square-lattice photonic crystal slabs (PCS's) which has rich resonant properties (quasiguided modes [2]) is used as a numerical example to calculate the optical coefficients and band structure of the PCS's model (shown in Fig.1).

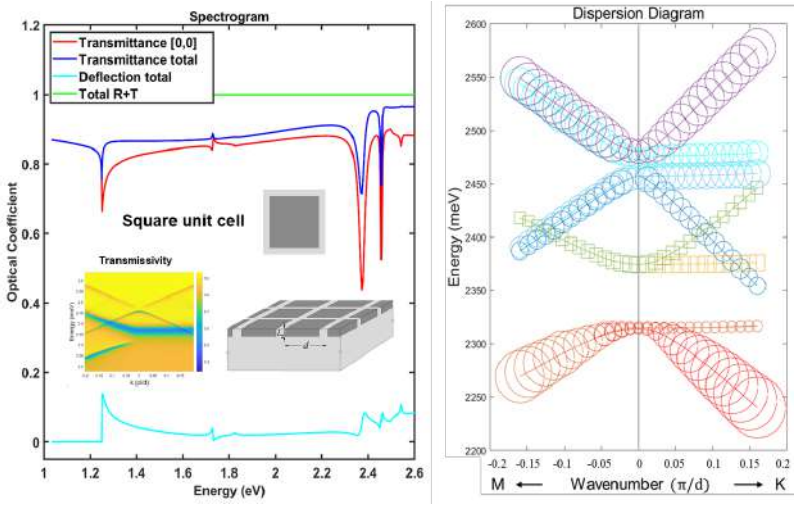


Figure 1. Optical coefficients and dispersion diagram (the imaginary parts of the eigen-energies are denoted by circles or squares with different sizes) of the square-lattice PCS's model.

Building on the SMM's ability to handle periodic structures, it can also be extended to simulate large-area metasurfaces, where electromagnetic simulations remain challenging. For example, metalenses, which are crucial for optical beam manipulation, have large physical dimensions compared to the optical wavelength, complicating accurate simulations. One solution is to apply a locally periodic approximation to aperiodic structures, neglecting the coupling between unit cells. To improve approximation accuracy and account for overlapping domains [3], larger supercells containing multiple unit cells (e.g., 3x3, 5x5, 7x7, etc.) are used to calculate the local field distribution.

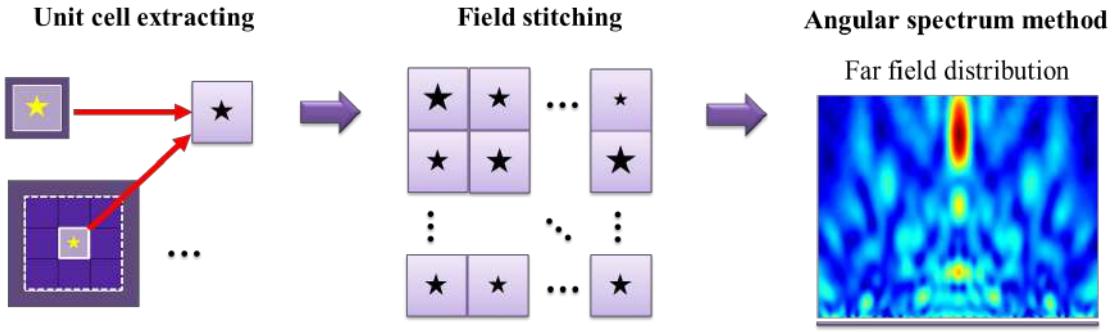


Figure 2. The procedure of the scattering-matrix-based field-stitching technique.

As illustrated in Fig. 2, the scattering-matrix-based field stitching technique developed in this study follows a three-step process. First, supercells of different sizes are employed to simulate the coupling modes of central unit cells. Second, the effective field distributions of these central unit cells are extracted from the supercell simulations and stitched together to reconstruct the complete field of the large-area metalens. To ensure smooth transitions at cell boundaries, a technique involving averaging the phases of fields in overlapping regions is applied. In the final step, the far-field focusing pattern is calculated by angular spectrum method. A 16λ-scale focusing dielectric metasurface consisting of 25x25 silicon disks is used as a numerical example to validate the method, with its far-field focusing pattern shown in Fig. 2. This process helps assess the focusing performance of the metalens, supporting further design and optimization since it substantially lowers time costs in comparison to full-wave simulation, owing to the parallelizability of the unit calculations and the reduced complexity.

Furthermore, the scattering-matrix-based algorithm and its eigenfrequency solver can be further developed to simulate the electromagnetic fields and band structures of emerging photonic structures, such as diffraction gratings with macroscopic moiré patterns and quasi-bound states in the continuum, as well as sources like oscillating point dipoles in addition to plane wave excitations. And the advancements of SMM will facilitate effective mode analysis, contributing to the optimized design of photonic devices.

References

1. Fornberg, B., “Finite difference formulas in the complex plane,” *Numer. Algorithms*, Vol. 90, No. 3, pp. 1305-1326, 2022.
2. S. G. Tikhodeev, A. L. Yablonskii, et al., “Quasiguided modes and optical properties of photonic crystal slabs,” *Phys. Rev. B*, Vol. 66, No. 4, pp. 045102, 2002.
3. Lin, Z. and S. G. Johnson, “Overlapping domains for topology optimization of large-area metasurfaces,” *Opt. Express*, Vol. 27, No. 22, pp. 32445-32453, 2019.

Directional near fields generated by small particles

Shubo Wang[1,2*]

[1]Department of Physics, City University of Hong Kong, Hong Kong, China
[2]City University of Hong Kong Shenzhen Research Institute, Guangdong, China
[*]corresponding author: shubwang@cityu.edu.hk

Abstract: Controlling the directionality of light radiation and scattering is essential to various optical applications. We show that small particles can be employed to generate directional near fields with broad applications in light routing, non-Hermitian sensing, and optical force manipulations.

Controlling the propagation direction of light to achieve directional radiation and coupling is a key objective of light manipulations. Recent studies have uncovered various mechanisms for manipulating the far-field and near-field directionality. In this talk, we show that small metallic particles can be applied to generate intriguing near fields with strong directionality. Specifically, we find that a subwavelength chiral helix particle, under the excitation of linearly polarized plane waves, can give rise to electric and magnetic dipoles with tunable phases and amplitudes [1]. These dipoles can form three types of directional sources—circular dipole, Huygens dipole, and Janus dipole—at the same frequency (such directional sources can also be realized with toroidal dipoles [2]). Therefore, the chiral particle can generate near fields that couple unidirectionally with guided waves. The spin, power flow, and reactive power of the near fields induce unidirectional couplings in three orthogonal directions, i.e., the chiral particle behaves like a “directional dipole dice”.

The circular dipole “face” of the chiral particle can give rise to a lateral optical force perpendicular to the propagation direction of the incident light, if the particle is placed on a substrate [3, 4]. Interestingly, the direction of the lateral force is decided by the spin of the circular dipole and thus the handedness of the chiral particle. For the particles with opposite handedness, the lateral force points in opposite directions. Thus, the mechanism can be applied to sort chiral particles or molecules. In addition, the emergence of the lateral force is accompanied by the directional excitation of surface waves (in the case of metal substrate) or guided waves (in the case of dielectric substrate) due to the property of spin-momentum locking.

Circular dipole can also be induced in small spherical particles under the illumination of circularly polarized light. For two spherical particles sitting on a waveguide, the excited circular dipoles can couple unidirectionally through the waveguide, protected by the spin-momentum locking of the guided wave. This unidirectional coupling naturally leads to a second-order non-Hermitian exceptional point [5], which does not rely on tuning system parameters such as loss or gain. At the exceptional point, the two particles exhibit dramatically different responses—one particle has a typical Lorentzian response, while strong interference happens to the other particle. By arranging multiple spherical particles on the waveguide, we can realize an arbitrary order exceptional point with its order directly decided by the number of the particles. The system exhibits enhanced sensitivity to external small perturbations due to the higher order exceptional point.

The work was supported by the Research Grants Council of the Hong Kong Special Administrative Region, China (CityU 11301820, CityU 11308223, CityU 21302018, C6013-18G, AoE/P-502/20, AoE/P-02/12) and the National Natural Science Foundation of China (12322416, 11904306).

References

[1] Y. Cheng, K. A. Oyesina, B. Xue, D. Lei, A. M. H. Wong, and S. Wang, "Directional dipole dice enabled by anisotropic chirality", Proceedings of the National Academy of Sciences 120, e2301620120 (2023).

[2] J. Jung, Y. Cheng, W. Xiao, and S. Wang, "Directional sources realised by toroidal dipoles", Physical Review A 110, 063510 (2024).

[3] S. Wang and C. T. Chan, "Lateral optical force on chiral particles near a surface", Nature Communications 5, 3307 (2014).

[4] C. Zhang, Y. Cheng, and S. Wang, "Enhanced optical forces on coupled chiral particles at arbitrary order exceptional points", Optics Express 31, 28929 (2023).

[5] S. Wang, B. Hou, W. Lu, Y. Chen, Z. Q. Zhang, and C. T. Chan, "Arbitrary order exceptional point induced by photonic spin-orbit interaction in coupled resonators", Nature Communications 10, 832 (2019).

Exploiting radially polarized beams to excite Bound States in the Continuum in periodic arrays of dipoles

L. Cerdán[1], J. R. Deop-Ruano[1], M. A. Martín[1], R. Martinez-Herrero[2], A. Manjavacas[1]

[1]Instituto de Química Física Blas Cabrera (IQF-CSIC), 28006, Madrid, Spain
[2]Departamento de Optica, Universidad Complutense de Madrid, 28040 Madrid, Spain
*corresponding author: l.cerdan@csic.es

Abstract: The exploitation of Bound States in the Continuum (BICs) -resonant eigenmodes with infinite *Q*-factors- promise the implementation of novel devices for many nanophotonic applications, but they are notoriously difficult to excite from the far-field. Here, we report their efficient excitation in periodic arrays of polarizable objects using radially polarized beams.

The last decade has witnessed an effervescent interest in exploiting Bound States in the Continuum (BIC) in both dielectric and plasmonic metasurfaces for many applications [1,2]: lasing, nonlinear optics, electromagnetically induced transparency, polarization conversion, and sensing, among others. These states -which are strongly resonant eigenmodes with eigenfrequencies laying within the radiation continuum- remain perfectly confined and cannot couple to the far-field, thus giving rise to infinite *Q*-factors. Nevertheless, small perturbations, like absorption losses or finite size effects, can destroy pure BICs and result in quasi-BICs, modes with large, but finite, *Q*-factors that can couple to the far field. But the same physical mechanism that gives rise to their diverging *Q*-factors makes their excitation from the far-field notoriously difficult.

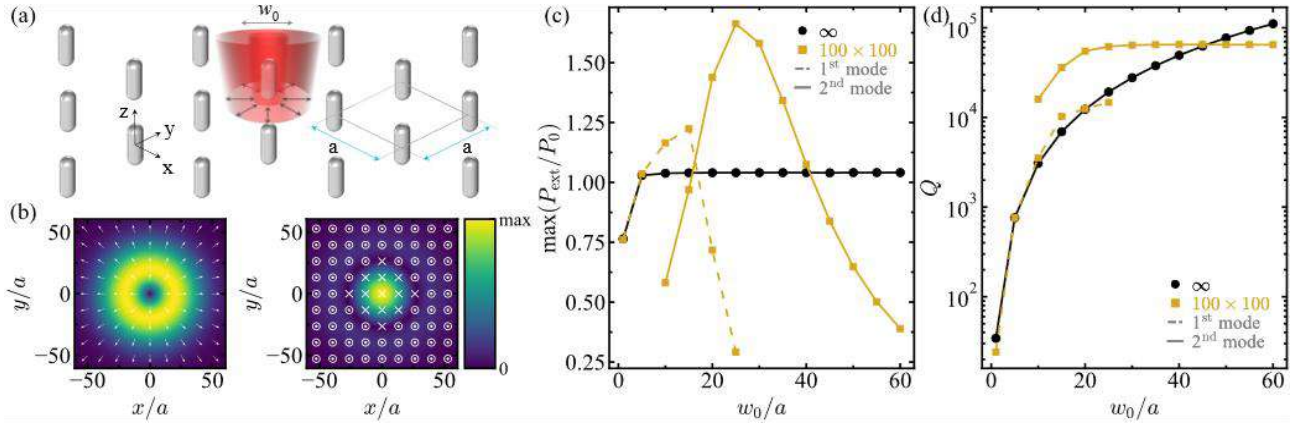


Figure 1. (a) The system under consideration consists of *z*-oriented loss-less elongated polarizable objects arranged in a square array of period *a*, which is excited by a radially polarized beam. (b) Spatial distribution across the array plane for the in-plane (left panel) and out-of-plane (right panel) components of the electric field for a radially polarized beam. (c) Maximum extincted power P_{ext} normalized to the incident power P_0 for infinite and finite arrays as a function of beam width. (d) *Q*-factor for infinite and finite arrays as a function of beam width.

Here, we report the excitation of quasi-BICs in periodic arrays of *z*-oriented elongated polarizable objects using structured beams (Fig. 1a). Exploiting a semianalytical approach based on the combination of the coupled

dipole model and the angular spectrum representation of a light beam [3], we demonstrate that tightly focused radially polarized beams are capable of exciting quasi-BICs more efficiently than any tilted plane wave [4]. For infinite square arrays (lattice period a) of loss-less objects with resonant wavelength $\lambda_r = 1.5a$, we show that increasing w_0 (a variable proportional to the beam width) leads to stronger and spectrally narrower collective resonances (Figs. 1c and 1d). Nevertheless, while the extinction efficiency saturates, the Q-factor increases exponentially with w_0, evidencing the excitation of a quasi-BIC. For finite arrays the behaviour is significantly different (Figs. 1c and 1d). For beam widths smaller than the array size, two different quasi-BICs are excited. The first mode initially follows the behaviour of the infinite array, to later vanish. For the second mode, the extinction efficiency and the Q-factor grow and significantly surpass those of the infinite array. More importantly, these conditions lead to much more efficient quasi-BIC excitation than for any tilted plane wave. For larger beam widths, the Q-factor saturates and the extinction efficiency worsens, eventually vanishing. Our results provide a solid theoretical framework to analyse, understand, and optimize the excitation of quasi-BICs in finite arrays by means of radially polarized beams.

This work was sponsored by Grant No.~PID2022-137569NB-C42 funded by MCIN/AEI/10.13039/501100011033. J. R. D-R. acknowledges support from a predoctoral fellowship from the MCIN/AEI assigned to Grant No. PID2019-109502GA-I00. L.C. acknowledges support from a Ramón y Cajal Research Fellowship, Grant RYC2022-038362-I, funded by MCIN/AEI/10.13039/501100011033 and by the European Social Fund Plus (ESF+).

References

1. Koshelev, K, Bogdanov, A., and Kivshar, Y., “Meta-optics and bound states in the continuum,” Sci. Bull. 64, 836, 2019
2. Kang, M., Liu, T., Chan, C. T., and Xiao, M., “Applications of bound states in the continuum in photonics,” Nat. Rev. Phys. 5, 659-678, 2023
3. Zundel, L., Deop-Ruano, J. R., Martínez-Herrero, R. and Manjavacas, A., “Lattice resonances excited by finite-width light beams,” ACS Omega 7, 31431, 2022
4. Cerdan, L., Deop-Ruano, J. R., Martín, M. A., Martínez-Herrero, R., Manjavacas, A., *in preparation*

Resonances in doubly anisotropic, high-index nanoplatelets

Bingying You[1,2], Tom T. C. Sistermans[1,2*], and Alberto G. Curto[1,2*]

[1] Photonics Research Group, Ghent University-imec, Ghent, Belgium
[2] Center for Nano- and Biophotonics, Ghent University, Ghent, Belgium

[*]Corresponding author: Alberto.Curto@UGent.be

Abstract: Optical anisotropy plays a crucial role in the manipulation of light. Its strength is, however, limited to low values in conventional materials. Transition metal dichalcogenides possess both high refractive index and high birefringence. Here, we investigate optical resonances in nanoplatelets with both geometrical and refractive index anisotropies to control light scattering and emission.

Anisotropy plays a crucial role in manipulating light as the basis for optical components such as polarizers, waveplates, or modulators and phenomena like phase matching in nonlinear optics. The functionality of these devices hinges primarily on the retardance between two orthogonal linear polarizations, which is proportional to both the thickness and the birefringence (Δn) of the material. A large birefringence is thus beneficial for the performance and compactness of such components. Birefringence is a tuning degree of freedom for nanophotonics, for example, in electro-optic modulators, waveguides with reduced cross-talk, and electro-optic polarization conversion. Beyond natural materials, metasurfaces and metamaterials can be constructed to achieve high anisotropy but suffer from losses and fabrication challenges. As a result, natural materials with higher anisotropy than conventional dielectrics or metals are in demand.

Transition metal dichalcogenides are promising birefringent materials due to their layered van der Waals structure, which naturally leads to a large intrinsic birefringence above unity. In particular, molybdenum disulfide (MoS_2) possesses one of the highest birefringences of all natural materials in the near infrared. Such a high birefringence is possible thanks to the presence of strong excitons. They endow MoS_2 with a high in-plane refractive index above 4.5 while making it possible to have higher out-of-plane index contrast than lower index dielectrics. A high refractive index also enables the existence of Mie-type resonances in MoS_2 nanostructures for enhancing and controlling light-matter interaction.

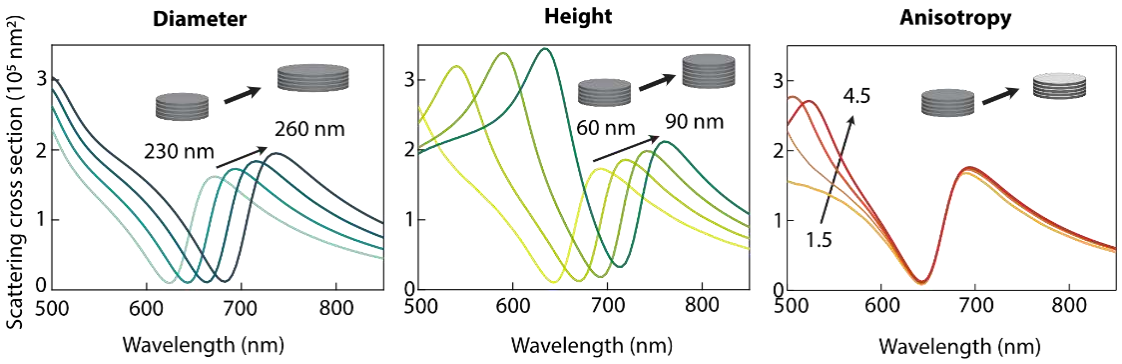


Figure 1. Different dependence of electric and magnetic dipole resonances on geometrical and optical anisotropy.

Here, we study the optical resonances sustained by nanoplatelets made of high refractive index material with high optical anisotropy. These nanoplatelets have both geometrical and refractive index anisotropies. Their high refractive index enables them to sustain electric and magnetic resonances. We find a distinct impact of changing geometric and birefringence on the tunability of electric and magnetic resonances, which we explain using multipolar expansions. Due to their double anisotropy, the optical response of nanoplatelets strongly depends on the direction of illumination, as different illumination conditions can lead to in-plane or out-of-plane electric and magnetic multipoles. We also show that nanoplatelets can control the polarization and directionality of the scattering radiation patterns. Finally, we show preliminary experimental results using MoS_2 nanoplatelets.

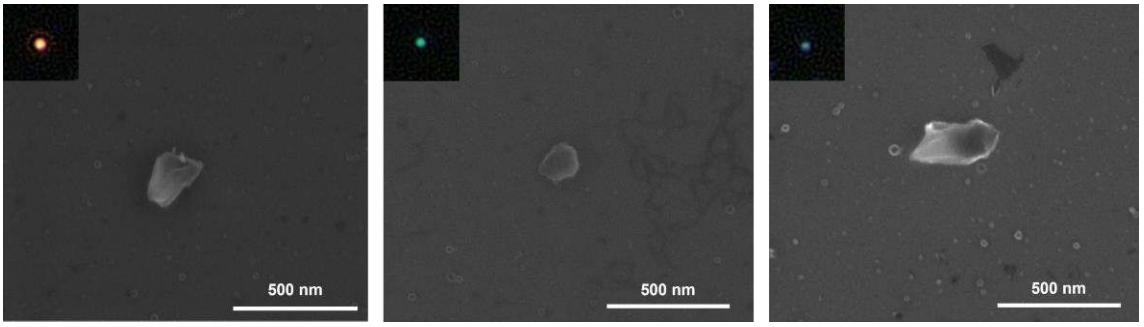


Figure 2. SEM image of MoS_2 nanoplatelets with varying sizes. The insert images are corresponding dark field images, where the nanoplatelet colors indicate different optical resonances.

In summary, high-refractive-index nanoplatelets with intrinsic out-of-plane anisotropy and large birefringence exhibit a wealth of electric and magnetic multipolar resonances that are sensitive to geometry and anisotropy in distinct manners. We envision that nanoplatelets could be used to enhance and direct light scattering and light emission, with applications in light-emitting devices and lasers.

References

1. Ermolaev, G. A., D. V. Grudinin, Y. V. Stebunov, *et al.*, "Giant optical anisotropy in transition metal dichalcogenides for next-generation photonics," *Nature Communications*, Vol. 12, No. 854, 2021.
2. Verre, R., D. G. Baranov, B. Munkhbat, J. Cuadra, M. Käll, and T. Shegai, "Transition metal dichalcogenide nanodisks as high-index dielectric Mie nanoresonators," *Nature Nanotechnology*, Vol. 14, 679-683, 2019.
3. Hinamoto, T., and Fujii, M., "MENP: an open-source MATLAB implementation of multipole expansion for nanophotonics," *Optics Express*, Vol. 4, No. 5, 1640–1648, 2021.

Analysis of a tunable terahertz waveguide using the frequency-dependent HIE-FDTD method

J. Shibayama[1*] and H. Miyao[1]
[1]Hosei University, Japan
shiba@hosei.ac.jp

Abstract

A tunable terahertz waveguide with InAs sidewalls and air buffers is efficiently analyzed using a newly developed frequency-dependent hybrid-implicit-explicit FDTD method based on the trapezoidal recursive convolution technique. The waveguide acts as a TE/TM-pass waveguide, while it acts as a TE-stop/TM-pass waveguide polarizer with the buffer being filled with water.

1 Introduction

Many devices have been investigated for communication, sensing, and imaging at terahertz (THz) frequencies. We have investigated a surface plasmon resonance (SPR) waveguide sensor in the THz regime [1]. For the sensor, only the TM wave is required as an input source, since the sensor operates on the TM wave. Therefore, we need a waveguide polarizer with TE-stop/TM-pass characteristics. Here we propose a tunable THz waveguide with InAs sidewalls and air buffers. The waveguide acts as a TE/TM-pass waveguide, while it acts as a TE-stop/TM-pass waveguide polarizer with the buffer filled with water. To efficiently analyze the polarizer, we also develop a frequency-dependent hybrid-implicit-explicit (HIE) FDTD method.

2 Discussion

The structure of the waveguide is shown in Fig. 1. The Si core dimension is $w = 50$ μm and $d = 60$ μm. InAs sidewalls with air buffers are placed on both sides of the core, in which $w_{\rm i} = 5$ μm and $t_{\rm b} = 12.5$ μm are used. The temperature is set to $T = 300$ K and the designed frequency is 1.3 THz.

Note that fine meshes should only be used in the horizontal (x) direction for accurate analysis of the thin InAs layer. In addition, InAs is a dispersive material at THz frequencies, which requires the frequency-dependent FDTD formulation [2]. Therefore, we newly formulate a frequency-dependent HIE-FDTD method, in which the implicit scheme is applied only in the x direction. The developed FDTD method greatly relaxes the Courant-Friedrichs-Lewy (CFL) condition, leading to a reduction in computational time with a larger time step size compared to the conventional explicit counterpart (e.g., [3]). In the following analysis, the spatial sampling widths are $\Delta y = \Delta z = 2.5$ μm, $\Delta x = 0.125$ μm. In this case, we can use a time step seize that is fourteen times as large as the explicit counterpart.

Fig. 2 shows the filed distributions where the buffers are filled with water. As can be seen, the TE wave is rapidly attenuated due to surface plasmon excitation, while the TM wave propagates through the waveguide, demonstrating the performance of the TE-stop/TM-pass characteristics. The present field distributions agree quite well with those obtained from the conventional explicit FDTD method (not illustrated) and the computational time is reduced to only 25%. The extinction ratio between the TE and TM modes is calculated to be 20 dB at

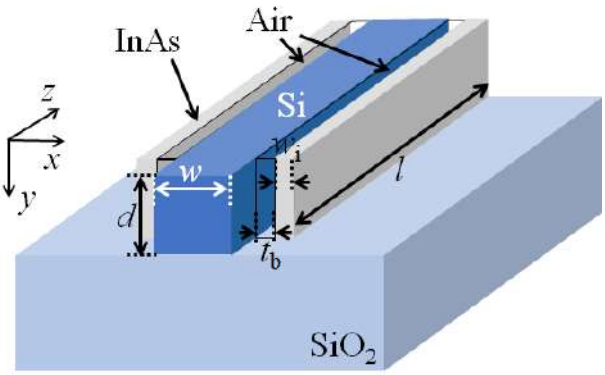
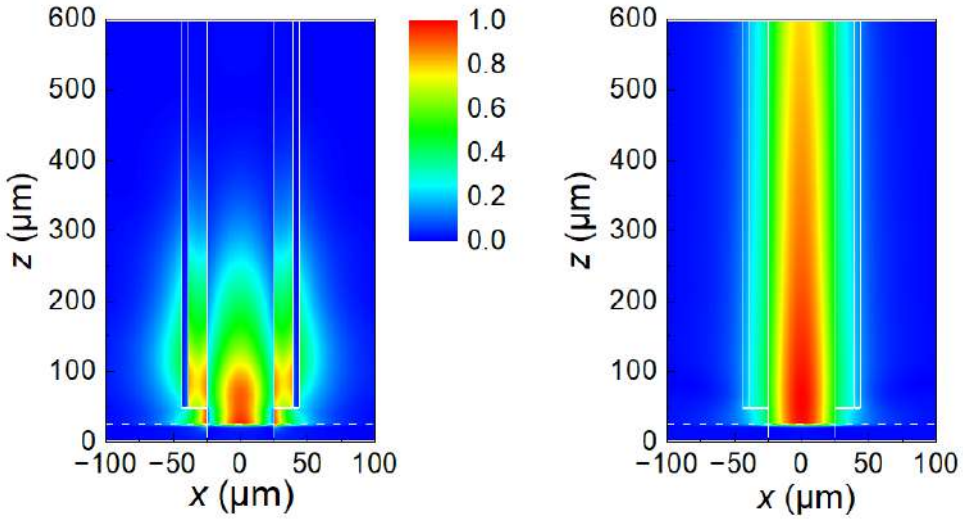


Figure 1: Configuration of a THz waveguide with InAs sidewalls and air buffers.



(a) TE wave

(b) TM wave

Figure 2: Field distributions.

around $z = 300$ μm. Incidentally, it is confirmed that the waveguide acts as a simple TE/TM pass waveguide for the case without the water in the buffers.

References

[1] Shibayama, J., K. Shimizu, J. Yamauchi, and H. Nakano, "Surface plasmon resonance waveguide sensor in the terahertz regime," *IEEE/OSA J. Lightw. Technol.*, Vol. 34, No. 10, pp. 2518-2525, 2016.

[2] Shibayama, J., R. Ando, A. Nomura, J. Yamauchi, and H. Nakano, "Simple trapezoidal recursive convolution technique for the frequency-dependent FDTD analysis of a Drude-Lorentz model," *IEEE Photon. Technol. Lett.*, Vol. 21, No. 2, pp. 100-102, 2009.

[3] Shibayama, J., T. Hara, M. Ito, J. Yamauchi, and H. Nakano, "Improved cylindrical HIE-FDTD method and its application to a metal disc-type surface wave splitter," *IEEE Microw. Wireless Compon. Lett.*, Vol. 29, No. 3, pp. 177-179, 2019.

Coupling quantum mechanical molecular excitations with localized surface plasmons using boundary element methods in the time-domain

S. Corni[1,2*]

[1]Dept. Chemical Sciences, Univ. Padua, Italy
[2]CNR Institute of Nanoscience, Modena, Italy
[*]corresponding author: stefano.corni@unipd.it

Abstract: Boundary element methods are powerful numerical tools to solve Maxwell equations, also involving plasmonic nanostructures. We have developed models where such electromagnetic descriptions are coupled with a quantum mechanical description of nearby molecules, specifically in the time domain, so to disclose basic mechanisms of the time-resolved process of molecular nanoplasmonics.

The optical properties of plasmonic nanostructures can be often described very accurately by electromagnetic modeling. This amounts to neglect most of the microscopic details of the nanostructure, treating it as a continuum medium characterized by its bulk dielectric function and its shape and boundaries. Among the different options to solve the resulting Maxwell equations for light-nanostructure interactions, surface integral approaches, numerically solved by boundary element methods (BEMs),[1,2] became popular for their computational efficiency and accuracy. Such methods are also most suitable to set up multiscale modeling approaches of molecular nanoplasmonic systems, i.e., nanostructures interacting with specific molecules. The latter can in fact be described by quantum chemistry methods coupled to BEM for the nanostructures.[3,4] Such modeling was initially limited to frequency domain description of optical phenomena. This however is not the natural framework to describe many of the currently investigated molecular nanoplasmonics phenomena, i.e., those where light pulses and time-resolved detection is used. We have therefore extended such approaches, in the quasi-static regime, to time-dependent versions and exploited their flexibility to interface them with various quantum chemistry descriptions and codes.[5,6] Specific applications ranges from time-resolved Surface Enhanced Raman spectroscopy[7] to hot carrier injections in molecules[8]

Acknowledgements, SC thanks European Union for funding under the grant PROID (European Union's Horizon 2020 under grant agreement no. 964363) and iSenseDNA (European Innovation Council under grant agreement no. 101046920)

References

1. García de Abajo, F. and Howie, A. "Retarded field calculation of electron energy loss in inhomogeneous dielectrics." Phys. Rev. B Vol. 65, 115418–17, 2002.
2. Hohenester, U. and Trügler, A. "MNPBEM - A Matlab toolbox for the simulation of plasmonic nanoparticles." Comput. Phys. Commun. 183, 370–381, 2012.
3. Corni, S. and Tomasi, J. "Enhanced response properties of a chromophore physisorbed on a metal particle." J. Chem. Phys. 114, 3739–3751, 2001.
4. Mennucci, B. and Corni, S. "Multiscale modelling of photoinduced processes in composite systems." Nat. Rev. Chem. 3, 315–330, 2019.

5. Dall'Osto, G., Gil, G., Pipolo, S. and Corni, S. "Real-time dynamics of plasmonic resonances in nanoparticles described by a boundary element method with generic dielectric function." J. Chem. Phys. 153, 184114, 2020.
6. https://github.com/stefano-corni/WaveT_TDPlas
7. Dall'Osto, G. and Corni, S. "Time-dependent surface-enhanced Raman scattering: A theoretical approach." J. Chem. Phys. 161, 044103, 2024.
8. Dall'Osto, G. et al. "Peeking into the Femtosecond Hot-Carrier Dynamics Reveals Unexpected Mechanisms in Plasmonic Photocatalysis." J. Am. Chem. Soc. 146, 2208–2218, 2024.

The Fourier Modal Method, equipped with Adaptive Spatial Resolution, simplified for shallow gratings

B. Guizal[1*]

[1]Laboratoire Charles Coulomb (L2C), UMR 5221 CNRS- Université de Montpellier, F-34095 Montpellier, France
[*]corresponding author: brahim.guizal@umontpellier.fr

Abstract: We present a simplification of the well-known Fourier Modal Method (FMM) equipped with Adaptive Spatial Resolution (ASR) concept for gratings with subwavelength heights. We show that in this case it is possible to compute the scattering matrix of the structure by solving only one eigenvalue problem (instead of three) which reduces the most expensive computational part of the FMMASR algorithm. This approach is very efficient and thus suitable for periodic metasurfaces.

The Fourier Modal Method[1] is one of the most versatile and efficient methods for modeling diffraction from gratings. This is why it is suitable for modeling metasurfaces based on binary gratings. The problem with this approach is that for metallic structures, it is necessary to truncate the Fourier series representing the fields to a high order implying the use of large matrices (especially in the case of crossed gratings). This situation can be improved by using the ASR concept[2] to accelerate the convergence rate and thus reduce the size of the matrices in play. Still, this remains demanding from the computational point of view, for certain applications, because the heart of the FMM is based on the solution of an eigenvalue problem. This later has a cost scaling with the third power of the dimension of the matrices involved. This can be a severe limitation and hinder the use of the FMM.

On the other hand, an interesting class of metasurfaces is made of gratings with subwavelength thicknesses. In this special case, it is possible (via a Taylor series expansion of the phase propagation matrix) to simplify the FMMASR is such a way that it is no longer needed to solve any eigenvalue problem[3]. This proves to be very efficient in reducing the computational cost.

After recalling the principle of the FMMASR and the details of the corresponding algorithm, I will show how the assumption of subwavelength height leads to a simplified scattering matrix where it is sufficient to solve one eigenvalue problem. Numerical examples will be presented to support this new algorithm.

References

1. L. Li, “New formulation of the Fourier Modal Method for crossed surface-relief gratings,” J. Opt. Soc. Am. A 14, 2758-2767, 1997.
2. B. Guizal, et al., “Reformulation of the eigenvalue problem in the Fourier modal method with spatial adaptive resolution,” Opt. Lett. 34, 2790-2792, 2009.
3. J. Li, et al., “Efficient Rigorous Coupled-Wave Analysis Without Solving Eigenvalues for Analyzing One-Dimensional Ultrathin Periodic Structures,” IEEE Access, Vol. 8, 198131-198138, 2020.

Photothermal Engineering in Graphene Nanoplasmonics

J. D. Cox[1,2*]

[1]POLIMA—Center for Polariton-driven Light−Matter Interactions, University of Southern Denmark, DK-5230 Odense M, Denmark
[2]Danish Institute for Advanced Study, University of Southern Denmark, DK-5230 Odense M, Denmark
[*]corresponding author: cox@mci.sdu.dk

Abstract: We theoretically explore the photothermal response of localized plasmons supported by graphene nanostructures. Our simulations reveal intriguing possibilities to achieve unity-order optical modulation, strong nonlinear light-matter interactions, and chiral-optic effects by resonantly exciting plasmons sustained by absorbed photothermal energy.

Plasmons in electrically doped graphene offer extreme electromagnetic field confinement and active tunability, uniquely addressing the limitations of their counterparts in noble metals. In addition, the linear electronic band structure and atomic thickness of graphene, which are at the origin of its high optoelectronic tunability, together with its low heat capacity, give rise to a substantial photothermal response: optical energy absorbed in graphene is rapidly converted to heat within ~10s of femtoseconds, such that the two-dimensional electron gas reaches temperatures of several thousand Kelvin when illuminated by pulses of moderate (~1 J/m2) optical fluence, and gradually cools by transferring energy to phonons on ~1 picosecond timescales [1].

Here we theoretically explore unique possibilities to leverage the thermal activation and control of localized plasmons in graphene nanostructures for controlling light-matter interactions at the nanoscale. We first discuss the photothermal response of small graphene nanoislands, characterized using atomistic quantum mechanical simulations, and the conditions under which their supported plasmon resonances undergo unity-order changes triggered by the absorption of single photons [2]. We then explore the thermal activation of mid- and near-infrared plasmons in mesoscale graphene nanoribbons (GNRs) of ≤10 nm width, revealing their capability to drive a large coherent nonlinear optical response associated with harmonic generation and the optical Kerr effect [3]. Combined ab initio modelling and self-consistent perturbation theory reveals prominent quantum finite-size effects in these GNRs that impact their supported thermoplasmons, which can be optically induced by fluences commensurate with those used in ultrafast optical experiments. Finally, we investigate thermal magnetoplasmons (TMPs) in graphene nanodisks at finite temperature and in the presence of a static perpendicular magnetic field [4]. Specifically, we show that TMPs in graphene undergo strong hybridization with transitions between thermally populated Landau levels, presenting opportunities to control chiral absorption and chiral thermal emission in a metasurface comprised of a graphene nanodisk array and a gold mirror in a Salisbury screen configuration.

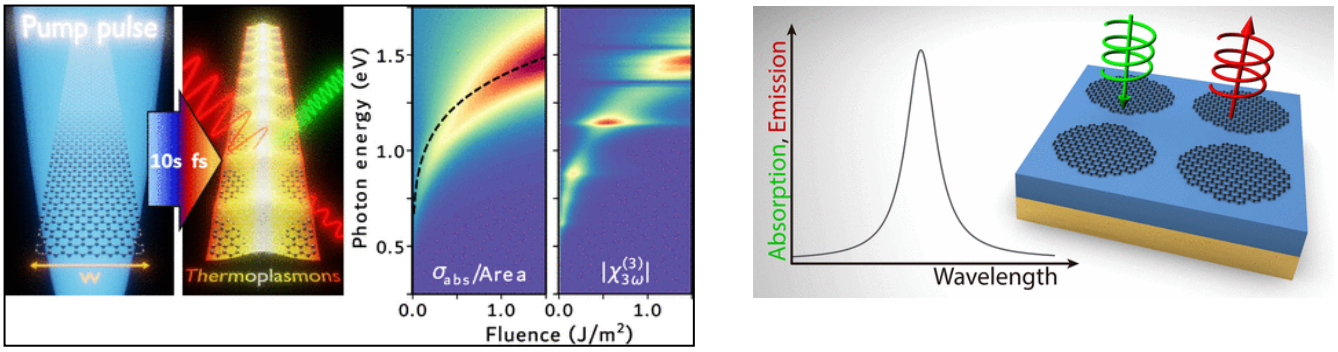


Figure 1 – (left panel) Transient thermoplasmons in narrow graphene nanoribbons that can be probed in ultrafast nonlinear spectroscopy [3]. (right panel) Perfect chiral absorption and chiral emission driven by thermal magnetoplasmons in a graphene nanodisk array [4].

Acknowledgements: J.D.C. is a Sapere Aude research leader supported by Independent Research Fund Denmark (grant no. 0165-00051B). The Center for Polariton-driven Light-Matter Interactions (POLIMA) is funded by the Danish National Research Foundation (Project No. DNRF165). Part of the computation in this project was performed on the DeiC Large Memory HPC system managed by the eScience Center at the University of Southern Denmark.

References

1. Mics, Z., K.-J. Tielrooij, K. Parvez, S. A. Jensen, I. Ivanov, X. Feng, K. Müllen, M. Bonn, and D. Turchinovich, "Thermodynamic picture of ultrafast charge transport in graphene," Nat. Commun., Vol. 6, 7655, 2015.
2. Cox, J. D. and F. J. García de Abajo, "Single-plasmon thermo-optical switching in graphene," Nano Lett., Vol. 19, 3743, 2019.
3. Jelver, L. and J. D. Cox, "Nonlinear thermoplasmonics in graphene nanostructures," Nano Lett., Vol. 24, 13775, 2024.
4. Eriksen, M. H., J. R. Deop-Ruano, J. D. Cox, and A. Manjavacas, "Chiral light-matter interactions with thermal magnetoplasmons in graphene nanodisks," Nano Lett., Vol. 25, 313, 2025.

Multiphysics Topology Optimization for Optimal Photon-Electron Interaction in Geometrically Tailored Quantum-Well Environments

Rasmus Ellebæk Christiansen[1,2,*], Ole Sigmund[1,2]

[1] Department of Civil and Mechanical Engineering, Technical University of Denmark,
Nils Koppels Allé Building 404, Kongens Lyngby, 2800, Denmark.
[2] NanoPhoton - Center for Nanophotonics, Technical University of Denmark,
Ørsteds Plads 345A, Kongens Lyngby, 2800, Denmark
[*]corresponding author: raelch@dtu.dk

Abstract: We present a multi-physics-based Topology-Optimization framework for maximizing photon-electron interaction by co-location of an electronic and an optical state, solely through tailoring of the environment geometry. Hereby, we seek to achieve electron confinement without the need for embedding quantum dots of different materials, enabling simpler, scalable fabrication.

High-fidelity conversion between optical (photon) and electrical (electron) signals in optical interconnects is critical to the operation of the vast data centers and communication networks underpinning modern society. If such reliable signal-conversion can be achieved at the few-photon/-electron level at the nanoscale, it may be possible to exploit near-lossless information transport offered by photons for realizing on-chip energy-efficient opto-electronic computational devices useful in the green transition and for the next generation of machine learning systems, among others.

Existing devices demonstrating few-particle interaction at nanoscale are often based on quantum dots (QDs); tens of nanometer-sized particles, of different material composition than the background medium, offering near-perfect spatial confinement of electrons due to the electronic energy barrier offered by the QD [1]. Exact positioning of the QDs is required for spatial co-location of the electrons with the photons, which may be geometrically confined to deep sub-wavelength focal spots using extreme dielectric confinement (EDC) [2]. Consistent and stable nano-meter-precise positioning of QDs is an unsolved problem, however.

An alternative to using QDs for electron confinement are the use of quantum wells (QWs); a layer of material confining the electronic states to two dimensions (2D) encapsulated in the lateral (third) dimension by some background medium. Atomic-scale precision in the lateral placement of QWs in a scalable fashion has been achieved, however by the nature of the QWs, electrons are free to roam in the horizontal dimensions, significantly reducing their spatial co-location with the photons in existing EDC devices.

Inspired by recent modelling work [3], we develop a multi-physics topology-optimization [4] based framework for spatial co-location of photons and electrons in the QW solely by geometric means. We tailor EDC structures simultaneously supporting electronic potential barriers, recovering strong spatial confinement of the electrons in all spatial dimensions, hereby co-locating the two particles. We will present our multi-physics framework used to model the photons and electrons assuming time-harmonic field behavior with appropriate boundary conditions truncating the modelling domain. That is, we use a wave-equation derived from Maxwells equations to model the photonic states.

$$\nabla \times \nabla \times \mathbf{E}(\mathbf{r}) - \frac{\omega^2}{c^2}\varepsilon_r(\mathbf{r})\mathbf{E}(\mathbf{r}) = \mathbf{0}, \qquad \mathbf{r} \in \Omega_{EM}$$

Here **E** denotes the electric field, ω the angular frequency, c the speed of light, ε_r the relative permittivity, Ω_{EM} the modelling domain and **r** the spatial coordinate. A wave equation derived from the Schrödinger equation is used to model the electronic states. Which for a single electron takes the form,

$$-\frac{\hbar^2}{2}\nabla \cdot \left(\boldsymbol{m}_{eff,e}(\boldsymbol{r})^{-1} \cdot \nabla\right)\psi_e + (V(\boldsymbol{r}) - E)\psi_e = 0, \qquad \mathbf{r} \in \Omega_{\mathrm{QM}}$$

Here, $\hbar$ denotes planks constant over two pi, m_{eff} the effective mass of the electron, V the background potential, E the electron energy, ψ_e the electronic wave function and Ω_{QM} the modelling domain. We define the normalized overlap of the two wave-functions as our figure of merit to be maximized.

$$\Phi = \int_{\Omega_T} \frac{|\mathbf{E}(\xi, \mathbf{r})|}{\int_{\Omega_{\mathrm{EM}}} |\mathbf{E}(\xi, \boldsymbol{r})|\, d\boldsymbol{r}} \cdot \frac{|\psi_e(\xi, \boldsymbol{r})|}{\int_{\Omega_{\mathrm{QM}}} |\psi_e(\xi, \boldsymbol{r})|\, d\boldsymbol{r}} d\boldsymbol{r}$$

Where ξ denotes the design field controlling the device geometry and Ω_T the target overlap domain. We present the topology optimization model, a set of optimized geometries as well as a study of the effect of imposing various fabrication constraints on the designs.

Acknowledgements: Our work was funded by Danmarks Grundforskningsfond (DNRF147).

References

1. Uppu, R. et al, *Scalable integrated single-photon source*, Science Advances, 6 (50), eabc8268, 2020.
2. Albrechtsen, M. et al, *Nanometer-scale photon confinement in topology-optimized dielectric cavities*, Nature Communications, 13, 6281, 2022.
3. Kountouris, G. et al, *Lithographically defined quantum dot with subwavelength confinement of light*, Physical Review B, 110 (24), L21301, 2024.
4. Christiansen, R. E. & Sigmund, O. *Inverse design in photonics by topology optimization: tutorial* Journal of the Optical Society of America B, 38 (2), 496, 2021.

Metasurfaces with Integrated MEMS structures as Tunable Elements for Spoof Surface Plasmon Polaritons

L. Franke[1], S. Klingel[1], and M. Rahm[1,*]

[1]Department of Electrical and Computer Engineering and Research Center OPTIMAS, Erwin-Schroedinger-Strasse, RPTU Kaiserslautern-Landau, 67663 Kaiserslautern, Germany

[*]corresponding author: marco.rahm@rptu.de

Abstract: By proper design, we tailor the dispersion of spoof surface plasmon polaritons on metasurfaces in a wide frequency range to implement on-chip networks with tunable properties, as e.g. tunable filters and beam steering leaky wave antennas. The practical implementation relies on the integration of MEMS into the metasurface unit cells.

Advancing on-chip communication at higher frequencies depends on miniaturizing plasmonic networks. While static metasurfaces reliably guide SSPPs in a broad range of frequencies, real-time reconfigurability at microwave or terahertz ranges remains challenging. Current solutions primarily integrate graphene monolayers with metasurfaces [1,2].

Here, we designed and implemented a tunable low-pass filter for spoof surface plasmon polaritons on a fishbone metasurface. In this structure, the fishbones are formed by MEMS bridges, whose bending can be continuously tuned by application of a bias voltage. Without bias voltage, the surface plasmon polaritons can freely pass the filter and travel from the transmitting horn antenna to the receiving horn antenna (see Fig. 1). By increasing the bias voltage and thus changing the bending curvature of the fishbone bridges, the transmission of the filter can be continuously tuned. In our case, the low-pass filter was operated at a cut-off frequency of 83 GHz. We achieved continuous tuning in the attenuation band with a maximum of 15 dB. The applied approach is readily scalable to higher frequencies, including the terahertz frequency range.

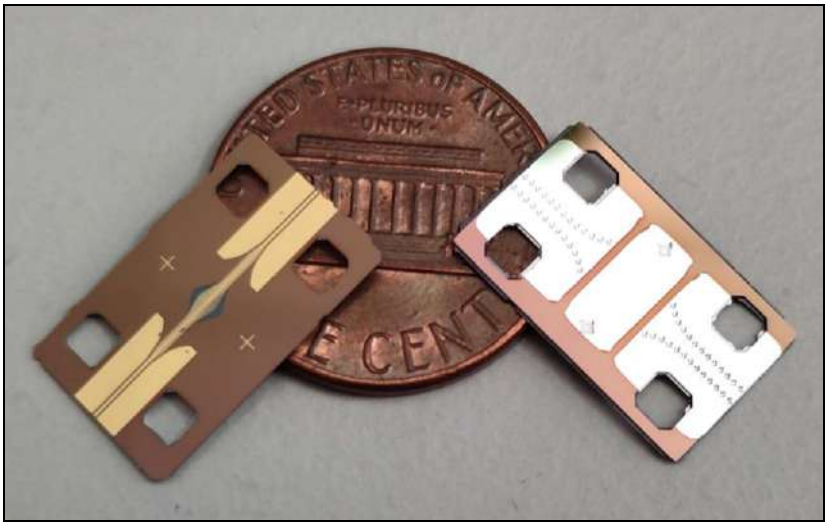


Fig. 2: Photograph of a MEMS-based fishbone metasurface, including the horn antennas.

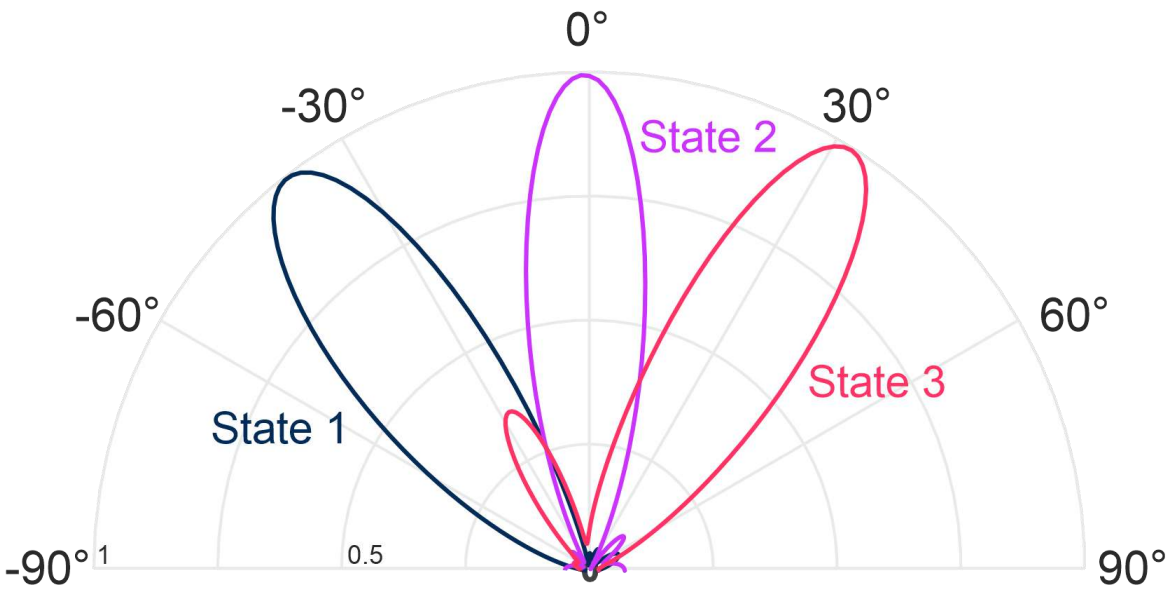


Fig. 2: Simulated beam steering at 57.5 GHz by a MEMS-based metasurface for three different states.

As another example, we designed a beam steering leaky wave antenna that can deflect the beam within a range of more than 60° at an operating frequency of 57.5 GHz. The metasurface again consists of a fishbone structure with tunable MEMS bridges as fishbones. In this case however, the MEMS bridges periodically vary in length, thus forming a diffraction grating that couples the surface plasmon polaritons to a free space propagating mode even without the application of a bias voltage. When a bias voltage is applied, however, the MEMS bridge bending strongly depends on the bridge length, which allows us to deliberately tune the diffraction grating period and modulus. As a result, the diffracted beam can be efficiently steered. Fig. 2 shows the simulated beam steering of microwaves at 57.5 GHz for three different states, where state 1 corresponds to no bias voltage, state 2 to a bias voltage of 105 V and state 3 to a bias voltage of 120 V.

We acknowledge the financial support of the project by the German Research Foundation (project number 458851938, GZ RA 1903/6-1).

References

1. A. -Q. Zhang,W. B. Lu, Z. -G. Liu, B.Wu and H. Chen, ”Flexible and Dynamically Tunable Attenuator Based on Spoof Surface Plasmon Polaritons Waveguide Loaded With Graphene,” IEEE Transactions on Antennas and Propagation, vol. 67, no. 8, pp. 5582-5589 (2019).
2. Feng, M., Zhang, B., Ling, H., Zhang, Z., Wang, Y., Wang, Y., Zhang, X., Hua, P., Wang, Q., Song, A. and Zhang, Y., ”Active metal–graphene hybrid terahertz surface plasmon polaritons. Nanophotonics,” vol. 11, no. 14, pp. 3331-3338 (2022).

GSTCs: A connection to exact spherical multipoles

Hossein Allahverdizadeh[1], Karim Achouri[1*]
[1]École Polytechnique Fédérale de Lausanne (EPFL), Switzerland
karim.achouri@epfl.ch (corresponding author)

Abstract

Metasurfaces are subwavelength structures that manipulate both local and nonlocal electromagnetic properties, enabling interesting phenomena. Conventional methods like the Generalized Sheet Transition Conditions (GSTC) focus primarily on far-field calculations and often overlook near-field distributions. In this work, we extend the GSTC method by using a multipolar decomposition to connect near-field properties with far-field scattering, offering clearer physical insights. Our method is able to accommodate for oblique incidence by accounting for higher-order multipoles, offering significant advances over traditional approaches that were limited to normal incidence. Additionally, our method properly accounts for the presence of different media on both sides of the metasurface, allowing for effective generalization to various background materials, including layered substrates and embedded elements. By overcoming previous challenges in adapting multipolar decomposition for environments with different media and oblique incidence, our method creates a more systematic approach to interpreting metasurface behaviors in complex scenarios.

"Metasurfaces exhibit fascinating phenomena by manipulating the electromagnetic properties of local elements and introducing nonlocal effects throughout the structure, allowing researchers to flexibly control wave scattering properties. Several modeling techniques have been developed to offer reliable methodologies for describing the effects of these structures, among which the Generalized Sheet Transition Conditions (GSTC) method is a key approach [1]. The GSTC consists in calculating fitted susceptibility tensors based on far-field incident and scattered waves, considering an equivalent imaginary boundary sheet. Although the GSTC show promising results, it predominantly emphasizes far-field calculations, with limited attention to the near-field distribution. Moreover, the technique has been mostly limited to dipolar responses with local interactions.

In this study, we use a multipolar decomposition as a bridge to connect near-field characteristics to the GSTC by calculating equivalent currents for the sheet and the corresponding near-field densities. This approach not only enables a deeper understanding of complex near-field distributions, particularly for intricate unit cell structures and phenomena like Bound States in the Continuum (BICs), but also provides insights into the physical effects within the unit cell. Using this method, susceptibility tensor calculations become less opaque and more systematic. This approach sheds new light on the susceptibility tensors, transforming it from a 'black box' into a tool with tangible physical interpretation.

Additionally, we extend our method to accommodate oblique incidence, addressing limitations in previous studies that focused solely on normal incidence. Our approach introduces new contributions from higher-order multipoles in angular regimes. This generalization is not achieved merely by incorporating additional higher-order multipoles; rather, it involves accounting for the transverse components of the wave vector present in oblique incidence. These transverse components can excite extra resonances within the object, leading to novel contributions in both radiative and non-radiative regimes. In complex scenarios, such as those involving accidental BICs, it becomes essential to investigate these methods thoroughly and map the resulting multipolar distributions to their radiation characteristics, thereby elucidating the interactions among the emergent modes.

Furthermore, adapting multipolar decomposition to different background materials has proven challenging in previous works. Until now, there was no straightforward method for cases involving multi-media environments and oblique incidence. A common approach based on Green's functions has been both challenging and computationally intensive, particularly when layered substrates are considered: breaking the structure inversion symmetry typically leads to the emergence of higher-order multipoles and makes its implementation more challenging [2]. By contrast, our method employs boundary conditions, treating the metasurface as an equivalent current sheet with an effective surface current given by [3, 4]

$$\mathbf{J}_{\mathrm{s}} = j\omega\mathbf{p} + \nabla\times\mathbf{m} - \frac{j\omega}{2}\nabla\cdot\mathbf{Q} - \frac{1}{2}\nabla\times(\nabla\cdot\mathbf{S}) + \ldots + \frac{(-1)^{n-1}j\omega}{n!}\nabla^{n-1}\cdot(\mathbf{P}_n) + \frac{(-1)^{n-1}}{n!}\nabla^{n-1}\cdot(\nabla\times\mathbf{M}_n), \quad (1)$$

where $\mathbf{J}_{\mathrm{s}}$ is expressed in terms of the multipolar components $\{\mathbf{p}, \mathbf{m}, \mathbf{Q}, \mathbf{S}, \mathbf{P}, \mathbf{M}\}$ that respectively correspond to electric dipole, magnetic dipole, electrical quadrupole, magnetic quadrupole, n^{th}-order electric multipole and n^{th}-order magnetic multipole. The figure below compares the fields scattered obliquely by a metasurface, computed using COMSOL and our method. The subscript c denotes the results of COMSOL, while g represents those obtained using the GSTC method.

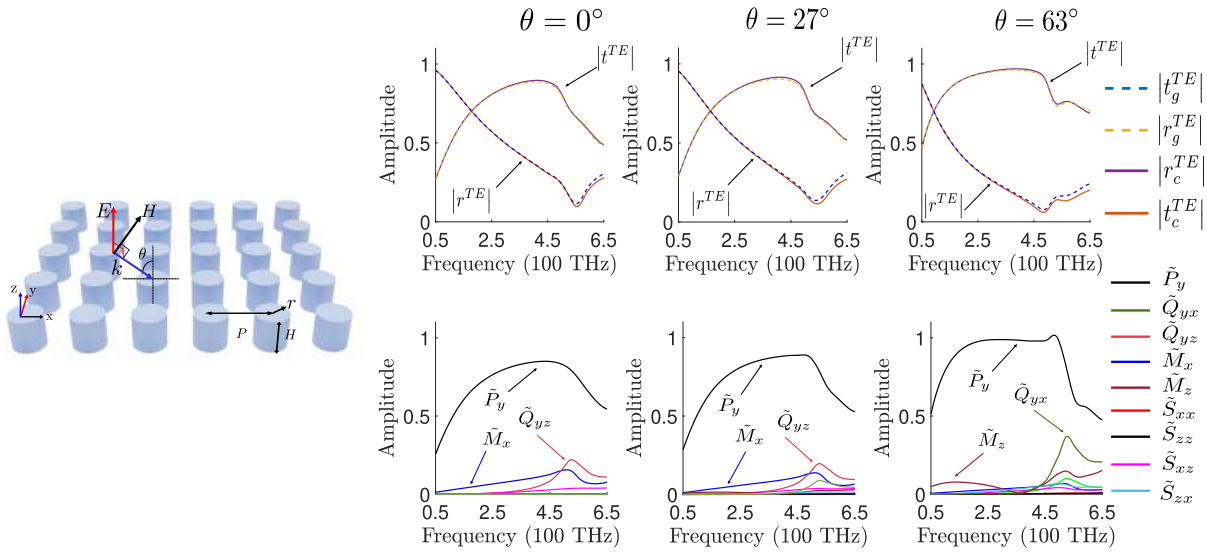


Figure 1: Simulation and theoretical results for nano-gold cylinders for $P = 225$ nm and $H = 95$ nm and $r = 100$ nm under TE illumination for three incidence angles of $\theta = 0°, 27°, 63°$.

We acknowledge funding from the Swiss National Science Foundation (project TMSGI2_218392).

References

[1] K. Achouri and C. Caloz, *Electromagnetic Metasurfaces: Theory and Applications*. Hoboken, NJ: Wiley-IEEE Press, 2021.

[2] L. Novotny and B. Hecht, *Principles of Nano-Optics*. Cambridge: Cambridge University Press, second edition ed., 2012.

[3] K. Achouri, V. Tiukuvaara, and O. J. F. Martin, "Spatial symmetries in nonlocal multipolar metasurfaces," *Adv. Photon.*, vol. 5, June 2023.

[4] S. Nanz, *Toroidal Multipole Moments in Classical Electrodynamics*. Wiesbaden: Springer Fachmedien Wiesbaden, 2016.

META 2025, MALAGA - SPAIN, JULY 22–25, 2025

Physics informed Bayesian optimization for efficient solution of inverse problems in nanophotonics

I. Sekulic[1*], P. I. Schneider[1], M. Hammerschmidt[1], and S. Burger[1,2]
[1]JCMwave GmbH, Germany
[2]Zuse Institute Berlin, Germany
Corresponding author: ivan.sekulic@jcmwave.com

Abstract: Efficient solution of inverse problems is ubiquitous across many disciplines in engineering and physics. In this manuscript, we introduce physics-informed multi-channel Bayesian optimization (BO) and apply it to inverse design problems in nanophotonics and nanometrology. By learning the vector-valued physical properties of numerically simulated systems, from which the final cost is constructed, our approach achieves faster convergence compared to other optimization methods.

Bayesian decision theory combined with Gaussian processes (GPs) [1] has emerged as a robust machine learning tool for approximating and optimizing different cost functions associated with the physical process under investigation. Gaussian process posteriors are constructed by applying Bayesian conditioning on all observed cost evaluations, creating a stochastic model that represents the underlying objective function. This technology is particularly useful in the context of inverse device design due to its inherent ability to quantify model uncertainty in the unexplored regions of device's parameters, where the observed cost evaluations are sparse. Such uncertainty quantification is essential for the development of efficient active learning algorithms, where the candidate designs are chosen selectively in order to improve the overall search process and decrease the total number of iterations. In practice, when dealing with nanophotonic devices of arbitrary shapes and materials, solving an inverse problem and finding an optimal device design for a given functionality entails a series of calls to Maxwell's numerical solver which is often time- and resource-intensive [2]. The Bayesian algorithm effectively reduces the number of forward solver evaluations needed to find good device candidates by strategically balancing exploration of the search space with exploitation of the promising parameter regions, leveraging information from all previous cost evaluations resulting in sample-efficient search processes.
The inverse design task in nanophotonics is typically formulated as an optimization problem, where the final scalar objective to be minimized in the space of device's parameters is defined as the L_2 norm between the target vector $\mathbf{y}$, representing the desired device functionality, and the candidate vector $\mathbf{y}'$ obtained by numerical simulation of the structure suggested by the optimizer. Directly modeling the scalar objective $\|\mathbf{y} - \mathbf{y}'\|_2$ with GP inherently leads to a loss of information as this objective is strictly positive in the search space, whereas the individual components of the vector-valued functions $\mathbf{y}$ and $\mathbf{y}'$ can take on both positive and negative values. The consequences of this information loss can result in a slower convergence of the classical BO and suboptimal designs.
To tackle this issue, we propose multi-output Gaussian processes to learn the components of physically meaningful vector-valued observation $\mathbf{y}'$ directly, from which the final objective surrogate is constructed. This approach allows us to extract more information from the underlying physical processes leading to the more accurate surrogate model of the final objective. As a result, we dramatically accelerate inverse problem solving and reach better final structure designs

compared to classical single-channel BO and several well known heuristic methods. Additionally, we extend this concept to the optimization of scalar objective functions derived from an *arbitrary* non-linear function of components of $\mathbf{y}'$, significantly broadening the applicability of our approach to a wide range of inverse problems.
As a representative example, here we demonstrate an inverse design of a nanostructured beam splitter, aiming to distribute light equally across all diffraction orders [3]. Therefore, the final design objective subject to minimization can be defined as the variance function of the simulated diffracted power fluxes with the constraint on the specified total transmission efficiency. In each iteration of the algorithm, we simulate the beam-splitter structure with finite-element method implemented in the solver *JCMsuite* [4] and extract the diffracted power flux vector $\mathbf{y}'$ which we learn with multi-output GP. The final variance objective is assembled from these *learned* quantities and minimized with the help of acquisition function of choice. From Figure 1 it is clear that multi-channel BO outperforms single-channel BO and heuristic methods in the number of iterations needed to find a good beam-splitter candidate.

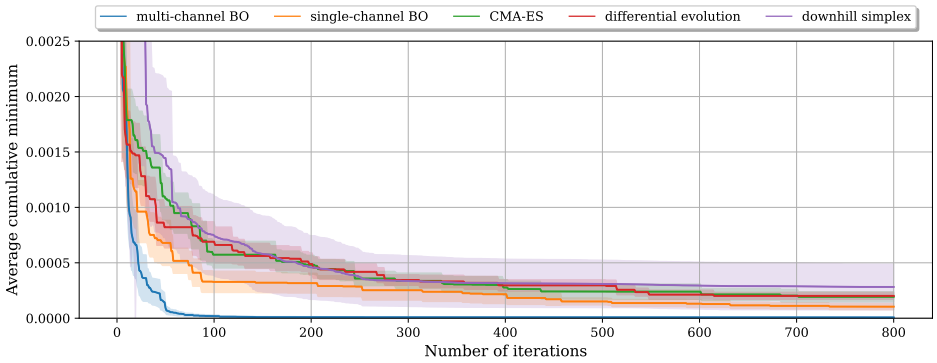


Figure 1: Benchmark of different optimization approaches on a beam-splitter example. The bold lines represent the mean convergence trends averaged over 10 runs, and the shaded areas indicate respective standard deviations.

Funding information The project has received funding from the German Federal Ministry of Education and Research (BMBF). Grant No. 01 IS 24 005 (NanoMaC) and from the German Federal Ministry for Economic Affairs and Energy (BMWK), Grant No. 50WM2253 (AI-QUADRAT).

References

1. Rasmussen C. E. and C. K. I. Williams, *Gaussian Processes for Machine Learning*, (MIT Press, Cambridge, MA, 2006).

2. Schneider P. I., Santiago X. G., Soltwisch V., Hammerschmidt M., Burger S. and Rockstuhl C., "Benchmarking Five Global Optimization Approaches for Nano-optical Shape Optimization and Parameter Reconstruction," *ACS Photonics*, Vol.6, pp. 2726–2733, 2019.

3. Ni Y., Chen S., Wang Y., Tan Q., Xiao S. and Yang Y., "Metasurface for Structured Light Projection over 120° Field of View," *Nano Lett.*, Vol. 20, pp. 6719–6724, 2020.

4. Pomplun J., Burger S., Zschiedrich L. and Schmidt F., "Adaptive finite element method for simulation of optical nano structures," *Phys. Status Solidi (b)*, Vol. 244, pp. 3419–3434, 2007.

Free-Electron Optical Nonlinearities in Heavily Doped Semiconductors: From Fundamentals to Integrated Photonics

G. Álvarez-Pérez[1,*], H. Hu[1], M. Ortolani[2, 3, 4], and C. Ciracì[1]

[1]Istituto Italiano di Tecnologia, Center for Biomolecular Nanotechnologies, Via Barsanti 14, 73010 Arnesano, Italy

[2]Istituto di Fotonica e Nanotecnologie, Consiglio Nazionale delle Ricerche, Via del Fosso del Cavaliere 100, Rome, 00133, Italy

[3]Department of Physics, Sapienza University of Rome, Piazzale Aldo Moro 5, 00185 Rome, Italy

[4]Istituto Italiano di Tecnologia, Center for Life Nano- and Neuro-Science, Viale Regina Elena 291, Rome, 00161, Italy

[*]corresponding author: gonzalo.alvarezperez@iit.it

Abstract: Heavily doped semiconductors have emerged as an enabling platform for mid-infrared photonics, leveraging free electrons to achieve strong and tunable nonlocal-nonlinear light-matter interactions. In this talk, we will discuss recent theoretical and experimental studies on third harmonic generation and Kerr nonlinearity in heavily doped semiconductors, in which hydrodynamic contributions dominate.

Heavily doped semiconductors have emerged as a promising platform mid-infrared photonics, providing tunable optical properties with low optical losses. These materials achieve their unique optical behavior through free-electron densities on the order of 10^{18}-10^{19} cm^{-3}, which allows precisely tuning the plasma wavelengths simply by adjusting doping levels. Importantly, free-electrons in heavily doped semiconductors exhibit quantum hydrodynamic behavior, which together with their low effective electron mass can leads to strong nonlocal and nonlinear light-matter interactions. Moreover, heavily doped semiconductors are compatible with already mature fabrication processes, making them a compelling alternative to traditional noble metal-based plasmonics.

The behavior of these materials can be understood and predicted using a hydrodynamic theory (HT) that captures free-electron dynamics, accounting for quantum pressure, nonlocal electron density variations, and convective dynamics, leading to a more accurate description of both linear and nonlinear optical responses, including nonlinear optical effects up to the third order [1]. While these effects are typically negligible in metals, they dominate in heavily doped semiconductors due to their lower carrier density. We will discuss how recent experiments on third-harmonic generation (THG) in InGaAs nanoantennas have revealed that hydrodynamic nonlinearities dominate over traditional lattice contributions [2]. These hydrodynamic contributions boost THG efficiency to control and enhance optical nonlinearities in plasmonic semiconductor nanostructures.

Unlike noble metals, where nonlinear interactions are largely confined to surfaces, these semiconductors support charge density waves known as longitudinal bulk plasmons (LBPs), which extend deep into the material. LBPs are intrinsically nonlocal excitations that fulfill $\varepsilon(\omega, \mathbf{k}) = 0$, where ε is the permittivivty and ω and $\mathbf{k}$ are the frequency and wavevector respectively. LBPs can trigger exceptionally large nonlinearities. Building on this, we have developed a theoretical framework to describe Kerr-type nonlinearities by combining metallic gap plasmons strongly coupled to LBPs in hybrid nanopatch antennas [3]. In this design, LBPs provide a large nonlinear interaction volume, while gap plasmons confine light to subwavelength dimensions, amplifying the nonlinear response. Using a time-domain method to solve hydrodynamic-Maxwell equations, we have demonstrated optical bistability at a ultralow threshold of 1 mW/μm. This effect arises from a feedback loop in which the Kerr nonlinearity shifts the LBP resonance, increasing reflectance hysteresis by 60%, a feature that

could be crucial for applications in optical memory and logic gates. Additionally, we study the electrostatic tuning of these nonlinear properties using metal-oxide-semiconductor (MOS) structures with gold electrodes and ultra-thin hafnium dioxide layers [4]. Our theory incorporates electrostatic and hydrodynamic frameworks to describe the electronic dynamics, demonstrating electrically tunable linear and nonlinear modulation. Specifically, applying a voltage bias dynamically modulates the free-electron density from depletion to accumulation, effectively tuning the plasma wavelength with a sensitivity of 0.89 μm/V. This control reduces bistability thresholds to just 10 μW, critical for next-generation reconfigurable photonic devices.

Finally, we translate these effects into practical photonic circuits. We have designed hybrid waveguides incorporating a 3.5 μm InGaAs core, evanescently coupled to a 30 nm heavily doped InGaAs layer, supporting free-electron Kerr-type nonlinearities [5]. This configuration supports long-propagating modes with very high nonlinear coefficients, surpassing traditional waveguides. Based on this, we design a Mach-Zehnder interferometer capable of achieving 60% transmission modulation as a function of the input power.

These advances position heavily doped semiconductors as promising platform for mid-IR photonics by combining highly nonlinear and nonlocal responses with electrostatic gating for tunability, with potential for ultra-fast (<1 ps switching), low-power photonic devices. Moreover, the compatibility of heavily doped semiconductors with existing foundry-compatible fabrication techniques makes large-scale adoption feasible.

References

1. De Luca, F. et al. “Free electron nonlinearities in heavily doped semiconductors plasmonics”. Phys. Rev. B 103 (11), 115305 (2021).
2. Rossetti, A. et al. “Control and enhancement of optical nonlinearities in plasmonic semiconductor nanostructures”. Light: Sci App, in press.
3. Hu, H. et al. “Low-Power Threshold Optical Bistability Enabled by Hydrodynamic Kerr Nonlinearity of Free Carriers in Heavily Doped Semiconductors”. ACS Photonics 11 (11), 4812-4817 (2024).
4. Hu, H. et al. “Modulating Low-Power Threshold Optical Bistability by Electrically Reconfigurable Free-Electron Kerr Nonlinearity”. arXiv:2412.14082 (2024).
5. Álvarez-Pérez, G. et al. “Ultrahigh free-electron Kerr nonlinearity in all-semiconductor waveguides for all-optical nonlinear modulation of mid-infrared light”. To be submitted.

Tunable plasmonic metasurfaces with epsilon-near-zero semiconductors: The case for a quantum carrier model

Masoud Shahbaninezhad,[1,2,3] Lora Ramunno,[2,3] and Pierre Berini[1,2,3,*]

[1]School of Electrical Eng. and Comp. Sci., University of Ottawa, Ottawa, ON K1N 6N5, Canada
[2]Department of Physics, University of Ottawa, Ottawa, ON K1N 6N5, Canada
[3]NEXQT Institute, 25 Templeton St., Ottawa, ON K1N 6N5, Canada
[*]corresponding author: pberini@uottawa.ca

Abstract: We model MOS capacitors using the drift-diffusion, density-gradient and Schrödinger-Poisson theories, connecting carrier distributions to permittivity distributions via the Drude model, then to electrodynamic computations to determine the optical performance of devices. This comprehensive approach enables accurate predictions of the voltage-gated performance of tunable plasmonic metasurfaces and high-speed electroabsorption modulators.

Resonant nanometallic structures, such as plasmonic nanoantennas, are essential to the conversion of light to surface plasmon-polaritons (SPPs) localized to ultra-small volumes. Such structures can provide highly enhanced fields, strong confinement, high surface sensitivity, and can double as a device electrode for applying voltages or passing currents to active regions in optoelectronic devices. In optoelectronics, metallic nanostructures supporting SPPs can be exploited for high-performance beam-steering devices and electro-optic modulators [1-6].

Metal oxide semiconductor (MOS) capacitors are useful electronic structures for enabling tunable metasurfaces [1-5] or high-speed electroabsorption modulators [6-8] where the metal contact also operates as a plasmonic nanostructure. Indium tin oxide (ITO) is of interest as the semiconductor in such MOS structures, as the real part of its optical permittivity can be driven through zero to become negative under accumulation, enabling epsilon-near-zero (ENZ) effects which further enhance fields in tandem with plasmonic enhancement. The carrier density profile produced under accumulation in such MOS capacitors is required to determine the associated permittivity profile following the carrier dispersion effect. The permittivity profiles are then used in optical computations to determine the gated optical response of surface plasmons supported by nanostructures incorporating MOS structures.

The carrier density profile in MOS capacitors can be computed under gating using two classical theories - conventional drift-diffusion (CDD) and density-gradient (DG) - and a self-consistent Schrödinger-Poisson (SP) quantum theory [7]. Under accumulation the predictions made by the CDD and SP models differ considerably, such that the former results in one ENZ point but the latter leads to two, as can be appreciated from Fig. 1. Consequently, the CDD model significantly underestimates perturbations of SPPs and yields incorrect details in SPP fields near ENZ points. The discrepancy is large enough to invalidate the CDD model in MOS structures on ENZ materials under accumulation, strongly motivating a quantum carrier model in this regime. Once calibrated the DG model approximates well the SP model while being computationally more efficient.

We discuss application of these models to tunable metasurfaces [5] and high-speed electroabsorption modulators [8]. Our approach consists in modelling the electrostatic performance of the MOS capacitor using the CDD, DG and SP theories, then connecting the resulting carrier distributions to permittivity distributions via the Drude model, and then carrying out electrodynamic computations to determine the optical performance of

devices. This comprehensive approach enables accurate predictions of the voltage-gated performance of tunable metasurfaces and high-speed electro-optic modulators.

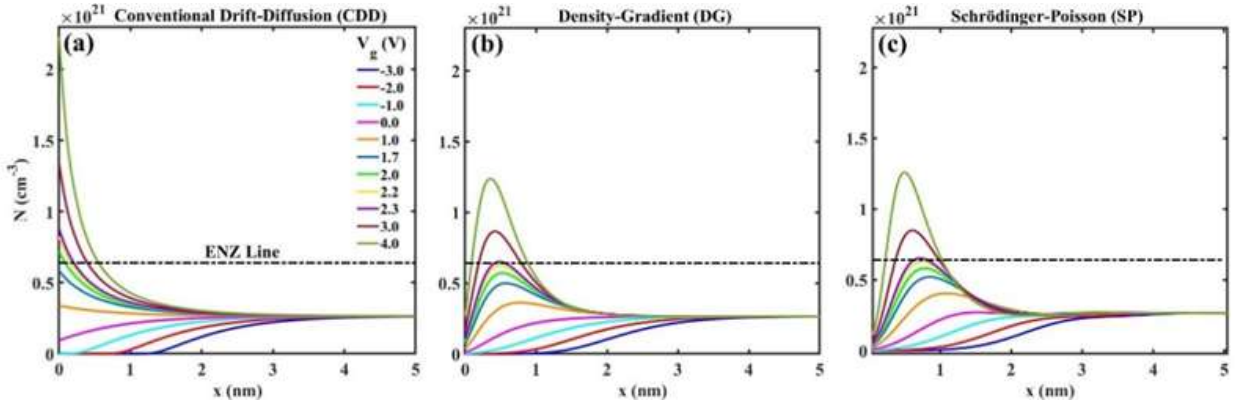


Fig. 1. 1D carrier density *vs*. distance from an insulator (HfO_2) ITO interface into ITO, for a MOS structure, at different bias voltages (V_g), obtained using: (a) CDD, (b) DG, and (c) SP models. The carrier density required to produce ENZ in ITO is highlighted as the horizontal black dash-dot line.

References

1. Berini, P., "Optical Beam Steering Using Tunable Metasurfaces," ACS Photonics, Vol. 9, pp. 2204-2218, 2022
2. Calà Lesina, A., Goodwill, D., Bernier, E., Ramunno, L., Berini, P., "Tunable Plasmonic Metasurfaces for Optical Phased Arrays," IEEE J Sel. Top. Quant. Electr., Vol. 27, 4700116, 2021
3. Calà Lesina, A., Goodwill, D., Bernier, E., Ramunno, L., Berini, P., "On the performance of optical phased array technology for beam steering: effect of pixel limitations," Opt. Express, Vol. 28, pp. 31637-31657, 2020
4. Rashid, S., Walia, J., Northfield, H., Hahn, C., Olivieri, A., Calà Lesina, A., Variola, F., Weck, A., Ramunno, L., Berini, P., "Helium ion beam lithography and liftoff," Nano Futures, Vol. 5, 025003, 2021
5. Mayoral-Astorga, L.-A., Shabaninezhad, M., Northfield, H., Ntais, S., Rashid, S., Lisicka-Skrzek, E., Mehrvar, H., Bernier, E., Goodwill, D., Ramunno, L., Berini, P., "Electrically tunable plasmonic metasurface as a matrix of nanoantennas," Nanophotonics, Vol. 13, pp. 901–913, 2024
6. Dhingra, N., Mehrvar, H., Berini, P., "Broadband plasmonic modulator operating with the fundamental TM or TE modes of a planarized silicon waveguide," Optics Express, Vol. 31, pp. 22481-22496, 2023
7. Shabaninezhad, M., Ramunno, L., Berini, P., "Tunable plasmonics on epsilon-near-zero materials: the case for a quantum carrier model," Optics Express, Vol. 30, pp. 46501- 46519, 2022
8. Shabaninezhad, M., Mehrvar, H., Berini, E., Ramunno, L., Berini, P., "Plasmonic electro-optic modulators based on epsilon-near-zero materials: comparing the classical drift-diffusion and Schrödinger-Poisson coupling models," Optics Express, Vol. 33, pp. 4474-4490, 2025

An FFT-accelerated PML-BIE method for 3D acoustic scattering problems in layered media

Hangya Wang[1] and Wangtao Lu[1*]
[1]Zhejiang University, China
wangtaolu@zju.edu.cn (corresponding author)

Abstract

For a 3D acoustic scattering problem in a two-layer medium with an axisymmetric interface, we use PML to truncate the unbounded domain, PML transformed Green's functions to derive boundary integral equations, and design FFT-accelerated high-accuracy quadrature rules. Numerical examples demonstrate the effectiveness of the PML-based BIE solver.

1 Introduction

This paper is concerned with three-dimensional acoustic wave scattering in two-layer media, where the two homogeneous layers are separated by a locally perturbed plane featuring an axially symmetric perturbation. A fast novel boundary integral equation (BIE) method is proposed to solve the scattering problem within a cylindrical perfectly matched layer (PML) truncation. We use PML-transformed Green's functions to derive BIEs in terms of single- and double-layer potentials for the wave field and its normal derivative on the boundary of each truncated homogeneous region. These BIEs, combined with interface and PML boundary conditions, form a complete system that accurately approximates the scattering problem. An FFT-based approach is introduced to efficiently and accurately discretize the surface integral operators in the BIEs, where a new kernel splitting technique is developed to resolve instabilities arising from the complex arguments in Green's functions. Numerical experiments demonstrate the efficiency and accuracy of the proposed method, as well as the exponential decay of truncation errors introduced by the PML. Readers are referred to [1] for details.

2 Equations

As shown in Fig 1(a), the scattered field u^{s} due to a given incident wave u^{inc} is governed by:

$$\Delta u^{\mathrm{s}}(\boldsymbol{r}) + \omega_j^2 u^{\mathrm{s}}(\boldsymbol{r}) = 0, \quad \text{for} \quad \boldsymbol{r} = (x, y, z) \in \Omega_j, \tag{1}$$

$$u^{s,1}\big|_\Gamma - u^{s,2}\big|_\Gamma = u_{\mathrm{ref}}^{\mathrm{inc},2}\Big|_\Gamma - u_{\mathrm{ref}}^{\mathrm{inc},1}\Big|_\Gamma, \tag{2}$$

$$\frac{\partial u^{s,1}}{\partial \boldsymbol{\nu}}\bigg|_\Gamma - \frac{\partial u^{s,2}}{\partial \boldsymbol{\nu}}\bigg|_\Gamma = \frac{\partial u_{\mathrm{ref}}^{\mathrm{inc},2}}{\partial \boldsymbol{\nu}}\bigg|_\Gamma - \frac{\partial u_{\mathrm{ref}}^{\mathrm{inc},1}}{\partial \boldsymbol{\nu}}\bigg|_\Gamma, \tag{3}$$

$$\lim_{|\boldsymbol{r}|\to\infty} |\boldsymbol{r}| \left(\partial_{|\boldsymbol{r}|} - \mathbf{i}\omega_j\right) u^s = 0, \quad \text{in} \quad \Omega_j, \quad j = 1, 2, \tag{4}$$

where Γ and the two domains Ω_j are all axisymmetric. For $\boldsymbol{r} = (\rho\cos\theta, \rho\sin\theta, z) \in \mathbb{R}^3$, the cylindrical PML is defined by the complex stretching $\tilde{\boldsymbol{r}}(\boldsymbol{r}) = (\tilde{\rho}\cos\theta, \tilde{\rho}\cos\theta, \tilde{z})$ where

$$\tilde{\rho}(\rho) = \rho + \mathbf{i}\int_0^\rho \sigma_\rho(t)dt, \quad \tilde{z}(z) = z + \mathbf{i}\int_0^z \sigma_z(t)dt.$$

The complexified scattered field $\tilde{u}^s(\boldsymbol{r}) = u^s(\tilde{\boldsymbol{r}}(\boldsymbol{r}))$ satisfies

$$\nabla \cdot \left(\mathbf{A}\nabla \tilde{u}^{s,j}\right) + \omega_j^2 J \tilde{u}^{s,j} = 0, \quad \text{in} \quad \Omega_j, \quad j = 1, 2. \tag{5}$$

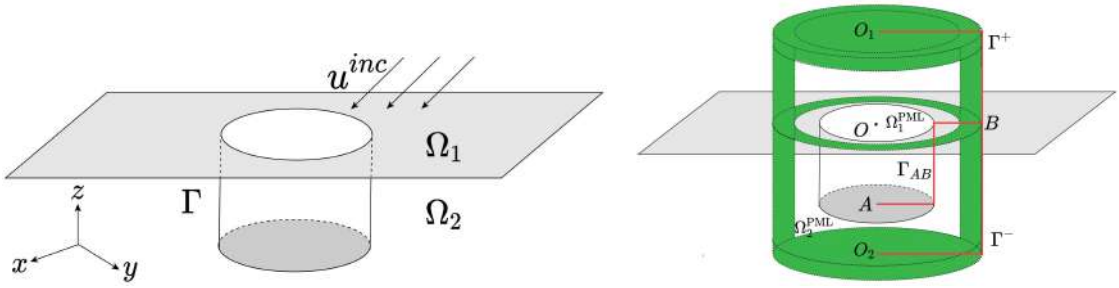
By using the complexified Green's functions $\tilde{G}^j(\boldsymbol{r}; \boldsymbol{r}') = \frac{e^{i\omega_j \text{dist}(\boldsymbol{r};\boldsymbol{r}')}}{4\pi \text{dist}(\boldsymbol{r};\boldsymbol{r}')}$, we derive two governing BIEs on the truncated interface Γ_{AB} due to the PML:

$$(\tilde{\mathcal{K}}^j_{AB} - \tilde{\mathcal{K}}^0 1)\tilde{u}^{s,1} \approx \tilde{\mathcal{S}}^j_{AB} \partial_{\boldsymbol{\nu}_c} \tilde{u}^{s,1}, \quad \text{on} \quad \Gamma_{AB}, \tag{6}$$

where $\tilde{\mathcal{S}}^j_{AB}$ and $\tilde{\mathcal{K}}^j_{AB}$ are single- and double-layer integral operators defined only on Γ_{AB} and $\tilde{\mathcal{K}}^0$ is the double-layer operator for the complexified Laplacian. By complexifying the interface conditions (2) and (3) with the cylindrical PML, and by numerically discretizing the BIEs (6), we are able to compute $\tilde{u}^s$ with high accuracy.

3 Figures and Tables

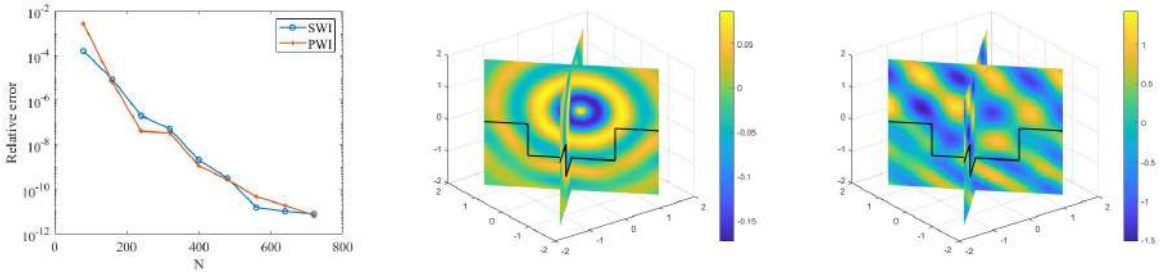
Figure 1(a) shows the profile of the scattering problem. Figure 1(b) shows the truncation by a cylindrical PML. When the perturbed part of Γ is a cylinder, Figure 2(a) shows the accuracy



(a) (b)

Figure 1: (a) Profile of a 3D layered medium. (b) The 3D illustration of the cylindrical PML truncation.

of the numerical solutions for a sufficiently strong PML. Figure 2 (b) and (c) show the field patterns on some slices of the computational domain.



(a) (b) (c)

Figure 2: (a) Relative errors against the number of discretization points for a strong enough PML. (b) and (c) are the real parts of the total field for spherical and plane wave incidences, respectively.

References

[1] H. Wang, W. Lu, An FFT-accelerated PML-BIE Solver for Three-Dimensional Acoustic Wave Scattering in Layered Media, arXiv preprint arXiv:2412.11162, 2024.

Inverse design of large and complex metaoptics systems

Bryan Stone[1*], Evan Heller[2], Li-Ce Hu[3], Rob Scarmozzino[2], Mayank Bahl[2], Ziwei Zhu[4], Maryvonne Chalony[5], Yijun Ding[4], and Chenglin Xu[2]

[1]Synopsys Inc., Marlborough MA 1752, USA
[2]Synopsys Inc., Ossining NY 10562, USA
[3]Synopsys Inc., Hsinchu, Taiwan
[4]Synopsys Inc., Pasadena, CA 91101, USA
[5]Synopsys Inc., Hyeres 83400, FRANCE
[*]Corresponding author: bryans@synopsys.com

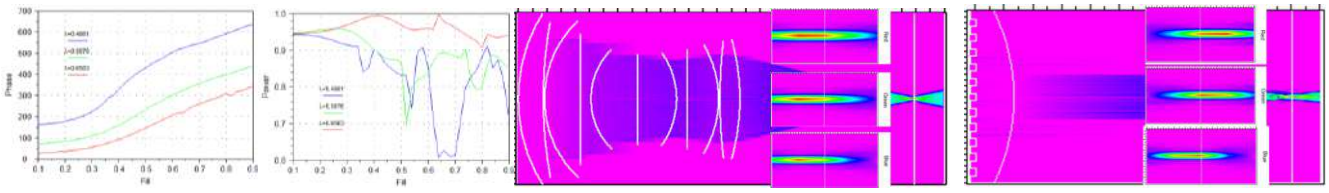
Abstract

The fully automated inverse design tools developed at Synopsys can be used for large and complex metaoptics systems, such as hybrid metalens systems, to reduce physical size and specify complex metasurfaces to achieve high performance. Minimal design experience is required of designers because of pre-built knowledge in the design tools.

Summary

MetaOptic Designer (MOD) [1], has been widely used to design various metaoptics devices because it is easy to use and requires minimal design knowledge. Its effectiveness and accuracy have been validated both numerically and experimentally for simple applications, such as holographic displays [2] and LiDAR systems [3]. In this paper, we apply MOD to more complex systems.

The first example is a hybrid system co-designed in CODE V and MOD with a singlet to replace a double Gauss refractive lens system with six pieces. The meta-atom used for the metasurface is an Si_3N_4 pillar on a glass substrate with a period of 0.4μm. Its transfer function, both phase and amplitude, is shown Fig. 1(a). As shown in Fig. 1(d), the hybrid system can focus RGB light similarly to the refractive lens system [Fig. 1(c)], but it is 5 times smaller in physical size.



(a) (b) (c) (d)

Fig. 1 Transfer function: (a)phase and (b)amplitude; Focus of RGB (c)refractive lenses and (d)hybrid system.

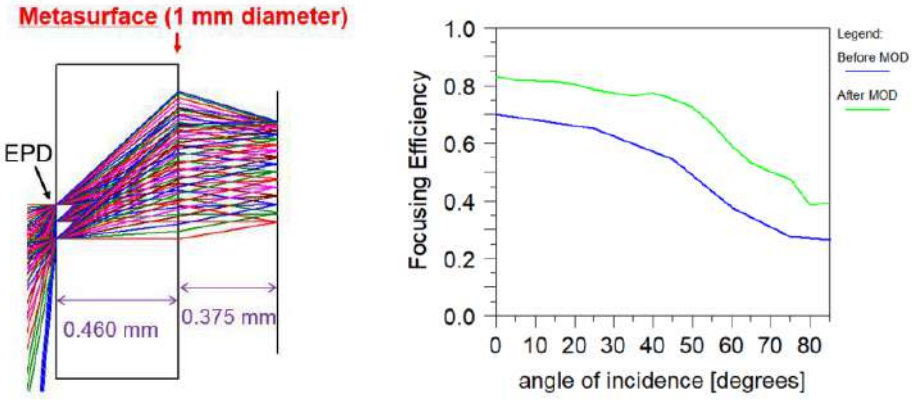
The performance of the hybrid system in terms of both absolute focusing efficiency (AFE) and Strehl ratio for different wavelengths and different FOVs has been calculated using CODE V [4] and summarized in Table 1. The simple hybrid system can image surprisingly well, although the blue light experiences relatively low efficiency due to low transmission, as shown in Fig. 1(b).

Table 1. Absolute focusing efficiency & Strehl ratio

Wavelength \ FOV	0°	10°	20°	28°
0.6563μm (R)	68.14% & 0.744	66.07% & 0.781	64.15% & 0.730	67.74% & 0.739
0.5876μm (G)	74.31% & 0.862	69.72% & 0.882	68.94% & 0.835	69.90% & 0.831

0.4861μm (B)	69.70% &0.807	56.14% & 0.791	43.52% & 0.685	39.85% & 0.694

The second example is an ultra-wide FOV metalens, which is very challenging to design with a single tool. Here we combine ray-based and wave-based design tools [5], using CODE V to do the initial design shown in Fig. 2(a), then further optimize it in MOD. Comparing the AFE before and after further optimization in MOD demonstrates the AFE has been improved significantly as shown in Fig. 2(b).



(a) (b)

Fig. 2 (a) Initial design in CODE V, (b) Further optimization in MOD with better results

As demonstrated in Ref. [6], multi-metasurface systems perform better than a single metasurface. With the same Si meta-atom library as used in Ref. [6], we quickly and easily created a similar design as shown in Fig. 3. Details will be reported at the META 2025 conference.

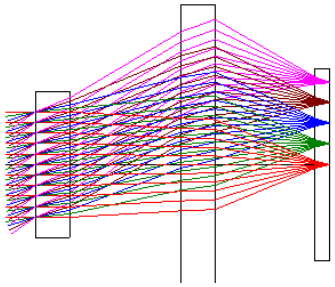


Fig. 3 Initial design of the doublet metasurfaces

References

[1] https://www.synopsys.com/photonic-solutions/rsoft-photonic-device-tools/metaoptic-designer.html

[2] H. L. Liu, T. K. Yang, and P. Yu, "Design and Fabrication of Meta-Optical Elements for Beam Shaping," META 2024, Toyama, Japan, July 2024.

[3] Loucif, A., Chalony, M., Majorel, C., Kuperman, Q., & Genevet, P. (2024, June). Design and characterization of metasurfaces for LIDAR applications. In *Optical Design and Engineering IX* (Vol. 13019, pp. 228-236). SPIE.

[4] https://www.synopsys.com/optical-solutions/codev.html

[5] Hu, Li-Ce, and Yijun Ding. "Ultra-wide angle metalens design with ray-based and wave-based tools." *Optical Design and Testing XIII*. Vol. 12765. SPIE, 2023.

[6] Mattinson, Fredrik, et al. "Latest advancements at NILT on flat metalens based camera modules in near infrared." *Current Developments in Lens Design and Optical Engineering XXIII*. Vol. 12217. SPIE, 2022.

Recent Progress in the Design and Simulation of Large-Scale Metalenses

J. Niegemann[1*], D. Huynh[2], Han-Hsiang (Michael) Cheng[3], Thibault Leportier[1], Dylan McGuire[1]

[1]Ansys Canada Ltd., Canada
[2]Ansys Germany GmbH, Germany
[3]Ansys Japan K.K., Japan
[*]corresponding author: jens.niegemann@ansys.com

Abstract: This presentation discusses recent advances in the design and simulation of large-scale metalenses. We will present a complete simulation workflow from the design of individual meta-atoms to the simulation of complete optical systems. Future directions for research and potential industrial applications are highlighted.

Metalenses are composed of meticulously arranged meta-atoms with sub-wavelength structures. By fine-tuning the geometry and location of these individual elements, we can control the phase, amplitude, and polarization of transmitted or reflected light. Recent advancements in the simulation and fabrication of metalenses [1] have garnered significant interest from both academia and industry. However, the design and optimization of large-scale metalenses remains challenging, necessitating the development of improved simulation methods and the utilization of modern high-performance computing (HPC) systems.

The first step in metalens design often is the construction of a meta-atom database. Here, we will discuss and compare different numerical methods to simulate individual meta-atoms. Specifically, we present the respective strengths and weaknesses of the finite-difference time-domain (FDTD) method and the rigorous coupled-wave analysis (RCWA) approach for this purpose. With a suitable database in hand, the next step typically is the optimization of the arrangement of meta-atoms to achieve the desired overall metalens response. We will again compare different approaches with a focus on adjoint methods which have been particularly effective in the optimization of large-scale lenses.

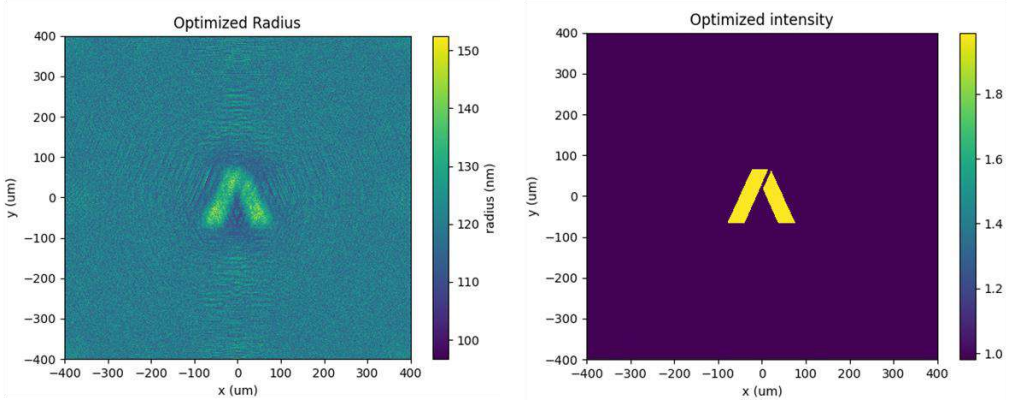


Figure 1. Optimization results for pillar shaped meta-atoms: The optimized radius distribution (left) and intensity in the image plane (right) is shown for a stylized letter “A”.

Optimization is typically performed using approximations such as the local periodic approximation (LPA), making it crucial to verify the final design before manufacturing. To this end, we demonstrate the utilization of multi-GPU systems to conduct full-scale FDTD simulations of optical metalenses with diameters exceeding 1

mm. Once the individual metalens design is finalized and verified, engineers often need to simulate the entire optical system, which may include a combination of traditional optical elements and metalenses. Raytracing is generally the preferred method for such simulations; however, accurately incorporating metalenses in raytracing simulations without compromising efficiency or accuracy remains a challenge. We show that the recently developed Windowed Fourier Transform (WFT) method [2]maintains the expected performance of raytracing while handling metalenses more accurately than previous methods.

References

1. Y. He, B. Song and J. Tang, “Optical metalenses: fundamentals, dispersion manipulation, and applications,” Front. Optoelectron. Vol. 15, No. 24, 2022.
2. Ziwei Zhu, Zhaocheng Liu, and Changxi Zheng, "Metalens enhanced ray optics: an end-to-end wave-ray co-optimization framework," Opt. Express 31, 26054-26068, 2023.

Study of the radiative properties of quasi-bound states in the continuum in dimer gratings using the Quasi-normal mode method

E. Centeno[1*], V. Kalt[2], Rafik Smaali[1], Antoine Moreau[1]

[1]Université Clermont Auvergne, Clermont Auvergne INP, CNRS, Clermont-Ferrand, France

[2]Université de Lyon, Laboratoire Hubert Curien, UMR 5516, Université Jean Monnet, Saint-Etienne, France

[*]corresponding authors: emmanuel.centeno@uca.fr

Abstract: We study the radiating properties of dimer grating supporting quasi-bound states in the continuum (QBICs) with a novel approach based on the quasi-normal mode method. This approach allows an accurate calculation of the Purcell factor, light extraction and radiative enhancement coefficients for a unique quantum emitter.

Increasing the light matter interaction in photonic nanostructures is fundamental for lighting, communication, imaging, and medicine applications. Metasurfaces, photonic crystals and gratings are today essential nanophotonics platforms used to both enhance the spontaneous emission and extract the emitted light [1]. Optical bound states in the continuum (BICs) constitute an elegant solution to boost the photoluminescence quantum yield. BICs are eigen electromagnetic modes with forbidden radiation or equivalently infinite Q-factors. These BICs must be converted into quasi-BICs (QBICs) of high but finite Q-factors so that they can radiate toward the external medium [2]. The calculation of the radiative properties of nanophotonic structures supporting QBICs is thus crucial for realizing efficient emissive devices. Many such numerical studies use a dipole source placed within the periodic cell [1,3]. However, this approach assumes that periodic emitters produce coherent radiation, in contrast to the inherently incoherent nature of the spontaneous emission process. The periodic set of coherent emitters also introduces spurious interferences that prevent the accurate calculation of radiative properties at off – Γ points. To avoid this issue, the reciprocity principle can be used to calculate the radiated power in the far field emitted by a single quantum emitter in a periodic structure [4]. However, this method fails when dealing with photonic systems supporting dark modes such as BICs since external coupling with a plane wave is forbidden. In this context, the quasi-normal mode (QNM) method appears as an interesting approach as the radiated field of a single non-periodic dipole is reconstructed from the eigenmodes of the structure [5]. In this work, we develop a QNM theory to calculate the radiative properties of a dimer grating which supports QBICs. With this approach we can calculate the normalized decay rate (Fp) as well as the Light Extraction Efficiency (LEE) for a unique quantum emitter (QE). These two factors can be combined to calculate the Radiative Enhancement (RE), product of the LEE and the normalized decay rate.

The dimmer grating consists of a supercell period 2D, made of TiO_2 ribbons of width $w \pm \Delta w$ with $w = D/2$ and height h =150 nm above a quartz substrate. We denote the gap distance $L \pm \Delta L$. The ribbons are embedded within a TEOS layer of 200 nm height. To determine the geometry of the dimmer grating, we introduce the coefficients $\alpha = \Delta w/2w$ and $\beta = \Delta L/2L$. For the regular grating with $\alpha = 0$ and $\beta = 0$ presents a BIC at the Γ-point, for the wavelength of 681.67 nm.

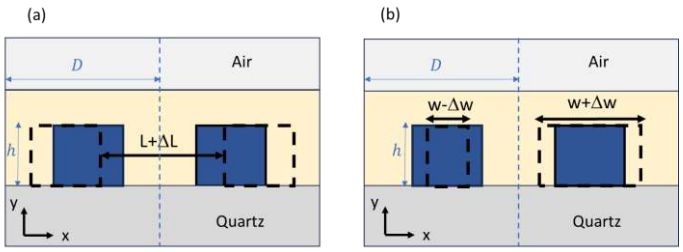


Figure 1: schematic of a dimer grating.

When the in-plane symmetry of the grating is broken by varying the position or the size of the ribbons, the BIC transforms into a QBIC, enabling radiation in the normal direction. To analyze this dynamic, we determine the evolution of the resonant wavelength and Q-factor in the (α, β) parameter space as shown Fig. 2a-b.

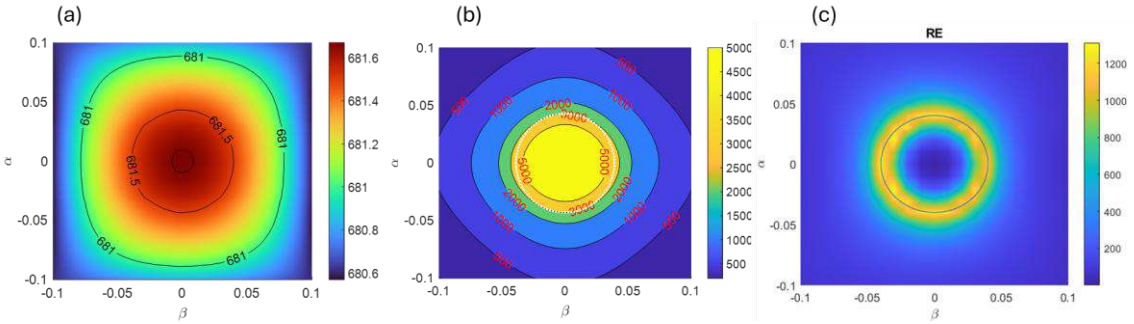


Figure 2:(a), (b), (c) represents respectively the resonant wavelength of the QBIC, the Q-factor and the RE in the parameter space (α, β). The white circle in (b) corresponds to the iso-wavelength λ_0 = 681.5nm.

To get a high Q-factor (larger than 3000) and a feasible dimer grating, we focus on the resonant iso-wavelength of $\lambda_0 = 681.5$ nm. Next, we use the QMN expansion to calculate the RE in the normal direction and for the target wavelength for the QBIC. We observe that the RE reaches very large values up to 1600 when a weak modification of 4\% is either introduced for the size or the gap distance of the dimer. This approach allows us to design the optimal dimer grating able to enhance the spontaneous emission at a given emission direction.

The authors thank the French “Agence Nationale de la Recherche” in the framework of the COULEURS project (ANR-22-CE39-0013).

References

1. A. Vaskin, R. Kolkowski, A. F. Koenderink, and I. Staude, “Light-emitting metasurfaces”, Nanophotonics Vol. 8, 1151 (2019)
2. S. I. Azzam and A. V. Kildishev, “Photonic bound states in the continuum: from basics to applications”, Advanced Optical Materials Vol.9, 2001469 (2021).
3. P. Ding, L. Shao, J. Wang, Y. Li, F. Zeng, and E. Liang, “Enhanced light extraction with silicon nanoantenna arrays for white light led applications”, Optical and Quanum Electronics Vol. 49, 1 (2017)
4. S. Zhang, E. R. Martins, A. G. Diyaf, J. I. Wilson, G. A. Turnbull, and I. D. Samuel, “Calculation of the emission power distribution of microstructured oleds using the reciprocity theorem”, Synthetic Metals Vol. 205, 127 (2015).
5. C. Sauvan, J.-P. Hugonin, I. S. Maksymov, and P. Lalanne, “Theory of the spontaneous optical emission of nanosize photonic and plasmon resonators”, Physical Review Letters Vol. 110, 237401 (2013).

Effect of top metallic contacts on energy conversion performances for near-field thermophotovoltaics

M. Antezza
University of Montpellier, Laboratoire Charles Coulomb, Montpellier, France
and
Institute Universitaire de France, Paris, France
mauro.antezza@umontpellier.fr

Abstract: We study Effect of top metallic contacts on energy conversion performances for near-field thermophotovoltaics. We find behaviors differing substantially from those predicted by previous simplistic approaches, with significant impact on the net radiative power absorbed by the cell and, consequently, on the generated electrical power.

The design of metallic contact grids on the front side of thermophotovoltaic cells is critical since it can cause significant optical and electrical resistive losses, particularly in the near field. However, from the theoretical point of view, this effect has been either discarded or studied by means of extremely simplified models like the shadowing methods, that consist in simply ignoring the fraction of the semiconductor surface covered by metal. Our study [1], based on a rigorous three-body theoretical framework and implemented using the scattering matrix approach with the Fourier modal method augmented with adaptive spatial resolution, provides deeper insight into the influence of the front metal contact grid. This approach allows direct access to the radiative power absorbed by the semiconductor, enabling the proposal of an alternative definition for the thermophotovoltaic cell efficiency. By modeling this grid as a metallic grating, we demonstrate its significant impact on the net radiative power absorbed by the cell and, consequently, on the generated electrical power. Our analysis reveals behaviors differing substantially from those predicted by previous simplistic approaches.

References

1. Youssef Jeyar, Kevin Austry, Minggang Luo, Brahim Guizal, Yi Zheng, Riccardo Messina, Rodolphe Vaillon, and Mauro Antezza, arXiv:2412.04258 (2024)

The technology and commercialization strategy of next-generation computational electrodynamics

Zongfu Yu[1], Shanhui Fan[1,2], Jianming Jin[1,3]

1. Flexcompute Inc, Watertown, MA, USA
2. Department of Electrical Engineering, Stanford University, Stanford CA, USA
3. Department of Electrical and Computer Engineering, UIUC, Champaign, IL, USA

In the rapidly evolving fields of photonics and radio frequency (RF) engineering, accurate and efficient electromagnetic (EM) simulations are essential for driving innovation. However, traditional EM solvers often struggle to keep pace with the growing complexity of modern designs and fail to fully leverage emerging algorithms and computational technologies.

This talk will explore the future of electromagnetic solvers in the era of cloud computing, GPUs, and AI. We will discuss how these advancements enable unprecedented speed and efficiency in tackling complex engineering challenges, including the design and fabrication of photonic integrated circuits (PICs), mission-critical electromagnetic compatibility (EMC) analysis, and AI-driven optimization for next-generation antenna design. By embracing these cutting-edge technologies, EM solvers can unlock new possibilities for faster, more accurate, and more scalable simulations, accelerating progress in photonics and RF engineering.

Inverse design and knowledge discovery in nanophotonics through integration of shape optimization and machine learning algorithms

Reza Marzban and Ali Adibi

School of Electrical and Computer Engineering, Georgia Institute of Technology

Short Abstract: This talk is focused on a new approach for inverse design and knowledge discovery in large-scale nanostructures by combining topological optimization and machine-learning algorithms to enable the optimization of all structural and physical parameters while providing better visualization of the input-output relationship for knowledge discovery through dimensionality reduction.

Summary: With great progress in fabrication technologies, new classes of nanophotonic and metaphotonic devices with a very large number of design parameters have been realized. The large number of design parameters along with the nonuniqueness of the optimal solution has necessitated new approaches for both the design of these structures and providing insight into their operation (i.e., knowledge discovery). Two major classes of these approaches are based on machine learning and shape optimization (e.g., topological optimization) techniques, each with positive aspects and shortcomings.

This talk is focused on a new hybrid approach for the inverse design and knowledge discovery in large-scale nanostructures by combining the unique features of topological optimization and machine-learning algorithms. This approach allows for optimization of all design parameters including geometrical features and physical (e.g., material) parameters of passive and active nanophotonic structures. In addition, by using properly trained dimensionality reduction techniques, visualization of the input-output relationship and knowledge discovery are facilitated, and computational complexity is reduced.

In addition to describing the fundamental aspects of this hybrid technique, its applications to forming functional metaphotonic devices for wavefront engineering will be discussed, and the potentials of this approach as a new paradigm in the design of large-scale nanophotonic structures will be covered.

Adiabatic time modulations vs. Photonic time interfaces

M. Antyufeyeva[1,2], and V. Pacheco-Peña[1*]

[1] School of Mathematics, Statistics and Physics, Newcastle University, Newcastle upon Tyne, NE1 7RU, United Kingdom
[2] V. N. Karazin Kharkiv National University, 4, Svobody Square, Kharkiv, 61022, Ukraine
[*]corresponding author: victor.pacheco-pena@newcastle.ac.uk

Abstract: We develop an in-depth theoretical study on the potential properties of temporal adiabatic modulations of the refractive index of the medium where a wave travels. The results are compared with the field distribution produced by photonic time interfaces demonstrating the potential to mimic time refracted signals.

As it is known, wave propagation can be tailored by *shaping the space* where a wave propagates. i.e., one can place objects of different dimensions and materials (spatial inhomogeneities) along the path where a wave propagates. While such wave control is carried out in the frequency domain where inhomogeneities are only spatially dependent (three spatial dimensions), the recent introduction of time as an additional degree of freedom has opened many opportunities to further manipulate wave-matter interactions [1–3]. One of such examples are photonic time interfaces where the optical properties of the medium where a wave propagates rapidly changes in time from one value to a different value at a certain time [4]. Ideally, time interfaces are modelled using Heaviside functions (or step functions) where the optical properties (permittivity, permeability, refractive index) abruptly change in time). Recent experimental works have demonstrated the existence of time interfaces from water waves up to the optical regime [5–7]. These works are clear evidence that, as long as the time modulation is faster than the period of the wave traveling inside the medium, the main features of time interfaces will still exist (backward and forward waves, frequency conversion, etc.) despite non-zero rising/falling times[8–17].

The main challenge in this context is the fast modulation of the optical properties of the material where a wave propagates which may require complex experimental setups to achieve. Recently, it has been shown that adiabatic modulations can indeed be used to, for instance, reduce the backward wave produced by time interfaces while still enabling frequency conversion [18]. Such scenario is indeed the temporal equivalent of a spatial tapering of waveguides, for instance. However, an interesting question is: is it indeed possible to fully mimic time interfaces using adiabatic modulations of the optical properties of the material where a wave propagates?

Inspired by the opportunities that time varying and spacetime metamaterials can open for a four-dimensional wave control and the importance of time interfaces as the equivalent of spatial interfaces in the time domain, in this work we study the potential of smooth modulation of the optical properties of materials [19]. Specifically, we consider a cavity filled with a material having a time dependent refractive index. For the sake of simplicity, we focus our attention on the case where the impedance remains constant for all times while the permittivity (and then the corresponding permeability) is changed from ε_1 to ε_2 in time following the general expression $\varepsilon(t) = (A\varepsilon_1 + \varepsilon_2 - \varepsilon_1)A^{-1}$ with $A = 1 + e^{-\gamma(t-t_0)}$, and with γ as a parameter used to change the rise/fall time (Δt). As it will be shown in detail during the conference, our theoretical analysis (carried out using the Evolutionary Approach to Electromagnetics in time domain, EAE [20]) allows us to calculate full analytical expressions for the rising/fall times that produce the same total mode amplitudes inside the cavity as that produced by a temporal interface. In order words, we will show how, indeed, there are some rise/fall times for smooth modulation of the optical properties of the medium where it is possible to mimic the same response as the time refracted signal produced by time interfaces. These results may open further potential experimental demonstrations of time

interfaces by relaxing the need of fast time modulated media.

Acknowledgements, V.P.-P. would like to thank the support of the Leverhulme Trust under the Leverhulme Trust Research Project Grant scheme (No. RPG-2020-316 and RPG-2023-024). M.A. acknowledges the British Academy and CARA for support through the Researcher at Risk Fellowship programme.

References

1. C. Caloz and Z.-L. Deck-Léger, "Spacetime Metamaterials — Part I : General Concepts," IEEE Trans Antennas Propag **68**(3), 1569–1582, 2020.
2. V. Pacheco-Peña, D. M. Solís, and N. Engheta, "Time-varying electromagnetic media: opinion," Opt Mater Express **12**(10), 3829, 2022.
3. T. T. Koutserimpas and F. Monticone, "Time-varying media, dispersion, and the principle of causality [Invited]," Opt Mater Express **14**(5), 1222, 2024.
4. F. Morgenthaler, "Velocity Modulation of Electromagnetic Waves," IEEE Trans Microw Theory Tech **6**(2), 167–172, 1958.
5. V. Bacot, M. Labousse, A. Eddi, M. Fink, and E. Fort, "Time reversal and holography with spacetime transformations," Nat Phys **12**(10), 972–977, 2016.
6. H. Moussa, G. Xu, S. Yin, E. Galiffi, Y. Ra'di, and A. Alù, "Observation of temporal reflection and broadband frequency translation at photonic time interfaces," Nat Phys **19**(6), 863–868, 2023.
7. R. Tirole, S. Vezzoli, E. Galiffi, I. Robertson, D. Maurice, B. Tilmann, S. A. Maier, J. B. Pendry, and R. Sapienza, "Double-slit time diffraction at optical frequencies," Nat Phys **19**(7), 999–1002, 2023.
8. V. Pacheco-Peña and N. Engheta, "Temporal aiming," Light Sci Appl **9**(129), 1–12, 2020.
9. V. Pacheco-Peña and N. Engheta, "Antireflection temporal coatings," Optica **7**(4), 323, 2020.
10. J. E. Vázquez-Lozano, V. Pacheco-Peña, and I. Liberal, "Mirrors without spatial boundaries," arXiv:2502.13901, 2025.
11. G. Castaldi, V. Pacheco-Peña, M. Moccia, N. Engheta, and V. Galdi, "Exploiting space-time duality in the synthesis of impedance transformers via temporal metamaterials," Nanophotonics **10**(14), 3687–3699, 2021.
12. D. Ramaccia, A. Alù, A. Toscano, and F. Bilotti, "Temporal multilayer structures for designing higher-order transfer functions using time-varying metamaterials," Appl Phys Lett **118**(10), 101901, 2021.
13. X. Wang, M. S. Mirmoosa, and S. A. Tretyakov, "Controlling surface waves with temporal discontinuities of metasurfaces," Nanophotonics **12**(14), 2813–2822, 2023.
14. O. Silbiger and Y. Hadad, "Inverse design of time-varying transmission-line filters for broadband spatial signal processing," Phys Rev B **111**(5), 2025.
15. L. Bar-Hillel, A. Dikopoltsev, A. Kam, Y. Sharabi, O. Segal, E. Lustig, and M. Segev, "Time-refraction and time-reflection above critical angle for total internal reflection," arXiv:2311.15070, 2023.
16. V. Pacheco-Peña and N. Engheta, "Temporal equivalent of the Brewster angle," Phys Rev B **104**(21), 214308, 2021.
17. V. Pacheco-Peña, Y. Kiasat, D. M. Solís, B. Edwards, and N. Engheta, "Holding and amplifying electromagnetic waves with temporal non-Foster metastructures," arXiv 2304.03861, 2023.
18. E. Galiffi, S. Yin, and A. Alú, "Tapered photonic switching," Nanophotonics **11**(16), 3575–3581, 2022.
19. M. Antyufeyeva and V. Pacheco-Peña, "Emulating photonic time interfaces via smooth temporal transitions," arXiv:2411.19847, 2024.
20. F. Erden and O. A. Tretyakov, "Excitation by a transient signal of the real-valued electromagnetic fields in a cavity", Phys Rev E **77**, 056605, 2008.

Spin-mediated radiative caloritronics

P. Ben-Abdallah[1,*]

[1] *Laboratoire Charles Fabry, UMR 8501, Institut d'Optique, CNRS, Université Paris-Saclay, 2 Avenue Augustin Fresnel, 91127 Palaiseau Cedex, France*

The Spin Hall effect [1–3] and its inverse counterpart [4–8] are fundamental phenomena in condensed matter physics that have greatly contributed to the progress of modern spintronics. These effects harness the interaction between charge currents and spin dynamics in materials. The Spin Hall effect involves the generation of a transverse spin current when an electric current flows through a material, whereas the inverse Spin Hall effect describes the conversion of a spin current into a charge current, oriented perpendicularly to both the spin current and an externally applied electric field.

In this presentation, I will explore the thermal analogs of these effects, which arise from photon exchanges in networks of magneto-optical materials subjected to an external magnetic field. I will examine how the spin angular momentum of thermal photons interacts with radiative heat flux, which serves as a medium for heat transfer.

First, I will discuss how a temperature gradient within these systems can generate a transverse heat flux and a spatial variation in spin angular momentum [9–11], demonstrating the thermal equivalent of the Spin Hall effect. Then, I will introduce the concept of an inverse thermal Hall effect [12], where a gradient in spin angular momentum within non-reciprocal systems drives a heat flux. This effect opens up new possibilities for thermal management strategies that leverage the localized control of light's spin angular momentum.

The interaction between the spin momentum of light and heat transport introduces an additional degree of freedom, paving the way for innovative energy conversion devices and advanced thermal management technologies.

---

* Electronic address: pba@institutoptique.fr

[1] M. I. Dyakonov and V. I. Perel, JETP Lett. 13, 467 (1971).
[2] J. E. Hirsch, Phys. Rev. Lett. 83, 1834 (1999).
[3] Y. K. Kato, R. C. Myers, A. C. Gossard, and D. D. Awschalom, Science 306, 1910 (2004).
[4] E. Saitoh, M. Ueda, H. Miyajima and G. Tatara, Appl. Phys. Lett. 88, 182509 (2006).
[5] S. O. Valenzuela and M. Tinkham, Nature (London) 442, 176 (2006).
[6] H. Zhao, E. Loren, H. van Driel and A. Smirl, Phys. Rev. Lett. **96**, 246601 (2006).
[7] L. K. Werake, B. A. Ruzicka, and H.Zhao, Phys. Rev. Lett. **106**, 107205 (2011).
[8] J. Sinova, S.O. Valenzuela, J. Wunderlich, C.H. Back and T. Jungwirth, Rev. Mod. Phys. **87**, 1213 (2015).
[9] P. Ben-Abdallah, Phys. Rev. Lett. **116**, 084301 (2016).
[10] A. Ott, P. Ben-Abdallah, and S.-A. Biehs, Phys. Rev. B **97**, 205414 (2018).
[11] S.-A. Biehs, R. Messina, P. S. Venkataram, A. W. Rodriguez, J. C. Cuevas, and P. Ben-Abdallah, Rev. Mod. Phys. **93**, 025009 (2021).
[12] P. Ben-Abdallah, Inverse Spin Thermal Hall Effect in Non-Reciprocal Photonic Systems, to appear Phys. Rev. Lett. arXiv:2410.15691

Predictive Modeling for Ultrafast Photothermal Effects in Nanophotonic Systems

Alessandro Alabastri[1,2]

[1]Department of Electrical and Computer Engineering, Rice University, USA
[2]Smalley-Curl Institute, Rice University, USA
*corresponding author: alabastri@rice.edu

Abstract: This work summarizes recent advances in computational methods to describe ultrafast photothermal phenomena in nanophotonic systems. We introduce predictive modeling frameworks integrating electronic dynamics and thermal diffusion, enabling optimized design and enhanced performance in applications such as photocatalysis, photothermal cancer therapy, and solar steam generation.

Recent developments in nanophotonics have opened unprecedented opportunities for controlling and utilizing electromagnetic energy at the nanoscale, particularly in systems where plasmonic nanostructures convert light into hot electrons and, eventually, localized heating. Accurate modeling of these ultrafast phenomena is critical for applications ranging from photocatalysis to cancer therapy.

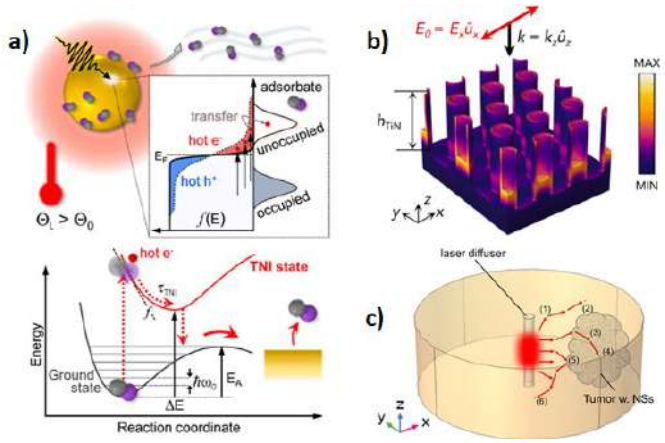


Fig. 1. **a)** Modeling approach for the ultrafast dynamics of plasmonic HCs in the presence of an adsorbate [1]. *Adapted with permission from ACS Nano 2024, 18, 29, 18933–18947. Copyright 2024 American Chemical Society* **b)** TiN metasurfaces as quasi-2D broadband solar absorbers [2]. **c)** Scheme for Nanoparticle Assisted Photothermal Therapy (NAPTT) [3]. *Adapted from Nano Energy, 83, 105828, 2021, Elsevier*

We have developed an original theoretical approach—the Generalized Extended Two-Temperature Model (GE2TM)—to simulate ultrafast energy transfer from plasmonic hot carriers to molecular adsorbates on metallic nanoparticle surfaces [1], Fig. 1a. This approach, accounting for spatial, temporal, and energy resolutions, clarifies how hot electron dynamics and photothermal effects compete during femtosecond-pulsed illumination, leading to nontrivial dependencies on pulse duration, photon energy, and nanostructure geometry. Our framework demonstrates how pulsed illumination conditions can optimize energy transfer efficiency and reaction rates significantly beyond steady-state scenarios.

Upon hot carrier relaxation and electron-phonon scattering, electromagnetic energy is transferred to lattice vibrations as heat. Such heat dissipation in confined dissipative structures can lead to nanoscale heat sources with various applications. For example, we explored the use of ultrathin plasmonic metasurfaces for efficient solar

steam generation [2], Fig. 1b. Our scalable titanium nitride nanocavity arrays achieved over 90% broadband absorption within 250 nm thickness, enabling rapid localized heating and high-performance steam generation. Numerical simulations elucidated the role of quasi-two-dimensional heat dissipation regimes in significantly accelerating evaporation processes, marking a substantial improvement over traditional solar absorbers.

Besides leading to phase changes as in water evaporation, localized heat can also induce other structural changes, such as thermal ablation in live tissues. In this context, we proposed a comprehensive model for nanoparticle-assisted photothermal cancer therapy [3], Fig. 1c. This model combines Monte Carlo-like simulations of photon trajectories, detailed light-to-heat conversion calculations, and bioheat transfer equations that incorporate temperature-dependent tissue properties. By spatially and temporally modulating the laser intensity, we showed that thermal ablation volumes could be increased by 44% while reducing illumination time by 33%, significantly enhancing therapeutic efficiency.

Overall, these computational advances collectively provide robust predictive tools crucial for optimizing nanophotonic designs across diverse photothermal applications, pushing forward our ability to manipulate nanoscale energy transfer processes with precision and efficacy.

References

[1] A. Schirato et al., "Quantifying Ultrafast Energy Transfer from Plasmonic Hot Carriers for Pulsed Photocatalysis on Nanostructures," ACS Nano, 2024.
[2] L. Mascaretti et al., "Solar steam generation on scalable ultrathin thermoplasmonic TiN nanocavity arrays," Nano Energy, 2021.
[3] G.N. Naidu et al., "Routes to Optimizing Photothermal Cancer Therapy through a Comprehensive Theoretical Model," ACS Photonics, 2024.

Terahertz Parametric Detection: High Sensitivity and Applications in Nondestructive Testing

K. Murate[1*], S. Mine[1,2], and K. Kawase[1]

[1] Department of Electronics, Nagoya University, Furocho, Chikusa, Nagoya, 464-8603, Japan
[2]2RIKEN, 519-1399 Aramakiaoba, Aoba, Sendai, 980-0845, Japan
[*]corresponding author: murate@nuee.nagoya-u.ac.jp

Abstract: Terahertz parametric detection offers high sensitivity and, when combined with an injection-seeded terahertz parametric generator, enables measurements with a high dynamic range of 125 dB. We recently found that this technique has a relatively large incident angle tolerance. Here, we evaluate this tolerance and report on its THz scanner application.

Terahertz (THz) parametric detection upconverts THz waves to a near-infrared (NIR) Stokes beam using the inverse process of injection-seeded THz wave parametric generator (is-TPG) [1-4]. This method achieves exceptional detection sensitivity (130 zJ [5]) and dynamic range (125 dB) by combining with is-TPG. It enables various applications, including reagent detection through shields and real-time spectroscopic imaging [1, 6]. This detection process uses THz waves as a seed beam to generate the NIR Stokes beam via upconversion, satisfying a non-collinear phase-matching condition. Typically, THz waves are injected through a Si prism coupler due to the refractive index (nTHz = 5.2) of MgO-doped $LiNbO_3$. However, experiments revealed that detection is possible without an Si prism or strict phase-matching angles, demonstrating large incident angle tolerance. Here we evaluate this tolerance and report on its application in THz scanner measurements.

Firstly, we examined the angular tolerance of THz parametric detection by measuring detection sensitivity at various angles (Fig. 1 (b-e)) and comparing it with 64°(Fig.1 (a)), the non-collinear phase-matching angle. As shown in Fig. 1(f), the input THz wave was generated by is-TPG with a frequency of 1.28 THz. A microchip Nd:YAG laser (wavelength: 1064 nm; pulse width: ~500 ps; output power: 20 mJ after amplification) was used as the pump source, and was split into two beams for is-TPG and THz parametric detection. The THz wave from is-TPG was injected into the $LiNbO_3$ crystal, and the detection Stokes beam was observed with an NIR pyroelectric detector. The input THz wave was attenuated by a calibrated neutral density (ND) filter, and the minimum detectable energy was measured.

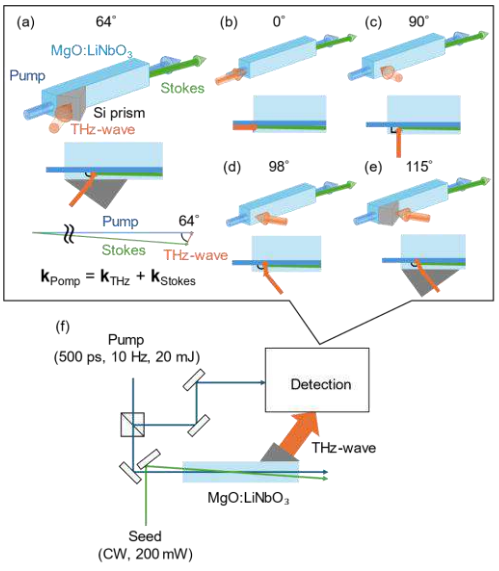


Fig. 1 (a) General THz parametric detection, (b)–(e) the various THz-wave angles of incidence tested: (b) 0°, (c) 90°, (d) 98°, and (e) 115°. (f) Experimental setup overview.

Figure 2 shows the measured minimum detectable energy at each of the angles shown in Fig. 1. THz waves were detected over a very large angular range, from 0° coaxial with the pump beam to 115° in the direction opposite to the pump beam. In the case of conventional is-TPG, the tolerance of the incident angle of the seed beam to the Stokes beam during THz wave generation is as tight as ± 0.03° (FWHM), whereas this condition was significantly relaxed to ±55° (FWHM) in our detection

experiment.

Next, utilizing this large tolerance, we demonstrated a terahertz scanner as shown in Fig. 3. The terahertz wave output from the is-TPG was shaped into a vertically elongated beam using a cylindrical lens and irradiated onto the measurement sample. The transmitted terahertz wave was focused onto a $LiNbO_3$ crystal for parametric detection, transferring the terahertz image onto the detection Stokes beam. By utilizing the large incident angle tolerance, both the terahertz wave and the pump beam were directed onto the same crystal surface. This approach, compared to conventional side-face incidence, enhances the spatial overlap between the pump beam and the terahertz wave, potentially improving image resolution. The detection Stokes beam was then observed using a near-infrared camera to acquire a one-dimensional image of the terahertz wave. The sample was scanned laterally in discrete steps using a translation stage, and the obtained one-dimensional Stokes images were arranged in sequence to reconstruct a two-dimensional image.

The sample, printed with the letters 'T' and 'H' using silver nanoparticle ink, as shown in Fig. 3, was measured at 1.5 THz, and the results are shown in Fig. 4. In both cases, the sample shape was successfully reconstructed, demonstrating the functionality of the scanner.

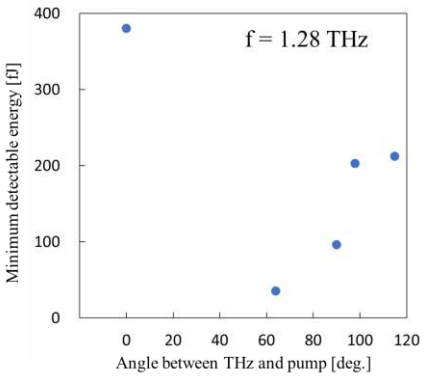


Fig. 2 Minimum detectable sensitivity for each angle of incidence

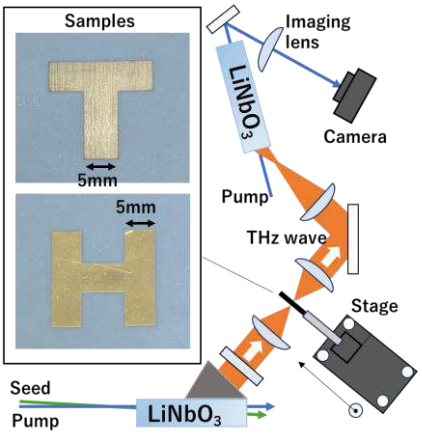


Fig. 3 Setup of THz scanner

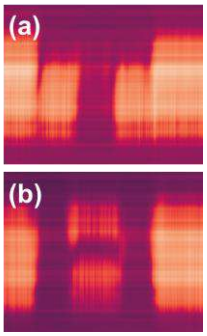


Fig. 4 Imaging result of (a) 'T' and (b) 'H' using THz scanner.

Acknowledgements The authors appreciate the fruitful discussions with Prof. S. Ohno from Tohoku University, and Dr. S. Hayashi from National Institute of Information and Communications Technology. This work was partially supported by Japan Science and Technology Agency (JST) ASPIRE Program (JPMJAP2340) and FOREST Program (JPMJFR212J), and Japan Society for the Promotion of Science KAKENHI (22J20963, 24K00943).

References

[1] K. Murate, S. Mine, and K. Kawase, "Terahertz Parametric Generators and Detectors for Nondestructive Testing Through High-Attenuation Packaging Materials," IEEE J Sel Top Quantum Electron, **29**, 5, pp. 1–13, 2023.
[2] K. Murate, R. Kawaguchi, S. Hayashi, and K. Kawase. "Pulse Burst Multiwavelength Terahertz-Wave Spectroscopic Measurement Using Parametric Wavelength Conversion," IEEE Trans Terahertz Sci Technol, **13**, 5, pp. 561-564, 2023.
[3] S. Mine, K. Kawase, and K. Murate, "Cascaded Terahertz Parametric Generation Under Noncollinear Phase-Matching Condition," J Infrared Milli Terahz Waves, **45**, 1, pp. 116–123, 2024.
[4] S. Mine, N. Yamamoto, K. Kawase, and K. Murate, "Collinear injection-seeded terahertz parametric generator," APL Photonics, **9**, 3, Art. No. 036103, 2024.
[5] H. Sakai, K. Kawase, and K. Murate, "Highly sensitive multi-stage terahertz parametric detector," Opt Lett, **45**, 14, pp. 3905–3908, 2020.
[6] K. Murate, S. Mine, Y. Torii, H. Inoue, and K. Kawase, "Wide dynamic range and real-time reagent identification and imaging using multi-wavelength terahertz parametric generation and machine learning," Sci Rep, **13**, 1, p. 12743, 2023.
[7] R. Guo, S. Ohno, H. Minamide, T. Ikari, and H. Ito, "Highly sensitive coherent detection of terahertz waves at room temperature using a parametric process," Appl Phys Lett, **93**, 2, 2008.

Understanding collective excitations in finite-sized arrays using discrete-dipole approximation

J. Kelavuori[1], A. Panahpour[1], and M. J. Huttunen[1*]

[1]Tampere University, Finland
[*]corresponding author: mikko.huttunen@tuni.fi

Abstract: Full-wave simulations of diffractive resonances can be accurate but slow. Semi-analytical methods based on lattice-sum calculations provide faster alternatives, with recent adaptations revealing that high-Q metasurfaces can be achieved with small arrays in slow-light environments. Furthermore, lattice-wide simulations not resorting to periodic boundary conditions offer valuable insights into lattice's inter-particle dynamics.

Plasmonic–diffractive metasurfaces have emerged as flat-optics alternatives for lasing [1] and nonlinear optics [2]. Strong light–matter interaction emerging from decreased plasmonic losses naturally improve the capabilities of traditional plasmonic devices based on nanoparticles (NPs). The properties of such structures are often computed using full-wave simulations, such as finite-element or finite-difference schemes. However, such simulations can be moderately slow even when monopartite arrays are investigated while using periodic boundary conditions. This makes designing metasurfaces iteratively with such tools cumbersome, also restricting possibilities to study properties of multipartite arrays.

Semi-analytical computational schemes, such as T-matrix method [3], discrete-dipole approximation (DDA) and lattice-sum approach (LSA) [4], offer faster alternatives for calculating optical properties of metasurfaces. As the name suggests, DDA approximates each NP as point-like dipole, coupled through the electric-dipole radiation pattern, while in T-matrix method electric and magnetic multipoles can be readily included. DDA however offers the fastest scheme due to decreased complexity and is adequate for most metasurface designs. The LSA reduces the computational complexity even further by assuming that each particle experiences identical scattered fields over a finite number of unit cells.

Use of periodic boundary conditions in LSA or full-wave simulations makes it impossible to study collective mode formation in metasurfaces at larger-than-unit cell distances. However, such effects could play a strong role in more realistic arrays consisting of finite number of NPs. As an example, we show in Figure **1** how lattice-wide phase dynamics are important even in periodic arrays of identical scatterers. In Figure **1a),** the plasmonic–diffractive resonance shifts by 10 nm when excited with a Hermite-Gaussian TEM_{20} mode as opposed to fundamental Gaussian mode, due to changed inter-particle phase dynamics across the entire 80×80 plasmonic NP array. This dynamics persists even under plane-wave excitation (Figure **1b)**. Interestingly the dynamics may also explain the observed larger-than-unity transmissions [5], at wavelengths close to the resonance. Given light is not collected over the whole array, the optical power from the outer parts can drive the middle parts due to imperfect phase accumulation, resulting in apparent negative extinction. The dipole-moment distributions in the insets illustrate interesting pattern formation.

In most implementations of the semi-analytical methods, homogeneous surroundings of the NPs are assumed, corresponding to NPs coupling through free-space Green's functions. Recently, we constructed the dipole approximation of LSA inside a mirror waveguide [6]. Surprisingly, this modification revealed interesting dynamics in diffractive resonances; namely their Q-factor is proportional to the group index of refraction of the

surroundings in finite systems, as depicted in Figure **1d)**. This discovery suggests that high-Q metasurfaces could be achieved already with small particle counts, given slow-light can be achieved in the surroundings.

We acknowledge the support of the Flagship of Photonics Research and Innovation (PREIN) funded by the Research Council of Finland (grant no. 320165).

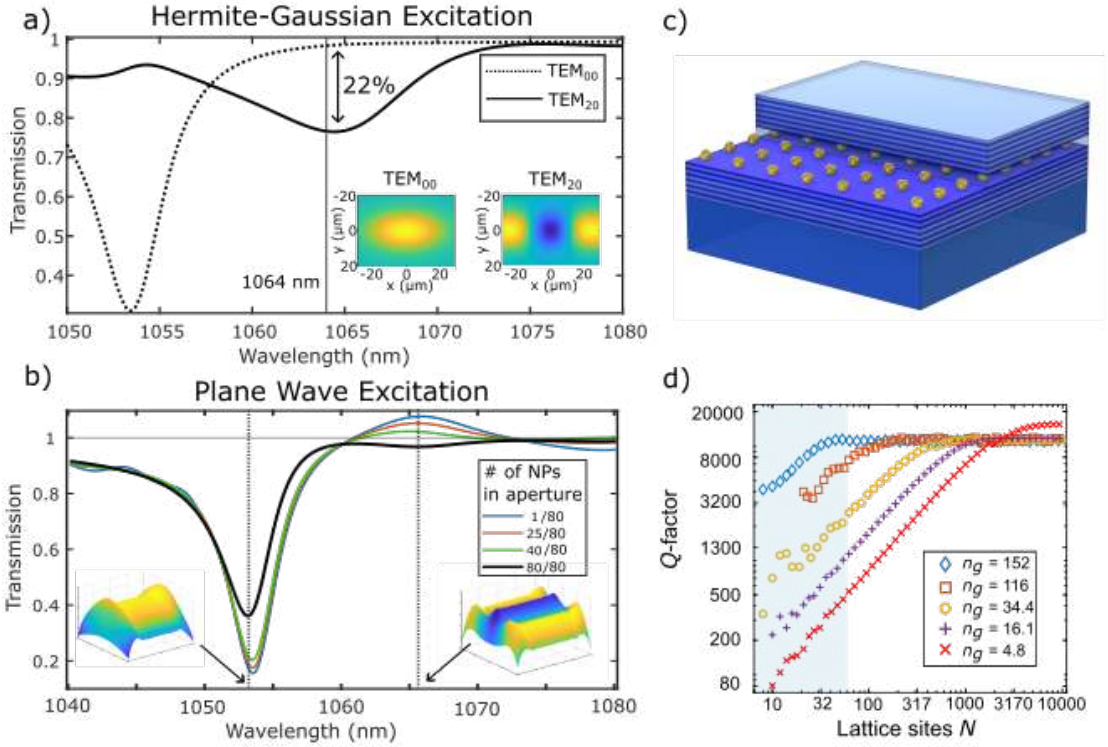


Figure 1 a) Transmission of a plasmonic 80x80 array with different excitation fields (shown in insets). b) Array transmission with plane-wave incidence as a function of collection aperture, demonstrating larger-than-unity transmission. Apertures are centered to the middle of the array. The insets show dipole moments distributions (with a 0.7 red phase difference between yellow and blue colors). c) Schematic of NP array inside mirror waveguide. d) Q-factor dependence on lattice size and the surroundings group refractive index.

References

1. Hakala, T., Rekola, H., *et al.* ”Lasing in dark and bright modes of a finite-sized plasmonic lattice, ” Nat. Commun. Vol. 8, 13687, 2017
2. Stolt, T., Vesala, A., *et al.* ”Multiply-resonant second-harmonic generation using surface lattice resonances in aluminum metasurfaces,” Opt. Express Vol. 30, pp. 3620–3631, 2022
3. Beutel, D., Fernandez-Corbaton, I., and Rockstuhl, C., “treams – a T-matrix-based scattering code for nanophotonics,” Comput. Phys. Commun., Vol. 297, 109076, 2024
4. Huttunen, M. J., Dolgaleva, K., *et al*, “Ultra-strong polarization dependence of surface lattice resonances with out-of-plane plasmon oscillations,” Opt. Express, vol. 24, pp. 28279–28289, 2016
5. Bin-Alam, M.S., Reshef, O., *et al.* “Ultra-high-Q resonances in plasmonic metasurfaces,” Nat Commun, vol. 12, No. 974, 2021.
6. Kelavuori, J., Panahpour, A., and Huttunen, M. J., ” Dispersion-induced Q-factor enhancement in waveguide-coupled surface lattice resonances,” Phys. Rev. B, vol. 110, 195422, 2024

Super-bound States in the Continuum in One-dimensional Gratings on a Substrate

Nan Zhang and Ya Yan Lu*
Department of Mathematics, City University of Hong Kong, Kowloon, Hong Kong
Corresponding author: mayylu@cityu.edu.hk

Abstract: Super-bound states in the continuum (super-BIC) are useful, since they are associated with ultrahigh Q resonances for a wide range of wavevectors. Existing super-BICs are mostly found in periodic structures with up-down mirror symmetry. We show super-BICs in simple gratings on a substrate.

We consider a 1D grating on a substrate with refractive index $n_s = 1.45$, assuming the cladding is air. Each period of the grating consists of two rectangular segments with refractive index $n_1 = 1.45$ and $n_2 = 2.55$, height h_1 and h_2, width w and $L \in w$, respectively, where L is the period. A BIC in such a structure is a guided Bloch mode with frequency ω_* and Bloch wavevector β_* satisfying $\omega_*/c > |\beta_*|$, where c is the speed of light in vacuum. The resonant modes with β near β_* have quality factor $Q \sim 1/|\beta \in \beta_*|^m$, where m typically equals 2. Super-BICs are those with $m \geq 4$ [1,2]. In applications such as lasing, super-BICs are preferred [3].

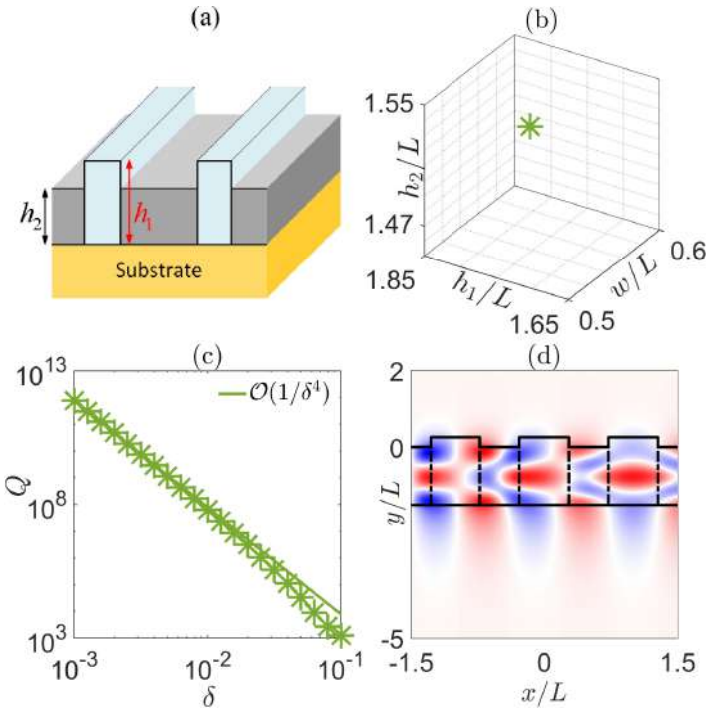


Figure 1: (a) A 1D grating on a substrate; (b) parameter values for an off-Γ super-BIC; (c) Q factor of resonant modes near the super-BIC; (d) electric field distribution of the super-BIC.

As shown in Fig. 1(a), the grating structure with a substrate does not have up-down mir-

ror symmetry. It is easy to find at-Γ BICs (with $\beta_* = 0$) that are protected by the reflection symmetry in the periodic direction. Since the radiation channels above and below the grating are different, it is not easy to find off-Γ BICs (with $\beta_* \neq 0$). It is challenging to find super-BICs (either at-Γ or off-Γ) in structures without the up-down mirror symmetry. We can show that to find an at-Γ super-BIC (actually, there two types with $m = 4$ and 6, respectively), it is necessary to tune two parameters, and to find an off-Γ super-BIC with $m = 4$, it is necessary to tune three parameters. We have developed an efficient numerical method to calculate the super-BIC and the structural parameters together. In Fig. 1(b), we show the values of h_1, h_2 and w to realize an off-Γ super-BIC. Figure 1(c) give a validation that $m = 4$. The electric field distribution of this super-BIC is shown in Fig. 1(d).

The authors acknowledge support from the Research Grants Council of Hong Kong Special Administrative Region, China (Grant No. CityU 11305021).

References

1. Bulgakov, E., G. Shadrina, A. Sadreev, and K. Pichugin, "Super-bound states in the continuum through merging in grating," *Phys. Rev. B*, Vol. 108, 125303, 2023.

2. Zhang, N. and Y. Y. Lu, "Perturbation Theory for Resonant States near a Bound State in the Continuum," *Phys. Rev. Lett.*, Vol. 134, 013803, 2025.

3. Hwang, M.-S., H.-C. Lee, K.-H. Kim, K.-Y. Jeong, S.-H. Kwon, K. Koshelev, Y. Kivshar, and H.-G. Park, "Ultralow-threshold laser using super-bound states in the continuum," *Nat. Commun.*, Vol. 12, 4135, 2021.

Inferring structure from fundamental limits

S. Molesky[1*], P. Chao[2], A. Amaolo[3] and A. W. Rodriguez[3]

[1]Department of Engineering Physics, Polytechnique Montreal,CAN
[2]Department of Mathematics, Massachusetts Institute of Technology, USA
[3]Department of Electrical and Computer Engineering, Princeton University, USA
[*]corresponding author: sean.molesky@polymtl.ca

Abstract: We show that the fields calculated during the computation of limits via Lagrange duality can be used to improve the performance of inverse design.

The recognition that the constraints implied by any set of linear differential equations can be reformulated to restate the optimization problems encountered in photonic inverse design as a quadratically constrained quadratic program (QCQP) and then convexified via Lagrange duality has proven to be a powerful means of determining fundamental performance limits[1]. As soon as the constraints of total real and reactive power conservation are imposed, the subtle interplay between chosen material properties, device size, wave physics, and attainable objective values for basic scattering quantities is captured to a remarkable extent, including the onset of well-known asymptotics such as quasi-statics and geometric optics, and the possibility of creating resonances[2]. More importantly, through the generalization of considering any number of local power conservation constraints, these convexification methods have been found to be remarkably predictive of what is possible for range of technologically relevant electromagnetic processes; limits coming within a factor of ten of topology optimized structures have been found for variety of basic absorption, scattering and field transformation functions as well as more complex objectives like surface-enhanced Raman scattering.

In this presentation, we demonstrate that the fields computed when calculating performance limits via duality can also directly inform structural discovery through inverse design. Focusing on the exemplary problem of local density of states enhancement, we find that topology optimization initialized with structures derived from duality analysis consistently produces performance gains of roughly an order of magnitude, for sufficiently large design domains, relative to current methods. These results strongly suggest presently untapped potential in photonic inverse design, and highlight a number of open question concerning the mathematical structure of electromagnetic inverse design problems and related convexifications.

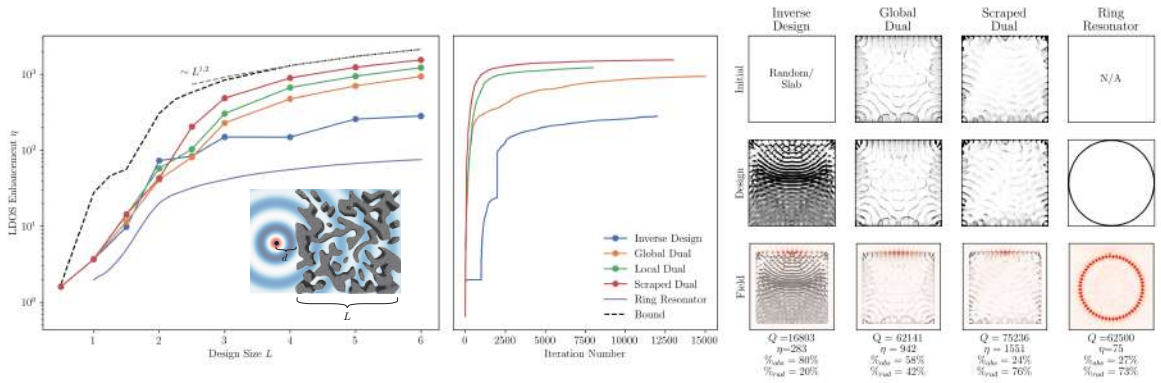


Fig.1: The figure illustrates a comparison between the design method that will be described during this presentation and topology optimization, starting from standard initializations, for the exemplary test problem of enhancing the local density of states (LDOS) outside of a structurable design region, separated by a tenth of a wavelength. Left: LDOS enhancement of for various optimization strategies as a function of the design size L. The solid line indicates the performance of a finetuned ring resonators for reference. Middle: Performance progression as a function of the number of optimization iterations completed for the various initializations. Right: Structures and profiles of the dominant mode field at $L = 6$ for the various design schemes.

Acknowledgments. We acknowledge the support by a Princeton SEAS Innovation Grant and by the Cornell Center for Materials Research (MRSEC). S.M. acknowledges financial support from the Canada First Research Excellence Fund via the Institut de Valorisation des Données (IVADO) collaboration. Simulations were performed on computational resources managed and supported by Princeton Research Computing, a consortium of groups including the Princeton Institute for Computational Science and Engineering (PICSciE) and the Office of Information Technology's High Performance Computing Center and Visualization Laboratory at Princeton University.

References

1. Chao, P., Strekha, B., Kuate Defo, R., Molesky, S. and Rodriguez, A.W., “Physical limits in electromagnetism,” Nat. Rev. Phys, Vol. 4, No. 8, 543-559, 2022.
2. Molesky S, Chao P, and Rodriguez A. W., “Hierarchical mean-field T operator bounds on electromagnetic scattering: Upper bounds on near-field radiative Purcell enhancement,” Phys. Rev. Research, Vol. 2, No. 4, 043398, 2020.

Stokes Solitons and PT-Symmetric Coupled Cavities: Two Paths to Mode-Locking Without Saturable Absorbers

Takasumi Tanabe*, Ryo Otake, Riku Imamura, and Heng Wang

Department of Electronics and Electrical Engineering, Keio University, Japan
*corresponding author: takasumi@elec.keio.ac.jp

Abstract: Through numerical analyses, we demonstrate that robust mode-locking can be achieved without the use of saturable absorbers by either exploiting stimulated Raman scattering in dispersion-engineered microresonators or by operating near exceptional points in PT-symmetric coupled cavities.

Mode-locked lasers play a pivotal role in applications such as ultrafast spectroscopy, precision metrology, and high-speed optical communications. Traditionally, achieving mode-locking relies on incorporating saturable absorbers (SAs) into laser cavities, which provide intensity-dependent losses to generate short pulses. However, integrating SAs into high-Q microresonators [1] can degrade their Qs, motivating alternative approaches that circumvent the need for natural SA materials. Our numerical study explored two promising paths in this direction, both of which leverage the unique optical properties of microresonators to generate pulses without the use of conventional SAs.

One approach exploits stimulated Raman scattering in a dispersion-engineered silica microresonator (inset Fig. 1(a)) [2]. By carefully tailoring the group-velocity dispersion profile, it becomes possible to favor Raman comb generation over four-wave mixing (Fig. 1(a) and 1(b)), thereby producing Stokes solitons in a single device (Fig. 1(c)). In this design, the dispersion near the pump wavelength is set to be normal, while both the Stokes and anti-Stokes wavelength regions are engineered to exhibit anomalous dispersion. This arrangement suppresses conventional parametric effects near the pump while supporting intense Raman gain. Numerical simulations based on the Lugiato-Lefever equation with Raman gain indicate that when the pump is a continuous wave, stimulated Raman scattering dominates, resulting in a broad comb that then transitions to a soliton regime in the Stokes region. The resulting pulse is well-localized in time and exhibits a characteristic envelope in frequency space, confirming stable mode-locking without the need for an additional SA.

In these simulations, the anti-Stokes dispersion proves to be significant: mode-locking is achieved only when the anti-Stokes region also falls within the anomalous dispersion regime, as this ensures phase matching and free spectral range alignment across the different spectral components. Indeed, the free spectral range in the anti-Stokes band must closely match that of the Stokes region for strong pulse formation to occur. This condition is achieved by tailoring wedge angles and layer thicknesses in the disk resonator. By stacking three layers with different wedge angles (inset Fig. 1(b)), the device achieves normal dispersion around the pump wavelength and anomalous dispersion, where solitons are desired.

A second approach demonstrates that a coupled-cavity system with gain and loss (Fig. 1(d)) can induce mode-locking by mimicking an artificial SA effect near a parity-time symmetry breaking point, known as an exceptional point (EP) [3]. This design employs two microcavities: one with high Q and another with lower Q. Light initially couples from the high-Q, gain-bearing cavity into the lossy cavity, where it dissipates to a large extent. Yet, when the circulating light intensity rises due to the Kerr effect in the gain cavity, the refractive index shift modifies the resonance frequencies, causing an instantaneous decoupling of the two cavities and, thus, temporarily reducing the net loss. The net effect is analogous to SA: at high intensities, the system's loss

effectively drops, allowing stronger pulses to form and reinforcing mode locking.

Central to this mechanism is the system's proximity to an EP, where small changes in refractive index cause drastic shifts in the complex eigenfrequencies of the coupled resonators (Fig. 1(e)). Simulations based on coupled nonlinear Schrödinger equations reveal that, when tuned near the EP, even modest changes in refractive index yield significant modulation of the system's Q. This capability translates directly to more effective pulse shaping. Numerical results indicate that a stable single-pulse mode-locked state is achieved, resulting in a nearly transform-limited pulse (inset Fig. 1(e)). Importantly, parameter scans indicate that mode-locking is most likely to occur when the initial coupling Q places the system just below the EP.

Comparing the two methods underscores the growing trend of replacing natural SAs with inherent physical effects in high-Q microresonators. Stimulated Raman scattering in engineered dispersion regimes and PT-symmetric coupling near EP both offer effective, power-efficient ways to generate ultrashort pulses. These concepts not only simplify the design and fabrication of integrated mode-locked lasers but also open up new degrees of freedom, such as external control of coupling strength, precise dispersion engineering, or platform materials, all of which can significantly enhance performance. While further exploration of device physics and more sophisticated experimental validations will be needed to confirm the scalability of these designs, the early results are promising. They reveal pathways to achieve mode-locked pulses with minimal physical overhead, high repetition rates, and potentially wide optical bandwidth. Ultimately, these breakthroughs may spur new advances in integrated photonics, ultrafast science, and next-generation optical communication systems.

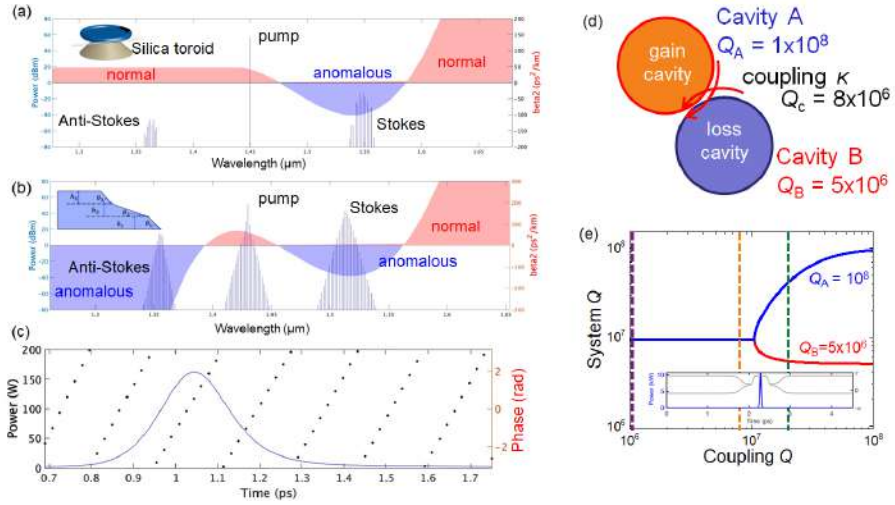


Fig. 1. (a) Raman comb generation with normal dispersion in the anti-Stokes regime, exhibiting no mode locking. Inset: Schematic of the silica toroid cavity under investigation. (b) Raman comb generation with anomalous dispersion in the anti-Stokes regime, enabling mode-locking in the Stokes band. Inset: cross-section of a cavity featuring the tailored dispersion profile. (c) Mode-locked Stokes pulse corresponding to (b). (d) Coupled-cavity system with high- and low-Q resonators. (e) Imaginary part of the complex eigenvalue versus the coupling Q, revealing an exceptional point (EP) where strong Q modulation occurs. Inset: numerically obtained mode-locked pulse.

References

1. T. Kumagai, *et al.*, J. Appl. Phys. **123**, 233104 (2018).
2. R. Otake, *et al.*, *Nonlinear Photonics (NP2024)*, JTu1A.40, Quebec, Jul. 28-Aug. 1 (2024).
3. R. Imamura, *et al.*, Opt. Express, **32**, 22280 (2024).

This work was supported by MEXT Q-LEAP (JPMXS0118067246).

19th International Congress on Artificial Materials for Novel Wave Phenomena – Metamaterials 2025
Amsterdam, The Netherlands, Sep. 1st –6th, 2025

Quantum Effects in Nanophotonic Light–Matter Interactions

P. André D. Gonçalves [1]

[1] POLIMA – Center for Polariton-driven Light–Matter Interactions, University of Southern Denmark, Campusvej 55, DK-5230 Odense M, Denmark
padgo@mci.sdu.dk

Abstract **– Advances in fabrication and spectromicroscopy techniques have enabled unprecedented access to quantum mechanical effects underlying various nanophotonic phenomena, challenging their description solely within classical electrodynamics. Here, I will present a suite of quantum-informed theoretical frameworks for accurately describing light–matter interactions in nanophotonics and discuss how these approaches provide new insights and unlock new capabilities. Topics will include quantum corrections to plasmon spectra and plasmon-enhanced light–matter interactions, as well as the exploration of quantum effects governing electron–light–matter interactions in various electron-beam-based spectroscopies of current interest.**

Advances in topology optimization for nanophotonics

Antonio Calà Lesina[1,2,3]
[1]Hannover Centre for Optical Technologies, Leibniz University Hannover, 30167 Hannover, Germany
[2]Cluster of Excellence PhoenixD, Leibniz University Hannover, 30167 Hannover, Germany
[3]Institute for Transport and Automation Technology, Leibniz University Hannover, 30823 Garbsen, Germany
antonio.calalesina@hot.uni-hannover.de

Abstract: Inverse design methods based on topology optimization can uncover nanophotonic structures in 3D with free-form shapes beyond human intuition, and optical functionalities not obtainable with conventional design methods. This talk highlights the recent achievements of my team in topology optimization for nanophotonics and integrated optics.

Advances in computing capabilities and inverse design methods have recently enabled the discovery and engineering of novel and unconventional nanophotonic devices. By exploring large design spaces one can find new conceptual free-form designs that provide a solution to complex optimization problems, thus unlocking advanced optical functionalities. Gradient-based topology optimization is a robust inverse design technique that allows us to explore large design spaces in a computationally efficient manner. This is due to efficient techniques for the calculation of the gradient, such as the adjoint method. This talk focuses on the recent achievements of my research group in computational nanophotonics and inverse design via topology optimization, which include:

- the inverse design of nanostructures made of arbitrary dispersive optical materials thanks to a formulation of the adjoint method in the time domain [1],
- the optimization of metallic and dielectric nanostructures and metasurfaces to achieve broadband absorption [2, 3],
- anapole effects in plasmonic meta-atoms that can be exploited as building blocks for transparent metasurfaces and metamaterials [4],
- integrated beam splitters designed via topology optimization to achieve arbitrary phases at the output ports [5], and
- the topology optimization of nanostructures where the aim is to achieve a desired multipolar response in order to engineer the nanoantenna's scattering properties [6].

This work was supported by the Deutsche Forschungsgemeinschaft (DFG, German Research Foundation) under Germany's Excellence Strategy within the Cluster of Excellence PhoenixD (EXC 2122, Project ID 390833453), and the Research Grants CA 2763/2-1 (Project ID 527470210) and CA 2763/6-1 (Project ID 544158178). The computing time was granted by the Resource Allocation Board and provided on the supercomputer Lise and Emmy/Grete at NHR@ZIB and NHR@Göttingen as part of the NHR infrastructure (project nip00059).

References

1. Gedeon, J., E. Hassan, and A. Calà Lesina, "Time-Domain Topology Optimization of Arbitrary Dispersive Materials for Broadband 3D Nanophotonics Inverse Design," *ACS Photonics*, Vol. 10, No. 11, pp. 3875–3887, 2023.

2. Gedeon, J., I. Allayarov, A. Calà Lesina, and E. Hassan, "Time-domain topology optimization of power dissipation in dispersive dielectric and plasmonic nanostructures," *IEEE Trans Antennas Propag*, 2025.

3. Gedeon, J., I, Allayarov, E. Hassan, and A.Calà Lesina, "Topology optimization of a super-absorbing thin-film semiconductor metasurface," arXiv:2502.19352, 2025.

4. Hassan, E., A. B. Evlyukhin, and A. Calà Lesina, "Anapole Plasmonic Meta-Atoms for Nearly Transparent Metamaterials," *Laser Photon Rev*, Vol. 19, No. 5, 2400118, 2025.

5. Nanda, A., M. Kues, and A. Calà Lesina, "Exploring the fundamental limits of integrated beam splitters with arbitrary phase via topology optimization," *Opt Lett*, Vol. 49, No. 5, pp. 1125–1128, 2024.

6. Bahmani, S., A. Evlyukhin, E. Hassan, and A. Calà Lesina, "Inverse design of nanophotonic meta-atoms with desired multipoles," Proc. SPIE 12991, Nanophotonics X, 129911Q, 2024.

Graphene-based optoelectronics: simulations and design

S. Doukas[1], I. Katsantonis[2,3], E. Lidorikis[4], A. C. Tasolamprou[1]

[1] Department of Physics, National and Kapodistrian University of Athens, Athens 15784, Greece
[2]Institute of Electronic Structure and Laser, Foundation of Research and Technology Hellas, 71110, Heraklion, Greece
[3] University of Crete, Department of Material Science and Engineering, 71003, Heraklion, Greece
[4]Department of Materials Science and Engineering, University of Ioannina, Ioannina 45110, Greece
[*]corresponding author: atasolam@phys.uoa.gr

Abstract: We present a self-consistent multiphysics simulation framework for modeling the optoelectronic response of graphene-based devices in THz. The model accounts its thermodynamic response, offering valuable insights into the ultrafast processes that define graphene's behavior under strong THz fields. Two examples of ultrafast and nonlinear modulators are discussed.

Graphene’s unique optical and electronic properties—such as its remarkably high carrier mobility, broad-spectrum optical absorption, and strong nonlinear optical response—make it an exceptional material for ultrafast and tunable photonics [1-3]. Its ability to integrate seamlessly into plasmonic and dielectric structures allows for highly efficient light-matter interactions and significant enhancements in field confinement. Nonlinear effects, particularly in the THz regime, are significantly amplified through electrostatic gating and interactions with intense THz pulses, which induce substantial changes in graphene’s conductivity via carrier heating. This carrier heating leads to changes in the material’s electronic properties, which in turn modify its optical response. Furthermore, embedding graphene in metamaterials, especially topological photonic crystals, results in an even greater enhancement of harmonic generation. This is achieved by exploiting the engineered interface states within these structures, which facilitate even stronger localized field enhancement. The unique combination of these features creates a powerful synergy that promises not only to drive forward the development of advanced, efficient nonlinear optical devices for next-generation photonic systems, ranging from communication technologies to quantum information processing.

We present a self-consistent multiphysics simulation framework that models graphene’s nonlinear response under strong THz illumination, providing a comprehensive approach that aligns well with experimental observations. This framework offers critical insights into graphene’s carrier dynamics and enables predictive device engineering, making it a versatile tool for designing advanced graphene-based optoelectronic components. The study investigates self-action and third-harmonic generation, utilizing a well-established simulation framework [4,5] to model graphene’s response under THz illumination. Coupled opto-thermal calculations enable us to extract photo-induced carrier heating, track the redistribution of carriers, and assess the impact of these processes on both linear and nonlinear conductivity of graphene. By integrating these computational methods, we aim to provide deeper insights into the fundamental mechanisms driving THz-induced nonlinear effects in graphene-based topological photonic structures.

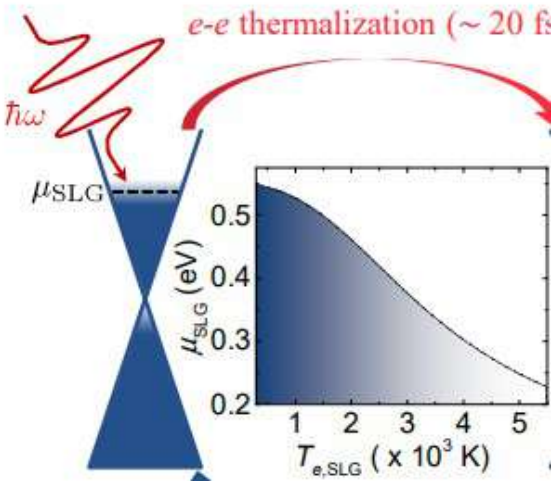


Figure 1: Charge carrier distribution evolution in graphene under THz excitation. Energy absorption raises carrier temperature, redistributing charge carriers. Middle graph: decrease in chemical potential as temperature increases.

To validate our framework, we apply it to a practical graphene-based optoelectronic device: a Salisbury screen configuration with a ionic liquid layer between monolayer graphene and a grounded gold backplate. Our results, compared with experimental data, confirm the accuracy of our approach [1]. At low field strengths, the device exhibits near-perfect absorption at 2.3 THz due to destructive interference effects. As the THz field strength increases, graphene's conductivity is significantly modulated by carrier heating, leading to a rapid shift in the absorption spectrum. Additionally, we investigate graphene ribbons placed within a photonic crystal topological cavity. By leveraging the coupling between topological surface states and plasmonic resonances in graphene ribbons, we design novel configurations to efficiently extract third-harmonic waves. This approach combines advanced modeling tools with material assumptions, enabling the development of a robust framework that supports both forward (transmission) and backward (reflection) propagation of the generated waves. The synergy between these factors enhances the system's efficiency and versatility, opening up applications in nonlinear optics and photonics. Notably, since no back reflector is required, the device operates effectively in both transmission and reflection modes.

Acknowledgment

This work was supported by the Hellenic Foundation for Research and Innovation (H.F.R.I.) under the "Basic Research Financing", National Recovery and Resilience Plan (Greece 2.0), (Project Number:14830, PhoToCon).

References

1. A. D. Koulouklidis et al., "Ultrafast Terahertz Self-Induced Absorption and Phase Modulation on a Graphene-Based Thin Film Absorber," *ACS Photonics*, vol. 9, no. 9, pp. 3075–3082, Sep. 2022.
2. H. A. Hafez, S. Kovalev, K. Tielrooij, M. Bonn, M. Gensch, and D. Turchinovich, "Terahertz Nonlinear Optics of Graphene: From Saturable Absorption to High-Harmonics Generation," *Adv. Optical Mater.*, vol. 8, no. 3, p. 1900771, Feb. 2020.
3. A. C. Tasolamprou et al., "Experimental Demonstration of Ultrafast THz Modulation in a Graphene-Based Thin Film Absorber through Negative Photoinduced Conductivity," *ACS Photonics*, vol. 6, no. 3, pp. 720–727, Mar. 2019.
4. S. Doukas, P. Mensz, N. Myoung, A. C. Ferrari, I. Goykhman, and E. Lidorikis, "Thermionic graphene/silicon Schottky infrared photodetectors," *Phys. Rev. B*, vol. 105, no. 11, p. 115417, Mar. 2022.
5. S. Doukas, A. D. Koulouklidis, S. Tzortzakis, M. Kafesaki, E. Lidorikis, and A. C. Tasolamprou, "A self-consistent simulation framework for modelling graphene-based optoelectronics in the THz regime," in *2024 Eighteenth International Congress on Artificial Materials for Novel Wave Phenomena (Metamaterials)*, Chania, Greece: IEEE, Sep. 2024, pp. 1–3.

Focusing of heat flux radiated by magneto-optical nanoemitters in the presence of a magnetic-field

L. Rihouey[1], P. Ben-Abdallah[1], and R. Messina[1*]
[1]Laboratoire Charles Fabry, UMR 8501, Institut d'Optique, CNRS
Université Paris-Saclay, 2 Avenue Augustin Fresnel, 91127 Palaiseau Cedex, France
Corresponding author: riccardo.messina@institutoptique.fr

Abstract: We describe the near-field heat flux radiated by magneto-optical nanoemitters close to a substrate in the presence of a magnetic field. We demonstrate that this can induce an amplification of the flux and a focusing of the Poynting field at the substrate interface, opening promising perspectives for heat-assisted magnetic-recording technology.

The development of fluctuational electrodynamics and the discovery that radiative heat flux can be strongly amplified in the near field have paved the way to several applications including heat-assisted magnetic recording (HAMR) [1, 2]. In HAMR, a small surface area of a magnetic material is heated to raise its temperature close to the Curie temperature, where its magnetic coercivity is weak. Then by applying a magnetic field a new magnetic state can be recorded inside the material. While the hot spot area should be minimized to approach the superparamagnetic limit, radiative heat focusing by a conventional scanning probe microscope is constrained by the emission pattern of its tip in the near-field regime. In a recent work [3] a theory describing heat flux radiated in the near-field regime by several interacting nanoemitters has been introduced, demonstrating that the thermal energy can be focused and amplified into smaller spots than single emitters.

We extend this study to magneto-optical many-body systems [4] whose optical properties can be manipulated by applying a magnetic field. Our system consists of N spherical having equal radius r, placed in vacuum and in proximity of a substrate. Following the approach of [5], we derive the Poynting vector at any position. This formalism is then applied to the scenario of a single emitter made of InSb (a magneto-optical material recently studied in the context of near-field radiative heat transfer [6]) close to a substrate made of SiC.

We study the maximum of the Poynting vector below the nanoemitter and its Full Width Half Maximum (FWHM) as a function of the applied magnetic field B for different radii r of the nanoparticle. The results, shown in Fig. 1(a,b), highlight a non-monotonic behavior, according to which the maximum Poynting vector (FWHM) first increases (decreases) as a function of B, then decreases (increases), by reaching values even below (above) the reference one for $B = 0$ [7]. This highlights an ideal scenario as a function of B, since it shows the existence of an optimal magnetic field for which not only is the local heat flux quantitatively increased, but it is also more focused on the surface of the substrate.

We performed a detailed spectral investigation of the effect. We first analyze the spectrum of the Poynting vector below the nanoparticle, shown in Fig. 1(c,d). For $B = 0$ we remark two resonances, one at higher frequencies corresponding to SiC, one at lower frequency stemming from the InSb nanoparticle. It is known that the presence of a magnetic field induces the appearance of two further InSb resonances. The effect is manifest in Fig. 1(c), where we remark the existence of an optimal field for which one of this resonances matches the one of SiC, thus leading to a strong amplification.

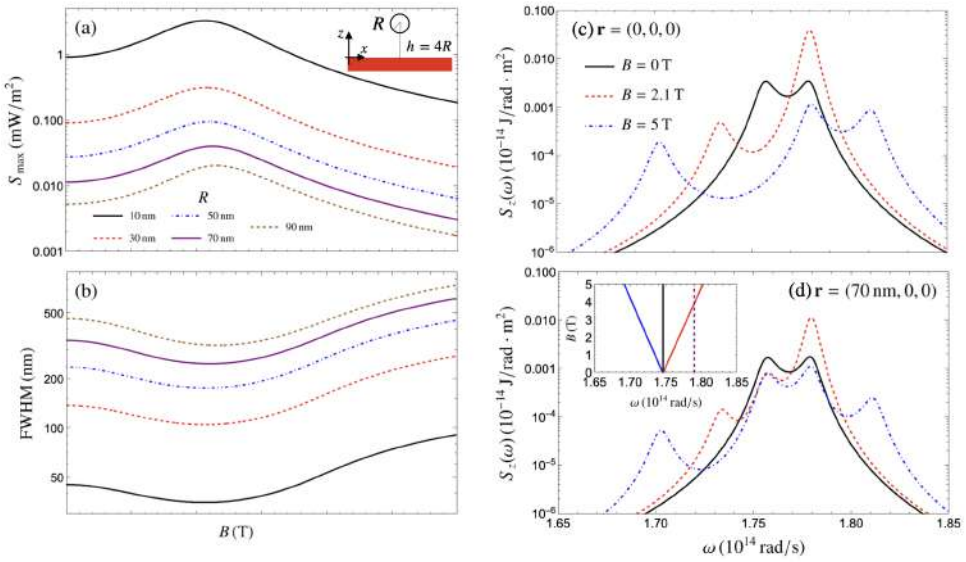


Figure 1: (a) Poynting vector $S_{\max}$ below the nanoparticle, placed at $(0, 0, 4r)$, and (b) FWHM as a function of the applied magnetic field B for different radii (see legend). (c-d) Spectral decomposition of the z component of the Poynting vector at (c) the origin and (d) at $(70\,\text{nm}, 0, 0)$, for different values of the applied magnetic field (see legend). The inset of (d) shows the three resonances of InSb, the vertical dashed purple line the resonance frequency of SiC.

To explain the reduction of FWHM, we present [Fig. 1(d)] the spectral analysis at a different coordinate, corresponding to half the FWHM at $B = 0$. We observe that the enhancement at the peak frequency (the resonance of SiC) is less pronounced. This can be attributed to the fact that the almost monochromatic nature of the heat flux is a purely near-field effect: it strongly depends on the distance and is more pronounced right below the nanoparticle. Although the heat flux is amplified on the entire surface, the distance-dependent amplification is stronger right below the nanoparticle and is at the origin of the desired reduction of FWHM.

References

1. Challener, W. A. et al., "Heat-assisted magnetic recording by a near-field transducer with efficient optical energy transfer", *Nat. Photonics*, Vol. 3, p. 220 (2009).

2. Stipe, B. C. et al., "Magnetic recording at 1.5 Pb m^{-2} using an integrated plasmonic antenna", *Nature Photonics*, Vol. 4, p. 484 (2010).

3. Ben-Abdallah, P. "Multitip Near-Field Scanning Thermal Microscopy", *Phys. Rev. Lett.*, Vol. 123, p. 264301 (2019).

4. Biehs, S.-A. et al., "Near-field radiative heat transfer in many-body systems", *Rev. Mod. Phys.*, Vol. 93, p. 025009 (2021).

5. Messina, R. et al., "Fluctuation-electrodynamic theory and dynamics of heat transfer in systems of multiple dipoles", *Phys. Rev. B*, Vol. 88, p. 104307 (2013).

6. Ben-Abdallah P. "Photon Thermal Hall Effect", *Phys. Rev. Lett.*, Vol. 116, p. 084301, (2016).

7. Rihouey, L. and P. Ben-Abdallah and R. Messina, "Deep sub-wavelength scale focusing of heat flux radiated by magneto-optical nanoemitters in the presence of an external magnetic-field", *J. Quant. Spectrosc. Radiat. Transfer*, Vol. 333, 109322 (2025).

Bounds as blueprints: towards optimal and accelerated photonic inverse design

Pengning Chao[1], Alessio Amaolo[2], Sean Molesky[3], and Alejandro W. Rodriguez[4*]

[1]Department of Mathematics, Massachusetts Institute of Technology, Cambridge, MA, USA
[2]Department of Chemistry, Princeton University, Princeton, NJ, USA
[3]Department of Engineering Physics, Polytechnique Montreal, Montreal, Quebec, Canada
[4]Department of Electrical and Computer Engineering, Princeton University, Princeton, NJ, USA
[*]corresponding author: arod@princeton.edu

Abstract: In pursuit of optimal photonic designs, substantial progress has been made on two complementary fronts: bottom-up structural optimizations (inverse design) discover complex high-performing structures but offer no guarantees of optimality, while top-down field optimizations (convex relaxations) reveal fundamental performance limits but offer no guarantees that structures meeting these limits exist. We bridge the gap between these two parallel paradigms by presenting a ``verlan" method that exploits local and global wave information encoded in performance bounds to guide inverse design towards better-performing structures. Structures informed by limits outperform standard (random) inverse-design initializations by close to an order of magnitude and approach fundamental performance limits within a factor of two, highlighting the possibility of accessing significant untapped performance improvements.

The design of optical components has relied for many decades on a small number of well-understood physical mechanisms for light control, e.g. index guiding, photonic bandgaps, and material resonances. However, with growing freedom for structuring materials down to the nanoscale and increasing demands on device functionality and complexity, this paradigm is currently being partially supplanted by computational inverse design: structural optimization over an enormous number of parameterizing degrees of freedom [1-2]. The high-dimensional and nonconvex nature of the inverse design problem often leads to uncertainty (Fig. 1, center): adjoint gradient-based algorithms are generally necessary for navigating the high-dimensional design space, and if an optimization fails to achieve a desired level of performance, it may be that either the algorithm is "stuck" in a sub-par local optimum, or that the desired performance is physically impossible to achieve. To address this uncertainty, recent progress has been made on elucidating fundamental limits to photonic performance which no structure may exceed (e.g. duality limits shown in Fig. 1, top right) [3]. The key to such performance bounds rests on a reformulation of the structural design problem to an optimization over fields (instead of geometry) subject to power conservation constraints that are quadratic functions of the fields (Fig. 1, top left).

When there is a significant performance gap between bounds and existing designs, the situation is intriguing: are the limits loose, signifying a large duality gap, or are there as-yet undiscovered superior designs? The wave nature of light allows for complicated interference patterns that create many local structural optima (Fig. 1, center). Moreover, photonic devices often rely on physical effects that are highly sensitive to small structural perturbations (e.g., high-quality resonances, multipole cancellation, localized fields), making structural optimization numerically ill-conditioned. Photonic inverse design with adjoint gradients is thus strongly contingent on the starting point, and given the high dimensional design space, it is impossible to exhaustively sample different initializations. We report a novel method that exploits Lagrangian dual limits to extract structure templates for guiding and accelerating inverse design [4]. To differentiate from existing initialization methods based primarily on random sampling and to emphasize the role of duality, we refer to our new approach as "verlan" design. We apply verlan extraction in conjunction with topology optimization to discover 2D structures

that maximize the Purcell enhancement of nearby out-of-plane point sources, an ill-conditioned and challenging structural optimization problem. Verlan inverse designs achieve over one thousand-fold Purcell enhancement despite the choice of a low-index and lossy medium, outperforming random initializations by nearly an order of magnitude and approaching performance limits to within a factor of two. Our results represent a significant step towards a practical general-purpose framework for integrating performance limits and inverse design.

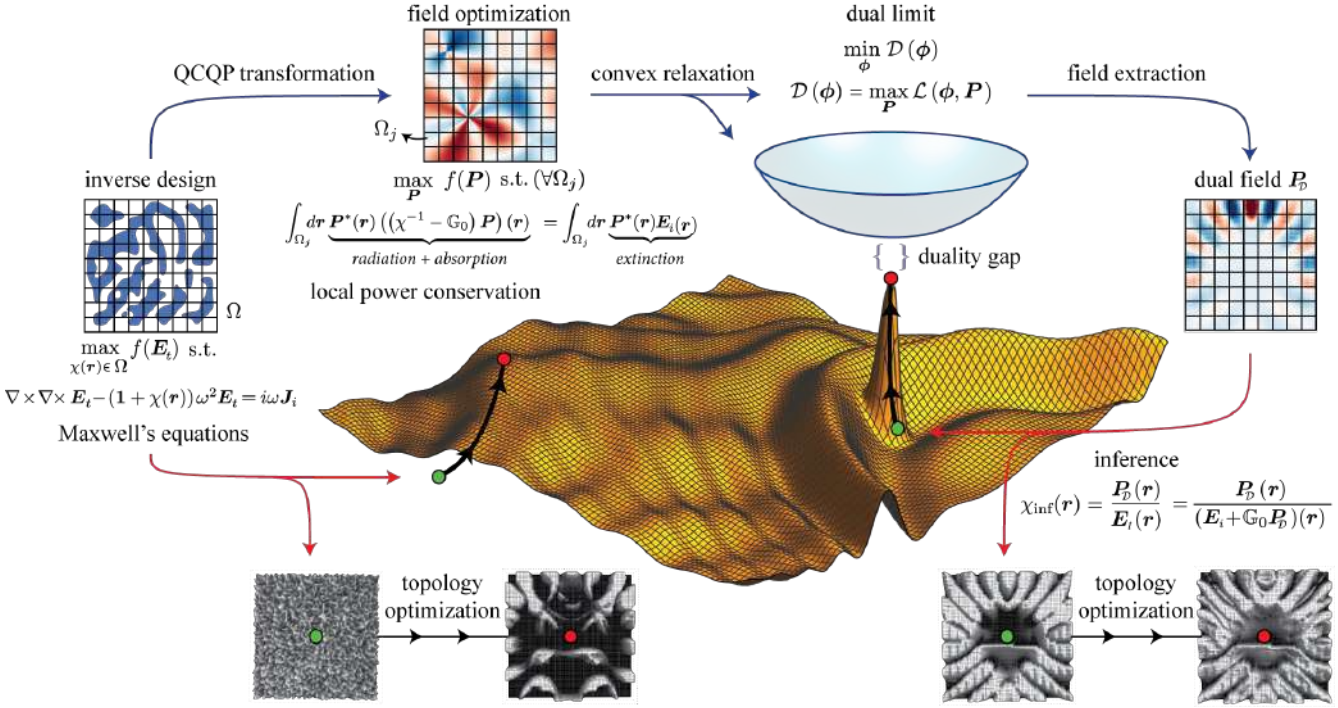


Figure 1: Schematic of verlan design methodology. The optimization landscape of photonic design—illustrated as a surface—is often very complicated, exhibiting ill-conditioning and many local optima which can trap gradient-based (adjoint) algorithms. Limits to device performance can be evaluated by transforming the inverse design problem into a quadratically constrained quadratic field optimization program (QCQP) that is then relaxed (e.g. Lagrange duality) to obtain limits on achievable performance. In contrast to structural optimization, the dual program (minimization over Lagrange multipliers) is convex, with a unique global optimum corresponding to the tightest bound. The "polarization" associated with the dual optimum encodes global characteristics of optimal fields. Retracing these set of transformations illustrates the major steps involved in our verlan method: the original inverse design problem is converted into a QCQP over the polarization field, which is then convexified via Lagrange duality to produce a dual polarization field. A material profile is then inferred from the dual fields and used to initialize local optimization (e.g. topology optimization).

References

1. J. S. Jensen and O. Sigmund, Topology optimization for nano-photonics, Laser & Photonics Reviews 5, 308 (2011)
2. S. Molesky, Z. Lin, A. Y. Piggott, W. Jin, J. Vuˇckovi´c, and A. W. Rodriguez, Inverse design in nanophotonics, Nature Photonics 12, 659 (2018).
3. P. Chao, B. Strekha, R. Kuate Defo, S. Molesky, and A. W. Rodriguez, Physical limits in electromagnetism, Nature Reviews Physics 4, 543 (2022)
4. P. Chao, Alessio Amaolo, S. Molesky and A. W. Rodriguez, Bounds as blueprints: towards optimal and accelerated photonic inverse design, ArXiv:2504.10469 (2025)

Nonlinear-nonlocal flat optics for space-time image processing

C. De Angelis[1,2,*]

[1]CNIT and Department of Information Engineering, University of Brescia, via Branze 38, Brescia, 25123, Italy.
[2]Istituto Nazionale di Ottica, Consiglio Nazionale delle Ricerche, via Branze 45, Brescia, 25123, Italy
[*]Corresponding author: costantino.deangelis@unibs.it

Abstract: Digital signal processing has revolutionized many fields of science and engineering, but it still shows critical limits; a long-sought solution is optical analog computing. We demonstrate here that nonlinear phenomena combined with engineered nonlocality in flat optics can be leveraged to synthesize Volterra kernels able to outperform linear devices.

In this work, I will present our recent findings on the use of nonlocality and nonlinearity for image processing in space and time. Flat-optics devices exhibiting a linear local (LL) response are defined by a position-dependent linear transfer function $T_{LL}(\mathbf{r})$, which can be locally tailored by engineering metaatoms arranged within metasurfaces. An input signal, defined in real space as $I_\omega(\mathbf{r})$, is filtered linearly and locally, and transformed into an output $O_\omega(\mathbf{r})=T_{LL}(\mathbf{r})I_\omega(\mathbf{r})$. Wavefront engineering is arguably the most prominent application for LL systems [1]. Spatial dispersion, i.e., nonlocality, is usually regarded as a nonideality in LL flat-optics devices. However, the nonlocal response of metasurfaces has been recently indicated as an effective means to achieve advanced functionalities based on the independent control of spectral and angular selectivity [2].

To date, investigations into nonlocality have primarily focused on the linear-optics regime. The action of linear nonlocal (LN) systems is well described by a k-dependent transfer function $T_{NL}(\mathbf{k})$, which describes how the metasurface filters the angular spectrum of an input function, according to $O_\omega(\mathbf{k})=T_{NL}(\mathbf{k})I_\omega(\mathbf{k})$. Nonlocal metasurfaces are well suited for analog computing and image processing. For example, n-th order differentiation is easily achieved with transfer functions of type (jk)n, while integration is obtained by synthesizing transfer functions of the type (jk)1/n [3].

Despite the advantages, linear approaches — both local and nonlocal — face limitations related to the restricted numerical aperture and frequency bandwidth, and the inherent linearity of the mathematical operations that one can engineer. Here I show that the combination of nonlinear and nonlocal effects in the same flat-optics device is a powerful strategy to achieve advanced image processing and analog computing functionalities with reduced structural complexity and increased efficiencies in terms of angular and frequency bandwidth [4, 5].

The concept of image processing with nonlinear flat optics is illustrated in figure 1. The input image is a pump field (ω_0 in figure 1) with its polarization and space-time structure which impinges on a nonlinear nonlocal thin film. The space-time dependent structure of the generated second harmonic ($2\omega_0$ in figure 1) is used to extract key features of the input image. By exploring the simple scenario of a uniform thin film, we demonstrate edge detection in space and in time. In our proposed nonlinear flat-optics solution, the non-resonant nature of the nonlinear interaction allows edge detection over a broadband spectrum with ultra–high contrast.

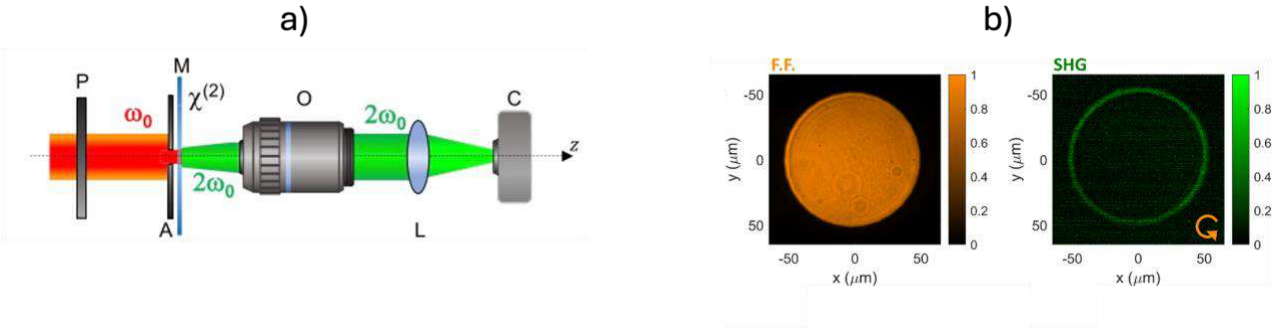


Figure 1. a): Setup for image processing with a nonlinear flat-optics element. P (polarizer); A (aperture); M (flat-optics element/metasurface); O (objective); L (lens); C (camera). b): example of edge detection on a circular aperture.

Our results indicate that Volterra kernels of nonlinear nonlocal flat optics can open new opportunities in applications such as image processing, item recognition for computer vision, high-contrast and high-resolution microscopy, implementation of nonlinear functions for analog deep learning.

References

1. Hail, C.U., Foley, M., Sokhoyan, R. et al., “High quality factor metasurfaces for two-dimensional wavefront manipulation” Nat Commun 14, 8476 (2023).
2. Overvig, A. and Alù, A., “Diffractive nonlocal metasurfaces,” Laser Photonics Rev. 16, 2100633 (2022).
3. Kwon, H., Sounas, D., Cordaro, A., Polman, A. and Alù, A. “Nonlocal Metasurfaces for Optical Signal Processing,” Phys. Rev. Lett., 121, 173004 (2018).
4. de Ceglia, D., Alù, A., Neshev, D. N. and De Angelis, C., “Analog image processing with nonlinear nonlocal flat optics,” Opt. Mater. Express 14, 92 (2024).
5. Arregui Leon, U., Franceschini, P., Sergaeva, O., Tognazzi, A., Rocco, D., Carletti, L., de Ceglia, D., Della Valle, G., and De Angelis, C., "Event detection via THz generation with flat nonlinear optics [Invited]," Opt. Mater. Express 15, 307-318 (2025).

Deep learning based inverse design approach for infrared phonon-polariton microstructures: a SiC-array toy model

E. Cannavò[1,*], O. K. C. Jackson[2], D. Baiocco[1], E. Bozdogan[1], S. De Liberato[2,3], and A. Tredicucci[1]

[1]Dipartimento di Fisica "E. Fermi", Università di Pisa, Largo Pontecorvo 3, Pisa, Italy
[2]School of Physics and Astronomy, University of Southampton, Southampton, SO17 1BJ, United Kingdom
[3]Istituto di Fotonica e Nanotecnologie – Consiglio Nazionale delle Ricerche (CNR), Piazza Leonardo da Vinci 32, Milano, Italy

[*]Corresponding author: emmanuele.cannavo@phd.unipi.it

Abstract: We present a one-shot deep learning approach to the inverse design of microstructures whose absorption spectra are tuned to allow the selective detection of a specific chemical species. We test the approach in a periodic array of silicon carbide surface phonon polariton microresonators.

In the last decade, Deep Learning (DL) approaches have become increasingly popular for solving a numerous technological and scientific problems. More specifically, DL has recently started competing with global optimization algorithms and adjoint methods as the tool of choice for inverse design in the field of nanophotonics, showing noteworthy achievements when working on systems such as photonic crystals, nano-scatterers, gratings, Bragg mirrors, etc. While data generation and training of the DL model might require significant computational effort, high evaluation speed, differentiability, and the possibility of obtaining latent representations of complex data can give DL an edge over more conventional inverse design methodologies[1,2].

The usage of Surface Phonon Polaritons (SPhPs) in nanophotonics has demonstrated great promise for sub-wavelength light confinement in polar dielectrics[3]. The significant reduction of optical losses and wide availability of polar crystals makes SPhPs a viable alternative to plasmonic systems. These modes can be excited between the longitudinal optical and transverse optical phonon frequencies, in the so-called Reststrahlen band of the dielectric which, for most materials of interest, spans the Terahertz and mid-infrared ranges of the spectrum[3].

In the present work, we showcase a DL model aimed at inverse-designing a nanostructure whose absorption spectrum is matched to the spectral signature of a specific chemical substance in its gaseous or liquid state; to this end, we built a simple model of a SiC (Reststrahlen band from 25 to 29 THz) nanoarray and applied the DL algorithm to it.

Data generation is carried out by producing absorption spectra of SiC nanostructures, like the ones showed in Figure 1(a) and 1(b), varying the pillars' dimensions and the parameters of the unit cell of the periodic array. The simulated spectra are computed using the Electromagnetic Waves, Frequency Domain module of the COMSOL Multiphysics package. For the training process, a direct, one-shot network is adopted, in the form of a conditional variational autoencoder. The loss function depends on the overlap between the absorption spectra of the SiC microstructure and of the chemical species of interest, in proximity of its dominant spectral signature. The DL approach is here initially applied to a simple and well-studied system, with a limited parameter space, in order to allow for a straightforward evaluation of the obtained results. Its success paves the way toward applications to more complex structures, with possible applications to radiative cooling[5] and gas sensors[6].

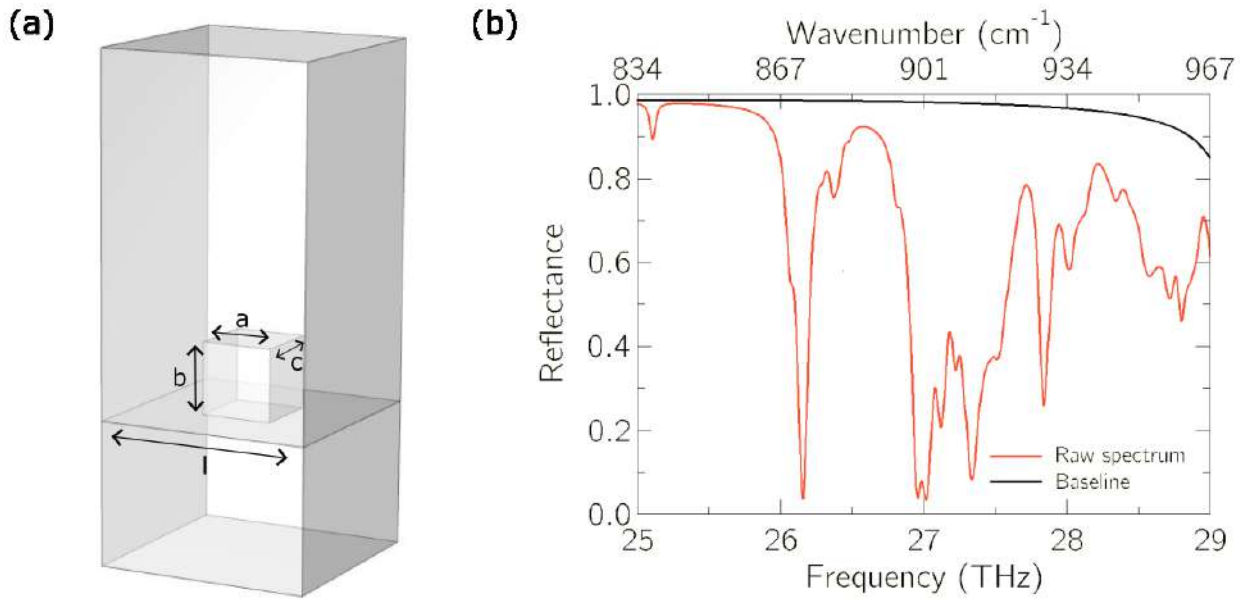


Figure 1: (a) Schematics of the unit cell simulated in COMSOL Multiphysics: a SiC parallelepiped-shaped microresonator of edges *a*, *b* and *c* on top of a substrate of the same material, with air above it. The square-based cell is repeated in two dimensions with periodicity *l*. (b) An example of a reflectance spectrum for a cell with $a = b = c = 1$ μm and $l = 3$ μm, compared with the SiC baseline. This is the raw spectrum computed by COMSOL, to be converted in an absorption one.

Acknowledgements

We acknowledge financial support under the National Recovery and Resilience Plan (NRRP), Mission 4, Component 2, Investment 1.1, Call for tender No. 1409 published on 14.9.2022 by the Italian Ministry of University and Research (MUR), funded by the European Union – NextGenerationEU – Project: Mid-Infrared Nanophotonics for Sustainability (MINAS) – CUP I53D23006670001 - Grant Assignment Decree No. 1381 adopted on 1.9.2023 by the Italian Ministry of University and Research (MUR).

References

1. Khaireh-Walieh, A., D. Langevin, P. Bennet, O. Teytaud, A. Moreau, and P. R. Wiecha "A newcomer's guide to deep learning for inverse design in nano-photonics," Nanophotonics, Vol. 12, No. 24, 4387–4414, 2023.
2. Wiecha, P. R., A. Arbouet, C. Girard, and O. L. Muskens, "Deep learning in nano-photonics: inverse design and beyond," Photonics Res., Vol. 9, B182, 2021.
3. Gubbin, C. R., S. De Liberato, and T. G. Folland "Surface phonon polaritons for infrared optoelectronics," J. Appl. Physics, Vol. 131, No. 3, 030901, 2022.
4. Lu, G., C. R. Gubbin, J. R. Nolen, T. G. Folland, K. Diaz-Granados, I. I. Kravchenko, J. A. Spencer, M. J. Tadjer, O. J. Glembocki, S. De Liberato, and J. D. Caldwell "Collective Phonon−Polaritonic Modes in Silicon Carbide Subarrays," ACS Nano, Vol. 16, No. 1, 963-973, 2022.
5. Lee, M., G. Kim, Y. Jung, K. R. Pyun, J. Lee, B.-W. Kim, and S. H. Ko "Photonic structures in radiative cooling," Light Sci Appl, Vol. 12, 134, 2023.
6. Panigrahi, P. V., B. Chandu, and N. Puvvada "Recent Advances in Nanostructured Materials for Application as Gas Sensors," ACS Omega, Vol. 9, No. 3, 3092-3122, 2024.

Nanophotonic Design for Augmented Reality Displays: Opportunities and Challenges

Christina Spaegele[1]

[1]Meta, United States
cspaegele@meta.com

Abstract: This talk explores the opportunities and challenges of computational design for nanophotonic components in Augmented Reality (AR) devices. It discusses the stringent requirements for AR displays, the potential of nanophotonics, and the complexities introduced by factors like unwanted artifacts and fabrication constraints in achieving high-performance AR displays.

Augmented Reality (AR) has the potential to fundamentally change how we interact with digital information by integrating it into our physical environment in a seamless and intuitive way. To achieve this vision, it is essential to develop displays that can blend in with reality without causing visual obstructions or disrupting the user's perception of their surroundings. This necessitates a large field of view display with variable focus that can fit within the form factor of a typical sunglass and is efficient enough for an all-day use.

While significant progress has been made in this area, further breakthroughs in Materials, OptoElectronics and Photonics are necessary to meet the stringent requirements for size, quality, efficiency, and cost. Nanophotonic components hold great promise for enabling the development of high-performance AR displays due to their lightweight nature, potential for smaller footprint, and increased control of light-matter interactions. However, the combination of increased design freedom with the need to consider factors such as unwanted artifacts and fabrication constraints introduces substantial design complexity. This talk gives an overview of the opportunities and important parameters for the computational design of nanophotonic components in Augmented Reality devices.

Hybrid Silicon Metamaterial combining Microstructured Silicon surface with Silicon / Silicon Dioxide multilayer as a Selective Emitter for Thermophotovoltaic Applications

Karam Choukri*, Maha Ben Rhouma, Armande Hervé, Elodie Richalot, and Elyes Nefzaoui
ESYCOM lab, Univ Gustave Eiffel, CNRS UMR 9007, F-77454 Marne-la-Vallee, France
*corresponding author : karam.choukri@univ-eiffel.fr

Abstract

We propose a broadband selective emitter for thermophotovoltaic applications, combining a microstructured doped silicon surface with a Si/SiO_2 multilayer. This structure enhances emissivity in the above bandgap spectral region (i.e., for wavelengths shorter than λ_{gap}) while suppressing emissivity in the below bandgap region (i.e., for wavelengths longer than λ_{gap}) over a broad spectral range. The structure composition and properties are optimized using a Particle Swarm Optimization algorithm.

Thermophotovoltaic (TPV) systems convert thermal radiation into electricity and are generally made of two main components: an infrared radiation emitter, and a photovoltaic (PV) cell. Selective emitters are often used to tune the spectral range of emitted radiation for a better match with the used PV cell bandgap in order to increase the overall system efficiency. The design and optimization of selective emitters has become a key research focus in the TPV community during the past two decades. Various structural designs of selective emitters have been developed for TPV systems, including metal-dielectric multilayer [1], as well as 1D and 2D photonic crystals (PC) [2,3].

In this work, we propose a silicon based selective emitter (SE) to take benefit of the widespread and affordability of silicon micro and nano-fabrication techniques. The proposed SE combines a PC made of Silicon and Silicon Dioxide deposited on a periodic array of triangular grooves etched in a heavily doped silicon substrate (Figure 1). The emitter radiative properties are calculated using the transfer matrix method (TMM) combined with the effective medium theory (EMT). In this approach, the grooves are considered as a stack of layers composed of a mixture of silicon and air, with different volume fractions depending on the depth. The silicon volume fraction goes from zero above the grooves tip to 1 in the silicon bulk. The effective permittivity of each layer is calculated using the Bruggeman homogenization equation. Using the TMM, we compute the spectral reflectance and absorptance of the whole structure.

The simulation results of the triangular Si grooves grating show that the gradual change in the refractive index of the Si/air mixture with altitude enhances the optical impedance matching between the air and the material's surface, thereby improving light absorption, which exceeds 99% between 1 and 5 μm for a groove height of 10 μm. In order to evaluate the spectral performance of the triangular grooves, we calculate the spectral efficiency η_{sp}, which represents the fraction of power emitted by the thermal emitter at its expected operation temperature (we consider $T = 1500$ K in our case) in the above bandgap spectral range of the considered TPV cell (up to 1.7 μm, corresponding a GaSb cell, $E_g = 0.72$ eV).

$$\eta_{\text{sp}} = \frac{\int_{\lambda_{\min}}^{\lambda_{\text{gap}}} \epsilon_\lambda(T,\lambda) \cdot E_{b\lambda}(T,\lambda)\, d\lambda}{\int_{\lambda_{\min}}^{\lambda_{\max}} \epsilon_\lambda(T,\lambda) \cdot E_{b\lambda}(T,\lambda)\, d\lambda}, \text{ with } E_{b\lambda}(T,\lambda) = \frac{2hc^2}{\lambda^5}\left(\frac{1}{e^{\frac{hc}{\lambda KT}} \in 1}\right)$$

Where ϵ_λ is the emissivity of the structure, $E_{b\lambda}$ is the spectral blackbody emissive power, $\lambda_{\text{gap}} = 1.7\mu m$ is the wavelength corresponding to the bandgap energy of the cell. In our calculations,

we have considered $\lambda_{\min} = 1\mu m$ and $\lambda_{\max} = 5\mu m$. Different doping levels (from 10^{18} to $5 \times 10^{19}\,\mathrm{cm}^{-3}$) and groove heights (from 500 nm to 10 μm) have been considered and the spectral efficiency does not exceed 25%. Optimizing the emissivity is therefore essential to maximize the power that will be converted by the TPV cell. For this purpose, we use a 1D PC alternating Si and SiO_2 layers on the top of the doped Si grooves to filter radiation at wavelengths above the bandgap (ABG) wavelength, hence improving spectral efficiency.

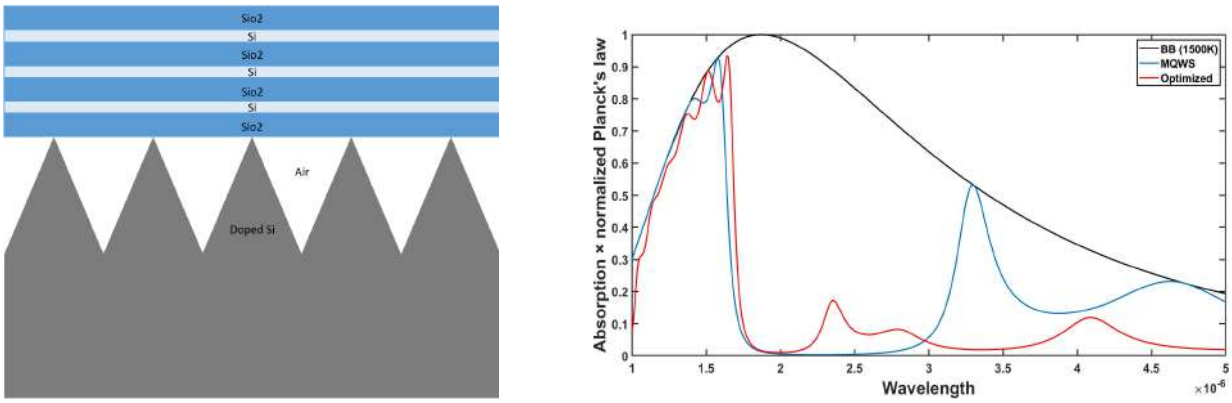


Figure 1: (a) The proposed selective emitter: a photonic crystal on triangularly grooved Si periodic grating with a doping concentration of $5 \times 10^{19}\,\mathrm{cm}^{-3}$. (b) Comparison of the absorption weighted by Planck's law at 1500 K between a quarter-wave structure (MQWS) and the optimized structure.

Some works have already proposed this strategy using PC filter with quarter-wave stack (MQWS) thicknesses [4]. This strategy leads in our case to a spectral efficiency up to ($\eta_{sp\%}$=49.47 %). Further optimization of the PC layers thicknesses would enable broadening of the photonic bandgap and increasing the spectral efficiency. We used the Particle Swarm Optimization (PSO) method for this optimization task. A random population of p structures (particles) is initially generated. Each particle has an initial position and velocity within the search space. The position coordinate in each dimension defines the value of a parameter of the multilayer structure, the thickness in our case. The particles are allowed to move within the search space, i.e. to vary the layers thickness, looking for an optimum. At each step of their movement and of the optimization algorithm, the emissivity of each particle is calculated using the TMM and compared to the target emissivity. After this comparison, the position x_i and velocity v_i of each particle i are updated taking into account the particle inertia (its velocity), memory (its knowledge of previous positions performances) and information provided by other particles (the position of the best performing particle) [5]. This method leads in our case to an optimized design exhibiting a spectral efficiency $\eta_{sp} = 71.45$ %.

References

[1] Bhatt, Rajendra, Ivan Kravchenko, and Mool Gupta. *Solar Energy* 197 (2020): 538-545.

[2] Zhou, Zhiguang, Omar Yehia, and Peter Bermel. . *Journal of Nanophotonics* 10.1 (2016): 016014-016014.

[3] Reyu Sakakibara, Veronika Stelmakh, Walker R. *Solar Energy Materials and Solar Cells*, 238, (2022): 0927-0248.

[4] Mao, Lei, and Hong Ye. *Renewable Energy* 35.1 (2010): 249-256.

[5] Nefzaoui, Elyes, Jérémie Drevillon, and Karl Joulain. *Journal of Applied Physics* 111.8 (2012): 84316 - 84316.

Accelerating Proximity-Field Nanopatterning: GPU-Optimized Electromagnetic Solvers for Complex 3D Nanostructure Design

Dohyeon Lee[1,2], Moosung Lee[1,2†], Bakytgul Yerenzhep[3], Myungjoon Kim[4], Herve Hugonnet[1,2], Seokwoo Jeon[3], Jonghwa Shin[4], and YongKeun Park[1,2,5*]

[1]Department of Physics, Korea Advanced Institute of Science and Technology (KAIST), Daejeon 34141, Republic of Korea

[2]KAIST Institute for Health Science and Technology, KAIST, Daejeon 34141, Republic of Korea

[3]Department of Material Science and Engineering, Korea University, Seoul 02841, Republic of Korea

[4]Department of Material Science and Engineering, KAIST, Daejeon 34141, Republic of Korea

[5]Tomocube Inc., Daejeon 34109, Republic of Korea

[†]Institute for Functional Matter and Quantum Technologies, Allmandring 13, 70569 Stuttgart, Germany

[*]corresponding author: yk.park@kaist.ac.kr

Abstract: We enhance the phase mask design process of proximity-field nanopatterning by integrating a GPU-accelerated convergent Born series solver with gradient-based optimization. This method outperforms FDTD in 2D and 3D simulations, enabling efficient, high-contrast nanostructure design. Our approach advances PnP, expanding its potential for complex 3D nanofabrication.

1. Introduction

Enhancing productivity in 3D nanoprinting is crucial for advancing applications in energy storage, sensors, photonic devices, and microrobotics. Among various techniques, proximity-field nanopatterning (PnP) stands out for its ability to balance high productivity with satisfactory spatial resolution. This method relies on coherent light passing through a phase mask to generate intricate 3D hologram patterns within a photoresist. However, traditional approaches for designing phase masks often result in low-contrast patterns, limiting the complexity of achievable nanostructures.

Recent developments integrating numerical simulations with optimization algorithms have addressed these challenges by enabling high-contrast patterns. Gradient-based optimization has proven effective for refining phase mask designs iteratively. However, designing large-scale phase masks remains computationally demanding, particularly for multi-layered structures requiring 3D simulations. Traditional methods like the finite-difference time-domain (FDTD) approach struggle with computational feasibility, making large-scale designs impractical.

Frequency-domain solvers provide simulation results using less computational resources by eliminating time-stepping and improving accuracy for steady-state scattering analysis. Even though those approaches have been validated in previous studies, they suffer from scalability issues, especially for simulating three-dimensional (3D) space.

This work proposes a convergent Born series frequency-domain solver that enhances computational efficiency and stability. This solver stably works for 3D simulation by ensuring mathematical stability. Coupled with GPU acceleration, this solver significantly reduces simulation time and extends the applicability of PnP for complex nanostructure fabrication.

2. Result

We compared the design results with an FDTD-based design tool in a 1D periodic phase mask to validate our approach. This setup mimics a PnP process where a normal plane wave illuminates the phase mask, creating a desired diffraction pattern. Our solver achieves a 2.6-fold speedup in CPU-based computation compared to a commercial FDTD solver and a 30-fold speedup when using GPU.

Further, we extended our approach to 2D phase masks, designing structures that generate specific interference patterns such as a focal point, a single helix, and a double helix. These designs were optimized using 3D electromagnetic simulations and GPU acceleration, reducing computation time per iteration to 45 seconds—several hours faster than a CPU-based reference solver. The optimized phase masks effectively directed light into the desired patterns, demonstrating the feasibility of generating complex chiral nanostructures using normal plane wave illumination alone.

3. Conclusion

This study demonstrates the practical inverse design of 2D phase masks capable of generating intricate 3D holograms while significantly reducing computational costs. We enable rapid and reliable optimization of large-scale phase masks by integrating GPU-accelerated frequency-domain solvers into the PnP process. This approach opens new possibilities for scalable, high-contrast nanopatterning with applications across photonics, sensors, and other advanced nanomanufacturing fields.

References

[1] Lee, Dohyeon, et al. "Fast Free-Form Phase Mask Design for Three-Dimensional Photolithography Using Convergent Born Series." ACS Photonics (2025).

[2] Osnabrugge, Gerwin, Saroch Leedumrongwatthanakun, and Ivo M. Vellekoop. "A convergent Born series for solving the inhomogeneous Helmholtz equation in arbitrarily large media." Journal of Computational Physics 322 (2016): 113-124.

[3] Vettenburg, Tom, Simon AR Horsley, and J. Bertolotti. "Calculating coherent light-wave propagation in large heterogeneous media." Optics Express 27.9 (2019): 11946-11967.

[4] Nam, Sang-Hyeon, et al. "Photolithographic realization of target nanostructures in 3D space by inverse design of phase modulation." Science Advances 8.21 (2022): eabm6310.

[5] Hughes, Tyler W., et al. "Adjoint method and inverse design for nonlinear nanophotonic devices." ACS Photonics 5.12 (2018): 4781-4787.

Tailoring the design space of structurally colored stretchable materials

B. Abdennadher[1], M. Saba[1], U. Steiner[1], and M. Kolle[2]
[1]Adolphe Merkle Institute, Switzerland
[2]Massachusetts Institute of Technology, USA
bilel.abdennadher@unifr.ch

Abstract

Large scale-structural colored streachable material was recently developed. We aim to parametrize its design space using two surface roughness parameters: the autocorrelation length and the Root Mean Square. By tuning roughness, we control diffuse and specular scattering, enhancing light diffusion and minimizing iridescence for improved sensing applications.

Large-scale, structural colored stretchable material was recently developed. We aim to parametrize its design space using two surface roughness parameters: the autocorrelation length and the Root Mean Square. By tuning roughness, we control diffuse and specular scattering, enhancing light diffusion and minimizing iridescence for improved sensing applications.

Structurally colored stretchable material was recently fabricated using Lippmann photography and photosensitive elastomers [1]. This process generates refractive index variations in the material, making it act as a distributed Bragg reflector. We aim to expand these materials' design space and improve their scattering properties by mainly controlling their surface roughness. Specifically, we want to modify the light scattering behavior—from specular to more diffuse—and minimize iridescence by tuning the roughness of the photonic material itself and adding a rough, transparent, thick top layer. Thus, this approach will provide new possible applications of these materials in optical sensors.

The idea behind using a rough top coat is to introduce initial diffusion before the light interacts with the Bragg reflector; this broadens the scattered light cone and enhances total diffusion. Selecting a thick top coat of the photonic material simplifies our analytical model. Since the thickness exceeds the coherence length of light, we can treat the system from a far-field perspective, allowing intensities to add up more straightforwardly. Additionally, assuming that the top coat is homogeneous and transparent, no scattering occurs within it, ensuring that light propagates through it without more diffusion.

To model the scattering behavior, we consider a system composed of three sequential scattering events: (1) transmission from air into the rough top coat, (2) reflection at the interface between the top coat and the photonic material, and (3) transmission back into the air from the top surface. By tuning the roughness of both the photonic material and the top coat, we can control the balance between specular and diffuse scattering.

For a fixed incident angle $(\theta_{\text{in}}, \varphi_{\text{in}})$ and a fixed observation angle $(\theta_{\text{out}}, \varphi_{\text{out}})$, the total intensity results from contributions spanning all possible intermediate angles (θ_1, φ_1) and (θ_2, φ_2), accounting for the cumulative scattering effects. Here, θ represents the polar angle, and φ is the azimuthal angle. The resulting sequence of interactions is described as:

$$I(\theta_{\text{in}}, \varphi_{\text{in}}, \theta_{\text{out}}, \varphi_{\text{out}}) = \int_{\theta_1} \int_{\varphi_1} \int_{\theta_2} \int_{\varphi_2} T_1(\theta_{\text{in}}, \varphi_{\text{in}}, \theta_1, \varphi_1) \cdot R(\theta_1, \varphi_1, \theta_2, \varphi_2) \cdot T_2(\theta_2, \varphi_2, \theta_{\text{out}}, \varphi_{\text{out}}) \tag{1}$$

$$\cdot \sin(\theta_1) \cdot \sin(\theta_2)\, d\theta_1\, d\varphi_1\, d\theta_2\, d\varphi_2 \tag{2}$$

To quantify intensities in both transmission cases T_1, T_2, and in reflection R, we adapt the Generalized Harvey-Shack (GHS) Method, a semi-analytical model used to describe the scattering signature of light on moderately rough surfaces. In the literature, only a numerical model using GHS was provided for the reflection scenario [2, 3]. Therefore, we aim to extend it to include the transmission case. This extension will enable us to provide a precise prediction of angular light behavior and will allow us to link the total angular spread intensity of the system to two main roughness parameters: the autocorrelation length (lateral distance) and the root mean square (height distribution).

To better understand the core concept of the Generalized Harvey-Shack Method [2, 3], this theory aims to provide a linear system that characterizes the scattering signature of a material depending on its surface parameters. As empirical experiments show a shift-invariance behavior of the scattered light when looked at from different incident angles, this suggests the existence of a Surface Transfer Function that universally describes the scattering behavior. This function is an analogy to the linear system formulation in image formation, particularly the Optical Transfer Function OTF, which characterizes the system's ability to transfer contrast and detail from an image object to its image. The Surface Transfer Function is given by the normalized autocorrelation function of the Pupil function of the scattering process (describing amplitude and phase variation due to roughness). The Fourier transform of the Surface Transfer Function represents the angular intensity variation of the propagation vectors in the far field, which is our primary interest to measure.

References

[1] B. H. Miller, H. Liu, M. Kolle, "Scalable optical manufacture of dynamic structural colour in stretchable materials," *Nature Materials*, Vol. 21, pp. 1014–1018, 2022.

[2] V. E. Johansen, "Preparing the generalized Harvey–Shack rough surface scattering method for use with the discrete ordinates method," *Optical Society of America A*, Vol. 32, No. 2, pp. 186-194, 2015.

[3] A. Krywonos., J. E. Harvey, and N. Choi, "Linear systems formulation of scattering theory for rough surfaces with arbitrary incident and scattering angles," *Optical Society of America A*, Vol. 28, No. , pp. 1121-1138, 2011.

Efficient lookup table computation for the design of metalenses leveraging propagation phase

A. Locatelli[1*], M. Gandolfi[1], D. Rocco[1], O. Sergaeva[1], and C. De Angelis[1]

[1]Department of Information Engineering, University of Brescia, Italy
[*]corresponding author: andrea.locatelli@unibs.it

Abstract: We introduce an efficient technique to accelerate the computation of lookup tables for the design of metalenses leveraging propagation phase. Our approach determines the phase imposed by each meta-atom through an analysis of the modal properties of a uniform waveguide array cross-section.

Research in the field of optical metasurfaces has been experiencing a rapid growth in the last decade, with potential applications in a plethora of different scenarios [1]. In particular, metalenses have attracted the interest of the scientific community thanks to the possibility of replacing conventional bulky optical components for wavefront shaping with flat-optics devices [2]. In this framework, impressive experimental results have already been reported in the literature, see e.g., fabrication of a 100-mm diameter metalens composed of billions of nanostructures [3]. As a matter of fact, design rules which are commonly used for metalenses are based on a combination of pre-calculated lookup tables for the meta-atoms, cumbersome 3D full-wave simulations of the real device, and optimization techniques needed to refine the efficiency. In a nutshell, the development of efficient numerical models plays a pivotal role in metalens design and research (see e.g. [4, 5]).

Two different physical mechanisms have been proposed so far to get meta-atoms imposing the required phase change, which is in the $0-2\pi$ range. The first approach exploits modulation of the propagation delay in a truncated waveguide structure [6], whereas the main alternative technique relies on scattering by nanoresonators characterized by properly engineered Mie resonances [7]. Hereinafter we focus on the first paradigm, i.e., metalenses based on guiding effect in high-index pillars. The goal of this work is indeed to demonstrate a fast and accurate technique accelerating the computation of the phase imposed by each meta-atom as a function of one or more geometrical parameters. We propose to model the metasurface under exam as a waveguide array, by considering both the dielectric and the air band of the periodic structure. In particular, the plane wave impinging onto the metalens is projected onto the mode profiles of the two bands, and the overall imposed phase is then estimated by weighing the propagation constants of the modes through an overlap integral. This technique considers both coupling between the (identical) meta-atoms and excitation of multiple bands. At the same time, computational efficiency is extremely high since fast modal analysis of 2D structures is sufficient for the generation of the complete lookup table for a 3D metalens.

As an example, we consider a 2D metalens composed of a periodic 1D arrangement (along x-axis) of silicon bricks ($n = 3.3$) in air. Each high-index brick has height $h = 1050$ nm, and the width W can be varied between 100 and 500 nm to get the required $0-2\pi$ phase variation (see Fig. 1a). It should be noted that the structure is invariant along the z-axis. Furthermore, incident light is a plane-wave polarized along x-axis at the wavelength of 1550 nm. The lookup table can be generated by using 2D full-wave simulations wherein a plane-wave is launched from a 1D port, and phase is evaluated by collecting the transmitted field with another port on the opposite side of the metalens (see blue lines in Figs. 1b and 1c). These results can be compared with the outcomes of approximate techniques. On one hand, we applied the simplest model that describes the metalens as a collection

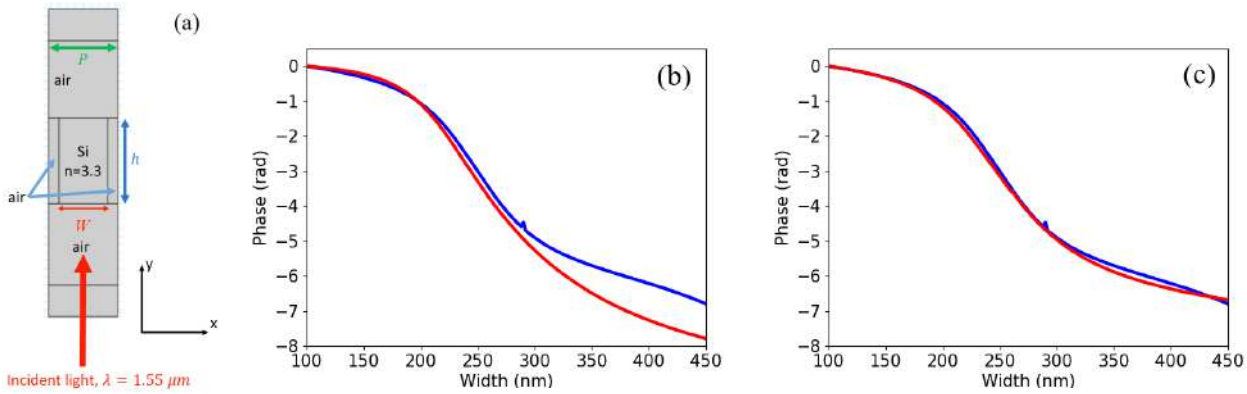


Figure 1. (a) Schematic view of the unit cell of the 2D metalens. Phase lookup table of the metasurface as a function of the width W evaluated from full-wave simulations (blue lines) and approximate models (red lines). (b) Single-waveguide model. (c) Waveguide-array model with multiple-band excitation.

of isolated waveguides. In this scenario, the phase can be estimated as $\Phi = \beta h$, where β is the propagation constant of the TM guided mode of a 1D slab waveguide. Fig. 1b demonstrates that agreement with full-wave simulations is decent, but far from being satisfactory for design of a real device. On the other hand, in Fig. 1c we report the lookup table obtained by modeling the metalens as a 1D waveguide array characterized by a dielectric band, which is generated by the coupled guided modes of the neighboring slabs, and by an air band. In stark contrast with the previous case, agreement with full-wave simulations is quite good over the entire width range.

We envisage that the reported results open the way to a fast and accurate generation of libraries of meta-atoms for design of metalenses leveraging propagation phase with realistic 3D geometries. Furthermore, investigation of the behavior of the described modeling procedure with tilted incidence is underway. Last, but not least, the possibility of exploiting this technique to refine the lookup table approach by also including the effects due to the modulation of the geometrical parameters along the surface of the metalens can be explored.

The authors acknowledge financial support from the Italian Ministry for University and Research and the European Union – Next Generation EU Mission 4 Component 1, as part of PRIN 2022 project DOSE (CUP D53D23001350006), PRIN 2022 project GRACE6G (CUP D53D23001250001), PRIN PNRR 2022 project FLAIRS (CUP D53D23016160001).

References

1. Kuznetsov, A., et al., “Roadmap for optical metasurfaces,” ACS Photon., Vol. 11, No. 3, pp. 816-865, 2024.
2. Lalanne, P., and P. Chavel, “Metalenses at visible wavelengths: past, present, perspectives,” Laser Photon. Rev., Vol. 11, No. 3, 1600295, 2017.
3. Park, J.S., S. Lim, A. Amirzhan, H. Kang, K. Karrfalt, D. Kim, J. Leger, A. Urbas, M. Ossiander, Z. Li, and F. Capasso, “All-glass 100 mm diameter visible metalens for imaging the cosmos,” ACS Nano, Vol. 18, No. 4, pp. 3187-3198, 2024.
4. Wenjin, X., H. Zhang, A. Gopal, V. Rokhlin, and O. Miller, “Fullwave design of cm-scale cylindrical metasurfaces via fast direct solvers,” arxiv preprint., arXiv:2308.08569v1, 2023.
5. Dainese, P., L. Marra, D. Cassara, A. Portes, J. Oh, J. Yang, A. Palmieri, J. Rodrigues, A. Dorrah, and F. Capasso, “Shape optimization for high efficiency metasurfaces: theory and implementation,” Light Science Appl., Vol. 13, 300, 2024.
6. Basilio-Ortiz, J., and I. Moreno, “Unveiling invariant optical properties of dielectric meta-atoms,” Nano Lett., Vol. 24, No. 16, pp. 4987-4992, 2024.
7. Gigli, C., Q. Li, P. Chavel, G. Leo, M. Brongersma, and P. Lalanne, “Fundamental limitations of Huygens’ metasurfaces for optical beam shaping,” Nano Lett., Vol. 15, No. 8, 2000448, 2021.

Modeling microstructured optical fibers using boundary element method

M. A. Ayela[1*], J.R. Poirier[1], F. Surre [2] and H.C. Seat [3]
[1]Laplace, Université de Toulouse, INPT, UPS, Toulouse, France
[2]James Watt School of Engineering, University of Glasgow, UK
[3]LAAS, Université de Toulouse, CNRS, INP, Toulouse, France
ayela@laplace.univ-tlse.fr (corresponding author)

Abstract

In this study, we use the Boundary Element Method (BEM) to analyze the propagation modes and characterize the electromagnetic field distribution in the hexapolar microstructured optical fibers (MOFs). More specifically, we are interested in the proportion of the field located in an outer corona surrounding the air holes, a key region for loss engineering and the sensitivity of fiber optic sensors. Our results show that BEM provides better accuracy in calculating propagation modes than traditional methods such as finite element method.

1 Introduction

Microstructured optical fibers (MOFs) have attracted growing interest due to their light guiding properties, enabling advanced applications in telecommunications, optical sensors and biophotonics [1]. In this context, it is essential to understand and optimize the electromagnetic field distribution in these fibers, particularly in the corona outside the air holes, a key region influencing sensor losses and sensitivity [2]. To carry out this analysis, we use BEM, which offers an effective alternative to traditional methods such as the finite element method (FEM), notably by reducing computational complexity and improving the accuracy of propagation mode calculations. In this study, we analyze the distribution of the electromagnetic field, denoted RSI, in the 1 and 2 regions of the hexapole microstructured fiber.We evaluate this proportion for each propagation mode to identify evanescent modes that generate a very large RSI in the 1 region. This analysis enables us to identify and propose optimal configurations of the hexapole MOF for optical sensing.

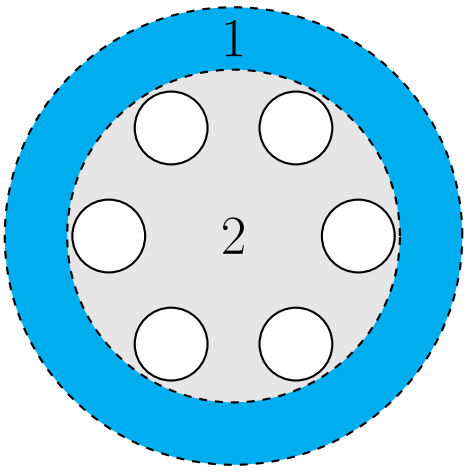


Figure 1: Hexapolar microstructured fiber.

The fraction of the total power located in the region 1 and 2 is evaluated as:

$$RSI = \frac{\int_{(1,2)} \Re(E_x H_y - E_y H_x) dxdy}{\int_{total} \Re(E_x H_y - E_y H_x) dxdy} \quad (1)$$

where Ex, Ey, Hx et Hy are the transverse electric and magnetic fields

2 Boundary element method

The integral approach we have adopted is based on the formulation developed in [3]. It corresponds to an eigenvalue problem where the eigenvectors represent the transverse or longitudinal components of the field at the interfaces, in other words, at the boundary of the Ω_l air holes. Every components u of the electromagnetic field of the mode satisfies the following Green's representation formula:

$$u(\mathbf{r}) = \pm \left(\int_{\partial\Omega_j} G(\mathbf{r}, \tilde{\mathbf{r}}) \frac{\partial u(\tilde{\mathbf{r}})}{\partial(\tilde{\mathbf{r}})} \mathrm{d}s(\tilde{\mathbf{r}}) \; - \int_{\partial\Omega_j} \frac{\partial G(\mathbf{r}, \tilde{\mathbf{r}})}{\partial(\tilde{\mathbf{r}})} \, u(\tilde{\mathbf{r}}) \mathrm{d}s(\tilde{\mathbf{r}}) \right), \; \mathbf{r} \notin \partial\Omega_j \,, \tag{2}$$

The table highlights the RSI and complex effective indices for two modes, revealing a strong asymmetry in energy distribution between regions, with a first mode mainly confined to a specific region (RSI=99.01%) and a second mode showing a more balanced distribution (RSI=62.63%).

MOF.	**neff**	**RSI**	
		RSI_1	RSI_2
MODE.[1]	$1.4453952 + j3.1952e-08$	0.96%	99.01%
MODE.[2]	$1.2973449 - j5.8943e-11$	62.63%	37.35%

Table 1: Relative sensitivity values in each region

3 Conclusion

In this study, we analyzed hexapolar microstructured optical fibers using the boundary element method, focusing on the proportion of the electromagnetic field in a corona external to the air holes. Our results show that this approach offers a better possibility of calculating higher-order propagation modes than conventional methods, notably the finite element method. In addition, we have highlighted the influence of the fiber's geometric parameters on field distribution, and proposed optimized configurations to improve sensitivity and minimize losses. These results pave the way for new fiber designs suitable for applications in telecommunications, optical sensors and biophotonics, where precise control of field distribution is essential.

4 Acknowledgements

This work was supported in part by the French National Research Agency under Grant ANR-21-CE04-0002-01 and in part by LAAS-CNR's micro and nanotechnologies platform, a member of the Renatech french national network.

References

[1] Ahmed, K., and Morshed, M. "Design and numerical analysis of microstructured-core octagonal photonic crystal fiber for sensing applications," *Sensing and Bio-Sensing Research*, Vol. 7, 1-6, 2016. (2016).

[2] Islam, M. I., Ahmed, K., Sen, S., Chowdhury, S., Paul, B. K., Islam, M. S and Asaduzzaman, S. "Design and optimization of photonic crystal fiber based sensor for gas condensate and air pollution monitoring," *Photonic Sensors*, Vol. 7, pp. 234-245, 2017.

[3] Poirier, J. R. and Perrussel, R. "Solution of a nonlinear eigenvalue problem from photonic crystal fiber applications discretized by a boundary element method," *Engineering Analysis with Boundary Elements*, Vol. 168, No. 105928, 2024.

Cosine beams for near-field space division multiple access in 6G communications and beyond

S. Droulias*, G. Stratidakis, and A. Alexiou

Department of Digital Systems, University of Piraeus, Piraeus 18534, Greece

*corresponding author: sdroulias@unipi.gr

Abstract: In this work, we propose the family of cosine beams that satisfy the orthogonality condition, offering a multitude of communication modes for multiple access in the near-field. We introduce the concept of near-field space division multiple access (NF-SDMA) to enable spatial multiplexing and capacity improvements for 6G near-field wireless connectivity.

Wireless communications are nowadays shifting to higher frequencies and the utilization of large radiating apertures for manipulating the wavefront of the radiated wave, to acquire curvature beyond the typical far-field planar form. For example, focused beams are ideal for concentrating the power at controllable distances and small areas, a key element for energy efficient communications and localization applications [1,2]. Such beams could be used in a multiple access scheme, to boost connectivity to unprecedented performance levels. Multiple access offers the advantage of having several users simultaneously served with minimum interference and maximum resource allocation. It relies on the orthogonality of beams, a key element for successfully retrieving the information assigned to different beams, even though all such beams may coexist. For example, in classical far-field space division multiple access (SDMA) it is possible to distinguish multiple users at different angles, due to the angular beam orthogonality. Despite the various attempts, to date, the design of near-field multiple access schemes relies primarily on the utilization of focused beams, which are either entirely non-orthogonal or achieve orthogonality only asymptotically [3]. Hence, a multiple access scheme based on beams that have strictly zero correlation, is still missing.

Consider a transmitter (Tx), such as a uniform planar array (UPA), centered at the origin of the coordinate system, with its plane extending on the *xy*-plane, as shown in Fig.1(a). A receiver (Rx) is located at distance L, with its surface also residing on the *xy*-plane. The Tx generates beams that propagate along the *z*-axis, the *E*-field of which at the observation point $\mathbf{r} = (x,y,z)$ is $\mathbf{E}(\mathbf{r}) = \mathbf{E}(x,y,z)$. The correlation of two such beams $\mathbf{E}_1(x,y,z)$, $\mathbf{E}_2(x,y,z)$ at distance $z = L$, as defined in terms of their inner product on the transverse *xy*-plane, is written as

$$C = \frac{\iint_{-\infty}^{+\infty} E_1(x,y;L)E_2^*(x,y;L)dxdy}{\sqrt{\iint_{-\infty}^{+\infty} |E_1(x,y;L)|^2 dxdy}\sqrt{\iint_{-\infty}^{+\infty} |E_1(x,y;L)|^2 dxdy}} \quad (1)$$

where E_1, E_2 are the magnitudes of the *E*-field vectors.

In this work we propose cosine beams as a family of beams that satisfy the near-field orthogonality property, i.e. $C = 0$. A cosine beam is a beam formed by the superposition of two waves traveling at opposite oblique angles [4]. The distance z_{max} marks the cosine beam range, i.e. the propagation distance for which the standing wave is formed in the transverse (*xy*) plane, as shown in Fig.1(a). Such beams offer the necessary condition $C = 0$ (see Fig.1(b),(c)), offering a multitude of communication modes, as shown in Fig.1(d),(e). By applying a global phase of the form $kx \sin\theta$ at the Tx, the beam can be steered towards any desirable angle θ.

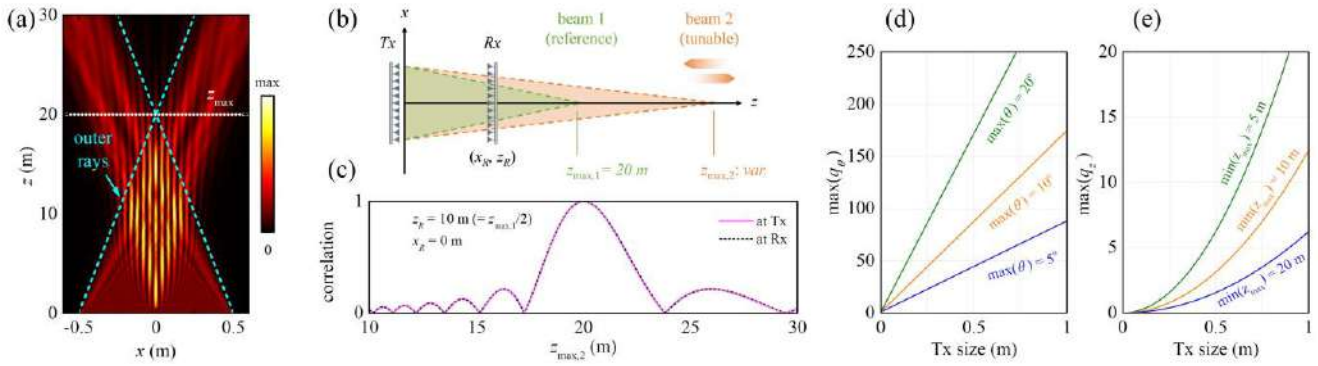


Figure 1. Cosine beams for NF-SDMA. (a) Intensity of numerically propagated beam, using an array of size 1 m. The operation frequency is 150 GHz. (b) Schematic illustration of two cosine beams generated by a transmitter (Tx) and directed towards the receiver (Rx), located at (x_R, z_R). Beam 1 has fixed $z_{max,1}$ = 20 m, and is used as reference. Beam 2 has tunable z_{max}, accounting for a multitude of cosine beams. (c) Beam correlation at the Tx and the Rx, as a function of $z_{max,2}$, for Rx of size 1 m, located at (x_R = 0 m, z_R = 10 m). (d) Maximum number of communication modes per maximum steering angle, max(q_θ), as a function of the array size; examples for max(θ) = 5°, 10°, 20°, the maximum angle at which the cosine beams are steered. (e) Maximum number of communication modes per minimum convergence distance, max(q_z), as a function of the array size; examples for $z_{max} \geq$ 5 m, 10 m, 20 m.

We provide analytical expressions for the cosine beam orthogonality and we prove theoretically that there is a countable set of mutually orthogonal beams, all propagating along the same direction. We also prove that the same conclusion holds for beams propagating along different directions, providing an ideal means for multiple access in both the angular and the distance domain. For different Tx sizes, we numerically verify that the orthogonality of the proposed beams is successfully retrieved at a receiver that resides in the near-field of the transmitter, and is also robust to displacements of the receiver. With the aid of cosine beams, we introduce the concept of near-field SDMA (NF-SDMA) to bring into the near-field the classical far-field SDMA and its benefits, which are essential for novel near-field applications in future wireless communications.

Acknowledgements

This work was supported by the European Commission's Horizon Europe Programme under the Smart Networks and Services Joint Undertaking INSTINCT project (Grant Agreement 101139161).

References

1. Droulias S., Stratidakis G., and Alexiou A., "Near-field engineering in RIS-aided links: Beamfocusing analytical performance assessment," IEEE Access, vol. 12, pp. 29 536–29 546 (2024).
2. Stratidakis G., Droulias S. and Alexiou A., "Perceptive, Resilient, and Efficient Networks: Programming the Wireless Environment with Reconfigurable Intelligent Surfaces," in IEEE Veh. Technol. Mag., vol. 19, no. 4, pp. 36-43 (2024).
3. Ouyang C., Wang Z., Chen Y., Mu X. and Zhu P., "A Primer on Near-Field Communications for Next-Generation Multiple Access," in Proceedings of the IEEE, vol. 112, no. 9, pp. 1527-1565 (2024).
4. Droulias S., Stratidakis G., and Alexiou A., "Near-field orthogonality and cosine beams for near-field space division multiple access in 6G communications and beyond," https://arxiv.org/abs/2408.13190 (submitted).

Impact of disorder on the radiative efficiency of bound states in the continuum in dimer gratings

V. Kalt[1], E. Centeno[2*], R. Smaali[2], A. Moreau[2]

[1]Université de Lyon, Laboratoire Hubert Curien, UMR 5516, Université Jean Monnet, Saint-Etienne, France

[2]Université Clermont Auvergne, Clermont Auvergne INP, CNRS, Clermont-Ferrand, France

Corresponding author: emmanuel.centeno@uca.fr

Abstract: A dimer grating is engineered to increase the light emission of a dipole source in the normal direction through the transformation of a bound state in the continuum (BIC) into a quasi-BIC (QBIC). We study the effect of controlled and structural disorder on the structure.

The design of photonic structures capable of enhancing the emission of quantum emitters is an active area of research [1] with applications in lighting, imaging... The performance of those structures is measured by the radiative enhancement (RE), product of the emitters normalized decay rate and the light extraction efficiency. Periodic gratings supporting symmetry-protected BICs have been proposed as an efficient solution to increase light emission in off-normal directions [2,3]. In this work, we study a dimer grating where asymmetry is introduced to transform the BIC into a QBIC radiating at the Γ point.

The dimer grating of period $2 \times D = 2 \times 420$ nm is built from TiO_2 ribbons of height $h = 150$ nm and width $w = \frac{D}{2}$ separated by a distance L. A 200 nm TEOS cover layer protects the grating and contains a dipole which is centered between the dimer elements and emits light at a wavelength $\lambda = 618.5$ nm. Figure 1 presents the two kinds of perturbations we consider: width variations $w \pm \Delta w$ and gap variations $L \pm \Delta L$, respectively characterized by parameters $\alpha = \frac{\Delta w}{w}$ and $\beta = \frac{\Delta L}{L}$. All simulations are performed using the quasi-normal mode method [4].

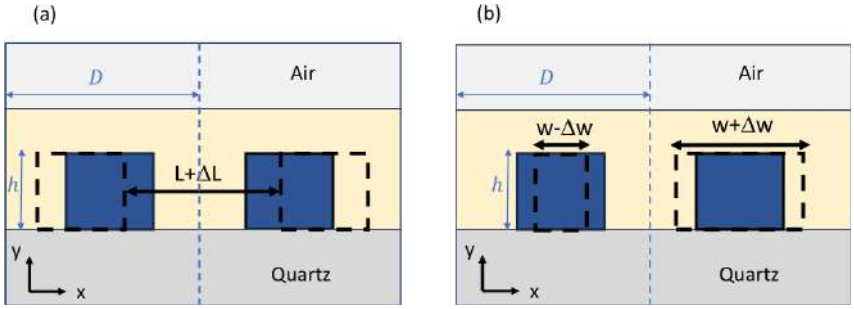


Figure 1: Schematic of a dimer grating made of two TiO_2 ribbons embedded in a TEOS layer. (a) and (b) are respectively modified gap $L \pm \Delta L$ and widths w±Δw dimer gratings.

The symmetry of the dimer structure ($\alpha = \beta = 0$) leads to a BIC existing at the Γ point. The infinite Q-factor of the mode increases the dipole emission through the Purcell effect but prevents the light extraction from the structure, resulting in a null radiative enhancement. Through a breaking of the dimer symmetry induced by α and β perturbations, we observe a radiative enhancement at the Γ point which can be explained as the transformation of the BIC into a QBIC with a lower Purcell factor but a non-zero light extraction efficiency. RE values up to 1600 are obtained in the normal direction with the dimer grating. RE values for both structures are presented in figure 2.

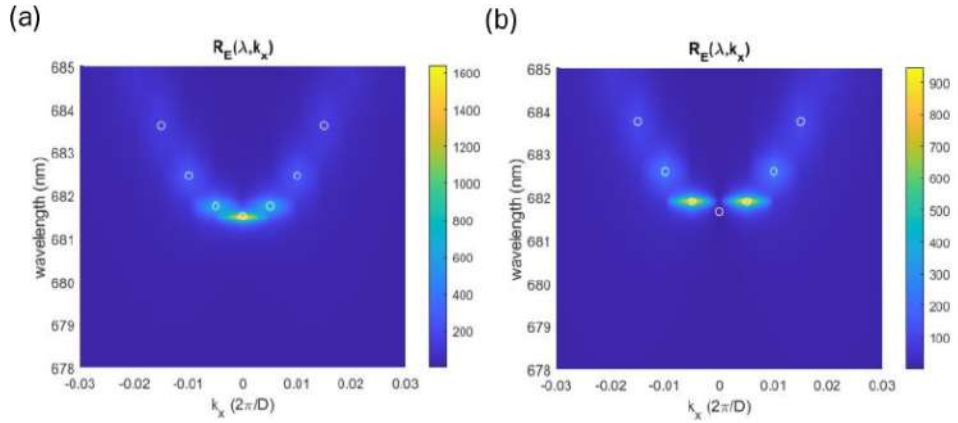


Figure 2: Directive radiative enhancement coefficient $R_E(\lambda, k_x)$ calculated: (a) for the dimer structure with $\alpha = 0$ and $\beta = 0.08$, (b) for the regular grating with $\alpha = 0$ and $\beta = 0$.

Structural disorder induced by fabrication imperfection is another source of asymmetry. It is known that BICs and QBICs are sensitive to this kind of disorder [5]. We study its effect on the dimer structure by independently randomly perturbing the position and width of the elements in a supercell. Results presented in figure 3 show that structural disorder on the ribbon's width greatly reduces the RE by splitting the QBIC energy on multiple wavelength. Conversely, the dimer structure is robust to structural disorder on the position of the elements.

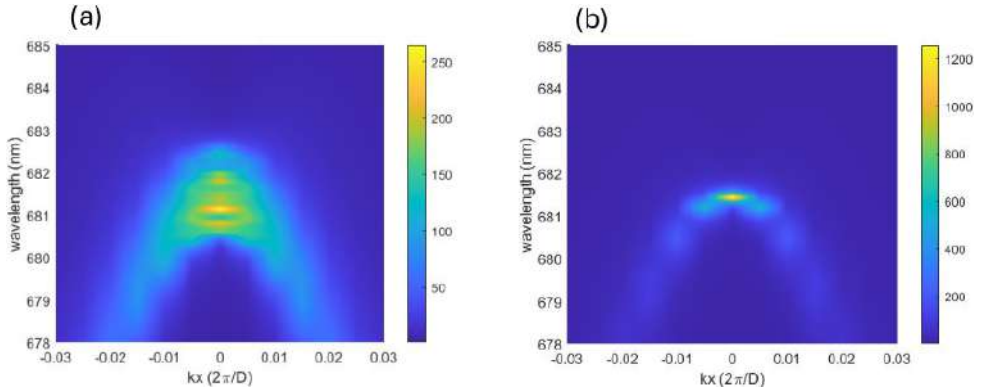


Figure 3: Average $R_E(\lambda, k_x)$ for the dimer grating with ($\alpha = 0$, $\beta = 0.08$) calculated for a perturbation strength $\delta = 1.2\%$: (a) when disorder only affects the width of the ribbons, (b) when disorder only impacts the position of the ribbons.

The authors thank the French "Agence Nationale de la Recherche" in the framework of the COULEURS project (ANR-22-CE39-0013).

References

1. A. Vaskin, R. Kolkowski, A. F. Koenderink, and I. Staude, "Light-emitting metasurfaces", Nanophotonics Vol. 8, 1151 (2019)
2. S. Farazi and S. Tadigadapa. "Coherent light-emitting metasurfaces based on bound states in the continuum" Nanophotonics, vol. 13, no. 16, 2024, pp. 2915-2924
3. L. Liu, R. Wang, Y. Sun, Y. Jin and A. Wu. "Fluorescence enhancement of PbS colloidal quantum dots from silicon metasurfaces sustaining bound states in the continuum" Nanophotonics, vol. 12, no. 15, 2023, pp. 3159-3164.
4. C. Sauvan, J.-P. Hugonin, I. S. Maksymov, and P. Lalanne, "Theory of the spontaneous optical emission of nanosize photonic and plasmon resonators", Physical Review Letters Vol. 110 (2013).
5. E. Maslova, M. Rybin, A. Bogdanov, and Z. Sadrieva. "Bound states in the continuum in periodic structures with structural disorder" Nanophotonics, vol. 10, no. 17, 2021, pp. 4313-4321.

Metamaterials: novel trends and applications

Dynamic *in-situ* photoluminescence lifetime imaging of halide anion exchange in $CsPbBr_3$ nanocrystals

P. Liška[1,2*], P. Klok[1,2], J. Král[3], T. Musálek[1,2], R. Kuželová[1,2], P. Viewegh[1,2] and T. Šikola[1,2]

[1]Institute of Physical Engineering, Faculty of Mechanical Engineering, Brno University of Technology, Czech Republic
[2]CEITEC, Brno University of Technology, Czech Republic
[3]Department of Nuclear Chemistry, Faculty of Nuclear Sciences and Physical Engineering, Czech Technical University in Prague, Czech Republic
[*]corresponding author: Petr.Liska1@vutbr.cz

Abstract: Lead halide perovskites, with their unique structural and optical properties like bright photoluminescence and highly tunable band gap have gathered significant attention due to their enormous number of optoelectronic applications. In this work, we demonstrate in-situ photoluminescence lifetime imaging and describe the kinetics of halide anion exchange inside $CsPbBr_3$ nanocrystals.

Nanocrystalline lead halide perovskites (LHPs) have recently emerged as prominent low-dimensional semiconductors due to their combination of bright direct optical transitions, unique structural and optical properties, room-temperature stable excitonic states [1], and single-photon emission capabilities [2]. Their straightforward and cost-effective synthesis from abundant elements makes LHPs an appealing, high-performance alternative to conventional optoelectronic materials [3]. Initially developed for photovoltaic applications, achieving light-conversion efficiencies surpassing 26%, LHPs are now gaining recognition as versatile materials for a variety of optoelectronic uses, including gamma radiation detectors and scintillators [4].

Among the LHPs, the all-inorganic $CsPbBr_3$ perovskite stands out for its unique optical and structural properties such as low non-radiative losses, high tolerance to structural defects, and bright, narrow photoluminescence (PL) emission in the green region of the visible spectrum (~2.4 eV/520 nm) with quantum yields exceeding 90% and a linewidth of approximately 56 meV (12 nm) in its nanocrystalline form [5, 6]. Due to its inherent ionic nature, the electronic structure and optical properties of $CsPbBr_3$ can be tuned across the entire visible spectrum [(1.4–3.6) eV] by incorporating different halides [7]. This band gap engineering offers not only an enormous amount of potential optoelectronic applications but also a significant insight into molecular dynamic processes in such nanosized systems.

In this work, we demonstrate *in-situ* observation of halide anion exchange kinetics in $CsPbBr_3$ nanocrystals dispersed in a toluene solution by photoluminescence lifetime imaging with state-of-art Leica Stellaris Falcon 8 Fluorescence Lifetime Imaging Microscope (FLIM). The $CsPbBr_3$ nanocrystals dispersed in toluene are placed into a micro-cuvette system and halides (I, Cl) are introduced to the solution through injection of their precursors (CsI, ZrI, DDACl) dispersed either in isopropyl alcohol or toluene. The wideband sensing of FLIM allows for real-time observation of the halide exchange in $CsPbBr_3$ (Figure 1), which is revealed by recording the photoluminescence lifetime of the perovskite chemical phases. This allows for determination of the reaction's kinetics, reveals intermittent perovskite phases and helps to elucidate the underlying physical and chemical processes.

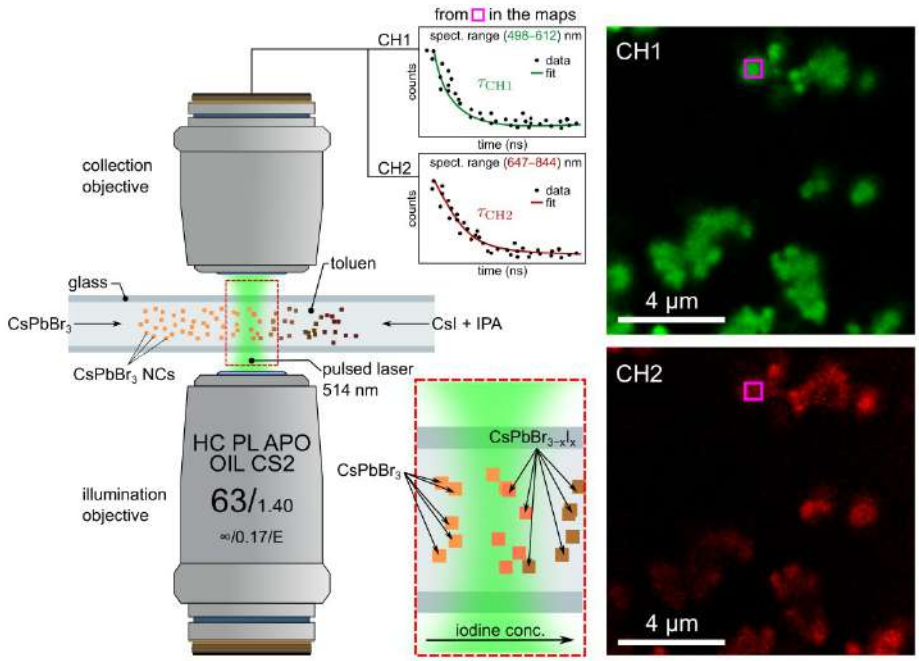


Figure 1 Schematics of the *in-situ* photoluminescence lifetime imaging of halide anion exchange in $CsPbBr_3$ nanocrystals.

The authors acknowledge financial support from the Czech Science Foundation (grant No. 25-17500S), ThermoFisher Scientific, CzechNanoLab (project LM2023051, MEYS CR), and the Light Microscopy Core Facility, IMG, Prague (MEYS LM2023050, RVO 68378050-KAV-NPUI).

References

1. Iragashi, H. "Correlation between Single-Photon Emission and Size of Cesium Lead Bromide Perovskite Nanocrystals," J. Phys. Chem. Lett., Vol. 14, No. 9, 2441-2447, 2023.
2. Shamsi, J. "To nano or not to nano for bright halide perovskite emitters," Nat. Nanotechnol., Vol. 16, No. 11, 1164-1168, 2021.
3. Hartono, N.T.P. "Stability follows efficiency based on the analysis of a large perovskite solar cells ageing dataset," Nat. Comm., Vol. 14, No. 1, 2023.
4. Král, J. "Towards high loading cesium lead halide nanocomposites for radiation detection," J. Phys. Materials, Vol. 8, No. 1, 2024.
5. Kovalenko, M.V. "Properties and potential optoelectronic applications of lead halide perovskite nanocrystals," Science, Vol. 358, No. 6364, 2017.
6. Liška, P. "Correlative imaging of individual $CsPbBr_3$ nanocrystals: Role of isolated grains in photoluminescence of perovskite polycrystalline thin films," J. Phys. Chem. C, Vol. 127, No. 25, 12404-12413, 2023.
7. Akkerman, Q.A. "Tuning the Optical Properties of Cesium Lead Halide Perovskite Nanocrystals by Anion Exchange Reactions," J. Am. Chem. Soc., Vol. 137, No. 32, 10276-10281, 2015.

Anisotropic response of hybridized collective plasmon modes of 2D-metal nanoparticle arrays assembled on periodically corrugated sapphire substrates

Maciej Wiesner [1]*, Ephraim T. Mathew [2], Andriy E. Serebryannikov [1], Jacek Jenczyk[2], Igor latsunskyi[2], Szymon Murawka[2], Mikołaj Lewandowski [2]

[1] Faculty of Physics, Adam Mickiewicz University, Uniwersytetu Poznańskiego 2, 61-614 Poznań, Poland

[2] NanoBioMedical Centre, Adam Mickiewicz University, Wszechnicy Piastowskiej 3, 61-614 Poznań, Poland

Abstract

Anisotropic 2D metal nanoparticles (2D-MNP) of radius *r*, which form arrays on corrugated sapphire, show in-phase longitudinal plasmon hybridization from strong inter-particle coupling. This hybridization includes anisotropic plasmonic responses dependent on the inter-particle distance *S*, excitation polarization angle *σ*, and pumping (laser) wavelength, making the substrates suitable for applications requiring tunable plasmonic properties.

Structural and Optical Characterization:

In the fabricated 2D-MNP arrays, sapphire templates subjected to thermal annealing have been utilized, resulting in periodic corrugations. Au films of various thicknesses (2–10 nm) were deposited to form the grains with the average diameters of ~30 nm. Atomic force microscopy (AFM) confirmed the anisotropic in-plane ordering of Au grains on the corrugated substrates. Reflection and transmission spectra were obtained for different polarization angles (σ = 0°, 45°, and 90°) by using ellipsometry. The shifts in plasmon resonance wavelengths (λ_p) with increasing Au thickness have been shown.

Results and Discussion

Plasmon Hybridization and Anisotropic Response

Far-field measurements revealed longitudinal bonding and transverse anti-bonding plasmon modes in the arrays. The wavelength λ_p is red-shifted while increasing the Au thickness, that is attributed to strong inter-particle coupling. These effects were stronger pronounced for the samples with smaller corrugation periods *P*, indicating the importance of precise inter-particle distances in anisotropic plasmonic behavior.

Electromagnetic (EM) simulations reveal near-field distributions consistent with the experimental results. These distributions show the enhanced coupling in the arrays with $S < r$, producing the localized plasmonic hotspots. The anisotropic plasmonic response has further been confirmed by measuring reflectance spectra for different polarizations, by highlighting the role of inter-particle distance in tuning the plasmonic modes.

SERS Enhancement Mechanism

The polarized SERS measurements showed the strong anisotropic enhancements for phenyl-thiolate analytes. Excitation at λ_{exc}=633 nm produced significant SERS dichroism, with lower-frequency Stokes peaks ($\lambda_{Stokes1}$) exhibiting $cos^2(\sigma)$ dependency, while higher-frequency peaks ($\lambda_{Stokes2}$) follow $sin^2(\sigma)$ dependency. The observed differences were linked to the near-field enhancement factors, *g* and g^s, which are associated, respectively, with the plasmonic coupling and the ordering of 2D-MNP arrays:

$$I_{SERS}(\lambda_{exc}) \propto |\alpha_R|^2 |gg^s|^2 I_{exc}(\lambda_{exc}) \quad (1)$$

where I_{SERS} is intensity of the emitted SERS peaks and I_{exc} is intensity of laser light.

At λ_{exc} = 785 nm, the anisotropy in SERS enhancement is more pronounced, as it relies on the dipole scattering intensity influenced by the array's ordering. The comparison of flat and corrugated templates indicates that smaller corrugation periods *P* can produce higher enhancements, demonstrating the interplay between nanoparticle arrangement and plasmon resonance tuning.

Implications for SERS Applications

The combination of the distributed hotspots and broader plasmonic resonances makes the proposed substrates ideal for reliable and reproducible SERS sensing. The observed anisotropic SERS effects provide new insights into the possible role of plasmon hybridization in optimizing SERS performance. The dichroic behavior observed at Stokes peaks highlights the potential of the substrates of the used type in advanced sensing applications, particularly in polarized SERS techniques.

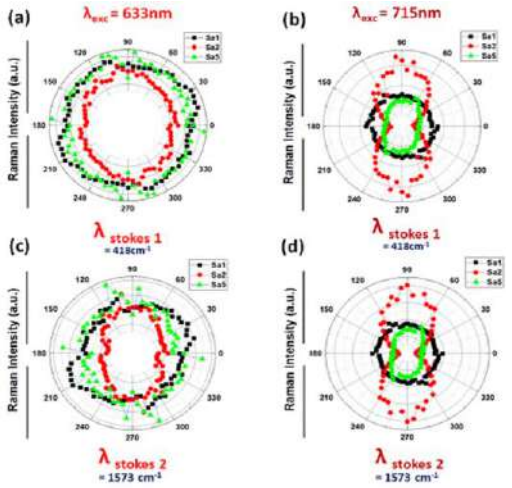


Figure 1. (a) and (c): example of SERS dichroism for $\lambda_{Stokes1}$ and $\lambda_{Stokes2}$ peaks on flat sapphire (sample Sa1) and corrugated sapphire, Sa2 (P=30nm) and Sa5 (P=150nm) samples measured for $\Delta\sigma = 5^o$ at λ_{exc} = 633nm. (b) and (d): example of SERS dichroism for $\lambda_{Stokes1}$ and $\lambda_{Stokes2}$ peaks on Sa1, Sa2 and Sa5 samples measured for $\Delta\sigma = 5^o$ at λ_{exc} = 785nm.

Conclusions

The ordered 2D-MNP arrays with the inter-particle spacing S smaller than the radius r were fabricated by depositing non-percolated ultrathin Au films onto the corrugated sapphire templates. The golden grains with diameter d nucleated anisotropically onto the templates with period $P \approx d$. In contrast, the templates with $P \gg d$ produced disordered grain nucleation. *First, the novelty of the results presented here is an anisotropic response of the collective plasmon modes arising in the 2D-MNP arrays, depending on the polarization azimuthal angle σ*. The simulated spectra and EM near-field distributions confirm this anisotropy and reveal plasmon hybridization. *The second interesting conclusion from SERS experiments states that the transverse collective plasmon modes excited at λ_{exc}=633nm< λ_p depend primarily on S rather than the extent of order in the MNP arrays.* It is supported by similar absolute SERS intensities at σ=90^o for flat substrate $P \approx d$, and substrate with $P \gg d$. Conversely, at λ_{exc}=785 nm > λ_{LP1}, the absolute SERS intensities at σ=90^o and σ=0^o are varied among the investigated samples, indicating that the ordering of MNP arrays affects the dipole mode scattering intensity and contributed to anisotropic SERS enhancement. *The third important outcome of our investigation is the SERS dichroism dependence on λ_{exc}, λ_p, and σ.* The lower-frequency Stokes-shifted peaks ($\lambda_{Stokes1}$), being closer to λ_p and λ_{exc}, exhibit a $cos^2(\sigma)$ dependency, that is consistent with the $|E|^4$ mechanism. In contrast, higher Stokes-shifted peaks ($\lambda_{Stokes2}$) follow a $sin^2(\sigma)$ dependency, being driven by variations of the enhancement factors (g at λ_{exc} and g^s at λ_{Stokes}) that validates the EM near-field mechanism of SERS. Finally, the essential criteria for reliable, reproducible, and feasible SERS measurements, such as distributed hotspots, broad resonance peaks (enabling wider Stokes-shifted ranges), and near-field enhancements up to 10^{10}, were successfully met.

Acknowledgments

The studies were supported by two programs: the LaSensA project carried out under the M-ERA.NET 2 scheme (European Union's Horizon 2020 research and innovation programme, grant No. 685451) and co-funded by the Research Council of Lithuania (LMTLT), agreement No. S-M-ERA.NET-21-2, the National Science Centre of Poland, project No. 2020/02/Y/ST5/00086, and the Saxon State Ministry for Science, Culture and Tourism (Germany), grant No. 100577922, as well as from the tax funds on the basis of the budget passed by the Saxon State Parliament. Moreover; the IDUB Mini grant (internationalization of scientific research at the Doctoral School of the Adam Mickiewicz University, grant No. 054/13/SNŚ/0043).

Etching-free rare earth doped meta-surfaces made by pulsed laser deposition

Antoine BERNARD[1], Antonio PEREIRA[1], Hai-Son NGUYEN[2], Sébastien CUEFF[2], Tam NGUYEN[2], Christian SEASSAL[2], Etienne CLEYET-MERLE[1], Yannick GUYOT[1], Alban GASSENQ[1,*]

[1] Institut Lumière Matière, UMR5306, CNRS, UCBL, Lyon, France

[2] Institut des Nanotechnologies de Lyon, UMR 5270, CNRS, ECL, INSA, UCBL, Lyon, France

[*]alban.gassenq@univ-lyon1.fr

Abstract: Etching is a complex and costly method for making nano-structuration in photonics. In this work, we present an innovative approach to fabricate meta-surfaces without etching, using Pulsed Laser Deposition combined with liftoff processing to enhance rare earth emission.

Rare earth based micro- and nano-photonics are promising for applications in quantum optics or telecommunication [1], [2]. Materials such as Y_2O_3 and Al_2O_3 are suitable hosts for lanthanide ions, including Erbium (for telecom wavelength) and Europium (for visible light applications). However, their microfabrication requires etching processes, which currently increases the cost and limits the design flexibility of devices [2], [3], [8]. In 2021, we have demonstrated for the first time that micro-strips of Y_2O_3:Eu^{3+} could be fabricated ~~are possible to make~~ without etching by combining Pulsed Laser Deposition (PLD) with liftoff processing [4]. Later on, we have extended our technic~~s~~ to other materials, including Al_2O_3 with Er doping [5] and we have improved the resolution fabrication down to few micrometers [6]. More recently, we have also shown that beam filtered PLD can provide high quality films suitable for waveguide applications [7]. Finaly, we are now exploring etching-free photonic crystals, showing very promising results for nano-metric structurations.

Figure 1-a illustrates the PLD principle. A high-fluence laser is focused on a target, ejecting a high kinetic energy plume that deposits matter onto a substrate. This directive method enables thus the production of high-quality layers at room temperatures, surpassing other methods in certain aspects. Following this, a lithography step is performed (Figure 1-b), after which lift-off processing can be performed directly after deposition (Figure 1-c) to create micro or nanostructures (Figure 1-d) [4]. Nevertheless, several optimizations are required, such as the control of the photoresist sidewall slopes (Figure 1-b), the layer quality (Figure 1-c) and the clean liftoff process to obtain smooth sidewalls (Figure 1-d).

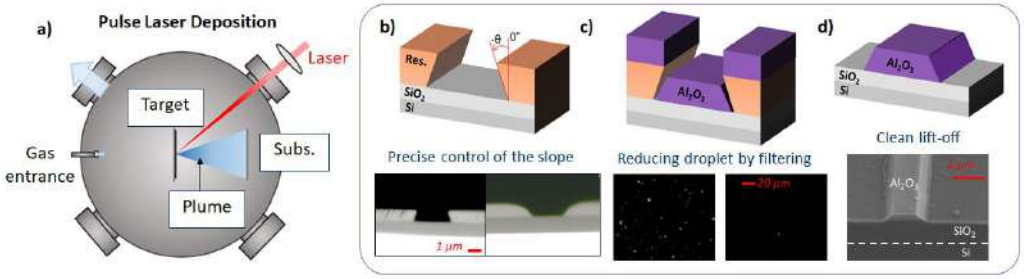


Figure 1 : a) Pulsed laser deposition technics; Processing and optimization for b) slope control of the lithography, c) layer quality improvement and d) clean liftoff

Figure 2 shows examples of rare-earth-doped microstructures with various shapes, such as micro-bowls arrays (Figure 2-a), gratings (Figure 2-b), ring resonators (Figure 2-c), nanopillars (Figure 2-d) and photonic crystals (Figure 2-e). In addition to the cost advantage, this approach provides access to new shapes, such as micro-bowls or localized doped rings, that are challenging to achieve using conventional methods (ANR project IDEAL 2025-28 in progress). The deposited thicknesses are intrinsically linked to the photosensitive resin thickness, with a typical thickness ratio of approximately 1:3. This allows the fabrication of structures around 500 nm thick with micrometric resolution (e.g., waveguides, infrared gratings) or thinner layers, approximately 100 nm layers, with sub-micrometric resolution (e.g., micro pillars or photonic crystals).

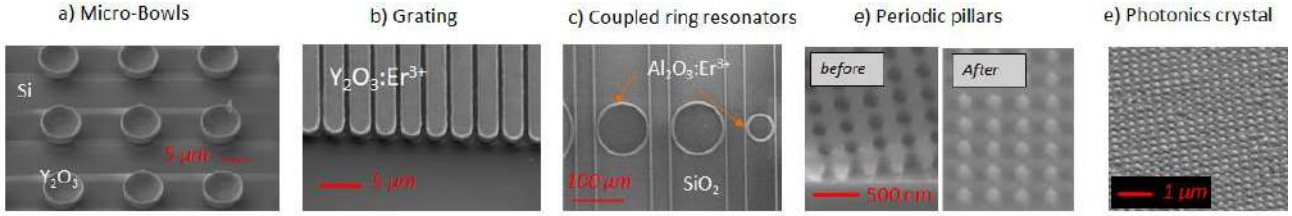


Figure 2: SEM imaging for a) arrays of micro bowls, b) grating, c) ring resonator, periodic pillar and e) photonics crystal.

Figure 3 presents optical characterizations of the fabricated devices, including the photoluminescence of microstrip for various materials and doping configurations [4], [5] (Figure 3-a) and the modified reflectivity showing the Erbium photoluminescence enhancement (Figure 3-b and c) [6]. Furthermore, we recently demonstrated low-losse waveguides made of Al_2O_3, achieving losses as low as 2 dB/cm [7].

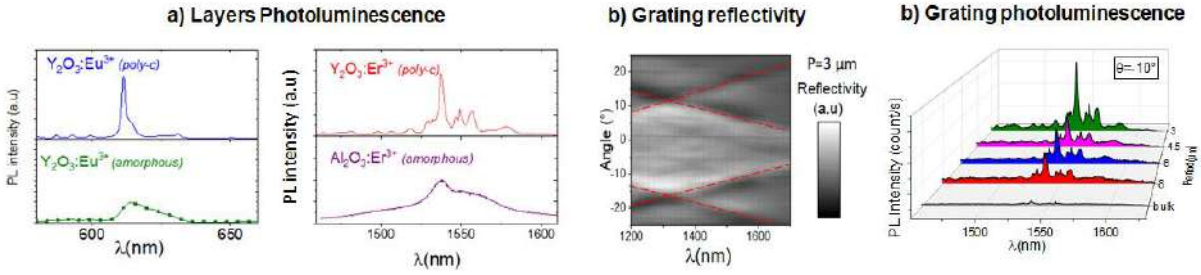


Figure 3 : Photoluminescence measurements in microstrip with different materials and doping [4], [5] *; b) reflectivity measurement in 3µm period grating and c)associated photoluminescence as a function of the grating period* [6]

This work highlights the significant potential of our approach combining PLD and liftoff-for fabricating innovative devices with rare earth doping. It could also be extended to other materials and applications currently constrained by etching limitations.

References

[1] Ruskuc et al., *Nature*, **2022**, https://doi.org/10.1038/s41586-021-04293-6.

[2] Hendriks et al., Adv. Phys. X, 2021, https://doi.org/10.1080/23746149.2020.1833753.

[3] Cao et al., *Appl. Surf. Sci.*, **2016**, https://doi.org/10.1016/j.apsusc.2016.01.092.

[4] Gassenq et al., *Opt. Express*, **2021**, https://doi.org/10.1364/oe.416450.

[5] Gassenq et al., *Appl. Phys. A*, **2023**, https://doi.org/10.1007/s00339-023-06549-6.

[6] Gassenq et al., *Opt. Lett.*, **2023**, https://doi.org/10.1364/OL.486893.

[7] Bernard et al., *Submitt. to Appl. Phys. Lett.*, **2024**.

[8] Hoang et al., *ACS Photonics*, **2017**, https://doi.org/10.1021/acsphotonics.7b00177.

We thank the Nanolyon plateform member of the French Renatech network for the clean room facility.

Lattice Resonances in Bipartite Arrays of Nanostructures for Tailored Optical Responses

J. J. Alvarez-Serrano[1*], J. R. Deop-Ruano[1], L. Cerdán[1], V. Aglieri[2], A. Toma[2] and A. Manjavacas[1]

[1]Instituto de Química-Física "Blas Cabrera" (IQF-CSIC), Madrid, Spain.

[2]Istituto Italiano di Tecnologia, Genova, Italy.

[*]juanjose.alvarez@csic.es

Abstract: Bipartite, two-dimensional periodic arrays stand as promising platforms for photonic applications. By controlling the nanoparticle positioning within the unit cell, we demonstrate that these systems can be exploited to achieve perfect absorption and to excite out-of-plane lattice resonances at normal incidence, which exhibit outstanding quality factors.

Lattice resonances are collective modes supported by periodic arrays of nanoparticles, arising from their coherent interactions [1]. While monopartite configurations (arrays with only one particle per unit cell) provide the simplest setting for observing these modes, bipartite arrays offer a compelling avenue for exploration. In particular, controlling the relative positioning of the two nanoparticles within the unit cell serves as a powerful tool for tailoring and accessing remarkable optical phenomena not achievable in monopartite systems. Here, we demonstrate that bipartite systems can be leveraged to achieve perfect absorption in planar arrays and to excite out-of-plane lattice resonances at normal incidence. Furthermore, the resonances exhibit higher quality factors and greater tunability than traditional methods seeking similar goals, which makes these bipartite arrays as promising platforms for advanced optical applications.

Figure 1 summarizes the main results discussed in this communication, with Figure 1(a) presenting a schematic of the bipartite arrays under consideration in their most general form.

Placing the first particle at the origin and the second at the center of the unit cell cancels all electric-magnetic interactions between the nanostructures. In this configuration, purely electric and magnetic lattice resonances will not interact, allowing for their independent tuning. Such an effect can be leveraged to achieve perfect absorption by overlapping electric and magnetic lattice resonances (LRs) [2]. This principle can be demonstrated in a bipartite system composed of gold and silicon nanoparticles, which act as sources of electric- (ED) and magnetic dipolar (MD) resonances, respectively. Figure 1(b) demonstrates how, by carefully controlling the lattice period, the wavelengths at which these resonances overlap is precisely tuned, enabling for the perfect absorption effect.

Alternatively, a position like $(x, y) = (a_x/4, a_y/4)$ enables interactions that couple in-plane (x or y) and out-of-plane coordinates (z). In particular, the interaction between in-plane dipoles can induce an out-of-plane dipole moment, allowing for the excitation of out-of-plane lattice resonances at normal incidence [3]. This approach offers a significant advantage over conventional methods that rely on oblique incidence excitation, which often degrade the quality of the resonance and limit their applicability in integrated devices. As illustrated in Figure 1(c), by working with a bipartite array of silver nanospheres in vacuum we are able to generate out-of-plane lattice resonances with outstanding quality factors, advantageous for applications in lasing and biosensing.

Thus, our work paves the way for the design of bipartite arrays of nanostructures as platforms for advanced optical effects, enabling their exploitation in a wide range of photonic applications.

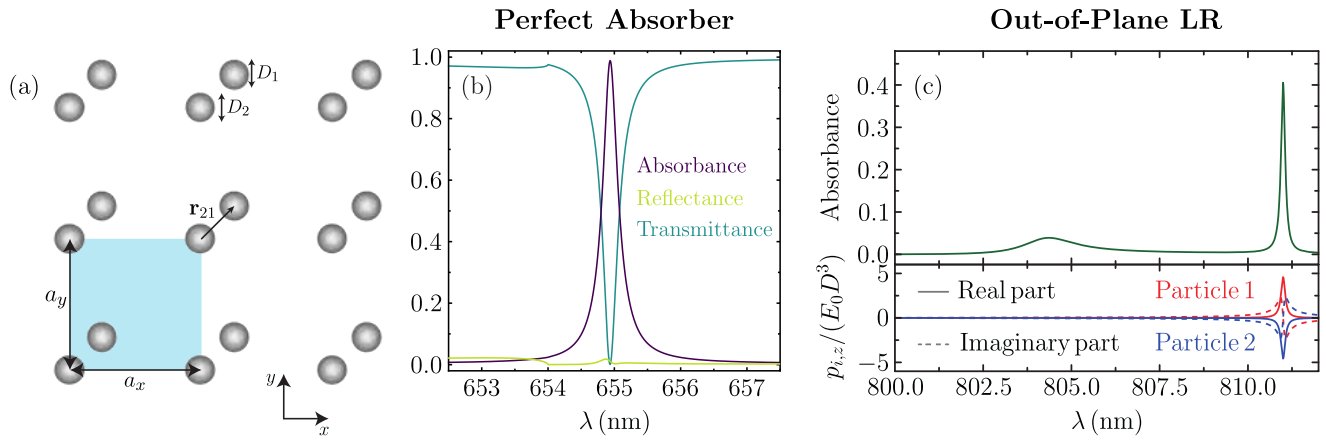


Figure 1. (a) Schematics of the bipartite systems under consideration. (b) Perfect absorber, achieved with a bipartite array that contains a gold and a silicon nanoparticle. The geometrical parameters of the system are: $a_x = 654$nm, $a_y = 649$nm, $D_{Au} = 98$nm, $D_{Si} = 140$nm, and $\boldsymbol{r_{21}} = (a_x/2, a_y/2, 0.0)$. (c) Excitation of an out-of-plane lattice resonance under normal incidence (λ~811nm) in a bipartite, square array composed of equal silver nanospheres. The parameters in this case are: $a_x = a_y = 800$nm, $D_{Ag} = 160$nm, and a relative position of $\boldsymbol{r_{21}} = (a_x/4, a_y/4, 0.0)$.

This work has been supported by grants PID2022-137569NB-C42, PID2019-109502GA-I00, and PID2019-104268GB-C21 funded by MCIN/AEI/10.13039/501100011033, a 2022 Leonardo Grant for Researchers in Physics from the BBVA, and a "La Caixa" Foundation Fellowship with code LCF/BQ/DR24/12080025.

References

1. Auguié, B., and Barnes, W. L., "Collective Resonances in Gold Nanoparticle Arrays", Phys. Rev. Lett, 101, 143902, 2008.
2. Cerdán, L., Deop-Ruano, J. R., Alvarez-Serrano, J. J., and Manjavacas, A., "Perfect Absorption with Independent Electric and Magnetic Lattice Resonances in Metallo-Dielectric Arrays," Adv. Opt. Mater., 2302737, 2024.
3. Alvarez-Serrano, J. J., Deop-Ruano J. R., Aglieri, V., Toma, A., and Manjavacas, A., "Normal Incidence Excitation of Out-of-Plane Lattice Resonances in Bipartite Arrays of Metallic Nanostructures", ACS Photonics, 11, 1, 301 – 309 2024.

Design of Complex Liquid Crystal Photonic Devices

Peter Ropač[1,2*], Yu-Tung Hsiao[3], Žiga Černe[1], Brecht Berteloot[3,+], Yera Ussembayev[3], Inge Nys[3], Jeroen Beeckman[3], Kristiaan Neyts[3,4,5] and Miha Ravnik[1,2,6]

[1]Faculty of Mathematics and Physics, University of Ljubljana, Ljubljana, Slovenia
[2]Institute Jožef Stefan, Ljubljana, Slovenia
[3]ELIS Department, Ghent University, Ghent, Belgium,
[4]Department of Electronic and Computer Engineering, The Hong Kong University of Science and Technology, Hong Kong SAR,
[5]State Key Laboratory of Advanced Displays and Optoelectronics Technologies, Hong Kong, SAR
[6]International Institute for Sustainability with Knotted Chiral Meta Matter, Hiroshima, Japan.
[+]now associated with IMEC, Leuven, Belgium
[*]Corresponding author: peter.ropac@fmf.uni-lj.si

Abstract:
We demonstrate and discuss two approaches to designing complex liquid crystal (LC) photonic devices – shape and topology optimization. The methods are applied to LC filters, holograms and waveguides. The latter two were manufactured using photopatterning. With these design and manufacturing techniques we design high performance liquid crystal photonic devices.

Optical elements based on liquid crystals (LCs) are widely used for different applications due to their mechanical and electro-optical properties. The optical birefringence is actively exploited in LC-based optical devices [1], [2], [3]. With photoalignment, it is possible to create alignment patterns with very fine features, but the characteristic length scale of the LC is a necessary consideration during the design of LC optical devices. The design can be adjusted for the relaxation of the LC, by computing the full director configuration simulation or approximated with various mapping functions. Computer-generated holograms (CGHs) are promising for many applications [4], [5], [6]. The CGHs are 2D phase or amplitude patterns which when illuminated by a coherent light source are reconstructed into a 2D or 3D image in space. Optical waveguides are essential for tele- and data communication technology. In existing waveguide platforms, the propagation of light is realized efficiently, but for modulation and routing, hybrid integration with other material systems is often necessary [7], [8], [9]. Topology optimization is a powerful computational inverse design method that has been applied in engineering and scientific research to design and optimize structures with optimal physical or mechanical properties. Topology optimization for photonics is enabling the design of improved optical/photonic components and devices [10], [11], [12].
We design LC optical filters with specific transmission spectra using topology optimization. We design short-pass filters in various wavelength ranges which can work as standalone devices or be integrated into soft matter waveguides. We explore other transmission spectra such as Gaussian or linear. We developed a shape optimization design framework based on Signed Distance Functions (SDFs), where we can construct complex geometry and vector fields completely parametrically. A Python implementation of this framework is available in SPOMSO [13]. Using this approach and the photopatterning manufacturing method, we realize 3D waveguides in the bulk of the LC, by only defining the anchoring patterns on the surface. We show straight and curved waveguides with various radii of curvature and discuss the associated losses [14]. Another approach to design of complex geometry is by using topology optimization. We developed a topology optimization-based algorithm which generates phase-only 2D computer-generated holograms - TO-CGH [15]. With our algorithm, we can enforce design, manufacturing,

and material constraints. The liquid crystal-based computer-generated phase-only holograms are also manufactured using photoalignment. We further develop the algorithm to use different far-field solvers and to support full RGB holograms.

References

[1] J. Beeckman, K. Neyts, and P. J. M. Vanbrabant, "Liquid-crystal photonic applications," *Optical Engineering*, vol. 50, no. 8, p. 81202, 2011, doi: 10.1117/1.3565046.

[2] I. Nys, B. Berteloot, and K. Neyts, "Photoaligned Chiral Liquid Crystal Grating with Hysteresis Switching," *Adv Opt Mater*, vol. n/a, no. n/a, p. 2201289, 2022, doi: https://doi.org/10.1002/adom.202201289.

[3] C. Yoo *et al.*, "Dual-focal waveguide see-through near-eye display with polarization-dependent lenses," *Opt. Lett.*, vol. 44, no. 8, pp. 1920–1923, Apr. 2019, doi: 10.1364/OL.44.001920.

[4] D. Pi, J. Liu, and Y. Wang, "Review of computer-generated hologram algorithms for color dynamic holographic three-dimensional display," *Light Sci Appl*, vol. 11, no. 1, p. 231, 2022, doi: 10.1038/s41377-022-00916-3.

[5] V. R. Curtis, N. W. Caira, J. Xu, A. G. Sata, and N. C. Pégard, "DCGH: Dynamic Computer Generated Holography for Speckle-Free, High Fidelity 3D Displays," in *2021 IEEE Virtual Reality and 3D User Interfaces (VR)*, 2021, pp. 1–9. doi: 10.1109/VR50410.2021.00097.

[6] C. Jin, C. Liu, R. Shi, and L. Kong, "Precise 3D computer-generated holography based on non-convex optimization with spherical aberration compensation (SAC-NOVO) for two-photon optogenetics," *Opt. Express*, vol. 29, no. 13, pp. 20795–20807, Jun. 2021, doi: 10.1364/OE.426578.

[7] S. Y. Siew *et al.*, "Review of Silicon Photonics Technology and Platform Development," *J. Lightwave Technol.*, vol. 39, no. 13, pp. 4374–4389, Jul. 2021, [Online]. Available: https://opg.optica.org/jlt/abstract.cfm?URI=jlt-39-13-4374

[8] H. Ma, A. K.-Y. Jen, and L. R. Dalton, "Polymer-Based Optical Waveguides: Materials, Processing, and Devices," *Adv. Mater.*, vol. 14, no. 19, pp. 1339–1365, Sep. 2002, doi: https://doi.org/10.1002/1521-4095(20021002)14:19<1339::AID-ADMA1339>3.0.CO;2-O.

[9] S. Kang, G. Dong, J. Qiu, and Z. Yang, "Hybrid glass optical fibers-novel fiber materials for optoelectronic application," *Opt. Mater.: X*, vol. 6, p. 100051, 2020, doi: https://doi.org/10.1016/j.omx.2020.100051.

[10] J. S. Jensen and O. Sigmund, "Systematic design of photonic crystal structures using topology optimization: Low-loss waveguide bends," *Appl Phys Lett*, vol. 84, no. 12, pp. 2022–2024, 2004, doi: 10.1063/1.1688450.

[11] A. M. Hammond, A. Oskooi, M. Chen, Z. Lin, S. G. Johnson, and S. E. Ralph, "High-performance hybrid time/frequency-domain topology optimization for large-scale photonics inverse design," *Opt. Express*, vol. 30, no. 3, pp. 4467–4491, Jan. 2022, doi: 10.1364/OE.442074.

[12] B. S. Lazarov, F. Wang, and O. Sigmund, "Length scale and manufacturability in density-based topology optimization," *Archive of Applied Mechanics*, vol. 86, no. 1, pp. 189–218, 2016, doi: 10.1007/s00419-015-1106-4.

[13] P. Ropač, "SPOMSO: SDF based geometry generation," Jun. 21, 2024, *Zenodo*: 1.2.3. doi: 10.5281/zenodo.8090670.

[14] P. Ropač *et al.*, "Liquid Crystal 3D Optical Waveguides Based on Photoalignment," *Adv Opt Mater*, p. 2402174, 2024, doi: 10.1002/ADOM.202402174.

[15] P. Ropač, Y.-T. Hsiao, B. Berteloot, M. Ravnik, and J. Beeckman, "Material-Constrained Optimization of Liquid Crystal-Based Holograms," *Adv Opt Mater*, vol. 12, no. 26, p. 2400972, 2024, doi: https://doi.org/10.1002/adom.202400972.

Meta-Cracks in Thin Films for Ultrasensitive Strain Monitoring

Jae-Hwan Lee[1,2], Seung-Kyun Kang[1,2,3,4*]

[1] Department of Materials Science and Engineering, Seoul National University, Republic of Korea
[2] Research Institute of Advanced Materials (RIAM), Seoul National University, Republic of Korea
[3] Interdisciplinary Program of Bioengineering, Seoul National University, Republic of Korea
[4] Nano Systems Institute SOFT Foundry, Seoul National University, Republic of Korea
[*]corresponding author: kskg7227@snu.ac.kr

Abstract: Mechanical metamaterials enable novel behaviors like tunable crack openings in thin metal films. These "meta-crack" sensors, combining high sensitivity and conformal contact, outperform conventional sensors. Leveraging Poisson-induced contraction and metamaterials, they offer adjustable sensitivity and strain range, with applications in bio-diagnostics like real-time stroke detection, revolutionizing healthcare innovations.

Mechanical metamaterials offer insights into novel mechanical behaviors by inducing unexpected deformations in conventional materials. In this study, we explore the unique phenomenon of crack opening in thin metal films, which exhibits distinctive behavior when coupled with a metamaterial structure. Thin-film crack sensors are advantageous due to their simple fabrication process, thin profile, and ability to achieve conformal contact with various surfaces, enabling broad applicability. The induced cracks in the thin film result in significant changes in electrical conductivity even under minor deformations, making them highly sensitive sensors. Unlike conventional sensors, the key feature lies not in binary on/off resistance changes but in the Poisson-induced contraction, which prevents immediate separation of crack surfaces. This creates transient contact areas, maintaining sensor functionality. However, this mechanism can also reduce sensitivity. By incorporating metamaterial structures, we successfully controlled the crack opening behavior, allowing tunable sensor sensitivity and an extended measurable strain range.[1] Furthermore, we demonstrate the application potential of these "meta-crack" sensors in bio-diagnostics, including real-time stroke detection.[1] This presentation will cover the deformation mechanisms, sensor applications, and practical implementations of these advancements, highlighting their potential in healthcare and beyond.

Figure 1a demonstrates through SEM imaging that cracks with meta-structured substrates exhibit faster interface opening under tensile strain compared to those without meta structures.[1] The meta-crack sensor is composed of a crack-induced conductive Mo layer (50 nm thick), a MoO_3 adhesive layer (15 nm thick), and a substrate featuring an auxetic structure. The substrate combines a PBAT base matrix (30 μm thick) and a PLA auxetic structure (10 μm thick). With a Poisson's ratio of -0.9, the sensor achieves a gauge factor at least four times higher than conventional crack sensors at a strain of 3×10^{-3}, delivering an exceptional strain resolution in the 10^{-5} range.

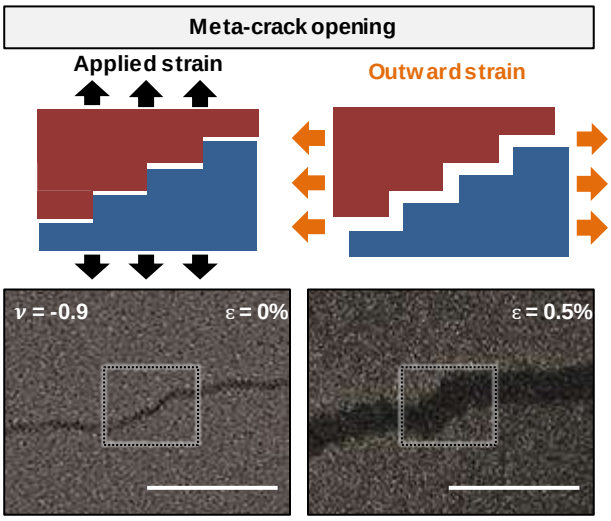


Figure 1. Illustration and SEM images highlight the step-shaped crack boundaries and their response to vertical tensile strain (5×10^{-3}) in meta-cracks characterized by a Poisson's ratio of -0.9. (This material is reproduced with permission from Jae-Hwan Lee et al., "Hypersensitive meta-crack strain sensor for real-time biomedical monitoring," Science Advances, Vol. 10, eads9258 (2024). DOI: 10.1126/sciadv.ads9258. © 2024)[1]

References

1. Jae-Hwan Lee et al., Hypersensitive meta-crack strain sensor for real-time biomedical monitoring.*Sci. Adv.***10**,eads9258(2024). DOI:10.1126/sciadv.ads9258.

Strong-Field Tunable Light-Generating Metasurfaces

E. Almeida[1,2*], M. D. Feinstein[1*], and G. Trivizas[1]

[1]Queens College, City University of New York, United States of America
[2]The Graduate Center of the City of New York, United States of America
[*]corresponding author: euclides.almeida@qc.cuny.edu

Abstract: We present a new class of all-optically tunable, light-generating metasurfaces. By coupling virtual excitons in two-dimensional semiconductors with off-resonant photons from a strong field, we attain ultrafast spectral and amplitude control of harmonic generation in nonlinear metasurfaces. Our work represents a significant advancement in the development of compact light sources.

Nonlinear metasurfaces are a special class of compact light-generating photonic platform, where light's parameters such as amplitude, phase and polarization can be controlled with nanoscale precision[1]. This powerful control has allowed multiple demonstrations such as nonlinear holography, imaging and generation of entangled photons[1-3]. Active tuning in ultrafast temporal scales will greatly expand the capabilities of nonlinear metasurfaces, in particular for all-optical information processing. However, most all-optical control schemes rely on resonant excitation, limiting their tuning rate to the lifetime of electronic excitations, which range from hundreds of femtoseconds (hot-electrons) to picoseconds (electron-hole recombination).

Here, we introduce a novel approach to attain ultrafast control of coherent light generation from metasurfaces by coupling an off-resonant strong laser field to virtual excitons in two-dimensional semiconductors. The scheme for all-optical tuning is illustrated in Figure 1(a), and is based on the AC Stark effect. A broadband femtosecond fundamental pulse (red pulse) excites a monolayer WS_2, with its third-harmonic emission (blue pulse) slightly above the excitonic resonance (613 nm). A second strong, off-resonant beam (green pulse, 800 nm), with electric field amplitude exceeding 10^8 V/m, couples to the virtual excitons, as depicted in the energy level diagram in Figure 1(b). This strong light-matter coupling induces a blue shift of the exciton peak and, consequently, the third-harmonic spectrum, which can be tuned by the gate pulse energy (Figure 1(c)). Since this interaction involves only virtual excitons, the tuning mechanism is in principle instantaneous with the gate pulse. However, nonlinear absorption of the gate beam can slow the tuning rate to the picosecond regime (Figure 1(d)).

Figure 1(e) shows self-tunable third-harmonic generation in a plasmon-exciton metasurface that utilizes only the intensity of the fundamental beam as the tunable parameter. The metasurface consists of an arrays of gold nanorods on monolayer WS_2 fabricated using near-field inverse design[4] (Figure 1(f)). The spectrum of the third-harmonic is tunable by up to 40 meV. This large tunability enables new applications such as a dynamic beam steering, as shown in figure 1(f). Under illumination by a circularly-polarized strong field, a periodic array of rotating rods on WS_2 generates third harmonic at an angle defined by the periodicity of the array, the helicity of the input pulse, and the central wavelength of the third harmonic beam. As we control the intensity of the fundamental pulse, the angle of the emitted third harmonic beam is tuned due to the change of the peak third-harmonic spectrum.

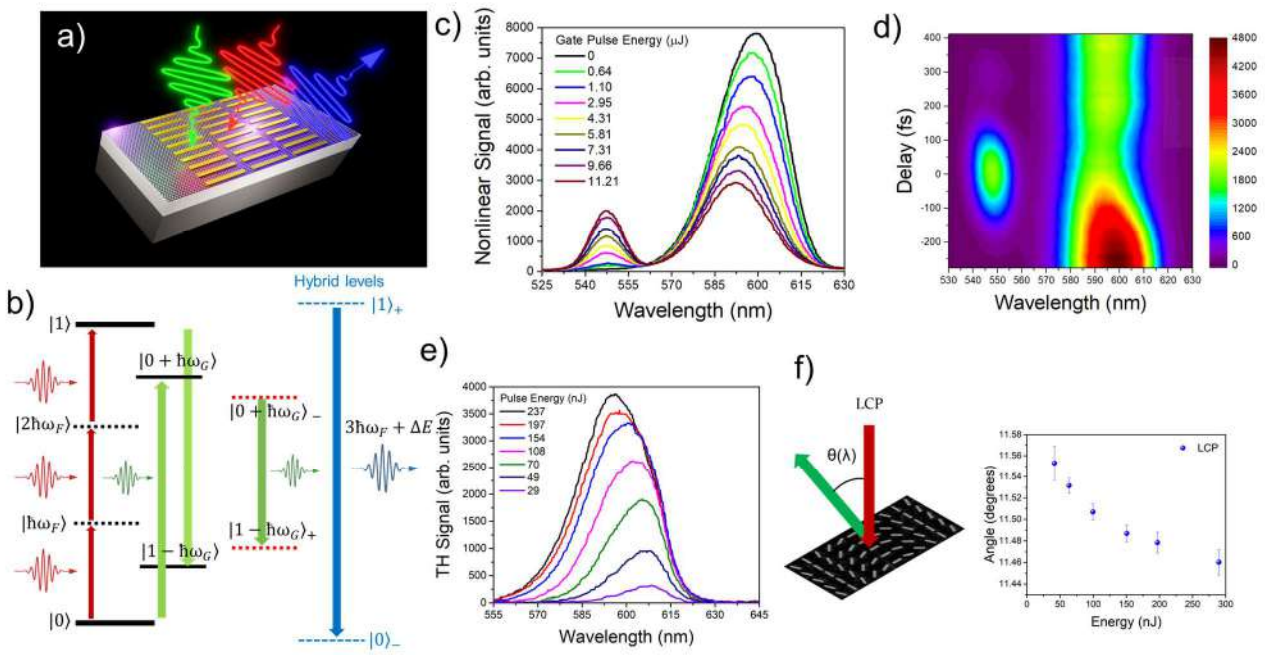


Figure 1. Tuning nonlinear metasurfaces with strong fields. a) Illustration of the tuning process. Fundamental pulse (red), control (green), third-harmonic (blue). b) Energy levels for the gated third harmonic generation. c) Third harmonic spectrum of monolayer WS_s as a function of the gate pulse energy. d) Ultrafast time-delayed measurements. e) Self-tunable metasurface, showing the TH spectra for various pulse energies of the fundamental beam. f) Self-beam steering in a phase-controlled nonlinear metasurface.

The authors acknowledge support from the Air Force Office of Scientific Research under grant number W911NF-23-1-0156. Support for this work was provided by a PSC-CUNY Award, jointly funded by The Professional Staff Congress and The City University of New York

References

1. Li, G., S. Zhang and T. Zentgraf, "Nonlinear Photonic Metasurface," Nature Reviews Materials 2, 17010 (2017)
2. Almeida, E., O. Bitton and Y. Prior, "Nonlinear Metamaterials for Holography," Nature Communications 7, 12533 (2016)
3. Santiago-Cruz, T. et al., "Resonant Metasurfaces for Generating Complex Quantum States," Science 377, 991 (2022).
4. Blechman, Y., et al., "Strong Coupling at Room Temperature Achieved by Nanoscale Inverse Design," ACS Photonics 10, 2494 (2023).

An all Al Terahertz Metasurface with Friedrich-Wintgen Bound States in the Continuum

T. Aikawa[1], G. M. Rodriguez-Barrios[2], Z. Li[3], A. Baydin[2], J. Kono[2], W. Sims[3], P.-Y. Chen[1], T. A. Searles[1], and Z. A. Chase[1*]

[1]Department of Electrical and Computer Engineering, University of Illinois Chicago, USA
[2]Department of Electrical and Computer Engineering, Rice University, USA
[3]Department of Physics, Morehouse College, USA
[*]corresponding author: chase8@uic.edu

Abstract: An all Al metasurface, through numerical evaluation and THz-TDS spectroscopy, shows enhanced light-matter interaction via the presence of multimode ultra strong coupling (USC) with FW-BIC's occurring near the anti-crossings.

The phenomena of ultra strong coupling (USC), has applications in low loss on-chip communication, nonlinear harmonic generation, and will be critical for quantum computing architectures including the growing sector of quantum information technology [1,2]. USC can be achieved by placing a resonator inside a cavity with distinct resonances for both the resonator and cavity. The resulting interaction between the two resonances is exhibited through a spectral line splitting which is the creation of an upper and lower polariton. The polaritons are quasi-particles that have properties of both light and matter. The cavity creates a photon field, and the resonator creates a matter excitation. The coupled light-matter interaction creates these quasi-particles known as polaritons. When the strength of the coupling between the two becomes a significant fraction of the resonant frequency such that the frequency splitting is 10% of the resonant frequency it is said to be in the USC regime. For quantum computing platforms, the stronger the coupling the more efficient qubit-photon coupling can become which provides shorter operation times. The USC regime also allows the possibility of replacing quantum gates just by their very nature due to the natural evolution of a USC system. [3] In quantum information technology, particularly quantum computation, the core idea is to use multiple interconnected quantum systems to perform calculations, enabling the use of numerous qubits. The strength of the coupling between qubits determines the speed at which a quantum computer can process information. Exploring this phenomenon in the terahertz (THz) region is crucial, as it provides a greater communications bandwidth compared to microwave frequencies. FW-BIC's occur in cavities as a function of continuous parameter (i.e. the length of the ribbon as it is varied in the cavity). This interference induces an anti-crossing which results in part of the polariton to vanish becoming an FW-BIC. [4,5] FW-BIC's have found many applications in laser, demultiplexers and filters. [4]

Figure 1(a) shows a unit cell of the metasurface consisting of a 200 nm thick Al thin film that consists of the cavity-dipole system on a 150 μm thick quartz substrate. The cavity-dipole system is comprised of a cavity that is 280 μm x 30 μm and a ribbon that is 10 μm wide with its length parametrically varied from 50 to 270 μm. Numerical calculations were performed using ANSYS HFSS to predict the spectral response of the structure which was illuminated at normal incidence under a TE polarized wave. Periodic boundary conditions are applied to mimic the periodic unit cell. The ribbon displays a dipole resonance. As the ribbon is varied parametrically the dipole resonance changes as well. The dipole resonance sweeps the frequency range that overlaps with the second and third cavity modes. This effect causes two anti-crossings to occur in our metasurface. The contour

plot of Fig. 1(b) shows anti-crossing at zero-detuning to be at ~0.784 THz, respectively with a rabbi splitting (ΩR) of 0.17 for the third cavity mode. The second cavity mode at 0.584 THz also has an anti-crossing with the with a rabbi splitting (ΩR) of 0.19 showing that this structure results in multimode USC. The near field coupling strength derived from the two-band Hamiltonian show FW-BIC at 0.72 and 0.51 THz. We show an enhanced light-matter interaction that can be utilized for various optical applications in a small, compact device.

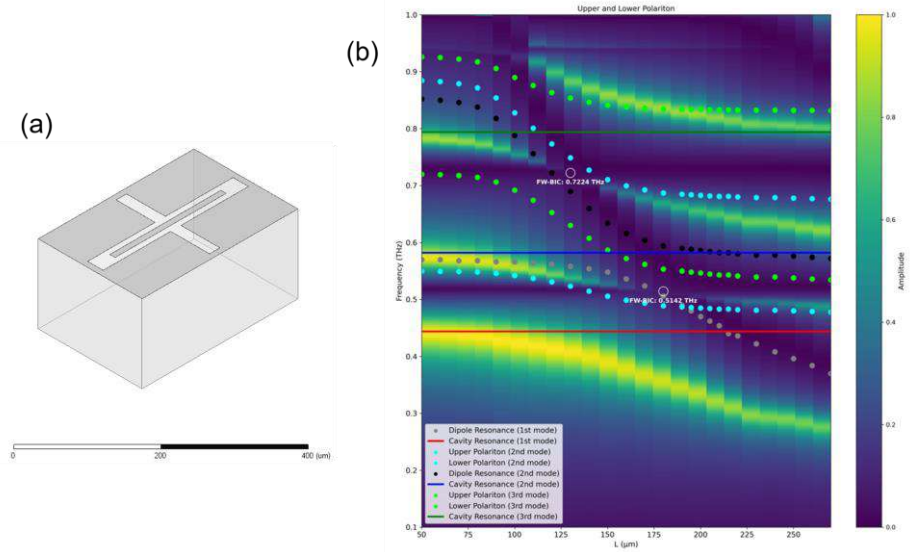


Figure 1: (a) This is the unit cell of the metasurface. (b) Contour plot of the transmission of the metasurface as the ribbon is parametrically varied. Green and light blue dots indicate the upper and lower polaritons for the third and second cavity modes.

Acknowledgements: We would like to thank DOE Award #: 0000276559 for funding this project.

References

1. S. Joseph et al., Nanophontics 10, (2021).
2. A. Blais et al., Phys Rev. A 69, 062320 (2004).
3. A. Laucht et al., Nanotechnology 32, 162003 (2021).
4. C. W. Hsu et al., Nature Reviews Materials 1.9, 16048 (2016).
5. M. Amrani et al., Phys. Rev. B 106, 125414 (2022).

300-GHz-band metasurface technology for wireless communication and sensing

A. Pander*, H. Kagami, D. Kitayama, H. Matsunaga, and H. Takahashi

[1]NTT Device Technology Labs., NTT Corporation, 3-1 Morinosato-Wakamiya, Atsugi, Kanagawa, 243-0198, Japan

*Corresponding author: adam.pander@ntt.com

Abstract: 300-GHz-band transmission-type metasurfaces for signal coverage extension in wireless communication and high-resolution sensing applications were designed, fabricated, and evaluated. Gradient beamforming devices with steering angles between 18° and 38° and collimating lenses based on 3-bit quantization were fabricated as self-standing devices which makes them perfect candidates for future sub-THz applications.

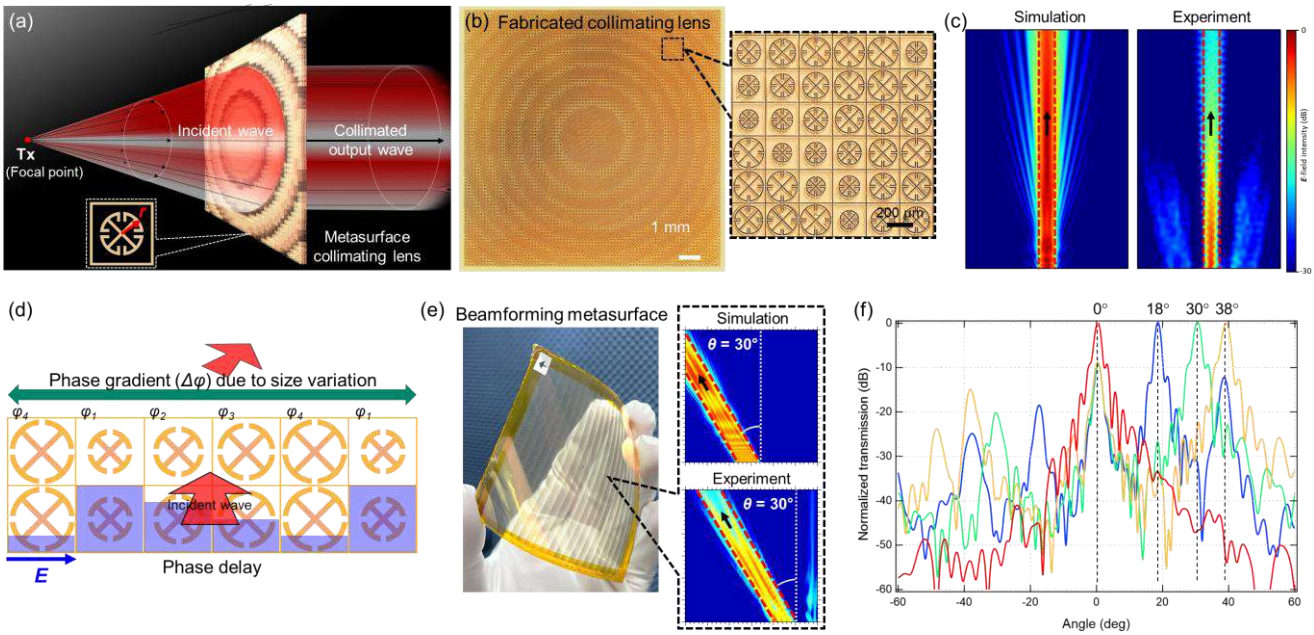


Fig. 1. (a) Schematic of operating of collimating metasurface lens. (b) Fabricated metasurface lens and (c) obtained in simulation and experiment near ***E*** field results. (d) Schematic of operation of gradient beamforming metasurface. (e) Fabricated metasurface beamformer and near ***E*** field results for beam steering angle of 30°. (f) Far-field characteristics for beamforming metasurfaces at 300 GHz band.

With advancements in high-frequency semiconductor technologies, major attention has been brought to sub-terahertz waves (millimeter-wave) due to their unique characteristics, like high directivity, wide bandwidth, or very distinctive absorption spectra. Millimeter waves, especially between 30 and 300 GHz, became a major development target for high-capacity wireless communication networks with data rates over 100 Gb/s, and high-resolution sensors for short-range applications and object recognition [1,2]. However, an increase in operation frequencies generally leads to the degradation of signal-to-noise ratios (SNR) and data rates in the system, due to strong atmospheric attenuation, non-line-of-sight propagation (high linearity), and free space path losses [3]. To cope with these challenges, in both wireless communication and radar sensing, various beamforming and beam shaping techniques were developed to allow for desired beam radiation patterns, beam scanning, or spectral selectivity. Among these techniques, metasurface-based devices, both passive and active, have been intensively studied as an enabling technology and an alternative to complex conventional designs [4].

In this work, we present a diversity of devices at the 300 GHz band, including gradient beamforming metasurfaces for signal coverage expansion in wireless communication and multiple types of lenses for precise beam collimation and focusing. All the devices were fabricated using an in-house developed process to allow for multilayer metasurface structures that exhibit superb characteristics.

Fig. 1(a) shows an operation schematic of a metasurface lens composed of continuous 2π phase controllable multilayer metamaterial cells based on Jerusalem cross geometry that were organized into radial patterns with 3-bit quantization (eight steps) with phase step $\Delta\varphi = 45°$ between each zone. The radius of each zone was optimized to provide beam collimation of the incident wave from the transceiver (Tx) antenna placed at a close distance (20 mm) from the device. An example of a fabricated device operating at 300 GHz is shown in Fig. 1(b). As shown, radial zones are clearly defined in the image, while the inset confirms the high quality of the fabrication and the high level of alignment of each metamaterial layer (5 layers in total). The quality of beam collimation was evaluated by the electric near-field distribution maps, showing good consistency between the experiment and the simulation results. The data shown in Figs. 1(a-c) relates to the control of the beam collimation for high-resolution sensing applications in 300 GHz.

Fig. 1(d) shows a schematic of a phase gradient beamforming metasurface used for beam forming of the incident wave during wave transmission through the device. Similar to the sensing, the designed cells exhibit continuous 2π phase controllability as a response to radius variation. By the combination of different-sized metamaterial cells, the metasurface exhibits a desired transmission phase gradient across its surface, allowing for bending the beam into a predesigned direction (0 ~ 38° in this work). Fig. 1(e) shows fabricated gradient beamforming metasurface and near-$\boldsymbol{E}$-field results confirming beam steering at 30°. The obtained experimental results were in good agreement with the simulation. Additionally, as shown, fabricated metasurface devices exhibited good optical transparency and flexibility, expanding the range of potential use cases in wireless communication applications. Fig. 1(f) shows far-field results obtained for various beamforming angles in this work at 300 GHz. The main lobes in the graph correspond to the designed beam steering angles for all metasurface devices.

In this study, transmission-type metasurface devices for wireless communication and sensing are discussed and combine low loss, good transmission efficiency, broadband operation, and good control of output wave characteristics at 300 GHz. Additionally, good flexibility, optical transparency, and self-standing design were achieved making the presented devices a prospecting technology for future applications in sub-THz.

References

[1] M. Inomata, W. Yamada, N. Kuno, M. Sasaki, K. Kitao, M. Nakamura, T. Tomie, and Y. Oda, “Sub-terahertz propagation characteristics up to 150 GHz for 6G mobile communication systems”, Int. J. Microw. Wirel. Technol. 15(1), 51–58, 2023.

[2] L. Daniel, and M. Gashinova, “Sub-THz Radar Imagery for Automotive Application”, in Proceedings of the 19th European Radar Conference, 261–264, 2022.

[3] International Telecommunication Union Recommendation ITU-R P.676-12, “Attenuation by Atmospheric Gases and Related Effects”, 2019.

[4] A. Pander, D. Kitayama, H. Kagami, and H. Takahashi, “Multilayer-laminated optically transparent 300-GHz-band transmissive beamforming metasurface for wireless communication”, Opt. Exp. 32(14). 24772–24786, 2024.

Tunable beamsplitter based on continuous transition between a planar metasurface and a Brewster metafilm

Yasuhiro Tamayama[1*], and Yugo Shibata[1]

[1] Department of Electrical, Electronics and Information Engineering, Nagaoka University of Technology, Japan
*corresponding author: tamayama@vos.nagaokaut.ac.jp

Abstract: We develop a method for realizing a beamsplitter with a tunable splitting ratio using a metamaterial with deep subwavelength thickness. We numerically verify that the splitting ratio can be controlled by the arrangement of the constituent meta-atoms without changing the structure of the meta-atoms.

Controlling the reflectance and the transmittance is one of the most fundamental issues in the application of electromagnetic waves. It has already been shown that an arbitrary complex reflectance can be achieved in a metasurface with a ground plane and that an arbitrary complex transmittance can be achieved in a Huygens metasurface [1]. In addition to the control of either the reflectance or the transmittance, simultaneous control of the reflectance and the transmittance is also important. In this study, we develop a method for controlling the absolute values of the reflectance and the transmittance simultaneously in a broad frequency range using metamaterials.

First, we theoretically analyze the reflectance and the transmittance of a single-layer resonant metamaterial. Based on the coupled mode theory [2], the reflectance and the transmittance is calculated to be

$$r = -\frac{2k}{k^2+1}\frac{\gamma_\mathrm{r}}{-\mathrm{i}(f-f_0)+\gamma_\mathrm{r}+\gamma_\mathrm{nr}}, \quad (1)$$

$$t = 1-\frac{2}{k^2+1}\frac{\gamma_\mathrm{r}}{-\mathrm{i}(f-f_0)+\gamma_\mathrm{r}+\gamma_\mathrm{nr}}, \quad (2)$$

where f is the frequency of the incident wave, f_0 is the resonance frequency of the metamaterial, γ_r (γ_nr) is the radiative (non-radiative) loss of the metamaterial, k is the ratio of the radiation from the metamaterial in the propagation direction of the reflected wave to that of the transmitted wave. In the case of γ_nr =0, the absolute value of $r(f=f_0)$ [$t(f=f_0)$] can be varied in the range from 1 to 0 (0 to 1) by varying k in the range from 1 to 0. Assuming that the constituent meta-atom acts as an infinitesimally small dipole, k is equal to $\sin(45^\circ-\theta)/\sin(45^\circ+\theta)$ in the configuration of Fig. 1. Thus, k can be controlled in the range from 1 to 0 by varying θ in the range from 0° to 45°. Note that in the case of θ=0° (θ=45°), the single-layer metamaterial corresponds to a planar metasurface (Brewster metafilm [3]).

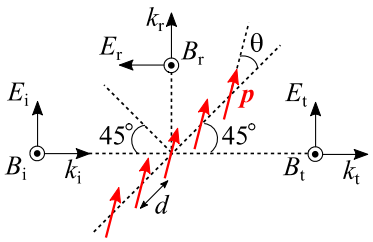


Fig. 1. The relationship between the electromagnetic fields and the electric dipoles induced in the meta-atoms. In the numerical simulation, d=16mm.

Now we verify the above theory numerically. We use a dipole resonator shown in Fig. 2(a) as the constituent meta-atom. The dipole resonator is assumed to be fabricated on a dielectric substrate (FR-4) and covered by the same dielectric as shown in Fig. 2(b) to simply decrease the resonance frequency in a realistic manner. We numerically analyze a metamaterial composed of the dipole resonator arranged as shown in Fig. 1. The calculated reflection and transmission spectra are shown in Figs. 3(a)-3(c). The absolute value of the reflectance (transmittance) at the resonance frequency decreases (increases) with increasing θ as shown in Fig. 3(d).

We gather from the above result that a tunable broadband beamsplitter may be realized using a metamaterial with deep subwavelength thickness that exhibits high reflectance in a broad frequency range for θ=0°. Then we

design and analyze a metamaterial composed of the structure shown in Fig. 2(c). Although this structure is a two-layer structure, the thickness is much smaller than the wavelength. The reflection and transmission spectra of the metamaterial for θ=0°, 15°, 24°, and 33° are shown in Fig. 4. The absolute value of the reflectance is high in a broad frequency range for θ=0° and broadband beamsplitters with different splitting ratio are realized by only varying θ.

In conclusion, we developed a method for realizing a tunable broadband beamsplitter based on the continuous transition between a planar metasurface and a Brewster metafilm. This result would be useful for realizing compact broadband beamsplitters with low losses especially in the low frequency region such as the microwave and the terahertz regions.

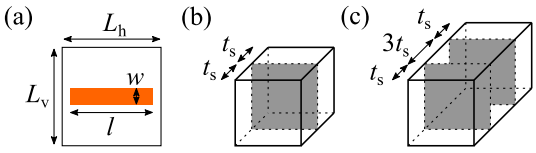


Fig. 2. (a) Schematics of the structure of the dipole resonator, (b) the structure of the meta-atom, and (c) the unit structure of the two-layer metamaterial. The dipole resonator is at the gray plane. In the numerical simulation, w=0.5mm, l=14mm, t_s=0.8mm, L_h=15mm, L_v=4mm.

The authors gratefully thank Satoshi Tomita for helpful discussion. This research was supported by the Japan Society for the Promotion of Science (JSPS) Grants-in-Aid for Scientific Research (KAKENHI) under Grant No. JP21K04192 and by the Japan Science and Technology Agency (CREST Grant No. JPMJCR2101).

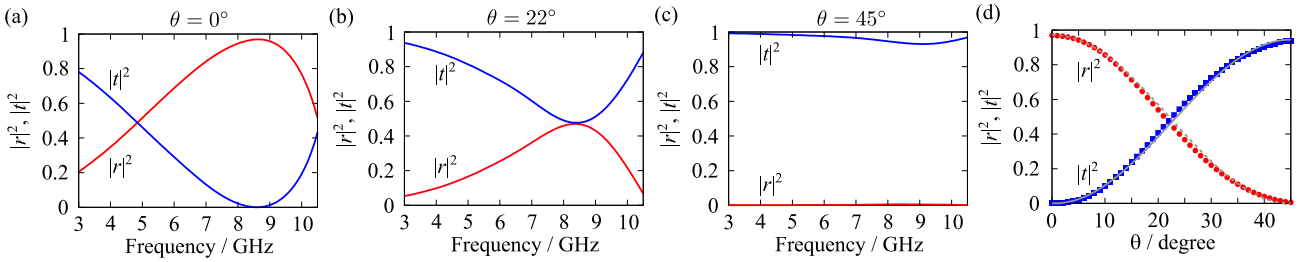


Fig. 3. The reflection and transmission spectra of the single-layer metamaterial for (a) θ=0°, (b) 22°, and (c) 45°. (d) The θ dependences of the reflectance and the transmittance at the resonance frequency. The gray curves are the theoretical fits.

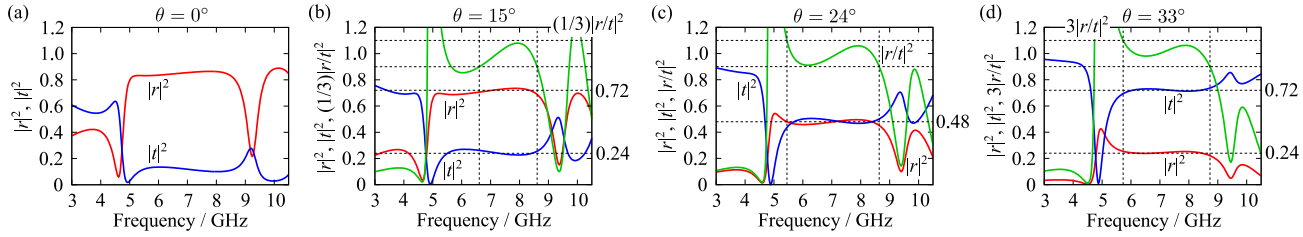


Fig. 4. The reflection and transmission spectra of the two-layer metamaterial for (a) θ=0°, (b) 13°, (c) 24°, and (d) 33°.

References

1. Chen, M. *et al*., "Huygens' metasurfaces from microwaves to optics: a review," Nanophotonics Vol. 7, No. 6, 1207–1231, 2018.
2. Christopoulos, T. *et al*., "Temporal coupled-mode theory in nonlinear resonant photonics: From basic principles to contemporary systems with 2D materials, dispersion, loss, and gain," J. Appl. Phys. Vol. 136, No. 1, 011101, 2024.
3. Tamayama, Y. and Yamamoto, H. "Broadband Control of Group Delay Using the Brewster Effect in Metafilms," Phys. Rev. Appl. Vol. 18, No. 1, 014029, 2022.

Plasmonic Enhanced Si-based Hot Electron Photodetector for SWIR Range

D.Cristea [*], R.Tomescu , G. Craciun and A.Dinescu

National Institute for Research and Development in Microtechnologies - IMT Bucharest, Romania
[*]corresponding author: dana.cristea@imt.ro

Abstract: We explored various architectures for plasmonic-enhanced Si Schottky photodetectors for SWIR, aiming at enhancing light absorption, hot electron generation and collection. The combination of grating-like electrodes with a nanostructured thin metal layer demonstrated the most promising results, with responsivities reaching the range of tens of mA/W at telecom wavelengths.

SWIR photodetectors are required in a wide range of applications with high societal impact, such as remote monitoring and surveillance, imaging systems, firefighting, sensing (e.g. humidity, temperature, gas, bio-chemical), contaminant detection, optical metrology, optical communications [1-3]. Despite the recent development of various photodetectors based on a range of materials (InGaAs, Ge, InAs, colloidal quantum dots, 2D metal chalcogenides, polymers, etc.) [1], all-Si photodetectors remain of significant interest because they can be easily integrated with Si electronic circuits [2,5]. Silicon becomes transparent to photons with energies below its 1.12 eV bandgap. However, the internal photoemission (IPE) process in a Schottky barrier enables sub-bandgap photodetection making thus silicon devices suitable for operation in the SWIR range [2-5]. IPE-based devices typically consist of a metal surface in contact with a semiconductor forming a Schottky barrier. Photons are absorbed by the metal and excite hot electrons. The electrons with energy higher than the Schottky barrier and sufficient momentum in the direction of the Schottky barrier can be injected into the silicon and contribute to the photocurrent. Thus, hot-electron devices on Si offer an alternative to the existing technologies for SWIR detectors, which require either expensive epitaxial growth or bonding of multi-layer structures, or quantum dots based on toxic materials (Pb, Hg). The key benefits of these photodetectors include high speed, simple fabrication process, and small dimensions, which are comparable to those of highly integrated electronic circuits. The main drawback of the internal photoemission process over a bulk metal/semiconductor Schottky junction is the low efficiency due to the low absorption of incident light by the metal, the broad hot electron energy distribution, and the momentum mismatch of electron waves between the silicon and the metal. However, plasmonic nanostructures have been shown to improve light absorption and enhance the electric field, leading to a more efficient generation of hot carriers [4,6]. Furthermore, the energy levels of the hot carriers generated by plasmon decay are higher than those generated by direct light absorption [6].

In recent years, a number of solutions for improving the responsivity of plasmonic Si photodetectors have been proposed, including the use of nanoparticles, thin/nanostructured metal layers [2,3,9], Si surface nanostructuring [5,10,11] and complex 3D structures/metasurfaces [13]. However, the responsivity remains still low (units of A/W for λ=1300-1500 nm).

In order to enhance light absorption, hot electron generation and collection, we conducted a series of experiments on different architectures for the front-side and backside electrodes. One solution that was pursued involved the use of plasmonic nanostructures, which were obtained by means of vacuum deposition of very thin Ag layers (15–50 nm), followed by thermal annealing. Nanostructured layers composed of flattened nano-hemispheres have been obtained. The diameter of these nanostructures varies between 10 and 500 nm, depending on the initial thickness of the Ag layer and the annealing process parameters. The nanostructured Ag

layer acts as plasmonic metasurface that improves both light absorption and the efficiency of hot electrons generations. In addition, experiments have been conducted with very thin discontinuous Ag and Au layers (2-6 nm in mass equivalent) composed of nanoparticles partially interconnected. Devices with Ag and Au nanostructured layers on n-Si demonstrate high responsivities, reaching 7-12 mA/W at telecom wavelengths for both front and back-side illumination. The second approach involved the combination of grating-like Au electrodes with as-deposited, very thin nanostructured Au or Ag layers. This approach yielded a 5-fold improvement of the responsivity, likely attributable to enhanced absorption coupled with improved collection of the carriers at the electrodes.

Similar experiments were conducted with Al plasmonic structures on p-Si. The responsivity was slightly higher, but also the dark current was higher (lower barrier). The next step is to place plasmonic nanostructures on both front and backside of the chip.

Acknowledgements: This work was funded from the project "National Platform for Semiconductor Technologies", contract no. G 2024-85828/390008/27.11.2024, SMIS code 304244, co-funded by the European Regional Development Fund under the Program for Intelligent Growth, Digitization, and Financial Instruments.

References

1. Cao, F., Liu, L., Li, L. “Short-wave infrared photodetector”, Materials Today 62, 327–349, 2023.
2. G. Kim et al.: Scalable hot carrier–assisted silicon photodetector array based on ultrathin gold film, Nanophotonics; 13(7): 1049–1057, 2024.
3. Krayer, L. J., Tennyson, E. M, Leite, M. S. and Munday, J. N. “Near-IR imaging based on hot carrier generation in nanometer-scale optical coatings,” ACS Photonics, Vol. 5, 306−311, 2018.
4. Diels, W., Steyaert M. and Tavernier, F. "Schottky Photodiodes in Bulk CMOS for High-Speed 1310/1550 nm Optical Receivers, "IEEE Journal of Selected Topics in Quantum Electronics, Vol. 24, 1-8, 2018.
5. Dong, Y., Li, J., Liang, W., Nan, X., Wen, L., and Chen Q. “CMOS-Compatible Broad-Band Hot Carrier Photodetection with Cu−Silicon Nanojunctions”, ACS Photonics, Vol.9, 3705−3711, 2022.
6. Goswami, A., Kim, A.S., and Cai, W. “Exploring the synergy between hot-electron dynamics and active plasmonics: A perspective” J. Appl. Phys., Vol.136, 100901, 2024.
7. Khurgin, J., Yu. Bykov, A., Zayats, A. V. “Hot-electron dynamics in plasmonic nanostructures: fundamentals, applications and overlooked aspects”, eLight Vol. 4, 15, 2024.
8. Zhang, C., Luo Y., Maier, S.A and Li, X. “Recent Progress and Future Opportunities for Hot Carrier Photodetectors: From Ultraviolet to Infrared Bands”, *Laser Photonics Rev16*, 2100714,2022,
9. Okamoto, S, et al., Facilely Fabricated Zero-Bias Silicon-Based Plasmonic Photodetector in the Near-Infrared Region with a Schottky Barrier Properly Controlled by Nanoalloys, ACS Appl. Mater. Interfaces, Vol.16, 8984–8992 (2024).
10. Zhai, Y., Li, Y., Ji, J., Wu, Z., and Wang Q. “Hot Electron Generation in Silicon Micropyramids Covered with Nanometer-Thick Gold Films for Near-Infrared Photodetectors” ACS Appl. Nano Mater. Vol. 3, 149−155, 2020.
11. C.Zhang et al., Plasmonic Nanoneedle Arrays with Enhanced Hot Electron Photodetection for Near-IR Imaging, Adv. Funct. Mater. Vol. 33, 230436, 2023.
12. K-T Lin, et. al., “Silicon-based embedded trenches of active antennas for high responsivity omnidirectional photodetection at telecommunication wavelengths,” ACS Appl Mater Interfaces Vol. 11, 3150–3159, 2019.
13. L.Zhang, et al., Highly responsive silicon-based hot-electron photodetector with self-aligned metamaterial interdigital electrode, Appl. Phys. Lett. 122, 031101, 2023.

Tailoring the RF fields in MRI: A new compact multi-layer metamaterial design combining a hexagonally-structured artificial dielectric with electric and/or magnetic dipoles

Rita Schmidt [1,2]

[1]Department of Brain Sciences, Weizmann Institute of Science, Israel,
[2]The Azrieli National Institute for Human Brain Imaging and Research, Weizmann Institute of Science
[*]corresponding author: rita.schmidt@weizmann.ac.il

Abstract: We established a new framework of MRI-beneficent artificial materials to tailor the RF transmit and receive fields, combining an artificial dielectric with a set of electric and/or magnetic dipoles. This combination provides high flexibility to plan the possible enhancement, as well as a higher efficiency and a very compact structure.

Magnetic Resonance Imaging (MRI) has become a staple of medical diagnostics, providing indispensable diagnostics information. Its influence can be extended even more by boosting the sensitivity, which would translate into shorter scan duration and greater scan resolution. In recent years, metamaterial designs have been developed in the field of MRI to increase SNR and efficiency for passive designs and for new RF coil's designs[1-5]. In our lab, we explored a hybrid metamaterial-based structures, combining a high-permittivity dielectric layer and a set of electric and/or magnetic dipoles[4]. We implemented this design in MRI applications achieving local signal enhancement in the vicinity of the structure. Our recent works[6,7] also showed that non-uniform distribution of the copper strips can be utilized to further extend the degrees of freedom to tailor the resulting RF transmit field and to reduce the power deposition.

Taking the next step forward, we recently replaced the high permittivity dielectric layer with artificial dielectric (AD) design, introducing a new framework to design a compact and flexible metasurfaces for MRI. In this design, the AD comprises of shifted short copper strips arranged in hexagons and a dielectric (relative permittivity, εr=2.6) substrate in-between (Fig.1). Introducing a hexagonal arrangement of the sub-units achieves an optimally condensed distribution and thus provides a wide range of artificial dielectric properties. As was shown before[8], the combination of overlapping copper strips generates a network of capacitors. We show that the AD structure can also be combined with another layer of electric and/or magnet dipoles, which can be used to control the resonant frequency and the achieved RF transmit field enhancement. To achieve much smaller dimensions (16x11.2 cm^2), AD layer was attached to two additional AD layers with diagonally shifted configurations (See Fig.1B).

To characterize and examine the proposed structures, EM simulations, including eigen mode solver and time domain, and measurements in 7T MRI were performed. All the simulations were carried out using CST Microwave Studio, Darmstadt, Germany. The most relevant resonant mode of interest for MRI - the lowest transverse-electric (TE) mode (with large penetration depth) was examined. Similar distribution was achieved by the TE_{01} mode with an actual dielectric layer and with an AD (Fig.2). A resonant structure at ~298 MHz was achieved for all configurations (Fig.2). A time domain simulation with an RF coil and a phantom showed B_1^+ field enhancement of ×1.25, ×1.35, and ×2.35 for AD, dielectric and the combined resonant "Triple Hexa" setup, respectively. Scans were performed on 7T Terra, Siemens, with an 8Tx/32Rx Nova coil and a cylindrical oil phantom. The MRI scan with the "triple-Hexa" showed 4-fold enhancement for the square root of the image intensity (Fig.3), which can

be approximated as B_1^+ enhancement (assuming the signal is proportional to B_1^{+2}).

This study shows a new design of a metamaterial that can provide very compact resonant structures at 7T MRI. Another advantage of this design that no lumped elements are required. The combined design provides high flexibility to plan a range of possible enhancements.

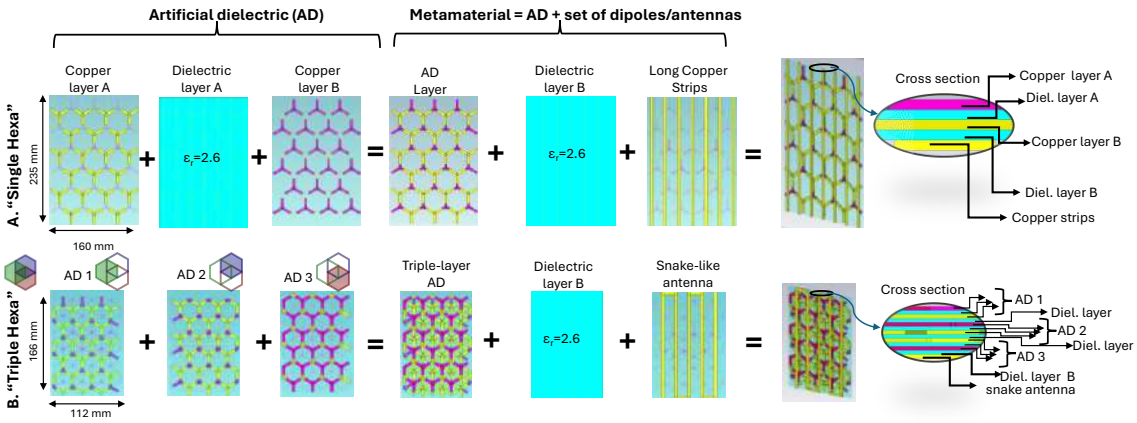


Fig.1. Schematics of the metamaterial design. A) "Single-Hexa", B) "Triple-Hexa"

Acknowledgements: This project is supported by the Israel Science Foundation.

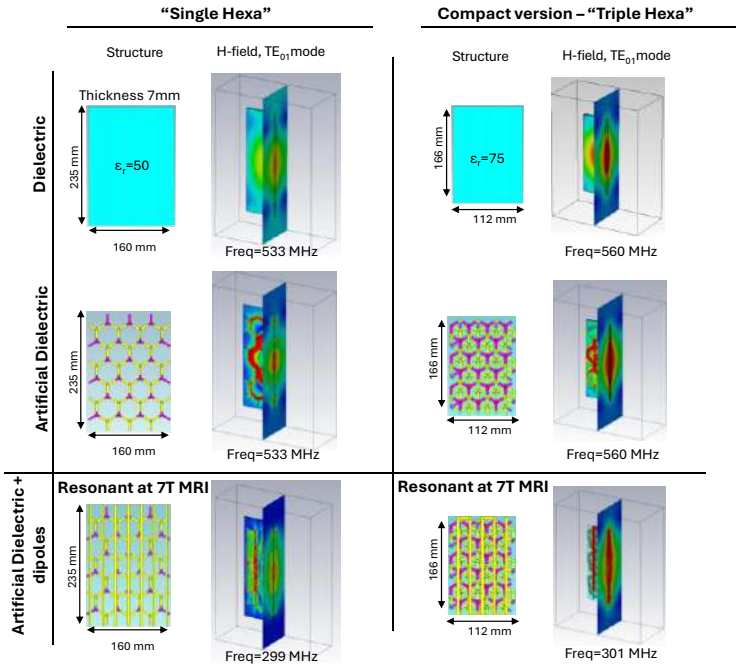


Fig.2. H-field of the TE_{01} mode for each AD and the metamaterial configuration. The AD H-field is also compared with a dielectric layer of 7 mm thickness with the same resonant frequency.

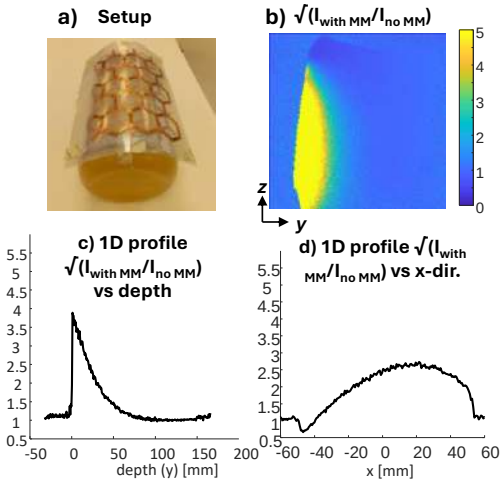


Fig.3. MRI experiment. a) photo of the setup, b-d) Ratio map ($I_{with\ MM}/I_{no\ MM}$) and 1D profiles of images acquired with and without the "triple-Hexa".

References

1. Motovilova, E., Huang, S. Y. IEEE Trans. Microwave Theory Techn. 67, 615–625,2019.
2. Lippke, M., Stoja, E., Philipp, D., Konstandin, S., Jenne, J., Bertuch, T., & Günther, M. IEEE, 668-671, 2022.
3. Slobozhanyuk, A. P., Poddubny, A. N., Raaijmakers, A. J., van den Berg, C. A., Kozachenko, A. V., Dubrovina, I. A., … & Belov, P. A. *Adv Mater*, Vol.28, No.9, 1831-1831, 2016.
4. Schmidt, R., Slobozhanyuk, A., Belov, P., & Webb, A. *Sci Rep*, Vol.7, No. 1, 1-7, 2017.
5. Webb, A., Shchelokova, A., Slobozhanyuk, A., Zivkovic, I., & Schmidt, R. Magn Reson Mater Phy. Vol. 36, No. 6, 875-894, 2022.
6. Maurya, S. K., & Schmidt, RACS Applied Materials & Interfaces, 16(36), 47284-47293, 2024.
7. Maurya, S. K., & Schmidt, RSensors, 24(7), 2250, 2024.
8. Koloskov, V., Brink, W. M., Webb, A. G. & Shchelokova, A. Magnetic Resonance in Med 92, 869–880, 2024.

Breaking the Diffraction Limit: Far-Field Super-Resolution Imaging Via Metasurfaces and Holography

P. Salami[1] and L. Yousefi[2*]

[1]School of Electrical and Computer Engineering, College of Engineering, University of Tehran, Tehran, Iran
[2]School of Engineering and Informatics, University of Sussex, Falmer, UK
[*]corresponding author: l.yousefi@sussex.ac.uk

Abstract: In this presentation, we discuss the innovative methods we have developed to surpass the diffraction limit using metasurfaces. By designing metasurfaces to transform evanescent waves into propagating modes and utilizing holography, we achieve super-resolution imaging. Full-wave simulations demonstrate that our proposed techniques can retrieve feature sizes as small as λ/14.

Irregularities on a surface smaller than the wavelength of light generate evanescent waves that decay rapidly as they move away [1]. The loss of this information enforces the diffraction limit, restricting optical systems from resolving details smaller than $\lambda/2NA$, where λ is the light wavelength and NA is the numerical aperture [2].

To overcome this barrier, near-field techniques like NSOM utilize probes to capture evanescent waves, achieving nanometer resolution [3]. However, these methods are slow and have a limited field of view. To enable far-field imaging, approaches such as hyperlenses and superlenses have been introduced [4]. Hyperlenses, composed of hyperbolic metamaterials, magnify sub-wavelength details but are challenging to fabricate due to their curved structure. Superlenses use gratings to convert evanescent waves into propagating modes, but multiple diffraction orders can create ambiguities in imaging, requiring the placement of a superlens before the grating to resolve this issue.

To overcome these challenges and remove the need for a superlens in far-field superlens approach, we employed plasmonic and dielectric metasurfaces [5,6] (see Figs. 1(a) and (b)). These metasurfaces manipulate the amplitude, phase, and polarization of incident waves, enabling the conversion of evanescent waves into propagating modes for sub-wavelength imaging (see Figs. 1(c) and (d)).

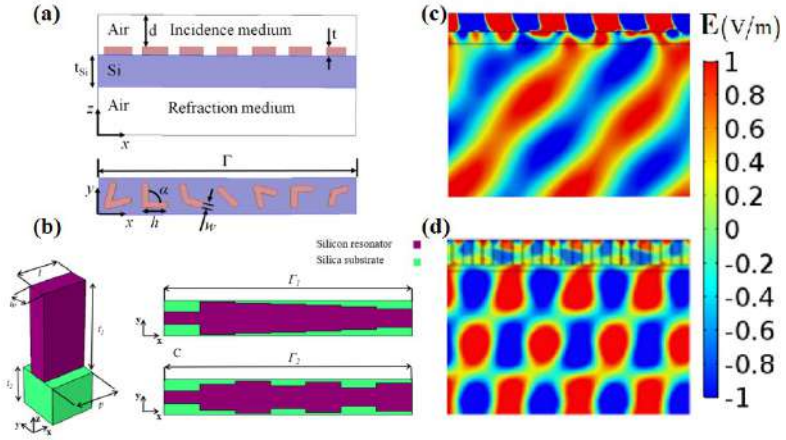


Figure 1. (a) Plasmonic [5], and (b) first and second order dielectric [6] metasurfaces used for sub-wavelength imaging. (c) Plasmonic [5], and (d) second order dielectric [6] metasurfaces convert evanescent waves with transverse wavenumbers of $1.7k_0$ and $2.6k_0$ into propagating modes, respectively.

Metasurfaces introduce a shift in the transverse wavenumber of incident waves, transferring evanescent waves with large transverse wavenumbers into the propagating region. Our previous studies [5,6] showed that in sub-wavelength imaging, scattered waves from the sub-wavelength features of the sample interact with only a few unit cells, preventing the excitation of higher-order modes. The typical reconstructed sub-wavelength images obtained using plasmonic [5] and high-order dielectric [6] metasurfaces, are shown in Figs. 2(a) and (b), respectively.

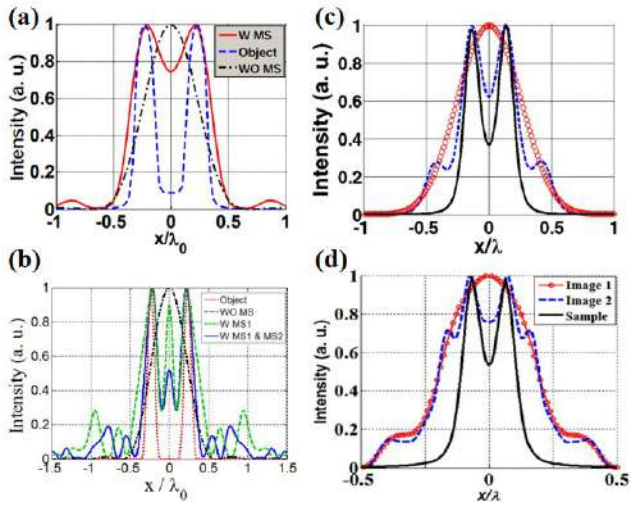


Figure 2. (a) λ/3.4 and (b) λ/5.5 resolution achieved using plasmonic and dielectric metasurfaces, respectively. (c) λ/7 and (d) λ/14 resolution achieved using one-step and two-step holography-based techniques, respectively.

For removing the need for nanostructures in sub-wavelength imaging, we propose holography-based techniques in Refs. [7,8]. These methods demonstrate that interference between a known reference wave and waves scattered from the sample, can shift sample angular spectrum, converting a range of evanescent waves into propagating ones. By recording interference patterns using photographic emulsions and applying reconstruction waves, scattered wavefronts are analyzed. Combining this data with the propagating range of sample angular spectrum enables sub-wavelength image reconstruction (see Figs. 2(c) and (d)).

References

1. Pendry, J. B. "Negative refraction makes a perfect lens," Phys. Rev. Lett., Vol. 85, No. 18, 3966–3969, 2000.
2. Born, M. and E. Wolf, Principles of Optics, 7th ed. Cambridge University Press, 1999.
3. Hecht, B., B. Sick, P. Wild, V. Deckert, R. Zenobi, J. F. Martin, and D. U. Pohl, "Scanning near-field optical microscopy with aperture probes: Fundamentals and applications," J. Chem. Phys., Vol. 112, 7761–7774, 2000.
4. Zhang, X., Z. Liu, "Superlenses to overcome the diffraction limit," Nature Mater., Vol. 7, No. 6, 435–441, 2008.
5. Salami, P., L. Yousefi, "Far-field subwavelength imaging using phase gradient metasurfaces," J. Lightw. Technol., Vol. 37, No. 10, 2317–2323, 2019.
6. Akbari-Chelaresi, H., P. Salami, and L. Yousefi, "Far-field sub-wavelength imaging using high-order dielectric continuous metasurfaces," Opt. Express, Vol. 30, No. 21, 39025–39039, 2022.
7. Salami, P., L. Yousefi, "Far-field imaging beyond the diffraction limit using waves interference," J. Lightw. Technol., Vol. 38, No. 8, 2322–2327, 2020.
8. Salami, P., L. Yousefi, "Super-resolution far-field sub-wavelength imaging using multiple holography," J. Opt. Soc. Am. B, Vol. 38, No. 3, 670–676, 2021.

Terahertz collimating metalens antenna based on a polarization-independent isotropic metasurface with high refractive index and low reflectance mounted on a resonant tunneling diode

Y. Saito[1], K. Sato[2], K. Tsuruda[3], and T. Suzuki[4*]

[1] Department of Electrical and Computer Science, Graduate School of Engineering, Tokyo University of Agriculture and Technology, Japan
[2] Department of Electrical and Electronic Engineering, Graduate School of Engineering, Tokyo University of Agriculture and Technology, Japan
[3] ROHM Co., Ltd., Japan
[4] Division of Advanced Electrical and Electronic Engineering, Institute of Engineering, Tokyo University of Agriculture and Technology, Japan
[*]corresponding author: takehito@go.tuat.ac.jp

Abstract: Measurements demonstrate that a terahertz collimating metalens antenna based on a polarization-independent isotropic metasurface with a high refractive index and low reflectance collimates terahertz waves from a resonant tunneling diode (RTD) in the 0.3-THz band. These results could pave the way for integrating metalens antennas with RTDs as on-chip devices.

The terahertz waveband is a promising candidate as a carrier frequency for next-generation wireless communications [1]. Various attractive terahertz continuous-wave (CW) sources have been developed [2,3], and optical elements for the collimation of terahertz waves are essential to propagate terahertz waves over long distances. We have reported collimating metalens antennas [4,5] that collimate terahertz waves for propagation toward the far field. However, the previously reported metalens antennas are made with a polarization-dependent metasurface with a high refractive index and low reflectance, and metasurfaces with polarization-independent isotropic optical properties would be very adaptable for integration with terahertz CW sources. In this paper, we propose a terahertz collimating metalens antenna based on a polarization-independent isotropic metasurface with a high refractive index and low reflectance in the 0.3-THz band.

Figures 1 (a) and (b) show terahertz collimating metalens antennas with 10- and 1.0-mm focal lengths. Figure 1(c) shows a cross-section view of a terahertz collimating metalens antenna composed of a dielectric substrate and circular metal disks. The collimating metalens antennas are fabricated by etching a dielectric substrate (cyclo-olefin polymer film) coated with metal (copper) on the front and back of the substrate. Figure 2 shows the experimental system to measure the directivity of a terahertz collimating metalens antenna mounted on an RTD. The distance h between the metalens antenna and receiver is 65 mm, longer than the far-field distance of 44 mm for Fig. 1(a) and 6.7 mm for Fig. 1(b). Figures 3 (a) and (b) show the measured directivity of the metalens antenna with a 10-mm focal length mounted on the RTD. The collimating metalens antenna enhances the directivity of the RTD 3.1 times for a rotation angle γ of 0 degrees and 2.7 times for 90 degrees. The measurements are normalized with the maximum directivity of the RTD set to 1.0. Figures 4 (a) and (b) show the measured directivity of the metalens antenna with a 1.0-mm focal length mounted on the RTD. The collimating metalens antenna enhances the directivity of the RTD 1.6 times for a rotation angle γ of 0 degrees and 1.7 times for 90 degrees. The measurements are normalized with the maximum directivity of the RTD set to 1.0. The terahertz collimating metalens antennas collimate terahertz waves with the polarization directions along the x- and y-axes radiated from the RTD.

The metalens antennas with 10- and 1-mm focal lengths are fabricated and mounted on a resonant tunneling diode (RTD) to enhance the directivity. The metalens antennas could be integrated with various terahertz CW sources for applications in the terahertz band in next-generation (6G and 7G) wireless communications and advanced imaging applications.

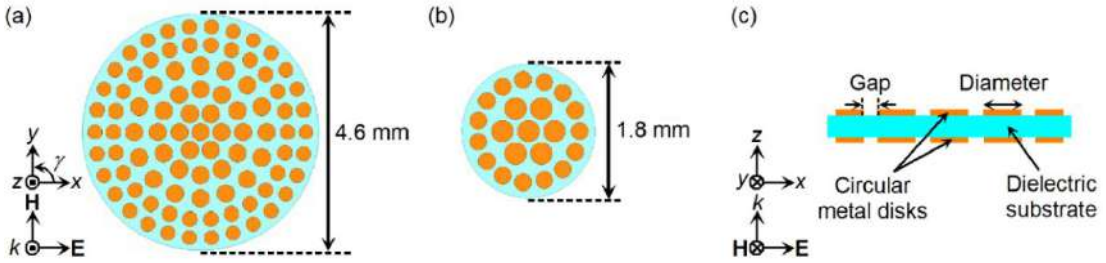


Fig. 1 Full model of terahertz collimating metalens antennas with (a) 10- and (b) 1.0-mm focal lengths. (c) Cross-section view of the terahertz collimating metalens antenna.

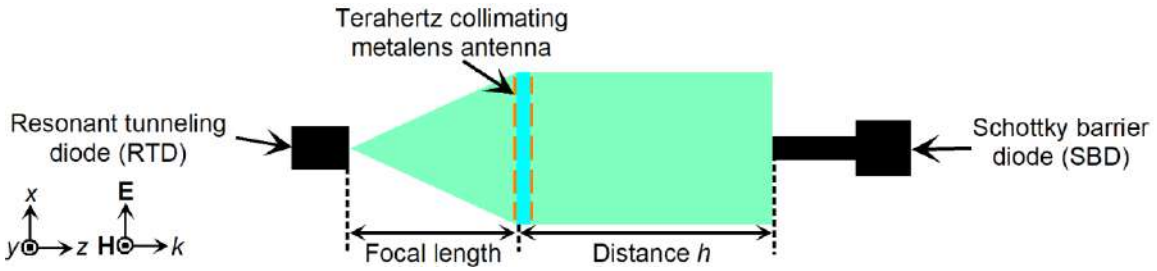


Fig. 2 Schematic of experimental system to measure the directivity of a metalens antenna mounted on an RTD.

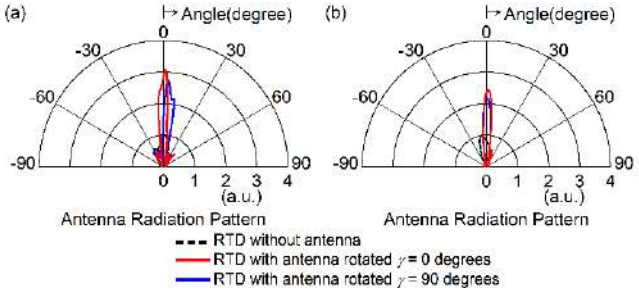


Fig. 3 Directivity of a metalens antenna with a 10-mm focal length mounted on an RTD in the (a) *xz*- and (b) *yz*-planes.

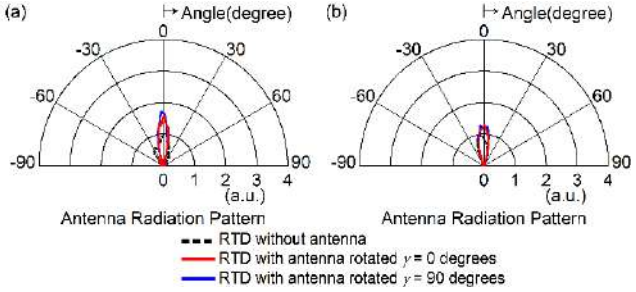


Fig. 4 Directivity of a metalens antenna with a 1.0-mm mounted on an RTD in the (a) *xz*- and (b) *yz*-planes.

Acknowledgements

This research was supported by Fusion Oriented REsearch for disruptive Science and Technology (FOREST) from the Japan Science and Technology Agency (JST) (JPMJFR222I), Grants-in-Aid for Scientific Research (B) from the Japan Society for the Promotion of Science (JSPS) (24K01376), and Grant-in-Aid for Challenging Research (Exploratory) from the Japan Society for the Promotion of Science (JSPS) (24K21617).

References

1. S. Dang, O. Amin, B. Shihada, and M.-S. Alouini, "What should 6G be?," Nat. Electronics, Vol 3, No. 1, 20–29, 2020.
2. S. Hayashi, A. Ito, M. Hitaka, and K. Fujita, "Millimeter-wave generation with a room-temperature nonlinear quantum cascade laser," J. Vac. Sci. Technol. B, Vol 42, No.4, 040601, 2024.
3. T. Hagelschuer, H. Richter, M. Wienold, X. Lü, B. Röben, L. Schrottke, K. Bierman, H. T. Grahn, and H.-W. Hübers, "A Compact 4.75-THz Source Based on a Quantum-Cascade Laser With a Back-Facet Mirror," IEEE Trans. Terahertz Sci. Technol., Vol 9, No. 6, 606–612, 2019.
4. T. Suzuki., K. Endo, J. Kim, K. Tsuruda, and M. Sekiya, "Metalens mounted on a resonant tunneling diode for collimated and directed terahertz waves," Opt. Express, Vol 29, No. 12, 18988, 2021.
5. K. Endo, M. Sekiya, J. Kim, T. Suzuki, "Resonant tunneling diode integrated with metalens for high-directivity terahertz waves," Applied Physics Express, Vol 14, No. 8, 082001 2021.

Hybrid Gold–Vanadium-Dioxide Tunable Plasmonic Devices

V. Křápek[1*], R. Řepa[1], J. Liška[1], P. Kepič[1], J. Kabát[1], M. Horák[1], and T. Šikola[1]

[1]Brno University of Technology, Technická 2, 616 69 Brno, Czechia

krapek@vutbr.cz (corresponding author)

Abstract

The lateral arrangement of self-assembled VO2 nanoparticles and gold nanostructures fabricated by electron beam lithography is presented as a suitable platform for hybrid tunable plasmonic devices. Two specific tunable devices are demonstrated: Electric-magnetic switches and resonance-energy switches.

Vanadium dioxide (VO_2) exhibits a metal-insulator transition near room temperature (68 °C), which can be exploited in tunable plasmonic devices with compelling functions. However, devices based solely on VO_2 suffer from a large optical absorption and low chemical stability of VO_2 [1].

In our contribution, we present a hybrid material platform that combines high-quality crystalline self-assembled VO2 nanoparticles [2] with lithographically defined gold nanostructures in a lateral arrangement [Fig. 2(a) shows an example of a fabricated device]. In this way, we benefit from both the tunability of VO_2 and the high conductivity of gold. Lithography is performed only on gold, which brings the desired design flexibility while preventing damage to VO_2. Finally, the lateral arrangement minimizes the amount of VO_2 and thus contributes to the high quality of the devices.

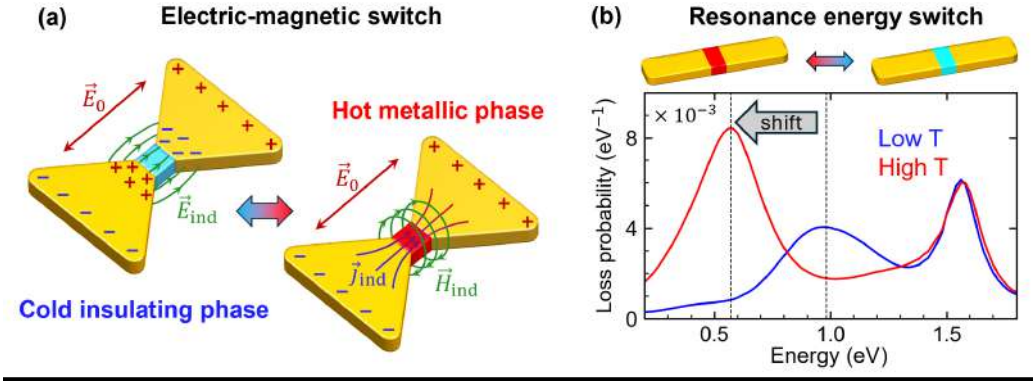


Figure 1: a) Conceptual design of the electric-magnetic switch. Gold wings (yellow) are connected with a VO_2 bridge (cyan or red). When cold, the bridge is insulating, resulting in charge accumulation near the bridge and a formation of the electric hot spot (as in the bowtie plasmonic antenna). When hot, the bridge is conducting, resulting in the funneling of the electric current and a formation of the magnetic hot spot (as in the diabolo antenna). (b) Conceptual design of the resonance energy switch (top). It is designed as a dimer of gold nanorods connected with a VO_2 bridge. A low-temperature dimer of two short nanorods separated by the insulating bridge transforms upon heating into a single nanorod with gold part connected with the conducting bridge. This process is accompanied by a pronounced shift in the plasmon resonance energy, as demonstrated in the calculated electron energy loss spectra (bottom).

We demonstrate two tunable plasmonic devices based on the above-mentioned material platform: (1) Electric-magnetic switches, in which either an electric or magnetic hot spot is formed, following a design from Ref. [3]. Such switches might find application e.g. in THz spectroscopy of magnetic transitions [4], to which they can introduce a temporal resolution or facilitate nonlinear spectroscopy by promoting either electric or magnetic transitions. (2) Resonance-energy switches, in which the spectral profile of the scattering or absorption is controlled, with possible applications in fine tuning of thermochromic smart windows. The concept of the switches is demonstrated in Fig. 1.

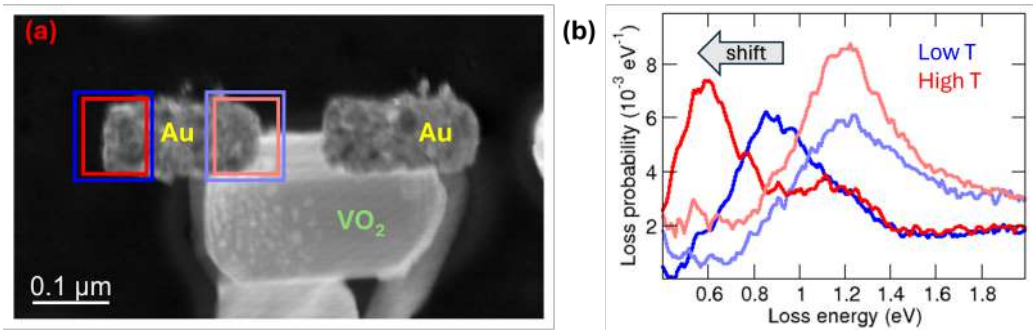


Figure 2: a) Annular dark-field image of a hybrid plasmonic device acting as a resonance-energy switch. A VO_2 nanoparticle and gold nanorods are indicated. (b) Electron energy loss spectra of the same switch taken at the low temperature where VO_2 is insulating (blue) and the high temperature where VO_2 is metallic (red). The energy shift observed for one of the plasmon resonances is indicated with the gray arrow. The color of the spectra corresponds to the color of the squares in panel (a) indicating the regions where the spectra were retrieved.

Both devices were characterized by analytical electron microscopy [in particular, electron energy loss spectroscopy] and electrodynamic simulations. A proof of concept for the resonance-energy switch is in Fig. 2. The observed shift of the lowest plasmon resonance shown in Fig. 2(b) agrees remarkably well to the prediction of Fig. 1(b).

References

[1] Krpenský, J., M. Horák, J. Kabát, J. Planer, P. Kepič, V. Křápek, and A. Konečná, "Analytical electron microscopy analysis of insulating and metallic phases in nanostructured vanadium dioxide," *Nanoscale Adv.*, Vol. 6, pp. 3338–3346, 2024.

[2] Horák, M., P. Kepič, J. Kabát, M. Hájek, F. Ligmajer, A. Konečná, T. Šikola, and V. Křápek, "Efficient nanoscale imaging of solid-state phase transitions by transmission electron microscopy demonstrated on vanadium dioxide nanoparticles," *arXiv*, pp. 2408.11972, 2024.

[3] Křápek, V., A. Konečná, M. Horák, F. Ligmajer, M. Stöger-Pollach, M. Hrtoň, J. Babocký, and T. Šikola, "Independent engineering of individual plasmon modes in plasmonic dimers with conductive and capacitive coupling," *Nanophotonics*, Vol. 9, No. 3, pp. 623–632, 2020.

[4] Tesi, L., D. Bloos, M. Hrtoň, A. Beneš, M. Hentschel, M. Kern, A. Leavesley, R. Hillenbrand, V. Křápek, T. Šikola, and J. van Slageren, "Plasmonic Metasurface Resonators to Enhance Terahertz Magnetic Fields for High-Frequency Electron Paramagnetic Resonance," *Small Methods*, Vol. 5, No. 9, pp. 2100376, 2021.

van der Waals metamaterials for photonics enabled by FIB lithography

A. C. Liapis[1*], X. Cui[1], N. Shang[1], H. Kaaripuuro[1], J. C. Arias-Muñoz[1] X. Cheng[1], and Z. Sun[1]

[1]QTF Centre of Excellence, Department of Engineering and Nanosciences, Aalto University, Finland

Corresponding author: andreas.liapis@aalto.fi

Abstract: Nanostructured multilayer 2D materials are a promising alternative to traditional bulk nonlinear materials for on-chip photonics. Here we present a universal approach for patterning such materials based on Focused-Ion-Beam lithography. We fabricate high-quality microdisk resonators and other photonic nanostructures and characterize them as a platform for linear and nonlinear optics.

Van der Waals (vdW) materials are promising candidates for next-generation nanophotonics and optoelectronics thanks to their exceptional optical, electrical, thermal, and mechanical properties arising from their unique anisotropic structure, in which two-dimensional sheets of covalently-bound atoms are held together by relatively weak vdW forces to form multi-layer structures and bulk crystals. Overcoming these vdW interactions allows layers to be peeled off by mechanical exfoliation, resulting in flakes with controllable thickness down to a single atomic layer. The pristine dangling-bond-free surfaces of these layers enable the arbitrary stacking of heterogeneous materials without being constrained by lattice mismatch. Such heterostructures have been used to create optoelectronic devices with unprecedented functionalities [1, 2].

Even in bulk form, vdW materials exhibit monolayer-like excitonic behavior and in many cases their nonlinear optical performance far exceeds those of traditional platforms [3]. However, the potential of vdW materials as a platform for integrated photonics remains largely unexplored, as the fabrication of high-quality nanostructures out of these materials using traditional nanopatterning approaches poses significant challenges [4].

In this work we demonstrate a versatile and universal (material agnostic) approach for high-quality patterning of vdW multi-layer flakes and their heterostructures based on Focused-Ion-Beam lithography. Crucially, we employ a protective layer to minimize unwanted damage and parasitic ion implantation during milling. Our technique enables us to pattern a wide range of fundamental photonic building blocks such as waveguides, resonators, photonic crystals, and metasurfaces (Figure 1), which serve as a robust platform for exploring both linear and nonlinear optical phenomena. By controlling both the in-plane (via patterning) and out-of-plane (via stacking) structure, we are able to create metamaterials with precisely-tailored optical properties. This approach unlocks the untapped potential of vdW-based metamaterials for high-performance integrated nonlinear photonics and optoelectronics.

This work was supported by Research Council of Finland (352780, 352930, 353364, 360411, 359009, 365686, and 367808), the Research Council of Finland Flagship Programme (320167, PREIN), the EU H2020-MSCA-RISE-872049 (IPN-Bio), the Jane and Aatos Erkko foundation and the Technology Industries of Finland centennial foundation (Future Makers 2022), and ERC

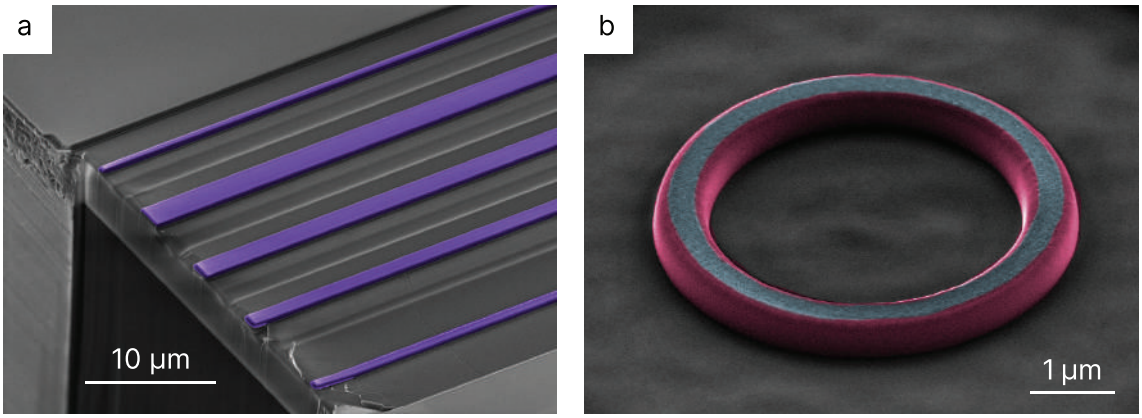


Figure 1: False-color Scanning Electron Micrographs of fabricated vdW photonic structures: (a) a series of MoS_2 waveguides of different widths, and (b) a h-BN microring resonator with ultra-smooth sidewalls. The blue ring seen in (b) is what remains of the protective layer after FIB milling, and is removed in a subsequent processing step.

(834742). The authors acknowledge the provision of facilities and technical support by Aalto University OtaNano – Nanofabrication Centre for sample fabrication.

References

1. Cui, X., *et al.*, "Miniaturized spectral sensing with a tunable optoelectronic interface," *Sci. Adv.*, Vol. 11, No. 4, eado6886, 2025.

2. Uddin, M. G., *et al.*, "Broadband miniaturized spectrometers with a van der Waals tunnel diode," *Nat. Communications*, Vol. 15, No. 1, 571, 2024.

3. Autere, A., *et al.*, "Nonlinear optics with 2D layered materials," *Adv. Mater*, 30, 1705963, 2018.

4. Cui, X., *et al.*, "On-chip photonics and optoelectronics with a van der Waals material dielectric platform," *Nanoscale*, 14, 9459–9465, 2022.

NIR to Visible Upconversion Luminescence from Single Rare-earth doped Nanoparticles on Self-assembled Chiral Metasurfaces

A. Ahmed[1], K.Y. Chiok[1], S. May[2], A. Baride[2], R.B. Anderson[1], S. Zhou[1], S. Smith[1]

[1]South Dakota School of Mines and Technology, Rapid City, South Dakota, USA
[2]University of South Dakota,Vermillion, South Dakota, USA

Corresponding author email: Steve_Smith@mailaps.org

Abstract: We observe circularly polarized NIR-to-visible upconversion luminescence (UCL) from single β-$NaYF_4$:Yb^{3+}:Tm^{3+} upconverting nanoparticles (UCNPs) supported on self-assembled chiral metasurfaces[1]. A circular-polarized luminescence microscope images the left and right circularly polarized emission from single particles randomly placed on the substrate. We use time- and energy-resolved single particle imaging to assess the plasmon-enhanced radiative decay and polarization of upconversion luminescence from nanoparticles supported on self-assembled metasurfaces, composed of self-assembled tetrahedral Au nanoparticles. We obtain a statistical description of UCL emission enhancement in the Tm-doped UCNPs and map out the statistical distribution of excitation and luminescence enhancement on plasmonic substrates[2–4]. We use both wide field and confocal scanning spectroscopic imaging of single UCNPs on and off the plasmonic substrates in combination with energy and time resolved spectroscopy, and compare these results to a coupled rate equation analysis to elucidate the energy transfer upconversion enhancement mechanisms. The results obtained are compared to Finite Difference Time Domain (FDTD) calculations of the fields near the plasmonic substrate.

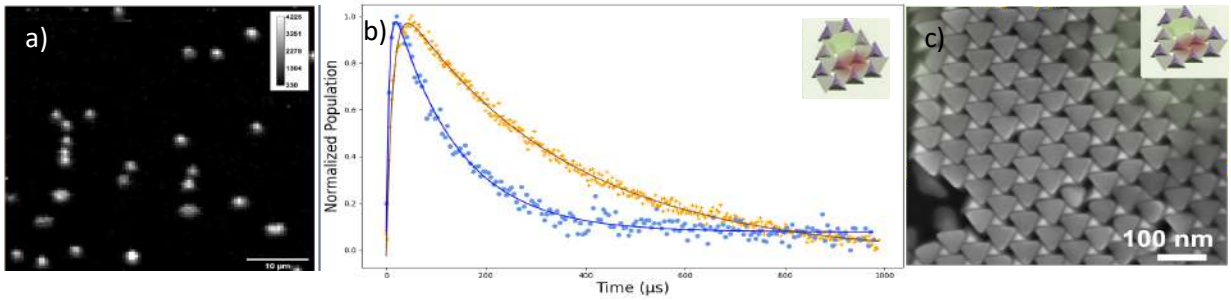


Figure 1: (**a**) Single particle upconversion luminescence (UCL) image (**b**) luminescence decay of isolated and plasmon-coupled upconverting nanoparticle (schematically shown in inset). (**c**) Chiral metasurface induces circularly polarized UCL (CP-UCL) (schematically shown in inset).

References:

(1) Zhou, S.; Li, J.; Lu, J.; Liu, H.; Kim, J. Y.; Kim, A.; Yao, L.; Liu, C.; Qian, C.; Hood, Z. D.; Lin, X.; Chen, W.; Gage, T. E.; Arslan, I.; Travesset, A.; Sun, K.; Kotov, N. A.; Chen, Q. Chiral Assemblies of Pinwheel Superlattices on Substrates. *Nature* **2022**, *612* (7939), 259–265.

(2) Fisher, J.; Zhao, B.; Lin, C.; Berry, M. T.; May, P. S.; Smith, S. Spectroscopic Imaging and Power Dependence of NIR to Visible Upconversion Luminescence from NaYF4:Yb3+,Er3+ Nanoparticles on Nano-Cavity Arrays. *Journal of Physical Chemistry C* **2015**, *119* (44), 24976–24982.

(3) Hor, A.; Luu, Q.; May, P.; Berry, M.; Smith, S. Non-Linear Density Dependent Upconversion Luminescence Enhancement of β-NaYF4: Yb3 : Er3 Nanoparticles on Random Ag Nanowire Aggregates. *MRS Adv* **2016**, *1* (38), 2677–2682.

(4) Hossan, M. Y.; Hor, A.; Luu, Q.; Smith, S. J.; May, P. S.; Berry, M. T. Explaining the Nanoscale Effect in the Upconversion Dynamics of β-NaYF 4 :Yb 3+ , Er 3+ Core and Core–Shell Nanocrystals. *The Journal of Physical Chemistry C* **2017**, *121*, 16592–16606.

Relative illumination engineering of metalens

Qiu-Chun Zeng[1,2], Chen-Yi Yu[2], Wei-Lun Hsu[2], Che-Chin Chen[1], and Chih-Ming Wang[2,*]

[1]Taiwan Instrument Research Institute, National Applied Research Laboratories, Hsinchu, 30076, Taiwan
[2]Department of Optics and Photonics, National Central University, Taoyuan, 320371, Taiwan
[*]corresponding author: cmwang@cc.ncu.edu.tw

Abstract: The relative illumination of traditional lenses generally follows the Cosine Fourth Power Law. We proposed a metalens consisting of mixing-pitch meta-units to modulate the relative illumination. Our experimental results show that the relative illumination of our metalens at 30° is 4-folds higher than that at 0°. Our metalens offers promising potential for applications requiring specific illumination control, such as wide-angle imaging and oblique detection.

Machine vision is increasingly prevalent in daily life, with image input being a core component [1]. However, metalens-based imaging systems often suffer from strong relative illumination variations, causing the image center to appear significantly brighter than the edges. Most research on metalenses has focused on focusing quality and imaging performance within imaging optics [2-3]. In this work, we extend their application to non-imaging optics by leveraging metasurface amplitude modulation for illumination control. Traditional lenses follow the Cosine Fourth Power Law [4-5], causing illumination to drop at large field angles. Here, we employ a mixing-pitch meta-unit design to adjust relative illumination at different angles [6]. Experiments show that relative illumination at a 30° incident angle is twice as high as at 0°, making it useful for oblique image detection and wide-angle illumination compensation.

We investigate two metalens designs: single-pitch and mixing-pitch, both designed for 940 nm and using a telecentric optical setup. In the single-pitch case, Figures 1(a) and 1(b) show the simulated and measured focal spots at AOI = 0° and 45°, both 1.98 μm in size. The spots are symmetric due to the zero chief ray angle at all AOIs, enabling consistent imaging quality. The modulation transfer function (MTF) in Figure 1(c) confirms stable imaging across AOI = 0° to 60°, achieving 150 lp/mm at MTF = 0.3.

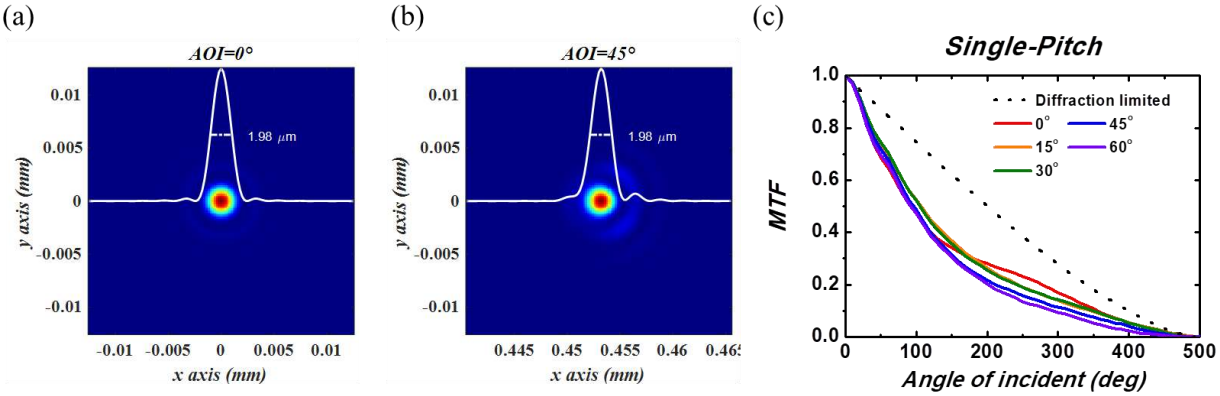


Figure 1. Simulated focal spot diagrams of the single-pitch metalens at an angle of incidence (AOI) of (a) 0° and (b) 45°. (c) Measured MTF curve for AOI values ranging from 0° to 60°.

For the mixing-pitch metalens, Figures 2(a) and 2(b) show smaller focal spots of 1.59 μm and 1.79 μm at AOI = 0° and 45°, respectively, improving resolution. The MTF diagram in Figure 2(c) shows a resolution of 170 lp/mm at MTF = 0.3, though a minor low-frequency drop is observed at AOI = 0°.

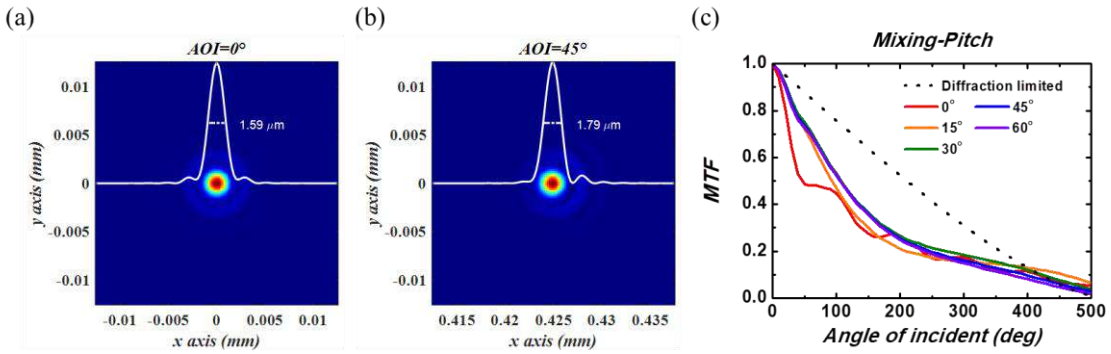


Figure 2. Simulated focal spot diagrams of the mixing-pitch metalens at an angle of incidence (AOI) of (a) 0° and (b) 45°. (c) Measured MTF curve for AOI values ranging from 0° to 60°.

Distortion characteristics across these cases are compared in Figure 3(a). The telecentric system exhibits -27% distortion at AOI = 40°, with the mixing-pitch metalens showing similar behavior. Relative illumination, a key factor in metalens applications, decreases with increasing AOI, causing uneven brightness. As shown in Figure 3(b), the telecentric metalenses exhibit a significant illumination drop. However, the mixing-pitch metalens effectively mitigates this issue. This improvement is due to using larger-period meta-atoms at the lens center, reducing central illumination and enhancing overall brightness uniformity.

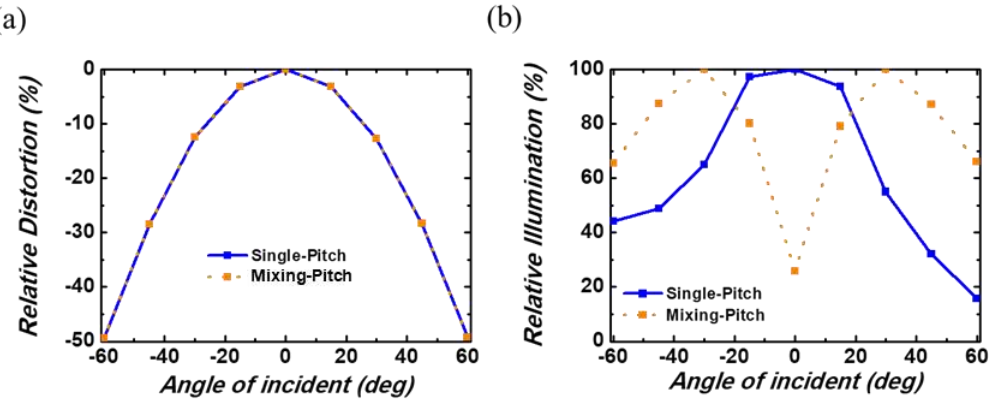


Figure 3. (a) Relative distortion and (b) relative illumination characteristics of the two metalens designs.

References

1. Hsu, W. L., C. F. Huang, and C. C. Tan, "High-resolution metalens imaging with sequential artificial intelligence models," Nano Lett., **23**(24), 11614–11620, 2023.
2. Engelberg, J., C. Zhou, and N. Mazurski, "Near-IR wide-field-of-view Huygens metalens for outdoor imaging applications," Nanophotonics, **9**(2), 361–370, 2020.
3. Martins, A., K. Li, J. Li, and H. Liang, "On metalenses with arbitrarily wide field of view," ACS Photonics, **7**(8), 2073–2079, 2020.
4. Luo, X. G., et al., "Recent advances of wide-angle metalenses: principle, design, and applications," Nanophotonics, **11(**1), 1–20, 2022.
5. Pu, M., et al., "Nanoapertures with ordered rotations: symmetry transformation and wide-angle flat lensing," Opt. Express, **25**(24), 31471–31477, 2017.
6. Yu, C. Y., Chen, Y. C., Zeng, Q. C., W. L. Hsu and C. M. Wang, "Optical performance of synthetic aperture metalens based on hybrid unit-cells," Mater. Sci. Semicond. Process., **170**, 107982, 2024.

Emerging fabrication technologies for all-dielectric periodic metastructures

L. Grinevičiūtė[1,2*], J. Nikitina[1], L. Ramalis[1], S. Indrisiunas[1], K. Staliunas[3,4]

[1]Department of Laser Technologies, Center for Physical Sciences and Technology, Vilnius, Lithuania
[2]Vilnius University, Faculty of Physics, Laser Research Center, Sauletekio Ave. 10, Vilnius, Lithuania
[3]ICREA, Passeig Lluís Companys 23, 08010, Barcelona, Spain
[4]UPC, Dep. de Fisica, Rambla Sant Nebridi 22, 08222, Terrassa (Barcelona), Spain

[*]Corresponding author: lina.grineviciute@ftmc.lt

Abstract: The method for structuring and oxidizing metallic layers on glass, creating transparent oxide metasurfaces with periodic patterns, is presented. Sub-micrometer periodicity gratings are formed using laser interference patterning of tantalum layers, followed by thermal oxidation. Applications of such metamaterials in laser optics will be discussed.

The topic of photonic crystals has been booming over the past decade. Various technologies can be combined to achieve fascinating phenomena in light-controlling meta-structures and photonic crystals. A conceptually novel mechanism of spatial filtering in the near-field domain has already been demonstrated using a nanostructured multilayer coating: a 2D photonic crystal structure with periodic index modulation along the longitudinal and transverse directions relative to the beam propagation [1,2]. Such a structure is built on a nano-modulated substrate, which provides transverse periodicity. The fabrication of complex periodic structures based on coatings involves dual challenges: the development of advanced technologies for both layer deposition and substrate preparation. Even though controlling the growth of layers with periodic patterns is challenging, ensuring the optical quality of substrates with submicron periodicities is also a very difficult task.

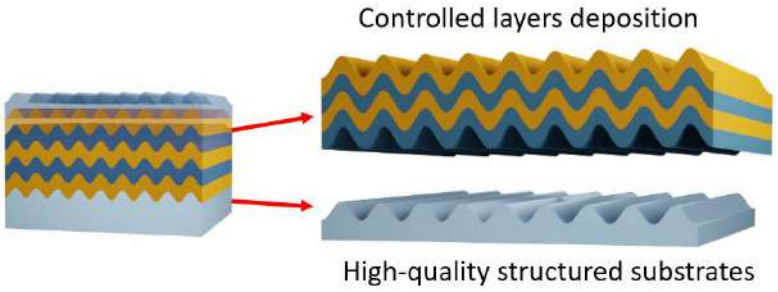


Fig. 1. The schematic representation with highlighted complexity of photonic structure fabrication by coatings.

Nano- and micro-structuring of glass surface for IR and visible spectrum applications is challenging due to the need of submicronic structures which involve complicated fabrication processes, especially while maintaining high surface quality in glass. The method proposed in this work involves the structuring and subsequent thermal oxidation of a thin metallic layer on a glass substrate [3]. Annealing of the structured metal layer produces a transparent fully inorganic oxide surface with periodic patterns, avoiding the subtleties of glass structuring.

In this work, a new method for the formation of sub-micrometer non-absorbing gratings with 750 nm periodicity is presented by direct laser interference patterning (DLIP) of thin tantalum layers on fused silica substrates followed by thermal oxidation by annealing. This method aims to improve the field of laser optics by providing a scalable and efficient method for the creation of precise metal-oxide photonic structures.

The patterned tantalum thin film sample was annealed using earlier estimated parameters: 2 ºC per minute heating rate up to 600 ºC, held for an hour, and cooled down to room temperature along with the furnace pace. Afterwards, captured surface morphologies of structured areas showed increased modulation depths and fill factor (Fig. 2). As it is inevitable during the oxidation process, attachment of oxygen atoms to metal causes material volumetric expansion.

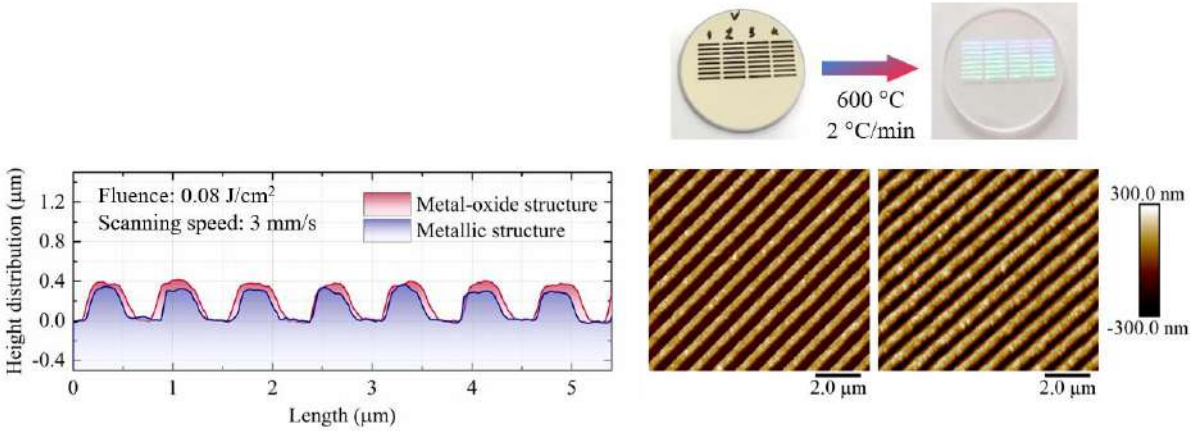


Fig.2. The comparison of 2D surface patterns before and after thermal oxidation.

This method could be expanded for fabrication of different periodicity or even 2D structures, such as meta surfaces suitable for at least to IR spectral band. Slightly smaller periodicities can be relatively easily achieved and much smaller (i.e. by factor of 10) periodicities cannot currently be easily fabricated using this method. DLIP can provide 2D patterns, therefore, this method can be used for 2D non-absorbing gratings.

In this work, a novel method for inorganic periodic structures formations is presented. Such surfaces are needed for 2D photonic structures fabrication based on coatings. The fabrication method proposed in this work involves the structuring and subsequent thermal oxidation of a thin metallic layer on a glass substrate. Annealing of the structured metal layer produces a transparent fully inorganic oxide surface with periodic patterns, avoiding the subtleties of glass structuring. The formation of sub-micrometer non-absorbing gratings with 750 nm periodicity is presented by direct laser interference patterning (DLIP) of thin tantalum layers on fused silica substrates followed by thermal oxidation by annealing.

During the conference presentation, the proposed technology will be discussed in a frame of fabrication process, applications and resistance to laser radiation. Additional insights on how coating technologies can improve the formation of periodic structures will also be shared.

Acknowledgements:

This project has received funding from the Research Council of Lithuania (LMTLT), agreement No. S-PD-24-94

References

[1] L. Grineviciute et al., “Nanostructured Multilayer Coatings for Spatial Filtering,” Adv. Optical Mater. 2001730 (2021)

[2] L. Grinevičiūtė, “Nanostructured optical coatings for the manipulation of laser radiation”, dissertation, Vilnius University, Center for Physical Sciences and Technology, (2021)

[3] J. Nikitina et al., “Submicron periodic structures in metal oxide coating via laser ablation and thermal oxidation”, Applied Surface Science Advances, 24, 100660 (2024)

Aluminum Nanoparticles for Photobleaching Resistance of Quantum Dots in Solution

Jérôme Plain[1*], Théo Duarte[1], Silvère Schuermans[1], Thomas Lerond[1], Jérôme Martin[1], Davy Gérard[1], Thomas Maurer[1], and Julien Proust[1]

[1]L2n, Université de technologie de Troyes and CNRS, Troyes, France
[*]corresponding author: jerome.plain@utt.fr

Abstract: We investigated aluminum nanoparticles (2–20 nm) synthesized via ion reduction in alkane solvents. Extinction spectroscopy revealed UV-range plasmon resonances matching Mie theory. These nanoparticles enhanced quantum dot emission by 1.75× and reduced photobleaching, absorbing emitted light. They hold promise as building blocks for nanophotonics and protecting emitters from degradation.

This study presents a novel method for synthesizing tiny aluminum nanoparticles (Al NPs) with diameters ranging from 2 to 20 nm and explores their potential applications in nanophotonics, particularly for enhancing the photobleaching resistance of quantum dots.

The synthesis process involves the reduction of aluminum ions in trace amounts of water present in alkane solvents like hexane or dodecane. This bottom-up approach allows to produce significant quantities of small, crystalline Al NPs that can serve as building blocks for more complex UV-dedicated plasmonic structures. The method is straightforward, cost-effective, and can be conducted in a standard chemistry laboratory without the need for expensive equipment.

Transmission Electron Microscopy (TEM) analysis revealed two families of Al NPs: a dominant population (99.9%) with an average diameter of 2.0 nm and a standard deviation of 1.2 nm, and a smaller population (0.1%) with an average diameter of 20 nm and a standard deviation of 10 nm. The size distribution of the nanoparticles can be controlled by modifying the water content in the solution, either by changing the alkane solvent or adjusting the temperature during synthesis.

Optical characterization of the Al NPs in hexane showed sharp extinction peaks in the UV range, indicating the presence of Localized Surface Plasmon Resonances (LSPRs). Two distinct peaks were observed: one at 206 nm (FWHM 25 nm) associated with the 2 nm nanoparticles, and another at 249 nm (FWHM 32 nm) corresponding to the dipolar LSPR of the 20 nm nanoparticles. Mie theory calculations confirmed that the particles are purely metallic, with the alkane solvent successfully preventing oxidation.

The study demonstrates the potential of these Al NPs for enhancing the photobleaching resistance of quantum dots in solution. The particles allowed for a global increase in the number of photons emitted by a factor of up to 1.75 compared to quantum dots alone. This enhancement is attributed to the high absorption of the Al NPs in the near UV region, which increases the absorption cross-section of nearby quantum emitters.

The unique properties of these Al NPs make them promising candidates for various applications in UV plasmonics and nanophotonics. Their ability to support LSPRs in the UV range opens possibilities for

developing new UV-LSPR-based nanotechnology, including highly sensitive UV Surface Enhanced Raman Spectroscopy (UV-SERS), high-energy LSPR-based nano-lasers, plasmonic photocatalysis, and UV optical lithography and data storage.

Furthermore, the compatibility of these Al NPs with UV excitation and emission of photo-emitters such as quantum dots and wide bandgap semiconductors suggests potential applications in developing nano-optical devices that leverage exciton-plasmon interaction mechanisms. The ability to control the size distribution of the nanoparticles also allows for tuning their optical properties, potentially extending their usefulness across a broader spectral range.

In conclusion, this study presents a significant advancement in the synthesis of small, crystalline aluminum nanoparticles and demonstrates their potential for enhancing the photobleaching resistance of quantum emitters. The method developed here provides a valuable tool for researchers in the fields of plasmonics and nanophotonics, particularly those focused on UV applications. Future work may explore the integration of these Al NPs into more complex nanostructures and investigate their performance in various optical and sensing applications.

References

1. Théo Duarte De Assuncao, Silvère Schuermans, Thomas Lerond, Jérôme Martin, Davy Gérard, Thomas Maurer, Jérôme Plain, and Julien Proust “Aluminum Nanoparticles for Photobleaching Resistance of Quantum Dots in Solution”, J Phys Chem C, article ASAP, DOI: 10.1021/acs.jpcc.5c00879

Chalcopyrite – Noble Metal Hybrids as Catalytic Nanoscale Metamaterials with Enhanced Interfacial Excitation Transfer

B.M. Reinhard[1,*]

[1]Boston University, Department of Chemistry and The Photonics Center, Boston University, Boston, MA 02215, United States

[*]corresponding author: bmr@bu.edu

Abstract: Chalcopyrite ($CuFeS_2$) nanocrystals provide collective quasistatic resonances in the visible where they can couple with plasmonic resonances of metal nanoparticles. Hybrid chalcopyrite – noble metal nanoparticles are introduced as catalytic nanoscale metamaterials that utilize energy and charge transfer mechanisms to generate excited charge carriers and provide chemical reactivity.

Chalcopyrite nanocrystals provide a quasistatic resonance in the visible range (~490 nm) of the electromagnetic spectrum that is associated with collective oscillations of bound electrons.[1] Integration of these nanocrystals into hybrid structures with noble metal nanoparticles provides unique opportunities for realizing new materials in which the building blocks are resonantly coupled or, alternatively, off-set to generate bi-resonant nanostructured metamaterials. Both types of structures have been implemented and direct energy transfer and photoelectrocatalytic properties have been investigated.[2,3]

Chalcopyrite nanocrystals can be incorporated into the evanescent field around noble metal nanoparticles by assembling a lipid coating around the metal nanoparticle that serves as matrix for chalcopyrite nanocrystals with a hydrophobic ligand shell. Two classes of chalcopyrite nanocrystal – noble metal nanoparticle hybrids will be discussed in this presentation: i.) Chalcopyrite nanocrystals with Au nanorods ($CuFeS_2$ NC – Au NR)[3] and ii.) Chalcopyrite nanocrystals with Ag nanospheres ($CuFeS_2$ NC – Ag NP)[2]. The vertical and longitudinal plasmon resonances of the Au nanorods used in ref[3] peaked at around 530 nm and 745 nm, respectively. The chalcopyrite nanocrystal resonance overlaps only with the vertical but not with the longitudinal plasmon mode of the Au nanorod. These bi-resonant hybrid nanostructures were found to enhance the hydrogen evolution reaction (HER) when excited at 730 nm in an acidic electrolyte and the oxygen evolution reaction (OER) when excited at 530 nm in a basic electrolyte.

A systematic investigation of the photoelectrocatalysis obtained with these materials indicated that the detected reactivity is consistent with a hot electron transfer in different directions based on the chosen excitation wavelength.[3] Excitation of the longitudinal resonance triggers the formation of hot electrons in the Au NRs. These hot electrons can be transferred to the chalcopyrite nanocrystals where they can trigger the HER ($2H^+ + 2e^- \rightarrow H_2$). Alternatively, excitation of the quasistatic resonance in the chalcopyrite nanocrystals results in the formation of hot electrons in the nanocrystals that can transfer to the Au nanorods in a process that generates reactive holes on the nanocrystals to facilitate the OER ($4OH^- - 4e^- \rightarrow 2H_2O + O_2$) on the nanocrystal surface. In addition to the generation of hot electrons and holes on the chalcopyrite nanocrystals, the specific surface properties of the $CuFeS_2$ nanocrystals also play a role in driving the chemical reactivity of the hybrid materials and will be discussed.

The presence of a quasistatic resonance in the nanocrystals that overlaps with the plasmon resonance of metal nanoparticles also provides opportunities for engineering direct energy transfer between the building

blocks. This was investigated through single particle spectroscopy of $CuFeS_2$ NC – Ag NP hybrids.[2] Single particle lineshape analysis revealed a broadening of the silver nanoparticle spectrum that was indicative of a decrease in plasmon lifetime due to the presence of the chalcopyrite nanocrystals. Importantly, the spectral broadening was observed to depend on the energetic overlap between the silver nanoparticle plasmon resonance and the quasistatic chalcopyrite nanocrystal resonance.[2] An analysis of the single particle data will be presented and examined in this presentation.

Overall, the experiments performed so far suggest that chalcopyrite nanocrystal – noble metal nanoparticle hybrids facilitate light driven and wavelength-dependent charge and energy transfer that can be utilized to drive energy-relevant chemical transformations. This presentation will develop the framework of the relevant interactions between the building blocks and highlight potential strategies to optimize the photocatalytic properties of these intriguing nanoscale metamaterials.

References

(1) Gaspari, R.; Della Valle, G.; Ghosh, S.; Kriegel, I.; Scotognella, F.; Cavalli, A.; Manna, L. Quasi-Static Resonances in the Visible Spectrum from All-Dielectric Intermediate Band Semiconductor Nanocrystals. *Nano Lett.* **2017**, *17* (12), 7691–7695. https://doi.org/10.1021/acs.nanolett.7b03787.

(2) Ouyang, T.; Chen, Y.-C.; Kundu, K.; Zhong, X.; Mei, Y.; Nalluri, A.; Dennis, A. M.; Reinhard, B. M. Direct Excitation Transfer in Plasmonic Metal-Chalcopyrite-Hybrids: Insights from Single Particle Line Shape Analysis. *ACS Nano* **2024**, *18* (32), 21565–21575. https://doi.org/10.1021/acsnano.4c07442.

(3) An, X.; Kays, J. C.; Lightcap, I. V.; Ouyang, T.; Dennis, A. M.; Reinhard, B. M. Wavelength-Dependent Bifunctional Plasmonic Photocatalysis in Au/Chalcopyrite Hybrid Nanostructures. *ACS Nano* **2022**, *16* (4), 6813–6824. https://doi.org/10.1021/acsnano.2c01706.

Narrow Conducting Polymer Plasmonics via Collective Lattice Resonance

D. Q. Lin[1], Y. L. Duan[1], P. Bandaru[1] and M. P. Jonsson[1*]

[1] Laboratory of Organic Electronics, Department of Science and Technology (ITN), Linköping University, Norrköping, SE-60174, Sweden

[*]corresponding author: magnus.jonsson@liu.se

Abstract

We improve quality factors (Q) of conducting polymer plasmonics by one order of magnitude through coupling with collective lattice resonance, and such nonlocal narrow resonance allows large extinction modulation depths during dynamic switching, which puts forward a key step in smart organic metasurfaces.

1 Summary

Conducting polymers with tunable redox states support dynamic switching of surface plasmon resonances for intelligent nano-optic metasurfaces. However, current polymer plasmons suffer from weak resonance intensities and low quality factors (Q < 2). Here, we achieve narrow conducting polymer plasmonics by coupling with collective lattice resonance (CLR) based on poly(3,4-ethylenedioxythiophene) (PEDOT) nanoantennas. We analyze the CLR-matching relationship between array factors of lattice and isolated polarizabilities of PEDOT nanoantenna units, and fabricated PEDOT arrays with well-matched sizes between array periodicities and nanoantenna dimensions, by using electron-beam lithography. The PEDOT arrays exhibit mid-infrared surface plasmon resonance (at the wavelength ranges of 2-4.5 μm) with linewidths of 0.3-0.5 μm, and Q can be up to 10-12, as one order of magnitude higher than previous works [1-4] (Q = 1-2). Furthermore, we can modulate large extinction depths of narrow plasmonic resonance (between ~5% and ~45%) through redox reactions of PEDOT materials. By addressing problems of broad and weak plasmonic resonances from conducting polymer nanoantennas, this work not only offers significant advances in the emerging field of nonlocal metasurfaces, but also shows feasibility of organic electronic materials for practical applications in active nano-optic systems.

2 Acknowledgements

The authors acknowledge support from the European Research Council (Consolidator Grant, 101086683), the Knut and Alice Wallenberg Foundation (Wallenberg Academy Fellow, 2019. 0163) and the Swedish Research Council (VR, 2020-00287).

References

1. Chen S*, et al.* "Conductive polymer nanoantennas for dynamic organic plasmonics," *Nat. Nanotechnol.* Vol. 15, 35-40, 2020.
2. Karst J*, et al.* "Electrically switchable metallic polymer nanoantennas," *Science* Vol. 374, 612-616, 2021.
3. Karki A*, et al.* "Electrical Tuning of Plasmonic Conducting Polymer Nanoantennas," *Adv. Mater.* Vol. 34, 2107172, 2022.

4. Lee S, *et al.* “Plasmonic polymer nanoantenna arrays for electrically tunable and electrode-free metasurfaces,” *J. Mater. Chem. A* Vol. 11, 21569-21576, 2023.

Bound-state-in-the-continuum dielectric bowtie metasurfaces for strongly enhanced light-matter interaction

Sergei Lepeshov[1], Nikolaj Balslev Hougs[1], and Søren Stobbe[1,2*]

[1] DTU Electro, Department of Electrical and Photonic Engineering, Technical University of Denmark, Lyngby, Kgs. Lyngby, Denmark
[2] NanoPhoton — Center for Nanophotonics, Technical University of Denmark, Lyngby, Kgs. Lyngby, Denmark
[*]corresponding author: ssto@dtu.dtu.dk

Abstract: Dielectric bowtie cavities allow confining light well below the diffraction limit without absorption and therefore enable greatly enhanced light-matter interactions. Here we present theoretical results showing that this enhancement may be harnessed in metasurfaces that support bound states in the continuum laterally confined to dielectric bowties.

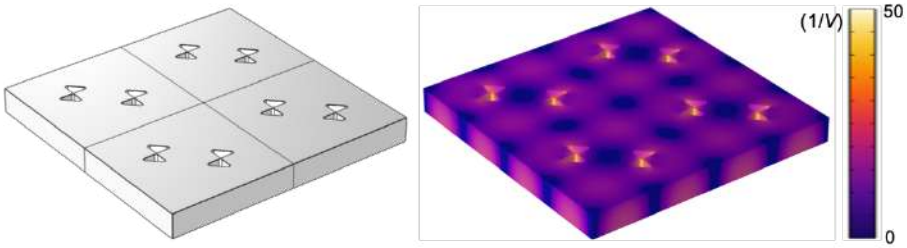


Figure 1. Left: Geometry of a metasurface with bowtie unit cells. Right: Simulated bound-state-in-the-continuum mode confining light more than 50 times below the diffraction limit in the silicon bridges at the center of the bowties.

The advent of dielectric bowtie cavities (DBCs) opens prospects for enhancing light-matter interaction[1] beyond what was previously considered possible owing to subdiffraction mode volumes[2-8]. Previous experimental works have considered single bowtie cavities, either realized by high-resolution nanofabrication[4,7] or self-assembly[5], while theoretical works span various inverse-design methods, nanobeam cavities, or topological building blocks, but a direct observation of increased spontaneous-emission rates have so far not been reported. Here we utilize a bowtie as a building block for a metasurface supporting as shown in Fig. 1. The structure supports bound states in the continuum[9] as shown in Fig. 2. In my talk, I will discuss recent theoretical results as well as experimental efforts towards measuring enhanced spontaneous-emission rates in bowtie structures.

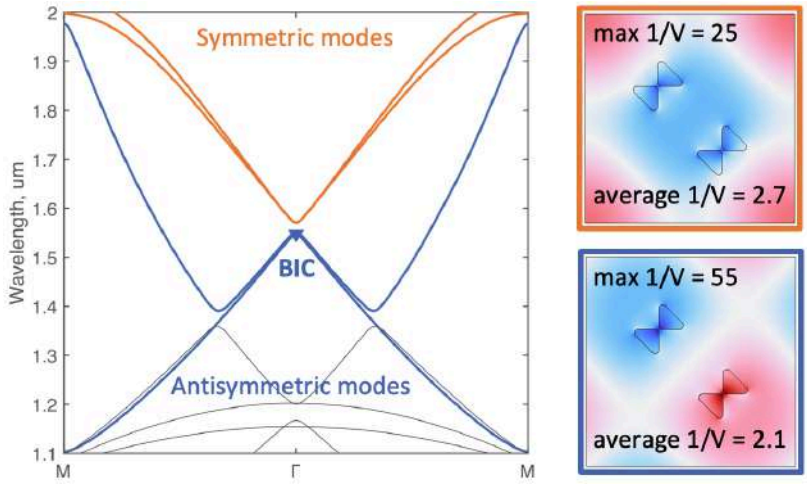


Figure 2: Calculated band structure exhibiting both symmetric and antisymmetric modes, and the latter includes a bound state in the continuum (BIC) with strong field enhancement in the bowtie region.

References

1. P. Lodahl, S. Mahmoodian, and S. Stobbe, "Interfacing single photons and single quantum dots with photonic nanostructures," Rev. Mod. Phys., vol. 87, p. 347, 2015.
2. A. Gondarenko, S. Preble, J. T. Robinson, C. W. Chen, and M. Lipson, "Spontaneous Emergence of Periodic Patterns in a Biologically Inspired Simulation of Photonic Structures," Phys. Rev. Lett., vol. 96, p. 143904, 2006.
3. H. Choi, M. Heuck, and D. Englund, "Self-Similar Nanocavity Design with Ultrasmall Mode Volume for Single-Photon Nonlinearities," Phys. Rev. Lett., vol. 118, p. 223605, 2017.
4. O. Albrechtsen, F. Vosoughi Lahijani, R. E. Christiansen, K. Q. Nguyen, R. Casses, O. Hansen, N. Stenger, O. Sigmund, E. Jansen, J. Mørk, and S. Stobbe, "Nanometer-scale photon confinement in topology-optimized dielectric cavities," Nat. Commun., vol. 13, p. 6281, 2022.
5. S. Babar, T. Weis, A. Tsoukalas, S. Kadkhodazadeh, G. Arregui, F. Vosoughi Lahijani, and S. Stobbe, "Self-assembled photonic cavities with atomic-scale confinement," Nature, vol. 624, p. 57, 2023.
6. M. Albrechtsen and S. Stobbe, "Two regimes of confinement in photonic nanocavities: bulk confinement versus lightning rods," Opt. Express, vol. 30, pp. 15458–15469, 2022.
7. M. Xiong, R. E. Christiansen, F. Schröder, Y. Yu, L. N. Casses, E. Semenova, K. Yvind, N. Stenger, O. Sigmund, and J. Mørk, "Experimental realization of deep sub-wavelength confinement of light in a topology-optimized InP nanocavity," Opt. Mater. Express, vol. 14, pp. 397–406, 2024.
8. A. Vladimirova, G. Arregui, S. Lepeshov, C. A. Rosiek, B. Vosoughi Lahijani, and S. Stobbe, "Waveguide and cavity quantum electrodynamics with topological bowtie modes," Phys. Rev. A, vol. 110, L061503, 2024.
9. S. Joseph, S. Pandey, S. Sarkar, and J. Joseph, “Bound states in the continuum in resonant nanostructures: an overview of engineered materials for tailored applications,” Nanophotonics, vol. 10 pp. 4175-4207 (2021).

Plasmonic Multilayers Metamaterials combining Nitrides, Oxynitrides and Transparent Conductors with novel, broad and tunable properties

C. Mancarella[1*], C. Hallqvist[1], S. Bossetti[1], L. Tovaglieri[1], G. Baiardi[1], A. Lamperti[2], D. Koutsogeorgis[3], N. Kalfagiannis[3,4], V. Caligiuri[5,6] A. De Luca[5,6], A. Li Bassi[1,7]

[1] Nanolab, Department of Energy, Politecnico di Milano, Via Ponzio 34/3, 20133, Milano, Italy
[2] CNR-IMM, Via C. Olivetti 2, 20864, Agrate Brianza (MB), Italy
[3] Nottingham Trent University, 50 Shakespeare Street, NG1 4FQ Nottingham, United Kingdom
[4] University of Ioannina, GR-451 10 Ioannina, Greece
[5] Department of Physics, Università della Calabria, Via P. Bucci - Cubo 31/C, 87036, Rende (CS), Italy
[6] CNR-Nanotec, Via P. Bucci - Cubo 31/C, 87036, Rende (CS), Italy
[7] CNST-IIT – Italian Institute of Technology, Via Rubattino 81, 20134, Milano, Italy
*cristina.mancarella@polimi.it

Abstract: Plasmonic effects enhance light-matter interactions for advanced metamaterials with tunable properties and broad spectral responses. Noble metals limit modulation beyond the visible range. This work develops novel meta-structures using alternative plasmonic materials (transparent conductors, nitrides, oxynitrides) to achieve customizable plasmonic properties from visible to infrared for extreme light control.

Optimizing solar energy conversion processes requires materials capable of harnessing the entire solar spectrum, from the visible (VIS) to the infrared (IR). In this context, plasmonics enables advanced control of light-matter interactions through plasmonic resonances [1]. Traditionally, noble metals such as gold (Au) have dominated due to their high-quality resonance in the VIS range, but their limited plasmonic tunability has driven research towards alternatives [2]. Transition metal nitrides, such as TiN, stand out due to their cost-effectiveness, thermal stability, and CMOS compatibility, offering tunable plasmonic responses in the VIS-NIR through compositional variations [3]. At the same time, oxynitrides (TiO_xN_y) are emerging as promising materials because they exhibit two epsilon-near-zero (ENZ) points, granting them a Double Epsilon-Near-Zero (D-ENZ) character. This property is highly beneficial for advanced optical phenomena, such as multiple resonances and enhanced nonlinear optics [4]. Another promising class of materials is represented by transparent conducting oxides (TCOs), such as Ta-doped TiO_2 ($Ta:TiO_2$), whose carrier concentration can be modulated to extend plasmonic properties into the IR range [2]. In this scenario, research focuses on developing metastructures based on alternative materials to enable multifunctional properties for applications in optoelectronics, biosensing, and nanophotonics. Hyperbolic Metamaterials (HMMs) are a key approach, as they feature anisotropic permittivity by alternating conductive ($\varepsilon_1 < 0$) and dielectric ($\varepsilon_1 > 0$) layers, enabling high-wavevector propagation and new light-confinement strategies [5].

In this study, thin films and multilayers based on $Ta:TiO_2$, TiN, and TiO_xN_y were developed and characterized using pulsed laser deposition (PLD) on cost-effective substrates (Si, glass). This technique allows precise control over composition and morphology during both growth and post-deposition treatments.

TiN/TiO_2 multilayers (**Fig.1(a)**) were explored as new candidates for HMMs, merging TiO_2 wide-bandgap semiconductor properties and TiN thermal stability. Optical characterization via spectroscopic ellipsometry revealed a broadband hyperbolic response between 600 and 2100 nm.

For oxynitrides, synthesis was optimized to incorporate oxygen while maintaining the TiN structure and preventing its transition to TiO_2. This challenge was addressed by fine-tuning deposition parameters such as base vacuum, oxygen and H_2-N_2 pressure. The resulting films exhibited a D-ENZ character, with tunable ε_1 crossings between 400 and 1700 nm (**Fig.1(b)**), opening new possibilities for their integration into multilayered broadband and multi-resonant HMMs, as it will be explained later.

With the final goal to extend plasmonic and optical functionalities of nanostructures far in the IR, Ta-doped TiO_2 TCO compact-conducting and porous-insulating films, obtained by varying solely the deposition pressure during PLD synthesis (1, 3, 6 Pa O_2) at fixed Ta doping content (5% or 10% at.), have been fully investigated from a material science perspective. The obtainment of metal-like and dielectric properties (**Fig.1(c)**) is allowed by the possibility to impose optoelectronic modification to the TCO upon tuning finely the oxygen content directly in the deposition process, that modifies morphology and stoichiometry, due to the inherent charge carrier density tunability owned by TiO_2-based TCOs. These results are fundamental to confirm the possibility to engineer HMM in the IR, which is impressive and quite unusual for a TCO (usually accomplished for AZO and ITO in the NIR up to 2 μm). Indeed, the next challenge is the experimental development of original nanostructures potentially working as HMM in the IR. Multilayers for this purpose have been synthetized with a simple one-step production by alternating metal-like (compact, crystalline) and insulating (nano-porous, amorphous) layers of the same Ta:TiO_2 TCO material, by varying the background pressure (1-6 Pa O_2) during the PLD deposition. As last but interesting remark, multilayers combining TiN, TiO_xN_y and Ta:TiO_2, definitely deserve additional research efforts, since it seems promising for achieving an exceptionally wide HMM behaviour, in multiple ranges, from VIS (TiO_xN_y is metal-like) to IR (Ta:TiO_2 is metal-like) (**Fig. 1(d)**).

Concluding, TCO (Ta:TiO_2) and nitride-based (TiN) alternative plasmonic nanomaterials merging multifunctional, tunable and broader plasmonic responses have been experimentally realized and characterized according to the tailored application. This work surely provides a starting guideline for designing real devices implementing cutting-edge alternative plasmonic materials, where the expected enhancement of light-matter interactions is at the core for technologically-relevant applications (thermal management in photovoltaics, plasmon-mediated broadband solar absorption/manipulation and photocatalysis).

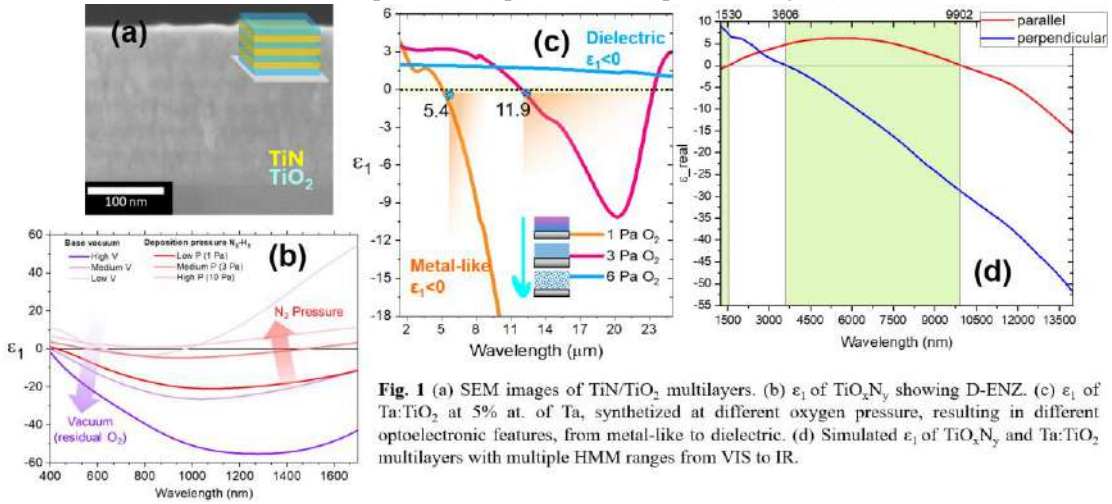


Fig. 1 (a) SEM images of TiN/TiO_2 multilayers. (b) ε_1 of TiO_xN_y showing D-ENZ. (c) ε_1 of Ta:TiO_2 at 5% at. of Ta, synthetized at different oxygen pressure, resulting in different optoelectronic features, from metal-like to dielectric. (d) Simulated ε_1 of TiO_xN_y and Ta:TiO_2 multilayers with multiple HMM ranges from VIS to IR.

[1] Naldoni, A. et al., "Solar-Powered Plasmon-Enhanced Heterogeneous Catalysis", Nanophotonics 5, 112–133, 2016

[2] Naik, G. V. et al., "Alterantive Plasmonic Materials: Beyond Gold and Silver", Adv. Mater. 25, 3264–3294, 2013

[3] Patsalas, P. et al., "Conductive nitrides: Growth principles, optical and electronic properties, and their perspectives in photonics and plasmonics", Mater. Science and Engineering R 123 1-55, 2018

[4] Braic, L., et al., "Titanium Oxynitride Thin Films with Tunable Double Epsilon-Near-Zero Behavior for Nanophotonic Applications", ACS Appl. Mater. Interfaces, 9, 29857−29862, 2017

[5] Shekhar, P. et al., "Hyperbolic metamaterials: fundamentals and applications", Nano Convergence, 1, 14, 2014.

Geometric approach based on optimal toric packings for photonic crystals and metamaterials design.

Alexander Itin[1]

[1]Hamburg University of Technology (TUHH), Hamburg, Germany
*E-mail/website: alx.itin@gmail.com /AI4science.de

Abstract

We introduce new classes of nanostructures—optimal toric packings of particles and their Voronoi tessellations—that exhibit remarkable properties for photonic and potentially for plasmonic/phononic crystals design. These structures connect the classical problem of optimal packings on tori with the development of optimized photonic architectures.

1. Introduction

Design of photonic crystals [1, 2, 3] with large bandgaps above a specified band is a well-known problem with diverse applications. Usually, such a design is achieved numerically using optimization methods or machine learning (ML) techniques. Optimality of the final designs is not easy to determine: combinatorial complexity of the design space is too large. Therefore, despite advances in numerical and ML techniques [4, 5], theoretical understanding of design principles of photonic bandgap structures remains being an important topic, and may be useful for many adjacent areas of scientific knowledge (e.g. plasmonics, phononics, and magnonics). In fact, in the field of photonic crystals, approximate design principles do exist thanks to insightful classic work of O.Sigmund and K. Hougaard [6]. Their conjecture linked optimal structures for bandgaps between bands n and n+1 to centroidal Voronoi tessellations (CVT): rods being placed at locations of CVT generators (in the case of transverse magnetic (TM) polarization), and walls of the CVT (in the case of transverse electric (TE) polarization). We found another mathematical approach [7]: optimal disc packings in square and triangular tori. While geometric idea behind CVT is some kind of uniformity in distribution of optical elements (coincidence of Voronoi tesselation generators with corresponding cell center of mass), optimal disk packings realise a simpler geometric objective: maximisation of minimal distance between the elements. Arrays of particles placed at the centers of optimally packed discs on tori and nets formed by walls of their Voronoi tessellations produce qualitatively different structures that sometimes significantly enlarge bandgaps. The new classes of periodic structures might have many applications in photonics and beyound. Optimal packing problems have arisen throughout the history of humankind, one of the most famous example is probably the Kepler problem concerning densiest arrangement of (many) identical spheres, where a close-packed structure was conjectured to be a solution [8]. It took more than 300 years to prove 2D version of the Kepler conjecture, and then much more difficult 3D case [8]. These results were about infinite space. We use somehow related and much more recent results for finite spaces [9]: optimal packings in "containers" with periodic boundary conditions. Indeed, even though a photonic crystal occupies an infinite space, it is obtained by periodic arrangement of a finite elementary unit cell. Considering a square or rhombic unit cell with periodic boundary, one obtains a square torus or triangular torus geometry, correspondingly [7]. Several mathematical and numerical methods had been used to find point configurations maximising minimal distance between points [9, 10, 11, 12]. In [7], we compared symmetry constrained CVT recipes of [6] with toric optimal configurations (OP). Here, we additionally study toric CVT configurations (tCVT, with generators of centroidal Voronoi tesselations being distributed on tori *without* symmetry restrictions). Part of the achieved advantage of OP over CVT comes from absence of symmetry restrictions. It is therefore logical to study also tCVT without those symmetry restrictions. We find that they are able to outperform toric OP in certain (rare) cases.

2. CVT, toric CVT, and toric OP configurations for photonic bandgap structures

.

Toric optimal packing configurations studied in [7] are illustrated on Fig. 1. CVT configurations of [6] with symmetry restrictions are shown on Fig. 2 and toric CVT configurations (without symmetry restrictions) are shown in Fig. 4. Here we illustrate only the square lattice geometry, for the triangular lattice case see [6, 7]. Bandgaps of optimised structures are shown in Fig. 3. Permittivity of the inclusions is the same as in Ref.[6]: $\varepsilon = 11.56$, while host media is air with $\varepsilon = 1$. 1-parameter optimisation (with only radius of rods or width of wires being the optimisation parameter) was applied to OP structures and obtained in this way OP_1 structures were compared with topology optimised (TO) structures of [6] (CVT_{top}), and with 1-parameter optimised CVT and tCVT structures (CVT_1 and tCVT_1, correspondingly). If 1-parameter optimisation is comparable with or better than TO (which involves hundreds of parameters), it is a clear sign of success. Indeed the

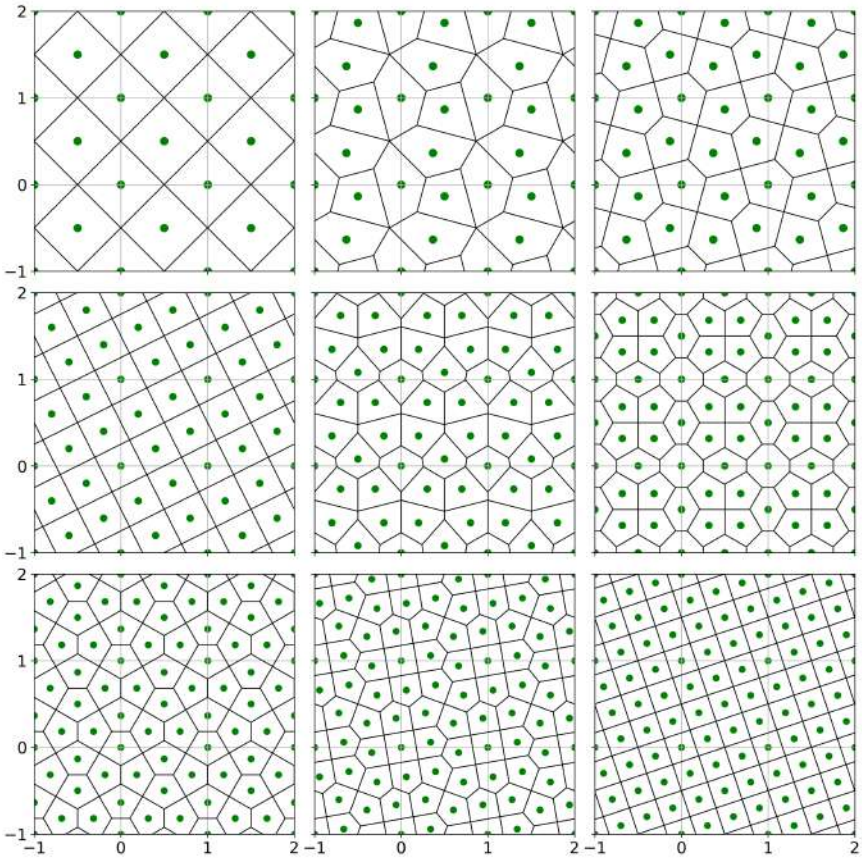


Figure 1: Optimal packing configurations (green dots) and their Voronoi tesselations (black lines) from N=2 (top left) to N=10 (bottom right). Each panel shows 3x3 supercell (numbers just mark the unit cells)

OP_1 structures clearly have certain advantages compared to classic CVT structures of [6]. In square lattice geometry, bandgaps of CVT structures for TE modes cannot reach levels that are achieved in triangular lattice geometry (approx. 52 %). However, for OP_1 structures, surprisingly, it is possible. In some cases OP_1 structures for TM modes also outperform CVT_{top}. One of the most peculiar structures arises at N=4 and N=8: for TM modes, arrays of points form one of the Archimedean square-triangular patterns, and for TE modes its corresponding Voronoi tesselations form Cairo pentagonal tiling [14, 15]. For triangular lattice geometry, the optimal packing recipe allows to predict "magic" band numbers where maximal bandgaps can be achieved [7]. Toric CVT structures (without symmetry restrictions) are shown in Fig. 4. We use results of [13] where toric CVT configurations were achieved using L-BFGS method. These structures, unlike OP, are not unique: there could be many different realisations, in particular it is possible to find fully hexagonal patterns in most cases. In some cases (e.g. N=5), toric CVT configurations coincide with toric OP structures. We chose fully hexagonal toric CVT patterns where it was possible, and found that for N=4 and N=8 they outperform toric OP structures (Cairo pentagonal tilings). At the same time, neither CVT nor toric CVT property, even being supplied with fully hexagonal patterning, is not enough to ensure optimal photonic bandgap: hexagons should also be somehow "round", e.g. for N=7 tCVT performs considerably worse than either OP or CVT (Fig 3c).

3. Further connections to art, math, and physics

.

Cairo tesselation [14, 15] is encountered in architecture, decorative design, and crystallography, but was not used in photonic crystals yet, to the best of our knowledge. In architecture, it can be found in Cairo (obviously), but also in Hamburg ([14, 15], see also Fig.6) and some other cities.

Mathematically, it is connected to one of the 11 Archimedean tilings via duality (see Fig.5). Archimedean tilings were already studied from the point of view of photonic structure design, but not from the point of view of optimal packings.

When discussing low-contrast limit of photonic bandgap structures, some kind of optimal packings in reciprocal space appear [17, 18].

Some of the structures of [7] may hopefully find applications in topological photonics and plasmonics: e.g. Ref.[16] studied lasing in arrays of quadrumers, while our N=4 configurations provides another route for packing of quadrumers on lattice.

There are certain connections with phononic structures

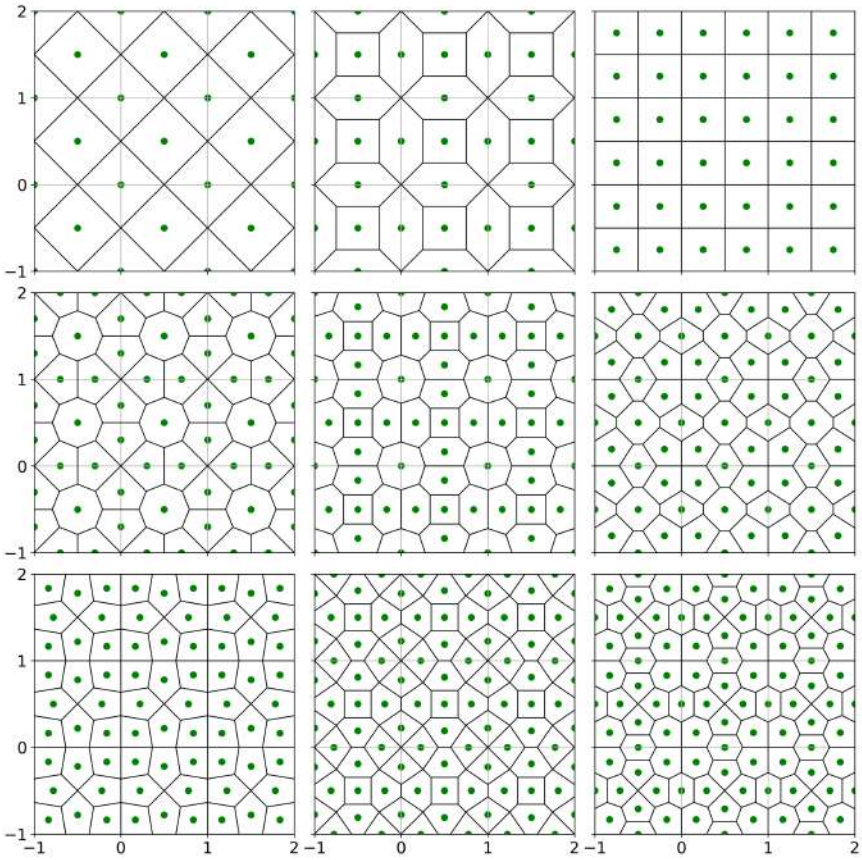


Figure 2: Centroidal Voronoi tesselations with symmetry constraints (black lines) and their generators (green dots) from N=2 (top left) to N=10 (bottom right). Each panel shows 3x3 supercell (numbers just mark the unit cells)

studied in [19].

4. Conclusions

. Splitting the process of topology optimisation on two steps, as suggested in [6], with the first step being purely geometric one, is very attractive and inspirational idea. So far systematic applications of this approach have been done in photonics, but it should be possible to extend to other realms of physics: plasmonics, phononics, etc. A peculiar historical fact is worth noting: in the very same year the first bandgap structure was ever discussed [3] (1887), a study appeared on an optimal geometric structure realising tiling of space [20]. These two scientific fields remain being intrinsically connected, providing interesting new findings. In [7] and here we considered toric optimal packing configurations and toric CVT configurations which sometime demonstrate certain advantages compared to classic CVT configurations of [6].

Acknowledgement

Useful and inspiring discussions with Ole Sigmund, Carsten Rockstuhl, Alexander Petrov, Manfred Eich, Andreas Tittl, Michael Berry are greatly acknowledged. Some funding for conferences participation was kindly provided by German Research Foundation (DFG) via SFB 986 “Tailor-made Multi-scale Materials Systems: M3”, Project 192346071.

References

[1] E. Yablonovitch, Inhibited Spontaneous Emission in Solid-State Physics and Electronics, *Phys. Rev. Lett.* 58, 2059, 1987.

[2] S. John, Strong localization of photons in certain disordered dielectric superlattices, *Phys. Rev. Lett.* 58, 2486, 1987.

[3] Lord Rayleigh Sec.R.S., XVII. On the maintenance of vibrations by forces of double frequency, and on the propagation of waves through a medium endowed with a periodic structure, *The London, Edinburgh, and Dublin Philosophical Magazine and Journal of Science* 24:147, p.145-159, 1887

[4] T. Christensen, et al. Predictive and generative machine learning models for photonic crystals,

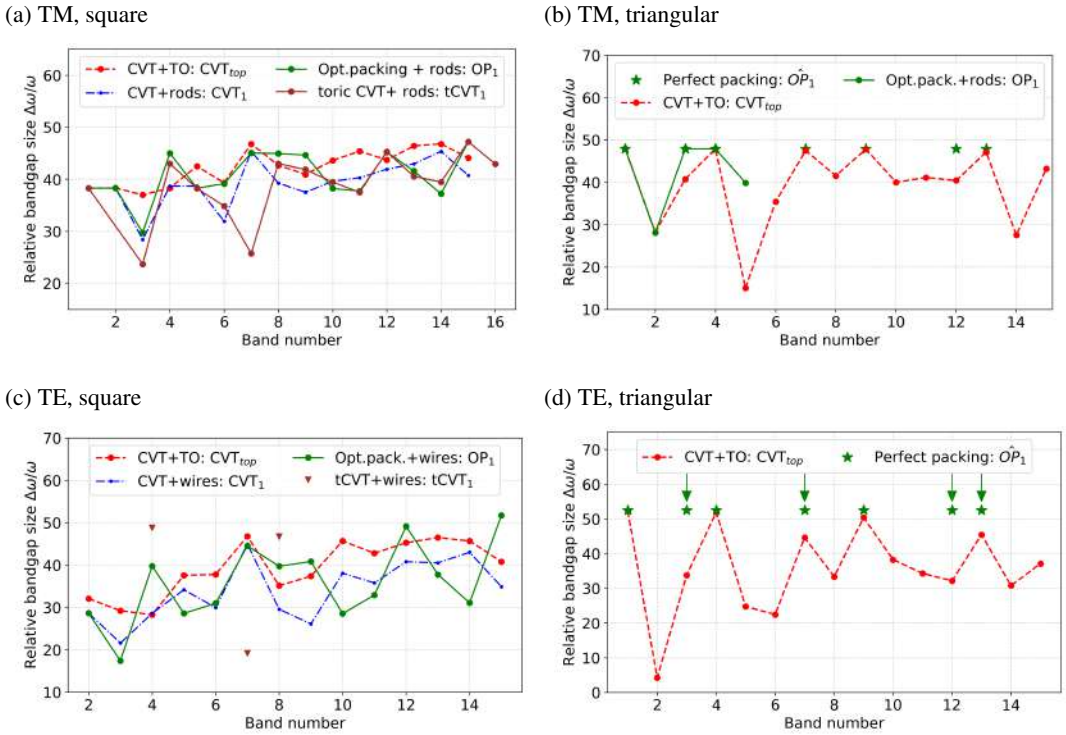


Figure 3: Relative bandgap vs. band number for square lattice geometry (left panels) and triangular lattice (right panels). Upper(bottom) panels: TM(TE) modes. Dot-dashed line ("CVT+rods(wires): CVT_1"): configurations realising centroidal VT (CVT) are taken from Ref. [6], and circular rods of equal radius are placed at each point of the configuration for TM modes, or wires of equal width are placed along walls of VT for TE modes. The rod radius (wire width) is optimised to achieve the highest bandgap (1-parameter optimisation). Dashed line ("CVT+TO: CVT_{top}"): results of Ref.[6], where topology optimisation was done on top of CVT. Solid line ("Opt.packing+ rods(wires): OP_1" for TM(TE) modes): our results, where configurations are obtained from optimal packing solutions and circular rods of equal and optimised radius are placed there for TM modes, or wires of optimised width are placed along walls of VT for TE modes. Triangles denote $tCVT$ configurations (CVT without symmetry constraints). Stars denote perfect packing solutions (close-packed structures), those VT in TE case produce honeycomb-like structures with maximal bandgaps. They are realised for "magic" band numbers $N = 1, 4, 9$ found both in [6] and in our approach [7], and at additional "magic" band numbers $N = 3, 7, 12, 13$ obtained via our approach only [7] (highlighted by vertical arrows).

Nanophotonics 9, 4183, 2020.; Nikulin et.al, Machine learning models for photonic crystals band diagram prediction and gap optimisation, *Photonics and Nanostructures-Fundamentals and Applications* 52, 101076, 2022.

[5] C. Loh et.al., Surrogate- and invariance-boosted contrastive learning for data-scarce applications in science, *Nat. Commun.* 13, 4223, 2022; A.Schurov et. al, Invariant multiscale neural networks for data-scarce scientific applications, arxiv:2406.08318 (2024).

[6] O.Sigmund and K. Hougaard, Geometric properties of optimal photonic crystals, *Phys. Rev. Lett.* 100, 153904, 2008.

[7] A.Itin, Geometric approach to design of photonic crystals and metamaterials via optimal toric packings, *Phys. Rev. B* 111, L121404, 2025.

[8] D.Weaire, A Short History of Packing Problems, *Forma* 14, 279 ,1999.

[9] O.R.Musin, A.V.Nikitenko, Optimal Packings of Congruent Circles on a Square Flat Torus, *Discrete Comput Geom* 55, 1, 2016.

[10] R.Connelly and W.Dickinson, Periodic planar disc packings, *Philos. Trans. R. Soc. A* 372, 20120039, 2014.

[11] R.Connely et.al, Packings of equal disks in a square torus, *Discrete Comput. Geom.* 58, 614, 2017.

[12] V. Voloshinov, S. Smirnov, Optimal packings of congruent circles on a square flat torus as mixed-integer nonlinear optimization problem, *Supercomputing. Communications in Computer and Information Science* 1129., 2019.

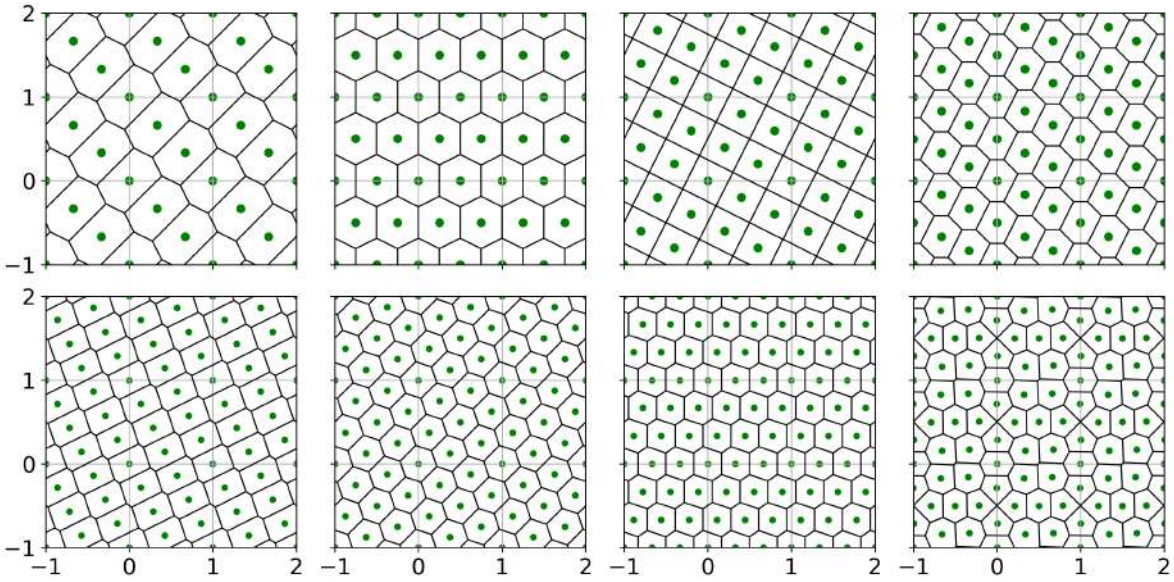


Figure 4: Toric centroidal Voronoi tesselations (black lines) and their generators (green dots) from N=3 (top left) to N=10 (bottom right). Each panel shows 3x3 supercell

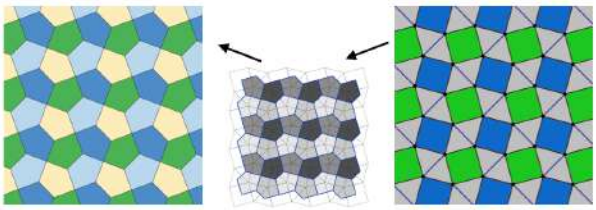


Figure 5: The Cairo pentagonal tiling (left), an Archimedean square-triangular tiling (right), and duality procedure transforming them between each other is in the center

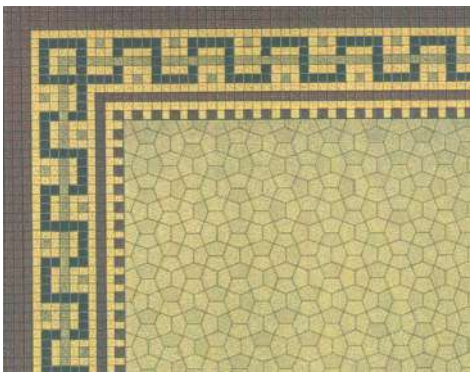


Figure 6: Photo of floor tiling from catalog of Villeroy & Boch, between 1900 and 1920. In Laeiszhalle music pavilion in Hamburg, constructed in 1908, the floor in the foyer is covered with such tiles. [15]

[13] D. -M. Yan, K. Wang, B. Levy and L. Alonso, Computing 2D Periodic Centroidal Voronoi Tessellation, Eighth International Symposium on Voronoi Diagrams in Science and Engineering, QingDao, China, pp. 177-184, 2011.

[14] F. Morgan, My Undercover Mission to Find Cairo Tilings. Math Intelligencer 41, 19 (2019).

[15] In the beginning of 20th century Villeroy & Boch created a line of ceramic floor tiles in the Cairo tiling pattern, being used in the foyer of the Laeiszhalle in Hamburg, Germany. (David Bailey, personal communication).

[16] R.Heilmann, G.Salerno, J.Cuerda, T.K. Hakala, and P.Törmä, Quasi-BIC Mode Lasing in a Quadrumer Plasmonic Lattice, *ACS Photonics* 9, 224, 2022.

[17] P.N.Dyachenko, Yu.V.Miklyaev, Band structure calculations of 2D photonic pseudoquasicrystals obtainable by holographic lithography, *Proc. of SPIE* 6182, 61822I, 2006.

[18] L. Maiwald et al, Control over Light Emission in Low-Refractive-Index Artificial Materials Inspired by Reciprocal Design, *Adv. Optical Materials* 10, 2100785, 2022.

[19] I. Nadejde, Pushing the limits of complete omnidirectional bandgaps in 2D nonsymmorphic single-phase phononic crystals, *Appl. Phys. Lett.* 123, 132201 (2023).

[20] Lord Kelvin (Sir William Thomson), On the Division of Space with Minimum Partitional Area, *Philosophical Magazine* 24, 503, 1887.

Germanium Metalenses for Long-Wavelength Infrared Spectroscopy Applications

J. H. Mendoza-Castro[1,2*], G. Piscopo[2,3], A. S. Vorobev[3,4], T. Piwonski [4], A. D'Orazio[2], G. Magno[2], B. Lendl[1] and L. O'Faolain[3,4]

[1] Institute of Chemical Technologies and Analytics, TU Wien, Getreidemarkt 9/164, Vienna, 1060, Austria.
[2] Department of Electrical and Information Engineering, Politecnico di Bari, Via E. Orabona, 4, 70126 Bari, Italy
[3] Centre for Advanced Photonics and Process Analysis, Munster Technological University, T12 T66T, Cork, Ireland
[4] Tyndall National Institute, T12 PX46 Cork, Ireland
[*]corresponding author: jesus.mendoza-castro@tuwien.ac.at

Abstract: We report the design and anticipated fabrication of Germanium metalenses on Ge and ZnSe platforms in the long-wavelength infrared (12–15 μm). Integrated into indirect absorption spectroscopy systems, they enable miniaturization for BTEX detection (Benzene, Toluene, Propane), addressing the need for compact optical components in the LWIR range.

Many Volatile Organic Compounds (VOCs) have strong fundamental vibrational absorption bands in the long-wavelength infrared (LWIR) region, making this spectral range particularly advantageous for their detection [1]. The pronounced absorption features in this range enable highly sensitive and selective VOC identification, even in complex gas mixtures, overcoming the limitations of shorter-wavelength methods.

Recent advances in indirect spectroscopy, such as photothermal [2] and photoacoustic spectroscopy [3], offer high selectivity and sensitivity. However, miniaturization remains challenging due to the limited availability of mid-IR optical components, including sources, detectors, and efficient beam-shaping elements. While recent developments in high-power LWIR sources [1] open new possibilities, conventional optics remain constrained by diffraction limits and bulky designs.

Metastructures [4], particularly long-wavelength metalenses [5], present a promising solution by enabling compact, high-performance optical elements for mid-IR applications [6]. These structures enhance light-matter interactions, surpass the limitations of traditional optics, and facilitate system integration for next-generation LWIR spectroscopy. In this work, we explore engineered meta-optics for focusing and collimation, designed to operate at the absorption bands of three VOCs, advancing miniaturized sensing technologies.

The selected absorption bands for Propane (13.36μm), Toluene (13.71μm), and Benzene(14.85μm) are highlighted in Fig. 1(a) with color-coded dashed lines. To increase the fabrication possibilities of the proposed design for indirect LWIR spectroscopy, two alternative platforms are considered. The first approach involves Ge on ZnSe, whose refractive index contrast is shown in Fig. 1(a). The second consists of a monolithic unit cell based entirely on Ge. Both systems have good compatibility with available photolithography-based fabrication processes and are derived from the structure presented in Fig. 1(b). As illustrated in Fig. 1(b), the design consists of Ge nanopillars with a thickness of t=7μm and a unit cell periodicity of P=5μm while the in-plane geometry is varied through the ratio d/P, where d represents nanopillar diameter. P is guaranteed to be subwavelength, $P<\lambda/n_{\mathrm{ZnSe}}$, to ensure the contribution primarily comes from the zeroth diffraction order. Additionally, $P<\lambda/2NA$ is set to allow high numerical aperture (NA). A minimum feature size of 1 μm is also ensured for fabrication.

Rigorous Coupled Wave Analysis (RCWA) is used to compute the amplitude and phase response that characterize the proposed Ge/ZnSe platform under normal incidence within the wavelength range of 13.3–14.9 μm. Fig. 1(c–e) illustrates that, in all cases, the phase response reaches at least 2π, while the amplitude response appears to be decoupled from the phase response, with transmission exceeding 90%.

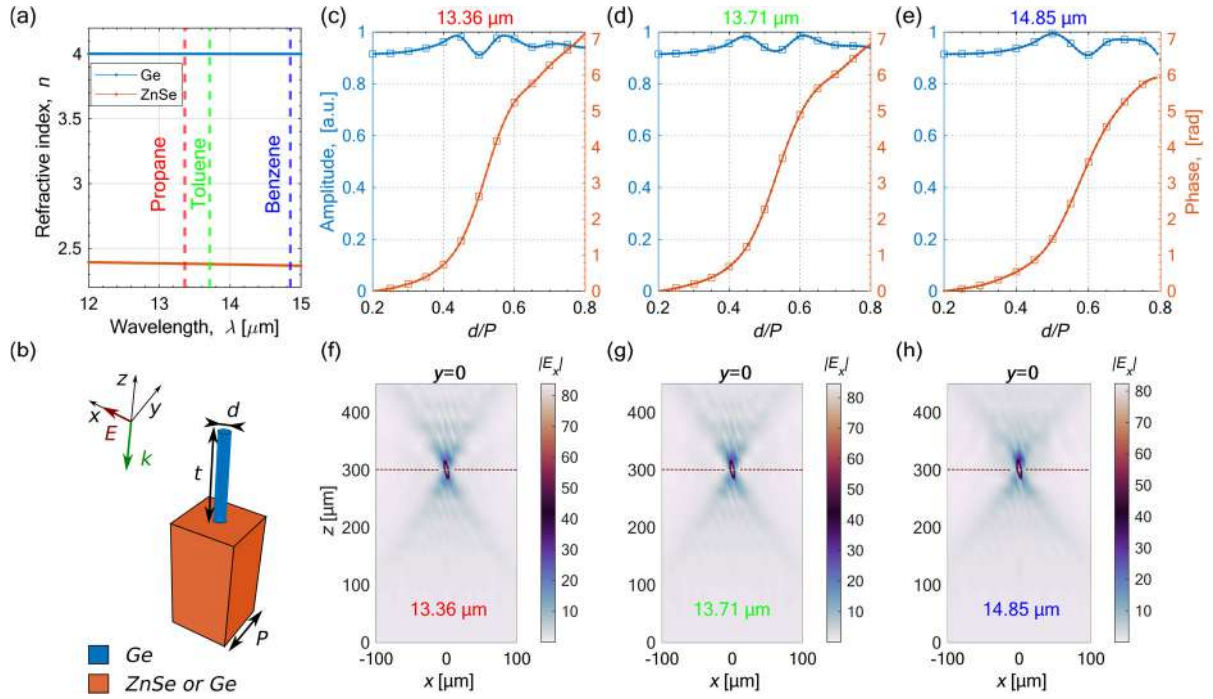


Fig. 1. (a) Refractive index of Ge and ZnSe. (b) Ge unit cell on a ZnSe substrate or bulk Ge. (c-e) Simulated amplitude and phase as a function of the filling fraction (d/P). The meta-atom response is computed when illuminated at the absorption band wavelengths in (a): Propane, Toluene, and Benzene. (f-g) Cross-section of the simulated diffracted beam along the z-axis for a metalens designed with a 300 μm focal length, 700μm diameter and NA = 0.8.

The composed meta-element library is then used to design three different high-NA (0.8) metalenses with a focal length of 300 μm, optimized for the absorption wavelength of the target VOCs, as shown in Fig. 1(f–h).

The monolithic unit cell, despite having a limited amplitude transmission as low as 60%, still exhibits 2π phase coverage for the two lowest wavelength bands. However, when implemented in a metalens design, its focusing efficiency is estimated to be lower than the 90% achieved with the bi-material unit cell. Fabrication in bulk Ge, requires a smaller P value, if not increases secondary diffraction effects, potentially reducing overall efficiency. However, single-material systems offer simpler fabrication compared to Ge grown on ZnSe.

With ongoing fabrication, we aim to integrate these metadevices into photothermal and photoacoustic spectroscopy, leveraging their compactness and flexible optics to overcome LWIR limitations.

Acknowledgments: E.U. Horizon 2020 research and innovation programme under the Marie Skłodowska-Curie Grant Agreement No. 860808 (OPTAPHI), the EVOQUE Project Grant Agreement No 101135764, and the MetaSPECS Project funded by the Science Foundation Ireland (SFI) project ID 21/FFP-A/10002.

References

[1] De Palo, R. *et al.*, "Quartz-Enhanced Photoacoustic Sensors for Detection of Eight Air Pollutants," *Advanced Photonics Research*, vol. 4, no. 6, p. 2200353, 2023, doi: 10.1002/adpr.202200353.

[2] Ricchiuti, G. *et al.*, "Photothermal spectroscopy on-chip sensor for the measurement of a PMMA film using a silicon nitride micro-ring resonator and an external cavity quantum cascade laser," *Nanophotonics*, Mar. 2024, doi: 10.1515/nanoph-2024-0033.

[3] Kinjalk , K. *et al.*, "Highly selective and sensitive detection of volatile organic compounds using long wavelength InAs-based quantum cascade lasers through quartz-enhanced photoacoustic spectroscopy," *Applied Physics Reviews*, vol. 11, no. 2, p. 021427, Jun. 2024, doi: 10.1063/5.0189501.

[4] Kotlyar, V. V. *et al.*, "Thin high numerical aperture metalens," *Opt. Express, OE*, vol. 25, no. 7, pp. 8158–8167, Apr. 2017, doi: 10.1364/OE.25.008158.

[5] Nalbant, H. C. *et al.*, "Transmission optimized LWIR metalens," *Appl. Opt., AO*, vol. 61, no. 33, pp. 9946–9950, Nov. 2022, doi: 10.1364/AO.469805.

[6] Heiden, J. T. and Jang, M. S. "Design framework for polarization-insensitive multifunctional achromatic metalenses," *Nanophotonics*, vol. 11, no. 3, pp. 583–591, Jan. 2022, doi: 10.1515/nanoph-2021-0638.

Study of active and bleached TDBC dye devices for photonics applications

B. Zerbo[1], K. Gadedjisso-Tossou[2], C. Symonds[1], J-M Benoit[1], J. Bellessa[1], A. Gassenq*[1]

[1]Institut Lumière Matière, UMR5260 CNRS-UCBL, Lyon, France;

[2]Laboratoire de Physique des Matériaux et Composants à Semi-conducteurs (LPMCS), Université de Lomé, Togo;

*corresponding author: alban.gassenq@univ-lyon1.fr

Abstract: We have investigated local photo-bleaching in TDBC dye layers for grating and strong coupling applications. This method allows to be modulate the refractive index both locally and spectrally, enabling the patterning of micro-devices with spectral modulation. We will present fundamental properties and fabricated devices, highlighting the high potential of such material.

Tetrachloro Diethyl Benzimidazo Carbocyanine (TDBC) layers are highly promising for photonic applications due to their significant oscillator strength, narrow absorption spectrum, local photo-bleaching capabilities, and cost-effective fabrication. They were primarily utilized in aggregation and strong coupling studies [1], but also in other works like light concentration [2] and absorption enhancement [3]. However, the intrinsic properties of TDBC layers are not yet fully understood and require further investigations to fully harness their potential, especialy regarding their bleaching properties (i.e., photochemical alteration of a molecule that renders it non-fluorescent) and the fabrication process [4].

Over the past few years, we have studied various TDBC micro-devices, demonstrating that micro-structures with resolution~~s~~ down to 1 µm can be successfully fabricated for strong coupling applications [5] and grating fabrication [6]. Additionally, we have investigated the intrinsic properties of the material. Using Raman spectroscopy, we have shown that even a slight change in the molecule can result in a significant modification of the oscillator strength [7].

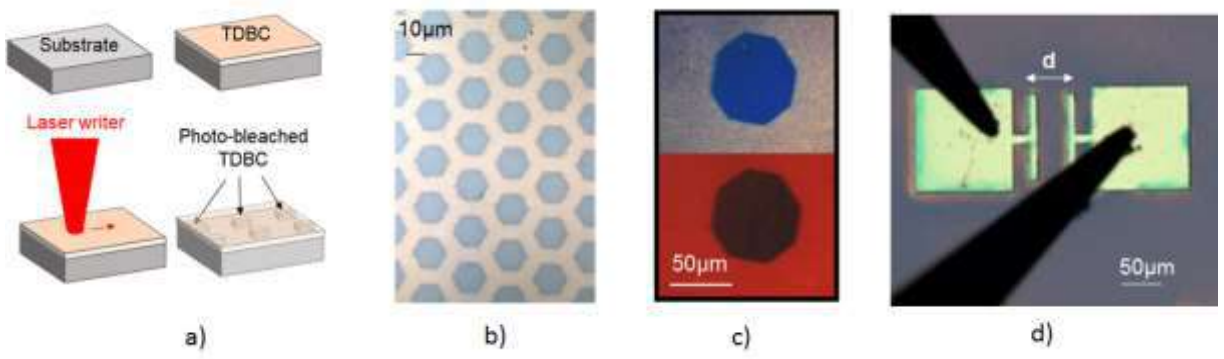


Figure 1 : a) process flow of the local photo-bleaching using a laser writer; fabricated sample observed with an optical microscope in b) bright field on Ag and in c) bright field and fluorescence on SiO_2; d) electrical characterization

Figure 1-a illustrates the process flow used to locally bleach such layers. TDBC layers, 17 nm thick, are spin-coated onto substrates and then exposed using a laser writer (µPG Heidelberg) [5,6] or fluorescence microscope. Figures 1-b and c show examples of fabricated structures with polygons exposed on Ag layer or SiO_2 substrate,

respectively. Images were captured using an optical microscope in both fluorescence and bright field (BF) modes. In the BF image, we can see that the refractive index is modulated at the microscale, as the TDBC becomes transparent in the bleached regions. In fluorescence mode, no emission is detected in the bleached regions, as expected. Furthermore, we investigated how the refractive index changes as a function of the bleaching. The Drude-Lorentz model, which is widely used in the literature, involves four constant material parameters: f_{osc} (the oscillator strength), Eg (the energy of the HOMO-LUMO transition), ΔE (the absorption spectral width), and ε_0 (the constant part of the dielectric function). After bleaching, only the fundamental transition around the 590 nm wavelength range is modified in the refractive index [9].

Finally, we explored different new significant parameters such as layer thickness influence, surface roughness, layer conductivity (Figure 1-d), the use of PDAC (Poly Diallyldimethyl Ammonium Chloride) as a hang layer highlighting the need for more investigation of these layers to fully leverage the potential of this promising material for future applications.

References

[1] A. Bard, S. Minot, J-M. C. Symonds, A. Gassenq, F. Bessueille, C. de la Vega, K. Chevrier, Y. De Wilde, V. Krachmalnicoff, Extended hybridization and energy transfer in multimaterial polaritonic metasurfaces, Adv. Opt. Mater. 10 (2022) 2200349 https://doi.org/10.1002/adom.202200349

[2] A. Cacciola, C. Triolo, O. Di Stefano, A. Genco, M. Mazzeo, R. Saija, S. Patanè, S. Savasta, Subdiffraction Light Concentration by J-Aggregate Nanostructures, ACS Photonics. (2015) https://doi.org/10.1021/acsphotonics.5b00197

[3] M.A. Castillo, C. Estévez-Varela, W.P. Wardley, R. Serna, I. Pastoriza-Santos, S. Núñez-Sánchez, M. Lopez-Garcia, Enhanced Light Absorption in All-Polymer Biomimetic Photonic Structures by Near-Zero-Index Organic Matter, Adv. Funct. Mater. 32 (2022) 1–26 https://doi.org/10.1002/adfm.202113039

[4] A. Sorokin, I. Ropakova, S. Wolter, R. Lange, I. Barke, S. Speller, S. Yefimova, Y. Malyukin, S. Lochbrunner, Exciton Dynamics and Self-Trapping of Carbocyanine J-Aggregates in Polymer Films, J. Phys. Chem. C. 123 (2019) 9428–9444 https://doi.org/10.1021/acs.jpcc.8b09338

[5] C. de la Vega, E. Bailly, K. Chevrier, J-P. Hugonin, A. Gassenq, J-M. Benoit, J. Bellessa, J-J. Greffet, Y. De Wilde, and V. Krachmalnicoff, Plasmon-Mediated Energy Transfer between Two Systems out of Equilibrium, ACS Photonics. 10 (2023) 1169–1176 https://doi.org/10.1021/acsphotonics.2c01931

[6] A. Gassenq, K. Chevrier, A. Bard, J. Benoit, C. Symonds, J. Bellessa, Selective grating obtained by dye micro-structuration based on local photo- bleaching using laser writer, Appl. Opt. 59 (2020) 5697–5701 https://doi.org/10.1364/AO.393103

[7] A. Gassenq, Y. Pipon, G. Montagnac, O. Boisron, V. Martinez, A. Bard, J. Benoit, J. Bellessa, Raman investigation of local photo-bleaching in TDBC dye layer for photonics applications, J. Raman Spectrosc. (2022) 6–9 https://doi.org/10.1002/jrs.6303

[8] K. Gadedjisso-Tossou, T. Albaric, A. Habouria, D. Lian, C. Symonds, J-M. Benoit , J. Bellessa and A. Gassenq, Refractive Index Evaluation in Active TDBC Layers for Photonics Applications, Photonics (2024), 11-9, https://doi.org/10.3390/photonics11090802

The authors would like to thank the CNRS Africa fellowship for funding.

Quasi three dimensional gold plasmonic metasurfaces for enhanced harmonic generation and light conversion to UV

Shroddha Mukhopadhyay[1], Ana Conde-Rubio[2], Agustín Mihi[2], Jose Trull[1], Maria Antonietta Vincenti[3], Michael Scalora[4], Crina Cojocaru[1]

[1] Department of Physics, Universitat Politècnica de Catalunya, Rambla Sant Nebridi 22, 08222 Terrassa (Barcelona), Spain
[2] Institute of Materials Science of Barcelona, ICMAB – CSIC, 08193 Bellaterra (Barcelona), Spain
[3] Department of Information Engineering – University of Brescia, Via Branze 38, 25123 Brescia, Italy
[4]Aviation and Missile Center, US Army CCDC, Redstone Arsenal, AL 35898-5000, USA
[*]corresponding author: userid@institution.edu

Abstract: We report a combined experimental-theoretical investigation on nanoscale light-matter interaction in quasi-3D photonic crystals of gold. Using ultrafast optical pulses we produce strongly localized surface plasmon resonances in the metal-dielectric interface, to enhance nonlinear frequency conversion from visible/NIR to ultraviolet ranges.

Plasmonic nanostructures under resonant conditions create strong spatial confinement of the electromagnetic field near the surface of the metal, which in turn enhances light-matter interaction and generates very large surface nonlinearities and enhanced frequency conversion, a fundamental step towards building coherent and efficient nano-scale UV light sources. The resonant properties are determined by the geometrical (shape, size, sharpness) and physical parameters (dielectric functions) of both the metal and surrounding dielectric materials [1-4].

In this work we explore crystals consisting of large area, periodically patterned arrays of cylindrical wells along x and y dimensions, with diameters of $d \sim 367\text{nm}$, imprinted in film of SU8 photoresist ($h_{SU8} \sim 390\text{nm}$), and center-to-center spacings of $p \sim 800\text{nm}$. The nanostructure is coated with uniform deposition of gold ($h_{Au} \sim 50\text{nm}$), coating both the top surface and the recessed regions, resulting in quasi-3D plasmonic crystals (Fig. 1(a)). The top layer is a 2D array of nano-holes in gold films, with a second, physically separate level of isolated gold disks at the bottoms of the embossed wells (Fig. 1(b)).

Our detection system and precise calibration enables us to detect and quantify third harmonic generation (THG) efficiencies, and corroborate our theoretical and experimental observations of shape, spectral width, and maximum amplitude of the spectral response. Fig. 1(c) shows the narrow spectral linewidth plasmonic resonance centered around 789 nm. The sharp dip in reflection is a result of complete absorption of incident light and its localization at the metal-air interface inside the holes (Fig. 1(d) inset). The spectral position of the resonance precisely depends on the geometrical parameters of the structure, such as p, d, h_{Au}, h_{SU8} and hence is highly tunable.

The spectral response of the TH emission ocurring in the UV (centered at 263 nm) is depicted in Fig. 1(d), the experimentally retrieved data as the curve with red dots, showing a maximum THG enhancement factor of 98. The theoretical prediction, calculated by FDTD (blue curve in Fig. 1(c)), shows a maximum enhancement of 108. The periodicity of the structure can diffract the generated TH. The total efficiency, which is the sum of the zeroth and first diffraction orders, when scaled to the TH reference signal originating from the unpatterned portion of the gold sample, measured exactly in the same experimental conditions, gives us the total enhancement factor of ~ 400 times.

Fig. 1 Sample description (a) 2D side view of the quasi-3D plasmonic crystal, (b) 3D view to show the two

layers of periodicity (c) The plasmonic resonance at normal incidence (d) Simulated and experimentally detected enhancement profile of the THG enhancement around the wavelength of resonance (Inset : E field localization inside the holes).

Acknowledgement

SM, JT, and CC acknowledge Spanish Agencia Estatal de Investigación (project no. PID2023-148620NB-I00) and US Army Research Laboratory Cooperative Agreement N◦ W911NF-22-2-0236 issued by US ARMY ACC-APG-RTP.

References

1. Kauranen, M. and Zayats, A., "Nonlinear plasmonics", Nature Photonics, Vol. 6, 737–748, 2012.
2. Falamas, A. and Tosa, V. and Farcau, C., "Hybrid architectures made of nonlinear-active and metal nanostructures for plasmon-enhanced harmonic generation", Optical Materials 88, 653-666, 2019.
3. Mukhopadhyay, S. and Rodriguez-Suné, L. and Cojocaru, C. et al, “Three orders of magnitude enhancement of second and third harmonic generation in the visible and ultraviolet ranges from plasmonic gold nanogratings,” APL Photonics, Vol. 8, 046108, 2023.
4. Matricardi, C. and L. Garcia-Pomar, J. and Molet, P. et al, "High-Throughput Nanofabrication of Metasurfaces with Polarization-Dependent Response", Advanced Optical Materials 8, 2000786, 2020.

Technology of formation and new areas of application of composite metastructures based on aluminum oxide

Ekaterina N. Muratova*, Dmitry. A. Kozodaev, Anton A. Bobkov, Maxim V. Mesh and Vyacheslav A. Moshnikov

NT-MDT BV, Hoenderparkweg 96 b, 7335 Apeldoorn, The Netherlands

Corresponding author: Ekaterina N. Muratova (e-mail: e.muratova@ntmdt.nl

ABSTRACT The basis of a scientific and technological breakthrough at the nanoscale is the use of new, previously unknown properties and functionality of materials. New devices require the development of new materials with atomically smooth interfaces. Therefore, this paper examines modern metamaterials based on porous anodic alumina (PAA), and presents prospects for the development of micro- and nanoelectronics, including a wide range of innovative nanodevices and miniature systems using PAA. The features of anodizing aluminum foil are considered. Nanosized layers and membranes based on PAA with ordered nanoscale capillaries with a pore diameter from 20 nm to 200 nm and an aspect ratio of up to 500 are obtained. Study of structure and morphology using AFM, SEM and RBS techniques. The results of studying the optical properties (in the range of 200 nm - 16 μm) made it possible to propose a method for diagnosing a porous structure based on an analysis of optical transmission spectra. Possible areas of application of structures based on PAA, including in popular new generation devices, have been demonstrated.

INDEX TERMS areas of application, diagnostic methods, membranes, metamaterials, nanoelectronics, porous anodic alumina, biomedical application, optical transmission spectra, Rutherford backscattering.

I. INTRODUCTION

To date, a number of effective methods for creating nanostructures have been developed, among them the methods based on the principle of self-formation are extremely important [1-9]. Self-formation methods include various mechanisms for ordering nanoparticles into structures with a given shape and size. The simplicity of electrochemical methods for obtaining porous materials and the ability to control their properties by changing the formation mode make them convenient objects for studying physical phenomena in nanostructures. The most studied materials obtained by the electrochemical etching method are porous silicon and porous anodic alumina (PAA) [9-15]. To date, the most widely accepted model of the formation of the porous structure of aluminum oxide is based on the hypothesis of the mechanism of formation of the ordered honeycomb structure of the PAA layer. According to this hypothesis, a possible source of forces arising between neighboring cells is mechanical stress associated with the increase in volume during the formation of aluminum oxide. More detailed theoretical ideas about pore formation can be found in the works.

In this work, the main emphasis is on the formation of nanoporous aluminum oxide. Membranes based on it are in demand in nanotechnology and microbiology [12, 16-17], nuclear physics [18-22], since they have a number of unique properties (high aspect ratio, optical transparency, biological inertness), as well as mechanical strength, thermal stability and chemical resistance.

The complexity of separating such porous anodic films from the substrate limits the prospects for their use as free membranes (masks, matrices) with the required topological and geometric parameters of pores. Thus, the formation of mechanically strong PAA membranes with ordered through pores - capillaries of micro- and nanoscales in thin (~10 μm) aluminum foil is an actual task.

The aim of this work is a comprehensive study of the processes of controlled formation and self-formation of nano- and microporous membranes based on aluminum oxide and the possibilities of using them as nanosized capillary matrices and masks for various purposes in micro- and nanoengineering.

II. EXPERIMENTAL

Since the aim of the work was to form through single-axis oriented capillary membranes based on aluminum oxide, the main object of the study was aluminum foil with a thickness of ~ 10 μm. Particular attention was paid to the technology of

preliminary preparation of its surface and the actual process of electrochemical anodization, as well as to the study of the structure, geometry and physical characteristics of porous membranes.

For the reproducibility of the membrane manufacturing technology, it is necessary to study the microstructure of the original aluminum foil, since the size and crystallographic orientation of the grains of the anodized foil determine the homogeneity of the layer and the shape of the pores. In the course of the work, special attention was paid to the technology of preliminary preparation of the surface of aluminum foil with a thickness of ~ 10 μm and the process of electrochemical anodization itself. The first stage of the study was the preparation of the foil within the framework of such processes as mechanical faceting (Fig. 1a) and surface polishing, as well as recrystallization during thermal annealing. Surface faceting largely determines the topological and geometric parameters of the pore formation process and the pore habit (Fig. 1b).

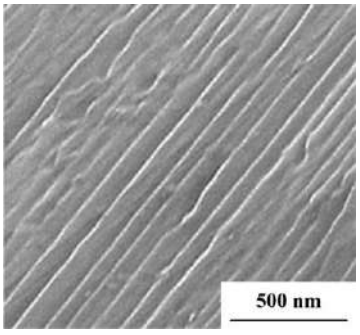


FIGURE 1. SEM images of aluminum foil after faceting process.

Using a local X-ray structural analysis method (inverse Laue imaging), a study of the recrystallization of aluminum foil and determination of grain orientation was carried out (Fig. 2).

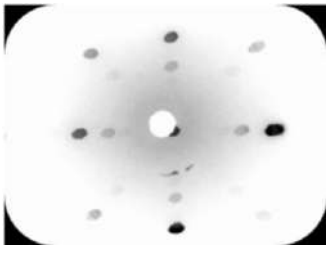


FIGURE 2. Reverse Lauegram of aluminum foil after annealing at T = 650 ºC for t = 6 h

The results showed that high-temperature annealing leads to the formation of single-crystal grains, and on the Lauegram taken in the center of the sample, clear reflections corresponding to the (100) orientation of this grain are observed.

In order to form PAA membranes, aqueous solutions of sulfuric and orthophosphoric acids with the addition of 10-15% glycerol were used as electrolytes in this work. The production technology is described in detail in [23], Table 1 provides generalized data, where U_A is the anodizing voltage, t is the time, T is the temperature, d_{pore} is the pore diameter, C_{pore} is the pore concentration.

TABLE 1. Aluminum anodizimg parameters

electrolyte	H_2SO_4+15% glycerol	H_3PO_4	H_3PO_4+10…15% glycerol
U_A, V	20–27	80	120–150
t, min	3…5	20	10…17
T, ˚C	5…7	-5…+5	0…7
d_{pore}, *nm*	20–30	80–100	180–220
C_{pore}, $1/\mu m^2$	350	50	20

To obtain through membranes, technological stages of chemical and electrochemical etching of samples from the back side were introduced.

The study of the parameters of the porous structures was carried out using scanning electron, atomic force and optical microscopy. A technique based on the analysis of optical transmission spectra in a wide range (from 200 nm to 15 μm) of wavelengths was also used.

IV. RESULTS AND DISCUSSION

A comprehensive study of PAA showed [15, 18, 23] that by varying the technological conditions of anodization (electrolyte composition, voltage/current density, temperature and process time), it is possible to control the structural parameters of the porous layer (Fig.3): pore diameter (from 20 to 200 nm), distance between pore centers (from 40 to 250 nm), and thickness of the porous layer (from 200 nm to 30 μm).

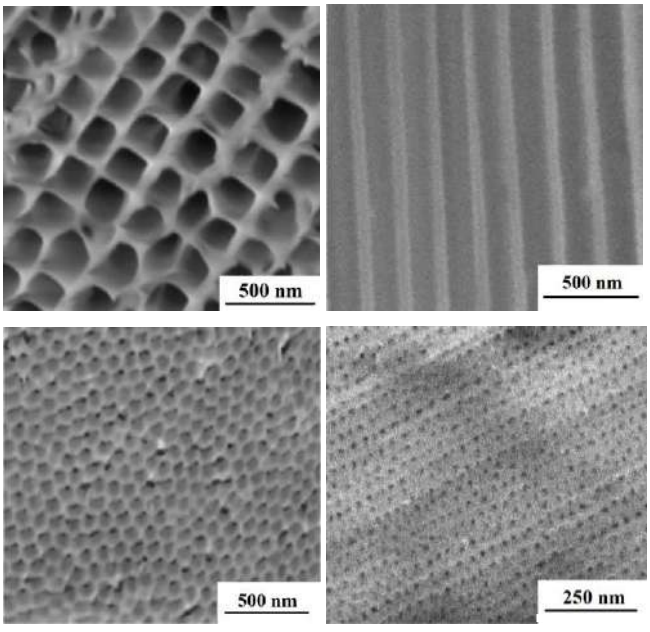


FIGURE 3. SEM images of PAA with different pore geometries

The results showed that by choosing the method of preliminary processing of the initial aluminum foil (faceting, polishing, thermal annealing), it is possible to control the shape of the pores: square, hexagonal, round.
The results of the study of optical transmission spectra are presented in Fig. 4 [24].

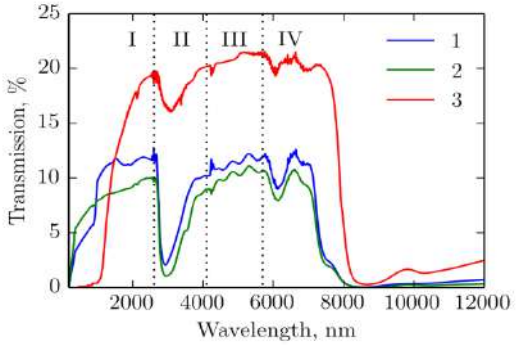


FIGURE 4. Optical transmission spectrum for PAA-based membranes in a wide range of wavelengths (1–5 in the text)

The transmission spectrum contains zones that allow for express characterization of the membrane: to estimate the average pore size and size distribution (section 1), membrane thickness (section 4), the presence of residual products (sections 2 and 5), and to identify the membrane material as aluminum oxide (section 3).

IV. APPLICATION AREAS

This article presents new applications of nanoporous membranes with a system of uniaxially oriented capillaries: as a material for attenuating thermal radiation from the human body, nanoscale masks for channeling ion beams, growth platforms for lab-on-a-chip, and filters for a liposome extruder.

A. SHIELDING COATINGS

The first application is related to the fact that nanoporous PAA membranes significantly reduce the transmission of IR radiation in the range from 8 to 14 μm [24]. The maximum thermal radiation of biological objects (at a wavelength of ≈ 10 μm) is located within the above-mentioned limits. As studies using IR Fourier spectroscopy have shown, for the por-Al2O3 membrane, a section of significant radiation attenuation is observed in the range from 7.5 to 14 μm (Fig. 4, sections 5).

The data obtained using FTIR spectroscopy are fully confirmed by studies conducted using a thermal imager (SDS INFRARED hotfind LXT). As an example, these membranes were used to attenuate the thermal radiation of the human body. Fig. 9 presents the results of thermal imaging studies and shows that a 15 μm thick PAA membrane located on a 5 mm thick fluoroplastic ring holder provides effective shielding of the thermal radiation of the human body, while the recorded change in the temperature difference from the biological object in the presence and absence of the membrane is at least 4˚–5˚.

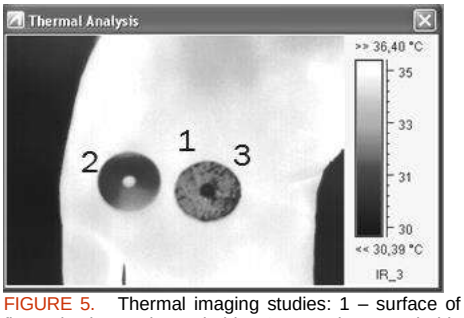


FIGURE 5. Thermal imaging studies: 1 – surface of biological object, 2 – fluoroplastic membrane holder, 3 – membrane on holder

Thus, it can be said that, despite the optical transparency in the visible range (Fig. 7, section 1), por-Al2O3 membranes significantly weaken the transmission of radiation in the mid-IR range (λ = 8-13.5 μm), which can allow them to be used as filters for absorbing radiation from biological objects.

B. TEMPLATES FOR HIGH-ENERGY ION BEAMS

PAA membranes with through nanocapillaries were considered as nanoscale templates for high-energy ion beams [30-32]. For this purpose, they were studied for the effect of passage of a helium ion beam with an energy of 1.5–2 MeV. Figure 6 shows the Rutherford backscattering (RBS) spectrum for a mask–template with a pore diameter of ≈ 20 nm. A sample containing a "heavier" element, in particular, hafnium (Hf), was placed behind the membrane as a "recording" medium–target.

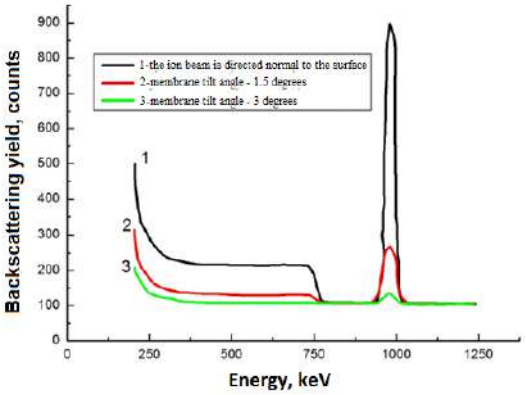


FIGURE 6. The energy spectrum of backscattered He+ ions with an energy of 1200 keV. The black curve is the spectrum along the normal direction; the red curve is the spectrum when the deviation is 1.5 degrees from the normal; the blue curve is the spectrum when the deviation is 3 degrees.

Even a slight deviation of the membrane from the normal (1.5˚…3˚) with respect to the direction of propagation of the ion beam leads to a decrease in the yield of backscattered ions from the HfO_2 target and, consequently, to a decrease in the recorded current. Thus, the created and studied

membrane–templates ensure the performance of the functions of channeling a high-energy ion flow.

It has been established that the coefficient of accelerated ion transmission through the membrane can reach 60% [18, 24]. This allows spatial localization of the ion impact on the substrate with nanoscale resolution.

Thus, PAA matrices, depending on their geometric parameters, can expand the capabilities of RBS.

C. BIOMEDICAL APPLICATION

Porous ordered structures are of particular interest for filtering various media. The authors of this work consider the possibility of using PAA membranes as a growth platform for bacterial colonies, as well as a filter for homogenizing liposomes. In this case, it is important to select membranes with certain geometric parameters.

To achieve the stated goals, microporous membranes obtained by both anodization through a photoresistive mask and microchannel plates were used in the work (Fig. 7).

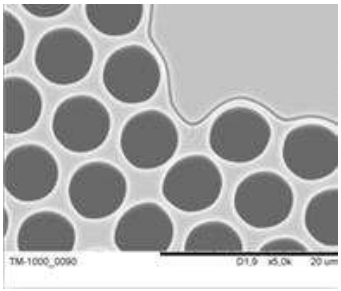


FIGURE 7. SEM image of the edge of a microchannel plate

The method of layer-by-layer molecular deposition of Al_2O_3 was considered as a method for precision control of the pore diameter. As a result of the work, growth cells were formed, which represent a microporous structure (Fig. 8), the bottom of which is a nanoporous layer of aluminum oxide.

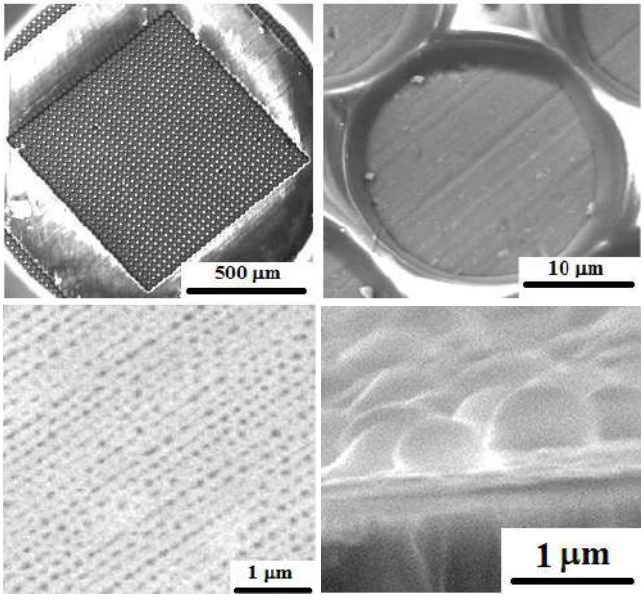


FIGURE 8. SEM images of a PAA membrane after photolithography and electrochemical anodization: a) membrane with a photolithographic pattern of micropores, b) a fragment of a micropore with nanocapillaries, c) nanocapillaries, d) membrane with bacterial colonies

Through this porous bottom, the nutrient medium entered the bacteria located in the micropore due to capillary action. As a result, the bacterial colonies were able to survive.

In addition, a liposomal extruder was developed for homogenizing liposomes (Fig. 9). The key element of such a device is a nanoporous membrane. The diameter of the membrane pores determines the size of the liposomes passing through it.



FIGURE 8. Photo of the final model of the liposome extruder

The optimal pore size in this case is 200 nm in diameter. The process of electrochemical anodization under properly selected technological conditions makes it easy to achieve this.

V. CONCLUSION

In this paper, the technology of self-formation of porous membranes with a system of ordered uniaxially oriented nanosized (pore diameter from 20 nm and more) capillaries based on aluminum oxide with an aspect ratio of up to 500 by electrochemical anodization of aluminum foil with a thickness of tens of microns was described. The structure and optical properties of ordered through membranes of nanoporous aluminum oxide were studied depending on the process conditions.

A method for diagnosing a porous structure based on the analysis of optical transmission spectra is proposed. The results of the studies showed that zones are identified in the transmission spectrum that allow express characterization of the membrane by the main structural and geometric parameters. It is shown that nanoporous membranes based on aluminum oxide significantly reduce the transmission of IR radiation in the range from 8 to 14 µm, which corresponds to the spectral region of IR radiation of biological objects. They also ensure the performance of channeling functions for a high-energy flow of helium ions with an energy of 1.5–2 MeV.

The possibilities of using PAA membranes for biomedical purposes, namely as a growth platform for bacterial colonies and a filter for homogenization of liposomes, are considered.

REFERENCES

[1] L.B. Hamad, B.S. Khalaf and N.M.Faleh, "Analysis of static and dynamic characteristics of strain gradient shell structures made of porous nano-crystalline materials", *Adv. Mater. Res*. 2019, 8, pp. 179–196. https://doi.org/10.12989/amr.2019.8.3.179.

[2] E.N. Muratova and V.A. Moshnikov "The use of nanomaterials from electronics to medicine", International Conference on Advanced Materials and Nanotechnology for a Green and Sustainable future (ICAGS-2023). Maharaja's College, Ernakulam, Kerala, India, 5th to 6 th of December 2023, pp.7–9.

[3] S. Feng and W. Ji, "Advanced nanoporous anodic alumina-based optical sensors for biomedical applications", *Front. Nanotechnol*. 2021, 3, pp. 678275. https://doi.org/10.3389/fnano.2021.678275.

[4] J.T. Domagalski, E. Xifre-Perez, and L.F. Marsal, "Recent Advances in Nanoporous Anodic Alumina: Principles, Engineering, and Applications", *Nanomaterials* 2021, 11, pp. 430. https://doi.org/10.3390/nano11020430.

[5] Y. Spivak, E. Muratova, V. Moshnikov, A. Tuchkovsky, I. Vrublevsky and N. Lushpa, "Improving the Conductivity of the PEDOT:PSS Layers in Photovoltaic Cells Based on Organometallic Halide Perovskites", *Materials*, 2022, 15 (3), pp. 990. https://doi.org/10.3390/ma15030990

[6] V .Moshnikov, E. Muratova, A. Aleshin, A. Maksimov, G. Nenashev, I. Vrublevsky, N. Lushpa, A. Tuchkovsky, A. Zhilenkov and O. Kichigina, "Controlled Crystallization of Hybrid Perovskite Films from Solution Using Prepared Crystal Centers", *Crystals*. 2024; 14(4), pp. 376. https://doi.org/10.3390/cryst14040376

[7] G. V. Nenashev, A. N. Aleshin, A.A. Ryabko, I. P. Shcherbakov, V. A. Moshnikov, E. N. Muratova, V. M. Kondratev and I. A. Vrublevsky, "Effect of barium doping on the behavior of conductivity and impedance of organic-inorganic perovskite films" *Solid State Communications*, Vol. 388, 2024, pp.115554, https://doi.org/10.1016/j.ssc.2024.115554

[8] E.N. Muratova, V.A. Moshnikov and A.A. Zhilenkov, "Development of Model Representations of Materials with Ordered Distribution of Vacancies", *Crystals* 2024, 14, pp.1095. https://doi.org/10.3390/cryst14121095

[9] E. Muratova, D. Kozodaev, V. Moshnikov and Yu. Spivak, "AFM for monitoring interphase interfaces of solar cells" European Materials Research Society. B. Advancing sustainable organic photovoltaics: from experiments and materials to applications and device models. Convention & Exhibition Centre of Strasbourg (France), from May 27 to 31, 2024, pp. 00370

[10] A. Ruiz-Clavijo, O. Caballero-Calero and M. Martín-González, "Revisiting anodic alumina templates: From fabrication to applications" *Nanoscale* 2021, 13, 2227–2265. https://doi.org/10.1039/d0nr07582e.

[11] E. Davoodi, M. Zhianmanesh, H. Montazerian, A.S. Milani, M. Hoorfar, "Nano-porous anodic alumina: Fundamentals and applications in tissue engineering", *J. Mater. Sci. Mater. Med*. 2020, 31, 60. https://doi.org/10.1007/s10856-020-06398-2

[12] R.P. Alvarez-Carrizal, J.A. Rodríguez-García, D.A. Cortés-Hernández, S.J. Esparza-Vázquez and E. Rocha-Rangel, "Manufacture of Al2O3/Ti composite by aluminum bonding reaction for their use as a biomaterial", *Adv. Mater. Res*. 2021, 10, pp. 331–341. https://doi.org/10.12989/amr.2021.10.4.331.

[13] S. Manzoor, M.W. Ashraf, S. Tayyaba, M.I. Tariq and M.K. Hossain, "Recent Progress of Fabrication, Characterization, and Applications of Anodic Aluminum Oxide (AAO) Membrane", *A Review. Comput. Model. Eng. Sci*. 2022, 135, pp. 1007–1052.

[14] V. Romero and J. Benavente, "Electrochemical Characterization of Nanoporous Alumina-Based Membranes with Different Structure and Geometrical Parameters by Membrane Potential Analysis" *Micro* 2022, 2, pp.475–487. https://doi.org/10.3390/micro2030029.

[15] N.V. Lushpa, Dinh Huu Tai, K.V. Chernyakova, I.A. Vrublevsky, E.N. Muratova, Yu.M. Spivak and Moshnikov V.A. "Using the method of SEM image processing to study the morphology of porous anodic alumina films" Chapter 13 in book "New Materials: Preparation, Properties and Applications in the Aspect of Nanotechnology" Edited by Andrey G. Syrkov and Kirill L. Levine, Published by Nova Science Publishers 2020, ISBN: 978-1-53617-090-0, pp. 125-132.

[16] S. Feng and W. Ji, "Advanced Nanoporous Anodic Alumina-Based Optical Sensors for Biomedical Applications", *Front. Nanotechnol.* 2021, 3, pp.678275. https://doi.org/10.3389/fnano.2021.678275.

[17] Yu. M. Spivak, E. N. Muratova, V. P. Bezverkhniy and V. A. Moshnikov, "Porous Aluminum Oxide for Medical Applications Including Targeted Drug Delivery", *Nanobiotechnology Reports*, 2023, Vol. 18, Suppl. 1, pp. S37–S47. DOI: 10.1134/S2635167623600773.

[18] A.A. Shemukhin and E.N. Muratova, "Investigation of transmission of 1.7-MeV He^+ beams through porous alumina membranes", *Tech. Phys. Lett*. 2014, 40, pp.219–221. https://doi.org/10.1134/S1063785014030110.

[19] S. Pinilla, T. Campo, J.M. Sanz, F. Márquez and C. Morant, "Highly ordered metal-coated alumina membranes: Synthesis and RBS characterization", *Surf. Coat. Technol*. 2019, 377, pp.124883. https://doi.org/10.1016/J.SURFCOAT.2019.08.012.

[20] V. V. Luchinin, V. A. Moshnikov, E. N. Muratova and R. Sh. Samigullin, "Formation of ordered nanoscale capillary membranes based on anodic alumina", *Jour. of Physics: Conference Series*, 2015. V. 586. pp. 012008.

[21] Z. Zhu, D. Zhu, R Lu, "The experimental progress in studying of channeling of charged particles along nanostructure" *Proc. of SPIE, Bellingham.* WA, 2005. V. 5974. pp.13.

[22] N. Stolterfoht and Y. Yamazaki, "Guiding of charged particles through capillaries in insulating materials", Phys. Rep. 2016, 629, pp. 1–107. https://doi.org/10.1016/j.physrep.2016.02.008.

[23] E.N. Muratova, A.A. Ponomareva, A.A. Shemukhin, Y.V. Balakshin, A.P. Evseev, V.A. Moshnikov, A.A. Zhilenkov and O.Y. Kichigina, "The Influence of the Structural Parameters of Nanoporous Alumina Matrices on Optical Properties", *Metals* 2024, 14, pp.651. https://doi.org/10.3390/met14060651.

[24] L.B. Matyushkin, E.N. Muratova and M.F. Panov, "Determination of the alumina membrane geometrical parameters using its optical spectra" *Micro Nano Lett*. 2017, 12, pp.100–103. https://doi.org/10.1049/mnl.2016.0353.

Parity-Time and quasi-normal modes in Photonics, Plasmonics, Acoustics

Fermi arcs in dielectric resonators

N. Solodovchenko[1,2], M. Bochkarev[1], K. Samusev[1,3], A. Bogdanov[1,2], and M. Limonov,[1,3*]

[1]School of Physics and Engineering, ITMO University, Saint-Petersburg 197101, Russia
[2]Harbin Engineering University, Qingdao 403 266404, China
[3]Ioffe institute, St. Petersburg, 194021, Russia
[*]corresponding author: m.limonov@metalab.ifmo.ru

Abstract: Fermi arcs in coordinate space link topological degeneracies, with surface Fermi arcs linking Weyl points and bulk Fermi arcs linking exceptional points. We present the results of an experimental observation of a bulk Fermi arc in a single dielectric ring resonator.

Topological photonics arises as a bridge between the properties of bulk and surface states, with non-Hermitian systems possessing unique topological features that are absent from their Hermitian counterparts [1–3]. An important example of the combination of non-Hermitianity and topology is provided by Fermi arcs. By breaking the parity or time-reversal symmetry of a Hermitian system, the Dirac point in coordinate space splits into two or four Weyl points of opposite chiralities, and by adding losses, the Dirac point splits into two exceptional points of opposite chiralities. In this case, two pairs of Weyl points with opposite topological charges are connected by two surface Fermi arcs, and a pair of exceptional points is connected by a bulk Fermi arc, and along the arc the eigenvalues coincide, while the eigenfunctions differ [4]. Confirmation of the theory faces serious technological and experimental difficulties and, to our knowledge, has only been achieved once for a surface and once for a bulk Fermi arcs. Four Weyl points and helicoidal surface Fermi arcs connecting them have been experimentally observed in a 3D photonic crystal composed of metallic inclusions [5]. The emergence of a bulk Fermi arc and half topological charges were experimentally observed in a 2D periodic photonic crystal [6]. Note that in both cases complex objects were used as experimental samples and the question of observing such topological features on a single resonator remained open. We have previously demonstrated the existence of a bulk Fermi arc in a single dielectric ring resonator with a rectangular cross-section in our calculations [3] and now report an experimental observation of this striking feature of non-Hermitian systems.

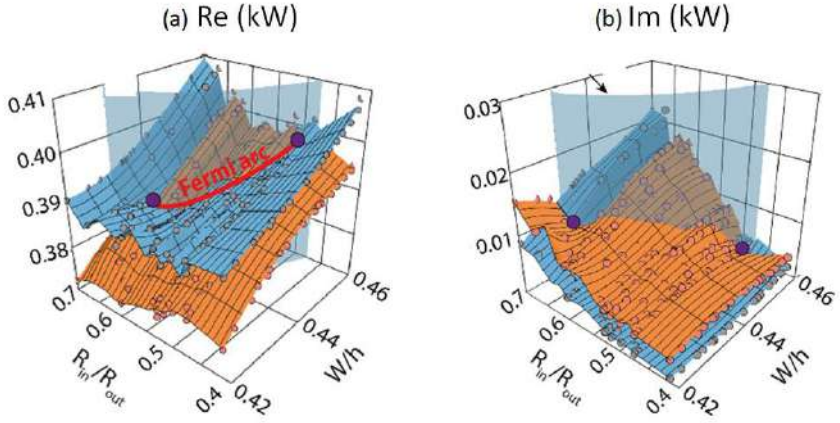


Figure 1. Double Riemann sheet for the Real (a) and Imaginary (b) parts of the eigenvalues, obtained by connecting the experimental points (shown as dots). The two purple dots show the positions of the experimental EPs. The red line shows the resulting experimental bulk Fermi arc.

Based on our theoretical work [3], we determined the ranges of geometric parameters R_{in}/R_{out} and $(R_{out}-R_{in})/h$ of a ring resonator for observing a bulk Fermi arc. To obtain a sufficiently dense grid of parameters, 203 ring resonators were manufactured and experimentally measured. It should be noted that the results of processing the experimental spectra were in excellent agreement with the data of numerical calculations. Based on 203 experimental spectra, two intersecting Riemann sheets were constructed, two exceptional points were determined, which for the eigenvalues Re(kW) were connected by a continuous Fermi arc belonging to both sheets, which does not happen when two sheets Im(kW) intersect (Figures 1a,b). Figure 1 presents the first, as far as we know, experimental observation of a bulk Fermi arc for a single resonator.

This work was funded by the Russian Science Foundation (Project No. 23-12-00114).

References

1. Ozawa, T., H. M. Price, A. Amo, N. Goldman, M. Hafezi, L. Lu, M. C. Rechtsman, D. Schuster, J. Simon, O. Zilberberg, and I. Carusotto, "Topological Photonics, " Rev. Mod. Phys., Vol. 91, 015006, 2019.
2. Bochkarev M., N. Solodovchenko, K. Samusev, and M Limonov, "Topology and curvature effects in the photonics of ring–split ring–cuboid transitions", Materials Today, Vol. 80, 179-186, 2024.
3. Solodovchenko, N., K. Samusev, and M. Limonov, "Quadruplets of exceptional points and bound states in the continuum in dielectric rings", Phys. Rev. B, Vol. 109, 075131, 2024.
4. Özdemir, Ş. K. "Fermi arcs connect topological degeneracies," Science 359, 996, 2018.
5. Yang, B., Q. Guo, B. Tremain, R. Liu, L. E. Barr, Q. Yan, W. Gao, H. Liu, Y. Xiang, J. Chen, C. Fang, A. Hibbins, L. Lu, S. Zhang, "Ideal Weyl points and helicoid surface states in artificial photonic crystal structures," Science, 359, 1013 (2018).
6. Zhou, H., C. Peng, Y. Yoon, C.W. Hsu, K. A. Nelson, L. Fu, J. D. Joannopoulos, M. Soljačić, and B. Zhen, "Observation of bulk Fermi arc and polarization half charge from paired exceptional points," Science, Vol. 359, 1009–1013, (2018).

Bright and dark soliton blending stabilized by non-Hermitian potentials in Kerr ring cavities

S. B. Ivars [1], M. Botey [1], K. Staliunas[2], and R. Herrero[1*]

[1] Departament de Fisica, Universitat Politecnica de Catalunya (UPC), Rambla Sant Nebridi 22, 08222, Terrassa, Barcelona, Catalonia, Spain

[2] Institucio Catalana de Recerca i Estudis Avancats (ICREA), Passeig Llus Companys 23, E-08010, Barcelona, Spain
[*]corresponding author: ramon.herrero@upc.edu

Abstract: Bright and dark solitons, separately observed in systems with opposite dispersion, are blended in a hybridized scenario by introducing periodic non-Hermitian potentials in the damped-driven nonlinear Schrödinger equation. New patterns, solitonic structures, and molecules are generated, become accessible, and can be stabilized.

We consider the damped-driven nonlinear Schrödinger equation as a normal form describing a large variety of systems, Eq. (1), and in particular Kerr ring cavities. The system exhibits a resonance for particular values of detuning, δ, that is tilted by the nonlinearity, and shows bistability of two homogeneous states for defocusing dispersion (normal group velocity dispersions in Kerr cavities) [1]. As a consequence, stationary localized structures, dark solitons, arise as spatial orbits close to homoclinic cycles between the two homogeneous states, and organized in a collapsed snaking diagram of S_n branches. For anomalous group velocity dispersions, the upper homogeneous state suffers a Modulation Instability generating periodic patterns. In this case, bright solitons appear as homoclinic cycles between the pattern and the lower stable homogeneous state organized in a standard homoclinic snaking diagram of S^Z branches. These two disjoined scenarios in the formation of localized structures become blended by introducing a stationary non-Hermitian potential $V(x)$ in the system:

$$\frac{\partial \psi}{\partial t} = -i\frac{\partial^2 \psi}{\partial x^2} - (1+\delta i)\psi + 2i|\psi|^2\psi + V(x)\psi + h, \quad V(x) = m\cos\left(\frac{2\pi px}{L}\right)e^{-i\phi} \tag{1}$$

Considering negative dispersion in a spatial window of length L and p potential periods, the upper homogeneous state becomes modulated and acquires a pattern character. It allows the stabilization of patterns with the potential periodicity and the mixing of dark solitons, already existing for this dispersion sign, and bright solitons, all organized in a complex scenario merging collapsed and standard homoclinic diagrams. New families of differently shaped solitons arise by the resulting crossbreeding of bright and dark solitons. The stabilization of patterns as soliton trains, allows new connections between patterns and the modulated homogeneous states [2]. Particularly stable molecules as combination of dark solitons with small n values arise, $\{S_n, S_n\}$, while combinations of large n solitons generate $\{S^Z, S^Z\}$ molecules, see Fig. 1 a). More interesting is the combination of solitons $\{S^Z, S_n, S_n\}$ generating combinations of bright solitons or even more complex combinations like $\{S^Z, S_n, S_{n+1}, S_{n+1}, S_n\}$ as two kinds of dark solitons mixing corresponding to consecutive branches in the collapsed snaking diagram, Fig, 1 b).

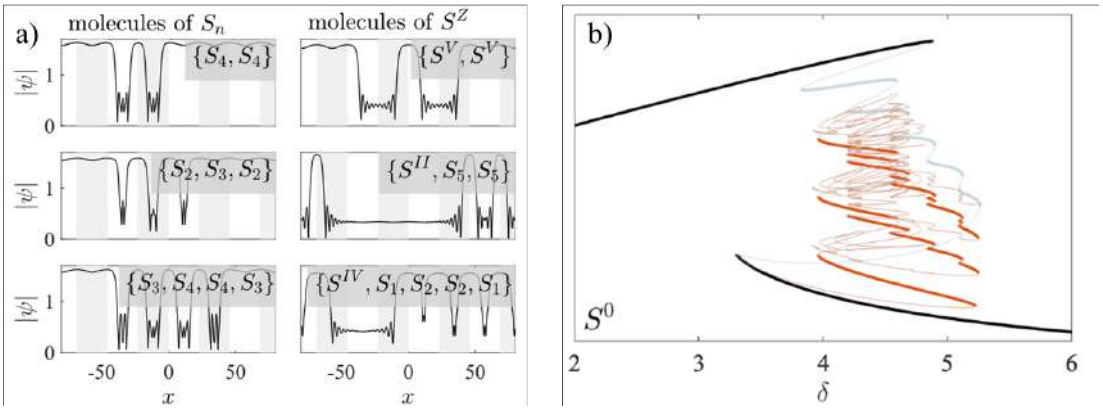


FIG. 1: a) Molecules as combinations of dark and bright solitons. b) Bifurcation diagram of homogeneous solutions (black), patterns (blue), and solitons and molecules (red) for a) m=0.15 and ϕ=6.

For large enough potential amplitudes the bistability of homogeneous states totally disappear, and the lower state acquires the pattern character allowing molecules of bright solitons of the form $\{S^Z, \ldots, S^Z\}$. The system symmetry induces disjoined odd and even families of molecules, see Fig. 2.

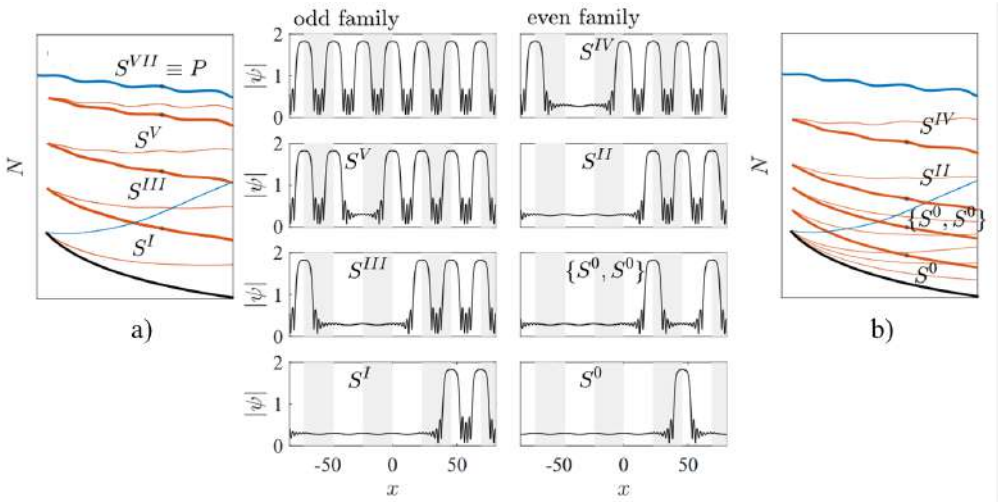


FIG. 2: a) Molecules as combinations of bright and dark solitons. b) Bifurcation diagram of homogeneous solutions (black), patterns (blue), and solitons and molecules (red) for a) m=0.7 and ϕ=6.

This work was supported by the Spanish government via PID2022-138321NB-C21 and Generalitat de Catalunya via 2021 SGR 00606.

References

1. C. Godey, I. V. Balakireva, A. Coillet, and Y. K. Chembo, Physical Review A 89, 063814 (2014).
2. S. B. Ivars, C. Milian, M.Botey, R. Herrero, K. Staliunas, Physical Review Letters, 133(9), 093802, 2024.

Active Parabolic Waveguide Amplifiers with Non-Hermitian Mode Control

M. N. Akhter[1], R. Herrero[1], K. Staliunas[1, 2] and M. Botey[1]

[1] Departament de Física, Universitat Politècnica de Catalunya (UPC), Barcelona, Catalonia, Spain

[2] Institució Catalana de Recerca i Estudis Avancats (ICREA), Barcelona, Catalonia, Spain

*corresponding author: muriel.botey@upc.edu

Abstract: We demonstrate a non-Hermitian mode management mechanism in nonlinear parabolic waveguide amplifiers, exploiting asymmetric mode growth via refractive index and gain/loss modulations. This enables flexible mode combination, higher-order mode excitation, and photon concentration into the lowest-order Hermite mode for all-optical cleaning. The effect is analytically predicted, numerically validated, and robust.

In the present paper, we propose a modal management scheme for active nonlinear systems such as multimode fiber amplifiers. The scheme exploits simultaneous longitudinal non-Hermitian modulations of the propagation constant and of the gain/loss coefficient with a transverse profile (see Fig. 1a), which recently showed effective all-optical mode-cleaning in parabolic multimode optical waveguides [1]. Indeed, non-Hermitian photonics allows for managing the flow of light, from laser stabilization to the control of optical turbulence, among others [2-6].

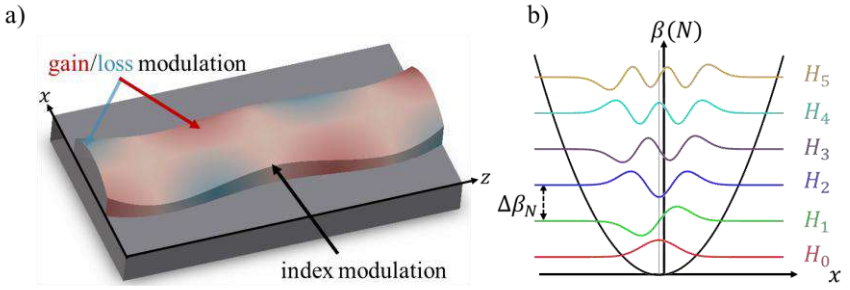


Figure 1. a) Periodically modulated active parabolic waveguide, the index modulation along the propagation direction, z, is accounted for by the fiber snaking, and the gain/loss modulation is antisymmetric in the transverse direction as indicated by the colors. b) First transverse Hermitte-Gauss modes of the unmodulated waveguide, with equidistant mode spacing $\Delta\beta_N$.

The proposal takes advantage of the equidistant mode solutions in unmodulated parabolic nonlinear MMFs, see Fig. 1b. The nonlinearity saturates the growth of the mode amplitudes, leading to particular mode configurations. Under the introduction of particular non-Hermitian modulations, which, in the simplest form, may be expressed as: $V(x,z) = V(z)V(x) = [m_{re}cos(qz) + im_{im}\, cos(qz + \phi)]\,(x/x_0)e^{-x^2/x_0{}^2}$, it is possible to control the mode distribution and, therefore, the beam shape. The effect is also analytically predicted using a mode-expansion approach, showing good agreement with the full model calculations based on the complex Ginzburg–Landau equation, the governing equation for light propagation along the active multimode fibers in CW or quasi-CW (long pulses) regimes. Irrespective of the initial conditions of the input beam, the system evolves toward the same final state, which only depends on the system parameters, see Fig. 2 [7]. In particular, all-optical mode cleaning is also possible; see the A case in Fig. 2, which may represent an alternative to various

attempts to address randomization [8].

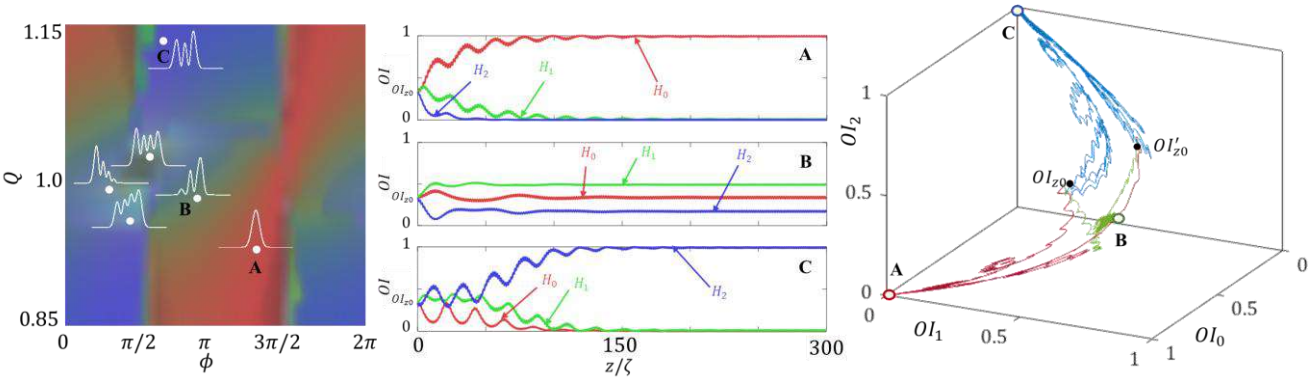


Figure 2. Left: Map of the participation of each mode into the final eigenmode, as a function of the wavenumber of the non-Hermitian normalized modulation $Q = q/\Delta\beta_N$ and phase ϕ for $m_{re} = m_{im} = 0.6$. Middle: Evolution of the participation, *OI*, of the first three modes, H_1, H_2, and H_3 along the modulated amplifier, distance normalized to the self-imaging period of the waveguide $\zeta=2\pi/\Delta\beta_N$. Right: Phase space evolution of *OI*, for two different initial conditions with mode relative intensity distributions, OI_{z0} and OI'_{z0}, being $OI_1 = OI_2 = OI_3 = 33.33\%$ and $OI'_1 = 6\%$, $OI'_2 = OI'_3 = 47\%$ for the above-mentioned modulations. The final states are labeled A, B, and C and marked with a circle corresponding to points the points shown on the map.

This work received funding from the Horizon 2020 program project MEFISTA (Project No 861152) and from the Spanish Ministry of Science, Innovation, and Universities (MICINN) under Project No. PID2022-138321NB-C21.

References

1. M. N. Akhter, S. B. Ivars, M. Botey, R. Herrero and K. Staliunas, Physical Review Letters, vol.131, no. 4, pp. 043604, 2023.
2. Li, H. Wei, M. Cotrufo, M. Chen, S. Mann, X. Ni, B. Xu, J. Chen, J. Wang, S. Fan, C. Qiu, A. Alù, L. Chen, Nature Nanotechnology, vol. 18, no. 7, pp. 706-720, 2023.
3. R. El-Ganainy, M. Khajavikhan, D. N. Christodoulides and S. K. Ozdemir, Communications Physics, vol. 2, no. 1, pp. 37, 2019.
4. W. W. Ahmed, R. Herrero, M. Botey, Y. Wu and K. Staliunas, Physical Review Applied, vol. 14, no. 4, pp. 044010, 2020.
5. S.B. Ivars, M. Botey, R. Herrero, K. Staliunas, Non-Hermitian control of optical turbulence in systems with fractional dispersion. Chaos, Solitons & Fractals, 165, 112774, 2022.
6. J. M. Pardell, R. Herrero, M. Botey and K. Staliunas, Optics express, vol. 29, no. 15, pp. 23997-24009, 2021.
7. M. N. Akhter, M. Botey, R. Herrero, K. Staliunas, APL photonics, vol. 9, no. 10, pp. 106115, 2024.
8. E. Deliancourt, M. Fabert, A. Tonello, et al., OSA Continuum, vol. 2, no. 4, pp. 1089-1096, 2019.

Exceptional points and large chirality in coupled photonic waveguides

Alice De Corte[1], Stefanos Fr. Koufidis[2], Martin W. McCall[2], and Bjorn Maes[1]

[1]University of Mons, Micro- and Nanophotonic Materials Group, Research Institute for Materials Science and Engineering, Mons, Belgium
[2]Imperial College London, Department of Physics, London, United Kingdom
*corresponding author: alice.decorte@umons.ac.be

Abstract: In coupled waveguides, exceptional points can stem from the coupling of either counter-propagating modes or co-propagating modes. We utilize both methods, by implementing extreme chirality in a homogeneous waveguide, thereby realizing backward mode propagation, and by inserting a chiral material in the slot between waveguides exhibiting balanced gain and loss.

Exceptional points (EPs) are critical junctures in a system's parameter space where eigenvalues and eigenvectors coincide [1]. In waveguiding systems, EPs result in the convergence of multiple eigenmodes into a single mode, leading to remarkable dispersion relations nearby the merging point(s). In a photonic configuration comprising two coupled waveguides, EPs can be achieved in two main ways, using either counter-propagating modes or co-propagating modes. The first method relies on the coupling of a standard waveguide with one exhibiting negative phase velocity [1]. The second method utilizes non-Hermitian Hamiltonians, particularly those adhering to PT-symmetry, with conventional coupling between waveguides exhibiting balanced gain and loss [2]. Here, we harness giant values of chirality to achieve EPs using both approaches. First, we adopt Pendry's chiral route to negative refraction [3], coupling counter-propagating modes in waveguides made of homogeneous extremely chiral media [4]. Secondly, we alter the coupling between modes of PT-symmetric waveguides by varying the chirality of the material in the gap that separates them.

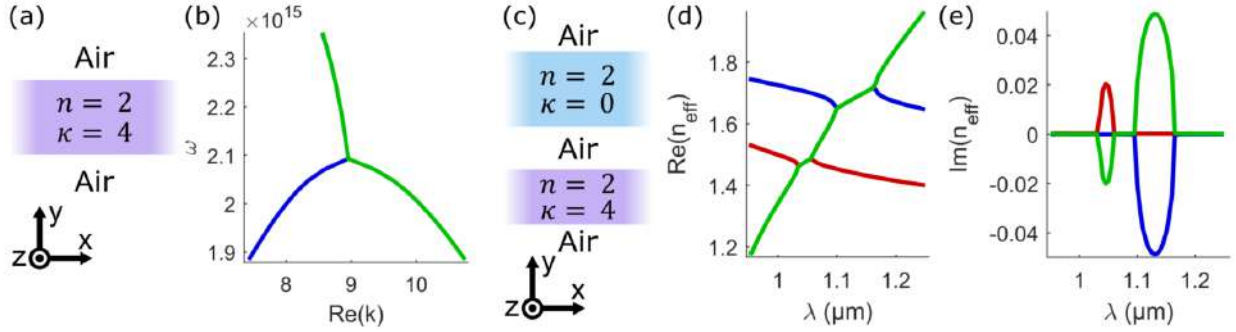


Figure 1. (a) Schematic of a 150nm thick chirowaveguide, with n = 2 and κ = 2n, embedded in vacuum, and (b) dispersion ω(k) of two of its modes. (c) Schematic of a 300nm thick dielectric slab coupled to a 130nm thick chirowaveguide, separated by 200nm, and (d) real and (e) imaginary parts of the effective indices of three modes [4].

Homogeneous chiral media, characterized by a chirality parameter κ, exhibit backward-propagating waves when their chirality reaches extreme values, i.e. $|\kappa| > n$, n being the medium's refractive index [4]. The phase velocity and power flow of these waves have opposite directions. Guided modes with these properties can be brought about in waveguides made of extremely chiral media, along with standard forward-propagating modes [4]. The interaction of counter-propagating modes, of great interest for EP generation, is numerically confirmed by simulating a single chiral slab surrounded by vacuum, as depicted in Fig. 1(a). A backward-propagating mode, characterized by a negative slope of ω(k) (green in Fig. 1(b)), couples with a forward-propagating mode (blue in

Fig. 1(b)) to create an EP ($\lambda \approx 900$ nm) and the signature "fork" dispersion of PT-symmetric structures. This coupling can also be observed between the counter-propagating modes of two distinct waveguides, one achiral and the other with giant chirality (Fig. 1(c)). Figs. 1(d,e) display the real and imaginary effective indices of two forward-propagating modes (blue and red) and one backward-propagating mode (green). Complex-index zones are brought about by the crossings of counter-propagating modes ($\lambda \approx 1.05\mu$m and 1.15 μm), with EPs at each end. The width and magnitude of these zones increase as the waveguide separation decreases, resulting in increased coupling, so that they can eventually merge.

EPs can also be achieved in PT-symmetric waveguides with balanced gain and loss. As the amount of gain and loss increase in the waveguides, controlled by a parameter γ, guided modes transition from a PT-symmetric regime with real effective indices to a PT-broken regime, with complex effective indices. The transition between these two regimes is the EP, that has previously been shown to be displaced by the introduction of chirality in the slot that separates these waveguides (configuration shown in Fig. 2(a)) [2]. We observe a similar behavior when chirality is increased to extreme values: the characteristic forks of PT-symmetric waveguides also appear for large chirality parameters κ, and their EPs are displaced as κ increases. For any κ, modes are PT-symmetric for small gain and loss ($\gamma < \gamma_{EP}$) and PT-broken beyond a gain-loss threshold ($\gamma > \gamma_{EP}$). For a fixed amount of gain and loss, this creates a succession of PT-symmetric and PT-broken regimes as κ varies (Figs. 2(b,c)).

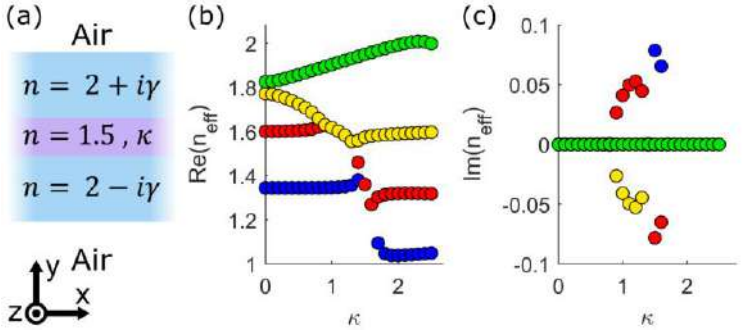


Figure 2. (a) Schematic of two 100nm thick achiral slab waveguides with gain and loss (2±iγ) separated by a 12nm thick chiral slab, and (b) real and (c) imaginary parts of the effective indices of four modes.

Meta-media advancements have enabled significant progress in accessing giant chiral values across various spectral realms [5], enabling giant controllable chirality. Utilizing these materials in coupled waveguide configurations provides an additional way of tailoring the mode dispersion, and in particular to manipulate the position of EPs, offering innovating perspectives for integrated photonics.

A.D.C. holds a FRIA grant from F.R.S.-FNRS; S.F.K. is a Bodossaki Foundation scholar. The SIMPHOTONICS MATLAB toolbox mode solver was developed at Laboratoire Charles Fabry by Mondher Besbes.

References

1. Mealy, T. and F. Capolino, "Exceptional points of degeneracy with indirect band gap induced by mixing forward and backward propagating waves," Phys. Rev. A, Vol. 107, p. 012214, 2023.
2. De Corte, A., M. Besbes, H. Benisty and B. Maes, "Chiral materials to control exceptional points in parity-time-symmetric waveguides, " Phys. Rev. A, Vol. 109, p. 023531, 2024.
3. Pendry J. B., "A chiral route to negative refraction," Science, Vol. 306, pp. 1353–1355, 2004.
4. De Corte, A., S. F. Koufidis, M. W. McCall and B. Maes, "Exceptional points in negatively refracting chirowaveguides due to giant chirality," Phys. Rev. A, Vol. 110, p. 053513, 2024.
5. Katsantonis, I. et al., "Strong and broadband pure optical activity in 3D printed THz chiral metamaterials," Advanced Optical Materials, Vol. 11, p. 2300238, 2023.

Exceptional Points in Open Quantum Systems: A Quantum Channel Approach

Jensen Li[1,2], Wai Chun Wong,[2] Bei Zeng,[3]

[1]*Department of Physics, Hong Kong University of Science and Technology, Clear Water Bay, Hong Kong, China*

[2]*Department of Engineering, University of Exeter, EX4 4QF, UK*

[3]*Department of Physics, The University of Texas at Dallas, Richardson, Texas 75080, USA*

Abstract: We propose interpolating quantum channels to construct exceptional points. We show that a second-order exceptional point emerges by interpolating two quantum channels. Quantum circuits are constructed to verify the exceptional point on a nuclear magnetic resonance quantum computer. A classical metasurface simulation of the quantum channel will also be discussed.

Exceptional points (EPs), where eigenvalues and eigenvectors coalesce, are key signatures of non-Hermitian systems and have been demonstrated in a wide range of classical wave systems. While the origin of exceptional points dates back to parity-time (PT) symmetry and extensions of quantum mechanics, their realization in the quantum regime has only recently been demonstrated by considering the semi-classical Hamiltonian of quantum systems. Phase transitions and chiral state transfer around such EPs have been observed in trapped ions and cold atoms [1,2]. Furthermore, although semi-classical Hamiltonians can be probed using post-selection techniques, the full quantum dynamics of open quantum systems extends far beyond these approximations. For instance, decoherence and noise from a Markovian environment play a crucial role, necessitating the use of the Lindblad master equation. In this framework, EPs must be analyzed in terms of the eigenvalue and eigenvector degeneracy of the Liouvillian superoperator, which governs the evolution of the density matrix [3]. Quantum EPs have also been proposed in non-Markovian systems, where memory effects cannot be neglected and the dynamics deviate from standard Markovian descriptions [4].

Here, we pursue a systematic approach to constructing exceptional points (EPs) by interpolating quantum channels. As an example, we consider the interpolation of two single-qubit quantum channels, defined as

$$\mathcal{E} = (1-p)\mathcal{E}_1 + p\mathcal{E}_2,$$

where p is the probability of applying channel $\mathcal{E}_2$ and $1-p$ is the probability of applying channel $\mathcal{E}_1$. The resulting overall quantum channel $\mathcal{E}$ is completely positive and trace-preserving (CPTP), transforming an input 2×2 density matrix ρ into an output state ρ'. The two quantum channels $\mathcal{E}_1$ and $\mathcal{E}_2$ are expressed in Kraus representation using Pauli matrices as follows:

$$\mathcal{E}_1[\rho] = \frac{1}{2}\sqrt{\sigma_x}\rho\sqrt{\sigma_x}^{\dagger} + \frac{1}{4}\sigma_y\rho\sigma_y + \frac{1}{4}\sigma_z\rho\sigma_z,$$

$$\mathcal{E}_2[\rho] = \frac{1}{4}\rho + \frac{1}{4}\sigma_x\rho\sigma_x + \frac{1}{2}\sigma_y\rho\sigma_y.$$

These channels are specifically chosen so that $\mathcal{E}_2$ has purely real eigenvalues, representing the “symmetric” phase, while $\mathcal{E}_1$ has a complex conjugate pair of eigenvalues, representing the “broken” phase in conventional terminology. By interpolating between these two channels, which belong to different phases, a transition is enforced, ensuring that an exceptional point (EP) emerges at a certain value of p where both eigenvalues and eigenvectors coalesce.

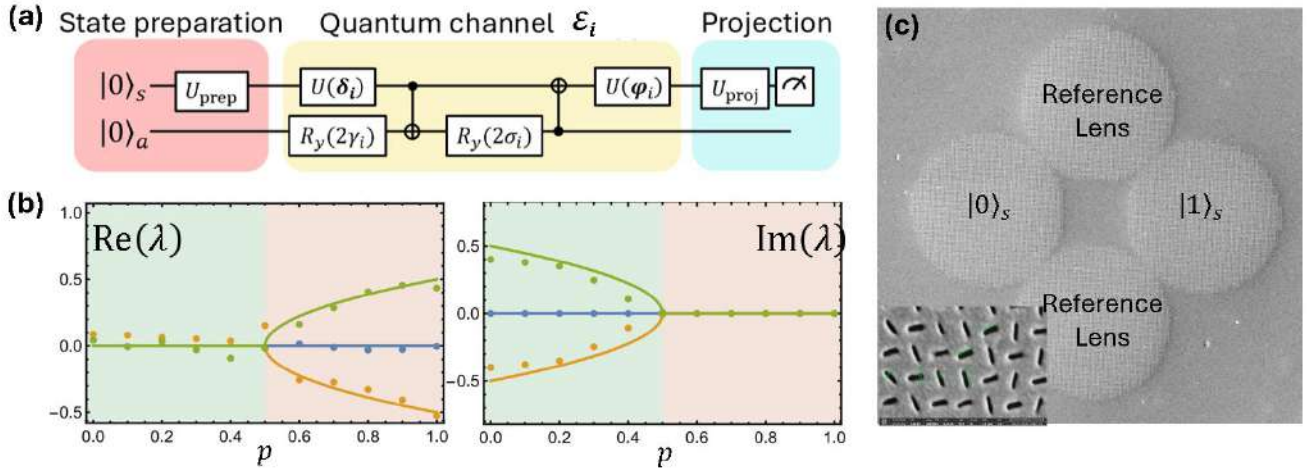


Figure 1 (a) Quantum circuit for the implementation of the single-qubit quantum channel (denoted with subscript s). A total of two qubits are used with one ancilla qubit (denoted with subscript a). The two quantum channels $\mathcal{E}_1$ and $\mathcal{E}_2$ are implemented in the middle block. The left and the right blocks contain unitary operations U_{prep} and U_{proj}, which are used for preparing different input states and projecting to different measurement bases to perform quantum process tomography. (b) Real and imaginary parts of the eigenvalues of the interpolated channel $\mathcal{E}$. Lines (symbols) are showing the model (experimental) results. (c) A metalens array for purely classical simulation of a quantum channel.

To verify our approach, we employ a two-qubit quantum computer (SpinQ) based on nuclear magnetic resonance (NMR) qubits, implementing the quantum channel with statistical averaging approach. Figure 1(a) illustrates the quantum circuit, which implements either $\mathcal{E}_1$ and $\mathcal{E}_2$ using CNOTs, rotations, and 1-qubit unitary operators for diagonalization. The quantum channel is applied to different input states, prepared by U_{prep}, while the output states are measured with different bases using U_{proj}, effectively carrying out quantum process tomography. The eigenvalues of the interpolated channel $\mathcal{E}$ are then plotted in Fig. 1(b) as symbols, with solid lines representing model predictions. A second-order EP is identified at $p = 0.5$. Only three eigenvalues are plotted while the forth eigenvalue remains 1 due to the trace-preserving property. While not shown here, generalizing to additional channels for interpolation results in higher-order EP structures. For instance, adding one more channel for interpolation can lead to the emergence of a third-order EP and an EP-line. Furthermore, our approach of interpolating quantum channels to obtain EPs can be straightforwardly extended to a larger number of qubits.

Finally, we also discuss a purely classical analog of such a quantum simulation, using a metalens array to simulate a one-qubit quantum channel. Figure 1(c) shows such a meta-lens array with two signal lenses in representing the two signal qubit states $|0\rangle_s$ and $|1\rangle_s$ while the reference lenses are for extracting complex transmission amplitudes for diffraction from the two signal lens into different directions through interferometry.

References

1. L. Ding, K. Shi, Q. Zhang, D. Shen, X. Zhang, and W. Zhang, Physical Review Letters 126, 083604 (2021).
2. Z. Ren, D. Liu, E. Zhao, C. He, K. K. Pak, Jensen Li, and Gyu-Boong. Jo, Nature Physics 18, 385 (2022).
3. J.-W. Zhang, J.-Q. Zhang, G.-Y. Ding, J.-C. Li, J.-T. Bu, B. Wang, L.-L. Yan, S.-L. Su, L. Chen, F. Nori, et al., Nature Communications 13, 6225 (2022).
4. J.-D. Liu, P.-C. Kuo, N. Lambert, A. Miranowicz, F. Nori, Y.-H. Chen, Nature Communications 16, 1289 (2025).

Resonant states of photonic time crystals

A.C. Valero[1*], S. Gladyshev[1], D. Globosits[2], S. Rotter[2], E. A. Muljarov,[3] and T. Weiss[1]

[1]Institute of Physics, University of Graz, and NAWI Graz, 8010 Graz, Austria

[2]Institute for Theoretical Physics, Vienna University of Technology (TU Wien), 1040 Vienna, Austria

[3]School of Physics and Astronomy, Cardiff University, Cardiff CF24 3AA, United Kingdom

Corresponding author: adria.canos-valero@uni-graz.at

Abstract: Realizing photonic time crystals in optics requires imparting fast temporal modulations to nanostructures of finite spatial extent. We show that these systems exhibit cavity effects driven by resonant states, which dominate their exotic optical response. We present a general framework to calculate these eigenmodes, uncovering their underlying non-Hermitian physics.

In recent years, the exploration of photonic time crystals has captivated the metamaterials community, offering intriguing possibilities for controlling light through periodic temporal modulation of material properties. The latter gives rise to a momentum bandgap [1]. Inside the bandgap, there exists a solution of Maxwell's equations that parametrically amplifies light over time [2]. However, realistic optical implementations will require imparting temporal modulations in complex nanostructures. These spatially-structured photonic time crystals differ fundamentally from their bulk counterparts, with their behavior governed by optical resonances, as sketched in Fig.1(a) for the case of a dielectric slab. Resonant phenomena have been predicted to strongly influence and even decrease the modulation thresholds for the observation of light amplification [3]. Hence, there is an urgent need for a rigorous theory of resonances, that can guide the design of realistic photonic time crystals in the optical regime.

In static structures, it is well known that resonances are directly related to their resonant states (or quasinormal modes), i.e. source-free solutions of Maxwell's equations for outgoing waves and complex eigenfrequencies [4,5]. However, the physics of these eigenmodes in photonic time crystals has yet to be explored.

In this contribution, we will close this gap and present a resonant state theory of photonic time crystals of arbitrary geometry. Our formalism provides profound physical insights into their resonant properties and uncovers several key phenomena. We discover that, for an arbitrary periodic modulation, the original resonant states spawn an infinite number of "replicas", which correspond to new resonant states of the modulated system, manifesting as new resonances in the optical spectra. An example is shown in Fig.1(b) for the case of a time-modulated dielectric slab. It can be seen that, in addition to the conventional Fabry-Pérot resonance, new 'replica modes' emerge in the complex frequency spectrum.

Crucially, we also identify the inherently resonant mechanism behind parametric amplification in such structures, which cannot be explained using the momentum bandgap of bulk materials. We find that the latter occurs when the modulation induces one of the eigenfrequencies to cross the real axis, introducing gain. This can happen more easily for eigenfrequencies with small imaginary parts, for which we derive explicit design rules. For instance, Figure 1(c)-(d) shows the design of a parametric resonance in a realistic Bragg microcavity, sketched in Fig.1(d). Choosing a weakly radiative mode of the static structure as a starting point [Figure 1(c)], we quantitatively predict the formation of a parametric resonance for permittivity modulations of less than 0.16%. Due to its generality, we anticipate our framework will play a

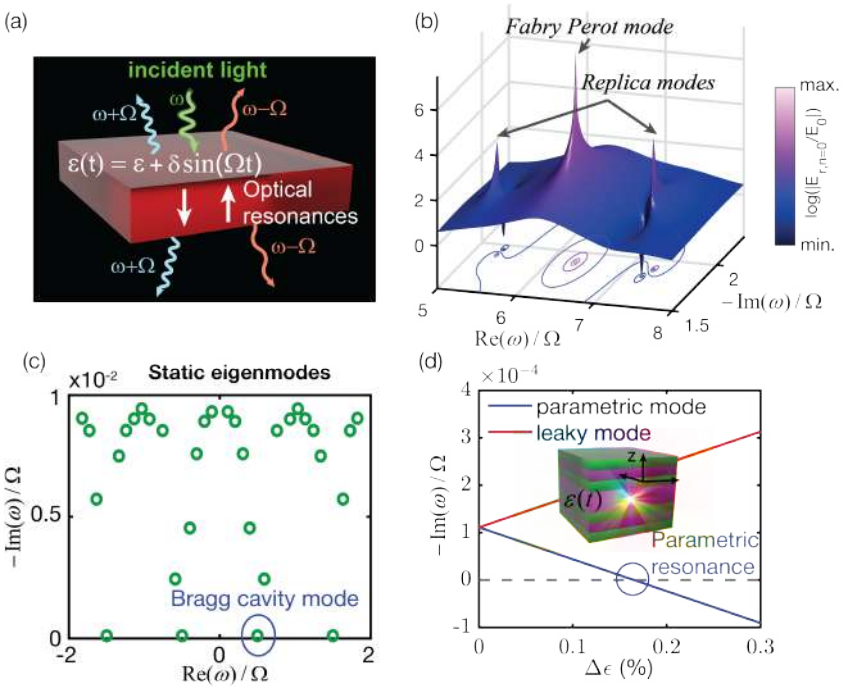


Figure 1: (a) Illustration of a time-modulated dielectric slab illuminated by a plane wave. The plane wave excites a series of optical resonances, directly linked to the slab eigenmodes. (b) Reflected field amplitudes from a modulated slab in the complex frequency plane. (c) Static eigenmodes of a Bragg microcavity. (d) Imaginary parts of the eigenfrequencies of the eigenmodes spawning from the Bragg cavity mode in (c) vs. modulation amplitude.

prominent role in the emerging field of space-time optics.

References

1. M. M. Asgari, P. Garg, X. Wang, M. S. Mirmoosa, C. Rockstuhl, and V. Asadchy, "Theory and applications of photonic time crystals: a tutorial," *Advances in Optics and Photonics*, vol. 16, no. 4, pp. 958–1063, 2024.

2. M. Lyubarov, Y. Lumer, A. Dikopoltsev, E. Lustig, Y. Sharabi, and M. Segev, "Amplified emission and lasing in photonic time crystals," *Science*, vol. 377, no. 6604, pp. 425–428, 2022.

3. X. Wang, P. Garg, M. Mirmoosa, A. Lamprianidis, C. Rockstuhl, and V. Asadchy, "Expanding momentum bandgaps in photonic time crystals through resonances," *Nature Photonics*, pp. 1–7, 2024.

4. P. Lalanne, W. Yan, K. Vynck, C. Sauvan, and J.-P. Hugonin, "Light interaction with photonic and plasmonic resonances," *Laser & Photonics Reviews*, vol. 12, no. 5, p. 1700113, 2018.

5. S. Both and T. Weiss, "Resonant states and their role in nanophotonics," *Semiconductor Science and Technology*, vol. 37, no. 1, p. 013002, 2021.

Trapping light at an exceptional point

A.C. Valero[1*], Z. Sztranyovszky[2], E.A. Muljarov[3], A. Bogdanov[4] and T. Weiss[1]

[1]Institute of Physics, University of Graz, and NAWI Graz, 8010 Graz, Austria

[2]School of Chemical Engineering, University of Birmingham, Birmingham B15 2TT, United Kingdom

[3]School of Physics and Astronomy, Cardiff University, Cardiff CF24 3AA, United Kingdom

[4]Harbin Engineering University, Sansha Road 1777, Qingdao 266404, China

Corresponding author: adria.canos-valero@uni-graz.at

Abstract: Bound states in the continuum and exceptional points are unique singularities of non-Hermitian systems. We demonstrate that multiple bound states in the continuum can merge into a single exceptional point, creating a novel kind of singularity. This state combines non-radiative behavior with extreme sensitivity, opening new prospects for nanoscale sensing.

Open systems inherently imply interaction with the surrounding space via the exchange of energy. They can be found in both classical and quantum systems, involving acoustical or optical waves [1]. A remarkable consequence of non-hermiticity is the emergence of *exceptional points* (EPs) in the eigenenergy spectra. EPs are spectral singularities where at least two eigenvectors and their associated eigenvalues coalesce [2]. In close proximity to an EP, the eigenvalues exhibit a strongly enhanced sensitivity to perturbations, making them prospective for nanophotonic sensing applications [2, 3].

Another type of singularities of open systems are *bound states in the continuum* (BICs). BICs are localized states that are embedded in the continuous spectrum of radiation modes, yet do not radiate away [4]. Nowadays, they are actively investigated in nanophotonics, owing to their remarkable ability to boost and fine-tune light-matter interactions [5].

Despite the intense attention received by the two kinds of singularities, an intriguing question has remained unanswered: *can two or more BICs coalesce into an EP?*.

We answer positively to this question and show, based on general principles, that perfect BICs can merge into a single EP, creating a novel kind of singularity, an "exceptional bound state in the continuum" (EP-BIC), that combines non-radiative behavior with extreme sensitivity [6].

In this contribution, we will provide general rules for their observation in nanophotonic systems. For instance, a simple design that supports EP-BICs is depicted in Fig. 1(a). We consider a stack of two dielectric metasurfaces supporting symmetry-protected BICs [6]. When changing the separation distance between the metasurfaces, the near field interaction between the BICs can be modified. Upon introducing a small amount of ohmic losses k in the top metasurface, an EP-BIC emerges at some critical separation [Fig. 1(b)]. Both theory (solid lines) and numerical simulations (grey dots) show excellent agreement. Near the EP-BIC, the fields of the two BICs become almost identical, as can be seen in the inset of Fig. 1(b). Moreover, they are still BICs, as no waves propagate out of the plane of the structure.

Upon breaking the in-plane symmetry of the bilayer metasurface [e.g. introducing an off-center hole of surface S_h, see Fig. 11(c)], EP-BICs, like conventional BICs, span quasi-BICs that can be probed from the far field. In stark contrast, however, we have found that the resulting quasi-BICs are much more sensitive to small perturbations. Fig. 1(c) plots a comparison between the changes in the decay rates (i.e. the losses) of a conventional BIC and EP-BICs with two and three coalescing BICs, respectively. It can be confirmed that the latter two have a much larger response to perturbations.

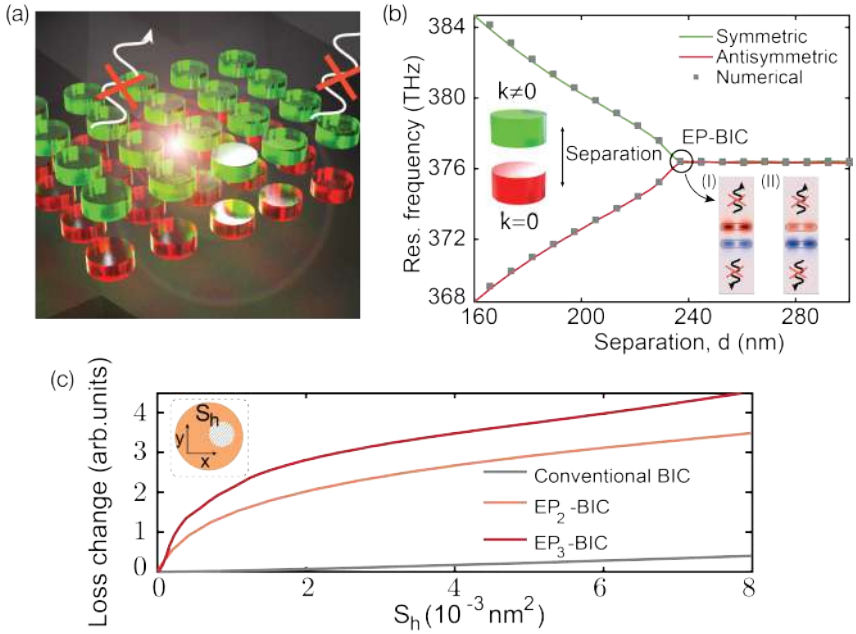


Figure 1: (a) Artistic representation of a bilayer metasurface supporting an exceptional bound state in the continuum. (b) Resonance frequencies of the BICs as a function of the separation between the two metasurfaces and field distributions of the BICs near the EP-BIC. (c) Comparison between the changes in the loss rates of a conventional BIC and EP-BICs of second (EP_2-BIC) and third order (EP_3-BIC) as a function of S_h (details in text). Inset: depiction of the perturbation.

In conclusion, we have shown that an arbitrary number of ideal BICs can coalesce into an EP, forming an EP-BIC, and validated our theoretical predictions with numerical simulations of a realistic bilayer metasurface operating in the visible. The new state inherits the properties of both singularities, as it does not radiate, but also becomes extremely sensitive to perturbations [6]. Therefore, besides their fundamental interest, EP-BICs are exciting candidates for the realization of EP sensors at the nanoscale.

References

1. Y. Ashida, Z. Gong, and M. Ueda, "Non-hermitian physics," *Advances in Physics*, vol. 69, no. 3, pp. 249–435, 2020.

2. M.-A. Miri and A. Alù, "Exceptional points in optics and photonics," *Science*, vol. 363, no. 6422, Jan. 2019.

3. A. C. Valero, V. Bobrovs, T. Weiss, L. Gao, A. S. Shalin, and Y. Kivshar, "Bianisotropic exceptional points in an isolated dielectric nanoparticle," *Physical Review Research*, vol. 6, no. 1, p. 013053, 2024.

4. C. W. Hsu, B. Zhen, A. D. Stone, J. D. Joannopoulos, and M. Soljačić, "Bound states in the continuum," *Nature Reviews Materials*, vol. 1, no. 9, pp. 1–13, 2016.

5. K. Koshelev, S. Lepeshov, M. Liu, A. Bogdanov, and Y. Kivshar, "Asymmetric Metasurfaces with High-Q Resonances Governed by Bound States in the Continuum," *Phys. Rev. Lett.*, vol. 121, no. 19, p. 193903, Nov. 2018.

6. A. C. Valero, Z. Sztranyovszky, E. A. Muljarov, A. Bogdanov, and T. Weiss, "Exceptional bound states in the continuum," *Physical Review Letters*, 2025, accepted for publication.

Spherical representation of (anti-)parity-time states of Bragg gratings

Tianyi Hao,[1] Pavel Cheben,[1,3] Jens H. Schmid,[3] and Pierre Berini[1,2,4,*]

[1]School of Electrical Engineering and Computer Science, University of Ottawa, Ottawa, K1N 6N5, Canada
[2]NEXQT Institute, University of Ottawa, Ottawa, K1N 6N5, Canada
[3]National Research Council Canada, Ottawa, K1A 0R6, Canada
[4]Department of Physics, University of Ottawa, Ottawa, K1N 6N5, Canada
[*]corresponding author: pberini@uottawa.ca

Abstract: Parity-time (PT) symmetry and anti-PT symmetry are two types of non-Hermitian Hamiltonian systems. Waveguide Bragg gratings with phase-shifted perturbations in real and imaginary refractive index can reach any (anti-)PT symmetry state. A spherical surface of the grating design space is proposed, illustrating (un)broken and exceptional point (anti-)PT symmetry states. Grating design examples are presented and discussed.

Non-Hermitian Hamiltonians have drawn vigorous interest in photonics [1]. A non-Hermitian Hamiltonian H is Parity-Time (PT) symmetric if it commutes with the PT operator [H,PT]=0, or anti-PT symmetric if it anti-commutes with the PT operator {H,PT}=0, where P is the parity operator and T is the time reversal operator [2, 3]. In an open system, the eigenvalues of H can be real or complex and the eigenvectors can merge or differ from those of the (anti-)PT operator. Eigen analysis determines the state of H as (Anti-)PT symmetric [1-3], or anyonic PT symmetric [4], with unbroken, broken or exceptional point (EP) states. Vortex beams [5], PT symmetric lasers [6], unidirectional reflection [7,8], coherent perfect absorption [9], and chiral polarizers [10] are applications that are realized in different PT states of an open system.

Consider a non-Hermitian Hamiltonian H, having complex eigenvalues, satisfying [4]:

$$\mathrm{PTH} = e^{2i\theta}\mathrm{HPT} \tag{1}$$

where θ is the phase of an eigenvalue. When $\theta = n\pi$ ($n \in \mathrm{Z}$), we have $\mathrm{PTH} = \mathrm{HPT}$ and the system is PT symmetric. When $\theta = n\pi \pm \pi/2$, we have $\mathrm{PTH} = -\mathrm{HPT}$ and the system is anti-PT symmetric. Cases where θ takes on other values correspond to non-Hermitian Hamiltonians that are neither PT symmetric nor anti-PT symmetric. A Bragg grating with gain and loss, and coupling between the forward and backward propagating modes, has a refractive index distribution $n(z)$ along the z (propagation) direction that can be written as [11]:

$$n(z) = n_{\mathrm{ave}} + \Delta n_r \sin\left(\frac{2\pi}{\Lambda} z\right) + \mathrm{j}\Delta n_{\mathrm{i}} \cos\left(\frac{2\pi}{\Lambda} z + \theta\right) \tag{2}$$

where n_{ave} is the average uniform complex refractive index, Δn_r and Δn_i are the strength of the real and imaginary index perturbations, Λ is the period of the grating, and θ is an additional phase offset between the real and imaginary index perturbations. Note that the real and imaginary perturbations have a $\pi/2$ phase shift for $\theta = 0$, and that θ is the same as in Eq. 1. n_{ave} and Λ satisfy $\Lambda = (m\lambda_B/|2n_{\mathrm{ave}}|)$ where m is the grating order, and λ_B is the Bragg wavelength. In Eq. 2, $\theta \in [0,\ 2\pi]$ (mod(2π)), the perturbation amplitudes Δn_r and Δn_i have the same period Λ, and n_{ave} determines the central (Bragg) wavelength of the grating. These parameters are independent of each other and can be used to define a spherical surface.

The general perturbation distribution implied by Eq. 2 can be represented by a sphere of radius $r = |n_{\mathrm{ave}}|$, azimuthal coordinate θ (identical to θ in Eqs. 1 and 2), and polar coordinate $\varphi = \mathrm{acos}(\Delta n_i - \Delta n_r)/(\Delta n_i +$

Δn_r), as sketched in Fig. 1 [11]. All possible (anti-)PT symmetric states can be illustrated on this sphere: the blue ring corresponds to anti-PT symmetric gratings ($\theta = n\pi \pm \pi/2$), whereas the yellow ring corresponds to PT symmetric gratings ($\theta = n\pi$). The northern hemisphere ($\varphi \in [0, \pi/2)$) has $\Delta n_r > \Delta n_\mathrm{i}$, which corresponds to symmetry unbroken states, whereas the southern hemisphere ($\varphi \in (\pi/2, \pi]$) corresponds to symmetry broken states with $\Delta n_r < \Delta n_\mathrm{i}$. The equatorial black ring corresponds to $\Delta n_r = \Delta n_\mathrm{i}$ and $\varphi = \pi/2$ indicating exceptional points that separate broken and unbroken states. The north pole ($\varphi = 0$) corresponds to $\Delta n_\mathrm{i} = 0$ which yield gratings with a real index perturbation, whereas gratings at the south pole ($\varphi = \pi$) have an imaginary index perturbation with $\Delta n_\mathrm{r} = 0$. The performance of gratings located at various points on this sphere will be discussed.

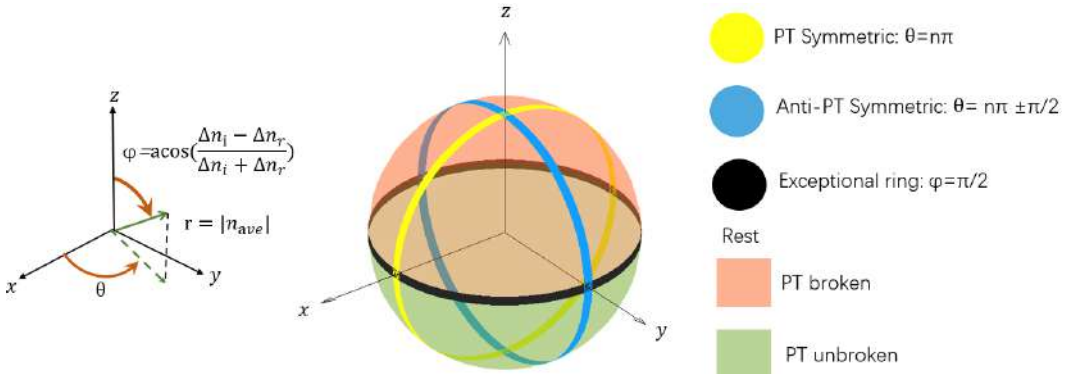


Fig. 1. Spherical representation of Eq. 2 with regions of the sphere identifying (anti-)PT symmetric states [11].

References

1. A. Li, H. Wei, M. Cotrufo, W. Chen, S. Mann, X. Ni *et al*., "Exceptional points and non-Hermitian photonics at the nanoscale," Nat. Nanotechnol. 18, 706–720 (2023).
2. C. M. Bender, "Introduction to PT-symmetric quantum theory," Contemp. Phys. 46, 277–292 (2005).
3. Y. L. Fang, J. L. Zhao, Y. Zhang, D. X. Chen, Q. C. Wu, Y. H. Zhou *et al*., "Experimental demonstration of coherence flow in PT- and anti-PT-symmetric systems," Commun Phys. 4, 223 (2021).
4. G. Arwas, S. Gadasi, I. Gershenzon, A. Friesem, N. Davidison, and O. Raz, "Anyonic-parity-time symmetry in complex-coupled lasers," Science Advances 8, eabm7454 (2022).
5. P. Miao, Z. Zhang, J. Sun, W. Walasik, S. Longhi, N. M. Litchinitser, *et al*., "Orbital angular momentum microlaser," Science 353, 464–467 (2016).
6. H. Benisty, V. B. Perrière, A. Ramdane, *et al*., "Parity-time symmetric gratings in 1550 nm distributed-feedback laser diodes: insight on device design rules," J. Opt. Soc. Am. B 38, C168-C174 (2021).
7. M. Kulishov, J. M. Laniel, N. Bélanger, J. Azaña, and D. V. Plant, "Nonreciprocal waveguide Bragg gratings," Opt. Express 13, 3068–3078 (2005).
8. T. Hao, and P. Berini, "Directional coupling with parity-time symmetric Bragg gratings," Opt. Express 30, 5167-5176 (2022).
9. Y. Sun, W. Tan, H. Q. Li, J. Li, and H. Chen, "Experimental demonstration of a coherent perfect absorber with PT phase transition," Physical Review Letters 112, 143903 (2014).
10. Y. Wei, Z. H. Zhou, Y. Chen, Y. Ding, J. Dong, and X. Zhang, "Anti-parity-time symmetry enabled on-chip chiral polarizer," Photonics Research 10, 76-83 (2022).
11. T. Hao, P. Cheben, J. H. Schmid, and P. Berini, "Parity-time and anti-parity-time states of Bragg gratings and their representation in spherical coordinates," Opt. Express 32, 45521-45530 (2024).

Field localization Metamaterial for stable Pseudo Parity-Time Symmetrical wireless power transfer system.

Abdulrahman Alsaadi[1,2], Inki Kim[1,2*]

[1]Department of Biophysics, Institute of Quantum Biophysics, Sungkyunkwan University, Suwon, Republic of Korea
[2] Department of Intelligent Precision Healthcare Convergence, Sungkyunkwan University, Suwon, Republic of Korea
[*]Corresponding author: inki.kim@skku.edu

Abstract: Wireless power systems suffer from low efficiency and performance instability. Our system provides extended-range power transfer using the physics of parity-time symmetry and metamaterials, increasing transfer efficiency stability against distance fluctuations with the ability to localize the power from a larger transmitter to smaller size receiver.

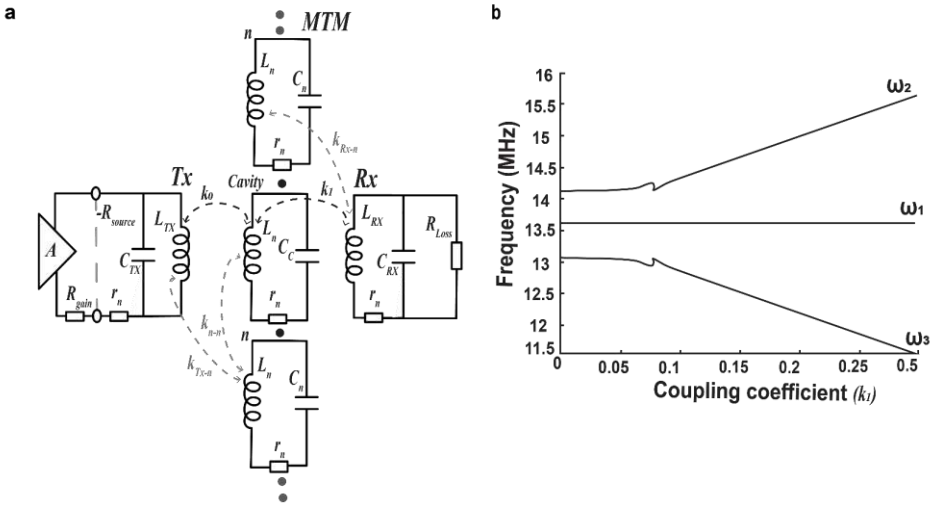


Figure 1. (a) Circuit schematic of Pseudo PT-WPT. (b) Real parts of eigenfrequencies for the field localized WPT Pseudo PT- WPT

systems have limitations in range, efficiency of transmission and Transmitter (Tx) to receiver (Rx) size ratio. This work proposes a stable and extended range wireless power transfer system utilizing parity-time symmetry (PT-symmetry) and electromagnetic metamaterials (MTM) to address these limitations. Our wireless power transfer system Pseudo PT-symmetry (PT) can be implemented in WPT systems by introducing a gain element into the circuit equivalent to the loss element. As shown in Fig.1(a), it is denoted as (-R), which is equivalent to load resistance (RL) [1]. The system can be modeled as the non Hermitian Hamiltonian as presented in equation (1). We adopt a pseudo-PT symmetric approach by making $g_1 = k_0^2\gamma/k_1^2 + \gamma_{s2}\gamma$ in our wireless power transfer system because it relaxes the strict requirement that the coupling coefficients between the transmitter and the cavity ($k0$) and between the cavity and the receiver ($k1$) must be equal[2]..

$$H = \begin{pmatrix} \omega_{\mathrm{Tx}} + ig & -ik_0 & 0 \\ -ik_0 & \omega_{\mathrm{Cav}} - i\gamma_{s2} & -ik_1 \\ 0 & -ik_1 & \omega_{\mathrm{Rx}} - i\gamma \end{pmatrix} \qquad (1)$$

$$\omega_1 = \omega_{\mathrm{Cav}},\ \omega_{2,3} = \omega_0 \pm \sqrt{k_{\mathrm{eff}}^2 - (g-\gamma)^2} \qquad (2)$$

The eigenvalues of equation (1) shows that such system supports three real eigen values as shown in Fig.1(a), and equation

(2), which makes it robust against fluctuations in coupling coefficient (k1). The inclusion of an electromagnetic metamaterial slab enables the system to transfer power effectively from a larger Transmitter (Tx) to smaller receiver (Rx). Fig.2(a), shows our metamaterial (MTM) that is made of Megahertz spiral resonators that each act as a unit cell, when arranged periodically the structure will behave as a metamaterial with the unique negative refractive index and by making a defect in the structure by tuning one of the unit cells to operate at a lower resonance frequency will make the structure to act as meta lens with hotspot that confines the field into one spot [3]. Electromagnetic wave simulations show that the metamaterial effectively confines the magnetic field (h-field), as shown in Fig. 2(c), surpassing the capabilities of the PT system without Metasurface. Measured results shows that our proposed wireless power transfer system posses stable and high efficiency compared to conventional wireless due to the inclusion of the field localization metamaterial and pseudo party time symmetry design conditions .

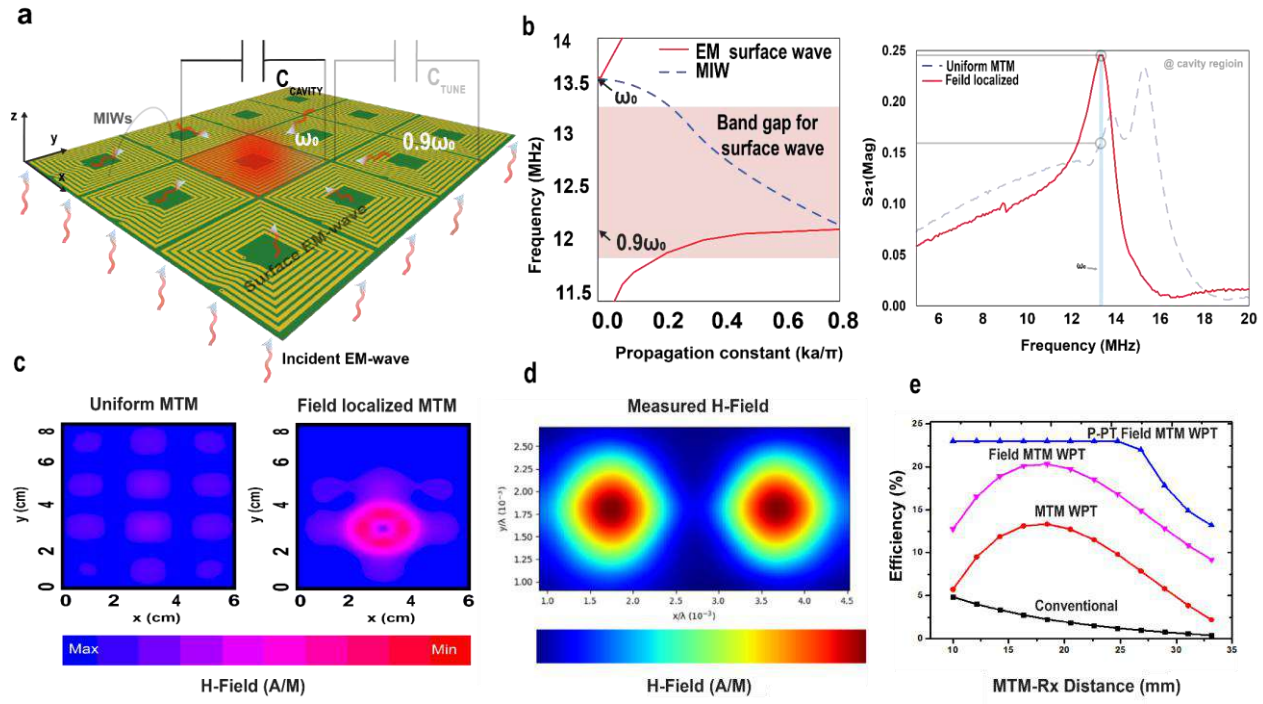


Figure 2. (a) Field localization concept (b) Dispersion characteristics of propagating waves. (c) Simulated H-field for localized MTM and Uniform MTM (d) Measured H-field localization for two cavities simultaneously. (e) Measured H-field localization for two cavities

References

1. Sakhdari, M., Hajizadegan, M., & Chen, P. Y. (2020). "Robust extended-range WPT PT-symmetric platform." Physical Review Research, 2(1), 013152. vol. 68, no. 3, pp. 1569-1582 (2020).
2. Hao, Xianglin, et al. "Frequency-stable robust wireless power transfer based on high-order pseudo-Hermitian physics." Physical Review Letters 130.7 (2023): 077202.
3. H. N. Bui, J. -S. Kim and J. -W. Lee, "Design of Tunable Metasurface Using Deep Neural Networks for Field Localized WPT," IEEE Access, vol. 8, pp. 194868-194878 (2020).

New Advances in Metamaterials and Their Functional Applications

Dynamical Manipulation of Terahertz Waves based on Moiré Metamaterials

Jin Zhang[1*], and Zhipei Sun[1]

[1]QTF Centre of Excellence, Department of Electronics and Nanoengineering, Aalto University, FI-02150 Espoo, Finland.
[*]Corresponding author: jin.zhang@aalto.fi

In recent years, moiré metamaterials have emerged as a fascinating and promising area of research, offering unique and unprecedented opportunities for controlling and manipulating electromagnetic waves. These artificially designed structures feature unit cells that are twisted or rotated relative to each other, leading to the emergence of novel properties and behaviors. Twisting introduces a new degree of freedom in the design of metamaterials, enabling the creation of complex and tunable responses that are unattainable with traditional designs. The properties of these materials can be finely tuned by adjusting the twist angle, providing a versatile platform for exploring new physical phenomena and developing advanced functional materials.

In this paper, we propose a bilayer graphene-based metamaterial for the tunable manipulation of THz waves. The structure, as depicted in Figure 1(a), consists of a moiré metamaterial. Figure 1(b) presents a zoomed-in view of the moiré metamaterial, which comprises, from bottom to top, a metallic back plate, a silicon substrate, a SiO_2 insulating layer, and two graphene strips with a mutual twist angle $\Delta\theta$. Figures 1(c) and 1(d) illustrate the graphene strips and the twisted layers with $\Delta\theta = 40°$, respectively, where the moiré patterns are clearly visible in the overlapped regions. Furthermore, the surface conductivity of graphene can be dynamically controlled by applying a bias voltage, thus enabling the manipulation of THz waves. When THz waves are normally illuminated on the surface of the moiré metamaterials, the simulated reflection spectra, shown in Figures 1(e) and 1(f), demonstrate the independent manipulation of amplitude and frequency.

This study sets up a new paradigm for tunable metamaterials, which is expected to find extensive applications in advanced THz device and communication system.

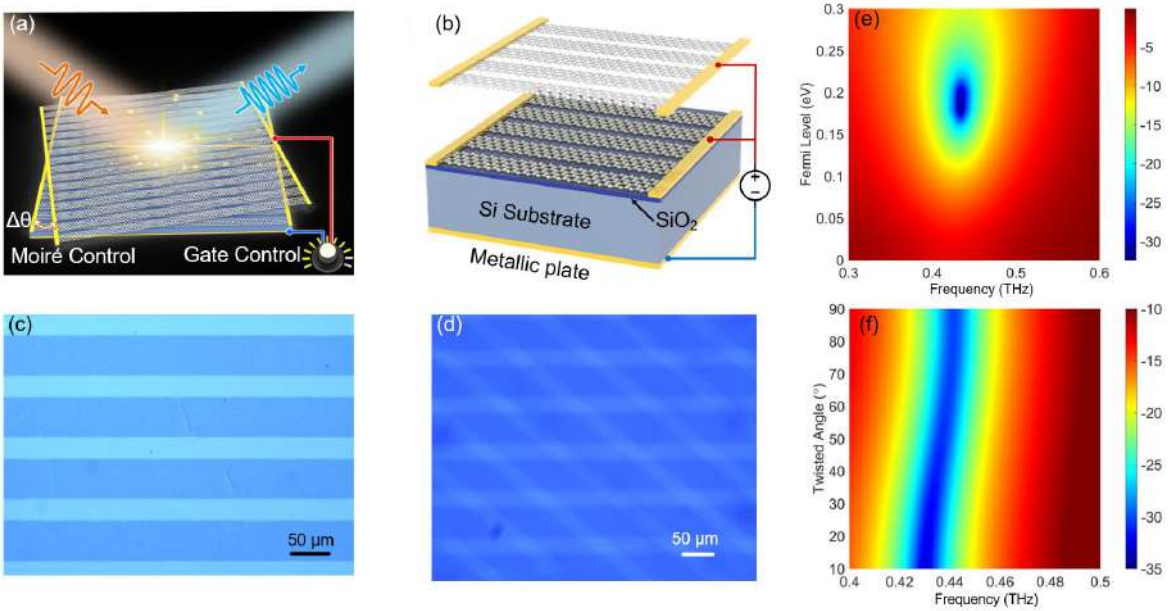


Figure 1 (a) Conceptual features and (b) schematic depiction of the graphene-based moiré metamaterial. Optical images of (c) graphene strips and (d) moiré patterns with $\Delta\theta = 40°$. Refleciton spetra as a function of (e) Fermi level and (f) twisted angle.

Dual-band acoustic topological metalaterials with valley-locked waveguide sates

C. L. Ding[1*], Yang Sun[1]

[1]Smart Materials Laboratory, School of Physical Science and Technology, Northwestern Polytechnical University, Xi'an 710129, People's Republic of China
[*]corresponding author: dingchanglin@nwpu.edu.cn

Abstract: we present two kinds of valley topological metamaterial with topological valley-locked waveguide sates (TVWSs) composed of local resonant meta-atoms or meta-molecules.The work frequency can be tuned by the geometry size of local resonant structures. Arraying the two structures together, the composite topological metamaterial can realize TVWSs in two bands.

Acoustic topology is a hot spot in recent year, because Acoustic topological insulator presents topological transport with defect immunity, backscattering immunity, and robust edge states.[1-4] Although some ATIs have been achieved by phononic crystals based on Bragg scattering, the narrow work frequency band related to the lattice constant limits their applications.[5-8] Acoustic metamaterials (AMs)[7-10] based on local resonance are another kind of candidate for the design of ATIs.[11, 12]

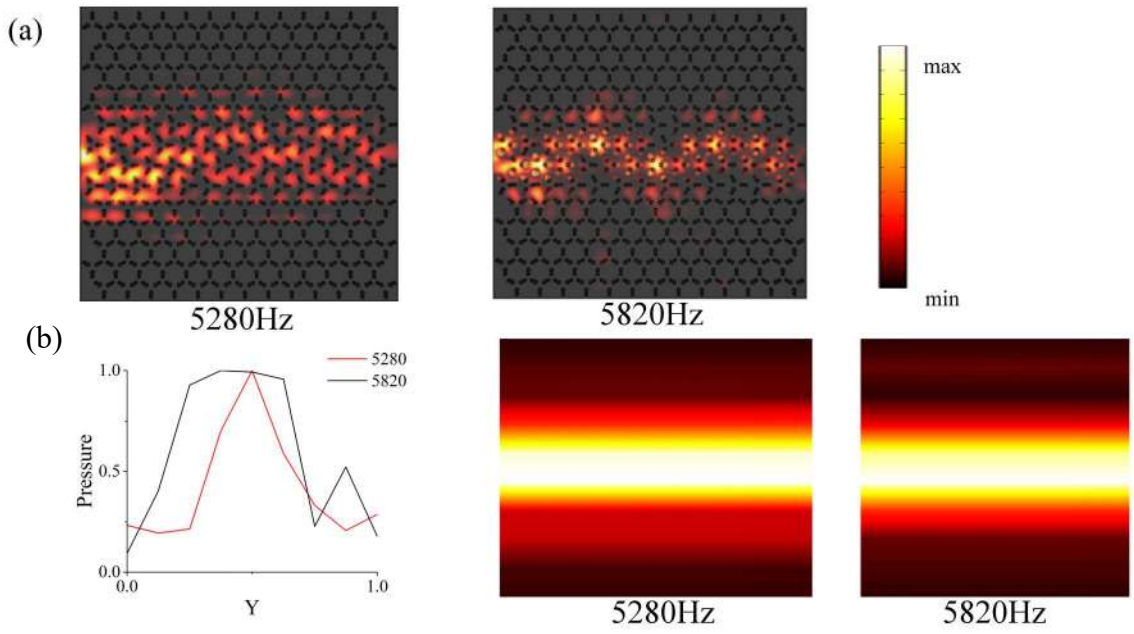


Fig. 1 (a) Simulated absolute acoustic pressure distributions of sample at frequencies of 5280 Hz and 5820 Hz . (b) Experimental measured sound pressure distribution and the corresponding sound pressure curve at the right end of sample.

In this paper, we create a structure consisting of three metamaterial sections that incorporate valley properties achieving the creation of topological waveguides states in two frequency bands with valley-locked modes. The simulation and experimental results show that the the energy will be transmitted in the wide

region without any reflections in two frequency ranges of 5280 Hz and 5820 Hz as shown in Fig. 1, which could have promising implications for manipulating acoustic waves and transmitting information effectively.

References

1. K. v. Klitzing, G. Dorda, and M. Pepper, "New Method for High-Accuracy Determination of the Fine-Structure Constant Based on Quantized Hall Resistance," Phys. Rev. Lett. 45, 494, 1980.
2. R. B. Laughlin, "Anomalous Quantum Hall Effect: An Incompressible Quantum Fluid with Fractionally Charged Excitations," Phys. Rev. Lett. 50, 1395, 1983.
3. M. Z. Hasan and C. L. Kane, "Colloquium: Topological insulators," Rev. Mod. Phys. 82, 3045, 2010.
4. X. L. Qi and S. C. Zhang, "Topological insulators and superconductors," Rev. Mod. Phys. 83, 1057, 2011.
5. R. Fleury, D. L. Sounas, C. F. Sieck, M. R. Haberman, and A. Alù, "Sound isolation and giant linear nonreciprocity in a compact acoustic circulator," Science 343, 516, 2014.
6. C. He, X. Ni, H. Ge, X. C. Sun, Y. B. Chen, M. H. Lu, X. P. Liu, and Y. F. Chen, "Acoustic topological insulator and robust one-way sound transport," Nat. Phys. 12, 1124, 2016.
7. C. L. Ding, Y. B. Dong, Y. B. Wang, J. B. Shi, S. L. Zhai, and X. P. Zhao, "Acoustic metamaterials and metasurfaces composed of meta-atoms and meta-molecules," J. Phys. D: Appl. Phys. 55, 253002, 2022.
8. C. L. Ding, Y. B. Dong, and X. P. Zhao, Research advances in acoustic metamaterials and metasurface, Acta Phys. Sin. (Beijing, China) 67, 194301, 2018.
9. H. J. Chen, H. Li, S. L. Zhai, C. L. Ding, L. M. Hao, C. R. Luo, and X. P. Zhao, "Ultrasound acoustic metamaterials with double-negative parameters," J. Appl. Phys. 119, 204902, 2016.
10. C. L. Ding, H. J. Chen, S. L. Zhai, and X. P. Zhao, "Acoustic metamaterial based on multi-split hollow spheres," Appl. Phys. A 112, 533, 2013.
11. Y. B. Wang, Y. B. Dong, S. L. Zhai, C. L. Ding, C. R. Luo, and X. P. Zhao, "Reconfifigurable topological transition in acoustic metamaterials," Phys. Rev. B 102, 174107, 2020.
12. C. L. Ding, J. B. Shi, Y. B. Dong , Y. Bai , S. L. Zhai, and X. P. Zhao, "Dual-band acoustic higher-order topological metamaterial composed of meta-atoms and meta-molecules," Phys. Rev. B 108, 094103 (2023)

Optical near-field enhancement by metal particles at higher-order plasmon resonances

Sagar Sehrawat[1*] and Andriy Shevchenko[1]

[1]Department of Applied Physics, Aalto University, P.O. Box 13500, FI-00076 Aalto, Finland
[*]Corresponding author: sagar.sehrawat@aalto.fi

Abstract: We demonstrate that higher-order plasmon resonances in small groups of metal nanoparticles or their arrays can significantly enhance optical near-fields, exceeding the most common dipole-induced enhancement. The finding is important for the development of new approaches to the design of plasmonic devices, such as plasmonic sensors and nonlinear optical components.

Metal nanoparticles showing plasmon resonances can confine and enhance optical fields at the nanoscale, resulting in a wide range of applications, e.g., in optical sensing, photocatalysis, surface enhanced Raman spectroscopy, and nonlinear optics. Usually, localized plasmon resonances are used to enhance optical near-fields via the electric-dipole excitations, and higher-order excitations are considered to be much weaker. However, we have recently shown that hybridization of multipole excitations of different orders can lead to both narrowband and bright light scattering by a pair of nanoparticles [1]. We have also found that a strong near-field enhancement can appear in the gap between two particles at a hybrid dipole-octupole resonance in a metal nanosphere dimer [2] or at a quadrupole-octupole resonance in a nanodisc trimer [3]. The effect is explained by the fact that higher-order multipole resonances are relatively dark, showing a higher Q-factor and a better field trapping than the electric dipole resonance. This effect can be further enhanced in an array of such particles by coupling their higher-order plasmon resonance to a lattice resonance of the structure.

In Fig. 1(a), the intensity enhancement spectrum of light in the gap between two silver nanospheres is shown by the black solid line and the spectrum of the excited electric current density around the gap by the blue dashed line. The silver dimer is shown in the inset. The radius of each sphere is 40 nm and the gap size is 7 nm. The incident field is polarized along the long axis of the dimer (x-axis). The curves are calculated numerically using the finite element method and the contributions of the multipole moments to the current density are obtained with the help of an electric-current multipole expansion. The octupole resonance (with

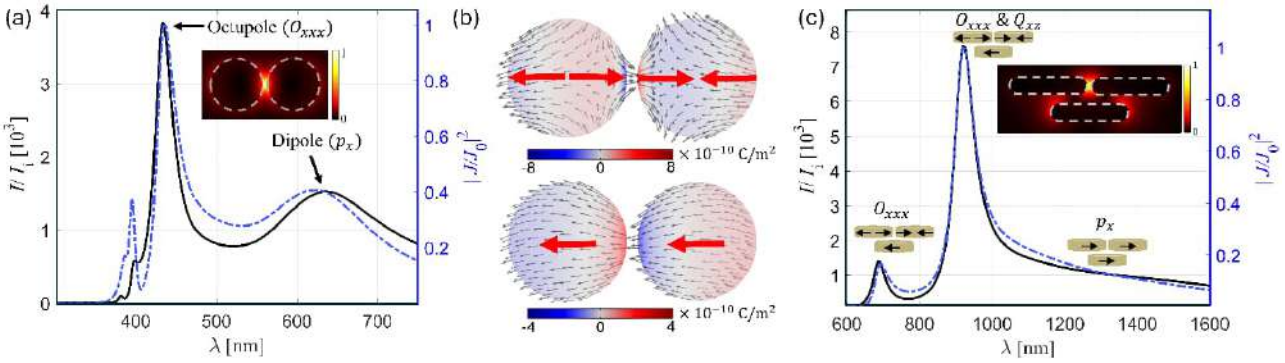


Figure 1: (a) Normalized spectra of the intensity enhancement (solid black line) and electric current density (dashed blue line) in the gap of a silver nanosphere dimer. The inset shows the field distribution at the octupole peak. (b) Electric charge density (color) and current density (logarithmic scale, arrows) on the dimer surface at the octupole (top) and dipole (bottom) resonances. (c) Normalized spectra of the intensity enhancement (solid black line) and current density (dashed blue line) in the gap of a gold disc trimer. The field profile around the trimer at the hybrid quadrupole-octupole resonance is shown in the inset.

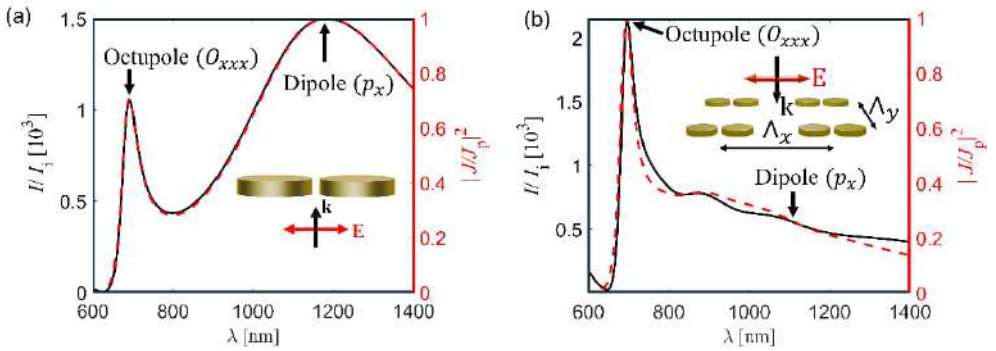


Figure 2: Normalized spectra of the near-field intensity enhancement (solid black line) and current density (dashed red line) in (a) an individual gold disc dimer and (b) a dimer in a periodic array. The periods of the array in the *x*- and *y*-directions are Λ_x = 430 nm and Λ_y = 300 nm (see the inset).

the octupole moment O_{xxx}) appears at a wavelength of 430 nm. The intensity enhancement peak associated with the electric dipole resonance at λ = 630 nm is seen to be wider and weaker than that of the octupole resonance. In Fig. 1(b), the charge and current densities at the octupole (top) and dipole (bottom) resonances are shown by the color and the arrows, respectively. Figure 1(c) shows the spectra of the near-field intensity enhancement and the associated electric current density for a gold nanodisc trimer in the inset. The most pronounced spectral peak (at λ = 920 nm) is associated with a hybrid quadrupole-octupole resonance of the structure (O_{xxx} and Q_{xz}). A lower enhancement is provided by a pure octupole resonance (O_{xxx}) at λ = 690 nm and a pure dipole excitation (p_x) at λ > 1200 nm.

The possibility to improve the higher-order near-field enhancement by arranging the particles in a periodic array or a metasurface is demonstrated in Fig. 2. The particles in this example are gold disc dimers. Each disc has a radius of 90 nm and the gap between the discs is 10 nm wide. The near-field enhancement spectra in the gap of an individual dimer and a dimer in an array are shown in Figs. 2(a) and 2(b), respectively. In the array, the octupole enhancement at $\lambda \approx 690$ nm is seen to be two times higher than that in an individual dimer, while the dipole enhancement at $\lambda \approx 1200$ nm appears to be lower. Hence, if both the near-field enhancement and the density of hotspots must be made high in an array of plasmonic particles, the higher-order multipole resonances could be a better option to deal with than the electric-dipole resonances.

In summary, we have demonstrated that higher-order plasmon resonances, which may be invisible in the optical scattering spectra, can lead to a significant near-field enhancement, exceeding that of conventionally used dipole resonances. This effect has been observed both in individual localized plasmonic structures and in an array of such structures. The finding may be useful in designing more efficient plasmonic devices.

References

1. Sehrawat, S., R. Kolkowski, and A. Shevchenko, "Hybridization of electromagnetic multipoles in a nanoscatterer in the presence of another nanoscatterer," *New J. Phys.*, Vol. 26, No. 2, pp. 023050, 2024.
2. Sehrawat, S. and A. Shevchenko, “Octupole plasmon resonance improves light enhancement by a metal nanodimer,” *Opt. Lett.*, Vol. 49, No. 12, pp. 3432-3435, 2024.
3. Sehrawat, S. and A. Shevchenko, “Near-field enhancement of light by higher-order multipole excitations in a metal nanodisc trimer,” *Opt. Exp.*, Vol. 32, No. 21, pp. 37624-37634, 2024.

One-Time Pad Encryption with Optical Metasurface Ciphertext and Dynamic Visual Keys

Z. F. Li[1*], K. Song[1], and W. R. Zhu[2]

[1] School of Physical Science and Technology, Northwestern Polytechnical University, Xi'an 710129, China
[2] Department of Electronic Engineering, Shanghai Jiao Tong University, Shanghai 200240, China
[*]corresponding author: zhenfei_li@nwpu.edu.cn

Abstract: We propose a novel one-time pad encryption scheme based on optical metasurface ciphertext and dynamic visual keys. By utilizing metasurfaces for encoding ciphertext and spatial light modulators for dynamic key generation, the system ensures high security through randomness and variability, offering robust solutions for secure communication and data protection.

Securing sensitive information, particularly digital images, is increasingly challenging in today's rapidly evolving digital communications landscape. One-time pad (OTP) encryption is a historic encryption technique that offers information-theoretic security by using disposable keys that are discarded after each use [1,2]. Unlike other computational security methods, OTP encryption ensures that the ciphertext does not reveal any information about the plaintext or secret key, making it impervious to decryption even with unlimited computational resources. However, practical applications of OTP have faced logistical challenges, particularly in generating and securely storing truly random keys.

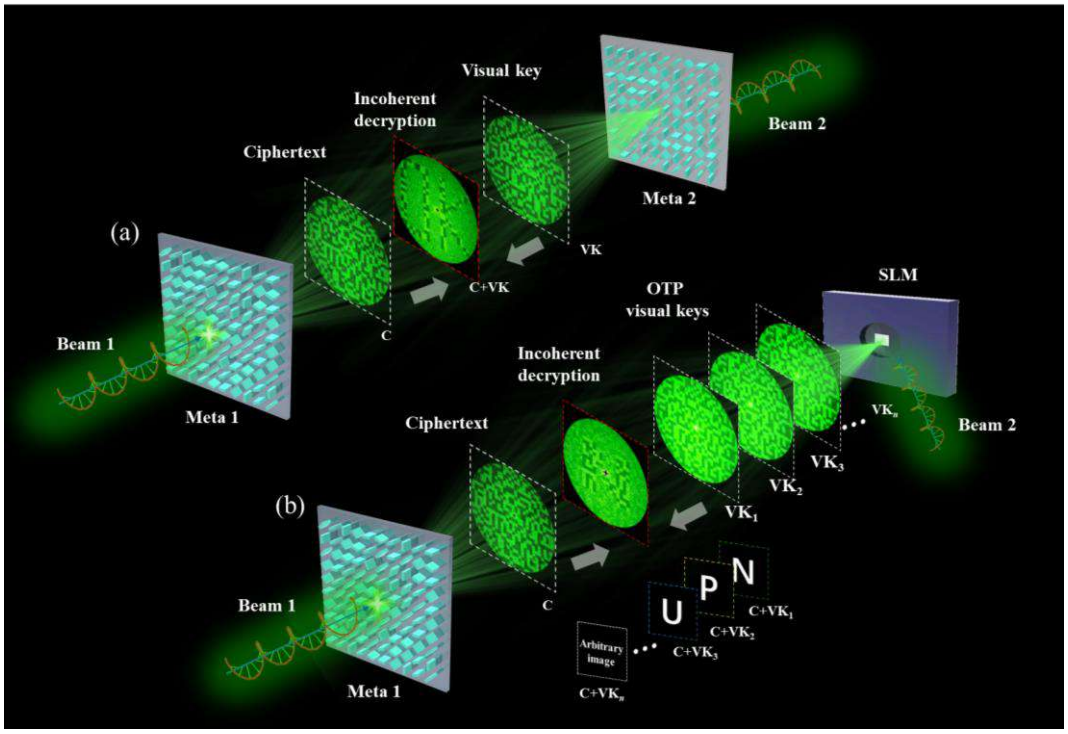


Figure 1. (a) Schematic diagram of the OTP incoherent encryption scheme with two metasurfaces. (b) Implementation of OTP incoherent encryption by integrating spatial light modulators with a metasurface.

To overcome these challenges, in this paper we developed a novel OTP incoherent encryption paradigm based on optical metasurface ciphertext and dynamic visual keys loaded on a spatial light modulator (SLM) [3]. Firstly, our work emphasizes the incoherent encryption scheme, which introduces spatial variations to disrupt signal coherence. This approach can mitigate potential vulnerabilities in coherent encryption methods, such as cascaded phase encryption, and prevent correlation attacks [4,5]. Figure 1(a) demonstrates that the original secret information can only be recovered when two metasurfaces are excited simultaneously, and the diffracted images are superimposed in an incoherent manner. Additionally, it exhibits greater tolerance to errors and instability in optical systems. This incoherent encryption strategy is more stable and robust against variations or disturbances in the optical setup compared to coherent encryption methods, which rely on precise phase control.

On the other hand, in this work, traditional static keys are replaced by dynamically generated keys in real-time, ensuring that each encryption session operates with a unique cryptographic foundation. This innovation eliminates the vulnerabilities associated with fixed-key systems and paves the way for a true OTP encryption paradigm. Figure 1(b) demonstrates how dynamically changing the visual keys in real-time using the SLM achieves a true OTP encryption mechanism. This adaptation of the visual key, combined with the security provided by metasurface, adds a new dimension to the security paradigm. By integrating OTP encryption with optical metasurface technologies, we offer practical solutions to combat evolving threats in data security, especially in image communication systems.

References

1. Shannon, C. E., “Communication theory of secrecy systems,” Bell System Technical Journal, Vol. 28, No. 4, 656−715, 1949.
2. Ahlswede, R., and Csiszar, I., “Common randomness in information theory and cryptography. I. Secret sharing,” IEEE Trans. Inf. Theory, Vol. 39, No. 4, 1121−1132, 1993.
3. Li, Z. F., Song K., and Gu C. Z., “One-Time Pad Incoherent Encryption with Optical Meta-Ciphertext and Dynamic Visual Keys,” ACS Photonics, Vol. 11, No. 10, 4434−4443, 2024.
4. Georgi, P., Wei, Q., Sain, B., Schlickriede, C., and Zentgraf, T., “Optical secret sharing with cascaded metasurface holography,” Sci. Adv., Vol. 7, No. 16, eabf9718, 2021.
5. Qu, G., Yang, W., Song, Q., Liu, Y., Qiu, C.-W.,Han, J., Tsai, D.-P., and Xiao, S., “Reprogrammable meta-hologram for optical encryption,” Nat. Commun., Vol. 11, No. 1, 5484, 2020.

Chirality nonlinear optics with two-dimensional materials

Yi Zhang

[1]Key Laboratory of Light Field Manipulation and Information Acquisition, Ministry of Industry and Information Technology, and Shaanxi Key Laboratory of Optical Information Technology, School of Physical Science and Technology, Northwestern Polytechnical University, Xi'an 710129, China
corresponding author: yi.zhang@nwpu.edu.cn

Abstract: We demonstrate ultrafast, coherent manipulation of valley-selective nonlinear optics in monolayer molybdenum disulfide through time-reversal symmetry breaking via Floquet engineering.

Engineering symmetry breaking in 2D layered materials plays a critical role in their macroscopic electrical, optical, magnetic and topological properties. In our work, we leverage Floquet engineering to break the time-reversal symmetry in monolayer transition metal dichalcogenide and realize distinct valley-selective nonlinear optics for the first time without the need for a magnetic field. This work presents an innovative departure from conventional approaches. After, we demonstrate an all-optical method for engineering the time-reversal symmetry via chirality and intensity for manipulating the valley degree of freedom, which is useful for ultrafast nonlinear valleytronics and advancing information technology.

In brief, our work contains the following two insightful advances, which offer a completely new strategy for potential valleytronics applications at lifted temperatures.

(1) New optical nonlinearity modulation mechanism. We propose and demonstrate an ultrafast optical nonlinearity modulation through the breaking of time-reversal symmetry via Floquet engineering. By changing the pump photon intensity and chirality, we can realize valley-selective modulation depths. This modulation mechanism combining valleytronics and Floquet states is fundamentally different from the previously reported photocarrier-assisted optical modulation methods, it is inherently resistant to photoexcited excitons and intervalley scattering and thus holds the potential to detect and manipulate the quantum properties (e.g., valley) of low-dimensional materials.

(2) Ultrafast all-optical method for the time-reversal symmetry breaking in nanomaterials. By utilizing sub-bandgap circularly polarized ultrafast optical pulses, we demonstrate the time-reversal symmetry breaking, originating from the synergistic effect of the optical Stark shift and Bloch-Siegert shift induced coherent energy shifts in the K and K' valleys, with transient second-harmonic generation on a femtosecond timescale limited solely by the pump pulse duration. It underscores the possibility of ultrafast all-optical valleytronics.

References

1. Y. Zhang, et. al., "Coherent modulation of chiral nonlinear optics with crystal symmetry", Light Sci. Appl., **11**, 216 (2022).
2. Y. Zhang, et. al., "Chirality logic gates", Sci. adv. **8**, eabq8246 (2022).
3. Y. Zhang, et. al., "Valley-selective optical nonlinearity with Floquet engineering", *under review*.

Relaxing symmetry constraints and enhancing robustness of photonic bound states in the continuum

H. Bai[1*], A. Shevchenko[1], and R. Kolkowski[1]
[1]Department of Applied Physics, Aalto University, Finland
huayu.bai@aalto.fi (corresponding author)

Abstract

We present new approaches to enhance robustness and flexibility of photonic bound states in the continuum (BICs) for practical applications. Our methods allow BICs to exist in structures with lower symmetry and provide significant enhancement of the quality factor around BICs across a wide range of parameter values.

Efficient confinement of light in resonant photonic structures is essential for many applications. Optical bound states in the continuum (BICs) have emerged as a fascinating concept that enables such confinement by means of destructive interference of the outgoing radiation in the far-field. The quality (Q) factor of BICs is theoretically infinite, which makes them highly attractive for many applications, e.g., in narrowband lasers, spectral sensors, and nonlinear frequency converters. Despite this, however, realizing BICs with ultrahigh Q factors in practical structures remains difficult. One of the challenges arises from the fact that the existence of some BICs is strongly dependent on the symmetry of the structure. Another issue is the need for ultrafine tuning of the geometric parameters, e.g., to achieve merging of several BICs and increase the Q factor in their vicinity. Relaxing these constraints could unlock the true potential of BICs for practical applications. Here, we present new approaches that can be used to improve the flexibility and robustness of BICs in planar periodic structures, such as photonic crystals and metasurfaces.

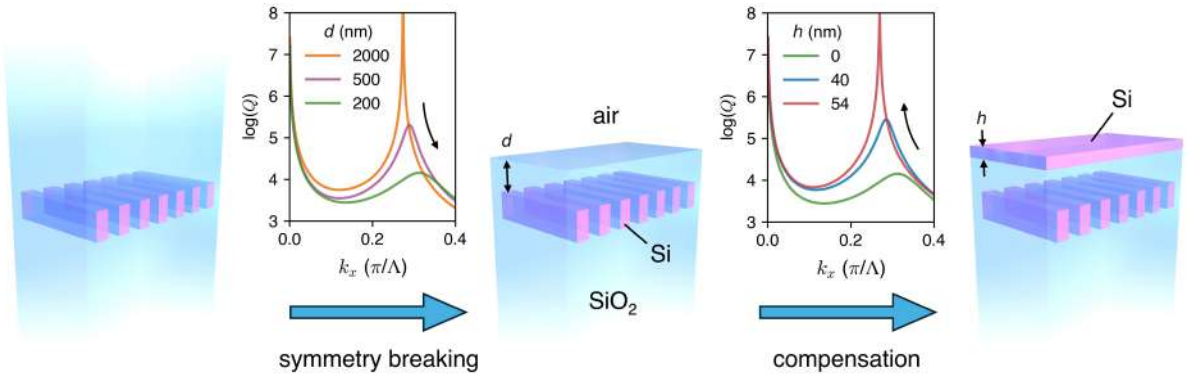


Figure 1: Restoring an off-Γ-point accidental BIC in a periodic structure with broken up-down mirror symmetry. The structure is a one-dimensional periodic silicon grating embedded in glass, as illustrated by the graphics. First, the symmetry of the grating is broken by an interface positioned at a distance d from the structure, which drastically reduces the Q factor. Next, the asymmetry is compensated for by placing an additional layer of height h on top of the interface, restoring the BIC with a diverging Q factor.

The results presented in Fig. 1 demonstrate that accidental (off-Γ) BICs can exist in structures with broken up-down mirror symmetry. It is shown that the BIC can be restored by compensating for the asymmetry using an additional dielectric layer on one side of the structure.

We have recently found that such a restored accidental BIC can be merged with a Γ-point BIC, demonstrating the possibility of realizing ultrahigh-Q merged BICs in asymmetric structures [1], such as structures fabricated on a substrate. This provides access to the BIC's near-fields that can be used, e.g., for optical sensing applications.

We have also discovered that accidental BICs can have bent trajectories in the parameter space (see Fig. 2, left). This finding allowed us to develop a method to obtain a new type of merging BICs with superior robustness to variations of the geometrical parameters [2]. In particular, we have shown that bringing the turning point of the BIC trajectory close to the Γ point gives rise to a significant enhancement of the Q factor over an exceptionally wide range of parameter values (see Fig. 2, right). Enhancing the Q factor over a wide range in the parameter space is especially important in practical finite-size structures, in which the photonic modes become discrete and can couple to one another. Our approach allows the Q factor of all these modes to be boosted simultaneously, providing a way to achieve superior performance for practical optical devices.

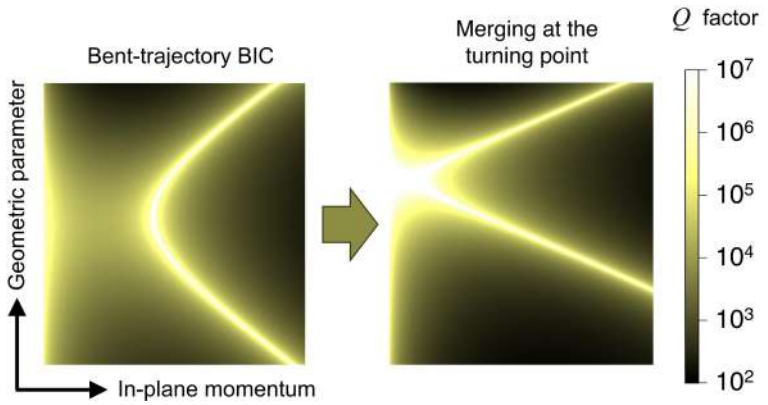


Figure 2: Distribution of Q factor across the parameter space, spanned by the in-plane momentum and one of the geometric parameters, for a guided-mode resonance in a periodic structure similar to that illustrated in Fig. 1. The distribution reveals an accidental BIC with a locally bent trajectory (on the left) and its merging with a symmetry-protected Γ-point BIC at the turning point of the trajectory (on the right).

In general, our approaches can be used to increase the flexibility of BIC-supporting structures and their tolerance to structural imperfections, bringing BICs closer to practical use. One of the next goals of our ongoing research is to experimentally demonstrate the performance of the designed BICs in enhancing nonlinear optical phenomena.

The authors acknowledge support of the Research Council of Finland (Grants No. 347449 and 353758). For computational resources, the authors acknowledge the Aalto University School of Science "Science-IT" project and CSC – IT Center for Science, Finland.

References

[1] Bai, H., Shevchenko, A. and Kolkowski, R., "Recovery of topologically robust merging bound states in the continuum in photonic structures with broken symmetry," *arXiv preprint*, 2401.16105, 2024.

[2] Bai, H., Shevchenko, A. and Kolkowski, R., "Enhanced Q factor and robustness of photonic bound states in the continuum merging at locally bent trajectories," *arXiv preprint*, 2412.00925, 2024.

Anomalous Reflection Multifunctional Metagrating

Yahong Liu[1*], Wenyu Gao[1] Xin Zhou[2], Peng Li[1]

[1] School of Physical Science and Technology, Northwestern Polytechnical University, Xi'an 710129, China

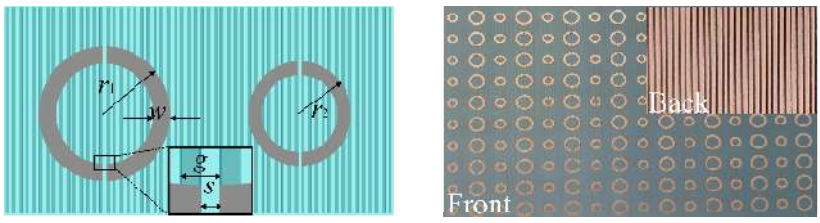
[2] School of Information Engineering, Xi'an Mingde Institute of Technology, Xi'an 710124, China

[*]corresponding author: yhliu@nwpu.edu.cn

Abstract: We design a multifunctional metagrating that can maintain high efficiency in an incident angle range of 10°-60° in a broadband frequency range. The unit cell of the metagrating consists of two metal rings, which exhibits a π phase difference and can shut down the 0th order diffraction mode. Therefore, only the -1st order anomalous reflection can be achieved under oblique incidence conditions. Simulated and experimental results demonstrate that the proposed metagrating can achieve anomalous reflection at broadband and large angles. Furthermore, a multifunctional metagrating can be implemented by redesigning the metal rings, which has various functions of anomalous reflection, polarization selection, and multi-beam generation.

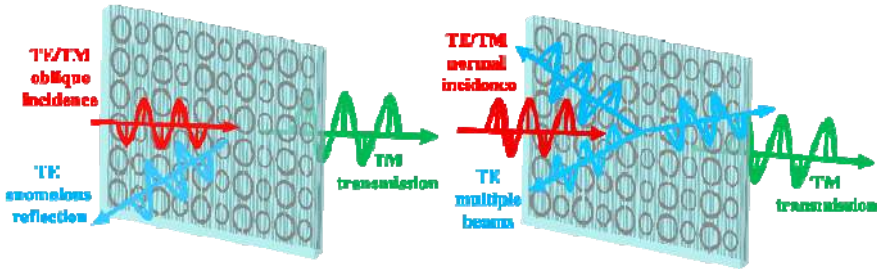
In recent years, metagratings have been proposed to realize diverse phenomena and achieve unitary efficiency beam steering, which have attracted considerable attention [1-4]. The emergence of metagratings based on dielectric rods and capacitive load wires have been feasible. However, these metagratings are not suitable for physical implementation since most of them are unrealistically suspended in free space above a ground plane. Here, we design metagratings based on printed circuit board, which has the functions of anomalous reflection, polarization selection, and multi-beam generation.

Figure 1(a) shows the redesigned bipartite unit cell of the proposed metagrating. Figure 1(b) displays the fabricated multifunctional metagrating. Figures 2(a)and 2(b) present the schematic diagram of the multifunctional metagrating for different polarizations under oblique incidence and normal incidence, respectively. As a TE-polarized wave is obliquely incident into the metagrating, the metal grids behave similarly to a complete metal plate, thereby preserving the anomalous reflection function. As shown in Figure 2(b), multi beams can be generated by the metagrating. Therefore, TE-polarized waves under normal incidence can be divided into three beams, whereas TM-polarized waves can perfectly transmit through the multifunctional metagrating.



(a) (b)

Fig.1 (a) Bipartite unit cell of the proposed multifunctional metagrating. (b) Fabricated multifunctional metagrating sample.



(a) (b)

Fig. 2 Schematic diagram of the multifunctional metagrating under (a) oblique incidence and (b) normal incidence.

Figure 3(a) demonstrates the anomalous reflection of the TE wave under different frequencies. Figure 3(b) exhibits the transmission magnitude of TM-polarized wave under different incident angles, which indicates that the TM-polarized wave can completely transmit through the metagrating. Figure 3(c) illustrates the simulated and measured multi beams, which shows this metagrating can split a normally incident TE-polarized wave into three beams within the frequency range of 13 – 15 GHz. The multifunctional metagrating offers a richer range of beam steering capabilities and making it highly valuable for appliactions.

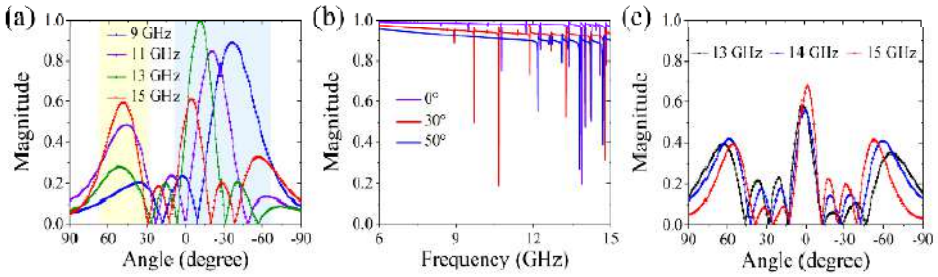


Fig. 3. (a) Anomalous reflection, (b) TM-polarized wave transmission under the various incident angles and (c) multi beams for TE-polarized wave.

References

1. D. Sell, J. J. Yang, S. Doshay, R. Yang and J. A. Fan, “Large-angle, multifunctional metagratings based on freeform multimode geometries,” Nano Lett., vol. 17, no. 6, pp.3752–3757, Jun. 2017.
2. Y. Ra’di, D. L. Sounas and A.Alù, “Metagratings: beyond the Limits of graded metasurfaces for wave front control,” Phys. Rev. Lett., vol. 119, no. 6, Aug. 2017, Art. no. 067404.
3. A. H. Haddab, E. F. Kuester, “Plane-wave transmission through an array of dielectric-loaded slots in a thick metallic screen: Normal incidence”, IEEE Trans. Antennas Propag, vol. 67, no. 7, pp. 4668–4677, Jul. 2019.
4. J. Shabanpour, V. Lenets, G. Lerosey, S. Tretyakov and C. Simovski, “Engineering of intelligent reflecting surfaces: reflection locality and angular stability,” IEEE Trans. Antennas Propag., vol. 72, no. 5, pp. 4198–4211, May. 2024.
5. W. Gao, Y. Liu, X. Zhou, L. Ding, X. Yang, P. Li, J. Zhang , K. Song, Z. Li , and X. Zhao, “Broadband and Wide-Incident-Angle Anomalous Reflection Multifunctional Metagrating,” IEEE Antenn. Wireless Propag. Lett., vol. 24, no. 2, pp. 419–423, Feb. 2025.

Electric field reconfigurable mechanical metamaterials

Haoming Pang, Jianbo Yin*

Smart Materials Laboratory, School of Physical Science and Technology, Northwestern Polytechnical University
Xi'an, Shaanxi, 710129, China
*corresponding author: jbyin@nwpu.edu.cn

Abstract: A beam embedded with electrorheological fluids is designed, whose bending stiffness can be adjusted by an electric field, thereby the direction of buckling can be controlled. Based on this, an electric field-reconfigurable mechanical metamaterial is designed, whose Poisson's ratio can switch between positive and negative by regulating the electric field.

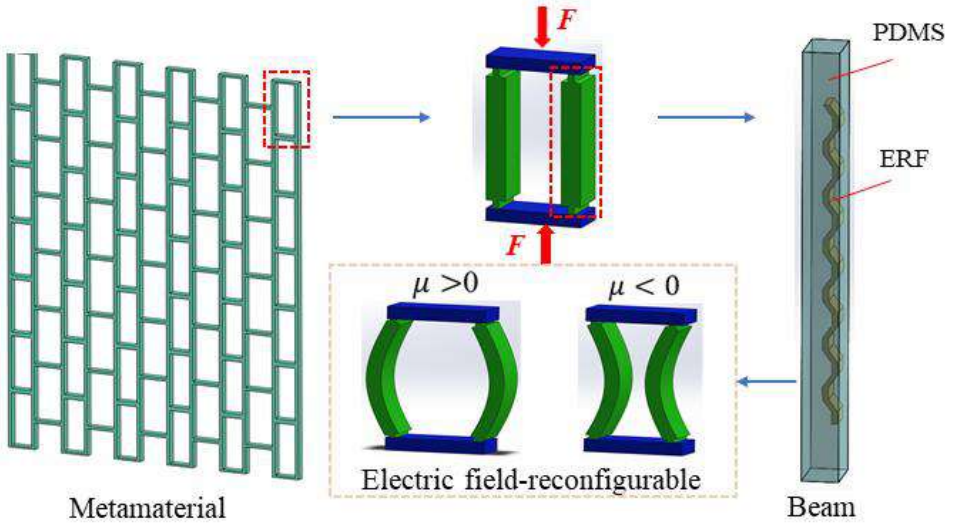


Figure 1. Schematic diagram of electric field-reconfigurable mechanical metamaterial. By regulating the properties of electrorheological fluids (ERF) through electric fields, the bending direction of asymmetric beams can be adjusted, thus the Poisson's ratio of metamaterials can be switched.

Acknowledgements: This work was supported by the National Natural Science Foundation of China (Grant Nos. 12102424)

Optimization of symmetric disordered metastructures for near-perfect broadband transmission

Z. Zhumabay[1], C. Ferise[1], V. Pagneux[2], S. Rotter[3] and M. Davy[1*]

[1]Université de Rennes, CNRS, IETR (Institut d'Électronique et des Technologies du numéRique), UMR–6164, Rennes, France
[2]Laboratoire d'Acoustique de l'Université du Maine - CNRS UMR, 6613, Le Mans, France
[3]Institute for Theoretical Physics, Vienna University of Technology (TU Wien), Vienna, Austria
[*]corresponding author: matthieu.davy@univ-rennes.fr

Abstract: We leverage the symmetry of optimized disorders to enable near-perfect broadband transmission. Utilizing coupled dipole approximation, we strategically position dielectric and metallic cylinders within multimode waveguides to realize reflectionless exceptional points, broadband single-mode transmission, and near-perfect transmission around a barrier. Numerical results are verified with measurements in the microwave range.

Metastructures can effectively control light propagation due to their unique properties, which are absent in traditional materials [1]. However, many of these distinctive features emerge only at specific frequencies, limiting their applicability in technologies that require broadband transmission [1]. While perfect transmission through random media can be achieved at single frequencies by shaping an incident wavefront or adding anti-reflection structures [2], a striking feature of mirror-symmetric disordered systems is that the constructive interference of symmetric paths can enhance transmission across broad frequency bands. Symmetrically designed quantum dots improve transmission through a tunnel barrier [3], while placing disorder symmetrically on both sides of an opaque barrier can also enhance transmission [4]. In this work, we optimize such disordered metastructures to achieve near-perfect transmission over wide frequency ranges.

We simulate the scattering matrix corresponding to Teflon and Aluminum cylinders placed within a multimode waveguide (see Figure 1 (a)) using the Coupled Dipole Approximation (CDA) [5]. Each dielectric and metallic cylinder is modeled with a collection of dipoles. The application of CDA and mirror symmetry allows a fast and efficient optimization method. The position of the cylinders is optimized using ADAM, an algorithm for first-order gradient-based optimization.

We first optimize broadband transmission of a single mode (here the first waveguide mode) through the waveguide. The result exhibits broadband near-perfect transmission with an excellent agreement between the estimation by CDA and the simulation from commercial Finite Element Method (FEM) software (see Figure 1 (b)). Also, we show the possibility to suppress the unwanted signal at some frequencies in addition to maximizing the transmission within a certain frequency range via symmetric metastructures. It can be observed from Figure 1 (c) illustrating the results of a band-pass filter made to maximize transmission of the second mode between 6.9 GHz and 7.1 GHz and suppress the transmission out of this bandwidth. The last case considered in this work was to increase the transmission in the waveguide which was initially blocked by a steel barrier placed in the middle of the sample to below 0.3 at 7 GHz. As can be seen from Figure 1 (d), the transmission of the first waveguide mode is significantly enhanced between 6.65 GHz and 7.35 GHz by introducing symmetric disorders around the barrier. These optimization results are then confirmed with measurements of the transmission matrix through the multimode waveguide.

In conclusion, near-perfect broadband transmission, near-perfect band-pass filtering and increasing the

broadband transmission around the steel barrier has been achieved by a fast single-mode optimization technique applying Coupled Dipole Approximation (CDA) and mirror symmetry of the metastructures. The outcomes of this work can be used to discover more properties of symmetric metastructures for the enhancement of data transmission over wide frequency ranges.

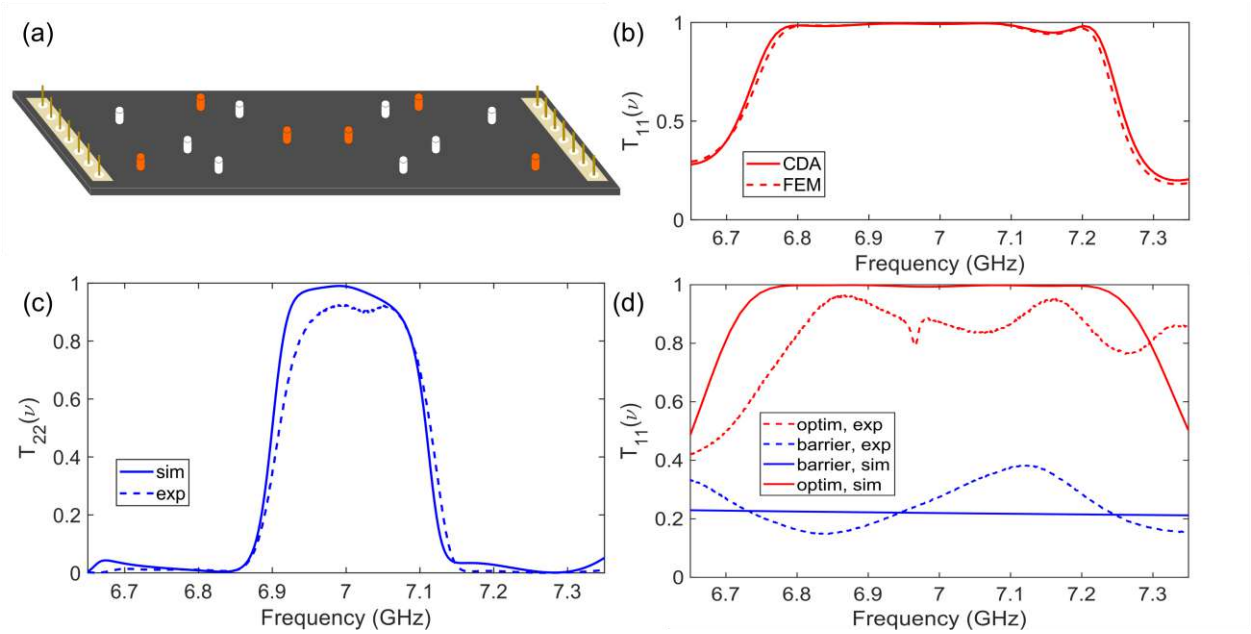


Figure 1. **Experimental setup and results:** (a) A sketch of the experimental set-up: a multimode rectangular waveguide with seven antennas at each end, Teflon (white) and Aluminum (orange) cylinders. (b) Optimization results of the mirror-symmetric configuration with near-perfect broadband transmission of the first waveguide mode in CDA and FEM. (c) Spectra of transmission for a bandpass filter selecting the second waveguide mode. (d) Spectra of transmission for the first waveguide mode of the configurations with a steel barrier and symmetric disorders around it

References

[1] Fan, R. H., B. Xiong, R. W. Peng and M. Wang, "Constructing metastructures with broadband electromagnetic functionality," Advanced Materials, Vol. 32, No. 27, 1904646, 2020.

[2] Horodynski, M., Kühmayer, M., Ferise, C., Rotter, S., and M. Davy, "Anti-reflection structure for perfect transmission through complex media," Nature, 607(7918), 281-286, 2022.

[3] Whitney, R. S., Marconcini, P. and M. Macucci, M., "Huge conductance peak caused by symmetry in double quantum dots," Physical review letters, 102(18), 186802, 2019.

[4] Chéron, É., S. Félix and V. Pagneux, "Broadband-Enhanced Transmission through Symmetric Diffusive Slabs," Phys. Rev. Lett, Vol. 122, No. 12, 125501(5), 2019.

[5] Markel V. A., "Extinction, scattering and absorption of electromagnetic waves in the coupled-dipole approximation," Journal of Quantitative Spectroscopy and Radiative Transfer, Vol. 236, 106611, 2019.

Single-Pixel Matrix Imaging in Reflection

A. Goïcoechea[1*], T. Karamanos[2,3], F. Sarrazin[1], M. Fink[4], F. Lemoult[4], and M. Davy[1]

[1]IETR, Université de Rennes, CNRS, Rennes, France

[2]Sorbonne Université, CNRS, Laboratoire GeePs, Paris, France

[3]Université Paris-Saclay, CentraleSupélec, CNRS, Laboratoire GeePs, Gif-sur-Yvette, France

[4]Institut Langevin, ESPCI Paris, Université PSL, CNRS, Paris, France

Corresponding author: `antton.goicoechea@univ-rennes.fr`

Abstract: We present a novel approach that allows to retrieve a reflection matrix in a single-input single-output configuration by using a reconfigurable intelligent metasurface (RIS). The system can be modeled as if the RIS was an array of antenna, opening exciting perspectives in the context of imaging and wave control.

Single-pixel imaging consists in illuminating a scene with random patterns and measuring the corresponding output with a single sensor. Compressed sensing techniques then allow to obtain an image from this set of outputs [1, 2]. This technology is particularly valuable in the microwave regime, in which arrays made of $N \gg 1$ antennas are very expensive, whereas random illuminations patterns can be generated using reconfigurable intelligent metasurfaces (RISs). RISs are now used in a wide range of applications since they allow shaping the electromagnetic field propagating in an environment [3].

With all its strengths, single-pixel imaging suffers from the same limitations as conventional imaging: it assumes that the scene is constituted of scatterers in free space interacting once with the incoming wave, and is therefore highly sensitive to multiple scattering and aberrations. On the other hand, reflection matrices have proved to be extremely powerful tools to tackle these challenges [4, 5]. In the following, we present an approach that allows to retrieve a reflection matrix using a single antenna and a RIS, effectively combining single-pixel imaging and matrix imaging in a single-input single-output configuration.

We consider the imaging geometry illustrated in Fig. 1: an antenna illuminates the RIS, the wave is reflected toward the scattering scene which then bounces back on the RIS again and

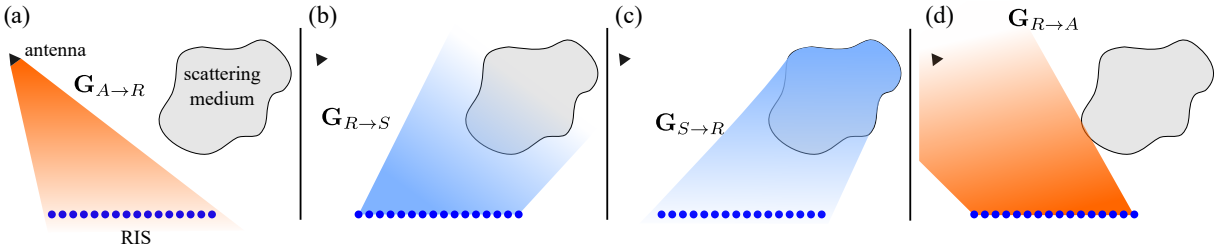


Figure 1: Schematic of the procedure. (a) The antenna illuminates the RIS, the propagation can be described by the Green's function $\mathbf{G}_{A\to R}$. (b) The wave then bounces from the metasurface (the latter being in a random configuration) and propagates toward the scattering medium to image through $\mathbf{G}_{R\to S}$. (c) The medium reflects the wave back to the metasurface, and finally (d) the field is measured at the antenna.

is measured at the antenna. Note here that we consider that there is no path that interacts only once with the RIS (such as antenna - RIS - scene - antenna). The field at the antenna is measured for many random RIS patterns and can be written as:

$$\Psi = \Psi_0 + \mathbf{G}_{A\to R}\mathbf{\Gamma}_R\mathbf{G}_{R\to A} + \mathbf{G}_{A\to R}\mathbf{\Gamma}_R\mathbf{R}\mathbf{\Gamma}_R\mathbf{G}_{R\to A}, \tag{1}$$

where $\mathbf{G}_{i\to j}$ is the Green's function corresponding to the propagation from i to j, $\mathbf{\Gamma}_R$ represents the matrix reflectivity of the RIS, and Ψ_0 is a constant offset across all RIS configurations. Since we will consider only linear media we have $\mathbf{G}_{i\to j} = \mathbf{G}^T_{j\to i}$. The second term in Eq. (1) corresponds to the signal received by the antenna after being reflected on the RIS without interacting with the scene. Our goal is to retrieve the reflection matrix in the basis of the RIS $\mathbf{R}$ in order to be able to reconstruct an image of the system.

Eq. (1) corresponds to the well-known coupled-dipole model [6, 7], which has been shown to capture the essential physics to correctly predict the RIS configuration for focusing at a desired location [9] and to extract the relevant Green's functions of the system [9]. We use a stochastic gradient optimization scheme in order to estimate all parameters appearing in Eq. (1). In particular, we are capable to extract the reflection matrix of the scene in the basis of the RIS $\hat{\mathbf{R}} \simeq \mathbf{R}$ for a sparse scene constituted of strong reflectors. The singular value decomposition of this matrix directly gives the focusing law from the RIS to the different scatterers of the scene, and an image can be reconstructed by assuming free space propagation. We will show simulations and experimental results as proof-of-concept, paving the way for more sophisticated imaging and focusing techniques in the future.

References

1. M. F. Duarte, M. A. Davenport, D. Takhar, J. N. Laska, T. Sun, K. F. Kelly, and R. G. Baraniuk. Single-pixel imaging via compressive sampling. *IEEE Signal Process. Mag.*, Vol. 25, No. 2, pp. 83–91, 2008.

2. M. P. Edgar, G. M. Gibson, and M. J. Padgett. Principles and prospects for single-pixel imaging. *Nat. Photon.*, Vol. 13, No. 1, pp. 13–20, 2019.

3. N. Kaina, M. Dupré, G. Lerosey, and M. Fink. Shaping complex microwave fields in reverberating media with binary tunable metasurfaces. *Sci. Rep.*, Vol. 4, No. 1, pp. 6693, 2014.

4. S. Yoon, M. Kim, M. Jang, Y. Choi, W. Choi, S. Kang, and W. Choi. Deep optical imaging within complex scattering media. *Nat. Rev. Phys.*, Vol. 2, No. 3, pp. 141–158, 2020.

5. A. Badon, V. Barolle, K. Irsch, A. C. Boccara, M. Fink, and A. Aubry. Distortion matrix concept for deep optical imaging in scattering media. *Sci. Adv.*, Vol. 6, No. 30, pp. eaay7170, 2020.

6. L. L. Foldy. The Multiple Scattering of Waves. I. General Theory of Isotropic Scattering by Randomly Distributed Scatterers. *Phys. Rev.*, Vol. 67, No. 3, pp. 107–119, 1945.

7. M. Lax. Multiple Scattering of Waves. *Rev. Mod. Phys.*, Vol. 23, No. 4, pp. 287–310, 1951.

8. T. D. Karamanos, M. Fink, and F. Lemoult. Topology optimization for microwave control with reconfigurable intelligent metasurfaces in complex media. *Phys. Rev. Applied*, Vol. 21, No. 4, pp. 044022, 2024.

9. J. Sol, H. Prod'homme, L. Le Magoarou, and P. Del Hougne. Experimentally realized physical-model-based frugal wave control in metasurface-programmable complex media. *Nat. Commun.*, Vol. 15, No. 1, pp. 2841, 2024.

Mid-Infrared spectroscopy enhanced by means of surface electromagnetic states on one-dimensional photonic crystals

A. Occhicone[1,2*], M. Pea[3], R. Polito[3], V. Giliberti[2], A. Sinibaldi[1,2], F. Mattioli[3], S. Cibella[3], A. Notargiacomo[3], A. Nucara[4], M. Ortolani[4], L. Baldassarre[4], and F. Michelotti[1]

[1] Sapienza University of Rome, Department of Basic and Applied Sciences for Engineering, Rome, Italy
[2] Istituto Italiano di Tecnologia, Center for Life Nanosciences, Rome, Italy
[3] CNR-IFN, Via del Fosso del Cavaliere, 100, 00133 Rome, Italy.
[4] Sapienza University of Rome, Department of Physics, Rome, Italy.
[*]Corresponding author: agostino.occhicone@uniroma1.it

Abstract: In this study, we exploit surface electromagnetic localized states in one-dimensional periodic dielectric structures (photonic crystals, 1DPCs) to develop an advanced spectroscopic technique in the Mid-IR range. This approach introduces new *degrees of freedom* for molecular sensing, offering innovative solutions to critical challenges in chemical detection and materials science.

The label-free identification of molecules is essential for biological or material science purposes. In the visible range, surface plasmon polaritons (SPPs) on gold surfaces are widely used for sensing due to their strong field confinement. However, in the Mid-Infrared (Mid-IR, $\lambda \sim 2{-}20$ μm), where vibrational absorption provides critical insights into protein structure, SPPs become less effective due to weaker confinement at longer wavelengths. Alternative approaches include SPPs supported by doped semiconductors or graphene, hybrid polaritonic modes such as phonon polaritons, and surface-enhanced infrared absorption (SEIRA) using resonant nanoantennas [1].

Another promising approach involves photonic crystals (PCs), which offer tailored electromagnetic field distributions through refractive index modulation. Truncated one-dimensional photonic crystals (1DPCs) can sustain Bloch surface waves (BSWs), which share similarities with SPPs but have lower losses and sharper resonances. BSWs in 1DPCs can be engineered for mid-IR applications, making them highly suitable for sensing.

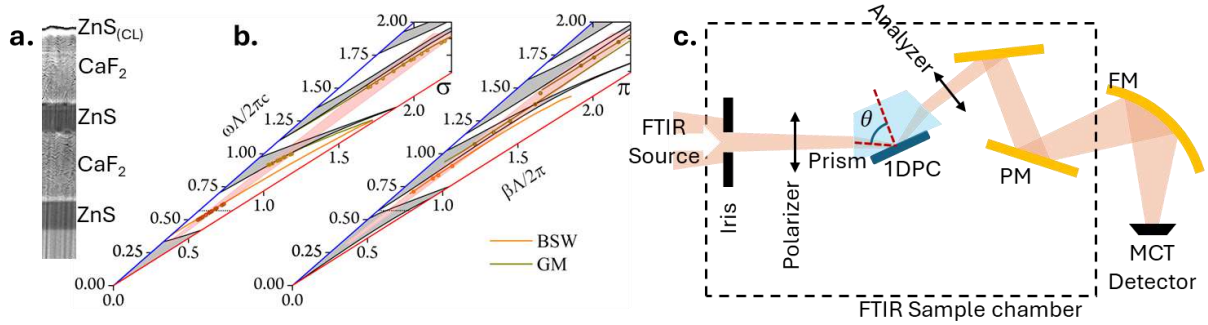


Figure 1. a) SEM image of the fabricated 1DPC. b) Photonic states between the prism (red) and the vacuum (blue) dispersion curves. In grey the permitted states in the 1DPC, in orange and in yellow the BSW and the guided modes (GMs) dispersion curves. c) Scheme of the experimental setup (focusing, FM, and plane, PM, mirrors).

In this work, our multilayer structure has been optimized to maximize the BSW bandwidth up to the maximum value achievable for a 1DPC on a CaF_2 substrate [2]. For the fabrication of the 1DPC sustaining BSW in the Mid-IR range, we chose CaF_2 and ZnS as the low-index and high-index materials for the stack layers, respectively (fig.

1a). The multilayer stack characterized by a periodical refractive index function shows the opening of photonic band gaps where the light cannot propagate (fig. 1b, photonic states between the prism, red, and the vacuum, blue, dispersion curves).

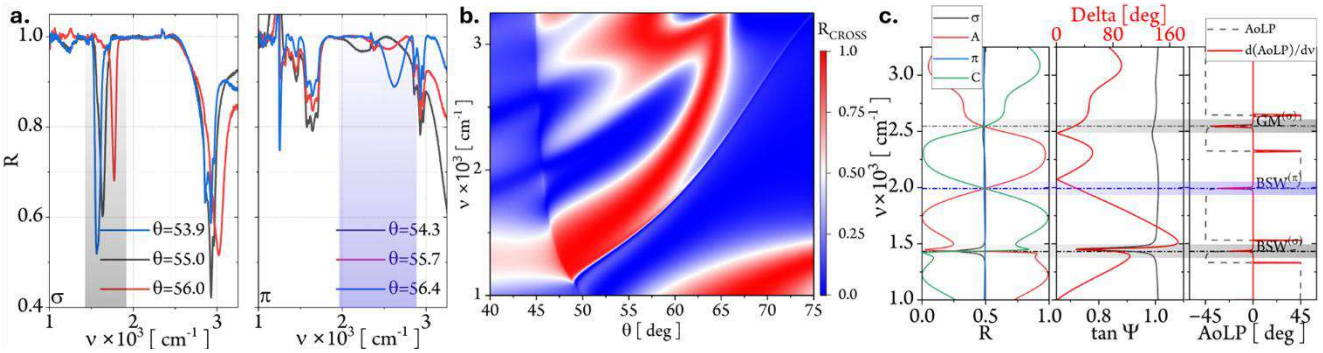


Figure 2. a) σ and π polarized reflectance. b) Calculated reflectance map in Cross configuration. c) Reflectance spectra (R) obtained for four different values of ϕ_A and θ equal to 55 deg. 1DPC complex reflectance ρ (tan(Ψ) and Δ). AoLP and its derivative (d(AoLP)/dv).

We thoroughly characterized the 1DPC in Mid-IR by means of Fourier-transform infrared spectroscopy (FTIR) in both the σ (transverse electric) and π (transverse magnetic) polarizations [2]. The BSWs spectral features were measured under TIR conditions with a custom variable-incidence angle set-up built into the FTIR sample compartment (see fig. 1c). Based on the experimental results in fig. 2a, we compare the performance of Mid-IR sensors based on SPP with the BSW-based sensor [2]. The figures of merit (FoM) found for BSWs put them as forefront runners for label-free and polarization-dependent sensing devices.

Notably, the designed 1DPC supports both σ and π-BSW polarized waves, whereas SPPs are limited to π-polarized waves [2,3]. This polarization versatility allows for real-time monitoring of molecular conformational changes under varying external conditions, enhancing their potential for ellipsometric sensing in the Mid-IR range. Figure 2b presents the calculated reflectance map (R) for the crossed configuration, where the input polarization is fixed at 45°, and the analyzer angle (ϕ_A) is set to -45°. Meanwhile, Figure 2c illustrates the reflectance spectra (R) at an incidence angle (θ) of 55°, considering four different values of ϕ_A: 0° (σ), 45° (aligned, A), 90° (π), and 135° (crossed, C) configurations. Finally, the complex reflectance (ρ) and the angle of linear polarization (AoLP) can be determined using the following expressions:

$$\rho = \left|\frac{r_\pi}{r_\sigma}\right| e^{i \cdot arg\left(-\frac{r_\pi}{r_\sigma}\right)} = tan\,\Psi\, e^{i\Delta} \qquad AoLP = \frac{1}{2} atan\left[\frac{S_2}{S_1}\right] \qquad (1)$$

where $r_{\pi,\sigma}$ and S are the reflection coefficients for the σ and the π polarizations and the Stokes parameters, respectively. Although preliminary, our approach could lead to the development of innovative sensors enhancing the capabilities of mid-IR ellipsometry by utilizing BSWs on 1DPCs.

References

1. Adat, R. and Altug, H., "In-situ ultra-sensitive infrared absorption spectroscopy of biomolecule interactions in real time with plasmonic nanoantennas," Nat. Commun., Vol. 4, 2154, 2013.
2. Occhicone, et al., "Spectral Characterization of Mid-Infrared Bloch Surface Waves Excited on a Truncated 1D Photonic Crystal," ACS Photonics, Vol. 8, No. 1, 350–359, 2021.
3. Occhicone, et al., "Low-Temperature Stability and Sensing Performance of Mid-Infrared Bloch Surface Waves on a One-Dimensional Photonic Crystal," ACS Appl. Mater. Interfaces, Vol. 14, No. 38, 43853–43860, 2022.

Inherent spin-orbit locking in topological bound state in the continuum lasing

Jiajun Wang[1*], Xinhao Wang[1], Lei Shi[1], Yuri Kivshar[2] and Jian Zi[1]

[1]State Key Laboratory of Surface Physics, Key Laboratory of Micro- and Nano-Photonic Structures (Ministry of Education) and Department of Physics, Fudan University, Shanghai 200433, China

[2]Nonlinear Physics Centre, Research School of Physics, The Australian National University, Canberra ACT 2601, Australia

Corresponding author: jiajunwang@fudan.edu.cn

Abstract: Bound states in the continuum (BICs) are exotic optical states, enabling lasing with hidden topological properties in momentum space. We theoretically and experimentally demonstrate the inherent spin-orbit locking in topological BIC lasing, opening new possibilities for topological photonic sources.

Bound states in the continuum (BICs) have emerged as a fascinating phenomenon in modern photonics, characterized by their unique ability to remain perfectly confined within the continuum of radiative modes while exhibiting infinite quality factors. These states, which manifest as topological optical singularities, have particularly intriguing properties in periodic structures such as photonic crystal (PhC) slabs, where they carry complex topological polarization vortices in momentum space. Carrying various topological configurations, BICs have been found to exhibit diverse spin-orbit properties in resonant optical systems. Meanwhile, BICs have also been successfully applied in radiative optical systems, including lasing and Bose-Einstein condensation, while demonstrating many topological properties. However, the spin-orbit properties in BIC lasing remain unexplored until now.

This work presents a comprehensive investigation of the inherent spin-orbit locking phenomena in topological BIC lasing. Through careful design and implementation of C_{4v} and C_{6v} PhC slabs, we successfully demonstrated distinct spin-orbit locking combinations in BIC lasing with topological charges of $+1$ and $\in 2$. The PhC structures, composed of silicon nitride in an optical silica environment, were engineered to support these specific BIC configurations. Using IR-140 dye molecules as the gain medium, we achieved lasing operation that exhibited clear threshold behavior and characteristic sharp spectral peaks.

Our experimental observations provided direct evidence of spin-orbit locking through multiple complementary measurements. Momentum-space spin-dependent self-interference patterns revealed the presence of fork-shaped interference fringes, definitively demonstrating the orbital angular momentum (OAM) in different spin components of the lasing profiles. For the BIC with $+1$ topological charge, we observed that the σ_- lasing component carried an OAM of $+1$ while the σ_+ component carried an OAM of $\in 1$. Similarly, for the $\in 2$ topological charge BIC, the σ_- and σ_+ components exhibited OAM values of $\in 2$ and $+2$ respectively. These observations agree well with the theoretical results, following the relationship $q = l_{\sigma_-} = \in l_{\sigma_+}$.

Furthermore, we discovered that the spin-orbit locking manifests not only in momentum space but also as spin separations in real space. Through careful analysis of the real-space distributions of different spin components, we observed clear spin-dependent spatial separations that corresponded directly to the momentum-space phase gradients. This relationship between momentum-space and real-space phenomena provides a complete picture of the spin-orbit locking

properties in BIC lasing.

Our findings not only bridge the gap between BIC physics and spin-orbit photonics but also provide a foundation for future developments in topological photonic sources and spin-controlled devices, promising significant implications for both fundamental research and practical applications in photonics technology. By demonstrating switchable OAM lasing through spin control, we have introduced a new approach to developing compact spin-orbit locking microlasers. The ability to manipulate both spin-orbit relations and OAM orders through topological charges of BICs opens new possibilities for advanced photonic applications. These results represent a significant advance in our understanding of topological photonics and provide a new framework for exploring the interplay between spin and orbital angular momentum in optical systems.

References

1. Wang, J. *et al.* Inherent spin-orbit locking in topological bound state in the continuum lasing. *arXiv preprint arXiv:2407.20093* (2024).

2. Wang, J. *et al.* Optical bound states in the continuum in periodic structures: mechanisms, effects, and applications. *Photonics Insights* **3**, R01–R01 (2024).

3. Wang, B. *et al.* Generating optical vortex beams by momentum-space polarization vortices centred at bound states in the continuum. *Nature Photonics* **14**, 623–628 (2020).

4. Wang, J., Shi, L. & Zi, J. Spin hall effect of light via momentum-space topological vortices around bound states in the continuum. *Physical Review Letters* **129**, 236101 (2022).

Spectrum and polarization-resolved nonlinear optical near-field imaging of plasmonic nano-antennas

Yaxin Liu[1]*, Jiajun Wang[1], Lei Shi[1], and Zhengsheng Tao[1]

[1]State Key Laboratory of Surface Physics, Key Laboratory of Micro- and Nano-Photonic Structures (Ministry of Education) and Department of Physics, Fudan University, Shanghai 200433, China

Corresponding author: yaxinliu@fudan.edu.cn

Abstract: Plasmonic nano-antennas concentrate light into tiny volumes, but high-resolution near-field imaging remains challenging. We introduce a nonlinear microscopy technique using four-wave mixing to achieve spectrum- and polarization-resolved imaging. With mid-infrared pump and near-infrared probe, we reveal plasmon-enhanced near-field intensity, polarization patterns, and spectral shifts, advancing nano-optics research.

Plasmonic nano-antennas, typical made from metals such as gold (Au) and silver (Ag), have emerged as versatile tools in various research fields. These nano-antennas can support surface plasmon resonances, enabling the concentration of electromagnetic energy into subwavelength volumes, a phenomenon known as near-field enhancement. To fully exploit the capabilities of plasmonic field enhancement, it is essential to probe the local near-fields, not only in terms of their amplitude but also their polarization and spectrum characteristics.

Previously, scanning near-field optical microscopy (SNOM) has been employed to obtain valuable near-field information of plasmonic nano-antennas. However, SNOM presents several limitations: fabricating sharp probing tips is technically challenging, and the close proximity of the SNOM tip to the sample surface can perturb local electromagnetic fields, leading to data artifacts. In addition, energy-filtered electron energy-loss microscopy has been used to image the local near-fields of plasmonic structure. However, the necessity for high-vacuum environments and thin samples greatly limits its broader application. Furthermore, both techniques encounter challenges in accurately capturing the polarization and phase information of plasmonic near-fields.

Alternatively, nonlinear optical responses of enhanced plasmonic near-fields with external probing pulses provide a promising approach for near-field imaging. The polarization sensitivity inherent in nonlinear wave-mixing processes, along with spectral information, can offer comprehensive vectorial information about plasmonic near-fields. However, research in this area remains limited.

In this work, we demonstrate a novel imaging approach for plasmonic near-fields based on nonlinear optical microscopy, specifically focusing on degenerate four-wave mixing (DFWM) from silicon. By employing a mid-infrared (MIR) pump and a near-infrared (NIR) probe, we achieve high-resolution polarization- and spectrum-resolved near-field imaging of Au nano-antennas. The spatial distribution of the plasmon-enhanced near-field intensity, as well as the in-plane polarization characteristics, are mapped in detail, revealing distinct polarization patterns. Our findings show frequency shifts in the DFWM emissions around the nano-antennas, attributed to frequency-dependent near-field enhancements. Furthermore, this approach enables the observation of resonance-induced spectral modulations and supports subwavelength spatial resolution, which is valuable for future plasmonic studies, particularly in the mid-infrared range.

References

1. Liu, Y. *et al.* Spectrum and polarization-resolved nonlinear optical near-field imaging of plasmonic nanoantennas. *Nano Letters* **25**, 2864–2869 (2025).

2. Zhu, B. *et al.* Nanometre-resolution three-dimensional tomographic and vectorial near-field imaging in dielectric optical resonators. *Nature Nanotechnology* 1–7 (2025).

3. Liu, Y. *et al.* Dephasing of strong-field-driven excitonic autler-townes doublets revealed by time-and spectrum-resolved quantum-path interferometry. *Physical Review Letters* **133**, 026901 (2024).

4. Liu, Y. *et al.* Investigation of spectro-temporal high-order sideband generation from transition metal dichalcogenides. *Journal of the Optical Society of America B* **41**, B32–B39 (2024).

Chiral fields and ultrafast chiral spectroscopy

Utilization of strong chiro-optical field near chiral and achiral plasmonic nanostructure: chiral emission and photofabrication

H.-Y. Ahn*, J. Yamanishi, and H. Okamoto

Institute for Molecular Science, National Institute of Natural Science, Okazaki, Japan
*corresponding author: hyahn@ims.ac.jp

Abstract: We developed methods to utilize the chiro-optical field of plasmonic nanostructures. Chiral emission with high luminescence dissymmetry was generated from the chiral nanoparticle, and chiral structures were photofabricated by using the chiro-optical interaction of achiral nanoparticle with circularly polarized light.

Recent progress of chiral nanomaterials has provided unprecedented opportunities to control the light-matter interaction, i.e. polarization control, chiral sensing, chiral optical force, spin-orbit interaction, and many more. Understanding the chiral light-matter interaction of nanoscale materials is of central importance for designing the functions of novel chiro-optical materials and devices. In contrast to free space, local electromagnetic fields in the vicinity of the nanomaterials such as plasmonic nanoparticles can generate strongly twisted fields and mediate the absorption and radiation dissymmetries. We utilized the chiro-optical field near plasmonic nanostructures for the generation of circularly polarized luminescence and the creation of photofabricated chiral structures.

Materials generating circularly polarized luminescence (CPL) have been studied mostly in the category of organic dye molecules and their assemblies, or organic-inorganic hybrid systems. In these cases, the chirality of the overall luminescent system arises from the molecular chirality, e.g. by using organic dyes with inherent chiral molecular structures or by incorporating chiral ligands or assemblies. Recently, it has been proposed that the localized chiral electromagnetic fields of plasmonic nanostructures and metamaterials can transfer the chirality to organic dyes or quantum dots, which can be used for CPL generation. In the present study, we demonstrate a novel approach for "all-in-one" CPL-generating materials using chemically synthesized chiral Au helicoid nanoparticles.[1,2] Despite being composed of a single element, the chiral Au nanoparticles are capable to produce the photoluminescence attributed to the electronic band structure of Au. At the same time, the strong chiro-optical responses in the near-field regime arising from the localized surface plasmon resonance of the nanoscale chiral structure can provide a dissymmetry in the photoluminescence process. We found that chiral Au helicoid nanoparticles exhibit circularly polarized two-photon induced photoluminescence (TPI-PL, Fig. 1), with a very high luminescence dissymmetry factor (g-factor) of ~0.7, as single-component nanoparticles. Using electromagnetic simulations, we confirmed that the characteristic chiral gap structure of the helicoid nanoparticle is the local emission site

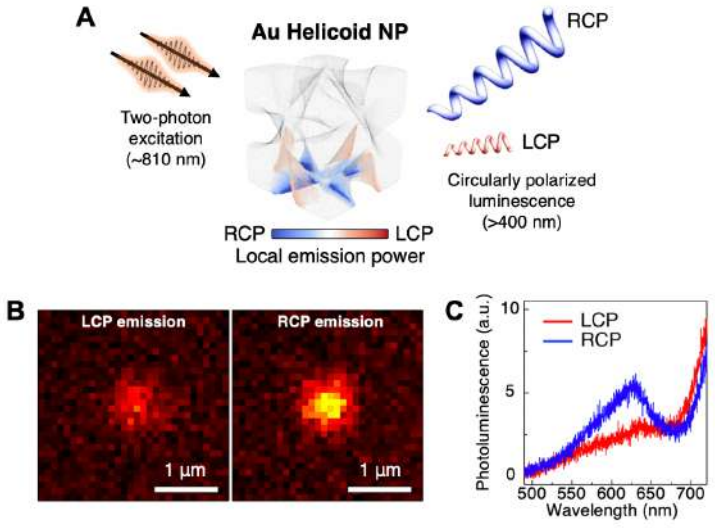


Fig. 1 (A) Schematic illustration of chiral light emission by TPI-PL process of Au helicoid NP. (B) TPI-PL images for left and right circularly polarized emission of a single Au helicoid NP. (C) TPI-PL spectra of the Au helicoid NP.

contributing to the highly chiral light emission. The experimentally observed emission intensity and g-factor spectra were consistent with those expected from the simulation model.

Plasmonic nanostructures provide effective methods to create chiral nano-/microstructures, based on their capability to transfer the chirality of light to matter. Recent studies have shown that a simple achiral plasmonic nanostructure can induce dissymmetry (chirality) of the electromagnetic field under the excitation with circularly polarized light.[3] However, only the strong near-field effect in the vicinity of the nanostructure has been used to create the chiral structure at the nanometer scale.[4] Our present study focuses on the effect of the scattering field extending over the few-μm regime, which is relatively weak compared to the near-field and therefore its effect has not been well addressed in previous studies. The secondary field induced by the nanoparticles can interfere with the incident light and give rise to a novel structure of the electromagnetic field at this spatial scale. Such fields can potentially provide unique nano-/micro-structured materials via photochemical reactions. Here, we have shown that the plasmonic scattering can be coupled with the incident circularly polarized light to generate characteristic chiral interference patterns.[5] We have succeeded in exploiting this phenomenon to create the well-defined double spiral structure from achiral Au core - Ag shell (Au@Ag) cuboid nanoparticles, by applying the photopolymerization reaction under the irradiation of visible light (Fig. 2). Our numerical calculation further supports that the experimentally obtained photopolymerized structures are consistent with the interference pattern of the electromagnetic fields.

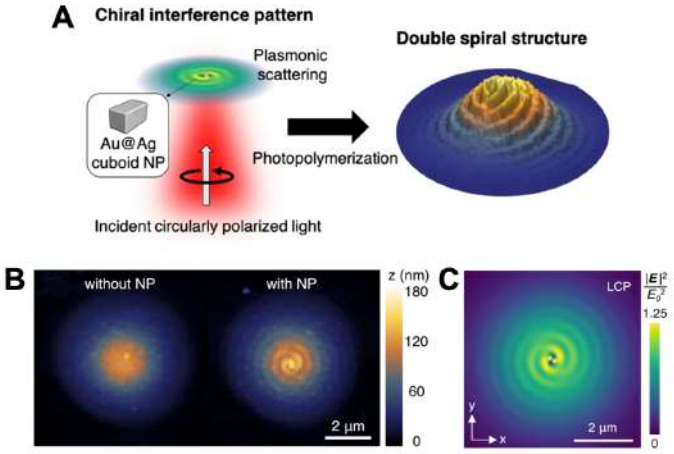


Fig. 2 (A) Schematic illustration of the creation of double spiral structure. (B) AFM images of photofabricated structures with (right) or without (left) Au@Ag NP under LCP irradiation. (C) FDTD simulated electric field near Ag cuboid NP under LCP irradiation.

The authors thank Drs. T. Narushima, K. Q. Le, R. M. Kim, and Prof. Ki Tae Nam for their contributions. This work was supported by Grants-in-Aid for Scientific Research (KAKENHI Nos. JP16H06505, JP21H04641, JP21K18884, and JP22H05135).

References

1. H.-E. Lee, H.-Y. Ahn, J. Mun, Y. Lee, M. Kim, N. H. Cho, K. Chang, W. S. Kim, J. Rho, and K. T. Nam, Nature Vol. 556, 360–365, 2018.
2. H.-Y. Ahn, K. Q. Le, T. Narushima, J. Yamanishi, R. M. Kim, K. T. Nam, H. Okamoto, Adv. Opt. Mater. Vol. 12, 2400699, 2024.
3. S. Hashiyada, T. Narushima, H. Okamoto, J. Phys. Chem. C Vol. 118, 22229–22233. 2014.
4. K. Saito and T. Tatsuma, Nano Lett. Vol. 18, 3209–3212, 2018.
5. H.-Y. Ahn, T. Narushima, H. Okamoto, J. Phys. Chem. C Vol. 128, 7159–7168, 2024.

Chiral Stark shift – tweezing molecules in enantiofashion

R. M. Jones[1], N. Mayer[1], S. Patchkovskii[2], E. Pisanty[1], and M. Khokhlova[1*]
[1]King's College London, WC2R 2LS London, UK
[2]Author Max-Born-Institute, 12489 Berlin, Germany
margarita.khokhlova@kcl.ac.uk (corresponding author)

Abstract

We present an experimentally realisable scheme for all-electric dipole trapping of chiral molecules in an enantioselective fashion. Our theory shows that light with chirality structured in time induces a chiral Stark shift resulting in trapping of the chosen enantiomer in the laser beam, while the other enantiomer is shaken away.

Ultrafast chirality

Chirality has been proven to play a vital role for living nature, emphasising the importance of its study across sciences with one of the key problems being chiral recognition – the creation of methods telling apart right-handed molecules from their mirror, left-handed, companions. As an illustration of this massive campaign of chiral study spread, it has recently become an emerging frontier in ultrafast physics, with vivid progress achieved in the strong laser field interaction with chiral molecules [1].

Chiral Stark shift

We introduce a new effect from the realm of ultrafast physics – chiral Stark shift [2]. We theoretically show that the common Stark shift can be turned into its chiral counterpart if a chiral molecule is illuminated by synthetic chiral light [3]. This opens a way to turn Stark-shift-based phenomena into enantiosensitive, or chiral, ones. We demonstrate it within the example of free-induction decay steered by synthetic chiral light in the shape of a tricolour chiral (TRICC) field structured in space and time. We show that an excited chiral molecule accumulates an enantiosensitive quantum phase due to perturbative interactions with the TRICC field. The resulting spatial phase gradient steers the free-induction decay (FID) beam in opposite directions for left- and right-handed enantiomers, revealing the chirality of the molecule – the scheme we call FID labelling of enantiomers, and demonstrating the potential of the chiral Stark shift.

Chiral optical tweezers

Optical tweezers have proven to be an extremely powerful and versatile tool for trapping and manipulating matter from atoms to micron-scale objects. One long-lasting dream, which has yet to be realised, is the enantiosensitive trapping of chiral objects in an optical tweezer: an optical trap which will keep, say, the right-handed version of a molecule, but will reject (and, indeed, eject) its left-handed mirror version, providing an optical solution to an essential task of the chemical and pharmaceutical industries over the past 200 years. A chiral optical trap, however, has remained elusive to standard methods, as linear chiroptical phenomena rely on magnetic-dipole and electric-quadrupole interactions, and these are dominated by the much stronger electric-dipole contribution.

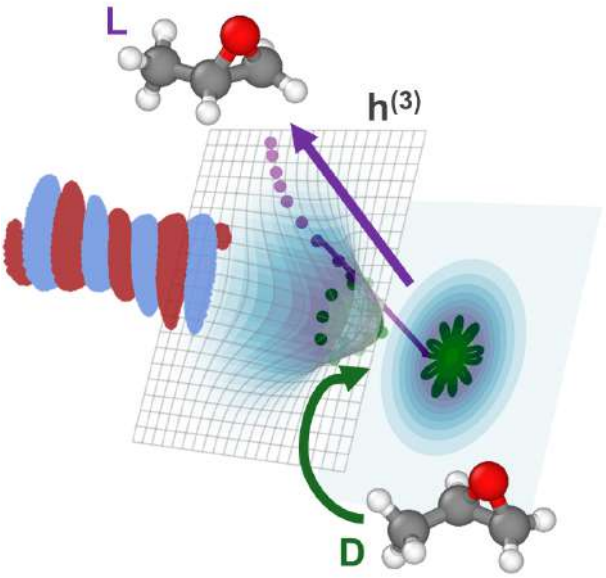


Figure 1: Cartoon for chiral optical tweezers catching D-methyloxirane, while L-enantiomer is sent off the laser TRICC beam with the nonlinear correlation function $h^{(3)}$ responsible for trapping.

Here we leverage recent developments in chiral nonlinear optics, direct brainchildren of attosecond and ultrafast science, which permit pure electric-dipole interactions in the ultrafast regime, built around SCL [3] as the main tool: a multicolour light field, which couples to a multi-photon chiral molecular pseudoscalar [4], that exhibits its chirality over time. We construct a tightly-focused TRICC beam, designed to be globally chiral [2]. We demonstrate how this leads to the highly efficient enantioseparation of small molecules using only electric-dipole transitions that give rise to a nonlinear (three-photon) chiral Stark shift.

This chiral Stark shift, the product of a molecular and a light-field pseudoscalar, which is tuned through the relative phases and frequencies of the TRICC field, permits the enantiosensitive optical trapping of a specific enantiomer – a Chiral Optical Tweezer – in the same way that the the linear achiral Stark shift enables standard optical tweezers [5]. We analyse the nonlinear susceptibility of the molecule of choice to optimise the TRICC-beam frequencies, and we show that results in a realistic trap in the presence of a cold buffer gas.

References

[1] Ayuso D., Ordonez A., and Smirnova O., "Ultrafast chirality: the road to efficient chiral measurements," *Phys. Chem. Chem. Phys.*, Vol. 24, p. 26962, 2022.

[2] Khokhlova M., Pisanty E., Patchkovskii S. et al., "Enantiosensitive steering of free-induction decay," *Sci. Adv.*, Vol. 8, p. eabq1962, 2022.

[3] Ayuso D., Neufeld O., Ordonez. et al., "Synthetic chiral light for efficient control of chiral light–matter interaction," *Nat. Photon.*, Vol 13, p. 866, 2019.

[4] Beaulieu S., Comby A., Descamps D. et al., "Photoexcitation circular dichroism in chiral molecules," *Nat. Phys.*, Vol. 14, p. 484, 2018.

[5] Jones R. M., Mayer N., Patchkovskii S. et al., "Chiral Optical Tweezers – efficient enantioseparation of molecules," in preparation

Knotted topologies in the polarization state of bichromatic light

E. Pisanty
Attosecond Quantum Physics Laboratory, Department of Physics,
King's College London, Strand WC2R 2LS London, United Kingdom
emilio.pisanty@kcl.ac.uk

Abstract

I will present recent work on the fundamental polarization singularities available to polychromatic light. The presence of multiple colours, coherent with each other, allows light to have higher-order internal symmetries, which permits new topologies, and new conserved quantities, as well as novel optical singularities.

Optical singularities are often separated into scalar vortices (such as phase vortices) and vector vortices, which contain singularities of the polarization field at their heart, and which are typically symmetric under rigid spatial rotations about the axis of the singularity. Vector vortices, however, are unstable objects, and they are liable to separate into fundamental polarization singularities when they propagate through turbulent media.

These fundamental polarization singularities of light – typically known as C-points – are generally symmetric under coordinated rotations: that is, transformations which rotate the spatial dependence of the fields by an angle θ and the field polarization by a fraction $\gamma\theta$ of that angle, as generated by 'mixed' angular momenta of the form $L + \gamma S$. Generically, the coordination parameter γ has been thought to be restricted to integer or half-integer values [1].

In this talk I will show that this constraint is an artifact of the restriction to monochromatic fields, and that a much wider variety of optical singularities is available when one considers polychromatic beam combinations that contain more than one frequency.

Building upon this I will show that these new optical singularities present novel field topologies, isomorphic to torus knots, and I will show how they can be characterized both analytically and experimentally [2]. I will also show that the generator for the symmetry group of these singularities, whose algebraic structure is deeply related to the torus-knot topology of the beams, is conserved in nonlinear optical interactions [3]. Finally, I will report on recent work studying tightly-focused versions of the same beams, where the longitudinal component of the fields induces a novel nonlinear measure of optical chirality, which carries a 'vortex of chirality' [4].

References

[1] Ballantine, K.E. et al. "There are many ways to spin a photon: Half-quantization of a total optical angular momentum," *Sci. Adv.*Vol. 2, p. e1501748, 2016.

[2] Pisanty, E. et al."Knotting fractional-order knots with the polarization state of light," *Nat. Photon.* Vol. 13, p. 569, 2019.

[3] Pisanty, E. et al. "Conservation of torus-knot angular momentum in high-order harmonic generation," *Phys. Rev. Lett.* Vol. 122, p. 203201, 2019.

[4] Mayer, N. et al. Chiral topological light for detection of robust enantiosensitive observables," *Nat. Photon.* Vol. 18, p. 1155, 2024.

Deep Learning and Nano-optics: Designing nanoscale polaritonic effects in twisted chiral multilayers of vdW materials

L.F. Álvarez-Tomillo[1,2]

[1] *Department of Physics, University of Oviedo 33006, Oviedo, Spain*

[2.] *Center of Research on Nanomaterials and Nanotechnology, CINN (CSIC-Universidad de Oviedo), El Entrego 33940, Spain.*

*Corresponding author: luciafernandez@uniovi.es

Abstract: This talk builds on recent advances in hyperbolic nanooptics, introducing a neural-network-based approach to design phonon polariton propagation in twisted multilayers. We achieve on-demand control—including canalization and bi-canalization—in previously unexplored frequency ranges, demonstrating a powerful strategy for tailoring light–matter interactions at the nanoscale.

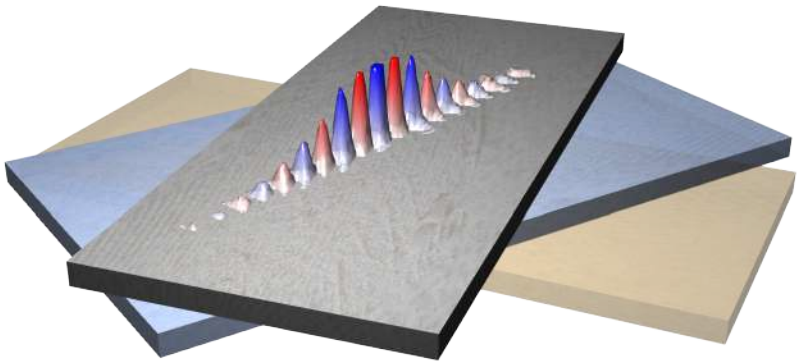


Figure 1: Schematic representation of the desired polaritonic propagation in real space, used as input to the neural network (NN). The NN accurately predicts the structural parameters (t, θ, and ω) for one or multiple configurations.

Summary: Polaritons—dipole excitations in matter coupled to electromagnetic fields—in van der Waals[1, 2] (vdW) crystals enhance light–matter interactions through extreme field confinement and long lifetimes. In some natural crystals, their dispersion adopts a hyperbolic shape, enabling "hyperbolic light" to travel only along specific directions. This gives rise to highly non-intuitive phenomena such as negative reflection and refraction, canalization[3], ray-like propagations[4] and deeply subwavelength focusing. These unique capabilities have driven rapid advances in nano-optics, enabling unprecedented control of light at the nanoscale. However, despite these exciting advances, nano-optics still presents a major limitation: obtaining propagations on demand, i.e. by design.

In this work, we overcome this limitation through the combined use of a **neural network and twisted polaritonic multilayers**. Our method enables **inverse design**, making it possible to **demonstrate desired (and thus novel) polariton propagations** by obtaining accurate predictions of subsequently fabricated multilayer configurations. Interestingly, this method efficiently handles possible system degeneracies, identifying multiple multilayer structures that give rise to the same desired propagations at the nanoscale.

References:

1. Ma, W. *et al.* In-plane anisotropic and ultra-low-loss polaritons in a natural van der Waals crystal. *Nature* **562**, 557–562 (2018).
2. Álvarez-Pérez, G. *et al.* Infrared Permittivity of the Biaxial van der Waals Semiconductor α-MoO3 from Near- and Far-Field Correlative Studies. *Advanced Materials* **32**, 1908176 (2020).
3. Duan, J. *et al.* Multiple and spectrally robust photonic magic angles in reconfigurable α-MoO3 trilayers. *Nat Mater* **22**, 867–872 (2023).
4. Álvarez-Cuervo, J. *et al.* Unidirectional ray polaritons in twisted asymmetric stacks. *Nat Commun* **15**, 9042 (2024).

Acknowledgments

We acknowledge the support from the European Research Council under Consolidator grant no. 101044461, TWISTOPTICS and the Spanish Ministry of Science and Innovation (State Plan for Scientific and Technical Research and Innovation grant number PID2022-141304NB-I00), projects PID2023-148359NB-C21 and CEX2023-001286-S (financed by MICIU/AEI/10.13039/501100011033) and the Government of Aragon through Project Q-MAD.

Chiral far-field signature of single achiral gold nano-antennas

A. Mildner[1], A. Horrer[2], P. Weiss[3], S. Dickreuter[1], P. C. Simo[1], D. Gérard[2], D. P. Kern[1], and M. Fleischer[1*]

[1]Institute for Applied Physics and Center LISA[+], University of Tübingen, Germany
[2]Light, nanomaterials, nanotechnologies (L2n), Université de Technologie de Troyes, France
[3]Physical Institute, University of Tübingen, Germany
[*]Corresponding author: monika.fleischer@uni-tuebingen.de

Abstract: Optical chirality is most commonly associated with geometrically chiral nanostructures. By spectrally analyzing single planar achiral nanostructures with two dipolar plasmonic resonances, it can be shown that the polarization state of the emitted light is determined by chiral near-fields, leading to a chiroptical far-field response.

Chirality presents an important concept in chemistry and biology. It is manifest in the characteristic optical properties of chiral structures under interaction with chiral light [1,2]. Yet, the far-field response of achiral nanostructures is widely reported to be invariant to the handedness of the optical excitation. The dipolar electric resonances of plasmonic nano-antennas are commonly determined from the structures' white-light dark-field scattering spectra. The spectra of planar achiral particles with a long and short geometric axis, such as nano-rods or nano-rectangles, display two resonances at longer and shorter wavelengths. Using a polarizer, these modes can be excited selectively. In such measurements, no chiroptical far-field response is observed.

The situation changes when a second polarizer is introduced in the beam path, acting as an analyzer. The resonance positions of the two contributing modes start to shift depending on the analyzer angle, indicating an interplay between the spectrally overlapping modes (see Figure 1) [3]. Simulations show electric near fields of opposite circular polarization at different locations around the particle. The near-field chirality is transformed to an optical chirality flux in the far-field [4]. The relevant parameter determining the interplay is the relative phase between the electrical fields of the eigenmodes. This phase shift can be entered into a description of the system via an analytical dipole model, by which the intensity of the electric far-field radiation can be derived [3].

Experimental, numerical and analytical findings thus confirm that both chiral and achiral nano-antennas can exhibit chiral near-fields that are transmitted to a chiral far-field emission due to phase shifts and interference between the antenna's dipolar plasmonic resonances. The corresponding polarimetric measurements may, e.g., be utilized to determine the orientation of gold nanorods through identifying the orientation of their longitudinal dipolar modes [5].

Support from the French Agence Nationale de la Recherche (grant ANR-17-CE24-0039) and the European Union's FEDER fund, the nano'mat platform and the French RENATECH+ network is gratefully acknowledged.

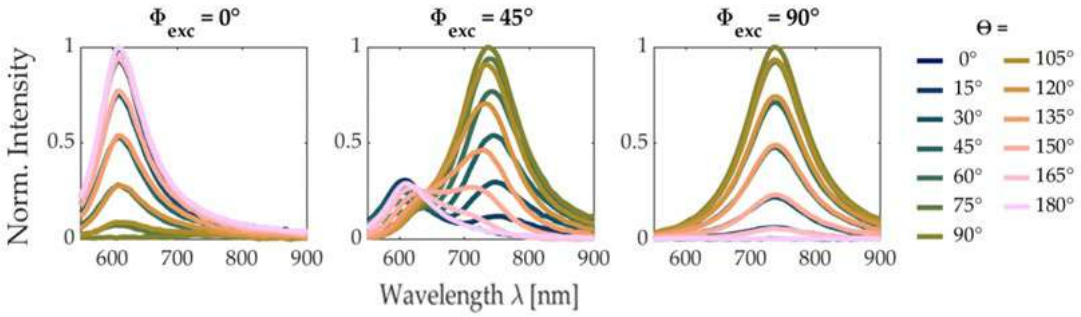


Figure 1: Dark-field scattering spectra of an achiral rectangular gold nano-antenna under excitation with linearly polarized white light under three different angles Φ_{exc}, measured with analyzation angles Θ between 0° and 180°. Under 0° excitation, only the transversal localized surface plasmon resonance, and under 90° excitation, only its longitudinal counterpart is detected with varying intensities. Under 45° excitation, a relative spectral shift of the resonances is observed in addition to an intensity modulation, indicating a chiroptical response.

References

[1] Wu, W., M. Pauly, "Chiral plasmonic nanostructures: recent advances in their synthesis and applications", Materials Advances 3, 186-215, 2022.

[2] Mun, J., M. Kim, Y. Yang, T. Badloe, J. Ni, Y. Chen, C.-W. Qiu, J. Rho, "Electromagnetic chirality: from fundamentals to nontraditional chiroptical phenomena," Light: Sci. Appl. 9, 139, 2020.

[3] Mildner, A., A. Horrer, P. Weiss, S. Dickreuter, P. C. Simo, D. Gérard, D. P. Kern, M. Fleischer, "Decoding polarization in a single achiral gold nanostructure from emitted far-field radiation," ACS nano 17, 25656–25666, 2023.

[4] Poulikakos, L. V., P. Gutsche, K. M. McPeak, S. Burger, J. Niegemann, C. Hafner, D. J. Norris, "Optical chirality flux as a useful far-field probe of chiral near fields," ACS Photonics 3, 1619−1625, 2016.

[5] Simo, P. C., A. Mildner, D. P. Kern, M. Fleischer, "Dipole determination by polarimetric spectroscopy yielding the orientation of gold nanorods," Small Science 2400340, 2025.

Enantiosensitive exceptional points for exceptional detection of molecular chirality

N. Mayer[1,2*], A. Löhr[2], N. Moiseyev[3,4], M. Ivanov[2,3,5,6], and O. Smirnova[2,3,7]
[1] Attosecond Quantum Physics Laboratory, King's College London, London, UK
[2] Max-Born-Institut, Berlin, Germany
[3] Department of Physics, Technion-Israel Institute of Technology, Haifa, Israel
[4] Institute of Advanced Studies in Theoretical Chemistry, Technion-Israel Institute of Technology, Haifa, Israel
[5] Department of Physics, Imperial College London, London, United Kingdom
[6] Department of Physics, Humboldt Universität zu Berlin, Berlin, Germany
[7] Technische Universität Berlin, Berlin, Germany
*nicola.1.mayer@kcl.ac.uk

Abstract

We introduce the concept of enantiosensitive exceptional points – non-Hermitian degeneracies whose position in parameter space is sensitive to the handedness of an open system. We apply the concept for the development of novel highly sensitive and robust methods to detect molecular chirality, from single molecules to racemic mixtures.

Non-Hermitian Hamiltonians (NH) describe open systems where energy and/or matter is exchanged between the system and its surrounding environment. The parameter space of these systems can host branch points, commonly known as exceptional points (EPs), where the eigenvalues and eigenstates of the Hamiltonian coalesce. The presence of EPs in NH physics leads to a plethora of remarkable phenomena, such as topological population transfer between the eigenstates or the enhanced sensitivity of NH systems to external perturbations. Owing to their generality, these effects are ubiquitous and have been observed in many different experimental platforms, from atomic and molecular media to photonic and optical materials [1].

Here, we apply these EP-based non-Hermitian phenomena to the problem of detection of molecular chirality. In particular, we show that the position of EPs in open chiral systems depends on their handedness, paving the way for the development of much needed highly sensitive and topologically robust chiral methods that can work in racemic mixtures and detect small variations of enantiomeric excess [2].

First, we show that selective excitation of chiral enantiomers can be achieved by coupling a chiral molecule to the continuum using a three-color field (Fig.1a). By tuning the field configuration, we achieve highly efficient topological population transfer between the adiabatic states of only one of the molecular enantiomers, while its mirror twin is left in the initial state. The phenomenon survives orientational averaging, paving the way for topologically robust enantiosensitive separation of chiral molecules in racemic gaseous mixtures.

Then, we demonstrate that enantiosensitive EPs in photodissociating chiral molecules can amplify weak chiral effects induced by the magnetic component of chiral light fields. (Fig.1b). Specifically, we show that we can control the amount of dissociated chiral molecules in a racemic mixture in an enantioselective fashion by changing the interaction time between the molecule and the field. Our results show chiral dichroic effects on the order of $\simeq 10\%$, which are orders of magnitude larger compared to the the typical $\simeq 0.1\%$ efficiency of standard approaches that employ the magnetic component of light for the detection of chirality.

Finally, we devise a chiral sensor based on a twisted non-Hermitian optical fiber interacting via evanescent modes with a solution of chiral molecules (Fig.1c). By engineering the gain/loss

profile of the optical fiber, we show that the position of EPs in the parameter space depends directly on the enantiomeric excess of the solution $ee = C_R \in C_L$ (where $C_{R/L}$ is the concentration of right/left molecules). We then couple linearly polarized light into the fiber and analyze the rotation angle θ and the ellipticity ξ of the propagating light. If the chiral fiber is tuned to an EP corresponding to a given enantiomeric excess $ee^{(0)}$, small variations $\epsilon = ee \in ee^{(0)}$ in the relative concentrations of right- or left-handed molecules lead to fast variations of the rotation angle θ and ellipticity ξ of the light at the end of the fiber. Changing the fiber parameters, the sensor can be made to be highly sensitive to small variations around any given value of the enantiomeric excess $ee^{(0)}$.

Our work is a first step in an exciting new direction at the crossroad beteween the development of new enantiosensitive techniques and non-Hermitian physics. While chirality is a ubiquitous phenomenon present in a wide range of temporal and length scale, any realistic system is open to the environment and can be therefore described in the non-Hermitian language. Here we show that non-Hermitianity can provide a much needed enhancement of chiral phenomena, while chiral interactions open new avenues for the exploitation of EP-induced effects.

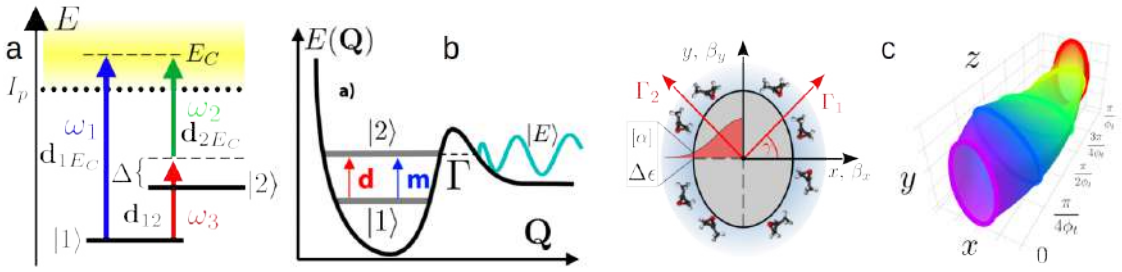


Figure 1: Open chiral systems with enantiosensitive EPs. **(a)**: A photoionizing chiral molecule driven by a three-color field in the electric dipole approximation, where we drive enantiosensitive topological population transfer; **(b)**: a photodissociating chiral molecule driven by the electric and magnetic component of a single-color field, where we show enantiosensitive photodissociation and stabilization; **(c)** a chiral twisted non-Hermitian fiber interacting with a solution of chiral molecules via evanescent fields, where we show highly sensitive detection of small variations of enantiomeric excess.

Acknowledgements

This project has received funding from the EU Horizon 2020 (grant agreement No 899794) and European Union (ERC, ULISSES, 101054696). This work is funded by UK Research and Innovation (UKRI) under the UK government's Horizon Europe funding guarantee (grant number EP/Z001390/1). Nimrod Moiseyev acknowledges the Israel Science Foundation (ISF) grant No. 1757/24 for a partial support.

References

[1] Özdemir, S *et al.* "Parity–time symmetry and exceptional points in photonics," *Nat. Mater.*, Vol. 18, pp. 783-798, 2019.

[2] Mayer, N. *et al.*, "Enantiosensitive positions of exceptional points in open chiral systems," *arXiv*, 2502.18963, 2025.

Ultrafast Light-Matter Interaction in Photocatalytic Systems

X-ray techniques for probing and inducing ultrafast dynamics at nanoscale

N. Agarwal[1]

[1]Elettra Sincrotrone Trieste, Italy

Naman.agarwal@elettra.eu

Abstract: I will overview X-ray techniques for probing ultrafast nanoscale dynamics, with a focus on Coherent Diffraction Imaging (CDI) and X-ray Transient Grating Spectroscopy (XTG). I will present recent results on imaging ultrafast phase transition in VO2 using CDI and discuss the application of XTG to induce and probe nanoscale dynamics.

Understanding photoinduced dynamics with femtosecond-picosecond temporal and nanometer spatial resolution is crucial for optimizing and efficient control of next-generation devices. X-ray Free Electron Lasers (XFELs) have advanced the study of element-specific material dynamics with unparalleled temporal and spatial resolution. In this talk, I will give an overview of X-ray techniques for investigating ultrafast nanoscale dynamics in solid thin-film systems, focusing on Soft X-ray Coherent Diffraction Imaging (CDI) and X-ray Transient Grating Spectroscopy (XTG). I will present our recent findings on imaging heterogeneity in the ultrafast metal-insulator phase transition in VO2 using coherent diffraction imaging, and discuss the application of XUV transient grating to induce and probe nanoscale dynamics.

Sensitizing diamond to visible light to increase electron emission under solar radiation.

P. O'Keeffe[1, *], G. Ammirati[2], A. Bellucci[3], D. Catone[2], F. Martelli[2], M. Mastellone[3], S. Orlanducci[4], A. Paladini[1], R. Polini[3,4], R. Salerno[3], F. Toschi[2], D. M. Trucchi[3], S. Turchini[2], V. Valentini[3]

[1]Istituto di Struttura della Materia-CNR (ISM-CNR), EuroFEL Support Laboratory (EFSL), 00015 Monterotondo Scalo, Italy.
[2]Istituto di Struttura della Materia-CNR (ISM-CNR), EuroFEL Support Laboratory (EFSL), 100 Via del Fosso del Cavaliere, 00133 Rome, Italy.
[3]Istituto di Struttura della Materia-CNR (ISM-CNR), DiaTHEMA Lab, 00015 Monterotondo Scalo, Italy.
[4]Dipartimento di Scienze e Tecnologie Chimiche, Università di Roma "Tor Vergata", Via della Ricerca Scientifica, 1, 00133 Roma, Italy.
[*]corresponding author: patrick.okeeffe@ism.cnr.it

Abstract: In this work we aim to exploit the negative electron affinity of the surface of hydrogenated diamond combined with the efficient absorption of visible light by plasmonic nanoparticles to emit electrons using solar light. We postulate that by combining plasmonic nanoparticles with diamond it is possible to simultaneously increase the photoductivity of the diamond and to enhance photemission of electrons from the surface. The role of diamond defects in this process is discussed.

Combining plasmonic metal nanoparticles with wide bandgap semiconductor materials has been demonstrated to be an effective way to sensitize these materials to sub-bandgap light.[1] This is often used as a strategy to improve the photocatalytic properties of these materials.

In this work, we focus our efforts on diamond as it has the very interesting property of having a negative electron affinity at its surface when it is hydrogenated. This property can lead to numerous useful applications such as a cold cathode or as a clean source of solvated electrons. The problem is that diamond has a band gap of 5.5 eV and therefore this process only works with VUV light ($\lambda < 213$ nm).

We have fabricated several separate systems based on the combination of plasmonic nanoparticles with diamond which show that exciting the plasmonic resonance of the metal nanoparticles can lead to a strong enhancement of the emission of electrons from the diamond surface.

The first of these is a system involving nanodiamonds coupled with gold nanoparticles in aqueous solution which has been shown to be a source of solvated electrons following interaction with visible light. In this case, the presence of solvated electrons was verified by using an ultrafast pump-probe experiment in which a visible light pump was used to excite the plasmon resonance of the gold nanoparticles while a white light probe was used to optically detect the formation of the solvated electron in the first picoseconds after the excitation.

The next system attempted was to fabricate an array of nanoparticles embedded below the surface of a thin film of diamond. Initial attempts with Aluminium as the plasmonic material were not successful[3] while successive fabrication using silver showed the required properties[4]. Using this system, it was possible to demonstrate both increased photoconductivity and emission of electrons into vacuum using visible light. Based on the details of the above measurements we propose a mechanism involving plasmonically enhanced visible-light absorption by defect states at the Ag/Diamond interface which increases the photoconductivity of

the material combined with photoemission from occupied surface states with electronic transport through defects.

Subsequent samples in which diamond films are grown on Silicon substrates have been examined with synchrotron radiation and pump-probe techniques to verify the above-proposed mechanisms and to optimize the efficiency of the process.

References

1. Catone D., Di Mario L., Martelli F., O'Keeffe P., Paladini A., Pelli Cresi J.S., Sivan A.K., Tian L., Toschi F. and Turchini S. “Ultrafast optical spectroscopy of semiconducting and plasmonic nanostructures and their hybrids” Nanotechnology, Vol.32, No. 2, 025703, 2020.
2. Orlanducci S., Ammirati G., Bellucci A., Catone D., Gontard L.C., Martelli F., Matassa R., Paladini A., Toschi F., Turchini S., and O’Keeffe P. "Gold-diamond Nanocomposites Efficiently Generate Hydrated Electrons upon Absorption of Visible Light" ACS Applied Optical Materials Vol. 2, No. 6, 1180-1187, 2024.
3. Bellucci A., Campanari V., Mastellone M., O'Keeffe P., Paladini A., Polini R., and Trucchi D.M., “Optical characteristics of nanostructured aluminium/diamond composite systems in the visible range,” Diamond and Related Materials, Vol. 132¸109669, 2023.
4. Bellucci A., Mastellone M., Catone D., O'Keeffe P., Martelli F., Ammirati G., Paladini A., Turchini S., Toschi F., Santagata A., Pace M. L., Polini R., Salerno R., Valentini V., and Trucchi D. M., “Plasmonic Silver Nanoparticles Facilitate Electron Emission from Diamond upon Sun-Like Excitation” ChemPhotoChem , 9, e202400202, 2025.

Time-resolved Raman spectroscopy in photoexcited MoS2: transient doping, resonance effects and electron-phonon coupling

C.Fasolato[1,2*], A.M. Finardi[3,4], M. Capeccia[2], A. Giugni[3,4], R. Cucini[4], E. Cappelluti[5], G. Panaccione[4], F. Sacchetti[4,6], P. Postorino[2], C. Petrillo[6,7], and G. Rossi[3,4]

[1]Istituto dei Sistemi Complessi (ISC)-CNR, Italy
[2]Dipartimento di Fisica, Università Sapienza, Rome, Italy
[3]Dipartimento di Fisica, Università di Milano, Italy
[4]Istituto Officina dei Materiali (IOM)-CNR, Italy
[5]Istituto di Struttura della Materia (ISM)-CNR, Italy
[6]Dipartimento di Fisica e Geologia, Università di Perugia, Italy
[7]AREA Science Park, Trieste, Italy
[*]corresponding author: claudia.fasolato@cnr.it

Abstract: I will present a time-resolved Raman spectroscopy (TRRS) study on the layered semiconductor MoS_2, under resonant optical pumping with the excitonic gap at Brillouin zone K point. TRRS allows mapping the redistribution of energy among the system degrees of freedom, from the photoexcited electronic subsystem to specific zone-center phonon modes.

MoS_2 belongs to the class of graphene-like, layered materials called transition metal dichalcogenides (TMDs). Semiconducting TMDs, like MoS_2, show an indirect to direct bandgap transition when the system is exfoliated down to the monolayer structure, which makes them promising materials for future applications in optoelectronics and related fields [1]. Unravelling the relaxation pathways of photoexcited electrons in such systems, and specifically their coupling with the lattice degrees of freedom, is of great applicative interest.

Time-resolved Raman spectroscopy (TRRS) can provide direct access to the electron-phonon coupling dynamics, as well as the incoherent phonon relaxation [2]. The aim of our experiment is studying the deexcitation dynamics of MoS_2 after impulsive optical pumping of the excitonic bandgap. At the SPRINT-NFFA facility, we have carried out a TRRS study on the system, monitoring the temporal evolution of two specific Raman active features, namely the out-of-plane A_{1g} mode and the in-plane E^1_{2g} mode, after the photoexcitation. Equilibrium Raman spectroscopy studies have linked the modification of such phonon lineshapes to doping effects, providing the background for studying the optically induced, transient doping of the system [3,4,5]. To explore the effect of dimensionality on the system relaxation dynamics, the experiment was performed on both bulk and monolayer MoS_2, revealing significant differences in the phenomenology and relaxation timescales. The role of the substrate on the monolayer deexcitation dynamics was explored by selecting substrates with different electrical and thermal properties.

After presenting the results of the TRRS study, I will discuss their perspective integration in a multi-messenger, time-resolved spectroscopy study, coupling the time resolved photon and electron spectroscopies available at the SPRINT-NFFA facility (CNR-IOM@Elettra, Trieste, Italy).

Acknowledgements: G.P. and P.P. acknowledge support from Progetto PRIN 2022 “BEST-WIN” PNRR Next Generation EU – CUP B53D23004530006. E.C. acknowledges support from MUR, PRIN Project

2022WS9MS4. M.C., E.C. and G.P. acknowledge financial support from PNRR MUR project PE0000023-NQSTI. This work was performed in the framework of the NFFA-SPRINT facility, supported by MUR as the Activity of International Relevance NFFA, (www.Trieste.NFFA.eu).

References

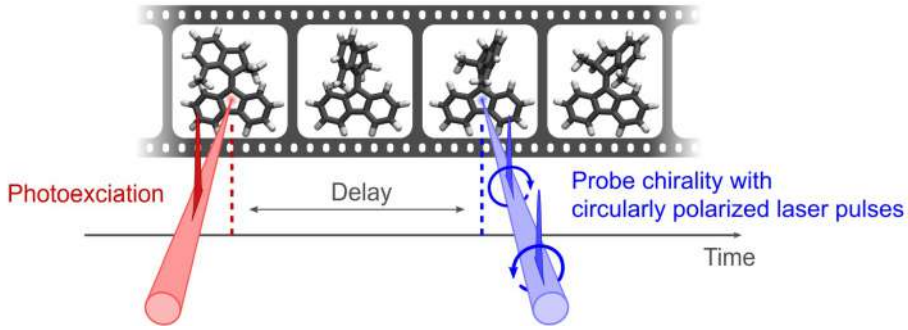
1. X. Zhang, et al., Chem Soc Rev, Vol. 44, No. 9, 2757, 2015.
2. S. Han, et al., Optics Express, Vol. 27, No. 21, 29949, 2019.
3. G. Kukucska, et al., Physica Status Solidi B, Vol. 254, No. 11, 1700184, 2017.
4. B. Chakraborty, et al., Phys Rev B, Vol. 85, No. 16, 161403, 2012.
5. M. Yamamoto, et al., J Phys Chem C, Vol. 117, No. 48, 25643, 2013.

Ultrafast chiral spectroscopy for stereocontrolled photochemistry

M. Oppermann[1*]

[1]Department of Chemistry, University of Basel, Klingelbergstrasse 80, CH-4056 Basel
[*]corresponding author: malte.oppermann@unibas.ch

Abstract: We present an ultrafast circular dichroism technique to capture the dynamics of chiral excited states in solution. By combining sub-picosecond time resolution with high chiral sensitivity, we resolve the stereochemical evolution of photoexcited molecules, such as a chiral Fe(II) spin-crossover complex and a chiral lanthanide complex with circularly polarized luminescence.



The incorporation of chiral structures into photochemical systems is a powerful strategy to control their functions [1]. For example, uni-directional molecular motors, chiral photocatalysts, and chiral metal nanostructures have achieved exceptional levels of stereocontrol over mechanical motion, energy transfer, and electric charge-carriers on the nanoscale. However, the direct characterization of the underlying chiral excited states remains a formidable experimental challenge, due to a lack of analytical techniques that combine high chiral sensitivity in solution with ultrafast time resolution [2].

To address this challenge, we have developed an ultrafast circular dichroism technique that measures the absorption difference of left- and right-circularly polarized laser pulses in photoexcited chiral molecules [3]. Through an ultra-sensitive broadband detection scheme, we are thus able to capture ultrafast changes in molecular chirality and follow the stereochemical evolution of the associated photoexcited states with sub-picosecond time resolution. On this basis we are now able to resolve chiral photochemical dynamics in real-time, which I will illustrate via two examples: 1) the identification and control of a chiral reaction coordinate in the spin-crossover dynamics of Fe(II) complexes [4], and 2) the resolution of the energy and chirality transfer dynamics in a chiral lanthanide-based OLED complex with circularly polarized luminescence (CPL) [5].

References

1. J. R. Brandt, F. Salerno, and M. Fuchter, Nat. Rev. Chem. 1, 0045 (2017)
2. M. Oppermann, CHIMIA 78, 45-49 (2024)
3. M. Oppermann, B. Bauer, T. Rossi, F. Zinna, J. Helbing, J. Lacour, and M. Chergui, Optica 6, 56 (2019)
4. M. Oppermann F. Zinna, J. Lacour, and M. Chergui., Nat. Chem. 14, 739-745 (2022)
5. J. L. Lunkley, D. Shirotani, Y. Kazuaki, K. Sumio, and G. Muller, J. Am. Chem. Soc. 130, 13814-13815 (2008)

Elucidating Charge Transfer Processes in Plasmonic and Semiconductor Photocatalysts

G. Tagliabue[1]

[1]Laboratory of Nanoscience for Energy Technologies (LNET), EPFL, 1015 Lausanne, Switzerland

[*]corresponding author: giulia.tagliabue@epfl.ch

Abstract: The combination of optical nanoantennas and scanning photoelectrochemical microscopy opens new door for the in-situ investigation of non-equilibrium charge transfer processes.

In the last decade, optical nanoantennas have revolutionized light manipulation and control at the nanoscale. Interestingly, generation of hot carriers in metals upon light absorption have opened new pathways for controlling activity and selectivity of photo(electro)chemical processes. Concurrently, semiconductor nanostructures enable optimization of charge transport and light absorption. Yet, fundamental questions remain about the microscopic details of these complex light-matter interactions.

I will first present our recent results on quantifying the energy-resolved injection probability of hot electrons and hot holes across the metal/semiconductor interface. We demonstrate the importance of small scale nanoantennas to maximize the chance of ballistic collection and we unravel microscopic details of charge transfer via inner or outer sphere pathways [1,2,3]. Furthermore, I will show how morphology of semiconducting nanostructures dramatically impacts the performance of solar redox flow batteries [4,5,6]. In particular, we demonstrate that high photovoltages are attainable in single-material photoanode, enabling unassisted recharging up to high state of charge. Overall, using an internal quantum efficiency perspective, our work unravel the interplay of light absorption, charge generation and in plasmonic and semiconducting photocatalysts.

References

1. Kiani F., Tagliabue G. - High‐Aspect Ratio Au Microflakes via Gap‐Assisted Synthesis – Chemistry of Materials 34 (3), 1278-1288
2. F Kiani, AR Bowman, M Sabzehparvar, CO Karaman, R Sundararaman, G Tagliabue - Transport and Interfacial Injection of d-Band Hot Holes Control Plasmonic Chemistry - ACS Energy Letters 8 (10), 4242-4250, 2023
3. F Kiani, AR Bowman, M Sabzehparvar, R Sundararamn, G Tagliabue, Distinguishing Inner and Outer-Sphere Hot Electron Transfer in Au/p-GaN Photocathodes, Nano Letters 2024 24 (50), 16008-16014
4. Ma J., Oh K., Tagliabue G. - Understanding Wavelength-Dependent Synergies between Morphology and Photonic Design in TiO2-Based Solar Powered Redox Cells – Journal of Physical Chemistry C 2022
5. Ma J, Pan Z., Tagliabue G., High-Performance Hematite Photoanodes for Unassisted Recharging of Solar Redox Flow Battery. Sol. RRL, 8: 2400477.
6. Ma J, Sabzehparvar M, Pan Z., Tagliabue G. Nanostructured Fe2O3/CuxO heterojunction for enhanced solar redox flow battery performance, J. Mater. Chem. A, 2025, 13, 1320-1329

Quantum Light Emitters and Photonic Heterogeneous Integration

Room-temperature quantum emission from interface excitons in mixed-dimensional heterostructures

N. Fang[1,2], Y. R. Chang[1,2], S. Fujii[2,3], D. Yamashita[2,4], M. Maruyama[5], Y. Gao[5], C. F. Fong[1,2], D. Kozawa[1,2,6], K. Otsuka[1,7], K. Nagashio[8], S. Okada[5], Y. K. Kato[1,2*]

[1]Nanoscale Quantum Photonics Laboratory, RIKEN Cluster for Pioneering Research, Saitama 351-0198, Japan
[2]Quantum Optoelectronics Research Team, RIKEN Center for Advanced Photonics, Saitama 351-0198, Japan
[3]Department of Physics, Keio University, Yokohama 223-8522, Japan
[4]Platform Photonics Research Center, National Institute of Advanced Industrial Science and Technology (AIST), Ibaraki 305-8568, Japan
[5]Department of Physics, University of Tsukuba, Ibaraki 305-8571, Japan
[6] Research Center for Materials Nanoarchitectonics, National Institute for Materials Science, Ibaraki, Japan
[7]Department of Mechanical Engineering, The University of Tokyo, Tokyo 113-8656, Japan
[8]Department of Materials Engineering, The University of Tokyo, Tokyo 113-8656, Japan
[*]corresponding author: yuichiro.kato@riken.jp

Abstract: We report on interface excitons in mixed-dimensional heterostructures consisting of two-dimensional tungsten diselenide and one-dimensional carbon nanotubes. Localization of low-energy interface excitons is indicated by extended lifetimes as well as small excitation saturation powers. Photon correlation measurements confirm antibunching at room temperature.

The development of van der Waals heterostructures has introduced unconventional phenomena that emerge at atomically precise interfaces. For example, interlayer excitons in two-dimensional transition metal dichalcogenides show intriguing optical properties at low temperatures. Here we report on room-temperature observation of interface excitons in mixed-dimensional heterostructures consisting of two-dimensional tungsten diselenide and one-dimensional carbon nanotubes [1].

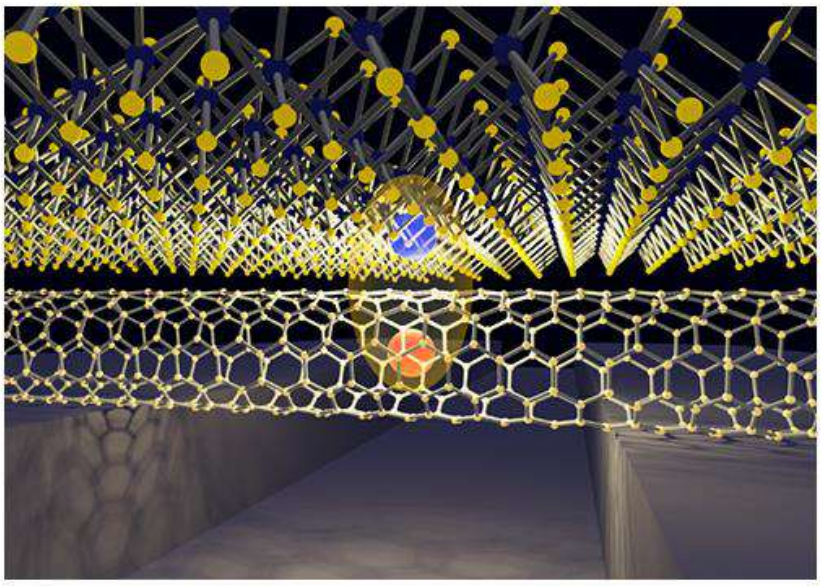


Figure 1: Schematic of an interface exciton in a mixed-dimensional heterostructure.

The mixed-dimensional heterostructures are fabricated by transferring a tungsten diselenide flake on top of the carbon nanotubes using the anthracene-assisted transfer technique [2,3]. The heterostructures are entirely free standing to preclude substrate effects (Fig. 1). Room-temperature photoluminescence spectroscopy is employed to investigate interface excitons within the heterostructure. Bright emission peaks originating from the interface are identified, spanning a broad energy range within the telecommunication wavelengths. The effect of band alignment is investigated by systematically varying the nanotube bandgap, and we assign the new peaks to interface excitons as they only appear in type-II heterostructures. Time-resolved photoluminescence measurements reveal extended lifetimes of the interface excitons, whereas excitation power dependence shows that emission saturates at low powers. These characteristics suggest room-temperature localization of the low-energy interface excitons. To elucidate the quantum nature of the interface excitons, we conduct photon correlation measurements. The second-order correlation exhibits a clear antibunching dip at zero delay. With mixed-dimensional van der Waals heterostructures where band alignment can be engineered, new opportunities for quantum photonics are envisioned.

Work supported by JSPS (KAKENHI JP22K14624, JP22K14625, JP21K14484, JP22K14623, JP22H01893, JP21H05233, JP22F22350, JP23H00262, JP20H02558) and MEXT (ARIM JPMXP1222UT1135). Y.R.C. is supported by JSPS (International Research Fellow). N.F. and C.F.F. are supported by the RIKEN Special Postdoctoral Researcher Program. We thank the Advanced Manufacturing Support Team at RIKEN for technical assistance.

References

1. N. Fang, Y. R. Chang, S. Fujii, D. Yamashita, M. Maruyama, Y. Gao, C. F. Fong, D. Kozawa, K. Otsuka, K. Nagashio, S. Okada, Y. K. Kato, “Room-temperature quantum emission from interface excitons in mixed-dimensional heterostructures,” Nature Commun. **15**, 2871 (2024).
2. K. Otsuka, N. Fang, D. Yamashita, T. Taniguchi, K. Watanabe, Y. K. Kato, “Deterministic transfer of optical-quality carbon nanotubes for atomically defined technology,” Nature Commun. **12**, 3138 (2021).
3. N. Fang, Y. R. Chang, D. Yamashita, S. Fujii, M. Maruyama, Y. Gao, C. F. Fong, K. Otsuka, K. Nagashio, S. Okada, Y. K. Kato, “Resonant exciton transfer in mixed-dimensional heterostructures for overcoming dimensional restrictions in optical processes,” Nature Commun. **14**, 8152 (2023).

Designer van der Waals Materials for Quantum Optical Emission

Shengxi Huang

Department of Electrical and Computer Engineering & Department of Materials Science and NanoEngineering, Rice University, Houston, TX 77005

shengxi.huang@rice.edu

Abstract: We report new atomic engineering approaches on van der Waals materials to generate high quality single photon emitters. Our approaches include atomic substitution through plasma treatment, in-situ doping, and manipulating layer thickness and polarization. Such approaches have led to single photon emission with high purity, high brightness, and high stability.

Key words: single photon purity, Debye-Waller factor, atomic substitution, transition metal dichalcogenide, hexagonal boron nitride

Designer van der Waals (vdW) materials offers enormous opportunities to tune material properties for various applications. Isolated, optically-active defects generated in vdW materials could lead to single photon emission. 2D vdW materials as host materials for single photon emission hold various advantages, such as high optical extraction efficiency from the atomically-thin layered materials, and readiness to integrate with on-chip photonic and electronic devices. However, single photon emission from 2D vdW materials typically suffers from low purity and lack of controllability, due to the sensitivity of these atomically-thin materials to external dielectric environments, surface defects and adsorbents, and strains and wrinkles introduced during material processing. This talk introduces our recent efforts to improve the single photon purity and controllability in vdW materials. We developed novel defect structures that can overcome several current issues, and explored their electronic structure and tunability in optical emission. Through a combination of approaches, including strain engineering, heterostacking, employing optical selection rules for excitation and detection, optimization of material synthesis and handling, we were able to achieve high purity (> 98%) for single photons emitted from 2D transition metal dichalcogenides (TMDs) at cryogenic temperature and in hBN at room temperature. This work provides deep insights into the electronic, spin, and valley properties of TMDs and hBN. It also paves the way towards the

application of 2D vdW materials for quantum optical applications. The materials engineering approaches developed here can be applied to the optimization of other optical and quantum materials.

Spatial Resolution Enhancement by Quantum Entanglement

Zhe He

Shandong Institute of Advanced Technology, China

*corresponding author: zhe.he@iat.cn

Abstract: Quantum imaging surpasses the classical limit of spatial resolution without the need for labeling by measuring the second-order correlation functions of entangled photons. Here, we discuss the mechanism and methods of resolution enhancement by using a type-I BBO quantum source.

Classical imaging techniques are typically restricted by the diffraction limit of light. To overcome this challenge, quantum phenomena can be applied to enhance imaging capabilities. Resolution enhancement arises from measuring the second-order correlation functions of entanglement photons [1]. The entanglement state of photons could be generated by the spontaneous parametric down-conversion (SPDC) of a type-I BBO source:

$$\Psi(\boldsymbol{r}_s,\boldsymbol{r}_i) = \sum_{\boldsymbol{k}_s,\boldsymbol{k}_i} e^{-i\boldsymbol{k}_s\cdot\boldsymbol{r}_s} e^{-i\boldsymbol{k}_i\cdot\boldsymbol{r}_i} |\boldsymbol{k}_s,\boldsymbol{k}_i\rangle, \quad (1)$$

where $|\boldsymbol{k}_s,\boldsymbol{k}_i\rangle$ represents the biphoton state in the momentum domain, and the wavevectors $\boldsymbol{k}_s,\boldsymbol{k}_i$ obey the phase matching condition.

We experimentally use the signal and idler photons generated by the BBO source for wide-field imaging [2]. The classical spatial resolution is evaluated by analyzing the point spread function (PSF) of the signal photon. Additionally, when measuring the second-order correlation function, the PSFs of both the signal and idler photons together create an equivalent PSF. This narrows the bandwidth of the second-order correlation function by a factor of two compared to the original PSF. As a result, the effective spatial resolution of the entangled photons is halved compared to that of the signal photon.

Measuring the second-order correlation function of two light beams often requires the photon counting detectors [3]. However, in our approach, we utilize both the signal and idler photons to illuminate the object and a reference plane, which requires a two-dimensional detector to resolve the correlation between symmetrical pixels. To achieve this, we employ an electron-multiplying charge-coupled device (EMCCD) camera, which captures the entangled photons with a 1000 Hz frame rate. Additionally, we utilize a reconstruction algorithm to extract the correlation information from the EMCCD, achieving the image with enhanced resolution.

We acknowledge the support from Taishan Scholars Program (No. tsqn202306316), Shandong Excellent Young Scientists Fund (No. 2024HWYQ-081), and the National Natural Science Foundation of China under grant No. 12404413.

References

[1] X. Yue, H. Wu, J. Wang, and Z. He, “Quantum super-resolution imaging: a review and perspective,” *Nanophotonics*,

doi: 10.1515/nanoph-2024-0597, 2025.

[2] Z. He, Y. Zhang, X. Tong, L. Li, and L. V. Wang, “Quantum microscopy of cells at the Heisenberg limit,” *Nat. Commun.*, vol. 14, no. 1, 2023

[3] Y. Zhang, Z. He, X. Tong, D. C. Garrett, R. Cao, and L. V. Wang, “Quantum imaging of biological organisms through spatial and polarization entanglement,” *Sci. Adv.*, vol. 10, no. 10, p. eadk1495, 2024.

Towards top-down integrated quantum photonics based on color centers in hBN

A. Delteil[1*]

[1] Université Paris-Saclay, UVSQ, CNRS, GEMaC, 78000, Versailles, France
[*]aymeric.delteil@uvsq.fr

Abstract: We present the quantum optical properties and controlled integration of single-photon sources created in the 2D material hexagonal boron nitride (hBN) by local irradiation with an electron beam. This technique yields high-quality color centers with reproducible emission wavelength in the visible range, enabling scalable integration into monolithic devices for applications in quantum technologies.

Control in position and wavelength of high quality quantum emitters is crucial for implementing a top-down approach in solid-state quantum technologies. In this context, 2D materials bring new opportunities in the field, with specific integration techniques at the ultimate scale of single atomic layers.

We recently demonstrated the local generation of quantum emitters ("B centers") with reproducible wavelength and high-quality photophysics in the visible range [1]. The B centers are created by local irradiation in a scanning electron microscope (fig. 1). They exhibit narrow and reproducible spectra, with a stable and bright emission in the visible range. I will first present their optical properties, including coherence, indistinguishability and quantum efficiency, inferred using quantum optics techniques, such as resonant laser excitation combined with photon correlations [2-4], Hong-Ou-Mandel interference [5] and the Purcell effect [6]. I will also present their controlled integration into monolithic photonic devices [7]. Altogether, the controlled generation of coherent quantum emitters in a 2D material opens appealing perspectives in quantum photonics, with applications in optical quantum technologies.

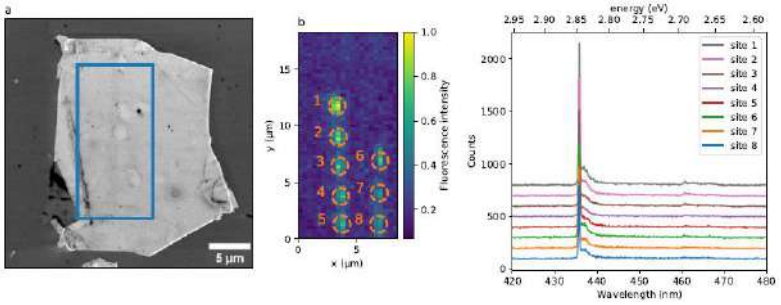


Fig. 1 (a) hBN flake (single crystal of a few tens of nanometers thickness).
(b) Confocal photoluminescence map showing color center luminescence in 8 irradiation sites.
(c) Emission spectra of the eight sites, revealing similar narrow emission lines.

References

1. Fournier, C., Plaud, A., Roux, S., Pierret, A., Rosticher, M., Watanabe, K., Taniguchi, T., Buil, S., Quélin, X., Barjon, J., Hermier, J.-P., and Delteil, A. "Position-controlled quantum emitters with reproducible emission wavelength in hexagonal boron nitride," Nat. Commun., Vol. 12, 3779, 2021.

2. Fournier, C., Watanabe, K., Taniguchi, T., Buil, S., Barjon, J., Hermier, J.-P., and Delteil, A. “Investigating the fast spectral diffusion of a quantum emitter in hBN using resonant excitation and photon correlations,” Phys. Rev. B, Vol. 107, No. 19, 195304, 2023.
3. Gérard, D., Buil, S., Hermier, J.-P., and Delteil, A. “Crossover from inhomogeneous to homogeneous response of a resonantly driven hBN quantum emitter,” arXiv:2411.07202, 2024.
4. Delteil, A., Buil, S., and Hermier, J.-P. “Photon statistics of resonantly driven spectrally diffusive quantum emitters,” Phys. Rev. B, Vol. 109, No. 15, 155308, 2024.
5. Fournier, C., Roux, S., Watanabe, K., Taniguchi, T., Buil, S., Barjon, J., Hermier, J.-P., and Delteil, A. “Two-photon interference from a quantum emitter in hexagonal boron nitride,” Phys. Rev. Appl., Vol. 19, L041003, 2023.
6. Gérard, D., Pierret, A., Fartas, H., Bérini, B., Buil, S., Hermier, J.-P., and Delteil, A. “Quantum efficiency and vertical position of quantum emitters in hBN determined by Purcell effect in hybrid metal-dielectric planar photonic structures,” ACS Photonics, Vol. 11, 5188, 2024.
7. Gérard, D., Rosticher, M., Watanabe, K., Taniguchi, T., Barjon, J., Buil, S., Hermier, J.-P., and Delteil, A. “Top-down integration of a hBN quantum emitter in a monolithic photonic waveguide,” Appl. Phys. Lett., Vol. 122, 264001, 2023.Lastname, F. M. and F. M. Lastname, “Title of the journal paper,” Journal Title Abbreviation, Vol. 34, No. 10, 1064–1076, 1986.

Deterministic Formation of Single Organic Color Centers in Single-Walled Carbon Nanotubes

D. Kozawa[1,2,3], Y. Shiota[2,4*], and Y. K. Kato[1,2*]

[1]Quantum Optoelectronics Research Team, RIKEN Center for Advanced Photonics, Saitama, Japan
[2]Nanoscale Quantum Photonics Laboratory, RIKEN Cluster for Pioneering Research, Saitama, Japan
[3]Research Center for Materials Nanoarchitectonics, National Institute for Materials Science, Ibaraki, Japan
[4]Department of Applied Physics and Physico-Informatics, Keio University, Yokohama, Japan
kozawa.daichi@nims.go.jp (corresponding author)

Abstract

We develop a deterministic technique for creating single organic color centers in carbon nanotubes via in-situ photochemical reaction. By monitoring discrete photoluminescence changes, we precisely control the formation of individual color centers. Photon antibunching confirms their quantum nature, demonstrating the potential of atomically defined quantum emitters for quantum photonic devices.

Quantum light sources that emit single photons on demand are crucial for advancing quantum technologies, including quantum communication, quantum computing, and quantum sensing. Various solid-state systems, such as nitrogen-vacancy centers in diamond, semiconductor quantum dots, and defects in two-dimensional materials, have demonstrated single-photon emission. However, practical implementation requires quantum light sources that operate at room temperature and within the telecom wavelength range. Overcoming material limitations and optimizing emission efficiency remain key challenges in this field.

Single-walled carbon nanotubes (SWNTs) have emerged as a promising platform for quantum light sources due to their unique one-dimensional structure, exceptional optical properties, and intrinsic compatibility with telecom wavelengths [1–3]. A significant advancement in this field has been the introduction of localized color centers in SWNTs, enabling single-photon emission at room temperature. However, the deterministic control over the formation of these quantum defects remains a challenge. Specifically, precise control the number and spatial positioning of defects is critical for scalability, yet existing fabrication techniques often lack the required precision.

In this work, we present a novel technique for the deterministic creation of single organic color centers in SWNTs using an *in-situ* photochemical reaction (Fig. 1). By monitoring discrete intensity changes in photoluminescence (PL) spectra during the functionalization process, we identify and control the formation of individual color centers. The reaction is halted upon the observation of the discrete PL intensity increase, enabling control over the photochemical reaction to form single color centers.

We perform a statistical analysis of PL spectra from individual color centers to quantitatively assess the distribution of color center types, providing insight into the reproducibility of defect formation. Furthermore, position-controlled color center formation is demonstrated and validated using PL imaging, confirming spatial precision in defect placement. To assess the quantum nature of the created defects, we conduct photon correlation measurements, which reveal photon antibunching—a hallmark of single-photon emission. This result establishes that quantum defects can be reliably generated using our proposed method.

Our findings demonstrate a scalable approach for deterministic single-photon emitter fabrication in SWNTs, addressing a critical challenge in quantum photonics. By providing precise

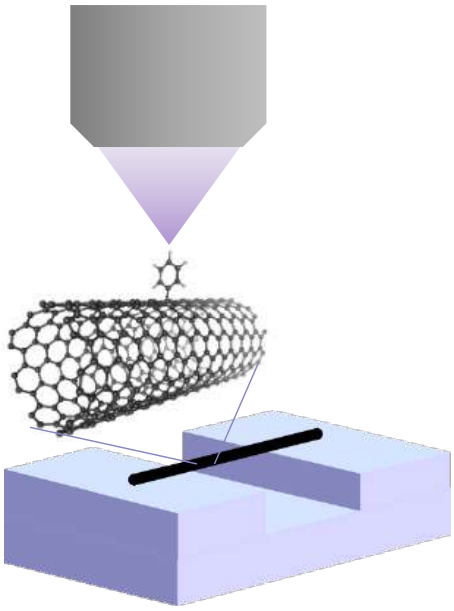


Figure 1: A schematic of *in-situ* photochemical reaction in a air-suspended SWNT where we deterministically create single organic colors using iodobenzene.

control over defect formation, our technique paves the way for integrating SWNT-based quantum light sources into practical quantum communication and computing applications. The ability to generate telecom-compatible single-photon emitters at room temperature further enhances the viability of SWNTs as a platform for future quantum technologies.

Acknowledgements

This work is supported in part by JSPS (KAKENHI JP24H01210, JP23K23161, JP23H00262), JST (JPMJAP2310), the Canon Foundation, the Mitsubishi Foundation, and MEXT (ARIM JPMXP1222UT1136). We thank the Advanced Manufacturing Support Team at RIKEN for technical assistance.

References

[1] Kozawa, D., Wu, X., Ishii, A., Fortner, J., Otsuka, K., Xiang, R., Inoue, T., Maruyama, S., Wang, Y., and Kato, Y. K. "Formation of organic color centers in air-suspended carbon nanotubes using vapor-phase reaction," *Nature Commun., Vol. 13, 2814, 2022*.

[2] Ishii, A., He, X., Hartmann, N. F., Machiya, H., Htoon, H., Doorn, S. K., and Kato, Y. K. "Enhanced single photon emission from carbon nanotube dopant states coupled to silicon microcavities," *Nano Lett., Vol. 18, 3873, 2018*.

[3] Yu, B., Naka, S., Aoki, H., Kato, K., Yamashita, D., Fujii, S., Kato, Y. K., Fujigaya, T., Shiraki, T. "Ortho-substituted aryldiazonium design for the defect configuration-controlled photoluminescent functionalization of chiral single-walled carbon nanotubes," *ACS Nano, Vol. 16, 21452, 2022*.

Lattice Symmetry Guided Spin Dynamics in Supramolecular Assemblies

Xuedan Ma

[1] Department of Materials Science and NanoEngineering, Rice University, Houston, TX, 77005, USA

[2] Center for Nanoscale Materials, Argonne National Laboratory, Lemont, IL, 60439, USA

Synthetic soft materials mimicking biological structures are promising for many applications in fields such as photovoltaics and photocatalysis. For these applications, a deep understanding of charge- and energy-transfer mechanisms is required to build more efficient devices. In this work, we investigate self-assembled 2D supramolecular structures using angle-resolved photoluminescence (PL) imaging techniques and decompose the optical transition dipoles in the supramolecular structures. Combining these optical studies with Monte Carlo simulations, we reveal the important role played by lattice symmetry in charge dissociation, transport, and recombination, as well as the exciton spin states. These mechanistic findings have important implications for engineering soft materials towards efficient energy conversion and photocatalytic applications.

Nanoscale magnetic field imaging based on NV center in diamond: instruments and applications

Pengfei Wang[1]

[1]CAS Key Laboratory of Microscale Magnetic Resonance and School of Physical Sciences, University of Science and Technology of China, Hefei 230026, China, Country
[*]corresponding author: wpf@ustc.edu.cn

Abstract: Based on the solid-state spin sensors in diamond, we have developed scanning nitrogen-vacancy probe microscope for magnetic measurement with a spatial resolution up to 10 nm. We have carried out dark matter detection, *in situ* single cell magnetic resonance imaging, and harmonic spin wave generations in vortex-like spin texture.

The nitrogen vacancy (NV) center in diamond has been studied as an atomic-scale sensor for magnetic resonance technique in the past decade. It was demonstrated the ability to detected the magnetic field from as weak as a single electron or nuclear spin. The combination of nitrogen vacancy center and the scanning probe microscope can bring the single spin sensor to the sample and obtain the magnetic stray field image of the interesting target including the spin textures, current density and spin dynamics. To push forward the application, we have built several scanning NV probe microscope for study. ‘

In this talk, I will give a brief talk on scanning NV probe miscroscope and applications in our lab:

1) We fabricated the scanning NV matrix probe to improve the yielding and decrease the NV-sample distance[1]. The probe contains a 7 × 7 NV nanopillar matrix. It also allows us to adjust the diamond-sample parallelism to allow a better contact.
2) We develop a controller with lock-in amplifier and multi-channel ADC and DAC for spin manipulation and scanning feedback[2].
3) We realized the *in situ* magnetic resonance imaging on a single cutted liver cancel cell. The spatial resolution achieved 10 nm and we also combine the magnetic resonance imaging and transmittive electron microscopy[3].
4) We study the magtisms in topological magnetic film with skymions[4,5], antiferromagnetic spin textures[6] and spin dynamics in magnetic vortex.
5) Beyond the magnetic field imaging, we develop the electric field image and achieve a spatial resolution of 30 nm.

References

1. Guo, M. et al. A flexible nitrogen-vacancy center probe for scanning magnetometry. Review of Scientific Instruments 92, 055001, 2021.
2. Liang, K. et al. Field-programmable-gate-array based hardware platform for nitrogen-vacancy center based fast magnetic imaging. Review of Scientific Instruments 95, 024701, 2024.
3. Wang, P. et al. Nanoscale magnetic imaging of ferritins in a single cell. Science Advances 5, eaau8038, 2019.

4. Cheng, Z. et al. Observation of magnetic domain patterns with tilted uniaxial anisotropy using a single-spin magnetometer. Phys Rev B 105, 064433, 2022.
5. Wang, C.-J. et al. Formation of magnetic biskyrmions mediated by an intrinsic emergent monopole-antimonopole pair. npj Quantum Materials 7, 78, 2022.
6. Ding, Z. et al. Observation of Uniaxial Strain Tuned Spin Cycloid in a Freestanding BiFeO3 Film. Advanced Functional Materials 33, 2213725, 2023.

Cavity quantum electrodynamics with single photon emitters in 2D crystals

C Antón-Solanas[1,*]

[1]*Depto. Física de Materiales, INC, IFIMAC, Universidad Autónoma de Madrid, Madrid, Spain*

*carlos.anton@uam.es

Abstract: Weak light-matter coupling conditions allow to generate bright single photon emission from solid-state sources. In this talk we will present results on quantum dots in monolayers of WSe_2 (and defects in hexagonal Boron Nitride) that are coupled to a tunable Fabry-Pérot microcavity, rendering a bright single photon emission.

The nanoscale control of light-matter interactions allows to create new optoelectronic devices for a wide span of nonlinear and quantum photonic applications. A key part of this endeavour is the exploration of novel materials, which reveal unique properties that can be tailored to specific applications. Regarding the implementation of solid-state single photon sources, relevant emergent materials for quantum light emission are quantum dots in transition metal dichalcogenides monolayers, perovskite quantum dots, or also defects in hexagonal boron nitride nanocrystals. [1]

An optimal single-photon source should satisfy three essential criteria: (1) the emission of photons "*on demand*", (2) emit one photon at a time, and (3) high degree of temporal coherence and uniformity in the properties of emitted photons (spectrum, polarization, spatial mode). Achieving this ideal quantum performance relies on using a resonant cavity to enhance the emitter's spontaneous decay rate via the Purcell effect.

In the first part of this talk, we will present recent advancements in generating single photons from atomically thin WSe_2 monolayers. Local stress within these monolayers creates a confining potential that traps single excitons, resulting in single-photon emission. By embedding these quantum dots in a cryogenic Fabry-Pérot optical cavity, we achieve record emission-efficiency levels. [2] We also study the filtering cavity effects on the temporal coherence of the emitted single photons via Michelson interferometry. [3] Initial quantum communication tests with these sources further demonstrate their viability for single-photon applications. [4]

In the latter part of the talk, I will discuss our experimental progress with an alternative material platform: single defects in hexagonal boron nitride. This emitter, operable at ambient conditions and integrated with a Fabry-Pérot cavity, offers a promising option for cryogenic-free quantum optical applications, including free-space quantum key distribution.

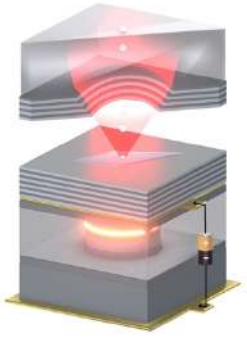


Figure 1: Schematic of the single photon device, composed by a quantum emitter in a hexagonal boron nitride monolayer,

embedded in a reconfigurable Fabry-Pérot open cavity.

References

[1] M. Esmann, S. C. Wein, and C. Antón-Solanas, Solid-State Single-Photon Sources: Recent Advances for Novel Quantum Materials, Advanced Functional Materials **34**, 2315936 (2024).

[2] J.-C. Drawer et al., Monolayer-Based Single-Photon Source in a Liquid-Helium-Free Open Cavity Featuring 65% Brightness and Quantum Coherence, Nano Lett. **23**, 8683 (2023).

[3] V. N. Mitryakhin et al., Engineering the Impact of Phonon Dephasing on the Coherence of a ${\mathrm{WSe}}_{2}$ Single-Photon Source via Cavity Quantum Electrodynamics, Phys. Rev. Lett. **132**, 206903 (2024).

[4] T. Gao, M. von Helversen, C. Antón-Solanas, C. Schneider, and T. Heindel, Atomically-thin single-photon sources for quantum communication, Npj 2D Mater Appl **7**, 1 (2023).

Exciton, charge and spin lattices in moiré heterostructures

A. Högele[1]

[1]Fakultät für Physik, Munich Quantum Center and Center for NanoScience, Ludwig-Maximilians-Universität München, Geschwister-Scholl-Platz 1, 80539 München, Germany
[*]corresponding author: alexander.hoegele@lmu.de

Abstract: Semiconductor van der Waals heterostructures with near-resonant band alignment and non-commensurate lattices such as MoSe2/MoTe2 [1] and MoSe2/WS2 [2] constitute peculiar model systems for excitons, charges and spins localized on moiré lattices. Being robust against mesoscopic lattice reconstruction [3] due to sizable lattice mismatch, they exhibit canonical periodic moiré potentials, while near-resonant band alignment induces hybridization of exciton states across the constituent layers. Using cryogenic optical spectroscopy of moiré excitons, we study the effects of correlated charge and spin ordering in such moiré heterostructures with different twist-angle configurations, highlighting emergent magnetism phenomena on effective monolayer and bilayer Hubbard triangular lattices [4]. Moreover, by employing open cavities, we establish control over neutral and charged moiré exciton-polaritons in the regime of strong light-matter coupling [5], thereby expanding the realm of moiré phenomena in van der Waals heterostructures.

References

1. S. Zhao, X. Huang, R. Gillen, Z. Li, S. Liu, K. Watanabe, T. Taniguchi, J. Maultzsch, J. Hone, A. Högele, and A. S. Baimuratov, Hybrid moiré excitons and trions in twisted MoTe2-MoSe2 heterobilayers, Nano. Lett. 24, 4917 (2024).
2. B. Polovnikov, J. Scherzer, S. Misra, X. Huang, C. Mohl, Z. Li, J. Göser, J. Förste, I. Bilgin, K. Watanabe, T. Taniguchi, A. Högele, and A. S. Baimuratov, Field-Induced Hybridization of Moiré Excitons in MoSe2/WS2 Heterobilayers, Phys. Rev. Lett. 132, 076902 (2024).
3. S. Zhao, Z. Li, X. Huang, A. Rupp, J. Göser, I. A. Vovk, S. Yu. Kruchinin, K. Watanabe, T. Taniguchi, I. Bilgin, A. S. Baimuratov, and A. Högele, Excitons in mesoscopically reconstructed moiré heterostructures, Nat. Nanotechnol. 18, 572 (2023).
4. B. Polovnikov, J. Scherzer, S. Misra, H. Schlömer, J. Trapp, X. Huang, C. Mohl, Z. Li, J. Göser, J. Förste, I. Bilgin, K. Watanabe, T. Taniguchi, A. Bohrdt, F. Grusdt, A. S. Baimuratov, and A. Högele, Implementation of the bilayer Hubbard model in a moiré heterostructure, arXiv:2404.05494 (2024).
5. J. Scherzer, L. Lackner, B. Han, B. Polovnikov, L. Husel, J. Göser, Z. Li, J.C. Drawer, M. Esmann, C. Bennenhei, F. Eilenberger, K. Watanabe, T. Taniguchi, A. S. Baimuratov, C. Schneider, and A. Högele, Correlated magnetism of moiré exiton-polaritons on a triangular electron-spin lattice, arXiv:2405.12698 (2024).

Electrical control of quantum emitters in van der Waals crystals

Jieun Lee[1*]

[1]Department of Physics and Astronomy, Seoul National University, Korea
[*]corresponding author: lee.jieun@snu.ac.kr

Abstract: In this talk, we present our recent works on electrically excited quantum emission in *h*-BN by the voltage applied across 2D heterostructure composed of a graphene/*h*-BN/$NbSe_2$ stack. We also introduce van der Waals material, α-MoO_3, as an emerging platform for room temperature quantum emitters.

Quantum emitters in 2D van der Waals crystals have attracted much recent attention due to their emission properties retained down to atomically thin layers which allows potential integration with various materials with optical, electrical, and magnetic structures.

In the first part of the talk, we will discuss the electrical control of quantum emitters in *h*-BN. Through the heterostructure integration of *h*-BN with metallic 2D materials including graphene and $NbSe_2$, we demonstrate the electrical generation of quantum light emission from *h*-BN atomic defects [1]. By applying voltages between graphene and $NbSe_2$ electrodes sandwiching *h*-BN host material, we observe localized electroluminescence at the overlapped edge of the electrodes which exhibited the photon intensity increasing linearly with the tunneling current. The second-order correlation function measurement performed under the application of a voltage at zero time delay displayed the value below 0.5, confirming the electrically pumped non-classical light generation. From the band structure analysis of graphene/*h*-BN/$NbSe_2$ heterostructure, we found that the work function manipulation of the contact electrodes has enabled the effective supply of charge carriers to atomic defect sites leading to the creation of photon emission with high probability.

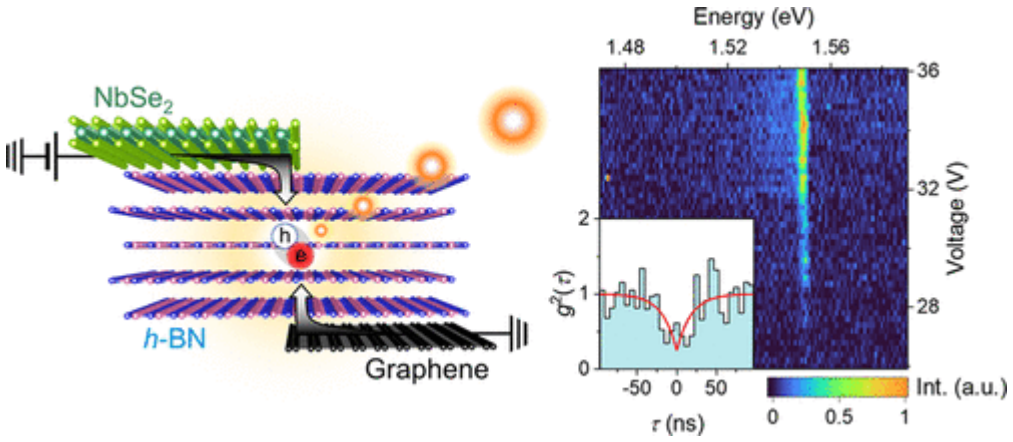


Figure 1. Graphene/*h*-BN/$NbSe_2$ heterostructure and electrically induced quantum light emission.

In the second part of the talk, we introduce our recent work on the observation of quantum emitters in α-MoO_3 [2]. α-MoO_3 is a van der Waals semiconductor with the bandgap of 3 eV, which has been extensively studied in 2D transistors and optoelectronic devices. Due to its high dielectric constant and capability to manipulate charge densities, 2D heterostructures involving α-MoO_3 have found applications in the development of efficient light-emitting devices and photodetectors. Previously, defect-related emissions have been reported in α-MoO_3, but only ensemble measurements have been observed so far. By exfoliating thin layers of α-MoO_3 and

applying thermal annealing process, we observe quantum emission from localized defect sites of α-MoO_3. The second-order correlation function measurement shows the antibunching dip, the emission wavelength is distributed in the range between 560 and 620 nm, the photon intensity reaches nearly 1 Mcounts/s, and the luminescence is observable up to room temperature. Using DFT calculations, an oxygen vacancy center is found as a promising candidate for the observed emitters from calculated photon energy, excited state lifetime, and spectral lineshape of phonon sidebands.

Our results on quantum emitters in van der Waals materials and heterostructures will be potentially beneficial for the optoelectronic implementations of quantum devices for quantum information science.

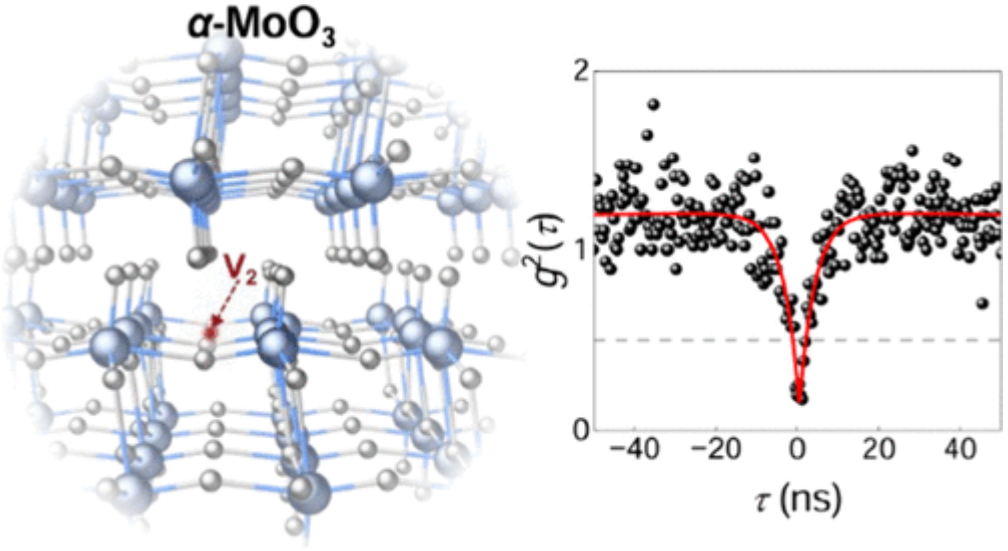


Figure 2. Crystal structure of α-MoO_3 defect center and the second-order correlation function measurement.

References

1. M. Yu, J. Lee, K. Watanabe, T. Taniguchi and J. Lee, "Electrically pumped *h*-BN single-photon emission in van der Waals heterostructure," ACS Nano, 19, 504 (2025).
2. J. Lee, H. Wang, K.-Y. Park, S. Huh, D. Kim, M. Yu, C. Kim, K. S. Thygesen and J. Lee, "Room temperature quantum emitters in van der Waals α-MoO_3," Nano Letters, 25, 1142 (2025).

Atomically Thin Near Infrared Quantum Light Emitters

Han Htoon

Center for Integrated Nanotechnologies, Los Alamos National Laboratory, Los Alamos NM, USA
htoon@lanl.gov

Abstract: This talk will highlight our recent efforts on the development of three 2D material-based quantum light emitters capable of operating in near-infrared spectral regime.

Quantum emitters that operate at near-infrared (NIR) wavelengths, particularly those within the telecom band, hold significant technological importance. The alignment of these SPEs with established fiber optic technologies – characterized by minimal photon loss at the telecom wavelengths – facilitates the seamless integration of quantum and classical communication infrastructures. Two-dimensional (2D) materials have recently emerged as promising materials for quantum light generation, owing to their high photon extraction efficiency, facile coupling to external fields, and seamless integration into photonic circuits. However, most of the 2D material-based quantum emitters reported to date operate at the wavelength <1 μm.

Here in this talk I will present three new 2D quantum emitters capable of wavelength tunable single photon emission across 1000-1600 nm NIR spectral range and operation at liquid nitrogen temperatures. The QEs were realized via nano-pillar-based strain-engineering of few-layer $MoTe_2$ [1] and InSe [2] and MoS_2/WSe_2 heterostructures [3]. The emission wavelengths of $MoTe_2$ and InSe QEs can be tuned with layer-thickness over the entire NIR range covering both O and C telecommunication bands [1, 2], making them ideally suited for the implementation of quantum photonic technologies over the existing optical-fiber-based telecommunication networks. Hanbury Brown and Twiss experiments conducted at 10 K reveal clear photon antibunching. The photon antibunching can be observed up to liquid nitrogen temperature (77 K) in case of $MoTe_2$ quantum emitters. Density-functional-theory calculations and scanning-tunneling-microscopy analyses are conducted on InSe multi-layer to gain insights into the electronic structures and defect states, elucidating the origins of the SPEs.

We have utilized MoS_2/WSe_2 heterostructure as a model system to investigate how strain engineering can be applied to manipulate the interlayer exciton formed at the interface of van der Waal materials [3]. We discovered a new type of quantum light emitting state where an electron residing in the sulfur-vacancy state ~200 meV below the MoS_2 conduction band edge form an optically active excitonic transition with a hole in the hybridized Γ band of MoS_2/WSe_2 heterointerface. The QEs emit in 900-1050 nm range and can operate up to 77K. While this emission is out of the telecommunication band, our approach unlocks the freedom of combining arbitrary 2D semiconductors for building IXs with desired emission energy and extending this strategy for engineering interfacial Γ point transitions in other 2D heterostructures, for instance, in MoS_2/WS_2. Given that monolayer TMDCs emit in the visible spectral range can be combined to generate IXs that emit in the NIR, our findings pave the way for extending the operational wavelength of 2D quantum light sources into the technologically important yet rarely reached NIR regime. Our strategy of creating site-controlled QEs from the defect-bound IXs signifies a paradigm shift in 2D quantum photonics research, moving from engineering intralayer exciton in monolayer structures towards IXs in 2D heterostructures.

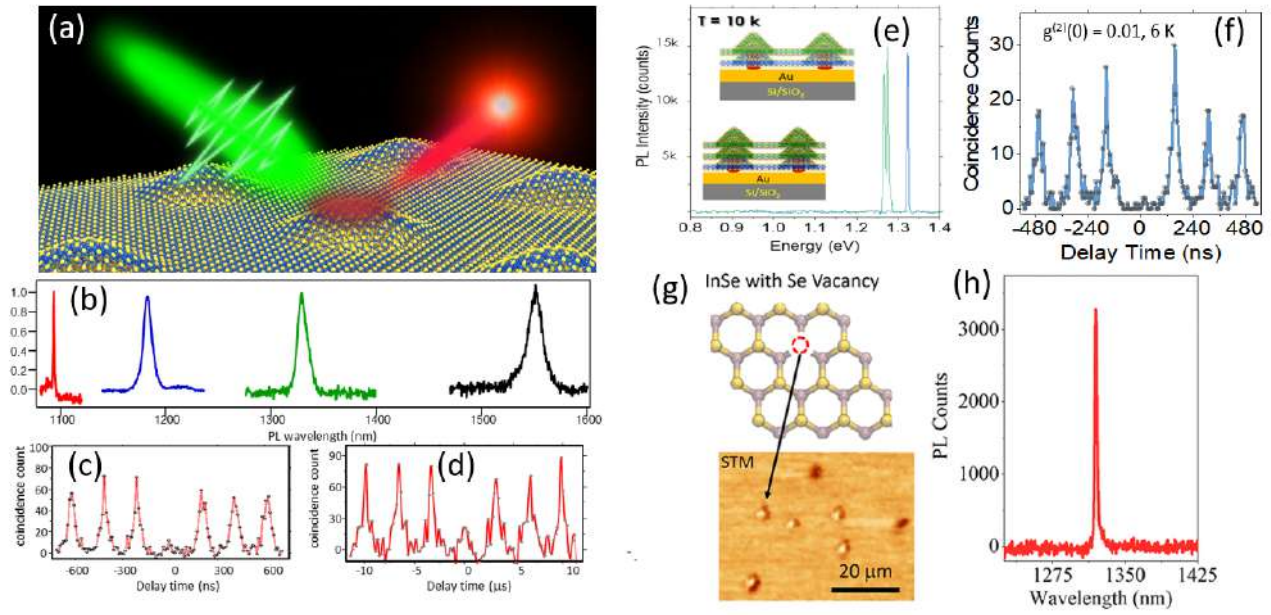


Fig. (a) Schematic illustration of nano-pillar strain-engineering of 2D materials. (b) Wavelength tuning of QE realized in $MoTe_2$ with flake thickness. (c, d) Second order photon correlation $g^{(2)}$ of QEs emitting at 1100 nm and 1550 nm, respectively. (e) PL spectra of quantum emitter realized in MoS_2/WSe_2 and sample structure. (f) $g^{(2)}$ trance of a QE. (g) Atomic structure and STM image of InSe film. (h) PL spectrum of a InSe QE.

References

1. Zhao, H., Pettes, M. T., Zheng, Y. & Htoon, H. Site-controlled telecom-wavelength single-photon emitters in atomically-thin MoTe2. *Nature communications* **12**, 1-7 (2021).
2. Zhao, H., Hus, S. M., Chen, J., Yan, X., Lawrie, B. J., Jesse, S., Li, A.-P., Liang, L. & Htoon, H. Telecom-Wavelength Single-Photon Emitters in Multilayer InSe. *ACS Nano*, doi:10.1021/acsnano.4c13888 (2025).
3. Zhao, H., Zhu, L., Li, X., Chandrasekaran, V., Baldwin, J. K., Pettes, M. T., Piryatinski, A., Yang, L. & Htoon, H. Manipulating Interlayer Excitons for Near-Infrared Quantum Light Generation. *Nano Letters* **23**, 11006-11012 (2023).

Strained two-dimensional semiconductors toward straintronics

Jin Myung Kim[1], Soyeong Kwon[1], and SungWoo Nam[1*]

[1]University of California, Irvine, USA
[*]corresponding author: sungwoo.nam@uci.edu

Abstract: We report strain-induced exciton transport in monolayer WSe_2 across microns at room temperature via steady-state pump-probe measurement. Wrinkle architecture enabled optically-resolvable local strain (2.4%) and energy gradient (49 meV/μm) to WSe_2. We observed strain gradient induced flux of high-energy excitons transported to the nearest energy minima with high transport efficiency.

Optoelectronic information processing is an appealing platform for ultrafast, energy-efficient signal computing and optical communication beyond electronic devices[1,2]. Excitons in atomically-thin two-dimensional (2D) semiconductors, including transition metal dichalcogenides (TMDs), have potential for integrated optoelectronic circuits and interconnects because they are strongly bound, stable even at room temperature[3,4] and can carry rich quantum information as demonstrated in valleytronics[5,6] and antibunched photon emission[7,8]. The overarching requirement for development of such 2D excitonic devices is to realize localization and controlled transport of exciton for logic operation and data transfer. However, because bosonic excitons are charge-neutral, electrical modulation of exciton flux is thus far limited to particular exciton subtypes such as charged trions or interlayer excitons with out-of-plane dipole moments. On the other hand, heterogeneous strain engineering via elastic deformation is a universally applicable technique to manipulate exciton flux because local strain directly tunes the electronic band structure, and results in built-in potential in the form of a bandgap gradient, which funnels excitons to regions with lowest energy without charges or aligned dipoles.

Strain-induced exciton drift/funneling was first experimentally demonstrated in irreversibly deformed bulk semiconductors at cryogenic temperatures. In contrast, exciton funneling in 2D semiconductors can be achieved at ambient temperatures because of

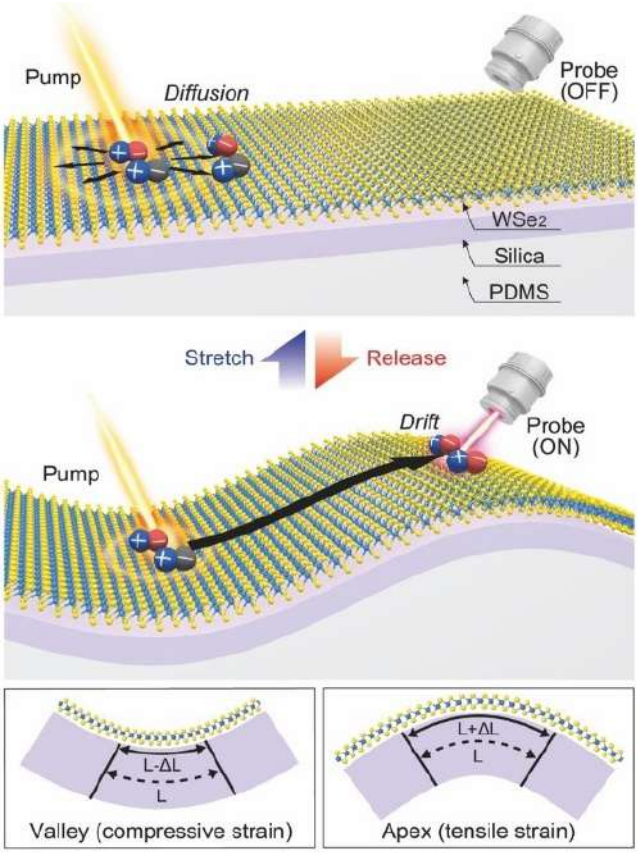


Figure 1. Heterogeneous strain engineering of exciton transport in monolayer WSe_2 via soft wrinkle architecture. Schematic diagram of mechanically reconfigurable wrinkle architecture made of multiple thin films on PDMS including silica skin layer, WSe_2, and encapsulating PMMA layer (not shown in the schematic). Tensile and compressive strain is applied to WSe_2 at apex and valley of the wrinkle architecture, respectively.

reduced dielectric screening and resultant strong exciton binding energy[3,4]. Additionally, the unique mechanical features arising from the atomic thinness of 2D semiconductors, such as high in-plane strength and low bending stiffness, enable strain-sensitive and reversible strain-exciton coupling. Upon these advantages and theoretical prediction in strain engineered atomic materials, strain-induced exciton funneling has been investigated in 2D semiconductors deformed by nano-indentation, 3D nanostructured substrates and trapped gas, or buckle-delaminated by substrate shrinkage. However, experimental demonstration of 2D exciton funneling has been mostly limited to indirect evidence such as photoluminescence (PL) enhancement, comparison of spectral shifts or spatial profiles, and PL emission center shift in spatiotemporally resolved PL. In addition, recent studies of nano-indented TMDs also showed either exciton-trion conversion or limited exciton funneling under nanoscale local strain. Thus, it is unclear if limited observations of strain-induced 2D exciton funneling is a result of the inherent factors, such as short ambient lifetime or trion conversion of 2D intralayer excitons, or extrinsic factors such as insufficient strain and sub-diffraction strain gradient. Accordingly, quantitative elucidation of how efficiently strain can induce exciton funneling and what physical parameters should be considered for practical design of straintronic optoelectronic devices remains elusive thus far.

Here, we present strain-engineered exciton drift in monolayer tungsten diselenide (WSe_2) using pump-probe measurements at ambient temperature. We employed three-dimensional soft wrinkle architecture to create optically-resolvable and mechanically reconfigurable lateral strain gradient from the apex (tensile) to the valley (compressive) of WSe_2 wrinkles (**Fig. 1**). Straintronic switching was made possible by tailoring exciton motion from isotropic diffusion to directional drift. We observed strain-induced exciton drift over micrometer scale distances with high transport efficiency demonstrated by pump-probe characterization. We established a theoretical strain-exciton coupling model based on time-resolved PL measurement and simulation, which revealed strong influence of strain gradient on exciton decay and transport dynamics. We further demonstrated a theoretical model of straintronic exciton router functional at GHz frequency. Our work presents new opportunities for exploring exciton transport and localization for quantum straintronic devices and quantum excitonic phase transitions.

We gratefully acknowledge support from the AFOSR (FA2386-17-1-4071, FA2386-21-1-4129 and FA9550-23-1-0134), NSF (MRSEC DMR-1720633, CMMI-2135734, CMMI-2306039, ECCS-2201054, and CBET-2035584), and ONR (N000142412533).

References

1. Miller, D. A. B. Rationale and challenges for optical interconnects to electronic chips. Proc. IEEE 88, 728–749 (2000).
2. O'Brien, J. L., Furusawa, A. & Vučković, J. Photonic quantum technologies. Nat. Photonics 3, 687–695 (2009).
3. Mueller, T. & Malic, E. Exciton physics and device application of two-dimensional transition metal dichalcogenide semiconductors. npj 2D Mater. Appl. 2, 29 (2018).
4. He, K. et al. Tightly bound excitons in monolayer WSe2. Phys. Rev. Lett. 113, 026803 (2014).
5. Schaibley, J. R. et al. Valleytronics in 2D materials. Nat. Rev. Mater. 1, 16055 (2016).
6. Unuchek, D. et al. Valley-polarized exciton currents in a van der Waals heterostructure. Nat. Nanotechnol. 14, 1104 (2019).
7. Koperski, M. et al. Single photon emitters in exfoliated WSe2 structures. Nat. Nanotechnol. 10, 503–506 (2015).
8. Palacios-Berraquero, C. et al. Large-scale quantum-emitter arrays in atomically thin semiconductors. Nat. Commun. 8, 15093 (2017).

Fundamental Limits of Boron-Vacancy Spin Dynamics in Hexagonal Boron Nitride

Benjamin J. Lawrie[1], Yueh-Chun Wu[1], Abhishek B. Solanki[2], Ian Gallagher[1], Hamza Ather[3,4], Aravindh Shankar[2], Priyo Adhikary[2], Owen Matthiessen[2,4], Xingyu Gao[3], Demid Sychev[2-4], Alexei Lagoutchev[4], Tongcang Li[2-4], Yong P. Chen[2-4], Vladimir M. Shalaev[2-4], Pramey Upadhyaya[2], Huan Zhao[5], Ivan Vlassiouk[5]

[1]*Materials Science and Technology Division, Oak Ridge National Laboratory, Oak Ridge, Tennessee, 37830 USA*
[2]*Elmore Family School of Electrical and Computer Engineering, Purdue University, West Lafayette, IN 47907, USA*
[3]*Department of Physics and Astronomy, Purdue University, West Lafayette, Indiana 47907, USA*
[4]*Birck Nanotechnology Center, Purdue University, West Lafayette, Indiana 47907, USA*
[5]*Center for Nanophase Materials Sciences, Oak Ridge National Laboratory, Oak Ridge, Tennessee, 37830 USA*
[*]Corresponding author: lawriebj@ornl.gov

Abstract: We probe the spin-relaxation dynamics of boron-vacancy spin defects in hBN and show that T_1 is strongly sensitive to the applied magnetic field, especially at low temperatures. Moreover, we explore the effect of the boron vacancy formation on the fundamental limits of T_1 and T_2 in these 2D spin defects.

Boron-vacancy (V_b^-) spin defects in hexagonal boron nitride (hBN) are drawing increasing interest as resources for quantum sensing of spin ordering and spin fluctuations in van der Waals heterostructures. The V_b^- ground state is a spin triplet state ($S = 1$) that is further split into $m_s = 0, \pm 1$ sublevels by a zero-field splitting of $3.5\ GHz$. The ground state splitting is sensitive to external magnetic fields via the Zeeman effect and electric fields via the Stark effect, enabling the spin defects to serve as in situ probes of these quantities with diffraction-limited spatial resolution. The sensitivity of these defects to external magnetic fields at $DC - GHz$ frequencies is closely related to the linewidth of the ground-state spin transition, the lattice environment of the host material, and the intrinsic spin-relaxation time (T_1) and decoherence time (T_2). While T_1 is influenced by spin-spin interactions and spin-phonon interactions, T_2 is governed by the coupling of the ground state spin with the nuclear spins in the environment. The effect of a small T_2 can be circumvented by applying appropriate microwave pulse sequences to filter the environmental noise. However, the upper limit of the effective T_2 time is determined by the T_1time. Therefore, it is critical to understand the nature of the relaxation dynamics of the V_b^-defects as the community begins to develop new approaches to quantum sensing with 2D spin defects.

We initially focus on magnetic field and temperature dependent spin relaxation dynamics of V_b^-defects for fields of $0 - 7\ T$ (corresponding to ground-state splitting $\sim 3.5\ to\ 200\ GHz$) and temperatures of $2 - 300\ K$. Spin relaxation processes at low temperatures are commonly ascribed to two-phonon processes or Orbach type processes due to coupling with quasilocalized phonons. We show here that, while the measured spin contrast is relatively independent of field, the T_1 time is strongly field dependent with the maximum measured T_1 occuring around $1.8\ T$, suggesting an intrinsic magnetic-field-dependent relaxation mechanism.

In order to better understand the intrinsic limitations to T_1 and T_2 for V_b^-, we patterned V_b^-defects in hBN by electron, neutron, He^+ and Ar^+ irradiation on both bulk substrates and freestanding STEM membranes. The room temperature spin-lattice relaxation time for these samples shows a strong anticorrelation with defect density, decreasing from 15 μs at low defect densities to <1 μs at high defect densities. This observation, together with the measured field-dependent T_1 suggests that a combination of dipolar spin-spin interactions and resonant cross-relaxation mechanisms may serve to limit T_1 in typical hBN samples. However, neutron irradiated freestanding hBN membranes appear to exhibit substantially reduced unwanted defect bands, and preliminary measurements suggest that these samples may exhibit improved T_1 as a result. Additional ongoing relaxometry measurements are utilizing scanning NV microscopy to probe cross-relaxation interactions in hBN with nanoscale spatial

resolution. Finally, if time allows, we will also discuss ongoing experiments focused on milliKelvin temperature-dependent probes of T_1 and T_2 for V_b^- and for carbon spin-defects in hBN. Together, these results provide insights into the nature of spin-spin and spin-phonon coupling in 2D quantum sensors and highlight the potential of these defects for quantum sensing in high magnetic fields and milliKelvin environments.

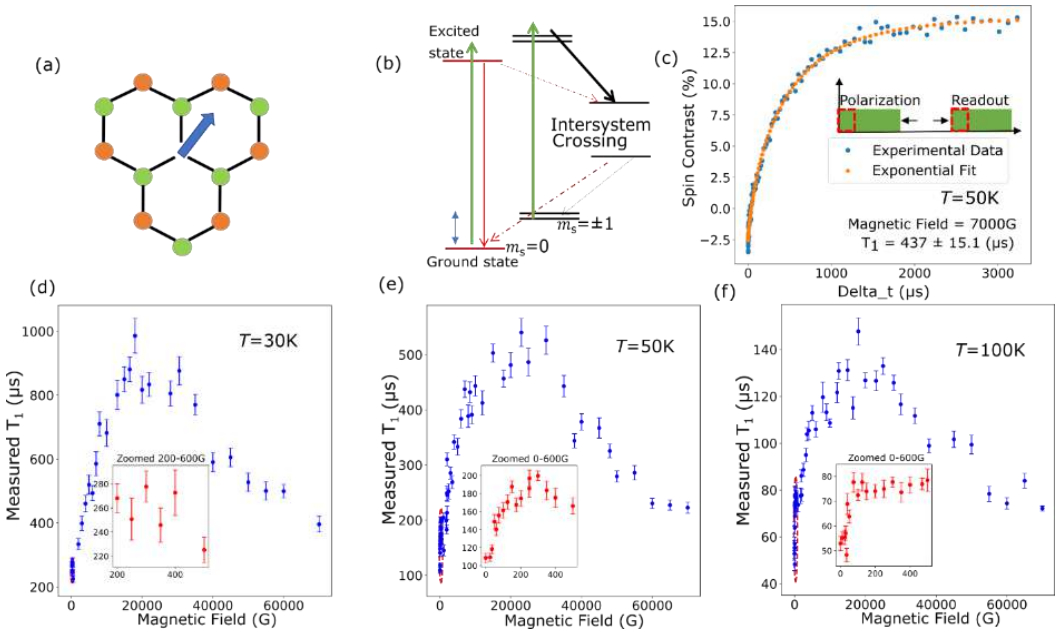


Figure 1. (a) Schematic of boron-vacancy center. The blue arrow represents the out of plane spin dipole. (b) The energy level diagram of boron-vacancy center in hBN. (c) Measured T_1 relaxation curve and exponential fit for an external field of $7000\ G$ and a $50K$ sample temperature. The experimental pulse sequence is shown in the inset. (d, e, f) Measured T_1as a function of applied external magnetic field up to 7 T at temperatures of 30, 50, 100 K.

This research was sponsored by the U.S. Department of Energy, Office of Science, Basic Energy Sciences, Materials Sciences and Engineering Division and by the Quantum Science Center, a National Quantum Information Science Research Center supported by Office of Science. Sample preparation and scanning NV microscopy was supported by the Center for Nanophase Materials Sciences, which is a U.S. Department of Energy Office of Science User Facility.

Diamond Color Center for In-Memory Computing

Xiaodong Yan[1,2,3]
1. Department of Materials Science and Engineering, University of Arizona, Tucson, AZ 85719
2. Department of Electrical and Computer Engineering, University of Arizona, Tucson, AZ 85719
3. Wyant College of Optical Sciences, University of Arizona, Tucson, AZ 85719

Abstract: This presentation will discuss our recently work on the diamond color center and elucidate our efforts to interpret and harness the unique emission property, which lead to novel IMC functionalities.

In-memory computing[1] (IMC) is an emerging technology designed to overcome the limitations of the von Neumann bottleneck by drawing inspiration from the human brain and enabling highly parallel data processing. However, developing IMC devices and hardware capable of handling vast amounts of information while maintaining sustainability and power efficiency presents significant challenges. Addressing these challenges requires novel materials with exceptional physical properties.

Diamond color centers[2], widely studied in quantum science and technology for their unique optical properties, remain largely unexplored for IMC applications. In this presentation, I will introduce our recent research on diamond color centers and detail our efforts to interpret and harness their distinct emission properties, which unlock novel IMC functionalities. I will discuss the underlying mechanisms of our diamond color centers, supported by both experimental and theoretical insights. Finally, I will demonstrate how their reconfigurable nature enables bio-realistic neuromorphic functionalities, paving the way for energy-efficient IMC architectures optimized for artificial intelligence and machine learning hardware accelerators.

References

1. A. Sebastian et al, *Nat. Nanotech.* 15, 529 (2020)
2. T. Muller et al, *Nat. Commun.* 5, 3328 (2014)

A Colloidal Quantum Dot on a Hybrid Nanoantenna as an Ultrafast and Efficient Single Structured Photon Source for Room Temperature High Dimensional Quantum Communications

Ronen Rapaport[1, 2,*]

[1]*Racah Institute of Physics, The Hebrew University of Jerusalem, Jerusalem 9190401, Israel*
[2]*The Center for Nanoscience and Nanotechnology, The Hebrew University of Jerusalem, Jerusalem 9190401, Israel*
[*]*ronen.rapaport@mail.huji.ac.il*

Abstract: We demonstrate ultrabright, highly directional single photon sources operating at room temperature, utilizing a colloidal quantum dot positioned on a hybrid nanoantenna device, that produces structured photons. We then demonstrate two high-dimensional quantum key distribution protocols, by encoding and decoding qudits on different degrees of freedom of these structured photons.

Deterministic GHz-rate single photon sources (SPS) at room-temperature would be essential components for various quantum applications. Our on-chip single photon source utilzes a ‘giant’ colloidal quantum dot (gQD) deterministically bound to a complex monolithic photonic resonator constructed of a gold nanocone responsible for the rate enhancement, enclosed by a circular Bragg antenna for emission directionality [1-6]. A repeatable process accurately binds a gQD that show highly stable, blinkingless emission to the tip of the antenna-embedded super-sharp nanocone. As a result we achieve simultaneous >20-fold emission rate enhancement, with sub-ns emission lifetimes, and a record-high directionality, leading to an increase in the observed single-photon brightness by more than two orders of magnitude. Our device results in a usable photon emission rates of tens of MHz, thus enabling ultrafast light-matter interfaces for quantum communications at ambient conditions. We further demostrate a practical plug-and-play SPS with an antenna device which allows back optical pumping of the quantum dots and a front directional single photon emission with high single photon purity and an almost unity colllection efficiency [7], as well as a direct coupling to a fiber without any additional coupling optics.

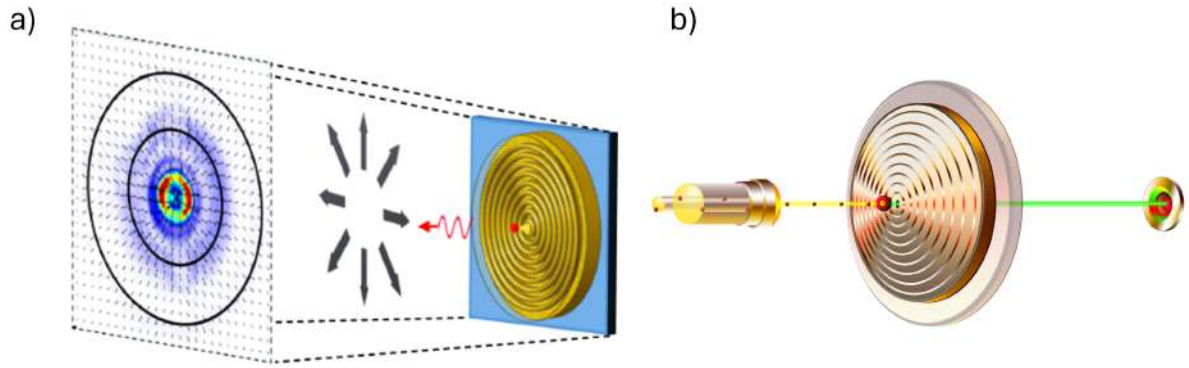


Figure 1:(a) Schematic sketch of the SPS emitting radially polarized single photons, with an experimental back focal plane image exhibiting a 'donut' shape structure associated with radial polarization. (b) Sketch of fiber coupled SPS with back excitation and forward highly directional emission directly coupled into an optical fiber

To demonstrate the relevance of our SPS for real quantum communication applications, we experimentally emulate two high-dimensional quantum key distribution (HDQKD) protocols. HDQKD is a promising avenue to address the inherent limitations of basic QKD protocols.
First, we demonstrate a HDQKD protocol by encoding information in a high-dimensional (d=3) space of the orbital angular momentum of the photons [8]. Our experimental configuration incorporates two spatial light modulators for encoding and decoding the spatial information carried by individual photons. We

demonstrate experimentally secure qudit transmission exceeding one secure bit per photon, thus already beating the traditional d=2 QKD capacity [8].
Finally, we show a new concept for encoding high-dimentional quantum information on single photons from our SPS, taking advantage of the high-quality vector-beam radial polarization nature of the emitted photons from the resoator-antenna device [9], to encode information on mutually unbiased hybrid spatial-polarization modes with d=4, establishing the feasibility of utilizing high radiative quantum yield gQD-based SPS as a practical avenue for HDQKD applications.

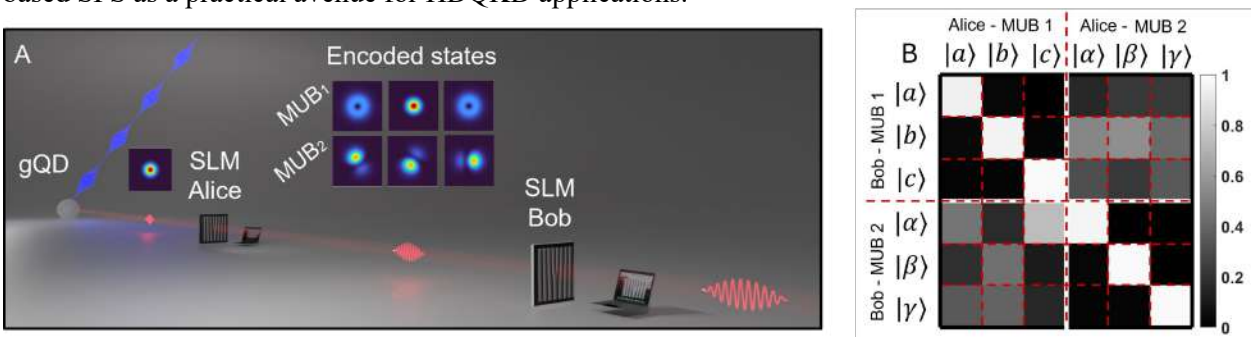


Figure 2: (A) A visualization of the experimental process: a pulsed laser excites a gQD, generating single photons that are encoded with spatial information by Alice's SLM and projected onto corresponding modes by Bob's SLM. (B) Projection measurements: normalized

References

[1] Hamza Abudayyeh and Ronen Rapaport, *Quantum Sci. Technol.* **2** 034004 (2017)
[2] Abudayyeh et al., ACS Nano 15, 11, 17384 (2021)
[3] Abudayyeh et al., APL Photonics 6, 036109 (2021)
[4] Abudayyeh et al., ACS Photonics 6, 446 (2019)
[5] Livneh et al., Nanoletters 16, 2527 (2016)
[6] Waltrich et al., New Journal of Physics 23, 113022 (2021)
[7] B Lubotzky, et al., Nano Letters 24, 2, 640-648 (2024)
[8] D. Halevi, et al., Optica Quantum 2, 5, 351–357 (2024)
[9] A Nazarov, Y Bloom et al., ACS Photonics 11, 10, 4453-4460 (2024)

Quantum Light in a Moiré Heterostructure

Mauro Brotons-Gisbert

Institute for Photonics and Quantum Sciences, Heriot-Watt University, Edinburgh, UK

The unique physical properties of two-dimensional materials, combined with the ability to stack unlimited combinations of atomic layers with arbitrary crystal angle, has unlocked a new paradigm in designer quantum materials. For example, when two different monolayers are brought into contact to form a heterobilayer, the electronic interaction between the two layers results in a spatially periodic potential-energy landscape: the moiré superlattice [1]. The moiré superlattice can create flat bands and quench the kinetic energy of electrons, giving rise to strongly correlated electron systems. Further, single particle wave packets can be trapped in the moiré potential pockets with three-fold symmetry C_3 symmetry to form interlayer exciton (IX) 'quantum dots' which can emit single photons [2,3].

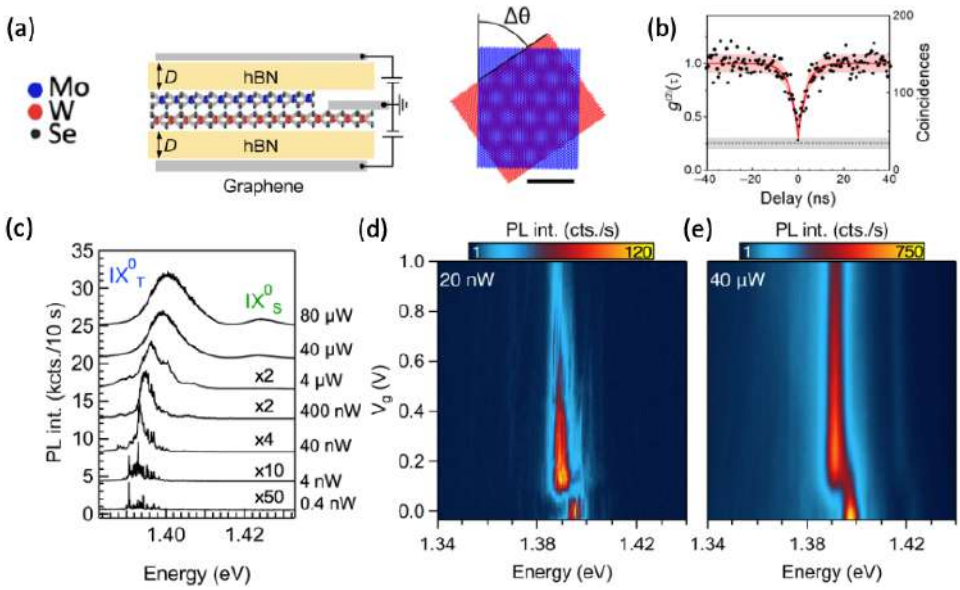


Figure 1. (a) Sketch of the dual-gated $WSe_2/MoSe_2$ heterobilayer. Graphite layers are used as contacts for top, bottom, and heterobilayer, while hBN layers (D = 18 nm) are used as dielectric spacers. **(b)** Second-order photon correlation statistics of a moiré-trapped IX under CW excitation. **(c)** Power dependence of moiré-trapped IXs. **(d)**, **(e)**, Gate-voltage controlled PL of IXs in the neutral ($0 < V_g \leq 0.1$ V) and electron doping regime ($V_g \geq 0.1$V) at P_{exc} =20 nW (d) and P_{exc} =40 μW (e) at 4K.

In this talk, I will review our recently published results on the creation of moiré-trapped IXs. First, I will present the continuous evolution from a few trapped IXs to an ensemble of IXs with both triplet and singlet spin configurations in a gate-tunable 2H-$MoSe_2/WSe_2$ heterobilayer [Figs. 1(a) and 1(c)] [4]. I will then discuss signatures of dipolar interactions in the IX ensemble regime, which, when combined with magneto-optical spectroscopy, reveal that both the narrow quantum-dot-like and broad ensemble emission originate from IXs trapped in moiré potentials with the same atomic registry [4].

Furthermore, electron doping leads to the formation of negative on-site IX trions with a binding energy of ~7 meV in both the low- and high-IX-density regimes [Figs. 1(d) and 1(e)] [4]. At low IX densities, additional electron doping results in a sequential filling of empty superlattice sites, giving rise to a Coulomb staircase—stepwise changes in IX trion emission energy due to Coulomb interactions with carriers at nearest-neighbor moiré sites [5].

Finally, I will discuss the presence of three distinct species of localized negative IX trions with contrasting spin-valley configurations in the IX ensemble regime [4]. These findings not only identify the origin of IX emission in $MoSe_2/WSe_2$ heterobilayers but also underscore the crucial role of Fermi-level control, dipolar interactions, and Coulomb effects in these highly tunable quantum materials.

[1] H. Yu *et al*. *Sci. Adv*. **3**, e1701696 (2017).
[2] K. Seyler, *Nature* **567**, 66 (2019).
[3] H. Baek *et al*., *Sci. Adv*. **6**, eaba8526 (2020).
[4] Brotons-Gisbert *et al*., *Phys. Rev. X* **11**, 031033 (2021).
[5] H. Baek *et al*., *Nature Nanotech*. **16**, 1237 (2021).

Increased Formation of Silicon-Vacancies in Diamond by Sub-Bandgap Light Irradiation during Annealing

Coleman Cariker[1], Yifan Yao[2], Andre Schleife[2], Michael Titze[1,*]

[1]Sandia National Laboratories, Albuquerque, NM, USA
[2]Departement of Materials Science and Engineering, University of Illinois Urbana-Champaign, Urbana, IL, USA
[3]Materials Research Laboratory, University of Illinois Urbana-Champaign, Urbana, IL, USA
[4]National Center for Supercomputing Applications, University of Illinois Urbana-Champaign, Urbana, IL, USA
[*]corresponding author: mictitz@sandia.gov

Abstract: This study investigates the brightness enhancement of silicon-vacancy (SiV) centers in diamond through UV irradiation during post-implantation annealing. Results show a 15% increase in photoluminescence brightness, attributed to improved SiV formation due to reduced divacancy density, suggesting potential for optimized manufacturing of single defect sites for quantum applications.

Color centers in diamond, particularly silicon-vacancy (SiV) centers, have garnered significant attention due to their potential applications in quantum information science (QIS). SiV are advantageous because they can couple electronic spins with optical photons and can be manufactured at scale. SiV are interesting candidates for QIS due to low electron-phonon coupling and high brightness, leading to an overall high quantum efficiency.

The fabrication of SiV centers typically involves silicon ion implantation followed by annealing. However, this process can lead to collateral damage in the diamond lattice, resulting in the formation of defects like divacancies (VV). The formation of SiV requires a monovacancy adjacent to a silicon substitutional defect, but the presence of VVs complicates this process. During annealing, monovacancies become mobile at around 900 K, but they are more likely to encounter another vacancy than an implanted silicon ion, leading to the formation of VVs that persist until approximately 1100 K, resulting in a low yield of SiV centers.

To address the issue of low SiV yield, previous work has explored charging vacancies during annealing, which can reduce the number of VVs [1]. These studies have shown that generating excess charges during ion implantation can suppress VV formation through Coulomb repulsion. However, this method typically requires implantation of additional ion species, introducing more vacancies. Alternatively, optical excitation, particularly using UV light, has emerged as a promising technique for defect manipulation by modifying electron distributions.

This study combines density functional theory (DFT) simulations and experimental methods to investigate the effects of UV irradiation during post-implantation annealing on the dissociation of VVs and the yield of SiVs [2]. DFT simulations are used to analyze mid-gap energy levels and the binding energy of VVs, while experimental measurements assess the Si to SiV activation yield through scanning photoluminescence (PL).

DFT calculations were performed using the Vienna Ab-initio Simulation Package (VASP) to investigate the optical spectrum and binding energies of VVs and SiVs. The electronic structure and binding energy of VV-related states was analyzed, revealing that UV excitation could destabilize VVs. The destabilized VVs can then be easily dissociated, facilitating the formation of SiVs. The binding

energy of SiVs was found to be higher than that of VVs, indicating that SiVs formed following VV dissociation will be stable complexes.

Silicon ions were implanted into diamond samples using a focused ion beam (FIB) implanter. Following implantation, the samples were annealed at 800 °C for 24 hours, with UV light exposure during the annealing process. Half the sample was blanked during IV irradiation, allowing for the comparison of PL brightness between UV-irradiated and non-irradiated regions of the sample.

Spectrally resolved photoluminescence (PL) confirms the presence of silicon-vacancy (SiV) centers, shown in Figure 1(a). The activation yield of SiVs per implanted ion is assessed by PL maps containing approximately 300 SiV locations for both the UV blanked and irradiated regions. In the UV blanked region, PL yield is assume to be 3%, resulting in an average of 9 ± 3 SiV defects per location [3]. A representative implant area is shown in Figure 1(b). On the UV irradiated side, individual SiV brightness is assumed to be the same, such that from the observed brightness a number of SiV contributing to the emission can be extracted. A detailed analysis of individual spot brightnesses is shown in Figure 1(c) and indicates a 15-20% increase in brightness in the UV-irradiated region compared to the blanked region, attributed to a higher number of active SiVs resulting from reduced divacancy (VV) density.

Further optimization of annealing temperature and UV exposure duration could enhance SiV brightness. In conclusion, this research highlights the potential of using sub-bandgap light irradiation in during annealing to enhance the formation of SiV centers in diamond, paving the way for advancements in quantum technologies and other applications reliant on these unique color centers.

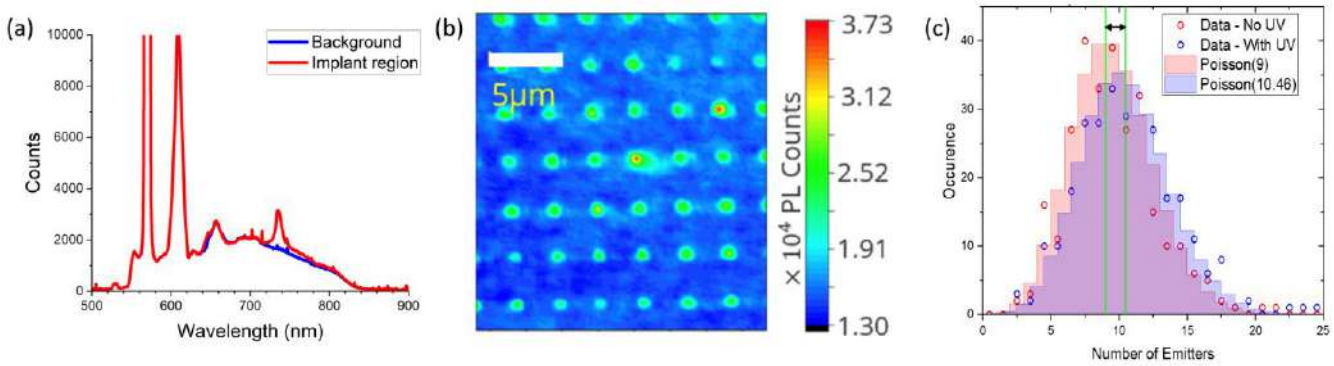


Figure 1 (a) PL spectrum comparing the implanted region and background. The peak at 737 nm confirms that PL is due to SiV. (b) PL map showing the implanted array of SiV. (c) Comparison of ~300 implant regions for both UV blanked and irradiated region, showing a 15 % increase in SiV formation.

Acknowledgement

Sandia National Laboratories is a multimission laboratory managed and operated by National Technology & Engineering Solutions of Sandia, LLC, a wholly owned subsidiary of Honeywell International Inc., for the U.S. Department of Energy's National Nuclear Security Administration under contract DE-NA0003525.

References

[1] J. Mah*, et al.*, APS March Meeting, 2024; [2] Y. Yao*, et al.*, APS March Meeting, 2023; [3] M. Titze*, et al.*, Nano Letters, 22, 8, 3212-3218, 2022

Quantum Transport and Spin-Valley Control in Monolayer $MoTe_2$ for Photonic Integration

M. A. Campbell[1], **T. J. McSorley**[1], **J. Liu**[1], **and L. A. Jauregui**[1,*]

[1]Department of Physics and Astronomy, University of California, Irvine, CA 92697, USA
[*]corresponding author: lajaure1@uci.edu

Abstract: We demonstrate quantum transport in monolayer $MoTe_2$ with engineered Ohmic contacts via $RuCl_3$. High mobility and Zeeman-split oscillations reveal broken spin-valley degeneracy. Integrated with prior advances in high-quality growth and strain-tunable emission, our results establish monolayer $MoTe_2$ as a promising platform for hybrid quantum photonic and light-emitting devices.

Monolayer $MoTe_2$ offers a compelling platform for quantum photonics, combining a direct bandgap (~1.1 eV), strong excitonic interactions, and large spin-orbit coupling. However, realizing its potential in quantum light-emitting and photonic integrated systems has been limited by contact resistance and instability under ambient conditions. Here, we report a heterostructure approach using α-$RuCl_3$ as a charge-transfer substrate to enable Ohmic contacts and cryogenic magneto-transport in monolayer $MoTe_2$. The resulting devices exhibit high hole mobility (> 4,000 $cm^2/V \cdot s$) and clear Shubnikov–de Haas oscillations for $B > 2.3$ T. At higher fields ($B > 7$ T), oscillation splitting indicates broken spin-valley degeneracy with a large effective g-factor ($g^* \approx 10.8$), supporting spin- and valley-selective phenomena (as shown in Figure 1). Raman and photoluminescence studies confirm significant strain and heavy hole doping, the latter leading to exciton quenching and altered recombination dynamics.

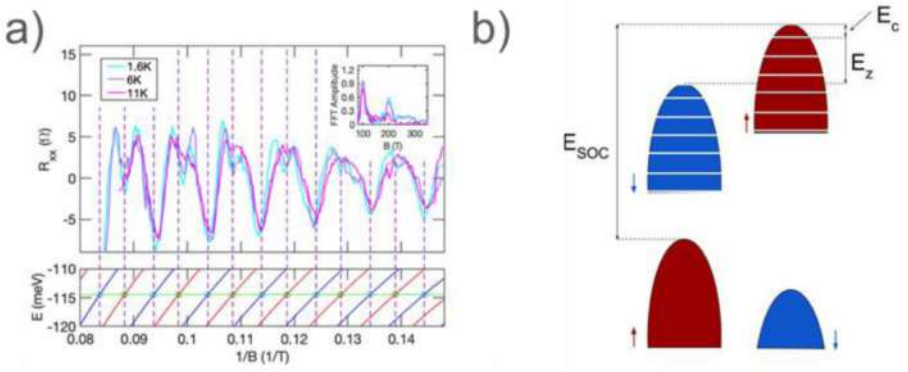


Figure 1a) High field ΔR_{xx} vs. $1/B$ at 3 representative temperatures, T = 1.6K, 6K, and 11K. Inset: FFT of ΔR_{xx} vs. $1/B$ at different Ts. Lower panel: simulated Landau fan diagram using our extracted parameters for a Fermi energy EF = -115meV, where the dips in ΔRxx are aligned with the Landau levels (LLs) from two spin-polarized bands. Red and blue lines correspond to spin up and spin down respectively. b) Schematic of the K and K' bands in MoTe2 under a high magnetic field that creates discrete LLs, separated by the cyclotron energy Ec. B lifts the degeneracy of the K and K' bands through the Zeeman energy $EZ = g * \mu BB$, where μB is the Bohr magneton and g^* is the effective Landé g-factor.

These findings complement recent progress in strain engineering of van der Waals heterostructures on piezoelectric substrates, where tunable electrical properties were demonstrated via dynamic lattice deformation [1], and leverage our previously reported method for growing high-quality $MoTe_2$ crystals with long-lived excitonic species [2,3]. Together, these advances establish a pathway for photonic integration of monolayer $MoTe_2$ with tunable optical and quantum transport properties. The demonstrated control over contacts, doping, and exciton behavior positions this system as a versatile building block for hybrid quantum light-emitting and electrically driven two-dimensional optoelectronic platforms.

Acknowledgements, L.A.J. acknowledges the support from the NSF-CAREER (DMR 2146567). T.M. acknowledges support from the Eddleman Quantum Institute (EQI) through the EQI graduate research fellowship.

References

1. McSorley, T. J., et al, "Dynamic Carrier Modulation via Nonlinear Acoustoelectric Transport in van der Waals Heterostructures," Arxiv:2503.16033.
2. Yepez-Rodriguez, S., et al, "Rydberg exciton states and near-infrared light-emitting diode in monolayer $MoTe_2$ devices," Arxiv:2403.19189.
3. Jauregui, L. A., et al, "Electrical control of interlayer exciton dynamics in atomically thin heterostructures," Science, 366, 6467, 870-875, 2019.

From Light to Matter: Controlling Excitons for Quantum Innovation

Libai Huang[1*]

[1] Purdue University, West Lafayette, IN, 47907, USA
[*]corresponding author: libai-huang@purdue.edu

Abstract: I will discuss our latest discoveries on how we manipulate exciton quantum phases in two-dimensional moiré superlattices. These superlattices have the potential to serve as solid-state analogues to ultracold gases for quantum simulations. We applied transient photoluminescence and ultrafast reflectance microscopy to image non-equilibrium exciton phase transitions.

At the most fundamental level, transport of energy carriers (such as electrons and excitons) in the solid state is determined by their quantum wavefunctions and the interactions with their surroundings. However, studying this transport at the quantum level is challenging because excitons lose their quantum coherent properties extremely quickly, on the subpicosecond timescale, and are confined to nanometer-scale regions. To truly probe transport in the quantum regime, we need experimental techniques that capture both their spatial and temporal dynamics.

To tackle this challenge, my research group has developed advanced imaging techniques that combine optical microscopy with ultrafast spectroscopy. These methods allow us to visualize exciton transport at the nanoscale to the mesoscale across a wide range of temperatures. I will discuss our latest discoveries on how we manipulate excitons in two-dimensional moiré superlattices. These superlattices have the potential to serve as solid-state analogues to ultracold gases for quantum simulations. A key open question is the coherence and dynamics of the quantum phases arising from photoexcited moiré excitons, particularly amid dissipation. Here we use transient photoluminescence and ultrafast reflectance microscopy to image non-equilibrium exciton phase transitions. Counterintuitively, experimental results and theoretical simulations indicate that strong long-range dipolar repulsion freezes the motion of the Mott insulator phase for over 70 ns. In mixed electron–exciton lattices, reduced dipolar interactions lead to diminished freezing dynamics. These findings challenge the prevailing notion that repulsion disperses particles, whereas attraction binds them. The observed phenomenon of frozen dynamics due to strong repulsive interactions is characteristic of highly coherent systems, a feature previously realized exclusively in ultracold gases.

Quantum optical description of nanophotonic systems

Johannes Feist[1,2*]

[1] Departamento de Física Teórica de la Materia Condensada, Universidad Autónoma de Madrid, E-28049 Madrid, Spain
[2] Condensed Matter Physics Center (IFIMAC), Universidad Autónoma de Madrid, E-28049 Madrid, Spain
[*]corresponding author: johannes.feist@uam.es

Abstract: We show how to obtain a quantum-optics like description in terms of a few discrete "cavity" modes for the quantum light-matter interaction in arbitrary nanophotonic structures, while still taking into account the full nanophotonic complexity of light propagation and emission.

The control of the interaction between quantum emitters using nanophotonic structures holds great promise for quantum technology applications, while its theoretical description for complex nanostructures is a highly demanding task as the electromagnetic (EM) modes form a high-dimensional continuum. We here introduce an approach that permits a quantized description of the full EM field and its coupling to various emitters through a small number of discrete modes, without any restrictions on the emitter level structure. The low computational demand of this method makes it suitable for studying dynamics for a wide range of parameters. We illustrate the power of our approach for various hybrid metallodielectric structures.

Additionally, we show how to extend the approach to give direct access to photon correlations of the emitted light resolved in space, frequency, time and polarization for arbitrary electromagnetic environments. While experimental measurements of photon correlations have become routine in laboratories, theoretical access to these quantities for the light generated in complex nanophotonic devices remains a major challenge. Current methods are limited to specific simplified cases and lack generality. Within the macroscopic QED framework, we develop a practical tool to compute electric field correlations for complex quantum systems by including lossy two-level systems that act as field detectors within the system. The method correctly accounts for fully retarded light propagation to the detectors. We demonstrate the effectiveness and robustness of the proposed technique by studying the photon correlations of one and two emitters in close proximity to a plasmonic nanoparticle. The simulations show that even in these relatively simple configurations, the light statistics exhibit a strong angular dependence. These results highlight the importance of going beyond conventional quantum-optical approaches to fully capture the analysed physical effects and enable the study of the quantum light generation in realistic nanophotonic devices.

References

1. I. Medina, F. J. García-Vidal, A. I. Fernández-Domínguez, and J. Feist, "Few-Mode Field Quantization of Arbitrary Electromagnetic Spectral Densities", Phys. Rev. Lett. 126, 093601, 2021.
2. M. Sánchez-Barquilla, F. J. García-Vidal, A. I. Fernández-Domínguez, and J. Feist, "Few-mode field quantization for multiple emitters", Nanophotonics 11, 4363, 2022.
3. M. Lednev, D. Fernández de la Pradilla, F. Lindel, E. Moreno, F. J. García-Vidal, and J. Feist, "Spatially resolved photon statistics of general nanophotonic systems", arXiv:2411.19777, 2024

Thin Film Materials and Device Platforms for Quantum Photonics and Sensing Applications

Yong P. Chen[1,2,*]

[1]Purdue University, USA
[2]Aarhus University, Denmark
[*]corresponding author: yongchen@alum.mit.edu

Abstract: Functional optical thin film materials that can be incorporated into various heterostructures and (hybrid) device platforms are important for a wide range of quantum photonics and sensing applications. Of particular interests are 2D/thin film insulators/semiconductors that host optically active (quantum) emitters/sensor platforms such as 1) color centers, esp. NV-like spin defects; and 2) excitons, including Rydberg excitons that may also feature strong nonlinear interactions.

We will present our recent work developing and characterizing various thin film materials and device platforms for quantum photonics and sensing applications based on 1) spin defect centers in (exfoliated) h-BN, particularly with spin-selective excitations[1], exhibiting potentials in sensing magnetic fields and magnetic materials; and 2) exciton/Rydbergs in 2D/thin film semiconductors such as (exfoliated) transition metal dichalcogenides (TMDCs) and (synthesized) Cu_2O (grown by oxidization of Cu thin films/foils)[2,3], exhibiting potentials in sensing dielectric environment and other phase transitions in materials.

We acknowledge partial support from DOE, DOD, NSF, and Villum Foundation.

References

1. Mohammad Abdullah Sadi, Luca Basso, David A Fehr, Xingyu Gao, Sumukh Vaidya, Emmeline G Riendeau, Gajadhar Joshi, Tongcang Li, Michael E Flatté, Andrew M Mounce, Yong P Chen, “Spin-State Selective Excitation in Spin Defects of Hexagonal Boron Nitride”, arxiv:2506.04448.
2. Kinjol Barua, Samuel Peana, Arya Deepak Keni, Vahagn Mkhitaryan, Vladimir Shalaev, Yong P. Chen, Alexandra Boltasseva, Hadiseh Alaeian, "Bottom-up Fabrication of 2D Rydberg Exciton Arrays in Cuprous Oxide", Communications Materials 6, 21 (2025)
3. Akshay Agrawal,Kinjol Barua,Nithin Abraham,Hadiseh Alaeian,Yong Chen, “Effect of Strain and Grain Boundaries on Rydberg Excitons in Thin Films of Cuprous Oxide”, MRS 2025, CH02.10.04

Enhanced quantum emission via epsilon-near-zero materials

Sven Stengel[1], Abhishek Solanki[2], Hamza Ather[2], Pei-Gang Chen[2], Jae Ik Choi[2], Brandon M. Triplett[2], Mustafa Ozlu[2], Kyu Ri Choi[2], Alexander Senichev[2], Wallace Jaffray[1], Alexei S. Lagoutchev[2], Marcello Ferrera[1], Alexandra Boltasseva[2], and Vladimir M. Shalaev[2*]

[1]Heriot-Watt University, Edinburgh, EH14 4AS, Scotland, United Kingdom

[2]Purdue University, Birck Nanotechnology Center, West Lafayette, Indiana 47907, United States of America

[*]corresponding author: shalaev@purdue.edu

Abstract: Near-infrared quantum emitters have huge potentials in quantum technologies, especially for integrated photonics. By coupling PbS/CdS quantum dots to a CMOS-compatible epsilon-near-zero index substrate, we show improved emission directionality, increased saturation intensity and a 30-fold lifetime reduction, leading the way to advanced quantum optics applications.

Single photon emitters with near-infrared (NIR) emission at telecom wavelengths show significant potentials for optical quantum applications, specifically for integrated quantum photonic sensing and computation. Recent investigations related to quantum emitters demonstrate increased emission when they are coupled to an epsilon-near-zero (ENZ) environment. This can be attained by structural engineering of metamaterials and/or cut-off frequency of collection channels [1-4]. Further effects associated with the coupling to an ENZ environment include altering the emission directionality of radiative antennas due to electric field expulsion effects [5-7].

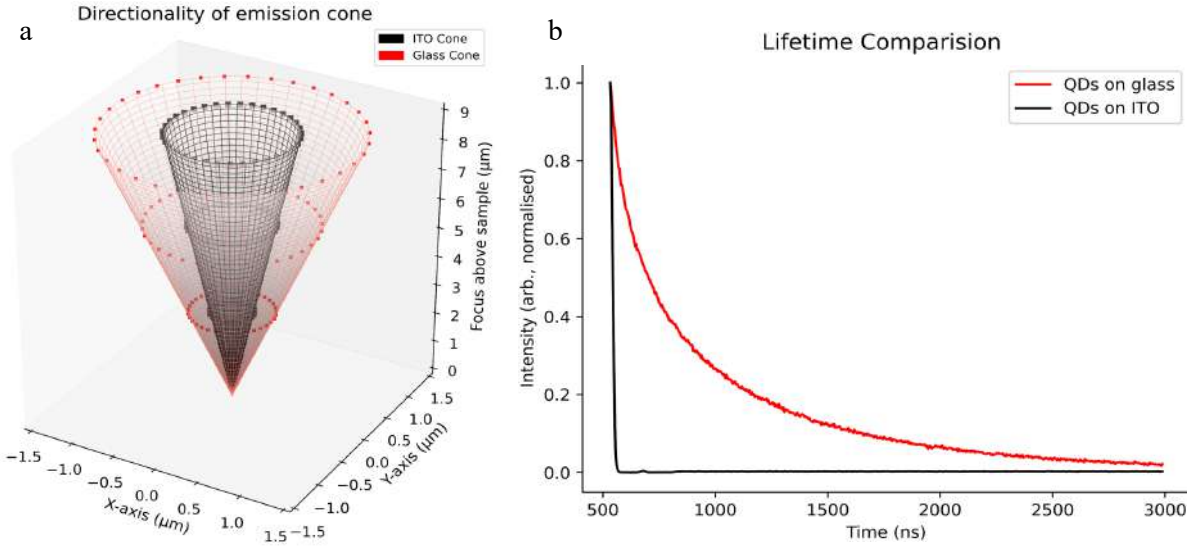


Figure 1: Modified emission properties of PbS/CdS quantum dots (QDs) via coupling to an epsilon-near-zero substrate. a) Emission cones for both QDs on indium tin oxide (ITO – black cone) and glass (red cone). An angular emission narrowing from 17.5° to 8.8° is reported. b) Comparison of emission lifetime for QDs on ITO vs QDs on glass. Quantum emitters placed on the ITO thin film display a thirty-fold reduction of emission lifetime if compared to emitters on the glass film.

Expanding on these findings, we experimentally tested emission and directionality improvements in quantum emitters coupled to an ENZ substrate. Specifically, we analyzed PbS/CdS (core/shell) quantum dots (QDs) on an indium tin oxide (ITO) substrate, where the broad crossover wavelength (1320 nm) closely aligns with the QD emission peak at 1350 nm. This coupling led to an increase in the relative intensity by a factor of four due to a narrowing of the emission cone from 17.5° to 8.8° for QDs on glass compared to those placed on ITO, respectively (see Fig.1,a). Additionally, a thirty-fold reduction in emission lifetime was recorded (see Fig.1,b) by comparing the same systems.

These results highlight the largely unexplored potential of transparent conductive oxides (TCOs) in integrated quantum optics applications at telecom wavelengths. With their ultra-fast optical nonlinearities, CMOS compatibility, and exceptional thermal and optical durability, TCOs can provide a robust foundation for key applications in all-optical photonics and integrated quantum optics [8, 9].

M.F. acknowledges economic support from EPSRC project ID: EP/X035158/1 and AFOSR (EOARD) under Award No.FA8655-23-1- 7254. Purdue team acknowledges support from the U.S. Department of Energy, Office of Basic Energy Science, Division of Materials Sciences and Engineering under Award DE-SC0017717 and the Air Force Office of Scientific Research (AFOSR) under Award FA9550-22-1-0372.

References

1. M. Lobet, I. Liberal, E. N. Knall, M. Zahirul Alam, O. Reshef, R. W. Boyd, N. Engheta, and E. Mazu, “Fundamental Radiative Processes in Near-Zero-Index Media of Various Dimensionalities,” ACS Photonics 7, 1965−1970 (2020)
2. J.K. So, G. H. Yuan, C. Soci, and N. I. Zheludev, “Enhancement of luminescence of quantum emitters in epsilon-near-zero waveguides,” Appl. Phys. Lett. 117, 181104 (2020)
3. R. Fleury, and A. Alu, “Enhanced superradiance in ENZ plasmonic channels,” Phys. Rev. B 87, 201101(R) (2013).
4. M. Y. Shalaginov, et al. “Enhancement of single-photon emission from NV centers with TiN/(Al,Sc)N hyperbolic metamaterial” Las. Phot. Rev. 9 (1), 120-127 (2015)
5. F. J. Rodríguez-Fortuño, A. Vakil, and N. Engheta, “Electric Levitation Using ENZ Metamaterials,” Phys. Rev. Lett. 112. 033902 (2014).
6. Y. Wu, X. Hu, F. Wang, J. Yang, C. Lu, Y. Liu, H. Yang, and Q. Gong, “Ultracompact and Unidirectional On-Chip Light Source Based on Epsilon-Near-Zero Materials in an Optical Communication Range,” Phys. Rev. Applied 12, 05402 (2019).
7. J. Kim, A. Dutta, G. V. Naik, A. J. Giles, F. J. Bezares, C. T. Ellis, J. G. Tischler, A. M. Mahmoud, H. Caglayan, O. J. Glembocki, A. V. Kildishev, J. D. Caldwell, A. Boltasseva, and N. Engheta, “Role of epsilon-near-zero substrates in the optical response of plasmonic antennas,” Optica 3, 339-346 (2016).
8. W. Jaffray, S. Stengel, F. Biancalana, C. B. Fruhling, M. Ozlu, A. Boltasseva, & M. Ferrera (2024). Spatio-spectral optical fission in time-varying subwavelength layers. arXiv preprint arXiv:2406.04917.
9. W. Jaffray, S. Saha, V. Shalaev, A. Boltasseva, and M. Ferrera, “Transparent conducting oxides: from all-dielectric plasmonics to a new paradigm in integrated photonics,” Adv. Opt. Photon. 14, 148-208 (2022).

Integration of single-defect carbon nanotube photon sources into waveguide circuits for quantum applications

C. Deleau[1*], C. F. Fong, [1,2], F. L. Sebastian[3], J. Zaumseil[3] and Y. K. Kato[1,2]
[1]Quantum Optoelectronics Research Team, RIKEN Center for Advanced Photonics, Saitama 351-0198, Japan
[2]Nanoscale Quantum Photonics Laboratory, RIKEN Cluster for Pioneering Research, Saitama 351-0198, Japan
[3]Institute for Physical Chemistry, Universität Heidelberg, Heidelberg, Germany
[*]corresponding author: clement.deleau@riken.jp

Abstract:
In this research, functionalized carbon nanotube single photon emitters are implemented in waveguide circuits for the development of chip-integrated quantum photonic applications at room temperature. Carbon nanotubes are drop-coated or deterministically positioned on waveguide cavities after which autocorrelation study and photoluminescence spectra demonstrate both single photon propagation and cavity enhancement.

Currently a rapidly growing research field at the heart of many emerging technologies, photonic integrated circuits (PIC) have enabled the realization of mass-manufacturable, stable, resilient and compact optical circuits for a large panel of applications. Environmental monitoring and telecommunications systems involving PICs are already commercially available and there is strong evidence that integrated quantum photonics applications will soon follow that path. However, scalable chip-integration of quantum light sources generating single photons at room temperature remains limited with current technologies [1]. Carbon nanotubes (CNTs) have been proposed as promising candidates but have yet to be demonstrated in functional quantum photonics circuits due to the stringent conditions indispensable for producing and manipulating photons with pure states [2,3]. To overcome these issues, a rigorous approach is required to find and implement on-chip solutions for proper CNT excitation and emission, waveguide coupling, further spectral filtering and adequate optical modulation [1]. The objective of this research is to develop such tools as a technological starting point for CNT-based quantum PIC applications.

Firstly, as a result of thorough excitonic analysis involving spectral, lifetime, polarization, brightness and autocorrelation measurements, (6,5) carbon-nanotubes with single defects have firstly been identified as a promising choice for chip integration [3]. A photonic integrated circuit characterization platform and associated automation algorithms have subsequently been realized and implemented to a photoluminescence measurement set-up for CNT circuit coupling analysis. Following, different types of photonic circuit fabrication processes have been developed and optimized in cleanroom. These circuits technologies have been used to realize a large variety of photonic nanostructures such as couplers, resonators, interferometers, waveguides, gratings or cavities.

CNTs have then been implemented both by drop-casting or deterministic positioning techniques and coupled to these circuits on evanescently coupled grating cavities that allow Purcell effect enhancement, demonstrating a sharpened and magnified photon-emission into waveguides. Finally, we also demonstrated single-photon emission at room temperature and waveguide photonic coupling of a deterministically positioned CNT in a low fluorescence lithium niobate waveguide circuit, readily available for electro-optical modulator processing. This way, we hope to demonstrate the first functional quantum PIC application that strives from CNT emission properties.

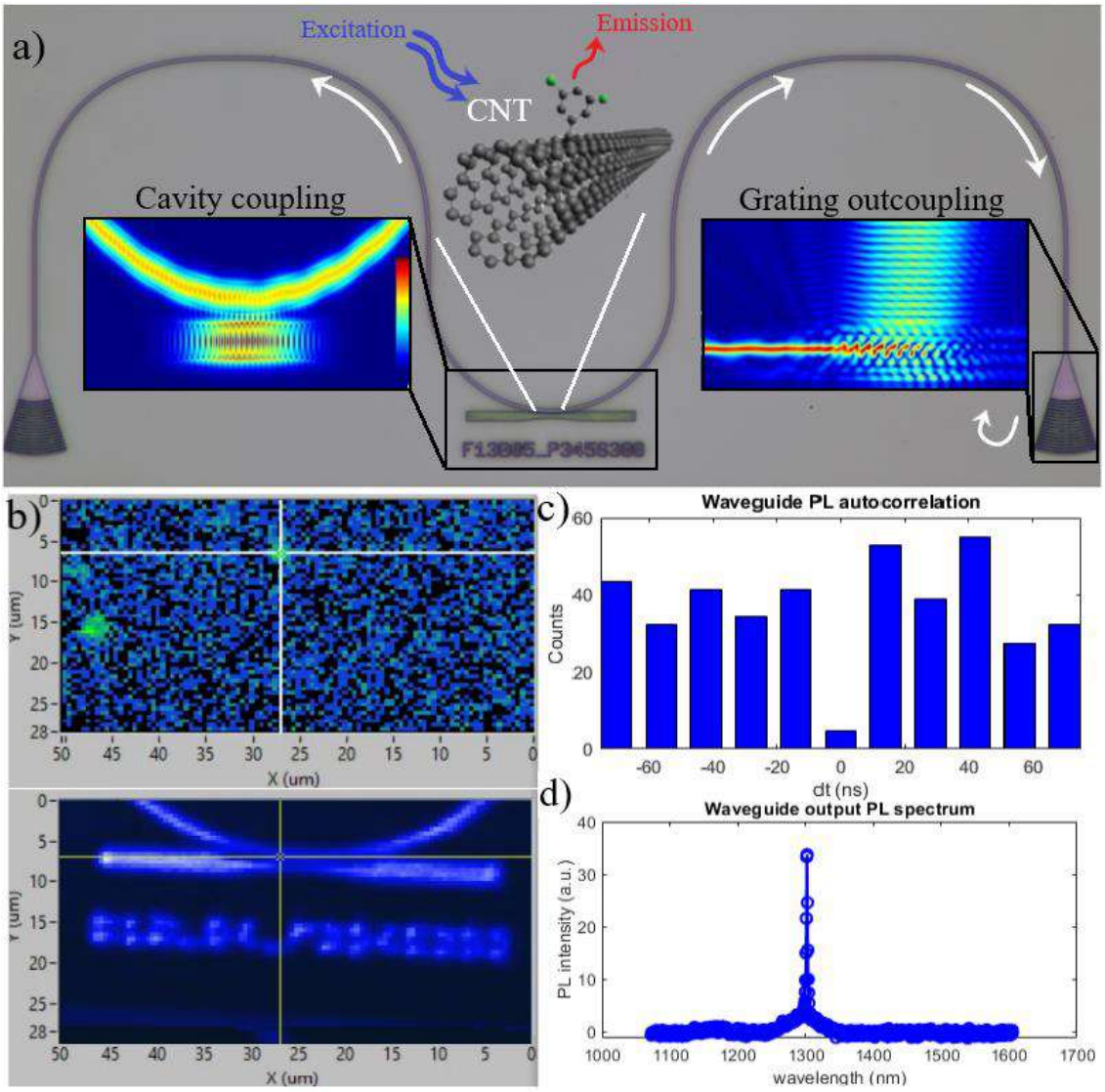


Figure 1. a) CNT coupling waveguide circuit and principle illustration, b) Photoluminescence and topography mapping of a waveguide cavity with stamped CNT, c) Autocorrelation measurement of the stamped CNT waveguide structure and d) example of PL spectrum measured from CNT-coated cavitiy waveguide

References

1. G. Moody, V. J. Sorger, D. J. Blumenthal, P. W. Juodawlkis, W. Loh, C. Sorace-Agaskar, A. E. Jones, K. C. Balram, J. C. F. Matthews and A. Laing, "2022 Roadmap on integrated quantum photonics", J. Phys. Photonics 4, 012501 (2022).
2. A. Baydin, F. Tay, J. Fan, M. Manjappa, W. Gao and J. Kono, "Carbon Nanotube Devices for Quantum Technology", Materials 15, 1535 (2022).
3. F. L. Sebastian, N. F. Zorn, S. Settele, S. Lindenthal, F. J. Berger, C. Bendel, H Li, B. S. Flavel, J. Zaumseil*, "Absolute Quantification of sp3 Defects in Semiconducting Single-Wall Carbon Nanotubes by Raman Spectroscopy", J. Phys. Chem. Lett. 13, 3542-3548 (2022)

Work supported by JSPS (KAKENHI JP24KF0092 and JP23H00262), JST (ASPIRE JPMJAP2310) and MEXT (ARIM JPMXP1224UT1073). We thank the Advanced Manufacturing Support Team at RIKEN for technical assistance.

Quantum fluctuations in the propagation of light through a dielectric medium

Arghadip Koner[1*], Sricharan Raghavan-Chitra[1], and Joel-Yuen Zhou[1*]

[1]Department of Chemistry and Biochemistry, University of California, San Diego, United States
[*]corresponding author: akoner@ucsd.edu

Abstract: Classical linear optics traditionally dictates light propagation through media. However, in high-Q cavities, rare quantum vacuum fluctuations imprint additional information about the medium, beyond the linear susceptibility, directly onto the linear response, revealing novel quantum corrections to the classical framework and enabling new quantum-enhanced insights into material response.

Light is traditionally understood to propagate through dielectric media according to classical linear optics, where the material's refractive index, determined by its linear susceptibility, dictates the propagation and intensity of light. In the field of molecular polaritonics, this translates to the success of transfer matrix-based methods in modeling the linear spectra of the cavity strongly coupled to N=10^6-10^{10} molecules. This observation stands in stark contrast to the quantum electrodynamics (QED) perspective, which predicts quantum and nonlinear effects in the polaritonic dynamics due to the strong interaction between the light and the matter.

We solve this apparent contradiction in molecular polaritonics by modeling the polaritonic linear response using input-output theory. By mapping the polariton problem to a quantum impurity model, we show that in the thermodynamic limit ($N\to\infty$), the polaritonic linear response is completely captured by the linear susceptibility of the molecular ensemble, leading to the success of classical optics. We further obtain a general expression for the linear response of molecular polaritons, which evidences that this classical optical description is only correct in the thermodynamic limit and, in fact, there is a previously overlooked hierarchy of (finite-size) $1/N$ corrections containing signatures of nonlinear molecular processes like Raman scattering mediated by the quantum vacuum fluctuations of the cavity. These corrections lead to new features in the linear spectra beyond those predicted by classical optics, but are small due to an emergent separation of timescales in polariton dynamics and hence excluded from the spectra due to limited resolution in the low-Q cavities typically used in the experiments.

We further demonstrate that this departure from the conventional framework of light propagation is more general and becomes essential when photons are confined in a high-Q cavity, rare quantum vacuum fluctuations, and quantum correlations between the light and the matter can imprint additional information about the medium, beyond what is captured by the linear susceptibility, directly onto the electric field amplitude.

To reveal this effect, we studied a high-Q microtoroid resonator with analytes adsorbed on its surface and probed via a tapered optical fiber. The prolonged photon lifetimes and three-dimensional confinement permit a long interaction window, allowing the light field to "wait" for those entropically unlikely quantum vacuum fluctuations to occur and to imprint Raman signatures onto the linear absorption signal. This pathway to retrieving Raman details through linear absorption offers exciting possibilities in sensing technology, eliminating the need for intense light sources directly shining on the sample or complex phase matching and enabling straightforward implementation, reliable benchmarking, and straightforward signal enhancements. To underscore its experimental feasibility, we rigorously perform noise analyses using state-of-the-art technology, demonstrating that the observed signal clearly rises above the noise floor, indicating immediate applicability.

Unlike other weak-coupling phenomena, such as Purcell enhancement, which rely on increased decay pathways, our approach leverages photon confinement and long-lived modes to access rare, vacuum-mediated processes in the linear regime. This work expands the conceptual boundaries of weak-coupling cavity QED and opens new directions in linear and nonlinear optics, nanophotonics, precision spectroscopy, and quantum-enhanced sensing.

Acknowledgements: This work was supported as part of the Center for Molecular Quantum Transduction (CMQT), an Energy Frontier Research Center funded by the U.S. Department of Energy, Office of Science, Basic Energy Sciences under Award No. DESC0021314

References

1. J. Yuen-Zhou[†*] and A. Koner[†*], "Linear response of molecular polaritons", J. Chem. Phys. 160, 154107 (2024)..
2. A. Koner and J. Yuen-Zhou*, "Hidden nonlinear optical susceptibilities in linear polaritonic spectra", arXiv.2411.09039 (2024).
3. S. Raghavan-Chitra and A. Koner[*] and J. Yuen-Zhou, "High Q microtoroids reveal rare quantum events" (submitted)

Functional materials for tunable and reconfigurable photonics

VO_2 Nanoparticles: Phase-transition Properties and Optical Memory Demonstration

F. Ligmajer[1,2*], P. Kepič[1], M Horák[1], J. Kabát[1,2],
M. Hájek [2], A. Konečná[1,2] and T. Šikola[1,2]

[1]Brno University of Technology, CEITEC, Czech Republic
[2]Brno University of Technology, Faculty of Mechanical Engineering, Czech Republic

filip.ligmajer@vutbr.cz (corresponding author)

Abstract

In our work, we analyze phase transitions in single VO_2 nanoparticles, revealing statistical variations in their transition temperature, steepness, and phase stability. We also demonstrate a multilevel optical memory near room temperature. Our findings clarify nanoscale hysteresis mechanisms and establish VO_2 nanoparticles as a promising platform for advanced nanophotonic devices.

1 Introduction

Phase-change materials, known for their ability to transition between solid phases with distinct optical properties, are crucial for advancements in nanophotonics. They enable applications such as tunable metasurfaces and integrated photonic memories, where optical memory states are controlled by materials exhibiting multiple phases. Vanadium dioxide (VO_2) represents an efficient platform for volatile memory applications such as neuromorphic computing and reconfigurable metasurfaces due to its insulator-to-metal transition (IMT) at approximately 68°C. Single-crystal VO_2 nanoparticles (NPs) exhibit phase transitions at even lower temperatures, making them highly promising for enhancing bit compactness and reducing energy consumption. The coexistence of insulating and metallic phases at nanoscale offers an opportunity to expand the memory capacity of VO_2-based devices. However, previous studies have focused on VO_2 films and NP ensembles rather than individual NPs, which are essential for practical applications in optical data storage and tunable metasurfaces [1, 2].

In our study, we employ scanning transmission electron microscopy techniques to investigate phase transitions in individual VO_2 NPs [3]. Using electron energy loss spectroscopy (EELS) and annular dark-field (ADF) imaging, we investigated the spatial distribution of coexisting phases and hysteretic behaviors within NPs in real time. By analyzing hundreds of VO_2 NPs, we discovered that the transition width (the temperature range required to completely switch a NP from one phase to another) of IMT is three times greater than that of MIT. During backward MIT, on the other hand, the transitions of the NPs are very abrupt (narrow MIT widths) but spread over a larger temperature window. These results help to explain the behavior of polycrystalline VO_2 films, where the grain structure influences macroscopic phase transition properties. Leveraging the observed phase coexistence in VO_2 NPs, we also demonstrated a multi-level optical memory device. By controlling the IMT termination temperature, we were able to stabilize different transmission levels close to room temperature. While individual NPs do not seem to support stable coexisting phases at low temperatures, we show that carefully designed NP ensembles can enable persistent memory states. These findings strengthen the case for VO_2 as a viable material for low-power, high-density optical data storage and processing applications, neuromorphic computing, and integrated photonic circuits.

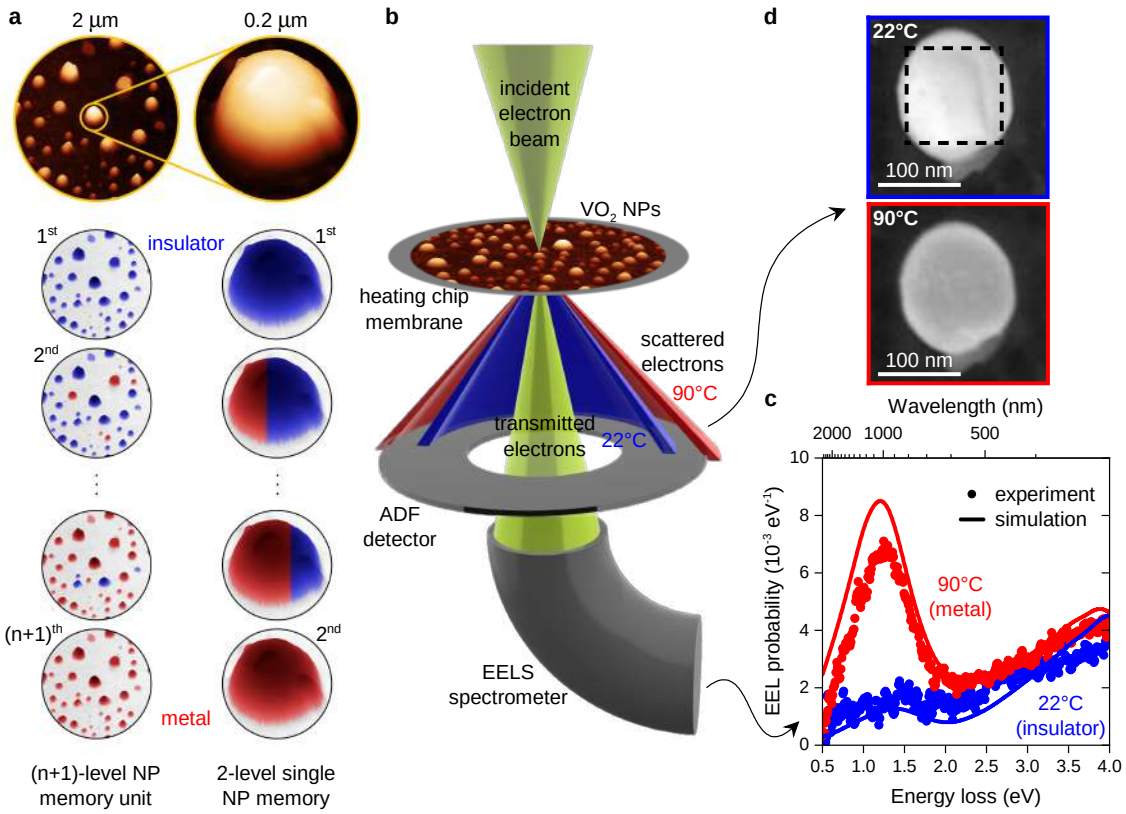


Figure 1: VO_2 NP memory and the measurement setup. (a) Concept of a VO_2 NP memory unit based on coexisting insulator (blue) and metal (red) phases within a single VO_2 NP. The left column corresponds to (n + 1)-level memory based on an n-NP ensemble, and the right column corresponds to a 2-level single-NP memory. The illustration uses real atomic force microscopy (AFM) images of our samples. (b) Scheme of EEL spectroscopy and ADF measurement of VO_2 NPs at different temperatures. (c) Measured and simulated EEL spectra of a 130 nm VO_2 NP on a SiN membrane in the insulator (22 °C; blue) and metal (90 °C; red) phases. (d) ADF images of the NP in (c) at the listed temperatures. The dashed rectangle highlights the area over which EEL spectra in (c) were spatially integrated.

2 Acknowledgements

This conference contribution is supported by the Grant Agency of the Czech Republic (25-18336M). We acknowledge CzechNanoLab Research Infrastructure supported by MEYS CR (LM2023051) for the financial support of the measurements and sample fabrication.

References

[1] Kepič, P., Ligmajer, F., Hrtoň, M., Ren, H., de S Menezes, L. and Maier, S. A. "Optically Tunable Mie Resonance VO_2 Nanoantennas for Metasurfaces in the Visible," *ACS Photonics*, Vol. 8, No. 4, pp. 1048–1057, 2021.

[2] Aigner, A., Ligmajer, F., Rovenská, K., Holobrádek, J., Idesová, B., Maier, S. A. and Tittl, A. "Engineering of Active and Passive Loss in High-Quality-Factor Vanadium Dioxide-Based BIC Metasurfaces," *Nano Letters*, Vol. 24, No. 35, pp. 10742–10749, 2024.

[3] Kepič, P., Horák, M., Kabát, J., Hájek, M., Konečná, A., Šikola, T. and Ligmajer, F. "Coexisting Phases of Individual VO_2 Nanoparticles for Multilevel Nanoscale Memory," *ACS Nano*, Vol. 19, No. 1, pp. 1167–1176, 2025.

Deep learning enabled programmable silicon photonics using low-loss phase change material Sb_2Se_3

O. L. Muskens[1*], S. Blundell[1,2], T. Radford[1], D. Lawson[1], I. A. Ajia[1], L. Rozaqi[1], P. Deoli[1], D. Trubacs[1], P. R. Wiecha[3], A. Politi[1], D. J. Thomson[2] and I. Zeimpekis[2,4]

[1]Physics and Astronomy, Faculty of Engineering and Physical Sciences, University of Southampton, UK
[2]Optoelectronics Research Centre, Faculty of Engineering and Physical Sciences, University of Southampton, UK
[3]LAAS, Université de Toulouse, CNRS, 31031, Toulouse, France
[4]Electronics and Computer Science, Faculty of Engineering and Physical Sciences, University of Southampton, UK

[*]corresponding author: o.muskens@soton.ac.uk

Abstract: The ability to program optical devices using non-volatile phase change materials with low losses is of importance in a wide range of applications. An overview will be presented of the developed materials platform together with proposed strategies of designing programmable devices using a deep learning neural network.

Programmable photonics using non-volatile phase change materials (PCMs) holds tremendous potential for next-generation technologies such as photonic computing, AI and quantum circuits [1]. Our group has introduced antimony selenide (Sb_2Se_3) as an ideal material for programmable silicon photonics [2,3]. Sb_2Se_3 offers low losses at near-infrared wavelengths including the telecommunications bands, a refractive index closely matched to silicon allowing for seamless integration into silicon-on-insulator (SOI) platforms, and a moderate crystallization temperature of around 200°C. Reversible switching over one million cycles is in principle possible [4], indicating endurance suitable for a range of applications requiring moderate numbers of switching cycles.

A topic of considerable interest is whether it is possible to achieve freeform control of light in integrated platforms similar to what is achieved using wavefront shaping in free space optics. The equivalent of a spatial light modulator would be the implementation of digitally programmable multi-port devices based on multimode interferometer (MMI) devices [3,5]. We have proposed to use patterns of weakly scattering perturbations imprinted onto the device to effectively mix modes and produce a fully programmable unitary operation. In order to find the appropriate patterns, our team has been able to successfully apply methods from neural network inverse design as a route alternative to more traditional topology optimization [5]. Recently we have implemented a neural-adjoint approach, where a forward surrogate network is used in combination with a gradient optimization scheme [6]. We successfully designed unitary operators using a coupled-waveguide array (CWG). The CWG holds advantages over MMIs by reducing the number of internal modes, thus reducing the outcoupling challenge, however at the cost of a slightly larger footprint.

The role of the thickness of the PCM used in SOI platforms is another parameter of considerable importance. In a series of systematic experimental studies [7] we look at the effect of increasing the thickness of Sb_2Se_3 from 20 nm – 100 nm thickness (Figure 1). A large increase in optical phase shift is achieved by increasing the thickness, resulting in a switching length over which π phase-shift can be achieved (L_π) of around 5 μm. The reduced phase shift comes at the cost of increased losses in the crystalline phase due to scattering by polycrystalline domains.

When applied to the digital programming of a MMI device, the number of pixels can be reduced down from above 30 pixels for the thinnest films to below 10 pixels for the thicker Sb_2Se_3 layers, thus indicating a potential reduction in complexity and write times for programmable devices.

In conclusion, our work combines experimental and theoretical advances in programmable photonic devices exploiting low-loss phase change technology and direct optical writing. Both coupled-waveguide and multimode interference based programmable devices hold promise as an alternative for existing interferometer meshes.

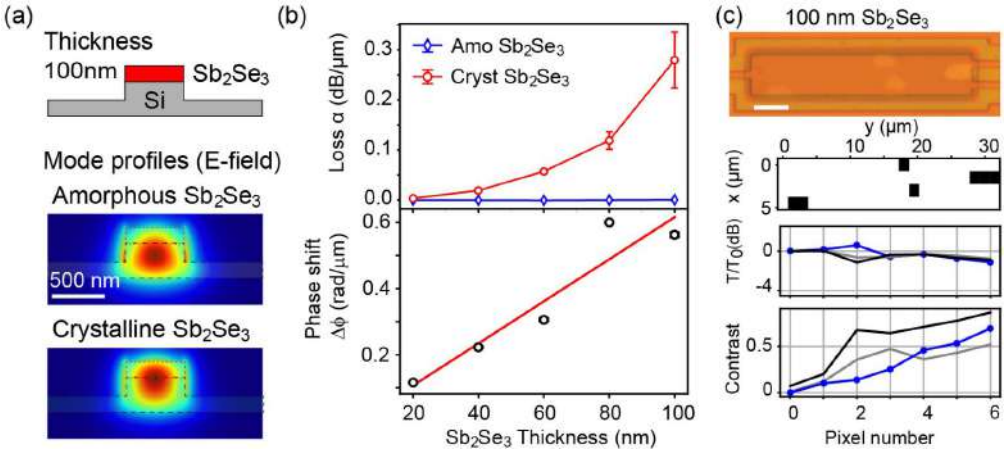


Figure 1. (a) Cross sectional view of hybrid Sb_2Se_3/Silicon waveguide with calculated mode profiles for amorphous and crystalline states. (b) Experimental losses and induced optical phase shift versus Sb_2Se_3 thickness. (c) Demonstration of switching on MMI with 100nm thick Sb_2Se_3 layer, showing switching with 6 pixels using crystalline pixels on amorphous Sb_2Se_3 background.

References

1. Prabhathan, P. et al. "Roadmap for phase change materials in photonics and beyond," iScience 26, 107946, 2023.
2. Delaney, M., Zeimpekis, I., Lawson, D., Hewak, D. W., Muskens, O. L. "A new family of ultralow loss reversible phase-change materials for photonic integrated circuits: Sb_2S_3 and Sb2Se3," Adv. Func. Mater. 30, 2002447, 2020.
3. Delaney, M., Zeimpekis, I., Du, H., Yan, X., Banakar, M., Thomson, D. J., Hewak, D. W., Muskens, O. L. "Nonvolatile programmable silicon photonics using an ultralow-loss Sb_2 Se_3 phase change material," Science Adv. 7, 3500–3516, 2021.
4. Lawson, D., Blundell, S., Ebert, M., Muskens, O. L., Zeimpekis, I., "Optical switching beyond a million cycles of low-loss phase change material Sb_2Se_3," Opt. Mater. Expr. 14, 22–38, 2024.
5. Dinsdale, N. J., Wiecha, P. R., Delaney, M., Reynolds, J., Ebert, M., Zeimpekis, I., Thomson, D. J., Reed, G. T., Lalanne, P., Vynck, K., O. L. Muskens, "Deep learning enabled design of complex transmission matrices for universal optical components," ACS Photon. 8, 283–295, 2021.
6. Radford, T. W., Wiecha, P. R., Politi, A., Zeimpekis, I. and Muskens, O. L., "Inverse Design of Unitary Transmission Matrices in Silicon Photonic Coupled Waveguide Arrays Using a Neural Adjoint Model," ACS Photon. doi:10.1021/acsphotonics.4c02081, 2025.
7. Blundell, S., Radford, T., Ajia, I. A., Lawson, D., Yan, X., Banakar, M., Thomson, D. J., Zeimpekis, I. and Muskens, O. L., "Ultracompact programmable silicon photonics using layers of low-loss phase-change material Sb2Se3 of increasing thickness," arXiv:2409.12582, 2025.

Tunable conducting polymer mid-IR plasmonic microantenna arrays

Pravallika Bandaru, Mohammad Shaad Ansari, Aleksandr Poliakov, Suraya Kazi, and Magnus P. Jonsson*

Laboratory of Organic Electronics, Department of Science and Technology (ITN), Linköping University, SE-601 74 Sweden
*corresponding author: magnus.jonsson@liu.se

Abstract: Actively tunable mid-IR plasmonic antennas show prospects for a broad range of applications, which rely on efficiently switchable materials. Here, we investigate the tunable mid-IR plasmonic response of conducting polymer microantenna arrays and demonstrate efficient and reversible on/off switching capability.

Summary: Although noble metals like gold and silver show strong plasmonic resonances, their tunability is limited due to fixed carrier density. Recently, Chen *et al*., introduced PEDOT (poly[3,4-ethylenedioxythiophene]) based dynamically tunable conducting polymer nanoantennas exhibiting plasmonic resonances in the near-IR regime. [1] These resonances could be chemically or electrically switched on/off by controlling the polaronic charge carrier concentration of the polymer, which switches the polymer between metallic (oxidized) and dielectric (reduced) states. [2,3]

Here, I will present our recent results on PEDOT microantenna arrays with plasmonic resonances at longer wavelengths in the mid-IR spectral range. [4] We find that the antenna arrays can provide clear asymmetric Fano-type plasmon resonances with peak position controlled by antenna size or array periodicity. Furthermore, we demonstrate complete and reversible chemical on/off switching of the mid-IR plasmonic response. This study can contribute to the developments in applications such as active mid-IR beam steering, active thermal sources, and the adaptive radiative cooling technology.

References

1. Chen, S. *et al*., “Conducting polymer nanoantennas for dynamic organic plasmonics,” *Nat. Nanotechnol*., 15, 35-40, 2020.
2. Karki, K. *et al*., “Electrical Tuning of Plasmonic Conducting Polymer Nanoantennas,” *Adv. Mater*., 34, 13, 2107172, 2022.
3. Chen, S. and Jonsson, M. P., “Dynamic Conducting Polymer Plasmonics and Metasurfaces,” *ACS Photonics*., 10, 3, 571-581, 2023.
4. Bandaru, P. *et al*., “Tunable mid-IR conducting polymer plasmonic antenna arrays,” (In manuscript).

Programmable Polariton Nanophotonics with Phase-Change Materials

L. Conrads[1], and T. Taubner[1,*]
[1] I. Institute of Physics (IA), RWTH Aachen University, Germany

[*]corresponding author: taubner@physik.rwth-aachen.de

Abstract: We exploit the non-volatile insulator-to-metal transition of the plasmonic phase-change material In_3SbTe_2 for optical programming surface polariton resonators on polar crystals and doped semiconductors. The strongly confined resonance modes are investigated with scanning near-field optical microscopy. This study enables rapid prototyping of reconfigurable polariton resonators even with anisotropic 2D-materials.

Tailoring light-matter interaction is essential to realize nanophotonic components and can be achieved with polaritons, an excitation of photons coupled with the collective (plasmon) oscillation of charge carriers in metals and semiconductors or with phonons in polar crystals and 2D-materials leading to Surface Plasmon Polaritons (SPPs) and Surface Phonon Polaritons, (SPhPs), respectively. [1] Based on a reversible change in their refractive index [2], Phase-change materials (PCMs) enabled the modification of SPhPs propagation [3] and the on/off switching of SPhP resonators [4]. While ultraconfined resonances are in principle possible by restricting these polaritons to cavities, the directing writing of launching and resonator structures in PCMs has been so far elusive. Recently, the plasmonic PCM In_3SbTe_2 (IST) was introduced for programmable nanophotonics due to the ability of reversibly switching from an amorphous dielectric to a crystalline metallic state in the infrared. [5] This material IST has also enabled the fast fabrication of infrared metasurfaces for tailoring thermal emission [6] and infrared beam shaping on demand [7]. Here, now apply IST for the creation and modification of polaritonic cavities.

We investigate surface phonon polariton resonators optically programmed via laser irradiation in the plasmonic PCM IST on top of the phonon polariton hosting polar crystal silicon carbide with scanning near-field optical microscopy (s-SNOM). Circular resonators are reconfigured in their diameters to shift the resonance modes accordingly. In addition, smaller resonator diameters facilitate stronger field confinements up to a value of $\lambda/35$. The vast flexibility of direct programming resonators is highlighted by investigating square and triangular resonators featuring complex field distributions according to their unusual shape.[8]

Moreover, we apply the same principle to study infrared SPPs on doped semiconductors CdO and InAs covered with thin layers of PCMs. Conventionally, the small polariton confinement and the dispersion close to the light line aggravate real-space observation of SPPs in bulk materials in the infrared. Increasing the SPP confinement with thin dielectric layers modifies the SPP dispersion and allows for direct fabrication of resonators by locally switching the PCM.[9]

The concept of directly programming polariton resonators with PCMs without cumbersome fabrication techniques facilitates sub-wavelength polaritonic devices such as biosensors or optical data storage systems. The combination of PCMs with polariton-hosting materials can be easily extended to 2d hyperbolic and anisotropic crystals featuring lower losses and higher polariton propagation lengths. In most recent work, we investigate hyperbolic phonon polaritons in hBN above optically programmed resonator structures with IST and studied the different resonance modes. Polariton lensing is demonstrated with focusing structures and the focal point is tuned by reconfiguring the IST structures below.

Acknowledgements: The authors acknowledge support by the Deutsche Forschungsgemeinschaft (DFG No. 518913417 & SFB 917 “Nanoswitches”).

References

1. Basov, D.N. et al., “Polariton panorama” *Nanophotonics* **10**, 549-577 (2021)
2. Wuttig, M. et al., “Phase-change materials for non-volatile photonic applications” *Nat. Photon*. **11**, 8 (2017)
3. Chaudhary, K. *et al.* “Polariton nanophotonics using phase-change materials.” Nat. Commun. **10**, 4487 (2019).
4. Sumikura H. et al, “Highly-confined and switchable mid-infrared surface phonon polariton resonances of planar circular cavities with a phase change material”, Nano Lett. **19,** 2549 (2019).
5. Heßler, A. et al., “In_3SbTe_2 as a programmable nanophotonics material platform for the infrared” *Nat. Commun.* **12**, 924 (2021)
6. Conrads, L. et al., “Reconfigurable and Polarization‐Dependent Grating Absorber for Large‐Area Emissivity Control Based on the Plasmonic Phase‐Change Material In_3SbTe_2” Adv. Opt. Mat. **11**, 8 (2023)
7. Conrads, L. et al. “Infrared beam-shaping on demand via tailored geometric phase metasurfaces employing the plasmonic phase-change material In_3SbTe_2” arXiv:2408.05044 (2024)
8. Conrads, L. et al., “Direct programming of confined surface phonon polariton resonators with the plasmonic phase-change material In_3SbTe_2” Nat. Commun. **15**, 3472 (2024)
9. Conrads, L. et al., “Real-space imaging of confined infrared surface plasmon polaritons on doped semiconductors covered with phase-change materials” Sci. Adv. **11**, eadr6844 (2025)

Zero-static-power photonics using chalcogenide metacoatings with engineered volatile and non-volatile transitions

Behrad Gholipour[1*], Avik Mandal[1], Joshua Perkins[1], Mahirah Zaini[1], Abbas Sheikh Ansari[1], Yihao Cui[1] , Kwanghyun Kim[1]

[1]Nanoscale Optics Lab, Electrical and Computer Engineering Dept, University of Alberta
[*]corresponding author e-mail: bgholipo@ualberta.ca

Abstract: We show that non-resonant, subwavelength nanoscale patterning that enables dispersion engineering of chalcogenide glasses through lithography-free, bottom-up growth and patterning techniques, paves the way to the realization of metacoatings with tunable optoelectronic properties without any stoichiometric changes to chemical composition through glancing angle deposition and interlayer nanostructuring techniques.

Training and running large artificial intelligence (AI) and machine learning (ML) models as well as emerging large language models (LLM's) and the push towards online learning, inference and, more broadly, artificial general intelligence (AGI), require staggering amounts of energy to train in years to come.

This is largely due to current hardware architectures' reliance on volatile transitions (for signal routing, switching and processing) such as carrier modulation and thermo-optic effects in silicon and its derivatives, transparent conducting oxides, and ferroelectrics. This creates an intense need for active thermal load management as volatile transitions require power to be maintained to the device at all times. This is a major obstacle to scaling up to increasingly dense chips and racks in hyperscale AI-centric data centres that would need ever more spacious rack layouts or energy-intensive cooling solutions to deal with the generated heat resulting from the volatile nature of all transitions used on the chip level. Going forward, zero-static power architectures are needed on the fundamental processing and memory component layers to enable scalable and environmentally sustainable systems.

The most scalable non-volatile transition available to us in nature is the phase transition commonly observed in chalcogenide semiconductors that relies on the reversible atomic rearrangement of an alloy using thermal, electrical, or optical stimuli between a reflective high conductivity crystalline and a transparent highly resistive amorphous phase. To this end, here we show that using phase change metacoatings, subwavelength thickness layers of chalcogenide phase change alloys nanostructured through bottom-up growth techniques can enable control of static optical properties as well as volatile and non-volatile transitions, with a view to photonic integrated circuits that will be the workhorse of emerging hyperscale AI-centric data centers. Notably, in these architectures, the mitigation of high insertion losses when introducing many of these alloys to the vicinity of waveguide platforms due to their inherent absorption across this band has resulted in devices with larger than necessary lateral footprints and/or poor modulation contrasts and an incessant search for low-loss/high switching contrast alloys.

Chalcogenide phase-change materials (PCMs) are high refractive index dielectrics across the visible/telecom band. We show that by making use of this high refractive index, mach-zender modulators (MZM's) with built-in memory functionality and zero static power consumption,

capable of 2π phase shifts, can be realized with active lateral footprints down to 10 μm. Furthermore, the patterning of these alloys on the subwavelength scale has demonstrated high-quality factor optically resonant devices under the umbrella of metamaterials and metasurfaces. In this realm, subwavelength nanostructuring can also offer non-resonant dispersion engineering of a given dielectric/plasmonic material. We show that non-resonant, lithography-free, subwavelength patterning, which enables dispersion engineering of chalcogenide glasses, paves the way to the realization of alloys with tunable static optoelectronic properties.

We then go on to show that volatile and non-volatile optical transitions can be tuned and engineered in PCMs without the need for stoichiometric changes to chemical composition through glancing angle deposition and interlayer nanostructuring, enabling ultra-compact phase/intensity modulators with tunable insertion losses.

Acknowledgments
This work was supported by the Canadian Natural Sciences and Engineering Research Council (NSERC), Alberta Innovates and Future Energy systems institute.

Reconfigurable Nonlocal Metasurfaces

A. Alù[1,2]

[1]Photonics Initiative, Advanced Science Research Center, City University of New York, New York, NY 10031, USA
[2] Physics Program, Graduate Center, City University of New York, New York, NY 10016, USA
[*]corresponding author: aalu@gc.cuny.edu

Abstract: In this talk, I will discuss my group's recent work in the area of nonlocal metasurfaces, with an emphasis on reconfigurability and temporal transformations. The field of metasurfaces has been blossoming in recent years, but the need for fast and diverse reconfigurable response remains an outstanding challenge to be competitive as a photonic platform. In this context, we have explored various approaches, from thermal to electro-optical and all-optical modulations, leveraging the long-range collective interactions stemming from nonlocal metasurface designs to facilitate the reconfigurability control.

Metasurface tuning based on carrier manipulation

A. Tognazzi[1,2,*]
[1]Università degli Studi di Palermo, viale delle Scienze, Palermo 90128, Italia
[2]Istituto Nazionale di Ottica (INO-CNR), via Branze 45, Brescia 25123, Italia
Corresponding author: andrea.tognazzi@unipa.it

Abstract: Tuning the optical response of nanoscale objects can be achieved through different carrier types. We demonstrate two distinct approaches: all-optical modulation via free-carrier injection in silicon metasurfaces and iontronic tuning in organic mixed conductors. These strategies enable fast, broadband, and energy-efficient control, paving the way for next-generation tunable photonic devices.

Metasurfaces provide a versatile platform for shaping electromagnetic fields at the subwavelength scale, enabling control over polarization, wavefront, and nonlinear effects. However, achieving tunability in their optical response remains challenging due to the nanoscale dimensions of their building blocks. The ability to induce abrupt changes in phase and amplitude is essential for applications such as focusing, polarization control, nonlinear frequency conversion, and wavefront manipulation. Various strategies have been explored to achieve nanoscale control of metasurface behavior, leveraging liquid crystals, phase-change materials, and carrier excitation [1]. Among the fastest tuning mechanisms, electrical and optical stimuli offer promising solutions; however, achieving a large modulation depth often comes at the cost of slower response times. Here, we present two distinct approaches that exploit different types of carriers—electrons and ions—to achieve tunability with both high speed and large modulation depth. First, we demonstrate all-optical tuning in silicon metasurfaces by controlling free-carrier dynamics, enabling ultrafast modulation of optical properties. Second, we introduce iontronically controllable PEDOT:PSS films to create spatially varying refractive index profiles, allowing for phase control without the need for nanoscale patterning. Our results pave the way for next-generation tunable photonic devices, combining high-speed operation with energy efficiency and broad spectral tunability.

First, we employ free carrier excitation in Si to perform all-optical modulation in a high-contrast index grating (HCG). The HCG linear spectral properties are design by means of rigorous coupled wave analysis (RCWA) to obtain a sharp spectral feature, related to a guided mode resonance, in the third telecommunication window. The sharp spectral feature rigidly shifts upon carrier excitation through a pump beam in the Si absorption region, giving rise to large reflectivity modulation as shown in Fig. 1a. The spectral and temporal response can be described by means of a coupled rate equation model, to describe the out-of-equilibrium dielectric constant modifications, and RCWA to take into account the HCG geometry [2].

As an alternative approach to show the crucial role that carrier manipulation plays in tuning nanoscale devices, we now focus on a different type of carriers, namely positive ions in PEDOT:PSS. By properly arranging the electrical contacts in a three-terminal transistor configuration it is possible to control the refractive index of the material by inducing a migration of positive ion carriers [3]. Unlike previous capacitive configurations, our approach allows to induce a spatially varying control electric field between the source and drain electrodes, which results in a spatially varying refractive index (as shown in Fig. 1b). It is thus possible to achieve

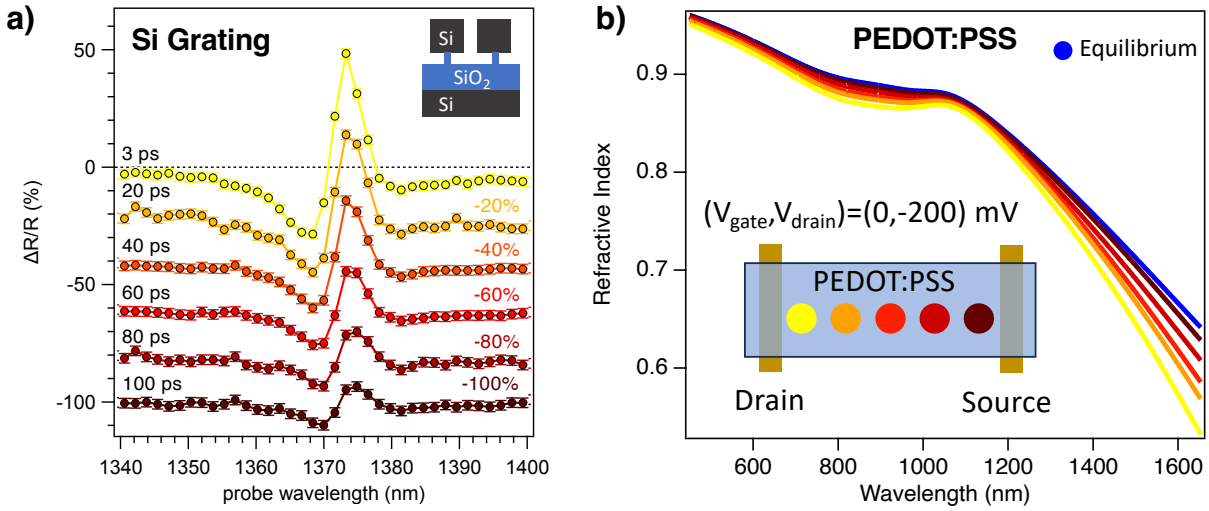


Figure 1: a) Experimental differential reflectivity as a function of the probe wavelength at different time delays. The inset display the cross-section of the metasurface. b) Refractive index real part as a function of the wavelength at four different positions between the source and drain electrodes. The inset shows the top view of the device.

a control over the phase of the electric field through the PEDOT:PSS film in a dynamic way without any patterning by changing only the drain potential V_{drain}.

Our findings enable next-generation tunable photonic devices with high speed, energy efficiency, and broad spectral control.

This work was partially supported by the European Union under the Italian National Recovery and Resilience Plan (NRRP) of NextGenerationEU, of partnership on "Telecommunications of the Future" (PE00000001 - program "RESTART"), S2 SUPER – Programmable Networks, Cascade project PRISM - CUP: E13C22001870001.

References

1. Saifullah, Y., Y. He, A. Boag, G.-M. Yang and F. Xu "Recent Progress in Reconfigurable and Intelligent Metasurfaces: A Comprehensive Review of Tuning Mechanisms, Hardware Designs, and Applications," *Adv. Sci.*, Vol. 9, No. 33, pp. 2203747, 2022.

2. Tognazzi, A., P. Franceschini, O. Sergaeva, L. Carletti, I. Alessandri, G. Finco, O. Takayama, R. Malureanu, A. V. Lavrinenko, A. C. Cino, D. de Ceglia and C. De Angelis "Giant photoinduced reflectivity modulation of nonlocal resonances in silicon metasurfaces," *Adv. Photonics*, Vol. 5, No. 6, pp. 066006–066006, 2023.

3. Franceschini, P., A. Tognazzi, V. M. Demartis, L. Carletti, E. Menshikov, I. Alessandri, A. C. Cino, F. Torricelli, C. De Angelis and M. A. Vincenti, "Iontronically Tunable Broadband Graded Index Films," *Adv. Opt. Mater.*, Early view, pp. 2402410, 2024.

Dynamic Optical Control with VO_2 Metasurfaces

R. Camacho-Morales[1]

[1]ARC Centre of Excellence for Transformative Meta-Optical Systems (TMOS), Department of Electronic Materials Engineering, Research School of Physics, The Australian National University, Canberra, ACT 2600, Australia
*rocio.camacho@anu.edu.au

Abstract: We design reconfigurable VO_2-based metasurfaces for tuneable optics and imaging. By leveraging the phase transition of VO_2, we achieve a high transmission contrast ($\Delta T = 0.73$) at telecommunication wavelengths and demonstrate switchable imaging between phase contrast and brightfield modes, enabling dynamic control for advanced optical and computational imaging applications.

Metasurfaces are planar arrays of nanostructures engineered to manipulate electromagnetic waves with exceptional control. Their ability to tailor optical responses at the nanoscale has garnered significant attention. However, conventional metasurfaces face a fundamental limitation: their optical properties are fixed upon fabrication, observing a single optical response. To address this constraint, extensive research has focused on developing reconfigurable metasurfaces that dynamically control electromagnetic waves in response to external stimuli. Various tuning mechanisms have been explored, including carrier doping, mechanical deformation, and phase transitions [1].

In our work, we utilise vanadium dioxide (VO_2), a phase-change material, to design reconfigurable metasurfaces. When heated above its critical temperature (T_c = 68°C), VO_2 undergoes a transition from an insulating to a metallic state inducing a significant change in its optical properties, particularly in the near-infrared spectral range. This transition is volatile, as VO_2 naturally returns to its insulating state upon cooling to room temperature [2].

In the first part of my presentation, I will present our results on a VO_2-based metasurface designed for tuneable transmission. Specifically, I will discuss our approach to maximising the transmission contrast ($\Delta T = T_i - T_m$) of nanostructured VO_2 at telecommunication wavelengths. To achieve this, we developed numerical tools for electromagnetic simulations and structural optimisation, establishing the fundamental transmission limits for various geometries, including multilayer stacks and high-dimensional nanostructures. Our optimised design achieved a maximum transmission contrast of $\Delta T = 0.73$, with the corresponding VO_2 structure shown in Figure 1a. These findings provide a benchmark for future VO_2-based tuneable transmission filters [3].

In the second part of my presentation, I will introduce a VO_2 metasurface designed for switchable imaging, enabling dynamic control between phase contrast and brightfield imaging. Brightfield microscopy is a widely used imaging technique for examining microscopic samples that create contrast through amplitude variations via absorption. However, it cannot visualize phase variations in transparent samples, such as biological specimens. To address this limitation, we leverage the phase transition of VO_2 to design a metasurface that converts phase variations into intensity variations when VO_2 is in its insulating state. In contrast, brightfield imaging is enabled when VO_2 transitions to its metallic state. The metasurface consists of a silicon photonic crystal deposited on a VO_2 thin film. The photonic crystal is composed of a hexagonal array of cylindrical holes etched into an

amorphous silicon layer, supported by a quartz substrate (Figure 1b). This structure enables dynamic switching between different imaging modalities, highlighting the potential of VO_2-based metasurfaces for advanced imaging applications.

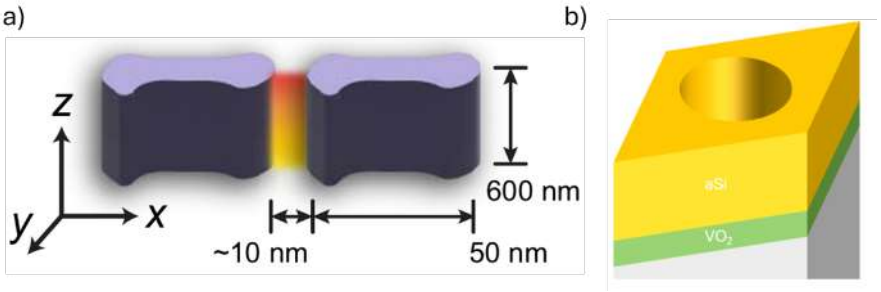


Figure 1. Optimal geometries of VO_2 nanostructures obtained for a) maximising transmission contrast ΔT and b) switchable imaging.

These results demonstrate the potential of VO_2-based metasurfaces for dynamically reconfigurable optical systems, paving the way for advancements in tuneable optical devices and computational imaging.

References

1. Q. He, S. Sun, and L. Zhou, “Tunable/Reconfigurable Metasurfaces: Physics and Applications,” *Research*, Vol. 2019, 1-16, 2019.
2. S. Cueff, J. John, Z. Zhang, J. Parra, J. Sun, R. Orobtchouk, S. Ramanathan, P. Sanchis, “VO_2 nanophotonics,” *APL Photonics*, Vol. 5, 110901, 2020.
3. B. Li, R. Camacho-Morales, N. Li, A. Tognazzi, M. Gandolfi, D. de Ceglia, C. De Angelis, A. Sukhorukov, and D. Neshev, "Fundamental limits for transmission modulation in VO2 metasurfaces," *Photon. Res.*, Vol. 11, B40-B49, 2023.

Hybrid integration of ferroelectric oxides in silicon photonics platform

Ana-Maria Statie[1], Pablo Bedoya-Ríos[1], Clément Ben Braham[1,2], Alicia Ruiz-Caridad[4], Ali El Boutaybi[1], Roy Prosopio[1], Sebastian Alvarez Ortega[1], Jonathan Peltier[1,2], Daniele Melati[1], Etienne Herth[1], Samson Edmond[1], Ali Belarouci[3], Eric Cassan[1], Delphine Marris-Morini[1], Panagiotis Karamanis[5], Michel Rérat [5], Guy Aubin[1], Regis Orobtchouk[3], Léopold Virot[2], Yohan Désières[2] Carlos Alonso-Ramos[1], Philippe Lecoeur[1], Sylvia Matzen[1], Thomas Maroutian[1], Laurent Vivien[1]

[1] Université Paris-Saclay, CNRS, Centre de Nanosciences et de Nanotechnologies, C2N – Palaiseau, France

[2] Université Grenoble Alpes, CEA-LETI, Minatec, 17 rue des Martyrs, F-38054 Grenoble

[3] Université de Lyon, Institut des Nanotechnologies de Lyon, INSA Lyon, CNRS, UMR 5270, Lyon

[4] Institut de Recerca en Energia de Catalunya, Spain

[5] Institut des Sciences Analytiques et de Physico-Chimie pour l'Environnement et les Matériaux, CNRS, Université de Pau et des Pays de l'Adour, France

[6] Laboratoire Photonique, Numérique et Nanosciences (LP2N), CNRS, University of Bordeaux, Institut d'Optique d'Aquitaine, Talence, France

[*]corresponding author: laurent.vivien@c2n.upsaclay.fr

Abstract: To overcome the limitations of silicon, hybrid integration of materials is required including ferroelectric oxides to develop efficient Pockels based optical modulators.

Silicon photonics has emerged as a promising platform to address future challenges in many applications, including data communications, sensing, and optical communications, among others. However, the properties of silicon alone are not enough to overcome key limitations related to speed, power consumption, and scalability. In particular, silicon exhibits strong two-photon absorption (TPA) at telecom wavelengths and is centrosymmetric, which limits the use of its nonlinear optical properties, such as the Kerr and Pockels effects. To address these challenges, new strategies have focused on integrating novel materials into the silicon photonics platform.

The presentation will explore recent developments in materials with optical properties that complement those of silicon and silicon nitride. It will also highlight the integration of ferroelectric oxides including Lithium Niobate and doped zirconia (ZrO_2), into silicon photonics platforms. In particular, doped zirconia, which is compatible with Si technology, offers several advantages: it exhibits low propagation loss, a large bandgap energy that prevents TPA, a wide transparency window ranging from ultraviolet to mid-infrared, and supports both Kerr and Pockels effects, along with light emission[1,2]. These properties make doped zirconia a promising candidate for addressing key challenges in silicon photonics.

References

1. Ruiz-Caridad, A.; Marcaud, G.; Ramirez, J. M.; Zhang, J.; Duran-Valdeiglesias, E.; Lafforge, C.; Largeau, L.; Maroutian, T.; Matzen, S.; Collin, S.; others Erbium-doped yttria-stabilized zirconia thin layers for photonic

applications. IEEE Journal of Quan- tum Electronics 2019, 56, 1–7.
2. Ruiz-Caridad, A. et al. Erbium-Doped Yttria-Stabilized Zirconia Thin Layers for Pho- tonic Applications. IEEE Journal of Quantum Electronics 2020, 56, 1–7.1064–1076, 1986.

Phase change material programmed photonics: plasmonic, dielectric, and interband resonances

Robert E Simpson[1*], Eleanor Gaggs[1], Daniel Chambers-Sims[1], Nur Qalishah Adanan[2], Simon Wredh, Ting Yu Teo[2], Li Lu[2], Liu Yan[3,4], Zhaogang Dong[2,3,4], and Joel K W Yang[2]

[1]School of Engineering, University of Birmingham, UK
[2]Singapore University of Technology and Design, Singapore
[3]Quantum Innovation Centre (Q.InC), A*STAR, Singapore
[4]Institute of Materials Research and Engineering (IMRE), A*STAR, Singapore
[*]corresponding author: r.e.simpson.1@bham.ac.uk

Abstract:

Chalcogenide phase change materials are being actively developed to tune the optical response of 3D displays, beam steering, and optical trap devices. We are studying dynamic control of metasurfaces through three different types of resonances, namely dielectric, plasmonic, and interband.

We aim to develop programmable metasurfaces composed of meta-atoms that can be progressively tuned across a full π-rad phase delay. We envision these materials finding widespread applications in 3D displays, beam steering devices, and dynamic optical traps for controlling cold atom clouds. The resonant frequency of a meta-atom can be controlled by either changing its size and geometry or by changing the intrinsic optical properties of the material from which it is composed. This talk focuses on the latter by exploiting dielectric, plasmonic, and interband resonances within chalcogenide phase change materials[1-6].

Many sulfide, selenide, and telluride materials (chalcogenides) exhibit multiple stable structural states at room temperature[7]. Structural transitions between these states can lead to large changes to the electronic band structure, which in turn produces refractive index contrast. In comparison to the negligible change in refractive index of oxides, like SiO_2, which is stable in glassy and crystalline forms (quartz), the refractive index contrast in phase change chalcogenides can be enormous. For example, the mid-infrared refractive index of the phase change material, $Ge_2Sb_2Te_5$ (GST), goes from ~4 to ~6 when it crystallizes[8], and the crystallization can occur in just 500 ps[9]. Clearly, these properties make chalcogenide phase change materials attractive for tuning and/or programming photonic devices.

We have now discovered, designed, and optimized a wide range of phase change materials that can be used to tune optical devices. In principle there are fundamentally two ways that these materials can be used in optical devices: (1) by using the change in their optical absorption (imaginary component of refractive index), or (2) by exploiting their change in the real component of refractive index. For metasurfaces composed of resonant meta-atoms, we have focused on developing ways to tune the real component of refractive index. Typically, we have been patterning these materials into meta-atoms and changing their dielectric resonances at below band gap energies via crystallization and amorphisation[2,5]. However, several tellurides, including elemental tellurium, are now providing a new option with interband resonances, using above bandgap light.

This talk will introduce our progress moving from infrared dielectric resonances in the common narrow bandgap tellurides, such as GST, to the discovery of Sb_2S_3, which has a band gap sufficiently large to allow dielectric resonances in the visible spectrum[1]. Finally, we will reconsider narrow bandgap tellurides, which can exhibit interband plasmonic-like resonances in the visible spectrum[10]. The presentation will introduce the intrinsic physical traits of these materials that allow them to support different resonances, and it will also show examples and demonstrations of how we exploited these resonances in tuneable metasurface devices.

Acknowledgements: E.G, D.C-M, N.Q.A and S.W are grateful for their PhD studentships from EPSRC, DSTL, and the Singapore MoE. Z.D. would like to acknowledge the funding support from the Agency for Science, Technology and Research (A*STAR) under its MTC IRG (Project No. M22K2c0088), SUTD Kickstarter Initiative (SKI) grant with the award No. SKI 2021_06_05, and National Research Foundation via Grant No. NRF-CRP30-2023-0003.

References

1 Dong, W. *et al.* Wide Bandgap Phase Change Material Tuned Visible Photonics. *Adv Funct Mater* **29**, doi:10.1002/adfm.201806181 (2018).

2 Lu, L. *et al.* Tunable Mie Resonances in the Visible Spectrum. *arXiv preprint arXiv:2107.07081* (2021).

3 Dong, W. L., Qiu, Y. M., Yang, J., Simpson, R. E. & Cao, T. Wideband Absorbers in the Visible with Ultrathin Plasmonic-Phase Change Material Nanogratings. *J Phys Chem C* **120**, 12713-12722, doi:10.1021/acs.jpcc.6b01080 (2016).

4 Liu, H. *et al.* Rewritable color nanoprints in antimony trisulfide films. *Sci Adv* **6**, eabb7171, doi:10.1126/sciadv.abb7171 (2020).

5 Moitra, P. *et al.* Programmable Wavefront Control in the Visible Spectrum Using Low-Loss Chalcogenide Phase-Change Metasurfaces. *Adv Mater* **35**, e2205367, doi:10.1002/adma.202205367 (2023).

6 Zamiri, G. *et al.* Interband plasmonic nanoresonators for enhanced thermoelectric photodetection. *Nanophotonics*, doi:10.1515/nanoph-2024-0752 (2025).

7 Wuttig, M. & Yamada, N. Phase-change materials for rewriteable data storage. *Nat Mater* **6**, 824-832, doi:10.1038/nmat2009 (2007).

8 Chew, L. T. *et al.* in *Proc Spie.* 103451B (International Society for Optics and Photonics).

9 Loke, D. *et al.* Breaking the Speed Limits of Phase-Change Memory. *Science* **336**, 1566–1569-1566–1569 (2012).

10 Toudert, J. & Serna, R. a. Interband transitions in semi-metals, semiconductors, and topological insulators: a new driving force for plasmonics and nanophotonics. *Opt. Mater. Express* **7**, 2299–2325-2299–2325 (2017).

Scalable Architectures for Photonic Compute-In-Memory Using Nonvolatile Optical Materials

Sadra Rahimi Kari[1], **Paolo Pintus**[2,3], **N. Youngblood**[1,*]

[1]Department of Electrical and Computer Engineering, University of Pittsburgh, USA
[2]Department of Electrical and Computer Engineering, Univ. of California, Santa Barbara, CA, USA
[3]Department of Physics, University of Cagliari, Cagliari, Italy
[*]corresponding author: nathan.youngblood@pitt.edu

Abstract: Photonic processors offer a route to analog computation with ultra-low latency and high efficiency. By combining nonvolatile optical materials (both phase-change and magneto-optic) with integrated photonics, we enable scalable photonic compute-in-memory architectures for high-speed matrix-vector operations in machine learning applications.

Photonics information processing strategies offer the unique ability to perform analog computation with ultra-low latency and high efficiency. However, designing compact and reconfigurable photonic architectures which scale well is a challenge. The combination of bistable optical materials (such as phase-change materials like $Ge_2Sb_2Te_5$) and integrated photonics is a promising approach which enables nonvolatile optical memory on-chip with low drift, compact footprint, and high-speed readout. This talk will focus on developing robust and scalable photonic memories using phase-change and magneto-optic materials (Ce:YIG)—together with wavelength division multiplexing and "in-memory" computing techniques—to enable high-speed matrix-vector operations for machine learning applications. Our work addresses key limitations in photonic compute-in-memory through two complementary nonvolatile optical memory technologies that enable practical, scalable architectures.

We introduce a multifunctional photonic memory cell that integrates phase-change materials ($Ge_2Sb_2Se_4Te_1$ and Sb_2Se_3) with a foundry-compatible PN junction in a micro-ring resonator. This hybrid approach uniquely combines coarse nonvolatile tuning via the PCM with high-speed volatile fine-tuning using the PN junction. Under forward bias, the junction acts as a microheater to program the PCM, while under reverse bias, it enables rapid adjustment of weights through the plasma dispersion effect. This dual functionality achieves a 400-fold increase in volatile tuning speed and a 10,000-fold improvement in efficiency over traditional approaches, with static power dissipation below 640 pW per device. We demonstrate 3.8-bit precision (14 distinct nonvolatile levels) while significantly extending effective cycling endurance by reducing the frequency of PCM reprogramming.

Addressing the fundamental endurance limitation of PCMs, we've also developed a non-reciprocal magneto-optic memory cell that leverages cerium-substituted yttrium iron garnet (Ce:YIG) on silicon micro-ring resonators. By simultaneously exciting clockwise and counterclockwise propagating modes in the resonator, we encode weights through the differential transmission resulting from magneto-optically induced resonance splitting. This approach delivers unprecedented performance: 2.4 billion programming cycles without degradation, 1 ns programming speed, 143 fJ/bit energy consumption, and approximately 3.5-bit precision. The non-reciprocal architecture also provides symmetric positive and negative weighting with improved extinction ratio while requiring smaller phase shifts than reciprocal approaches.

Both memory technologies integrate into a "broadcast and weight" architecture for matrix-vector multiplication, where our innovations specifically address the critical bottleneck of weight update time and energy. The multifunctional PCM-PN memory dramatically improves programming efficiency, while the non-reciprocal magneto-optic memory transforms the endurance limitation, enabling frequent reprogramming for large-scale computing algorithms. These developments represent significant steps toward practical photonic computing architectures capable of meeting the demands of next-generation machine learning applications, with future work focusing on increasing integration density, improving modulation efficiency, and further optimizing materials and device structures to enhance performance.

Acknowledgements: Parts of this work were funded by AFOSR, the National Science Foundation, the Autonomous Region of Sardinia via the 'Mobilità Giovani Ricercatori (MGR)' programme of the University of Cagliari; the Italian Ministry of University and Research via the PRIN PNRR 2022 project 'Magneto-optic Integrated Computing (MAGIC)', and the Fondazione di Sardegna.

References

1. Sadra Rahimi Kari, Marcus Tamura, Zhimu Guo, Yi-Siou Huang, Hongyi Sun, Chuanyu Lian, Nicholas Nobile, John Erickson, Maryam Moridsadat, Carlos A. Ríos Ocampo, Bhavin J Shastri, Nathan Youngblood, "High-Speed Multifunctional Photonic Memory on a Foundry-Processed Photonic Platform," Optica 12(1), 31-38 (2025).
2. Paolo Pintus, Mario Dumont, Vivswan Shah, Toshiya Murai, Yuya Shoji, Duanni Huang, Galan Moody, John E. Bowers, Nathan Youngblood, "Integrated nonreciprocal magneto-optics for photonic in-memory computing," Nature Photonics 19, 54-62 (2025).

Multifunctional materials for plasmonics in extreme conditions

A. Calzolari[1,2]

[1] CNR-NANO Istituto Nanoscienze, I-41125 Modena IT

[2] Department of Mechanical Engineering and Materials Science, Duke University, Durham, NC, USA; and Center for Autonomous Materials Design, Duke University, Durham, NC, USA

[*]corresponding author: arrigo.calzolari@nano.cnr.it

Abstract: By combining thermodynamics approaches, first principles simulations and experimental techniques we investigate and discover multifunctional materials (nitrides and high-entropy carbides) that combine tunable plasmonic properties in the near-IR/vis range and high mechanical and thermal resistance for applications in extreme and harsh conditions.

The manipulation of light on the deep subwavelength scale is essential for enhancing light-matter interactions and improving the performance of nanophotonic and thermal devices. The unique properties of plasmonic materials made them essential for a plethora of applications, ranging from energy to automotive, from wireless to medical and IoT. In particular, discovering multifunctional materials with tunable plasmonic properties, capable of surviving harsh environments (e.g., high temperature, and chemical or mechanical abrasion) is critical for advanced optical, thermal, and aerospace applications.

Here, we adopt massive high-throughput computational techniques, based on density functional theory, to design and characterize tunable plasmonic materials active in the near-IR and visible range. Starting from simple transition-metal crystals (such as nitrides) [1,2], we investigate the role of composition, off-stoichiometry and structural disorder in TiNx compounds [3], and we provide an efficient strategy to fine engineering stable, easy-to-grow hyperbolic metamaterial superlattices [4,5], with selected optical and extraordinary mechanical properties (e.g. hard materials).

Finally, by combining computational thermodynamics and first principles electronic structure techniques that allows us to predict synthesizable single-phase solid-state solutions (DEED) [6], we propose high-entropy transition-metal carbides (HECs) [7], which yielded plasmonic properties from room temperature to 1500K, as demonstrated by multi-technique experiments (ellipsometry, REELS, TEM-EELS) at varying temperature (see Figure 1). This new class of plasmonic materials may foster previously unexplored optical/mechanical applications (e.g. aerospace and security systems) in extreme conditions and ultra-high temperature.

We acknowledge the National Centre for HPC, Big Data and Quantum Computing (ICSC), funded under the National Recovery and Resilience Plan (NRRP), Mission 04 Component 2 Investment 1.4, NextGenerationEU, Award Number:CN00000013; and MUR-PRIN Project AMONIX - Amorphous conductors as a new route for plasmonics (2023-2025).

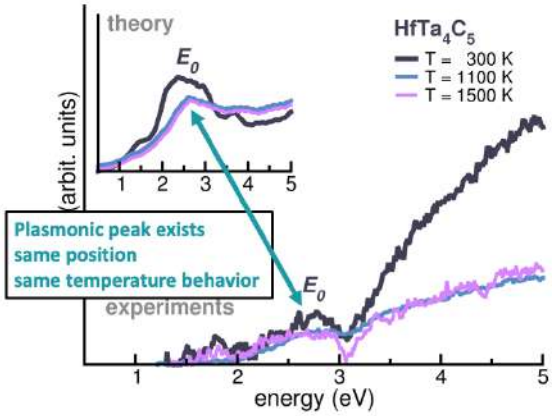


Figure 1: Comparison between experimental and theoretical (inset) EELS spectra of high entropy HfTa4C5 as a function of temperature. Image adapted from Ref. [7].

References

1. Catellani, A. and A. Calzolari, "Plasmonic properties of refractory titanium nitride", Phys. Rev. B Vol. 95, 115145, 2017.
2. Shah, D., Al. Catellani, H. Reddy, N. Kinsey, V . Shalaev, A. Boltasseva, and A. Calzolari, "Controlling the Plasmonic
3. Properties of Ultrathin TiN Films at the Atomic Level", ACS Photonics Vol. 5, 2816-2424, 2018.
4. Catellani, A., P. D'Amico, and A. Calzolari "Tailoring the plasmonic properties of metals: The case of substoichiometric titanium nitride", Phys. Rev. Mater. Vol. 4, 015201, 2020.
5. Catellani , A. and A. Calzolari, "Tailoring the plasmonic properties of ultrathin TiN films at metal-dielectric interfaces", Opt. Mater. Exp. Vol. 9, 1459, 2019.
6. Calzolari, A., A. Catellani, M. B. Nardelli, M. Fornari, "Hyperbolic Metamaterials with Extreme Mechanical Hardness" Adv. Opt. Mater. Vol. 9, 2001904, 2021.
7. Divilov, S., et al. "Disordered enthalpy–entropy descriptor for high-entropy ceramics discovery", Nature Vol. 625, 66, 2024.
8. Calzolari, A., C. Oses, C. Toher, M. Esters, X. Campilongo, S. P. Stepanoff, D. E. Wolfe, S. Curtarolo "Plasmonichigh-entropy carbides" Nature Commun. Vol. 13, 5993, 2022.

Semimetal-based nanostructured thin films for sustainable reconfigurable plasmonics and photonics

Fernando Chacon-Sanchez[1], **Marina García-Pardo**[1], **Johann Toudert**[1], **and Rosalía Serna**[1*]

[1]*Instituto de Optica, CSIC, Serrano 121, 28006 Madrid, Spain*
[*]Corresponding author: rosalia.serna@csic.es

Abstract: Elemental semimetal nanostructures (Bi, Sb) offer sustainable platforms for plasmonics and photonics, extending spectral range beyond that of noble metals. They enable advanced functionalities such as perfect absorption, structural coloration, and tunable optical responses via phase transitions, positioning them as versatile materials for next-generation optoelectronic and nanophotonic applications.

Plasmonic nanostructures and metasurfaces based on noble metals are well established as transformative components in sensing, imaging and photonic devices, owing to their ability to dramatically enhance light–matter interactions. However, the limited availability and high cost of these metals have stimulated extensive efforts to identify alternative materials that not only substitute noble metals, but also extend their operational spectral range and introduce novel functionalities to further advance nanophotonic performance. In this regard, semimetals have recently emerged as a promising class of unconventional platforms for both plasmonic and photonic applications.

In particular, the semimetals bismuth and antimony are relatively abundant elements in earth's crust that have emerged as promising candidates for sustainable photonic technologies due to its unique optical properties, moderate processing temperature, and low environmental impact. Whereas traditional noble metals whose plasmonic behavior is dominated by conduction electrons, in the case of Bi and Sb the origin of their plasmonic behavior relies on “interband plasmons” that arise from prominent interband transitions in the ultraviolet–visible range. As a consequence of these interband transitions it is derived the appearance of a spectral range with negative values in the real part of the permittivity at visible wavelengths, and an exceptionally high refractive index. For the case of Bi it has been shown that the refractive index can approach values as large as 10 in the infrared regime [1-2]. Making use of these unique properties we have designed and successfully fabricated metasurface thin film architectures based on Bi-nanostructures to enable different functionalities that include among others subwavelength perfect absorbers and efficient structural color devices [4-5]. In addition, Bi low melting point (~271 °C) facilitates energy-efficient manufacturing and enables a reversible solid–liquid phase change that allows modulating its optical response. Upon melting, Bi switches to a Drude-like metallic behavior with increased free-carrier contributions, while supercooled liquid states further expand the range of tunable optical responses. Making use of this properties we have developed reconfigurable photonic meta-surfaces for optical switching presenting state-of-the-art values for reversibility and cyclability [6-7].

In this presentation I will review these recent results and discuss how these robust transitions can be harnessed for fast optical modulators, multilevel data storage, and reconfigurable photonic circuits, especially where intermediate supercooled states enable analog tuning. Beyond switching applications, Bi strong

visible–UV absorption and high infrared refractive index hold promise for advanced sensors, photovoltaics, and thermal imaging devices.

Acknowledgements: This work has been partly funded by the Spanish research grants, ASSESS (TED2021-129666B-C21 and C22) and ALPHOMENA (PID2021-123190OB-I00f), funded by MCIN/AEI/ 10.13039/501100011033 and by the European Union NextGenerationEU/PRTR and the European Regional Development Fund (ERDF).

References

1. Toudert, J.; Serna, R.; Camps, I.; Wojcik, J.; Mascher, P.; Rebollar, E.; Ezquerra, T. A. Unveiling the Far Infrared-to-Ultraviolet Optical Properties of Bismuth for Applications in Plasmonics and Nanophotonics. J. Phys. Chem. C, Vol. 121, No. 6, 3511–3521, 2017.
2. Toudert, J.; Serna, R. Interband Transitions in Semi-Metals, Semiconductors, and Topological Insulators: A New Driving Force for Plasmonics and Nanophotonics [Invited]. Opt. Mater. Express, Vol. 7, No. 7, 2299, 2017.
3. Toudert, J.; Serna, R.; Pardo, M. G.; Ramos, N.; Peláez, R. J.; Maté, B. Mid-to-Far Infrared Tunable Perfect Absorption by a Sub - Lambda/100 Nanofilm in a Fractal Phasor Resonant Cavity. Opt. Express, Vol. 26, No. 26, 34043–34059, 2018.
4. Chacon-Sanchez, F.; de Galarreta, C. R.; Nieto-Pinero, E.; Garcia-Pardo, M.; Garcia-Tabares, E.; Ramos, N.; Castillo, M.; Lopez-Garcia, M.; Siegel, J.; Toudert, J.; Wright, C. D.; Serna, R. Building Conventional Metasurfaces with Unconventional Interband Plasmonics: A Versatile Route for Sustainable Structural Color Generation Based on Bismuth. Adv. Opt. Mater. Vol. 12, No. 10, 2302130, 2024.
5. Chacon-Sanchez, F.; Serna, R. Semimetal/Substrate Cavities Enabling Industrial Materials for Structural Coloring. ACS Appl. Opt. Mater. Vol. 3, No. 3, 727–736, 2025.
6. Alvarez-Alegria, M.; Siegel, J.; Garcia-Pardo, M.; Cabello, F.; Toudert, J.; Haro-Poniatowski, E.; Serna, R. Nanosecond Laser Switching of Phase-Change Random Metasurfaces with Tunable ON-State. Adv. Opt. Mater. Vol. 10, No. 3, 2101405, 2022.
7. Garcia-Pardo, M.; Nieto-Pinero, E.; Petford-Long, A. K.; Serna, R.; Toudert, J. Active Analog Tuning of the Phase of Light in the Visible Regime by Bismuth-Based Metamaterials. Nanophotonics Vol. 9, No. 4, 885–896, 2020.

Combining Phase Change Materials with soft-NIL dielectric metasurfaces for large-scale tunable optics

M. Putero[1*], O. Meskini[1,2], Y. Ramanda[3], J. Remondina[1], V. Malgras[3], B. Sciacca[3], F. Schenk[4], M. Yarema[4], and D. Grosso[2,3]

[1] Aix Marseille Univ, CNRS, IM2NP, Marseille, France
[2] Solnil, Marseille, France
[3] Aix Marseille Univ, CNRS, CINaM, Marseille, France
[4] Chemistry and Materials Design Group, ETH Zürich, Zürich, Switzerland
[*]corresponding author: magali.putero@univ-amu.fr

Abstract: Metasurfaces, composed of sub-wavelength nanostructures, enable precise light control but are typically static. Integrating Phase Change Materials (PCMs) allows tunability for real-time photonic devices. However, conventional fabrication is costly and complex. This work explores combining soft Nano Imprint Lithography with other methods to create low-cost, large-area tunable metasurfaces.

Managing the propagation of light and its properties with ever greater control and efficiency has become a major challenge in nanophotonics. This can be achieved using large arrays of sub-wavelength metallic or dielectric nanostructures known as metasurfaces. These structures are typically static, "fixed-by-design", meaning that their optical properties are predeterminated by their design. The next major milestone in metasurface development is the integration of tunability by incorporating Phase Change Materials (PCMs) such as $Ge_xSb_yTe_z$ or low-loss Sb_2S_3 alloys. Since PCM alloys can reversibly switch between their amorphous and crystalline states, exhibiting distinct optical and electronic contrast, they are ideal candidates for coupling with dielectrics metasurfaces. This approach enables the development of tunable photonic devices[1–3] (e.g. waveguides, phase shifters, absorbers…) capable of dynamically altering displayed information in real time. However, in most cases, integrating PCM in photonic devices relies on conventional top-down microfabrication techniques (standard lithography, lift-off, etching) which are costly, complex, difficult to implement on chalcogenides, and result in limited active surface areas.

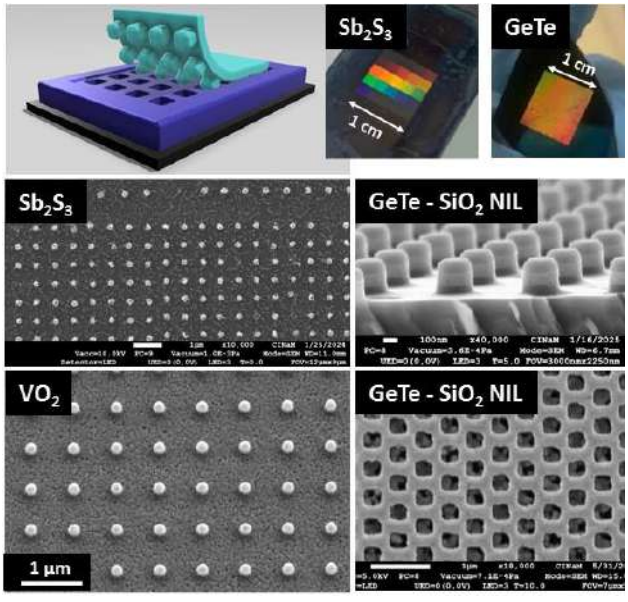


***Fig. 1**: Soft-NIL process scheme and SEM images & photos of various metasurfaces obtained by direct soft-NIL of inorganic based inks (Sb_2S_3, VO_2) or by combining soft-NIL dielectric metasurface with PCM (GeTe).*

In this work, we present recent progress, key achievements and future perspectives on combining soft Nano Imprint Lithography (soft-NIL) methods[4,5] with other methods (such as liquid deposition[6] or PVD) to elaborate PCM metasurfaces with various structural features (e.g. pillars or well arrays) of different dimensions and pitches (see Fig.1). Conducted in collaboration with Solnil, this research aims to move beyond traditional

fabrication methods to achieve low-cost, large-area active metasurfaces on diverse substrates. Finally, initial demonstrations of the switching capabilities of such metasurfaces will also be presented.

References

1. Hosseini, P., Wright, C. D. and Bhaskaran, H. "An optoelectronic framework enabled by low-dimensional phase-change films." Nature 511, 206–211 (2014).
2. Conrads, L. et al. "Infrared Resonance Tuning of Nanoslit Antennas with Phase-Change Materials." ACS Nano 17, 25721–25730 (2023).
3. Laprais, C. et al. "Reversible Single-Pulse Laser-Induced Phase Change of Sb_2S_3 Thin Films: Multi-Physics Modeling and Experimental Demonstrations." Adv. Opt. Mater. 2401214, 1–13 (2024).
4. Checcucci, S. et al. "Multifunctional Metasurfaces Based on Direct Nanoimprint of Titania Sol–Gel Coatings." Adv. Opt. Mater. 7, 1801406 (2019).
5. Modaresialam, M., Chehadi, Z., Bottein, T., Abbarchi, M. and Grosso, D. "Nanoimprint lithography processing of inorganic-based materials." Chem. Mater. 33, 5464–5482 (2021).
6. Schenk, F. M. et al. "Phase-Change Memory from Molecular Tellurides." ACS Nano 18, 1063–1072 (2024).

Programmable Infrared Geometric Phase Metasurfaces with the Plasmonic Phase-Change Material In_3SbTe_2

L. Conrads[1,*], and T. Taubner[1]
[1] I. Institute of Physics (IA), RWTH Aachen University, Germany

[*]corresponding author: conrads@physik.rwth-aachen.de

Abstract: We exploit the non-volatile insulator-to-metal transition of the plasmonic phase-change material In_3SbTe_2 for optical programming metasurfaces for infrared beam-shaping. We tailor the geometric phase of metasurfaces with rotated crystalline In_3SbTe_2 rod antennas to achieve beam steering, lensing, optical vortex beams and holography. Our approach enables rapid-prototyping of customized infrared meta-optics.

Conventional optical elements are bulky and limited to specific functionalities, contradicting the increasing demand of miniaturization and multi-functionalities. Optical metasurfaces enable tailoring light-matter interaction at will, especially important for the infrared spectral range which lacks commercially available beam-shaping elements. A convenient approach for programming plasmonic metasurfaces relies in direct laser writing nanoantennas directly with the novel plasmonic phase-change material PCM In_3SbTe_2 (IST). IST can be reversibly switched from an amorphous dielectric phase to a metallic crystalline one upon laser irradiation.[1] This material has been previously exploited for resonance tuning by reconfiguring the antenna shapes themselves [2,3], tailoring thermal emission of metasurfaces [4,5], and programming surface polariton resonators [6,7] directly. However, rapid-prototyping of complex IST metasurfaces for real-world applications has not been shown yet. Tailored phase-modulated metasurfaces with the plasmonic PCM IST promise arbitrary beam-shaping in the infrared spectral range.

Here, we exploit direct laser writing for programming large-area infrared metasurfaces at 9 µm operation wavelength and investigate their respective functionalities. First, we demonstrate beam steering metasurfaces with varied supercell periods to obtain different beam deflection angles. Second, we design and investigate a metalens with a focal length of 11.5 cm. Third, we exploit the orbital angular momentum of light and verify the mediated topological charges by revealing the spiral intensity pattern. Then, the phase profile of a metasurface hologram is designed with the Gerchberg-Saxton algorithm and combined with the phase profile of a magnifying lens, highlighting an easy way for combining multiple functionalities within a single metasurface. Finally, we use a diffractive neural network for designing a single hologram metasurface featuring two different hologram patterns at certain distances behind the metasurface.[8]

The concept of directly programming metasurfaces with IST antennas is much simpler, more cost-effective and faster compared to cumbersome fabrication techniques such as conventional lithography involving multiple costly and complex etching and design steps. The turnaround times of designing, fabricating and characterizing a new functional metasurface is only a fraction compared to established fabrication methods of metasurfaces. The operation wavelength of the metasurfaces is only given by the length of the rotated antennas and can be easily scaled to target the entire infrared range. Hence, our demonstrated concept paves the way towards fabrication of large-area metasurfaces within hours, enabling rapid-prototyping of customized infrared meta-optics for sensing, imaging and quantum information.

Acknowledgements: The authors acknowledge support by the Deutsche Forschungsgemeinschaft (DFG No. 518913417 & SFB 917 “Nanoswitches”).

References

1. Heßler, A. et al., “In_3SbTe_2 as a programmable nanophotonics material platform for the infrared” *Nat. Commun.* **12**, 924 (2021)
2. Heßler, A., Conrads, L. et al., “Reconfiguring Magnetic Infrared Resonances with the Plasmonic Phase-Change Material In_3SbTe_2” *ACS Photon*. **9**, 5 (2022)
3. Conrads, L. et al., “Infrared resonance tuning of nanoslit antennas with phase-change materials” ACS Nano **17**, 24 (2023)
4. Conrads, L. et al., “Reconfigurable and Polarization‐Dependent Grating Absorber for Large‐Area Emissivity Control Based on the Plasmonic Phase‐Change Material In_3SbTe_2” Adv. Opt. Mat. **11**, 8 (2023)
5. Giteau, M, Conrads, L. et al., “Switchable Narrowband Diffuse Thermal Emission With an In_3SbTe_2 -Based Planar Structure” Laser Photonics Rev. 2401438 (2024)
6. Conrads, L. et al., “Direct programming of confined surface phonon polariton resonators with the plasmonic phase-change material In_3SbTe_2” Nat. Commun. **15**, 3472 (2024)
7. Conrads, L. et al., “Real-space imaging of confined infrared surface plasmon polaritons on doped semiconductors covered with phase-change materials” Sci. Adv. **11**, eadr6844 (2025)
8. Conrads, L. et al. “Infrared beam-shaping on demand via tailored geometric phase metasurfaces employing the plasmonic phase-change material In_3SbTe_2” arXiv:2408.05044 (2024) *under review in Nat. Commun.*

Physics of Low-loss Phase Change Material (Sb_2Se_3) Enabled Nanophotonic Metasurface

P.Deoli[1*], O.L. Muskens[1], I. Zeimpekis[2,3] and **K.Sun[3]**

[1]Physics and Astronomy, Faculty of Engineering and Physical Sciences, University of Southampton, UK
[2]Optoelectronics Research Centre, Faculty of Engineering and Physical Sciences, University of Southampton, UK
[3]Electronics and Computer Science, Faculty of Engineering and Physical Sciences, University of Southampton, UK

[*]**corresponding author: pd1d23@soton.ac.uk**

Abstract: This research aims to develop an active, continuously reconfigurable metasurface by integrating a low-loss chalcogenide phase-change material, Antimony Selenide (Sb_2Se_3), with a Silicon dielectric metasurface. The objective is to create a metasurface that should be able to modulate various aspects of light, including amplitude modulation, comprehensive 2π phase control and dynamic optical switching.

Metasurfaces facilitate control over optical phenomena such as transmission, reflection and polarisation, paving the way for compact and efficient devices beyond the limits of traditional optics [1]. While passive metasurfaces have driven advancements, their fixed optical properties post-fabrication limit real-time adaptability. To overcome this limitation, active tunable metasurfaces have been developed, which can respond to external stimuli such as electric, thermal or optical inputs [2]. Among various strategies for achieving tunability, this research focuses on the integration of Phase change materials (PCMs), specifically the chalcogenide Sb_2Se_3. Sb_2Se_3 is a low loss chalcogenide capable of undergoing rapid and reversible phase transition between amorphous and crystalline states. This transition can be triggered by optical, thermal or electrical stimuli. Unlike traditional chalcogenides such as GST and GSST, Sb_2Se_3 offers minimal absorption loss in both the Amorphous and crystalline phases, particularly in the NIR region around 1550nm telecommunications wavelength [3].

To explore tunable optical responses, this study involves integration of Sb_2Se_3 with a silicon-based – dielectric metasurface. The silicon metasurface was fabricated using deep UV lithography (**Figure 1**), followed by Sb_2Se_3 coating via RF magnetron sputtering and thermal annealing to induce crystallization.

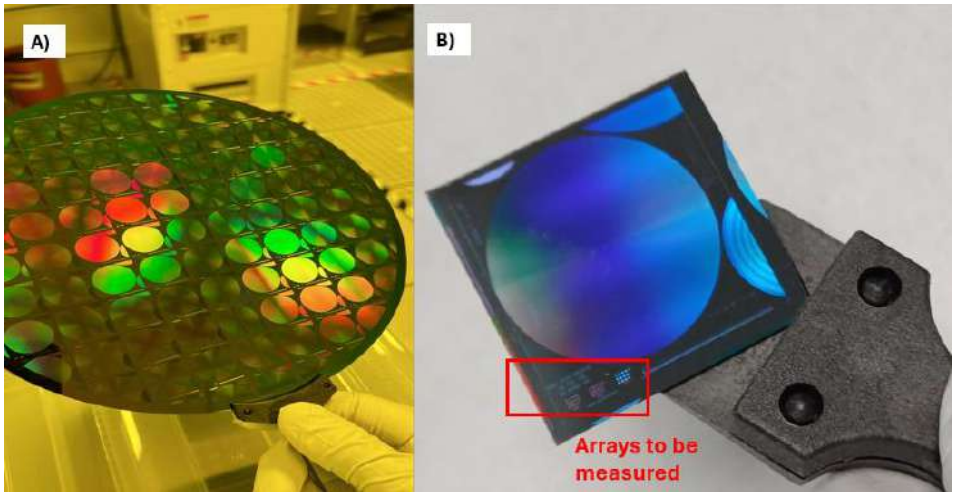


Figure 1: A) The metasurface reticle duplicated multiple times on the wafer. B) Chip cleaved from the wafer for deposition and measurements.

A protective ZnS: SiO2 capping layer was added to prevent oxidationa and ensure stability. Post fabrication, SEM imaging was conducted to examine the pillar geometry and to measure the thickness of the deposited PCM (**Figure 2**). The results revealed that the pillars exhibited rounded cone shape rather than intended square profile. To account for these structural variations, we employ modelling using the finite-difference time-domain (FDTD) method in Lumerical, optimising the design and analysing the effects of the geometry and phase change material on resonance tuning.

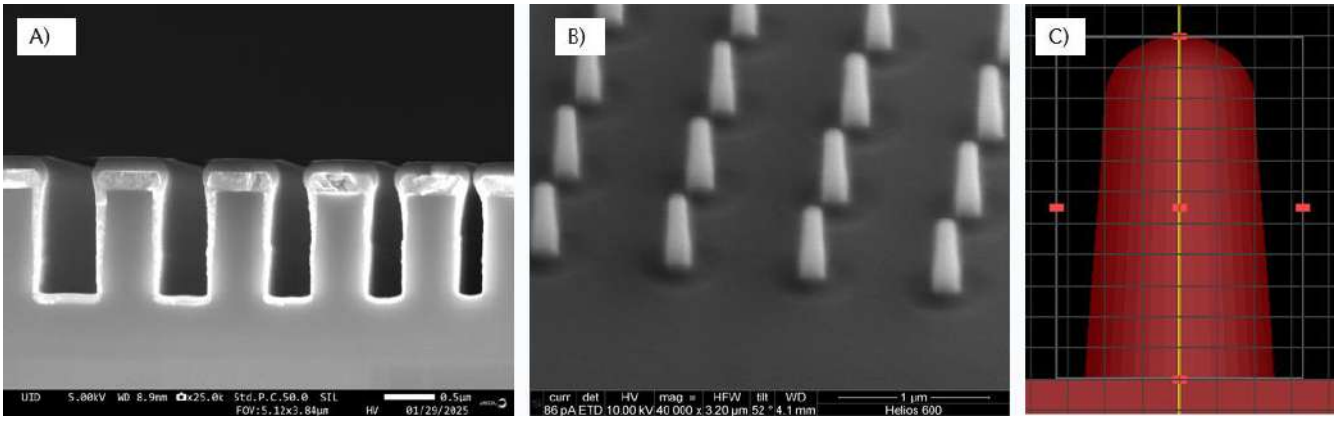


Figure 2: A) SEM cross-section of test bars showing the deposited PCM. B) Tilted view of 300nm wide pillars, providing insight into the vertical geometry of the pillars. C) Rounded cone model of the silicon pillars simulated in the Lumerical FDTD.

Initial experimental results demonstrate that the phase transitions of Sb_2Se_3 enable effective amplitude control and Mie resonance tuning. The Mie resonances redshifted upon the integration of Sb_2Se_3 and are further influenced by the dimensions of the metasurface. The metasurface exhibits high transmission with minimal loss, providing distinct contrasts between the amorphous and crystalline states of PCM. This makes it a promising candidate for telecommunications applications, including high-speed data transfer and optical modulators.

Currently, we are focusing on laser induced phase transition in the PCM to achieve optical switching. Moving forward, we aim to assess continuous switching performance by testing the metasurfaces stability and durability under multiple switching cycles. This will involve evaluating optical properties and ensuring consistent and reproducible control. In conclusion, the research focuses on developing a reprogrammable metasurface that alters both amplitude and phase while ensuring consistent efficiency across multiple switching cycles.

References

[1] H. T. Chen, A. J. Taylor, and N. Yu, “A review of metasurfaces: Physics and applications,” Jun. 16, 2016, *Institute of Physics Publishing*. doi: 10.1088/0034-4885/79/7/076401.

[2] T. Cui, B. Bai, and H. B. Sun, “Tunable Metasurfaces Based on Active Materials,” Mar. 07, 2019, *Wiley-VCH Verlag*. doi: 10.1002/adfm.201806692.

[3] M. Delaney, I. Zeimpekis, D. Lawson, D. W. Hewak, and O. L. Muskens, “A New Family of Ultralow Loss Reversible Phase-Change Materials for Photonic Integrated Circuits: Sb2S3 and Sb2Se3,” *Adv Funct Mater*, vol. 30, no. 36, Sep. 2020, doi: 10.1002/adfm.202002447.

Development of a New Reconfigurable Nanophotonic Platform Based on Spin Modulation

L. Mascaró-Burguera[1], J. Parra[1], R.Torres-Cavanillas[2], T. Mengual[1], L.M. Máñez-Espina[1], P. Sanchis[1], A. Díaz-Rubio[1] and E. Pinilla-Cienfuegos*[1]

[1]Nanophotonics Technology Center, Universitat Politècnica de València, 46022, València, Spain
[2]Institut de Ciència Molecular, Universitat de València, 46980, Paterna, Spain
*epinilla@ntc.upv.es (corresponding author)

Abstract

Reconfigurable integrated photonic devices rely on phase-change materials for their ability to transition between states with distinct optical properties under external stimuli. In this work, we present a novel reconfigurable photonic switch that operates at room temperature, utilizing integrated spin crossover nanoparticles to enable efficient, reversible switching with enhanced performance.

Multiple platforms have been developed for integrated photonics, such as InP, SiN, and GaAs. However, these technologies require specialized fabrication facilities and are not compatible with CMOS processes. In contrast, Silicon-on-Insulator (SOI) can benefit from existing microelectronics infrastructureproviding a cost-effective and scalable solution. Despite this, silicon lacks intrinsic electro-optic modulation capabilities, a limitation that can be addressed through the integration of active materials. Phase-change materials (PCMs), such as transition metal oxides and dichalcogenides, serve as active media for integrated photonics. Their distinct optical properties in different phases enable the development of reconfigurable nanophotonic devices. However, traditional PCMs still present significant drawbacks. For instance, VO_2 undergoes a volatile phase transition near room temperature (RT), affecting its stability [1], while the crystalline phase of GeSbTe (GST) exhibits a high extinction coefficient, resulting in significant optical losses in certain applications [2].

Both of these problems can be overcome using specially designed PCMs based on the spin crossover (SCO) phenomenon. SCO materials provide a versatile platform for actively tuning optical properties, as they can transition between low-spin and high-spin states in response to external stimuli such as temperature, pressure, or light. These transitions are also associated with changes in volume, magnetic behavior, electrical properties and color (Fig 1.a). Moreover, these materials can be chemically engineered to tailor their properties for specific applications [3] while maintaining their hysteretic behavior (and consequently, their bistability) even at the nanoscale [4]. By incorporating SCO nanoparticles (NPs) into a polymer matrix, it is possible to harness their advantageous properties while mitigating fabrication challenges.

In this work, we present a reconfigurable optical switch by integrating PMMA-embedded SCO NPsinto silicon micro-ring resonators (MRRs), enabling efficient and tunable performance (Fig 1.b). The distinct hysteretic optical response, with a width of approximately 25 ^{o}C and centered near room temperature, enables a reliable bistable switch for low-power integrated photonics (Fig 1.c). The results of our work pave the way for a novel kind of reconfigurable, low powered, low-cost and reliable integrated photonic devices based on polymer-integrated SCO nanomaterials. This could enable dynamic, on-demand control of optical signals in real time, facilitating a wide range of applications, from data processing to adaptive optical systems.

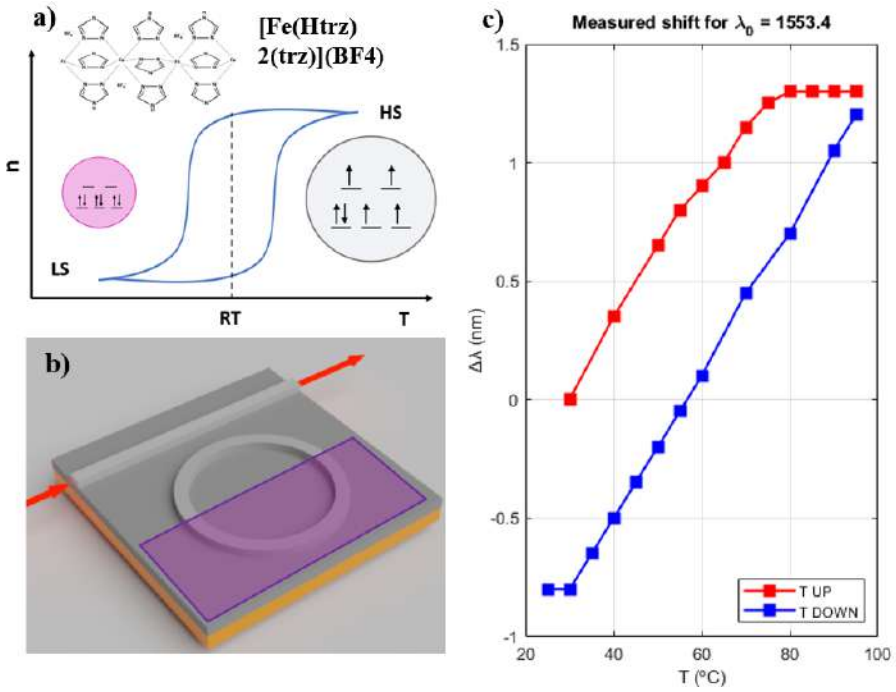


Figure 1: (a) Schematic hysteresis loop of the $[Fe(Htrz)_2(trz)](BF_4)$ NPs. (b) Windowed MicroRing Resonator. (c) Measured hysteresis loop at $\lambda_0 = 1553.4$ nm. Red represents heating and blue cooling. The experimental width is around 25 ^{o}C.

Acknowledgements

This project has been funded by the AGENCIA ESTATAL DE INVESTIGACIÓN of Ministerio de Ciencia e Innovacion (PID2021-128442NA-I00), and the European Regional Development Fund (ERDF) (IDIFEDER/2020/041, IDIFEDER/2021/061).

References

[1] R.M. Briggs, I.M. Pryce, and H.A. Atwater, "Compact silicon photonic waveguide modulator based on the vanadium dioxide metal-insulator phase transition", *Opt. Express*, Vol. 18, No. 11, pp. 11192-11201, 2010.

[2] J.H. Ko, Y.J. Yoo, Y.Lee, H. Jeong and Y. M. Song, "A review of tunable photonics: Optically active materials and applications from visible to terahertz", *iScience*, Vol. 25, No. 8, pp. 104727, 2022.

[3] J. R. Galán-Mascarós, E. Coronado, A. Forment-Aliaga, M. Monrabal-Capilla, E. Pinilla-Cienfuegos, and M. Ceolin, "Tuning Size and Thermal Hysteresis in Bistable Spin Crossover Nanoparticles", *Inorg. Chem*, Vol.49, No.11, 5706–5714, 2010.

[4] G. Molnár, S. Rat, L. Salmon, W. Nicolazzi and A. Bousseksou, "Spin Crossover Nanomaterials: From Fundamental Concepts to Devices",*Adv Mater*, Vol.30, No.5, pp. 17003862, 2018.

Dynamic Local Strain Engineering in Suspended 2D Materials

Eric Herrmann, Sai Rahul Sitaram, Ke Ma, S M Jahadun Nobi, and Xi Wang*

Department of Materials Science and Engineering, University of Delaware, Newark, DE 19716, USA
*Corresponding author: wangxi@udel.edu

Abstract: This talk presents a novel platform for dynamically engineering local strain in suspended 2D materials via nano-indentation. We demonstrate a measurable and reversible shift in the photoluminescence spectra in suspended two-dimensional materials. We further show that various types of strain distributions can be designed.

Strain engineering in two-dimensional (2D) semiconductors has recently unveiled captivating nanophotonic phenomena, including localized bandgap tuning, exciton funneling, and the development of site-specific single-photon emitters. Despite notable advancements in the theoretical framework surrounding nanoscale strain engineering, experimental efforts face challenges due to unintended strain in solid-state devices, complicating the connection between local strain environments and material responses. We have developed a novel strain engineering platform aimed at exploring complex strain distributions by transferring 2D material flakes onto closely patterned nanostructures, facilitating the investigation of various strain distributions like uniaxial, biaxial, and triaxial strain within one flake. The strong emission from thicker flakes makes gallium selenide (GaSe) an excellent candidate for examining the correlation between local strain and optical responses. In this presentation, we will discuss the dynamic local strain engineering of suspended 2D material flakes using a unique micromechanical spring that features specially designed nanoscale probes to induce symmetry-controlled localized strain. By conducting strain engineering measurements on suspended 2D materials instead of patterned substrates, we eliminate unintended strain effects from the surrounding environment. This research establishes a new platform for enhancing the quantitative understanding of material properties in relation to complex local strain in two-dimensional materials for quantum photonics applications.

Central to our approach is the design and fabrication of a silicon-on-insulator (SOI) based micro-spring with patterned nanoscale probes (MTS) at its apex, as shown in Figure 1(a,b). While AFM probe-based indentation induces in-plane biaxial strain at the point of contact, control over the probe geometry introduces an additional degree of freedom to tune the local strain distribution. Specifically, the MTS is designed to induce out-of-plane deformation and in-plane strain in suspended 2D materials by mechanical force, which allows for continuous tuning of the strain magnitude while performing optical and electrical characterization. The dynamic strain engineering platform has been applied to study tunable photoluminescence (PL) in 2D materials at room temperature, as shown in Figure 2(c,d).

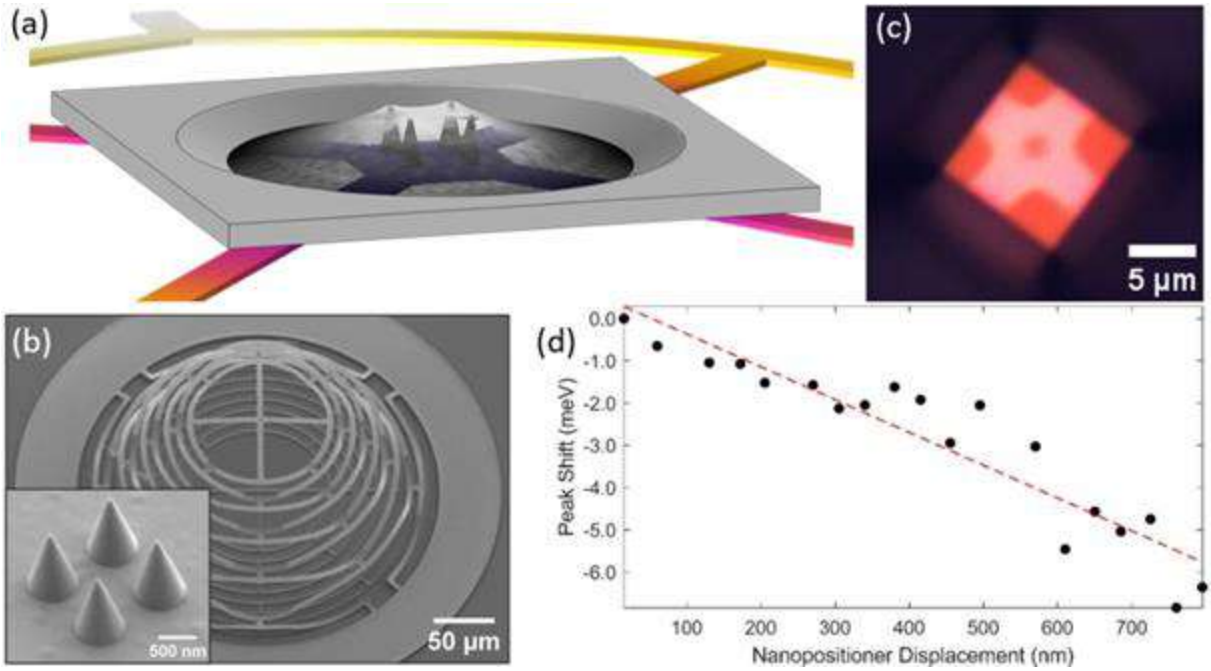


Figure 1 (a) Schematic of an MTS for inducing switchable out-of-plane deformations in suspended 2D materials. (b) SEM images of a fabricated MTS. The inset shows tips at the center of the spring. (c) Optical image of a flake of GaSe suspended on a square aperture and in contact with an MTS. (d) The center wavelength of PL red-shifts when the MTS induces higher out-of-plane deformation (larger strain).

Acknowledgements. This research was primarily supported by NSF DMR-2128534.

META Quantum Nanophotonics Workshop

Polarization-entangled photon pair generation from an epsilon-near-zero metasurface

Wenhe Jia[1,2], Grégoire Saerens[2], Ülle-Linda Talts[2], Helena Weigand[2], Robert J. Chapman[2], Liu Li[1], Rachel Grange[2,*], Yuanmu Yang[1,*]

[1] Department of Precision Instrument, Tsinghua University, China

[1]State Key Laboratory of Precision Measurement Technology and Instruments, Department of Precision Instrument, Tsinghua University, Beijing 100084, China.

[2]Optical Nanomaterial Group, Institute for Quantum Electronics, Department of Physics, ETH Zurich, Zurich 8093, Switzerland.

[*]corresponding authors: grangera@ethz.ch or ymyang@tsinghua.edu.cn

Abstract: We introduce and experimentally demonstrate a nanoscale polarization-entangled photon pair source utilizing a plasmonic metasurface that is strongly coupled to an epsilon-near-zero (ENZ) material.

Polarization-entangled photon pair sources are essential for diverse quantum technologies, such as quantum communication, computation, and imaging. However, the generation of complex polarization-entangled quantum states has long been constrained by the available nonlinear susceptibility tensor of natural nonlinear crystals, necessitating a cumbersome and intricate setup for additional coherent superposition or post-selection. In this study, we introduce and experimentally demonstrate a nanoscale polarization-entangled photon pair source utilizing an artificially-engineered metamaterial platform. This platform is based on a plasmonic metasurface that is strongly coupled to an epsilon-near-zero (ENZ) material. By precisely engineering resonances at both pump and signal/idler wavelengths, and leveraging the field enhancement provided by the ENZ effect, the photon pair generation efficiency of the 68-nm-thick metasurface is significantly boosted. More notably, the ENZ metasurface platform facilitates versatile manipulation of the system's anisotropic second-order nonlinear susceptibility tensor, enabling direct control over the polarization states of the photon pairs, which leads to the generation of a polarization-entangled Bell state without the need for additional components. Our approach opens a new avenue for the simultaneous photon pair generation and quantum state engineering in a compact platform.

Lighting the Future: Advancing Quantum Nanophotonics with Forward & Inverse Designs

Lin Wu*

Singapore University of Technology and Design (SUTD), 8 Somapah Road, Singapore 487372

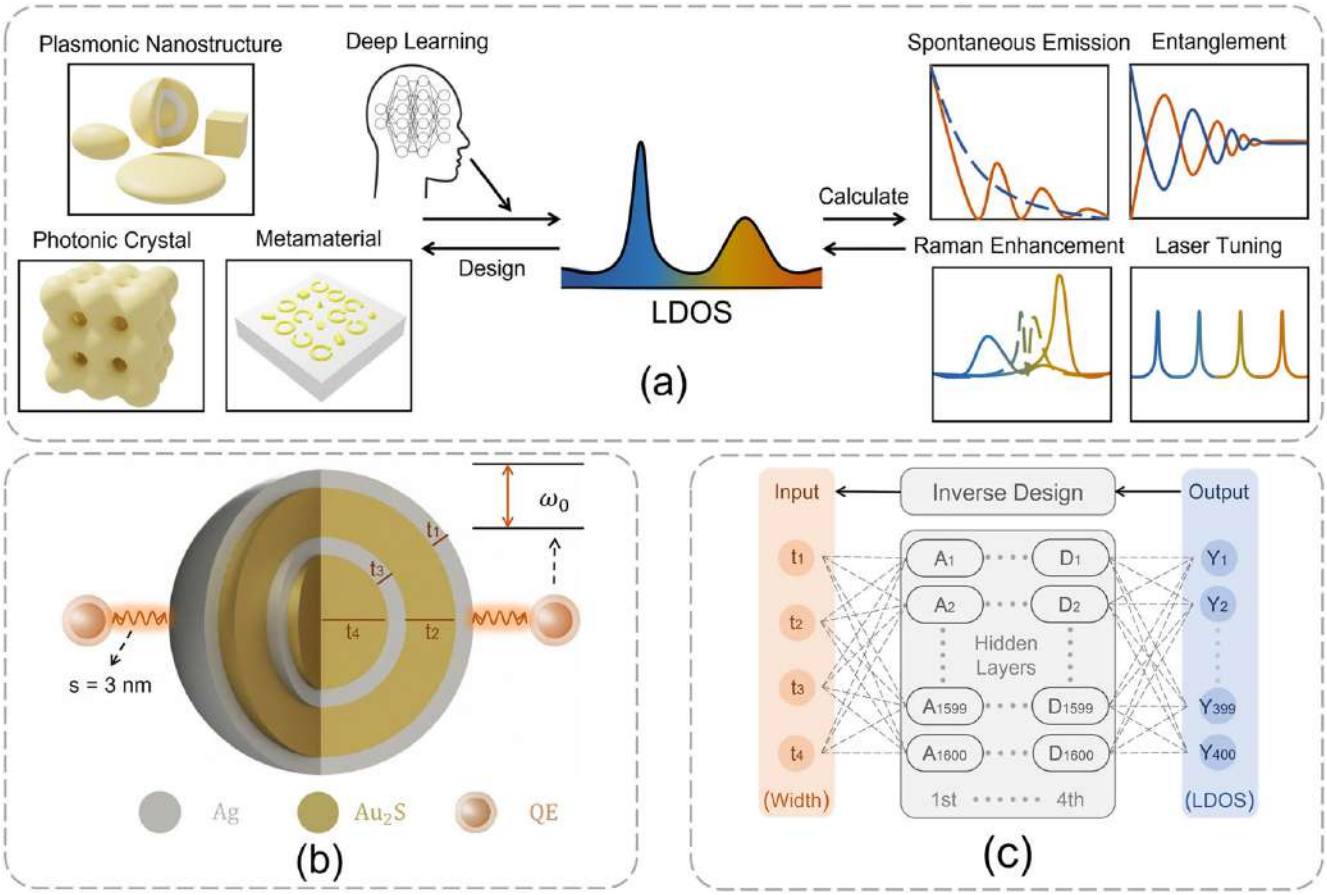
*Corresponding author: lin_wu@sutd.edu.sg

Abstract: This talk explores cavity quantum electrodynamics (Cavity-QED) design strategies from forward and inverse perspectives, highlighting case studies like quantum plasmonic sensing. We introduce advancements in quantum nanophotonics, combining the local density of states with deep learning to innovate and optimize design processes, offering a transformative pathway for quantum photonics.

We will revisit our theoretical proposals in forward design, presenting new experimental insights through case studies such as quantum plasmonic immunoassay sensing[1] and the recent demonstration of deterministic positioning and alignment of single-molecule excitons in plasmonic nanodimers for strong coupling[2]. Additionally, we will introduce our multidimensional hotspot nanoengineering approach for deterministic plexcitonic strong coupling at the single-emitter level, with a focus on substrate-mediated hotspot engineering[3] and the spectral localization of single-nanoparticle plasmons through photonic substrate engineering[4].

Furthermore, we will explore an innovative all-plasmonic spatio-spectral localized (SSL) system consisting of a gold bowtie array on a gold substrate[5], producing high-Q spectral-localized modes through the lattice's collective response, particularly surface lattice resonance (SLR). This SSL system enables tunable coupling between localized surface plasmon resonance (LSPR) and SLR, facilitating precise alignment with quantum emitters to form quasi-bound states that protect room-temperature quantum coherence. We will also discuss a generalized model[6] for probing spectral hole-burning (SHB) mechanisms in non-Hermitian scattering problems, advancing the design of tailored optical devices with enhanced performance.

Recent advances in inverse-design approaches have reshaped the landscape of nanophotonic structures by enabling the discovery of optical designs based on desired functional characteristics. Most studies so far have focused on light's interaction with these nanophotonic structures. However, when quantum emitters (QEs)—such as atoms, molecules, and quantum dots—are introduced to couple with these structures, the light-matter interactions become more complex, creating the rapidly evolving field of quantum nanophotonics. Quantum functionalities depend on the intrinsic properties of the QE and the electromagnetic environment it experiences, often described by the local-density-of-states (LDOS). We introduce a generalized inverse-design framework in quantum nanophotonics[7], using LDOS as a bridge to connect nanophotonic structures with quantum functional characteristics. As a case study, we examine a system where QEs are placed on a single multilayer shell–metal–nanoparticle (SMNP). By applying fully connected neural networks to model the LDOS of SMNP, we inverse-design and optimize its geometry based on LDOS to achieve desirable quantum characteristics in two quantum nanophotonic problems: spontaneous emission and entanglement. Our work introduces deep learning into the quantum optics domain, advancing the design of quantum devices.



References

1. Kongsuwan N., Xiong X., Bai P., You J. B., Png C. E., Wu L., Hess O. "Quantum plasmonic immunoassay sensing," **Nano Lett.**, Vol. 19, No. 9, 5853–5861, 2019.
2. Liu R. M., Geng M., Ai J. D., Fan X. Y., Liu Z. X., Lu Y. W., Kuang Y. M., Liu J. F., Guo L. J., Wu L. "Deterministic positioning and alignment of a single-molecule exciton in plasmonic nanodimer for strong coupling," **Nat. Commun.**, Vol. 15, 4103, 2024.
3. Xiong X., Lai Y. M., Clarke D., Kongsuwan N., Dong Z. G., Bai P., Png C. E., Wu L, Hess O. "Control of plexcitonic strong coupling via substrate-mediated hotspot nanoengineering," **Adv. Opt. Mater**. Vol. 10, No. 17, 2200557, 2022.
4. Liu R. M., Ai J. D., Zhou W. J., Zhu J. F., Liu G. X., Feng S. H., Li W., Liu J. F., Wu L. "Unlocking spectral localization of single-nanoparticle plasmons through photonic substrate engineering," **Phys. Rev. Lett**. (under review).
5. Zhou W. J., Lu Y. W., Liu J. F., Liu R. M., Ang L. K., Hess O., Wu L. "Spatio-spectral localized modal coupling for room-temperature quantum coherence protection," **Nanophotonics** (in press).
6. Zhou W. J., Liu J. F., Liu R. M., Zhu J. F., Gromyko D., Qiu C.W., Wu L. "Probing spectral-hole-burning in non-Hermitian scatterings: Differentiating far-field interference and near-field coupling," **ACS Photonics**, Vol. 11, No. 11, 4671–4681, 2024.
7. Liu G. X., Liu J. F., Zhou W. J., Li L. Y., You C. L., Qiu C.W., Wu L. "Inverse design in quantum nanophotonics: Combining local-density-of-states and deep learning," **Nanophotonics**, Vol. 12, No. 11, 1943–1955, 2023.

Superresolution for Nanometer-Scale Optical Imaging

Robert W. Boyd
Department of Physics, University of Ottawa, Ottawa, ON Canada
Institute of Optics, University of Rochester, Rochester, NY USA
boydrw@mac.com

Abstract: Quantum imaging is a research area that seeks to produce "better" images using quantum methods. We review recent research in this field, especially in the context of applications in biomedicine.

Traditional microscopy is limited in its resolution to approximately 400 nm. Many objects of interest to technology and biomedicine, for example, have feature sizes of much smaller dimensions. In this talk, we review methods to achieve higher resolution. One means to achieve superresolution, and the topic of this presentation, is to use quantum imaging methods.

Quantum imaging is a research area that seeks to produce "better" images using quantum methods. The image can be better in one of several different ways. It might possess better spatial resolution, it might display better signal-to-noise ratio, or it might be able to be formed using a very small number of photons. From an operational standpoint, we can consider quantum imaging to be an imaging modality that seeks to exploit the quantum properties of the transverse structure of light fields. In this presentation, we describe several different recent examples of advances in the field of quantum imaging.

One such example is afforded by quantum phase imaging. Many biological materials, especially cellular materials, possess very small contrast in terms of the amplitude of a light field transmitted through the material. However, the transmitted field does show significant structure in terms of the phase of the transmitted light. Many of these materials are optically quite fragile and cannot withstand a high intensity light field. High intensities are required for certain applications such as short-exposure imaging to monitor the dynamical changes in the structure of the material. The problem with optical damage is aggravated through use of short illumination wavelengths, which are normally required in order to obtain good spatial resolution of the image. These difficulties can largely be mitigated through use of quantum imaging methods. For example, quantum imaging can make optimum use of a small number of photons in an image-bearing field. Also, the spatial resolution can be limited not by the wavelength of light being used but by some fraction $1/N$ of this wavelength, where N is the number of photons in the quantum state that interrogates the object to be imaged. A quantum phase-imaging setup similar to the one used in our recent work is shown in Fig. 1. In our work, we were able to achieve a spatial resolution 1.7 times better than that of a classical imaging system with the same numerical aperture. Moreover, the measured phase shift of the light transmitted through the sample was 2.0 times larger than that of a classical imaging system.

Other examples of quantum imaging methods will be described in this talk. Quantum imaging has been shown to be a versatile method for enhancing the performance of optical imaging systems. One can expect additional improvements in imaging performance to be developed in the coming years.

Reference

1. Black, A. N., L. D. Nguyen, B. Braverman, K. T. Crampton, J. E. Evans, and R. W. Boyd, "Quantum-enhanced phase imaging without coincidence counting," Optica Vol.10, 952-958, 2023.

Nanophotonic interfaces for integrated quantum technologies

H. Siampour*

School of Mathematics and Physics, Queen's University Belfast, University Road, Belfast BT7 1NN, UK
* h.siampour@qub.ac.uk

Abstract: In this talk, I will present my research on developing nanophotonic interfaces for integrating solid-state quantum emitters. This includes nanoscale optical positioning of single emitters in nanomaterials for efficient waveguide/cavity coupling, plasmonic enhancement of single-photon emission at the zero-phonon line, and deterministic photon-emitter interfaces in chiral nanophotonic waveguides.

The development of chip-integrated optical components for the scalable implementation of solid-state qubits has become a key focus in advancing photonic quantum technologies, such as quantum communication, as well as distributed quantum computing and sensing. A critical aspect of integrating these systems is on-chip excitation, where quantum emitters are excited via waveguide modes rather than locally.[1] This approach enables precise quantum operations and device miniaturization, making it particularly relevant for deterministic photon-emitter interfaces.[2] In such systems, controlling light polarization and propagation within waveguides facilitates the unidirectional transfer of spin-carrying photons (flying qubits) between solid-state emitters (stationary qubits).[3]

Furthermore, leveraging slow-light effects in photonic crystal waveguides or nanoscale confinement of light in plasmonic waveguide-cavity systems leads to a significant enhancement of the spontaneous emission rate due to the Purcell effect.[2,4] This enhancement is particularly important for suppressing decoherence sources in solid-state environments and improving coherent operation.

In this talk, I will discuss recent progress in developing nanophotonic interfaces for the chip-integration of solid-state quantum emitters. I will cover nanoscale optical positioning of nanodiamonds containing single emitters for efficient waveguide excitation[1], plasmonic cavity coupling for the realization of Purcell-enhanced coherent photons[4] and unidirectional waveguide coupling[5]. Experimental results demonstrate a 42-fold enhancement of the spontaneous emission rate of nitrogen-vacancy (NV) emitters coupled with a plasmonic cavity. Additionally, precise placement of a nanodiamond at the constructive interference node of a Bragg reflector enables unidirectional emission coupling into a plasmonic waveguide mode.

In the second part of this talk, I will introduce a remote excitation protocol for deterministic photon-emitter interfaces in a quantum dot (QD)-waveguide system. In this approach, a single QD is excited in-plane via a photonic crystal waveguide through its nearest p-shell optical transition.[3] By exploiting the chirality of the waveguide mode, we achieve both directional absorption and emission, leading to a substantial enhancement in directional contrast, as measured for the Zeeman components of the waveguide-coupled QD.

Our remote excitation scheme achieves high directionality ($\geqslant 0.95$) across approximately 56% of the waveguide area, significantly overlapping with the Purcell-enhanced region where the electric field intensity peaks. In contrast, local excitation methods – using an out-of-plane excitation beam focused directly on the QD – achieve only ~25% overlap. This enhanced approach increases the likelihood of placing QDs in regions with both high Purcell enhancement and high directionality. Experimental results show a six-fold enhancement in the decay rate of a chirally coupled QD, achieving 90% directional contrast under remote excitation. This

corresponds to a β-factor of ~97%, as confirmed by FDTD simulations. This remote p-shell excitation protocol sets a new benchmark for waveguide quantum optics, effectively combining Purcell enhancement with high directionality. It lays the foundation for on-chip excitation in spin-based solid-state quantum technologies operating in the high β-factor regime.

References

1. Siampour, H. et al. On-chip excitation of single germanium vacancies in nanodiamonds embedded in plasmonic waveguides. *Light: Science & Applications* 7, 61 (2018).
2. Siampour, H. et al. Observation of large spontaneous emission rate enhancement of quantum dots in a broken-symmetry slow-light waveguide. *npj Quantum Information* 9, 15 (2023).
3. Germanis, S. et al. Waveguide excitation and spin pumping of chirally coupled quantum dots. *arXiv*:2502.00218.
4. Siampour, H. et al. Chip-integrated plasmonic cavity-enhanced single nitrogen-vacancy center emission. *Nanoscale* 9, 17902-17908 (2017).
5. Siampour, H. et al. Ultrabright single-photon emission from germanium-vacancy zero-phonon lines: deterministic emitter-waveguide interfacing at plasmonic hot spots. *Nanophotonics* 9, 953-962 (2020).

Nanoscale Gap-Plasmon-Enhanced Superconducting Photon Detectors at Single-Photon Level

Yu-Jung Lu[1,2]*

[1]Research Center for Applied Sciences, Academia Sinica, Taipei 11529, Taiwan
[2]Department of Physics, National Taiwan University, Taipei 10617, Taiwan
*E-mail: yujunglu@gate.sinica.edu.tw

Single-photon detectors have been widely studied for decades because of their unique capability to resolve photon numbers, enabling many applications in quantum information technologies. Compared to other types of single-photon detectors, niobium nitride (NbN) superconducting nanowire single-photon detectors are promising candidates and are commercially available today. However, the absorption coefficient of superconducting NbN in the visible range is typically low, resulting in low quantum efficiency and low signal-to-noise ratios. In the present work, we use a novel approach to enhance the visible-light photoresponse in NbN superconducting microwire photon detectors (SMPDs) by integrating them with gap plasmon resonators (GPRs). This talk describes how we observe the plasmonic NbN SMPDs can achieve a 233-fold enhancement in the phonon-electron interaction factor (γ) compared to pristine NbN SMPDs under resonant conditions with illumination at 532 nm. The nonlinear photoresponse in the visible region is attributed to the gap-plasmon resonances that disrupt the Copper pairs that break the superconducting state to normal. In addition, an impressive detection efficiency of 98% was achieved using these plasmonic SMPDs. Our results open new opportunities for designing sensitive quantum detectors for quantum information processing, quantum optics, imaging, and sensing at visible wavelengths. The detailed mechanisms and possible applications will be discussed.

Reference

1. Jing-Wei Yang, Tzu-Yu Peng, Daniel D. A. Clarke, Frank Daniel Bello, Jia-Wern Chen, Hao-Chen Yeh, Wei-Ren Syong, Chi-Te Liang, Ortwin Hess,* and **Yu-Jung Lu***, Nanoscale Gap-Plasmon-Enhanced Superconducting Photon Detectors at Single-Photon Level. *Nano Lett.* 23, 11387–11394 (2023)

Quantum Radar with Undetected Photons

Diego Dalvit
Los Alamos National Laboratory
dalvit@lanl.gov

Abstract: Quantum sensing promises to revolutionize sensing applications by employing quantum states of light or matter as sensing probes. Photons are the clear choice as quantum probes for remote sensing because they can travel to and interact with a distant target. Existing schemes are mainly based on the quantum illumination framework, which requires a quantum memory to store a single photon of an initially entangled pair until its twin reflects off a target and returns for final correlation measurements. Existing demonstrations are limited to tabletop experiments, and expanding the sensing range faces various roadblocks, including long-time quantum storage and photon loss and noise when transmitting quantum signals over long distances. We propose a novel quantum sensing framework that addresses these challenges using quantum frequency combs with path identity for remote sensing of signatures (“qCOMBPASS”). The combination of one key quantum phenomenon and two quantum resources, namely quantum induced coherence by path identity, quantum frequency combs, and two-mode squeezed light, allows for quantum remote sensing without requiring a quantum memory. The proposed scheme is akin to a quantum radar based on entangled frequency comb pairs that uses path identity to detect/range/sense a remote target of interest by measuring pulses of one comb in the pair that never flew to target, but that contains target information ``teleported" by quantum-induced coherence from the other comb in the pair that did fly to target but is not detected. This work was recently published in

D.A.R. Dalvit et.al., Quantum Frequency Combs with Path Identity for Quantum Remote Sensing, PRX **14**, 041058 (2024).

Controlling Multiple Quantum Dots using Structured Light

Suraj Goel[1], Sheena Shaji[1], Julian Wiercinski[1], Antoine Borel[1], Natalia H. Valencia[1], Moritz Cygorek[1], Erik Gauger[1], Brian Gerardot[1] and Mehul Malik[1]*

[1]Institute for Photonics and Quantum Sciences, Heriot-Watt University, Edinburgh, United Kingdom
*corresponding author: m.malik@hw.ac.uk

Abstract: We demonstrate the control of multiple, distinct quantum dots on one cryogenic sample via spatial light modulation, allowing us to observe cooperative emission from up to five dots and Hong-Ou-Mandel interference from two dots enabled by multi-plane optical circuits.

Semiconductor quantum dots are bright and deterministic sources of narrow linewidth single photons that play a vital role in quantum optical technologies, with applications ranging from quantum communication networks and photonic quantum computing. Platforms that involve processing multiple photons at the same time often employ a single quantum emitter providing a stream of photons which are then multiplexed in time [1]. This approach introduces a bottleneck in the generation rates of multi-photon quantum states, significantly limiting the scalability of such architectures. Moreover, the time-space demultiplexer used in these platforms often introduces line-shifts between the multiplexed photons, poorly affecting their indistinguishability. One could potentially introduce additional quantum dots from independent samples to improve this scalability, however this would require additional cryostats owing to the cooling requirements of these quantum dot samples. The ability to collect and manipulate light from multiple independent quantum emitters located randomly on a single sample promises a path towards scalability but remains an outstanding challenge. Here we demonstrate this capability by spatially structuring the optical excitation and collection modes to coherently control and observe quantum interference from up to five distinct quantum dots located on one sample.

In our approach, we employ structured excitation and collection with spatial light modulators (SLMs) to search for, identify, and specifically address nominally identical quantum dots that emit indistinguishable photons. Additionally, the structured collection can be used to erase the spatial “which dot” information of the indistinguishable photons coupled into a single-mode fiber (single core of multi-core fiber as shown in Fig. 1a) to induce cooperative emission [2,3]. Using this technique, we are able to scale the distance between two accessible quantum dots on a single sample by more than 40 times as compared to the previous state of the art (Fig. 1b) when considering measurement-induced cooperativity [2]. Using our scalable technique, we are able to observe bunching in the second-order coherence of cooperatively emitted photons from up to n=5 quantum dots for the first time, as shown in Fig. 1c.

We can go one step further and employ a programmable linear optical circuit implemented on a multi-plane light converter (MPLC) [4] to multiplex and interfere the collected photons from independent quantum dots. The use of an MPLC enables the programmability of optical circuits in the spatial degree-of-freedom of light. This is achieved via an inverse-design technique known as a wavefront matching, where a circuit is implemented by multiple phase screens and free-space propagation, allowing us to realise arbitrary operations on the emitted photons [5]. As a proof-of-concept demonstration, we program a 2x2 beam-splitter operation within the MPLC allowing photons from two independent quantum dots to interfere. The photon statistics are measured as a

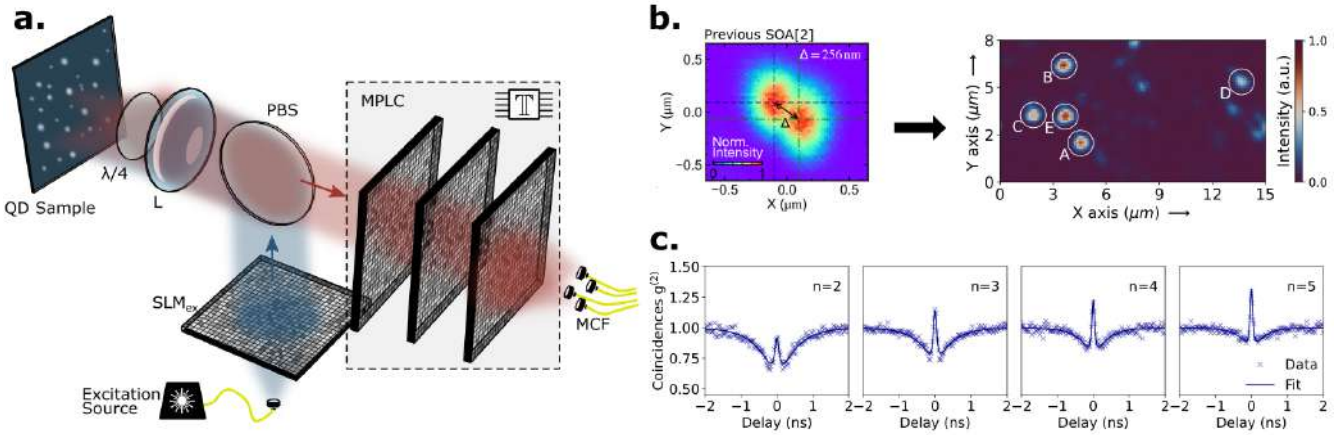


Fig. 1: Control of single-photon emission from multiple quantum dots using multi-plane light conversion (MPLC)}: (a) Structured excitation using a spatial light modulator (SLM_{ex}) is used to simultaneously excite multiple quantum dots (QDs) on a sample. The corresponding emission is manipulated by a multi-plane light converter (MPLC) to be coupled into individual channels of a multi-core fibre (MCF). (b) Characterised map of five independent quantum dots (labelled A-E) on a sample compared to previous state of the art (adapted from Ref. [2]). (c) Measurement-induced cooperative emission of up to five indistinguishable emitters obtained from the second-order correlation function measured via a Hanbury Brown and Twiss setup. Note that only one MCF core is used in this measurement.

second-order correlation function between light from different cores of the multi-core fiber, resulting in a two-photon Hong-Ou-Mandel dip. In this experiment, we observe a zero-delay HOM visibility of approximately 80%, successfully violating the bound necessary to demonstrate quantum interference. We are currently working towards scaling this up in terms of the number of dots and the programmability of our circuits. Our method serves as a powerful tool for interconnecting optical circuits with quantum dots and paves the way towards scalable and efficient quantum information processing.

References

[1] N. Maring, A. Fyrillas, M. Pont, E. Ivanov, P. Stepanov, N. Margaria, W. Hease, A. Pishchagin, A. Lemaˆıtre, I. Sagnes et al., "A versatile single-photon-based quantum computing platform," Nat. Photonics 18, 603–609 (2024).

[2] Z. X. Koong, M. Cygorek, E. Scerri, T. S. Santana, S. I. Park, J. D. Song, E. M. Gauger, and B. D. Gerardot, "Coherence in cooperative photon emission from indistinguishable quantum emitters," Sci. Adv. 8, eabm8171 (2022).

[3] M. Cygorek, E. D. Scerri, T. S. Santana, Z. X. Koong, B. D. Gerardot, and E. M. Gauger, "Signatures of cooperative emission in photon coincidence: Superradiance versus measurement-induced cooperativity," Phys. Rev. A 107, 023718 (2023).

[4] S. Goel, M. Tyler, F. Zhu, S. Leedumrongwatthanakun, M. Malik, and J. Leach, "Simultaneously sorting overlapping quantum states of light," Phys. Rev. Lett. 130, 143602 (2023).

[5] S. Goel, S. Leedumrongwatthanakun, N. H. Valencia,W. McCutcheon, A. Tavakoli, C. Conti, P.W. Pinkse, and M. Malik, "Inverse design of high-dimensional quantum optical circuits in a complex medium," Nat. Phys. 20, 232–239 (2024).

META 2025, MALAGA - SPAIN, JULY 22–25, 2025

Multimode and collective strong coupling in plasmonic nanocavities

A. Crookes[1], B. Yuen[1], and A. Demetriadou[1]
[1]University of Birmingham, UK
Corresponding author: a.crookes@bham.ac.uk

Abstract: Strong coupling in plasmonic nanocavities is often treated within a single mode approximation. However, here we show that off-resonant modes in-fact play a crucial role. In particular, we identify three regimes: single mode, multi-mode, and collective multimode strong coupling; advancing the understanding of quantum dynamics in realistic plasmonic nanocavities.

Plasmonic nanocavities provide a promising platform for exploring the quantum properties of light and matter. [1]. In particular, they enable a unique pathway to the strong coupling regime due to their deep subwavelength mode volumes [2]. However, most theoretical descriptions of strong coupling use a single-mode approximation – following their success in dielectric cavities. In contrast, plasmonic systems support a dense collection of modes that often also have large coupling strengths [3]. In general, the origin and impact of these modes on the quantum dynamics is not known.

In this work [4] we show that off-resonant plasmonic modes play a crucial role in strong coupling. In particular, we show that n strongly coupled plasmonic modes introduce up to $n(n+1)/2$ oscillation frequencies in the quantum dynamics. The amplitudes and frequencies of these oscillations depend on the detunings and coupling strengths of each mode and therefore, we also identify three distinct regions depending on these parameters: (i) single mode, (ii) multimode, and (iii) collective multimode strong coupling. In the single mode coupling regime, the quantum dynamics are governed by a single resonant mode. In the multimode coupling regime, the off-resonant modes become significant and produce multiple distinct oscillation frequencies, and in the collective coupling regime (which occurs past a critical dipole moment) the light-matter interaction is dominated by a single ultrafast oscillation. This ultrafast oscillation is due to the collective coupling with multiple modes, and is over one order of magnitude faster than if a single mode approximation is made. The collective multimode coupling regime is highlighted in Fig. 1

In Fig 1. (a) we show a single quantum emitter (QE) interacting with a common plasmonic system, the nanoparticle on mirror (NPoM) cavity. The electric field profile of the quasinormal modes (QNMs) in the gap centre are shown in Fig 1 (b) and are labelled with the index $\xi = (\ell 0)$. To determine their effect on strong coupling, we first consider a single QE with transition frequency $\omega_0 = \omega_{(10)} = 283$ THz and dipole moment $\boldsymbol{\mu} = 72\ \hat{\mathbf{z}}$ D. In Fig. 1 (c) we show the quantum dynamics when including interacting modes up to $\xi = (\ell_{\text{max}}0)$. For a single mode ($\ell_{\text{max}} = 1$) the QE exchanges energy with the cavity at a single (Rabi) frequency. However, as more modes are included in the interaction, the quantum dynamics become more complicated. In particular, when $\ell_{\text{max}} = 9$ the evolution is dominated by a single ultra-fast oscillation due to collective coupling with multiple modes.

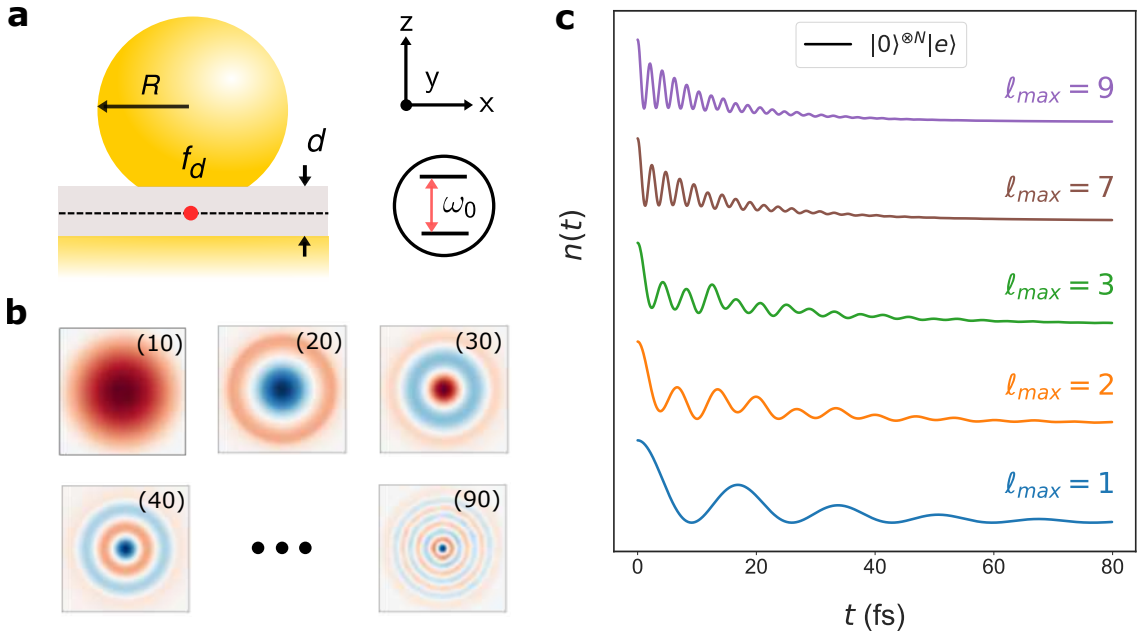


Figure 1: Multimode strong coupling **a** Schematic of a nanoparticle on mirror (NPoM) cavity; a single QE is placed at the gap centre. **b** Electric field $E_z(x, y, 0)$ of the first nine $\xi = (\ell 0)$ quasinormal modes (QNM's). **c** Evolution of the QEs excited state population $n(t)$ when including interacting modes up to $\xi = (\ell_{\max} 0)$ for $\ell_{\max} = 1, 2, 3, 7, 9$ where the QE has frequency $\omega_0 = \omega_{(10)} = 283$ THz and dipole moment $\boldsymbol{\mu} = 72\ \hat{\mathbf{z}}$ D

These insights advance the understanding of quantum dynamics in realistic plasmonic systems, and multimode cavities in general. In addition, the collective ultra-fast presents significant opportunities for enhanced precision and control of quantum systems, improved sensing, and for enabling faster and more efficient manipulation of quantum states in quantum information technologies.

AD gratefully acknowledges support from the Royal Society University Research Fellowship URF R1 180097 and URF R 231024, Royal Society Research grants RGS R1 211093, and funding from ESPRC grants EP Y008774 1 and EP X012689 1. AD, BY acknowledge support from Royal Society Research Fellows Enhancement Award RGF EA 181038, and AD, AC acknowledge funding from EPSRC for the CDT in Topological Design EP S02297X 1.

References

1. Tame, M. S. et. al. "Quantum Plasmonics," *Nature*, Vol. 9, pp. 329–340, 2013.

2. Chikkaraddy, R. et. al., "Single-molecule strong coupling at room temperature in plasmonic nanocavities," *Nature*, Vol. 535, pp. 127–130, 2016.

3. Kongsuwan, N. et al. "Plasmonic Nanocavity Modes: From Near-Field to Far-Field Radiation," *ACS Photonics*, Vol. 347, pp. 463–471, 2020.

4. Crookes, A., Yuen, B and Demetriadou, A. "Collective multimode strong coupling in plasmonic nanocavities," *arXiv*, 2024.

Colored Quantum Random Walks as a Route to Floquet States in Plasmonic Systems

Z. Jalali-Mola[1], O. Hess[1,*]
[1]School of Physics and CRANN Institute, Trinity College Dublin,
University of Dublin, Dublin 2, D02 PN40, Ireland
Corresponding author: ortwin.hess@tcd.ie

Abstract: Plasmonic and metasurface platforms enable exploration of topological Floquet phenomena in nanophotonics. We show that colored quantum random walks exhibit Floquet states without external driving. Using SU(3) symmetry, we uncover color-induced band mixing, topological bands, and bound states in the continuum, offering a new route to quantum photonic control.

Bound states in the continuum (BICs) are localized states that reside within bulk electronic or photonic dispersion bands, allowing for lossless transport and propagation. Building on this concept, topological bound states in the continuum (TBICs) incorporate key topological features—such as bulk-boundary correspondence and edge-state protection—to enable robust, backscatter-free transport and directional propagation [1–3].

Here, we show that lower-order dispersive TBICs naturally arise as Floquet systems via colored quantum random walks (cQRWs) on discrete lattice structures [4]. By employing the SU(3) group to describe the walker's spatial evolution, the cQRW inherently realizes Floquet dynamics without requiring external periodic driving. Through tunable rotation parameters, we reveal unconventional edge-state behaviors, including localized states within topological band gaps and dispersive TBICs that manifest as edge states embedded within bulk topological bands. These TBICs exhibit controllable group velocity and precise excitation dynamics, emerging as intrinsic features of the cQRW framework. CQRWs can be implemented in nanophotonic platforms, such as plasmonic metasurfaces or plasmonic waveguide networks, where the lattice comprises arrays of plasmonic nanoparticles or dielectric resonators forming a discrete periodic system. Here, the internal degrees of freedom—"colours"—are encoded through plasmonic mode hybridization, different polarization states, or spatial resonances, with periodic modulation inherently embedded in the system.

A discrete-time quantum random walk (QRW) evolves through a periodic sequence of unitary operators (U) acting on a Hilbert space composed of two subspaces: the particle's position states and the coin space. The coin operation is governed by rotations within the SU(3) group space, while the walker's motion is dictated by an alternating sequence of rotation and hopping operations. These operations, with tunable parameters and directions, define the walker's dynamics, which are encapsulated by the unitary operator:

$$\boldsymbol{U}(\theta_1,\theta_2)=\boldsymbol{T}_y\boldsymbol{R}(\theta_2)\boldsymbol{T}_x\boldsymbol{R}(\theta_1),\quad \boldsymbol{T}_i=|i,\mathfrak{R}\rangle\langle i,\mathfrak{R}|+|i-1,\mathfrak{G}\rangle\langle i,\mathfrak{G}|+|i+1,\mathfrak{B}\rangle\langle i,\mathfrak{B}|\,, \tag{1}$$

where, $\boldsymbol{T}_{x/y}$ are the hopping operators that control movement along the x and y directions respectively, and $\boldsymbol{R}(\theta)=e^{i\boldsymbol{S}\theta/2}$, is the coin rotation operator, defined using operators $\boldsymbol{S}$ from the SU(3) symmetry group.

To characterize the system's topology, we compute the Chern number for each energy band by numerically evaluating the band curvature. The obtained Chern numbers and the corresponding topological properties of the system, as functions of the rotation parameters (θ_1,θ_2),

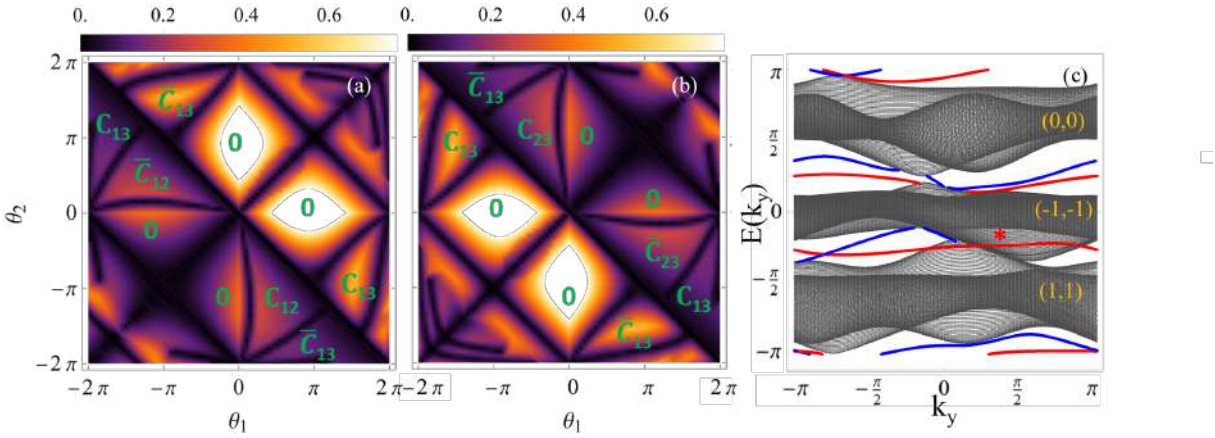


Figure 1: Energy gaps, Chern numbers and Edge States in the rotation plane (θ_1, θ_2). Panels (a) and (b) depict the energy gaps Δ_{12} and Δ_{23}, corresponding to the separations between the first and second bands and the second and third bands, respectively. The Chern number of each region is denoted as $(C_{ij} = (C_i = 1, C_j = -1) = -\bar{C}_{ij})$, indicating the topological characteristics of bands i and j. Panel (c) presents the energy spectrum of two semi-infinite structures, highlighting localized edge states. Edge states at the left and middle boundaries are distinguished by blue and red, respectively. The rotation parameters are set to $(\theta_{1L}, \theta_{2L}, \theta_{1R}, \theta_{2R}) = (\pi\ \ 3, -\pi, -2\pi, 3\pi)$.

are presented in Fig. 1, where green numbers indicate the values within each gapped region. Darker regions, where the energy gap closes, delineate the boundaries between distinct topological phases. We now examine scenarios involving media with non-trivial topological properties, ensuring at least one gap closing occurs between them. Analyzing different topological configurations of the QRW reveals that while both media share the same non-trivial topological characteristics, in addition to chiral edge states, mid-gap edge states also emerge. These states, marked by a red star in panel (c), coexist with the gapless bands but remain unhybridized with the bulk extended states. They appear as dispersive topological bound states in the continuum (TBICs) that are robust against random disorder. Unlike flat bands and higher-order TBICs, these TBICs arise within a semi-infinite configuration and exhibit a dispersive nature.

Acknowledgements, O.H. gratefully acknowledges funding from Research Ireland (formerly Science Foundation Ireland) via the METAQUANT Research Professorship Programme (Grant No. 18/RP/6236).

References

1. Yang,B. J. and Saeed Bahramy, M. and Nagaosa, N., "Topological protection of bound states against the hybridization," *Nature Communications*, Vol. 4, No. 1, pp. 1524, 2013.

2. Hu, Z. and Bongiovanni, D. and Jukić, D. and Jajtić, E. and Xia, S. and Song, D. and Xu, J. and Morandotti, R. and Buljan, H. and Chen, Z., "Nonlinear control of photonic higher-order topological bound states in the continuum," *Light: Science & Applications*, Vol. 10, No. 1, pp164, 2021.

3. Cerjan, A. and Jürgensen, M. and Benalcazar, W. A. and Mukherjee, S. and Rechtsman, M. C., "Observation of a Higher-Order Topological Bound State in the Continuum," *Phys. Rev. Lett.*, Vol. 125, No. 21, PP. 213901–213908, 2020.

4. Jalali-Mola, Z. and Hess, O., "Controlled Floquet Dynamics and Topological Bound States in Continuum via Colored Quantum Random Walks," *arXiv*:2503.17263, 2025.

Quantum metaphotonics

Broadband and bright photon pairs from periodically poled triple-resonance metasurface

Jihua Zhang[1,2,*], Chaoxin Shi[1,3], Jinyong Ma[2], Frank Setzpfandt[4], Thomas Pertsch[4], Chunxiong Bao[3], Jianjun Zhang[1,5] and Andrey A. Sukhorukov[2]
[1]Songshan Lake Materials Laboratory, Dongguan 523808, China
[2]ARC Centre of Excellence for Transformative Meta-Optical Systems (TMOS), Department of Electronic Materials Engineering, Research School of Physics, Australian National University, Canberra, ACT 2600, Australia
[3]School of Physics, Nanjing University, Nanjing 210093, China
[4]Institute of Applied Physics, Abbe Center of Photonics, Friedrich Schiller University Jena, Jena 07745, Germany
[5]Institute of Physics, Chinese Academy of Sciences, Beijing 100190, China
zhangjihua@sslab.org.cn (corresponding author)

Abstract

We propose a periodically poled triple-resonance metasurface capable of generating photon pairs with high brightness and broad bandwidth in both frequency and momentum.

Photon pairs from spontaneous parametric down-conversion (SPDC) with broad bandwidth are highly desired in many quantum technologies [1]. In particular, broad frequency and momentum bandwidths are essential for realizing the promise of quantum advantages in quantum communications and quantum metrology. However, achieving broad bandwidth in both frequency and momentum while maintaining a high rate remains a challenge for both conventional nonlinear crystals and recently emerging nonlinear metasurfaces [2–4]. In this work, we address this challenge by introducing a periodically poled triple-resonance metasurface comprising a binary silica grating atop a periodically poled lithium niobate (PPLN) film (Fig. 1a) [5].

As studied before [4], such a metasurface supports high-Q guided mode resonances (GMRs) to enhance SPDC. The novelty in this work lies in two aspects. First, here we not only excite GMRs at the photon-pair wavelengths (red lines in Fig. 1(b, c)), but also at the pump wavelength (blue lines in Figs. 1(b, c)), realizing the so-called triple-resonance SPDC. The quasi-phase matching (QPM) condition between three waveguide modes is further satisfied by using a PPLN film with a poling period determined by the phase mismatch between three waveguide modes. Second, we employ a binary grating design to simultaneously optimize the input coupling of the GMR at the pump wavelength and the output coupling of the GMRs at the photon-pair wavelengths during the SPDC.

With triple resonances, the sum frequency generation (SFG), and thus the inverse SPDC, is further amplified by more than four orders of magnitude when compared to the previous double-resonance case (Fig. 1d). Most interestingly, since GMRs have a weak dispersion along k_z and a linear dispersion along k_y (Fig. 1b), the triple-resonance SPDC is supported in a broad range near the degenerate point for the same pump. This leads to enhanced photon-pair generation with a broad momentum bandwidth even under a Gaussian pump (Fig. 1e). The photon-pair frequency is related to the resonance frequencies of the GMRs at each position and thus broadband as well. Overall, the predicted SPDC rate is as high as 102 MHz/mW with

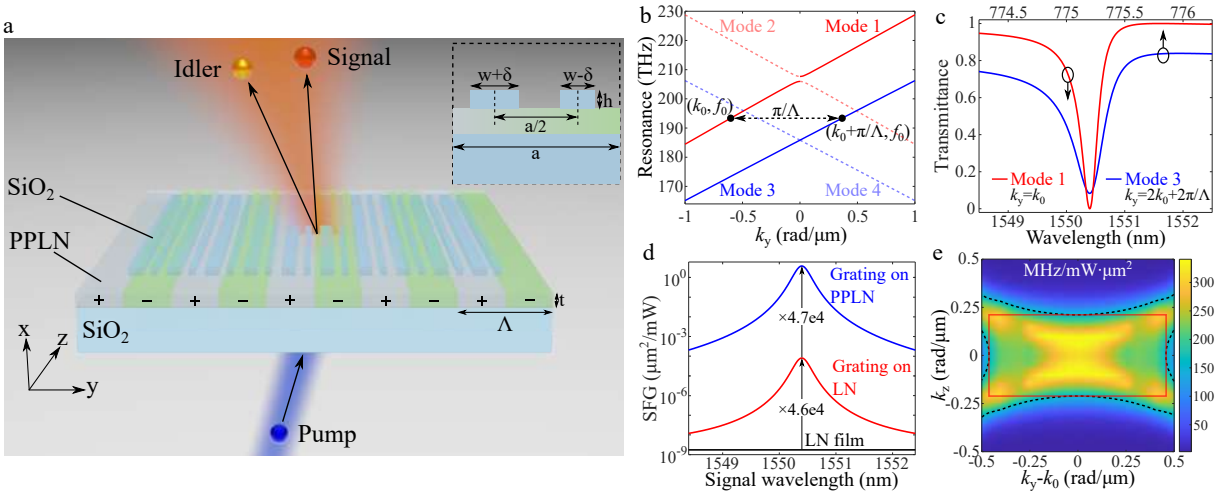


Figure 1: **a** Proposed metasurface including a binary SiO_2 grating ($h = 200nm$, $a = 810nm$, $w = 0.25a$, $\delta = 75nm$) on a PPLN film ($t = 300nm$, $\Lambda = 4a$). **b** Resonance frequency of the first- (Mode 1 & 2) and second-grating-order (Mode 3 & 4) GMRs as a function of k_y when $k_z = 0$. The coordinate axes are halved when plotting Modes 3 & 4. The GMRs at the two black dots satisfy the QPM condition in SPDC. **c** Transmission spectra of the metasurface near the photon-pair and pump wavelengths at the QPM directions. **d** SFG efficiency for the triple-resonance, double-resonance, and no-resonance cases. **e** SPDC spatial emission pattern from the metasurface under a Gaussian pump with a beam waist of $200\mu m$.

a frequency bandwidth of 165 nm around 1550 nm and a momentum bandwidth of 13° × 6°. This improves the state-of-the-art by more than 1000 times in rate and 10 times in bandwidths. Such a broadband and bright photon-pair source could stimulate the performance improvement of various free-space quantum photonic technologies, such as quantum imaging.

The authors acknowledge support from Guangdong Provincial Quantum Science Strategic Initiative (GDZX2303004, GDZX2200001), Songshan Lake Materials Laboratory (XMYS20230020, 24D1281G111), Innovation Program for Quantum Science and Technology (2021ZD0302300) (J.Z., C.S., J.Z.), the Australian Research Council (CE200100010) (J.Z., J.M., A.A.S.), the Deutsche Forschungsgemeinschaft (DFG, German Research Foundation) through the International Research Training Group (IRTG) 2675 "Meta-ACTIVE", project number 437527638 (T.P., F.S., A.A.S.) and the Collaborative Research Center (CRC) 1375 "NOA" (T.P., F.S.).

References

[1] K. G. Katamadze, A. V. Pashchenko, A. V. Romanova, and S. P. Kulik, *JETP Lett.*, 115, 581-595, 2022.

[2] T. Santiago-Cruz, S. D. Gennaro, O. Mitrofanov, S. Addamane, J. Reno, I. Brener, M. V. Chekhova, *Science*, 377, 991-995, 2022.

[3] W. Jia, G. Saerens, Ü. Talts, H. Weigand, R. J. Chapman, L. Li, R. Grange and Y. Yang, Sci. Adv. 11, eads3576, 2025.

[4] J. Zhang, J. Ma, M. Parry, M. Cai, R. Camacho-Morales, L. Xu, D. N. Neshev, and A. A. Sukhorukov, Sci. Adv. 8, eabq4240, 2022.

[5] J. Zhang, C. Shi, J. Ma, F. Setzpfandt, T. Pertsch, C. Bao, J. Zhang and A. A. Sukhorukov, arXiv:2502.08990, 2025.

Highly directional photon-emitter interactions in slow-light waveguides

H. Siampour*

School of Mathematics and Physics, Queen's University Belfast, University Road, Belfast BT7 1NN, UK
* h.siampour@qub.ac.uk

Abstract: In this talk, I will present our work on remote excitation of a single quantum emitter in a slow-light waveguide. Exploiting waveguide chirality, we achieve both directional absorption and emission, resulting in 90% directional contrast and a β-factor of ~97%. This approach advances waveguide quantum optics for spin-based quantum technologies.

The development of chip-scale quantum optical circuits has become a key focus in advancing quantum technologies, including computing, communication, and sensing. A critical component for integrating these systems is on-chip excitation, where quantum emitters are excited via waveguide modes rather than locally.[1] This approach enables precise quantum operations and device miniaturization, making it particularly relevant for chiral quantum systems. In such systems, controlling light polarization and propagation within waveguides enables unidirectional information transfer.[2]

A key parameter in waveguide quantum optics is the β-factor, which quantifies the coupling efficiency of emitted photons into the waveguide mode. High β-values are essential for observing quantum-optical effects, such as single-photon nonlinearities, and are especially significant when quantum emitters are placed at chiral points within the waveguide. At these points, emitters can introduce spin-dependent phase shifts, with potential applications in quantum spin-networks and spin-based quantum technologies. While significant progress has been made in chiral emission from quantum dots (QDs), directional absorption in such systems, particularly at high β-factors, remains largely unexplored.

In this talk, I will present our results on an integrated semiconductor chip where a single QD is excited in-plane via a photonic-crystal waveguide through its nearest p-shell optical transition.[3] By exploiting the waveguide mode's chirality, we achieve both directional absorption and emission, leading to a substantial enhancement in directional contrast, as measured for the Zeeman components of the waveguide-coupled QD. Our remote excitation scheme enables high directionality ($\geqslant 0.95$) across approximately 56% of the waveguide area, significantly overlapping with the Purcell-enhanced region where the electric field intensity peaks. In contrast, local excitation methods, which use an out-of-plane excitation beam focused directly on the QD, achieve only ~25% overlap. This enhanced approach increases the likelihood of placing QDs in regions with both high Purcell enhancement and high directionality.

We experimentally demonstrate a six-fold enhancement in the decay rate of a chirally coupled QD with 90% directional contrast under remote excitation, corresponding to a β-factor of ~97%, as calculated using FDTD simulations. Our remote p-shell excitation protocol sets a new benchmark for waveguide quantum optics, combining Purcell enhancement with high directionality, and lays the foundation for on-chip excitation in spin-based solid-state quantum technologies operating in the high β-factor regime.

References

1. Siampour, H. et al. On-chip excitation of single germanium vacancies in nanodiamonds embedded in plasmonic waveguides. Light: Science & Applications 7, 61 (2018).
2. Siampour, H. et al. Observation of large spontaneous emission rate enhancement of quantum dots in a broken-symmetry slow-light waveguide. npj Quantum Information 9, 15 (2023).
3. Germanis, S. et al. Waveguide excitation and spin pumping of chirally coupled quantum dots. arXiv:2502.00218.

Quantum metasurfaces of quantum emitters arrays

Uri Israeli[1], Ada Krasnosky[1], Itai David[1], Shahar Levi[1] , and Rivka Bekenstein

[1]Racah Institute of Physics, Hebrew University of Jerusalem, Jerusalem 91904, Israel
*corresponding author: rivka.bekenstein@mail.huji.ac.il

Abstract: We implement quantum metasurfaces by deterministically preparing atomic-like arrays in sub-wavelength spacing. These devices are promising tools for cavity-free quantum optics and the generation of large-scale atom-photon entanglement.

Light control has taken a new path following the invention of metasurfaces [1] with incredible manipulation of almost every light property by scattering. The new system we analyzed of quantum metasurfaces extended this control to quantum properties. Quantum metasurfaces are made out of two-dimensional atomic arrays that control light quantum state by scattering [2] without the need of nanostructures or cavities. This was soon followed by experimental realizations with ultra-cold atomic arrays [3,4] proposals employing these arrays for various quantum applications, such as extending quantum memory and generating entanglement [5,6]. However a system that will enable robustness and scalability is still to be found.

The basic principle behind quantum metasurfaces is that two-dimensional arrays of atoms can be prepared in superposition states of reflectivity and transparency. This is done by employing the enhanced response of subwavelength atomic arrays along with inter-atomic long-range interactions and quantum control [2]. Hence, scattering of single photons sequentially off these arrays generates atom-photon entanglement. While this analysis the employment of long-ranged Rydberg interactions that naturally display themselves in atomic systems, it is still lacks implantation with emitters that do no exhibit these properties. The latter would be crucial for implantations with quantum emitters is a solid-state based system, that naturally offers scalability.

Here, we present an implementation with atom-like emitters and specifically with Silicon-Vacancy centers in diamond [7]. In our new experiment we are able to prepare emitter-like arrays deterministically and probe the light-atom interaction. The next-generation low-temperature experiment we are currently working on will enable access to the long coherence time of the electronic spin of the Silicon-Vacancy centers. Employing this long coherence time along with our developed protocols [8,9] enables generation of large scale atom-photon entanglement.

References

1. Z. Bomzon, G. Biener, V. Kleiner, and E. Hasman, “Radially and azimuthally polarized beams generated by space-variant dielectric
2. R. Bekenstein, I .Pikovski, H. Pichler, E. Shahmoon *et. al.,* “Quantum metasurfaces with atom arrays”. Nat. Phys., 16(6):676–681, 2020.
3. Kritsana Srakaew, *et al., “*A subwavelength atomic array switched by a single rydberg atom”, 2022.
4. R Bekenstein and S. F. Yelin. “A switchable atomic mirror”. Nat. Phys., 19(5):619–620, 2023.
5. Asenjo-Garcia, H. Kimble, and D. E. Chang, “Optical waveguiding by atomic entanglement in multilevel atom arrays”, PNAS, 116, 51, 25503–25511, 2019.
6. O. Guimond, A. Grankin, D. Vasilyev, B. Vermersch, and P. Zoller, “Subradiant bell states in distant atomic arrays”, Phys. Rev. Lett. 122, 9, 093601, 2019.
7. N. Knall, C. M. Knaut, R. Bekenstein, D. R. Assumpcao, and P. L. Stroganov *et al.*, “Efficient source of shaped single photons based on an integrated diamond nanophotonic system,” Phys. Rev. Lett. 129, 053603, 2022.
8. P. N. T. Lloyd and R. Bekenstein, “Single atomic layer quantum holography”, Physical Review Research 7, p:L022014.
9. N. Antman-Ron, M Carmi, and R. Bekenstein, “Atom-Atom entanglement generation via collective states of atomic rings” , Physical Review Research 6, p:L042051

Shaping the emission directivity of single quantum dots in dielectric nanodisks exploiting Mie resonances

A. Genco[1*], C. Cruciano[1], D. Rocco[2], A. Tognazzi[3], A. Locatelli[2], L. Carletti[2], A. Fedorov[1], C. Trovatello[1], G. Di Blasio[1], I. Bargigia[1], C. Louca[1,5], P. Gubian[2], G. Tavani[1], L. Lovisolo[6], A. Tuktamyshev[7], L. C. Andreani[8], M. Galli[8], G. Cerullo[1], G. Leo[6], S. Sanguinetti[7], C. De Angelis[2], and M. Bollani[4]

[1]Politecnico di Milano, Piazza Leonardo Da Vinci 32, 20133, Milano, Italy
[2]University of Brescia, via Branze 38, 25123, Brescia, Italy
[3]University of Palermo, viale delle scienze 10, 90128, Palermo, Italy
[4]Institute of photonics and of nanotechnologies- National Researcher Council (IFN-CNR), LNESS laboratory, Piazza Leonardo Da Vinci 32, 20133 Milano, Italy
[5]Cavendish Laboratory, Department of Physics, JJ Thompson Ave, Cambridge, UK
[6]Matériaux et Phénomènes Quantiques, Université Paris Cité and CNRS, 10 rue A. Domon et L. Duquet, Paris, 75013 France
[7]University of Milano Bicocca via Cozzi 55, 20126 Milano, Italy
[8]University of Pavia, via Bassi 6, I-27100 Pavia, Italy
[*]corresponding author: armando.genco@polimi.it

Abstract: Manipulating the optical landscape of single quantum dots (QDs) is essential to increase the emitted photons output. In this work, we exploit the Kerker condition for precise control of single GaAs QDs emission directivity when embedded in AlGaAs nanocylinders, as proved by angle-resolved PL micro-spectroscopy experiments and confirmed by theory.

The convergence of quantum optics and nanophotonics has led to major advances in controlling light-matter interactions at the nanoscale. Quantum dots (QDs), as reliable single-photon emitters, are central to emerging quantum technologies in communication, computation, and sensing. Realizing their full potential requires precise control of their emission, which can be achieved by engineering the surrounding photonic environment to channel photons into well-defined optical modes [1]. Micro- and nano-optical architectures—such as gate-tunable microcavities, micropillars, and photonic crystal waveguides—have been developed to enhance photon extraction while preserving high indistinguishability (up to 99%) [2], achieving end-to-end efficiencies above 50% [3]. These structures also enable compact, chip-integrated designs.

Among emerging strategies, the Kerker condition has gained attention as a means to tailor the emission properties of QDs, by strategically integrating them with optical nanostructures. This unidirectional scattering mechanism is based on the interference of electromagnetic multipolar moments induced in the Mie scatterers [4]. The Kerker effect leverages interference between electric and magnetic dipole modes in Mie-resonant particles to achieve unidirectional scattering—either forward (in-phase, first Kerker condition) or backward (out-of-phase, second Kerker condition). All-dielectric nanostructures exploiting this principle offer a promising platform for QD integration [5], though experimental demonstrations remain limited.

Here, we tested both theoretically and experimentally the behavior of few GaAs-based QDs working as quantum emitters embedded within AlGaAs dielectric nanoresonators, and exploited the Kerker condition to modify the emission directivity based on the position of the QDs within the nanodisks.

We fabricated the optimized structures based on numerical simulations and measured their emission properties. By employing an innovative fabrication method, we created AlGaAs nanodisks on a AlO_x transparent

layer with a low number of QDs (about 8 -12 dots for cylinder) located at two different heights within the pillar, which correspond to forward and backward scattering Kerker conditions. Changing the vertical position of the dots by just 80 nm, we found a dramatic increase of the PL directivity from QDs due to the different Kerker condition. In fact, performing a statistical analysis on more than 150 QDs, we observed a dramatic enhancement of the PL intensity by more than one order of magnitude (about 14 times) when the emitters resided close to the top of the nanodisks, demonstrating the efficacy of the Kerker effect. Angle-resolved photoluminescence (PL) spectroscopy revealed a strong dependence of the angular emission pattern on the position of the QDs within the base area of the pillar. The experimental results aligned very well with the theoretical simulations.

The integration of QDs with nanostructures leveraging the Kerker condition not only advances our fundamental understanding of light-matter interactions, but also opens pathways to practical applications, from quantum information processing to advanced sensing technologies.

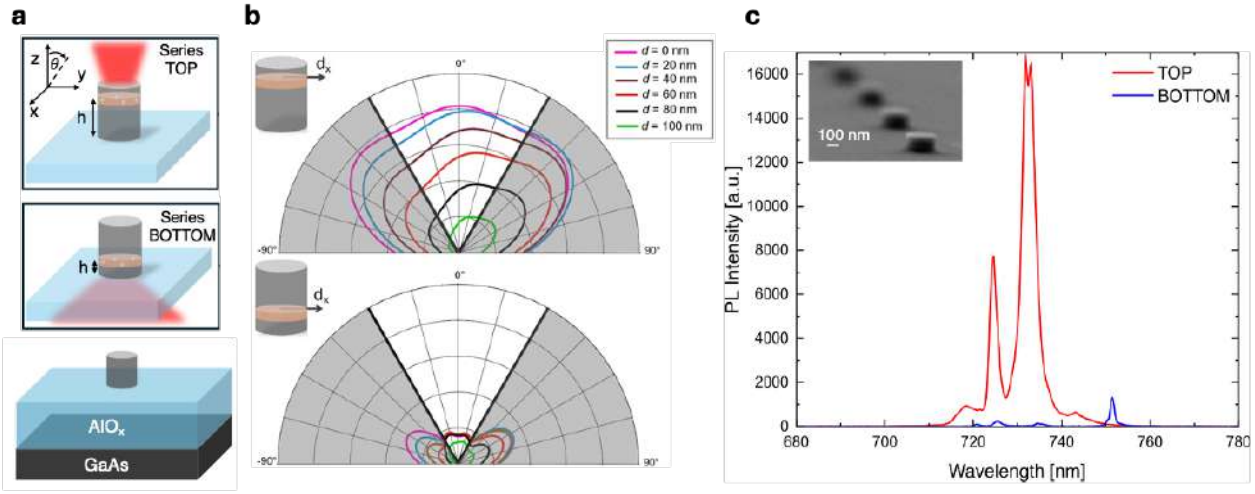


Figure 1: a) Top-Middle panels: Schematics of the QD-loaded nanodisks located at two different heights of the nanodisks for the series TOP and BOTTOM. Bottom panel: Representation of the final device structure after all the fabrication steps. b) Calculated radiation pattern in the air region as a function of the QD displacement along the x axis for the two reference heights of the series TOP and BOTTOM, highlighted by the insets. The gray area indicates the region outside the NA used in the experiment. c) PL spectra collected from two single nanodisks of the TOP and BOTTOM series respectively. Inset: SEM image of the fabricated nanodisks.

References

1. P. Lodahl, S. Mahmoodian, S. Stobbe, “Interfacing single photons and single quantum dots with photonic nanostructures”, Reviews of Modern Physics (2015), 87 (2).
2. Y. Arakawa, M. J. Holmes, “Progress in quantum-dot single photon sources for quantum information technologies: A broad spectrum overview”, Applied Physics Reviews (2020), 7 (2).
3. N. Tomm, et al. “A bright and fast source of coherent single photons.” Nature Nanotechnology 16.4 (2021): 399-403.
4. W. Liu, Y. S. Kivshar, “Generalized Kerker effects in nanophotonics and meta-optics” Optics Express (2018), 26 (10).
5. A. S. Solntsev, G. S. Agarwal, Y. S. Kivshar, “Metasurfaces for quantum photonics”, Nature Photonics (2021), 15 (5).

Metamaterials for Sustainable Energy and Environmental Solutions

Computational Design of Crystalline Chalcogenides for Intermediate-Band Solar Cells

M. Cagnoni[1]
[1]Politecnico di Torino, Italy
matteo.cagnoni@polito.it (corresponding author)

Abstract

Intermediate-band solar cells are a promising concept to exceed the Shockley-Queisser limit. Yet, photo-converting materials fully exploiting the intermediate-band paradigm remain elusive thus far. In this contribution, their possible realization with Earth-abundant crystalline chalcogenides is explored by state-of-the-art computational methods.

The intermediate-band solar cell is a concept developed to outperform today's commercial devices based on the Shockley-Queisser model. The latter employ a conventional semiconductor to convert sunlight photons into charge carriers, and selective contacts to order their motion and establish a net electric current (Figure 1a). The reliance on a single photon absorption onset (valence-conduction inter-band transitions) imposes a trade-off between photo-generated current and voltage. In fact, more carriers are available with a smaller valence-conduction gap (higher current), while more energy can be extracted per carrier with a larger one (higher voltage). This limits the maximum achievable efficiency to ∼30% [1, 2].

In intermediate-band solar cells, electronic states are introduced within the gap of the photo-converting material (Figure 1b). This allows electrons to be excited from the valence to the conduction band via an additional pathway that involves the absorption of two sub-gap photons. Compared to conventional semiconductors, the current-voltage trade-off is improved, because more charge carriers are photo-generated for the same valence-conduction band gap. As a result, the power conversion efficiency limit is boosted to ∼45% [3].

The potential to combine high performance with systemic simplicity makes intermediate-band solar cells very appealing. Yet, these devices have failed to outperform Shockley-Queisser ones thus far. This can be attributed to the use of sub-optimal photo-converting materials. In fact, these are often realized by heavily doping conventional semiconductors used in Shockley-Queisser solar cells, such as GaAs, to introduce the needed intermediate states. Not only the

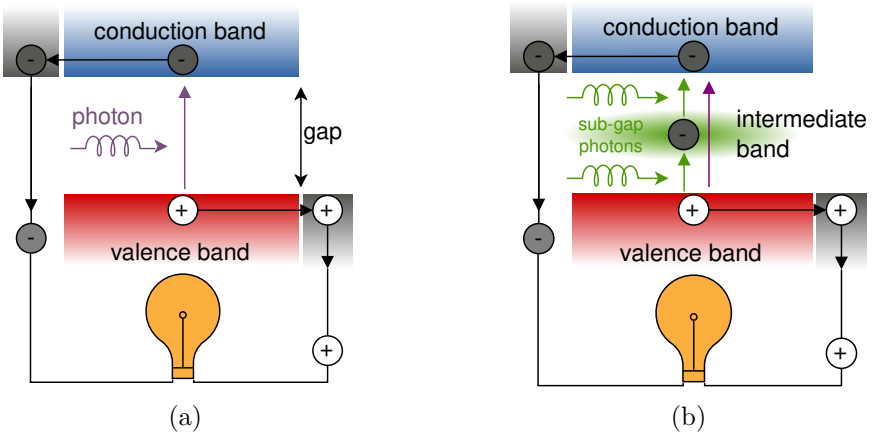


Figure 1: Working principle of a) Shockley-Queisser and b) intermediate-band solar cells.

resulting optical properties are far from optimal (for example, the valence-conduction band gap of GaAs is ∼1.4 eV, against the optimal value of ∼2.4 eV), but also the electrical properties are significantly degraded; indeed, the introduction of intermediate states as deep impurity levels strengthen Shockley-Read-Hall non-radiative recombination [4].

It has been argued that Shockley-Read-Hall non-radiative recombination can be inhibited by delocalizing the wave function of the intermediate states [5]. This can be accomplished by increasing the dopant concentration until the Mott transition occurs. Alternatively, one could use crystalline materials that inherently possess an intermediate-band electronic structure. This second approach is particularly appealing, because the intermediate-band paradigm is implemented by the material as it is, with possibly reduced fabrication complexity and better material quality. Yet, only a few studies have explored this concept, many of which only discuss the presence of an intermediate band, without subsequent material optimization and assessment of the corresponding solar cell efficiency limit [6, 7].

In this contribution, a step is made in this direction, by exploring the opto-electronic properties of Earth-abundant chalcogenides, such as IA:VIA compounds, and their possible optimization for intermediate-band solar cells. In particular, the following aspects are discussed, based on state-of-the-art computational methods:

1. optimization of electronic structure and optical properties by chemical substitution;
2. interplay between Fermi level position and intermediate-band solar cell efficiency limit;
3. possible approaches to adjust the Fermi level position by shallow defects.

Acknowledgements

The work has been carried out as part of the project *PhANTOM*, funded by the Italian Ministry of University and Research (MUR) through the National Recovery and Resilience Plan (PNRR) with the call *Young Researchers - Seal of Excellence* (CUP number: E13C22002920006).

References

[1] Shockley, W. and Queisser, H. J., "Detailed balance limit of efficiency of *p-n* junction solar cells," *J. Appl. Phys.*, Vol. 32, No. 3, pp. 510-519, 1961.

[2] Rühle, S., "Tabulated values of the Shockley-Queisser limit for single junction solar cells," *Sol. Energy*, Vol. 130, pp. 139-147, 2016.

[3] Luque, A. and Martí, A., "Increasing the efficiency of ideal solar cells by photon induced transitions at intermediate levels," *Phys. Rev. Lett.*, Vol. 78, No. 26, pp. 5014-5017, 1997.

[4] Okada, Y. et al., "Intermediate band solar cells: recent progress and future directions," *Appl. Phys. Rev.*, Vol. 2, No. 2, pp. 021302, 2015.

[5] Martí, A. et al., "Six not-so-easy pieces in intermediate band solar cell research," *J. Photonics Energy*, Vol. 3, No. 1, pp. 031299, 2013.

[6] Liu, Q. et al., "Natural intermediate band in I_2-II-IV-VI_4 quaternary chalcogenide semiconductors," *Sci. Rep.*, Vol. 8, No. 1, pp. 1604, 2018.

[7] Baquião, D. J. R. and Dalpian, G, M., "Computational screening of bulk materials with intrinsic intermediate band," *Comput. Mater. Sci.*, Vol. 158, pp. 382-388, 2019.

Radiative Cooling and Metalens for Advanced Micro-Concentrating Photovoltaic Systems

P. Testa[1*], M. Cagnoni[1], D. Osuna-Ruiz[2], A. E. Torres-García[2], M. Beruete[2], and F. Cappelluti[1]
[1]Politecnico di Torino, Italy
[2]Universidad Pública de Navarra, Pamplona, Spain
pietro.testa@polito.it (corresponding author)

Abstract

Aiming to advance next-generation photovoltaic architectures, we explore radiative cooling as a cooling system for multi-junction solar cells under high concentration. Additionally, we investigate the feasibility of metalenses for micro-concentrating photovoltaics, offering high design flexibility and compactness to enhance system efficiency.

To achieve high-efficiency photovoltaic systems, beyond improving the solar cells at the device level, two key approaches are better thermal management and concentrated photovoltaics (CPV). In this work, we investigate the potential of radiative cooling in high-concentration multi-junction (MJ) solar cells and the feasibility of a metalens-based micro-concentration system (μ-CPV). Radiative cooling, which relies on heat dissipation via infrared radiation through the atmospheric transparency window (8–13 μm), offers a cost-effective, passive approach for cooling solar cells [1]. Building on our previous findings on radiative cooling for MJ solar cells [2], we now focus on high-concentration scenarios. We demonstrate that placing a larger radiative cooler beneath the solar cell improves thermal management, achieving acceptable temperatures without the need for additional non-radiative systems. This approach is especially well-suited for CPV, where solar cells are significantly smaller than the system itself.

μ-CPV aims to enable compact, high-efficiency photovoltaic systems by miniaturizing CPV components, enhancing both performance and commercial viability [3]. However, such systems remain complex, particularly due to the need for multiple optical elements and the associated manufacturing challenges. Metalenses, with their design flexibility and compactness, offer a promising solution by integrating essential CPV requirements—such as uniform intensity and aberration correction—into a single optical component. Research in this area is still in its early stages, with some review papers addressing related aspects but not covering the practical realization of these metalenses, such as component dimensions [4]. To bridge this knowledge gap, we discuss the feasibility and challenges of developing metalens-based solar concentrators for μ-CPV, presenting preliminary results.

Figure 1a presents a schematic of our system, illustrating the detailed balance model for the solar cell/radiative cooler stack. The temperature is assumed to be uniform throughout the system and determined by the thermal equilibrium condition, set by zero net power exchange:

$$P_{\text{net}} = P_{\text{rad}}^{\text{RC}} \in P_{\text{atm}} + P_{\text{con}} + P_{\text{rad}}^{\text{SC}} + P_{\text{elec}} \in P_{\text{Sun}} = 0 \tag{1}$$

The terms related to the solar cell are calculated using the Shockley-Queisser model for series-connected MJ solar cells. The first three terms are scaled by the area ratio factor, $f_{\text{A}} = A_{\text{RC}}/A_{\text{SC}}$, to account for the radiative cooler larger area. More details are provided in [2]. Figure 1b shows the temperature of a three-junction (3J) solar cell, composed of GaP/GaAs/Ge (1.87/1.4/0.67 eV), for different concentration factors and area ratios, calculated by solving Equation 1. The solar cell temperature can be reduced to acceptable values ($T < 350$ K)

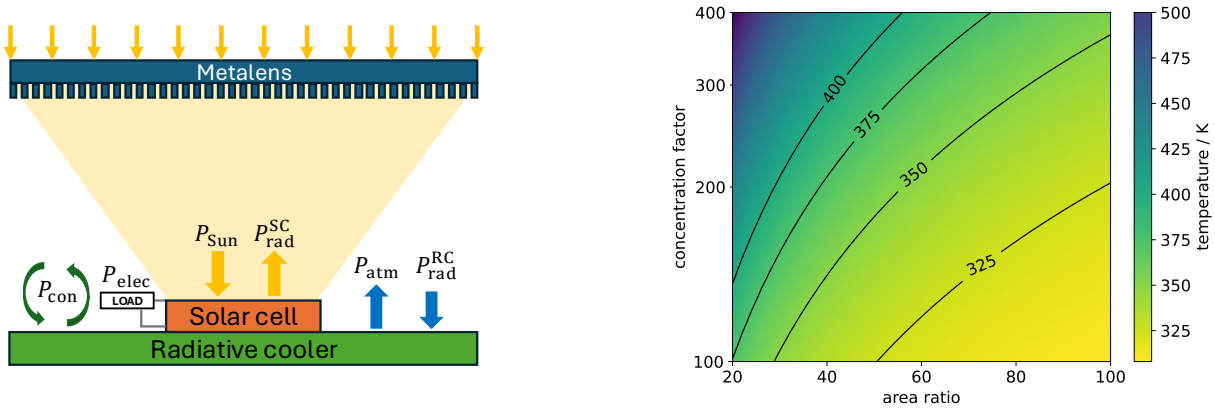


Figure 1: (a) Schematic of the system, illustrating the detailed balance model. (b) Temperature of the 3J solar cell for different concentration factors as a function of the area ratio.

for high concentration factors by simply increasing the radiative cooler's area in typical wind conditions ($h_c = 10.6\,\mathrm{Wm^{-2}K^{-1}}$) [1], as experimentally shown for a single junction solar cell in [5].

The metalens in Figure 1a acts as the concentrator in our system. Designing metalenses for μ-CPV requires satisfying key criteria such as broad bandwidth, uniform intensity, and achromatic performance. The achievable dimensions of an achromatic metalens are constrained by the group delay, as discussed in the literature [6]. We compute the geometric concentration factor, $C_g = A_{\text{metalens}}/A_{\text{solar cell}}$, and calculate the required group delay for various metalens sizes and numerical apertures. Using a non-imaging optics approach, we derive the phase profile and assess feasibility by comparing the calculated group delay with the maximum achievable values reported in the literature [7]. Given the small size of miniaturized solar cells [3], our results suggest that high concentration is theoretically achievable with metalenses for μ-CPV. In conclusion, the combination of radiative cooling and a metalens-based micro-concentration system shows strong potential for advancing next-generation photovoltaic systems.

Acknowledgements

This project has received funding from the European Union's Horizon 2020 Research and Innovation Program under grant agreement no. 964450.

References

[1] B. Zhao et al., "Radiative cooling: A review of fundamentals, materials, applications, and prospects," *Applied Energy*, vol. 236, pp. 489–513, Feb. 2019.

[2] P. Testa et al., "Detailed-balance assessment of radiative cooling for multi-junction solar cells under unconcentrated and low-concentrated light," *Solar Energy Materials and Solar Cells*, vol. 274, p. 112958, Aug. 2024.

[3] N. Jost et al., "Integrated Micro-Scale Concentrating Photovoltaics: A Scalable Path Toward High-Efficiency, Low-Cost Solar Power," *Solar RRL*, vol. 7, no. 16, p. 2300363, Aug. 2023.

[4] C. Zhang et al., "Planar metasurface-based concentrators for solar energy harvest: from theory to engineering," *PhotoniX*, vol. 3, no. 1, p. 28, Nov. 2022.

[5] Z. Wang et al., "Lightweight, Passive Radiative Cooling to Enhance Concentrating Photovoltaics," *Joule*, vol. 4, no. 12, pp. 2702–2717, Dec. 2020.

[6] S. Shrestha et al., "Broadband achromatic dielectric metalenses," *Light: Science & Applications*, vol. 7, no. 1, p. 85, Nov. 2018.

[7] S. Chang et al., "Achromatic metalenses for full visible spectrum with extended group delay control via dispersion-matched layers," *Nature Communications*, vol. 15, no. 1, p. 9627, Nov. 2024.

Advanced Light-Scattering Control for High-Performance Radiative Cooling Surfaces

R. Bravo-Pino[1*], J. S. Dolado[1,2], A. E. Torres-García[3], M. Beruete[3,4], and I. Liberal[3,4]

[1] Centro de Física de Materiales (CFM) CSIC-UPV/EHU); San Sebastián, 20018, Spain.
[2] Donostia International Physics Center (DIPC); San Sebastián, 20018, Spain
[3] Department of Electrical, Electronic and Communications Engineering, Public University of Navarre (UPNA); Pamplona, 31006, Spain.
[4] Institute of Smart Cities (ISC), Public University of Navarre (UPNA); Pamplona, 31006 Spain
[*]Email: rbravo008@ikasle.ehu.eus

Abstract: Multipole engineering is employed to enhance backscattering in core-shell spherical particles by optimizing the refractive index contrast. By aligning the electric dipole with the magnetic quadrupole in a TiO_2 particle, a significant increase in backscattering is achieved. These findings are highly relevant for passive radiative cooling applications.

Backscattering has been shown to play a crucial role in achieving high solar reflectance, as evidenced by studies that quantify its impact. These studies utilize simulations, asymmetry parameter analysis, and Maxwell/Mie theory-based methods to optimize their designs. In general, research incorporating specific backscattering calculations highlights its essential role in attaining high reflectance levels (Felicelli et al., 2022; Huang et al., 2021; Li et al., 2022; Lin et al., 2023).

Here, we study the enhancement of the backscattering of core-shell spherical particles by leveraging the refractive index contrast between the core and the shell using multipole engineering. By shifting the electric dipole to overlap with the magnetic quadrupole, we demonstrate that backscattering is significantly amplified (see Fig 1.), following a similar approach to that presented in the study by Liberal et al. (2015).

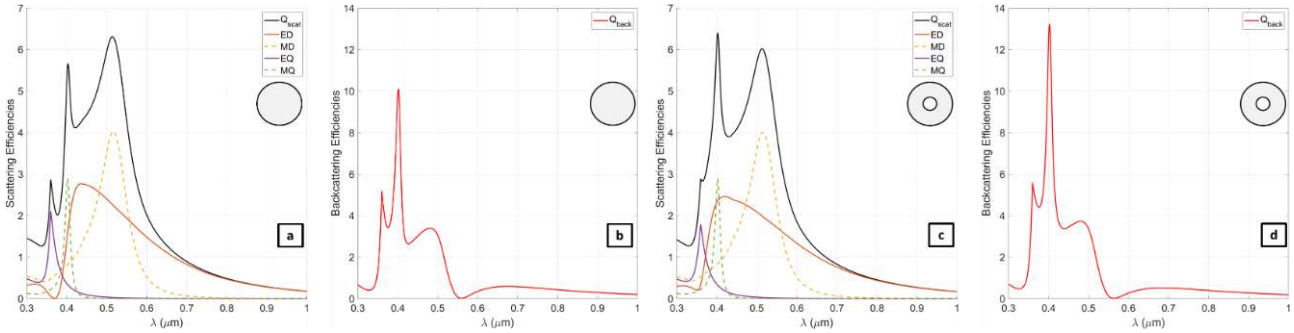


Figure 1. Evolution of the scattering after the transformation of a nanoparticle from a solid TiO_2 sphere (outer radius equal to 100 nm) to an air-cored core-shell (inner radius equal to 30 nm). (a and c) Scattering efficiency (black) and individual contributions from the electric (solid lines) and magnetic (dashed lines) multipoles. (b and d) Backscattering efficiencies for the homogeneous sphere and the core-shell particle.

Figure 1 (c-d) shows how even the amplification of backscattering directly affects the total scattering efficiency, creating a new maximum for that particle around 0.4 μm. Considering this effect, determining the optimal ratio between particle size and air gap dimensions within the core is essential to maximizing the improvement in scattering efficiency. Figure 2 shows the comparison of the ratio (Eq. 1) between backscattering/scattering efficiencies for an homogeneous particle and a core-shell one with a fixed air core equal

to 0.3 times the outer particle radius. These representations allow us to identify the optimal particle dimensions and core-shell configurations that maximize backscattering, showing that the ratio increase is more significant in core-shell particles and that the wavelength at which maximum backscattering occurs can be optimized by adjusting the outer radius.

$$Ratio = \frac{Q_{back}}{Q_{scatt}} \quad (1)$$

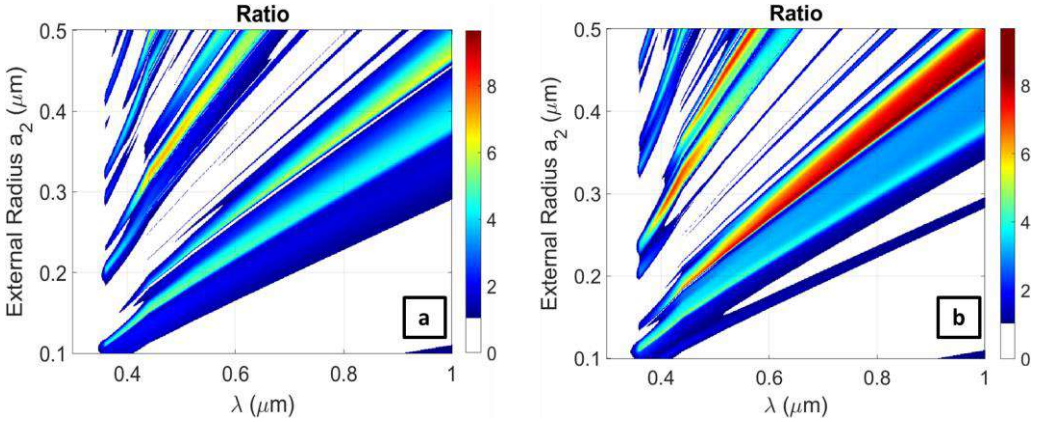


Figure 2. Heat map showing the ratio between Backscattering and Scattering efficiencies for different particle radii (from 0.1-0.5 µm). Values less than 1 are shown in white. (a) homogeneous TiO2 particle; (b) air-cored particle with radius equal to 0.3 times the shell radius.

In conclusion, multipole engineering allows for precise quantification of backscatter contributions from particle size and core-shell configurations. The next phase of this study involves employing FDTD simulations to design randomized particle clusters, enabling the development of structures with enhanced backscattering in the visible solar spectrum. This approach aims to achieve high broadband reflectance while improving net radiative cooling efficiency by minimizing parasitic solar absorption.

References

Felicelli, A., Katsamba, I., Barrios, F., Zhang, Y., Guo, Z., Peoples, J., Chiu, G., & Ruan, X. (2022). Thin layer lightweight and ultrawhite hexagonal boron nitride nanoporous paints for daytime radiative cooling. *Cell Reports Physical Science*, *3*(10), 101058. https://doi.org/10.1016/j.xcrp.2022.101058

Huang, J., Li, M., & Fan, D. (2021). Core-shell particles for devising high-performance full-day radiative cooling paint. *Applied Materials Today*, *25*, 101209. https://doi.org/10.1016/j.apmt.2021.101209

Li, P., Wang, A., Fan, J., Kang, Q., Jiang, P., Bao, H., & Huang, X. (2022). Thermo-Optically Designed Scalable Photonic Films with High Thermal Conductivity for Subambient and Above-Ambient Radiative Cooling. *Advanced Functional Materials*, *32*(5), 2109542. https://doi.org/10.1002/adfm.202109542

Liberal, I., Ederra, I., Gonzalo, R., & Ziolkowski, R. W. (2015). Superbackscattering from single dielectric particles. *Journal of Optics*, *17*(7), 072001. https://doi.org/10.1088/2040-8978/17/7/072001

Lin, K., Chen, S., Zeng, Y., Ho, T. C., Zhu, Y., Wang, X., Liu, F., Huang, B., Chao, C. Y.-H., Wang, Z., & Tso, C. Y. (2023). Hierarchically structured passive radiative cooling ceramic with high solar reflectivity. *Science*, *382*(6671), 691–697. https://doi.org/10.1126/science.adi4725

Making the MIRACLE Possible: Concrete as a Radiative Cooling Material

Jorge S. Dolado [1,2*], Guido Goracci[1], Ghizlane Moutaoukil[1], Ridwan O. Agbaoye[1], Miguel Beruete[3,4], Alicia E. Torres-García[3], Laura Carlosena[5], Iñigo Liberal[5], Achutha Prabhu[6], Jose A. Ibáñez[6], Nick Adams[7], Nicole van Lipzig[8], Karen Allacker[7]

[1] Centro de Física de Materiales (CFM) CSIC-UPV/EHU); San Sebastián, 20018, Spain.

[2] Donostia International Physics Center (DIPC); San Sebastián, 20018, Spain

[3] Department of Electrical, Electronic and Communications Engineering, Public University of Navarre (UPNA); Pamplona, 31006, Spain.

[4] Institute of Smart Cities (ISC), Public University of Navarre (UPNA); Pamplona, 31006 Spain

[5] Department of Engineering, Public University of Navarra (UPNA); Pamplona, 31006, Spain

[6] TECNALIA, Basque Research and Technology Alliance (BRTA), Derio 48160, Spain

[7] KU Leuven, Faculty of Engineering Science, Department of Architecture,

Kasteelpark Arenberg 1 – box 2431, Leuven, 3001, Belgium

[8] KU Leuven, Department Earth and Environmental Sciences, Celestijnenlaan 200E, 3001 Leuven, Belgium

[*]corresponding author: j.dolado@ehu.eus

Abstract: Over the past four years, the MIRACLE project has been dedicated to developing innovative cement-based materials with radiative cooling properties. This work highlights some of the most promising results achieved, emphasizing the significant impact of these new concretes in reducing building energy consumption and mitigating the urban heat island effect.

Radiative cooling technology [1] utilizes the atmospheric transparency window (8-13 μm), called Atmospheric Window (AW), to passively dissipate heat from the Earth to outer space. All bodies in the Earth are in continuous exchange of energy with the sun and the atmosphere, with a net balance of power that depends on the incoming solar and atmospheric radiation, the emitted radiation and non-radiative heat exchanges. The key concept here is that the incoming and reflected solar radiation is short wave (~0.5 μm), while the incoming and outgoing thermal radiation is long wave (~10 μm). This spectral separation underpins most of the technologies which have envisaged radiative cooling, and justifies why it is so relevant to search for materials with high solar reflectivity, high emissivity in the AW and low non-radiative heat losses (low U-values).

So far, this technology has attracted wide interest from both fundamental and applied sciences, due to its a priori potential in multiple applications like building cooling, renewable energy harvesting, or even dew water production. However, currently the development of this technology is in a bottleneck, where the scientific progress has been largely based on either (i) fanciful 1D and 2D photonic metamaterials [2,3] containing scarce and expensive materials with negligible potential impact in any real-world energy solution; or (ii) hierarchically porous polymer coatings [4,5] which can be scalable, but at the cost of expensive industrial manufacturing processes, sacrificing spectral selectivity performance and suffering unavoidable durability issues (e.g. ultraviolet UV degradation).

In this context, the MIRACLE project [6] envisioned a new science and technology to turn low-tech concrete and cement-based materials into high-tech eco-friendly photonic metamaterials. In particular, over the las four years the MIRACLE project has constructed and tested several revolutionary Photonic Meta-Concrete (PMC) devices whose response to light was engineered for exhibiting radiative cooling ability.

As a matter of fact, and after several works linking the microstructure and properties [7,8,9], some of the realizations of MIRACLE enabled new concrete formulations with very high solar reflectance and emissivity in the atmospheric window. Indeed, these concretes were capable of delivering positive cooling powers and remain in sub-ambient temperature regime even on very hot days under intense solar irradiation. Of course, these properties were obtained without compromising the intrinsic mechanical resistance and/or the *per se* good durability of the cementitious matrices, something pivotal for scaling the technology.

In the face of increasing global warming, these "miraculous" concretes play a crucial role in advancing Nearly-Zero-Energy Buildings (NZEB) and contributing to the global strategy for reducing CO_2 emissions. Our projections indicate that in hot regions where heating demand is minimal, these materials can lead to drastic reductions—over 50%—in building energy consumption and associated CO_2 emissions. Furthermore, our climatic studies confirm that these innovative concretes are highly effective in mitigating the urban heat island effect.

This work was supported by the MIRACLE project. This project has received funding from the European Union's Horizon 2020 research and innovation programme under grant agreement No 964450. JSD and MB acknowledge the grants nos. PID2022-137845NB—C21-C22 funded by MICIU/AEI/ 10.13039/501100011033, by ERDF/EU and the European Union NextGenerationEU/PRTR.

References

1. S. Chu, Y. Cui, and N. Liu, "The Path towards Sustainable Energy". Nature Materials, Vol. 16, 16-2, 2017
2. E. Rephaeli, A. Raman and S. Fan. "Ultrabroadband photonic structures to achieve high-performance daytime radiative cooling". Nano Letters Vol. 10, No 3(4), 1457-1461, 2013.
3. A. Raman, M. Anoma, L. Zhu. et al. "Passive radiative cooling below ambient air temperature under direct sunlight". Nature Vol. 515, 540–544, 2014
4. J. Mandal et al. "Hierarchically porous polymer coatings for highly efficient passive daytime radiative cooling", Science Vol. 362,315-319, 2018
5. K.D. Dobson, G. Hodes, Y. Mastai "Thin semiconductor films for radiative cooling applications", Solar Energy Materials and Solar Cells, Vol. 80, No. 3, 283-296, 2003
6. https://miracle-concrete.eu
7. J.M. Pérez-Escudero et al. "Suppressed-scattering spectral windows for radiative cooling applications". Optics Express Vol. 31, 6314-6326, 2023.
8. J.S. Dolado et al., "Radiative Cooling Properties of Portlandite and Tobermorite: Two Cementitious Minerals of Great Relevance in Concrete Science and Technology". *ACS Applied Optical Materials* Vol. **2**, No 6, 1000–1009, 2024
9. A. Torres *et al.* Towards Cooling Concrete: Evaluation of Cement and Cement Composites under Realistic Climatic Conditions. *Applied Thermal Energy* Vol. **265**, 125531, 2025.

Manipulation of silver thicknesses of patterned metal by nanosphere lithography and electroplating for a smart window

Cheng-Yuan Xiao[1] and Tsung-Yu Huang[1,*]

[1.]Department of Materials Engineering, Ming Chi University of Technology, New Taipei, Taiwan

[*] Author e-mail address: huang.tsungyu@mail.mcut.edu.tw

Abstract: By regulating solar heat, smart windows mitigate the overall vicious cycle fueled by global warming. Our electrochromic approach integrates electroplated silver and nanospheres, enabling transmittance from 0% to clarity. Surpassing traditional systems, this flexible technology delivers dynamic sun modulation, enhanced performance, and improved energy efficiency, significantly boosting global architectural sustainability.

In response to global warming, sustainable development has become a critical focus. Currently, buildings in both developed and developing countries consume a significant amount of energy, accounting for 30% to 50% of total societal energy consumption. Heating and cooling systems constitute 40% of the energy consumed by buildings. [1,2,3] As a result, achieving a balance between indoor comfort and energy savings has become a major challenge. To address this, scientists have proposed smart windows to enhance indoor temperature comfort while conserving energy. Smart windows utilize various mechanisms, such as thermochromic, photochromic, and electrochromic technologies, among which electrochromic windows offer the flexibility to switch modes according to environmental conditions. However, previous studies have shown that electrochromic mechanisms typically involve voltage-induced switching between two or more stages, lacking the desired flexibility. In this study, we propose a novel approach by combining nanosphere lithography with reactive ion etching (RIE) to create uniform and discontinuous nanospheres, as shown in **Figure 1(a)**. Subsequently, transparent electrode materials are deposited to form structured electrodes, followed by simple electrochemical deposition of a silver metal film. In the initial phase of this research, we used simulation software to ensure the reliability of the experiment and explored deposition parameters to achieve higher-quality transparent conductive electrodes. Silver plating was then employed to dynamically adjust transmittance. The result is a new type of transparent conductive electrode with dynamic tuning capabilities, allowing for a seamless transition between a transmitting window and a reflecting mirror, achieving electrochromic effects. In the early stages of the experiment, we used simulation software to model the structured electrode's behavior under applied voltage during electrochemical reactions. Over time, the thickness of the silver film changed, leading to significant variations in the window's transmittance, as illustrated in **Figure 1(b)**. In subsequent experiments, we tested the transmittance and resistivity of indium tin oxide and gold as transparent electrodes using electron beam evaporation and thermal evaporation techniques. This part of the study is crucial for the transparency of the window and the subsequent electrochemical mechanisms. Therefore, we measured the transmittance of the samples using UV-Vis and the resistivity of the films using a four-point probe, as shown in **Figure 2**. We will further optimize the parameters to enhance the performance of the transparent electrodes and conduct electrochemical experiments to achieve a final seamless smart window.

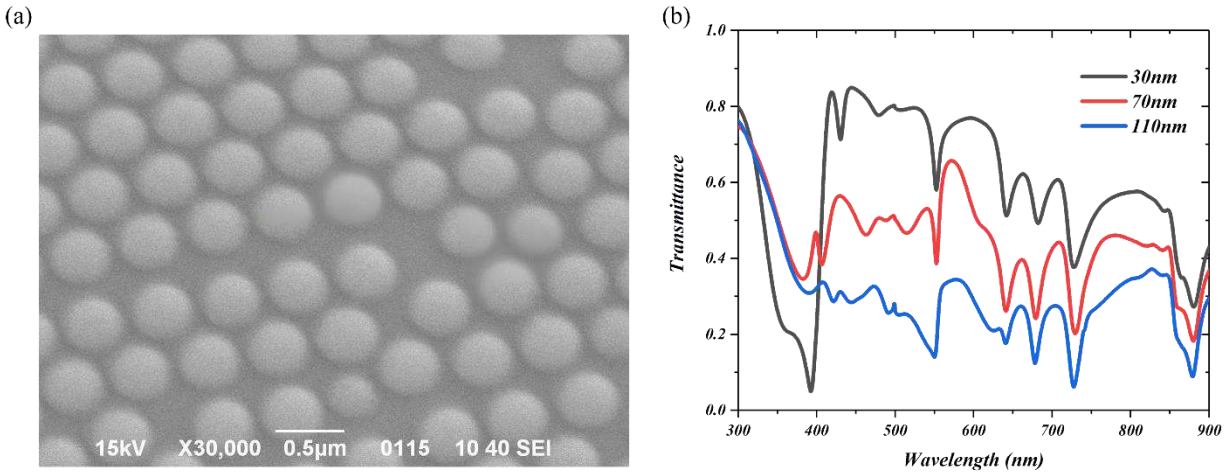


Figure 1. (a) SEM image of distributions of single-layered nanospheres. (b) Simulated transmittance under different metal thicknesses.

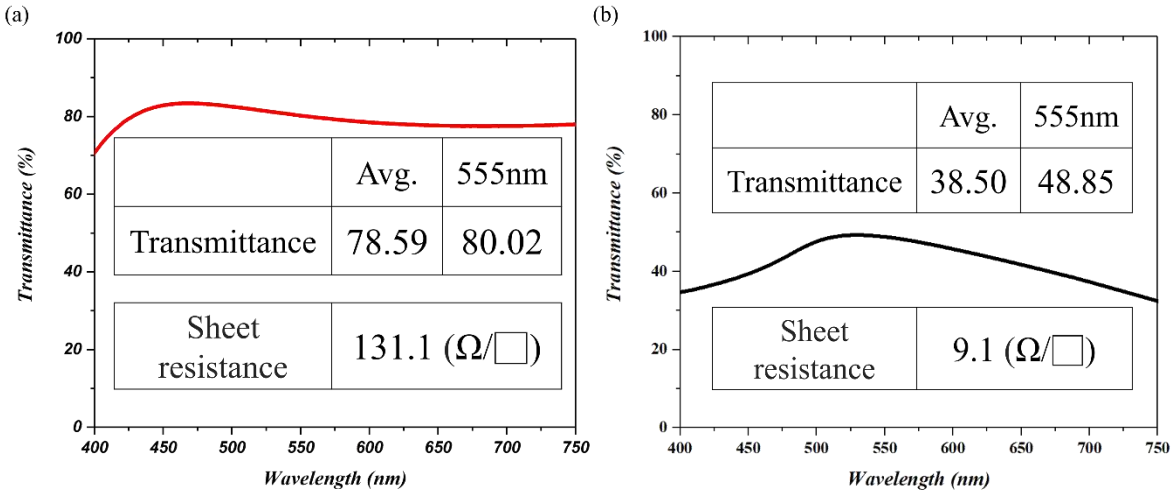


Figure 2. (a) UV-Vis measured transmittance spectrum of ITO and sheet resistance values measured by four-point probe. (b) UV-Vis measured transmittance spectrum of gold and sheet resistance values measured by four-point probe.

References

[1] Pérez-Lombard, Luis, José Ortiz, and Christine Pout. "A review on buildings energy consumption information." Energy and buildings 40.3 (2008): 394-398.

[2] Guo, Juquan, et al. "Recent progress in improving strategies of metal oxide-based electrochromic smart window." Green Energy and Resources 1.1 (2023): 100007.

[3] Piccolo, Antonio, and Francesca Simone. "Performance requirements for electrochromic smart window." Journal of Building Engineering 3 (2015): 94-103.

ITO-based heterostructures toward tunable windows and radiative cooling

E. Peci[1*], F. Marangi[2], E. Spotorno[1], F. Scotognella[2], M. Canepa[1], F. Bisio[3], M. Magnozzi[1]

[1]Dipartimento di Fisica, Università degli Studi di Genova, via Dodecaneso 33, 16146 Genova, Italy
[2]Politecnico di Torino, corso Duca degli Abruzzi 24, 10129 Torino, Italy
[3]CNR-SPIN, corso Perrone 24, Genova, Italy
[*]Corresponding author: ermes.peci@edu.unige.it

Abstract: solution-processed ITO-based thin films and heterostructures are investigated by spectroscopic ellipsometry for application as metamaterials in the visible and near-infrared spectral ranges. Effective medium approximations are used to assess their optical and structural properties, optimizing their design for smart windows. This study advances active photonic crystals for on-demand photonic devices.

Photonic crystals (PhCs) are complex multi-layered dielectric systems that allow the spectrally resolved management of electromagnetic radiation. In their passive form, their response is univocally fixed upon fabrication; conversely, active PhCs may reversibly vary their optical response upon application of an external stimulus. These systems can be exploited for several applications, including smart windows and tunable daytime radiative cooling [1]. By leveraging PhCs in this way, researchers aim to develop smart windows with on-demand photonic capabilities, significantly enhancing the efficiency of photonic and solar-energy devices.

Among the various approaches explored in this field, electric-field-tuned PhCs based on indium-tin oxide (ITO) have garnered significant attention. ITO, one of the most widely studied transparent-conductive oxides (TCOs), exhibits remarkable tunability in its optical properties, making it a prime candidate for such applications. In this poster, we present a detailed ellipsometric characterization of ITO-based thin films and ITO/silica multilayers fabricated using solution-processing techniques [2]. We exploit the diagnostic capabilities offered by spectroscopic ellipsometry to evaluate the relation between the spin casting deposition parameters and the resulting optical and structural (i.e. porosity, surface roughness) properties of the films. Additionally, we utilize effective medium approximation (EMA) models, originally developed to describe nanocrystalline ITO films [3], to extract and interpret the broad-band optical properties of both individual layers and complex multilayer structures. By implementing EMA-based modeling, we aim to refine and optimize the design of ITO-based coatings for tunable radiative cooling applications.

This approach not only enhances our fundamental understanding of the material system but also facilitates the development of next-generation smart coatings, paving the way for more efficient and adaptive thermal management solutions in architectural and energy-related technologies.

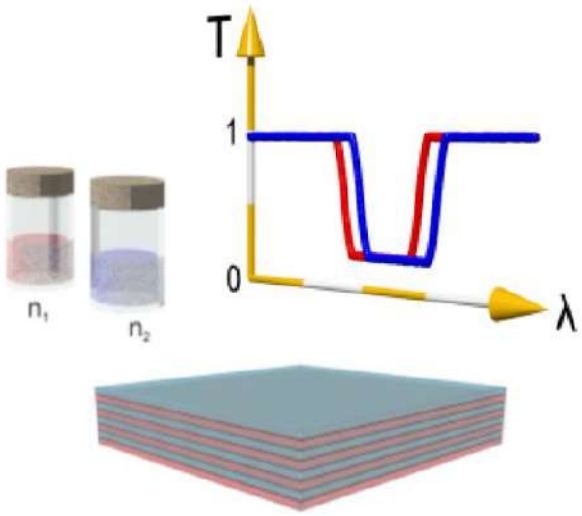


Figure 1. Concept for a tunable photonic crystal based on a Bragg reflector design, where one of the two materials is a transparent-conductive oxide.

Authors acknowledge financial support under the National Recovery and Resilience Plan (NRRP), Mission 4, Component 2, Investment 1.1, Call for tender no. 104 PRIN 2022 published on 2.2.2022 by the Italian Ministry of University and Research (MUR), funded by the European Union – NextGenerationEU – Project Title ERACLITO – CUP B53D2300904006 and Call for tender no. 1409 PRIN PNRR 2022 published on 14.9.2022 by the Italian Ministry of University and Research (MUR), funded by the European Union – NextGenerationEU – Project Title ARCO – CUP B53D23027690001. This project received funding from the European Research Council (ERC) under the European Union's Horizon 2020 research and innovation programme (ERC-H2020 PAIDEIA GA 816313).

References

1. Raman, A. P., Anoma, M. A., Zhu, L., Rephaeli, E., and Fan, S., "Passive radiative cooling below ambient air temperature under direct sunlight". *Nature*, Vol. 515, No. 7528, 540-544, 2014.
2. Moscardi, L., Paternò, G.M., Chiasera, A., Sorrentino, R., Marangi, F., Kriegel, I., Lanzani, G., and Scotognella, F., "Electro-responsivity in electrolyte-free and solution processed Bragg stacks". *J. Mater. Chem. C*, Vol. 37, No. 8, 13019-13024, 2020.
3. Sygletou, M., Marangi, F., Varas, S., Chiasera, A., Canepa, M., Scotognella, F., and Bisio, F., "Effective medium optical modelling of indium tin oxide nanocrystal films". *Phys. Chem. Chem. Phys.*, Vol. 24, No. 9, 5317-5322, 2022.

Optical antennas and metasurfaces: fundamentals and applications of enhanced light-matter interactions

Chiral Symmetry Breaking in Chiral Crystallization on Mie-Resonant Metasurface

Hiromasa Niinomi*[1], Kazuhiro Gotoh[2,3], Naoki Takano[1], Miho Tagawa[4], Iori Morita[5], Akiko Onuma[1], Hiroshi Y. Yoshikawa[6], Ryuzo Kawamura[7], Tomoya Oshikiri[1,8], and Masaru Nakagawa[1]

[1]Institute of Multidisciplinary Research for Materials, Tohoku University, Japan
[2]Graduate School of Science and Technology, Niigata University, Japan
[3]Interdisciplinary Research Center for Carbon-Neutral Technologies, Niigata University, Japan
[4]Institute of Materials and Systems for Sustainability, Nagoya University, Japan
[5]Research Institute of Electrical Communication, Tohoku University, Japan
[6]Graduate School of Engineering, Osaka University, Japan
[7]Department of Chemistry, Saitama University, Japan
[8]Research Institute for Electronic Science, Hokkaido University, Japan
*corresponding author hiromasa.niinomi.b2@tohoku.ac.jp

Abstract: We found that approximately 18％ of large crystal enantiomeric excess (CEE) is observed in sodium chlorate chiral crystallization from a solution on a Mie resonant silicon (Si) metasurface excited by circularly polarized light. Numerical analyses implied that the CEE was caused by chiral optical force acting on chiral crystalline clusters.

Chiral light-matter interaction between circularly polarized light (CPL) and chiral materials has motivated researchers to control chirality of materials by CPL such as chiral photosynthesis by CPL.[1] However, the resulting chiral asymmetry is known to be very small and typical enantiomeric excess (e.e.) is 0.5-2%.[2] This situation arises from intrinsically weak chiral light-matter interaction between CPL and chiral materials. It is necessary for chirality control by light to enhance chirality of light. Recently, it has been discovered that the chiral light-matter interaction can be enhanced by enhancing the optical chirality of light field.[3] The light field with optical chirality stronger than that of CPL is called superchiral field. Recent numerical simulations have shown that superchiral fields can be generated in near-fields of Mie resonance in dielectric nanoparticles.[4] The question whether the superchiral field causes e.e. larger than that induced by CPL attracts much attention. However, it is not easy to evaluate e.e. in the chiral products synthesized in the nano-scaled superchiral near-field because the amount of the product is very small. This hinders the demonstration of effectiveness of superchiral near-field on chiral synthesis. A system including amplification process of the chiral products is necessary to investigate the effectiveness of the superchiral field. Here, we focused on chiral crystallization, where achiral molecules solidify into chiral crystal, by regarding rapid crystal growth after the chiral nucleation as an amplification process. We demonstrate that statistically significant CEE can be observed by inducing sodium chlorate ($NaClO_3$) chiral crystallization from a solution on a Mie-resonant silicon (Si) metasurface whose near-field of Mie resonance is expected to be superchiral.[5]

A metasurface with polycrystalline Si (poly-Si) nanodisk square array was fabricated by ultraviolet nanoimprint lithography. A platinum-palladium thin film (1 nm) was coated on the metasurface by sputtering. Mie resonance at 532 nm was confirmed by comparing dark-field spectrum and finite-difference time-domain (FDTD) simulations. Chiral crystallization of $NaClO_3$ was induced from microdroplets of aqueous solution on the metasurface by the irradiation with 532 nm continuous-wave *l*- and *r*-CPL focused by an inverted optical microscope. The handedness of the resulting crystals was identified using a polarized microscope. Chiral asymmetry of the obtained crystals was evaluated by counting each enantiomorph out of 100 crystallizations with the metasurface and 25 crystallizations without the metasurface using *l*- and *r*-CPL, respectively.

The 25 crystallizations without the metasurface using *l*- and *r*-CPL yielded 13 *d*-crystals and 13 *l*-crystals, respectively. On the other hand, the 100 crystallizations with the metasurface using *l*- and *r*-CPL yielded 57 *l*-crystals and 61 *d*-crystals, respectively. These results indicate the effectiveness of superchiral field beyond CPL. The magnitude of enantioselective optical force acting on $NaClO_3$ chiral crystalline clusters due to the excitation of superchiral field was estimated to be in the order of 1 fN in the vicinity of the Si nanosidks by FDTD method. Several previous studies have shown that a few fN force can transport nanoparticles with the radius of several tens of nanometers in liquids. Therefore, the enantioselective optical force can be the cause of the large CEE by changing the incident frequency of *d*- and *l*-chiral crystalline clusters to a crystal nucleus.

References

1. Kagan, H. et al., "Photochemistry with circularly polarized light. Synthesis of optically active hexahelicene" *J. Am. Chem. Soc*., Vol. 93, No. 9, 2353–2354, 1971.
2. Feringa, B. L. et al., "Absolute Asymmetric Synthesis: The Origin, Control, and Amplification of Chirality" *Angew. Chem. Int. Edit.*, Vol. 38, No. 23, 3418–3438, 1999.
3. Tang, Y. et al., "Optical Chirality and Its Interaction with Matter" *Phys. Rev. Lett.*, Vol. 104, (2010) 163901, 2010.
4. Solomon, M. L. et al., "Nanophotonic Platforms for Chiral Sensing and Separation" *Acc. Chem. Res.*, Vol. 53, No. 3 588–598, 2020.
5. Niinomi, H. et al., "Mie-Resonant Nanophotonic-Enhancement of Asymmetry in Sodium Chlorate Chiral Crystallization" *J. Phys. Chem. Lett.*, Vol, 15, No.6, 1564–1571, 2024.

PURCELL BROADENING AND LAMB SHIFT FOR DNA-ASSEMBLED NEAR-INFRARED QUANTUM EMITTERS

Sachin Verlekar[1*], Maria Sanz-Paz[2], Mario Zapata-Harrera[3], Mauricio Pilo-Pais[2], Karol Kolataj[2], Ruben Esteban[3], Javier Aizpurua[3], Guillermo P. Acuna[2] and Christophe Galland[1]

[1] EPFL, Switzerland
[2] University of Fribourg, Switzerland
[3] CFM-MPC San Sebastian, Spain
[*]corresponding author: sachin.verlekar@epfl.ch

Abstract: We harness the precision of DNA origami to assemble single fluorophores within plasmonic nanocavities. We observe an interplay of quantum effects, including giant Purcell broadening and pronounced Lamb shifts. These effects enable substantial spectral reshaping by redirecting the single molecule's emission into detuned near-infrared plasmonic modes.

Leveraging our scalable DNA-origami approach, we explore the plasmonic modes of nano-dimers and tailor them in nano-dimer-on-mirror (NDoM) plasmonic nanocavities to create a distinct radiative near-infrared (NIR) plasmonic mode. In these hybrid structures, a single fluorophore is precisely positioned within a narrow gap—on the order of 4–5 nm—between gold nanoparticles, ensuring that the Purcell factor is maximized while the gap remains tightly confined. This configuration not only enhances the local density of optical states (LDOS) but also paves the way toward achieving lifetime-limited emission, a crucial requirement for generating indistinguishable single photons for quantum nanophotonic applications.
Our experimental study, carried out at both room and cryogenic temperatures, reveals that coupling the fluorophore to the engineered nanocavity leads to dramatic spectral reshaping. Specifically, while the bare fluorophore exhibits a narrow zero-phonon line (ZPL) under low-temperature conditions, embedding it in an NDoM configuration induces a significant broadening of the ZPL—attributable to an enormous Purcell enhancement—and a pronounced Lamb shift that red-shifts the emission. This cooperative interplay between Purcell broadening and the Lamb shift facilitates energy transfer from the primary visible emission into a far-detuned NIR mode, even when the plasmonic resonance lies well outside the natural emission bandwidth of the molecule.

By independently engineering both the radiative and total LDOS, our nanocavity platform unlocks new regimes of cavity quantum electrodynamics (QED) where electronic transitions, molecular vibrations, and photonic modes interact in a highly controlled manner. The robust design allows us to decouple the radiative decay rate from nonradiative losses, thereby optimizing the emission properties of the coupled system. Detailed electromagnetic simulations confirm that the radiative efficiency and Purcell factor can be fine-tuned by altering the nanocavity geometry and the precise positioning of the fluorophore, a feature that is pivotal for achieving tailored spectral responses. The experimental data corroborate these predictions, demonstrating not only an enhancement of the overall photon budget but also a selective feeding of emission into the NIR mode.

These findings have significant implications for the development of broadband single photon sources, which are essential for secure quantum communication protocols and scalable quantum information processing. By exploiting the giant Purcell effect and the associated Lamb shift, our approach circumvents limitations inherent

to traditional organic emitters, offering a pathway to realize lifetime-limited single photon emission. Moreover, the platform is versatile enough to accommodate different fluorophores, allowing for fine adjustments of the spectral output based on specific application requirements.

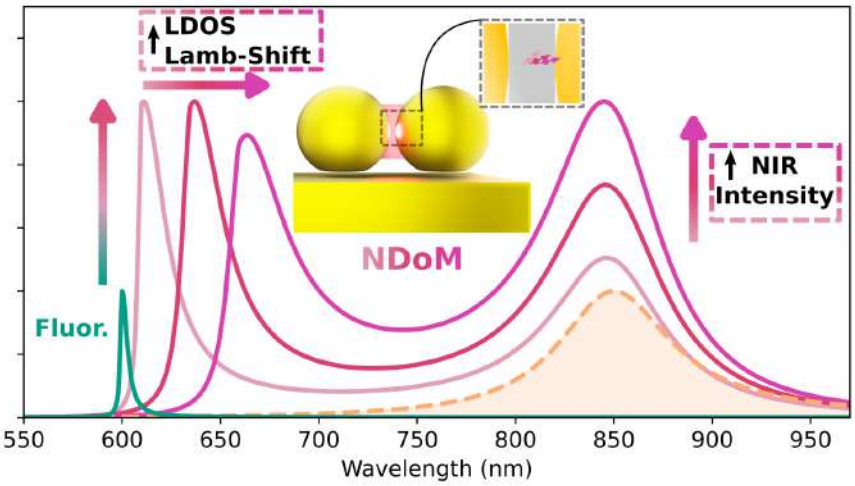


Figure 1 – Single fluorophores embedded in nano-dimer on mirror (NDoM) structures experience fluoroscence enhancement as well as Purcell broadening, leading to coupling to the NIR plasmonic mode, and pronounced fluorescence reshaping

In summary, our work demonstrates a powerful method for manipulating light–matter interactions at the single-molecule level. The ability to reshape emission spectra by harnessing engineered plasmonic modes, coupled with the control over LDOS, heralds a new era in nanoplasmonic cavity QED. This advance not only enhances our understanding of fundamental photonic processes but also lays the groundwork for practical applications in quantum optics, including the realization of indistinguishable photon sources and highly efficient NIR emitters.

Funding

This work received funding from the European Union's Horizon 2020 research and innovation program under Grant Agreement No. 820196 (ERC CoG QTONE). C.G. also acknowledges the support from the Swiss National Science Foundation (project numbers 170684 and 198898). M.Z.-H., R.E., and J.A. acknowledge funding from grant PID2022-139579NB-I00 funded by MICIU/AEI/10.13039/501100011033 and by "ERDF/EU A way of making Europe" from grant no. IT 1526-22 from the Basque Government for consolidated groups of the Basque University, as well as by the European Union (NextGenerationEU) through the Complementary Plans (Grant No. PRTR-C17.I1) promoted by the Ministry of Science and Innovation within the Recovery, Transformation, and Resilience Plan of Spain, and part of the activities of the IKUR strategy of the Department of Education promoted by the Department of Education of the Basque Government. G.P.A. acknowledges support from the Swiss National Science Foundation (200021_184687) and from the National Center of Competence in Research Bio-Inspired Materials NCCR (51NF40_182881).

References

1. Verlekar, S. et. al. "Giant Purcell Broadening and Lamb Shift for DNA-Assembled Near-Infrared Quantum Emitters." *ACS Nano* **2025**, *19* (3), 3172–3184.

Mechanically Tunable Optical Responses in Silicon Nanospheres Square Lattice Array Metasurface Fabricated via Bottom-up Process

Yongan Hu[1], Patrick T. Probst[1], Mojtaba Karimi Habil[1], Hiroshi Sugimoto[1]*, Minoru Fujii[1]**

[1]Electrical and Electronic Engineering, Kobe University

*Corresponding author: sugimoto@eedept.kobe-u.ac.jp
**Corresponding author: fujii@eedept.kobe-u.ac.jp

Abstract: We fabricate a 2-dimensional (2D) square lattice array of silicon nanospheres on a polydimethylsiloxane (PDMS) substrate from a colloidal suspension of silicon nanospheres by a bottom-up process, and demonstrate the reflectance modulation via switching on and off the lattice Kerker effect by uniaxial strain.

1. Introduction

In a 2D array of resonant nanoparticles, resonance of individual nanoparticles interferes with the lattice mode of the periodic structure producing a collective lattice resonance (CLR), whose resonance properties depend strongly on the lattice constant[1]. The property of the CLR can be controlled by external stimuli like mechanical deformation[2]. In this work, we produce a large area 2D square lattice array (0.7 cm × 1 cm) of crystalline silicon nanospheres (Si NSs) having Mie resonances in the visible and near-infrared range on a flexible PDMS substrate, and demonstrate that the reflectance spectra are modulated by mechanical force via the lattice Kerker effect. We start with numerical simulations of the reflectance spectra to find the condition where the lattice Kerker effect occurs. We then produce a 2D square lattice array of Si NSs from the colloidal suspension[3] and demonstrate the reflectance modulation by uniaxial strain.

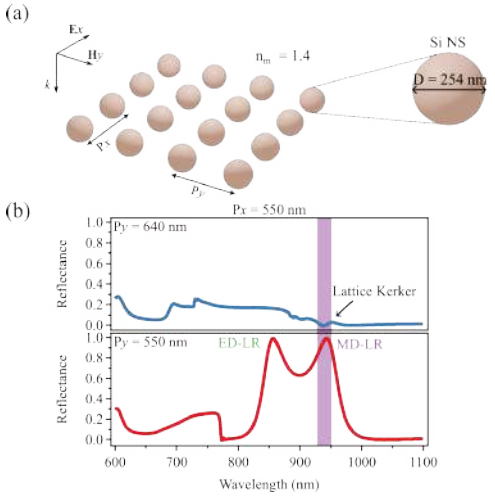


Figure 1. (a) Model structure of a Si NS 2D array. Si NSs are embedded in a medium with the refractive index of 1.4. The NS array is illuminated from the top by a plane wave polarized in the *x*-direction. (b) Calculated reflectance spectra. (red) P*x* = 550 nm, P*y* = 550 nm, (blue) P*x* = 550 nm, P*y* = 640 nm.

2. Numerical simulation

Figure 1a shows a model structure of a Si NSs 2D square lattice array embedded in PDMS (n_m = 1.4). The diameter of a Si NS is 254 nm. The 2D array is illuminated from the normal to its surface by a *x*-polarized plane wave. Figure 1b (red) shows the calculated reflectance spectrum when the lattice constants in the *x* (P*x*) and *y* (P*y*) directions are 550 nm. The two resonance peaks are lattice resonances arising from the electric dipole resonance (ED-LR) and magnetic dipole resonance (MD-LR) of Si NSs. When P*y* is increased to 640 nm at fixed P*x* (blue), the reflectance at ~ 940 nm almost disappears. This is due to the red shift of the ED-LR resonance, which causes the overlapping with the MD-LR resonance. Overlapping of the two resonances cancels the far field radiation (lattice Kerker effect) and suppresses the reflectance strongly. Therefore, by dynamically controlling the lattice constant, we can modulate the reflectance.

3. Preparation of Si NS square lattice array by a bottom-up process

In order to experimentally demonstrate dynamic control of the reflectance in 2D array of Si NSs, we produce it from the colloidal suspension[3] shown in Figure 2a. The transmission electron microscope (TEM) image shows that Si NSs are well defined with a high sphericity. Figure 2b shows the capillary-force assisted particle assembly procedure of the 2D array. We use a square lattice hole array made on PDMS as a template. The hole diameter is 300 nm, and the pitch is 550 nm. To fill the holes with Si NSs, a Si NSs suspension with the average diameter of 254 nm is dropped on the template and dragged by a guiding glass. Figure 2c shows a scanning electron microscope (SEM) image of the produced Si NS square lattice array. The holes are selectively filled with single Si NSs of almost the same size.

4. Mechanical modulation of the reflectance

Figure 2d (red) shows the measured reflectance spectra of the fabricated 2D array under the *x*-polarized light illumination. Peaks assigned to ED-LR and MD-LR are observed. When the 2D array is stretched in the *y*-direction with the strain of 15% (blue), the reflectance at ~ 910 nm is strongly suppressed. This is consistent with the calculated results in Figure 1b and can be explained by the lattice Kerker effect. The observed reflectance modulation is reversible for at least 100 times stretching-releasing cycles.

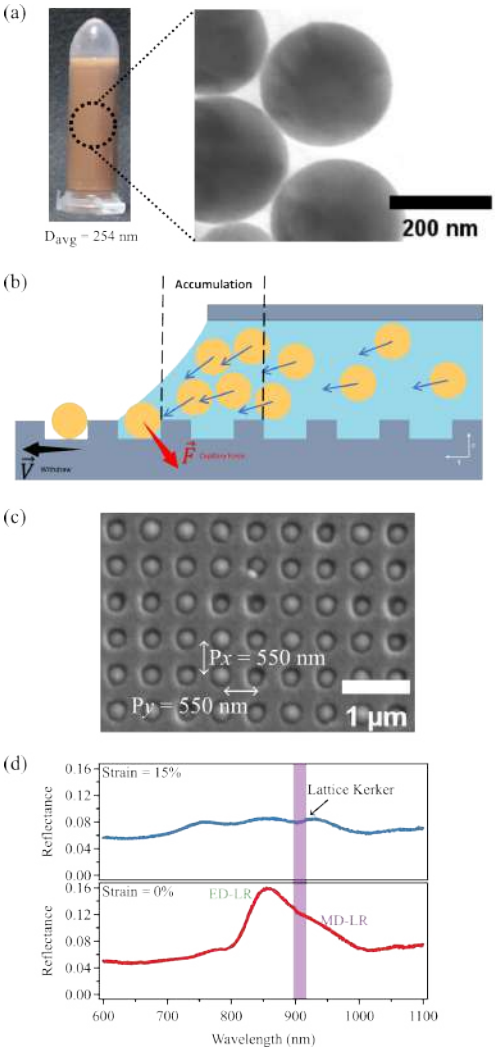


Figure 2. (a) Photo of colloidal suspension of Si NSs, and corresponding TEM image. (b) Schematic illustration of the procedure to fill holes in a template with Si NSs. (c) SEM image of a Si NS 2D array. (d) Measured reflection spectra. (red) Without strain, and (blue) 15% strain in y-direction.

5. Conclusion

We have succeeded in producing a Si NS square lattice array from the colloidal suspension on a flexible PDMS substrate by a bottom-up process. The 2D array shows ED-LR and MD-LR reflectance peaks in the visible and near-infrared range, and the peak wavelengths can be controlled by mechanical strain. We showed that overlapping the two resonances results in strong suppression of the reflectance due to the lattice Kerker effect. The reflectance modulation is reversible for at least 100 times, and thus the produced flexible metasurface works as a mechano-tunable optical component.

References

(1) Babicheva, V. E.; Evlyukhin, A. B. "Resonant Lattice Kerker Effect in Metasurfaces With Electric and Magnetic Optical Responses. Laser Photon", Rev., Vol. 11, No. 6, 1–10, **2017**.

(2) Gupta, V.; Probst, P. T.; Goßler, F. R.; Steiner, A. M.; Schubert, J.; Brasse, Y.; König, T. A. F.; Fery, A. "Mechanotunable Surface Lattice Resonances in the Visible Optical Range by Soft Lithography Templates and Directed Self-Assembly", ACS Appl. Mater. Interfaces, Vol. 11, No. 31, 28189–28196, **2019**.

(3) Sugimoto, H.; Okazaki, T.; Fujii, M. "Mie Resonator Color Inks of Monodispersed and Perfectly Spherical Crystalline Silicon Nanoparticles", Adv. Opt. Mater., Vol. 8, No. 12, 2000033, **2020**.

Enhanced linear and nonlinear single-particle spectroscopy within plasmonic nanocavities

O.S. Ojambati

Department of Applied Nanophotonics, Faculty of Science and Technology,

University of Twente, the Netherlands

o.s.ojambati@utwente.nl

Abstract: Plasmonic nanocavities localize and enhance optical fields in sub-diffraction-limited mode volume. Here, we harness the nanocavity to reveal linear and nonlinear optical signatures of sub-10 nm particles. The beauty of our approach is that it also enables label-free spectroscopy of freely diffusing single proteins, elucidating parameters that modify the dynamics.

Sub-diffraction-limited particles play crucial roles in nanomedicine, spectroscopy, catalysis, biomedical imaging, and nano-devices. Observing and imaging the tiny particles (diameter < 10 nm) in a label-free way is an interesting challenge for many optical techniques, due to the low scattering cross-section of these particles.

In this talk, I will describe how plasmonic nanocavities enhance the optical signatures of individual sub-10nm particles. Plasmonic nanocavities confine optical fields to extremely low mode volume (< 50 nm^3), and efficiently localize intense light intensity on the nanoparticles. Moreover, the nanocavity also enhances the scattered field by the nanoparticle, thereby enabling enhanced linear and nonlinear spectroscopy.

We demonstrate that the nanocavity enables the detection of a single metallic nanoparticle down to 1.8 nm in diameter [2]. The nanoparticle inside the nanocavity forms a strongly-coupled system revealed as anti-crossing modes in darkfield extinction spectroscopy. The strong coupling effect provides a nonlinear wavelength dependence on the nano-object diameter, which results in a high sensitivity.

Furthermore, we harness the subwavelength spatial confinement in the nanocavity to probe third-order optical nonlinearity of individual nanoparticles [3]. We performed Z-scan technique on the nanocavity, which enables accurate determination of nonlinear parameters, namely, the nonlinear refractive index and nonlinear absorption coefficient. Quantifying these parameters of individual nanoparticles is essential for nano-optical devices such as optical limiters, saturable absorbers, and optical switches. Our results remarkably show the nonlinear optical properties can be measured using only a few photons per pulse.

Additionally, we develop coupled nanocavities to probe the dynamics of individual proteins. The coupled nanocavities form a metasurface that enhances optical fields in unconstrained space. Our fast time-dependent surface-enhanced Raman spectroscopy measurement demonstrates that single protein dynamics is largely influenced by several factors, including surface functionalization, acidity of solvent, and electrostatics interactions.

References

1. M. Wang, T. Wang, O.S. Ojambati, T.J. Duffin, K. Kang, T. Lee, E. Scheer, D. Xiang, C.A. Nijhuis, “Plasmonic phenomena in molecular junctions: principles and applications” Nat. Rev. Chem. 6 (10), 681-704 (2022).
2. M.R. Aghdaee and O. S. Ojambati. "Optical detection of single sub-15 nm objects using elastic scattering strong coupling." arXiv preprint arXiv:2411.02341 (2024).
3. A. Kumari, M.R. Aghdaee, M. Van de Voorde, O.S. Ojambati, "Few photons probe third-order nonlinear properties of nanomaterials in a plasmonic nanocavity", Adv. Opt. Mater. (accepted) arXiv:2411.02315 (2025).

DNA Origami-Based Rhodium Dimers as a New Type of UV-Plasmonic Nanoantennas

Karol Kołątaj[1*], Nicco Corduri[1], Guillermo Acuna[1*]

[1] Department of Physics, University of Fribourg, Chemin du Musée 3, Fribourg CH 1700, Switzerland

[*]corresponding authors: guillermo.acuna@unifr.ch, karol.kolataj@unifr.ch

Abstract: The DNA origami technique has been extensively used to arrange plasmonic nanoparticles for various photonic applications. Here, we present a new type of such nanoantennas based on UV-active rhodium nanocubes, which can be used for label-free fluorescence or resonance-SERS measurements of biologically important molecules, such as proteins and DNA.

Plasmonic nanoparticles have attracted considerable attention due to their ability to concentrate light at the nanoscale, resulting in significant enhancements of phenomena such as surface-enhanced Raman scattering (SERS) and fluorescence. To fully exploit the potential of plasmonic nanosystems, it is necessary to arrange nanoparticles in precise configurations with high accuracy. One of the most effective methods for synthesizing plasmonic nanoantennas is the DNA origami technique, which enables the precise, programmable assembly of nanoparticles into highly ordered structures, resulting in enhanced optical properties that cannot be achieved through traditional synthesis methods.

So far, all plasmonic nanostructures created using this technique have employed nanoparticles with optical responses in the visible and infrared regions. However, recent advances have made it possible to synthesize nanoparticles with a broader range of optical properties, including those that interact with ultraviolet (UV) light.[1] UV-active nanoparticles offer interesting possibilities, as many biological molecules absorb light in this range. For example, use of such nanoparticles enabled the label-free measurement of protein autofluorescence.[2] As a result, constructing DNA origami-based nanodevices with UV nanoparticles opens new avenues for detecting biologically relevant molecules, such as proteins and DNA, through fluorescence and resonance-SERS measurements.

In this contribution, we present the synthesis of plasmonic nanoantennas based on DNA origami and rhodium nanocubes, which is the first report of the use of UV-plasmonic nanoparticles to construct such nanosystems. Firstly, we optimized a detachment of polyvinylpyrrolidone (PVP) from the nanoparticle surface, which was later exchanged with DNA strands. The resulting DNA-functionalized Rh nanoparticles were precisely arranged on the surface of DNA origami, creating plasmonic nanoantennas, as shown in Figure 1a, with a remarkable 72% yield. These nanostructures are well-suited for applications in surface-enhanced Raman scattering (SERS) and fluorescence enhancement. To evaluate the performance of the constructed nanostructures in enhancing light-matter interactions, we conducted optical simulations, as shown in Figure 1b. Additionally, we examined the optical responses of nanoparticles with different shapes (see Figure 1c) to identify the optimal configuration for future nanosystems.

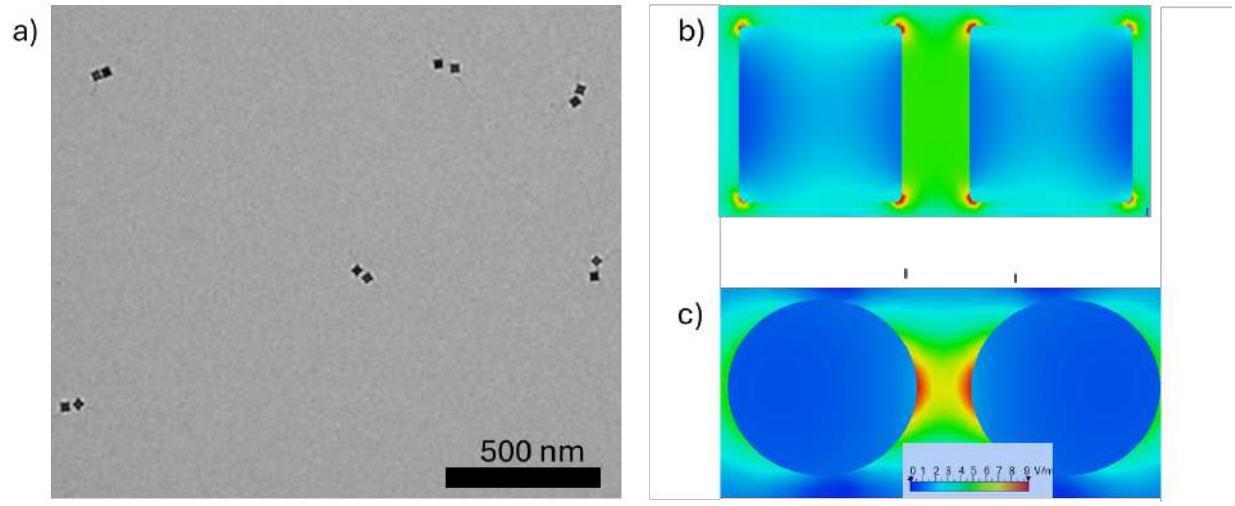


Figure 1. (a) TEM image of a rhodium nanocube dimer connected through DNA origami. (b) and (c) 2D E-field maps of NP dimers composed of rhodium nanocubes and nanospheres, respectively, with a 10 nm gap.

References

1. Zhang, X.; Li, P.; Barreda, A.; Gutierrez, Y.; Gonzalez, F.; Moreno, F.; Everitt, H. O.; Liu, J. Size-Tunable Rhodium Nanostructures for Wavelength-Tunable Ultraviolet Plasmonics. *Nanoscale Horiz.* 2016
2. Roy, P.; Zhu, S.; Claude, J.-B.; Liu, J.; Wenger, J. "Ultraviolet Resonant Nanogap Antennas with Rhodium Nanocube Dimers for Enhancing Protein Intrinsic Autofluorescence," *ACS Nano*, Vol. 17, No. 22, 22418–22429, 2023.

Solving Maxwell's Equations Using Polarimetry Alone

J. Olmos-Trigo[1*]
[1]Faculty of Optics and Optometry, Universidad Complutense de Madrid, Madrid 28037, Spain.
Corresponding author: jolmostrigo@gmail.com

Abstract: Maxwell's equations are solved when the amplitude and phase of the electromagnetic field are determined. Generally, the Stokes parameters can only capture the amplitude and polarization state of the electromagnetic field in the radiation (far) zone. Therefore, the measurement of the Stokes parameters is, in general, insufficient to solve Maxwell's equations. In this talk, we solve Maxwell's equations for a set of objects widely used in Nanophotonics using the Stokes parameters alone. Our method for solving Maxwell's equations endows the Stokes parameters an even more fundamental role in the electromagnetic scattering theory.

The determination of the amplitude and phase of the electromagnetic field at all points in space solves Maxwell's equations [1]. Currently, electromagnetic software packages can provide the numerical solution to Maxwell's equations. However, solving Maxwell's equations in the optical laboratory is nearly infeasible. One needs to measure the components of the scattered field at all points of the radiation zone. On top of that, the internal field induced in the excited object is experimentally inaccessible. In stark contrast, the Stokes parameters can be readily measured using a photodiode and waveplates [2]. The Stokes parameters can capture the amplitude and polarization state of the electromagnetic field in the radiation (far) zone. Therefore, the measurement of the Stokes parameters is, in general, insufficient to solve Maxwell's equations.

In this talk, we demonstrate that a measurement of the Stokes parameters at a single scattering angle is sufficient to solve Maxwell's equations for a set of objects [3, 4]. Notably, several works have tackled such objects in different branches of Nanophotonics. To the best of our knowledge, this study represents the first method capable of solving Maxwell's equations experimentally and from a measurement of the Stokes parameters. This feature endows the Stokes parameters, mostly used to get insight into the polarization state of the electromagnetic radiation, an even more fundamental role in the electromagnetic scattering theory.

References

1. James Clerk Maxwell, "Viii. a dynamical theory of the electromagnetic field," Philosophical transactions of the Royal Society of London, 459–512 (1865).

2. George Gabriel Stokes, "On the composition and resolution of streams of polarized light from different sources," Transactions of the Cambridge Philosophical Society 9, 399 (1851).

3. Olmos-Trigo, Jorge. "Solving maxwell's equations using polarimetry alone." Nano letters 24.28 (2024): 8658-8663.

4. Olmos-Trigo, Jorge. "Revealing the Electric and Magnetic Nature of the Scattered Light." ACS photonics 11.9 (2024): 3697-3703.

Multivalency Studied at the Single Molecule Level via Plasmon Enhanced Fluorescence

K.R. Okholm[1], S.W. Nooteboom[2], P. Zijlstra[2] and D. S. Sutherland[1*]

[1]Interdisciplinary Nanoscience Center (iNANO), Faculty of Natural Sciences, Aarhus University, Denmark
[2]Dept. Appl. Physics and Science Education, Eindhoven University of Technology, The Netherlands
[*] duncan@inano.au.dk

Abstract: Plasmon enhanced fluorescence was used to allow the study of weak dynamic interactions during multivalent binding at the single molecule level at the microsecond timescale. Molecular architecture changes the interactions and here we extend the concept of effective concentration to separate effects from size and structure/flexibility.

Summary:

The interaction of macromolecules via multiple weak interactions, so called multivalency, is a key feature present throughout nature for example in the recognition of pathogens by the immune system or the activation of signaling pathways via a concentration dependent pathway. The dynamic intramolecular interactions allow strong binding of a macromolecule to a multivalent target via the summation of multiple weak interactions. The avidity, the apparent increased binding affinity, is conceptually understood as a local concentration effect leading to enhanced rebinding of the individual binding motifs of a multivalent molecule. Overall avidity can be measured via a range of techniques but the study of dynamic intramolecular interactions is only accessible via single molecule approaches such as single molecule FRET. Current approaches are generally limited to millisecond timescales while many biological interactions and dynamics occur on the microsecond timescale. Here we present a plasmon-enhanced fluorescence platform to give highly enhanced photon count and potential for faster measurements in the microsecond regime [1]. We apply this approach to the study of multivalency with the nanoparticle as a multivalent, ligand-presenting object [2]. Using a Holliday Junction (HJ) as a model system we binding of constructs being 1, 2 and 3 ligands and study the role of construct structure and size on avidity. The HJ shows structure-dependent restriction of binding with limited binding of the third ligand. Addition of flexible extensions leads to overall reduced avidity from the longer arms and reduced local concentration, but importantly with activated trivalent binding. The dynamics within a single binding event can give information on the switching between states and the rate of binding/rebinding of the individual monovalent interactions within the multivalent interaction. We develop a theoretical framework extending the concept of effective concentration to separate effects from size from effects such as molecular structure and flexibility. Using the single molecule multivalent binding platform we study the role of ligand concentration and demonstrate super-selectivity for trivalent constructs [2]. The approach based on plasmonic nanoparticle-enhanced fluorescence gives a distance-based signal which both facilities single molecule measurements with low back ground and signal enhancement, but also enables the study of dynamics with a single molecule binding event Making use of the high time resolution in the microsecond regime we study intramolecular dynamics during bivalent binding events allowing the study of binding/unbinding of individual interactions within a multivalent binding[1].

We demonstrate that single molecule studies of multivalent constructs can measure avidity and dynamics of multivalent binding events and has the potential to guide the design of multivalent therapeutic constructs.

Acknowledgements:

This work was funded within the DNRF center of excellence DNRF 135 and by the European Commision un der the ERC (grant agreement No 864772 and Grant Agreement 860914)

References:

1. Nooteboom, S. W., K. R. Okholm, V. Lamberti, B. Oomen, D.S. Sutherland and P. Zijlstra, “Real-time microsecond dynamics of single biomolecules probed by plasmon-enhanced fluorescence” Nano Letters Vol. 24, No. 37, 11641-11647, 2024
2. Okholm, K. R., S. W. Nooteboom, V. Lamberti, S. Dey, P. Zijlstra and D.S. Sutherland, “Single-molecule multivalent interactions revealed by plasmon-enhanced fluorescence” ACS Nano, Vol. 18, No.52, 35429–35442. 2024

Controlling the light emission of quantum emitters using plasmonic nanoantennas

M. Zapata-Herrera[1*], L. Montaño-Priede[2], N. Zabala[1,2,3], R. Esteban[1,2] and J. Aizpurua[1,3,4]
[1]Donostia International Physics Center, Paseo Manuel de Lardizabal 4, 20018 Donostia-San Sebastián, Spain.
[2]Materials Physics Center CSIC-UPV/EHU, Paseo Manuel de Lardizabal 5, 20018 Donostia-San Sebastián, Spain.
[3]Department of Electricity and Electronics, University of the Basque Country (UPV/EHU), 48080, Bilbao, Spain.
[4]Ikerbasque, Basque Foundation for Science, María Díaz de Haro 3, 48013 Bilbao, Spain.
[*]corresponding author: mario.zapatah@ehu.eus

Abstract: We investigate light emission control from single emitters using plasmonic nanostructures. Analyzing various plasmonic configurations, we offer general insights into the enhancement of the emitted photoluminescence and other key parameters like radiative decay rates, Purcell factors and quantum yields, to guide the design of novel devices for future nanophotonic applications.

Optical nanoantennas are nanostructures that strongly interact with light through the excitation of localized surface plasmonic resonances. These resonances result from the collective oscillations of free electrons within the metal, generating enhanced electromagnetic fields in subwavelength volumes. This phenomenon has been exploited in numerous applications in nanophotonics, including enhanced spectroscopy, sensing, and imaging.

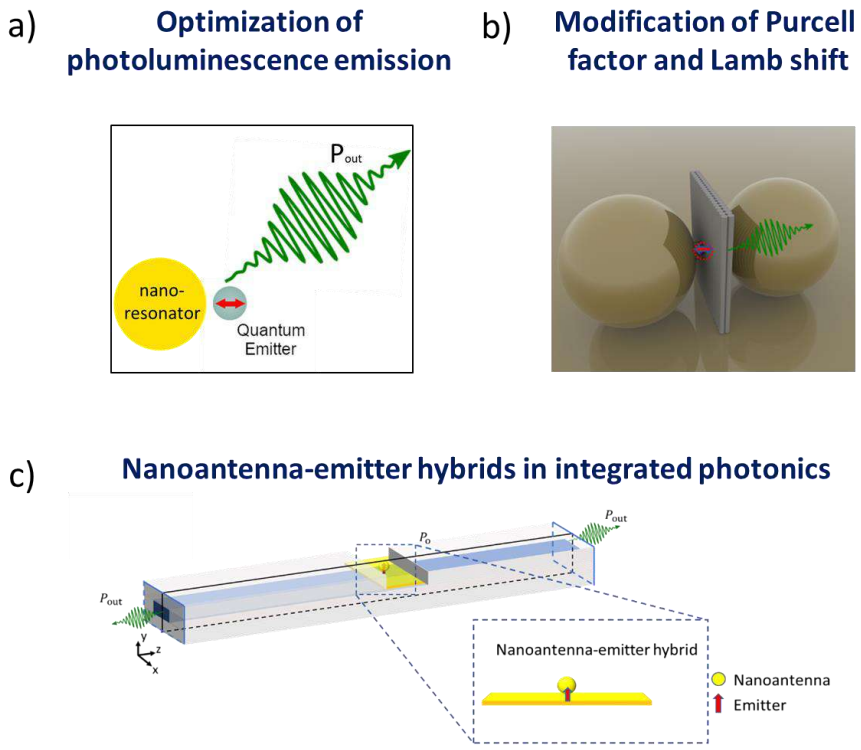


Figure 1. Light emitted from single emitters placed in a variety of plasmonic scenarios: a) A quantum emitter in close proximity to a single nanoresonator. b) Fluorophore placed in a plasmonic nanocavity within a nanodimer on a mirror (NDoM) configuration. c) Nanoantenna-emitter coupled to an etched SiN waveguide.

Notably, plasmonic nanoantennas can serve as a versatile platform for controlling the efficiency of light emission and the optical properties of single emitters—such as organic molecules, quantum dots, or nitrogen-vacancy centers in nanocrystals—by modifying their electromagnetic environment.

In this work, we present a comprehensive theoretical investigation of the light emitted from single emitters placed in diverse plasmonic scenarios (see Figure 1), focusing in the following key aspects:

i) We explore how plasmonic nanoantennas—varying in shape and size— modify the photoluminescence emission of a single emitter across multiple plasmonic configurations (Figure 1a). These include single and dimer gold nanorod antennas, plasmonic nanocavities, patch nanoantennas, and hybrid photonic-plasmonic cavities [1-4].

ii) We show that the emission spectra from a single molecule can be tailored by placing it within a plasmonic nanocavity formed by a gold nanodimer deposited on a mirror substrate, which radically alters the local photonic environment and introduces a very large Purcell Factor and Lamb Shift (Figure 1b). The theoretical predictions are in good agreement with the experimental results of collaborators that use DNA origami techniques to precisely position emitters within the nanoantennas [5].

iii) We explore the integration of an antenna-emitter hybrid system with a waveguide, to achieve efficient emission of light into the latter. Specifically, we consider a nanoparticle-on-a-mirror (NPoM) structure with a quantum dot positioned at the narrow gap between a metallic nanoparticle and a metallic surface [6], which are coupled to a SiN waveguide [7] (Figure 1c).

This work thus provides a comprehensive guide for enhancing light emission from quantum emitters using plasmonic nanostructures, offering insights for future advancements in the design of nanophotonic devices and on-chip applications.

References

1. Montaño-Priede. J. L., et al. “An Overview on Plasmon-enhanced Photoluminescence via Metallic Nanoantennas”. Nanophotonics, 13(26): 4771–4794, 2024.
2. Gupta. V., et al. Emission Enhancement of Colloidal Quantum Dots Confined in Double Disc Nano-antennas with Controlled Exposing of the Gap Opening”. In preparation.
3. Barreda, A. I., et. al. Hybrid Photonic-Plasmonic Cavities Based on the Nanoparticle-on-a-Mirror Configuration. Photonics Res. 9 (12), 2398, 2021.
4. Barreda, A. I., et. al. Hybrid Photonic-Plasmonic Cavity Design for Very Large Purcell Factors at Telecommunication Wavelengths. Phys. Rev. Appl. 18 (4), 044066, 2022
5. Verlekar, S., et al. Giant Purcell broadening and Lamb shift for DNA-assembled near-infrared quantum emitters. ACS Nano, 19, 3, 3172–3184, 2025.
6. de Aberasturi, et al. Modern Applications of Plasmonic Nanoparticles: From Energy to Health. Adv. Opt. Mater, 3 (5), 602–617, 2015.
7. Zapata-Herrera, M. et al. Design Strategies to Optimize Light Emission from Plasmonic Antenna-Emitter Hybrids into Waveguides. In preparation

Plasmonic Nanoparticles as Enhancers for WGM Single-Molecule Sensing and Chiral Molecule Detection

Frank Vollmer[1]

[1]University of Exeter, Department of Physics & Living Systems Institute, U,K.

[*]corresponding author: f.vollmer@exeter.ac.uk

Abstract: Plasmonic nanoparticles enhance optical fields. I demonstrate the application of plasmonic enhancers in Whispering Gallery Mode (WGM) sensing using optical microcavities. These enhancers have enabled significant advances in thermo-optoplasmonic (TOP) sensing of single molecules, including measurements of their absorption cross-sections, enzyme thermodynamics, and protein dynamics. They have also facilitated the development of microlasers with single atomic ion and molecule sensitivity, the detection and discrimination of neurotransmitters down to attomolar concentrations, and the observation of nanoparticle catalysis through plasmonic tip engineering. Furthermore, I present recent progress in the use of plasmonic enhancement for the detection of chiral molecules, ranging from monolayers and bilayers to nanoscale shells.

References:

Ghamari, S., Wu, HY., Pedireddy, S. *et al.* Plasmonic nanorod and dimer chiral molecule sensing from cysteine monolayer to bi-layers and multilayered shells. *npj Biosensing* **2**, 17 (2025). https://doi.org/10.1038/s44328-025-00036-z

M. C. Houghton, N. A. Toropov, D. Yu, S. Bagby, F. Vollmer, Single Molecule Thermodynamic Penalties Applied to Enzymes by Whispering Gallery Mode Biosensors. *Adv. Sci.* 2024, 11, 2403195. **https://doi.org/10.1002/advs.202403195**

Nikita A. Toropov, Matthew C. Houghton, Deshui Yu, Frank Vollmer, Thermo-Optoplasmonic Single-Molecule Sensing on Optical Microcavities. ACS Nano, 18, 1936-0851 **https://doi.org/10.1021/acsnano.4c00877**

Fluorescence color-routing and steering with a single dielectric nanoparticle

M. Sanz-Paz[1,2*], N. Siegel[1], G. Serrera[3], J. González-Colsa[3], F. Zhu[1], H. Sugimoto[4], P. Albella[3], and G. P. Acuna[1]

[1]Department of Physics, University of Fribourg, Chemin du Musée 3, Fribourg CH-1700, Switzerland
[2]Sorbonne Université, CNRS, Institut des NanoSciences de Paris, INSP, F-75005 Paris, France
[3]Group of Optics, Department of Applied Physics, University of Cantabria, 39005, Santander, Spain.
[4]Department of Electrical and Electronic Engineering, Graduate School of Engineering, Kobe University, Rokkodai Nada, Kobe 657-8501, Japan
*corresponding author: maria.sanz-paz@insp.upmc.fr

Abstract: Nanoscale photon sources exhibit a dipole-like emission pattern, limiting their incorporation into on-chip devices. Nanoantennas can control their radiation pattern, but often involve lossy plasmonic nanoparticles. Here, we show that a single dielectric nanoparticle can direct the emitted light of a nearby nanoemitter, allowing for geometrical and spectral light routing.

Summary: Nanoscale photon sources such as fluorescent molecules exhibit a dipole-like emission pattern, significantly limiting the amount of light that can be collected and hampering their incorporation into flat on-chip optical components. Therefore, developing directional optical emitters with tunable angular responses in the visible range is crucial for applications ranging from designing efficient integrated optical systems to high-sensitivity screening of molecular species. While optical antennas have been introduced to control the radiation pattern of nanoemitters, the overall sizes of the reported systems are typically larger than the wavelength of the radiation, and the designs often involve high-loss plasmonic nanoparticles. Researches attempts to design compact directional plasmonic antennas rely on achieving unidirectional emission through interference between electric multipoles. Alternatively, interference between electric and magnetic resonances have recently been explored as an alternative to enhance nanoantenna directivity based on the Kerker condition. However, this approach remains largely unexplored. However, this unidirectional emission happens only for complex structures, for specific positions of the emitter around the nanoantenna and in a narrow wavelength.

Individual low-loss high-index dielectric nanoparticles (HID NPs) can overcome these limitations as they can also generate electric and magnetic dipole responses, whose interference can strongly affect their scattering pattern.[29] It has been theoretically shown that a single HID NP is sufficient to direct the light emitted by a neighboring dipole.[1,2] Moreover, a single HID NP promises to have more advantages, as it has been proposed to be able to reverse this directionality depending on the emission wavelength,[2] and to be able to either collect or reflect the emitted light by tuning the particle-emitter distance.[1] However, those effects have never been demonstrated experimentally, mainly due to the difficulties of placing an individual dipole emitter in the proximity of the NPs with high accuracy.

In this work we show, for the first time, that emission directionality can be tuned at the single-molecule level using a single silicon nanoparticle that is deterministically coupled to a single fluorescent molecule using the DNA origami technique. This approach allows manipulation of the emitter's position relative to the Si NP with

nanometer precision. By varying the emitter-NP distance, NP size, and fluorescent molecule (and thus emission range), it is demonstrated that a silicon nanoparticle functions as a broadband directional nanoantenna in the visible range with high robustness to geometrical variations, as opposed to commonly used designs. We further show that a displacement of the emitter around the NP can yield to a change in the emission angle (beam steering behavior), which, so far, has only been theoretically predicted.[3] Furthermore, we observed, for the first time with a single nanoparticle, a change in emission direction as a function of the emission wavelength, i.e., color routing,[2] with a strong dependence on the distance between the NP and the emitter. This results as well in a change in the collector/reflector behavior of the NP at certain wavelengths as theoretically predicted.[1]

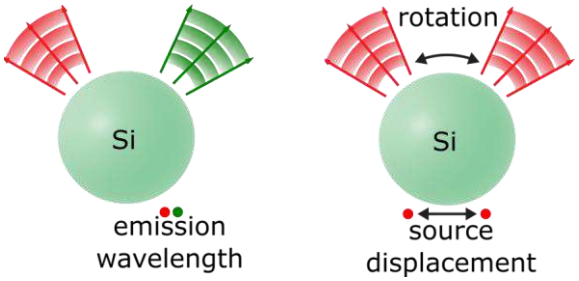


Figure: *sketch of spectral and geometrical fluorescence routing with a single silicon nanoparticle.*

References

1. Rolly, B.; Stout, B.; and Bonod, N. "Boosting the Directivity of Optical Antennas with Magnetic and Electric Dipolar Resonant Particles," Opt. Express 2012, 20 (18), 20376.
2. Krasnok, A. E.; Miroshnichenko, A. E.; Belov, P. A.; and Kivshar, Y. S. "All-Dielectric Optical Nanoantennas," Opt. Express 2012, 20 (18), 20599.
3. Krasnok, A. E.; Simovski, C. R.; Belov, P. A.; and Kivshar, Y. S. "Superdirective Dielectric Nanoantennas," Nanoscale 2014, 6 (13), 7354–7361.

Fabrication of Plasmonic Lattices through Optical Printing

A. J. Pereyra[1], M. C. Mina Villarreal[1], A. Manjavacas[2], J. J. Álvarez-Serrano[2], F. D. Stefani[3], J. Gargiulo[1], and I. L Violi[1]*

[1]Instituto de Nanosistemas (INS), Universidad Nacional de San Martín (UNSAM), Buenos Aires, Argentina
[2]Instituto de Química Física Blas Cabrera (IQF), CSIC, Madrid, Spain
[3]Centro de Investigaciones en Bionanociencias (CIBION), Consejo Nacional de Investigaciones Científicas y Técnicas (CONICET), Buenos Aires, Argentina
*corresponding author: ivioli@unsam.edu.ar

Abstract: Metal nanoparticle arrays support lattice plasmon resonances with enhanced optical and photothermal responses. In this work, we fabricate square grids of 100 nm colloidal Au NPs with tunable parameters through optical printing and explore how lattice spacing and size affect resonance properties, also comparing experimental results with simulations.

Metal nanoparticles (NPs) act as nanoantennas in the visible range due to their localized surface plasmon resonances (LSPR), allowing them to efficiently collect light, concentrate it in nanoscale volumes, and transfer its energy to the material's charge carriers and phonons.[1] Thus, they act as sources of electromagnetic fields, charge, and heat at the nanoscale, which can be tuned remotely by using light. These capabilities have given rise to the field of nanoplasmonics and motivated the use of NPs in numerous nanotechnology applications. When NPs are arranged in ordered arrays, collective modes can emerge, known as lattice plasmon resonances.[2] These collective modes show an enhanced optical response compared to individual NP resonances, with higher quality factors. Additionally, collective resonances can be tuned by modifying lattice parameters and exhibit enhanced photothermal responses.[3] While the properties of these lattices have been extensively studied through simulations, their fabrication and experimental demonstration remain challenging.

In this work, we use the optical printing technique, which enables the deposition of arbitrary colloidal NP arrays on substrates.[4] The versatility of this method in modifying lattice parameters, such as diameter of the NPs (d), size of the array (N) and interparticle distance (a) (Figure 1 a), allows us to fabricate arrays of spherical gold NPs in a simple manner, a morphology that is difficult to achieve using other methods like lithography. We present here the fabrication of different square periodic arrays of 100 nm spherical Au NPs having different a and N (Figure 1b), investigating how these parameters influence the presence and intensity of lattice resonances. We also compared the optical response with simulations, considering the intrinsic disorder of the arrays due to the fabrication method, obtaining excellent agreement between them.

This work contributes to the development of new photonic devices for light and heat manipulation at the micro- and nanoscale.

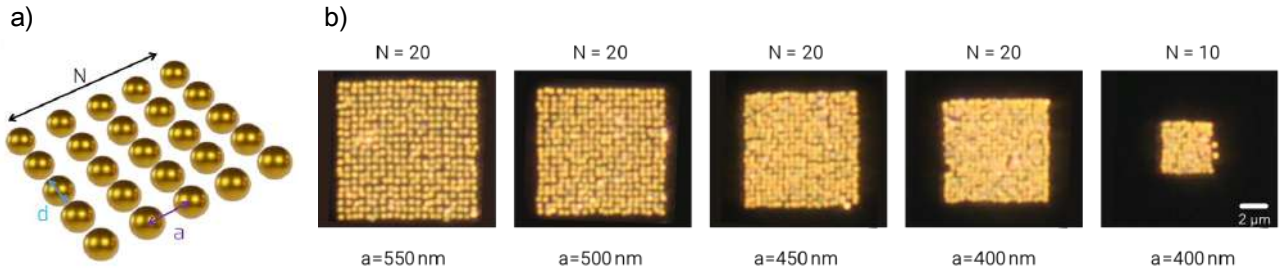


Figure 1: a) Scheme of a plasmonic lattice and their tunable parameters; b) Plasmonic lattices of different sizes (*N*) obtained by optical printing 100 nm (*d*) Au NPs at different interparticle distances (*a*).

References

1. Giannini, V.; Fernández-Domínguez, A. I.; Heck, S. C.; Maier, S. A., "Plasmonic Nanoantennas: Fundamentals and Their Use in Controlling the Radiative Properties of Nanoemitters," Chem. Rev., 111 (6), 3888–3912, 2011.
2. (Cherqui, C.; Bourgeois, M. R.; Wang, D.; Schatz, G. C., "Plasmonic Surface Lattice Resonances: Theory and Computation," Acc. Chem. Res., 52 (9), 2548–2558, 2019.
3. Zundel, L.; Malone, K.; Cerdán, L.; Martínez-Herrero, R.; Manjavacas, A., "Lattice Resonances for Thermoplasmonics," ACS Photonics, 10 (1), 274–282, 2023.
4. Violi, I. L.; Martinez, L. P.; Barella, M.; Zaza, C.; Chvátal, L.; Zemánek, P.; Gutiérrez, M. V.; Paredes, M. Y.; Scarpettini, A. F.; Olmos-Trigo, J.; Pais, V. R.; Nóblega, I. D.; Cortes, E.; Sáenz, J. J.; Bragas, A. V.; Gargiulo, J.; Stefani, F. D., "Challenges on Optical Printing of Colloidal Nanoparticles," J. Chem. Phys., 156 (3), 2022.

Cooperative electron-vibron interactions in Surface-Enhanced Raman Scattering (SERS)

Miguel Ángel Martínez-García[1], and Diego Martín Cano[1*]

[1] Departamento de Físíca Teórica de la Materia Condensada and Condensed Matter Physics Center (IFIMAC), Universidad Autónoma de Madrid, Madrid, Spain

[*]corresponding author: diego.martin.cano@uam.es

Abstract: We identify cooperative electron-vibron interactions between near-resonant and non-resonant electronic levels in SERS. Using an open-system quantum model, we demonstrate how Raman interference leads to large modifications in SERS peak intensities. This mechanism generates enhanced nonclassical photon correlations, reshaping conventional assessments of optomechanical contributions in SERS spectra and quantum observables.

The discovery of significant enhancements in Raman molecular signals near metallic surfaces, attributed to surface plasmons and charge-transfer effects, paved the way for the initial experimental validations of single-molecule vibrational spectroscopy and the initiation of SERS research. Despite strong supporting evidence of these findings, there have been debate and discrepancies regarding the mechanisms responsible for generating SERS and explanations for anomalous spectroscopic features when compared to conventional Raman spectroscopy [1]. Motivated by the need to elucidate such SERS processes, several pioneering studies have investigated cavity optomechanical models, treating vibrations and photons with equal complexity to account for their nonlinear contributions in off-resonance [2] and near-resonance SERS [3], respectively.

In this work we identify cooperative electron-vibron interactions occurring between both near-resonant and non-resonant electronic levels [4]. By developing an open-system quantum model based on fundamental molecular interaction principles, we illustrate how Raman interference, involving both resonant and non-resonant components, can lead to several orders of magnitude modifications in SERS peak intensities beyond previous optomechanical predictions. This cooperative optomechanical mechanism enables the generation of strongly enhanced nonclassical correlations between Stokes and anti-Stokes photons, observable via photon-counting measurements. Our findings reveal coherent Raman enhancements and suppressions that reshape conventional assessments of the optomechanical contribution to SERS spectra and its quantum mechanical signatures.

Acklowledgments: We acknowledge financial support from the Ramon y Cajal program (RYC2020-029730-I) and the fellowship (LCF/BQ/PI20/11760018) from “La Caixa” Foundation (ID 100010434) and from the European Union’s Horizon 2020 research and innovation program under the Marie Sklodowska-Curie Grant No. 847648. We also acknowledge financial support from the MCINN Projects No. PID2021-126964OB-I00 (QENIGMA) and No. TED2021-130552B-C21 (ADIQUNANO), and the CAM project Sinérgico CAM 2020 Y2020/TCS- 6545 (NanoQuCo-CM).

References

1. Zrimsek, A. et al., “Single-molecule chemistry with surface-and tip-enhanced Raman spectroscopy,” Chem. Rev. 117, No. 11, 7583–7613, 2016.

2. Roelli, P., Galland, C., Piro, N., and Kippenberg, T. J., “Molecular Cavity Optomechanics as a Theory of Plasmon-Enhanced Raman Scattering,” Nature Nanotechnology 11, No. 2, 164–69 (2016)
3. Neuman, T., Esteban, R. Giedke, G., Schmidt, M. K., and Aizpurua, J., “Quantum Description of Surface-Enhanced Resonant Raman Scattering within a Hybrid-Optomechanical Model,” Phys. Rev. A 100, No. 4, 043422 (2019).
4. Martínez-García, M. Á., and Martín-Cano, D., “Coherent Electron-Vibron Interactions in Surface-Enhanced Raman Scattering (SERS),” Phys. Rev. Lett. 132, No. 9, 093601 (2024).

High-Refractive-Index and Flexible SiC Nanoantenna Stickers

S. Murai[1], H. Maruyama[1], JTY Tse[1], H. Gao[1], K. Tanaka[1]

[1] *Department of Material Chemistry, Graduate School of Engineering, Kyoto University, Nishikyo-ku, Kyoto,615-8510 Japan*
*corresponding author: murai@dipole7.kuic.kyoto-u.ac.jp

Abstract: We fabricated a periodic SiC nanoparticle array embedded in a flexible polymer. Photoluminescence enhancement was demonstrated by placing it on the top of phosphor (YAG:Ce^{3+}) plate. the SiC sticker outperforms the TiO_2 nanoantenna sticker with identical design.

Silicon carbide (SiC) can be a good Mie-tronics ingredient because of its higher refractive index and a lower extinction coefficient than those of TiO_2 [1]. In the research field of power-electronics, SiC is intensively explored as wide-bandgap semiconductors. Heavy demands from the power-electronics community to reduce the numbers of crystalline defects and dislocations have developed high-quality crystal growth technologies of these materials, and the nanophotonics research community can make use of these crystals to fabricate metasurfaces.

We fabricated a periodic SiC nanoparticle array embedded in a flexible polymer, which is applicable as a sticker to stick to any clean surfaces to control light [2]. Starting from the epitaxial 3C-SiC thin films on Si substrates, the nanoparticle array was fabricated by combining electron beam lithography and dry etching. After coating the nanoparticles with a polydimethylsiloxane (PDMS) film, the Si substrate on the backside was etched away to obtain the free-standing SiC nanoparticle array embedded in the PDMS film. The optical measurements show that the resultant nanoantenna sticker supports surface lattice resonances. Because of the flexibility of the sticker, the resonances can be tuned by mechanical deformations. Photoluminescence enhancement was demonstrated by placing it on the top of phosphor plate.

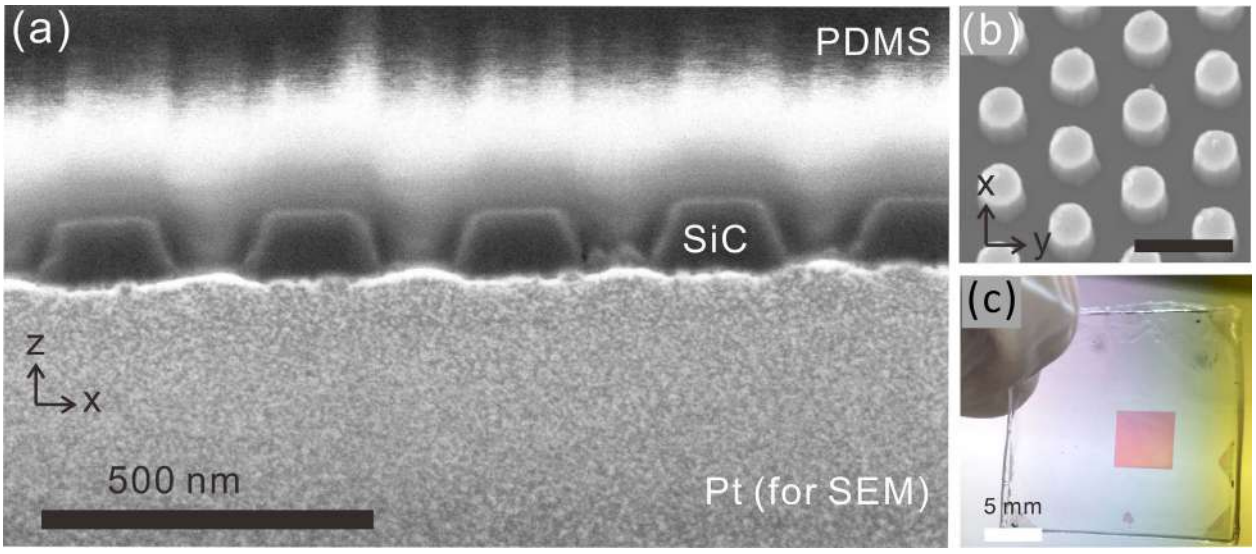


Fig.1: (a,b) SEM images. (a) Cross-sectional view after embedded in the PDMS. (b) Top-view after Ni etching. (c) Optical view of the SiC nanoantenna embedded in the PDMS layer.

References

1. H. Maruyama, et al., ***Jpn. J. Appl. Phys.***, accepted. 2. H. Maruyama, et al., to be submit

Acknowledgments

We acknowledge financial support from Kakenhi & Bilateral programs, Japan.

Chiral sensing with degenerate quasi-bound states in the continuum

D. Shakirova[1*], A. C. Valero[1], A. Bogdanov[2,3], and T. Weiss[1]
[1]Institute of Physics, University of Graz, and NAWI Graz,
Universitätsplatz 5, Graz 8010, Austria
[2]Qingdao Innovation and Development Center of Harbin Engineering University,
Qingdao, 266500, China
[3]School of Physics and Engineering, ITMO University, 191002, St. Petersburg, Russia
diana.shakirova@uni-graz.at (corresponding author)

Abstract

Dielectric nanoresonators have proven to be efficient platforms for chiral sensing due to high-quality-factor resonant states that increase chiral light-matter interaction and boost circular dichroism. We theoretically show that a proper combination of such resonant states significantly increases the chiroptical response to a level that should be measurable in experiments.

1 Results and discussion

Chirality is a non-identity of an object to its mirror image. This fundamental property is inherent in many organic molecules, chemical compounds, and drugs, and crucially affects living organisms. The same molecules of the opposite handedness (enantiomers) can act as a drug or a toxin, respectively [1]. Therefore, the detection of molecular handedness is a cornerstone problem of biology, chemistry, and medicine. Measuring circular dichroism (CD), which is the difference in absorbance of left-handed (L) and right-handed (R) circularly polarized light by chiral molecules, is a standard approach to distinguish the opposite enantiomers. The main obstacle is extremely small values of CD signal in a natural chiral medium. This is where nanophotonics comes into play. The use of resonant states of plasmonic and dielectric nanostructures allows us to significantly enhance chiral light-matter interaction and increase CD [2, 3].

Recently, a general electromagnetic theory of chiral light-matter interaction in arbitrary resonators has been developed [4]. In the framework of this theory, the chiroptical response can be disentangled into a sum of five contributions, namely, nonresonant interaction, resonance shift, changes in the excitation and emission of resonances, and modal crosstalk.

In this study, we explore the later mechanism, the modal crosstalk, and implement it on a dielectric metasurface [Fig. 1(a)] that supports quasi-bound states in the continuum (quasi-BICs) – resonant states with extremely high quality factors, which have attracted a lot of attention in the nanophotonic community over the last decades [5]. We demonstrate that a proper combination of quasi-BICs guarantees a huge boost of the chiroptical response, including the differential transmittance $\Delta T = T_{\mathrm{L}} \in T_{\mathrm{R}}$. By selecting two nearly degenerate, orthogonally polarized quasi-BICs, we demonstrate a ΔT enhancement on the order of 10^3 and an absolute value of ΔT on the order of 10^{-2} [Fig. 1(b)], which seems feasible for detection in standard spectrometers.

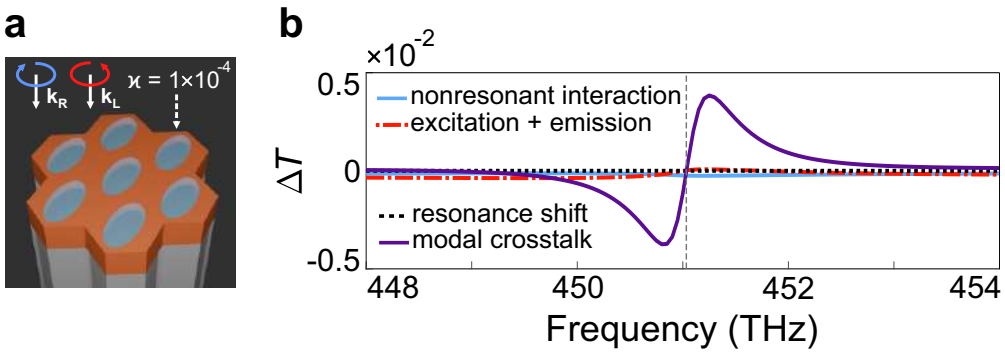


Figure 1: (a) Dielectric metasurface design with an inserted chiral analyte. (b) The chiroptical response ΔT from the system. ΔT is disentangled into five mechanisms (changes in the excitation and emission of the resonances are united into one class), and the modal crosstalk unambiguously dominates.

References

[1] E. Thall, "When Drug Molecules Look in the Mirror," *J. Chem. Educ.*, Vol. 73, No. 6, pp. 481–484, 1996.

[2] E. Mohammadi et al., "Nanophotonic Platforms for Enhanced Chiral Sensing," *ACS Photonics*, Vol. 5, pp. 2669–2675, 2018.

[3] S. Yoo and Q-H. Park, "Metamaterials and chiral sensing: a review of fundamentals and applications," *Nanophotonics*, Vol. 8, No. 2, pp. 249–261, 2019.

[4] S. Both et al., "Nanophotonic Chiral Sensing: How Does It Actually Work?," *ACS Nano*, Vol. 16, pp. 2822–2832, 2022.

[5] K. Koshelev et al., "Subwavelength dielectric resonators for nonlinear nanophotonics," *Science*, Vol. 367, pp. 288–292, 2020.

Full-Stokes polarimetric microscopy using cross-grating wavefront microscopy (polar-CGM)

Baptiste Marthy, Khosro Z. Kamali, Mikael Käll, Guillaume Baffou*

[1]Institut Fresnel, CNRS, Aix Marseille University, Centrale Med, Marseille, France
[2] Department of Physics, Chalmers University of Technology, Göteborg, Sweden
*corresponding author: guillaume.baffou@fresnel.fr

Abstract: We associate a 4-polarization camera with a 4-wave diffraction grating to achieve single-shot imaging of the vectorial electromagnetic field associated to nanostructures at the sample plane of an optical microscope. We illustrate the technique on lithographic and colloidal nanoparticles and metasurfaces.

Optical characterization methods in nanophotonics may be complex to implement, or fall short by providing only basic light intensity measurements, overlooking the intricate complexity inherent in many nanophotonic structures, in terms of spectral or polarization response. To address these limitations, we introduce an optical microscopy technique, both powerful and simple to implement, designed to capture the full complex vectorial electromagnetic field at the image plane of a microscope. This technique is based on the implementation of a 4-wave diffraction grating (QLSI grating [1]), associated with a polarized camera. We show how this advance enables quantitative tensorial characterization of nanophotonics sample, namely the determination of the complex polarizability tensor of anisotropic nanoparticles, and the mapping of the complex optical conductivity tensor of 2D materials and metasurfaces. This accessible method enables a detailed and comprehensive exploration of nanophotonic samples, paving the way for enhanced metrology, understanding and control of light-matter interactions at the nanoscale.

References

1. G. Baffou, “Quadriwave lateral shearing interferometry: applications in nanophotonics and biology”, ACS Photonics, ACS Photonics Vol. 10, 322-339, 2023.
2. S. Khadir, D. Andrén, P. C. Chaumet, S. Monneret, N. Bonod, M. Käll, A. Sentenac, G. Baffou, “Full optical characterization of single nanoparticles using quantitative phase imaging”, Optica Vol. 7, 243-248, 2020.
3. S. Khadir, D. Andrén, R. Verre, Q. Song, S. Monneret, P. Genevet, M. Käll, G. Baffou, “Metasurface optical characterization using quadriwave lateral shearing interferometry”, ACS Photonics Vol. 8, 603-613, 2021.
4. https://github.com/baffou/PhaseLAB

Au Core/Nanoporous Shell SERS Nanoprobe for Ultrasensitive Detection of Small Pesticide Molecule

Ryeong Myeong Kim[1], Afsana Mimi[1], and Eun-Ah You[1]

[1]1 Division of Biomedical Metrology, Medical Metrology Group, Korea Research Institute of Standards and Science (KRISS)

[*]corresponding author: eayou@kriss.re.kr

Abstract: We developed a nanoporous gold core–shell SERS nanoprobe enabling sensitive thiram detection down to 10^{-8} M. Incorporating TFMBA as an internal standard allows simultaneous evaluation of nanoparticle quality and concentration. This versatile platform offers potential for environmental monitoring, food safety, and biomedical diagnostics.

The rapid and sensitive detection of small pesticide molecules is essential for environmental monitoring and food safety. Here, we present a highly efficient surface-enhanced Raman spectroscopy (SERS) nanoprobe featuring a gold core surrounded by a nanoporous shell, synthesized via a dealloying strategy. The nanoporous structure serves as a network of SERS hotspots, significantly amplifying the Raman signal while providing a high surface area for small pesticide molecules to efficiently penetrate and bind within the pores. This ensures precise and selective detection at ultralow concentrations. To enhance the probe's functionality, we incorporated 4-trifluoromethylbenzoic acid (TFMBA) as a Raman reporter on the gold core. Acting as an internal standard, TFMBA enables dual functionality: in the dry state, its characteristic Raman signals allow assessment of nanoparticle quality, such as synthesis efficiency and structural integrity. In solution, the TFMBA signal provides a quantitative measure of nanoparticle concentration, ensuring reliable and consistent performance during pesticide detection. After systematic optimization, the nanoprobe demonstrated exceptional sensitivity, detecting thiram molecules at concentrations as low as 1×10^{-8} M in the dry state, with a broad detection range from 1×10^{-2} to 1×10^{-8} M. In aqueous solution, the nanoprobe achieved quantitative detection over a range of 1×10^{-2} to 1×10^{-6} M, with a detection limit of 1×10^{-6} M. Additionally, we developed an SNP-based visualization method for intuitive detection of pesticides at concentrations as low as 10^{-8} M. We envision that this nanoporous Au core/SERS nanoprobe, with its universal SERS hotspots and internal standards like TFMBA, could extend beyond pesticide detection to enable sensitive detection of larger biomarkers, such as antibodies, highlighting its potential as a versatile tool for environmental monitoring, food safety, and biomedical diagnostics.

Advanced Theoretical Methods for Nanoplasmonics and Molecular Plasmonics

Emission Quenching in Plasmonics – Understanding and Countering It

Jacob B. Khurgin
Johns Hopkins University

Plasmonic structures are well known for enhancing light emission through the Purcell effect. While they significantly increase radiative decay rates, this does not always translate to higher overall emission efficiency. In fact, in many cases, the efficiency can be lower than that of emitters without plasmonic enhancement—a phenomenon known as luminescence quenching.

In this talk, I will present a simple coupled-mode theory that attributes quenching to emission into higher-order nonradiative modes of plasmonic structures. This framework allows for the strategic placement of emitters to optimize efficiency. Moreover, the theory reveals that breaking symmetry mixes radiative and nonradiative modes, thereby mitigating quenching—an effect observed in dimers, nanoantennas, and disordered plasmonic structures. Finally, the model also provides insight into why quenching does not occur in plasmon-enhanced Raman scattering.

Modeling Plasmonics and Molecular Plasmonics from an Atomistic Perspective

C. Cappelli[1,2 *]

[1] Scuola Normale Superiore, Piazza dei Cavalieri, 7, 56126, Pisa, Italy
[2]IMT School for Advanced Studies, Piazza San Francesco, 55100, Lucca, Italy
[*]corresponding author: chiara.cappelli@sns.it

Abstract: This study presents an atomistic yet classical approach coupled to a QM Hamiltonian, to predict plasmonic properties of nanostructured materials. The method enables large-scale simulations, also capturing quantum effects. Remarkably, it accurately reproduces computed reference data and experiments.

The optical response of plasmonic nanostructures can be tuned by varying their shape, size, and chemical composition [1]. Peculiar phenomena arise when a molecular system is adsorbed on the surface of plasmonic materials, ranging from surface-enhanced spectroscopies to photocatalysis [2]. The accurate description of the optical properties of the plasmonic substrates is thus crucial for an understanding of the physical phenomena occurring at the plasmon resonance frequency.

We present an atomistic, yet classical, approach to predict the plasmonic properties of nanostructures of complex shapes. The method is general enough to describe any plasmonic material, including noble metal nanoparticles (Ag and Au) [3] and metal alloys [4]. The approach is also coupled to a quantum mechanical (QM) description of the molecular system adsorbed on the nanostructure surface [5]. The resulting mixed QM/classical method is then extended to various spectral signals, e.g. surface-enhanced Raman scattering.

We show that our classical approach for plasmonics can correctly reproduce reference ab initio data [3], and experimental trends [3-4], and can be applied to large-scale nanoplasmonic simulations (more than 1 million atoms). By properly accounting for the atomistic discretization of matter, we can accurately describe the nanoplasmonics of systems dominated by quantum effects, such as subnanometer junctions [3,6], geometrical defects [8], and Gold picocavities [8]. Finally, we discuss the current challenges in the prediction of surface-enhanced spectroscopies, analyzing the performance of our methods, also by comparison with experiments [5].

This work has received funding from the European Research Council (ERC) under the European Union’s Horizon 2020 research and innovation programme (grant agreement No. 818064).

References

1. Kelly, K. L. et al., J. Phys. Chem. B, Vol. 107, 668, 2003.
2. Langer, J. et al. ACS Nano, Vol. 14, 28, 2019.
3. Giovannini T. et al., ACS Photonics, Vol. 9, 3025, 2022.
4. Nicoli, L. et al. Front. Photon., 1199598, 2023.

5. Lafiosca P. et al., J. Chem. Theory Comput., Vol. 19, 3616, 2023.
6. Giovannini T. et al., Nanoscale, 11, 6004, 2019.
7. Zanotto S. et al. ACS Photonics, 10, 394, 2023.
8. T. Giovannini et al. in preparation.

A computational Maxwell solver for nonlocal Feibelman parameters in plasmonics

Lorenz Huber[1] and **Ulrich Hohenester**[1*]

[1]Institute of Physics, University of Graz, Universitätsplatz 5,8010 Graz, Austria
[*]corresponding author: ulrich.hohenester@uni-graz.at

In extreme vicinity of metallic nanoparticles, quantum surface effects play a significant role. We develop a computational Maxwell solver based on the boundary element method, accounting for quantum corrections through mesoscopic boundary conditions with nonlocal Feibelman parameters. We demonstrate the versatility and accuracy of our approach for various model systems.

Optical excitation of plasmonic nanoparticles allows light confinement in subwavelength volumes and can lead to strong field enhancements (1). When dealing with sharp particle features, gaps, or quantum emitter field variations on the nanometer scale, quantum surface effects become significant.
Recently, it has been suggested to account for such quantum effects through mesoscopic boundary conditions (2) that incorporate frequency-dependent Feibelman parameters (3). In this paper, we develop the methodology and implement mesoscopic boundary conditions into a computational Maxwell solver based on the boundary element method (BEM) (4). Unlike previous approaches (5), we additionally consider Feibelman parameters that are nonlocal in the parallel direction to the metal interface, providing a more accurate description of quantum effects as suggested by recent results from time-dependent density functional theory simulations (6).

We further developed a modified Mie theory incorporating nonlocal Feibelman parameters and show for sodium spheres perfect agreement with BEM simulations. When refining the mesh discretization in the BEM approach, the numerical error is shown to monotonically decrease. Notably, the computational cost of the novel scheme is comparable to that of normal BEM simulations, making our approach ideal for future investigations of different particle geometries and materials. This would make Feibelman parameters accessible to a broader community and would establish mesoscopic boundary conditions as an integral part of plasmonics simulations.

We acknowledge Tomáš Neuman, Antton Babaze, Andrei Borisov, and Javier Aizpurua for providing nonlocal Feibelman parameters obtained from ab-initio calculations and for their valuable discussions. This work has received support from the FWF under project P 37150**.**

References

1. U. Hohenester, “Nano and Quantum Optics”, Springer Cham, Switzerland (2020).
2. Y. Yang, D. Zhu, W. Yan, A. Agarwal, M. Zheng, J. D. Joannopoulos, P. Lalanne, T. Christensen, K. K. Berggren, and M. Soljacic, “A general theoretical and experimental framework for nanoscale electromagnetism”, Nature 576, 248 (2019).
3. P. J. Feibelman, “Surface electromagnetic fields”, Prog. Surface Science. 12, 287 (1982).
4. L. Huber and U. Hohenester, "A computational Maxwell solver for nonlocal Feibelman parameters in plasmonics", J. Phys. Chem. C 129, 250 (2025).
5. U. Hohenester and G. Unger, “Nanoscale electromagnetism with the boundary element method”, Phys. Rev. B 105, 075428 (2022).
6. A. Babaze, T. Neuman, R. Esteban, J. Aizpurura, and A. G. Borisov, “Dispersive surface-response formalism to address nonlocality in extreme plasmonic field confinement”, Nanophotonics 12, 3277 (2023).

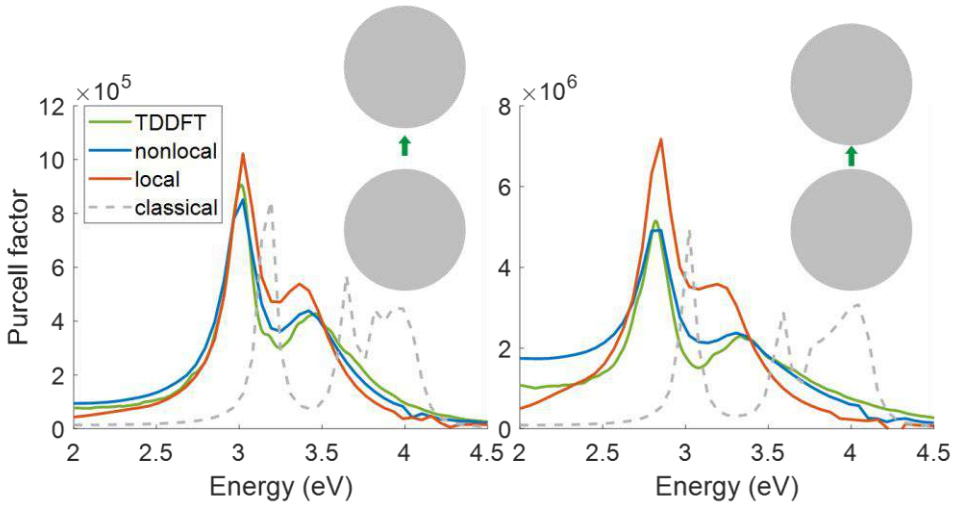


Figure. 1: Dipole in the gap region of two sodium spheres. The spheres have a diameter of 7 nm and a gap distance of 2,33 nm (left) and 1,32 nm (right). The dipole is z-oriented and located in the middle of the two spheres. The spectra show the Purcell factor of the dipole in between the dimer structure derived with TDDFT (6) calculation, BEM simulations (4) based on nonlocal and local Feibelman parameters, and classical Maxwell approach.

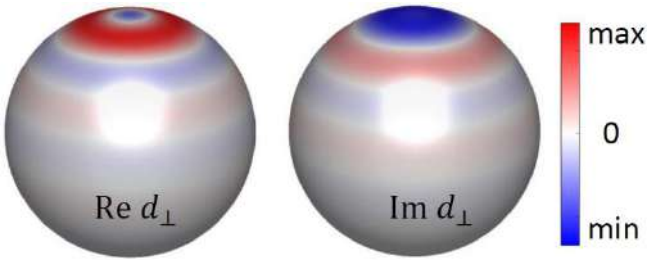


Figure. 2: Real and imaginary part of the Feibelman parameter $d_\perp(\boldsymbol{r}_\parallel - \boldsymbol{r}'_\parallel)$ used in our simulation (4) (in arbitrary units) for a sphere of 7 nm in diameter and a for a photon energy of 3.3 eV with $\boldsymbol{r}_\parallel$ being the position of the north pole.

Time-dependent quantum/continuum modeling of plasmon-enhanced electronic circular dichroism

L. Biancorosso[1], P. D'Antoni[1], S. Corni[2], M. Stener[1] and E. Coccia[1*]
[1]Dipartimento di Scienze Chimiche e Farmaceutiche, Università di Trieste (Italy)
[2]Dipartimento di Scienze Chimiche, Università di Padova (Italy) & Istituto Nanoscienze-CNR (Italy)
* Corresponding author: ecoccia@units.it

Abstract: We present a multiscale real-time approach to study plasmonic effects of a metal nanoparticle (NP) on the electronic circular-dichroism spectrum of a chiral molecule interacting with it. The method is based on a quantum description of the molecular system is coupled to a classical representation of the NP.

The enhanced sensitivity and response of chiral molecules in the presence of NPs have been thoroughly investigated experimentally [1], and theoretical literature was dedicated to a dipole-like description of the chiral molecule [2], usually within a master equation for the quantum states of the molecule.
Modeling the plasmonic-enhanced CD spectrum within the quantum-chemistry framework, beyond a dipole-like representation of the molecule, is a fundamental step to support experimentalists in the prediction and rationalization of the recorded data. It is a challenging task for theory because a large and complex system, generically composed of a NP and a molecule, has to be properly simulated.
The presented multiscale method is characterized by a quantum (QM) description of the chiral moiety, whereas the NP is treated according to a polarizable continuum model extended to nanoparticles [3]. The QM/continuum method is applied to the electronic CD (ECD) of methyloxirane (MOX) and peridinin (PID) at various distances (1, 3, and 5 nm) with respect to a gold NP surface. While no remarkable effect is observed for methyloxirane at any studied distance, an enhancement appears when the peridinin lies at 1 nm and the pulse is linearly polarized perpendicularly to the molecular axis, with the ECD signal centered at 4.1 eV increased by a factor of around 20. These results are rationalized looking at the gap between the plasmonic peak of the NP at around 2.5 eV and the molecular excitations: the smaller the gap between molecular and plasmonic excitations, the larger the plasmonic enhancement of the ECD signal. If the gap is too large, plasmon effects are negligible, as in the case of MOX; instead, since the PID lowest excitations are close to the NP plasmon, the effect of the induced plasmon field is remarkable and determines an enhancement approximately of a factor 20 with a pulse polarization perpendicular to the NP surface. This effect decreases with the distance between NP and PID, as the amplitude of the induced field decreases.
Moreover, ECD peaks are selectively enhanced due to the favorable coupling between the pulse polarization and the combined effect of electric and magnetic dipole moments.
This approach allows one to go through the electronic structure and dynamics of chiral molecules for obtaining a realistic description of plasmon-mediated ECD spectra, e.g., paving the way to applications to molecules of biological relevance interacting with nanostructures of experimental interest.

Financial support from ICSC-Centro Nazionale di Ricerca in High Performance Computing, Big Data, and Quantum Computing, funded by the European Union-NextGenerationEU is

gratefully acknowledged.

References

1. B. M. Maoz., Y. Chaikin, A. B. Tesler, O. B. Elli, Z. Fan, A. O. Govorov, and G. Markovich, "Amplification of Chiroptical Activity of Chiral Biomolecules by Surface Plasmons", *Nano Lett.*, Vol. 13, pp. 1203 (2013)

2. A. O. Govorov, Z. Fan, P. Hernandez, J. M. Slocik, and R. R. Naik, "Theory of Circular Dichroism of Nanomaterials Comprising Chiral Molecules and Nanocrystals: Plasmon Enhancement, Dipole Interactions, and Dielectric Effects',' *Nano Lett.*, Vol. 10, pp. 1374 (2010)

3. L. Biancorosso, P. D'Antoni, S. Corni, M. Stener and E. Coccia, "Time-dependent quantum/continuum modeling of plasmon-enhanced electronic circular dichroism", *J. Chem. Phys.*, Vol. 161, pp. 214104 (2024)

Modelling hot carrier generation, relaxation and extraction in large metallic nanoparticles

Johannes Lischner[1*]

[1]Imperial College London, United Kingdom
[*]corresponding author: j.lischner@imperial.ac.uk

Abstract: The decay of localized surface plasmons results in the generation of energetic or "hot" electrons and holes which can be harvested for applications in photovoltaics and photocatalysis. I will describe an atomistic theory of hot-carrier properties which allows the modelling of nanoparticles consisting of more than one million atoms.

Localized surface plasmons in metallic nanoparticles give rise to very strong light absorption. The decay of these excitations results in the generation of energetic or "hot" electrons and holes which can be harvested and harnessed for applications in photovoltaics, photocatalysis and light sensing. To optimize hot carrier production in devices, a detailed theoretical understanding of the relevant microscopic processes, including light-matter interactions, plasmon decay and hot electron thermalization, is needed. In my talk, I will describe a material-specific theory of hot-carrier generation and relaxation in metallic nanoparticles which combines a classical description of the electromagnetic radiation with large-scale atomistic quantum-mechanical simulations. I will present results for hot carrier distributions in spherical nanoparticles of gold, silver and copper and discuss the relative importance of interband and intraband transitions as function of nanoparticle size. Next, I will describe how CO_2 reduction performance of gold nanoparticles can be enhanced by changing the nanoparticle shape. Finally, I will discuss an approach to capture the effect of adsorbed molecules on the plasmon decay which enables the description of chemical interface damping.

Theory of imaging molecules using light in a scanning tunneling microscope

T. Neuman[1*]

[1]Institute of Physics of the Czech Academy of Sciences, Cukrovarnická 112/10, Prague 16 200, Czechia
[2]Author Affiliation, Country
[*]corresponding author: neuman@fzu.cz

Abstract: I will discuss the theoretical description and interpretation of techniques employing light in a scanning tunneling microscope. These techniques, including STM-induced electroluminescence, photocurrent generation, or tip-enhanced photoluminescence provide sub-molecular optical resolution and reveal atomic-scale molecular properties mostly related to the molecule's excited states, hardly accessible otherwise.

Advancements in scanning tunneling microscopy (STM), a technique where electrons tunnel between an atomically sharp probing tip and a sample supported by a conducting substrate, brought a breakthrough that allowed combining electron tunneling with light (electromagnetic wave) illumination and detection and thus lead to the advent of atomic-scale optical or optically assisted microscopy in an STM (STM plus light, STML). Several techniques lie under the umbrella of STML (see Fig. 1), including the STM-induced electroluminescence (STMEL) [1], its inverse, the generation of tunneling photocurrents in STM (PSTM) [2], or the tip-enhanced photoluminescence (TEPL) [3], to name a few. Each of these techniques provides a different, often complementary, view on the microscopic properties of the molecule. In this contribution I will focus on their theoretical description and interpretation.

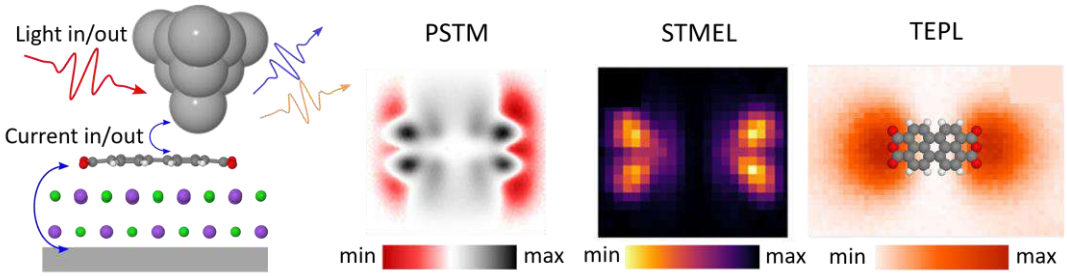


Figure 1. Schematic of the STM setup composed of the microscope tip, the molecule and the substrate including 2ML of NaCl (left) and examples of experimental images of photocurrents obtained with PSTM, and photon maps obtained with STMEL [4] and TEPL, respectively, of the perylenetetracarboxylic dianhydride molecule.

The optical resolution of these techniques originates in the highly localized interaction between the molecular excitations, characterized by the oscillating electron transition density, and the optical excitations in the STM tip-substrate cavity. The latter has its origin in the collective electron resonances, localized plasmons, that are hosted by the tip-substrate "cavity" and that give rise to an electric field oscillating at optical frequencies that is strongly localized around the atomically sharp apex of the STM tip. The interaction of the molecular excitation with the plasmons leads, on the one hand, to the enhanced coupling of incident light with the molecule and, on the other hand, tip-enhanced spontaneous emission of the molecular excitation giving rise to radiation into the far field. The detailed mechanism leading to sub-molecular optical imaging, however, depends on the specifics of the STML method.

TEPL can be considered as the optically purest of the mentioned techniques as it solely relies on interactions

between plasmons, the external laser illumination and the molecular excitation. I will discuss the theoretical details of plasmon—molecular exciton coupling that allow for optical imaging of molecular excitations going beyond the standard selection rules of light-matter interaction governing standard optical microscopy [5].

In STMEL, the molecule can most usually be excited by the sequential resonant tunneling of electrons where electrons are exchanged in several steps between the tip and the molecule and the molecule and the substrate. This process can lead to the transient change of the molecular charge followed by its return to the original charged state, however, hosting now an optical excitation (i.e. an electron-hole pair). As I will show, the tip-mediated tunneling step leaves its fingerprint in the population of the excited state through the density of states of the "active" molecular orbital (MO) involved in the tunneling process and is thus an inextricable part of the optical image obtained by scanning with the tip across the molecule and recording the intensity of the emitted light. The emitted light can be post-processed by analyzing its tip-position—dependent spectral properties to reveal details about the microscopic properties of the molecule such as the charge-transfer character of its excitation [6].

The spatial dependence of the tip-mediated tunneling step is the prime mechanism giving rise to PSTM, where tip-position-dependent currents are detected upon photoexciting the molecule. One can thus image the "active" MOs contributing to the sequential deexcitation of the molecule via resonant charge transfer processes. I will detail this mechanism using a recent example of a molecular radical where an excited state was imaged using this technique [7]. The analysis of the spatially resolved photocurrents revealed the multiconfigurational character of the molecule's doublet excited state, a feature influencing the optical properties of a broad range of radical emitters that are nowadays considered for application in optoelectronics as their efficiency is not hindered by the spin statistics (presence of dark triplet states) associated with closed shell systems.

TN acknowledges the Lumina Quaeruntur fellowship of the Czech Academy of Sciences.

References

1. Qiu, X. H., G. V. Nazin, and W. Ho, "Vibrationally Resolved Fluorescence Excited with Submolecular Precision", Science, Vol. 299 No. 5606, 542, 2003
2. Imai-Imada, M., H. Imada, K. Miwa, Y. Tanaka, K. Kimura, I. Zoh, R. B. Jaculbia, H. Yoshino, A. Muranaka, M. Uchiyama, and Y. Kim, "Orbital-resolved visualization of single-molecule photocurrent channels", Nature, Vol. 603, No. 7903, 829, 2022.
3. Yang, B., G. Chen, A. Ghafoor, Y. Zhang, Y. Zhang, Y. Zhang, Y. Luo, J. Yang, V. Sandoghdar, J. Aizpurua, Z. Dong, and J. G. Hou, "Sub-nanometre resolution in single-molecule photoluminescence imaging", Nat. Photonics, Vol. 14, 693, 2020.
4. Doležal, J., S. Canola, P. Hapala, R. C. de Campos Ferreira, P. Merino, and M. Švec, "Real Space Visualization of Entangled Excitonic States in Charged Molecular Assemblies", ACS Nano, Vol. 16, No. 1, 1082–1088, 2022.
5. Neuman, T., R. Esteban, D. Casanova, F. J. García-Vidal, and J. Aizpurua, "Coupling of Molecular Emitters and Plasmonic Cavities beyond the Point-Dipole Approximation", Nano Lett., Vol. 18, No. 4, 2358, 2018.
6. Roslawska, A., T. Neuman, B. Doppagne, A. G. Borisov, M. Romeo, F. Scheurer, J. Aizpurua, and G. Schull, "Mapping Lamb, Stark, and Purcell Effects at a Chromophore-Picocavity Junction with Hyper-Resolved Fluorescence Microscopy", Phys. Rev. X, Vol. 12, No. 1, 011012, 2022.
7. De Campos Ferreira, R., Sagwal, A., Doležal, J., Neuman, T., Švec, M., "Disentangling the components of a multiconfigurational excited state in isolated chromophore", arXiv:250209347, 2025.

Multiscale modelling insights on plasmon-assisted hot-carrier injection driving carbon dioxide reduction on rhodium nanocubes

M. Marsili[1*], G. Dall'Osto[2], M. Vanzan[3], D. Toffoli[2], M. Stener[2], S. Corni[4] and E. Coccia[2]

[1]Dipartimento di Fisica e Astronomia "Augusto Righi", Università di Bologna , Italy
[2]Dipartimento di Scienze Chimiche e Farmaceutiche, University of Trieste, Italy
[3]Dipartimento di Fisica, University of Milan, Italy
[3]Dipartimento di Scienze Chimiche, Università di Padova, Italy
[*]corresponding author: margherita.marsili@unibo.it

Abstract: In the case of carbon dioxide reduction, it was experimentally shown that the presence of a rhodium nanocube under illumination leads to the selective production of methane against carbon monoxide. Using a multiscale computational approach, based on accurate (GW-BSE) electronic-structure calculations for the "active site" and a classical representation of the rest of the nanostructure, we show that selectivity is due to a (predominantly) direct hole injection from rhodium to the reaction intermediate that favours the bonding of the proper molecular fragment to the surface.

It is well known that the presence of a plasmonic nanoparticle strongly affects the optical response of molecules, leading to significant effects such as surface enhanced Raman scattering, surface enhanced infrared absorption and metal enhanced fluorescence.Moreover, in recent years, plasmonic metallic nanostructures have emerged as a new family of photocatalysts, enhancing rates and increasing selectivity of important chemical reactions such as H_2 splitting and CO_2 reduction to methane [1].

When explaining the selectivity enhancement, hot carriers, i.e., energetic, non thermal electrons and holes generated upon plasmonic decay within the metal nanostructure, are thought to play a fundamental role. Nevertheless disentangling the effects of hot carrier dynamics from those of the other possibly concurrent phenomena such as reaction barriers lowering in excited state pathways, resonance of near fields with intramolecular transitions, and local increase of temperature, might be really hard from an experimental perspective. In this framework, theoretical modelization of these phenomena directly probing the role played by hot carriers are especially important to grasp the microscopic mechanism at play. However, theoretically modeling plasmonic-generated hot carriers and their effects is especially challenging due to the inherent multiscale nature of the system and to the kind of phenomena that are at play [1].

Recently [2], the simulation of the simultaneous electronic dynamics of molecule and nanoparticle has been achieved by combining a time-dependent configuration interaction approach for the molecule, and a description of the nanoparticle as a continuous dielectric of given shape and dielectric function within the polarizable continuum model approach. This approach was later extended to include the description of the molecule's electronic structure and neutral excited states at the GW-BSE level which correctly accounts for electronic level alignment at interfaces and charge transfer excitations [3].

In 2017, Zhang et al. demonstrated that in a hydrogen-rich environment, in the presence of rhodium nanocubes, CO_2 is reduced to a 60:40 ratio mixture of CH_4 and CO. However, in the presence of an external electromagnetic pulse matching the optical absorption of the nanocubes, the selectivity toward CH_4 rises to values above 90% [4]. The effect was tentatively assigned to hot-electron injection in antibonding orbitals of a reaction intermediate based on ground state density functional theory (DFT) calculations for CHO adsorbed on a model Rh(100) surface.

We performed extensive simulations of the electronic dynamics of the system, looking for possible charge transfer effects using the previously described multiscale computational approach, based on accurate (GW-BSE) electronic-structure calculations. In our simulations, the Rh nanoparticle is represented as a continuous dielectric nanocube of 37 nm edge, as in the experiment, characterized by the empirical Rh dielectric function $\epsilon(\omega)$, and

edge curvature equal to Rh atomic radius. One of the vertices of the nanocube is cut perpendicular to the (111) direction. Above the cut, at the atomic interlayer distance, an atomistic Rh19 cluster is set, mimicking the vertex itself. Adsorbed to the cluster is a CHO fragment, being the CHO dissociation into CH + O the rate-determining step in the thermally activated reaction toward CH4. The carrier dynamics is triggered by a Gaussian-enveloped electric field pulse centered at 3.4 eV, taken from the experimental work, and close to the plasmonic resonance of the rhodium nanocube. The results of our dynamics show that it is hole injection that speeds up the pathway leading to CH_4 production, by making the CHO fragment's oxygen more reactive. The microscopic mechanism of the injection was also analysed, showing that direct photoinduced charge transfer is prevailing for the nanocube thanks to the electromagnetic enhancement effect associated with the metal NP electronic resonance [5].

References

1. M. Vanzan, M. Marsili, npj Comput Mater 10, 222 (2024)
2. S. Pipolo, S. Corni, J. Phys. Chem. C 120, 28774 (2016)
3. M. Marsili, S. Corni J. Phys. Chem. C 126, (2022)
4. X. Zhang et al., Nat. Commun., 8, 14542 (2017)
5. G. Dall'Osto et al. J. Am. Chem. Soc. 146, 2208 (2024)

Active Control of Smith-Purcell Radiation Emission using 2D Nanoribbons

Eduardo J. C. Dias[1*], Theis P. Rasmussen[1], Álvaro Rodríguez Echarri[2], F. Javier García de Abajo[3,4], Joel D. Cox[1,5]

[1] POLIMA – Center for Polariton-driven Light-Matter Interactions, Univ. of Southern Denmark, 5230 Odense, Denmark
[2] Max-Born-Institut, 12489 Berlin, Germany
[3] ICFO – Institut de Ciencies Fotoniques, 08860 Castelldefels (Barcelona), Spain
[4] ICREA – Institució Catalana de Recerca i Estudis Avançats, 08010 Barcelona, Spain
[5] Danish Institute for Advanced Study, Univ. of Southern Denmark, 5230 Odense, Denmark
[*]corresponding author: dias@mci.sdu.dk

Abstract: We propose a theoretical approach to actively control Smith-Purcell radiation emission using 2D (graphene/TMD) nanoribbons. By tuning doping levels via electrical gating or optothermal doping, we achieve precise control of emission directionality, enabling light focusing and steering, with implications for spectroscopy, sensing, and communication applications.

Smith-Purcell radiation [1], a phenomenon arising from the interaction between charged particles and periodic structures, holds great importance for various applications, from particle accelerators to broadband radiation sources. In this study, we propose a novel approach to actively control and tune the emission of Smith-Purcell radiation in free space by leveraging the tunable properties of graphene and transition metal dichalcogenides (TMD) nanoribbons (Fig. 1a). Specifically, by adjusting the optical properties of individual ribbons within an array (namely their polarizability), we can customize the interference pattern that arises on the far-field, thus achieving precise control over the directionality of Smith-Purcell radiation. Notably, the doping level of graphene can be actively tuned through electrical gating, thus providing our system with a versatile set of knobs to control the emission properties of the array with a large degree of precision. Through extensive parameter optimization, we identify optimal combinations of parameters to maximize control over the emission process to allow for the control of both near-field and far-field distributions respectively aiming at active light focusing and steering (Fig. 1b).

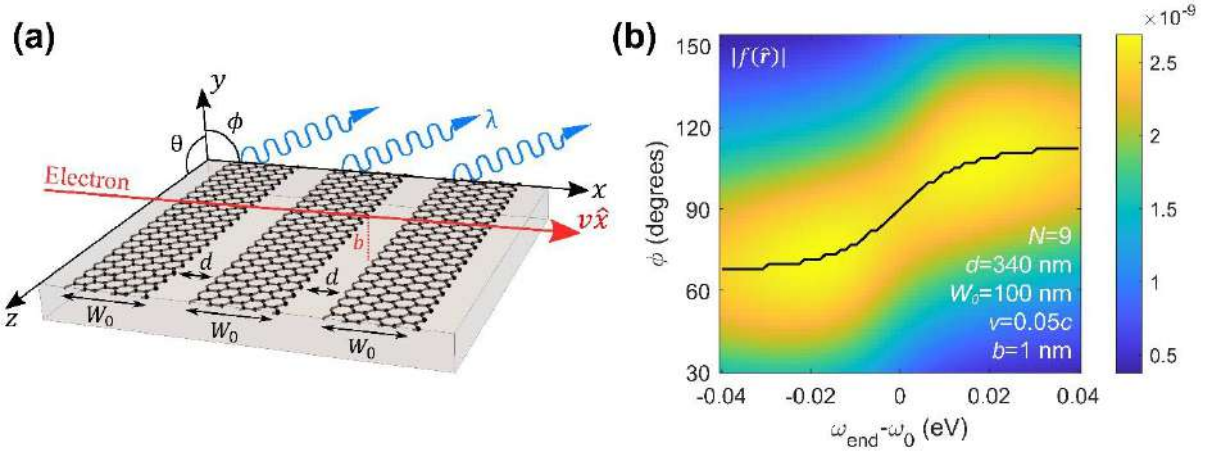


Figure 1. (a) Proposed setup composed of a periodic array of N 2D ribbons of width W_0 and spacing d. An electron flies with velocity v parallel and at a distance b to the ribbon's plane. Smith-Purcell emission of a wavelength λ is marked in blue. **(b)** Angular distribution of the far-field intensity $|f(\hat{r})|$ (for $\theta = 0$) of 9 graphene ribbons as a function of the difference in plasmon frequencies between the outmost (ω_{end}) and central (ω_0) ribbons, taken to vary linearly between ribbons. The black curve indicates the far-field intensity maxima which shows a steering ability ranging up to $\pm 20°$.

Furthermore, we explore alternative mechanisms for achieving a controllable optical response in each ribbon. Promisingly, optothermal doping can be obtained by employing spatially-modulated high-intensity laser pulses that locally change the electron temperature in graphene or TMD ribbons with diffraction-limited resolution, which translates into an ultrafast spatial-dependent modulation of their response [2]. This mechanism enables the fine-tuning of the emission characteristics which can be actively controlled by changing the illumination profile. Importantly, this mechanism provides a practical platform for the experimental investigation of such effects while offering insights into the underlying physics governing the ultrafast thermal dynamics in such systems.

Our findings pave the way for the development of advanced Smith-Purcell radiation sources with highly tailored and dynamically controllable emission properties, thereby unlocking new opportunities for innovative applications in areas such as spectroscopy, precision sensing, optical communication, and other fields requiring versatile and tunable radiation sources.

References

1. S.J. Smith, and E.M. Purcell, Visible light from localized surface charges moving across a grating, Physical Review 92, 1069 (1953).
2. E.J.C. Dias, R. Yu, and F.J. García de Abajo, Thermal manipulation of plasmons in atomically thin films. Light Sci Appl 9, 87 (2020).

Nonadiabatic dynamics of plasmon-mediated photochemistry

Yu Zhang[1]
[1]Theoretical Division, Los Alamos National Laboratory, Los Alamos, NM, 87544, USA
Corresponding author: zhy@lanl.gov

Abstract: Heterogeneous catalysis of adsorbates on metallic surfaces mediated by plasmons has the potential to achieve controllable reaction selectivity. However, the underlying physics of plasmon-mediated chemical transformations is very challenging to delineate. This talk will present our developments in theory and numerical methods for plasmon-mediated chemistry and the physical insights obtained.

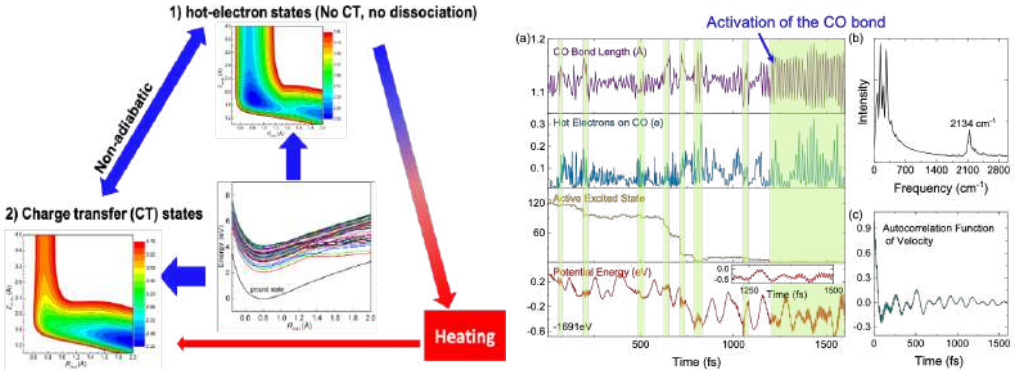


Figure 1: a) a) Different mechanisms of plasmon-mediated chemical transformations, including e hot carrier generation through surface plasmon excitation, followed by charge transfer to molecular antibonding orbitals, leading to bond dissociation. (b) A nonadiabatic molecular dynamics (NMAD) approach that treats all possible mechanisms—such as charge transfer, and electron-nuclear coupling—on an equal footing, providing a comprehensive framework for simulating plasmon-driven reactions

Introduction. Surface plasmon polaritons (SPPs) and localized surface plasmon resonances (LSPRs) are collective oscillations of electrons in conductors excited by electromagnetic modes. Surface plasmons results in concentration of light in the near-field around the particle interfaces, which enables efficient spatial control of charge and energy fluxes in a variety of applications. However, surface plasmons suffer from significant dissipation, with most of the plasmon's energy loss due to Landau damping leading to hot electron-hole (e-h) pairs. Several recent efforts have proposed the possible extraction of these energetic carriers before dissipation takes place, which has simulated the application of hot carriers to several branches of applied physics, chemistry, and materials and energy sciences [1].

Plasmon-mediated chemical transformation. Plasmon-driven reactions hold great promise for guiding chemical transformations with light, especially by exploiting the energetic electrons (hot carriers) that emerge from surface plasmon decay in metallic nanostructures. We have undertaken a series of computational investigations to illuminate how these hot carriers can activate and dissociate molecules or modify adsorbate–surface interactions on gold clusters.

First, the microscopic mechanism of H_2 dissociation in a plasmonic nanoparticle system was examined [2]. Our NAMD simulation revealed that, upon photoexcitation, hot carriers generated in gold nanoparticles transfer to the antibonding orbital of H_2, driving dissociation.

Interestingly, when H_2 is symmetrically placed in the gap of a dimer configuration, sequential charge transfer rapidly depletes the antibonding state, suppressing dissociation. Breaking this symmetry by displacing the molecule, however, restores dissociation, suggesting that nanoparticle geometry could offer a route for controlling reaction pathways.

But the Jellium model used in Ref. [2] lacks atomistic details. Insights from PESs built on the ab initio atomistic model are essential for a more in-depth understanding of plasmon chemistry. Hence, we employed time-dependent density functional theory (TDDFT) and quantum dynamics to investigate the potential energy surface of H_2 on a smaller Au_6 cluster and their photoinduced dynamics [3]. Our diabatization approach revealed two distinct categories of electronic states: those associated with hot electrons remaining in the metal, and those linked to charge transfer (CT) into the H_2 antibonding orbital. H_2 dissociation occurs efficiently only when transitions between these two states (from metal to CT) take place. Hence, controlling the funneling of population into these CT states is essential for plasmon-mediated chemical transformations.

To study all possible mechanisms on an equal footing, we implemented a TD-DFTB-based trajectory surface-hopping approach [4]. This methodology enabled us to treat hot-electron relaxation, charge transfer, and local heating in a unified framework. We then applied this approach to investigate plasmon-mediated heterogeneous catalysis involving CO adsorbed on an Au_{20} cluster [5]. After plasmon excitation, hot carriers shuttle between the Au_{20} and CO, activating the CO stretch via electron-vibration coupling. By tracking ensembles of trajectories, we estimated an overall $\sim$40% efficiency for plasmon-mediated transformations under these conditions. This work highlights how partial charge transfer, carrier migration, and molecular vibrational excitation interplay on ultrafast timescales to drive chemical transformations.

Acknowledgements

The authors acknowledge the support from the US DOE, Office of Science, Basic Energy Sciences, Chemical Sciences, Geosciences, and Biosciences Division under Triad National Security, LLC ("Triad") contract Grant 89233218CNA000001 (FWP: LANLECF7). LANL is operated by Triad National Security, LLC, for the National Nuclear Security Administration of the U.S. Department of Energy (contract no. 89233218CNA000001).

References

1. B. Weight, X. Li, Y. Zhang*, Theory and modeling of light-matter interactions in chemistry: current and future. *Phys. Chem. Chem. Phys.*, 25, 31554 (2023)

2. Y. Zhang*, T. Nelson, S. Tretiak, H. Guo, G. C. Schatz, Plasmonic Hot-Carrier-Mediated Tunable Photochemical Reactions. *ACS Nano.* 2018, 12, 8415-8422.

3. Q. Wu, L. Zhou, G. C. Schatz, Y. Zhang*, H. Guo*, Mechanistic Insights into Photocatalyzed H2 Dissociation on Au Clusters. *J. Am. Chem. Soc.* 142, 13090 (2020).

4. X. Wu, S. Wen, H. Song, T. Frauenheim, S. Tretiak, C. Yam, Y. Zhang*. Nonadiabatic molecular dynamics simulations based on time-dependent density functional tight-binding method *J. Chem. Phys.*, 157, 084114 (2022)

5. X. Wu, T. van der Heide, S. Wen, T. Frauenheim, S. Tretiak, C. Yam, Y. Zhang*. Molecular dynamics study of plasmon-mediated chemical transformations *Chem. Sci.*, 14, 4714 (2023)

Polaritonic Index: A Computational Tool for Classifying Hybrid Light-Matter Excitations in Metal-Molecule Systems

L. Cascino[1,2], R. Messina[1,2], S. Corni[3,4], and S. D'Agostino[1,2,5*]

[1]Mathematics and Physics Department "E. De Giorgi", University of Salento, Lecce, 73100, Italy
[2]Institute of Nanotechnology, National Research Council (CNR-NANOTEC), Lecce, 73100, Italy
[3]Department of Chemical Sciences, University of Padova, via Marzolo 1, Padova, 35100, Italy
[4]CNR-Institute of Nanoscience, Via Campi 213/A, Modena, 41125, Italy
[5]Center for Biomolecular Nanotechnologies, Istituto Italiano di Tecnologia (IIT), Arnesano, Lecce, 73100, Italy
[*]corresponding author: stefania.dagostino@nanotec.cnr.it

Abstract: Polaritonic chemistry exploits light-matter interactions to control chemical reactions. This study develops the Polaritonic Index (PI), a Python tool useful to classify electronic excitations in hybrid metal-molecule systems. Tested on systems of azobenzene (single or multiple molecules) interacting with Ag clusters, PI enables to control polariton-induced changes in photochemical processes.

Introduction

Polaritonic chemistry is an emerging interdisciplinary field that explores the interaction between light and matter to manipulate chemical reactions. This research employs Time-Dependent Density Functional Theory (TDDFT) to investigate how photonic modes, such as localized surface plasmon in metal nanoparticles, influence molecular potential energy surfaces (PESs). The primary objective is to develop a computational framework that enables precise control over photochemical processes, with potential applications in photopharmacology and opto-stimulation. Hybrid systems composed of metal nanoparticles and molecular emitters present challenges due to their complex molecular-plasmonic interactions, often leading to phenomena like charge-transfer states and polaritonic states. To address these challenges, a novel computational tool, the Polaritonic Index (PI), was developed to characterize and classify electronic excitations, distinguishing between molecular, metallic, and hybrid states.

Results

The Polaritonic Index (PI)[1] is implemented in a Python-based computational tool designed to analyze electronic excitations in hybrid metal-molecule systems. It employs transition density analysis to classify excitations into three categories: metal ($0 \leq PI \leq 1$), hybrid ($1 < PI < 10$), and molecular (≥ 10). The PI is determined using a mathematical formula (1) that quantifies the relative contributions of molecular and metallic components in an excitation:

$$PI(\omega_k) = \frac{\Delta\rho_{mol}}{\Delta\rho_{cluster}} = \frac{\sum_{I=1}^{Q_{mol}} \sum_{i=1}^{N} e^{-\left[\frac{(\vec{r_i}-\vec{R_I})^2}{2\sigma_i^2}\right]} |\Delta\rho(\vec{r_i},\omega_k)|}{\sum_j^{Q_{mol}} Z_j \cdot N_j}. \qquad (1)$$

In this context, $\Delta\rho_{mol}$ and $\Delta\rho_{cluster}$ represent electron density changes on the molecule and metallic cluster for a given excitation at frequency ω_k. The index I runs over the molecule's atoms (Q_{mol}), while i runs over the grid points. Here, $\vec{r_i}$ and $\vec{R_I}$ denote a grid point and atomic position, respectively. The standard deviation $\sigma_i = w_i \cdot rad$ is defined by a weight factor and a radius (covalent, van der Waals, or atomic), determining the charge distribution's spatial extent.

Since PI alone does not distinguish between charge-transfer (CT) and polaritonic states, the "D

distance" metric[2] was incorporated to precisely differentiate them by measuring spatial charge distribution changes between ground and excited states.

The PI tool was tested on a system consisting of an azobenzene molecule and a silver cluster. Azobenzene, a photoswitch, exhibits strong coupling with metal clusters under specific configurations[3]. By systematically varying the azobenzene dihedral angle, the research examined how molecular excitation properties changed due to plasmonic interactions. Through computational analysis, the hybrid system excitations were mapped as a function of dihedral angles, revealing clear trends in hybridization strength. Results showed that states exhibiting strong hybrid character required further refinement of classification thresholds to better differentiate between charge-transfer and polaritonic states.

Additionally, the PI was also tested on a system composed of a metal cluster and an ensemble of molecules, demonstrating its applicability in more complex hybrid systems.

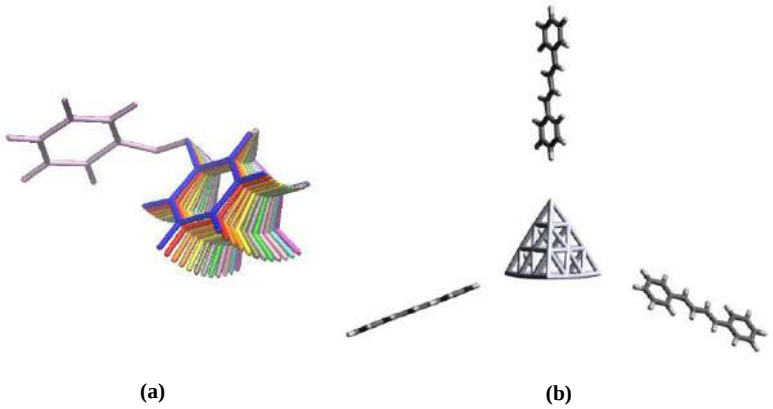


Fig 1: (a) Geometries of azobenzene molecule obtained by varying dihedral angle (CNNC). (b) Hybrid system composed of a silver cluster and three molecules of stilbene.

Conclusions

This study developed a computational approach for analyzing and classifying electronic excitations in hybrid metal-molecule systems. The Polaritonic Index provides a novel, systematic framework for distinguishing excitation types, with applications in understanding and controlling photochemical reactions. Testing on the azobenzene-silver system demonstrated the method ability to analyze hybrid states and identify charge-transfer contributions. Future work will refine classification thresholds and expand the methodology to more complex systems, further advancing polaritonic chemistry as a tool for tunable photoreactions.

Acknowledgements: S. D'Agostino thanks the Project PNRR I-PHOQS of CNR-NANOTEC.

References

1. Cascino L., Messina R., Corni S., and D'Agostino S., "Polaritonic Index". DOI: 10.5281/zenodo.14236666.
2. Le Bahers T., Adamo C., and Ciofini I. "A qualitative index of spatial extent in charge-transfer excitations." J. Chem. Theory Comput., Vol. 7, No. 8, 2498-2506, 2011.
3. Cascino L., Corni S., and D'Agostino S. "Revealing the Interplay between Hybrid and Charge Transfer States in Polariton Chemistry", J. Phys. Chem. C, Vol. 128, No. 7, 2024.

Optical properties of Au-based nanoparticles

M. Vanzan[1], G. Becatti[1], S. Zinzani[1], R. Plakaj[2], M. Stener[2], and F. Baletto[1,*]

[1]Physics Department, University of Milan, via Celoria 16, 20133 Milano, Italy
[2] Dipartimento di Scienze Chimiche e Farmaceutiche, Università di Trieste, via Giorgieri 1, 34127 Trieste, Italy.
[*]corresponding author: francesca.baletto@unimi.it

Abstract:

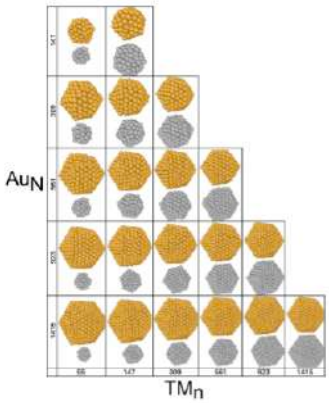
By classical MD simulations, we model the coalescence of Au-hybrid nanostructures -bimetallic nanoantennas- introducing proper geometrical descriptors to capture the kinetics of the process.

We calculate the absorption and ECD spectra employing TDDFT as in the AMS/ADF/polTDDFT tool[2], contrasting them against classical electromagnetic prediction from the pyGDM library.

Summary

We model the growth process by means of classical molecular dynamics simulations, using the package LoDiS and metal-metal interaction from the second-moment approximation of the tight-binding (TBSMA)[1]. The choice of those potentials resides in their accuracy in predicting surface diffusion processes. We focus on coalescence, see Fig. 1, where two initial seeds of Au and of another transition metal (TM), collide to form a larger nanoobject. We select TM among Au, Ag, Pd, Pt, Rh. We limit our analysis to icosahedral seeds being a likely geometry for the considered TMs at seed-sizes between 0.7 – 3.2 nm. To track the evolution of AuTM, we compute global, semi-local, and local structural descriptors with the aim of identifying (i) the kinetics of the shrinking process; (ii) and the most significant transition during the evolution of the so-formed AuTM. We sample our MD trajectories, at least 200 ns long, every 0.1 ns after 1 ns the contact time, see Fig. 1.

The AuTM shape classification follows the common neighbour analysis (CNA) signature, that detects the local connectivity of each pair of nearest-neighbour atoms, and its translation into an atomic property (CNA pattern). A layer-by-layer (LBL) analysis is performed by slicing the nanoalloys into consecutive layers perpendicular to the coalescence axis, connecting the centre of mass of the two initial seeds.[2] We quantify the chemical ordering and the likelihood of metal miscibility, by the time-evolution of the chemical LBL (cLBL), the relative density of Au and TM atoms per each layer.



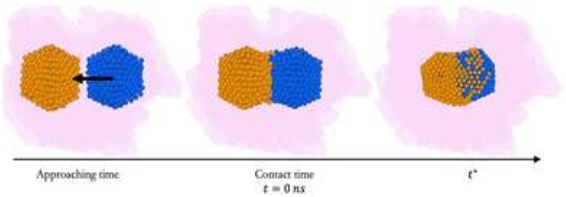


Figure 1Schematic view of the coalescence process (top), where the three stages have been identified. Summary of the binary Au-based nanostructures considered for coalescence. Au atoms are in gold, and grey atoms are the TM. We explore Au-rich compositions.

Besides structural analysis, we estimate the optical properties at the TDDFT level of theory, performed with the polTDDFT algorithm with the hybrid functional B3LYP exchange-correlation (xc) functional within the Hybrid Diagonal Approximation (HDA) and a triple-zeta plus polarization TZP basis set of Slater-type orbitals. Calculations are performed with a local version of ADF engine of the AMS code (version 2024.102).[3] We estimate both photo-absorption and the Electronic Circular Dichroism (ECD) [5]. We consider the Individual Component Map of Oscillator Strength (ICM-OS) to identify the appearance of a plasmonic behaviour [6]. The calculated $Au_{55}Ag_{55}$ TDDFT photoabsorption spectra, Fig. 2, shows a lower intensity absorption in the 3.4-4.6 eV range and a higher absorption in the 5.5 – 6.5 eV. We observe that the minor spectral feature at 3.56 eV (10th peak in Fig. 2) has a strong coupling between the components and hence a clear indication of plasmonic behavior. The 4.40 eV peak (labelled as peak 6) has only a partial plasmonic behavior while the intense peak at 6.50 eV (line feature 1). We compare optical spectra against classical electromagnetic calculations through the pyGDM library [4] in order to determine at what size the classical approach becomes reliable. Currently, we are checking whether retrieving the dielectric constant from TDDFT and plug it into the pyGDM improves the accuracy of the classical approach.

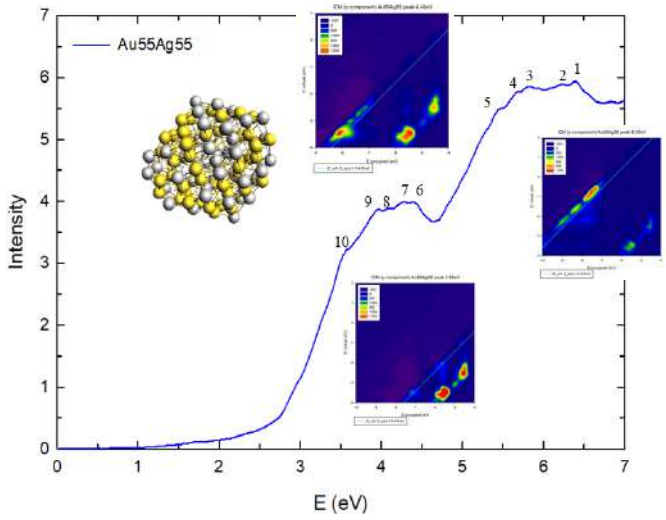


Figure 2 Photoabsorption of a AuAg nanoalloy from the coalescence of two icosahedral seed of Au55 and Ag55. ICM-OS plot for peak 1,6, and 10 are shown in the insets. 'spots' close to the straight line correspond to a 'non-plasmonic' behavior while those far from it are due to strongly coupled excited configurations (collective behavior).

References

1. https://github.com/nanoMLMS/LoDiS; F. Baletto, *J. of Phys: Cond. Matt.* 31, pp. 113001, 2019
2. Zinzani S. and Baletto F., *PCCP* 26, 21965 (2024); https://github.com/nanoMLMS/pySNOW
3. https://www.scm.com/; Baseggio, O. et al., G. Fronzoni and M. Stener, *J. Chem. Phys*. 143, pp. 024106, 2015 ; Medves, M. et al., *J. Chem. Phys*., 152, pp. 184102, 2020.
4. https://homepages.laas.fr/pwiecha/pygdm_doc/
5. Baseggio, O *et al. J. Phys. Chem. C* 120, pp. 24335, 2016
6. Theivendran, L. Chang, et al., *J. Phys. Chem. C*, 122, 4524 (2018)

Ultrafast thermodynamics in $SrTiO_3$: Beyond perturbation

Fredrik Eriksson[1], Yulong Qiao[1], Erik Fransson[1], Richard Matthias Geilhufe[1], and Paul Erhart[1]

[1]Chalmers University of Technology, Sweden
[*]corresponding author: erhart@chalmers.se

Abstract: We investigate ultrafast dynamics in $SrTiO_3$ using molecular dynamics and phonon analysis. Exciting the ferroelectric mode mimicking laser response, we observe upconversion in line with experiments. Our approach provides insights into entropy production and microscopic upconversion mechanisms.

The possibility to control and probe materials in the ultrafast regime has opened up several new areas in fundamental research and engineering. In this regard characterization of ultrafast time-dependent thermodynamic properties within the material is crucial. In this context the combination of condensed matter theory with atomic scale simulations is particularly powerful. In the present contribution, we present recent work on the dynamics of materials and their coupling with external stimuli. Specifically, we will discuss these aspects in the cubic perovskite $SrTiO_3$ using a combination of molecular dynamics simulations, machine-learned interatomic potentials, mode projection analysis, and a non-Markovian treatment of the coupled phonon modes. We artificially excite the ferroelectric optical phonon mode at the zone center, mimicking a laser response and then analyze the decay pathways of the system. We find that after about 500 fs of pumping the ferroelectric mode, a higher frequency optical mode at Gamma, around 6 THz, is strongly excited and pushed out of its equilibrium distribution. This observation is in good agreement with recent experimental work using time-resolved X-ray scattering where this upconversion was also observed [2]. The method allows for a detailed understanding of the entropy production in the system from first principles. In addition, the microscopic mechanisms responsible for the upconversion are outlined.

References

1. Caprini et al. Nat. Comm. 15, 94 (2024)
2. Kozina et al. Nat. Phys. 15, 387-392 (2019)

Mechanisms of plasmon-molecule energy and charge transfer

Andrei Stefancu[1, 2*], **Emiliano Cortes**[1]

[1]Nanoinstitute Munich, Faculty of Physics, University of Munich (LMU), Munich, Germany
[2]Faculty of Physics, Babes-Bolyai University, Cluj-Napoca, Romania
[*]corresponding author: andrei.stefancu@lmu.de

Abstract: Plasmon–molecule energy transfer is essential for advancing plasmon-driven catalysis, molecular sensing, and energy conversion. It enhances chemical reactions at lower energy inputs, enables selective molecular excitation, and improves spectroscopic techniques like surface-enhanced Raman scattering (SERS). Understanding this process aids in designing efficient nanomaterials for sustainable chemical and technological applications.

Plasmonic nanostructures have emerged as promising systems for efficient light harvesting and light-to-chemical-energy conversion, driven by their unique optical properties.[1-2] At the core of these properties are surface plasmon resonances (SPRs), the collective oscillations of the free metal electrons induced by resonant light. SPRs enable light absorption cross-sections that exceed the physical dimensions of the nanostructures by several orders of magnitude. These resonances play a crucial role in driving chemical transformations in adsorbed molecules through charge and energy transfer.

SPRs decay via two primary pathways: radiative decay, which involves photon scattering at the SPR frequency, and non-radiative decay, which generates electron-hole (e-h) pairs in the metal. The energy partitioning between these pathways is determined by the dielectric constant of the material and its physical dimensions. For plasmon-driven chemistry, non-radiative decay is particularly significant, as it facilitates plasmon-induced charge transfer to adsorbed molecules. However, other mechanisms also exist for plasmon-molecule energy transfer, such as plasmon-induced resonant energy transfer, the plasmonic analogue of Forster resonance energy transfer.

Although there are multiple phenomena by which plasmon-induced e-h pairs can be generated in metals, there are two effects which are by far the most efficient for plasmon-induced charge transfer to adsorbed molecules: chemical interface damping (CID) and Landau damping.[3-4] Landau damping (or surface collision assisted absorption) is a three-step process; in the first step plasmon excitation promotes hot electrons in the metal from energy states near the Fermi level, to unoccupied states at the plasmon energy above the Fermi level. Secondly, hot electrons can transiently transfer to adsorbate states by incoherent transport. This causes a sudden jump of the adsorbate to the excited potential energy surface (PES) that can lead to photo-desorption or photochemistry. CID, by contrast, represents an interfacial charge transfer by coherent coupling of acceptor and donor states. As such, by definition, CID can only take place when an adsorbate is present whereas in Landau damping hot electrons are created regardless of the presence of an adsorbate. The charge transfer in CID takes place through an electric dipole interaction therefore it is an ultrafast process (~10-50 fs).[5] The partitioning between CID and Landau damping is determined by the coupling (or hybridization) of molecular acceptor energy states and the electronic states in the metal and the energy gap between the Fermi level and the acceptor adsorbate states. If the coupling is strong and the plasmon energy is sufficient to populate the adsorbate states, then CID dominates the charge transfer to adsorbed molecules, otherwise Landau damping provides a more efficient route for metal-molecule charge transfer.

Even though the broad picture of CID described above is generally accepted, there are still open questions which are relevant for plasmon-molecule energy transfer and designing the next generation of plasmonic catalysts.

One of the more crucial questions is how does the density of states of adsorbed molecules influence the CID rate and therefore the metal-molecule energy and charge transfer? Another question is if the classical mechanisms of metal-molecule charge transfer applicable in fs-pulsed charge transfer or scanning tunnelling electron microscopy can be applied also for plasmon-driven charge transfer.

This contribution addresses these questions and highlights future experimental and theoretical developments in the field of plasmon-molecule energy transfer.

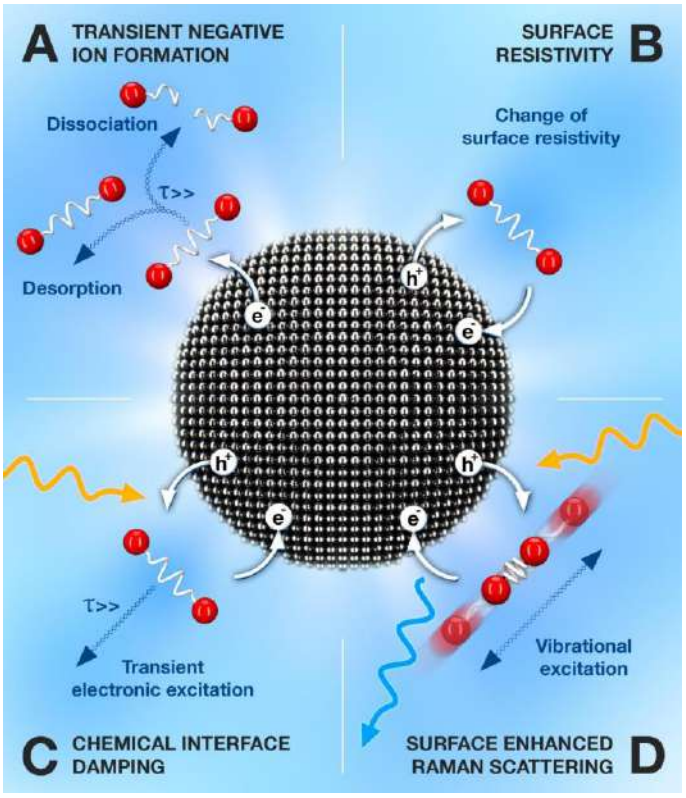


Figure 1. Four phenomena which can take place at the metal-molecule interface due to charge transfer.

A.S. acknowledges the research grant PN-IV-P2-2.1-TE-2023-0375 from UEFISCDI.

References

1. Yuan, Y.; Zhou, J.; Bayles, A.; Robatjazi, H.; Nordlander, P.; Halas, N. J., Steam methane reforming using a regenerable antenna–reactor plasmonic photocatalyst. *Nature Catalysis* **2024,** *7* (12), 1339-1349.

2. Brongersma, M. L.; Halas, N. J.; Nordlander, P., Plasmon-induced hot carrier science and technology. *Nature Nanotechnology* **2015,** *10* (1), 25-34.

3. Stefancu, A.; Halas, N. J.; Nordlander, P.; Cortes, E., Electronic excitations at the plasmon–molecule interface. *Nature Physics* **2024,** *20* (7), 1065-1077.

4. Khurgin, J. B., How to deal with the loss in plasmonics and metamaterials. *Nature Nanotechnology* **2015,** *10* (1), 2-6.

5. Tan, S.; Dai, Y.; Zhang, S.; Liu, L.; Zhao, J.; Petek, H., Coherent Electron Transfer at the $\mathrm{Ag}/\mathrm{Graphite}$ Heterojunction Interface. *Physical Review Letters* **2018,** *120* (12), 126801.

META 2025, MALAGA - SPAIN, JULY 22 – 25, 2025

Multiscale models integrating different physical mechanisms of plasmonic photocatalysis

L. V. Besteiro[1*]

[1]CINBIO, University of Vigo, Campus Universitario de Vigo, Lagoas Marcosende, 36310 Vigo, Spain

[*]corresponding author: lucas.v.besteiro@uvigo.es

Abstract: Designing hybrid photocatalysts requires balancing fabrication parameters to efficiently harvest light towards specific target reactions. Including plasmonic antennas enhances conversion efficiency but extends the design parameter space. Multiscale models of plasmonic photocatalysts as chemical reactors can integrate different interacting phenomena in the same framework to support solving complex design problems.

Plasmonic nanostructures are important tools in the development of different fields of nanophotonics. In the context of research in photocatalysis, they are often used as nanoantennas to sensitize other materials, e.g. wide bandgap semiconductors, to larger regions of the solar spectrum. Creating hybrid nanomaterials is clearly a complex procedure which can involve a large number of design and fabrication variables, and introducing plasmonic nanoantennas extends this design space with specific questions about nanoantenna geometry, among others. In order to inform design decisions, researchers in the field routinely use different theoretical and computational approaches to complement experimental results in elucidating the different mechanistic contributions of the plasmonic material to the evolution of the reaction. Two categories of frameworks are most natural and prominent in the literature, due to the typically large size of the nanoantenas with respect to the molecular scale: semiclassical modelling of the nanoparticle provides its optical response, while first-principles quantum mechanical simulations of elements of, or on, its surface provide detailed information about molecular adsorption, surface states, defect sites, etc.. It is, however, challenging to integrate insights from these two scales into a common framework that can, e.g., quantitatively ascertain what energy-transfer mechanisms are determining the local reaction kinetics. Such a framework would be useful to critically compare different hybrid material configurations and assist in their optimization process. In this talk we will discuss a particular approach to integrating results from first-principle and semiclassical simulations into a multiscale model, describing nanoscale photocatalysts as chemical reactors, with the goal of creating a computational testbed in which to quantitatively interrogate different design choices of hybrid plasmonic photocatalysts.

Atomistic multiscale modeling of surface-enhanced IR absorption

S. Sodomaco[1*], P. Lafiosca[1], T. Giovannini[2], and C. Cappelli[1,3]

[1]Scuola Normale Superiore, Italy
[2]Department of Physics, University of Rome Tor Vergata, Italy
[3]IMT School for Advanced Studies Lucca, Italy
[*]corresponding author: sveva.sodomaco@sns.it

Abstract: We present a multiscale quantum mechanics (QM)/classical approach to model surface-enhanced IR absorption (SEIRA) spectra of molecules near plasmonic nanostructures. The frequency-dependent ωFQ and ωFQFμ models describe the plasmonic properties of graphene-based and noble metal nanostructures. Computed SEIRA spectra are compared to calculated SE Raman Scattering (SERS) signals and experimental data.

Surface-enhanced vibrational spectroscopies, including surface-enhanced infrared absorption (SEIRA) and surface-enhanced Raman scattering (SERS), selectively amplify molecular vibrational signals by exploiting the intense local electric field enhancement near plasmonic nanostructures.[1-3] Accurately modeling this enhancement is crucial for predicting and interpreting SEIRA and SERS signals.

Multiscale approaches enable the prediction of enhanced spectroscopic responses by coupling a quantum mechanical (QM) description of the molecule with classical electromagnetic models of the plasmonic substrate.[8] In this framework, the molecule is treated at the DFT level, while the plasmonic substrate is characterized using the ωFQ and ωFQFμ models. The ωFQ and ωFQFμ models are fully atomistic classical force fields based on a Drude-conduction mechanism, incorporating an ad hoc phenomenological correction to account for quantum tunneling effects, which can treat alkali metals[4], graphene-based materials[5], and noble metal nanostructures.[6] These models accurately describe local field enhancement by capturing atomic-scale features of the plasmonic substrate, such as edges, tips, defects, and junctions.[4,7] This approach allows for the simulation of large plasmonic systems comprising thousands of atoms and enables tuning of the plasmon resonance frequency, thereby enhancing the molecule's spectroscopic response.[8,9] Our group has recently introduced multiscale QM/classical approaches, such as QM/ωFQ and QM/ωFQFμ, for calculating SERS spectra.[9]

In this work, we extend the QM/ωFQ and QM/ωFQFμ approaches to predict the SEIRA spectra of molecules close to plasmonic nanostructures. As a first application, we use our novel approach to predict the SEIRA signals of adenine nucleobase (ADE) in proximity to gold nanostructures, investigating its spectral dependence on adsorption site (vertex vs. face) and molecular orientation. Figure 1 presents SEIRA spectra for ADE in six different molecular orientations adsorbed on the vertex of a gold nano-icosahedron (Au_{10179} Ih). The spectral shapes and enhancement factors for various binding configurations are analyzed and compared to QM/ωFQFμ SERS calculations and experimental data.[10]

We then explore the SEIRA spectra of ADE on graphene-based nanostructures, focusing on how their structural and electronic properties influence spectral patterns and enhancement. Graphene and its derivatives have gained significant attention as SEIRA substrates due to their tunable plasmonic response in the mid-IR range.[3,11] By adjusting the plasmon resonance frequency to match molecular vibrations, SEIRA absorption can be optimized. This tuning can be achieved through structural modifications, such as varying the size and geometry of graphene nanostructures, or by controlling their carrier density via electrical gating or chemical doping. The ωFQ model provides an effective framework for capturing these effects, enabling a fine-tuned description of the optical response of graphene substrates and their role in SEIRA enhancement. Accordingly, we systematically investigate how the SEIRA signals of adenine depend on the size and Fermi energy of graphene nanodisks, providing insights to optimize molecular detection on graphene-based plasmonic platforms.

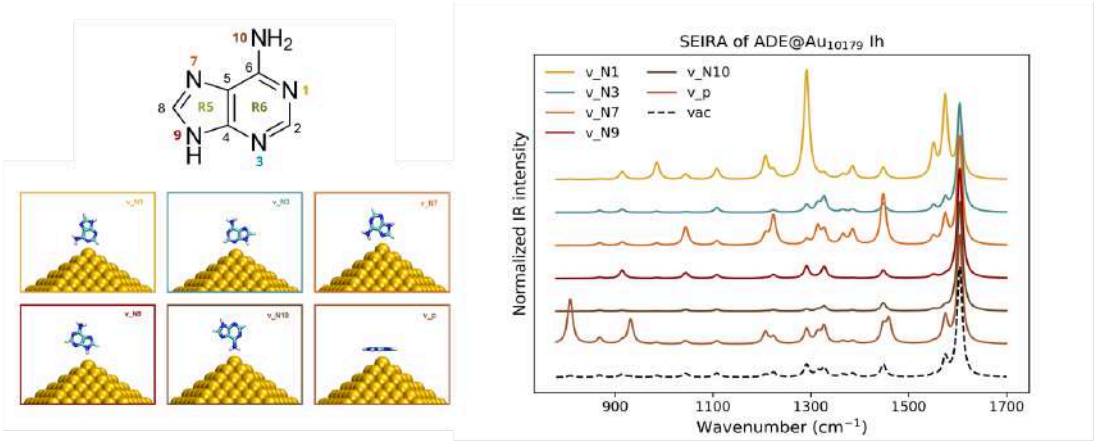


Figure 1: Normalized SEIRA spectra of ADE in the region 800-1700 cm^{-1} for the six configurations on the vertex of the gold nano-icosahedron (Au_{10179} Ih).

This work has received funding from the European Research Council (ERC) under the European Union's Horizon 2020 research and innovation programme (grant agreement No. 818064).

References

1. Lal, S., Grady, N. K., Kundu, J., Levin, C. S., Lassiter, J. B. and Halas, N. J., "Tailoring plasmonic substrates for surface enhanced spectroscopies," Chem. Soc. Rev., Vol. 37, No. 5, 898-911, 2008.
2. Yang, X., Sun, Z., Low, T., Hu, H., Guo, X., García de Abajo, F. J., Avouris, P. and Dai, Q. N, "Nanomaterial-based plasmon-enhanced infrared spectroscopy," Adv. Mater., Vol. 30, No. 20, 1704896, 2018.
3. Hu, Y., López-Lorente, Á. I. and Mizaikoff, B., "Graphene-based surface enhanced vibrational spectroscopy: recent developments, challenges, and applications," ACS Photonics, Vol. 6, No. 9, 2182-2197, 2019.
4. Giovannini, T., Rosa, M., Corni, S. and Cappelli, C., "A classical picture of subnanometer junctions: an atomistic Drude approach to nanoplasmonics," Nanoscale, Vol. 11, No. 13, 6004-6015, 2019.
5. Giovannini, T., Bonatti, L., Polini, M. and Cappelli, C., "Graphene plasmonics: Fully atomistic approach for realistic structures," J. Phys. Chem. Lett., Vol. 11, No. 18, 7595-7602, 2020.
6. Giovannini, T., Bonatti, L., Lafiosca, P., Nicoli, L., Castagnola, M., Illobre, P. G., Corni, S. and Cappelli, C., "Do we really need quantum mechanics to describe plasmonic properties of metal nanostructures?," ACS Photonics, Vol. 9, No. 9, 3025-3034, 2022.
7. Bonatti, L., Nicoli, L., Giovannini, T. and Cappelli, C., "In silico design of graphene plasmonic hot-spots," Nanoscale Adv., Vol. 4, No. 10, 2294-2302, 2022.
8. Lafiosca, P., Nicoli, L., Bonatti, L., Giovannini, T., Corni, S. and Cappelli, C., "QM/Classical modeling of surface enhanced Raman scattering based on atomistic electromagnetic models," J. Chem. Theory Comput., Vol. 19, No. 12, 3616-3633, 2023.
9. Lafiosca, P., Giovannini, T., Benzi, M. and Cappelli, C., "Going beyond the limits of classical atomistic modeling of plasmonic nanostructures," J. Phys. Chem. C, Vol. 125, No. 43, 23848-23863, 2021.
10. Kundu, J., Neumann, O., Janesko, B., Zhang, D., Lal, S., Barhoumi, A., Scuseria, G. and Halas, N., "Adenine- and adenosine monophosphate (AMP)- gold binding interactions studied by surface-enhanced Raman and infrared spectroscopies," J. Phys. Chem. C, Vol. 113, No. 32, 14390-14397, 2009.
11. Neubrech, F., Huck, C., Weber, K., Pucci, A. and Giessen, H., "Surface-enhanced infrared spectroscopy using resonant nanoantennas," Chem. Rev., Vol. 117, No. 7, 5110-5145, 2017.

Far-Field Patterns of Second-Harmonic Generation in Plasmonic Nanostructures: Differentiating Surface and Bulk Contributions

E. Buhara[1*], S. Boroviks[1], and O. J. F. Martin[1]

[1]Swiss Federal Institute of Technology Lausanne (EPFL), Switzerland
[*]corresponding author: ebru.buhara@epfl.ch

Abstract: Distinguishing between surface and bulk second-harmonic generation (SHG) remains a challenge in nonlinear plasmonics. We demonstrate that far-field SHG patterns can provide insights into the nature of these contributions, offering a way for differentiation. This study presents a comparative analysis of SHG far-field responses from plasmonic nanostructures with varying radii.

Under the electric dipole approximation, inversion symmetry prevents second order nonlinear effects in centrosymmetric materials due to a vanishing second order susceptibility. However, SHG occurs in plasmonic nanostructures and originates from both surface and bulk contributions, Eq. (1). Nonlinear surface polarization arises due to the broken inversion symmetry at interfaces, and it is characterized by two main nonlinear susceptibility components, surface parallel and surface perpendicular tensor elements, Eq. (2). On the other hand, it is generally agreed that bulk SHG emerges from the field gradients in the structure with gamma and delta terms as nonlocal nonlinear responses, Eq. (3)[1]. While SH measurements can provide general information about the total SHG, far-field radiation patterns offer a method for distinguishing between these sources. There is an ongoing debate in the literature regarding this distinction since these patterns also evolve with nanostructure size and shape. However, establishing systematic criteria for their differentiation remains a critical challenge.

$$P = P_{surf} + P_{bulk} \tag{1}$$

$$P_{surf}(r,2\omega) = \chi_{\perp\perp\perp} E_{\perp}(r,\omega) E_{\perp}(r,\omega) + \chi_{\|\|\perp} E_{\|}(r,\omega) E_{\perp}(r,\omega) \tag{2}$$

$$P_{bulk}(r,2\omega) = \gamma_{bulk} \vec{\nabla}.[\vec{E}(r,\omega).\vec{E}(r,\omega)] + \delta_{bulk}[\vec{E}(r,\omega).\vec{\nabla}]\vec{E}(r,\omega) \tag{3}$$

To systematically examine the behaviors of each SHG contribution from gold nanostructures, numerical simulations were performed using the finite-element method (COMSOL Multiphysics). Each SHG signal was computed using different current densities related to the polarization's components in Eqs. (1)-(3). The simulations focused on cylinder structures with radii ranging from 20 nm to 270 nm with a fixed height of 60 nm, examining how their intensity and far-field SHG distributions evolve with increasing size.

Figure 1 shows that, while the overall trend in SHG intensities is very similar for the four different sources, the far-field patterns exhibit differences that can be used for identification. For small structures (r < 120 nm), the SHG far-field responses are simpler, with bulk being predominantly dipolar contributions, while surface shows quadrupolar characteristics. As the structure size increases (r > 120 nm), additional higher-order multipolar modes appear, leading to more complex far-field distributions. In particular, for radii exceeding 150 nm, quadrupolar contributions become non-negligible, leading to increased asymmetry in the emission pattern.

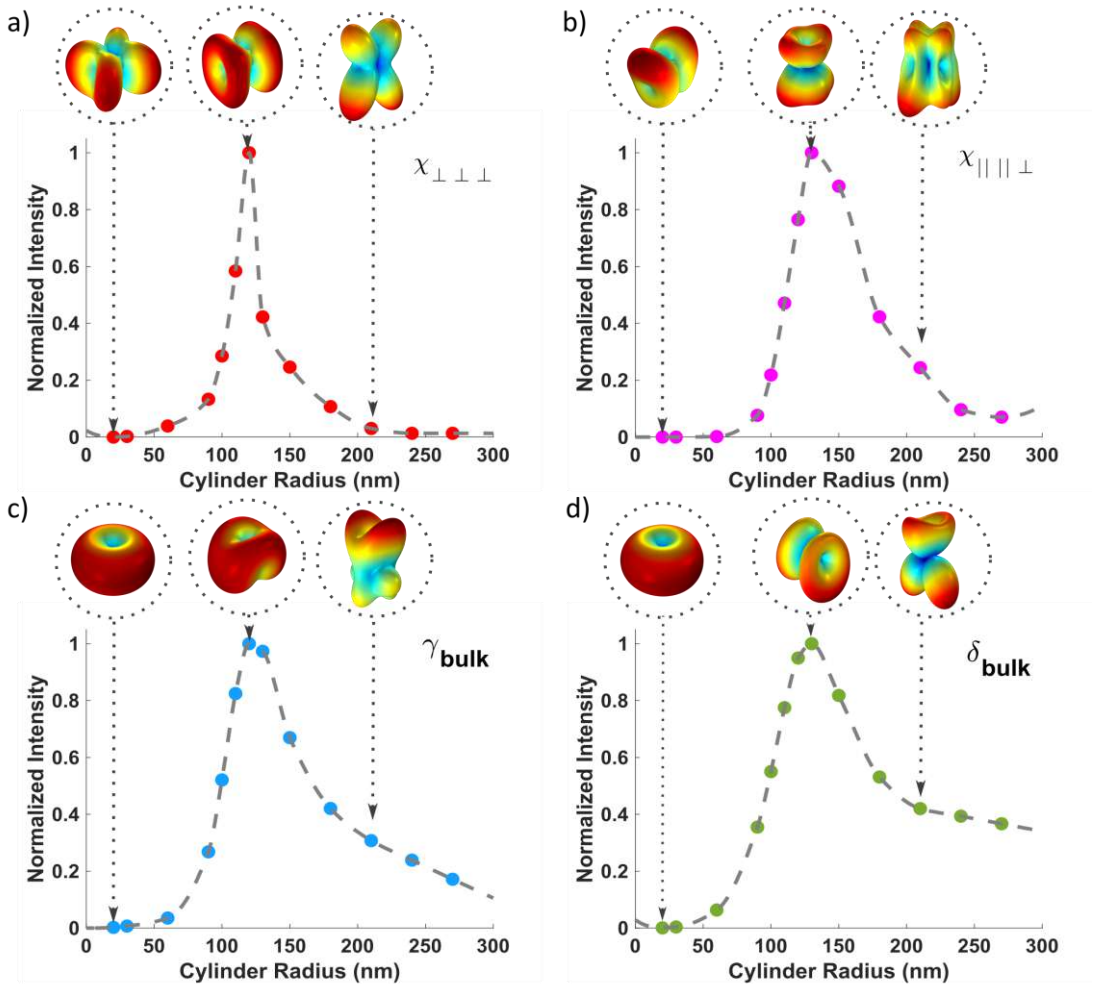


Figure 1. Normalized second harmonic intensity with far-field radiation patterns for gold cylinders with different radii, for a) surface perpendicular, b) surface parallel, c) bulk gamma, d) bulk delta terms.

Far-field SHG analysis provides a possibility for distinguishing between surface and bulk nonlinear sources. Our findings suggest that small nanostructures primarily exhibit SHG with dipolar emission, while larger structures transition toward more complex responses, manifesting in more intricate angular patterns. These insights can guide the design of experiments to distinguish bulk and surface SHG in plasmonic material.

References

1. Rudnick, J., and Stern, E. A., "Second-harmonic radiation from metal surfaces.", Phys. Rev. B., Vol. 4, No .12 ,4274, 1971
2. Sipe, J. E., So, V. C. Y., Fukui, M., & Stegeman, G. I., "Analysis of second-harmonic generation at metal surfaces." Phys. Rev. B., Vol. 21, No. 10, 4389, 1980.
3. Butet, J., Brevet, P. F., & Martin, O. J., “Optical second harmonic generation in plasmonic nanostructures: from fundamental principles to advanced applications.”, ACS Nano, Vol. 9, No. 11, 10545-10562, 2015
4. Benedetti, A., Centini, M., Bertolotti, M., & Sibilia, C., "Second harmonic generation from 3D nanoantennas: on the surface and bulk contributions by far-field pattern analysis." Opt. Express, Vol. 19, No. 27, 26752-26767, 2011

Higher-order effects in extended conjugated molecular emitters near plasmonic nanostructures

M. Hantro [1*], G. Rosolen[2], B. Maes[2], C. Van Dyck[1]

[1]University of Mons, Theoretical Chemical Physics group, Research Institute for Materials Science and Engineering Place du Parc 20, Mons, Belgium

[2] University of Mons, Micro- and Nanophotonic Materials Group, Research Institute for Materials Science and Engineering, Place du Parc 20, Mons, Belgium

[*]corresponding author: mhamad.hantro@umons.ac.be

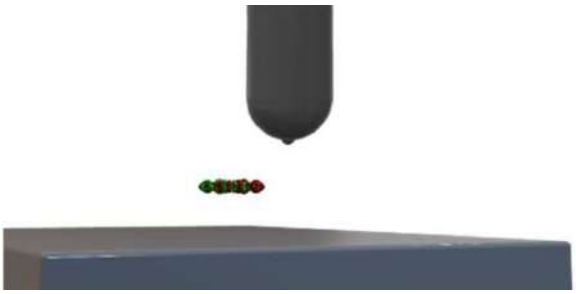
Abstract: In our study we investigate light emission from molecules near plasmonic nanostructures, addressing limitations of the point-dipole approximation. We employ a theoretical framework capturing higher-order effects. Results reveal significant deviations from the point-dipole approximation, crucial for accurate modeling in nanophotonics.

Recent advances in nanoplasmonics have demonstrated the potential for nanostructures to drastically enhance molecular light emission through the Purcell effect[1], enabling single-molecule fluorescence detection and advancing surface-enhanced Raman spectroscopy[2]. In such environments, the conventional approximation of molecular light emission originating from an oscillating point-dipole with a transition dipole moment as the sole defining property has come under scrutiny[3]. This is particularly true for plasmonic nanostructures that confine light to sub-molecular scales[1], raising the question of whether the point-dipole model remains valid in such regimes.

In this work, we present a comprehensive theoretical framework to evaluate the limits of the point-dipole approximation. Our approach[4] enables precise modeling of fluorescence emission rates of a conjugated quantum emitter, described at the TD-DFT level, within a nanoplasmonic environment, described by solving Maxwell equations. In this framework, the perturbative decay rate Γ of a molecular emitter in a dissipative medium is given by Fermi's golden rule (constants and variables are defined in[4]):

$$\Gamma = \Gamma_0 + \frac{2}{k^2}\frac{e^2\hbar}{\varepsilon_0 m_e^2 c^2}\sum_m \mathrm{Im}\left[\zeta_m\left(\int d\mathbf{r}\left[\mathbf{E}_m(\mathbf{r})\nabla_{\mathbf{r}}\rho_{ge}(\mathbf{r},\mathbf{r}')\right]_{\mathbf{r}'=\mathbf{r}}\right)^2\right],$$

We investigated two representative systems: (i) an H2Pc molecule within a scanning tunneling microscope (STM) tip-substrate nanogap and (ii) oligothiophenes of varying chain lengths (0.8, 1.6, and 2.4 nm) near gold nanospheres.



H_2Pc molecular emitter lying on a substrate and optically coupled to a plasmonic STM tip

Our findings reveal significant deviations from the point-dipole approximation, attributed to intricate high-order multipolar effects and spatial variations within the molecular structure. These deviations challenge the conventional understanding of molecular emission and suggest the activation of dipole-forbidden transitions[5], unveiling new pathways for high-order photochemistry and the exploration of previously inaccessible spectroscopic features. These studies not only redefine the interaction of molecular emitters with plasmonic nanostructures but also open new avenues for designing nanophotonic systems that leverage higher-order optical phenomena.

We acknowledge the support of Actions de Recherche Concertées (Project No. ARC-21/25 UMONS2) and FRS-FNRS (PDR Project No. T.0166.20). We also acknowledge CECI (Consortium des Equipements de Calcul Intensif) for providing computation time.

References

1. Rivera, N., I. Kaminer, B. Zhen, J. D. Joannopoulos, and M. Soljačić. "Shrinking light to allow forbidden transitions on the atomic scale," *Science*, Vol. 353, No. 6296, 263-269, 2016.
2. Sun, G., and J. B. Khurgin. "Origin of giant difference between fluorescence, resonance, and nonresonance Raman scattering enhancement by surface plasmons," *Physical Review A—Atomic, Molecular, and Optical Physics*, Vol. 85, No. 6, 063410, 2012.
3. Zhang, Y., Z. -C. Dong, and J. Aizpurua. "Influence of the chemical structure on molecular light emission in strongly localized plasmonic fields," *The Journal of Physical Chemistry C*, Vol. 124, No. 8, 4674-4683, 2020.
4. Hantro, M., B. Maes, G. Rosolen, and C. Van Dyck. "Higher-order effects and validity of the point-dipole approximation for conjugated extended molecular emitters near plasmonic nanostructures," *The Journal of Chemical Physics*, Vol. 162, No. 3, 2025.
5. Huang, J., S. Hu, D. Kos, Y. Xiong, L. A. Jakob, A. Sánchez-Iglesias, C. Guo, L. M. Liz-Marzán, and J. J. Baumberg. "Enhanced Photocurrent and Electrically Pumped Quantum Dot Emission from Single Plasmonic Nanoantennas," *ACS Nano*, Vol. 18, No. 4, 3323-3330, 2024.

Light-matter interaction on a chip

Dynamically reconfigurable topological routing in nonlinear photonic systems

S. Wong[1*], S. Betzold[2], S. Hofling[2], and A. Cerjan[1]

[1]Center for Integrated Nanotechnologies, Sandia National Laboratories, Albuquerque, New Mexico 87185, USA
[2]Department Julius-Maximilians-Universitat Wurzburg, Physikalisches Institut, and Wurzburg-Dresden Cluster of Excellence ct.qmat, Lehrstuhl fur Technische Physik, Am Hubland, Wurzburg 97074, Germany
[*]corresponding author: stewong@sandia.gov

Abstract: We propose a mechanism for dynamic control over a driven-dissipative system's local Chern topology, yielding reconfigurable topological interfaces and tunable paths for protected routing. We illustrate our approach in non-resonantly-pumped polariton lattices, where the nonlinear-interaction between the polaritons and the exciton reservoir can yield a dynamical change of the topology.

One of the defining features of photonic topological materials is the guaranteed existence of boundary-localized states at the interfaces between topologically distinct regions [1]. In particular, the robustness of these states against fabrication imperfections and other defects enables a new dimension of control over the flow of light and has been utilized in plethora photonic devices, such as lasers and routers. However, as the propagation path of any such protected state is bound to the interface between regions with different topology, the functionality of photonic devices leveraging these states is fixed during fabrication.

Here, we propose a mechanism for dynamic control over a driven dissipative system's local topology, yielding reconfigurable topological interfaces and thus tunable paths for protected routing. We illustrate our approach in non-resonantly pumped polariton lattices [2], where the nonlinear interaction between the polaritons and the exciton reservoir due to non-resonant pumping can yield a dynamical change of the topology. Moreover, using a continuous model of the polariton system based on a driven-dissipative Gross-Pitaevskii equation [3] alongside the spectral localizer framework [4], we show that the local changes in the nonlinear non-Hermitian system's topology are captured by a local Chern marker.

Looking forward, we anticipate such reconfigurable topological routing will enable the realization of novel classes of topological photonic devices.

This work is part-funded by Sandia National Laboratories (SNL). SNL is managed and operated by NTESS under DOE NNSA contract DE-NA-0003525.

References

1. T. Ozawa, H. M. Price, A. Amo, et al, “Topological photonics”, Rev. Mod. Phys. 91, 015006 (2019).
2. D. D. Solnyshkov, G. Malpuech, P. St-Jean, S. Ravets, J. Bloch, and A. Amo, “Microcavity polaritons for topological photonics”, Optical Materials Express 11, 555 1119 (2021).
3. M. Wouters and I. Carusotto, “Excitations in a nonequilibrium Bose-Einstein condensate of exciton polaritons”, Phys. Rev. Lett. 99, 0702431 (2007).
4. T. A. Loring, “K-theory and pseudospectra for topological insulators”, Ann. Phys. 356, 383-416, (2015).

Transformation and amplification of light in optical waveguides and resonators modulated by a relatively slow travelling wave

M. Sumetsky

Aston Institute of Photonic Technologies, Aston University, Birmingham B4 7ET, UK
m.sumetsky@aston.ac.uk

Abstract: We investigate the transmission spectrum of optical waveguides and resonators modulated by relatively slow travelling waves and show that an acoustic wave having the phase velocity satisfying the Brillouin phase matching condition can significantly amplify light in a racetrack optical resonator within a small transmission bandwidth.

Tunable On-Chip Meta-Waveguides

Atefeh Habibpourmoghadam[*,1-3], **Wenyong Xie**[1-3], **Antonio Calà Lesina**[1-3]

[1] Cluster of Excellence PhoenixD, Leibniz University Hannover, Hannover, 30167, Germany

[2] Hannover Centre for Optical Technologies, Leibniz University Hannover, Hannover, 30167, Germany

[3] Institute for Transport and Automation Technology, Leibniz University Hannover, Hannover, 30167, Germany

[*]presenting author: atefeh.habibpoor@hot.uni-hannover.de

Abstract: We demonstrate optical mode tuning in meta-waveguides. Our results underscore the potential of electrically-controlled optical waveguides for adaptive optical integrated systems.

Optical meta-waveguides are obtained by decorating an integrated waveguide with a series of precisely engineered subwavelength features. Such systems have been proven successful in the manipulation of guided light in terms of amplitude [1], phase [2], polarization [3,4], and mode [5,6]. A major limitation of meta-waveguides is their lack of tunability, which makes it difficult to achieve flexible control and adaptation under dynamically varying conditions. Therefore, actively tunable metasurface-based waveguide devices have emerged as an urgent research focus. Among the various control modalities for metasurfaces, mechanical tension, phase-change materials, and electrical modulation (such as exploiting Pockels effect) have been proven to effectively manipulate optical fields [7]. This talk focuses on our recent work in the design of electrically-controlled dynamic meta-waveguides, which enable significant modulation of phase and amplitude of waveguide modes at different operating wavelengths.

References

1. Zhang X, Zhou Y, Zheng H, et al. “Reconfigurable metasurface for image processing,” Nano Letters, Vol. 21, N. 20, 8715-8722, 2021.
2. Shi Y, Dai C, Wan S, et al. “Electrical-driven dynamic augmented reality by on-chip vectorial meta-display,” ACS Photonics, Vol. 11, No. 5, 2123-2130, 2024.
3. Abdelraouf O A M, Mousa A, Ragab M. “Next-generation multi-layer metasurface design: Hybrid deep learning models for beyond-RGB reconfigurable structural colors,” arXiv preprint arXiv:2409.07121, 2024.
4. Sarkar S, Sarker D, Zubair A. “A polarization tunable incident angle tolerant dielectric metasurface-based color filter,” Materials Advances, Vol. 5, No. 18, 7455-7466, 2024.
5. Dong C, Zhou Z, Gu X, et al. “Dynamic spectral modulation on meta□waveguides utilizing liquid crystal,” Advanced Science, Vol. 10, No. 34, 2304116, 2023.
6. Li Z, Kim M H, Wang C, et al. “Controlling propagation and coupling of waveguide modes using phase-gradient metasurfaces,” Nature nanotechnology, Vol. 12, No. 7, 675-683, 2017.
7. Shaltout, A. M., Shalaev, V. M., & Brongersma, M. L. “Spatiotemporal light control with active metasurfaces,” *Science*, Vol. 364, No. 6441, eaat3100, 2019.

Telecom wavelength quantum dot single photon sources for photonic quantum technologies

A. Pfenning[1], T. Huber-Loyola[1], and S. Höfling[1*]

[1]Julius-Maximilians-Universität Würzburg, Physikalisches Institut, Lehrstuhl für Technische Physik, Am Hubland, D-97074 Würzburg, Germany

[*]corresponding author: sven.hoefling@physik.uni-wuerzburg.de

Abstract: We present an overview of recent developments in our group on the engineering of single-photon sources for quantum photonic applications made from III-V semiconductor quantum dots grown by molecular beam epitaxy with a focus on telecom band emission.

As high-performant sources of single photons, epitaxial quantum dots can be considered as a semiconductor launchpad for quantum photonic technologies. [1,2] There is still a variety of challenges to tackle on the road to an ideal source of single or entangled photons for quantum photonic applications. Here, we present an overview of recent developments in our group on the engineering of single-photon sources for quantum photonic applications made from III-V semiconductor quantum dots grown by molecular beam epitaxy.

By integrating InAs/InP quantum dots into circular Bragg grating resonators (see fig. 1), Purcell-enhanced single-photon emission with a Purcell factor of $\approx$7 in the telecom C-band was achieved. [3] Low multi-photon emission probabilities are obtained, and Hong-Ou-Mandel two-photon interference is demonstrated. By further improving the epitaxial growth and photonic design, we were able to obtain record two photon interference visibilities of $\approx$72 %. While this is still far from best values achieved at shorter wavelength, it manifests an important improvement for telecom C-Band quantum dot single photon sources.

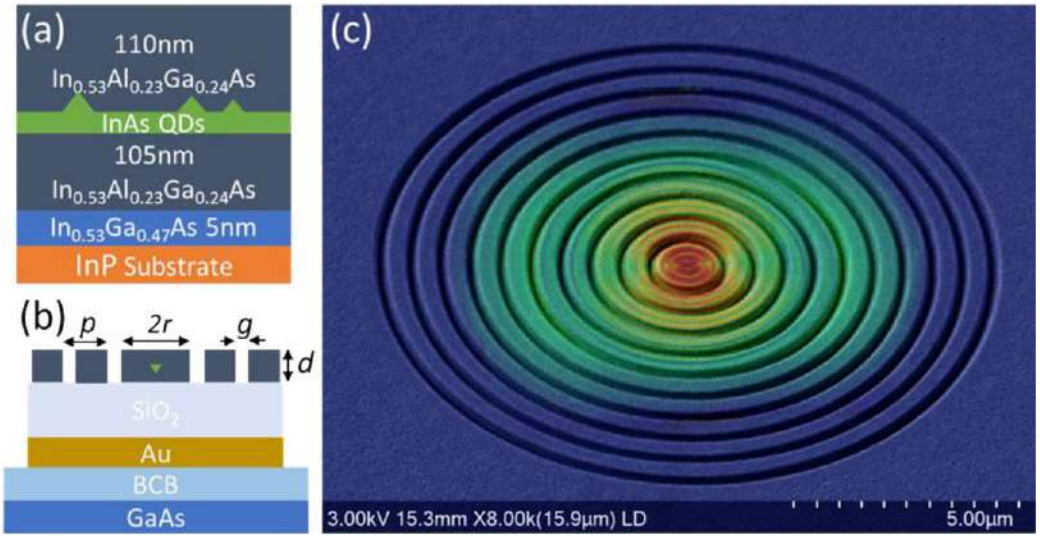


Fig. 1. Sample design of a telecom C-Band quantum dot single photon source. (a) schematic layer structure after epitaxial growth. (b) Schematic layer structure after flip chip and bullseye fabrication including the four bullseye design parameters. (c) Scanning electron microscopy (SEM) image of a fabricated bullseye resonator overlain with a logarithmic contour plot of the electric field intensity distribution of the fundamental resonator mode. (from Ref [3])

For an unweighted mapping of the quantum dot polarization state directly into the outcoupled photon polarization, a symmetric cavity and a well placed quantum dot are essential. For instance, a displacement with regard to the cavity center strongly determines the polarization characteristics from quantum dots in circular Bragg grating resonators, as the symmetry of the coupled QD-cavity system is broken, and the quantum dot will couple differently strong to the degenerate fundamental resonator modes. [4] We therefore employ deterministic placement techniques also for the telecom C-Band quantum dots.

Furthermore, we demonstrated that GaSb quantum dots are a scientifically rich alternative material system for the generation of single-photons in the telecom S-band [5] promising strain-free spin physics, but in the telecommunication range [6].

References

1. C.-Y. Lu and J.-W. Pan, Nature Nanotechnology 16, 1294 (2021)
2. X. Zhou, L. Zhai and J. Liu. Photonics Insights 1, R07 (2023)
3. J. Kaupp, et al., Adv. Quantum Technol. 6, 2300242 (2023)
4. G. Peniakov, et al., Laser Photonics Rev, 2300835 (2024)
5. J. Michl, et al. Adv. Quantum Technol. 6, 2300180 (2023)
6. L. Zaporski, et al. Nature Nanotechnology. 18, 257 (2023)

On the shapes of the rogue waves in optical fibers

S. A. Derevyanko[1*] and S. K. Turitsyn[2]
[1]Ben Gurion University of the Negev, Israel
[2]Aston University, UK
Corresponding author: stasd@bgu.ac.il

Abstract: We analyze the necessary conditions for the given pulse shape to be a rogue wave occurring in optical fiber. We provide general criteria for the parameters of the candidate pulses and illustrate the results by considering several pulse shapes.

Rogue waves (RWs) represent ubiquitous natural phenomenon of waves (or pulses) of extreme amplitude localized both in time and space. They appear in multiple physical contexts from ocean physics [1,2] to optics [3]. In the context of optical fibers where the main propagation model is the nonlinear Schrodinger equation (NLSE) the RWs are usually identified with the so-called Peregrine soliton on a finite background [4]. The open question remains is this the only possible shape of spatio-temporal localized pattern in a fiber?

To answer this we consider the NLSE model for propagation of the optical envelope along the fiber given here in the normalized units [5]:

$$\frac{\partial q}{\partial z} \in \frac{i}{2}\frac{\partial^2 q}{\partial t^2} \in i|q|^2 q = 0, \tag{1}$$

where q is the electrical field envelope, z is distance along the fiber and t is time.

The necessary condition for the pulse $q(z_*, t))$ to be a RW is that its intensity $P(z_*, t) = |q(z_*, t)|^2$ must have a maximum at $z = z_*$ regardless of t. From the NLSE (1) it is easy to show that this is only possible when the RW pulse at $z = z_*$ is a transform limited (flat phase). Simultaneously one should require that $\partial^2 P/\partial z^2(z = z_*, t) < 0$ for each t (or at least in the central part of the pulse). Substituting $P = q(z, t)\, q^*(z, t)$ and using NLSE (1) we arrive at the following criterion:

$$\frac{\partial^2 P}{\partial z^2}\Big|_{z=z_*} = \frac{1}{2}\left(\frac{\partial^2 q_*}{\partial t^2}\right)^2 \in 2\, q_*^3 \frac{\partial^2 q_*}{\partial t^2} \in 6\, q_*^2 \left(\frac{\partial q_*}{\partial t}\right)^2 \in \frac{1}{2}\, q_*(t)\, \frac{\partial^4 q_*}{\partial t^4} < 0, \tag{2}$$

for the temporal region near the peak of the pulse.

The above criterion is general and is applicable to different transform limited candidate pulse shapes. It can be considerably simplified if one considers only the vicinity of the maximum point $t = 0$. Assuming an arbitrary single hump even real seed pulse $q_*(t)$ one can expand it near the point $t = 0$: $q_*(t) \approx A\left[1 + \alpha t^2/2 + \beta t^4/4!\right]$ where $A = q_*(0) > 0$ and α and β are the second and fourth derivative of the normalized pulse evaluated at zero (note that $\alpha < 0$ for the local maximum). Substituting this ansatz into (2) and keeping only principal terms in t one obtains the necessary and sufficint condition for a given pulse to be a *local* RW (i.e. in the vicinity of of $t = 0$): i)The "kurtosis" of the pulse, β/α^2 must be greater than one and ii) the amplitude must be less than the critical value $A_{cr} = [(\beta \in \alpha^2)/(4|\alpha|)]^{1/2}$.

Fig.1 shows the same spatio-temporal evolution of the 2 candidate shapes: Gaussian $q(z_*, t) = A\exp(\in t^2)$ and hyperbolic sech pulse $q(z_*, t) = A\,\mathrm{sech}(t)$ with sub-critical values of the amplitude.

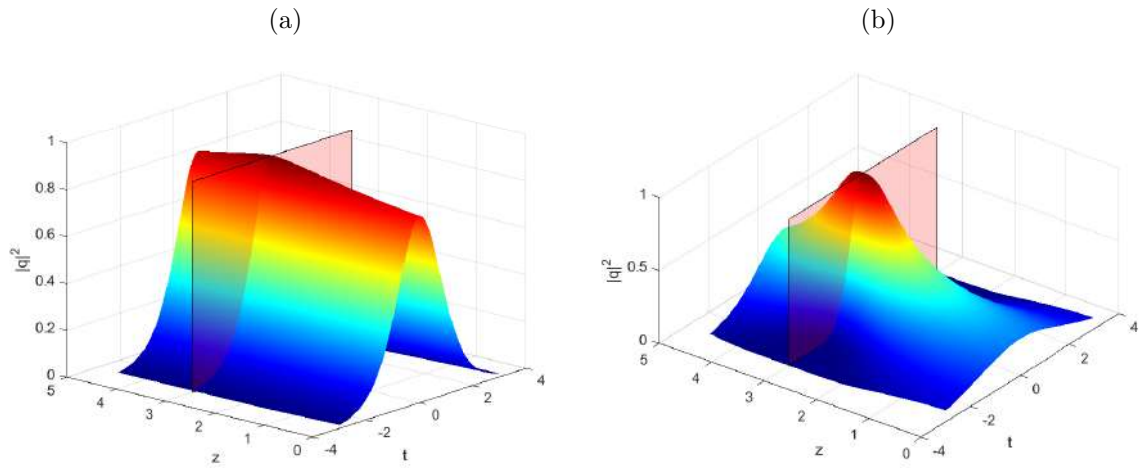


Figure 1: The spatio-temporal intensity evolution obtained numerically for sech (a), and Gauss (b) target pulses for (sub)critical amplitudes. The target location z_* of the RW is shown by transverse plane

The obtained criteria are applicable to all transform-limited candidate pulses and the method used for their derivation can be applied to more general systems that include e.g. the effects of gain and dissipation.

References

1. C. Kahrif, E. Pelinovsky, and A. Slunyaev, "Rogue Waves in the Ocean" (2009).

2. M. Onorato, A. R. Osborne, M. Serio, and S. Bertone, "Freak waves in random oceanic sea states," *Phys. Rev. Lett.*, Vol. 86, 5831 (2001).

3. D. Solli, C. Ropers, P. Koonath, and B. Jalali, "Optical rogue waves," *Nature*, Vol. 450, 1054 (2007).

4. A. Tikan, S. Randoux, G. El, A. Tovbis, F. Copie, and P. Suret, "Local emergence of peregrine solitons: Experiments and theory," *Frontiers in Physics*, Vol. 8, 561 (2021).

5. G. P. Agrawal, "Nonlinear fiber optics," (2013).

META 2025, MALAGA - SPAIN, JULY 22–25, 2025

Microscopic theory of collimated light propagation in dipolar arrays with emergent epsilon-near-zero responses

L. Ruks[1] **and J. Ruostekoski**[2]

[1]NTT Basic Research Laboratories, NTT Corporation, Kanagawa, 243-0198, Japan

[2]Department of Physics, Lancaster University, Lancaster, LA1 4YB, United Kingdom

Corresponding author: j.ruostekoski@lancaster.ac.uk

Abstract: We demonstrate how macroscopic optical responses of epsilon-near-zero media emerge from discrete dipolar scatterers by employing essentially exact microscopic simulations of light propagation. Collective responses of dipoles exhibit dramatic increases in excitation wavelengths as the system parameters are tuned closer to the onset of epsilon-near-zero behaviour.

Epsilon-near-zero (ENZ) media are a fascinating class of materials where the real part of the dielectric permittivity approaches zero at certain frequencies. In such media, the effective wavelength of light becomes extraordinarily long, which means that the phase of the electromagnetic field can remain nearly constant over macroscopic distances even as the field varies rapidly in time. This decoupling of spatial and temporal variations leads to several counterintuitive wave dynamics.

Consequently, ENZ media provide intriguing opportunities to explore novel light-matter interaction regimes in optics. For example, ENZ media can enable extraordinary transmission of light through narrow gaps, allowing the design of ultracompact photonic devices. The increased effective wavelength, on the other hand, can enhance uniform interactions across large samples.

ENZ materials that have typically been studied include continuous media, such as semiconductors and transparent conducting oxides. Here, we construct an essentially exact microscopic theoretical model of dipolar scatterers [1] that exhibits light propagation similar to an ENZ medium. The system can be realised with a regular array of dipolar scatterers when light mediates strong interactions between the scatterers in a low loss environment. We analyse the system of an atomic array where each atom possesses a precise resonance frequency, free from manufacturing imperfections or non-radiative absorption losses. This allows us to harness and utilise cooperative, non-local atom responses that arise from these strong interactions.

In Fig. 1, we demonstrate the transition of light propagation within the medium towards the near-zero regime in a lattice formed from $N_x = 25$ square array layers. This is revealed in Fig. 1(b) by a dramatic increase in the effective wavelength of the dipolar wave excited within the medium as the detuning of the beam is varied. The amplitudes are well-described as a sum $\mathcal{P}_+ e^{i\ell k_x' a} + \mathcal{P}_- e^{-i\ell k_x' a}$ of oppositely traveling waves, where ℓa (for $\ell = 0, 1, 2, \ldots$) indicate the dipole positions in the array. We fit these to $\mathcal{P}_\ell$ to extract a medium wavenumber k_x' for light that ranges from $k_x' = 0.25$ down to $k_x' = 0.03k$ – an effective wavelength of approximately 33λ. The slow variation of the excitation amplitude is further reflected in the phase accumulated across the layers in Fig. 1(c), which may remain almost constant across the entire sample in the most extreme case. Extracting the phase refractive index $n_p = k_x'/k \to 0$, these results demonstrate, using essentially exact microscopic calculations, how a near-zero medium for light emerges from collective scattering in atomic lattices. Finally, in Fig. 2, we show how the effective wavenumber and light transmission for a five-layer sample depends on the laser frequency and the lattice spacing.

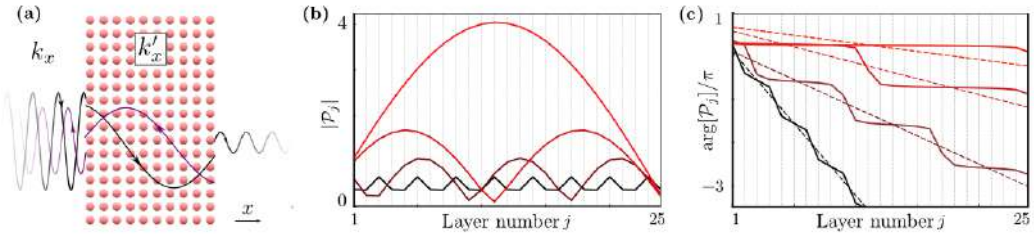


Figure 1: **Emergence of an ENZ medium response in light propagation through an array of discrete dipoles.** (a) Schematic of a plane wave transmitted through a dipolar array, stacked in infinite planar lattices along the x axis. Excitation (b) amplitude and (c) phase of the atomic dipoles. The effective wavelength of the excitation becomes longer as the laser frequency approaches the ENZ. condition.

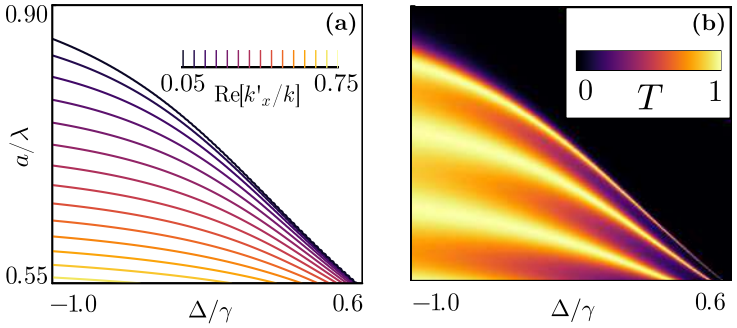


Figure 2: (a) Real part of the medium wavenumber k'_x, normalized to the free-space wavenumber k, and (b) transmittivity T. Here, detuning Δ (normalized to free-space linewidth γ) and lattice spacing a, normalized to wavelength λ, are varied within the transmission band for five layers.

In conclusion, we demonstrate through microscopic, atom-by-atom simulations the emergence of macroscopic ENZ medium response, enabling us to extract a microscopic mechanism of dipolar interactions behind this fascinating phenomenon.

References

1. Ruks L., Ballantine, K. E., and Ruostekoski, J. "Negative refraction of light in an atomic medium," *Nature Comm.* Vol. 16, 1433 (2025).

Anapole Response with Polarization-Independent Properties of a Trimer-Based Dielectric Metasurface

A. B. Evlyukhin[1,2*], **V. R. Tuz**[3,4]

[1]Institute of Quantum Optics, Leibniz University Hannover, Welfengarten 1, Hannover 30167, Germany
[2]Cluster of Excellence PhoenixD, Leibniz University Hannover, Hannover 30167, Germany
[3]International Center of Future Science, Jilin University, 2699 Qianjin Street, Changchun 130012, China;
[4]V. N. Karazin Kharkiv National University, 4, Svobody Square, Kharkiv 61022, Ukraine
*corresponding author:evlyukhin@iqo.uni-hannover.de

Abstract: Features of anapole state occurrence in a dielectric metasurface formed by trimer-based clusters (meta-atoms) have been revealed. Manifestation of anapole has been found in near-field distribution and wave transmission and reflection properties by a trimer-based metasurface.

The anapole phenomenon has attracted considerable attention in the field of metamaterials as a possible realization of nonradiative objects [1]. The optical anapole arises as a composite of electric dipole and toroidal dipole moments that does not produce any far-field emission due to the complete destructive interference of their similar emission patterns. In this state, the near fields appear to be strongly localized inside the particles, while their far-field emission is significantly suppressed. Due to the suppression of the scattered fields, the incident wave passes through the meta-atoms without distortion, resulting in a state of complete transmission (zero reflection) of the metamaterial at the anapole excitation wavelength. Thus, the anapole offers a new way to achieve the invisibility (cloaking) effect for lossless dielectric metamaterials based on the suppression of radiation scattering.

In this work we comprehensively study the anapole phenomenon in cluster systems of dielectric particles, considering the conditions for the anapole manifestation both in individual trimers of disk-shaped particles and in a metamaterial composed of such trimers [2]. Our analytical approach is based on the multipole expansion method and the secondary multipole expansion technique. They allow us to relate the anapole to the trimer multipole moments and individual multipole moments of its constituent particles. The manifestation of the anapole in a two-dimensional metamaterial (metasurface) is confirmed by checking the resonance states in the reflected field, as well as from the near-field electromagnetic patterns obtained from full-wave numerical simulations. It is shown that the anapole excitation in trimers leads to a polarization-independent suppression of reflection with a resonant enhancement of local electromagnetic fields in the metasurface. Finally, an experimental verification of the theoretical results is presented and discussed.

References

1. R. M. Saadabad, L. Huang, A. B. Evlyukhin, and A. E. Miroshnichenko, “Multifaceted anapole: from physics to applications”, Opt. Mat. Express, Vol. 12, 1817-1837, 2022.
2. V. R. Tuz and A. B. Evlyukhin, “Polarization-independent anapole response of a trimer-based dielectric metasurface,” Nanophotonics, Vol. 10, 4373–4383, 2021.

Cascade Enhancement of Magnetic Purcell Effect and Efficient Collection of Photons in Hybrid Topological Structure

Zihan Mo[1], Yali Jia[1], Zhaohua Tian[1], Qi Liu[1], Zhengyang Mou[1], Yu Tian[1], Qihuang Gong[1], and Ying Gu[1,2*]

[1]State Key Laboratory for Mesoscopic Physics, Department of Physics, Peking University, Beijing 100871, China
[2] Hefei National Laboratory, Hefei 230088, China
[*]corresponding author: ygu@pku.edu.cn

Abstract: We theoretically demonstrate that both cascade enhancement and high collection efficiency of emitted photons from a single emitter can be achieved simultaneously in a topological photonic crystal containing a resonant dielectric nanodisk.

1. Introduction

The unique properties of topological photonics, including topological robustness and anti-scattering, bring new opportunities for the development of single photon sources. Barik et al. first proposed the chiral coupling between quantum emitters and edge states in topological photonic crystals (PCs). After that, Purcell enhancement is demonstrated with topological corner states, topological slow light in valley PCs, and topological Su-Schrieffer-Heeger cavity modes. Unfortunately, their Purcell factor is not very high, almost on the same order as that in photonic crystals. Recently, nonscattering large Purcell enhancement is obtained in the topological photonic structure containing a plasmonic nanoantenna, but still suffers from low quantum yield due to an intrinsic metallic loss. So, that both high photon emission rates and high quantum yield simultaneously exist under topological protection remains an issue.

2. Model & Results

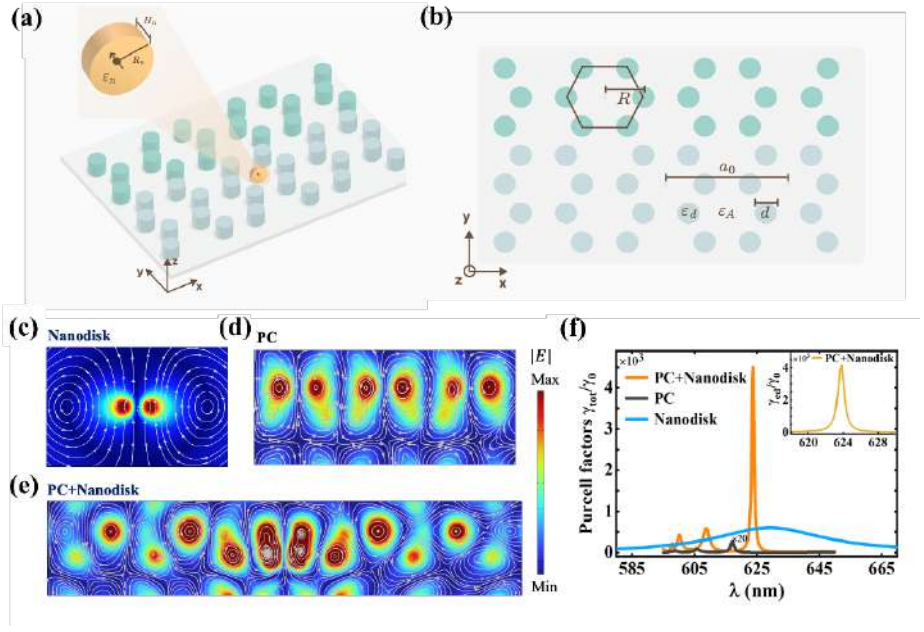


Fig. 1. (a) Schematic diagram of the hybrid structure of topological photonic crystal-nanodisk. (b) Schematic diagram of honeycomb photonic crystal. (c) The electric field in the xy plane of the magnetic dipole resonance in a bare nanodisk,

where the white streamlines indicate the direction of the magnetic field. (d) The electric field of the edge state in the xy plane of the bare PC. (e) The electric field of the edge state in the xy plane of the topological hybrid structure. (f) The total Purcell factors γ_{tot}/γ_0 in the bare nanodisk, bare topological PC, and the hybrid structure. The inset is the Purcell factor γ_{ed}/γ_0 along the edge state propagation in the hybrid structure.

We now investigate the cascade enhancement of magnetic emission in the hybrid structure. If a magnetic emitter is used to excite the nanodisk, then its magnetic dipole resonance can be viewed as a large equivalent dipole interacting with the edge states, which achieves the cascade enhancement of the magnetic emitter. As shown in Fig. 1(f), when a quantum emitter is placed at the center of a nanodisk, the maximum magnetic Purcell factor γ_{tot}/γ_0 can reach 4504. While in bare topological PC, the maximum Purcell factor is only 14. When there is only a dielectric nanodisk, the Purcell factor at the resonance is 604. Therefore, much stronger emission enhancement can be achieved in the hybrid structure than in the bare topological PC and the bare dielectric nanodisk.

For practical application of single photon sources, besides a large emission rate, efficient collection of photons is also extremely important. For a nanodisk in free space, emitted photons are difficult to collect and utilize. In the topological hybrid structure, the topological PC can guide the photons that were previously scattered to the surroundings into the edge states. If the collection efficiency is defined as $\beta = \gamma_{ed}/\gamma_{tot}$, β can reach 93% [inset in Figure 1(f)]. The high collection efficiency in the hybrid structure comes from the large nearfield overlapping between an equivalent large magnetic dipole and the edge state as well as anti-scattering of topological state [Fig. 1(e)]. In previously reported enhanced emission via hybrid structures containing a metallic nanoantenna, the quantum yield is not very high. But here, owing to no absorption loss in dielectric structures and anti-scattering property of edge states, the quantum yield is almost equal to the collection efficiency; i.e., almost all the emitted photons can be used for on-chip photonic devices. It is worth noting that the narrow line width in the hybrid structure also comes from the fact that edge states can collect scattered photons.

3. Conclusion

In summary, we have proposed a mechanism for the cascade enhancement and efficient collection of emitted photons under topological protection. A hybrid structure integrating a topological PC and nanodisk is designed in which the magnetic dipole resonance of the nanodisk can be equivalent to a large magnetic dipole to interact with the edge state. The large near-field overlapping between the resonant nanodisk and the edge state enhances the magnetic emission through a cascade effect. At the same time, emitted photons can be efficiently guided to propagate in the edge state channel, achieving a collection efficiency exceeding 90% due to the robustness of the edge state. The low loss of the dielectric structure and the anti-scattering properties of the topological mode make the quantum yield almost equivalent to the collection efficiency; that is, almost all of the emitted photons can be used in on-chip photonic devices. The mechanism proposed here enhances the spontaneous emission rate of the emitter while achieving large collection efficiency under topological protection, which will provide practical use for ultrabright and stable on-chip single photon sources. It also provides new insights for the study of cavity quantum electrodynamics in topological structures.

References

1. Y. Jia, Z. Tian, Q. Liu, Z. Mou, Z. Mo, Y. Tian, Q. Gong, and Y. Gu, “Cascade Enhancement and Efficient Collection of Single Photon Emission under Topological Protection,” Nano Lett. 24, 12277 (2024).

Bottom-up approaches, new fabrication routes and ENSEMBLE3

Mie resonant silicon particles via bottom-up synthetic routes and assembled into 2D metasurfaces

G. L. Drisko[1*], M. A. Parker[1], L. Roach[1], M. L. DeMarco[1], M. Gonidec[1], P. Rosa[1], B. A. Korgel[2], V. Ponsinet[2], P. R. Wiecha[3], A. N. Grigorenko[4], and P. Barois[1]

[1] Univ. Bordeaux, CNRS, Bordeaux-INP, ICMCB, UMR 5026, F-33600 Pessac, France.

[2] McKetta Department of Chemical Engineering, 200 E Dean Keeton St, The University of Texas at Austin, Austin, TX 78712, USA.

[3] Univ. Bordeaux, CNRS, CRPP, UMR 5031, F-33600 Pessac, France.

[4] LAAS, Université de Toulouse, CNRS, 31000 Toulouse, France.

[5] Department of Physics and Astronomy, University of Manchester, Manchester, M13 9PL, UK.
[*]corresponding author: glenna.drisko@icmcb.cnrs.fr

Abstract: Mie resonant silicon particles have strong scattering and thus are highly desirable building-blocks in metamaterials and metasurfaces. However, most silicon resonators are produced via top-down fabrication methods. We present two bottom-up fabrication methods followed by particle self-assembly, producing a silicon-based metasurface having a certain degree of disorder, and yet a high quality factor.

Silicon has a relatively high refractive index in the visible, coupled with low light absorption above 400 nm, making it a highly effective scatterer for visible frequencies.[1] In spite of the excellent optical properties of silicon, material scientists turn to other materials, such as titanium dioxide, due to the difficulty in synthesizing nanoscaled silicon resonant units. The difficulty in producing silicon particles stems from its propensity to oxidize upon exposure to air, the low reduction potential of the precursors and the relative danger associated with handling silicon precursors. Typically, either extreme synthesis conditions, very unstable silicon precursors or very strong reductants are used to create silicon through bottom-up chemistry. Even so, obtaining the necessary diameters for visible light scattering, e.g. 75-200 nm in diameter, is a challenge via bottom-up methods.[1] A variety of top-down methods have provided excellent proof-of-concept examples,[2] but these are typically more expensive and cumbersome to scale-up than are bottom-up methods. Thus, we have spent the last several years striving to discover a new solution-based synthesis method to make resonant silicon units.

Here we report two different synthesis techniques. The first is a redox reaction, where two different silicon precursors are combined at ambient temperature and pressure to generate Mie resonant silicon particles. The size of the particles is tuned via solvent selection and by the precursor ratio.[3,4] The refractive index of a single particle resulting from this redox synthesis technique was extracted by fitting the Lorentz Mie theory to the interference pattern generated at 532 nm.[4] The refractive index was found to be 4.08, which is similar to bulk silicon (4.14) at this wavelength. The slight difference in refractive index can be attributed to a small amount of amorphous material or inclusions within the particle. Although this technique allows the particle size to be tuned from 45-230 nm in diameter, and thus covers the entire visible spectrum, the particles suffer from polydispersity. We are currently working to reduce the size dispersion within a batch, but in the meantime, we decided to explore a second synthetic pathway towards resonant particles with higher conformity.

Synthesis of amorphous silicon particles between 400 nm to several microns in diameter is possible by

decomposing trisilane (Si_3H_8) in supercritical hexane.[5] These particles display multipolar resonances that can be improved upon thermal annealing to increase the degree of silicon crystallinity.[6] Moreover, the polydispersity within a batch can be as low as 5%, which is very low for a bottom-up fabrication technique. Previously, we were able to decrease the size of the silicon core to diameters compatible with dipole scattering in the visible by combining the trisilane precursor with a silicon coordination complex, bis-(N,N-diisopropylbutylamidinate) dichlorosilane ($[(i\text{-PrN})_2C(n\text{-Bu})]_2SiCl_2$).[7] This resulted in an amorphous silicon core between 130-160 nm in diameter, surrounded by a silica shell of tunable dimensions between 10-115 nm.[7] Here, we report an extension of this work, where trisilane is replaced by hexasilane (Si_6H_{12}), while keeping other aspects of the synthesis equivalent to the previous report. The exchange of the silane precursor resulted in silicon cores with a much higher degree of crystalline character, as noted by Raman and XRD analysis. The oxide shell is thinner (approximately 25 nm) and the total particle diameter increases to between 350-600 nm, depending on the precursor concentration in the reactor during synthesis.

These particles were then assembled into a metasurface via an interfacial self-assembly at a liquid-gas phase boundary, and then deposited onto a quartz substrate. The particles formed islands of crystalline particle placement within a largely disordered assembly. The optical properties of these particles were measured using variable angle spectroscopic ellipsometry. Lattice modes were observed, with a strong magnetic resonance of high quality factor at around 945 nm. We are currently comparing the experimental results to simulation to confirm these surprising experimental findings. If the results prove to be real, this pathway opens the possibility of making large scale metasurfaces through an all bottom-up method.

MAP, LR, and GLD were supported by the European Research Council (ERC) under the European Union's Horizon 2020 research and innovation programme ("Scatter", Grant agree-ment No.948319).

References

1. De Marco, M. L., Semlali, S., Korgel, B. A., Barois, P., Drisko, G. L., Aymonier, C. "Silicon-Based Dielectric Metamaterials: Focus on the Current Synthetic Challenges," Angew. Chem. Int. Ed. Vol. 57, No. 17, 4478-4498, 2018.
2. Staude, I., Schilling, J. "Metamaterial-inspired silicon nanophotonics" Nat. Photonics, Vol. 11, 274-284, 2017.
3. Parker, M. A., De Marco, M. L., Castro-Grijalba, A., Ghoridi, A., Portehault, D., Pechev, S., Hillard, E. A., Lacomme, S., Bessière, A., Cunin, F., Rosa, P., Gonidec, M. and Drisko, G. L. "Size-tunable silicon nanoparticles synthesized in solution via a redox reaction" Nanoscale, Vol. 16, 7958-7964, 2024.
4. Parker, M. A., Khaddad, S., Fares, N., Ghoridi, A., Portehault, D., Bonhommeau, S., Amarouchene, Y., Rosa, P., Gonidec, M., Drisko, G. L. "Unveiling the Potential of Redox Chemistry to Form Size-Tunable, High-Index Silicon Particles" Chem. Mater. Vol. 36, 22, 10986-10993, 2024.
5. Pell, L. E., Schricker, A. D., Mikulec, F. V. and Korgel, B. A. "Synthesis of amorphous silicon colloids by trisilane thermolysis in high temperature supercritical solvents" Langmuir, Vol. 20, 6546–6548, 2004.
6. Shi, L., Harris, J. T., Fenollosa, R., Rodriguez, I., Lu, X., Korgel, B. A., Meseguer, F. "Monodisperse Silicon Nanocavities and Photonic Crystals with Magnetic Response in the Optical Region" Nature Commun., Vol. 4, 1904, 2013.
7. De Marco, M. L., Jiang, T., Fang, J., Lacomme, S., Zheng, Y., Baron, A., Korgel, B. A., Barois, P., Drisko, G. L., Aymonier, C. "Broadband Forward Light Scattering by Architectural Design of Core-Shell Silicon Particles" Adv. Funct. Mater. Vol. 31, 26, 2100915, 2021.

Resonant hybrid nanostructures based on 2D semiconductors for advanced optoelectronics

I. Staude[1,2,3*], **Z. Fedorova**[1,2**]

[1]Institute of Solid State Physics, Friedrich Schiller University Jena, Max-Wien-Platz 1, 07743 Jena, Germany
[2]Institute of Applied Physics, Abbe Center of Photonics, Friedrich Schiller University, Albert-Einstein-Str. 15, 07745 Jena, Germany
[3]Max Planck School of Photonics, Hans-Knöll-Straße 1, 07745 Jena, Germany
[*]corresponding author: isabelle.staude@uni-jena.de
[**]corresponding author: zlata.fedorova@iuni-jena.de

Abstract: We present recent advances in integrating 2D transition metal dichalcogenides (TMDs) with resonant nanostructures for optoelectronics. Our work explores hybrid architectures combining 2D TMDs with dielectric metasurfaces and plasmonic nanoantennas, as well as nanopatterning strategies that preserve optical properties. We discuss fabrication challenges, performance, light-matter interactions in such hybrid systems and their prospects for next-generation optoelectronics.

Summary

2D transition metal dichalcogenides (TMDs) are highly promising atomically thin semiconductor materials for photonic applications due to their direct bandgap in the monolayer phase, strong photoluminescence, pronounced excitonic effects, high nonlinearity, and unique valley properties with potential for classical and quantum information processing. Their two-dimensional nature facilitates effective integration into nanophotonic architectures, while their exceptional optical properties and tunability make them ideal for compact, fast, and functional optoelectronic devices. The development of hybrid nanostructures based on 2D TMDs is a rapidly evolving field, with applications ranging from light-emitting metasurfaces and tunable lenses to ultrafast wavefront shaping and holography. Advancing these applications requires novel fabrication strategies for integrating TMDs with resonant photonic nanostructures.

In this talk, we discuss our recent progress in hybrid TMD-based nanophotonics, including their coupling to high-index dielectric metasurfaces and plasmonic nanoantennas. We explore how excitonic properties, charge carrier dynamics, and coherence effects influence light-matter interactions in these systems. Additionally, we present advances in nanopatterning techniques that allow precise structuring of TMDs while maintaining their optical functionality, enabling applications such as ultrathin holograms and reconfigurable photonic devices. In summary, we provide an overview of fabrication strategies, integration challenges, and recent advances in resonant hybrid nanostructures based on 2D TMDs.

Metal oxide metasurfaces elaborated by nanoimprint and derived methods

D. Grosso[1,2*], B. Kerzabi,[1] M. Abbarchi[1] M. Putero,[3] A. Gourdin,[1] M. bouabdellaoui,[1] E. Daher, and L. Weber[1]

[1] Solnil SAS, 95 rue de la république, 13002, Marseille, France (badre.kerzabi@solnil.com)
[2] Center for Interdisciplinary for Nanoscience of Marseille, CINaM, UMR 7325, Campus de Luminy – Case 913, 13288 Marseille, France
[3] Institut of Materials Microelectronics and Nanosciences of Provence, IM2NP, Avenue escadrille Normandie Niemen 13 397, UMR 7334, Marseille, France
[*]corresponding author: david.grosso@univ-amu.fr

Abstract: Sol-gel chemistry combined to direct nanoimprint lithography was developed to elaborate robust metal-oxide meta-surfaces. Different material/structures systems, dedicated to biosensing (DNA sequencing), high LIDT optics (Lasers), augmented reality and structural colours applications, are presented.

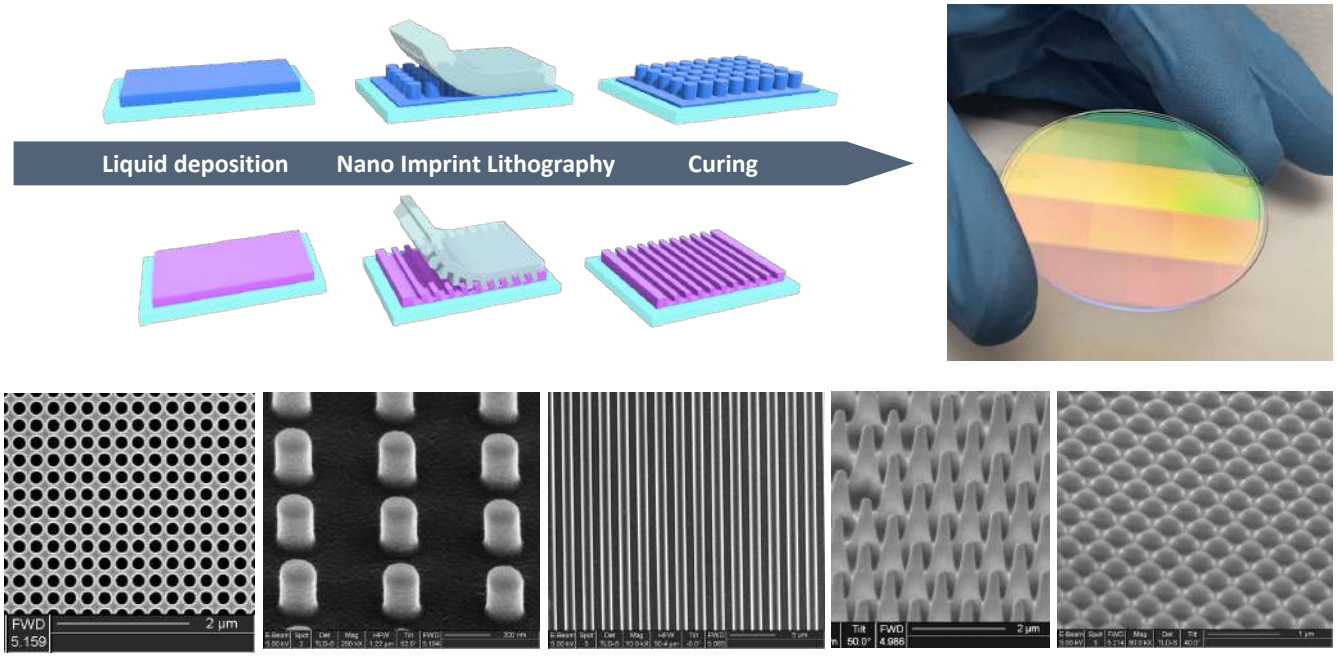


Figure 1 : Schemes of the NIL method and SEM images of different metaatom arrays composed of metal oxides.

Conventional top-down fabrication methods for metasurfaces are often cumbersome and expensive (both CapEx and production costs). Here, we showcase the use of Soft-Nano-Imprint-Lithography (soft-NIL) as a scalable, cost-effective, and CMOS-compatible method for directly imprinting sol-gel precursor inks into metasurfaces of metal oxides (e.g. SiO_2, TiO_2, Al_2O_3, Nb_2O_3, $CaTiO_3$, etc. see Fig. 1). Photonic metasurfaces can be prepared with vertical aspect ratios up to 7, on diverse substrates such as glass, fused silica, sapphire, and silicon wafers. A precise adjustment of the chemical precursors and nano-imprint conditions ensure faithful replicas over large areas: the method is scalable up to 200 mm wafers, limited only by the plate-to-plate machinery employed. The resulting materials offer controlled, on-demand refractive indices ranging from 1.12 to 2.7@520 nm with zero extinction for passive photonic devices and extremely low haze. Combinations of two metal oxides, on the same

metasurfaces, exhibiting extreme contrasts in optical constants or/and in chemical affinity can be prepared through a novel liquid deposition technique based on capillarity infiltration. Various metasurface designs addressing diverse functionalities,[1-6] including controlled-wetting surfaces, light-harvesting coatings, diffraction gratings for light in and out coupling, multispectral filters, enhanced spectrally and spatially controlled emitting surfaces, waveguides, structural colour coatings, anti-reflection coatings, and flow cells for DNA sequencing have been developed. This work highlights the potential of soft-NIL in advancing the field of optical metasurfaces and paves the way for their widespread applications in next-generation devices.

REFERENCES

1. Zeinab Chehadi, Michele Montanari, Nicoletta Granchi, Mehrnaz Modaresialam, Mathieu Koudia, Mathieu Abel, Magali Putero, David Grosso, Francesca Intonti, and Marco Abbarchi. Soft Nano-Imprint Lithography of Rare-Earth-Doped Light-Emitting Photonic Metasurface**, Advanced Optical Materials,** 10, 21, 2022, 2201618, DOI 10.1002/adom.202201618.
2. Modaresialam, M.; Bordelet, G.; Chehadi, Z.; O'Byrne, M.; Favre, L.; Putero, M.; Abbarchi, M.; Grosso, D. Enhanced Refractive Index Sensitivity through Combining a Sol-Gel Adsorbate with a TiO_2 Nanoimprinted Metasurface for Gas Sensing. 2021, **ACS Applied materials & interfaces**. DOI:10.1021/acsami.1c13248
3. M; Chehadi, Z; Bottein, T; Abbarchi,; Grosso, D. Nanoimprint Lithography Processing of Inorganic-Based Materials (review). Modaresialam, 2021, **Chemistry of Materials**. DOI: 10.1021/acs.chemmater.1c00693
4. Bochet-Modaresialam, Mehrnaz; Claude, Jean-Benoit ; Grosso, David ; Abbarchi, Marco. Methylated Silica Surfaces Having Tapered Nipple-Dimple Nanopillar Morphologies as Robust Broad-Angle and Broadband Antireflection Coatings. **ACS Appl. Mater. Inter. 2020**, 3, 5231-5239, DOI: 10.1021/acsanm.0c00646.
5. S. Checcucci, T. Bottein, M. Gurioli, L. Favre, D. Grosso, M. Abbarchi. Multifunctional metasurfaces based on direct nanoimprint of titania sol-gel coatings. **Adv. Opt. Mater.** 2019 7, 10, AN 1801406. DOI: 10.1002/adom.201801406
6. Faustini, Marco, Cattoni, Andrea, Peron, Jennifer, Boissiere, Cedric, Ebrard, Paul, Malchere, Annie, Steyer, Philippe, and Grosso, David.Dynamic Shaping of Femtoliter Dew Droplets. **ACS NANO**, 12, **2018**, 3243-3252. **DOI:** 10.1021/acsnano.7b07699

Template-assisted self-assembly of Functional Metasurfaces for Advanced Photonic Applications

Sezer Seçkin[1] and Tobias A.F. König[1-4,*]
[1]Leibniz-Institut für Polymerforschung Dresden e.V.,
Hohe Straße 6, 01069 Dresden, Germany
[2]Center for Advancing Electronics Dresden (cfaed), Technische Universität Dresden,
Helmholtzstraße 18, 01069 Dresden, Germany
[3]Faculty of Chemistry and Food Chemistry,
Technische Universität Dresden, Bergstraße 66, 01069 Dresden, Germany
[4]Dresden Center for Intelligent Materials (DCIM),
Technische Universität Dresden, Hallwachsstraße 3, 01069 Dresden, Germany
[*]corresponding author: koenig@ipfdd.de

Abstract: The ability to fabricate nanophotonic metasurfaces with precise structural control, scalable fabrication, and tunable optoelectronic properties is central to advancing next-generation sensing, energy, and spectroscopy applications. Recent breakthroughs in **template-assisted self-assembly (TASA)** enable the bottom-up fabrication of high-quality and defect-free metasurfaces by using **pre-synthesized nanoparticles, responsive polymer matrices, and tailored templates**. This approach minimizes material waste, reduces energy consumption, and integrates **top-down lithographic precision** with **bottom-up self-organization**, achieving large-area patterning with nanoscale precision [1].

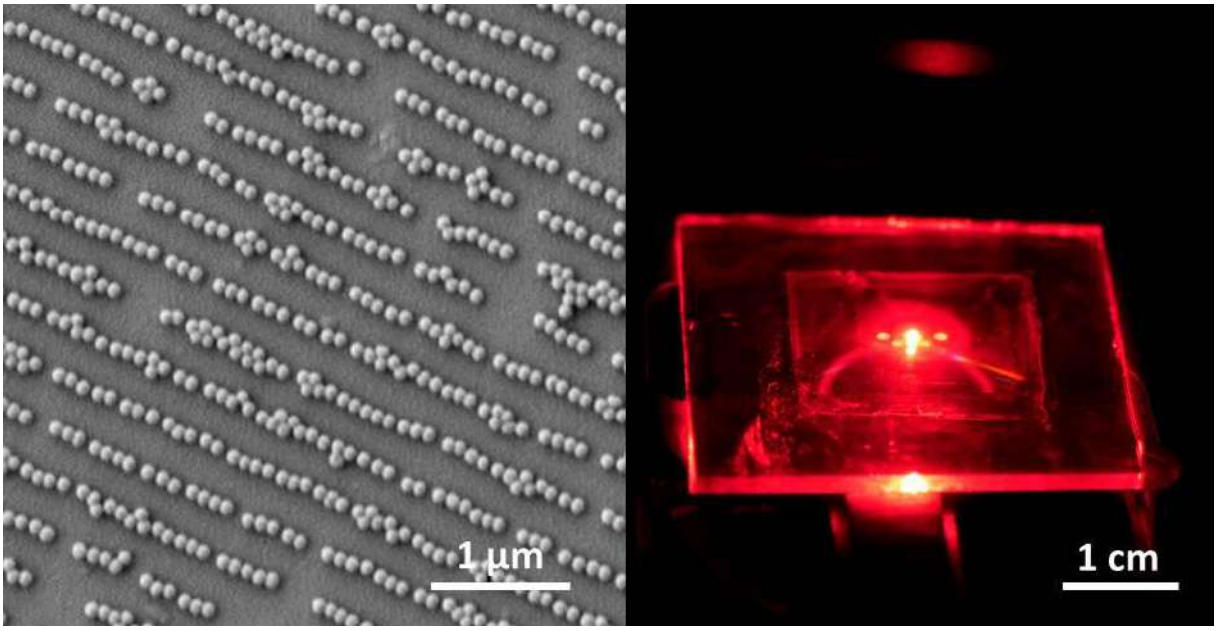


Figure: *Template-assisted self-assembly facilitates the bottom-up fabrication of ordered plasmonic and semiconducting metasurfaces on a centimeter scale. By integrating scalable colloidal assembly with top-down templating, this approach enables the precise alignment of resonator geometries with numerically optimized designs, achieving targeted optical properties with minimal loss. This sustainable and reproducible fabrication route aligns with the special session "SP14. Bottom-up approaches, new fabrication routes and ENSEMBLE3" mission of advancing novel crystal growth techniques and functional nanostructures for next-generation photonic applications.*

We demonstrate a **scalable and reproducible self-assembly process** to fabricate light-emitting and plasmonic metasurfaces with predefined periodicities and enhanced optical properties. Our method facilitates the fabrication of metasurfaces with **tunable photonic bandgaps, chiroptical responses, and directional radiation control** using **soft lithographic templating and controlled colloidal deposition** [2]. In particular, we report a **13-fold enhancement of directional photoluminescence** in perovskite-based metasurfaces, the highest observed to date [3]. In addition, by optimizing the concentrations, we achieve **waveguide-integrated grating couplers** in a single self-assembly step, extending the applicability of our approach to **nonlinear optics and integrated photonic circuits**.

Beyond light emission, we extend our fabrication strategy to **colloidal lasing metasurfaces** with record-low lasing thresholds of **0.6 mJ cm^{-2}**, achieved through **soft-lithographic distributed feedback (DFB) resonators** [4]. Additionally, leveraging the **self-assembled plasmonic particle gratings**, we demonstrate a **43-fold enhancement in SERS signal**, providing a high-sensitivity and uniform Raman response over large areas [5]. This result is achieved by tuning the lattice resonance and super-radiant plasmon mode along the particle chain, significantly improving signal strength while reducing surface coverage by 73%. The combination of colloidal self-assembly and template-assisted fabrication provides a sustainable route to tailor metasurface geometries and optimize light-matter interactions for **bioimaging, sensing, and energy-efficient display technologies**. Our work aligns with **ENSEMBLE3's mission** to contribute to **scalable bottom-up fabrication strategies** that bridge **fundamental research and industrial applications** in **advanced materials and nanophotonics**.

The Volkswagen Foundation supported this work through a Freigeist Fellowship awarded to TK.

References

1. Sarkar, S., & König, T. A. "Nano-engineering of functional metasurfaces by template-assisted self-assembly," *Nano-Engineering at Functional Interfaces for Multi-Disciplinary Applications*, Vol. 34, No. 10, 209–229, 2025.
2. Gupta, V., Sarkar, S., Aftenieva, O., Tsuda, T., Kumar, L., Schletz, D., et al. "Nanoimprint Lithography Facilitated Plasmonic ‐ Photonic Coupling for Enhanced Photoconductivity and Photocatalysis," *Adv. Funct. Mater.*, Vol. 31, No. 36, 2105054, 2021.
3. Aftenieva, O., Brunner, J., Adnan, M., Sarkar, S., Fery, A., Vaynzof, Y., & König, T. A. "Directional amplified photoluminescence through large-area perovskite-based metasurfaces," *ACS Nano*, Vol. 17, No. 3, 2399–2410, 2023.
4. Aftenieva, O., Sudzius, M., Prudnikau, A., Adnan, M., Sarkar, S., Lesnyak, V., et al. "Lasing by Template ‐ Assisted Self ‐ Assembled Quantum Dots," *Adv. Opt. Mater.*, Vol. 11, No. 6, 2202226, 2023.
5. Seçkin, S., Singh, P., Jaiswal, A., & König, T. A. "Super-radiant SERS enhancement by plasmonic particle gratings," *ACS Appl. Mater. Interfaces*, Vol. 15, No. 36, 43124-43134, 2023.

Multi-Oriented Self-Assembled Hexagonal Arrays for Isotropic Plasmonic Reflectors

Gil Cardoso[1], Frédéric Hamouda[1], Vy Yam[1]*, Béatrice Dagens[1]

[1] Université Paris-Saclay, CNRS, Centre de Nanosciences et de Nanotechnologies, 91120, Palaiseau, France

*corresponding author: vy.yam@c2n.upsaclay.fr

Abstract: We compare optical properties of different large area self-assembled hexagonal plasmonic metasurfaces, with a correlated-disorder plasmonic metasurface fabricated by e-beam lithography. By adjusting geometric arrangements of plasmonic nanostructures and their density, we obtain metasurfaces capable of isotropically modifying the reflectivity spectrum of transparent substrates without inducing diffraction or diffusion.

Photonic metasurfaces based on plasmonic nanoparticles (NP) on glass have proven their relevance for applications such as planar lenses [1], surface coloring [2], transparent displays for visualisation and augmented reality (AR) systems [3]. Indeed, NP based metasurfaces are used to functionalize plates to obtain high reflectivity at specific wavelengths by choosing the size and shape of the NPs, while preserving good transparency in the entire visible range thanks to an appropriate spatial density and arrangement of the NPs. In particular, correlated disorder patterns of plasmonic nanocylinders have led to reflectivity improvement at one chosen color, with good transparency on the entire visible range and any angle of observation [4]. However, the fabrication of metasurfaces with this type of structure is done by e-beam lithography since it requires high-positional control, which is not compatible with the fabrication on large surfaces.

The approach we use to increasing nanopatterning surfaces is to combine soft UV nanoimprint lithography (soft UV-NIL) with self-assembly (S-A) of nanostructures as described in [5,6]. Fig. 1(a) shows a so fabricated S-A metasurface with hexagonal array of silver NPs with a diameter of 130 nm and a pitch of 200 nm on glass substrate. In order to develop transparent semi-reflective plates for AR systems, we compare the optical responses of these large-area metasurfaces to the responses of those made of correlated disordered patterns well controlled by electron-beam lithography. First, we study NPs spatial arrangement impact by analyzing the structure factor S(q) of the fabricated metasurfaces, i.e., the response of the structure versus its scattering vector q. We consider that the relevant angular observation range is [16°-60°]. Then we evaluate the plasmonic resonance effects by measuring the metasurfaces optical transmission and reflection by using an ellipsometer.

Finally, the fabricated samples have been tested in a laboratory head-up-display (HUD) system (Fig.1(d), (e)): the displayed image is orange, corresponding to a wavelength of 590 nm. It appears more brilliant on the areas covered by the metasurface (roughly delimited by the white dotted line) with respect to the non-functionalized areas for both the ‘S-A metasurface’ and the ‘e-beam metasurface’. Furthermore, the view of the landscape through the metasurfaces is clear in the both cases, but darker in the case of the ‘S-A metasurface’. In both cases, diffraction and diffusion effects are not visible as predicted by the structure factor analysis. The intensity reduction is due to the spatial density of the nanostructures on the surface. Indeed, the nanostructures interspacing is of 200 nm in the case of the ‘S-A metasurface’ versus 274 nm in the case of the ‘e-beam metasurface’. Whereas hexagonal compact arrangement leads to sharper reflected and transmitted images, such a fabrication method will be relevant only if the spatial density of the final metasurface can be controlled.

We propose to reduce the spatial density by ‘removing’ 50% of the NPs, using a ‘reduction mask’ made of large islands positioned following a correlated disorder arrangement that do not induce diffraction or scattering in the

visible domain (Fig.1(a-c)). We evaluate numerically the impact of this reduction by varying the average distance between islands d, from 1 to 10 µm. Corresponding structure factors S(q) have been simulated (Fig.2(a)), using the experimentally obtained NP arrangement of sample of Fig.1(a). For d=1 µm, the peak induced by the correlated disorder arrangement is positioned in the observation range, whereas it is shifted toward lower q values when d increases. At the same time, a pedestal appears at the bottom of the hexagonal compact diffraction peak. It is attributed to the convolution of the structure factor from the initial structure with the structure factor from the masking structure (ring shape associated with the correlated disorder). It diminishes when the islands periodicity and consequently size increases: S(q) of the mask structure becomes concentrated on smaller values of q meaning it is confounded with S(q) of the S-A structure. This can be clearly understood in the 2D S(q) in Fig.2(b), where these ring shapes appear around the areas with larger values. This decrease of the q vector associated with the structure factor of the correlated disorder mask also affects diffusion in the observation range. A distance d=10 µm (and above) is sufficient to minimize diffraction and scattering effects.

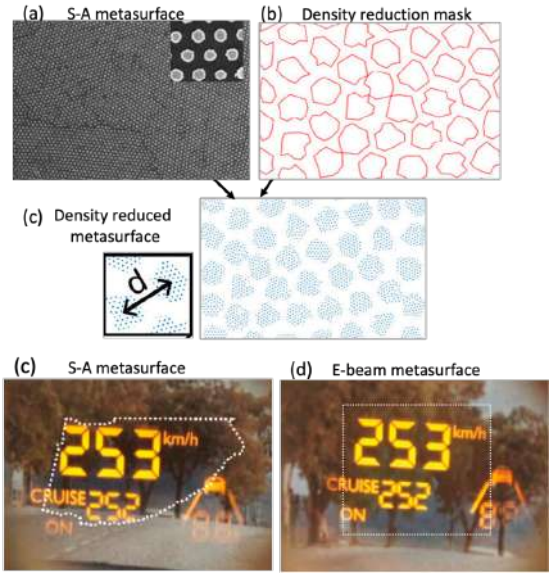


Fig.1: (a) S-A metasurface formed with a hexagonal array of silver NP on glass substrate, (b) and (c): spatial density reduction by half of (a): mask and principle. (d) and (e): qualitative assessment of the reflection in a HUD system fo respectively S-A and e-beam samples.

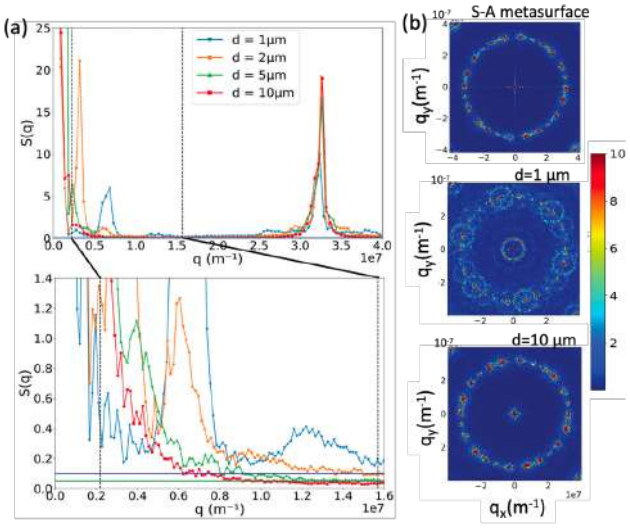


Fig. 2: *(a) numerical structure factors of the S-A structure with different island distances, for a constant average spatial density. Bottom: zoom on the observation range (b) 2D structure factor of the original S-A structure and the density-reduced structures with the 3 different island distances.*

Finally, such fabricated S-A metasurfaces with a sub-wavelength period appears to be robust in terms of transparency quality and fabrication process on large surfaces. The additional control of their average spatial density paves the way for the widespread use of such structures for augmented reality.

This work was partly supported by the French RENATECH cleanroom network and the General Council of Essonne.

References

1. Khorasaninejad M, *et al.,* 2016 Metalenses at visible wavelengths: Diffraction-limited focusing and subwavelength resolution imaging *Science* **352** 1190–4
2. Si G, *et al.,* 2013 Reflective plasmonic color filters based on lithographically patterned silver nanorod arrays *Nanoscale* **5** 6243
3. Saito, K. & Tatsuma, T., "A transparent projection screen based on plasmonic Ag nanocubes," Nanoscale 7 20365–8, 2015.
4. Bertin, H., *et al*., "Correlated Disordered Plasmonic Nanostructures Arrays for Augmented Reality," ACS Phot. 5, 2661–2668, 2018.
5. Cardoso, G., *et al*, "Improved PDMS mold fabrication by direct etch with nanosphere self-assembly mask for Soft UV-NIL subwavelength metasurfaces fabrication," Microelec. Eng. 258 111755, 2022.
6. Cardoso G., *et al,* "Controlling Isotropic Reflectivity with Multi-Oriented Self-Assembled Hexagonal Arrays in Plasmonic Metasurfaces," Adv. Optical Mater. 2024, 2401547.

Multifunctional composite materials based on nanoparticles-doped blue-phase liquid crystals for advanced tunable photonic devices

K. Orzechowski[1*], C.-T. Wang[2], O. Strzeżysz[3], W. Lewandowski[4], and T. R. Woliński[1]

[1]Faculty of Physics, Warsaw University of Technology, Koszykowa 75, 00-662 Warsaw, Poland
[2]Department of Photonics, National Sun Yat-sen University, No.70 Lianhai Rd., Kaohsiung 80424, Taiwan
[3]Institute of Chemistry, Military University of Technology, Kaliskiego 2, 00-908 Warsaw, Poland
[4]Faculty of Chemistry, University of Warsaw, Pasteura 1, 02-093 Warsaw, Poland
[*]corresponding author: kamil.orzechowski@pw.edu.pl

Abstract: Our work explores the optical properties of blue-phase liquid crystals doped with gold nanoparticles. These structures exhibit tunable optical properties, enhanced thermal stability, and significant potential for applications in electro-optical modulation, switching, tunable filters, and sensing, making them ideal for emerging photonic technologies.

The concept of photonic crystals – materials that provide access to photonic bandgap analogous to the electronic bandgap of semiconductors – has revolutionized technologies focused on controlling light flow[1]. This breakthrough has enabled the development of versatile photonic materials that allow precise engineering of light propagation, enhancing or suppressing emission within specific spectral ranges and affecting both frequency and time domains[2]. When these properties are tuned to the visible spectrum and the material responds to external stimuli, it becomes possible to develop systems with easy naked-eye readout to external stress. Among the promising materials with intriguing capabilities are blue-phase liquid crystals (BPLCs). Initially designed for high-speed display systems, BPLCs have recently been applied to a wide range of photonic technologies[3].

The applicability of BPLCs stems from their unique hierarchical structure, which comprises chiral, double-twist cylinders (DTCs, Fig. 1a), arranged into metastable body-centered cubic (BPI) and simple cubic (BPII) lattices, as schematically shown in Figs. 1b and 1c, respectively. These lattices exist within a narrow temperature range of 0.5 to 5 K and have unit cell sizes of a few hundred nanometers. The key distinction between BPI and BPII phases lies in the spatial organization of LC defects, i.e. a network of disclination lines. Such structures translate to strong interactions with visible light, resulting in vivid reflected coloring due to a 3D photonic bandgap and optical rotatory power due to their optical activity. Additionally, BPLCs exhibit optical isotropy and polarization insensitivity on a macroscopic scale for wavelengths outside of the resonance band, induced birefringence, and sub-millisecond response times under an electric field. These characteristics position BPLCs as 3D soft crystals with photonic properties that can be altered by external stimuli such as temperature, electric and magnetic fields, pressure, and alignment layers (i.e., boundary conditions).

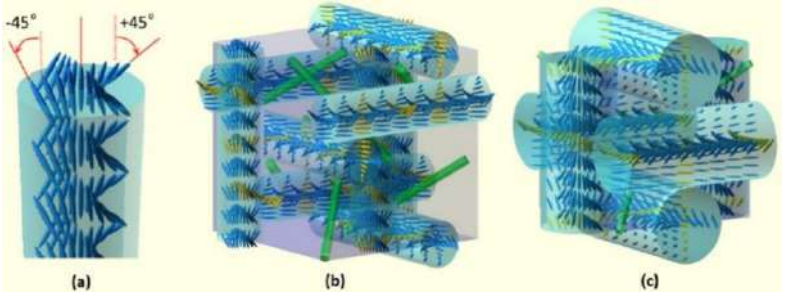


Fig. 1 Scheme of molecular ordering in: (a) DTC, and cubic structures corresponding to a unit cell of (b) BPI and (c) BPII. Orange molecules mean connected helices in neighboring DTCs, and green rods correspond to an array of LC disclinations.

Such hierarchical structures with isotropic defects in BPs make them a promising 3D template for doping with nanoparticles (NPs) and other nanomaterials[4]. This results in tunable nanostructures that are attractive for numerous photonic applications, offering improved electro-optical properties and new funcionalities.

Incorporating functionalized nanoparticles (e.g., gold nanoparticles coated with custom-designed LC-like ligands) into BPLCs can lead to shorter reaction times, reduced threshold voltage, and Bragg wavelength shifting, with the magnitude depending on NP concentration (Fig. 2a). Additionally, NP doping can significantly enhance thermal stability of BPs and provide supplementary functionality. This functionality includes the dynamic steering of optical properties in BPs (such as Bragg wavelength shifting, Fig. 2b) by an optical field, due to the plasmonic effect induced by gold nanoparticles.

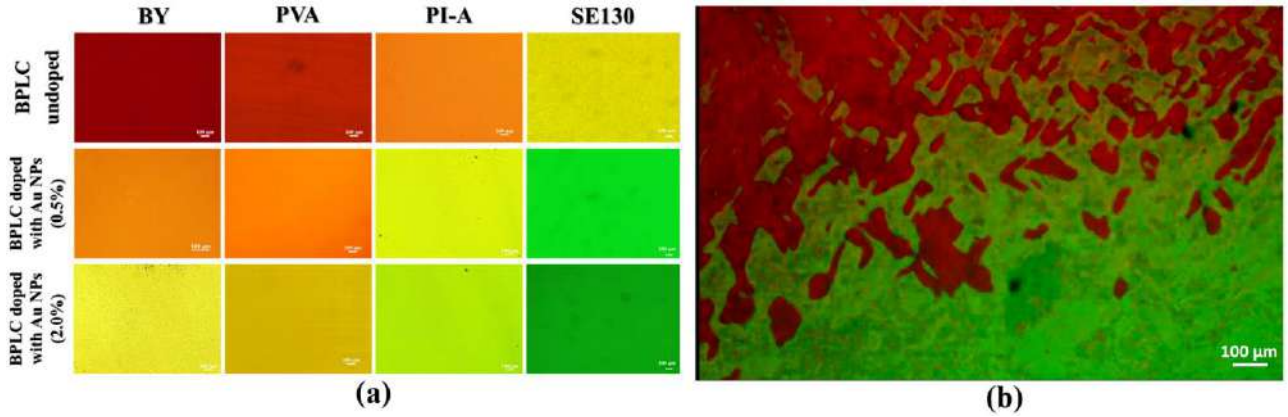


Fig. 2 Examplary photonic bandgap modulation in BPLCs by using: (a) synergistic action of alignment layers and gold nanoparticles, and (b) optical field.

Our research highlights the optical properties of photonic microstructures based on BPLCs doped with gold NPs. These photonic structures exhibit promising tunable optical properties with enhanced thermal stability. This improvement is achieved through a chemical and nanotechnological approach to create BPLC composites with gold NPs coated with LC-like ligands. The investigated BPLC-based photonic microstructures show significant potential for applications in electro-optical modulation and switching, as well as tunable filters and sensing capabilities. These systems offer superior transmission properties, making them highly suitable for emerging tunable photonic devices.

Research was funded by the Warsaw University of Technology within the Excellence Initiative: Research University (IDUB) program. K.O. acknowledges support from the National Science Centre Poland under the MINIATURA grant no. 2023/07/X/ST3/00943.

References

1. Yablonovitch, E., “Inhibited Spontaneous Emission in Solid-State Physics and Electronics,” Phys. Rev. Lett. 58, 2059–2062, 1987.
2. Joannopoulos, J. D., Villeneuve, P. R. and Fan, S., “Photonic crystals: putting a new twist on light,” Nature 386, 143–149, 1997.
3. Yang, Y. et al., “Bioinspired Color-Changing Photonic Polymer Coatings Based on Three-Dimensional Blue Phase Liquid Crystal Networks,” ACS Appl. Mater. Interfaces 13, 41102–41111, 2021.
4. Orzechowski, K. et al., “Achiral Nanoparticle-Enhanced Chiral Twist and Thermal Stability of Blue Phase Liquid Crystals,” ACS Nano 16, 20577–20588, 2022.

Numerical modelling of controlled light amplification in liquid crystal micro-structures

J. Zaplotnik[1,2], U. Mur[1,3], I. Muševič[2,1], and M. Ravnik[1,2,*]

[1] Faculty of Mathematics and Physics, University of Ljubljana, Slovenia
[2] Department of Condensed matter, Jožef Stefan Institute, Slovenia
[3] Department of Engineering Science, University of Oxford, UK
[*] Corresponding author: miha.ravnik@fmf.uni-lj.si

Abstract: Self-assembled dye-doped liquid crystals, in combination with printed polymer micro-structures, can form devices that perform as micro-lasers. Here we present numerical simulations of light coupling into and between such structures, their lasing characteristics, and optical control of laser emission intensity.

Liquid crystals possess the ability to self-organize into a variety of microstructures – such as 1D periodic cholesteric liquid crystal (CLC) layers, nematic and cholesteric droplets – which can be exploited for optical applications. These structures can function as optical micro-resonators and, when combined with dyes, also as micro-lasers [1,2]. Furthermore, liquid crystals can be combined with various 3D printed polymer micro-structures, for example, polymer waveguides.

In this work, we present numerical studies employing the finite-difference frequency-domain (FDFD) method and steady-state ab initio laser theory (SALT) [3], which enable precise identification of photonic crystal band-edge modes [4] and defect modes [5] in 1D geometries, as well as whispering gallery modes (WGM) in nematic droplets and a variety of resonant modes in Bragg-onion cylindrical CLC structures [6]. The FDFD method and SALT further allow for a comparison of quality factors and lasing thresholds of different modes across various geometries and material parameters. Additionally, the finite-difference time-domain (FDTD) method [7], coupled with equations describing saturable optical gain materials, as implemented in the Meep software package [8], is utilized to simulate light coupling into liquid crystal resonators, to model pulsed lasing from such micro-structures, and to develop protocols involving sequences of multiple light pulses with varying wavelengths, polarizations, and intensities enabling all-optical control of light amplification. These simulations provide valuable insights for further optimizing micro-lasers and their potential future applications in photonic microcircuits as all-optical logic gates.

References

1. Coles, H. and S. Morris, “Liquid-crystal lasers”, Nat. photonics, Vol. 4, No. 10, 676–685, 2010.
2. Muševič, I., “Liquid-crystal micro-photonics,” Liq. Cryst. Rev., Vol. 4, No. 1, 1–34, 2016.
3. Esterhazy, S., D. Liu, M. Liertzer, A. Cerjan, L. Ge, K. G. Makris, A. D. Stone, J. M. Melenk, S. G. Johnson, and S. Rotter, “Scalable numerical approach for the steady-state ab initio laser theory”, Phys. Rev. A, Vol. 90, No. 2, 023816, 2014.
4. Zaplotnik, J, U. Mur, D. Malkar, A. Ranjkesh, I. Muševič, and M. Ravnik, “Photonic eigenmodes and transmittance of finite-length 1D cholesteric liquid crystal resonators”, Sci. Rep., Vol 13, No. 1, 16868, 2023.
5. Zaplotnik, J, U. Mur, I. Muševič, and M. Ravnik, “Photonic defect modes in cholesteric liquid crystal resonators with

embedded isotropic layers", Opt. Express., Vol 32, No. 20, 34564--34581, 2024.

6. Mur, U, J. Zaplotnik, I. Muševič, and M. Ravnik, "Photonic eigenmodes of 2D cylindrical cholesteric liquid crystal resonators", *to be submitted*.
7. Taflove, A., A. Oskooi, and S. G. Johnson, "Advances in FDTD computational electrodynamics: photonics and nanotechnology", Artech house, 2013.
8. Oskooi, A. F., D. Roundy, M. Ibanescu, P. Bermel, J. D. Joannopoulos, and S. G. Johnson, "MEEP: A flexible free-software package for electromagnetic simulations by the FDTD method", Comput. Phys. Commun., Vol. 181, No. 3, 687–702, 2010.

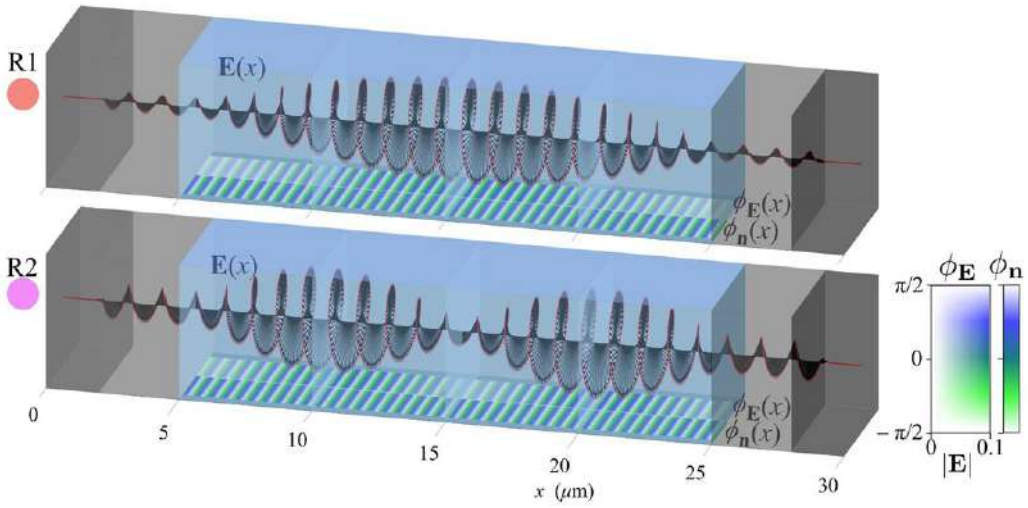


Figure 1: Electric field profiles of two modes (R1 and R2) with highest quality factors on the red side of the photonic bandgap in a planar CLC cell. Colors at the bottom surface show the orientation of electric and director field [4].

A Scalable Fabrication Method for High-Efficiency Photocatalytic Metasurfaces

Parvaneh Mokarian –Tabari[1,2*]

[1] Advanced Materials and BioEngineering Research Centre (AMBER), Trinity College, The University of Dublin, Ireland
[2] School of Chemistry, Trinity College, The University of Dublin, Dublin 2, Ireland
[*]corresponding author: parvaneh.mokarian@tcd.ie

Abstract: We present a bottom-up fabrication approach for highly efficient photocatalysis using a gold-silicon metasurface, where gold nanoparticles are confined within nanopatterned porous silicon. This design enhances charge separation, prevents recombination, and increases photocatalytic activity. Our findings highlight scalable, nanostructured metasurfaces for advanced environmental and energy applications.

Fabrication and design

The nanoporous silicon metasurface was fabricated using block-copolymer self-assembly, enabling the creation of a highly ordered nanostructured template. The use of polystyrene-block-polymethyl methacrylate (PS-b-PMMA) diblock copolymer allowed precise control over pore size and arrangement. After etching, the resulting silicon metasurface contained well-defined nanopores of approximately 25 nm in diameter (Figure 1). Gold nanoparticles were then deposited into these nanopores, with each cavity accommodating up to two nanoparticles. This controlled metasurface confinement prevents agglomeration, maintains high surface area availability, and enhances nanoparticle coupling, leading to improved charge carrier dynamics. The confined metasurface structure also ensures optimal interaction between AuNPs and Si, promoting effective Schottky junction formation for better charge separation.

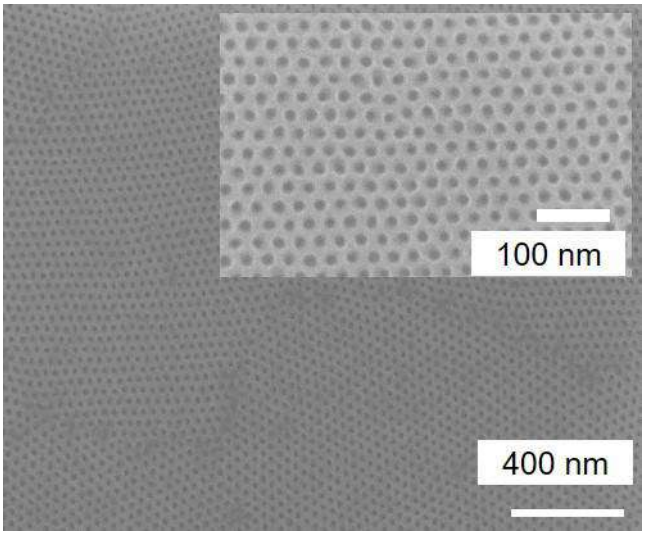


Figure 1. Si nanopore template.[1]

Photocatalytic Performance and Mechanism

Photocatalysis plays a crucial role in environmental sustainability, offering pathways for water purification, air purification, and renewable energy generation. However, the efficiency of conventional photocatalysts is often limited due to rapid charge carrier recombination and inefficient light absorption. In this work, we introduce a novel bottom-up approach for fabricating a highly efficient, reusable photocatalyst by confining gold nanoparticles (AuNPs) within a nanopatterned porous silicon (Si) metasurface. This structured metasurface enhances charge separation, prevents recombination, and significantly improves photocatalytic performance compared to traditional methods.

The photocatalytic efficiency of the AuNP-Si metasurface was tested by evaluating the degradation of methyl orange (MO) dye under UV light (λ = 353 nm). The results showed near-complete degradation of MO within 90 minutes, compared to 70% degradation for randomly dispersed AuNPs on silicon and only 15% degradation for bare silicon. This dramatic enhancement is attributed to three main factors:

1. Enhanced Charge Separation: The Schottky junction formed at the AuNP/Si interface facilitates rapid electron-hole separation, minimizing recombination losses.
2. Increased Surface Area: The nanoporous metasurface provides abundant active sites for catalytic reactions, ensuring more efficient dye adsorption and degradation.
3. Confined Plasmonic Effects: While the system primarily operates via charge transfer rather than plasmonic resonance at this UV wavelength, simulations suggest that enhanced near-field effects at visible wavelengths could further boost performance.

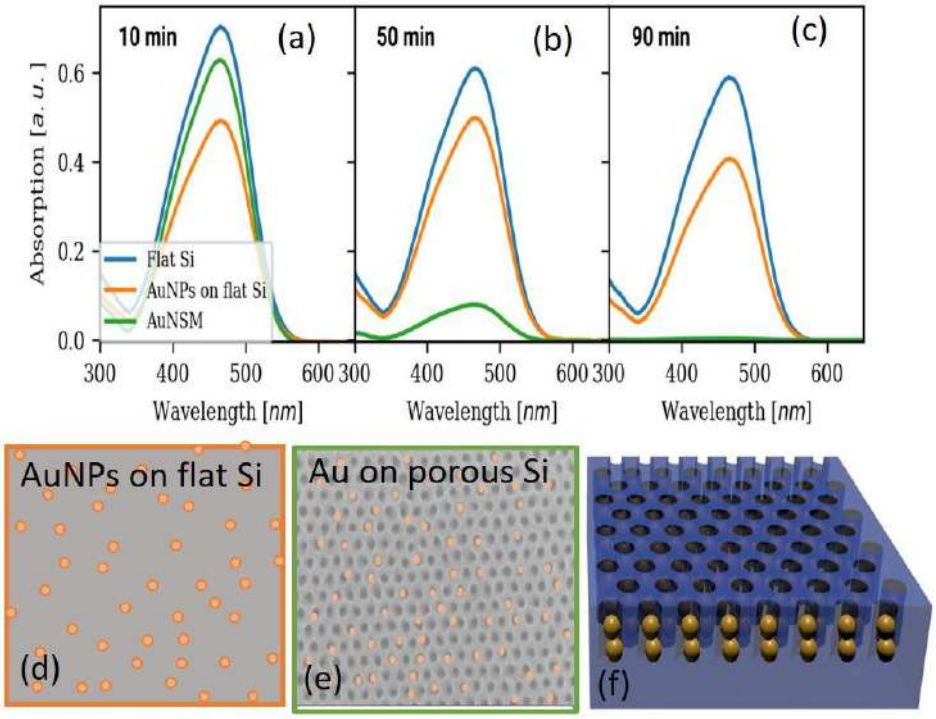


Figure 2. UV–vis absorption spectra of MO dye after degradation after (a) 10, (b) 50, and (c) 90 min on flat Si, AuNPs on flat Si (d), and AuNPs confined in Si pores. (f) Schematic of the metasurface.[1]

Finite Element Method (FEM) simulations revealed that the nanoporous metasurface led to increased power loss density, indicating a higher generation of charge carriers compared to flat silicon or dispersed AuNPs. This confirms that nanoparticle confinement within nanocavities improves photocatalytic efficiency through a combination of charge transfer mechanisms and field enhancement effects.

This work presents a scalable and cost-effective bottom-up approach to engineering high-performance photocatalysts through nanopatterning and particle confinement. By leveraging block-copolymer templating and metal nanoparticle incorporation, we achieve a robust metasurface with superior photocatalytic efficiency. Future work will focus on::

- Extending the study to visible-light-driven photocatalysis by optimising nanoparticle size and material composition.
- Investigating the long-term recyclability and stability of AuNP-Si metasurface for real-world water treatment applications.
- Exploring other semiconductor-metal nanoparticle combinations for enhanced photocatalytic performance.

This research highlights the potential of structured nanomaterials in environmental decontamination and sustainable energy applications, paving the way for the next generation of efficient photocatalysts.

References

1. Mir S H, Jennings B D, Akinoglu G E, Selkirk A, Gatensby R and Mokarian-Tabari P, 2021, Enhanced dye degradation through multi-particle confinement in a porous silicon substrate: a highly efficient, low band gap photocatalyst, Adv. Opt. Mater. 9 2002238.

Harnessing plasmonic phenomena in glass composites obtained by crystal growth techniques

P. Piotrowski,[1,2*] G. Vadivel,[1] K. Wyrwas,[1] P. Paszke,[1,2] R. Nowaczyński,[2] H. Surma,[1] N. Kongsuwan,[3,4] J. Toudert,[1] O. Hess,[5] D. A. Pawlak[1,2]

[1]Centre of Excellence ENSEMBLE[3] sp. z o.o., Wolczynska 133, 01-919 Warsaw, Poland
[2]Faculty of Chemistry, University of Warsaw, Pasteura 1, 02-093 Warsaw, Poland
[3]Quantum Technology Foundation (Thailand), 98 Soi Ari, Bangkok 10110, Thailand
[4]Thailand Center of Excellence in Physics, Ministry of Higher Education, Science, Research and Innovation, Bangkok 10400, Thailand
[5]School of Physics and CRANN Institute, Trinity College Dublin, Dublin 2, Ireland
[*] corresponding author: piotr.piotrowski@ensemble3.eu

Abstract: Volumetric glass materials grown by micro-pulling-down technique will be presented, particularly from the perspective of their enhanced optical properties upon doping with plasmonic nanoparticles.

Plexcitonic systems integrate plasmonic properties with excitonic emission, leading to enhanced system performance characterized by rapid and intense luminescence. These features are particularly desirable for applications in optoelectronic devices, ultrafast optical switches, and quantum information science.

In this study, we present optically active volumetric materials fabricated using the micro-pulling-down method. By employing the NanoParticle Direct Doping (NPDD) technique, we create nanocomposites with tailored plasmonic properties, enabling the observation of enhanced optical responses. This innovative approach, developed in our laboratory, facilitates the direct introduction of plasmonic nanoparticles into glass matrices, allowing precise control over their electromagnetic characteristics. Consequently, we can fine-tune localized surface plasmon resonances (LSPR) to optimize targeted effects, such as the photoluminescence (PL) enhancement of quantum dots.

By integrating advanced material fabrication with comprehensive characterization, our research paves the way for cost-effective photonic devices with enhanced functionalities.

Acknowledgements
The authors thank the ENSEMBLE[3] Project carried within the International Research Agendas Programme (MAB/2020/14) of the Foundation for Polish Science co-financed by the European Union under the European Regional Development Fund and the Teaming Horizon 2020 programme of the European Commission (GA No. 857543) for supporting this work.

Bottom-up wet-chemical synthesis of nanometals assisted by ultrafast irradiation

A. Guerrero-Martínez

Departamento de Química Física, Universidad Complutense de Madrid, Avda. Complutense s/n, 28040 Madrid, Spain
aguerrero@quim.ucm.es

Abstract: Metal nanoparticles' unique optical properties have driven research into their synthesis for nanoplasmonic devices. Ultrafast pulse lasers enable precise control of electron dynamics, leading to uniform nanoparticle production and controlled assembly. This advances applications in photonics, sensing, and catalysis by enhancing optical functionality and structural precision.

Over the past two decades, there has been significant interest and progress in the development and application of metal nanoparticles, primarily driven by their distinctive and highly tunable optical properties. The remarkable ability of gold nanoparticles to interact with light stems from their localized surface plasmon resonances (LSPRs), which are collective oscillations of conduction electrons induced by an electromagnetic field. These unique optical characteristics have opened up numerous possibilities for developing advanced nanoplasmonic devices with tailored functionalities, ranging from biosensing and imaging to photothermal therapy and optoelectronics.

In this context, a substantial body of research has focused on the rational bottom-up synthesis and controlled assembly of metal nanoparticles to achieve desired optical responses. The ability to engineer these nanoparticles with precision has been made possible through a deeper understanding of the mechanisms governing the interaction between light and nanostructures. A key driver of this progress has been the use of ultrashort-pulse laser technologies, which have provided critical insights into the complex electron dynamics underlying light-nanoparticle interactions.

This presentation will explore the transformative role of pulse lasers, particularly femtosecond and nanosecond pulses, in uncovering the fundamental processes that occur during light-matter interactions in metal nanoparticles. When nanometals are exposed to femtosecond pulse lasers, LSPRs are excited, triggering a series of ultrafast physical and electronic processes. These include rapid electron thermalization within hundreds of femtoseconds, followed by lattice relaxation on the picosecond timescale, and eventual environmental coupling, which can result in controlled surface melting of the nanoparticles. In contrast, nanosecond pulse irradiation leads to a fundamentally different response. The extended pulse duration causes overlapping excitation and relaxation processes, which typically result in uncontrolled melting and fragmentation of the nanoparticles due to excessive heat accumulation.

The ability to precisely control these laser-induced phenomena has paved the way for innovative methods to produce highly monodisperse nanometals. For instance, femtosecond pulse laser irradiation has been successfully used to refine polydisperse colloidal solutions, generating nanoparticles with exceptional uniformity and size control (Figure 1).[1] Furthermore, pulse laser irradiation has emerged as a powerful tool for the controlled synthesis of hollow nanometals,[2] and nanoalloys with tunable compositions and defined numbers of atoms.[3]

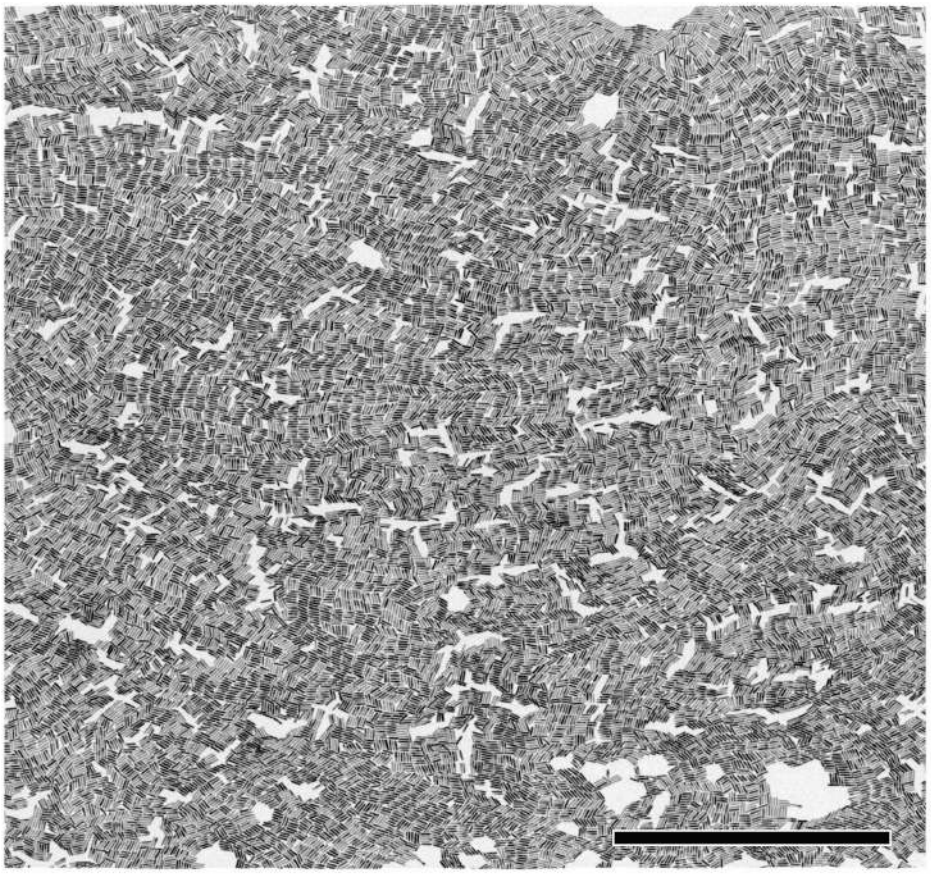


Figure 1. Gold nanorods prepared by bottom-up synthesis and ultrafast irradiation (scale bar, 1 μm)

Overall, the insights gained from pulse laser studies have not only deepened our fundamental understanding of plasmonic interactions at the nanoscale but have also driven technological advancements in nanofabrication and material design. The ability to tailor the optical properties of gold nanoparticles through laser-based synthesis and assembly holds immense potential for a wide range of applications in photonics, sensing, and catalysis.

References

1. González-Rubio, G., Díaz-Núñez, P., Rivera, A., Prada, A. Tardajos, G., González-Izquierdo, J., Bañares, L., Llombart, P., Macdowell, L. G., Palafox, M. A., Liz-Marzán, L. M., Peña-Rodríguez, O. and A. Guerrero-Martínez, "Femtosecond laser reshaping yields gold nanorods with ultranarrow surface plasmon resonances", Science, 358, 640–644, 2017.
2. Sánchez-Pérez, F., Borrell-Grueiro, O., Casasnovas-Melián, A., Ramos-Ramos, D., Guerrero-Martínez, A., Bañares, L., Prada, A., Valencia, F. J., Kohanoff, J., Crespillo, M. L., Olivares, J., Rivera, A. and O. Peña-Rodríguez, "Formation of hollow silver nanoparticles under irradiation with ultrashort laser pulses", Nanophotonics, 13, 1149-1157, 2024.
3. Triviño-Sánchez, S., Xu, R., González-Izquierdo, J., Bañares, L., Cano, I., Pérez-Juste, J., Guerrero-Martínez, A. and G. González-Rubio, "Colloidal gold-palladium-platinum alloy nanospheres with tunable compositions and defined numbers of atoms" Nanoscale, 2025, DOI: 10.1039/D4NR04898A.

Tailored Photonic Bandgap in Liquid Crystalline Cellulose Ether Mesophases: Harnessing Self-Assembly Kinetics and Polymer Chain Mobility

C. A. C. Chazot[1*], S. G. Fine[1], and C. Guo[1]

[1]Department of Materials Science and Engineering, Northwestern University, United States
[*]corresponding author: cchazot@northwestern.edu

Abstract: We investigate liquid crystal self-assembly kinetics and chiroptical properties in cholesteric cellulose ether mesophases. *In-situ* reflectivity measurements reveal the impact of polymer diffusivity and chain elasticity on photonic bandgap development. Our findings guide the design of structurally colored gels and composites with stable, angle-dependent optical properties and reversible colorimetric functions.

Cholesteric liquid crystalline (LC) mesophases based on cellulose ethers, such as ethyl cellulose and hydroxypropyl cellulose, have garnered significant attention for their ability to exhibit macroscopic structural color and chiroptical properties. This long-range helical arrangement consists of stacked nematic pseudo-layers, where the continuous change in refractive index allows selective reflection of part of the electromagnetic spectrum and a tailored photonic bandgap. When the helicoidal pitch matches the wavelength of visible light, dynamic structural colors emerge, driven by the spacing and twisting angles between isoclines (planes of constant orientation). This results in stimuli-responsive optical properties that are sensitive to environmental changes such as mechanical strain, humidity, and temperature.

Despite extensive studies, the time scales involved in the multiscale self-assembly of cholesteric LCs, from the formation of helical secondary structures to mesogen packing and microscopic domain development, remain underexplored.[1] This research discusses how polymer chain mobility, influenced by molecular weight, concentration, and viscoelastic properties, determines the evolution of the photonic bandgap based on the onset of kinetic trapping in the mesophase. A quantitative relationship between the kinetics of structural color formation after shear deformation and cholesteric order development at both nano- and microscales in the gel mesophase is established.[2] Utilizing rheology alongside static and time-resolved reflectivity measurements, the study highlights the strong influence of polymer diffusivity and chain elasticity on self-assembly and order relaxation kinetics in cholesteric cellulose ether gels. The developed phenomenological model can assess the structure–property relationships of various soluble polysaccharide LC mesophases, providing key design guidelines for developing and processing structurally colored cholesteric mesophases.

Further investigation into solvent photopolymerization and the trapping of cholesteric order in a composite reveals its effect on selective reflectivity. Using ethyl cellulose-poly(acrylic acid) (EC-PAA) films as a model system, the balance between EC chain mobility and solvent photopolymerization kinetics is explored to understand the preservation of cholesteric texture and optical properties. The findings demonstrate that realignment or disruption of chiral nematic order during PAA chain growth only occurs for low molecular weight (i.e. high chain mobility) EC. Time-resolved studies during UV curing, including in-situ reflection spectroscopy and rheometry, reveal that rapid polymerization reactions and reduced polysaccharide mobility help maintain the photonic bandgap and angle-dependent reflectivity in solid composite films.

Through the development and application of these fundamental design principles, the research demonstrates that self-assembly kinetics can be leveraged to create composites with spatially-controlled photopatterned bandgaps, tailored angle-resolved reflectivity, and reversible colorimetric functions. These findings provide

critical insights into the interplay between polymerization kinetics and cholesteric texture evolution, paving the way for advanced chiral nematic composites with spatial and temporal control over dynamic chiroptical properties.

This work was primarily supported by a seed grant from the Paula M. Trienens Institute for Energy and Sustainability at Northwestern University and an Army Research Laboratory (ARL) Early Career Program (ECP) Award (Award no. W911NF-25-1-0082), both awarded to C.A.C. C.. S.G.F. also gratefully acknowledges support from the Ryan Fellowship and the International Institute for Nanotechnology (IIN) at Northwestern University. C. G. was primarily supported through the Meister research-as-work-study program in the Department of Materials Science and Engineering at Northwestern University.

References

1. Fine, S. G., Chazot, C. A. C., “Unraveling the Governing Mechanisms Behind the Chiral Nematic Self-Assembly of Cellulose-Based Polymers”, Chemistry of Materials, Vol. 35, No. 21, 2023.
2. Fine, S. G., Branovsky, S. E., Chazot, C. A. C., “Structural Color Out of the Blue: A Quantitative Framework for the Self-Assembly Kinetics of Cholesteric Cellulosic Mesophases”, Biomacromolecules, Vol. 5, No. 8, 2024.

3D Topological Insulator-Based Eutectic Heterostructures: Fabrication and Potential Applications

K. Bandopadhyay[1*], K. Markus[1], A. Materna[1], F. Mazzola[2], C. Polley[3], M. Tonouchi[4], R. Hillenbrand[5], D. A. Pawlak[1, 6]

[1] ENSEMBLE[3] Centre of Excellence, Wolczynska 133, 01-919 Warsaw, Poland
[2] CNR – SPIN, University of Napoli, Federico II, 21 - 80126 Napoli, Italy
[3] MAX IV Laboratory, Lund University, 221 00 Lund, Sweden
[4] Institute of Laser Engineering, Osaka University, 2-6 Yamada-oka, Suita, Osaka 565-0871, Japan
[5]CIC nanoGUNE BRTA and Department of Electricity and Electronics at UPV/EHU, Donostia-San Sebastián, Spain
[6] Chemistry Dept. University of Warsaw, Pasteura 1, 02-093 Warsaw, Poland
[*] corresponding author: kingshuk.bandopadhyay@ensemble3.eu

Abstract: We report the fabrication of three-dimensional topological insulator heterostructures using a single-step bottom-up approach based on directional solidification. These materials exhibit atomically smooth interfaces, preserving topological surface states and enabling hetero-junction formation. This scalable approach paves the way for advancements in spintronics, quantum computing, and novel optoelectronic applications.

Three-dimensional (3D) topological insulators (TIs) have garnered significant interest for their unique quantum properties, particularly their topologically protected, gapless surface states. These materials are promising for topological spintronics and quantum computing due to their robust surface conduction channels, which are resistant to backscattering from nonmagnetic impurities[1]. However, practical implementation is hindered by challenges such as environmental sensitivity, a low surface-to-volume ratio, and the need for controlled material heterojunctions to enhance functionality. Addressing these issues is crucial for advancing TI-based technologies.

In this work, we demonstrate the successful fabrication of 3D TI heterostructures using a simple, fast, and scalable single-step directional solidification technique. This bottom-up approach enables the formation of eutectic composite materials, where two distinct crystalline phases naturally grow in an ordered structure with atomically smooth interfaces. Unlike conventional heterostructure fabrication methods such as molecular beam epitaxy or exfoliation-transfer techniques, which require multiple steps and precise environmental control, directional solidification provides a robust alternative that efficiently overcomes key challenges associated with 3D TIs. The resulting heterostructures exhibit well-defined lamellar micro/nanostructures, which preserve topological surface states while facilitating the formation of stable electronic junctions. This controlled fabrication process enables precise interface engineering between different TI phases or between TIs and adjacent functional materials, optimizing charge transport and spintronic behavior for device applications. Furthermore, the single-step nature of this process ensures reproducibility and scalability, making it suitable for large-scale production.

To confirm the presence of topologically protected metallic surface states and evaluate heterojunction formation, a range of advanced characterization techniques were employed. Spectroscopic and electronic measurements validated the existence of surface states, while transport studies revealed the formation of built-in heterojunctions within the heterostructures. The ability to naturally form these junctions in a single growth process marks a significant advancement in integrating TIs with functional device architectures.

We synthesized multiple TI-based eutectic composites, incorporating various second-phase materials such as metals, semiconductors, ferromagnetic, antiferromagnetic, and superconducting compounds to explore exotic interfacial phenomena. For instance, in the Sb_2TeSe_2-Sb_2Se_3 composite, where Sb_2TeSe_2 is a p-type TI and Sb_2Se_3 is a promising photovoltaic material, we confirmed the presence of topological surface states at the Fermi energy in Sb_2TeSe_2. Additionally, FTIR measurements revealed multiple peaks in the THz region. To further investigate their origin, THz nanoscopy was conducted at different THz frequencies, revealing clear optical property contrasts between different phases and at the interface. Beyond this system, additional eutectic composites—including Bi_2Te_3-Te, Sb_2Te_3-Te, Bi_2Te_3-BiTeI, Bi_2Te_3-Mn, SbTeI-Sb_2Te_3, Fe_7Se_8 -Bi_2Se_3 - were synthesized for further exploration.

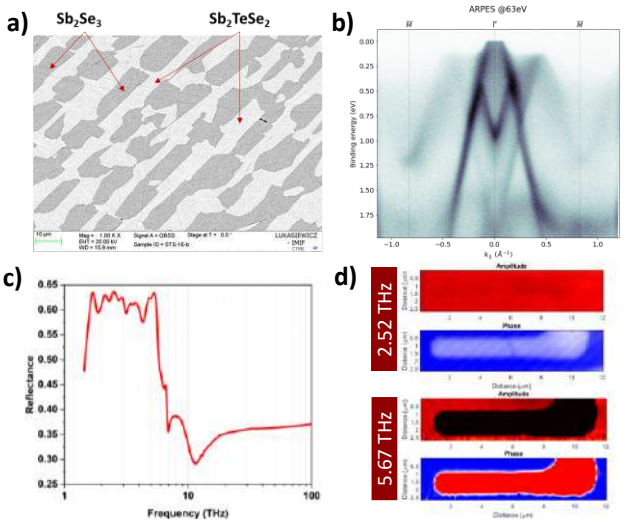


Figure 1. Sb_2TeSe_2-Sb_2Se_3 TI-based eutectic heterostructure a) SEM measurement, phase identification of Sb_2TeSe_2 and Sb_2Se_3 phases, b) μARPES measurement on Sb_2TeSe_2 phase confirms the presence of surface states with p-type doping, c) FTIR spectra with the presence of multiple peaks in THz region d) THz nanoscopy shows phase specific response at different THz frequencies.

These results align with recent studies on TI-based heterostructures, which emphasize the importance of interface quality and material stability in optimizing topological transport properties[2-3]. The successful demonstration of scalable heterostructure fabrication via directional solidification establishes a foundation for future investigations into exotic quantum phenomena, including topological superconductivity and novel magnetoelectric effects.

The authors thank ENSEMBLE[3] Project (MAB/2020/14) which is carried out within the International Research Agendas Programme (IRAP) of the Foundation for Polish Science co-financed by the European Union under the European Regional Development Fund and Teaming Horizon 2020 programme (GA. No. 857543) of the European Commission and the project of the Minister of Science and Higher Education "Support for the activities of Centers of Excellence established in Poland under the Horizon 2020 program" under contract No. MEiN/2023/DIR/3797.

References

1. Pesin, D.; MacDonald, A. H., Spintronics and pseudospintronics in graphene and topological insulators. *Nat Mater* **2012,** *11* (5), 409-16.

2. Bandopadhyay, K.; Buza, M.; Chen, C.; Materna, A.; Szlachetko, K.; Piotrowski, P.; Surma, H. B.; Borysiuk, J.; Diduszko, R.; Barinov, A.; Chen, Y. L.; Kaminska, M.; Pawlak, D. A., Self-organized topological insulator heterostructures via eutectic solidification of Bi2Te3-Te. *Next Materials* **2024,** *5*, 100252.

3. Murakami, F.; Serita, K.; Kawayama, I.; Murakami, H.; Bandopadhyay, K.; Materna, A.; Urbas, A. M.; Pawlak, D. A.; Tonouchi, M., Probing photocarrier dynamics in a Bi2Te3–Te eutectic p–n junction with a laser terahertz emission microscope. *APL Materials* **2023,** *11* (3), 031102.

Bottom-up Design of Isotropic Auxetic Metamaterials via Kolmogorov-Arnold Networks

H. Y. Huang[1*]

[1]School of Aeronautics, Northwestern Polytechnical University, China
[*]corresponding author: huangheyuan@nwpu.edu.cn

Abstract: This study introduced a data-driven structural design strategy and established a mapping between design parameters and mechanical responses for classical missing rib auxetic metamaterials via Kolmogorov-Arnold Networks. The predicted mean squared error for the stress dataset was 0.81%, only one-fourth of that achieved by multilayer perceptron models of equivalent width.

1. Structural Design

As shown in Figure 1(j), this study established tensile performance evaluation criteria at every 30° within the -90° to 90° range and uniformly assessed the variations in stress-strain curves of identical structures across different directions. The ultimate design objective was to develop an isotropic auxetic metamaterial with consistent stress-strain performance throughout the entire 0°-360° circumferential range.

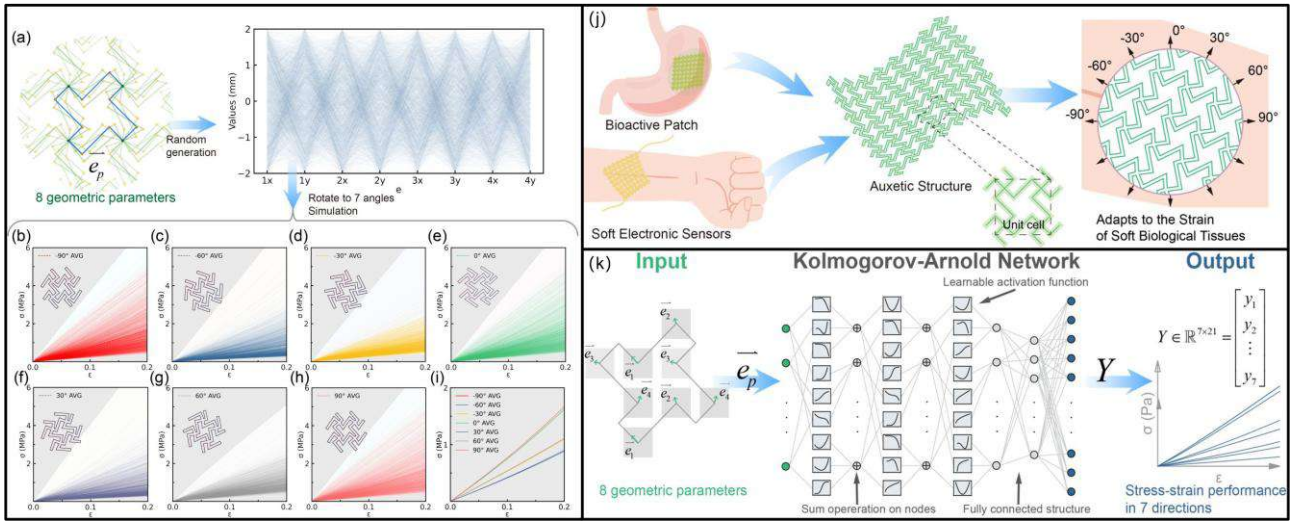


Figure 1. (a) Random generation results of the vectors; Distributions of the stress-strain datasets for generated structures under (b) -90°, (c) -60°, (d) -30°, (e) 0°, (f) 30°, (g) 60° and (h) 90°; (i) Average mechanical performance; (j) Design principles of metamaterials; (k) Workflow for KAN predictions.

To further expand the design space and identify auxetic metamaterials with isotropic properties, we introduced random perturbations to the design parameters of the basic structure, thereby enhancing the variability of the resulting configurations. By adjusting multiple parameters, structures with diverse mechanical response characteristics were generated, leading to the creation of a stress-strain dataset for multi-directional auxetic structures. This dataset served as the foundation for bottom-up design to identify optimal configurations.

2. KAN Prediction

This study randomly generated eight design parameter vectors, after which the results were shown in Figure 1(a). The parameter vectors were passed to the simulation model, and rotation angles were controlled in seven

directions. Through computational analysis, a total of 2,500 sets of nominal stress data per direction (17,500 entries in total across all seven directions) were obtained. Figure 1(b)–(h) illustrated the distribution of these 2,500 sets of results for each direction ranging from -90° to 90°. The dashed lines represented the mean value in each direction, serving as the foundation for subsequent training and optimization. As illustrated in Figure 1(k), the KAN was designed to replace the traditional MLP module in the training process. The training pipeline, built upon the PyTorch library and the Pykan library began by standardizing the input vector with Scikit-learn's StandardScaler to ensure a uniform distribution of input data.

3. Bottom-up Design

This study employed a genetic algorithm in conjunction with the KAN to achieve bottom-up optimization for isotropic stress and the best solution was named as Model III. Figure 2(a)-(b) compared the stress-strain relationships of Model III under multiple orientations in terms of predictions, simulations, experiments, and the stress dataset. The results indicated that the mean squared errors of the predicted, simulated, and experimental data are below 0.05%, confirming that Model III achieved a highly uniform and isotropic stress distribution. As illustrated in Figure 2(c)-(d), Model III were nearly circular across all directions and showed the lowest MSE, demonstrating that it achieved a more uniform isotropic response and underscoring the outstanding performance of the combined KAN and genetic algorithm.

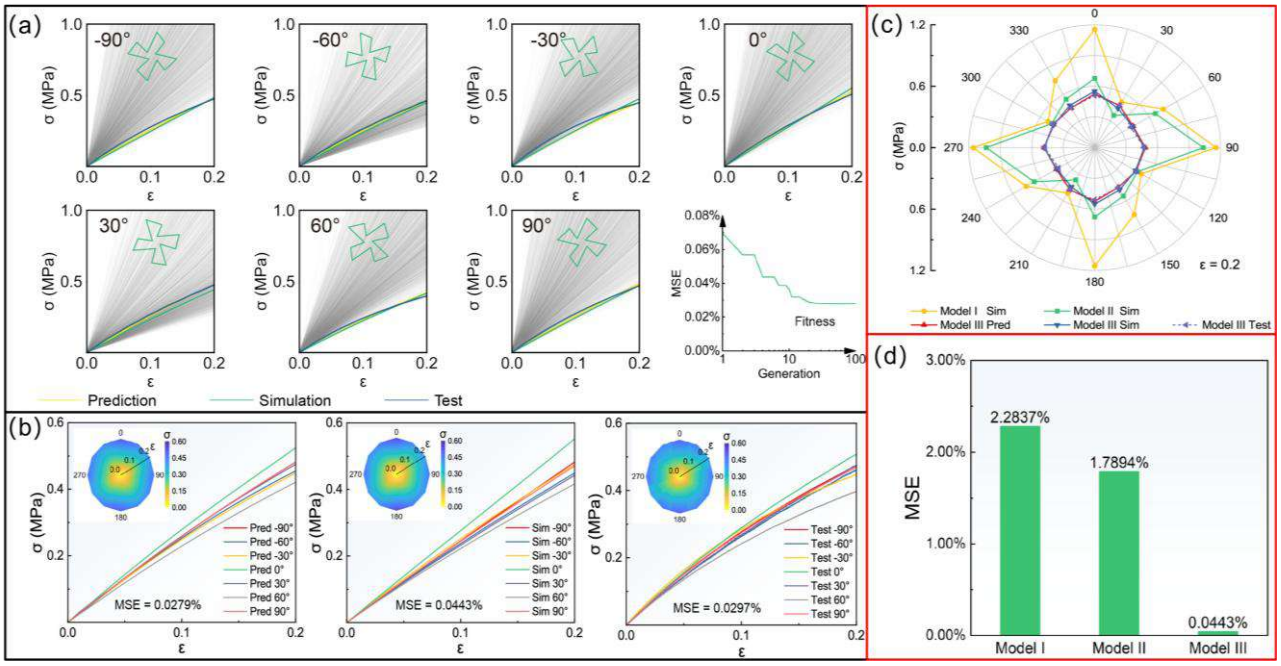


Figure 2. Bottom-up design combining KAN and genetic algorithm: (a) Comparison of predicted, simulated, and experimental stress results for Model III and genetic algorithm converges over generations; (b) Uniformity evaluation of predicted, simulated, and experimental stress responses of Model III; (c) Specific stress distribution at a strain of 0.2; (d) Comparison of average MSE.

Acknowledgements

This work was supported by the National Natural Science Foundation of China (No. 12141203); the Fundamental Research Funds for the Central Universities (No. D5000230052); the Shaanxi Innovation Ability Support Plan Project Funds (No. 2024RS-CXTD-29).

Grow with the flow: Bottom-up synthesis of anisotropic plasmonic nanoparticles within microfluidic channels

M. Lonza,[1,2] G. A. Vinnacombe-Willson,[1,3] F. Bevilacqua,[1] L. Scarabelli,[2,*] and L. M. Liz-Marzán[1,3,4,*]

[1]Author Affiliation, Country1BioNanoPlasmonics Laboratory, CIC biomaGUNE, Basque Research and Technology Alliance (BRTA), Miramon Pasealekua, 194, Donostia-San Sebastián, 20014, Gipuzkoa, Spain
[2]Department of Chemistry and Process & Resource Engineering, ETSIIT, University of Cantabria, Av. de los Castros, s/n, 39005 Santander, Spain 3CIBER de Bioingeniería, Biomateriales y Nanomedicina
[3](CIBER-BBN), 20014 Donostia-San Sebastián, Spain
[4]Ikerbasque, Basque Foundation for Science, 48013 Bilbao, Spain
*corresponding author: leonardo.scarabelli@unican.es; llizmarzan@cicbiomagune.es

Abstract: Bottom-up colloidal synthesis is the "gold standard" approach for preparing plasmonic gold nanomaterials with select compositions, sizes, and shapes, with high uniformity.[1] Here, we take a chemical approach towards translating traditional colloidal synthesis to *in situ* growth – the direct formation of morphology-controlled nanostructures directly on a substrate surface.

While *in situ* growth has been explored in the past, the quality of the fabricated nanostructures tends to have lower quality – low shape yield, high polydispersity, and limited control over the plasmonic response – compared to colloidally prepared nanostructures.[2] Additionally, many *in situ* growth schemes still rely on the implementation of colloidal seeds.[3] In this work, we aim to address this gap in synthetic know-how, with the specific goal of developing methods for fabricating gold nanostars and nanorods *in situ* on the internal walls of microfluidic channels without the use of colloidal synthesis or self-assembly. Taking a systematic approach, we were able to identify that increasing the competition between colloidal nanoparticle formation in the flowing growth solution and nucleation on the surface is necessary to facilitate successful formation of the desired nanoparticles on the substrate surface (**Figure 1A**).

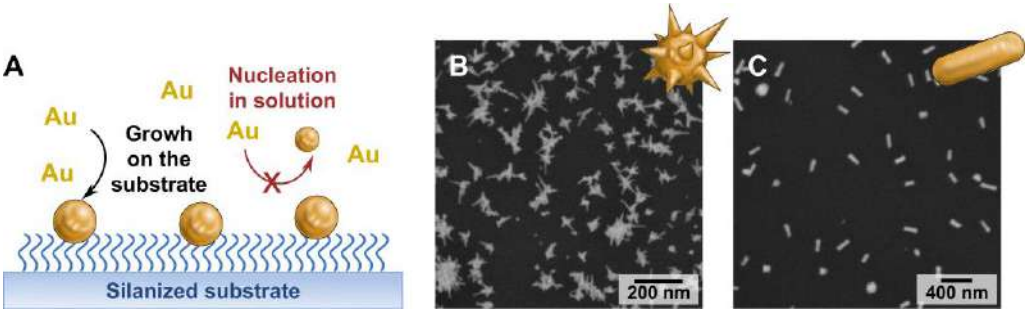


Figure 1. A: Schematic of the competition between colloidal nucleation and *in situ* growth of nanoparticles on the substrate. **B,C:** Scanning electron microscopy images of the gold nanostars (**B**) and nanorods (**C**) grown *in situ.*

Moreover, we identified key aspects of the growth conditions affecting shape yield, *i.e.*, nanoparticle density, growth solution composition, and flow rate. The extinction of the nanoparticles could also be modified *in situ* (~600 nm to 1100 nm) by changing the composition of the growth solution. Overall, tuning the chemical environment, we attain >90% shape yield for nanostars and ~80% for nanorods (**Figure 1B,C**), which in the latter case, represents a significant improvement, with previous reports obtaining only ~20-37% yield.

Ultimately, the fabricated plasmonic-microfluidic chips have the potential to be implemented in applications such as biological and chemical sensors and in microfluidic platforms incorporating 2D and 3D *in vitro* cellular models.

Acknowledgements: This work was funded by the European Research Council (ERC Advanced Grant 787510, 4DbioSERS) and MICIU/AEI/10.13039/501100011033/ FEDER/UE (PID2023-151281OB-I00). G.A.V.-W. acknowledges support from the European Union's Horizon Europe research and innovation programme under the Marie Skłodowska-Curie grant agreement No. 101105300 (PLASMOSTEMFATE). L.S. acknowledges support from the European Research Council (ERC Starting Grant 101115164, NANOGROWDIRECT). F.B. and L.M.L.-M. acknowledge funding from KU Leuven internal funds (C14/22/085).

References

1. Liz-Marzán, L. "Colloidal Synthesis of Plasmonic Nanomaterials." CRC Press, 2020.
2. Vinnacombe-Willson, G.A., Conti, Y., Stefancu, A., Weiss, P.S., Cortés, E., Scarabelli, L. "Direct Bottom-Up In Situ Growth: A Paradigm Shift for Studies in Wet-Chemical Synthesis of Gold Nanoparticles," Chem. Rev., Vol. 123, No. 13, 8488-8529.
3. Vinnacombe-Willson, G.A., Lee, J. K, Chiang, N., Scarabelli, L., Yue, S., Foley, R., Frost, I., Weiss, P.S., Jonas, S.J. "Exploring the Bottom-Up Growth of Anisotropic Gold Nanoparticles from Substrate-Bound Seeds in Microfluidic Reactors," ACS Appl. Nano Mater., Vol. 6, No. 8, 6454-6460.

Beyond Threshold: Geometry Matrix Modeling of Active Plasmonic Nanoparticles

N. Recalde[1], K. Caicedo[4], M. Mora[1], A. Aradian[3], M. Infusino[1,2], M. A. Iatì[2], R. Saija[5], O. M. Maragó[2], A. Veltri[1,2*]

[1]Universidad San Francisco de Quito, Ecuador

[2]Institute of Chemical and Physical Processes (IPCF-CNR), Messina, Italy

[3]Université de Bordeaux, CNRS, CRPP, UMR5031, F-33600 Pessac, France

[4]Institute of Applied Sciences and Intelligent Systems (ISASI-CNR), Napoli, Italy

[5]Università degli Studi di Messina, Messina, Italy

Corresponding author: aveltri@usfq.edu.ec

Abstract: We introduce the *Geometry Matrix* formalism, a modular framework for modeling active plasmonic nanoparticles in the quasi-static and Mie regimes. This approach predicts threshold gain conditions, emission spectra, and modal instabilities in gain-assisted metal nanostructures, offering a unified perspective on plasmonic nano-resonators and improving predictive modeling for plasmonic spasers.

The interaction of light with active plasmonic nanostructures is fundamental to emerging nanoscale light sources, quantum plasmonics, and plasmonic computing architectures. Predicting their emission properties and stability requires a robust electrodynamic framework that accounts for both geometric confinement and gain-assisted nonlinearities.

In this work, we introduce the Geometry Matrix formalism, a versatile analytical framework that systematically describes the optical response of active plasmonic nanoparticles, including both single-metallic and nano-shell architectures. By solving a self-consistent eigenvalue problem, this model determines the threshold gain, time evolution, and spectral emission characteristics in gain-assisted plasmonic nanostructures.

Unlike conventional modal analysis, the Geometry Matrix approach provides a direct connection between nanoparticle shape, multipolar plasmonic modes, and their stimulated emission dynamics. The Geometry Matrix formalism enables an analytical treatment of plasmonic spasers in both the quasi-static and Mie regimes. In these cases, a fully self-consistent description is possible, provided that nonlinear saturation effects are neglected. In the quasi-static approximation, the EM fields are limited to the dipolar mode, allowing for compact analytical formulations. When extended to the Mie regime, it incorporates full electrodynamic effects, enabling an accurate description of subwavelength spasers and their far-field signatures.

The system's evolution is governed by a matrix equation where $\mathbf{A}$ encodes both structural and gain-dependent properties, enabling direct modeling of threshold conditions and dynamical instabilities. We find that this governing set can be written in the following form:

$$\frac{d\mathbf{q}}{dt} = \mathbf{A} \cdot \mathbf{q} + \mathbf{b}, \tag{1}$$

where the vector $\mathbf{q}$ collects the electromagnetic mode components. The complete physical description of the system is encapsulated in the matrix $\mathbf{A}$, which we refer to as the geometry

matrix since it originates from the boundary conditions and depends explicitly on the system's geometry. The vector **b** is related to the excitation field; the non-resonant external pumping mechanisms appear in termos of the population inversion both in **A** and **b**. This formulation provides a self-contained, time-dependent electrodynamical model for gain-assisted spherically symmetric particles, offering a direct pathway to analyze their emission properties, instabilities, and nonlinear dynamics.

In the quasi-static nanoshell geometry, this approach allows analytical solutions in the saturation regime, revealing the rich spectral behavior of gain-assisted plasmonic systems in the emission regime. This framework is particularly relevant for designing ultracompact plasmonic nanolasers, tailoring metamaterial-based light sources, and engineering new active nanophotonic devices.

We acknowledge financial support from the European Union (NextGeneration EU), through the MUR-PNRR projects PE0000023-NQSTI and SAMOTHRACE (ECS00000022), the PRIN2022 "Cosmic Dust II" (2022S5A2N7), and carried out within the Project "Space It Up" funded by ASI and MUR – Contract n. 2024-5-E.0 - CUP n. I53D24000060005.

References

1. A. Veltri, A. Chipouline, and A. Aradian, "Multipolar, time-dynamical model for plasmonic nanoparticle spasers," *Scientific Reports*, vol. 6, no. 33018, 2016.

2. A. Aradian, K. Caicedo, A. Cathey, M. Infusino, and A. Veltri, "Emission dynamics and spectrum of a nanoshell-based plasmonic nanolaser spaser," *Nanophotonics*, vol. XX, 2024.

3. N. Recalde, D. Bustamante, M. Infusino, and A. Veltri, "Dynamic multi-mode Mie model for gain-assisted metal nano-spheres," *Materials*, vol. 16, no. 5, 2023.

Deterministic Bottom-Up Fabrication of Plasmonic Nanostructures on Tapered Optical Nanofibers via Blurred Electron Beam Deposition

A. Balena[1*], M. D'Amato[1], M.F. Kashif[2,3], C. Ding[1], M. De Vittorio[2,4], F. Pisanello[2], A. Bramati[1]

[1] Laboratoire Kastler Brossel, Sorbonne Université, CNRS, ENS-PSL Research University, Collège de France, France
[2] Istituto Italiano di Tecnologia - Center for Biomolecular Nanotechnologies, Italy
[3] Università degli Studi di Napoli Federico II – Department of Electric Engineering and Information Technologies, Italy
[4] Technical University of Denmark - Department of Health Technology Drug Delivery and Sensing, Denmark
[*]corresponding author: antonio.balena@lkb.upmc.fr

Abstract: We present a bottom-up method for fabricating plasmonic nanostructures on tapered optical nanofibers using Blurred Electron Beam Induced Deposition. The technique enables sub-20 nm precision, and the nanostructures show polarization-sensitive scattering, and directional emission, offering a versatile platform for on-fiber plasmonics with applications in sensing, light routing, and quantum photonics.

Localized surface plasmon resonances (LSPRs)[1] in subwavelength metallic nanostructures offer a powerful route to enhance light–matter interaction at the nanoscale, enabling a wide spectrum of applications ranging from biosensing[2] and optical manipulation[3] to quantum photonics[4]. In particular, coupling plasmonic structures to waveguides or fiber platforms[5] has recently emerged as a strategy to realize scalable, robust nanophotonic architectures. However, most existing efforts focus on multimode fibers and rely on stochastic[7] or self-assembled plasmonic structures, preventing deterministic control at the single-mode/single-structure level. Single-mode tapered optical nanofibers (TNFs)[6], with subwavelength diameters and strong evanescent fields, represent an ideal platform for achieving enhanced plasmonic interaction with precise mode confinement. Despite this potential, the deterministic integration of metallic nanostructures onto TNFs remains a challenge, primarily due to their mechanical fragility and incompatibility with conventional high-energy nanofabrication techniques.

To overcome this limitation, we introduce Blurred Electron Beam Induced Deposition (BEBID), a bottom-up fabrication method that enables the deterministic growth of platinum nanopillars and nanoantennae directly onto suspended single-mode TNFs with sub-20 nm spatial precision. In contrast to standard Focused EBID (FEBID), our approach deliberately defocuses the electron beam to reduce local pressure and mechanical stress on the fiber during deposition. This strategy allows for the nucleation of discrete plasmonic structures without damaging the nanometric, suspended substrate. The process was implemented in a dual-beam FIB/SEM system using a $MeCpPtMe_3$ precursor, with the degree of beam blurring matched to the desired nanopillar diameter.

We first assessed the mechanical compatibility of BEBID with subwavelength TNFs under varying fabrication parameters. We optimized the process to obtain high-fidelity nanopillars with diameters down to 100 nm and target heights of 300–500 nm. Energy-dispersive X-ray spectroscopy (EDX) and SEM analysis confirmed that the structures exhibit excellent geometric repeatability, with intra-sample diameter variation below 1% and inter-sample variation around 8%. Post-deposition plasma oxidation was employed to remove carbon content from the composite, increasing the Pt fraction to ~65% by volume. Optical characterization was carried out by coupling light into the TNF and recording the scattering spectra and polarization dependence from

individual nanostructures. Monomers and closely spaced dimers were investigated, showing a polarization-dependent response and a distinct ~50 nm redshift in the extinction spectra for dimers, indicating hybridized LSPR modes in the nanogap. Polar plots of scattered intensity exhibited cosine-squared behavior consistent with the anisotropic evanescent field profile, and the experimental Degree of Linear Polarization (DoLP) reached 0.92 in dimer structures, in good agreement with Finite-Difference Time-Domain (FDTD) simulations.

Furthermore, simulations of multi-pillar arrays on the TNF surface showed that increasing the number of nanopillars from one to six gradually narrows the far-field scattering lobe, concentrating the emission into a ~90° forward-propagating angular range. This directional behavior highlights the potential of BEBID-fabricated plasmonic structures as building blocks for light routing and on-fiber nanoantennae.

In conclusion, BEBID enables reliable and precise bottom-up fabrication of plasmonic nanostructures on otherwise inaccessible photonic substrates, such as suspended single-mode TNFs. The technique combines spatial accuracy, structural control, and optical functionality in a single-step process, marking a significant advancement over conventional top-down approaches. Future developments could extend this platform to different materials via precursor switching, or to complex nanophotonic arrays with tailored geometries, including Yagi-Uda antennas and emitter-coupled configurations. The deterministic nature of BEBID also opens avenues for hybrid integration with solid-state quantum emitters, where the precise spatial registration between emitter and antenna is crucial for optimized coupling. We envision that this approach will support emerging applications in quantum photonics, fiber-based sensing, and directional light emission control at the nanoscale.

Acknowledgments: This work is funded by the European Union's Horizon 2020 research and innovation programme under the Marie Skłodowska-Curie Actions grant agreement (no. 101106602).

References

1. Maier, S. A., "Plasmonics: Fundamentals and Applications", Springer US, New York, 2007.
2. Minopoli, A., Acunzo, A., Della Ventura, B., Velotta, R., "Nanostructured Surfaces as Plasmonic Biosensors: A Review", Adv Mater Interfaces, Vol. 9, No. 2101133, 2022.
3. Zhang, Y., Min, C., Dou, X., Wang, X., Urbach, H. P., Somekh, M. G., Yuan, X., "Plasmonic tweezers: for nanoscale optical trapping and beyond", Light Sci Appl, Vol. 10, No. 1, 2021.
4. Koenderink, A. F., "Single-photon Nanoantennas", ACS Photonics, Vol. 4, No. 710, 2017.
5. Zheng, D., Pisano, F., Collard, L., Balena, A., Pisanello, M., Spagnolo, B., Mach-Batlle, R., Tantussi, F., Carbone, L., De Angelis, F., Valiente, M., de la Prida, L. M., Ciracì, C., De Vittorio, M., Pisanello, F., "Toward plasmonic neural probes: SERS detection of neurotransmitters through gold nanoislands decorated tapered optical fibers with sub-10 nm gaps", Advanced Materials, Vol. 35, No. 2200902, 2023.
6. Hoffman, J. E., Ravets, S., Grover, J. A., Solano, P., Kordell, P. R., Wong-Campos, J. D., Orozco, L. A., Rolston, S. L., "Ultrahigh transmission optical nanofibers", AIP Adv, Vol. 4, No. 67124, 2014.
7. Sugawara, M., Xuan, Y., Mitsumori, Y., Edamatsu, K., Sadgrove, M., "Plasmon-enhanced single photon source directly coupled to an optical fiber", Phys Rev Res, Vol. 4, No. 043146, 2022.

Helicity Preserving Metasurface Mirrors for THz Applications

J. Yan[1], I. Katsantonis[1], S. Papamakarios[1,2], P. Konstantakis[1,3], M. Loulakis[1], Th. Koschny[4], M. Farsari[1], M. Kafesaki[1,3] and S. Tzortzakis[1,3,*]

[1]Institute of Electronic Structure and Laser, FORTH, Heraklion, Greece
[2]Department of Physics, National and Kapodistrian University of Athens, Athens, Greece
[3]Materials Science and Engineering Department, University of Crete, Heraklion, Greece
[4]Ames laboratory and Department of Physics and astronomy, Iowa State University, Iowa, USA

[*]corresponding author: stzortz@iesl.forth.gr

Abstract: We present metasurface mirrors that achieve perfect helicity-preserving reflection for circular polarization and cross-polarized reflection for linear polarization in the THz spectrum, without the need for a back-reflector. Validated via THz time-domain spectroscopy, the designs enable advanced applications in molecular chirality sensing and broadband polarization control.

Metasurfaces have emerged as a groundbreaking optical platform, enabling precise control over electromagnetic wave propagation [1-3]. Here we demonstrate how specific metasurface mirrors that operate in the low THz spectrum can achieve ideal reflection properties over either narrowband or broadband spectra depending on the design of the metasurface mirror [4]. The metasurface consists of a simple two-bar resonator structure designed for optimized polarization control, see Fig. 1.

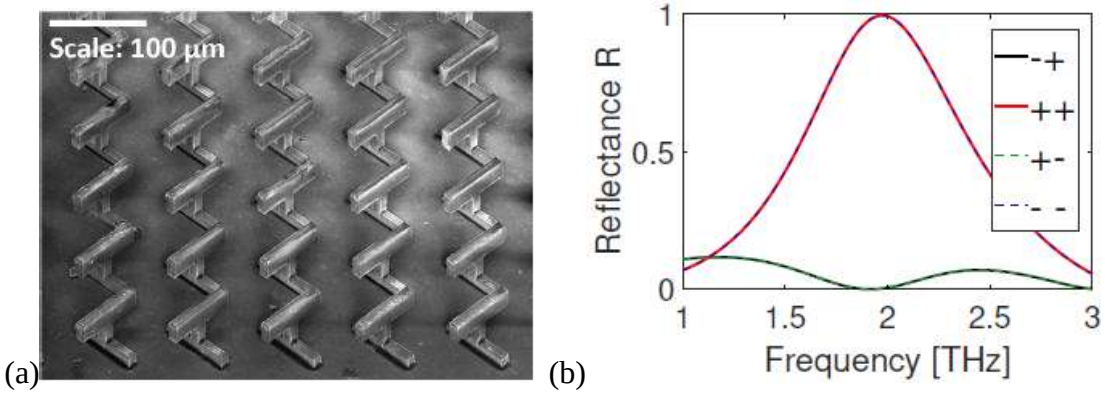


Fig. 1 a) SEM images of the fabricated metallized metasurface structures, b) Numerically calculated reflection response of the metasurface to normally incident CP waves, perfect co-polarized reflection is demonstrated.

The metasurface design provides perfect cross-polarized reflection for linearly polarized waves and perfect helicity-preserving reflection for circularly polarized waves. This effect is attributed to the Pancharatnam-Berry phase, which imparts an additional geometric phase to the reflected wave. The proposed metasurfaces are fabricated using 3D direct laser writing, followed by electroless silver plating for metallic coverage. The fabricated structures were experimentally validated through THz time-domain spectroscopy, demonstrating strong agreement with theoretical predictions.

Applications of such metasurfaces include beam steering and focusing by engineering the phase gradient of the reflected wave. Additionally, its helicity-preserving properties make it highly valuable in molecular chirality sensing and enantiomer detection, which have important implications for chemistry and life sciences. Furthermore, the study explores the potential of translating this concept to the optical frequency range using a fully dielectric version of the metasurface, extending its applications to high-frequency photonics.

Acknowledgements: This research work was supported by the Horizon 2020 RISE Project (CHARTIST, 101007896), the European Union under the call “EIC Pathfinder Open 2022” (Project PULSE, project no. 101099313). Also, it was co-funded by the Stavros Niarchos Foundation (SNF) and the Hellenic Foundation for Research and Innovation (H.F.R.I.) under the 5th Call of “Science and Society” Action – “Always Strive for Excellence – Theodore Papazoglou” (Project Number: 9578.), H.F.R.I. "2nd Call for H.F.R.I. Research projects to support faculty members and Researchers" (project number: 4542), and European Union project FABulous (HORIZON-CL4-2022- TWIN-TRANSITION- 01-02, GA:101091644). Work at Ames national Laboratory was supported by the Department of Energy (Basic Energy Sciences, Division of Materials Sciences and Engineering) under Contact No DEAC02-07CH11358.

References

[1] N. Yu and F. Capasso, “Flat optics with designer metasurfaces,” *Nature Materials*, vol. 13, no. 2, pp. 139–150, 2014.

[2] J. P. B. Mueller, N. A. Rubin, R. C. Devlin, B. Groever, and F. Capasso, “Metasurface polarization optics: Independent phase control of arbitrary orthogonal states of polarization,” *Physical Review Letters*, vol. 118, no. 11, 2017.

[3] F. Ding, A. Pors, and S. I. Bozhevolnyi, “Gradient metasurfaces: A review of fundamentals and applications,” *Reports on Progress in Physics*, vol. 81, no. 2, 2018.

[4] J. Yan, I. Katsantonis, S. Papamakarios, P. Konstantakis, M. Loulakis, Th. Koschny, M. Farsari, S. Tzortzakis, and M. Kafesaki, “3D-printed mirror-less helicity preserving metasurface "mirror" for THz applications,” *under review*

Composite plasmonic nanoparticles with extraordinary optical properties: Nanolasing, artificial magnetism, and spatial dispersion

A. Aradian[1*], K. Caicedo[2,3], R. Dwivedi[1], A. Cathey[4], M. Mora[3], M. Infusino[3], K. Vynck[5], A. Veltri[3], and A. Baron[1]

[1]Centre de Recherche Paul Pascal, University of Bordeaux & CNRS, Bordeaux, France
[2]Istituto di Scienze Applicate e Sistemi Intelligenti (ISASI) - CNR, Italy
[3]Universidad San Francisco de Quito, Quito, Ecuador
[4]Max Planck Institute for Plasma Physics, Garching, Germany
[5]Institut Lumière Matière, University Claude Bernard Lyon 1 & CNRS, Lyon, France
[*]corresponding author: ashod.aradian@crpp.cnrs.fr

Abstract: Nanoparticles form a wide-spread class of objects with multiples applications in the field of nanophotonics and optics. I will present two examples of plasmonic nanoparticles whose composite internal structures enable extraordinary optical properties: gain-metal nanoshells allowing nanolasing, and dense plasmonic clusters displaying artificial magnetism and spatial dispersion.

Progress over recent decades in the controlled synthesis of nanoparticles with various shapes, materials, and internal structure has allowed to extend their properties into previously unexplored regimes of light-matter interaction at the nanoscale. This is notably the case for nanoparticles inclusive of plasmonic components, capable of enhancing the interaction with light through resonances with the free-electron gas in the metal.

In this talk, I will present two examples of plasmonic nanoparticles whose composite internal structures enable extraordinary optical properties: (i) gain-metal hybrid nanoshells allowing nanolasing, and (ii) dense plasmonic clusters displaying artificial magnetism and spatial dispersion.

My first example will be about nanolasing: plasmonic nanolasers have triggered unabated interest in the past twenty years, as they could provide compact and versatile nanosized light sources. We studied theoretically [1] a hybrid nanoshell system made of an active (gain) medium core and a silver shell geometry as shown in Fig. 1(a), assuming that the gain medium is provided with some energy input through external pumping. We used a time-dependent model of the fields and polarizations inside and outside the nanoshell, with the help of optical Bloch equations and the free-electron equation of motion. We showed that above a certain level of gain in the system (i.e., above a certain intensity of pumping), the nanoshell starts to lase. We studied the dynamics of lasing above this threshold and find that it is single-mode (dipolar only). After a transient, the nanolaser reaches a steady state of emission where the intensity of the emitted field is constant, but its complex field amplitude is submitted to slow rotations in time. Such behavior is commonly known as a “frequency pull-out” effect in the field of classical lasers. Interestingly, while pull-out effects are responsible for minute shifts of laser frequencies in macroscopic lasers, we find that in the nanoshell laser, these effects are comparatively huge; so much that they reshape the spectrum of emission [see Fig. 1(b)] and are ultimately responsible for defining the emission linewidth of the nanolaser. This novel finding is a strikingly different paradigm as compared to standard laser physics, and expands the current knowledge on nanolasers,

The second example of complex nanoparticles I will present concerns dense plasmonic clusters. Clusters of

particles in general have been an extensive topic of research in nanophotonics and especially in metamaterials, where they could provide useful new properties. Dense plasmonic clusters are notoriously difficult to investigate due to strong, multiple interparticle couplings. We studied [2] spherical clusters as shown in Fig. 1(c), made of hundreds of small, randomly-packed plasmonic nanoparticles (gold nanoparticles with radius 7 nm) with variable particle densities. We set to determine whether their electromagnetic behavior could be appropriately described as that of a sphere made of a homogeneous medium [Fig. 1(c)] with effective parameters, like electric permittivity, magnetic permeability, etc. (so-called "homogenization"). Such effective descriptions, when possible, are interesting because they are intuitive and computationally-efficient for use in calculations.

To this purpose, we calculated the scattering of an incoming wave onto such clusters by means of high-precision T-matrix numerical simulation, and compared results with the scattering response of spheres made with a fictitious homogeneous medium. The values of the constitutive parameters of the fictitious medium were determined through careful fitting, so that the response of the homogeneous spheres accurately reproduced that of the cluster. To reach such a fitting for clusters with densities above 40%, we found that the equivalent medium had to include spatial dispersion effects, namely: (i) artificial optical magnetism, which is arising solely by virtue of interparticle couplings within the clusters (no magnetism is present in the individual gold nanoparticles) [Fig. 1(d)]; (ii) longitudinal waves in the medium, localized near the cluster borders. Our description should be seen as an attempt at providing a better and more consistent approach of dense cluster systems, but still easy to understand physically.

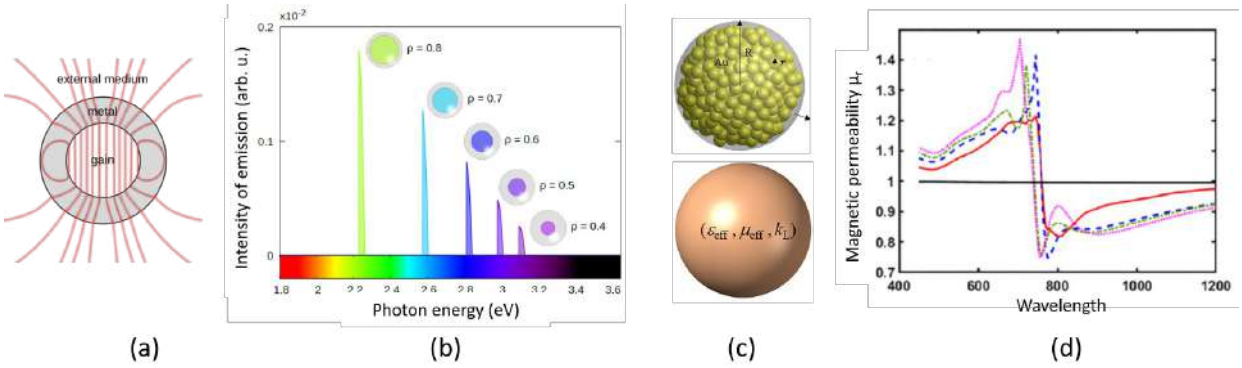


Figure 1. (a) Nanoshell geometry for lasing. **(b)** Emission spectra obtained for nanoshells with various aspect ratios ρ of the internal-to-external radii. **(c)** top, dense spherical cluster of small gold nanoparticles used in T-matrix simulations; bottom, equivalent homogeneous sphere made of an effective medium with spatial dispersion. **(d)** The magnetic permeability μ_r of the homogeneous medium vs. wavelength (different curves correspond to different cluster sizes) is seen to deviate from unity (artificial magnetism).

References

1. Aradian, A., K. Caicedo, A. Cathey, M. Mora, N. Recalde, M. Infusino and Alessandro Veltri, "Emission dynamics and spectrum of a nanoshell-based plasmonic nanolaser spaser," Nanophotonics, Vol. 13, 4817, 2024.
2. Dwivedi, R., A. Aradian, V. Ponsinet, K. Vynck and A. Baron, "Effective-medium description of dense clusters of plasmonic nanoparticles with spatial dispersion," Phys. Rev. A, Vol. 109, 023507, 2024.

Light scattering of hyperuniform-disordered metasurfaces

A. Sprafke,[1,2*] P. M. Piechulla,[3] D. Tesch,[1] P. Dhawan,[1] C. Rockstuhl,[4,5] R. B. Wehrpohn[1]

[1]Institute of Physics, Martin Luther University Halle-Wittenberg, Germany
[2]Center for materials science, Martin Luther University Halle-Wittenberg, Germany
[3]Institute of Theoretical Solid State Physics, Karlsruhe Institute of Technology, 76131 Karlsruhe, Germany
[4]Institute of Nanotechnology, Karlsruhe Institute of Technology, 76131 Karlsruhe, Germany
[*]corresponding author: alexander.sprafke@physik.uni-halle.de

Abstract: We explore scattering metasurfaces employing hyperuniform disorder (HuD), a special spatial arrangement in the realm of disorder. By engineering spatial correlations in arrays of scatterers, HuD metasurfaces combine characteristics of ordered and random configurations, enabling tailored angular scattering and expanding design flexibility for photonic devices.

Optical metasurfaces are typically highly ordered and fabricated with precision using expensive tools [1]. However, the inherent imperfections in large-scale nanophotonic devices, along with recent advances in bottom-up nanofabrication techniques and design strategies, have highlighted the potential benefits of incorporating disorder to achieve specific optical functionalities [2]. Within the realm of correlated disorder exists the exotic subclass of hyperuniform disorder. In these, density fluctuation are suppressed on large length scales and therefore its representation in fourier space, e.g. the structure factor $S(\boldsymbol{q})$, features vanishing components at the origin, $S(\boldsymbol{q} \to 0) = 0$ [3].

For optical metasurfaces comprising identical scatterers arranged in a HuD array (Figure 1), we find that hyperuniformity enables a novel leverage to tailor light scattering via the precise interplay of form factor f (property of individual scatterer) and structure factor S (property of array). The interplay of f and S is particularly strong when employing Mie resonances with their pronounced scattering cross section [4].

A further focus of our related work are scalable bottom-up fabrication methods of photonic HuD structures [5,6]. Large-area metasurfaces with controlled disorder and without the constraints and expenses typically associated with top-down manufacturing facilitate cost-effective production and also broaden the potential integration of HuD for light management in optoelectronic devices such as solar cells and OLEDs [7,8,9,10].

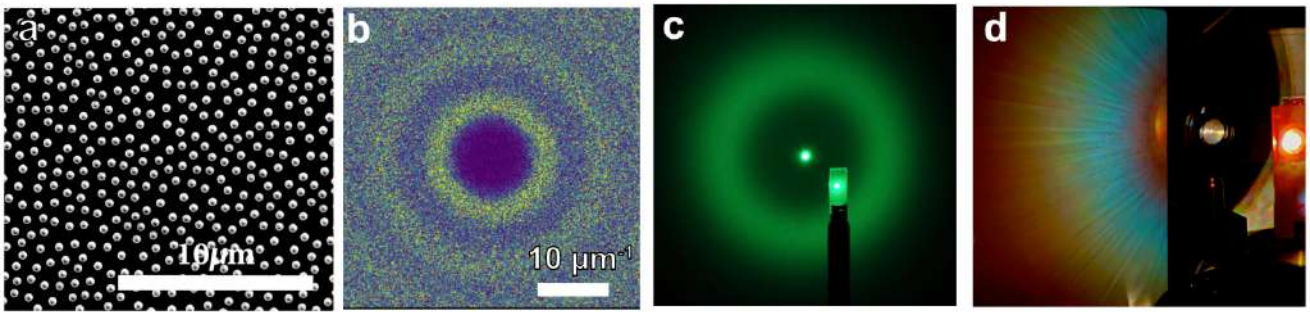


Figure 1 (a) Hyperuniform-disordered array of a-Si Mie scatterers. (b) Structure factor of array. Projection of forward scattering of array onto a screen using (c) green and (d) white laser light.

References

1. S. A. Schulz *et al.*, "Roadmap on photonic metasurfaces," *Appl. Phys. Lett.*, 124, 260701, 2024, doi: 10.1063/5.0204694.
2. P. Lalanne, M. Chen, C. Rockstuhl, A. Sprafke, A. Dmitriev, and K. Vynck, "Disordered Optical Metasurfaces: Basics, Properties, and Applications," *Adv. Opt. Photon.* 17, 2025, doi: 10.1364/AOP.537175.
3. S. Torquato, "Hyperuniform states of matter," *Phys. Reports*, 745, 2018, doi: 10.1016/j.physrep.2018.03.001.
4. P. M. Piechulla, B. Fuhrmann, E. Slivina, C. Rockstuhl, R. B. Wehrspohn, and A. N. Sprafke, "Tailored Light Scattering through Hyperuniform Disorder in Self-Organized Arrays of High-Index Nanodisks," *Adv. Opt. Mater.*, 9, 2100186, 2021, doi: 10.1002/adom.202100186.
5. P. M. Piechulla *et al.*, "Fabrication of Nearly-Hyperuniform Substrates by Tailored Disorder for Photonic Applications," *Adv. Opt. Mater.*, 6, 1701272, 2018, doi: 10.1002/adom.201701272.
6. P. M. Piechulla, R. B. Wehrspohn, and A. N. Sprafke, "Toward Hyperuniform Disorder via Self-Assembly of Bidisperse Colloidal Patterns at an Electrode," *Adv. Mater. Interfaces* 10, p. 2201395, 2022, doi: 10.1002/admi.202201395.
7. P. Dhawan, M. Gaudig, A. Sprafke, P. Piechulla , R.B. Wehrspohn, and C. Rockstuhl, "Anti-Reflective Graded-Index Metasurface with Correlated Disorder for Light Management in Planar Silicon Solar Cells," *Adv. Opt. Mater.* 12, 2302964, 2024, doi: 10.1002/adom.202302964.
8. P. M. Piechulla, Y. J. Donie, R. B. Wehrspohn, U. Lemmer, G. Gomard, and A. N. Sprafke, "Correlated Disorder Substrate-Integrated Nanodisk Scatterers for Light Extraction in Organic Light Emitting Diodes," *Adv. Opt. Mater.* 11, 202557, 2023, doi: 10.1002/adom.202202557.
9. P. M. Piechulla *et al.*, "Antireflective Huygens' Metasurface with Correlated Disorder Made from High-Index Disks Implemented into Silicon Heterojunction Solar Cells," *ACS Photonics* 8, 3476–3485, 2021, doi: 10.1021/acsphotonics.1c00601.
10. P. Dhawan *et al.*, "On the reliability of the collective coordinate method to simulate metasurfaces with correlated disorder used for light management," *J. Opt. Soc. Am. B* 40, B8, 2023, doi: 10.1364/JOSAB.476859.

Tailoring the spontaneous emission of magnetic dipole transitions with plasmonic multipods

J. Davis[1], S. Bidault[2], M. Mivelle[3], M. Tréguer-Delapierre[4], and A. Baron[1,5*]

[1]Université de Bordeaux, CNRS, CRPP, UMR 5031, F-33600, France

[2]Institut Langevin, ESPCI Paris, Université PSL, CNRS, F-75005 Paris, France

[3]Sorbonne Université, CNRS, Institut des Nanosciences de Paris, INSP, F-75005 Paris, France

[4]Université de Bordeaux, CNRS, ICMCB, UMR5026, F-33600 Pessac, France

[5]Insitut Universitaire de France, 1 rue Descartes, F-75231 Paris Cedex 05, France

Corresponding author: alexandre.baron@u-bordeaux.fr

Abstract: Plasmonic multipod structures composed of N metallic satellites around a dielectric core are designed and optimized to serve as bright, efficient and robust sources of magnetic light. Our approach based on quasi-normal mode analysis reveals that structures with at least tetrahedral symmetry exhibit far superior behavior compared to structures with poor symmetry.

Plasmonic multipods (or N-pods) are complex composite particles composed of a low index dielectric core and N metallic satellites distributed symetrically on the core (see Fig. 1(a)). They have garnered a lot of attention in recent years because they exhibit strong magnetic dipole moments [1, 2]. The Purcell effect can be leveraged in such structures to enhance the spontaneous emission of magnetic dipole transitions – naturally weak processes – while simultaneously suppressing the electric dipole transition [3]. Here, we investigate the optical emission of magnetic dipole transitions in such N-pod structres and optimize their geometries. We resort to quasi-normal modes (QNMs) for analysis, which provides a major advantage over conventional real-frequency methods by significantly reducing the parameter space exploration and offering deep physical insight. We demonstrate that N-pods, well within current fabrication capabilities (see for instance [2, 4]), are excellent candidates to achieve a large, orientation- and volume-independent magnetic Purcell factor with reduced Ohmic losses. Furthermore, we successfully suppress electric dipole transitions, achieving a magnetic branching ratio exceeding 95% across nearly all N-pod particles. For highly symmetrical designs, optimization of the core and satellite radii predicts radiated magnetic Purcell factors exceeding 180.

For each N-pod, we consider structures composed of a silica core with a fixed radius of $r = 42.5$ nm, surrounded by N silver satellites of radius r_{sat}, which is treated as a variable. The satellites are positioned according to solutions of the Thomson problem. These structures support both magnetic and electric dipole quasi-normal modes (QNMs) (see Fig. 1(c,d)). The satellite sizes are varied, and the magnetic Purcell factor is defined as γ_m/γ_0, where γ_m is the decay rate of a magnetic dipole positioned at the core center, and γ_0 is the corresponding free-space decay rate. This factor is evaluated for three principal dipole orientations and then averaged over all possible orientations (see Fig. 1(e) for an example).

This procedure is repeated for various values of N, revealing that the maximum average Purcell enhancement generally increases with the number of satellites, though it exhibits non-trivial sensitivity to dipole orientation (see Fig. 1(f)). A Figure of Merit (FOM) is introduced to account for: (i) robustness against dipole orientation and polydispersity, (ii) the branching ratio β_m, defined as the ratio of the magnetic to electric Purcell factors, and (iii) quantum efficiency. After optimizing this FOM, our results indicate that highly symmetric multipods—particularly

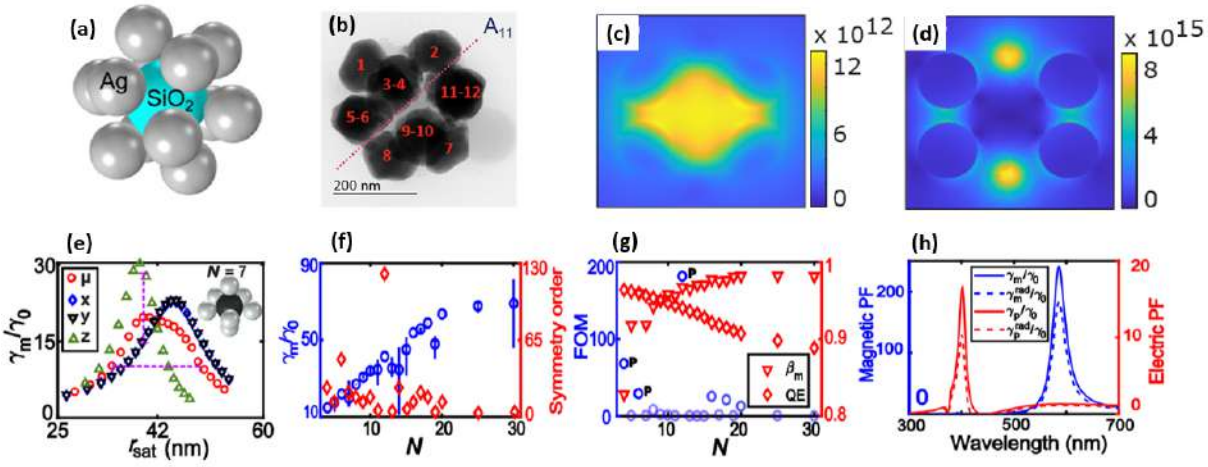


Figure 1: (a) Illustration of a 12-pod consisting of a silica core and Ag satellites. (b) TEM image of a typical 12-pod fabricated via nanochemistry (adapted from [2]). (c) FEM simulation of the absolute value of the modal magnetic field QNM. (d) Corresponding simulation for the electric field of the electric dipole QNM. (e) Example of the (x, y, z)-averaged and orientation-averaged evolution of the magnetic Purcell enhancement as a function of satellite radius for a 7-pod. (f) Optimized magnetic Purcell enhancement and symmetry orders as a function of the number of satellites in the multipod. (g) Dependence of the optimized figure of merit (FOM) on N, highlighting the superiority of the dodecapod structure ($N = 12$) and other highly symmetric N-pods (Platonic polyhedra are indicated with a P). The red triangles represent the branching ratio β_m, while the red diamonds denote the quantum efficiency (QE). (c–g) Computed for structures with a fixed silica core radius of $r = 42.5$ nm. (h) Optimized spectral variations of the magnetic Purcell factor for a dipole positioned at the center of a dodecapod (blue). The corresponding electric Purcell enhancement is shown in red.

those corresponding to Platonic solids—perform exceptionally well compared to all other structures (see Fig. 1(g)).

A full optimization of the magnetic Purcell factor, considering both core and satellite radii as parameters, identifies dodecapod structures with Purcell factors as high as 250 and radiation factors reaching 180 for the magnetic dipole transition.

References

1. V. Many, R. Dézert, E. Duguet, A. Baron, V. Jangid, V. Ponsinet, S. Ravaine, P. Richetti, P. Barois, and M. Tréguer-Delapierre, "High optical magnetism of dodecahedral plasmonic meta-atoms," *Nanophotonics*, vol. 8, no. 4, pp. 549–558, 2019.

2. L. Lermusiaux, V. Many, P. Barois, V. Ponsinet, S. Ravaine, E. Duguet, M. Tréguer-Delapierre, and A. Baron, "Toward huygens' sources with dodecahedral plasmonic clusters," *Nano Letters*, vol. 21, no. 5, pp. 2046–2052, 2021.

3. M. Sanz-Paz, C. Ernandes, J. U. Esparza, G. W. Burr, N. F. Van Hulst, A. Maitre, L. Aigouy, T. Gacoin, N. Bonod, M. F. Garcia-Parajo, *et al.*, "Enhancing magnetic light emission with all-dielectric optical nanoantennas," *Nano letters*, vol. 18, no. 6, pp. 3481–3487, 2018.

4. A. Désert, J. Morele, J.-C. Taveau, O. Lambert, M. Lansalot, E. Bourgeat-Lami, A. Thill, O. Spalla, L. Belloni, S. Ravaine, *et al.*, "Multipod-like silica/polystyrene clusters," *Nanoscale*, vol. 8, no. 10, pp. 5454–5469, 2016.

Integration of plasmonic metamaterials in sensing and photocatalytic technologies via scalable fabrication techniques

Anastasiia Zaleska, Wayne Dickson, Francesco Lotti, Anatoly Zayats

Department of Physics, King's College London, UK
*corresponding author: anastasiia.zaleska@kcl.ac.uk

Abstract: Plasmonic metamaterials have been widely used for many application, including optical sensing and photocatalysis. Here we will discuss the fabrication techniques that were used to achieve low-cost and scalable nanosensor technology for hydrogen detection and photocatalyst system for reduction of CO2. We will also discuss in-situ optical characterization methods that can improve device performance and sensitivity during the fabrication process.

Intriguing electromagnetic coupling in eutectic ZnO-$ZnWO_4$ from visible to medium infrared range

E. Petronijevic[1,*], A. Belardini[1], M. C. Larciprete[1], M. Centini[1], G. Leahu[1], R. Li Voti[1] M. Tomczyk[2,3], P. Osewski[4], P. Piotrowski[2,3], D. A. Pawlak[2,3,4], and Concita Sibilia[1]

[1]Univesità di Roma La Sapienza, Dip.SBAI- Via Scarpa 16,00161 Roma, Italy
[2]Centre of Excellence ENSEMBLE3 sp. z o.o., Wólczyńska 133, 01-919 Warsaw, Poland
[3]Department of Chemistry, University of Warsaw, Pasteura Street 1, Warsaw, Poland
[4]Łukasiewicz Research Network – Institute of Microelectronics and Photonics, Wólczyńska 133, 01-919 Warsaw, Poland
[*]emilija.petronijevic@uniroma1.it

Abstract: Bottom-up approaches in fabrication of eutectic metamaterials has opened new routes in designing intriguing electromagnetic properties. Here we show remarkable behavior of ZnO-$ZnWO_4$ eutectic, from second harmonic generation and polarization-dependent luminescence in the visible to metamaterial response in the medium infrared range.

Eutectic composites are self-assembled materials with properties different from those of the constituent materials. Here we investigate zinc oxide-zinc tungstate (ZnO-$ZnWO_4$) eutectic, in which parallel ZnO thin layers (lamellae) are self-organized and embedded in a dielectric $ZnWO_4$ matrix in a fairly regular manner. The samples were fabricated by means of the micro-pulling-down (μ-PD)[1,2], resulting in $\approx$240 nm ZnO lamellae (inset in Fig. 1). ZnO phase was of high quality and crystallinity, as confirmed by a strong exciton emission at room temperature in the blue range.

We start by exciting the eutectic with linearly polarized light at 370 nm and monitor its photoluminescence (PL). PL is governed by an unique refractive-index-matching condition between the ZnO and biaxial $ZnWO_4$ matrix[3], which leads to its strong polarization dependence. Fig. 1 shows PL spectra for the different orientation of the excitation beam nm with respect to the lamellae. The condition for a strong PL enhancement is when the incident polarization is orthogonal to the lamellae. This was further confirmed by numerical analysis with commercial finite-difference-time-domain electromagnetic solver[4]. The same polarization dependence is exhibited in the PL signal in the output, as the PL exits the sample prevalently with the polarization "orthogonal-to-lamellae".

We further show that such samples exhibit optimized nonlinear optical properties. Specifically, we demonstrate efficient optical second harmonic generation (SHG) at pumping wavelength of 800 nm. The eutectic composite relies on the specific crystallographic orientation of the constituent materials: the c-axis of ZnO naturally orients perpendicular to the growth direction, ending up in the plane of the sample. Contrary to the single ZnO crystal, this ensures the best condition for phase matching in SHG when the sample is excited at the normal incidence. Finally, we show that in the IR atmospheric window (8-14 μm), eutectic ZnO-$ZnWO_4$ behaves as a self-assembled metamaterial with strong polarization dependence. As such, it shows great potential for the development of photonics components in the IR.

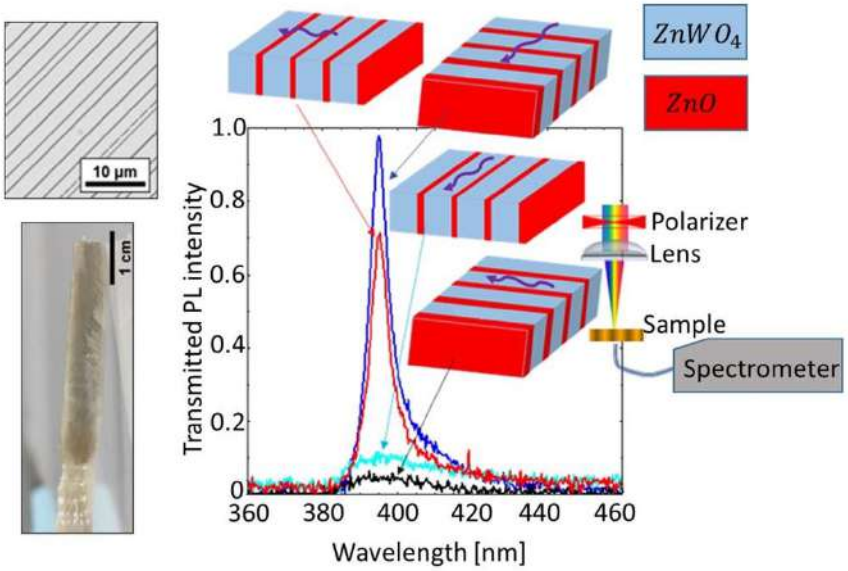


Figure 1. PL intensity of the eutectic depends on the polarization of the excitation beam with respect to the lamellae; inset: SEM image of ZnO-$ZnWO_4$ (top) and the sample photo (bottom).

In conclusion, we strongly believe that the micro-pulling-down route of eutectic material fabrication could be further used in designs where large-scale and cost-effective eutectic devices are needed. Our experimental results demonstrate the potential of lamellae-based eutectics for the development of both passive and active polarization-sensitive optical devices in various spectral ranges.

The authors thank the ENSEMBLE^3 Project carried within the Teaming for Excellence Horizon 2020 program of the European Commission (GA No. 857543), and the International Research Agendas Program (MAB/2020/14) of the Foundation for Polish Science co-financed by the European Union under the European Regional Development Fund and Teaming Horizon 2020 program of the European Commission

References

1. P. Osewski *et al.*, "New Self-Organization Route to Tunable Narrowband Optical Filters and Polarizers Demonstrated with ZnO–$ZnWO_4$ Eutectic Composite," Adv. Opt. Mater. 8, 1901617 (2020).
2. M. Tomczyk *et al.*, "Bulk nanocomposite made of ZnO lamellae embedded in the $ZnWO_4$ matrix: growth from the melt," J. Mater. Sci. 56, 11219 (2021).
3. P. Osewski *et al.*, "Self-Phase-Matched Second-Harmonic and White-Light Generation in a Biaxial Zinc Tungstate Single Crystal," Sci. Rep. 7, 1 (2017).
4. E. Petronijevic *et al.*, "ZnO-ZnWO4 eutectic: enhanced electromagnetic behaviour from visible to MIR," Adv. Mater. 2206005 (2022).

Non-Hermitian Photonics: Topological, Disordered and Quantum systems

Emission of emitters into the bulk or photonic graphene

Francesco Ciccarello[1]

[1*]University of Palermo, Italy

[*]corresponding author: francesco.ciccarello@unipa.it

Abstract: We study emission properties of quantum emitters coupled to a 2D honeycomb lattice of coupled resonators, a setup by now within reach in some experimental platforms.

We show that, by combining non-local coupling ("gian atom") with an engineered synthetic electric field, an atom in the bulk can emit chiral light orthogonal to the electric field without the need for breaking time reversal symmetry of the lattice.

We additionally study emitters coupled to the latttice edge. We show that, for suitable edge geometry (e.g. zigzag or bearded) vacuum Rabi oscillations, long-range excitation transfer and long-range dipole-dipole dispersive interactions can occur.

Enhanced Sensing Using Hysteresis Loops near Exceptional Points

A. Suntharalingam[1], L. Fernandez-Alcazar[1,2,3], P. Fabian Wagner-Boian[3], M. Reisner[1], U. Kuhl[4], T. Kottos[1,*]

[1]Wave Transport in Complex Systems Lab, Department of Physics, Wesleyan University, Middletown, CT 06459, United States

[2]Institute for Modeling and Innovative Technology, IMIT (CONICET - UNNE), W3404AAS, Corrientes, Argentina

[3]Physics Department, Natural and Exact Science Faculty, Northeastern University of Argentina, W3404AAS, Corrientes, Argentina

[4]Université Côte d'Azur, CNRS, Institut de Physique de Nice (INPHYNI), 06200, Nice, France

[*]corresponding author: userid@institution.edu

Abstract: The Riemann Surface near exceptional point degeneracies (EPD) of nonlinear systems with dynamical parity-time symmetry demonstrates the formation of a hysteresis loop whose width scales sublinearly with the distance from the EPD. We show that this hysteresis can be utilized as a noise-resilient measurand for ultrasensitive sensing.

Sublinear resonant deviations from an exceptional point degeneracy (EPD) has been recently promoted as a sensing scheme. However, there is still an ongoing debate whether the sensitivity advantage is negated by an increase in fundamental noise – especially when active elements induce self-oscillations. In this case, nonlinearities are crucial in stabilizing amplifying modes and mitigating noise effects. A drawback is the formation of hysteresis loops that signal a transition to unstable modes. This can only be alleviated by precise cavity symmetry management. Here, utilizing two coupled nonlinear RLC tanks with balanced amplification and attenuation, we demonstrate that an explicit symmetry violation, induced by sweeping the resonant detuning of the RLC tanks, reveals a hysteresis loop near the EPD whose width scales sublinearly with the inter-tank coupling. Our proposal re-envisions this disadvantageous feature as a sensing protocol with diverging sensitivity, enhanced signal-to-noise ratio, and self-calibration without requiring delicate symmetry control. As such, it opens new avenues in metrology as well as for optical/RF switching and triggering.

References

1. Suntharalingam, A. and Fernandez-Alcazar, L. and Wagner-Boian, F. and Reisner, M. and Kuhl, U., and Kottos, T. "Symmetry violation-driven hysteresis lopps as measurands for noise-resilient sensors," submitted (2025).

Light Tra[pping by Non-Hermitian Thin Films

L. Grineviciute[1], I. Lukosiunas[2], J. Nikitina[1], I. Meskelaite[2], D. Gailevicius[2], and K. Staliunas[3,4,*]

[1]Center for Physical Sciences and Technology, Savanoriu Ave. 231, LT-02300 Vilnius, Lithuania
[2]Vilnius University, Laser Research Center, Sauletekio Ave. 10, Vilnius, Lithuania
[3]UPC, Dep. de Fisica, Rambla Sant Nebridi 22, 08222, Terrassa, Spain
[4]ICREA, Passeig Lluís Companys 23, 08010, Barcelona, Spain

[*]corresponding author: kestutis.staliunas@icrea.cat

Abstract: One of the exceptional features of non-Hermitian systems is the unidirectional wave interactions. At a particular (exceptional) point the situation can be achieved, that the external radiation is efficiently coupled into the system, but the internal radiation cannot escape backwards. We realize this idea in non-Hermitically modulated thin films, consisting of a Hermitian part - the periodic corrugation of the surfaces of a film, and a non-Hermitian part - the modulation of losses along the film. We prove numerically and demonstrate experimentally that the incident radiation, coupled with such a non-Hermitian thin film, is unidirectionally trapped into a planar mode of the film, does not escape from the film (or escape weakly due to experimental imperfections), and is efficiently absorbed there.

One of the exceptional features of non-Hermitian systems is the unidirectional wave interactions. Simultaneous modulation of the real and the imaginary part of the interaction potentials (of the refractive index and the gain/loss in the case of optical systems) can result in unequal coupling coefficients between the fields of different parts of the system. The unidirectional coupling can be arranged between internal fields and external radiation as well. At a particular (exceptional) point, the situation can be achieved, that the external radiation is coupled into the system, but the internal radiation cannot escape backwards. In this way, the incident radiation can be trapped inside the non-Hermitian system and, eventually, can be efficiently absorbed there.

We realize this idea in non-Hermitically modulated thin films, see Fig.1. The modulation consists of a Hermitian part – the periodic corrugation of the surfaces of a thin film, and a non-Hermitian part – the modulation of losses on the surface of the film. We prove numerically and demonstrate experimentally that the incident radiation, coupled with such a non-Hermitian thin film, is unidirectionally trapped into a planar mode of the film, does not escape from the film (or escape weakly due to experimental imperfections), and is efficiently absorbed there.

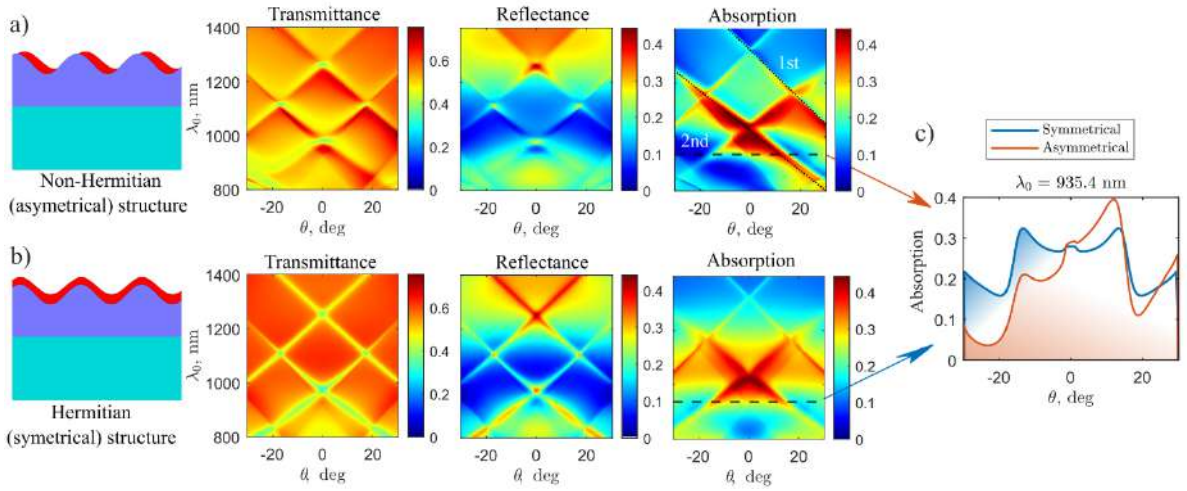


Figure 1. a) Non-Hermitian planar waveguide, with periodically modulated surface and the absorbing layer (red color) followed by the transmittance, reflectance and indirectly calculated absorption maps, b) the reference configuration with uniformly distributed absorber along the modulated planar structure with transmission, reflection and absorption maps; c) The calculated angular absorption profiles for the scheme with asymmetrically (red) and symmetrically (blue) distributed losses (cross-sections of absorption maps for the fixed wavelength of 935.4 nm).

We design the structure by analytic estimations and numerical simulations (Fig.1); we fabricate the structure by physical vapor deposition (titanium dioxide - TiO_2) on nanostructured substrates, and nonuniformly deposit the absorber by magnetron sputtering with the glancing angle method (nickel - Ni); we record the angular transmission/reflection profiles, and we reconstruct angle – asymmetric absorption map. Asymmetric absorption (asymmetry factor 2) is mediated by the left-/right-propagating waveguiding modes of the thin film, in good correspondence with the theoretical estimations, Fig.1. Finally, we prove the asymmetric absorption by photo-thermal measurements (measuring the increase of the temperature of the sample depending on the angle of illumination) [1].

References

1. L. Grineviciute, I. Lukosiunas, J. Nikitina, I. Meskelaite, A. Selskis, D. Gailevicius, and K. Staliunas, Light Trapping by Non-Hermitian Thin Films, submitted 2024, https://arxiv.org/abs/2410.15101

Disordered gain-loss coupled systems investigated by tracking Petermann factors upon applying continuous gradients.

H. Amyar[1],M. Besbes[1] and H. Benisty[1*],

[1]Laboratoire Charles-Fabry (LCF), Institut d'Optique Graduate School, Univ. Paris-Saclay, Palaiseau, France

[*]Corresponding author: henri.benisty@institutoptique.fr

Abstract: We study the advent of exceptional points in 2D disordered gain-loss systems. While disorder breaks them, a real-part gradient may restore their sharpness. We track this through the Petermann factor, providing a new kind of system's "signature". We explore whether specific subsystems are also diagnosed through more direct response analysis.

In disordered gain-loss systems, the balance between coupling and gain/loss that occurs in ideal 2-units gain-loss systems (N=2) is generally missing, so that genuine Exceptional Points (EPs) appear as smooth features. However, it is known that a proper detuning of the real-part of the Hamiltonian (the indices in the case of PT-symmetry in photonics) can "heal" the system and restore the characteristic EP singularities [1, 2].

We generalize this approach for an arbitrary multi-element system (from N=4 to 10 in our first studies), by imposing a spatial gradient, that affects the real part of the index of the j-th element according to $\Delta n_j = A_x x_j + A_y y_j$. The spirit is somehow analogous to imposing a Stark effect on cloud of interacting atoms immobilized in some matrix. Furthermore, our system is 2-dimensional, so that it rather resembles a bundle of fibers with arbitrary organization, albeit invariant in the third direction z for the time being.

To check the effect of this gradient on the "healing" of EPs, we monitor both the variation of the eigenvalues and the Petermann factor (or a synthetic version thereof, to account for all modes). This latter factor is a safer indication that we go through an EP. It directly reports on the maximal non-hermitic "signal" at the singular EP, whereas finding a "steep slope" of eigenvalues is a fuzzier assessment of an EP.

We compare the results of a toy mode (coupled mode theory, thus only NxN matrices are involved) and of a finite-element simulation capitalizing on the SimPhotonics Matlab Toolbox[3], using typical index values of waveguides that provide confinement and evanescent waves in tractable proportions (n=1.7 for cylindrical core waveguides, in a n=1.5 matrix). Typical results are shown in Fig.1.

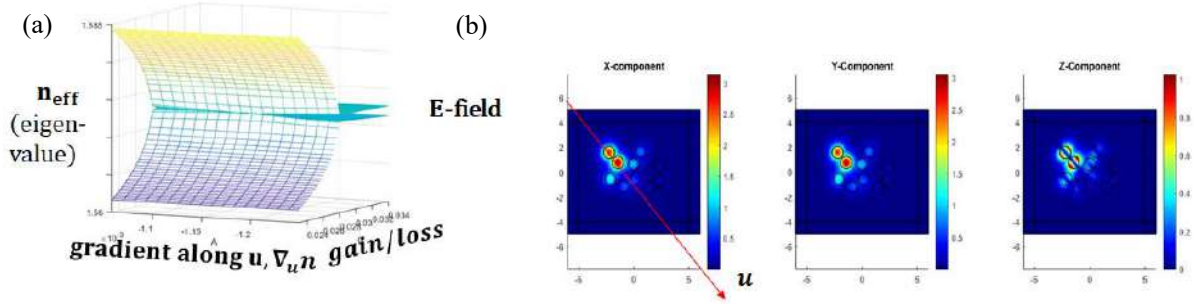


Fig.1 (a) Real part of effective index vs the gain-loss parameter *g* and the gradient *A* along *u* direction; (b) the X,Y,Z vector components of the E-field eigenmode in the *x,y* plane, at the EP. Black circles are the ten waveguides, identical before applying the gradient. The EP mostly stems from the top-left waveguide pair.

By probing the effect of a gradient in any direction, a kind of "Resonance imaging" of the Petermann factor is made, in the gradient space. Examples for a simple N=4 case and a complex N=10 case calculated by a toy-model of coupled-mode theory is shown in Fig.2.

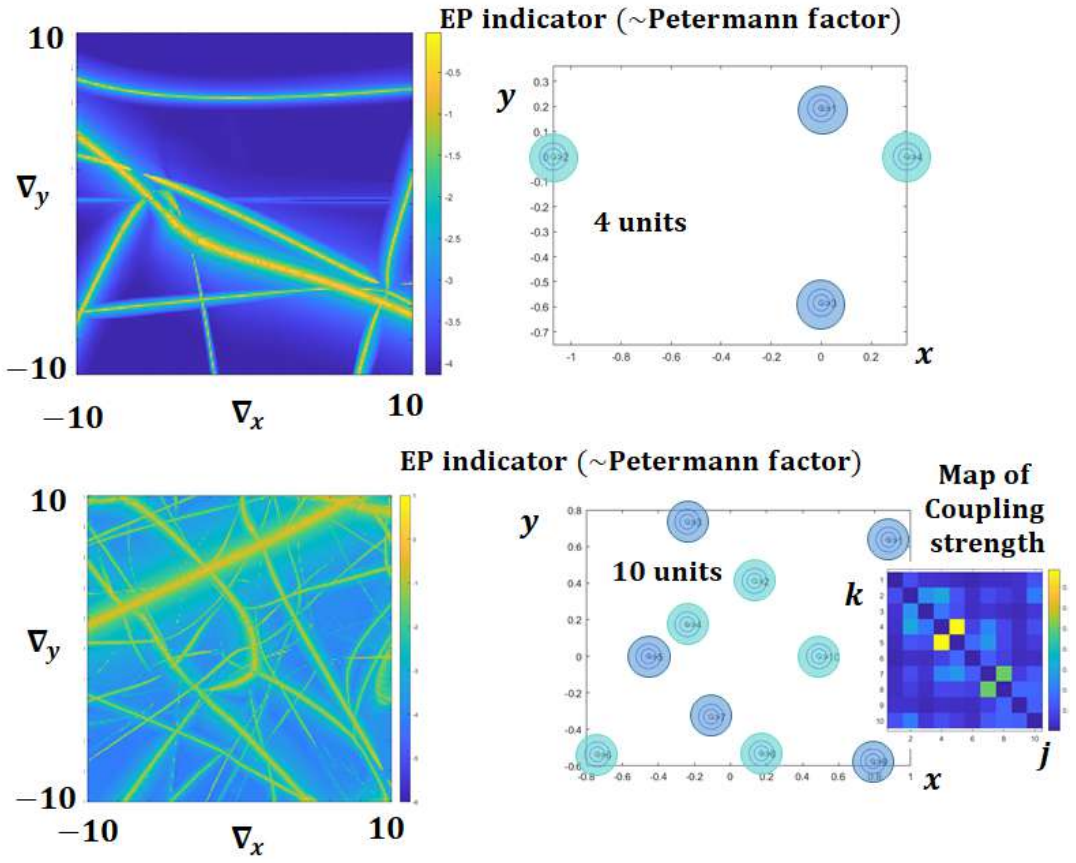


Fig.2 : Example of "gradient map" of EP indicator for a N=4 system (top) and an N=10 one (bottom) with two different bleu-green nuances for gain/loss. The coupling is distance-dependent, a map of their strength is indicated for the bottom case (inset to the right).

We will discuss the case of realistic models, and the use of the Petermann factor as the indicator. We also wish to discuss ways to visualize which vectors are involved in the large Petermann factor by adding noise and looking at the resulting perturbation.

This work was partially funded by the French Agence Nationale pour la Recherche (project "PARTISYMO", contract number N° ANR-18-CE24-0024).

References

1. Benisty, H., C. Yan, A. Degiron and A. Lupu. "Healing Near-PT-Symmetric Structures to Restore Their Characteristic Singularities:Analysis and Examples," IEEE J Lightwave Technol., Vol. 30, 2675–2683, 2012.
2. Nguyen, N. B., S. A. Maier, M. Hong and R. F. Oulton, "Recovering parity-time symmetry in highly dispersive coupled optical waveguides," New J. Phys. Vol.18, 125012(1–8) 2016.
3. https://github.com/SimPhotonicsFMM/Sources, M. Besbes, 2024.

Causal structure of interacting Weyl points in acoustic crystals

H. T. Teo[1], G.-G. Liu[1,2], Y. Ge[3], H.-y. Zou[3], W.-C. Chiu[4], H. Chen[1], Y. Long[1], S.-q. Yuan[3], A. Bansil[4], H.-x. Sun[3,5*], G. Chang[1†], and B. Zhang[1,6‡]

[1]Division of Physics and Applied Physics, School of Physical and Mathematical Sciences, Nanyang Technological University, Singapore 637371, Singapore
[2]Research Center for Industries of the Future, School of Engineering, Westlake University, Hangzhou, 310030, China
[3]Research Center of Fluid Machinery Engineering and Technology, School of Physics and Electronic Engineering, Jiangsu University, Zhenjiang 212013, China
[4]Department of Physics, Northeastern University, Boston, MA 02115, USA
[5]State Key Laboratory of Acoustics, Institute of Acoustics, Chinese Academy of Sciences, Beijing 100190, China
[6]Centre for Disruptive Photonic Technologies, Nanyang Technological University, Singapore 637371, Singapore
corresponding authors: *jsdxshx@ujs.edu.cn, †guoqing.chang@ntu.edu.sg, ‡blzhang@ntu.edu.sg

Abstract: Interactions between relativistic particles are governed by causality, represented by spacetime light cones. However, the causal relations between interacting quasiparticles remains elusive despite their conical dispersions. By dynamically driving an acoustic analogue of charge density wave, we experimentally extend the causal structure to interacting Weyl quasiparticles in three-dimensional acoustic crystals.

Dynamics of relativistic particles is governed by the Dirac equation. The massless solution reduces to the Weyl equation that hosts conical dispersions, whose gradient being the speed of light. Although often described in the single-particle formalism, relativistic particles can also interact with each other, whose occurrence is determined by the causal relation in the theory of relativity. Spacetime light cones, alternatively, the speed of light, in turn determine the causal structure of interacting particles.

The Weyl equation has been extended to quasiparticle excitations, but finite separation in momentum space prohibits interactions between Weyl points. Originated from solid-state systems [1], a dynamical charge density wave (CDW) can lift the lattice translational symmetry, thus allowing Weyl points to interact out of equilibrium. While the dynamics of interacting Weyl points remains elusive upon general CDW driving, the causality inherent to interacting quasiparticles also remains unexplored despite hosting relativistic dispersions.

Analogous to spacetime light cones [Fig. 1(a)], Weyl quasiparticles have been theoretically proposed to host causal structure due to its conical dispersions in energy-momentum space, with group velocity as the gradient [2]. Based on the position of a Weyl point relative to the neighbouring Weyl cone, the causal structure can be determined [Fig. 1(b)], where interaction only happens in energy-like dispersion.

In this work, we report on the first experimental realization of the causal structure in a three-dimensional (3D) acoustic Weyl semimetal. We start from an acoustic Weyl semimetal [3, 4], whose unit cell depicted in Fig. 2(a). It consists of 3D printed solid resin with air in the remaining regions, where the rotation angle θ of the fan-like structure controls the transition between energy-like and momentum-like regions. By doubling the unit cell, an acoustic analogue of CDW interaction is then applied by rotating opposite angles in neighbouring layers.

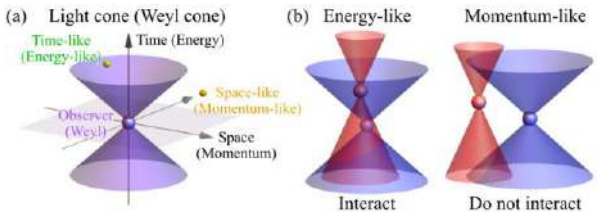


FIG. 1. (a) Causal structure of a Weyl cone is analogous to a spacetime light cone. Region within (outside) Weyl cone is named as energy-like (momentum-like) region. (b) Weyl cones in energy-like region interact, but Weyl cones in momentum-like region do not interact.

While hosting two Weyl cones along KH path [Fig. 2(b)], the bands are folded into the reduced Brillouin zone (BZ) upon unit cell doubling [Fig. 2(c)], exhibiting energy-like dispersion at θ = 35°. The causal structure takes effect by opening an energy gap upon the CDW interaction [Fig. 2(d)]. Reversely, the momentum-like dispersion (θ = 50°) is shown in Figs. 2(e)-2(f). By applying CDW, the gapless dispersion remains intact between the pair of Weyl points [Fig. 2(g)]. In the fabricated acoustic lattices [Fig. 3(a)], we also experimentally probe the causal structure by measuring the transmission in energy gap [Fig. 3(b)].

Our work provides an ideal platform to test causal connections in macroscopic classical wave systems. Based on the freedom to tune the energy-momentum separations between Weyl points, this acoustic demonstration also enriches the study of interactions between CDW-driven quasiparticles.

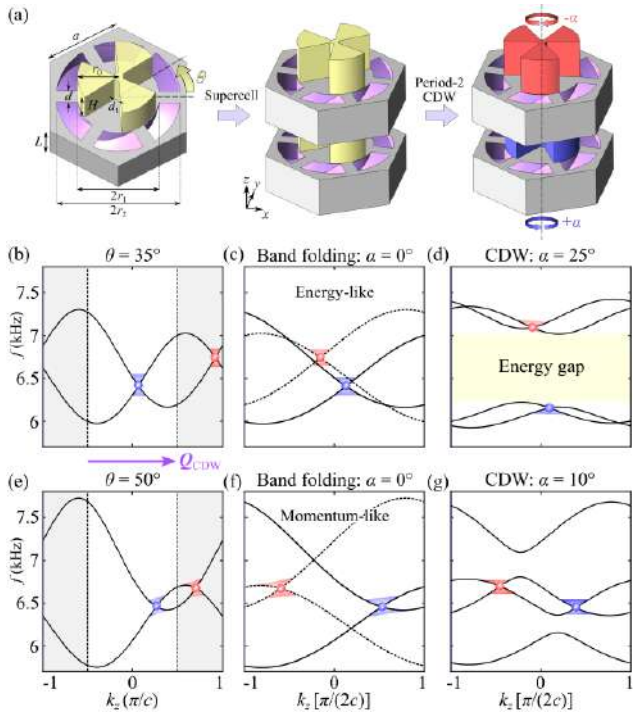


FIG. 2. (a) Unit cell of the acoustic crystal. After unit cell doubling, CDW is introduced via opposite rotation in neighbouring layers. (b) Bulk dispersion of the single-layer unit cell at θ = 35° along KH path. (c) Band folding in the reduced BZ with energy-like dispersion, then CDW is applied in panel (d). Panels (e) to (g) depict the momentum-like region with θ = 50°.

This research is supported by Singapore National Research Foundation Competitive Research Program under Grant No. NRF-CRP23-2019-0007, Singapore Ministry of Education Academic Research Fund Tier 2 under Grant No. MOE-T2EP50123-0007, and Tier 1 under Grant No. RG139/22 and RG81/23. Y.G., H.-y.Z., S.-q.Y., and H.-x.S. are supported by the National Natural Science Foundation of China (Grants No. 12274183, 12174159 and 51976079), the National Key R&D Program of China (Grant No. 2020YFC1512403), the Research Project of State Key Laboratory of Mechanical System and Vibration (Grant No. MSV202201) and the Postgraduate Research and Practice Innovation Program of Jiangsu Province (Grant No. KYCX22 3603).

References

1. Peierls, R. E., "Quantum theory of solids", Clarendon Press, Oxford (1996).
2. Chiu W.-C., Chang G., Macam G., et al., "Causal structure of interacting Weyl fermions in condensed matter systems," Nat. Commun., Vol. 14, 2228 (2023).
3. Xiao M., Chen W.-J., He W.-Y., and Chan C. T., "Synthetic gauge flux and Weyl points in acoustic systems," Nat. Phys., Vol. 11, 920 (2015).
4. Li F., Huang X., Lu J., Ma J., and Liu Z., "Weyl points and Fermi arcs in a chiral phononic crystal," Nat. Phys., Vol. 14, 30 (2017).

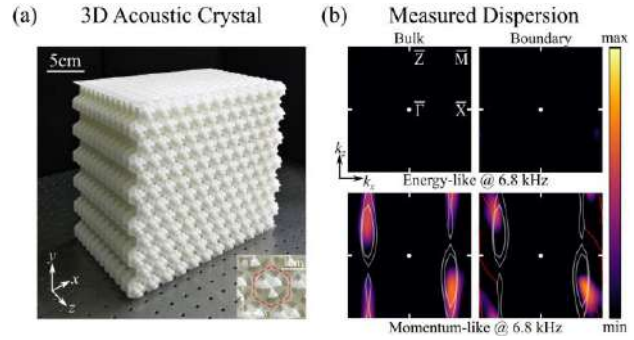


FIG. 3. (a) Perspective and side view (inset) of the 3D artificial acoustic crystal with the unit cell enclosed by the red lines. (b) Measured isofrequency surfaces of energy-like and momentum-like samples at 6.8 kHz, where bulk and boundary measurements are illustrated. The white (red) lines depict the simulated bulk (boundary) isofrequency surfaces.

META 2025, MALAGA - SPAIN, JULY 22–25, 2025

Intrinsic Non-Hermiticity in Photonic Floquet Topological Insulators with Genuine Temporal Modulation

J. Wang[1], H. Qin[1], Z. Zhang[1], and R. Fleury[1*]
[1]Laboratory of Wave Engineering, School of Electrical Engineering, EPFL, Lausanne, Switzerland
Corresponding author: romain.fleury@epfl.ch

Abstract: Photonic topological insulators (TIs), inspired by condensed matter TIs, exhibit intrinsic non-Hermitian properties due to the Maxwell equation's nature, particularly in Floquet TIs. This study peeks into these phenomena through a double-laced Floquet Su-Schrieffer-Heeger (SSH) model, revealing amplified and attenuated topological interface states via microwave experiments leveraging semiconductor varactors' nonlinearity.

Photonic topological insulators (TIs), as a successful analogue to TIs in condensed matter systems, have become a promising and prosperous topic. Following F. D. M. Haldane's pioneering proposal [1], a surge of publications in static photonic TIs has been witnessed during the past few decades, which are further furnished by non-Hermiticity and Floquet time modulation. Both non-Hermitian and Floquet TIs have been attracting research interest as indispensable branches of the photonic TIs' family tree. They enrich the underlying physics in equilibrium systems with more general non-equilibrium properties, opening avenues towards novel topologically protected states.

A remarkable nuance arises as one attempts to subsume photonic TIs into the established theoretical framework for condensed matter systems. Distinct from common senses in condensed matter physics, it has been noticed that the topological classification of photonic systems based on the Maxwell equation falls generically into a non-Hermitian context [2]. To clarify, a system subjected to the Schrödinger equation with Hamiltonian $H^\dagger \neq H$ is referred to as a non-Hermitian system here. While enclosing the Maxwell wave with the Schrödinger equation, Hermiticity is not naturally granted even in lossless materials as permittivity ϵ and permeability μ are not identical. A scaling proportional to $Z = \sqrt{\mu/\epsilon}$ of the field variables is required to preserve the Hermiticity of a system with fixed ϵ and μ. This conversely implies inevitable non-Hermiticity when Z varies either spatially or temporally, which has been validated in several previous publications [2,3]. Consequently, non-Hermitian TIs are possible to be realized in a Floquet manner, which is known as parametric instability in temporally modulated systems.

To capture this intrinsic non-Hermiticity in a Floquet TI, a double-laced Su-Schrieffer-Heeger (SSH) chain is employed as a phenomenological toy model. The lower and upper chain stand for the electric and magnetic field respectively, and couplings are exclusively present as mutual interactions between upper and lower sites (shown in Fig. 1(a)). Temporal modulations with staggered phase are introduced to the couplings from magnetic sites to electric sites, while those from electric sites to magnetic sites are fixed as constant. Following the analysis routine of Floquet TIs, we then evaluate the Floquet evolution operator over one period under open boundary condition (OBC), as well as the micromotion operator within one period under periodic boundary condition (PBC) to obtain the phase diagram (see Fig. 1(b)). As expected, topologically protected edge states possessing non-unitary eigenvalues appear, signifying temporally amplified or attenuated behavior (see Fig. 1(c)). The emergence of such states can be interpreted from the phase diagram [4] (see Fig. 1(b)). Unstable edge states are left in the gap

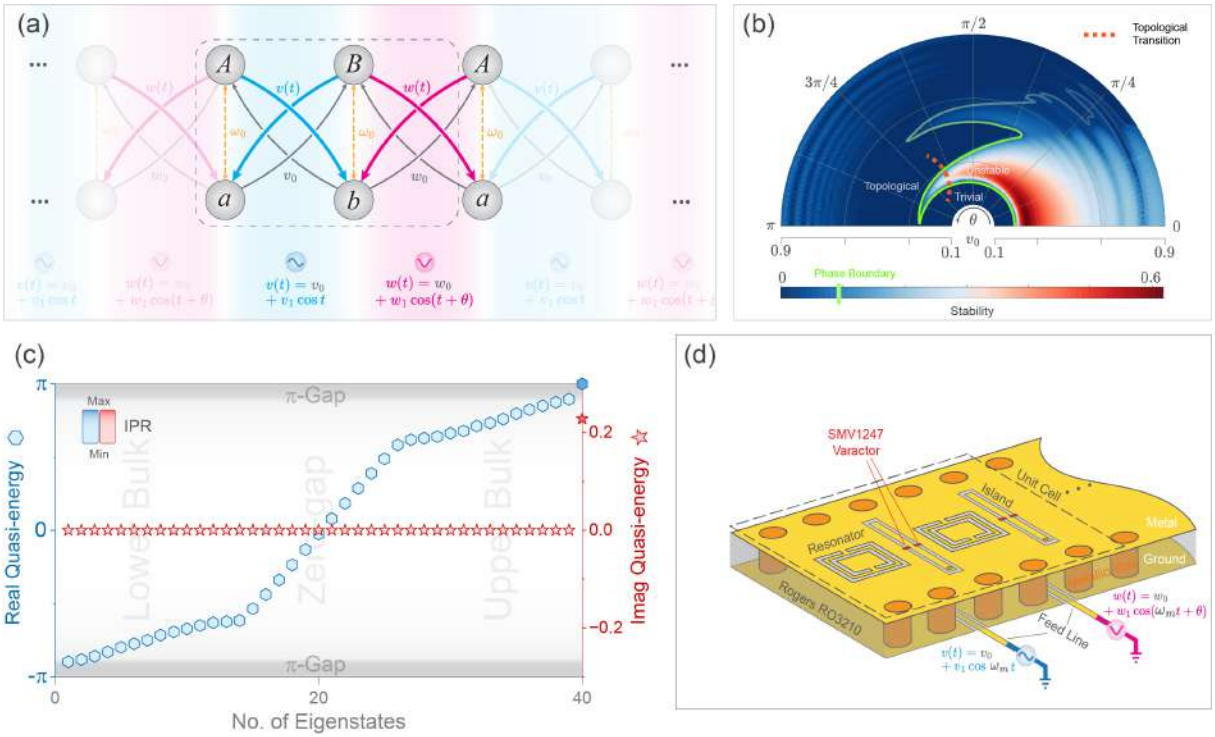


Figure 1: (a) The schematic of the double-laced Floquet Su-Schrieffer-Heeger (SSH) chain. (b) The phase diagram. (c) Eigenvalues calculated under the open boundary condition (OBC). (d) The experimental setup.

when topological phase transition and PT phase transition occur simultaneously.

Genuine temporal modulation is the key to experimental implementation, whereas a lot of previous publications focus on synthetic Floquet TIs. Leveraging the signal modulation capability of semiconductor varactors reported in Ref. [3], we designed a microwave platform aiming at working frequencies of several GHz (see Fig. 1(d)). A substrate integrated waveguide (SIW) and complementary split ring resonators (CSRRs) assist band structure engineering. Shunted with varactors SMV1247, slots separating every two CSRRs effectively modulate the electromagnetic coupling between them, leading to the topological unstable states we describe above.

J.W., H.Q., Z.Z. and R.F. acknowledge funding from the Swiss State Secretariat for Education, Research and Innovation SERI (contract no. MB22.00028).

References

1. F. D. M. Haldane and S. Raghu, "Possible Realization of Directional Optical Waveguides in Photonic Crystals with Broken Time-Reversal Symmetry," *Physical Review Letters*, vol. 100, no. 1, Jan. 2008.

2. K. Y. Bliokh, D. Leykam, M. Lein, and F. Nori, "Topological non-Hermitian origin of surface Maxwell waves," *Nature Communications*, vol. 10, no. 1, Feb. 2019.

3. J. Park et al., "Revealing non-Hermitian band structure of photonic Floquet media," *Science Advances*, vol. 8, no. 40, Oct. 2022.

4. G. Engelhardt, M. Benito, G. Platero, and T. Brandes, "Topological instabilities in AC-Driven bosonic systems," *Physical Review Letters*, vol. 117, no. 4, Jul. 2016.

Geometrical Phase Resonators

Y. Kawaguchi[1], D. Smirnova[2], F. Komissarenko[1,3], D. Kafeeva[1], S. Kiriushechkina[1], A. Vakulenko[3], J. Allen[4], M. Allen[4], A. B. Khanikaev[3*]

[1]Department of Electrical Engineering, The City College of New York, New York, NY 10031, USA
[2]Research School of Physics, The Australian National University, Canberra, ACT 2601, Australia
[3]Optics & Photonics, CREOL, UCF, Orlando, FL 32816, USA
[4]Air Force Research Laboratory, Munitions Directorate, Eglin AFB, Eglin, FL 32542, USA
[*]corresponding author: alexander.khanikaev@ucf.edu

Abstract: We introduce a new type of resonators defined solely by a geometrical phase. Topological boundary modes undergo an adiabatic evolution that gives rise to the geometrical phase of 360 deg. without propagation phase. This renders the resonance condition independent from its shape and length, which we confirmed by simulations and experiments.

Geometrical phases, originally introduced by Pancharatnam in optics [1], and generalized by Berry for quantum system [2], have been crucial for explaining a plethora of physical phenomena, from Foucault pendulum to polarization and phases of quantum matter [3]. Besides these purely fundamental interest, geometrical phases have recently attracted interest in a more applied context, including in metasurfaces, for redefining the fundamental laws of refraction [4], and controlling optical pseudo-spins [5].

In the context of resonators, evolution of the polarization state in Mobius strip-shaped ring resonators has been recently shown to alter resonant modes and shift them spectrally. Indeed, the addition of the geometrical phase ϕ_G to the propagation phase $\phi_P = \beta \cdot l$ accumulated in by the wave with the wavenumber β, twisted and bended into a ring of circumference l, yields a modified resonance condition $\phi_G + \phi_P = 2\pi N$, where N is the order of the resonance, which leads to the change of standing wave pattern and the spectral shift [6]. These exciting results allow one to envisage even more unusual resonances, which would not even require propagation and, while being spatially extended $l \neq 0$, would solely rely on the geometrical phase for the resonance to occur. This immediately imposes the following conditions: (i) vanishing propagation constant in such waveguides $\beta = 0$ and (ii) the net geometrical phase values of $\phi_G = 2\pi N$.

Here we demonstrate that both these conditions can be fulfilled in a topological photonic system emulating the Dirac physics and endowed with pseudospin degrees of freedom. We theoretically predict that two independent evolutions of the topological boundary modes in a 4-dimensional synthetic Hilbert space, both parametrized by the position withing the closed (ring-)resonator, give rise to the net geometrical phase of 2π. Numerical simulations and experimental observations in Fig. 1 unequivocally confirm our prediction. Moreover, our results confirm that, due to its purely geometrical nature, the resonance exhibits spectrally stability with respect to any deformations in resonator's shape and changes in its length.

We acknowledge support by the Simons Collaboration on Extreme Wave Phenomena, the Office of Naval Research award #N00014-24-1-2483, and the National Science Foundation award #2328993. J.A. and M.A. gratefully acknowledge support from the CLAWS Applied Research for the Advancement of Priorities program of the Office of the Secretary of Defense.

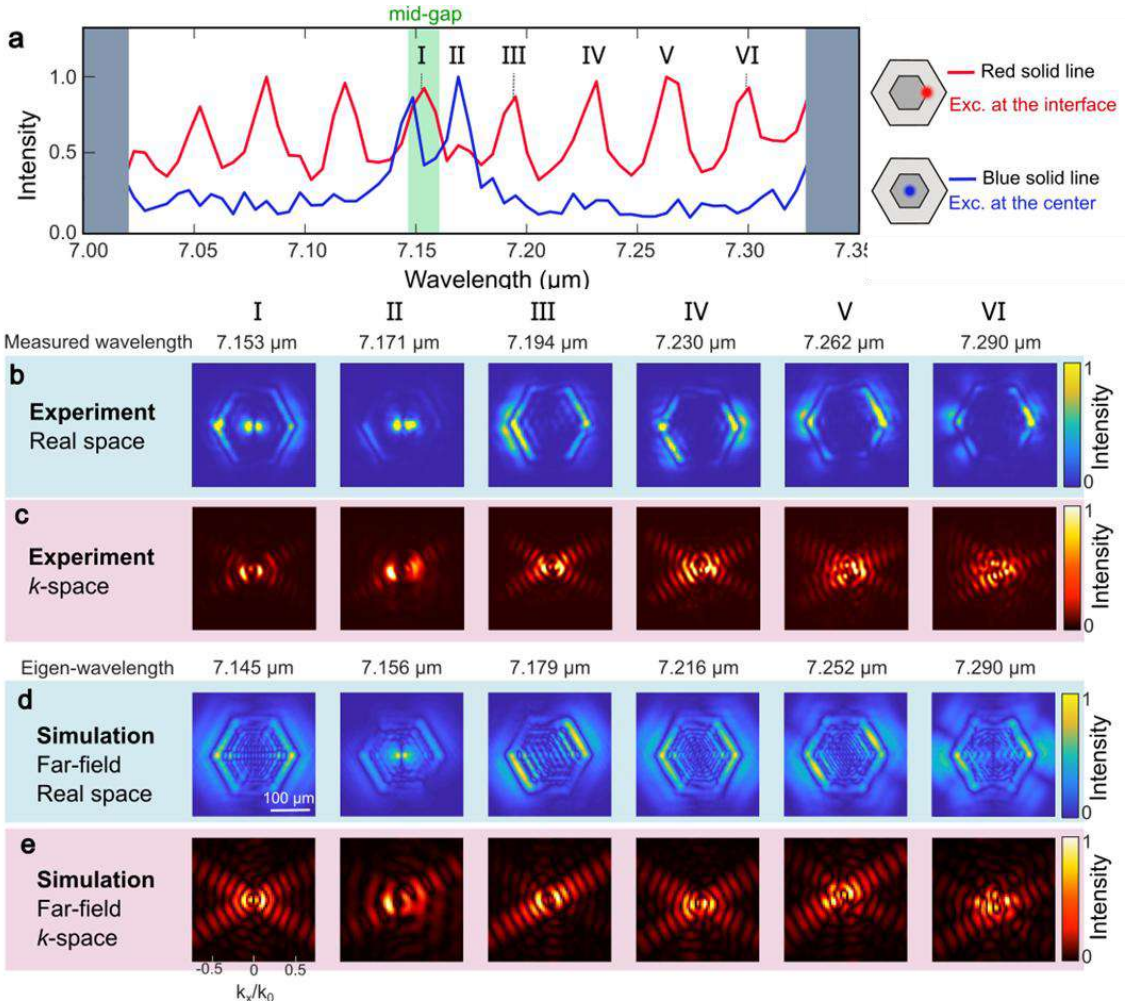


Figure 1. **Experimental and simulation results for hexagonal Spin-Valley-Hall ring resonator**. **a**. Experimental reflection spectra. The linearly polarized excitation was used to excite the interface (red solid line) and the center of ring resonator (bule solid line). **b**. Experimental real space images at resonance peaks. **c**. Experimental k-space images. **d**. Simulated far-field real space images. **e**. Simulated far-field k-space images.

References

1. Pancharatnam, S., "Generalized Theory of Interference, and Its Applications. Part I. Coherent Pencils," Proc. Indian Acad. Sci. A., Vol. 44, No. 5, 247–262, 1956.
2. Berry, M. V., "Quantal Phase Factors Accompanying Adiabatic Changes," Proceedings of the Royal Society A., Vol. 392, No. 1802, 45–57, 1984.
3. Resta, R. and D. Vanderbilt, “Theory of Polarization: A Modern Approach,” In: Physics of Ferroelectrics. Topics in Applied Physics, Vol 105. Springer, Berlin, Heidelberg, 2007.
4. Jisha, C. P., S. Nolte, and A. Alberucci, “Geometric Phase in Optics: From Wavefront Manipulation to Waveguiding,” Laser & Photonics Reviews, Vol. 15, 2100003, 2021.
5. Kawaguchi, Y., D. Smirnova, F. Komissarenko, et al., “Pseudo-spin switches and Aharonov-Bohm effect for topological boundary modes,” Sci. Adv., Vol. 10, eadn6095, 2024.
6. Wang, J., S. Valligatla, Y. Yin, et al., “Experimental observation of Berry phases in optical Möbius-strip microcavities,” Nat. Photon., Vol. 17, 120–125, 2023.

Are lasing zero modes always topological?

M. Alizadeh [1], S. K. Ozdemir[1], A. M. Yacomotti,[2] and R. El-Ganainy [1]

[1]Department of Electrical and Computer Engineering, Saint Louis University, Saint Louis, MO 63103, USA
[2]Centre de Nanosciences et de Nanotechnologies, CNRS, Universit´e Paris-Sud, Universit´e Paris-Saclay, 10 Boulevard Thomas Gobert, 91120 Palaiseau, France

Abstract:- It is often implicitly assumed that lasing zero modes inherit the spectral and spatial properties of their linear counterparts—an assumption that overlooks the critical role of nonlinear interactions inherent in laser systems. Contrary to this belief, we demonstrate that the interplay between coupling rates, dissipation, and gain saturation nonlinearity in laser arrays can significantly alter the mode structure. In particular, these effects can delocalize otherwise well-confined linear topological states, signaling a breakdown of the conventional bulk-boundary correspondence in the nonlinear lasing regime.

The interplay between non-Hermitian and topological physics has attracted considerable attention recently. Among the natural physical systems where these two concepts can emerge is laser systems. In one dimension, topological lasers can be implemented in SSH array under alternating pumping profile under which the system respects particle-hole symmetry [1]. Experimental observation of such laser array has been reported using different material platforms [2-4]. A fundamental underlying assumption associated with topological lasers is that lasing zero modes inherit their properties from the corresponding linear array in the absence of nonlinear effects such as gain saturation. In other words, even after the inclusion of the nonlinear effects, it was assumed that the lasing zero mode still resembles the corresponding linear zero mode. Given the important role that nonlinear effects play in laser dynamics, it is not clear if and when this assumption is valid. This in turn begs the following question: do the zero modes of topological laser arrays always operate as intended?

In this work, we investigate this fundamental question. In particular, we study how the nonlinear gain saturation impacts the intensity profile associated with the zero lasing mode when the underlying linear array operates in the topological phase. The following matrix equation describes the evolution of the complex fields [5]:

$$\frac{da}{dt} = (G - i\Omega - D - i\kappa) \quad , \quad (1)$$

Where a is the vector describing the field amplitudes a_n in resonator n, and G is a diagonal matrix whose non-zero elements represent the intensity dependent gain. The matrices Ω and D are also diagonal with their elements given by $\Omega_{nn} = \omega_n$ and $D_{nn} = \gamma_n$, where ω_n and γ_n are the resonant frequency and loss coefficient of resonator n, respectively. Finally, the matrix κ encodes the information about the coupling profile between the various elements of the laser arrays. The configuration of the SSH laser array is shown in figure 1.

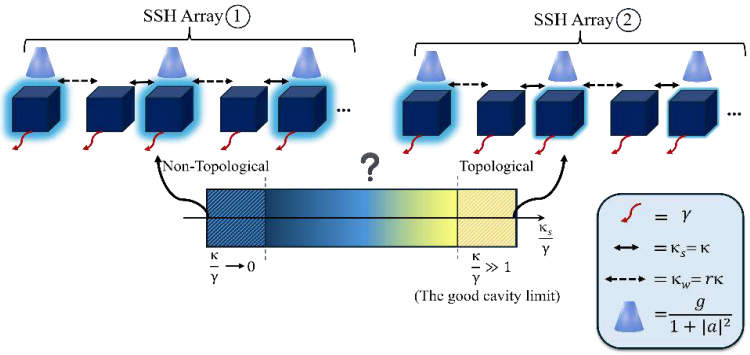


FIG. 1. Schematic of the SSH laser arrays in two extreme cases: (1) when $\kappa/\gamma \to 0$ featuring nearly decoupled elements; and (2) $\kappa/\gamma >> 1$ The pumping scheme and design parameters are also explained on the figure.

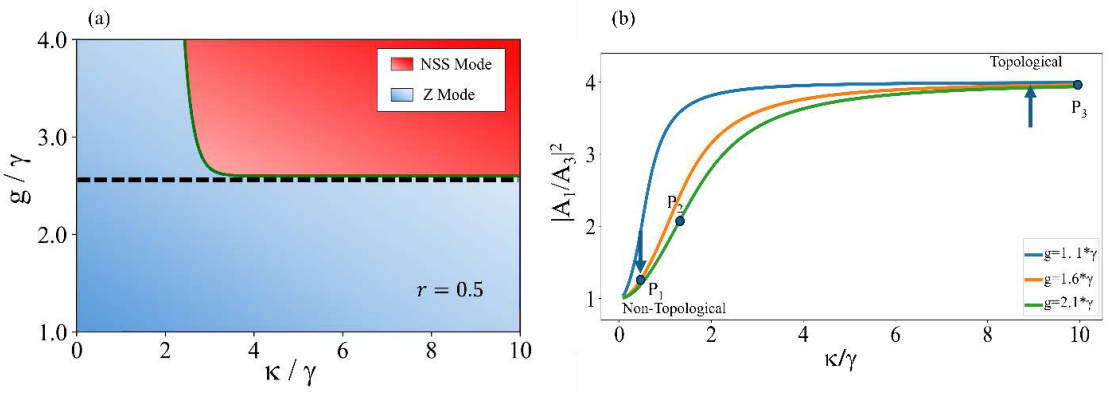


FIG. 2. Panel (a) plot the stability phases of the SSH laser array studied in this work. Two operating regions are shown: Zero Mode (Z Mode) and Non-Steady-State Mode (NSS Mode). (b) The intensity ratio plot of the SSH array for three different gain values, showing three different working regimes: 1 – Non-Topological, 2 – Transient, and 3 – Topological.

Figure 2 (a) depicts the stability diagram for an SSH laser array similar to that in Fig.1 but made of seven elements. As shown in the figure, the system operates in the steady-state zero-mode regime only when the gain below a certain threshold defined by the dashed black line. Figure 2(b) plots the ratio between the intensity in the third and first cavity of stable zero modes as a function of κ/γ (see Fig1 for the definition κ) of for three different values of the gain. For relatively small values κ/γ, the laser elements act as decoupled cavities, and the intensity ratios across the pumped sites remain nearly uniform, deviating from the expected linear topological profile. As κ/γ increases, the system enters a transient regime whose width is influenced by the gain level — higher gain leads to stronger nonlinear effects and a broader transition region. For $\kappa/\gamma \gg 1$, the system reaches a topological regime.

These results highlight that the nonlinear SSH laser array cannot be inherently classified as topological, contrary to common assumptions in the literature. Our study shows that lasing zero modes do not always inherit the spatial structure of their linear counterparts. Specifically, even when the linear zero mode is localized, nonlinear gain saturation can lead to a delocalized lasing mode with nearly equal intensities across the pumped sites. In essence, gain-induced nonlinearity can disrupt the bulk-boundary correspondence—even when it holds in the linear, non-Hermitian limit.

References

1. H. Schomerus, Opt. Lett. **38**, 1912 (2013).
2. P. St-Jean, V. Goblot, E. Galopin, A. Lemaître, T. Ozawa, L. Le Gratiet, I. Sagnes, J. Bloch, and A. Amo, *Nature Photonics* **11**, 651 (2017).
3. H. Zhao, P. Miao, M. H. Teimourpour, S. Malzard, R. ElGanainy, H. Schomerus, and L. Feng, Nature Communications **9**, 981 (2018)
4. M. Parto, S. Wittek, H. Hodaei, G. Harari, M. A. Bandres, J. Ren, M. C. Rechtsman, M. Segev, D. N. Christodoulides, and M. Khajavikhan, Phys. Rev. Lett.
5. S. Malzard and H. Schomerus, New Journal of Physics **20**, 063044 (2018).

Non-Hermitian topology solely from optical loss modulation

A. Hashemi[1], E. L. Pereira[2], H. Li [3], J. L. Lado[2] and A. Blanco-Redondo[1*]
[1]CREOL, The College of Optics and Photonics, University of Central Florida, Orlando, FL 32816, USA
[2]Department of Applied Physics, Aalto University, 02150 Espoo, Finland
[3]Nokia Bell Labs, 21 JJ Thomson Avenue, Cambridge, CB3 0FA, UK
Corresponding author: andrea@creol.ucf.edu

Abstract: We report the observation of topology arising solely from optical loss modulation. Specifically, we implement a non-Hermitian generalization of the Aubry-André-Harper model in a programmable integrated photonics platform, where the loss of each element can be controlled precisely, showing that loss modulation, alone, can be create topology in photonic systems.

The last decade has seen a flurry of research in non-Hermitian topological photonics [1], revealing exotic symmetries, such as that of parity-time [2], with no analogous in Hermitian systems, and enabling impactful applications such as topological lasers and sensors . All experiments to date have relied on the introduction of loss and/or gain in systems that were already topological in their Hermitian version [3], or have used gain in an indirect way to engineer the coupling of a Hermitian (closed) system [4]. In 2018, Takata and Notomi proposed that topological phases could potentially arise solely from gain and loss modulation [5], but an experimental proof of this had remained elusive due to the difficulty of accurately controlling loss in optical platforms. Here, we experimentally demonstrate that topology can arise exclusively from loss modulation in a photonic system that is non-topological in the absence of loss modulation [6].

Our experimental platform is a programmable hexagonal mesh of silicon photonics Mach-Zehnder interferometers, as shown in Fig. 1(a). In 2024, we demonstrated that this platform can be used to implement Hermitian topological Hamiltonians, thanks to its possibility of being reconfigured into arrays of coupled ring resonators with tunable ring-to-ring couplings and resonant frequencies [7]. Here, we show that the imaginary part of the onsite potential of the rings, i.e. the loss, can also be accurately controlled [6]. We use this newly discovered capability to implement a non-Hermitian generalization of the Aubry-André-Harper model, theoretically discussed in [8], where the rings are uniformly coupled, while exhibiting sinusoidal onsite loss modulation, leading to the following effective Hamiltonian:

$$H = \sum_{n=0}^{N-2} \left(t\hat{a}_n^\dagger \hat{a}_{n+1} + h.c. \right) \in i \sum_{n=0}^{N-1} \left[v_1 + v_2 \sin\left(2\pi n\alpha + \delta\right) \right] \hat{a}_n^\dagger \hat{a}_n, \tag{1}$$

where $\hat{a}_n^\dagger$ and $\hat{a}_n$ are creation and annihilation operators in site n, t is the coupling between neighboring sites, α is the inverse of the loss modulation period, δ represents the modulation phase, v_2 is the amplitude of the modulation, and v_1 is a uniform loss introduced to compensate the gain induced by sinusoidal gain/loss modulation.

Figure 1(a) shows a commensurate configuration of this model, with a modulation period a modulation period of $1/\alpha = 4$ and a phase parameter $\delta = 3\pi/4$, where the periodicity of the sinusoidal loss function – indicated by the dashed black line in Fig.1(b) – aligns with the lattice periodicity. Incommensurate cases have also been demonstrated [6]. This system's eigenfrequencies are shown by the dot markers in Fig.1(c), where the edge (bulk) states are highlighted in red

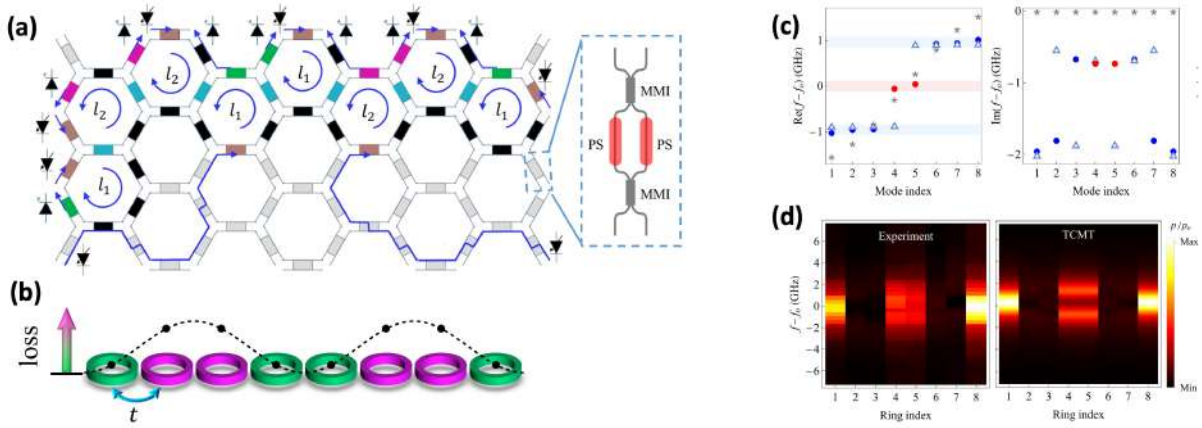


Figure 1: (a) Programmable integrated photonics platform. (b) Implemented loss modulation. (c) Eigenfrequencies. (d) Measured (left) and simulated (right) local density of states.

(blue). For contrast, Fig.1(c) also shows the eigenfrequencies of a trivial system, devoid of loss modulation (asterisks) and a similar conmensurate configuration where the phase parameter δ is chosen so that the arrangement does not support any edge mode. The experimentally measured local density of states (LDOS) spectrum is presented in the left panel of Fig.1(c), showing good matching with the temporal coupled mode theory (TCMT) simulations. For excitation frequencies matching the eigenfrequency of the edge modes the LDOS spectrum exhibits pronounced intensity localization at the chain's edges, a signature of the presence of edge states. These results highlight the appearance of topological edge states solely from loss modulation.

A.B.-R. is supported by the NSF award no. 2328993. E.L.P. is supported by the Nokia Industrial Doctoral School in Quantum Technology. J.L.L. is supported by the Academy of Finland Projects No. 331342 and No. 358088 and the Jane and Aatos Erkko Foundation.

References

1. Nasari, H., Pyrialakos, G., Christodoulides, D. & Khajavikhan, M. "Non-Hermitian topological photonics," *Opt. Mater. Express*, 13, 870-885, 2023.

2. Feng, L., El-Ganainy, R. & Ge, L. "Non-Hermitian photonics based on parity–time symmetry," *Nature Photonics*, 11, 752-762, 2017.

3. Weidemann, S., Kremer, M., Longhi, S. & Szameit, A. "Topological triple phase transition in non-Hermitian Floquet quasicrystals," *Nature*, 601, 354-359, 2022.

4. Liu, Y., Jung, P., Parto, M., Christodoulides, D. & Khajavikhan, M. "Gain-induced topological response via tailored long-range interactions," *Nature Physics*, 17, 704-709, 2021.

5. Takata, K. & Notomi, M. "Photonic Topological Insulating Phase Induced Solely by Gain and Loss," *Phys. Rev. Lett.*. 121, 213902, 2018.

6. Hashemi, A., Pereira, E., Li, H., Lado, J. & Blanco-Redondo, A. "Observation of non-Hermitian topology from optical loss modulation," *ArXiv Preprint ArXiv:2411.08729*, 2024.

7. On, M., Ashtiani, F., Sanchez-Jacome, D., Perez-Lopez, D., Yoo, S. & Blanco-Redondo, A. "Programmable integrated photonics for topological Hamiltonians," *Nature Communications*, 15, 629, 2024.

8. Pereira, E., Li, H., Blanco-Redondo, A. & Lado, J. "Non-Hermitian topology and criticality in photonic arrays with engineered losses," *Phys. Rev. Res.*, 6, 023004, 2024.

Use of Complex Time Delay to Control Propagation Through Generic Non-Hermitian Scattering Systems

Isabella Giovannelli[1], Nadav Shaibe[1], Jared Erb[1], Thomas M. Antonsen[1], and Steven M. Anlage[1*]

[1] Physics Department, University of Maryland, College Park, MD 20742-4111 USA
[*]corresponding author: anlage@umd.edu, website: https://anlage.umd.edu

Abstract: We establish the physical meaning of the imaginary part of complex time delay through experiments. We find universal statistics for complex time delay and utilize its divergences to identify a large variety of scattering singularities, including new ones that we create with our microwave graph and billiard experiments.

The scattering matrix S linearly relates the vector of incoming waves to outgoing wave excitations, and contains an enormous amount of information about the scattering system and its connections to the scattering channels. Time delay is one way to extract information from S, and the transmission time delay τ_T is a complex (even for Hermitian systems with unitary scattering matrices) measure of how long a wave excitation lingers before being transmitted [1,2]. The real part of τ_T is a well-studied quantity, but the imaginary part of τ_T has not been systematically examined experimentally, and theoretical predictions for its behavior have not been tested. Here we experimentally test the predictions of Asano, *et al*. [3] for the imaginary part of transmission time delay in a non-unitary scattering system. We utilize Gaussian time-domain pulses scattering from a 2-port microwave graph [2] supporting a series of well-isolated absorptive modes to show that the carrier frequency of the pulses is changed in the scattering process by an amount in agreement with the imaginary part of the independently determined complex transmission time delay, $\mathrm{Im}[\tau_T]$, from frequency-domain measurements of the sub-unitary S matrix [4]. Our results also generalize and extend those of Asano, *et al*., establishing a means to predict pulse propagation properties of non-Hermitian systems over a broad range of conditions.

From the experimentally measured multi-port scattering (S)-matrices of one-dimensional graphs, a two-dimensional billiard, and a three-dimensional cavity, we calculate the complex Wigner-Smith, as well as each individual reflection and transmission time-delays. The complex reflection time-delay differences between each port are calculated, [2] and the transmission time-delay differences are introduced for systems exhibiting non-reciprocal scattering [5]. Large time-delays are associated with scattering singularities such as coherent perfect absorption, reflectionless scattering, slow light, and uni-directional invisibility. We demonstrate that the large-delay tails of the distributions of the real and imaginary parts of each time-delay quantity are superuniversal, independent of experimental parameters: wave propagation dimension D, number of scattering channels M, Dyson symmetry class β, and uniform attenuation η [5]. The tails determine the abundance of the singularities in generic scattering systems, and the superuniversality is in direct contrast with the well-established statistics of unitary systems, where the distribution tail depends explicitly on the values of M and β. We relate the statistics to the topological properties of the corresponding singularities [5-9]. Although the results presented here are based on classical microwave experiments, they are applicable to any non-Hermitian wave-chaotic scattering system in the short-wavelength limit, such as optical or acoustic resonators.

This work was supported by NSF/RINGS under grant No. ECCS-2148318, ONR under grant N000142312507, DARPA WARDEN under grant HR00112120021.

References

1. Lei Chen, Steven M. Anlage, and Yan V. Fyodorov. Generalization of Wigner time delay to subunitary scattering systems. Phys. Rev. E, **103**, L050203, (2021).
2. Lei Chen and Steven M. Anlage, "Use of Transmission and Reflection Complex Time Delays to Reveal Scattering Matrix Poles and Zeros: Example of the Ring Graph," Phys. Rev. E **105**, 054210 (2022).
3. M. Asano, K. Y. Bliokh, Y. P. Bliokh, A. G. Kofman, R. Ikuta, T. Yamamoto, Y. S. Kivshar, L. Yang, N. Imoto, Ş K. Özdemir, and F. Nori, "Anomalous time delays and quantum weak measurements in optical micro-resonators," Nat. Commun. **7**, 13488 (2016).
4. Isabella L. Giovannelli and Steven M. Anlage, "A Physical Interpretation of Imaginary Time Delay." arXiv:2412.13139 (2024).
5. Nadav Shaibe, Jared M. Erb, and Steven M. Anlage, "Superuniversal Statistics of Complex Time-Delays in Non-Hermitian Scattering Systems," arXiv:2408.05343 (2024).
6. Jared M. Erb, Nadav Shaibe, Robert Calvo, Daniel Lathrop, Thomas Antonsen, Tsampikos Kottos, Steven M. Anlage, "Novel Topology and Manipulation of Scattering Singularities in Complex non-Hermitian Systems." arXiv:2411.01069 (2024).
7. Lei Chen, Tsampikos Kottos, and Steven M. Anlage, "Perfect Absorption in Complex Scattering Systems with or without Hidden Symmetries," Nature Communications **11**, 5826 (2020).
8. Jared Erb, David Shrekenhamer, Timothy Sleasman, Thomas M. Antonsen, and Steven M. Anlage, "Control of the Scattering Properties of Complex Systems By Means of Tunable Metasurfaces," Acta Physica Polonica A **144** (6), 421-428 (2023).
9. Lei Chen, Steven M. Anlage, Yan V. Fyodorov, "Statistics of Complex Wigner Time Delays as a counter of S-matrix poles: Theory and Experiment," Phys. Rev. Lett. **127**, 204101 (2021).

Fock space skin effects in many-body systems

Masatoshi Sato

Yukawa Institute for Theoretical Physics, Kyoto University
msato@yukawa.kyoto-u.ac.jp

Abstract: Non-Hermiticity enables macroscopic accumulation of bulk states, named non-Hermitian skin effects. The non-Hermitian skin effects are well-established for single-particle systems, but their proper characterization for general systems is elusive. In this talk, I will discuss a general criterion of non-Hermitian skin effects, which works for any finite-dimensional system evolved by a linear operator. The applicable systems include many-body systems and network systems. A system meeting the criterion exhibits enhanced non-normality of the evolution operator, accompanied by exceptional characteristics intrinsic to non-Hermitian systems. Applying the criterion, I will argue a new type of non-Hermitian skin effect in many-body systems, the Fock space skin effect. I also discuss the Fock space skin effect-induced slow dynamics, which gives an experimental signal for the Fock space skin effect.

References

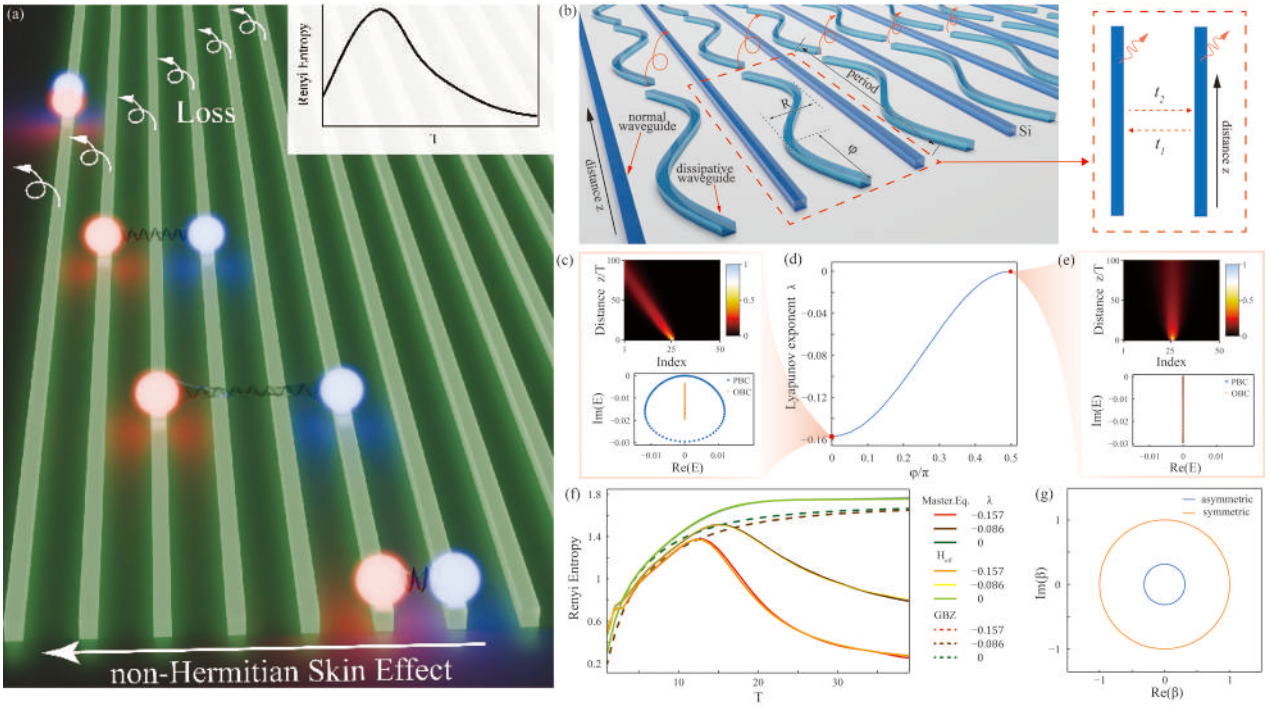
1. K. Shimomura, and M. Sato, “General Criterion for Non-Hermitian Skin Effects and Application: Fock Space Skin Effects in Many-Body Systems,” Phys. Rev. Lett. 133, 136502 (2024).

Quantum Walks of correlated photons in non-Hermitian photonic lattices

C.Sheng*, H. Liu, and S. N. Zhu
National Laboratory of Solid State Microstructures and School of Physics, Collaborative Innovation Center of Advanced Microstructures, Nanjing University, Nanjing, Jiangsu 210093, China
*corresponding author: csheng@nju.edu.cn

Abstract: We propose and experimentally realize quantum walks of two indistinguishable photons in engineered non-Hermitian photonic lattices. We have successfully observed the unidirectional behavior of quantum walks caused by the skin effect. Moreover, we reveal the suppression of entanglement that is caused by the skin effect in non-Hermitian systems.

Entanglement entropy characterizes the correlation of multiparticles and unveils the crucial features of open quantum systems. However, the experimental realization of exploring entanglement in non-Hermitian systems remains a challenge. In parallel, quantum walks have offered the possibility of studying the underlying mechanisms of non-Hermitian physics, which includes exceptional points, the non-Hermitian skin effect, and non-Bloch phase transitions. Unfortunately, these studies have only involved and prevailingly focused on the behavior of a single particle.



(a) The structured one-dimensional non-Hermitian lattice and Rényi entanglement entropy. (b) The designed system consists of an array of identical straight waveguides, with the auxiliary waveguide in the middle controlling their coupling. R is the Floquet radius, ϕ is the geometric phase, T is the period length, and the z axis indicates the propagation direction of waveguides. On the right is the schematic of effective coupling and dissipations. (c), (e) The asymmetric case and the symmetric case. (d) The relevance of the Lyapunov exponent to the geometric phase ϕ. (f) Rényi entropy calculated from the effective Hamiltonian and the master equation (solid lines). The corresponding results after the similarity transformation with GBZ are shown by the dashed lines. (g) The GBZ derived from the effective Hamiltonian.

In this work, we propose the use of silicon-on-insulator (SOI) technology to construct a non-Hermitian system comprising silicon waveguide arrays that can manipulate non-Bloch behavior. To exhibit the non-Hermitian feature of this engineered photonic lattice, we first experimentally realize quantum walks of single photons and observe the unique non-Hermitian evolution behavior of the wave dynamics of single photons in the bulk far from the edge. Crucially, we next study the quantum walks of two indistinguishable photons in the bulk and reveal the impact of non-Hermitian properties on the dynamics of quantum correlations. We finally explore the suppression of entanglement entropy of correlated photons in non-Hermitian systems and demonstrate that the nature of non-Hermicity plays a central role in entanglement evolution, which has been verified both experimentally and theoretically.

References

1. M. Y. Gao, C. Sheng, Y. L. Zhao, R. Y. He, L.L. Lu, W. Chen, K. Ding, S. N. Zhu, H. Liu, Quantum walks of correlated photons in non-Hermitian photonic lattices, Physical Review B 110, 094308, 2024.
2. R. Y. He, Y. L. Zhao, C. Sheng, J. C. Duan, Y. Wei, C.W. Sun, L.L. Lu, Y.X. Gong, S. N. Zhu, H. Liu, Experimental realization of quantum walks near synthetic horizons on photonic lattices, Physical Review Research 6, 013223, 2024.

Algebraic skin effect in higher-dimensional non-Hermitian metamaterials

Li Mingyang[1], **Lin Jing**[1,a *], and **Ding Kun**[1,b *]

[1]Department of Physics, State Key Laboratory of Surface Physics, and Key Laboratory of Micro and Nano Photonic Structures (Ministry of Education), Fudan University, Shanghai 200438, China

[a]jing_lin@fudan.edu.cn, [b]kunding@fudan.edu.cn

Abstract: This work establishes criteria for algebraic skin effect (ASE) in 2D reciprocal non-Hermitian metamaterials, demonstrating power-law decay via anisotropic optical axes and geometry. A photonic crystal design validates ASE's quasi-long-range interactions, revealed through impurity-induced spectral/dynamic responses. The framework can be extended to 3D systems and classical waves.

Metamaterials have unlocked unprecedented control over light by leveraging novel mechanisms to expand their functionality. Non-Hermitian physics further enhances the tunability of non-Hermitian metamaterials (NHMs) through phenomena such as the non-Hermitian skin effect (NHSE), enabling applications like directional amplification. The higher-dimensional NHSE manifests unique effects, including the algebraic skin effect (ASE), which features power-law decay instead of exponential localization, allowing for quasi-long-range interactions. In this work, we establish apparent criteria for achieving ASE in two-dimensional reciprocal NHMs with anisotropic and complex dielectric tensors. By numerically and theoretically demonstrating ASE through mismatched optical axes and geometric structures, we reveal that ASE is governed by a generalized Fermi surface whose dimensionality exceeds that of the Fermi surface. We then propose and validate a realistic photonic crystal design for ASE, which is experimentally accessible. Two infinitesimal impurities at the NHM boundary have further been introduced to demonstrate the quasi-long-range interaction nature of ASE from both the spectra and dynamics. Our recipe for ASE provides a versatile pathway for broader generalizations, including three-dimensional structures, synthetic dimensions, and other classical wave systems, paving the way for advancements in non-Hermitian photonics.

References

1. J. B. Pendry, Negative refraction makes a perfect lens, Phys. Rev. Lett. 85, 3966 (2000).
2. K. Ding, G. Ma, M. Xiao, Z. Q. Zhang, and C. T. Chan, Emergence, coalescence, and topological properties of multiple exceptional points and their experimental realization, Phys. Rev. X 6, 021007 (2016).
3. K. Zhang, C. Shu, and K. Sun, Algebraic non-Hermitian skin effect and unified non-Bloch band theory in arbitrary dimensions, arXiv:2406.06682.

Reflectionless transient excitation in complex media

C. Ferise[1], P. del Hougne[1*], and M. Davy[2]
[1]University of Rennes, CNRS, IETR - UMR 6164, Rennes F-35000, France
[2]École Polytechnique Fédérale de Lausanne, Laboratory of Wave Engineering, 1015 Lausanne, Switzerland
Corresponding author: matthieu.davy@univ-rennes.fr

Abstract: Reflectionless states corresponding to the zeroes of the reflection matrix enable reflectionless coupling of waves to a scattering sample. Here, we present a matrix approach to identifying these zeroes and determining the corresponding spatio-temporal input wavefronts. Theoretical results are verified experimentally in the microwave range within disordered multi-channel cavities.

In recent years, significant progress has been made in controlling the spatial and/or temporal shape of waves propagating through disordered scattering media. In particular, reflectionless excitation of a structure with monochromatic waves is possible when a zero of the reflection matrix lies on the real axis. This is for instance the case of coherent perfect absorption, a surprising interference phenomenon for which the incident radiations are fully absorbed within a lossy medium, or perfect transmission of waves. However, even a complex zero can be engaged by modulating the input wavefront in both space and time [1]. For a complex zero z_n of the reflection matrix, reflection is suppressed within the excitation interval for an excitation being a monochromatic signal at frequency $\mathrm{Re}[z_n]$ modulated with an exponentially increasing envelope at the rate $\mathrm{Im}[z_n]$ [1]. When the incident signal is interrupted, the energy accumulated within the medium leaks out through the channels. This concept of virtual perfect absorption is a promising concept for energy storage, sensing and transient application of optical forces. However, identifying the input wavefronts giving reflectionless transient excitation in disordered samples has remained a challenge, especially in the regime of overlapping resonances.

In this talk, we present a general approach based on a multispectral transport matrix, which fill this gap [2]. We demonstrate that a judicious singular value decomposition of this matrix enables optimal spatiotemporal wavefront shaping for arbitrary wave-control functionalities. Using measurement of the transport matrix, $\mathcal{H}(\nu)$, with the frequency ν, describing the linear relationship between N incoming channels, $x(\nu)$, and M outgoing channels, $y(\nu)$, $y(\nu) = \mathcal{H}(\nu)x(\nu)$, we extend the monochromatic input-output relationship to the time domain on both input and output sides via a discrete Fourier transform (DFT). We obtain a unified linear relationship between the spatiotemporal input and output wavefronts $x(t)$ and $y(t)$ as $y(t) = Hx(t)$, where H is the multi-channel multispectral operator, linking the spatial and temporal DoFs of a coherent input wavefront to those of the corresponding output wavefront. Using a singular value decomposition of H, we identify the spatio-temporal input wavefronts corresponding to reflectionless within the excitation interval.

Theoretical results are verified within a disordered quasi-2D electromagnetic cavity shown in Fig. 1(a) operating at a frequency range between 8 and 9 GHz. The channels are coax-to-waveguide transitions. In order to inject spatio-temporally sculpted signals in situ, we generate baseband signals between 0 and 1 GHz on an FPGA board at a sampling rate of 4 GS/s that are then analogically upconverted in the frequency range 8-9 GHz. We coherently record the spatio-temporal output signals with an ultra-wideband multi-channel oscilloscope using a sampling rate of 40 GS/s.

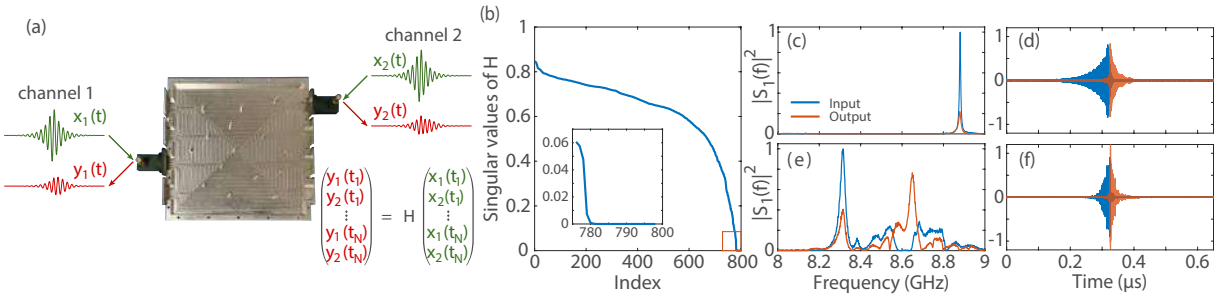


Figure 1: (a) Photographic image of our quasi-2D disordered cavity ($L = W = 205.74$ mm, $h = 10.16$ mm) with the top plate removed to show the inside. One coax-to-waveguide transition is attached at each side of the cavity, yielding a two-channel scattering system. The inset illustrates our spatio-temporal matrix formalism. (b) Singular value spectrum of H. (c-f) Experimentally measured output signals upon coherent spatio-temporal in situ injection of 2 different right singular vectors of H associated with near-zero singular values. For each considered state, we display the injected (blue) and outcoming (red) time-varying signals on the left channels (d,f), as well as the corresponding signal spectra averaged over both channels (c,e).

We display on Fig. 1(b) the singular value (SV) spectrum of H for the particular choice of the same input and output temporal intervals. We can observe that the largest SV, $\lambda_1 = 0.81$, remains below unity due to the inevitable presence of absorption in our experimental setup while multiple of the smallest SVs of H are extremely close to zero. This demonstrates that in the transient regime, the reflected signal intensity can be suppressed very efficiently. We experimentally validate our approach by injecting *in situ* these states. We observe in Fig. 1(c-e) that our approach identifies two types of VPA states: input wavefronts corresponding to either isolated or multiple zeroes. In both cases, the reflection from the sample is extremely small during the excitation time - Fig. 1(d-f) - while the energy is released once the excitation is stopped.

Beyond reflectionless states, our formalism more generally enables optimal spatiotemporal control of output waves. We will also present the possibility of delivering the maximum possible amount of energy within a time interval. Finally, we explore the possibility of exciting states that have the same spatial and temporal input and output patterns, generalizing the recent concept of time-harmonic (monochromatic) scattering-invariant states [3] from the harmonic regime to the time-varying regime.

References

1. D. G. Baranov, A. Krasnok, and A. Alù, "Coherent virtual absorption based on complex zero excitation for ideal light capturing," *Optica*, Vol. 4, No. 12, pp. 1457–1461, 2017.

2. Ferise, P. del Hougne, and M. Davy "Optimal matrix-based spatiotemporal wave control for virtual perfect absorption, energy deposition, and scattering-invariant modes in disordered systems," *Phys. Rev. Applied*, Vol. 20, No. 5, pp. 054023, 2023.

3. Pai, J. Bosch, M. Kühmayer, S. Rotter, and A. P. Mosk, "Scattering invariant modes of light in complex media," *Nat. Photonics*, Vol. 15, No. 6, pp. 431–434, 2021.

Optimal focusing on non-linear targets embedded within complex media

A. Goïcoechea[1*], Jakob Hüpfl[2], Stefan Rotter[2], F. Sarrazin[1], M. Davy[1],
[1]IETR, Université de Rennes, CNRS, 35000 Rennes, France
[2]Institute for Theoretical Physics, Vienna University of Technology (TU Wien), A-1040 Vienna, Austria
Corresponding author: antton.goicoechea@univ-rennes.fr

Abstract: We present a noninvasive matrix approach enabling detection and focusing on any nonlinear target embedded within a complex medium. By measuring a reflection matrix for two different incident powers, the local perturbation induced by the nonlinearity is used to identify the spatio-temporal incident wavefronts focusing on the target.

Controlling wave interactions in inhomogeneous media presents a significant challenge with applications spanning optical and acoustic imaging, wireless communications, wireless power transfer, and sensing [1]. In multiple scattering media, waves experience strong attenuation, making it particularly difficult to deliver energy deep within disordered environments. While wavefront shaping techniques can help mitigate the effects of disorder, their effectiveness relies on feedback mechanisms to precisely tailor the incident wavefront in space or time. To avoid invasive manipulation of the environment for field measurements, recent approaches have emerged that rely on slight perturbations of the medium [2]. Any internal change within a disordered sample is inherently encoded in the random speckle pattern generated by the complex interaction between the incident wave and the medium. Motion or local alterations in the target's scattering properties can thus act as a guidestar for optimal wavefront shaping.

In this work, we present a novel noninvasive method for detecting and focusing on electronic devices by leveraging their nonlinear response [3]. This approach (i) operates in the monochromatic regime and (ii) remains independent of the specific type of nonlinearity. Furthermore, our approach eliminates the need to measure the target device's higher harmonic response or any other frequency-shifted signal. It also does not require any prior knowledge on the medium or on the target. Specifically, we demonstrate the ability to focus a wave on a target embedded within a complex two-dimensional environment and show that programmable environments can enhance the intensity received by the target at a single frequency.

More precisely, we show theoretically that a singular value decomposition of the difference matrix $\Delta S = S^{\alpha+d\alpha} \in S^{\alpha+d\alpha}$ found from measurement of the scattering matrix S at two input powers α and $\alpha + d\alpha$ is equal to the number of point-like nonlinearities with the singular vectors identifying the input wavefront for maximal focusing on the non-linear target. We then verify experimentally the theoretical results using a two-dimensional scattering system working in the microwave range in which a nonlinear target is embedded. The target first consists of a high-Q dielectric cylinder coupled in its near field to a wire antenna connected to a low-noise amplifier. We show that at the resonance of the dielectric cylinder, a strong enhancement of the intensity at the target's position is observed for an input wavefront determined from ΔS. We then extend our results to the time-domain and demonstrate spatio-temporal focusing on the non-linearity. Finally, the non-linear element is embedded within a three-dimensional multichannel enclosure made programmable using reconfigurable intelligent surfaces. We rely on an optimization of these metasurfaces to enhance the signal on the non-linearity.



Figure 1: (a) Photograph of the experimental setup. A (nonlinear) low-noise amplifier is coupled to a resonant dielectric cylinder through a wire antenna. The scattering matrix is measured using seven antennas at the left interface. (b) Intensity map within the system around the target for an optimized illumination.

Our monochromatic technique is broadly applicable, enabling spatio-temporal focusing on nonlinear targets and working for any type of nonlinearity, even when the specific response is unknown. Our approach applies to various wave phenomena, offering potential applications in wireless power transfer, bioelectronics, and enhancing Wi-Fi signal focusing on smartphones in complex environments.

References

1. H. Cao, A. P. Mosk, and S. Rotter, "Shaping the propagation of light in complex media", *Nat. Phys.* vol. 18, pp. 994341, 2022.

2. M. Horodynski, M. Kühmayer, A. Brandstötter, K. Pichler, Y. V. Fyodorov, U. Kuhl, and S. Rotter, "Optimal wave fields for micromanipulation in complex scattering environments," *Nat. Photonics*, vol. 14, no. 3, pp. 149–153, 2020.

3. A. Goïcoechea, J. Hüpfl, S. Rotter, F. Sarrazin, and M. Davy, " Detecting and Focusing on a Nonlinear Target in a Complex Medium", 2024. [Online] Available: http://arxiv.org/abs/2407.07932

Correlation between topological effects in photonic crystal slabs: a theoretical and experimental exploration of BIC, Weyl points and Fermi arcs

Karen Caicedo, Silvia Romano, Gianluigi Zito, Ivo Rendina and Vito Mocella*

[1]Institute for Applied Physics and Intelligent Systems (ISASI-CNR), via P. Castellino 111, Napoli, Italy
*corresponding author: vito.mocella@cnr.it

Abstract: We present a theoretical-experimental framework that reveals how bound states in the continuum, Weyl points and Fermi arcs are connected in photonic crystal slabs. A novel setup allowing high-precision equi-frequency surface measurements confirms these topological phenomena and their far-field polarisation singularities, enabling robust device designs for optical communication and quantum technologies.

The correlation between bound states in the continuum (BICs), Weyl points and topology in photonic systems represents a new frontier in solid-state physics; however, the experimental characterisation of these connections remains incomplete. Here, we present a novel theoretical model that establishes a correlation between photonic BICs, Fermi arcs, Weyl points and singularities in far-field radiation, validating it through high-precision experimental measurements of equi-frequency surfaces (EFSs) in photonic crystal slab (PhCs).

Notably, and in contrast to previous approaches [1-3], our theoretical framework does not require in-plane symmetry breaking of the PhCs yet it shows excellent agreement with high-precision measurements of the EFS.

By studying iso-frequency surfaces—the photonic analogs of electronic Fermi surfaces—we gain key insights into the topological properties of far-field polarization states. These surfaces reveal how the geometry of momentum space underpins the emergence of topological charges, which govern polarization singularities in the far-field radiation pattern. This effect is especially prominent in PhCs supporting BICs, where small deviations near the Γ-point can dramatically alter topological charge distributions and the resulting polarization singularities.

Remarkably, our measurements demonstrate that Fermi arcs connect C-points located at Weyl points, which are strongly tied to photonic BICs viewed as real eigenstates in a non-Hermitian system (Figure 1).

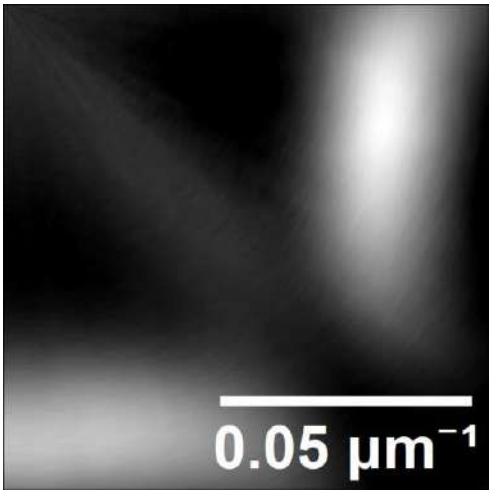


Figure 1. An open EFS measured at a wavelength of 534 nm near the Γ-point, located in the upper left corner, corresponds to Fermi arcs.

Even without any material or structural chirality, we observe chiral behavior in the far-field transmitted field around the BIC condition for both positive and negative angles with respect to the Γ-point—an unambiguous signature of the presence of a Weyl point. These findings advance our fundamental understanding of topological photonic phenomena and highlight the robustness of BICs under varying symmetry conditions. In addition, the capability of precise characterisation of EFS, particularly near the Γ point, provides new tools for designing photonic devices with controllable topological properties and potential applications in optical communications and quantum computation.

K.C and V.M., acknowledge PNRR MUR project PE0000023-NQSTI and PRIN PNNR - 2022X4W28 if any, for funding the present work.

References

1. Zhou, H. *et al.* Observation of bulk Fermi arc and polarization half charge from paired exceptional points. *Science* **359**, 1009–1012 (2018).
2. Zhen, B. *et al.* Spawning rings of exceptional points out of Dirac cones. *Nature* **525**, 354–358 (2015).
3. Chen, W., Yang, Q., Chen, Y. & Liu, W. Evolution and global charge conservation for polarization singularities emerging from non-Hermitian degeneracies. *Proc National Acad Sci* **118**, e2019578118 (2021).

Multi-order exceptional points in higher dimensions

A. A. Athanasopoulos[1,2] D. Kaltsas[1] K. G. Makris[1,2]
[1]ITCP-Physics Department, University of Crete, Heraklion, 71003, Greece
[2] Institute of Electronic Structure and Laser (IESL) – FORTH, Heraklion, 71110, Greece
aathanasopoulos@physics.uoc.gr

Abstract: We introduce a new class of Multi-order Exceptional Points (MoEPs) in 2D and 3D non-Hermitian systems. These MoEPs are Higher-order Exceptional Points (HEPs) coexisting at the same gain-loss parameter. We analyze their ultra-sensitivity using pseudospectra, highlighting their potential applications in precision sensing for optical systems.

Actual physical systems are always subject to external perturbations due to coupling to the environment, and that is why non-Hermitian (NH) Hamiltonians are widely used in many areas of physics. Quite intriguing are the parity-time ($\mathcal{PT}$) symmetric optical systems, like coupled optical waveguides, which under specific conditions, reveal fascinating characteristics like the Exceptional Points (EPs). It has been recently shown experimentally [1], that near these points, the system's sensitivity is enhanced, since the system's first order response to a perturbation "ε" exhibits a nonlinear dependence. EPs in one-dimensional lattices have been extensively studied, both in theoretical and experimental level [2, 3]. In our work, we present a direct method to generate multiple and higher order exceptional points in two- and three-dimensions, based on Kronecker sums of the corresponding one-dimensional lattices, that already exhibit EPs.

Multi-order exceptional points arise when a system hosts multiple exceptional points of different orders. This can be achieved by applying the Kronecker sum to two nilpotent sublattices, each containing at least one exceptional point. This is happening because if we apply the Kronecker sum on two matrices that represent different one dimensional systems, we get a matrix which effectively describes a two dimensional system. Based on our findings, when combining matrices associated with exceptional points of orders N_1 and N_2, the resulting system exhibits higher-order exceptional points with orders ranging from $|N_1 \in N_2| + 1$ to $N_1 + N_2 \in 1$, with an increasing increment of two. This idea extends to higher dimensions as well—for instance, applying the Kronecker sum to three nilpotent matrices results in a system with multiple and higher EPs in three dimensions.

In order to elucidate our method, let us consider the matrix $\mathcal{H}_{2,3}$ as the Kronecker sum of $\mathcal{H}_2$ and $\mathcal{H}_3$ matrices, which exhibit second- and third-order exceptional points, respectively. These matrices could model one-dimensional configurations consisting of two and three coupled optical waveguides. The couplings along the x-direction depend solely on the original matrix $\mathcal{H}_3$, while the couplings along the y-direction are determined by $\mathcal{H}_2$. The onsite potentials are a combination of those from both $\mathcal{H}_2$ and $\mathcal{H}_3$. The corresponding schematic representation of the lattice described by $\mathcal{H}_{2,3}$ is shown in the left panel of Fig. 1. In our case, summing matrices with an EP2 and an EP3 produces multi-order exceptional point of orders two and four.

To characterize, the sensitivity of the system to external perturbations, we calculate the associated pseudospectra of $\mathcal{H}_{2,3}$, defined as: $\sigma_\varepsilon(\mathcal{H}_{2,3}) = \quad \mathrm{z} \quad \mathbb{C}, \mathrm{z} \quad \sigma(\mathcal{H}_{2,3} + V)$ with $||V|| \leq \varepsilon$, with $\sigma(M)$ denoting the eigenvalues of matrix M [5]. For instance, under a small perturbation ($\varepsilon = 10^{-3}$), two distinct clouds emerge; differing in size and reflecting the presence of two exceptional points of different orders (Fig. 1 middle panel). This is happening because, to first

order approximation the response of the system to a perturbation ε is proportional to: $\varepsilon^{-1/n}$, with n being the order of the corresponding EP. This response is closely tied to the system's dynamics, in the $\mathcal{PT}$ unbroken regime ($g < g_{crit} = 1$). The power of the system is an oscillating function, with its behavior strongly dependent on the initial input (Fig. 1 right panel).

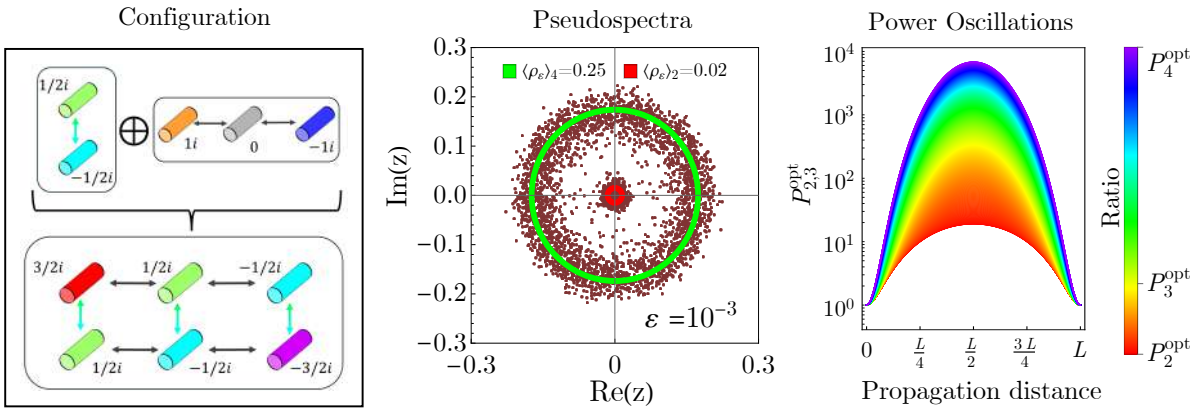


Figure 1: (Left) Schematic illustration of the Kronecker sum method with the $\mathcal{H}_{2,3}$ matrix. (Middle) Pseudospectrum in the complex plane of the $\mathcal{H}_{2,3}$ lattice. (Right) Power oscillations observed around the two exceptional points in the $\mathcal{PT}$ -unbroken regime, shown for various initial conditions.

In conclusion, in our work we present a new type of non-Hermitian singularities, the multi-order exceptional points and present a method to construct them in two- and three- dimensional lattices. The proposed geometries are experimentally relevant and are derived based on the Kronecker sum of two or three nilpotent matrices, each corresponding to a one-dimensional system. Remarkably, the MoEPs demonstrate significant sensitivity to external perturbations across various orders, highlighting their potential use for novel sensing applications.

This project was funded by the European Research Council (ERC-Consolidator) under the grant agreement No. 101045135 (Beyond_Anderson) and by the Hellenic Foundation for Research and Innovation (HFRI) through the 4th Call for HFRI PhD Fellowships (Fellowship Number: 10638.) and the 5th Call of the "Science and Society" Action, titled "Always strive for excellence – Theodoros Papazoglou" (Project Number: 11496, "PSEUDOTOPPOS").

References

1. H. Hodaei, et al., "Enhanced sensitivity at higher-order exceptional points", Nature **548**, 187 (2017).

2. E. M. Graefe, U. Günther, H. J. Korsch, and A. E. Niederle, "A non-Hermitian symmetric Bose–Hubbard model: Eigenvalue rings from unfolding higher-order exceptional points", J. Phys. A, **41**, 255206 (2008).

3. M. H. Teimourpour, R. El-Ganainy, A. Eisfeld, A. Szameit, and D. N. Christodoulides, "Light transport in $\mathcal{PT}$ -invariant photonic structures with hidden symmetries", Phys. Rev. A **90**, 053817 (2014).

4. D. Kaltsas, I. Komis, and K. G. Makris, "Higher order exceptional points in infinite lattices", Opt. Lett. **47**, 4447 (2022).

5. L. N. Trefethen, A. E. Trefethen, S. C. Reddy, and T. A. Driscoll, "Hydrodynamic stability without eigenvalues", Science **261**, 578 (1993).

META 2025, MALAGA - SPAIN, JULY 22 – 25, 2025

Lasing and coherent perfect absorption beyond canonical PT-symmetry using electrically-injected DFB lasers with complex-coupled Bragg grating

Y. Liang[1], Y. El Droubi[1], J.R. Coudevylle[1], L. Ferlazzo[1], X. Lafosse[1], F. Maillard[1], A. Garreau[3], A. Wilk[3], O. Delorme[3], H. Benisty[2], A. Ramdane[1], and A. Lupu[1*]

[1]Centre de Nanosciences et de Nanotechnologies, CNRS, Université Paris-Saclay, Palaiseau, 91120, France

[2]Laboratoire Charles Fabry de l'Institut d'Optique LCFIO, Université Paris-Saclay, Palaiseau, 91120, France

[3]III-V Lab, 1 avenue Augustin Fresnel, 91767 Palaiseau Cedex, France
[*]corresponding author: anatole.lupu@c2n.upsaclay.fr

Abstract: An analysis of lasing and coherent perfect absorption beyond canonical Parity-Time symmetry using internal emission of electrically-injected complex-coupled Bragg grating distributed feedback lasers a operated in a strong coherent feedback regime provided by an ultra-short micro-mirrors confined external cavities is reported.

The objective of this work is to investigate the behavior of complex-coupled distributed feedback (C-C DFB) lasers in a seemingly previously unexplored regime of very strong coherent feedback provided by an ultra-short micro-mirrors-defined external cavity. In our recent publication [1] we provided a proof-of-principle demonstration of Coherent Perfect Absorption (CPA) exploiting a C-C DFB laser's own internal emission reinjected from an ultra-short short external cavity mirror instead of the two beams of conventional CPA implementations. It is worth noting that the DFB lasers used in our work have an arbitrary facet termination, highly reflective outer mirrors, and an additional external cavity. Thus, this study goes well beyond canonical PT-symmetric systems such as the bare C-C DFB, but keeps in its nutshell the key feature that CPA and lasing behavior are based on the principle of constructive-destructive interference in a gain-loss modulated structure.

The results of our modeling study based on the threshold gain analysis of DFB laser poles are shown in Figure 1. As can be seen, the facet termination indeed has a strong impact on the threshold gain level of DFB lasers. However, there is a substantial difference between the threshold gain behavior observed in Fig. 1a for a metal Bragg grating DFB laser (shown in Fig. 1c) and that of a C-C DFB laser (Fig. 1b) with phased modulations of both dielectric and metal Bragg gratings (shown in Fig. 1d). Namely, the region delineated by the yellow color in Fig. 1b, which corresponds to the lower threshold gain areas, represents about 80% of the total parametric area. This should be compared to only about 50% of the total color map area corresponding to a similar gain level in the case of a metal grating DFB laser, as shown in Fig. 1a. This feature of C-C DFB lasers would result in a larger production yield of lasers with acceptable performances.

Furthermore, as we demonstrated in [1], ultra-short external-mirror-confined cavity-assisted C-C DFB lasers also exhibit higher spectral purity behavior than their metal grating DFB counterparts. To further compare the performances of C-C DFB lasers versus metal DFB lasers, we enhanced the aspects related to the impact of DFB laser facet termination by considering a configuration where the DFB lasers are confined at both ends with 95% external cavity reflection dielectric mirrors deposited on the cleaved fibers. The schematic of the experimental setup is shown in Figure 2a. Preliminary results regarding the variation of the emission power itself of DFB lasers with respect to the mirror position as a function of the piezoelectric actuator voltage, presented in Figures 2b and 2c for the metal and C-C DFB lasers, respectively, corroborate the trends of modeling predictions.

Notably, the ratio of the color map area corresponding to the lasing behavior (red region colors) is almost

twice as large for the C-C DFB laser compared to the DFB metal grating devices despite the latter operating at a higher injection current (40 mA vs. 30 mA for C-C DFB).

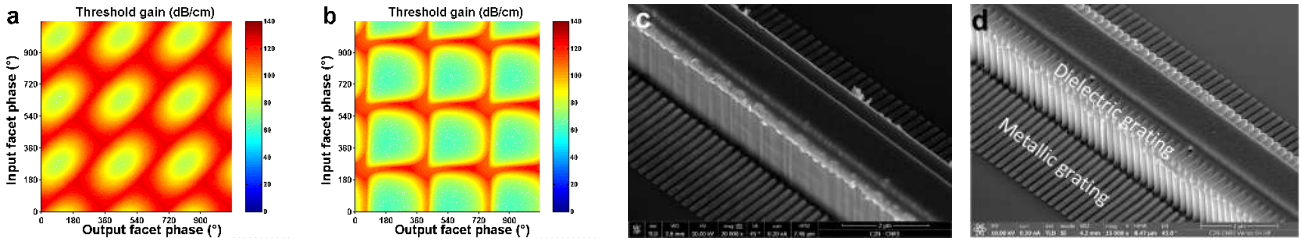


Figure 1: a) Color map showing variation of the threshold gain level as a function of input and output facets termination for metal Bragg grating DFB (a) and C-C DFB (b); SEM micrographs of metal Bragg grating DFB (c) and C-C DFB (d).

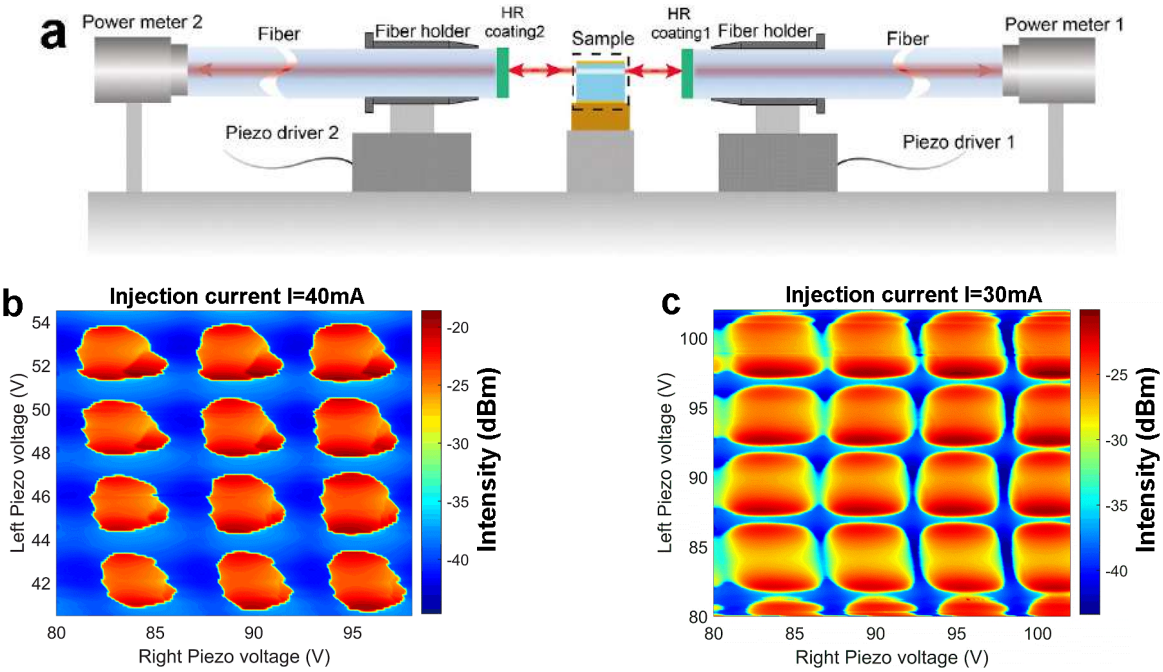


Figure 2: a) Schematic of DFB laser confined from both ends with ultra-short external mirror confined cavities; Color map showing variation of the fiber collected laser emission intensity for metal Bragg grating DFB (b) and C-C DFB (c).

It is also worth noting that CPA effects are also more pronounced in the case of external double-cavity confined DFB lasers, a devicethat appears as a promising test vehicle both from the point of view of practical applications, such as laser modulator, and for more fundamental concepts related to light-by-light manipulation.

Acknowledgements

This work was partially funded by the French Agence Nationale pour la Recherche (project “PARTISYMO”, contract number N° ANR-18-CE24-0024). Funding by the China Scholarship Council is acknowledged by Y. L (grant number 201906750021). This work was partly supported by the RENATECH network and the General Council of Essonne.

References

1. Y. Liang, J.-R. Coudevylle, H. Benisty, A. Ramdane, A. Lupu, “Strong Laser Emission Modulation by Coherent Perfect Absorption Inside Complex-Coupled Distributed Feedback Laser Diodes,” Small, 21(1), 2570003 (2025).

Chiral and non-chiral swift mode conversion through adiabaticity engineering

D. Wang[1], W.-X. Huang[2], B. Zhou[1], W. Yu[1], P.-C. Cao[1],
Y.-G. Peng[1], Z.-Y. Zhou[3], H. Chen[1], X.-F. Zhu[1], Y. Li[1*]
[1]College of Information Science and Electronic Engineering,
Zhejiang University, China
[2]School of Physics and Innovation Institute,
Huazhong University of Science and Technology, China
[3]Department of Physics, Zhejiang Sci-Tech University, China
eleying@zju.edu.cn (corresponding author)

Abstract

We propose a method that dynamically engineers adiabaticity in the evolution of non-Hermitian systems, enabling both chiral and nonchiral mode conversion. This approach addresses speed and chirality challenges in EP encircling without relying on a specific model, facilitating dynamic manipulation of nonadiabatic processes and accelerating operations with selectable mode conversion patterns.

1 Introduction

Non-Hermitian systems can exhibit exceptional points (EPs) where eigenvalues and eigenstates coalesce. EPs have been extensively studied for their unique properties in the field of photonics, acoustics and beyond, which can be implemented for single-mode lasing, loss-induced transmission enhancement, unidirectional invisibility. The eigenvalues of these non-Hermitian Hamiltonians form a self-intersecting Riemann surface, causing the initial eigenstate to be irrecoverable after completing a loop around an EP. Mode conversion can be achieved by adiabatically encircling an EP, but only in one direction (e.g., counterclockwise, CCW). In the opposite direction (e.g., clockwise, CW), the Hamiltonian transitions to a lower imaginary Riemann sheet, leading to a nonadiabatic jump and subsequent recovery of the initial state. This asymmetric mode conversion highlights the chirality of EP encircling and has sparked significant research interest, particularly in applications such as optical communications, quantum control, and optical isolators.

Despite notable progress, the EP encircling scheme faces two fundamental problems. Firstly, the adiabatic requirement limits mode conversion speed, impacting operational efficiency and mode decay. Recent approaches, like Hamiltonian hopping and selected loops, aim to accelerate evolution but are hindered by extreme parameters and low-loss eigenstates, restricting broader applicability. Secondly, controlling chirality in mode conversion is constrained. Conventional schemes permit only chiral mode conversion (mode A $\rightarrow$ B in CCW, mode A $\rightarrow$ A in CW). Recent findings shows potential for non-chiral mode recovery (mode A $\rightarrow$ A in CCW and CW) via a non-encircling-EP loop path, however, the specific outcome depends on the path details. And non-chiral mode conversion (mode A $\rightarrow$ B in CW and CCW) remains insufficiently explored, reportedly achievable only with specific starting points in the evolution process. Addressing speed and chirality challenges in EP encircling requires an efficient and model-independent solution, as existing works rely on specific models, paths, or Hamiltonians, necessitating broader approaches. Adiabaticity offers potential solutions but lacks adequate exploration. Existing

schemes focus on maintaining proximity to the Riemann surface throughout the encircling operation, with occasional jumps, yet fail to consider the degree of adiabaticity at each instant. A systematic method to quantify and control instantaneous adiabaticity is currently absent, impeding efficiency optimization. Furthermore, non-adiabaticity engineering has been overlooked, with previous approaches either avoiding non-adiabatic processes in mode conversion or limiting non-adiabatic jumps between Riemann sheets in mode recovery. The active introduction and control of non-adiabatic processes remain rare, limiting the ability to accelerate operations and freely select mode conversion patterns. Overall, an on-demand approach addressing the speed and chirality challenges in EP encircling is urgently needed, with adiabaticity playing a crucial role that requires further attention.

We introduce dynamic adiabaticity engineering for non-Hermitian Hamiltonian evolution, achieving equivalent quality to conventional quasi-adiabatic evolution in one-fourth of the time. Our method facilitates both chiral and non-chiral mode conversions on a single path. By optimizing velocity at each local point based on quantified adiabaticity, we transcend the adiabatic/non-adiabatic dichotomy, integrating both processes within a unified framework. Importantly, our methodology allows deviation from the Riemann surface, offering an alternative to strict adherence or jumps between surfaces. Implemented in a microwave waveguide system, our approach demonstrates superior speed and mode purity. Moreover, it extends beyond optical systems, being applicable to various non-Hermitian systems. Our work enhances understanding of adiabaticity in non-Hermitian systems and provides insights for advancing mode converters. The dynamic adiabaticity engineering method is a promising approach for achieving efficient and high-quality evolution in non-Hermitian systems.

2 Acknowledgements

This work is supported by the National Key R & D Program of China under Grant No. 2022YFA1405200, the National Natural Science Foundation of China (NNSFC) under Grants No. 92163123 and No. 52250191, the Zhejiang Provincial Natural Science Foundation of China under Grant No. LZ24A050002.

References

[1] Y. Ashida, Z. Gong, and M. Ueda, Non-Hermitian physics, Adv. Phys. 69, 249 (2020).

[2] J. Doppler, A. A. Mailybaev, J. Böhm, U. Kuhl, A. Girschik, F. Libisch, T. J. Milburn, P. Rabl, N. Moiseyev, and S. Rotter, Dynamically encircling an exceptional point for asymmetric mode switching, Nature (London) 537, 76 (2016).

[3] X. Shu, A. Li, G. Hu, J. Wang, A. Alù, and L. Chen, Fast encirclement of an exceptional point for highly efficient and compact chiral mode converters, Nat. Commun. 13, 2123 (2022).

[4] D. Guéry-Odelin, A. Ruschhaupt, A. Kiely, E. Torrontegui, S. Martínez-Garaot, and J. G. Muga, Shortcuts to adiabaticity: Concepts, methods, and applications, Rev. Mod. Phys. 91, 045001 (2019).

[5] H. Nasari, G. Lopez-Galmiche, H. E. Lopez-Aviles, A. Schumer, A. U. Hassan, Q. Zhong, S. Rotter, P. LiKamWa, D. N. Christodoulides, and M. Khajavikhan, Observation of chiral state transfer without encircling an exceptional point, Nature (London) 605, 256 (2022).

[6] J.-T. Bu et al., Enhancement of quantum heat engine by encircling a liouvillian exceptional point, Phys. Rev. Lett. 130, 110402 (2023).

Complex continuation exceptional point and its role in eigenvalue knots for open boundary lattices

Yuancheng Zhao and Kun Ding*

Department of Physics, State Key Laboratory of Surface Physics, and Key Laboratory of Micro and Nano Photonic Structures (Ministry of Education), Fudan University, Shanghai 200438, China
*corresponding author: kunding@fudan.edu.cn

Abstract: Non-Bloch EPs are not merely straightforward generalizations of Bloch EPs. We define complex continuation EPs (CCEPs) and non-Bloch Fermi arcs (NBFAs) connecting CCEPs, clarify the distinction between non-Bloch EPs and CCEPs, and show that CCEPs and NBFAs in OBC knots mirror Bloch EPs and non-Hermitian Fermi arcs in PBC knots.

Exceptional points (EPs) are unique non-Hermitian degeneracies with fascinating properties, particularly in lattice systems. EPs under periodic boundary conditions (PBCs) that reside in the Brillouin zone are called Bloch EPs, resulting in phenomena like eigenvalue braiding and knots. The disparity between the PBC and open boundary condition (OBC) spectra illustrates the Bloch EPs may not be observable for NH lattices under OBC, leading to non-Bloch EPs. Recent studies reveal that non-Bloch EPs can emerge even in single-band cases, unlike Bloch EPs, which are limited to multiband systems. This undoubtedly shows that non-Bloch EPs are not merely straightforward generalizations of Bloch EPs. To explore this, we deploy the reciprocal non-Hermitian Lieb lattice, which supports observable Bloch EPs, and alter the geometry to make them disappear. By analytic continuation wavenumbers to complex domain, Bloch EPs naturally generalize to complex continuation EPs (CCEPs), which typically do not lie on the OBC spectra. We then examine the generalized Brillouin zone and its intersection with CCEPs, showing that the CCEP, even with its energy on the OBC spectra, is still distinct from the non-Bloch EP. Non-Bloch Fermi arcs (NBFAs) connecting CCEPs determine the OBC eigenvalue braiding and knots, generalizing the Bloch EP phenomena. We finally demonstrate a transition in OBC eigenvalue knots with CCEPs, NBFAs, and non-Bloch EPs, revealing their respective roles.

References

1. K. Ding, C. Fang, and G. Ma, Non-Hermitian topology and exceptional-point geometries, Nat. Rev. Phys. **4**, 745 (2022).
2. Y.-M. Hu, H.-Y. Wang, Z. Wang, and F. Song, Geometric origin of non-Bloch PT symmetry breaking, Phys. Rev. Lett. **132**, 050402 (2024).
3. Y.-X. Xiao, K. Ding, R.-Y. Zhang, Z. H. Hang, and C. T. Chan, Exceptional points make an astroid in non-Hermitian Lieb lattice: Evolution and topological protection, Phys. Rev. B **102**, 245144 (2020).
4. Y. Li, X. Ji, Y. Chen, X. Yan, and X. Yang, Topological energy braiding of non-Bloch bands, Phys. Rev. B **106**, 195425 (2022).

Nano-Lasers, Spasers, and Nanostructures with Quantum Elements

Geometric Antibunching and Directional Shaping of Photon Anticorrelations

B. Durá-Azorín[1,2,3*], A. Manjavacas[3], and A. I. Fernández-Domínguez[1,2]
[1]Departamento de Física Teórica de la Materia Condensada,
Universidad Autónoma de Madrid, E-28049 Madrid, Spain.
[2]Condensed Matter Physics Center (IFIMAC), Universidad Autónoma de Madrid, E-28049 Madrid, Spain.
[3]Instituto de Química Física Blas Cabrera (IQF), CSIC, 28006 Madrid, Spain.
[*]corresponding author: blas.dura@uam.es

Abstract: In this work, we investigate the directional characteristics of photon statistics in dimers of quantum emitters placed in different photonic environments. We find a new mechanism for photon anticorrelation, termed as *geometric antibunching*, that is completely agnostic to the quantum state of the emitters and emerges from quantum interference effects.

Although temporal photon statistics have been a cornerstone since the beginning of the field of quantum optics, the second order spatial coherence has been greatly overlooked. In this work [1], we present a comprehensive description of the spatial characteristics of photon anticorrelations in quantum emitters placed in different photonic environments. For their analysis, we construct a two-point second-order correlation function, $g^{(2)}(\mathbf{r}, \mathbf{r'})$, that allows us to find a new mechanism for photon anticorrelation, termed as *geometric antibunching*. This phenomenon is completely agnostic to the quantum state of the emitters and emerges from quantum interference effects due to the indistinguishability of different two-photon optical pathways. Finally, we explore its occurrence in emitters placed in the vicinity of a flat substrate and a nanosphere, demonstrating that these *geometrical zeros* are not a coincidence of free-space [2, 3] but a general property of the photonic environment where the emitters are placed. We also demonstrate its tunnability through the different material and geometric parameters of these structures.

By decomposing the electric field operator into optical-path and polarization terms we derive the expression for the normalized two-point second-order correlation function for the QE dimer

$$g^{(2)}(\mathbf{r}, \mathbf{r}') = \frac{|\Psi(\mathbf{r}, \mathbf{r}', \mathbf{r}_1, \mathbf{r}_2)|^2 \langle \hat{\sigma}_1^\dagger \hat{\sigma}_2^\dagger \hat{\sigma}_1 \hat{\sigma}_2 \rangle}{\langle I \rangle \langle I' \rangle}$$

where the quantum state of the dimer is encoded in the steady-state expected value of the σ_1 and σ_2 operators and the function Ψ captures the optical-path dependence of the wavefunction of the two-photon states generated by the quantum emitters. The phenomenon referred to here as geometric antibunching occurs when the function Ψ vanishes at two pairs of points, causing $g^{(2)}(\mathbf{r}, \mathbf{r'})$ to be zero. This effect arises independently of the specific quantum state of the dimer, making it unaffected by factors such as pumping, emitter interactions, or decoherence.

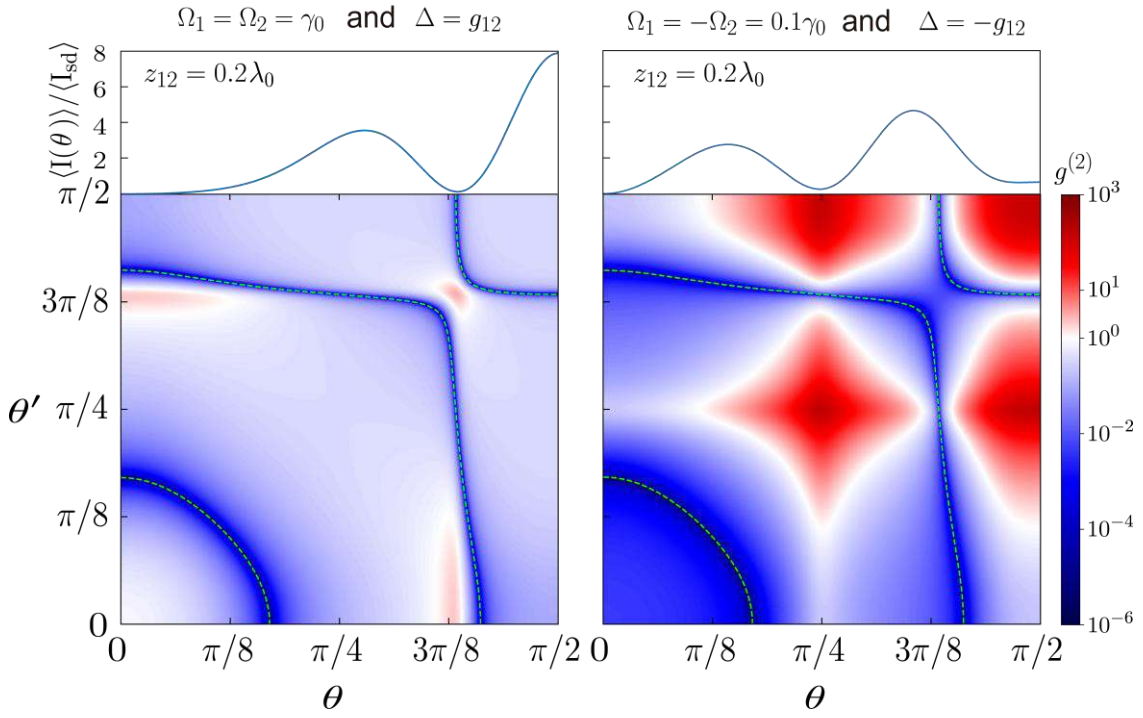


Figure 1. Maps of directional correlations, $g^{(2)}(\theta, \theta')$, for a vertically oriented QE dimer placed above a perfect mirror (z1 = 0.6 λ_0 and z2 = 0.8 λ_0). The polar angles θ, θ' represent the directions in the far-field where light is detected. The laser drivings (Ω_1 and Ω_2) and detuning (Δ) are set to target the Bell symmetric (left) and antisymmetric (right) states of the QE dimer. The upper panels show directional intensity plots in both scenarios, normalized to $\langle I_{sd}\rangle$ (the emission of a single emitter in free space at $\theta=\pi/2$). Green dashed curves indicate geometric antibunching zeros, where $g^{(2)}(\theta, \theta')$ vanishes independently of the quantum state of the emitters.

Our work opens the door to developing new strategies to control and harness quantum light by incorporating the spatial degrees of freedom in its theoretical description. Moreover, it puts forward a number of design ideas that can promptly be implemented for single-photon generation in nanophotonic platforms. We foresee efficient and versatile quantum light sources based on our findings, with application in quantum information and quantum sensing technologies.

This work has been generously supported by MCIN/AEI/10.13039/501100011033/FEDER under projects PID2021-126964OB-I00, TED2021-130552BC21, and PID2022-137569NB-C42. BDA and AIFD also thank the support from the European Union's Horizon Program through grant 101070700.

References

1. B. Durá-Azorín, A. Manjavacas, A. I. Fernández-Domínguez, *arXiv*, (2024)
2. C. Skornia, J. von Zanthier, G. S. Agarwal, E. Werner, H. Walther, *Phys. Rev. A* **64**, 063801 (2001)
3. S. Ritcher, S. Wolf, J. von Zanthier, F. Schmidt-Kaler, *Phys. Rev. Res.* **5**, 013163 (2023)

Exploring extreme dielectric confinement for Nano-lasers

Y. Yu[1,2*], M. Xiong[1,2], Y. Berdnikov[1,2], S. K. Borregaard[1,2], A. H. Dubré[1,2], E. Semenova[1,2], K. Yvind[1,2], and J. Mørk[1,2]

[1]Department of Electrical and Photonics Engineering, Technical University of Denmark, Ørsteds Plads 345A, 2800 Lyngby, Denmark
[2]NanoPhoton - Center for Nanophotonics, Ørsteds Plads 345A, 2800 Lyngby, Denmark
[*]corresponding author: yiyu@dtu.dk

Abstract: In this talk, I will present our recent work on nanolasers that leverage extreme dielectric confinement to localize both photons and electrons, achieving a sub-diffraction-limited mode volume and continuous-wave lasing at room temperature. This approach enhances light-matter interactions, lowers the lasing threshold, and paves the way for ultra-efficient optoelectronic devices.

Efficient light capture in space and time is vital for fundamental physics and applications like lasers. Conventional lasers are large and energy-intensive, restricting their applications such as on-chip optical links. Achieving ultra-efficient microscopic lasers requires compact, low-loss cavities with strong spatial confinement. Since Purcell's insight on cavity-enhanced emission, minimizing optical mode volume (V_{mod}) has been a key goal. Plasmonic structures achieve sub-diffraction confinement but suffer from ohmic losses and low Q-factors [1]. In contrast, dielectric nanostructures with sharp geometries enable sub-diffraction hotspots while maintaining high Q-factors [2-5]. While minimizing V_{mod} enhances quantum light sources with a single emitter at the cavity antinode, it inadequately quantifies light-matter interactions in lasers. Effective enhancement requires spatial localization of both light and carriers, as interaction strength depends on their spatial overlap

$$V_{\mathbf{I}} = 1 / \left(\int N_{\mathrm{p}}(\mathbf{r}) N_{\mathrm{c}}(\mathbf{r}) d\mathbf{r} \right) \tag{1}$$

Here, we define $V_{\mathbf{I}}$ as the light-matter interaction volume and find that the laser threshold is proportional to $V_{\mathbf{I}}$. $N_{\mathrm{p}}(\mathrm{r})$ and $N_{\mathrm{c}}(\mathrm{r})$ are the normalized photon and carrier densities. Eq. (1) shows that minimizing laser threshold requires considering both photon and carrier spatial distributions to minimize $V_{\mathbf{I}}$.

Here we explore extreme dielectric confinement (EDC) for lasers. The EDC laser (Fig. 1(a)) achieves a V_{mod} of $0.88(\lambda/2n)^3$—less than half that of the smallest point-defect photonic crystal (PhC) laser. Such a V_{mod} below the diffraction limit is due to the narrow nanobridge at the center (Fig. 1(b)). We fabricated the structures in an InP quantum-well membrane [5] with a passivation step to mitigate surface recombination, a key challenge for active nanostructures. The laser is optically pumped with a CW light source at room temperature. For comparison, we also evaluate a PhC laser counterpart. We measure laser thresholds by varying the pump focal plane, which controls the spatial distribution of $N_{\mathrm{c}}(\mathrm{r})$. The measurements align closely with our developed 2D laser model (Fig. 1(c)), which incorporates the spatial distributions of photons, carriers, spontaneous emission, and the pumping profile. Thresholds are lowest at the focal plane and increase as excitation disperses. The EDC laser exhibits over 10 dB threshold reduction compared to the PhC laser (Fig. 1(d)).

To quantify carrier localization, we define the carrier volume $V_{\mathrm{car}} = \int N_{\mathrm{c}}(\mathbf{r}) d\mathbf{r} / \max\{N_{\mathrm{c}}(\mathbf{r})\}$. We found that the EDC laser achieves a V_{car} an order of magnitude smaller than that of the PhC laser. Assuming Gaussian distributions for $N_{\mathrm{p}}(\mathrm{r})$ and $N_{\mathrm{c}}(\mathrm{r})$, we find $V_{\mathbf{I}}=V_{\mathrm{mod}}+\Gamma V_{\mathrm{car}}$. Since typically, V_{car} exceeds V_{mod} in nanostructures,

making its reduction more critical in minimizing V_I.

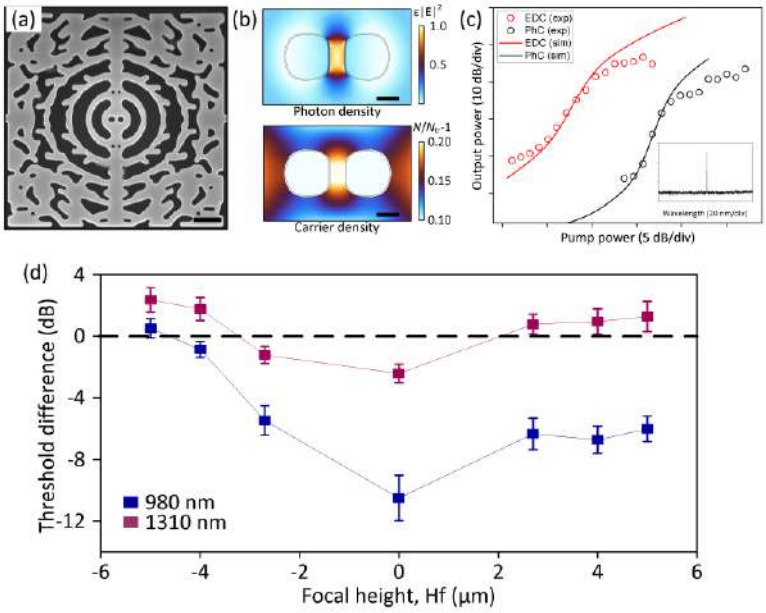


Fig. 1. (a) SEM image of the EDC laser. Scale bar: 1 μm. (b) Calculated photon (top) and carrier (bottom) densities showing strong co-localization at the cavity center. Scale bar: 100 nm. (c) Laser characteristic comparison between the EDC (red) and PhC laser (black). Inset: lasing spectrum of the EDC laser. (d) Measured threshold difference between the EDC and PhC laser ($\Delta P_{th} = P_{th,EDC} - P_{th,PhC}$) at different pump focal positions.

In conclusion, we investigate extreme dielectric confinement of both photons and electrons in lasers, demonstrating a room-temperature CW nanolaser with a sub-diffraction-limited mode volume and a significantly reduced laser threshold. The EDC laser minimizes the interaction volume, a new concept we introduce, while maintaining high gain and *Q*-factor. This would enable unprecedented light-matter interaction levels, with implications beyond light sources.

Acknowledgement: This work was supported by the Danish National Research Foundation (DNRF147 NanoPhoton), the European Research Council (ERC) (834410 FANO), and the Villum Fonden via the Young Investigator Program (42026 EXTREME).

References

1. Khurgin, J. “How to deal with the loss in plasmonics and metamaterials,” Nat. Nanotech, Vol. 10, 2–6, 2015.
2. Hu, S. and Weiss, S. M. “Design of photonic crystal cavities for extreme light concentration,” ACS photon, Vol. 3, 1647–1653, 2016.
3. Choi, H., Heuck, M. and Englund, D. “Self-similar nanocavity design with ultrasmall mode volume for single-photon nonlinearities,” Phys. Rev. Lett, Vol. 118, 223605, 2017.
4. Wang, F., Christiansen, R. E., Yu, Y., Mørk, J. and Sigmund, O. “Maximizing the quality factor to mode volume ratio for ultra-small photonic crystal cavities,” Appl. Phys. Lett, Vol. 113, 241101, 2018.
5. Xiong, M., Christiansen, R. E., Schröder, F., Yu, Y., Casses, L. N., Semenova, E., Yvind, K., Stenger, N., Sigmund, O. and Mørk, J. “Experimental realization of deep sub-wavelength confinement of light in a topology-optimized InP nanocavity,” Opt. Mat. Express, Vol. 14, 397–406, 2024.

Light goes Nano:

The T-matrix method in nanoplasmonics with active gain media

M. A. Iatì[1*] **and R. Saija**[1,2]

[1]CNR-Istituto per i Processi Chimico Fisici, Messina, Italy
[2]Dip. di Scienze Matematiche e Informatiche, Scienze Fisiche e Scienze della Terra, Università di Messina, Italy
[*]corresponding author: mariaantonia.iati@cnr.it

Abstract: The T-matrix method is a powerful approach to study the opto-plasmonic behaviour at the nanoscale. Particle shape, composition, material hybridization, and degree of aggregation affect optical properties and forces. This implies the need for an accurate theoretical modeling paving the way to applications in photothermal therapy, enhanced spectroscopy, and spasing.

1. Introduction

The Transition matrix (T-matrix) is a powerful method to study the opto-mechanical behaviour of metal nanoparticles and nano-aggregates [1]. The technique is based on the multipole expansions of the electromagnetic fields and can be applied to many scatterer models, from nano-shell particles to composite structures and aggregates of spherical monomers. A key point of this approach is that it offers both an analytical and numerical solution to the scattering problem, surpassing other computational approaches in terms of efficiency and accuracy. Furthermore, the T-matrix allows to perform an analytical evaluation of the scattering characteristics averaged over particle orientation. This is a key feature which results in a significant saving in computational time. The T-matrix has proven to be a very reliable tool to describe plasmon coupling in metal nanoparticles, with a detailed description of the near-field plasmon interaction [2].

The T-matrix also offers a comprehensive description of the mechanical effects of light on nanostructures and has proven to be particularly suitable to describe optical trapping of composite and arbitrary-shaped particles [3].

2. Opto-mechanical behaviour in hybrid nanostructures

Hybrid nanostructures exhibit a peculiar optical behaviour since they combine the plasmonic properties with those of the hybrid components, affecting also optical forces and torques acting on the particles [4]. We will discuss, through several case studies, how material hybridization can promote accurate control of the mechanical effects of light. Optical forces on systems composed of metal nanoparticles and molecular emitters [4], as well as multi-shells with alternating metal and dye-doped layers are investigated computationally [5], with a focus on the resonant interplay between plasmonic structures and gain media. Understanding this behaviour will pave the way to many applications, such as photothermal therapy, enhanced spectroscopy, and spasing.

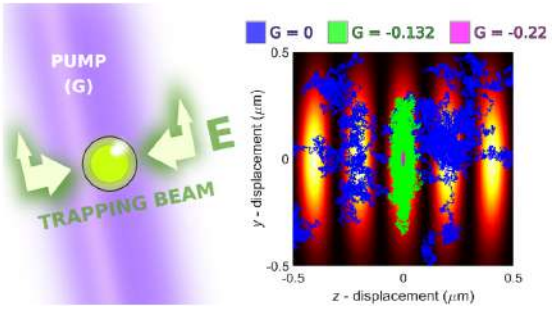


Figure 1: (left) A core-shell particle composed by a metal shell and a dye-doped dielectric core, under the action of a pumped field (purple). (right) The counterpropagating laser beam intensity is projected on the yz plane. Nanoparticle trajectories are plotted for several gain G values showing the tightest confinement at the highest gain. Taken from [4].

We acknowledge financial support from the European Union (NextGeneration EU), through the MUR-PNRR projects PE0000023-NQSTI and SAMOTHRACE (ECS00000022), the PRIN2022 "Exo-CASH" (2022J7ZFRA), "EnantioSelex" (2022P9F79R), and carried out within the Project "Space It Up" funded by ASI and MUR – Contract n. 2024-5-E.0 - CUP n. I53D24000060005.

References

1. Borghese, F. , Denti, P., and Saija, R. "Scattering from model nonspherical particles," 2nd ed., Springer, Berlin, 2007.
2. Amendola, V., Pilot, R., Frasconi, M., Maragò, O. M., & Iatì, M. A. "Surface plasmon resonance in gold nanoparticles: a review", Journal of Physics: Condensed matter, Vol. 29 (20), 203002, 2017.
3. Polimeno, P., et al. "Optical tweezers and their applications" , Journal of Quantitative Spectroscopy and Radiative Transfer, Vol. 218, 131-150, 2018.
4. Polimeno, P., et al. "Gain-assisted optomechanical position locking of metal/dielectric nanoshells in optical potentials", ACS Photonics, Vol. 7, 1262–1270, 2020.
5. Pezzi, L., Iatì, M. A., Saija, R., De Luca, A., and Maragò, O. M. "Resonant coupling and gain singularities in metal/dielectric multishells: Quasi-static versus T-matrix calculations", The Journal of Physical Chemistry C, Vol. 123 (48), 29291-29297, 2019.

Emission landscape and spectrum of plasmonic nanoshell lasers

K. Caicedo[1*], M. Infusino[2], A. Aradian[3] and A. Veltri[2]

[1]Istituto di Scienze Applicate e Sistemi Intelligenti (ISASI) - CNR, Italy
[2]Universidad San Francisco de Quito, Quito, Ecuador
[3]University of Bordeaux & CNRS, Bordeaux, France
[*]corresponding author: karen.caicedo@na.isasi.cnr.it

Abstract: We present comprehensive modeling of gain-enhanced metallic nanoshells, analyzing their lasing characteristics through optical Bloch equations coupled to free-electron dynamics. By comparing symmetric and antisymmetric plasmon resonances and examining detuning effects between gain and resonance frequencies, we identify optimal conditions for emission thresholds, spectral tunability, and frequency pull-out dynamics.

Recent advancements in nanophotonics have opened promising possibilities for miniaturized optical devices, particularly through metallic nanoshell structures (Fig. 1). These nanoshells, characterized by specific geometric configurations, effectively enhance nanoscale light-matter interactions. A pivotal development involves gain-doped metallic nanoshells, where optical gain materials embedded within a plasmonic metallic shell overcome inherent metallic losses, enabling coherent photon emission (lasing) at nanoscale dimensions [1].

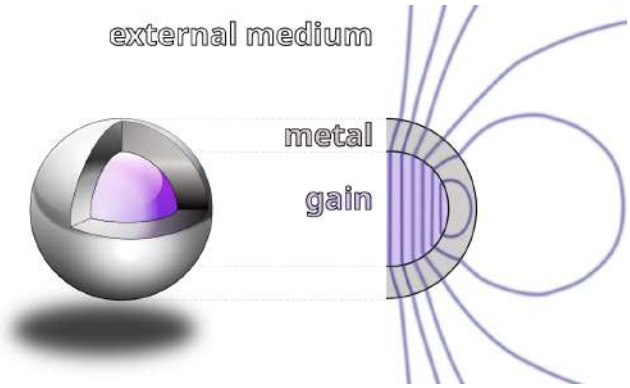


Figure 1. A spherical nanoshell particle, with a gain medium filling the core and a metallic shell, placed into an external medium.

This presentation provides a detailed modeling approach to investigate gain-enhanced nanoshell systems, emphasizing their lasing characteristics and the intricate relationship between structural features and optical behaviors [2,3]. The theoretical framework applied incorporates time-dependent optical Bloch equations, which describe population dynamics within the gain medium, coupled to free-electron motion in the metallic shell. This comprehensive model captures system behaviors both below [2] and above the lasing threshold [3]. Previous studies have successfully applied this method to other configurations, such as spherical nanoparticles immersed in gain media, allowing insights into lasing instabilities at threshold conditions [4].

Our current study extends beyond previous work, exploring two novel avenues. Firstly, we address the distinct properties of the nanoshell's two inherent plasmon resonances—symmetric and antisymmetric—whose frequencies depend strongly on the geometric aspect ratio of the nanoshell [3,5]. Unlike earlier generic treatments, we systematically analyze and compare these resonances, optimizing the necessary gain levels to achieve efficient lasing.

Secondly, we examine the consequences of detuning between the gain medium's emission frequency and the plasmonic resonance frequency [5]. Traditionally, gain frequencies are matched precisely to resonance frequencies for simplified theoretical treatment and optimal gain conditions. However, we explore the physical implications of frequency detuning, analyzing its effects on critical lasing parameters such as gain threshold, lasing frequency, spectral width, and frequency pull-out dynamics. Detuning introduces additional tunability, broadening the potential applications of nanoscale lasers.

Acknowledgments
K.C and V.M., acknowledge the PRIN PNNR - 2022X4W28 project for funding the present work.

References

1. Bergman, D. and M. Stockman, M. “Surface plasmon amplification by stimulated emission of radiation: quantum generation of coherent surface plasmons in nanosystems,” Phys. Rev. Lett., Vol. 90, 027402, 2003.
2. Caicedo, K., Cathey, A., Infusino, M., Aradian, A., and Veltri, A. “Gain-driven singular resonances in active core-shell and nano-shell plasmonic particles,” J. Opt. Soc. Am. B, Vol. 39, No. 1, 107–116, 2022.
3. Aradian, Caicedo, K., A., Cathey, A., Mora, M., Recalde, N., Infusino, M., and Veltri, A . “Emission dynamics and spectrum of a nanoshell-based plasmonic nanolaser spaser,” Nanophotonics, Vol. 13, 4817-4837, 2024.
4. Veltri, A., Chipouline, A., and Aradian, A. “Multipolar, time-dynamical model for the loss compensation and lasing of a spherical plasmonic nanoparticle spaser immersed in an active gain medium,” Sci Rep, Vol. 6, 2016.
5. Caicedo, K., Infusino, M., Aradian, A., and Veltri, A. (in preparation).

Interface Engineering in Surface Plasmon Polariton Nanolasers for Integrated Photonic Applications

Y. -H. Chou[1,2,3*]

[1] Department of Photonics, National Cheng Kung University, Tainan, 70101, Taiwan
[2] Program on Key Materials, Academy of Innovative Semiconductor and Sustainable Manufacturing, National Cheng Kung University, Tainan, 70101, Taiwan
[3] Meta-nano Photonics Center, National Cheng Kung University, Tainan, 70101, Taiwan
[*]corresponding author: tnc@gs.ncku.edu,tw

Abstract: We report interface-engineered SPP nanolasers featuring optimized dielectric-metal coupling, enabling ultracompact mode confinement, low-threshold lasing, and substrate-free transferability for scalable integration.

Surface plasmon polariton (SPP) nanolasers have emerged as promising candidates for subwavelength light sources due to their ability to confine electromagnetic energy beyond the diffraction limit[1]. However, traditional designs relying on rigid substrate-bound configurations face limitations in mode confinement, integration flexibility, and overall optical performance. In this work, we present a new architecture of substrate-free, interface-engineered SPP nanolasers that enables enhanced electromagnetic confinement, significantly lowered lasing threshold, and robust operation across diverse substrate environments[2-5]. Our approach emphasizes precise control of the metal-dielectric-semiconductor interface to tailor plasmonic modes while achieving structural versatility for photonic integration. The device structure is based on a metal–insulator–semiconductor (MIS) configuration. Unlike conventional devices fabricated directly on substrates, our process introduces a sacrificial layer beneath the metal film, allowing for complete release and transfer of the nanolaser structure to arbitrary surfaces. This method offers both structural reconfigurability and potential compatibility with flexible or biologically relevant substrates.

ZnO nanowires were selected as the gain medium for their superior optical properties in the ultraviolet regime. ZnO exhibits a wide direct bandgap of ~3.37 eV and a large exciton binding energy of approximately 60 meV, which facilitates efficient excitonic emission even at room temperature[3]. These characteristics, coupled with strong oscillator strength and compatibility with well-established nanowire growth techniques, make ZnO an ideal candidate for ultraviolet plasmonic nanolasing applications. Moreover, its refractive index profile supports strong light confinement within nanoscale geometries, crucial for coupling with surface plasmon polaritons. To guide the cavity design and optimize the plasmonic interaction, we conducted comprehensive finite element method (FEM) simulations. The simulations evaluated the impact of key parameters including metal type, metal thickness, dielectric material, dielectric thickness, and ZnO nanowire geometry. Among candidate plasmonic metals, aluminum and silver were compared due to their favorable permittivity in the UV range. A dielectric spacer of Al_2O_3 was selected for its high bandgap, low optical loss, and conformal deposition via ALD. The resulting structure produced an effective mode volume of approximately 0.008 λ^3 in the Al-based substrate-free configuration, calculated using the standard definition[1]:

$$V_m = \frac{W_m}{\max[W(r)]} = \frac{1}{\max[W(r)]} \iiint W(r) d^3r \quad (1)$$

W(r) is the spatial distribution of the electromagnetic energy density. For comparison, the same nanowire cavity

on a conventional substrate yields a mode volume of around 0.027 λ^3. This represents a substantial improvement in confinement, attributed to the removal of the substrate and optimized dielectric-metal coupling. The field exhibits strong localization at the nanowire–dielectric–metal interface, as shown in Figure 1.

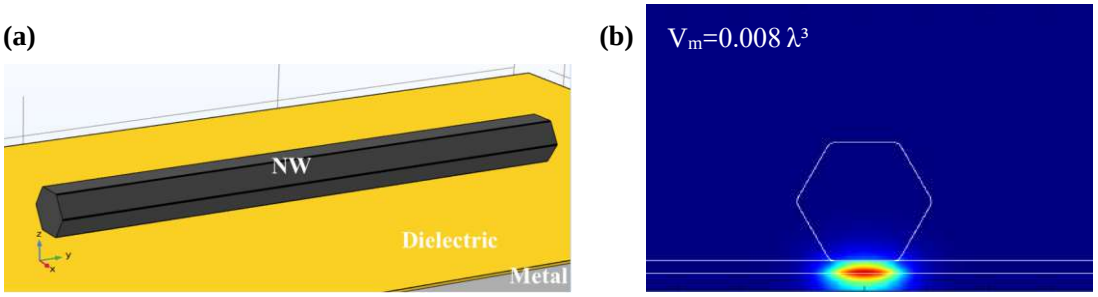


Figure 1. (a) Schematic of the simulated metal–insulator–semiconductor (MIS) nanolaser structure, consisting of a ZnO nanowire (NW) placed on an Al_2O_3 dielectric spacer atop a single-crystalline aluminum film. (b) Simulated electric field intensity distribution ($|E|^2$) in the cross-sectional plane, illustrating strong field confinement at the ZnO–dielectric–metal interface. The calculated mode volume is approximately 0.008 λ^3 under substrate-free configuration.

The combination of precise interface engineering and substrate-free construction offers several advantages over conventional SPP laser platforms. Not only does it enhance the Purcell factor and reduce the required gain, but it also allows for nontraditional integration pathways such as in flexible electronics, implantable sensors, and compact optical interconnects. Moreover, the entire process is compatible with scalable fabrication techniques, and the choice of materials ensures CMOS process compatibility.

Acknowledgements This research received support from National Science and Technology Council (NSTC), under Contract Numbers NSTC 113-2112-M-006-031. The author expresses gratitude for the utilization of the 2204 equipment, which belongs to the Core Facility Center of National Cheng Kung University (NCKU).

References

1. Oulton, R. F., V. J. Sorger, T. Zentgraf, R.-M. Ma, C. Gladden, L. Dai, G. Bartal and X. Zhang, “Plasmon lasers at deep subwavelength scale,” Nature, Vol. 461, No. 7264, 629–632, 2009.
2. Chou, Y.-H., K.-B. Hong, Y.-C. Chung, C.-T. Chang, B.-T. Chou, T.-R. Lin, S. M. Arakelian, A. P. Alodjants, and T.-C. Lu, “Metal for plasmonic ultraviolet laser: Al or Ag?,” IEEE J. Sel. Top. Quantum Electron., Vol. 23, No. 6, 4601907, 2017.
3. Chou, B.-T., Y.-H. Chou, Y.-M. Wu, Y.-C. Chung, W.-J. Hsueh, S.-W. Lin, T.-C. Lu, T.-R. Lin, and S.-D. Lin, “Single-crystalline aluminum film for ultraviolet plasmonic nanolasers,” Sci. Rep., Vol. 6, 19887, 2016.
4. Chou, Y.-H., B.-T. Chou, C.-K. Chiang, Y.-Y. Lai, C.-T. Yang, H. Li, T.-R. Lin, C.-C. Lin, H.-C. Kuo, S.-C. Wang, and T.-C. Lu, “Ultrastrong mode confinement in ZnO surface plasmon nanolasers,” ACS Nano, Vol. 9, No. 4, 3978–3983, 2015.
5. Cheung, W.-S., I. Huang, Z. Y. Wu, P.-Y. Chang, H.-C. Hsu, Y.-P. Lan, and Y.-H. Chou, “Advancements in nanoscale coherent emitters: The development of substrate-free surface plasmon nanolasers,” APL Photonics, Vol. 9, No. 1, 016103, 2024.

Enhancement of lasing and spasing phenomena via individual, periodic and complex plasmonic resonators

D. Vass[1,2], A. Szenes[1,2], M. Waldhauser[1], E. Tóth[1], O. Fekete[1], B. Bánhelyi[2,3], and M. Csete[1,2*]

[1] University of Szeged, Department of Optics and Quantum Electronics, Dóm tér 9, H-6720 Szeged, Hungary
[2] Wigner Research Center for Physics, Konkoly-Thege Miklós út 29-33, Budapest H-1121, Hungary
[3] University of Szeged, Department of Computational Optimization, Árpád tér 2, H-6720 Szeged, Hungary
[*]corresponding author: mcsete@physx.u-szeged.hu

Abstract: Amplification, nanolasing and spasing phenomena can be controlled by designing individual nanoresonators of different composition that are randomly distributed, periodically arranged along 1D gratings, compose 3D multilayers and construct 2D patterns of a miniarrays. By considering the local impact of the plasmonic nanoresonators, the 4D optimization enables tailored lasing characteristics.

The judicious design of nanoresonator (NR) patterns enables the optimization of lasing characteristics, by improving the pump and probe related phenomena via coupled modes [1]. In this work, the coupled Maxwell and rate equations were solved by considering the local **E**-field distribution as a nonlinear term in the gain. Via numerical pump-and-probe computations the near-field enhancement, far-field optical responses and optical cross-sections were determined above the dye concentration-E_{pump} field parameter space, to distinguish near-field amplifier, far-field emitting laser and spaser operation regions. The lasing /spasing was proven based on the threshold behavior and line-width narrowing /negative extinction cross-section. Asymmetrical frequency pulling and counter-intuitive pump dependence was demonstrated, according to the non-Hermitian nature of plasmonic NRs [2, 3]. Metamaterial retrieval was realized to extract the effective parameters of NR composites.
Individual nanoresonators of various core-shell compositions were optimized, and the impact of the configuration and dye concentration on the mode competition, far-field emission distribution and quantum efficiency was determined [4]. The concentration corresponding to the minimal spaser threshold was determined for NRs of different composition. Various NRs were randomly implanted into extended targets and it was proven via time-domain computations that the near-field and energy deposition of counter-propagating short laser pulses can be balanced via optimized distributions [5]. Arrangement of the NRs into multilayers of periodic patterns allowed for designing amplifying mirror, impedance matched amplifier and epsilon-near-zero media that operate at the center, lower and upper edge of their plasmonic band gaps, respectively. On the dispersion maps modes resulting in the highest near-field enhancement, light tunneling and allowing for phase synchronization were identified at composition dependent tilting. Achievement of the coherent perfect absorption was demonstrated along hyperbolas on the dye concentration-E_{pump} map, for counter-propagating beams. Propagation direction and relative phase independent perfect transmission capable of ensuring cloaking was demonstrated. It was shown that the FOM=out-coupled intensity/FWHM can be maximized by aligning NRs along the turning lines of long-range propagating surface plasmon polaritons that can be coupled in specific azimuthal orientations of one-dimensional dielectric-metal gratings seeded by dye. Multispectral control of plasmonic lasing was demonstrated via coupled modes on the convex and concave complex structures constructed with Babinet complementary miniarrays of a central nanoring and satellite nano-crescent NRs. The threshold behavior and line-width narrowing is more well defined in transmittance /reflectance in complementary orientations of convex /concave patterns, the stimulated emission is slightly /considerably pulled spectrally and is neighbored by ASE.

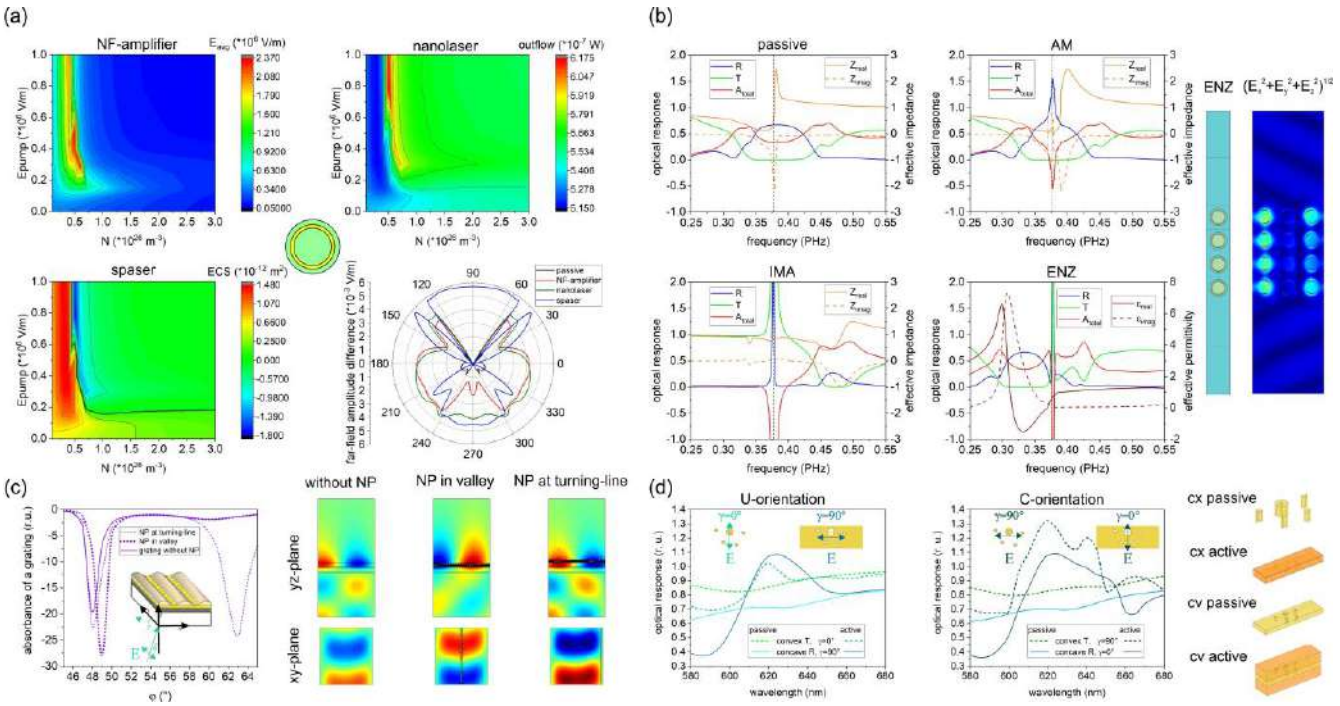


Figure 1. Comparison of (a) dye-concentration-E_{pump} maps and polar angle distributions of emission in passive, near-field amplifier, nanolaser and spaser individual CS NRs; (b) optical responses and effective parameters of passive, amplifying mirror, impedance matched amplifier and ENZ CS quad-layers (inset: instantaneous E(t) of a backward collective mode); gain in absence and presence of NRs in the valley and on turning lines of E_y, on a multilayer grating in azimuthal orientations resulting in efficient long-range SPP coupling (insets: instantaneous $E_y(t)$); transmission and reflection in complementary orientations of passive and decay-length-scaled gain medium coated convex and concave Babinet complementary patterns (insets: illumination configurations).

Acknowledgement: This work was supported by the National Research, Development and Innovation Office (NKFIH) of Hungary, projects: "Nanoplasmonic Laser Inertial Fusion Research Laboratory" (NKFIH-2022-2.1.1-NL-2022-00002) and "National Laboratory for Cooperative Technologies" (NKFIH-2022-2.1.1-NL-2022-00012) in the framework of the Hungarian National Laboratory program.

References

1. Azzam, S. I., A. V. Kildishev, R-M. Ma, C-Z. Ning, R. Oulton, V. M. Shalaev, M. I. Stockman, J-L. Xu, X. Zhang, "Ten years of spasers and plasmonic nanolasers," Light: Science & Applications, Vol. 9, 90, 2020.
2. Aradian, A., K. Caicedo, A. Cathey, M. Mora, N. Recalde, M. Infusio, and A. Veltri, "Emission dynamics and spectrum of a nanoshell-based plasmonic nanolaser spaser," Nanophotonics, Vol. 13, No. 26, 4817-4837, 2024.
3. Benzaouia, M., A. D. Stone and S. G. Johnson, "Nonlinear exceptional-point lasing with ab initio Maxwell-Bloch theory," APL Photonics, Vol. 7, 121303, 2022.
4. Szenes A., D. Vass, O. Fekete, E, Tóth, B. Bánhelyi and M. Csete, "Active individual nanoresonators optimized for lasing and spasing operation," Nanomaterials, Vol. 11, No. 5, 1322, 2021.
5. Vass D., A. Szenes, E. Tóth, B. Bánhelyi, I. Papp, T. Bíró, L. P. Csernai, N. Kroó, and M. Csete, "Plasmonic nanoresonator distributions for uniform energy deposition in active targets," Opt. Mater. Express, Vol. 13, No. 1, 9-27, 2023.

Plasmonic slot waveguides: a quantum leap in nonlinear nanophotonics

L. Rojas Yanez[1], H. Hu[3], C. Ciracì[3], J.A. Scott[1,2], L. Sortino[4], M. Toth[5,6], P. G. Zotev[7], A. I. Tartakovskii[7], and S. Palomba[1,2]*

1. Institute for Photonics and Optical Sciences, School of Physics, University of Sydney, Sydney, NSW, Australia
2. University of Sydney Nano Institute, The University of Sydney, Camperdown, Australia
3. Istituto Italiano di Tecnologia, Center for Biomolecular Nanotechnologies, Lecce, Italy
4. Chair in Hybrid Nanosystems, Nanoinstitute Munich, Faculty of Physics, Ludwig-Maximilians-Universität München, Germany
5. School of Mathematical and Physical Sciences, University of Technology Sydney, Ultimo, Australia
6. ARC Centre of Excellence for Transformative Meta-Optical Systems, University of Technology Sydney, Ultimo, Australia
7. Department of Physics and Astronomy, University of Sheffield, Sheffield, UK
* Electronic address: stefano.palomba@usyd.edu.au

Abstract: In this work, we theoretically show that integrating epsilon-near-zero materials within metal–dielectric–metal slot waveguides would boost the nonlinear conversion efficiency, exhibiting unprecedented nonlinear optical conversion efficiency in an ultra-compact device. Furthermore, we have developed a novel nanofabrication process flow to fabricate these slot waveguides with high aspect ratio and sub-nm gaps.

Interest and excitement in nanophotonics—the study and control of light-matter interactions at the nanoscale—are driven by the ability to confine light to volumes well below a cubic wavelength, and, thereby, achieve extremely high intensities. This leads to light-matter interactions of unprecedented localization and strength. Such extreme behaviour—both in terms of field enhancement and localization—can be achieved using plasmonic nanostructures, which concentrate light in regions much smaller than the wavelength of light, reducing the excitation power and, under certain conditions, removing phase-matching requirements in the nonlinear regime. In this study, we theoretically demonstrate that the metal–dielectric–metal (MDM) slot waveguides, consisting of a thin dielectric layer embedded between metal films, provide the strongest confinement and that integrating epsilon-near-zero (ENZ) materials into the slot significantly improves the nonlinear conversion efficiency of these structures. The results show that the degenerate four-wave mixing (DFWM) conversion efficiency of these ENZ-MDM structures surpasses that of regular plasmonic structures and their dielectric counterparts, even under low pump power conditions, and remains robust despite higher losses in the ENZ material (Figure 1a).

Creating such extremely compact devices requires advanced nanofabrication methods capable of overcoming the limitations of conventional approaches; in response to this, we have developed a novel lithographic process flow based on Carbon Electron Beam Induced Deposition (C-EBID). Using a carbon hard mask prepared via C-EBID (Figure 1b), we overcome focused ion beam resolution limits and fabricate close-to-ideal slot waveguides with high aspect ratios. The effectiveness of this approach has been demonstrated by successfully preparing MDM slot waveguides with 10 nm gaps and straight side walls (Figure 1c), showing a significant advancement in the preparation of optically active nanostructures. Overall, these results underscore the potential for applications, for example, in quantum optics, where extreme compactness and high efficiency in harnessing pure and strong nonlinearities become crucial.

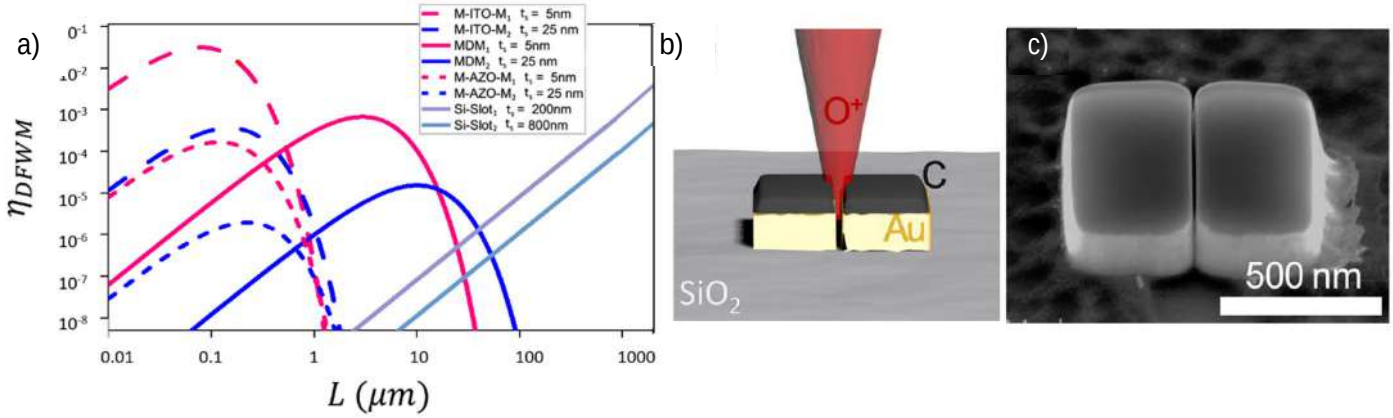


Figure 1: (a) Comparison of DFWM conversion efficiency of M–ENZ–M (using two ENZ materials: ITO and AZO), MDM, and Si-Slot waveguides for two different spacer thicknesses (t_s) when each structure is driven at the maximum threshold power of MDM1 (P_{th} =0.32) for fairness. (b) Schematic illustrating important features of nanofabrication workflow. (c) SEM image of Au dimer structure with ~10 nm gap.

Round Table: Nanolasers: prospects and challenges

Ashod Aradian
University of Bordeaux, France

Abstract: This roundtable is open to everybody, whether they attended or not the "nanolaser" SP17 session. This will be a time to discuss and exchange views informally around the following themes, as well as others: (i) challenges and prospects in the field of nanolasers, (ii) state of the theory versus the state of experiments, (iii) nanolasers versus classical lasers, (iv) what are the obstacles towards the commercialization of nanolaser-based devices? All colleagues are more than welcome to participate.

Laser cooling of hybrid nanoparticles

O. M. Maragò[1,*], A. Veltri[1,2], M. Infusino[1,2], R. Saija[1,3], M. A. Iatì[1]
[1]CNR-Istituto per i Processi Chimico Fisici, Messina, Italy
[2]Colegio de Ciencias e Ingenieria, Universidad San Francisco de Quito, Quito 170901, Ecuador
[3]Dip. di Scienze Matematiche e Informatiche, Scienze Fisiche e Scienze della Terra, Università di Messina, Italy
[*]corresponding author: onofrio.marago@cnr.it

Abstract: After an introduction to optical forces at the nanoscale, we discuss some ideas on laser cooling of hybrid nanostructures, where localized surface plasmons are coupled to excitons, and of gain-assisted nanoparticles, where the strong coupling between plasmons and excitons controls their optomechanical behavior.

Optical forces are the consequence of momentum conservation in the light-matter interaction [1,2]. In recent years, their applications for pushing, trapping, and manipulation of particles resulted in a wide range of applications in the nanoscience, life sciences, physics, and engineering [3]. Their averaged components can be separated in a conservative contribution, responsible for the operation of optical tweezers, and in a dissipative one, crucial for laser cooling of the particle centre-of-mass [1].

Here, we discuss on the hybridization of optical forces by studying the control and engineering of mechanical effects of light in the presence of plasmon-exciton coupling [4,5]. Optical forces on exemplar systems composed of plasmonic particles and quantum emitters [4] are investigated theoretically by extending the theoretical framework used for atoms in the dipole approximation. Prospects for laser cooling and optomechanical manipulation of gain-assisted systems [5,6] will be discussed.

We acknowledge financial support from the European Union (NextGeneration EU), through the MUR-PNRR projects PE0000023-NQSTI and SAMOTHRACE (ECS00000022), the PRIN2022 "Cosmic Dust II" (2022S5A2N7), “EnantioSelex” (2022P9F79R), and carried out within the Project “Space It Up” funded by ASI and MUR – Contract n. 2024-5-E.0 - CUP n. I53D24000060005.

References

1. Jones, P. H., Maragò, O. M., Volpe, G. Optical Tweezers: Principles and Applications, Cambridge University Press, Cambridge (UK), 2015.
2. Polimeno, P., et al. “Optical tweezers and their applications,” Journal of Quantitative Spectroscopy and Radiative Transfer 218, 131-150, 2018.
3. G. Volpe, O. M. Maragò, H. Rubinsztein-Dunlop, et al., “Roadmap for Optical Tweezers”, J. Phys. Photonics 5, 022501, 2023.
4. Ridolfo, A., Saija, R., Savasta, S., Jones, P. H., Iati, M. A., Maragò, O. M. “Fano-doppler laser cooling of hybrid nanostructures”, ACS Nano, 5(9), 7354-7361, 2011.
5. Polimeno, P., et al. “Gain-assisted optomechanical position locking of metal/dielectric nanoshells in optical potentials,” ACS Photonics 7, 1262–1270, 2020.
6. Aradian, A., Caicedo, K., Cathey, A., Mora, M., Recalde, N., Infusino, M., & Veltri, A. “Emission dynamics and spectrum of a nanoshell-based plasmonic nanolaser spaser”, Nanophotonics 13, 4817-4837 (2024).

Electrically-biased Surface Plasmon Nanolaser with a Hyperbolic Metasurface

Jun-Yu Wu[1], and Tsung-Yu Huang[1,*]

[1] Department of Materials Engineering, Ming Chi University of Technology, New Taipei City, Taiwan, 243303

[*] Email: huang.tsungyu@mail.mcut.edu.tw

Abstract: In this study, we employed a hyperbolic metasurface of alternating air and metallic stipes for demonstration of the nanolaser. The hyperbolic metasurface provides three-dimensional confinement of surface plasmons, enabling smaller physical and modal volumes compared to others. Furthermore, the minimal volume facilitates miniaturization and integration of photonic integrated circuits efficiently.

Current surface plasmon (SP) nanolasers mostly used Fabry-Perot resonant for the SP cavity, which can only achieve two-dimensional confinement. This limits the interaction between surface plasmons and the material, leading to higher lasing thresholds. Furthermore, most nanolasers are optically excited and lack electrical excitation designs, making integration with integrated circuits difficult and relying on external excitation light sources.

To address these issues, we propose the design of a hyperbolic metamaterial interface, which allows surface plasmon polaritons to be confined in three dimensions, significantly enhancing laser efficiency and enabling electrical excitation. In this design, we introduce laterally arranged air trenches on the metal surface to form a hyperbolic metamaterial interface. The momentum mismatch between the hyperbolic interface and the continuous metal prevents surface plasmon polaritons from coupling into the surrounding continuous metal, thus achieving confinement within the resonator. Additionally, since the air trenches are arranged along the x-direction in this structure, surface plasmon polaritons are confined in the x-direction due to the wave vector mismatch of the hyperbolic interface. In the y-direction, confinement is achieved based on traditional Fabry-Perot resonance. Moreover, we anticipate that the use of a silver thin film as the top electrode and highly-doped gallium arsenide as the bottom electrode will make electrical excitation possible, as shown in **Figure 1(a)**.

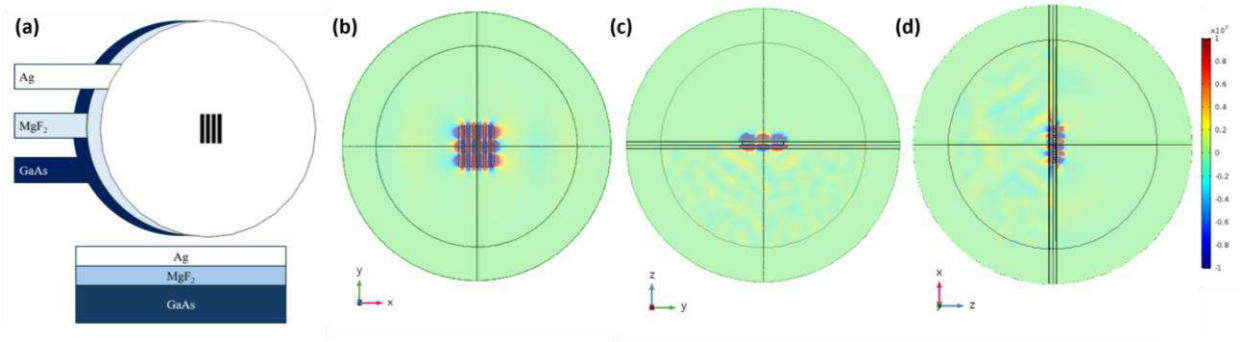


Figure 1. (a) Scheme of the hyperbolic metasurface and its (b) top, (c)y-z and (d) x-z views.

We used finite element simulation to verify whether the results met our expectations. Based on the structure shown in **Figure 1(a)**, we built a system consisting of a gallium arsenide (GaAs) substrate, magnesium fluoride (MgF_2), and a continuous silver with air trenches. **Figure 1(b)** presents the simulation results of the designed resonant cavity. According to the results, it is evident that the surface plasmon is effectively confined in all three

dimensions by the hyperbolic metasurface. To further investigate the performance of this resonant cavity, we conducted in-depth calculations. As shown in **Figure 2(a)**, the quality factor of this mode is 81.445; the Purcell factor is 9467.35; the physical volume is 0.01584 μm³; the modal volume is 4.6663×10^{-4} μm³; and the normalized modal volume is 5.2298×10^{-3}. Therefore, based on the modal volume, it is clear that this structure successfully breaks the diffraction limit, achieving a subwavelength resonant cavity with a high quality factor.

(a)

Quality factor	81.445
Purcell factor	9467.35
Mode volume	0.01584 μm³
Physical volume	4.6663×10^{-4} μm³
Normalized mode volume	5.2298×10^{-3}

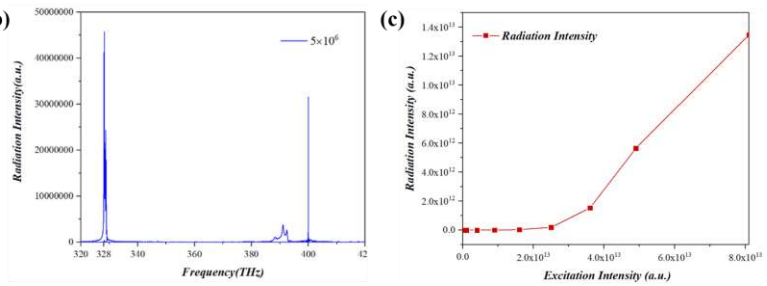


Figure 2、(a)resonance cavity quality (b)At a pump intensity of 2.5×10^{13}, laser excitation occurs. (c)The nonlinear relationship between laser radiation intensity and pump intensity is observed.

To further observe the laser performance, we used the finite difference time domain (FDTD) method to calculate the laser excitation intensity under different pump intensities. As shown in **Figure 2(b)**, with a pump Intensity of 2.5×10^{13}, we observed successful excitation of the laser in the 328 THz range. For a deeper analysis of the laser threshold characteristics, as shown in **Figure 2(c)**, before the threshold, the radiation intensity remained at a low level, changing linearly with the increasing pump intensity. Once the threshold was surpassed, stimulated radiation dominated, and the radiation intensity showed a rapid and significant increase. As shown in **Figure 2(c),** the laser threshold is approximately 2.5×10^{13}, which provides further evidence that this structure can successfully support a laser.

In summary, by employing the hyperbolic metasurface as a resonant cavity of the nanolaser, we successfully achieved three-dimensional confinement of surface plasmon polaritons, resulting in a high quality factor of 81.445. Furthermore, the modal volume was reduced to 4.6663×10^{-4} μm³. We also successfully simulated laser excitation using this resonant cavity, demonstrating a low threshold. Therefore, this nanolaser is expected to serve as a promising source for future integrated circuit applications.

References

1. Kwon, S.-H., et al., *Surface plasmonic nanodisk/nanopan lasers.* IEEE Journal of Quantum Electronics, 2011. **47**(10): p. 1346-1353.
2. Zhang, Q., et al., *A room temperature low-threshold ultraviolet plasmonic nanolaser.* Nature communications, 2014. **5**(1): p. 4953.
3. Oulton, R.F., et al., *Plasmon lasers at deep subwavelength scale.* nature, 2009. **461**(7264): p. 629-632.

Optical tweezers: a powerful and versatile micro- and nano manipulation tool with applications from space to spaser

M. Infusino[1,2*], K. Caicedo[4], M. A. Iatì[2], O. M. Maragó[2], M. Donato[2], A. Veltri[1,2]

[1]Universidad San Francisco de Quito, Ecuador

[2]Institute of Chemical and Physical Processes (IPCF-CNR), Messina, Italy

[4]Institute of Applied Sciences and Intelligent Systems (ISASI-CNR), Napoli, Italy

Corresponding author: minfusino@ipcf.cnr.it

Abstract: In this work, we demonstrate the versatility of Optical Tweezers as a manipulation tool, using them for trapping and identifying extraterrestrial analogues. We also theoretically show that they serve as an experimental system for detecting the onset of spasing in gain-assisted plasmonic nanoshells.

Optical tweezers (OT) are tools made of light for the contactless pushing, trapping, and manipulation of objects, ranging from atoms to light sails [1]. They have evolved into sophisticated instruments and have been employed in a broad range of applications in the life sciences, physics, engineering and nano-technology. Here we discuss two applications of the technique on two physical systems that radically differs in terms of size, scope and context.

In the first application we use OT coupled to Raman spectroscopy in the framework of cosmic dust analysis and identification. Very recently Optical Raman Tweezers (ORTs) have been successfully used to trap, manipulate, and analyze spectra coming from micrometeorites and cosmic dust [2].

In this work we push forward the challenge by proposing ORTs as a tool to identify biosignatures on extraterrestrial mineral samples. In particular we analyzed extraterrestrial mineral analogues artificially doped with organic molecules of interest.

In the second application we considered OT as a tool that can be used to characterize the optical properties of gain-assisted plasmonic nanoshell and that might offer an experimental proof of the system ability to sustain spaser emission. In particular we demonstrated theoretically that a pump-probe optical tweezers set-up can be successfully used to detect the spaser/nanolaser emission transition. In the amplification regime—below the emission threshold—the nanoparticle's dipole moment remains proportional to the external trapping (probe) field. This leads to a predictable force landscape, as demonstrated in earlier work using optical tweezers and sub-threshold gain materials [3].

Above the threshold, however, the dipole moment becomes essentially independent of the trapping field [4], driven instead by gain-sustained emission. In this regime, the spatial structure of the pump governs the optomechanical response, resulting in force landscapes that are radically different from the pre-threshold, linear-optics regime.

This transition manifests as a measurable change in trapping behavior, providing a localized, near-field probe of spaser emission. This approach offers a complementary perspective to far-field spectroscopy, enabling a direct experimental link between spasing and nanolasing phenomena.

Aknowledgments

We acknowledge financial support from the European Union (NextGeneration EU), through the MUR-PNRR projects PRIN2022 "Cosmic Dust II" (2022S5A2N7), PE0000023-NQSTI, and carried out within the Project "Space It Up" funded by ASI and MUR – Contract n. 2024-5-E.0 - CUP n. I53D24000060005.

References

1. P. H., Maragò, O. M., Volpe, G. "Optical Tweezers: Principles and Applications", Cambridge University Press, Cambridge (UK), 2015.

2. A. Magazzú et al."Investigation of Dust Grains by Optical Tweezers for Space Applications" ApJ 942 11 (2023)

3. P. Polimeno et al., "Gain-Assisted Optomechanical Position Locking of Metal/Dielectric Nanoshells in Optical Potentials," *ACS Photonics*, vol. 7, no. 5, pp. 1262–1270, 2020.

4. A. Aradian et al., "Emission Dynamics and Spectrum of a Nanoshell-Based Plasmonic Nanolaser Spaser," *Nanophotonics*, 2024.

Plasmonics and Nanophotonics: Fundamentals and Applications

Quantum Beam Splitting on Metasurfaces: Principles and Applications

Yu Tian[1,2], Qi Liu[1,2], Xuan Liu[3], Zhaohua Tian[1], Shuyun Su[1], Guixin Li[4], Xifeng Ren[5], Qihuang Gong[1,2] and Ying Gu[1,2,*]

[1]State Key Laboratory for Mesoscopic Physics, Department of Physics, Peking University, Beijing, China
[2]Beijing Academy of Quantum Information Sciences, Beijing, China
[3] Beijing University of Technology, China
[4] Southern University of Science and Technology, China
[5] University of Science and Technology of China, China
[*]corresponding author: ygu@pku.edu.cn tian-yu@stu.pku.edu.cn

Abstract: We reveal the properties of quantum beam splitting on local and nonlocal metasurfaces, functioning as a series of parallel two-port beam splitters and a set of independent four-port beam splitters, respectively, which can manipulate various quantum states. We further demonstrate quantum logic gates on a single metasurface.

1. Introduction

Metasurfaces are planar structures that can control all degrees of freedom of light at nanoscale, which as an excellent platform for beam splitting (BS). Based on the responses are localized or not, they can be classified as local and nonlocal metasurfaces [1]. Here, we reveal the parallel two-port BS on local metasurfaces and independent four-port BS on nonlocal metasurfaces, which has different responses on incident wavelengths, angles and polarizations [2,5]. Based on that, we demonstrate the engineering of quantum states and realization of quantum logic gates on a single metasurface [3,4].

2. Results

2.1 BS on local metasurface

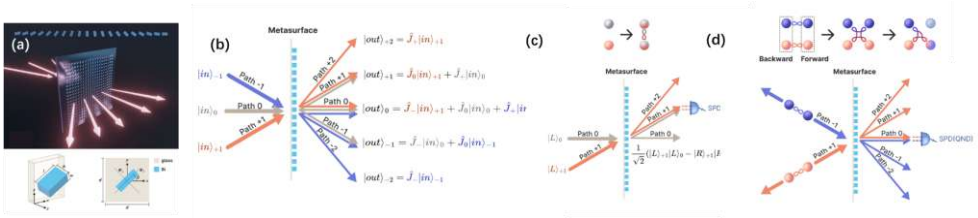


Figure 1 Parallel BS principle and its application in entanglement generation and fusion. (a) The schematic of parallel BS on local metasurface. (b) Parallel BS for three incident beams. (c) Entangled state preparation and (d) entanglement fusion under parallel BS.

Consider a local metasurface encoded with geometric phase gradient, as shown in Fig. 1(a). Along with the polarization conversion, it can deflect part of the incident light. Based on this, the metasurface has a parallel BS capability [2]. Fig. 1(b) shows the condition that three beams are incident from paths 0, ± 1. Each beam is split into three beams, while interference occurs in this process, with transformation matrix like:

$$\begin{bmatrix} |R_{out}\rangle_{+1} \\ |L_{out}\rangle_{0} \\ |R_{out}\rangle_{0} \\ |L_{out}\rangle_{-1} \end{bmatrix} = \begin{bmatrix} \cos\Delta & i\sin\Delta & 0 & 0 \\ i\sin\Delta & \cos\Delta & 0 & 0 \\ 0 & 0 & \cos\Delta & i\sin\Delta \\ 0 & 0 & i\sin\Delta & \cos\Delta \end{bmatrix} \begin{bmatrix} |R_{in}\rangle_{+1} \\ |L_{in}\rangle_{0} \\ |R_{in}\rangle_{0} \\ |L_{in}\rangle_{-1} \end{bmatrix}. \quad (1)$$

Such the BS can support various classical and quantum operations [3]. Fig. 1(c) shows the generation of entangled state with two parallel BS processes from direct product states. The parallel BS also can fuse entangled photon pairs in to a larger-scale entangled state, as shown in Fig1. (e). It can be further extended to support richer quantum operations, such as quantum CZ gate.

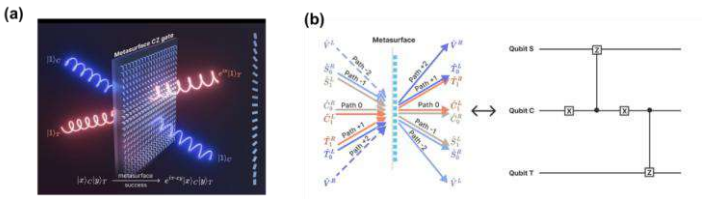


Figure 2 (a) Schematic diagram of polarization-encoded quantum CZ gate on single local metasurface; (b) Scheme of a cascaded quantum CZ gate.

Using the parallel BS with flexible splitting ratio, we can realize a CZ gate (Fig. 2(a)) or a cascaded CZ gate (Fig. 2(b)) on a single local metasurface. Taking advantage of the polarization-path correlation feature of paralle BS, both polarization-encoded and path-encoded CZ gates can be realized on the same metasurface [4].

2.2 BS on nonlocal metasurface

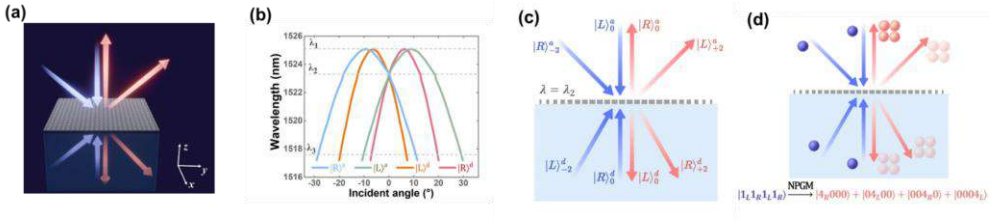


Figure 3 (a) Schematic of four-port BS on nonlocal metasurfaces; (b) Angular dispersion relations; (c) Four-port BS at λ_2; (d) Four-mode four-photon NOON state preparation on a metasurface.

Different from the above local metasurfaces, nonlocal metasurfaces exhibit selectivity of incident wavelengths and angles. Consider a nonlocal metasurface encoded with geometric phase gradient, as shown in Fig. 3(a). It can split one incident beam into four output beams symmetrically. Combining with the angular dispersion relations depicted in Fig. 3(b), we reveal that a series of independent four-port BS with selectivity of incident wavelengths, angles and polarization [5], just like the four-port BS at λ_2 shown in Fig. 3(c) with the transformation matrix like:

$$\begin{bmatrix} |R\rangle_{+2}^{d} \\ |L\rangle_{0}^{d} \\ |R\rangle_{0}^{a} \\ |L\rangle_{+2}^{a} \end{bmatrix}_{out} = \begin{bmatrix} 0.44e^{-i\times27^\circ} & 0.57e^{-i\times64^\circ} & 0.48e^{i\times91^\circ} & 0.50e^{-i\times44^\circ} \\ 0.57e^{-i\times63^\circ} & 0.45e^{-i\times60^\circ} & 0.49e^{-i\times96^\circ} & 0.48e^{i\times113^\circ} \\ 0.48e^{i\times92^\circ} & 0.49e^{-i\times96^\circ} & 0.59e^{-i\times115^\circ} & 0.42e^{-i\times95^\circ} \\ 0.50e^{-i\times44^\circ} & 0.48e^{i\times111^\circ} & 0.41e^{-i\times96^\circ} & 0.59e^{-i\times41^\circ} \end{bmatrix} \begin{bmatrix} |L\rangle_{-2}^{d} \\ |R\rangle_{0}^{d} \\ |L\rangle_{0}^{a} \\ |R\rangle_{-2}^{a} \end{bmatrix}_{in} \quad (2)$$

With this four-port BS, we can prepare four-mode four-photon NOON states, which are encoded in spatial modes and polarization modes, simultaneously, as shown in Fig. 3(d).

In summary, we reveal the BS properties on local and nonlocal metaasurfaces, which exhibit a series of parallel two-port BS and independent four-port BS, respectively. We further demonstrate its application in quantum state engineering, including entanglement manipulation, quantum CZ gates and NOON state preparation.

References

1. Kunal Shastri and Francesco Monticone, Nonlocal flat optics, Nat. Photonics, 17(36), 2023
2. Qi. Liu, Yu Tian, et al., Parallel beam splitting based on gradient metasurface: from classical to quantum, Opt. Express, 32(18), 31389-31404, 2024.
3. Qi Liu, Yu Tian, et al, Multiphoton path-polarization entanglement through a single gradient metasurface, Adv. Photon. Nexus, 4(2), 026002 2024.
4. Qi. Liu, Yu Tian, et al., Quantum CZ Gate based on Single Gradient Metasurface, revised to Light Sci. Appl.
5. Yu Tian, Qi Liu, et al, Near-symmetric multiport beam splitting for four-mode high-NOON state preparation on nonlocal metasurface, arXiv, 2408,14002, 2024

Birefringence-Driven Chiral Resonances in Lithium Niobate Metasurfaces

Bo Wang[1,*], Tingyue Zhu[1], and Junjie Li[1]

[1]Beijing National Laboratory for Condensed Matter Physics, Institute of Physics, Chinese Academy of Sciences, 100190 Beijing, China
[*]Corresponding author: wangbo2014@iphy.ac.cn

Abstract: We demonstrate that the birefringence of lithium niobate (LN) material can induce strong coupling between two resonant modes of an LN metasurface, leading to hybridized elliptically polarized modes with opposite chirality. This achieves a giant chiral optical response, even though both the material and structure are achiral.

One of the remarkable capabilities of metasurfaces is to increase chiral-optical response by creating chiral resonant modes on metasurfaces, which can exhibit near-unity circular dichroism (CD) signals under normally incident light. Chiral resonant modes on metasurfaces usually result from geometric chirality of the building structures, such as subwavelength helices [1], some simpler asymmetric shapes with mirror symmetry broken [2], or asymmetric lattice [3]. In this study, we demonstrate that the intrinsic birefringence of lithium niobate (LN) can induce strong coupling between two resonant modes in a planar LN metasurface, leading to the formation of hybridized modes with opposite chirality [4].

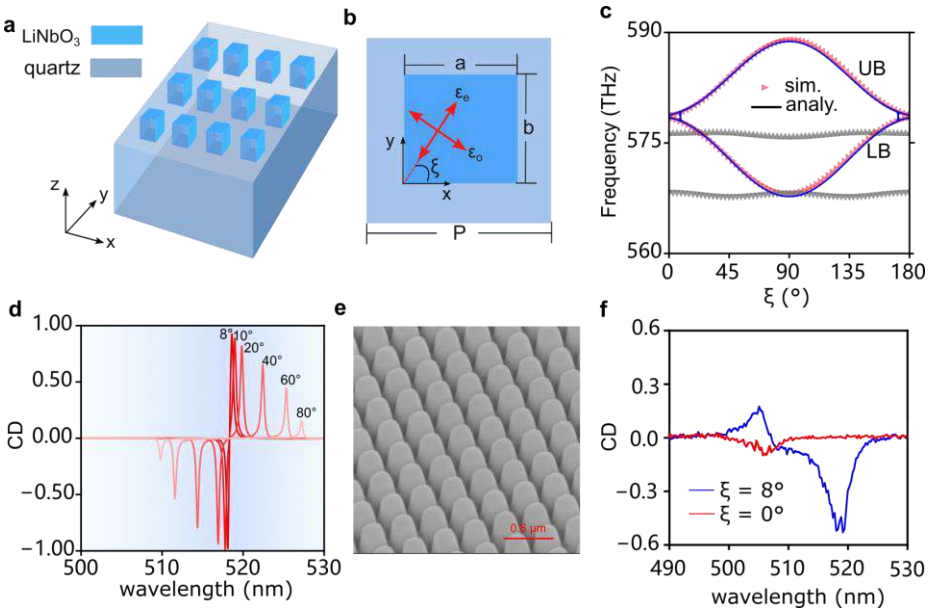


Figure 1 a, b Schematic of LN metasurface structure. c Simulated and analytic resonant frequencies. d, Simulated CD spectra. e, SEM images of the fabricated LN metasurfaces. f, Measured CD spectra.

Figures 1a and 1b show the structure of the LN metasurface. It is composed of periodic LN nanocubes, which are arranged in a square lattice with period p = 340 nm on a fused quartz substrate. Crystalline LN has negative uniaxial

birefringence with $n_o - n_e \approx 0.06$ in the visible spectral range. We show that this birefringence can induce the coupling between two resonant modes when the optical axis is rotated. The resonant frequencies of the mixed resonant modes are governed by an effective Hamiltonian,

$$\mathcal{H} = \begin{bmatrix} p_1 + \kappa_1 \sin^2\xi & \kappa \sin(2\xi)/2 \\ \kappa \sin(2\xi)/2 & p_2 + \kappa_2 \sin^2\xi \end{bmatrix}^{-1} \begin{bmatrix} \omega_1 p_1 & 0 \\ 0 & \omega_2 p_2 \end{bmatrix} \quad (1)$$

This effective Hamiltonian is verified by full wave simulations, as show in Figure 1c. We show that these resonant modes are chiral, presenting nearly full circular dichroism signals, as shown in Figure 1d. For the experiment demonstration, we fabricated the proposed metasurfaces on a commercially available LN films with the thickness of 300 nm on quartz substrate. The LN films were patterned with electron beam lithography and etched with inductively coupled plasma reactive ion etching technique. The scanning electron microscope images of the fabricated LN metasurfaces are shown in Figure 1e. The measured CD spectra, as shown in Figure 1f, validate the main features of our theoretical prediction of the chiral resonant modes induced by the birefringence. The discrepancies between experimental and simulated CD signals are attributed to dimensional deviations and slanting sidewalls in the real samples.

This work highlights a new approach to controlling chiroptical effects by leveraging material birefringence, offering a powerful tool for applications in nonlinear chiral metaphotonics. The results are significant because they demonstrate how achiral materials and structures can be combined to exhibit giant chirality, opening new avenues for the design of chiral optical devices.

This work was supported by National Key Research and Development of China (Grants No. 2023YFF0715902 and 2023YFF0721901), the National Natural Science Foundation of China (Grants No. 12074420, No. U21A20140, No. 12304463, and No. 12204527), and the Chinese Academy of Sciences through the Project for Young Scientists in Basic Research (YSBR-021). This work is also technically supported by Extreme Condition User Facility (SECUF).

References

1. Esposito, V. Tasco, F. Todisco, M. Cuscun`a, A. Benedetti, M. Scuderi, G. Nicotra, and A. Passaseo, Nano Lett.,16, 5823 (2016).
2. A. Overvig, N. Yu, and A. Alù, Phys. Rev. Lett. 126, 073001 (2021).
3. I. Toftul, P. Tonkaev, K. Koshelev, F. Lai, Q. Song, M. Gorkunov, and Y. Kivshar, Phys. Rev. Lett. 133, 216901(2024).
4. B. Wang, T. Zhu, Y. Liu, H. Yang, R. Pan, J. Li, to be published on Phys. Rev. Lett.

Exploring Mesoscopic Plasmonics by Integrating Transformation Optics and Feibelman *d* Parameters

Fan Yang[1*]
[1]College of Physics, Sichuan University, Chengdu, Sichuan 610065, China
fyang@scu.edu.cn (corresponding author)

Abstract

Classical electrodynamics falls short in capturing plasmonic responses at the mesoscopic scale. Therefore, we introduce an innovative analytical framework that synergizes transformation optics with Feibelman d parameters. This approach offers a more efficient pathway to explore electronic nonclassical effects in complex nanostructures, surpassing the limitations of traditional density functional methods.

1 Introduction

The mesoscopic scale has garnered significant attention as it serves as a bridge between continuous medium descriptions and pure quantum mechanical frameworks. At this scale, the classical permittivity fails to accurately depict optical responses due to the emergence of nonclassical electron effects, such as nonlocality and electron spill-out. A comprehensive consideration of these quantum effects typically demands a time-intensive time-dependent density functional approach. Alternatively, the hydrodynamic model has been proposed to numerically investigate these nonclassical effects. Analytical methods for studying these nonclassical effects have been largely confined to flat surfaces, nanowires, and spherical particles. The advent of transformation optics has opened the door to analytical solutions for complex nanostructures. However, prior works utilizing transformation optics to study nonclassical effects have predominantly focused on the nonlocal effect of electrons, neglecting other nonclassical contributions. This incomplete description has motivated us to extend the existing analytical model. An elegant approach to incorporate the quantum effects dominant at the mesoscopic scale involves the use of Feibelman d parameters. By integrating the d parameter into the boundary conditions, both nonlocal and electron spill-out effects are accounted for.

2 Results

We consider a sodium nanowire dimer as a prototype to validate our theoretical approach, as depicted in Fig. 1(a). The inset of Fig.1(a) shows the electron distribution near the metal surface, where n_0 and n_1 represent the ground state and excited state of the electron, respectively. The electron distribution can be quantified using the surface d parameter, defined as

$$d_\perp = \frac{\int r n_1(r)\mathrm{d}r}{\int n_1(r)\mathrm{d}r} \qquad d_\parallel = \int \frac{n_0(r) \in n_j}{n_{ion}}\mathrm{d}r, \tag{1}$$

where the integration is performed along the direction normal to the metal interface, and n_j (n_{ion}) denotes the jellium (ion) density. We obtained these d parameters using quantum hydrodynamic model for a flat metal surface. The d parameter, being a surface response function, is solely determined by the materials forming the interface, allowing its application of d parameter in plasmonic structure with arbitrary shape.

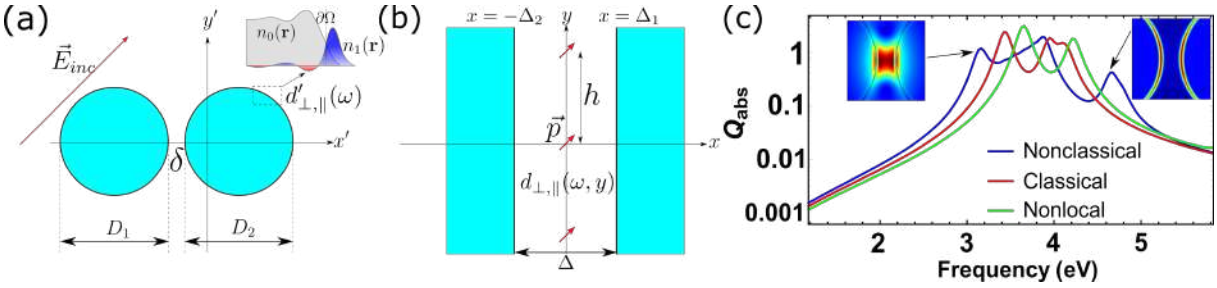


Figure 1: Integration of transformation optics and Feibelman d parameter. (a) The dimer consists of two closely spaced nanowires with diameters D_1 and D_2, separated by a gap δ. (b) The nanowire dimer is mapped into an MIM structure, with relevant geometric parameters labeled. (c) Absorption spectrum obtained by combining transformation optics and d parameters.

Direct calculation for the structure in Fig. 1(a) is challenging. Therefore, we transform it into a simpler metal-insulator-metal (MIM) geometry, as shown in Fig. 1(b). The incident plane wave in Fig. 1(a) is converted into a dipole array in Fig. 1(b), where the material permittivity remains unchanged during the transformation. However, the d parameter is not conserved in this transformation. In the dimer frame, the d parameter is solely a function of frequency, whereas in the transformed slab frame, it becomes both frequency and coordinate dependent. The relationship between the d parameter in the dimer frame $d'_{\perp,\parallel}$ and the d parameter in the MIM frame $d_{\perp,\parallel}$ is given by [1]

$$\frac{d_{\perp,\parallel}}{d'_{\perp,\parallel}} = \left|\frac{\mathrm{d}z}{\mathrm{d}z'}\right| = \frac{2h}{\pi g}\left|\sinh\left(\frac{\pi}{h}z\right)\right|^2, \tag{2}$$

where $z' = x' + iy'$ ($z = x + iy$) is complex coordinates in the dimer (MIM) frame.

With the d parameter in the slab frame, we can now analytically calculate the field profile and absorption in the presence of nonclassical effects. This transformation significantly simplifies analytical calculations. By integrating transformation optics and d parameters, we successfully reproduce the red-shift caused by electron spill-out and identify the emergence of the Bennett mode (Fig. 1(c)). This integrated framework provides a versatile tool for analytically investigating a wide range of nonclassical phenomena at the mesoscopic scale, including charging effects [2], DC biasing [3], mode coupling, and nonlinearities.

3 Acknowledgements

F.Y. acknowledges the financial support from the National Natural Science Foundation of China (Grant No. 12204328), Sichuan Science and Technology Program (Grant No. 2024NSFSC1351), and the Fundamental Research Funds for the Central Universities.

References

[1] **F. Yang** and K. Ding, "Transformation optics approach to mesoscopic plasmonics," *Phys. Rev. B* 105, L121410 (2022).

[2] D. Xiang, H. Zhang, L. Stella, and **F. Yang**, "Quantum description of a charged plasmonics nanowire dimer," *Phys. Rev. B* 109, 245407 (2024).

[3] C. Wen, F. Gao, and **F. Yang**, "Tunable Plasmonic Bandwidth Broadening via DC Electrical Bias," *under review.*

Near-field Spacetime Imaging of THz Surface Plasmon Polaritons in Graphene

Simon Anglhuber[1], Martin Zizlsperger[1], Eva A. A. Pogna[2], Yaroslav A. Gerasimenko[1], Anastasios D. Koulouklidis[1], Imke Gronwald[1], Svenja Nerreter[1], Leonardo Viti[3], Miriam S. Vitiello[3], Rupert Huber[1], and Markus A. Huber[1*]

[1]Department of Physics and Regensburg Center for Ultrafast Nanoscopy (RUN), University of Regensburg, 93040 Regensburg, Germany
[2]Istituto di Fotonica e Nanotecnologie, Consiglio Nazionale delle Ricerche (CNR-IFN), Milano, I-20133, Italy
[3]NEST, CNR – Istituto Nanoscienze and Scuola Normale Superiore, Piazza San Silvestro 12, 56127, Pisa, Italy
[*]corresponding author: markus.huber@ur.de

Abstract: Field-resolved terahertz near-field microscopy enables direct spatiotemporal mapping of polariton dynamics in graphene with subcycle temporal resolution. The spacetime maps yield key parameters of the polariton, like group and phase velocities as well as its damping. Femtosecond control of non-equilibrium polariton propagation is achieved by optical excitation.

Surface polaritons – light-matter excitations at interfaces – are widely studied for their strong field confinement and high propagation velocities, making them ideal for nanoscale waveguides and sensors [1]. Typically, near-field microscopy maps polariton dispersions frequency by frequency, yet real-space field-resolved detection of polaritons by broadband pulses (spacetime imaging) can offer new insights into their properties [2,3].

Here, we investigate surface plasmon polaritons (SPPs) in graphene using spacetime imaging in the terahertz spectral domain and manipulate their dynamics via ultrafast photoexcitation [4]. A terahertz pulse (red transient) is coupled to a sharp metallic tip of a near-field microscope and launches surface polaritons (Fig. 1a). These polaritons reflect at edges of the sample and return to the tip, yielding a delayed scattering response (blue transient). Additionally, an instantaneous scattering response appears due to the direct dielectric tip-sample interaction (green transient). By recording scattered waveforms at different distances to a graphene edge and subtracting the spatially homogeneous response we can directly trace the spatiotemporal evolution of the SPP wave packet (Fig. 1b, blue spheres). Very prominently, the electric field of the polariton is delayed in time with distance to the edge, yielding insights into the group and phase velocities of the polariton wave packet. The full propagation dynamics are captured by one global fit of all recorded traces (Fig. 1b, solid lines), revealing the decay of the wave due to damping (1/e decay length of ~2.31 µm) and the respective phase (~0.081c) and group (~0.045c) velocities (Fig. 1c). Additionally, our approach can be expanded to full 2D images, mapping distinct propagation directions at different edges (Fig. 1d). Access to the time domain also allows probing nonequilibrium dynamics with femtosecond precision (Fig. 1e). Ultrafast visible light pulses transiently modify graphene's conductivity, enabling subcycle SPP amplitude control (Fig. 1f) – much faster than electrostatic gating – paving the way for ultrafast plasmonic logic devices.

Beyond graphene, this method can be applied to a wide range of materials including anisotropic polaritons in black phosphorus and α-MoO_3, topological insulator surface modes, and other systems utilizing electro-optic sampling of scattered fields. Finally, the method offers an intuitive approach to visualize non-equilibrium polariton propagation, e.g. upon photoexcitation. With these abilities, phenomena like ultrafast plasmon amplification by optical pumping or Bloch polaritons could be directly investigated.

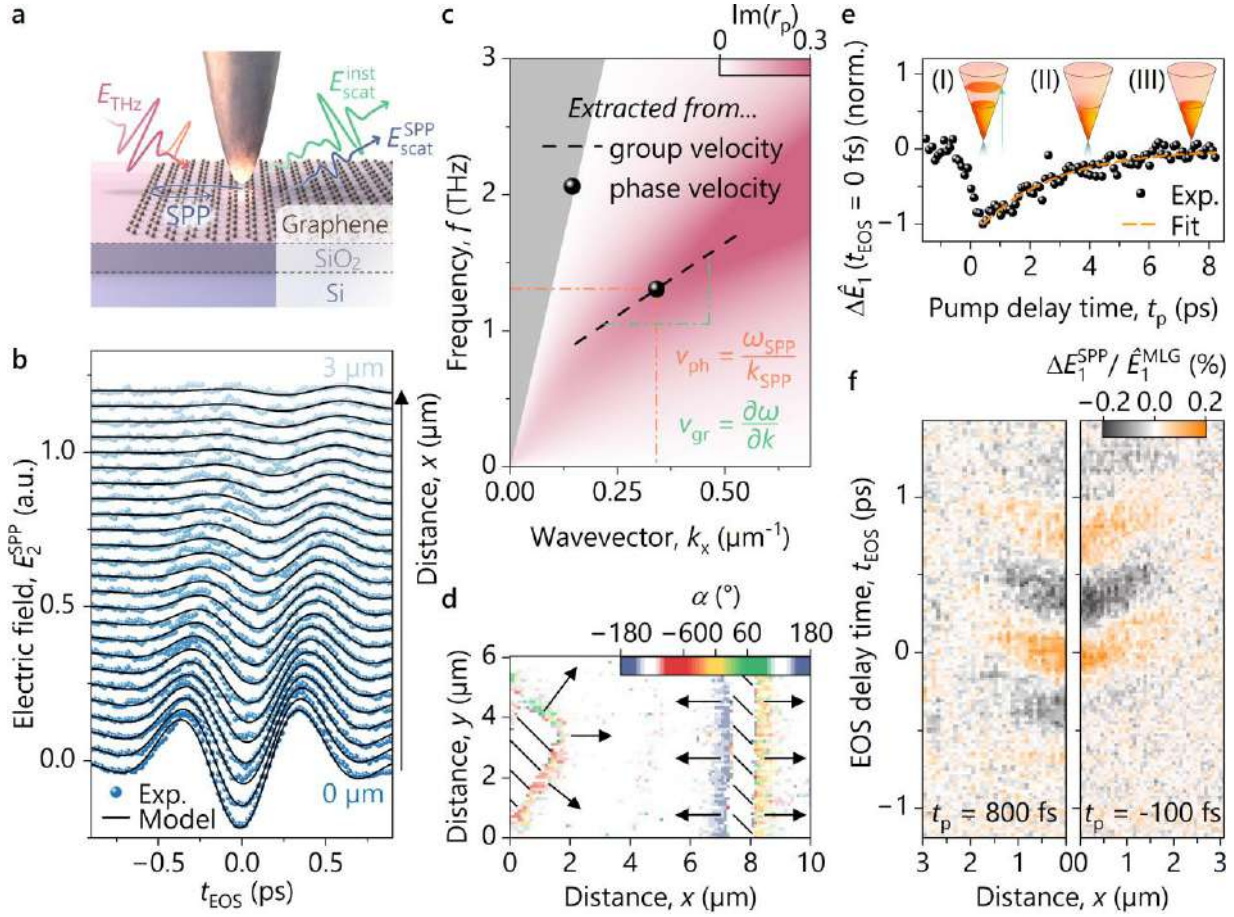


Figure 1. Time-domain imaging and ultrafast control of surface plasmon polaritons (SPPs) in graphene. a, Schematic: A THz pulse (red) incident on a tip launches SPPs, which reflect at the sample edge (blue arrows). The tip's scattered response comprises an instantaneous component (green) and a delayed component from propagating SPPs (blue). A pump pulse (orange) can be used for photoexcitation. **b,** Electric field of the propagating SPP for different distances to a graphene edge (x = 0 µm). A global fit (black lines) yields the polaritons' group and phase velocities as well as damping. **c,** Phase and group velocities determine the position and linear slope of the dispersion relation of the polariton (black sphere and dashed line). Background: Numerically calculated dispersion relation of the multilayer sample system. **d,** Extending the model to two dimensions allows one to visualize the propagation directions on a larger graphene sample. **e,** Photoexcitation (515 nm, 140 fs) of graphene creates a non-equilibrium carrier distribution (I), thermalizing to a Fermi-Dirac distribution (II). The pump-induced change of the electric peak field on graphene features a decrease with an exponential recovery (orange fit) to equilibrium (III). **f,** Map of the pump-induced change on the SPP's electric field for two pump delay times (t_p = 800 fs, left; t_p = -100 fs, right). Tuning the pump arrival time allows the SPP to be changed with femtosecond precision.

References

1. Basov, D. N., *et al.*, "Polariton panorama," Nanophotonics, Vol. 10, No. 1, 549–577, 2020.
2. Mitrofanov, O., *et al.*, "Probing terahertz surface plasmon waves in graphene structures," Appl. Phys. Lett., Vol. 103, No. 11, 111105, 2013.
3. Xu, S., *et al.*, "Electronic interactions in Dirac fluids visualized by nano-terahertz spacetime interference of electron-photon quasiparticles," Sci. Adv., Vol. 10, No. 43, eado5553, 2024.
4. Anglhuber, S., *et al.*, "Spacetime imaging of group and phase velocities of THz surface plasmon polaritons in graphene," Nano Lett., Vol. 25, No. 6, 2125–2132, 2025.

SP18-1

Plasmonic effects on the crystal transformation and emission control of luminescence particles

Hairong Zheng*, Huan Chen, Chengyun Zhang, Zhenglun Fu, Zhenglong Zhang_

School of Physics and Information Technology, Shaanxi Normal University, Xian, China, 710119

*Corresponding author: hrzheng@snnu.edu.cn

Abstract: Plasmonic effects produced by the metal nanostructures have presented potential applications in the field of spectral regulation including the intensity enhancement and lifetime reduction. It is also found that the plasmonic effect can help to drive fast in-situ crystal structure transformation.

Surface plasmon of metal nanostructures can produce significant local field effect under proper radiation, which can effectively control the optical spectral property and matter structure. For example, in the system of plasmonic nanocavity with rare earth doped nanoparticle, the luminescence decay time is reduced by 3 orders and emission intensity enhanced enormously. With assistance of localized surface plasmon resonance of Au nanoparticles, polycrystalline NaYF4 particle transforms to single crystal Y2O3 in tens of milliseconds, which opens an easy and rapid in situ way to achieve single crystal particle by taking advantage of plasmon-induced thermal and catalysis effects. In this talk, the luminescence regulation and crystal transformation of optical particles induced by surface plasmon effect of a tilted plasmonic nanocavity and metal nanostructures will be presented, and corresponding mechanism will be discussed too.

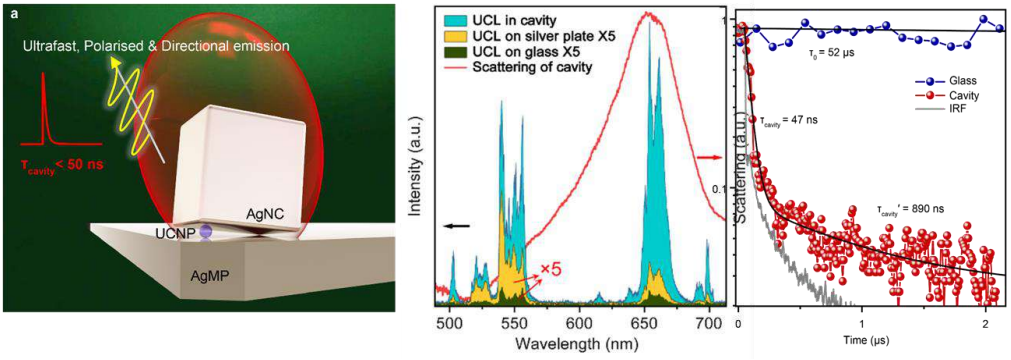


Figure 1. A titled plasmonic nanocavity with a hexagonal $NaGdF_4$:20 mol%Yb^{3+}/2 mol%Er^{3+} particle and experimental observation on the luminescence emission and decay.

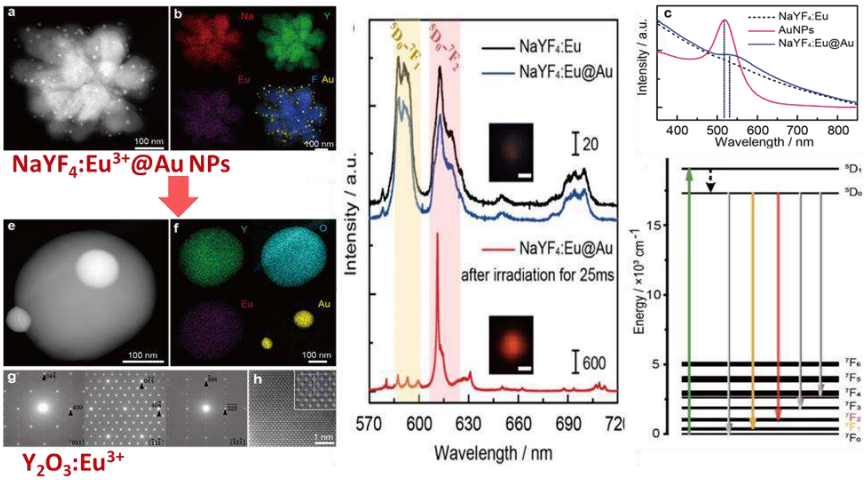


Figure 2. Transformation of polycrystalline $NaYF_4$ particle to single crystal Y_2O_3 with assistance of localized surface plasmon resonance of Au nanoparticles.

References:

1. Chen, H. *et al.*, Sub-50-ns ultrafast upconversion luminescence of a rare-earth-doped nanoparticle, *Nature Photonics*, **2022**, 16(9): 651–657.

2. C Zhang, *et.al.*, Plasmon-driven rapid in situ formation of luminescence single crystal nanoparticle, *Small*, **2019**, 1901286.

Memristive nanogaps with biophoton-like properties as a building block for advanced nanophotonic applications

M. Ćwierzona[1,2], D. Singh[1], K. Malchow[1], S. Hamdad[1] and A. Bouhelier[1*]
[1]Laboratoire Interdisciplinaire Carnot de Bourgogne, UMR 6303 CNRS, Université de Bourgogne Europe, 2100 Dijon, France
[2]Institute of Physics, Nicolaus Copernicus University, ul. Grudziadzka 5, 87-100 Torun, Poland
[*]corresponding author: alexandre.bouhelier@u-bourgogne.fr

Abstract: We demonstrate that memristive nanogaps can emit light during resistive switching, replicating key properties of biophotons observed in neurons. This dual electronic-photonic functionality enables new approaches for on-chip light generation, high-speed optical communication, and nanoscale optoelectronic integration, expanding the role of memristors in neuromorphic computing and advanced nanophotonic applications.

The need for more efficient computing units is rising with the recent emergence of energy-hungry Artificial Intelligence (AI) accelerators. Memristive networks can be used in Spiking Neural Networks technologies to implement biology-inspired information processing methods to create ultra-low power computing devices[1]. While the electrical properties of memristors are widely studied, their ability to emit photons is still relatively unexplored. Here, we focus on single memristive nanogaps, which release photons during resistive switching induced by an applied electric field (Figure 1). Resistive switching is usually achieved by stimulating the device with ramping voltage or applying several predefined voltage pulses of similar amplitude. Depending on the stimulation conditions, the device can be in a volatile state, i.e., it self-returns to the initial, high-resistive state after stopping the voltage stimulation, or it may be in a non-volatile state, allowing it to retain the high-conductance state after the voltage stimulation is finished. Rapid changes in conductance caused by the intrinsic dynamics of atomic diffusion typical for memristors operated in the volatile state provide the conditions needed to observe light emission in artificial neurons. This light emission replicates several key attributes of biophotons emitted by neurons during brain activity, including self-generation, stochasticity, broad spectral coverage, sparsity, and correlation with electrical activity[2].

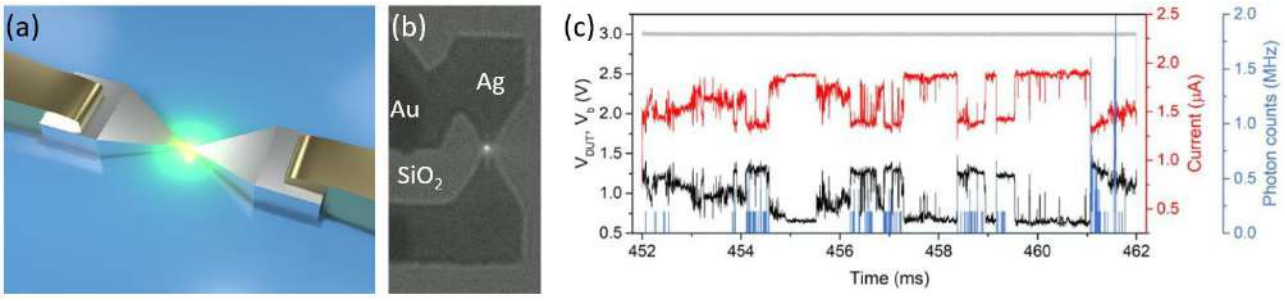


Figure 1. (a) Visualization of memristor light emission. (b) Bright-field image of memristive nanogap during light emission. (c) Time traces of the current flowing through the artificial memristive neuron (red trace), the actual voltage dropped at the memristor (black trace), and the photon emission (blue trace) during a single 10 ms voltage pulse of 3V (grey trace).

Several mechanisms leading to light emission in metal-insulator-metal memristors have been identified, including electron trap luminescence[3], inelastic tunneling[4], and overbias emission[4]. Depending on the voltage stimulation history of the memristive junction, the same device can exhibit emission resulting from one or a combination of the aforementioned mechanisms. Many luminescent point defects spanning a wide energy window can be present in the switching matrix even before the stimulating voltage is applied[5]. In addition, electroluminescence defects can also be self-generated during the switching process due to the formation and aggregation of oxygen vacancies, which provide a strong source for the memristors' photon emission. We also observe electromagnetic radiation with photon energies exceeding the kinetic energy of electrons given by the stimulating voltage when the memristor undergoes volatile switching. This emission is described by a thermal radiation model, where hot carriers radiatively decay to optical modes with an effective temperature surpassing 2000 K.

Our findings expand the capabilities of memristors to include not only their electrical but also optical properties. This is the first step towards developing more complex memristive devices that could operate with electrons and photons simultaneously. Exploring this kind of dual functionality enables new approaches for on-chip light generation, high-speed optical communication, and nanoscale optoelectronic integration, expanding the role of memristors in neuromorphic computing and advanced nanophotonic applications.

References

1. Le Gallo, M., M., Khaddam-Aljameh, R., Stanisavljevic, et al., "A 64-core mixed-signal in-memory compute chip based on phase-change memory for deep neural network inference", Nat Electron 6, 680–693, 2023
2. Malchow, K., T., Zellweger, B., Cheng, A., Leray, J., Leuthold, and A., Bouhelier, "Self-Induced Light Emission in Solid-State Memristors Replicates Neuronal Biophotons," ACS Nano, 18, 35, 240004-24011, 2024
3. Cheng, B., T., Zellweger, K., Malchow, X., Zhang, et al., "Atomic scale memristive photon source," Light: Science & Applications,11, 78, 2022
4. Hamdad, S., K., Malchow, D., Avetisyan, et al., "Overbias and Quantum Tunneling in Light-Emitting Memristors", Phys. Rev. Applied 20, 024057, 2023
5. Salh, R., "Defect Related Luminescence in Silicon Dioxide Network: A Review," Crystalline Silicon - Properties and Uses, InTech, 2011

Electrically driven functional plasmonic nanocavities

Pan Wang

State Key Laboratory of Extreme Photonics and Instrumentation, College of Optical Science and Engineering, Zhejiang University, Hangzhou 310027, China
*corresponding author: nanopan@zju.edu.cn

Abstract: In this work, based on single-crystal metallic building blocks, we demonstrate electrically driven functional plasmonic nanocavities with multifunctionality.

Enhancement and active control of light-matter interactions at the atomic scale is important for developing next-generation nanophotonic and quantum optical devices. However, it is challenging to realize with conventional dielectric photonic nanostructure. In this work, based on single-crystal metallic building blocks, we demonstrate electrically driven functional plasmonic nanocavities with multifunctionality. First, we will introduce the fabrication of ultrasmooth single-crystal gold flakes with tunable thickness down to 1 nm and an atomic level prevision [1]. Then, we introduce the realization of low-loss plasmonic nanocaivites by depositing single-crystal gold nanocubes on an ultra-smooth, single-crystal gold flake, which are separated by a nanometer-thick alumina as the dielectric layer. Benefitting from the single-crystal structure of the used building blocks, as-fabricated plasmonic nanocavities have a low loss which approaches the theoretical optical quality limit [2,3]. Finally, we demonstrated electrical integration of plasmonic nanocavities, by applying a low bias across the nanometer-thick gap of the nanocavites, active modulation of strong coupling and electroluminescence were realized [4].

Electrically driven functional plasmonic nanocavities provide a versatile platform for strong enhancement and active control of atomic-scale light-matter interactions and open opportunities for developing next-generation optoelectronic and quantum optical devices that can seamlessly interface electronics and photonics at the nanoscale.

References

1. Chenxinyu Pan, Yuanbiao Tong, Haoliang Qian, Alexey V. Krasavin, Jialin Li, Jiajie Zhu, Yiyun Zhang, Bowen Cui, Zhiyong Li, Chenming Wu, Zhenxin Wang, Lufang Liu, Linjun Li, Xin Guo, Anatoly V. Zayats, Limin Tong, Pan Wang, Large area single crystal gold of single nanometer thickness for nanophotonics. *Nat. Commun.* **15**, 2840 (2024).
2. Lufang Liu, Alexey Krasavin, Junsheng Zheng, Yuanbiao Tong, Pan Wang, Xiaofei Wu, Bert Hecht, Chenxinyu Pan, Jialin Li, Linjun Li, Xin Guo, Anatoly Zayats, and Limin Tong, Atomically smooth single-crystalline platform for low-loss plasmonic nanocavities. *Nano Lett.* **22**, 1786 (2022).
3. Zhenxin Wang, Lufang Liu, Di Zhang, Alexey V. Krasavin, Junsheng Zheng, Chenxinyu Pan, Enxing He, Zifan Wang, Shengchengao Zhong, Zhiyong Li, Mengxin Ren, Xin Guo, Anatoly Zayats, Limin Tong, and Pan Wang, Effect of mirror quality on optical response of nanoparticle-on-mirror plasmonic nanocavities. *Adv. Optical. Mater.* **11**, 2201914 (2023).
4. Junsheng Zheng, Ruoxue Yang, Alexey Krasavin, Zhenxin Wang, Yuanjia Feng, Longhua Tang, Linjun Li, Xin Guo, Daoxin Dai, Anatoly Zayats, Limin Tong, Pan Wang, Active control of excitonic strong coupling and electroluminescence in electrically driven plasmonic nanocavities. arXiv:2409.14742.

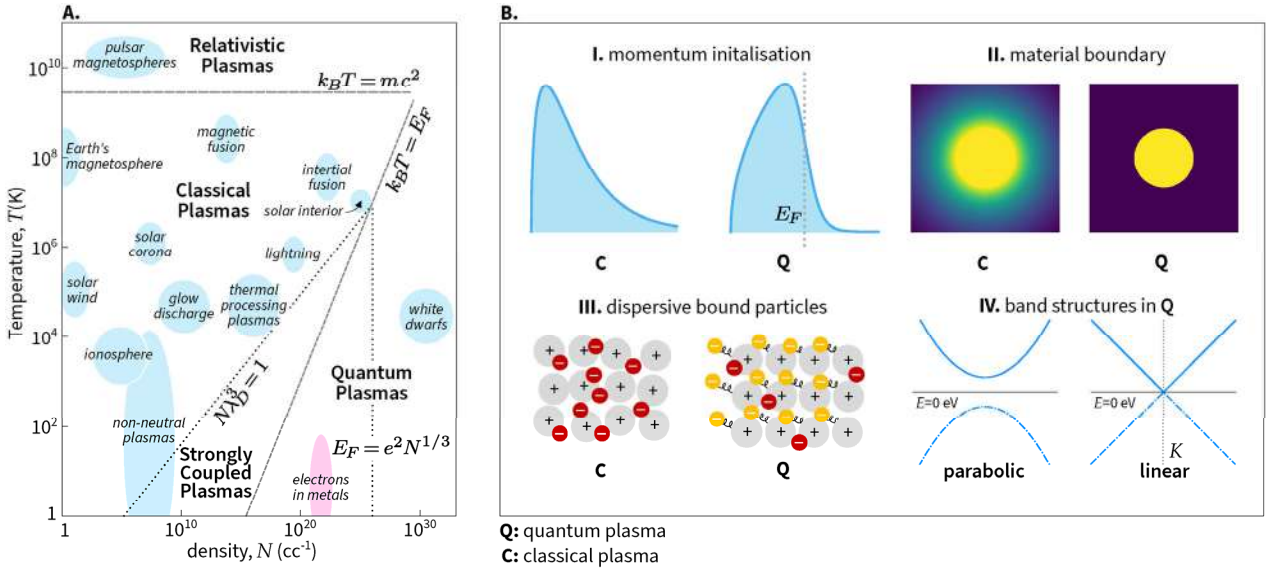
Particle-in-Cell (PIC) Simulations for Next-Gen Nanoscopic Photonics and Plasmonics

Lin Wu*

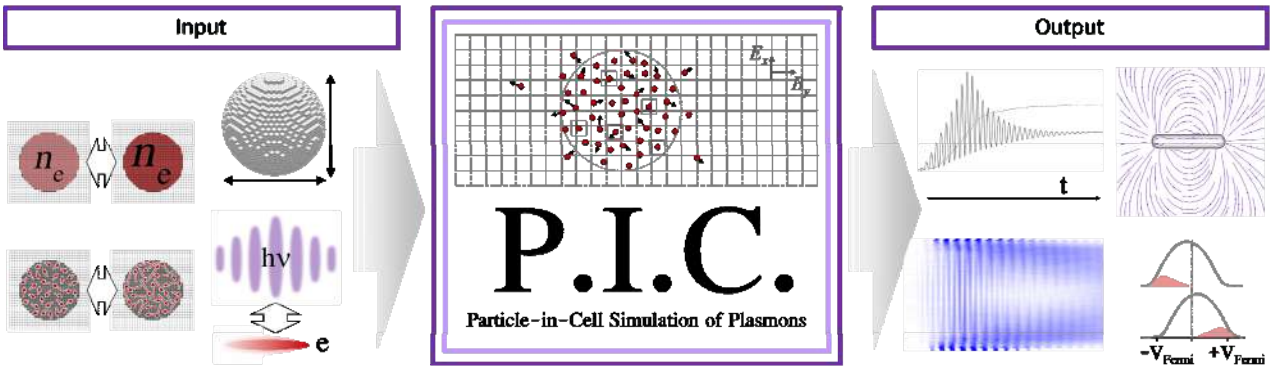
Singapore University of Technology and Design (SUTD), 8 Somapah Road, Singapore 487372
*Corresponding author: lin_wu@sutd.edu.sg

Abstract: Room-temperature metals and semi-metals, acting as cold quantum plasmas, enable Particle-in-Cell (PIC) simulations for next-gen nanoscopic studies in photonics and plasmonics. Our recent work examines graphene antennas and nonlinear electron transport in graphene plasmon resonators, revealing novel even-order nonlinearities for frequency-tunable infrared upconversion.

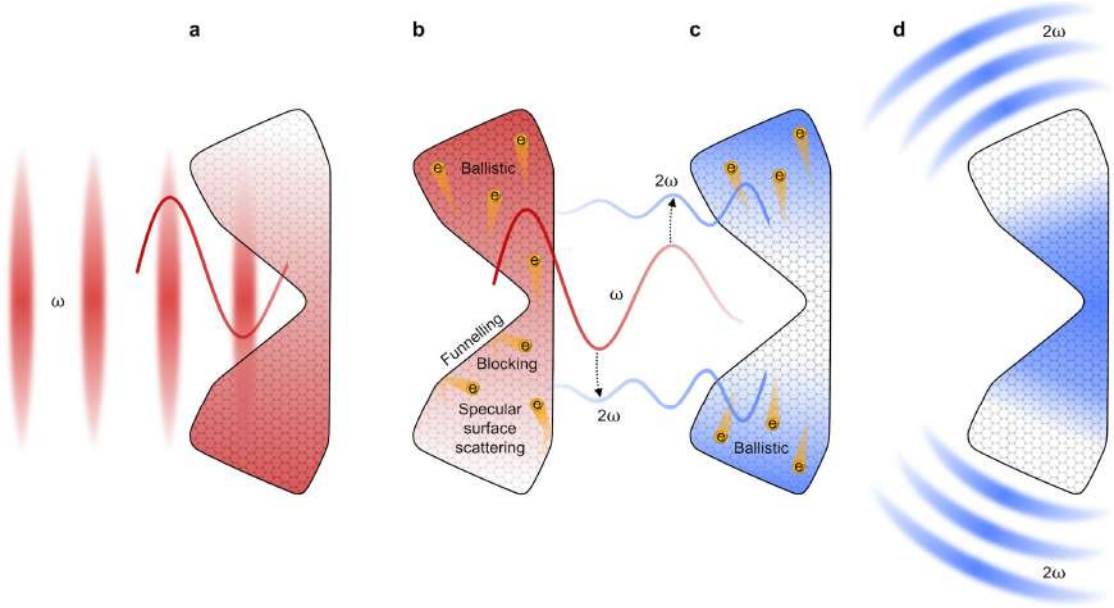
Since the 1940s, computational simulations have revolutionized physics, particularly in electromagnetism, where the interaction of charged particles governs many phenomena. Plasmas, often linked to extreme environments, can also be found in solid materials like metals and semi-metals, where quasi-free electrons behave as quantum plasmas. Traditional methods like Finite-Difference Time-Domain (FDTD) and Finite Element Method (FEM) effectively model static dielectric functions but struggle with dynamic materials, especially in quantum plasmas where electron dynamics significantly impact behavior. The Particle-in-Cell (PIC) method, traditionally used for plasmas, models both the electromagnetic field and charged particle motion self-consistently, making it ideal for simulating quantum plasmas in time-dependent scenarios[1-4].



In PIC simulations, resonator geometry, excitation source, electron density, and initial energy distribution are defined. Maxwell's equations and Vlasov's equations of motion are solved iteratively to update the electromagnetic field and particle dynamics. The particle velocity is deposited as current density for Maxwell's solver, and the particle pusher interpolates the field at each particle's position. This approach directly calculates the electric field, particle position, and momentum, allowing the derivation of parameters like plasmon amplitude, decay times, and particle distributions.



We recently proposed a new mechanism for second-harmonic generation via geometrically rectifying, or funnelling, ballistic electrons in THz optical resonators[4]. Our PIC simulations show that femtosecond electron-surface scattering is crucial in this process. We distinguish electron funnelling from nonlocal plasmonic drag and bulk Dirac anharmonicity, demonstrating that funnelling can reduce the required field intensity for second-harmonic generation by 3-4 orders of magnitude. We provide design guidelines for funnelling-induced second-harmonic generation, including resonance mode matching and material selection. This approach enables low-field, geometrically tunable THz upconversion and rectification, effective from sub-10 THz to tens of THz in graphene.



References

1. Ding W. J., Lim J. Z. J., Do H.T.B., Xiong X., Mahfoud Z., Png C. E., Bosman M., Ang L. K., Wu L. "Particle simulation of plasmons," **Nanophotonics**, Vol. 9, No. 10, 3303-3313, 2020.
2. Do H.T.B., Ding W. J., Mahfoud Z., Wu L., Bosman M. "Electron dynamics in plasmons," **Nanoscale**, Vol. 13, 2801-2810, 2021.
3. Ngirmang G. K., Do H.T.B., Liu G. X., Bosman M., Wu L. "Particle-in-cell simulations of quantum plasmas," **Computer Physics Communications** (under review), arXiv:2501.07465.
4. Do H.T.B., Ngirmang G. K., Wu L., Bosman M. "Nonlinear optical resonances from ballistic electron funnelling," **ACS Nano** (minor revision), arXiv:2411.09212.

Hyperbolic photonic topological insulators and quantum sources

Lu He, and Xiangdong Zhang*

Key Laboratory of advanced optoelectronic quantum architecture and measurements of Ministry of Education, Beijing Key Laboratory of Nanophotonics & Ultrafine Optoelectronic Systems, School of Physics, Beijing Institute of Technology, 100081 Beijing, China.

*zhangxd@bit.edu.cn

In this talk, we will introduce hyperbolic photonic topological insulators and their application. We experimentally realize hyperbolic photonic topological insulators on silicon chips using coupled ring resonators and hyperbolic topological quantum sources. They show the higher utilization efficiency of resonators, showing great potential for integrated quantum chips.

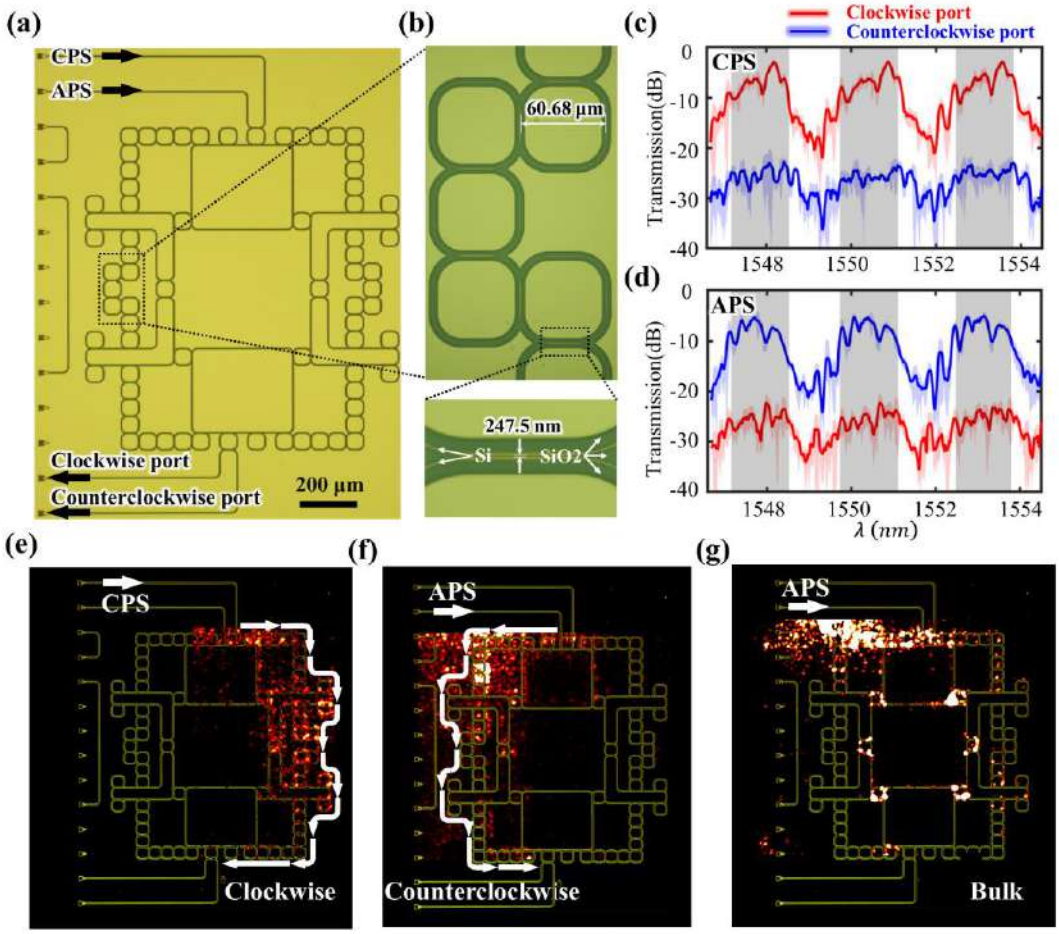


Fig. 1. Hyperbolic photonic topological insulators.

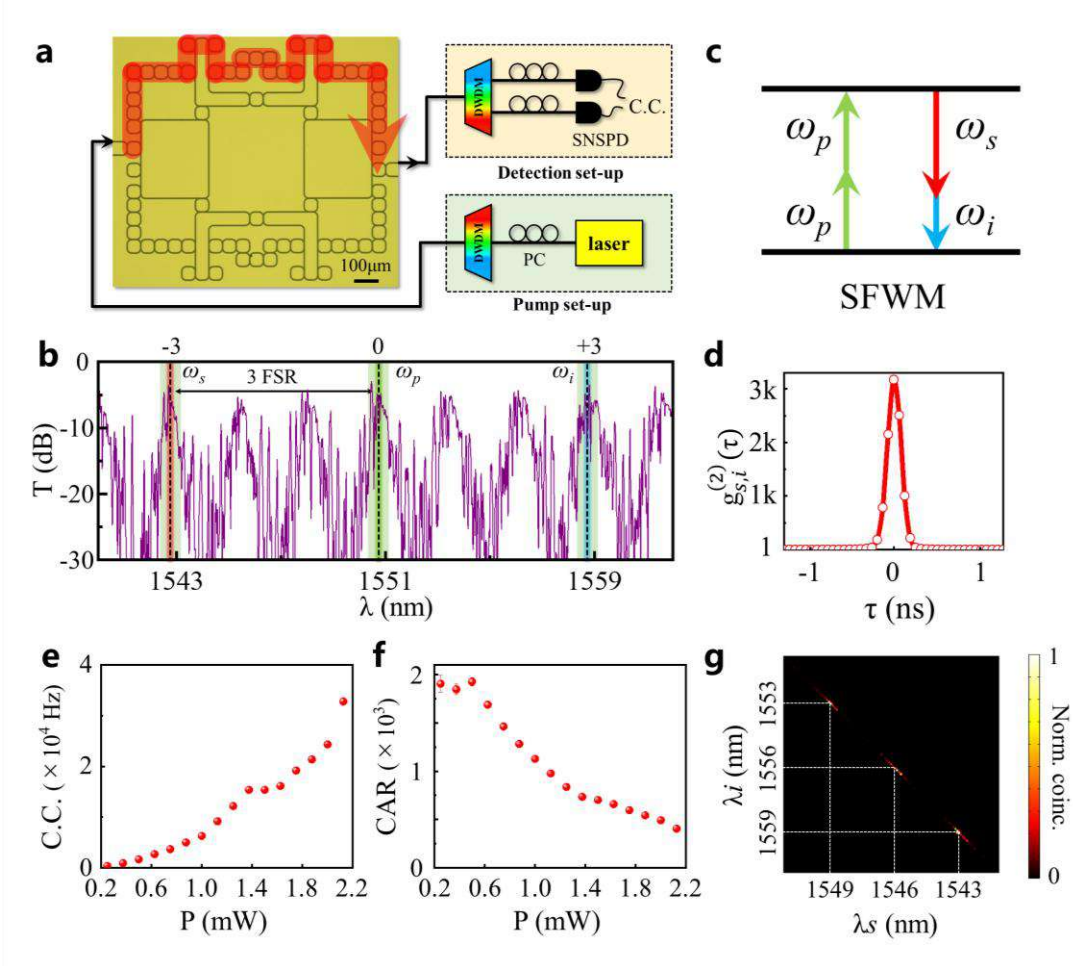


Fig. 2. Hyperbolic Topological Quantum Sources.

Reference

[1] L. Huang, L. He, W. Zhang, et al. Hyperbolic photonic topological insulators. Nat. Commun. 15, 1647 (2024). https://doi.org/10.1038/s41467-024-46035-y

[2] L. He, L. Huang, W. Zhang, et al. Hyperbolic Topological Quantum Sources. Adv. Sci. 2417708 (2025). https://doi.org/10.1002/advs.202417708

Chiral plasmonic nanoparticle-molecule hybrids for circularly polarized OLEDs

Lei Shao[1*]

[1]State Key Laboratory of Optoelectronic Materials and Technologies, Guangdong Province Key Laboratory of Display Materials and Technologies, School of Electronics and Information Technology, Sun Yat-sen University, Guangzhou 510275, China

[*]corresponding author: shaolei5@mail.sysu.edu.cn

Abstract: We demonstrate circularly polarized organic light-emitting diodes with an emission dissymmetry factor of 0.31 based on the assembly of chiral plasmonic nanoparticles and supramolecular aggregates. The chiral nanoparticles serve as the chiral scaffold and chiral optical nanoantenna to modulate the circularly polarized absorption and emission of the supramolecular chromophores.

Organic light-emitting diodes (OLEDs) supporting the direct emission of circularly polarized (CP) light are essential for numerous technologies. It is challenging to achieve CP-OLEDs with large dissymmetry (g_{EL}) factors and high external quantum efficiencies (EQEs). In this work, we have developed CP-OLEDs exhibiting extraordinary circularly polarized electroluminescence (CPEL) asymmetry (emission dissymmetry factor $g_{EL} \approx 0.31$) and luminous efficiency (EQE $\approx$ 2.5%) based on (chiral plasmonic nanoparticle)–(molecule aggregate) hybrids. The chiral nanoparticles (NPs) serve as scaffolds directing the chiral stacking of molecule aggregates to generate chiral excitons or plasmonic nanoantennas polarizing emitted photons. The proposed method only involves the design of the emissive layer and does not require any specialized changes on the OLED device architecture or molecular modification on the chromophore. Our strategy is therefore compatible with the current manufacturing technology of OLEDs and can also be applied to devices with different structures. We believe designing (chiral NP)–(molecule aggregate) hybrids with both strong chiral excitonic and plasmonic properties will bring further improvement of the circular polarization asymmetry in the EL emissions. In addition, the capability of chiral plasmonic NPs in controlling the chiroptical properties of supramolecular chromophores enables rich chiral plasmon–exciton interactions at the single-nanostructure level, making chiral plasmonic NPs promising candidates for constructing other chiral photoelectric devices, such as non-reciprocal nanoscale light sources and deterministic spin–photon interfaces for quantum networks, without the need for precision design and complex manufacturing.

Acknowledgements: We acknowledge the support from the National Natural Science Foundation of China (62375290, 2024YFA1209003, 62411560271, 12088101), the Pearl River Talent Recruitment Program (2019QN01C216) and the Science and Technology Planning Project of Guangdong Province (2023B1212060025).

References

1. Zheng, J. P., Fu, Y., Wang, J., Zhang, W., Lu, X. H., Lin, H.-Q., Shao, L. and Wang, J. F. "Circularly polarized OLEDs from chiral plasmonic nanoparticle-molecule hybrids," Nat. Commun., Vol. 16, 1658, 2025.

Strong coupling with excitons and one-dimensional photonic crystal modulated plasmonic nanocavities

Xiulai Xu *

School of Physics, Peking University, China
*corresponding author: xlxu@pku.edu.cn

Abstract: Strong light-matter interaction with plasmonic nanocavities with challenges like Ohmic losses, low quality factor and precise emitter positioning, makes it difficult for real applications. Here, we demonstrate room-temperature strong coupling by integrating plasmonic nanostructures with 2D materials, photonic crystals, and quantum dots, resulting in reduced exciton numbers and improved stability.

Plasmonic nanocavities can achieve strong light-matter interactions by confining electromagnetic fields below the diffraction limit. However, challenges such as Ohmic losses, low quality factor, and sensitivity to emitter positioning have hindered deterministic coupling at the single-quantum level. We systematically addressed these limitations through innovative cavity designs, integrating plasmonic nanostructures with photonic crystals, ultimately enabling room-temperature strong coupling with lowest exciton numbers using two-dimensional (2D) materials.

Firstly, we demonstrated robust plasmon-exciton coupling using gold bowtie nanocavities and mechanically exfoliated MoS_2 layers. By utilizing gold-assisted exfoliation and wet transfer techniques, large-area MoS_2 flakes were deterministically placed over bowtie arrays, achieving Rabi splitting of 80-110 meV. Due to the ultrasmall mode volume (~10^3 nm^3) and in-plane field localization, strong coupling at room temperature was desmonstrated with a reduced exciton number to N $\approx$ 40-48 (Figure 1a).

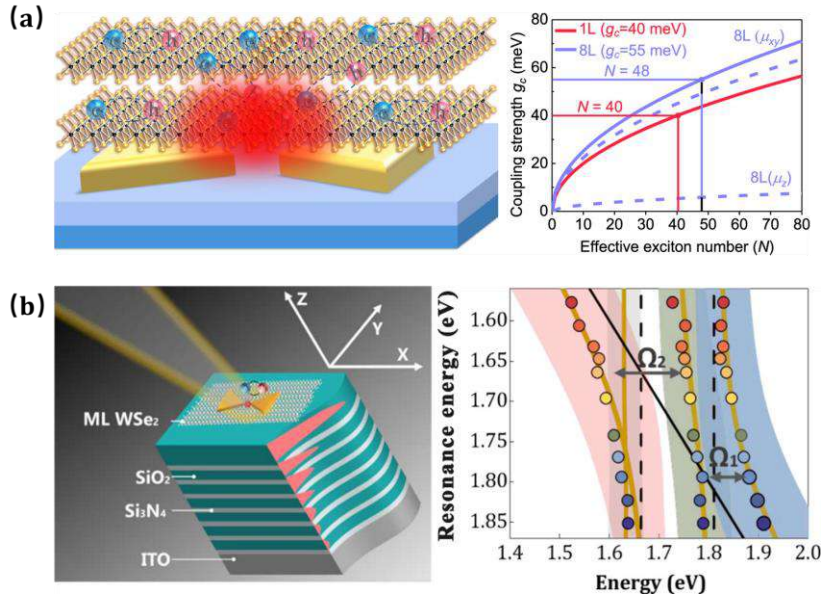


Figure 1 Strong coupling of 2D excitons with bowtie nanocavity at low exciton number. (a) Robust plasmon-exciton coupling with monolayer and few layer MoS_2. (b) Strong coupling using one-dimensional photonic crystal modulated bowtie with an exciton number less than 10.

Recently, we introduce a hybrid cavity nanostructure consist of bowtie nanocavity and one-dimensional photonic crystal (1DPC) to further compress mode volumes and tailor electric fields via Bloch surface waves (Figure 1b). The 1DPC composed of alternating Si_3N_4/SiO_2 layers strongly suppress the plasmon damping and enhanced in-plane field components, with a plasmonic mode volume down to 446 nm^3. Experimentally, we achieve a Rabi splitting of 186 meV with monolayer WSe_2, corresponding to an effective exciton number of about 8.

To extending this platform to strong coupling at the single quantum level, we embedded CdSe/ZnS quantum dots (QDs) in the hybrid cavity's nanogap. The uniform electric field distribution in nanogap indicates a robust coupling strength for the variations of QDs position. Dark-field scattering spectra show a stable Rabi splitting of approximately 170 meV for single QDs. The hybrid cavity's robustness against fabrication imperfections and quantum dot position marks a critical step toward scalable quantum photonic circuits.

References

1. Yang, L. et, al. "Strong light–matter interactions between gap plasmons and two-dimensional excitons under ambient conditions in a deterministic way" Nano Letters. Vol. 22, No. 6, 2177–2186, 2025
2. Fu, B. et, al. "Enhanced light–matter interaction with Bloch surface wave modulated plasmonic nanocavities" Nano Letters. Vol. 5, No. 2, 722–729, 2025
3. Fu, B. et, al. "Enhanced light–matter interaction with Bloch surface wave modulated plasmonic nanocavities" Submitted.

Control of polaritons in low-dimensional nanomaterials

Qing Dai[1, 2*]

[1] Shanghai Jiao Tong University, China
[2] National Center for Nanoscience and Technology, China
[*]corresponding author: daiqing@sjtu.edu.cn

Abstract: Our research explores the manipulation of polaritons in low-dimensional nanomaterials for efficient on-chip optoelectronic interconnects. Key advances include enhanced excitation in van der Waals materials, precise transmission control in heterostructures, and graphene-plasmonic infrared sensing, providing novel solutions for nanoscale optical manipulation and advanced sensing applications.

Polaritons are well-established carriers of light, electrical signals, and even heat at the nanoscale. Achieving control over it is pivotal for the realization of nanoscale manipulation of light signals and even heat within on-chip devices. Our research focuses on efficient excitation, precise manipulation, and high-sensitivity detection of polaritons in one-dimensional to two-dimensional nanomaterials within complex dielectric environments and has achieved a series of original breakthroughs.

In terms of **excitation**, we have developed a new theoretical model for electronic excitation[1,2] and a novel excitation source based on synthetic waves of complex frequency[3,4]. These advancements have significantly enhanced the excitation efficiency of polaritons in van der Waals materials, providing new insights into the design of on-chip light sources.

For **manipulation**, through employing techniques such as suspension[1,5], heterostructures[6], chemical doping[5,6], and electrical modulation[7], we have achieved precise control over the transmission modes, propagation distance, and directions of polaritons, enabling phenomena such as negative refraction[7] and in-plane cloaking[8].

Regarding **detection**, we have developed an infrared sensing chip enhanced by graphene plasmons, enabling high-sensitivity infrared spectroscopy at the nanoscale[9-11]. This technology has been applied in biological sample analysis and catalysis research, demonstrating its potential for advanced sensing applications.

Our research presents innovative solutions for nanoscale optical manipulation and advanced sensing applications, paving the way for the development of highly integrated optoelectronic interconnect chips.

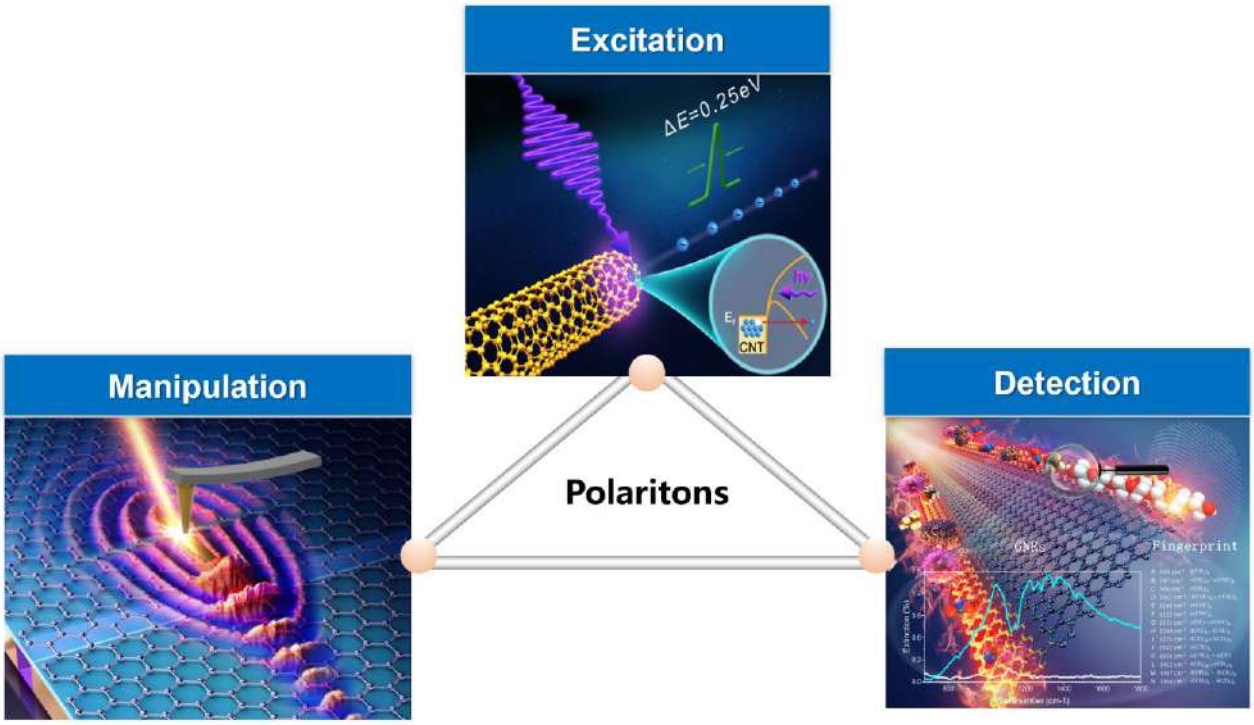


Figure 1. Excitation, manipulation, and detection of polaritons in low-dimensional nanomaterials

References

1. Li, N. et al. "Direct observation of highly confined phonon polaritons in suspended monolayer hexagonal boron nitride," Nat. Mater., 20, 43-48, 2021.
2. Guo, X. et al. "Hyperbolic whispering-gallery phonon polaritons in boron nitride nanotubes," Nat. Nanotechnol., 18, 529-534, 2023.
3. Guan, F. et al. "Overcoming losses in superlenses with synthetic waves of complex frequency," Science, 381, 766-771, 2023.
4. Guan, F. et al. "Compensating losses in polariton propagation with synthesized complex frequency excitation," Nat. Mater., 23, 506-511, 2024.
5. Hu, H. et al. "Active control of micrometer plasmon propagation in suspended graphene," Nat. Commun., 13, 1465, 2022.
6. Hu, H. et al. "Doping-driven topological polaritons in graphene/α-MoO_3 heterostructures," Nat. Nanotechnol., 17, 940-946, 2022.
7. Hu, H. et al. "Gate-tunable negative refraction of mid-infrared polaritons," Science, 379, 558-561, 2023.
8. Teng, H., et al. "Steering and cloaking of hyperbolic polaritons at deep-subwavelength scales," Nat. Commun., 15, 4463, 2024.
9. Hu, H. et al. "Far-field nanoscale infrared spectroscopy of vibrational fingerprints of molecules with graphene plasmons," Nat. Commun., 7, 12334, 2016.
10. Hu, H. et al. "Gas identification with graphene plasmons," Nat. Commun., 10, 1131, 2019.
11. Wu, C. et al. "Ultrasensitive mid‐infrared biosensing in aqueous solutions with graphene plasmons," Adv. Mater., 34, 2110525, 2022.

Thermal Emission Control and Applications of Metasurfaces

Xiaohe Shang[1], Ye Zhang[1], Fan Zhong[2], Shining Zhu[1] and Hui Liu[1*]

[1] Collaborative Innovation Center of Advanced Microstructures, National Laboratory of Solid State Microstructures, School of Physics Nanjing University Nanjing, China;
[2] Key Laboratory of Quantum Materials and Devices of Ministry of Education, School of Physics, Southeast University, China
[*]corresponding author: liuhui@nju.edu.cn

Abstract: We propose an integrated metasurface-based thermal emission chip with multi-degree-of-freedom control (wavelength, polarization, direction) and advanced detection. These innovations enable precise infrared emission and detection for industrial inspection, medical diagnosis, and environmental monitoring by leveraging bound states in the continuum, micro-area thermal imaging, and AI-assisted signal analysis.

In recent years, thermal emission has attracted considerable research interest due to its significant potential in applications such as radiative cooling, near-field heat transfer, and thermophotovoltaics. Current efforts in thermal emission control and detection typically rely on micro-nano structures like multilayer films and photonic crystals, with relatively little attention given to the role of metasurfaces in thermal emission. This gap in research limits the precise control of thermal emission across multiple degrees of freedom, including wavelength, polarization, and direction, restricting further advancements in infrared light sources and detection technologies.

To address this challenge, our research group has proposed a metasurface-based thermal emission chip design to enable precise multi-degree-of-freedom control and detection of thermal emission[1]. Our work in thermal emission control has achieved significant milestones, including directional control of thermal emission[2,3], the application of topological and non-Hermitian systems in thermal emission[4,5], and the development of metasurface chips for wavelength, polarization, and spatial multiplexing, along with their application in indirect spectral detection[6,7].

Building on these achievements, we have proposed the development of a multifunctional, integrated metasurface-based thermal emission chip and a corresponding detection system. This includes (1) a polarization vortex thermal emission chip designed using bound states in the continuous(BICs); (2) polarization angle-resolved thermal emission measurement and micro-area thermal imaging characterization techniques; and (3) an artificial intelligence-assisted system for the efficient detection of complex spectral mixtures. These innovations provide new approaches to achieving precise multi-degree-of-freedom control of thermal emission and demonstrate the feasibility of translating thermal emission chips from theoretical design to practical applications. Furthermore, we have outlined an integrated technological path for their use in infrared detection. Moving forward, we will continue to explore the mechanisms for multi-degree-of-freedom control in thermal emission chips, providing both fundamental innovation and practical engineering solutions for applications in industrial inspection, medical diagnosis, and environmental monitoring.

References

1. Chu, Q. *et al.* Controlling thermal emission with metasurfaces and its applications. *Nanophotonics* **13**, 1279–

1301 (2024).

2. Zhang, X., Liu, H., Zhang, Z. G., Wang, Q. & Zhu, S. N. Controlling thermal emission of phonon by magnetic metasurfaces. *Sci. Rep.* **7**, 41858 (2017).
3. Zhang, X., Zhang, Z., Wang, Q., Zhu, S. & Liu, H. Controlling Thermal Emission by Parity-Symmetric Fano Resonance of Optical Absorbers in Metasurfaces. *ACS Photonics* **6**, 2671–2676 (2019).
4. Zhong, F. *et al.* Angle-Resolved Thermal Emission Spectroscopy Characterization of Non-Hermitian Metacrystals. *Phys. Rev. Appl.* **13**, 014071 (2020).
5. Zhong, F., Zhang, Y., Zhu, S. & Liu, H. Probing mid-infrared surface interface states based on thermal emission. *Opt. Express* **29**, 35216 (2021).
6. Chu, Q. *et al.* Integrated thermal emission microchip based on meta-cavity array. *Nanophotonics* **11**, 4263–4271 (2022).
7. Chu, Q. Q., Zhang, F. Y., Zhang, Y., Zhu, S. N. & Liu, H. Indirect measurement of infrared absorption spectrum through thermal emission of meta-cavity array. *Opt. Express* **31**, 39832 (2023).

Plasmon-Modified Light Emission from Monolayer Semiconductors

Hong Wei*

Institute of Physics, Chinese Academy of Sciences, Beijing 100190, China
*corresponding author: weihong@iphy.ac.cn

Abstract: The extraordinary properties of surface plasmons in metal nanostructures make it possible to enhance and manipulate light-matter interaction at the nanoscale. In this talk, I will present our work on the interaction between plasmonic nanostructures and monolayer transition metal dichalcogenides, with the focus on the light emission properties.

Metal nanostructures supporting surface plasmons can concentrate light into nanoscale volumes, enabling the manipulation of light beyond the diffraction limit. Two-dimensional semiconductor materials such as transition metal dichalcogenides possess unique optical properties, showing large application potentials. The combination of plasmonic nanostructures and two-dimensional semiconductor materials provides a versatile platform for investigating light-matter interaction at the nanoscale.

In this presentation, I will introduce our research on the coupling systems of plasmonic nanostructures and monolayer transition metal dichalcogenides. The interaction between them can not only lead to the plasmon-exciton strong coupling shown by the spectral splitting in the scattering or transmission spectra, but also modify the photoluminescence and Raman scattering properties of the monolayer semiconductors.

High-Contrast Ratio Optical Switching in multilayer Fabry-Perot Cavities with Phase Change Materials

Ruhao Pan[1*], Bo Wang[1], Zhiyang Tang[1], and Junjie Li.[1]

[1] Beijing National Laboratory for Condensed Matter physics, Institute of Physics, Chinese Academy of Sciences, Beijing 100190, China.

[*]corresponding author: panruhao@iphy.ac.cn

Abstract: This work proposed a multilayer Fabry-Perot (FP) cavity to achieve optical switches with high contrast ratio by introducing the $Ge_2Sb_2Se_4Te$ (GSST) as phase change material. Due to the distinctive FP resonances for the amorphous and crystalline GSST, a high contrast ratio of 2410/735 can be obtained by simulation/experiment.

Optical switches are widely utilized in the fields of optical communicating, computing, and data storage, and thus attracted tremendous attention of researchers[1, 2]. However, it is still a challenge to achieve high contrast ratio switches simultaneously with the advantages of compact size, low fabrication cost, and easy integration. Here, we design a multilayer FP cavity by introducing the GSST for its low intrinsic loss, high optical contrast, and non-volatile property[3] as shown in **Fig. 1**. The index changes of the GSST during the phase-change process contribute to the change of FP resonance, resulting in the reflectance with distinctive level for the amorphous and crystalline states, which resulting in an optical switching capacity at the communication band. The operating wavelength can be continuous tuned from 1460 nm to 1630 nm by modulating the thickness of the GSST and the dielectric layers in the cavity, meaning that our switches cover the “S”, “C”, and “L” band. The highest contrast ratio of 2410/735 can be obtained by simulation/experiment for the optimized thickness of the phase-change material (PCM). Interestingly, the contrast ratio of the switches can be tuned in the range of 570-730 by the GSST with different crystallization ratios for which can be continuously regulated by the annealing temperature. The demonstration of optical switches with GSST showing great advantages of small footprint, high contrast ratio, and low fabrication cost, providing a new strategy for the design of optical communication systems and data storage devices.

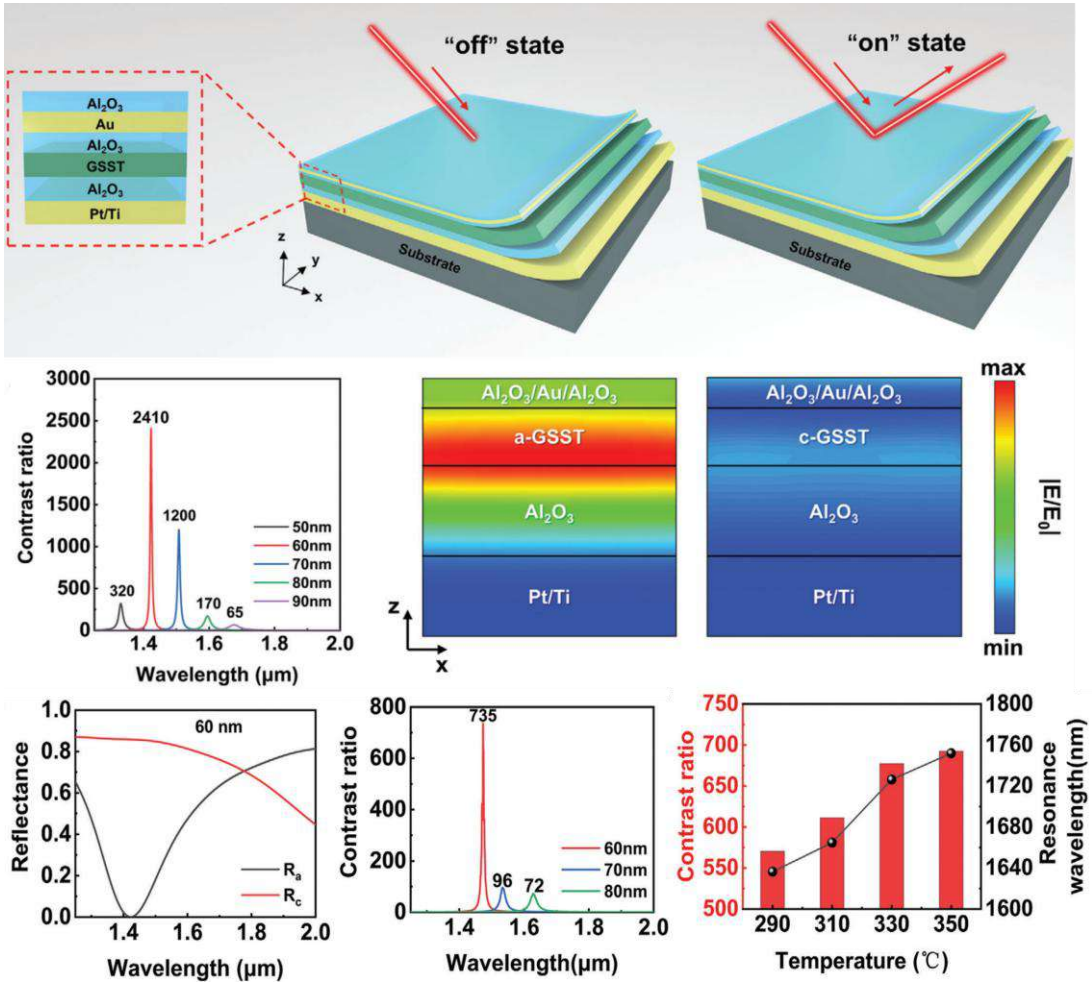


Fig. 1: The design of the GSST-based multilayer optical switches with its optical properties.

References

[1] Zhu Z, Wen Y, Li J, et al. Metasurface-enabled polarization-independent lcos spatial light modulator for 4k resolution and beyond. Light, science & applications, 2023, 12: 151

[2] Srivastava YK, Chaturvedi A, Manjappa M, et al. Mos2 for ultrafast all-optical switching and modulation of thz fano metaphotonic devices. Advanced Optical Materials, 2017, 5: 1700762

[3] Zhang Y, Fowler C, Liang J, et al. Electrically reconfigurable non-volatile metasurface using low-loss optical phase-change material. Nat Nanotechnol, 2021, 16: 661-666

Monte Carlo Simulation for Dense Nanoparticle Dispersion with Rigorous Treatment of Particle Types and Distributions

Changgyun Noh[1], Seokhwan Min[1], and Jonghwa Shin[1*]

[1]Korea Advanced Institute of Science and Technology, 291 Daehak-ro, Yuseong-gu, Daejeon, Republic of Korea
[*]corresponding author: qubit@kaist.ac.kr

Abstract: We develop Monte Carlo-based optical simulation for nanoparticle dispersion with high accuracy and versatility. Our approach incorporates dependent scattering with structure factor and rigorously accounts for particle types and distributions. It is applicable to various structures, including multimodal probability density functions, multi-shell configurations, and multi-composition structures, enabling comprehensive optical analysis.

Nanoparticle dispersion is used to tailor a structure's optical properties by exploiting the scattering effects of the nanoparticles. Therefore, it is widely used in applications such as optical diffusers, antireflective coatings, displays, and radiative cooling due to its ease of processing and scalability. Accordingly, extensive research is underway to predict accurately the optical performance of this structure. For instance, methods that solve Maxwell's equations, such as the Finite-Difference Time-Domain (FDTD), Finite Volume (FV), and Finite Element Method (FEM)—are employed to predict the behavior of electromagnetic waves. However, these approaches are computationally expensive and time-consuming.

Consequently, a simulation tool that combines Monte Carlo methods with Mie theory is proposed to more efficiently predict the optical characteristics of this structure. However, previous studies either neglected inter-particle correlations or assumed that uniform size and type of nanoparticles are dispersed in the medium. Consequently, when the particle volume fraction is high or the probability density function is multimodal, the simulation results deviate from the experimental results. Therefore, we calculate the scattering cross section and phase function for overall particles in the dispersion based on Mie theory, ensuring accurate computations even for nanoparticle dispersions with bimodal or random distributions. In addition, we calculate the structure factor to account for the interaction between particles. These corrections are applied to the scattering cross section and phase function, as shown in Eqs. (1) and (2), and employed in the Monte Carlo simulation. In the equations, ζ is the near-field factor for accuracy, and $S(\theta)$ is the structure factor.

$$C_{sca,corr} = |\zeta|^2 \int_{\phi=0}^{2\pi} \int_{\theta=0}^{\pi} \frac{dC_{sca}}{d\Omega} S(\theta) \sin\theta \, d\theta d\phi \tag{1}$$

$$\Phi_{\mathrm{corr}}(\theta) = S(\theta)\Phi(\theta) \tag{2}$$

Unlike previous studies that calculated effectively, our approach computes the scattering properties of all particles within the structure. As a result, the simulation can be applied not only to structures containing solid spherical particles but also to those including various types of particles, such as multi-shell particles, and able to deal with dispersions with nanoparticles of varying sizes. This is illustrated in Fig. 1 below.

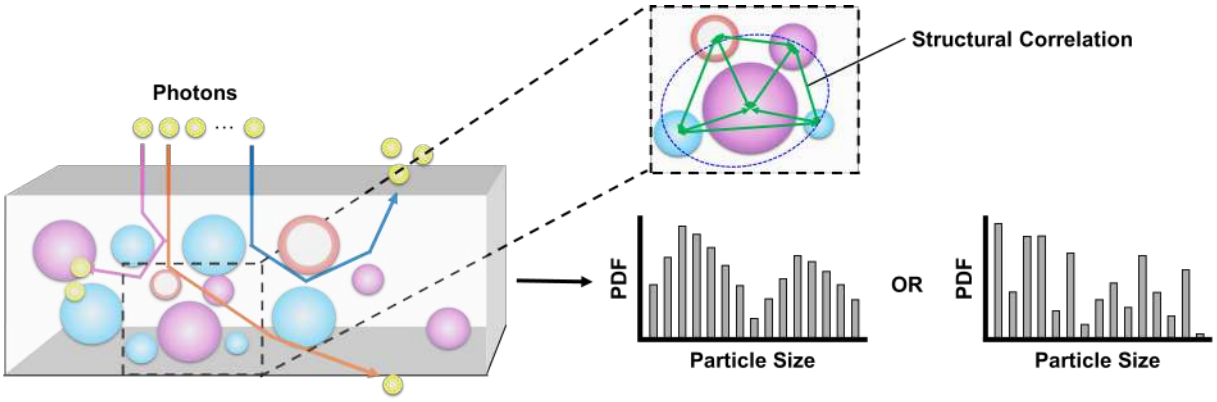


Figure 1. Schematic figure of simulation

This simulation can be utilized to accurately design nanoparticle dispersions composed of multiple particles and multi-layered structures. Therefore, we design the color paints with multilayer nanoparticle dispersions. The bottom layer contains TiO_2 nanoparticles for high reflection, while the layers above consist of Ag/SiO_2 core-shell nanoparticles. By controlling the SiO_2 core size, Ag shell thickness, the volume fraction of the nanoparticles, and the thickness of the layer, we can tune the reflection spectrum to achieve the desired paint color. As a result, by dispersing Ag/SiO_2 nanoparticles, we design paint with absorption peaks, thereby achieving a wide range of colors. Figure 2 illustrates one of the designed structures, along with their corresponding spectra and color under D65 illumination.

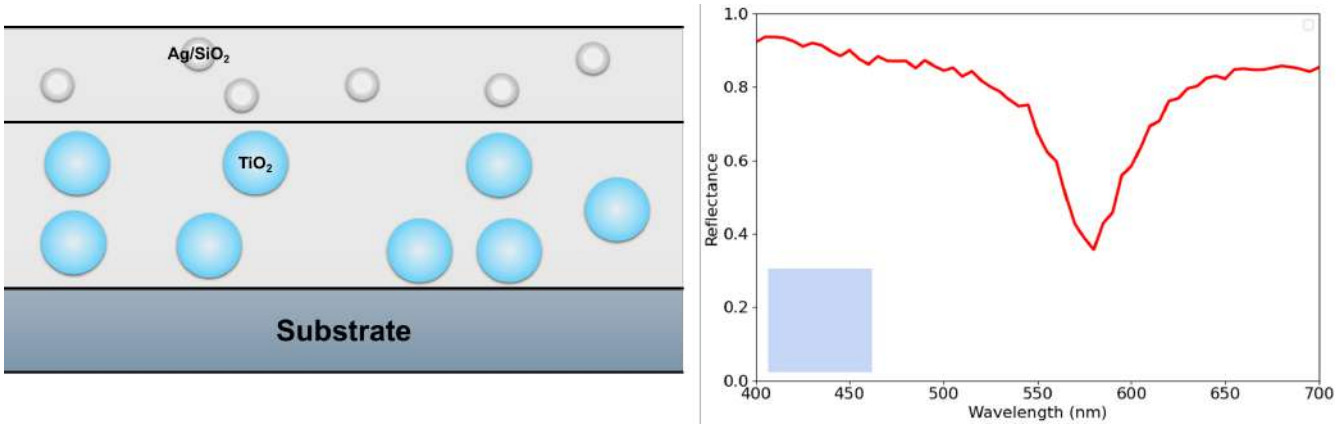


Figure 2. Multilayer nanoparticle color paint and its spectra and color

References

1. S. Kumar, and C. L. Tien, "Dependent Absorption and Extinction of Radiation by Small Particles," J. Heat Transfer., Vol. 112, No. 1, 178-185, 1990.
2. L. Wang, S. L. Jacques, and L. Zheng, "MCML – Monte Carlo modeling of light transport in multi-layered tissues," Comput. Methods Programs Biomed., Vol. 47, No. 2, 131-146, 1995.
3. X. Li, J. Peoples, Z. Huang, Z. Zhao, J. Qiu, and X. Ruan, "Full Daytime Sub-ambient Radiative Cooling in Commercial-like Paints with High Figure of Merit," Cell Rep. Phys. Sci., Vol. 1, No. 10, 100221, 2020.

Strong near-field enhancement through SPhP and LSP coupling on CdO gratings

P. Ibañez-Romero[1], M. Villanueva Blanco[1], E. Martinez Castellano[1], J. Yeste[2], F. Gonzalez-Posada[3], T. Taliercio[3], V. Muñoz-Sanjosé[2] , M. Montes Bajo[1], and A. Hierro[1]
[1] ISOM, ETSIT Telecomunicación, Universidad Politécnica de Madrid, Madrid, Spain
[2] Departament de Física Aplicada i Electromagnetisme, Universitat de València, Burjassot, Spain
[3] Univ. Montpellier, IES. UMR 5214, F-34000, Montpellier, France

The coupling between plasmonic modes and phonons enables new approaches for tailoring optical properties and controlling light at the nanometer scale. Here, we demonstrate the dramatic amplification of the near-field driven by the coupling of sapphire's localized surface phonon polaritons and localized surface plasmons in CdO gratings.

CdO stands out as the best semiconductor for plasmonic applications in the mid-IR [1] thanks to its high plasma frequency and low losses. When nanostructured, it can host localized surface plasmons (LSP) whose resonant frequency can be tuned via nanostructure geometry. On the other hand, polar dielectrics, like sapphire, have drawn increasing attention in the last years due to their ability to host localized surface phonon polaritons (LSPhP) [2]. These modes allow sub-diffraction confinement in the mid-IR and very sharp resonances paired with extremely low losses [3]. We demonstrate the progressive coupling between CdO LSP and the LSPhP held by the sapphire-air interface by adequate design of CdO nanostripes. Experimental spectra obtained through Fourier Transformed Infrared Spectroscopy are backed by a Finite Element Methods model showing outstanding near field enhancement at the coupling frequency.

A set of samples was designed and fabricated using a novel protocol developed in-house. The process is illustrated in Figure 1a. It begins with the MOCVD deposition of CdO films on top of a r-plane sapphire wafer. Then, standard e-beam lithography followed by ICP etching is used to define periodic nanostripes (Figure 1b), with a period d=2 μm and an opening (w) from 1 μm to 200 nm. From now onwards we will use the fill factor (w/d) to refer to the geometry of the samples, ranging from 0.9 to 0.5.

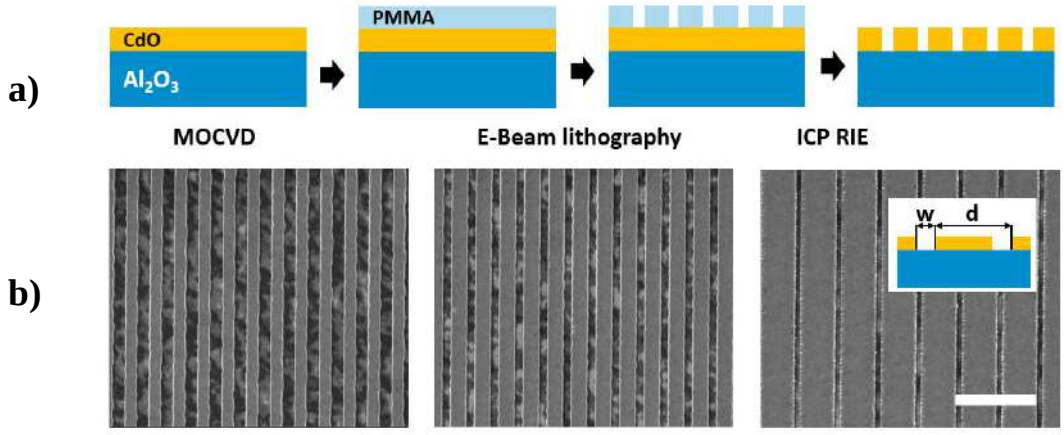


Figure 1. a) Processing scheme of the CdO nanostripes. b) SEM images of nanostripes with fill factors ranging from 0.5 (leftmost) to 0.9 (rightmost). The white bar measures 4 μm. The inset shows the design parameters.

The plasmonic response of the samples shown above is displayed in Figure 2a, where the black line corresponds to reflectivity measurements and the blue and red line are extracted from a FEM model, yielding a very high agreement. Starting with the sample with 0.5 fill factor, the response is characterized by a broadband LSP centered at 1400 cm^{-1} and a LSPhP located in sapphire's Reststrahlen band. As the fill factor increases (i.e the separation between stripes decreases and the stripe width increases), the LSP shifts towards lower energies effectively coupling with the LSPhP and thus increasing the overall absorption (red line) of the system at the latter's resonant frequency. Finally, when the distance between the stripes is small (fill factor 0.9) the LSP and the LSPhP become resonant, and the latter is shifted to slightly higher energies. At such frequency, the interaction in the near field is outstanding. The intensity of the electric field at the LSPhP frequency is plotted for the three samples in Figure 2b. When the LSP and the LSPhP are fully coupled, the intensity enhancement is around 1200, proving to be an outstanding platform for the observation of rare optical effects and its application in sensing systems and IR sources.

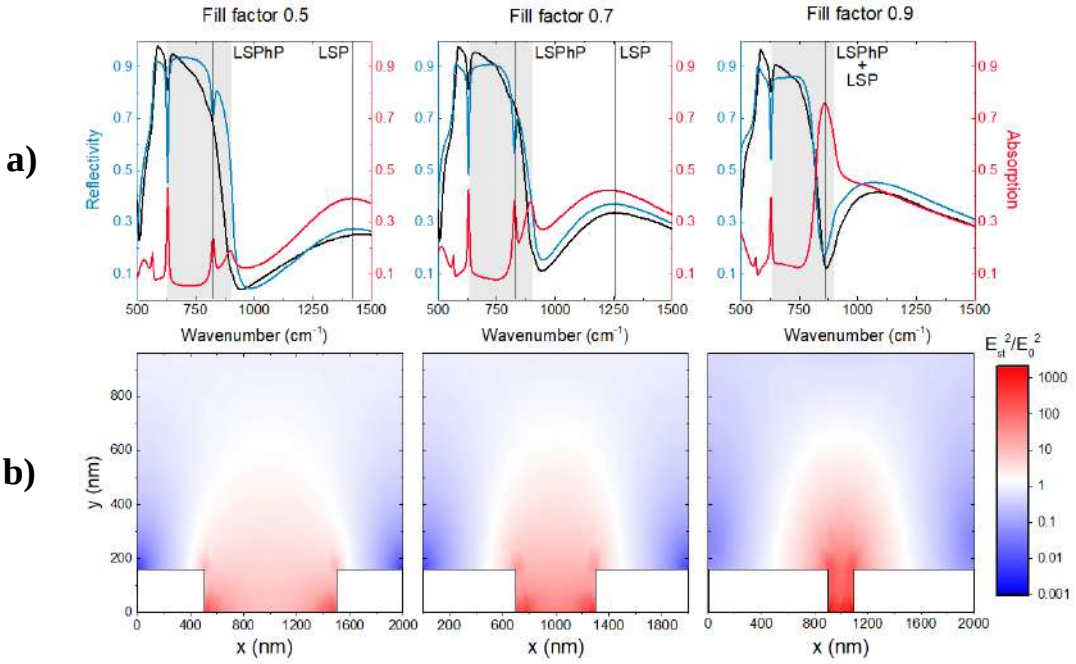


Figure 2. a) Measured (black) and modeled (blue) reflectance spectra for different fill factor nanostripes along with the modeled absorption (red). The shaded area corresponds to sapphire's Restsrahlen band. b) Near field simulations for different fill factors. The enhancement is obtained by comparing the electric field distribution with and without the stripes.

This work was supported by: Project PID2020-114796RB-C2 funded by MCIN/ AEI /10.13039/501100011033/; Project PDC2023-145827-C2 funded by MICIU/AEI /10.13039/501100011033/ and by European Union Next Generation EU/ PRTR; Generalitat Valenciana under Project No. PROMETEU/2021/066; P. I and J. Y. acknowledge the FPU 27 (Formación de Profesorado Universitario) predoctoral contract from the Spanish Ministry of Science, Innovation, and Universities.

[1] J. D. Caldwell *et al.*, "Low-loss, infrared and terahertz nanophotonics using surface phonon polaritons," *Nanophotonics*, vol. 4, no. 1, pp. 44–68, Apr. 2015.

[2] T. Wang, P. Li, B. Hauer, D. N. Chigrin, and T. Taubner, "Optical Properties of Single Infrared Resonant Circular Microcavities for Surface Phonon Polaritons," *Nano Lett.*, vol. 13, no. 11, pp. 5051–5055, Nov. 2013, doi: 10.1021/nl4020342.

[3] R. Hillenbrand, T. Taubner, and F. Keilmann, "Phonon-enhanced light–matter interaction at the nanometre scale," *Nature*, vol. 418, no. 6894, pp. 159–162, Jul. 2002, doi: 10.1038/nature00899.

Energy and momentum distribution of surface plasmon-induced hot carriers

C. G. O. Weiß[1*], T. Eul[2], E. Prinz[1], B. Stadtmüller[3], and M. Aeschlimann[1]
[1]Department of Physics and Research Center OPTIMAS, University of Kaiserslautern-Landau, Germany
[2]Institute of Experimental and Applied Physics, University of Kiel, Germany
[3]Institute of Physics, University of Augsburg, Germany
Corresponding author: weissc@rptu.de

Abstract: Spectroscopic differences between photoexcited and surface plasmon polariton-induced hot electrons reveal distinct energy and momentum distributions. Time-resolved photoemission electron spectroscopy captures their dynamics in real- and momentum-space, enabling a clear separation of both carrier types. These results provide new insights into plasmonic energy conversion and hot electron generation.

Are the spectroscopic properties of plasmon- and photon-induced carriers fundamentally different? This question is crucial for the advancement of plasmonic energy conversion. Electrons excited at bulk plasmon resonance show a distinct distribution in energy and momentum space [1], while the electron distribution of surface plasmon-induced carriers is still under debate [2]. To address this issue for surface plasmons, we aim to separate the energy and momentum distributions of surface plasmon polariton-induced hot electrons from those of photoexcited ones. Exciting a circular ring-slit geometry with radially and azimuthally polarised light, we can clearly separate the plasmon and photon-induced hot carriers in space and time with two measurements. Our time-resolved photoemission electron microscope is then able to capture their signatures in real time. In this contribution, we show that there are spectroscopic differences between photoemitted electrons and those generated by plasmoemission in the centre of the structure.

References

1. Reutzel, M. et al., "Nonlinear Plasmonic Photoelectron Response of Ag(111)," *Phys. Rev. Lett.*, Vol. 123, p. 017404, 2019.

2. Hartelt, M. et al., "Energy and Momentum Distribution of Surface Plasmon-Induced Hot Carriers Isolated via Spatiotemporal Separation," *ACS Nano*, Vol. 15, No. 12, pp. 19559–19569, 2021.

Electromagnetically induced transparency and lasing without inversion in chiral molecules

Somasree Pal [1], Ambaresh Sahoo[1], Raju Adhikary[1], Matteo Venturi[1], Giovanna Salvitti[1], Carino Ferrante[2], Davide Tedeschi[1], Paola Benassi[1,2], Massimiliano Aschi[1], Andrea Marini[1,2*]

1. Department of Physical and Chemical Sciences, University of L'Aquila, Via Vetoio, 67100 L'Aquila, Italy
2. CNR-SPIN, c/o Dip.to di Scienze Fisiche e Chimiche, Via Vetoio, Coppito (L'Aquila) 67100, Italy

*corresponding author: andrea.marini@univaq.it

Abstract: We study how molecular chirality influences electromagnetically induced transparency and lasing without inversion, revealing key chiroptical effects and quantum coherence phenomena. These insights are essential for advancing spectroscopic techniques, improving the detection and characterization of chiral molecules, and enhancing applications in quantum optics and molecular spectroscopy.

Chiral sensing plays a key role in the pharmaceutics because the specific enantiomeric form of drugs affects their functionality and toxicity [1], and thus nanophotonic-based platforms [2] are promising for nanomedicine. Here we focus on the behavior of a single chiral molecule in vacuum, Fluorooxirane, as a model system for exploring quantum coherence phenomena. Fluorooxirane, chosen for its rigid chiral scaffold despite its instability, was subjected to both a strong pump field and a signal field without any temporal delay. The interaction revealed interesting results, sparking hypotheses about the observation of Electromagnetically Induced Transparency (EIT) or Lasing Without Inversion (LWI) under these conditions.

We developed an analytical model using the N-level approximation, which was then reduced to a two-level system. The density matrix equation was solved perturbatively to derive analytical expressions for the coherences of both the pump and signal fields:

$$\begin{aligned}\dot{\rho}_{1,i} &= \left[i\left(\omega_i - \omega_1\right) - \frac{\gamma_i}{2} \right] \rho_{1,i} + \frac{1}{i\hbar} \rho_{1,i} \left(\overline{d_{i,i}} - \overline{d_{1,1}} \right) \cdot \left[\overline{E_P}(t) + \overline{E_S}(t) \right] \\ &+ \frac{1}{i\hbar} \left\{ \overline{d_{1,i}} \cdot \left[\overline{E_P}(t) + \overline{E_S}(t) \right] + \overline{m_{1,i}} \cdot \left[\overline{B_P}(t) + \overline{B_S}(t) \right] \right\}\end{aligned} \tag{1}$$

From above equation (1) The interaction between coherences is mediated by the interaction Hamiltonian, involving three dipole moments: the static electric dipole moment, the electric transition dipole moment, and the magnetic transition dipole moment arising from molecular chirality, resulting in transparency and amplification effects. We further employ the Chiral Optical Theorem to calculate the rate of absorption of energy, starting from its classical counterpart by evaluating the current density and molecular absorption:.

$$\sigma_{\text{abs}} = -\frac{1}{I_0}\frac{dU}{dt} = -\frac{\omega}{\varepsilon_0 c} \operatorname{Im} \left\{ \begin{aligned} &\overline{\hat{n}_E} \cdot \left[\hat{\alpha}_{dE}{}^{*} : \overline{\hat{n}_E}^{*} \right] + \frac{1}{c^2} \left(\overline{\hat{k}} \times \overline{\hat{n}_E} \right) \cdot \left[\hat{\alpha}_{mB}{}^{*} : \left(\overline{\hat{k}} \times \overline{\hat{n}_E}^{*} \right) \right] \\ &+ \frac{1}{c} \overline{\hat{n}_E} \cdot \left[\hat{\alpha}_{dB}{}^{*} : \left(\overline{\hat{k}} \times \overline{\hat{n}_E}^{*} \right) \right] + \frac{1}{c} \left(\overline{\hat{k}} \times \overline{\hat{n}_E} \right) \cdot \left[\hat{\alpha}_{mE}{}^{*} : \overline{\hat{n}_E}^{*} \right] \end{aligned} \right\} \tag{2}$$

From equation (2) we determine the absorption cross section which depends over the orientation of the molecule and polarization of light. By analyzing the linear response, nonlinear response and the molecular orientation of the molecule we observed Electromagnetically Induced Transparency (EIT) at very low intensity 100 MW/ cm^2.

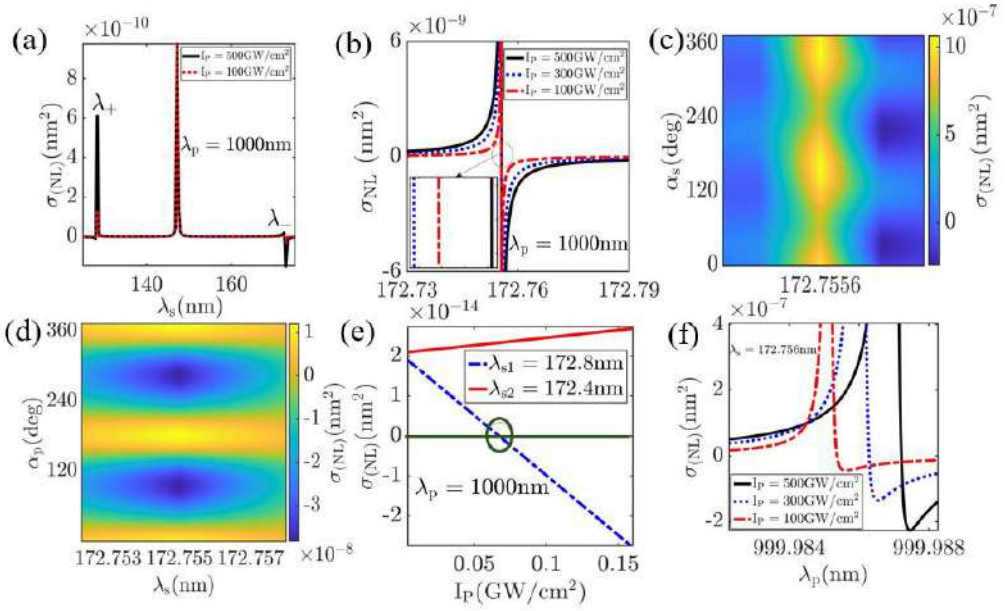


Fig. 1 (a–f) Dependence of the nonlinear absorption cross-section on various parameters for Fluorooxirane in vacuum.**(a, b, f)** Variation of the nonlinear absorption cross-section as a function of the signal wavelength, considering a fixed pump wavelength λ_P =1000nm ,while increasing the pump intensity I_P =100,300,500 GW/cm^2 .**(c, d)** Influence of the angle of linear polarization of the signal field and pump field on the nonlinear absorption cross-section, with the pump intensity fixed at I_P = 500 GW/cm^2.**(e)** Dependence of the nonlinear absorption cross-section on the pump intensity, with a fixed pump wavelength λ_P =1000nm for two distinct signal wavelengths λ_S =172.8nm,172.4nm. The marked line in this plot highlights the emergence of Electromagnetically Induced Transparency (EIT) as a function of increasing intensity.**(f)** Dependence of the nonlinear absorption cross-section on the pump wavelength, while progressively increasing the pump intensity I_P =100,300,500 GW/cm^2.All plots are obtained with fixed damping rate **(a-f)** Υ=1.15*10^{7}s^{-1} for Fluro oxirane in vacuum. We observe, additional peaks appear on top of the primary absorption peak, indicating frequency mixing between the pump and signal fields. The nonlinear response dependence on pump intensity reveals that the absorption cross-section of the molecule can either increase or decrease depending on the signal field wavelength, eventually reaching zero, as observed in Figure **(e)**. This phenomenon, known as Electromagnetically Induced Transparency (EIT), occurs when the molecule effectively ceases to absorb light. In this regime, the population remains unchanged since the pump field is not resonant with the molecular transition. Instead of promoting electrons from the lower to the upper level, the pump field induces coherence at the signal frequency due to the molecule's static electric dipole moment. This coherence modulates the absorption through interference, potentially leading to gain. This mechanism, referred to as Lasing Without Inversion (LWI), enables signal amplification without requiring population inversion.

References

1. L.A. Nguyen, H. He, and C. Pham-Huy. "Chiral drugs: an overview.",IJBS 2.2, 85 (2006)
2. M. Venturi, R. Adhikary, A. Sahoo, C. Ferrante, I. Daidone, F. Di Stasio, A. Toma, F. Tani, H. Altug, A. Mecozzi, M. Aschi, A. Marini, "Plasmon-enhanced circular dichroism spectroscopy of chiral drug solutions", J. Chem. Phys., Vol. 159, No. 15, p. 154703 (2023)

Influence of the plasmonic lattice Kerker effect on second-harmonic generation

S. Boroviks[1*], B. S. Garcia[1], and O. J. F. Martin[1]

[1] Nanophotonics and Metrology Laboratory, École Polytechnique Fédérale de Lausanne (EPFL), Switzerland
[*]corresponding author: sergejs.boroviks@epfl.ch

Abstract: We study the Kerker effect associated with the excitation of multipolar surface lattice resonances and its influence on nonlinear optical response. Observing that the appearance of the Kerker effect is associated the strong absorption, we show that it diminishes second-harmonic generation despite strong near-field enhancement.

A surface lattice resonance (SLR) is a Fano-type resonance that occurs in two-dimensional arrays of plasmonic nanoparticles [1]. Emerging from the diffractive coupling of localized surface plasmon resonances, the SLR features a sharper linewidth (i.e. higher quality factor). Typically, the dipolar response is considered in the limit of small particles; however larger nanoparticles arranged in arrays with subwavelength periodicity (referred to as metasurfaces) support higher order multipolar modes [2]. This allows to achieve more intricate behavior, such as unidirectional scattering, known as lattice Kerker effect (KE) [3].

An example of such a structure and its optical response (reflection spectrogram) is shown in Fig. 1. We perform numerical simulations (Fig. 1 a, b) and experimental validations (Fig. 1 c, d), which agree fairly well. Intriguingly, we observe that the KE is accompanied by the appearance of a bound state in the continuum (BIC) mode that is not excitable at normal incidence. However, it manifests in the reflection spectrogram as a quasi-BIC mode, which becomes observable at off-normal incidence.

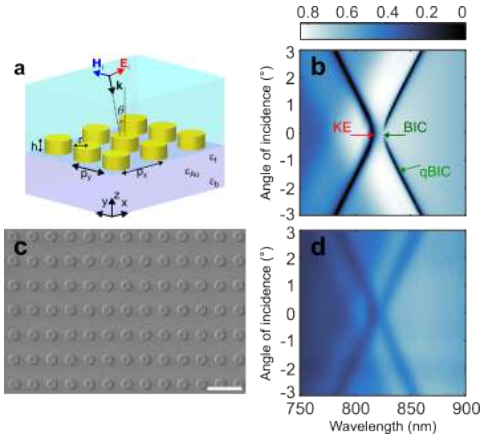


Figure 1

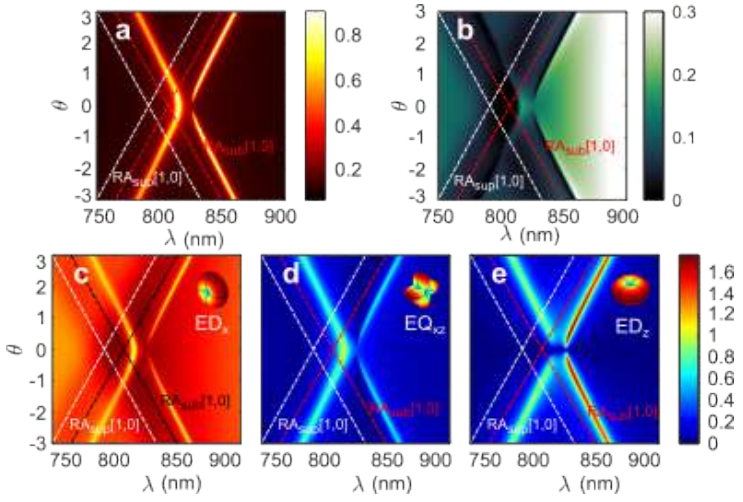


Figure 2

To gain further insights into the physical mechanisms behind the KE, we study the absorption (Fig. 2a) and transmission (Fig. 2b) of the system, and we perform multipole decompositions (Fig. 2c-e). As can be seen, the KE occurs in the vicinity of Rayleigh anomaly (RA) and is associated with very strong absorption induced by excitation of electric dipole along *x*-axis direction (ED_x) and electric quadrupole in *xz*-plane (EQ_{xz}). In turn, the quasi-BIC mode is associated with the dipole oriented along the *z*-axis.

Further, we experimentally study the nonlinear optical response of the system, in particular second-harmonic generation (SHG). Although several works [4-6] suggest that excitation of the SLR in a plasmonic metasurfaces enhances the nonlinear optical response, our findings indicate that it is not always the case. As shown in Fig. 3, the linear reflection minima associated with the KE correspond to the SHG minima, whereas maximum is achieved at the linear reflection maximum, which is associated with the dipolar resonance. We attribute the observed behavior to the competition between the absorption and the near-field enhancement. Although, in the limit of small particles, some degree of absorption is beneficial for SHG [7], in the case of the SLR-mediated KE, the absorption overtakes the benefits of the strong electric field at the surface of the nanoparticles and diminishes the SHG.

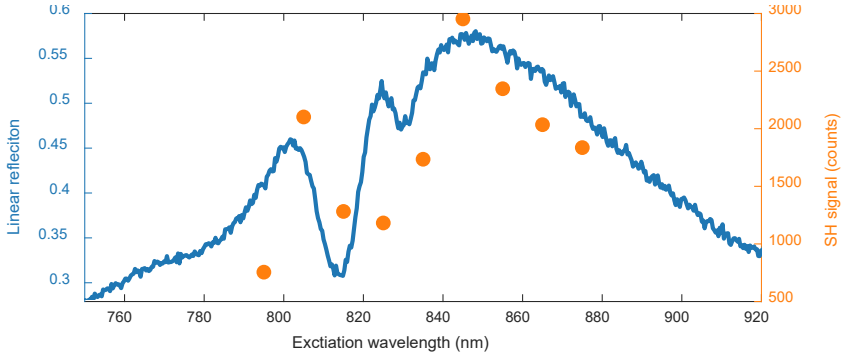


Figure 3

References

1. Kravets, V.G., et al "Plasmonic Surface Lattice Resonances: A Review of Properties and Applications", Chem. Rev. 118, 12, 5912 (2018).
2. Babicheva, V.E., Evlykhin, A.B. "Metasurfaces with Electric Quadrupole and Magnetic Dipole Resonant Coupling", ACS Photonics 5, 5, 2022 (2018).
3. Babicheva, V.E., Evlykhin, A.B. "Resonant Lattice Kerker Effect in Metasurfaces With Electric and Magnetic Optical Responses", Las. Photon. Rev. 11, 6, 1700132 (2017).
4. Liu, A.-Y., et al. "Third Harmonic Generation Enhanced by Generalized Kerker Condition in All-Dielectric Metasurfaces", Adv. Opt. Mater., 11, 19, 2300526 (2023).
5. Han, A., et al. "Second harmonic generation in metasurfaces with multipole resonant coupling", Nanophotonics 9, 11, 3545 (2020).
6. Hooper, D.C. et al. "Second Harmonic Spectroscopy of Surface Lattice Resonances", Nano Lett. 19, 1, 165 (2019).
7. Butet, J., et al. "Maximizing Nonlinear Optical Conversion in Plasmonic Nanoparticles through Ideal Absorption of Light", ACS Photonics 3, 8, 1453 (2016).

Plasmon-enhanced vibrational circular dichroism in plasmonic nanostructures incorporating chiral drugs

R. Adhikary[1], M. Venturi[1], G. Salvitti[1], A. Sahoo[1], C. Ferrante[2], P. Benassi[1,2], F. Di Stasio[3], A. Toma[3], H. Altug[4], M. Aschi[1], and A. Marini[1,2*]

[1]Department of Physical and Chemical Sciences, University of L'Aquila, Via Vetoio, L'Aquila 67100, Italy
[2]CNR-SPIN, c/o Dip.to di Scienze Fisiche e Chimiche, Via Vetoio, L'Aquila 67100, Italy
[3]Istituto Italiano di Tecnologia, Via Morego 30, Genova 16136, Italy
[4]Institute of Bioengineering, Ecole Polytechnique Federale de Lausanne (EPFL), Lausanne 1015, Switzerland
[*]corresponding author: andrea.marini@univaq.it

Abstract: We investigate the chiroptical response of plasmonic nanostructures based on Aluminum-doped zinc oxide (AZO) and a layer of pharmaceutical chiral drug solutions. We systematically study the localized surface plasmon resonances (LSPRs) to enhance the vibrational circular dichroism (VCD) of the chiral drug solution to develop innovative chiroptical sensing techniques.

Chiral sensing plays a crucial role in numerous scientific disciplines, particularly in pharmaceutical industries, biotechnology, and pharmacology, where detection of specific enantiomers of a chiral molecule is important for toxicity [1] and functionality assessment. Despite the capabilities of advanced chiral sensing techniques to precisely detect enantiomeric imbalances, compatibility with real-time analysis and wider nanomedicine applications is still in high demand. Here, we investigate plasmon-enhanced VCD facilitated by the LSPRs in AZO-based plasmonic nanostructures embedding realistic chiral drug solutions, specifically an isotropic assembly of Ladarixin (adopted to treat diabetes patients because of its ability to serve as a dual allosteric inhibitor of CXCR1, CXCR2, and CXCL8 (IL-8) receptors) dissolved in water. Employing a robust computational approach [2], we calculate the bi-anisotropic optical parameters of the chiral sample considering a dilute molecular number density $n_{mol} = 10^{-2}$ nm^{-3}. We model the LSPRs of the considered nanostructures, see Fig. 1, within the electrostatic limit through an analytical approach leading to the calculation of their absorption cross-sections. In turn, we obtain the VCD differential absorption cross-section (VCDDA) $\Delta\sigma = \sigma_R - \sigma_L$, where σ_R and σ_L represent the respective absorption cross-section upon excitation by right and left circular polarization radiation. By measuring such VCDDA, it is possible to retrieve the enantiomeric imbalance $\Delta n_{mol} = n^{(S)}_{mol} - n^{(R)}_{mol}$ as $\Delta\sigma$ is proportional to Δn_{mol}. Thanks to intense near-field confinement generated by the LSPRs, we attain a plasmon-induced VCDDA enhancement factor ranging from $\simeq 3$ to $\simeq 20$. Our findings have the potential to design promising chiroptical sensing platforms capable of investigating the chirality of molecular systems at the nanoscale level.

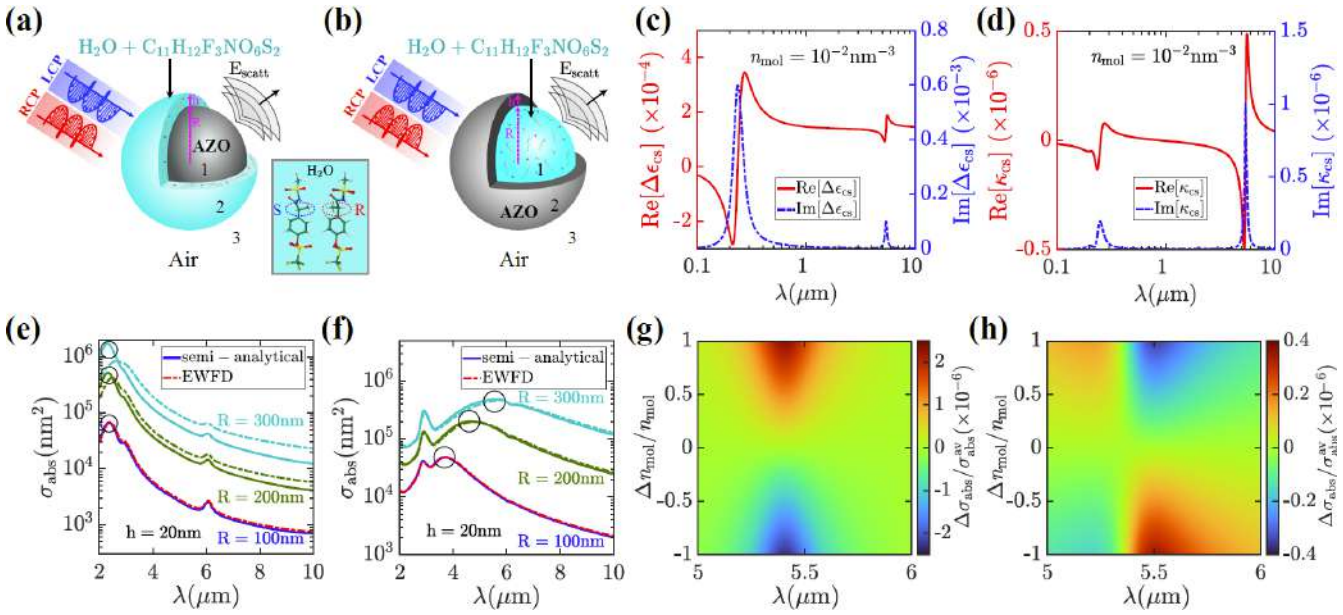


Fig. 1: Schematic of (a) Type-1 plasmonic nanostructure consisting of Al-doped ZnO (AZO) nanosphere of radius R surrounded by an aqueous Ladarixin layer with thickness h, immersed in air, (b) Type-2 plasmonic nanostructure which contains AZO-based nanoshell with inner/outer radii R/R+h, embedding aqueous Ladarixin at its core and immersed in air. Dependence of (c) relative dielectric permittivity $\epsilon_r(\lambda)$ and (d) chiral parameter $\kappa(\lambda)$ over vacuum wavelength λ, evaluated at a fixed molecular density n_{mol} of R and S-Ladarixin dissolved in water. Dependence of the absorption cross-section $\sigma_{abs}(\lambda)$ of (e) Type-1 and (f) Type-2 nanostructures over λ upon excitation by right circular polarization for several R and fixed h = 20 nm. Dependence of the relative vibrational circular dichroism differential absorption over λ and enantiomeric imbalance evaluated for (g) Type-1 and (h) Type-2 nanostructures with R = 100 nm and h = 20 nm.

References

1. Nguyen, L. A., He, H., & Pham-Huy, C. “Chiral drugs: an overview,” Int J Biomed Sci., Vol. 2, No. 2, 85, 2006.
2. Venturi, M., Adhikary, R., Sahoo, A., Ferrante, C., Daidone, I., Di Stasio, F., ... & Marini, A. “Plasmon-enhanced circular dichroism spectroscopy of chiral drug solutions,” J. Chem. Phys. Vol. 159, No. 15, 2023.

Possibility of the zinc oxide refractive index changing to explanation the shift of the of the ZnO/Ag nanocomposites related LSPR peak due to magnetic field pre-treatment

S. M. Redko[1*], G. V. Milenin[1], V. V. Shvalagin[2], O. A. Kapush[1], A. V. Fedorenko[1], R. A. Redko[1]

[1] V. Lashkaryov Institute of Semiconductor Physics of the National Academy of Sciences of Ukraine, Ukraine
[2] L. Pysarzhevskii Institute of Physical Chemistry of the National Academy of Sciences of Ukraine, Ukraine
[*]corresponding author: redko.fotya@gmail.com

Abstract: The modeling of the absorbance of ZnO/Ag nanocomposites with MiePlot 4.16 Software were carried out to obtain information about principal possibility of LSPR peak position changing due to changing of ZnO nanoparticles refractive index due to magnetization in external magnetic field. Obtained results are in good agreement with experiment.

The blue shift of LSPR peak from 450 to 410 nm due to magnetic field (60 mT) pre-treatment of the ethanol solution of ZnO nanoparticles has been detected [1]. It was quite unexpected because undoped ZnO, actually, is paramagnetic material and any action of external magnetic field should not lead to any changing in LSPR peak position of ZnO/Ag nanocomposites, which were prepared after magnetic field action doe to photocatalytic reduction of silver. However, observed feature may take place when the magnetization of ZnO nanoparticles is occurred in external magnetic field [2]. This is relatively a new phenomenon, when nanostructures of inorganic materials exhibit ferromagnetic-like properties [3]. This is mainly due to the presence of defects – vacancies and interstitial atoms. Thus, observe in [1] shift can take place due to some changes in ZnO nanoparticles, as carrier of ferromagnetic properties. Naturally that magnetization of these nanoparticles may take place. And due to this magnetization the changing of refractive index could occurs. The last thing could result to LSPR peak shift as well as it was observed in [4].

To confirm this assumption the modeling with MiePlot 4.16 Software was carried out. For refractive index of silver (shell) Palik database was used. Core/shell radii of ZnO/Ag structure for modelling were assumed to be 2.5/6.0 nm. Fig. 1 (*a-f*) demonstrates shift of LSPR peak position due to changing of refractive index of zinc oxide core. As can be seem from this figure, principal possibility of proposed assumption was confirmed. However, for complete agreement with experimental results further investigations are required. According to [2, 3] the surface of ZnO nanoparticles has ferromagnetic-like properties while the core remains paramagnetic ones. So, three layers model (paramagnetic core/ferromagnetic surface/silver shell) is required to more accuracy modeling.

This work was supported by the IEEE program "Magnetism for Ukraine".

References

1. Redko, R., V. Shvalagin, G. Milenin, S. Redko and A. Sarikov, Shift of plasmon resonance in silver nanoparticles: effect of magnetic field pre-treatment, Materials Research Express Vol. 11, No. 10, 105012, 2024.
2. Ren, H. and G. Xiang, “Morphology-Dependent Room-Temperature Ferromagnetism in Undoped ZnO Nanostructures”, Nanomaterials Vol. 11, No.12, 3199, 2021.
3. Sundaresan A., and C.N.R. Rao, “Ferromagnetism as a universal feature of inorganic nanoparticles”, Nano Today Vol.

4, No. 1, 96-106, 2009.

4. Anggraeni K., M. Riswan, P.D. Jayanti, D.L. Puspitarum, H. Ardiyanti, P.E. Swastika, N.I. Istiqomah, M. Arifin and E. Suharyadi, “Microstructure, magnetic, and surface plasmon resonance studies of green-synthesized ferrite nanoparticles for biosensor applications”, Journal of Magnetism and Magnetic Materials Vol. 614, 172727, 2025.

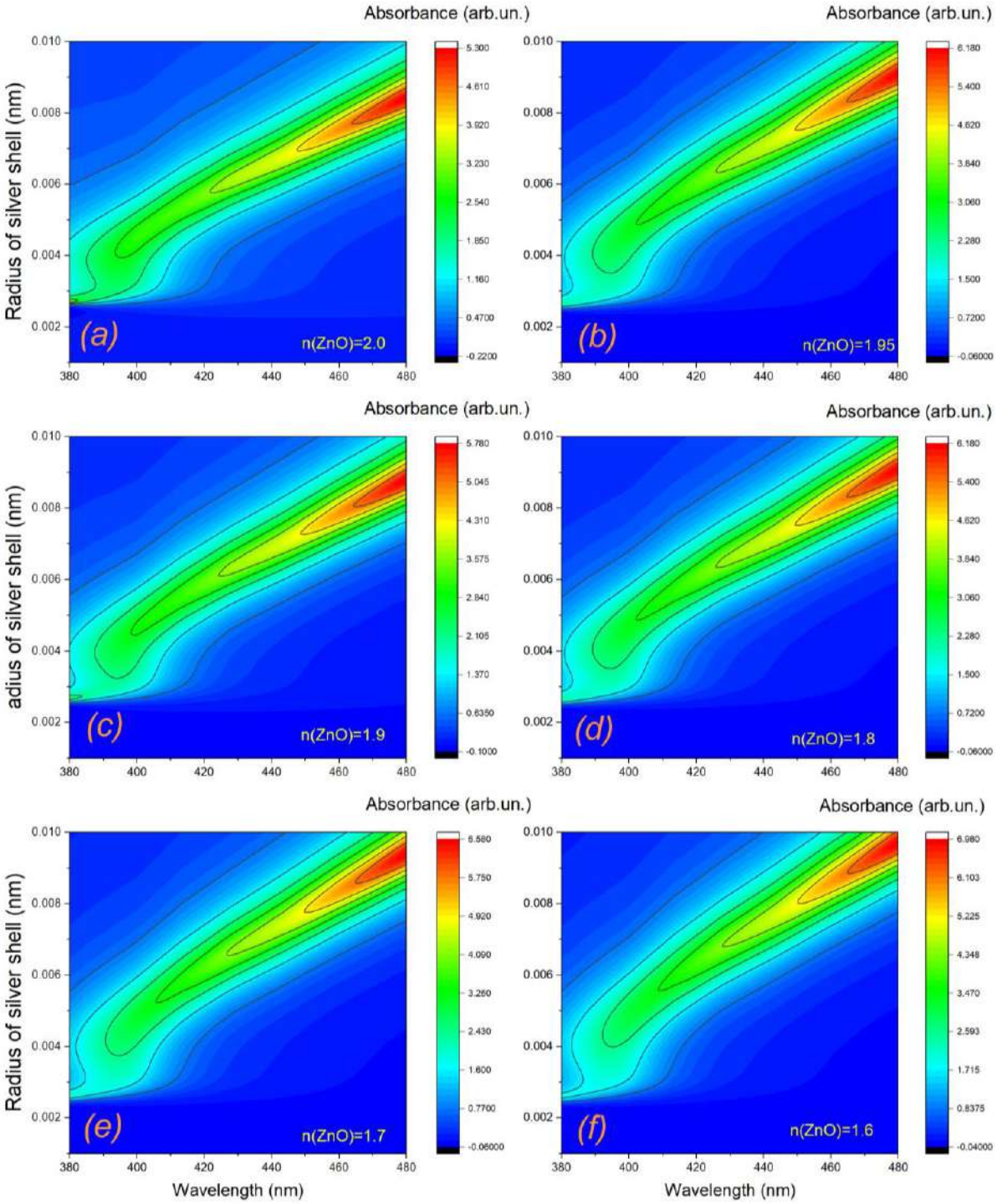


Fig. 1. Maps of modelled absorbance spectra of ZnO/Ag core/shell nanostructures for different refractive index of zinc oxide

Quantum Quasinormal Mode Theory for Dissipative Nano-Optics and Magnetodielectric Cavity Quantum Electrodynamics

L. Meschede[1], D. D. A. Clarke[1], and O. Hess[1*]
[1]School of Physics and CRANN Institute, Trinity College Dublin, Dublin 2, Ireland
Corresponding authors: clarked5@tcd.ie, ortwin.hess@tcd.ie

Abstract: The rapid evolution of nanoscale architectures for cavity quantum electrodynamics has posed crucial challenges for the theory of non-hermitian systems. We introduce a formalism for the quantization of quasinormal modes in the presence of magnetodielectric media, enabling a unified and rigorous approach for simulating photonic, plasmonic and magnonic cavities.

Introduction: Quantum nanophotonics has recently forged a rich nexus of nanotechnology with photonic quantum information processing, offering remarkable prospects for driving quantum technologies down to nanoscale spatial and ultrafast temporal regimes, whilst simultaneously elevating their functionality towards ambient temperatures [1]. In particular, nanoscale architectures for cavity quantum electrodynamics (cQED) are poised to play an instrumental role in next-generation quantum technologies, whereby the confined photonic, plasmonic or magnonic modes of a resonator can become inextricably intertwined with the excitonic, phononic or spin-related excitations of matter, giving rise to a panorama of polaritons and facilitating such quintessential functionalities as single-qubit coherent control, single-photon non-linearities and quantum sensing. The unprecedented pace of experimental progress in this field has placed evermore ambitious demands on the power and predictive scope of theoretical methodologies, where the development of fully quantum dynamic approaches that capture polaritonic effects in three-dimensional (3D), dispersive and non-hermitian, magnetodielectric cQED systems has become imperative.

To this end, we propose a quantum quasinormal mode (QNM) formalism for addressing problems in dissipative nano-optics and magnetodielectric cQED. Our approach offers a unified and rigorous, yet practical simulation methodology for photonic, plasmonic and magnonic cavities interacting with quantum emitters and spin qubits, paving the way towards a fully quantum-mechanical description of such phenomena as quantum nanoplasmonic coherent perfect absorption, lasing in $\mathcal{PT}$-symmetric photonic systems, magnonic strong coupling and cavity-mediated spin-photon interfaces at the nanoscale.

Quantum QNM theory: Our theory is formulated within the framework of macroscopic QED, which describes the quantized electromagnetic field in the presence of arbitrary, 3D, dispersive and lossy, linear media characterized by permittivity $\varepsilon(\mathbf{r},\omega)$ and permeability $\mu(\mathbf{r},\omega)$ distributions. The electric field operator satisfies the equation

$$\nabla\times\mu^{-1}(\mathbf{r},\omega)\nabla\times\hat{\mathbf{E}}(\mathbf{r},\omega)-\frac{\omega^2}{c^2}\hat{\mathbf{E}}(\mathbf{r},\omega)=\mathrm{i}\mu_0\omega\mathbf{j}_{\mathrm{N}}(\mathbf{r},\omega)\ ,\ \hat{\mathbf{E}}(\mathbf{r})=\int_0^\infty \mathrm{d}\omega\,\hat{\mathbf{E}}(\mathbf{r},\omega)\ , \tag{1}$$

with the noise current density

$$\hat{\mathbf{j}}_{\mathrm{N}}(\mathbf{r},\omega)=\omega\sqrt{\frac{\hbar\varepsilon_0}{\pi}}\sqrt{\Im(\varepsilon(\mathbf{r},\omega))}\hat{\mathbf{f}}_{\mathrm{e}}(\mathbf{r},\omega)+\sqrt{\frac{\hbar}{\mu_0\pi}}\nabla\times\left(\sqrt{-\Im(\mu^{-1}(\mathbf{r},\omega))}\hat{\mathbf{f}}_{\mathrm{m}}(\mathbf{r},\omega)\right)\ , \tag{2}$$

which stands in accordance with the fluctuation-dissipation theorem and ensures the preservation of the fundamental commutation relations. The bosonic operators $\hat{\mathbf{f}}_{\mathrm{e}}(\mathbf{r},\omega)$, $\hat{\mathbf{f}}_{\mathrm{m}}(\mathbf{r},\omega)$ correspond to the joint excitations of the electromagnetic-field-dressed media (polaritons) and diagonalize the Hamiltonian of the system. Note that this formula can also be generalized for materials that exhibit amplification in certain domains, in which the creation and annihilation operators switch roles [2]. By utilizing the classical dyadic Green's function $G(\mathbf{r},\mathbf{r},\omega)$, the electric field operator can be formally expressed as

$$\hat{\mathbf{E}}(\mathbf{r}) = \mathrm{i}\mu_0 \int_0^\infty \mathrm{d}\omega\, \omega \int \mathrm{d}^3 r\, G(\mathbf{r},\mathbf{r}',\omega)\hat{\mathbf{j}}_{\mathrm{N}}(\mathbf{r},\omega)\ . \tag{3}$$

To circumvent the large and practically cumbersome continuum of modes, we employ a discrete QNM expansion of the Green's function, ascertained via an auxiliary field eigenvalue technique with a complex coordinate transformation, tantamount to perfectly matched layers (PMLs) [3]. In the classical theory, a complete set of QNM/PML modes $\tilde{\mathbf{E}}_\mu(\mathbf{r})$ is obtained that can be orthogonalized and normalized, and which are capable of reconstructing the Green's function and scattered fields in a compact domain containing the resonator. Inspired by this idea, we can also use effective PML media within the quantum theory, which are themselves magnetodielectric materials with gain components in the 3D case. In this way, radiation losses are converted into material losses within the PMLs, and the regularization of the QNM fields renders feasible their quantization. Although the PMLs are treated like real materials in this approach, which exhibit fluctuations according to Eq. (2), it can be shown that in the unmapped region, all the N-point correlation functions of the electric and magnetic fields are unaltered by the presence of the PMLs and thus the correct quantum dynamics are reproduced. If we use these QNM/PML modes to expand the electric field operator, an effective Hamiltonian for the system can be derived that involves off-diagonal mode coupling terms $\hbar\tilde{\omega}_{\mu\nu}\hat{a}_\mu^\dagger\hat{a}_\nu$ and the usual coupling of the modes to a continuum of bath modes, where all the coupling coefficients can be calculated directly from the electromagnetic properties of the system. From that point, standard methods and approximations for treating dissipative cQED systems, like the derivation of Langevin and master equations in the presence of few-level emitters and spin qubits, can be used to establish a fully time-dependent quantum treatment.

Conclusions: Commencing from macroscopic QED, we have introduced a formalism for the quantization of QNMs in the presence of dissipative magnetodielectric media, enabling a unified and rigorous approach for simulating photonic, plasmonic and magnonic cQED phenomena.

Acknowledgments: The authors gratefully acknowledge funding from Research Ireland (formerly Science Foundation Ireland) via Grants No. 18/RP/6236 and 22/QERA/3821.

References

1. Clarke, D. D. A., O. Hess, "Near-field strong coupling and entanglement of quantum emitters for room-temperature quantum technologies", *PhotoniX*, Vol. 5, No. 1, pp. 33–41, 2024.

2. Raabe, C., D. G. Welsch, "QED in arbitrary linear media: Amplifying media", *Eur. Phys. J.: Spec. Top.*, Vol. 160, No. 1, pp. 371–381, 2008.

3. Yan, W., R. Faggiani, and P. Lalanne, "Rigorous model analysis of plasmonic nanoresonators", *Phys. Rev. B*, Vol. 97, No. 20, pp. 205422(1)–(10), 2018.

Large Purcell Enhancement with High-Quality Factor in Dielectric Nanoantenna-Microtoroid Structure

Zihan Mo[1], Yali Jia[1*], Xinchen Zhang[1], Yu Tian[1], and Ying Gu[1,2*]

[1]State Key Laboratory for Mesoscopic Physics, Department of Physics, Peking University, Beijing 100871, China
[2] Hefei National Laboratory, Hefei 230088, China
[*]corresponding author: ygu@pku.edu.cn

Abstract: By combining the advantages of the high-quality factor of microtoroids and the ultra-small mode volume of a nanoantenna, we theoretically achieve large Purcell enhancement with narrow linewidth in dielectric nanoantenna-microtoroid structure.

1. Introduction

Single-photon sources with high emission rates are crucial components of rapidly developing on-chip quantum devices. Enhancing the Purcell effect at the single quantum level contributes to improving the performance of single-photon sources. Meanwhile, the high-quality characteristic of spontaneous emission spectrum facilitates the realization of single-photon emission. However, it is difficult to meet the above two requirements at the same time. Dielectric structures with high refractive index and low loss have been developed through the theory of Mie resonance, which confines the electric or magnetic field inside and around the nanostructure. Although dielectric nanostructures own a small mode volume, the great scattering losses limit their applications. The high-Q whispering gallery microcavities (WGMs) ultra-localize the cavity's electric field, resulting in an extremely narrow spontaneous emission spectrum. Unfortunately, the Purcell factors of WGMs based on dielectric materials are only tens to hundreds due to the large mode volume. In order to achieve Purcell enhancement with high-quality factor, the idea of designing hybrid micro-nano structures has been considered. The dielectric nanoantenna has a small mode volume and no absorption loss, but the photons are scattered around and difficult to collect. The WGMs localizing the electric field excellently are expected to build a natural photon collection channel for nanoantenna to guide the scattered photons into the WGMs. Thus, it is possible to achieve high-Q Purcell enhancement in low-loss dielectric hybrid structures.

2. Model & Results

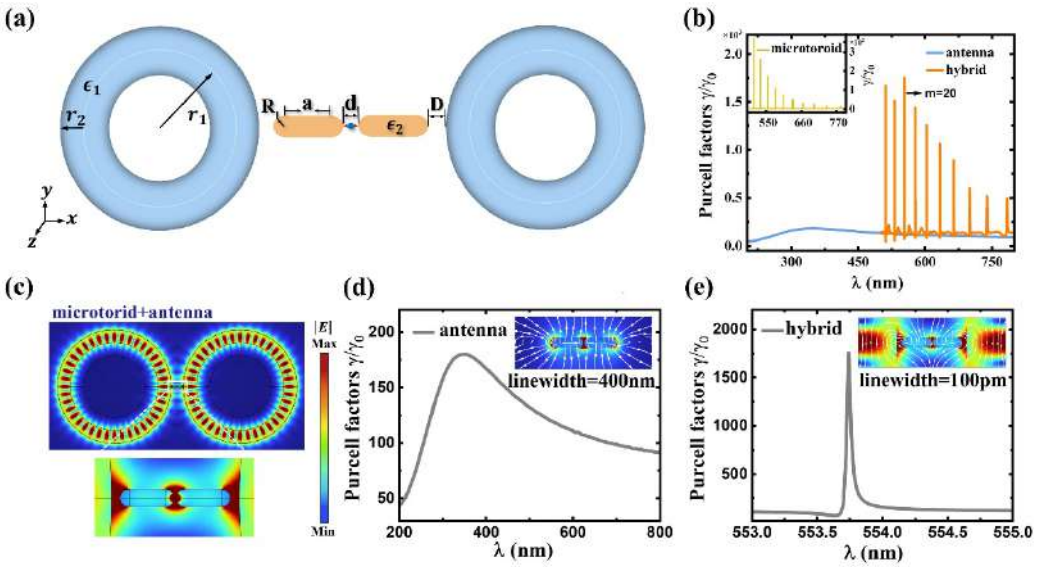


Fig. 1. (a) The schematic of the dielectric nanoantenna-microtoroid structure. The x-polarized quantum emitter is located at the center of the nanoantenna. (b) The Purcell factor of single dielectric nanoantenna and hybrid structure. Inset: the Purcell factor of single microtoroid. (c) The electric field of the xy plane (wavelength at 553.74 nm) in the hybrid structure when the azimuthal mode number m = 20. (d) The linewidth of the spontaneous emission spectrum for the single dielectric nanoantenna. Inset is the electric field and energy flow diagram of the nanoantenna. (e) The linewidth of the spontaneous emission spectrum for the hybrid structure at azimuthal mode number m=20. Inset is the partial electric field and energy flow diagram of the hybrid structure.

The schematic diagram of the proposed system is shown in Fig. 1(a), where the dielectric nanoantenna is coupled to the microtoroids through a nanoscale gap $D = 20nm$. Two WGMs are both microtoroids of $r_1 = 1000nm$ and $r_2 = 300nm$. The dielectric constant of the microtoroids is $\varepsilon_1 = 3.13$, which can be made by Al_2O_3 material. A dielectric nanoantenna with radius $R = 20nm$, length $a = 80nm$, gap $d = 5nm$, and dielectric constant $\varepsilon_2 = 12$ is inserted between two microtoroids, and its material can be considered as GaP. Then, an x-polarized quantum emitter is placed into the gap of the nanoantenna. The local field at ends of the nanoantenna is coupled with the evanescent field of microtoroids, so that the photons originally scattered are bound in the microtoroids [Fig. 1(c)]. It can be seen from the electric field diagram of Fig. 1(c) that the whispering gallery mode in the hybrid structure is still well maintained.

As shown in Fig. 1(b), the large Purcell enhancement has been achieved in dielectric nanoantenna-microtoroid structure. The maximum Purcell factor γ/γ_0 can reach 1752 at the azimuthal mode number of microtoroids m=20. Compared to the Purcell factors of 155 for single GaAs microdisk, 580 for microtoroid, and 47 for silicon nanoantenna arrays, we demonstrate a significant enhancement in the spontaneous emission rate. For the azimuthal mode number m ranging from 15 to 22, the Purcell factors of the hybrid structure are all greater than 500. A single dielectric nanoantenna achieves a maximum Purcell factor of only 180 when the emitter is located in the gap. For the bare whispering gallery mode at wavelength 500-800 nm [inset in Fig. 1(b)], when the emitter is placed close to the outer surface, the maximum Purcell factor reaches 372. Therefore, we can achieve stronger emission enhancement in the hybrid structure than individual dielectric nanoantenna or dielectric microtoroids.

For high-performance single-photon sources, the spontaneous emission spectrum also exhibits high-Q characteristic to facilitate practical applications. In our mechanism, the linewidth of the nanoantenna is reduced from hundreds of nanometers to the order of hundreds of picometers in the hybrid structure [Fig. 1(d), Fig. 1(e)]. The photons are difficult to collect and utilize in a single nanoantenna [inset in Fig. 1(d)], which leads to the broadening of the spontaneous emission spectrum. In the hybrid structure, the microtoroid alters the electromagnetic environment around the nanoantenna, which creates a natural photon collection channel for the scattered photons from the nanoantenna. As shown in the energy flow line of the inset in Fig. 1(e), the scattered photons can be guided into the microtoroids. The narrowed linewidth of the spontaneous emission spectrum is conducive to the realization of single photon emission.

3. Conclusion

In this work, we theoretically demonstrate large Purcell enhancement with high-quality factor in dielectric nanoantenna-microtoroid structure.

References

1. Z. Mo, Y. Jia, X. Zhang, Z. Tian, Y.Tian, and Y. Gu, "Large Purcell Enhancement with Narrow Linewidth in All-Dielectric Nanoantenna-Microtoroid Structures," Revised to Chin. Opt. Lett.

New Materials for Photonics (Graphene, MoS2, WS2, etc

On-chip Refractive Index Sensors in 200 mm Wafer Silicon Technology

S. Reiter[1], A. Sengül[1], C. Mai[2], C. Alvarado Chavarin[2], C. Wenger[2], I. A. Fischer[1,*],

[1]BTU Cottbus-Senftenberg Experimentalphysik und funktionale Materialien, Erich-Weinert-Straße, 03046 Cottbus, Germany,
[2]IHP - Leibniz Institut für innovative Mikroelektronik, Im Technologiepark 25, 15236 Frankfurt (Oder), Germany
[*]corresponding author: inga.fischer@b-tu.de

Abstract: We present electrooptical characterization results for Ge photodetectors with TiN nanohole arrays as miniaturized sensors for the detection of refractive index changes. Fabrication was carried out in cost-effective CMOS compatible 200 mm wafer Si technology.

Integrated biosensors have potential applications ranging from agriculture to personalized medical diagnostics. Commercial plasmonic biosensing predominantly relies on external instruments, such as microscopes or spectrometers, which limits miniaturization. This challenge can be addressed with on-chip refractive index (RI) sensors that employ plasmonic nanostructures for compact sensing approaches. Specifically, the integration of plasmonic nanohole arrays (NHAs) with Ge photodetectors constitutes a promising device concept [1], which can potentially be realized on the cost-effective silicon platform. In these devices, changes in the RI of a medium adjacent to the NHAs are directly converted to electrical signals, i.e. photocurrent variations. Compared to the realization of a proof-of-concept device [1], transitioning the device concept to large-scale production necessitates modifications for compatibility with CMOS manufacturing processes, introducing additional constraints in fabrication and design [2, 3].

Here, we present results of the electrooptical characterization of on-chip refractive index sensors for the detection of RI changes. Fabrication was carried out in CMOS compatible 200 mm wafer Si technology. In our devices, plasmonic NHAs made from sputtered TiN are combined with Ge photodetectors for an operating wavelength range between 1200 and 1550 nm. We present optical characterization results for the plasmonic NHAs alone as well as responsivity spectra of the on-chip RI sensors, with devices submerged in different liquids for the detection of changes in bulk RI (Fig. 1). In our devices, plasmonic resonances induced in the TiN NHA lead to dips and peaks in the responsivities of the Ge photodetectors. A change in refractive index of the liquid above the nanohole array can be seen to induce peak shifts as a result of changes in the optical properties of the NHA. In simulation, the transmission through the TiN NHA is calculated using the commercial FDTD simulation software Ansys Lumerical and the sensor responsivity is then obtained by multiplying the result with responsivity spectra obtained from a reference device without the NHAs [1]. While there are qualitative differences between simulation and experimental results, the sensitivity is well reproduced by simulation results and exceeds 900 nm/RIU. Large damping in TiN leads to broadening of resonances, we present strategies to modify the NHAs in order to improve sensing performance together with first experimental results.

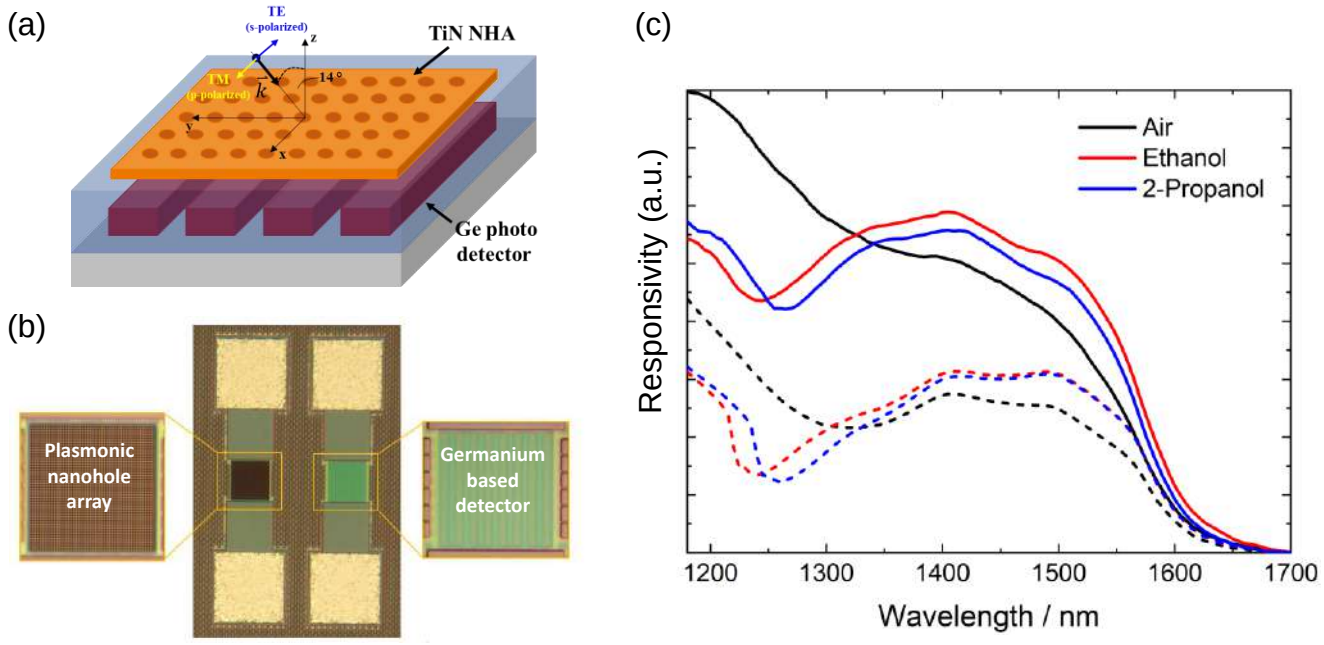


Fig. 1 (a) Schematic view of the device concept [3] (b) Microscope images of the devices with and without TiN nanohole arrays (c) device responsivities in air and submerged in liquids with different refractive indices ($n_{Ethanol}$ = 1.353 and $n_{2\text{-}Propanol}$ = 1.369) obtained from simulation (dashed lines) and experiment (solid lines).

Our results indicate that integrating NHAs with Ge photodetectors is an interesting approach for on-chip RI sensing, achievable with standard industrial manufacturing techniques, and we report performance metrics such as sensor resolution. Our work can be a starting point for the development of cost-efficient on-chip RI sensors on the silicon platform.

The authors would like to thank the financial support by the Federal Ministry of Education and Research of Germany under grant numbers 16ES1131 and 16ES1128 K.

References

1. Augel, L., Kawaguchi, Y., Bechler, S., Körner, R., Schulze, J., Uchida, H., and Fischer, I.A., "Integrated Collinear Refractive Index Sensor with Ge PIN Photodiodes," ACS Photonics, Vol. 5, 4586–4593, 2018.
2. Reiter, S., Han, W., Mai, C., Spirito, D., Jose, J., Zöllner, M., Fursenko, O., Schubert, M. A., Stemmler, I., Wenger, C., and Fischer, I. A., "Titanium Nitride Plasmonic Nanohole Arrays for CMOS-Compatible integrated refractive index sensing: influence of layer thickness on optical properties," Plasmonics, Vol. 18, 831–843, 2023.
3. Mai, C., Peczek, A., Kroh, J., Jose, J., Reiter, S., Wenger, C., Fischer, I. A., "Towards a CMOS compatible refractive index sensor: cointegration of TiN nanohole arrays and Ge photodetectors in a 200 mm wafer silicon technology," Optics Express, Vol. 32, 29099-29111, 2024.

Tunable impedance matching layer based on piezoelectric materials with external circuits

Han Jia[1*], and Yuzhen Yang[1]

[1] Institute of Acoustics, Chinese Academy of Sciences, Beijing 100190, People's Republic of China
[*]corresponding author: hjia@mail.ioa.ac.cn

Abstract: A tunable impedance matching layer is designed and fabricated. It is composed of periodical piezoelectric disks with shunting capacitors. An external digital control system is introduced to adjust the effective acoustic impedance of the PZT disks through digital potentiometers and microprogrammed control unit, enabling digital manipulation of wave transmission.

In this work, a digital metalayer is designed to control the elastic wave transmission. The schematic diagram of the proposed digital metalayer is illustrated in Fig. 1. The digital metalayer consists of eight PZT disks, and each disk is connected to a corresponding external electric impedance Z. The metalayer as a tunable medium is inserted between two rods to form a digital wave transmission control system.

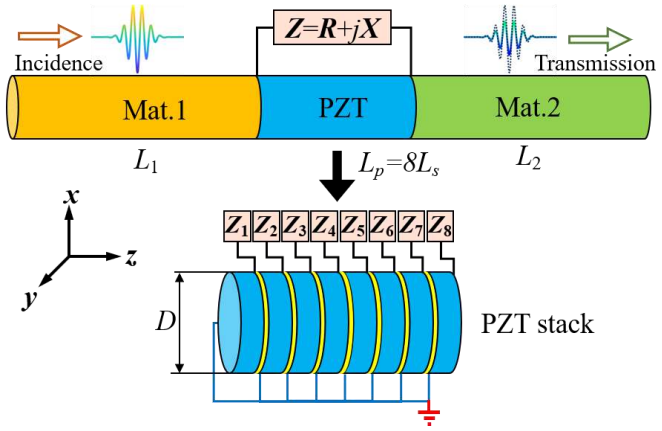


Fig. 1 The schematic diagram of the transmission energy control by the interlayer PZT stack with PSCs.

The amplitude modulation of the transmitted waves versus C_e (external electric impedance) around 30kHz and 60kHz are measured and shown in Figs. 2(a) and 2(b), respectively. Here, the incident signals are Gaussian pulses with a narrow bandwidth of 2kHz. It can be seen that the amplitudes are obviously affected by C_e for both measurements. In order to exhibit clearly the effect of the external capacitance C_e on the wave energy transmission, the curves of transmitted amplitude versus frequency with different values of C_e are shown in Figs. 2(c) and 2(d). The value of C_e is adjusted from -8.5nF to 7.35nF. The 'Wo' represents the case that SS and PMMA rods are bonded directly without the digital metalayer, while the 'Op' represents the case that the PZT disks are in the open-circuit state. It can be observed that the max values of the 'Op' curves are over three times than those of the 'Wo' curves at 30kHz and 60kHz. Since the initial acoustic impedance of the PZT disk is between SS and PMMA, the wave transmission energy increases when the PZT disks are inserted. When the SCCs connect with the PZT disks, the transmitted amplitudes can be further adjusted by the digital wave transmission control system. Compared with 'Op' curves at 30kHz and 60kHz, the max values of transmitted amplitudes increase about 35% when $C_e = -0.86\text{nF}$. The transmitted amplitudes can also be turned down by the same system. The min values

of transmitted amplitudes are almost 45% of the 'Op' curves when $C_e = -1.0\text{nF}$. The digital metalayer has an excellent adjustment capacity in wave energy transmission at both 30kHz and 60kHz.

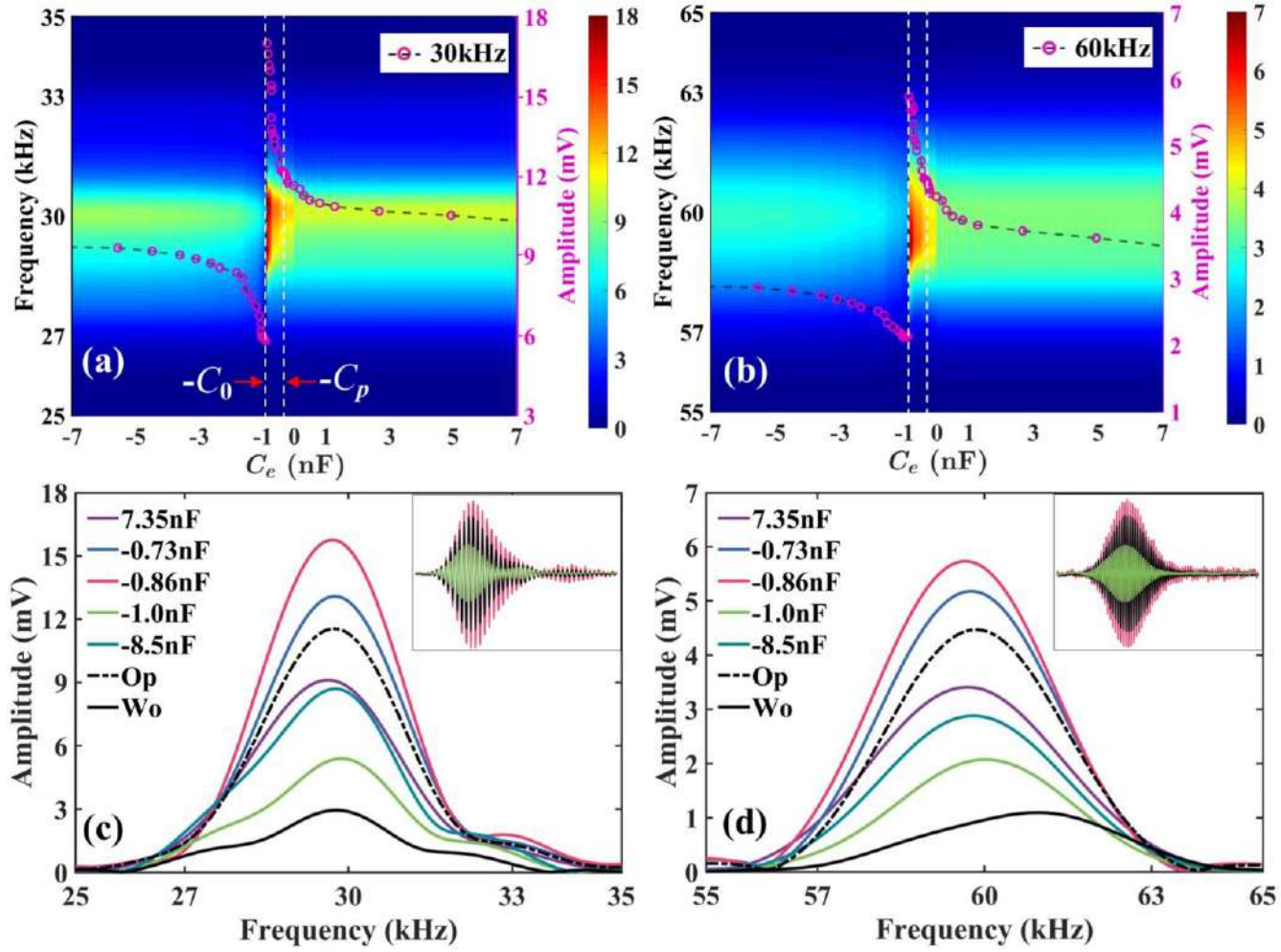


Fig. 2 Transmission spectra and curves of 30kHz and 60kHz with the external capacitance C_e.

References

1. Hong, G. F., Jia, H., Yang, Y., Yang, Y. H., Yang, Y. Z., Yang, J. and Yuan, X. J "Title of the journal paper" J. Appl. Phys. , Vol. 136, 144503, 2024.
2. Wu, J. E., Yang, Y. Z., Jia, H., Xu, X. Y., Yang, J., He, Z. J., and Deng, K "A tunable gradient impedance matching layer based on piezoelectric materials with external circuits," J. Appl. Phys. , Vol. 128, 064502, 2020.

Side-Coupled Fabry-Perot based on Multi-Slot Subwavelength Grating Metamaterials for Sensing Applications

S. Hadi Badri[1,2], Artem S. Vorobev[1,2], Liam O'Faolain[1,2]

[1]Centre for Advanced Photonics and Process Analysis, Munster Technological University, T12 P928, Cork, Ireland

[2]Tyndall National Institute, Lee Maltings, Dyke Parade, T12 R5CP, Cork, Ireland

[*]corresponding author: hadi.badri@mtu.ie

Abstract: We present a highly sensitive side-coupled Fabry-Perot (FP) photonic sensor with multi-slot subwavelength grating (SWG) metamaterials, which enhances light-matter interaction through strong optical confinement in slot regions. The sensor, fabricated on a silicon-on-insulator (SOI) platform, exhibited a measured sensitivity of 520 nm/RIU when tested with NaCl solutions of varying concentrations. The SWG-based mirrors feature a broadband photonic bandgap, enhancing the sensor's versatility and making it a promising platform for biochemical sensing, environmental monitoring, and chemical analysis.

1. Introduction

Silicon photonic sensors on SOI platforms provide compact, cost-effective, and high-performance solutions for sensing. Their CMOS compatibility enables full integration, supporting portable lab-on-a-chip systems for point-of-care and home healthcare. Incorporating subwavelength grating (SWG) metamaterials into photonic sensors significantly enhances sensitivity by increasing optical field overlap with the analyte, making SWG-based sensors highly promising [1, 2].

This work focuses on an FP-based photonic sensor employing a multi-slot SWG structure, where strong optical field confinement in slot regions boosts light-matter interaction and enhances sensing performance. Additionally, the SWG-based mirrors exhibit a broadband photonic bandgap, improving sensor robustness and allows for the detection of various analytes, making the design adaptable for different sensing applications.

2. Device Design and Working Principle

The sensor structure, depicted in Fig. 1, consists of a side-coupled FP cavity with a multi-slot SWG metamaterial configuration. SWGs are created by periodically interleaving the silicon core with low-index materials. When the period ($P_{SWG,x}$) is much smaller than the operating wavelength, the structure

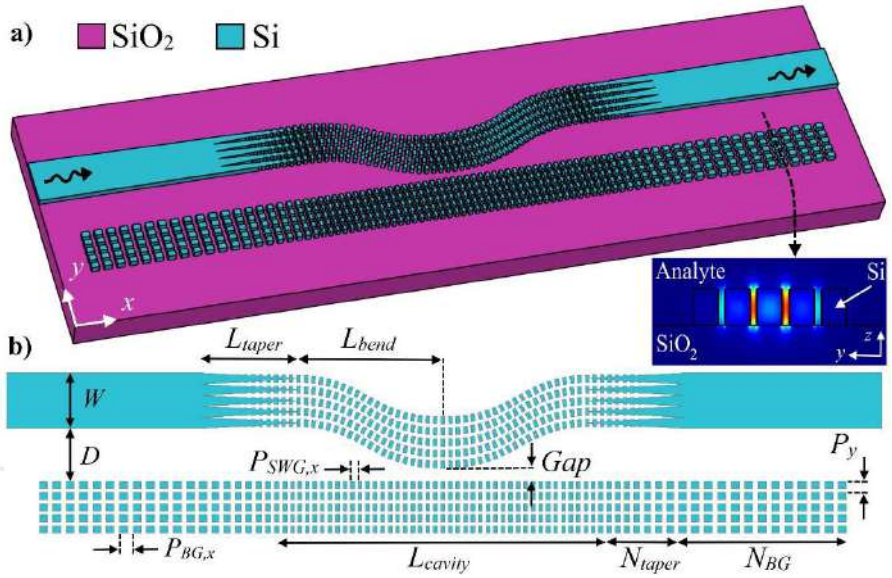


Fig. 1 a) 3D schematic and b) top-view of the sensor. Electric field distribution illustrates strong mode confinement in slots.

behaves as a lossless homogeneous medium, as diffraction and reflection effects are negligible. However, for larger periodicities ($P_{BG,x}$), the structure enters the Bragg reflection regime, creating mirrors in the FP cavity [3]. The designed SWG mirrors possess a broadband photonic bandgap, which enhances reflection across a wide range of wavelengths. This broader spectral coverage increases sensor flexibility, allowing it to function effectively across different operating wavelengths and detect a variety of analytes with improved stability. The optical mode distribution shows strong confinement in the slots, enhancing light-matter interaction and sensor sensitivity. To optimize mode matching and reduce insertion loss, tapers were employed. The geometrical parameters of the fabricated device are P_y=450 nm, $P_{BG,x}$=490 nm, $P_{SWG,x}$=250 nm, N_{BG}=500, N_{taper}= 100, L_{taper}=21 µm, L_{bend}= 110 µm, L_{cavity}= 62.5 µm, *Gap*= 400 nm, W=2.25 µm, and D= 13.8 µm. The gap between the slots in the y-axis is fixed to 100 nm.

3. Experimental Results

The photonic structure was fabricated on a 220 nm-thick silicon layer atop an 8 µm-thick SiO_2 insulator. Patterning was performed using electron beam lithography, followed by inductively coupled plasma etching. The sensor was tested by placing a drop of deionized (DI) water on its surface. The corresponding transmission spectrum, illustrating the sensor's broadband response, is shown in Fig. 2(a). Subsequently, NaCl solutions with concentrations of 5, 10, and 20 mg/mL were applied, and the transmission spectra were recorded, as shown in Fig. 2(b). The key performance metrics of a refractive index sensor include sensitivity (S) and limit of detection (LOD). Our sensor achieved a sensitivity of $S=\Delta\lambda/\Delta n$=520 nm/RIU, determined by the ratio of the resonance wavelength shift ($\Delta\lambda$) to the corresponding refractive index change (Δn). The quality factor, defined as $Q=\lambda_{res}/FWHM$, where $FWHM$ is the full-width at half maximum, was measured to be Q=4200. The smallest detectable refractive index change is calculated as $LOD=FWHM/S$ and was found to be $LOD=7.1\times10^{-4}$ RIU.

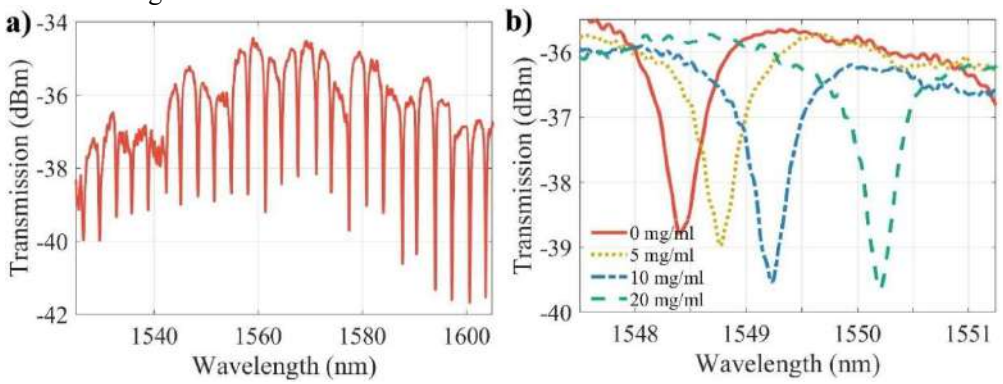


Fig. 2. Transmission spectrum for a) DI water and b) varying NaCl concentrations.

4. Conclusion

This work demonstrates a highly sensitive photonic sensor based on a side-coupled FP cavity with multi-slot SWG metamaterials. The strong field confinement in the slot regions enhances light-matter interaction, leading to an experimental sensitivity of 520 nm/RIU. This result highlights the potential of the proposed sensor for applications in biochemical sensing, environmental monitoring, and lab-on-chip systems.

5. Acknowledgment

This publication has emerged from research funded by Research Ireland through the postdoctoral fellowship held by S.H.B., under project ID: GOIPD/2024/774. The authors also acknowledge financial support from Research Ireland through research centre IPIC, 12/RC/2276_P2.

References

[1] W. Cheng, S. Ye, B. Yuan, J. H. Marsh, and L. Hou, "Subwavelength grating cascaded microring resonator biochemical sensors with record-high sensitivity," *ACS photonics,* vol. 11, no. 8, pp. 3343-3350, 2024.

[2] S. H. Badri, "Transmission resonances in silicon subwavelength grating slot waveguide with functional host material for sensing applications," *Optics & Laser Technology,* vol. 136, p. 106776, 2021.

[3] P. Cheben, R. Halir, J. H. Schmid, H. A. Atwater, and D. R. Smith, "Subwavelength integrated photonics," *Nature,* vol. 560, no. 7720, pp. 565-572, 2018.

On-Chip Lasers on Waveguides: A Meta-Morphosis in Waveguide Imaging!

Oliver Olsson[1*], Khosro Zangeneh Kamali[1], Erik Strandberg[2], Hana Šípová-Jungová[1], and Mikael Käll [1*]

[1]Department of Physics, Chalmers University of Technology, 412 96, Gothenburg, Sweden
[2] Department of Microtechnology and Nanoscience, Chalmers University of Technology, 412 96 Gothenburg, Sweden
[*]corresponding author: ooliver@chalmers.se, mikael.kall@chalmers.se

Abstract: Scattering-based microscopy with an evanescent field enhances signal-to-noise by suppressing background. Waveguides generate evanescent waves, but edge-coupling of light is difficult to use. Bonding a VCSEL to a waveguide platform enables an easy coupling via a grating coupler. Integrating a metasurface into the VCSEL tilts emission, improving waveguide excitation.

Scattering-based microscopy offers an alternative to conventional fluorescence microscopy [1] with certain configurations achieving super-resolution through techniques like structured illumination [2] or coherent light [3]. Compared to fluorescence, scattering microscopy has several advantages: 1) it is *label-free*, there is need for fluorescent tags; 2) it allows unlimited experiments, as it does not suffer from photobleaching; and; 3) it avoids saturation effects that limit fluorophore-based detection rates [4].

To suppress the background and only collect the scattered light, darkfield imaging (DF) and total internal reflection (TIR) are frequently used. In TIR, an *evanescent field* is generated which induces scattering from the object. Another way to achieve evanescent fields is to couple the excitation light to a waveguide. Multiple configurations have been realized using materials such as silicon dioxide and a polymer [5], microscope slides [6], or silicon nitride [7]. However, existing platforms rely on external lasers for end-coupling into the waveguide, making them complex to operate and more susceptible to external disturbances.

Integrating a laser directly onto a waveguide enables the fabrication of a fully on-chip illumination source. This approach eliminates the need for additional equipment and creates a scattering-based TIR illumination platform compatible with standard microscopes.

Vertical cavity surface emitting lasers (VCSELs) are well-suited for integrated photonics due to their high conversion efficiency and the ability for wafer-scale testing. However, perfectly vertical illumination from a VCSELs onto a grating coupler compromises efficiency [8]. To improve this, the light needs to strike the grating coupler at an angle. Tilting the VCSEL package can create this angle, but it comes at the cost of flatness and wafer scalability [9].

A promising solution to achieve the desired coupling angle is to directly inscribe a metasurface onto the VCSEL's substrate. This configuration maintains high coupling efficiency without sacrificing scalability or flatness. A concept image can be viewed in Figure 1.

VCSELs have also recently been used in label-free imaging in both darkfield and TIR modalities, where a monolithically integrated metasurface deflects the beam at a high angle, enabling the application [10]. Building on this, we are now expanding the concept by coupling VCSEL light into a silicon nitride waveguide, providing more uniform illumination with ultralow background noise and a wider field of view.

This work was funded by the Knut and Alice Wallenberg Foundation and performed in part at Myfab Chalmers.

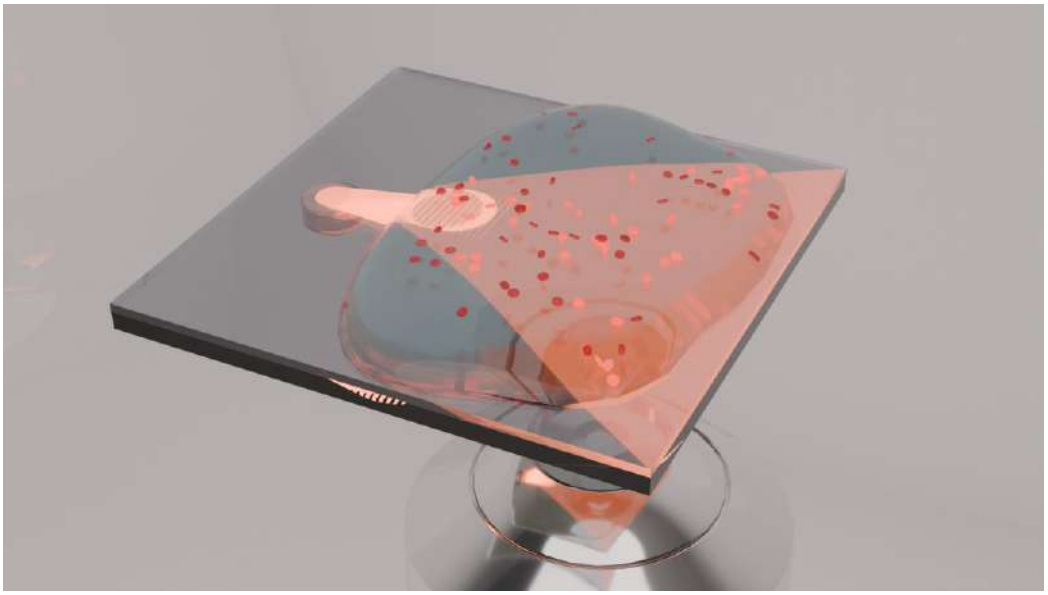


Figure 1 Concept image of a VCSEL with a metasurface illuminating a grating coupler with an angle. the grating couple light into a planar waveguide.

References

1. Astratov, V.N., et al., *Roadmap on Label-Free Super-Resolution Imaging.* Laser & Photonics Reviews, 2023. **17**(12): p. 2200029.
2. Heintzmann, R. and T. Huser, *Super-Resolution Structured Illumination Microscopy.* Chemical Reviews, 2017. **117**(23): p. 13890-13908.
3. Jünger, F., P.V. Olshausen, and A. Rohrbach, *Fast, label-free super-resolution live-cell imaging using rotating coherent scattering (ROCS) microscopy.* Scientific Reports, 2016. **6**(1): p. 30393.
4. Priest, L., J.S. Peters, and P. Kukura, *Scattering-based Light Microscopy: From Metal Nanoparticles to Single Proteins.* Chemical Reviews, 2021. **121**(19): p. 11937-11970.
5. Agnarsson, B., et al., *Evanescent Light-Scattering Microscopy for Label-Free Interfacial Imaging: From Single Sub-100 nm Vesicles to Live Cells.* ACS Nano, 2015. **9**(12): p. 11849-11862.
6. Yang, S., et al., *Waveguide-based microscope slide for label-free high-resolution imaging.* Applied Physics Letters, 2024. **125**(6).
7. Helle, Ø.I., et al., *Structured illumination microscopy using a photonic chip.* Nature Photonics, 2020. **14**(7): p. 431-438.
8. Goyvaerts, J., et al., *Enabling VCSEL-on-silicon nitride photonic integrated circuits with micro-transfer-printing*. Optica, 2021. **8**(12): p. 1573.
9. Jahed, M., et al., *Angled Flip-Chip Integration of VCSELs on Silicon Photonic Integrated Circuits.* Journal of Lightwave Technology, 2022. **40**(15): p. 5190-5200.
10. Juodėnas, M., et al., *High-angle deflection of metagrating-integrated laser emission for high-contrast microscopy.* Light: Science & Applications, 2023. **12**(1).

Excitation of multiple Fano resonances through broadband oblique-wire-bundle metamaterial absorbers and targeted molecules

Kai-Lin Hsiao[1] and Tsung-Yu Huang[1,*]
[1]Department of Materials Engineering, Ming Chi University of Technology, New Taipei, Taiwan
[*]corresponding author: huang.tsungyu@mail.mcut.edu.tw

Abstract: To improve the absorption sensitivity of sensors, we have studied the absorption interaction with multiple functional groups in the sample through oblique wire bundle (OWB) metamaterial absorber with molecular functional groups' absorption. We developed four Fano resonances with three PMMA functional groups and one carbon functional group for better sensitivity.
Keyword: oblique-wire-bundle (OWB), metamaterial absorber, Fano resonance.

1. Introduction

To detect ingredients from an unknown sample with higher sensitivity and specificity is crucial especially regarding food safety and chemical detection. To achieve such a goal, a detection method without labelling procedure should be developed. There appeared many different techniques for detection of chemical structures such as mass spectroscopy, nuclear magnetic resonance spectroscopy, infrared spectroscopy, Raman spectroscopy, etc., and infrared absorption and Raman scattering provide footprints of compositions of a sample and are both applied in so many different fields such as bio-, chemical- and gas-sensors. Besides, signals from both the two methods could be further enhanced through surface modification, also known as surface enhanced infrared absorption (SEIRA)[1–3]and surface enhanced Raman scattering (SERS)[4–6]. Among these different methods, one promising kind of SEIRA is to couple a narrow absorption band from molecules' vibration modes to a broadband absorption often introduced by a metamaterial for excitation of Fano resonance that revealed high quality resonance, extended interaction time due to slow group velocity and spectrum reversal for a better signal to noise ratio.

In this work, we designed an oblique wire bundle (OWB) metamaterial absorber on substrate. There is a 150-nanometer-thick layer of aluminum and an MgF_2 seed layer. Through advanced electron beam lithography technology and electron gun evaporator, in the experiment, MgF_2 presents a shape of a rectangular frustum due to the undercutting of the resist during the lithography process. The sample was then placed on the platform of an electron gun evaporator with a tilt angle of 86 degrees to ensure a coverage length of 1430 nm, ensuring that the metal nanowires only grew on top of the seed layer during deposition. Since the OWB metamaterial absorber has a broadband absorption spectrum, we expect that the OWB metamaterial absorber can exhibit a strong Fano resonance, and for comparison, **Figure 1** depicts the scheme and the absorbance spectra of the OWB and planar metamaterial absorbers at x- and y-polarized incidence. The OWB metamaterial absorber has a bandwidth of up to 111 THz (69 to 180 THz) in the x-polarization range of 100 to 180 THz, and a wider bandwidth in the y-polarization range. In contrast, the planar metamaterial has an absorption peak of 0.6 with a bandwidth of 15.65 THz under x-polarization. It is worth pointing out that the small peak/valley metamaterial absorber at 70.5 THz frequency in the OWB and planar spectra can be attributed to the stretching vibration mode of C=O in CO_2. Here, there is an absorption peak in the spectrum of an OWB metamaterial absorber, but there is an absorption dip in the spectrum of a planar absorber, which may originate from the background and the changes in the CO_2 concentration measured by the device. Nevertheless, due to the larger hot spot area and stronger field enhancement, the OWB metamaterial absorber enhances the modes vibrating from CO_2, resulting in stronger absorption compared to the planar metamaterial absorber.

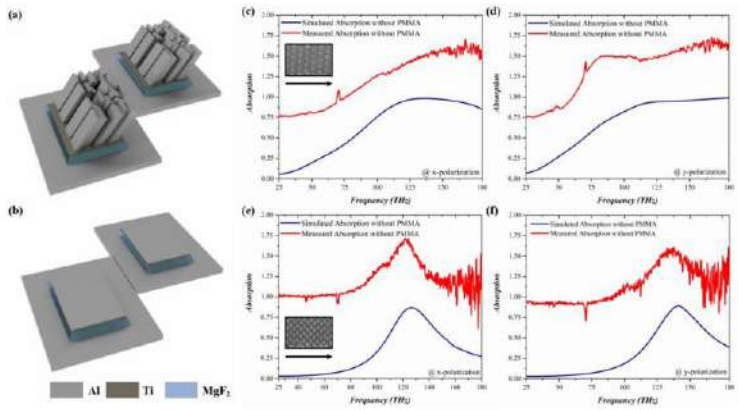


Figure 1. Schemes of (a) an oblique wire bundle (OWB) and (b) planar metamaterial absorbers. Measured and simulated absorption spectra of (c, d) oblique wire bundle (OWB) and (e, f) planar metamaterial absorbers.

From the blue curve in **Figure 2**, it can be seen that the OWB metamaterial absorber favors the Fano resonance of all four vibration modes, and the line shapes are clearly asymmetric, which indicates the Fano resonance; in addition, the signal is stronger at y-polarization incidence, at 88.5 and 90 THz compared with that at x-polarization incidence, which is evidence of the better enhancement of the y-polarization. On the other hand, the planar metamaterial absorber exhibits Fano resonance only for the strongest vibrational mode with the least damping, i.e., the O = C = O stretching mode of CO_2, and only a superposition of absorption for the other three modes. Nevertheless, planar metamaterial absorbers can improve the absorption compared to PMMA absorbers.

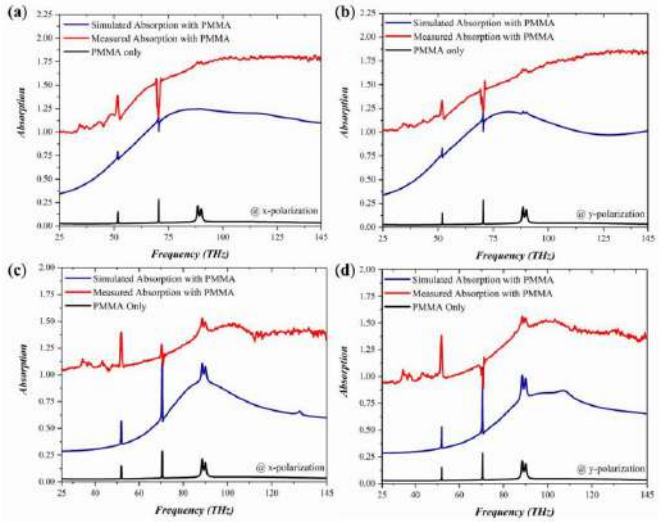


Figure 2. Measured and simulated absorption spectra of the (a, b) OWB and (c, d) planar metamaterial absorbers under the x- and y-polarizations with PMMA. The OWB metamaterial absorber could couple to all the four molecular vibration modes and developed Fano resonance while the planar metamaterial absorber could only couple to the vibrational mode of CO_2 with a superposition behaviour for all the other three modes from PMMA.

References

1. Autore, M. et al. Boron Nitride nanoresonators for phonon-enhanced molecular vibrational spectroscopy at the strong coupling limit. Light Sci. Appl. 7, 17172 (2018).
2. Dayal, G., Chin, X. Y., Soci, C. & Singh, R. High-Q Plasmonic Fano Resonance for Multiband Surface-enhanced infrared absorption of Molecular Vibrational sensing. Adv. Opt. Mater. 5, 1600559 (2017).
3. Lin, C. T., Yen, T. J. & Huang, T. Y. PVC Detection through a hybrid SEIRA substrate and refractive Index Sensor based on Metamaterial Perfect absorbers. Coatings. 11, 789 (2021).
4. Lee, B. S., Lin, D. Z. & Yen, T. J. A Low-cost, highly-stable surface enhanced Raman scattering substrate by Si Nanowire Arrays Decorated with au nanoparticles and au backplate. Sci. Rep. 7, 4604 (2017).
5. Wang, H., Kundu, J. & Halas, N. J. Plasmonic nanoshell arrays combine surface-enhanced vibrational spectroscopies on a single substrate. Angew. Chem. Int. Ed. 46, 9040–9044 (2007).
6. Fan, X. et al. Three-dimensional SERS sensor based on the sandwiched G@AgNPs@G/PDMS film. Talanta. 233, 122481 (2021).
7. Durmaz, H. A graphene-metal hybrid biosensor for SEIRA spectroscopy applications. Opt. Commun. 550, 130020 (2024).

Slanted Anisotropic Metasurfaces for Enhanced Reflectance Minimization in CMOS Image Sensors

M. Cho[1], and J. Shin[1*]

[1]Department of Materials Science and Engineering, KAIST, Daejeon 34141, Republic of Korea.
[*]corresponding author: qubit@kaist.ac.kr

Abstract: We propose a slanted anisotropic metasurface (SAMS) to minimize reflectance in silicon photodetectors by adapting to incidence angle and polarization variations. Using slanted TiO_2 elliptical nanodisks, our SAMS achieves broadband antireflection in the visible spectrum over ±40° angles through enhanced impedance matching, promising improved optical performance.

Silicon photodetectors in CMOS image sensors suffer from significant reflection losses, reducing light absorption and overall efficiency. To mitigate this, antireflective coatings (ARC) are commonly applied. However, conventional single-layer ARCs (1-ARC) rely solely on film thickness as the primary structural parameter, limiting their broadband antireflection capabilities across varying incidence angles and polarization states. The fundamental limitations of 1-ARC arise from several factors: (1) The refractive index (n, k) values of conventional ARC materials remain relatively constant, making it difficult to maintain impedance matching across the entire visible spectrum. As a result, a design optimized for a single wavelength becomes ineffective at shorter and longer wavelengths, leading to residual reflectance at the spectral edges. (2) The angle of incidence varies significantly depending on the position of the silicon photodetector (Si PD) within the CMOS sensor array. While different ARC thicknesses could provide better antireflection for specific angles, fabricating spatially varying film thicknesses across the sensor is impractical. (3) Traditional ARC materials lack anisotropic optical properties, and even if anisotropic materials are used, 1-ARC designs cannot align the optical axis according to the spatial distribution of the Si photodetector surface. These limitations result in persistent impedance mismatch across broader angular ranges and polarization conditions, particularly at oblique incidence. In addition to 1-ARC, various anti-reflection techniques like multilayer coatings, nanoparticles, surface texturing, and metasurfaces [1-3] have been explored, mainly for uniform incident angles in solar panels. However, CMOS image sensors face varying angles and polarization across the silicon photodetector, making broadband reflectance reduction still an unresolved challenge.

To overcome these challenges, we propose a slanted anisotropic metasurface (SAMS) that dynamically adapts to the spatially varying incidence conditions in CMOS image sensors. As shown in Figure 1(a), the SAMS consists of slanted TiO_2 elliptical nanodisks arranged in a triangular lattice on a crystalline Si substrate. The structural parameters were optimized using a particle swarm optimization (PSO) algorithm to minimize reflectance for specific incidence angles and polarization states.

Objective function F, is defined as

$$F = \frac{\sum_{400}^{700} R_{p-pol} + \sum_{400}^{700} R_{s-pol}}{Total\ points} \quad (1)$$

In Equation (1), $R_{\text{p-pol}}$ and $R_{\text{s-pol}}$ represent the reflectance for p-polarized and s-polarized light, respectively, calculated over the visible wavelength range from 400 nm to 700 nm. The total points corresponds to the wavelength intervals used within this range. By optimizing slanted design, we can introduce artificial dispersion and give controlled anisotropy, enabling enhanced impedance matching across a wide range of incidence angles and polarization conditions. To illustrate the performance of the SAMS, we present reflectance results for normal incidence (θ=0°) and oblique incidence (θ=30°) as representative cases. Figures 1(b) and (c) compare the reflectance spectra of the SAMS and a conventional 1-ARC under these conditions. At normal incidence, Figure 1(b) shows that the SAMS achieves near-zero reflectance across the visible spectrum, significantly outperforming the 1-ARC. For oblique incidence, Figure 1(c) demonstrates that the SAMS maintains low reflectance for both s- and p-polarized light, whereas the 1-ARC still exhibits relatively higher reflectance due to impedance mismatch.

By leveraging its slanted nanostructures, the SAMS provides broadband antireflection in the visible spectrum for incidence angles up to ±40°, offering a scalable and robust solution for next-generation CMOS image sensors. With its superior optical performance compared to traditional ARC approaches, the SAMS enables improved light collection efficiency, making it highly suitable for high-performance imaging applications (Detailed research findings will be presented in the conference poster session).

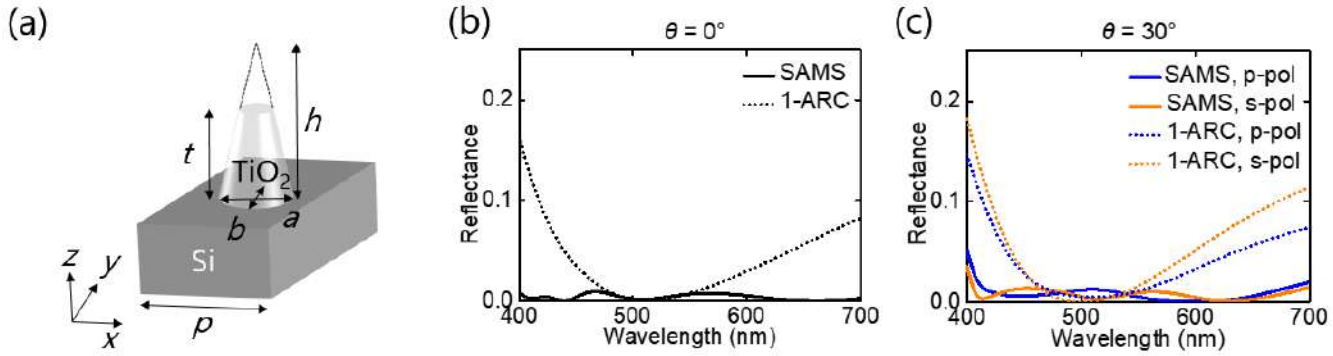


Figure 1. Reflectance spectra of the SAMS and 1-ARC, optimized at specific incidence angles with an azimuthal angle of φ=0°. (a) Unit cell design of the SAMS, composed of TiO_2 elliptical nanodisks arranged in a triangular lattice on a crystalline Si substrate. (b, c) Reflectance spectra for incidence angles of θ=0° and 30° for the SAMS (solid lines) and 1-ARC (dashed lines). The spectra show s-polarized light in orange and p-polarized light in blue.

I acknowledge the APMD research group at KAIST for their valuable contributions and support to this research.

References

1. Pecora, E. F., A. Cordaro, P. G. Kik, and M. L. Brongersma, "Broadband Antireflection Coatings Employing Multiresonant Dielectric Metasurfaces," *ACS Photonics*, Vol. 5, No. 11, 4456–4462, 2018.
2. Lee, N., M. Xue, J. Hong, J. van de Groep, and M. L. Brongersma, "Multi-Resonant Mie Resonator Arrays for Broadband Light Trapping in Ultrathin c-Si Solar Cells," *Adv. Mater.*, Vol. 35, No. 29, 2210941, 2023.
3. Cordaro, A., J. van de Groep, S. Raza, E. F. Pecora, F. Priolo, and M. L. Brongersma, "Antireflection High-Index Metasurfaces Combining Mie and Fabry-Pérot Resonances," *ACS Photonics*, Vol. 6, No. 2, 453–459, 2019.

Analysis of the temperature sensitivity of split ring resonator metamaterials

M. Töfferl[1,2*], A. Schossmann[1,2], and A. Bergmann[1,2]
[1]Graz University of Technology, Austria.
[2]Christian Doppler Laboratory Structured Matter Based Sensing, Austria.
m.toefferl@tugraz.at (corresponding author)

Abstract

The temperature sensitivity of a metamaterial that operates as a passive sensing device in the millimeter-wave regime is analyzed. Broad-side coupled split-ring resonators are manufactured on two glass substrates, with a dielectric spacer between them. The sensor effect is the tuning of the resonance frequency due to a temperature-dependent change in the permittivity of the dielectric spacer. The experiment shows a sensitivity of $(10.5 \pm 1.0)\,\mathrm{MHz/°C}$.

1 Introduction

Millimeter-wave metamaterials have gained importance in different applications because of their applicability as wireless sensors. For temperature sensing this can be beneficial given the constraints in temperature range and mechanical setup [1]. Different designs have been proposed depending on the target temperature range, for example [2] showed a metamaterial design with double split-ring resonators filled with sea water and a temperature range of 10°C to 30°C. Kairm et. al [3] used a closed ring resonator design to propose a sensor system for 450°C to 800°C. Temperature sensors based on mm-wave metamaterials can be implemented with a separate read-out element and allows to sense the temperature locally. The approach in this work with metamaterials is the additional feature of sensing temperature at the same location without interfering with wiring and electronics.

2 Metamaterial design

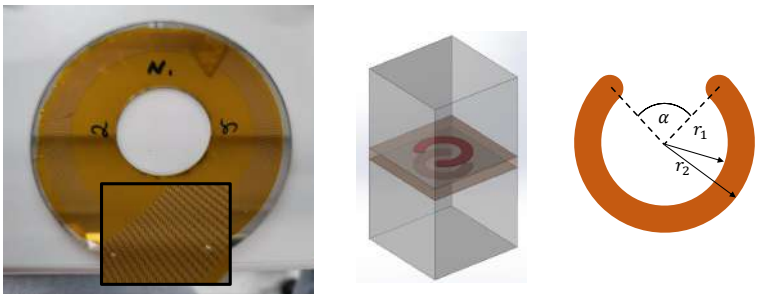


Figure 1: Metamaterial design under test, $r_1 = 140\,\mu\mathrm{m}$, $r_2 = 230\,\mu\mathrm{m}$, $\alpha = 90°$.

For the metamaterial design we chose broadside-coupled split ring resonators (BCSRR) which are processed on two separate glass disks. The glass disks are 700 µm thick and are glued together (polysiloxane) with a separation film (Kapton) holding a layer of glue on both sides. The nominal thickness of the film with the glue is 140 µm. A simulation was done to estimate

the size of the rings based on the permittivity of the used materials. The target resonance frequency of the metamaterial was designed to be in the range of 60 GHz to 70 GHz. In this range commercial mm-wave chips are available for read-out. The size parameters for the split rings are shown in fig. 1. The backside of one of the disks is coated with a thin layer of titanium to reflect the incoming waves and measure the reflection spectrum of the metamaterial.

3 Measurement results

The reflection spectra of the metamaterial were recorded using a Vector Network Analyzer (VNA). The horn antenna was placed directly above the metamaterial at a distance of 15 mm.

For the temperature measurement we used the ambient room temperature of a temperature stabilized laboratory as this has a sinusoidal variation from 21° to 23°. A Pt100 temperature sensor as reference was mounted on the metamaterial and for every 30 s a reflection spectrum (S11) and a temperature value was recorded. From the measurement data the resonance minimum was calculated and plotted as a time series with the temperature data. (see fig. 2). From the data we calculated the Pearson correlation coefficient to estimate the correlation of the temperature T to $f_{\min}$ and the temperature inertia of the system. We assumed a linear relation as the temperature difference is only $\Delta T \approx 2°$. The data gives Person coefficient of 0.919 with a time shift of 4 minutes coming from the temperature inertia of the setup. The linear fit for the temperature and the resonance frequency yields to a sensitivity of (10.5 ± 1.0) MHz/°C.

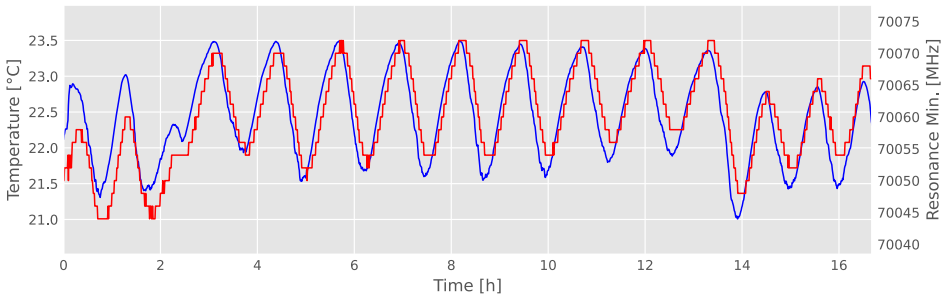


Figure 2: Time series of temperature and resonance minimum for the metamaterial.

4 Acknowledgements

The financial support by the Austrian Federal Ministry of Labour and Economy, the National Foundation for Research, Technology and Development and the Christian Doppler Research Association is gratefully acknowledged.

References

[1] Sun, Z., "A Dual Resonance Frequency-Selective Surface Temperature Sensor With Linear Frequency–Temperature Behavior" *IEEE Sensors Journal*, Vol. 23, No. 9, pp. 9382–9389, 2023.

[2] Ekmekci, E. and Turhan-Sayan, G., "Multi-functional metamaterial sensor based on a broadside coupled SRR topology with a multi-layer substrate" *Applied Physics A*, Vol. 110, pp. 189–197, 2013.

[3] Kairm, H., "Concept and Model of a Metamaterial-Based Passive Wireless Temperature Sensor for Harsh Environment Applications" *IEEE Sensors Journal*, Vol. 15, No. 3, pp. 1445-1452, 2014.

All-Optical Phase Modulation of mm-waves for Beam Steering Applications

G. Neville White[1*], I. R. Hooper[1], F. Burton[2], D. B. Phillips[1], and E. Hendry[1]

[1]School of Physics and Astronomy, University of Exeter, Stocker Road, Exeter, EX4 4QL, UK
[2]BT, Adastral Park, Martlesham Heath, Ipswich, IP5 3RE, UK
[*]Corresponding author: gn257@exeter.ac.uk

Abstract: 6G technologies will require fast and efficient mm-wave beam steering, yet methods to achieve this are still evolving. Here, we experimentally demonstrate a novel mm-wave spatial light modulator based on an optically controlled metasurface. Our system is capable of arbitrary beam shaping – including multicasting and orbital angular mode generation.

With the rapidly increasing demand for high-speed communication systems, high efficiency reconfigurable beam-steering technologies are essential to support high-frequency operations beyond the GHz and into the THz regime [1]. Here, we present the design and implementation of a novel reconfigurable mm-wave metasurface, capable of arbitrary spatially-varying phase modulation of reflected beams. This control is achieved all-optically, by photo-activating local areas of the surface to dynamically encode target phase holograms. We demonstrate high-precision beam focusing, steering, orbital angular momentum mode generation and beam splitting (multicasting) at 50 GHz. Our approach enables dynamic control reflected beam direction and shape, while substantially reducing the hardware complexity in comparison with conventional phased arrays. Furthermore, numerical simulations and experimental results demonstrate significant improvements in beamforming efficiency, steering accuracy, and focusing power at 50 GHz, compared to standard amplitude-only modulation [2,3]. Our concept is scalable to THz frequencies, holding promise for next-generation 6G networks and applications in low-latency communication and high-speed data transfer networks.

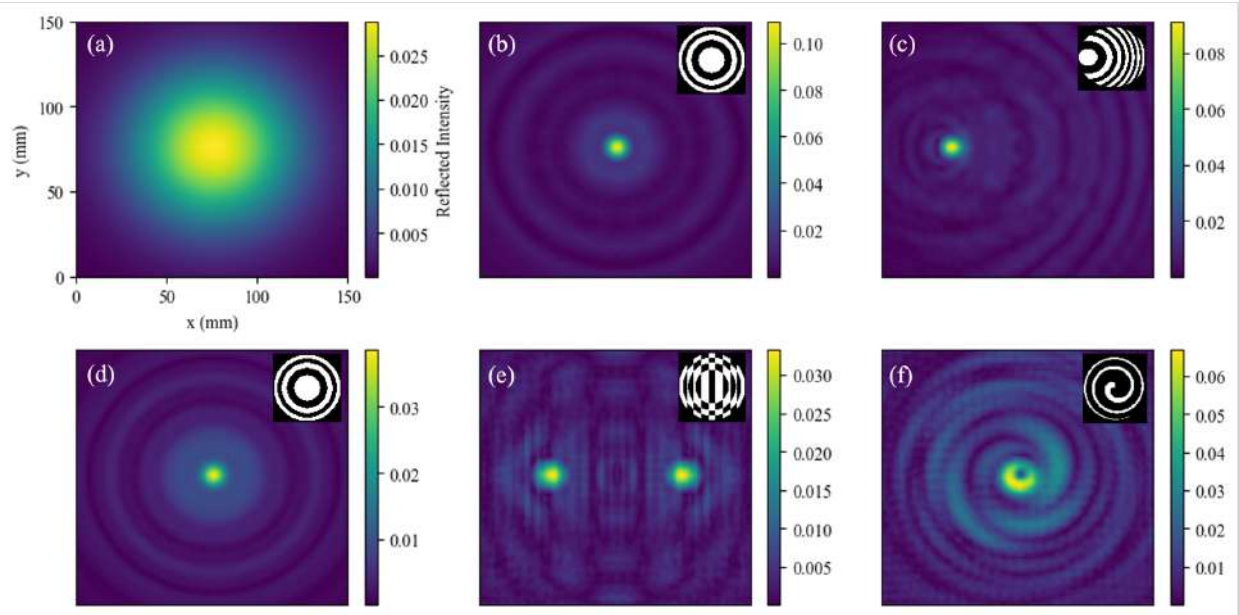


Figure 1. Modelled values of beam steering at 47.5GHz, with their appropriate Fresnel Lens, for (a) Unfocused beam (b) Focused beam (c) Focused beam, steered 15° (d) Focused beam using an amplitude modulator (e) Multicast Beam (f) Generation of an OAM beam.

I.R.H acknowledges support from the EPSRC, UK, via the A-Meta Project (EP/W003341/1) and the META4D Programme Grant (EP/Y015673/1)

References

1. Rahm, M., J.S. Li, and W.J. Padilla, THz Wave Modulators: “A Brief Review on Different Modulation Techniques,” *J Infrared Milli Terahertz Waves* 34, 1–27, 2013.
2. Gallacher, T.F., R. Sondena, D. A. Robertson and G. M. Smith, "Optical Modulation of Millimeter-Wave Beams Using a Semiconductor Substrate," *IEEE Transactions on Microwave Theory and Techniques,* Vol. 60, No. 7, 2301-2309, 2012.
3. Gallacher, T.F., D. A. Robertson and G. M. Smith, “The Photo-Injected Fresnel Zone Plate Antenna: Optoelectronic Beam Steering at mm-Wave Frequencies” *IEEE Transactions on Antennas and Propagation*, Vol. 61, No. 4, 1688-1696, 2013.

Optimized Bilayer Meta-Substrate for Hyper-Sensitive Strain Monitoring

Jae-Hwan Lee[1,2], Junsang Lee[3], Seung-Kyun Kang[1,2,4,5*]

[1] Department of Materials Science and Engineering, Seoul National University, Republic of Korea
[2] Research Institute of Advanced Materials (RIAM), Seoul National University, Republic of Korea
[3] Weldon School of Biomedical Engineering, Purdue University, United States
[4] Interdisciplinary Program of Bioengineering, Seoul National University, Republic of Korea
[5] Nano Systems Institute SOFT Foundry, Seoul National University, Republic of Korea
[*]corresponding author: kskg7227@snu.ac.kr

Abstract: We present an optimized bilayer meta-substrate for hyper-sensitive strain sensing, achieving a near-ideal Poisson's ratio of -1. By tuning the geometrical factors of auxetic structures, we maximize gauge factor performance beyond conventional designs. Experimental validation confirms enhanced sensitivity, demonstrating the potential for precision biomechanical monitoring and next-generation flexible sensors.

Real-time detection of ultra-small deformations in complex structures is crucial for advanced biomechanical engineering. While flexible strain sensors offer adaptability to various shapes, their sensitivity remains inferior to spectroscopic imaging techniques. Crack-based strain sensors utilizing Meta-Cracks exhibit significantly high strain resolution of 10^{-5} scale, capable of detecting infinitesimal strain through a novel crack-opening mechanism.[1] These sensors achieve exceptional GFs exceeding 1000 at strains as low as 10^{-4} when integrated with substrates exhibiting a Poisson's ratio of -0.9.[1] The hypersensitivity is attributed to a crack-opening behavior that remains independent of orientation, as verified through simplified models and finite element analysis.[1]

Building upon the previous study on strain sensors utilizing Meta-Cracks[1], we investigate the role of meta-substrate design in optimizing sensor sensitivity. While prior work employed reference auxetic structures without systematic characterization of Poisson's ratio effects, our study strategically tailors the mechanical properties of bilayer meta-substrates to enhance strain sensitivity. By precisely engineering the geometry of the meta-material layer, we achieve a Poisson's ratio close to -1, which maximizes crack opening efficiency and strain-induced resistance changes. This approach integrates theoretical modeling, finite element simulations, and experimental validation to establish an optimized design paradigm for meta-substrates in strain sensing applications.

We successfully fabricated and tested a meta-substrate-integrated strain sensor with a near-optimal Poisson's ratio (-1). Figure 1 shows the normalized crack gap distance (D/D_0) presenting continuously increasing states in all orientations under −0.9 Poisson's ratio, and getting saturated to the same crack opening rate, while presenting the crack narrowing behavior in specific orientations under 0.3 Poisson's ratio. Experimental results of Meta-Crack sensor with a Poisson's ratio of near -1 confirmed a substantial increase in sensitivity, surpassing prior auxetic designs. This advancement opens new avenues for hyper-sensitive, conformal, and biocompatible

strain sensors applicable to biomedical monitoring, soft robotics, and precision mechanical diagnostics. Moreover, this research contributes to the fundamental understanding of meta-material mechanics in functional sensor applications and provides a scalable design methodology for next-generation flexible electronic devices.

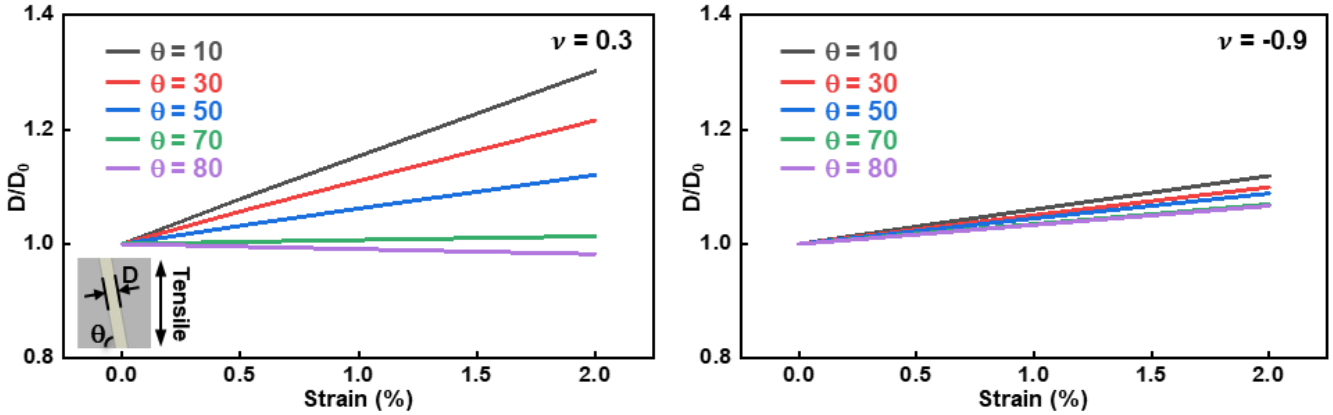


Figure 1. Verification of crack gap widening rate with various crack shapes, with angles of 10°, 30°, 50°, 70°, and 80° under positive Poisson's ratio (0.3) and negative Poisson's ratio (−0.9) based on FEA. (This material is reproduced with permission from Jae-Hwan Lee et al., "Hypersensitive meta-crack strain sensor for real-time biomedical monitoring," Science Advances, Vol. 10, eads9258 (2024). DOI: 10.1126/sciadv.ads9258. © 2024)[1]

References

1. Jae-Hwan Lee, et al., Hypersensitive meta-crack strain sensor for real-time biomedical monitoring. *Sci. Adv.* **10.51**, eads9258 (2024). DOI:10.1126/sciadv.ads9258.

A Broadband Artificial Magnetic Conductor Utilising Magnetodielectric Substrate and Multilayered Metasurface

C. P. Gallagher[1], S. J. Berry[2], C. R. Lawrence[2], and A. P. Hibbins[1]
[1]The University of Exeter, United Kingdom
[2]QinetiQ, United Kingdom
c.gallagher2@exeter.ac.uk (corresponding author)

Abstract

We present an artificial magnetic conductor comprising a multilayered metasurface and a magnetodielectric composite. The metasurface confines the electric field, prioritizing the bandwidth enhancement of the relative permeability over the reduction from the relative permittivity. This design achieves a 110% bandwidth (300-1100 MHz) with a significantly sub-wavelength height <15 mm.

1 Introduction

Microwave metasurfaces are technology enablers that present the unprecedented ability to control the interaction between matter and electromagnetic waves. Applications such as electromagnetic filtering [1], broadband absorption [2], beamforming [3] and antenna miniaturisation [4] have all seen enhancements in recent years owing to the development of microwave metasurfaces. However, there are still limitations on the bandwidth that can be achieved with microwave metasurfaces when using standard dielectric substrates. Broadband technologies can be developed using magnetodielectric composites to enhance the bandwidth, but these rely heavily on developing composites that have significantly higher relative permeability than relative permittivity. This is no simple task for microwave applications, as the permeability is considerably lower than at, for example, 10s of MHz. Here we present a multilayered metasurface that, on resonance, confines the electric field outside the magnetodielectric composite. This confinement of the electric field means the bandwidth enhancing effects of the relative permeability in the composite takes precedence over the diminishing effects arising from the relative permittivity. Using this design, an artificial magnetic conductor is presented for operation over the frequency range 300 – 1100 MHz, boasting a bandwidth in excess of 110%. The total height of the artificial magnetic conductor is 15 mm, corresponding to a size less than $\frac{\lambda}{28}$ for the central operating frequency (700 MHz). We present simulation results for the operation of an equiangular spiral antenna when using this AMC as the groundplane for the antenna, and compare these results for simulations of the performance of the same antenna in freespace. The AMC groundplane allows design and fabrication of conformal antennas for communications that will have a minimal footprint in terms of depth. These AMC groundplanes are hence important for the development of communications antennas in, for example, the aerospace industry where antennas would ideally conform to the shape of the aircraft fuselage, and require as little internal space as possible.

2 Acknowledgements

Dr. Gallagher is grateful for the financial support provided by the strategic coollaboration between The University of Exeter and QinetiQ Ltd, supporting his position as a Senior Industrial Research Fellow at Exeter.

3 Figures and Tables

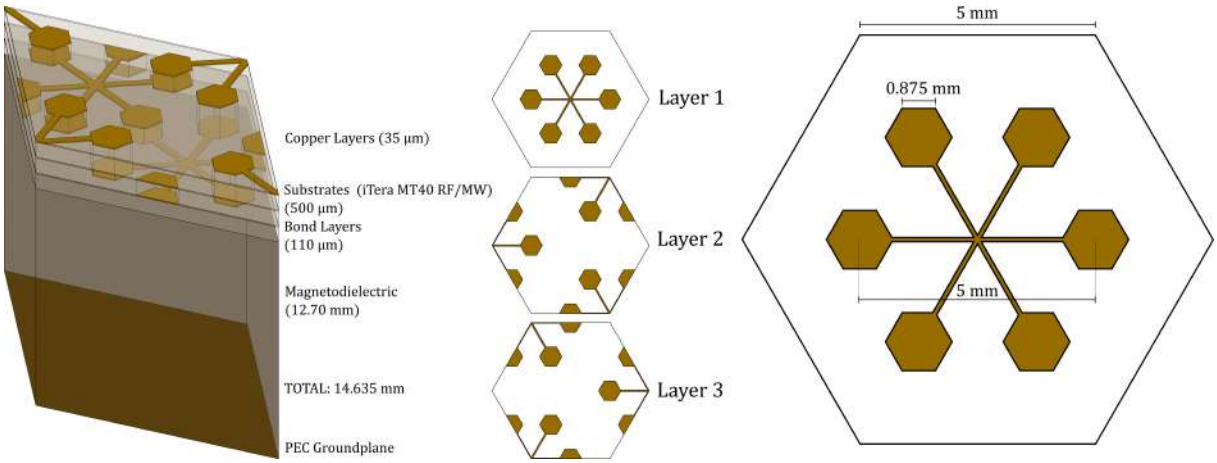


Figure 1: Schematics showing the unit cell for the AMC, as well as how each layer of the metasurface is offset.

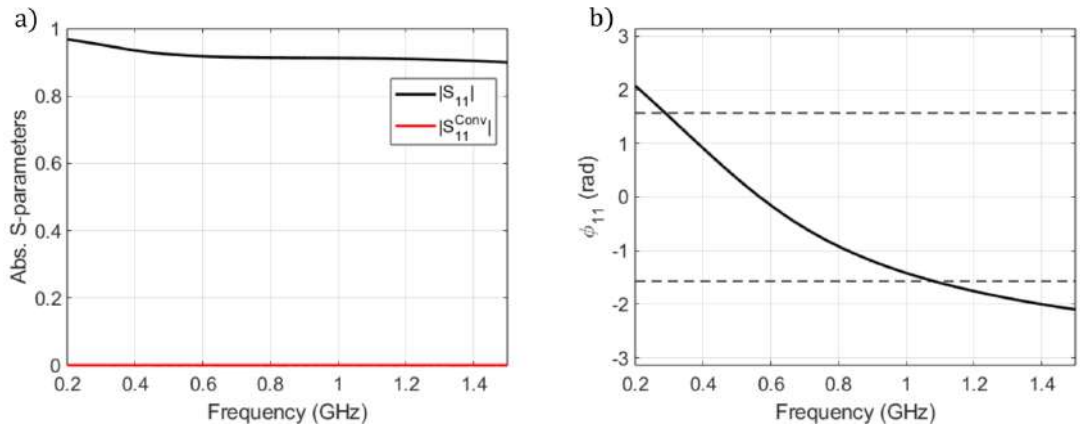


Figure 2: Graphs showing simulation results for a) the absolute values for the reflection (S_{11}) with and without polarisation conversion and b) the reflected phase for the conserved signal.

References

[1] C. P. Gallagher, J. K. Hamilton, I. R. Hooper, J. R. Sambles, A. P. Hibbins, C. R. Lawrence, and J. Bows, "Multi-resonant tessellated anchor-based metasurfaces," *Sci. Rep.*, vol. 13, no. 1, pp. 1–10, 2023.

[2] Y. Luo, L. Huang, J. Ding, W. Liu, B. Sun, C. Xie, H. Yang, and J. Wu, "Flexible and transparent broadband microwave metasurface absorber based on multipolar interference engineering," *Opt. Express*, vol. 30, pp. 7694–7707, Feb 2022.

[3] J. R. Capers, S. J. Boyes, A. P. Hibbins, and S. A. R. Horsley, "Designing metasurfaces to manipulate antenna radiation," in *2021 XXXIVth General Assembly and Scientific Symposium of the International Union of Radio Science (URSI GASS)*, pp. 1–4, 2021.

[4] Y. Song, P. Zhang, Y. Liu, K. Duan, L. Huang, and M. Li, "Broadband circular polarized composite spiral antenna using two-layer amc," in *2019 Photonics & Electromagnetics Research Symposium - Fall (PIERS - Fall)*, pp. 1197–1203, 2019.

A Simplified Approach to 3D Spherical Cloaking Using Shell Based Dielectric Metamaterials

Chen, Guan-Wen[1,*], Huang, Jing-Hao[1,*], Ren, He-Jun[1,*], and Huang, Tsung-Yu[1,*]

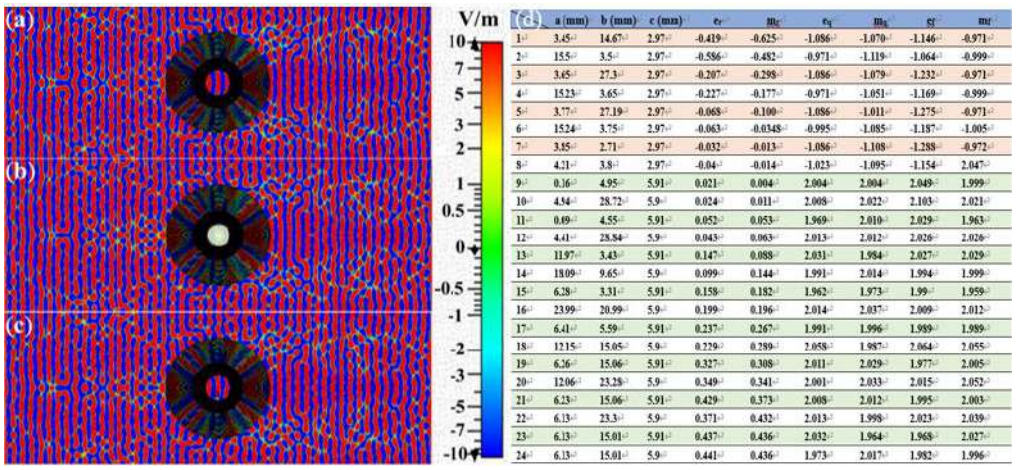
1 Department of Materials Engineering, Ming Chi University of Technology, New Taipei, R.O.C., Taiwan 243303

[*]corresponding author: huang.tsungyu@mail.mcut.edu.tw

Abstract: We propose a 3D spherical reciprocal invisibility cloak using shell-based dielectric metamaterials, minimizing scattering and ensuring effective concealment. The cloak operates from 2.8 to 4.33 GHz with 1.63 GHz bandwidth, offering simpler design, broader bandwidth, and improved fabrication feasibility for transformation optics applications.

Traditional invisibility cloaks based on transformation optics (TO) and scattering cancellation face challenges such as customization requirements, bandwidth limitations, and fabrication complexity. To address these issues, we propose a 3D spherical reciprocal invisibility cloak, composed of shell-based dielectric metamaterials, which can be fabricated using advanced ceramic manufacturing techniques.

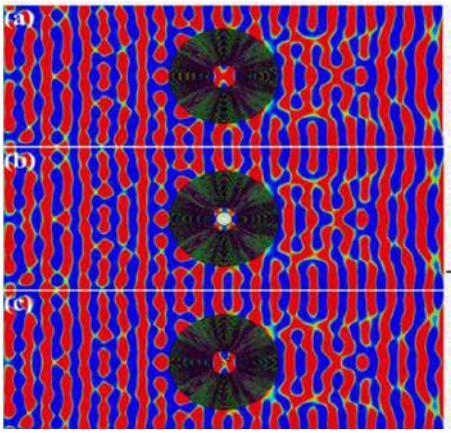
Figure 1 presents the structural parameters and simulated electric field distribution of the 24-layered reciprocal cloak. The cloak is designed with anisotropic material properties, where odd layers correspond to TE modes and even layers to TM modes. The simulation results confirm that the cloak effectively minimizes scattering and maintains smooth wavefronts, ensuring the concealment of hidden objects. The scattering cross-section analysis indicates variations of 8.44% and 1.11% along the θ and ϕ directions, with an average field deviation of 7.2%, verifying its excellent cloaking performance. To further evaluate the cloak's efficiency, Figure 2 presents the simplified design parameters and corresponding electric field distribution. Figure 2 demonstrates the simplified cloak's material parameters and field distribution. Here, c (mm) represents the shell thickness, while ε and μ values correspond to the anisotropic material properties of different layers. Through optimized design, the number of metamaterial layers is reduced, significantly improving computational efficiency. Additionally, the simulation results show that the cloak operates within the frequency range of 2.8 GHz to 4.33 GHz, with an average relative deviation below 7%, ensuring effective concealment of hidden objects. The cloak achieves a total bandwidth of 1.63 GHz, exhibiting excellent frequency response performance. Compared with existing designs, our cloak features a simpler structure, broader bandwidth, and improved fabrication feasibility. Moreover, we provide the anisotropic material properties of the shell-based dielectric metamaterials, including permittivity (ε) and permeability (μ), applicable to both TE and TM modes, ensuring the cloak's performance and manufacturability. The study confirms that the proposed spherical reciprocal invisibility cloak effectively conceals both metallic and dielectric objects, making it suitable for optical camouflage, radar stealth, and electromagnetic wave control. This approach provides a scalable solution for next-generation transformation optics applications.



(d)

	a (mm)	b (mm)	c (mm)	ε_r	μ_φ	ε_φ	μ_θ	ε_θ	μ_r
1	3.45	14.67	2.97	-0.419	-0.625	-1.086	-1.070	-1.146	-0.971
2	155	3.5	2.97	-0.586	-0.482	-0.971	-1.119	-1.064	-0.999
3	3.65	27.3	2.97	-0.207	-0.298	-1.086	-1.079	-1.232	-0.971
4	1523	3.65	2.97	-0.227	-0.177	-0.971	-1.051	-1.169	-0.999
5	3.77	27.19	2.97	-0.068	-0.100	-1.086	-1.011	-1.275	-0.971
6	1524	3.75	2.97	-0.063	-0.0348	-0.995	-1.085	-1.157	-1.005
7	3.85	2.71	2.97	-0.032	-0.013	-1.086	-1.108	-1.288	-0.972
8	4.21	3.8	2.97	-0.04	-0.014	-1.023	-1.095	-1.154	2.047
9	0.16	4.95	5.91	0.021	0.004	2.004	2.004	2.049	1.999
10	4.54	28.72	5.9	0.024	0.011	2.008	2.022	2.103	2.021
11	0.69	4.55	5.91	0.052	0.053	1.969	2.010	2.029	1.963
12	4.41	28.84	5.9	0.043	0.063	2.013	2.012	2.026	2.026
13	11.97	3.43	5.91	0.147	0.088	2.031	1.984	2.027	2.029
14	18.09	9.65	5.9	0.099	0.144	1.991	2.014	1.994	1.999
15	6.28	3.31	5.91	0.158	0.182	1.962	1.973	1.99	1.959
16	23.99	20.99	5.9	0.199	0.196	2.014	2.037	2.009	2.012
17	6.41	5.59	5.91	0.237	0.267	1.991	1.996	1.989	1.989
18	12.15	15.05	5.9	0.229	0.289	2.058	1.987	2.064	2.055
19	6.26	15.06	5.91	0.327	0.308	2.011	2.029	1.977	2.005
20	12.06	23.25	5.9	0.349	0.341	2.001	2.033	2.015	2.052
21	6.23	15.06	5.91	0.429	0.373	2.008	2.012	1.995	2.003
22	6.13	23.3	5.9	0.371	0.432	2.013	1.998	2.023	2.039
23	6.13	15.01	5.91	0.437	0.436	2.032	1.964	1.963	2.027
24	6.13	15.01	5.9	0.441	0.436	1.973	2.017	1.952	1.996

Figure 1. Structural Parameters and Simulated Electric Field Distribution of the 24-Layered Reciprocal Cloak. (a) Electric field distribution without hidden objects. (b) Field distribution when the hidden object is a copper sphere. (c) Field distribution when the hidden objects are a silicon cuboid and a copper ellipsoid. (d) Structural parameter table of the shell-based dielectric metamaterials.



(d)

	c (mm)	εθ	μφ	εφ	μφ
1	6	-1.007	-	-	-0.993
2	6	-	**-1.007**	**-0.993**	-
3	6	2.013	-	-	1.981
4	6	-	**2.013**	**1.981**	-

Figure 2. Simplified Design Parameters and Field Distribution of the Reciprocal Cloak. (a) Retrieved material parameters. (b) Simulated field distribution without hidden objects. (c) Field distribution when the hidden object is a larger conductive object (copper sphere). (d) Parameters from simplified design of the reciprocal cloak.

References

1. 1. Alù, A. & Engheta, N. Cloaking a Sensor. *Physical Review Letters* 102, (2009).
2. 2. Lai, Y., Chen, H., Zhang, Z.-Q. & Chan, C. Complementary Media Invisibility Cloak that Cloaks Objects at a Distance Outside the Cloaking Shell. *Physical Review Letters* 102, 093901 (2009).
3. 3. Semouchkina, E., Werner, D. H., Semouchkin, G. B. & Pantano, C. An infrared invisibility cloak composed of glass. *Applied Physics Letters* 96, 233503-233503–3 (2010).
4. 4. Landy, N. & Smith, D. R. A full-parameter unidirectional metamaterial cloak for microwaves. *Nature Materials* 12, 25–28 (2013).

Water-based cylindrical metamaterials with radial anisotropy for electric field enhancement and suppression

J. Brandt[1*], H. Renner[1], D. Langer[2], M. Eich[1,3] A. Koelpin[2] and A. Petrov[1,3]

[1]Institute of Optical and Electronic Materials, Hamburg University of Technology, Hamburg, Germany
[1]Institute of High-Frequency Technology, Hamburg University of Technology, Hamburg, Germany
[2]Institute of Functional Materials for Sustainability, Helmholtz Zentrum Hereon, Geesthacht, Germany
[*]corresponding author: julia.brandt@tuhh.de

Abstract: In this paper, we study how a cylindrical shell made from a radially anisotropic material can modify the electric field inside an isotropic core, either by enhancing or suppressing it. We present a water-air metamaterial that enhances electric fields by 10 dB across a broad frequency range.

We consider a radially anisotropic cylinder with a diagonal permittivity tensor in cylindrical coordinates, with components in the radial, azimuthal and axial directions [1]. An electric field which is polarized in the polar plane is influenced by the radial component ε_r and the azimuthal component ε_θ. In the scope of the quasi-static approximation, such cylinders can be constructed by a metamaterial of wedges or of shells, as shown in Figure 1b and described in reference 2. The anisotropy ratio defined by $v^2 = \varepsilon_\theta / \varepsilon_r$ is less than or greater than 1, respectively. The electric field inside a radially anisotropic cylinder is proportional to r^{v-1}, where r is the radial coordinate. This implies that in the case of a wedge metamaterial, the electric fields theoretically increase to infinity as they approach the cylindrical axis, while in the case of a multi-shell metamaterial, the electric fields are suppressed.

For practical reasons, we consider core-shell cylinders with an empty core of finite size in which the electric fields are enhanced or suppressed. These have an isotropic core of radius a, surrounded by a shell of a radially anisotropic material, forming a cylinder of radius b (Figure 1a). Although the electric field in the shell (whether isotropic or anisotropic) is not uniform, the electric field in the isotropic core material remains constant. We can define an enhancement factor A for the electric field in the core, which is: $E_{core} = A\, E_0$, where E_0 is the incident electric field. This factor has already been derived in previous work [3,4]. As the anisotropy ratio v approaches zero, A approaches b/a. If v instead goes to infinity, A tends to zero.

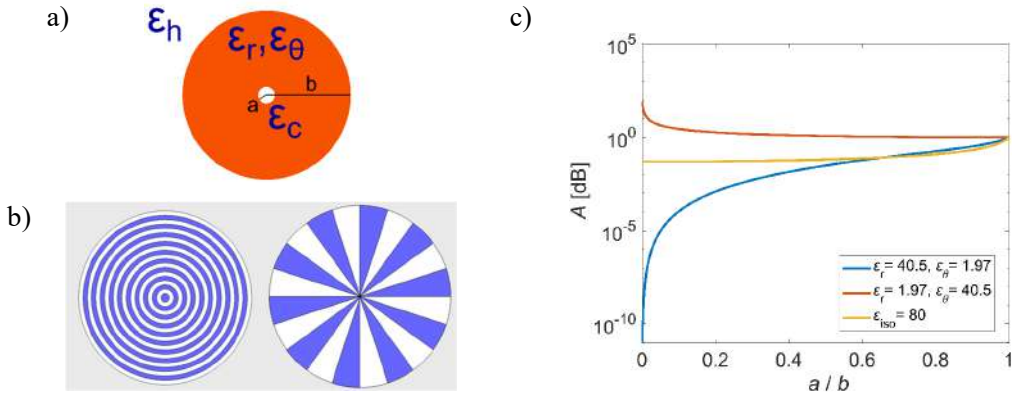


Figure 1. a) Schematic of a radially anisotropic core-shell cylinder. b) Schematic of the shell and wedge metamaterial realization. c) Enhancement factor for water-air metamaterials in the effective medium approximation as a function of the core-to-cylinder radius ratio for a water content of 50%.

To achieve a significant permittivity contrast, we chose to study water-air metamaterials in the microwave frequency range. At a frequency of 1 GHz, water has a permittivity of 80 and is nearly lossless. Figure 1c shows the enhancement factors of such cylinders as a function of the core-to-cylinder ratio. These theoretical considerations are valid in the quasi-static regime. In our experiments the enhancement is also affected by Mie resonances with the structure. Employing radially anisotropic structures with an optimized water content of 20%, we can smooth out these resonances and achieve a broadband enhancement of an incident electric field by 10 dB (Figure 2a).

We fabricated the wedge structure by 3D printing a polymer scaffold with an outer diameter of 6 cm and an empty core of 6 mm. Water was then filled into the designated areas (blue for visualization purposes). A horn antenna is used to direct an electromagnetic field onto the structure, while the power is measured in the air-filled core. The experimental setup is shown in Figure 2b. In Figure 2a, we plot the calculated intensity enhancement in dB scale of the printed structure alongside that of the pure metamaterial. The differences in these results are due to the effect of the polymer scaffold.

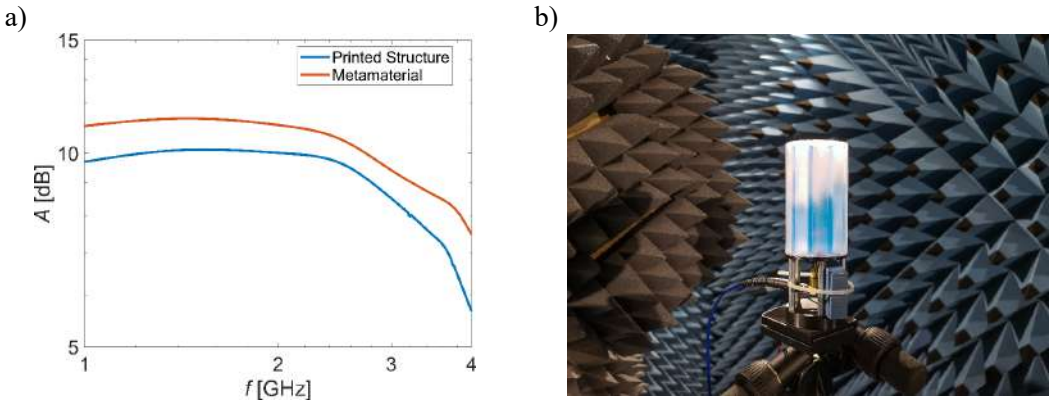


Figure 2. a) Calculated enhancement factor as a function of frequency for the water-air metamaterial and the printed structure. B) 3D printed structure in the measurement chamber with water in the wedge areas

In summary, we have developed a metamaterial-based, non-resonant and omnidirectional antenna which relies solely on water and air. The electric field enhancement is achieved through an effectively radially anisotropic shell. Similar to the wedge metamaterial, we aim to fabricate a water-based multi-shell cylinder designed to cloak its core material.

JB, ME and AP thank Dassault Systèmes for providing their simulation software “CST Studio Suite”.

References

1. Chen, H. L. & Gao, L. Anomalous electromagnetic scattering from radially anisotropic nanowires. Phys. Rev. A 86, 107 (2012).
2. Zhang, Y.-L., Pendry, J. B. & Lei, D. Y. Radial anisotropy from a geometric viewpoint: Topological singularity and effective medium realization. Phys. Rev. B 96, 035430 (2017).
3. Yu, X. & Gao, L. Nonlinear dielectric response in partially resonant composites with radial dielectric anisotropy. Physics Letters A 359, 516–522 (2006).
4. Kettunen, H., Wallén, H. & Sihvola, A. Cloaking and Magnifying Using Radial Anisotropy. Journal of Applied Physics 114, 044110 (2013).

On-chip angle-scanning scattering microscopy with all-dielectric metasurfaces and surface-emitting lasers

K. Zangeneh Kamali[1*], O. Olsson[1], E. Strandberg[2], H. Jungová[1], and M. Käll[1]

[1]Department of Physics, Chalmers University of Technology, 412 96, Gothenburg, Sweden

[2]Department of Microtechnology and Nanoscience, Chalmers University of Technology, 412 96, Gothenburg, Sweden

Corresponding author: khosro.zangeneh@chalmers.se

Abstract: Here, we propose a miniaturized imaging system based on integrating scattered light spatial frequencies under angled illumination. We employ spatially arranged vertical-cavity surface-emitting lasers to configure the azimuthal beam rotation. This, integrated with silicon and gallium arsenide metasurfaces, facilitates fast biological specimens imaging beyond the classical diffraction limit.

Fluorescence microscopy offers a way to achieve sub-wavelength resolution in cell images; however, photobleaching and motion blur hinder its effectiveness. Consequently, there is a need to develop rapid marker-free imaging systems. In an optical system, the highest resolvable spatial frequencies of the image are constrained by the numerical aperture of the objective lens. Angled illumination is recognised as an effective method for capturing higher spatial frequencies, thus improving image contrast and resolution. The 2π azimuthal rotation of the angled illumination has been utilised as a strategy to construct a synthetic aperture that maximises the collected spatial frequencies [1, 2]. While this method produces images with higher resolution and contrast, in practice, the image acquisition speed of the system is limited to 100 Hz due to the use of scanning mirrors [3]. An elegant solution for miniaturizing optical systems is found in the combination of vertical-cavity surface-emitting lasers (VCSEL) with metasurfaces [4, 5]. Metasurfaces consist of a collection of sub-wavelength-sized structures and can replicate and combine the functions of traditional bulk optical elements as well as surpass their capabilities by manipulating the phase of the incident field with sub-wavelength resolution. The application of VCSELs as the light source for metasurfaces ranges from biosensing [5, 6] to the generation of holographic images [7].

Here, we suggest a novel approach for performing fast 2π rotational angled microscopy and enhancing its image acquisition rate. We leverage VCSEL-based meta-optical systems to miniaturize conventional 2π rotational angled microscopes (Fig. 1b). The meta-device is constructed from VCSELs with a working wavelength of 980 nm arranged in a circular pattern to facilitate rotational illumination (Fig. 1c). Each of the VCSELs can be electrically switched at speeds of tens of gigabits per second. We design a Pancharatnam–Berry metasurface to function as a half-wave plate, rotating the output VCSEL polarization to the required state (Fig. 1d). The inherent divergence of a VCSEL is exploited for spatial broadening of the beam as it propagates through a glass spacer, thus achieving the beam diameter required for illumination. A polarization-independent metalens is engineered to collimate the beam (Fig. 1e). A phase-gradient metasurface (Fig. 1f) deflects light to the imaging spot at an angle of 70 degrees. It is worth noting that, due to the very large incident angles, aside from the light portion that decouples through scattering, the input beam undergoes total internal reflection (TIR) and

will not be captured by the imaging system. This implies that the metasurface/VCSEL-based 2π-rotating microscope can be operated in TIR mode.

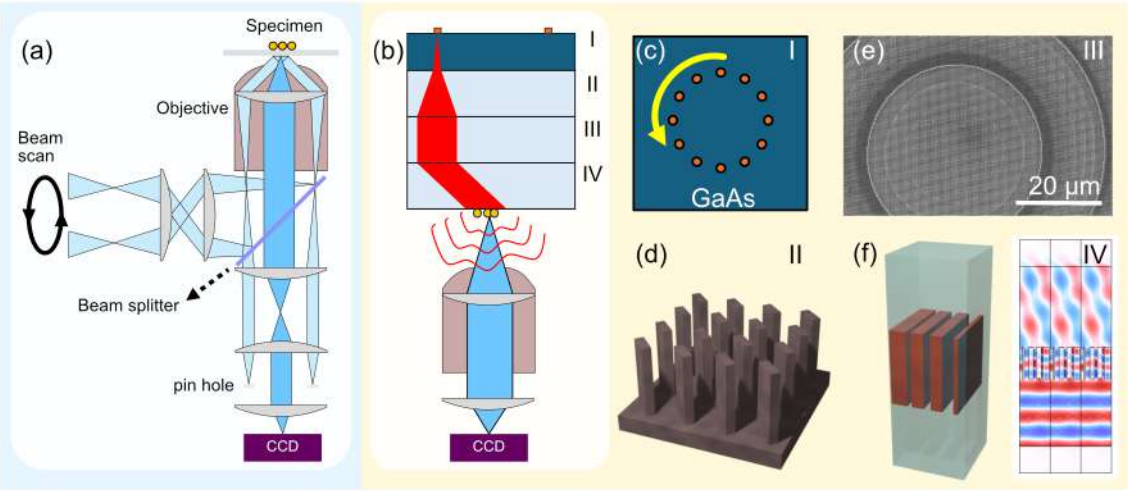


Figure 1: *On-chip* 2π*-rotating coherent microscopy.* (a) Schematics of a conventional rotational microscopy setup, adapted from [1]. (b) Conceptual schematics of a surface-emitting laser-based on-chip device with integrated all-dielectric metasurfaces for 2π-rotating microscopy. (c) Top view of the device with individually addressable vertical-cavity surface-emitting lasers (VCSEL). (d) Design of a GaAs metasurface acting as a phase-retarding plate. (e) Scanning electron micrograph of a silicon metalens for laser beam collimation. (f) Design of a silicon metagrating and electromagnetic simulation results for high-angle beam deflection.

Our research findings may facilitate the commercialization of on-chip microscopes if combined with flat imaging optics and detectors, decreasing their image acquisition time and making them more affordable and widely accessible. Moreover, the substantial enhancement in acquisition speed provided by this approach will reduce motion blur due to Brownian particle diffusion, resulting in sharper images.

This work was funded by the Knut and Alice Wallenberg Foundation and performed in part at Myfab Chalmers.

References

1. Ruh, D., et al., "Superior contrast and resolution by image formation in rotating coherent scattering (ROCS) microscopy," *Optica*, Vol. 5, No. 11, pp. 1371–1381, 2018.

2. Cotte, Y., et al., "Marker-free phase nanoscopy," *Nat. Photonics*, Vol. 7, p. 113-117, 2013.

3. Jünger, F., et al., "100 Hz ROCS microscopy correlated with fluorescence reveals cellular dynamics on different spatiotemporal scales," *Nat. Commun.*, Vol. 13, p. 1758, 2022.

4. Xie, Y-Y., et al., "Metasurface-integrated vertical cavity surface-emitting lasers for programmable directional lasing emissions," *Nat. Nanotechnol.*, Vol. 15, pp. 125–130, 2020.

5. Shitrit, N., "Surface-emitting lasers meet metasurfaces," *Light Sci. Appl.*, Vol. 13, p. 37, 2024.

6. Juodėnas. M, et al., "High-angle deflection of metagrating-integrated laser emission for high-contrast microscopy," *Light Sci. Appl.*, Vol. 12, p. 251, 2023.

7. Pan, G., "Harnessing the capabilities of VCSELs: unlocking the potential for advanced integrated photonic devices and systems," *Light Sci. Appl.*, Vol. 13, p. 229, 2024.

Design and Fabrication of Parity-Time Symmetric Optical Waveguides for Unidirectional Propagation of Light

I. Meskelaite[1*], K. Staliunas[1,2,3], and D. Gailevicius[1]

[1]Laser Research Center, Faculty of Physics, Vilnius University, Sauletekio Ave. 10, 10223, Vilnius, Lithuania

[2]ICREA, Passeig Lluís Companys 23, 08010, Barcelona, Spain

[3]UPC, Dep. de Fisica, Rambla Sant Nebridi 22, 08222, Terrassa (Barcelona), Spain

Corresponding author: `indre.meskelaite@ff.stud.vu.lt`

Abstract: A parity-time symmetric optical waveguide enabling unidirectional propagation of light is proposed. Its numerical investigation via the finite-difference time-domain method and experimental realization by means of femtosecond direct laser writing is presented. A possible application of such a device is foreseen in optical neural networks.

Due to the associated higher speed and lower power consumption, optical neural networks (ONNs) have recently emerged as a promising computing modality. Consequently, a growing research effort is invested in the development of novel hardware architectures that implement the artificial neural networks (ANNs) by means of different optical devices [1].

Here, as our first step in this direction, we aim to achieve unidirectional propagation of light. To this end, we propose a specially designed optical waveguide that respects the parity-time (PT) symmetry of non-Hermitian photonics [2]. Such a structure exhibits different reflectivities depending on the propagation direction of light, and could, therefore, serve in controlling the propagation of light. To fulfill this requirement, both the real and imaginary parts of the structure's effective refractive index must be periodically modulated and phase-shifted with respect to each other. A conceptual design of such a waveguide is shown in Figure 1(a). In this work, we focus on the design and fabrication of the proposed PT-symmetric structure.

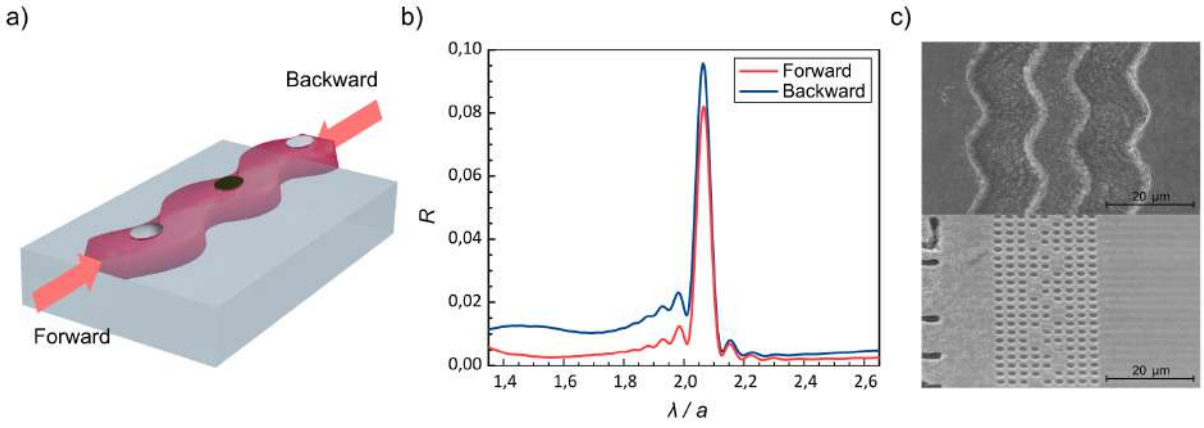


Figure 1: PT-symmetric structure for unidirectional propagation of light. (a) Conceptual design of a periodically modulated dielectric waveguide with metallic islands deposited on top. (b) Simulated forward and backward reflectivities of the device as a function of wavelength λ normalized to the modulation period a. (c) SEM images of fsDLW ridge and PhC waveguides.

We study the propagation of light through the device under investigation using the finite-difference time-domain (FDTD) method. The initial numerical investigation of a non-optimized PT-symmetric waveguide structure (see Figure 1(b)) already indicates a difference in the reflectivity R for light incident in the forward and backward directions. With a careful further optimization of the design, as well as an appropriate choice of the constituting materials, the reflection from one side could be significantly suppressed and increased – from the other, therefore, maximizing the contrast ratio between the two.

Finally, to realize the proposed PT-symmetric structure experimentally, we employ femtosecond direct laser writing (fsDLW). Several different approaches to waveguide fabrication are tested, including laser-ablated ridge and photonic crystal (PhC) waveguides. Scanning electron microscope (SEM) images of the latter implementations are presented in Figure 1(c).

References

1. Shastri, B. J., A. N. Tait, T. Ferreira de Lima, W. H. P. Pernice, H. Bhaskaran, C. D. Wright, and P. R. Prucnal, "Photonics for artificial intelligence and neuromorphic computing," *Nat. Photonics*, Vol. 15, pp. 102–114, 2021.

2. Huang, Y., Y. Shen, C. Min, S. Fan, and G. Veronis, "Unidirectional reflectionless light propagation at exceptional points," *Nanophotonics*, Vol. 6, No. 5, pp. 977–996, 2017.

Towards an Inverse-Designed Low-Cost Waveguide Absorber

Christoph Schmidt[1*], Alexander Schossmann[1,2], and Alexander Bergmann[1,2]
[1]Graz University of Technology, Inffeldgasse 33/I, 8010 Graz, Austria
[2]Christian Doppler Laboratory for Structured Matter Based Sensing, 8010 Graz, Austria
Corresponding author: christoph.schmidt@tugraz.at

Abstract: The paper introduces an inverse-designed waveguide absorber optimized for minimum reflections within the frequency range of 60 GHz to 90 GHz, with a structure that is manufacturable with cost-efficient 3D SLA printing. Validation of simulations indicates similar or even better performance than traditional absorbers, exhibiting an improved Voltage Standing Wave Ratio of 1.03.

1 Introduction

Waveguide absorbers with high return loss are crucial in microwave engineering, especially for terminating ports with impedance-matched loads. This is done by using special material (e.g., graphite or ferrite), removing impedance discontinuities, and ensuring a complete energy transfer into the absorber. Conventional absorbers, however, are constructed from specialized materials and require precise machining, leading to high costs. [1] Conversely, a 3D-printed methodology has demonstrated promising outcomes as a low-cost alternative. However, it depends on the empirical shape and material selection [2]. This work presents a novel methodology for a inverse-designed waveguide absorber, optimized to minimize reflections within the frequency range of 60 GHz to 90 GHz. Utilizing Inverse Design (ID), we propose a compact and cost-effective absorber that can be manufactured by consumer-grade 3D Stereolithography (SLA) printing techniques.

2 Inverse Design Formulation

Using ID, one may identify counterintuitive structures by Topology Optimization (TopOpt). The given problem is based on Maxwell's wave equation (Eq. 2) aiming to minimize the reflection coefficient S_{11} at the waveguide termination. The S_{11} parameter is used to determine the power dissipation. The gradient-based MMA solver is used for optimization. The optimization problem is formulated as a set of $N = \texttt{len}(\texttt{range}(60, 0.5, 90)\text{GHz}) = 61$ discrete sub-problems.

$$\max_{\varepsilon_r} \frac{1}{N} \sum_{N} \left(1 - |S_{11}|^2\right) \quad \text{with} \quad S_{11} = \frac{\int_{\partial\Omega} (\boldsymbol{E} - \boldsymbol{E}_1) \cdot \boldsymbol{E}^*}{\int_{\partial\Omega} (\boldsymbol{E} - \boldsymbol{E}_1) \cdot \boldsymbol{E}} \tag{1}$$

$$\text{s. t.:} \quad \nabla \times \left[\boldsymbol{\mu}_r^{-1} (\nabla \times \boldsymbol{E})\right] - \left(\omega^2 \mu_0 \boldsymbol{\varepsilon} - \mathrm{i}\omega\sigma\right) \boldsymbol{E} = \boldsymbol{0} \tag{2}$$

To guarantee a manufacturable design, the Solid Isotropic Material with Penalization (SIMP) method employing a Filter- and Threshold approach (Eq. 3) and a continuation scheme is utilized [3, 4]. We employ the continuous optimization variable $\theta_c \in [0, 1]$, which is subjected to filtering to remove small features ($\theta_c \to \theta_f$) and is then thresholded to enforce a near binary (black and white) designs ($\theta_f \to \theta$). The variable θ is then mapped linearly (Eq. 4) to the relative permittivity ε_r and the loss tangent $\tan\delta$.

$$0 \leq \theta_c \leq 1, \quad \theta_f = \theta_c + r_f^2 \nabla^2 \theta_f, \quad \theta = \frac{\tanh(\beta \cdot \eta) + \tanh(\beta(\theta_f - \eta))}{\tanh(\beta \cdot \eta) + \tanh(\beta(1 - \eta))} \tag{3}$$

$$\varepsilon_r = \varepsilon_{r,\text{Opt}} + \theta(\varepsilon_{r,\text{Air}} - \varepsilon_{r,\text{Opt}}), \quad \tan\delta = \tan\delta_{Opt} + \theta(\tan\delta_{Air} - \tan\delta_{Opt}) \tag{4}$$

3 Simulation and Verification

The 2D design is based on a *WR12* waveguide geometry, ensuring compatibility with standard components. The optimization domain measures 10 mm × 30 mm and is enclosed within a metal cavity. For the simulation's material parameters, standard 3D SLA printing resin properties ($\varepsilon_r = 2.76$; $\tan\delta = 0.025$) [5] have been taken.

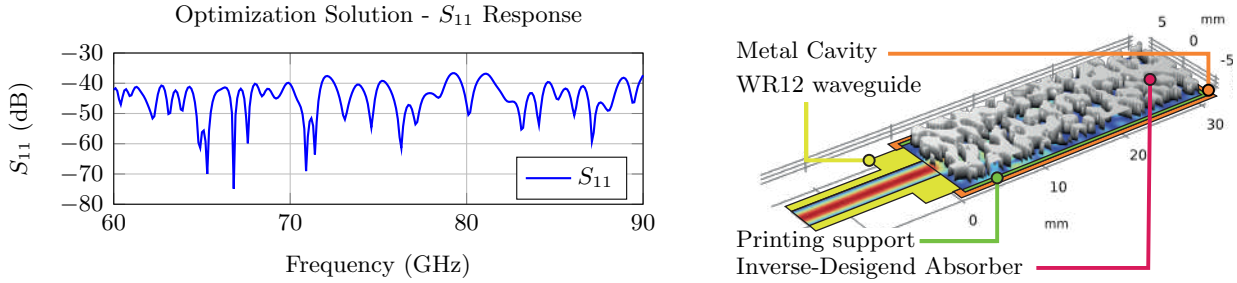


Figure 1: S_{11} spectra of the simulation and the corresponding optimized design.

A summary of the performance comparison regarding return loss and VSWR (Voltage Standing Wave Ratio) between the inverse-designed absorber and a commercially available WR-12 waveguide load is presented in Table 1.

Table 1: Comparison of WR-12 Waveguide Loads

	Frequency (GHz)	**Return Loss (dB)**	**VSWR** (Maximum)
Our Design	60–90	−36 to −75	1.03 : 1
Pasternack PE-W12TR1001	60–90	> −20	1.2 : 1
Flann 26040 Terminations	60.5–92	> −35	1.035 : 1

4 Conclusion and Outlook

This work introduces an inverse-designed waveguide absorber as a cost-effective alternative to traditional calibration loads. A compact and efficient design is achieved, demonstrating comparable or better performance in simulations across the 60 GHz–90 GHz range. The results indicate that good performance is achievable within a small area of 30 mm × 10 mm. The structure is designed for fabrication using commercially available 3D SLA printing, ensuring easy manufacturability. Future work will focus on fabricating the inverse-designed absorber and experimentally validating its performance regarding simulated results, including the return loss and overall absorption efficiency in a controlled measurement setup.

References

1. F. Nazari, F. Ghorbani, M. Khak, P. Soh, and H. Aliakbarian, "A thin and low-cost scalable waveguide load absorber," vol. 137, p. 153820. [Online]. Available: https://linkinghub.elsevier.com/retrieve/pii/S143484112100217X
2. Y. Arbaoui, V. Laur, A. Maalouf, P. Queffelec, D. Passerieux, A. Delias, and P. Blondy, "Full 3-D Printed Microwave Termination: A Simple and Low-Cost Solution," vol. 64, no. 1, pp. 271–278. [Online]. Available: http://ieeexplore.ieee.org/document/7355417/
3. M. P. Bendsøe and O. Sigmund, *Topology Optimization*. Springer Berlin Heidelberg. [Online]. Available: http://link.springer.com/10.1007/978-3-662-05086-6
4. F. Wang, B. S. Lazarov, and O. Sigmund, "On projection methods, convergence and robust formulations in topology optimization," vol. 43, no. 6, pp. 767–784. [Online]. Available: https://link.springer.com/10.1007/s00158-010-0602-y
5. M. Forstmeier, M. Yuan, S. Perini, M. Lanagan, and B. Foley, "Dielectric characterization of paraelectric particle-loaded polymer matrix composites and commercial photoresins at W-band frequencies," vol. 9, no. 2, p. e13458. [Online]. Available: https://linkinghub.elsevier.com/retrieve/pii/S2405844023006655

Terahertz liquid crystal transmissive metasurface with in-plane switching structure

Wei Zhu[1,2], Sheng Wang[1,2], Hangbing Guo[1,2], Jingbo Wu[1,2,3*], Kebin Fan[1,2,3], Caihong Zhang[1,2,3], Biaobing Jin[1,2,3], Huabing Wang[1,2,3], Jian Chen[1,2,3] and Peiheng Wu[1,2,3]

[1] Research Institute of Superconductor Electronics (RISE), School of Electronic Science and Engineering, Nanjing University, Nanjing, China
[2] Key Laboratory of Optoelectronic Devices and Systems with Extreme Performances of MOE, School of Electronic Science and Engineering, Nanjing University, Nanjing, China
[3] Purple Mountain Laboratories, Nanjing, China
[*]corresponding author:jbwu@nju.edu.cn

Abstract: Liquid crystal (LC) metasurfaces exhibit excellent tunability in multidimensional control of terahertz waves. We design a programmable metasurface with in-plane switching to enhance the response speed of LC. The simulated spectral response agrees well with the experimental results, manifesting its applications in the fields of computational imaging and dynamic holography.

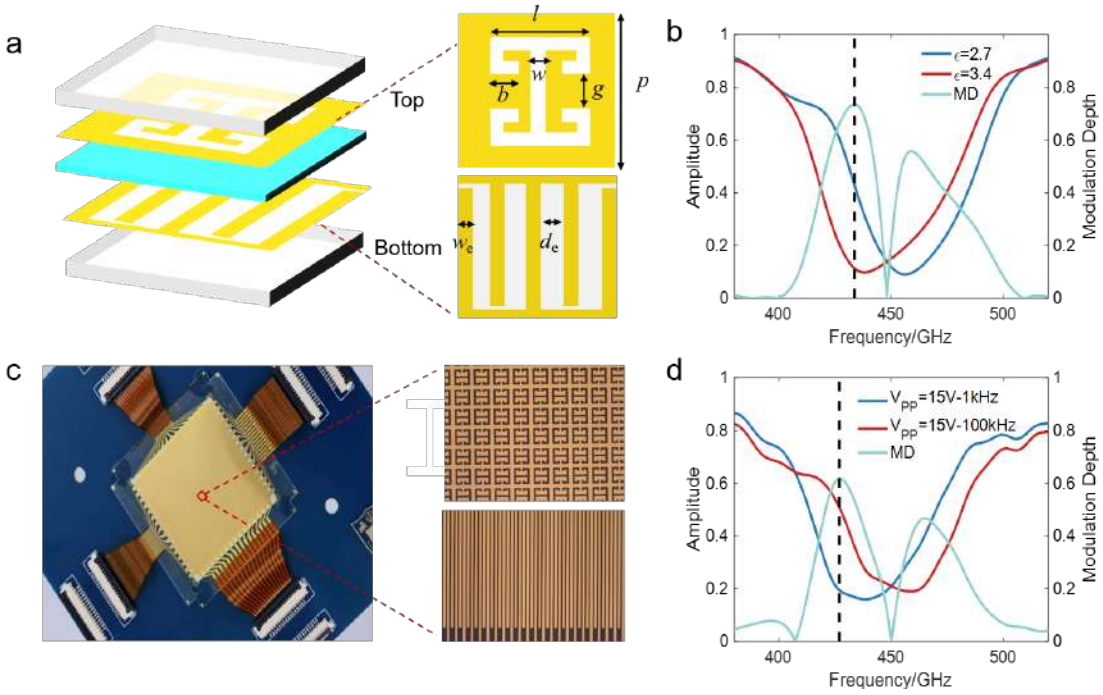


Figure 1 Device structure and spectral response of LC programmable metasurface. (a) Schematic of the unit cell structure and the diagram of metal layers. (b) Simulated THz transmission spectra using dual-frequency LC. (c) Optical image and microscopic image of fabricated devices. (d) Measured THz transmission spectra using dual-frequency LC.

We propose an LC-based programmable transmissive metasurface[1] with a fast response time. Figure 1a illustrates the structure of a unit cell and the diagram of the top and bottom metallic layers. From top to bottom, the unit cell consists of quartz substrate, gold layer, LC, gold layer, and quartz substrate. The thickness of both top and bottom quartz substrates is 500 μm, while that of the gold layer is 300 nm. The geometrical parameters

of the metal layers are defined as follows: p = 300 μm, b = 50 μm, l = 240 μm, g = 30 μm, w = 30 μm, w_e = 30 μm and d_e = 8 μm. A 10-μm-thick dual-frequency LC (Jiangsu Hecheng Display Technology, DP002-016) was selected as the spacer, as it exhibits a large birefringence at 0.2–1.1 THz and does not need an alignment layer to define the orientation of LC molecules. The loss tangent of the LC is set to 0.058.

The unit cell is numerically modeled and the simulated spectral response of the metasurface is presented in Fig. 1b. The results reveal a substantial switching contrast around 438 GHz, where the normalized transmission amplitude varies from 0.5 to 0.16. The modulation depth (*MD*) is defined as $MD = \frac{T_{off} - T_{on}}{T_{off}}$, where T denotes the signal amplitude and the calculated *MD* reaches up to 68%.

The optical image of the fabricated metasurface and its microscopic image are shown in Fig. 1c. Figure 1d illustrates the measured transmission amplitude response under biased voltage with different frequencies. The peak-to-peak voltage is set to 15 V. The dual-frequency LC is controlled by saturation voltages at 1 kHz and 100 kHz for the "on" and "off" states, respectively. The fabricated device achieves a maximum *MD* of 62.5% at 428 GHz, with the normalized transmission amplitude varying from 0.48 to 0.18. The experimental results show good agreement with the simulations, with slight frequency deviation primarily attributed to fabrication tolerances.

Table 1 Comparison of the dual-frequency LC response time under vertical field switching(VFS) and in-plane switching (IPS)

	Normal Switching	IPS
τ_{on}	7.8 ms	38.8 ms
τ_{off}	502.4 ms	48.4 ms
τ_{all}	510.2 ms	87.2 ms

Subsequently, the response time of the device was measured under both VFS and IPS conditions, with the results summarized in Table 1.

In conclusion, we demonstrate that the combination of IPS and dual-frequency LC effectively enhances the response speed of the programmable metasurface[2][3]. The design shows great potential for applications in computational imaging and dynamic holography.

References

1. Cui, T., Qi, M., Wan, X. et al. "Coding metamaterials, digital metamaterials and programmable metamaterials," Light Sci Appl. Vol. e218, No.3, 2014.
2. Chen CC, Chiang WF, Tsai MC, et al. "Continuously tunable and fast-response terahertz metamaterials using in-plane-switching dual-frequency liquid crystal cells," Optics Letters. Vol. 40, No. 9, 2021-2024, 2015.
3. Kowerdziej R, Wrobel J, Kula P. "Ultrafast electrical switching of nanostructured metadevice with dual-frequency liquid crystal," Scientific Reports. 9, 2019.

Calculating analogue solutions to PDEs with waves

R. G. MacDonald[1], A. Yakovlev[2], and V. Pacheco-Peña[1*]

[1] School of Mathematics, Statistics and Physics, Newcastle University, Newcastle Upon Tyne, NE1 7RU, United Kingdom

[2] School of Engineering, Newcastle University, Newcastle Upon Tyne, NE1 7RU, United Kingdom
[*]corresponding author: victor.pacheco-pena@newcastle.ac.uk

Abstract: An electromagnetic (EM) wave-based method of computing approximate analogue solutions to the Helmholtz equation is presented. This is done by exploiting a grid-like network of metatronic circuits at microwave frequencies. The behavior of the network is analogous to a numerical finite difference grid.

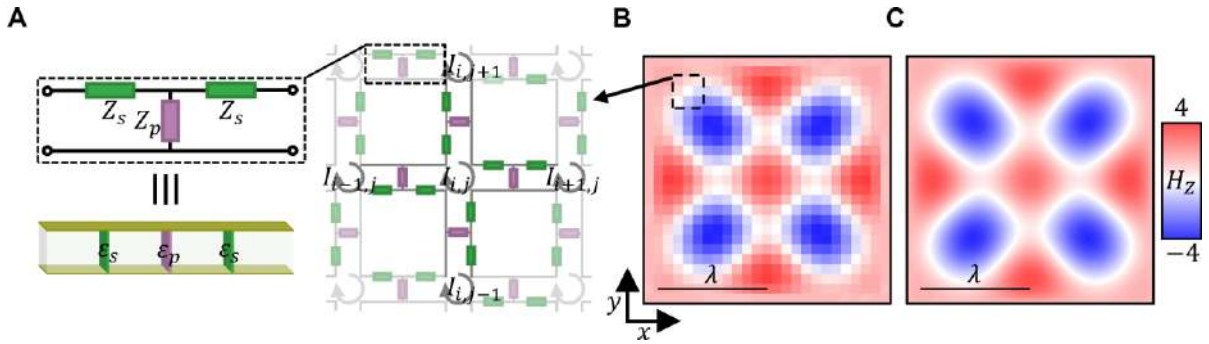


Figure 1. A. (Right) Circuit representation of a PDE solving network designed to solve the Helmholtz equation. The unit cell consists of a junction having four T-circuits (top-left) connected in series. (Bottom-left) Waveguide based-metatronic circuit implementation of a T-circuit. **B.** Numerical simulation for a $\mathbf{25 \times 25}$ network of waveguide based metatronic T-circuits solving a $\boldsymbol{g|_{\partial\Omega} = 1}$, $\boldsymbol{h = 0.2}$, $\boldsymbol{k = 3}$ boundary value problem **C**. Analytical solution.

In recent years, the advantages of electromagnetic (EM) waves, such as an inherent capability for parallel operations, have been exploited to enable high-speed computing operations[1]. EM wave-based processors have been demonstrated performing digital (or quasi-digital)[2] and analogue[1] operations, including elementary switching[3–8], differentiation[9–11], integration[12,13] and convolution[13,14]. Additionally, computationally intensive tasks, such as integral[15,16] or partial differential equation[17–19] (PDE) solving has also been reported. As it is known, analogue PDE solvers can be implemented using circuits[20]. The behavior of such networks is analogous to numerical finite difference grids, with the junctions between circuit elements acting as grid points. Similar approaches have been utilized to solve the Poisson equation $[\nabla^2 g(x,y) = 0]$ at higher frequencies[17,18].

Motivated by the potential applications of metatronic circuits for analogue computing, in this work we present a method of solving PDEs in the form of the Helmholtz equation $[\nabla^2 g(x,y) + k^2 g(x,y) = 0]$ by exploiting a network of waveguide-based metatronic T-circuits at microwave frequencies. A schematic representation of this network is presented in Fig. 1A. Like the previously discussed methods, the network emulates an area of finite difference simulation space with the PDE parameters (grid separation h and wavenumber k) determined by the emulated impedances of the metatronic circuit elements (Z_s and Z_p). Numerical simulation results obtained using CST Studio Suite®, for a 25×25 network solving a $g|_{\partial\Omega} = 1$, $h = 0.2$, $k = 3$ Dirichlet boundary value problem are presented in Fig. 1B. Analytical results for the same scenario are depicted in Fig. 1C As it can be seen, there is a clear agreement between the results indicating the PDE solving network is producing an accurate solution.

This work was supported by the Leverhulme Trust under the Leverhulme Trust Research Project Grant scheme (No. RPG-2020-316 and RPG-2023-024).

References

1. Zangeneh-Nejad, F., Sounas, D. L., Alù, A. & Fleury, R. Analogue computing with metamaterials. *Nat Rev Mater* **6**, 207–225 (2020).
2. Singh, P., Tripathi, D. K., Jaiswal, S. & Dixit, H. K. All-Optical Logic Gates: Designs, Classification, and Comparison. *Advances in Optical Technologies* **2014**, 1–13 (2014).
3. Yakovlev, A. & Pacheco-Peña, V. Enabling High-Speed Computing with Electromagnetic Pulse Switching. *Adv Mater Technol* **5**, 2000796 (2020).
4. MacDonald, R. G., Yakovlev, A. & Pacheco-Peña, V. Amplitude-Controlled Electromagnetic Pulse Switching Using Waveguide Junctions for High-Speed Computing Processes. *Advanced Intelligent Systems* **2200137**, 2200137 (2022).
5. Rogers, W., Johnson-Richards, C., Yakovlev, A. & Pacheco-Peña, V. Perfect splitting in rectangular-waveguide junctions for analog computing. *Phys Rev Appl* **21**, 054054 (2024).
6. Pal, A., Ahmed, M. Z. & Swarnakar, S. An optimized design of all-optical XOR, OR, and NOT gates using plasmonic waveguide. *Opt Quantum Electron* **53**, 84 (2021).
7. Matos Barreto, P. P. & Rodriguez-Esquerre, V. F. Fully Integrated AND and OR Optical Logic Gates. in *Latin America Optics and Photonics Conference* vol. 26 Th3A.2 (OSA, Washington, D.C., 2018).
8. Ventisei, A., Yakovlev, A. & Pacheco-Peña, V. Exploiting Petri Nets for Graphical Modelling of Electromagnetic Pulse Switching Operations. *Adv Theory Simul* **2100429**, 2100429 (2021).
9. Knightley, T., Yakovlev, A. & Pacheco-Peña, V. Neural Network Design of Multilayer Metamaterial for Temporal Differentiation. *Adv Opt Mater* **11**, 2202351 (2023).
10. Zhang, J., Ying, Q. & Ruan, Z. Time response of plasmonic spatial differentiators. *Opt Lett* **44**, 4511 (2019).
11. MacDonald, R. G., Yakovlev, A. & Pacheco-Peña, V. Time derivatives via interconnected waveguides. *Sci Rep* **13**, 13126 (2023).
12. Bezus, E. A., Doskolovich, L. L., Bykov, D. A. & Soifer, V. A. Spatial integration and differentiation of optical beams in a slab waveguide by a dielectric ridge supporting high-Q resonances. *Opt Express* **26**, 25156 (2018).
13. Silva, A. *et al.* Performing Mathematical Operations with Metamaterials. *Science (1979)* **343**, 160–163 (2014).
14. Park, M. & Park, Y. Metasurface-Based Imagers Enabled Arbitrary Optical Convolution Processing. *Light Sci Appl* **11**, 10–11 (2022).
15. Mohammadi Estakhri, N., Edwards, B. & Engheta, N. Inverse-designed metastructures that solve equations. *Science (1979)* **363**, 1333–1338 (2019).
16. Tzarouchis, D. C., Mencagli, M. J., Edwards, B. & Engheta, N. Mathematical operations and equation solving with reconfigurable metadevices. *Light Sci Appl* **11**, 263 (2022).
17. Sun, S. *et al.* Induced homomorphism: Kirchhoff's law in photonics. *Nanophotonics* **10**, 1711–1721 (2021).
18. Miscuglio, M. *et al.* Approximate analog computing with metatronic circuits. *Commun Phys* **4**, 196 (2021).
19. MacDonald, R. G., Yakovlev, A. & Pacheco-Peña, V. Solving partial differential equations with waveguide-based metatronic networks. *Advanced Photonics Nexus* **3**, (2024).
20. Kron, G. Electric circuit models of partial differential equations. *Electrical Engineering* **67**, 672–684 (1948).

A Metamaterial Coherent Detector for mmWave Operation

N. Rozman[1], O. Khatib[2], and W. J. Padilla[2,*]

[1]Leidos Inc., USA
[2]Duke University, USA
[*]corresponding author: willie.padilla@duke.edu

Abstract: A coherent detector, that is both sensitive to phase and amplitude, has yet to be established at high frequencies. To address this gap, we experimentally demonstrate a frequency, phase, and power-sensitive metamaterial coherent detector (MCD) for operation at millimeter (mmW) wavelengths.

Metamaterials have become a promising choice for developing high-frequency components because they can be tailored to cover a wide range of the electromagnetic spectrum through geometric tuning. Metamaterial detectors can leverage engineered absorption in order to measure electromagnetic signals. Metamaterial absorbers have been experimentally demonstrated for a wide variety of applications, including hyperspectral imaging [1], refractive index sensing, and IR detection [2]. Electromagnetic metamaterial absorbers may be fashioned from metal-based metamaterials, [3] or from all dielectric structures, [4] both of which achieve near-unity absorption A at a desired frequency, $f0$. [5]

Our approach leverages two port excitation from opposite sides of the absorber, which can be modeled by temporal coupled mode theory (TCMT), that provides is a general framework useful for describing idealized resonant systems with an added weak disturbance. [6] In this case, the metamaterial is strongly absorbing when radiation of equal power is incident from both sides and is in-phase (symmetric absorber) or out-of-phase (anti-symmetric absorber). In electromagnetic wave absorbers, the perturbation represents a weak coupling of the resonant systems together, and the method is analogous to time-dependent perturbation theory. [7]

In this work, we experimentally demonstrate a metamaterial coherent detector (MCD) whose response is dependent on both the amplitude and phase of an incident electromagnetic wave. The coherent detector uses a metal-based anti-symmetric metamaterial absorber with an integrated pyroelectric material (Fig. 1a). The metasurface was designed to detect incident mmWave radiation at $f_0 = 91.5$ GHz when two out of phase counter-propagating beams are applied to both sides of the detector (Fig. 1c and 1e).

To demonstrate the coherent nature of the detector, the back reflecting mirror was moved

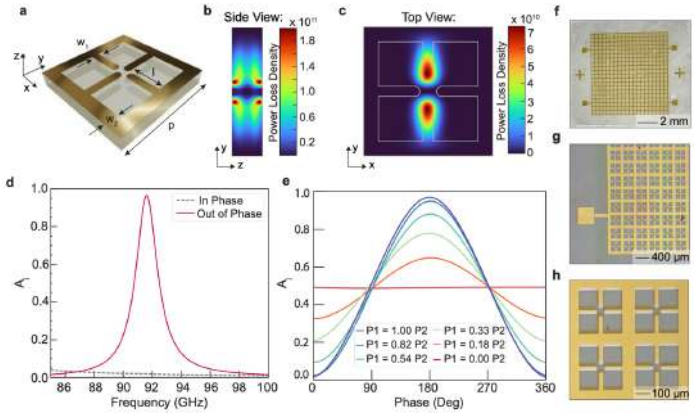


Figure 1 - Frequency, phase, and power-sensitive metamaterial coherent detector. (a) Rendered schematic of the unit cell geometry comprised of two identical patterned metamaterial layers on both sides of a pyroelectric thin film. (b,c) Simulation of the power loss density for out-of-phase excitation at the resonance frequency. (d) Frequency-dependent absorption is shown for out-of-phase (red, solid) and in-phase (gray, dashed) radiation. (e) Normalized phase-sensitive absorption for varying, uneven port power excitation. (f) Image of the coherent detector and. (g,h) optical microscopy images of the metamaterial pattern.

along the optical axis (z-axis of Fig. 2) in a direction away from the device, effectively modifying the phase difference $\Delta\phi$ of radiation incident on the metasurface. Experimental measurements of the detected metamaterial pyroelectric current (Imm) as a function of mirror distance are plotted in Fig. 2b-d for three different operating frequencies. The dependence of the detected metamaterial pyroelectric current as a function of mirror position, or $\Delta\phi$, is plotted as the blue curve for 80 GHz (Fig. 3b), red curve for 91.5 GHz (Fig. 2c), and green curve for 100 GHz (Fig. 2d). The detected signal oscillates as a function of mirror position, or $\Delta\phi$, demonstrating phase-dependent absorptance. As expected, the amplitude of the detected pyroelectric current is relatively small at frequencies of 80 and 100 GHz, with peak values of approximately I_{mm} = 40 pA and Imm = 35 pA, respectively, which is attributed to the lower absorptance values realized by the metasurface.

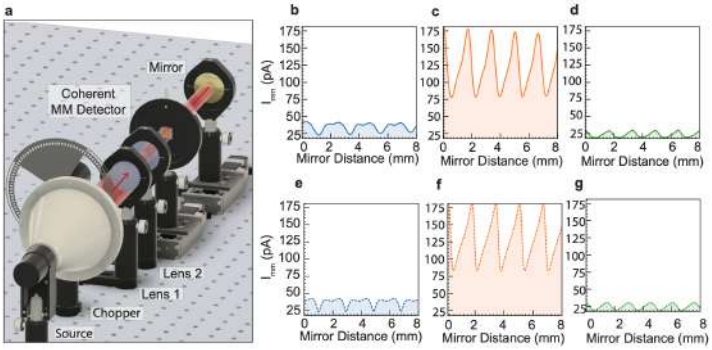


Figure 2 - (a) A schematic depicting the optical configuration used to experimentally test the metamaterial coherent detector. Experimental (b-d) and theoretical (e-g) pyroelectric current signal at frequencies of 80 GHz (b,e), 91.5 GHz (c,f), and 100 GHz (d,g) as a function of mirror distance.

In summary, our study has successfully conceptualized, simulated, and experimentally validated the first metamaterial coherent pyroelectric detector. Our design was specifically tailored for frequency-selective coherent detection of mmW radiation, but it can be scaled to operate at other electromagnetic bands. WOur study has successfully conceptualized, simulated, and experimentally validated the first metamaterial coherent pyroelectric detector. Our design was specifically tailored for frequency-selective coherent detection of mmW radiation, but it can be scaled to operate at other electromagnetic bands. Our investigation highlights the detector's sensitivity to frequency, phase, and power. This work marks a significant stride in coherent detection, opening avenues for advancements in high-frequency detectors. Our findings lay the groundwork for further exploration and development in this domain, promising potential innovations in the field of metamaterial-based detectors.

References

1. X. Liu, T. Starr, A. F. Starr, and W. J. Padilla, "Infrared spatial and frequency selective metamaterial with near-unity absorbance," Phys. Rev. Lett. 104 (2010).

2. A. Ishikawa and T. Tanaka, "Metamaterial absorbers for infrared detection of molecular self-assembled monolayers," Sci. Reports 5 (2015).

3. N. I. Landy, S. Sajuyigbe, J. J. Mock, et al., "Perfect metamaterial absorber," Phys. Rev. Lett. 100 (2008).

4. X. Liu, K. Fan, I. V. Shadrivov, and W. J. Padilla, "Experimental realization of a terahertz all-dielectric metasurface absorber," Opt. Express 25, 191 (2017).

5. X. Ming, X. Liu, L. Sun, and W. J. Padilla, "Degenerate critical coupling in all-dielectric metasurface absorbers," Opt. Express 25, 24658 (2017).

6. W. Suh, Z. Wang, and S. Fan, "Temporal coupled-mode theory and the presence of non-orthogonal modes in lossless multimode cavities," IEEE J. Quantum Electron. 40, 1511–1518 (2004).

7. J. R. Piper and S. Fan, "Total absorption in a graphene monolayer in the optical regime by critical coupling with a photonic crystal guided resonance," ACS Photonics 1, 347–353 (2014)

Tunable nanostructured metamaterial with epsilon-near-zero transition layer

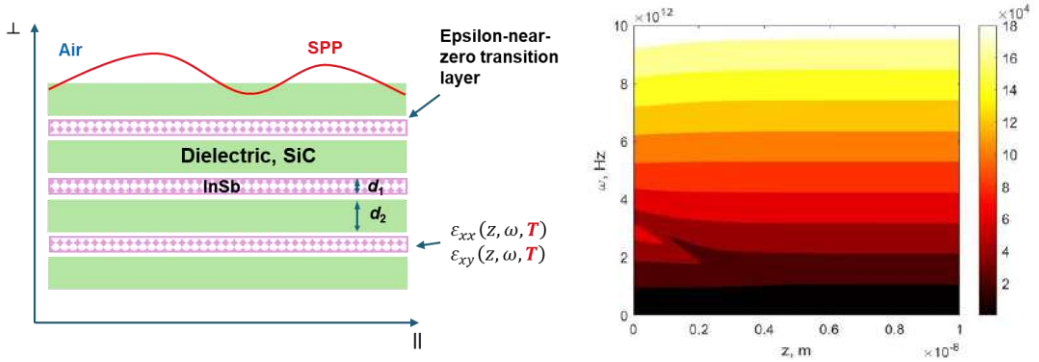
T. Gric[1], E. Rafailov[2]

[1] Department of Electronic Systems, Vilnius Gediminas Technical University, Vilnius, Lithuania
[2] Aston University, Birmingham, UK
*corresponding author: Tatjana.gric@vilniustech.lt

Abstract: Propagation of surface plasmon polaritons at the boundary of semiconductor based nanostructured metamaterial with epsilon-near-zero transition layer is investigated. The dispersive properties are altered by a dielectric function being temperature dependent allowing for sensing applications.

The metamaterials offer much-needed atypical material features to help with the subwavelength concentration of electromagnetic fields, which is the focus of nanophotonics research [1]. By investigating propagation of surface plasmon polaritons (SPPs) at the boundary of semiconductor based nanostructured metamaterial with epsilon-near-zero transition layer, we demonstrate that the surface plasmon's dispersion along with the absorption is altered by a continuous dielectric function that is temperature dependent opening the wide avenues for sensing applications.

A continuous function $\varepsilon(z)$ of the normal to the interface coordinate z describes the properties of the nanostructured metamaterial structure due to the existence of the transition layer. It should be topologically equal to a kink, however the major results for the spectrum of SPP are not sensitive to the particular form of $\varepsilon(z)$ [2]. Here, we'll look at a semiconductor-based metamaterial heterostructure made up of stacked anisotropic semiconductor sheets separated by dielectric layers, as schematically shown in Figure 1.



(a) (b)

Fig. 1. Diagram showing the contact between air and an infinitely layered nanostructured metamaterial made of alternating dielectric and semiconductor layers (a). Real part of the propagation constant β (b). Herein, d_1=6 nm, d_2=10 nm, T=350K.

To describe the optical response of such a system, we employ the effective-medium technique [3], which is suitable when the wavelength of the light in question is substantially larger than the thickness of any layer. It is based on the average of the structure parameters. The effective homogeneous media for the semi-infinite periodic structure are thus still covered in this work.

By matching the tangential components of the electrical and magnetic fields, the dispersion relation for the

surface modes localized at the boundary separating an anisotropic media and dielectric is inferred at the interface. Because the relevant layers are represented by semiconductors, we assume that the permittivities $\varepsilon_{xx,xy}(\omega)$ are frequency dependent.

It should be mentioned that the frequency range of surface wave existence may be significantly controlled by adjusting the permittivities and thicknesses of the layers [4] utilized in the metamaterial. One must evaluate the tangential components of the electric and magnetic fields at the interface and generate a single surface mode with the propagation constant in order to determine the unique dispersion relation for the surface modes restricted at the interface between metamaterial and air [5].

$$\beta(z,\omega) = k\sqrt{\frac{\left(1-\varepsilon_{||}(z,\omega)\right)\varepsilon_{\perp}(z,\omega)}{1-\varepsilon_{\perp}(z,\omega)\varepsilon_{||}(z,\omega)}}, \tag{1}$$

where k is the wavevector's absolute value in vacuum and β is the wavevector component parallel to the interface.

References

1. Cai, W. and V. Shalaev, Optical Metamaterials: Fundamentals and Applications (Springer, New York, 2010).
2. Litchinitser, N. M., A. I. Maimistov, I. R. Gabitov, R. Z. Sagdeev, and V. M. Shalaev, "Metamaterials: Electromagnetic enhancement at zero-index transition," Opt. Lett., Vol. 33, 2350, 2008.
3. Zhang, X., Y. Wu, „Effective medium theory for anisotropic metamaterials," Sci Rep, Vol. 5, 7892, 2015.
4. Gric, T. "Surface-plasmon-polaritons at the interface of nanostructured metamaterials," Prog. Electromagnetics Res., Vol. 46, 165–172, 2016.
5. Iorsh, I., A. Orlov, P. Belov, and Y. Kivshar, "Interface modes in nanostructured metal-dielectric metamaterials," Appl. Phys. Lett., Vol. 99, No. 15, 151914, 2011.

Optical characterization of barium titanate from the visible to mid-infrared range by using Mueller-matrix spectroscopic ellipsometry

Jiwon Kang[1,2], Nina Hong[3], Martin Thomaschewski[1], Prachi Thureja[1], Sangjun Han[2], Harry A. Atwater[1*], and Min Seok Jang[1,2*]

[1]Thomas J. Watson Laboratory of Applied Physics, California Institute of Technology, Pasadena, California 91125, USA
[2]School of Electrical Engineering, Korea Advanced Institute of Science and Technology, Daejeon 34141, Republic of Korea
[3]J.A. Woollam Co. Inc., Lincoln, Nebraska 68508, USA
[*]corresponding authors: haa@caltech.edu (H. A. Atwater) and jang.minseok@kaist.ac.kr (M. S. Jang)

Abstract: Barium titanate (BTO) displays diverse exotic characteristics, therefore, various studies on its engineering have been conducted. However, accurate optical constants of BTO have not been reported. Here, we firmly determined the complex refractive index of BTO from the visible to the mid-infrared range by using Mueller-matrix spectroscopic ellipsometry on BTO.

Barium titanate ($BaTiO_3$, BTO) is one of the earliest reported lead-free ferroelectric polydomain crystal materials, first documented in the 1940s [1]. Numerous studies on BTO have been conducted to analyze and engineer its exotic physical characteristics—including ferroelectricity, pyroelectricity, piezoelectricity, and biocompatibility—which primarily originate from differences in the bonding energy of ionic bonds (Ba^{+2}/TiO_3) and covalent bonds (Ti/O) [2]. Additionally, the high dielectric constant (ε_r > 2,000) of a-axis BTO facilitates various applications, such as multilayer ceramic capacitors, ferroelectric tunnel junctions, and positive temperature coefficient thermistors. BTO exhibits a tetragonal structure (symmetry group *P*4*mm*) at room temperature with anisotropy between the crystallographic c-axis and the other axes. From an optical perspective, BTO shows low optical losses from the near-ultraviolet to near-infrared range, along with transparency, and the Pockels effect, an ultrafast second-order linear electro-optic effect, enables the development of diverse optical components and nonlinear optical systems. In order to accurately characterize the Pockels tensor coefficients of BTO, its intrinsic complex refractive indices must be precisely determined to observe refractive index modulation under an applied electric field. However, the absence of accurate optical constants of anisotropic BTO along ordinary and extraordinary axes due to the ferroelectric multidomain makes it difficult to utilize BTO as an active matrix of nanophotonic devices.

Standard spectroscopic ellipsometry (SE) is a widely used, efficient, and non-destructive optical measurement technique for determining materials' optical thickness and refractive index. The measurement quantities are based on the complex ratio of *p*- to *s*-polarized Fresnel reflection coefficients, corresponding to the two on-diagonal elements of the 2 × 2 complex-valued Jones matrix. While SE effectively quantifies the amplitude and phase ratio of completely polarized light, it struggles to describe the non-ideal polarization states of light, which can frequently arise in anisotropic materials. To overcome these limitations, Mueller-matrix (MM) SE extends the analysis by employing 4 × 4 real-valued Mueller matrices and 4 × 1 Stokes vectors, offering a comprehensive representation of polarization effects, including depolarization and cross-polarization [3]. This capability enables precise optical characterization of complex optical systems and intricate materials.

In this work, we optically characterize the refractive indices, extinction coefficients, and birefringence of BTO across a broad spectral range, from the visible to the mid-infrared range, using transmission and reflection measurement modes. Due to the presence of multi-domains in a-axis BTO, where the c-axis lies in the sample

plane but lacks macroscopic long-range order, we introduce a smearing effect to the Euler angle associated with the optic axis in our ellipsometry model. This modeling approach allows us to extract a single set of ordinary and extraordinary refractive indices consistent for both a-axis and c-axis BTO samples. Furthermore, we utilize strong interference fringes observed in the ellipsometry data, caused by the differing phase velocities of the *p*- and *s*-polarized waves propagating through the sample. These fringes enhance sensitivity to birefringence in the transparent region. To further refine our measurements of the extremely low extinction coefficients (k) in regions where the sample remains partially transparent, we incorporate transmittance data from UV-Vis spectrometry and FTIR measurements. Finally, to validate our fitted data, we calculate rigorous coupled-wave analysis and finite element method simulations, the results of which closely align with the experimental data. We envision that our work will contribute to flourishing BTO-based nanophotonic devices such as photonics integrated circuits and active metasurfaces in various operating ranges, leveraging the physically fitted and practically verified optical characteristics of BTO.

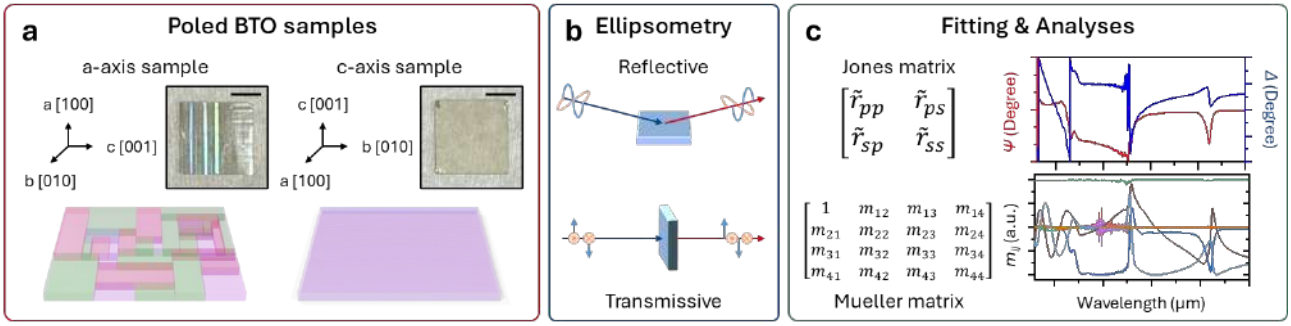


Figure. Schematic illustration of our workflow. (a) Poled BTO samples with a-axis and c-axis orientations. The a-axis BTO sample exhibits a ferroelectric multidomain structure. Scale bar: 2 mm. (b) Spectroscopic ellipsometry was performed for both reflective and transmissive measurements. (c) The acquired ellipsometry data were fitted and analyzed to extract physical optical constants using Jones matrices and Mueller matrices, respectively.

Acknowledgement

This research was supported by Culture, Sports and Tourism R&D Program through the Korea Creative Content Agency (KOCCA) grant funded by the Ministry of Culture, Sports and Tourism in 2024 (RS-2024-00332210), Basic Science Research Program through the National Research Foundation of Korea (NRF) funded by the Ministry of Education (RS-2024-00413441), and the Ministry of Science and Technology (2022R1A2C209209513, RS-2024-00416583, RS-2024-00414119). This work was also supported by the Air Force Office of Scientific Research Meta-Imaging MURI under grant no. FA9550-21-1-0312 and the Caltech Space Solar Power project.

References

1. Wu, B. “Barium Titanate: a New Ferro-Electric,” Nature, Vol. 157, No. 808, pp. 808, 1946.
2. Karvounis, A., Timpu, F., Vogler-Neuling, V. V., Savo, R. and Grange, R. “Barium titanate nanostructures and thin films for photonics,” Adv. Opt. Mater., Vol. 8, No. 2001249, 2020.
3. Hilfiker, J. N., Hong, N. and Schoeche, S. “Mueller matrix spectroscopic ellipsometry,” Adv. Opt. Technol. Vol. 11, No. 3, pp. 59–91, 2022.

Optical characterization of periodic subwavelength structures composed of polycyclic aromatic hydrocarbons

K. Morita[1], H. Okamoto[1,2], and K. Imura[1*]

[1] Department of Chemistry and Biochemistry, School of Advanced Science and Engineering, Waseda University, Japan
[2]Institute for Molecular Science, Japan
[*]Corresponding author: imura@waseda.jp

Abstract: Perylene crystals were irradiated by electron-beam to induce chemical reactions. Mass spectrum shows oligomerization of the molecules. Raman spectroscopic analysis of the product indicates that dimers are produced. Periodic subwavelength structure was fabricated on perylene crystals. Scattering spectrum of the structure shows a peak originated from the diffraction effect.

Polycyclic aromatic hydrocarbons (PAHs) consisted of several aromatic rings show broad absorption band and high luminescence quantum yields. For this reason, the PAHs are promising for organic optoelectrical devices.[1] PAHs can be oligomerized by the irradiation of high energy beams such as ultraviolet and electron beam (e-beam). By precisely controlling the e-beam irradiation, the oligomerization of the PAHs and the reaction area can be controlled. In this way, fabrication of periodic subwavelength structures with the oligomerized PAHs are feasible. In this study, we prepared the oligomer of perylene molecules by the e-beam irradiation and fabricated subwavelength periodic structures of the perylene oligomer using the space-selective reaction.

Powder of the perylene was heated to prepare the crystal on the sample substrate by the sublimation. Then, the crystal was placed in a low-vacuum scanning electron microscope and the e-beam was irradiated to the surface of the crystal. To fabricate the periodic structures, the sample substrate was raster-scanned by the closed loop piezo stage. The morphology of the sample was evaluated by an atomic force microscope (AFM). Mass of the reaction products was evaluated by the matrix assisted laser desorption/ionization mass spectrometry. Optical properties of the products were evaluated by extinction, Raman, and photoluminescence (PL) spectroscopy. Scattering and PL properties of the periodic structure were evaluated by dark-field (DF) and the confocal microscope, respectively.

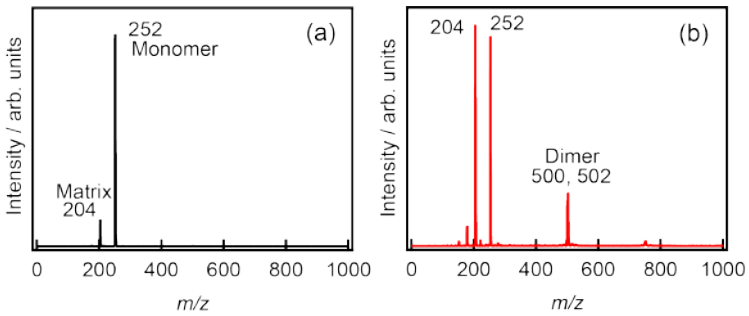


Figure 1. Mass spectra of the crystal (a) without and (b) with the e-beam irradiation.

Figure 1(a,b) shows the mass spectra taken on the crystal without and with the e-beam irradiation, respectively. In Fig. 1(a), the spectrum shows the ion peaks at m/z = 204 and 252, which are assignable to the matrix and the monomer, respectively. On the other hand, in Fig. 1(b), the spectrum shows the peaks at m/z = 500 and 502, in addition to m/z = 204 and 252. The peaks at m/z = 500 and 502 are assignable to the molecular species that the

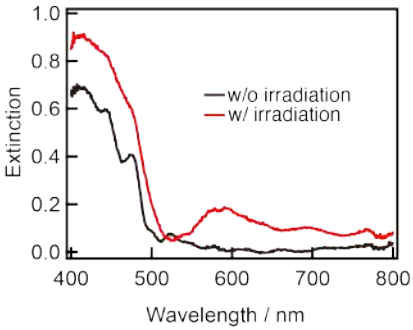


Figure 2. Extinction spectra of the crystal without (black) and with (red) the e-beam irradiation.

mass is 2 or 4 smaller than that of the perylene dimer. This result implies the formation of the one or two C-C bonds after releasing two or four H atoms.

Figure 2 shows the extinction spectra taken on the crystal without (black) and with (red) the e-beam irradiation. The irradiated crystal shows the increase of the absorption in the longer wavelength region compared to that of the neat crystal. This indicates that the formation of the perylene polymer with the extended π-conjugated molecular orbital. By using the Raman spectroscopy, the molecular structure was investigated and found that the perylene molecule was oligomerized to dimer with ribbon-like shape.

The periodic dotted pattern with a pitch of 600 nm was fabricated on the perylene crystal. Figure 3(a) shows the AFM image of the fabricated structure. The black area represents the surface of the crystal. We found from the figure that the irradiated area was protruded from the crystal surface. Figure 3(b) shows the line profile along the red line shown in Fig. 3(a). Height and width of the protrusion were determined to be ~50 nm and ~300 nm, respectively. This result indicates that the reaction area can be controlled with subwavelength scale.

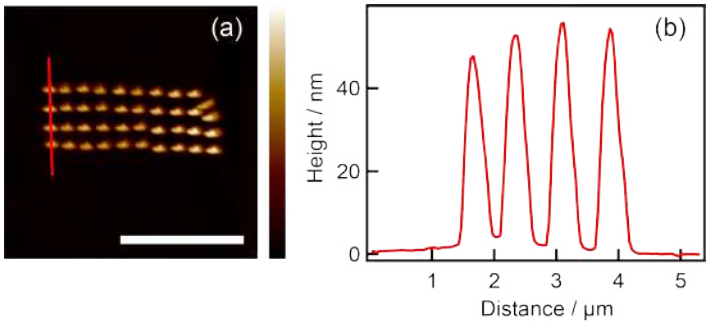


Figure 3. (a) AFM image of the dotted pattern on the perylene crystal. Scale bar: 5 μm. (b) Line profile along the red line shown in (a).

Figure 4(a,b) shows the DF scattering images of the structure in Fig. 3 taken at the wavelengths of 870 and 460 nm, respectively. In the figures, black square shows the fabricated area of the periodic structure, and the white dashed line shows the edge of the crystal. In Fig. 4(a), the edge of the crystal shows the strong scattering, and the dotted area show only minor signal. On the other hand, in Fig. 4(b), the dotted area shows the strong signal. Figure 4(c,d) shows the DF scattering spectra at the edge of the crystal and the periodic structure, respectively. In Fig. 4(c), the spectrum shows a broad scattering peak at ~690 nm. In contrast, in Fig. 4(d), the spectrum shows a sharp peak near 450 nm. The peak is only observable on the periodic structure area, and thus origin of the peak is attributed to the diffraction effect of the periodic structure.

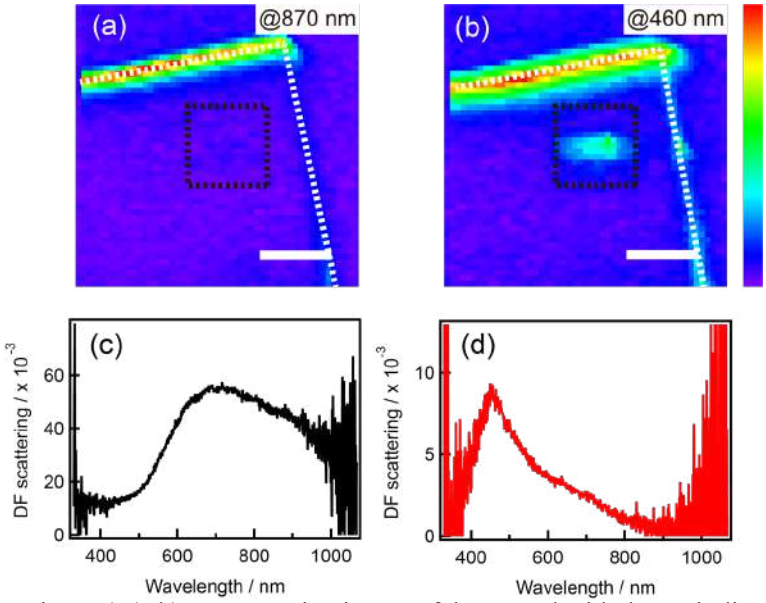


Figure 4. (a,b) DF scattering image of the crystal with the periodic structure shown in Fig. 3 taken at 870 and 460 nm, respectively. Scale bars: 5 μm. Black square shows the fabricated area of the periodic structure, and white dotted line shows the edge of the crystal. (c,d) DF scattering spectra taken at the edge of the crystal and the periodic structure, respectively.

References

1. Liu, Z., Fu, S., Liu, X., Narita, A., Samorì, P., Bonn, M., and Wang, H. I., "Small Size, Big Impact: Recent Progress in Bottom-Up Synthesized Nanographenes for Optoelectronic and Energy Applications," Adv. Sci., Vol. 9, 2106055, 2022.

Spatio-spectral fission through time-varying layers

Wallace Jaffray[1] , Sven Stengel[1] , Fabio Biancalana[1] , Colton Bradley Fruhling[2] , Mustafa Ozlu[2] , Michael Scalora[3] , Alexandra Boltasseva[2] , Vladimir M. Shalaev[2] and Marcello Ferrera[1,*]

[1]Institute of Photonics and Quantum Sciences, Heriot-Watt University, SUPA, Edinburgh, EH14 4AS, UK

[2]Elmore Family School of Electrical & Computer Engineering and Birck Nanotechnology Center, Purdue University, West Lafayette, Indiana 47907, USA

[3]FCDD-AMT-MGR, DEVCOM AvMC, Charles M. Bowden Research Center, Redstone Arsenal, AL 35898-5000, USA

[*]corresponding author: m.ferrera@hw.ac.uk

Abstract: Transparent conducting oxides are highly-doped semiconductors exhibiting remarkable nonlinear optical properties in the near-infrared spectrum—a feature previously overlooked despite their long-standing application in photovoltaics and touchscreens. Here we report the spatio-spectral fission of an ultra-fast pulse trespassing a thin film of aluminium zinc oxide with a non-stationary refractive index.



Figure 1. – Spatio-spectral fission of an optical pulse trespassing a non-stationary ultra-thin layer. The scheme can also describe a fs-pulse going through an optically pumped subwavelength film of aluminium zinc oxide operating at the cross-over wavelength.

The theory of wave propagation in non-stationary media originated from the concept of time-varying permittivity [1]. Experimental demonstrations of the effects of time-varying media on light propagation first emerged in plasma physics under the name of photon acceleration. In these settings, significant effects can be observed when photons interact with a plasma undergoing an abrupt electron density transition [2], [3].

More generally, when a propagating wave encounters a sudden change in the environmental refractive index, it experiences a phenomenon known as time refraction [2], [3], [4], [5]. This effect is analogous to the behavior of a wave at a spatial material interface and results in a frequency shift of the photon, described by the equation $\omega_1 n_1 = \omega_2 n_2$, where ω_1 and ω_2 are the angular frequencies before and after the time boundary, and n_1 and n_2 are the refractive indices before and after the transition. In its differential form, $d\omega/\omega = dn/n$, this equation explicitly states that a large change in the refractive index over a very short time is required for a frequency conversion process to be experimentally measurable.

Due to this requirement, substantial experimental advancements in time-varying materials have been slow, despite their vast potential and intrinsic scientific interest. Typically, real-world temporal index changes are either extremely fast or large, but these two characteristics generally exclude each other [6]. Recently, transparent conducting oxides (TCOs) have proven of critical importance in overcoming this trade-off in the near-infrared region. These materials possess a bandwidth exceeding 260 nm [7], [8] and enable unity changes in the refractive index [8].

In this work, an ultra-thin time-varying layer is attained by optically pumping a sub-wavelength film of aluminum zinc oxide (AZO) operating in its near-zero-index (NZI) region. The optical excitation induces a steep

refractive index gradient, initially increasing and then decreasing, thereby exerting opposite effects on the front and back of a synchronized probe. Consequently, the transmitted pulse undergoes spatial splitting into two halves, each containing approximately half of the total spectral power (see Fig.1). These two "fission products" also exhibit strong spectral shifts that are opposite in sign for each half and centered around the NZI carrier wavelength. Our analytical model, adapted from the generalized spatio-temporal Snell's law for subwavelength time-varying layers, quantitatively accounts for all measurable macroscopic parameters, including spectral shifts, angular shifts, and energy redistribution. The spatio-spectral fission observed here represents one of the most extreme nonlinear optical phenomena occurring over deeply subwavelength propagation lengths. These findings open new possibilities for the temporal engineering of material optical properties while also providing insights into previously reported results that did not account for the spatial distribution of the propagating pulse.

M.F. acknowledges economic support from EPSRC project ID: EP/X035158/1, and AFOSR (EOARD) under Award No.FA8655-23-1-7254. A.B. and V.M.S. acknowledge support by the U.S. Department of Energy, Office of Basic Energy Sciences, Division of Materials Sciences and Engineering under Award DE-SC0017717.

References

1. F.R. Morgenthaler "Velocity Modulation of Electromagnetic Waves," IRE Transactions on Microwave Theory and Techniques, 6, 2, 167–172, (1958).
2. J. T. Mendonça and P. K. Shukla, "Time Refraction and Time Reflection: Two Basic Concepts," Phys Scr, 65, 2,160–163, (2002)
3. J. T. Mendonca, Theory of Photon Acceleration. (2001)
4. F. Biancalana, A. Amann, A. V. Uskov, and E. P. O'Reilly, "Dynamics of light propagation in spatiotemporal dielectric structures," Phys Rev E Stat Nonlin Soft Matter Phys, 75, 4, 046607, (2007)
5. E. Galiffi et al., "Photonics of time-varying media," Advanced Photonics, 4, 1, 014002 (2022)
6. J. B. Khurgin, M. Clerici, and N. Kinsey, "Fast and Slow Nonlinearities in Epsilon Near-Zero Materials," Laser Photon Rev, 15, 2, 2000291, (2021)
7. W. Jaffray et al., "Near-zero-index ultra-fast pulse characterization," Nat Commun, 13, 1, (2022)
8. E. Lustig et al., "Time-refraction optics with single cycle modulation," Nanophotonics, 12, 12, (2023).

Circularly Polarized Photoluminescence in TmIG/TMDs Heterostructures

T. López-Carrasco[1*], D. Vaquero-Monte[1], M. Cosset-Chéneau[1], C. V. Phuoc[2], J. Jong-Ryul[2] and M. H. D. Guimarães[1]

[1]Zernike Institute of Advance Materials, The Netherlands
[2]Department of Material Science and Engineering, Chungnam National University, Republic of Korea
[*] m.t.lopez.carrasco@rug.nl

Abstract: Next-generation communication technologies require miniaturization and more energy-efficient devices. Two-dimensional materials provide a promising platform for advancing atomic-scale applications. Here, we demonstrate control of circularly polarized photoluminescence in a WS_2 monolayer placed on thulium iron garnet substrate under linearly polarized excitation by switching the magnetization direction.

Information transfer between nanoscale devices is a major bottleneck in integrated circuits due to high energy consumption. This process is hindered by short spin relaxation lengths, requiring the conversion of spin information into charge currents, which increases power dissipation. Replacing electrons with photons as information carriers offers a promising solution to reduce energy consumption and enhance speed through optical interconnects.

Two-dimensional (2D) materials provide an ideal platform for achieving this goal. In the monolayer state, they exhibit new properties that differ from the bulk. Transition metal dichalcogenides (TMDs) are 2D semiconductors which show a direct bandgap in the monolayer limit. This, combined with the enhancement of Coulomb interactions in low-dimensional systems lead to the formation of tightly bound excitons. Furthermore, these materials present strong spin-orbit interaction and naturally break spatial inversion symmetry, resulting in optical selection rules for the K and K' valleys, where each valley couples with a different helicity of circularly polarized light. By combining TMDs with magnetic materials, it is possible to modify their band structure and induce new properties in the system. These characteristics make TMDs a promising platform for encoding magnetic information into light polarization.

However, due to the degeneracy of the K and K' valleys, efficiently generating circularly polarized light using linearly polarized excitation is unachievable. By Integrating TMDs with magnetic materials we can break the degeneracy allowing the selectively excitation of one of the valleys, resulting in the control of the light emission. Through proximity effect between 2D magnets and monolayer TMDs, an exchange field can emerge, inducing Zeeman splitting in the energy levels breaking the degeneracy of the two valleys. Additionally, spin-dependent charge transfer can offer a non-radiative decay channel which leads to preferentially light emission from a single valley. These phenomena have been demonstrated using 2D magnets such as CrI_3 and $CrBr_3$ [1,2,3]. However, the major drawbacks of these materials are their air instability and low Curie temperatures, significantly below room temperature, making experiments challenging and limiting their practical applications.

In this work [4], we use the magnetic proximity effect between Thulium Iron Garnet (TmIG) [5] and TMDs to generate circularly polarized photoluminescence after exciting with linearly polarized light (Figure 1). TmIG is a magnetic material that is air-stable, has a Curie temperature well above room temperature, and a switching field in the millitesla range making it ideal for applications. We show a degree of polarization of the emitted photoluminescence depends on the magnetization direction, establishing a link between the emitted light and the magnetization of TmIG.

We observe that changing the magnetization direction of TmIG results in a switch in the helicity of the circular polarization of the emitted light in a tungsten-based TMD (WS_2). Additionally, we detect a redshift in the excitonic peak associated with magnetization confirming the proximity interaction between the TMD and TmIG. This study opens the possibility of encoding magnetization information into light polarization offering a novel platform for

more energy-efficient optical interconnections in integrated circuits.

We acknowledge the financial support by the Zernike Institute for Advanced Materials and the European Union (ERC, 2DOPTOSPIN, 101076932). Views and opinions expressed are however those of the author(s) only and do not necessarily reflect those of the European Union or the European Research Council. Neither the European Union nor the granting authority can be held responsible for them.

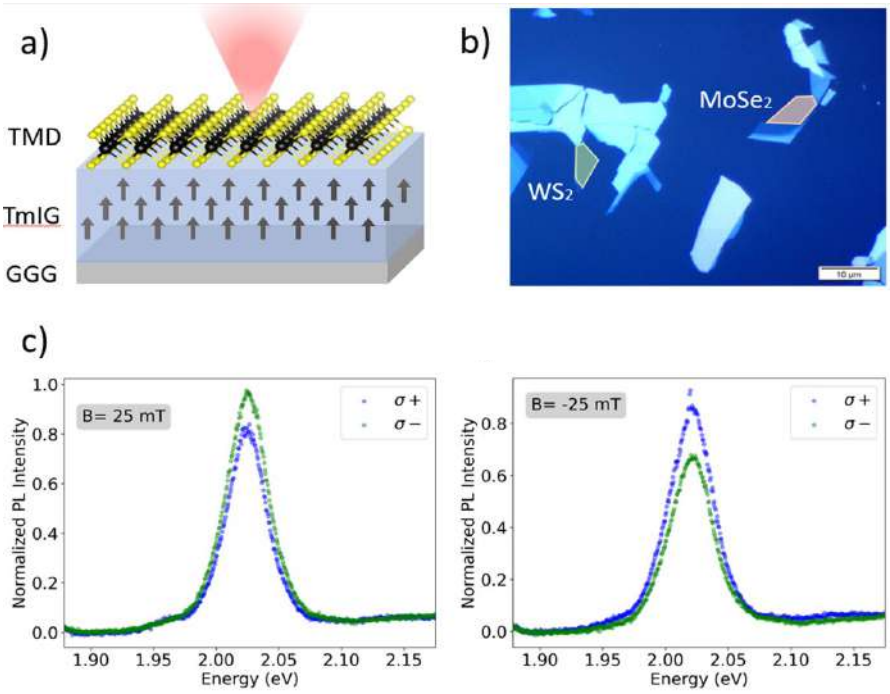


Figure 1. (a) Schematic of the studied system: a 10 µm-thick thulium iron garnet (TmIG) layer grown on a gadolinium galium garnet (GGG) substrate with a TMD monolayer on top. (b) Optical microscope image of WS_2 and $MoSe_2$ monolayers deposited on the TmIG substrate. (c) Photoluminescence spectrum of the WS_2 monolayer at 80 K, showing a switch in right- and left-handed circularly polarized light intensity when the TmIG magnetization is saturated in opposite directions.

References

1. Zio-Bio, Y. et al "The magnetic proximity effect at the MoS^2/CrI^3 interface", J. Phys.: Condens. Matter, 34, 035002, 2022.
2. Wenli, Z. et al, "Manipulation on valley-pseudospin in 2D WTe^2/CrI^3 van der Waals heterostructure by magnetic proximity effect, Applied surface science, 647, 158986, 2024.
3. Ciorciaro, L., et al, "Observation of Magnetic Proximity Effect Using Resonant Optical Spectroscopy of an Electrically Tunable $MoSe^2/CrBr^3$ Heterostructure" Phys. Rev. Lett. 130, 019901 (2023)
4. Lopez Carrasco, T. et al, [In preparation]
5. Duong, V. D. , et. al "Interfacial roughness driven manipulation of magnetic anisotropy and coercivity in ultrathin thulium iron garnet films", Journal of Alloys and Compounds, Vol. 927, 2022, 166800, 2022.

Electrical control of light emission process of two-dimensional materials on the nanoscale

Elysé Laurent[1*], Elizabeth Boer-Duchemin[1], Séverine Le Moal[1], Guillaume Schull[2], Stéphane Berciaud[2], Eric Le Moal[1]

[1]Institute of Molecular Sciences of Orsay (ISMO), France

[2]Institute of Materials Physics and Chemistry of Strasbourg (IPCMS), France

[*]corresponding author: elyse.laurent@universite-paris-saclay.fr

Abstract: A scanning tunneling microscope (STM) is used to tailor the excitonic properties of transition metal dichalcogenides (TMD). We demonstrated STM-induced generation of neutral and charged excitons in TMD monolayers and achieved full control of the TMD photoluminescence quantum yield at a submicrometer scale.

A scanning tunneling microscope (STM) is used to electrically activate the luminescence of two-dimensional (2D) materials within a nanoscale tunnel junction, in order to spatially resolve the variations of the excitation quantum efficiency on the nanometer scale. An optical microscope and spectrometer is used to spatially, angularly, and spectrally resolve the emitted light, in order to investigate the emission processes and identify the involved excitonic species. In this way, we demonstrate the STM-induced generation of neutral and charged excitons in monolayer transition metal dichalcogenides (TMD) [1,2]. Moreover, we introduce a new technique that makes it possible to monitor in real space the effects of locally injected charge carriers on the radiative quantum efficiency of TMDs, which was not possible using the techniques reported until now. In our technique, the wide-field laser-induced photoluminescence (PL) microscopy image of molybdenum diselenide ($MoSe_2$) monolayers is captured while charge carriers are injected into the monolayers via electron tunneling from (or to) the tip of an STM. As shown in Figure 1, we found that local electron injection into the $MoSe_2$ monolayer induces a long-range quenching of the PL intensity of the TMD. Conversely, we show that we can enhanced the PL response of the $MoSe_2$ monolayers by inverting the bias voltage polarity between the STM tip and the TMD.

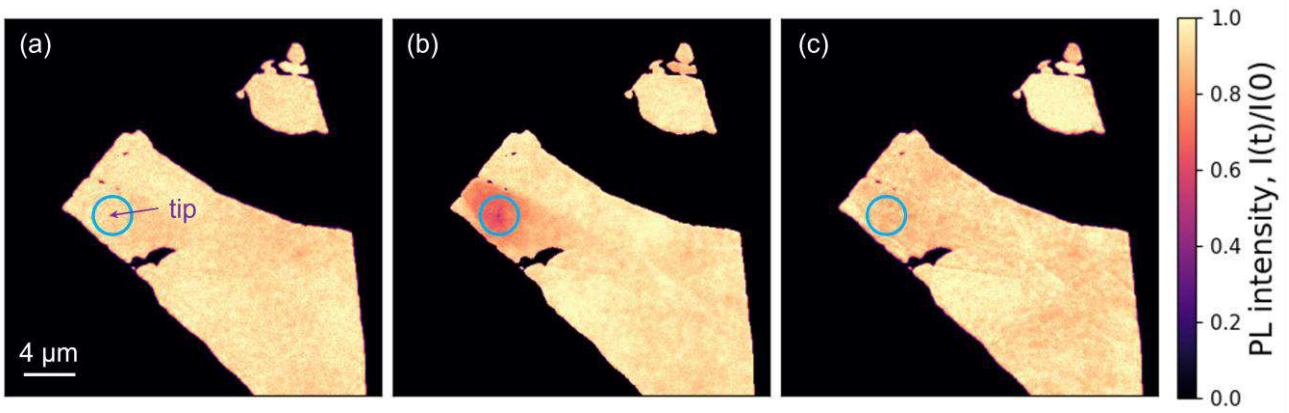


Figure 1: PL quantum yield of two $MoSe_2$ monolayers deposited onto an indium tin oxide (ITO) coated glass cover slip. The image (a) was taken before inducing a tunneling current through the sample. The image (b) was taken while inducing a tunneling current through the sample. The image (b) was taken while inducing a

tunneling current through and the image (c) was taken several seconds after cutting the tunneling current.

Our results show that the presence of the electrically biased STM tip and the tunneling current acts as a gate nanoelectrode, which locally modifies the charge carrier density and thus the luminescence properties of the TMD monolayer. In a series of experiments where we periodically varied the setpoint current or the potential applied to the junction, we show the role played by this effect in STML measurements, in particular the impact this effect has on the current-dependent linearity of the electroluminescence process. These results, presented here for the first time, shed new light on the mechanisms at the heart of STML in 2D semiconductors.

References

1. D. Pommier, et al, Physical Review Letters, 123 (2019) 027402.
2. R. J. Peña Román, et al, Physical Review B, 106 (2022) 085419.

TMDCs' Monolayer PL Enhancement Using h-BN and SiO_2 Gratings

M. Bakhshikhah[1*], C. Palekar[3], Y.Yang[3], M. Podhorský[3], B. Sankar Sahoo[3], S. Machchhar[3], I. Limame[3], M. Ries[3], M. Hrtoň[2], J. Liška[1], T. Šikola[1, 2], and S. Reitzenstein[3]

[1]Central European Institute of Technology, Brno University of Technology, Brno, Czech

[2]Institute of Physical Engineering, Faculty of Mechanical Engineering, Brno University of Technology, Brno, Czech Republic

[3]Institute of Solid State Physics, Faculty of Mathematics and Natural Sciences, Technical University Berlin, Berlin, Germany

[*]corresponding author: mahan.bakhshikhah@ceitec.vutbr.cz

Abstract: Light-matter interactions in transition-metal dichalcogenides (TMDCs) for optoelectronic applications enable advanced nanophotonics functionalities. This work demonstrates photoluminescence enhancement in TMDCs monolayer on patterned SiO_2 and h-BN using an optical microcavity approach. The method enables efficient light confinement to optimize light-matter interactions in two-dimensional materials at room temperature.

1. Introduction

Atomically thin TMDCs with the chemical formula MX_2 (M = Mo, W and X = Se, S) exhibit unique optical properties and electronic structures for two-dimensional optoelectronic applications such as photodetectors, photovoltaics, and light emitters. TMDCs like WS_2, MoS_2, WSe_2, and $MoSe_2$ show an indirect-to-direct bandgap transition with large excitonic (i.e., coupled electron-hole pairs) binding energy ranging from 1.5 – 2 eV when thin down to a monolayer. Therefore, their photoluminescence (PL) quality is higher than that of their bulk counterparts. Consequently, excitons dominate the optical and electrical properties of these materials[1], [2], [3], [4]. Most 2D TMDCs show a direct bandgap with large excitonic binding energy in the visible wavelength range [5]. Tungsten disulfide (WS_2) monolayers show unique and promising properties compared to other TMDCs monolayers for optoelectronic applications. Notably, WS_2's high excitonic binding energy results in better light-matter interaction that enhances light absorption and emission [6]. WS_2 monolayers exhibit a higher photoluminescence quantum yield (QY) than MoS_2, making them more effective for light-emitting devices. Also, WS_2 direct bandgap (~2 eV) makes it better suited for visible light optoelectronic applications such as photodetectors and photovoltaics, unlike $MoSe_2$ and WSe_2 which have bandgaps in the near-infrared region. However, light-matter interaction with atomically thin materials such as TMDCs is generally weak [7]. In this presentation, we report on improving the light-matter interaction to enhance the PL properties of a TMDCs material, namely WS_2.

2. Fabrication

We prepared h-BN flakes by exfoliation and transfer from a bulk crystal to a Si/SiO_2 substrate. After that, we patterned the flakes to fabricate linear gratings using electron beam lithography (EBL) and reactive ion etching (RIE). Then we transferred exfoliated WS_2 monolayers on h-BN and SiO_2 gratings.

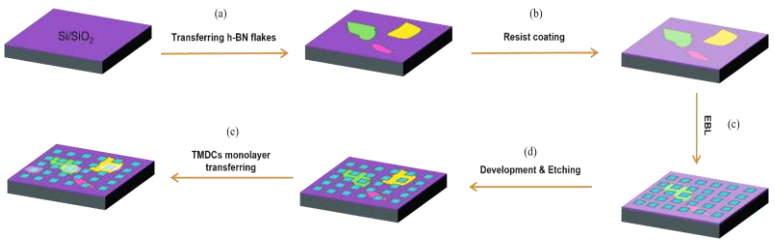


Figure 1. Nanofabrication process (patterning). (a) h-BN flakes transferring on the substrate (not-to-scale drawing), (b) CSAR coating, (c) patterning using EBL on top of the h-BN and SiO_2, (d) development and etching by RIE, (e) TMDCs monolayers transferring on h-BN and SiO_2 gratings after removing CSAR.

3. Results and Discussion

The results of the WS_2 treatment are shown in Figure 2. The PL enhancement was 2-fold for SiO_2 and more than 2-fold for h-BN grating based on PL peak area. This value can certainly be increased by optimization of fabrication parameters (e.g., pitch and groove size).

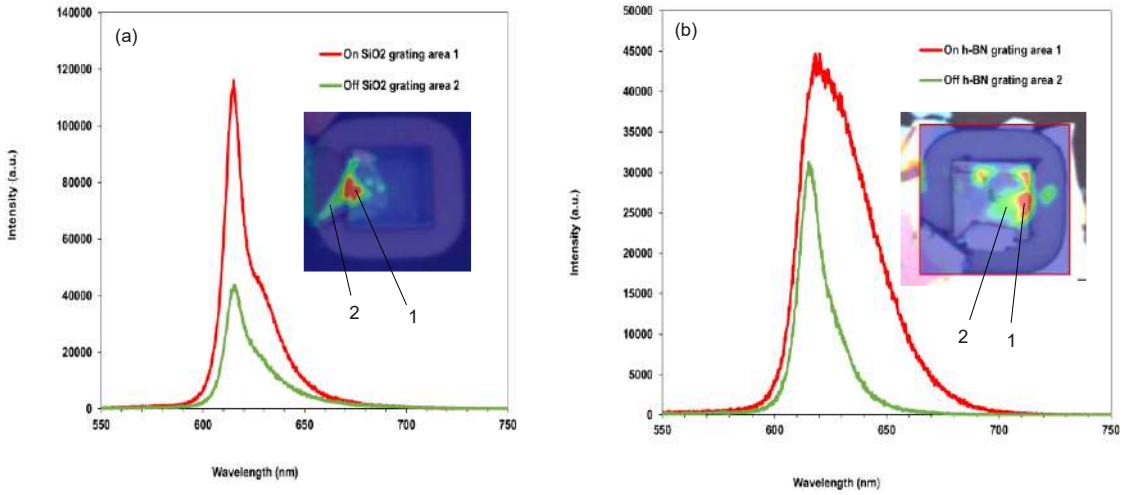


Figure 2. Enhancement of a WS_2 monolayer PL on SiO_2 and h-BN gratings: (a) PL spectra of the monolayer on and off the SiO_2 grating (the inset shows the PL map), (b) PL spectra of the monolayer on and off the h-BN grating (the inset shows the PL map).

4. Conclusion

We have proved that the proposed method based on the application of h-BN and SiO_2 gratings is capable of improving the PL of WS_2 monolayers. In the next step, we will find the optimum grating parameters to obtain the maximum PL enhancement.

Acknowledgments

This research has been carried out with the financial support of Technical University Berlin and the CzechNanoLab project LM2023051, funded by MEYS CR. JAROSLAV KOČA BRIDGE FUND 2024 project is acknowledged for its financial support in continuing the project.

References

[1] S. Tongay *et al.*, "Broad-range modulation of light emission in two-dimensional semiconductors by molecular physisorption gating," *Nano Lett*, vol. 13, no. 6, pp. 2831–2836, Jun. 2013, doi: 10.1021/nl4011172.

[2] S. V. Sivaram *et al.*, "Spatially Selective Enhancement of Photoluminescence in MoS 2 by Exciton-Mediated Adsorption and Defect Passivation," *ACS Appl Mater Interfaces*, vol. 11, no. 17, pp. 16147–16155, May 2019, doi: 10.1021/acsami.9b00390.

[3] L. Yuan and L. Huang, "Exciton dynamics and annihilation in WS2 2D semiconductors," *Nanoscale*, vol. 7, no. 16, pp. 7402–7408, Apr. 2015, doi: 10.1039/c5nr00383k.

[4] U. Krishnan, M. Kaur, K. Singh, M. Kumar, and A. Kumar, "A synoptic review of MoS 2 : Synthesis to applications," Apr. 01, 2019, *Academic Press*. doi: 10.1016/j.spmi.2019.02.005.

[5] Q. Vadis, C. Qiu, T. Zhang, G. Hu, and Y. Kivshar, "Quo Vadis, Metasurfaces?," 2021, doi: 10.1021/acs.nanolett.1c00828.

[6] C. Li, D. Sang, S. Ge, L. Zou, and Q. Wang, "Recent Excellent Optoelectronic Applications Based on Two-Dimensional WS2 Nanomaterials: A Review," Jul. 01, 2024, *Multidisciplinary Digital Publishing Institute (MDPI)*. doi: 10.3390/molecules29143341.

[7] M. Amani *et al.*, "Recombination Kinetics and Effects of Superacid Treatment in Sulfur- and Selenium-Based Transition Metal Dichalcogenides," *Nano Lett*, vol. 16, no. 4, pp. 2786–2791, Apr. 2016, doi: 10.1021/acs.nanolett.6b00536.

Nanophotonics and Plasmonics Applications

Transfer Learning for the Design of a Composite Metasurface Unit Cell in the K_a-Band

Alexander Wolff[1], Lukas Mueller[1], Steffen Klingel[1], and Marco Rahm[1]

[1]RPTU Kaiserslautern-Landau, Department of Electrical and Computer Engineering and Research Center OPTIMAS, Kaiserslautern, D-67663, Germany
[*]corresponding author: alexander.wolff@rptu.de

Abstract: Training data is a sparse resource when designing neural networks to describe the scattering parameters of metamaterials based on their geometry. Using transfer learning, we have reduced the necessary training data for a neural surrogate model of a tunable composite metasurface unit cell by more than an order of magnitude.

Neural networks have been shown to accelerate the design process of artificial electromagnetic materials (AEM) by several orders of magnitude [1]. Yet, training an accurate neural network requires a substantial amount of training data to be obtained beforehand. This training data is typically specific to a particular set of geometrical and material parameters of the described AEM. However, transfer learning allows us to generalize training data to other AEM-problems [1, 2].

We apply transfer learning to the design of a metasurface unit cell for the use in 5G and 6G wireless communication. In this context, metasurfaces can improve the signal-to-noise ratio of a mobile user by redirecting and focusing an electromagnetic wave onto the user area [3]. To decrease side lobes, it is beneficial to tune the phase of the reflected wave from the metasurface between 0° and 360° while keeping the reflectivity invariant. A composite structure of two varactor-tunable dipoles, as illustrated in Figure 1 (left), can achieve these requirements when tuned correctly [4]. The structure comprises two metallic dipoles of different length on top of a FR-4-substrate. The bottom layer of the PCB is covered entirely by a ground plane. The bias circuitry for the varactors was neglected in the coarse design phase to accelerate the training data generation. The goal was to investigate whether transfer learning could reduce the number of simulations of the dipole-dipole structure as inherently needed to train a direct model of the structure in Fig. 1. This was examined by comparing the required simulations for training a direct model to those needed when first training a model on a single dipole and then applying a transfer model to learn the coupling between two dipoles, ultimately describing the same structure.

The objective of the transfer learning process was to train a model to accurately characterize the S_{11} parameters of a single dipole, before feeding them into a transfer model designed to learn the coupling effects between two dipoles to describe the S_{11} parameters of the structure shown in Fig. 1. For this purpose, we first simulated and extracted the S_{11} parameters of a single dipole dependent on the four parameters {D, L_i, H, C_{var}}. Based on this data, we trained a multi-layer perceptron (MLP) to output the S_{11} parameters of a single dipole in a frequency range between 18 GHz and 34 GHz. The MLP had 4 input neurons, 4 hidden layers with 200 neurons each and 706 output neurons that represented the concatenation of Re(S_{11}) and Im(S_{11}) at 353 discrete frequency samples. In order to train the transfer model regarding the coupling between two dipoles, we used the S_{11} parameters of the first model as input for a second MLP of the same size that learned the dipole-dipole coupling dependent on the distance d between the two dipoles. The second MLP was trained on simulation data previously obtained from numerically calculating the S_{11} parameters of the unit cell in Fig. 1.

In order to evaluate the benefit of this transfer learning scheme, we calculated the mean squared error (MSE) of the transfer-learned MLP over a test dataset for different sizes of training datasets. The result is illustrated by the solid red line in Fig. 1 (right). We see that the MSE reaches 0.05 with only 29 training simulations. In comparison, the solid blue line in Fig. 1 (right) represents a reference MLP of the direct model of the structure in Fig. 1. This reference network requires 583 simulations to yield a MSE of 0.05. As a result, the transfer-learning scheme decreased the number of training samples of the composite unit cell by more than an order of magnitude.

Although transfer learning requires additional simulations to train the single dipole, these simulations are typically faster due to the smaller and less complex geometry. Furthermore, the simulations of the single dipole can be recycled for composite unit cells with different coupling geometries between the dipoles.

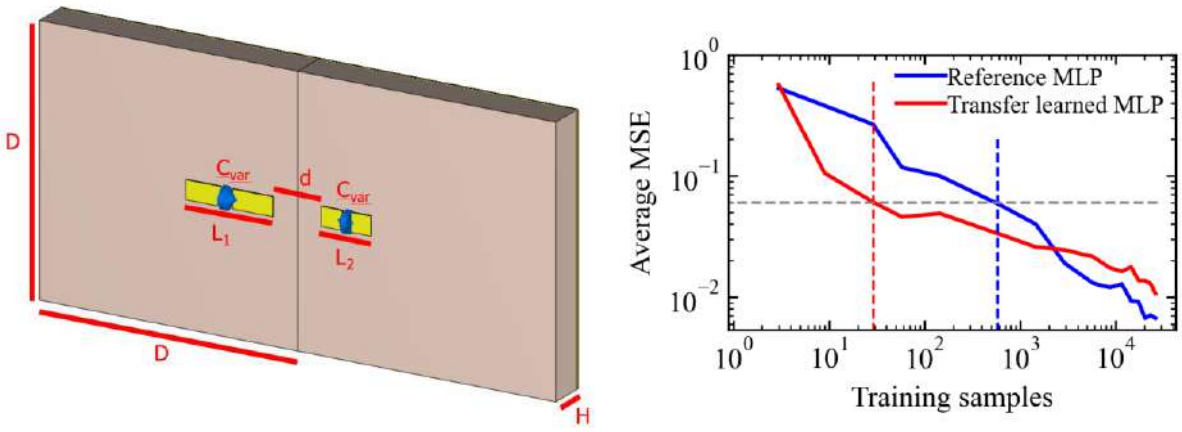


Figure 1

(left) Composite unit cell for a tunable metasurface with high reflection phase shift. The dipoles are split in the middle and the gap is bridged by a varactor diode. The backside of the FR-4 substrate is covered with a ground plane.

(right) Test set average mean squared error of the multi-layer perceptron (MLP) for different training sample sizes in the case of the transfer-learned network (red) and the reference direct network (blue). The transfer-learned MLP requires an order of magnitude fewer training data of the coupled dipole structure than the reference MLP.

Acknowledgements

The authors acknowledge the financial support by the Federal Ministry of Education and Research of Germany in the project “Open6GHub” (grant number: 16KISK004).

References

1. Khatib, O., Ren, S., Malof, J. and Padilla, W., “Deep Learning the Electromagnetic Properties of Metamaterials – A Comprehensive Review ,” Advanced Functional Materials, Vol. 31, No. 31, 2101748, 2021.
2. Peng, R., Ren, S., Malof, J. and Padilla, W., “Transfer Learning for Metamaterial Design and Simulation,” Nanophotonics, Vol. 13, No. 13, 2323–2334, 2024.
3. Wu, Q., Zhang, S., Zheng, B., You, C. and Zhang, R., “Intelligent Reflecting Surface-Aided Wireless Communications: A Tutorial,” IEEE Transactions on Communications, Vol. 69, No. 5, 3313-3351, 2021.
4. Zhu, B., Zhao, J. and Feng, Y., “Active impedance metasurface with full 360° reflection phase tuning,” Scientific Reports, Vol. 3, No. 1, 3059, 2013.

Broadband Field Prediction via Parameter-Efficient Electromagnetic Surrogate Solver

Chanik Kang[1†], Joonhyuk Seo[1†], Changkyun Lee[2] and Haejun Chung[1,2]
[1]Department of Artificial Intelligence, Hanyang University, Seoul, Republic of Korea
[2]Department of Electronic Engineering, Hanyang University, Seoul, Republic of Korea
haejun@hanyang.ac.kr (corresponding author)
[†]These authors contributed equally to this work.

Abstract

We propose a parameter-efficient electromagnetic surrogate solver that predicts broadband field distributions from discrete wavelength data. Using wave-informed multiplicative encoding and Fourier group convolutional shuffling, our approach reduces parameters by 74% and improves the accuracy of untrained wavelength prediction by 80.5%, outperforming state-of-the-art models.

1 Introduction

Electromagnetic simulations based on Maxwell's equations are essential for photonic device design but are computationally intensive [1]. For electric field prediction, traditional surrogate solvers that are trained under fixed conditions struggle to generalize across a continuous wavelength spectrum [2]. To overcome this limitation, we introduce two key method Wave-Informed Multiplicative Encoding (WIME) and Fourier Group Convolutional Shuffling (FGCS) which together enable efficient and accurate prediction of electric fields over a broad spectrum while drastically reducing parameter complexity.

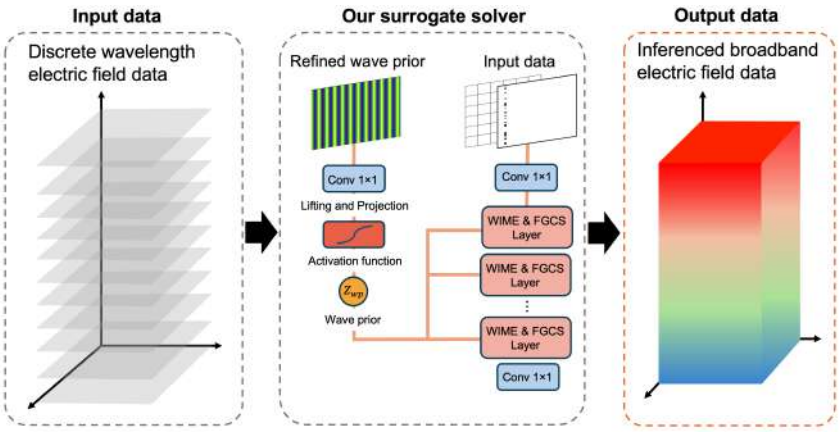


Figure 1: Schematic illustration of the proposed overall framework.

Our approach overcomes the high computational cost and limited generalization ability of traditional methods by integrating two key components. First, WIME extracts condition embeddings from a refined wave prior defined as $\mathcal{W}_x = e^{j\frac{2\pi}{\lambda}x\mathbf{1}^T\Delta l_x}$ and $\mathcal{W}_z = e^{j\frac{2\pi}{\lambda}\mathbf{1}z^T\Delta l_z}$ where x and y are the coordinates. Δl_x, Δl_z, and λ are the simulation step sizes and wavelength, respectively. These embeddings are processed with shallow 1×1 convolution layers and injected into every network layer via element-wise multiplication, adaptively modulating feature maps

to account for wavelength variations. Second, the FGCS operator efficiently reduces parameters by factorizing the Fourier transform along horizontal and vertical dimensions [3]. By leveraging weight sharing and channel shuffling, it achieves a compact yet expressive representation while preserving essential spectral features.

Our surrogate model thus approximates the mapping from material properties to field distributions, enabling fast inference over continuous wavelengths. Figure 1 illustrates the overall architecture of our surrogate solver, where WIME and FGCS are integrated to condition the model and reduce parameters effectively. Figure 2 compares our method with a state-of-the-art surrogate solver [2], demonstrating a 74% reduction in parameters and enhanced prediction accuracy for wavelengths not observed during training.

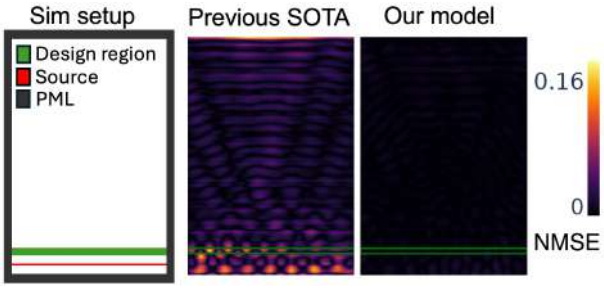


Figure 2: Model error evaluation at 410nm, the unobserved wavelength with maximal error.

Our surrogate solver achieves state-of-the-art performance by accurately predicting broadband electromagnetic fields from a limited set of discrete wavelength data. The proposed WIME and FGCS enable robust generalization to unseen wavelengths while significantly reducing computational burden, paving the way for faster and more efficient photonic device simulation.

2 Acknowledgements

This work was supported by the National Research Foundation of Korea (NRF) grant (RS-2024-00338048 and RS-2024-00414119) funded by the Republic of Korea's MSIT (Ministry of Science and ICT), under the Global Research Support Program in the Digital Field program (RS-2024-00412644) supervised by the IITP (Institute of Information and Communications Technology Planning & Evaluation); Culture, Sports and Tourism R&D Program through the Korea Creative Content Agency grant funded by the Ministry of Culture, Sports and Tourism in 2024 (RS-2024-00332210); Artificial Intelligence Graduate School Program (RS-2020-II201373, Hanyang University) supervised by the IITP; the artificial intelligence semiconductor support program to nurture the best talents (IITP(2024)-RS-2023-00253914) grant funded by the Korea government; and by the MSIT (RS-2023-00261368) grant funded by the Korea government.

References

[1] Chanik Kang, Chaejin Park, Myunghoo Lee, Joonho Kang, Min Seok Jang, and Haejun Chung, "Large-scale photonic inverse design: computational challenges and breakthroughs," *Nanophotonics*, doi:10.1515/nanoph-2024-0127, 2024.

[2] Jiaqi Gu, Zhengqi Gao, Chenghao Feng, Hanqing Zhu, Ray Chen, Duane Boning, and David Pan, "Neurolight: A physics-agnostic neural operator enabling parametric photonic device simulation," *Advances in Neural Information Processing Systems*, vol. 35, pp. 14623–14636, 2022.

[3] Alasdair Tran, Alexander Mathews, Lexing Xie, and Cheng Soon Ong, "Factorized Fourier Neural Operators," *arXiv preprint arXiv:2111.13802*, 2021.

Superscatterers for tailoring electromagnetic interactions: Radar Visibility and Scattering Suppression

P. Ginzburg[1,*]
and D. Vovchuk[1], A. Mikhailovskaya[1], M. Tsukerman[1], K. Grotov[1], A. Kharchevskii[1], D. Kolchanov[1], D. Dobrykh[1]
T. Salgals[2], V. Bobrovs[2]

[1]Department of Electrical Engineering, Tel Aviv University, Ramat Aviv, Tel Aviv, 69978 Israel
[2]Institute of Telecommunications Riga Technical University, Azenes Street 12, Riga, 1048 Latvia
[*]corresponding author: pginzburg@tauex.tau.ac.il

Abstract: Experimental demonstration of superscattering is among the long-standing challenges in electromagnetic theory. We will present several strategies to design superscatterers with the aid of generic optimization and demonstrate their state-of-the-art performances experimentally. A solution to an emerging problem of small UAV tracking and monitoring with radar-visible superscatterers will be demonstrated.

The presentation is based on our recent works [1-8] and on a large set of new unpublished data. On top of our published results, we will demonstrate novel extremely broadband superscatterers, fabricated with the aid of additive technologies, and all-angle all-polarization corona-virus-like devices, whose operation encompasses both resonant phenomena and constructively interfering creeping wave interactions. The results will be supported with experimental data, considering both indoor and outdoor demonstrations.

Electromagnetic scattering on subwavelength structures has always been a subject of extensive investigations owing to fundamental challenges and applied rewards, related to its maximization or suppression. The maximal possible scattering into a single multipole is called a channel limit. A dipolar single channel limit (the maximal scattering cross-section, which a small resonant lossless dipole can approach) is $3\lambda^2/(2\pi)$, where λ is a free space wavelength. Subwavelength structures, bypassing the single channel limit, are called super-scatterers. While there is no fundamental upper bound on a scattering cross section, quite a few theoretical limits, with Cho-Harrington being the most commonly used, have been proposed to account for possible practical aspects. Bypassing those limits requires accommodating several resonant multipoles, constructively interfering at nearly the same frequency. In this case, a significant near-field accumulation in the vicinity of lossy materials, accompanied by an extremely low fabrication tolerance, are the main known factors limiting the practical demonstration of super-scatterers. Regardless of their particular realization, they all share the same design principles. The first one is the choice of a material platform. Since high near-field accumulation necessarily implies having high Ohmic losses, constitutive components should be carefully chosen. The second criterion is the capability to perform extensive electromagnetic optimization. In the case of compact structures, internal resonances tend to repel each other, opening frequency gaps. In this contribution, we will demonstrate several conceptually different strategies to design and experimentally demonstrate superscattering. The following sections survey our results. Novel and conceptually different architectures will also be demonstrated at the conference. A strong emphasis will be placed on practical outdoor demonstrations, related to tagging small radar cross-sections (RCS) with super scattering devices. Those will be shown to play a dramatic role in the detection, rendering initially weakly detectable objects to highly visible targets, subject to convenient and reliable radar-based monitoring.

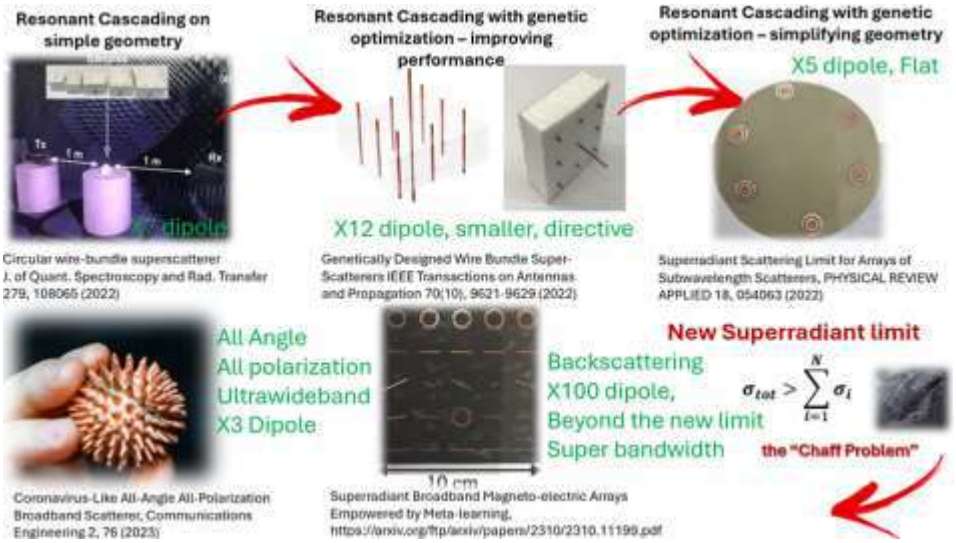


Fig. 1: Brief survey of our strategies for Superscattering devices – wire bundles, split-ring resonator arrays, magneto-electrical genetically designed arrays, and 3D-printed topologically optimized structures.

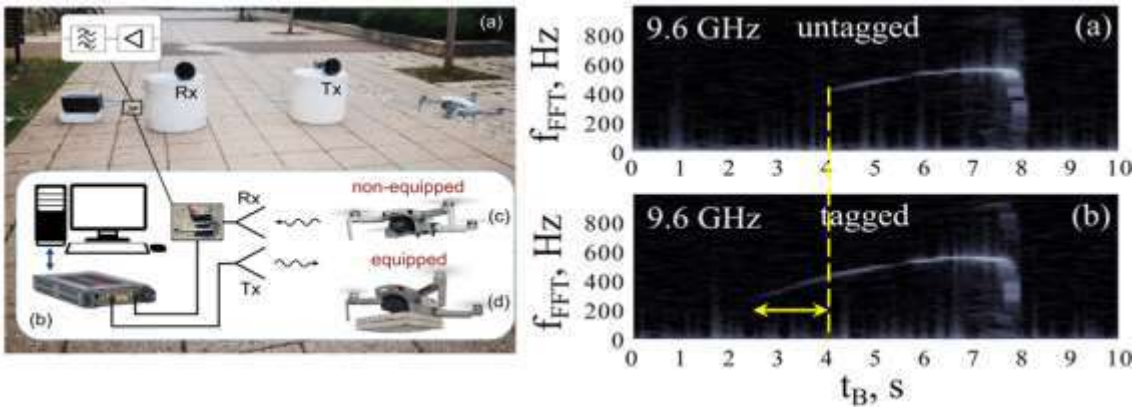


Fig. 2: (Left). Photographs from an outdoor experiment. (Right) Short-Time Frequency Transform for the untagged and tagged flights at different carrier frequencies of the used CW radar. The advantage in detectability (x10 in range) is demonstrated.

References

1. K. Grotov et al., "Genetically Designed Wire Bundle Super-Scatterers," IEEE Trans Antennas Propag, Oct. 2022, doi: 10.1109/TAP.2022.3177531.
2. A. Mikhailovskaya *et al.*, "Superradiant Scattering Limit for Arrays of Subwavelength Scatterers," *Phys Rev Appl*, vol. 18, no. 5, p. 054063, Nov. 2022, doi: 10.1103/PHYSREVAPPLIED.18.054063/FIGURES/8/MEDIUM.
3. S. Kosulnikov *et al.*, "Circular wire-bundle superscatterer," *J Quant Spectrosc Radiat Transf*, vol. 279, p. 108065, Mar. 2022, doi: 10.1016/J.JQSRT.2022.108065.
4. V. Kozlov, D. Vovchuk and P. Ginzburg, "Radar Range Deception With Time-Modulated Scatterers," in *IEEE Transactions on Antennas and Propagation*, vol. 71, no. 5, pp. 4486-4491, May 202
5. V. Kozlov, D. Vovchuk and P. Ginzburg, "Direction of Arrival Deception With Time-Modulated Scatterers," in *IEEE Transactions on Radar Systems*, vol. 1, pp. 90-95, 2023
6. D. Vovchuk, et. al., "Micro-Doppler-Coded Drone Identification", https://arxiv.org/abs/2402.04368, 2024.
7. Kozlov V, Kharchevskii A, Rebenshtok E, Bobrovs V, Salgals T, Ginzburg P. Universal Software Only Radar with All Waveforms Simultaneously on a Single Platform. *Remote Sensing*. 2024; 16(11):1999.
8. Vovchuk, D., Uziel, G., Machnev, A. *et al.* Genetically synthesized supergain broadband wire-bundle antenna. *Commun Eng* **3**, 101 (2024).

Conditional Normalizing Flow Surrogate for Monte Carlo Prediction of Radiative Properties in Nanoparticle-Embedded Layers

Fahime Seyedheydari[1], Kevin Conley[2], and Simo Särkkä[3]

[1,3]Department of Electrical Engineering and Automation (EEA), Aalto University, Espoo, Finland
[2]Department of Chemistry and Materials Science, Aalto University, Espoo, Finland
*corresponding author, E-mail: fahime.seyedheydari@aalto.fi

Abstract

We present a probabilistic, data-driven surrogate model for predicting the radiative properties of nanoparticle embedded scattering media. The model uses conditional normalizing flows, which learn the conditional distribution of optical outputs, including reflectance, absorbance, and transmittance, given input parameters such as the absorption coefficient, scattering coefficient, anisotropy factor, and particle size distribution. We generate training data using Monte Carlo radiative transfer simulations, with optical properties derived from Mie theory. Unlike conventional neural networks, the conditional normalizing flow model yields full posterior predictive distributions, enabling both accurate forecasts and principled uncertainty quantification. Our results demonstrate that this model achieves high predictive accuracy and reliable uncertainty estimates, establishing it as a powerful and efficient surrogate for radiative transfer simulations.

1. Introduction

Monte Carlo (MC) simulations, are a foundational tool in modeling radiative transfer through scattering and absorbing media, with widespread applications in thermal engineering [1], biomedical optics [2], and in materials science [3]. The Monte Carlo for Multi-Layered Media (MCML) algorithm by Wang et al. [4], originally developed for biological tissues, has been extensively adapted for other types of layered media.

In previous work [5], we applied the MC method to study the optical properties of a particle-containing layer at low volume fractions. This method involves launching a large number of photons at normal incidence into the layer, where they are either transmitted, reflected, or absorbed. Despite advances in GPU-based parallel processing, MC simulations remain computationally expensive for high-throughput applications. In this work, we combine the MC method with Mie theory to model radiation transport in layers with low particle volume fractions.

While MC simulations are accurate and physically grounded, they remain computationally intensive, especially when repeated across a high-dimensional input space of wavelengths, particle sizes, and material properties. Despite the efficiency gains achieved through parallel processing on GPUs, large-scale or repeated simulations continue to be computationally prohibitive in high-throughput applications such as design optimization or inverse scattering problems.

To address this limitation, surrogate models have been introduced to approximate the forward mapping from physical parameters to optical responses, enabling significant cost reduction while preserving accuracy [6, 7]. Fully connected neural networks (FCNNs), in particular, have demonstrated strong performance in learning deterministic relationships from Monte Carlo-generated data. With sufficient training data, neural networks can approximate complex functions and provide fast, accurate predictions [8]. Such networks have been successfully applied to surrogate modeling tasks, including the design of thin-film photovoltaic cells and other optical systems [7].

Deterministic neural networks lack the capacity to quantify uncertainty—an essential feature for applications such as photonic material design and uncertainty-aware simulations [9]. We propose a probabilistic surrogate model based on Conditional Normalizing Flows (CNFs), which transform a simple base distribution (e.g., standard Gaussian) into a complex target distribution through invertible transformations [10, 11, 12]. By conditioning this transformation on physical input parameters (e.g., μ_a, μ_s, g, and ρ), CNFs learn the conditional distribution $p(\mathbf{x} \mid \mathbf{y})$, where $\mathbf{y}$ denotes the input parameters and $\mathbf{x}$ represents the radiative spectral outputs. To overcome the computational burden of radiative transfer in scattering media, we generated training data using Monte Carlo simulations executed on a high-performance server at Aalto University.

The proposed CNF framework enables the generation of diverse and physically consistent outputs for a given input, thereby capturing the inherent uncertainty in radiative transfer simulations. It produces posterior predictive distributions, allowing for both mean predictions and associated confidence intervals—an essential feature for uncertainty-aware modeling. By maintaining consistency with Monte Carlo-generated training data, the framework ensures physical interpretability and robustness. To validate its effectiveness, we train a RealNVP-based CNF model on MC-simulated datasets. The model successfully predicts full spectral profiles of reflectance, absorbance, and transmittance with high accuracy while also providing well-calibrated uncertainty estimates. Model performance is

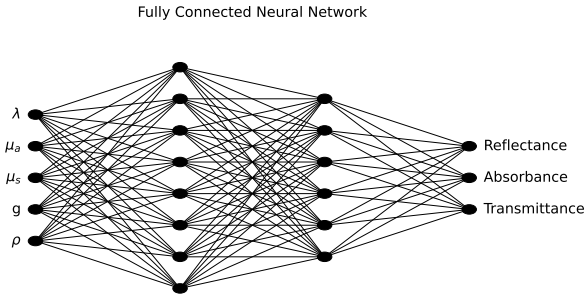


Figure 1: A schematic representation of the fully connected neural network.

rigorously assessed through cross-validated posterior sampling and comparisons against deterministic neural network baselines.

2. Methods

The proposed surrogate modeling framework is structured around two main components: data generation via Monte Carlo simulations and probabilistic modeling using CNFs. We begin by providing an overview of this framework and its rationale. Subsequent subsections describe the data generation process, the architecture of the CNF model, the training objective, and the inference procedure in detail.

2.1. Data Generation and Preprocessing

To train the CNF model, we generated a comprehensive dataset using Monte Carlo radiative transfer simulations, specifically designed for layered media embedded with nanoparticles. Each simulation corresponds to a folder containing detailed input parameters and the resulting output spectra.

The input parameters include the wavelength-dependent absorption coefficient (μ_a), scattering coefficient (μ_s), anisotropy factor (g), and the particle size distribution function (ρ). These parameters represent the key physical and optical properties that influence light transport within the medium.

For each simulation, the Monte Carlo method outputs the spectral properties of the system, including total reflectance (computed as the sum of specular and diffuse components), absorbance, and transmittance.

All input features are preprocessed by stacking and reshaping them into a unified feature vector representing each sample. The corresponding outputs are vectorized in a similar manner, resulting in a structured dataset compatible with neural network training. A schematic overview of the network architecture used for modeling is provided in Figure 1.

2.2. Conditional Normalizing Flow Architecture

We employ a CNF framework to model the conditional distribution of radiative spectral outputs given input physical parameters. The CNF is based on a Real-valued Non-Volume Preserving (RealNVP) transformation, which provides a scalable and invertible mapping between a simple latent distribution and a complex target distribution [13]. In our case, the target distribution corresponds to spectral quantities such as total reflectance, absorbance, and transmittance, conditioned on high-dimensional input features extracted from the optical and material properties.

Starting from a standard Gaussian latent variable $\mathbf{z} \sim \mathcal{N}(\mathbf{0}, \mathbf{I})$, where $\mathbf{z} \in \mathbb{R}^D$ is a latent vector of the same dimensionality as the output and $\mathbf{I}$ is the identity covariance matrix, we define an affine mapping:

$$\mathbf{x} = \exp\big(\log s(\mathbf{y})\big) \odot \mathbf{z} + t(\mathbf{y}),$$

where $\log s(\mathbf{y})$ and $t(\mathbf{y})$ are the log-scale and shift vectors produced by a conditioner neural network, and $\odot$ denotes element-wise multiplication. This structure ensures that the transformation is differentiable and invertible, making it suitable for both sampling and likelihood estimation. Here, the functions $s(\mathbf{y})$ and $t(\mathbf{y})$ are parameterized by neural network weights ψ.

To compute the conditional likelihood $p(\mathbf{x} \mid \mathbf{y})$, we apply the change-of-variables formula. Due to the affine nature of the transformation, the Jacobian determinant simplifies to the sum of log-scale terms:

$$\log p(\mathbf{x} \mid \mathbf{y}) = \log p(\mathbf{z}) + \sum_{j=1}^{D} \log s_j(\mathbf{y}),$$

where $p(\mathbf{z})$ is the log-density under the standard normal prior. This formulation enables the model to learn expressive conditional distributions and supports principled uncertainty quantification via posterior sampling. For a full derivation of the conditional log-likelihood, see Supplementary Material, Section 5.

2.3. Training Objective

The CNF model is trained to maximize the likelihood of the observed output data given the input features. This is achieved by modeling the conditional distribution $p(\mathbf{x} \mid \mathbf{y})$ using a bijective transformation applied to a latent variable sampled from a standard multivariate normal distribution. Specifically, we learn a mapping from latent space to data space through neural networks that output data-dependent shift and scale parameters.

Given a training pair $(\mathbf{y}^{(i)}, \mathbf{x}^{(i)})$, the model first computes the inverse transformation to recover the corresponding latent variable:

$$\mathbf{z}^{(i)} = g_\psi^{-1}(\mathbf{x}^{(i)}, \mathbf{y}^{(i)}) = (\mathbf{x}^{(i)} - t(\mathbf{y}^{(i)})) \oslash \exp(\log s(\mathbf{y}^{(i)})),$$

where $t(\mathbf{y})$ and $\log s(\mathbf{y})$ are the shift and log-scale vectors predicted by the conditioner neural network with parameters ψ, and $\oslash$ denotes element-wise division.

The conditional log-likelihood is then computed using the change-of-variables formula derived earlier:

$$\log p_\psi(\mathbf{x}^{(i)} \mid \mathbf{y}^{(i)}) = \log p(\mathbf{z}^{(i)}) + \sum_{j=1}^{D} \log s_j(\mathbf{y}^{(i)}),$$

where $\log p(\mathbf{z}^{(i)}) = -\frac{1}{2}\left(\|\mathbf{z}^{(i)}\|^2 + D\log(2\pi)\right)$, since $\mathbf{z}^{(i)} \sim \mathcal{N}(\mathbf{0}, \mathbf{I})$.

To train the model, we maximize the total log-likelihood over the dataset. Equivalently, the training objective is to minimize the negative log-likelihood loss:

$$\mathcal{L}(\psi) = -\frac{1}{N}\sum_{i=1}^{N} \log p_\psi(\mathbf{x}^{(i)} \mid \mathbf{y}^{(i)}).$$

This objective is minimized using stochastic gradient descent with the Adam optimizer. By learning parameters ψ that maximize the likelihood of the observed data, the model captures the full conditional distribution and generates accurate, uncertainty-aware predictions of spectral responses.

2.4. Training Procedure

The model is trained using stochastic gradient descent with the Adam optimizer to minimize the negative log-likelihood objective. Training is conducted over 20,000 epochs using mini-batches. At the beginning of each epoch, the training data is shuffled to promote generalization and to avoid learning spurious patterns. For each mini-batch, the conditioner network computes the shift and log-scale parameters, defines the transformed distribution, evaluates the loss, and updates the model weights via backpropagation.

To ensure robust evaluation and reduce variance in performance estimates, we employ 5-fold cross-validation. The dataset is partitioned into five subsets, and training is repeated five times, each time using a different subset for validation and the remaining subsets for training. This yields five independently trained models. Model checkpoints are saved at the end of each fold to facilitate ensemble predictions and uncertainty estimation. The key steps of the training process are summarized in Algorithm 1.

Algorithm 1 Conditional Normalizing Flow Training

Require: Dataset $\{X, Y\}$, epochs number T, batch size B
Ensure: Trained conditioner network

```
Initialize the conditioner network and Adam optimizer with learning rate 10^-4
for epoch = 1 to T do
    Shuffle the training data {X, Y}
    Partition the data into mini-batches of size B
    for each mini-batch (x_batch, y_batch) do
        (shift, log_scale) ← conditioner_net(x_batch)
        Define transformed distribution:
        p(y_batch | x_batch) = N(shift, exp(log_scale))
        Compute loss: L = − log p(y_batch | x_batch)
        Update conditioner network via backpropagation
    end for
end for
return Trained conditioner network =0
```

2.5. Inference and Sampling

After training, the CNF model is used to generate probabilistic predictions for new, unseen input configurations. Each input, represented by a high-dimensional vector of physical parameters, is passed through the conditioner network to compute the corresponding shift and log-scale vectors. These parameters define an affine transformation applied to latent samples drawn from a standard normal distribution, producing samples from the output distribution.

Specifically, given a new input $\mathbf{y}_{\text{new}}$, the conditioner network outputs $t(\mathbf{y}_{\text{new}})$ and $\log s(\mathbf{y}_{\text{new}})$. A set of latent vectors $\mathbf{z} \sim \mathcal{N}(\mathbf{0}, \mathbf{I})$ is sampled and transformed into output predictions $\mathbf{x}$ using the mapping:

$$\mathbf{x} = \exp(\log s(\mathbf{y}_{\text{new}})) \odot \mathbf{z} + t(\mathbf{y}_{\text{new}}),$$

where $\odot$ denotes element-wise multiplication. This procedure is repeated across all models obtained from cross-validation, enabling ensemble sampling from the posterior predictive distribution.

The resulting samples are aggregated to compute the posterior mean and standard deviation for each spectral quantity. These statistics yield the predicted response along with its associated uncertainty. A 95% confidence interval is computed as $\hat{x}_{\text{mean}} \pm 1.96 \cdot \hat{\sigma}$, providing interpretable and calibrated probabilistic forecasts of total reflectance, absorbance, and transmittance for previously unseen physical inputs.

2.6. Model Evaluation and Predictions

Model evaluation is performed using the negative log-likelihood (NLL) computed on the validation sets during cross-validation. This metric quantifies how well the predicted conditional distributions align with the observed spectral responses and serves as a principled objective that is consistent with the training loss. Lower NLL values indicate higher model confidence and better agreement with the data.

To assess predictive performance, we compare the posterior means of the predicted outputs with the ground-truth spectral values across the wavelength domain. Additionally, the model provides standard deviations and confidence intervals, enabling uncertainty quantification for each prediction. These intervals offer valuable insights into the model's reliability, particularly in the context of noisy or underdetermined physical systems.

In the following section, we present detailed comparisons between the predicted and true values, including graphical analyses with uncertainty bands. These evaluations underscore the model's ability to generalize to unseen inputs and to provide well-calibrated probabilistic forecasts across a variety of optical configurations.

3. Results and Discussion

To evaluate the performance of our trained CNF model, we perform predictive inference on previously unseen data. The test input consists of wavelength-dependent optical properties—namely, the absorption coefficient (μ_a), scattering coefficient (μ_s), anisotropy factor (g), and particle size distribution (ρ)—which are concatenated into a single

input vector and reshaped to match the input dimensionality expected by the trained model.

Predictions are generated using the ensemble of models obtained from 5-fold cross-validation. For each fold, the corresponding trained CNF model outputs shift and log-scale vectors conditioned on the test input. These parameters define a conditional Gaussian distribution from which we draw multiple samples (10,000 per model). The generated outputs are then transformed via the RealNVP bijector to yield predictive samples of the total reflectance, absorbance, and transmittance. The predictions from all five folds are aggregated to compute the posterior mean and standard deviation across the spectral domain, enabling robust estimation of both the predicted mean and associated uncertainty.

Figure 2 presents a direct comparison between the NF-predicted mean spectra (solid lines) and the true Monte Carlo-generated values (dashed lines) for all three optical properties. The NF model achieves excellent agreement with the true values across the full wavelength range. Both reflectance and absorbance curves are accurately captured, including sharp transitions, while transmittance remains consistently modeled even in low-signal regions. This highlights the capacity of the CNF model to generalize across complex radiative behaviors in nanoparticle-laden media.

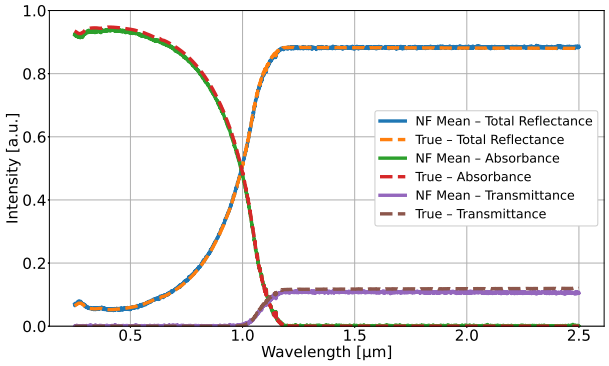


Figure 2: Comparison between conditional Normalizing Flow model predictions (solid lines) and true simulation outputs (dashed lines) for total reflectance, absorbance, and transmittance across the spectral range.

The high degree of overlap between predicted and true spectra confirms the accuracy of the CNF framework. The model remains stable in smooth spectral regions and accurately captures sharp spectral transitions. These results validate both the expressiveness of the CNF architecture and the robustness of the training strategy—including cross-validation and posterior sampling. Overall, the CNF model demonstrates strong generalization capabilities and reliability as a surrogate for fast, uncertainty-aware predictions in radiative transfer modeling.

Figures 3 present individual comparisons between the CNF-predicted spectral properties and the corresponding ground truth values for (a) total reflectance, (b) absorbance, and (c) transmittance. Each plot displays the posterior predictive mean (solid black line), the true Monte Carlo simulation output (dashed blue line), and a 95% confidence interval (shaded blue region) derived from posterior sampling. The close visual agreement between the predicted and true values highlights the model's ability to faithfully capture spectral behavior across the entire wavelength range.

The confidence intervals remain relatively uniform across most of the spectrum, reflecting high predictive certainty. Even near the sharp spectral transition around 1.1 μm, the model maintains well-calibrated uncertainty, indicating robust learning and effective generalization in data-sparse or high-gradient regions. This behavior aligns with expected uncertainty dynamics in such scenarios. Notably, the true values consistently fall within the predicted bounds, further validating the reliability of the CNF model's uncertainty estimates.

These findings confirm that the CNF model delivers both accurate point predictions and well-calibrated epistemic uncertainty quantification. Such reliable uncertainty estimates are crucial in optical modeling scenarios, where prediction confidence directly impacts experimental design, material selection, and downstream decisions. The strong performance demonstrated here suggests significant potential for extending this CNF-based approach to more complex forward and inverse problems in optical characterization.

While the conditional normalizing flow (CNF) model delivers accurate predictions and well-calibrated uncertainty estimates, it is worth noting that, in certain regions, the 95% confidence intervals occasionally extend into negative values. Although mathematically permissible within the probabilistic framework of the model, such negative bounds are physically non-interpretable for radiative properties like reflectance, absorbance, and transmittance, which are inherently non-negative. This outcome highlights a known limitation of the current modeling approach. As part of our future work, we plan to enhance the model structure and incorporate additional constraints to ensure that both the predictive means and the corresponding confidence intervals remain consistent with physical reality.

4. Conclusions

This work introduced a probabilistic surrogate modeling framework based on Conditional Normalizing Flows (CNFs) to predict the spectral radiative properties—total reflectance, absorbance, and transmittance—of nanoparticle-embedded scattering media. Trained on synthetic data generated via Monte Carlo simulations combined with Mie theory-derived optical parameters, the model provides a fast, data-driven alternative to computationally expensive simulations.

The CNF framework successfully captures complex, wavelength-dependent optical behavior across a broad spectral range. Through 5-fold cross-validation and detailed uncertainty quantification, we demonstrated its abil-

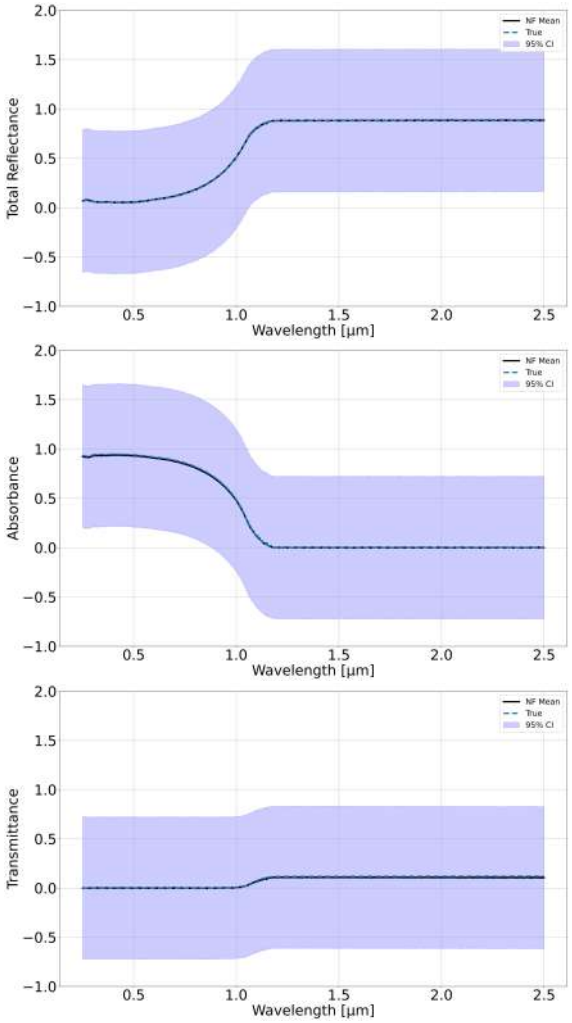


Figure 3: Posterior predictions of (a) Total Reflectance, (b) Absorbance, and (c) Transmittance obtained from the CNF model. The solid black line indicates the predictive mean, the dashed blue line represents the true simulation output, and the shaded region denotes the 95% confidence interval computed from posterior samples.

ity to generalize to unseen inputs while producing well-calibrated posterior distributions. These predictive distributions enable interpretable confidence intervals and support robust, uncertainty-aware inference.

Our findings establish CNFs as powerful tools for forward modeling in optical and materials science. The probabilistic nature of the model is particularly advantageous in scenarios where predictive confidence is essential, including optical device design, inverse scattering, and experimental planning. Future extensions could explore support for more diverse particle geometries, higher concentrations, or multilayer systems—thereby broadening the relevance of the method in advanced photonics and nanomaterials research.

Finally, we acknowledge that the model's confidence intervals can occasionally extend into negative values, which—although mathematically valid within the probabilistic framework—may be physically non-interpretable for radiative properties. Addressing this limitation is an important direction for future model development, ensuring that both predictive means and confidence intervals remain consistent with the underlying physics.

5. Supplementary Material: Derivation of the Conditional Log-Likelihood in CNF

Latent Variable and Forward Mapping: Let $\mathbf{z} \in \mathbb{R}^D$ be a latent variable drawn from a standard multivariate Gaussian distribution:

$$\mathbf{z} \sim \mathcal{N}(\mathbf{0}, \mathbf{I}),$$

where $\mathbf{I} \in \mathbb{R}^{D\times D}$ is the identity matrix. We define an affine transformation to generate the observed variable $\mathbf{x} \in \mathbb{R}^D$ conditioned on an input $\mathbf{y}$:

$$\mathbf{x} = \exp\big(\log s(\mathbf{y})\big) \odot \mathbf{z} + t(\mathbf{y}),$$

where $\log s(\mathbf{y}) \in \mathbb{R}^D$ is the log-scale vector output by the conditioner network, $t(\mathbf{y}) \in \mathbb{R}^D$ is the shift vector from the same network, and $\odot$ denotes element-wise (Hadamard) product. This transformation is invertible and differentiable, making it suitable for both sampling and density estimation.

Change of Variables Formula: Given the invertible transformation $f_\psi : \mathbf{z} \mapsto \mathbf{x}$, the conditional log-probability $p(\mathbf{x} \mid \mathbf{y})$ is computed using the change-of-variables formula:

$$\log p(\mathbf{x} \mid \mathbf{y}) = \log p(\mathbf{z}) - \log \left|\det \left(\frac{\partial \mathbf{x}}{\partial \mathbf{z}}\right)\right|.$$

Jacobian Determinant: The Jacobian matrix $\frac{\partial \mathbf{x}}{\partial \mathbf{z}}$ is diagonal because the transformation is element-wise. Each diagonal entry is given by:

$$\frac{\partial x_j}{\partial z_j} = \exp(\log s_j(\mathbf{y})) = s_j(\mathbf{y}).$$

Hence, the determinant is:

$$\left|\det \left(\frac{\partial \mathbf{x}}{\partial \mathbf{z}}\right)\right| = \prod_{j=1}^{D} s_j(\mathbf{y})$$

$$\log \left|\det \left(\frac{\partial \mathbf{x}}{\partial \mathbf{z}}\right)\right| = \sum_{j=1}^{D} \log s_j(\mathbf{y})$$

Latent Density: The log-density of $\mathbf{z} \sim \mathcal{N}(\mathbf{0}, \mathbf{I})$ is:

$$\log p(\mathbf{z}) = -\frac{1}{2}\left(\|\mathbf{z}\|^2 + D\log(2\pi)\right).$$

Combining the two components, the final expression for the conditional log-likelihood is:

$$\log p(\mathbf{x} \mid \mathbf{y}) = \log p(\mathbf{z}) + \sum_{j=1}^{D} \log s_j(\mathbf{y}),$$

where $\mathbf{z} = f_\psi^{-1}(\mathbf{x}, \mathbf{y}) = (\mathbf{x} - t(\mathbf{y})) \oslash \exp(\log s(\mathbf{y}))$.

Acknowledgement

The AI-TranspWood project, HORIZON-CL4–2023-RESILIENCE- 01–23 (Grant Agreement 101138191), is gratefully acknowledged. This project is co-funded by the European Union. Views and opinions expressed are however those of the author(s) only and do not necessarily reflect those of the European Union or HaDEA. Neither the European Union nor the granting authority can be held responsible for them.

References

[1] H. Azarkish and M. Rashki, "Reliability and reliability-based sensitivity analysis of shell and tube heat exchangers using monte carlo simulation," *Appl. Therm. Eng.*, vol. 159, p. 113842, 2019.

[2] A. Doronin and I. Meglinski, "Online object oriented monte carlo computational tool for the needs of biomedical optics," *Biomed. Opt. Express*, vol. 2, no. 9, pp. 2461–2469, 2011.

[3] F. Seyedheydari, K. Conley, P. Ylä-Oijala, A. Sihvola, and T. Ala-Nissila, "Electromagnetic response and optical properties of anisotropic cusbs2 nanoparticles," *JOSA B*, vol. 39, no. 7, pp. 1743–1751, 2022.

[4] L. Wang, S. L. Jacques, and L. Zheng, "MCML-Monte Carlo modeling of light transport in multi-layered tissues," *Comput. Methods Programs Biomed.*, vol. 47, no. 2, pp. 131–146, 1995.

[5] K. Conley, S. Moosakhani, V. Thakore, Y. Ge, J. Lehtonen, M. Karttunen, S.-P. Hannula, and T. Ala-Nissila, "Silica-silicon composites for near-infrared reflection: A comprehensive computational and experimental study," *Ceram. Int.*, vol. 47, no. 12, pp. 16 833–16 840, 2021.

[6] D. Lu and D. Ricciuto, "Efficient surrogate modeling methods for large-scale earth system models based on machine-learning techniques," *Geosci. Model Dev.*, vol. 12, no. 5, pp. 1791–1807, 2019.

[7] M. Kaya and S. Hajimirza, "Surrogate based modeling and optimization of plasmonic thin film organic solar cells," *Int. J. Heat Mass Transf.*, vol. 118, pp. 1128–1142, 2018.

[8] I. Goodfellow, *Deep learning*. MIT press, 2016, vol. 196.

[9] Y. Gal and Z. Ghahramani, "Dropout as a bayesian approximation: Representing model uncertainty in deep learning," in *international conference on machine learning*. PMLR, 2016, pp. 1050–1059.

[10] D. Rezende and S. Mohamed, "Variational inference with normalizing flows," in *International conference on machine learning*. PMLR, 2015, pp. 1530–1538.

[11] I. Kobyzev, S. J. Prince, and M. A. Brubaker, "Normalizing flows: An introduction and review of current methods," *IEEE Trans. Pattern Anal. Mach. Intell.*, vol. 43, no. 11, pp. 3964–3979, 2020.

[12] J. H. Park, J. Lee, and J. Hwang, "Solving inverse problems using normalizing flow prior: Application to optical spectra," *Phys. Rev. B*, vol. 109, no. 16, p. 165130, 2024.

[13] C. Durkan, A. Bekasov, I. Murray, and G. Papamakarios, "Neural spline flows," *NeurIPS*, vol. 32, 2019.

Optical Polarization modulation based on metasurfaces

Chen Chen*

College of Engineering and Applied Sciences, Nanjing University, Nanjing, 210093, China
*corresponding author: chenchen2021@nju.edu.cn

Abstract: We realized independent wavefront manipulation of different polarization channels including two cross-polarizations, and co- and two cross-polarizations, applications like achromatism, polarimetry and encryption were successively demonstrated.

Metasurfaces, emerging as innovative flat optical devices, facilitate the development of thin and lightweight optical elements with precisely engineered wavefronts. Benefiting from the plentiful freedoms of the anisotropic meta-atoms, flexible manipulation of polarization can be achieved.

The fundamental phase modulation method for spin light is the PB phase, which is determined by the varying orientation angles of each meta-atom, constrained by intrinsic symmetry. Unlike the global effects of the PB phase in spin light manipulation, we propose a novel local phase modulation mechanism based on planar chiral meta-atoms. This mechanism enables efficient and independent phase control for different spin lights [1]. Utilizing such two cross-polarizations modulation, we can realize a folded pancake metalens with polarized space-folding effect [2], and an achromatic metalens out of the size limitation. Considering the co-polarization light channel [3], we can realize three independent channels: one co-spin channel and two cross-spin channels. Leveraging this chiral modulation, we propose a non-interleaved single-pixel polarimetry scheme that achieves high spatial resolution through mutual interference information [4]. Applying interferometric methods to Poincaré beams, we introduce the concept of perfect high-dimensional Poincaré beams with expanded degrees of freedom. By cascading two arrayed metasurfaces, we can independently engineer more beam properties, significantly enhancing the key and encoding spaces for optical encryption, thereby achieving high security levels and large information capacities [5]. Such tri-polarization-channel wave front control can further be extended for the arbitrary polarization state [6]. We envision that such polarization manipulation based on metasurfaces could bring in more intriguing applications in the near future.

References:

1. Chen, C. et al. “Metasurfaces with Planar Chiral Meta-Atoms for Spin Light Manipulation”. Nano Lett. 21,1815,2021.
2. Chen, C. et al. “Bifacial-metasurface-enabled pancake metalens with polarized space folding”. Optica, 9, 1314, 2022.
3. Chen, C. et al. “Highly efficient metasurface quarter-wave plate with wavefront engineering”. Adv. Photon. Res. 2, 2000154, 2021.
4. Chen, C. et al. “Neural network assisted high-spatial-resolution polarimetry with non-interleaved chiral metasurface”. Light Sci. Appl. 12, 288, 2023.
5. Ji, J. et al. “High-dimensional Poincaré beams generated through cascaded metasurfaces for high-security optical encryption”. PhotoniX 5, 13, 2024.
6. Li, S. et al, “Metasurface Polarization Optics: Phase Manipulation for Arbitrary Polarization Conversion Condition”. Phys. Rev. Lett. 134, 023803, 2025.

All-optical ultrafast polarization switching with nonlinear plasmonic metasurfaces

Heng Wang, Guixin Li*

Department of Materials Science and Engineering, Southern University of Science and Technology, Shenzhen 518055, China

*corresponding author: ligx@sustech.edu.cn

Abstract: We demonstrate all-optical ultrafast polarization switching of second harmonic waves with nonlinear plasmonic metasurfaces. By leveraging geometric phase controlled symmetry-selective polarization switching via second-harmonic generation, ~520 fs switching time, ~97% modulation depth and dual-channel switching are achieved. The metasurface platform offers promising applications in ultrafast optical information processing.

Optical switching has important applications in optical information processing, optical computing and optical communications. The long-term pursuit of optical switch is to achieve short switching time and large modulation depth. Among various mechanisms, all-optical switching based on Kerr effect represents a promising solution. However, it is usually difficult to compromise both switching time and modulation depth of a Kerr-type optical switch. To circumvent this constraint, symmetry selective polarization switching via second harmonic generation (SHG) in nonlinear crystals has been attracting scientists' attention. Here, we demonstrate the all-optical ultrafast polarization switching of second harmonic waves with the nonlinear plasmonic metasurfaces working in the near infrared regime. By using the concept of geometric phase, the linear polarization directions of the second harmonic waves could be well controlled by the linear polarization direction and time delay of the two pump waves. A switching time of ~520 femtoseconds and a near-unity modulation depth of ~97% were experimentally achieved. In addition, we also demonstrate the dual-channel all-optical ultrafast switching by designing the distributions of the meta-atoms. This work represents an important progress in the fields of nonlinear optics and optical information processing. The metasurface platform is easy to be scaled up and allows for the design of parallel switching channels. The metasurface platform proposed here may open new routes for developing all-optical ultrafast switches and would benefit the area of optical information processing.

References

1. H. Wang, Z. Hu, J. Deng, X. Zhang, J. Chen, K. Li, G. Li, "All-optical ultrafast polarization switching with nonlinear plasmonic metasurfaces," *Sci. Adv.*, Vol. 10, No. eadk3882, 2024.

Chaos-based communication in synthetic temporal lattices

Chenyu Liu[1], Bing Wang[1*], and Peixiang Lu[1]
[1]School of Physics and Wuhan National Laboratory for Optoelectronics and, Huazhong University of Science and Technology, Wuhan 430074, China.
[*]corresponding author: wangbing@hust.edu.cn

Abstract: We presents a tunable nonlinearity method in synthetic temporal lattices via opto-electric feedback, experimentally demonstrating bistability-to-chaos transitions and constructing a high-entropy chaos-based encryption system. The findings enable advanced secure communication schemes within synthetic dimension platforms.

Main results:

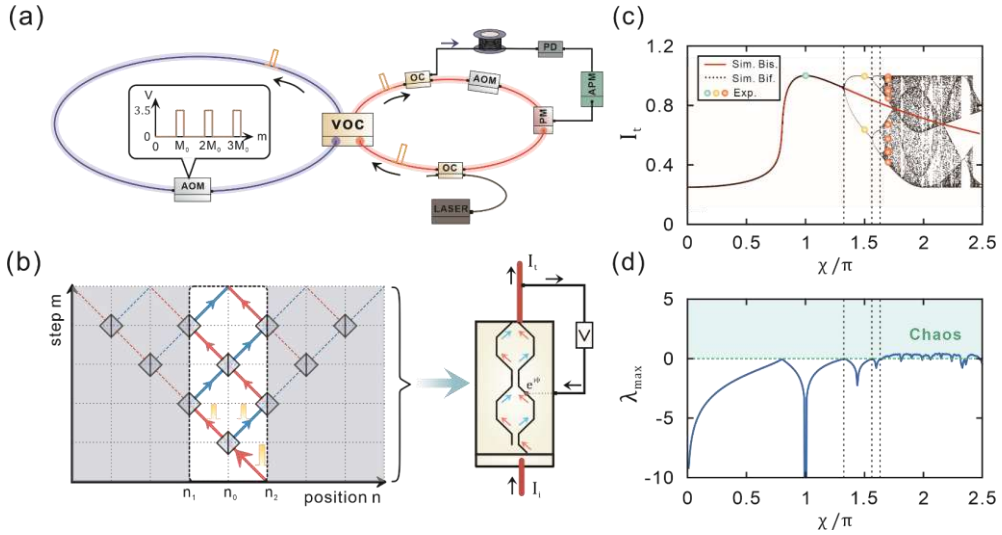


Fig. 1. a. Schematic experimental setup of temporal lattices based on two coupled fiber loops with a length difference. **b.** Schematic diagram of the synthetic temporal mesh lattice and temporal feedback system. **c.** Bifurcation diagram. **d.** The maximal Lyapunov exponent corresponding to the bifurcation diagram in **c**, the green region means chaos behavior emerge.

Based on two coupled fiber loops with difference lengths and an opto-electric circuit shown in Fig. 1a, we first construct temporal nonlinear feedback system (Fig. 1b). Assuming the temporal feedback system operates continuously, with the nonlinear phase feedback time negligible compared to the system's response time and the final output intensity stabilizing at a constant value, two functional relationships between transmittance and phase can be described as

$$T = \sin^4\beta + \cos^4\beta - \frac{1}{2}\sin^2(2\beta)\cdot\cos\phi, \tag{1}$$

$$T = \frac{\phi}{\chi I_i}, \tag{2}$$

where χ is the nonlinear feedback coefficient. This allowed us to derive a simulated bistable curve illustrating the relationship between χ and the outgoing light intensity It, as shown in Fig. 1c. Due to the discreteness of temporal

synthetic lattices underlying the temporal nonlinear feedback system, the feedback phase becomes discretized and exhibits iterative variations rather than continuous changes. Therefore, as the nonlinear coefficient increases, the lower branch of bistable curve transitions through a sequence of period-doubling bifurcations, ultimately leading to chaotic behavior. Figure 1c displays the bifurcation diagram illustrating the transition from bistable behavior to chaos as ϕ is discretized. The maximal Lyapunov exponent curve shown in Fig. 1d corresponding to the bifurcation diagram, in which maximal Lyapunov exponent λ_{max} is positive in the chaotic region and negative in region without chaos.

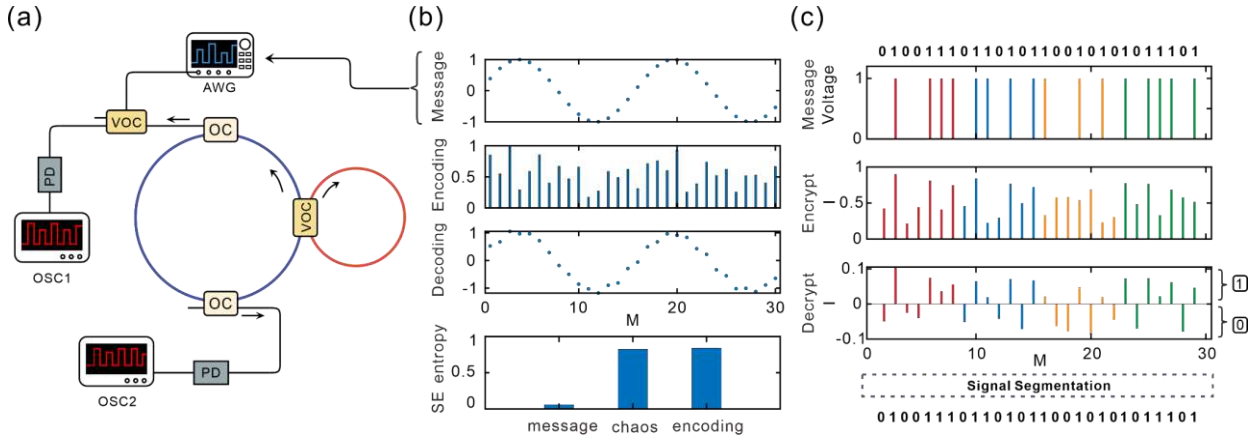


Fig. 2. a. Experimental and theoretical implementation of temporal chaotic encryption transmitter. **b.** Experimental results of chaotic encryption and decryption of waveform message. **c.** Experimental results of chaotic encryption and decryption of binary message.

Figure 2a is the experimental setup of temporal chaos transmitter. The chaotic pulse sequences generated by the nonlinear coupled fiber loops are extracted via an OC in the long loop. These sequences are modulated by a VOC, which incorporates message through an arbitrary waveform generator (AWG). The modulated chaotic signal is then detected by a photodetector (PD) and displayed on oscilloscope 1 (OSC1). The unmodulated chaotic signal is extracted using a separate set of OC and PD and recorded by OSC2. Figure 2b and 2c are the experimental and simulation results of the chaotic encryption and decryption processes of waveform he binary message.

This work represents the first experimental realization of temporal chaos in synthetic lattices and paves the way for advanced chaos-based communication with high-security encryption.

Acknowledgements: This work is supported by the National Natural Science Foundation of China (No. 12374305, No. 12021004, No. 12147151, No. 62305122 and No. 12204185).

References

1. A. Regensburger *et al.*, "Parity-time synthetic photonic lattices," Nature, Vol. 488, 167-171, 2012.

Enhancement of Light-Matter Interaction in Topological Waveguides and Resonators

M. Brauckmann[1,3,*], E. Narváez Castañeda[1,3], D. Siebert[2,3], B. Brecht[1,3], J. Förstner[2,3], and T. Zentgraf[1,3]
[1]Department of Physics, Paderborn University, Warburger Straße 100, 33098 Paderborn, Germany
[2]Department of Electrical Engineering, Paderborn University, Warburger Straße 100, 33098 Paderborn, Germany
[3]Institute for Photonic Quantum Systems (PhoQS), Warburger Straße 100, 33098 Paderborn, Germany
michael.brauckmann@uni-paderborn.de (corresponding author)

Abstract

The quantum valley Hall effect is used to arrange different topological areas with specific topological properties and customize waveguides and resonators to study enhanced light-matter interactions.

1 Introduction

Topological waveguides display novel possibilities of controlling light in on-chip structures. Here the quantum valley Hall effect is used as a foundation to design topological valley photonic crystal structures which relies on a broken inversion symmetry of the topological area. [1]
Superlattices of holes with different sizes, etched into a silicon on insulator wafer, are used to open up a bandgap in the photonic crystal slab [2]. The bandgap can be further tuned through changing hole sizes and the lattice constant. Combining two different topological areas breaks the spatial-inversion symmetry of the overall topological area and edge states arise at the interface. These edge states create one directional waveguides with tunable transmission windows and low losses as shown in Figure 1. Since silicon offers high non-linearity for light-matter interaction the topological waveguide provide a platform for tuning direction as well as wavelength range for these processes. In order to further enhance light-matter interaction within the topological structures we build triangular topological resonators which couple to the nearby topological waveguides as shown in Figure 2.

2 Figures and Tables

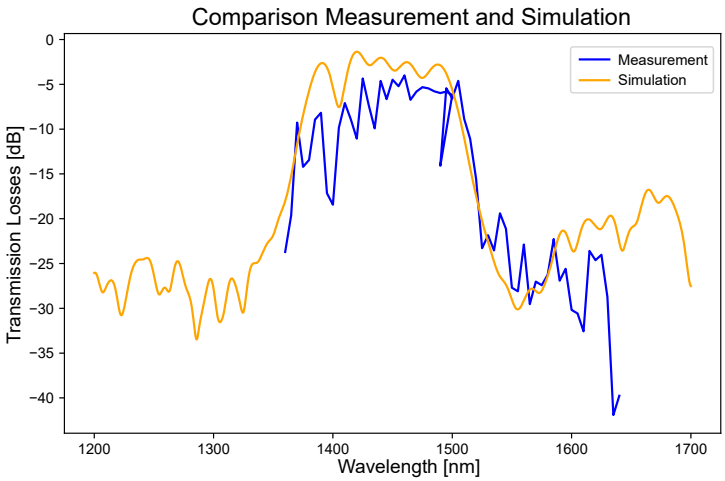


Figure 1:
The losses of a topological waveguide for wavelength between 1350 nm and 1640 nm are shown. The reduced topological losses can be recognized both in the experiment and in the simulation and are in agreement.

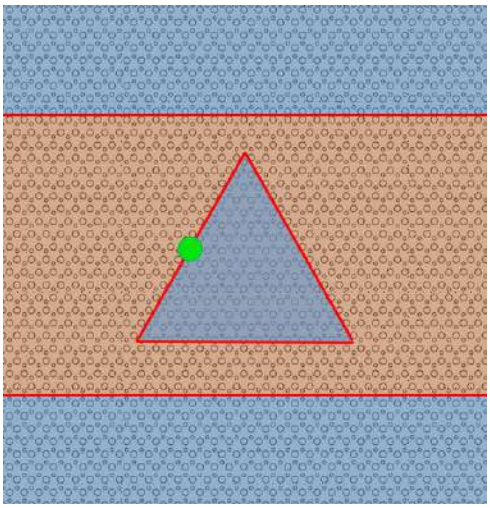


Figure 2:
The figure shows a schematic drawing of the resonator that should enhance linear and non-linear effects. The different topological areas are highlighted and the interfaces are marked red. The green dot indicates a possible position of a pump laser.

References

[1] Ma, T., Shvets, G. "All-Si valley-Hall photonic topological insulator," *New Journal of Physics*, Vol. 18, No. 2, pp. 025012, 2016

[2] He,XT. et al., "A silicon-on-insulator slab for topological valley transport," *Nat. Commun.*, Vol. 10, No. 1, pp. 872, 2019

Pixelated plasmonic metasurfaces as a platform for sensing applications in mid-IR

Amirmostafa Amirjani[1*] and Ewald Janssens[1*]

[1] Quantum Solid State Physics, Department of Physics and Astronomy, KU Leuven, 3001 Leuven, Belgium
[*]Corresponding authors: Amirmostafa.Amirjani@kuleuven.be and Ewald.Janssens@kuleuven.be

Abstract:

In this study, we present the pixelated plasmonic metasurface for detecting mid-infrared molecular fingerprints and for the chemical identification and compositional analysis of surface-bound analytes. The pixelated plasmonic metasurface successfully detected the molecular fingerprints of glucose (1 nM) in the wavenumber range of 1000 cm^{-1} to 1800 cm^{-1}.

Plasmonic metasurfaces are two-dimensional arrays of metallic nanoantennas (meta-atoms) with subwavelength thicknesses and spacings and spatially varying phase responses. Plasmonic metasurfaces promise a paradigm shift in optics by replacing traditional bulky optical elements, e.g., beam deflectors, lenses, waveplates, vortex generators, and holograms, with ultrathin, lightweight, and easy-to-integrate two-dimensional optical interfaces [1,2]. Furthermore, plasmonic metasurfaces have an ultrathin thickness on the order of tens of nanometers, are easy to fabricate, support field confinement beyond the diffraction limit, and have the potential to respond on the timescale of a few femtoseconds. These properties are unparalleled in traditional optical elements, which makes them a promising candidate for sensing applications, especially in the mid-IR range. However, because of the mismatch between mid-IR wavelengths and dimensions of molecules, the sensitivity of mid-IR spectroscopy is limited when detecting signals from nanometer-scale samples.

This drawback can be addressed by exploiting the strong near-field enhancement of the plasmonic metasurfaces. If the metasurface resonance is spectrally overlapped with the absorption fingerprints of the molecule, the enhanced molecule-resonator coupling can lead to a change in either the frequency or the strength of the resonance, from which the molecular fingerprints can be extracted [3]. The idea of pixelated metasurfaces helped to tune the resonance wavelength and the electromagnetic field enhancement at specific wavelengths. In this study, we successfully fabricated plasmonic metasurfaces with reflectance resonances in the molecular fingerprint region (Figure 1) from 1000 cm^{-1} to 1800 cm^{-1}.

Figure 1(a) shows the schematic illustration of the fabricated pixelated plasmonic metasurface according to different scaling factors (S), and it can be inferred that the resonances of each pixel (shown in Figure 1(b)) covered the molecular fingerprint region entirely. Upon the addition of glucose (1 nM) on top of the plasmonic metasurface, specific changes can be observed in the frequency or intensity of the resonances (Figure 1(b, middle row)), which can be attributed to the absorption fingerprint of glucose. These reflectance differences were translated to a 2D map using a Python code from which the signature of the glucose molecule can be seen clearly. As can be inferred, this platform can enhance, detect, and differentiate the absorption fingerprints of glucose (as a model) without the need for complex instrumentation.

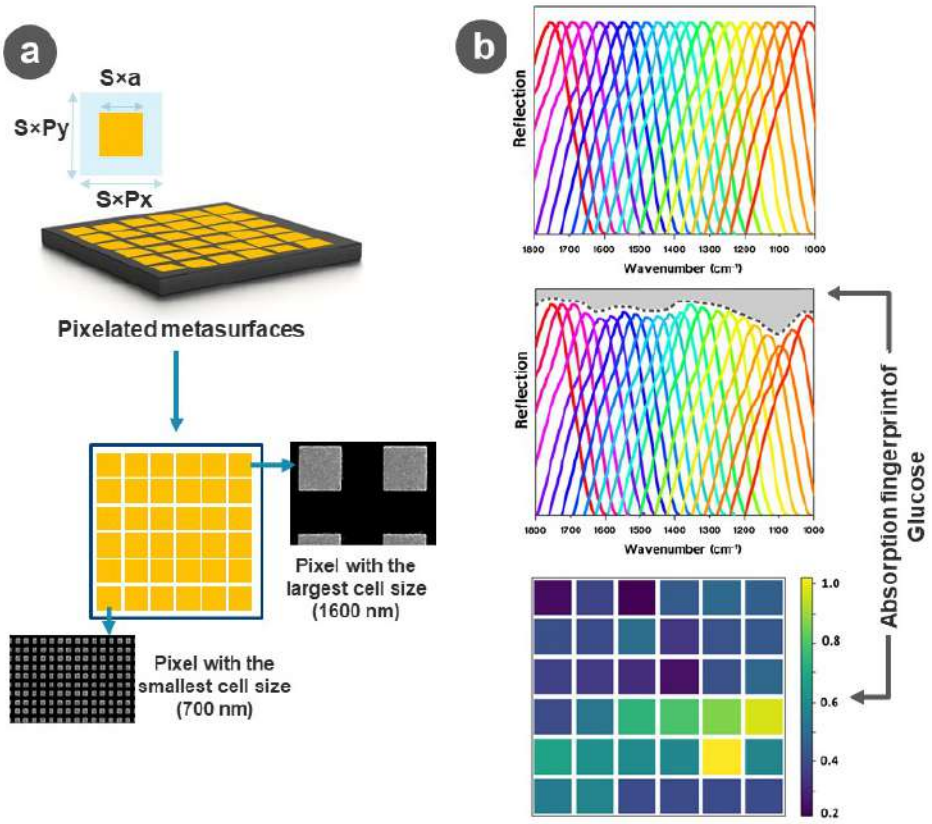


Figure 1. (a) Schematic illustration of the fabricated plasmonic metasurfaces containing 36 pixels with different cell sizes according to the scaling factor (S). (b) Resonance spectra of each pixel before (top row) and after (middle row) the addition of the analyte (Glucose (1 nM) in this case). The bottom row shows the 2D barcode-like map of reflectance difference.

This concept showed promising applications for detecting mid-infrared molecular fingerprints for the chemical identification and compositional analysis of surface-bound analytes. We aim to use the developed barcode-like sensor to detect different molecules and realize the multiplexed sensing in the mid-IR range.

References

1. Song, M. *et al.* (2022) 'Versatile full-colour nanopainting enabled by a pixelated plasmonic metasurface', *Nature Nanotechnology*, 18(1), pp. 71–78.
2. Liang, Y., Tsai, D.P. and Kivshar, Y. (2024) 'From local to nonlocal high-Q Plasmonic Metasurfaces ', *Physical Review Letters*, 133, 053801.
3. Tittl, A. *et al.* (2018) 'Imaging-based molecular barcoding with pixelated dielectric metasurfaces', *Science*, 360(6393), pp. 1105–1109.

A phenomenon of noise avalanche in bosonic chains with random off-diagonal disorder and its quantum quenching

V. Stefanov[1*], A. Stefanov[1], L. Sirota[2], G. Slepyan[3], and D. Mogilevtsev[3,4]

[1]Institute of Applied Physics, University of Bern, Switzerland

[2]School of Mechanical Engineering, Tel Aviv University, Tel Aviv University, Israel

[3]School of Electrical Engineering, Tel Aviv University, Tel Aviv University, Israel

[4]B.I.Stepanov Institute of Physics, NAS of Belarus, Belarus

Corresponding author: vladislav.stefanov@unibe.ch

Abstract

We discuss a sharp increase in photon number noise in bosonic chains with off-diagonal disorder. This "noise avalanche" occurs under coherent excitation of a bosonic mode, leading to super-thermal photon bunching in the lattice. Single-photon excitation of an another mode can quench the avalanche, while classical excitation only slows it.

1 Introduction

Study of coupling between closely situated waveguides often discusses an influence of coupling randomness on field propagation through waveguides. This randomness eventually leads to an asymptotically equal field energy distribution between the waveguides, regardless of the initial states. This phenomenon was shown to be common in systems with noisy coupling (i.e., the so-called 'off-diagonal disorder') [1]. Here we report an counterintuitive phenomenon that can arise in coupled bosonic systems with random off-diagonal disorder: a noise avalanche.

2 Model and the noise avalanche demonstration

The chain model can be considered as a generalization of the much discussed Su–Schrieffer–Heeger [2] (SSH) and is described by the Hamiltonian $H = H_0 + V(t)$, where the time-independent non-random part H_0 describes the unitary SSH chain of $N+1$ resonant coupled bosonic modes:

$$H_0 = \sum_{j=1}^{N}(v_j a_j^\dagger a_{j+1} + v_j^* a_{j+1}^\dagger a_j), \quad V(t) = \sum_{j=1}^{N}(\mu_j(t) a_j^\dagger a_{j+1} + \mu_j^*(t) a_{j+1}^\dagger a_j), \tag{1}$$

with $a_j^\dagger$ and a_j being bosonic creation and annihilation operators for the j-th mode of the chain; v_j are the interaction constants. The off-diagonal random disorder affecting the chain we take as described by the random addition to the Hamiltonian $V(t)$, where $\mu_j(t)$ are random zero-mean classical variables $\langle \mu_j(t) \rangle_c = 0$, where $\langle \ldots \rangle_c$ denotes classical averaging over the noise realizations. We assume that noises between each pair of modes are independent,

$$\langle \mu_j(t)\mu_k(\tau)\rangle_c = \langle \mu_j(t)\mu_k^*(\tau)\rangle_c = 0, \quad \forall j \neq k.$$
$$\langle \mu_j^*(t)\mu_j(\tau)\rangle_c = \gamma_j \delta(t-\tau), \quad \langle \mu_j(t)\mu_j(\tau)\rangle_c = \kappa_j \delta(t-\tau).$$

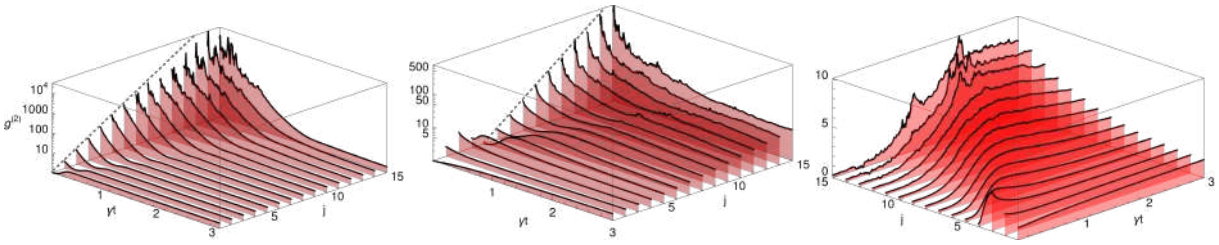
We concentrated our attention on the peculiar phenomenon arising for just one mode initially excited in the coherent state with other modes initially in the vacuum state [3]. This phenomenon is a sudden jump of the photon number noise in the initially empty modes at the very early

stages of dynamics. For long chains of coupled modes this jump turns to the avalanche: the normalized second-order correlation function grows exponentially. However, an additional single-photon excitation quenches the avalanche [3].

We found a simple analytical estimate at the initial time point for the avalanche growth and differences in dependence on the character of noise. For real κ_j one has

$$g^{(2)}_{j+1}(0) \approx \left(2 + \frac{\kappa_j^2}{\gamma_j^2}\right)^j . \tag{2}$$

We have performed numerical Monte-Carlo (MC) simulation demonstrating the effect, particular case is shown in Figure 1.



(a) (b) (c)

Figure 1: Normalized second order correlation functions of a system (1) for j-th mode is calculated via MC simulation with the number of realization is $K = 3 * 10^5$ and the number of time sub-intervals is $M = 300$ (see details in [3]). (a) The first mode is initially excited in a coherent state with the amplitude $\alpha_1 = 10$ and $v = 5\gamma$, $\nu = 0.5$; (b) the first mode is in a coherent state with the amplitude $\alpha_1 = 10$ and the fifth mode is in the amplitude $\alpha_5 = 1$ and $v = 0$, $\nu = 1$; (c) the first mode is in a coherent state with the amplitude $\alpha_1 = 10$ and the fifth mode is initially excited in the single-photon Fock state; all other unmentioned modes are initially in the vacuum state. Dashed lines show a curve (a) 2.36^{j-1} and (b) 2^{j-5} as limit case (2) for $t = 0$.

3 Conclusions

An obvious use of the considered systems with random off-diagonal disorder might be for generation of bunched and super-bunched states in well-defined spatial modes. Such sources are of high demand nowadays for ghost imaging, LIDAR ranging based on intensity correlations or quantum tomography [4, 5]. Additionally, the considered phenomena can be useful for breeding sub-Poissonian states from a combination of a single-photon and coherent inputs.

References

[1] Yusipov I. et al., "Localization in open quantum systems," *Phys. Rev. Lett.* Vol. 118, No. 7, pp. 070402, 2017.

[2] Su W. P., Schrieffer J. R., and A. J. Heeger, "Solitons in polyacetylene," *Phys. Rev. Lett.*, Vol. 42, No. 25, pp. 1698, 1979.

[3] Stefanov, V. et al., "Noise avalanche and its quantum quenching in bosonic chains with random off-diagonal disorder," arXiv:2501.12290.

[4] Chizhevsky, V. N. et al., "Versatile VCSEL source of thermal and super-thermal light," *Opt. Lett.*, Vol. 49, No. 21, pp.6245-6248, 2024.

[5] Harder G. et al., "Tomography by noise," *Phys. Rev. Lett.*, Vol. 113, No 7, pp. 070403, 2014.

PEEM based near-field imaging of plasmonic topological Harper nanochains

Qiuchen Yan[1*], Boheng Zhao[2], Xiaoyong Hu[1], and Qihuang Gong[1]

[1]Peking University, China
[2]Tsinghua University, China
[*]corresponding author: qiuchenyan@pku.edu.cn

Abstract: We propose a novel approach to regulate coupling intensity by integrating gold nanodisks with connecting waveguides. The topological properties of Aubry-André-Harper configuration are directly characterized using photoemission electron microscopy. This work provides direct in-situ measurements of topological states at nanoscale, advancing the practical applications of integrated plasmonic topological photonics.

Photoemission electron microscopy (PEEM) with ultrahigh spatial-temporal resolution can be a good platform to measure the plasmonic modes in the near field and the time field[1]. We have successfully explored the near-field mode distributions and the topological dynamic responses of topological edge states (TESs) in the Aubry-André-Harper (AAH) nanochains. The wavelength-dependent mode distributions of AAH chains are well demonstrated by PEEM instruments, which provides a reliable approach for the multidimensional regulation of TESs and explains the dynamic evolution process of TESs from a fundamental physics perspective.

Here, we report a novel strategy of weaving gold nanodisks with waveguides to realize an ultracompact on-chip-integrated plasmonic topological insulator with an AAH configuration[2]. The on-chip plasmonic topological insulator is constructed by gold nanodisks that are connected by short gold waveguides with different widths, meeting the extremely strict precision requirement of coupling parameters for sample nanofabrication and suppressing the influence of plasmon hotspots. Furthermore, we discover a transition between symmetric and asymmetric boundary modes of the plasmonic topological nanodisk chains with increasing nanochain length, corresponding to variations in the value of parameter ϕ of AAH model. This work advances the foundational research and practical applications of controlling synthetic dimensions in optical micro/nano-scale AAH models, providing robust support for the development of plasmonic topological photonics. By addressing the challenges in this field, the work lays a foundation for the development of advanced photonic devices and information processing chips, enabling further exploration and innovation in the realm of topological photonics.

References

1. Qiuchen, *et.al.* “Near-field imaging and time-domain dynamics of photonic topological edge states in plasmonic nanochains,” Nano Lett., Vol. 21, No. 21, 9270–9278, 2021.
2. Qiuchen, *et.al.* “Near-field imaging of synthetic dimensional integrated plasmonic topological harper nanochains,” Nat. Commun. accepted.

Slot Mode Optomechanical System for Mass Sensing

C. Thrideep[1], M. Belov[2], and W. Hiebert[1,2*]

[1] Department of Physics, University of Alberta, Edmonton, Alberta, Canada T6G 2E1

[2] Nanotechnology Research Centre, National Research Council Canada, 11421 Saskatchewan Dr NW, Edmonton, Alberta, Canada T6G 2M9

[*]corresponding author: Wayne.Hiebert@nrc-cnrc.gc.ca

Abstract: Optomechanical systems have demonstrated their significance in sensing applications. We study a slot mode optomechanical system where in a THz optical mode from a Photonic Crystal (PhC) cavity is coupled to a MHz mechanical mode of the cantilever to construct an effective mass sensitive device specifically operating at low-frequency region.

Improving ultimate mass sensitivity in resonant NEMS is achieved by the best combination of smallest mass resonator (m_{eff}), highest signal-to-noise-ratio (SNR) and largest mechanical quality factor Q represented by the figure of merit:

$$\frac{\delta f}{f} = \frac{m_{eff}}{QSNR} \tag{1}$$

The primary tension in this figure of merit comes from the fact that shrinking device size tends to lose both readout signal and drive efficiency and thus diminishes SNR. In previous work using a cantilever coupled to a racetrack optical resonator [1], it was shown that drive efficiency has a maximum for an optimum optical quality factor and that larger optomechanical coupling provides larger amplitude. It was further shown [2] that readout laser frequency could be tuned for cancellation of optomechanical nonlinearity potentially allowing relatively large driven amplitude. Shrinking the device to improve mass sensitivity would quickly diminish the optomechanical coupling value (G) which would endanger SNR in both the ability to resolve noise floor and the ability to drive a large peak amplitude. While adding optical power could partially mitigate SNR losses, this path is not available due to two-photon absorption nonlinearity limitations in the silicon system. The critical improvement required to solve this problem is one of increasing G in this system, even while maintaining or reducing coupled mass. This drives our present motivation for methods to increase G between a cavity and a low mass mechanical element. For a slot-mode system, the redistribution of energy into the slot should allow an increase to G per unit volume of coupling mechanical element, due to the increased sensitivity of the mode to the surface position boundary conditions. The use of a PhC better localizes the mode energy to the cantilever region also increasing G. Further, the mode energy in the slot may allow slightly higher optical powers due to reduced two photon absorption. Altogether, this motivates the choice of PhC with slot waveguide for best mass sensitivity.

In slot-mode optomechanical devices, the coupling of photonic and phononic beams is utilized to enhance the optomechanical coupling strength beyond what is achievable in single nanobeam crystals. We consider the integration of Silicon PhC with cantilevers on either side which essentially behave as a slot mode optomechanical system. A modified inline coupling technique in reflection mode is used to couple light into the cavity by manipulating losses at the mirrors [3]. To achieve this, the coupling end of the waveguide is provided with only 1 to 5 holes to access different coupling regimes. We utilized COMSOL to model our slot-mode optomechanical system, considering both photonic and phononic bandgap. The PhC- cantilever system was fabricated, and the

chip underwent testing through a pump and probe system to evaluate the device's mass sensitivity. We were able to realize a mass sensitivity of 51zg despite the encountered temperature fluctuation noise. This aligns with the notion that our shorter cantilever demonstrated an improved G of 0.12 GHz/nm, as compared to the value achieved by our research group for a longer cantilever coupled to a racetrack resonator.

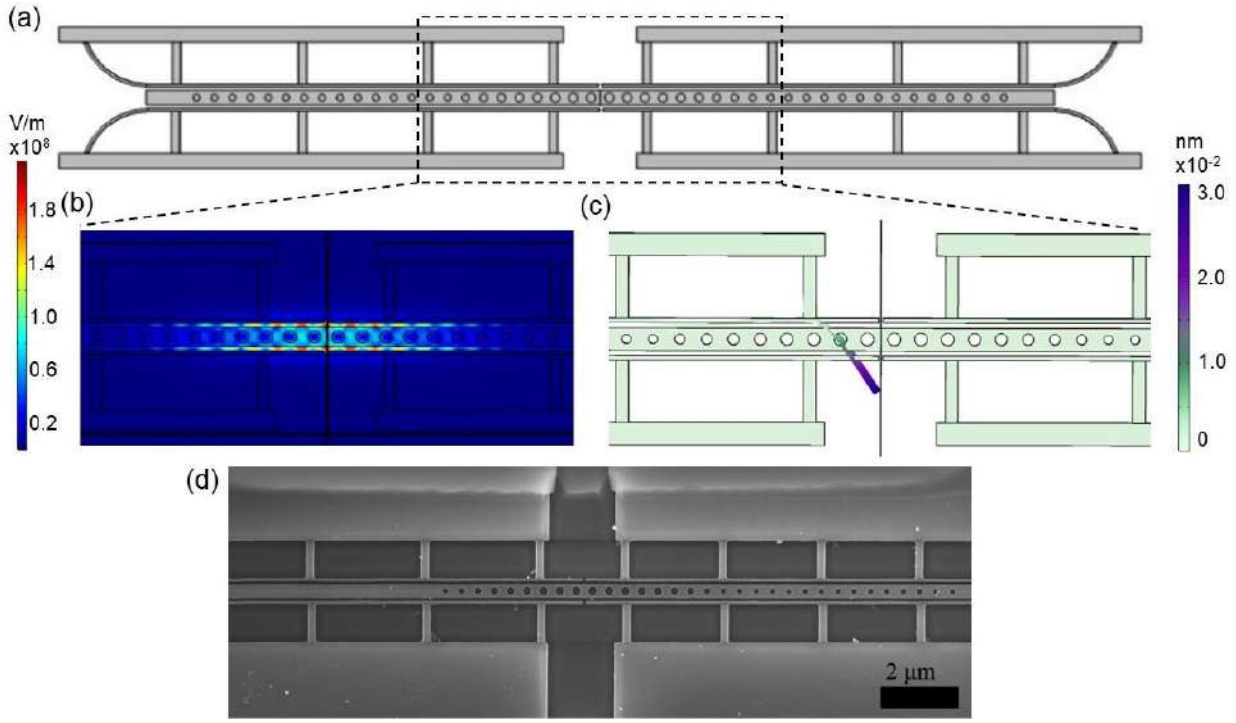


Fig. 4. (a) An illustration of Si Photonic Crystal-Cantilever Slot mode Optomechanical system. The FEM simulation of (b) First mode of optical resonance (c) Mechanical resonance of the cantilever (d) Scanning Electron Microscope Image (SEM) of the optomechanical device fabricated on SOI with one mirror on the coupling end

Acknowledgements

The authors acknowledge Applied NanoTools Inc. for the help with device fabrication. The work was supported by the Natural Sciences and Engineering Research Council of Canada and by Alberta Innovates.

References

1. J. Westwood-Bachman, T. Lee, and W. Hiebert, "Efficient actuation design for optomechanical sensors," Opt. Express 28, 32349–32362 (2020).
2. J. N. Westwood-Bachman, T. Firdous, A. E. Kobryn, et al., "Isolation of optomechanical nonlinearities in nanomechanical cantilevers," Phys. Rev. A 105, 053517 (2022).
3. K. E. Grutter, M. I. Davanço, K. C. Balram, and K. Srinivasan, "Invited article: Tuning and stabilization of optomechanical crystal cavities through nems integration," APL Photonics 3 (2018).

Incoherent Dielectric Tensor Tomography for Robust 3D Birefringence Imaging Using Non-Interferometric System

Juheon Lee[1], Herve Hugonnet[1], Chulmin Oh[1], YongKeun Park[1,*]

[1] Department of Physics, Korea Advanced Institute of Science and Technology (KAIST), Daejeon, Republic of Korea
[*]Corresponding author: yk.park@kaist.ac.kr

Abstract: We present an incoherent dielectric tensor tomography (DTT) technique for robust three-dimensional birefringence imaging of anisotropic materials. Unlike conventional DTT methods that rely on temporally coherent light and interferometry—making them vulnerable to mechanical vibrations and speckle noise—our system utilizes temporally incoherent illumination and a non-interferometric architecture.

Birefringence is an optical property observed in anisotropic materials, where the refractive index (RI) varies depending on the polarization of incident light. This polarization-dependent RI arises from the internal molecular alignment and structural anisotropy of the material. Consequently, three-dimensional (3D) birefringence imaging has become a valuable tool in both industrial and biomedical fields for analyzing the internal orientation and organization of target samples [1,2].

Recently, dielectric tensor tomography (DTT) has emerged as a powerful technique for 3D birefringence imaging, offering a more comprehensive characterization of anisotropic structures by reconstructing the full 3×3 dielectric tensor at each spatial position [3,4,5]. Unlike conventional holotomography, which measures a scalar RI value per voxel, DTT captures the vectorial nature of light–matter interactions by accounting for both the local molecular orientation and the polarization state of light. This tensorial approach provides fundamentally richer information on anisotropic optical behavior within the sample.

However, conventional DTT systems typically rely on interferometric setups with temporally coherent illumination, making them prone to mechanical vibrations and speckle-induced artifacts. To overcome these limitations, we propose a novel incoherent DTT framework based on a non-interferometric imaging system combined with modulated illumination.

Our system employs two temporally incoherent LED light sources and a spatial light modulator (SLM) to control both the incident wavefront and polarization states. A polarized beam splitter is used to direct the modulated light onto the sample, which is sequentially illuminated with a series of polarization-encoded wavefronts. For each illumination condition, the resulting 2D diffraction patterns are recorded at the image plane.

To reconstruct the full 3×3 dielectric tensor, we compute polarization-dependent optical transfer functions using the known input and analysis polarization states. Because a single measurement cannot capture all tensor components, multiple acquisitions with varied SLM modulation patterns and polarization configurations are performed, enabling comprehensive tensor recovery [3].

For validation, we experimentally measured a liquid crystal droplet with a well-known radial molecular alignment. The reconstructed orientation field closely matches the expected structure, and the resulting birefringence tomograms clearly reveal a positive uniaxial anisotropy within the droplet.

In addition, we applied our method to thick biological tissue samples from colon cancer patients. The 3D birefringence information of the collagen network within the tumor microenvironment was accurately reconstructed and quantitatively analyzed, demonstrating the applicability of our approach to complex biological

specimens.

These results demonstrate that our incoherent DTT framework provides a robust and noise-resilient approach for high-fidelity 3D birefringence imaging of anisotropic samples. By eliminating the need for interferometry and coherent illumination, the system significantly enhances experimental stability and reduces speckle artifacts, enabling reliable tensor reconstruction even in challenging biological and material contexts. The ability to retrieve the full dielectric tensor in a label-free and quantitative manner opens new avenues for investigating molecular alignment and structural anisotropy in diverse applications ranging from soft matter physics to cancer pathology.

Acknowledgements

This work was supported by National Research Foundation of Korea grant funded by the Korea government (MSIT) (RS-2024-00442348, 2015R1A3A2066550, 2022M3H4A1A02074314), Institute of Information & communications Technology Planning & Evaluation (IITP; 2021-0-00272) grant funded by the Korea government, the Ministry of Trade, Industry and Energy (MOTIE) and Korea Institute for Advancement of Technology (KIAT) through the International Cooperative R&D program (P0028463), and the Korean Fund for Regenerative Medicine (KFRM) grant funded by the Korea government (the Ministry of Science and ICT and the Ministry of Health & Welfare) (21A0101L1-12).

References

1. Needleman, D. & Dogic, Z. Active matter at the interface between materials science and cell biology. Nat. Rev. Mater. 2, 17048 (2017).
2. Priestly, E. Introduction to Liquid Crystals. Springer Science & Business Media (2012).
3. Shin, S., Eun, J., Lee, S.S. et al. Tomographic measurement of dielectric tensors at optical frequency. Nat. Mater. 21, 317–324 (2022).
4. Oh, C., Hugonnet, H., Lee, J. et al. Extending Rytov Approximation to Vector Waves for Tomography of Anisotropic Materials. Phys. Rev. Lett. 134(6), 068101 (2025).
5. Hugonnet, H., Oh, C., Lee, J. et al. Vectorial inverse scattering for dielectric tensor tomography: overcoming challenges of reconstruction of highly scattering birefringent samples. Opt. Express 31(18), 29654–29663 (2023).

3D Strain Tensor Analysis in micro-indented glass via Dielectric Tensor Tomogram

Juheon Lee[1], YongKeun Park[1,*]

[1] Department of Physics, Korea Advanced Institute of Science and Technology (KAIST), Daejeon, Republic of Korea
[*]corresponding author: yk.park@kaist.ac.kr

Abstract: Dielectric tensor tomography (DTT) enables 3D visualization of strain in materials through optical birefringence. Applying the stress-optic law, we determine principal strains and orientations in micro-indented glass, revealing density variations and crack propagation. Our findings highlight DTT's potential for non-destructive strain analysis and characterization of complex strain distributions.

Assessing mechanical stress and strain is essential for optimizing mechanical components and preventing failures. Optical birefringence, which is sensitive to molecular alignment induced by mechanical stress, serves as a valuable tool for studying stress and strain in materials. A recently developed technique, dielectric tensor tomography (DTT), enables the reconstruction of 3D optical anisotropic structures.[1] In this study, we employ DTT to visualize the 3D strain tensor in micro-indented glass samples. By applying the stress-optic law, we determine the principal strains and their orientations, uncovering variations in density and crack propagation patterns. Our findings demonstrate the potential of DTT for non-destructive strain analysis and its effectiveness in characterizing complex strain distributions in materials.

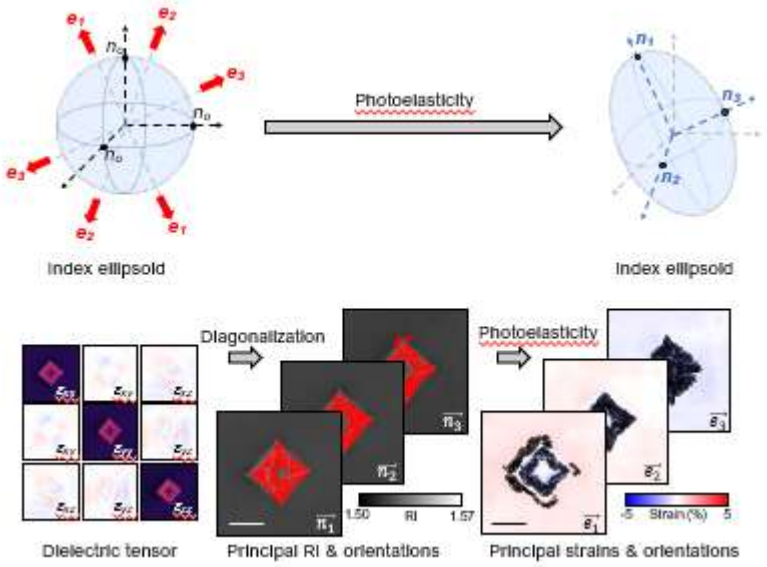


Fig1. Photoelasticity and reconstruction principle of strain tensor.

Acknowledgements

This work was supported by National Research Foundation of Korea grant funded by the Korea government (MSIT) (RS-2024-00442348, 2015R1A3A2066550, 2022M3H4A1A02074314), Institute of Information & communications Technology Planning & Evaluation (IITP; 2021-0-00272) grant funded by the Korea government, the Ministry of Trade, Industry and Energy (MOTIE) and Korea Institute for Advancement of

Technology (KIAT) through the International Cooperative R&D program (P0028463), and the Korean Fund for Regenerative Medicine (KFRM) grant funded by the Korea government (the Ministry of Science and ICT and the Ministry of Health & Welfare) (21A0101L1-12).

References

1. Shin, S., Eun, J., Lee, S.S. et al. Tomographic measurement of dielectric tensors at optical frequency. Nat. Mater. 21, 317–324 (2022).

Generation of high-efficiency bi-functional holography with metasurfaces

Changhong Dai[1†], Tong Liu[2†], Dongyi Wang[3*], Lei Zhou[1,4*]

1. State Key Laboratory of Surface Physics, Key Laboratory of Micro and Nano Photonic Structures (Ministry of Education), Shanghai Key Laboratory of Metasurfaces for Light Manipulation and Department of Physics,
Fudan University, Shanghai 200438, China
2. Department of Physics and Institute for Advanced Study, The Hong Kong University of Science and Technology, Clear Water Bay, Kowloon, Hong Kong, China
3. Department of Physics, The University of Hong Kong, Hong Kong 999077, China
4. Collaborative Innovation Centre of Advanced Microstructures,
Nanjing 210093, China

*corresponding author: Dongyi Wang, Email: physwang@hku.hk
Lei Zhou, E-mail: phzhou@fudan.edu.cn

Abstract: Here we propose a generic approach to design ultra-thin and high-efficiency metasurfaces for multiple holographic images' generation. Utilizing high-efficiency reflective meta-atoms exhibiting incident-spin-delinked reflection phases governed by geometric and resonant mechanisms, distinct holographic images can be generated by the metasurface with the thickness ~ 1/4 λ and efficiencies ~ 48.08%.

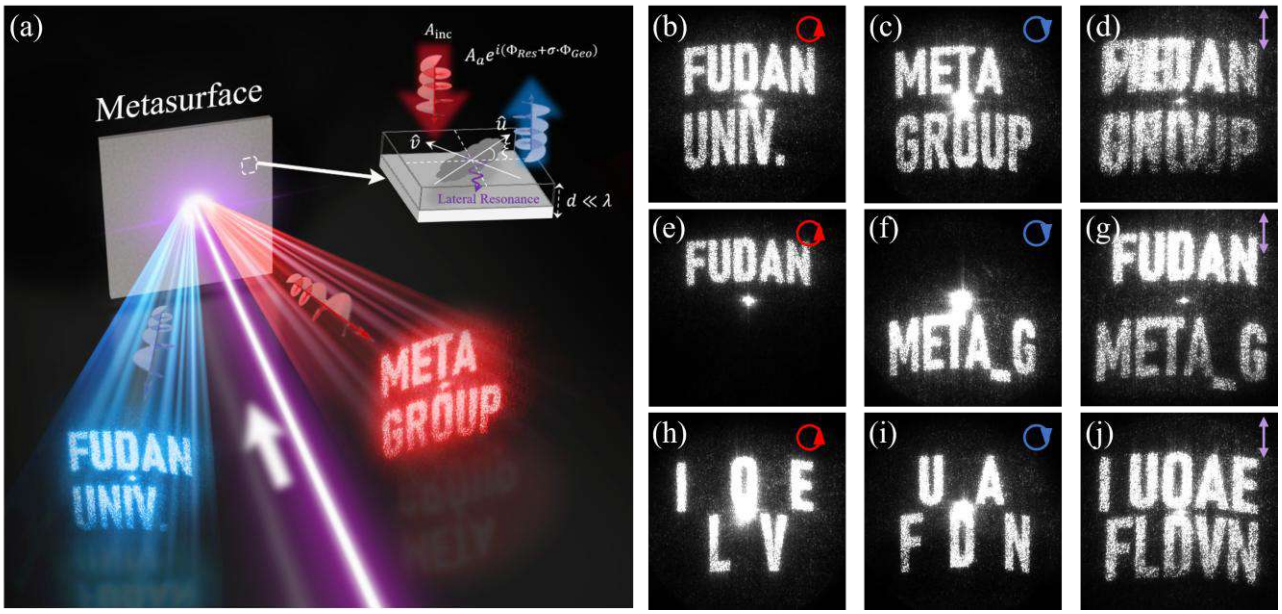


Fig. 1 Bifunctional holography generation based on metasurface. (a) The schematics of bifunctional holography generation with ultra-thin and high efficiency metasurfaces. Experimental demonstrations of varied kinds of bifunctional holography generation at incidences of different polarizations: (b) full-screen bi-functional meta-hologram; (c) split-screen bi-functional meta-hologram; (d) information-encrypted bi-functional meta-hologram.

Generation of holography has garnered increasing interests for its broad applications in modern photonics[1]. However, conventional generation technology requires complex setups, unfavorable for on-chip photonics

applications. Though employment of metasurface in holography generation have been studied recently, meta-holograms realized so far still suffer from imbalances between device thickness and working efficiency/ performance[2].

In this work, designing a series of meta-atoms in MIM configuration exhibiting reflection phases governed by both resonant and geometric mechanisms, we construct bi-functional meta-holograms based on phase distributions retrieved from two distinct holographic images[3]. Suppressing the undesired normal mode by:

$$A_n = |r_{uu}+r_{vv}|/2 = 0 \tag{1}$$

Under the condition of which, the reflected wave of the meta-atom can be expressed by $\boldsymbol{R}|\sigma\rangle = A_a e^{i(\Phi_{Res}+\sigma\cdot\Phi_{Geo})}|\text{-}\sigma\rangle$, containing both a spin-*independent* resonant phase $\Phi_{Res} = (\Phi_u+\Phi_v)/2\text{-}\pi/4$ and a spin-*dependent* geometric phase $\sigma\cdot\Phi_{Geo}$. With the GS algorithm, the reflection-phase distributions to generate distinct holographic images can be retrieved as $\Phi^{m}_{tar,|+\rangle}(\vec{r})$ and $\Phi^{m}_{tar,|-\rangle}(\vec{r})$, Thus with $\Phi^{m}_{tar,|\sigma\rangle}(\vec{r}) = \Phi_{Str}(\vec{r})+\sigma\Phi_{Geo}(\vec{r})$, we have

$$\begin{cases} \Phi_{Str}(\vec{r}) = \dfrac{\Phi^{m}_{tar,|+\rangle}(\vec{r})+\Phi^{m}_{tar,|-\rangle}(\vec{r})}{2} \\ \Delta\Phi(\vec{r}) = \pm\pi \\ \xi(\vec{r}) = \dfrac{\Phi^{m}_{tar,|+\rangle}(\vec{r})-\Phi^{m}_{tar,|-\rangle}(\vec{r})}{4} \end{cases} \tag{8}$$

Which provides an explicit guidance for metasurface design. Following this design strategy, we design and experimentally realize three different kinds of bi-functional meta-holograms. As shown in Fig. 1 (b,c), the first metadevice displays two different full screen patterns on the imaging plane at left circular polarized (LCP) and right circular polarized (RCP) incidences respectively, and simultaneously displays both components at the linear polarized (LP) incidence[Fig. 1 (d)]. Similar bifunctional holographic images exhibit for the split-screen meta-hologram as demonstrated in Fig 1 (e-g). The third metadevice can be applied to information encryption. Carefully arranging the two groups of desired character patterns, we find that while effective information (i.e., “I LOVE” and “FUDAN”) can be correctly displayed as the device is shined by LCP and RCP light beams [Fig. 1(h,i)], respectively, no meaningful information can be obtained as the incident light changes to the LP beam [Fig. 4(j)]. The efficiencies are evaluated to be ~35% in experiments and ~48% in numerical calculations.

In conclusion, we propose a generic strategy to realize bi-functional meta-holograms and experimentally verify the concept with three different metadevices including an information-encrypted one in the telecom frequency domain. The proposed meta-platform can find many applications in future integration photonics.

Acknowledgements: This work was funded by National Key Research and Development Program of China (Grant No. 2022YFA1404700), National Natural Science Foundation of China (Grant Nos. 12221004, 62192771) and Natural Science Foundation of Shanghai (Grant Nos. 23dz2260100).

References

[1] D. Gabor, “A new microscopic principle,” Nature, vol. 161, no. 4098, pp. 777–778, 1948.

[2] D. Wen, F. Yue, G. Li, et al., "Helicity multiplexed broadband metasurface holograms," Nat. Commun., vol. 6, pp. 8241, 2015.

[3] C. Dai, T. Liu, D. Wang, and L. Zhou "High-efficiency generation of bi-functional holography with metasurfaces" Nanophotonics, https://doi.org/10.1515/nanoph-2024-0677, 2025.

Theoretical Analysis of Recoil Force Generated by Stimulated Emission of Higher-Order Optical Vortices

Y. Umekawa[1*], T. Horai[1], M. Ashida[1], and H. Ishihara[1,2]

[1] Graduate School of Engineering Science, Osaka Univ., Japan
[2]Ritsumeikan Semiconductor Application research center (RISA), Ritsumeikan University, Japan
[*]corresponding author: umekawa@laser.mp.es.osaka-u.ac.jp

Abstract: The mechanical recoil force generated in a material by stimulated emission occurs in the direction opposite to the propagation of light. In this study, we theoretically elucidate the rotational motion of nanoparticles induced by recoil force from higher-order optical vortices, considering nonlinear optical responses.

Optical manipulation has been studied since Ashkin's discovery in 1970 as a technique for the non-destructive manipulation of microscopic materials [1]. In particular, resonant optical manipulation, which significantly enhances optical forces, is effective for manipulating nanomaterials [2]. Recently, we proposed an optical manipulation method based on stimulated emission, focusing on the fundamental optical property of luminescence [3]. Stimulated emission induces a recoil force in the direction opposite to light propagation, which overcomes the conventional limitation due to absorption saturation, and this has been quantitatively demonstrated theoretically [4]. Furthermore, this method has been verified experimentally [5][6]. However, photobleaching from prolonged high-intensity laser irradiation remains a challenge, hindering long-distance recoil force observation. Therefore, in this study, we focus on fluorescent nanodiamonds (NV-NDs), which are resistant to photobleaching. Additionally, by employing optical vortices with orbital angular momentum (OAM) as the light source, we explore novel light-matter interactions. Optical vortices propagate with a helical wavefront and are known to induce rotational motion in materials. We previously proposed that stimulated emission induced by optical vortices could reverse the rotational force on dye molecules [7], but its experimental demonstration has been challenging. In this study, we theoretically analyze the reversal of the rotational direction of NV-NDs in room-temperature water and demonstrate that rotational motion can be controlled. Furthermore, we discuss the effects of higher-order optical vortices on rotational motion. While the relationship between higher-order OAM and optical vortices has been previously discussed [8], this study rigorously examines the nonlinear optical response and elucidates the relationship between recoil force from stimulated emission and OAM, providing new physical insights into optical manipulation through optical vortices.

The optical force is evaluated using the time-averaged Lorentz force [9]:

$$\langle \mathbf{F} \rangle = \frac{1}{2} \Re \left[\sum_{\omega} \int \mathrm{d}\mathbf{r} \{ \nabla \mathbf{E}^{*}(\mathbf{r}, \omega) \} \cdot \mathbf{P}(\mathbf{r}, \omega) \right], \tag{1}$$

where, $\mathbf{E}(\mathbf{r}, \omega)$ is the incident electric field and $\mathbf{P}(\mathbf{r}, \omega)$ is the polarization. The incident electric field is modeled as a Laguerre-Gaussian (LG) beam, which is a paraxial eigenmode of the Helmholtz equation.

The resonant polarization is determined through non-perturbative solutions of the density matrix equation of motion. This enables the precise calculation of the nonlinear optical response of the material. The non-resonant polarization is evaluated using the Clausius-Mossotti relation, since the target material is an NV-ND with a 50 nm diameter. In the computational model, an NV-ND is modeled as a five-level system. The assumed experimental

setup involves two excitation LG beams propagating in the same direction, along with an additional stimulated LG beam. The excitation LG beams are configured so that their rotational forces almost cancel each other out, with their wavefronts rotating in opposite directions and their output power adjusted accordingly. Additionally, to prevent interference, the wavelengths of the two excitation LG beams are tuned within the absorption range of the NV-ND. As a result, the rotational force induced by the stimulated LG beam becomes dominant. Finally, room-temperature water is considered as the solvent. The motion of the nanodiamond in the solvent is analyzed using the Langevin equation.

Since p and l represent the radial and azimuthal mode indices, respectively, this study first considers a simple system with (p,l)=(0,1). As a result, the analysis reveals a significant difference in the rotational motion of the NV-ND and an undoped nanodiamond (undoped-ND) within just 0.1 seconds of laser irradiation. Specifically, it is demonstrated that the NV-ND can overcome thermal fluctuations and rotate opposite to the optical vortex, even in room-temperature water. Furthermore, this study examines the resonant and non-resonant components of the rotational force on the NV-ND as the OAM varies. The results are shown in Figure 1. As the orbital angular momentum increases, the ring radius expands, while the rotational force remains nearly constant. The trends observed in these computational results are also consistent with previous studies. The insights from this study advance the understanding of optical vortex–nanomaterial interactions and open new possibilities for optical manipulation.

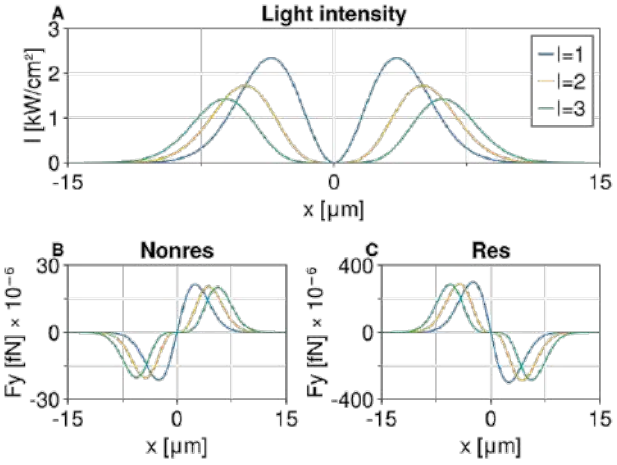


Fig1. Computational results of the optical vortex when varying the orbital angular momentum.
A: X-axis dependence of the optical vortex intensity.
B, C: Non-resonant and resonant components of the rotational force acting on the NV-ND.

References

1. Ashkin, A., "Acceleration and Trapping of Particles by Radiation Pressure," *Phys. Rev. Lett.* **24**, 156 (1970).
2. Ishihara, H., "Optical manipulation of nanoscale materials by linear and nonlinear resonant optical responses," *Adv. Phys. X* **6**, 1885991 (2021).
3. Kudo, T. and Ishihara, H., "Proposed nonlinear resonance laser technique for manipulating nanoparticles," *Phys. Rev. Lett.* **109**, 087402 (2012).
4. Horai, T., Wada, T., Saito, Y., Makino, Y., Ashida, M., and Ishihara, H., "Proposed Optical Manipulation of Nanoparticles to Access and Select Emission Lines," *Nano Lett.* **25**, 2785 (2025).
5. Kudo, T., Louis, B., Sotome, H., Chen, J.-K., Ito, S., Miyasaka, H., Masuhara, H., Hofkens, J., and Bresolí-Obach, R., "Gaining control on optical force by the stimulated-emission resonance effect," *Chem. Sci.* **14**, 10087 (2023).
6. Ito, S., Mizoguchi, T., Mori, M., Koga, M., Sotome, H., Tamura, M., Ishihara, H., and Miyasaka, H., "Nanoscopic Photomechanical Motion of Small Particles Induced by Optical Force due to Positive and Negative Photoabsorption by Excited States of Molecules," *J. PHYS. CHEM. C* **128,** 4859 (2024).
7. Hoshina, M., Yokoshi, N., and Ishihara, H., "Nanoscale rotational optical manipulation," *Opt. Express* **28**, 14980 (2020).
8. Curtis, J. E., and Grier, D. G., "Structure of Optical Vortices," *Phys. Rev. Lett.* **90**, 13001 (2003).
9. Iida, T. and Ishihara, H., "Theory of resonant radiation force exerted on nanostructures by optical excitation of their quantum states: From microscopic to macroscopic descriptions," *Phys. Rev. B* **77**, 245319 (2008).

Computing metalens array for programmable quantum algorithms and complex-to-complex discrete Fourier transform

R. S. Tanuwijaya[1], **S. Lap**[1], **W. C. Wong**[1], **T. An**[1], **W. Y. Tam**[1], **J. Li**[1,2*]

[1]Department of Physics, The Hong Kong University of Science and Technology, Clear Water Bay, Hong Kong
[2]Department of Engineering, University of Exeter, Exeter, United Kingdom
[*]corresponding author: jensenli@ust.hk

Abstract: Photonic computing offers a promising platform for accelerating highly parallel tasks, including neural networks. We present a computing metalens array scheme for programmable quantum algorithms and complex-to-complex DFT. The scheme incorporates error correction through multi-focal point focusing and phase reconstruction. Experimental results demonstrate accuracy with random inputs amplitude and phase.

The growing demand in machine learning and artificial intelligence has brought focus into research of more energy efficient alternatives to traditional electronic computing frameworks. Photonic computing emerges as a promising platform, offering advantages such as higher speed, larger bandwidth, lower power consumption, and enhanced parallelization capabilities [1]. Due to their inherent ability to achieve parallelization at the physical level, photonic computers excel in tasks requiring high degrees of parallelism.

Metasurfaces – two-dimensional arrays of nanostructures, is a promising platform for free-space photonic computing, which offers higher bandwidth and greater parallelism compared to on-chip methods [2]. However, free-space approach is often susceptible to errors due to misalignment of the optical elements. To addresses this issue, we adopt a metalens array approach to generate multiple focal points. This approach localizes the output field, which embeds redundancy and allows error correction.

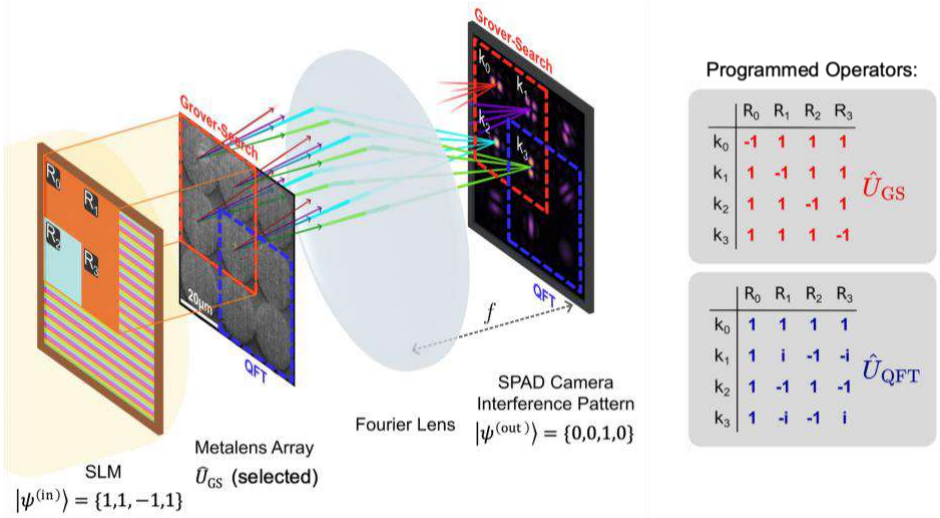


Fig 1 Computing metalens array for programmable quantum algorithms. An SLM selectively excites the metalens array to select the algorithm and prepares the two-qubit input state $|\psi^{(in)}\rangle$. Each metalens diffracts the beam into four directions, with amplitude and phase modulated by the U-matrix. The interference patterns of the diffracted beams in the same direction are projected onto the Fourier plane, where the intensity profile yields the output state $|\psi^{(out)}\rangle = \hat{U}|\psi^{(in)}\rangle$ by decoding constructive/destructive interference feature.

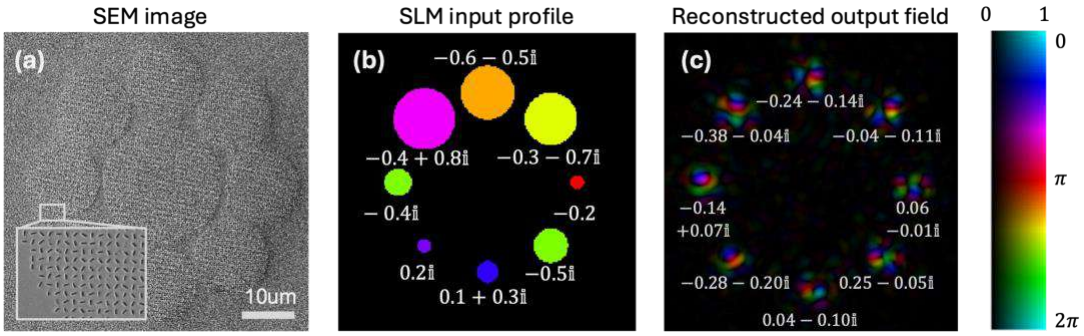


Fig 2 Computing metalens array for complex-to-complex DFT. (a) SEM image of eight circumferential signal metalenses and an additional central reference metalens. Each signal metalens is designed to focus light on 8 focal points, which phase delay designed according to DFT_8 matrix. The reference metalens is used to reconstruct the complex phase of the field at the focal plane. **(b)** A typical input vector encoded as complex illumination profile, with arbitrary input amplitude and phase. The amplitude is proportional to illumination radius (black region indicates no illumination), while the phase will be set directly by the SLM phase (represented as hue in the plot). **(c)** Reconstructed output field, experimentally obtained by combining four camera images with varying reference metalens incident phases $\phi_R = \{0°, 90°, 180°, 270°\}$. The output vector can be extracted by reading the complex value of the pixel at the center of each complex interference pattern.

Here, we highlight two examples on the same metalens-array platform for matrix-vector-multiplication (MVM). Our scheme encodes the input vector as the illumination profile using a spatial light modulator (SLM), and the matrix as the metasurface transmission profile. The output vector is decoded from the interference pattern, which is imaged at the focal plane of the metalens array. The first example demonstrates programmable quantum algorithms at countable photon regime [3], as shown in Fig. 1. The programmability comes from the selective excitation of the SLM and selective observation of the interference pattern. The second work extends this framework for complex-to-complex computation, demonstrating discrete Fourier transform (DFT) [4]. Typically, reconstructing the complex phase necessitates additional optical elements or computation. Our design addresses this by incorporating a built-in reference metalens, where phase reconstruction can be performed by iterating four phases of incident light on the reference metalens. Consequently, we experimentally demonstrate DFT with O(n) time complexity and effective error control, as shown in Fig. 2

Acknowledgements: The work is supported by the Hong Kong RGC (Grant Nos. 16304524, 16306521, R6015-18, STG3/E-704/23N, and AoE/P-502/20) and by the Croucher Foundation (Grant No. CF23SC01).

References

1. B. J. Shastri, A. N. Tait, T. Ferreira De Lima, W. H. P. Pernice, H. Bhaskaran, C. D. Wright, and P. R. Prucnal, Photonics for artificial intelligence and neuromorphic computing, Nat. Photonics **15**, 102 (2021).
2. J. Hu, D. Mengu, D. C. Tzarouchis, B. Edwards, N. Engheta, and A. Ozcan, Diffractive optical computing in free space, Nat Commun **15**, 1525 (2024).
3. R. S. Tanuwijaya, H. Liang, J. Xi, W. C. Wong, T. K. Yung, W. Y. Tam, and J. Li, Metasurface for programmable quantum algorithms with classical and quantum light, Nanoph **13**, 927 (2024).
4. R. S. Tanuwijaya, S. Lap, W. C. Wong, T. An, W. Y. Tam, J. Li. Metalens array for complex-valued optical discrete Fourier transform, arXiv preprint, 2502.08770 (2025).

Single-shot optical imaging of plasmonic nanoparticles: orientation, polarization anisotropy, aspect ratio

P. Bouchal[1], P. Dvořák[1], M. Hrtoň[1], K. Rovenská[1], V. Křápek[1*], R. Chmelík[1], T. Šikola[1], and Z. Bouchal[2]

[1]Brno University of Technology, Technická 2, 616 69 Brno, Czechia

[2]Department of Optics, Palacký University, Olomouc 771 46, Czechia

krapek@vutbr.cz (corresponding author)

Abstract

We demonstrate single-shot wide-field optical imaging of plasmonic nanoparticles visualizing their orientation and aspect ratio, in conventional far-field methods hidden below the diffraction limit. The capability of the method is demonstrated in the time-resolved imaging of the electrophoretic deposition process or the Brownian motion imaging using plasmonic nanorods.

Plasmonic nanoparticles can be used to shape (confine, enhance, and direct) the light at the nanoscale, building upon their ability to support localized surface plasmons and making them suitable optical probes for sensing and imaging. The most common shapes are nanospheres and nanorods. The nanorods offer the benefit of anisotropic optical properties, which makes them suitable for orientation sensors in the conformation and dynamics studies of biological systems as well as for novel plasmonic-based nanoimaging devices [1]. The orientation imaging of the nanorods is thus highly desirable, although it is significantly hindered by their deeply subwavelength dimensions. An overview of available methods is provided in Ref. [2].

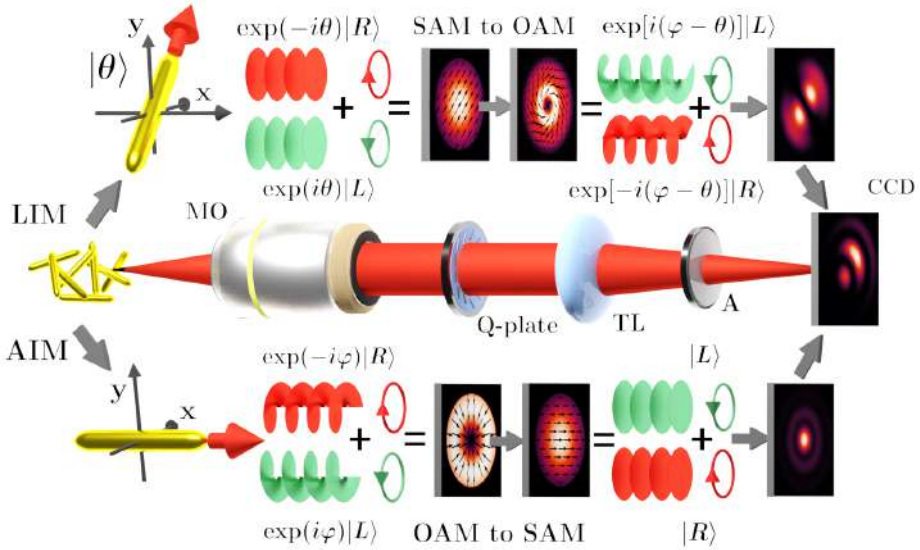


Figure 1: Left to right: A plasmonic nanorod either in LIM (top) or in AIM (bottom) scatters the light field with a specific spin and orbital angular momentum, transformed by the Q-plate to form characteristic PSF in the image plane. For a general nanorod orientation (middle), both LIM and AIM fields propagate independetly through the optical column (due to orthogonal polarization) and interfere in the image plane after polarization projection by the analyzer (A).

In our contribution, we report a new method for single-shot three-dimensional orientation imaging of plasmonic nanorods. We utilize a dark-field transmission optical microscope with an add-on imaging module that exploits a Q-plate for conversions between spin and orbital angular momentum of the light scattered by the nanorods. In this way, the orientation of nanorods is imprinted into the polarization and geometric phase of the scattered light and transformed into characteristic point spread functions (PSF), which are detected and utilized to retrieve the orientation angles of the nanorod. The principle of the method is visualized in Fig. 1. We consider two specific modes: the lateral imaging mode (LIM) with the nanorod perpendicular to the optical axis and the axial imaging mode with the nanorod parallel to the optical axis. In both cases, the spin or orbital angular momentum of the scattered light is shaped by the optical system to produce characteristic PSF: double helix PSF for LIM and the Airy disk for AIM. For a general nanorod orientation, the resulting image is formed by the interference of both specific components of the light fields. A calibration measurement comparing the orientation image of the nanorods to a reference scanning electron microscopy image allowed us to estimate the accuracy of the method by a standard deviation of 2.5° [2]. We have also developed an extension that allows to characterize the polarization anisotropy of the nanorods which can be related to their aspect ratio [3]. Our orientation imaging method can be generalized to other dipole light sources, e.g., quantum emitters.

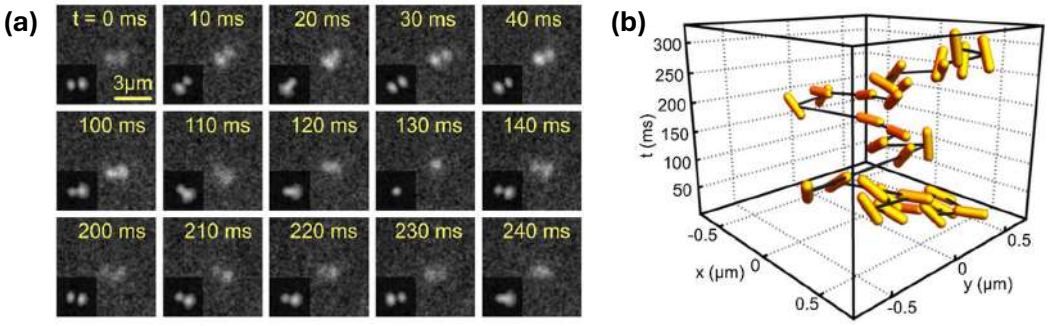


Figure 2: 3D orientation imaging of nanorods moving by Brownian motion. (a) Gradual variations in the axial and polar angles of a single nanorod are reflected in variations in the detected image patterns taken with a time step of 10 ms. (b) Reconstruction of the single nanorod 3D orientation during its Brownian motion.

To demonstrate the capability of the orientation imaging we present in Fig. 2 a study of a Brownian motion of a nanorod (length 71 nm, diameter 25 nm) dispersed in a water droplet. The method was also successfully applied in the time-resolved imaging of the electrophoretic deposition process [3] or the live cell imaging using plasmonic nanorods [2].

This work was supported by Czech Science Foundation, grant No. 25-17500S.

References

[1] Chang, W.-S., J. W. Ha, and L. S. Slaughter, L. S.;"Plasmonic Nanorod Absorbers as Orientation Sensors.," *Proc. Natl. Acad. Sci. U. S. A.*, Vol. 107, No. 7, pp. 2781–2786, 2010.

[2] Fordey, T. et al., "Single-Shot Three-Dimensional Orientation Imaging of Nanorods Using Spin to Orbital Angular Momentum Conversion," *Nano Lett.*, Vol. 21, pp. 7244–7251, 2021.

[3] Bouchal, P., P. Dvořák, M. Hrtoň, K. Rovenská, R. Chmelík, T. Šikola, and Z. Bouchal, "Single-Shot Aspect Ratio and Orientation Imaging of Nanoparticles," *ACS Photonics*, Vol. 10, pp. 3331–3341, 2023.

Investigation of structural and optical properties of tungsten doped VO_2-Au plasmonic switchable material

Shraddha Shukla[1], Urvashi Solanki[1], Abhishek Prasad[2], P. Mandal[1]*

[1]Department of Physics, Applied Science Cluster, School of Advanced Engineering, UPES, Dehradun-248007, India

[2]Department of Physics, H.N.B. Garhwal University, Badshahi Thaul Campus, Tehri Garhwal-249199, India

Corresponding author: pmandal@ddn.upes.ac.in

Abstract

We have developed tungsten doped VO_2-Au switchable material with needle-like morphology through hydrothermal synthesis and post growth thermal annealing method. Structural studies confirm the grown samples are mixture of various polymorphs of VO_2 (VO_2 (M), VO_2 (B) and VO_2 (R)) which is further supported by vibrational studies using Raman spectroscopy.

The metal-to-insulator (MIT) transition of VO_2 close to room temperature (~68°C) makes it a prominent candidate for various applications, such as, reflective/transmissive smart windows, photonic and optoelectronic switching devices, sensors and actuators design, energy storage and conversion, and more [1]. However, utilizing VO_2 for devices operating around room temperature is considerably challenging due to its high critical temperature. Research on lowering down its critical temperature and high differential reflection/transmission is required. Present work explores an effective way of manipulating structural, optical and thermochromic properties of tungsten (W) doped VO_2 in the presence of plasmonic gold.

Pristine VO_2 and W doped VO_2 (VO_2:W, at different weight percent (wt%) % of W: 1.5%. 3%, 4.5% and 6%) are prepared using hydrothermal synthesis (at 200°C ± 10 °C) and high temperature thermal annealing method (at 500°C ± 15 °C) in the presence of argon gas. Subsequently, VO_2:W and gold (Au) are mixed at different wt % (ratio of VO_2:W and Au), such as, 1:1 (sample A), 5:1 (sample B) and 10:1 (sample C). All these samples are thermally annealed at 300°C ± 15 °C.

Structural studies using X-ray diffraction (XRD) show doped samples contain three polymorphs of VO_2 (VO_2(B), VO_2(M) and VO_2(A)) (JCPDS card no. 01-082-0661, 00-009-0142, 01-081-2392 and 01-079-1655) (Figure-1). Also, dominance of VO_2 (B) is indicated in pristine VO_2 which decreases with increasing dopant concentration. Dominance of VO_2 (M) is evident too. Considering the peak at 2θ=25°, crystallite size for 1.5% W doped sample is larger than pristine VO_2, which surprisingly decreases with increasing W% (Table-1).

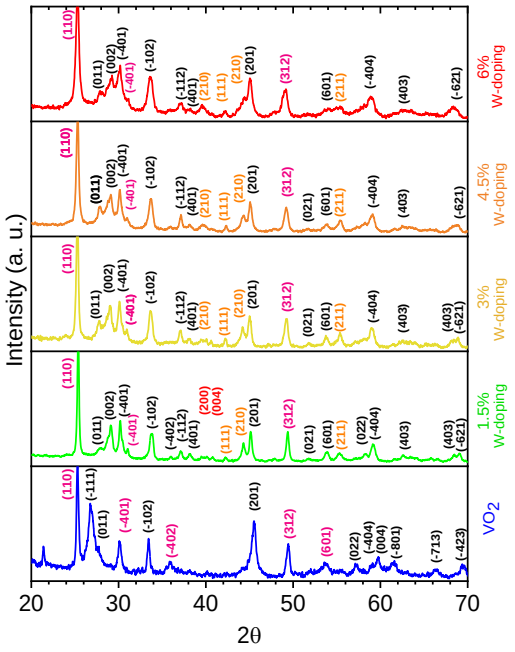


Fig. 1 XRD spectra of different W doping percentage (Black- VO_2(M), Pink- VO_2(B), Red- VO_2(A) and Orange- VO_2(A)).

Table. 1 Change in crystallite size with W doping percentage

Doping %	K	λ (nm)	θ (Radian)	β	D (nm)
Pure VO_2	0.94	0.154	12.65	0.27	29.97
1.5% W-VO_2	0.94	0.154	12.685	0.25	32.37
3% W-VO_2	0.94	0.154	12.635	0.31	26.11
4.5% W-VO_2	0.94	0.154	12.650	0.33	23.12
6% W-VO_2	0.94	0.154	12.645	0.46	18.39

Raman spectroscopic measurements show samples corresponds to polymorphic phases of VO_2 as observed from XRD measurements (Figure-2). XRD and Raman measurements on VO_2:W in the presence of gold show no change in characteristic peaks correspond to polymorphs of VO_2. These observations indicate the retainment of switching characteristics of VO_2 polymorphs intact. Needle-like structure (as observed from scanning electron microscope (SEM)) can be used for further investigation of MIT transition temperature (using differential scanning calorimetry (DSC)), resistive switching and optical/thermal switching characteristics for optoelectronic applications.

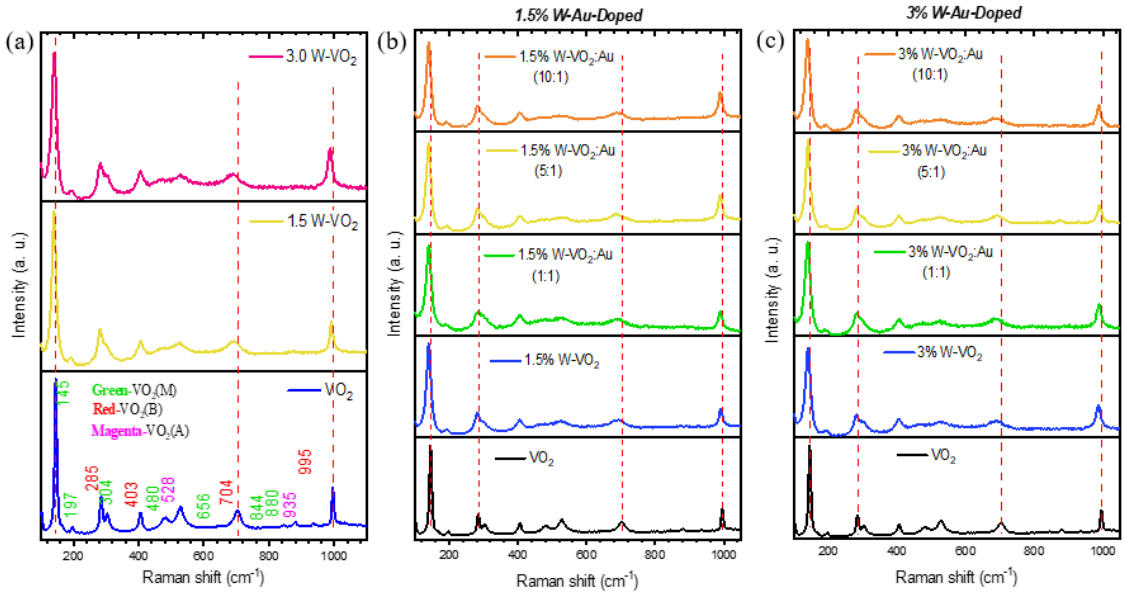


Fig. 2 Raman spectra of (a) pure VO_2 when compared with 1.5% and 3% W-doped VO_2 (VO_2:W), (b) 1.5% VO_2:W when compared with VO_2:W-Au, and (c) 1.5% VO_2:W when compared with VO_2:W-Au.

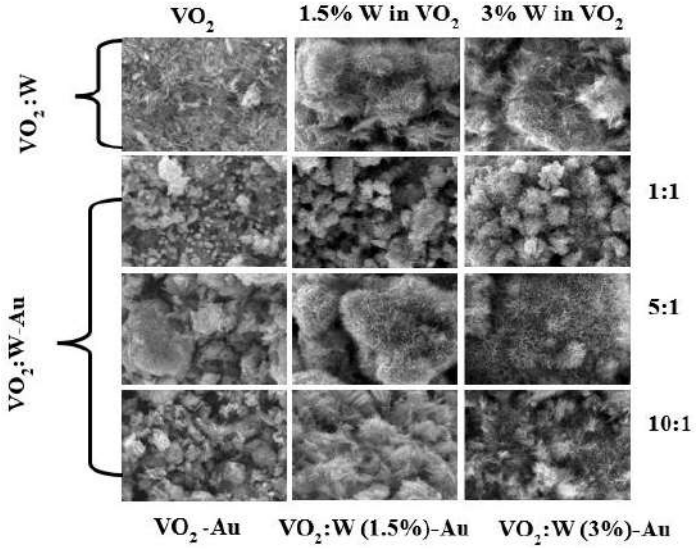


Fig. 3 SEM images of VO_2:W (top row) and VO_2:W-Au (second row: (1:1), third row: (5:1) and bottom row (10:1)). Scale bar is 2 μm for all the images.

References

[1] Y. Cui *et al.*, "Thermochromic VO2 for Energy-Efficient Smart Windows," Sep. 19, 2018, *Cell Press*. doi: 10.1016/j.joule.2018.06.018.

Strong coupling of chiral light with chiral matter: a macroscopic study

N. S. Salakhova[1*], S. A. Dyakov[1], I. A. Smagin[1*], I.M. Fradkin[1] and N. A. Gippius[1]

[1]Skolkovo Institute of Science and Technology, the territory of the Skolkovo Innovation Center, Bolshoy Boulevard, 30, bld. 1, Moscow 121205, Russia

[*]corresponding author: Natalia.Salakhova@skoltech.ru

Abstract: We studied the strong coupling of chiral light with chiral material by incorporating the Lorentz pole into macroscopic chirality parameter: dielectric permittivity, magnetic permeability, and chirality coefficient. Our study demonstrates significantly distinct behaviors between the material's enantiomers, offering a promising approach for their detection and selective differentiation.

The detection and selection of chiral organic molecules with different handedness are critical for numerous applications in pharmacology, biology, and chemistry. Due to their similar size and chemical structure, the most promising approach is to exploit subtle differences in their optical responses when interacting with an electromagnetic field. Consequently, enhancing the interaction between chiral light and chiral matter is essential for developing advanced techniques that enable handedness-selective optical detection of chiral molecules. One effective strategy to achieve this involves creating resonators that support photonic modes with non-zero electromagnetic handedness, allowing differential interaction with left- and right-handed chiral molecules [1,2]. Recent studies have investigated chiral polaritons—strong couplings between chiral light and individual chiral molecules at the microscopic scale [3]. However, when chiral molecules are introduced into resonator hotspots, their electric and magnetic transition dipole moments significantly influence the overall system. This effect becomes particularly pronounced at high molecular concentrations.

In this study, we investigate the interaction between a chiral medium and photonic modes within a resonator from a macroscopic perspective. Specifically, we examine a Fabry-Perot resonator featuring dielectric mirrors that preserve handedness. These mirrors are engineered using a combination of dielectric Bragg mirrors and a one-dimensional photonic crystal slab, creating a layer with high artificial anisotropy. They are optimized to achieve near-unity reflection while maintaining the handedness of light over a broad spectral range. This design enables the Fabry-Perot cavity to support photonic modes with high electromagnetic chirality for both handednesses. Notably, these modes become distinct when the rotational angle between the upper and lower mirrors deviates from integer multiples of π [4]. To describe the resonant medium inside the cavity, we introduced macroscopic parameters to model the chiral material. Rather than focusing on individual molecules, we represented the medium using effective properties: dielectric permittivity, magnetic permeability, and a chirality coefficient. The chirality coefficient, also known as the Pasteur parameter, quantifies the medium’s macroscopic chirality and establishes a coupling between the electric and magnetic fields in the constitutive relations. Materials with opposite signs of the Pasteur parameter correspond to media composed of enantiomers with opposite handedness.

Our results demonstrate that using a chiral medium with a constant macroscopic chirality parameter enables the separation of modes with different electromagnetic chirality, even when the rotational angle between the mirrors equals πn. Furthermore, introducing a resonant chiral medium—modeled by incorporating a Lorentz pole into its macroscopic parameters—leads to the emergence of chiral strong light-matter coupling. Furthermore, the mode

splitting near the resonant wavelength varies depending on the value of the chirality parameter.

A particularly intriguing regime occurs when the chirality coefficient satisfies the condition $|\chi|=\varepsilon^{1/2}/2$. In that case materials with opposite values of chirality coefficient would be in different light and matter coupling regimes. Under these circumstances, media with opposite chirality coefficients exhibit distinct light-matter coupling regimes. For instance, a medium with positive chirality may exhibit strong coupling between the chiral electromagnetic field and the medium, while a medium with negative chirality remains in a weak coupling regime. This behavior reverses for modes of the opposite handedness.

These findings offer exciting prospects for developing advanced methods to detect chiral molecules with different handedness, even in high-concentration conditions where molecular resonance significantly influences cavity modes.

References

1. Feis, J., Beutel, D., Köpfler, J., Garcia-Santiago, X., Rockstuhl, C., Wegener, M., & Fernandez-Corbaton, I., ”Helicity-preserving optical cavity modes for enhanced sensing of chiral molecules,”.Physical review letters,**124(3)**, 033201 (2020).
2. Tang, Y., & Cohen, A. E., “Enhanced enantioselectivity in excitation of chiral molecules by superchiral light,” Science, **332(6027)**, 333-336 (2011).
3. Baranov, D. G., Schäfer, C., & Gorkunov, M. V., “Toward molecular chiral polaritons,” ACS Photonics, **10(8)**, 2440-2455 (2023).
4. Riso, R. R., Castagnola, M., Ronca, E., & Koch, H., “Chiral polaritonics: cavity-mediated enantioselective excitation condensation,’ Reports on Progress in Physics, **88(2)**, 027901 (2025).
5. Dyakov, S. A., Salakhova, N. S., Ignatov, A. V., Fradkin, I. M., Panov, V. P., Song, J. K., & Gippius, N. A, “Chiral light in twisted fabry–pérot cavities,” Advanced Optical Materials, **12(12)**, 2302502 (2024).

Integrated Spectral Sensitivity as Physics-Based Figure of Merit for Spectral Transducers in Optical Sensing

F. L. McCluskey[1*], A. van Klinken[1], and A. Fiore[1]

[1]Eindhoven University of Technology, Netherlands
[*]corresponding author: f.l.mccluskey@tue.nl

Abstract:

We introduce Integrated Spectral Sensitivity, a novel figure of merit for optical sensors, derived from the Cramér–Rao lower bound. This metric quantifies transducer performance across various readout methods, improving sensor design. We apply it to two transducer types, offering insights into optimizing spectral sensing systems for enhanced precision.

Optical sensors which use spectral transducers play a very important role in mapping a physical, chemical or biological phenomena or change in environment. Traditional figures of merit which aim to aim estimate the performance of these transducers are often independent of the readout system used in combination with these transducers. This creates practical challenges since different transducers achieve optimal performance with varying types of readout systems. A new physics-based figure of merit, the Integrated Spectral Sensitivity, is introduced to take into account both parts of the system and is used as a framework to enable a more appropriate transducer design and optimisation.

The sensing system in the paper consists of a spectral transducer that converts changes in the target measurand into spectral shifts, which are detected using a readout system. The study analyses different transducer types and readout methods, comparing their performance using the newly introduced Integrated Spectral Sensitivity metric. This Integrated Spectral Sensitivity is derived from the already known Cramér Rao lower bound, which sets a limit on measurement precision of sensing systems based on spectral transduction, but has no assumption on the data analysis method. This simple FoM is applied to two different types of transducer responses, namely a single peak spectrum (ie. a photonic crystal resonance) and a multipeaked response (achieved with a Fabry-Pérot).

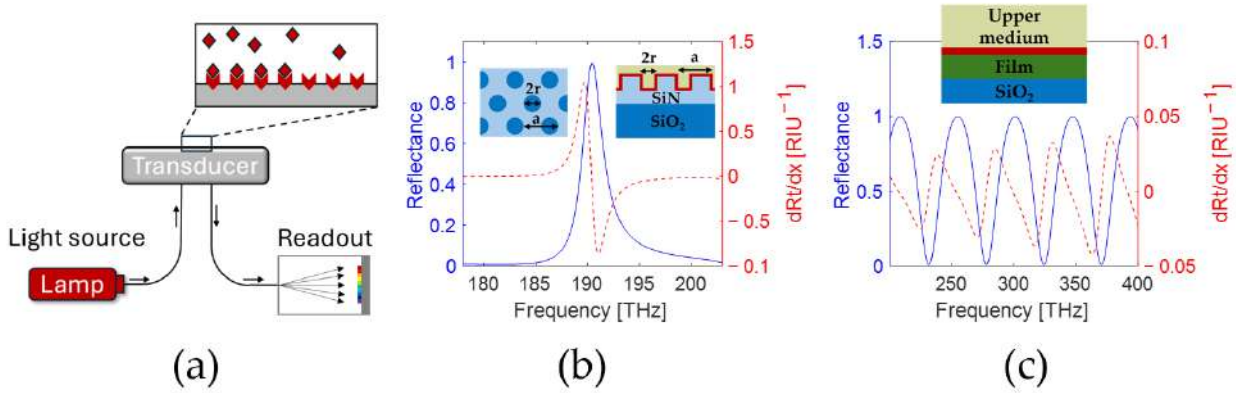


Figure 1. (a) Schematic representation of the sensing system. Reflectance spectrum (blue) of (b) a photonic crystal (insets) and (c) a Si/SiO_2 multilayer (inset) and its derivative with respect to the measurand (red).

From the analytical expression of the CRLB, we can derive a more general FoM based on certain assumptions, which allows us to implement the type of readout used. It is defined as an integral of the squared sum of the reflectance derivative times the transmission functions of the readout channels, thus incorporating both parts of the sensing system. The mathematical formulation of Integrated Spectral Sensitivity is given by:

$$S_{\int ¿} = \frac{1}{\Delta \nu} \sqrt{\sum_{i=1}^{n} \left(\int_{\nu_{min}}^{\nu_{max}} \frac{\partial R_t(\nu)}{\partial x} T_i(\nu) d\nu \right)^2} \quad ¿ \quad (1)$$

Where R_t represents the reflectance function of the transducer, derived as a function of x which is the parameter of interest, T_i is the response functions of the readout channels chosen and $\Delta \nu$ is the spectral range.

This now more general FoM is then used as a comparison of performance for both types of transducers, with more specific assumptions made on the characteristics of the readout. This introduces the concepts of spectrometric and ideal readouts, as two different examples of approaches to assess performance. The spectrometric readout is a description of different closely spaced frequency bands in space or in time, which commonly represents an array of filters or photodetectors. The ideal readout assumes that all available spectral information is optimally used without being constrained by practical limitations such as detector noise or resolution. This gives the maximum achievable precision in determining the measurand based on the transducer's spectral response, and not on the data analysis method.

The application of $S_{\int ¿¿}$ to single-resonance transducers, such as photonic crystal resonators, reveals that optimal performance is achieved when the transducer linewidth matches the readout system resolution, which contradicts the common assumption that narrower linewidths always improve sensitivity. The framework is also applied to multi-resonance transducers like Fabry-Pérot cavities, which demonstrates a decrease in performance compared to photonic crystals.

From these two cases of readout methods, simpler expressions of $S_{\int ¿¿}$ can be derived depending on the method used. Thanks to these new expressions, we can analyse the impact of the design parameters of the transducers on its overall performance and evaluate the performance of different transducer types in a specific label-free biosensing application, demonstrating that the proposed method offers novel insights and highlights new possibilities for transducer design.

This research was partially funded under NWO TTW Project No. 19942 (F.L.M.) and NWO TTW Project No. 16670 (A.v.K.).

Fabrication of Porous Au Nanowires on Flexible Substrates Featuring High- Density Nanogaps via Nanotransfer Printing for SERS

H. J. An[1,2], B. K. Ju[1*], and J. Y. Jung[2*]

[1]Nano-Conversgence Mechanical System Research Division, Korea Institute of Machinery and Materials, Daejeon 34103, Republic of Korea
[2]Dislay and Nanosystem Laboratory, School of Electrical Engineering, Korea University, Seoul 12841, Republic of Korea
[*]Corresponding author: bkju@korea.ac.kr (B.K.J.); jjy2121@kimm.re.kr (J.Y.J.)

Abstract: We report hierarchically porous Au nanostructures fabricated via nanotransfer printing to achieve sub-10 nm gaps and ultradense hotspots on flexible substrates. These structures showed a 9.6-fold SERS enhancement over flat Au nanowires using 4-mercaptobenzoic acid. The results demonstrate the significance of structural design in plasmonic systems [1,2].

1. Introduction

Surface-Enhanced Raman Spectroscopy (SERS) enhances molecular signals through localized surface plasmon resonances, where sub-10 nm gaps generating dense hotspots that greatly improve sensitivity [3].

2. Fabrication and SERS Performance

Figure 1 shows the morphology of Au NWs and P-Au NWs. Figure 2 illustrates the stacking process and SERS results. The porous structure forms nanogaps with an average spacing of 10.22 nm. Single-layer P-Au NWs exhibited 9.6-fold higher SERS intensity than Au NWs using 4-mercaptobenzoic acid, with a markedly steeper increase observed for P-Au NWs.

3. Conclusion

The integration of porous nanostructures and nanotransfer printing increases contact areas, promoting strong plasmonic coupling at cross-junctions, and enables high-performance SERS substrates on flexible platforms. Our P-Au NWs with ultradense nanogaps demonstrate enhanced signal amplification and strong potential for applications in flexible sensing, catalysis, and photonics.

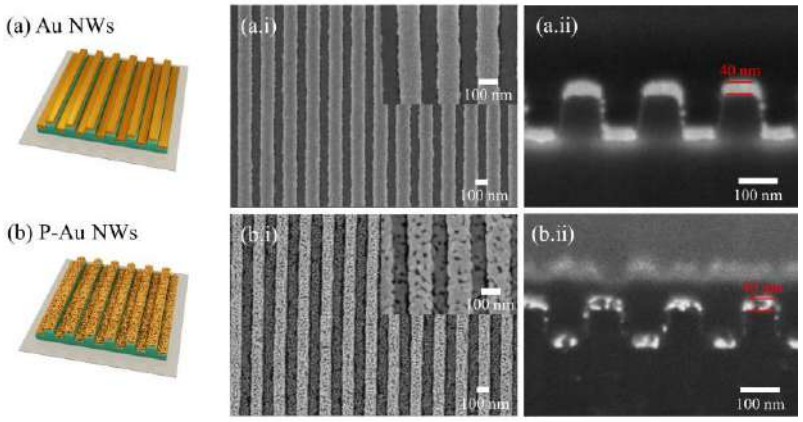


Figure 1. Morphology of (a) Au NWs and (b) P-Au NWs on flexible substrates: (a, b) Schematic; (a.i, b.i) top-view SEM images; (a.ii, b.ii) cross-sectional FIB-SEM images.

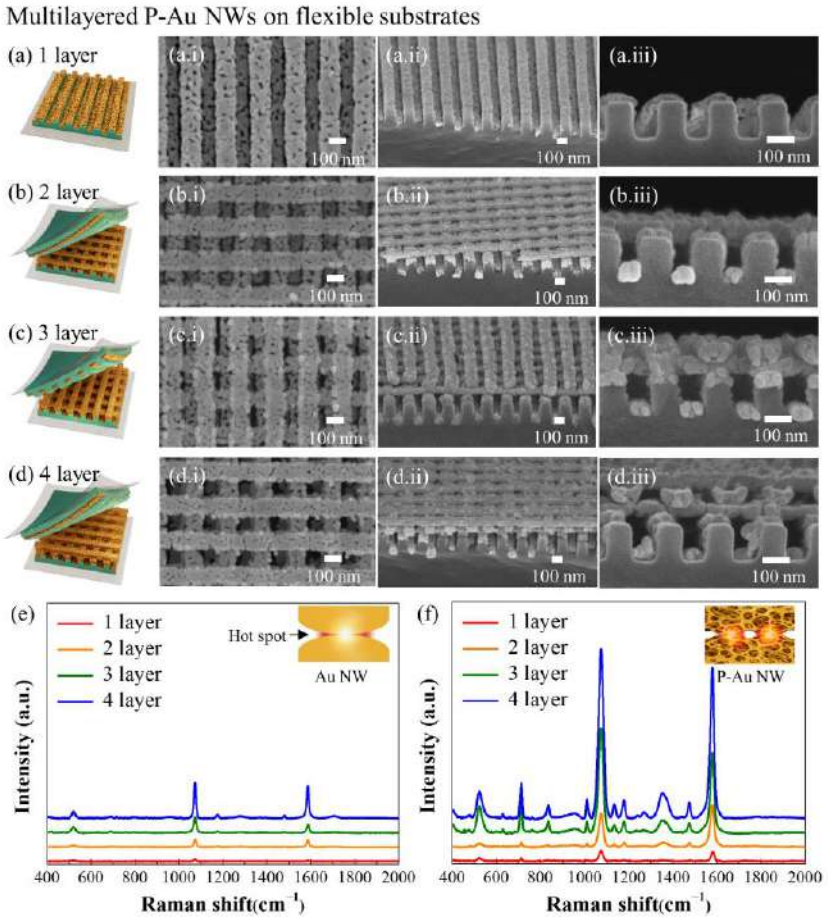


Figure 2. Structural and SERS characterization of multilayered P-Au NWs on flexible substrates via nanotransfer printing. (a–d) Schematic and SEM images of 1-4 layer stacks: (a.i-d.i) top view, (a..ii-d.ii) tilted (30°), and (a.iii-d.iii) cross-sectional images. (e-f) SERS spectra of stacked (e) Au NWs and (f) P-Au NWs; insets show hotspot schematics.

Acknowledgements: This work was supported by National Research Foundation, grant No. RS-2024-00408446; Korea Institute of Machinery and Materials, grant No. NK 255D.

References

1. Zhao, Z.-J., Shin, S.-H., Choi, D.-G., Park, S.-H., and Jeong, J.-H. "Shape-Controlled 3D Periodic Metal Nanostructures Fabricated via Nanowelding", Small, pp. 1703102, 2017.
2. Cho, S. H., Baek, K.-M., Han, H. J., Kim, M., Park, H., and Jung, Y. S. "Selective, Quantitative, and Multiplexed Surface-Enhanced Raman Spectroscopy Using Aptamer-Functionalized Monolithic Plasmonic Nanogrids Derived from Cross-Point Nano-Welding", Adv. Mater, Vol. 30, pp. 2000612, 2020.
3. Jeong, J. W., Arnob, M. M. P., Baek, K.-M., Lee, S. Y., Shih, W.-C., and Jung, Y. S. "3D Cross-Point Plasmonic Nanoarchitectures Containing Dense and Regular Hot Spots for Surface-Enhanced Raman Spectroscopy Analysis", Adv. Mater, Vol. 28, pp. 5695-8704, 2016.

Metasurface-enabled Dynamic Focusing Arrays for Transport of Multiple Particles

Hyeonhee Kim[1], Taeyong Chang[1,2], Joonkyo Jung[1], and Jonghwa Shin[1,*]

[1]Department of Materials Science and Engineering, KAIST, Daejeon, 34141, Republic of Korea
[2] Division of Physics & Applied Physics, NTU, 50 Nanyang Ave, 639798, Singapore
[*]corresponding authors: qubit@kaist.ac.kr

Abstract: We introduce and experimentally demonstrate, for the first time, metasurface-driven dynamic focusing arrays designed to accurately transport multiple microparticles along customized routes. By exploiting interference between polarization-multiplexed holographic images, our method enables simultaneous, precise movement of optically trapped microparticles.

Here, we propose metasurface-enabled dynamic focusing arrays capable of precisely transporting multiple microparticles along arbitrary trajectories. Optical forces have been widely investigated for particle manipulation in various fields, including nanophotonics, biomedical sciences, laser optics, and microfluidics, enabling functionalities such as optical sorting, tweezing, and conveying. Although spatial light modulators (SLMs) have previously enabled dynamic optical field control to transport particles along arbitrary pathways by applying phase gradients, precise particle manipulation through an optical trap array remains challenging [1]. Prior metasurface studies aiming to form optical trap arrays have either been limited to static focusing arrays or discrete holographic field state changes without demonstrating experimental trapping or dynamic particle transport [2, 3, 4].

Our work experimentally demonstrates dynamic, precise control of multiple optical traps generated from polarization-multiplexed metasurfaces. We achieve continuous and precise movement of optical focusing spots along user-defined trajectories by overlapping and dynamically interfering two polarization-dependent states. This capability allows multiple microparticles to be simultaneously trapped and conveyed with high precision over substantial distances, overcoming previous limitations. Our experimental validation confirms the reliable and precise transport of microparticles along trajectories, demonstrating significant potential for applications in microfluidic channels, particle sorting systems, and biomedical devices.

This research advances optical particle manipulation by integrating the unique advantages of metasurface-based focusing arrays with dynamic optical field control, enabling sophisticated micro-manipulation tasks previously unattainable with conventional SLM-based or static metasurface approaches.

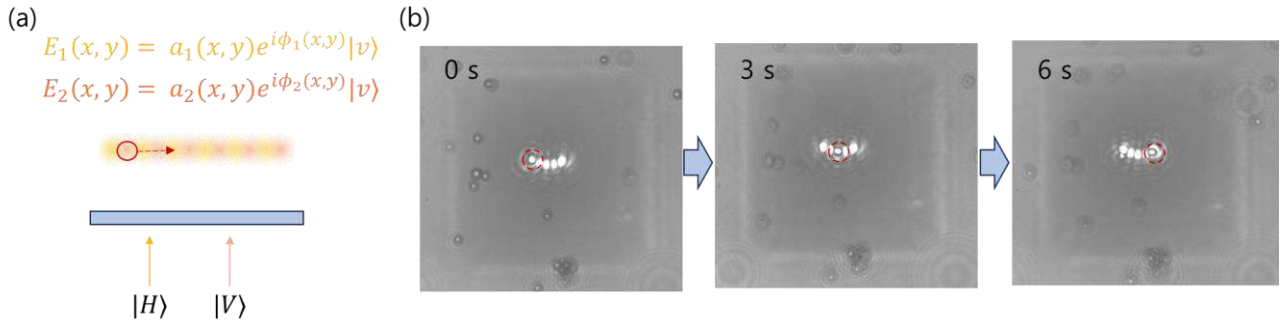


Figure 1. (a) Schematic of the optical conveyor. The metasurface generates two distinct holographic field states under orthogonally polarized incidences. (b) Experimental demonstration of optical transport of a 3-μm particle. Red dotted circles indicate a dielectric polystyrene particle trapped in optical hotspot arrays, showing its movement along the conveyor path over time.

References

1. Niu, Kai., Zhao, Shangdong., Tao, Shaohua., and Wang, Fuliang., "Long distance and direction-controllable conveyor for automatic particle transportation based on optical tweezers." Sensors and Actuators A: Physical 333, 113223, 2022
2. Huang, Xiaoyan., Yuan, Weijun., Holman, Aaron., Kwon, Minho., Masson, Stuart. J., Gutierrez-Jauregui, Ricardo., Asenjo-Garcia, Ana., Will, Sebastian., and Yu, Nanfang., "Metasurface holographic optical traps for ultracold atoms." *Progress in Quantum Electronics* 89, 100470, 2023
3. Wang, Ruoxing., Ansari, Muhammad. Afnan., Ahmed, Hammad., Li, Yan., Cai,Wenfeng., Liu, Yanjun., Li, Songtao., Liu, Jianlong., Li, Li., and Chen, Xianzhong., "Compact multi-foci metalens spectrometer." *Light: Science & Applications*, Vol 12, No. 1, 2023.
4. Zhou, Tao., Du, Juan., Liu, Yongsheng., and Zang, Xiaofei., "Helicity multiplexed terahertz multi-foci metalens." *Optics Letters*, Vol. 45, No. 2, 463-466, 2020.

Spectrally tailored surface-enhanced Raman spectroscopy (SERS) with polarization-sensitive metasurface

J. Lövgren[1] and A. Xomalis[1*]

[1] Nanoscale Spectroscopies Group, Department of Electronic Systems,
Norwegian University of Science and Technology, Trondheim, Norway
[*]corresponding author: angelos.xomalis@ntnu.no

Abstract: While SERS is a powerful sensing technique with single-molecule resolution, plasmonic SERS antenna arrays lack precise spectral control. Here, we present a metasurface with polarization-dependent optical resonances designed to overlap with individual vibrational modes of a molecule. Spectrally tailored SERS has applications in biosensing, molecular optomechanics and plasmon-based nano-optics.

I. INTRODUCTION

SERS utilizes plasmonic resonances to enhance the intrinsically low Raman scattering of molecules, providing a versatile spectroscopy method [1]. However, the optical linewidth of typical plasmonic array resonances is far greater than the vibrational resonances (Raman modes) of molecules, prohibiting plasmon-enhanced sideband-resolved spectroscopy. Recent configurations for spectrally tailored SERS comprise either photonic crystal cavity-antenna structures [2] or hybrids of antennas coupled to Fabry-Perot microcavities [3]. While these approaches offer tunable spectrally tailored Raman mode enhancements, they demand advanced nanofabrication and layering of nanophotonic structures, limiting widespread use. Here we demonstrate an approach for spectrally tailored molecular SERS based on polarization dependent resonances of a single-layer metasurface.

II. STRUCTURE DESIGN AND FABRICATION

A 100 nm thick Au film was deposited on a Si substrate by E-beam evaporation (K.J. Lesker, PVD 200). Quadratic holes in a rectangular lattice were patterned into the Au film using focused ion beam milling (FIB, FEI Helios G4 UX). Two samples with rectangular hole arrays are presented here, both with holes of dimensions 250x250 nm^2 and periodicity 750 nm in the x direction (see Figure 1a for definition of x and y directions). The periodicity in the y direction of the two samples is different: 780 nm and 800 nm, respectively.

III. OPTICAL MEASUREMENTS AND SIMULATION

White light reflectance nanoscale measurements were performed in an in-house built setup capable of both broadband reflectance measurements and Raman spectroscopy. Each metasurface is shown to have different resonance features when illuminated with light polarized along the x and y directions (Figure 1b, c), with the resonance being redshifted for larger periodicities. Comparing the two demonstrated metasurfaces, we see that the resonance emerging for y polarized light can be shifted independently of the resonance for x polarized light. The resonance of the metasurface can be shifted to the spectral position of selected Raman peaks of biphenyl-4-thiol (BPT) on demand (Figure 1d). The experimental results are supported by finite-difference time-domain (FDTD Ansys Lumerical) simulations (dashed lines, Figure 1b, c).

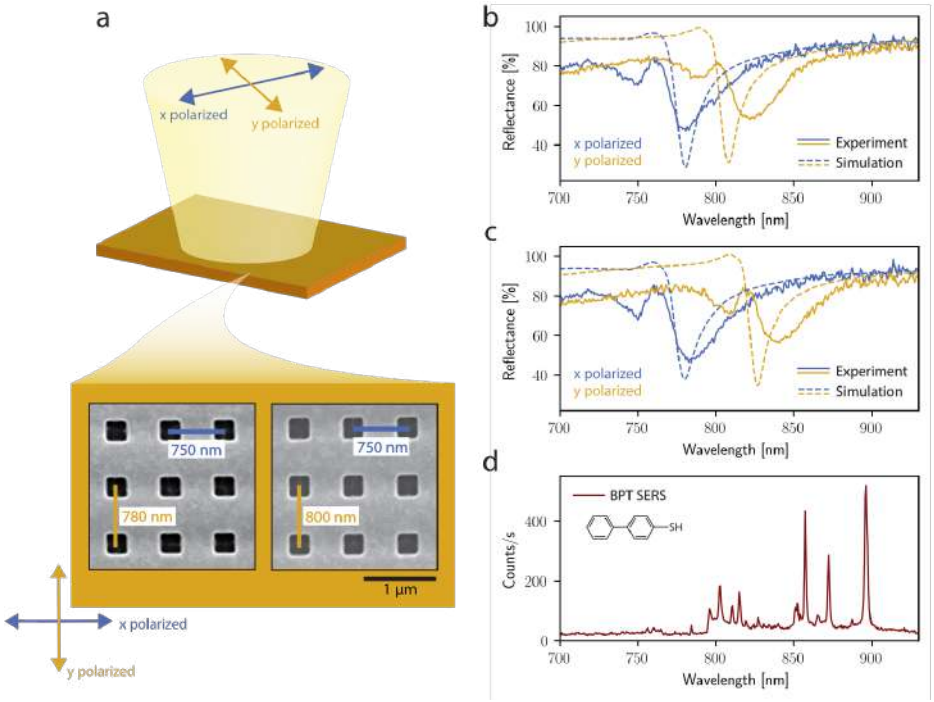


Figure 1. (a) Schematic of excitation of the metasurface by x (blue) and y (yellow) polarized light and SEM images of the two evaluated metasurfaces. **(b,c)** Broadband reflectance measurements (solid) and simulations (dashed) of metasurfaces with periodicity 780 nm (b) and 800 nm (c) in the y direction, using x (blue) and y (yellow) polarized light. Both metasurfaces have a periodicity of 750 nm in the x direction. **(d)** Standard surface-enhanced Raman spectroscopy (SERS) of biphenyl-4-thiol (BPT), using a 785 nm laser for excitation.

IV. CONCLUSION

Utilizing a polarization sensitive metasurface, we show how to perform spectrally tailored SERS otherwise challenging with conventional plasmonic nanoconstructs. Here we design, fabricate and experimentally characterize such metasurfaces, demonstrating resonances promising for spectrally tailored and sideband-resolved SERS. Our results are in good quantitative agreement with full-wave simulations, indicating the quality of the fabricated metasurfaces.

ACKNOWLEDGEMENTS

We acknowledge the NTNU Rector AVIT fund (949024104). The Research Council of Norway is acknowledged for the support to the Norwegian Micro- and Nano-Fabrication Facility, NorFab, project number 295864.

References

1. R. Arul et al., "Giant mid-IR resonant coupling to molecular vibrations in sub-nm gaps of plasmonic multilayer metafilms", *Light Sci. Appl.*, vol. 11, no. 1, p. 281, 2022.
2. I. Shlesinger et al., "Integrated Sideband-Resolved SERS with a Dimer on a Nanobeam Hybrid", *Phys Rev Lett*, vol. 130, no. 1, p. 016901, 2023.
3. I. Shlesinger et al., "Hybrid cavity-antenna architecture for strong and tunable sideband-selective molecular Raman scattering enhancement", *Sci. Adv.*, vol. 9, no. 51, p. eadj4637, 2023.

Strong light-matter interaction of Chlorophyll-a molecules on plasmonic arrays

Yadav Rohit Umashankar, Parinda Vasa*

Department of Physics, Indian Institute of Technology Bombay, Mumbai, India
*Corresponding author, E-mail: parinda@iitb.ac.in

Abstract

Here, we demonstrate strong exciton-photon coupling between photosynthetic light-harvesting complexes i.e., Chlorophyll-a molecules, and a surface lattice resonance of periodically patterned Silver nanodisk arrays. The high-quality factor and delocalized field modes of lattice resonances enable efficient studies of optical responses and energy transfer in strongly coupled photosynthetic pigments.

1. Introduction

Strong light-matter coupling provides a sophisticated and effective approach to altering the energy landscapes of excited states in organic semiconductors[1]–[3]. This interaction allows for the tuning of their chemical and photophysical properties without requiring any chemical modifications to the material itself. Noble metal nanoparticles have been extensively studied for their remarkable optical properties, particularly their ability to support localized surface plasmon resonances. These resonances exhibit strong optical field confinement and are highly sensitive to changes in the surrounding environment, making them valuable for various applications[4]–[6]. The disadvantage of a single nanoparticle resonance in studying strong interaction is, it shows relatively broad and localized resonance which requires the organic molecules to be close to nanoparticles and hence it limits the coupling strength as well as signal strength from coupled molecules. However, when these nanoparticles with certain shapes and sizes are arranged periodically, they can support lattice resonances with much higher quality factors and delocalization of the electric field, known as surface lattice resonances (SLR)[7]. As these lattice resonances are more distributed between the nanostructures, it allows a greater number of organic molecules to interact and couple to these open cavity modes. Chlorophyll-a is a key photosynthetic pigment located in the light-harvesting antenna of plants, where it plays an essential role in absorbing light energy and efficiently transferring excitation energy to the reaction center.[8]. Thus, Chlorophyll-a molecules offer significant potential for artificial photosynthesis research, serving as a versatile biomolecular platform to explore optical responses, energy transfer mechanisms, and their applications in photovoltaics, light-harvesting systems, and photosensors.[9]–[11]. Here, we showed the strong radiative interaction between molecular excitations of chlorophyll-a molecules and delocalized optical fields of silver nanodisk arrays. Our observations indicate that strong coupling enhances the absorption of chlorophyll-a and introduces tunability across a broad spectral range, and more importantly the coupled systems made of open plasmonic cavities and organic semiconductors are more suitable for device applications and further study.

2. Materials and Experimental Method

The photosynthetic chlorophyll-a material, with 85% purity extracted from spinach, was purchased from Sigma Aldrich. The stock solution of chlorophyll-a was prepared by dissolving 1 mg in 1 mL of Ethanol. The experimental solution was prepared by mixing 70 µL of the stock solution with 20 µL of a 15 mg/mL PVA solution in deionized water, which served as the matrix. The reflectance spectrum obtained from the 50 nm silver film coated with the prepared solution at 1500 rpm reveals distinct absorption bands characteristic of chlorophyll-a molecules. The absorbance spectrum had been fitted with the Lorentz dispersion model to obtain the absorption peaks. It shows the strongest peak at 660 nm $Q_y(0\rightarrow0)$ corresponding to the pure electronic transition from the ground vibronic state to the ground vibronic state of the first excited electronic state. Other vibronic transitions are shown at 618 nm $Q_y(0\rightarrow1)$ and 572 nm $Q_y(0\rightarrow2)$. Figure 1 shows the fitted absorbance data, showing the corresponding absorption peaks.

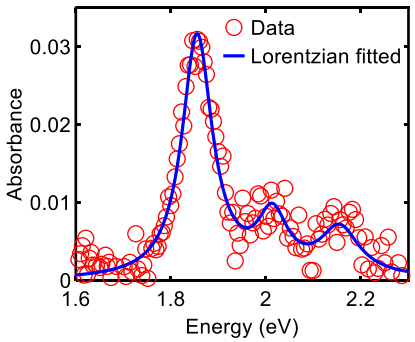


Figure 1: Absorption spectrum of Chlorophyll-a fitted with Lorentz dispersion model.

Nanodisk arrays were fabricated through electron beam lithography using Raith 150 Two. Rf sputtering of 15 nm ITO was done on the fused silica substrates to reduce the charging effect because of e-beam exposure during lithography. Bilayer resists Polymethyl Methacrylate (PMMA) of 495K A4% and 950K A2% have been used as e-beam resist. The size of the arrays was kept at 25 µm x 25 µm. The nanodisk diameter (120 nm–160 nm) and period (280 nm–410 nm) were adjusted to maintain a constant filling factor, which is

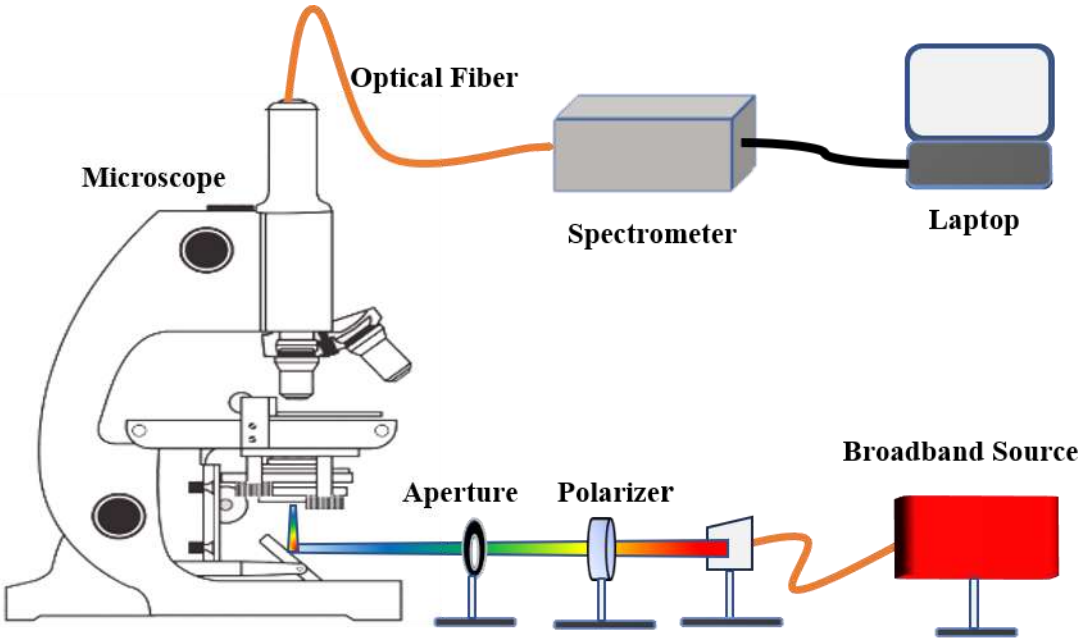


Figure 2: Schematic diagram of the experimental setup

ratio of nanodisk area to unit cell area of 13% across all arrays. Metallization of 70 nm silver has been done through an e-beam evaporator. Figure 3 shows the scanning electron microscope (SEM) image of the fabricated nanostructures.

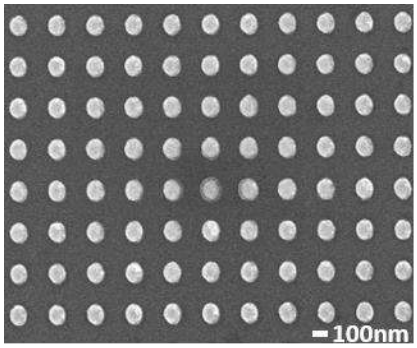


Figure 3: Scanning electron microscope (SEM) image of the fabricated silver nanodisk.

Optical transmission measurements were performed on the nanodisk arrays both before and after coating with chlorophyll-a. The schematic diagram of the experimental setup is presented in Figure 2. It comprises an Energetic-99X LDLS broadband light source, a linear polarizer, an aperture for beam shaping, a mirror, a microscope-based sample mounting and collection system, and a spectrometer connected to a laptop for data acquisition. The collimated light from the source is first passed through the polarizer to control the polarization state of the incident beam. The aperture ensures that only the central portion of the beam is used, improving spatial coherence. The beam is then directed by the mirror towards the microscope, which focuses the light onto the sample placed on a mechanical stage with micrometer-resolution movement. The transmitted light is collected through a high numerical aperture objective and guided via optical fiber to the spectrometer, where the transmission spectrum is recorded. This setup enables precise, polarization-resolved optical characterization of the nanostructures.

3. Results and Discussion

3.1. Measuring the dispersion relation

Transmission measurements performed on the nanodisk arrays, prior to chlorophyll-a coating, reveal that the array resonance energies shift from 1.7 eV to 2.1 eV as the array period increases from 280 nm to 410 nm. Since the filling factor is maintained at a constant 13%, the nanodisk diameter scales proportionally with the period. This tunability highlights the strong dependence of the plasmonic resonance on the lattice geometry. Figure 4 shows the transmittance spectrum of a few arrays.

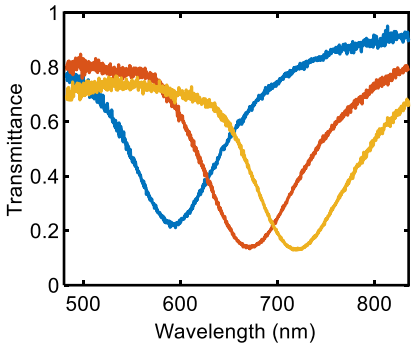


Figure 4: Transmittance spectrum of arrays having diameters and periods as d=125 nm p=300 nm (blue curve), d=145 nm p=355 nm (brown curve), d=165 nm p=405 nm (yellow curve).

To obtain the dispersion relation of these array resonances, the transmittance spectrum was fitted with the Fano line shape function[12]–[14]. The general expression for the line-shape function is given as:

$$R(w,\phi) = \sum_{i=1}^{m} \left| a_i + \frac{b_i * e^{i*\phi_i} * \Gamma_{radi}}{w - w_{0i} + i * \Gamma_{radi}} \right|^2 \qquad (1)$$

The array resonances obtained through fitting the transmittance spectrum were employed in getting the dispersion relation. Figure 5a shows the Fano-fitted transmittance spectrum of an array having a diameter of 125 nm and a period of 300 nm. Whereas, Figure 5b shows the obtained dispersion relation showing the variation of resonance energies of different arrays as a function of the array period.

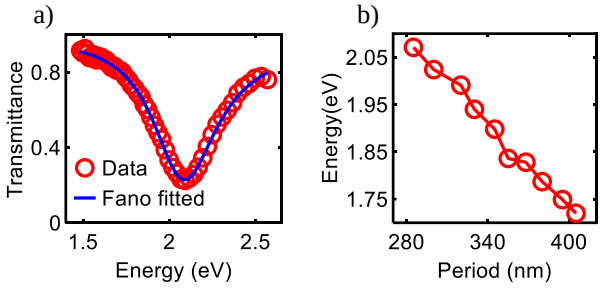


Figure 5: (a) Fano-fitted transmittance spectrum of a nanodisk array with 125 nm diameter and 300 nm period, having a fitting error of 2–3 meV. (b) Extracted dispersion relation illustrating the variation of resonance energy with array periodicity.

Transmittance spectra of the strongly coupled system were recorded after coating the sample with the chlorophyll-a solution. The dispersion relation of the coupled system was extracted by fitting the transmittance spectra with a Fano lineshape function, revealing the characteristic anti-crossing behavior at the excitonic resonance. Figure 6a shows the transmittance spectrum of the coupled system fitted with the Fano lineshape, while Figure 6b presents the extracted dispersion relation, obtained using the fitted resonance positions of the upper and lower polaritonic branches.

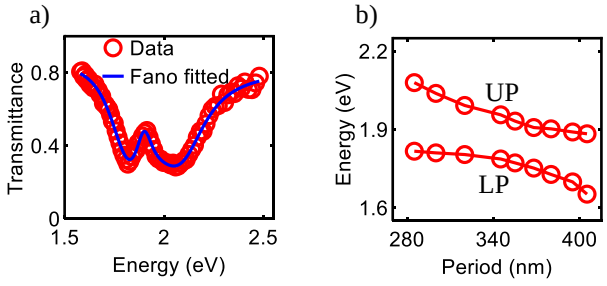


Figure 6: a) Fano-fitted transmittance spectrum of the nanodisk array with 125 nm diameter and 300 nm period, forming a strongly coupled system. (b) Dispersion relation showing the upper (UP) and lower (LP) polaritonic branches.

To model the observed anti-crossing behavior, the extracted dispersion relation was fitted using a coupled oscillator framework. This quantitatively describes the light-matter interaction.

3.2. Modeling the dispersion relation

When molecular aggregates undergo strong coupling with surface lattice resonances (SLR), they form hybrid polaritonic states that exhibit ultrafast decay dynamics on the timescale of a few femtoseconds. The strength of the strong interaction or Rabi splitting energy between the hybrid states is given as[15]

$$\hbar\Omega_R = 2 * d * \sqrt{\frac{\hbar * w_c * N}{2 * \varepsilon_0 * V}} \qquad (2)$$

where d is the dipole moment of the oscillator, V is the mode volume, and N is the number of molecules or oscillators. The linear optical behavior of this hybrid structure can be effectively described using a coupled harmonic oscillator model, where the exciton and surface lattice resonances are represented as complex Lorentzian oscillators[16]. According to the model, the UP and LP hybrid mode frequencies are given by

$$w_{UP/LP} = \frac{w_x + w_{spp}}{2} \pm 0.5 * \sqrt{(w_x - w_{spp})^2 + 4 * \Omega_R^2} \qquad (3)$$

Where W_x and W_{SPP} represent the complex frequency of the exciton and SLR. Figure 7a shows the coupled oscillator model fitting of the extracted dispersion relation, yielding a Rabi splitting energy of approximately 180 ± 6 meV. Figure 7b presents the transmittance spectra of all nanodisk arrays, illustrating the evolution of the upper and lower polaritonic branches and clearly demonstrating the strong coupling behavior.

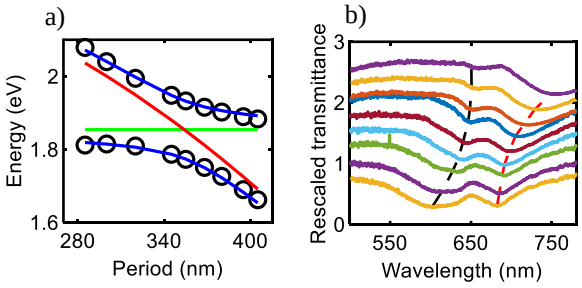


Figure 7: a) Fitted dispersion curve using the coupled oscillator model (blue line), showing a Rabi splitting energy of approximately **180 ± 6 meV**. The surface lattice resonance (SLR) dispersion is shown in red, and the excitonic absorption is represented by the green curve. b) Transmittance spectrum of different arrays in coupled form showing upper and lower polaritonic dips.

These results confirm the realization of strong coupling between the excitonic transition of chlorophyll-*a* molecules and the surface lattice resonances of silver nanodisk arrays, as evidenced by a clear anti-crossing behavior in the dispersion and a Rabi splitting energy of approximately 180 ± 6 meV. Such strong light-matter interaction offers a unique

platform to probe and manipulate the optical response of photosynthetic pigments under hybridized polaritonic states.

4. Conclusion

In summary, we have demonstrated strong coupling between chlorophyll-*a* molecules and the surface lattice resonances of silver nanodisk arrays, evidenced by a pronounced anti-crossing in the dispersion relation and a Rabi splitting of approximately 180 ± 6 meV. The coupled oscillator model effectively captures the hybridization behavior, indicating the formation of exciton–plasmon polaritonic states. This hybrid system provides a promising route to investigate the fundamental optical properties of photosynthetic pigments under modified photonic environments. By placing chlorophyll-*a* molecules in the strong coupling regime, we gain new opportunities to explore energy level modifications, polaritonic mode tuning, and potential coherence effects within biomolecular systems.

Such interaction-driven modifications can offer insights into how light-matter coupling can influence or enhance natural energy transfer pathways. Furthermore, the ability to manipulate excitonic states using nanophotonic structures may prove useful in designing artificial photosynthetic systems, sensitive bio-sensors, and low-threshold polaritonic devices. Overall, this work highlights the potential of plasmonic architectures in advancing our understanding and control of bio-excitonic systems at the nanoscale.

5. Acknowledgments

The authors gratefully acknowledge the financial support provided by the Department of Science and Technology (DST), Government of India. The fabrication work was carried out at the Centre of Excellence in Nanoelectronics (CEN), IIT Bombay, whose infrastructure and technical assistance are also duly acknowledged.

6. References

[1] D. G. Lidzey, D. D. C. Bradley, M. S. Skolnick, T. Virgili, S. Walker, and D. M. Whittaker, Strong exciton-photon coupling in an organic semiconductor microcavity, *Nature*, vol. 395, no. 6697, pp. 53–55, 1998.

[2] Y. M. Lee, S. E. Kim, and J. E. Park, Strong coupling in plasmonic metal nanoparticles, *Nano Converg.*, vol. 10, no. 1, 2023.

[3] P. Vasa, Exciton-surface plasmon polariton interactions, *Adv. Phys. X*, vol. 5, no. 1, 2020.

[4] A. V. Whitney *et al.*, Localized surface plasmon resonance nanosensor: A high-resolution distance-dependence study using atomic layer deposition, *J. Phys. Chem. B*, vol. 109, no. 43, pp. 20522–20528, 2005.

[5] W. A. Murray, J. R. Suckling, and W. L. Barnes, Overlayers on silver nanotriangles: Field confinement and spectral position of localized surface plasmon resonances, *Nano Lett.*, vol. 6, no. 8, pp. 1772–1777, 2006.

[6] B. Auguié and W. L. Barnes, Collective resonances in gold nanoparticle arrays, *Phys. Rev. Lett.*, vol. 101, no. 14, pp. 1–4, 2008.

[7] K. Yang, X. Yao, B. Liu, and B. Ren, Metallic Plasmonic Array Structures: Principles, Fabrications, Properties, and Applications, *Adv. Mater.*, vol. 33, no. 50, pp. 1–21, 2021.

[8] L. O. Björn, G. C. Papageorgiou, R. E. Blankenship, and Govindjee, A viewpoint: Why chlorophyll a?, *Photosynth. Res.*, vol. 99, no. 2, pp. 85–98, 2009.

[9] J. Du, T. Teramoto, K. Nakata, E. Tokunaga, and T. Kobayashi, Real-Time Vibrational Dynamics in Chlorophyll a Studied with a Few-Cycle Pulse Laser, *Biophys. J.*, vol. 101, no. 4, pp. 995–1003, 2011.

[10] S. Mackowski *et al.*, Metal-enhanced fluorescence of chlorophylls in single light-harvesting complexes, *Nano Lett.*, vol. 8, no. 2, pp. 558–564, 2008.

[11] M. Szalkowski, J. D. Janna Olmos, D. Buczyńska, S. Maćkowski, D. Kowalska, and J. Kargul, Plasmon-induced absorption of blind chlorophylls in photosynthetic proteins assembled on silver nanowires, *Nanoscale*, vol. 9, no. 29, pp. 10475–10486, 2017.

[12] M. F. Limonov, M. V. Rybin, A. N. Poddubny, and Y. S. Kivshar, Fano resonances in photonics, *Nat. Photonics*, vol. 11, no. 9, pp. 543–554, 2017.

[13] D. V. Nesterenko, S. Hayashi, and Z. Sekkat, Asymmetric surface plasmon resonances revisited as Fano resonances, *Phys. Rev. B*, vol. 97, no. 23, pp. 1–12, 2018.

[14] B. Luk'Yanchuk *et al.*, The Fano resonance in plasmonic nanostructures and metamaterials, *Nat. Mater.*, vol. 9, no. 9, pp. 707–715, 2010.

[15] P. Vasa, Strong Light-Matter Interaction, in *digital Encyclopedia of Applied Physics*, Wiley-VCH Verlag GmbH & Co. KGaA, pp. 1–30,2019.

[16] P. Vasa and C. Lienau, Strong Light-Matter Interaction in Quantum Emitter/Metal Hybrid Nanostructures, *ACS Photonics*, vol. 5, no. 1, pp. 2–23, 2018.

Ultrastrong Coupling of $Si_{1-x}Ge_x$ Parabolic Quantum Wells to Terahertz Microcavities

S. Cibella[1*], M.Gambelli[1], L. Baldassarre[2] , T. Venanzi[2] , F. Berkmann[3] , E. Talamas Simola[4] , L. DiGaspare[4] , E. Campagna[4] , C. Corley-Wiciakh [5], G. Capellini[4,6] , M. Virgilio[7] , G. Scalari[8], M. Ortolani[2,9], and M. De Seta[4]

[1] CNR, Institute for Photonics and Nanotechnologies, Rome, Italy

[2] Sapienza Univ. of Rome, Department of Physics, P.le A. Moro 5, 00185 Rome, Italy

[3] Experimental Physics and Functional Materials, BTU Cottbus, 03046 Cottbus, Germany

[4]Università Roma Tre, Department of Sciences, Rome, Italy

[5]ESRF - The European Synchrotron, Grenoble, France

[6]IHP GmbH, Frankfurt am Oder, Germany

[7]Università di Pisa, Department of Physics, Pisa, Italy

[8] Institute for Quantum Electronics, ETH Zurich, Switzerland

[9]Istituto Italiano di Tecnologia, Center for Life Neuro and Nano Sciences, Rome Italy

[*] sara.cibella@ifn.cnr.it

Abstract: Using semiconductor-metal patch cavities, we demonstrate ultrastrong coupling at room temperature between conduction sub-band states in $Si_{(1-x)}Ge_x$ heterostructures and THz cavity photons. At the resonant frequency of 3.1 THz, we observe an anticrossing splitting of 1.4 THz, corresponding to a coupling ratio in excess of 0.2.

Control and manipulation of quantum states by light are increasingly important for both fundamental research and applications [1]. This can be achieved, among other techniques, through the strong coupling between light and intersubband transitions (ISBT) in semiconductor quantum wells, typically observed at THz frequencies in integrated lithographic optical cavities [2,3]. Here, we explore the possibility of achieving ultrastrong coupling at room temperature between conduction sub-band states in $Si_{1-x}Ge_x$ heterostructures and THz cavity photons fabricated with a potentially silicon-CMOS-compliant process. Our system is based on $Si_{1-x}Ge_x$ parabolic quantum wells (PQW) [4] with a transition at $\omega_0 = 3.1$ THz embedded in THz patch-antenna microcavities array resonating between 2 and 5 THz depending on the antenna length. We realized a stack of 25 identical $Si_{1-x}Ge_x$ QWs grown by chemical vapor deposition on a Si wafer [6]. We then fabricated the cavities acting as square patch antennas with a highly doped semiconductor ground plane and etched sidewalls to improve the field confinement inside the cavity. In this first demonstration, we achieved anti-crossing at 3.1 THz with spectroscopically measured Rabi frequency $\Omega_R \simeq 0.7$ THz ($\Omega_R/\omega_0 \simeq 0.2$, i.e. ultrastrong coupling). The present group-IV semiconductor material platform can be extended to the 5−12 THz range, where these semiconductors are transparent, as opposed to the III−V compound semiconductors plagued by strong THz optical phonon absorption. Moreover, the intersubband transition in parabolic quantum wells hosted by the nonpolar $Si_{1-x}Ge_x$ crystal lattice is robust against carrier density and temperature variations, making the strength of the coupling only weakly temperature-dependent from 10 to 300 K. In Fig. 1 are visible the reflection spectra measured on two samples having different cavities array periodicity P filled with identical doped PQWs compared to an undoped sample (in grey). The spectra show the results for different cavity dimensions from 7 to 14 um. The present understanding [5] of the strong coupling

conditions in a group-IV semiconductor material may be exploited in the future to realize optoelectronics devices operating in the THz frequency range at room temperature in a fully CMOS compatible platform.

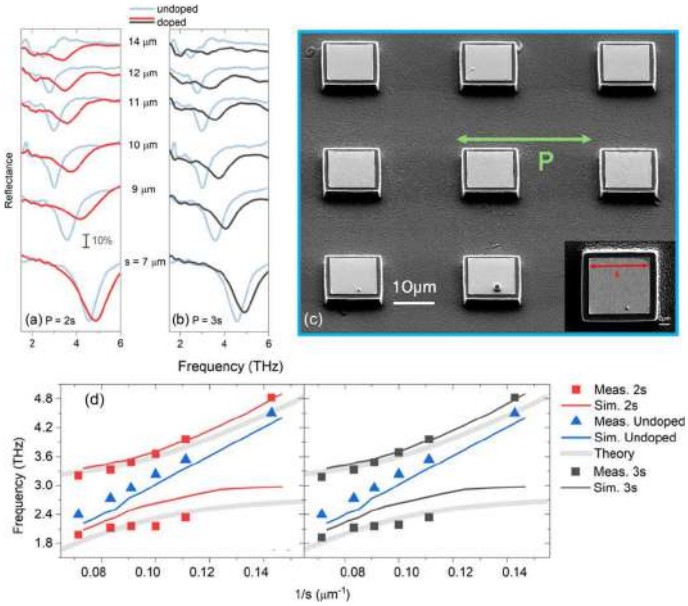


Figure1: (a) Reflection spectra of the cavity arrays with P = 2s (red curves); the gray curves are the reflection spectra of identical cavities fabricated on a sample with undoped PWQs. (b) Reflection spectra of cavities filled with identical doped PQWs but P = 3s. (c) a portion of an array of patch cavities with a unit cell dimension P = 3s; inset: detail of an individual patch cavity with s = 11 μm, where s is the width of the metallic patch.(d): Polariton dispersion as determined by a bi-Lorentzian fitting of the data in (a, b), respectively.

M.D.S., M.O., and S.C. acknowledge support from Italian MIUR grant PRIN 2022 "Strong light−matter coupling manipulation in SiGe QWs at terahertz frequencies" CUP F53D23001190006.

References

1. Rajabali, S.; Markmann, S.; J.chl, E.; Beck, M.; Lehner, C. A.; Wegscheider, W.; Faist, J.; Scalari, G. "An ultrastrongly coupled single terahertz meta-atom". Nat. Commun. 13, 2528 (2022).
2. Forn-Díaz, P.; Lamata, L.; Rico, E.; Kono, J.; Solano, E. "Ultrastrong coupling regimes of light-matter interaction". Rev. Mod. Phys. 91, 025005 (2019).
3. Todorov, Y.; Andrews, A. M.; Sagnes, I.; Colombelli, R.; Klang, P.; Strasser, G.; Sirtori, C. "Strong light-matter coupling in subwavelength metal-dielectric microcavities at terahertz frequencies" Phys. Rev. Lett. 102, 186402 (2009
4. Stark, D., Mirza, M., Persichetti, L. , Montanari, M., Markmann, S. , Beck, M., Grange, T. , Birner, S:,Virgilio, M., Ciano, C., Ortolani, M., Corley, C., Capellini, G., Di Gaspare, L., De Seta, M., Paul, D. J., Faist, J. ,Scalari, G.; THz intersubband electroluminescence from n-type Ge/SiGe quantum cascade structures. Appl. Phys. Lett. 8 March 2021; 118 (10): 101101
5. Berkmann F., Venanzi T., Baldassarre L, Campagna E.,Talamas Simola E., Di Gaspare L., Corley-Wiciak C., Capellini G., G. Nicotra, Sfuncia G., Notargiacomo A., Giovine E., Cibella S., Virgilio M., Scalari G., De Seta M., and Ortolani M. "Ultrastrong coupling of Si1–xGex parabolic quantum wells to terahertz microcavities" ACS Photonics 11, 7, 2776-2786 (2024); https://doi.org/10.1021/acsphotonics.4c00641

Nanoscale Time-Resolved Photoluminescence Mapping of $CsPbBr_3$ Nanocrystals via Near-Field Optical Microscopy

P. Klok[1, 2*], P. Viewegh[1, 2], P. Liška[1, 2], V. Křápek[1, 2], Z. Nováček[1], M. Kratochvíl[3], F. Ulč[1], J. Čecháček[1], J. Spousta[1, 2], and T. Šikola[1, 2]

[1]Institute of Physical Engineering, Faculty of Mechanical Engineering, Brno University of Technology, Technická 2, 61669 Brno, Czech Republic
[2]Central European Institute of Technology, Brno University of Technology, Purkyňova 123, 61200 Brno, Czech Republic
[3]Institute of Physical and Applied Chemistry, Faculty of Chemistry, Brno University of Technology, Purkyňova 464/118, 61200, Brno, Czech Republic
[*]corresponding author: 208733@vutbr.cz

Abstract: We demonstrate time-resolved photoluminescence (tr-PL) mapping with sub-diffraction resolution (~150 nm) in aperture-type scanning near-field optical microscopy (a-SNOM) of $CsPbBr_3$ nanocrystals. This method allows to correlate structural and optoelectronic properties, revealing the impact of nanoscale heterogeneities on recombination dynamic and enhancing nanoscale characterization for optoelectronic applications.

Lead halide perovskites (LHPs), particularly $CsPbBr_3$ nanocrystals, have emerged as highly promising materials for optoelectronic applications [1], exhibiting exceptional optoelectronic properties, such as high photoluminescence quantum yield [2], long non-radiative recombination lifetimes [3]. However, a detailed understanding of these properties necessitates advanced characterization techniques capable of resolving spatial and temporal dynamics at the nanoscale [4].

Traditional far-field photoluminescence (PL) and tr-PL spectroscopy methods provide insights into charge-carrier dynamics and recombination mechanisms but are diffraction-limited. Consequently, they fail to resolve nanoscale heterogeneities that significantly impact the optoelectronic behavior of LHPs. This limitation underscores the necessity of a non-destructive, high-resolution optical technique for nanoscale characterization.

To address this challenge, we present an approach that integrates aperture-type scanning near-field optical microscopy (a-SNOM) with tr-PL to achieve sub-diffraction-limited resolution in the study of carrier recombination dynamics in $CsPbBr_3$ nanocrystals. Our experimental setup enables pixel-by-pixel correlation of structural topography, PL intensity, and tr-PL decay dynamics within a single scan, providing a comprehensive nanoscale characterization framework.

Using this technique, we demonstrate tr-PL mapping of $CsPbBr_3$ nanocrystals with a spatial resolution of ~150 nm. This multimodal approach allows direct visualization of charge-carrier recombination dynamics, revealing significant spatial variations in lifetime distributions, spectral shifts, and carrier diffusion. By directly correlating these findings with structural features, we gain critical insights into morphology-dependent optoelectronic behavior.

This study establishes near-field excited tr-PL as a powerful tool for nanoscale characterization of perovskites. By enabling simultaneous nanoscale mapping of topography, PL, and tr-PL dynamics, this method provides essential insights into local recombination mechanisms, paving the way for the optimization of perovskite-based devices. By advancing nanoscale characterization capabilities, our approach contributes to the broader goal of developing high-performance perovskite-based optoelectronic technologies.

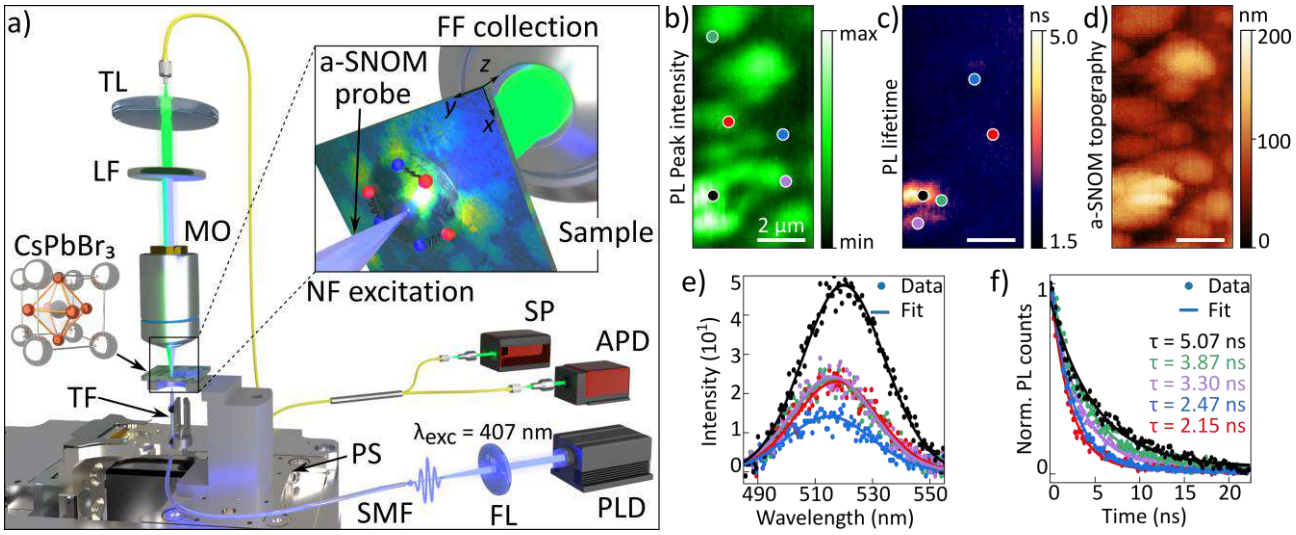


Figure 1: (a) Schematic of the experimental setup, integrating a pulsed laser diode (PLD), single-mode optical fiber (SMF), piezo stage (PS), tuning fork (TF) with an a-SNOM probe, 50× magnifying objective (MO), longpass filter (LF), tube lens (TL), avalanche photodiode (APD), and spectrograph (SP). The inset illustrates near-field (NF) excitation of photoluminescence (PL) in $CsPbBr_3$ nanocrystals. (b) NF excited PL intensity map fitted using a Gaussian function. (c) tr-PL lifetime map revealing spatial variations in carrier lifetimes. (d) Topographic map obtained via a-SNOM probe using shear-force feedback. (e) Representative PL spectra at selected locations, fitted with Gaussian functions. (f) tr-PL decay curves at corresponding points, fitted using a single-exponential decay model.

The author acknowledges the support of the Brno Ph.D. Talent Scholarship, funded by the Brno City Municipality, financial support from the Czech Science Foundation (grant No. 25-17500S), CzechNanoLab Research Infrastructure supported by MEYS CR (LM2023051), and the Light Microscopy Core Facility, IMG, Prague, Czech Republic, supported by MEYS – LM2023050 and RVO – 68378050-KAV-NPUI, for their support with the FLIM (Leica Stellaris 8 Falcon) presented herein.

References

1. Stoumpos, C. C. et al., "Crystal Growth of the Perovskite Semiconductor $CsPbBr_3$: A New Material for High-Energy Radiation Detection," Cryst. Growth Des., Vol. 13, No. 17, 2722–2727, 2013.
2. Stasio, D. F. et al., "Near-Unity Photoluminescence Quantum Yield in CsPbBr3 Nanocrystal Solid-State Films via Postsynthesis Treatment with Lead Bromide," Chem. Mater., Vol. 29, No. 18, 7663–7667, 2017.
3. Cheng, H. et al., "Understanding and minimizing non-radiative recombination losses in perovskite light-emitting diodes," J. Mater. Chem. C, Vol. 10, No. 37, 13590–13610, 2022.
4. Delport, G. et al., "Imaging Carrier Transport Properties in Halide Perovskites using Time-Resolved Optical Microscopy," Adv. Energy Mater., Vol. 10, No. 26, 1903814, 2020.

Super-resolution Imaging Using Photonic Nanojet Generated by a Cylinder

M. H. Shor Peled1 and A. Karabchevsky1,2*

1 School of Electrical and Computer Engineering, Ben Gurion University of the Negev, Israel

2 Department of Physics, Lancaster University, LA1 4YB, United Kingdom

*Corresponding author: alinak@bgu.ac.il

Abstract: We present a sub-diffraction limit imaging approach using the Photonic Nanojet (PNJ) effect in tapered fibers. By analyzing the PNJ generated by upright dielectric cylinders, we achieve extended working distances without compromising resolution. This label-free method enables non-invasive nanoscale imaging, offering new possibilities for biological and material science applications.

The resolution limit of conventional optical imaging techniques, imposed by the diffraction of light, restricts the ability to observe nanoscale structures with high precision. This limitation presents significant challenges in understanding biological systems at the nanoscale, which is crucial for gaining insights into disease mechanisms and cellular processes. As a result, there is a growing need for advanced imaging techniques that go beyond the diffraction limit of traditional microscopy [1]. To address this, we utilize the Photonic Nanojet (PNJ) effect, which generates high-intensity, narrow light beams through dielectric structures under plane wave illumination [2].

We demonstrate the resolution of sub-diffraction limit grid lines using a tapered fiber, showcasing its capability in imaging nanoscale structures. Further, we explore the PNJ characteristics by illuminating upright dielectric cylinders with varying diameters (8 to 16 microns). Through experimental imaging and computational simulations, we analyze the full width at half maximum (FWHM) and working distance of the generated PNJ. Our findings indicate that while the FWHM remains relatively constant across different cylinder diameters, the working distance increases with larger diameters. This extended working distance enhances imaging versatility, particularly for applications requiring non-invasive techniques.

By optimizing the fiber diameter to balance resolution and working distance, our approach offers a label-free, sub-diffraction limit imaging solution. This method is particularly advantageous for imaging specimens sensitive to damage from electron microscopy or high-power imaging systems, opening avenues for safer and more effective nanoscale imaging in biological and material sciences.

The research reported in the manuscript was funded by Israel Science Foundation (ISF no. 2598/20).

References

1. Karabchevsky, Alina, et al. "Super-Resolution Imaging and Optomechanical Manipulation Using Optical Nanojet for Nondestructive Single-Cell Research." Advanced Photonics Research 3.2 (2022): 2100233.
2. Luk'yanchuk, Boris S., et al. "Refractive index less than two: photonic nanojets yesterday, today and tomorrow." Optical Materials Express 7.6 (2017): 1820-1847.

Plasmon-enhanced photovoltaics, photocatalysis, and solar fuels

Randomness in self-assembled photonic crystals

Duanduan Wan[1]

1 School of Physics and Technology, Wuhan University, Wuhan 430072, China

*corresponding author: ddwan@whu.edu.cn

Abstract: Randomness arising from thermal noise is almost inevitable in self-assembled colloidal crystals and is generally believed to be detrimental to photonic band gaps (PBGs). In this talk, I will present a counterintuitive example in which randomness actually enhances PBGs and discuss its effects on the width of PBGs.

Unlike top-down design, self-assembly, as a bottom-up method, offers advantages such as low cost, low energy consumption, and the ability to produce crystals over large areas. However, randomness arising from thermal noise is almost inevitable in self-assembled colloidal crystals. In this talk, we will present a counterintuitive example where randomness actually benefits photonic band gaps (PBGs) and explore the effects of particle randomness on the width of PBGs. Additionally, we will discuss the realization of chiral photonic crystals using self-assembly approaches.

References

1. D. Wan and S. C. Glotzer. “Unexpected dependence of photonic band gap size on randomness in self-assembled colloidal crystals”, Phys. Rev. Lett. 126, 208002 (2021).
2. Z. Qin, T. Liu, and D. Wan. “Effects of orientational and positional randomness of particles on photonic band gap”, Phys. Rev. B 107, 174110 (2023).
3. T. Liu, H.-K. Chan and D. Wan. “Chiral photonic crystals from sphere packing”, Soft Matter, 19, 7313, (2023). [Selected as the back cover]

Impact of Realistic 3D Hole Shapes on Photonic Crystal Surface Emitting Laser (PCSEL) Performance

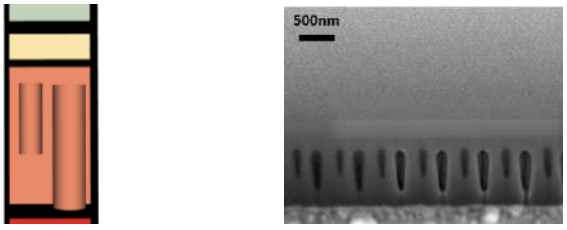
A. Vukovic[1*], P. Sewell[1], B. Lang[2], K. Boyan, S Rihani[2], D. Moodie[2], N. Hattasan[2], G. Berry[2]

[1]George Green Institute for Electromagnetics Research, Faculty of Engineering, University of Nottingham, Nottingham, UK
[2]Huawei Technologies Research and Development, Ipswich, United Kingdom
[*]corresponding author: ana.vukovic@nottingham.ac.uk

Abstract: PCSEL lasers utilize a photonic crystal layer to scatter the light in the vertical direction. However, the practical etching limitations result in hole scatterers not having an ideal cylindrical shape. Using a 3D numerical method the paper investigates the impact of realistic hole shapes on PCSEL characteristics and performance.

Photonic Crystal Surface Emitting Lasers (PCSELs) are a relatively new type of surface emitting lasers that incorporate a photonic crystal layer that uses in-plane scattering to enhance optical feedback and scatters the light vertically. PCSELs that lase with a small divergence angle and CW output power of 50 W have been reported [1]. The photonic crystal pitch, size and shape of the air holes need to be engineered to optimise the Q-factor, maximise the threshold difference between the lasing mode and higher order modes and to control the far field emission pattern. In order to do this accurately full three-dimensional (3D) nature of the PCSEL unit cell needs to be accounted for and combined with the realistic model of the laser gain.

In this paper we extend the analysis of the PCSELs by investigating how the true shape of the etched holes affects the lasing spectrum of the PCSEL. Fabrication limitations mean that the vertical shape of the etched holes is not of ideal cylindrical shape and that the etching depth depends on the overall diameter of the hole, i.e. smaller holes will be etched with smaller depths than larger holes. An example of double lattice 3D PC unit cell with ideal cylindrical profile that is assumed in the theoretical analysis is shown in Fig.1a). SEM image of the fabricated sample is shown in Fig.1b) where it can be seen that the shapes of the holes are not cylindrical but of tapered design and rounded at both ends.



a) b)

Figure 1. Detail of the photonic crystal unit cell with: a) ideal cylindrical holes, b) SEM image of the fabricated photonic crystal.

PCSELs are commonly modelled using Effective Index type methods that eliminate the vertical epitaxy by approximating the 3D structure with an equivalent two-dimensional (2D) one and thus are not able to accurately characterise 3D features of PCSEL geometry. Full 3D analysis can be done using Finite Difference Time Domain (FDTD) method (FDTD) and Transmission Line Modelling (TLM) method [2]. Time-domain electromagnetic methods that deploy unstructured meshes that can tackle increasingly complex, multi-scale and multi-physics problems are being continually developed. Although not as well known as FDTD, the TLM

framework offers distinctly valuable features namely: a) no need for mass lumping in order to obtain an explicit time-stepping algorithm and, b) unlike the FDTD method, it calculates the electric and magnetic fields at the same point and at the same time step, ensuring the unconditional stability which is of particular importance for modelling of complex materials and for large scale simulations [2]. Recently, a TLM method formulated on the unstructured tetrahedral mesh has been extended to include the model of realistic laser gain by combining the polarization equation that relates carrier dynamics in the lasing media with the macroscopic Maxwell's equations [3].

As PCSELs contain many thousands of PC unit cells it is adequate to approximate it with an infinitely periodic structure using a 3D unit cell with periodic boundary conditions. The PCSEL vertical epitaxy is shown in Fig.2a) and is comprised of following layers (from top to bottom): 2040 nm thick InP cavity (n = 3.20), 185 nm thick MQW (n =3.37), spacer of 170 nm thickness (n = 3.20), infill layer of 25 nm thickness (n = 3.40), 600 nm deep photonic crystal and InP substrate of 1500 nm thickness (n = 3.20). A perfectly reflecting mirror is placed at the top of InP cavity and matched boundary conditions are placed at the bottom of the InP substrate where light escapes and constitutes the useful output of the laser. The photonic crystal is comprised of air holes (n = 1) etched into a InGaAsP slab (n = 3.40). The photonic crystal has lattice constant a = 408nm. The larger hole has a diameter of 143 nm and depth of 600 nm, the smaller hole has the diameter of 105 nm and depth of 325 nm and they are separated by 450 nm. Figure 2b) compares the lasing spectrum of the PCSEL with ideally etched holes and with a realistic hole. It can be seen that the vertical hole shape has a significant impact on the lasing frequency spectrum. Similarly to the measured lasing spectra in Fig.2c) the simulated results predict multimodal lasing output but are shifted down in wavelength. The full paper will discuss in more detail the impact of the realistic shape on the modes that are supported in the structure and the carrier dynamics.

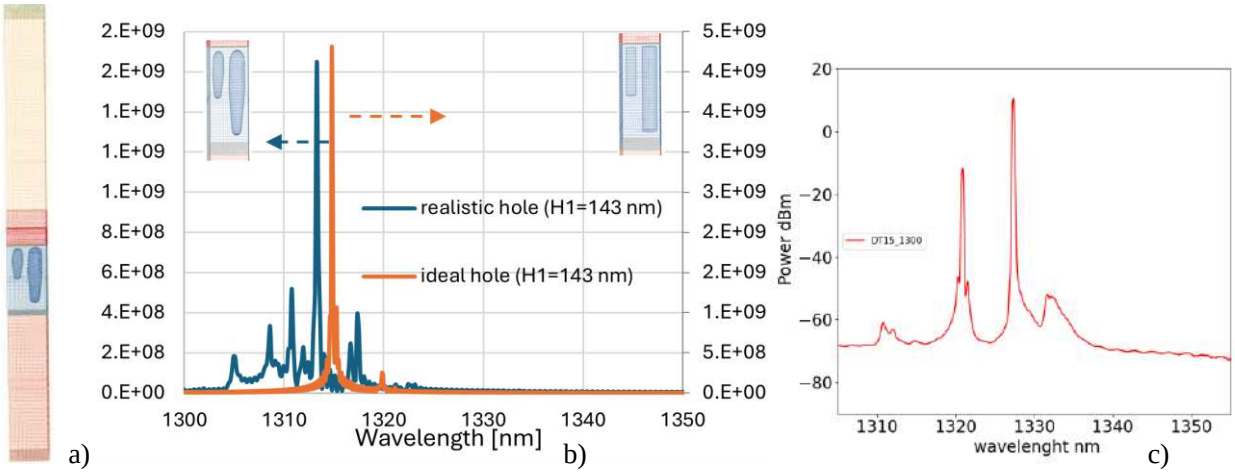


Figure 2. a) Vertical epitaxy of the 3D PCSEL unit cell with realistically etched holes and b) lasing spectrum of the PCSE with ideal cylindrical holes and realistically etched holes and c) measured lasing spectrum of fabricated PCSEL.

References

1. Yoshida M., Katsuno S., Inoue T., *et al.*, "High-brightness scalable continuous-wave single-mode photonic-crystal laser," Nature 618, 727–732 2023.
2. Sewell P., Benson T.M., Christopoulos C., Thomas D. W. P., Vukovic A., Wykes J., "Transmission Line modelling (TLM) based upon unstructured tetrahedral meshes", IEEE Trans on MTT, Vol.53, pp.1919-1928, 2005.
3. Vukovic A, et all, "Laser PCSEL Model in Unstructured TLM Method", International workshop on PCSEL, Birmingham, November 2024.

From Photonic Time-Crystals to Gravitational Waves

M. W. McCall and S. F. Koufidis*

Blackett Laboratory, Department of Physics, Imperial College London, London SW7 2AZ, United Kingdom
*corresponding author: steven.koufidis20@imperial.ac.uk

Abstract: Building on the band structure and optical response of synthetic photonic time crystals, we explore the temporal analogs of quasi-crystals and optical activity via coupled-wave theory. We thence extend this framework to investigate the interaction of light waves with Nature's quintessential space-time grating: the gravitational wave.

Incorporating time as an additional degree of freedom for *tripping the light fantastic* has given rise to the temporal analog of photonic crystals, which, under certain conditions, feature regions where waves are amplified rather than attenuated. The key ingredient in this parametric amplification process is the periodic modulation of the relative permittivity, akin to conventional photonic crystals but in *time* rather than space. Since these exotic modulations require pumping certain crystals, such as ITO, it hardly comes as a surprise that de-synchronizations may well occur. Thus, by treating the temporal medium as a temporal quasi-crystal—wherein the permittivity is an *almost*-periodic function of time—we observe in Fig. 1(a) that for a specific tone-spacing, almost-periodicity surprisingly outperforms perfect periodicity [1]. On the other hand, the temporal analog of optical activity—where the permittivity, permeability, and chirality are periodic functions of time—reveals that a wave traversing such a temporal slab will not only be amplified but also rotated [see Fig. 1(b)]. Moreover, the amplification is handedness-specific: two bandgaps form in Brillouin space, one for right-handed modes and one for left-handed modes [2]!

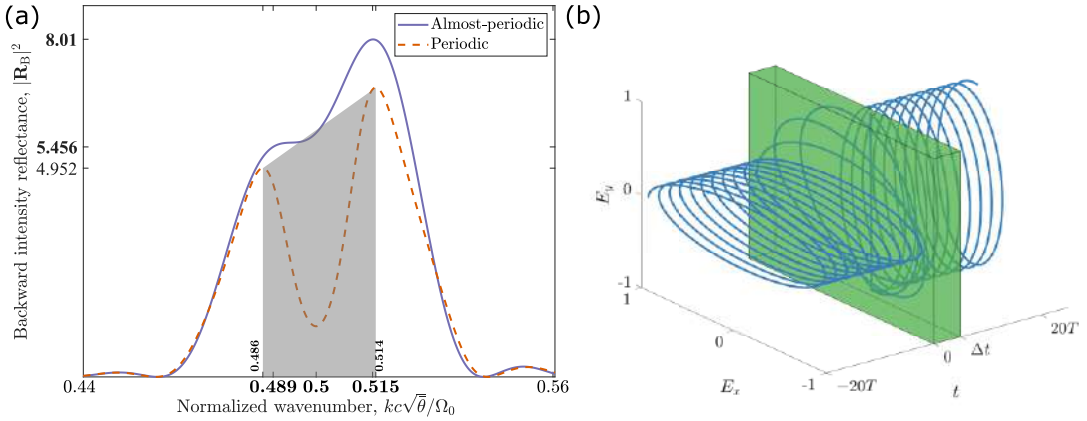


Fig. 1 (a) Optical response of an *almost*-periodic temporal slab: almost-periodicity outperforming perfect periodicity [1]. (b) As waves traverse a time-periodic chiral slab, the **E**-field is at once rotated *and* amplified [2].

Hitherto, we have been discussing purely temporal meta-media. We may now move on to spatio-temporal modulations. This category of meta-gratings has garnered significant attention in recent years, with the concept of "traveling wave modulation" and synthetic velocity in meta-optics not only promising exciting new ways of manipulating light but also proposing entirely new physical mechanisms to achieve, e.g., gain via the compression of lines of force [3]. Here, we pose the question: Are meta-media truly the only route towards realizing spatio-temporal gratings? Insofar as *synthetic* gratings are concerned, obviously yes! However, Nature has gone a step further! Indeed, one may conceptualize gravitational waves (GWs)—the fundamental spacetime perturbations—

as “luminal moving gratings” [see Fig. 2(a)]. These dynamic fluctuations induce effective refractive index modulations that interact with electromagnetic waves (EMWs), thereby providing a signature of their presence.

Within linearized gravity and in a source-free curved spacetime, the electromagnetic 4-potential satisfies a wave equation in which gravity is contained within the derivatives of the Christoffel symbols. If the metric perturbation is taken as a plane GW, and the total electromagnetic 4-potential is expressed as the sum of an incident and, say, two scattered EMWs, then fully *covariant* coupled-wave theory reveals that first-order synchronous sidebands have 4-wavevectors $k_{(+1)\mu} = k_{(inc)\mu} + K_\mu$ and $k_{(-1)\mu} = k_{(inc)\mu} - K_\mu$, wherein K_μ is the 4-wavevector of the GW, whereas $k_{(inc)\mu}, k_{(\pm1)\mu}$ those of the EMWs. These phase-matching conditions, simultaneously conserving both *energy* and *momentum*, occupy an intermediate regime between static and temporal Bragg gratings. The interaction is independent of any specific frequency and, unlike conventional Bragg scattering, does *not* support backscattering. Estimation of the interaction lengths between the EMWs’ coupling, mediated by the GW, reveals that for high-frequency, strong-field GWs, the interaction lengths shown in Fig. 2(b) appear plausible.

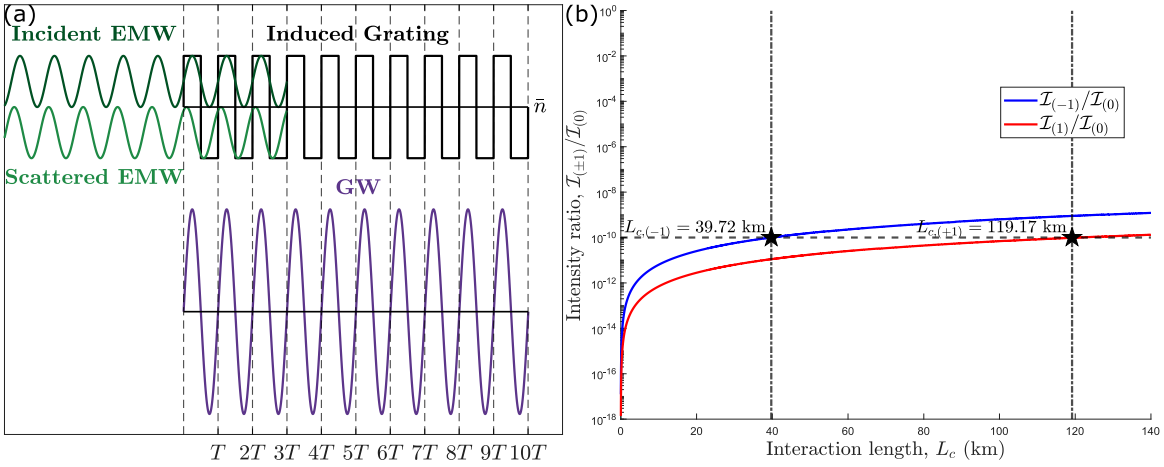


Fig. 2 (a) A luminally propagating plane GW induces a periodic spatiotemporal modulation in the refractive index. (b) Interaction lengths in the coupling process of EMWs, mediated by the scaffold formed by the GW.

Interactions between EMWs and GWs within a covariant coupled-wave framework predict observable sidebands in the electromagnetic spectrum. This direction-preserving mechanism for the indirect detection of gravitational radiation through incoherent electromagnetic sources aims to inspire an all-optical analog experiment for GW detection in laboratory settings using synthetic gratings [4].

M. W. M. and S. F. K. are supported by a Kickstarter Research Project funded by the Department of Physics at Imperial College London. S. F. K. thanks the Bodossaki Foundation for its financial support since 2021.

References

1. Koufidis, S. F., T. T. Koutserimpas, F. Monticone, and M. W. McCall, “Enhanced scattering from an almost-periodic slab,” Phys. Rev. A, Vol. 110, L041501, 2024.
2. Koufidis, S. F., T. T. Koutserimpas, F. Monticone, and M. W. McCall, “Electromagnetic wave propagation in time-periodic chiral media,” Opt. Mater. Express, Vol. 14, 3006, 2024.
3. Pendry, J. B., E. Galiffi, and P. A. Huidobro, “Gain mechanism in time-dependent media,” Optica, Vol. 8, 636, 2021.
4. Harwood, A. C., S. Vezzoli, T. V. Raziman, C. Hooper, R. Tirole, F. Wu, S. A. Maier, J. B. Pendry, S. A. R. Horsley, and R. Sapienza, “Super-luminal synthetic motion with a space-time optical metasurface,” arXiv:2407.10809, 2024.

Multiple unidirectional chiral zero modes arising from a large Chern number in 2D photonic crystals

Weiyuan Tang[1,#], Hsun-Chi Chan[1,#], Shaojie Ma[2], Chuang Tan[1], Biye Xie[3], Kazuki Hasebe[1,4], Nicholas X. Fang[5], and Shuang Zhang[1*]

[1]Department of Physics, The University of Hong Kong, Hong Kong, China

[2]Department of Optical Science and Engineering, Fudan University, Shanghai, China

[3]School of Science and Engineering, The Chinese University of Hong Kong, Shenzhen, China

[4]National Institute of Technology, Sendai College, Sendai, Japan

[5]Department of Mechanical Engineering, The University of Hong Kong, Hong Kong, China

[#]These authors contributed equally to this work

Corresponding author: `shuzhang@hku.hk`

Abstract: We experimentally demonstrate the presence of four unidirectional chiral zero modes originating from large Chern numbers in 2D gyromagnetic topological photonic semimetals. Our findings experimentally validate the intrinsic connection between the chiral zero modes and topological fermions, offering the potential to advance large-capacity and highly efficient photonic devices.

Chiral zero mode (CZM) appears as the zeroth Landau level of the quantized dispersions in the presence of a gauge field [1]. The number of chiral zero modes is dictated by the topological charge of the fermion point [2]. Despite the proposal of effective Hamiltonians to achieve multiple Chiral zero modes - which possess substantial practical applications, such as improving mode density and coupling efficiency in compact multimode waveguide devices - the realization of multiple Chiral zero modes arising from a large Chern number has remained elusive. Here, we have experimentally observed multiple unidiretional CZMs in a 2D topological photonic system with large gap Chern numbers under external magnetic fields [3]. Our findings on multiple unidirectional CZMs not only experimentally validate the index theorem on chiral Landau bands for topological semimetals [2] but also open up possibilities for the enhancement of the capacity and coupling efficiencies of wave transmission and processing devices, including large-scale topological photonic circuit with compact multimode routing.

References

1. Armitage, N. P., Mele, E. J., and Vishwanath, A. " Weyl and Dirac semimetals in three-dimensional solids," *Rev. Mod. Phys.*, Vol. 90, pp. 015001, 2018

2. Zhao, Y. X. and Yang, S. A. "Index Theorem on Chiral Landau Bands for Topological Fermions," *Phys. Rev. Lett.*, Vol. 126, pp. 046401, 2021.

3. Tang, W. and Chan, H. -C. et al."Multiple unidirectional chiral zero modes arising from a large Chern number in 2D photonic crystals," 2025. (to be submitted)

Demonstration of a Broadband Polarization Control Device for Terahertz Waves Using Silicon Photonic Crystals

H. Yamane[1*], Y. Yamada[1], Y. Kondo[1], T. Ehiro[1], M. Fujita[2], and S. Murakami[1]

[1]Osaka Research Institute of Industrial Science and Technology, Japan
[2]Graduate School of Engineering Science, Osaka University, Japan
[*]corresponding author: yamane.hidemasa@orist.jp

Abstract: A broadband, high-efficiency terahertz polarization converter is developed using a silicon photonic crystal with elliptical through-holes. Experimental and numerical results demonstrate its broadband half-wave plate function (0.30–0.50 THz). The device achieves high transmission with minimal loss due to biaxial anisotropy, enabling efficient terahertz polarization control using all-silicon structures.

Terahertz (THz) waves have been attracting significant attention as a promising form of electromagnetic radiation, offering new possibilities for Beyond 5G and 6G communication systems as well as biomedical imaging due to their broadband characteristics. However, practical utilization of THz waves faces challenges, including strong absorption by atmospheric water vapor and oxygen, which hinders long-distance propagation, and increased propagation losses in conventional metal-based systems as the frequency increases. To address these challenges, devices utilizing high-purity silicon as a dielectric material have gained attention. Silicon exhibits high transparency in the THz range and has a refractive index of approximately 3.4. Additionally, MEMS fabrication techniques allow for the creation of photonic crystals and metamaterials, paving the way for efficient THz optical control [1]. Polarization control of THz is essential for applications such as polarization multiplexing in communication, spectroscopy, and THz imaging. Recent developments include various metamaterial structures such as ring resonators and multilayer prism-based wave plates that demonstrate broadband performance in the THz range [2-4]. These approaches suffer from issues such as absorption losses in metal-based designs, complex fabrication processes, and challenges in miniaturization.

This study aims to create a broadband, high-efficiency polarization converter using only silicon wafers with a simplified fabrication process. To achieve broadband and uniform polarization control, it is crucial to design optical properties with appropriate frequency dispersion for each anisotropic axis, which is nontrivial. Electromagnetic response simulations were conducted to determine the size parameters, leading to the identification of a structure that functions as a broadband half-wave plate in the THz range.

Figure 1(a) shows a schematic diagram of the silicon photonic crystal half-wave plate in this study. A two-dimensional anisotropic photonic crystal is considered by periodically patterning elliptical through-holes in a rhombic lattice on a silicon substrate. The thickness of the silicon substrate is denoted as d, the short and long axes of the elliptical holes as a and b, respectively, and their periodicities along each axis as α and β. These directions are defined as the x- and y-axes, respectively. Here, using d as the unit, the parameters are set as follows:

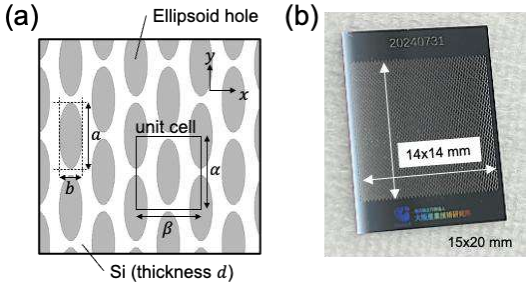


Figure 1 (a) Schematic diagram of silicon photonic crystal. (b) Photo of fabricated half-wave plate.

$$a/d = 0.160, b/d = 0.455, \alpha/d = 0.450, \beta/d = 0.500 \quad (1)$$

High-resistance silicon substrates (resistivity >10 kΩ·cm, thickness 200 μm) were used to fabricate the photonic crystal designed theoretically. Photolithography and deep reactive ion etching were employed to create through-elliptical holes in the silicon wafer. As an example, a half-wave plate was fabricated based on eq. (1) with d = 800 μm. The thickness of 800 μm was achieved by stacking four identical elements, each processed on a single 200 μm-thick silicon wafer. The element is shown in Figure 1(b).

The optical properties of the fabricated devices were evaluated using a THz time-domain spectrometer. A polarized wave tilted 45 degrees with respect to the axis of the photonic crystal was incident, and the transmitted wave was detected. Figure 2(a) shows the transmission spectrum. The red and blue lines represent the spectra of the transmitted wave with polarization parallel ($T_{\parallel}$) and orthogonal ($T_{\perp}$) to the polarization of incident wave, respectively. The solid lines indicate numerical calculations, and the dashed lines represent experimental measurements. The transmittance $T_{\parallel}$ remains close to zero over the broadband range of 0.30–0.50 THz, while $T_{\perp}$ increases to nearly 1. This is due to the photonic crystal exhibiting biaxial anisotropy along the minor and major axes of the ellipse. The phase difference for each axis is shown in Figure 2(b). The phase difference is approximately π radians over a broad bandwidth in the range of 0.30–0.50 THz.

The silicon photonic crystal polarization control device fabricated in this study demonstrates high transmission with minimal absorption loss, owing to its all-silicon composition. Unlike multilayer metamaterial structures [2, 3], it is composed solely of silicon, allowing for a simpler and more straightforward fabrication process. Compared to conventional prism-based wave plates [4], it can remain thin and compact even when scaled to a larger aperture. The desired thickness was achieved by stacking multiple thin silicon wafers, avoiding the challenges associated with high-aspect-ratio etching. The ability to batch-process multiple devices on a single thin silicon wafer significantly reduces manufacturing time and costs, thereby making this approach highly practical.

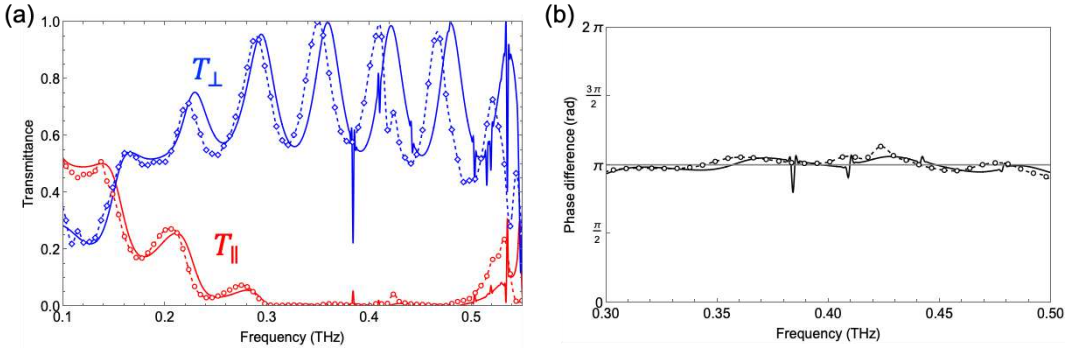


Figure 2 (a) Spectra of the transmitted wave with polarization parallel ($\boldsymbol{T}_{\parallel}$) and orthogonal ($\boldsymbol{T}_{\perp}$) to the polarization of incident wave, respectively. (b) Phase difference between polarizations along the minor and major axes of the ellipse.

References

1. Gao, W., Yu, X., Fujita, M., Nagatsuma, T., Fumeaux, C. and Withatachumnankul, W., "Effective-medium-cladded dielectric waveguides for terahertz waves", Opt. Express, vol. 27, 38721-38734, 2019.
2. Wen, X. and Zheng, J., "Broadband THz reflective polarization rotator by multiple plasmon resonances", Opt. Express, vol. 22, 28292-28300, 2014.
3. Han, Z., Ohno, S., Tokizana, Y., Nawata, K., Notake, T., Takida, Y. and Minamide, H., "Thin terahertz-wave phase shifter by flexible film metamaterial with high transmission", Opt. Express, vol. 25, 31186-31196, 2017.
4. Kawada, Y., Yasuda, T., Nakanishi, A., Akiyama, K., Hakamata, K. and Takahashi, H., "Achromatic prism-type wave plate for broadband terahertz pulses", Opt. Letters, vol. 39, 2794-2797, 2014.

Topological line singularities in scattering matrix and bound states in the continuum

Wenzhe Liu[1,2*], Yuan-Song Zeng[3], Geng-Bo Wu[3], and C. T. Chan[2]

[1]Institute for Nanoelectronic Devices and Quantum Computing, Fudan University, China

[2]Department of Physics and Institute for Advanced Study,
The Hong Kong University of Science and Technology, Hong Kong SAR

[3]State Key Laboratory of Terahertz and Millimeter Waves and Department of Electrical Engineering,
City University of Hong Kong, Hong Kong SAR

Corresponding author: wzliu@fudan.edu.cn

Abstract: We reveal that bound states in the continuum function as robust chain points pinning together nodal lines in scattering matrices. These singularities induce observable phase vortices and persist even when symmetry is broken, providing a new framework for understanding topological protection in open photonic systems.

We present a novel framework revealing that scattering matrices of photonic systems host continuous lines of topological singularities in frequency-momentum space. While previous studies of topological photonics primarily focused on Hamiltonian matrices of closed systems, our work demonstrates that open systems characterized by scattering matrices exhibit rich topological structures with distinct properties. In lossless systems with mirror symmetry, we identify diabolic points (DPs) that form continuous nodal lines (NLs) where eigenvalues intersect linearly. Material loss transforms these into exceptional lines (ELs), where both eigenvalues and eigenvectors coalesce. Most significantly, we discover that bound states in the continuum (BICs) act as robust "chain points" that pin together nodal lines, creating nodal chain structures that persist even when mirror symmetry is broken.

The theoretical mechanism behind these phenomena emerges from the properties of reflective metasurfaces described by 2×2 scattering matrices. Mirror symmetry enforces zero inter-channel coupling when the in-plane wavevector lies in the mirror plane, creating eigenvalue degeneracies that form nodal lines in frequency-momentum space. BICs represent a special case where the resonance bandwidth approaches zero, resulting in an abrupt 2π phase jump in the eigenphase. This phase discontinuity ensures eigenvalue crossings along mirror-symmetric directions, generating nodal lines that intersect precisely at the BIC. Our theoretical analysis shows that when modifying structures to break mirror symmetry while preserving C_2 rotational symmetry, nodal chain points at BICs remain robust, while regular degeneracies disappear. This confirms a special topological protection mechanism of BIC-associated nodal chains beyond conventional symmetry requirements.

To verify these theoretical predictions, we conducted experiments using PCB-based metasurfaces operating at microwave frequencies. The experimental setup consisted of a reflective metasurface with periodic rectangular slots formed on a dielectric substrate backed by a metallic mirror. Using circular polarizers and vector network analyzers, we mapped the cross-circularly polarized reflection phase across different incident angles. These angle-resolved phase measurements revealed characteristic phase vortices at the predicted positions in frequency-momentum space, validating the presence of nodal lines converging at BICs.

The topological features we discovered have practical applications in wavefront engineering. We demonstrated the generation of spatiotemporal optical vortices using our metasurface structures, where phase vortices in the cross-polarization scattering create distinct optical signatures. More fundamentally, our work unifies previously separate concepts in topological photonics—BICs and nodal lines—through the scattering matrix framework. This connection provides new design principles for robust photonic devices that maintain functionality despite structural imperfections.

By establishing the relationship between BICs and nodal chains in scattering matrices, our research advances fundamental understanding of topological protection in open photonic systems. These findings open new avenues for exploring complex topological structures in higher-dimensional scattering matrices, non-Hermitian systems, and across different wave phenomena, potentially leading to novel approaches for designing advanced photonic devices for sensing, communications, and quantum information applications.

Acknowledgement

W.L. and C.T.C. are supported by Hong Kong RGC (CRS_HKUST601/23 and AoE/P-502/20). Y.-S.Z. and G.-B.W. are supported by the Research Grants Council of Hong Kong (CityU 21207824).

References

1. Chen, J., Liu, W., Wang, J. et al. "Topological Singularities in Metasurface Scattering Matrices: From Nodal Lines to Exceptional Lines," *arXiv preprint*, arXiv:2411.04666, 2024.

Harnessing Anisotropic Photonic Crystals for Advanced Chiral Mirrors

A. Alessandrini[1*], L. di Mauro Villari[1], L. Assogna[1], M. Silvestri[1], M. Venturi[1], C. Ferrante[2], P. Benassi[1,2], D. Tedeschi[1], A. Marini[1,2]

[1] Department of Physical and Chemical Sciences, University of L'Aquila, Via Vetoio, 67100 L'Aquila, Italy
[2] CNR-SPIN, c/o Department of Physical and Chemical Sciences, Via Vetoio, Coppito (L'Aquila) 67100, Italy
[*]corresponding author: andrea.alessandrini1@student.univaq.it.

Abstract: We leverage the optical torque from anisotropic media for polarization control, designing ultra-compact uniaxial layered stacks that form chiral photonic crystals with >99% reflectance for one circular polarization depending on the reciprocal orientation of the extraordinary axes of neighboring layers.

We conduct a detailed theoretical analysis of the proposed device, identifying optimal conditions for a very high reflectance for one circularly polarized (CP) component and very high transmittance for the other one, according to the specific relative orientations of the extraordinary axes of neighbouring slabs and on their thicknesses. Realization of chiral metamaterials and metasurfaces exhibiting comparable characteristics involves complex, costly, and time-consuming nanoscale fabrication. Moreover, high absorption and ohmic losses limit the performance of plasmonic metasurfaces [1].

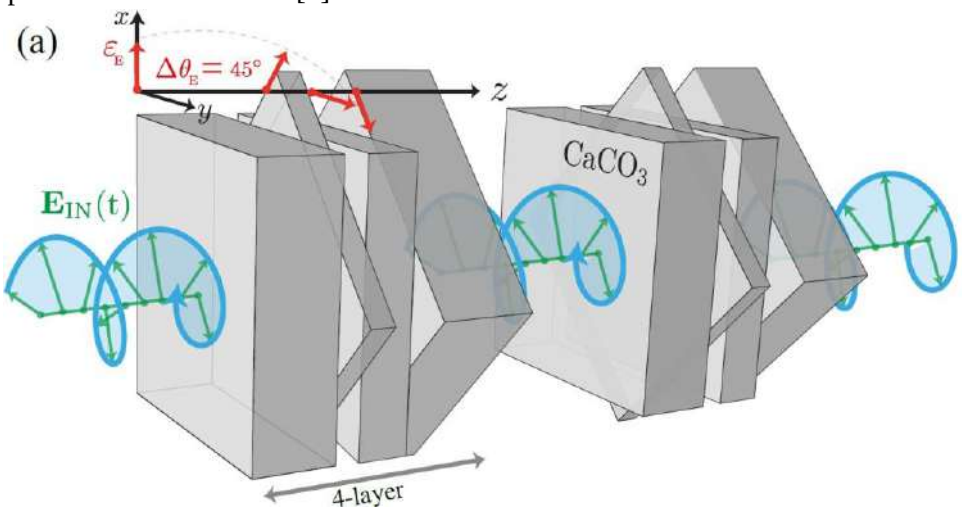


Figure 1. (**a**) Schematic of the optical system consisting of *N* four-layer stacks of uniaxial anisotropic calcite. Each layer has a defined thickness and an extraordinary axis progressively rotated relative to the *x* – axis. The mirror is illuminated by an electromagnetic field with arbitrary vacuum wavelength, incidence angle, and polarization. For simplicity, we assume circular polarization for the incident field.

We introduce a device leveraging a straightforward yet powerful physical mechanism: the optical torque density exerted by an anisotropic medium on the electromagnetic (EM) field [2]

$$\boldsymbol{\tau}_V^{EM} = -\mathbf{P}\times\mathbf{E} = -\mathbf{D}\times\mathbf{E}. \qquad (1)$$

We analyze a monochromatic plane electromagnetic wave incident at an arbitrary angle, employing the transfer matrix approach for birefringent layered media introduced by Yeh [3]. To quantify the local chirality density of the EM field, we also consider the optical chirality [4,5],

$$C = \frac{1}{2}\left[\mathbf{E}\cdot\left(\nabla\times\mathbf{D}\right)+\mathbf{H}\cdot\left(\nabla\times\mathbf{B}\right)\right]. \tag{2}$$

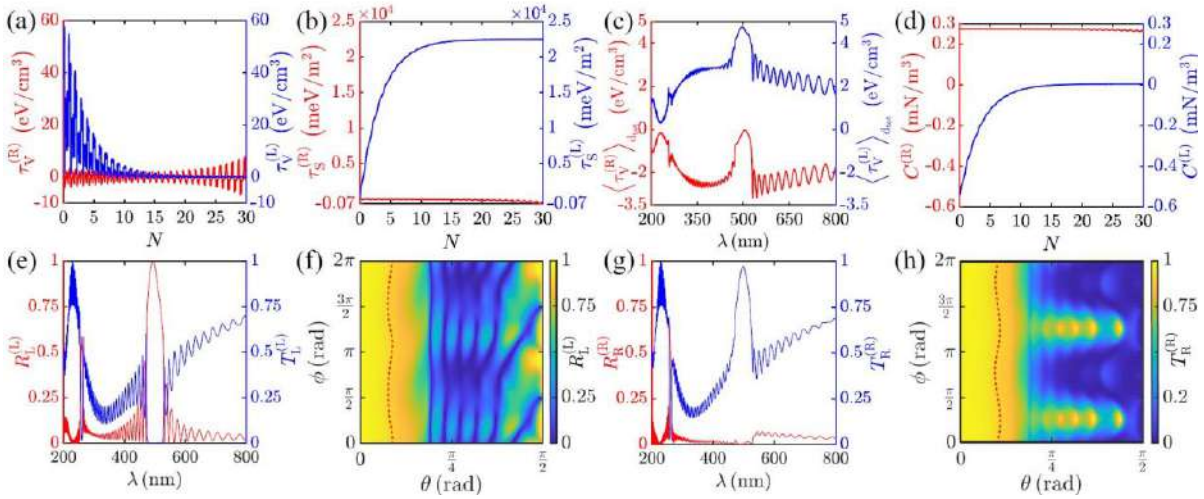


Figure 2. Normally incident EM field with λ=500 nm unless otherwise specified. (**a**) Optical torque volume density for right- and left-circularly polarized (RCP and LCP) light. For RCP, it oscillates around zero, resulting in a negligible net effect. For LCP, it is significant initially, as the device tries to force the opposite polarization, then decreases to zero. This indicates that the electric field amplitude vanishes during forward propagation, leading to near – complete LCP reflection. (**b**) Integral of the optical torque volume density along the propagation coordinate *z*. It remains near zero for RCP light but increases rapidly for LCP one until saturation. (**c**) Wavelength dependence of the length – averaged optical torque density for both normally incident RCP and LCP light. (**d**) Optical chirality for normally incident RCP and LCP light. It remains positive for RCP, while for LCP, it starts negative and increases toward zero. (**e**) Reflectance and transmittance of LCP light for incident LCP light. (**f**) Reflectance of LCP light as a function of the incidence angle. For θ values up to the red dashed line, it exceeds 0.90, and for normal incidence it is >0.99. (**g**) Reflectance and transmittance of RCP light with incident RCP light. (**h**) Transmittance of RCP light as a function of the incidence angle. For θ values up to the red dashed line, it exceeds 0.90.

This device represents a promising candidate for a new class of miniaturizable (the system characterized in Fig. 2 has a total thickness of 4.578 μm) circular polarizers, offering low – absorption, cost – effective fabrication, and suitability for applications in quantum technologies and polarization-sensitive optical detectors.

References

1. Khaliq, H. S., A. Nauman, J. W. Lee and H. R. Kim, “Recent Progress on Plasmonic and Dielectric Chiral Metasurfaces: Fundamentals, Design Strategies, and Implementation”, Adv. Opt. Mater., Vol. 11, No. 16, 2300644, 2023.
2. Beth, R. A., “Mechanical Detection and Measurement of the Angular Momentum of Light”, Phys. Rev., Vol. 50, No. 2, 115–125 (1936).
3. Yeh, P., “Electromagnetic propagation in birefringent layered media”, Josa, Vol. 69, No. 5, 742–756, 1979.
4. Tang, Y. and A. E. Cohen, “Optical chirality and its interaction with matter”, Phys. Rev. Lett., Vol. 104, No. 16, 163901, 2010.
5. Vázquez-Lozano, J. E. and A. Martinez, “Optical chirality in dispersive and lossy media”, Phys. Rev. Lett., Vol. 121, No. 4, 043901, 2018.

Thermal Dissipation in Pillar-Based Optomechanical Resonators: Comparing Monolithic Silicon and Hybrid Silicon-Silicon Dioxide Nanopillars

V. González-Morote[1*], D. Alonso-Tomás[1], M. Poblet[1], N. E. Capuj[2], A. Romano-Rodríguez[1], and D. Navarro-Urrios[1]

[1]MIND-IN2UB, Electronics and Biomedical Engineering Department at University of Barcelona

[2]Depto. Física, Universidad de La Laguna, 38200 San Cristóbal de La Laguna, Spain

*corresponding author: vgonzalezmorote@ub.edu

Abstract

We study thermal dissipation in optomechanical crystal geometries with monolithic silicon and hybrid silicon/silicon dioxide nanopillars. Finite-element simulations and a pump-probe technique reveal 11 MHz and 2 MHz thermal relaxation rates for monolithic and hybrid nanopillars, respectively, enabling accurate calibration of thermal effects in photonic crystal for force sensing applications.

Advances in fabrication methods have facilitated the creation of high-quality nanoscale optomechanical crystals (OMCs), integrating high-Q mechanical resonators with high-Q optical cavities [1]. Optomechanical cavities, characterized by an optical cavity created by introducing a defect within a photonic crystal functioning in the near-infrared spectrum, are notably significant within this category. Nanopillar-based OMCs offer a promising platform for on-chip sensing and photonic integration [2]. However, managing their thermal properties is vital for maintaining both stability and performance of the device. Silicon (Si) is widely used in optomechanical systems due to its high thermal conductivity, while the incorporation of silicon dioxide (SiO_2) can drastically modify thermal dissipation. In this work, we compare the thermal decay rates of monolithic silicon and hybrid silicon-silicon dioxide nanopillars through two different approaches, combining simulations and a frequency-domain pump–probe measurement.

We fabricate monolithic silicon and hybrid silicon/silicon dioxide nanopillar resonators by etching arrays of cylindrical pillars with top radii around 100 nm. The monolithic silicon nanopillars have a bottom radius 50 nm smaller than the top portion (see Figure 1a), while the hybrid nanopillars incorporate a SiO_2 segment at the base with the same radius as the top (see Figure 1b). The overall cavity structure, including periodic nanopillars and photonic crystal mirrors, is illustrated in Figure 1c.

Finite-element simulations (COMSOL) model the optical mode at telecom wavelengths and track the heat flow. By introducing an internal heating source that is subsequently switched off, we obtain the thermal decay time (τ_{th}). Figures 1d and 1e show finite-element simulations of thermal relaxation in monolithic and hybrid nanopillars, revealing respective dissipation rates of about 7.67 MHz and 2.22 MHz.

Experimentally, we employ a frequency-domain pump–probe method to evaluate the heat dissipation rate of nanostructures. The nanostructures are designed to behave as an optical cavity supporting at least two optical modes. One mode is resonantly pumped with a laser that heats the optical cavity by light absorption and the other mode is excited with a probe laser of low power that coherently detects the modulation of the spectral position of the mode due to the thermo-optic effect.

The thermal response induced by the pump laser modulation can be read on the probe laser. Figure 1f shows the measured transmission at the modulation frequency for monolithic

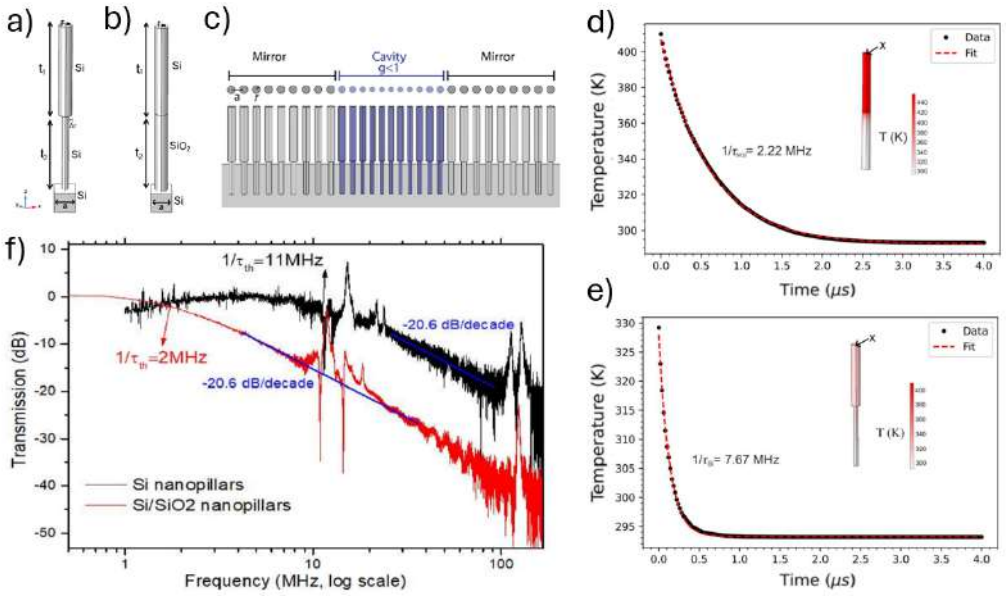


Figure 1: (a) Monolithic silicon nanopillar cross-section. (b) Hybrid silicon/silicon dioxide nanopillar cross-section. (c) Schematic of the 1D photonic crystal cavity, illustrating alternating pillars forming mirror sections and a defect region. (d) Experimentally obtained frequency-domain measurements (black/red) indicating different dissipation rates, while (e) and (f) show corresponding finite-element thermal simulations.

(black) and hybrid (red) nanopillars. By locating the cut-off (roll-off) frequency, we extract thermal dissipation rates around 11 MHz for monolithic silicon nanopillars and 2 MHz for hybrid structures, consistent with the differences in thermal conductivity ($\sim$ 1–2 $\mathrm{W\,m^{-1}K^{-1}}$ for SiO_2 vs. $> 100\,\mathrm{W\,m^{-1}K^{-1}}$ for crystalline Si) [3].

In conclusion, we have measured the thermal decay rates of monolithic silicon and hybrid silicon-silicon dioxide nanopillar OMCs, demonstrating dissipation rates of $\sim$ 11 MHz and $\sim$ 2 MHz, respectively. This dual validation—finite-element simulations and frequency-domain pump–probe measurement—enables the understanding and calibration of thermal effects on the optical and mechanical properties of these novel photonic crystal geometries. Consequently, thermal contributions from optical heating can be accurately factored into force sensing measurements.

References

[1] Aspelmeyer, M., T. J. Kippenberg, and F. Marquardt, "Cavity optomechanics," *Rev. Mod. Phys.*, Vol. 86, No. 4, pp. 1391–1452, 2014.

[2] Jaramillo-Fernandez, J., M. Poblet, D. Alonso-Tomás, *et al.*, "Strong Cavity-Optomechanical Transduction of Nanopillar Motion," *ACS Nano*, Vol. 18, No. 35, pp. 24550–24557, 2024.

[3] Lee, S. M. and D. G. Cahill, "Heat transport in thin dielectric films," *J. Appl. Phys.*, Vol. 81, No. 2590, 1997.

Mechanism and Demonstration of Interference and Multi-port Switching in Silicon Topological Photonics

X.-X. Wang[1*], S. Okada[2], T. Maekawa[1], L. Hu[1], X. Hu[1,3], and T. Amemiya[1]

[1]School of Engineering, Institute of Science Tokyo, Tokyo 152-8552, Japan

[2]Photonic ICT Research Center, National Institute of Information and Communications Technology, Tokyo 184-8795, Japan

[2]Institute for Quantum Science and Technology, Department of Physics, Shanghai University, Shanghai 200444, China

Corresponding author: `xingxiang.w.4839@m.isct.ac.jp`

Abstract: We demonstrate the principle of manipulating topological states towards a multi-port interferometric switch, leveraging the geometric phase degree of freedom in a silicon photonics platform with Dirac-type dispersions.

I. Introduction

The Kekulé-distorted honeycomb photonic crystal (PhC) enables a photonic quantum spin Hall effect (QSHE) [1], which offers a robust way to manipulate electromagnetic (EM) waves. This topological photonic state works across a broad frequency range, from microwaves to visible light at room temperature. Made entirely of semiconductor material, it is compatible with modern nanofabrication technology and can be integrated with existing semiconductor photonic devices.

Here, we investigate a novel scattering phenomenon in a bent topological interface based on this platform, and demonstrate both theoretically and experimentally an 2-in-2-out interferometric switching effect. We show that this switching effect can be also realized in an extended 6-way junction. The switching effect occurs within an extremely small region in the PhC ($< 1\mu m \times 1\mu m$) compared to any other existing photonic switches.

II. Interferometry switching effect of photonic topological states

In this work, we investigate the bent interface between the trivial and topological PhCs by a perturbative approach. The topological interfacial states propagating along the angle θ is described by the zero-energy Jackiw-Rebbi mode $|\theta, +\rangle = F(d)[|p_+\rangle, |d_+\rangle][1, i\exp(-i\theta)]^T$ [2, 3]. We found that a shift of the global phase $\psi(\theta)$ is induced when the topological interfacial state

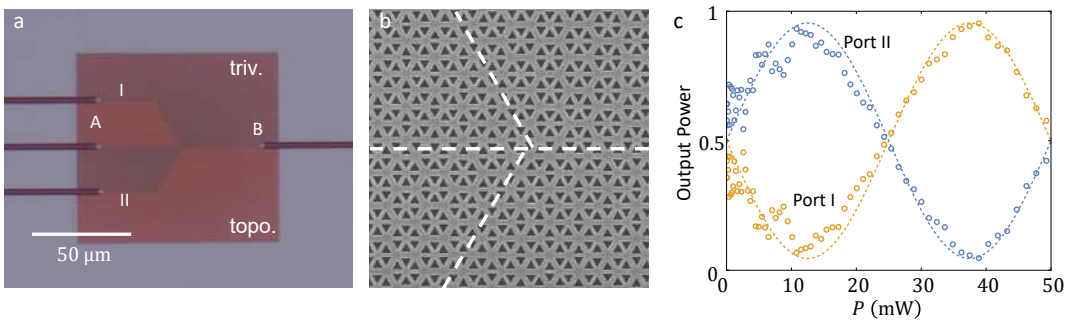


Figure 1: (a) Optical microscpe image near the PhC. (b) SEM image of the 4-way junction. (c) Experimental result of the interferometry switching effect.

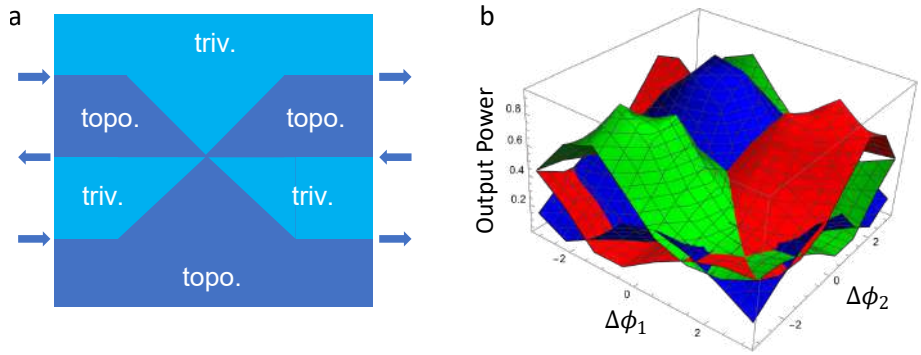


Figure 2: Interferometry switching effect of a 3-in-3-out junction.

is scattered by the bend, which is revealed as exactly half of the bending angle

$$\psi(\theta_{\text{out}}) = \psi(\theta_{\text{in}}) \exp[i(\theta_{\text{out}} - \theta_{\text{in}})/2]. \tag{1}$$

The phase shift above is understood as a geometric phase acquired by the spin-$\frac{1}{2}$ spinor wavefunction of the topolgical interface state at a bend.

We experimentally fabricate a silicon topological PhC with a 2-in-2-out structure on an SOI wafer, as shown in Fig. 1(a and b), where the two horizontal interfaces serve as the input ports. The scattering matrix of this 4-way junction can be precisely solved according to Eq. (1). By simultanuously exciting two input ports with a phase difference $\phi = \phi_{\text{A}} - \phi_{\text{B}}$, the power distribution at two output ports are evaluated as

$$P_1 = \frac{1}{2}(1 - \sin\phi), \quad P_2 \quad = \frac{1}{2}(1 + \sin\phi). \tag{2}$$

It is known from Eq. (2) that the switching effect happens at $\phi = \pi/2$ and $\phi = 3\pi/2$, where the output power is fully directed to port 2 and port 1, respectively. The experimentally measured switching effect is depicted in Fig. 1c (blue and yellow circles), which is in full agreement with the theoretical analysis (dashed lines).

We reveal that the switching effect can be also realized in an extended 6-way (3-in-3-out) junction, by controling the phase difference between the three input ports, as depicted in Fig. 2.

Acknowledgments

This work is supported by JST-CREST (JPMJCR18T4), JSPS (JPJSBP-120219942) and JST-ASPIRE (23837157).

References

1. Long-Hua Wu and Xiao Hu. Scheme for Achieving a Topological Photonic Crystal by Using Dielectric Material. *Phys. Rev. Lett.*, 114(22):223901, June 2015.

2. Xiao-Chen Sun and Xiao Hu. Topological ring-cavity laser formed by honeycomb photonic crystals. *Phys. Rev. B*, 103(24):245305, June 2021.

3. Xing-Xiang Wang, Zhiwei Guo, Juan Song, Haitao Jiang, Hong Chen, and Xiao Hu. Unique Huygens-Fresnel electromagnetic transportation of chiral Dirac wavelet in topological photonic crystal. *Nat. Commun.*, 14(1):3040, June 2023.

Spin-Valley Topological Photonics

Ekta[1], Vikram[1], Brijesh Kumar[1], Abhishek Kumar[2], Anshuman Kumar[1]
[2]Jawaharlal Nehru Centre for Advanced Scientific Research, Bengaluru, India
[1]Indian Institute of Technology Bombay, Mumbai 400076, India
*Email: anshuman.kumar@iitb.ac.in

Abstract: This research focuses on the design and fabrication of topological photonic crystals (TPCs) using Electron Beam Lithography (EBL). Through Fourier imaging and COMSOL simulations, the study investigates the topologically protected waveguiding properties, highlighting the robustness of TPCs to defects and their potential for efficient, reliable optical applications.

Keywords: Topology, Photonic cavities, Kagome lattices, Rashba effect, COMSOL.

Introduction

Direct-bandgap monolayers of transition metal dichalcogenides (TMDs) offer promising potential for atomic scale spin-optical light sources, owing to their unique valley-dependent optical selection rules. In this study, we present a spin-valley laser incorporating a WS_2 mono- layer within a high-Q heterostructure microcavity, designed to support photonic spin-valley resonances. This Rashba monolayer laser exhibits inherent spin polarization, high spatial and temporal coherence, and symmetry driven robustness, achieving valley coherence in the WS_2 monolayer under arbitrary pump polarization at room temperature. The integration of spin-valley microcavities within monolayers expands opportunities for both classical and quantum coherent spin-optical sources, leveraging interactions between electron and photon spins.

This study presents the development of a spin-optical monolayer laser that leverages spin-valley modes generated by the photonic Rashba effect, induced through inversion symmetry (IS) breaking in a Kagome photonic crystal slab with a bound state in the continuum (Γ-BIC). By precisely tuning the orientation of anisotropic nanoholes, a photonic Rashba type spin splitting of the Γ-BIC is achieved, leading to the formation of oppositely polarized ±K spin-valley modes, which enhance spin-dependent light–matter interactions with zero group velocity. The laser's spin-valley optical microcavity is engineered by interfacing inversion asymmetric (IaS) and inversion symmetric (IS) photonic lattices, creating laterally confined resonant modes with high Q factors. This design facilitates coherent, spin-polarized emission from ±K valley excitons in the WS_2 monolayer (in Fig1), resulting in a quasi-single-mode Rashba laser with high spatiotemporal coherence and symmetry-protected robustness.

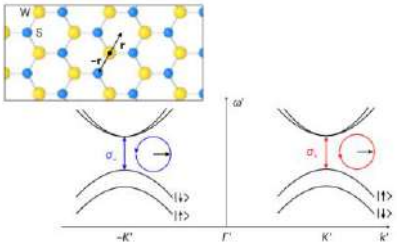


Fig:1 Valley contrasting optical selection rules of WS_2 monolayer.

Experimental Methods

In planar Kagome lattices with elliptical nanoholes were fabricated on a silicon nitride film using electron-beam lithography and reactive-ion etching techniques, followed by the integration of a highly crystalline WS_2 monolayer supported by a poly methyl methacrylate (PMMA) layer for structural stability. The Kagome lattice was chosen due to its geometric frustration properties, similar to those observed in electron spins within antiferromagnets, contributing to highly degenerate ground states with distinct chiral spin configurations. Two primary configurations were implemented: one exhibiting uniform inversion symmetry (IS) with

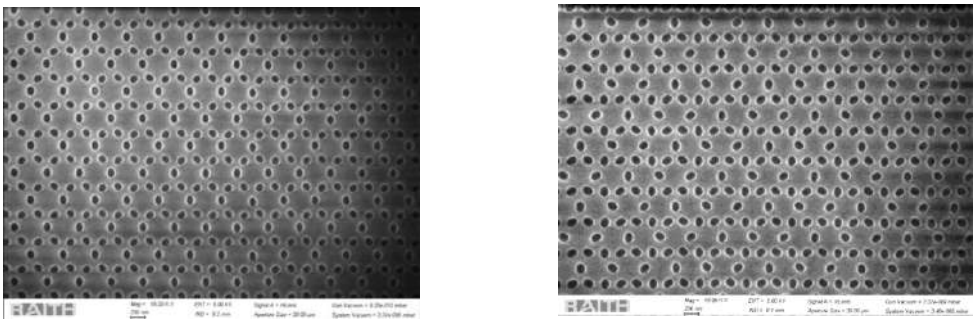


Figure 2: SEM image of IS and IaS photonic spin-like lattice**.**

q=0 and the other featuring a staggered inversion asymmetric (IaS) configuration with q=√3 × √3 chirality distributions. The orientation angles of the elliptical nanoholes within these Kagome lattices were designed to align with these two spin-like lattice configurations, as confirmed by scanning electron microscopy (SEM) images in Fig2.

Results and Discussion

COMSOL Multiphysics simulations model the band structure of optical spin-split dispersions centered around 620 nm, a wavelength optimized to align with the photoluminescence range of the WS_2 monolayer. By tuning the anisotropic nanohole dimensions in photonic spin-like lattices, coupling between nanoholes and photonic modes is enhanced, enabling effective spatial polarization control and high geometric phase efficiency via spin-orbit interaction. This interaction creates spin-split dispersions in momentum space through the photonic Rashba effect. Outside this range, geometric phase efficiency decreases sharply, causing the IS and IaS photonic spin-like lattices to converge toward a similar band structure as the Rashba effect diminishes. Future experiments will aim for Rashba monolayer lasing in the spin-valley microcavity, targeting high spatial and temporal coherence with tunable valley polarization at room temperature. By selectively pumping the WS_2 monolayer, researchers plan to achieve directional, spin-polarized emission through coherent superposition of valley excitons and to control Rashba lasing properties with pump polarization, enhancing coherence and phase correlation in the valley excitons.

Acknowledgment

We acknowledge LOQM IITB and CEN IITB for their support in fabrication and for providing the essential resources needed to carry out this research.

References

1. Rong, K., Duan, X., Wang, B. et al. Spin-valley Rashba monolayer laser. Nat. Mater. 22, 1085–1093 (2023).
2. Duan, Xiaoyang, et al. ”Valley-addressable monolayer lasing through spin-controlled Berry phase photonic cavities.” Science 381.6665 (2023): 1429-1432.
3. D. Bisharat, R. Davis, Y. Zhou, P. Ban- daru and D. Sievenpiper, ”Photonic Topological Insulators: A Beginner’s Introduction [Electro-magnetic Perspectives],” in IEEE Antennas and Propagation Magazine, vol. 63, no. 3, pp. 112-124, June 2021.

Emitting properties of a-Si:C:H-coated 2D-opaline photonic crystals

S. I. Pavlov[1*]. M. E. Bochkarev[2], S. A. Dyakov[3], V.G. Golubev[1], S.A. Grudinkin[1], M. F. Limonov[2] and A. B. Pevtsov[1]
[1]Ioffe Institute, Russia
[2]ITMO University, Russia
[3]Skolkovo Institute of Science and Technology, Russia
Pavlov_Sergey@mail.ioffe.ru (corresponding author)

Abstract

Two-dimensional (2D) photonic crystals (PhC) are fabricated from opal slabs coated with an a-Si:C:H emitting layer. The optical response of the emitting 2D PhC's near Γ-point of the Brillouin zone have been studied. A significant increase in the luminescence intensity in the visible spectral range has been demonstrated in the synthesized structures.

1 Introduction

2D PhC's are currently as considered one of the most promising dielectric media for achieving enhance light emission by increasing the probability of radiative recombination, described by the Purcell factor [1]. In this work, we studied the possibility of increasing the photoluminescence (PL) intensity of an a-Si:C:H emitting layer, resulted from interaction with the modes of a 2D PhC fabricated on the basis of an opal slab. Such interaction can be realized if the a-Si:C:H emission is located above the photonic band gap, where various radiative modes of the photonic crystal can exist within the light cone [2]. The spectral position of the PL contour can be easily varied by changing the content of carbon in the a-Si:C:H film. The full width at the half-maximum (FWHM) of the PL contour of a-Si:C:H reaches a value of 0.6-0.7 eV.

2 Results

The samples of the opal slabs being studied include opal films [2-3 monolayers (ML) of a-SiO_2 spheres of diameter 520 nm with a spread in diameter smaller than 3] grown on fused silica substrates. The a-Si_{1-x}:C_x:H layer with a thickness of 250 nm was deposited on opal film by the plasma-enhanced chemical vapor deposition (PECVD) technique in a capacitive reactor at various relative flows of silane (SiH_4) and methane (CH_4). The optical thickness of the layers was monitored in-situ by the laser beam interference pattern. Carbon content in the film is x = 0.58, which corresponds to PL peak at 1.7 eV and refractive index n = 2.2 [3].

Angle-resolved optical spectra were measured using a Fourier imaging spectroscopy technique. For PL measurements, a 405 nm laser diode illuminates the sample by the from the backside. The spectral resolution of the setup is 0.17 nm, whereas the angular resolution is not less than 0.4° [4]. Theoretical analysis of the optical response of the structure included numerical calculations of the structure's eigenmodes and angle-resolved spectra performed by a Fourier modal method in the scattering matrix form.

The experimental and theoretical angle-resolved PL spectra are presented in Fig. 2(a, b) Due to a broad PL band in the range of 500–1000 nm, the PL spectra contain many peaks resulted from interaction processes of the a-Si:C:H emitting clusters with PhC modes near Γ-point of

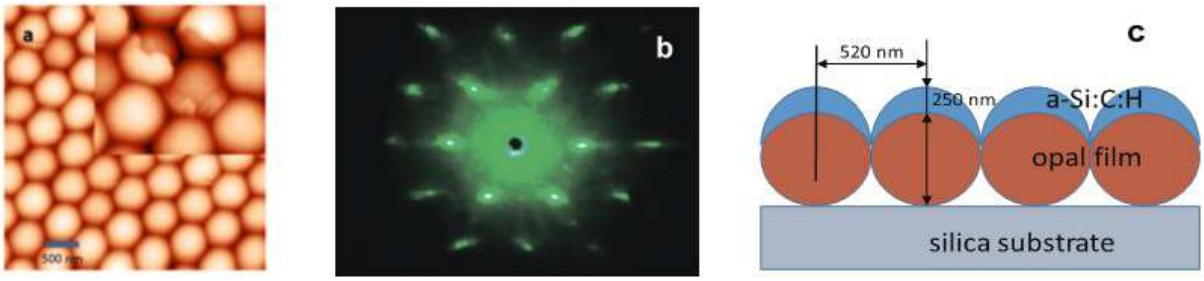


Figure 1: AFM image of the a-Si:C:H/opal slab (a). Insert: a fragment of the structure where the aSi:C:H film is partially absent and SiO2 spheres are exposed. Laser diffraction pattern of an a-Si:C:H/opal slab (b). Schematic view of the structure used in scattering matrix method calculations. Only one monolayer of SiO2 spheres is shown for simplicity (c).

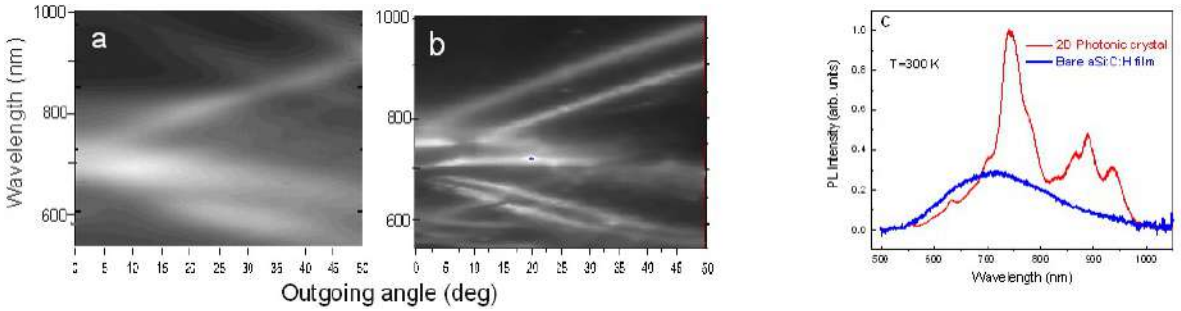


Figure 2: Experimental (a) and theoretical (b) angle-resolved photoluminescence spectra measured in p-polarization. Comparison of PL spectrum of the PhC with PL spectrum of the a-Si:C:H bare film (c).

the Brillouin zone. Figure 2c shows PL spectra from PhC slab coated with a-Si:C:H layer (a) and bare a-Si:C:H film (b) measured near Γ-point of the Brillouin zone. It is seen remarkable increasing PL intensity from PhC slab.

Finally, we have studied the angle-resolved PL spectra of 2D opal coated with a thin luminescent a-Si:C:H film. Since the measurements were carried out near the Γ-point of the Brillouin zone of the PhC, it can be assumed that the observed PL lines of different widths correspond to the interaction of the radiation of a-Si:C:H nanoclusters with PhC modes of different nature. The calculations of the PhC band diagram showed that in such structures it is possible to observe radiative modes located inside the light cone and characterized by a small group velocity, which appear in the PL spectra in the form of relatively broad, intense lines.

References

[1] M. Pelton, Modified spontaneous emission in nanophotonic structures," Nature Photonics, Vol. 9, pp. 427-435, 2015.

[2] A. Mahdavi, G. Sarau, J. Xavier et al, "Maximizing photoluminescence extraction in silicon photonic crystal slabs", Sci. Rep., Vol. 6, pp. 25135, 2016.

[3] R. Carius, "Optical gap and photoluminescence properties of amorphous silicon alloys", JPhilos. Mag., Vol. B 804, No. 4, pp. 741-753, 2000.

[4] S.I Pavlov, I. M. Fradkin, S. A. Dyakov et al, "Bound states in the continuum in a waveguide structure covered by a two-dimensional square array of gold nanodisks", Phys. Rev., B, Vol. 108, pp. 205425, 2023.

Interplay of Two Structures of Nano-Modulated Thin Films

Lucciano A. Letelier[1,*], Julianija Nikitina[1], Lina Grineviciute[1], Kestutis Staliunas[2,3]

[1]Center for Physical Sciences and Technology (FTMC), Savanoriu Ave. 231, LT-02300 Vilnius, Lithuania
[2]ICREA, Passeig Lluís Companys 23, 08010, Barcelona, Spain [3] UPC, Departamento de Fisica, Rambla Sant Nebridi 22, 08222, Terrassa (Barcelona) Spain

[*]corresponding author: Lucciano.letelier@ftmc.lt

Abstract: Fano resonances in periodically nano-modulated thin films are known to produce narrow bandgaps in frequency and angular domains [1,2]. At resonance, the incident wave couples to the planar waveguiding mode of the film, resulting in zero transmission and 100% reflection [3]. The bandwidth of these resonances is proportional to the coupling coefficient between the incident radiation and the waveguiding mode. In this work, we demonstrate that combining two closely spaced resonances can create extremely narrow high-pass bands in transmission, with a theoretically tunable passband width that can approach zero in wavelength-angle space.

This study investigates frequency and angular filters based on Fano resonances (FR) in periodically nano-modulated thin films, which exhibit zero transmission and 100% reflection at resonance under near-normal incidence conditions. The research focuses on the coupling between incident waves and planar waveguide modes, exploring the interaction of left- and right-propagating waveguide modes. When these modes are in close proximity, a high-transmission band emerges between the resonances, achieving 100% peak transmission with a theoretically infinitely narrow bandwidth. Analytical models, derived under weak modulation ($h0 \ll dz$) and strong confinement ($n \gg 1$) approximations, describe the resonant coupling conditions and propagation wavenumbers of the modes.

The transmission resonances in the angle-wavelength can be derivated using a coupled equations for the Fabry-Perot (FP) modes of the film giving the following expression:

$$t(\theta,\lambda) = \frac{1}{1+\sum_m \frac{i\Delta\lambda_m}{\lambda-\lambda_m(\theta)}} \qquad (1)$$

Where λ_m represent the wavelength of the m-order resonance. In presence of two resonances (1) indicates that the transmission reaches unity at a particular point between the resonances and whereas being zero at resonances, θ and $\boldsymbol{\lambda}$ represents the incidence angle and wavelength of the source .

The numerical study using FDTD methods for the structures using the previously mentioned criteria (weak

modulation and strong confinement), allow us to sweep several parameters to choose the optimal design to fabricate and measure the transmission maps.

To find the best structure several simulations with one structure was performed to find the sharpest resonance, this single thin layer, was used to develop the dual configuration for this research.

Tilting these structures is possible to shift the transmission maps in the angle space allowing us to get a eye-shape filter for angle and wavelength, this is observed in figure 1, where the Numerical simulations and experimental measures are compared.

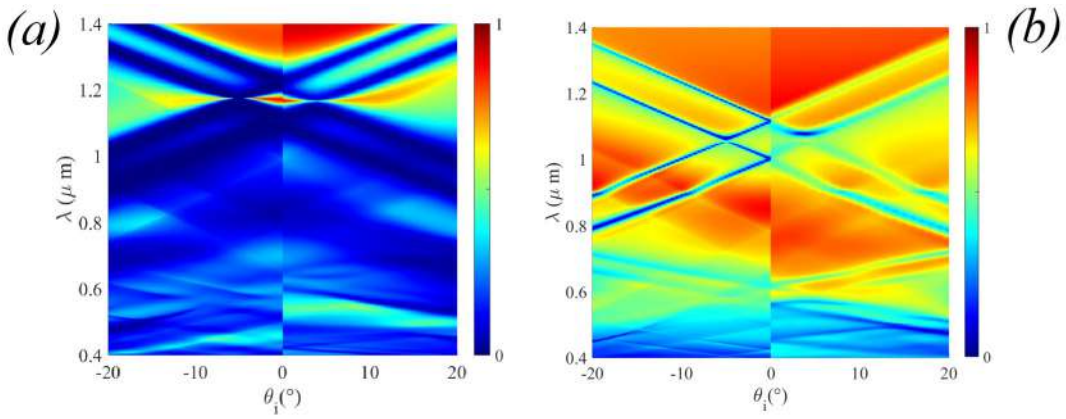


Fig. 1. Comparison of Numerical simulation (left side) and Experimental measure (right side) of this double periodical structures for (a) S polarization and (b) P polarization, tilted by 10 degrees respect each other.

This research shows the possibility of create a adaptable filter in the angle-wavelength domain by choosing the geometry of the mentioned structure, and also by changing the tilting angle between the structures, taking advantage of the Fano resonance that exist in the thin layers.

Acknowledgments

This work has received funding from the Research Council of Lithuania (LMTLT), agreement no. S-LT-TW-24-9.

References

1. L. Grineviciute, J. Nikitina, C. Babayigit, and K. Staliunas, Appl. Phys. Lett. 118, 131114 (2021).
2. L. Grineviciutė, C. Babayigit, D. Gailevičius, E. Bor, M. Turduev, V. Purlys, T. Tolenis, H. Kurt, and K. Staliunas, Applied Surface Science 481, 353 (2019).
3. L. Lukosiunas, L. Grineviciute, J. Nikitina, et al., Phys. Rev. A 107, L061501 (2023).1064–1076, 1986.

Calculation of density of states in a one-dimensional photonic biosensor

Francis Segovia-Chaves
Grupo de Física Teórica, Universidad Surcolombiana, Neiva-Huila. Colombia
Corresponding author: francis.segovia@usco.edu.co

Abstract: Using Green's functions we calculate the local density of states in a one-dimensional photonic biosensor. The insertion of a cavity with a refractive index of four types of cells: Normal, Jurkat, PC12, and MCF-7. By increasing the dielectric constant, we observe that the localized mode shifts to shorter frequencies.

In a scattering system described by a dielectric constant $\epsilon(\overrightarrow{r})$, the dyadic Green's function $\mathbf{G}(\overrightarrow{r}, \overrightarrow{r}')$ in real space satisfies:

$$\overrightarrow{\nabla} \times \overrightarrow{\nabla} \times \mathbf{G}(\overrightarrow{r}, \overrightarrow{r}') - k^2 \mathbf{G}(\overrightarrow{r}, \overrightarrow{r}') = \widehat{I}\delta(\overrightarrow{r} - \overrightarrow{r}') \tag{1}$$

In Eq. (1), $\overrightarrow{k}$ and $\widehat{I}$ represent the wave vector and the unit dyad, respectively. Using the Fourier expansion method, $\mathbf{G}(\overrightarrow{r}, \overrightarrow{r}')$ is given by:

$$\mathbf{G}(\overrightarrow{r}, \overrightarrow{r}') = \frac{1}{2\pi} \int e^{i\overrightarrow{k}_{\parallel} \cdot (\overrightarrow{\rho} - \overrightarrow{\rho}')} \mathbf{g}(\overrightarrow{k}_{\parallel}, z, z') d\overrightarrow{k}_{\parallel}, \tag{2}$$

$$\mathbf{g}(\overrightarrow{k}_{\parallel}, z, z') = \int e^{-i\overrightarrow{k}_{\parallel} \cdot (\overrightarrow{\rho} - \overrightarrow{\rho}')} \mathbf{G}(\overrightarrow{r}, \overrightarrow{r}') d(\overrightarrow{\rho} - \overrightarrow{\rho}') \tag{3}$$

where $\mathbf{g}(\overrightarrow{k}_{\parallel}, z, z')$, $\overrightarrow{k}_{\parallel} = (k_x, k_y)$, $\overrightarrow{\rho}$ is the transverse coordinate, and $\overrightarrow{r} = (\overrightarrow{\rho}, z)$. By substituting Eq. (2) into Eq. (1), the wave equation in the reciprocal space for the dyadic Green's function is:

$$\begin{bmatrix} -k^2 - \partial_z^2 & 0 & ik_{\parallel}\partial_z \\ 0 & k_{\parallel}^2 - k^2 - \partial_z^2 & 0 \\ ik_{\parallel}\partial_z & 0 & k_{\parallel}^2 - k^2 \end{bmatrix} \begin{bmatrix} g_{nxx} & g_{nxy} & g_{nxz} \\ g_{nyx} & g_{nyy} & g_{nyz} \\ g_{nzx} & g_{nzy} & g_{nzz} \end{bmatrix} = \widehat{I}\delta(z - z') \tag{4}$$

Fig. 1 illustrates the heterostructure consists of alternating polymer layers: layer A (PS) and layer B (PMMA). The polymer thicknesses are quarter-wavelength, $d_A = \frac{an_B}{n_A + n_B}$ and $d_B = \frac{an_A}{n_A + n_B}$. Fig. 2 shows the calculated LDOS for normal (Fig. 2(a)), Jurkat (Fig. 2(b)), PC12 (Fig. 2(c)), and MCF-7 (Fig. 2(d)) cells, with dielectric constants of 1.822, 1.932, 1.946, and 1.962, respectively. In the PBG region, we see that the appearance of confined photonic modes accompanied by a maximization of the LDOS, implying an elevated spontaneous emission rate within the cavity. PCs are sensitive to increases in the dielectric constant within the cavity, causing a shift of the confined mode to lower frequencies, as shown in Fig. 3. The results indicate an LDOS increase from 0.834 for the normal cell to 1.477 for the Jurkat cell, 1.471 for the PC12 cell, and 1.464 for the MCF-7 cell. The effects of pressure on the LDOS for our biosensor are presented in Figure 3.

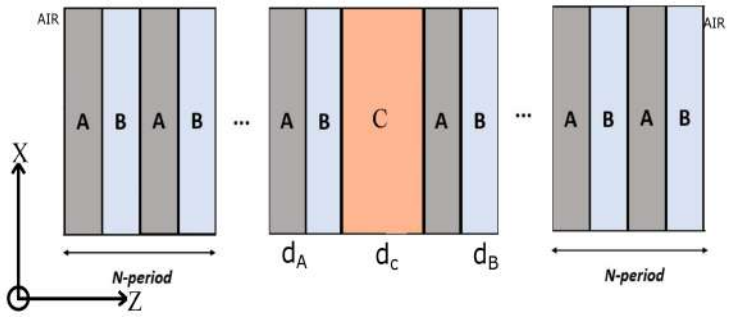


Figure 1: Representation of a 1D-PC with a cavity surrounded by N layers of materials A and B.

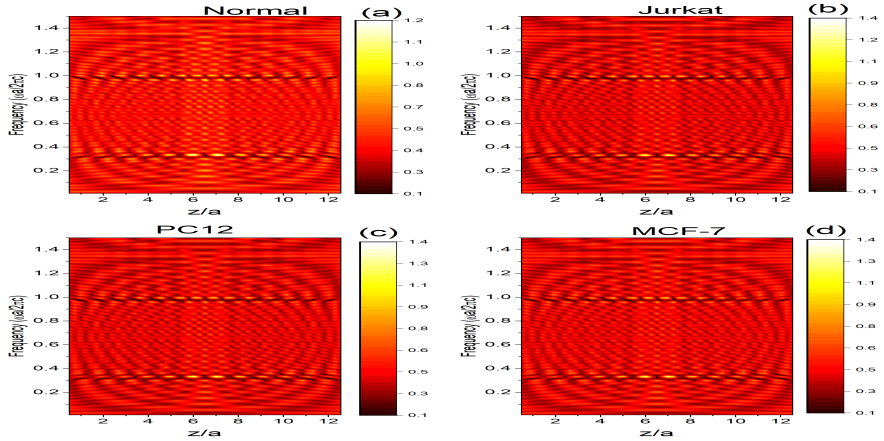


Figure 2: LDOS as a function of frequency for cells: a) normal, b) Jurkat, c) PC12, and d) MCF-7.

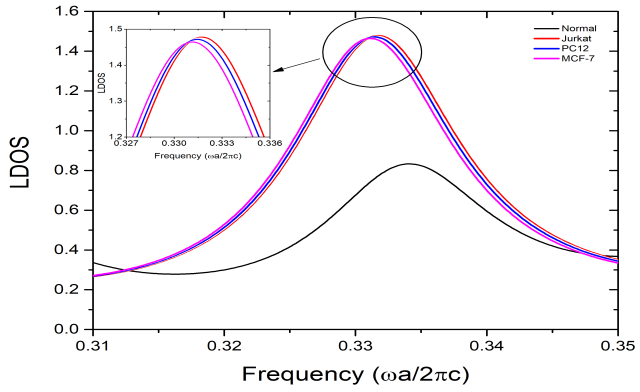


Figure 3: LDOS for different types of cells infiltrated into the cavity.

References

1. Segovia, F., Navarro E., H. Vinck "Local density of states for different cancer cells in a one-dimensional photonic biosensor," *Mater. Res. Express*, Vol. 12, pp. 026201, 2025.

2. A. Maradudin, D. Mills, "Scattering and absorption of electromagnetic radiation by a semi-infinite medium in the presence of surface roughness," *PRB B*, Vol. 11, pp. 1392, 1975.

Confined mode shift in a photonic crystal with a cavity infiltrated by CHIKV cells

F. Segovia-Chaves
Grupo de Física Teórica, Universidad Surcolombiana, Neiva-Huila. Colombia.

*corresponding author: francis.segovia@usco.edu.co

Abstract: We calculate the transmittance spectrum in a defective one-dimensional photonic crystal. The cavity is filled with CHIKV-infected cells. We find a resonant peak inside the photonic band gap. Increasing the pressure decreases the confinement of the defective mode due to the decrease in quality factor.

The total transfer matrix for the defective structure $Air/(AB)^N C/(AB)^N/Air$, is given by.

$$M = \begin{pmatrix} M_{11} & M_{12} \\ M_{21} & M_{22} \end{pmatrix} = D_0^{-1}[M_A M_B]^N M_C [M_A M_B]^N D_0 \quad (1)$$

where D_0 is the dynamic matrix of the air. The transmittance T is calculated with the matrix elements M_{11} of Eq. (1), $\mathbb{T} = \left|\frac{1}{M_{11}}\right|^2$. Using the transfer matrix method, we calculate the transmittance spectrum.

Fig. 1 shows in two panels the behavior of the transmittance spectrum with increasing external pressure for normal plasma cells, keeping both temperatures constant (T=4.2K).

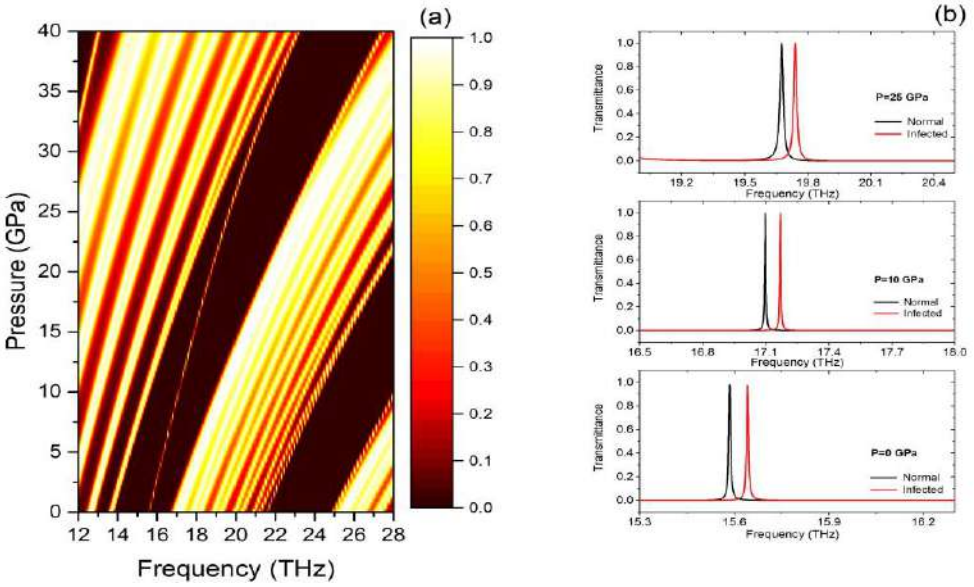


Figure 1. a) Transmittance spectrum as a function of applied pressure in a defective 1D-PC with a cavity infiltrated by normal plasma cells. b) Transmittance spectrum for normal (black line) and CHIKV-infected (red line) plasma cells for three different values of hydrostatic pressure.

The transmittance spectra for normal and infected cells of platelets (see Fig. 2 (a)) and uric acid (see Fig. 2 (b))

are shown in Fig. 2. For platelets, the maximum confined energy in the cavity is reached for 6GPa, where the quality factor is 3015.56 and 3011.79 for normal and infected cells, respectively. The energy stored in the cavity is quantified by the quality factor (Q), determined by the ratio of a resonant cavity frequency to the linewidth of the cavity mode. The energy decreases for pressures higher than 6GPa, as shown in Fig. 2(c).

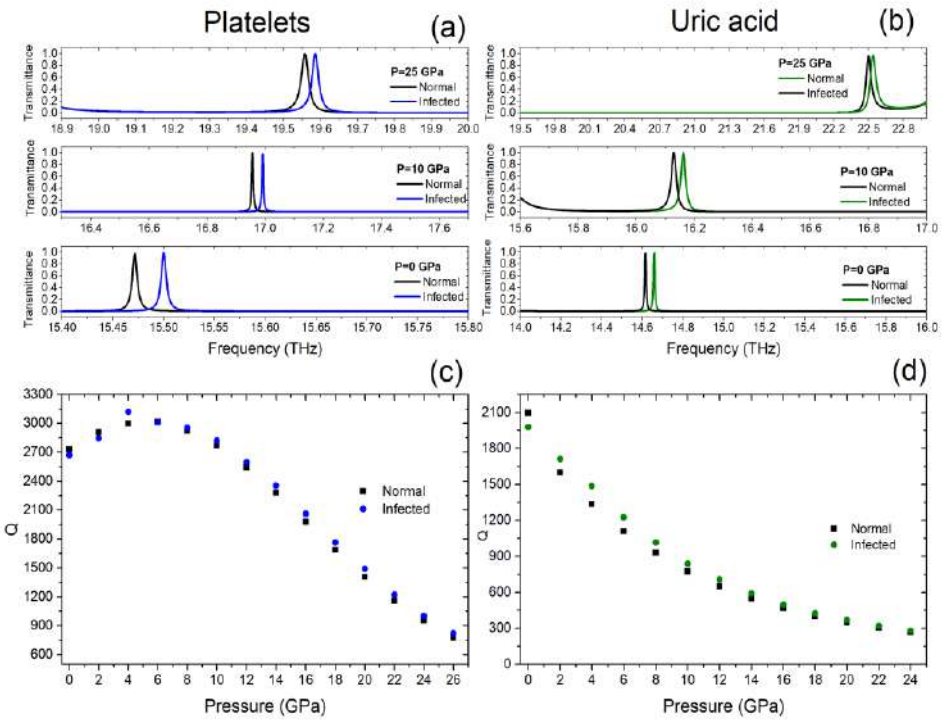


Figure 2. Transmittance spectrum for three values of applied pressure in a cavity infiltrated by cells: a) normal (black line) and infected (blue line) platelets, and b) normal (black line) and infected (green line) uric acid. Quality factor as a function of applied pressure for (c) platelets and (d) uric acid.

References

1. J. Joannopoulos, S. Johnson, R. Meade, Photonic crystals: molding the flow of light, Princenton University Press, 2007.
2. Lipson, R. H., C. Lu, Photonic crystals: a unique partnership between light and matter. Eur. J. Phys. 30 (2009) S33.

Photonic Routing in a Multiple-Input Valley Photonic Crystal Junction

C. Johnson-Richards[1], R. G. MacDonald[1*], A. Yakovlev[2] and Victor Pacheco-Peña[1]

[1] School of Mathematics, Statistics and Physics, Newcastle University, Newcastle Upon Tyne, NE1 7RU, United Kingdom.
[2] School of Engineering, Newcastle University, Newcastle Upon Tyne, NE1 7RU, United Kingdom
[*]victor.pacheco-pena@newcastle.ac.uk

Abstract: Topological waveguides have demonstrated their potential to enable the design of photonic circuits without scattering from defects such as sharp bends. In this work the routing of information using multiple inputs at a 6-port topological valley junction is investigated by calculating the scattering that defines the proposed structure.

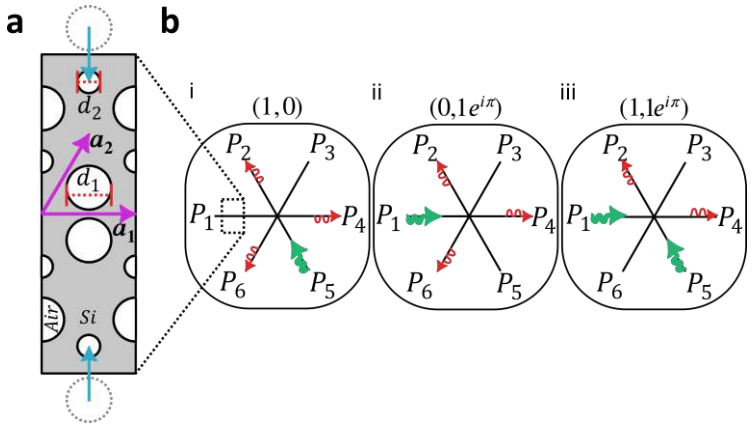


Figure 1. (a) Schematic of the center of a VPC waveguide. (b) Schematic of the routing performance at a 6-port VPC junction for three input logical combination pairs (port 1, port 5).

Valley photonic crystals (VPCs) can be used to design topological waveguides (VPC waveguides) with high transmission while being resilient to sharp turns or defects/obstacles [1–4]. Multiple VPC waveguides can be connected to form junctions. It has been shown that signals incident from one VPC waveguide will be restricted to be coupled only to other waveguides with the same valley type [5]. This property has been exploited to design four port junctions that emulate linear computing operations [6]. VPC waveguide junctions can also be represented by a scattering matrix so that they may be studied analytically [7,8]. In this communication we push forward the ideas in previous work from our group in the context of linear computing with parallel plate [9–13] and rectangular [14] waveguide junctions and move towards a solution that may function at higher frequencies using topologically protected waveguides [7]. To do this, we make use of a numerically extracted scattering matrix to investigate the possible linear routing operations that a 6-port junction may support with two or more inputs.

A schematic of the VPC waveguide is included in Figure 1a with the hexagonal unit cell vectors labeled as $\boldsymbol{a_1}$ and $\boldsymbol{a_2}$ respectively. The VPC waveguide is designed with a lattice constant, $a = 340$ nm, with a silicon (Si) background (grey) and two Air (white) holes each with different diameters of $d_1 = 0.24a$ and $d_2 = 0.12a$ respectively (labelled in Figure 1a). To design the 6-port junction, five additional VPC waveguides were rotated around a central point by $\pi/3$ radians. A frequency dependent scattering matrix, $\boldsymbol{S}$, was then extracted following [7,8]. The scattering of two input signals at the 6-port junction was then represented by a vector of phasors in the form, $\boldsymbol{X}_{\text{input}} = [x_1, 0,0,0, x_5, 0]$, where x_1 and x_5 were changed through three input combination pairs of

$(x_1, x_5) = (1,0), \left(0,1e^{i\pi}\right), (1,1e^{i\pi})$ respectively. Then, for each pair the resulting output signals were calculated using, $\boldsymbol{X}_{\text{output}} = \boldsymbol{S}\boldsymbol{X}_{\text{input}}$. This calculation produced $|\boldsymbol{X}_{\text{out}}|^2 \approx [0,0.33,0,0.33,0,0.33]$ for the first two input combinations shown in Figure1b(i-ii) and $|\boldsymbol{X}_{\text{out}}|^2 \approx [0,1.00,0,1.00,0,0.00]$ for the third input combination shown in Figure1b(iii). In this configuration, it can be observed that at port 6 the output signal can emulate an XOR gate (when defining the low/high classification threshold within the range $0 < |x_6|^2 < 0.33$). Additionally, when the output is observed at ports 2 and 4 (and considering a classification threshold $0.33 < |x_n|^2 < 1,\ n = 2,4$) the output signal can emulate an AND gate. During the conference the full details of the 6-port VPC waveguide design, the extraction of the scattering matrix and evaluation of its computing operation will be fully discussed. This will include numerical simulation of each input combination as well as different configurations such as a three-input case and a study of the performance of the junction with holes removed.

This work was supported by the Leverhulme Trust under the Leverhulme Trust Research Project Grant scheme (No. RPG-2020-316 and RPG-2023-024).

References

1. Ozawa, T. *et al.* Topological photonics. *Rev. Mod. Phys.* **91**, 015006 (2019).
2. Bisharat, D., Davis, R., Zhou, Y., Bandaru, P. & Sievenpiper, D. Photonic Topological Insulators: A Beginner's Introduction [Electromagnetic Perspectives]. *IEEE Antennas Propag. Mag.* **63**, 112–124 (2021).
3. Qi, Z. *et al.* Electrical tunable topological valley photonic crystals for on-chip optical communications in the telecom band. *Nanophotonics* **11**, 4273–4285 (2022).
4. Ma, J., Xi, X., Li, Y. & Sun, X. Nanomechanical topological insulators with an auxiliary orbital degree of freedom. *Nat. Nanotechnol.* **16**, 576–583 (2021).
5. Chen, Y. *et al.* Topologically Protected Valley-Dependent Quantum Photonic Circuits. *Phys. Rev. Lett.* **126**, 230503 (2021).
6. Chao, M.-H. *et al.* Novel optical XOR/OR logic gates based on topologically protected valley photonic crystals edges. *J. Opt.* **23**, 115002 (2021).
7. Johnson-Richards, C., Yakovlev, A. & Pacheco-Peña, V. Topological Valley Photonic Waveguides: Scattering matrix evaluation for linear computing. *arXiv:2412.02388* (2024).
8. Lévêque, G., Pennec, Y., Szriftgiser, P., Amo, A. & Martínez, A. Scattering-matrix approach for a quantitative evaluation of the topological protection in valley photonic crystals. *Phys. Rev. A* **108**, 043505 (2023).
9. Yakovlev, A. & Pacheco-Peña, V. Enabling High-Speed Computing with Electromagnetic Pulse Switching. *Adv. Mater. Technol.* **5**, 2000796 (2020).
10. Pacheco-Peña, V. & Yakovlev, A. Computing with Square Electromagnetic Pulses. in 465–492 (2021). doi:10.1142/9789811235740_0016.
11. MacDonald, R. G., Yakovlev, A. & Pacheco-Peña, V. Amplitude-Controlled Electromagnetic Pulse Switching Using Waveguide Junctions for High-Speed Computing Processes. *Adv. Intell. Syst.* **4**, 2200137 (2022).
12. Ventisei, A., Yakovlev, A. & Pacheco-Peña, V. Exploiting Petri Nets for Graphical Modelling of Electromagnetic Pulse Switching Operations. *Adv. Theory Simul.* **5**, 2100429 (2022).
13. MacDonald, R. G., Yakovlev, A. & Pacheco-Peña, V. Solving partial differential equations with waveguide-based metatronic networks. *Adv. Photonics Nexus* **3**, (2024).
14. Rogers, W., Johnson-Richards, C., Yakovlev, A. & Pacheco-Peña, V. Perfect splitting in rectangular-waveguide junctions for analog computing. *Phys. Rev. Appl.* **21**, 054054 (2024).

Near-unity Index Meta-surfaces and Design of Thermally Emitting Meta-surfaces for Catalysis

Joel Y.Y. Loh[1]

[1] Department of Electrical and Electronic Engineering, University of Manchester, Manchester, M13 9PY
E-mail: joel.loh@manchester.ac.uk

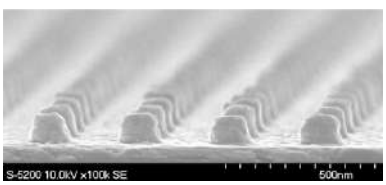
Abstract: A metamaterial of index <1 achieves near-perfect absorption over 400nm range in visible, enhancing CO_2 adsorption through broadband plasmonic fields and angular invariance. Further, adjoint optimization of thermal metamaterials enable coupling with CO_2 vibrational modes. Atomic simulations confirm the enhanced gas absorption due to CO_2 activation energy barrier decrease to 0 eV.

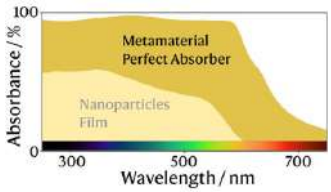
Summary

The absorption of gas-sensing metals and dielectrics offers a breakthrough in conventional material-based engineering. This approach involves meticulously engineering the electric permittivity (ε) and magnetic permeability (μ) by arranging and shaping meta-atoms, creating a meta-surface with desired properties. This surface can achieve several electromagnetic effects, including optical impedance matching and peak absorption spectrum matching of vibrational modes.

Figure 1 shows the cross-sectional microscopy of 90nm copper on a gold layer [1] (**Figure 1a**). The optical absorption spectrum of the meta-surface is wider and higher than that of a film of nanoparticles (**Figure 1b**). For a randomly distributed nanoparticle film, most absorption is due to internal scattering of incident light, with a copper plasmonic absorption edge at 600nm. For the meta-surface, the edge is extended to 650nm.

To show the difference in the underlying EM mechanism, we show the results associated with the conventional effective medium theory and the boundary sheet theory. **Figure 1c** shows the real component of the index, and the calculated absorption spectrum of the meta-surface nano-cube array and periodicity, using the MG effective medium theory. The absorption spectrum is similar to that of the nanoparticle film but not the meta-surface, and while the refractive index is close to 1, it is still high enough to induce reflection. A different refractive index theory is needed. Using the boundary sheet theory, we calculated that the meta-surface has an index real component below 1 (**Figure 2a**). This means that the metamaterial scatters or reflects minimal light because light effectively does not see any scattering medium. This is revealed by the electric field intensity spectrum (**Figure 2b**), which showed that while a nanoparticle film only shows strong plasmonic fields at the resonance wavelength of ~600nm, the plasmonic field in the meta-surface covers 350nm to 650nm. Such a range of plasmonic energies can likely enhance the adsorption of gas molecules through an energy ladder of charge injection. The in-situ FTIR spectroscopy showed a large increase in absorption in the 1050−1220 cm^{-1} band under 1 sun illumination (**Figure 2c**), which is associated with adsorbed methoxy (*CH_3O) or gaseous CH_3OH species. By contrast, the particle film showed relatively small absorption changes in the same band. This separate hydrogenation pathway suggests an additional indirect charge transfer that is present in the meta-surface, even though the nanoparticle film should also exhibit plasmonic effects.





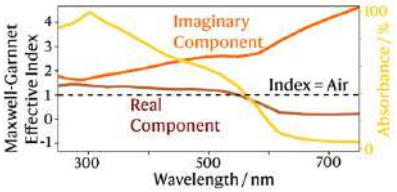


Figure 1. The cross-sectional microscopy image of the meta-surface (left). The optical absorption spectra of the fabricated meta-surface and uniform ZnO / Cu film (right). Effective medium theory shows the real and imaginary components of the refractive index of a Cu layer with a low volumetric filling ratio. Also shown is the simulated absorption spectrum of the Cu layer, which does not match the experimental absorption spectrum.

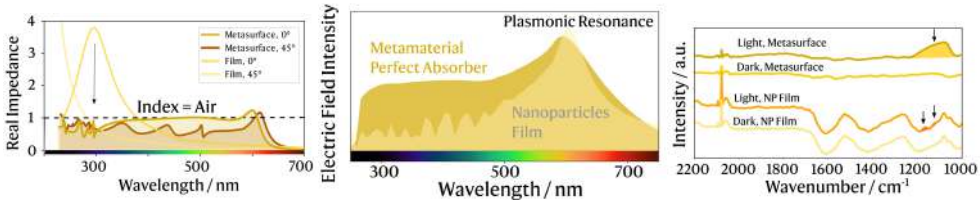


Figure 2. The Boundary Sheet theory shows the real impedances of the meta-surface and ZnO / Cu film. Average electric field intensities between the nano-cubes at the optimal periodicity, and nano-cubes with random periodicities, such that it is considered a nanoparticle film. The meta-surface impedance shows minor changes in profile whereas the film shows significant changes both across the spectrum and incident angle. Fourier transform infrared spectra of the meta-surface and quartz fiber surface coating under 250 °C temperature and CO_2 and H_2 flow, compared between under dark and light conditions.

In another example of meta-surface behavior for thermal emission, we show a multilayer metal-dielectric periodic array is able to generate either a broader peak matching the asymmetric O=C=O bond at ~2420 cm^{-1}. Adjoint optimization involving 2nd derivative softmax functions enables fast convergence of meta-surface design and thicknesses with near-zero error to the desired wavelength (**Figure 3a**). With adjoint method we were able to generate broadband and narrowband emitting designs matching the O=C=O bond (**Figure 3b**), an example is shown in Figure 3c. DFT simulations indicate with a slight asymmetric stretching of the CO2 bond by < 10% of the bond length, enables its chemisorption activation barrier to be reduced to 0 eV.

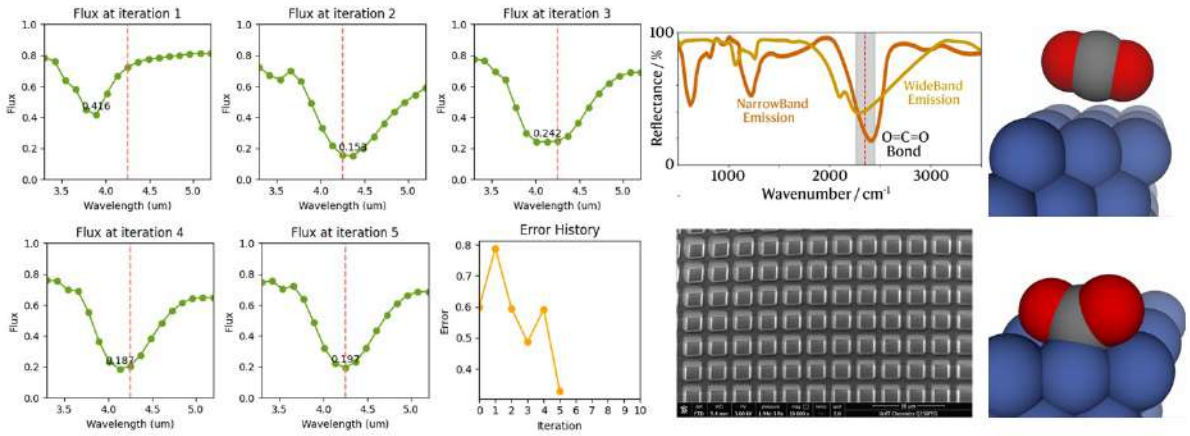


Figure 3. Adjoint method optimization of multilayer metal-dielectric The near-field thermal radiation of the meta-surface as determined by stochastic theory calculations. The wideband emitter shows higher radiation power than the narrowband emitter at 2 to 5 μm distance from the surface.

References

1. Joel Loh, Mahdi Safari, Chengliang Mao, Camilo J. Viasus, George V. Eleftheriades, Geoffrey A. Ozin, Nazir P. Kherani, "Near-Perfect Absorbing Copper Metamaterial for Solar Fuel Generation" ACS *Nano Lett. 2021, 21, 21, 9124–9130*

Polarization-Dependent Au Nanopillar Array for Resonance-Driven Photocatalysis

Ning Lyu[1,2], Anjalie Edirisooriya[2], Zelio Fusco[2], Fiona Beck[2], Christin David[1,3]

[1]IFTO, Friedrich-Schiller-Universität Jena, 07743 Jena, Germany
[2]School of Engineering, Australian National University, Canberra ACT2600, Australia
[3]University of Applied Sciences Landshut, Am Lurzenhof 1, 84036 Landshut, Germany
[*]corresponding author: ning.lyu@uni-jena.de

Abstract: A polarization-dependent metasurface of elliptical Au nanopillars selectively catalyzes reactions via localized surface plasmon resonance. Asymmetric nanopillars allow tuning the resonance wavelengths to maximize yield under x-polarization while suppressing activity under y-polarization, demonstrating a promising approach for controlling selectivity in multibranched reactions.

Photocatalysis holds significant potential for sustainable energy conversion, enabling chemical processes such as water splitting and CO_2 reduction [1]. These reactions typically involve multistep electron transfers, leading to the simultaneous formation of multiple products [2], [3]. However, efficiently harnessing solar energy while achieving selective product conversion remains a challenge. To address this, we focused on precisely controlling a single-step reaction: the N-demethylation of Methylene Blue (MB), activated by light within the 530–710 nm wavelength range [4]. We designed a polarization-dependent metasurface (Figure 1c) that exhibits localized surface plasmon resonance (LSPR) at a specific wavelength, allowing reaction control by tuning the polarization of incident light [5].

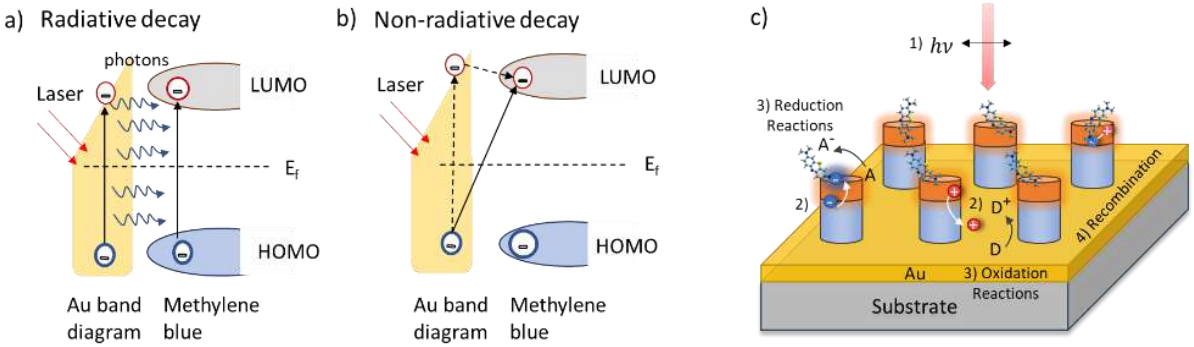


Figure 1. Metasurface nanostructure and photocatalysis mechanisms: a) LSPR radiative decay provides optical near-field enhancement for photocatalysis in MB. b) LSPR non-radiative decay provides direct and indirect hot electrons for reactions. c) Photocatalysis mechanisms on a Au-TiO_2 hybrid nanopillar array.

Metasurfaces feature nanoscale structures that enable precise tuning of optical properties by modifying their geometry. Elliptical TiO_2 and Au nanopillars with asymmetric diameters exhibit polarization-dependent optical behavior. A hybrid nanopillar array was modeled using the finite element method (FEM) and fabricated via a top-down approach with electron beam lithography (EBL). Under transverse magnetic (TM) mode illumination, the nanopillars exhibit peak absorption at 620 nm, aligning with the laser wavelength to activate the MB reaction. In contrast, absorption decreases in the transverse electric (TE) mode, suppressing the reaction, while the peak redshifts to 800 nm due to asymmetry along this direction.

To evaluate catalytic performance, surface-enhanced Raman spectroscopy (SERS) was used for real-time

monitoring of the N-demethylation reaction. The reaction yield was quantified by integrating the Raman peak of the product at 480 cm^{-1}, providing insight into reaction rate manipulation. By switching laser polarization from TE to TM, the yield increased from 4.7 to 9.8 over 10 seconds under consistent illumination conditions on the same sample.

This study demonstrates the potential of tunable metasurfaces for precise control of light-driven reactions, offering promising applications in selective photocatalysis. Utilizing advanced nanofabrication techniques, we engineered nanoscale morphologies to tailor optical properties, enabling targeted activation or suppression of specific reaction pathways. These metasurfaces provide a powerful strategy for selectively catalyzing optical resonance-driven reactions by modulating intermediate steps. Future research will explore the integration of tunable materials, such as phase-change materials, and extend this approach to complex multibranched reactions, including CO_2 reduction. This method presents a versatile solution for optimizing multistep reaction pathways, crucial for enhancing conversion efficiency in renewable fuel production.

Acknowledgements: This work is supported by the German Research Foundation DFG (Deutsche Forschungsgemeinschaft) through funding of the International Research Training Group IRTG 2675 (Gepris 437527638). The authors acknowledge access to NCRIS facilities (ANFF-ACT Node) at the Australian National University.

References

[1] Y. Ma, X. Wang, Y. Jia, *et al.*, *Chem. Rev.*, vol. 114, no. 19, pp. 9987–10043, Oct. 2014.
[2] Z. Fusco, A. Edirisooriya, N. Lyu, *et al.*, in Semiconductors and Semimetals., Elsevier, 2024.
[3] J. L. White, M. F. Baruch, J. E. Pander, *et al.*, *Chem. Rev.*, vol. 115, no. 23, pp. 12888–12935, Dec. 2015.
[4] Z. Fusco, K. Catchpole, and F. J. Beck, *J. Mater. Chem. C*, vol. 10, no. 19, pp. 7511–7524, 2022.
[5] S. Zhao, Z. Fusco, and F. J. Beck, *Optica*, vol. 9, no. 9, p. 1084, Sep. 2022.

Cofactor Regeneration in Enzyme Membrane Reactors by Photoenzymatic Methods: A Biomimetic Light-Harvesting Platform with Ionic Porphyrins for CO_2 Reduction

Zhibo Zhang, Manuel Pinelo*

[2]Department of Chemical and Biochemical Engineering, Technical University of Denmark, Søltofts Plads 228A, 2800 Lyngby, Denmark

*corresponding author: mp@kt.dtu.dk

Abstract: Photoenzymatic platforms enable efficient cofactor regeneration for enzymatic reactions requiring redox cycling. We present an ionic porphyrin-based light-harvesting system that enhances NADH regeneration and enzymatic CO_2 reduction. By optimizing photonic absorption and charge transfer, this biomimetic approach improves energy conversion, demonstrating potential for sustainable photocatalysis and solar-driven biomanufacturing.

Summary:

Cofactor regeneration is a fundamental challenge in enzymatic processes requiring redox reactions, particularly in biomanufacturing, carbon capture, and sustainable chemical synthesis. Many enzymatic reactions depend on nicotinamide adenine dinucleotide ($NADH/NAD^+$), but the high cost and instability of NADH hinder industrial scalability. Photoenzymatic regeneration of NADH, inspired by natural photosynthesis, provides a sustainable approach by utilizing solar energy to drive electron transfer, enabling efficient cofactor recycling and continuous enzymatic conversion of CO_2 (1).

In this study, a biomimetic ionic porphyrin-based platform was developed to enhance light-driven NADH regeneration and integrate it into a photoenzymatic CO_2 reduction system, demonstrating a scalable approach to solar-driven biocatalysis. The core innovation is the use of ZnTPyPBr, an ionic porphyrin photosensitizer that mimics chlorophyll's light-harvesting function while overcoming the limitations of conventional porphyrins. Ionic functionalization significantly improves hydrophilicity and charge separation, reducing charge recombination and aggregation, which are two major bottlenecks in nonionic porphyrin-based systems (2). The photonic efficiency of ZnTPyPBr results in a threefold higher NADH regeneration rate compared to its nonionic counterparts, offering a highly stable and efficient alternative to traditional semiconductor-based photocatalysts, which often suffer from poor stability and back-electron transfer losses (3).

The photoenzymatic membrane integrates a cascade enzymatic system immobilizing formate dehydrogenase (FDH), formaldehyde dehydrogenase (FaldDH), and alcohol dehydrogenase (ADH) to achieve CO_2 reduction to methanol. In this system, continuous NADH regeneration drives a sevenfold increase in methanol production compared to free enzyme systems, demonstrating the significance of sustained NADH availability in overcoming kinetic limitations (1). Additionally, the membrane modification with polydopamine (PDA) and polyethyleneimine (PEI) enhances enzyme stability and facilitates local CO_2 capture, further boosting reaction efficiency (4).

This study, which will be presented along with other potential photocatalytic platforms for cofactor regeneration, highlights the potential of bioinspired photonic materials for scalable solar-driven enzymatic processes, offering a sustainable alternative for biomanufacturing, artificial photosynthesis, and CO_2 utilization. By using ionic porphyrins for efficient cofactor regeneration, this approach aims at future developments in solar-driven biocatalysis, green chemistry, and renewable fuel production (3).

References

1. Zhang, Z., Tong, J., Meng, X., Cai, Y., Ma, S., Huo, F., Luo, J., Xu, B-H., Zhang, S., & Pinelo, M. (2021). Development of an Ionic Porphyrin-Based Platform as a Biomimetic Light-Harvesting Agent for High-Performance Photoenzymatic Synthesis of Methanol from CO_2. ACS Sustainable Chemistry & Engineering, 9(34), 11503–11511.
2. Obert, R., & Dave, B. C. (1999). Enzymatic conversion of carbon dioxide to methanol: Enhanced methanol production in silica sol-gel matrices. Journal of the American Chemical Society, 121(49), 12192-12193.
3. Wang, Y., Sun, J., Zhang, H., Zhao, Z., & Liu, W. (2018). Tetra(4-carboxyphenyl)porphyrin for efficient cofactor regeneration under visible light and its immobilization. Catalysis Science & Technology, 8(9), 2578-2587.
4. Yadav, R. K., Baeg, J.-O., Oh, G. H., Park, N.-J., Kong, K.-j., Kim, J., Hwang, D. W., & Biswas, S. K. (2012). A photocatalyst-enzyme coupled artificial photosynthesis system for solar energy in production of formic acid from CO_2. Journal of the American Chemical Society, 134(28), 11455-11461.

Plasmonically Enhanced Solar Water Splitting with TiO_2/Au/Pt Nanoparticles in three-dimensional porous PDMS Substrates

N. Albenge[1*], F. Laible[1], S. Glocker[1], and M. Fleischer[1]

[1]Institute for Applied Physics and Center LISA[+], Tübingen, Germany
[*]nicolas.albenge@uni-tuebingen.de

Abstract: Green hydrogen can be generated in a water-splitting process using solar energy and photocatalytic titanium dioxide. When this is brought into contact with gold and platinum nanoparticles and assembled on inner surfaces of transparent porous PDMS substrates for high absorption, the efficiency of the hydrogen generation reaction can be enhanced.

The current vastly growing global demand for ecologically green hydrogen (H_2) leads to many scientific studies on efficient H_2 generation based on renewable energy sources. Following the suggestions of the hydrogen ladder, the generated green H_2 should be used as the chemical itself, for example in the production of green ammonia for fertilizers, for hydrogenation processes or in steel production, and not as an energy source in cars or trucks [1]. In cases where there is no alternative to H_2, so far it is generated out of natural gas with a 99% share and thus drives climate change and globe pollution.

One method to generate green H_2 is electrolysis. Here, solar energy is indirectly transformed, using solar cells providing the necessary potential difference for water splitting reactions at two electrodes in a water bath. In this project, a more direct solar energy conversion method, namely photocatalysis, is investigated. Using the semiconducting photocatalyst titanium dioxide (TiO_2) with its large bandgap of 3.2 eV, light in the UV-regime leads to the creation of electron-hole pairs under photo-absorption with a potential difference high enough to drive water splitting reactions. Combining it with metallic nanoparticles (NPs), an increase in the water splitting efficiency can be observed [2]. This increase originates from the plasmonic behavior of gold (Au) NPs, which enable the absorption of wavelengths also in the visible spectrum. The excited localized surface plasmon of the Au particles can resonantly decay into hot electrons or holes that are injected into the conduction or valence band of TiO_2, providing more electron-hole pairs to enhance the redox reaction rates involved in water splitting. Efficiency can be further improved by reducing the amount of electron-hole recombination inside TiO_2. This can be achieved by adding catalytically active platinum (Pt) NPs [3].

Three-dimensional, highly porous PDMS structures that are fabricated by using commercial sugar cubes as a template (see Figure 1) [4] serve as substrates offering large inner surfaces for different material constellations realized out of TiO_2, Au and Pt (see Figure 2). In comparison to two-dimensional systems, these PDMS substrates can hold many more NPs, accessible to incoming light because of their transparency, enhancing absorption. A first constellation of a random NP distribution inside the three-dimensional substrate was achieved and its H_2 generation proven. The fabrication process, resulting structures and analysis by gas sensors will be presented.

Support by the Vector Stiftung (Grant number: P2021-0129) is gratefully acknowledged.

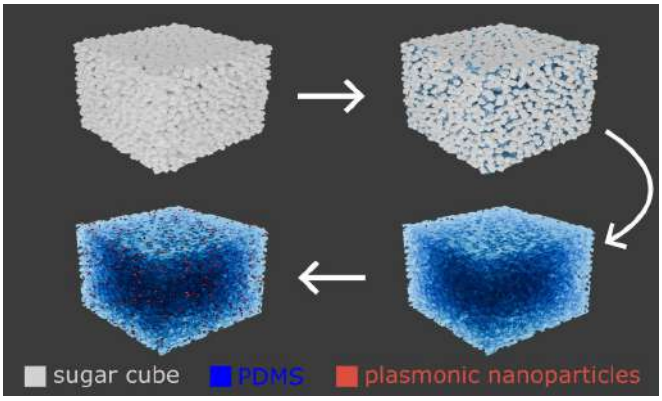
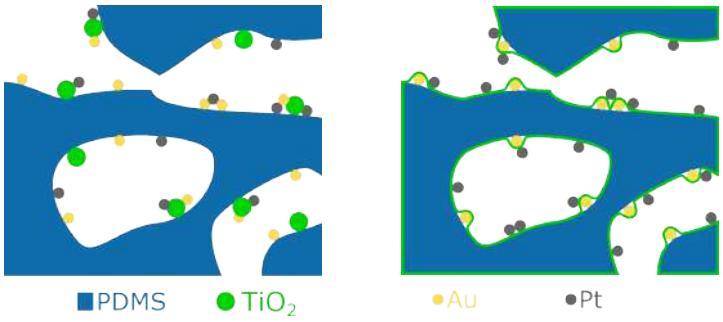


Fig. 1: PDMS substrate fabrication starting with a commercial sugar cube [4]. After filling the interstices between the sugar crystals with liquid PDMS and hardening the PDMS, the sugar cube can be dissolved in water. A three-dimensional transparent PDMS substrate with a large internal surface is realized. Residual PDMS-crosslinkers from its hardening process act as reducing sites for chemically grown metallic NPs.



(a) (b)

Fig. 2: Cross-sectional schematic view of randomly distributed TiO_2-, Au- and Pt-NPs (a) and randomly distributed Au-NPs with a TiO_2 thin film and randomly distributed Pt-NPs (b) inside three-dimensional porous PDMS substrates.

References

1. Liebreich, M., Liebreich Associates, https://www.liebreich.com/hydrogen-ladder-version-5-0/, 2023, accessed last on 21.02.2025.
2. Kim, H. J., S. H. Lee, A. A. Upadhye, I. Ro, M. I. Tejedor-Tejedor, M. A. Anderson, W. B. Kim and G. W. Huber, "Plasmon-Enhanced Photoelectrochemical Water Splitting with Size-Controllable Gold Nanodot Arrays," ACS Nano, Vol. 8, No. 10, 10756–10765, 2014.
3. Wang, F., R. J. Wong, J. H. Ho, Y. Jiang and R. Amal, "Sensitization of Pt/TiO_2 Using Plasmonic Au Nanoparticles for Hydrogen Evolution under Visible-Light Irradiation," ACS Applied Materials & Interfaces, Vol. 9, No. 36, 30575–30582, 2017.
4. Choi, S.-J., T.-H. Kwon, H. Im, D.-I. Moon, D. J. Baek, M.-L. Seol, J. P. Duarte and Y.-K. Choi, "A Polydimethylsiloxane (PDMS) Sponge for the Selective Absorption of Oil from Water", ACS Applied Materials & Interfaces Vol. 3, No. 12, 4552-4556, 2011.

Plasmonic Metasurfaces as Solar Absorption Enhancers for the Perovskite Thin Film Solar Cells

S. Mamykin[1*], I. Mamontova[1], R. Redko[1], O. Shtykalo[1], T. Lunko[1], I.Dmytruk[2], O.Yeshchenko[2], O. Fedotov[2], N.Berezovska[2], A. Pinchuk[3]

[1]V. Lashkaryov Institute of Semiconductor Physics, NAS of Ukraine, Ukraine

[2]Taras Shevchenko National University of Kyiv, Ukraine

[3]Department of Physics and Energy Sciences, University of Colorado at Colorado Springs, USA

[*]corresponding author: mamykin@isp.kiev.ua

Abstract: Perovskite thin films are promising materials for next-generation photovoltaic technologies, but their widespread adoption is limited by stability issues and lead toxicity. This study proposes plasmonic perovskite solar cells with Au@SiO_2 core-shell nanoparticles, which enhance efficiency, reduce the active layer thickness, and improve stability under real-world conditions.

Perovskite thin films have emerged as highly promising materials for next-generation photovoltaic technologies. Their solution-based fabrication process offers the potential to significantly reduce production costs, paving the way for widespread adoption of perovskite solar cells. However, two critical challenges hinder their large-scale implementation [1]: the instability of perovskites in real-world conditions and the reliance on toxic lead in their composition. This research aims to address these issues by developing plasmonic perovskite solar cells (PPSC) with enhanced power conversion efficiency, thinner active layers, and improved stability.

The proposed PPSC design has a multilayered structure. The base is a fluorine-doped tin oxide coated glass. A hole transport layer of PEDOT is followed by a cesium-lead-iodide perovskite layer, which may include a monolayer of gold core - silica shell (Au@SiO2) nanoparticles (NPs). The electron transport layer consists of either ZnO or TiO_2. Finally, a continuous electrical contact layer made of Au or Al thin film is deposited on top. This film serves both as a protective encapsulation surface, preventing perovskite degradation, and as a plasmonic cavity surface, where the electric field is enhanced in the gap between the Au@SiO_2 NPs monolayer and metal film, forming a hybrid plasmon polariton - gap modes [2].

Metal halide perovskite quantum dots (QDs) and clusters are critical for enhancing the efficiency of plasmonic solar cells [3]. Their band gap energy can be tuned by adjusting their size or composition. The photoluminescence of perovskite QDs is characterized by narrow emission bands and a high quantum yield, making them highly suitable for photovoltaic applications. The small size of the QDs, along with their tolerance to defects, ensures improved performance and durability. The use of perovskite QDs containing "inks" will enable scalable, cost-effective fabrication methods, such as spin-coating, to produce large-area solar cells.

The finite-difference time-domain computational method is used to estimate the enhancement of light absorption and the electric field, as well as for design optimization for enhanced efficiency and reduce material usage. By incorporating Au@SiO_2 NPs and optimizing the multilayer architecture, the proposed solar cells are expected to increase power conversion efficiency, reduce the use of toxic lead, and improve stability under atmospheric conditions.

The results of FDTD calculations of the absorption spectra of the solar cell (glass substrate – ITO (300 nm) – PEDOT (100 nm) – perovskite $CsPbI_3$ (100 nm) – ZnO (50 nm)) without plasmonic part and the plasmonic

solar cell (glass substrate – ITO (300 nm) – PEDOT (100 nm) – Au@SiO_2 NP monolayer (Au core diameter 40 nm, SiO_2 shell 3nm) – perovskite $CsPbI_3$ (100 nm) – ZnO (50 nm) – Al (100 nm)) containing the plasmonic cavity metasurface are peresenten in Fig. 1(a). Due to the thin-film structure of the solar cell, the spectra contain interference fringes. However, it can be seen that in the entire visible range and in the near IR up to 1200 nm, the presence of a plasmonic metasurface provides a noticeable enhancement of light absorption. Fig. 1(b) demonstrates the spectral dependence of the absorption enhancement factor for perovskite solar cell containing plasmonic metasurface in relation to the same solar cell without plasmonic metasurface. It is seen that the maximum enhancement is achieved at 960 nm that most probably is related to the excitation at this wavelength of the plasmon gap mode which is the eigenmode of the Au@SiO_2 NP monolayer – Al film plasmonic cavity. The assumption that the wavelength of 960 nm corresponds to the plasmonic cavity gap mode is confirmed by calculations of the absorption spectra for different distances between the surfaces of neighboring Au@SiO_2 NPs in the monolayer, Fig. 1(c). It can be seen that decreasing the distance between the NPs leads to a blue shift of the band with a maximum at 960 nm, while the spectral position of the other bands remains unchanged. Thus, the calculations have proven the effectiveness of incorporating a plasmon metasurface inside the photoactive layer of a solar cell to enhance light absorption.

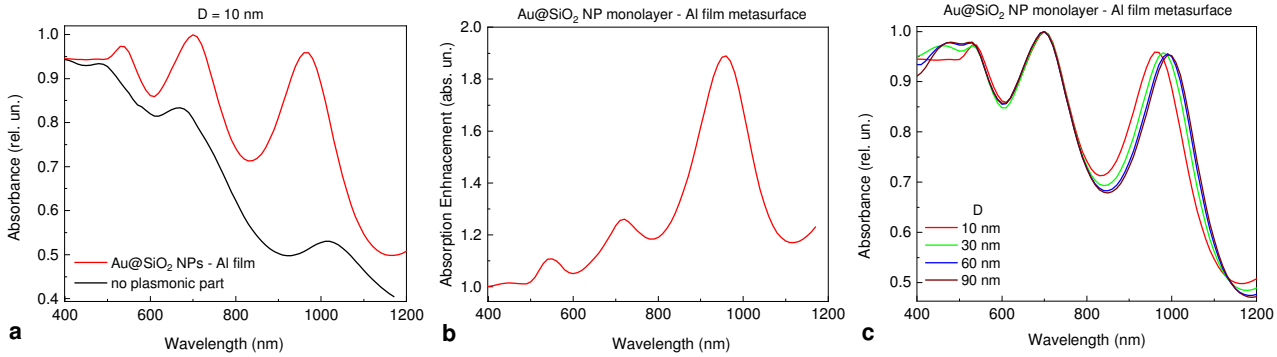


Figure 1. (a) – Calculated absorption spectra of perovskite solar cell with Au@SiO_2 NP monolayer – Al film plasmonic cavity metasurface (red line) and the same solar cell without plasmonic metasurface. (b) – Spectral dependence of the absorption enhancement factor for perovskite solar cell containing plasmonic metasurface in relation to the same solar cell without plasmonic metasurface. (c) – Calculated absorption spectra of perovskite solar cell with Au@SiO_2 NP monolayer – Al film plasmonic cavity metasurface with different distance D between the surfaces of neighboring Au@SiO_2 NPs in the layer. (a) and (b) correspond to D=10 nm.

Acknowledgements. This work was partially supported by the NATO SPS project G6197 “Plasmonically Enhanced Perovskite Thin-Film Solar Cells”.

References

1. Y. Rong, Y. Hu, A. Mei, H. Tan, M. I. Saidaminov, S. I. Seok, M. D. McGehee, E. H. Sargent, and H. Han, "Challenges for commercializing perovskite solar cells," Science, Vol. 361**,** No. eaat8235, 6408, 2018.
2. O. A. Yeshchenko, V. V. Kozachenko, A. P. Naumenko, N. I. Berezovska, N. V. Kutsevol, V. A. Chumachenko, M. Haftel, and A. O. Pinchuk, "Gold nanoparticle plasmon resonance in near-field coupled Au NPs layer/Al film nanostructure: dependence on metal film thickness," Photonics Nanostructures: Fundam. Appl., Vol. 29, 1-7, 2018.
3. L. Hu, Q. Zhao, S. Huang, J. Zheng, X. Guan, R. Patterson, J. Kim, L. Shi, C. Lin, and Q. Lei, "Flexible and efficient perovskite quantum dot solar cells via hybrid interfacial architecture," Nat. Commun., Vol. 12, No. 1, 466, 2021.

Plasmonic Gold Nano-Dendrites for Efficient CO_2 Reduction: Tailored Architectures and Enhanced Multi-Electron Pathways

Anjalie Edirisooriya[1], Ning Lyu[1,2], Zelio Fusco[1], Fiona Beck[1]
[1]School of Engineering, Australian National University, Canberra ACT2600, Australia
[2]IFTO, Friedrich-Schiller-Universität Jena, 07743 Jena, Germany

Abstract: A scalable plasmonic gold nano-dendrite catalyst enhances multiple electron transfer and carbon-carbon (C–C) coupling in CO_2 reduction reactions (CO_2RR). The dendritic morphology allows tuning of plasmonic resonance energies to optimize reaction efficiency, demonstrating a promising approach for enhancing product selectivity in CO_2 conversion.

Photocatalysis plays a pivotal role in sustainable energy conversion by driving chemical transformations such as CO_2 reduction into valuable products. However, selectively promoting multi-electron transfer pathways and C–C coupling remains a significant challenge[1]. To address this, we developed plasmonic gold nano-dendrites using a single-step electrodeposition process under controlled current and voltage conditions. By systematically varying the deposition parameters, we were able to tailor the dendrite morphology, optimizing localized surface plasmon resonance (LSPR) effects to maximize catalytic performance[2].

The structural and optoelectronic properties of the gold dendrites were characterized using scanning electron microscopy (SEM), X-ray diffraction (XRD), and high-resolution cathodoluminescence spectroscopy (CL). CL analysis provided critical insights into local photon density of states (LDOS) and hotspot formation, demonstrating the excitation of abundant plasmonic resonances at high-curvature regions within the dendritic architecture, which are essential for plasmon-driven charge transfer. CO_2RR efficiency was evaluated in a standardized photocatalytic reactor under continuous-wave (CW) solar illumination. Gas chromatography was employed to identify and quantify the reaction products, confirming an increased yield of multi-electron reduction products. Photoelectrochemical (PEC) measurements provided direct insights into hot electron generation and internal quantum efficiency. Additionally, spectral response analysis with a monochromator-assisted CW light source revealed wavelength-dependent catalytic activity, with peak efficiency observed in the visible range. High-resolution CL spectroscopy further demonstrated the excitation of abundant plasmonic resonances at high-curvature regions within the dendritic architecture.

Electrochemical CO_2RR experiments demonstrated that Au dendrites efficiently produced C_{2+} products. Upon light illumination, the Faradaic efficiency (FE) for C_2 species increased compared to electrochemical measurements in the dark. The catalysts exhibited improved charge transfer kinetics and enhanced multi-electron pathways, driven by plasmon-induced charge separation. Spectroscopic analysis confirmed prolonged hot carrier lifetimes, correlating with increased catalytic activity and selective C–C bond formation.

Catalyst degradation was assessed post-reaction using energy-dispersive X-ray spectroscopy (EDS) and XRD to analyze structural integrity and elemental composition changes after prolonged electrochemical and photoelectrochemical reduction. The results showed that the Au dendrites maintained their structural and catalytic stability over extended reaction cycles.

This study demonstrates the potential of tailored gold nano-dendrites for plasmon-enhanced CO_2 reduction, offering a tunable approach for selective multi-electron transfer and C–C bond formation. By leveraging plasmonic excitations, reaction pathways can be directed toward the formation of C_2 species through energy transfer mechanisms. Moreover, optimizing the optical response of photocathodes with plasmonic resonances introduces a new degree of control in designing highly efficient and selective photo-electrocatalysts. Future research will focus on dynamic plasmonic tuning through external stimuli to further enhance catalytic performance, with the goal of advancing sustainable fuel production and carbon valorization.

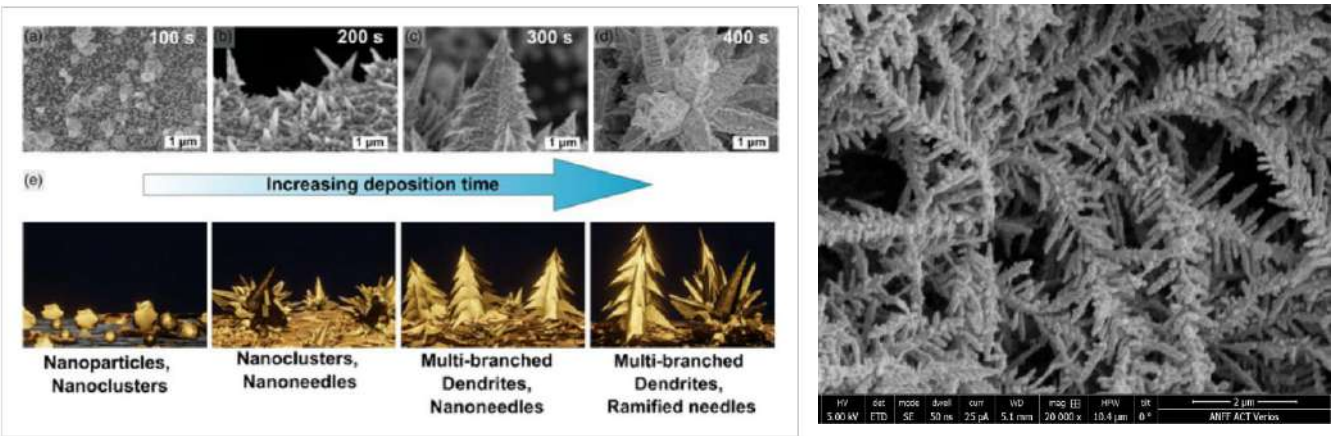


Figure 1. a) Representative SEM images of the Au nanostructures self-assembled with an applied current of 5 mA cm^{-2} at the different electrodeposition times of 100, 200, 300, and 400 s, respectively [3]. b) Scanning electron micrograph of the Au dendritic architectures on stainless steel mesh.

References

1. Z. Fusco and F. J. Beck, "Advances in fundamentals and application of plasmon-assisted CO2 photoreduction," *Nanophotonics*, vol. 13, no. 4, pp. 387-417, 2024.
2. Z. Fusco, K. Catchpole, and F. J. Beck, "Investigation of the mechanisms of plasmon-mediated photocatalysis: synergistic contribution of near-field and charge transfer effects," *Journal of Materials Chemistry C*, vol. 10, no. 19, pp. 7511-7524, 2022.
3. Z. Fusco, A. Riaz, C. David, and F. J. Beck, "Cathodoluminescence Spectroscopy of Complex Dendritic Au Architectures for Application in Plasmon-Mediated Photocatalysis and as SERS Substrates," *Advanced Materials Interfaces*, vol. 10, no. 3, p. 2202236, 2023.

Theoretical comparison of longitudinal and transverse interactions between plasmon and electron-hole pairs in Ag thin film

S. Inoue[1*], T. Inaoka[2], and H. Ishihara[1,3]

[1] Graduate School of Engineering Science, Osaka Univ., Japan
[2]Graduate school of Engineering and Science, Univ. of the Ryukyus, Japan
[3]Ritsumeikan Semiconductor Application research center (RISA), Ritsumeikan University, Japan
[*]corresponding author: inoue.s@opt.mp.es.osaka-u.ac.jp

Abstract: Plasmon excitations in metals generate hot carriers, crucial for photoelectric conversion. While conventional theories attribute carrier generation to Landau damping, recent experiments reveal an unexplained IQE peak. Our theory shows that the radiative coupling produces resonant effects near the light energy, offering a compelling explanation for the observed IQE enhancement.

Fundamental excitations in a metallic system can be categorized into two distinct types: plasmon excitations and electron-hole pair (e-h pair) excitations. It is well established that optical excitation of plasmons at a metal surface can lead to the generation of high-energy e-h pairs, known as hot carriers, which exist beyond thermal equilibrium. The injection of these hot carriers into semiconductors or molecular systems facilitates photoelectric conversion within the visible to near-infrared spectral range. This phenomenon is particularly promising for applications in photovoltaic and photocatalytic devices [1]. However, to enhance conversion efficiency, further research is necessary. Achieving efficient photoelectric conversion requires the rapid transfer of plasmonic energy into hot carriers. Conventional theoretical approaches have typically described the hot carrier generation as a relaxation process caused by Landau damping [2]. It has been argued by Yamada [3] that this damping arises from the residual longitudinal interactions between plasmon and electron-hole pairs in the Bohm & Pines theory [4], and since this relaxation rate is described in a manner independent of the incident photon energy, the internal quantum efficiency (IQE) spectrum, which quantifies photoelectric conversion efficiency normalized by photon absorption, has been considered to be proportional to the density of states of electron-hole pair excitation. However, recent experimental observations indicate that the IQE spectrum exhibits a pronounced peak near the plasmon resonance energy [5]. This spectral feature cannot be solely attributed to a relaxation mechanism, highlighting the need for a more microscopic theoretical framework. To address this unresolved issue and explore new avenues for efficient photoelectric conversion, we have formulated a novel theory of metal optical responses. Bohm and Pines quantized plasmon and e-h pair excitations respectively, and constructed a theoretical model that can discuss the energy transfer between them only in bulk systems without coupling to light [4]. Therefore, we expanded their theory to finite systems with surfaces and constructed a theory that describes the further generalized optical response of idealized metals. In our theory, the Hamiltonian of the thin metallic film shown in Fig. 1(a) is expressed as follows:

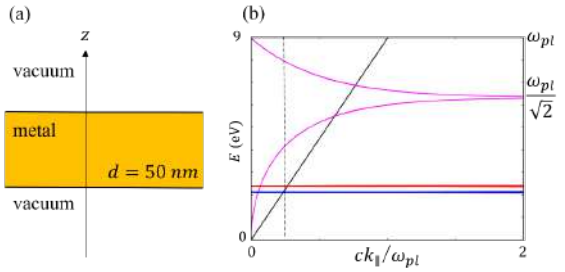


Fig.1: (a) Schematic view of metal film. (b)Dispersion relation of electrostatic plasmon (magenta) and specific e-h pairs (red,blue).

$$H = \sum_{\mu\mu'} \left(\hbar\omega_{\mu}^{(\mathrm{pl})}\delta_{\mu\mu'} + Z_{\mu\mu'}(\omega)\right)\hat{A}_{\mu}^{\dagger}\hat{A}_{\mu'} + \sum_{\nu} \hbar\omega_{\nu}^{(\mathrm{e-h})}\hat{B}_{\nu}^{\dagger}\hat{B}_{\nu} + \sum_{\mu\nu}\left(g_{\mu\nu}^{(L)} + g_{\mu\nu}^{(T)}(\omega)\right)A_{\mu}^{\dagger}\hat{B}_{\nu} + \mathrm{H.c.} \quad (1)$$

where $\hat{A}_{\mu}^{\dagger}(\hat{A}_{\mu})$is creation (annihilation) operator of plasmon and $\hat{B}_{\nu}^{\dagger}(\hat{B}_{\nu})$is creation (annihilation) operator of e-h pair. $\mu\,(=\boldsymbol{k}_{\parallel},m)$ is the index for in-plane and z-direction wavenumbers of the plasmon and $\nu\,(=\boldsymbol{k}_{\parallel},\boldsymbol{K}_{\parallel},n,n')$ is the index for the in-plane and z direction wavenumbers of the e-h pair excitations, respectively. $\hbar\omega_{\mu}^{(\mathrm{pl})}\left(\hbar\omega_{\nu}^{(\mathrm{e-h})}\right)$ are the energy quanta of plasmon (e-h pair) and expressed as follows:

$$\hbar\omega_{\mu}^{(\mathrm{pl})}=\frac{\hbar\omega_{pl}}{\sqrt{2}}\left[1-(-1)^{m}e^{-|\boldsymbol{k}_{\parallel}|d}\right] \quad (2)$$

$$\hbar\omega_{\nu}^{(\mathrm{e-h})}=\frac{\hbar^{2}}{2m^{*}}\left[\boldsymbol{k}_{\parallel}^{2}+2\boldsymbol{k}_{\parallel}\cdot\boldsymbol{K}_{\parallel}+\frac{\pi^{2}(n'^{2}-n^{2})}{d^{2}}\right] \quad (3)$$

where ω_{pl} represents the plasma angular frequency. $Z_{\mu\mu'}(\omega)$ is the radiative correction for plasmon, and the dispersion relation for coupled system of light and plasmon is given by the equation $\mathrm{Det}|S|=0$ with the matrix $S_{\mu\mu'}$:

$$S_{\mu\mu'}=\left(\hbar\omega_{\mu}^{(\mathrm{pl})}-\hbar\omega\right)\delta_{\mu\mu'}+Z_{\mu\mu'}(\omega) \quad (4)$$

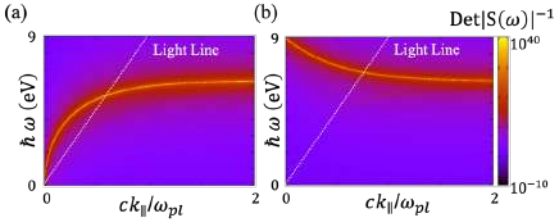


Fig.2: Dispersion relation for coupled system of light and plasmon in Ag film with thickness of 50nm. SR-SPP and LR-SPP appear as a surface mode of even plasmon (a) and odd plasmon (b).

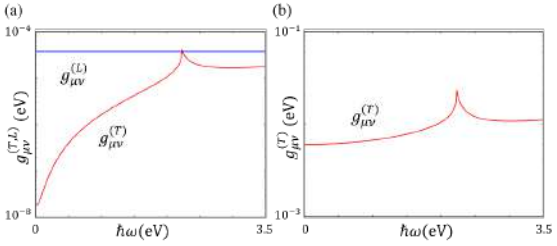


Fig.3: Comparison of incident photon energy dependency of $\boldsymbol{g^{(L)}}$ (blue) and $\boldsymbol{g^{(T)}(\omega)}$ (red). (a) m=0, n= 185, n'=220. (b) m=0, n= 180, n'=220.

Our analysis, applied to a 50nm-thick Ag film, reveals the well-known dispersion of Short- and Long-Range Surface Plasmon Polariton (S(L)R-SPP) (see Fig. 2(a), (b)). $g^{(L)}$ is the residual longitudinal interactions between plasmon and e-h pairs and gives landau damping as already mentioned. However, in the case of the surface system with light coupling, radiative transverse coupling $g^{(T)}(\omega)$ occurs. Comparing $g^{(L)}$ and $g^{(T)}(\omega)$, we get the interesting results regarding the parity of the polarization in z-direction. When the parity of plasmon (m) and e-h pairs (n'-n) are mismatched, $g^{(T)}(\omega)$ is less than $g^{(L)}$ regardless of incident photon energy (see Fig. 3(a)). However, when they are matched, we found that some combinations of plasmon and e-h pairs cannot interact via longitudinal field but can be coupled strongly via transverse field (see Fig. 3(b)). This fact is not addressed by conventional theories based on Landau damping, which considers only residual longitudinal interactions. Moreover, the radiative coupling $g^{(T)}(\omega)$ depends on frequency and increases resonantly near the light energy, which is a highly promising clue to explain the experimentally observed peak structure of IQE. In our future work, we plan to investigate the population dynamics of this system and analyze in detail the novel hot carrier generation process arising from this radiative coupling.

References

1. Clavero, C., "Plasmon-induced hot-electron generation at nanoparticle/metal-oxide interfaces for photovoltaic and photocatalytic devices," Nat. Photonics, Vol. 8, 95-103, 2014.
2. Besteiro, L. V., X. -T. Kong, Z. Wang, G. Hartland and A. O. Govorov, "Understanding Hot-Electron Generation and Plasmon Relaxation in Metal Nanocrystals," ACS Photonics, Vol. 4, 2759–2781, 2017.
3. Yamada, K., "On the mechanism of the Landau damping," J-STAGE, Vol. 5 633-639, 1960.
4. Bohm, D. and D. Pines, "A Collective Description of Electron Interactions," Phys. Rev., Vol. 92, 609-625, 1953.
5. Shi, X., K. Ueno, T. Oshikiri, Q. Sun, K. Sasaki and H. Misawa, "Enhanced water splitting under modal strong coupling conditions," Nat. Nanotechnol., Vol. 13, 953-958, 2018.

Laser Cavities, Photovoltaic, and Light-Emitting Technologies

Enhancing Anti-reflective Coating Performance through Binary Optimization of Structural Parameters with Concurrent Material Selection and Thickness Optimization

S. Jung[1] and E. Lee[1*]

[1] Department of Electronic Engineering, Kyung Hee University, Republic of Korea
[*]corresponding author: eleest@khu.ac.kr

Abstract: Optimizing planar multilayer coatings is challenging due to vast parametric space and complex requirements. This study proposes an adaptive scheme using active learning for concurrent material selection and thickness optimization. Applied to antireflective coatings for infrared camera, it identified a five-layer design with 0.47% reflectance, reducing computational cost.

Optimizing planar multilayer optical coatings remains challenging due to the extensive parametric space and complex figure-of-merit constraints. This study presents an adaptive thickness approach incorporating active learning for simultaneous material selection and thickness optimization. Thickness is adaptively sampled within a continuous spectrum, while material status is represented as a discrete binary variable to enable flexible design exploration. Within this scheme, we evaluate three machine learning (ML) models—Gaussian process regression (GPR)[1], factorization machines (FM)[2], and field-aware factorization machines (FFM)[3]—as surrogate functions, alongside ML-specific optimization algorithms such as discrete particle swarm optimization (PSO)[4], artificial bee colony optimization (ABC)[5], and simulated annealing (SA)[6].

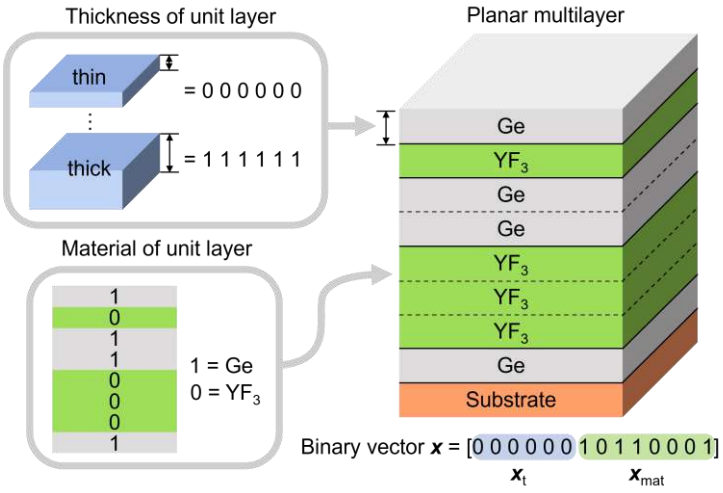


Figure 1. Schematic diagram of encoding optical coatings to binary vector

Optimization results showed that nearly all algorithms identified lower FoM values compared to conventional optimization with fixed thickness, with the optimized structures exhibiting greater thickness variation. In the benchmarking study of Ge-YF_3 antireflective coating for a Si substrate, the adaptive scheme discovered a high-performance five-layer structure using a more sparse dataset than the conventional

optimization with fixed thickness, achieving an average reflectance of 0.47%.

Acknowledgement

This research was supported by the Quantum Computing Based on Quantum Advantage Challenge Research (RS-2023-00255442) funded by the Korea government (MSIT).

References

[1] Schulz, E., Speekenbrink, M. & Krause, A. “A tutorial on Gaussian process regression: Modelling, exploring, and exploiting functions.” *J. Math. Psychol.* Vol. 85, pp. 1-16, 2018.

[2] Rendle, S., “Factorization Machines” in *2010 IEEE International Conference on Data Mining*, pp.995-1000, 2010.

[3] Juan, Y., Zhuang, Y., Chin, W.-S. & Lin, C.-J. “Field-aware Factorization Machines for CTR Prediction” in *Proceedings of the 10th ACM Conference on Recommender Systems*, pp.43–50, 2016.

[4] Kennedy, J. and Eberhart, R. “Particle swarm optimization” in *Proceedings of ICNN'95 - International Conference on Neural Networks.*, Vol.4, pp.1942-1948, 1995.

[5] Karaboga, D. & Basturk, B., “A powerful and efficient algorithm for numerical function optimization: artificial bee colony (ABC) algorithm,” *Journal of Global Optimization*, Vol.**39**, pp.459-471, 2007.

[6] Kirkpatrick, S., Gelatt, C. D. and Vecchi, M. P., “Optimization by Simulated Annealing,” *Science* Vol. 220, pp. 671-680, 1983.

High Purcell Values from Inverse Design of Bullseye Cavities by Machine Learning

F M. Sanchez, C. Everly, L.M. Weituschat, L.N. Goduguluri, P.K. Anwla and P. A. Postigo*

[1] The Institute of Optics, University of Rochester, Rochester, New York 14627, USA
*corresponding author: ppostigo@ur.rochester.edu

Abstract: We present a Tandem Neural Network (TNN) approach for the inverse design of Bullseye cavities, optimizing Purcell enhancement and emission efficiency. This method reduces computational demands, integrates fabrication constraints, and generalizes across materials, enabling efficient design of photonic structures with high performance and applicability to other complex cavity systems.

Developing and optimizing photonic devices and other nanostructure electromagnetic devices presents a computationally intensive task. Much optimization relies on finite-difference time-domain or finite element analysis simulations, which can become very computationally demanding for finely detailed structures and dramatically reduce the available optimization space. [1] Circular Bragg Grating cavities (aka “Bullseye”) are widely used in single photon sources due to their moderate Purcell enhancement and excellent emission directionality. Although fundamentally simple, the design of Bullseye cavities demands computationally intensive and time-consuming iterations for optimization, and is limited in performance due to designer intuition, particularly when the number of adjustable parameters is large. Therefore, the inverse design of a Bullseye cavity is ideal, where geometry is determined as a function of target cavity performance instead of calculating cavity performance based on geometry. Here, we demonstrate that a Tandem Neural Network (TNN) architecture for the inverse design of Bullseye cavities can optimize Purcell enhancement and collimation efficiency at target resonant wavelengths within a training dataset. We describe how to implement this approach for a dielectric-based Bullseye cavity with a resonant wavelength of 690nm, achieving a comparatively high Purcell enhancement of 32 and an extraction efficiency of 0.60. We also report the fabrication of Bullseye cavities and the measured optical quality factors (Q) for some TNN-designed Bullseye cavities, which match the design well. Furthermore, we demonstrate the technique's generalizability to other materials and Bullseye geometries. We also illustrate how to incorporate fabrication constraints to tailor the design to minimum feature sizes and/or layer thickness. This technique not only significantly reduces design and simulation time while uncovering new favorable geometries for Bullseye cavities but could also be extended to other multiparameter photonic cavity systems.[2]

References

1. M. Sanchez, C. Everly, and P. A. Postigo, "Advances in machine learning optimization for classical and quantum photonics," J. Opt. Soc. Am. B 41, A177-A190 (2024) DOI: 10.1364/JOSAB.507268
2. J. Guimbao, L. Sanchis, L. Weituschat, J. M. Llorens, M. Song, J. Cardenas, and P. A. Postigo “Numerical Optimization of a Nanophotonic Cavity by Machine Learning for Near-Unity Photon Indistinguishability at Room Temperature”, ACS Photonics 2022 9 (6), 1926-1935 DOI: 10.1021/acsphotonics.1c01651

High-efficiency metasurface color routers inverse-designed via accelerated genetic algorithms

Hyoseok Park[1, 2†], Samuel Kim[3†], Yeonsang Park[1, 2*], Myungjae Lee[3*]

[1]Department of Physics, Chungnam National University, Daejeon, 34134, Korea
[2]Institute of Quantum Systems, Chungnam National University, Daejeon, 34134, Korea
[3]Department of Materials Science and Engineering, Seoul National University, Seoul, 08826, Korea
[†]H.P and S.K equally contributed to this work.
[*]corresponding authors: Y.P. (yeonsang.park@cnu.ac.kr) and M.L. (myungjae@snu.ac.kr).

Abstract: Metasurface color routers surpass color-filter arrays in image sensors by directing specific wavelengths of light to corresponding pixels. We inverse-designed a metasurface color router with high efficiency using a genetic algorithm accelerated by a U-net. The fabricated router shows efficiencies with 73 %, 69 %, and 45 % for RGB.

Conventional image sensors discriminate colors through the absorption by color filter arrays (CFAs). Since CFAs transmit only light of the desired color and absorb other colors, the theoretical maximum efficiency of CFA-based image sensors is restricted to approximately one-third. By contrast, metasurface color routers (MCRs), which are made of dielectric nanostructures that refract light depending on the wavelength, discriminate colors without absorption losses by directing light with specific color into the desired pixels in an image sensor. Therefore, an MCR can overcome the fundamental limitations of conventional image sensors with CFAs and show improved efficiency in color imaging as shown in Fig. 1 [1, 2]. In this work, we present an MCR with high routing efficiency that is enabled by inverse design using an accelerated genetic algorithm (GA) and demonstrated its enhanced performance experimentally.

GAs have been used to optimize MCR structures. However, GA-based optimization often faces challenges because simulating candidate structures is computationally expensive, limiting the exploration of potential designs. To address this, we replaced direct simulations with a U-Net neural network, trained to predict optical responses of given structures, thereby accelerating GA-based optimization. We trained the U-Net with electric-field (E-field) distribution datasets for approximately 140,000 structures, each consisting of a 16×16 array of randomly placed silicon nitride (Si_2Ni_3) nanopillars at three wavelengths (450 nm, 550 nm, and 650 nm for blue, green, and red, respectively). These datasets were produced using a finite-difference time-domain (FDTD) simulator (Lumerical FDTD). Once trained, the U-Net rapidly provides E-field dataset for any given structure, allowing the GA to explore millions of potential designs far more efficiently. After over 4,000 iterative generations, we identified an optimized MCR with peak routing efficiencies of 72.9% at 650 nm (red), 68.6% at 550 nm (green), and 45.1% at 450 nm (blue) as shown in Fig. 2.

The optimized MCR design was fabricated on a quartz substrate by depositing a 600 nm-thick Si_3N_4 layer, defining structures with an electron-beam lithography, and etching using inductively coupled plasma-reactive ion etching. To verify the routing performance, hyperspectral imaging with a xenon lamp and a high-numerical-aperture objective was performed on the fabricated MCR. Figure 2(b) shows both simulation and experimental results simultaneously and confirms that the two results are in excellent agreement. It means that our GA accelerated by U-Net neural network works well and is very efficient in optimizing MCR structure.

This study demonstrates a powerful framework for accelerating inverse-design processes, significantly

reducing computational overhead while enabling a broader exploration of design space. We expect that this approach not only paves the way for future high-efficiency MCRs but also can be applied for designing a wide range of nanophotonic device.

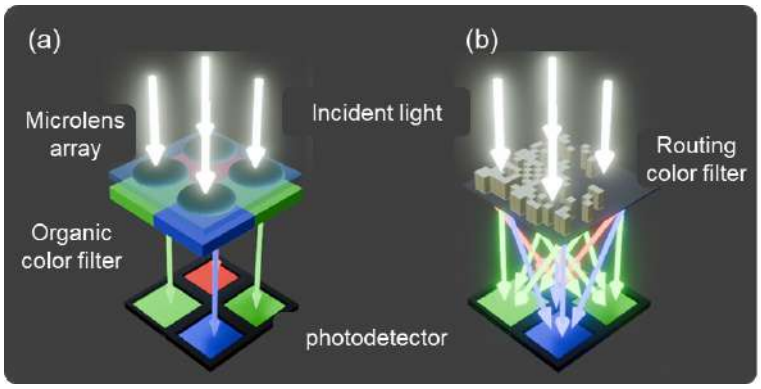


Figure 1. Schematics of comparison between (a) a conventional image sensor with color-filter array and (b) a metasurface color router.

(a) (b)

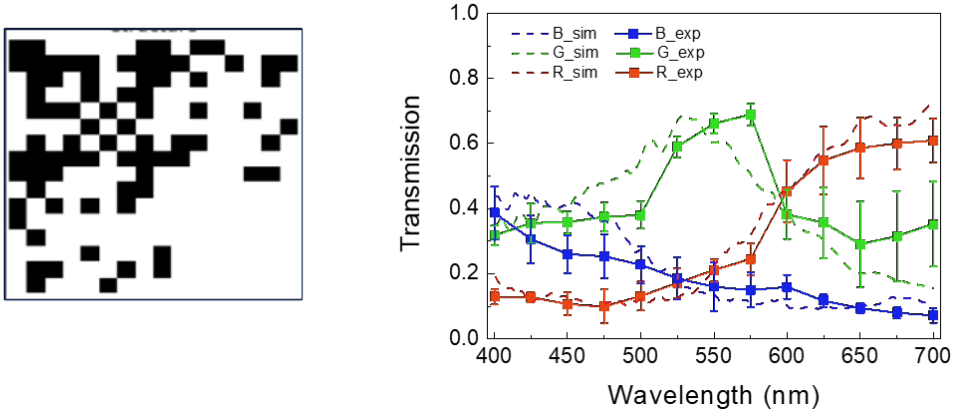


Figure 2. (a) Schematics of a high-efficiency MCR structure inverse-designed by an accelerated GA. (b) The solid lines represent the simulated transmission spectra of the optimized metasurface color router design, while the scatter points with error bars show the measured transmission of the fabricated device.

Acknowledgements

This work was supported by the Technology Innovation Program Development Program (00235080) funded by the Ministry of Trade, Industry & Energy (MOTIE, Korea), and by the Basic Science Research Program through the National Research Foundation of Korea (NRF) funded by the Ministry of Education (RS-2020-NR049597).

References

1. X. Zou, Y. Zhang, R. Lin, G. Gong, S. Wang, S. Zhu, Z. Wang, Pixel-level Bayer-type colour router based on metasurfaces, Nature Communications 13 (2022) 3288.
2. J. Li, Q. Zhang, H. Yang, T. Lei, L. Du, X. Wang, J. Bu, Q. Chen, Y. Liu, Z. Xie, Single-layer Bayer metasurface via inverse design, ACS Photonics 9 (2022) 2607-2613.

Experimental realization of convolution processing in photonic synthetic dimensions

Xinyuan Hu[1], Bing Wang[1*], Chenzhi Qin[1] and Peixiang Lu[1]

[1]School of Physics and Wuhan National Laboratory for Optoelectronics and, Huazhong University of Science and Technology, Wuhan 430074, China.
[*]corresponding author: wangbing@hust.edu.cn

Abstract: We use synthetic photonic lattice constructed from two coupled fiber loops to design an optical convolution processing unit, achieving the arbitrary convolution operations. The convolution process is completed with two phase modulators and two intensity modulators, which the convolution kernels can be dynamically reconfigured through phase and intensity modulation.

Main results:

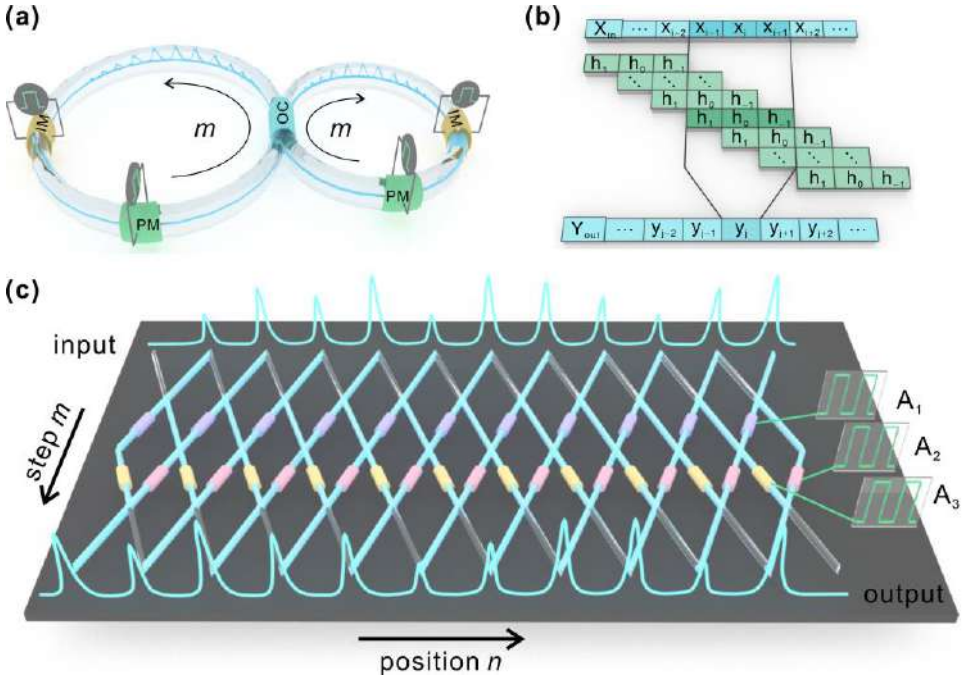


Fig. 1 Schematic diagram of the synthetic photonic lattice convolutional operation unit. **a.** Schematic of coupled fiber circuit to create the temporal lattice. **b.** Schematic of 2D convolution. **c.** Schematic of the synthetic lattice drawn based on the pulse evolution in the two coupled fiber loops in (a) and the convolution operation cell indicated by the blue grid.

Figure 1(a) and 1(c) show the evolution and construction of a synthetic temporal lattice through the mapping of pulses in two coupled fiber loops. The pulse sequences can be conceptually mapped to the "node-link" model by position n and step m of the synthetic temporal lattice. Additional phase shifts ϕ_n^m, ψ_n^m and intensity modulations G_n^m, F_n^m are introduced via a phase modulator (PM) and a Mach-Zehnder modulator (MZM)[1]. A convolution kernel of size $1\times M$ is designed by utilizing M steps of optical pulse propagation. Figure 1(b) constructs the most common and versatile 1×3 convolution kernel $[h_1\ h_0\ h_{-1}]$. The relevant pulse X_{in} is injected into the short loop at step $m = 0$, and the convolution result is obtained after two steps of modulation

$$\begin{cases} u_n^3 = C_1[A_v^1 A_v^2 u_{n-1}^0 + (A_v^1 A_u^2 + A_u^1 A_v^2)u_{n+1}^0 - (A_u^1 A_u^2 / t^2)u_{n+3}^0] \\ v_n^3 = iC_2\left[A_v^1 A_v^2 u_{n-3}^0 + (A_u^1 A_v^2 - A_v^1 A_u^2 t^2)u_{n-1}^0 + A_u^1 A_u^2 u_{n+1}^0\right] \end{cases}, \quad (1)$$

where, u_n^m and v_n^m represent the complex amplitudes of the pulses in the short and long loops, respectively, $\sin^2(\beta)/\cos^2(\beta)$is the splitting ratio of the central optical coupler ($\beta \in [0, \pi/2]$), and $A_u^m = G_n^m e^{i\phi_n^m}$, $A_v^m = F_n^m e^{i\psi_n^m}$ are the overall phase and intensity modulations applied to the loops. Here, $C_1 = -\sin^2(\beta)\cos(\beta)$, $C_2 = \sin(\beta)\cos^2(\beta)$, $t^2 = \sin^2(\beta)/\cos^2(\beta)$. By setting $X_{in} = [\ldots\ x_{i-1}\ x_i\ x_{i+1}\ldots]^T = [\ \ldots\ u_{n_1-2}^0\ \ u_{n_1}^0\ \ u_{n_1+2}^0\ \ \ldots\ ]^T$, $Y_{out} = [\ldots\ y_{j-1}\ y_j\ y_{j+1}\ldots]^T = [\ldots\ u_{n-1}^M\ \ u_{n+1}^M\ \ u_{n+3}^M\ldots]^T$, we obtain $y_j = h_1 x_{i-1} + h_0 x_i + h_{-1} x_{i+1}$, which corresponds to the classical form of convolution

$$y_j = H_{j,i} x_i = \sum_i h_{j-i} x_i = \sum_i h_i x_{j-i}\,. \quad (2)$$

Figure 2 demonstrates the process of convolution using the temporal photonic lattice convolution processing unit, where the convolution kernel [1 2 1] is employed. The figure illustrates the image convolution processing flow (the left figure), the corresponding electronic control signals and optical signal flow (the middle figure), the experimental setup (the right figure), and the evolution of the convolution pulse amplitude in the temporal photonic lattice (The bottom image in the middle).

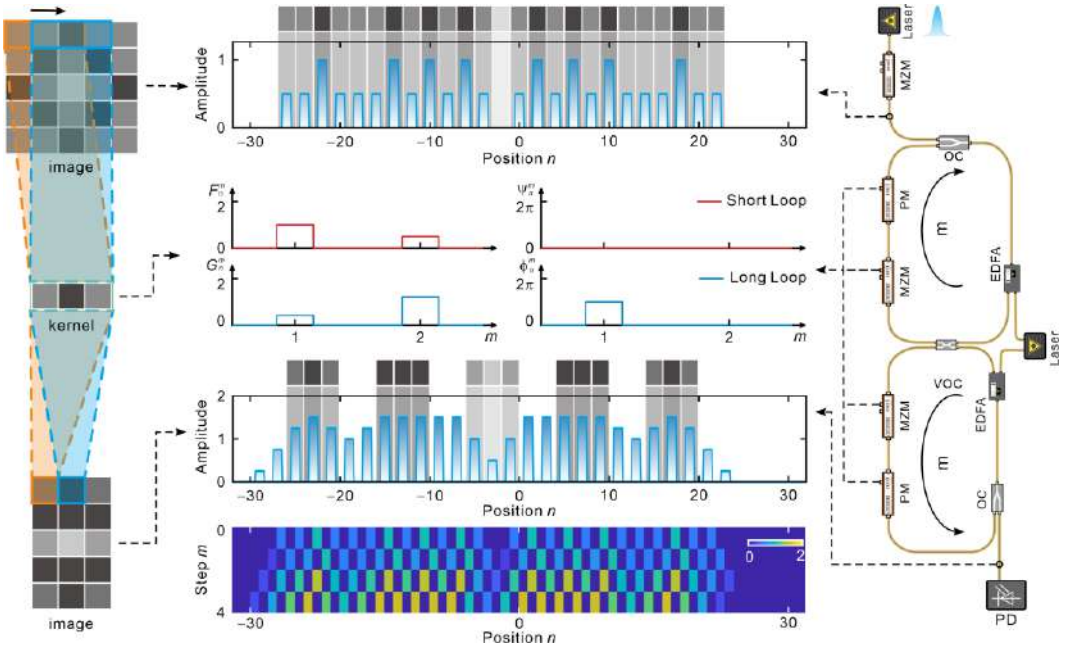


Fig. 2. Schematic diagram of image processing in a temporal photonic lattice.

Acknowledgements: The work was supported by National Natural Science Foundation of China (No. 12374305, No. 12021004, No. 12147151, No. 62305122, No. 12204185 and No. 12204185).

References

1. X. Hu *et al*., "Observing the collapse of super-Bloch oscillations in strong-driving photonic temporal lattices," *Advanced Photonics*.

Learning Higher-Order Interactions with Factorization Machine for Material Design

S. Hwang[1], S. Kim[2], T. Luo[3*] and E. Lee[1*]

[1]Department of Electronic Engineering, Kyung Hee University, Gyonggi-Do, Yongin-Si, 17104, South Korea
[2]National Centor for Computational Sciences, Oak Ridge National Laboratory, Oak Ridge, TN 37830, USA
[3]Department of Aerospace and Mechanical Engineering, University of Notre Dame, Notre Dame, IN 46556, USA
[*]tluo@nd.edu (T. Luo)
[*]eleest@khu.ac.kr (E. Lee)

Abstract:
Factorization Machine (FM) has been used for effectively designing optical systems, it is limited in expressing complex systems. To overcome this limitation, we propose higher-order factorization machine (HOFM). Compared to FM, HOFM predict more accurately than FM and find better optimal structures in optical systems.

Introduction

Optimizing structural parameters is important for improving performance in material science. The 2nd-order factorization machine (FM)[1] has been used for modeling optimal structures and predicting optical systems by factorizing pairwise interactions between two variables. However, FM has limitations in capturing intricate relationships among numerous system features and multiple variables. To overcome this limitation, we use a higher-order factorization machine (HOFM)[2], which has supplementary parameters up to the third interaction. In this study, we verify the predictive fidelity and efficiency of the surrogate model in optimizing optical design (e.g. Transparent Radiative Cooler (TRC)[3]) by 3rd-order FM compared to 2nd-order FM. To evaluate the designed structure, we define figure of merit (FOM), given by:

$$\mathrm{FOM} = \frac{10\int_{300}^{2500}\left(TI_{ideal}(\lambda) - TI_{designed}(\boldsymbol{\lambda})\right)^2 \mathrm{d}\lambda}{\int_{300}^{2500} S(\boldsymbol{\lambda})^2 \,\mathrm{d}\lambda}, \quad (1)$$

where , $S(\boldsymbol{\lambda})$, $TI(\lambda)$ respectively denotes the solar spectral irradiance, and transmitted irradiance.

Results and Discussion

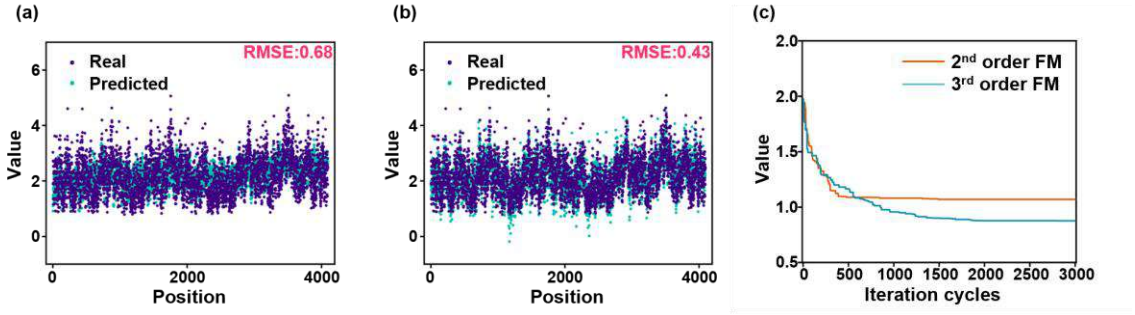


Figure1. The performance comparison between 2nd-order FM and 3rd-order FM with a TRC as a testbed. (a) and (b) is the accuracy of the surrogate model obtained from 2nd-order FM and 3rd-order FM, respectively. (c) Convergence of FOM values for iterative FMs integrated with active learning algorithms.

For the benchmarking analysis, the FOM of the TRC system is investigated by evaluating all possible material combinations and plotted as purple dots in Fig1. We made surrogate model obtained from FMs by training 500 randomly sampled binarized discrete data points in 2^{12} (= 4,096). The value of these 2nd-order and 3rd-order FM's surrogate models are shown as cyan dots in Fig.1 a and Fig.1 b respectively. 3rd-order FM shows better accuracy of TRC system than 2nd-order FM (Figs. 1a,b). The fact that the RMSE of 3rd-order FM (0.43) is lower than that of 2nd-order FM (0.68) supports it. This can be concluded as showing that the third order interactions are helpful for capturing the complex features in optical systems.

We perform active learning combined with both 2nd order or 3rd order FM (Fig. 1c) 10 times, each with a different initial training dataset for ensuring the reliable results. Solid lines denote the average minimum FOM values with 10 different datasets for each active learing iteration. It can be guaranteed that active learning combined with 3rd-order FM finds better optical structures on average.

The performance analysis demonstrates the enhanced surrogate modeling capabilities and optimization efficiency of 3rd-order FM compared to 2nd-order FM. Accordingly, our study indicates that 3rd-order FM-based active learning serves as a highly effective approach for material design, yielding optimally refined results. Moreover, we anticipate that quantum computing techniques can be incorporated into this 3rd-order FM active learning framework to optimize large-scale material optimization [4, 5].

Acknowledgement
This research was supported by the Quantum Computing Based on Quantum Advantage Challenge Research (RS-2023-00255442) funded by the Korea government (MSIT).

References

[1] S. Rendle, "Factorization machines." pp. 995-1000.

[2] M. Blondel, A. Fujino, N. Ueda *et al.*, "Higher-order factorization machines," *Advances in neural information processing systems,* vol. 29, 2016.

[3] S. Wang, T. Jiang, Y. Meng *et al.*, "Scalable thermochromic smart windows with passive radiative cooling regulation," *Science,* vol. 374, no. 6574, pp. 1501-1504, 2021.

[4] S. Kim, W. Shang, S. Moon *et al.*, "High-performance transparent radiative cooler designed by quantum computing," *ACS Energy Letters,* vol. 7, no. 12, pp. 4134-4141, 2022.

[5] A. Mandal, A. Roy, S. Upadhyay *et al.*, "Compressed quadratization of higher order binary optimization problems." pp. 126-131.

Deep Learning and Nano-optics: Designing nanoscale polariton propagations in twisted van der Waals multilayers

L. F. Álvarez-Tomillo[1,2], J. Álvarez-Cuervo[1,2], P. Calvo-Barlés[3,4], S. G. Rodrigo[3,5], E. Terán-García[1,2], A. Taragaza Martín-Luengo[1,2], K. V. Voronin[6,7], A. Y. Nikitin[7,8], L. Martín-Moreno[3,4*], P. Alonso-González[1,2*]

[1] Department of Physics, University of Oviedo 33006, Oviedo, Spain

[2.] Center of Research on Nanomaterials and Nanotechnology, CINN (CSIC-Universidad de Oviedo), El Entrego 33940, Spain.

[3] Instituto de Nanociencia y Materiales de Aragon (INMA), CSIC-Universidad de Zaragoza, Zaragoza 50009, Spain

[4]Departamento de Física de la Materia Condensada, Universidad de Zaragoza, 50009 Zaragoza, Spain

[5]Departamento de Física Aplicada, Universidad de Zaragoza, 50009 Zaragoza, Spain

[6]Universidad del Pais Vasco/Euskal Herriko Unibertsitatea, 20080 Donostia/San Sebastián, Basque Country, Spain

[7]Donostia International Physics Center (DIPC), Donostia-San Sebastián, Spain.

[8]IKERBASQUE, Basque Foundation for Science, Bilbao 48013, Spain

[*]Correspondence to: lmm@unizar.es, pabloalonso@uniovi.es

Abstract: We demonstrate the design of nanoscale phonon polariton propagations by combining artificial intelligence and nanophotonics. Using neural networks and twisted α-MoO_3 multilayers, we achieve desired polariton propagations such as canalization and bi-canalization in unexplored frequency ranges, showcasing a powerful method for on-demand control of light at the nanoscale.

The field of nano-optics or nanophotonics has advanced rapidly, enabling unprecedented control of light at the nanoscale. One of the main driving forces behind this progress is the discovery of a variety of polaritons in van der Waals[1,2] (vdW) multilayers with never-before-observed properties, such as unidirectional[3] or ray-like propagations[4]. However, despite these exciting advances, nano-optics still presents a major limitation: obtaining propagations on demand, i.e. by design.

In this work, we overcome this limitation through the combined use of a **neural network** a**nd twisted polaritonic multilayers (Fig. 1)**. Our method enables **inverse design**, making it possible to **demonstrate desired (and thus novel) polariton propagations** by obtaining accurate predictions of subsequently fabricated multilayer configurations. Interestingly, this method efficiently handles possible system degeneracies, identifying multiple multilayer structures that give rise to the same desired propagations at the nanoscale.

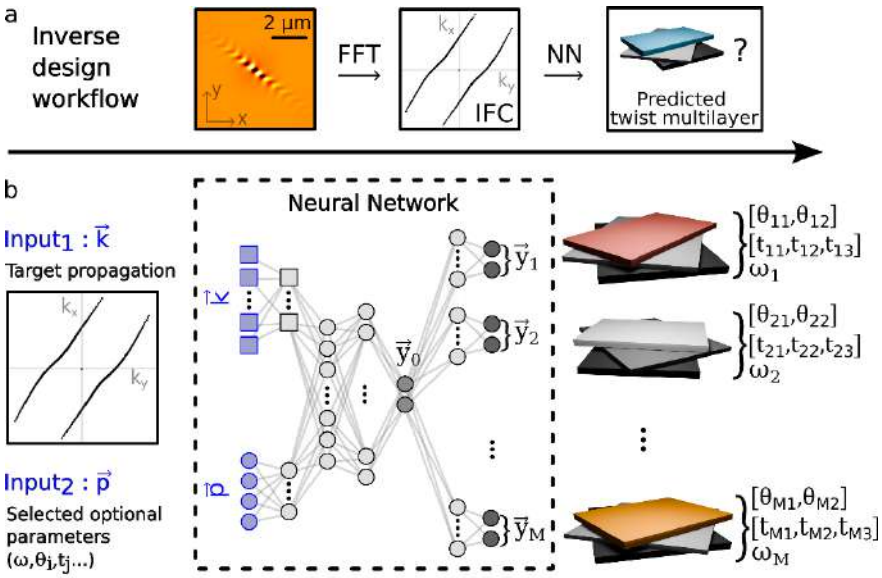


Figure 1: Designing nanoscale light propagation by combining deep learning and twistoptics. a) Schematic representation of the inverse design workflow using a NN in twistoptics. The desired polaritonic propagation in real space is transformed into an IFC that serves as input1 to the NN which predicts the optimal multilayer structure. b) The NN operates as a unified model with a set of M branches that allow finding multivalued solutions. The overall NN, trained with the customized loss function as described in ref. 5, accurately predicts the structure parameters ($\vec{\theta}$, $\vec{t}$, and ω) for one or multiple configurations.

References

1. Ma, W. *et al.* In-plane anisotropic and ultra-low-loss polaritons in a natural van der Waals crystal. *Nature* **562**, 557–562 (2018).
2. Álvarez-Pérez, G. *et al.* Infrared Permittivity of the Biaxial van der Waals Semiconductor α-MoO3 from Near- and Far-Field Correlative Studies. *Advanced Materials* **32**, 1908176 (2020).
3. Duan, J. *et al.* Multiple and spectrally robust photonic magic angles in reconfigurable α-MoO3 trilayers. *Nat Mater* **22**, 867–872 (2023).
4. Álvarez-Cuervo, J. *et al.* Unidirectional ray polaritons in twisted asymmetric stacks. *Nat Commun* **15**, 9042 (2024).

Laser Generation with Metal-Free Carbogenic Quantum Dots

D. Hernández-Pinilla[1,2*], B. K. Barman[1], and T. Nagao[1,3]

[1]International Center for Materials Nanoarchitectonics (MANA-NIMS), Tsukuba 305-0044, Japan
[2]Dept. of Physics of Materials, Universidad Autónoma de Madrid (UAM), Madrid 28049, Spain
[3]Dept. of Condensed Matter Physics, Hokkaido University, Sapporo 060-0810, Japan

[*]corresponding author: david.hernandezp@uam.es

Abstract: Different types of newly synthetized eco-friendly, low-cost carbon quantum dots (CDs) are evaluated to achieve carbon-based laser devices utilizing planar micro-cavities. The results constitute a step forward towards developing alternative eco-friendly carbon-based light-emitting devices aimed to replace current ones based on costly rare-earth and toxic metal elements.

In the last years, intense research efforts have been made in search of new strategic luminescent materials aimed to replace costly rare-earth and toxic metal elements as well as scarce semiconductors. On this account, a unique emerging class of metal-free luminescent materials known as carbon dots (CDs) has been successfully developed via low-cost methods, exhibiting intense photoluminescence and high stability together with excellent biocompatibility and environmental sustainability [1-3]. The outstanding properties of this promising new material has led to the development of proof-of-concept applications in sensing, photocatalysis, and bio-imaging among other fields. However, most of the reported CDs exhibit broad emissions that hinder their implementation in practical applications where commercial semiconductor quantum dots, rare earths and organic dyes are commonly used (LEDs, bio-labeling detection…). For this reason, CDs systems displaying narrowband emissions are essential to achieve the required technological breakthrough for the development of cutting-edge practical applications.

In this work, we made use of the excellent fluorescence properties of our synthetized metal-free, eco-friendly, and low-cost CDs to realize a CDs laser system with reduced linewidth [3]. Sputtered planar nano-photonic structures composed of low-loss materials were assembled to form a Fabry-Perot laser planar micro-resonator that allow exceptionally high reflectance spectral regions. This architecture realizes an excellent electromagnetic field confinement in the CDs gain media, thus providing appropriate optical gain to the system. Upon supplying an adequate amount of pump power, laser threshold is observed and single-mode narrow blue laser emission is finally achieved. The results constitute a step forward towards the development of novel eco-friendly carbon-based light-emitting devices.

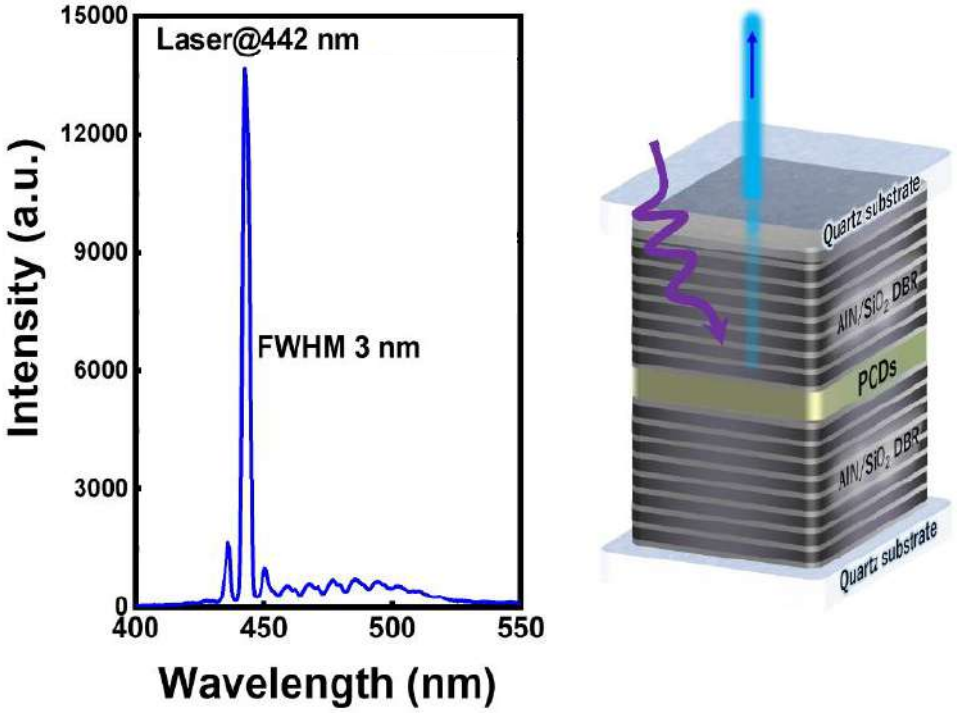


Figure 1: Narrowband laser emission from a CD-based laser system. Pump wavelength corresponds to UV radiation and lasing wavelength falls within the blue spectral region. A sputtered planar micro-cavity is utilized as micro-resonator.

References

1. Liu, J. J., Li, R. and Yang, B, "Carbon Dots: A new Type of Carbon-based nanomaterial with wide applications", ACS Cent. Sci., Vol. 6, No. 12, 2179-2195, 2020.
2. Barman, B. K., Nagao, T. and Nanda, K. K, "Dual roles of a transparent polymer film containing dispersed N-doped carbon dots: A high-efficiency blue light converter and UV screen", Appl. Surf. Sci., Vol. 510, 145405, 2020.
3. Barman, B. K., Hernández-Pinilla, D., Cretu, O., Ohta, R., Okano, K., Shiroya, T., Sasai, J., Kimoto, K. and Nagao, T, "New insight into fluorescent polymeric carbon dots for solid-state laser device", ACS Sustain. Chem. Eng., Vol. 11, No. 33, 12291-12303, 2023.

AlGaInAs/InP microcavities for unidirectional and single mode lasing

You-Ling Chen
State Key Laboratory of Integrated Optoelectronics, Institute of Semiconductors, Chinese Academy of Sciences, Beijing 100083, China
*corresponding author: ylchen@semi.ac.cn

Abstract: A dual-port square microresonator for single-mode lasing has been fabricated, capable of providing two optical sources simultaneously for optical signal processing. Moreover, a deformed circular-side triangular microresonator is fabricated with unidirectional light emission, which has potential applications in portable and highly sensitive far-field detection of nanoparticles.

1. Introduction

Whispering-gallery mode (WGM) optical microcavities have found a wide range of applications such as highly sensitive bio/chemical sensing, and microlasers. However, light emission is isotropic in a traditional WGM microlaser. To realize efficient extraction and collection of light, the emission should be tailored. Here we report two schemes of realizing directional laser emission using semiconductor microcavities, benefiting the integration with other optoelectronic devices.

2. Dual-port square microresonator for directional single-mode lasing

For the cavity material of AlGaInAs quantum wells, we demonstrate experimentally a dual-port square microresonator for single-mode lasing with a side-mode-suppression ratio (SMSR) exceeding 40 dB. By connecting waveguides at two opposite vertices, the quality factor for the antisymmetric mode (ASM) is much higher than that of the symmetric mode (SM), enabling nondegenerate single-mode lasing.

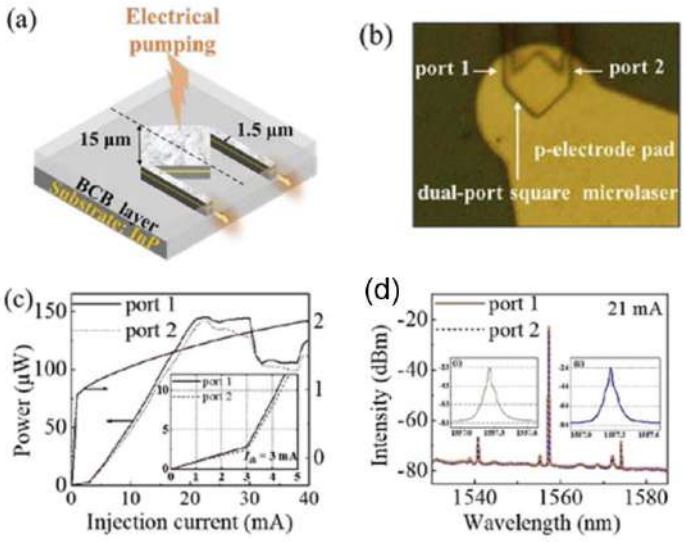


Fig. 1 (a) Schematic diagram of the dual-port square microcavity. (b) Microscopic image of the microlaser. (c) Output power coupled to MMF from two ports and V-I curve at 293 K versus continuous injection current; the inset is the enlarged view of the V-I curve for the injection current range of 0-5 mA. (d) Emission spectra for ports 1 and 2 independently at the injection current of 3 mA.

3. Deformed circular-side triangular microresonator for unidirectional lasing

A waveguide-connected deformed circular-side triangular microresonator (CTM) is designed and fabricated, as illustrated in Fig. 2.

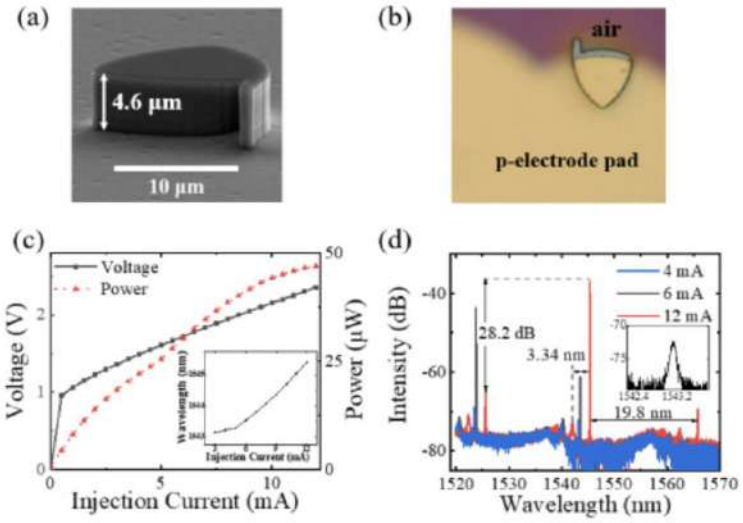


Fig 2. (a) SEM image of the circular side triangular microlaser after ICP etching. (b) Microscopic image of the CTM with p-electrode. (c) Integral ball output power and voltage versus continuous-wave injection current. The inset shows the wavelength of the main lasing mode versus the injection current. (d) Lasing spectra at injection currents of 4, 6, and 12 mA. The inset shows the detailed spectra at 4 mA near the wavelength of 1543.15 nm.

The far field light emission pattern is illustrated in Fig. 3. Fig. 3 (b) is the detailed experimental far field pattern for $I = 12$ mA. Unidirectional light emission from arc side 1 with a divergence angle of about 38° is obtained.

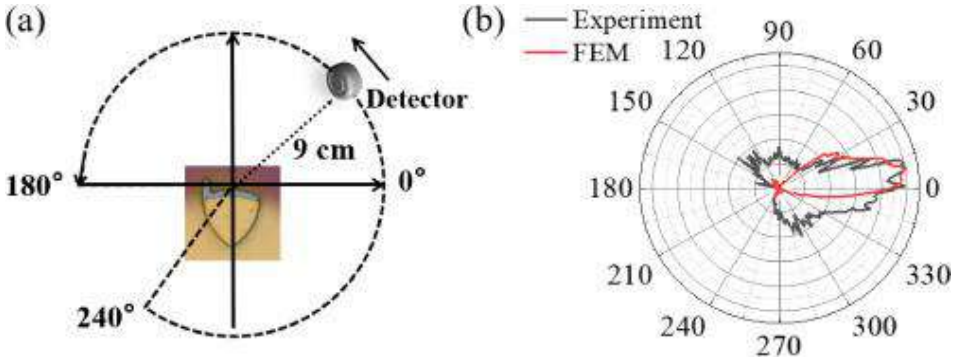


Fig. 3. **(a)** Schematic diagram of the experimental far field light emission test. **(b)** Experimental (black) and theoretical (red) far field pattern at the injection current of 12 mA.

Refences

1. K. Yang, Y. L. Chen, et al. “Single-mode lasing in an AlGaInAs/InP dual-port square microresonator,” Opt. Lett. 47, 3672 (2022)
2. W. Wang, Y. L. Chen, et al. “Unidirectional light emission in a deformed circular-side triangular microresonator,” Opt. Express 31, 14560 (2023).

Fabrication of bound states in the continuum laser cavity compatible with standard semiconductor technology

K. Bogdanowicz[1,2*], L. Stanco[1], W, Glowadzka[2], T. Fas[3], J. Suffczynski[3], M. Ekielski[1], J. Muszalski[1] , T. Czyszanowski[2], A. Szerling[1]

[1] Łukasiewicz Research Network – Institute of Microelectronics and Photonics, 02-668 Warsaw, Lotnikow 32/46, Poland
[2] Lodz University of Technology – Institute of Physics , 93-005 Lodz, Wolczanska 217/221, Poland
[3] University of Warsaw – Faculty of Physics, Pasteura 5, 02-093 Warsaw, Poland
[*]Karolina.bogdanowicz@imif.lukasiewicz.gov.pl

Abstract: The work demonstrates fabrication of the laser cavity with broken symmetry based on bound states in the continuum (BICs). A fabrication process for a 1D dielectric grating was developed to realize a newly designed cavity, achieving a mechanically stable laser, manufactured using standard semiconductor technology.

The research objective was to design a grating with broken symmetry relative to the plane of the periodic structure to achieve bound states in the continuum (BIC). This was pursued by developing a method for producing dielectric nanophotonic structures intended to replace one of the classically used Distributed Bragg reflector (DBR) in a vertical-cavity surface-emitting laser (VCSEL), epitaxially grown on a GaAs substrate (see Fig. 1a). The periodic structure enables the replacement of the upper distributed Bragg reflector (DBR) layer in VCSELs, resulting in a miniaturized device without compromising laser efficiency, while simplifying the manufacturing process, thus enhancing production efficiency and reducing costs on a larger scale. Existing lasers utilizing this idea have been created in a form of difficult to produce membranes with limited applications. Our solution provides a mechanically stable laser, manufactured using standard semiconductor technology.

The key aspect of the technology is the formation of subwavelength gratings with precisely defined geometry, in which the period *L*, the fill factor *F* and the etching depth *H* are designed to reflect a specific wavelength of light. Another important requirement is to make the grating in a material characterized by a refractive index lower than the index of the substrate material on which the grating is formed. The grating constructed in this way generates an antisymmetric mode and is an element of the cavity in which the DBR is designed to reflect specific, non-zero diffraction orders - usually the first one.

The goal was to establish a process for creating a 1D dielectric grating with straight and smooth walls to achieve an antisymmetric mode. High-precision electron beam lithography was employed to create the grating pattern, which was subsequently transferred to the substrate material via reactive ion etching (RIE). Numerical simul a) s were utilized to optimize the dimensions of the grating structure. For the epitaxial substrate with central wavelength at Λ_{DBR}= 995nm, optimal grating parameters were *L* = 910nm, *H* = 380nm, *F* = 0.5, *L-a* = 455nm. These dimensions can vary based on the e-beam dose, development time, and the parameters selected for the plasma etching process, therefore achieving the designed configuration is a challenge. To mitigate the impact of individual process steps on the final dimensions of the structure, a 10x10 matrix was established, accounting for period variations (*L*) from 902 to 920 nm and etched stripe width (*L-a)* from 420 to 520 nm, while maintaining constant dimensions: etched depth (*H*) at 0.38 μm and total oxide thickness at 0.8 μm. An etching procedure was developed, considering the influence of process gas pressure on wall shape and etch rate. Studies indicated that using lower pressure in the RIE etching process resulted in a higher etch rate and positively influenced the inclination of the etched walls, producing a more rectangular profile.

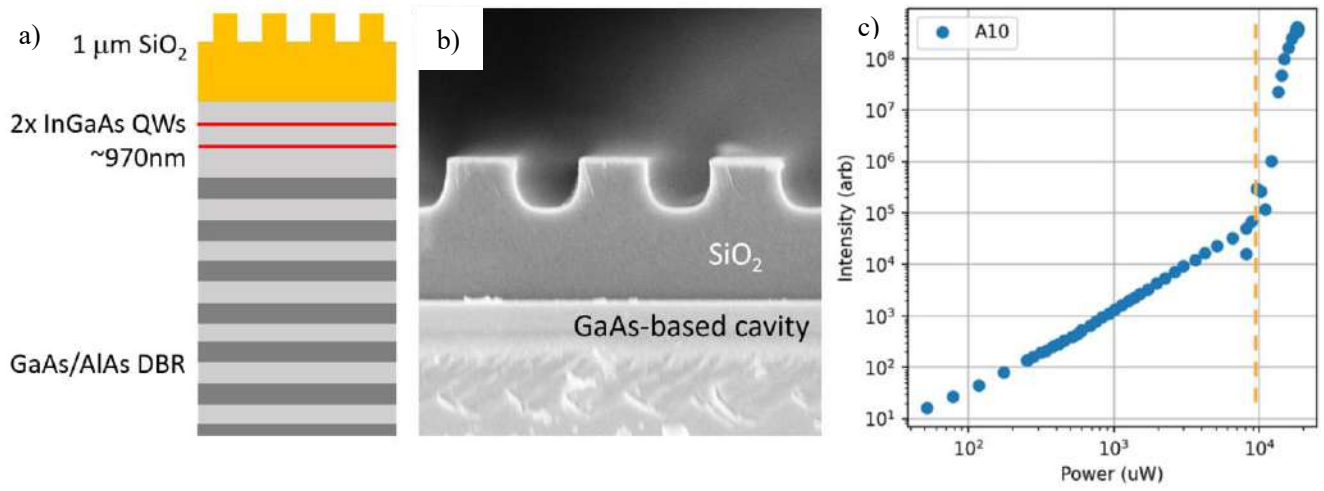


Figure 1 -Schematics of BIC-based cavity a), SEM image of cavity cross-section b), the dependence of the relative power emitted by the laser on the relative excitation power c)

The result of the research was the creation of a structure optimized in terms of dimensions, meeting the design requirement defined at the beginning of the work. The quality of the structure was checked by observations using a scanning electron microscope (see Fig. 1b), and its optical properties were characterized. Photoluminescence measurements were performed on the structure produced in this way, using a Mira Seed pulsed laser with a pulse length of 20 fs and an excitation wavelength of 755 nm. The tests performed at a temperature of 10 K showed lasing action of the structure for a minimum power of 10 mW of the excitation laser (Fig. 1c), as well as the presence of a polarization vortex, which confirms the occurrence of BIC in the structure.

This research was financially supported by the Polish National Center of Science within the project SONATA BIS 13 under grant no. 2023/50/E/ST7/00698 and European Union's Horizon Europe Research and Innovation Programme under grant agreement No. 101069490

Multicolor Scintillators Coupled with Physics-Aware Postprocessing Allows Energy-Resolved X-ray Imaging of Medical Contrast Agents

S. Min[1,2], S. Choi[1], S. Pajovic[3], S. Vaidya[4], N. Rivera[5], S. Fan[6], M. Soljačić[1,4], and C. Roques-Carmes[1,6*]

[1]Research Laboratory of Electronics, Massachusetts Institute of Technology, USA
[2]Department of Material Science and Engineering, Korea Advanced Institute of Science and Technology, Republic of Korea
[3]Department of Mechanical Engineering, Massachusetts Institute of Technology, USA
[4]Department of Physics, Massachusetts Institute of Technology, USA
[5]Department of Physics, Harvard University, USA
[6]E. L. Ginzton Laboratories, Stanford University, USA
[*]corresponding author: chrc@stanford.edu

Abstract: We present an end-to-end reconstruction framework that combines a three-layer multicolor scintillator with a physics-aware postprocessing algorithm to allow energy-resolved X-ray imaging. Using this framework, we demonstrate the simultaneous identification of iodine and gadolinium-based contrast agents from body tissues through simulations of a computational phantom.

Conventional X-ray imaging often relies on scintillators to convert impinging X-rays into visible light, which is then detected by image sensors. In a typical clinical setting, X-rays generated from an X-ray tube with a broadband energy spectrum passes through the specimen, and a grayscale image sensor is used to map the scintillation intensity from all incident X-ray energies into the same intensity channel. Such a single-channel setup is only able to record the energy-integrated absorption level of each region of the specimen (i.e., the source-spectrum-weighted average of the linear attenuation coefficient over the incident energy range).

This is a significant drawback for applications in which material identification is important such as medical contrast imaging and nondestructive inspection at security checkpoints. Energy-resolved imaging is particularly crucial for contrast imaging, where it is known that blood containing contrast agents are difficult to distinguish from calcium-rich media such as bones and calcified stones that also attenuate X-ray strongly [1,2]. Nevertheless, commonly used iodine or gadolinium-based contrast agent have characteristic absorption K-edges at 33 and 50 keV, respectively. Therefore, an appropriately designed energy-resolved imaging scheme would allow the contrast agents and calcium-rich media to be distinguished from one another based on each media's unique energy-dependence of X-ray absorption.

In our work, we present a general framework for energy reconstruction in X-ray imaging that combines a three-layer multicolor scintillator with a physics-aware postprocessing algorithm in an end-to-end approach (Fig. 1a). Through this, we demonstrate three-bin energy-resolved X-ray imaging tailored for identifying contrast agents for medical applications (Fig. 1b-d). In our framework, the multicolor scintillator acts as a physical "pre-processor" that preserves and encodes the energy information of incident X-rays onto an RGB detector. The scintillators used for the multilayer stack were carefully selected such that each energy bin is preferentially absorbed in different target scintillators, each with a different emission color. The postprocessing algorithm extracts the energy information from the size and color of the scintillation "spots" recorded on the RGB detector. All simulations were done using GEANT4, an *ab initio* Monte Carlo simulation tool for high-energy particle-matter interactions [3].

This work is supported in part by the DARPA Agreement No.~HO0011249049, as well as being also

supported in part by the U. S. Army Research Office through the Institute for Soldier Nanotechnologies at MIT, under Collaborative Agreement Number W911NF-23-2-0121.

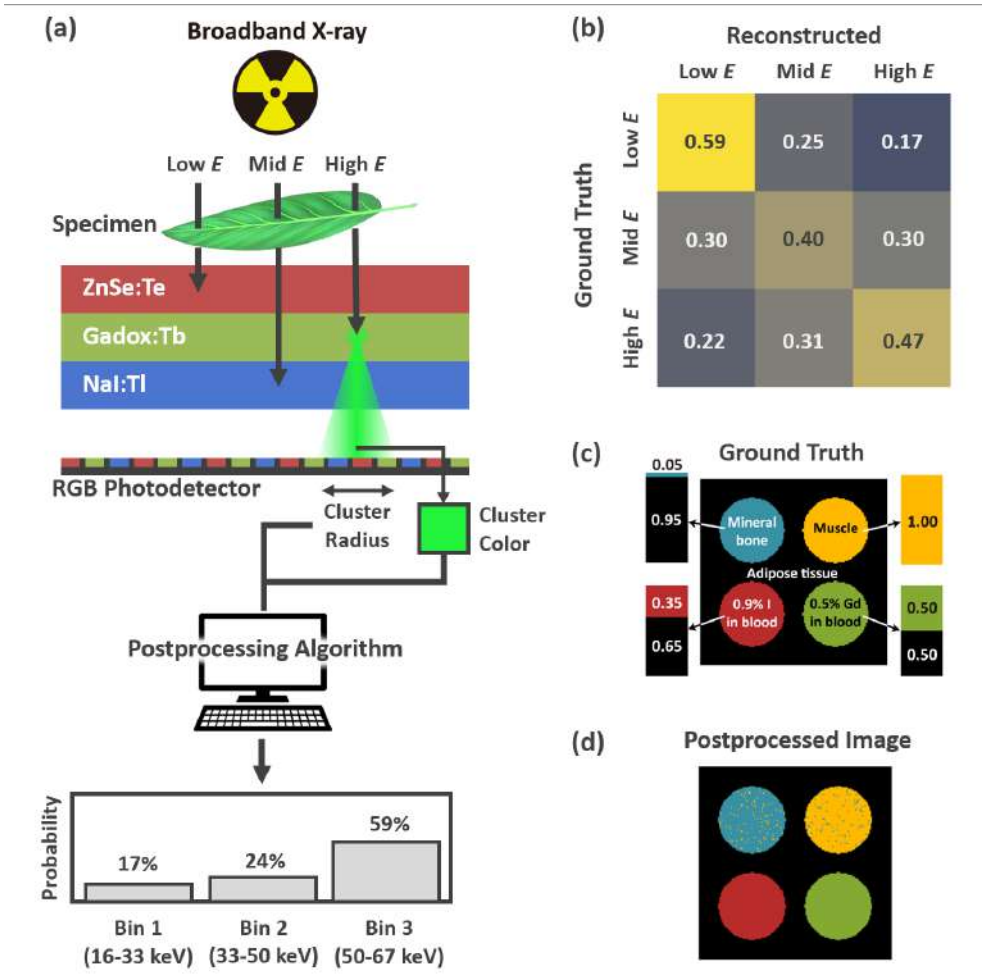


Figure 1. a) End-to-end energy reconstruction framework. X-rays with a broadband energy distribution passes through a specimen to be incident on the multicolor scintillator. The absorption depth is dependent on the X-ray energy. The size and color of the resulting scintillation spot is passed to a postprocessing algorithm, which computes the probabilities that the original X-ray could have been from each energy bin. **b)** Simulated confusion matrix for the mapping from the ground truth to the reconstructed energy bins. **c)** Ground truth computational phantom. **d)** Simulated postprocessed image using our energy reconstruction framework under low detector noise.

References

1. Riederer, S. J. and C. A. Mistretta, "Selective iodine imaging using K-edge energies in computerized x-ray tomography," Med. Phys., Vol. 4, No. 6, 474–481, 1977.
2. De Vries, A., E. Roessl, E. Kneepkens, A. Thran, B. Brendel, G. Martens, R. Proska, K. Nicolay and H. Grűll, "Quantitative Spectral K-Edge Imaging in Preclinical Photon-Counting X-Ray Computed Tomography," Invest. Radiol., Vol. 50, No. 4, 297–304, 2015.
3. Agostinelli, S., J. Allison, K. Amako, J. Apostolakis, H. Araujo, P. Arce, M. Asai, D. Axen, S. Banerjee, G. Barrand *et al*., "GEANT4–a simulation toolkit," Nucl. Instrum. Methods Phys. Res. A, Vol. 506, No. 3, 250–303, 2003.

Versatile Design Approach of Switchable On-Chip Emitter-Coupled Meta-Optics Photon Source

S. im Sande[1*], Torgom Yezekyan[1], Y. Kan[1], D. Komisar[1], C. Wu[1], S. Kumar[1], N. Q. Adanan[2], G. Zamiri[2], J. K. W. Yang[2], S. I. Bozhevolnyi[1], F. Ding[1]

[1] University of Southern Denmark, Centre for Nano Optics, Campusvej 55, 5230, Odense, Denmark

[2]Singapore University of Technology and Design (SUTD), 8 Somapah Road, 487372 Singapore, Republic of Singapore

* corresponding author: soim@mci.sdu.dk

Abstract –We showcase a versatile metasurface-enabled design method for multichannel photon sources that enables arbitrary polarization control over multiple channels with distinct directions by exploiting the nonradiative interaction between quantum emitters and surrounding scattering meta-atoms. Furthermore, the integration of phase-change materials allows for the switching between multiple functionalities.

Solid-state quantum emitters (QEs) need to compensate several drawbacks to be purposefully used in quantum technologies. To overcome these issues bulky components are needed, which, however, are disadvantageous for implementation in devices. Some of the issues can be resolved by integrating QEs in photonic metasurfaces. [1,2] Embedding the QEs in nanocavities improves emission rates via the Purcell effect. However, simulatneous control of polarization states or directionality of the emission remains challenging. [3,4] Recently, on-chip plasmon-QE coupled metasurfaces have shown improvements in the control of the emission properties. [5] The QE excites surface plasmon polaritons (SPPs) that are outcoupled by the surrounding metasurface, resulting in defined polarization states.

We demonstrate a universal on-chip QE-coupled meta-optics platform that unlocks full DoFs in shaping the polarization states and direction in multiple channel emission by using metallic metaatoms with half-wave plate (HWP) functionality. These metaatoms are arranged around a QE, that is separated by a thin silica layer from a silver substrate. A quantum emitter with the dipole orientation out of plane decays mostly into radially outoing SPPs. By surrouding the QE emitter by a nanostructure the SPPs are outcoupled into the farfield. Therefore, it is possible through careful design of the metasurface that surrounds the QE to manipulate the outcoupled light with regard to propagation direction and polarization. HWP metaatoms have shown great capabilities in the manipulation of polarizations and the shaping of wavefronts. At each point surrounding the emitter the necesasary resonance and geometric phase can be calculated to outcouple the SPP into the desired photon state.

The versatility of this approach can be extended through the integration of phase-change materials (PCM) disc in the center of the structure surrounding the QE. This allows to selectively absorb the SPPs in certain directions before reaching the metasurface. Therefore, dividing the surrounding metasurface into segments with different functionalities allows for selective emission properties depending on the state of the phase-change, surpressing the emission of metasurface segments where the SPP is absorbed.

Polarization measurements at wavelength of 670nm show a S3-parameter value of -0.94 for single channel left-circularly polarized emission averaged over the entirety of the spot. Additionally, a metasurface, that directs 45°-linearly polarized (aLP) and 135°-linearly polarized (bLP) light into −y and y-direction showcase the multi-channel performance of this design principle. The measured avergaed S2-parameter values for this metasurface are +0.95 and −0.94.

Furthermore, the versatility of the design method is highlighted by fabricating a metasurface directing aLP and LCP light in different spatial directions (Fig. 1). This metasurface achieves avergaged S-parameters of +0.79

(S2) and −0.93 (S3) due to cross talk between the two non-orthogonal polarizations. In the second metasurface the intensities are reversed. In this case, the averaged S-parameter values are +0.79 (S2) and −0.92 (S3).

Simulations with an integrated PCM disc surrounding the QE made of Sb_2S_3 show a contrast in the signal between amorphous and crystalline close to unity allowing for an extension of this approach to a switchable multi-channel approach. However, the integration of the PCM discs slightly reduces the polarization purity.

Finally, it should be noted that this platform can be implemented for various wavelengths through thoroughly designing the metaatoms (i.e., dimensions and material).

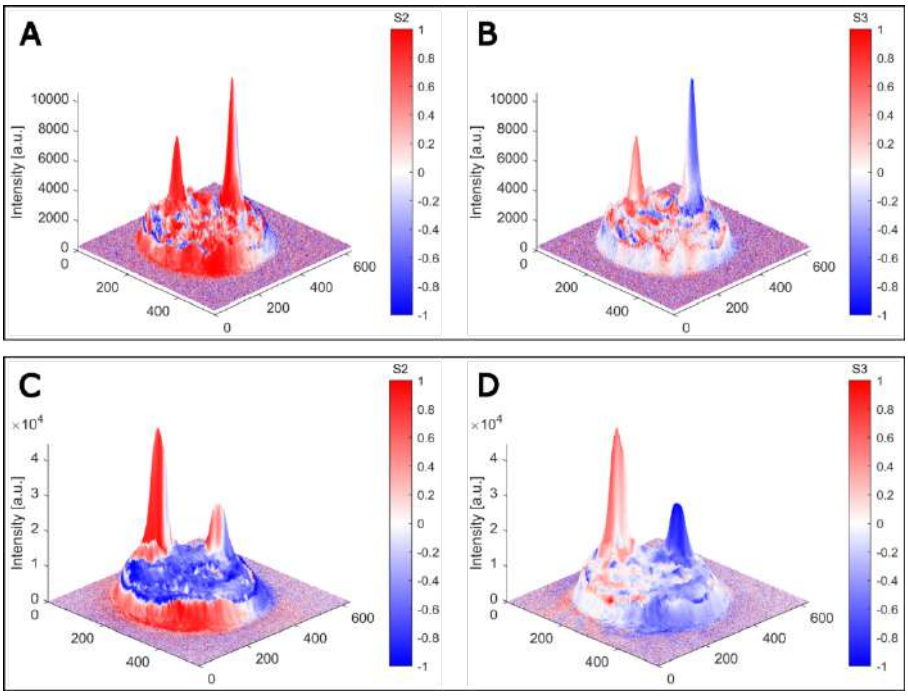


Fig. 1. Experimental demonstration of multi-beam emission with versatile polarization states and reversed intensity distributions. A+B Intensity plots with a color overlay showing measured Stokes parameters (S2, S3 respectively) with aLP+LCP states. C+D Intensity plots with a color overlay showing measured Stokes parameters (S2, S3 respectively) with reversed intensities of aLP+LCP states.

Acknowledgements

This work was funded by the Villum Fonden (Award in Technical and Natural Sciences 2019 and Grant No. 37372) and Danmarks Frie Forskningsfond (1134-00010B). Y.K. acknowledges the support from European Union's Horizon Europe research and innovation programme under the Marie Skłodowska-Curie Action (Grant agreement No. 101064471).

References

1. A. S. Solntsev, G. S. Agarwal, and Y. Y. Kivshar, "Metasurfaces for quantum photonics," Nat. Photonics, vol. 15, no. 5, p. 327, 2021.
2. F. Ding and S. I. Bozhevolnyi, "Advances in quantum meta-optics," Materials Today, vol. 71, pp. 63-72, 2023.
3. U. Stella et al., "Enhanced directional light emission assisted by resonant bloch surface waves in circular cavities," ACS Photonics, vol. 6, p. 2073, 2019.
4. N. Livneh et al., "Highly directional room-temperature single photon device," Nano Lett., vol. 16, p. 2527, 2016.
5. S. Jia et al., "Multichannel single-photon emissions with on-demand momentums by using anisotropic quantum metasurfaces," Adv. Mater., vol. 10, p. 2212244, 2023.

Micro/Nano Fabrication and Characterization Techniques

Phononic hyperbolic metamaterial with ZnO/(Zn,Mg)O heterostructures

J. Inglés-Cerrillo[1], P. Ibañez-Romero[1], R. Fandan[1], J. Pedrós[1], N. Le Biavan[2], D. Lefebvre[2], M. Hugues[2], J-M. Chauveau[2,3], M. Montes Bajo[1,*], A. Hierro[1,*]

[1]ISOM, ETSIT Telecomunicación, Universidad Politécnica de Madrid, Madrid, Spain
[2]Université Côte d'Azur, CNRS, CRHEA, 06560 -Valbonne, France
[3]Université Paris-Saclay, UVSQ, CNRS, GEMaC, Versailles, France
[*]Corresponding authors: miguel.montes@upm.es, adrian.hierro@upm.es

We design a phonon-driven negative index metamaterial (NIM) using ZnO/(Zn,Mg)O heterostructures, demonstrating tunable hyperbolic behaviour via Mg content and layer thicknesses. Experimentally, we achieve type I hyperbolic dispersion in four samples. Spectroscopic characterization and calculations of modes dispersion and isofrecuency curves confirm the negative frequency dispersion.

Stacked semiconductor hyperbolic metamaterials (HMMs) exhibit opposite signs of the real part of the dielectric function along the directions parallel ($\varepsilon_{\parallel}$) and perpendicular ($\varepsilon_{\perp}$) to the surface plane. Type I HMMs ($\varepsilon_{\parallel} > 0$ and $\varepsilon_{\perp} < 0$) have been of special interest given their negative refraction capabilities [1,2]. Various approaches have been explored to achieve Type I HMMs, including arranging materials in periodic structures [3], designing plasmonic structures [2] and, only recently, the first phononic HMM was demonstrated using superlattices supporting surface phonon polaritons (SPhPs) [4]. Given the higher quality factor observed in SPhP materials compared to plasmonic materials [5], phonon modes hold promise for attaining low-loss, sub-diffraction-limited optical modes using SPhP excitations, hence our focus on this approach.

This study presents the demonstration of a Type I phononic HMM formed by ZnO/(Zn,Mg)O heterostructures. Our approach begins by designing the heterostructure using the transfer matrix method (TMM) to find the conditions that the structure needs to satisfy so that a Type I HMM spectral region exists. We control the epsilon-near-zero character of the alternating layers by shifting the LO phonon frequency of the ternary alloy via the Mg content. For this purpose, the HMM is studied as a function of two parameters: the thickness ratio of the layers (d_{ZnO}/d_{ZnMgO}) and the Mg concentration ([Mg]) in the ternary layers. **Figure 1** shows the peak value of the figure of merit (FOM), defined as $\mathrm{Re}[k_{\perp}]/\mathrm{Im}[k_{\perp}]$ and typically accepted for characterizing anisotropic NIMs [2], as a function of both parameters.

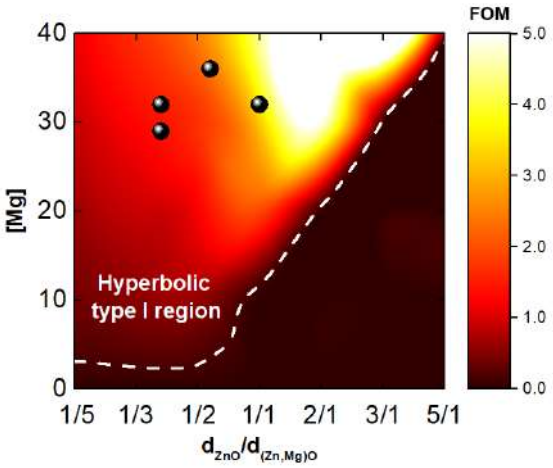


Figure 1: Calculated peak value of the FOM as a function of [Mg] and the layer thickness ratio. FOM is set to zero in the areas of the map where there is no type I hyperbolic region. The white dashed line defines the boundary between the region of parameter combinations for which a type I region is found and those for which it is not. The black dots indicate the experimental samples used in this work.

Once the combination of parameters needed to obtain a Type I HMM region is identified, we fabricate four samples (marked as black dots in **Figure 1**) which satisfy these conditions and characterize them experimentally by carrying out reflectance measurements in a FTIR spectrometer. For each sample, we then fit the measurements to the Gervais model, obtaining the dielectric functions of the two

constituent materials, ε_{ZnO} and ε_{ZnMgO}, from which we build ε∥ and ε⊥ by employing effective medium theory, and verify that this effective dielectric function exhibits Type I HMM behavior in a specific region.

The results of the study outlined above have been performed for all four samples, with **Figure 2** showing the results for one of the samples. First, we use attenuated total reflectance spectroscopy to report the presence of an SPhP mode in each sample, located within the type I hyperbolic region. Next, by employing the TMM, we demonstrate that this mode exhibits negative frequency dispersion, which is a hallmark of type I hyperbolic modes, and finally, isofrequency curve (IFC) calculations further confirm the hyperbolic behavior.

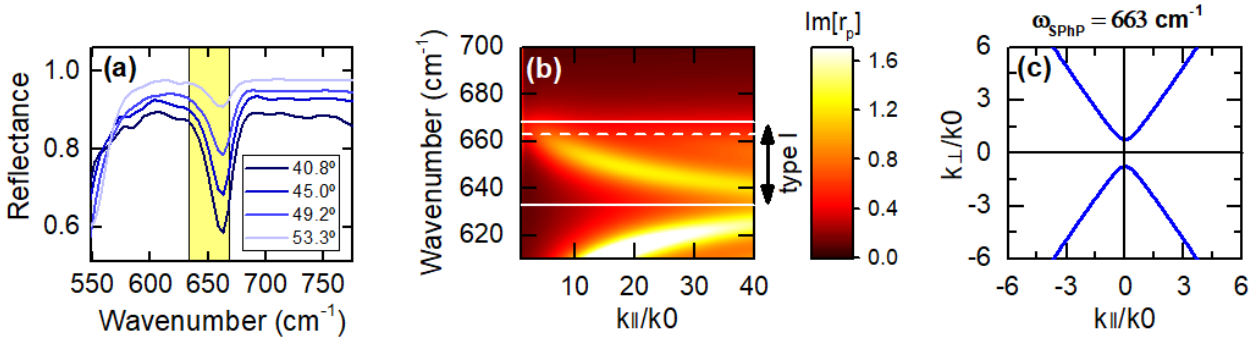


Figure 2: For one selected sample: (a) Measured ATR curves in p-polarization at different angles of incidence. The type I HMM behavior is highlighted in yellow. (b) Calculated polariton dispersion curves, computed with the TMM. Solid white reference lines show the region where the type I behavior has been found (635–668 cm^{-1}). (c) Calculated IFC of this sample for a frequency of 663 cm^{-1}, where the SPhP excitation is measured, and which lies within the type I hyperbolic region. This frequency is marked in (b) with a white dashed line. As expected, the IFC shows a hyperbolic shape characteristic of type I hyperbolic region. k∥ and k⊥ are the parallel and perpendicular components (with respect to the surface) of the wavevector, respectively. Both variables are normalized to k0, the wavevector in vacuum.

In summary, we have performed a detailed analysis of the design rules to obtain a phononic type I HMM using a realistic ZnO/(Zn,Mg)O heterostructure. Our study shows that increasing the Mg content in the ternary layers enhances the type I behavior, and that the optimal layer thickness depends on the Mg content. After examining the conditions for achieving a type I HMM, we experimentally validate this concept using four different samples.

This work was supported by: Project PID2020-114796RB-C2 funded by MCINN/ AEI /10.13039/501100011033/; Project PDC2023-145827-C2 funded by MICIU/AEI /10.13039/501100011033/ and by European Union Next Generation EU/ PRTR and EU Horizon 2020 Research and Innovation Program under grant agreement No. 665107 (project ZOTERAC); P. I. acknowledges the FPU predoctoral contract from the Spanish Ministry of Science, Innovation, and Universities (MICIU).

References

1. Naik, G., *et al.*, "Demonstration of Al:ZnO as a plasmonic component for near-infrared metamaterials", PNAS, Vol. 109, No. 23, 8834-8838, 2012.
2. Hoffman, A., *et al.*, "Negative refraction in semiconductor metamaterials", Nature Materials, Vol. 6, 946-950, 2012.
3. Suang, Z., *et al.*, "Experimental demonstration of near-infrared negative-index metamaterials", Phys. Rev. Lett., Vol. 95, 137404, 2007.
4. Ratchford, D.C., *et al.*, "Controlling the Infrared Dielectric Function through Atomic-Scale Heterostructures", ACS Nano, Vol. 13, No. 6, 6730-6741, 2019.
5. Caldwell, J.D., *et al.*, "Low-loss, infrared and terahertz nanophotonics using surface phonon polaritons", Nanophotonics, Vol. 4, No. 1, 44-68, 2015.

UAPO Diffracted Field by a PEC-Backed Chiral Half-Sheet

G. Riccio[1*], F. Ferrara[2], G. Gennarelli[3], R. Guerriero[2], and F. Chiadini[2]

[1]D.I.E.M. - University of Salerno, Italy
[2] D.I.In. - University of Salerno, Italy
[3] I.R.E.A. - C.N.R., Naples, Italy
[*]corresponding author: griccio@unisa.it

Abstract: A Uniform Asymptotic Physical Optics solution is provided to evaluate the plane wave diffraction by a uniaxial anisotropic chiral half-sheet with a perfect electrical conductor backing. The incidence direction is assumed to be perpendicular to the linear edge of the chiral sheet.

This summary deals with the evaluation of the diffracted field occurring when an incident plane wave travels in the free space and hits the upper surface of a uniaxial anisotropic chiral sheet with thickness *d* and a perfect electrical conductor (PEC) backing. At the best authors' knowledge, analytical solutions of this canonical problem don't exist in literature.

The structure thickness permits considering the plane wave diffraction by an equivalent impenetrable half-plane having the edge coincident with the *z*-axis of a useful coordinate system (see Fig. 1). The angle ϕ' defines the incidence direction and the polar co-ordinates ρ,ϕ describe the position of the observation point *P*.

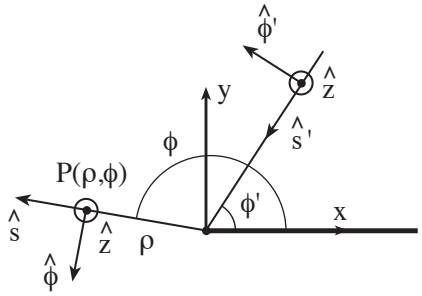


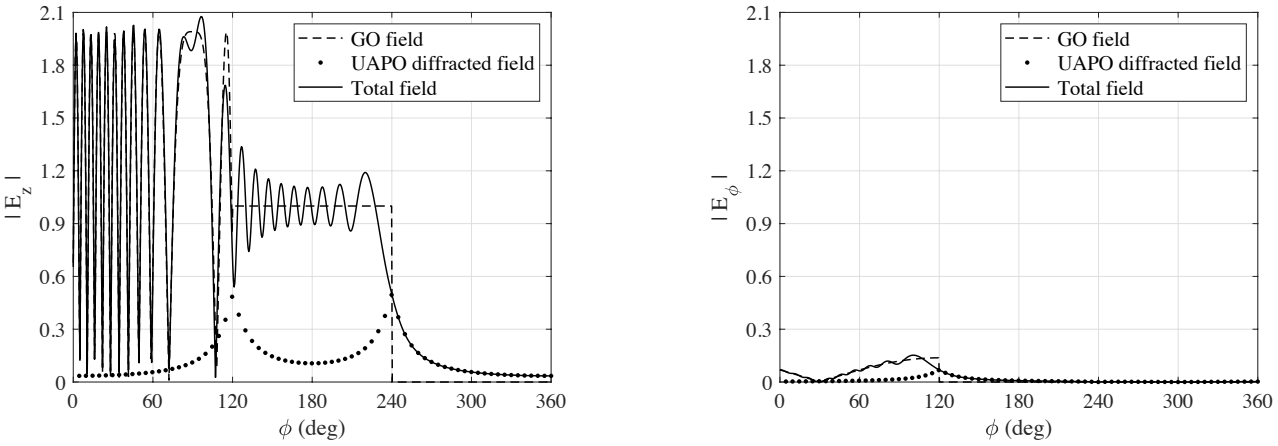
Figure 1. Geometry of the diffraction problem.

The Uniform Asymptotic Physical Optics (UAPO) approach is able to furnish an analytical solution to the tackled problem by adopting electric and magnetic PO equivalent surface currents as radiating sources. According to [1], if $\underline{E}^i = E_0^i \exp(j\beta_0 \rho \cos(\phi - \phi'))\hat{z}$ is the electric field associated to the incident plane wave, the resulting UAPO diffracted field can be so expressed:

$$\begin{pmatrix} E_z^d(\rho,\phi) \\ E_\phi^d(\rho,\phi) \end{pmatrix} = E_0^i \frac{\exp(-j\pi/4)}{2\sqrt{2\pi\beta_0}} \frac{\exp(-j\beta_0\rho)}{\sqrt{\rho}} \frac{F^d\left(2\beta_0\rho\cos^2\left(\frac{\phi \pm \phi'}{2}\right)\right)}{\cos\phi + \cos\phi'} \begin{pmatrix} (1-R_{22})\sin\phi' - (1+R_{22})\sin\phi \\ -R_{12}(\sin\phi' + \sin\phi) \end{pmatrix} \quad (1)$$

where β_0 is the free-space propagation constant and F^d is the transition function of the Uniform Geometrical Theory of Diffraction (UTD) [2]. The coefficients R_{12} and R_{22} are elements of the 2x2 reflection matrix related to the standard plane of incidence and are obtained by applying the boundary conditions at the upper and lower interfaces of the chiral material. In particular, the presence of a PEC support guarantees the total internal reflection of the eigenwaves at the lower interface.

Figure 2 refers to a uniaxial chiral sheet that is characterized by thickness $d = 0.05\lambda_0$, permeability parameters $\mu_t = \mu_n = \mu_0$, permittivity parameters $\varepsilon_t = 2.7\varepsilon_0$, $\varepsilon_n = 3.4\varepsilon_0$, and chirality parameter $\kappa = 1.9$. Parameters and wavelength λ of free space are denoted by the index "0". In particular, co- and cross-polar field components are shown in (a) and (b), respectively, when $E_0^i = 1$ and $\rho = 6\lambda_0$. The discontinuities of the Geometrical Optics (GO) field are compensated by the contribution of the UAPO diffracted field at the shadow boundaries $\phi = 120°$ and $\phi = 240°$, thus gaining a continuous total field as expected.



(a) (b)

Figure 2. Co- and cross-polar field components when $\rho = 6\lambda_0$ and $\phi' = 60°$.

References

1. Riccio, G., G. Gennarelli, F. Ferrara, R. Guerriero and F. Chiadini, "UAPO diffraction contribution by uniaxially anisotropic chiral half-planes," Int. J. Microwave Opt. Tech., Vol. 18, 593–600, 2023.
2. Kouyoumjian, R. G. and P. H. Pathak, "A uniform geometrical theory of diffraction for an edge in a perfectly conducting surface," Proc. IEEE, Vol. 62, pp. 1448–1461, 1974.

Enhanced chiral sensing in epsilon-near-zero metamaterials

A. Paul[1], M. Venturi[1], R. Adhikary[1], L. D. M. Villari[1], G. Salvitti[1], C. Ferrante[2], D. Tedeschi[1], F. D. Stasio[3], A. Toma[3], H. Altug[4], and A. Marini[1,2]

1. Department of Physical and Chemical Sciences, University of L'Aquila, Via Vetoio, L'Aquila 67100, Italy
2. CNR-SPIN, c/o Dip.to di Scienze Fisiche e Chimiche, Via Vetoio, Coppito, L'Aquila 67100, Italy
3. Istituto Italiano di Tecnologia, Via Morego 30, Genova 16136, Italy
4. Institute of Bioengineering, Ecole Polytechnique Federale de Lausanne (EPFL), Lausanne 1015, Switzerland
Corresponding author: ashiskumar.paul@univaq.it

Abstract

We report enhanced optical activity in the epsilon-near-zero regime in a chiral metamaterial composed of metallic nanospheres randomly dispersed in a chiral drug solution. Our results are relevant for developing innovative devices capable of detecting the chirality of low-volume samples with applications in nanomedicine and pharmaceutics.

In recent years, chiroptical sensing has emerged as the cornerstone of detecting specific enantiomeric forms of chiral biomolecules, including pharmaceutical chiral drugs, because the two enantiomers often exhibit different behavior and functionality. Current state-of-the-art chiral sensing techniques that measure enantiomeric excess of chiral mixtures, such as nuclear magnetic resonance and high-performance chromatography, are limited by macroscopic drug volumes and unsuitable for real-time analysis and on-chip integration schemes. Recent progress in nanophotonic metamaterials fabrication has enabled advanced chiroptical sensing techniques, including plasmon-enhanced circular dichroism (CD) and optical rotatory dispersion (ORD) spectroscopy [1, 2], to quantify enantiomeric imbalance in chiral drug solutions.

Here, we propose an ultrasensitive chiroptical sensing method based on epsilon-near-zero (ENZ) effective parameters of metallic nanospheres (NS) randomly dispersed in aqueous reparixin (a pharmaceutical molecule currently used in clinical studies, including COVID-19 and acute respiratory distress syndrome) with dilute molecular $\approx 10^{-2}\text{nm}^{-3}$ density. The proposed setup is illustrated in Fig. 1(a). In the limit of dilute drug solution, the effective bi-anisotropic optical parameters of reparixin dissolved in water are evaluated through a previously reported combined molecular dynamics simulation and quantum mechanical ensemble average approach [3]. Note that the chirality parameter of the chiral medium is determined solely by the mixing (magnetoelectric) polarisability, which flips sign for opposite enantiomers and enantiomeric imbalance. Due to the near-field and electromagnetic interactions, chiral molecules induce optical chirality in the plasmonic spectra of the metal NSs. Working in the quasi-static limit, we calculate the NS's induced electric, magnetic, and magnetoelectric polarizabilities [Figs. 1(b-d)]. The dielectric response of the metal is accounted for by the Lorentz-Drude model. Next, we apply Maxwell-Garnett's effective medium theory to account for the local field corrections and derive the effective constitutive relations of the chiral MM given by,

$$\begin{aligned} \mathbf{D}(\mathbf{r}) &= \epsilon_0\epsilon_{\text{eff}}\mathbf{E}_0(\mathbf{r}) \in \frac{i}{c}\kappa_{\text{eff}}\mathbf{H}_0(\mathbf{r}) \\ \mathbf{B}(\mathbf{r}) &= \frac{i}{c}\kappa'_{\text{eff}}\mathbf{E}_0(\mathbf{r}) + \mu_0\mu_{\text{eff}}\mathbf{H}_0(\mathbf{r}) \end{aligned} \tag{1}$$

where ϵ_{eff}, μ_{eff}, κ_{eff}, and κ'_{eff} are the effective optical constants for the bulk nanosphere-chiral medium, Each of them is a function of the NS filling fraction f and impinging wavelength λ. We observe enhanced ORD and CD in the ENZ regime $\text{Re}[\epsilon_{\text{eff}}(f,\lambda)] \approx 0$ of the bulk, as illustrated in Figs. 1(e)-(g). Our results hold potential applications in the development of ultrasensitive photonic probes to detect molecular chirality at the nanoscale level.

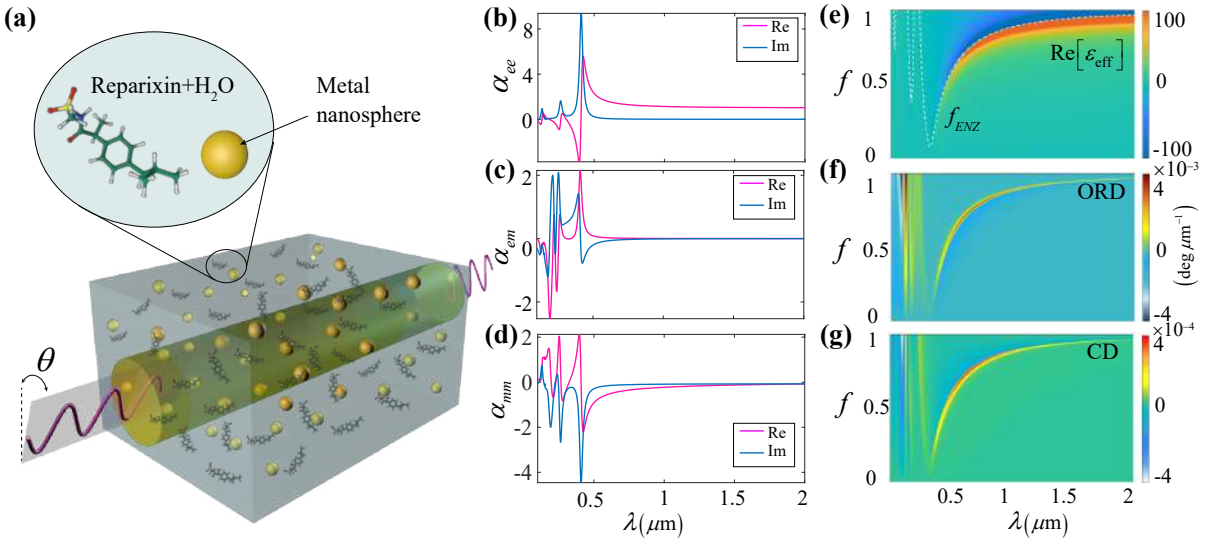


Figure 1: Fig. 1 **(a)** Schematic illustration of the proposed chiral metamaterial composed of silver nanospheres randomly dispersed in aqueous Reparixin solution. **(b)-(d)** Real and imaginary parts of the induced electric (α_{ee}), magnetoelectric (α_{em}), and magnetic (α_{mm}) polarizabilities of a nanosphere. **(e)** Effective permittivity of the bulk medium plotted against filling fraction f of the nanospheres and incident wavelength λ. The dashed line represents the ENZ filling fraction. The calculated **(f)** ORD and **(g)** CD spectra. Enhancement is observed near the ENZ regime.

References

[1] Govorov, A. O. and Z. Fan, "Theory of Chiral Plasmonic Nanostructures Comprising Metal Nanocrystals and Chiral Molecular Media," *ChemPhysChem.*, Vol. 13, No. 10, pp. 2551-2560, 2012.

[2] Ayuso, D., A. F. Ordonez, and O. Smirnova, "Ultrafast chirality: the road to efficient chiral measurements," *Phys. Chem. Chem. Phys.*, Vol. 24, pp. 26962-26991, 2022.

[3] Venturi, M., R. Adhikary, A. Sahoo, C. Ferrante, I. Daidone, F. Di Stasio, A. Toma, F. Tani, H. Altug, A. Mecozzi, M. Aschi, and A. Marini, "Plasmon-enhanced circular dichroism spectroscopy of chiral drug solutions," *J. Chem. Phys.*, Vol. 159, pp. 154703, 2023.

Enhanced frequency conversion by plasmonic-dielectric metasurfaces with high-Q quasi-BICs in the visible spectral range

T. Stolt[1*], H. Bai[1], A. Shevchenko[1], and R. Kolkowski[1]
[1]Department of Applied Physics, Aalto University, FI-00076 Aalto, Finland

timo.stolt@aalto.fi (corresponding author)

Abstract

We numerically demonstrate plasmonic-dielectric metasurfaces with narrow-band resonances in the visible spectral range, showing exceptionally high quality factors ($Q \sim 6400$). These arise from hybridization between guided modes of different order. We predict up to 750-fold enhancement of second- and third-harmonic generation in these metasurfaces, revealing their potential for nonlinear nanophotonics.

Periodic metasurfaces with high-quality-factor (high-Q) resonances, such as quasi-bound states in the continuum (qBICs), show great potential for enhancement of nonlinear optical phenomena in highly compact structures [1, 2]. Typically, qBICs are realized in structures made of absorption-free all-dielectric materials, avoiding the use of lossy components, such as plasmonic nanoparticles. However, under certain conditions qBICs can be realized in plasmonic metasurfaces as well, leading to unique combinations of extremely high Q factors with strong local field enhancement inherent to resonant plasmonic systems [3, 4]. Here, by combining plasmonic nanoparticle arrays with dielectric slab waveguides (see Fig. 1a), we design hybrid metasurfaces that can exhibit qBICs with exceptionally high Q factors in the visible spectral range. By using a second-order nonlinear material for the waveguide, we show that the designed qBICs can boost the second- and cascaded third-harmonic generation (SHG, THG) by almost three orders of magnitude.

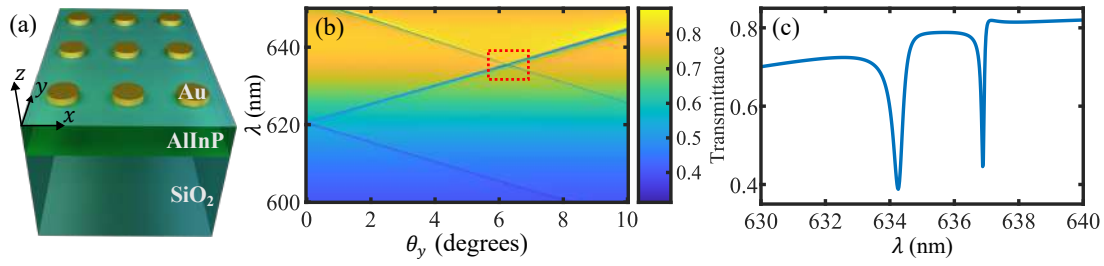


Figure 1: (a) Illustration of the designed metasurface. (b) Transmittance of TE-polarized light, calculated for the studied metasurface as a function of wavelength and incidence angle (θ_y). The dashed box indicates the location of the anticrossing between the two guided-mode resonances. (c) Transmittance spectrum at $\theta_y = 5.75°$, showing a bright and a dark hybrid resonance (qBIC).

The main component of our metasurface is a slab waveguide (thickness 400 nm) made of aluminum indium phosphide (AlInP). We choose AlInP due to its high refractive index (> 3), negligible absorption loss at $\lambda > 500$ nm, and relatively high intrinsic second-order susceptibility ($\chi^{(2)}$). The properties of this material are currently studied in our group. To obtain a qBIC, we place a rectangular array of gold nanodisks (radius 40 nm, height 40 nm) on the waveguide (see

Fig 1a). The periods along the x and y directions are set to 150 and 210 nm, respectively. The resulting dispersive guided-mode resonances (see Fig 1b) originate from TE-polarized guided modes of different orders. By changing the incidence angle θ_y (residing in the yz plane), we make the resonances intersect and anticross with each other. The anticrossing gives rise to a bright and dark hybrid mode, following a mechanism described in Ref. [4]. The dark mode is a qBIC with linewidth $\Delta\lambda \approx 0.1$ nm at $\lambda = 636.9$ nm, corresponding to $Q \approx 6400$ (Fig 1c).

To showcase the potential of the studied structures for nonlinear optical applications, we simulated the SHG and cascaded THG from the designed metasurface. We assumed a TM-polarized pump to be incident on the metasurface at $\theta_y = 5.75°$ (i.e., having significant E_y and E_z components) in the wavelength range between 1260 and 1280 nm. Due to the $\chi^{(2)}$-tensor symmetry of AlInP, this results in SHG fields in the range from 630 to 640 nm that are co-polarized with the qBIC (i.e., have a significant E_x component). Furthermore, we evaluated the cascaded THG at 420-427 nm, resulting from mixing of the SHG with the fundamental fields. We have found that both the bright mode and the qBIC give rise to strong resonant enhancement of the SHG and THG emission (up to 750- and 400-fold, respectively; see Fig 2).

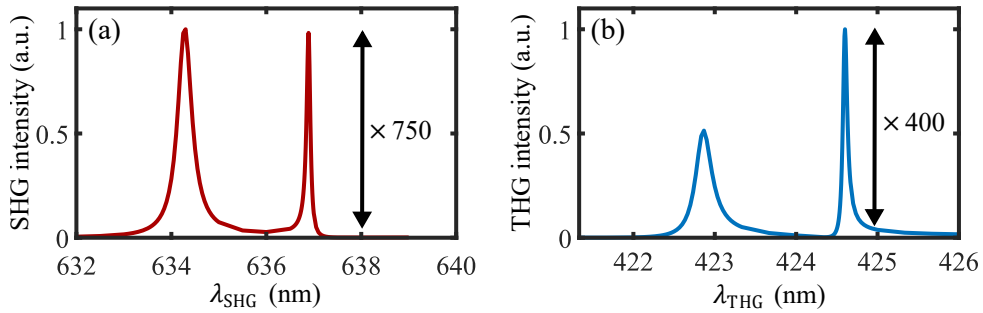


Figure 2: Calculated spectrally-resolved (a) SHG and (b) cascaded THG from the designed metasurface, with SHG wavelengths near the hybrid resonances.

To conclude, by combining a plasmonic nanoparticle array with a nonlinear dielectric slab waveguide, we have obtained a metasurface hosting hybrid plasmonic-photonic resonances that result from the coupling between guided modes of different orders. One of these resonances is a qBIC with $Q \sim 6400$, which is exceptionally high for a plasmonic system in the visible spectral range. We have shown that both hybrid resonances can boost SHG and cascaded THG by almost three orders of magnitude. Experimental demonstration of these predictions is a target of our ongoing research.

The authors acknowledge support of the Research Council of Finland (Grants No. 347449 and 353758). For computational resources, the authors acknowledge the Aalto University School of Science "Science-IT" project.

References

[1] Vabishchevich, P. and Y. Kivshar, "Nonlinear photonics with metasurfaces," *Photon. Res.* Vol. 11, No. 2, pp. B50-B64 (2023)

[2] Anthur, A. P. et al., "Continuous Wave Second Harmonic Generation Enabled by Quasi-Bound-States in the Continuum on Gallium Phosphide Metasurfaces," *Nano Lett.*, Vol. 20, No. 12, pp. 8745-8751, 2020.

[3] Assam, S. I. et al., "Formation of Bound States in the Continuum in Hybrid Plasmonic-Photonic Systems," *Phys. Rev. Lett.*, Vol. 121, No. 25, p. 253901, 2018.

[4] Kolkowski, R. and A. Shevchenko, "Enabling infinite Q factors in absorbing optical systems," *Nanophotonics*, Vol. 12, No. 17, pp. 3443-3454, 2023.

Phase-Matched Second-Harmonic Generation from Metasurfaces Inside Multipass Cells

M. Mekhael[1], T. Stolt[1], A. Vesala[1], H. Rekola[2],
T. K. Hakala[2], R. Fickler[1], and M. J. Huttunen[1*]
[1]Photonics Laboratory, Physics Unit, Tampere University, FI-33014 Tampere, Finland
[2]Center for Photonics Sciences, University of Eastern Finland,
P.O. Box 111, FI-80101, Joensuu, Finland
mikko.huttunen@tuni.fi

Abstract

We demonstrate scalable enhancement of second-harmonic generation (SHG) from metasurfaces using multipass cells, where the pump interacts multiple times with the metasurface. We achieve phase matching with superlinear dependence on the number of passes, promising applications in diverse nonlinear optics.

1 Introduction

Nonlinear metasurfaces and metamaterials have recently emerged as a promising solution to realize thin nonlinear devices. These artificial structures, composed of sub-wavelength building units, can exhibit properties not (easily) achieved in natural materials. Despite their advantages, nonlinear metamaterials have not yet found real-world applications, where they could outperform existing nonlinear material systems, such as nonlinear waveguides [1], fibers [2], or crystals [3]. This lack of applications is mainly related to the still-too-low conversion efficiencies of nonlinear metamaterials.

In this work, we introduce a straightforward approach to enhance nonlinear responses of metamaterials (and thus their conversion efficiencies), by incorporating them inside multipass cells and allowing the pump beam to pass through the metamaterial several times as demostrated in Fig. 1a. We experimentally demonstrate a tenfold enhancement in the SHG signal from a plasmonic metasurface after 9 passes [4]. Our results show a superlinear dependence of the SHG signal on the number of passes N, confirming a successful phase matching. Importantly, this demonstrated approach is generic, offering compatibility with various existing enhancement techniques and metamaterials.

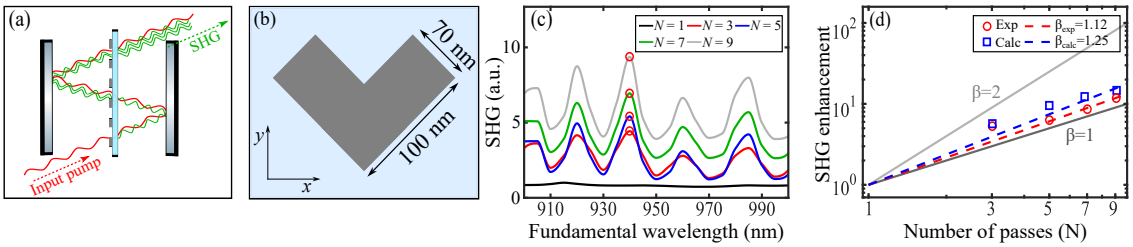


Figure 1: (a) A schematic showing the phase-matched SHG emission in case of 3 passes of the pump beam through the metasurface device. (b) A schematic representing a single V-shaped nanoparticle from the metasurface. (c) Measured SHG signal for different number of passes N. (d) The enhancement factor of the SHG signal as a function of the number of passes N.

2 Results and discussion

In our experiments, we used a sample consisting of V-shaped aluminum nanoparticles [Fig. 1b] deposited on a 0.5 mm-thick SiO_2 substrate. The nanoparticles were randomly positioned (being, however, similarly oriented). The sample was designed to have localized surface plasmon resonance (LSPR) around 420 nm for x-polarized incident light. We utilized the optical phase shifts induced by the LSPR to phase match SHG signal inside the multipass cell. The phase-matching condition was fulfilled for numerous pump wavelengths in our pump wavelength range from 900 to 1000 nm [see Fig. 1c]. The measured phase-matching wavelengths agree well on the ones calculated with a semi-analytical model [5].

Notably, the SHG response exhibited a superlinear dependence (SHG $\propto N^{\beta_{\text{exp}}} = N^{1.12}$) on the number of passes N [Fig. 1d], confirming successful phase matching. In the ideal scenario of a lossless and perfectly phase-matched sample, the SHG signal would exhibit a quadratic dependence on the number of passes N (SHG $\propto N^{\beta_{\text{ideal}}}$, where $\beta_{\text{ideal}} = 2$) [6]. However, various loss mechanisms, including transmission losses and beam intensity changes during propagation, result in a measured scaling factor less than 2. In future, we plan to fabricate metasurfaces directly on top of the mirrors or replace the mirrors with highly-reflecting metasurfaces. This would reduce the amount of normal dispersion, simultaneously increasing the achievable β. Such demonstrations could pave the way towards ultra-thin, tunable, and multifunctional nonlinear devices, eliminating the need for complex fabrication procedures.

3 Acknowledgements

The authors acknowledge the support of the Academy of Finland (Grant No. 308596), the Flagship of Photonics Research and Innovation (PREIN) funded by the Research Council of Finalnd (Grants No. 320165 and 320166). TS acknowledges also Jenny and Arttu Wihuri Foundation for doctoral research grant. TKH acknowledges Research Council of Finalnd project number (322002). RF acknowledges the support of the Research Council of Finalnd through the Academy Research Fellowship (332399).

References

[1] D. Dimitropoulos, V. Raghunathan, R. Claps, and B. Jalali, "Phase-matching and nonlinear optical processes in silicon waveguides," *Opt. Express*, vol. 12, pp. 149–160, 2004.

[2] A. Bétourné, Y. Quiquempois, G. Bouwmans, and M. Douay, "Design of a photonic crystal fiber for phase-matched frequency doubling or tripling," *Opt. Express*, vol. 16, pp. 14255–14262, 2008.

[3] W. Zhang, H. Yu, H. Wu, and P. S. Halasyamani, "Phase-Matching in Nonlinear Optical Compounds: A Materials Perspective," *Chem. Mater.*, vol. 29, pp. 2655–2668, 2017.

[4] M. Mekhael, T. Stolt, A. Vesala, H. Rekola, T. K. Hakala, R. Fickler, and M. J. Huttunen, "Phase-Matched Second-Harmonic Generation from Metasurfaces Inside Multipass Cells," *ACS photonics*, vol. 11, 2024.

[5] T. Stolt, J. Kim, S. Héron, A. Vesala, Y. Yang, J. Mun, M. Kim, M. J. Huttunen, R. Czaplicki, M. Kauranen, J. Rho, and P. Genevet, "Backward Phase-Matched Second-Harmonic Generation from Stacked Metasurfaces," *Phys. Rev. Lett.*, vol. 126, No. 3, pp. 033901, 2021.

[6] R. W. Boyd, "Nonlinear Optics, Third Edition," (Academic, 2008).

Nonlinear Enhancement from Epsilon-near-zero Material-based Metasurface Structure

S. P. Mahato[1*], **V. Rastogi**[1,2]

[1]Department of Physics, Indian Institute of Technology Roorkee, INDIA 247667

[2]Center for Photonics and Quantum Communication Technology, Indian Institute of Technology Roorkee, Uttarakhand, INDIA 247667

[*]Corresponding author: sp_mahato@ph.iitr.ac.in

Abstract: We numerically investigate nonlinear responses produced by Epsilon-near-zero (ENZ) material-based metasurface structure. Here we show that our proposed structure can produce a large nonlinear response with the change in refractive index, Δn, exceeding 2 near the ENZ wavelength range, even at very low pump fluence in the near-infrared spectral range.

Nonlinear effects offer vast opportunities across a wide range of applications like all-optical signal processing, optical computing, beam steering as well as sensing and detection. The size and energy efficiency of nonlinear optical devices are largely dependent on the strength of the nonlinear optical response of the materials from which they are made. Therefore, using conventional materials of weak nonlinear response, it is difficult to realize sub-wavelength all-optical devices. Therefore, materials exhibiting significantly stronger nonlinear optical responses are essential for developing highly dense on-chip optical devices.

Recent studies have shown that materials with vanishingly small permittivity, known as epsilon-near-zero (ENZ) materials, display remarkable linear and substantial nonlinear responses [1]. Transparent conducting oxides (TCOs like ITO, AZO, CdO etc.) are one of the most favorable materials as an ENZ material, in which optical properties can be easily tuned by manipulating the carrier concentrations [2]. In terms of nonlinear response, a thin film of TCOs can result in large nonlinearity around the ENZ wavelength of that material [3]. Here, we report a novel metasurface structure, as shown in Fig. 1(a), composed of an array of gold rings placed on a thin layer of cadmium oxide (CdO), which is situated on a silica (SiO_2) substrate. In this configuration, the CdO thin film functions as an epsilon-near-zero (ENZ) material. This proposed design demonstrates a significantly enhanced nonlinear response compared to traditional thin-film ENZ materials, and the required pump fluence is also comparably very small. The real part of the permittivity of the ENZ material used in this study vanishes at $\lambda \approx 1500$ nm as shown in Fig. 1(b). Here, two important resonance phenomena were observed in our structure; one is ENZ resonance

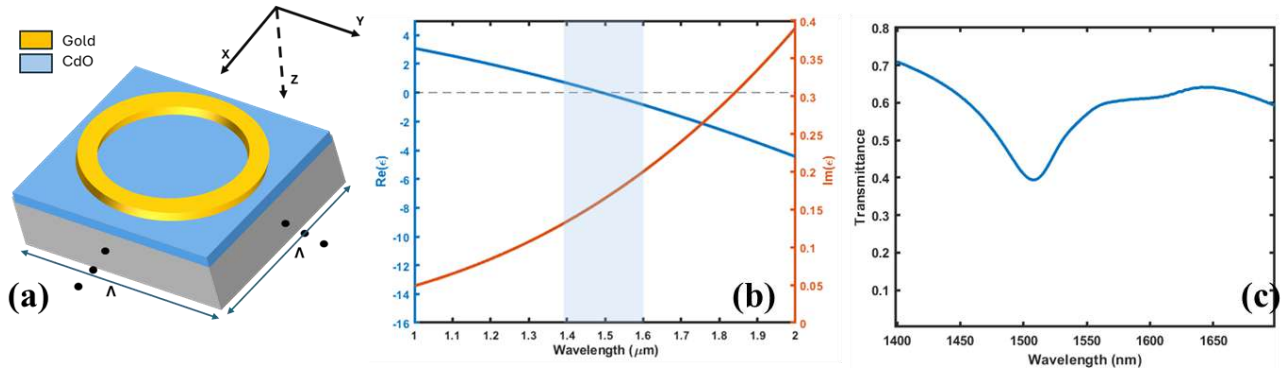


Figure 1: (a) Unit cell of our proposed metasurface structure, (b) Real and imaginary permittivity component of CdO layer, and (c) Linear optical transmittance of the proposed structure

supported by the thin layer of CdO due to electric field confinement within this layer near ENZ wavelength. And, the other one is the dipolar resonance of the metal ring array. We chose the metasurface parameters in such a way that both resonances significantly coincide with each other and the corresponding transmission spectrum is shown in Fig. 1(c). We then investigated the nonlinear responses using two-temperature model [4]. The optical nonlinearity observed in TCOs is governed by the heating of electrons via optical excitation of short-pulse laser source. As the laser pulse is applied, the electron temperature rises to the peak and then rapidly drops due to electron lattice interaction. After laser pulse absorption, the dynamics of both electron (T_e) and lattice (T_l) temperatures in CdO thin film can be described by the following sets of equations, with the relevant parameters defined in ref. [3]

$$C_e \frac{\partial T_e}{\partial t} = -g_{ep}(T_e - T_l) + \frac{N}{2\tau_{ee}} \quad (1)$$

$$C_l \frac{\partial T_l}{\partial t} = g_{ep}(T_e - T_l) + \frac{N}{2\tau_{ep}} \quad (2)$$

$$\frac{\partial N}{\partial t} = -\frac{N}{2\tau_{ee}} - \frac{N}{2\tau_{ep}} + P \quad (3)$$

For solving the equations, 100 fs pump pulses with wavelengths near the ENZ region and a very small pump fluence of 20 μJ/cm^2 are used. We find that a large change in electron temperature is due to the absorption of pump pulses, and it causes a significant manipulation in the optical properties of CdO film in terms of plasma frequency.

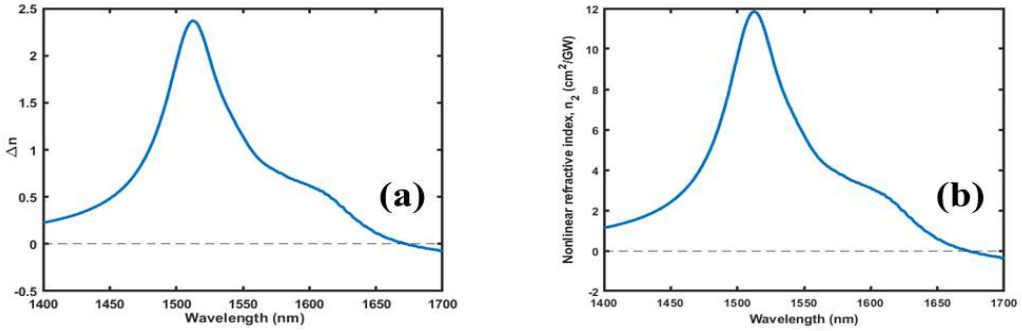


Figure 2: (a) Effective index change (Δn) and (b) Nonlinear refractive index of our proposed structure

Figure 2(a) shows the change in the effective refractive index (Δn) of the proposed structure which confirms that near the ENZ wavelength range Δn exceeds 2. The wavelength dependence of the nonlinear refractive index (n_2) is shown in Fig. 2(b). We observe that here the maximum value of n_2 is 11.83 cm^2/GW, which is almost 3 orders of magnitude greater than that of bare CdO film, as determined in ref. [5]. In conclusion, our findings can offer the possibility to develop low-power nonlinear nano-optical devices with drastically reduced footprints.

References

1. Caspani, L., Kaipurath, R. P.M., Clerici. M., Ferrera. M., Roger, T., Kim. J. & Faccio. D., "Enhanced nonlinear refractive index in ε-near-zero material." Phys. Rev. Lett, Vol. 116, 233901, 2016.
2. Jaffray, W., Saha, S., Shalaev, V. M., Boltasseva, A., & Ferrera, M. "Transparent conducting oxides: from all-dielectric plasmonics to a new paradigm in integrated photonics." AOP, Vol. 14, No. 2, 148-208, 2022.
3. Alam, M. Z., De Leon, I., & Boyd, R. W. "Large optical nonlinearity of indium tin oxide in its epsilon-near-zero region." Science, Vol. 352, No. 6287, 795-797, 2016.
4. Carpene, E. "Ultrafast laser irradiation of metals: Beyond the two-temperature model." Phys. Rev. B, Vol. 74, No. 024301, 2006.
5. Wu, Y., Wang, Y., Wang, M., Ma, H., Jiang, H., Yao, J., Zhao, Y., Yu, K.M. and Shao, J., "Tailoring epsilon-near-zero wavelength and nonlinear absorption properties of CdO thin films by Mo doping." Appl. Phys. Lett., Vol. 125, No. 1, 2024.

Polarization-Dependent Anapole States in Elliptical Nanodisks for Nonlinear and Filtering Applications

M.E.Kjellberg*, H. Kylhammar, and S. Anand

Department of Applied Physics, School of Engineering Sciences, KTH Royal Institute of Technology, Albanova University Center, Roslagstullsbacken 21, 106 91 Stockholm, Sweden

*corresponding author: mikkokj@kth.se

Abstract: We demonstrate anapole states in vertically stacked Si nanodisks by leveraging the high refractive index contrast between Si and SiO_2, simplifying fabrication. By extending this to elliptical disks, we achieve polarization-dependent dual-wavelength anapole excitation. This platform offers strong field enhancements, enabling advanced nonlinear optical applications and wavelength filtering.

The ability of sub-wavelength all-dielectric nanostructures to confine light in the visible and infrared spectral regions through Mie resonances offers significant potential for enhancing light-matter interactions, particularly in optoelectronic and nonlinear optics applications [1]. In this context, optical anapole states in Si nanodisks not only enable high optical field confinement but also offer novel ways for manipulating light scattering [2,3]. Furthermore, by vertically stacking nanodisks, the degree of field confinement can be significantly enhanced, opening new avenues for advanced photonic device design [4].

Anapole states, characterized by suppressed far-field radiation and enhanced optical field confinement, are highly sought after for nanophotonic applications. By utilizing the high refractive index contrast between Si ($n \approx 3.5$) and SiO_2 ($n \approx 1.45$), we design vertically stacked Si nanodisks that support anapole states without requiring complex fabrication steps. This approach simplifies production and enables strong light-matter interactions. Additionally, we show wavelength selective transmission/reflection by tailoring the dimensions and arrangement of nanodisks, enabling functions such as filters and structural coloration.

Elliptical nanodisk stacks introduce geometric anisotropy, enabling polarization-dependent anapole excitation at two distinct wavelengths [5]. When light is polarized along the major axis, the anapole mode occurs at a shorter wavelength, while polarization along the minor axis shifts it to a higher wavelength. This dual-wavelength behavior, controlled by the aspect ratio of the elliptical disks, provides a versatile platform for nonlinear processes, paving the way for advanced devices like tunable frequency converters and ultrafast optical switches.

Acknowledgements: The work is supported by the Swedish Research Council – Vetenskapsrådet, grant 2019-05321 and the Swedish Energy Agency – Energimyndigheten; grant 49227-1 and P2023-01371.

References

1. A. I. Kuznetsov, A. E. Miroshnichenko, M. L. Brongersma, Y. S. Kivshar, and B. Luk'yanchuk, "Optically resonant dielectric nanostructures," Science **354**, (2016).
2. A. E. Miroshnichenko, A. B. Evlyukhin, Y. F. Yu, R. M. Bakker, A. Chipouline, A. I. Kuznetsov, B. Luk'yanchuk, B. N. Chichkov, and Y. S. Kivshar, "Nonradiating anapole modes in dielectric nanoparticles,"

Nat Commun **6**, 8069 (2015).
3. Y. Yang and S. I. Bozhevolnyi, "Nonradiating anapole states in nanophotonics: from fundamentals to applications," Nanotechnology **30**, 204001 (2019).
4. F. Vennberg, A. P. Ravishankar, and S. Anand, "Manipulating light scattering and optical confinement in vertically stacked Mie resonators," Nanophotonics **11**, 4755–4764 (2022).
5. M. Kjellberg, F. Vennberg, A. P. Ravishankar, and S. Anand, "Polarization-Enabled Tuning of Anapole Resonances in Vertically Stacked Elliptical Silicon Nanodisks," Advanced Photonics Research 5 (11), 2400009 (2024).

Deep and vertical etching technique using hydrogen fluoride gas for glass-based metasurfaces

Y. Ono[1*], K. Sano[1], A. Ueno and Y. Hayashi[1]

[1]Innovative Technology Laboratories, AGC Inc., Japan
[*]corresponding author: yoshitaka.ono@agc.com

Abstract: This report introduces a glass-etching technique using hydrogen fluoride gas, where the photoresist, which typically acts as a mask, serves as a catalyst. This technique, enabling selective, faster, deeper, and more vertical etching than conventional reactive-ion etching, is promising for glass-based metasurface applications.

The demand for lightweight and compact metasurfaces in practical applications is growing, with recent research extending beyond monochromatic light to visible and ultraviolet (UV) regions. In the visible region, thin films of TiO_2 and SiN are widely used, although glass, commonly used for optical lenses, is also a promising candidate.[1] In the UV region, silica glass (pure SiO_2) offers advantages as a substrate,[2] and direct processing of glass substrates may lead to cost reduction. However, conventional reactive-ion etching (RIE) techniques suffer from mask erosion, resulting in tapered shapes and limited etching depth, which adversely influence the performance and application of glass-based metasurfaces.[1] Additionally, RIE exhibits low selectivity when etching glass, leading to low rates and throughput owing to single-wafer processing. Therefore, a batch processing method enabling deep and vertical glass etching is required.

For nearly 10 years, we have been investigating glass etching using hydrogen fluoride (HF) gas. HF gas etches glass by fluorinating its oxide groups.[3] Leveraging this, we discovered that photoresist, typically used as an etching mask, acts as a catalyst when exposed to high-temperature HF gas, enabling a novel selective-etching method[4] named advanced gas-phase chemical reaction for anisotropic catalyst etching (AGC-ACE). Figure 1 presents a schematic of AGC-ACE. After patterning the resist on silica glass using i-line photolithography, etching is performed with HF gas. The catalyst is then removed using oxygen plasma. The core of this method is the catalytic effect of the resist, which accelerates etching in the coated areas, while uncoated areas exhibit minimal reaction. Consequently, only the area under the resist is selectively etched. Density functional theory calculations suggest that this catalytic mechanism involves interactions between -OH groups in the resist polymer and H from the HF gas, which activate F and promote nucleophilic reactions with Si.

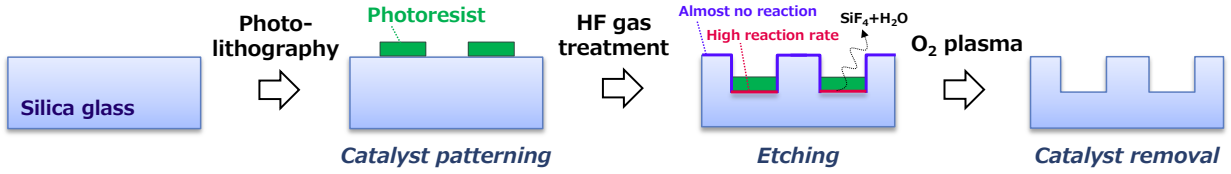


Figure 1. Schematic of AGC-ACE

Figures 2(a)–(d) show scanning electron microscopy (SEM) images captured before and after HF gas treatment. The resist-coated areas are selectively etched, confirming the conceptual illustration in Figure 1. Structures processed by RIE (Figure 2(c)) exhibit an 85° tapered shape, whereas AGC-ACE (Figure 2(d)) achieves nearly vertical etching with an angle of less than 1°. Moreover, the etching rate is 2.6 times higher (1.3 μm/min) than that of RIE (0.5 μm/min). As AGC-ACE is a plasma-free process, it enables batch processing. This allows the simultaneous treatment of multiple wafers, thereby significantly increasing throughput.

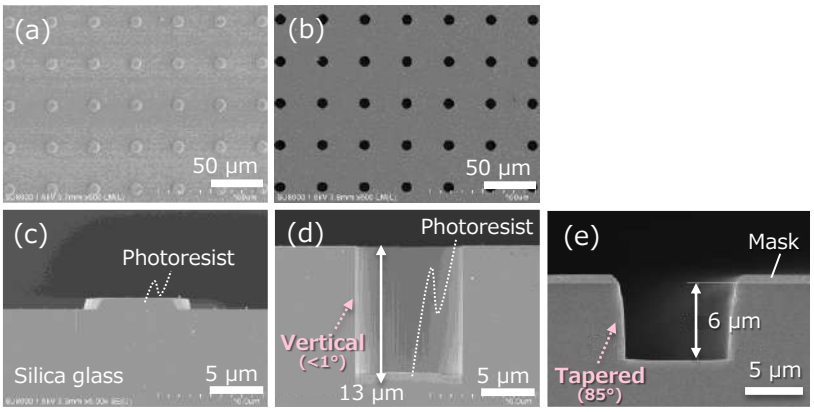


Figure 2. SEM images of silica glass before HF gas etching (a, c), after HF gas etching (b, d), and after RIE (e)

Figure 3 shows SEM images of microfabricated silica glass structures produced using AGC-ACE. High verticality is achieved in both trench and dense pillar structures. Unlike RIE, where the resist is consumed, the resist acts as a catalyst in AGC-ACE, enabling unlimited etching depth. In fact, successful etching up to 100 μm depth has been demonstrated. Furthermore, pillars with a diameter of 500 nm and depth of 25 μm (aspect ratio: 50) have been fabricated, which was impossible with conventional techniques. As the resolution is determined by photolithography, sub-100 nm fabrication has been achieved by changing the patterning method.

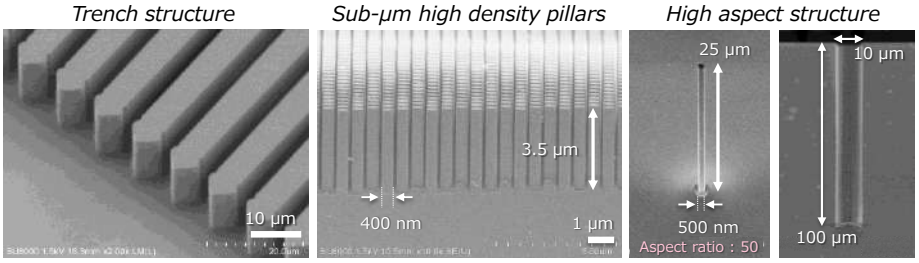


Figure 3. SEM images of silica glass substrate fabricated using AGC-ACE

AGC-ACE enables high-throughput etching of glass with excellent verticality and depth in a batch process. Therefore, it is expected to enable the low-cost fabrication of high-efficiency glass-based metasurfaces, overcoming limitations of conventional methods. We will present the most recent work towards applying this method to fabricate visible metasurfaces.

References

[1] Park, J. S., S. Zhang, A. She, W. T. Chen, P. Lin, K. M. A. Yousef, J. X. Cheng and F. Capasso, "All-glass, large metalens at visible wavelength using deep-ultraviolet projection lithography," Nano Lett., Vol. 19, 8673, 2019.

[2] Zhang, C., S. Divitt, Q. Fan, W. Zhu, A. Agrawal, Y. Lu, T. Xu and H. J. Lezec, "Low-loss metasurface optics down to the deep ultraviolet region," Light Sci. Appl., Vol. 9, 55, 2020.

[3] Ono, Y., Y. Hayashi, S. Urashima and H. Yui, "Glass etching with gaseous hydrogen fluoride: Rapid management of surface nano-roughness," Int. J. Appl. Glas. Sci. Vol. 13, 1, 2022.

[4] Sano, K. Y. Ono, R. Tobinaga, Y. Imamura, Y. Hayashi and T. Yanagitani, "Atmospheric gas-phase catalyst etching of SiO_2 for deep microfabrication using HF gas and patterned photoresist," ACS Appl. Mater. Interfaces, Vol. 16, 22657, 2024.

Gold nanostructure gratings produced using direct laser writing with pulse energy-dependent morphology for SERS substrates

K. Vilkevičius[1*], I. Ignatjev[2], G. Niaura[2], and E. Stankevičius[1]

[1]Department of Laser Technologies, Center for Physical Sciences and Technology, Savanoriu Ave. 231, Vilnius, Lithuania
[2]Department of Organic Chemistry, Center for Physical Sciences and Technology, Sauletekio Ave. 3, Vilnius, Lithuania
[*]corresponding author: kernius.vilkevicius@ftmc.lt

Abstract: Direct laser writing is a versatile tool for producing free-form periodic arrays of gold nanostructures by modification. Pulse energy, grating period, and film thickness lead to variations in produced structure morphology, which in turn provide tunable resonant properties. The formation and application of such structures for SERS are presented.

Periodic gratings of plasmonic nanostructures provide the ability to efficiently couple plasmonic modes leading to an enhancement and improvement of their properties. Grating-coupling of the plasmonic modes achieved by a periodic array provides the flexibility and compactness of the platform where an additional element as a prism is not required for the excitation. Therefore, rapid, scalable, and reproducible fabrication of such structures is of high importance for practical applications and mass production. In this work, we employ a direct laser writing (DLW) technique using a sharply focused femtosecond laser beam onto the metal surface to achieve a single-step formation of free-form arrays with high precision. Variation in fs-pulse energy leads to the formation of distinct morphologies of the structures [1,2] produced with single pulses – bumps, cones, and jets (Figure 1a,b). Additionally, adjustments in the grating period and gold film thickness provide additional control of the structure shape [3]. This, in turn, allows for a more accurate manipulation of plasmonic properties.

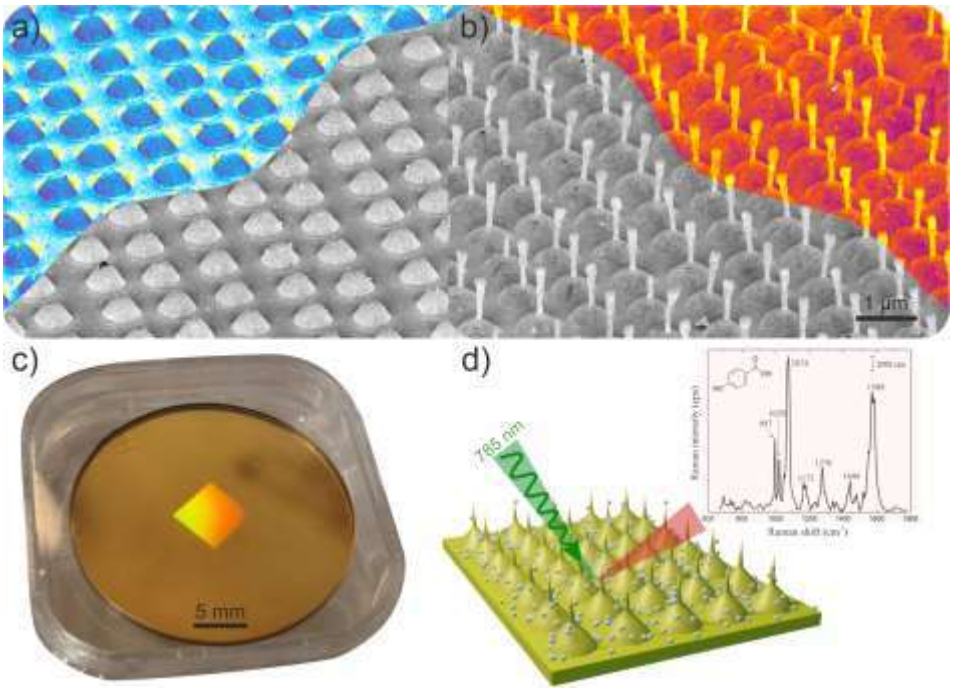


Figure 1. a) Periodic array of gold bumps. b) Periodic array of gold jets. c) Large-scale gold grating used as a SERS platform. d) Raman measurements using 4-MBA and obtained SERS spectrum.

This study investigates the influence of DLW-produced structure shape on the plasmon resonance and evaluates their applicability for surface-enhanced Raman spectroscopy (SERS). Large-scale arrays of 5×5 mm^2 were produced on thin gold films of varying thickness from 50 nm to 200 nm (Figure 1c) using femtosecond laser pulses. The formation with different pulse energies at various thicknesses leads to a great control of structure shape, with small bumps being similar in all thin films, and jets changing their shape depending on the gold layer thickness. Morphological changes significantly affect the enhancement of the local electromagnetic field, leading to variations in the signal enhancements [4]. Using 4-mercaptobenzoic acid as a Raman reporter, we examined the impact of structure shape and film thickness influence on the measured Raman signals (Figure 1d). The main 2 characteristic bands of 4-MBA at 1074 cm^{-1} and 1589 cm^{-1} were examined to determine the enhancement factor. While bumps achieved only a 10^5-order enhancement factor, its order can be increased at jet-like structures up to 10^7. Moreover, since structures are produced in a grating, the results also correspond to a repetitive manner at each structure.

The authors acknowledge the Research Council of Lithuania (LMT, Lithuania) for the received funding under project No. S-MIP-23-32.

References

1. Korte F., Koch J. and Chichkov B. “Formation of microbumps and nanojets on gold targets by femtosecond laser pulses” Appl. Phys. A, Vol. 79, 879-881, 2004.
2. Pavlov D., Syubaev S., Kuchmizhak A., Gurbatov A., Vitrik O., Modin E., Kudryashov S., Wang X., Juodkazis S. and Lapine M., “Direct laser printing of tunable IR resonant nanoantenna arrays” Appl. Surf. Sci., Vol. 469, 514-520, 2019.
3. Vilkevičius K., Tsibidis G. D., Selskis A., Stratakis E. and Stankevičius E., “Formation of highly tunable periodic plasmonic structures on gold films using direct laser writing,” Adv. Opt. Mater., Vol. 12, No. 20, 2400172, 2024.
4. Vilkevičius K., Ignatjev I., Selskis A., Niaura G. and Stankevičius E., “Tuning SERS performance through the laser-induced morphology changes of gold nanostructures,” Appl. Surf. Sci., Vol. 660, 160003, 2024.

Comparative Study of Nanocrystalline Dy_2O_3 Thin Films deposited on Sapphire and Silicon Wafers by Means of Electron Beam

Faisal Alresheedi
Department of Physics, College of Science, Qassim University, Buraidah 51452, Saudi Arabia.
F.alresheedi@qu.edu.sa

Abstract:

In this work, we reported a comparative study of dysprosium oxide (Dy_2O_3) thin films deposited on sapphire and silicon substrates by electron beam evaporation technique. X-ray diffraction (XRD) was used to investigate the crystal structural of Dy_2O_3 thin films, which showed that all films possess a polycrystalline nature and possess a cubic-type structure. The average crystallite size was calculated and it shows that the film deposited on the silicon substrate is slightly larger than the film deposited on the sapphire substrate. Scanning electron microscopy (SEM) was employed to investigate the morphological characteristics of the thin films. The film grown on the sapphire substrate has a granular surface while the film grown on the silicon substrate has a more compact surface and is free of pores. Spectroscopic ellipsometry (SE) was used to obtain the optical constants of both thin films. The reflectance of both samples was examined using UV-Vis spectrophotometry, with the findings demonstrating that the deposited layer on the sapphire substrate serves as a preferable choice for creating an improved anti-reflective layer in compared to a silicon layer.

References

1. Ramay, Shahid M., et al. "Magnetron sputtered Dy_2O_3 with chromium and copper contents for antireflective thin films with enhanced absorption." Journal of Rare Earths 37.9 (2019): 989-994.
2. Singhal, Kiran, et al. "Studies on Synthesis, Physical and Optical Properties of Dysprosium Ion-Doped Transparent Heavy Metal Oxide Glasses." Key Engineering Materials 1001 (2024): 57-64.
3. Ganvir, V. Y., et al. "Investigation of dysprosium oxide substitution on physical, electrical and dielectric properties in sodium borosilicate glass system." Journal of Molecular Structure 1302 (2024): 137381.
4. Snetkov, I. L., et al. "Magneto-optical Faraday effect in dysprosium oxide (Dy2O3) based ceramics obtained by vacuum sintering." Optics Letters 43.16 (2018): 4041-4044.
5. Bhat, R., Qayoom, M., Dar, G. N., & Want, B. (2020). Structural, dielectric, optical and magnetic studies of dysprosium doped iron oxide nanostructures. Materials Chemistry and Physics, 245, 122764.

Metrology of singular metasurfaces

Y. Tahmi[1,2], M. Ansquer[2], P. M. Coulon[1], S. Chenot[1], V. Brandli[1], B. Wattellier[2], P. Genevet[3] and S. Khadir[1]

[1]Université Côte d'Azur, CNRS-CRHEA, Rue Bernard Gregory, Valbonne, 06560, France.

[2]Phasics, Parc Technologique de Saint Aubin, Saint-Aubin, 91190, France.

[3]Department of Physics, Colorado School of Mines, 1523 Illinois Street, Golden, CO, 80401, USA

[*]corresponding author: samira.khadir@crhea.cnrs.fr

Abstract: This study employs quadriwave lateral shearing interferometry (QLSI) to characterize singular metasurfaces generating optical vortex beams. By analyzing effective refractive index (ERI) and Pancharatnam-Berry (PB) phase metasurfaces, we demonstrate QLSI's accuracy in detecting phase errors, non-integer topological charges, and complex multi-vortex configurations, offering robust phase metrology for advanced photonic applications.

Photonic orbital angular momentum (OAM) is a fundamental property of light that results from its wavefront structure. OAM beams, also known as vortex beams, exhibit a helical phase distribution, leading to a central phase singularity where intensity is zero. This property is quantified by the topological charge (TC), which determines the number of phase twists in one wavelength. OAM has applications in optical communication, [1] imaging, microscopy, [2] and quantum information processing due to its capacity for encoding multiple information states. Traditional methods of OAM generation, such as spiral phase plates and spatial light modulators, suffer from size constraints and limited design flexibility. To address these issues, metasurfaces (MSs) have emerged as a powerful alternative, allowing precise phase manipulation at a subwavelength scale [3]. However, discrepancies between theoretical design and experimental fabrication necessitate robust phase characterization techniques. Interferometric methods, previously used for this purpose, are highly sensitive to noise. This study employs quadriwave lateral shearing interferometry (QLSI) as an alternative, [4] offering a more accurate characterization of singular MSs. We demonstrate that QLSI can be effectively applied to achieve high precision phase metrology of arbitrary singular MSs, imprinting either high-order integer or non-integer OAMs. Specifically, we showcase the technique's ability to detect fabrication imperfections and their influence on the generated vortex beams. This is achieved by studying various MS designs based on effective refractive index (ERI) and Panchratnam-Berry (PB) phase. We also studied vortex-like MSs with non-integer topological charges and complex multi-vortex configurations.

A comparative analysis of ERI and PB MS-based vortex beams was conducted by fabricating and characterizing MSs with TCs ranging from 1 to 10. QLSI measurements confirmed that PB MSs had lower phase errors than ERI MSs due to better fabrication tolerance and phase discretization. Far-field intensity profiles showed that both MS types generated the expected vortex beams; however, PB MSs exhibited more accurate donut-shaped intensity profiles. The superior performance of PB MSs was attributed to their higher phase discretization capability and lower sensitivity to fabrication errors.

We further characterized MSs generating vortices with non-integer TCs ranging from 0.1 to 1. QLSI successfully retrieved the phase profiles for non-integer vortices with high accuracy. This capability is particularly interesting for MS-based vortex metrology, where non-integer TCs may arise from design or fabrication errors. By leveraging a straightforward optical characterization approach, we identified singular

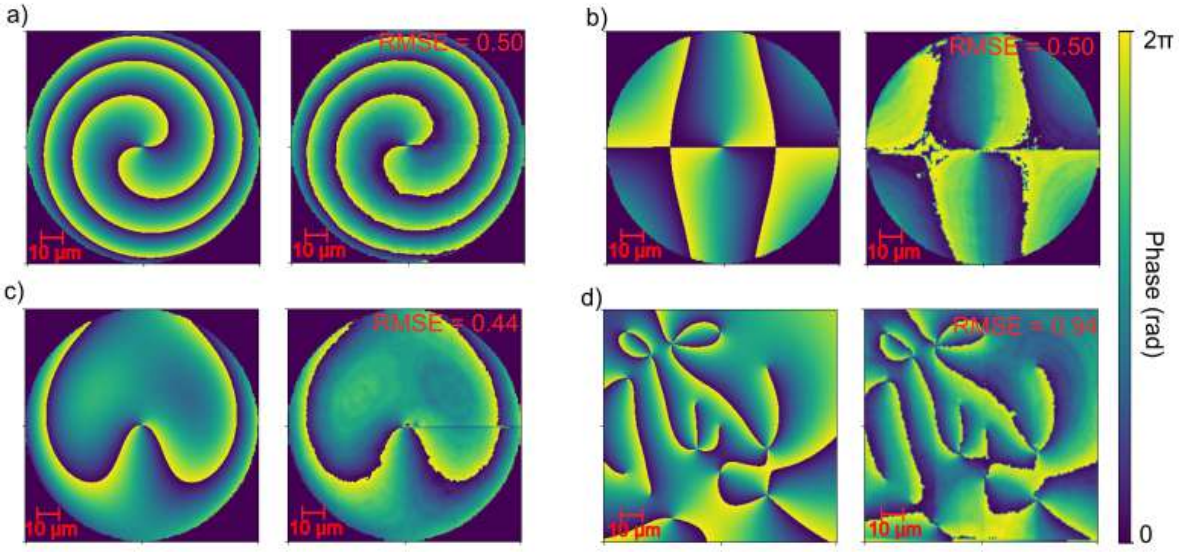


Figure 1: Characterization of PB MS with multi-vortices and other optical functionalities. Design (left) and measured (right) phase profile for vortex of CT=2 associated with a lens profile (a), astigmatism aberration profile (b) and coma aberration profile (c). d) Design (left) and measured (right) phase profile MS caring 15 vortices with TCs ranging from -4 to 4.

wavefront discrepancies without relying on expensive and intricate morphological analyses.

The versatility of QLSI in characterizing complex phase profiles is further demonstrated by analyzing metasurfaces (MSs) designed to generate multiple optical vortices and those incorporating additional optical functionalities, such as lens aberrations described by Zernike polynomials. The characterization results are benchmarked against their designed profiles, as shown in Fig. 1. Several examples illustrate the combination of a vortex with a TC of 2 and different phase profiles: a lens profile (Fig. 1a), astigmatism (Zernike moment Z_2^2) (Fig. 1b), and coma (Zernike moment Z_3^1) (Fig. 1c). In each case, the designed phase maps (left) are compared with the measured phase profiles (right). A strong qualitative agreement between the designed and retrieved profiles is evident, further supported by the root mean square error (RMSE) values of approximately 0.5 rad. The minor discrepancies observed primarily arise from measurement noise, design limitations, and fabrication imperfections, with numerical artifacts from the phase unwrapping process being particularly noticeable in Fig. 1b. Figure 1d presents the designed (left) and measured (right) phase profiles for an MS generating 15 vortices with TC values ranging from -4 to 4. The retrieved phase profile closely matches the designed structure; however, as the complexity of the phase distribution increases, the RMSE value slightly rises to 0.94 rad. This increase is likely due to the greater intricacy of the phase structure, making it more susceptible to minor deviations.

Acknowledgments: SK acknowledges financial support from French National Research Agency ANR Project VERDICT (ANR-22-CE42-0021)

References

1. J. Wang et al., “Terabit free-space data transmission employing orbital angular momentum multiplexing.” Nat. Photonics 6, 488–496, 2012
2. D. G. Grier, “A revolution in optical manipulation.” Nature 424, 810–816, 2003.
3. H. Ren, G. Briere, et al. “Metasurface orbital angular momentum holography” Nature Commun., 10, 2886, 2019
4. S. Khadir, D. Andrèn, et al. “Metasurface optical characterization using quadriwave lateral shearing interferometry,” ACS Photonics 8 (2), 603, 2021.

Thermal-Mechanical Coupling Performance of the Printable Al-Si Alloy Antisymmetric Lattice Metastructure

J. Q. Yan[1], Y. D. Gao[1], and H. Y. Huang[1*]

[1]School of Aeronautics, Northwestern Polytechnical University, China
[*]corresponding author: huangheyuan@nwpu.edu.cn

Abstract: This study investigated the mechanical behavior of four lattice structures using AlSi12Fe2.5Ni3Mn4, a newly developed alloy. A novel antisymmetric anti-buckling lattice cell (ASLC-B) based on a rotation reflection multistage design was developed. Quasi-static compression tests showed that ASLC-B outperformed the other three types in energy absorption, and heat transfer efficiency.

1. Structural Design

As shown in **Figure 1(a)**, by using a one-rod core of the PLC as the basis and performing a 180° rotation reflection within the plane of the structure's spatial center, a newly designed antisymmetric lattice cell (ASLC) was obtained. Then, a secondary cross-core has been incorporated into the rod core for anti-buckling constraint, resulting in a pyramid anti-buckling lattice cell (PLC-B) and antisymmetric anti-buckling lattice cell (ASLC-B).

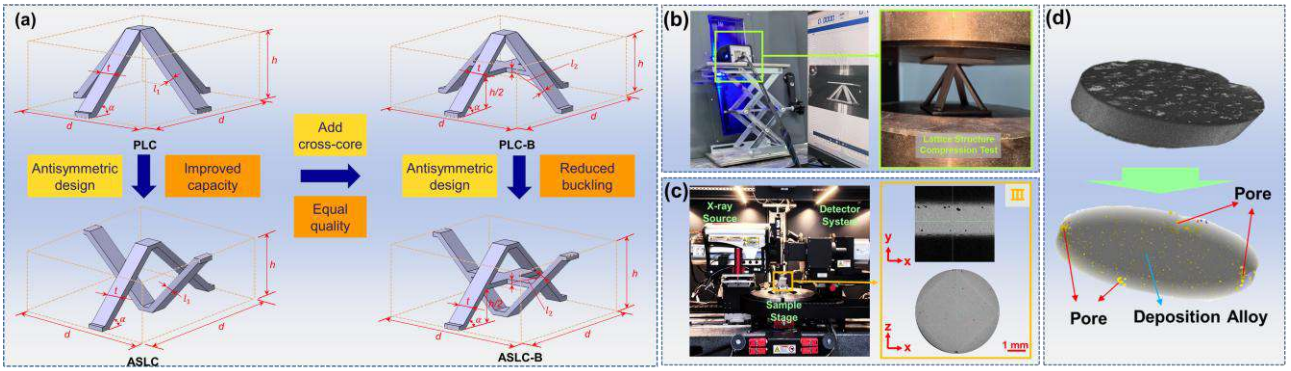


Figure 1. (a) Designing concept of lattice cells; (b) Schematic of lattice cells quasi-static compression test device; (c) Micro-CT device and the schematic of scanning results; (d) Distribution and 3D morphology of pores.

2. Test and Characterization

The lattice structure test pieces fabricated using SLM technology included PLC, PLC-B, ASLC, ASLC-B designs. The laser power for printing was 360W, with a scanning speed of 1250mm/s and a scanning spacing of 0.14mm. The tests were conducted using an MTS-E42 Universal Testing Machine equipped with a 500°C Environmental Box at a loading rate of 1mm/min. The compression test setup and the actual loading conditions were illustrated in **Figure 1(b)**.

The porosity of the printed lattice structures was analyzed using CT technology. For this purpose, an X-ray Micro-CT system (model: ZEISS Xradia 620 Versa) equipped with a 120kV voltage and 25W output power was employed to inspect the AlSi12Fe2.5Ni3Mn4 lattice structure. **Figure 1(c)** displayed the setup of the scanning device and the images of the scanning results obtained from different directions. By applying the global gray threshold to the Micro-CT reconstructed volume model, the pore distribution and morphology were determined in detail, as shown in **Figure 1(d)**. The porosity values ranged from as low as 0.307% to as high as 0.583%. After fitting and calculating the curve, the average porosity of the test piece was determined to be 0.454%.

3. Results and discussion

The comparison leveraged quantified indicators of structural performance, including the load-to-weight ratio (F_b), specific energy absorption (SEA), mean crushing force (MCF), crushing force efficiency (CFE), and structural stiffness (K)[1-3]. **Figure 2(a)** offered a comprehensive comparison of the load-bearing efficiency of the four lattice cells at 25°C and 200°C. **Figure 2(b)** offered a comprehensive comparison of the load-bearing efficiency of ASLC-B(AlSi10Mg) and ASLC-B at 25°C and 200°C. **Figure 2(c)** showed the N_{uL}-R_{eH} curves of four configurations, and the comparison showed that ASLC-B had the highest heat transfer efficiency.

At temperatures of 25°C and 200°C, the ultimate load of ASLC-B increased by 36.04% and 38.85% respectively, compared to PLC. Additionally, the heat transfer efficiency increased by 27.34%. Moreover, when comparing different materials, ASLC-B exhibited a 39.39% (25°C) and 44.14% (200°C) higher load-bearing capacity than ASLC-B(AlSi10Mg).

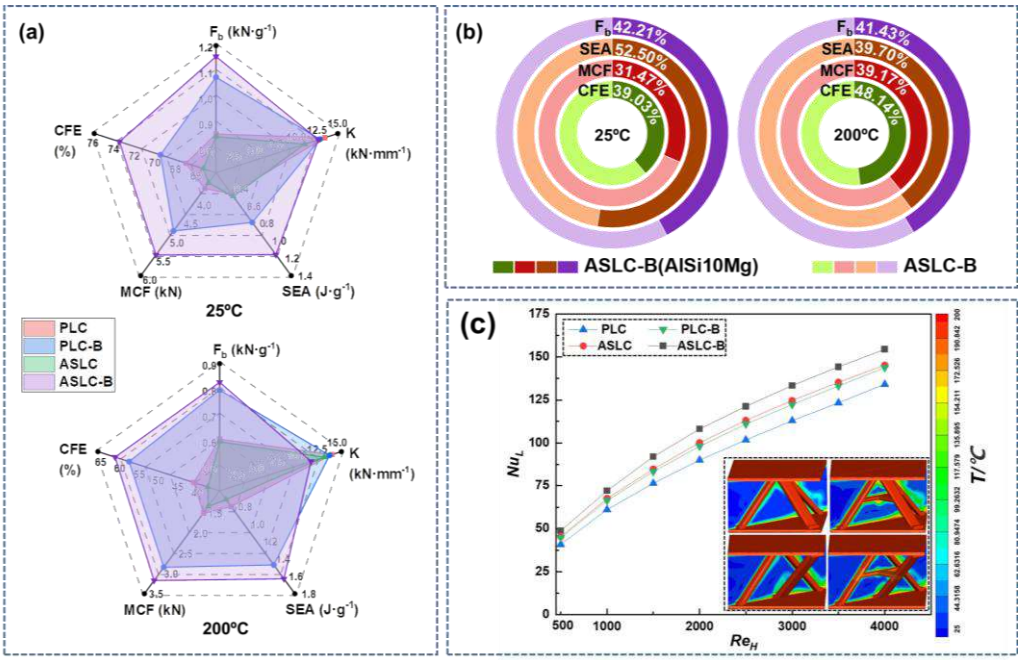


Figure 2. (a) Comparison of PLC, PLC-B, ASLC, and ASLC-B; (b) Comparison of ASLC-B(AlSi10Mg) and ASLC-B; (c) N_{uL}-R_{eH} curves.

Acknowledgements

This work was supported by the National Natural Science Foundation of China [grant number 12141203]; the Fundamental Research Funds for the Central Universities [grant number D5000230052]; the Shaanxi Innovation Ability Support Plan Project Funds [grant number 2024RS-CXTD-29].

References

1. F.L. Li, J.K. Gan, L. Zhang, H.L. Tan, E. Li, B. Li, Enhancing impact resistance of hybrid structures designed with triply periodic minimal surfaces, Compos. Sci. Technol., 245 (2024) 17.
2. H. Wang, D.W. Tan, Z.P. Liu, H.F. Yin, G.L. Wen, On crashworthiness of novel porous structure based on composite TPMS structures, Eng. Struct., 252 (2022) 15.
3. B.Y. Zhang, L. Wang, J. Zhang, Y.X. Jiang, W. Wang, G.H. Wu, Deformation and energy absorption properties of cenosphere/aluminum syntactic foam-filled circular tubes under lateral quasi-static compression, Int. J. Mech. Sci., 192 (2021) 14.

Large area metalenses for the generation of vector beams

D. Bonaldo[1*], A. Vogliardi[2], G. Ruffato[2], S. Dal Zilio[3], V. Apolloni[2] and F. Romanato[2,3]
[1]Department of Information Engineering, University of Padova, Italy
[2]Department of Physics "G. Galilei", University of Padova, Italy
[3]CNR-IOM Istituto Officina dei Materiali, Trieste, Italy
daniele.bonaldo.2@phd.unipd.it (corresponding author)

Abstract

Given their unprecedented control over the degrees of freedom of light, metalenses showed great potential for structuring light. In this work centimeters-wide metalenses for the generation of self-accelerating vector beams are designed, fabricated and characterized.

Metasurfaces gained a lot of attention for their capacity to tune materials' properties. The field of structured light hugely benefits from metasurfaces, since the ability to spatially tune the light beams' degrees of freedom has always been a technological challenge. Moreover, metasurfaces can display anisotropic behaviour, enabling the polarization to be controlled with spin-decoupled meta-atoms [1]. In common types of light beams, only phase and intensity are spatially tuned, but thanks to recent advances in optical devices, light beams with a spatially-varying polarization state, the so-called vector beams, are gaining new interest. Applications of vector beams are reported in microscopy, communication and encryption. Regarding the application of metasurfaces for generating vector beams, multiple references can be found but they are limited to small sizes [3,4]. While size is not a limiting factor for research, larger devices may be needed for certain applications. For example, Gaussian-Bessel beams exhibit longer non-diffracting length if generated by larger optics. For applications involving structured light in free-space telecommunication, large optics are required to propagate signals for long distances [5]. Large metalenses are challenging for every step of their development: bigger memories are needed for simulating their response, huge amount of pattern data is to be generated and conveyed to the lithography tool, lithography takes longer and is subject to stricter stitching requirements.

In this work, we designed, fabricated and characterized spin-decoupled metalenses up to 2cm-wide for the generation of vector beams, working at 1310 nm of wavelength.

A spin-decoupled metalens is able to control the phase of a spin state independently of the other. This can be accomplished by designing a set of meta-atoms that act as half-wave plates (HWP): they exhibit spin-dependent and spin-independent phase contributions which can be respectively tuned by rotating and reshaping the pillar. A library of HWP meta-atoms was generated through FEM simulations and encoded in an ASCII file.

The metalens was designed to generate a self-accelerating propagating-variant Bessel beam. Such beam displays a non-linear focal curve in the non-diffracting range of the Bessel-like beam [6], which can be interpreted as the constructive interference of bundles of rays coming from circles of the input plane with different radii and center position. Moreover, a radius-dependent angular orbital momentum term was added, so that their Bessel order increased with propagation. The local meta-atom shapes and rotations were calculated to match the phase needed for such optical transformations.

In order to represent the pattern efficiently, shapes and rotations were encoded as losslessly-compressed bitmap images. Compared to a standard structure-reference-based GDS file, this encoding was 140 times more efficient. After some lithography-related preprocessing, the library file and images were fed to an algorithmic patterning script of the electron beam lithography

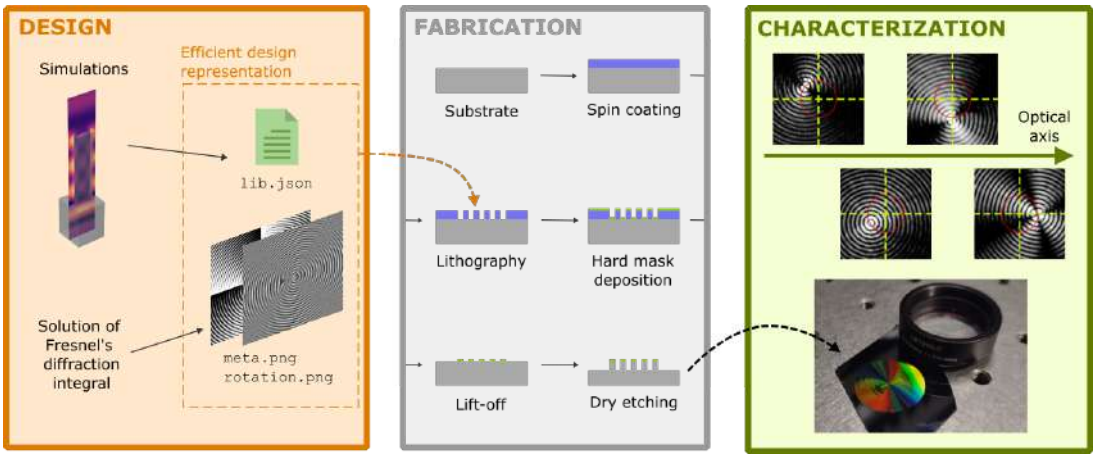


Figure 1: Scheme of the design, fabrication and characterization phases. Regarding characterization, the images were taken by shifting the image-collecting objective. On the low-right, the metalens is compared with a inch-sized lens.

(EBL) tool. Fabrication involved a two-phase protocol. First, a resist was patterned on a silicon substrate through EBL. In the second phase, the pattern was transferred to the underlying silicon by means of hard mask deposition, lift off and dry etching.

Devices were characterized on an optical bench. By shifting the image-collecting objective along the optical axis, the beam clearly shifted its center and the Bessel order increased, showing the desired self-accelerating behaviour.

Acknowledgements

This work was partially supported by the European Union under the Italian National Recovery and Resilience Plan (NRRP) of NextGenerationEU, partnership on "Telecommunications of the Future" (PE0000001–program "RESTART").

References

[1] Xu, H. X., Han, L., Li, Y., Sun, Y., Zhao, J., Zhang, S., and Qiu, C., "Completely Spin-Decoupled Dual-Phase Hybrid Metasurfaces for Arbitrary Wavefront Control" *ACS Photonics*, Vol. 6, No. 1, pp. 211-220, 2018.

[2] Holleczek, A., Aiello, A., Gabriel, C., Marquardt, C., and Leuchs, G., "Classical and quantum properties of cylindrically polarized states of light" *Opt. Express*, Vol. 19, pp. 971-9736, 2011.

[3] Kotlyar, V. V., Stafeev, S. S., Nalimov, A. G., O'Faolain, L., and Kotlyar, M. V., "A dual-functionality metalens to shape a circularly polarized optical vortex or a second-order cylindrical vector beam" *Photonics and Nanostructures*, Vol. 43, 100898, 2021.

[4] Vogliardi, A., Ruffato, G., Dal Zilio, S., Bonaldo, D., and Romanato, F. "Dual-functional metalenses for the polarization-controlled generation of focalized vector beams in the telecom infrared" *Sci Rep*, Vol. 13, 10327, 2023.

[5] Ferrari, M., Romanato, F., and Ruffato, G. "Design of a free-space optical link based on multipole-phase division multiplexing" *Opt. Express*, Vol. 33, No. 3, pp. 4957-4977, 2025.

[6] Chremmos, I. D., Chen, Z., Christodoulides, D. N., and Efremidis, N. K., "Bessel-like optical beams with arbitrary trajectories" *Opt. Lett.*, Vol. 37, pp. 5003-5005, 2012.

Application of micro-CT technology in performance characterization of composite materials under extreme temperatures

Xiaoyang Ren[1, #], Yaguang Dai[1, 2, #], Meiying Zhao[1, 3], Heyuan Huang[1, 3*]

[1] Northwestern Polytechnical University, China
[2] Shenyang Aircraft Design and Research Institute, China
[3] National Key Laboratory of Aircraft Configuration Design, China
[#] Xiaoyang Ren and Yaguang Dai contributed to this work equally.
[*]Corresponding author: huangheyuan@nwpu.edu.cn

Abstract: This paper delves deep into the application of Micro-CT technology in the performance characterization of composite materials. It elaborately expounds how this technology precisely reveals the internal structures and defects, and analyzes its vital significance for accurately evaluating composite properties.

Introduction

Traditional methods for characterizing the performance of composite materials mainly present numerical results (such as load, stress, etc.). The amount of information that can be reflected in this form is very limited, and it lacks intuitiveness. In contrast, micro-CT technology, with its advantages such as non-destructive testing, high-resolution imaging, three-dimensional visualization, and high detection efficiency, provides a feasible way to efficiently obtain internal information, preserve the original state of the sample, and accurately present the fine structures[1-3].

Experiment

In this paper, the Micro-CT technology is applied to detect the area around the holes of the bolted joint structure of carbon fiber composite materials under 150℃, and the internal damage forms and distribution laws are discussed. The schematic diagram of the sampling part and experimental devices are shown in **Figure 1**.

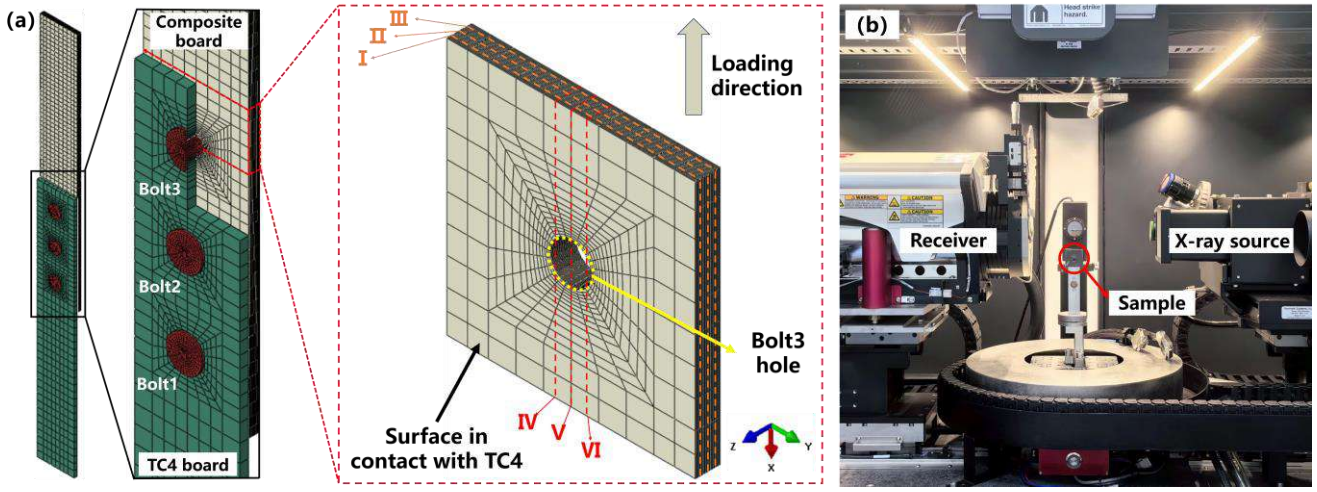


Figure 1 (a) Schematic diagram of the sampling part; (b) experimental devices.

The test piece is a hybrid bolted connection structure of T1000/BMI composite material and TC4 metal. The sample is taken from the area around the hole near the clamping end of the composite material plate. The three-dimensional reconstructed image obtained after Micro-CT scanning is shown in **Figure 2(a-b)**.

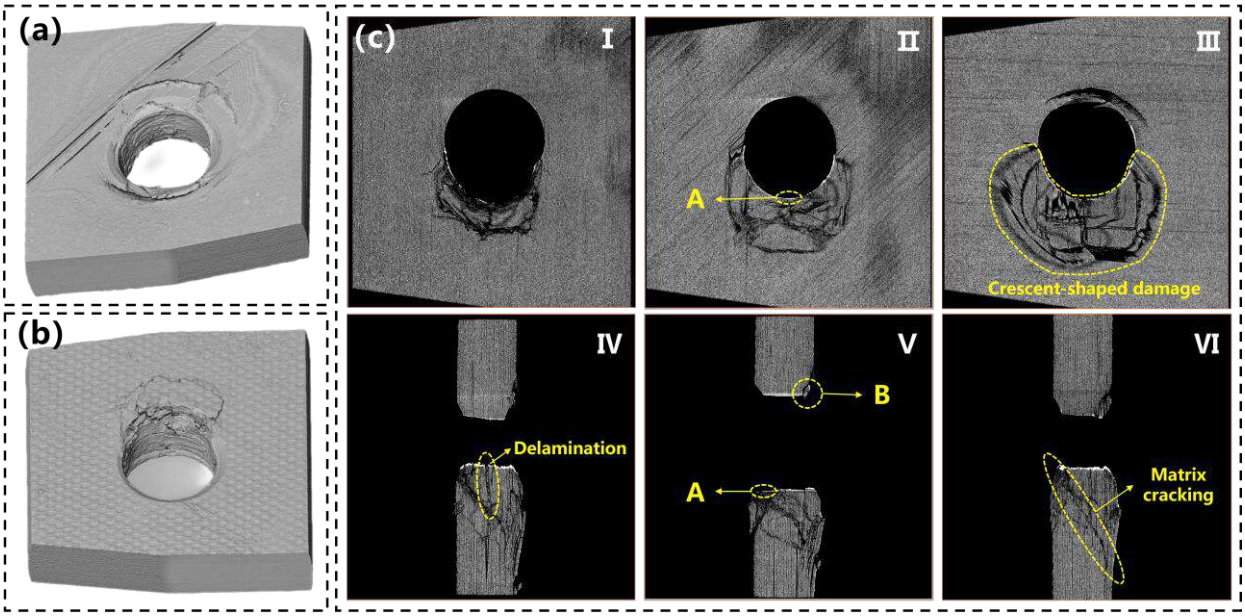


Figure 2 Results of the three-dimensional scanning: (a) the surface in contact with the TC4; (b) the reverse side; (c)the cut section diagrams in xy and xz directions (sections I to VI are intercepted according to Figure 1)

Results and Discussion

As can be seen from **Figure 2**, the extrusion damage (internal shadow) of the composite laminate shows a trend of gradually increasing from the inner side to the outer side, and a mixed damage of laminate delamination and matrix cracking has occurred. The extrusion damage is symmetrically distributed along the central position of the bolt hole, that is, the distribution laws of Section IV and Section VI obtained by micro-CT are basically the same. The damage on the outer side of the laminate at Section V in the middle of the bolt hole is weaker than that at Section IV and Section VI, but the damage on the inner side is stronger, reflecting that the vertical extrusion effect of Position A on the laminate is more obvious. At Position B, the outer plane of the composite laminate within a certain range has also been damaged.

In summary, Micro-CT technology can intuitively and efficiently assist in detecting the internal damage of the test piece without causing any damage, thereby facilitating the analysis of the mechanism.

Acknowledgements

This work was supported by the National Natural Science Foundation of China [grant number 12141203]; the Northwestern Polytechnic University Doctoral Dissertation Innovation Foundation [grant number CX2023083]; the Fundamental Research Funds for the Central Universities [grant number D5000230052].

References

1. Tang, C., J. Zou, Y. Xiong, Automatic reconstruction of closely packed fabric composite RVEs using yarn-level micro-CT images processed by convolutional neural networks (CNNs) and based on physical characteristics. Composites Science and Technology, Vol. 252, 110616, 2024.
2. Ye, J., H. Cai, L. Liu, Microscale intrinsic properties of hybrid unidirectional/woven composite laminates: Part I experimental tests. Composite Structures, Vol. 262, 113369, 2021.
3. Huang, W., P. Causse, V. Brailovski, Reconstruction of mesostructural material twin models of engineering textiles based on Micro-CT Aided Geometric Modeling. Composites Part A: Applied Science and Manufacturing, Vol. 124, 105481, 2019.

Submicron Periodic Structures in Metal Oxide Thin Film via Laser Ablation and Thermal Oxidation

J. Nikitina[1*], S. Indrišiūnas[1], T. Tolenis[1,2], M. Andrulevičius[3], L. Ramalis[1], L. Grinevičiūtė[1]

[1]Department of Laser Technologies, Center for Physical Sciences and Technology, Vilnius, Lithuania
[2]ELI Beamlines Facility, Extreme Light Infrastructure ERIC, Dolní Břežany, Czech Republic
[3]Institute of Materials Science, Kaunas University of Technology, Kaunas, Lithuania
[*]corresponding author: julianija.nikitina@ftmc.lt

Abstract: Direct laser interference patterning of metal layer followed by thermal oxidation for the fabrication of fully inorganic transparent submicron periodic structures, avoiding complexities of direct patterning of dielectric materials.

Periodic structures, featuring periodic modulation of optical constants, exhibit polarization control, spectral and angular selectivity of light and thus were found extremely useful for laser radiation manipulation. However, fabrication technologies of periodic structures have to face strict requirements for laser optics, especially for high-power systems. Despite a sub-micrometer scale of periodicity required for visible and infrared spectral region applications, the following significant criteria are optical transparency and durability, which require a completely inorganic composition of all constituent materials. Polymers are quite easily processed and can be transparent in the target spectral regions, but they exhibit lower optical resistance than fully inorganic materials such as metal oxides [1]. However, direct patterning of the dielectric materials is non-trivial, especially if sub-micrometric periodicity is required with sufficiently low surface roughness. To get around a direct patterning of metal oxides, a thin metallic layer deposited on a glass substrate can be structured. Subsequent annealing promotes a metal oxidation reaction, producing a fully inorganic, transparent periodic surface structure on a glass substrate.

The fabrication method proposed in our work [2] involves the structuring and subsequent thermal oxidation of a thin metallic layer on a glass substrate, as schematically shown in Fig. 1. For this, thin tantalum metal films were formed on fused silica substrates using ion beam sputtering technology. The pristine thin film samples were thermally annealed in an ambient atmosphere under various conditions (varying annealing temperature and heating rate) to evaluate optimal oxidation conditions for the structured thin film. Investigating the structural, optical, and chemical characteristics of various annealing procedures applied to tantalum thin films offered insights into the optimal parameters for thin film thermal oxidation. Thus, to avoid high optical losses and reach the purest Ta_2O_5 composition, 600 °C annealing temperature and 2 °C/min heating rate were used.

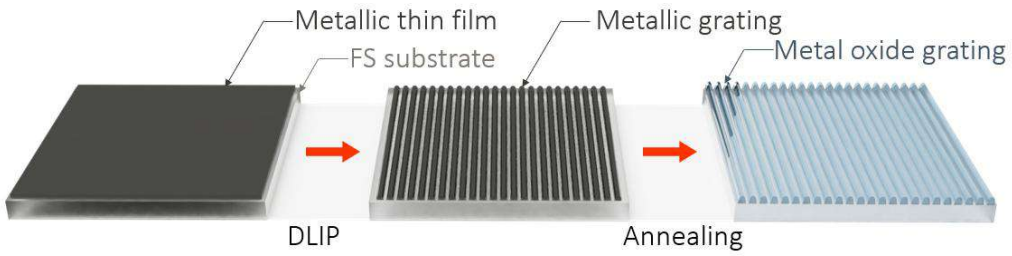


Figure 1. Fabrication steps of submicron periodic surface structure in metal oxide thin film, including Direct Laser Interference patterning (DLIP) of metallic layer and thermal oxidation (annealing).

Linear periodic structures – gratings – in thin metallic films were formed via the Direct Laser Interference Writing (DLIP) technique. The two-beam interference pattern was produced from the second harmonic (515 nm wavelength) laser beam of 7 ps short pulses. The resulting period of the linear interference pattern on the sample was 750 nm, with the laser spot size diameter at a $1/e^2$ level of 1.36 mm. After forming the grating structure by DLIP, the last step was annealing to complete metal oxidation, thus forming non-absorbing gratings. The structured films were annealed using the optimal parameters obtained from the investigation of as-grown films. The characterization results of the formed grating structure in thin films before and after annealing are summarized in Fig. 2. The atomic force microscope captured surface morphology images show increased modulation depths and fill factor, as shown in Fig. 2a. As it is inevitable during the oxidation process, the attachment of oxygen atoms to metal causes material volumetric expansion. Generally, the average modulation depth has increased from 280 to 420 nm, and the fill factor has increased by approximately 10 % for metal oxide structures.

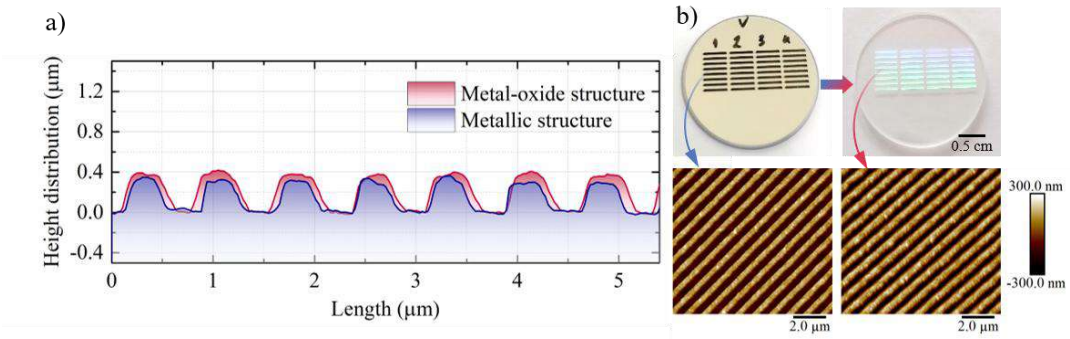


Figure 2. a) The atomic force microscope captured cross-sections and b) images of the patterned niobium thin film sample before (metallic structure) and after (transparent metal-oxide structure) annealing at niobium oxidation temperature.

The presented method of direct laser interference patterning of metal layers followed by thermal oxidation by annealing has been proven effective for obtaining sub-micrometer non-absorbing gratings. No absorption has been detected by spectrophotometric measurements, which allows the use of the developed nanostructures for high-intensity laser optics applications. This investigation shows that this method can overcome the problems associated with traditional glass microstructuring and is a promising route for developing advanced optical elements.

Acknowledgements:
This work was supported by the PerFIN project from the Research Council of Lithuania (LMTLT), agreement No S-MIP-22–80.

References

1. A. Žukauskas, et al., ‘Effect of the photoinitiator presence and exposure conditions on laser-induced damage threshold of ORMOSIL (SZ2080)’, Optical Materials, vol. 39, 2015.
2. J. Nikitina, et al., ‘Submicron periodic structures in metal oxide coating via laser ablation and thermal oxidation’, Applied Surface Science Advances, vol. 24, 2024.

Optical biosensor for rapid detection of medical biomarkers based on Bound States in the Continuum

Magdalena Zadura[1,2], Weronika Głowadzka[1,2], Karolina Bogdanowicz[1,2], Piotr Polak[1], Joanna Jankowska-Śliwińska[1], Kamil Kosiel[1], Krzysztof Piskorski[1], Marek Ekielski[1], Tomasz Czyszanowski[2], Anna Szerling[1]

[1] *Łukasiewicz Research Network - Institute of Microelectronics and Photonics, al. Lotników 32/46, 02-668 Warsaw, Poland*

[2] *Photonics Group, Institute of Physics, Lodz University of Technology, ul. Wolczanska 219, 90-924 Łódź, Poland*

[*] *corresponding author:* magdalena.zadura@imif.lukasiewicz.gov.pl

Abstract: We present an optical biosensor for detecting the protein S of COVID-19. Based on a low-refractive-index contrast subwavelength grating, we employ Fano resonance for high-sensitivity detection. The platform, fabricated using E-beam lithography and plasma etching, can be adapted for various biomarkers, including cancer-related proteins and pathogens.

Introduction

Various biosensors are currently being developed to detect analytes such as biomolecules and biological cells. These sensors hold significant potential for applications in diagnostic systems and screening tests.

Biosensors can be classified based on the type of signal transducer used, including electrochemical, mechanical, and optical sensors. Examples include electrochemical sensors, chemiluminescence and colorimetric sensors, surface plasmon resonance (SPR) sensors, localized surface plasmon resonance (LSPR) sensors, fluorescence-based sensors, fiber-optic sensors, terahertz-based biosensors, and surface-enhanced Raman spectroscopy (SERS) sensors [1,2], among others.

The design of biosensors varies significantly, particularly in terms of recognition elements, which depend on the specific of analytes [2] they are designed to detect. Electrochemical sensors operate by detecting electrochemical changes, such as variations in conductance, current, and potential, which may result from redox reactions [3]. Optical biosensors, on the other hand, detect changes in the properties of transmitted or reflected light, such as wavelength, intensity, and polarization [3]. They are highly sensitive to alterations in the optical properties of their environment, including changes in the refractive index.

Biosensors have enormous potential, particularly in medical applications, where they are used in diagnostic systems and screening tests. They can detect bacteria [4] and viruses [5,6], as well as various molecular and cellular analytes that serve as predictive, prognostic, or diagnostic biomarkers, such as glucose [7]. These biosensors employ diverse biorecognition elements, including proteins (antibodies, enzymes), nucleic acid probes

(deoxyribonucleic acid (DNA), ribonucleic acid (RNA)), and other specific biomolecules immobilized on the transducer surface [8,9].

Results

In this work, we present the design of an optical sensor for detecting the S protein of COVID-19. The sensor can be easily adapted to detect other viruses or cancer-related proteins without altering its fundamental design. The structure is based on a low-refractive-index contrast subwavelength grating (LC-SG) (Fig.1), which has been shown to support Friedrich–Wintgen Bound States in the Continuum (FW-BICs) that are non-radiative states in trully periodic configuration, and create high quality factor resonances in real-world realisations. This type of BIC is highly sensitive to environmental changes since resonating optical field interacts significantly with surroundings. Consequently, a structure based on FW-BIC exhibits an immediate response to variations in the surrounding environment or thickness, manifested as a spectral shift or a decrease in the quality factor. This characteristic makes it an ideal optical sensor.

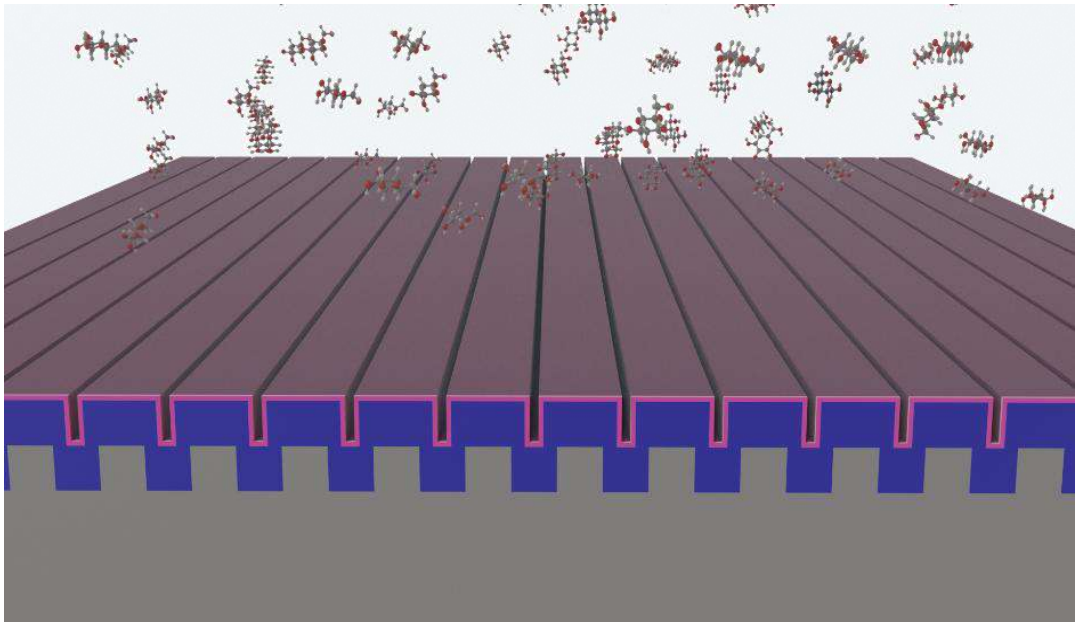


Fig. 1. Biosensor concept.

This sensor operates by exploiting changes in reflection or transmission resulting from the modification of Fano resonance conditions. Our approach involves creating subwavelength quasi-periodic structures, both one- and two-dimensional, made of polymer and coated with an inorganic layer (for example, HfO_2 or ZrO_2) with properly designed thickness to reveal a resonance peak (Fig. 2). The development of the sensor's platform involves a multi-step process. Firstly, the structures are designed based on numerical modeling, taking into account the desired sensing properties. Subsequently, E-beam lithography and plasma etching are used for master stamp fabrication. Next, the achieved stamp is replicated into the polymer. An inorganic coating with designed and precisely controlled thickness and optical properties is deposited onto the fabricated structures to enhance the sensor's performance. In the next step, the sensor surface is biofunctionalized, enabling

immobilization of specific bioreceptors that show particular affinity to the designed analytes, which are selected medical biomarkers in this case. These steps are crucial due to the challenges associated with preparing organic layers on polymers and achieving an effective layer for detection.

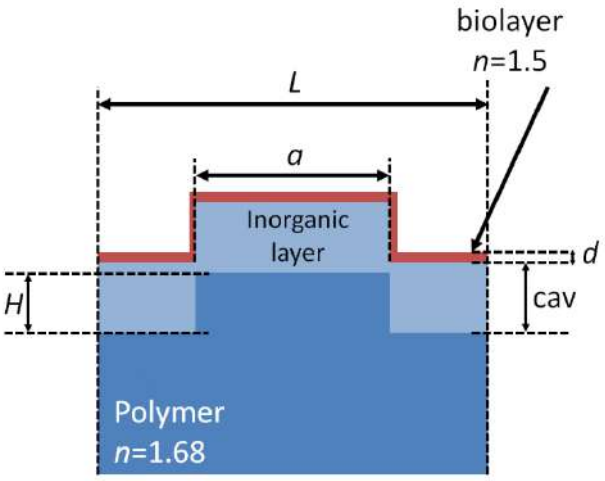
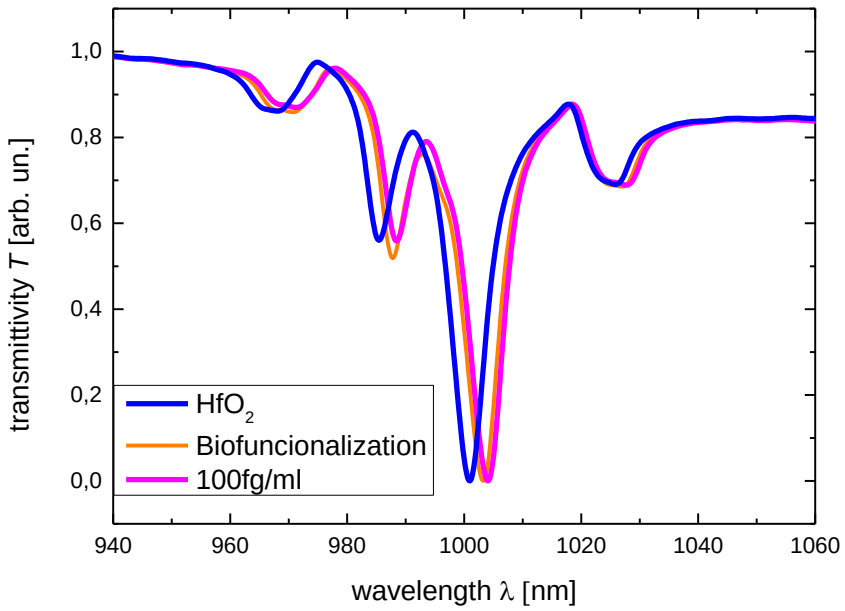


Fig. 2 Subwavelength quasi-periodic structures (a - 214 nm, L - 560 nm; H= 120 nm, cav(HfO_2)=319 nm).

The detection mechanism primarily relies on the optical response of the biosensor. The presence of analytes induces a spectral shift of the Fano resonance (Fig. 3), which is caused by modifying the biolayer thickness. First, the response is shifted after the biofunctionalization process (Fig. 3, orange line) and then again after the detection of 100 fg/mL of protein S (Fig. 3, pink line)



.

Fig. 3. The spectral shift of the Fano resonance, which is caused by the modification of the layer thickness.

This optical sensor platform holds significant potential for the detecting a variety of medical biomarkers, including analytes related to pathogens, cancer biomarkers, and others. By leveraging the unique properties of Fano resonance and utilizing engineered subwavelength quasi-periodic structures with specially designed optical coatings, the sensor can be tailored for detecting selected biomarkers.

References

[1] Chaudhry Ge *et al*., Cancer and disease diagnosis -Biosensor as potential diagnostic tool for biomarker detection J Adv Pharm Technol Res;13:243-7 (2022)

[2] M.R. Hasan *et al*., Recent development in electrochemical biosensors for cancer biomarkers detection, Biosens. Bioelectron.: X, 8, 100075, (2021)

[3] do Couto, Beatriz Serrano. "Nanophotonic Biosensors for Melanoma Diagnostics and Therapy Monitoring." (2022).

[4] Piestrzyńska M., Dominik M., Kosiel K. *et al*., Ultrasensitive tantalum oxide nano-coated long-period gratings for detection of various biological targets. Biosens. Bioelectron.;133:8–15 (2019)

[5] Jankowska-Śliwińska, J. *et al*., Electrochemical sensors for fast and non-invasive detection of SARS-CoV-2 at an early stage of infection, poster presentation, ETPN 2022, Braga, Portugal 20-23.06.2022

[6] Kosiel, K. *et al*., Optical fiber sensor for SARS-CoV-2 detection, poster presentation, ETPN 2022, Braga, Portugal 20-23.06.2022

[7] Kaczmarski, J., Jankowska-Śliwińska, J. *et al*., IGZO MESFET with enzyme-modified Schottky gate electrode for glucose sensing , JJAP Journal; 58 (9) 090603, doi: 10.7567/1347-4065/ab1a65 (2019)

[8] G. Yang *et al*., Recent advances in biosensor for detection of lung cancer biomarkers, Biosens. Bioelectron., 141, p. 111416, (2019)

[9] Morales MA *et al*., Guide to Selecting a Biorecognition Element for Biosensors. Bioconjug Chem. 2018 Oct 17;29(10):3231-3239 (2018)

Broadband Anti-Reflectance by Disordered Si Nanodisks for Thin-Film Solar Cells

H. Kylhammar*, S. Zayouna, A. Dumitrescu, M.E. Kjellberg, and S. Anand

Department of Applied Physics, School of Engineering Sciences, KTH Royal Institute of Technology, Albanova University Center, Roslagstullsbacken 21, 106 91 Stockholm, Sweden
*corresponding author: hannaky@kth.se

Abstract: We design and fabricate spatially disordered Si nanodisks by colloidal lithography for broadband antireflection and light trapping. Absorption is optimized for thin-film solar cells through control of the geometrical features, dimensions, and density of the nanodisks. For comparison, periodic arrangements with unit cells containing more than one disk are investigated.

The development of semiconductor based metasurfaces enables light management for a wide range of optoelectronic device applications[1]. Dielectric nanostructure arrays provide significant improvement in antireflection and light trapping for thin-film solar cells[1-3].

The Mie resonant nanodisks are designed to induce forward scattering, implying a strong dependence on the nanodisk dimension and shape for the desired antireflection and wavelength dependent light scattering. Effective refractive index-matching improves the anti-reflection further and is controlled through nanodisk packing density as well as through disk height profile. Arranging nanodisks in a disordered array minimizes the effects from spatial correlation,[4,5] and provides weaker angular dependence compared to periodic arrays, which is beneficial for solar cell applications.

In this study, we utilize colloidal lithography to fabricate disordered Si nanodisk arrays on Si substrates (and thin films). Negatively charged polystyrene nanoparticles are adsorbed on a positively charged layer (polydiallyldimethylammonium, PDDA) on a silicon substrate forming a disordered, self-assembled mask. The interparticle spacing is controlled by the ionic strength of the particle suspension medium. The nanodisk height profiles can be controlled by changing the conditions of the dry etch process. We investigate the antireflective properties of disks of varying height profiles, ranging from nearly cylindrical to tapered and conical.

The measured reflectance of the fabricated arrays is compared with finite-difference time-domain (FDTD) simulations. Separately, for comparison FDTD simulations of the reflectance are performed for periodic structures, specifically considering a square lattice with a basis composed of 1 and 2 nanodisks. The scattering profiles from single nanodisks and from arrays are simulated and optimized to generate forward scattering into the Si substrate for targeted wavelengths to increase the path length for absorption. Our results show both the geometrical size and shape of the nanodisks and their spatial arrangement are important for enhancing solar light absorption in thin film Si solar cells.

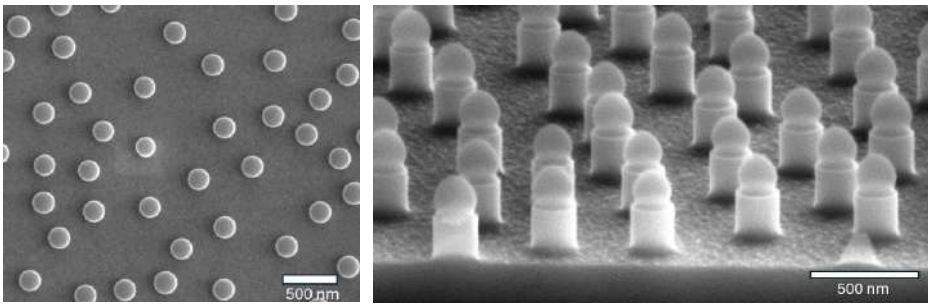


Figure 1. Left: Spatially disordered polystyrene nanoparticles (etch-masks) dispersed on Si substrate. Right: Si nanodisks fabricated by a pseudo-Bosch process; the remnant mask particles are also visible.

Acknowledgements: The work is supported by the Swedish Energy Agency – Energimyndigheten, grant no. P2023-01371.

References

1. Son Tung Ha, Li Q., Yang, J.K.W., Demir H.V., Brongersma M.L., and Kuznetsov A.I. ” Optoelectronic metadevices”, Science **386**(6725), eadm7442 (2024).
2. Kjellberg M., Ravishankar A.P., and Anand S. “Enhanced Absorption in InP Nanodisk Arrays on Ultra-Thin-Film Silicon for Solar Cell Applications,” Photonics, 9, no. 3: 157, (2022).
3. Visser, D., Chen, D.Y., Désières, Y., Ravishankar A.P., and Anand S. ”Embossed Mie resonator arrays composed of compacted TiO_2 nanoparticles for broadband anti-reflection in solar cells” *Sci Rep* **10**, 12527 (2020).
4. Vennberg, F., Ravishankar A.P. and Anand S., “Manipulating light scattering and optical confinement in vertically stacked Mie resonators,” Nanophotonics, Vol. 11, No. 21, 4755–4764, (2022).
5. Piechulla P.M., Fuhrmann B., Slivina E., Rockstuhl C., Wehrspohn R.B., Sprafke A.N. “Tailored Light Scattering through Hyperuniform Disorder in Self-Organized Arrays of High-Index Nanodisks,” Adv. Optical Mater. **9**, 2100186, (2021).

Silicon pn-Junction Quantum Instability formed by Wafer-bonding

Sung Hoon Cho[1], Petr Moroshkin[2], Damir Kulzhanov[2], Jimmy Xu[2], and Ki Tae Nam[1*]

[1]Department of Materials Science and Engineering, Seoul National University, Seoul, Korea
[2]Division of Engineering and Department of Physics, Brown University, Providence, Rhode Island, USA
[*]corresponding author: nkitae@snu.ac.kr

Abstract: We report a novel bistable current-voltage behavior observed in a Si pn-junction formed by direct wafer bonding at cryogenic temperatures below 30K. The phenomenon, driven by a 6nm SiO_2 barrier layer at the interface, reveals negative differential resistance and suggests potential applications in high-performance and quantum devices.

As the semiconductor industry prepares for the "post-Moore" era, the pursuit of further performance improvements through traditional miniaturization techniques has become increasingly challenging. To overcome these limitations, leading semiconductor companies such as Intel, Samsung, and TSMC are focusing on the development of advanced 2.5D packaging technology with direct wafer bonding. This innovative approach connects chips directly without the use of bumps, offering significant benefits, including reduced transmission delays, minimized parasitics, and enhanced power management and heat dissipation. These advantages make direct wafer bonding a critical technology for the development of high-performance semiconductor devices. Simultaneously, the growing demand for higher performance, as well as advancements in quantum computing, has pushed the exploration of silicon electronics into the cryogenic temperature regime.

In this study, we present a novel phenomenon observed in the cryogenic operation of a silicon p-n junction, formed by direct wafer bonding. The p-type and n-type silicon wafers, heavily doped to achieve desired electrical properties, were bonded together using this direct wafer bonding technique. The electrical properties of the junction were measured using metal ohmic contacts on both the top and bottom surfaces. At room temperature, the device exhibited typical diode current-voltage (I-V) characteristics. However, when the device was tested at cryogenic temperatures below 30K, an unexpected S-shaped I-V characteristic emerged, which became more pronounced as the temperature was reduced. This change in I-V behavior resulted in a bistable current switching response when sourcing voltage, attributed to the presence of negative differential resistance between the two stable states.

A key factor contributing to this intriguing behavior is the formation of a 6 nm thick silicon dioxide (SiO_2) barrier layer at the metallurgical interface between the p-type and n-type wafers during the wafer bonding process. This layer plays a crucial role in the switching mechanism and in the observed negative differential resistance. Our study, supported by computational modeling simulations, provides valuable insights into the underlying mechanisms driving this bistable behavior. Furthermore, it suggests potential applications for this novel functionality in the development of high-performance and quantum computing devices, where such switching properties could be leveraged for innovative use cases in next-generation electronics.

Cost-effective and mass production of meta-hologram using photolithography and Nanoimprint lithography

Chanwoong Park[1], Seungyeon Lee[1], Hansang Sung[1], Jaein Park[1], Heon Lee[1,*]

[1] Department of Materials Science and Engineering, Korea University, Seoul, 02841 Republic of Korea

[*]corresponding author: heonlee@korea.ac.kr

Abstract: This study introduces a cost-effective, scalable manufacturing technique for metasurfaces using ArF scanner and nanoimprint lithography. The process allows high-throughput production with an 8-inch master stamp. A demonstration meta-hologram using TiO_2 nanoparticle-embedded resin achieved optical efficiencies of 44.8%, 32.3%, and 22.9% at different visible wavelengths.

A metasurface is a two-dimensional plane designed to have optical properties that do not exist in nature by arranging meta-atoms smaller than the wavelength of light. The shape and arrangement of the meta-atoms are designed differently depending on the purpose of the metasurface. When incident light passes through the metasurface, meta-atoms change the phase and amplitude of the light, resulting in unique optical properties that cannot be found in natural materials. These engineered electromagnetic responses enable precise control over light propagation, scattering, and focusing at the subwavelength scale. Using these remarkable properties, metasurfaces are applied to various fields such as metalenses, metaholograms, waveguides, cloaking, and color filters.

Small and lightweight optical devices are increasingly required in markets such as home appliances, automobiles, optical fiber and medical imaging. The miniaturization of optical systems like lenses becomes more important as devices become smaller and more compact. Traditional optical components rely on phase accumulation through propagation, necessitating specific thicknesses and curvatures that limit miniaturization. High-resolution hologram technology, lightening and miniaturization of devices are essential for immersive virtual reality (VR) and augmented reality (AR) experiences, where user comfort and portability are crucial factors. However, with current hologram technology, it is difficult to implement realistic images and reduce the form factor of the device simultaneously. Metasurfaces offer a promising solution to these problems by enabling optical functionality within ultracompact form factors, but issues such as manufacturing cost, yield, and productivity must be addressed before widespread commercialization can be achieved.

Electron-beam lithography (EBL) is generally used to fabricate metasurfaces for high-resolution patterning. Since the size of the meta-atoms constituting the metasurface is subwavelength (typically 100-500 nm for visible light applications), EBL is preferred for the accuracy of the designed patterns, allowing precise control of meta-atom geometry at nanometer resolution. However, EBL has significant limitations for commercialization because it is expensive, has low productivity, and is difficult to use for forming patterns over large areas. EBL irradiates electron beams one by one to produce patterns in a serial writing process, resulting in slow writing speed and narrow writing area. This point-by-point patterning approach makes EBL impractical for mass production scenarios where throughput and cost-effectiveness are essential considerations.

To overcome these limitations, photolithography using argon fluoride (ArF) laser has been employed to manufacture master stamps. This technique, widely used for high-resolution patterning in the semiconductor industry, operates at 193 nm wavelength and allows the production of metasurfaces much faster and over larger areas than EBL, though cost remains an issue when producing metasurfaces with photolithography alone due to the expensive equipment

required. ArF immersion lithography, which increases resolution by introducing a liquid medium between the final lens element and the wafer surface, enables feature sizes below 40 nm, suitable for many metasurface applications.

Nanoimprint lithography (NIL) presents an efficient method to reduce the cost of fabricating metasurfaces. Unlike conventional processes that require thin film deposition and etching in multiple steps under vacuum conditions, NIL can be performed much more easily and quickly than EBL through a simple mechanical embossing process. Once a master stamp is created, replica molds can be produced continuously as long as the stamp remains intact, dramatically improving throughput and reducing per-unit costs. By combining photolithography and NIL, it's possible to enhance productivity in metasurface fabrication while compensating for the cost disadvantage of using photolithography exclusively, creating a scalable approach suitable for industrial applications.

In this study, we demonstrated a platform for one-step printing of millimeter-scale metahologram patterns on a wafer scale using this combined approach. By preparing a resin with dispersed TiO_2 nanoparticles (NPs), researchers have created a high refractive index material with low extinction coefficient in the visible region, essential for efficient light manipulation. The NIL process using this TiO_2 nanoparticle-embedded-resin (nano-PER) forms meta-atoms on the substrate without requiring a vacuum process, further simplifying manufacturing. The direct patterning of nanoparticle-embedded resins eliminates several processing steps typically needed in conventional metasurface fabrication.

The fabricated metahologram demonstrated excellent performance across the visible spectrum, operating effectively with all three primary colors (RGB). It achieved maximum efficiencies of 60.7% at 450 nm (blue), 45.1% at 532 nm (green), and 38.5% at 635 nm (red), respectively. This broadband efficiency across RGB wavelengths is particularly significant for full-color holographic applications, enabling more vibrant and realistic holographic displays. These results suggest that EBL, which has been hindering the commercialization of metaholograms, can be successfully replaced by highly productive photolithography and NIL processes, potentially enabling widespread adoption of metasurface technology in consumer applications.

References

1. Park, C., Kim, W., Kim, Y., Sung, H., Park, J., Song, H., Kim, K., Oh, D. K., Kang, H., Jeon, N., Rho, J., & Lee, H. High-throughput fabrication of large-scale metaholograms via one-step printing. *Advanced Optical Materials*, *12*(9), 2301562.

Mass Production of Metasurfaces Using $BaTiO_3$ Nanoparticle-Embedded Resin (nano-PER)

Seungyeon Lee[1], Chanwoong Park[1], Hansang Sung[2], Heon Lee[1*],

[1, 2]Department of Materials Science and Engineering, Korea University, Republic of Korea
[*]corresponding author: heonlee@korea.ac.kr

Abstract: In this study, we fabricated a high-performance meta-hologram using $BaTiO_3$ nanoparticle-embedded resin (nano-PER) via nanoimprint lithography. $BaTiO_3$ offers a high refractive index, low extinction coefficient, and ferroelectric properties. By uniformly dispersing these nanoparticles in nano-PER, we developed an optimized resin and mass-produced meta-holograms.

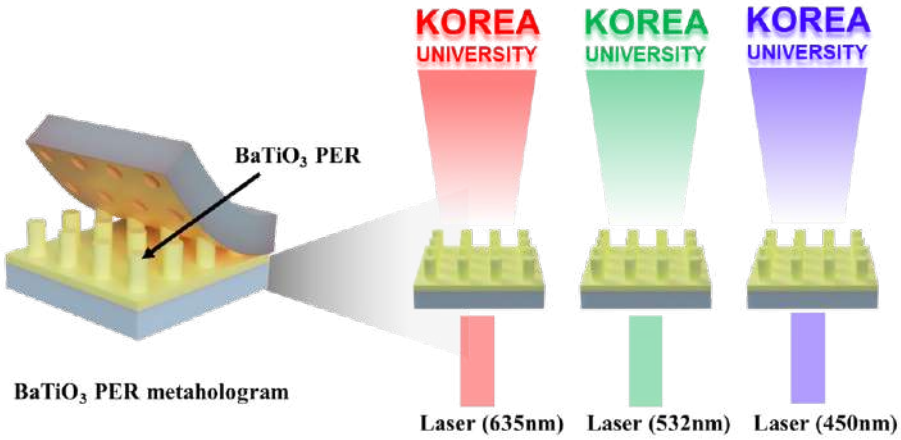


Figure 1. Schematic of meta-holograms fabricated using nanoimprint lithography

Recently, metasurfaces have received significant attention for various applications including metalenses, metaholograms, cloaking, waveguides, and color filters. They are also increasingly being integrated into various fields such as augmented reality (AR), virtual reality (VR), 3D displays, and medical imaging technologies.[1] Metasurfaces consist of meta-atoms arranged in specific structures on a 2D plane, with each meta-atom having a subwavelength size smaller than the incident light's wavelength. When light passes through the metasurface, the meta-atoms induce a phase shift, changing the phase and amplitude of the light and shaping the wavefront, giving the metasurface unique optical properties. By adjusting the arrangement, shape, and size of the meta-atoms, it is possible to control the phase and amplitude of the light.[2] Specifically, metaholograms encode desired images into the metasurface, which are displayed when light passes through it. Metaholograms can overcome the limitations of traditional holography technologies by providing a thin and lightweight alternative to bulky optical devices, while also enabling high-resolution images through the precisely designed meta-atoms.[3]

Despite their promise, fabricating metaholograms presents several challenges. Metaholograms require precisely arranged structures at the nanometer scale, making high-resolution lithography techniques essential for their fabrication. Nanoimprint lithography (NIL) is an efficient and cost-effective method that offers low manufacturing costs, high throughput, and the ability to produce high-resolution patterns. NIL makes the formation of precise nanostructures simple, ensuring the high resolution and accuracy that are critical for

determining the performance and quality of metaholograms. Moreover, NIL can be used for patterning with various materials, including polymers, dielectric materials, and ceramics, making it adaptable for a wide range of applications. [4]It is also suitable for large-area patterning and compatible with flexible substrates, making it ideal for mass production and use across different substrate types. [5]NIL is a cost-effective alternative to costly techniques such as electron-beam lithography or those requiring vacuum environments. The reusability of the master stamp further enhances its cost-efficiency, providing significant economic benefits for metasurface production.[6]

In this study, we propose a method to fabricate wafer-scale metahologram patterns using NIL and a newly developed $BaTiO_3$ -based resin in a single process. $BaTiO_3$ is a ferroelectric material with a high refractive index and low extinction coefficient in the visible spectrum. [7] By dispersing $BaTiO_3$ nanoparticles (NPs) into a thermal curable resin, we developed a $BaTiO_3$ nanocomposite resin (nano-PER) with ferroelectric properties and nano-formability. The $BaTiO_3$ nano-PER enables precise fabrication of nanostructures on a 2D plane and allows for the recording of electrical signals due to its ferroelectricity. [8]Additionally, its high refractive index facilitates phase modulation of light in the visible spectrum. Using this resin, we performed an NIL process to form meta-atoms composed of $BaTiO_3$ nanoparticles directly on a substrate without requiring additional vacuum process. The fabricated metaholograms achieved an efficiency of 34.2% at a blue light wavelength (λ = 450 nm), demonstrating the combined excellence of the optical properties of the BaTiO-based resin and the precision of the NIL process. This work opens up new possibilities for high-efficiency and commercially viable metaholograms and suggests promising applications in optical and electronic devices.

References

1. Chen, H. T., Taylor, A. J. & Yu, N. "A review of metasurfaces: Physics and applications", "*Reports Prog. Phys.",* 79, (2016).
2. Bukhari, S. S., Vardaxoglou, J. & Whittow, W. "A metasurfaces review: Definitions and applications.","*Appl. Sci."* 9, (2019).
3. Lee, G. Y., Sung, J. & Lee, B. "Recent advances in metasurface hologram technologies.","*ETRI J.",* 41, 10–22 (2019).
4. Park, C. *et al.* "High-Throughput Fabrication of Large-Scale Metaholograms via One-step Printing.", "*Adv. Opt. Mater.",* 2301562, 1–6 (2024).
5. Kim, J. *et al.* "8″ Wafer-Scale, Centimeter-Sized, High-Efficiency Metalenses in the Ultraviolet." "*Mater. Today*",, 1–7 (2024).
6. Lee, M. H., Huntington, M. D., Zhou, W., Yang, J. C. & Odom, T. W. Programmable soft lithography: Solvent-assisted nanoscale embossing. *Nano Lett.* 11, 311–315 (2011).
7. Weigand, H. C. *et al.* "Nanoimprinting Solution-Derived Barium Titanate for Electro-Optic Metasurfaces.", "*Nano Lett.",* 24, 5536–5542 (2024).
8. Jiang, B. *et al.* "Barium titanate at the nanoscale: Controlled synthesis and dielectric and ferroelectric properties." "*Chem. Soc. Rev.",* 48, 1194–1228 (2019).

Fabrication and study of Nd-doped BCT-based dielectric ceramics for functional metamaterial applications

J. Makowska[1*], K. Feliksik[1], M. Adamczyk-Habrajska[1] and B. Wodecka-Dus[1]

[1] University of Silesia, Faculty of Science and Technology, Institute of Materials Engineering, 75 Pułku Piechoty 1A, 41-500 Chorzow, Poland;

[*]corresponding author: jolanta.makowska@us.edu.pl

Abstract: Nd-doped $Ba_{0.75}Ca_{0.25}TiO_3$ ceramics were synthesized using the solid-state method to improve dielectric properties. Due to their low losses and thermal stability, these materials show strong potential for applications in functional metamaterials.

Barium titanate ($BaTiO_3$, BT) is one of the most important electroceramic materials due to its excellent dielectric and ferroelectric properties [1–3]. Its performance can be significantly improved through chemical modification, particularly by doping with ions at A and/or B sites of the perovskite structure. Among these, doping with rare-earth elements like neodymium (Nd^{3+}) offers a promising route to enhancing dielectric behavior, reducing losses, and stabilizing phase transitions [4–9]. Additionally, processing parameters such as sintering temperature are known to play a crucial role in tuning the microstructure and electrical performance of BT-based ceramics [10-15].

Recent developments in ceramic-based dielectric metamaterials have highlighted the potential of such materials as low-loss, tunable alternatives to metal-based metamaterials, with applications in electromagnetic and energy systems, non-Hermitian physics, and components with near-zero or negative refractive index [16].

In this work, Nd-doped $Ba_{0.75}Ca_{0.25}TiO_3$ (BCT:Nd) ceramics were synthesized via the conventional solid-state reaction method, using high-purity oxides and carbonates as starting materials. The study aimed to modify the structural and dielectric properties of BCT ceramics through rare-earth element doping, in view of their potential use in functional metamaterial devices. The phase composition of the synthesized ceramics was confirmed by X-ray diffraction (XRD), indicating the formation of a single-phase perovskite structure. Basic microstructural observations using scanning electron microscopy (SEM) showed that sintering temperature and Nd incorporation affected grain growth and morphology. Dielectric measurements were performed as a function of temperature (from room temperature up to 200 °C) and frequency (1 kHz to 1 MHz). The incorporation of Nd significantly influenced the dielectric response, improving thermal stability and reducing dielectric losses — both essential for the performance of high-frequency metamaterial systems. The results demonstrate that Nd doping effectively enhances the functional properties of BCT-based ceramics, supporting their application in tunable and low-loss dielectric components for metamaterials, such as phase shifters, resonators, and adaptive electromagnetic devices.

References

1. Roberts, S., “Dielectric constant of barium titanate at high temperatures,”*Phys. Rev.*, Vol. 76, No. 7, 989–999, 1949.
2. Megaw, H. D., “Origin of ferroelectricity in barium titanate and other perovskite-type crystals,” *Acta Crystallogr.*, Vol. 5, No. 6, 739–749, 1952.
3. Johnson, C. J., “Some dielectric and electrooptic properties of $BaTiO_3$ single crystals,” *Appl. Phys. Lett.*, Vol. 7, No. 7, 221–223, 1965.
4. Khedhri, M. H., N. Abdelmoula, H. Khemakhem and R. Douali, “Structural, spectroscopic and dielectric properties of

Ca-doped $BaTiO_3$," *Appl. Phys. A*, Vol. 125, No. 193, 2019.
5. Gromov, O. G., A. P. Kuz'min, G. B. Kunshina, E. P. Lokshin and V. T. Kalinnikov, "Preparation of powder barium titanate," *Inorg. Mater.*, Vol. 42, No. 2, 176–181, 2006.
6. Ma, N., B. P. Zhang, W. G. Yang and D. Guo, "Phase structure and nano-domain in high performance of a TiO_3 piezoelectric ceramics," *J. Eur. Ceram. Soc.*, Vol. 32, No. 5, 1059–1066, 2012.
7. Wang, P., Y. Li and Y. Lu, "Enhanced piezoelectric properties of $(Ba_{0.85}Ca_{0.15})(Ti_{0.9}Zr_{0.1})O_3$ lead-free ceramics by optimizing calcination and sintering temperature," *J. Eur. Ceram. Soc.*, Vol. 31, No. 1, 11–17, 2011.
8. Zheng, P., J. L. Zhang, S. F. Shao, Y. Q. Tan and C. L. Wang, "Piezoelectric properties and stabilities of CuO-modified $Ba(Ti,Zr)O_3$ ceramics," *Appl. Phys. Lett.*, Vol. 94, No. 3, 032902, 2009.
9. Rached, A., M. A. Wedern, A. Belkahla, J. Dhahri, K. Khirouni, S. Alaya and R. J. Martín-Palma, "Effect of doping in the physico-chemical properties of $BaTiO_3$ ceramics," *Physica B*, Vol. 596, 412343, 2020.
10. Sandi, D. K., A. Supriyanto and Y. Iriani, "The effects of sintering temperature on dielectric constant of barium titanate ($BaTiO_3$)," *Mater. Sci. Eng.*, Vol. 107, 012069, 2016.
11. Ulfa, U., K. Kusumandari and Y. Iriani, "The effect of temperature and holding time sintering process on microstructure and dielectric properties of barium titanate by co-precipitation method," *AIP Conf. Proc.*, Vol. 2202, 020036, 2019.
12. Wang, X. H., R. Z. Chen, Z. L. Gui and L. T. Li, "The grain size effect on dielectric properties of $BaTiO_3$ based ceramics," *Mater. Sci. Eng. B*, Vol. 99, No. 2, 199–202, 2003.
13. Ren, X. C., W. L. Nie, Y. Bai and L. J. Qiao, "Effect of sintering temperature and oxygen atmosphere on electrocaloric effect of $BaTiO_3$ ceramics," *Eur. Phys. J. B*, Vol. 88, No. 232, 2015.
14. Vittayakorn, N., "Dielectric properties of bismuth doped barium titanate ($BaTiO_3$) ceramics," *J. Appl. Sci. Res.*, Vol. 2, No. 12, 1319–1322, 2006.
15. Yusoff, N. H., R. A. M. Osman, M. S. Idris, K. N. Dhaniah, K. Muhsen and N. I. M. Nor, "Dielectric and structural analysis of hexagonal and tetragonal phase $BaTiO_3$," *AIP Conf. Proc.*, Vol. 2203, 020038, 2020.
16. Luo, W., S. Yan and J. Zhou, "Ceramic-based dielectric metamaterials," *Interdiscip. Mater.*, Vol. 1, No. 1, 2022. DOI: 10.1002/idm2.12012.

Synthesis and Characterization of Dielectric Metamaterials Based on BLTF Ceramics

B. Wodecka-Dus[1*], M. Adamczyk-Habrajska[1], and J. Makowska[1]

University of Silesia, Faculty of Science and Technology, Institute of Materials Engineering, 75 Pułku Piechoty 1A, 41-500 Chorzow, Poland;
[*]corresponding author: beata.wodecka-dus@us.edu.pl

Abstract: Dielectric BLTF metamaterials with a perovskite structure were obtained using solid-state synthesis. Analysis of the microstructure, crystal structure, and electrical properties confirmed their high dielectric permittivity and low dielectric losses. Increasing Fe^{3+} doping significantly enhances the piezoelectric properties, indicating their potential for modern technological applications..

Dielectric metamaterials based on ceramics have attracted significant interest in recent years due to their high dielectric permittivity, relatively low dielectric losses, and other outstanding functional properties (e.g., ferroelectric, piezoelectric, dielectric, and magnetic) relevant to various resonance effects, their simple crystal structure, excellent multipolar tunability, and good environmental adaptability [1–5]. Compared to structures composed of discrete components (capacitance or inductance) in metal-based metamaterials at high frequencies, a single ceramic dielectric block can perform a basic resonance function, indicating that the structure of ceramic-based dielectric metamaterials is simpler and their preparation more convenient [6–9].

The aim of this study was to produce ceramics with the general formula $Ba_{1-x}La_xTi_{1-y}Fe_yO_3$ (BLTF) for concentrations x=0.004 and y=0.001, 0.002, 0.003, 0.004, characterized by a perovskite-type ABO_3 structure. These materials were obtained by conventional ceramic powder synthesis based on the solid-state reaction method (MOM method) using simple oxide powders, followed by free sintering and uniaxial hot pressing to densify the obtained powder materials.

All ceramic powders underwent thermal analysis (TG/DTA) and differential thermogravimetric analysis (DTG). The chemical composition of BLTF powders was determined by energy-dispersive X-ray spectroscopy (EDS). The microstructure of the resulting powders and BLTF ceramics was examined using scanning electron microscopy (SEM). EDS analysis confirmed the assumed chemical compositions for all ceramic powders. The crystal structure of BLTF ceramics was studied using X-ray diffraction. At room temperature ($T_r<T_C$), the obtained ceramic exhibits a single-phase, tetragonal structure with space group P4mm. An increase in iron content slightly reduces the unit cell volume.

BLTF ceramics exhibit a classical phase transition, high dielectric permittivity (ε), and low dielectric loss tangent values (tgδ), both at room temperature and in the phase transition region. Analysis of temperature-dependent DC conductivity revealed the presence of a positive temperature coefficient of resistivity (PTCR) in the phase transition region [10]. The dependence of piezoelectric coefficients on iron content in BLTF ceramics was determined using quasi-static and resonance methods. The results show that the addition of 0.3mol% Fe^{3+} ions to the ceramic structure increased the piezoelectric coefficient d_{33} to a maximum value of 159pC/N [11]. The electrical properties of BLTF ceramics were tested using impedance spectroscopy in the frequency range of 20Hz–2MHz and temperature range of 20–580°C. To ensure the consistency of the measured data, the obtained impedance spectra were analyzed using the Kramers–Kronig method. The use of an equivalent circuit proposed by the authors allowed for the extraction of grain and grain boundary resistivity. Based on the plot of the natural

logarithm of resistivity versus the inverse absolute temperature, the activation energies for conduction processes were determined. The values indicated that the iron dopant in the BLTF ceramic played a key role in grain and grain boundary conductivity [12].

This review summarizes recent advances in ceramic-based BLTF dielectric metamaterial technologies for electromagnetic applications. Following the developmental trends of modern physics, multifunctional devices realized solely with ceramic-based dielectric metamaterials are expected to evolve rapidly. They may be integrated into many other devices, offering broad application prospects in the future.

References

1. Zhu, W., Xiao, F., Kang, M., and Premaratne, M. “Coherent perfect absorption in an all‐dielectric metasurface,” Appl. Phys. Lett., Vol. 108, No. 12, 121901, 2016.
2. Zhao, Q., Kang, L., Du, B., et al. “Experimental demonstration of isotropic negative permeability in a three‐dimensional dielectric composite,” Phys. Rev. Lett., Vol. 101, No. 2, 027402, 2008.
3. Zhou, H. Y., Liu, X. Q., Zhu, X. L., and Chen, X. M. “Cryptococcal meningitis mimicking cerebral infarction: a case report,” J. Am. Ceram. Soc., Vol. 101, No. 5, 1999–2002, 2018.
4. Zhang, B., Li, L., and Luo, W. “Oxygen vacancy regulation and its high frequency response mechanism in microwave ceramics,” J. Mater. Chem. C, Vol. 6, No. 39, 11023–11034, 2018.
5. Baranov, A., and Oh, Y. J. “Microwave frequency dielectric properties of hexagonal perovskites in the $Ba_5Ta_4O_{15}$–$BaTiO_3$ system,” J. Eur. Ceram. Soc., Vol. 25, No. 14, 3451–3457, 2005.
6. Levine, B. “Bond susceptibilities and ionicities in complex crystal structures,” J. Chem. Phys., Vol. 59, No. 3, 1463–1486, 1973.
7. Li, L., Wang, J., Ma, H., et al. “Achieving all‐dielectric metamaterial band‐pass frequency selective surface via high‐permittivity ceramics,” Appl. Phys. Lett., Vol. 108, No. 12, 122902, 2016.
8. Zeng, X., Zhang, G., Xi, X., Li, B., and Zhou, J. “Terahertz transmission of square‐particle and rod structured $TbFeO_3$ metamaterials,” Mater. Lett., Vol. 234, 66–68, 2019.
9. Jeon, D. H., Reisner, M., Mortessagne, F., Kottos, T., and Kuhl, U. “Non‐Hermitian CT‐symmetric spectral protection of nonlinear defect modes,” Phys. Rev. Lett., Vol. 125, No. 11, 113901, 2020.
10. Wodecka-Duś, B., Bara, M., Adamczyk-Habrajska, M., Goryczka, T., Dzik, J., and Szalbot, D. “Dielectric and electrical properties of BLT ceramics modified by Fe ions,” Materials, Vol. 13, No. 24, 5623, 2020.
11. Wodecka-Duś, B., Kozielski, L., Makowska, J., Bara, M., and Adamczyk-Habrajska, M. “Fe-doped barium lanthanum titanate as a competitor to other lead-free piezoelectric ceramics,” Materials, Vol. 15, No. 3, 1–12, 2022.
12. Adamczyk-Habrajska, M., Wodecka-Duś, B., Goryczka, T., and Makowska, J. “Impedance spectroscopy of Fe and La-doped $BaTiO_3$ ceramics,” Crystals, Vol. 14, No. 2, 131, 2024.

Fabrication of optical phase elements in bulk sapphire by ultrashort pulses

E. Aleksandravičius[1*], G. Kontenis[1], I. Meškėlaitė[1] and D. Gailevičius[1]

[1]Vilnius university, Laser Research Center, Saulėtekio ave. 10, Vilnius, Lithuania
[*]corresponding author: edvinas.aleksandravicius@ff.vu.lt

Abstract: Sapphire possesses many desirable properties for use in photonics, however there are many challenges when it comes to fabricating optical phase elements in it. We show that the use of ultrashort pulses <100 fs can alleviate many of these issues, particularly the formation of cracks in larger structures.

The aim of this study is to fill the gap in available research on the fabrication of geometric phase elements in sapphire. The use of sapphire is desirable due to its excellent thermal stability and conductivity, broad transmission spectrum, high optical damage threshold, chemical inertness, and nonlinear properties, which could lead to interesting interplay with various phase elements. Because of these properties, sapphire is commonly used as a substrate for the deposition and subsequent direct laser writing of other materials. Still, there are very few examples of fabricating phase elements in sapphire itself, with much of the present literature focusing instead on the use of the induced nanogratings[1] or chemical etching of the modified material[2]. The core of this research is a parametric study of direct laser writing in sapphire aiming to circumvent the issues of the sapphire crystal cracking, induction of mechanical stress, and formation of nanogratings, all of which reduce the quality of any fabricated phase element. We note that the availability of high pulse energies for pulse durations down to >200 fs allowed us to explore these phenomena in some regard. However, improvements given by <100 fs have not been realized in the context of high repetition rates and high pulse energies.

We fabricated single-layer phase diffraction gratings to help evaluate the modified refractive index contrast and multi-layered spatial filtering photonic crystals to assess the formation of cracks in the sapphire. We used crossed-polarizer microscopy to evaluate the formation of nanogratings and the induction of mechanical stress. The determination of the crystal's cracking and strain-induced failure is performed by standard bright-field microscopy.

The results show that using ultrashort pulses down to 60 fs can significantly improve the quality of the fabricated elements. Shorter pulse durations significantly shift the fabrication window, the optimal pulse energy being nearly double that of 240 fs pulses. The formation of cracks can be seen in Figure 1. Fig. 1 (a) and (c) show single- and multi-layered structures fabricated with 240 fs, while (b) and (d) – structures fabricated with 60 fs, respectively. The structure (a) (240 fs) already shows some signs of small cracks, particularly at the corners and edges; on the other hand, (b) (60 fs) appears to be nearly ideal. However, a much more significant difference can be seen in the multi-layered structures, with (c) (240 fs) exhibiting large-scale cracks, rendering the structure entirely unusable, whereas (d) (60 fs) shows only minor defects. Therefore, we can conclude that the use of shorter pulses leads to reduced mechanical stress and, thus, reduced likelihood of cracking. However, the effect on the formation of nanogratings appears negligible. Additionally, the refractive index contrast induced by the material modification at optimal pulse energies does not show a significant dependence on pulse duration. Regardless, by employing 60 fs laser pulses, we could fabricate high-quality optical phase elements, such as photonic crystal spatial filters and phase diffraction gratings.

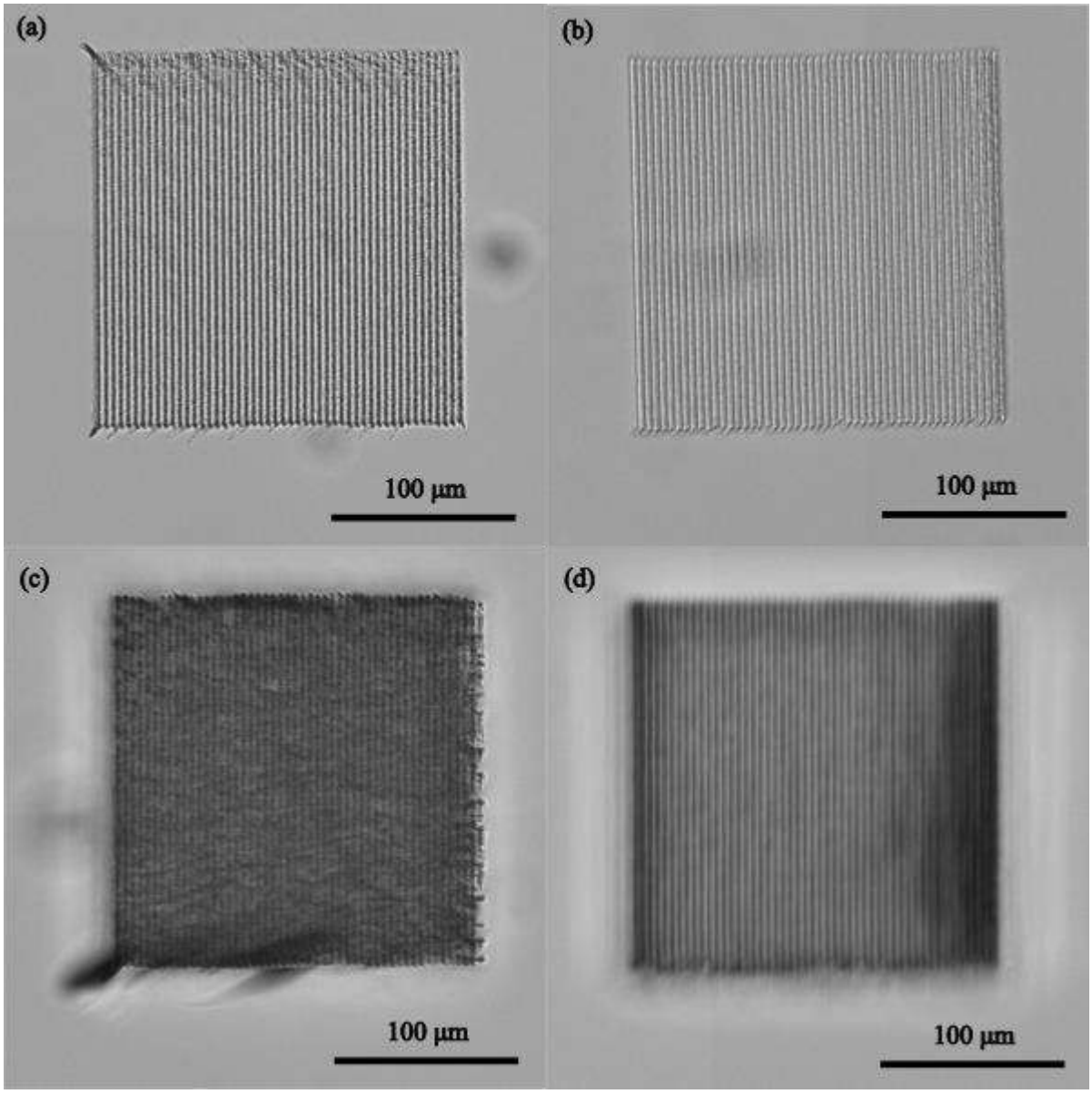


Figure 1. Microscope images of single-layer structure (a) and multi-layer structure (c) fabricated with 240 fs pulses and single-layer structure (b) and multi-layer structure (d) fabricated with 60 fs pulses.

This research has been funded by the Research Council of Lithuania, project S-MIP-23-49, "Supercontinuum generation in super-diffracting bulk photonic crystals".

References

1. Shuai Xu, Hua Fan, Zhen-Ze Li, Jian-Guan Hua, Yan-Hao Yu, Lei Wang, Qi-Dai Chen, and Hong-Bo Sun, "Ultrafast laser-inscribed nanogratings in sapphire for geometric phase elements," Opt. Lett. 46, 536-539 (2021).
2. Yi-An Chen, Kun-Chieh Chien, I-Te Chen and Chih-Hao Chang, "Sapphire nanophotonics: Fabrication challenges and optical properties," Micro Nano Eng., 14, 100115 (2022).

Acoustic, Seismic, and Thermal Metamaterials

Dual-Directional Acoustic Metamaterial Absorber for Noise Reduction

Tzu-Hsuan Chan[1], **and Tsung-Yu Huang**[1,*]

[1]Department of Materials Engineering, Ming Chi University of Technology, New Taipei City, Taiwan, 243303
[*] Email: huang.tsungyu@mail.mcut.edu.tw

Abstract: This study explores an acoustic metamaterial with dual-directional absorption, allowing sound waves to enter from two perpendicular directions for multi-directional noise absorption. This study utilizes a 3D printer to create Lego bricks, which can be assembled. Users can customize the structure as needed. This design enhancing flexibility for various environments.

This study improves the limitations of traditional acoustic metamaterial absorbers, which are primarily designed with a single opening and thus cannot effectively absorb sound waves from orthogonal directions. To address this issue, we propose a sound-absorbing structure with dual openings, utilizing a quasi-Helmholtz resonance mechanism. This mechanism is like that of a conventional Helmholtz resonator, where sound wave resonated within the cavity. When sound waves impinged on the metamaterial, the air inside the cavity vibrated, generating thermo-viscous losses that gradually converted acoustic energy into thermal energy, thereby achieving effective absorption. As shown in **Figure 1(a)**, our designed acoustic metamaterial revealed a 4 folded symmetry, consisting of four sealed side resonance cavities and a central resonance cavity, with two openings at both the x- and y-axes. The proposed acoustic metamaterial absorber achieves a high absorption rate of 97% at 990 Hz, demonstrating excellent acoustic absorption performance. Additionally, the overall thickness is only 1/30 of the working wavelength, achieving a subwavelength miniaturized design. Furthermore, for the sound waves incident along the x- or y-axis, the absorption peak remains the same, confirming the ability of dual directional incidences. Besides, it was observed that the cavity thickness would affect the absorption performance of the acoustic metamaterials. As shown in **Figure 1(b)**, when the thickness increases to 4 mm from 2 mm, the absorption peak significantly decreases. ◦

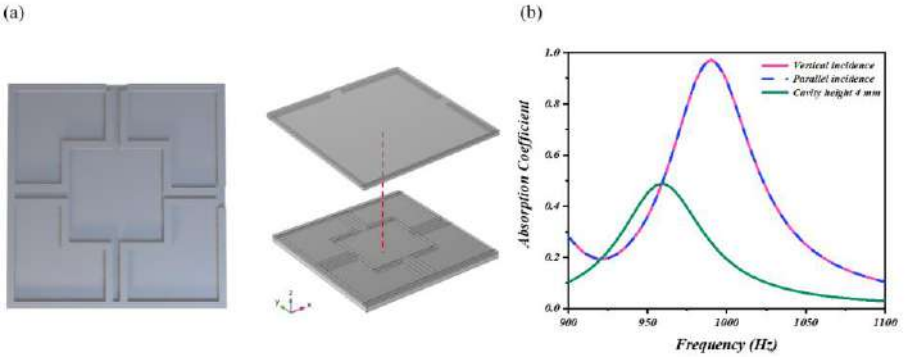


Figure 1. (a) Schematic diagram of the proposed acoustic metamaterial absorber, (b) absorption spectra for sound waves incident from the vertical and parallel directions, as well as the absorption spectrum for a cavity height of 4 mm.

Taking a step further, as shown in **Figure 2(a)**, we utilized a 3D printer to print LEGO-like components, which were then assembled into the designed acoustic metamaterial absorber. We found that by adjusting the structural parameters, the absorption frequency range could be further tuned to match different application needs. As shown in **Figure 2(b)**, simply modifying the structural parameters of the model allows for changes the

absorption frequency of the acoustic metamaterial. Additionally, the LEGO-style assembly method using 3D printing not only enhances design flexibility but also enables users to fine-tune the structure according to their needs, further optimizing the absorption frequency range and providing an efficient and adjustable noise control solution.

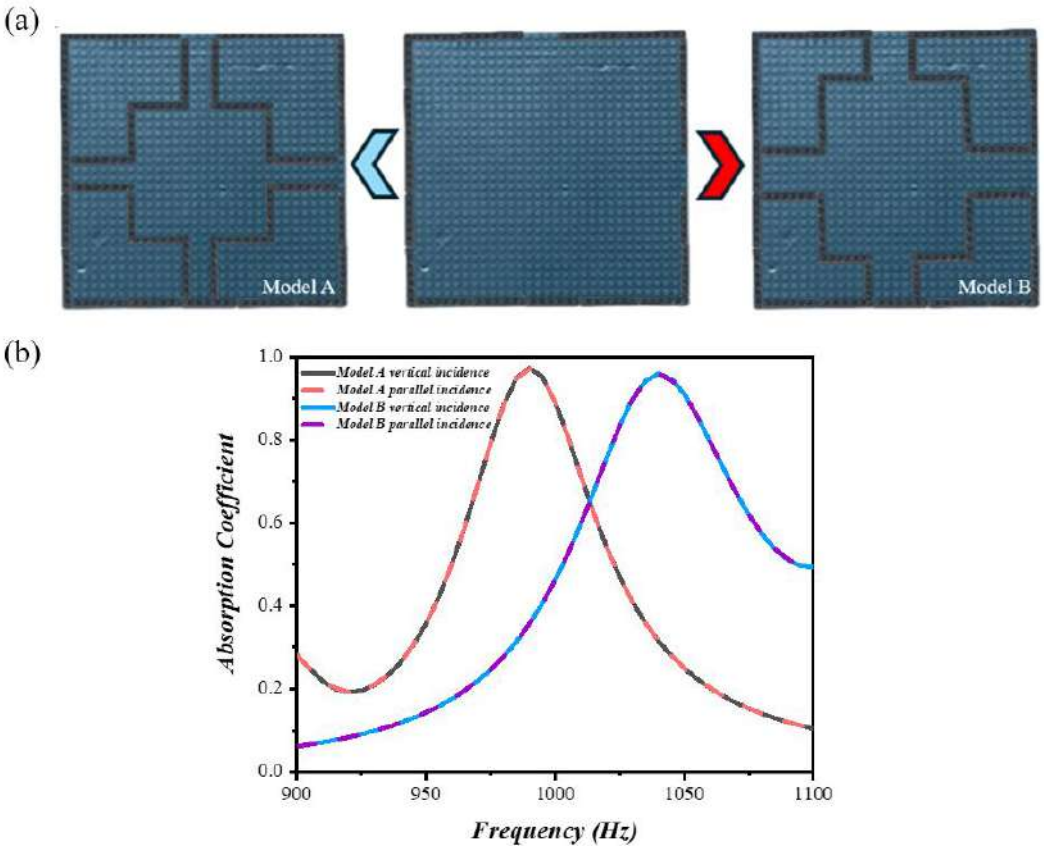


Figure 2. (a) 3D-printed LEGO-like blocks that can be arranged into different acoustic metamaterials. (b) Absorption spectra of Model A and Model B.

In summary, this study features a symmetric bidirectional absorption structure with a subwavelength thickness. The proposed acoustic metamaterial achieves a high sound absorption efficiency of 97% at 990 Hz, demonstrating excellent potential in noise control applications and offering significant practical usage.

References

1. Guan, Yi-jun, et al. "Ultra-thin metasurface-based absorber of low-frequency sound with bandwidth optimization." *Frontiers in Materials* 8 (2021): 764338.
2. Duan, Haiqin, et al. "Acoustic multi-layer Helmholtz resonance metamaterials with multiple adjustable absorption peaks." *Applied Physics Letters* 118.24 (2021).
3. Yang, Min, et al. "Optimal sound-absorbing structures." *Materials Horizons* 4.4 (2017): 673-680.

Bound states in the continuum of underwater phononic crystals

Yuzhen Yang[1*], Han Jia[1]

[1]Key Laboratory of Noise and Vibration Research, Institute of Acoustics, Chinese Academy of Sciences, China
[*]corresponding author: yangyuzhen@mail.ioa.ac.cn

Abstract: This study focuses on the bound states in the continuum of underwater phononic crystals, specifically examining symmetry-protected bound states and Fabry-Perot bound states. These bound states in the continuum enhances the potential for developing high-Q acoustic devices, which are of paramount importance for applications in underwater communication, imaging, and detection.

Acoustic resonators are the fundamental components of many modern acoustic devices and can be used as unit structures for acoustic metasurfaces to achieve arbitrary wavefront manipulation[1,2]. So far, most of the reported acoustic resonators exhibit relatively small quality factors, which hinders their application in the design of acoustic filters, sensors and other devices. Bound states in the continuum (BICs), also known as capture modes with infinite quality factors, have attracted widespread interests from researchers in the fields of optics and acoustics[3,4]. It is a non-radiative mode embedded in the continuous spectrum. Due to its excellent field confinement, it can enhance the interaction between waves and matters. On the basis of underwater phononic crystals, this work focuses on the formation mechanisms of different kinds of BICs in one-dimensional phononic crystals, such as symmetry-protected BICs and Fabry-Perot BICs. In addition, we explored the evolution characteristics of BICs in parameter space, such as merging and splitting. This work will provide potential applications in constructing ultra-high Q value underwater acoustic devices.

In single-layer square phononic crystals, symmetry-protected BICs were achieved in the case of incompatibility between mode symmetry and radiation channels. The sound pressure distributions of modes M2 and M4 in water are both odd symmetric at Γ point, which can not be excited by vertically incident plane waves. In the simulation, rotating square structures were used to break the symmetry of the phononic crystal, which is shown as in FIG.1(a). It was demonstrated that structural symmetry is a necessary condition for the formation of symmetry-protected BICs. By calculating the transmission spectra of various rotating structures, the disappearance of transmission valley linewidth was observed and the appearance of symmetry-protected BICs was verified, as shown in FIG.1(b).

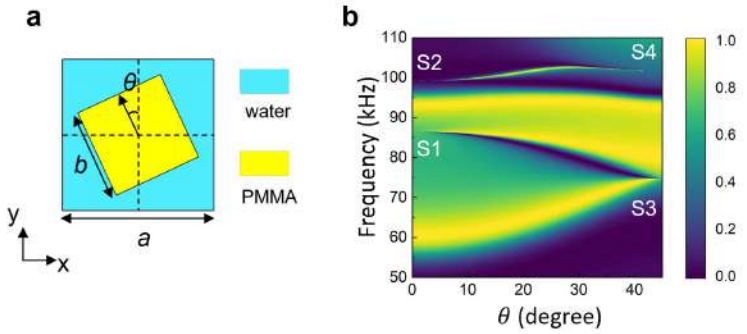


FIG.1 (a) Symmetry-broken unit cell. (b) Reflection spectrum with different rotation angles.

Then, we used bilayer structures that shown as in FIG.2(a) to form Fabry-Perot resonance between two

resonant systems. The distance between layers is adjusted to cause destructive interference in the external radiation channels. The simulated transmission spectrum is shown in FIG.2(b). At some specific distance, Fabry-Perot BICs are achieved when sound energy is localized between two layers and radiation is prevented. For different resonance modes of single-layer structure, the conditions for the formation of Fabry-Perot BICs can be achieved by changing the interlayer distance, and a periodic distribution is formed in the axial of parameter δ. Two broadband transmission valleys were observed in transmission spectra, and narrowband transmission peaks appeared in the broadband transmission valleys. The simulation result showed the disappearance of line width at the BICs formed within these transmission peaks.

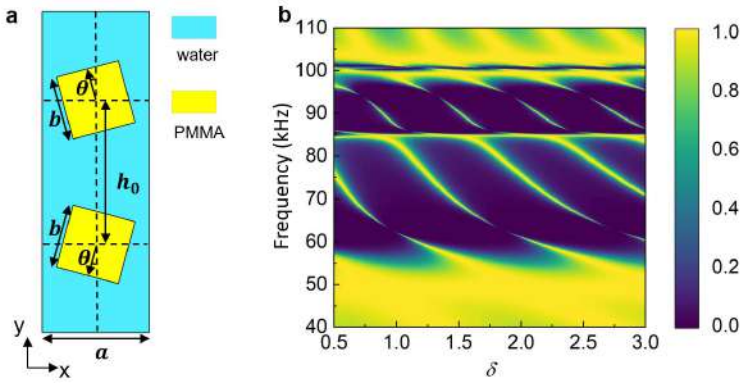


FIG.2 (a) Unit-cell composition of bilayer structure. (b) Transmission spectrum of bilayer phononic crystal with variable parameter δ.

By combining the Fabry-Perot resonance of bilayer structures with the coupled resonant modes in a single system, the Fabry-Perot BICs formed by two different resonant modes can be merged together, and the Q value divergence rate will change into $(\delta - \delta_0)^{-4}$, forming a high-order BIC. The merging BIC achieved a stable high-Q bound state in a larger parameter region. To accomplish this objective, we proposed bilayer rectangular structure. By changing two parameters about spacing distance δ and side length d, two Fabry-Perot BICs with the same symmetry merge together to form a single high-order BIC.

References

1. Z. Y. Liu, C. T. Chan, and P. Sheng, Analytic model of phononic crystals with local resonances, Phys. Rev. B, Vol. 71, No. 014103, 2005.
2. G. Lee, D. Lee, J. Park, Y. Jang, M. Kim, and J. Rho, Piezoelectric energy harvesting using mechanical metamaterials and phononic crystals, Commun. Phys, Vol. 5, No. 94, 2022.
3. K. Koshelev, S. Lepeshov, M. Liu, A. Bogdanov, and Y. Kivshar, Asymmetric metasurfaces with high-Q resonances governed by bound states in the continuum, Phys. Rev. Lett., Vol. 121, No. 193903, 2018.
4. P. Xie, Y. Deng, L. Zeng, Z. Liang, S. Shen, Q. Ding, H. Zhang, Z. Zhou, and W. Wang, Tunable interactions of quasibound states in the continuum with cavity mode in a metasurface microcavity hybrid, Phys. Rev. B, Vol. 106, No. 165408, 2022.

Tunable curved piezoelectric metasurface for flexural wave manipulation in cylindrical shells

Jie Xu, Youqi Zhang, Weihan Wang, and Zheng Li *

State Key Laboratory for Turbulence and Complex Systems, Department of Mechanics and Engineering Science, Peking University, Beijing 100871, China
*corresponding author: lizheng@pku.edu.cn

Abstract: A tunable curved piezoelectric metasurface is proposed here, which is attached on the surface of host cylindrical shell to achieve anomalous refraction of flexural waves. This study extends the research on elastic metasurfaces from planar structures to non-planar structures, and provides a new method for wave manipulation in cylindrical shells.

Non-planar structures such as cylindrical shells and conical shells are widely used in engineering fields, and the control of elastic wave and vibration in service is always a key issue [1]. Metasurface has received extensive attention due to its compact configuration and strong ability to manipulate the wave propagation [2]. Whereas, the current researches on elastic wave metasurface are mainly focused on wave manipulation in plates by planar metasurface. In this study, we design a curved piezoelectric metasurface, which consists of piezoelectric transducers with shunting negative capacitance circuits, and attached it on the surface of host cylindrical shell (shown in Figure 1) to realize the manipulation of flexural waves. Considering the anisotropy properties of piezoelectric transducers introduced by the curvature, the generalized Snell's law and diffraction law [3] for waves passing through the curved piezoelectric metasurface are obtained, and the wave motion characteristics in the cylindrical shell are analyzed. Then, the tunable ability of metasurface is investigated by adjusting the shunting circuits for the incident waves at different frequencies, and the symmetric and asymmetric transmissions of flexural waves in cylindrical shell are realized by designing the phase gradient distribution of metasurface.

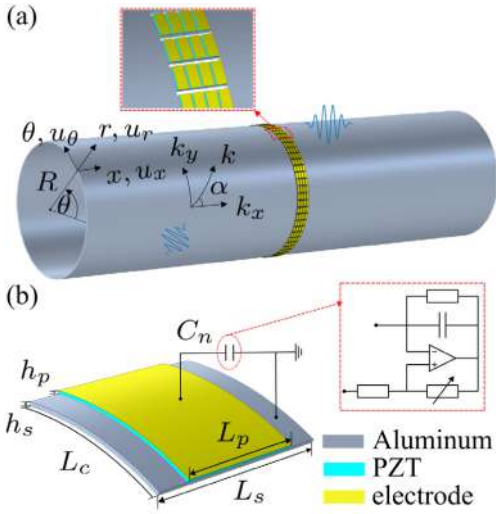


Figure 1. Schematic diagrams of (a) the host elastic cylindrical shell with a piezoelectric metasurface and (b) the basic unit cell of metasurface.

To verify the effectivencess and tunable ability of metasurface to manipulate flexural waves, numerical simulations are carried out. By altering the shunting circuits to design different distributions of phase gradient, the metasurface can achieve asymmetric and symmetric transmissions of flexural waves in cylindrical shell as shown in Figures 2(a) and (b), respectively. The transmission angle obtained by simulation is consistent with the theoretical value, which verifies the correctness of our metasurface model. In addition, results show that the proposed piezoelectric metasurface has the tunable ability in a wide frequency range by only adjusting the circuits and without changing its physical structure.

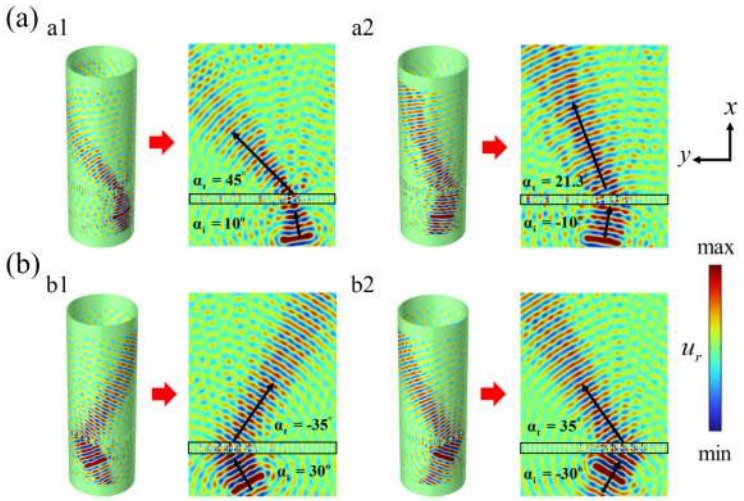


Figure 2. Asymmetric and symmetric transmissions at f=30 kHz: (a) radial displacement fields with incident angles $\alpha_i = \pm 10^\circ$, (b) radial displacement fields with incident angles $\alpha_i = \pm 30^\circ$.

In this paper, the concept of elastic metasurface is extended to apply in curved structures, and a tunable curved piezoelectric metasurface is proposed to realize the anomalous refraction of flexural waves in cylindrical shells. Our research could broaden the application of tunable piezoelectric metasurface and provide an efficient method for the wave manipulation in curved structures.

Acknowledgements

This research was supported by the National Natural Science Foundation of China under Grants No. 12232001 and No. 12172008.

References

1. Oukhai, E., Agounad, S., and Faiz, B., "Behaviour of circumferential and helical guided waves in two-layered composite cylindrical shell", Appl. Math. Model., Vol. 126, 266-286, 2024.

2. Chen, A. L., Wang, Y. S., and Wang, Y. F., et al., "Design of Acoustic/Elastic Phase Gradient Metasurfaces: Principles, Functional Elements, Tunability, and Coding", Appl. Mech. Rev., Vol. 74, No. 2, 020801, 2022.

3. Fu, Y. Y., Shen, C., and Cao, Y. Y., et al. "Reversal of transmission and reflection based on acoustic metagratings with integer parity design", Nat. Commun., Vol. 10, No. 1, 2326, 2019.

Design of tunable bound states in the continuum for flexural waves in elastic waveguide

Weihan Wang[1], Shixuan Shao[1], Rongyu Xia[2], and Zheng Li[1*]

[1] Department of Mechanics and Engineering Science, College of Engineering, Peking University, China
[2] Department of Applied Mechanics and Engineering, School of Aeronautics and Astronautics, Sun Yat-sen University, China
[*]corresponding author: lizheng@pku.edu.cn

Abstract: In this research, a tunable Friedrich-Wintgen bound state in the continuum (FW BIC) is designed to achieve an elastic waveguide with a high-quality factor. Numerical simulations and experimental tests are conducted to verify the formation of FW BIC. Furthermore, a perfect absorption of flexural waves can also be realized.

As engineering structures have become increasingly complex to meet the requirements of industries, the study of propagating guided waves within them presents a significant difficulty due to the characteristics of dispersion and multimodality. In addition, it poses a considerable obstacle for guided wave-based nondestructive testing techniques (NDT) [1]. Although diverse metamaterial-based sensors have been proposed to extract desired information from complex signals, most of them have many unit cells and are generally difficult to reach a high-quality factor (*Q*-factor). Consequently, the design of guided wave sensors with compact configuration and high *Q*-factor is of paramount importance.

In this study, we design a non-Hermitian electromechanical system, which integrates Friedrich-Wintgen bound states in the continuum (FW BICs) [2] into an elastic plate using two PZT (lead zirconic titanate) patches with shunting circuits, as shown in Figure 1. Each PZT patch can be a tunable resonator by altering the inductor in the circuit. It doesn't like metamaterials, FW BICs can be formed by two PZT patches and can exhibit a very high *Q*-factor. The complex eigenfrequency is calculated by using the finite element software COMSOL Multiphysics. Results not only exhibit the existence of a high *Q*-factor but also show the coupled mode of FW BICs. Experimental tests are also conducted to verify the numerical results.

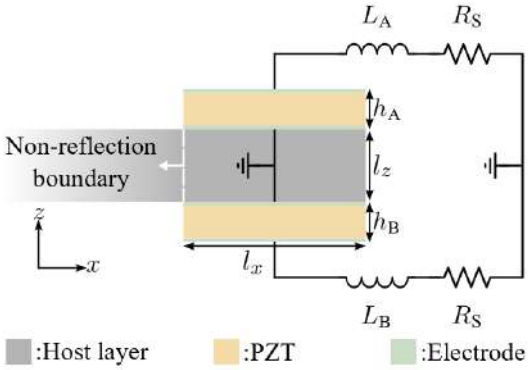


Figure 1. The non-Hermitian electromechanical system: A plate attached by two PZT (lead zirconic titanate) patches with shunted circuits.

For indicating the robustness and effectivity of FW BICs, the influences of manufacturing errors and material properties of host plate are discussed. By tuning the resonance frequency of resonators, the reduction in *Q*-factor can be repaired. And the designed FW BICs are observed within diverse host waveguides with different parameters. Furthermore, FW BICs can realize perfect absorption of flexural waves at the resonant frequency as shown in Figure 2, in which the critical coupling conditions $\Gamma = \Gamma_S$ and $\Gamma = \Gamma_A$ are separately for symmetric mode and antisymmetric mode, and the reflection ratio *R* is calculated by finite element method and temporal coupled-mode theory [3].

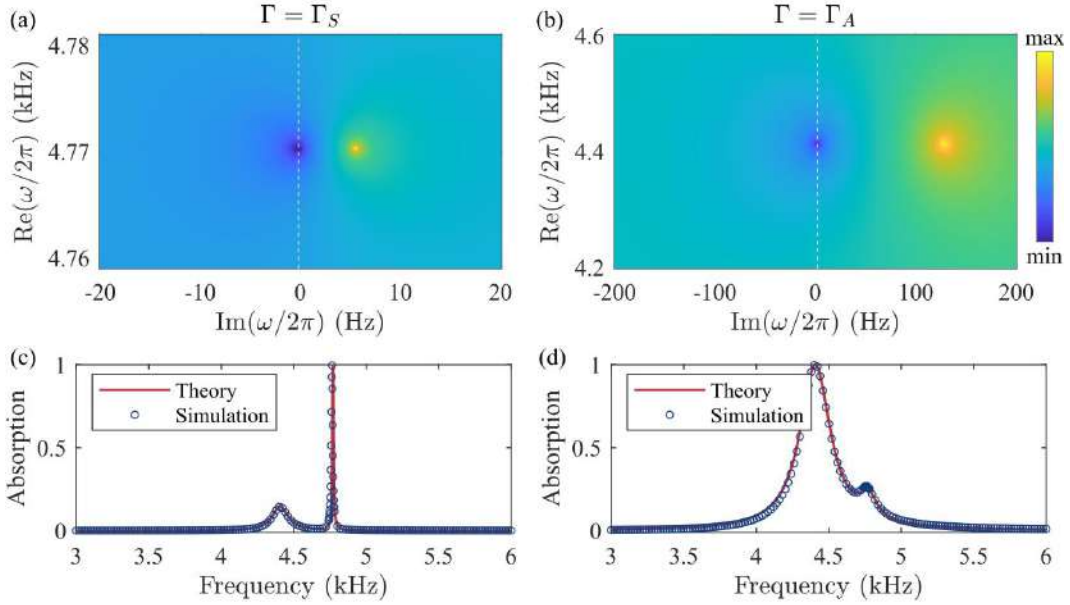


Figure 2. The $\log_{10}|R|$ in the complex frequency plane for (a) $\Gamma = \Gamma_S$ and (b) $\Gamma = \Gamma_A$, and the perfect absorption for (c) $\Gamma = \Gamma_S$ and (d) $\Gamma = \Gamma_A$.

In this research, we propose a tunable FW BIC in an elastic plate. Based on the FW BIC, the tunable resonance with a high *Q*-factor can be realized, and the perfect absorption of flexural wave can also be successfully achieved. Therefore, our research paves a new way for designing miniaturized high-*Q* sensors.

Acknowledgment

This work was supported by the National Natural Science Foundation of China under grants No. 12232001, No. 12172008 and No.12202012.

References

1. Mitra, M. & Gopalakrishnan, S. Guided wave based structural health monitoring: A review. *Smart Mater. Struct.*, Vol. 25, No. 5, 053001, 2016.
2. Hsu, C. W., Zhen, B., Stone, A. D., Joannopoulos, J. D. & Soljačić, M. Bound states in the continuum. *Nat. Rev. Mater.*, Vol. **1**, No. 9, 1–13, 2016.
3. Fan, S., Suh, W. & Joannopoulos, J. D. Temporal coupled-mode theory for the Fano resonance in optical resonators. *J. Opt. Soc. Am. A*, Vol. **20**, No.3 569–572, 2003.

Real-Time Manipulation of Spoof Surface Acoustic Waves via a Reconfigurable Coding Metasurface

Haoxiang Li[1,2*], Jie Hu[1*]

[1] College of information science and technology & College of artificial intelligence,

Nanjing Forestry University, Nanjing 210037, P.R.China

[2] Key Laboratory of Modern Acoustics, MOE, Institute of Acoustics, Department of Physics, Collaborative Innovation Center of Advanced Microstructures, Nanjing University, Nanjing 210093, P. R. China.

[*]corresponding author: hxli@njfu.edu.cn; hujie@njfu.edu.cn;

Abstract: In this paper, we design a tunable acoustic metasurface composed of Helmholtz-resonator-like digital-coding meta-atoms to realize the dynamic manipulation of spoof surface acoustic waves (SSAWs). By mechanically adjusting the resonator depth, we demonstrate a multifunctional and adaptive wavefront manipulation including acoustic focusing and Airy beam's generation.

Spoof surface acoustic waves (SSAWs), which is the direct acoustical analog of plasmon, can support strongly localized surface waves by metasurfaces and offer a toolset for acoustic imaging, communications, etc. For example, Liu manipulates two-dimensional acoustic vortices beyond the diffraction limit based on SSAWs. Li demonstrates the superwavelength self-healing of spoof surface sonic Airy-Talbot waves and realizes a high-quality, low-error, and high-capacity acoustic information transmission. However, the SSAWs cannot be controlled dynamically by these passive metasurfaces as the geometries of the unit cells are fixed, which restricts their application in emerging fields such as real-time signal encoding and adaptive wavefront manipulation. Here, we design a reconfigurable coding metasurface based on Helmholtz resonator unit cells, enabling flexible phase modulation of SSAWs through mechanical adjustment of the resonator depth. By selecting two units with a consistent transmission amplitude and a relative phase difference of 180° to construct a binary 1-bit encoding metasurface, we realize multiple functions of acoustic focusing and generation of Airy beam, as shown in Figs. 1(a) and (b).

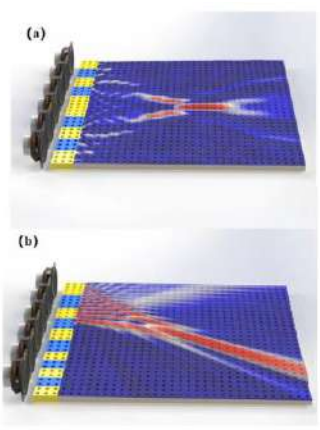
Our metasurface comprises two independent coding units, as shown in Fig. 1(c). The neck length l=1mm, the opening diameter w=7mm, the length and width of the substrate cavity are both a=18mm. The depth of the cavity h can be adjusted, corresponding to the two states of the coding units, "0" and "1". In order to determine the value of h, it is essential to calculate the dispersion curve of the SSAWs. The dispersion relation reflects the relationship between its wave vector k_x and the angular frequency ω, which can be derived as:

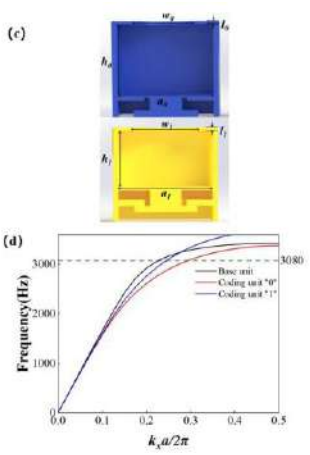
$$k_x = \frac{\omega}{c_0}\sqrt{1+\frac{\omega^2}{\left(\omega_{\mathrm{HR}}^2-\omega^2\right)^2}\left(\frac{\rho_0 c_0}{M_{\mathrm{HR}}a^2}\right)^2} \tag{1}$$

where $\rho_0 = 1.21\,\mathrm{kg/m^3}$ is the mess density of the air, c_0=343kg/m^3 is the speed of sound in air, $\omega_{\mathrm{HR}} = \sqrt{(\pi w^2 c_0^2)/(4lha^2)}$ is the resonance angular frequency of the resonator cavity, $M_{\mathrm{HR}} = 4\rho_0 l/\pi w^2$ is the acoustic mass. As shown in Eq. (1), the wave vector of SSAW is determined by the cavity depth h. According to the equation $\varphi = kL$ where L is the propagation distance, we can select two types of units which result in a 180°

phase difference in the SSAWs. We calculate the dispersion relation in Fig. 1(d), where the black curve represents the substrate structure, which begins to deviate from the dispersion line of the background air when the frequency exceeds 3000 Hz. In order to avoid thermal viscosity and anisotropy, we set the operation frequency at 3080Hz, which is slightly off-resonance. The red and blue curves show the dispersion relations of the two selected coding units (h_1=17mm, h_2=15mm).

To validate the effectiveness of the designed coding unit, we use this programmable metasurface to realize the acoustic focusing, as shown in Fig. 2(a). To implement the designed acoustic lens, we fabricate a metasurface composed of 32×20 units using 3D printing with PLA materials and establish an experimental setup as shown in Fig. 2(b). The experimental results not only demonstrate excellent focusing capabilities but also allows for arbitrary control of the focal point's position. Furthermore, we change the structure to generate an Airy beam and demonstrate its non-diffracting property, as shown in Figs. 2(g)-(j).





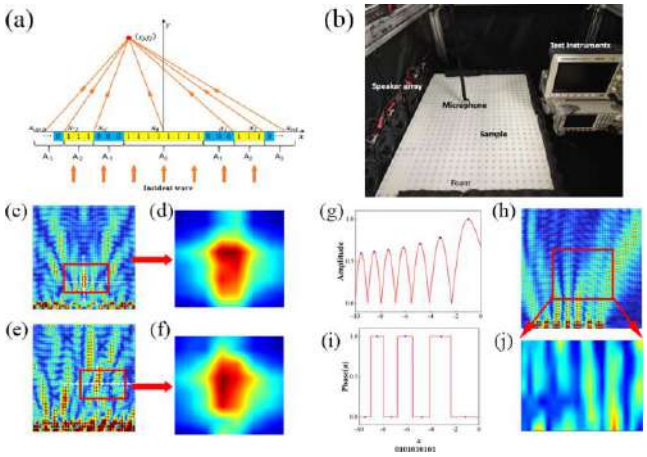


Figure 1 (left). Schematic of the reconfigurable metasurface, including (a) acoustic focusing, (b) Airy beam generation, (c) structural parameters of the encoding units "0" and "1", (d) dispersion relationship of the substrate and encoding units "0" and "1".

Figure 2 (right). (a) Schematic of acoustic focusing. (b) Experimental setup with speaker array, microphone, and test instruments. (c) Simulation of on-axis focusing. (d) Experimental on-axis focusing result. (e) Normalized intensity comparison for on-axis focusing. (f) Focal line intensity comparison for on-axis focusing. (g) Simulation of off-axis focusing. (h) Experimental off-axis focusing result. (g) Amplitude profile of an Airy beam, illustrating its characteristic oscillatory behavior. (h) Simulated propagation of an Airy beam, highlighting its self-bending behavior. (i) Phase profile of the Airy beam, showing a step-like structure. (j) Experimental propagation results of an Airy beam.

Acknowledgements.

This work is supported by the Natural Science Foundation of Jiangsu Province (grant No. BK20240659) and the Fundamental Research Funds for the Central Universities (grants No. 020414380195).

References

1. Jia, H., et al. Subwavelength imaging through spoof surface acoustic waves on a two-dimensional structured rigid surface. Appl. Phys. Lett. 103, 103505 (2013).
2. Li, H. X., et al. Superwavelength self-healing of spoof surface sonic Airy-Talbot waves. Nat. Commun. 14, 7633 (2023).
3. Lu, Y. X., et al. Acoustic rainbow trapping in cylindrical spoof waveguide. Applied Acoustics 231, 110502 (2025).

A Surface Integral Equation with Bianisotropic Impedance Boundary Conditions for Simulation of Acoustic Metasurfaces

J. Shao[1*], R. Chen[2], and H. Bagci[1]
[1]Computer, Electrical and Mathematical Science and Engineering (CEMSE) Division,
King Abdullah University of Science and Technology (KAUST),
Thuwal 23955-6900, Saudi Arabia
[2]School of Microelectronics, Nanjing University of Science and Technology,
Nanjing 210094, China
junze.shao@kaust.edu.sa (corresponding author)

Abstract

A surface integral equation with bianisotropic impedance boundary conditions is formulated and numerically solved using a Nyström method for simulation of acoustic metasurfaces. An acoustic splitter is simulated using the proposed method. Simulation results agree very well with analytic results demonstrating the method's validity and accuracy.

The rapid development of acoustic metasurfaces has generated significant interest in methods for simulation of acoustic metasurfaces. Direct simulation of a metasurface consisting of units cells in its native environment is challenging due to the difference of scale in the dimensions of propagation environment and the unit cell. To avoid this multiscale issue, in electromagnetics, the metasurface is replaced by a infinitesimally thin sheet with generalized sheet transition conditions (GSTCs) that enforce the response of the metasurface on the fields on the two sides of this sheet [1]. In acoustics, Willis coupling [2], which can be used for the same purpose, "connects" the velocity potentials on two sides of a metasurface, $\varphi_1(\mathbf{r})$ and $\varphi_2(\mathbf{r})$, using

$$\begin{bmatrix} \Delta\varphi(\mathbf{r}) \\ \Delta\partial_n\varphi(\mathbf{r}) \end{bmatrix} = \begin{bmatrix} b_{11}(\mathbf{r}) & b_{12}(\mathbf{r}) \\ b_{21}(\mathbf{r}) & b_{22}(\mathbf{r}) \end{bmatrix} \begin{bmatrix} \varphi_{\text{avg}}(\mathbf{r}) \\ \partial_n\varphi_{\text{avg}}(\mathbf{r}) \end{bmatrix}. \tag{1}$$

Here, $\Delta x(\mathbf{r}) = x_1(\mathbf{r}) - x_2(\mathbf{r})$, $x_{\text{avg}}(\mathbf{r}) = [x_1(\mathbf{r}) + x_2(\mathbf{r})]/2$, $\mathbf{r} \in S$, S is the surface of the infinitesimally thin sheet replacing the metasurface, ∂_n represents derivative along the direction normal to S (pointing from side 1 to side 2), and b_{ij}, $i, j = 1, 2$ are equivalent coupling coefficients. For a bianisotropic metasurface, one can easily derive the expressions for these coupling coefficients as

$$\begin{bmatrix} b_{11}(\mathbf{r}) & b_{12}(\mathbf{r}) \\ b_{21}(\mathbf{r}) & b_{22}(\mathbf{r}) \end{bmatrix} = \begin{bmatrix} 2\frac{Z_{11}(\mathbf{r})+Z_{12}(\mathbf{r})-Z_{21}(\mathbf{r})-Z_{22}(\mathbf{r})}{Z_{11}(\mathbf{r})+Z_{12}(\mathbf{r})+Z_{21}(\mathbf{r})+Z_{22}(\mathbf{r})} & \frac{4}{i\omega\rho_0}\frac{Z_{11}(\mathbf{r})Z_{22}(\mathbf{r})-Z_{21}(\mathbf{r})Z_{12}(\mathbf{r})}{Z_{11}(\mathbf{r})+Z_{12}(\mathbf{r})+Z_{21}(\mathbf{r})+Z_{22}(\mathbf{r})} \\ 4\frac{i\omega\rho_0}{Z_{11}(\mathbf{r})+Z_{12}(\mathbf{r})+Z_{21}(\mathbf{r})+Z_{22}(\mathbf{r})} & -2\frac{Z_{11}(\mathbf{r})-Z_{12}(\mathbf{r})+Z_{21}(\mathbf{r})-Z_{22}(\mathbf{r})}{Z_{11}(\mathbf{r})+Z_{12}(\mathbf{r})+Z_{21}(\mathbf{r})+Z_{22}(\mathbf{r})} \end{bmatrix}. \tag{2}$$

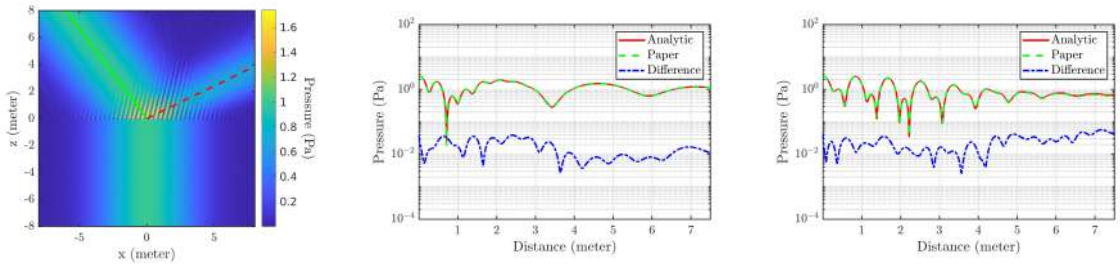
Here, Z_{ij}, $i, j = 1, 2$ are impedance matrix entries which relate the pressure and the normal component of the velocity on two sides of the metasurface, ω is the frequency, and ρ_0 is the density in the background medium where the metasurface resides.

Using the second Green identity, Kirchhoff-Helmholtz boundary integral equation can be formulated on S as [3]

$$\begin{aligned} \varphi^{\text{inc}}(\mathbf{r}) - S[\Delta\partial_n\varphi](\mathbf{r}) + D[\Delta\varphi](\mathbf{r}) &= \varphi(\mathbf{r}), \\ \partial_n\varphi^{\text{inc}}(\mathbf{r}) - D'[\Delta\partial_n\varphi](\mathbf{r}) + N[\Delta\varphi](\mathbf{r}) &= \partial_n\varphi(\mathbf{r}). \end{aligned} \tag{3}$$

Here, $\varphi^{\text{inc}}(\mathbf{r})$ is the incident potential, operators $S[x]$, $D[x]$, $D'[x]$ and $N[x]$ are given by

$$\begin{aligned} S[x](\mathbf{r}) &= \int_S G(\mathbf{r}, \mathbf{r}')x(\mathbf{r}')ds', \qquad D[x](\mathbf{r}) = \int_S \partial_{n'}G(\mathbf{r}, \mathbf{r}')x(\mathbf{r}')ds', \\ D'[x](\mathbf{r}) &= \int_S \partial_n G(\mathbf{r}, \mathbf{r}')x(\mathbf{r}')ds', \quad N[x](\mathbf{r}) = \int_S \partial^2_{nn'}G(\mathbf{r}, \mathbf{r}')x(\mathbf{r}')ds', \end{aligned} \tag{4}$$



(a) (b) (c)

Figure 1: (a) Pressure field on the $y = 0$ plane. Pressure field along (b) the green solid line and (c) the red dashed line.

and $G(\mathbf{r}, \mathbf{r}') = e^{ik_0|\mathbf{r}-\mathbf{r}'|}/4\pi|\mathbf{r} - \mathbf{r}'|$ is the Green function in the background medium with wave number k_0. By averaging Eq. (3) on two sides of S and combining resulting equation with Eq. (1), one can obtain

$$\begin{aligned} &\Delta\varphi(\mathbf{r}) - b_{11}(\mathbf{r})\tilde{D}[\Delta\varphi](\mathbf{r}) - b_{12}(\mathbf{r})N[\Delta\varphi](\mathbf{r}) + b_{11}(\mathbf{r})S[\Delta\partial_n\varphi](\mathbf{r}) + b_{12}(\mathbf{r})\tilde{D}'[\Delta\partial_n\varphi](\mathbf{r}) \\ &\qquad = b_{11}(\mathbf{r})\varphi^{\text{inc}}(\mathbf{r}) + b_{12}(\mathbf{r})\partial_n\varphi^{\text{inc}}(\mathbf{r}), \\ &\Delta\partial_n\varphi(\mathbf{r}) - b_{21}(\mathbf{r})\tilde{D}[\Delta\varphi](\mathbf{r}) - b_{22}(\mathbf{r})N[\Delta\varphi](\mathbf{r}) + b_{21}(\mathbf{r})S[\Delta\partial_n\varphi](\mathbf{r}) + b_{22}(\mathbf{r})\tilde{D}'[\Delta\partial_n\varphi](\mathbf{r}) \\ &\qquad = b_{21}(\mathbf{r})\varphi^{\text{inc}}(\mathbf{r}) + b_{22}(\mathbf{r})\partial_n\varphi^{\text{inc}}(\mathbf{r}), \end{aligned} \tag{5}$$

where '$\sim$' on the surface integral operators means the integration is evaluated in Cauchy principal value. Eq. (5) is a coupled system of equations in unknowns $\Delta\varphi(\mathbf{r})$ and $\Delta\partial_n\varphi(\mathbf{r})$. This system is discretized using a higher-order Nyström method [4].

The proposed method is used to simulate a metasurface that can split a normally incident beam into two directions θ_l and θ_r. The metasurface is a circular disk with a radius of 7 m located on the $z = 0$ plane and is excited by tapered plane wave at 689.8 Hz, and $\theta_l = 36.87°$ and $\theta_r = 64.16°$. S is discretized into a mesh of curvilinear triangular patches with an average edge length of 0.15 m, resulting in a total of 15 992 patches. On this mesh, unknowns $\Delta\varphi(\mathbf{r})$ and $\Delta\partial_n\varphi(\mathbf{r})$ are expanded using second-order basis functions. This results in a matrix system of dimension 191 904. An LU direct solver is used to solve this matrix system.

Fig. 1(a) visualizes the pressure field on the $y = 0$ plane. The splitting of the incident wave is clearly demonstrated. Fig. 1(b) and Fig. 1(c) plot the scattered pressure computed along the green solid and red dashed lines in Fig. 1(a). The proposed method achieves an error of 1.54% and 2.68% with respect to analytical results on these two lines, demonstrating its accuracy.

References

[1] Holloway, C. L. and E. F. Kuester, "A homogenization technique for obtaining generalized sheet-transition conditions for a metafilm embedded in a magnetodielectric interface," *IEEE Trans. Antennas Propag.*, vol. 64, no. 11, pp. 4671-4686, 2016.

[2] Hussein, E., M. Yarden, and A. Andrea, "Homogenization and design of acoustic Willis metasurfaces," *Phys. Rev. B*, vol. 103, no. 5, pp. 054306, 2021.

[3] Krishnasamy, G., L. W. Schmerr, T. J. Rudolphi, and F. J. Rizzo, "Hypersingular boundary integral equations: Some applications in acoustic and elastic wave scattering," *J. Appl. Mech.*, vol. 57, no. 2, pp. 404–414, 1990.

[4] Chen, R., Y. Shi, S. B. Sayed, M. Lu, and H. Bagci, "On the spurious resonance modes of time domain integral equations for analyzing acoustic scattering from penetrable objects," *J. Acoust. Soc. Am.*, vol. 151, no. 2, pp. 1064–1076, 2022.

Metamaterial two-sphere Newton's cradle

S. A. Pope[1*], and O. B. Wright[2,3]
[1]University of Sheffield, United Kingdom
[2]Hokkaido University, Japan
[3]Osaka University, Japan
Corresponding author: s.a.pope@sheffield.ac.uk

Abstract: We show that the collision dynamics of two pendulum-suspended mass-in-mass resonators, essentially a two "meta-atom" Newton's cradle, can be described using effective parameters. These effective parameters can assume non-conventional values compared to their conventional counterparts. This work paves the way for the development of new "collision-based metamaterial" structures.

While some aspects of collisions in metamaterials have been studied, e.g. [1], a common feature across previous work is a focus on multiple collisions and associated wave propagation. The fundamental processes involved in individual collisions in such metamaterials and their effect on the overall dynamics have not been extensively studied. We use the modified Newton's cradle as a suitable base system for our work. Assuming stiff shells and small angular displacements and ignoring effects such as acoustic waves in the supporting wires, we model a mass-in-mass locally resonant Newton's cradle as a one-dimension linear piecewise system. We show that the collision between two mass-in-mass resonators can be described using relevant effective parameters by defining the average velocities $\dot{x}_a$ of the two mass-in-mass spheres at the end of the collision as:

$$\dot{x}_{1,a} = \tfrac{1}{2}\left(CM_a \in CR_a\right)\dot{x}_{1,t_c}, \tag{1a}$$

$$\dot{x}_{2,a} = \tfrac{1}{2}\left(CM_a + CR_a\right)\dot{x}_{1,t_c}. \tag{1b}$$

We define an effective coefficient of restitution CR_a in the same manner as the conventional sense, but also an effective "coefficient of motion" CM_a as the ratio of the momentum after to that before the collision. $\dot{x}_{1,t_c}$ is the velocity of shell 1 at t_c the start of the collision. We derive the effective parameters by solving the linear equations for the collision, leading to:

$$CR_a = \tfrac{m}{m+m_r}\left(CR_e + \left(\hat{m}_{e,s}(t) * CR_e(t)\right)\big|_{t=t_s} \in \omega_r^2\left(\tfrac{d^2\hat{m}_{e,s}(t)}{dt^2}\tfrac{x_{r_1,t_c}}{\dot{x}_{1,t_c}} + \tfrac{d\hat{m}_{e,s}(t)}{dt}\tfrac{\dot{x}_{r_1,t_c}}{\dot{x}_{1,t_c}}\right)\Big|_{t=t_s}\right) \tag{2a}$$

$$CM_a = \tfrac{m}{m+m_r}\left(1 + \tfrac{m_r}{m}\tfrac{\dot{x}_{r,t_c}}{\dot{x}_{1,t_c}}\right). \tag{2b}$$

where

$$CR_e = \in \mathcal{L}^{-1}\left(\tfrac{\hat{m}_{e,s}s}{\hat{m}_e s^2+2\omega_c^2}\left(\tfrac{x_{r_1,t_c}}{\dot{x}_{1,t_c}}s + \tfrac{\dot{x}_{r,t_c}}{\dot{x}_{1,t_c}}\right) + \tfrac{s}{\hat{m}_e s^2+2\omega_c^2}\right)\Big|_{t=t_s},$$

$$CM_e = \mathcal{L}^{-1}\left(\tfrac{\hat{m}_{e,s}}{\hat{m}_e s}\left(s\tfrac{x_{r_1,t_c}}{\dot{x}_{1,t_c}} + \tfrac{\dot{x}_{r,t_c}}{\dot{x}_{1,t_c}}\right) + \tfrac{1}{\hat{m}_e s}\right)\Big|_{t=t_s},$$

$$\hat{m}_e = 1 + \tfrac{m_r}{m}\tfrac{\omega_r^2}{s^2+\omega_r^2} = 1 + \hat{m}_{e,s}.$$

Unlike effective parameters derived to understand wave propagation, these effective parameters are derived in the time domain since they are defined at the time t_s when the spheres separate.

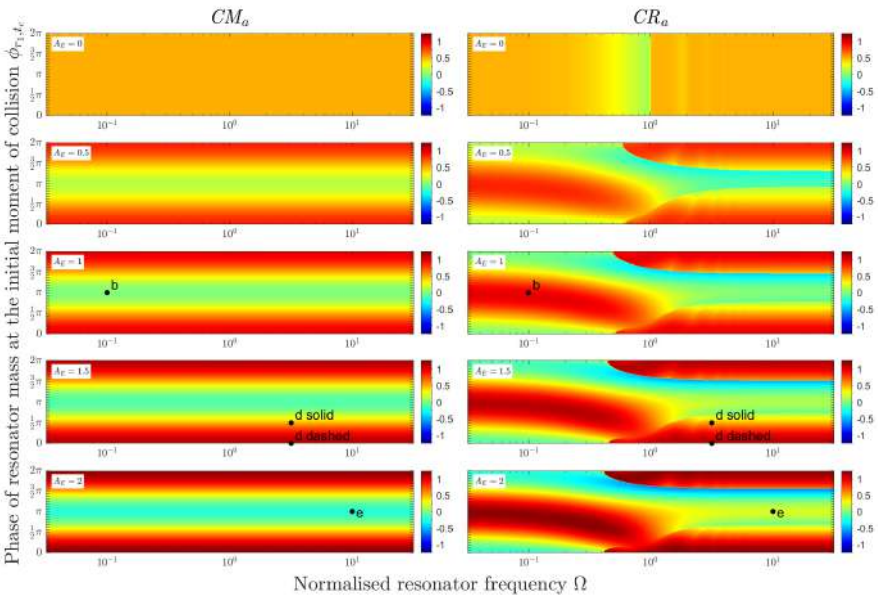


Figure 1: Density plots for the effective coefficients of motion, CM_a (left panels), and restitution, CR_a (right panels), for the mass-in-mass resonator system. Each plot represents the results for different initial conditions of the left-hand mass-in-mass system at the moment of collision.

The Laplace variable is s, $\mathcal{L}^{-1}$ the inverse Laplace operator, m and m_r the mass of the spherical shell and internal mass, ω_c and ω_r are the natural frequencies of the shell compression during collision and internal resonator respectively. The effective parameters are a function of the displacement x_{1,t_c} and velocity $\dot{x}_{1,t_c}$ of the resonant mass of shell 1 at the time of the impact.

Figure 1 shows density plots for the effective coefficients, with the horizontal axes showing the normalized frequency ratio $\Omega = \omega_r/\omega_c$. Conditions for a stiff shell are implemented using a steel shell with radius $R = 10$ mm and shell thickness $0.1R$, leading to $\omega_c/\omega_g = 4.7 \times 10^4$ for $m_r = m$, where ω_g is the pendulum frequency. The initial conditions of the internal resonator of shell 1 at the moment of collision are described in terms of A_E, the total energy of the resonator relative to the kinetic energy of a non-resonant shell of mass m (increasing down each column), and ϕ_{r_1,t_c}, the phase of the internal resonant mass relative to its undisturbed location (plotted on the vertical axis of each panel). It shows that CR_a can exceed 1, indicating that kinetic energy is being added to the spherical shells and also that it can take negative values. It shows that the CM_a, which is unity for conventional shells, can take positive/negative values associated with an effective addition/reduction of momentum to the system of spherical shells. This demonstrates that the mass-in-mass resonator system can exhibit a variety of responses depending on the resonator properties. As examples, the case indicated by the dot (b) is for approximately equal and opposite motion of the two outer spheres after collision, while (e) is a case when shell 1 bounces back and shell 2 remains stationary. Numerical simulations of the motion of the mass-in-mass resonators during and after collision verify these results.

SAP was supported by the UK Engineering and Physical Sciences Research Council through grant EP/T028661/1. OBW acknowledges Grants-in-Aid for Scientific Research from the Ministry of Education, Culture, Sports, Science and Technology (MEXT).

References

1. E. Kim, et al. , "Impact and blast mitigation using locally resonant woodpile metamaterials," *Int. J. Impact Eng.*, Vol. 101, pp. 24-31, 2017.

Basic Performance Test Results of a 3D Underwater Acoustic Metalens Using a Sensor Positioning Device in a Water Tank

S.-M. Kim[1*], B. Oh[2], Y.-S. Choo[1,3], J.-B. Jang[1,3], D. Lee[2], J. Rho[2], and S.-H. Byun[1,3]

[1]Korea Research Institute of Ships and Ocean Engineering, Korea
[2]Pohang University of Science and Technology, Korea
[3]Korea University of Science and Technology, Korea
[*]corresponding author: smkim@kriso.re.kr

Abstract: An underwater sensor positioning device was developed to control the hydrophone's location and the azimuth angle of tested metamaterial. Recently, a 3D underwater acoustic metalens was designed and fabricated using a 3D metal printing process. Basic performance tests with the positioning device in a tank showed a high focusing performance.

Various studies have been conducted on acoustic metamaterials for focusing underwater sound. Su et al. explored broadband underwater sound focusing using a 2D transparent pentamode lens [1], while Kim et al. investigated 3D acoustic metamaterial Luneburg lenses for broadband, wide-angle underwater ultrasound focusing [2]. In both cases, sound focusing was observed; however, in a water tank, the pentamode lens achieved an amplification of up to 4 dB, while Kim's study did not report the level of amplification achieved. Over the past decade, various experimental implementations of underwater lenses have emerged, driving further advancements in the acoustic field. However, despite their potential in the low-frequency range and the need for submerged applications, research remains limited, with most studies focusing on 2D lenses. To overcome low focusing efficiency and the limitations of 2D designs, a 3D Helmholtz resonator-based underwater acoustic metalens was recently designed and fabricated [3]. This paper presents the results of basic performance tests conducted in a large water tank ($35 \times 20 \times 9.6$ m^3).

A remotely operated underwater sensor positioning device was developed to control the location of a hydrophone along the x-, y-, and z-axes [4]. Additionally, a motor-driven rotator was incorporated to adjust the horizontal posture angle of the metamaterial being tested. Figure 1 presents a conceptual illustration along with a photograph of the device in a water tank. The device operates at depths exceeding 20 meters, with its position and angle automatically controlled by a PC. The measurement volume is approximately 1m × 1m × 1m, and the rotation angle spans a full 360 degrees.



Figure 1. Underwater sensor positioning device (a) conceptual illustration (b) photo

To verify the formation of plane waves in the water tank, sound field measurements were conducted. An omnidirectional transducer and a standard hydrophone were used to generate and measure the underwater sound

pressure. For the measurements, 2 ms-long burst tones ranging from 15 to 35 kHz were employed. Figure 2 presents an example of the measured magnitude and phase distribution at 25 kHz. The results confirm that the plane wave fields were successfully generated.

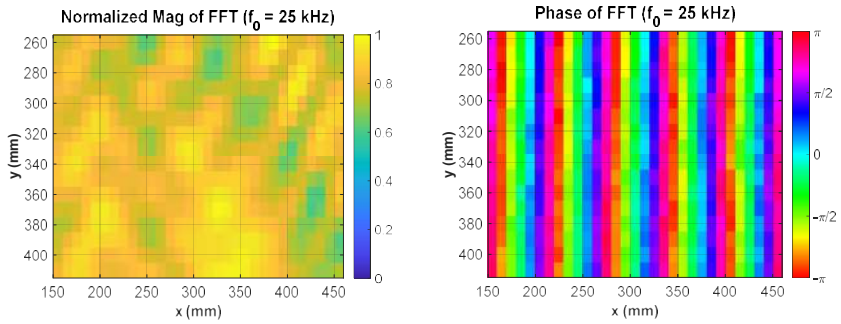


Figure 2. Measured underwater acoustic field in the water tank (a) normalized magnitude (b) phase

The 3D underwater acoustic metalens is fabricated using a 3D metal printing process, with a diameter of 240 mm. Its focusing performance is evaluated in a water tank using the same measurement techniques as those applied for plane wave analysis. Figure 3 illustrates the fabricated metalens mounted on the positioning device, along with an example of the measured sound distribution at 25 kHz. The results show that high sound focusing performance over 10 kHz band.

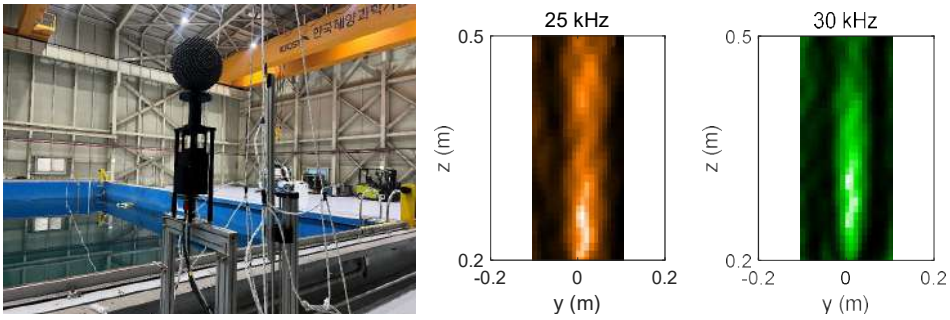


Figure 3. Focusing performance test results of 3D underwater acoustic metalens (a) photo of the metalens (b) measure focused underwater acoustic fields at 25 and 30 kHz

Acknowledgements: This research was supported by KRISO funded by Ministry of Oceans and Fisheries (PES5551).

References

1. Su, X., Norris, A. N., Cushing, C. W., Habermand, M. R. and Wilson, P. S., “Broadband focusing of underwater sound using a transparent pentamode lens,” J. Acoust. Soc. Am., Vol. 141, No. 10, 4408–4417, 2017.
2. Kim, J.-W., Hwang, G., Lee, S.-J. and Kim, S.-H., “Three-dimensional acoustic metamaterial Luneburg lenses for broadband and wide-angle underwater ultrasound imaging,” Mech. Sys. Sig. Proc., 109374, 2022.
3. Oh, B., Lee, D., Byun, S.-H, Kim, S.-M., Rho, J et al., "Underwater Willis lens for broadband low-frequency focusing," in preparation.
4. Kim, S.-M., Choo, Y.-S., Jang, J.-B., Oh, B., Lee, D., Rho, J. and Byun, S.-H., “Design of an underwater 3D positioning system for verifying focusing performance of underwater acoustic metamaterial in a water tank,” Metamaterals 2024, X-128–130, 2024.

Programmable sound wave transmission by active acoustic meta-layers

Shoubo Dai[1], Hao Gao[1], and Yegao Qu[1*]

[1]State Key Laboratory of Mechanical System and Vibration, Shanghai Jiao Tong University, Shanghai 200240, China

[*]corresponding author: quyegao@sjtu.edu.cn (Yegao Qu)

Abstract: We have developed a programmable acoustic meta-layer that can precisely control sound waves transmission while meeting ventilation requirements. The acoustic meta-layer can realize non-reciprocal transmission and frequency conversion. Further, various functions such as tunable anomalous refraction, wave focusing and self-bending beam can be realized by adjusting the phase distribution.

Achieving precise and flexible control over sound waves have always been the main focus of engineering and science. Acoustic metamaterials provide a novel technical platform for sound wave control [1, 2]. However, the design of acoustic devices often needs to consider environmental requirements such as ventilation, and the demand for compact and multifunctional acoustic devices is also increasing, which poses challenges to the design of the structure [3].

Based on the active control strategy, we propose, design and demonstrate an active acoustic meta-layer that achieves programmable and precise control of the incident sound field while ensuring ventilation. As shown in Figs. 1(a) and (b), the meta-layer consists of a supporting frame, piezoelectric patches and a feedforward control loop. A charge amplifier is attached to the sensing patches to acquire the sensing voltage V_s. Based on the sensing signal V_s and the designed transfer function H implemented in the digital controller, antisymmetric potentials V_a and -V_a are generated and applied to the actuators. This configuration ensures the control loop feedforward [4].

Assume a plane sound wave varying harmonically in time and with an amplitude of P_0 is incident forward to the active acoustic meta-layer, the transmission coefficient can be expressed as

$$T_f = s_{21} + \kappa_a \kappa_s H\left(e^{-ika} + e^{ika}\right), \tag{1}$$

where s_{21} are the complex scattering coefficients of the acoustic meta-layer, representing its transmissive properties. κ_s is the sensing coefficient, κ_a is the actuation coefficient, and a represents the distance from the actuator to the center of the active acoustic meta-layer. Based on Eq. (1), the transmission characteristics of sound wave can be arbitrarily regulated by adjusting the transfer function H. However, when the sound wave is backward incident, the transmission coefficient is expressed as

$$T_b = s_{21} - \kappa_a \kappa_s H\left(e^{-ika} + e^{ika}\right). \tag{2}$$

Therefore, the active acoustic meta-layer is intrinsically non-reciprocal. As an example, consider the complete suppression of a 4000 Hz forward incident sound wave, where $T_f = 0$, the corresponding transfer function H_0 can be calculated according to Eq. (1). As shown in Fig. 1(c), a set of time-domain numerical simulations are conducted to further verify the non-reciprocal sound wave suppression property and the stability of the system. As shown in Figs. 1 (d) and (e), compared with the transmitted signal without control, the forward incident transmitted signal after the acoustic meta-layer control is almost zero, while the backward incident transmitted signal is twice as much. To achieve single-frequency conversion, further processing of the transfer function H is required. By adjusting the time-varying transfer function, the actuation voltage is made to satisfy

$$V_a(t) = H_0 V_s(t) + A_n\left[V_s(t)\cos(\omega_n t) + \dot{V}_s(t)\sin(\omega_n t)/\omega\right], \tag{3}$$

where A_n controls the emitted wave amplitude of the conversion frequency, ω_n is the modulation frequency. As an example, in Figs. 1(f) and (g), frequency up conversion is achieved by applying $\omega_n = 2\pi \times 1000$ Hz.

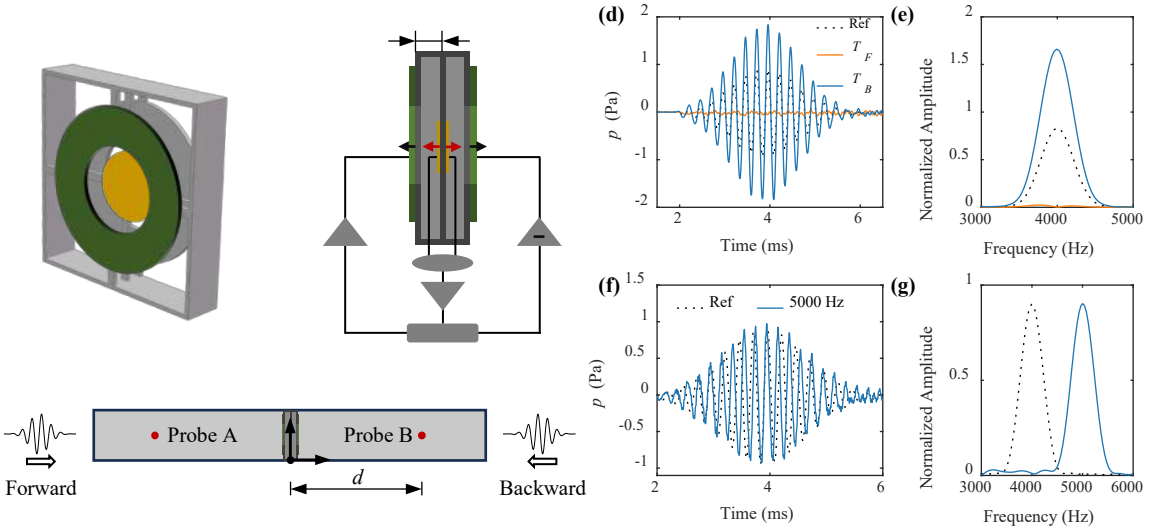


Figure 1. (a) Structural diagram of the active acoustic meta-layer; (b) design of the feedforward control loop; (c) schematic illustration of sound wave transmission modulated by the meta-layer; (d) time-domain transmission signals and (e) their spectra for non-reciprocal; (f) time-domain transmission signals and (g) their spectra after frequency conversion.

In addition, as shown in Fig. 2 (a), the meta-layer can also programmatically control the phase of the transmitted sound field. By distributing the array of meta-layers and individually programming the phase of each unit, tunable anomalous refraction, wave focusing, and self-bending beams can be achieved as shown in Figs 2 (b)-(c).

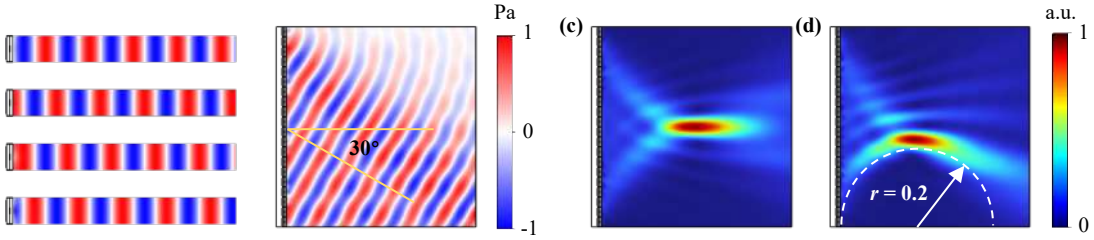


Figure 2. The transmitted pressure fields with the (a) phase shifts and (b) 30° refraction angle; spatial normalized distributions of acoustic intensity fields of the (c) acoustic focusing and the (d) acoustic self-bending.

Acknowledgements

This work was supported by the National Key R&D Program (Grant No. 2022YFB3902702), the National Natural Science Foundation of China (Grant Nos. U2141244, 12393781, 12121002, 12202260, 12202267).

References

[1] N. Gao, Z. Zhang, J. Deng, et al. Acoustic metamaterials for noise reduction: a review, Advanced Materials Technologies. 7 (2022) 2100698.

[2] S. Dai, Y. Zheng, J. Mao, et al. Vibro-acoustic control of a programmable meta-shell with digital piezoelectric shunting, International Journal of Mechanical Sciences. 255 (2023) 108475.

[3] C. Rubino, S. Liuzzi, G. Fusaro, et al. Balancing ventilation and sound insulation in windows by means of metamaterials: A review of the state of the art, Building and Environment. 275 (2025) 112780.

[4] Q. Wu, X. Zhang, P. Shivashankar, et al. Independent Flexural Wave Frequency Conversion by a Linear Active Metalayer, Physical Review Letters. 128 (2022) 244301.

An ultrasonic metamaterial based on Lieb lattice structures

A. Rehman[1*], D.A. Hutchins[1], P.J. Thomas[1], R. Römer[2], K.E. Sopińska[2], J. Im[1], P. Sheffield[1], S. Laureti[3]

[1]School of Engineering, University of Warwick, Coventry CV4 7AL, UK
[2]Department of Physics, University of Warwick, Coventry CV4 7AL, UK
[3]DIMES Dept., University of Calabria, 87036 Rende (CS), Italy.
[*]corresponding author: Anusha.Rehman@warwick.ac.uk

Abstract: This work proposes a polymer based acoustic metamaterial based on Lieb lattices, supporting energy localization at specific ultrasonic frequencies. The structure's tuneable bandgap and topologically-protected flat bands is demonstrated through simulations and experimental verification, leading to possible future applications in ultrasonic medical imaging, sensing, and acoustic manipulation.

The interaction of waves with periodic structures is a fundamental topic in physics [1]. In the context of acoustics, the periodic arrangement of materials gives rise to band structures that define the frequencies at which wave propagation is allowed or forbidden [2]. This phenomenon, known as band gaps, has been extensively studied in various wave systems, from photonic crystals to phononic crystals [3], where the periodicity of the material leads to the formation of band gaps that block wave propagation in specific frequency ranges. The discovery of such effects, initially explored for electronic waves in crystalline solids, has since been extended to mechanical and acoustic waves, providing significant insight into wave manipulation across a variety of systems [1].

In recent years, there has been an increase of interest in the development of acoustic metamaterials and phononic crystals, where the interplay between wave dynamics and the periodic structure can be exploited to control sound in novel ways [4]. In particular, the Lieb lattice has emerged as a key system due to its ability to support flat bands - frequency ranges where waves become non-dispersive. These flat bands are of great interest as they enable the localization of energy within specific regions of the material, often at particular lattice sites, due to interference effects. This phenomenon is especially significant in systems where energy localization can be selectively induced, such as in topologically protected states within the lattice structure.

In this work, we propose an acoustic metamaterial based on a Lieb lattice design, where the periodic arrangement of resonant cavities is tailored to support energy localization at specific frequencies. This structure consists of interconnected polymer cylinders with a diameter d = 1.079 mm. The length of the interconnections is set to be L = 1.079mm. The structure is designed for the wavelength λ = 6.075 mm such that the spacing between the diagonal sites is $\lambda/2$. These sites will act as defect sites for the formation of flat bands. We demonstrated the viability of the design through both numerical simulations and experimental verification. The initial numerical simulations were developed in COMSOL, followed by fabrication of the structure using a Digital Light Processing (DLP) 3D printer. We demonstrate that these localized modes occur at Lieb sites, where energy becomes confined within the structure. The geometrical

design of the unit cell plays a crucial role in tuning the bandgap and ensuring the desired frequency range for localization. Furthermore, the simulation results reveal that the energy localization is robust to perturbations in the lattice structure, suggesting the presence of topologically protected states.

Interestingly, the proposed design also allows for the adjustment of the bandgap through simple geometric modifications, which enables the system to be finely tuned for different frequencies of interest. This tunability presents an exciting opportunity for medical imaging, cloaking, lensing and further manipulation of localized signals [5].

In conclusion, this work introduces a new class of acoustic metamaterials based on the Lieb lattice, with potential applications in medical imaging, sensing, and other acoustic manipulation technologies. The combination of topologically protected flat bands, energy localization, and geometric tunability offers a promising avenue for advancing the capabilities of ultrasound and acoustic-based systems in various practical domains.

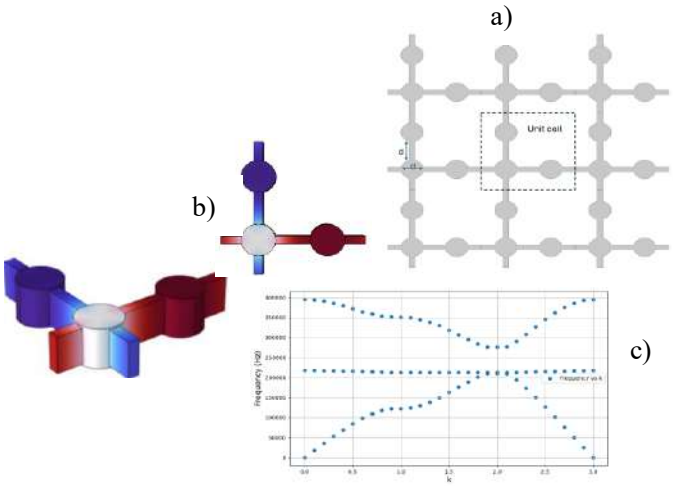


Figure 1 a) Schematic diagram of the proposed lattice structure with polymer defect sites. b) Simulated pressure field distributions of the acoustic FB. c) Band structure diagram of the defect lattice with a flatband at 218 kHz,

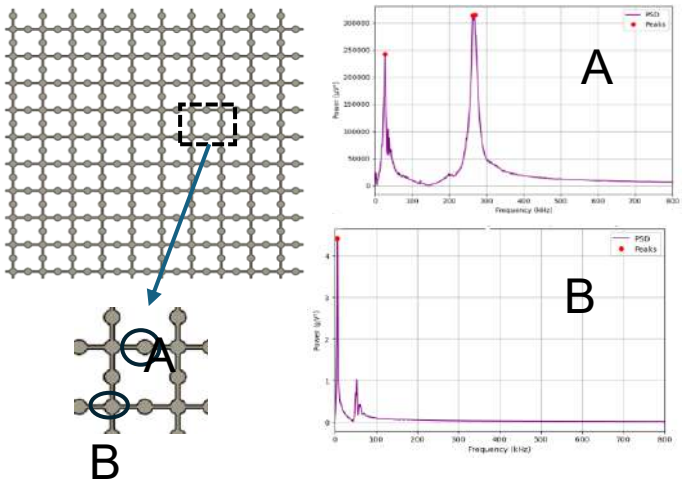


Figure 2 Experimental demonstration of Lieb and cubic sites. Graph A corresponds to the measurement at the Lieb site (A) where a strong signal at 260 kHz demonstrates localization of energy. Graph B corresponds to a location at the cubic site, where the much smaller detected signal corresponds to destructive interference effects.

References

[1] N. W. Ashcroft and N. D. Mermin, Solid State Physics (Saunders College, Philadelphia, 1976).

[2] Laude, V. (2020). Phononic Crystals. In *Phononic Crystals: Artificial Crystals for Sonic, Acoustic, and Elastic Waves, 2nd edition*. De Gruyter. https://doi.org/10.1515/9783110641189

[3] C. Danieli, A. Andreanov, D. Leykam and S. Flach, Flat band fine-tuning and its photonic applications, Nanophotonics 13, 21, 3925-3944 (2024)

[4] Tian-Xue Ma, Quan-Shui Fan, Chuanzeng Zhang, Yue-Sheng Wang; Acoustic flatbands in phononic crystal defect lattices. *J. Appl. Phys.* 14 April 2021; 129 (14): 145104.

[5] Ma, F., Huang, Z., Liu, C., & Wu, J. H. (2022). Acoustic focusing and imaging via phononic crystal and acoustic metamaterials. *Journal of Applied Physics*, *131*(1).

Plasmonics and Nano-Optics

Highly-efficient meta-surface for vectorial holography generation

Tong Liu[1†], Changhong Dai[2†], Dongyi Wang[3*], C. T. Chan[1], Lei Zhou[2,4]

1. Department of Physics and Institute for Advanced Study, The Hong Kong University of Science and Technology, Clear Water Bay, Kowloon, Hong Kong, China
2. State Key Laboratory of Surface Physics, Key Laboratory of Micro and Nano Photonic Structures (Ministry of Education), Shanghai Key Laboratory of Metasurfaces for Light Manipulation and Department of Physics, Fudan University, Shanghai 200438, China
3. Department of Physics, The University of Hong Kong, Hong Kong 999077, China
4. Collaborative Innovation Centre of Advanced Microstructures, Nanjing 210093, China

*corresponding author: Dongyi Wang, Email: physwang@hku.hk

Abstract: In this work, an efficient meta-platform is proposed and experimentally demonstrated for high-resolution *vectorial* holography generation at the incidence of arbitrary polarization. Employing a series of highly-efficient and ultra-thin single-structure metaatoms with arbitrarily designated scattered phases and polarization-conversion capabilities, various vectorial holographic images are experimentally realized at 1064 nm.

Holography is an important technology in modern optics for information recording and reconstruction[1], yet traditional methods for holography generation face the problems of bulky sizes, complex setups and low efficiencies, and most holograms generated so far are typically scaler ones[2]. Recently, metasurfaces, highly-efficient and ultra-thin artificial materials have been widely employed for complex electro-magnetic wave manipulation, and introduced to holography generation. However, employing composite metaatoms, the meta -holograms realized so far are still scaler ones, with the few attempts on vectorial ones of low efficiencies[3].

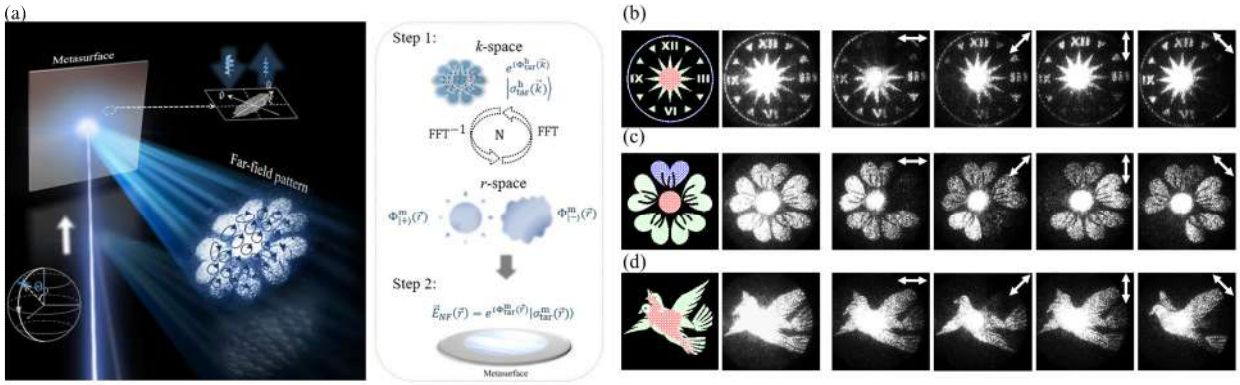


Fig. 1 The vectorial holography based on metasurface. (a) The schematics and design procedure of the vectorial meta-holograms. Experimental demonstrations of different vectorial holographic images and polarization filtered patterns for (b) a vectorial clock; (c) a vectorial flower; (d) a vectorial bird.

Here, by employing deep-subwavelength single-structure metaatoms, we propose and experimentally realize a general method for vectorial holography generation. As shown in Fig.1 (a), the method can be summarized as a two-step procedure: 1) firstly, decompose the target far-field vectorial holography into left-circular-polarized

(LCP) and right-circular-polarized (RCP) components, i.e. $A^{h}_{tar}(\vec{k})|\sigma^{h}_{tar}(\vec{k})\rangle = A^{h}_{tar,+}(\vec{k})|+\rangle_{\vec{k}} + A^{h}_{tar,-}(\vec{k})|-\rangle_{\vec{k}}$, here:

$$\begin{cases} A^{h}_{tar,+}(\vec{k}) = A^{h}_{tar}(\vec{k}) e^{-\frac{i\Psi^{h}_{tar}(\vec{k})}{2}} \cos\left(\frac{\Theta^{h}_{tar}(\vec{k})}{2}\right) \\ A^{h}_{tar,-}(\vec{k}) - A^{h}_{tar}(\vec{k}) e^{+\frac{i\Psi^{h}_{tar}(\vec{k})}{2}} \sin\left(\frac{\Theta^{h}_{tar}(\vec{k})}{2}\right) \end{cases} \quad (1)$$

then employ GS algorithm to retrieve the two nearfield planar sources (LCP and RCP sources) for generation of these two components; 2) secondly, construct the vectorial near-field planar source through the LCP and RCP components:

$$\vec{E}_{NF}(\vec{r}) = \frac{1}{\sqrt{I_+ + I_-}}\left[\sqrt{I_+}\, e^{i\Phi^{m}_{+}(\vec{r})}|+\rangle + \sqrt{I_-}\, e^{i\Phi^{m}_{-}(\vec{r})}|-\rangle\right] = e^{i\Phi^{m}_{tar}(\vec{r})}\begin{pmatrix} e^{-\frac{i\Psi^{m}_{tar}(\vec{r})}{2}}\cos\left(\frac{\Theta^{m}_{tar}(\vec{r})}{2}\right) \\ e^{+\frac{i\Psi^{m}_{tar}(\vec{r})}{2}}\sin\left(\frac{\Theta^{m}_{tar}(\vec{r})}{2}\right) \end{pmatrix}, \text{ where } \begin{cases} \Phi^{m}_{tar}(\vec{r}) = \frac{\Phi^{m}_{+}(\vec{r}) + \Phi^{m}_{-}(\vec{r})}{2} \\ \Theta^{m}_{tar}(\vec{r}) = 2\arctan\left(\frac{\sqrt{I_-}}{\sqrt{I_+}}\right) \\ \Psi^{m}_{tar}(\vec{r}) = \Phi^{m}_{-}(\vec{r}) - \Phi^{m}_{+}(\vec{r}) \end{cases} \quad (2)$$

Thus the Jones matrix for the target metasurface can be attained, and the geometric parameters of metaatoms for different vectorial meta-hologram design can be correspondingly retrieved from the FDTD simulated database.

Following this strategy, we design and experimentally demonstrate different meta-holograms. As shown in Fig. 1, at LCP incidence, the image directly collected by CCD [second panels of Fig.1 (b,c,d)] consist well with the target patterns [first panels of Fig.1 (b,c,d)]. Further placing a rotatable polarizer in front of the CCD as an analyzer, the filtered patterns illustrate the vectorial properties of the generated holography. Interestingly, the polarization filtered patterns of different images tell different stories. As shown in the third to sixth panel of Fig.1 (b), when the polarizer is tilted at 0° , 45° , 90° , 135° respectively, different parts of the vectorial holographic clock are "illuminated" in turn, as if the time passes. The third to sixth panel of Fig.1 (c) illustrate a vectorial holographic flower, the petals of which are "picked off" in turn as the analyser rotates to 0° , 45° , 90° , 135° respectively. As for the vectorial bird demonstrated in the third to sixth panel of Fig.1 (d), the bird is "flying" when the polarizer is rotated to different angles continuously.

To conclude, in this work, we establish a generic method to design meta-holograms employing ultra-thin single-structure metaatoms, which can generate designated vectorial holographic images under illuminations of light with an arbitrary polarization. Following this strategy, we experimentally illustrate different vectorial holographic images including vectorial clock, flower and bird, which exhibit interesting animations when the analyzer is continuously rotated to different angles.

Acknowledgements: This work was funded by National Key Research and Development Program of China (Grant No. 2022YFA1404700), National Natural Science Foundation of China (Grant Nos. 12221004, 62192771) and Natural Science Foundation of Shanghai (Grant Nos. 23dz2260100). Work done in Hong Kong is supported by Research Grants Council (RGC) of Hong Kong (AoE/P-502/20 and CRS_HKUST601/23).

References

[1] L. B. Lesem, P. M. Hirsch, and J. A. Jordan, 'The Kinoform: A New Wavefront Reconstruction Device', *IBM J. Res. Dev.*, vol. 13, no. 2, pp. 150–155, Mar. 1969.

[2] P. W. M. Tsang and T.-C. Poon, 'Review on the State-of-the-Art Technologies for Acquisition and Display of Digital Holograms', *IEEE Trans. Ind. Inform.*, vol. 12, no. 3, pp. 886–901, Jun. 2016.

[3] Q. Song *et al.*, 'Ptychography retrieval of fully polarized holograms from geometric-phase metasurfaces', *Nat. Commun.*, vol. 11, no. 1, p. 2651, May 2020.

Designing Temperature Invariant All-Dielectric Photothermal Metasurfaces

Gopal Narmada Naidu*, Can O Karaman, and Giulia Tagliabue

EPFL, Switzerland
*corresponding author: gopal.naidu@epfl.ch

Abstract: The diffusion-driven nature of temperature fields complicates spatial manipulation, making it challenging to achieve uniform or complex temperature distributions at the micro- and nanoscale. To address this, we developed an algorithm for designing temperature-invariant-all-dielectric photothermal metasurfaces, enabling precise, scalable thermal control and reconfigurable optical properties.

Shaping precise temperature fields at the micro- and nanoscales is a key challenge in nanotechnology, with applications in photonics, nanochemistry, biology, and microfluidics [1-4]. The diffusion-driven nature of temperature fields complicates spatial manipulation, posing challenges for applications requiring uniform or complex temperature distributions [5]. Thermonanophotonics, the study of photothermal effects in optical nanoantennas, has garnered significant attention in addressing this challenge. Moving beyond thermoplasmonic designs, all-dielectric nanophotonics has rapidly advanced in recent years, driven by resonant high-refractive-index dielectric and semiconductor nanostructures. These materials avoid the parasitic Ohmic losses inherent in plasmonics while offering strong optical nonlinearity and thermo-optical properties [6]. However, understanding and manipulating light-driven thermo-optical effects in large arrays of dielectric nanoantennas presents substantial challenges. Recent research, analyzed thermo-optical effects beyond a single nanoresonator, revealing that collective heating contributions in nanoresonator arrays strongly influence local absorption cross-sections and self-heating behavior. By optimizing nanoresonator size, array periodicity, and illumination wavelength, researchers demonstrated the ability to generate nontrivial spatial temperature profiles, including flat temperature distributions in 2D arrays of dissimilar silicon nanoresonators [7]. However, these studies primarily focused on silicon nanospheres embedded in uniform media, leaving substrate effects and non-spherical nanostructures as areas for further exploration.

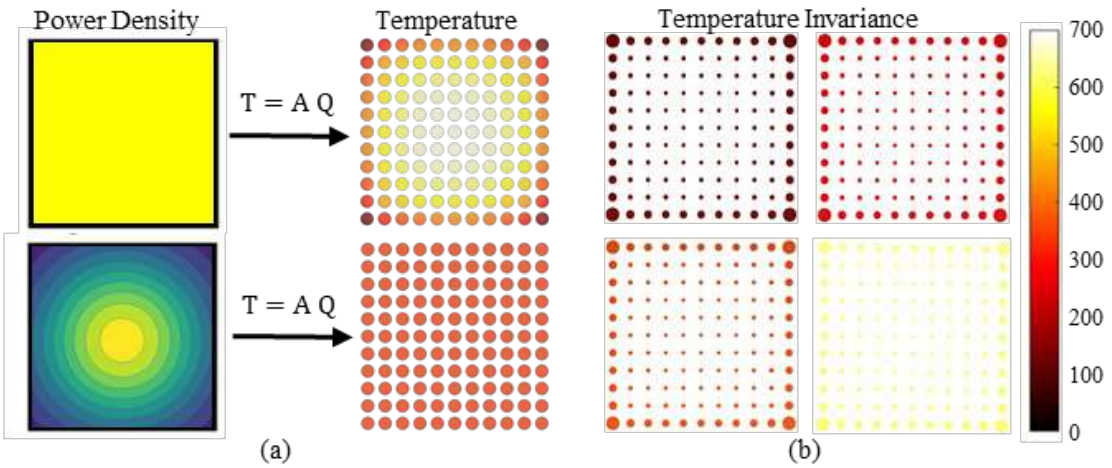


Fig.1(a) Power density distribution and the correspond temperature distribution over a 4μm x 4μm metasurface. (b) Temperature distributions over the designed metasurface under varying laser powers ($0.5 - 6$ mW/μm^2)

In this work, we developed an inversion algorithm to compute the thermal power density distribution for target temperature profiles on all-dielectric metasurfaces (Fig.1 (a)). Using a unit cell approach, we generated a library of optical absorption spectra for silicon nanodisks of varying radii and temperatures, accounting for the temperature-dependent refractive index of silicon [8]. The temperature field, modeled as a combination of self-heating and collective heating terms in a matrix formulation, was solved to determine the required thermal power distribution, which was then mapped to absorption cross-sections for a particle size distribution map. The study also addresses challenges posed by thermo-optical effects that impact the temperature-invariant performance of metasurfaces [9]. To mitigate this, we propose a design strategy for temperature-invariant all silicon metasurfaces, maintaining performance up to 600°C (Fig.1 (b)). Simulations validate our approach, demonstrating uniform and complex temperature distributions and reconfigurable optical properties, such as temperature-modulated transmission. This work combines thermal precision, scalability, and temperature stability, opening new avenues for nanotechnology and photonics.

References

1. Archetti, A., Lin, R.-J., Restori, N., Kiani, F., Tsoulos, T.V., Tagliabue, G., 2022. Thermally reconfigurable metalens. *Nanophotonics* 11, 3969–3980.
2. Cao, L., Barsic, D. N., Guichard, A. R., & Brongersma, M. L. 2007. Plasmon-Assisted Local Temperature Control to Pattern Individual Semiconductor Nanowires and Carbon Nanotubes. *Nano letters* 7(11), 3523–3527.
3. Molinaro, C., Bénéfice, M., Gorlas, A., Da Cunha, V., Robert, H.M.L., Catchpole, R., Gallais, L., Forterre, P., Baffou, G., 2022. Life at high temperature observed in vitro upon laser heating of gold nanoparticles. *Nature Communications* 13.
4. Ciraulo, B., Garcia-Guirado, J., De Miguel, I., Ortega Arroyo, J., Quidant, R., 2021. Long-range optofluidic control with plasmon heating. *Nature Communications* 12.
5. Baffou, G., Ureña, E.B., Berto, P., Monneret, S., Quidant, R., Rigneault, H., 2014. Deterministic temperature shaping using plasmonic nanoparticle assemblies. *Nanoscale* 6, 8984–8989.
6. Zograf, G.P., Petrov, M.I., Makarov, S.V., Kivshar, Y.S., 2021.All-dielectric thermonanophotonics. *Advances in Optics and Photonics* 13, 643.

7. Naef, A., Mohammadi, E., Tsoulos, T.V., Tagliabue, G., 2023. Light-Driven Thermo-Optical Effects in Nanoresonator Arrays. *Advanced Optical Materials* 11.
8. Karaman, O.C., Naidu, G. N., Bowman, A. R., Dayi, E. N., Tagliabue, G. Decoupling Optical and Thermal Responses: Thermo-optical Nonlinearities Unlock MHz Transmission Modulation in Dielectric Metasurfaces. arXiv:2412.00996.
9. Cohen, S.Z., Singh, D., Nandi, S., Lewi, T., 2023. Temperature invariant metasurfaces. *Nanophotonics* 12, 3217–3227.

Quantum Two-Photon Density-Matrix Holography with Metasurfaces

Qinmiao Chen[1], Guangzhou Geng[2], Hong Liang[1], Tailin An[1], Wai Chun Wong[1], Junjie Li[2*], Jensen Li[1*]

[1]Department of Physics, The Hong Kong University of Science and Technology, Clear Water Bay, Hong Kong
[2] Beijing National Laboratory for Condensed Matter Physics, Institute of Physics, Chinese Academy of Sciences, Beijing, 100191, China
[*]corresponding author: jensenli@ust.hk, jjli@iphy.ac.cn

Abstract: We demonstrate quantum density-matrix holography by leveraging the interaction between a metasurface and entangled photon pairs. The entanglement property of this quantum hologram is further examined using quantum hologram tomography. By projecting onto different polarization-Bell states, we reveal distinct, tailor-made holographic patterns at the level of the photon density matrix.

The versatile spin-orbit coupling capability of metasurfaces has already advanced classical optics and is now becoming useful in quantum optics. They can enhance nonlinear crystals for quantum sources [1], facilitate the generation of entanglement [2], and improve quantum imaging [3]. Here, we propose a novel density-matrix holography technique that combines a two-photon entangled source and a polarization-multiplexed metasurface, as illustrated in Figure 1(a), to construct a quantum hologram. In the circular polarization basis, the two-photon entangled state can be expressed as: $\psi = (|L\rangle_i|L\rangle_s - |R\rangle_i|R\rangle_s)/\sqrt{2}$, where L and R denote left-handed and right-handed circular polarization, respectively, and the subscripts i and s represent the idler and signal photons. A metasurface placed in the signal arm generates distinct complex holographic fields under different input/output polarization combinations. We now outline the methodology for realizing density-matrix holography. A polarization-multiplexed metasurface needs to be designed to operate on circular polarizations as follows:

$$\hat{M}|L\rangle = \alpha|L,"="\rangle + \beta|R,"+" + " \times "\rangle, \;\; \hat{M}|R\rangle = \alpha|R,"="\rangle + \beta|L,"+" - " \times "\rangle, \quad (1)$$

where $\hat{M}$ represents the metasurface operator, with α and β denoting its co-polarization and cross-polarization conversion coefficients, respectively. This metasurface enables three distinct holographic patterns depending on the polarization pair. The LL and RR polarization pairs produce an "="-shaped pattern, while the LR polarization pairs generate a superposition of "+" and "×" patterns. Similarly, the RL polarization pairs also yield a superposition of "+" and "×" patterns but with a π-phase difference. After interacting with the metasurface, the two-photon quantum hologram becomes

$$\Psi = (\alpha(|L\rangle_h|L\rangle_s - |R\rangle_h|R\rangle_s)|"="\rangle_s + \beta(|L\rangle_h|R\rangle_s + |R\rangle_h|L\rangle_s)|" \times "\rangle_s + \beta|L\rangle_h|R\rangle_s - |R\rangle_h|L\rangle_s)|"+"\rangle_s)/\sqrt{2} \quad (2)$$

From this equation, it is evident that different Bell states correspond to distinct holographic patterns as our target. To further explore the entanglement properties of the quantum hologram, we perform quantum hologram tomography. This allows us to reconstruct the pixel-resolved density matrix, capturing its two-dimensional distribution, and project it onto specific Bell states using density matrix to reveal the corresponding holographic patterns.

On the other hand, the unit cell of our design consists of a SiO_2 substrate with an amorphous silicon nanopillar. The tunable parameters include the nanopillar width (W), length (L), and azimuthal angle (θ). When the nanopillars are rotated by an azimuthal angle θ and expressed in the circular polarization basis, the Jones matrix J_{CP} can be formulated as:

$$J_{CP} = \begin{pmatrix} t_{LL} & t_{LR} \\ t_{RL} & t_{RR} \end{pmatrix} = \begin{pmatrix} |t|e^{i\varphi} & |t'|e^{i(\varphi'-2\theta)} \\ |t'|e^{i(\varphi'+2\theta)} & |t|e^{i\varphi} \end{pmatrix}, \quad (3)$$

where t_{xy} represents the transmission coefficient for y-polarization input, x-polarization output. The diagonal terms are governed by the propagation phase $\varphi = \arg(t_{LL}) = \arg(t_{RR})$, while the off-diagonal terms include an additional propagation phase $\varphi' = \arg(\sqrt{t_{LR}}\sqrt{t_{RL}})$. From equation (3), it can be seen that the rectangular nanopillar is capable of generating three distinct holograms through the combination of geometric and propagation phases.

Next, quantum hologram tomography was performed using {H, V, D, L} as the basis. As shown in Figure 1(b), different columns correspond to distinct polarization states of signal photons, while different rows represent various polarization states of idler photons. By analyzing these sixteen raw holograms, we successfully reconstructed the two-dimensional distribution of density matrices in the Bell-state basis, pixel by pixel. The diagonal elements, which represent the projection weights onto different Bell states, are specifically visualized in Figure 1(c). Finally, three distinct holograms were obtained through projections onto different Bell states (diagonal of density matrix), obtaining "+","=" and "×" as in equation (2). Density-matrix holography holds great potential for advancing quantum communication and high-dimensional information encryption while also offering valuable insights into metasurface-driven quantum optics.

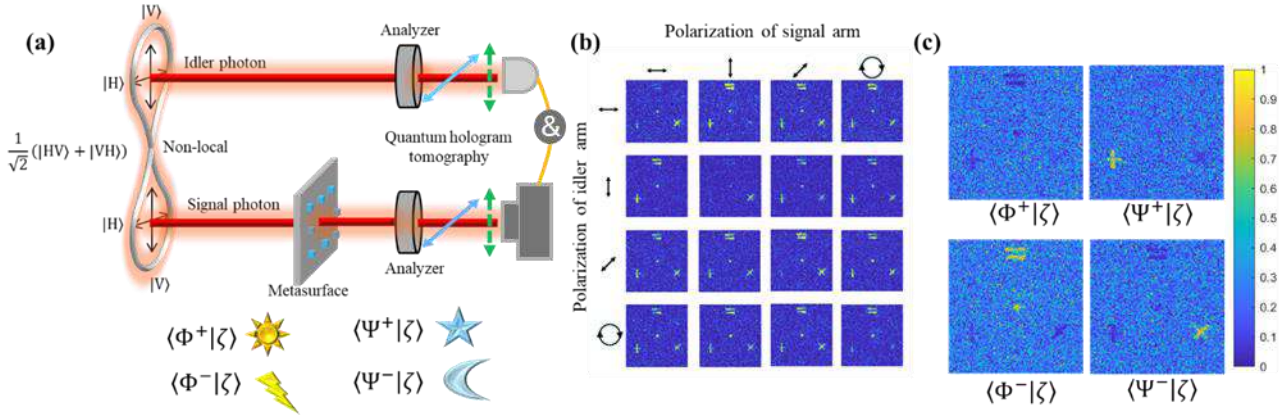


Figure1. (a) Schematic of density matrix holography. (b) Experimental results of quantum hologram tomography. (c) Projection to different Bell states (diagonal of density matrix) yields different holograms.

Acknowledgements: The work is supported by the Hong Kong RGC (Grant Nos. 16304524, 16306521, R6015-18, STG3/E-704/23N, and AoE/P-502/20) and by the Croucher Foundation (Grant No. CF23SC01).

References

1. L. Li et al., "Metalens-array–based high-dimensional and multiphoton quantum source", Science, 368,1487-1490, 2020.
2. T. Stav et al., "Quantum entanglement of the spin and orbital angular momentum of photons using metamaterials", Science, 361, 1101-1104, 2018.
3. J. Zhou et al., "Metasurface enabled quantum edge detection". Sci. Adv., 6, eabc4385, 2020.

A Dual Bound States in the Continuum Mid-IR Metasurface

G. Piscopo*[1,2], A. S. Vorobev[1,3], J. H. Mendoza-Castro[4], G. Magno[2] and L. O'Faolain[1,3]

[1]Centre for Advanced Photonics & Process Analysis, Munster Technological University, Cork, Ireland
[2]Department of Electrical and Information Engineering, Politecnico di Bari, Bari, Italy
[3]Tyndall National Institute, Cork, Ireland
[4]Institute of Chemical Technologies and Analytics, Technische Universität Wien, Austria
*Corresponding author: giovanni.piscopo@mycit.ie, g.piscopo1@phd.poliba.it

Abstract: We numerically demonstrate a dual Bound States in the Continuum metasurface operating in the Mid-IR region, with calculated Q-factors exceeding 10^5 and 10^6 and broad wavelength tunability. The choice of materials and structural dimensions makes our design a promising candidate for large-scale application as a highly efficient resonator.

Metasurfaces are engineered 2D nanostructures capable of manipulating light in ways that rarely occur in nature. Structurally, metasurfaces consist of a periodic or aperiodic arrangement of subwavelength elements that manipulate light at the nanoscale through the collective resonant behavior of individual meta-atoms. This characteristic has drawn the attention of researchers worldwide, leading to the exploration of metasurfaces in diverse applications including amplitude and phase control [1], focusing [2], enhanced light-matter interaction [3], sensing and spectroscopy [4], selective color reflection [5, 6], and high reflectivity mirrors [7, 8].

In recent years, a new kind of metasurface exploiting the Bound States in the Continuum (BICs) phenomenon has emerged, offering unprecedented light-mater interaction capabilities [9]. BICs were initially studied in quantum mechanics as a mathematical curiosity, however, only in recent years have they been explored in wave physics and photonics. By definition, BICs are non-radiating dark states that coexist within the radiative continuum while remaining fully decoupled from it [10].

In its "pure" form, a BIC has limited use in practice since it cannot couple with free-space light., However, by perturbating the meta-atom's symmetry, a controlled energy leakage can be achieved, enabling the excitation of super high Q-factors Fano resonances. These resonances are characterized by strong near-field enhancement and localization. In this contribution, we numerically investigate the influence of the asymmetry in a square block nanoresonator. Figure 1(a) shows the sketch of the proposed meta-atom. It consists of a square germanium (Ge) block with a single tapered side, positioned on a sapphire (Al_2O_3) layer and supported by a calcium fluoride (CaF_2) substrate. We selected Ge and CaF_2 for their wide transparency range in the Mid-IR region and we incorporate a thin Al_2O_3 layer to preserve CaF_2 from etching. The unit cell's symmetry is broken via the asymmetry parameter α, which controls the tapering angle on one side of the block.

We employed the 3D Rigorous Coupled-Wave Analysis (RCWA) method to simulate the unit-cell response. Periodic boundary conditions were applied along the *x*- and *y*-directions. A normally incident plane wave polarized along the y-axis excited the metasurface from the top. The transmitted power was measured. All materials were modelled as dispersive and lossless materials, given their minimal absorption in the Mid-IR region.

Figure 1 (b) – (c) reveal the excitation of two ultra-narrow Fano resonances, whose linewidth and spectral position depend on the degree of asymmetry. Particularly, Figure 1 (c) – (d) confirm that the Q-factor follows the expected α^{-2} power law, widely reported in literature, reaching values above 10^5 and 10^6 and asymptotically tending to infinity when the asymmetry parameter approaches to zero. Furthermore, extended simulations were performed to account for the smoothing of corner shapes observed in ongoing fabrication trials.

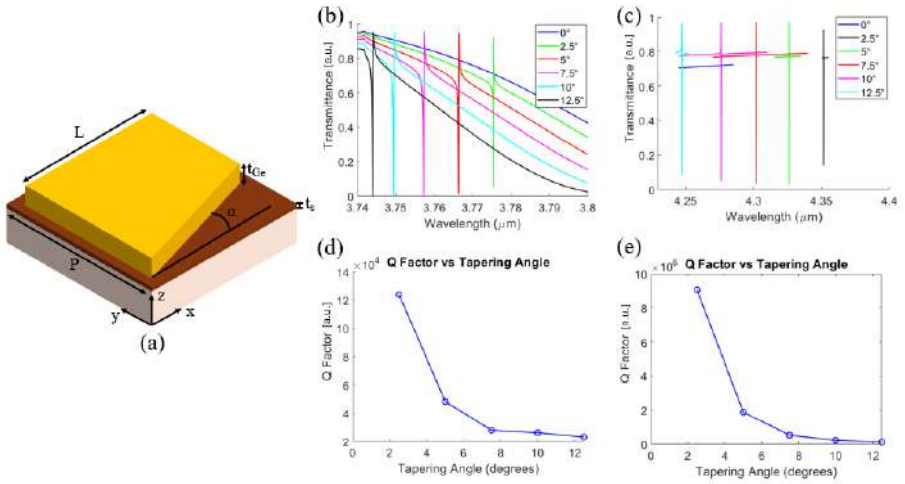


Fig. 1: (a) Sketch of the unit cell. The geometric parameters are $P = 2.65\ \mu m$, $L = 1.65\ \mu m$, $t_{Ge} = 0.2\ \mu m$ and $t_s = 0.011\ \mu m$. (b) – (c) Transmittance as a function of the asymmetry parameter α for both the excited resonances. As the asymmetry increases, the resonances exhibit blue-shift and broadening. (d) – (e) Q-factor as a function of α for both the excited resonances. As expected, Q-factor diverges as the asymmetry approaches to zero, following the α^{-2} power law.

This work presents a novel metasurface design capable of achieving dual band high-Q Fano resonances. The combination of tunable spectral response and Q-factor as well as the material selection and dimensions render our design an excellent candidate for large-scale application as a highly efficient Mid-IR Fano resonator.

Acknowledgements: This work has been developed under the MetaSPECS Project funded by the Research Ireland ID 21/FFP-A/10002.

References

1. Dagens, B.et al., "Direct Observation of Optical Field Phase Carving in the Vicinity of Plasmonic Metasurfaces," *Nano Lett.*, Vol. 16, No. 7, 4014–4018, 2016.
2. Kotlyar, V. V. et al., "Thin High Numerical Aperture Metalens," *Opt. Express*, Vol. 25, No. 7, 8158–8167, 2017.
3. Piscopo, G. et al., "Dielectric Meta-Platform for Mid-IR Enhancing Applications," *IEEE*, Vol. 1, No. 4, 1–4, 2024.
4. Mendoza-Castro, J. et al., "Unlocking Multi-Scenario Sensing Capabilities in the Mid-IR Using Polycrystalline Silicon Metasurfaces," *IEEE*, Vol. 1, No. 2, 1–2, 2024.
5. Filograno, F.et al., "Selective Color Reflection through Guided Mode Resonance Transparent Metasurfaces," *IEEE*, Vol. 1, No. 4, 1–4, 2024.
6. Magno, G.et al., "Multi-colour reflective metagrating with neutral transparency for augmented reality," Opt. Express, Vol. 32, 25545–25559, 2024.
7. Thottoli, A. et al., "Novel High Contrast Grating Hollow Core Waveguides for Enhanced Gas Spectroscopy," *EPJ Web Conf.*, Vol. 309, 109–109, 2024.
8. Magno, G. et al., "Multifunctional and reconfigurable graphene/liquid crystal-assisted asymmetrical Fabry-Pérot cavity for reflected light control," *Opt. Express*, Vol. 29, 27816–27829, 2021.
9. Liu, Z. et al., "High-Q Quasibound States in the Continuum for Nonlinear Metasurfaces," *Phys. Rev. Lett.*, Vol. 123, 253901, 2019.
10. Zhou, M. et al., "Selective Perturbation of Eigenfield Enables High-Q Quasi-Bound States in the Continuum in Dielectric Metasurfaces," *ACS Photonics*, 2024.

Dispersive Meta-lens Temperature Detector

Y. He[1], M. K. Chen[2,3], M. Huang[1], Y. Zhang[4], S. Shi[1*]

[1]School of Mechanical Engineering, Shanghai Jiao Tong University, China
[2]Department of Electrical Engineering, City University of Hong Kong, China
[3]The State Key Laboratory of Terahertz and Millimeter Waves, City University of Hong Kong, China
[4]Ministry Institute of Data and Information, Tsinghua Shenzhen International Graduate School, Tsinghua University, China.
[*]corresponding author: kirinshi@sjtu.edu.cn;

Abstract: Temperature measurement is crucial for energy transfer, particularly in extreme high-temperature environments. Traditional radiation thermometry struggle with bulky optical systems. We introduce Dispersive Meta-lens Temperature Detector (DMTD), which uses dispersive meta-lens to achieve miniaturized, high-precision temperature measurements with a reduced error (<0.32%), compared to state-of-the-art multi-spectral light-field thermometry (MSLF, <2%).

Our presentation will introduce the DMTD system, designed for high-precision temperature measurements. The performance of the DMTD system was validated through experiments on a high-temperature blackbody furnace. The experimental setup and captured dispersion image are shown in Figures 1(a), (b).

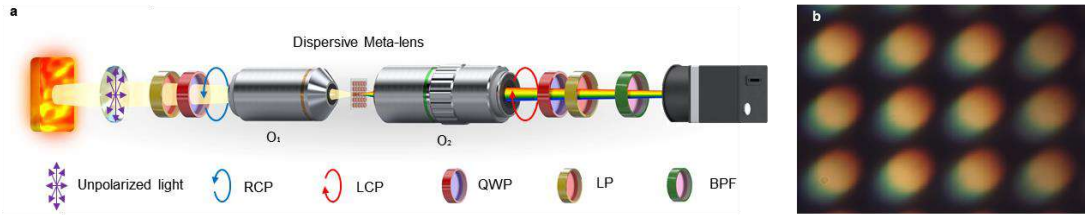


Figure 1. Experimental setup and local captured dispersion image.

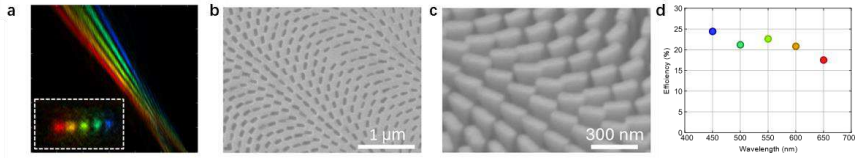


Figure 2. Meta-lens dispersion calibration results and SEM image.

The system consists primarily of a dispersive meta-lens array, an RGB image sensor, two objective lenses (10X and 20X), quarter-wave plates, and linear polarizers. The meta-lens is designed to cover the visible spectrum (450 nm to 650 nm) with a phase profile that disperses broadband light with the following phase profile:

$$\Phi(x, y, \lambda) = -\frac{2\pi}{\lambda}\left(\sqrt{(x-x')^2 + (y-y')^2 + f^2} - \sqrt{(x')^2 + (y')^2 + f^2}\right) \quad (1)$$

The focal spots (x', y') of long and short wavelength are designed at different lateral position.

The meta-lens was fabricated with TiO_2 rectangular nanopillars on a sapphire substrate, with a radius of 30 μm. Scanning electron microscope (SEM) images of the meta-lens are shown in Figures 2(b) and (c), and the efficiency and dispersed focal spots are measured and shown in Figure 2(d). For calibration, the DMT system was verified by switching filters at wavelengths (450, 500, 550, 600, and 650 nm in Figure 2(a)) to ensure precise wavelength decoding. The system was experimentally validated by capturing dispersed light-field images from a blackbody furnace, ranging from 1673K to 1873K in 10K intervals. The captured compressed images were decoded using Convex Spectral Compressive Sensing (SCS) and Reverse Dispersion Network (RDN) algorithms.

These methods allow the construction of hyperspectral images **V** from the compressed RGB information **S**. The basic reconstruction model is as follows:

$$\underset{\mathbf{V}}{\operatorname{argmin}} \| \boldsymbol{\Psi X V} - \boldsymbol{S} \|_2^2 + \alpha_1 \left\| \nabla_{xy} \boldsymbol{V} \right\|_1 + \beta_1 \| \nabla_{\lambda} \boldsymbol{V} \|_1 \tag{2}$$

Where **Ψ** and **X** are the shift and mapping operators. The reconstructed hyperspectral images for 21 wavelengths at 1873K are shown in Figure 3(a ~ d). Figure 3(e) displays well-matched spectral data for four temperature points. Comparisons of intensity profiles with the theoretical Planck's radiation law show that the SCS and RDN results correlate strongly with theoretical values, with correlation coefficients greater than 0.97 and 0.99, respectively.

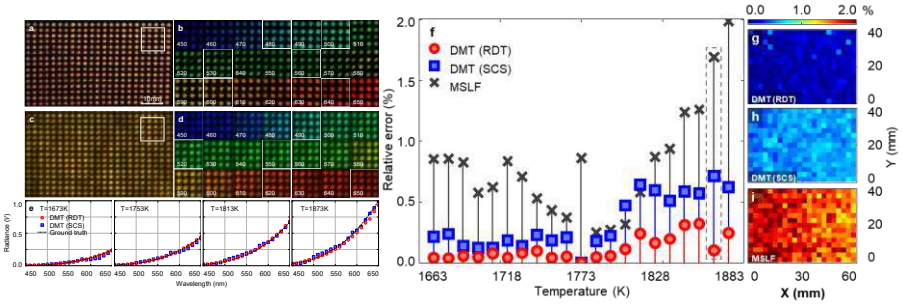


Figure 3. Reconstructed spectral intensity and temperature measured results of blackbody furnace.

Since each channel corresponds to the same temperature but different emissivity, temperature solving references the spectrum intensity of blackbody furnace at 1873K, and the optimization problem is defined as:

$$\min f(x) = \sum_{i=1}^{n} [T_i - E(T)]^2 \to 0 \tag{3}$$

Which can be solved using the Chameleon Swarm Algorithm (CSA) and compared with the state-of-the-art MSLF. As shown in Figure 3(f), the average relative error of DMT (RDN) (<0.32%) and DMT (SCS) (<0.7%) is much lower than that of state-of-the-art MSLF (<2%). What's more, the measured temperature of the blackbody shows a consistent distribution (as illustrated in Figure 3(g–i) which is recorded at 1863 K). This improvement is due to the hyperspectral radiation sampling, which leads to more accurate temperature and emissivity calculations.

In conclusion, the DMTD system offers an efficient and accurate method for measuring high-temperature radiation, with potential applications for infrared dispersive meta-lenses to achieve similar performance in low-temperature measurements.

References

1. Hua, X. et al, "Ultra-compact snapshot spectral light-field imaging." Nat. Commun. Vol. 13, No. 1, 2732, 2022.
2. Yao, C. et al, "Multi-spectral light-field imager for ultra-high temperature measurement". Opt. Express, Vol. 32, No. 18, 32094-32106, 2024.

Green Metasurface for Wearable ETA Radar Antenna Protection

M. E. de Cos Gómez[1*], Alicia Flórez Berdasco[1] and F. Las-Heras Andrés[1]

[1] TSC, Electrical Engineering Department. Universidad de Oviedo. Gijón, Spain
[*]corresponding author: medecos@uniovi.es

Abstract: An Eco-friendly metasurface solution to protect a wearable grid array antenna in 24.05-24.25 GHz band is designed. The overall device' size is 40 x 40 x 1.94 mm^3. The target application is collision avoidance to assist visually impaired individuals at short-medium distance.

The antenna is a key part of Electronic travel assistance (ETA) radar systems to assist visually impaired people. Wearable antennas must be compact, lightweight, comfortable to wear and not radiate towards the body. Moreover, they should be protected from impacts and inclement weather. To avoid degrading antenna performance, radomes should be transparent, i.e. provide high transmission and low reflection and absorption in the antenna operating band. Metasurfaces have been proposed to be used as radomes [1]. At 24 GHz the metallization designs of the unit cells must remain simple, allowing them to be fabricated using standard microwave circuit techniques. To contribute to circular economies and achieve sustainable development goals, electronic device designs must be based on green materials. Figure 1 shows the metasurface unit cell geometry and dimensions on eco-friendly polypropylene (PP) dielectric [2] and Aluminium (Al), the retrieved reflection and transmission coefficients for both TE and TM polarized incident plane waves. It is noteworthy that very high transmission and very low reflection is achieved within the target band (24.05-24.25GHz).

The angular stability of the metasurface to be used as radome is of prime importance. The designed metasurface is fully stable across the target frequency band (24.05- 24-25 GHz) under oblique incident TM polarized waves (see Figure 1 c)) for Phi=0º and almost fully stable (up-to θ=45º) for TE polarized waves.

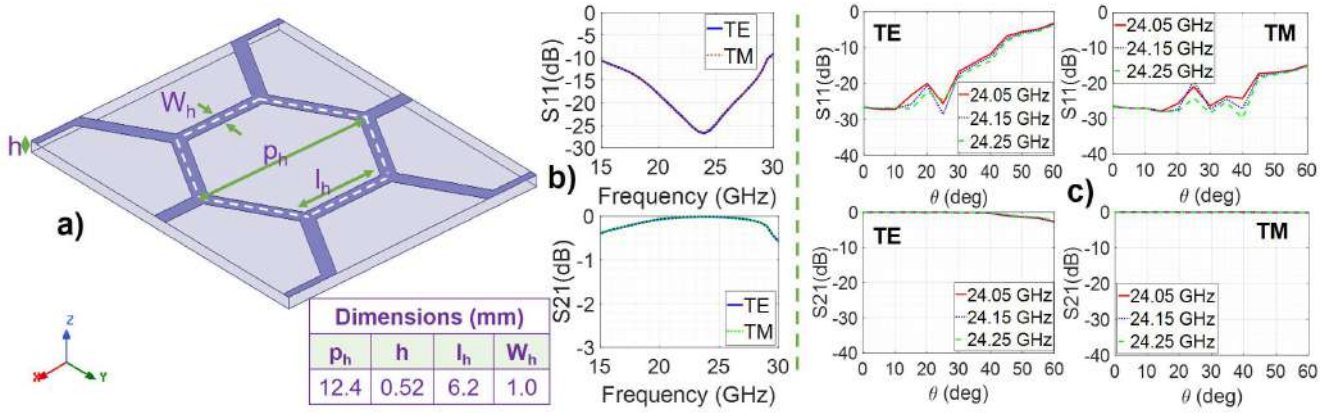
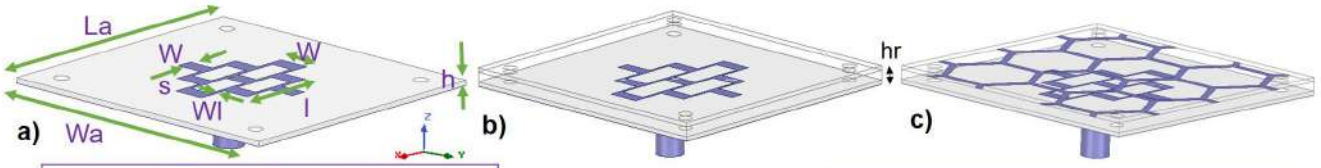


Figure 1. Metasurface: a) Unit cell; b) Reflection (S_{11}) and Transmission (S_{21}) coefficients; c) Angular stability.

Grid array antennas (GAA) [3] surpass conventional patch-type radiator arrays in terms of gain, cross-polarization control and bandwidth. A suitable GAA was designed on Al-cladded PP (Figure 2 a) and d)). According to Figure 3 e) the hexagonal metaradome (MTR-Hexagon) considerably overcomes a thin PP radome in terms of front to back ratio (FTBR) and radiation efficiency (η) at short distances from the GAA (hr= 0.7 and 0.9 mm) while provides similar peak realized gain (G). Prototypes of the GAA, the radome and MTR-hexagon

have been fabricated based on eco-friendly PP and Al using conventional milling machining (see Figure 3 a))



Dimensions (mm)						
La	Wa	h	l	Ws	W	Wl
40.8	40.8	0.52	10.6	1.9	4.7	0.4

d)

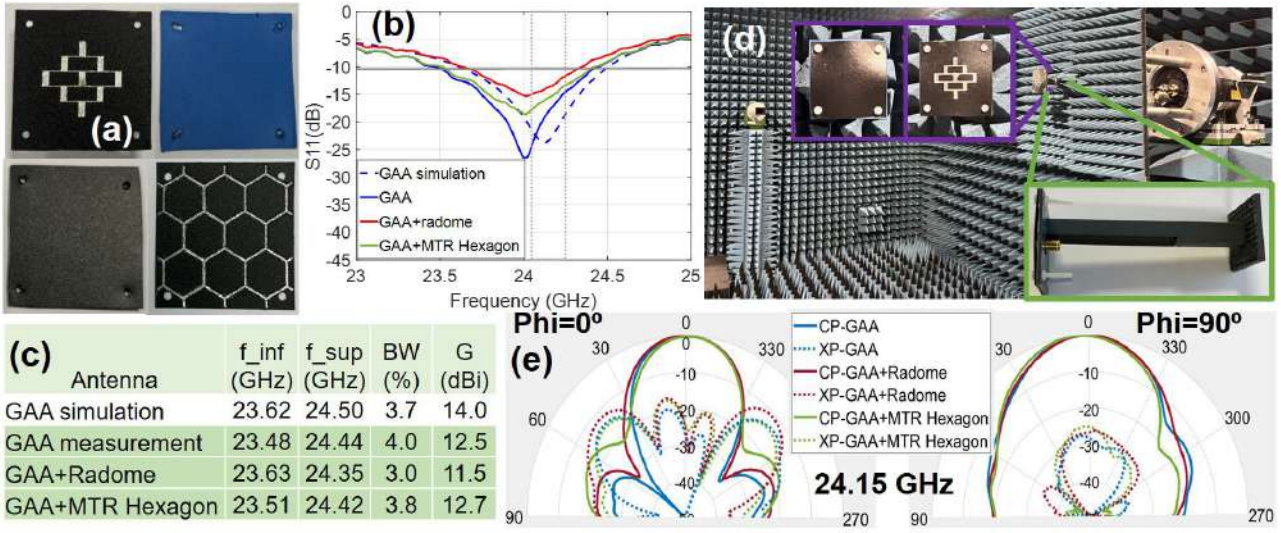
GAA						
G(dBi)	η(%)	FTBR (dB)	SLL (dB) ϕ=0°	HPBW (°) ϕ=0°	SLL (dB) ϕ=90°	HPBW (°) ϕ=90°
14	93	22.9	-30	30	-15	40

e)

	GAA +radome			GAA + MTR hexagon		
hr (mm)	G(dBi)	η(%)	FTBR (dB)	G(dBi)	η(%)	FTBR (dB)
0.3	12,0	69	23,2	12,4	81	22,0
0.5	12,8	77	24,4	12,5	74	19,0
0.7	13,2	81	23,5	13,2	84	35
0.9	13,4	83	23,8	13,2	86	35
1.2	13,7	86	23,9	12,8	86	26
1.4	13,8	88	24,5	13	86	22

Figure 2. Antenna under study: a) GAA; b) GAA+radome; c) GAA+Metaradome; Radiation properties of d) GAA and e) GAA+radome and GAA+MTR hexagon at different distances of radome and MTR from the GAA.

Measurements of the prototypes for hr=0.9mm show that the MTR-Hexagon provides wider impedance matching bandwidth (BW) and higher gain (G) than the radome (see Figure 3 b) and c)) while preserving the half-power bandwidth (HPBW) requirements (see Figure 3 e)).



(c)

Antenna	f_inf (GHz)	f_sup (GHz)	BW (%)	G (dBi)
GAA simulation	23.62	24.50	3.7	14.0
GAA measurement	23.48	24.44	4.0	12.5
GAA+Radome	23.63	24.35	3.0	11.5
GAA+MTR Hexagon	23.51	24.42	3.8	12.7

Figure 3. a) Fabricated prototypes; measurement results: b) S_{11}, c) Bw and G; d) anechoic chamber measurement set-up; e) radiation pattern cuts measurement results at 24.15 GHz.

This research was funded by Ministerio de Ciencia, e Innovación of Spanish Government and Spanish Research Agency under project META-IMAGER PID2021-122697OB-I00 and project TED2021-131975A-I00 and by the Government of Asturias-Sekuens/FEDER under grant IDE-2024-000693.

References

1. He, Y. and Eleftheriades, G. V., "A Thin Double-Mesh Metamaterial Radome for Wide-Angle and Broadband Applications at Millimeter-Wave Frequencies," in IEEE Trans. Antennas Propag, Vol. 68, No. 3, pp. 2176-2185, 2020.
2. de Cos Gómez, M.E.; et al. "PP-based 24 GHz wearable antenna". Wireless Networks, pp.1-16. 2023
3. Lin, Z., Wei, Z.X., Ping, Z.Y., "A microstrip grid array antenna for 24 GHz Doppler sensors". IEEE Asia-Pacific Conf. on Antennas and Propagation (APCAP), pp. 257- 258, 2012.

Meta-DRA Array for Mm-Wave Wearable ETA Radar Applications

Lara Prendes Suárez[1], M. E. de Cos Gómez[1*], and F. Las-Heras Andrés[1]

[1] TSC, Electrical Engineering Department. Universidad de Oviedo. Gijón, Spain
[*]corresponding author: medecos@uniovi.es

Abstract: A wearable artificial magnetic conductor backed dielectric resonator antenna array is designed for operation in 24.05-24.25 GHz band. The overall device' size is 24 x 24 x 7.37 mm^3. The target application is collision avoidance in aid to visually impaired people at short-medium distance.

Electronic travel assistance (ETA) radar systems are valuable for assisting visually impaired individuals by providing accurate and real-time environmental awareness, enhancing their mobility and safety. The antenna is a key element in radar's operation. For the target application, to alert of obstacles within a short to medium range (up to 2 meters), antenna radiation pattern beam-widths of 30-40 degrees are recommended [1]. In addition, to be wearable, the antenna must be compact, lightweight, comfortable to wear and not radiate towards the body. Dielectric resonator antennas (DRAs) offer high efficiency, wide bandwidth, and compact size, making them ideal for millimeter-wave frequency applications [2]. An artificial magnetic conductor (AMC) metasurface can be used to isolate a person's body from the wearable antenna and vice versa, so that neither the antenna's performance is degraded by the presence of the body, nor does the user receive high levels of radiation from the antenna [3], to comply with ICNIRP exposure guidelines. At such high frequencies, the metallization geometries of the unit cells cannot be very complex, so they can be manufactured using conventional microwave circuit techniques. Figure 1 shows the metasurface unit cell geometry and dimensions on RO3003 dielectric, the simulation set-up and the retrieved reflection coefficient phase and surface impedance for both TE and TM polarized incident plane waves. It is worth noting the wide AMC operating bandwidth achieved (29%), which includes the target band 24.05-24.25 GHz, and the high surface impedance at the 23.95 GHz resonant frequency.

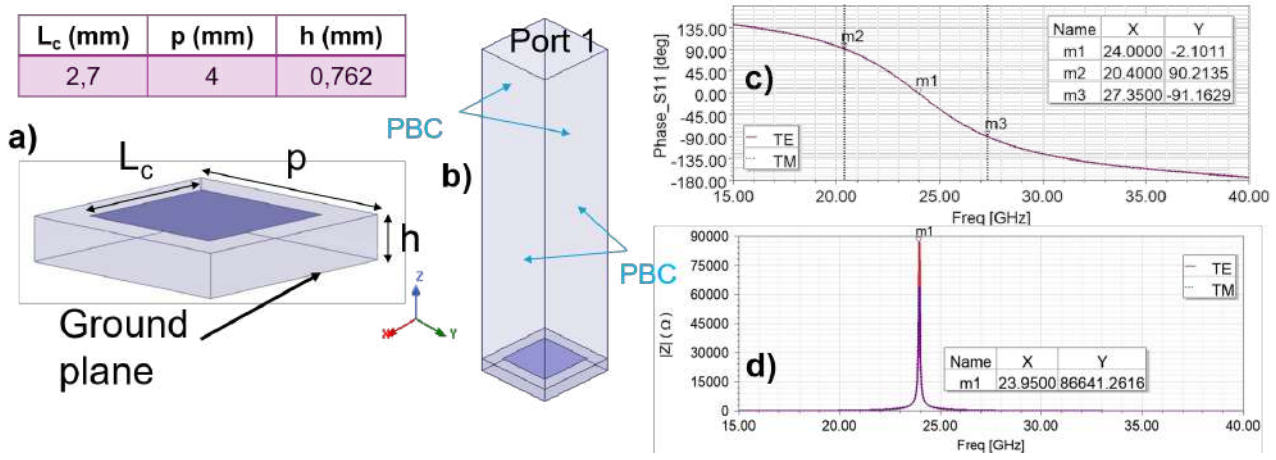


Figure 1. Metasurface: a) Unit cell; b) Simulation set-up; c) Reflection coefficient; d) Surface impedance.

The angular stability of the AMC to be combined with an antenna is of major importance. The designed AMC is fully stable under oblique incident TE and TM polarized waves (see Figure 2) throughout the target frequency band (24.05- 24-25 GHz).

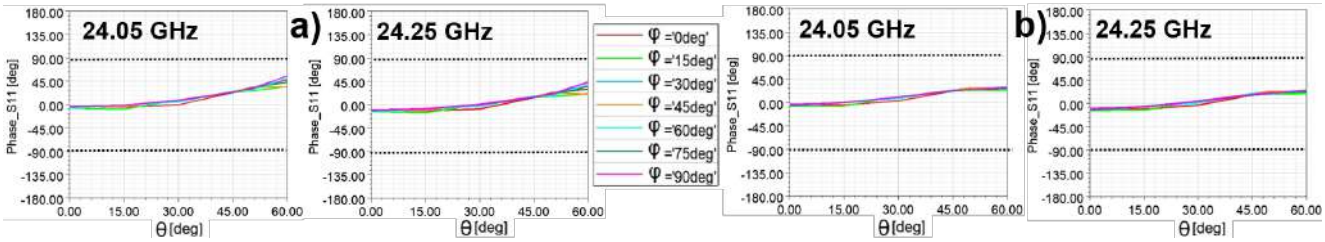
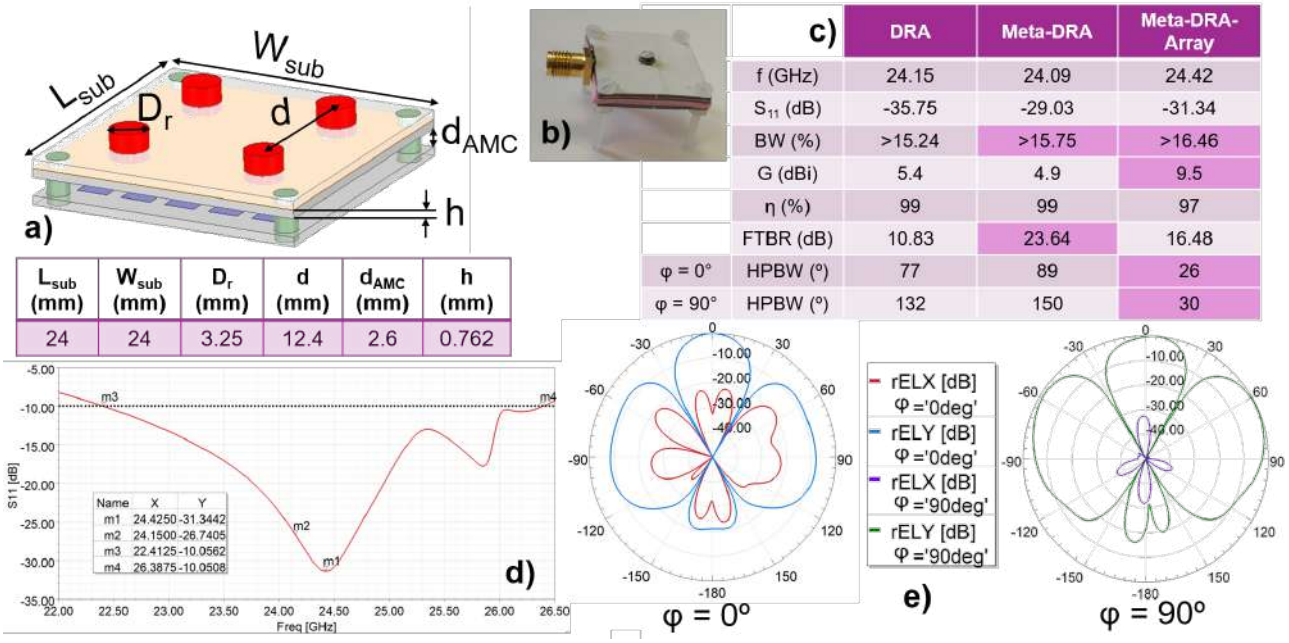


Figure 2. Metasurface angular stability under a) TE and b) TM polarized incident plane waves at the band edges.

A single element DRA provides wide bandwidth (BW) and high radiation efficiency (η) (Figure 3 c)), but exhibiting low front to back ratio (FTBR) level and not meeting the half-power bandwidth (HPBW) requirements. Adding an AMC to the DRA greatly improves the FTBR in the MTR-DRA, while preserving η, BW and gain (G), but slightly worsening the HPBW. Finally, Meta-DRA array (an AMC backed 2 x 2 element array) meets all the target application requirements, although the FTBR is reduced with respect to Meta-DRA.



L_{sub} (mm)	W_{sub} (mm)	D_r (mm)	d (mm)	d_{AMC} (mm)	h (mm)
24	24	3.25	12.4	2.6	0.762

c)	DRA	Meta-DRA	Meta-DRA-Array
f (GHz)	24.15	24.09	24.42
S_{11} (dB)	-35.75	-29.03	-31.34
BW (%)	>15.24	>15.75	>16.46
G (dBi)	5.4	4.9	9.5
η (%)	99	99	97
FTBR (dB)	10.83	23.64	16.48
φ = 0°	HPBW (°)	77	89	26
φ = 90°	HPBW (°)	132	150	30

Figure 3. Meta-DRA under study: a) Meta-DRA-Array and dimensions, b) Fabricated Meta-DRA, c) impedance matching and radiation properties, c) Meta-DRA-Array S_{11}(dB), d) Meta-DRA-Array radiation pattern cuts.

This research was funded by Ministerio de Ciencia, e Innovación of Spanish Government and Spanish Research Agency under project META-IMAGER PID2021-122697OB-I00 and project TED2021-131975A-I00 and by the Government of Asturias-Sekuens/FEDER under grant IDE-2024-000693.

References

1. Berdasco, A.F.; Laviada, J.; de Cos Gómez, M.E.; Las-Heras, F. "Performance evaluation of millimeter-wave wearable antennas for electronic travel aid". IEEE Trans. on Instrumentation and Measurement, Vol.72, 4507510. 2023
2. Liu, W.; Ma, B. and J. Pan, "24 GHz Dielectric Resonator Antenna for MMW Automotive Radar," IEEE 3rd Advanced Information Technology, Electronic and Automation Control Conf. (IAEAC), Chongqing, China, 2018, pp. 351-354.
3. Thangavelu, Y.; et al. "Design and SAR Analysis of an AMC-Integrated Wearable Cavity-Backed SIW Antenna". Micromachines 2024, 15, 1530

Aperiodic tiling-based metasurface design for angle- and polarization-tolerant structural color

Minyeul Lee[1], Suwan Jeon[2], and Jonghwa Shin[1*]

[1]Department of Materials Science and Engineering, KAIST, Daejeon, 34141 Korea
[2]Department of Nano-device & Display, Korea Institute of Machinery and Materials (KIMM), Daejeon, Korea
[*]corresponding author: qubit@kaist.ac.kr

Abstract: In this study, we present a novel metasurface design based on the 'Einstein' tile for achieving robust structural color under varying incident light conditions. Simulation results demonstrate that the aperiodic metasurface based on aperiodic unit cell exhibits improved incident angle and polarization tolerance compared to periodic metasurface.

Metasurface-based color generation offers advantages such as resistance to chemical discoloration and high resolution. However, structural colors from metasurfaces are often affected by different incident light conditions. Conventional periodic-array metasurface designs are sensitive to incident angle and polarization due to some phenomena from periodicity, such as diffraction, lattice resonance, and asymmetric resonance.

In this work, the 'Einstein' tile, which can cover a surface completely without periodicity [(1)], is introduced into the metasurface design to mitigate incident angle and polarization sensitivity. By breaking the periodicity of the metasurface through the 'Einstein' tile, this design induces enhanced incident angle and polarization tolerance.

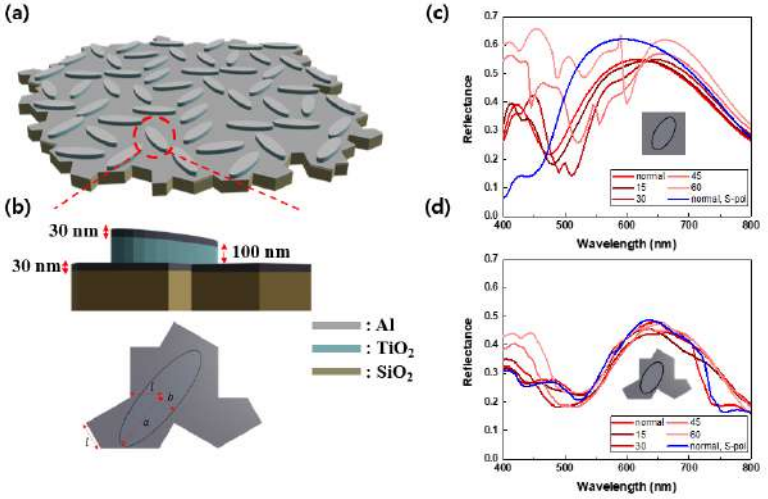
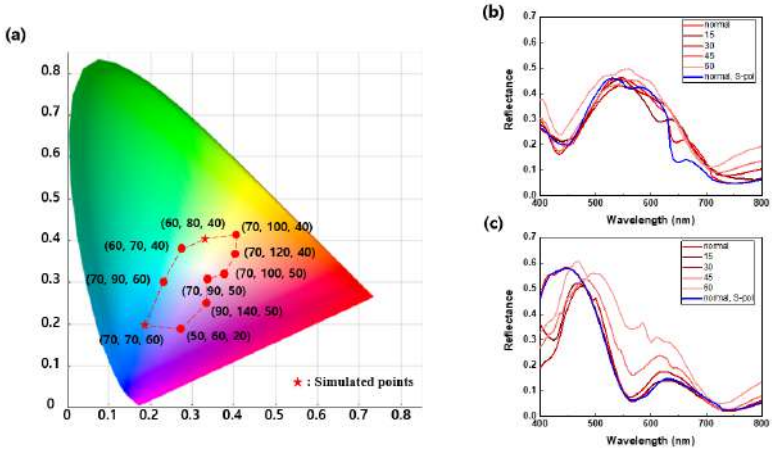


Figure 1. Schematic of the aperiodic metasurface for the structural color and the comparison between periodic and aperiodic metasurface. (a) The entire structure and (b) the aperiodic unit cell design of the aperiodic metasurface. Spectral reflectance of (c) periodic and (d) aperiodic metasurfaces with the same scatterer design.

Figure 1 depicts the schematic of the aperiodic metasurface and the comparison between a periodic and an aperiodic metasurface. As illustrated in Fig. 1(a), the scatterers are aperiodically arranged on the metasurface due

to the ‘Einstein’ tile. The aperiodic unit cell design for this aperiodic metasurface is shown in Fig. 1(b). The internal scatterer, a commonly used plasmonic resonator for the structural colors, is embedded within the ‘Einstein’ tile. This aperiodic unit cell induces aperiodicity and orientational randomness into the metasurface, like Fig. 1(a), and such properties contribute to improved tolerance under varying incident light conditions.

The simulation results of periodic and aperiodic metasurfaces with the same scatterer design are shown in Fig. 1(c-d). Conventional periodic metasurface exhibits high sensitivity under different incident angle and polarizations due to its periodic arrangement and anisotropic scatterer shape. In contrast, the proposed aperiodic metasurface effectively suppresses additional diffraction peaks near the 450 nm range, which appear in the periodic case, and achieves improved polarization tolerance. Thus, this aperiodic metasurface enhances incident angle and polarization tolerance by utilizing the aperiodic tile with conventional scatterer designs.



[Fig.2] (a) Color map of aperiodic metasurface with different structural parameters and (b-c) spectral reflectance under various incident light conditions for green and blue metasurfaces.

Figure 2 demonstrates the expandability of the aperiodic metasurface with different designs of the inside scatterer. Inset numbers are (*l, a, b*) structural parameters explained in Fig. 1(a). As shown in Fig. 2(a), the aperiodic metasurface can exhibit diverse structural colors by changing structural parameters of the aperiodic unit cell. This result shows the flexibility of the aperiodic metasurface so that we can simply design the aperiodic unit cell for diverse purposes, as we did in the periodic case.

The incident angle and polarization tolerance of two different structural parameter sets are also investigated and depicted in Fig. 2(b-c). The aperiodic metasurface for green and blue colors still exhibit tolerant spectral reflectance, similar to previous result in Fig. 1(d). This result represents that the aperiodic metasurface can be applied with various shapes or materials of scatterers for the proper performance with the additional incident angle and polarization tolerance.

References

1. Smith, David, et al. "An aperiodic monotile." *arXiv preprint arXiv:2303.10798* (2023).

Liquid Crystal-Based Asterisk-Shaped Millimeter-Wave Reflectarray for Reconfigurable Intelligent Surfaces

Junaid Ahmed Uqaili[1], Dayan Perez-Quintana[2], David Osuna Ruiz[1], and Miguel Beruete[1*]
[1]Department of Electric, Electronic and Communications Engineering, Public University of Navarra, 31006 Pamplona, Spain
[2]Department of Information Engineering and Mathematics, University of Siena, 53100 Siena, Italy
[*]corresponding author: miguel.beruete@unavarra.es

Abstract: This study introduces a low-cost, single-layer unit cell for reconfigurable reflectarray effectively targeting the frequency bands from 90 GHz to 120 GHz. The results demonstrate a reflection phase tunability of 208^{0} and low loss of 3.9 dB. The reflectarray is simulated as proof of concept for 1-D beam-steering applications.

Reconfigurable intelligent surfaces (RIS) have gained significant interest in both academia and the industry in recent years, as they offer a wide range of advantages for modern millimeter-wave (mmWave) wireless communication systems. To achieve electronic reconfigurability, the meta-atoms that make up these RIS have to be loaded with active elements such as PIN diodes, varactors, MEMs, transistors, graphene, phase-change materials, etc. Alternatively, tunable substrates such as liquid crystals (LCs) enable reconfigurability in reflectarrays (RAs), offering low power consumption, low insertion loss, continuous tunability, scalability, reliability, and cost-effectiveness. One of the pioneering liquid crystal (LC)-based reflectarrays (RA), consisting of a square patch at 35 GHz, was proposed in 2006 [1]. Following this work, several studies have explored the use of LC as a tunable substrate material capable of modifying the reflective phase of the unit cell (UC) when a quasistatic electric field is applied. Over the past two decades, after these initial pioneering efforts, LC compounds specifically designed for microwave and millimeter-wave frequencies have been developed. Some notable examples include GT3-230001 [2], GT5-26001 [3], GT7-290001 [4], C–09–2 [5], and LCM-1 [6], whose electrical parameters have been measured and extracted accordingly.

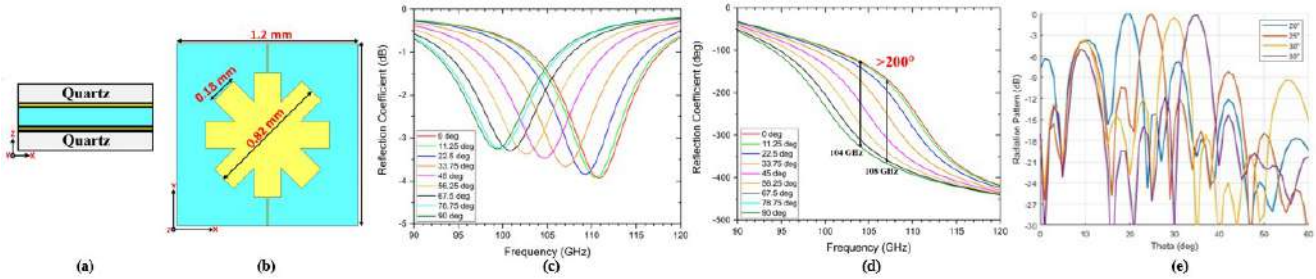


Figure 1: (a) Schematic View of the LC-based RA cell, cross-sectional view (b) Front View (c) Reflection coefficient magnitude in dB (d) Reflection phase in degrees (e) Simulated 1D radiation patterns at 105 GHz, illustrating beam steering to reflection angles of 20^{0}, 25^{0}, 30^{0}, and 35^{0}.

We analyze the performance of an LC-based RA using various LC formulations. The UC configuration consists of two parallel 400 µm quartz plates separated by a cavity filled with the LC, with a thickness of 40 µm, as shown in Figure 1 (a-b). The quartz plates act as the dielectric material, with a relative permittivity (ε_r) of 3.78 and dielectric loss tangent (tanδ) of 0.002. The UC is illuminated by a normally incident plane wave in the

transversal magnetic (TM) mode, with the electric field polarized along the x-axis. Its electromagnetic performance is analyzed and optimized using CST Microwave Studio™.

Our findings indicate a trade-off between reflection loss (RL) and maximum phase excursion (PE), as shown in Table 1. Among the tested compounds, LCM-1 and GT5 emerge as the most favorable options for applications requiring low RLs (< -2.2 dB), coupled with a maximum PE of approximately 188^0. On the other hand, GT7 and C-09-2 provide the best PE exceeding 200^0 but at the cost of a higher RL, around -4 dB. Therefore, if a RL of around -4 dB is acceptable and maximizing PE is a primary objective, GT7 and C-09-2 are the most suitable choices for such applications. Hereafter, the GT7-29001 is finally adopted in this work to achieve improved phase ranges and low RLs.

Table-1: Summary of performance evaluations for various LC compounds in RA based on an asterisk-shaped UC

	GT3-23001	**GT5-26001**	**GT7-29001**	**C–09–2**	**LCM-1**
Resonance Shifted from to (GHz)	110.9 to 102.3	110.8 to 100.5	110.8 to 99.4	99.3 to 112.4	109.2 to 100.5
Maximum loss (dB)	-4	-2.2	-3.9	-4	-1.76
Maximum Phase Excursion	175° at 106 GHz	188° at 106 GHz	208° at 105 GHz	217° at 104 GHz	168° at 106 GHz

To give an idea of the operation of the designs, Figure 1 (c-d) shows the reflection coefficient magnitude for different biasing states, particularized to the GT7-29001 LC compound. To capture all possible intermediate orientations of LC molecules, the LC tensor (α) is rotated incrementally from $\alpha = 0^0$ to 90^0. The resonant frequency shifts from 110.8 GHz to 99.4 GHz and maximum PE of 208^0 is obtained at 105 GHz. In the numerical analysis of a 1D beam steering scenario, a single row consisting of 1 × 33 UCs was considered. The design demonstrated the ability to steer the reflected beam to an angle of E_r=35^0, while the main reflection beam (specular reflection) remained at E_r=10^0, as shown in Figure 1 (e).

In summary, LC-based RA cell simulations demonstrated a wide 12 GHz bandwidth, with a maximum RL of -3.9 dB and a maximum PE of 208° at 105 GHz, showing a phase variation over 200° between 104 and 108 GHz. These findings highlight the potential of LC technology to enable reconfigurable devices for both mmWave and sub-mmWave applications, offering an effective solution for the demands of emerging technologies.

This project has received funding from the European Union's Horizon 2020 research and innovation programme under the Marie Sklodowska-Curie grant agreement No 101034285.

References

1. R. Marin, A. Moessinger, J. Freese and R. Jakoby. “Characterisation of 35 GHz Tunable Reflectarray Unit Cells Using Highly Anisotropic Liquid Crystal,” German Microwave Conference GeMiC, 2006.
2. R. Dickie et al. “Electrical characterisation of liquid crystals at millimeter wavelengths using frequency selective surfaces,” Electron. Lett., Vol. 48, No. 11, 611–612, 2012.
3. Jost, M., Reese, R., Nickel, M., Maune, H., & Jakoby, R. “Fully dielectric interference-based SPDT with liquid crystal phase shifters,” IET Microw. Antennas Propag., Vol. 12, No. 6, 850-857, 2017.
4. Guirado, R., Perez-Palomino, G., De La Rosa, P., Carrasco, E., & Quintana, X. “Electronically reconfigurable reflectarray antenna based on Single-Layer liquid crystal with independent Dual-Polarization control,” IEEE Trans. Antennas Propag., Vol 72, No. 7, 5626-5636, 2024.
5. Li, X., Zheng, G., Zhang, G., Yang, J., Hu, M., Li, J., Li, Y., Lu, H., & Yin, Z. “Highly Sensitive Terahertz Dielectric Sensor for Liquid Crystal,” Symmetry, Vol 14, No. 9, 1820, 2022.
6. Pérez-Quintana, D., Aguirre, E., Olariaga, E., Kuznetsov, S. A., Lapanik, V. I., Sutormin, V. S., Zyryanov, V. Y., Marcotegui, J. A., & Beruete, M. “Reconfigurable Millimeter-Wave reflectarray based on Low-Loss liquid crystals,”

IEEE Trans. Antennas Propag., Vol 72, No. 1, 531-541, 2023.

Polarization-Independent Huygens' Metasurfaces based on Split Ring Resonator for Highly Efficient Wavefront Formation at sub-THz bands

H. Kagami*, D. Kitayama, A. Pander, H. Matsunaga, and H. Takahashi

[1]NTT Device Technology Labs., NTT Corporation, 3-1 Morinosato-Wakamiya, Atsugi, Kanagawa, 243–0198, Japan
*Corresponding author: hibiki.kagami@ntt.com

Abstract: A polarization-independent design for Huygens' metasurfaces at sub-THz bands is proposed. Metasurfaces designed using an electric LC resonator exhibited 2π phase controllability and low transmission loss. With a cell size below 0.5λ even for polarization-independent design, a 38° beam deflection angle with 2-bit wavefront formation was achieved.

In response to the continuously increasing volume of wireless traffic, frequency bands above 100 GHz have been discussed to enable high-speed and high-capacity wireless communications. However, radio waves above 100 GHz exhibit high linearity that results in the formation of blind zones due to shielding effects in obstacles, which creates a significant challenge in practical applications. To solve this problem and provide a highly efficient polarization-independent performance that can accommodate polarization multiplexing and mitigate polarization fluctuations, propagation control using metasurfaces is required [1]. Since metasurfaces are formed by unit cells with a finite size, quantization of the gradient phase profile is necessary; however, the occurrence of phase quantization errors can lead to a decrease of the diffraction efficiency. To keep the diffraction efficiency degradation low (below 1 dB), a quantization number of 4 (0, π/2, π, 3π/2) or more is required [2]. Huygens' metasurfaces, which can exhibit a full 2π phase control with a small number of metallic layers, are suitable to keep the diffraction efficiency high. For the same quantization number, metasurfaces with smaller unit cells allow for larger deflection angles and fewer sidelobes. One way to reduce the cell size is to use split ring resonators (SRRs). While a few reports on SRR-based Huygens metasurfaces can be found, the distinctive features of SRRs make them difficult to use in polarization-independent designs. In this study, we investigate SRR-based Huygens' metasurface unit cells (size <0.5λ) that exhibit polarization-independent characteristics for future applications to polarization-multiplexed communication in the sub-terahertz band.

The basic metasurface unit cell used in this study is based on an SRR and features an electric LC (ELC) resonator (marked by a red contour line in Fig. 1(a)). By stacking two layers of ELCs, an electric dipole (ED) and magnetic dipole (MD) can be excited. However, simply stacking two layers of ELCs does not match the

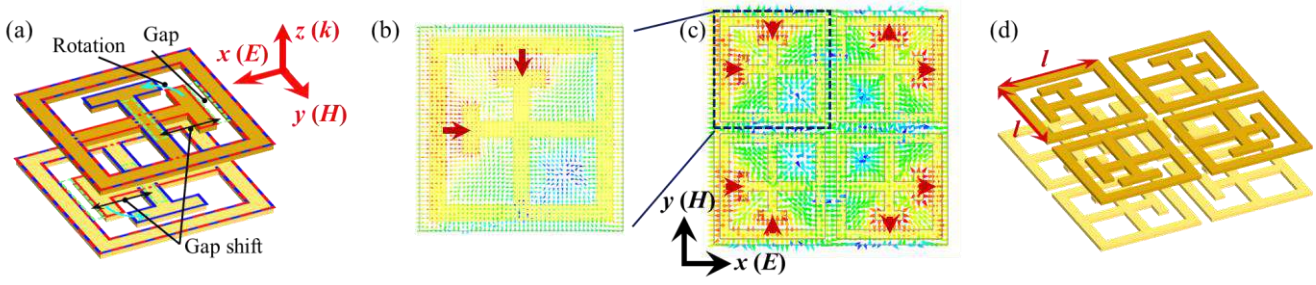


Fig. 1. (a) Geometry of ELC resonator unit cell. Red and blue regions correspond to *x*- and *y*- polarization. (b) ***E*** vector when *x*-polarization is incident on a basic unit cell synthesized to respond to both polarizations. (c) ***E***-field vector diagram for ***E***-field polarization along the *x*-axis of the unit cell, where the ***E*** fields in the *y*-direction cancel each other out. (d) Polarization- independent unit cell based on 4-fold rotational symmetry of ELC unit cell.

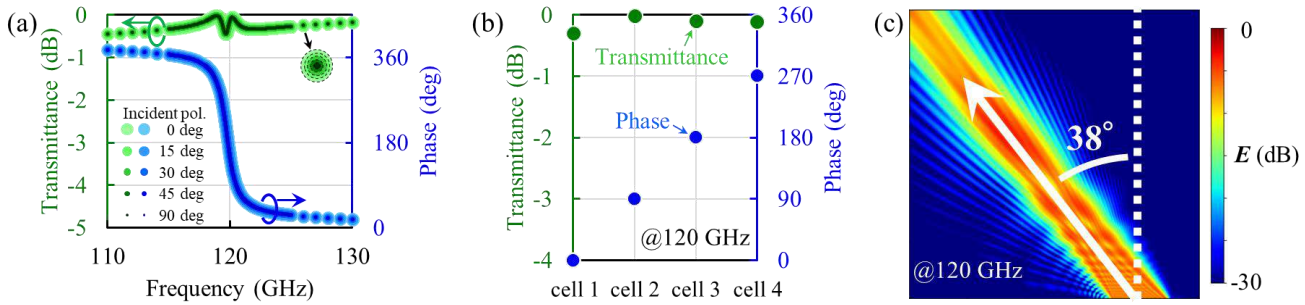


Fig. 2. (a) Transmission characteristics for the direction of the incident ***E*** field varied in 15° steps. (b) Unit cell transmission characteristics for π/2 phase variation caused by the change of parameter *l*. (c) Simulated near-field patterns of electromagnetic waves transmitted through a four-step phase-gradient metasurface.

frequencies of ED and MD. Therefore, offsetting the split part (gap) in both layers in the opposite directions (marked by arrows in Fig. 1(a)) is necessary so that the ED/MD resonance frequencies can be matched to form a Huygens' metasurface [3]. This structure correlates to a single polarization (*x*-polarization) where the electric field (***E***) vector aligns with the *x*-axis.

By 90° orthogonal rotation of basic ELC (red contour into blue contour cell in Fig. 1(a)) and a combination of both cells, an additional response can be obtained for vertically polarized (*y*-polarization) waves. However, as shown in the ***E*** field distribution (see Fig. 1(b)), when the electromagnetic wave is incident to the *x*-polarized wave, the local ***E*** field is excited in both orthogonal sections, and the polarization of the transmitted wave is rotated with respect to the incident wave. Therefore, we considered a unit cell (Fig. 1(c), (d)) structure obtained by a 4-fold rotational symmetry of the cell in Fig. 1(a). The EM simulation shows that the local ***E*** fields in the *y*-direction that are orthogonal to the incident ***E***-plane cancel each other in the entire unit cell (Fig. 1(c)). Similar EM field responses can be expected for both *x*- and *y*-polarized incident waves without polarization rotation. Simulation results of the transmission characteristics of this unit cell are shown in Fig. 2(a), where we can see that a phase shift of 2π is obtained with a transmission loss below 1 dB. The case where the incident polarization varies in 15° steps from 0° (*x*-pol.) to 90° (*y*-pol.) is also shown, demonstrating that the transmission characteristics remain the same regardless of the input polarization angle.

In this work, the change in transmission characteristics of the unit cell at 120 GHz to achieve four phase steps, as shown in Fig. 2(b), was obtained by the variation of the length *l* in Fig. 1(d). Next, we constructed a phase gradient metasurface using the discussed cell. The near-field simulation results shown in Fig. 2(c) confirm that small cells with a quantization number of 4 can produce a 38° beam deflection angle.

In conclusion, the proposed Huygens' metasurface structure can realize a low-loss polarization-independent transmissive metasurface with a quantization number of 4 or higher (phase change of 3π/2 or higher). The detailed experimental data analysis will be presented at the conference.

References

1. D. Kitayama, Y. Hama, K. Goto, K. Miyachi, T. Motegi, and O. Kagaya, "Transparent dynamic metasurface for a visually unaffected reconfigurable intelligent surface: controlling transmission/reflection and making a window into an RF lens," Opt. Exp. 29(18), 29292–29307, 2021.
2. I. Moreno, B. K. Gutierrez, M. M. Sanchez-Lopez, J. A. Davis, H. P. Khanal, and D. M. Cottrell, "Diffraction efficiency of stepped gratings using high phase-modulation spatial light modulators," Opt. Las. Eng., 126, 105910, 2020.
3. Q. Lou, C. Xue, and Z. N. Chen, "High-Efficiency Metalens Antenna Using Huygens' Metasurface With Glide Symmetric I-Shape Metal Strips," IEEE Trans. Ant. Prop., 69(11), 7394–7403, 2021.

Designing Impedances Surfaces for Simultaneous Anomalous Reflection and Polarisation Conversion

J.G. Smith[1], C.M. Hooper[1], N. Clow[2], A.P. Hibbins[1], I.R. Hooper[1], and S.A.R. Horsley[1]

[1]Department of Physics and Astronomy, Centre for Metamaterial Research and Innovation, University of Exeter, Exeter United Kingdom,

[2] DSTL, Porton Down Salisbury, Wiltshire, United Kingdom,
*corresponding author: jgs212@exeter.ac.uk

Abstract: We present a method for deriving the tensorial impedance distributions required for arbitrary anomalous reflections, with polarisation conversion. We demonstrate this by converting a normally incident Transverse Magnetic polarised plane wave into a 30° anomalously reflected plane wave that is also polarisation converted to both Transverse Electric and Circular polarisations.

Anomalous reflection metasurfaces are surfaces patterned on the order of the diffraction period [1,2], with a sub-patterning within this period that is graded to select a direction for the incident wave to be reflected into. Anomalous reflection metasurfaces have attracted attention for their applications in 5/6G communications and their ability to redirect signals in increasingly dense environments.

Previous research has shown that an optimal tensorial susceptance distribution for simultaneous anomalous reflection and polarisation conversion can be found through the matching of Floquet modes, however this method can be rather complex and has only been demonstrated with total polarization conversion [3].

In this work we present a novel alternative method of calculating the family of tensorial impedance distributions for any given field transformation, and apply it to the case of simultaneous anomalous reflection and polarisation conversion. This method can be applied to any field transformation, directly from expressions for the desired incident and reflected fields. We begin our design process by extending the equation presented in [4], finding the tensorial impedance required to satisfy the total incident and reflected fields to be

$$\boldsymbol{Z} = \frac{|\vec{E}|}{|\vec{H}|}\{e_1\left[\hat{h} \otimes \left(\hat{n} \times \hat{h}\right)^* + \left(\hat{n} \times \hat{h}\right)^* \otimes \hat{h}\right] + e_2\left(\hat{n} \times \hat{h}\right)^* \otimes \left(\hat{n} \times \hat{h}\right)^* + \alpha\hat{h} \times \widehat{h}\}. \quad (1)$$

Here $\hat{e}, \hat{h}$ are the unit vectors of the Electric and magnetic fields respectively, $\hat{n}$ is the surface normal of the impedance surface, e_1 and e_2 are the defined by $\vec{E} = e_1\hat{h} + e_2\left(\hat{n} \times \hat{h}\right)$, and $\vec{\mathrm{E}}, \vec{\mathrm{H}}$ are the electric and magnetic fields respectively. In the case of lossless problems the circle collapses to a point, retrieving a specific passive solution. However, in cases of partial polarization conversion and anomalous reflection where loss is required, we gain a range of solutions of $\boldsymbol{Z}$. In this talk we will show the test cases of anomalous reflection at $30°$ converting an incident TM polarised wave to either a TE or circularly polarized waves. We then verify the performance of this impedance distribution in 2D FEM modelling [5] before approximating the impedance distribution, for a frequency of 31 GHz, using a repeated supercell design formed of 10 dodecagonal copper patches of various sizes and rotations on a grounded dielectric [6]. The performance of the metasurfaces design can be seen in Fig 1. We chose a test case of TM to TE polarisation conversion similar to [3] as a demonstrator of "perfect" anomalous reflection, allowing for the maximum amount of power to be sent in the desired direction [7]. The reflectance magnitudes for this case are shown in Fig 1a with a peak in the m=-1 TE mode at the design frequency of 31 GHz

with corresponding nulls in the other reflected orders.The second case is chosen as a demonstration of the ease of control over the level of polarisation conversion that can be achieved with this method, where loss is now required due to the partial interference of the incident and reflected waves [7]. This case is shown in Fig 1b, where the reflected TE/TM m = -1 modes show a near equal proportion of around the design frequency of 31GHz. Fig 1c shows the phase difference between the m = -1 TE and TM modes π radians with an approximately 1GHz

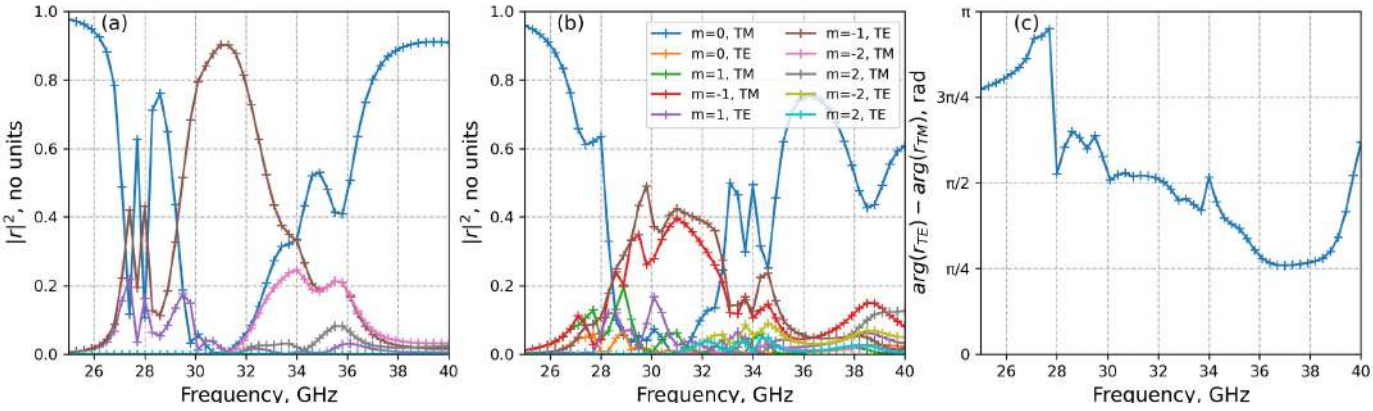


Figure 1 (a): Reflectance of the supercell design required for converting a Transverse Magnetic incident plane wave to a Transverse electric plane wave with a reflection angle of $\theta_r = 30°$ (b): Reflectance of the supercell design required for converting a Transverse Magnetic incident plane wave to a Circularly polarised plane wave with a reflection angle of $\theta_r = 30°$. (c) shows the phase difference between the TE and TM components of the -1 diffracted order modes of the surface shown in (b).

bandwidth either side of the design frequency.

We wish to acknowledge financial support from the Defence Science Technology Laboratory (DSTL). IRH acknowledges support from the EPSRC via the A-Meta International Centre to Centre Collaboration (Grant No. EP/W003341/1) and the Meta4D Programme Grant (EP/Y015673/1). SARH thanks the Royal Society and TATA for financial support (URF R211033). CMH acknowledges financial support from the Engineering and Physical Sciences Research Council (EPSRC) of the UK via the Exeter University Physics DTP. The authors would also like to acknowledge useful conversations with Kyle Arnold and James Capers.

References

1. F. Liu, D. -H. Kwon and S. Tretyakov, ”Reflectarrays and Metasurface Reflectors as Diffraction Gratings: A tutorial,” in IEEE Antennas and Propagation Magazine, vol. 65, no. 3, pp. 21-32, June 2023, doi: 10.1109/MAP.2023.3236278
2. N. Mohammadi Estakhri, A. Alu. ”Wave-front Transformation with Gradient Metasurfaces,” in Phys. Rev. X, vol. 6, pp. 041008, 2016.
3. C. Yepes, M. Faenzi, S. Maci, E. Martini; Perfect non-specular reflection with polarization control by using a locally passive metasurface sheet on a grounded dielectric slab. Appl. Phys. Lett. 7 June 2021; 118 (23): 231601. https://doi.org/10.1063/5.0048970
4. K. O. Arnold, C. Hooper, J. Smith, N. Clow, A. P. Hibbins, J. R. Sambles, S. A. R. Horsley. ”Non-Uniqueness of Metasurfaces for Wave Transformations,” 2024.
5. COMSOL Multiphysics® v. 6.2. www.comsol.com. COMSOL AB, Stockholm, Sweden.
6. Ventec VT6710, Ventec International Group
7. V. S. Asadchy, M. Albooyeh, S. N. Tcvetkova, A. Dıaz-Rubio, Y. Ra’di, and S.A. Tretyakov, “Perfect control of

reflection and refraction using spatially dispersive metasurfaces," Phys. Rev. B 94, 075142 (2016)

Topology optimization of blazed metasurfaces for high-efficiency spectrographs

S. Ans[1,2*], F. Zamkotsian[1], G. Demésy[2], Q. Tanguy[3], R. Salut[3], A. Mursa[3], and N. Passilly[3]
[1]Aix Marseille Univ, CNRS, CNES, LAM, Marseille, France
[2]Aix Marseille Univ, CNRS, Centrale Med, Institut Fresnel, Marseille, France
[3]FEMTO-ST, CNRS, UFC, Besançon, France
simon.ans@lam.fr (corresponding author)

Abstract

By benchmarking two Topology Optimization (TO) strategies, a metasurface grating is presented, developed using a 3D Finite Element model based on open-source softwares. It exhibits nearly 60% of average diffraction efficiency on the $\in 1^{\text{st}}$ diffraction order in reflection between 400 and 1500 nm.

1 Introduction

For Earth and Universe observation purpose, a new generation of compact spectro-imagers is being developed [1]. To efficiently disperse the incident light on a given diffraction order for a wider range of wavelengths than a grating with a sawtooth profile, a metasurface configuration is proposed. We have generalized our 2D conical code [2] to the 3D case using two approches. First, a natural development is the TO of the distribution of the relative permittivity ε_r into the design region based on the Finite Element mesh generated by the resolution of the Maxwell's Equations; ε_r is considered constant by part in each tetrahedron. Second, a pillar-based permittivity distribution is presented for a fabrication purpose; ε_r is considered constant by part inside manufacturable cuboids.

2 Theoretical model

The function of merit in the optimization process is the diffraction efficiency of the grating in reflection on the $\in 1^{\text{st}}$ order, for a plane wave incidence. This quantity is computed with an open-source code that solves the Maxwell's Equations in the frequency domain. Then, the Jacobian of this merit function is calculated using an adjoint method. The latter Jacobian is applied in a gradient descent to optimize the permittivity distribution that maximizes the objective. Finally, a binarization and a connectedness filter are added to obtain a readable shape. The theory, the in-house developed code and all the tools used are detailed in Ref. [2] for the conical incidence, namely for a mono-periodic grating with a 3D incident plane wave. However, the Partial Differential Equation (PDE) remains the same in 3D, namely for a bi-periodic pattern. The weak formulation is even simpler to write, nevertheless more costly to solve [3].

3 Pillar-based bi-periodic pattern

Though the mesh-based algorithm is an interesting proof of concept for the TO process – it provides very high-efficiency gratings – a pillar bi-periodic pattern is hereby presented, for it can be manufactured. As illustrated in Fig. 1a on a single period, it is made of 200 nm-high elementary pillars of Si_3N_4 (in blue) or air with 82.5 nm-long edges, deposited on a 50 nm

stopping layer of aluminum oxide (Al_2O_3, in orange). Such dimensions have already been etched with adjusted e-beam lithography [4].

Fig. 1b shows the spectral response of the proposed pattern on the [400,1500] nm wavelength range (two octaves), with an oblic incident plane wave which wavevector is not coplanar with (Oxz) nor (Oyz). It is moreover compared to the best spectral responses obtained with topology optimized, mesh-based, mono-periodic structures. Starting from a 1300 nm-high design region using the mesh-based algorithm with SiO_2, the average diffraction efficiency reaches 81% (red dashed graph). With a 300 nm-high design region and Si_3N_4, this value drops to 65% (black dotted graph). Finally, with the 200 nm-high Si_3N_4 pillars, the average efficiency is 58% (blue graph). As compared to the efficiency of the sawtooth profile of 46% (grey graph), a 26% improvement in relative terms is achieved.

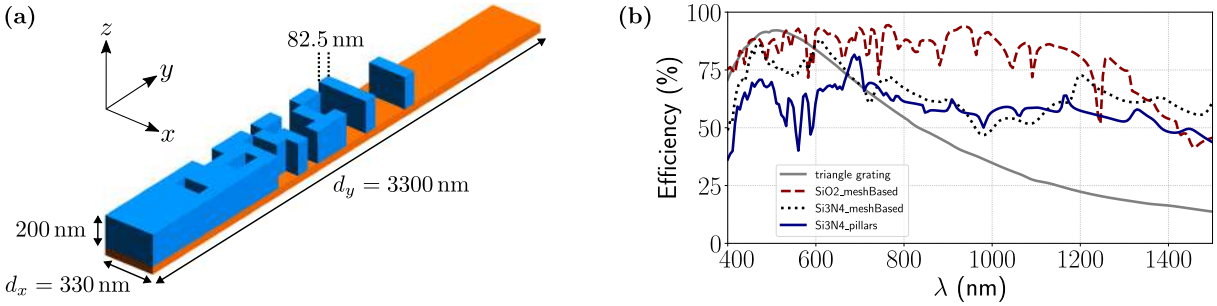


Figure 1: **(a)** Single period of the 3D structure. **(b)** Spectral responses on the $\in 1^{st}$ diffraction order for different structures.

4 Conclusion

The theoretical optimization of blazed metasurface gratings in broadband (two octaves, between 400 and 1500 nm) has led to a pillar-based design that can be manufactured. This structure exhibits a 58% of average diffraction efficiency on the $\in 1^{st}$ order, which is 26% higher than the sawtooth design in relative terms.

The next step of this project is to actually manufacture this structure using adjusted e-beam lithography and to analyse the feedback on the models, using far- and near-field characterization techniques.

Acknowledgements This work is partially funded by CNES and Thales Alenia Space with a PhD grant. It is also supported by the French RENATECH network with the FEMTO-ST technological facility MIMENTO, partially funded by the CNRS PEPS-INSIS program.

References

[1] Zamkotsian, F., Lanzoni, P., et al., "BATMAN @ TNG: instrument integration and performance," in *Proc. SPIE*, Vol. 10702, 107025P, 2018.

[2] Ans, S., Zamkotsian, F., and G. Demésy, "Topology optimization of blazed gratings under conical incidence," *J. Opt. Soc. Am. A*, Vol. 41, No. 8, pp. 1531–1543, 2024.

[3] Demésy, G., Zolla, F., Nicolet, A., et al., "Chapter 5: Finite element method," in *Gratings: Theory and Numeric Applications*, 2nd ed., E. Popov, ed., (Presses Universitaires de Provence, 2014).

[4] Ans, S., Demésy, G., Zamkotsian, F., et al., "Nanostructured blazed gratings for high performance spectrographs," in *Proc. SPIE*, Vol. 12990, 129900K-1, 2024.

Discrete multilevel metasurfaces for absorbers and antireflective layers

M. Kusko[1] and C. Kusko[1*]

[1]National Institute for R&D in Microtechnologies – IMT Bucharest , Romania

[*]corresponding author: cristian.kusko@imt.ro

Abstract: We numerically investigate dielectric nonresonant metasurfaces consisting in periodic arrays of blocks with different sizes and heights placed one on the top of the other. By adjusting the features of the blocks one can find enhanced functionalities of these metasurfaces such as absorbers or antireflecting layers.

Metasurfaces are two dimensional metamaterials, being essentially, periodic array of micro/nano antennas or resonating elements with subwavelength features, such that one can apply homogenization describing their properties in terms of effective material parameters. With applications ranging from antireflective layers and absorbers to metalenses or optical devices for wavefront control and manipulation, metasurfaces emerged as an important research direction in the field of flat optics [1].

One road to add another degree of freedom for increasing the possibility of tailoring the electromagnetic properties of the metasurfaces is to consider a multilayered metasurface by stacking arrays of elements with different geometric parameters one on the top of the other [2].

In this work, we perform a numerical analysis of multilevel dielectric metasurfaces consisting of a series of 2^N blocks with different sizes and heights placed one on the top of the other. We consider this number of levels since they can be practically realized by N standard photolithographic processes each of the followed by a etching process. The features of the blocks are much smaller than the wavelength such that the metasurface can be considered homogeneous. Also, the features of the blocks are chosen such that for the range of wavelengths of interest, the Mie resonances do not appear, the metasurfaces being non – resonant. In this quasi – static approach, we calculated the effective dielectric permittivites of each layer of blocks employing the circuit model [3,4]. By applying the transfer matrix method algorithm and the finite difference time domain method, we explore the potential of these configurations to be used as absorbers and antireflective layers.

Acknowledgements, This work was funded from the project "National Platform for Semiconductor Technologies",contract no. G 2024-85828/390008/27.11.2024, SMIS code 304244, co-funded by the European Regional Development Fund under the Program for Intelligent Growth, Digitization, and Financial Instruments and Romanian Core Program PNCDI 2022-2027 ”Advanced research in micro-nano-electronics, photonics, sensors and microsystems devices for societal applications-μNanoEl”, 2307/29.12.2022 (2023-2026), financed by the Ministry of Research, Innovation and Digitalization.

References

1. Hou-Tong Chen *et al* “A review of metasurfaces: physics and applications”, *Rep. Prog. Phys.* **79** 076401 (2016).
2. You Zhou, et al, ”Multilayer Noninteracting Dielectric Metasurfaces for Multiwavelength Metaoptics”, : Nano Lett.**18**, 7529−7537 (2018).

3. C. Kadlec et al, "Materials with on-demand refractive indices in the terahertz range", Optics Letters, 33, 2275 (2008).
4. Mihai Kusko, Cristian Kusko and Rebeca Tudor, “Simulation of antireflective structures in terahertz region”, IEEE International Semiconductor Conference Proceedings, 291, (2024).

Incoherent digital holography using multilayer metasurfaces for zeroth-order-light-free recording

T. Nobukawa*, R. Higashida, K. Imamura, Y. Maeda, and K. Hagiwara

Japan Broadcasting Corporation (NHK), Japan
*Corresponding author: nobukawa.t-eq@nhk.or.jp

Abstract: We propose and experimentally demonstrate an incoherent digital holography (IDH) system using multilayer metasurfaces. Unlike conventional IDH systems using a geometric-phase metalens, which suffer from noise caused by the zeroth-order light of the metalens, our proposed system exhibits exceptional robustness to such noise owing to its multilayer geometry.

1. Introduction

Incoherent digital holography (IDH) is a technique for recording holograms through the self-interference of a spatially incoherent light source [1]. To implement IDH, generating two beams with different defocus phases from the object light is necessary. One approach for generating two beams involves using a geometric-phase metalens [2] that generates two beams with the same intensities and opposite-sign defocus phases based on the geometric-phase. However, practical metalenses exhibit fabrication errors, leading to the generation of zeroth-order light. In IDH, zeroth-order light introduces undesired interference in the holograms, thereby degrading the quality of the reconstructed images. Optimizing the metalens fabrication process can help minimize zeroth-order light. However, even a few percent of zeroth-order light remain problematic in IDH due to the inherently low contrast of holograms.

Therefore, to address this issue, we propose a novel IDH system using multilayer metasurfaces. The proposed system effectively filters out zeroth-order light by incorporating geometric linear phases on each metasurface. Proof-of-principle experiments were conducted to prove that this system can successfully record holograms without the effect of zeroth-order light.

2. Principle of an incoherent digital holography system using multilayer metasurfaces

Figure 1 illustrates the schematic of the proposed IDH system, which comprises three geometric-phase metasurfaces. The spatially incoherent light from the object is first polarized using a polarizer. The polarized light is then divided into two parts with orthogonal circular polarizations by the first metasurface, which functions as a geometric-phase prism. If a fabrication error occurs in the first metasurface, zeroth-order light propagates along the optical axis. The second metasurface comprises three subregions. The center region filters out on-axis zeroth-order light, whereas the two outer regions function as geometric-phase prisms. The grating period of these outer regions is half that of the first metasurface. The divided beams are incident on the third metasurface that has the functions of the geometric-phase prism and geometric-phase metalens. The modulated light follows a common optical path, exhibiting different defocus phases and orthogonally circular polarization states. A polarization-sensitive image sensor captures the hologram with four-step phase shifts determined by the geometric-phase [1, 2]. From the captured image, the three-dimensional information of the object can be reconstructed using the phase-shifting method and diffraction calculations.

3. Proof-of-principle experiments

We used three metasurfaces composed of silicon nitride meta-atoms for the proof-of-principle experiment. The meta-atoms are designed to be nearly ideal half-wave plates with 120 × 240 × 700-nm^3 dimensions. The metasurfaces were fabricated using a multistep process, including plasma-enhanced chemical vapor deposition of a silicon nitride layer on fused glass, nanopatterning via electron beam lithography, and dry etching with a Cr hard mask. During dry etching, we intentionally under-etched samples to generate zeroth-order light. The diffraction efficiencies for the zeroth-order light of the fabricated metasurface were 78 % in average, which generally cannot be used in conventional IDH systems. To demonstrate the IDH functionality using the imperfect metasurfaces, we used a USAF test chart as the object and illuminated it with LED light. A bandpass filter with a center wavelength of 633 nm and a bandwidth of 10 nm was applied to enhance the temporal coherence of the light. The three metasurfaces modulated the transmitted light, and a polarization-sensitive image sensor captured its self-interference hologram. Figure 2(a) shows the captured hologram. By demosaicking the hologram and applying the phase-shifting and angular spectrum methods, we successfully reconstructed an image of a portion of the USAF test chart (Fig. 2(b)). These results show that the proposed system can successfully implement the IDH functionality without the effect of zeroth-order light of the imperfect metasurfaces.

4. Conclusions

We proposed and demonstrated IDH systems using multilayer metasurfaces. The proof-of-principle experiments show the proposed system is highly robust against zeroth-order light. In future work, we will evaluate the robustness of the system against zeroth-order light and optimize its geometry to improve image quality.

Acknowledgments

This work was partially supported by the "Advanced Research Infrastructure for Materials and Nanotechnology in Japan (ARIM)," of the Ministry of Education, Culture, Sports, Science and Technology (MEXT) (Grant No.: JPMXP1224UT1141), and a part of the fabrication process was conducted in Takeda Cleanroom, Center of The University of Tokyo for The Advanced Research Infrastructure for Materials and Data Hub.

References

1. Rosen, J., Vijayakumar, A., Kumar, M., Rai, M. R., Kelner, R. Kashter, Y., Bulbul, A. and Mukherjee, S. "Recent advances in self-interference incoherent digital holography," *Adv. Opt. Photonics,* Vol. 11, No. 1, 1–66, 2019.
2. Faraz, F., Tian, J., Abbasi, T. U. R. and Zhu, W. "Recent advances in geometric phase metasurfaces: principles and applications," *Adv. Phys. Res.*, Vol. 4, No. 2, 2400095, 2025.

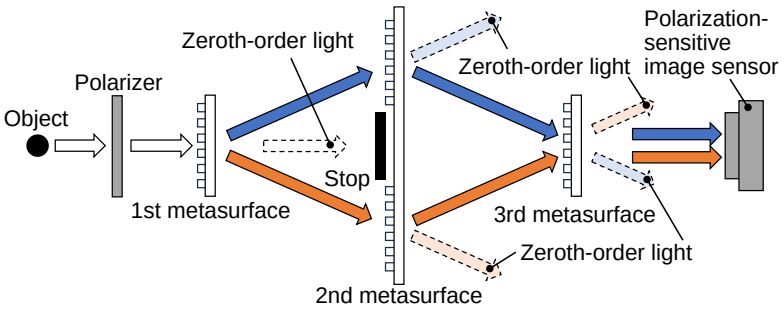


Figure 1. Schematic of the proposed IDH system.

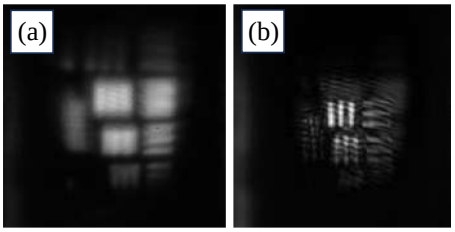


Figure 2. Proof-of-principle experimental results: (a) Hologram and (b) its reconstructed image.

Angle independent enhancing and diminishing metasurface with susceptibility-driven inverse design

S. Y. Golla*, Jian Cao, S. Salhi, Paula Nuño Ruano, Carlos Alonso-Ramos, Daniele Melati

Centre de Nanosciences et de Nanotechnologies, CNRS, Université Paris-Saclay, 91120 Palaiseau, France

sandeep-yadav.golla@universite-paris-saclay.fr

Abstract: This study presents metasurfaces for angle independent enhancement and diminution, designed and fabricated using analytical target phases derived from susceptibilities via generalized sheet transition conditions. Electric filed and far-field simulated results demonstrate precise doubling/halving of angular patterns even at extreme angles, enabling applications in beam shaping and steering.

1. Introduction

Achieving precise beam steering without losing directivity at higher angles has long been challenging in optics [2]. While metasurfaces have driven significant advancements, their performance is limited, especially at smaller pixel sizes, due to restricted numerical apertures. Angle-enhancing devices address wide-angle beam steering but face notable shortcomings. Passive metasurfaces perform optimally only within narrow design ranges, as their phase profiles approximate target phase maps rather than using rigorous analytical solutions, leading to limited efficiency and steering angles. Active metasurfaces offer tunability but face challenges like complexity, energy use, and dependence on actuation, limiting their practicality for compact applications. Current methods struggle to combine the flexibility of active metasurfaces with the simplicity of passive ones, especially for wide-angle beam steering and imaging. This paper presents an inverse design for angle-enhancing and -diminishing metasurfaces, starting with engineered susceptibility, converting it into the target phase, and using a lookup table method to design nano-pillars.

2. Susceptibilities of angle enhancing and diminishing metasurfaces

Electromagnetic wave propagation in a medium is governed by Maxwell's equations. For interfaces with metasurfaces (engineered arrays of nanoscale meta-atoms), the Generalized Sheet Transition Conditions (GSTCs) [1] describe the discontinuity:

$$n \times [\![\mathbf{E}]\!] = -i\omega\mu_0 \overline{\overline{\chi}}_{mm,0} \{\mathbf{H}_{\parallel}\}, \quad n \times [\![\mathbf{H}]\!] = i\omega\varepsilon_0 \overline{\overline{\chi}}_{ee,0} \{\mathbf{E}_{\parallel}\}. \tag{1}$$

where n is the vector normal to the surface of the interface, satisfying local orthonormal curvilinear basis (τ^1, τ^2, n) with tangential vectors τ^1 and τ^2. ω, μ_0 and ε are frequency , permittivity and permeability for free space. The $[\![\mathbf{A}]\!] = \mathbf{A}_+ - \mathbf{A}_-$ and $\{\mathbf{A}\} = (\mathbf{A}_+ + \mathbf{A}_-)/2$ are the difference, mean of the $\mathbf{A}_+, \mathbf{A}_-$ with $\mathbf{A} = \mathbf{E}, \mathbf{H}$. $\mathbf{A}_{pm}$ is the filed before and after the metasurface. On inverting the above equations and solving for the susceptibilities, we obtain

$$\chi_{ee,0}^{\tau^1\tau^1} = \frac{-1}{i\omega\varepsilon_0} \frac{[\![\mathbf{H}^0 \cdot \tau^2]\!]}{\{\mathbf{E}^0 \cdot \tau^1\}}, \chi_{ee,0}^{\tau^2\tau^2} = \frac{1}{i\omega\varepsilon_0} \frac{[\![\mathbf{H}^0 \cdot \tau^1]\!]}{\{\mathbf{E}^0 \cdot \tau^2\}}, \chi_{mm,0}^{\tau^1\tau^1} = \frac{1}{i\omega\mu_0} \frac{[\![\mathbf{E}^0 \cdot \tau^2]\!]}{\{\mathbf{H}^0 \cdot \tau^1\}}, \chi_{mm,0}^{\tau^2\tau^2} = \frac{-1}{i\omega\mu_0} \frac{[\![\mathbf{E}^0 \cdot \tau^1]\!]}{\{\mathbf{H}^0 \cdot \tau^2\}}. \tag{2}$$

By carefully selecting the injected and transmitted electromagnetic fields,$\mathbf{E}_{\pm}^0, \mathbf{H}_{\pm}^0$, the desired functionality of the metasurface can be inverse designed. For Transverse Electric (TE) $(\mathbf{E}_x, \mathbf{H}_y, \mathbf{E}_z)$ mode interacting with a metasurface designed to enhance or diminish the propagation angle, one possible configuration for the injected and transmitted electromagnetic fields is given by:

$$\mathbf{E}_{0,-}(x,y,z) = (1,0,1)\exp\left(-ik_0(x\sin(\theta_i) + y\cos(\theta_i))\right), \tag{3}$$

$$\mathbf{E}_{0,+}(x,y,z) = (1,0,1)\exp\left(-ik_0(x\sin(m\theta_t) + y\cos(m\theta_t))\right). \tag{4}$$

For angle doubling and halving, m takes the values 2 and $1/2$, respectively. The remaining field components can be derived using the corresponding Maxwell curl equations. The final expressions for the electric and magnetic susceptibilities are obtained by substituting the input/output fields from Eqs. (**??**)- (**??**) into Eqs. (2), and are as follows:

$$\chi_{\mathrm{ee}} = \frac{2\sqrt{\varepsilon_0/\mu_0}(1-t_{e/d}-r)}{\mathrm{j}\omega(1+t_{e/d}+r)}, \chi_{\mathrm{mm}} = \frac{2\sqrt{\mu_0/\varepsilon_0}(1-t_{e/d}+r)}{\mathrm{j}\omega(1+t_{e/d}-r)},$$

Here, $t_{e/d}$ and r represent the transmission and reflection coefficients, respectively, for the angle-doubling and angle-halving metasurfaces. For the case where $r = 0$ t is given by:

$$t_d = \frac{2\pi}{\lambda}\left(\frac{1}{2} - 2\left(\frac{n_t}{4n_i}\right)^2 \mp \frac{n_t}{4n_i}\left(\left(\frac{n_t}{2n_i}\right)^2+2\right)^{1/2}\right)^{1/2}\left(n_t - 2n_i\left[\frac{n_t}{4n_i} \pm \frac{1}{2}\left(\left(\frac{n_t}{2n_i}\right)^2+2\right)^{1/2}\right]\right),$$

$$t_e = \frac{2\pi}{\lambda}\left(\frac{1}{2} - 2\left(\frac{n_i}{4n_t}\right)^2 \mp \frac{n_i}{4n_t}\left(\left(\frac{n_i}{2n_t}\right)^2+2\right)^{1/2}\right)^{1/2}\left(-n_i + 2n_t\left[\frac{n_i}{4n_t} \pm \frac{1}{2}\left(\left(\frac{n_i}{2n_t}\right)^2+2\right)^{1/2}\right]\right)$$

The refractive indices of the incident and transmitted media at the metasurface interface are denoted by $n_{i/t}$. Angle-independent susceptibilities are achieved using generalized Snell's law, ensuring accuracy. These susceptibilities, including $t_{e/d}$ for the required phase profile, are used for inverse designing the metasurface.

Finite Difference Time Domain (FDTD) simulations of the metasurface were performed to analyze its angle-enhancing and angle-diminishing functions. Electric field maps and far-field patterns for incidence angles of 0 to 45 degrees are shown in Fig. 1. The refractive indices of SiO_2 (input medium) and air (output medium) are 1.48 and 1.0, respectively, with simulations over a $10\lambda \times 10\lambda$ region at a wavelength of $1.5\mu m$.

The far-field patterns show the metasurface maintains beam directivity at higher angles, with reduced intensity due to complex susceptibilities and partial transmittance. It effectively doubles the angle in the enhancer configuration and halves it in the diminisher configuration. The design performs reliably even at extreme angles, and no side lobes are present except at 90 degrees, confirming its ability to suppress unwanted scattering.

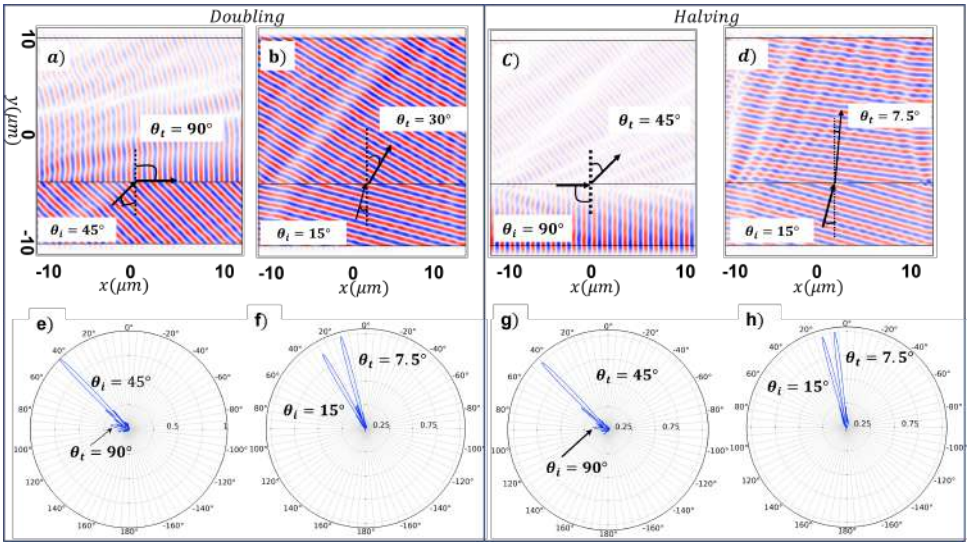


Fig. 1. Numerical simulations of the angle enhancing metasurface: a-d) Electric filed component of angle doubling metasurface for incidence range of ∠0 to ∠45; e-h) The associated farfield radiation pattern of angle doubling metasurface.

Conclusion. In conclusion, we designed an angle-doubling and halving metasurface that is independent of propagation angle, performs effectively at extreme angles, and offers a passive alternative to active metasurfaces.

Acknowledgments. This work has been supported by the European Research Council (ERC project BEAMS, grant agreement No. 101041131).

References

1. Lebbe, N. and Lanteri, S. and Golla, S. Y. and Genevet, P, *Susceptibility synthesis of arbitrary shaped metasurfaces*
2. G. A. Egorov and G. V. Eleftheriades, *Theory and Simulation of Metasurface Lenses for Extending the Angular Scan Range of Phased Arrays*, IEEE

Ring distributed metamaterial with phase cancellation for RCS reduction

O. Fernández[1*], R. Gonzalez[1], A. Gómez[1] and I. Barba[2]

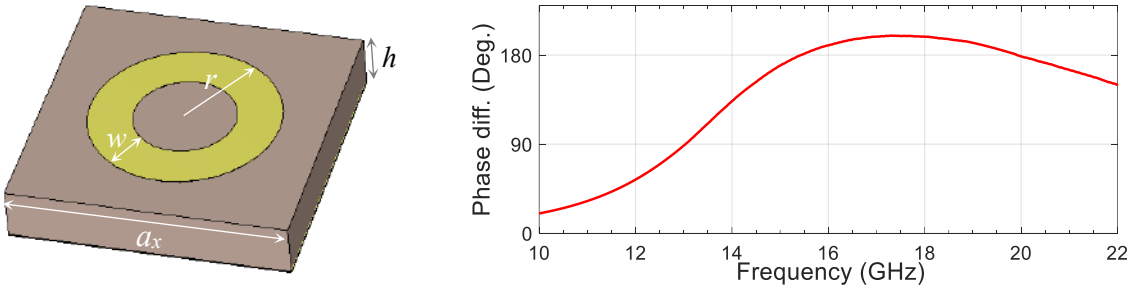
[1]Departamento de Ingeniería de Comunicaciones, Universidad de Cantabria, Santander, Spain.
[2]Departamento de Electricidad y Electrónica, Universidad de Valladolid, Valladolid, Spain
[*] corresponding author: fernanos@unican.es

Abstract: In this communication a phase cancellation metasurface is presented. The novelty of the proposed design resides on the combination of 4 structures based on the same unit cells but with slight modifications. This metasurface is designed to reduced monostatic RCS but also improve the diffuse scattering taking advantage of secondary lobes.

In electronic warfare applications, radar cross-section reduction is of vital importance to protect the integrity of fleets and infrastructures. Traditionally, techniques such as structural design with "special" geometries or the use of Radar absorbing Materials (RAM) have been used to reduce the radar signature. In recent years, metamaterials have been shown to be a good alternative to overcome the limitations of these traditional techniques, providing lighter structures (as opposed to RAM) and geometries suitable for the low observability of some parts of the infrastructures as antennas.

Phase-cancellation metasurfaces are one of the most commonly used techniques in the literature. The simplest structure combines two different types of cells which have a modulus reflection coefficient close to 1 and a phase offset of 180°. Each type of unit cell is grouped into tiles and both types of tiles are distributed over the metasurface. This technique significantly reduces the RCS for monostatic radar. However, it appears secondary lobes that represent a handicap for bi-static radar. In this paper, we focus on evaluating the impact of the type of tile distribution on the metasurface. Different approaches can be found in the literature. We start from the chessboard distribution [1] where two squared tiles (one of each type) are alternately distributed. The resulting bistatic RCS has four lobes. In [2] triangular tiles are used alternately distributed in a hexagonal supercell and its RCS has 6 lobes. Non-periodic distributions as in [3] with the tiles aligned without any specific pattern (i.e. random) can reduce the RCS by means of diffuse scattering thus reducing the bistatic radar.

In this communication we analyze a hybrid distribution that combines the advantages of different arrangements. This metasurface is based on the ring unit cell presented elsewhere [4]. Fig. 1a presents the main geometrical parameters of the Ring unit cell. We have selected a ring width of 1 mm and for the two-unit cells outer radius of



(a) (b)

Figure 1.- (a) Representation of the unit cell with the main parameters, a_x = 6 mm, w = 1 mm, substrate Rogers 4003C with h = 1.524 mm and cladding 35 μm. (b) Phase difference between the reflection coef. of unit cells with r = 1.6 and 2.4 mm.

2.4 and 1.6 mm. The phase difference between the two types of structures is represented in Fig. 1b. A 180º phase difference is obtained at about 15.5 GHz and 20 GHz.

The type of distribution provides a different interaction between the tiles thus affecting to the resultant phase cancellation. In this communication we propose a ring distributed metasurface that reduces the bistatic RCS in comparison with the chessboard and the random distribution. The proposed metasurface is formed by four structures distributed in rings as detailed in Fig. 2 a. In each structure a small variation of the generic unit cell or the default tile is done to provide whether a reduction of the broadside RCS or an increase of the diffuse. Fig 2b presents a comparison of the monostatic RCS for the three structures.

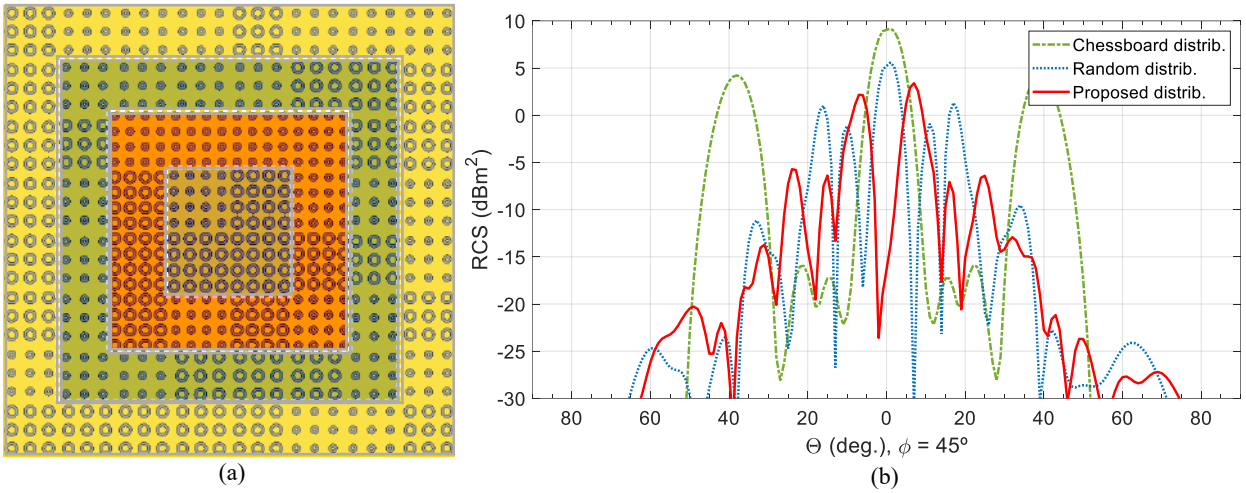


Figure 2.- (a) Proposed metasurface (b) Monostatic RCS of the proposed distribution compared with the chessboard and the random distribution.

Acknowledgements: This work was supported by the Spanish Ministry of Science and the European Union: MCIN/AEI /10.13039/501100011033 / FEDER, UE under Project PID2022-137619NB-I00.

References

1. J. C. Iriarte, M. Paquay, I. Ederra, R. Gonzalo and P. De Maagt, “RCS reduction in a chessboard like structure using AMC cells”, *2nd European Conference on Antennas and Propagation 2007* (EuCAP 2007), pp. 168–168. doi: 10.1049/ic.2007.1291.
2. W. Chen, C. A. Balanis and C. R. Birtcher, “Checkerboard EBG Surfaces for Wideband Radar Cross Section Reduction”, *IEEE Transactions on Antennas and Propagation*, vol. 63, no. 6, pp. 2636–2645, 2015, doi: 10.1109/tap.2015.2414440.
3. H. Zhang, Y. Lu, J. Su, Z. Li, J. Liu, and Y. (Lamar) Yang, “Coding diffusion metasurface for ultra-wideband RCS reduction,” *Electron. Lett.*, vol. 53, no. 3, pp. 187–189, Feb. 2017, doi: 10.1049/el.2016.3956
4. Zhang, G., Sui, S., Wang, A., Wang, J., Qu, S., & Wang, J. (2020). Coding metasurface for radar cross section reduction. *Proceedings of 2020 IEEE 3rd International Conference of Safe Production and Informatization, IICSPI 2020*, 52–55, doi: 10.1109/IICSPI51290.2020.9332391

Numerical investigation of Transverse-Mode Theory for Strongly Coupled Periodic All-Dielectric Metasurfaces

Pooja Uday Naik[1] **and Massimiliano Guasoni**[1*]

[1]Optoelectronics Research Centre, University of Southampton, United Kingdom.
[*]corresponding author: m.guasoni@soton.ac.uk

Abstract: Transverse mode behaviour has been investigated by modelling strongly coupled periodic nanoantenna array. Our study, unlike the Mie theory and look-up table approach—where individual nanoantenna modes and their interference are studied—considers the effect of coupling strength on the supermode of the array, offering new insights into light-matter interaction.

Metasurfaces have been widely studied as a powerful platform for manipulating light at the subwavelength scales, enabling applications in beam shaping, metalenses, and holography[1,2]. While traditional metasurface designs rely on localized Mie resonances, lattice modes, quasi-modes description, and look-up table approach[3-5], the models fail to capture the collective optical behaviour in the strong coupling regime, where interactions between neighbouring meta-atoms become significant. In this work, we numerically investigate the transverse-mode behaviour in periodic metasurfaces and introduce a 3-layer equivalent model that accurately predicts the phase response in the strong coupling regime.

The study models the periodic metasurface as an effective three-layer system, where the metasurface can be interpreted as a homogenized anisotropic slab. By analysing the forward and backward propagating waves and their interactions, the analytical formulation captures the behaviour of strongly coupled meta-atoms in a more intuitive manner than conventional scattering-based models. In the linear regime, the incident plane wave can be further decomposed as a combination of transverse modes, providing a simplified approach to predict the near-field and by extension shape the phase-coherent far-field response of the densely packed nanoantenna array.

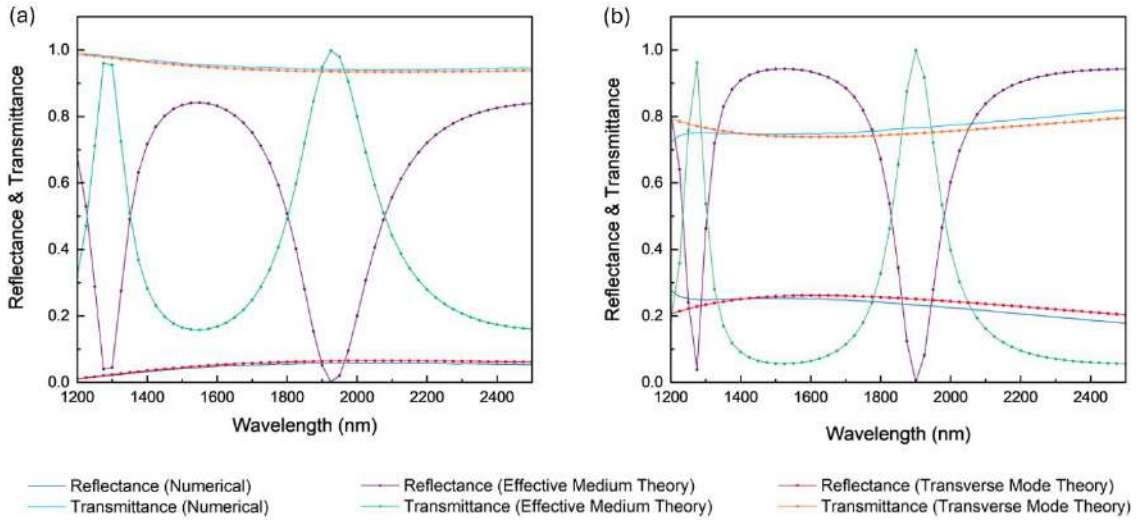


Figure 1: Transmittance and reflectance spectra of a periodic Si-air hollow-core nanoantenna array with period (P) = 1.5 as a function of incident wavelength for (a) normal incidence and (b) 55° incidence. The graphs compare numerical simulation results with EMT and the proposed transverse mode theory.

The transverse-mode approach differs fundamentally from standard effective medium theory (EMT) in how it treats light-matter interactions in metasurfaces. EMT homogenizes the structure, assuming the meta-atoms act independently and can be replaced by an averaged refractive index, which works well when particles are subwavelength and weakly interacting. However, in the strongly coupled regime, where meta-atoms are closely spaced, near-field interactions become significant, and the metasurface

behaves collectively, supporting lateral waves propagating along its plane[6]. Rather than treating the metasurface as a uniform bulk medium, the transverse-mode model views it as an effective thin slab that guides these lateral waves. This approach captures the phase-coherent nature of strongly coupled metasurfaces, enabling accurate descriptions of their phase response.

The predictions are verified using COMSOL Multiphysics by performing full-wave simulations and comparing it against the proposed transverse mode theory as shown in Figure 1. Here, silicon (Si) hollow-core nanoantennas filled with air with diameter and height of 400 nm are modelled. The optical response of the periodic array with period (P) = 1.5 has been investigated as a function of incident wavelength from 1200 nm to 2500 nm. A comparison between EMT and transverse mode theory has been made to showcase the accuracy of the proposed transverse mode theory model. In the case of EMT, the effective refractive index (n_{eff}) was determined using a weighted index approach, which fails to accurately capture the underlying physics of mode confinement and coupling. In contrast, transverse mode theory provides a more rigorous description of the system even with the change in the incident angle from normal incidence to 55° incidence, yielding results that exhibit strong agreement with numerical simulations, thereby offering a more precise characterization of the modal behaviour.

Our findings provide an alternative perspective on metasurface physics, offering a more unified framework for designing highly efficient wavefront-control devices. The proposed transverse mode theory can also be further extended to study aperiodic metasurfaces since the theory fundamentally depends on the coupling strength rather than the geometry of the individual meta-atom. By bridging gaps in existing theories, this work opens new avenues for inverse-designed metasurfaces and even nonlinear nanophotonics applications.

References

1. Genevet, P., Capasso, F., Aieta, F., Khorasaninejad, M., & Devlin, R. (2017). Recent advances in planar optics: from plasmonic to dielectric metasurfaces. *Optica*, *4*(1), 139-152.
2. Khorasaninejad, M., & Capasso, F. (2017). Metalenses: Versatile multifunctional photonic components. *Science*, *358*(6367), eaam8100.
3. Liu, B., Sain, B., Reineke, B., Zhao, R., Meier, C., Huang, L., ... & Zentgraf, T. (2020). Nonlinear wavefront control by geometric-phase dielectric metasurfaces: influence of mode field and rotational symmetry. *Advanced Optical Materials*, *8*(9), 1902050.
4. Zhao, W., Jiang, H., Liu, B., Song, J., Jiang, Y., Tang, C., & Li, J. (2016). Dielectric Huygens' metasurface for high-efficiency hologram operating in transmission mode. *Scientific Reports*, *6*(1), 30613.
5. Overvig, A. C., Shrestha, S., Malek, S. C., Lu, M., Stein, A., Zheng, C., & Yu, N. (2019). Dielectric metasurfaces for complete and independent control of the optical amplitude and phase. *Light: Science & Applications*, *8*(1), 92.
6. Lalanne, P., & Chavel, P. (2017). Metalenses at visible wavelengths: past, present, perspectives. *Laser & Photonics Reviews*, *11*(3), 1600295.

Polarization-multiplexed vectorial OAM holography based on dielectric metasurfaces

Joonkyo Jung[1], Hyeonhee Kim[1], and Jonghwa Shin[1,*]

[1]Department of Materials Science and Engineering, KAIST, Daejeon 34141, Republic of Korea
[*]corresponding author: qubit@kaist.ac.kr

Abstract: We propose novel metasurface holograms, where multiple vectorial holographic images can be encrypted into the polarization state and orbital angular momentum (OAM) of incident light. By expanding the multiplexing capability, we anticipate that our approach can find various applications such as optical information storage, secure encryption, and optical communications.

Metasurfaces, which are two-dimensional arrays of subwavelength nanostructures, have attracted tremendous interests by virtue of their versatile controllability over various characteristics of light such as amplitude, phase, and polarization. This controllability has made metasurfaces promising platforms for optical holograms. In addition, metasurfaces can be designed to operate differently depending on the states of incident light, e.g., polarization and wavelength. This multiplexing capability of metasurfaces has significantly increased the amount of information that can be encoded in a single metasurface.

The OAM of light has emerged as a new degree of freedom for augmenting the multiplexing capability of metasurface-enabled holograms [1, 2]. Since OAM is not bounded theoretically, it is expected to dramatically boost the information capacity. In an OAM-preserving hologram, the OAM of incident light is preserved at each pixel of the target images. By imposing an additional helical phase, this hologram becomes an OAM-selective hologram, where only incident light with the opposite helical phase can generate the target images with the fundamental Gaussian modes; by applying a fundamental Gaussian filter, only incident light with the desired topological charge can generate holographic images.

Even though there have been many studies related to OAM holograms, almost all of these studies are limited to intensity-only holographic image, which represent only a small portion of the information that the electric field can convey. Recently, based on polarization-multiplexed metasurfaces, a vectorial OAM hologram was suggested in [3]. However, in [3], both input polarization channels are exhausted to generate the vectorial holographic images because the polarization controllability of metasurfaces has not been fully utilized.

In this study, we propose a novel approach to encode different vectorial OAM holograms in different polarization-OAM channels with the desired topological charges as schematically represented in Figure 1. As numerically demonstrated in Figure 1, the proposed metasurfaces can generate three distinctive target images for each polarization-OAM channel, where the first one is corresponding to the amplitude and the second and third ones are corresponding to the polarization state. We believe that our approach overcoming the current limitations of OAM holography can pave a way toward further improved optical communications, optical encryption, and data storage.

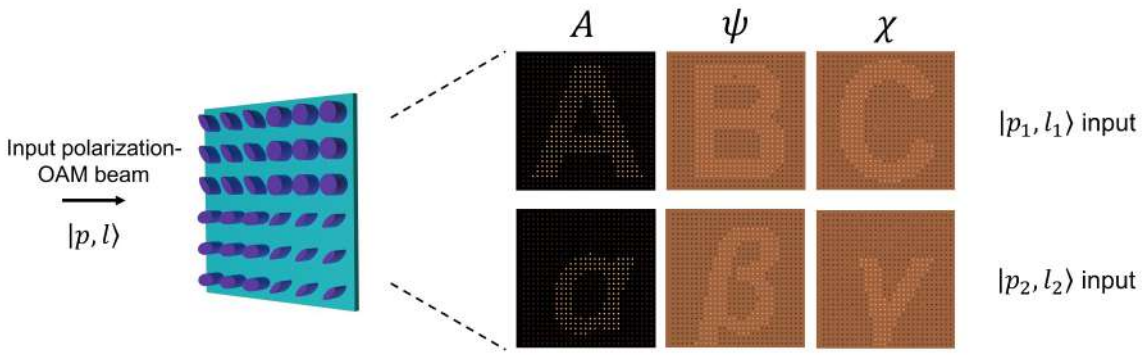


Figure 1. Schematic representation of polarization-multiplexed vectorial OAM holography. The state of an input OAM beam is defined by polarization states p and topological charge l. The right panels show the numerically calculated results of the amplitude A, and two angular values of ψ and χ, defining polarization state of the resulting vectorial field profile.

References

1. X. Fang, H. Ren, and M. Gu, "Orbital angular momentum holography for high-security encryption," *Nat. Photon*., **14**, 102-108 (2020).
2. H. Ren, et al., "Metasurface orbital angular momentum holography," *Nat. Commun.*, **10**, 2986 (2019).
3. Z. Yu, et al., "Spin-Orbit-Locking Vectorial Metasurface Holograph," *Advanced Materials*, 2415142 (2024).

Characterization of flat optical devices in a transformation optics context

M. Giloan

MG Data, Romania
corresponding author: mircea_giloan@yahoo.com

Abstract: Optical devices are mainly based on wave path and wave vector manipulation. This can be obtained by specifically designing the surface of the interface between two media. In the last years flat optical devices have been intensively studied. In this study flat optical devices are characterized as transformation optics media.

This theoretical study shows a general method for designing flat optical devices based on transformation optics. Optical devices consisting in flat media obtained by transforming only one coordinate of the free space have been considered. A proper control of the wave path and wave vector can provide a specific wave vector distribution at the output plane of the flat device [1]. This method can be used to design lenses, optical connectors and wave-shape transformers [2, 3]. Numerical computations consisting in Finite-Difference Time-Domain (FDTD) simulations confirm the proposed theoretical model. Figure 1 shows the FDTD simulation results for a designed flat optical device. This device transforms the wave generated by a dipole in a plane wave (see fig. 1(a)). The designed device has a square shape which can be observed in figure 1(b) which depicts the *xy* component of the electric permittivity tensor.

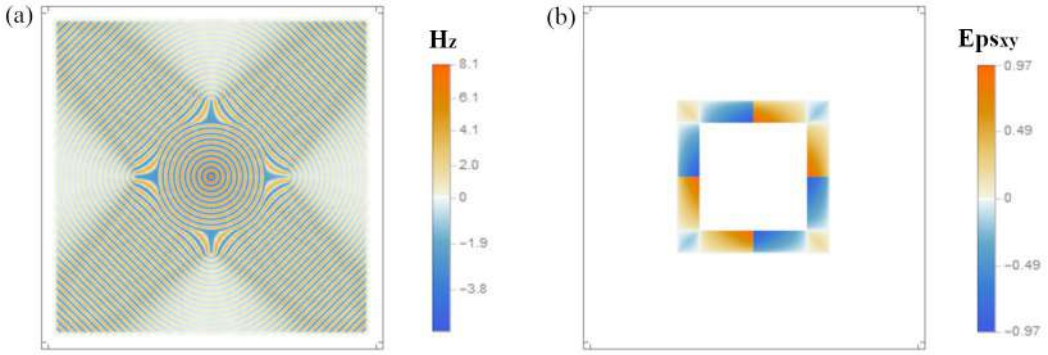


Figure 1. (**a**) Distribution of the magnetic field intensity (**Hz**) generated by a dipole source, transformed into plane waves after passing through a flat optical device. (**b**) Distribution of the *xy* component of the electric permittivity tensor of the transformation optics medium corresponding to the flat optical device.

References

1. Giloan, M. “Designing Devices for Wave-Vector Manipulation Using a Transformation-Optics Approach,” Phys. Rev. Applied, Vol. 8, No. 1, 014005, 2017.
2. Giloan, M. and R. Gutt, “Optical imaging system based on transformation-optics lenses,” J. Opt., Vol. 22, No. 1, 015103, 2019.
3. Giloan, M. and R. Gutt, “Designing flat optical devices for path and wave vector manipulation by space transformation along a fixed direction,” J. Opt. Soc. Am. B, Vol. 38, No. 1, 9–16, 2021.

Resistive Metamaterial based Ultrathin Broadband Microwave Absorber

Jyoti Yadav[1*], Kumar Vaibhav Srivastava[2], and J. Ramkumar[3]
[1]Materials Science Programme, IIT Kanpur, India
[2]Department of Electrical Engineering, IIT Kanpur, India
[3]Department of Mechanical Engineering, IIT Kanpur, India
Corresponding author: jyoti@iitk.ac.in

Abstract: A novel unit cell for broadband microwave absorber is proposed. This polarization insensitive absorber exhibits more than 90% absorption for (8.04 –19.30) GHz, covering X, and Ku bands. The absorption is maintained till incident angle 30° for both TE and TM modes. The absorption remains significant for higher angles, also.

1 Introduction

Microwave absorbers are strengthening their grip among the RF-Microwave research community. With diverse range of applications from strategic to civil domain, they are motivating quality research in the field. The applications range from RCS reduction, EM interference and shielding, clean anechoic chambers, to RF sensors, energy harvestors and solar cells. With increasing use of electromagnetic technologies in day to day lives, the demand for a high functioning low profile microwave absorber has also become significant. Multiple researches have been reported focusing on low profile, high transparency, high robustness, high environmental resilience, and easy fabrication processes.

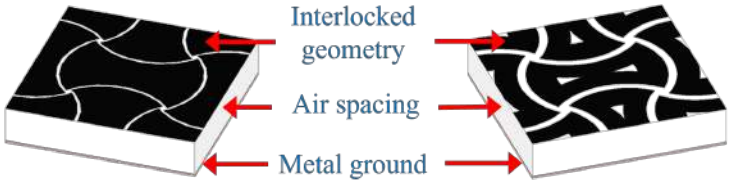


Figure 1: Interlocked unit cell based microwave absorber.

In this work, a novel unit cell is proposed with an improved absorption profile and miniaturized dimensions. This was achieved by fragmenting a patch-based geometry into interlocking tiles. Fragmentation of patch-based geometry gives rise to increased intra unit cell capacitance and helps in achieving the miniaturization of unit cell. Here, two unit cell designs are proposed and studied. One is interlocking loop-based geometry, and the other is interlocking patch-based geometry. Both the proposed absorbers exhibit more than 90% absorption for complete X and Ku band, and partial C and K bands. The proposed designs are insensitive to polarization due to 4∈fold geometrical symmetry of the unit cells. With stable TE mode performance upto 30°, and TM mode performance upto 45°, the proposed structure is reasonably stable against varying incident angle values.

2 Design and Analysis

In the presented work, two unit cell geometries are proposed and studied based on interlocking geometry. A typical absorber unit cell consists of a patterned resistive layer, backed by a thick air spacer and metal ground.

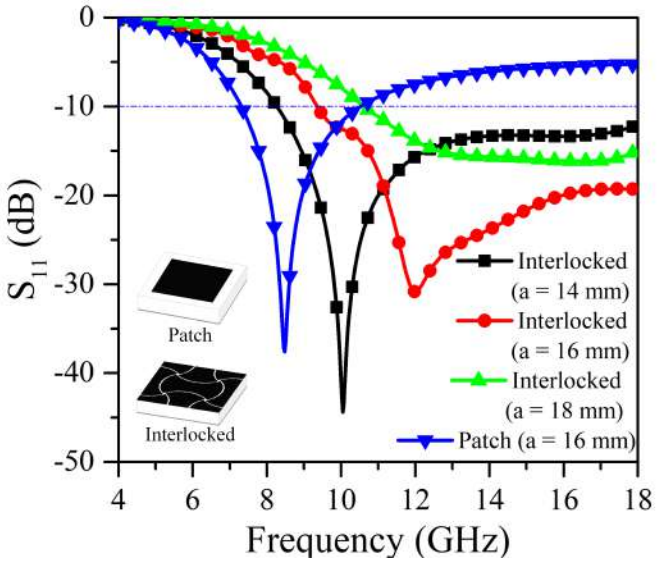


Figure 2: Comparative absorption profile of a resistive patch absorber against fragmented and interlocked geometry.

The design was achieved by fragmenting a square patch into 4 interlocked dumblelike structures. This is reflected and studied in Fig. 2. From the given plot, the two schemes are compared. This was done keeping the thickness, $t = 3mm$, constant for all the schemes. For interlocked schemes, the periodicity is also altered. It is inferred that most optimized performance is achieved for interlocked scheme with period, $a = 16mm$. However, all the interlocked schemes are better in terms of performance against square patch.

Further, two design schemes are proposed based on the interlocking scheme. The first one is interlocked loop-based unit cell geometry and the other one is interlocked patch-based geometry.

3 Conclusion

Wide-band resistive ink based novel absorber for C, X, Ku and K- bands is designed and studied. The possible applications of the proposed structure is in the RCS reduction of the structures where thin absorber profile is required. The proposed absorber is also conformable by the properties of the material choice made for the same.

Acknowledgment

The authors would like to acknowledge the members of Metamaterial lab at the Indian Institute of Technology Kanpur, India.

Tunable terahertz polarization converter based on liquid crystal

Sheng Wang [1], Wei. Zhu[1], Jingbo Wu[1,2*], Hangbing Guo [2], Caihong Zhang[1,2], Kebin Fan[1,2], Biaobing Jin[1,2], Jian Chen[1,2], and Peiheng Wu[1,2]

[1]Author Affiliation, Country1Research Institute of Superconductor Electronics (RISE) & Key Laboratory of Optoelectronic Devices and Systems with Extreme Performances of MOE, School of Electronic Science and Engineering, Nanjing University, Nanjing 210023, China
[2]Purple Mountain Laboratories, Nanjing 211111, China
[*]corresponding author: jbwu@nju.edu.cn

Abstract: We propose liquid crystal metasurface using split ring resonators for tunable polarization conversion in the terahertz band. The device achieves a polarization conversion ratio ranging from 98.7% to 4.8% and maintains high stability at incident angles from -30° to 30°, making it suitable for various terahertz applications.

Introduction

The polarization of electromagnetic waves is a fundamental property. The manipulation of polarization influences the anti-interference ability and quality of the signal. Conventional methods for terahertz (THz) polarization manipulation are based on natural materials that exhibit optical effects such as birefringence, total internal reflection, or magneto-optical rotation. Metasurfaces-based polarization converters[1,2] can achieve flexible and effective control of THz waves with advantages such as compact size, low profile, and low cost.

In this work, we present a novel device that can dynamically manipulate the polarization state of electromagnetic waves by integrating the liquid crystal layer into the metasurface. Liquid crystal is a tunable dielectric material that can change its orientation under an electric field. The unit cell has a metal-insulator-metal (MIM) structure. The liquid crystal layer is sandwiched between two metallic layers. By applying different voltages to the liquid crystal layer, we can switch the device between two states: the initial state (OFF) and the bias state (ON). The device can achieve a high polarization conversion ratio (PCR) 98.7% and a large modulation depth of 95.1% in the THz band.

Design of unit cell

As is shown in Fig. 1, the two metallic layers are made of 200 nm-thick gold film. The dielectric layer is liquid crystal. The upper metallic layer has a SRR pattern etched on it, and the lower metallic layer serves as the ground plane. The two metallic layers are separated by quartz glass, and the dielectric layer has a liquid crystal with a dielectric constant of 2.49 and a loss tangent of 0.06. The geometric parameters of the device are as follows: R_1 = 165 μm, R_2 = 107 μm, L = 360 μm, t_1 = 445 μm, t_2 = 500 μm, h = 25 μm.

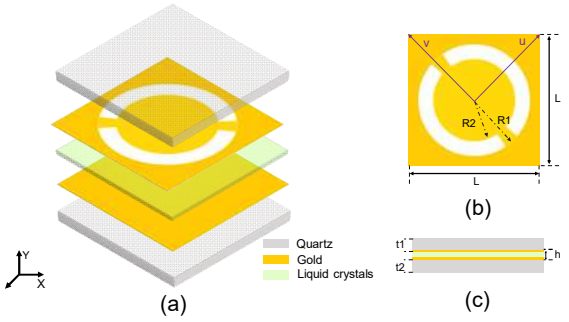


Fig. 1. Schematic of unit cell structure of the proposed tunable polarization converter. (a) 3-D view, (b)top view. (c)side view of the unit cell.

Simulation Results

As shown in Fig. 1b, the structure has a resonant ring with anisotropy, which creates a difference in the resonant frequency points of the electromagnetic waves along the U and V directions. This leads to a resonant phase difference. The MIM structure, filled with liquid crystal, acts as a variable capacitor. By rotating the liquid crystal molecules, the capacitance value of the capacitor changes, which alters the resonant frequency point and produces a tunable phase difference. We combine the ability of metasurface to manipulate electromagnetic waves with the tunable characteristics of the liquid crystal to achieve a tunable polarization converter device.

The reflection coefficient of a metasurface is defined as: $r_{xx} = \left|E^r{}_{xx}\right| / \left|E^i\right|, r_{xy} = \left|E^r{}_{xy}\right| / \left|E^i\right|$, where x and y are the polarization directions, and i and r represent the incident and reflected waves, respectively. The PCR of the converter is defined as $PCR = \frac{r_{xy}{}^2}{r_{xx}{}^2 + r_{xy}{}^2}$.

The device demonstrates broadband polarization conversion and large modulation depth, as shown by the simulation results. The co-polarized and cross-polarized reflection amplitudes in different liquid crystal states are presented in Fig. 2. In the frequency range of 0.380 -0.415 THz, the cross-polarized reflection amplitude is higher than the co-polarized reflection amplitude in the initial state of liquid crystal (OFF), with a maximum value of 0.77 at the center frequency. In the full-bias state of liquid crystal (ON), the cross-polarized reflection amplitude reaches a minimum value of 0.16, indicating that the reflection coefficient is inverted by switching the liquid crystal states. The PCR curve in the figure further illustrates the high modulation performance of the device. At 0.415THz, the PCR amplitude decreases from 98.7% to 4.8% by switching the liquid crystal states, achieving a modulation depth of 95.1%.

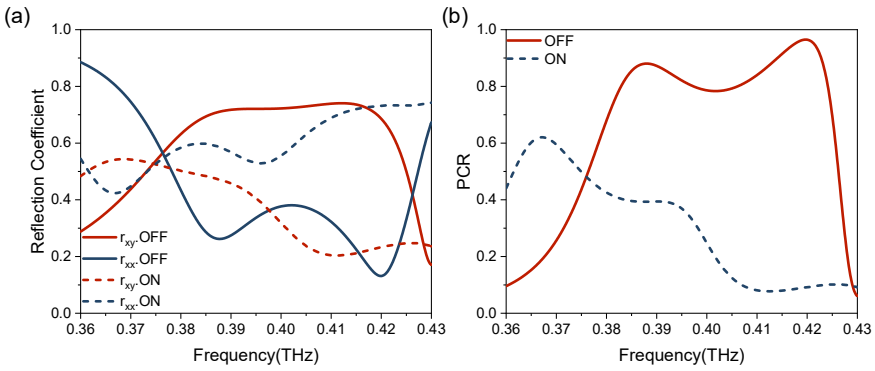


Fig. 2. (a) Simulated co-polariztion (r_{xx}) and cross-polarization (r_{yx}) reflection coefficients, (b) Calculated PCR values at ON and OFF state

References

1. A. Yu, D. Yu, Z. Yang, X. Guo, Y. Ren, X. Zang, A. V. Balakin, A. P. Shkurinov, and Y. Zhu, “Terahertz Broadband Polarization Conversion for Transmitted Waves Based on Graphene Plasmon Resonances,” Nanomaterials (Basel), vol. 11, no. 1, Dec 28, 2020.
2. Shi-Tong Xu, Fei Fan, Meng Chen, Yun-Yun Ji, and Sheng-Jiang Chang, “Terahertz polarization mode conversion in compound metasurface,” Applied Physics Letters, vol. 111, no. 3, 2017.

Complete asymmetric polarization conversion through zero-eigenvalued exceptional points of non-Hermitian metasurfaces

Donghak Oh1[1,†], Soojeong Baek[1,2,†], Sangha Lee[3,†], Kyungmin Lee[1], Jagang Park[4], Zhaowei Liu[2], Teun-Teun Kim[5], and Bumki Min[1,3*]

[1]Department of Physics, Korea Advanced Institute of Science and Technology (KAIST), Republic of Korea
[2]Department of Electrical and Computer Engineering, University of California, San Diego, USA
[3]Department of Mechanical Engineering, Korea Advanced Institute of Science and Technology (KAIST), Republic of Korea
[4]Department of Electrical Engineering and Computer Sciences, University of California, Berkeley, CA, USA
[5]Department of Physics, University of Ulsan, Republic of Korea
[*]corresponding author: bmin@kaist.ac.kr

Abstract: We propose a non-Hermitian metasurface that achieves complete asymmetric polarization conversion at an exceptional point with a zero eigenvalue by introducing gain. Numerical verification confirms this design, which converts right to left circular polarization, blocks the opposite conversion, and eliminates co-polarized transmission.

Non-Hermitian physics provides a unique avenue to reinterpret polarization optics [1-3]. At exceptional points (EPs), the eigenpolarization states merge into a single eigenpolarization, revealing the singular and topological polarization phenomena. To achieve a comprehensive understanding of these phenomena, it's essential to consider both the coalesced eigenpolarization and the eigentransmission. Here, we propose a non-Hermitian metasurface to achieve complete asymmetric polarization conversion (CAPC) at a chiral EP. In this work, the CAPC refers to the phenomenon of conversion from right (or left) to left (or right) circular polarization while blocking the opposite conversion and eliminating co-polarized transmission. The design exploits both zero eigentransmission and a coalesced circular eigenpolarization state at the chiral EP, which highlights an intriguing feature of eigenvalue-dependent polarization phenomena at the EP. Moreover, we demonstrate that the CAPC can enable achieving the highest level of circular dichroism in transmission, even without a three-dimensional helical chiral arrangement.

To verify the CAPC at the chiral EP, we performed a numerical simulation of a non-Hermitian metasurface composed of two orthogonally oriented nano-rod resonators on a gain substrate, designed for near-infrared operation. The resonators are designed to have the same resonance frequency under polarization along their major axes (Fig. 1A). In Fig. 1B, the numerically-extracted eigentransmission is plotted as a function of the input frequency and the imaginary part of the substrate permittivity. The zero-eigentransmission chiral EP gives rise to CAPC, validated by the near-vanishing of all Jones matrix elements except t_{LR} (Fig 1C).

Notably, this CAPC mechanism achieves a maximum circular dichroism in transmission (CDT), as indicated by the value nearing -1. This behavior is qualitatively different from the CDT observed in three-dimensional helical structures, which typically show differences in co-polarized transmission between RCP and LCP

incidence and zero-valued cross-polarized transmission. Furthermore, our planar design exhibits chirality by breaking in-plane mirror symmetry, yielding different responses to circularly polarized light incident from opposite directions. Consequently, asymmetric CAPC is observed, where incident light is converted to LCP for forward propagation and RCP for backward propagation, with the sign of maximal CDT being inverted for forward and backward propagation (Fig. 1D, E).

In conclusion, we propose an approach to achieve CAPC by leveraging a gain-integrated metasurface with zero-eigenvalued chiral EP. Our method numerically substantiates CAPC from a non-Hermitian perspective and provides a novel pathway to achieve asymmetric maximal CDT without the requirement for extrinsic chirality. This non-Hermitian approach opens up new possibilities for polarization optics, offering a powerful way to engineer polarization-dependent light matter interactions.

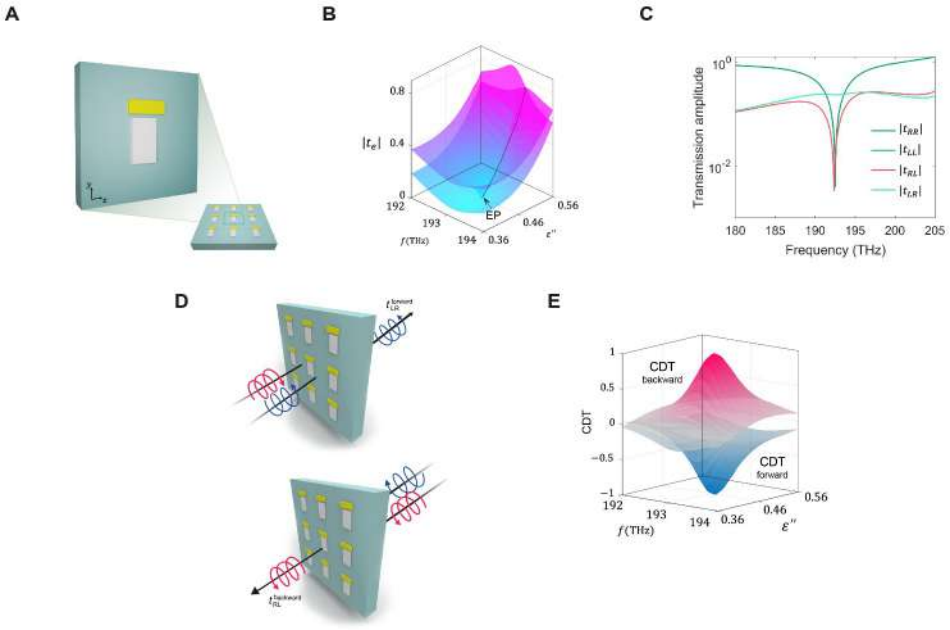


Fig. 1 (A) A schematic illustration of the gain-integrated non-Hermitian metasurfaces. (B) Numerically-extracted eigentransmission surfaces in a two-parameter space spanned by incident frequency and imaginary substrate permittivity. (C) Numerically-extracted transmission amplitudes near a zero-eigenvalued chiral EP. (D) A schematic illustration of an asymmetric polarization conversion taking place at a zero-eigenvalued chiral EP. (E) A plot of CDT in the two-parameter space, where the red and blue surfaces correspond to the CDT in the forward and backward propagation direction, respectively.

References

1. M. Kang, J. Chen, and Y. D. Chong, “Chiral exceptional points in metasurfaces,” Phys. Rev. A., vol. 94, no. 3, pp. 1–5, 2016
2. M. Lawrence et al., “Manifestation of PT symmetry breaking in polarization space with terahertz metasurfaces,” Phys. Rev. Lett., vol. 113, no. 9, pp. 1–5, 2014
3. S. Baek et al., “Non-Hermitian chiral degeneracy of gated graphene metasurfaces,” Light: Sci and Appl., accepted for publication, 2023

Singular Flat Band in Metallic Kagomé Lattice

Dongho Lee[1], Hyeon Gi Park[2], Donghak Oh[1], Yung Kim[2], Soojeong Baek[3], and Bumki Min[1,3*]

[1]Department of Physics, Korea Advanced Institute of Science and Technology, Republic of Korea
[2]Department of Physics, University of Ulsan, Republic of Korea
[3]Department of Mechanical Engineering, Korea Advanced Institute of Science and Technology, Republic of Korea
[*]corresponding author: bmin@kaist.ac.kr

Abstract: Our study focuses on reconstructing the singular flat band structure of a THz metallic Kagomé lattice, analyzing transmission spectra and eigenmodes, and confirming a singularity through quantum distance calculations.

Recent investigations into topological characteristics of quantum systems have increasingly centered on the quantum geometric tensor [1], with particular attention given to its real component, the quantum metric [2]. In this context, singular flat bands—characterized by discontinuous eigenstates at band touching points [3]—have emerged as a compelling platform for probing quantum metric-related phenomena. These bands, previously studied in phononic crystals [4] and waveguide arrays [5], are now gaining traction. Notably, the Kagomé lattice inherently supports such singular flat bands due to its distinct geometric structure [2]. In this study, we extract and investigate the singular flat band structure of a metallic Kagomé lattice, or Kagomé metasurface.

Drawing inspiration from the Kagomé lattice architecture [6], we developed a terahertz (THz) metasurface design (Fig. 1(a)) comprising thin gold disks arranged on a polyimide substrate, interconnected by gold bars. This metallic layer serves a pivotal role in our investigation—not merely as a static framework, but as a dynamic system wherein each disk accumulates an oscillating electric charge under electromagnetic wave excitation, alternating periodically between positive and negative values. To analyze the resulting complex band structure, we employed a coupled oscillator model integrated with the Euler–Lagrange formalism. The governing coupled charge equation is expressed as follows:

$$(\omega/\omega_0)^2\mathbf{q} = (4-\mathbf{A})(1+\kappa\mathbf{A})^{-1}\mathbf{q} \tag{1}$$

where $\mathbf{A}$ denotes the adjacency matrix of the Kagomé lattice in momentum space, $\mathbf{q}$ represents the vector of stored charge amplitudes, and κ is the coupling coefficient. Solving the resulting eigenvalue equation yields a three-band model (Fig. 1(b)), comprising a flat band, a parabolic band, and a lower-energy band. Notably, the parabolic band touches the flat band at the Γ point. The quantum distance of the flat band, measured from the propagation angle of 0°, is calculated as follows:

$$d^2 = 1 - \left|\left\langle q_0^{\mathrm{FB}} \middle| q_\varphi^{\mathrm{FB}} \right\rangle\right|^2 \tag{2}$$

where $\left|q_\varphi^{\mathrm{FB}}\right\rangle$ denotes the flat band eigenstate (Fig. 1(c)). The analytical expression for the quantum distance, derived from Eq. (2), yields a sinusoidal function with a maximum value of 1 and a periodicity of π.

Figure 2(a) presents the transmission spectra as functions of wavenumber and frequency, based on linearly polarized transverse input waves—TE_{00} and TM_{00} modes. Each polarization mode gives rise to distinct resonant frequencies. The combined spectral response reveals the presence of both flat and parabolic bands across all propagation angles. Owing to the C_6 rotational symmetry at the center of the hexagon, the transmission characteristics remain invariant under azimuthal rotation $\varphi \rightarrow \varphi + 60°$. By analyzing the transmission spectra with angular and polarization resolution, the full band structure can be reconstructed.

In summary, we have demonstrated the presence of a singular flat band structure in metallic Kagomé lattices engineered for terahertz-frequency operation. The extracted quantum distance near the singularity approaches unity, highlighting the promise of metallic Kagomé lattices as a viable platform for exploring unconventional phenomena linked to the quantum metric. The eigenstates of flat band can also be reconstructed via transmission intensities measured across six polarization states—horizontal–vertical (HV), diagonal–antidiagonal (DA), and right–left circular (RL) [7]. This enables experimental confirmation of the singular flat band, providing a reliable foundation for subsequent investigations into the system's quantum geometric and topological properties.

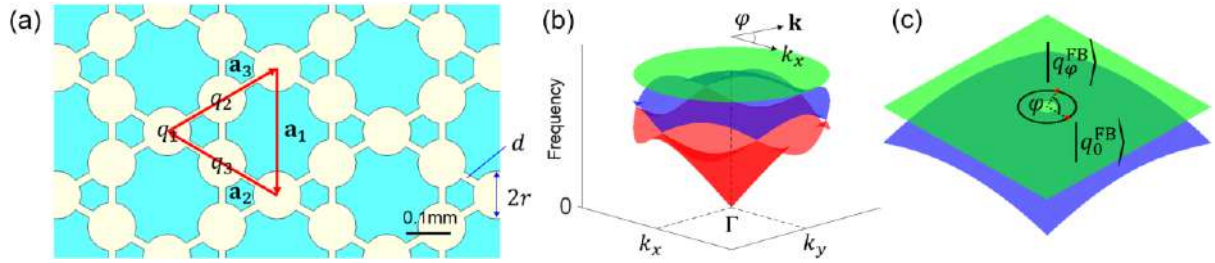


Fig.1. (a) Schematic illustration of the gold Kagomé lattice. The 200nm gold structure is on the 2μm polyimide substrate. $\mathbf{a}_i$ are unit-lattice vectors. Disk radius $r = 55\mu$m, bar width $d = 17\mu$m. (b) Analytical band structure of gold Kagomé lattice. Upper two bands are flat band and parabolic band, degenerating at the Γ point. $\mathbf{k}$ is parallel component of wavenumber of the incident wave, and φ is propagation angle of the incident wave. (c) View of the bands near the touching point. Both states have infinitesimal magnitude of momentum.

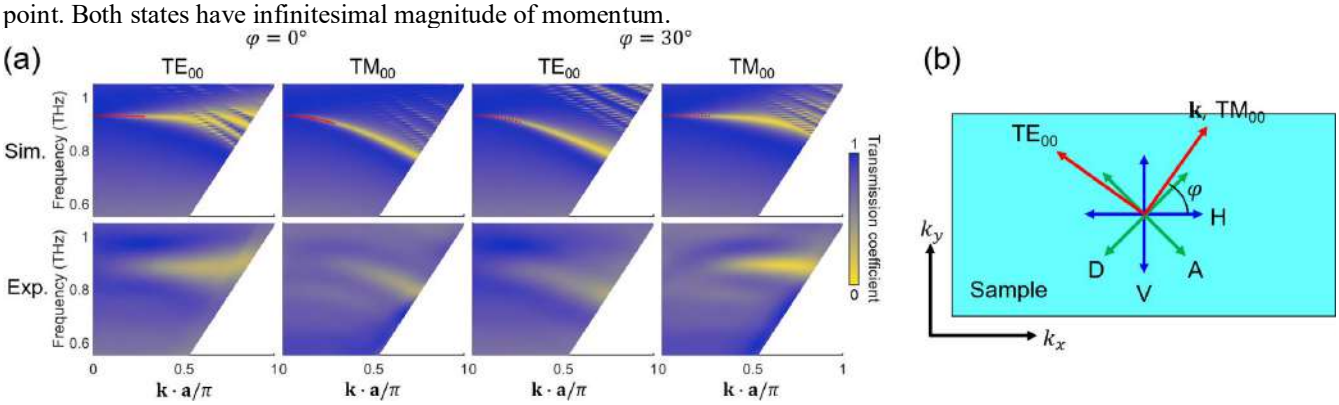


Fig.2. (a) Simulation and experiment result of angle- and polarization-resolved transmission spectra. The red dotted line is eigenmode solver simulation results. (b) Diagram of relation between input wave and linear polarizations.

References

1. Ma, Y.-Q. "Abelian and non-Abelian quantum geometric tensor," Physical Review B, 81, 245129, 2010.
2. Piéchon, F. "Geometric orbital susceptibility: Quantum metric without Berry curvature," Physical Review B, 94, 134423, 2016.
3. Rhim, J.-W. and Yang B.-J. "Singular flat bands," Advances in Physics: X, 6(1), 1901606, 2021.
4. Karki, P. and Paulose, J. "Non-singular and singular flat bands in tunable phononic metamaterials," Physical Review Research, 5, 023036, 2023.
5. Xie, Y. "Fractal-like photonic lattices and localized states arising from singular and nonsingular flatbands," APL Photonics, 6, 116104, 2021.
6. Nakata, Y. "Observation of flat band for terahertz spoof plasmons in a metallic kagomé lattice," Physical Review B, 85, 205128, 2012.
7. Bleu, O. "Measuring the quantum geometric tensor in two-dimensional photonic and exciton-polariton systems," Physical Review B, 97, 195422, 2018.

Design of a metasurface deflector integrated with a grating coupler to collimate a Gaussian beam from an optical fiber for vertical coupling

Suhee Shin[1], Jaewon Jang[1], Minsu Park[1], Yeonsang Park[12*]

[1]Department of Physics, Chungnam National University, Daejeon, Republic of Korea
[2]Institute of Quantum Systems, Chungnam National University, Daejeon, Republic of Korea
[*]corresponding author: yeonsang.park@cnu.ac.kr

Abstract: The light from an optical fiber has a very high divergence angle. We propose a metasurface that collimates the Gaussian beam and at the same time deflects it into a grating coupler. This enables the vertical coupling of the optical fiber and enhances the coupling efficiency.

In photonic integrated circuits (PICs), optical and electrical components are placed on a single substrate, which is called co-packaged optics (CPOs). Since CPOs are constructed on a low-loss substrate and are very compact, transmission power loss and delay time in CPOs can be decreased remarkably. Eventhough their advantages, the dimension of waveguides on the chip and a fiber core are very different in physical scale and therefore an interface structure to connect two components without the coupling loss is required. Since the emergence of metasurfaces, various practical photonic systems with high-performance such as a lens, a polarizer, and a spectrometer etc have been reported based on the advantage of dielectric metasurfaces that can freely control electromagnetic fields at the nanoscale.

Here, we propose an integration of a metasurface, working at 1550 nm, with a grating coupler to increase the coupling efficiency between a photonic integrated chip and an optical fiber. The metasurface collimates the light emitted from the fiber and enables vertical coupling. By executing finite difference time domain(FDTD) solver simultaneously, we found out that the light passing through the grating coupler is transmitted well into the waveguide. We expect that this technology will open new application of metasurfaces and give efficient solution for PICs that require high coupling efficiency between waveguides and optical fibers.

(a) (b)

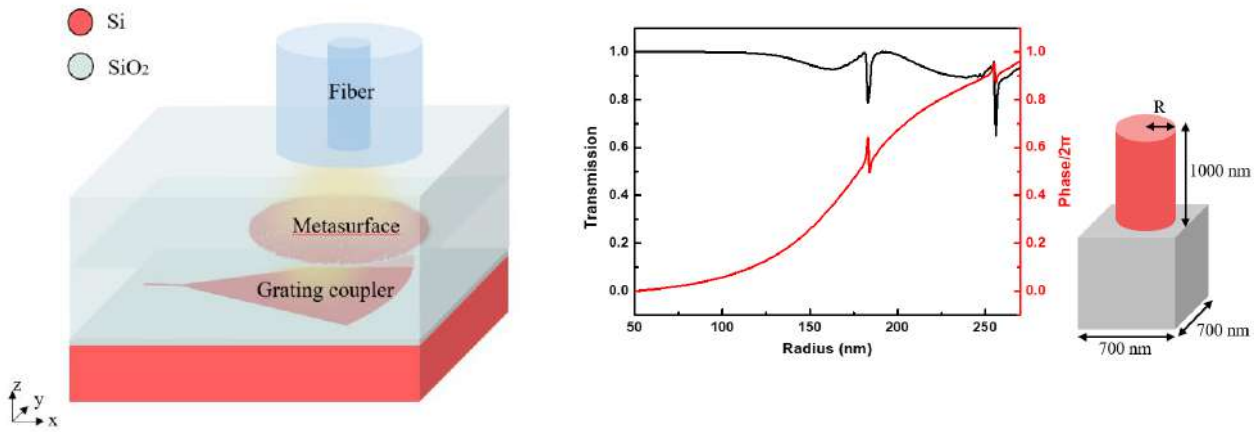


Figure 1. (a) Schematic of the metasurface integrated with a grating coupler. (b) Transmission and phase of the p eriodic Si nano-posts for different radius.

The emitted light beam from single mode optical fiber (SMF) has significant divergence. we used a single-

mode fiber, SMF-28e, manufactured by Thorlabs, which has a divergence of 5.44°, which is almost identical to the divergence of the fundamental Gaussian mode. we design for 1550 nm light with transverse electric field (TE) polarization of the waveguide, i.e., polarized along the y-direction.

We designed the silicon nano-posts with a height of 1000 nm on the SiO_2 background material and substrate, with a lattice constant of 700 nm. We performed the calculation using FDTD method and analyzed the transmission coefficient and phase of silicon nano-posts by varing the unit cell size a from 50 nm to 275 nm.

The phase profile that flattens the Gaussian wavefront is given as

$$\phi(x,y) = -\left[k\left(z + \frac{x^2+y^2}{2R(z)}\right) - \arctan(z/z_R)\right] \quad (1)$$

where z_R is the Rayleigh length and R(z) is the radius of curvature of the Gaussian wavefront and (x, y) is the Cartesian coordinate of the spatial phase profile.

The diffraction angle of the gradient metasurface can be obtained by following the Snell's law,

$$n_t sin\theta_t - n_i sin\theta_i = \frac{\lambda}{2\pi}\frac{d\phi}{dx} \quad (2)$$

Where n_t and n_i are the refractive index of the surrounding medium on the transmitted and incident siedes, in our design $n_t = n_i = 1.44$, θ_t is the deflection angle, θ_i is the incidence angle. According to the information of the well-known grating coupler, when the deflection angle is 9.7°, it is coupled to the grating coupler. The final phase profile of the metasurface can be obtained by linearly combining Equations (1) and (2).

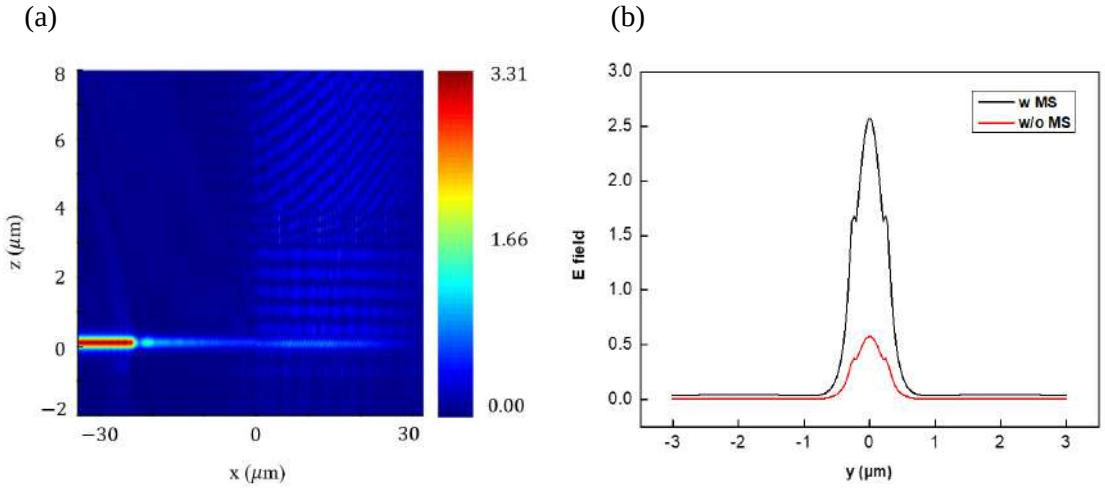


Figure 2. (a) xz-plane field profile showing transmission through the metasurface integrated grating coupler. (b) Waveguide E field magnitude with and without metasurface.

References

1. MAJUMDER, Sambuddha; RAVINDRAN, Sooraj. "Diffraction limited collimation of 1550 nm Gaussian beam from a single mode fiber using cylindrical metalens." *Optical and Quantum Electronics*, Vol. 56, No. 6, 1022, 2024.
2. Wu, Xingyu, et al. "Metasurface deflector enhanced grating coupler for perfectly vertical coupling." *Photonics*. Vol. 10. No. 4. MDPI, 2023.
3. KAR, Arunita, et al. "Realization of alignment-tolerant grating couplers for z-cut thin-film lithium niobate." *Optics Express*, Vol. 27, No. 11, 15856-15867, 2019.
4. DING, Yimin, et al. "Metasurface-dressed two-dimensional on-chip waveguide for free-space light field manipulation." *ACS Photonics*, Vol. 9, No. 2, 398–404, 2022.

Dual-functional metalenses for the generation of 2D and 3D structured beams

A. Vogliardi [1], G. Ruffato[1,2], D. Bonaldo[2], S. Dal Zilio[3] and F. Romanato[1,3,*]

[1]Department of Physics and Astronomy, University of Padova, Italy

[2]Department of Information Engineering, University of Padova, Italy

[3]IOM-Officina dei Materiali, Italy

*Corresponding author: filippo.romanato@unipd.it

Abstract

We report on spin-decoupled metasurfaces for compact generation of vector beams with non-separable polarization and spatial profiles, enabling three-dimensional light shaping along customizable spirals for applications in optical manipulation and quantum photonics.

Structured light has transformed optical beam shaping, enabling advanced control over phase, polarization, and orbital angular momentum (OAM). However, the generation of non-separable spin–orbit states often relies on bulky and complex optical setups. Metasurfaces overcome these limitations, offering compact, planar devices with full phase and polarization control. Here, we introduce a dual-functional metalens (DFML) paradigm that exploits spin-decoupled design to independently tailor right- and left-handed circular polarizations. This strategy paves the way for compact generation of complex 2D and 3D vector beams with arbitrary polarization structures.

Dual-functional metalenses are well-suited for structured vector beam generation, as they can impart distinct phase delays $e^{i\Phi^{\pm}}$ to orthogonal circular components. [1] A linearly polarized input state can be expressed as$|\vartheta\rangle = \frac{1}{\sqrt{2}}\left(|R\rangle e^{i\vartheta} + |L\rangle e^{-i\vartheta}\right)$ which, after passing through the metasurface, becomes:

$$J|\vartheta\rangle = \frac{1}{\sqrt{2}}\left(e^{i\vartheta}e^{i\Phi^{-}}|L\rangle + e^{-i\vartheta}e^{i\Phi^{+}}|R\rangle\right)$$

This spin-decoupled transformation enables the independent shaping of each polarization component, resulting in vector beams with non-separable spatial and polarization degrees of freedom. By engineering the phase profiles $\Phi^{\pm}$, arbitrary wavefront manipulation is possible. We demonstrate this concept through two representative cases: **3D helico-conical vector beams (HCVBs**, where the polarization pattern follows a spiraling intensity profile and evolves along the propagation axis due to the beam's caustic nature and **azimuthally-variant vector beams (AV-PVBs**, characterized by ring-shaped intensity profiles with spatially varying polarization and tunable phase gradients. 3D helico-conical vector can be obtained by imposing the following phase profiles to the experimental metasurface phase profile:

$$\Phi^{\pm}(r,\theta) = -i\left[a\left(\frac{r-r_0}{R}\right)(m\vartheta+\vartheta_0) \pm n\vartheta - \frac{kr^2}{2f}\right] \tag{1}$$

composed by an helico-conical $(a\left(\frac{r-r_0}{R}\right)(m\vartheta+\vartheta_0))$ and a focusing polarization independent $(-\frac{kr^2}{2f})$ phase terms plus an additional conical-independent but polarization-dependent phase gradient $(\pm n\vartheta)$. To demonstrate the versatility of the dual-functional metalens platform, we also investigated the generation of azimuthally-variant vector beams, characterized by structured polarization and phase profiles varying along a ring. To further enable this, the spin-dependent

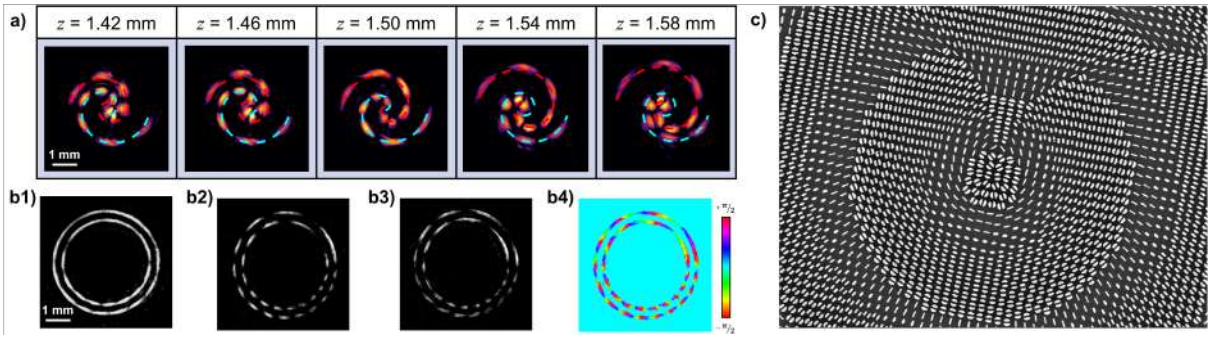


Figure 1: a) Measured double-arm helico-conical vector beam after filtering using a linear polarizer. Both the vectorial and 3D caustic nature are confirmed. b1) Intensity of generated double-ring azimuthally-variant perfect vector beam with linear phase gradient and encoding opposite vector states in the two annuli. Filtered acquisition of AV-PVB using a polarizer rotated by $+\pi/4$ (b2) and $-\pi/4$ (b3) shows both the azimuthally-variant nature of the beam and the different vector states of the annuli. b4) Reconstructed polarization state of the generated AV-PVB; colors refers to the local orientation of the polarization. c) SEM image of a fabricated DFML.

phase term $\Phi_{\pm\ell}$ is generalized to a more complex form $\Phi^{\pm}_{m,\ell_0,\ell_1}$, designed to impart an azimuthally varying phase gradient across the beam cross-section:

$$\Phi^{\pm}_{m,\ell_0,\ell_1}(r,\theta) = -\alpha r - k\sqrt{(r^2+f^2)} - f + \sum_{j=1}^{m}(-1)^{H_C^j}\left[\pm(\ell_0 + H_G^j\ell_1) \pm (-1)^{H_G^j}(\ell_1-\ell_0)\beta(m\cdot\varphi)\right]\varphi \tag{2}$$

where $\varphi \in \left((j-1)\frac{2\pi}{m}, j\frac{2\pi}{m}\right)$, for all $j = 1,\ldots,m$. $-\alpha r$ describes the phase profile associated with an axicon, while $\Phi_{lens} = -k\sqrt{(r^2+f^2)} - f$ provides the geometrically aberration-free focusing phase profile, where f is the focal length and $k = 2\pi/\lambda$ is the wavenumber. In addition, the function $\beta(\cdot)$ introduces a smoothly varying azimuthal phase gradient within each of the m sectors into which the ring is divided where, m defines the azimuthal sectors over the ℓ_0 the background topological charge, ℓ_1 controls the strength of the gradient and H_G^j and H_C^j are Heaviside-like binary functions that control the gradient sign and the local charge inversion within each sector. In both cases, it is possible to generate multiple beams using the same metalens using the phase equalization method. [2] Two DFML were fabricated using electron-beam lithography and inductive-coupled plasma reactive ion etching processes. The optical characterization their output field generating two-arm helico-conical vector beam and double-ring azimuthally-variant vector beams with linear phase gradients are depicted in Figure 1. The reported findings showcase the transformative potential of metasurfaces for generating complex structured light fields, specifically through meticulous design and nanofabrication that offers unprecedented control over the phase and polarization patterns in both two and three dimensions.

Acknowledgments: This work was founded by Project STRADA and partially supported by the European Union under the Italian National Recovery and Resilience Plan (NRRP) of NextGenerationEU.

References

1. Vogliardi, A., Ruffato, G., Bonaldo, D., Zilio, S. D., and Romanato, F. (2023). Silicon metaoptics for the compact generation of perfect vector beams in the telecom infrared. *Opt. Lett.*, 48(18), 4925-4928.

2. Vogliardi, A., Bonaldo, D., Dal Zilio, S., Romanato, F., and Ruffato, G. (2024). Helico-conical vector beams for intensity and polarization 3D light shaping. *Optica*, 11(12), 1628-1631.

Flat Optics for Hybrid Grafted Vortex Beams and Azimuthally Tailored Multispectral OAM Combs

Hammad Ahmed[1,*] and Xianzhong Chen[1]

[1]Institute of Photonics and Quantum Sciences, School of Engineering and Physical Sciences, Heriot-Watt University, Edinburgh, EH14 4AS, UK.

*Corresponding author: H.Ahmed@hw.ac.uk

Abstract: We demonstrate a compact flat-optics (metasurface) platform for generating and dynamically controlling hybrid grafted vortex beams and azimuthally tailored multispectral OAM combs. By superposing multiple helical phase profiles, beams with precisely customized topological charges and multispectral OAM spectra are achieved, offering new avenues for optical encryption, communications, and particle manipulation.

This work presents a novel metasurface-based approach for generating and controlling hybrid grafted vortex beams (GPVBs) and azimuthally tailored multispectral orbital angular momentum (OAM) combs, addressing key limitations in conventional optical systems. Grafted vortex beams [1], formed by combining multiple helical phase profiles, exhibit unique optical properties and offer promising applications in fields such as singular optics and quantum science. However, current methods for generating GPVBs rely on complex and bulky setups. Our approach utilizes a single metasurface to generate various superpositions of GPVBs with different topological charges, enabling the formation of asymmetric singularity distributions. The design allows the modulation of singularity positions via an initial phase difference, eliminating the need for intricate optical configurations.

In addition, we explore the generation of hybrid perfect vector vortex beams (GPVVBs) [2], which are produced by superimposing grafted vortex beams using a multifunctional metasurface. These hybrid beams have spatially variant polarization characteristics, providing enhanced design flexibility with multiple topological charge combinations. A rotating half-waveplate is introduced to dynamically control the hybrid beams, opening new possibilities for dynamic applications such as optical encryption and dense data communication.

Furthermore, the metasurface platform is extended to create multispectral OAM combs with customized mode spacings, enabling a compact and efficient solution for generating OAM spectra in multiple dimensions, and enhancing information capacity for optical communication and other emerging applications [3].

References

[1]. Ahmed, Hammad, et al. "Multichannel superposition of grafted perfect vortex beams." Advanced Materials 34.30 (2022): 2203044.

[2]. Ahmed, Hammad, et al. "Dynamic control of hybrid grafted perfect vector vortex beams." Nature Communications 14.1 (2023): 3915.

[3]. Ahmed, Hammad, et al. "Customizing Multicolored Orbital Angular Momentum Combs." Nano Letters (2025).

Tamm Plasmon for the enhancement of Light Matter Interaction

A. Rossini[1,2*], F. Marangi[2,3], C. Florindi[2,4], A. Pianetti[1,2], F. Lodola[2,4], F. Scotognella[3], G. Lanzani[1,2] and G. M. Paternò[1,2]

1. Department of Physics, Politecnico di Milano, Milano, Italy
2. Center for Nano Science and Technology, Istituto Italiano di Tecnologia, Milano, Italy
3. Department of Applied Science and Technology, Politecnico di Torino, Torino, Italy
4. Department of Biotechnology and Biosciences, University of Milano-Bicocca, Milano, Italy

andrea.rossini@polimi.it

Abstract

Tamm Plasmon (TP) modes, formed at the plasmonic layer-DBR interface, enable strong light confinement and coupling. This work explores TP modes ability to detect and modulate phenomena at the biotic-antibiotic interface, demonstrating their potential for advanced photonics and biological applications.

Introduction

Tamm Plasmon (TP) modes are a form of Surface Plasmon Resonance (SPR) that can be excited at the interface between a plasmonic layer and a distributed Bragg reflector (DBR). In recent years, interest in TP-based devices has significantly increased due to their unique properties, such as strong confinement of electromagnetic fields and efficient coupling of incident light to localized surface modes. These features make TP devices an ideal platform for the development of novel optoelectronic and photonics applications [1,2]. Previous studies [3] have demonstrated that introducing nanoscale corrugations on the free surface of the plasmonic layer can enable interactions between the confined electromagnetic field and the external interface of the device.

Here, we exploit these capabilities of TP modes to modulate phenomena at the biotic-abiotic interface. So, I discuss the TP-driven enhancement of the phototransduction activity of conjugated polymers at the interface with living cells, enabling photostimulation of biological signaling.

References

1. Kar, C., S. Jena, D.V. Udupa, and K. D. Rao, “Tamm plasmon polaritons in planar structure: A brief overview and applications”, Optics & Laser Technology, 159, 108928, 2023
2. Normani et al., “The impact of Tamm plasmons on photonic crystals technology”, Physica B: Condensed Matter, 645, 414253, 2022
3. Normani et al.,”Tamm Plasmon Resonance as Optical Fingerprint of Silver/Bacteria Interaction”, ACS Appl. Mater. Interfaces, 15, 27750-27758, 2023

Acoustically Driven Soft Metasurfaces

S. P. Selvin[1,2*], J. D. Carlstrom[1], Mohammad Taghinejad[1], and M. L. Brongersma[1]

[1]Geballe Laboratory for Advanced Materials, Stanford University; Stanford, CA, USA.
[2]Department of Electrical Engineering, Stanford University; Stanford, 94305, USA
[*]corresponding author: selvin@stanford.edu

Abstract: We utilize mechanically compliant materials in a nanophotonic resonator designed to trap light at dimensions comparable to gigahertz-scale acoustic displacements. This configuration enables rapid modulation and sculpting of optical fields, paving the way for fast, adaptable metasurfaces poised to advance future photonic technologies.

Mechanical approaches to controlling light remain among the most reliable methods and have been widely employed since optics began. Typically, such methods rely on physically shifting sizable optical parts, which inherently restricts the modulation speed. Reducing the scale of these movable components can help increase their speed. While significant progress in Micro-Electromechanical Systems (MEMS) has been made thanks to modern nanofabrication techniques [1,2], these systems generally cap out at only a few megahertz. Conversely, acoustic waves are among the fastest mechanical modulation schemes, but the small displacements involved have traditionally been insufficient to considerably affect optical fields.

In this work, we introduce a novel nanoscale opto-mechanical resonator that confines light to dimensions comparable to the typical displacements of gigahertz acoustic waves. By using mechanically compliant materials in tandem with an optical plasmon mode, we exploit surface acoustic waves to reshape the amplitude and phase of the optical field. Our results illustrate a notable resonance shift—extending from approximately 700 nm to 600 nm—and confirm modulation rates beyond 1 GHz. Furthermore, by tailoring the excitation profile of these acoustic waves, we achieve dynamic control of optical amplitude and phase distributions across the device surface, enabling beam steering and lensing without large-scale moving parts.

These findings mark a significant breakthrough in the field of acousto-optic modulation by proposing a flexible platform for high-speed modulation and precise manipulation of materials at nanometer and nanosecond scales. By designing mechanical components that match gigahertz acoustic displacements, we open new possibilities for advanced, dynamic optical metasurface technologies.

References

1. Meng, C. et al., “Dynamic piezoelectric MEMS-based optical metasurfaces,” Sci. Adv., Vol. 7, 2021.
2. Song, J. H. et al., “Nanoelectromechanical modulation of a strongly-coupled plasmonic dimer,” Nat. Commun., Vol. 12, No. 1, Dec. 2021.

Surface Enhanced Raman Spectroscopy (SERS) based on a polarization-insensitive nanoparticle-on-a-slit cavity with dielectric waveguide.

D. Arenas-Ortega[1], J. Redolat[1], A. Barreda[2], A. Griol[1], E. Pinilla-Cienfuegos[1*], A. Martínez[1*]

[1] Nanophotonics Technology Center, Universitat Politècnica de València, Camino de Vera, s/n, Edificio 8F, Valencia, 46022, Spain

[2]Department Electronic Technology, Carlos III University of Madrid, Avda. De la Universidad 30, Leganés, 28911, Spain

[*]corresponding author: epinilla@ntc.upv.es; amartinez@ntc.upv.es

Abstract: Nanoparticle on a slit (NPoS) is a nanometer cavity for extreme light confinement. In this work we present the simulation and characterization of a NPoS to work in the visible and infrared range with polarization-insensitive fashion for surface enhanced Raman spectroscopy (SERS).

In this work we present a new configuration for surface enhanced Raman spectroscopy with dielectric waveguides. The studied cavity is called nanoparticle on a slit. It is made of three structures, the first one is two patches of gold separated by a narrow slit of 120 nm, on top of the two patches a dielectric layer of a 1 nm thickness of a certain molecule is functionalized. The last part is a gold nanoparticle placed in the middle of the slit. Light is coupled in and out of the cavity by using a silicon nitride slot waveguide with a 200 nm air gap. A microscope image and a scanning electron image (SEM) of the studied structure are shown in Figure 1 b).

For the fabrication process, first, a gold infrared/visible light antenna made of two rectangular slits with 2500 nm length, 100 nm width and 50 nm thickness are deposited by metal evaporation. Then, the gold surface is functionalized with a self-assembled monolayer of Biphenil-4-thiol (BPT) [1], creating a dielectric interface with a nano-meter gap. In the slit between the two gold patches is placed accurately a gold spherical nanoparticle with 150 nm diameter. The nanoparticle is placed using a soft-lithography method. The method consists of using a PDMS stamp with micropillars to transfer the nanoparticle by capillarity onto the slit, as it is shown in Figure 1 a) [2].

Finite-difference time-domain simulations show that both TE and TM can excite the surface plasmon resonance of the nanoantenna at wavelengths around 750 nm. This resonance can be pushed towards the infrared region by changing the length of the strips. Furthermore, simulations show that the localized field in the BPT monolayer between the gold nanoparticle and the slit is perpendicular to the gold surface, independently of the polarization of the excitation mode. So, the excited vibrational states of the BPT molecule will remain the same.

The sample was characterized using a commercial Raman setup at an excitation wavelength of 633 nm. The light is coupled into the waveguide by means of a 50x objective, the incident mode excites the NPoS cavity and the Raman scattering of the BPT is propagated backwards by the slot waveguide and collected by the objective, as it is shown in Figure 1 c). BPT presents three main vibrational resonances related to the chemical bonds of the elements that compose the molecule. That vibrational resonance produces a certain Raman shift at 1090, 1280 and 1580 cm^{-1}, respectively. A typical Raman spectrum of BPT for bulk or Nanoparticle on a mirror (NPoM) cavity is plotted in Figure 1 d). Finally, in Figure 1 e) it is shown the measured Raman scattering of the BPT molecules that comprises the NPoS cavity. It can be noticed in Figure 1 f) that the signal measured for TM is more intense than that for the TE mode caused by the difference in the coupling efficiencies. Even though both

Raman scattering signals have the same order of magnitude, in contrast to other configurations, in which the Raman scattering signal for TE or TM will have different order of magnitude.

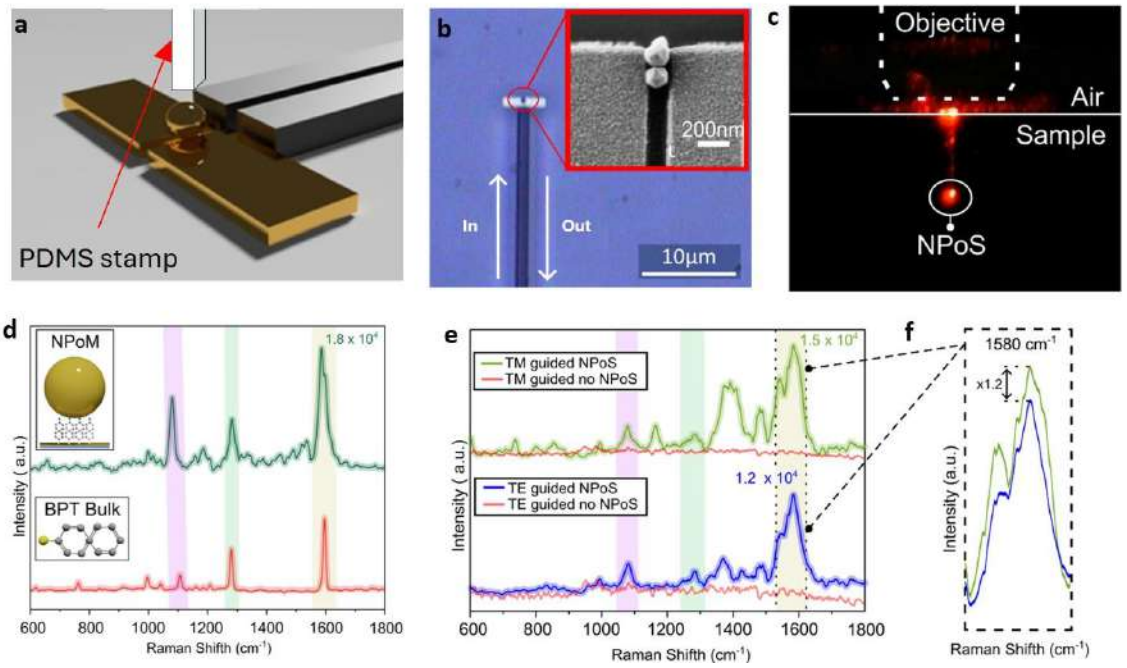


Figure 1. a) Schematic view of the soft-lithography method for accurate nanoparticle transfer using PDMS stamp. **b)** Microscope image and scanning electron microscope image of the NPoS structure. **c)** Experimental set-up configuration used to inject and collect light from the waveguide and excite the NPoS cavity. **d)** Nanoparticle-on-a-mirror BPT's Raman scattering signal and BPT bulk Raman scattering signal. **e)** NPoS BPT's Raman scattering signal excited by TM and TE modes of a slot Si_3N_4 waveguide**. f)** Zoomed image of the 1580 cm^{-1} vibrational resonance of the BPT.

References

1. Matei, D. G., H. Muzik, A. Gölzhäuser, and A. Turchanin, "Structural investigation of 1,1-biphenyl-4-thiol self-assembled monolayers on Au(111) by scanning tunneling microscopy and low-energy electron diffraction," *Langmuir*, Vol. 28, No. 39, 13905–13911, 2012.
2. Redolat, J., et al., "Accurate transfer of individual nanoparticles onto single photonic nanostructures," *ACS Appl. Mater. Interfaces*, Vol. 15, No. 3, 3558–3565, 2023.
3. Zhang, W., L. Huang, C. Santschi, and O. J. F. Martin, "Trapping and sensing 10 nm metal nanoparticles using plasmonic dipole antennas," *Nano Lett.*, Vol. 10, No. 3, 1006–1011, 2010.

Experimental observation of Bound States in the Continuum in fully semiconductor Subwavelength Gratings

W. Głowadzka[1,2*], T. Fąs[3], K. Gaur[4], F. Laudani[4], S. Tripathi[4], N. Heermeier[4], J. Suffczyński[3], S. Reitzenstein[4], T. Czyszanowski[2]

[1] Łukasiewicz – Institute of Microelectronics and Photonics, Poland
[2] Institute of Physics, Lodz University of Technology, Poland
[3] Institute of Experimental Physics, Faculty of Physics, University of Warsaw, Poland
[4] Institut für Festkörperphysik, Technische Universität Berlin, Germany

[*]corresponding author: weronika.glowadzka@imif.lukasiewicz.gov.pl

Abstract: Subwavelength Gratings (SGs) support Bound States in the Continuum (BICs), enabling high-quality factor resonances. To improve mechanical stability, vertically nonsymmetric SGs (VN-SGs) are formed by placing a GaAs membrane on an AlAs substrate. We demonstrate the first experimental observation of BICs in GaAs-AlAs SG, advancing toward future electrically pumped devices.

Subwavelength gratings (SGs) are periodic structures composed of high-refractive-index grating slabs, surrounded by lower-refractive-index material on both sides. When the material beneath the grating is air, the structure is referred to as a "membrane." In this configuration, it is possible to achieve an infinite quality factor (Q), indicating the presence of bound states in the continuum (BICs) [1]. A similar behavior is observed in vertically symmetric subwavelength gratings (VS-SGs), where the grating is symmetrically embedded in a low-refractive-index material. However, VS-SGs pose fabrication challenges and are mechanically fragile, particularly in the case of membranes.

To enhance mechanical stability, the vertical symmetry of the structure must be broken by placing the membrane onto a solid substrate, forming a vertically nonsymmetric subwavelength grating (VN-SG, Fig. 1). For practical applications, these structures are often envisioned for electrically pumped devices, requiring both high electrical and thermal conductivity of the membrane and substrate. In [2] we demonstrated that despite the low refractive index contrast (as small as Δn=0.04) between the membrane and the substrate, BICs can still emerge in VN-SGs. Furthermore, we showed that in finite structures, the localization of BICs in an infinite system corresponds to local maxima of the quality factor. In a system composed of a GaAs membrane on an AlAs substrate, quality factors on the order of 10^4 were observed in 2D simulations.

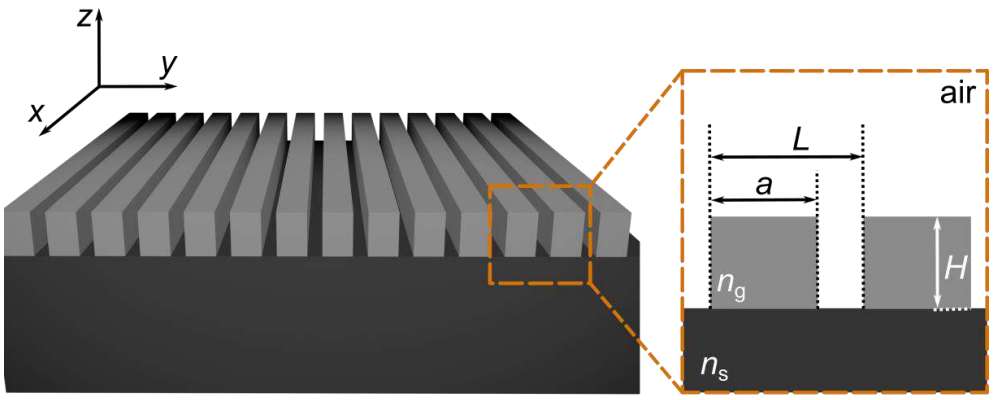


Figure 1. Vertically nonsymmetric subwavelength grating made of high refractive index grating (light gray) and bulky substrate (dark gray) with coordinate system (top panel). Bottom panel presents key parameters of a VN-SG namely refractive index of grating and substrate – n_g and n_s respectively, H – etching depth, a – width of a single stripe, L – period of the grating. In our work we demonstrate results for GaAs grating (n_g=3.52) and AlAs substrate (n_s =2.95).

In this study, we report the first experimental demonstration of BICs in real-world SGs that have been fabricated from GaAs grown on AlAs substrate. This configuration results in a fully monolithic semiconductor subwavelength grating, offering a robust and scalable platform for photonic applications. Our findings provide direct evidence of BIC formation in practical device structures, highlighting their potential for enhancing optical confinement and control in semiconductor-based systems. The successful realization of BICs in these structures represents a significant step toward achieving efficient light emission from SGs. Furthermore, these results open new possibilities for the integration of subwavelength gratings with electrically pumped devices, paving the way for the development of compact and high-performance semiconductor light sources.

This work is supported by the Polish National Center of Science within the project SONATA BIS 13 (grant no. 2023/50/E/ST7/00698).

References

1. Hsu, C., Zhen, B., Stone, A. et al. Bound states in the continuum. Nat Rev Mater 1, 16048, 2016
2. Głowadzka W., Wasiak M., Czyszanowski T., “True- and quasi-bound states in the continuum in one-dimensional gratings with broken up-down mirror symmetry,” Nanophotonics, vol. 10, no. 16, pp. 3979-3993, 2021

MEMS-tunable Multifunctional Optical Metasurfaces For Advanced Imaging

Z. H. Zhu[1,2,3,4*], C. Meng[1], M. W. Tang[2,3,4] , S. I. Bozhevolnyi[1] and K. Wei[2,3,4]

[1]Centre for Nano Optics, University of Southern Denmark, Campusvej 55, Odense DK-5230, Denmark

[2]Zhejiang Key Laboratory of Autonomous Optoelectronic Perception, College of Optical Science and Engineering, Zhejiang University, Hangzhou 310027, China

[3]ZJU-Hangzhou Global Scientific and Technological Innovation Center, Zhejiang University, Hangzhou 311215, China.

[4]State Key Laboratory of Extreme Photonics and Instrumentation，College of Optical Science and Engineering, Zhejiang University, Hangzhou 310027, China

[*]corresponding author: zhu@mci.sdu.dk

Abstract: The latest progress of piezoelectric MEMS tunable multifunctional optical metasurfaces (OMS) for advanced imaging is presented. Switching between different imaging modes can be achieved by varying the MEMS actuation voltages.

Optical metasurfaces (OMS) have emerged as transformative platforms for next-generation compact imaging systems by enabling precise light manipulation at subwavelength scales[1]. Among these, dynamic metasurfaces hold immense potential for realizing intelligent imaging devices with adaptive functionalities, such as tunable focal lengths and steerable focal spots. Recent advances leverage active materials like liquid crystals (LCs)[2] or phase-change materials (PCMs)[3] to achieve reconfigurability, yet fundamental limitations remain. LC-based systems suffer from polarization dependence and slow response times, while PCMs lack reversibility and speed. Conversely, approaches using 2D materials, though faster, exhibit weak modulation strength. To address these challenges, we propose a MEMS-integrated optical metasurface (MEMS-OMS) platform that combines a piezoelectric MEMS mirror with a plasmonic metasurface for dynamic wavefront shaping. Here, building on our developed MEMS-OMS platform, we designed a MEMS tunable bilayer metasurfaces as a varifocal lens operating at 800 nm wavelengths, under circularly polarized incidence.

Our MEMS-OMS design features a bilayer metasurface fabricated on a glass substrate assembled with a piezoelectric MEMS mirror (Fig.1). By applying an actuation voltage, the MEMS actuator induces out-of-plane nanoscale displacement of the mirror, thereby modulating the two-dimensional phase profiles of the reflected light. This tuning mechanism bypasses material limitations due to accessible refractive index changes, resulting in high efficiency and response speeds up to the MHz range. As a proof of concept, we demonstrate a metasurface that can switch the reflected light focusing at two distinct positions (i.e., different focal lengths and lateral shifts) by switching between two voltage sets. These functions are achieved by leveraging the design flexibility offered by the bilayer metasurface, where the displacement of the MEMS driven mirror is directly mapped to a customized phase distribution. Finite-difference time-domain (FDTD) simulations reveal that by switching the MEMS-OMS separation between 350 nm and 500 nm, varifocal lenses are achieved, indicating the distinct wavefront modulation encoded in the reflected light, which validates our design.

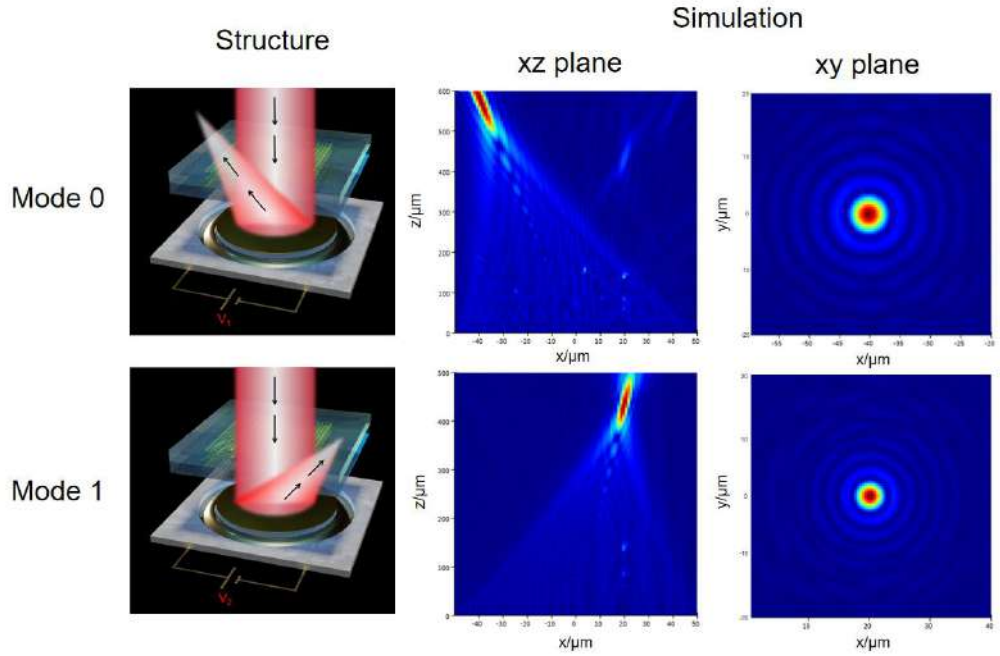


Fig.1 MEMS-OMS varifocal lens.

Looking ahead, this MEMS-OMS platform opens avenues for compact, multifunctional imaging systems. Applications span miniaturized endoscopic probes with adjustable focus, LiDAR systems with dynamically programmable scanning foci, and augmented reality (AR) displays requiring real-time aberration correction. We are also attempting to implement reconfigurable optical computing functions based on this configuration. This work emphasizes the synergistic effects between MEMS and meta-optics, which could potentially serve as a reliable platform for high-performance, adaptive optical systems.

References

1. Yu, N. and F. Capasso, “Flat optics with designer metasurfaces,” Nat. Mater., Vol. 13, 139–150, 2014.
2. Abdelraouf, O. A. M., Z. Wang, H. Liu, Z. Dong, Q. Wang, M. Ye, X. R. Wang, Q. J. Wang and H. Liu, “Recent Advances in Tunable Metasurfaces: Materials, Design, and Applicationsr,” ACS Nano, Vol. 16, No. 9, 13339–13369, 2022.
3. Ding F., Y. Yang and S. I. Bozhevolnyi, “Dynamic metasurfaces using phase-change chalcogenides,” Adv. Opt. Mater., Vol. 7, No. 14, 1801709, 2019.
4. Meng, C., P. C. V. Thrane, F. Ding, J. Gjessing, M. Thomaschewski, C. Wu, C. Dirdal and S. I. Bozhevolnyi, “Dynamic Piezoelectric MEMS-Based Optical Metasurfaces,” Sci. Adv., Vol. 7, No. 26, 5639, 2021.
5. Thrane, P. C. V., C. Meng, F. Ding and S. I. Bozhevolnyi, “MEMS Tunable Metasurfaces Based on Gap Plasmon or Fabry-Pérot Resonances,” Nano Lett., Vol. 22, 6951–6957, 2022.
6. Meng, C., P. C. V. Thrane, F. Ding and S. I. Bozhevolnyi, “Full-Range Birefringence Control with Piezoelectric MEMS-Based Metasurfaces,” Nat. Commun., Vol. 13, No. 1, 2071, 2022.

Evolution of Quantum Plasmonics in Relatively Large Doped Quantum Dots

D. Subedi, D. Dada and M. Mochena*
Florida A&M University
Tallahassee, FL, USA
***Corresponding author: mogus.mochena@famu.edu

Abstract: Two model Hamiltonians have been employed to investigate the evolution of plasmonics as a function of the number of electrons confined in a potential well in the first case[1] and a jellium model[2] in the second case. Here, we present results of DFT+U[3,4] as well as TDDFT studies on discrete crystal lattice.

Summary
The evolution of quantum plasmonics has been studied with two model Hamiltonians. In the first case, the conduction electrons are confined within a potential box and their oscillatory behavior was studied as a function of the number of electrons. In the second case, TDDFT study was applied to electrons distributed uniformly through a sphere or on the surface, confined by the jellium positive background charge. The jellium model is argued to apply in the highly doped limit. While these studies establish the evolution of plasmonics, in order to apply the findings, structural dependent studies must be performed to determine what materials manifest strong plasmonic behavior and why they do it. In particular, there are intriguing photodoping experimental results by two groups[5,6] that claim excitations of few electrons can lead to quantum plasmonics. This finding was only addressed at qualitative level in the jellium model by extrapolating the computational results obtained for highly doped QDs for which the jellium model is applicable. The model, however, cannot be justified in the limit of low level of doping where the discreteness of the lattice must be taken into account. Such findings are exciting on their own right from magneto-opics point of view as it is well established in diluted magnetic semiconductors, very few dopants lead to ferromagnetism. Thus, there is a potential to couple plasmonics with magnetism in the low doping limit.

Initially, we performed first principles calculations of density functional theory, with the Hubbard U correction, to see if localized surface plasmonic resonances can be sustained by doping a wide bandgap ZnO with few shallow donors of Ga. We distributed 3–6 dopants approximately uniformly, due to quasi-spherical geometry of the quantum dot, in the dilute doping limit. The uniform distribution of dopants in quantum dots has been reported experimentally. Although the dopant configurations are limited due to computational cost, our findings shed light on absorption trends. Results for quantum dots of 1.4 nm, passivated with pseudo-hydrogens, show that localized surface plasmonic resonances can be generated in the near infrared range. The absorption linewidths for such small-sized quantum dots are broad. We find that the resonance linewidth depends on the orientation of surfaces and the number of secondary peaks on the concentration of dopants. The absorption coefficients, as functions of the principal values of the dielectric tensor, indicate that an electric field with orientation parallel to that of the most symmetric surface will produce localized surface plasmonic resonances with high quality factors.

The broadness of the absorption spectral lines for a small QD led us to look into a larger ZnO QD. There are no studies of quantum plasmonics of large quantum dots of the size of Bohr excitonic radius

or less that take electronic and geometric structure of the quantum dots. In this work, we studied extensively the absorption spectra of a protype quantum dot of sizeable ZnO of approximately 3.0 nm in diameter consisting of 1580 atoms, doped with Ga, and Al in diluted limit with density functional theory (DFT) plus Hubbard corrections (U). The localized surface plasmon resonances (LSPRs) were then determined from the real part of the dielectric function by correlating the negative portion of it to resonant spectral lines. Our results show the sensitivity of the spectral lines to distribution of the dopants, the electronic structure of the dopants, the polarization of the electric field, and size of the quantum dots. Even though our findings are based on stoichiometrically simple ZnO, it shows that the DFT + U method with numerical atomic basis can be used at reasonable computational cost, in contrast to time dependent DFT, to study quantum plasmonics of few electrons taking into account electronic and geometric structures, which is currently missing.

Recently, we have extended our research to include the TDDFT approach to study the whole spectrum of doping and examine the evolution of quantum plasmonics. Our current computations of DFT+U of the 3.0 nm QD was studied with SIESTA code which can handle large QDs of the sizes used in experiments. SIESTA has recently incorporated capabilities to compute TDDFT, as a result we will be able to compare the DFT+U results with DFT + U ones. In addition, we are beginning to work with the Octopus code which is geared to studying TDDFT properties of large systems. The octopus code uses the real space grid to perform the computations unlike the reciprocal space commonly used in most codes. By attacking the quantum plasmonics problem from two different approaches, we hope to gain a comprehensive understanding of the phenomena. We will present our current findings in the talk.

References

1. P. K. Jain, “Plasmon-in-a-Box: On the Physical Nature of Few-Carrier Plasmon Resonances, “J. Phys. Chem. Lett. 5, 3112 (2014).
2. Zhang, H., Kulkarni, V., Prodan, E., Nordlander, P., and Govorov, A. O. “Theory of Quantum Plasmon Resonances in Doped Semiconductor Nanocrystals,” J. Phys. Chem. C 118, 16035 (2014).
3. J. A. Faucheaux, A. L. D. Stanton, and P. K. Jain, J. Phys. Chem. Lett. 5, 976 (2014).
4. M. Schimpf, N. Thakkar, C. E. Gunthardt, D. J. Masiello, and D. R. Gamelin, “Charge-Tunable Quantum Plasmons in Colloidal Semiconductor Nanocrystals,” ACS Nano 8, 1065
5. Dada, D., Kurian, G., Mochena, M. D. “Quantum plasmonics of few electrons in strongly confined doped semiconducting oxide: A DFT + U study of ZnGaO,” J. Appl. Phys. 131, 173101 (2022).
6. D. Dada and M. D. Mochena, A DFT + U Study of Absorption Spectra and Localized Surface Plasmon Resonances of few electrons in Doped ZnO Quantum Dots, arXiv:2401.00074, 2023.

Acknowledgement

D.D. and M.D.M were supported by the National Science Foundation Grant No. DMR-2013854. M.D.M. acknowledges computer time allocation (No. TG-DMR100055) from the Extreme Science and Engineering Discovery Environment (XSEDE) for Stampede at TACC, which was supported by the National Science Foundation Grant No. ACI-1548562. M.D.M. also acknowledges computer time at the carbon cluster of the Center for Nanoscale Materials at the Argonne National Laboratory and support from Dr. M. Chan.

Rainbow Trapping with Graded Triangular Grooves for Enhanced Raman Spectroscopy of Biomolecules

Yi Loh[1]

[1]National University of Singapore, SHINE Centre, Block E6, 5 Engineering Drive 1, Singapore

Abstract: Graded triangular gratings can be used for rainbow trapping biosensors. Wavelength-dependent phase reflection requires precise corrections to groove depths to achieve adiabatic condition. Optimized tapered grooves enable superior multiwavelength trapping and localized field intensities, boosting SERS sensitivity with enhancement factors up to 10^{10} for >10 nm molecules.

Summary: The concept of rainbow trapping, wherein different wavelengths are spatially localized at different positions along the graded structure, can enable broadband hyperspectral amplification of biomolecule model signals[1]. This can achieved by narrow slit grooves of high aspect ratios and graded depth over the grating length, in order to achieve adiabatic condition and field localization as well as multiwavelength trapping, yet the poor access of biomolecules to reach the bottom of these grooves is a major limitation. We show that graded triangular grooves (**Figure 1**) can achieve both adiabaticity[2,3] and sensing of large >10 nm sized molecules. Narrower grooves confine the plasmonic modes more tightly, while deeper grooves support multiple resonant modes.

One of the key findings is the significant influence of groove angle (**Figure 2**). Groove angles ~17.5°, 20°, and 25° were found to be critical in shaping the phase response and confinement characteristics of surface plasmon polaritons (SPPs) within the grooves. These angles determine the effective metal-insulator-metal (MIM) waveguide geometry that the groove forms and thus the propagation constant of the SPPs along the groove depth. The total reflection phase at the groove terminus is not constant in triangular grooves unlike slit grooves, which requires a wavelength-dependent phase shift correction to the groove depth. Theoretical estimations based on fixed parameter often underestimate the actual depth required for accurate resonance. Adjusting the groove depth by 10–20 nm across the visible to near-infrared spectrum brings theoretical predictions into better alignment with simulation and experimental data.

The triangular grooves are especially suitable for label-free biosensing applications. With groove widths on the order of 10 nm, these structures can effectively trap and enhance signals from small biomolecules, including hemoglobin, Rhodamine 6G, and lipid molecules (**Figure 3**). We report SERs enhancement factors as high as 5×10^{9}, which exceed those typically achieved with rectangular or cylindrical groove designs

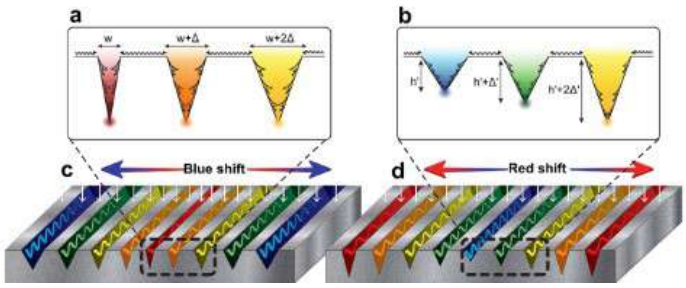


Figure 1. Schematic diagram of graded triangular gratings. (a) and (c) show that width-graded gratings undergo a blue shift, while conversely, (b) and (d) show that a depth graded grating undergoes a red shift. Nano-focusing at the top of the grating and intra-groove coupling are illustrated with arrows.

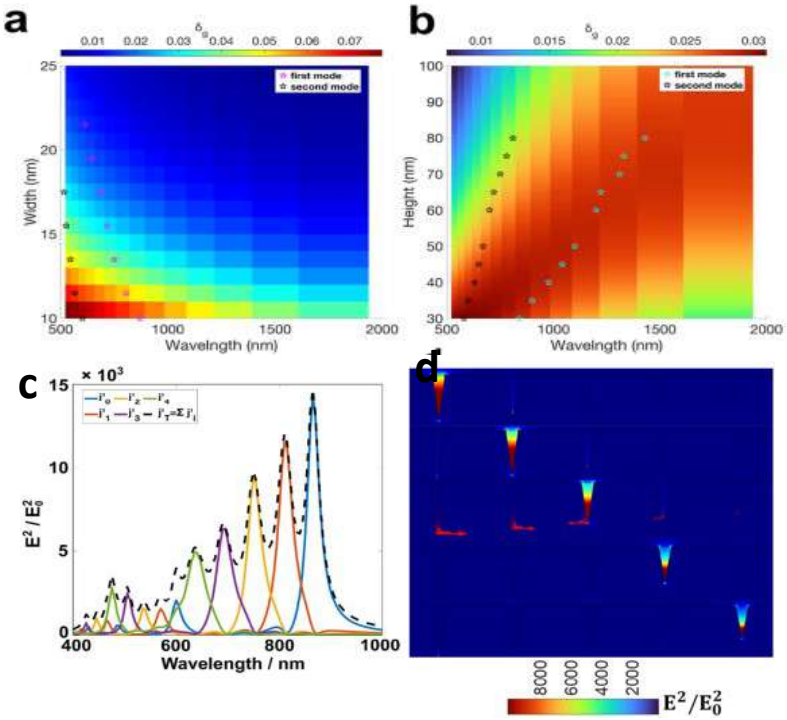


Figure 2. Variation of the adiabatic parameter for (**a**) width-graded gratings where the depth of the central grating is 30 nm, Δ = 5 nm, and w = 10 nm, and (**b**) depth-graded gratings where the width of the central grating is w' = 10 nm, Δ' = 2 nm, and d' = 50 nm. (**c**) Design of graded triangular gratings: localized field intensity inside depth graded grating: j_i, j'_i resembles the i-th groove inside the grating and j_T, j'_T is the total field intensity of all grooves. (**d**) COMSOL simulations of the electric field intensity inside the resonating groove. In addition, the E_x field is plotted with red arrows as an indication of the adiabatic mode transformation.

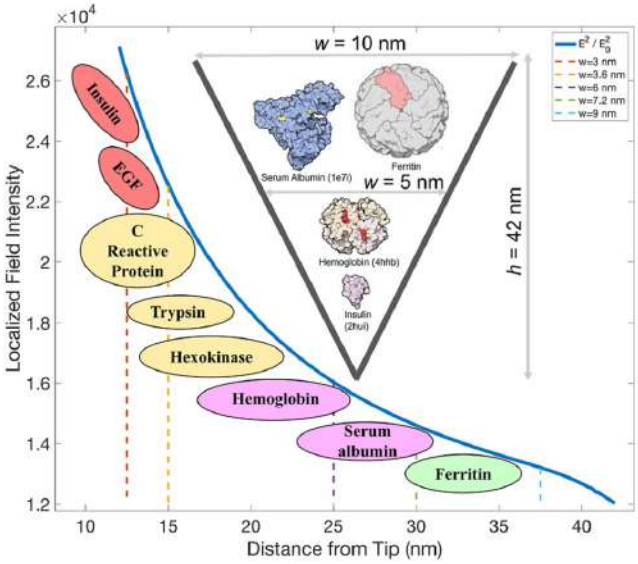


Figure 3. Various small and large bio-molecules fit within the triangular nano-groove with a width of 10 nm and a depth of 42 nm. Molecules smaller than 6 nm, which include hemoglobin, are likely to be detected under a high field greater than 1.5×10^4.

References

1. M. J. Banholzer et al. "Rationally designed nanostructures for surface-enhanced Raman spectroscopy," Chem. Soc. Rev. 37(5), 885–897 (2008)
2. M. Shayegannia et al., "Adiabatic mode transformation in width-graded nano-gratings enabling multiwavelength light localization," Sci. Rep. **11**(1), 669 (2021).
3. A. O. Montazeri et al., "Rainbow-trapping by adiabatic tuning of intragroove plasmon coupling," Opt. Express **24**(23), 26745 (2016)

Magnetic field induced shift in LSPR of photochemical synthesized ZnO/Ag nanocomposites

R. A. Redko[1], V. V. Shvalagin[2], G.V. Milenin[1], S.M. Redko[1]

[1] V. Lashkaryov Institute of Semiconductor Physics of the National Academy of Sciences of Ukraine, Ukraine
[2]L. Pysarzhevskii Institute of Physical Chemistry of the National Academy of Sciences of Ukraine, Ukraine
corresponding author: redko.rom@gmail.com

Abstract: The influence of the ZnO nanoparticles magnetic field pre-treatment on the position of the plasmon resonance peak in ZnO/Ag nanocomposites was detected. "Memory effect" during 30 days after magnetic field pre-treatment was observed. Possible physical mechanism related to feromagnetic-like behaviour of ZnO nanoparticles is discussed.

The ethanol solutions of the ZnO nanoparticles were placed in a constant and homogeneous weak magnetic field (B = 60 mT). Exposure time in the field was: 1 hour, 1 day and 5 days. These solutions were used for photocatalytic formation of ZnO/Ag nanoheterostructures under the action of UV irradiation. The production cycle was repeated during 30 days. During this time, the evolution of the obtained optical absorption spectra of solutions containing ZnO/Ag nanoparticles were measured on a Specord 210 spectrophotometer (relative to a cuvette with pure ethanol) and SEM microscopy data. For reliability of the received results the solution which was not exposed in magnetic field, but stored together with all samples at the same temperature conditions was used as a reference. Under the UV action, photocatalytic reduction of Ag (I) and the formation of a ZnO/Ag colloidal heterostructure occurs, which is characterized by an absorption maximum at 400–460 nm.

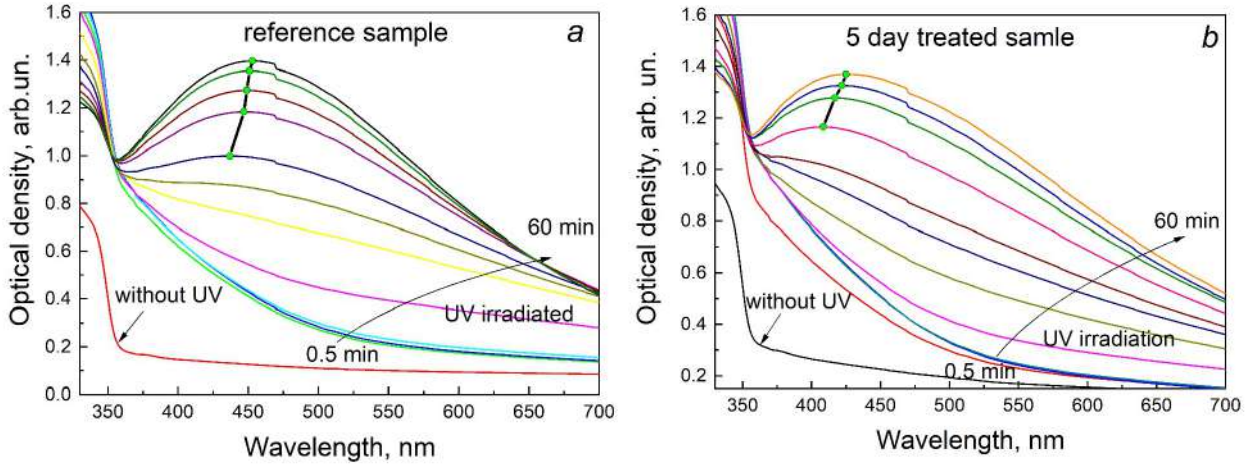


Fig. 1. OD spectra for the reference sample (a) and the pre-treated during 5 days (b) one at different UV radiation doses. The curves labeled ‘without UV’ are obtained for the solutions containing ZnO NPs, silver nitrate and sulfur before UV irradiation.

Moreover, increasing the UV dose leads to a long-wavelength displacement of this peak. These processes are characteristic for all studied samples. But the energy positions of the observed peak at low and maximum doses of weak magnetic field treatment do not match. It was found that within 30 days the final position of the maximum of plasmon absorption of the Ag, which were formed on ZnO cores, that have been undergone magnetic field treatment, slowly shifts to the position of the latter in the reference sample. The latter

circumstance indicates a "memory effect" that lasts for a month.

Ferromagnetic-like behavior of ZnO nanostructures was observed earlier [1, 2]. Not only for nanoparticles [3] but also for nanoflowers [4] and nanoroads [5]. So, physical mechanism of observed modification based on the fact, that a ZnO nanoparticle has a non-zero magnetic moment even without external field owing to the surface states formed by dangling bonds. This is not classical ferromagnetism of course. This moment appears due to oxygen vacancies present. Photoluminescence spectra testify about a lot of them – the broad intensity band near 500 nm, which usually related to V_O, was observed. The behavior of such nanoparticle is similar to the behavior of a ferromagnet in an external magnetic field. In other words, a ZnO nanoparticle will orient itself so to arrange its magnetic moment along the induction of the external field. Longer exposure of particle ensembles in the magnetic field will obviously orient more particles' magnetic moments. This can explain the observed shift of the plasmon absorption maximum, which was proportional to the duration of the magnetic field exposure of the solutions of ZnO nanoparticles in ethanol. The long-term effect observed during 30 days is most likely related to the thermal disordering of the system of "magnetized" ZnO nanoparticles, i.e. due to the thermal motion of atoms and molecules, the studied nanoparticles returned to their initial non-magnetized state.

The shift of SPR peak due to magnetic field influent was observer earlier [6, 7]. Authors relates observed features with the changes of refractive index of studied NPs due to the magnetization. Thus, we have tended to assume that in our case due to magnetization of ZnO NPs the refractive index of the near-surface region of ZnO has changed or/and the shape of ZnO/Ag nanocomposites may be changed due to this too. And all of these result in observed changes in LSPR of ZnO/Ag nanocomposites. The modeling with MiePlot 4.16 Software confirms principal possibility of this assumption

Regardless of the physical reasons and mechanisms of the observed phenomenon, MF pre-treatment may be used as an effective tool for manipulation of plasmon properties of silver-based nanoparticles, which is perspective for creation of new-generation sensor systems.

This work was supported by the IEEE program "Magnetism for Ukraine".

References

1. Ren, H. and G. Xiang, "Morphology-Dependent Room-Temperature Ferromagnetism in Undoped ZnO Nanostructures", Nanomaterials, Vol. 11, 3199, 2021.
2. Kisan, B., J. Kumar and P. Alagarsamy, "Experimental and first-principles study of defect-induced electronic and magnetic properties of ZnO nanocrystals", Journal of Physics and Chemistry of Solids, Vol. 146, 109580, 2020.
3. Zhang, Y. and E. Xie, "Nature of room-temperature ferromagnetism from undoped ZnO nanoparticles", Applied Physics A, Vol. 99, 955-960, 2010.
4. Bie, X., C. Wang, H. Ehrenberg, Y. Wei, G. Chen, X. Meng, G. Zou and F. Du, "Room-temperature ferromagnetism in pure ZnO nanoflowers", Solid State Sciences, Vol. 12, 1364-1367, 2010.
5. J. Wang, S. Hou, H. Chen, L. Xiang, "Defects-Induced Room Temperature Ferromagnetism in ZnO Nanorods Grown from ε-Zn(OH)2", The Journal of Physical Chemistry C, Vol. 118, 19469-19476, 2014.
6. Anggraeni, K., M. Riswan, P.D. Jayanti, D.L. Puspitarum, H. Ardiyanti, P.E. Swastika, N.I. Istiqomah, M. Arifin and E. Suharyadi, "Microstructure, magnetic, and surface plasmon resonance studies of green-synthesized ferrite nanoparticles for biosensor applications," Journal of Magnetism and Magnetic Materials, Vol. 614, 172727, (2025).
7. A.M. Panre, I.M. Yahya, J. Juharni, E. Suharyadi, "Magneto-optic surface plasmon resonance properties of core-shell Fe_3O_4@Ag nanoparticles", Advances in Natural Sciences: Nanoscience and Nanotechnology, Vol. 12, 045011, 2021.

Sequential Deposition of Silver Nanoparticles on Silicon Ripples for LSPR Anisotropy minimization and SERS Applications

Tarundeep Kaur Lamba[1,2*], Sebin Augustine[1,2], K.P. Sooraj[1,2], Mukesh Ranjan[1,2]

[1]Institute for Plasma Research, Bhat Gandhinagar, Gujarat, India 382428

[2]Homi Bhabha National Institute, BARC Training School Complex, Anushaktinagar, Maharashtra, India 400094

[*] tarundeep.lamba@ipr.res.in

Abstract: This work introduces the sequential deposition method for Ag-NPs on a silicon ripple substrate. This method enables the formation of nearly spherical NPs and prevents LSPR anisotropy. The concept is validated through detailed FDTD simulations, experiments, and SERS analysis, demonstrating its effectiveness in enhancing signal uniformity and intensity.

Surface-Enhanced Raman Spectroscopy (SERS) is a highly effective technique for detecting trace amounts of various molecules, finding applications in diagnostics, food safety, forensics, and more [1,2]. For SERS applications, optically isotropic arrays of metal nanoparticles (NPs) are crucial for achieving strong near-field coupling. One way to create such arrays involves low-energy ion beam sputtering (a bottom-up approach), which leads to the formation of regular ripple structures on the surface. These ripple patterns can be tailored by adjusting parameters like ion beam energy, incidence angle, and ion fluence [3], followed by the growth of metal NPs. However, the asymmetric ridges of these ripple patterns often lead to uniaxial growth [4], causing atoms to preferentially align along the ripples and resulting in elongated NP formation over time. In this study, silicon ripples with a typical wavelength of ~30 nm are used as a template as seen in Fig. 1(i). While these types of arrays (Fig. 1(ii)) often result in optically anisotropic substrates and their anisotropic SERS responses. For the first time, we employ the method of sequential deposition of silver (Ag)-NPs to produce isotropic SERS substrates as illustrated in Fig. 1(iii). This sequential deposition provides significant flexibility in fine-tuning the sphericity of the NPs while minimizing the anisotropy present in the sample.

At first, we performed the FDTD simulation to optimize the size and gap of our NP arrays to get optimized field enhancement. The key findings of the simulations are as follows: (i) As the gap (along the ripple 'd') increases, plasmonic coupling weakens, leading to a decrease in electric field enhancement. (ii) The interplay between the gap and aspect ratio significantly influences the shift in the Localized Surface Plasmon Resonance (LSPR) peak and field enhancement. (iii) Notably, when the aspect ratio satisfies 'a = b,' nearly spherical NPs form, ensuring uniform field enhancement along and across the ripple, as shown in Fig. 1(iv)-(vi).

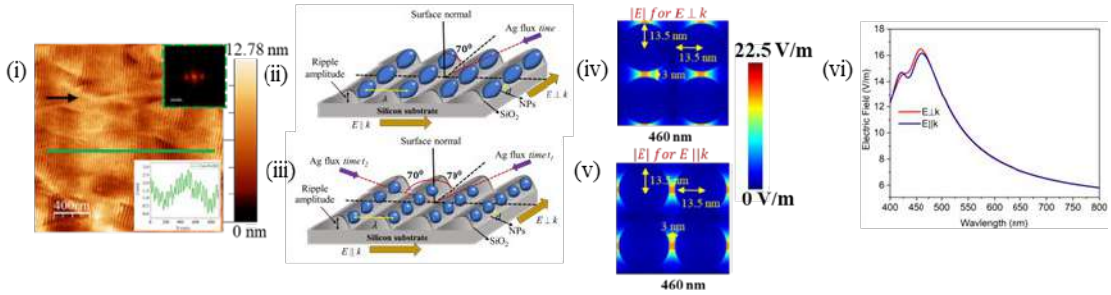


Fig.1 (i) AFM image of ripple pattern on silicon substrate with periodicity of ~ 30 nm. (ii) Schematic illustration of ripple formation on a silicon ripple, from single side deposition of Ag-NPs at an oblique angle of 70, and (iii)

Sequential deposition method for time t_1 and t_2. Electric field distribution for a particular frequency around the NPs using FDTD simulation for, (iv) E⊥k (v) E||k. (vi) Electric field vs wavelength spectra obtained for 'a'= 'b' with 'd' = 3 nm [5].

Four this study four samples were prepared: Ag-NPs deposited continuously for 60 min perpendicular to the ripple pattern (Ag_60_in) from one side and 60 min opposite to it (Ag_60_opp). Both these led to ellipsoidal NPs due to uniaxial growth (Fig. 2(i) and (iii)), causing elongation along the ripple. To avoid this uniaxial growth the novel concept of sequential deposition is employed where the Ag-NPs deposited 30 min from the direction beam and rotated the sample to deposit further 30 min from the opposite side (Ag_30+30_in) and vice versa (Ag_30+30_opp) as shown in Fig. 2(ii) and (iv). This resulted in nearly spherical NPs, with the aspect ratio decreasing from 1.69 (Ag_60_opp) to 1.24 (Ag_30+30_in). To investigate the LSPR anisotropy in the sample, reflection spectra measurements were carried out using the ellipsometry. For sample Ag_30+30_opp the shift in LSPR is decreases by 54 nm as shown in Fig. 3(i) leads to anisotropy minimization as compare to 209 nm for 60 min case. Furthermore, the effectiveness of this approach in SERS applications was validated using Crystal Violet (CV) dye at a concentration of 10^{-6} M. This sample exhibited the highest intensity while minimizing intensity variations across the substrate, rendering it nearly isotropic (Fig. 3(ii)).

This study demonstrates that the sequential deposition of Ag-NPs on silicon ripples facilitates the formation of low-aspect-ratio (almost spherical) NPs without requiring annealing, which would otherwise increase interparticle gaps via the Ostwald ripening process. The minimized LSPR shift and uniform SERS enhancement across the sample confirm the isotropic nature of the deposited NPs while preserving their regularity.

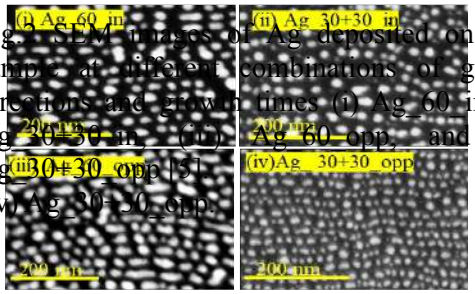


Fig.2 SEM images of Ag deposited on R-Si samples at different combinations of growth directions and grown times (i) Ag_60_in, (ii) Ag_30+30_in, (iii) Ag_60_opp, and (iv) Ag_30+30_opp [5].

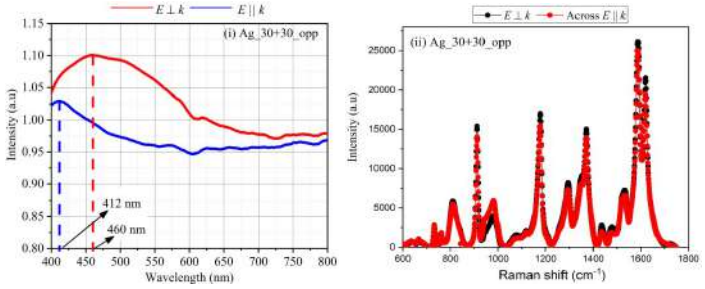


Fig.3 (i) Reflection spectra and (ii) SERS spectra of Ag_30+30_opp [5].

References

[1] B. Schreiber, et al., Large-scale self-organized gold nanostructures with bidirectional plasmon resonances for SERS, RSC Adv. 8 (40) (2018) 22569–22576, doi:10.1039/C8RA04031A.

[2] D. Gkogkou, et al., Polarization- and wavelength-dependent surface-enhanced raman spectroscopy using optically

anisotropic rippled substrates for sensing, ACS Sens. 1 (3) (2016) 318–323, doi:10.1021/acssensors.5b00176.
[3] M. Ranjan, “Predicting plasmonic coupling with Mie–Gans theory in silver nanoparticle arrays,” Journal of Nanoparticle Research, vol. 15, no. 9, p. 1908, Sep. 2013, doi: 10.1007/s11051-013-1908-7.
[4] S. Camelio, et al., “Sub-Wavelength Arrays of Metallic Nanoparticles for Polarization-Selective Broad-Band Absorbers,” Nanoscience and Nanotechnology Letters, vol. 5, no. 1, pp. 19–26, Jan. 2013, doi: 10.1166/nnl.2013.1418.
[5] T. K. Lamba, et al., “LSPR anisotropy minimization by sequential growth of Ag NPs on nanoripple patterned Si surface for SERS Application,” Surfaces and Interfaces, vol. 52, p. 104852, Sep. 2024, doi: 10.1016/j.surfin.2024.104852.

Plasmon-enhanced circular dichroism for chiral drugs enantiomeric discrimination

M. Venturi[1], R. Adhikary[1], A. Sahoo[1], C. Ferrante[2], M. Silvestri[1], G. Salvitti[1], D. Tedeschi[1], I. Daidone[1], F. Di Stasio[3], A. Toma[3], F. Tani[4], H. Altug[5], A. Mecozzi[1], M. Aschi[1], A. Marini[1,2]

1. Department of Physical and Chemical Sciences, University of L'Aquila, Via Vetoio, 67100 L'Aquila, Italy
2. CNR-SPIN, c/o Dip.to di Scienze Fisiche e Chimiche, Via Vetoio, Coppito (L'Aquila) 67100, Italy
3. Istituto Italiano di Tecnologia, Via Morego 30, Genova 16136, Italy
4. Max Planck Institute for the Science of Light, Staudtstr. 2, 91058 Erlangen, Germany
5. Institute of Bioengineering, École Polytechnique Fédérale de Lausanne (EPFL), Lausanne 1015, Switzerland
E-mail: andrea.marini@univaq.it

Abstract: This paper focuses on the surface plasmon polaritons potential at noble metals interface for enhancing chiroptical sensing of dilute chiral drug solutions. Circular dichroism is amplified by plasmonic resonances in a nano-scale drug volumes, showing relevant results for sensitive analysis of solvated reparixin, enabling advanced chiroptical sensor development.

Chiral sensing plays a key role in the pharmaceutics because the specific enantiomeric form of drugs affects their functionality and toxicity [1]. In this study, we explore the potential of surface plasmon polaritons at noble metal interfaces for surface-enhanced chiroptical sensing of dilute chiral drug solutions with nanoliter volumes. Such techniques are compatible with real-time analysis, lab-on-a-chip integration and wider nanomedicine applications. Here we focus on isotropic assemblies of reparixin (adopted as an inhibitor of the CXCR2 function, attenuating inflammatory responses for the treatment of hospitalized patients with COVID-19 pneumonia) solvated in water with dilute number molecular density $n_{mol} = n_{mol}^{(R)} + n_{mol}^{(S)} \approx 10^{-2}\text{nm}^{-3}$, where the number densities of R and S enantiomers are represented by $n_{mol}^{(R,S)}$. Our results are based on quantum chemical calculations adopting a hybrid computational approach that integrates Molecular Dynamics, time-dependent Density Functional Theory, and the Perturbed Matrix Method. [2]. The interactions between radiation and matter are analyzed from first principles using the density matrix formalism. The macroscopic optical parameters, such as dielectric permittivity, magnetic permeability, and chiral parameters of the dilute drug solution, are determined by perturbatively solving the density matrix equations within the dipole approximation. We evaluated the plasmon-enhanced circular dichroism differential absorption (CDDA) [3] in both the Otto and Kretschmann configurations.We attain a CDDA enhancement by a factor of ≈ 20 for silver metal substrate in the Otto configuration. In turn, by measuring the CDDA we can retrieve the enantiomeric imbalance in the drug solution. Our findings are relevant for the development of innovative chiroptical sensors capable of measuring the enantiomeric imbalance of nl volume chiral drug solutions.

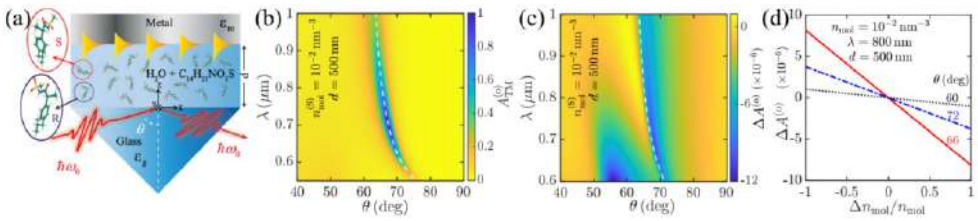


Fig. 1 (a) Schematic representation of plasmon-enhanced CD in the Otto configuration. The considered chiral sample is a solution of S and R reparixin enantiomers dissolved in water with molecular density n_{mol}. [(b) and (c)] Dependence of (b) TM absorbance $A_{TM}^{(o)}(\theta, \lambda)$ (for TM linear polarization excitation) and (c) CDDA $\Delta A^{(o)}(\theta, \lambda) = A_R(\theta, \lambda) - A_L(\theta, \lambda)$ (for circular polarization excitations) over the vacuum wavelength λ and the angle of incidence θ of the impinging radiation .The plots refer to a pure S reparixin enantiomer dissolved in water. (d) Dependence of CDDA over the enantiomeric number density imbalance $\Delta n_{mol} = n_{mol}^{(S)} - n_{mol}^{(R)}$ for several distinct incidence angles θ and fixed excitation vacuum wavelength λ = 800 nm. The dashed white curves in [(b) and (c)] indicate the SPP dispersion relation.

References

[1] Nguyen, L. A., He, H., and C. Pham-Huy. "Chiral drugs: an overview.",IJBS 2.2, 85, 2006
[2] Hess, B., Bekker, H., Berendsen, H. J. C., Frajie, J. C. E. M ,"A Linear Constraint Solver for Molecular Simulations ", J. Comput. Chem.,Vol. 81, p. 1463, 1997
[3] Venturi, M., Adhikary, R., Sahoo, A., Ferrante, C., Daidone, I., Di Stasio, F., Toma, A., Tani, F., Altug, H., Mecozzi, A., Aschi, M., Marini, A.," Plasmon-enhanced circular dichroism spectroscopy of chiral drug solutions " , J. Chem. Phys., Vol. 159, No. 15, p. 154703, 2023

Multiphysics Calculation of Plasmonic Photothermal Effects in Gold Nanorod Dimers: Influence of Size Mismatch

T. Zhou[1], M. V. Balois-Oguchi[1], and K. Kajikawa[1*]
[1]School of Engineering, Institute of Science Tokyo, Japan
kajikawa@ee.e.titech.ac.jp

Abstract

This study investigates the optical and photothermal behavior of gold nanorod dimers using finite element method. Our findings highlight the anti-correlation between near-field enhancement and photothermal efficiency resulting from size mismatch in gold nanorod dimers, providing valuable insights for optimizing the nanostructure design in plasmonic applications.

1 Introduction

Over the last decades, gold nanoparticles (GNPs) have greatly attracted interest in nanoscience due to their remarkable localized surface plasmonic resonance. The collective oscillation of free electrons in metals leads to intense light absorption and scattering as well as impressive near-field enhancement, which triggered many applications, such as biosensing, surface-enhanced Raman spectroscopy (SERS) and plasmon-enhanced second harmonic generation (SHG) [1]. Moreover, losses in the metal and the associated energy conversion from light to heat should also be a concern. On one hand, GNPs, serving as nanoscale heat sources, exhibit great potential in nanomedicine, such as plasmonic photothermal therapy, drug delivery and photothermal imaging. On the other hand, study of the heat transfer inside and around GNPs can help better understand the origin of the experimental observations in photonic applications [2].

In our research, the plasmonic optical and associated thermal responses of gold nanorod dimers (GNDs) in water under laser illumination are simultaneously investigated by employing multi-physics modeling via the finite element method (FEM). Our results highlight the anti-correlation between the light-to-heat energy conversion efficiency and local field enhancement when breaking the length asymmetry in GNDs.

2 Simulation Model

Computational models of GNDs were built and calculated using the FEM simulation software COMSOL Multiphysics (COMSOL). The study primarily focuses on gold nanorod monomers and dimers in water, as shown in Figure 1a. Each nanorod is 20 nm in diameter, and the total length is 41 nm. In the dimer structures, the interparticle gap is fixed at 1 nm, while the shorter rod length varies from 5 nm to 20 nm. The laser spot size is sufficiently large to ensure homogeneous illumination of the nanoparticles.

3 Results and Discussion

Figure 1b illustrates the absorption efficiency as a function of wavelength. The single nanorod (41 nm) exhibits the highest absorption peak at approximately 660 nm. For hetero-dimers, as the length of the shorter rod L_2 increases and the longer rod L_1 decreases, the absorption peak exhibits a blue shift and damped intensity. When the two rods in GNDs are of equal length

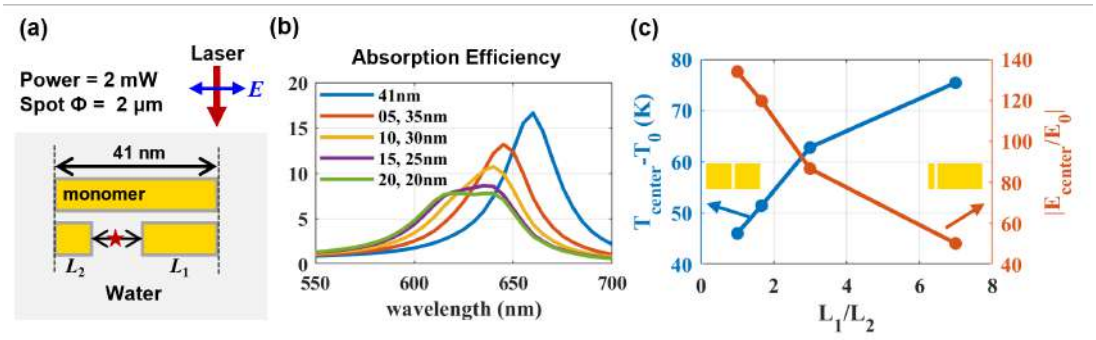


Figure 1: (a). Schematic of the gold nanorod monomer and dimers. The red star marks the gap center. (b). Absorption efficiency spectra of monomer and dimers with 1 nm gap. (c). Comparison of temperature rise (blue curve, left axis) and the local electric field enhancement (orange curve, right axis) at the gap center of GNDs excited by light of the LSPR wavelengths (i.e., peak wavelengths in (b)) as a function of length ratio.

(20, 20 nm), the absorption peak is the lowest, accompanied by a further blue shift and spectral broadening. The absorbed laser energy is converted into heat within the gold nanorods and subsequently dissipates into the surrounding water until thermal equilibrium is reached. The left axis of figure 1c presents the steady-state temperature at the gap center (marked by red star in figure 1a) between nanorods. Interestingly, the electromagnetic field enhancement at the same position (right axis of figure 1c) exhibits an inverse correlation with the temperature rise.

The anti-correlation in our findings can find its origin in the asymmetric energy distribution caused by size mismatch [3]. When the electron oscillation in each individual perfectly matches that of the other, the charges of equal magnitude and opposite sign on the facing faces can 'lock' electromagnetic energy within the gap. In contrast, length mismatch slows down the overall oscillation and drives the electromagnetic energy from one side to the other, so that the photons that cannot be 'locked' in the gap are absorbed and converted into heat within the metal .

Although the absorption and scattering are closely related to hot spots in GNPs, in techniques such as SERS and SHG, when we only concern the local field and temperature of certain hot spots, the extinction properties might mislead the design of GNPs. According to our findings, we propose gold nanorod homodimers as candidates for near-field optical applications, while size-mismached heterodimers can serve as nanoheat sources and highly sensitive biosensors.

4 Acknowledgements

Part of this study is supported by JST CREST (MJCR22B4) and JST SPRING (JPMJSP2180).

References

[1] Kelly, K. L., E. Coronado, L. L., Zhao, and G. C. Schatz, *J. Phys. Chem. B*, 107, 668-677, 2002.

[2] Baffou, G., F. Cichos, and R. Quidant, *Nature Mat.*, 19, 946-958, 2020.

[3] Slaughter L. S., Y. Wu, B. A. Willingham, P. Nordlander, and S. Link, *ACS Nano*, 4, 8, 4657-4666, 2010.

META 2025, MALAGA - SPAIN, JULY 22 – 25, 2025

Canalized Light Creates Directional and Switchable Surface Structures in Vanadium Dioxide

Daniel Kazenwadel[†], Noel Neathery[†], Peter Baum*

Universität Konstanz, Fachbereich Physik, 78464 Konstanz, Germany
[†]These authors contributed equally to this work
[*]corresponding author: peter.baum@uni-konstanz.de

Abstract: We create self-organized, re-writable, laser-induced periodic surface structures in single-crystalline vanadium dioxide. We discover anisotropic features from canalized surface plasmon polaritons that can only propagate along one crystal axis. All nanostructures remain mostly single-crystalline and preserve the material's sharp metal-to-insulator transition, enabling femtosecond switching by temperature or light.

Vanadium dioxide (VO_2) is a strongly correlated material with a first-order phase transition that changes the crystal structure from monoclinic to rutile at a temperature of $T_{trans} \approx 68^\circ$ C. At the same temperature, the material also switches from insulator to metal and its resistivity decreases by a factor of $>10^3$. The material is therefore a highly promising candidate for controllable and switchable nanophotonic devices and metamaterials. However, the fabrication of nanostructures of VO_2 is currently limited in size and quantity.

Here we investigate whether laser-induced periodic surface structures (LIPSS) can be induced in VO_2. Similar structures on other materials have found various applications in optics, structural coloring, friction reduction, dewetting or antibacterial surfaces, among many others [1]. We use large single crystals of VO_2 grown via liquid-flow crystallization [2] and hit their optically flat surface with ultrashort (300 fs) pulses of linearly polarized laser light with a center wavelength of 1030 nm. At high fluences this allows to produce periodic patterns orthogonal to the laser polarization (see Fig. 1a-d), that can be overwritten by exposure to laser light of other polarizations (Fig. 1e).

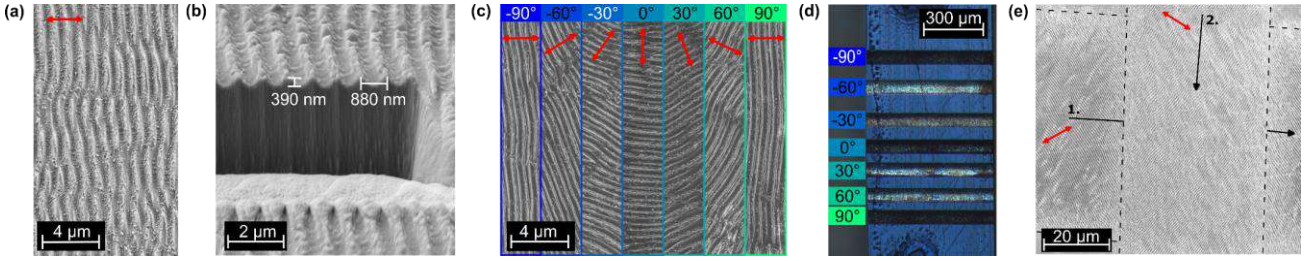


Fig. 1. Laser-induced surface structures on a VO_2 single crystal. (a) SEM image of the written structures in VO_2, writing fluence 400 mJ/cm^2 **(b)** SEM image of a cut with a focused ion beam through one of the structures. The grooves have a depth of ~390 nm and a periodicity of ~880 nm. **(c)** SEM images of the grooves for different laser polarizations (red). The grooves show a perpendicular orientation to the polarization of the incident light. **(d)** Cross-polarized light microscopy image of the structures for different laser polarizations. The wavelength-dependency of the optical response is evident by the different colors of the individual experiments. **(e)** Re-writing of LIPSS. A first laser (1) writes with ~30° polarization and then a second laser (2) writes at ~150°. The SEM image shows the results.

However, at lower fluences, another feature appears; a subharmonic pattern, that is oriented independently of the laser polarization.

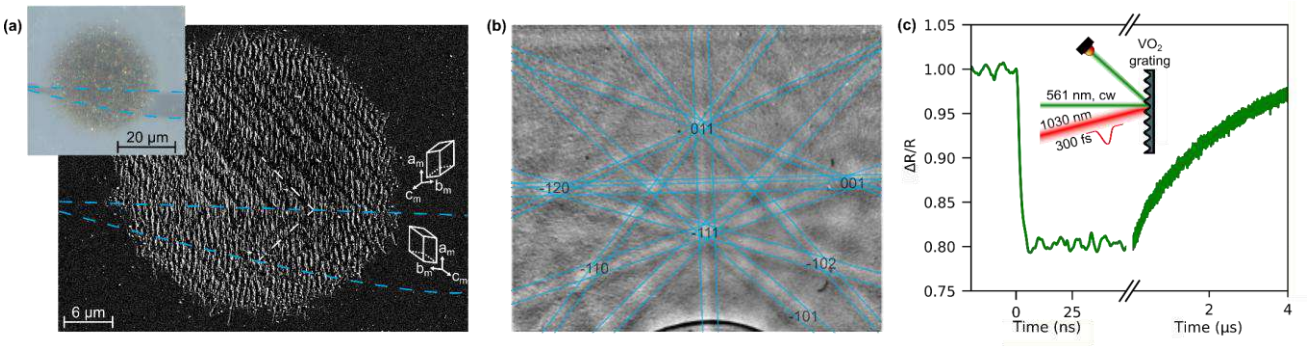


Fig. 2. Canalized light couples the ripple formation to the crystal structure. (a) Subharmonic structures with different directions (dashed white lines). The microscope image taken with crossed polarizers (inset) confirms that the different patterns belong to different crystal orientations (separated by dashed blue lines). **(b)** Electron back-scatter diffraction analysis proves the single-crystallinity of written structure and further confirms this coupling. **(c)** We pump our regular periodic surface structure with an ultrafast laser and observe the time-dependent refracted intensity of a green continuous wave laser with a fast diode. We see that the grating switches with approx. 2 ns, limited by the speed of the diode.

The low-temperature phase of VO_2 has a lower symmetry than the high-temperature phase. Therefore, some of our crystals exhibit rich domain structures that can be distinguished using polarized optical microscopy (insets in Fig. 3a). We now write the subharmonic structure on a domain boundary and see that the structures orient differently dependent on the orientation of the low temperature phase (Fig. 3a). Electron backscatter diffraction (Fig. 3b) identifies this orientation as orthogonal to the c_m-axis of the monoclinic low temperature phase. This points to the mechanism behind this crystal-coupled feature. In the low temperature phase, the dielectric constant of VO_2 is highly anisotropic [3] allowing the formation of surface plasmon polaritons only in the direction along cm, which leads to the formation of the anisotropic feature. At higher fluences, the material transforms into the nearly isotropic metallic state, where the patterns become dependent on the laser polarization.

Figure 2c shows how our written structures can be used as an ultrafast switchable diffraction grating. The single-crystallinity of the material is maintained during the nanostructuring process and allows for sharp hysteresis and femtosecond modulation of the refracted light.

Our results show that laser-induced surface structures in single-crystalline and anisotropic media can be generated with a large variety of geometries by utilizing and optimizing the transient femtosecond properties of photo-doped materials. The tools of femtosecond laser science in combination with correlated solid-state materials can therefore be used to create laser-induced nanostructures at unprecedented complexity. In turn, measurements of fabricated structures can provide insight into the underlying optical dynamics of surface plasmon polaritons or canalized light, time-frozen into the solid material. For applications, single-crystalline laser-induced surface structures with adjustable periodicity along polarization-controlled or crystallographic directions may therefore become a useful tool for producing active metamaterials on macroscopic scales.

References

1. J. Bonse, “Quo Vadis LIPSS? – Recent and Future Trends on Laser-Induced Periodic Surface Structures,” Nanomaterials Vol. 10, No. 10, 1950, 2020.
2. N. Sprinkart*, D. Kazenwadel*, R. Hartmann, P. Baum, “Liquid-diffusion-limited growth of vanadium dioxide single crystals,” Phys. Rev. Res., Vol. 5, No. 1, 013028, 2023.
3. H.W. Verleur, A.S. Barker, C.N. Berglund, “Optical properties of VO_2 between 0.25 and 5 eV,” Phys. Rev. Vol. 172, No. 3, 788–798, 1968.

Modelling, Fabrication and Characterization of Tunable Plasmonic Substrates for Designer Ultra-thin Optical Filters

Arka Jyoti Roy*, Sai Rama Krishna Malladi and Shourya Dutta-Gupta
Department of Materials Science and Metallurgical Engineering, Indian Institute of Technology Hyderabad, Telangana 502284, India
*Email: ms20resch11005@iith.ac.in

Abstract: Nanophotonic structures have been extensively used for realizing custom tailored flat optical elements. Amongst the various investigated structures, anisotropic gold nanoparticles have been a popular choice for different optical applications due to their aspect ratio dependent resonance. In this study, we demonstrate ultra-wide tunability via thermally driven shape change in highly anisotropic gold nano bipyramids. Using localized patterned heating of bipyramid substrates, we fabricate various patterns using these substrates with a tunable optical response (both reflectivity and transmission). Correlative microscopy, including in-situ TEM and in-situ optical spectroscopy with an integrated heating platform, is used to track the real-time changes in the optical response due to heating. Numerical modelling is also carried out to understand the far-field response and the underlying changes in the near-field of the bipyramid assemblies. These tunable substrates can potentially be used for designer ultra-thin optical filters for various applications.

1. Introduction

Anisotropic plasmonic nanoparticles are crucial components in making substrates for different applications [1, 2, 3]. The shape anisotropy and the size of the particles enables us to tune the resonance wavelength through a large spectral range. However, once the structures are prepared, it is quite difficult to tune or modify the resonance unless the structures are integrated with an active tuning medium [3]. Note that tunability of the resonance is beneficial for achieving the best performance from these structures when employed for a specific application. Amongst all the anisotropic particles, gold bipyramids and gold nanorods have emerged as the most popular candidates in terms of their spectral tunability right from the UV to the mid-IR range. From a near-field enhancement perspective, gold bipyramids typically exhibit a higher net near-field enhancement due to its smaller radius of curvature as compared to nanorods. In this study, we have developed thermally tunable plasmonic substrates based on self-assembled anisotropic gold bipyramids. *In-situ* reflection studies on substrates coated with anisotropic AuNPs give us a better understanding of shape change with a change in temperature [4]. This study opens a scope of easily controlling the fabrication of tunable substrates and optical filters for different applications [5]. By heating the substrates locally, we can prepare substrates with different LSPRs at different locations. This helps us to develop patterns or circuits with different LSPRs on the same substrate.

2. Methods

2.1. Synthesis of gold bipyramids

The synthesis of gold nano bipyramid (AuNBP) particles was carried out using a two-step seed-mediated growth method. A modified version of the method used by Li *et al.* [3] was employed for the synthesis. Briefly, in the first step, very small penta-twined nanoparticles (~5 nm) were synthesized by the rapid addition of NaBH4 to a

solution of $HAuCl_4$ and CTAB/CTAC. In the second step, this seed was injected into a growth solution (mention growth solution here) and stirred for 2 hours to achieve penta-twined AuNBP particles.

2.2 Self-assembled AuNBP substrates

Clean glass coverslips were functionalized by immersing them in a polyelectrolyte (PE) solution. In this method, the clean glass coverslip was first dipped in 1M NaCl solution for one minute and then transferred to 1M Poly-allylamine hydrochloride (PAH) solution for 10 minutes. The glass coverslips were then transferred to 1M NaCl solution for one minute, followed by 10 minutes in 1M Poly-4-styrene sulfonic acid (PSS) solution. This process was repeated in a cycle until five alternate layers of PSS and PAH were coated with PSS as the top layer. PSS was negatively charged and helped fix the positively charged AuNBPs on the glass coverslip surface. The AuNBP particles were purified and mixed with 1 M NaCl for a higher concentration of particles on the substrate surface. The PE-coated glass coverslips were then immersed in the AuNBPs solution and kept undisturbed for 4 hours. After 4 hrs, the substrate was gently washed with DI water and kept for drying at room temperature.

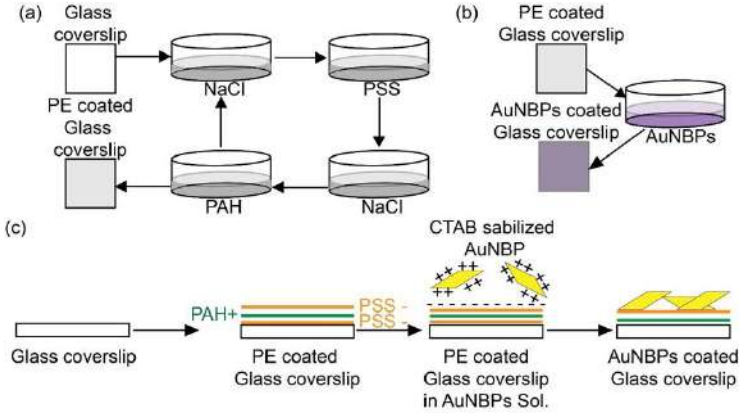


Figure 1. Schematics of substrate preparation. **(a)** Functionalization of glass coverslips by dipping in PE solutions of different surface charges. **(b)** Coating of these surface functionalized substrates in AuNBP solution. **(c)** Surface charge distribution and immobilization of AuNBPs on the surface.

3. Results and discussion

The synthesized AuNBP particles exhibit a resonance at around 800 nm. On heating the substrates to temperatures ranging from 200ºC to 400ºC, the substrate exhibit a strong color change from gray to purple and correspondingly, the resonance wavelength changes from around 800 nm to 550 nm. This is due to the change in the particle shape from anisotropic bipyramids to near-hemispherical nanoparticles. Subsequently, we patterned the self-assembled substrate through localized heating. The AuNBP substrate is placed over to copper plates which are placed on the heating stage. On heating, the substrate in contact with the copper strip exhibits a larger change in color due to larger temperature assisted shape change.

A major color change was observed at the area which was in contact with the copper plate figure 2(b). A significant shift of spectrum is observed on performing scanning of the substrate, showing a clear spectral difference between the region of contact and the surroundings, as shown in Figure 2(c). Figure 2(e) shows the collected spectrum from the contact region and two other regions near and far from the area of contact, as marked in Figure 2(b). figure 2(d) shows the corresponding SEM image of the marked region. The area 2 which was in contact with copper plate shows most particles turned spherical whereas area 1 which is far from the area of contact shows long bipyramid shaped particles. Figure 2(f) shows the particle aspect ratio distribution of

the three points, and we see that the aspect ratio at point 2 is nearly 1 whereas that of point 1 is about 1.5. This data proves the shape change is related to the color change, and it can be done locally.

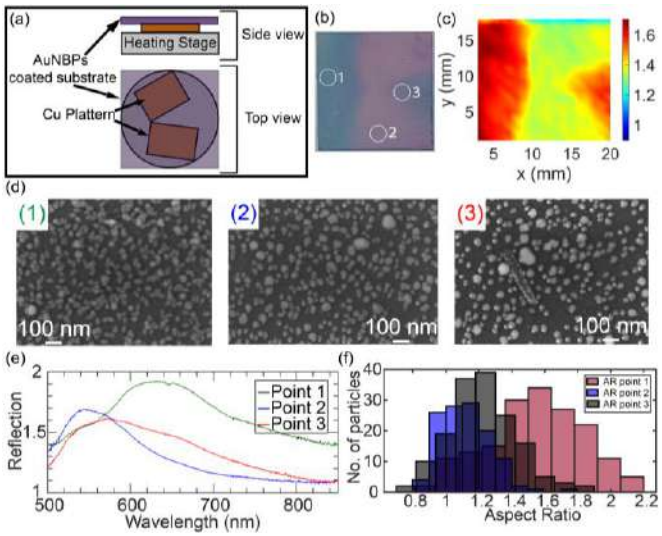


Figure 2 (a) Schematics of heating AuNBP substrates for developing patterns. (b) Shows the substrate with the pattern. (c) Spectral mapping of the substrate showing change in spectra in heated and unheated area. (d) SEM image of different points on the substrate which are exposed to different heating temperatures. (e) Shows the spectrum at the corresponding points. (f) Shows the particle aspect ratio distribution at these corresponding points.

Conclusions

In the current *in-situ* study, thermally driven resonance tuning in AuNBP substrates provides us with an facile approach for tuning the optical response of these structures. The heating temperature, holding time and nature of heating affect the shape change associated resonance shifts. This resonance shift is very large upto the tune of 300 nm when operating in the visible spectral domain. The *in-situ* studies enables us to track the realtime changes in the absorbance spectrum and lets us tailor these process more accurately. NThis setup helps gain a thorough understanding of the effect of rate heating required to achieve the desired change. We observe that the major changes occur during the heating cycle at 200ºC and 300ºC. Using simple parterning technique, we are able to realize patterns in the self-assembled gold-bypyramid samples. In future, this study can assist in the development of substrates with desired optical responses and structures.

Acknowledgement

The authors would like to acknowledge the financial support from the Ministry of Education granted to AJR. SDG would like to acknowledge funding support from the SERB Ramanujan Grant (SB/S2/RJN-126/2017), IIT Hyderabad SOCH Grant (IITH/BME/F110/SOCH4) and DST Nanomission Grant (DST/NM/NB/2018/118).

References

[1] L. A. Lane, X. Qian, and S. Nie, “SERS Nanoparticles in Medicine: From Label-Free Detection to Spectroscopic Tagging,” Chem. Rev., vol. 115, no. 19, pp. 10489–10529, 2015.

[2] Z. Wang, S. Zong, L. Wu, D. Zhu, and Y. Cui, “SERS-Activated Platforms for Immunoassay: Probes, Encoding

Methods, and Applications," Chem. Rev., vol. 117, no. 12, pp. 7910–7963, 2017.

[3] W. Li et al., "Shape Control beyond the Seeds in Gold Nanoparticles," Chem. Mater., vol. 33, no. 23, pp. 9152–9164, 2021.

[4] E. Mukherjee, J. Pillanagrovi, D. Bhatnagar, and S. Dutta-Gupta, "In situ optical spectroscopy for monitoring the assembly of gold nanoparticles for plasmonic applications," J. Appl. Phys., vol. 133, no. 7, 2023.

[5] N. Roostaei and S. M. Hamidi, "Plasmonic Eyeglasses Based on Gold Nanoparticles for Color Vision Deficiency Management," ACS Appl. Nano Mater., vol. 5, no. 12, pp. 18788–18798, 2022.

Thermal radiation forces on nanostructures with reduced symmetry

J. R. Deop-Ruano[1*], A. Manjavacas[1]

[1]Instituto de Química-Física "Blas Cabrera" (IQF-CSIC), Spain
[*]corresponding author: juan.deop@csic.es

Abstract: The fluctuations of the electromagnetic field produce a drag force on nanostructures moving with respect to a thermal radiation bath. We show that nanostructures with the appropriate symmetry properties are subject to a lateral force that significantly modifies their trajectory and a propulsion force that opposes the drag.

Fluctuations in the electromagnetic field, of both thermal and quantum origin, generate forces that play a crucial role in the motion of material structures. A key example is thermal radiation drag, which causes objects to decelerate as they move through a thermal radiation bath [1-2]. This effect arises from the Doppler shift of the thermal radiation bath in the frame comoving with the object: photons propagating with and against the trajectory experience redshift and blueshift, respectively, leading to different absorption rates.

The counterintuitive nature of the thermal radiation drag and its potential applications have led to increasing interest in recent years. However, prior studies have predominantly examined isotropic and homogeneous objects, simplifying the analysis but overlooking effects related to structural asymmetry.

In this study, we demonstrate that nanostructures with anisotropic optical properties experience both a lateral force and a torque when moving through a thermal radiation bath, as depicted in Figure 1(a) [3]. Remarkably, for highly anisotropic structures, the lateral force can be comparable in magnitude to the drag force, as shown in Figure 1(b). This leads to a strong modification of the trajectory, which tends to align with the direction of maximum polarizability. Interestingly, we find notable similarities between the motion of these nanostructures in a thermal radiation bath and the behavior of a wing in a viscous fluid.

Although anisotropy enables control over the trajectory of the nanostructure, its motion remains constrained by thermal drag. To overcome this limitation, we propose a bilayer structure composed of an absorbing and a reflecting material, which spontaneously accelerates when placed in a thermal environment with a different temperature [4]. This self-propulsion mechanism, powered by stored thermal energy, effectively acts as a thermal engine.

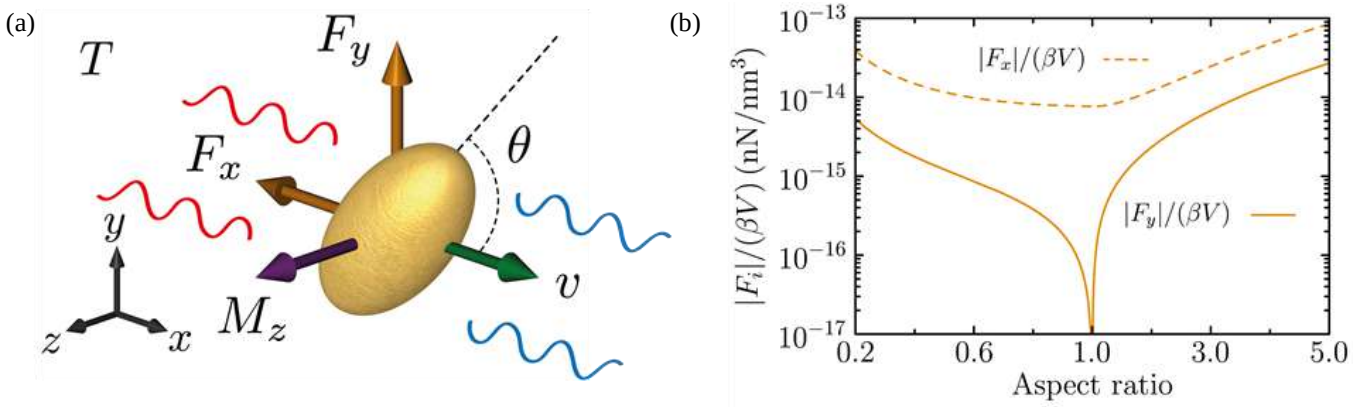


Figure 1. (a) Schematics of the system and (b) components of the force as a function of the aspect ratio.

References

1. Mkrtchian V., Parsegian V. A., Podgornik R., Saslow W. M., “Universal thermal radiation drag on neutral objects,” Phys. Rev. Lett., 91, 220801 (2003).
2. Volokitin A. I., “Friction force at the motion of a small relativistic neutral particle with respect to blackbody radiation” JETP letters, 101, 527 (2015).
3. Deop-Ruano J. R., Manjavacas A., “Thermal radiation force and torque on moving nanostructures with anisotropic optical response,” Phys. Rev. Lett., Accepted (2025)
4. Deop-Ruano J. R., García de Abajo F. J., Manjavacas A., “Thermal radiation forces on planar structures with asymmetric optical response,” Nanophotonics, 13, 25, 4569-4575 (2024)

Fourier Modal Method for Calculating Two-Dimensional Periodic Photonic Crystals with Chiral Inclusions

Ilia Smagin[1], **Sergey Dyakov**[1]
1. Skolkovo Institute of Science and Technology, Bolshoy Boulevard, 30, bld. 1, Moscow 121205, Russia

One of the main methods of theoretical investigation of resonances in layered periodic structures in nanophotonics is the Fourier Modal Method (FMM) in the form of a scattering matrix, based on the Fourier decomposition of electric and magnetic fields in layers homogeneous along the z axis. As far as we know, there are no publications in the literature that present a generalization of the Fourier modal method for the case of chiral substances in the most general anisotropic case. This work proposes to solve this scientific problem. In solving it, we will use an existing approach to take into account the cross coupling coefficients of local induction vectors and fields vectors, which consists in introducing a macroscopic chirality coefficient of a substance, by analogy with macroscopic permittivity and magnetic susceptibility.

It is necessary to increase light-chiral matter interaction for chiral molecules detection which is exactly what is achieved on the resonant responses. Scientific significance and novelty will be the Fourier-modal method generalization taking into account the factorization rules for mathematically correct Fourier transform of the material equation with chiral coefficients in the most general anisotropic case.

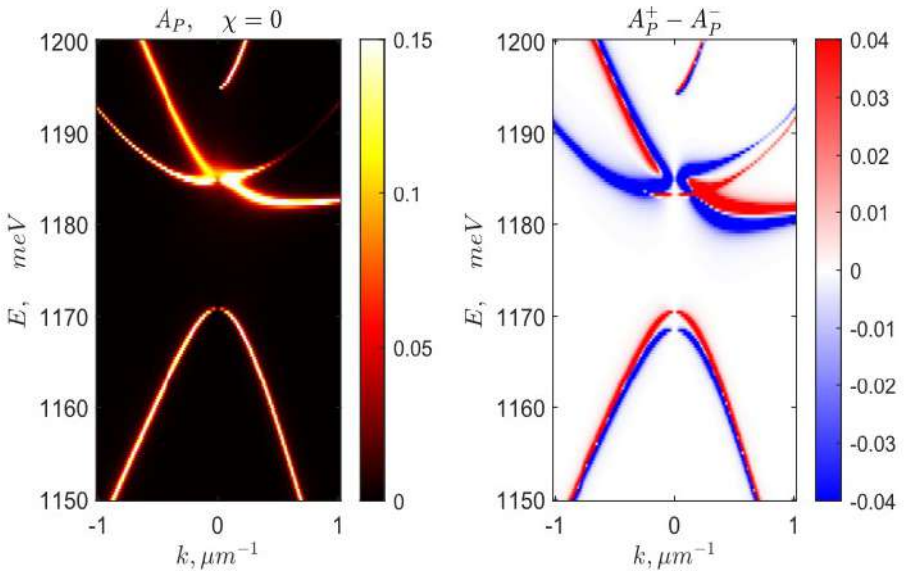


Fig. 1 Absorption spectrum in abstance of chirality (left) and the difference between spectra with different chiral coefficients sign (right).

As an example, using the FMM we got the absorption spectra demonstrated on the fig. 1. On the left panel the absorption spectrum above the light cone in the reciprocal space demonstrated for the case for which all the material is non-chiral, i.e. the chiral coefficient $\chi = \xi^* = 0$, while on the right panel the difference between the "+" and "-" chiral signs that chiral material has takes place. Namely, on the right side we have demonstrated the difference of the absorption spectra for $\chi_+ = \xi_+^* = \in 0.02i$ and $\chi_\in = \xi_\in^* = 0.02i$. On the abscissa axis the projection of the k-vector ($\mu k^{\in 1}$) in the main optical directions $M \in \Gamma \in X$ takes place while the ordinate axis indicates the wave energy in meV. In the presence of the non-zero chiral coefficients modes slightly change its energy position, which demonstrated on the right panel with red and blue colors.

References

[1] S.G. Tikhodeev and A.L. Yablonskii E.A. and Muljarov N.A. Gippius and T. Ishihara, Quasiguided modes and optical properties of photonic crystal slabs. Physical Review B, 2002, 66(4), 045102.

Interaction between Ag nanoparticles and excitons in organic light emtting diode: plasmonic enhancement and quenching

A. T. Diallo, N. Khiri, M. Chakaroun and A. Boudrioua

Laboratoire de Physique des Lasers, CNRS(UMR7538), Université Sorbonne Paris Nord 93430 Villetaneuse, France.
*corresponding author: boudrioua@univ-paris13.fr

Abstract: We report the effect of the distance between of Ag nanoparticles and the emitting layer of an OLED. A figure of merit is suggested, which includes LSPR, electrical and optical effects of nanoparticles.

Organic light-emitting diodes (OLEDs) are now widely available and increasingly used due to their low cost and great flexibility in design. Incorporating metallic nanoparticles (NPs) into OLED heterostructures presents a promising way to, significantly, enhance both optical and electrical performance. This improvement is, mainly, attributed to Localized Surface Plasmon Resonances (LSPR) [1], which have spurred ambitious developments and applications. However, the ability of plasmonic resonances to boost fluorescence strongly depends on the distance between the NPs and the emitter [2]. Moreover, these nanoparticles can enhance the local electric field at the excitation wavelength, thereby increasing the excitation rate. In addition, their scattering cross-section and antenna radiation pattern contribute to a more efficient out-coupling of the emitted light [3, 4]. Nevertheless, the mechanisms behind this enhancement remain not fully understood. One major challenge with metals is the inherent conductivity losses that may lead to emission quenching [3].

In this work, we present the investigation of the effects of metallic Ag-NPs randomly dispersed in a standard guest-host OLED by thermal evaporation during the fabrication process. We mainly study the interaction between the Ag-NP layer and excitons by varying the position of the Ag-NPs within the OLED stack. At each NP position, we compare the OLED performance with that of a reference device without NPs, and we provide an overall analysis of the variations in electroluminescence efficiency as a function of Ag-NP positioning relative to the exciton distribution in the emitting layer.

The typical OLED stack used in our experiments consists of the following layers: ITO/M-MTDATA as a 30 nm-thick hole injection layer (HIL), a 15 nm-thick NPD hole transport layer (HTL), a 30 nm-thick Alq_3 emitting layer (EML) doped with 1.5 wt% DCM to achieve red emission peaking at 620 nm, a 5 nm-thick BCP hole blocking layer (HBL), a 30 nm-thick Bphen electron transport layer (ETL), a 1 nm-thick LiF layer, and a 100 nm-thick Aluminum (Al) cathode. For the plasmonic devices, Ag-NPs with sizes ranging from 8 to 20 nm were evaporated and randomly dispersed within the OLED heterostructure during fabrication. The position of these NPs was varied using the NPB/Alq_3:DCM interface as a reference (see Figure 1).

Afterward, we analyzed the variations in electroluminescence efficiency as a function of the Ag-NP positioning relative to the exciton distribution within the EML. The experimental results (Figure 1) illustrate the interplay between enhancement and quenching effects induced by the Ag-NPs and their overall impact on the optical and electrical properties of the OLED. Two distinct physical phenomena must be considered, one near the cathode and the other near the anode (blue and green lines in Fig. 1), as well as the correlation between near-field and far-field effects. Specifically, figure 1 reveals two competing effects: on the one hand the LSPR amplification for large distances between the Ag-NPs and the emissive sites and on the other hand, the quenching effect by metallic NPs for short distances between the Ag-NPs and the emissive sites. On the anode side, for distances of 45nm and 30nm, the effect of the LSPR-exciton coupling is at the origin of the improvement in the overall

efficiency of the device. Regarding OLEDs with a distance less than or equal to 15 nm, the fall in efficiency can be attributed to the quenching of excitons by NPs. On the cathode side, the behavior of the NPs-OLED is quite different: the quenching phenomena is observed up to distance of 45nm. Besides, it should be indicated that the recombination area of excitons is mainly close to the NPB/Alq3: DCM interface.

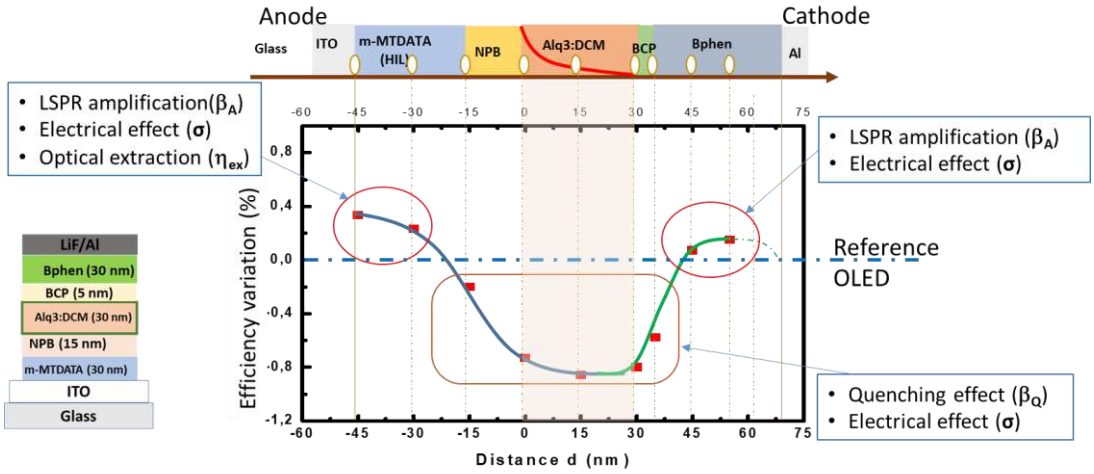


Figure 1 Experimental results of the efficiency variation vs Ag NPs-EML distance. Left and above: Typical OLED structure and the position of Ag NPs studied.

Nevertheless, other phenomena such as the influence of Ag-NPs on the charge carrier injection and transport (electrical effect) and their scattering effect, which influence the optical extraction, should be also taken into account in order to thoroughly understand the effect of metallic nanoparticles on the OLED structure performance. Eventually, our study enables us to suggest a figure of merit giving the total yield enhancement as following:

$$\eta = \sigma \beta_A \beta_Q \eta_{ex}$$

where σ accounts for NPs electrical effects, β_A and β_Q are LSPR amplification and plasmonic quenching, respectively and η_{ex} is related to NPs optical extraction effect.

The weight of each parameter will be analyzed and discussed. These experimental results allow us to assess the balance between amplification and quenching effects induced by the Ag-NPs, which is of a great interest in order to develop new generation of highly efficient OLED-based devices.

References

1. S. Khadir, M. Chakaroun, A. Belkhir, A. Fischer, O. Lamrous and A. Boudrioua, "Localized surface plasmon enhanced emission of organic light emitting diode coupled to DBR-cathode microcavity by using silver nanoclusters", Optics Express, 23(18), 23647-23659, 2015.
2. F. Wang, D. Li, D. Yang and D. Que, "The coupling between localized surface plasmons and excitons via Purcell effect", Nanoscale Research Letters, 7(1):669, 2012.
3. G. Sun, and B. Khurgin, "Theory of optical emission enhancement by coupled metal nanoparticles: An analytical approach", Appl. Phys. Lett. 98, 113116, 2011.
4. A. T. Diallo, M. Chakaroun, S. Khadir, S. Hamdad, J. U. Esparza-Villa, A. Maître and A. Boudrioua "Plasmonic effects of thermally evaporated aluminum nanoparticles on the electroluminescence of organic light-emitting diode subject to exciplex", J. Nanophoton. 13(1), 016004, 2019.

Enhanced Light Harvesting and Photothermal Conversion with Anisotropic Gold Nanoparticles

R. Miao,[1*] M. Bissoli, [1] and V. Amendola[1*]

[1] Department of Chemical Sciences, University of Padova, Italy
[*]corresponding author: runpeng.miao@phd.unipd.it

Abstract: Gold nanoparticles (Au NPs) face challenges in broadband light harvesting due to limited spectral coverage and low photothermal efficiency. This study compares spherical Au NPs with anisotropic Au nanostructures, including nanospheres and nanocorals, for enhanced absorption. Their optical and photothermal properties are tested in photo-thermoelectric generators for efficient energy conversion.

The increasing global energy demand and the urgent need to mitigate climate change necessitate innovative approaches to harness solar energy effectively. This study investigates the optical properties of anisotropic Au NPs and their potential applications in solar light harvesting and photo-thermoelectric conversion. The research focuses on synthesizing three distinct types of Au NPs—nanospheres (NSs), aggregated nanospheres (ANSs), and nanocorals (NCs)—and evaluating their performance in converting solar energy into usable forms.[1]

Firstly, the synthesis of Au NPs was achieved through laser ablation in liquid (LAL) using a Q-switched Nd:YAG laser, as shown in Figure 1(A). The process involved varying the concentration of hydrogen peroxide in the solvent to produce different nanoparticle morphologies, as shown in Figure 1 (B-D). Secondly, the optical properties of the synthesized nanoparticles were characterized using transmission electron microscopy (TEM) and numerical simulations based on the discrete dipole approximation (DDA) method. The study also included photothermal experiments to assess the efficiency of light-to-heat conversion across the ultraviolet (UV), visible (Vis), and near-infrared (NIR) regions of the solar spectrum.

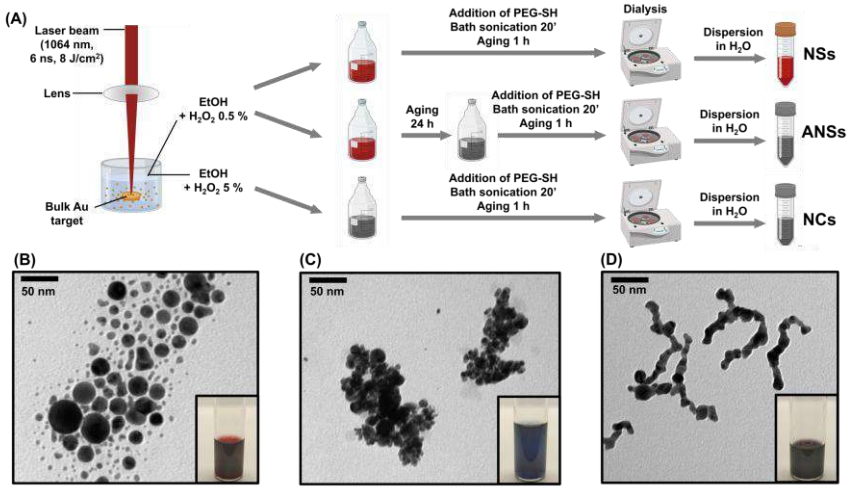


Figure 1 (A) Sketch of the synthesis workflow leading to the three types of Au NPs. (B) B–D) Representative TEM images of final Au NSs (B), ANSs (C), and NCs (D).

Furthermore, the results demonstrated that the optical properties of the Au NPs are significantly influenced by their morphology. The absorbance spectra indicated that the ANSs and NCs exhibited enhanced light absorption capabilities, particularly in the NIR region, compared to the NSs, which was shown in Figure 2 (A). This is crucial for maximizing solar energy capture, as more than half of the solar emission occurs at wavelengths longer than 700 nm.[2] The study also highlighted the importance of optimizing the absorptivity on

the hot side of photo-thermoelectric generators (TEGs) to enhance energy conversion efficiency. The findings suggest that the use of plasmonic materials, such as the Au NPs studied, could provide significant advantages in terms of device simplicity and scalability.

At last, the radar graph analysis revealed that the NCs achieved superior performance metrics, including a photothermal voltage of 0.244 V under Vis-NIR irradiation, which is 95% of the theoretical maximum. This performance is attributed to the synergistic effects of their unique structural features, which facilitate both light absorption and photothermal conversion. In contrast, while the ANSs showed higher absorbance in the visible range, their overall efficiency in energy conversion was lower than that of the NCs.

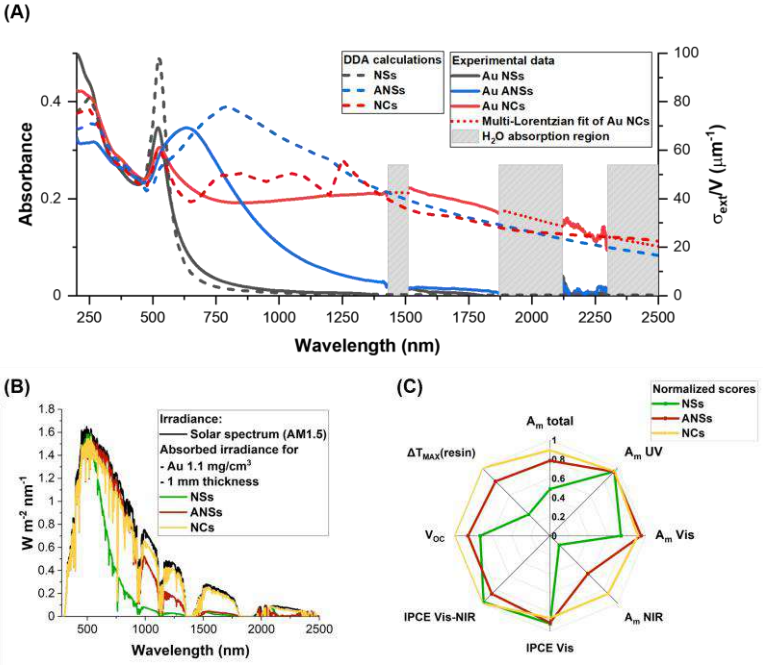


Figure 2 (A) Comparison of experimental absorption spectra and the volume-weighted average of calculated σ_{ext}/V for NSs, ANSs and NCs. (B) Comparative analysis of solar spectrum irradiance and absorbed spectral irradiance of the three Au NPs samples. (C) Radar graph for the comparative assessment of NSs, ANSs and NCs: solar-weighted absorption coefficient (A_m) for different spectral intervals (UV; Vis; NIR); IPCE under Vis and Vis-NIR irradiation; maximum VOC and temperature increase in resin (ΔT) reached under Vis-NIR irradiation at 1.02 ±0.01 $W \cdot cm^{-2}$.

In conclusion, this research underscores the potential of anisotropic gold nanoparticles as effective materials for solar light harvesting and photothermal applications. The ability of NCs to achieve high photothermal conversion efficiency positions them as promising candidates for future developments in sustainable energy technologies. The study contributes to the growing body of knowledge on nanomaterials for energy applications and highlights the need for further exploration of their properties and optimization strategies.

References

1. Miao, R., Bissoli, M. & Amendola, V. Optical Properties of Anisotropic Gold Nanoparticles for Solar Light Harvesting and Photo-Thermoelectric Conversion. *Adv. Opt. Mater.* (2024) doi:10.1002/adom.202402662.
2. NREL. Reference Air Mass 1.5 Spectra. *National Renewable Energy Laboratory (NREL)* (2019).

Self-assembly of high-quality single crystals of DNA-functionalized gold nanoparticle superlattices for *in-vivo* SERS detection

Taito Ikeuchi[1], Lidong Zhang[1], Saki Kozawa[1], Shoko Kojima[1], Hiromasa Niinomi[2], Makoto Kuwahara[3], Kotaro Hiramatsu[4], and Miho Tagawa[3*]

[1] Graduate School of Engineering, Nagoya University, Nagoya, Japan
[2] Institute of Multidisciplinary Research for Advanced Materials, Tohoku University, Sendai, Japan
[3] Institute of Materials and Systems for Sustainability, Nagoya University, Nagoya, Japan
[4] Faculty of Science, Department of Chemistry, Kyushu University, Fukuoka, Japan
[*]Corresponding author: tagawa.miho.z5@f.mail.nagoya-u.ac.jp

Abstract: Crystals of DNA-functionalized nanoparticle (DNA-NP) superlattices offer high design flexibility and excellent biocompatibility, making them promising for reliable *in-vivo* SERS sensing applications. In this study, we successfully fabricated superlattices consisting of Au-Ag core-shell nanostructures with precise control of their nano-gap distances, showing highly reproducible SERS effect.

Single crystals of DNA-functionalized gold nanoparticle superlattices are composed of periodic structures of gold nanoparticles linked by sequence-designed synthetic DNA molecules[1]. Due to their high degree of design freedom and well-defined periodic structure of plasmonic nanoparticles, they exhibit distinct optical properties such as Mie Resonance[2], Nonlinear optical effects[3], and Surface Enhanced Raman Scattering (SERS).

Recently, Raman-based vibrational imaging of biological cells and tissues has attracted considerable attention[4]. However, due to the inherently small scattering cross-section of Raman scattering, the scattered signals are typically weak, limiting sensitivity and temporal resolution. SERS is a powerful technique that can significantly improve the sensitivity of Raman scattering and enhance the temporal resolution[5]. DNA-functionalized gold nanoparticle (DNA-AuNP) crystals are promising optical SERS probes in biological sensing owing to their unique optical properties, reproducible structure, and excellent biocompatibility.

In this study, we fabricated high-quality DNA-AuNP single crystals and further processed these crystals to serve as optical SERS probes.

AuNPs were functionalized with thiol-modified DNA molecules. Single crystals of superlattices were fabricated through a self-assembly method, aiming for high-quality periodic structure. However, in the aqueous environment, inter-surface distances between nanoparticles within the DNA-AuNP crystal are relatively long, insufficient for the conditions required for strong near-field enhancement. To overcome this limitation, we subsequently induced the formation of core-shell structures on nanoparticles through Ag^+ ion reduction, concurrently contracting the DNA linkages between nanoparticles within the superlattice. Reduction of Ag^+ ions was carried out by adding L-sodium ascorbate, polyvinylpyrrolidone, and a low concentration of $AgNO_3$, each selected for controlled Ag shell formation. After washing the core-shelled nanoparticle crystals with $NaClO_4$ solution, additional higher concentration $AgNO_3$ was added for contracting of DNA[6]. Crystallinity of DNA-AuNP superlattice was verified by synchrotron-based small-angle X-ray scattering (SAXS) and it was confirmed that the crystal structure was maintained even after reduction. SEM analysis also confirmed the successful formation of periodic structures with nano-scale gaps and short-range order (Figure 1a).

To evaluate the SERS effect of the crystals, we performed Raman spectroscopy measurements. The crystals were washed again with $NaClO_4$ solution to remove residual $AgNO_3$, then mixed with Rhodamine B (Rh B) as the model analyte. Raman spectroscopy measurements were conducted in an aqueous environment, resulting in

consistent detection of Rh B at concentrations of 10 μM, 1 μM, and even 100 nM (Figure 1b). These results indicate that SERS enhancement within the crystal structure enabled highly sensitive molecular detection.

Boundary Element Method (BEM) simulations[7] were also conducted to elucidate the near-field properties. A three-dimensional nanoparticle array model, derived from SAXS analysis, was irradiated with a 532 nm plane wave which is same as that used in the Raman spectroscopic measurements, to assess electric field enhancement within the crystal. The simulations revealed strong electric field enhancement due to the periodic, nano-gapped structure of the superlattice. (Figure 1c).

In conclusion, we successfully fabricated DNA-functionalized nanoparticle superlattices maintaining short-range order, detected molecules at low concentrations in solution, and confirmed near-field enhancement inside crystals. Future research will focus on further characterizing their physical properties and exploring their applications in intracellular sensing.

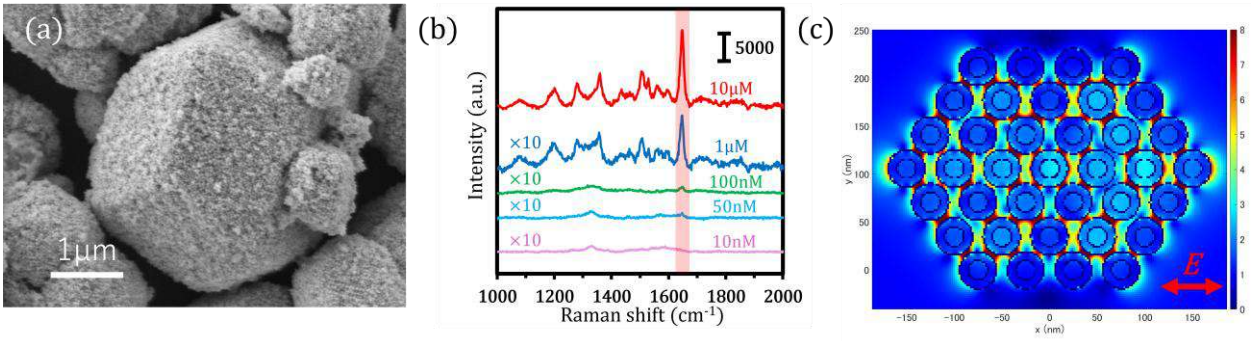


Fig. 1 (a) SEM image of DNA-AuNP crystals with Ag shells and contracted DNA. (b) Raman spectrum of RhB solution in different concentration, using crystals as SERS probes. (c) Electromagnetic field calculation using boundary element method with MNPBEM.

References

1. Sumi, Hayato., et al., “Designing a High-Crystallinity Nano-Gapped Particle Superlattice via DNA-Guided Colloidal Crystallization and Dehydration,” Crystal Growth & Design, Vol. 22, No. 6, 3708–3718, 2022.
2. Haobijam, Johnson. Singh., et al., “Optical Mie Scattering by DNA-Assembled Three-Dimensional Gold Nanoparticle Superlattice Crystals,” ACS Applied Optical Materials, Vol. 1, No. 1, 69–77, 2023.
3. Zhang, Ye., et al., “Nonlinear optical colloidal metacrystals”. Nature Photonics, Vol. 19, No. 1, 20–27, 2025
4. Hamada, Keisaku., et al., "Raman microscopy for dynamic molecular imaging of living cells," Journal of biomedical optics, Vol. 13, No. 4, 044027-044027, 2008.
5. Koike, Kota., et al., "Quantitative drug dynamics visualized by alkyne-tagged plasmonic-enhanced Raman microscopy," ACS Nano, Vol. 14, No. 11, 15032-15041, 2020.
6. Oh, Taegon., Sarah. S. Park, and Chad. A. Mirkin, "Stabilization of colloidal crystals engineered with DNA," Advanced Materials, Vol. 31, No.1, 1805480, 2019.
7. Hohenester, Ulrich. and Andreas. Trügler, "MNPBEM – A Matlab toolbox for the simulation of plasmonic nanoparticles," Computer Physics Communications, Vol. 183, No.2, 370-381 2012.

Frozen Plasmons on Uniformly Moving Surface

S. Azar[1], F. J. Rodríguez-Fortuño[1*]
[1]King's College London, Department of Physics, London, United Kingdom
Corresponding author: francisco.rodriguez_fortuno@kcl.ac.uk

Abstract: We revisited the problem of a dielectric medium moving uniformly along its surface, focusing on the dispersion relation of its surface modes. We discovered a mode with no group velocity, a frozen mode. Moreover, the surface motion induces a lateral force on a nearby source, maximised by frozen modes.

In our research we studied the reflection of light on a dielectric medium moving parallel to its surface at a fixed speed. Interesting phenomena linked to phase velocity of light have been discovered when the problem is studied through quantum mechanics [1]. However, we approached it from a classical standpoint mixing electromagnetism and special relativity, which revealed interesting features connected to the group velocity of light.

We started by deriving the reflection coefficients of a dielectric medium moving in the plane spanned by its surface. Starting from the s and p polarisation components of an arbitrary incident field we reconstruct the electric and magnetic fields before boosting them with Lorentz transformation. Then, in the rest frame of the surface, we reflect the fields and boost them back into the original frame. In general, we observe a mixing of polarisation in the reflected fields, which has been observed in [2], unless the motion of the surface is along the plane of incidence of the light. The motion of the surface modifies the dependence of the reflection coefficients on the wavevector transverse components, creating an asymmetry between the directions. This asymmetry has a direct impact on the dispersion relation of the surface and causes it to tilt, creating novel ways to excite surface plasmon polaritons (SPP) on the surface (Fig. 1).

It is now possible to excite more than one SPP along a given direction. For example, the negative frequency branch, curves up into the positive frequency domain [1]. Also, the positive branch curves down on one side, creating a maximum frequency point past which certain modes can no longer be excited. This maximum has a derivative equal to zero (see Fig. 1a) which means that there exists a mode with no group velocity, a frozen mode which was our main subject of study.

Another consequence of the asymmetry in the dispersion relation is the asymmetry induced in the emission of SPPs, which carry energy and momentum. This imbalance in momentum between the directions implies that a nearby source will experience a lateral optical force. Thus, we derived the expression of the force and showed that even if the source has no preferred direction of emission it will experience a force due to the motion of the surface. Furthermore, we found that it is possible to maximize the force by exciting the frozen modes mentioned before (Fig. 1b). In fact, studying other quantities such as the torque, the power emitted and the density of state we observed the same effect of enhancement at the frozen modes specifically.

The fields were also calculated and observed in the frame of the surface, from whose point of view the source is moving. From the point of view of the stationary surface, the frozen mode

corresponds to the situation in which the source is moving along the surface precisely at the group velocity of the surface plasmons, such that the source moves together with the envelope of the plasmons which it emits. Furthermore, it helped us understand other modes where the source moves faster than its plasmons, allowing us to fully interpret the dispersion relation and all the possible SPPs.

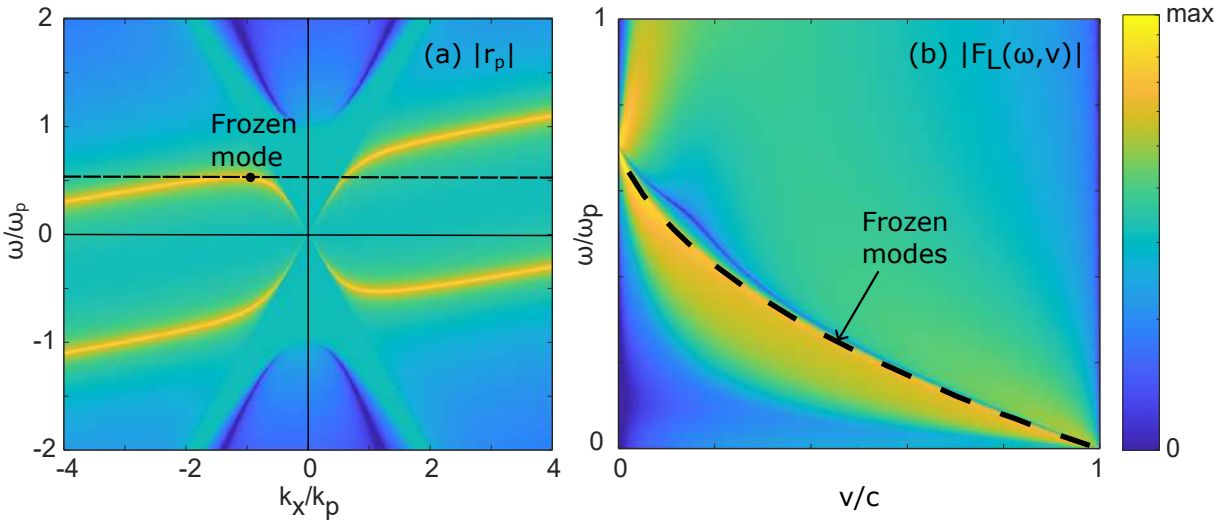


Figure 1: (a) Dispersion relation of the moving dielectric surface represented by the yellow lines, using a lossless Drude model for the relative permittivity of the surface. (b) Plot of the lateral force as a function of frequency (ω) and speed (v/c) with the frozen mode frequencies represented by the black curve.

S. A. acknowledges support from EPSRC doctoral studentship NMESFS 2024 and F. J. R. .F. acknowledges financial support from the EPSRC via the META4D Programme Grant (No. EP/Y015673/1)

References

1. S. Horsley, "Canonical quantization of the electromagnetic field interacting with a moving dielectric medium," *Physical Review A—Atomic, Molecular, and Optical Physics*, vol. 86, no. 2, p. 023830, 2012.

2. S. Horsley, M. Artoni, and G. C. La Rocca, "Radiation pressure on a moving body: beyond the doppler effect," *Journal of the Optical Society of America B*, vol. 29, no. 11, pp. 3136–3140, 2012.

Optical “writing” of stable single-atom features in plasmonic nanogaps

Paul Kerner[1], Rakesh Arul[1], Damien Thompson[2], Jeremy J. Baumberg[1]*, Bart de Nijs[1]*

[1]Nanophotonics Centre, Department of Physics, University of Cambridge, Cambridge, CB3 0HE, England, UK
[2]Department of Physics, Bernal Institute, University of Limerick, Limerick V94 T9PX, Ireland
*corresponding authors: jjb12@cam.ac.uk, bd355@cam.ac.uk

Abstract: We demonstrate all-optical creation and low-power readout of stable single-atom features in plasmonic nanogaps. These deterministically “written” picocavities exhibit week-long ambient stability in darkness, enabling applications in single-atom devices and catalysis.

The ever-stronger push for miniaturization has resulted in substantial interest towards observing and controlling the dynamics of matter at the level of single atoms. Devices that incorporate single-atom electronic components and memory are highly sought-after in nanoelectronics, while in catalysis single atoms on metal surfaces are key for interactions with molecules. Usually, atomic scale studies require disruptive electron beam techniques. Here, we show all-optical control over single gold atom dynamics through “writing”, “reading” and “storing” them within a plasmonic nanoarchitecture in ambient conditions [1].

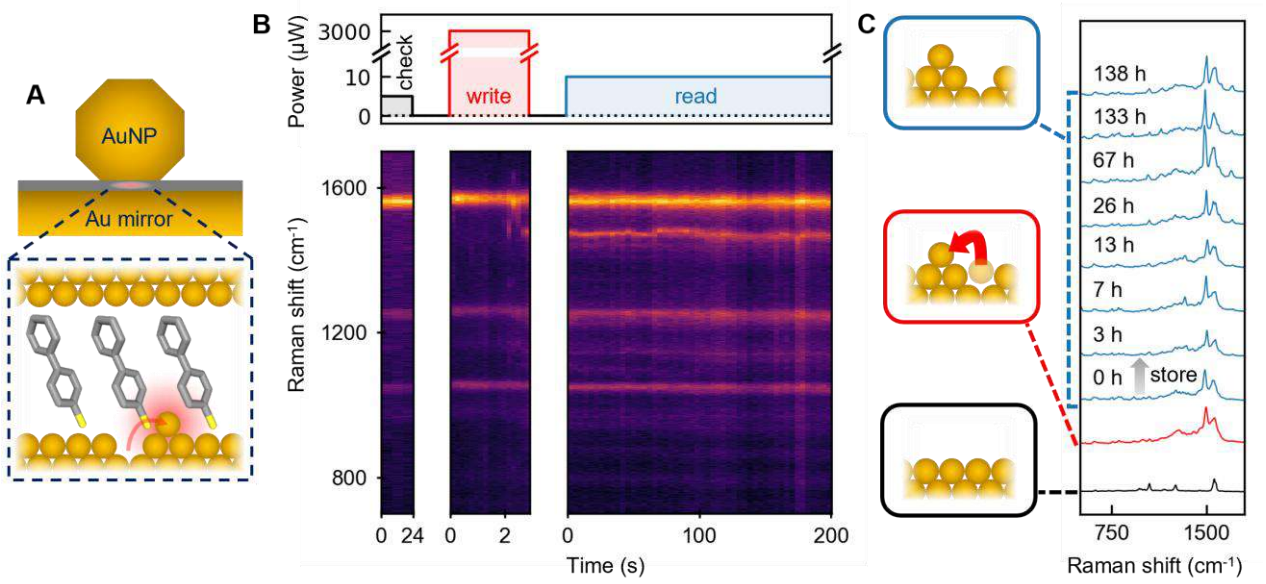


Fig. 1. (**A**) Top: nanoparticle-on-mirror (NPoM) structure, confining light to a nanogap filled with a biphenyl-4-thiol (BPT) monolayer (grey). Bottom: NPoM nanogap interior, where a gold adatom confines light to a picocavity (red) that perturbs one BPT molecule. (**B**) 633 nm laser irradiation power over the course of a typical *write-read* experiment with corresponding Raman time scans. (**C**) 633 nm excitation SERS spectra resulting from a *write-read* experiment on a picocavity over the course of a week, with increasing periods of dark storage between read spectra. Insets are inferred structure configurations corresponding to the spectra.

We use a nanoparticle-on-mirror (NPoM) architecture to plasmonically confine light within a ~1 nm gap between a gold mirror and gold nanoparticle. The nanogap is supported by a self-assembled monolayer of biphenyl-4-thiol (BPT) molecules, whose Raman spectra are visible due to the >108 enhancement in the gap. Illuminating the NPoM results in spontaneous new transient narrowband features termed “picocavities” [2,3].

These are found to be single gold adatoms lifting out of the gold surface, further confining light to sub-nm3 scales (Fig. 1A). Within this volume, the confinement is enough to discern Raman scattering of single BPT molecules next to the gold atom.

The adatoms preferentially form and decay at higher light powers, which we utilise for a write-read protocol. The NPoM is illuminated at ~mW 633 nm laser powers, allowing <10 s picocavity creation. Raman spectra are measured and automatically checked for adatom formation in real time. On strong peak appearance (adatom writing), laser powers are dropped to μW levels, at which it can be repeatedly read (Fig. 1B). This experiment is replicated on >1000 NPoMs at different write and read powers. Here 3 mW is found to be the optimal write power, while >75% of the adatoms survive for 200 s at <10 μW reads. Moreover, experiments where the same picocavity is read intermittently with extended dark periods in-between show picocavity stability for up to a week in ambient conditions (Fig. 1C). This shows the remarkable robustness of the adatom in ambient conditions.

Our study enables room-temperature, real-time optical manipulation of single atoms with week-long stability. These findings advance the integration of plasmonics into nanoelectronic devices and single-atom catalysis applications.

Acknowledgments: We thank support from the European Research Council (ERC) under the Horizon 2020 Research and Innovation Programme PICOFORCE (883703), and UK EPSRC EP/X037770/1. R.A. acknowledges support from St. John's College Cambridge and the Winton Programme for the Physics of Sustainability. B.d.N. acknowledges funding and support from the Royal Society (URF/R1/211162) and the EPSRC (EP/Y008294/1). D.T. acknowledges Research Ireland for support under Grant Number 12/RC/2275_P2 (SSPC) and for supercomputing resources at the Research Ireland and Higher Education Authority supported Irish Center for High-End Computing (ICHEC).

References

1. Kerner, P., R. Arul, D. Thompson, J. J. Baumberg and B. d. Nijs, "Optical control of single atom dynamics in plasmonic nanogaps", submitted.
2. Benz, F., M. K. Schmidt, A. Dreismann, R. Chikkaraddy, Y. Zhang, A. Demetriadou, C. Carnegie, H. Ohadi, B. De Nijs, R. Esteban, J. Aizpurua and J. J. Baumberg, “Single-molecule optomechanics in “picocavities””, Science 354, 726 (2016).
3. Lin, Q., S. Hu, T. Földes, J. Huang, D. Wright, J. Griffiths, E. Elliott, B. De Nijs, E. Rosta and J. J. Baumberg, “Optical suppression of energy barriers in single molecule-metal binding”, Sci. Adv. 8, eabp9285 (2022).

Resonant optical metasurfaces for eye-tracking applications

Vittorio Bonino[1*], Filippo Coviello[1,2], Pietro Baldin[2], Alberto Sivera[2], Rafael Bellei de Carvalho[2], Paolo Biagioni[2], Giuseppe Della Valle[2], Giovanni Isella[2], Roman Sordan[2], Gianluca Valentini[2], Giulio Cerullo[2], Anna Cesaratto[1], Tommaso Ongarello[1] and Jacopo Stefano Pelli Cresi[1]

[1]EssilorLuxottica Smart Eyewear Lab – Milano, Italy
[2]Dipartimento di Fisica, Politecnico di Milano – Milano, Italy
[*]corresponding author: vittorio.bonino@luxottica.com

Abstract: We propose an optical coupler with total internal reflected propagative modes to enhance signal detection in smart eyewear eye-tracking systems. Supporting surface lattice resonances, the metasurface is tuned to near-infrared wavelengths via geometric control of dielectric meta-atoms. Fabricated using electron-beam lithography, it achieves >80% visible transparency while enhancing infrared scattering at the lens.

Smart eyewear development requires careful integration to ensure the final device is both comfortable and functional, offering a lightweight and easy-to-wear solution. A key feature in these devices is eye-tracking technology, which detects and follows the user's gaze. This typically involves using infrared light to illuminate the eye and measuring the reflected light with photodetectors, enabling precise eye movement tracking [1]. The main challenges when embedding such systems into eyewear is minimizing form factor, reducing power consumption and computational load, all while maintaining high performances. In response to this, a recent proposal from a smart eyewear research team suggests a novel eye-tracking method that integrates photodetectors into the frame itself, positioned near the lens edge [2]. To enhance the photodetector signals, we suggest utilizing a metasurface (MS) with non-local properties, which can be applied to the lens. This metasurface enables surface lattice resonances (SLRs), created by the interaction of Rayleigh anomalies with meta-atom resonances, allowing for fine-tuned control of in-plane scattering efficiency [3].

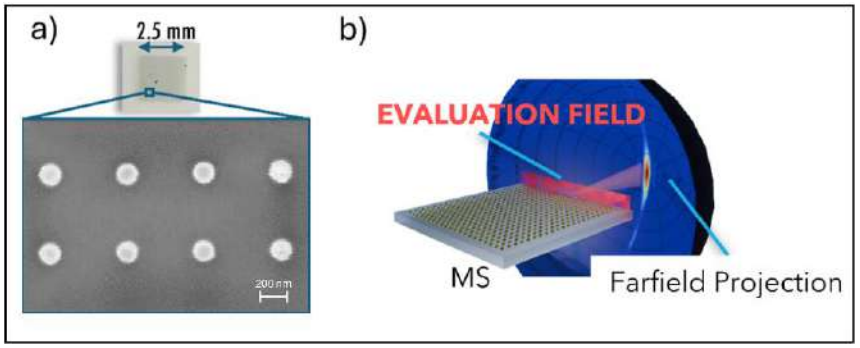


Figure 1: (a) Upper: Metasurface prototype consisting of meta-atoms arranged on a silicon oxide substrate. Lower: Scanning electron microscope (SEM) image of a portion of the metasurface. (b) Schematic representation of the in-plane scattering emitted from the metasurface.

By manipulating the geometric properties of the meta-atoms—such as their spacing, diameter, and height—we can control the scattering spectrum, aligning it with the near-infrared (NIR) LED's emission range used to illuminate the eye. This precise tuning ensures that the metasurface remains transparent to over 80% in the visible spectrum, enabling it to be applied directly on the lens without interfering with the user's see-through vision. In choosing materials, we focused on optical properties and considered two potential options: metallic and dielectric platforms. While metals like gold can facilitate plasmonic resonances, their optical losses in the visible spectrum might reduce overall transparency and the quality factor of the resonances. High-index dielectric materials, such as silicon, however, efficiently support resonances while minimizing visible spectrum losses, making them an ideal choice for photonic devices [4]. The metasurfaces were fabricated using electron-beam lithography (EBL), with material deposition and lift-off processes to finalize the structure. The optical performance of the device was evaluated using a specialized setup to measure both the transparency of the metasurface and the intensity of scattered infrared radiation at the lens surface.

This work was carried out in the Smart Eyewear Lab, a Joint Research Center between EssilorLuxottica and Politecnico di Milano.

References

1. Moritz Kassner et al. In proceeding of UbiComp '14 Adjunct conference. 1151–1160 (2014).
2. Crafa et al. In proceeding of ETRA' 24. 90, 1-7 (2024)
3. Castellanos et al. J. Appl. Phys. 125, 213105 (2019).
4. Joyce K. S. Poon et al., Adv. Opt. Photon. 16, 1-59 (2024)

Single Molecule Detection in hBN metasurfaces

S. Izadshenas*, K. Słowik
Institute of Physics, Faculty of Physics, Astronomy, and Informatics,
Nicolaus Copernicus University in Toruń, ul. Grudzikadzka 5, 87-100, Toruń, Poland
Corresponding author: s.izadshenas@umk.pl

Abstract: We report complementary hBN metasurface hosting embedded nanocavities. Comprehensive optical characterization reveals visible-regime high-Q resonances due to the quasi-bound states in the continuum, which produce a spatially uniform electric fields. The cavity field enables single-molecule surface-enhanced Raman spectroscopy, which we here consider for ATTO 610-doped ethanol. Results demonstrate strong absorption–emission enhancement and signal levels exceeding those of conventional plasmonic platforms.

This study is devoted to the design of a complementary all-dielectric metasurface formed hexagonal Boron Nitride (hBN) film, including cylindrical cavities. The optical response sustains high-Q resonances in the visible regime and uniform electric field inside the cavities due to the quasi-bound states in continuum [1, 2]. We investigate the single-molecule SERS process by considering a single ATTO 610 molecule in ethanol solvent inside the cavity. The schematic of the hBN metasurface with a single molecule inside a cavity is shown in Fig.1(a). The SERS intensity enhancement of a single molecule is investigated with equation (1) [3]:

$$I_{SERS} = |\frac{E(\mathbf{r},\omega)}{E_0(\mathbf{r},\omega)}|^2 \times F_p, \tag{1}$$

where $E(\mathbf{r},\omega)$, and $E_0(\mathbf{r},\omega)$ are electric fields in the molecule's position in hBN metasurface and free space, respectively. The F_p is the Purcell factor of a molecule inside the hBN cavity metasurface, defined as:

$$F = \frac{3}{4\pi^2}(\frac{\lambda}{n})^3 \frac{Q}{V_{\text{eff}}}, \tag{2}$$

where λ is the free-space resonant wavelength, n is the refractive index of the medium, Q is the quality factor of the resonance and V_{eff} is the effective mode volume. The effective mode volume can be calculated by:

$$V_{\text{eff}} = \frac{\int_{\text{V}} \varepsilon(\mathbf{r}) \left|\mathbf{E}(\mathbf{r})\right|^2 \mathrm{d}V}{\max\left[\varepsilon(\mathbf{r}) \left|\mathbf{E}(\mathbf{r})\right|^2\right]} \tag{3}$$

The SERS signal intensity in the logarithmic scale is shown as a function of the cavity diameter in Fig.1(b), demonstrating strong SERS intensity enhancement in larger volume compared to traditional plasmonic cavities. The SERS signal intensity enhancement in the hBN cavity with a diameter of 40 nm with respect to free space is around 10 orders of magnitude.

In summary, hBN metasurfaces offer exceptional potential for SERS spectroscopy, enabling both single-molecule detection and enhanced sensitivity of multi-molecule detection in coherent media.

The authors acknowledge the support from the National Science Centre, Poland (Project No. 2020/39/I/ST3/00526).

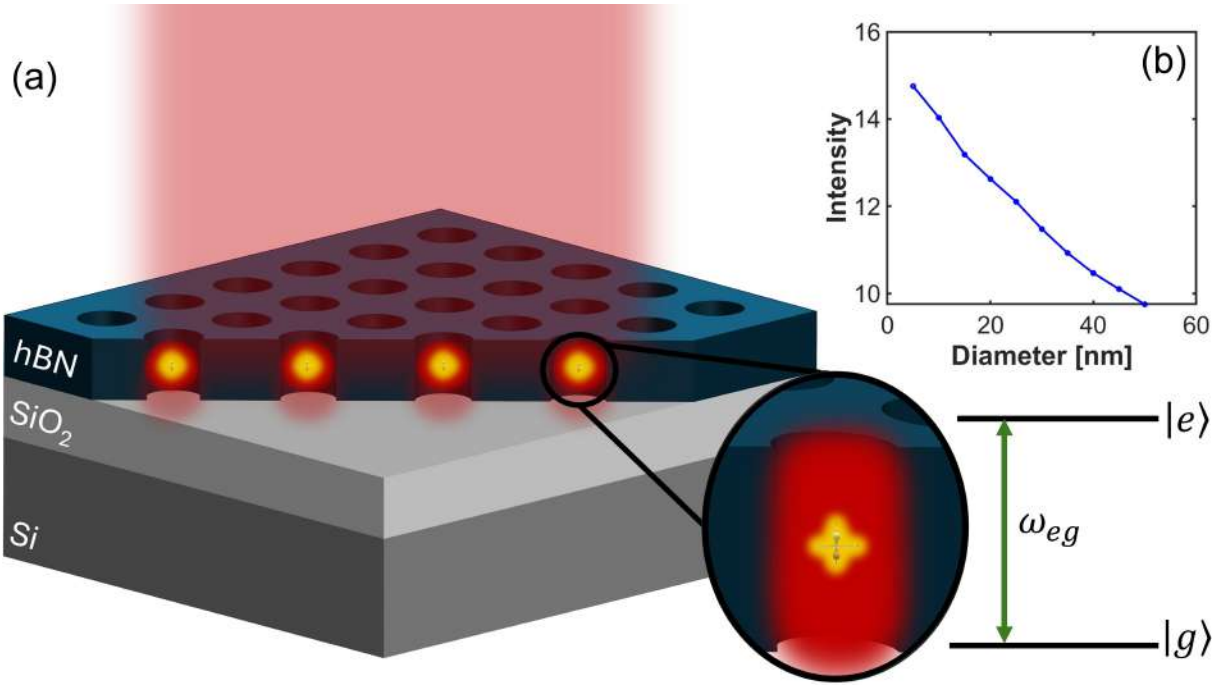


Figure 1: (a) HBN metasurface with a periodic array of cylindrical nanocavities, each hosting an ATTO 610 dye molecule. (b) SERS signal intensity enhancement of the hBN metasurface as a function of the cavity's diameter.

References

1. Tittl, A., Leitis, A., Liu, M., Yesilkoy, F., Choi, D.Y., Neshev, D.N., Kivshar, Y.S. and Altug, H., "Imaging-based molecular barcoding with pixelated dielectric metasurfaces," *Science*, Vol. 360, No. 6393, pp.1105-1109, 2018.

2. Kühner, L., Sortino, L., Tilmann, B., Weber, T., Watanabe, K., Taniguchi, T., Maier, S.A. and Tittl, A., "High-Q nanophotonics over the full visible spectrum enabled by hexagonal boron nitride metasurfaces," *Advanced Materials*, Vol. 35, No.13, p.2209688, 2023.

3. Bharadwaj, P., Deutsch, B. and Novotny, L., "Optical antennas," *Advances in Optics and Photonics*, Vol. 1, No. 3, pp.438-483, 2009.

Infrared Spectroscopy of Heavily Doped Germanium Crystals

Sergey G. Pavlov [1], Aravind N. Subramanian [2], R. Radhakrishnan Sumathi [2], S. Bin Anooz [2], Nikolay V. Abrosimov [2], Mariia Sidorova [3,1] and Heinz-Wilhelm Hübers [1,3]

[1] Institute of Optical Sensor System, German Aerospace Center, Berlin, Germany
[2] Leibniz-Institut für Kristallzüchtung, Berlin, Germany
[3] Humboldt Universität zu Berlin, Germany
*corresponding author, E-mail: sergeij.pavlov@dlr.de

Abstract

Infrared absorption spectroscopy, in transmission and reflectance modes, Raman scattering spectroscopy, X-ray rocking curve imaging analytics were used to characterize optical and structural properties of *n*-type and *p*-type bulk germanium crystals doped above the Mott transition. Such materials are being considered for mid-infrared technology as a counterpart to silicon-based devices.

1. Introduction

Heavily doped (HD) semiconductors are indispensable materials for realization of electronic and optoelectronic devices in particular because their properties bridge dielectric and metallic matter [1]. However, there is a lack of a comprehensive theoretical background that adequately explains all experimentally observed optical features, especially when the latter result from spectrally overlapping strong light-matter interaction. This upsurges the importance of empirical data on these materials and its direct analysis.

Germanium (Ge) crystals offers high mobility of charge carriers and possess low lattice absorption in the mid-infrared wavelength range that makes it one of the key materials for optoelectronic applications and sensing. Most of present research on HD Ge is focused on engineering approaches for a substitutional one-electron donor doped thin (typically not above 1 μm) films deposited on various substrates. Complex techniques using epitaxial and ion implantation methods were explored to overcome the natural limits of doping [2,3]. Note that many mid-infrared applications would require a thickness of a high-quality homogeneous material that exceeds the light wavelength. Such requirements can be addressed mainly by doped bulk crystals, which therefore remain the universal platform for multi-vector semiconductor technology.

We report on the characterization of optical and structural properties of *n*-type and *p*-type Ge crystals doped with single-electron substitutional impurities above the Mott transition, up to about the equilibrium solubility limit [4-6].

2. Crystal growth and characterization

All crystals were grown by the Czochralski (Cz) method or its modified variant, the so called “mini-Cz”, with the doping from the gas phase [4]. Concentration of the free charge carriers was estimated from calibrated resistivity measurements. The *p*-Ge crystals have large concentration of charge carriers than *n*-Ge; *p*-Ge ingots exhibit an axial doping gradient.

For the heavily doped (HD) *p*-Ge:Ga crystal (gallium concentration up to ~ 2×10^{20} cm^{-3}) [5] sections along this gradient (i.e. in the growth direction, Fig. 1a) were investigated. For a HD *n*-Ge:Sb (antimony concentration up to ~ 1.6×10^{18} cm^{-3}) and a HD *n*-Ge:P (phosphorus concentration up to ~ 2×10^{17} cm^{-3}), only sections perpendicular to the growth axis were measured.

The structural properties were analyzed using X-ray rocking curve imaging on the crystal sections along the growth axis. The 2D maps (intensities) of the rocking curves indicate an increased defect density at Ga concentrations above 10^{20} cm^{-3}, when HD Ge:Ga become multicrystalline.

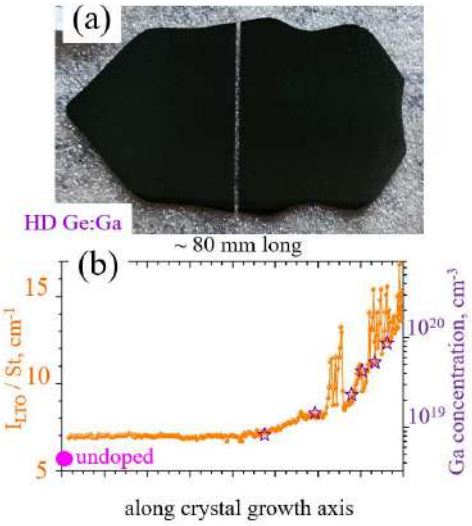


Figure 1. (a) A section along the HD Ge:Ga crystal growth (acceptor gradient) axis, the Ga concentration increases from the left to the right end; (b) Raman signal integrated absorption under the Ge LTO line over the LTO frequency, used to show the evolution of the LTO mode along the crystal growth axis; right axis – for the Ga concentration, the values marked as stars were obtained from calibrated resistivity measurements.

Raman spectra were recorded in the backscattering geometry using a WITEC 300 Alpha microscope providing a spatial resolution of 1.5 μm and a 532 nm laser. The spectra as it has been shown provide supplementary information on the concentration gradient as well as local lattice distortion (the latter – in the region of the ultra-high doping limit).

The first-order zone-centered LTO optical phonon exhibits a red shift in the energy and asymmetric line broadening. The large local deviations from the mean LTO frequency value (Fig. 1b) are most likely caused by strong structural changes, such as dislocation clusters towards the highly doped ingot end, which were observed using energy dispersive Laue spectroscopy [5].

The second-order Raman spectra show a strong increase in the scattering rates of the sum-phonon bands, expressed in line broadening, the intensity decrease of most of second-order bands and the appearance of defect-induced bands.

3. Infrared absorption spectroscopy

Infrared absorption spectra were collected with a Bruker Fourier-Transform spectrometer in transmission mode (normal incidence on the sample surface) and in reflection mode (biconic mode, 13° – 13°).

Transmission spectra of HD Ge crystals do not return useful information in the mid-infrared range for crystals doped above the Mott transition. This is apparently due to the strong free carrier absorption, which affects the spectra up to the bandgap absorption for *p*-Ge (Fig. 2).

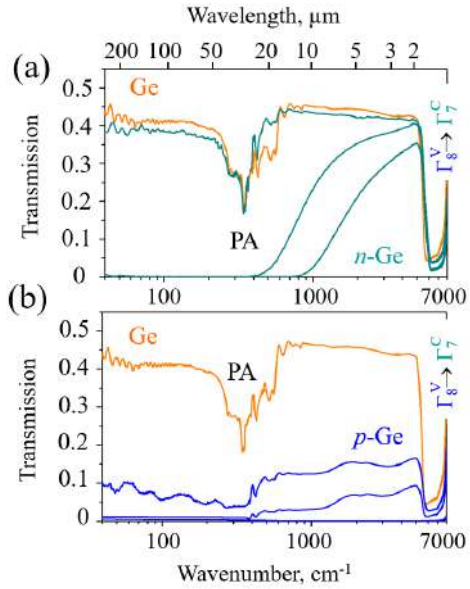


Figure 2. Transmission spectra of Ge samples doped below and above the Mott transitions, compared with the spectra of undoped Ge (residual acceptors below 10^{13} cm^{-3}). (a) Sb doped *n*-Ge, donor densities are $9.\times10^{14}$ cm^{-3}, 5.7×10^{17} cm^{-3}, 1.6×10^{18} cm^{-3}; (b) Ga doped *p*-Ge, acceptor densities are 1.1×10^{16} cm^{-3}, ~5×10^{18} cm^{-3}, ~5×10^{19} cm^{-3}. Interband transitions contributing to the integral absorption are shown. PA stays for multi-phonon absorption bands.

The samples doped below the Mott transitions exhibit non-vanishing transmission with the characteristic features of multi-phonon absorption (PA) bands (Fig. 2).

Infrared reflectance spectra of HD Ge reveal the impact of various optical processes contributing to infrared absorption: intraband absorption by free electrons ($e \rightarrow e$), including features associated with intervalley scattering in the conduction band of *n*-type Ge; intrasubband heavy and light holes ($hh \rightarrow hh$ and $lh \rightarrow lh$) and intersubband absorption by heavy-to-light hole transitions ($hh \rightarrow lh$) in *p*-Ge. Additionally, common for the both materials, interband absorption (dominating by) direct $\Gamma_8^{VB} \rightarrow \Gamma_7^{CB}$ transitions between the valence and conduction bands is clearly observed in the high-frequency region of the mid-infrared reflectance spectra. The frequency shift in the latter transition type illustrates the doping-induced bandgap narrowing [7] in a HD Ge.

4. Conclusions

Complementary (transmission and reflection) infrared absorption spectroscopy provides detailed information about optical properties of heavily doped germanium bulk crystals. At charge carrier densities above the Mott transition, mid-infrared transmission vanishes, while reflectance spectra indicate the transition between strong reflection and absorption regions.

Raman microscopy can be used to evaluate the local quality of HD Ge crystals, which is affected by local (dopant) and distributed (lattice) defects.

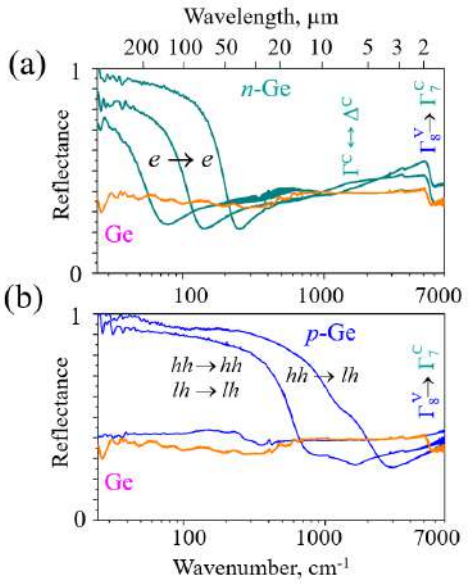


Figure 3. Reflectance spectra of HD Ge samples compared with the spectra of undoped Ge. (a) Sb doped HD *n*-Ge, donor densities are 1.4×10^{17} cm^{-3}, 5.7×10^{17} cm^{-3}, 1.6×10^{18} cm^{-3}. (b) Ga doped HD *p*-Ge, acceptor densities are 1.1×10^{16} cm^{-3}, ~5×10^{18} cm^{-3}, ~5×10^{19} cm^{-3}. Intrasubband $e \rightarrow e$, $hh \rightarrow hh$, $lh \rightarrow lh$, intersubband $hh \rightarrow lh$, interband $\Gamma_8 \rightarrow \Gamma_7$ as well as $\Gamma \rightarrow \Delta$ intervalley scattering transitions contributing to the integral absorption are shown.

Acknowledgements

The authors acknowledge partial support from the German Research Foundation (Deutsche Forschungsgemeinschaft) under DFG projects numbers 509105207 and 509113935.

References

[1] R. A. Abram, G. J. Rees, and B. L. H. Wilson, Heavily doped semiconductors and devices, *Adv. Phys.* 27 (6): 799–892, 1978.

[2] H. A. Tahini, A. Chroneos, R. W. Grimes, U. Schwingenschlögl, H. Bracht, Point defect engineering strategies to retard phosphorous diffusion in germanium, *Phys. Chem. Chem. Phys*. 15: 367-371, 2013.

[3] J. Kim, S. W. Bedell, D. K. Sadana, Multiple implantation and multiple annealing of phosphorus doped germanium to achieve n-type activation near the theoretical limit, *Appl. Phys. Lett*. 101: 112107, 2012.

[4] R. Radhakrishnan Sumathi, N. Abrosimov, K.-P. Gradwohl, M. Czupalla, J. Fischer, Growth of heavily-doped Germanium single crystals for mid-Infrared Applications, *J. Cryst. Growth*. 535: 125490, 2020.

[5] A. Subramanian, N. Abrosimov, A. Gybin, Ch. Guguschev, U. Juda, A. Fiedler, F. Bärwolf, I. Costina, A. Kwasniewski, A. Dittmar, R. Radhakrishnan Sumathi, Investigation of Doping Processes to Achieve Highly Doped Czochralski Germanium Ingots, *J. Electron. Mater.* 52: 5178–5188, 2023.

[6] Aravind N. Subramanian, M. P. Kabukcuoglu, C. Richter, U. Juda, R. Kernke, F. Bärwolf, E. Hamann, M. Zuber, N. V. Abrosimov, R. Radhakrishnan Sumathi, Growth of Boron-Doped Germanium Single Crystals by the Czochralski Method, *Cryst. Growth Des.* 25 (4): 1075–1081, 2025.

[7] C. Xu, J. Kouvetakis, and J. Menéndez, Doping dependence of the optical dielectric function in n-type germanium, *J. Appl. Phys.* 125: 085704, 2019.

Theoretical study and experimental validation of nonlocal metasurfaces for Augmented Reality

Pietro Baldin[1], Alberto Sivera[1], Rafael Bellei de Carvalho[1], Filippo Coviello[1,2], Vittorio Bonino[2], Jacopo Stefano Pelli Cresi[2], Anna Cesaratto[2], Tommaso Ongarello[2], Paolo Biagioni[1], Roman Sordan[1], Giovanni Isella[1], Gianluca Valentini[1], Giulio Cerullo[1], and Giuseppe Della Valle[1]

[1]Physics Department – Politecnico di Milano, piazza Leonardo da Vinci 32, 20133 Milan, Italy
[2]Smart Eyewear Lab – EssilorLuxottica, Via Giovanni Pascoli, 70/3, 20133 Milano, Italy
[*]corresponding author: giuseppe.dellavalle@polimi.it

Abstract:

Nonlocal metasurfaces are very promising solutions for advanced Augmented Reality (AR)-devices, but major challenges are still to be faced. This poster summarizes all the activities we have performed to achieve advanced nonlocal metasurfaces for this application, focusing on the theoretical studies and simulations, but also with experimental validations on structures fabricated at our facilities.

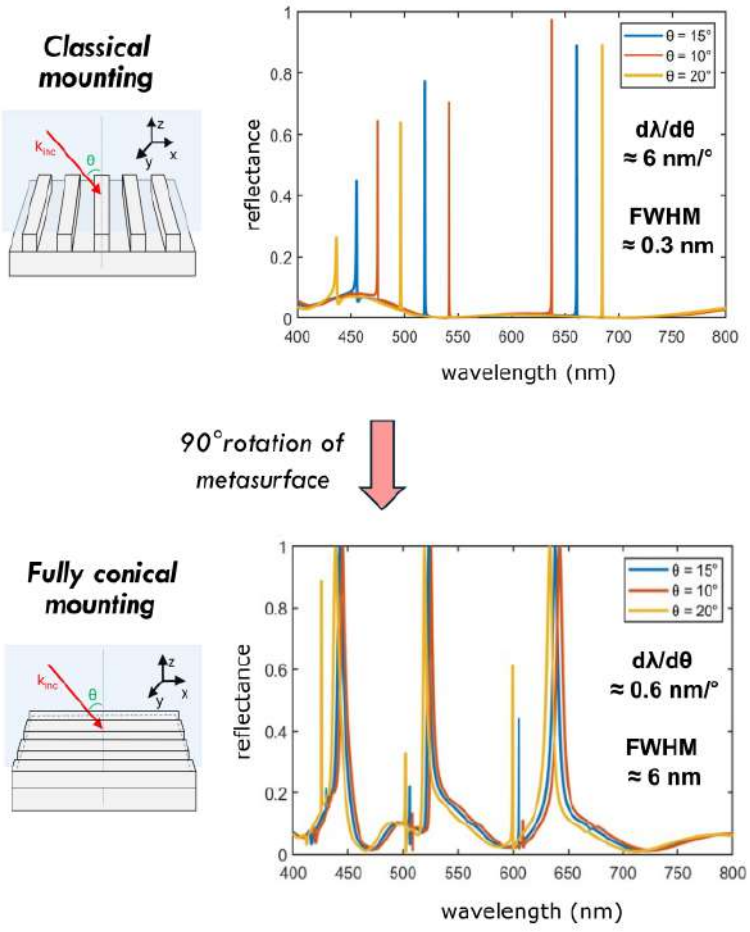


Figure 1. Differences between classical and fully-conical mountings in diffraction, with exemplary sketches of their setups and typical reflection spectra (for the 0th-diffraction order).

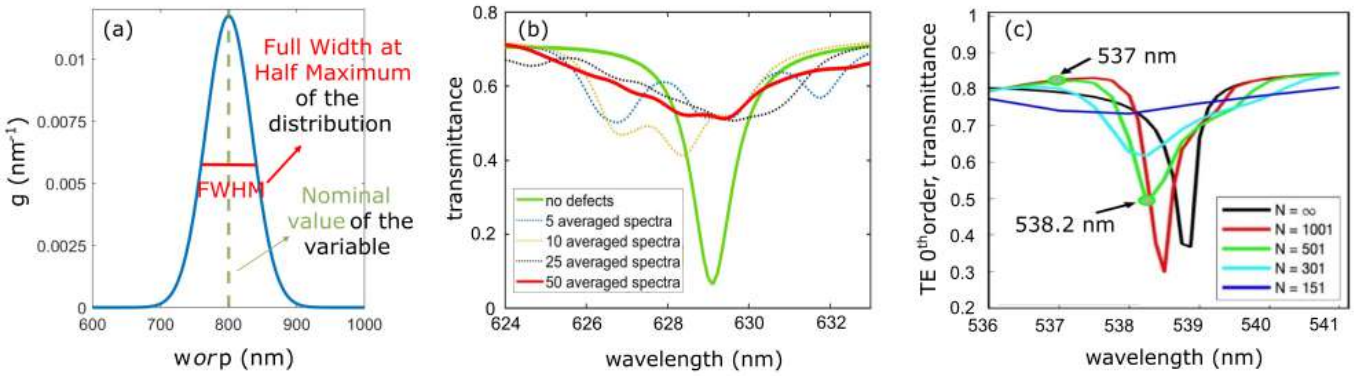


Figure 2. Modeling of geometrical defects and finite size effects in nonlocal metasurfaces. (a) gaussian-based distribution of geometrical defects; (b) simulation of periodicity defects of a grating-based structure, with the modeling of panel (a); (c) influence of finite size effects on the transmission spectrum of an exemplary structure (N is the number of simulated unit cells).

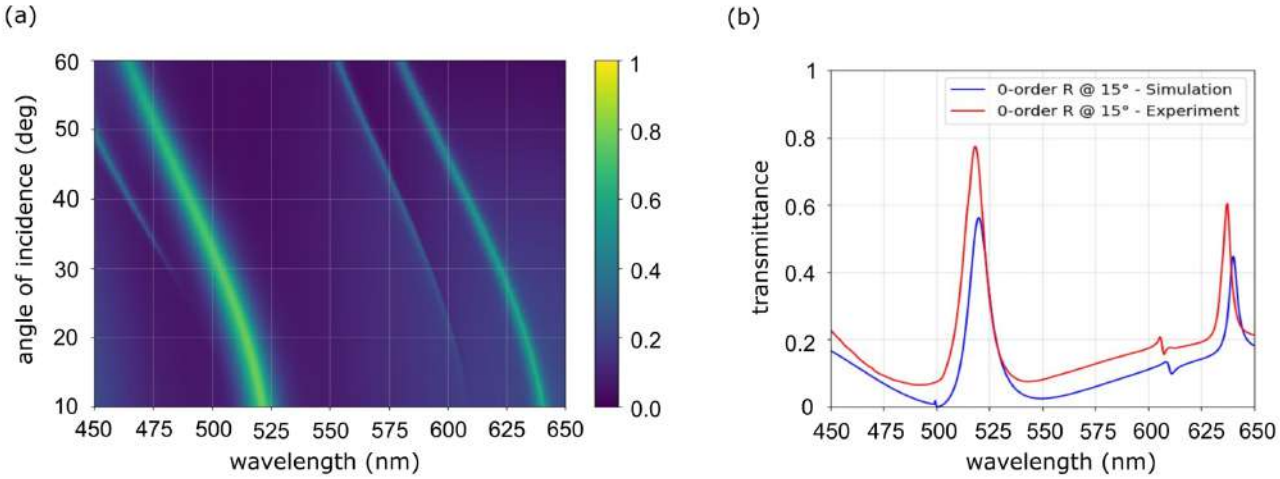


Figure 3. Experimental validation of numerical analyses on fabricated samples. (a) transmission colormap of an exemplary metasurface, highlighting the presence of resonant branches with reduced angular dispersion. (b) comparison between simulated and experimental spectra of the metasurface in panel (a), for an incidence angle of 15°.

This work was carried out in the Smart Eyewear Lab, a Joint Research Center between EssilorLuxottica and Politecnico di Milano.

References

1. Malek SC, Overvig AC, Alù A, Yu N. Multifunctional resonant wavefront-shaping meta-optics based on multilayer and multi-perturbation nonlocal metasurfaces. Light Sci Appl. 2022 Aug 3;11(1):246.
2. Z. Liu et al., Metasurface-enabled augmented reality display: a review, Adv. Photon., vol. 5, fasc. 03 (2023).
3. J.-H. Song et al., Non-local metasurfaces for spectrally decoupled wavefront manipulation and eye tracking, Nat. Nanotechnol., vol. 16, fasc. 11, pp. 1224–1230 (2021)

Suppressing photobleaching of j-aggregates via strong light-matter coupling

Yadav Rohit Umashankar, Parinda Vasa*

Department of Physics, Indian Institute of Technology Bombay, Mumbai, India
*Corresponding author, E-mail: parinda@iitb.ac.in

Abstract

Here, we experimentally investigate the suppression of photobleaching of cyanine dye j-aggregates when it is strongly coupled to propagating surface plasmons on planar silver film. The experimental technique involves the novelty of probing only the strongly coupled molecules for bleaching suppression in the Kretschmann configuration with no background from uncoupled molecules.

1. Introduction

Surface plasmon polaritons (SPPs) are spatially confined electromagnetic field modes at a metal-dielectric interface capable of generating intense near-field optical forces on ultrafast time scales[1]. When an organic emitter interacts with surface plasmon polariton (SPP) fields, it can form a hybrid system with new energy eigenstates called polaritonic states. This strong coupling is evidenced by an anti-crossing behavior in the dispersion relation, known as Rabi splitting[2,3]. It has been shown that chemical reactivity, charge, and exciton transport[4] can be modified under strong coupling conditions. The photobleaching effect is one such fundamental chemical property appearing in many organic molecules, suppressing the fluorescence of dye molecules and leading to irreversible photodamage. It limits the applications of organic electronic devices such as organic solar cells, electroluminescent devices, organic dye lasers, and molecular fluorescence[5]. Photobleaching occurs through photodynamic interactions, where dye molecules in an excited triplet state interact with atmospheric oxygen, which is also in its triplet state, via a charge transfer mechanism generating reactive oxygen species, which in turn chemically degrade the fluorophores[6,7]. Since polaritonic states are coherent hybrids of plasmons and excitons they have extremely short lifetimes (~ 10fs) far faster than typical intersystem crossing rates (10^{-8} to 10^{-3} seconds). This prevents efficient triplet state population, making polaritonic states highly effective in suppressing photobleaching reactions[8,9]. Recent studies have demonstrated that photobleaching of Rhodamine 6G molecules is significantly suppressed when the molecules are strongly coupled to surface plasmon polaritons (SPPs) on a 50 nm planar silver film using the Kretschmann configuration (KC). This suppression is evidenced by fluorescence intensity and lifetime measurements[10,11]. However, spectroscopic measurements involve the background of uncoupled molecules in the system. Here, we showed the experimental novelty in exciting and probing only the strongly coupled molecules with no background from uncoupled molecules. Time-dependent bleaching measurements were performed to obtain the bleaching curve from the reflectance spectrum in the Kretschmann configuration. The results demonstrated reduced photobleaching in strongly coupled j-aggregated molecules compared to the photobleaching observed when the sample was directly exposed to laser light.

2. Materials and Experimental Method

The commercially purchased water-soluble Cyanine dye 5,6-Dichloro-2-[[5,6-dichloro-1ethyl-3-(4sufobutyl) benzimidazole-2-ylidene] propenyl]-1-ethyl-3-(4-sulfobutyl) benzimidazolium hydroxide, inner salt, sodium salt (TDBC). A dye solution with Polyvinyl Alcohol (PVA) as a matrix was prepared by dissolving 1 mg of dye in 1 mL of a mixed solvent of Ethanol and PVA in a 4:1 ratio. The concentration of PVA was 25mg/ml in deionized water. The absorption spectrum of the dye in ethanol solvent exhibits a broad absorption peak at 525 nm. However, when spin-coated on a glass substrate, the spectrum shows an intense, narrow, red-shifted absorption band at 587 nm, indicating the formation of j-aggregates in the film form. The monomer and j-aggregate spectrum of the TDBC dye is shown in Figure 1.

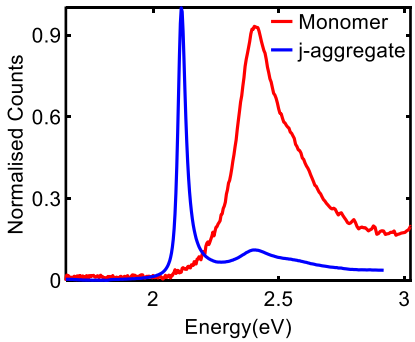


Figure 1: Absorption spectrum of TDBC monomer and j-aggregate.

The schematic diagram of the experimental setup is shown in Figure 2. It consists of a Tungsten-Halogen broadband source for reflectance measurements and a Supercontinuum pulsed laser source with wavelength selective filter for exposing the sample in the Kretschmann configuration. The spot size and beam path of the two sources have been made precisely coincided with the help of mirrors, beam splitter

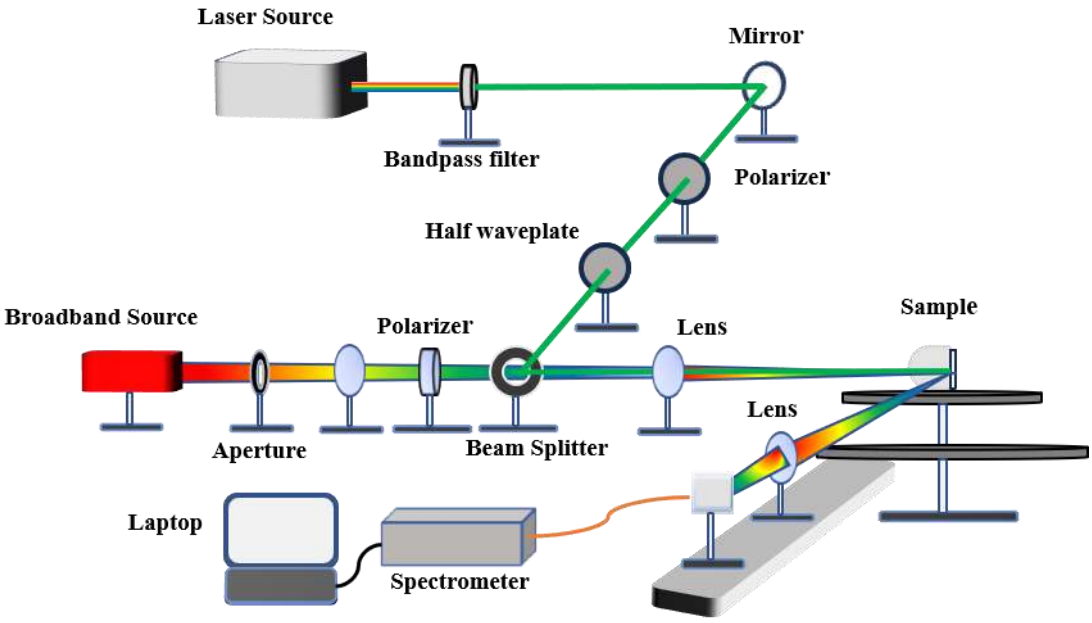


Figure 2: Schematic diagram of the experimental setup.

and lenses before they fell on the sample. This arrangement exposes the sample with a laser for a certain period and collects the reflectance spectrum from the same spot for the bleaching signature in the Kretschmann configuration. Polarizers have been introduced in the two paths to make both beams horizontally polarized. Since both exposing the dye and taking reflectance measurements are done in the Kretschmann configuration, the hallmark of bleaching is from the coupled molecules.

3. Results and Discussion

The angle-resolved reflection measurements were done to check for the signature of strong coupling through dispersion relation. The sample consists of a 50nm silver film spin-coated with the TDBC dye solution on it at 2000 rpm. The silver film was placed on the hemicylindrical prism, with index-matching oil.

3.1. Measuring the dispersion relation

To obtain the dispersion relation the angle-resolved reflection spectrum was fitted with the Fano line-shape function[12]–[14]. Figure 3a shows the Fano-fitted reflectivity spectrum at an angle of 46.5 degrees. Figure 3b shows the obtained dispersion relation, with the fitted parameter as resonance data points of upper and lower polaritonic branches. The expression for the Fano line shape function is given as

$$R(w,\phi) = \sum_{i=1}^{2} \left| a_i + \frac{b_i * e^{i*\phi_i} * \Gamma_{radi}}{w - w_{0i} + i * \Gamma_{radi}} \right|^2 \qquad (1)$$

Where a_1, b_1, ϕ_1, and a_2, b_2, ϕ_2, are the complex value parameters. The resonance positions of the upper and lower polaritonic branches obtained by Fano fitting the angle-resolved reflection spectrum is being used in getting the dispersion relation.

The dispersion relation shows the anti-crossing behavior at the j-aggregate absorption wavelength.

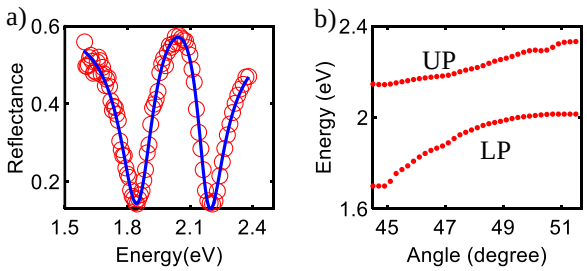


Figure 3: a) Reflection data (red circle) at 46.5degree angle fitted with Fano line-shape function (blue line). b) Dispersion relation showing the upper and lower polaritonic branches.

3.2. Modeling the dispersion relation

When molecular aggregates undergo strong coupling with surface plasmons, they form hybrid polaritonic states that exhibit ultrafast decay dynamics on the timescale of a few femtoseconds. The strength of the strong interaction or Rabi splitting energy between the hybrid states is given as[15]

$$\hbar\Omega_R = 2 * d * \sqrt{\frac{\hbar * w_c * N}{2 * \varepsilon_0 * V}} \qquad (2)$$

where d is the dipole moment of the oscillator, V is the mode volume, and N is the number of molecules or oscillators. The linear optical behavior of this hybrid structure can be effectively described using a coupled harmonic oscillator model, where the exciton and surface plasmon polaritons (SPPs) are represented as complex Lorentzian oscillators[16]. According to the model, the UP and LP hybrid mode frequencies are given by:

$$w_{UP/LP} = \frac{w_x + w_{spp}}{2} \pm 0.5 * \sqrt{(w_x - w_{spp})^2 + 4 * \Omega_R^2} \quad (3)$$

Where w_x and w_{spp} represents the complex frequency of the exciton and SPP. Figure 4a shows the contour plot of the angle-resolved reflection measurement done on the silver film without coating the TDBC dye. It shows the plasmon resonance varying from 1.6 eV to 2.4 eV. Whereas, Figure 4b shows the contour plot of the angle-resolved measurement for the coupled system. It shows the formation of a hybrid system with upper and lower polaritonic branches. The coupled oscillator model fitting of the dispersion relation gives the Rabi splitting energy around 365±6 meV.

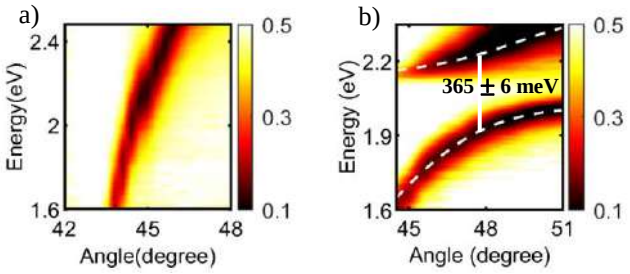


Figure 4: Contour plot of the angle-resolved reflection measurement a) On 50nm silver film without TDBC coating b) With TDBC coating.

For time-dependent bleaching information of the dye, the reflectance spectrum of the coupled system was recorded at a particular angle. The angle was chosen so the exposing laser wavelength can outcoupled through SPR in the Kretschmann configuration. The reflectance spectrum was recorded using a broadband source at different time intervals of laser exposure. Figure 5 shows the reflectance spectrum of the coupled system for various time intervals of laser exposure of wavelength 580nm in the Kretschmann configuration.

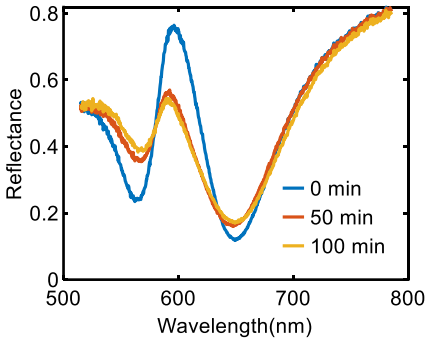


Figure 5: Reflectance spectrum at different time intervals of laser exposure of 580nm wavelength in Kretschmann configuration.

The bleaching of the dye reduces the number of active molecules participating in the coupling, which in turn decreases the Rabi splitting energy. As a result, the energy gap between the lower and upper polaritonic branches is reduced. It introduces inhomogeneous broadening due to variations in the dye's transition energies and partial photodamage. This broadens the polaritonic states. Here, we investigate the bleaching of the dye under strong coupling with SPPs in the Kretschmann configuration, analyzing its dependence on the exposure laser wavelength. The reflectance spectrum at different time intervals of laser exposure, for various exposure wavelengths, was fitted with a Fano profile to determine the resonance positions of the lower and upper polaritons. The results indicate that when the exposure wavelength is closer to the excitonic absorption, the polaritonic branches shift towards each other more significantly compared to when the exposure wavelength is farther from the excitonic absorption. This suggests that dye bleaching is more pronounced when the system exhibits excitonic-like behavior and is suppressed when it becomes plasmonic-like, farther from the excitonic absorption band. Table 1 shows the shifting of the resonances of the lower and upper polaritonic branches, as a function of bleaching time for different laser wavelength exposure.

Table 1: Resonances of Lower Polariton (LP) and Upper Polariton (UP) at different times for different laser wavelength exposures.

Time → Exposing laser wavelength ↓	0 (min)		100 (min)		Difference (0^{th}-100^{th})	
	LP (nm)	UP (nm)	LP (nm)	UP (nm)	LP (nm)	UP (nm)
580	649	563	645	570	4	7
550	661	564	659	568	2	4
520	607	508	606	511	1	3

The difference reflectance plots were obtained by subtracting the peak points of the reflectance spectrum at the 0th minute from those at various time intervals. This was done for different laser exposure wavelengths to analyze the changes over time. It presents the bleaching percentage for all laser exposure wavelengths in the Kretschmann configuration, along with direct dye bleaching at 590 nm exposure.

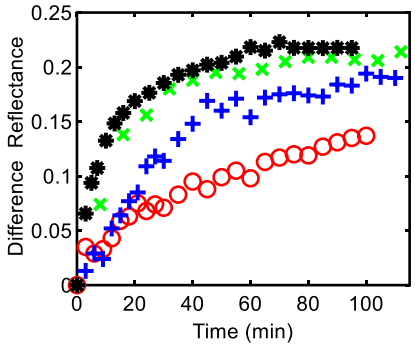


Figure 6: Bleaching curves for different laser wavelengths of exposure 1) 520nm (red circles) in KC 2) 550nm (blue plus) in KC 3) 580nm (green cross) in KC 4) 590nm (black asterisk) direct bleaching.

Table 2 summarizes the percentage of bleaching observed under different laser wavelengths for 50 minutes of exposure, comparing the Kretschmann configuration and direct bleaching. This comparison illustrates the suppression of bleaching under strong coupling conditions achieved in the Kretschmann setup. A bleaching of 20.39% was observed in

the J-aggregate dye upon direct exposure to a 590 nm laser for 50 minutes.

Table 2: Percentage bleaching suppressed for different exposing laser wavelengths.

Exposing laser Wavelength	%Bleaching data for 50^{th} minute	%Bleaching suppressed (Direct-KC)
520nm in KC	9.90	10.49
550nm in KC	16.0	4.39
580nm in KC	19.50	0.89

4. Conclusions

In this work, we investigated the photobleaching behavior of j-aggregating cyanine dye molecules under strong light-matter coupling with propagating surface plasmons supported by planar 50nm silver film. Using angle-resolved reflectance measurements in the Kretschmann configuration, we tracked bleaching dynamics by repeatedly probing the same spot during controlled laser exposure. Our results reveal that exposure at wavelengths far detuned from the excitonic absorption of the dye leads to significantly suppressed photobleaching compared to near-resonant excitation. This behavior contrasts with the direct bleaching observed under 590nm laser exposure in the non-Kretschmann configuration, where the excitation is near the excitonic absorption peak. Notably, the suppression of photobleaching is more effective when the polaritonic mode is plasmon like (off-resonance) than when it is more exciton-like (near resonance) indicating the role of photonic character in mitigating dye degradation. The observed suppression is attributed to the rapid relaxation dynamics of polaritonic states formed under strong coupling. This inhibits population of the triplet state and thus reduce the generation of reactive oxygen species responsible for fluorophore degradation. These results suggest that plasmon-exciton coupling can be an effective strategy to enhance photostability in dye-based optical systems.

Acknowledgements

We thank PD Dr. Sylke Blumstengel (Department of Physics, Humboldt University, Berlin) for providing TDBC (Cyanine dye) as resource material for this work.

References

[1] J. Zhang, L. Zhang, and W. Xu, Surface plasmon polaritons: Physics and applications, *J. Phys. D. Appl. Phys.*, vol. 45, no. 11, 2012.

[2] P. Vasa, Strong Light-Matter Interaction, in *digital Encyclopedia of Applied Physics*, Wiley-VCH Verlag GmbH & Co. KGaA, pp. 1–30, 2019.

[3] P. Vasa and C. Lienau, Strong Light-Matter Interaction in Quantum Emitter/Metal Hybrid Nanostructures, *ACS Photonics*, vol. 5, no. 1, pp. 2–23, 2018.

[4] J. A. Hutchison, T. Schwartz, C. Genet, E. Devaux, and T. W. Ebbesen, Modifying chemical landscapes by coupling to vacuum fields, *Angew. Chemie - Int. Ed.*, vol. 51, no. 7, pp. 1592–1596, 2012.

[5] B. H. Cumpston and K. F. Jensen, Photo-oxidation of polymers used in electroluminescent devices, *Synth. Met.*, vol. 73, no. 3, pp. 195–199, 1995.

[6] H. Horiuchi *et al.*, Photodegradation processes of cyanine dyes in the film state induced by singlet molecular oxygen, *J. Phys. Chem. B*, vol. 107, no. 31, pp. 7739–7746, 2003.

[7] A. Blázquez-Castro, Direct 1O2 optical excitation: A tool for redox biology, *Redox Biol.*, vol. 13, no. April, pp. 39–59, 2017.

[8] B. Munkhbat, M. Wersäll, D. G. Baranov, T. J. Antosiewicz, and T. Shegai, Suppression of photo-oxidation of organic chromophores by strong coupling to plasmonic nanoantennas, *Sci. Adv.*, vol. 4, no. 7, 2018.

[9] H. Horiuchi *et al.*, Suppression mechanism of the photodegradation of J-aggregate thin films of cyanine dyes by coating with polysilanes, *J. Phys. Chem. C*, vol. 115, no. 14, pp. 6902–6909, 2011.

[10] J. Anulyte, V. Zičkus, E. Buzavaitė-Verteliene, D. Faccio, and Z. Balevicius, Strongly coupled plasmon-exciton polaritons for photobleaching suppression, *Nanophotonics*, vol. 6528, 2024.

[11] N. Nefedkin, E. Andrianov, and A. Vinogradov, The Role of Strong Coupling in the Process of Photobleaching Suppression, *J. Phys. Chem. C*, vol. 124, no. 33, pp. 18234–18242, 2020.

[12] M. F. Limonov, M. V. Rybin, A. N. Poddubny, and Y. S. Kivshar, Fano resonances in photonics, *Nat. Photonics*, vol. 11, no. 9, pp. 543–554, 2017.

[13] D. V. Nesterenko, S. Hayashi, and Z. Sekkat, Asymmetric surface plasmon resonances revisited as Fano resonances, *Phys. Rev. B*, vol. 97, no. 23, pp. 1–12, 2018.

[14] B. Luk'Yanchuk *et al.*, The Fano resonance in plasmonic nanostructures and metamaterials, *Nat. Mater.*, vol. 9, no. 9, pp. 707–715, 2010.

[15] P. Vasa, Exciton-surface plasmon polariton interactions, *Adv. Phys. X*, vol. 5, no. 1, 2020.

[16] P. Vasa *et al.*, Ultrafast manipulation of the Rabi splitting in metal-molecular aggregate hybrid nanostructures, *Phys. status solidi c*, vol. 8, no. 4, pp. 1113–1116, Apr. 2011.

Nanostructures meet Perovskites: Advanced Applications and Future Challenges

META 2025, MALAGA - SPAIN, JULY 22 – 25, 2025

TAILORING THE METAL-INSULATOR TRANSITION OF RARE EARTH NICKELATES THIN FILMS TOWARDS OPTICAL APPLICATIONS

L. Matera[1*], J. Peiro[1], L. Divay[2], C. Galindo[2], P. Bortolotti[1], M. Bibes[1], L. Iglesias[1]

[1]Laboratoire Albert Fert, CNRS, Thales, Univ. Paris-Saclay, 91767 Palaiseau, France
[2]Thales Research & Technology, 91767 Palaiseau, France
[*]corresponding author: luigi.matera@cnrs-thales.fr

Abstract: Rare-earth perovskite nickelates, ReNiO3, are characterized by a large number of structural and physical properties, presenting a sharp metal-to-insulator transition, MIT. During the MIT, a rapid change of optical and electrical properties occurs. Here we will show how to tune the MIT and shift it around room temperature.

Correlated transition metal oxides (TMOs) are a class of materials that have attracted significant attention from the scientific community due to their remarkable electronic, magnetic, structural and optical properties. Within the TMOs, the family of the rare-earth perovskite nickelates, described by the general formula $RNiO_3$, with R a trivalent rare-earth (R = La, Pr, Nd, Sm, ..., Lu), is particularly interesting. These materials exhibit a wide range of structural and physical properties, forming a rich phase diagram [1]. With the exception of $LaNiO_3$, a remarkable phenomenon of nickelates is their sharp metal-to-insulator transition (MIT), during which rapid changes in optical and electrical properties occur. These changes could be leveraged in combination with nanostructures to endow new temperature-dependent functioalities to devices [2]. However, effectively exploiting these properties requires precise control of the MIT, adjusting its transition temperature and sharpness. Nowadays, the most studied materials for this purpose are part of the vanadium oxides family [3]. Unfortunately, their chemical inflexibility makes tuning their MIT temperature challenging.

In this work, we present our results on the growth of nickelates thin films by Pulsed Laser Deposition (PLD). We show how we were able to shift their MIT to room temperature by using a combination of Sm and Nd cations in $Sm_{1-x}Nd_xNiO_3$. In addition, we demonstrate the possibility to further modulate the MIT temperature and sharpness by changing the applied strain, i.e. using different crystalline substrates. Fourier-transform infrared spectroscopy, FTIR, reveals a significant change in optical reflectance during the transition, see Fig. 1. This pronounced temperature-driven infrared reflectance could enable various applications, including infrared camouflage. Our findings contribute to optimizing the properties of nickelates, facilitating their integration into next-generation nanostructured devices.

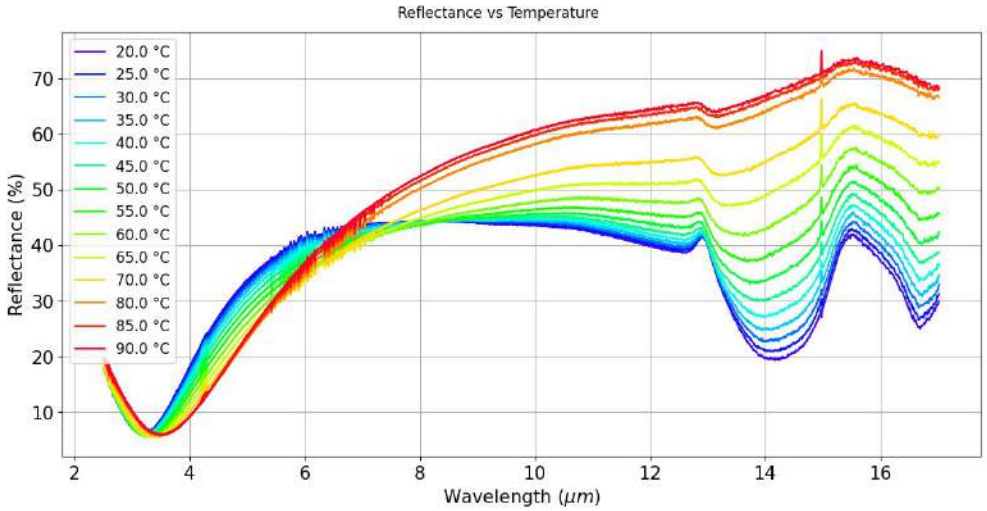


Fig. 1: Measured infrared reflectance for a $Sm_{0.85}Nd_{0.15}NiO_3$ grown on $LaAlO_3$ substrate. The measurement was performed while heating up. A significant increase in reflectance occurs above 8 um wavelengths. A decrease in reflectance is instead observed in the 4-6 um wavelength region

References

1. Catalano S, Gibert M, Fowlie J, Íñiguez J, Triscone JM, Kreisel J. "Rare-earth nickelates $RNiO_3$: thin films and heterostructures." Rep Prog Phys. 2018 Apr; 81(4):046501.
2. B. Khalichi, A. Ghobadi, A. K. Osgouei, Z. R. Omam, H. Kocer and E. Ozbay. "Phase-change Fano resonator for active modulation of thermal emission" Nanoscale, 2023, 15, 10783.
3. K. Tang, X. Wang, K. Dong, Y. Li, J. Li, B. Sun, X. Zhang, C. Dames, C. Qiu, J. Yao, J. Wu, A Thermal Radiation Modulation Platform by Emissivity Engineering with Graded Metal–Insulator Transition. Adv. Mater. 2020, 32, 1907071.

Electrically and Optically Driven Exciton-Polaritons in All-Perovskite Metasurfaces

A. Zacheo[1,2], Y. Wang[1,2], G. Adamo[1,2], and C. Soci[1,2,3*]

[1] Division of Physics and Applied Physics, School of Physical and Mathematical Sciences, Nanyang Technological University, Singapore 637371

[2] Centre for Disruptive Photonic Technologies, TPI, Nanyang Technological University, Singapore 637371

[3] National Centre for Advanced Integrated Photonics, Nanyang Technological University, Singapore 639798

[*]corresponding author: csoci@ntu.edu.sg

Abstract: Electrical control of exciton-polaritons is hindered by their inherent charge neutrality. We show that active perovskite metasurfaces allow optical and electrical generation of exciton-polaritons and control of their emission properties, including spin-polarized luminescence from Bose-Einstein condensates and electroluminescence from integrated light-emitting transistors.

Controllable suppression of non-Hermitian skin effects

C. Xu[1], Z. Q. Guan[1,2*], and H. X. Xu[1,2*]

[1]School of Physics and Technology, Center for Nanoscience and Nanotechnology, and Key Laboratory of Artificial Micro- and Nano-structures of Ministry of Education, Wuhan University, Wuhan 430072, Peoples R China
[2]Institute of Semiconductors, Henan Academy of Sciences, Zhengzhou 450046, Peoples R China
[*]corresponding author: zhiqiang.guan@whu.edu.cn; hxxu@whu.edu.cn

Abstract: The non-Hermitian skin effect (NHSE) characterized by the tendency of bulk states to concentrate toward the boundary is one of the most important and widespread phenomena within non-Hermitian Hamiltonian systems. Due to their topological origin, skin modes are usually robust and difficult to regulate. In our work, we engineered magnetic-field-like on-site and randomlike on-site potentials, and we found nonmonotonic and monotonic suppression patterns on skin modes. These suppression patterns represent characteristic transitions as the on-site potential shifts from order to disorder. Relying solely on on-site potential energy engineering, we develop a general strategy to control suppression of skin modes. By integrating with the scaling theory, we have extended the concept of controllable suppression of NHSEs to higher-dimensional systems.

Through potential energy engineering, we elucidated how a magnetic field affects skin modes that previously were emphasized for either suppression or enhancement. Though their topological origin, we developed a general strategy to control the suppression of skin modes, achieving both the robustness and controllable adjustability of skin modes. Finally, the concept of controllable suppression of skin modes was generalized to higher dimensions, addressing an important scenario often overlooked in higher dimensions. Moreover, this work only considered the most original Anderson localization and did not distinguish between strong and weak localization as well as weak antilocalization, and the richer connotation between the suppression of skin modes and localization, which need to be explored further.

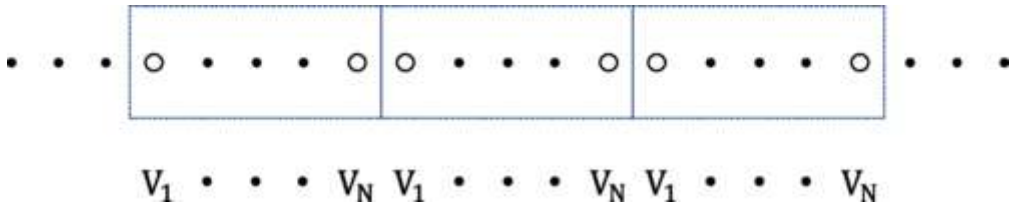


Fig.1 Schematic diagram of a one-dimensional single-atom chain considering on-site energies with period N. Dashed dots represent omitted atoms with potential energy V_i .

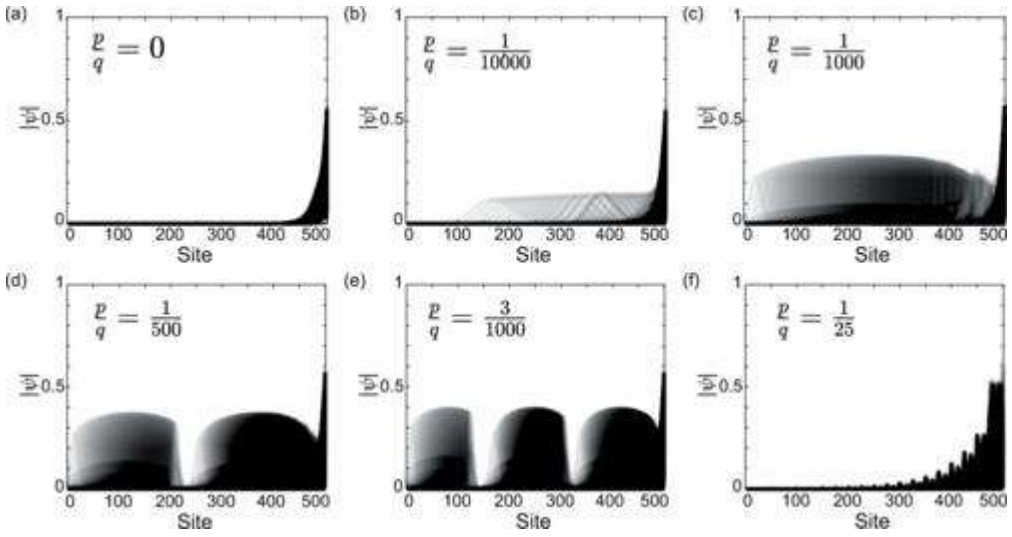


Fig.2 Skin modes suppression with magnetic flux $\phi = 2\pi \frac{\mathrm{p}}{q}$ in the Hofstadter model. Take $k_x = 0$, 500 atoms in the y-axis, and calculate state distribution under $t_x = 1, t_y^- = 0.9$, and $t_y^+ = 1.1$.

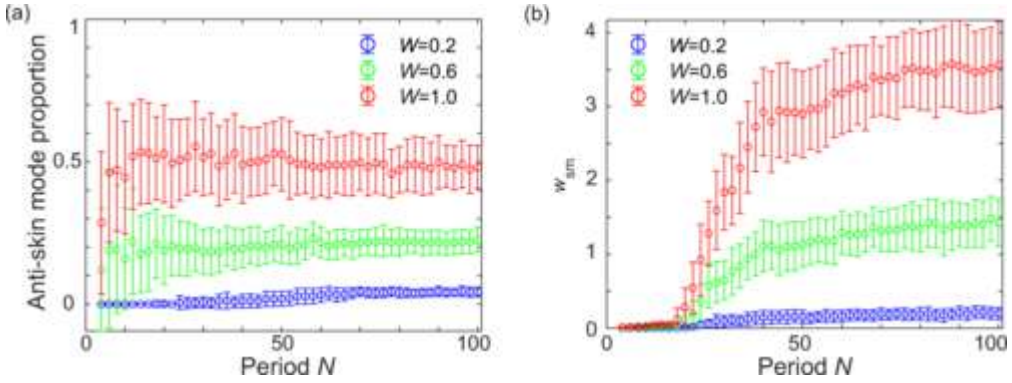


Fig.3 Antiskin mode proportion in total modes and skin mode weight $\mathrm{W_{sm}}$ under different period N. Parameters: $t_- = 0.9, t_+ = 1.1, V_{i \bmod N} \in [-W, W]$,L=100, and sampling times is 100.

References

1. Xu, C. “Controllable suppression of non-Hermitian skin effects,” Phys. Rev. B, Vol. 111, 024201, 2025

Indoor Energy Harvesting Enhancement With Nanostructured Grating Contact

Daniel Sarcanean[1], A. Barreda[1], B. García-Cámara[1], E. López-Fraguas[1], R. Vergaz[1*] and I. M. Seró[2]
[1]GDAF-UC3M, Displays & Photonics Applications Group, Universidad Carlos III de Madrid, Spain
[2]INAM-UJI, Institute of Advanced Materials, Universitat Jaume I de Castellón, Spain
Corresponding author: rvergaz@ing.uc3m.es

Abstract: We present a comprehensive study on the design of a dielectric TiO_2-based nanostructured metasurface into a novel perovskite solar cell with the aim of optimizing the power generation in indoor environments. An absorption improvement, and a consequent increment of the solar cell efficiency, with respect to the planar case, are obtained. Our findings highlight the potential of dielectric metasurfaces for next-generation photovoltaic devices.

Renewable energy is a must in a world with limited fossil fuels, and a strong impact on climate conditions. In this sense, solar energy is one of the most powerful alternatives, with currently 2 TW of energy installed, and a projection of 8 TW in 2030, according to the Global Solar Council [1]. Although silicon is the prevalent material worldwide, some alternatives appeared in recent years, such as organic or multi-junction cells, among others [2]. But there are still scenarios where power supply with these devices is far from the ideal case, like those indoors. In this context, Perovskite Solar Cells (PSC), known for their high absorption in the visible range and spectral tunability with material selection [3], may be a good choice [4]. Moreover, their efficiency can be further improved through metasurface engineering. High refractive index (HRI) dielectric nanostructures (e.g. Si, Ge, AlAs) are a good alternative to plasmonic nanostructures, due to their low ohmic losses in the visible and near-infrared spectral regions [5]. These HRI nanostructures have demonstrated the ability to perform a variety of functions such as phase tuners, directional filters, gratings, mirrors, etc. [6, 7]

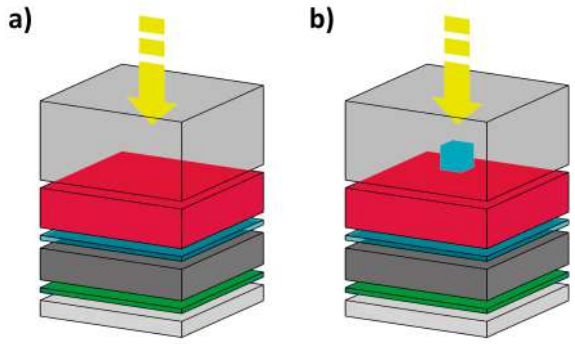


Figure 1: (a) Planar PSC reference composition. From top to bottom: silica (SiO_2), indium tin oxide (ITO) anode contact, poly(3,4-ethylenedioxythiophene) polystyrene sulfonate (PEDOT:PSS) as the Hole Transport Layer (HTL), FASI as active layer, fullerene (C_{60}) as Electron Transport Layer (ETL), and silver (Ag) as cathode. **(b)** Metasurfaced PSC with embedded dielectric on top of the ITO layer.

In this work, a novel formamidinium tin iodide ($FASnI_3$, or FASI) PSC was studied, intended to be used under indoor environments. The optical absorption in the photosensitive layer has been analyzed using the finite-difference time-domain (FDTD) method. The planar case (Fig. 1a) is taken as the reference starting point [8].

We investigated enhancement of absorption by embedding a dielectric metasurface into the former PSC (Fig. 1b), varying its geometry, location and material composition. By doing so, we disclosed which topologies were preferred to maximize the interaction of the field with the active layer, to provide light handling towards it and consequently increase the absorption. The factor chosen to discriminate against different structures was the optical efficiency (η), defined as in equation (1), in the range between 400 nm and 750 nm. In this equation, Abs(λ) is the spectral-dependent

absorption in the active layer, and $\mathrm{Irr}(\lambda)$ is the incident light irradiance, which corresponds to the LED luminaire in Figure 2. Using this irradiance as reference ensures that our optimization effort is effective for this indoor enhancement purpose.

$$\eta = \frac{\int_{\lambda_0}^{\lambda_f} \mathrm{Abs}(\lambda)\mathrm{Irr}(\lambda)\mathrm{d}\lambda}{\int_{\lambda_0}^{\lambda_f} \mathrm{Irr}(\lambda)\mathrm{d}\lambda} \tag{1}$$

In this contribution, we explored the case of a periodic array made of squared-base prismatic TiO_2 nanostructures (Fig. 1b) located on the ITO layer with a side base of 80 nm, demonstrating its feasibility to enhance efficiency for indoor environments by a 1.1 factor regarding the planar case, as shown in Fig. 2.

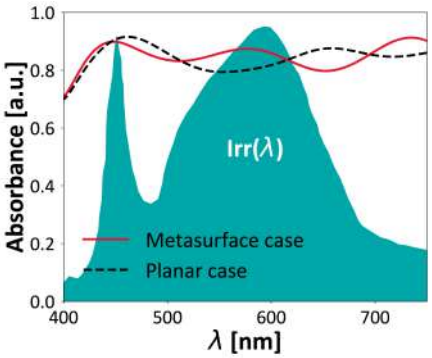


Figure 2: Absorbance spectra for the best case (red line) against the planar structure one (black dotted line). The LED luminaire is shown shaded in green for comparison.

Acknowledgements/Funding: A.B. thanks MICINN for the Ramon y Cajal Fellowship (grant No. RYC2021-030880-I). This work is part of the Projects STEP-UP (TED2021-131600B-C33) and PLEDs (PID2022-140090OB-C22) and HyQuaNa (PID2022-137857NA-I00), financed by the Spanish Ministry of Science and Innovation MCIN/AEI/10.13039-/501100011033, STEP-UP also by the European Union "NextGenerationEU"/PRTR", and PLEDs by "ERDF A way of making Europe".

References

1. Global Solar Council. (2024). Global Solar Council announces 2 terawatt milestone achieved for solar. https://www.globalsolarcouncil.org/news/global-solar-council-announces-2-terawatt-milestone-achieved-for-solar/

2. Nayak, P. K., Mahesh, S., Snaith, H. J., & Cahen, D. (2019). Photovoltaic solar cell technologies: Analysing the state of the art. *Nature Reviews Materials*, 4(4), 269–285. https://doi.org/10.1038/s41578-019-0097-0

3. Makarov, S., Furasova, A., Tiguntseva, E., Hemmetter, A., Berestennikov, A., Pushkarev, A., Zakhidov, A., & Kivshar, Y. (2019). Halide-Perovskite Resonant Nanophotonics. *Advanced Optical Materials*, 7(1), 1800784. https://doi.org/10.1002/adom.201800784

4. Chakraborty, A., Lucarelli, G., Xu, J, Skafi, Z., Castro-Hermosa, S., Kaveramma, A.B., Balakrishna, R. G., Brown, T.M. Photovoltaics for indoor energy harvesting, *Nano Energy*, 128, Part B, 2024, https://doi.org/10.1016/j.nanoen.2024.109932

5. Novotny, L., & Hecht, B. (2012). Principles of Nano-Optics (2nd ed.). *Cambridge University Press.* https://doi.org/10.1017/CBO9780511794193

6. Decker, M., Staude, I., Falkner, M., Dominguez, J., Neshev, D. N., Brener, I., Pertsch, T., & Kivshar, Y. S. (2015). High-Efficiency Dielectric Huygens' Surfaces. *Advanced Optical Materials*, 3(6), 813–820. https://doi.org/10.1002/adom.20140058

7. Terekhov, P. D., Babicheva, V. E., Baryshnikova, K. V., Shalin, A. S., Karabchevsky, A., & Evlyukhin, A. B. (2019). Multipole analysis of dielectric metasurfaces composed of nonspherical nanoparticles and lattice invisibility effect. *Physical Review B*, 99(4), 045424. https://doi.org/10.1103/PhysRevB.99.045424

8. Galve-Lahoz, S., Sánchez-Diaz, J., Echeverría-Arrondo, C., Simancas, J., Rodriguez-Pereira, J., Turren-Cruz, S.-H., Martinez-Pastor, J. P., Mora-Seró, I., & Delgado, J. L. (2024). Addressing ambient stability challenges in pure FASnI3 perovskite solar cells through organic additive engineering. *Journal of Materials Chemistry A*, 12(33), 21933–21943. https://doi.org/10.1039/D4TA03291H

Strong Light-Matter Coupling in Perovskite Quantum Dot Solids

F.J. Coto-Ruiz[1], R. Tao[2,3], C. Bujalance[1], L. Caliò[1], D.N. Dirin[2,3], M.V. Kovalenko[2,3] H. Míguez[1,*]

[1]Multifunctional Optical Materials Group, Institute of Materials Science of Sevilla, Consejo Superior de Investigaciones Científicas − Universidad de Sevilla, Sevilla, 41092, Spain
[2]Laboratory of Inorganic Chemistry, Department of Chemistry and Applied Biosciences, ETH Zürich, Zürich CH-8093, Switzerland
[3]EMPA – Swiss Federal Laboratories for Materials Science and Technology, Dübendorf CH-8600, Switzerland
[*]corresponding author: h.miguez@csic.es

Abstract: Recent advances in the monodispersity and ligand engineering of perovskite quantum dot dispersions have allowed the realization of high optical quality films amenable for integration in optical cavities. Rational and precise design of these resonators yields the formation of exciton-polaritons in quantum dot solids, opening new routes in optoelectronics.

Lead halide perovskite quantum dots (QDs) exhibit significant promise for optoelectronic applications, largely due to their bright and spectrally tunable photoemission characteristics. A recent breakthrough synthesis employing zwitterionic ligands has enabled the production of highly concentrated QD dispersions [1]. These dispersions can be processed into uniform films of controlled thickness that are free from scattering and display distinct excitonic transitions. The integration of these QD films into high-quality optical cavities has allowed for the first demonstration of strong coupling between confined photons and bound electron-hole pairs within a QD solid. [2] The resulting formation of hybridized exciton-polariton states leads to a fundamental reorganization of the system's optical properties. For instance, strongly coupled systems can absorb and emit light in spectral ranges where the uncoupled components show minimal optical activity [3]. This capability opens up opportunities for utilizing this interaction in various domains, including lasing, photodetection, catalysis, and chemistry.

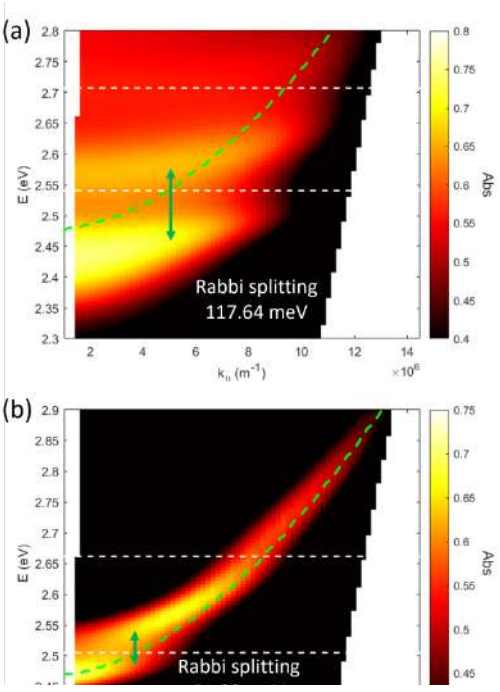


Figure 1 – Exciton-polariton energy dispersion relation for QD cavities capped with (a) PEA and (b) lecithin ligands

In this talk, we show that the coupling strength between QD excitons and cavity photons can be precisely controlled by adjusting the volume density of QDs within the film. To achieve this, we constructed two different optical resonators using QD films. These films were prepared from colloidal dispersions of CsPbBr3 QDs of similar size (approximately 6 nm in diameter), which were capped with two distinct zwitterionic ligands: C8C12-PEA [4] and lecithin [1]. The type of ligand used influences the spacing between particles in the QD solid. This

difference in spacing provides a way to manipulate the QD density in the film, and thus, the strength of the light-matter coupling. Figure 1 visually supports this, displaying the room-temperature absorption energy dispersion maps obtained from the two systems investigated. It is readily apparent that strong light-matter coupling was achieved in both cases, but with markedly different strengths. Our findings underscore the potential of employing ligand engineering as a tool to modulate coupling strength in QD polariton systems [5].

[1] Q. Akkerman et al. Controlling the nucleation and growth kinetics of lead halide perovskite quantum dots. Science 2022, 377, 1406−1412.
[2] C. Bujalance et al. Strong Light-Matter Coupling in Lead Halide Perovskite Quantum Dot Solids. ACS Nano 2024, 18, 4922−4931.
[3] C. Bujalance et al. Ultrastrong Exciton-Photon Coupling in Broadband Solar Absorbers. J. Phys. Chem. Lett. 2021, 12, 10706-10712.
[4] V. Morad et al. Designer phospholipid capping ligands for soft metal halide nanocrystals. Nature 2024, 626, 542-548.
[5] F.J. Coto-Ruiz, L. Caliò, H. D. Dirin, M.V. Kovalenko, H. Míguez. Tuning strong light-matter coupling in quantum dot solids by ligand engineering. *In preparation.*